A Conference of

ISES
International Solar Energy Society

Proceedings

EuroSun 2020

13th International Conference on Solar Energy for Buildings & Industry

Virtual

September 1st - 3rd 2020

www.eurosun2020.org

Organised by:

Cyprus University of Technology

Co-organised by:

University of West Attica

Supported by:

SHC
SOLAR HEATING & COOLING PROGRAMME
INTERNATIONAL ENERGY AGENCY

Professional Congress Organiser:

convin

CONVIN S.A.
29 K.Varnali str, 15233 Chalandri
Athens, Greece
+30210 6833600
+30210 6847700
www.convin.gr

Conference correspondence & updates:
info@eurosun2020.org
www.eurosun2020.org

Proceedings of the ISES EuroSun 2020 Conference – 13th International Conference on Solar Energy for Buildings and Industry

Edited by
Prof. Alexandros Charalambides, Cyprus University of Technology, Cyprus
Prof. Wolfgang Streicher, University of Innsbruck and ISES-Europe, Austria
Dr. Daniel Mugnier, Chairman IEA Solar Heating & Cooling Program
Chairs of EuroSun 2020

International Solar Energy Society
Wiesentalstr 50
79115 Freiburg
Germany

Tel: + 49 761 45906 – 0
Fax: + 49 761 45906 – 99
Email: hq@ises.org
Web: http://www.ises.org

ISBN: 978-3-9820408-2-0

Produced by:
International Solar Energy Society

EuroSun 2020 13th International Conference on Solar Energy for Buildings & Industry
Committee Members

Conference Chairs

Prof. Alexandros Charalambides
Cyprus University of Technology, Cyprus

Prof. Wolfgang Streicher
University of Innsbruck and ISES-Europe, Austria

Dr. Daniel Mugnier
Chairman IEA Solar Heating & Cooling Program

International Organising Committee

Alexandros Charalambides
Cyprus University of Technology, Cyprus

Andreas Häberle
HSR, Switzerland

Klaus Vajen
ISES & University of Kassel, Germany

John Kaldellis
University of West Attica, Athens, Greece

Wolfgang Streicher
University of Innsbruck, Austria

Kemal Gani Bayraktar
IZOCAM, Turkey

Torben Esbensen
Esbensen Consulting, Denmark

Joanna Costello
ISES, Germany

Arabella Liehr
ISES, Germany

Jennifer McIntosh
ISES, Germany

Stelios Choulis
Cyprus University of Technology, Cyprus

Pamela Murphy
IEA SHC Secretariat, USA

Local Organising Committee

Prof. John Kaldellis - Chair
University of West Attica, Athens, Greece

Prof. Alexandros Charalambides
Cyprus University of Technology, Cyprus

Prof. Kosmas Kavadias
University of West Attica

Dr. Andreas Ioannides
Johnsun Heaters Ltd

Filippos Milionis
CONVIN, Greece

Alkis Polyrakis
CONVIN, Greece

Theme Chairs

Solar Buildings
Maria Wall
Agis Papadopoulos

Solar Assisted District Heating and Cooling
Uli Jakob
Costas Balaras

Solar Heat for Industrial Processes
José González-Aguilar
Roza Christodoulaki

Domestic Hot Water and Space Heating
Ulrike Jordan
Dr. Bulent Yesilata

PV and PVT Systems for Buildings and Industry
Daniel Zenhäusern
Kosmas Kavadias

Solar Thermal Collectors and Solar Loop Components
Tomas Matuska

Thermal Storage
Manolis Souliotis

Testing & Certification
Korbinian Kramer
Vassiliki Drosou

Solar Resource and Energy Meteorology
Andreas Kazantzidis

Solar Education
Angelika Basch
Charalambos Malamatenios

Renewable Energy Strategies, Policies, SfF
Agnieszka Rządkowska
Venizelos Efthymiou

Renewable Energy Solutions for Isolated Systems (i.e. Islands)
Hans-Georg Beyer
Theocharis Tsoutsos
Dimitris Zafirakis

Renewable Energy System and Spatial Energy Planning
Wolfram Sparber
Andreas Poullikkas

Scientific Committee Reviewers

Stefan	Abrecht	Germany	Solar Heating Initiative
Mehmet Azmi	Aktacir	Turkey	Harran University
Sergio	Altomonte	Belgium	Université Catholique de Louvain
Costas	Balaras	Greece	Institute for Environmental Research & Sustainable Development, NOA
Angelika	Basch	Austria	Upper Austrian University Of Applied Sciences/ Strömstad Academy
Marco	Beccali	Italy	Università degli Studi di Palermo (DEIM)

Liliana O.	Beltran	USA	Texas A&M University
Christof	Biba	Switzerland	SPF / HSR
Philippe	Blanc	France	Mines ParisTech
Paolo	Bonato	Italy	Eurac Research
Francois	Boudehenn	France	CEA
Christoph	Brunner	Austria	AEE INTEC
Husamettin	Bulut	Turkey	Harran University
Rodrigo	Cáceres	USA	Georgia Tech
Carlos Alberto	Cadena	Argentina	UNSA
Marco	Calderoni	Italy	R2m Solution
Jose	Cardemil	Chile	P. Universidad Católica De Chile
Maria João	Carvalho	Portugal	LNEG
Laltu	Chandra	India	Indian Institute of Technology (BHU) Varanasi
Daniel	Chemisana	Spain	University of Lleida
Tomasz	Cholewa	Poland	Faculty of Environmental Engineering, Lublin University of Technology
Rosa	Christodoulaki	Greece	Centre For Renewable Energy Sources And Savings Fondation
Konstantinos	Christopoulos	Greece	University Of West Attica
Manuel	Collares Pereira	Portugal	Universidade de Evora
Cristian	Cortés	USA	University of California, San Diego
Alicia	Crespo	Spain	Universitat de Lleida - Greia
Sylvain	Cros	France	Ecole Polytechnique
Henrik	Davidsson	Sweden	Lund University
Pierre	Delmas	France	NEWHEAT SAS
Michael	Donn	New Zealand	Victoria University of Wellington School of Architecture
Vassiliki	Drosou	Greece	CRES
Jiangtao	Du	United Kingdom	University of Liverpool
Philip	Eames	UK	Loughborough University
Venizelos	Efthymiou	Cyprus	Foss
Aitziber	Egusquiza	Spain	Tecnalia
Michael	Epstein	Israel	Tel-Aviv University

Rodrigo	Escobar	Chile	Escuela de Ingeniería, Pontificia Universidad Católica de Chile
Istvan	Farkas	Hungary	Szent Istvan University
Angel G.	Fernandez	Spain	University of Lleida
Carlos M.	Fernández-Peruchena	Spain	National Renewable energy Centre (CENER)
Christian	Fink	Austria	AEE INTEC
Stephan	Fischer	Germany	ITGE
Juergen	Fluch	Austria	AEE - Institute for Sustainable Technologies
Daniela	Fontani	Italy	CNR
Márcio	Fonte-Boa Cortez	Brazil	UFMG
Judith	Franco	Agentina	INENCO-Argentina
Andrea	Frazzica	Italy	CNR-ITAE
Ramon	Frederick	Chile	
Simon	Furbo	Denmark	Technical University of Denmark
Niko	Gentile	Sweden	Lund University
Daniel	González i Castellví	Spain	AIGUASOL
Rodrigo	Guido Araujo	Brasil	PETROBRAS
Andreas	Häberle	Switzerland	SPF Institute for Solar Technology
Caroline	Hachem-Vermette	Canada	University Of Calgary
Mercedes	Haga	Chile	Universidad del Desarrollo
Andreas	Hauer	Germany	ZAE Bayern
Daniel	Herrera	Italy	Eurac Research
Carsten	Hoyer-Klick	Germany	German Aerospace Center (DLR)
Leticia	Jenisch Rodrigues	Brazil	UFRGS
Kosmas	Kavadias	Greece	University Of West Attica
Andreas	Kazantzidis	Greece	University of Patras
Jan	Kleissl	USA	Univ. of California at San Diego (UCSD)
Armin	Knotzer	Austria	AEE INTEC
Christian	Kok Skov	Denmark	PlanEnergi

Roland	Krippner	Germany	Nuremberg Tech, Faculty of Architecture
Fréderic	Kuznik	France	INSA-Lyon
Chrysovalantou	Lamnatou	Spain	University of Lleida
Ana	Lázaro	Spain	Unizar
J Owen	Lewis	Ireland	UCD Dublin
Gabriele	Lobaccaro	Norway	NTNU
Roberto	Lollini	Italy	EURAC
Yoann	Louvet	Germany	University of Kassel
Dirk	Mangold	Germany	Solites
Luis	Martín	Qatar	ISES
Luis	Martorelli	Argentina	Laboratorio De Optica Calibraciones Y Ensayos Fcag. Universidad Nacional De La Plata
Tomáš	Matuška	Czech Republic	Czech Technical University, UCEEB
Steven	Meyers	USA	Desert Genesis LLC
Andreu	Moià-Pol	Spain	Universitat De Les Illes Balears
Elielza	Moura de Souza Barbosa	Brazil	UFPE
Daniel	Mugnier	France	TECSOL
Urs	Muntwyler	Switzerland	Bern University of Applied Sciences BFH
Daniel	Neyer	Austria	Neyer Brainworks Gmbh
Jan Erik	Nielsen	Denmark	PlanEnergi
Philip	Ohnewein	Austria	AEE INTEC
Celso	Oliveira	Brazil	University of São Paulo
Janybek	Orozaliev	Germany	Institute of Thermal Engineering - Department of Solar and Systems Engineering, University of Kassel
Felix	Pag	Germany	University Of Kassel, Institute Of Thermal Engineering
Giorgos	Panaras	Greece	University of Western Macedonia
Mathaios	Panteli	UK	U Manchester
Christina	Papadimitriou	Cyprus	Foss/ucy
Christiana	Papapostolou	Greece	University Of West Attica
Philippe	Papillon	France	En Butinant l'Energie
Dimitrios	Pappas	United Kingdom	University of Manchester

Cedric	Paulus	France	CEA INES
Alan	Pino	Spain	University of Seville
Jesus	Polo	Spain	CIEMAT
David	Pozo Vazquez	Spain	Univ. of Jaen
Atul	Raturi	Fiji	The University of the South Pacific,Suva, Fiji
Jan	Remund	Switzerland	Meteotest AG
Dave	Renné	USA	Dave Renné Renewables, LLC
Esther	Rojas	Spain	CIEMAT
Celestino	Ruivo	Portugal	University of Algarve
Daniel	Ruiz-Bandera	Spain	RINA
Radim	Rybár	Slovakia	Technical University of Košice
Agnieszka	Rządkowska	Belgium	Eitci Institute
Eva	Schüpbach	Switzerland	Bern University of Applied Sciences BFH
Luis M.	Serra	Spain	Universidad de Zaragoza (
Manuel	Silva	Spain	Univ. Sevilla
Katharina	Simon	Germany	Wuppertal University
Manolis	Souliotis	Greece	University of Western Macedonia
Allan R.	Starke	Brazil	Federal University of Santa Catarina
Phedeas	Stephanides	United Kingdom	University of East Anglia (UEA)
Wolfgang	Streicher	Austria	University of Innsbruck
Christian	Tantolin	France	CEA INES
Danjana	Theis	Germany	htw saar
Chigueru	Tiba	Brazil	Universidade Federal De Pernambuco
Costas	Travasaros	Greece	Prime Laser Technology
Theocharis	Tsoutsos	Greece	Technical University of crete
Georgios	Tzanes	Greece	University of West Attica (UNIWA)
Klaus	Vajen	Germany	Universität Kassel
Loreto	Valenzuela	Spain	CIEMAT
Wim	Van Helden	Austria	AEE INTEC
Trajano	Viana	Brasil	TVc
Frank	Vignola	USA	Univ. of Oregon

Ping	Wang	Netherlands	Royal Netherlands Meteorological Institute (KNMI)
Werner	Weiss	Austria	AEE INTEC
Stefan	Wilbert	Spain	DLR
Izete	Zanesco	Brazil	School of Technology, Pontifical Catholic University of Rio Grande do Sul – PUCRS
Daniel	Zenhäusern	Switzerland	HSR SPF

Conference programme

Please note that conference times are in Eastern European Time Zone GMT+3 , the time in Athens, Greece.

Tuesday, September 1, 2020

	Track 1	Track 2	Track 3	Track 4
8:00 AM - 6:00 PM	How to use the Virtual Platform Click here to watch this video before the conference dates Visit the conference page for more detailed written instructions			
9:10 AM - 9:45 AM	Opening Session			
9:50 AM - 11:00 AM	Oral Presentations 1: Solar Buildings			
9:50 AM - 11:20 AM			Oral Presentations 3: PV and PVT Systems for Buildings and Industry	
9:50 AM - 11:30 AM		Oral Presentations 2: Solar Assisted District Heating and Cooling		
12:00 PM - 2:50 PM	Poster Session 1			
12:30 PM - 1:32 PM				Elsevier Workshop on How to get Scientific Paper published, Do's and Don'ts
3:00 PM - 3:25 PM	Keynote Lecture 1			
3:30 PM - 4:50 PM		Oral Presentations 5: Thermal Storage	Oral Presentations 6: Solar Resource and Energy Meteorology	
3:35 PM - 4:57 PM	Oral Presentations 4: Solar Heat for Industrial Processes | Testing & Certification			
5:15 PM - 5:38 PM	Networking Session: Solar Quiz The EuroSun2020 Conference Solar Quiz is a fun contest featuring questions on interesting facts and trivia in a domain of solar energy and renewables, as well as energy consumption.			
5:40 PM - 6:40 PM	Tuesday Virtual Social Session You will be randomly allocated to rooms with three more delegates every few minutes. Enjoy!			Organizing Committee Room 1

Wednesday, September 2, 2020

	Track 1	Track 2	Track 3	Track 4
8:00 AM - 6:00 PM	How to use this Virtual Platform Click here to watch this video before the conference dates Visit the conference page for more detailed written instructions			
9:30 AM - 9:51 AM	Keynote Lecture 2			
10:00 AM - 11:05 AM	Oral Presentations 7: Solar Thermal Collectors and Solar Loop Components | Testing & Certification			
10:00 AM - 11:10 AM		Oral Presentations 8: Thermal Storage		
10:00 AM - 11:20 AM			Oral Presentations 9: Renewable Energy System and Spatial Energy Planning	
11:40 AM - 12:08 PM	Keynote Lecture 3			
12:00 PM - 2:50 PM	Poster Session 2			

12:30 PM - 2:15 PM				REN21 Workshop on Public Support for Renewables: Do's and Don'ts Please click on the **Join as Panelist** button to join the Workshop.
3:00 PM - 3:22 PM	Keynote Lecture 4			
3:30 PM - 4:30 PM	Oral Presentations 10: Solar Buildings			
3:30 PM - 4:56 PM		Oral Presentations 11: Thermal Storage		
3:30 PM - 5:00 PM			Oral Presentations 12: Renewable Energy Strategies, Policies, Scientists for Future	
5:10 PM - 5:30 PM				Eurosun Roundtable on the Solar Thermal Industry Pledge
5:40 PM - 6:40 PM	Wednesday Virtual Social Session You will be randomly allocated to rooms with three more delegates every few minutes. Enjoy!			
6:40 PM - 7:40 PM				Organizing Committee Room 2

Thursday, September 3, 2020

	Track 1	Track 2	Track 3	Track 4
8:00 AM - 6:00 PM	How to use the Virtual Platform. Click here to watch this video before the conference dates Visit the conference page for more detailed written instructions			
9:30 AM - 9:57 AM	Keynote Lecture 5			
10:00 AM - 11:12 AM			Oral Presentations 15: PV and PVT Systems for Buildings and Industry	
10:00 AM - 11:37 AM		Oral Presentations 14: Domestic Hot Water and Space Heating		
10:10 AM - 11:40 AM	Oral Presentations 13: Solar Heat for Industrial Processes			
12:00 PM - 2:50 PM	Poster Session 3			
12:30 PM - 1:30 PM				Networking Session by GWNET: Women in Renewables
3:00 PM - 4:33 PM	Oral Presentations 16: Solar Assisted District Heating and Cooling			
3:00 PM - 4:39 PM		Oral Presentations 17: PV and PVT Systems for Buildings and Industry | Testing & Certification | Solar Education		
3:00 PM - 5:11 PM			Oral Presentations 18: Renewable Energy Solutions for Isolated Systems	
4:50 PM - 5:15 PM	Keynote Lecture 6			
5:20 PM - 6:06 PM	Closing Session			
6:10 PM - 7:10 PM	Thursday Virtual Social Session			

Table of Contents

Editorial

01. Solar Buildings

02. Solar Assisted District Heating and Cooling

03. Solar Heat for Industrial Processes

04. Domestic Hot Water and Space Heating

05. PV and PVT Systems for Buildings and Industry

06. Solar Thermal Collectors and Solar Loop Components

07. Thermal Storage

08. Testing & Certification

09. Solar Resource and Energy Meteorology

10. Solar Education

11. Renewable Energy Strategies, Policies, Scientists for Future

12. Renewable Energy Solutions for Isolated Systems (i.e. Islands)

13. Renewable Energy Systems and Spatial Energy Planning

Editorial

International Solar Energy Society EuroSun 2020 Proceedings

Editorial to the Proceedings of the 13th International Conference on Solar Energy for Buildings and Industry (EuroSun 2020)

Alexandros G. Charalambides, Wolfgang Streicher and Daniel Mugnier

1. Introduction

The 13th International Conference on Solar Energy for Buildings and Industry (EUROSUN 2020) of the International Solar Energy Society (ISES) was held virtually on 1-3 September 2020, in collaboration with the International Energy Agency (IEA) Solar Heating and Cooling (SHC). The Conference was organised in cooperation with the Cyprus University of Technology (CUT) and the University of West Attica. The Conference e-connected many researchers, renewable energy practitioners, students, government officials, media, and the general public, not only from Europe, but from around the world to learn about the latest development in renewable energy technologies and `their deployments. The Conference featured a variety of technical sessions, plenaries and keynote talks to stimulate discussions on how the world can achieve 100% renewable energy to meet all end use energy requirements; not just electricity, but also heating, cooling and transport applications.

Our planet is facing unprecedented changes as a result of climate change due to the use of fossil fuels and other sources of greenhouse gases. As such, countries around the world must focus on how to achieve a decarbonized world. Emphasis should be given to all aspects of our lives (from sustainable cities to the maritime sector) and solar energy is the key player in our efforts. Within Europe, the European Commission, as a response to these challenges, has set the European Green Deal. It is a new growth strategy that aims to transform the EU into a fair and prosperous society, with a modern, resource-efficient and competitive economy where there are no net emissions of greenhouse gases in 2050 and where economic growth is decoupled from resource use. Furthermore, in 2019, all Member States submitted their National Energy and Climate Plans (NECPs), that include new research, innovation and development opportunities over the next few years for all technologies, including of course solar energy. Ambitious targets have been set, that may not be ambitious enough however, given the urgency of the challenges the planet is dealing with and facing more of.

The worldwide success of renewable energy technologies, and solar energy in particular is remarkable, and it is what we are working for. In many cases solar technologies are already the most economical way to produce heat and electricity. But there is still way to go in order to rapidly achieve the goal of 100% renewable energy in all end-use sectors. Efficiencies must be increased, the costs of systems and services should be reduced further, and large energy storage systems have to be developed. We need a shift to thinking in terms of systems and a better understanding of the interaction of the heat, electricity and mobility sectors.

The challenges and opportunities of this energy transformation was the central theme of this Conference and these proceedings capture the many outstanding research papers that were presented at the Conference. A total of 214 technical abstracts had been submitted, and thanks to the superb efforts of the Theme Chairs, there were a total of 86 oral and 67 poster presentations at the Conference. 101 papers from these presentations are now published in these Proceedings. The papers cover a wide range of themes and topics, listed in the first pages of the proceedings. A full listing of the International and Local Organizing Committees as well as the Theme Chairs, is provided at the beginning of these proceedings.

The authors of this Editorial greatly appreciate your interest in these Conference Proceedings and look forward to your participation in future events of ISES and the IEA SHC Program.

© 2020. The Authors. Published by International Solar Energy Society
Selection and/or peer review under responsibility of Scientific Committee
Available at http://proceedings.ises.org

01. Solar Buildings

Integrated Daylight and Energy Evaluation of Passive Solar Shadings in a Nordic Climate

Agnieszka Czachura[1] and Henrik Davidsson[1]

[1] Energy and Building Design, Lund University, Lund (Sweden)

Abstract

Modern well-insulated and highly glazed buildings experience increased overheating, even in cold climates. The study focused on external and internal passive solar shadings on a south-oriented façade, having predetermined that external and internal shadings' main function is solar heat gain and glare protection, respectively. A daytime-occupied office space with several external shading geometry variations was simulated using an integrated daylight and energy approach aided by Radiance, Daysim, and EnergyPlus within Grasshopper. The method involved preparation of daylight-driven lighting schedules, and glare-driven internal blinds operation schedules for each design scenario, which were further applied to annual energy simulations. The interdependence of light in visible and thermal form, its impact on the building performance, and the resulting occupant response to the changing indoor conditions are core to this study. The comparative nature of the study allowed to evaluate thermal and visual performance of fixed external shadings in Nordic climates. The chief study findings highlight the gross impact of internal shading operation on overall building performance and indoor comfort, and the holistic benefit of external solar protection that includes reduction of total energy use and improvement of occupants' thermal and visual comfort.

Keywords: passive solar shading, daylight, energy use, glare, thermal comfort, overheating, cold climate

1. Introduction

The world's population, production, and energy consumption are growing, and according to the International Energy Agency (IEA, 2019), the world's total energy use has doubled in the span of the last three decade. The building sector is estimated to use about 40 % of the global energy, yet environmental and sustainable building regulations are fairly new – the energy-efficient practices to reduce the building consumption emerged in Europe in the 1990s. Even though only around 25 % of all European buildings are non-residential, it is estimated that their average specific energy consumption per floor area is 40 % more than of the residential sector (BPIE, 2011)

There is a scientific consensus regarding climate change, which affirms that global temperatures are rising (Cook et al., 2016). Lechner (2015) reminds that "one of the main reasons for regional differences in architecture is the response to climate". Sustainable design ensures buildings are tailored to maximise their performance, provide good indoor climate, and abide by their local environment. Heating demand gradually becomes a secondary issue even in traditionally heating-dominated climates (Grynning et al., 2014). Reduction of infiltration, lower U-values, highly glazed facades, and high internal heat loads of modern office buildings all contribute to overheating and consequently cooling loads much higher than in conventional leaky buildings. The importance of solar protection devices in reducing cooling loads, ensuring thermal comfort, and mitigating glare in a Swedish cold climate scenario was demonstrated by Wall and Bülow-Hübe (2003). ASHRAE (2017) reads that "the most effective way to reduce the solar load on fenestration is to intercept direct radiation from the sun before it reaches the glazing system". Researchers are in agreement that fenestration design must incorporate solar shading solutions in early building design stages, as it will have an immense effect on energy reduction and improvement of indoor comfort (Dubois, 1997; Haase et al., 2011; Poirazis et al., 2008). Still, the key functions of windows, which are daylighting and visual contact with the outdoor scene, should be preserved.

Solar shading devices can be placed externally or internally. Similarly, devices can be fixed or movable, and, in case of the latter, manually or automatically controlled. Passive shadings are those that do not require energy to function. Externally placed solar shadings are more effective in solar heat gain prevention than internal devices. Moreover, external shadings as fixed elements have higher life expectancy and are less prone to degradation, as opposed to movable ones that can induce operational energy, higher costs and maintenance (ASHRAE, 2017;

doi:10.18086/eurosun.2020.01.01 Available at http://proceedings.ises.org

Hammad and Abu-Hijleh, 2010). On the other hand, fixed shadings permanently block a portion of natural daylight, which may cause increased use of electric lights. Furthermore, they reach lower performance efficiencies than automated systems (Bakker et al., 2014).

Many studies debate occupant preferences regarding control systems and often discuss dissatisfaction with automated systems, however, there is no clear consensus about the patterns in which people respond to the indoor climate conditions (Zhang et al., 2018). A field study by Sadeghi et al. (2016) suggests that occupants express higher satisfaction with the indoor climate when they are allowed to adjust the control levels to their liking. The impact of occupant behaviour on building performance has been widely recognised. Simulated energy use can differ as much as three times when compared to the real-life occupant-interactive performance (Delzendeh et al., 2017). Therefore, the energy and daylight simulations should consider user control patterns as they will affect the overall results (van den Wymelenberg, 2012). The subject of human interactions is very complex and dependant on location, cultural inclinations, and acceptable comfort levels that are understandably subjective and varying.

Low solar angles, very common in higher latitudes, are difficult to shade with fixed external shadings, thus necessitate supplementation of vertical window blinds to satisfy comfort functions such as: radiant energy protection, privacy, brightness control (ASHRAE, 2017). Sporadic need for employment of internal blinds means they are typically movable and require a control strategy. Various control types and thresholds of internal blinds operation can be found in literature. A commonly used control measure variable is illuminance since internal blinds are closely associated with visual comfort rather than thermal comfort (van den Wymelenberg, 2012). The reason might be that in reality thermal comfort is harder to evaluate, measure, and also to sense by an occupant, since in a conditioned space the occupant might not be aware of excessive solar gain. Illuminance can be expressed simply in lux on a surface or in terms of glare. Daylight glare probability (DGP) is a method of calculating the likelihood of glare occurrence by analysing illuminances at occupant’s eye level (Wienold and Christoffersen, 2006). Its simplified version is an efficient way of predicting visual discomfort caused by extreme brightness or contrasts within a field of view (Wienold, 2009). DGP is expressed as a percentage and values above 40 % are expected to cause disturbing glare that might trigger an occupant to employ blinds. Internal blinds schedule can therefore be driven by DGP and this control method was found to be most accurately representing the average control behaviour in a study by da Silva et al. (2012) comparing different control types and thresholds.

Climate based dynamic simulation tools are widely used in today’s design process and performance evaluations (Kirimtat et al., 2016). Increasing number of studies underline the importance of an integrated daylight and energy performance analysis in a holistic approach that considers interdependency of visual and thermal dynamics in a building (Karlsen et al., 2016; Manzan, 2014; Tzempelikos and Athienitis, 2007). The fundamental correlation between daylight and energy is the use of electric lights. Since every lighting source emits heat, not only does daylighting impact the electrical energy use to power lights but also the demand for heating and cooling. State-of-the-art study on advanced shading systems listed a set of relevant criteria that can be used to make an informed design of a fenestration system (Kuhn, 2017). Those included solar heat gain reduction, thermal comfort, daylighting, visual comfort, view to the outside, etc. More recent studies put emphasis on human comfort in addition to thermal performance, as satisfaction with the indoor environment is linked to higher productivity and well-being of occupants (Day et al., 2019).

This paper presents a comparative study of external solar shadings in a cold Nordic climate. The issue of overheating is a rather new subject matter for heating-dominated climates, in recent years exacerbated by extensive insulation and airtight building envelopes. This study aims to address this gap and analyse passive solar shading solutions, externally fixed to an office room fenestration in the Stockholm weather scenario. Integrated simulation approach was used, including daylight and energy aspects with bespoke schedules governing the operation of internal zone control systems.

2. Method

The study was conducted on a theoretical typical office room – a ‘shoebox’ model. This reference model (Reinhart et al., 2013) had internal dimensions of 3.6 m × 8.2 m × 2.8 m. There was no outdoor shading context and surface boundary conditions were adiabatic, except for one south-oriented external wall on which a window was placed (Fig. 1). The window-to-wall ratio (WWR) was 84 %, which can be described as a highly glazed façade. WWR was measured against the internal wall dimensions and did not include frames. The modelling was done in

Rhinoceros 3D – a licence-based software, while Grasshopper simulation plugins were open-source, available online for free. The climate data used for annual simulations was an *epw file. It represented a typical meteorological year for Stockholm (Sweden).

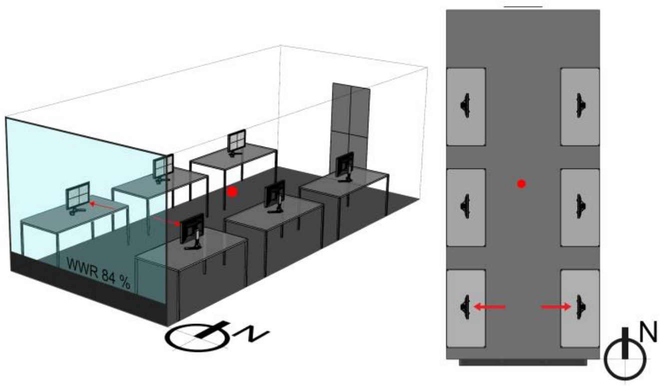

Fig. 1: Reference model (left: perspective view, right: top view)

There are six workstations available within the space of the reference model, but the permanent occupancy was set to four persons with a metabolic heat generation of 120 W person^{-1}. The occupancy time was 8AM to 6PM, seven days a week with summer daylight saving time from April to October. The equipment load was 8 W m^{-2}. Temperature setpoint (target air temperature during occupancy time) and setback (allowed air temperature outside of occupancy time) were 21 °C and 15 °C respectively for heating, and 25 °C and 30 °C for cooling. The external wall construction was an example of a typical highly insulated Swedish lightweight wall with the *U*-value of 0.13 W m^{-2} K^{-1}. The internal walls were also lightweight. Two window solutions were tested, their properties are listed in Table 1. The windows were triple-glazed, argon-filled.

Tab. 1: Glazing types and properties

Glass	Product name	*U*-value (W m^{-2} K^{-1})	*g*-value	τ_{vis}
Clear	Iplus top 3	0.6	0.5	0.7
Selective	Ipasol Ultraselect	0.5	0.26	0.54

The building had a set constant volume outdoor air supply of 0.35 l s^{-1} per square meter of floor area as is required by the Swedish building code (Boverket, 2011) with additional 7 l s^{-1} per person that meets a bronze criterion of Swedish Miljöbyggnad standard (SGBC, 2020). The system was equipped with a heat exchanger – an enthalpy wheel with sensible heat recovery efficiency of 81 %. Zone conditioning was set to the default EnergyPlus HVAC system called 'Ideal Air Loads'. With this system, all the heating and cooling is airborne, so the air alone has to meet the zone's thermal thresholds and the system is doing so by increasing the flow of air through the heater in a closed loop with no additional outdoor air intake.

The lighting load was obtained with Honeybee 0.0.64 Lighting Density Calculator component using default luminous efficacy for fluorescent T5 tubes, medium maintenance factor, and light illuminance level of 300 lux. The resulting lighting density was 6.9 W m^{-2}. The selected 300 lux work plane illuminance threshold is frequently found in recent literature and certifications (SGBC and BRE, 2018; USGBC, 2019) replacing the standard 500 lux threshold. This turn towards a lower required lighting level for an office space is motivated by a technological shift from paper- to computer-based office work (Richman, 2012).

The operation of electric lights was controlled with a manual on/off switch without dimming. Custom schedules were prepared using illuminance results at a sensor point from the annual daylight simulation. The sensor point was located at the centre of the zone at 0.8 m above the floor (marked in Fig. 1). The control can be perceived as automated rather than occupant controlled, as it does not account for real life user's behaviour patterns and reaction time. This manual control type can therefore be called 'active-user', as it is assumed that the user will react to the changing conditions without failure. Even though the method does not reflect realistic user patterns, its advantage is that it is straightforward and allows for comparative analysis of shading solutions and other factors. With this predictable type of control system, which is free of human factor, the resulting on/off schedule can by itself serve as a daylight metric to describe the daylighting quality of the zone. Percentage of occupancy time when the lights are switched on is thereby a reversed indicator of daylight utilisation.

Fixed external shading cases were devised for a south oriented façade, and the selection of solutions with their abbreviations and dimensions can be found in Table 2. Two sizes of each shading type were selected, so that the shading offsets correspond to roughly 40 % and 80 % of the window height. All fixed external shading geometries had a 20 % diffuse-only reflectance (no specular reflections).

Tab. 2: External shading types and depth sizes

Overhang (OH)	Horizontal louvers (HL)	Brise-soleil (BS)
100 cm, 200 cm	5×20 cm, 5×40 cm	100 cm, 200 cm
	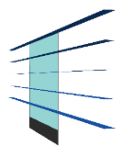	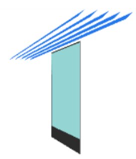

An overhang shading and horizontal louvers shading are both horizontal and have the same total depth and size of the shading elements, the latter is simply divided into smaller sections (e.g. OH: 100 cm = HL: 5 × 20 cm). From a geometrical perspective, those two shading designs intercept equal amount of direct solar radiation falling on the aperture.

Brise-soleil is a shading that is co-planar with the overhang and it has the same capacity to block direct solar radiation as the overhang, but as opposed to one, it is composed not of just one element but of multiple angled louvers that allow air, precipitation, and light to bounce through. The angle of the slats was 45°. The total horizontal offset of the brise-soleil was the same as for the overhangs, however, the resulting total added brise-soleil louvers length was 19 % less than of the overhang, which means less material can be used with BS type of solar shading.

While external shading device is intended primarily to intercept solar rays in order to protect the space from overheating, it can simultaneously provide a better visual comfort for the occupants by lowering the irradiance of the internal surfaces in the proximity to the aperture. To complement the function, internal blinds were provided additionally as a manually operated shading device that was set to active only in occurrence of disturbing glare, when the simplified daylight glare probability (DGP) result was higher than 0.4. DGP was simulated on the eye level of an occupant seated in the nearest workstation from the window, facing their computer screen placed against east or west wall side (marked in Fig. 1). For each design option a single internal blinds schedule was then obtained considering only the higher DGP value from the two occupant positions results. This method is straightforwardly based on probability of glare occurrence, which could mimic behaviour of an active user, but may not reflect real life occupant control patterns and does not account for passive user scenarios. When the blinds are down, the electric lights have to be switched on, as the blinds do not allow enough daylight to meet the lighting control illuminance threshold, they only manage to reduce the glare probability to an acceptable non-disturbing level. Furthermore, active blinds obstruct the view to the outside during the occupancy hours. This is a performance indicator describing the quality of the fenestration design as it carries information about the visual comfort occurrence. It was therefore used as an analysis metric to assess the visual quality of the space.

The study of shading designs integrated daylight and energy simulations into one workflow aiming to assess the fenestration performance in a more holistic approach. Annual daylight simulations were carried out using Radiance, while annual glare as DGP was calculated with Daysim analysis software, which is based on Radiance. Thermal modelling and energy simulations were performed in EnergyPlus. The geometries were modelled in Rhinoceros and Grasshopper, while the simulation setup was done in the Grasshopper environment using Ladybug and Honeybee plugin tools. The chart in Figure 2 illustrates the workflow method applied in this study. For the two workstations considered in glare analysis, the higher DGP result for a given hour was kept, consolidating two lists into one. Seeing from the chart, two types of results can be obtained: with and without internal blinds employment. When internal blinds were used, daylight-based lighting schedules had to be adapted to include electric lighting operation for the hours during which blinds were down. Having the operational schedules ready, energy simulation is the last step of the simulation workflow.

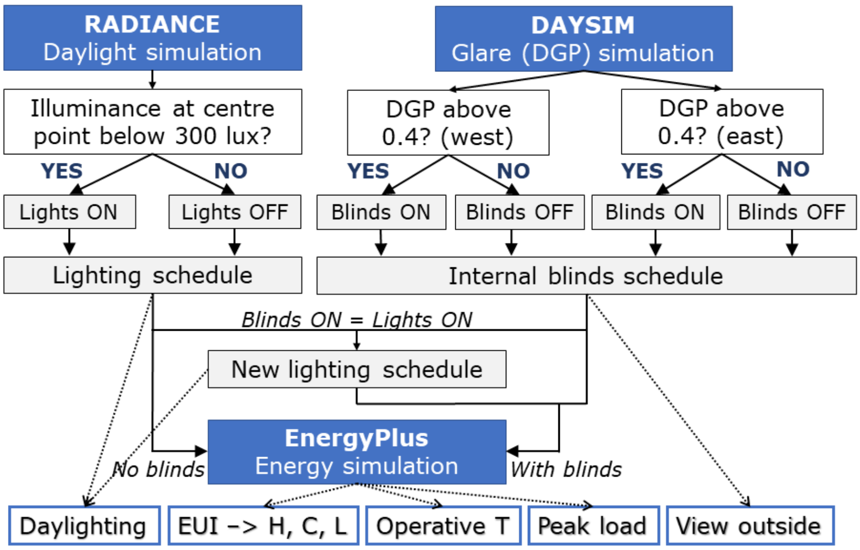

Fig. 2: Simulation workflow

The outputs of the analysis – listed at the bottom part of the chart in Fig.2 – are performance metrics that quantify and help describe the quality of design with regard to: daylight (daylighting), energy use intensity for heating cooling and lighting (EUI), thermal comfort (operative temperature), visual comfort (view outside), and system sizing (peak load).

3. Results

Figure 3 shows results of yearly electric lights use in the occupancy time (3 650 h annually) for investigated external shading cases, distinguishing between clear and selective glass type, as well as comparing the impact of internal blinds operation. Increased use of electrical lighting can be noticed for study cases where blinds schedules were implemented. In those cases, higher daylighting was often achieved by a fenestration design that featured an external shading device.

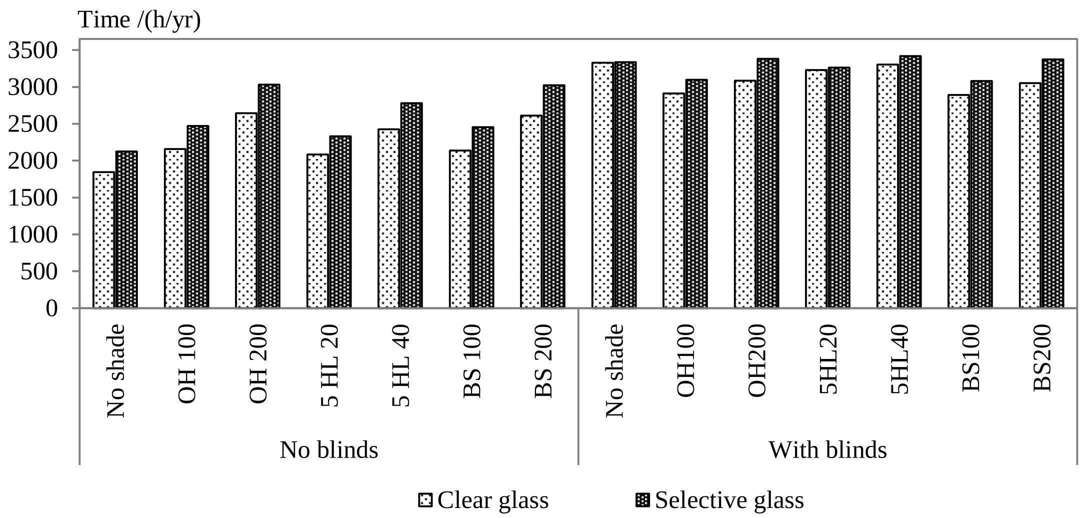

Fig. 3: Electric lighting use derived from daylight availability

Visual comfort expressed by "view to the outside" in Figure 4 indicates the annual availability of view to the outside during occupancy, enabled through low glare probability that entails that the internal blinds can remain open. The visual comfort and consequently the view availability improved dramatically with an external shading device. The graph in Fig. 4 presents percentage of the occupancy time when a) electric lights are required, thus low values are desired, b) occupants have an unobstructed view to the outside – higher values are desired. Noticeably, a given size of horizontal louvers shading compared to an overhang yielded higher artificial lighting use and also provided less hours with view to the outside, which indicates more frequent use of internal blinds with higher glare occurrence. Overhang and corresponding brise-soleil performed equally in that respect. Brise-soleil reduced the use of electric lights when compared to the respective overhang shading only by 1 %.

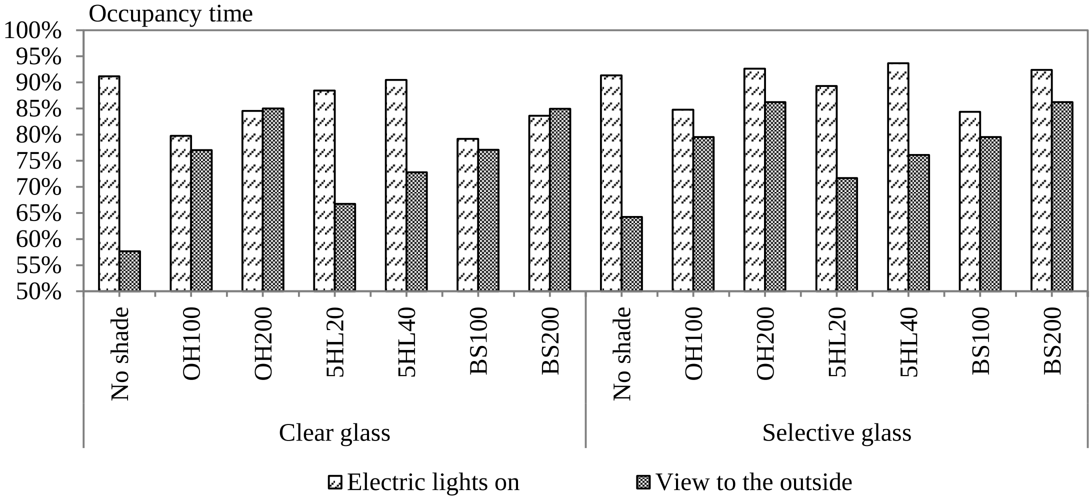

Fig. 4: Share of annual occupancy time with electric lights and view availability

Figure 5 compares the EUI for base cases of unobstructed windows without an external shading device. These cases were simulated with and without glare-driven internal blinds. When blinds were included, the energy results increased for all three energy use segments. The total EUI with internal blinds was higher than without internal blinds operation by 47 % and 41 % for clear and selective glass, respectively.

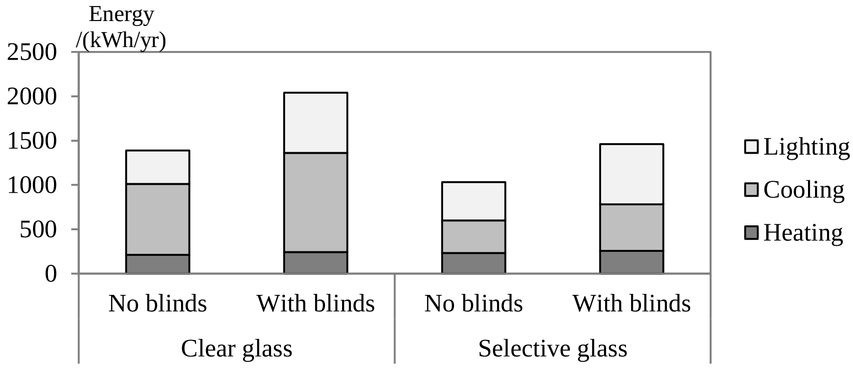

Fig. 5: Annual energy use for cases without an external shading

Considering annual energy use for the cases with external shadings and internal blinds being implemented, it can be seen from results in Fig. 6 that the window benefited from any external shading device regardless of the type of glass as the EUI decreased compared with the base cases (no shade). A large shading size on the clear glass window was better than the small, whereas for the selective glass window the difference with respect to the shading size was insignificant. The horizontal louvers type of shading yielded higher energy use than the corresponding overhang or a brise-soleil due to glare-induced high lighting load and extra internal solar gain added by radiation reflected from the louvers.

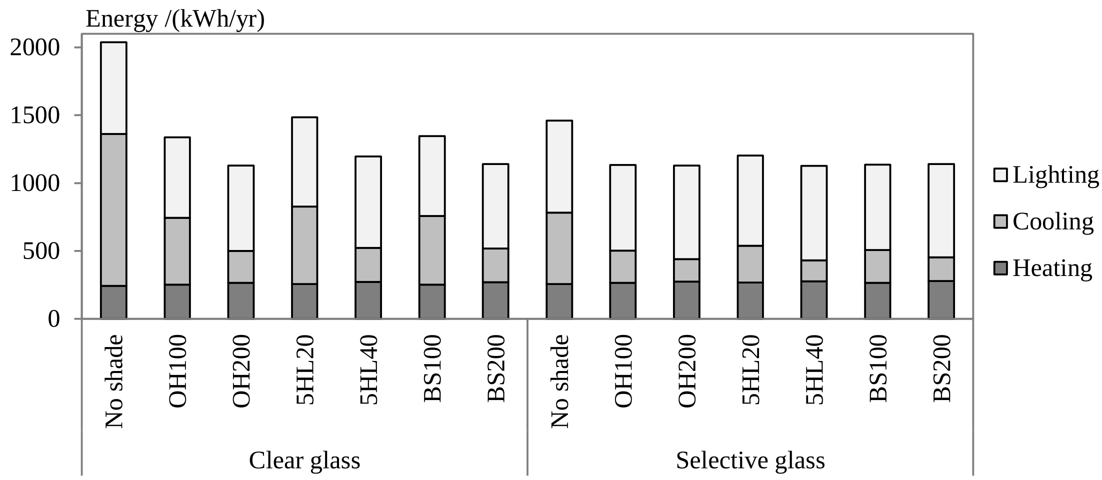

Fig. 6: Annual energy use for external shading cases with internal blinds operation

Thermal comfort metric is presented as a percentage of occupancy time when operative temperatures (equal to the average of mean radiant temperature and air temperature) exceeded the temperature setpoint of 25 °C (Fig. 7). Notably, external shadings improved summertime thermal comfort by means of operative temperatures, and even more effectively when combined with a selective glass window. Additionally, cooling peak loads and solar heat gains were minimised with selective glass cases, especially together with external shadings. System size assessed from cooling peak loads would transpire to be almost identical for large shading with clear glass and as for a small shading with selective glass cases.

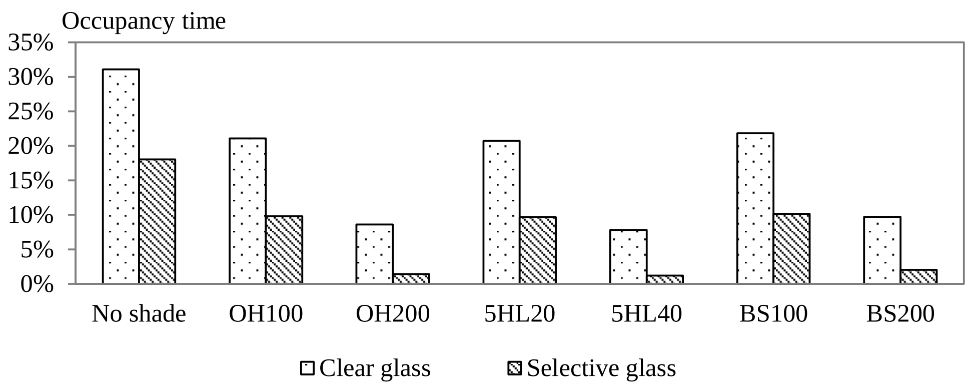

Fig. 7: Percentage of occupancy time with operative temperature exceeding 25 °C

4. Conclusions

The study intended to test, via computer simulations, various external shading geometries and glazing types placed on a south-oriented ‘shoebox’ office room aperture in a Nordic climate of Stockholm. It was done using means of integrated daylight and energy simulation approach. The main focus was the assessment of overheating issues in a modern highly insulated office space with a high thermal load. The study shows that interdependence of light, glare, and solar heat gain in buildings is a complex phenomenon that ought to be approached holistically, in an integrated manner. Its impact can be significant hence should be accounted for in performance assessments through routine implementation of integrated daylight and energy simulations. Other findings of this study were grouped into categories and listed.

Operational inferences:

- Internal shading systems, as glare protection, hinder both daylight and energy building performance.

- Occupant interaction with internal shading systems affects building performance assessments and should be accounted for, to avoid erroneous design inferences. More empirical studies on occupant interaction with building systems are needed.
- Building energy performance assessments require real-life operational schedules such as daylight-driven lighting or glare-driven blinds schedules for increased reliability.
- The authors claim that preparation of schedules for energy assessments, based on independent simulations of daylight and glare, is a complicated and time-consuming task, which highlights the need for more integrated and efficient simulation tools and workflows.

Fenestration design inferences:

- In a highly-glazed and well-insulated office in a Nordic climate, external shadings reduce overheating and improve occupant comfort, including visual comfort.
- In the absence of an external shading device, selective glass is a preferred glazing choice for a south-oriented window in the studied case, seeing as it reduces the annual energy use and improves occupant comfort.
- While external shadings were found inconsequential to the heating demand as they permit low-angle winter solar radiation, internal blinds increased the heating demand. The reason is that lower solar angles are likely to cause unwanted glare, which is mitigated by internal blinds, but consequentially, useful winter solar gains are also reduced.
- Brise-soleil type of external shading geometry is superior to a solid overhang due to higher daylight penetration, lesser material use, and more advantageous tilt angles for potential active solar integration on the building facade.
- Clear-glass window with a large overhang provided higher visual comfort (fewer glare occurrences), while an aperture with selective glass and a small overhang was more effective for summer thermal comfort (reduced overheating), albeit the same energy and daylight performance of these two cases.
- Overhang and horizontal louvers are two different shapes of external shading that intersect solar radiation equally; however, louvers pose a higher risk of glare, which impacts the operation of internal blinds and consequently worsens the energy and daylight building performance.

Future research on summer overheating in Nordic climates is highly encouraged, as it was shown that excessive solar radiation can negatively impact energy use and indoor comfort in a conventionally heating-dominated climate. The use of external solar shadings is not engrained in classic or modern Nordic architecture, but as was shown in this study, it might become essential from the standpoint of sustainable design. Moreover, there is a potential opportunity in utilizing external shading surfaces for active solar building integration (e.g. photovoltaic systems), which should be an interesting area for further exploration.

5. References

ASHRAE, 2017. 2017 ASHRAE Handbook: Fundamentals, ASHRAE Handbook Fundamentals Inch-Pound System. ASHRAE.

Bakker, L.G., Hoes-van Oeffelen, E.C.M., Loonen, R.C.G.M., Hensen, J.L.M., 2014. User satisfaction and interaction with automated dynamic facades: A pilot study. Building and Environment 78, 44–52. https://doi.org/10.1016/j.buildenv.2014.04.007

Boverket, 2011. Boverkets byggregler (BFS 2019:2) – föreskrifter och allmänna råd.

BPIE, 2011. Europe’s buildings under the microscope: A country-by-country review of the energy performance of buildings.

Cook, J., Oreskes, N., Doran, P.T., Anderegg, W.R.L., Verheggen, B., Maibach, E.W., Carlton, J.S., Lewandowsky, S., Skuce, A.G., Green, S.A., Nuccitelli, D., Jacobs, P., Richardson, M., Winkler, B., Painting, R., Rice, K., 2016. Consensus on consensus: a synthesis of consensus estimates on human-caused global warming. Environmental Research Letters 11, 48002. https://doi.org/10.1088/1748-9326/11/4/048002

da Silva, P.C., Leal, V., Andersen, M., 2012. Influence of shading control patterns on the energy assessment of office spaces. Energy and Buildings 50, 35–48. https://doi.org/10.1016/j.enbuild.2012.03.019

Day, J.K., Futrell, B., Cox, R., Ruiz, S.N., 2019. Blinded by the light: Occupant perceptions and visual comfort assessments of three dynamic daylight control systems and shading strategies. Building and Environment 154, 107–121. https://doi.org/10.1016/j.buildenv.2019.02.037

Delzendeh, E., Wu, S., Lee, A., Zhou, Y., 2017. The impact of occupants' behaviours on building energy analysis: A research review. Renewable and Sustainable Energy Reviews. https://doi.org/10.1016/j.rser.2017.05.264

Dubois, M.-C., 1997. Solar Shading and Building Energy Use: A Literature Review, Part 1. Lund.

Grynning, S., Time, B., Matusiak, B., 2014. Solar shading control strategies in cold climates - Heating, cooling demand and daylight availability in office spaces. Solar Energy 107, 182–194. https://doi.org/10.1016/j.solener.2014.06.007

Haase, M., Buvik, K., Dokka, T., Andresen, I., 2011. Design Guidelines for Energy Efficiency Concepts in Office Buildings in Norway. Design Principles and Practices 5, 667–694. https://doi.org/10.18848/1833-1874/CGP/v05i04/38156

Hammad, F., Abu-Hijleh, B., 2010. The energy savings potential of using dynamic external louvers in an office building. Energy and Buildings 42, 1888–1895. https://doi.org/10.1016/j.enbuild.2010.05.024

IEA, 2019. Key World Energy Statistics 2019. Paris.

Karlsen, L., Heiselberg, P., Bryn, I., Johra, H., 2016. Solar shading control strategy for office buildings in cold climate. Energy and Buildings 118, 316–328. https://doi.org/10.1016/j.enbuild.2016.03.014

Kirimtat, A., Koyunbaba, B.K., Chatzikonstantinou, I., Sariyildiz, S., 2016. Review of simulation modeling for shading devices in buildings. Renewable and Sustainable Energy Reviews. https://doi.org/10.1016/j.rser.2015.08.020

Kuhn, T.E., 2017. State of the art of advanced solar control devices for buildings. Solar Energy 154, 112–133. https://doi.org/10.1016/j.solener.2016.12.044

Lechner, N., 2015. Heating, cooling, lighting : sustainable design methods for architects., 4th editio. ed. John Wiley & Sons.

Manzan, M., 2014. Genetic optimization of external fixed shading devices. Energy and Buildings 72, 431–440. https://doi.org/10.1016/j.enbuild.2014.01.007

Poirazis, H., Blomsterberg, Å., Wall, M., 2008. Energy simulations for glazed office buildings in Sweden. Energy and Buildings 40, 1161–1170. https://doi.org/10.1016/j.enbuild.2007.10.011

Reinhart, C.F., Jakubiec, J.A., Ibarra, D., 2013. Definition of a reference office for standardized evaluations of dynamic facade and lighting technologies, in: Proceedings of BS2013: 13th Conference of International Building Performance Simulation Association. Chambéry, pp. 3645–3652.

Richman, E.E., 2012. Requirements for Lighting Levels [WWW Document]. Pacific Northwest National Laboratory. URL http://www.lumitronlighting.com/lighting_nowledge/LUX%20LEVEL_usace_Requirements%20for%20Lighting%20Levels.pdf (accessed 7.9.20).

Sadeghi, S.A., Karava, P., Konstantzos, I., Tzempelikos, A., 2016. Occupant interactions with shading and lighting systems using different control interfaces: A pilot field study. Building and Environment 97, 177–195. https://doi.org/10.1016/j.buildenv.2015.12.008

SGBC, 2020. Miljöbyggnad 3.1 Manual nybyggnad.

SGBC, BRE, 2018. BREEAM-SE New Construction 2017 Technical Manual 1.1.

Tzempelikos, A., Athienitis, A.K., 2007. The impact of shading design and control on building cooling and lighting demand. Solar Energy 81, 369–382. https://doi.org/10.1016/j.solener.2006.06.015

USGBC, 2019. LEED v4 for Building Design and Construction.

van den Wymelenberg, K., 2012. Patterns of occupant interaction with window blinds: A literature review. Energy and Buildings 51, 165–176. https://doi.org/10.1016/j.enbuild.2012.05.008

Wall, M., Bülow-Hübe, H., 2003. Solar Protection in Buildings. Part 2: 2000-2002. EBD-R--03/1.

Wienold, J., 2009. Dynamic daylight glare evaluation, in: Building Simulation 2009: Eleventh International IBPSA Conference. Glasgow, pp. 944–951.

Wienold, J., Christoffersen, J., 2006. Evaluation methods and development of a new glare prediction model for daylight environments with the use of CCD cameras. Energy and Buildings 38, 743–757. https://doi.org/10.1016/j.enbuild.2006.03.017

Zhang, Y., Bai, X., Mills, F.P., Pezzey, J.C.V., 2018. Rethinking the role of occupant behavior in building energy performance: A review. Energy and Buildings. https://doi.org/10.1016/j.enbuild.2018.05.017

Development of Indexes for the Form and Layout Design of Urban Residential Settlements in the West Plateau Region of China

Yu Liu[1], Yi Liu[1], Jin Wang[1], Wuxing Zheng[1], Teng Shao[1], Shangkai Hao[1], David Hou Chi Chow[2], Jingtao Du[2]

[1]Sustainable Building and Environmental Research Institute/Northwestern Polytechnical University, Xi'an (China)

[2] School of Architecture /University of Liverpool, Liverpool (U.K.)

Abstract

Solar radiation is the most important climate resource for human being. In order to achieve full acquisition and optimal distribution of solar radiation in urban residential settlements (URS), it is considered necessary to guide and control the form and layout design of URS. This research was conducted targeting URS in the west plateau region of China, which possesses abundant solar radiation resource. Firstly, web-based and on-site investigations were conducted, based on which typical building types and layout forms of URS in three representative cities in the researched region, as well as dimensions of typical residential buildings in such URS were identified, some living habits and needs of local residents in the researched region in wintertime were observed and recognized. Secondly, through software simulations, a number of different orientations, typical layout forms and sub-forms of URS were compared regarding their potential of solar radiation acquisition, based on which four indexes are proposed for guiding the design of URS in Lanzhou city. Finally, conclusions and limitations of the research are provided, and further researches are recommended.

Key-words: urban residential settlements (URS), form, layout, design, index, west plateau region, China

1. Introduction

The form and layout of urban residential settlements (URS) have a decisive influence on their potential accessibility to regional climate resources, including solar radiation resource. Design indexes are important in terms of guiding and control the direction of design. So far, few researches have been conducted to develop guiding and or control indexes for the form and layout design of URS concerning their potential of solar radiation acquisition. Supported by some national and provincial funded projects, a series of researches were conducted targeting URS in the west plateau region, which is also a solar resource intensive region, of China. Purpose of the research was to develop guiding indexes for the form and layout design of URS, in order to maximize their potential of solar radiation acquisition. Some results of the research are introduced in this paper.

2. A brief literature review

2.1. Overview

The accessibility of solar radiation in the high density urban areas (including URS) has attracted increasingly more interests of research worldwide in the last 20 years (Lundgren and Dahlberg, 2018, Hachem-Vermette and Singh, 2019, Hachem et al., 2012). A search of literature between 1999 and 2019 on the *Web of Science* database on the topic of community and solar energy shows a result of 3991 records with clear trend of continuous rise; while a similar search on CNKI, a Chinese literature database, shows a results of 179 records during the same period of time with no obvious trend, which implies a possible insufficiency of such research in China so far. (Fig. 1)

doi:10.18086/eurosun.2020.01.02 Available at http://proceedings.ises.org

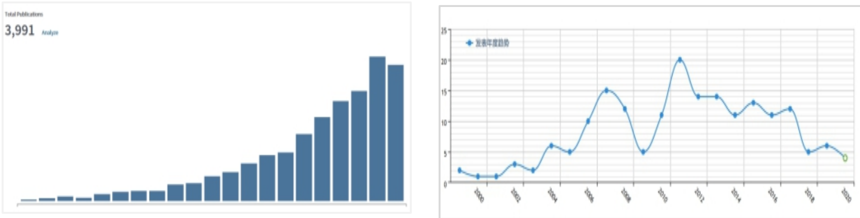

Fig. 1 Results of literature search on the topic of "community AND solar energy" (1999-2019)

Source：(left) Web of Science database; (right) CNKI database

2.2. Indexes in the existing standards in China

In the existing design standards in China, there are two types of guiding or control indexes that are directly related to the utilization or acquisition of solar radiation: type A. performance index, type B. design index. Examples of type A index include sunshine hours, sunshine effectiveness, solar radiation absorption rate of decorative materials, calculated temperature in passive solar heating room, daylight factor, shading coefficient, solar radiation correction coefficient, shading coefficient, solar radiation correction coefficient, etc. Examples of the type B index include coefficient of sunshine spacing, window to wall ratio, orientation of attached solar space, pitch of roof, proportion of the area of shading facilities against that of the transparent part of the exterior windows, etc. (Ministry of Housing and Urban-Rural Development of the People's Republic of China (MOHURD), 2012) (Ministry of Housing and Urban-Rural Development of the People's Republic of China (MOHURD), 2018) Overall, there are more Type A indexes, less Type B indexes. Most existing indexes are established at individual building scale and few at the residential community scale. This research intends to develop new Type B indexes for the form and layout design of URS in the west plateau region of China.

3. Investigations on URS in the west plateau region of China

A series of investigations were conducted targeting URS in three representative cities (Lanzhou, Xining and Lhasa) in the researched region. Some basic information of the three cities is listed in Tab. 1.

Tab. 1 Basic information of Lanzhou, Xining and Lhasa (Data source: SOLARGIS, http://solargis.cn)

	Lanzhou	Xining	Lhasa
latitudes	36.04	36.49	29.39
longitude	103.45	101.26	91.07
altitude（m）	1543	2697	3654
solar radiation (direct normal) (MJ/m^2Y)	4705	5526	9147
air temperature(yearly) (°C)	9.5	3.3	4.2

3.1. Web-based investigation

A number of digital map tools first compared, among which OpenStreetMap-OSM and Baidu Map were first identified as the ones that can meet the basic needs of the research. With a real scene function and possibility to check the height of buildings, Baidu Map was further utilized to identify the layout forms of URS and types of residential building in URS in Lanzhou, Lhasa and Xining.

1) Lanzhou city

Lanzhou is located on the Loess plateau, between two mountains, with the Yellow River running through the city. Web-based investigation in Lanzhou involved identification of typical forms of URS in the city area, as well as typical building types in the URS.

A total of 264 URS were identified on the digital map, in which 43 are mainly composed of *tower-type* buildings, 44 are composed of *plank-type* buildings, and 177 are composed of a mix of *tower & plank-type* buildings (in China, *tower-type* building refers to high-rise buildings that possess similar size of depth and width, which make them looked like towers, *plank-type* building refer to roughly cubic form buildings that possess a relatively small depth and larger width, which make them looked somewhat like planks; high-rise residential building refers to residential buildings that possess a height greater than 27m). Layout of the identified typical URS are mainly arranged in 3 different forms: *row, enclosed* and *fan. Row* refers a form of URS in which buildings are arranged largely in a range of rows; *enclosed* refers to a form of URS in which some buildings are arranged along the edge of the site, so form an enclosed or semi-enclose feeling of space inside the URS; *fan* refers to a form of URS in which buildings are arranged in a fan shape. *Row* and *enclosed* are the major forms in Lanzhou, while *fan* is a form that can suit special site conditions and it is not usually found in other cities. (see Fig. 2-3, Tab. 2-3)

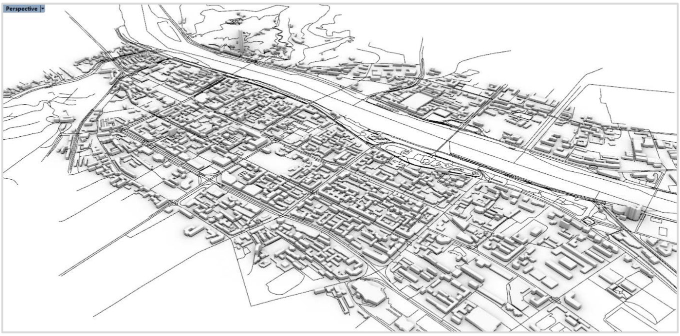

Fig. 2 Map of the dense urban area of Lanzhou city (source： OpenStreetMap-OSM, edited by Yi Liu)

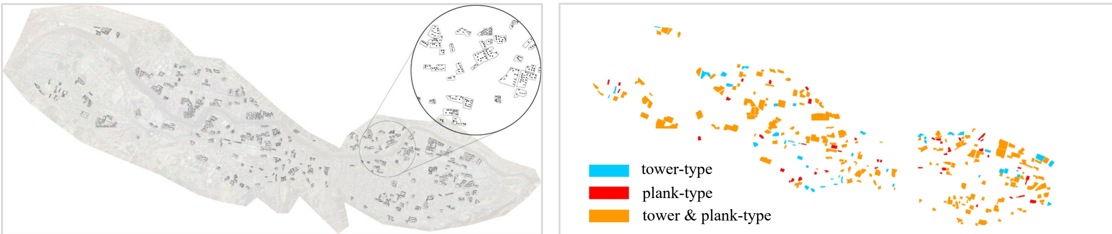

Fig. 3 Distribution of different types of URS in the dense city area of Lanzhou (source: Baidu Map, edited by Yi Liu)

2) Lhasa city

Lhasa is located on the Qinghai-Tibet plateau. Web-based investigation reveals that, layouts of URS in Lhasa are mainly arranged in 2 forms: *row* and *enclosed*, with the first one be the dominant form.

Two distinguished building styles are identified in Lhasa: *local* style and *inland* style. *Local* style refers to a kind of low-rise buildings evolved locally in Lhasa region. They are built with courtyards and their functional arrangement express a kind of traditional features in the Tibetan region. *Inland* style refers to the mid-rise and high-rise buildings without courtyards. Their functional layouts are largely the same as normal buildings in most inland cities in China, but their colors, symbols and decorations more or less possess clear local features. URS with *inland* style residential buildings can be further divided into three types: *plank, towe*r, and a mix of *tower & plank*, with the first one be the dominant type.

3) Xining city

Xining is also located on the Qinghai-Xizang plateau, north-east to Lhasa. Web-based investigation reveals that, URS in Xining are mainly arranged in two forms: *row* and *enclosed*, with the first be the dominant one. Residential buildings in the URS in Xining can be divided into three types: *plank*, *tower*, and a mix of *plank & tower*, also with the first be the dominant one.

A summary of building types and URS forms identified through web-based investigation is shown in Tab. 2.

Tab. 2 Building types and URS forms

<table>
<tr><th colspan="2">Cities</th><th colspan="3">Building types</th></tr>
<tr><td colspan="2">Lanzhou</td><td>high-rise/plank *</td><td>high-rise/tower</td><td>high-rise/tower & plank</td></tr>
<tr><td rowspan="2">Lhasa</td><td>Inland style</td><td>mid-rise/plank*
high-rise/plank</td><td>high-rise/tower</td><td>mid/high-rise/tower & plank</td></tr>
<tr><td>Local</td><td colspan="3">low-rise/plank with courtyard</td></tr>
</table>

style			
Xining	high-rise/plank *	high-rise/tower	high-rise/tower & plank

Cities	**URS forms**		
Lanzhou	row *	enclosed	fan
Lhasa	row *	enclosed	/
Xining	row *	enclosed	/

Note: * the dominant one

3.2. On-site investigation

1) Dimensions of buildings

On-site investigations show that, in Lanzhou city, the *plank* type residential buildings in URS usually possess a surface width of about 30 meters. When two buildings are placed side by side, the maximum width can reach 60 meters. The depth varies from about 14 to 30 meters. The width-to-depth ratio of a *tower* type building is usually about 1.45, while that of a *plank* type building with one unit is about 2.0, with two or more than two units is about 3.5, and maximum 4.61. In the newly constructed URS, building spacing all meet building standards for solar access; however, in the old ones, the space between buildings are obviously smaller.

2) Solar radiation on building surface

To reveal influence of direct solar radiation on building surfaces, infrared thermal image of facades and roofs of buildings inside URS in Lanzhou, Xining and Lhasa cities were collected by a small UAV with thermal infrared camera. The results show that solar radiation have obvious effect on the surface of buildings. A clear boundary line can be identified between the shaded and unshaded areas. The temperatures of external surface of buildings in areas with direct solar radiation are significantly higher than those in the shaded areas. Besides, orientations of buildings have a clear effect on their external surface temperatures. (see Tab.3)

Tab. 3 Thermal images of residential buildings in the researched region

Lanzhou (Jun.2019)	Photo	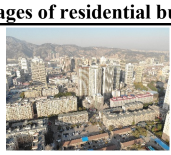		
	Thermal image	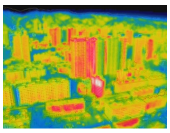	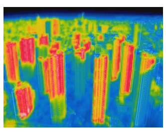	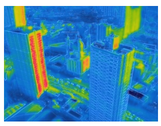
Xining (Jun.2020)	Photo			
	Thermal image	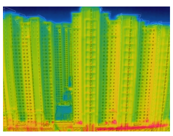	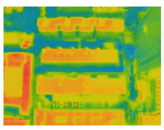	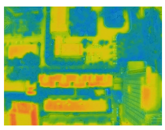
Lhasa (Jan.2020)	Photo			
	Thermal image	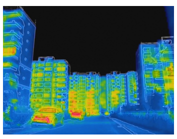	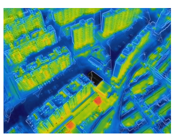	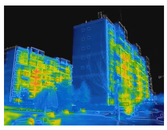

3) Living habits of local residents

On-site observations in URS in the researched region show that, “get out in the sun” in the warm and sunny days of wintertime is a common desire and even habit of many local residents . This is applicable for people of all ages and especially for the elderly, which implies a practical significance to maximize the wintertime solar radiation receiving potential of URS in the researched region.

4. Indexes for the form and layout design of URS

4.1 Orientation of URS

URS in Lanzhou city are taken as examples in the following simulation and discussion.

1) Model setting

According to the results of above-mentioned investigations, *row* and *fan* forms were selected to establish typical models of URS for further discussion. Setting of the models was the following: 25 individual buildings each with a dimension of 30m*15m*80m; the building cluster with a north-south spacing of 75m, and a gable spacing of 40m. All the settings meet the basic requirements of national and regional design standards for URS and residential buildings regarding solar access in winter time. (see Tab.4)

Tab. 4 Models of two typical layout forms of URS

Row		Fan	
plan	perspective	plan	perspective
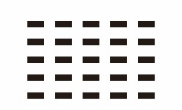	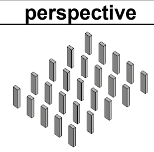	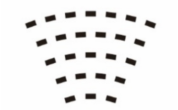	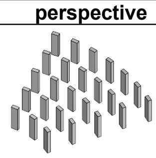

2) Results of simulation

Rhino's ladybug plugin was applied for the simulation. According to the *Technical Specification for Passive Solar Buildings* (DB62/T25-3079-2014), a regional building standard of Gansu Province, in which Lanzhou city is its capital city, the simulation period was set the same as its public heating period: from November 2 to March 14 of the following year, a total of 132 days. The total rotation angle of orientation was set at 360° and the step length of change was set at 10°.

Results of the simulations show that, in terms of solar radiation receiving potential, the optimal orientation of *row* forms is 10° south by west, while that of *fan* forms is south. For different orientations of *fan* forms, the difference of radiation level between south and 10° south by west orientation is very small. On the whole, the simulated results show a rough southward advantage, with southwest being slightly better than southeast orientation. (see Tab.5)

Therefore, from the perspective of solar radiation receiving potential, a guiding index for the orientation design of URS in Lanzhou is recommended as: Index ①--the percentage of orientation that is between *south* and *10° south by west*. A higher percentage means better solar radiation receiving potential, so should be encouraged.

Tab. 5 Optimal orientations of URS

Forms of URS	Optimal orientation		Forms of URS	Optimal orientation	
Row 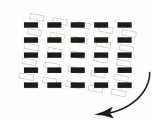	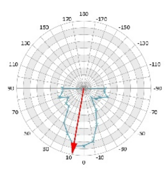	10° south by west	**Row-westward rotated** 	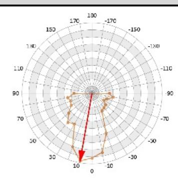	10° south by west

Fan

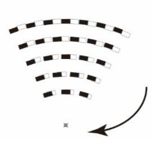

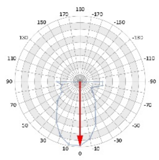

south

Fan-westward rotated

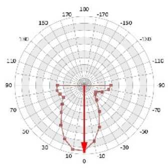

south

Note: red arrows indicate the optimal orientation for the best potential access to solar radiation

4.2 Layout of URS

1) Model setting

As mentioned before, typical layout of URS in Lanzhou can be classified into three forms: *row*, *enclosed* and *fan*. Considering that the overall layout of Lanzhou is related to the trend of the Yellow River that passes through the city, and the fact that many existing buildings in the city are set at 30° perpendicular to or parallel to the course of the river, an angle of 30° were set for the rotated sub-forms of URS.

For comparative purpose, different layout forms of URS in the simulation model were all set as a cluster of 25 buildings, in which 16 at surrounding positions and 9 at internal positions. Overall, 13 sub-forms of layout were established for simulation analysis. (see Tab.6)

Tab. 6 Forms and sub-forms of URS for simulation

Forms	Sub-forms		
Row	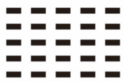	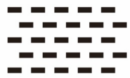	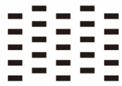
	No.**1** regular	No.**2** horizontally staggered	No.**3** vertically staggered
			
	No.**4** eastward rotated	No.**5** westward rotated	
	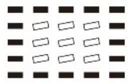	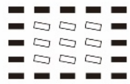	
	No.**6** inner part eastward rotated	No.**7** inner part westward rotated	
Enclosed	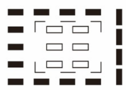	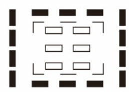	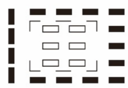
	No.**8** with 1 row of east-west facing building at the east side	No.**9** with 1 row of east-west facing building each at the east and the west side	No.**10** with 1 row of east-west facing building at the west side
Fan			
	No.**11** regular	No.**12** westward rotated	No.**13** eastward rotated

2) Results of simulation

Regarding solar receiving potential per unit building construction area, *Row* form in whole is higher than the other two forms. Among the 13 sub-forms, *Row-regular* form (No.1) is the highest, closely followed by *Row-inner part westward rotated* (No.7), *Row-inner part eastward rotated* (No.6), and *Row-westward rotated* forms (No.5); *Fan-eastward rotated* form is the lowest (No.13), followed by *Fan-westward rotated* form (No.12) (see Fig. 4 left)

Regarding solar radiation receiving potential per unit land area, *Fan-regular* form (No.11) is the highest, followed by *Row-regular* (No.1), *Row-inner part westward rotated* (No.7), *Row-westward rotated* (No.5) and *Row-inner part eastward rotated* forms(No.6); *Row-vertical staggered* from (No.3) is the lowest, followed by the three *Enclosed* sub-forms (No. 9, 8/10). (see Fig. 4 right)

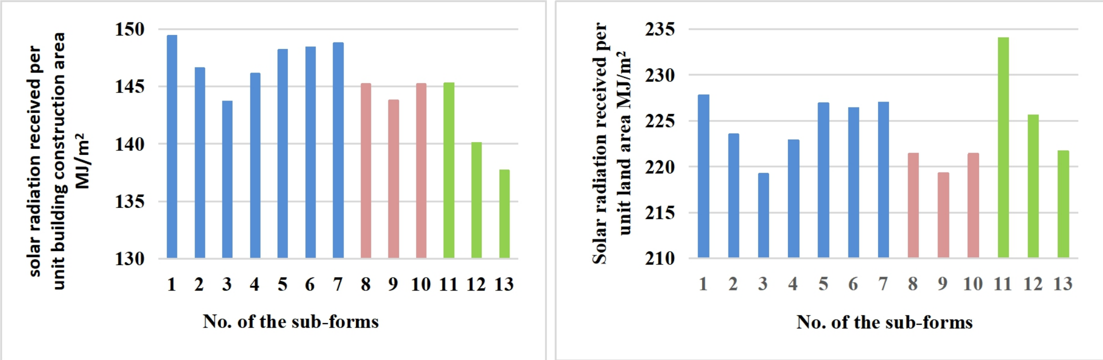

Fig. 4 Left: solar radiation received per unit building construction area（MJ/m²）; Right: solar radiation received per unit land area（MJ/m²）

Priorities of the sub-forms of URS regarding their solar radiation receiving potential per unit building construction area and per unit land area are listed in Tab.7.

Tab. 7 Priorities of the sub-forms of URS regarding their solar radiation receiving potential

Priorities	**Sub-forms of URS**	
	Solar radiation receiving potential per unit building construction area	**Solar radiation receiving potential per unit land area**
1	No.1 **Row**-regular	No.11 **Fan**-regular
2	No.7 **Row**-inner part westward rotated	No.1 **Row**-regular
3	No.6 **Row**-Inner part eastward rotated	No.7 **Row**-inner part westward rotated
4	No.5 **Row**-westward rotated	No.5 **Row**-westward rotated
5	No.2 **Row**- horizontally staggered	No.6 **Row**-inner part eastward rotated
6	No.4 **Row**-eastward rotated	No.12 **Fan**-westward rotated
7	No.11 **Fan**-regular	No.2 **Row**-horizontally staggered
8	No.10 **Enclosed**-with 1 row of east-west facing building at the west side No.8 **Enclosed**-with 1 row of east-west facing building at the east side	No.4 **Row**-eastward rotated
9	No.9 **Enclosed**-with 1 row of east-west facing building each at the east and the west side	No.13 **Fan**-eastward rotated
10	No.3 **Row**-vertically staggered	No.10 **Enclosed**-with 1 row of east-west facing building at the west side No.8 **Enclosed**-with 1 row of east-west facing building at the east side
11	No.12 **Fan**-westward rotated	No.9 **Enclosed**-with 1 row of east-west facing building each at the east and the west side
12	No.13 **Fan**-eastward rotated	No.3 **Row**-vertically staggered

Accordingly, four tentative indexes for the layout design of URS in Lanzhou are recommended as the following:

Index ②--the percentage of building construction area in the URS that is arranged in any of the following layout forms: *Row-regular* (No.1)*, Row-inner part westward rotated* (No.7), *Row-inner part eastward rotated* (No.6).

Index ③--the percentage of building construction area in the URS that is arranged in any of the following layout forms: *Fan-eastward rotated* (No.13)*, Fan-westward rotated* (No.12), *Row-vertically staggered* (No.3).

Index ④--the percentage of land area in URS that is arranged in any of the following layout forms: *Fan-regular* (No.11), *Row-regular* (No.1), *Row-inner part westward rotated* (No.7).

Index ⑤--the percentage of land area in URS that is arranged in any of the following layout forms: *Row-vertically staggered* (No.3), any of the three *Enclosed* form (No.9, 8/10).

For indexes ②and ④, a higher percentage means better solar radiation receiving potential, so should be encouraged; while for indexes ③and ⑤, a higher percentage means worse solar radiation receiving potential, so should be avoided when possible.

5. Conclusions, limitations and further researches

5.1 Conclusions

The building types and layout forms of URS in three typical cities (Lanzhou, Xining and Lhasa) in the west plateau region of China are discussed based on web-based investigations, on-site investigations and software simulations. Three typical building types (*plank*, *tower* and a mix of *plank & tower)*, as well as three typical layout forms (*row*, *enclosed* and *fan*) of URS were first identified in the investigated cities.

Simulations were then run targeting one dominant building type (high-rise/plank), two typical layout forms (*row* and *fan*) and thirteen sub-forms of URS that had been identified in Lanzhou city, based on the results of which five tentative indexes for guiding the form and layout design of URS were proposed as the following:

- Index ①--the percentage of orientation of buildings in URS that is between *south* and *10° south by west*.
- Index ②--the percentage of building construction area in URS that are arranged in any of the following layout forms: *Row-regular* (No.1)*, Row-inner part westward rotated* (No.7), *Row-inner part eastward rotated* (No.6).
- Index ③--the percentage of building construction area in URS that are arranged in any of the following layout forms: *Fan-eastward rotated* (No.13)*, Fan-westward rotated* (No.12), *Row-vertically staggered* (No.3).
- Index ④--the percentage of land area in URS that is arranged in any of the following layout forms: *Fan-regular* (No.11), *Row-regular* (No.1), *Row-inner part westward rotated* (No.7).
- Index ⑤--the percentage of land area in URS that is arranged in any of the following layout forms: *Row-vertically staggered* (No.3), any of the three *Enclosed* form (No.4-6).

For indexes ①, ②and ④, a higher percentage means better solar radiation receiving potential, so should be encouraged; while for indexes ③and ⑤, a higher percentage means worse solar radiation receiving potential, so should be avoided when possible.

5.2 Limitations and further researches

Limitations of this research mainly lie in four aspects: first, the simulation models, although were established based on statistical analysis of investigations, were highly abstracted and simplified, so could not fully reflect the complex conditions of URS in the real world; second, the proposed indexes were developed largely based on software simulations, the results of which have not yet been fully validated; third, the simulations were conducted only targeting URS in Lanzhou city, it is not yet clear if similar results could be achieved in other typical cities in the researched region; fourth, the practicability of the proposed indexes have not yet been tested.

Accordingly, further researches are recommended to: firstly, validate the simulation results by on-site surveys and measurements, etc.; secondly, conduct same researches in other typical cities in the researched region (e.g. Xining and Lhasa) to see if similar results could be achieved; and thirdly, apply the proposed indexes in real design practices to test their practicability, and base on which to adjust, deepen, or improve them when possible.

6. Acknowledgments

The research of this paper was supported by the National 13th Five-Year Key Research and Development Project of China (2016YFC0700200), the National Natural Science Foundation of China (52078422, 51908463), and the Shaanxi Provincial Key R&D Program - International Science and Technology Cooperation Program (2020KW-066).

7. References

Hachem-Vermette, C. & Singh, K. 2019. Mixed-use neighborhoods layout patterns: Impact on solar access and resilience. Sustainable Cities and Society, 51, 101771.

Hachem, C., Athienitis, A. & Fazio, P. 2012. Design Methodology of Solar Neighborhoods. Energy Procedia, 30, 1284-1293.

Lundgren, M. & Dahlberg, J. 2018. IEA SHC Task51/Report B2 Approaches, Methods and Tools for Solar Energy in Urban Planning.

Ministry of Housing and Urban-Rural Development of the People's Republic of China (Mohurd) 2018. Code of urban residential areas planning & design. Beijing.

Ministry of Housing and Urban-Rural Development of the People's Republic of China(Mohurd) 2012. Technical code for passive solar buildings. Beijing.

NUMERICAL ANALYSIS OF SOLAR RADIATION EFFECTS AT INDOORS WITH INTERNAL PARTITIONS AND EXTERNAL SOLAR SHADES

Ali Can Yelekci, Cem Keskin, M. Pınar Mengüç

Center for Energy, Environment and Economy (CEEE/EÇEM)

& Department of Mechanical Engineering

Ozyegin University, Istanbul, Turkey

Abstract

A numerical study is conducted to couple natural convection in an office space with thermal radiation due to solar radiation. The study specifically investigates the effect of partitions located between desks of the office space to develop a tool-box to determine the effect of windows on thermal and visual comfort of occupants. Three different partition cases (according to the aspect ratio of the partition to the ceiling height, which are 0.3, 0.5 and 1.0) were studied. Moreover, the effects of different designs of solar shades in front of windows were investigated. All walls other than the façade of the enclosure are assumed adiabatic, and the enclosure has a single window, which acts as a thermal radiative heat source. All surfaces are assumed to be gray-diffuse surfaces for calculation of thermal radiation. The solar radiation is analyzed for a perfect sunny day with both diffuse and direct sunlight, and for an overcast day with only diffuse sunlight. Based on the choice of partitions geometry, solar shade aspect ratios and the weather conditions, variations on the surface temperature distribution inside the office are analyzed.

Keywords: Solar radiation, Solar shade, Internal partition, Temperature distribution

1. Introduction

Partitions are used in offices to create personal space for occupants by separating them visually and creating sound insulation. However, if not designed properly, these semi-surrounded cubicles created by the partitions can cause thermal and visual discomfort of internal or external occupants due to unintended effects of thermal radiation and air flow in the office spaces.

There is a large body of literature on the effect of radiation to indoor thermal environment. An analytical and numerical model of radiation configuration factors and solar illumination parameters for a L-shaped room with opaque walls and clear windows was developed (Modest, 1982). Martyushev et al. (2014) numerically studied a cubical enclosure with heat source as a floor, by coupling natural convection and thermal radiation. They concluded that average convective heat transfer (based on dimensionless Nusselt number) is a decreasing, and average radiative Nusselt number is an increasing function of emissivity. Both are increasing function of Rayleigh number (another dimensionless number about the natural convective heat transfer in the medium). Cubical enclosure was numerically studied by Parmananda et al. (2018) with partitions on opposing walls while the other opposing walls were at temperature difference. They obtained that the partitions had little effect on convective Nusselt number but had considerable effect on radiative Nusselt number. Moreover, partitions are observed to cause local temperature differences near them. Xamán et al. (2008) developed a numerical model for a two-dimensional square cavity with a window. They achieved a correlation between the total Nusselt number and the Rayleigh number. The same numerical model was utilized for a study with various window sizes and locations by Olazo-Gómez et al. (2020). They concluded that the radiative heat transfer became lower than the convective heat transfer at higher values of solar irradiance, and the Nusselt numbers for convection and radiation transfer were lower at laminar flow than turbulent flow. Critical review on thermal radiation effects on thermal comfort was presented by Halawa et al. (2014). They emphasized the possible use of mean radiant temperature.

However, there are only a few studies available which explores the effect of thermal radiation coupled with natural convection in an enclosure to explore the thermal comfort of occupants. In addition, a detailed study of, surface

doi:10.18086/eurosun.2020.01.03 Available at http://proceedings.ises.org

temperature distribution due to solar thermal radiation within a three-dimensional office environment is missing. Purpose of this study is to shed light on thermal radiation effects of partitions in office spaces to provide better designed offices with better thermal comfort, and to develop more energy efficient spaces. Based on the results obtained, a series of conclusions are listed to achieve these goals.

2. Physical and Mathematical Model

The effects of solar thermal radiation on internal partitions in terms of surface temperatures considering thermal radiation is not studied extensively. The geometry for this study is based on an office at our academic building. The research question is investigated by conducting numerical simulations for various aspect ratios and weather conditions (see Tab. 1 for the list of cases). The solar heat flux and solid angle of the radiation incident on the window are assumed to be constant (changing only due to solar shade and weather condition). The diffuse solar irradiance is 10% of the direct solar irradiance. The walls, ceiling and floor are assumed to be adiabatic, except the window and façade, and all the surfaces are analyzed as gray-diffuse surfaces. The air inside of the geometry is assumed to be nonparticipating media. The inlet supplies air at 20° angle from the ceiling to four sides of the inlet cavity.

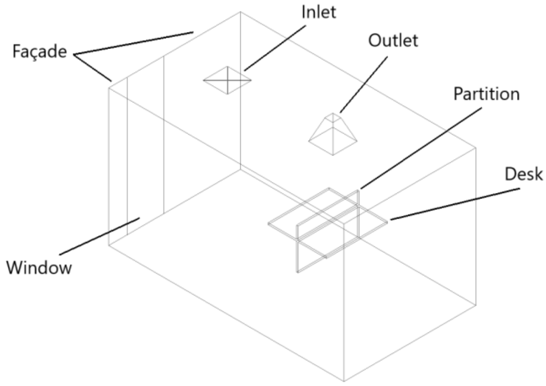

Fig. 1: Test geometry: An office with desks and partitions; window is allowing solar radiation in

Since the effect of the solar shade inside the enclosure is the concern of this study, solar shade will be added into the calculations by decreasing both direct and diffuse solar irradiances according to the aspect ratio of the solar shade. Same approach will be applied to the weather condition. For sunny cases both direct and diffuse solar irradiances will be active, but for overcast cases just the diffuse solar irradiance will be active for the model as shown on Tab. 1 for each case.

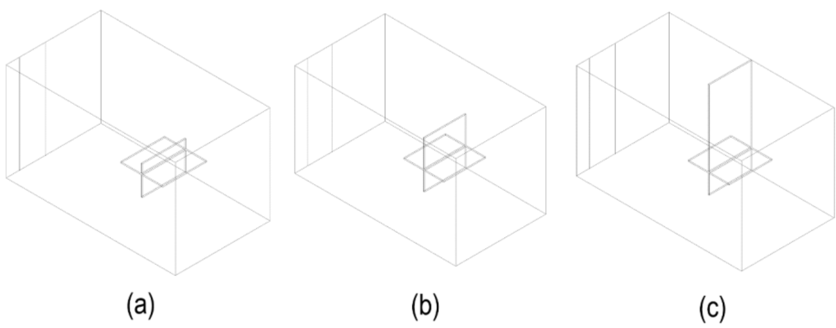

Fig. 2: Three test geometries for different sizes of partition; partition to ceiling aspect ratios used are (a) 0.30, (b) 0.50 and (c) 1.00

The material for walls and façade is chosen as concrete, for desk and partition it is wood (see Tab. 2 for material properties). Dimensions of the office are 3.25m x 5.8m x 3.36m. Window is 0.45m away from the side wall. Partition and desk are in the middle of the adjacent wall, both have thickness of 0.04m. Height of the desk is 0.7m. Thickness of the window and façade are 0.015m and 0.15m, respectively.

Tab. 1: List of cases studied

Case Number	Partition Aspect Ratio	Solar Shade Aspect Ratio	Weather Condition	Direct Solar Irradiance [W/m^2]	Diffuse Solar Irradiance [W/m^2]
1a	0.30	0.00	Sunny	1366	136.6
1b	0.50	0.00	Sunny	1366	136.6
1c	1.00	0.00	Sunny	1366	136.6
2a	0.30	0.50	Sunny	683	68.3
2b	0.50	0.50	Sunny	683	68.3
2c	1.00	0.50	Sunny	683	68.3
3a	0.30	0.00	Overcast	-	136.6
3b	0.50	0.00	Overcast	-	136.6
3c	1.00	0.00	Overcast	-	136.6
4a	0.30	0.50	Overcast	-	68.3
4b	0.50	0.50	Overcast	-	68.3
4c	1.00	0.50	Overcast	-	68.3

Tab. 2: Material properties

Material Name	Density [kg/m^3]	c_p [J/kgK]	k [W/mK]	Emissivity	Transmissivity
Concrete	2400	1000	0.8	0.94	-
Wood	800	1760	0.08	0.9	-
Glass	2500	840	0.8	0.1	0.8

For all CFD analysis continuity and conservation of mass equations need to be solved. Solution of the energy equation is also required if the problem involves heat transfer. Following Navier-Stokes equations constitute the required equations Çengel et al. (2015). The three dimensional continuity equation is

$$\frac{\partial p}{\partial t}+\frac{\partial (pu)}{\partial x}+\frac{\partial (pv)}{\partial y}+\frac{\partial (pw)}{\partial z}=0 \qquad \text{(Eq. 1)}$$

The three dimensional conservation of equations are

$$\frac{\partial (pu)}{\partial t}+\frac{\partial (pu^2)}{\partial x}+\frac{\partial (puv)}{\partial y}+\frac{\partial (puw)}{\partial z}=-\frac{\partial p}{\partial x}+\frac{1}{Re}\left[\frac{\partial \tau_{xx}}{\partial x}+\frac{\partial \tau_{xy}}{\partial y}+\frac{\partial \tau_{xz}}{\partial z}\right] \qquad \text{(Eq. 2)}$$

$$\frac{\partial (pv)}{\partial t}+\frac{\partial (puv)}{\partial x}+\frac{\partial (pv^2)}{\partial y}+\frac{\partial (pvw)}{\partial z}=-\frac{\partial p}{\partial y}+\frac{1}{Re}\left[\frac{\partial \tau_{xy}}{\partial x}+\frac{\partial \tau_{yy}}{\partial y}+\frac{\partial \tau_{yz}}{\partial z}\right] \qquad \text{(Eq. 3)}$$

$$\frac{\partial (pw)}{\partial t}+\frac{\partial (puw)}{\partial x}+\frac{\partial (pvw)}{\partial y}+\frac{\partial (pw^2)}{\partial z}=-\frac{\partial p}{\partial z}+\frac{1}{Re}\left[\frac{\partial \tau_{xz}}{\partial x}+\frac{\partial \tau_{yz}}{\partial y}+\frac{\partial \tau_{zz}}{\partial z}\right] \qquad \text{(Eq. 4)}$$

The energy equation is

$$\frac{\partial (E_T)}{\partial t}+\frac{\partial (uE_T)}{\partial x}+\frac{\partial (vE_T)}{\partial y}+\frac{\partial (wE_T)}{\partial z}=-\frac{\partial (up)}{\partial x}-\frac{\partial (vp)}{\partial y}-\frac{\partial (wp)}{\partial z}-\frac{1}{RePr}\left(\frac{\partial q_x}{\partial x}+\frac{\partial q_y}{\partial y}+\frac{\partial q_z}{\partial z}\right)+\frac{1}{Re}\left[\frac{\partial}{\partial x}\left(u\tau_{xx}+v\tau_{xy}+w\tau_{xz}\right)+\frac{\partial}{\partial y}\left(u\tau_{xy}+v\tau_{yy}+w\tau_{yz}\right)+\frac{\partial}{\partial z}\left(u\tau_{xz}+v\tau_{yz}+w\tau_{zz}\right)\right] \qquad \text{(Eq. 5)}$$

Accepted standard value for solar irradiance entering the atmosphere by Howell et al. (2016)

$$I_0 = 1366\ W/m^2 \qquad \text{(Eq. 6)}$$

Air mass is used to calculate the solar irradiance incident on the surface of the Earth after losing fraction of the irradiance throughout the atmosphere with corresponding solar zenith angle θ by Roumpakias et al. (2014)

$$AM = \frac{1}{cos\theta} \qquad \text{(Eq. 7)}$$

$$I_D = 1.1 \times I_0 \times 0.7^{AM^{0.678}} \qquad \text{(Eq. 8)}$$

Equations for the view factors and radiative heat transfer are retreived from Howell et al. (2016). View factor from surface 1 to surface 2 is

$$F_{1-2} = \frac{1}{A_1} \iint_{A_1 A_2} \frac{cos\theta_1\theta_2}{\pi S^2} dA_2 dA_1 \qquad \text{(Eq. 9)}$$

The view factors have reciprocity according to their surface areas

$$A_1 F_{1-2} = A_2 F_{2-1} \qquad \text{(Eq. 10)}$$

Radiative heat transfer inside a grey-diffuse enclosure consists of radiation incident on a surface irradiance, *G*, and radiation leaving the surface radiosity, *J*. Emissivity and absorptivity values are equal, emissivity and reflectivity are equal to 1.

$$\varepsilon_k = \alpha_k \qquad \text{(Eq. 11)}$$

$$\varepsilon_k + \rho_k = 1 \qquad \text{(Eq. 12)}$$

Radiative heat flux in terms of radiosity and irradiance are shown below

$$Q_k = q_k A_k = (J_k - G_k) A_k \qquad \text{(Eq. 13)}$$

$$J_k = \varepsilon_k \sigma T_k^4 + \rho_k G_k = \varepsilon_k \sigma T_k^4 + (1 - \alpha_k) G_k = \varepsilon_k \sigma T_k^4 + (1 - \varepsilon_k) G_k \qquad \text{(Eq. 14)}$$

Calculation of irradiance on a surface inside a grey-diffuse enclosure consists of sum of radiosity values multiplied by the view factors

$$A_k G_k = A_k J_1 F_{k-1} + A_k J_2 F_{k-2} + \cdots + A_k J_j F_{k-j} + \cdots + A_k J_k F_{k-k} + \cdots + A_N J_N F_{k-N} \qquad \text{(Eq. 15)}$$

$$G_k = \sum_{j=1}^{N} J_j F_{k-j} \qquad \text{(Eq. 16)}$$

Change of temperature of the surface due to solar irradiance involving conduction, convection and radiation is calculated by the following equation. Instead of $q_{solar} cos\theta$ in the equation I_D from the air mass calculation above can be implemented.

$$ka\left(\frac{\partial^2 T}{\partial x^2} + \frac{\partial^2 T}{\partial y^2} + \frac{\partial^2 T}{\partial z^2}\right) + \alpha_s q_{solar} cos\theta + \sigma\varepsilon_i [T_i^4 - T^4(x,y,z)] - \varepsilon_0 \sigma T^4(x,y,z) - h(T(x,y,z) - T_e) = mc_p \Delta T/\Delta t \qquad \text{(Eq. 17)}$$

Mean radiant temperature is a parameter used for thermal comfort analysis due to radiation by ASHRAE (2009).

$$T_r^4 = T_1^4 F_{p-1} + T_2^4 F_{p-2} + \cdots + T_N^4 F_{p-N} \qquad \text{(Eq. 18)}$$

3. Numerical Procedure

3.1. Validation and Mesh Independence

Validation study for the CFD model was done according to the experimental data obtained by Li et al. (1992) and numerical validation done by Gilani et al. (2016). The experiment was done for an enclosure empty other than a cubical heat. There was a single inlet and an outlet in the enclosure (can be seen on Fig. 3).

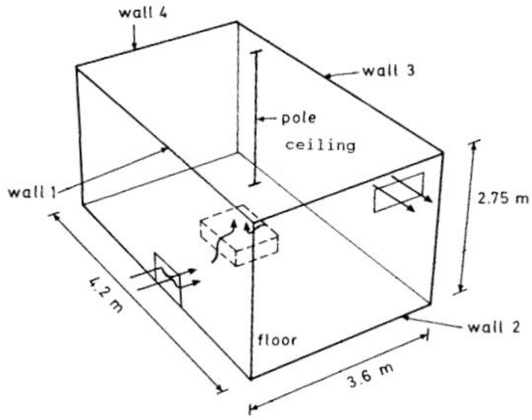

Fig. 3: Experimental test room geometry by Li et al. (1992)

B1 case from the experiment was chosen as the validation case by Gilani et al. (2016), due to most amount of result data available on the paper. According to Gilani et al. (2016) B1 case had 300W power output at the cubical heat source, all the walls were painted black, inlet air temperature and speed were 16 °C and 0.102 m/s. Measured ceiling and floor temperatures were 24.5 °C and 24 °C. Calculated heat transfer coefficient on the walls were 10 W/m^2-K. Pole (shown on Fig. 3) contained 22 thermocouples during the experiment and validation is done by those thermocouple readings. Fig. 4 indicates the aspect ratio of the point divided by the ceiling height as z/H on y-axis and temperature difference between local temperature and inlet temperature on x-axis validation was done for 0.3 million, 0.7 million and 1.25 million mesh elements. As the number of elements increase results slightly converged towards the experimental data for z/H of 0.1 to 0.4, rest remained unchanged. Due to similarity of the model size similar mesh with the validation case is used on this study, therefore a separate mesh independence analysis was not done for this study as well.

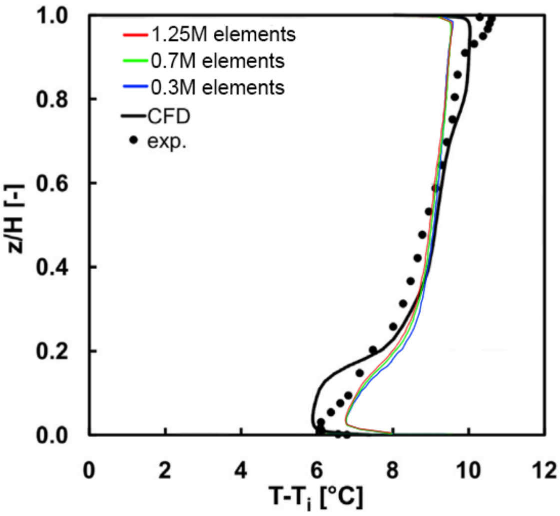

Fig. 4: Comparison of temperature on the pole between results of experimental (Li et al., 1992), CFD (Gilani et al., 2016) and current study (blue, green and red lines)

Validation of the CFD was done by ANSYS Fluent 19.2. Turbulence model was chosen as Shear-Stress Transport (SST) k-ω model according to Gilani et al. (2016). Boussinesq approximation was made to simulate the buoyancy effects properly sand air properties are; density is 1.17 kg/m^3, specific heat is 1006.95 j/kg-K, thermal conductivity is 0.026 W/m-K, viscosity is 1.83x10^{-5} kg/m-s and thermal expansion coefficient is 0.003 K^{-1}. Operating pressure and operating density are 101325 Pa and 1.17 kg/m^3. Radiation model was chosen as surface-to-surface (S2S) model. Pressure velocity coupling was chosen as Coupled Algorithm. Pressure discretization was chosen as PRESTO! to best analyze the natural convection due to buoyancy effects. Momentum and energy discretization are second order upwind. Maximum y* value of 1.8 was reached as in the validation study. For convergence criterion; continuity, x-velocity, y-velocity, z-velocity, k and omega were set to 10^{-3}, energy and radiation were set to 10^{-6}.

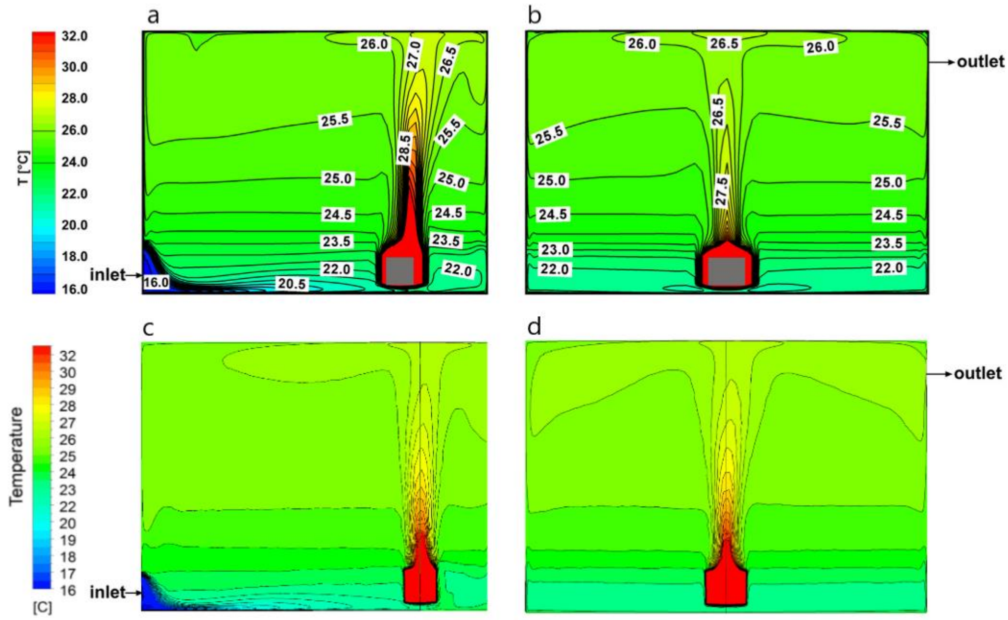

Fig. 5: Air temperature distribution comparison of Gilani et al. (2016) (a and b) to current study (c and d)

3.2. CFD Analysis

Physical and mathematical model described above is solved numerically using finite volume method by ANSYS Fluent software. The mesh is constructed from polyhedral elements with inflation on the walls with first layer thickness of 1 mm and total of 15 layers. Desk and partition are modeled as solid all other surfaces are given thickness on the boundary. Conduction heat transfer takes place inside of the desk and partition, through the window and façade. All the surfaces participate in convective and radiative heat transfer. Only façade and window have heat transfer with the environment, all other boundaries are modeled as adiabatic. Zenith angle of the Sun is 45° and the irradiance values are specified for each case above on Tab. 1. View factors were calculated using the ray tracing method with face to face basis and resolution is set to 100. Window is modelled as semi-transparent glass surface. All the models and properties used in this study are identical to the validation study explained at section 3.1. Weather parameters were set to average June weather in Istanbul as 25 °C air temperature and average wind speed of 4.7 m/s. Heat transfer coefficient on the outer surfaces of façade and window are assumed as 23 W/m^{2}K according to the paper by Vincent (2018). Inlet supplies 20 °C air with 1 m/s velocity to four sides of the inlet cavity with a 20° angle from the ceiling. Inlet was modelled according to Sun et al. (2005) without a diffuser to decrease the mesh size significantly. Outlet is modelled as a pressure outlet and has a decreasing cross-sectional area (can be seen on Fig. 1) to prevent reverse flow. Same decreasing outlet model was used at the validation study and it can be seen on Fig. 5 that it does not affect the temperature distribution.

4. Results and Discussion

Results are focused on the surface temperatures of desk and partition, since they are the closest surfaces to the occupant and will have the most effect on the occupant's thermal comfort. Desk and partition surfaces are analyzed in two groups for the opposing sides, which are facing the façade and facing the inside of the office. Effect of the partition on the air velocity is shown on Fig. 6 as velocity vectors around the partition and desk. Separation of flow and increase in vortices due to partition can be observed on theses figures as the partition aspect ratio increases. Also, the air velocity on the desk and partition at the side of the inlet increases with the increasing partition to ceiling aspect ratio. This might create thermal discomfort for the occupant near inlet at higher inlet speeds.

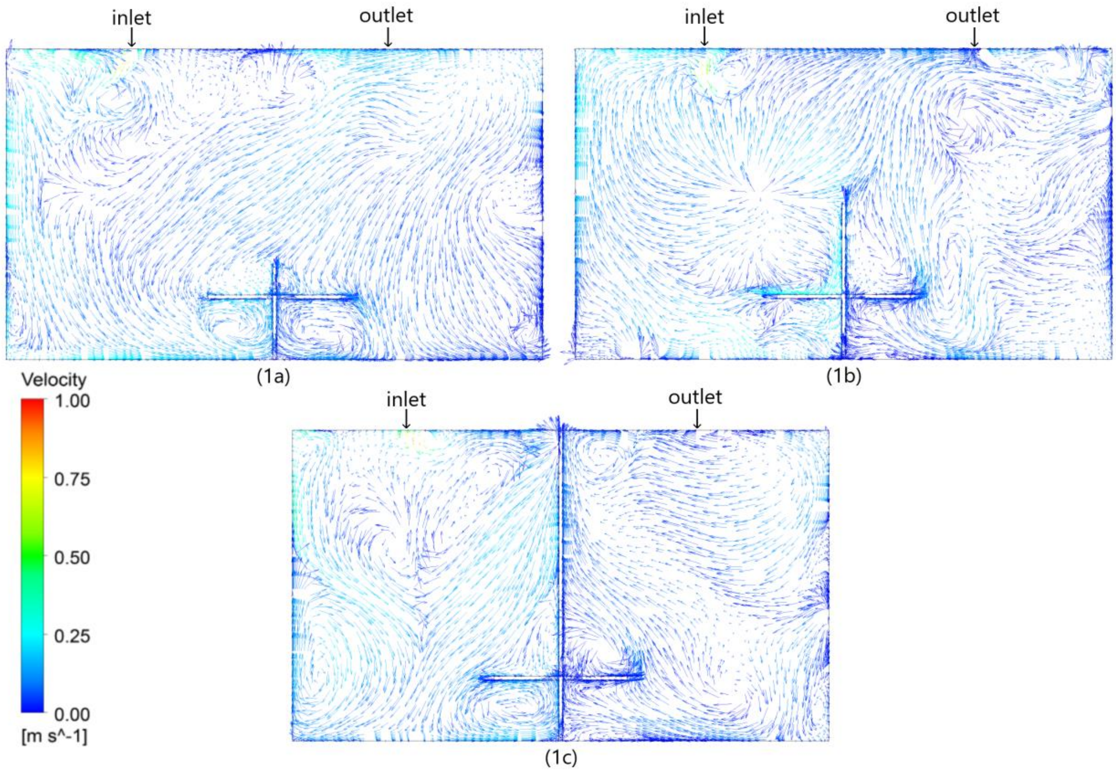

Fig. 6: Velocity contours on a plane at the middle of the desk (left side is facade)

Wall temperature contours are shown on Fig. 7 from an isometric viewpoint. Names under each contour represents the case name. On each row of Fig. 7 partition aspect ratio increases from left to right and solar radiation incident on the room decreases from top to the bottom. First row shows the sunny weather cases with no solar shade, second row shows the sunny weather cases with 50% solar shade coverage, third row shows the overcast weather cases with no solar shade and fourth row shows the overcast weather cases with 50% solar shade coverage on the window. As the case names go from 1 to 4 the solar radiation incident on the enclosure decreases. Lack of hot spot on the floor at the third and fourth lines of Fig. 7 is due to lack of direct solar irradiance at overcast weather cases. The colder spot near the top of the window and at the top of the wall between the partition and façade is due to ventilation hitting directly on to those walls.

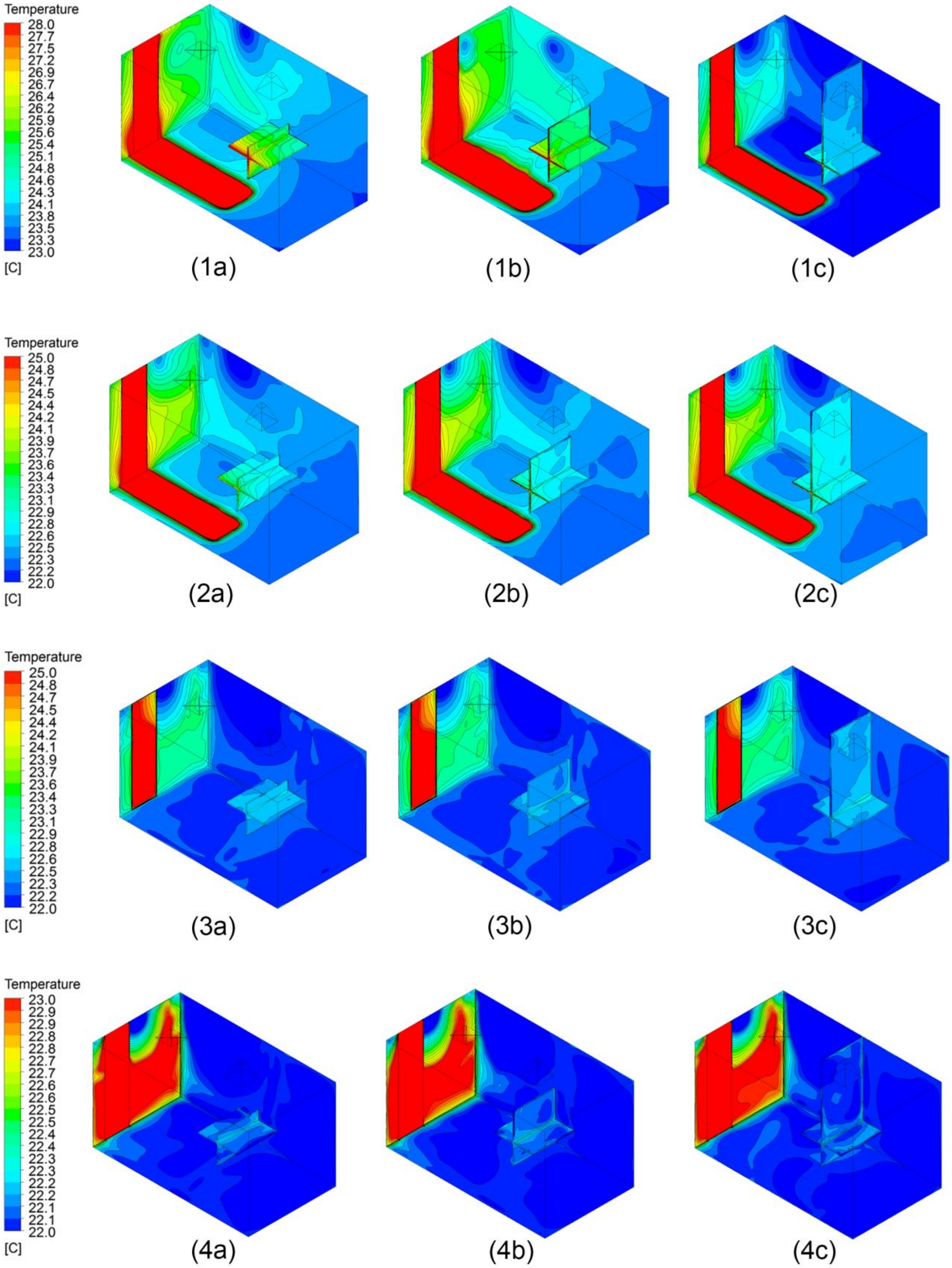

Fig. 7: Wall surface temperature contours for all cases with a different legend for each corresponding row

On the contours of Fig. 7 decrease in temperature contrast can be observed as the solar irradiance incident on the enclosure decreases. The effect of partition is minimal for the cases with no direct solar irradiance, since the affect of the partition on surface temperatures can be observed when there is solar radiation present in the enclosure. Surface temperature difference for the opposing sides of the desk and partition makes a peak at 0.5 partition aspect ratio (see Fig. 8). As the partition aspect ratio increases it blocks more solar radiation incident on the back of the enclosure, therefore prevents that region from heating but heats up the side of the desk facing façade even more due to increase in surface area and viewfactor of the partition. Inlet is located in between the façade and the partition (see Fig. 1) and quarter of the supplied air directly hits the wall between the façade and the desk and the flow separates from the wall to all sides. At partition aspect ratio of 1.0 flow cannot reach the back of the room, because the partition fully blocks the flow (see Fig.6.1c). This prevents the back of the enclosure from cooling down due to ventilation, but causes the region in between partition and façade to cool down more.

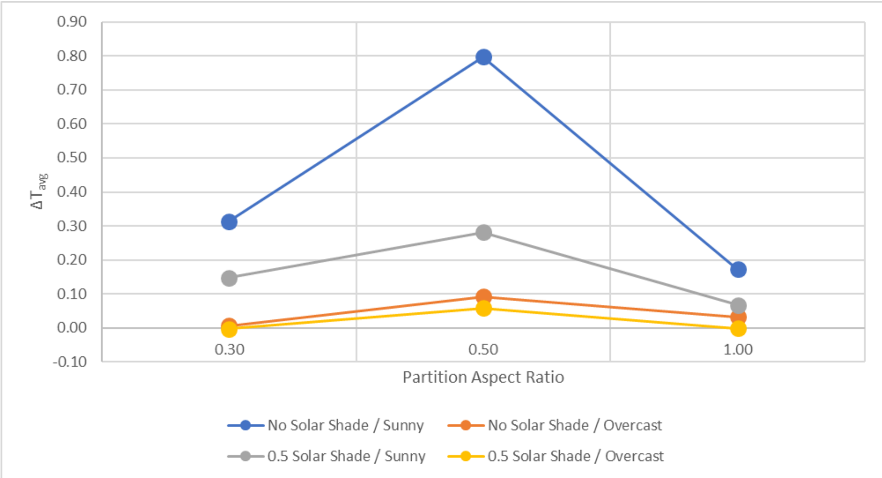

Fig. 8: Average surface temperature differences (ΔT_{avg}) on opposite sides of the desk and partition (facing façade and facing inside of the office space)

Average surface temperatures for the opposing sides of the desk and the partition are shown on Fig. 9. Surface temperatures decrease as the solar radiation incident on the enclosure decreases likewise the surface temperature difference between the opposing sides of the desk and partition decrease with decreasing solar radiation.

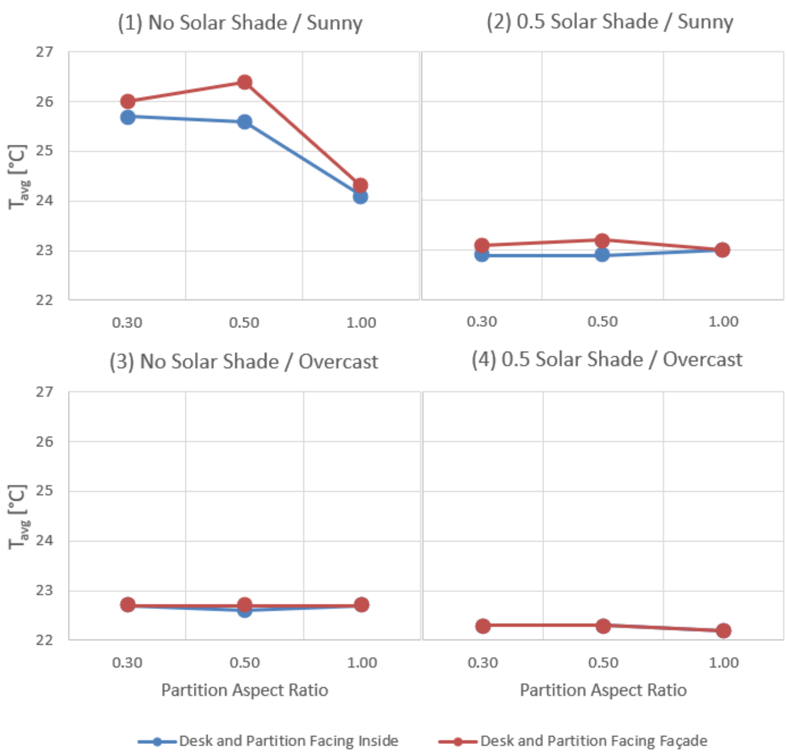

Fig. 9: Average surface temperatures for opposite sides of desk and partition at different partition aspect ratios

Average surface temperatures on the Fig. 9 are nondimensionalized on the Fig. 10 for better comparison inbetween cases due to the different temperature ranges at different cases. Nondimensionalization was done by dividing the average surface temperature to the maximum temperature on the desk and partition. Nondimensionalized plots also shows the temperature contrast. At lower the T_{avg}/T_{max} values there is higher temperature contrast (see Fig. 10). The side of the desk and partition facing façade has higher temperature contrast than the side facing inside of the enclosure. As the solar radiation incident on the enclosure decreases the temperature contrast decreases.

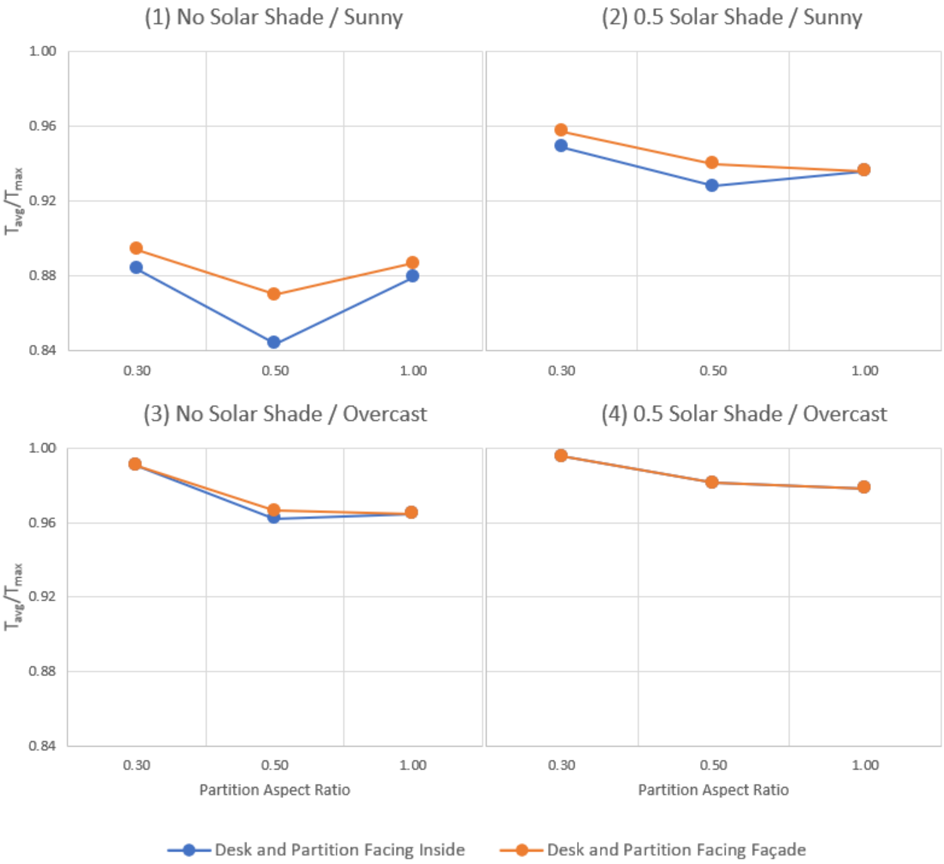

Fig. 10: Dimensionless average surface temperatures for opposite sides of desk and partition at different partition aspect ratios

5. Conclusion

A numerical study on the effect of indoor partitions has been studied for various external solar shade to window aspect ratios (0.0 and 0.5) and weather condition parameters (sunny and overcast) focused on surface thermal radiation. Surface to surface radiation model which is a gray-diffuse radiation model was utilized for this study. The results were evaluated as surface temperatures and the study focused on the surface temperatures of the desk and partition located at the office, because they are the closest surfaces to the occupants and have highest effect on mean radiant temperatures. Outcomes of the study are:

- Partition creates two zones with different temperature distributions and different air velocities.
- Increasing partition aspect ratio increases the air velocity near the partition and the desk at side facing façade, while decreasing the air velocity at the opposing side.
- Temperature difference at the opposing sides of the partition may cause thermal discomfort for the occupants, due to effected ventilation flow path inside of the office. Increase in air velocity may cause thermal discomfort due to increased convection on the occupant.
- Increasing partition to ceiling aspect ratio increases the temperature difference on the desk and partition for the opposing sides until the partition aspect ratio of 0.5, where the temperature difference peaks, then the temperature difference starts to decrease as the partition aspect ratio reaches 1.0. However, this peak point will alter for different office spaces, partition locations, air supply angles, air supply speeds and inlet locations.
- Partition and desk are the closest surfaces to the occupant, and they have the most effect on mean radiant temperature of the occupant. At higher temperature differences on opposing sides of partition and desk one side of the partition and desk is at higher temperature than the other, which means changing the partition aspect ratio changes the surface temperatures inside the office space and this changes the mean radiant temperature on the occupant causing thermal discomfort.
- Decreasing the solar radiation incident on the enclosure decreases the temperature contrast on the surfaces, therefore the visual comfort increases up until the point where there is enough light present.

6. References

- Atlanta, GA, USA: American Society of Heating, Refrigerating and Air-Conditioning Engineers, Inc; 2009 (S.I. Ed.).
- Çengel, Y.A., Ghajar, A.J., 2015. Heat and Mass Transfer Fundementals & Applications, fifth ed. McGraw-Hill Education, New York.
- Gilani, S., Montazeri, H., Blocken, B., 2016. CFD simulation of stratified indoor environment in displacement ventilation. Validation and sensitivity analysis. Building and Environment. 95, 299-313.
- Halawa, E., Hoof, J. V., Soebarto, V., 2014. The impacts of the thermal radiation field on thermal comfort, energy consumption and control—A critical overview. Renewable and Sustainable Energy Reviews. 37, 907-918.
- Howell, J.R., Mengüç, M.P., Siegel, R., 2016. Thermal Radiation Heat Transfer, sixth ed. Taylor & Francis, London.
- Li, Y., Sandberg, M., Fuchs, L., 1995. Vertical Temperature Profiles in Rooms Ventilated by Displacement: Full-Scale Measurement and Nodal Modelling. Indoor Air. 2, 225-243.
- Martyushev, S.G., Sheremet, M.A., 2014. Conjugate natural convection combined with surface thermal radiation in a three-dimensional enclosure with a heat source. International Journal of Heat and Mass Transfer. 73, 340–353.
- Modest, M.F., 1982. A general model for the calculation of daylighting in interior spaces. Energy and Buildings. 5(1), 69–79.
- Olazo-Gómez, Y., Xamán, J., Gijón-Rivera, M., Noh-Pat, F., Simá, E., Chávez, Y., 2020. Mathematical modelling of conjugate laminar and turbulent heat transfer in a cavity: Effect of a vertical glazed wall. International Journal of Thermal Sciences, 152, 106310.
- Parmananda, M., Dalal, A., Natarajan, G., 2018. The influence of partitions on predicting heat transfer due to the combined effects of convection and thermal radiation in cubical enclosures. International Journal of Heat and Mass Transfer. 121, 1179–1200.
- Sun, Y., Smith, T.F., 2005. Air flow characteristics of a room with square cone diffusers. Building and Environment. 40, 589-600.
- Vincent, P.B., 2018. CFD modelling for thermal comfort in an open workspace. eSim 2018, 276-285.
- Xamán, J., Arce, J., Álvarez, G., Chávez, Y., 2008. Laminar and turbulent natural convection combined with surface thermal radiation in a square cavity with a glass wall. International Journal of Thermal Sciences. 47(12), 1630–1638.

IMPACT OF NON-RESIDENTIAL LOAD PROFILES ON THE GRID-INTEGRATION OF BUILDING INTEGRATED PHOTOVOLTAIC (BIPV) SYSTEMS IN TWO DIFFERENT CLIMATE CONDITIONS

Fereshteh Poormohammadi[1, 2] and Johan Driesen[1, 2]

[1] ESAT-ELECTA, KU Leuven, Kasteelpark Arenberg 10 - box 2445, 3001 Leuven, Belgium

[2] EnergyVille, Thor Park 8300, 3600 Genk, Belgium

Summary

BIPV systems may satisfy electricity energy consumption of the building on an annual or monthly basis. However, the balance between on-site generation and the building energy consumption requires evaluation with a higher time resolution. One of the main barriers to this evaluation in simulated studies is the lack of building simulation (BES) tools to model the non-stochastic occupant interactions resulting in similar daily consumption profiles throughout a year. This paper investigates the impact of load profiles of a generic office room on the integration of building-integrated photovoltaic (BIPV) electricity generation by taking into account the load fluctuations due to the occupant behavior. Two locations of Seville (Spain) and Munich (Germany) representing two different European climate conditions are considered in the work. The consumption profile encompasses electricity for lighting, office appliances, heating, cooling, and ventilation. The simulation results show for fully electric consumption profile of the model, the annual cover factors change significantly when hourly values of the load matching indicators are considered also illustrating accurate seasonal and daily effects. Taking the average of the hourly values, the building shows a load cover factor of 0.21 and 0.31 for the locations of Munich and Seville, respectively.

Keywords: Load matching, Net zero energy building, BIPV, Stochastic consumption, Office buildings

1. Introduction

Climate change is recognized as a worldwide sustainability issue and requires serious considerations. To mitigate adverse environmental effects of this issue, in the building sector, many efforts towards achieving more energy-efficient and more decarbonized buildings have been made among them Net Zero Energy Building (Net ZEB) has gained growing attention (Berardi, 2015; Gonçalves et al., 2018). A Net ZEB is defined as a building connected to the grid that generates as much energy as it consumes annually (Salom et al., 2014; Sartori et al., 2012). In other words, Net Zero Energy Buildings must provide energy use of their consumers by integrating imported energy from the grid with on-site generation. The on-site generation is dedicated to the generation from available renewable energy sources.

Furthermore, the most viable renewable energy source which can be exploited for buildings is solar energy. Therefore, there is a broad consensus that Building Integrated Photovoltaic (BIPV) technology is the cornerstone of Net ZEBs (Goncalves et al., 2019). Taking into account that Net ZEBs sometimes have excessive generation than their consumption and have energy exported to the grid, their interplay with the grid is not same as typical buildings which are only importing energy from the grid. Therefore, design and evaluation of Net ZEBs integrating BIPV technology require a comprehensive analysis addressing the interplay between the building loads and on-site PV generation that is often called load matching (LM) phenomena (Goncalves et al., 2019).

Load matching analysis provides numeric indicators named cover factors in a yearly basis to study Net ZEBs. However, it has been realized that annual values of the cover factors do not provide a good understanding of the interplay between Net ZEBs and the grid. As a result, studies on Net ZEB concept have moved towards higher time resolution data, e.g. hourly data, either in simulation cases or real monitored cases (Salom et al., 2014; Sartori et al., 2012). Hourly values of the cover factors, namely load cover factor and supply cover factor, illustrate a good picture of the seasonal and daily pattern of the balance between the building demand and on-site generation. In simulated cases, however, non-stochastic occupant interactions modelled within a building simulated by using Building Energy Simulation (BES) tools result in non-stochastic similar daily consumption patterns (Salom et al., 2014). The work aims to study Net ZEB concept in non-residential buildings by

doi:10.18086/eurosun.2020.01.04 Available at http://proceedings.ises.org

simulating a representative office room with c-Si BIPV façades while stochastic consumption patterns are taken into account. The most widely used time resolution in building simulation, 1h resolution, is used to provide energy consumption and on-site generation for the representative office room to evaluate load matching phenomena. Two locations of Munich (Germany) and Seville (Spain) are considered as two representative climate conditions in Europe, the former one corresponding to temperate oceanic and the latter one corresponding to hot-summer Mediterranean climate condition.

Following this introduction, Section 2 brings the methodology beginning with the description of the representative office room with BIPV façades. Then, the simulation results of the stochastic power loads of the office room are presented. Section 3 provides performance evaluation of the office room in terms of load cover factor and supply cover factor for two selected climate conditions. Finally, the paper is closed with the main conclusions of the work presented in Section 4.

2. Methodology

Representative Office Room with BIPV Façades

An early stage building desing and simulation approach via simulation engines coupled into the CAD tools is adopted in this work (Han et al., 2018). The focus is on a conceptual office room (3 m high, 3 m wide, and 4.4 m deep) with windows towards the south. The architecture design of the representative office room is modelled in Rhinoceros 3D by using the parametric definition approach in Grasshopper environment (plug-in for Rhino) (Rutten, 2015). The construction and materials as well as thermal conditions have been defined to represent an energy-efficient built environment, for more detail information about the envelope properties the reader is referred to (Goncalves et al., 2019). Dynamic simulations of the defined architecture are done using the plug-ins embedded in Grasshopper environment namely Honeybee and Ladybug Tools (M Sadeghipour Roudsari, 2017; Mostapha Sadeghipour Roudsari et al., 2013). The tools connect Rhinoceros 3D to the valid simulation engines such as EnergyPlus and Daysim which are used for the energy simulations in the work presented here. The final definition of the office room in Rhino 3D is shown in Fig. 1.

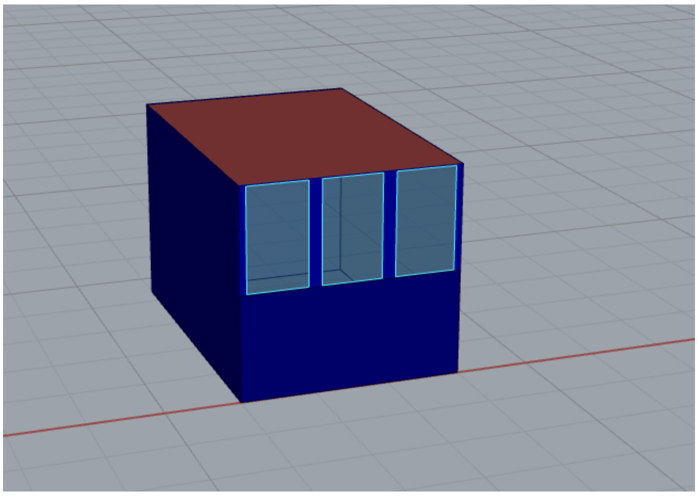

Fig. 1: Preview of the conceptual office room modelled in Rhino 3D

For sake of simplicity, it is assumed that the room is adjacent to the zones with similar thermal conditions on top and bottom, therefore adiabatic conditions are set for ceiling and floor, while the boundary condition for the walls is set to outdoors. All façades are covered by BIPV modules except the upper half of southern façade which is served as windows consisting of triple glazing with a U-value equals to 0.6 W/m-K, a 0.48 solar heat gain coefficient, and a 0.72 visible transmittance. The BIPV module used for the façades is inspired from works presented in (Gonçalves et al., 2018) and the material properties listed in Table 5 of the work presented in (Spiliotis et al., 2020) are used to model the thermal behavior of the BIPV modules. Each module is composed of c-Si cells, with a 14% cell efficiency, a rated power of 244 Wp, and an 80% inverter efficiency. Eastern and western façades are covered by six modules covering 79% of the surface area with the total PV generation of 1464 W. The façade towards north has four modules which generate 976 W in total and covering 77% of the surface. Southern façade has only two modules on the bottom half generating 488 W. Honeybee PV simulation relies on the EnergyPlus Photovoltaic generators, more information can be found in (Photovoltaic Arrays, EnergyPlus 8.0)

Climate Conditions

Using the office model described above, simulations are carried out for the two locations of Munich (Germany) and Seville (Spain) each representing a different climate condition in Europe. Weather data from the International Weather for Energy Calculations (IWEC) which are available in the format of EnergyPlus Weather (.epw) files are used to represent the locations. The main climate characteristics of the considered locations are summarized in Tab. 1.

Tab. 1: Annual average weather characteristics of the selected locations

Location	Latitude [°N]	Longitude [°E]	Global horizontal radiation [W m^{-2}]	Climate class
Munich (DE)	48.13	11.7	133	temperate oceanic
Seville (ES)	36.9	-2.4	220	hot-summer Mediterranean

Non-residential Power Loads

The representative model of this work is considered as a single-occupant office room. The first step to produce an annual stochastic consumption profile is to determine how stochastically the room is occupied throughout the year. There are different approaches for stochastic occupancy modeling, e.g. using a non-homogeneous Poisson process to simulate time series of occupancy states in a single office room proposed in (D. Wang et al., 2005), homogeneous Markov chain presented in (C. Wang et al., 2011), non-homogeneous two-state Markov chain introduced in (Page et al., 2008a), etc.

To produce the occupancy time series in this work, the non-homogenous Markov chain approach from the work presented in (Page et al., 2008b) is used. Time-varying transition probabilities used in the model are determined by using two inputs, namely a probability of presence over a typical week and a parameter called mobility factor (μ). To provide the inputs of the model, different occupant profiles from LESO-PB database (Zarkadis et al., 2014) corresponding to single-occupant office rooms are used to extract several weekly probabilities of presence. Different values of 0.1, 0.3, and 0.5 are used as μ to calibrate the model. The simulated occupancy time series from the extracted profiles show active occupancy hours with a minimum of 1600 hours and a maximum of 2050 hours during a typical year.

Finally, a time series of 1851 active occupancy hours is used as the "occupancy schedule" to occupy the representative office room in the work presented here. Fig. 2 shows this occupancy schedule assigned to the office model that is simulated in Ladybug tools. The internal gains related to the occupant is taken as 120 W/person, according to ISO 7730 (ISO 7730, 1994), corresponding to an activity level of seating, very light working during active occupancy hours.

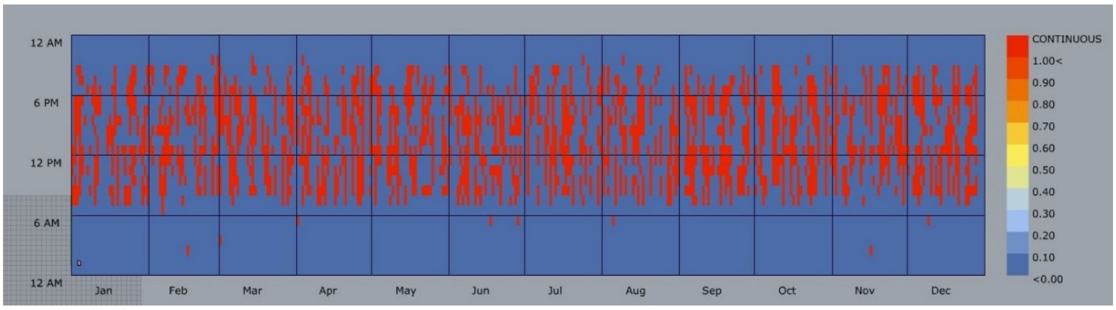

Fig. 2: Stochastic occupancy schedule assigned to the representative office room

After occupancy, the next step is to consider how the occupant interacts with the building systems to quantify the electricity consumption of the office. The most important interaction is the occupant's use of office plug-in appliances. The behavior is also modeled in this work based on the stochastic approaches from the literature. However, there are a few works dedicated to stochastic modeling of this occupant behavior in office buildings. The work presented in (Gunay et al., 2016) provides links between occupancy and use of plug-in loads by developing discrete likelihood distributions for five different time periods consisting of (a) occupancy periods, (b) absences less than 12 hours (intermediate breaks), (c) absences between 12 and 24 hours (nighttime), (d) absences between 24 and 72 hours (weekends), and (e) absences longer than 72 hours (vacations).

Two simplified and probabilistic approaches to predict the use of plug-in appliances in office buildings are presented in (Mahdavi et al., 2016). The work defines load fraction, the ratio between actual load and installed load at each time-step, as a function of occupancy. In the probabilistic approach, load fractions are formulated into three specific Weibull distributions corresponding to three different time periods. This probabilistic approach is adopted in the work presented here to produce the stochastic profile of the electricity consumed by the office appliances. The occupancy time series generated previously are used to map the active occupancy hours into three Weibull distributions corresponding to (a) occupied periods or intermediate absences shorter than one hour, (b) intermediate absences longer than one hour, or (c) outside working hours. The generated load fraction time series (Fig. 3) are used to calculate the energy consumption of the appliances by assuming 10 W/m^2 power density, as a conservative estimation (Mahdavi et al., 2016), for the representative office room. As in Fig. 3 can be seen between 7:00 to 19:00 load fraction is mainly greater than 0.6 and outside this period, the load fraction is mainly less than 0.3.

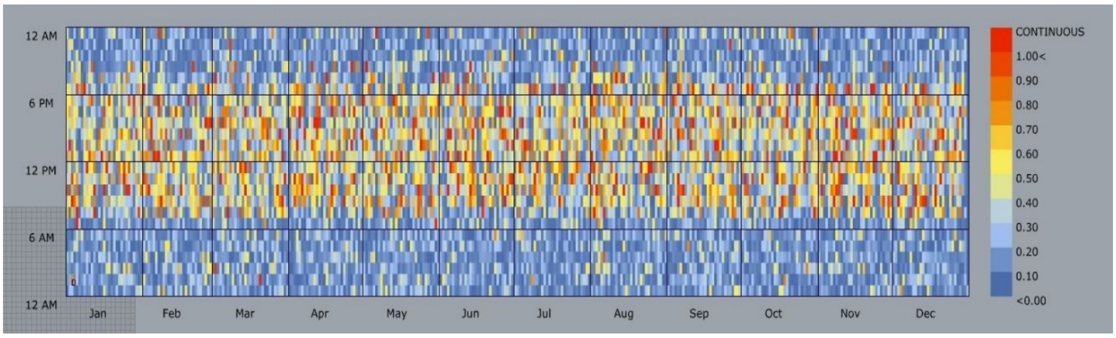

Fig. 3: Stochastic load fraction time series to calculate the energy consumption of the office appliances

To calculate the energy consumption due to the lighting, the amount of daylight inside the office room is simulated by using Daysim simulator integrated into Ladybug tools. The lighting schedule is linked to the stochastic occupancy schedule to always maintain 500 lux for a test surface 1 m above the floor area contributing to add 5 W/m^2 during active hours. Fig. 4 shows the simulated lighting schedule for the representative office room located in Munich. As it can be seen, during summer compared to winter, energy consumption due to the lighting is lower which is because of more available daylight and longer days during summer.

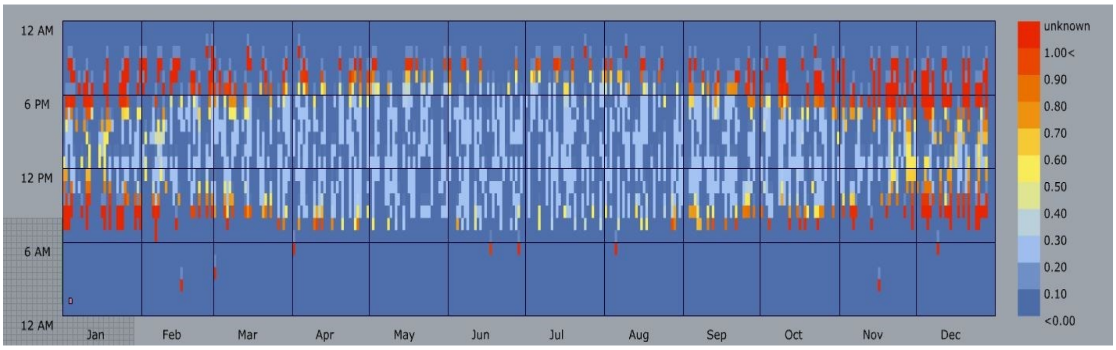

Fig. 4: Simulated lighting schedule (linked to the stochastic occupancy schedule) for the representative office room

To simulate the power consumed for heating, cooling, and ventilation, VAV with PFP boxes (ASHRAE Baseline Systems #8), recommended for non-residential buildings, is set as the HVAC of the office room. The cooling system is allowed to turn on when the indoor temperature is above 24°C during occupied hours, and during unoccupied hours, the indoor temperature is kept at 28°C. Similarly, the heating system is allowed to be activated when the indoor temperature is below 21°C during occupied hours, and the room space is kept at 17°C temperature during unoccupied hours. The room is ventilated at a rate of 0.0007 m^3/(s-m^2) and 0.007 m^3/(s-person) corresponding to the low-polluting buildings according to EN 15251 (CEN, 2007).

3. Results and Discussion

In this paper, the effect of the building integrated photovoltaic system on reducing the electricity consumption imported from the grid is quantified by the load factors. The cover factors include the load cover factor γ_l, the ratio to which the electrical demand is covered by the on-site electricity generation of the BIPV systems, and the supply cover factor γ_{PV} that is defined as the ratio to which the BIPV generation is used by the building represented in eq. 1 and eq. 2, respectively (system losses and storage are not considered in this work).

$$\gamma_l^{[t_1,t_2]} = \frac{\int_{t_1}^{t_2} \min(PV(t), l(t))dt}{\int_{t_1}^{t_2} l(t)dt} \qquad \text{(eq. 1)}$$

$$\gamma_{PV}^{[t_1,t_2]} = \frac{\int_{t_1}^{t_2} \min(PV(t), l(t))dt}{\int_{t_1}^{t_2} PV(t)dt} \qquad \text{(eq. 2)}$$

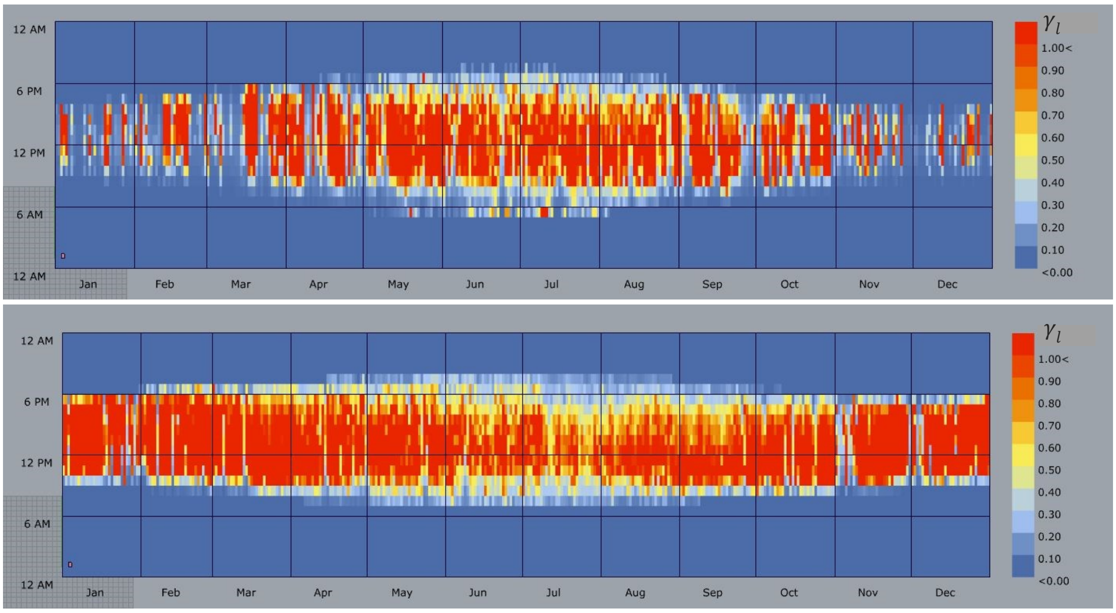

Fig. 5: Annual load cover factor with 1h resolution time for the representative office room located in Munich (up) and Seville (bottom)

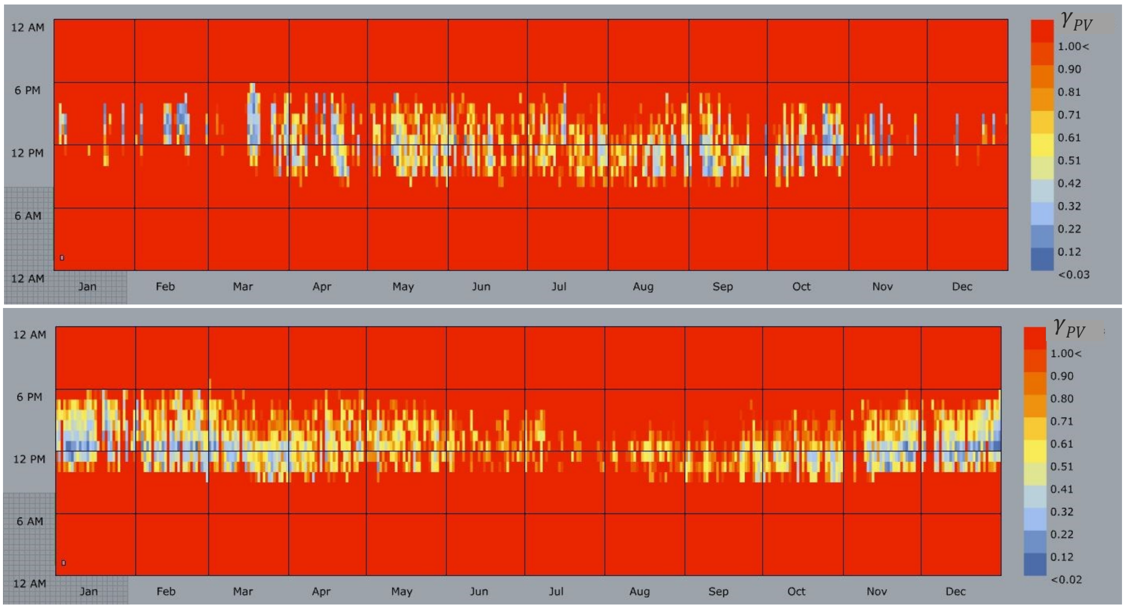

Fig. 6: Annual supply cover factor with 1h resolution time for the representative office room located in Munich (up) and Seville (bottom)

Simulation results of the load cover factor (γ_l) and the supply cover factor (γ_{PV}) for the office room with BIPV façades are illustrated in Fig. 5 and Fig. 6, respectively. In each figure, the upper profile shows the result of the simulation of Munich, and the bottom profile results from the simulation of the office room located in Seville. The cover factor takes a value between 0 (dark blue) to 1 (red). As can be seen in Fig. 5, comparing the profiles of Munich and Seville together, for Seville, greater load cover factor occurs from September to May and during May, June, July, and August, load cover factor decreases. The reason is because of the cooling loads during these months that increase the electricity demand, therefore the power generated by the BIPV systems is not sufficient to cover the building demand.

Conversely, for Munich as the upper profile in Fig. 5 shows, BIPV can cover the building demand for longer periods during the months of May, June, July, and August, while during September to April, the reduction of the load cover factor is evident. The reason is that during these months, not only the amount of solar energy is reduced due to shorter days and azimuth angle, but also heating loads due to the oceanic climate condition increase the building demand which results in low cover factors for that time period. In addition, the profiles of the supply cover factor shown in Fig. 6 represent the hours of the year during which the generation of the BIPV is more than the building demand and can be exported to the grid. The majority of the profiles are in red color which refers to the supply cover factor of 1 indicating either no generation by the BIPV systems (during the night) or the times that on-site generation is completely consumed by the building.

In general, it can be concluded that the load cover factor provides more useful information for evaluating the Net ZEB concept. The average of the hourly values indicates a load cover factor of 0.21 and 0.31 for Munich and Seville, respectively. While considering the yearly basis this indicator changes to 0.15 for Munich and to 0.5 for Seville. The daily effect of the building loads on the load cover factor can be seen in Fig. 7. In this figure, mean hourly values of load cover factors averaged over 4 months (January, April, July, and October), which are selected representing 4 seasons, are shown for each of the considered locations. It can be seen that Seville has smoother annual distributions, while there is a significant seasonal variation for Munich. For example, γ_l at 14:00 varies from 0.3 to 0.9, while at the same time, Seville has a variation from 0.81 to 0.95.

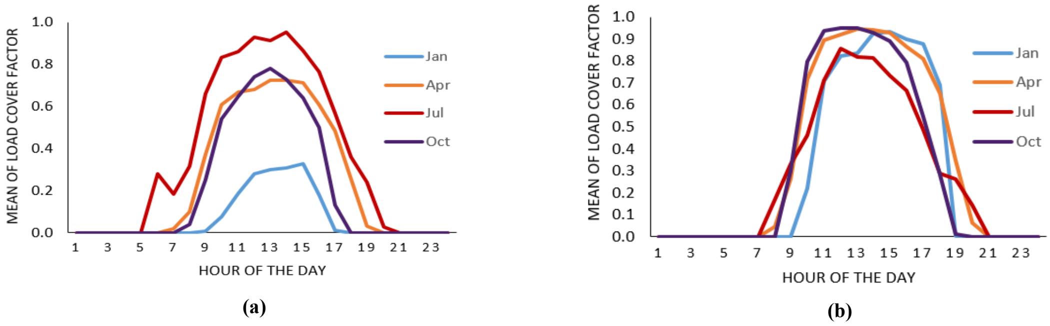

Fig. 7: Mean daily load cover factor for four selected months; (a) Munich, (b) Seville

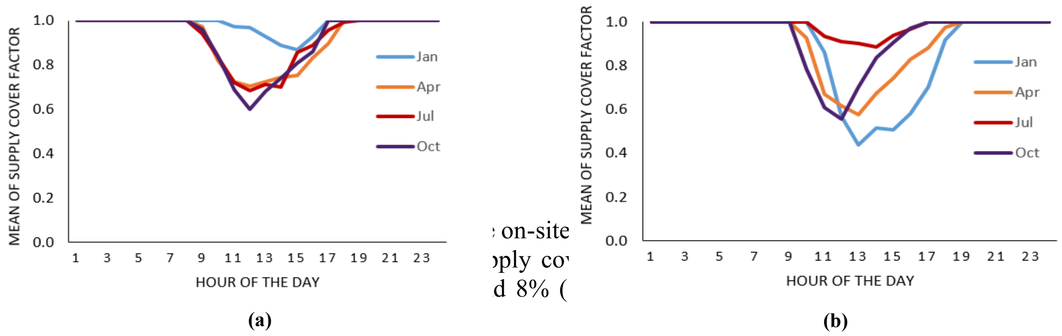

Fig. 8: Mean daily supply cover factor for four selected months; (a) Munich, (b) Seville

annually. In Munich, the building exports up to 3% of on-site generation in January at noon and in Seville, the lowest degree of export occurs during July for which the building exports up to 10% of the BIPV generation at 14:00. However, during the hours of maximum solar radiation, γ_{PV} varies between 0.68-0.93 and 0.44-0.9 for Munich and Seville, respectively.

4. Conclusion

In this paper, hourly values of the load matching indicators (namely, the load cover factor and the supply cover factor) were discussed for a conceptual office model for two different climate conditions. Stochastic consumption profiles were simulated by using the results of stochastic occupant behavior modelling implemented from the literature. Munich and Seville showed an annual cover factor of 0.21 and 0.31, respectively.

5. References

Berardi, U. (2015). Building energy consumption in US, EU, and BRIC countries. *Procedia Engineering*, *118*, 128–136.

CEN, E. (2007). 15251, Indoor environmental input parameters for design and assessment of energy performance of buildings addressing indoor air quality, thermal environment, lighting and acoustics. *European Committee for Standardization, Brussels, Belgium*.

Gonçalves, J., Spiliotis, K., Lehmann, J., Baert, C., Driesen, J., & Saelens, D. (2018). Experimental validation of a BIPV curtain wall model for building energy simulations. *Https://Abs. Green/Conference-Proceedings/*.

Goncalves, J., Van Hooff, T., & Saelens, D. (2019). Performance of BIPV modules under different climatic conditions. *WEENTECH Proceedings in Energy*, *September*, 107–115. https://doi.org/10.32438/wpe.6519

Gunay, H. B., O'Brien, W., Beausoleil-Morrison, I., & Gilani, S. (2016). Modeling plug-in equipment load patterns in private office spaces. *Energy and Buildings*, *121*, 234–249. https://doi.org/10.1016/j.enbuild.2016.03.001

Han, T., Huang, Q., Zhang, A., & Zhang, Q. (2018). Simulation-based decision support tools in the early design stages of a green building—A review. *Sustainability*, *10*(10), 3696.

Mahdavi, A., Tahmasebi, F., & Kayalar, M. (2016). Prediction of plug loads in office buildings: Simplified and probabilistic methods. *Energy and Buildings*, *129*, 322–329. https://doi.org/10.1016/j.enbuild.2016.08.022

normalisation, O. internationale de. (1994). *Moderate Thermal Environments: Determination of the PMV and PPD indices and specification of the conditions for thermal comfort*. International Organization for Standardization.

Page, J., Robinson, D., Morel, N., & Scartezzini, J.-L. (2008a). A generalised stochastic model for the simulation of occupant presence. *Energy and Buildings*, *40*(2), 83–98. https://doi.org/10.1016/J.ENBUILD.2007.01.018

Page, J., Robinson, D., Morel, N., & Scartezzini, J.-L. (2008b). A generalised stochastic model for the simulation of occupant presence. *Energy and Buildings*, *40*(2), 83–98. https://doi.org/10.1016/J.ENBUILD.2007.01.018

Photovoltaic Arrays: Engineering Reference — EnergyPlus 8.0. (n.d.). Retrieved August 27, 2020, from https://bigladdersoftware.com/epx/docs/8-0/engineering-reference/page-111.html

Reference - ASHRAE Baseline Systems – Sefaira Support. (n.d.). Retrieved August 28, 2020, from https://support.sefaira.com/hc/en-us/articles/204829529-Reference-ASHRAE-Baseline-Systems

Roudsari, M Sadeghipour. (2017). *Ladybug Tools*.

Roudsari, Mostapha Sadeghipour, Pak, M., & Smith, A. (2013). Ladybug: a parametric environmental plugin for grasshopper to help designers create an environmentally-conscious design. *Proceedings of the 13th International IBPSA Conference Held in Lyon, France Aug*.

Rutten, D. (2015). *Grasshopper3D*.

Salom, J., Joanna, A., Widén, J., Candanedo, J., & Byskov, K. (2014). *Analysis of load match and grid* *interaction indicators in net zero energy buildings with simulated and monitored data*. *136*, 119–131. https://doi.org/10.1016/j.apenergy.2014.09.018

Sartori, I., Napolitano, A., & Voss, K. (2012). Net zero energy buildings: A consistent definition framework. *Energy and Buildings*, *48*, 220–232.

Spiliotis, K., Gonçalves, J. E., Saelens, D., Baert, K., & Driesen, J. (2020). Electrical system architectures for building-integrated photovoltaics: A comparative analysis using a modelling framework in Modelica. *Applied Energy*, *261*, 114247.

Wang, C., Yan, D., & Jiang, Y. (2011). A novel approach for building occupancy simulation. *Building Simulation*, *4*(2), 149–167. https://doi.org/10.1007/s12273-011-0044-5

Wang, D., Federspiel, C. C., & Rubinstein, F. (2005). Modeling occupancy in single person offices. *Energy and Buildings*, *37*(2), 121–126. https://doi.org/10.1016/j.enbuild.2004.06.015

Zarkadis, N., Ridi, A., & Morel, N. (2014). A multi-sensor office-building database for experimental validation and advanced control algorithm development. *Procedia Computer Science*, *32*, 1003–1009. https://doi.org/10.1016/j.procs.2014.05.525

The Application of Solar Envelope Zoning for the Enhancement of Solar Access in a Density Populated Neighborhood

Javeriya Hasan[1], Miljana Horvat[1] and Kelsey Saunders[2]

[1] Ryerson University, Toronto (Canada)

[2] RDH Building Science, Toronto (Canada)

Abstract

The study examined the application of Solar Envelope Zoning for the enhancement of solar access in a densely populated neighborhood in Toronto. The purpose of the investigation is to find optimized envelope forms that could be integrated so that solar exposure to surfaces of adjacent buildings is maintained at least to a threshold limit of 4-6 hours daily, within limitations of existing zoning regulations.

Keywords: solar access, solar rights, solar envelope, Solar Envelope Zoning

1. Introduction

Rapid urbanization, the increasing effects of climate change, the need to reduce fossil fuels' dependency as well as to improve resiliency of the world's cities are all factors that are currently accelerating the shift toward renewable energy sources globally. In contemporary times, urban sustainability is characterized by the culmination of resilience in important sectors of the economy that includes energy, land use, water, transportation, and ecology. Moreover, it is pertinent to acknowledge that in the past few years, a number of studies worldwide have investigated the subject of energy resilience, which is evidence of its critical importance to policymakers, urban planners and researchers alike (Mola et al., 2018). It is now recognized that this form of resilience fundamentally entails focusing on the apparent nexus that now exists between a continuity in the supply of energy and a robust urban infrastructure based on optimum urban morphological characteristics, building forms and geometry. An efficient land utilization, which allows for the ready integration of passive design features and active technologies, provides the necessary context to achieving urban energy resilience. Therefore, it is necessitated that an optimum urban form is location-specific; it is designed to be in tune in its interaction with the natural environment, whilst simultaneously promoting socio-economic and environmental sustainability of the urban landscape (Sharifi & Yamagata, 2016).

2. Background

2.1. Solar access, urban density and solar rights

In light of the recent drive towards urban energy reliance, there has been renewed focus on reverting to principles of 'solar city' design in contemporary urban development (Byrne et al., 2015). Surfaces of urban buildings have been increasingly studied as potential locations for energy generation, particularly the rooftops and facades; whereby, this gradual shift in attention from traditional ground-based photovoltaic systems is noteworthy, evidently due to land usage and scarcity concerns. Therefore, in the backdrop of this Toronto-based study, it is pertinent to recognize that there exists tremendous potential for the adoption of solar centric systems for energy generation in Ontario alone, as Wiginton et al. (2010) have pointed in their study on the benefits of province wide roof-top generation, which can achieve a 30% reduction on reliance on the grid. In addition to this, if a wider application of Building Integrated Photovoltaic (BIPV) applications are also considered as a critical contributor to the energy supply, the resulting benefit can inevitably reduce this reliance further (Rosenbloom & Meadowcroft, 2014). As shown in the Compagnon (2004) study, the cities of today present great prospects for the implementation of appropriate technologies and passive features. Different urban morphological forms were analyzed, wherein based on the magnitude of insolation on the building facades, the potential for PV systems, passive solar and daylighting technologies were determined and this principally highlighted the need for meticulous planning right at the outset of any urban development. Therefore, to capitalize on such an opportunity, it is imperative that a solar ready urban neighborhood exists, and this may be somewhat lacking in today's urban centers.

There has been significant momentum on urban densification lately primarily due to the advantages this poses in terms of energy and land use. However, higher urban densities such as that due to high-rise buildings impact the availability of solar access to the vicinity, especially manifested as decreased solar exposure on adjacent buildings

doi:10.18086/eurosun.2020.01.05 Available at http://proceedings.ises.org

and public spaces. Energy resilience in urban quarters also hinges significantly on the benefits that accrue from solar gains, daylighting, and on-site power generation. It is therefore necessary that the risk of overshadowing is effectively tackled at the design stages of newer urban development. This process consequently leads to the optimization of building forms, thereby also accounting for the intricate relationship a development has with the its proximity (Lobaccaro & Frontini, 2014). Additionally, it has been shown that development density is correlated to environmental parameters such as Urban Heat Island (UHI) effect, outdoor solar access, and daylight penetration into indoor spaces (Chokhachian et al., 2020). Similarly, it has been shown that site orientation greatly influences the building density, whereby a higher density can be achieved as a trade-off for lower durations of solar access to spaces in the vicinity. Conversely, as the parametric study on a multi-floor apartment building in Dublin showed, lower solar exposure on adjacent buildings would inevitably augment the energy demand, evidently due to reduced daylighting, lower potential to generate electricity from onsite sources and lower solar gains (Bruce, 2008). At high urban densities, the solar irradiation was lower and hence, the performance of the passive technologies is also less. As development density increases, the rooftop solar potential also tends to decrease, thereby necessitating other building surfaces to be considered as plausible sites for an investigation (Ko et al., 2017). Moreover, the magnitude of insolation on building facades in dense urban centers is less than that of roofs; however, given the surface area involved, the total benefit that can be made from the former is significant.

This brings to the important subject of solar rights, which basically pivots on the need for guaranteeing solar access to the vicinity, when designing newer development. Capeluto and Shaviv (2001) investigated solar rights in the context of urban density and solar volume. They developed a simulation model to determine solar forms, which would effectively guarantee that chosen surfaces of buildings and the ground in the proximity were exposed to direct insolation. The solar rights envelope that resulted out of such a simulation was an irregularly formed mesh based on customized requirements i.e. a solar access duration and neighborhood geometry. The findings of their study showed that urban density and building height depend essentially on the street orientation and interbuilding distances. The highest urban density was calculated to be 180% or six floors, when neighborhood buildings were orientated along a North East-South West and East-West street (Capeluto & Shaviv, 2001). One of the approaches in defining the design constraints that help achieve the best solar exposure, whilst accounting for the influence of the surroundings, is the concept of ‘Solar Envelope Zoning’. Solar Envelope Zoning (SEZ) is referred to “as a spatial construct which defines where, within a lot, one may build without interfering with the solar access of adjacent lots. Solar envelopes set the height limitations for a lot in accord with land configuration and seasonal positions of the sun” (Osofsky, 1983, p. 642). First defined by Knowles in 1976, the objectives of SEZ include improving the solar access of adjacent buildings; reducing the instance of overshadowing; optimizing the duration and quality of solar exposure on building surfaces and maximizing the size of the neighborhood that can be developed (Knowles, 1981). SEZ accounts for the configuration of the site being studied, whereby the influence of nearby structures and obstacles are factored in the simulations also. Being primarily a result of a specific spatial-temporal context, Knowles (2003) suggests that factors such as Shadow Fence Height, street width and orientation and solar access cut-off times all influence the generated solar envelope form. According to Knowles (2003), “the solar envelope avoids unacceptable shadows above designated boundaries”, wherein the height of this boundary above the ground is referred to as the Shadow Fence Height (see Fig. 1).

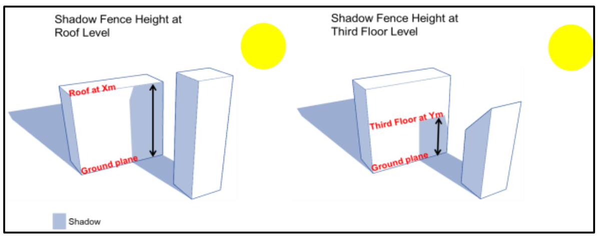

(a) **(b)**

Fig. 1: Two scenarios showing the concept of Shadow Fence Height. In (a), the Shadow Fence Height is at roof level and denoted as Xm. In (b), the Shadow Fence Height is at third-floor level and is denoted as Ym. Note the changed building form from (a) to (b); whereby, the roof shape in (b) is inclined and the overall building height is lower than (a). Also, in both scenarios, there was no overshadowing on the roof.

The size of the generated form is essentially dictated by variations in these factors; for example, a lower Shadow Fence Height would give rise to a more limited solar envelope form. Similarly, lower solar access cut-off times may result in larger volumes of solar envelopes generated (Knowles, 2003). In a study that looked at the implementation of a building prototype (based on principles of solar envelope zoning) in Thessaloniki, Greece, it was found to have higher levels of solar access, thereby creating potential for passive solar gains (Vartholomaios, 2015).

It is noteworthy that solar rights have varying interpretations depending upon the location in question; in some cases, it would entail guaranteed solar exposure to the ground whereas at other times, it would be a more wholistic concept encapsulating solar access to buildings (Li et al., 2019). Solar rights are typically inadequately addressed in the municipal regulations of many countries. Furthermore, depending upon the type of land use i.e. whether it is a residential or commercial area, the factors for the development of the solar envelope form may vary; for example, it could be made more strict in the case of a residential zone and relaxed for commercial areas (Hraška, 2020). It is important to bridge the disconnect between legislation and research through informed decisions on solar envelope zoning. This principally hinges on studies that are specific to the spatial and temporal context of the location in consideration.

2.2. The Toronto context

The city of Toronto, in Canada, is situated at latitude 43.65°N and 79.38°W, whereby the total annual global irradiation on horizontal surface is slightly above 1385 kWh/m^2 (The World Bank, 2019). This offers considerable potential in incorporating active and passive solar strategies in the city's-built environment. As one of the fastest growing cities in North America, booming construction of residential units in high-rise and mid-rise buildings caters to the increased interest in living in the city. Moreover, a study on designing Avenues and Mid-rise Buildings (BMI/Pace, 2010), and a change in building code that allowed wood construction in buildings up to 6 stories (Ontario Building Code, 2012) presented an excellent opportunity to address the urban growth challenge by taking advantage of existing wide avenues in the city, benefitting from an abundance of solar exposure, and introducing controlled neighborhood densification through construction of mid-rise buildings.

In 1995, Bosselmann et al.'s research investigated the morphological characteristics of the Toronto downtown core, which resulted in recommendations on urban design that would substantially enhance solar access in open spaces that included sidewalks and residential/commercial streets. Though the study holistically encompassed the subjects of wind, sun, and combined elements' effects on human thermal comfort in the public realm, it set a seminal framework to the plausible adoption of solar envelope zoning for newer development in Toronto. Building on a similar concept, the Toronto Mid-rise Guidelines study stipulated requirements based on building height and ROW; sidewalks; height of ground floor; frontal, side, and rear setback; building geometry and general urban morphological provisions along Toronto's Avenues. The study recommends as-of-right zoning for buildings that fall under the "Mixed-Use Areas and Employment Areas" (BMI/Pace, 2010, p. 3). In general, a building's maximum height depends upon the ROW width; the frontal and rear setback is stipulated to be at a 45º inclination, and the rear setback occurs at a minimum height of 10.5m. The guidelines also include a provision on the right to sunlight access, particularly in the case of sidewalks where five hours is the minimum specified duration. Despite the underlying focus on solar rights, the Toronto Mid-rise Guidelines' zoning method is almost constant and does not reflect any situation specific changes. This contrasts with the process of solar envelope zoning, which is essentially an adaptation to the "natural rhythm" of the location in context (BMI/Pace, 2010; Lepore, 2017, p. 17).

Also, as Toronto envisages a greenhouse gas (GHG) emissions target reduction by 2030, urban development guidelines such as the Toronto Green Standard (Version 3) promote the integration of renewable energy systems under certain criteria. Under the Tier 2 section, recommendations under the category of renewable energy technologies stipulate that buildings are designed to be solar ready. This essentially means that there exists an inherent flexibility to introduce renewable energy technologies such passive solar heaters, etc, in future. In a bid to achieve a minimum level of energy efficiency, developers are encouraged to attain higher tiers i.e. Tier 2 – Tier 4 status. These guidelines may be interpreted to indirectly support the inclusion of solar rights in newer development in Toronto, however currently, there exists no regulatory or legislative basis for enhanced solar access for buildings and open spaces (City of Toronto, 2018).

The purpose of this study is twofold: it entails a parametric study for a typical representative location along the Eglington Avenue West corridor and a case study based on an actual location i.e. the Eglington Avenue West/Bathurst intersection in Toronto. This location has been chosen as it is fast becoming a hub of commercial activity in Toronto due to improved transportation connectivity. Similarly, there are also plans for increased urban densification entailing mid-rise buildings via "as-of-right permissions" (City of Toronto, 2014, p. 77) along this corridor. Building forms would be generated based on three different types of zoning methods i.e. City of Toronto zoning, Toronto Mid-rise Guidelines and Solar Envelope Zoning. The developable densities (also indicated as Floor Space Index in this study) based on the Solar Envelope Zoning criteria of orientations, Shadow Fence Height, solar access cut-off times, Right of Way (ROW) width and environmental parameters would be compared to the Floor Space Index (FSI) from other zoning methods. The FSI is typically the "result of the gross floor area of a building divided by the area of the lot" (City of Toronto - Zoning By-Law, 2020, p. 23).

Additionally, it is pertinent to mention that over the past few years, a number of high-rise buildings (residential towers, with 40+ storeys) have been constructed along several main avenues in downtown and midtown Toronto, which substantially exceed the maximum height allowance as per zoning regulations. This evidently indicates that the height limitations (as seen in Tab. 1) are nearing obsoleteness and are thus not being strictly followed by developers. The developer typically applies for a location specific zoning by-law amendment, and the maximum height restriction is relaxed depending upon the development density that is desired to be achieved (City of Toronto, 2013). The implications of tall buildings constructed near low-rise residential single-family houses and other public spaces such as parks are well known. As documented by Bosselmann et al. (1995), the resulting microclimatic effects negatively impact thermal comfort levels due to the disruption of the natural sun and wind balance in the site that undergoes high-rise development. Providing analysis that would document benefits of urban densification through encouragement of midrise mixed-use buildings that could also provide adequate solar access on their own facades and avoid overshadowing surroundings is one of the main motivations of this study.

3. Methodology and Results

Building on this concept of solar rights, De Luca and Dogan (2019) recently introduced the 'subtractive method' for Solar Envelope generation, whereby this basically entailed a strategy of subtracting parts of the building form that overshadowed adjacent buildings. The results of their study showed that building forms generated through this method were larger in comparison to those based on the earlier approach of the 'additive strategy'. Similarly, the method also guaranteed that there was always direct solar access to all the adjacent buildings. Thus, this study aims to provide an insight on how solar access is guaranteed given the spatial and temporal variations of the solar irradiation.

The methodology entails identifying sun vectors incident on a given façade; selecting those that correspond to a threshold altitudinal angle and finally generating a solar envelope that meets the prescribed duration of 'solar window' i.e. four to six hours on the nearby buildings. Considering SEZ, the study also seeks to examine the impact of the street width and development density on the solar exposure on buildings located in a typical neighborhood. Finally, the solar envelope generated through this study would be compared to the conditions stipulated in the Toronto Zoning standard and the criteria for Mid-rise Buildings development. Preliminary findings of the study have highlighted the immense potential in estimating the extent of Solar Envelope Zoning that could be achieved in Toronto, wherein this may in future form the context of subsequent integration in mid-rise planning guidelines for the city.

3.1. The Process for the Parametric Study

For the parametric study, a typical location along the Eglington Avenue West corridor was chosen. The urban geometry and morphology of the area was studied, whereby the zone classifications were identified and dimensions pertaining to the ROW width, the lot depth, lot width and street orientation were determined (see Fig. 2 and Tab. 1). The roof morphology of a typical townhouse at the location of the study was emulated for the houses shown in the 3D model developed for the parametric study.

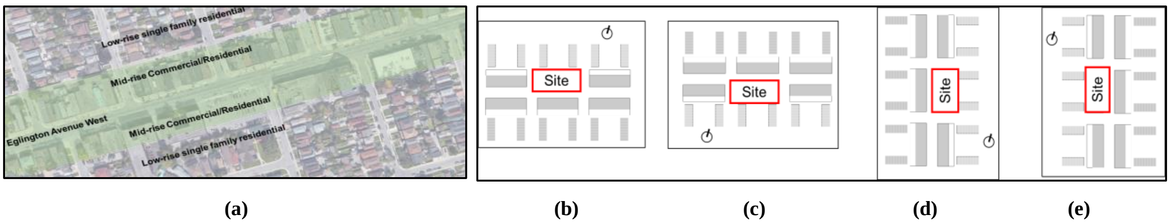

Fig. 2: (a) The typical representative location along the Eglington Avenue West corridor showing the different zoning classifications. The typical representative site layout (along the Eglington Avenue West corridor) under the indicating the view from different orientations (a) North-facing (b) South-facing (c) East-facing (d) West-facing

Tab. 1: The dimensions pertaining to the site in the parametric study

ROW width	Lot depth	Lot width	Street orientation	Maximum height of adjacent commercial buildings
27m	30m	75m	Tilted at an angle of 16.75º south of East	13.5m (with City of Toronto zoning specified FSI = 2.5)

The combination of Grasshopper and Rhino programs enable the development of solar envelope, which can used to make informed decisions on urban zoning and achieving a level of developable density (Niemasz et al., 2013). They facilitate the evaluation of the hourly- magnitude of solar potential, which is an integral component to the development of a customized solar map of any dense urban locality. Therefore, solar analysis simulations have been performed in Ladybug Version 0.0.69, which is an environmental analysis tool. This works with an interface in Grasshopper™, which is also now a plug-in integral to Rhino® Version 6. The input parameters for the solar envelope component in Ladybug Version 0.0.69 were of temporal and spatial nature (see Tab. 2).

Tab. 2: Details on the input parameters of the Ladybug Version 0.0.69 'SunPath' and 'SolarEnvelope' component

Input parameter	Description
_location	This would essentially connect to the location output of Ladybug Version 0.0.69's 'importEPW' component. The input to the 'importEPW' component is the 'Open Weather file', where the Toronto epw file 'CAN_ON_Toronto.716240_CWEC.epw' has been uploaded.
hour _day_ _month_	The '_hour_', '_day_' and '_month_' correspond to the analysis period. For this parametric study, the initial analysis period has been set for every 21st of the month from January to December. The time and hours of analysis has been adjusted based on the sensitivity factor investigated.
_baseSrf	The site limits (the dimensions are indicated in Tab. 1).
_obstacleCrvs	The surrounding context
maxHeight_	This is the maximum height that a building can have.
_sunVectors	This is an output of the Ladybug Version 0.0.69 'SunPath' component. The sun vectors are defined by the analysis period, location, and site orientation.
Ground floor height	4.5m
First floor and above height	3
Site area	2250m^2
The generated solar envelope form, which is a result of specific input parameters.	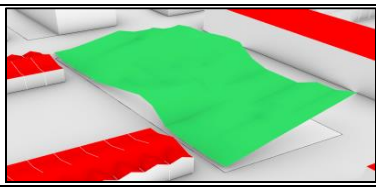

Similarly, information pertaining to the Toronto Mid-rise Guidelines and City of Toronto zoning was extracted for the respective FSI determination (see Tab. 3).

Tab. 3: The prescribed FSI, building height and setbacks as the three zoning methods: City of Toronto zoning, Toronto Mid-rise Guidelines and Solar Envelope Zoning

	City of Toronto zoning	Toronto Mid-rise Guidelines	Solar Envelope Zoning
Maximum building height	24m	ROW width	None
Maximum building FSI	2.5	None	
Setbacks	Varies depending on the building face considered. Typically, frontal setback is at a 45° inclination plane at a height equivalent to 80% ROW width.		

3.2. The Results for the Parametric Study

The sensitivity analysis for the parametric study initially involved setting a baseline combination of variables, and this essentially constituted as the baseline analysis (see Tab. 4). The categories of factors tested in the sensitivity analysis of the parametric study included orientation, Shadow Fence Height, solar access cut-off time and ROW width. Depending upon the variables examined, the number of sun-vectors[1] used to generate the solar envelope can reduce, thereby serving to enhance the development density. For example, reducing the solar access time or increasing the Shadow Fence Height would result in fewer sun vectors. It is noteworthy that the higher the sun-vectors generated, the more the restrictive are the conditions to generate the building form through Solar Envelope Zoning.

[1] Sun vectors are representations of hourly incident solar radiation from the sun to a point in space.

Tab. 4: Variables in the baseline analysis

Variable type	Description
Orientation	North The site is at the north side of the street
Shadow Fence Height	0m This is essentially the at the ground plane of the adjacent buildings in the context. This basically means that all the facades and roof surfaces of adjacent buildings will not be overshadowed during the solar access cut-off time.
Solar access cut-off time	10:00am – 4:00pm (6 hours)
ROW width	27m

1) Street Orientation

The baseline form was investigated vis a vis four different orientations i.e. the north facing side of the east-west street; the south-facing site for the east-west street; the east side of the north-south street and the west side of the north-south street. It is noteworthy that the building forms resulting from Toronto Mid-rise Guidelines and City of Toronto zoning are effectively independent of the orientations and are uniform irrespective to site changes. The shape and form of the building generated as per the Solar Envelope Zoning method varied greatly from the north, south, east to west orientations. It is observed that the building forms at the north-facing and east-facing orientations took up less proportion of the total site area, in comparison to the forms at the other orientations, which encompassed greater coverage of the area. As seen in Fig. 3, the building form generated at the south-facing (FSI = 3.56), west-facing (FSI = 2.61) and east-facing (FSI = 2.52) orientations have a higher Floor Space Index (FSI) compared to that of the City of Toronto zoning method. This essentially means that compared to the building form due to City of Toronto zoning method, the former has a higher gross floor area and essentially more floors in the same site area. The highest FSI of 3.55 was achieved when the building was south facing; this is characterized by a building height of 22.5m (corresponding to 7 floors) and a total gross floor area 7995 m^2. The lowest FSI of 1.78 was in the baseline case which was when the building was north facing; the building has a total height of 16.5m (corresponding to 5 floors) and a total gross floor area of 4000m^2. It is noteworthy that the gross floor achieved in former is about twice than that of the north facing building. From a development perspective, these results show that an appropriate site orientation (such as a site that is south-facing or west-facing) are critical for maximizing building gross floor area.

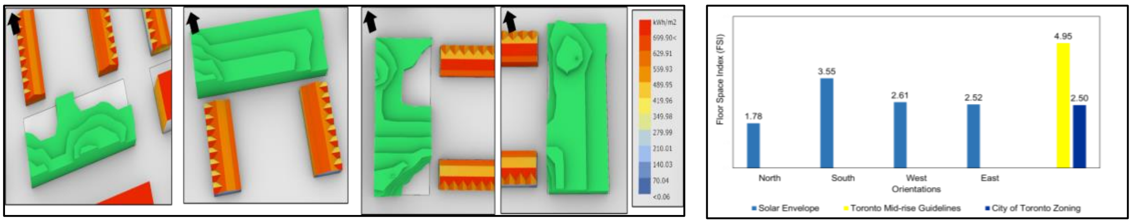

(a) (b) (c) (d) (e)

Fig. 3: Building forms through Solar Envelope Zoning (SEZ) (a) Baseline case: North-facing (b) South-facing (c) East-facing (d) West-facing. (e) Comparisons of Floor Space Index (FSI) between different SEZ building forms, Toronto Mid-rise Guidelines and City of Toronto Zoning

2) Shadow Fence Height

The analysis for Shadow Fence Height accounted for the vertical surfaces of adjacent residential buildings present at the north side of the site, which have a typical height of 10m: the total wall height is 6m while the depth of the roof is 4m. Thus, the baseline envelope (Shadow Fence Height at 0m) was compared to Shadow Fence Heights when it is at 3m and 6m corresponding to the second floor and roof level, respectively. These cut-off heights refer to solar access above the second-floor level and at the roof. In contrast to the case when the Shadow Fence Height is at 0m, these cut-offs can also be construed as there being a lower magnitude of solar radiation intensity on the facades, apparently due to the instance of overshadowing. With increasing Shadow Fence Height, the building volume due to Solar Envelope Zoning is observed to become larger, whereby this represents greater gross floor area and a higher development density. When the Shadow Fence is at 6m, the building FSI is 5.03; the building has a height of 22.5m (corresponding to 7 floors) and a gross floor area of 11,319m^2. The gross floor area in this case is about 2.8 times higher than that when the baseline case. Furthermore, the FSI achieved when the Shadow Fence Height is at roof level is higher than the FSI of the building form based on Toronto Mid-rise guidelines (4.95) and City of Toronto zoning (2.5). This indicates that easing the Shadow Fence Height restrictions can greatly augment the development density (see Fig. 4).

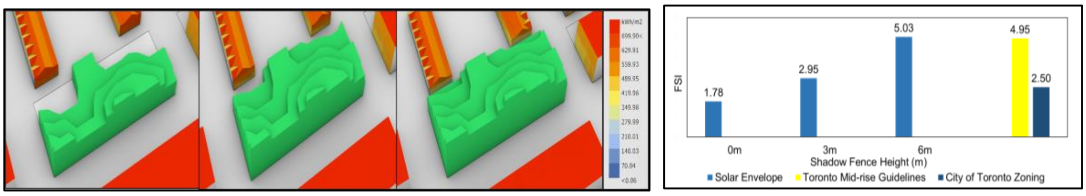

(a) (b) (c) (d)

Fig. 4: Building forms obtained by varying the Shadow Fence Height (a) 0m (b) 3m (c) 6m (d) FSI comparisons for different Shadow Fence Heights (m).

3) Solar access cut-off times

The solar access cut-off time is the duration during which solar access is guaranteed to adjacent surfaces. Several studies have looked at solar access cut-off time with the intent to examine the associated impact on health, work productivity and passive solar design. It is important to note that the recommended solar access cut-off time is 6 hours as per Knowles (2003). In this analysis, five solar access cut-off times were considered characterized by varying times and hours of analysis i.e. 9:00am to 3:00 pm (6 hours); 10:00am to 4:00pm (6 hours); 10:00am to 2:00pm (4 hours) and 11:00am to 1:00pm (2 hours) when the height of the building for generating the solar envelope was limited to 27m and 50m. As seen in Fig. 5, the shapes and forms of the buildings generated greatly varied; for example, the one for the cut-off time from 9:00am – 3:00pm is observed to have the most asymmetry in the form; covering the least proportion of the site area and having the lowest FSI of 1.26 (or a gross floor area of 2840m^2). The highest FSI of 5.81 was achieved when the solar access cut-off time was set as two hours and the maximum building height to generate the solar envelope at 50m. In this case, the building form has a height of 49.5m corresponding to 16 floors and a gross floor area of 13,083m^2. In both cases when the solar access cut-off time was 2 hours, the development density attained was higher than that through the City of Toronto Zoning method. This analysis showed that as the solar access cut-off times were reduced, the development density (constituting gross floor area and height of the building) greatly rose. However, it is also apparent that this occurred at the cost of solar radiation intensity on the adjacent facades, which decreased with iterations involving lower solar access durations.

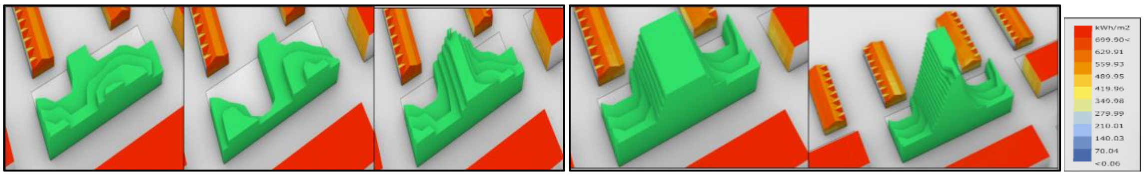

(a) (b) (c) (d) (e)

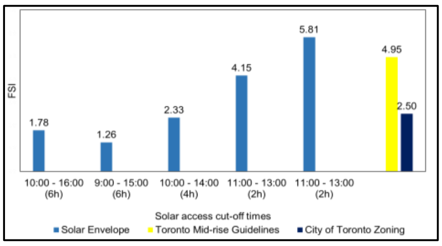

(f)

Fig. 5: Building forms for different solar access cut-off times (a) 10:00am – 4:00pm (6 hours) (b) 9:00am – 5:00pm (6 hours) (c) 10:00am – 2:00pm (4 hours) (d) 11:00am – 1:00pm (2 hours) – height = 27m (e) 11:00am to 1:00pm (2 hours) – height = 50m. (f) Comparisons of FSI between building forms corresponding to different solar access cut-off times

4) ROW width

The baseline was compared to three other ROW widths i.e. 20m, 33m and 42m. In this case, a south facing site was considered as the building form that would be impacted by changes in the ROW widths. As seen in Fig. 6, the building volume/FSI rises with increasing ROW width. The highest building FSI of 4.93 is inevitably reached when the ROW width is 42m; whereby, this corresponds to a building height of 49.5m characterized by 16 floors and a gross floor area of 11,088m^2. The lowest FSI of 2.90 corresponds to a ROW width of 20m, whereby the building height is 6 floors and a gross floor area of 6542m^2. The development density when ROW is 42m is 1.7 times greater than that when the ROW width is 20m. The results show that increasing the ROW width enhances the height/gross floor area of the building form generated.

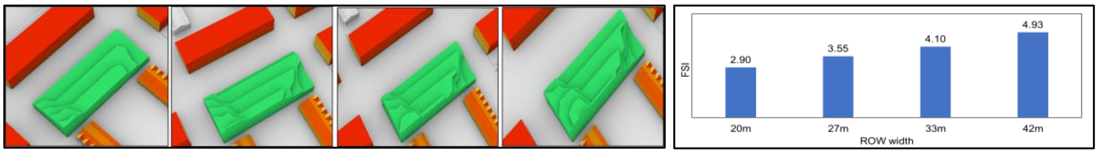

(a) (b) (c) (d) (e)

Fig. 6: Building forms for different Right of Way (ROW) (a) 20m (b) 27m (c) 33m (d) 42m (e) Building FSI pertaining to different Rights of Way (ROW)

3.3. The Process for the Case Study on Eglington Avenue West

The site in consideration for the Case Study was situated at the Eglington Avenue West/Bathurst intersection. The buildings in the vicinity have been zoned under either the commercial or residential categories, whereas the maximum height of buildings in this area vary between 16m to 24m (City of Toronto, 2013). A site map was imported in the Rhino® format from CADMapper, which is an online tool used to extract property maps (see Fig. 7). The site is situated at the south of the east-west street and is inclined at an angle of 16.75º south of the east orientation, whereby the ROW width is 27m. The analysis period has been set from 10:00am to 2:00pm (4 hours) at every 21st day of all the twelve months. The building form generated is hence referred to as the 'Baseline' in the subsequent section.

Fig. 7: The site layout at the Eglington Avenue West/Bathurst intersection

The site is located on the south side of the Eglington Avenue West street. Like the sensitivity analysis in the parametric study, the process of analysis for the case study involved establishing a baseline based on a combination of variables (see Tab. 5). There categories of factors tested in the sensitivity analysis of the parametric study included Shadow Fence Height, solar access cut-off time and environmental parameters.

Tab. 5: Variables in the baseline analysis

Variable type	Description
Orientation	South The site is at the south side of the street
Shadow Fence Height	0m This is essentially the at the ground plane of the adjacent buildings in the context. This basically means that all the facades and roof surfaces of adjacent buildings will not be overshadowed during the solar access cut-off time.
Solar access cut-off time	10:00am – 2:00pm (4 hours)
ROW width	27m

3.4. Results for the Case Study of the site at Eglington Avenue West/Bathurst

The south-facing baseline building form has an FSI of 4.49, whereby this is characterized by a building height of 22.5m (corresponding to 7 floors) and a gross floor area of 9912m^2. The baseline density is lower than that proposed for the site (FSI = 7.23) but higher than that due to City of Toronto Zoning (2.5) and only slightly lower than that due to Toronto Mid-rise Guidelines (4.95) (see Fig. 8). It is pertinent to mention that the differences in density are in effect due to the gross floor area, as the site area remains same irrespective of the zoning method. In the backdrop of the abovementioned sensitivity factors, the relationship between development density and solar access to adjacent sites will be subsequently investigated.

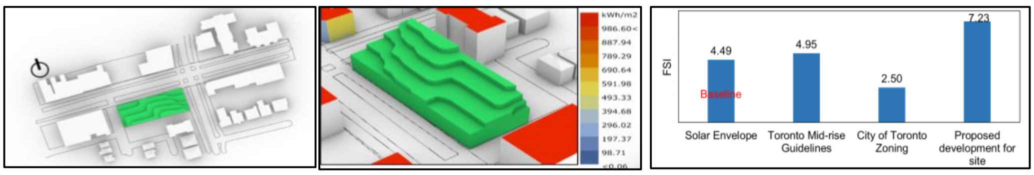

(a) (b) (c)

Fig. 8: (a) A plan view of the building form at the case study site (b) the side view of the building form based on Solar Envelope Zoning (SEZ) (c) Comparisons of FSI between different building forms SEZ building forms, Toronto Mid-rise Guidelines and City of Toronto Zoning

1) Shadow Fence Height

The buildings on the north side of the site are classified as commercial/residential, whereby the building heights range from 16m to 24m (corresponding to 4 to 6 floors). In the baseline analysis, the Shadow Fence Height was initially set at 0m (or the ground plane). The variables tested in the analysis for the category of Shadow Fence Height were 4.5m, 10.5m and 16.5m. As discussed in the parametric study, this essentially means that all the adjacent facades and roofs are not expected to be overshadowed above these cut-off heights. The volume of the building form generated is seen to steadily rise with an increasing Shadow Fence Height (0m to 16.5m). At a Shadow Fence Height of 4.5m, the FSI is 6.16 and the building height is 25.5m (corresponding to 8 floors) and a gross floor area of 13,642m^2 (see Fig. 9). This essentially means that in this building form, overshadowing will not occur at floors above the ground floor. Moreover, at 16.5m, which is roof level of a lot of the buildings in the area, solar access would only be on the roof. The resulting building has an FSI of 10.18; the total building height is 40.5m (corresponding to 13 floors) and a gross floor area of 22,472m^2, which is almost 2.27 times baseline case (9912m^2). The results show that increasing the Shadow Fence Height increases the development density, however solar access is compromised on the surfaces of the buildings in the vicinity.

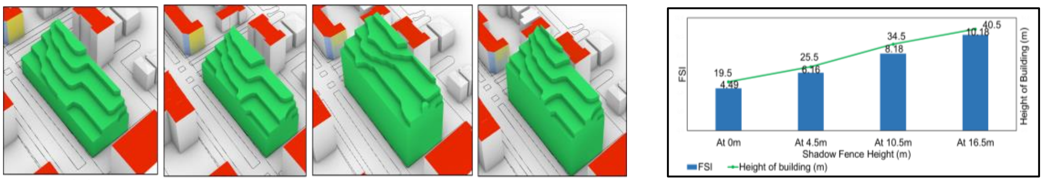

(a) (b) (c) (d) (e)

Fig. 9: Building forms obtained by varying the Shadow Fence Height (a) 0m (b) 4.5m (c) 10.5m (d) 16.5m Building forms obtained by varying the Shadow Fence Height (0m, 4.5m, 10.5m and 16.5m)

2) Solar access cut-off time

The solar access cut-off times studied were 10:00am to 4:00pm (6-hours); 9:00am to 3:00pm (6 hours); 10:00am to 2:00pm (4-hours) and 11:00am to 1:00pm (2 hours). The baseline building was based on a solar access cut-off time of 4-hours. For passive solar design, longer solar access windows are generally recommended. The volumes and FSIs of generated building forms increased with a decrease in the solar access cut-off time (6 hours to 2 hours). The highest FSI of 5.94 corresponding to a building height of 25.5m and gross floor area of 13,116m^2 occurred when the solar access cut-off time was from 11:00am to 1:00pm (2 hours). Moreover, the lowest development density occurred when the solar access cut-off time was from 9:00am to 3:00pm (6 hours), whereby the gross floor area in this case was about 6606m^2, which is about 2 times less than the case when the cut-off duration was 2 hours (see Fig. 10). With a decreasing duration of solar access, the roofs, facades, and other spaces in the vicinity are exposed to the sun for a shorter period. As seen in Fig. 10, solar access cut-off time and development density are inversely related, and this trade-off can be considered for achieving higher densities.

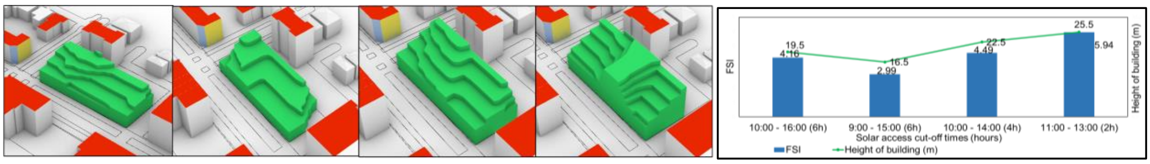

(a) (b) (c) (d) (e)

Fig. 10: Building forms obtained by varying the solar access cut-off times (a) 10:00am – 4:00pm (6 hours) (b) 9:00am – 3:00pm (6 hours) (c) 10:00am – 2:00pm (4 hours) (d) 11:00am – 1:00pm (2 hours). Maximum height = 27m (e) Comparisons of FSI of buildings based on different solar access cut-off times

3) Environmental parameters

The epw. file for Toronto presents a total of 8760 sun vectors corresponding to the total number of hours in the year. As the Capeluto and Plotnikov (2017) study showed, the number of sun vectors used in the analysis for solar envelope generation can be adjusted based on specified external conditions such as limitations on the global horizontal radiation and the dry bulb temperature. In this study, the environmental parameters tested pertaining to the sun vectors when (a) the dry bulb temperature is less than 18ºC; (b) Global Horizontal Radiation is more than 472 Wh/m^2; (c) (b) and 6-hours solar access time and (d) a combination of the parameters (a) and (b). Therefore, in the analysis, only sun vectors pertaining to these conditions are applicable. As seen in Fig. 11, the highest FSI of 8.00 is reached when the building form generated is characterized by sun-vectors in parameter (d). This is almost a uniform cuboid, which has a height of 25.5m (corresponding to 8 floors) and a gross floor area of 17,663 m^2. This building form also has a gross floor area about 1.78 times higher than the baseline case (9912m^2). This presents tremendous opportunity to achieve higher densities and concurrently maintain solar access within specified parameters, rather an all year-round approach as investigated in the parametric study earlier.

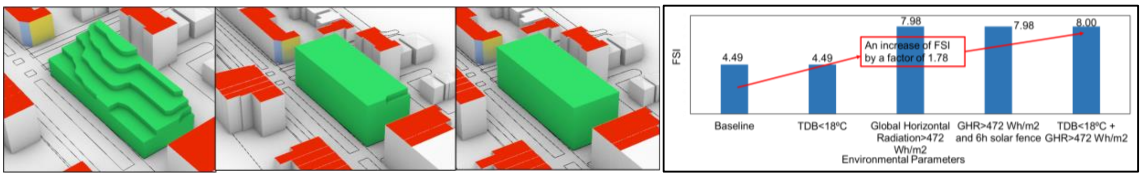

(a) (b) (c) (d)

Fig. 11: Buildings forms based on different environmental parameters (a) TDB<18°C (b) Global Horizontal Radiation>472 Wh/m^2 (c) TDB<18°C + Global Horizontal Radiation>472 Wh/m^2 (d) Comparisons of FSI of buildings based on different environmental parameters

4. Discussion

The study looked at a parametric analysis on a typical representative site along the Eglington Avenue West corridor and a case study based on an actual location at the Eglington Avenue West/Bathurst intersection. For the parametric study, a sensitivity analysis was carried out for four factors i.e. street orientation, Shadow Fence Height, solar access cut-off times and ROW width. Similarly, for the case study, three parameters i.e. Shadow Fence Height, solar access cut-off times and environmental parameters involving ambient temperature and threshold limits for Global Horizontal Radiation were investigated.

Whilst examining trends manifested in the results for the parametric and case study, important inferences regarding solar access and urban morphology were made. With regards to the FSI achieved, for majority of the factors tested, it was observed to be higher than that specified by City of Toronto Zoning (FSI = 2.5). The relationship between ROW width and Shadow Fence Height are directly proportional, whereby as they increase, the building FSI concurrently increases. In contrast, as the duration of solar access reduces, the FSI increases, hence this may be a relevant parameter for boosting building density. With regards to street orientation, clear deductions could not be made except that it is important to recognize that the street orientation can cause building FSI to greatly vary. In this case, the highest FSI of 3.55 was achieved when the building was south facing, followed by an FSI of 2.52 when it was east facing. Another important parameter to recognize is that a high Shadow Fence Height (at the roof level) brought about a building FSI of 5.03, which was higher than that of the Toronto Mid-rise Guidelines (FSI = 4.95). Similarly, a Shadow Fence Height of 3m, resulted in a building FSI of 2.95, which was substantially higher than the specified City of Toronto Zoning limit. For the case study, a Shadow Fence Height of 4.5m led to a building FSI of 6.15, which is substantially higher than that specified by the other zoning methods. It is however important to note that there is evidently a trade-off between attaining an all-encompassing solar access, which includes all the relevant façade surfaces and the roof and building density. An optimum approach of urban design may be characterized by compromise on Shadow Fence Height (designing for a higher height) to enhance the building FSI, however also acknowledging that solar access should be guaranteed beyond a threshold floor level or building surface area.

Although the findings showed that solar access can be shortened to augment building volume/FSI, it is necessary to appreciate the benefits solar exposure in terms of its temporal context (time and duration); these benefits may include improved human health and productivity, enhanced daylighting, passive solar gains during the Winter months and energy self-sufficiency through active technologies. Therefore, given both solar access and achieving higher building FSI is necessitated, the duration of solar access can be kept at a threshold limit. As the De Luca and Voll (2017) study showed, solar access cut-off requirements could be assigned to specific times of the year, such as between 11:00am to 3:00pm during the Winter months, rather than the whole year as performed in the analysis in this study. This method of solar envelope zoning would thus maintain the sensitive equilibrium between density and solar access. Moreover, it also important to identify the extent of solar access on nearby buildings. As this study has shown, a context-specific analysis can help generate a more optimum building form. For example, commercial buildings can be a greater beneficiary of implementing photovoltaic technologies, which can be installed on the facades. Therefore, there needs to be important considerations on the Shadow Fence Height and solar access cut-off times. Similarly, passive solar gains are important for residential buildings, which can be warmed up by the sun in the morning and noon and release the heat indoors at night. Thus, in this case too it is important to generate sun-vectors (used in the analysis) more attuned to local conditions.

In regards the environmental parameters studied, the combination of a dry bulb temperature less than 18ºC and a minimum Global Horizontal Radiation of 472 W/m2, resulted in a high building FSI of 8. This showed that specifying constraints such as a minimum ambient temperature and radiation intensity, a fewer number of sun-vectors would be involved in generating the building form through solar envelope zoning. This would be an effective strategy in optimizing building forms, based on say a season-based need for prolonged solar access on building surfaces. Similarly, through the application of relevant environmental parameters and solar access cut-off times, potential issues arising due to seasonal overheating and glare can be avoided.

5. Conclusion

The goal of this study was to investigate the impact of parameters pertaining to solar access on building density/FSI. The findings have hence highlighted that orientation, shadow fence height, solar access cut-off times, ROW width and environmental parameters had varying impact on the FSI of the building forms generated. A higher FSI can be achieved when limits pertaining to relevant factors are eased. For example, a lower solar access time, a greater shadow fence height, greater ROW width, setting limits on maximum outdoor temperature and radiation intensity reduce the number of sun-vectors needed to generate the building form, therefore potentially augmenting the resulting FSI. It is probable that a higher FSI may reduce the solar radiation on surfaces of buildings in the vicinity, whilst depending on the case, not significantly impact the roofs. A holistic approach needs to be adopted for the promotion of solar envelope zoning as a robust method for enhancing building FSI and guaranteeing solar access to the vicinity. This balance in strategy needs to focus on the nitty gritty pertaining to the vicinity; wherein, it accounts for the seasonal needs, functional use of buildings and key building surfaces that need to be guaranteed solar access.

6. References

BMI/Pace. (2010). *Avenues and Mid-Rise Buildings Study*. https://www.toronto.ca/city-government/planning-development/official-plan-guidelines/design-guidelines/mid-rise-buildings/Bosselmann, P., Arens, E., Dunker, K., & Wright, R. (1995). Urban form and climate: Case study, Toronto. *Journal of the American Planning Association*, *61*(2), 226–239. https://doi.org/10.1080/01944369508975635

Bosselmann, P., Arens, E., Dunker, K., & Wright, R. (1995). Urban form and climate: Case study, Toronto. Journal of the American Planning Association, 61(2), 226–239. https://doi.org/10.1080/01944369508975635

Bruce, G. (2008). High density, low energy: Achieving useful solar access for Dublin's multi-storey apartment developments. PLEA 2008 - Towards Zero Energy Building: 25th PLEA International Conference on Passive and Low Energy Architecture, Conference Proceedings, October.

Byrne, J., Taminiau, J., Kurdgelashvili, L., & Kim, K. N. (2015). A review of the solar city concept and methods to assess rooftop solar electric potential, with an illustrative application to the city of Seoul. *Renewable and Sustainable Energy Reviews*, *41*, 830–844. https://doi.org/10.1016/j.rser.2014.08.023

Capeluto, I. G., & Shaviv, E. (2001). On the use of "solar volume" for determining the urban fabric. *Solar Energy*, *70*(3), 275–280. https://doi.org/10.1016/S0038-092X(00)00088-8

Capeluto, I. G., & Plotnikov, B. (2017). A method for the generation of climate-based, context-dependent parametric solar envelopes. *Architectural Science Review*, *60*(5), 395–407. https://doi.org/10.1080/00038628.2017.1331334

Chokhachian, A., Perini, K., Giulini, S., & Auer, T. (2020). Urban performance and density: Generative study on interdependencies of urban form and environmental measures. *Sustainable Cities and Society*, *53*(April 2019), 101952. https://doi.org/10.1016/j.scs.2019.101952

City of Toronto. (2013). City of Toronto Zoning By-law. https://map.toronto.ca/maps/map.jsp?app=ZBL_CONSULT

City of Toronto. (2013). Tall Buildings Guidelines. https://www.toronto.ca/wp-content/uploads/2018/01/96ea-cityplanning-tall-buildings-may2013-final-AODA.pdf

City of Toronto. (2014). *EGLINTONconnects - Volume 2: The Plan: Recommendations and Implementation Strategies*. *2*(April), 117.

City of Toronto. (2018). *Toronto green standard v3*. https://www.toronto.ca/wp-content/uploads/2018/03/8f44-City-Planning-TGS-V3-4-storey-res-and-all-non-res.pdf

City of Toronto - Zoning By-law, Pub. L. No. 569–2013 (2020).

Compagnon, R. (2004). Solar and daylight availability in the urban fabric. *Energy and Buildings*, *36*(4), 321–328.

https://doi.org/10.1016/j.enbuild.2004.01.009

De Luca, F., & Dogan, T. (2019). A novel solar envelope method based on solar ordinances for urban planning. *Building Simulation*, *12*(5), 817–834. https://doi.org/10.1007/s12273-019-0561-1

De Luca, F., & Voll, H. (2017). Computational method for variable objectives and context aware solar envelopes generation. *Simulation Series*, *49*(11), 281–288. https://doi.org/10.22360/simaud.2017.simaud.037

Hraška, J. (2020). Approaches, Methods and Tools of Rights of Access to Sunlight around the World. *Slovak Journal of Civil Engineering*, *27*(4), 45–52. https://doi.org/10.2478/sjce-2019-0031

Knowles, R. . (2003). The solar envelope: Its meaning for energy and buildings. *Energy and Buildings*, *35*(1), 15–25. https://doi.org/10.1016/S0378-7788(02)00076-2

Knowles, R. L. (1981). *Sun Rhythm Form*. The MIT Press.

Ko, Y., Jang, K., & Radke, J. D. (2017). Toward a solar city: Trade-offs between on-site solar energy potential and vehicle energy consumption in San Francisco, California. *International Journal of Sustainable Transportation*, *11*(6), 460–470. https://doi.org/10.1080/15568318.2016.1274807

Lepore, M. (2017). The right to the sun in the urban design. *VITRUVIO - International Journal of Architectural Technology and Sustainability*, *2*(1), 25. https://doi.org/10.4995/vitruvio-ijats.2017.7459

Lobaccaro, G., & Frontini, F. (2014). Solar energy in urban environment: How urban densification affects existing buildings. *Energy Procedia*, *48*(1876), 1559–1569. https://doi.org/10.1016/j.egypro.2014.02.176

Mola, M., Feofilovs, M., & Romagnoli, F. (2018). Energy resilience: Research trends at urban, municipal and country levels. *Energy Procedia*, *147*, 104–113. https://doi.org/10.1016/j.egypro.2018.07.039

Niemasz, J., Sargent, J., & Reinhart, C. F. (2013). Solar zoning and energy in detached dwellings. *Environment and Planning B: Planning and Design*, *40*(5), 801–813. https://doi.org/10.1068/b38055

Ontario Building Code, Pub. L. No. O Reg. 332/12 (2012).

Osofsky, H. R. (1983). Solar Building Envelopes: A Zoning Approach for Protecting Residential Solar Access. The Urban Lawyer, 15(3), 637–652. http://www.jstor.org/stable/27893198

Rosenbloom, D., & Meadowcroft, J. (2014). Harnessing the Sun: Reviewing the potential of solar photovoltaics in Canada. *Renewable and Sustainable Energy Reviews*, *40*, 488–496. https://doi.org/10.1016/j.rser.2014.07.135

Sharifi, A., & Yamagata, Y. (2016). Principles and criteria for assessing urban energy resilience: A literature review. *Renewable and Sustainable Energy Reviews*, *60*, 1654–1677. https://doi.org/10.1016/j.rser.2016.03.028

Vartholomaios, A. (2015). The residential solar block envelope: A method for enabling the development of compact urban blocks with high passive solar potential. *Energy and Buildings*, *99*, 303–312. https://doi.org/10.1016/j.enbuild.2015.04.046

Wiginton, L. K., Nguyen, H. T., & Pearce, J. M. (2010). Quantifying rooftop solar photovoltaic potential for regional renewable energy policy. *Computers, Environment and Urban Systems*, *34*(4), 345–357. https://doi.org/10.1016/j.compenvurbsys.2010.01.001

© 2019 The World Bank, Source: Global Solar Atlas 2.0, Solar resource data: Solargis. downloaded https://solargis.com/maps-and-gis-data/download/canada

Study of the Influence of the Vertical/Horizontal Series Connections on the Photovoltaic Power Generation Potential on Building's Facades

Benjamin Govehovitch[1], Stéphanie Giroux--Julien[1], Léon Gaillard[2], Éric Peyrol[3] and Christophe Ménézo[2]

[1] University Claude Bernard Lyon 1 / CETHIL UMR CNRS 5008, Villeurbanne (France)

[2] University Savoie Mont-Blanc / LOCIE UMR CNRS 5271 / INES, Le Bourget-du-Lac (France)

[3] University Claude Bernard Lyon 1 / BioDyMIA, Lyon (France)

Abstract

In a context of urban densification, the exploitation of the solar potential of the facades of buildings is a promising way in order to meet the growing demand for energy whilst fighting against global warming – notably through BIPV (Building Integrated Photovoltaic technologies).The study presented in this paper focuses on the impact of the orientation of the series connection of photovoltaic (PV) panels installed on building facades. The solar potential of buildings is assessed considering the surrounding environment, using the ENVI-met urban micro-climate simulation software.

Keywords: BIPV, energy production, active facades, photovoltaic, ENVI-met

1. Introduction

Interest in building-integrated photovoltaic (BIPV) power generation technologies has been growing over the past two decades (Hagemann, 1996; Shukla et al., 2017; Saretta et al., 2020). These technologies are a promising way to make buildings producing energy from a renewable source.

Nevertheless, the predicted potential of energy production is often far away from the reported one. This is particularly true for the facades. This gap tends to be filled with new algorithms such as the one developed by (Redweik et al., 2013). But, despite the improvement brought by this algorithm, some phenomena that occur in urban environment are still not taken into consideration, notably the inter-building reflections and aeraulic phenomena.

The solar production potential of roofs has been the subject of studies for several decades (Sarralde et al., 2015). However, the interest in facades, although more recent (Díez-Mediavilla et al., 2019), highlights the fact that the level of irradiation of facades can be higher than that of roofs, depending on the latitude (especially in winter). Evaluating the solar potential in facades requires considering the environment close to the building. Indeed, different phenomena must be taken into account in relation to the case of an isolated building, including masking and shading of buildings on each other or inter-reflections between buildings. These phenomena are considered through the use of the urban micro-climate simulation software ENVI-met. The results of the simulations (facade irradiation level and surface temperature) are then used as input data for the photovoltaic production model.

The main goal of this study is to evaluate the influence of the direction of the series connections on the potential of the photovoltaic power generation of modules installed on facades of buildings. This paper falls into two main parts. First, the context of the study is put, as well as the developed model of PV production. Next, the results are presented and discussed.

2. Context of Study

The study reported here is carried out as part of the Interreg France-Swiss G2 Solaire, which aims to implement a solar cadaster on the scale of Greater Geneva. It involves the evaluation of the potential of production regarding the morphology of the neighborhoods. The final goal of this project is to achieve the energy transition in a context of urban densification by intensifying the use of solar energy in accordance with the technical and economical

doi:10.18086/eurosun.2020.01.06 Available at http://proceedings.ises.org

imperatives. In order to precisely assess the influence of all the phenomena that occur in urban environment, it is important to start from simplified cases, for which the evaluation of each phenomenon is easier.

2.1. Fictional Neighborhood

The modeled district shown in figure 1 is a fictional district, positioned at a location corresponding to the city of Geneva, Switzerland. The climate of Geneva is temperate, with mild and humid winters, and cooler summers than in subtropical climates and with variable weather.

The fictional district is inspired by the study of (Natanian et al., 2019). Unlike the study presented in this paper, the main goal of the one carried out by (Natanian et al., 2019) was to evaluate the energy load and daylight autonomy of buildings. Nonetheless, the morphologies of the neighborhoods used in this paper have demonstrated their impact. Thus, the interest focuses on the building number 5, which is particularly impacted by the surrounding buildings. In this neighborhood, all the buildings are 30 meters high, 20 meters wide and separated from each other by 20 meters. The spatial resolution is equal to 1 meter in each direction. Although expensive from the point of view of the computational time, this resolution allows to obtain a greater precision concerning the spatial heterogeneity in terms of solar irradiance on the facades and thus in terms of PV power generation.

The results presented in section 3 concern the south facade. Buildings 1, 2 and 3 can create shadows or reflections on building 5. Studies on the assessment of the photovoltaic potential of buildings consider surrounding buildings only as masks (therefore having a negative impact on solar potential). However, these buildings can also reflect part of the solar radiation, allowing a surface which is not facing the Sun to receive part of this radiation (which therefore contributes to an increase in terms of solar potential). In order to take these reflections into account, all the facades of the buildings in this district have a coefficient of reflection equal to 0.2, corresponding to that of conventional cement.

The studied days are the representative average days of each month of the year. The representative average day of the month is defined, according to the equation 1, as the day for which the meteorological conditions (including: irradiation level, temperature, wind speed and direction) for each hour are equal to the average of these conditions over all the days of the month. Carrying out the study over the whole year makes it possible to assess the evolution of the impact of the surrounding environment on the PV power generation potential.

$$X_{RAD}(t) = < X_i(t) >_{N_{day}} \qquad \text{(eq. 1)}$$

where X is the averaged variable, t is the time of the day, N_{day} is the number of days in the month, the subscripts i and RAD represent the i-th day of the month and the representative averaged day, respectively.

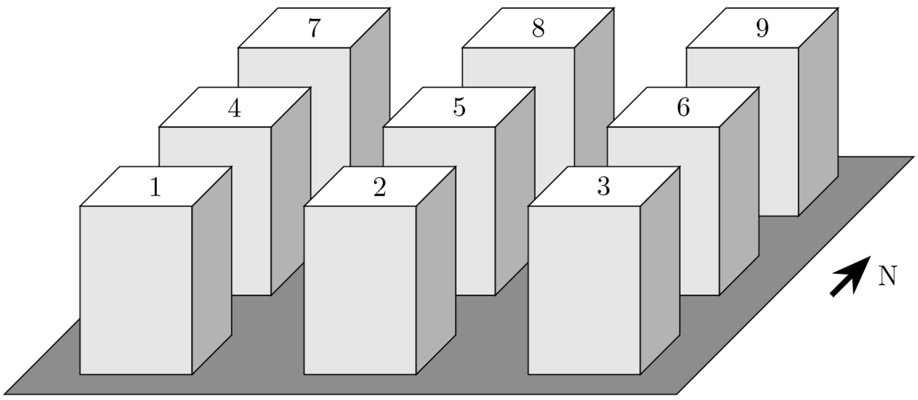

Figure 1: Fictional Studied Neighborhood – Geneva

2.2. Double-diode Model

The PV production model used is based on the double diode model developed by (Et-torabi et al., 2017). It is represented in figure 2. Owing to the similarity in their construction, the constituents of a photovoltaic (PV) panel can be approximated by one or more diodes to produce the desired electrical response. An example of a such a current-voltage characteristic curve is shown in figure 3.

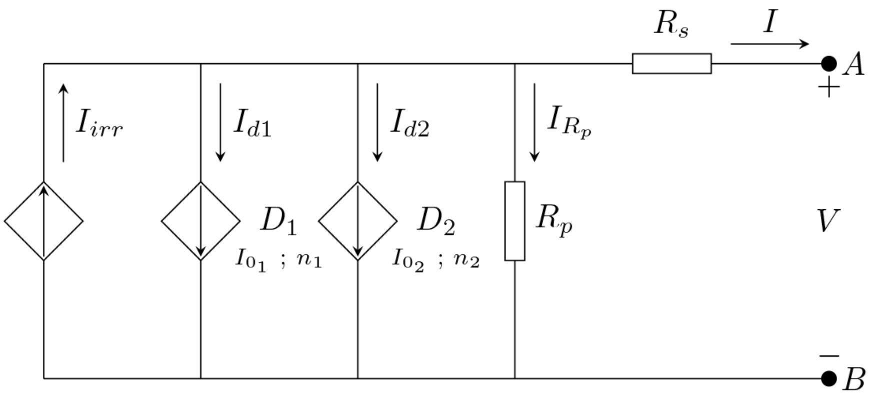

Figure 2: Double-diode Model Equivalent-Circuit

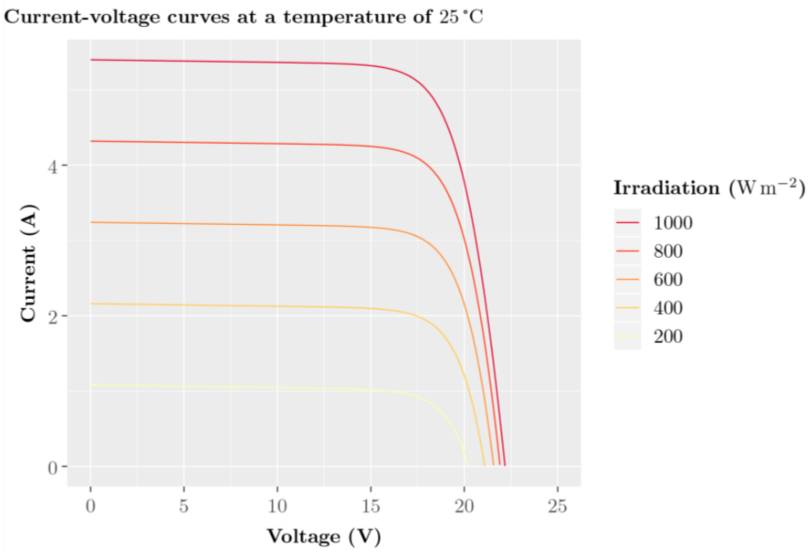

Figure 3: Current-voltage curves of the multicrystalline photovoltaic module TEX854

The purpose of the double diode model is to bring greater precision to the production model for low irradiation, compared to the single diode model (Humada et al., 2016). Indeed, an increasing number of diodes, although making the resolution of the model more complex, also makes it possible to take into account the evolution of the ideality factor of the diodes, which depends on the voltage to which the panel is subjected. For strong irradiations, the ideality factor is close to 1, while for lower irradiation levels, it approaches 2. This variation of the ideality factor is obtained by adding a second diode in parallel with the first (Gao et al., 2016). The electrical characteristics of the TEX854 multicrystalline PV panel used in this study are presented in Table 1.

Table 1: Electrical characteristics of the TEX854 photovoltaic module

Photovoltaic Module TEX854	
Rated voltage	18.0 V
Rated current	5.0 A
Open-circuit voltage	22.2 V
Short-circuit current	5.4 A
Temperature coefficient: short-circuit current	1.53 mA/C

Temperature coefficient: open-circuit voltage	-76.32 mV/C
Solar cells	36 (4 × 9)

3. Results and discussion

3.1. Irradiation on facade

An example of the irradiation profile on the south facade of building 5 at different time of October 16th, 2018 is shown in figure 4. The figure presents the total direct and diffuse solar radiation incident on the facade, including sky diffuse and ground reflected components The lower levels of irradiation on the facade are due to the shadow of buildings on the southern row. The mask that they create have an influence on the production profile, as discussed in section 3.2.

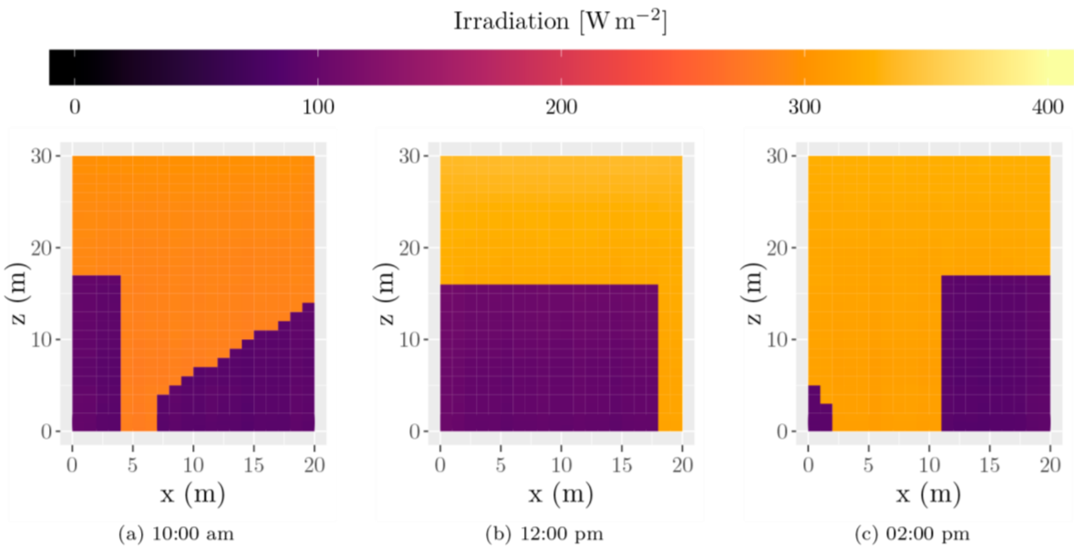

Figure 4: Irradiation on south façade of the building 5 on October 16th, 2018

3.2. Influence of the type of series connections on the production profile

Connecting the panels in series affects the current flowing through them. In the case of micro-inverters, each panel is electrically independent. Thus, the current-voltage couple of the PV panel is only dependent on its level of irradiation and its temperature. However, in the case of a series connection of several PV panels, the current flowing through them is equal to the lowest current flowing through all these panels. Different connection configurations are considered:

- one micro-inverter per PV panel,
- one inverter for all PV panels,
- one inverter for each vertical row,
- one inverter for each horizontal row.

The results of these different configurations obtained from the irradiation profiles (figure 4) are shown in figure 5 and 6. They correspond to a situation where the entire facade would be covered with PV panels. The case of micro-inverters (figures 5a and 6a) are the most favorable from the point of view of energy production. Indeed, only the area of the facade that is effectively hidden is affected. Thus, this case is taken as a reference for the calculation of the power generation drop. The case where all the panels are connected in series (figure 5b and 6b) are the least favorable cases. This is because the area of the facade, which is shaded also impacts the non-shaded area. The instantaneous production profile is like the case where the entire wall was shaded. Finally, the cases of vertical and horizontal connections (respectively figures 5c and 6c, and 5d and 6d) have an intermediate impact on the level of production potential. Indeed, the panels impacted by the shading are those effectively hidden, as well as those connected in accordance with the direction of the series connection.

The drop of power generation due to shadowing is depending on the time of the day. Indeed, on October 16th, 2018, this drop is higher in the case of a vertical series connection. The potential of instantaneous PV power generation for the case of the micro-inverters reaches 13.39 kW. This is reduced by 20.8 % with horizontal series connection (10.60 kW) and up to 40.0 % with vertical series connection (8.04 kW). Nonetheless, the drop of power generation due to the horizontal series connection is more important than that of vertical series connection the same day at 2:00 pm. Indeed, the drop of power generation reaches 27,3 % for the horizontal series connection against 20,5 % for the vertical series connection.

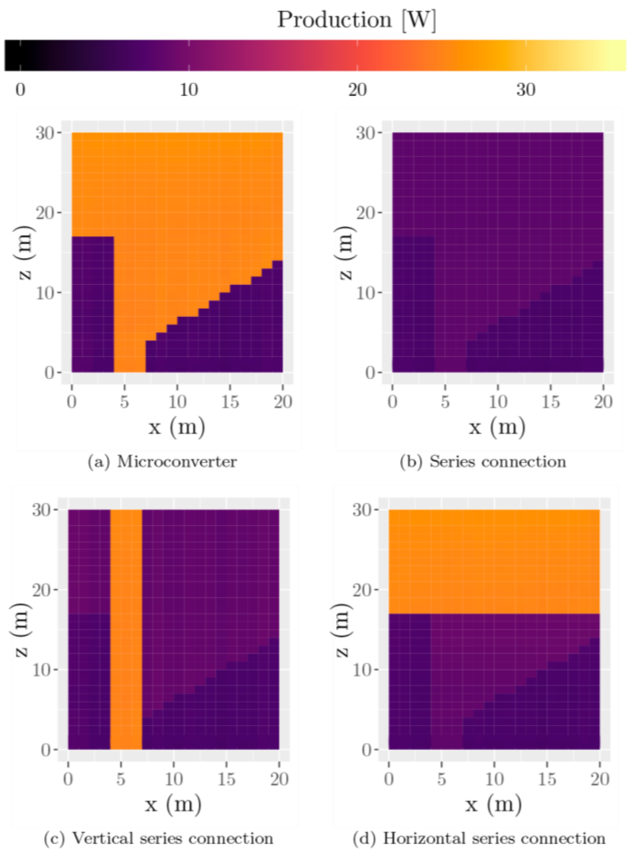

Figure 5: Power Generation Map on October 16th at 10:00 am, for different connection types

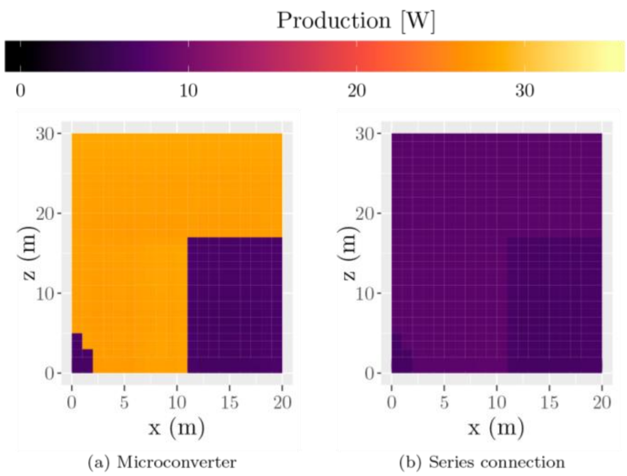

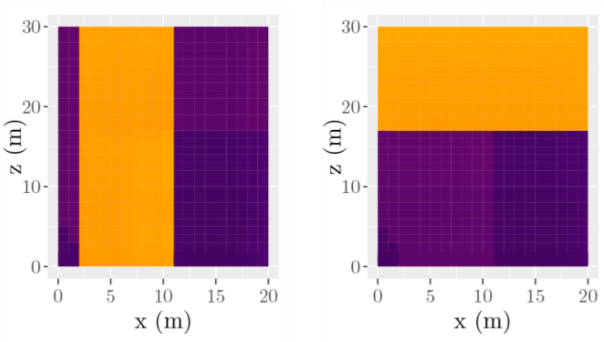

(c) Vertical series connection (d) Horizontal series connection

Figure 6: Power Generation Map on October 16th at 2:00 pm, for different connection types

3.3. Impact on the daily power generation

The different instantaneous production profiles presented in figure 5 and 6 have an impact on the daily production potential of the facade. The daily power generation, depending on the type of connection, is shown in figure 9.

As seen in the previous section, the case of a connection by micro-inverters is the least impacted by shading on the facade. Thus, the level of production is the highest regardless of the time of day. Conversely, the series connection impacts the production potential of all the panels. In this case, the level of production is the lowest throughout the day.

As seen in figure 5 and 6, the impact of the series connection on the energy production can alternatively be more important for the horizontal or the vertical series connection, depending on the time of the day. This alternance in terms of potential of power generation has an impact on the daily power generation profile.

Table 2 groups the differences in terms of power generation for representative average days of each month of the year, according to the type of connection of the PV panels. The production by micro-inverters is taken as a reference for the calculation of the drop of PV power generation.

Table 2: Drop of PV Power Generation[1] According to the Connection Type

Table Headers	Connection Type		
	Vertical Series Connection	Horizontal Series Connection	Series Connection
01 – January	-35.27 %	-36.83 %	-80.97 %
02 – February	-35.56 %	-24.49 %	-62.71 %
03 – March	-38.06 %	-15.00 %	-62.79 %
04 – April	-18.87 %	-4.46 %	-42.99 %
05 – May	-1.68 %	-0.44 %	-2.94 %
06 – June	-1.92 %	-0.51 %	-3.36 %
07 – July	-1.92 %	-0.58 %	-3.41 %
08 – August	-1.15 %	-0.38 %	-2.02 %
09 – September	-29.48 %	-9.67 %	-53.13 %
10 – October	-36.56 %	-17.90 %	-58.47 %
11 – November	-28.47 %	-27.40 %	-61.65 %
12 - December	-24.57 %	-35.20 %	-66.05 %

[1] Power generation by micro-inverters is taken as a reference

It appears that the case of the serial connection is the most impactful, with a loss of generation that can reach 80.97 % in January compared to the case of production by micro-inverters. This sharp decrease in production potential is since the smallest hidden square meter of the facade impacts the whole of it. Thus, this type of connection amounts to amplifying the phenomenon of shading of the facade. Regarding the influence of the orientation of the series connections, at the same time of the year, the horizontal and vertical series connections have a similar impact on the power generation with a drop of 36.83 % and 35.27 %, respectively.

This way, the table 2 offers a dual reading. The first reading is horizontal. Indeed, as can be seen in figure 7 as well, between the months of May and August, the impact of the series connection is very low (less than 5 % in the worst case). This can be explained by the sun's path. Indeed, between these two times of the year, the sun passes over the buildings (see figure 8). Thus, the shading effect is much less significant.

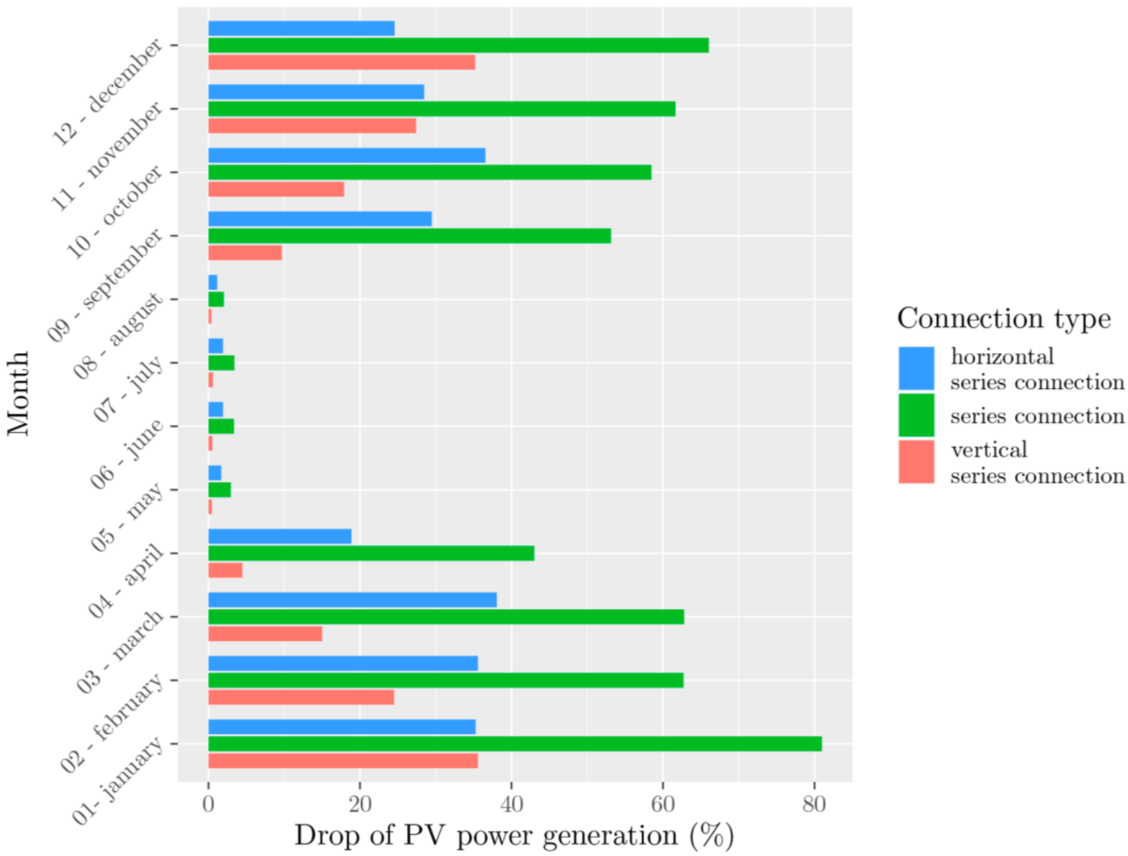

Figure 7: Comparison of the drops of PV power generation

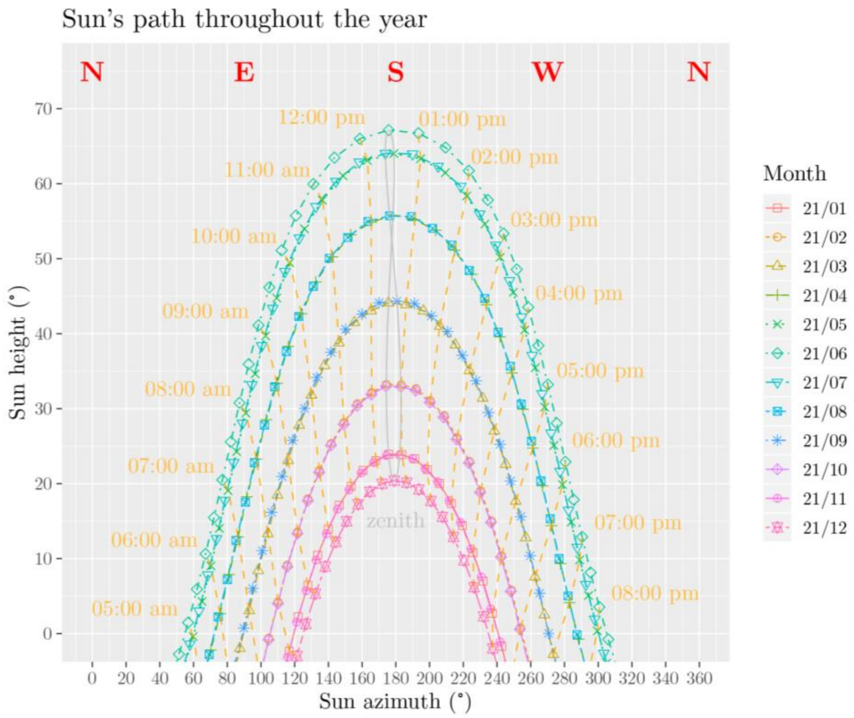

Figure 8: Annual sun's path over Geneva

The second reading is vertical. As aforementioned, the least positive case considering the power generation is the series connection. Regarding the direction of the series connection, except the months of December and January, the horizontal series connection appears as the solution to be preferred. In terms of energy production over the year, the horizontal series connection presents a drop of 14.4 %, compared with 21.1 % for the vertical one.

The energy production over a long period of time is not the only result arising from the study. Indeed, the evolution of the hourly power generation is clearly relevant. As can be seen in figure 9, the influence of the series connections depends on the time of the year as well as the time of the day. On the one hand, it appears that the energy production is barely impacted in May. On the other hand, for some time of the day, it can be more interesting to use vertical series connections than horizontal. For example, in figure 9a, the PV power generation with vertical series connection is higher than that of horizontal one at 11:00 am, 2:00 pm and 3:00 pm. The opposite is true for the rest of the day.

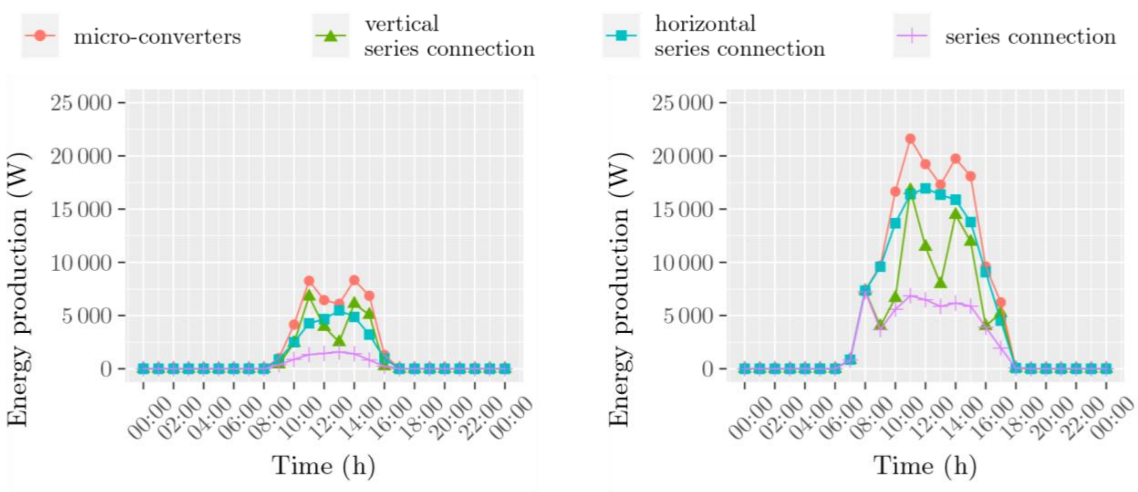

(a) January

(b) March

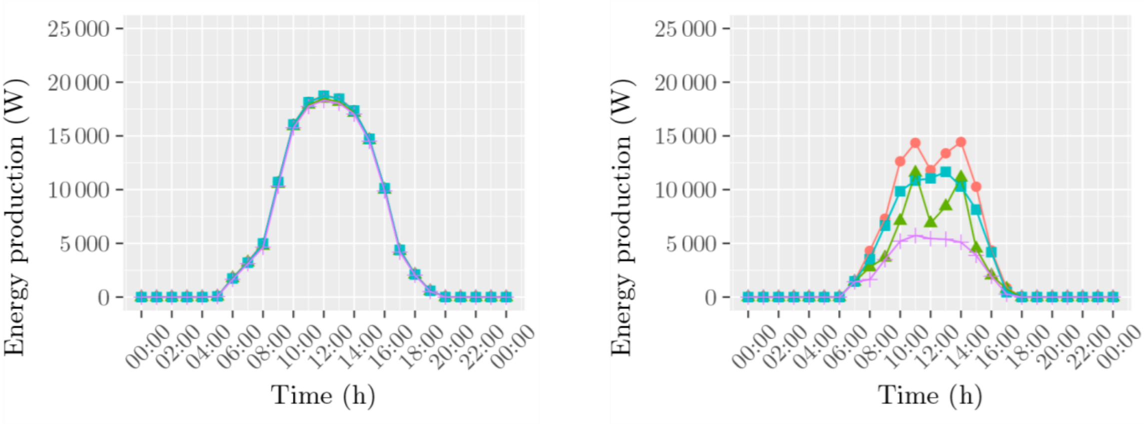

(c) May (d) October

Figure 9: Daily Power Photovoltaic Power Generation on South Facade

4. Conclusion and outlooks

Although generally less irradiated than roofs, facades have a significant solar potential in terms of PV power generation. Indeed, even if the production potential per square meter of a facade turns out to be lower than that of a roof, in a context of urban densification where buildings are always more vertical, the solar potential of the latter can become superior (Díez-Mediavilla et al., 2019).

The study presented here shows the importance of taking into account the surrounding environment when evaluating the solar potential of facades. Indeed, the shading created by neighboring buildings has a significant impact on the level of irradiation received on the surrounding facades. From the point of view of PV power generation potential, the series connection of the panels has a big impact. It appears, in this study, that a horizontal connection of the panels is to be preferred, most of the time. Nonetheless, adaptative solutions (real-time switching of the direction of the series connection) could be an efficient way to exploit the solar potential of the facades to the full, whilst complying with technical and economical constraints.

Moreover, the results presented in this paper relate to a fictitious neighborhood. To confirm these results, it is therefore important to extend this study to different morphologies of neighborhoods, including actual ones. In addition, the conclusions are drawn only from numerical results. In order to validate this model a confrontation between numerical results and measurements data should be carried out.

5. Acknowledgments

This work is supported by the Franco-Swiss Interreg research program: through the G2Solaire project.

6. References

Díez-Mediavilla, M., Rodríguez-Amigo, M., Dieste-Velasco, M., García-Calderón, T., & Alonso-Tristán, C. (2019). The PV potential of vertical façades: A classic approach using experimental data from Burgos, Spain. Solar Energy, 177, 192 – 199.

Et-torabi, K., Nassar-eddine, I., Obbadi, A., Errami, Y., Rmaily, R., Sahnoun, S., fajri, A. E.,& Agunaou, M. (2017). Parameters estimation of the single and double diode photovoltaic models using a gauss–seidel algorithm and analytical method: A comparative study. Energy Conversion and Management, 148, 1041 – 1054.

Gao, X., Cui, Y., Hu, J., Xu, G., & Yu, Y. (2016). Lambert w-function based exact representation for double diode model of solar cells: Comparison on fitness and parameter extraction. EnergyConversion and Management, 127, 443 – 460.

Hagemann, I. (1996). PV in buildings - the influence of PV on the design and planning process of a building. Renewable Energy, 8(1), 467 – 470. Special Issue World Renewable EnergyCongress Renewable Energy, Energy Efficiency and the Environment.

Humada, A. M., Hojabri, M., Mekhilef, S., & Hamada, H. M. (2016). Solar cell parameters extraction based on single and double-diode models: A review. Renewable and Sustainable Energy Reviews, 56, 494 – 509.

Natanian, J., Aleksandrowicz, O., Auer, T. (2019). A parametric approach to optimizing urban form, energy balance and environmental quality: The case of Mediterranean districts. Applied Energy, 254.

Redweik, P., Catita, C., Brito, M. (2013). Solar energy potential on roofs and facades in an urban landscape. Solar Energy, 97, 332 - 341.

Saretta, E., Bonomo, P., & Frontini, F. (2020). A calculation method for the BIPV potential of swiss façades at LOD2.5 in urban areas: A case from Ticino region. Solar Energy, 195, 150 –165.

Sarralde, J. J., Quinn, D. J., Wiesmann, D., & Steemers, K. (2015). Solar energy and urban morphology: Scenarios for increasing the renewable energy potential of neighbourhoods in London. Renewable Energy, 73, 10 – 17. Sustainable Development in Building and Environment (SuDBE) 2013.

Shukla, A. K., Sudhakar, K., & Baredar, P. (2017). Recent advancement in BIPV product technologies: A review. Energy and Buildings, 140, 188 – 195.

Validation process of a multifunctional and autonomous solar window block for residential buildings retrofit

Leire Minguez[1], Martino Gubert[1], Alexander Astigarraga[1] and Stefano Avesani[1]

[1] Institute for Renewable Energy, EURAC Research, Bolzano (Italy)

Abstract

In the framework of the EU H2020 project EnergyMatching, a catalogue of multifunctional and autonomous window renovation solutions was developed. Such catalogue is based on the Solar Window Block (SWB), which is a prefabricated window system that integrates a highly efficient window, a PV module, a shading system and a decentralized ventilation machine. The SWB aims at enhancing the energy performance and indoor comfort of existing residential buildings without adding electrical loads and simplifying the installation works. The development of the SWB was addressed through calculations, prototyping, testing campaign up to demo installation and monitoring. This paper focuses on the testing campaign validation process of this technology. Three main SWB configurations were designed and real scale prototypes manufactured, followed by dedicated tests to verify the operation of the system and its energy production-consumption matching performance. On the one hand, operational temperature tests showed a proper functioning of the electrical circuit of the system, as well as underlined the importance of the ventilative cooling of the electrical equipment. On the other hand, the energy matching performance tests showed the capability of the different SWB configurations to cover different demand profiles of the ventilation unit. Thanks to the holistic technology validation process, the executive SWB design has already implemented required modifications to assure safe functioning, easy installation and maintenance.

Keywords: energy efficiency, indoor comfort, BIPV, solar building, solar window block

1. Introduction

The retrofit of the existing building stock is being promoted by the EU Directives in terms of energy performance of buildings (2018/844/EU and 2012/27/EU) as one of the most relevant actions to reduce the building sector energy consumption, CO_2 emissions and therefore climate change risk. In a renovation intervention, windows are a crucial component due to their strong impact in the final achieved energy efficiency and comfort. Although their substitution is frequent, it is still a very delicate intervention because its correct installation influences significantly the building renovation final quality, that could be easily impoverished due to risk of wrong installation, of damages, of poor component performance as well as create excessive disturbance to occupants. To facilitate and secure the proper window installation, both in new and existing buildings, the use of a prefabricated insulating frame called “window block” is more and more used. Besides its decrease of thermal losses due to thermal bridges and increase of installation precision, it provides space for the integration of different components that could enhance energy efficiency and indoor comfort.

In the framework of the EU H2020 project EnergyMatching, a catalogue of multifunctional window blocks, called Solar Window Block (SWB) was developed for residential buildings retrofit (Andaloro, et al., 2018). The SWB is a prefabricated system composed by the following components: an insulating frame; a highly efficient timber-frame window; photovoltaic modules; automated shading and a decentralized ventilation machine. The SWB solutions provide valuable opportunities for enhancing the energy performance of existing buildings and increasing building occupants comfort, in terms of enhanced indoor air quality and daylighting control, with a unique easy-to-install system, without adding electrical loads to the building. In addition, these systems allow for effective integration of BIPV modules to maximize renewable energy sources exploitation through self-consumption, with a low disturbance on building occupants.

Three main SWB configurations were identified based on a joint technical feasibility and performance-based assessment of the different possible solutions (Andaloro, et al., 2018). The development process was characterized by an iterative design through several steps with progressive increase of details and analysis, such as: (a) thermal

doi:10.18086/eurosun.2020.01.07 Available at http://proceedings.ises.org

performance, (b) daylighting analysis, (c) energy matching performance, (d) technical integration of components and PV sizing. This process led to the identification and detail design of a catalogue of SWB solutions. The three main configurations contained in the catalogue integrate the PV modules on the sill, as a shading overhang or vertically in the façade. Some of the most important barriers identified were the fire prevention requirements, operation and maintenance needs, components integration and interfaces. Consequently, the required modifications were implemented in the prototypes final design, resulting in the manufacturing of three real scale mock-ups (Fig. 1).

Fig. 1: Solar Window Block mock-ups in the outdoor lab (from left to right: BIPV vertical, BIPV sill, BIPV overhang)

After the executive design and real scale prototypes manufacturing, the SWB development was followed by the demonstration in real operational environments, both in testing infrastructures and in a real building. Hence, the work presented in this paper aims at validating the SWB design through a dedicated testing campaign. Specifically, the testing phase focused on operational temperature tests of the electrical components in their compartment, and energy production and consumption matching tests under real conditions. Finally, lesson learnt from the prototypes design, manufacturing and testing activities was implemented in the SWB design for a real demo case building.

2. Methods

In order to validate the system before its installation in real buildings, an extensive testing campaign was performed. Initially, the manufacturing and assembly chain of the solution was validated through direct communication with the different component manufacturers and system integrator. Besides this, the functionality and robustness of the SWB and its components were verified through initial trials during the mock-ups commissioning. Once done the initial verifications, the testing campaign was focused on two main test types: operational temperature tests and system energy matching performance tests.

2.1. Summary of the SWB main features

The main features and components of the three tested SWB configurations are summarized in Tab. 1, and differ mainly by PV module positioning within the overall system: (i) in sill, (ii) in window overhang and (iii) vertical position next to window (Andaloro, et al., 2020). However, the position of the PV module impacts on other features of the system, such as the installed PV power (different PV cell technology and module size) and required electrical components. For example, the solution with the PV sill requires an additional electrical component (booster) increasing the output voltage to be able to charge the battery. Moreover, the PV position constraints the window position within the wall depth, which in turn has a significant effect in the SWB thermal bridges.

Apart from these differences, the concept behind the three SWB configurations is similar as well as its off-grid electrical connection scheme. As shown in Fig. 2, the energy produced by the PV module is used to charge the battery and to feed the ventilation machine. The circuit is controlled by the Maximum Power Point Tracker (MPPT), which controls the PV operation point, the battery charging process and the battery discharging process through the Ventilation Machine (VM).

Tab. 1: Summary of main features and installed components of the main SWB configurations

<table>
<tr><th colspan="2" rowspan="2">SOLAR WINDOW BLOCK

COMPONENTS</th><th>SWB 1 – BIPV SILL</th><th>SWB 2 – BIPV OVERHANG</th><th>SWB 3 – VERTICAL BIPV</th></tr>
<tr><td>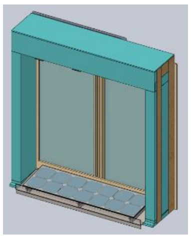</td><td>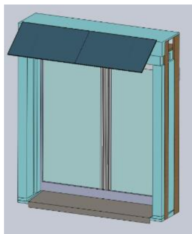</td><td>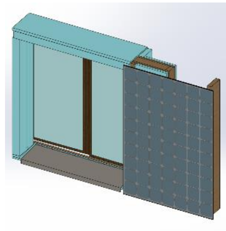</td></tr>
<tr><td colspan="2">GLAZING</td><td colspan="3">Triple glazing of 52.8mm total thickness (U glazing = 0.6 W/m²K)</td></tr>
<tr><td colspan="2">SHADING</td><td colspan="3">ScreenLine SL22W - V95 coated (reflective)</td></tr>
<tr><td rowspan="3">WINDOW BLOCK</td><td>WINDOW</td><td colspan="3">Versatile continental window (U frame = 0.91 W/m²K)</td></tr>
<tr><td>PV POSITION</td><td>On the sill</td><td>Overhang</td><td>Vertical</td></tr>
<tr><td>VM POSITION</td><td colspan="2">Above window</td><td>Next to window</td></tr>
<tr><td colspan="2">VENTILATION MACHINE</td><td colspan="3">Thesan Aircare ES (Max 20.6W)</td></tr>
<tr><td colspan="2">PV MODULE</td><td>c-Si (56 Wp)</td><td>a-Si (31 Wp)</td><td>c-Si (291 Wp)</td></tr>
<tr><td colspan="2">PV CLICK&GO</td><td colspan="3">Cosmos plug &play solution</td></tr>
<tr><td colspan="2">BATTERY</td><td>2x12V (Li-Fe-Po4)</td><td>1x24V (Lithium-ion)</td><td>2x12V (Li-Fe-Po4)</td></tr>
<tr><td colspan="2">MPPT</td><td>-</td><td colspan="2">Morningstar’s SunSaver MPPT</td></tr>
<tr><td colspan="2">MPPT & BOOSTER</td><td>Genasun GVB-8-Li-28.4V</td><td colspan="2">-</td></tr>
</table>

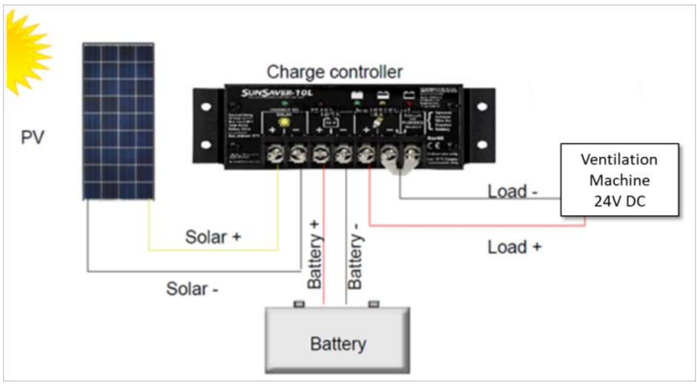

Fig. 2: Electrical connections scheme (without booster)

2.2. Operational temperature tests

The verification of the operation temperatures of the system was a first priority in the validation process, in order to identify the potential risk of fire due to the presence of electrical components within the window block. In fact, the VM, batteries and rest of electrical equipment are installed within a closed wooden compartment on top of the window block. A set of openings for the natural ventilation was designed and needed to be validated. In case of overheating of these components, besides the risk of fire, the system could not work properly if exceeding their maximum allowed operation temperatures (Tab. 3). Therefore, a dedicated test campaign was performed with the goal of verifying that the temperatures reached by the different components were acceptable and there was no risk of fire and malfunctioning of components.

These tests were performed in a prototype, containing the wood compartment with all the electrical equipment. The prototype represents the smallest wooden box design, representing thus the worst case in terms of overheating risk. This prototype was installed and tested in an indoor laboratory with an air temperature fixed to 25°C, in a set up that allowed air to flow naturally through the different ventilation grids foreseen in the system. All the electrical components, such as ventilation device, batteries, MPPT-controller and DC/DC controller, were installed. Normally, the real SWB is fed with the power generated by the PV module. However, in this indoor test, the lack of real PV power was substituted by a PV simulator Ametek ETS600X, which provides power in the same way as a PV module. This allows the MPPT-controller to work as it was connected to a PV panel in the different test scenarios.

During the tests, two air temperatures and four surface temperatures were monitored, together with the current and voltage of the battery and ventilation unit. In order to measure the temperatures five thermocouples were installed in the most representative positions, such as on the surfaces of battery, MPPT and DC/DC controller. The air temperature was measured next to the main electrical components and the air outlet ventilation holes, as shown in Fig. 3. The portable digital thermometer TM 947 SD with a resolution of 0.1°C and an accuracy of 0.5% of reading was used to monitor and record thermocouples data. However, the voltage and current measurements (1% and 2% of accuracy respectively), as well as the MPPT heat sink temperature measurement were done by the sensors embedded in the MPPT device. This data was monitored and gathered by the MSView software provided by SunSaver MPPT manufacturer. Both monitoring systems recorded data every 1 minute.

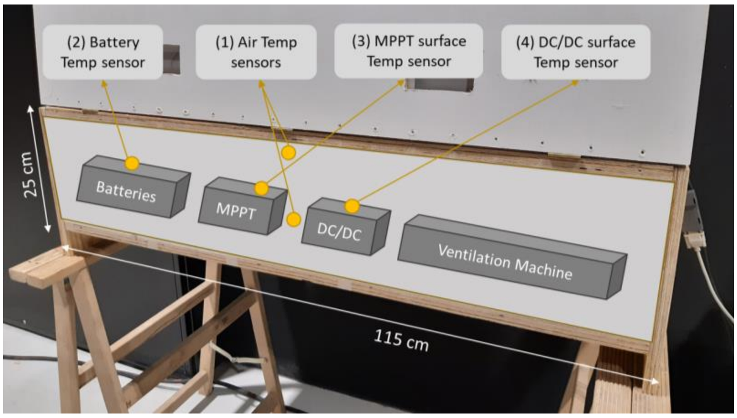

Fig. 3: Scheme of the operation temperature test mock-up and set-up

Besides the operation temperature verifications, these tests allowed to check the following aspects: (i) the real battery energy storage capacity and voltages related to different states of charge, (ii) battery charge and discharge strategy to be configured in the SunSaver MPPT and (iii) correct functioning of the MPP tracker. The implemented control strategy aimed at maximizing the PV power generation, while preventing the battery complete emptying and consequent system restart need. Fig. 4 shows an example of evolution of the battery state of charge and the main control parameters: (i) upper battery capacity limit (95%), (ii) depth of discharge (80%), (iii) status of charge at which disconnect the load (20%) and (iv) reconnect the load again (80%).

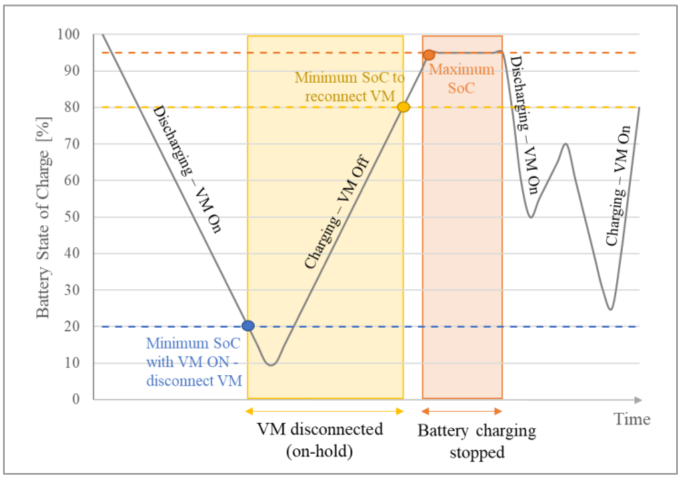

Fig. 4: Example of battery charging-discharging process along time and main control strategy parameters

When the battery reaches a minimum state of charge (20%), the system was programmed to disconnect the VM, aiming at being able to feed the inherent consumption of the system for certain time even if no power input from the PV modules occur. Once reached that minimum state, the VM continues disconnected until the battery is charged to 80%, with the goal of avoiding continuous VM switching on and off, and the consequent potential discomfort. Moreover, in order to define the battery charging strategy, such as the absorption and float voltage, the recommendations from the battery and MPPT manufacturers were considered.

The operation temperature tests were performed under the following different operation modes.

- Both open and closed box ventilation grids were considered (two configurations). Open configuration allowed natural ventilation through the electrical wooden compartment, as implemented in the SWB final design, while closed configuration represented the worst heat dissipation case.
- The power input from the PV simulator for charging the batteries was tested as per the following three configurations: (i) disabled, (ii) with constant maximum power supply equal to 300 Wp, which represents approximately the peak power of the largest PV module (configuration of SWB 3) and (iii) a more realistic variable power input generated by the largest PV module when receiving the highest irradiation daily profile in the year at the Italian demo case location and orientation.
- The consumption load that discharges the batteries, i.e. the ventilation machine, was tested both at the maximum fan speed and disactivated.

The prototype was tested in different operating modes resulting from the fully factorial combinations of the above described parameters, aiming at identifying the scenario that would lead to the highest temperatures. The number of tests amounts therefore to twelve (2x3x2).

2.3. Solar Window Block performance tests

Once the adequate functioning of the electrical components was verified under indoor controlled conditions, the SWB electrical energy matching performance tests were conducted. The whole SWB system performance was tested in an outdoor laboratory with the following goals: (a) The verification of the energy matching KPIs among the BIPV production, the consumption profiles of the ventilation machine and the battery; (b) The measurement of the temperatures of the system during operation to check its correct and safe functioning; (c) The validation of the developed theoretical models; (d) The assessment of the durability and robustness of the electrical system and components.

The SWB performance tests were done on the manufactured real scale mock-ups shown in Fig. 1, which represent the three above described SWB configurations integrating all the components (section 2.1). Hence, each of them is in the off-grid setup. Therefore, the system performance was tested with the same operation mode as in the real conditions, i.e. the ventilation machine could be fed only by the energy produced by the PV modules and stored in the batteries. The prototypes were positioned facing South in order to test them in the optimal orientation and identify thus the limitation of the technology under real, but best oriented conditions. They are being monitored since mid-June 2020.

During these tests, the electrical parameters of the different components were monitored, i.e. voltage and current of PV module, batteries and ventilation machine. In addition, operation temperatures of the PV modules, batteries and MPPT controller, as well as solar irradiance were measured. For that purpose, a complete set of sensors were installed in the three prototypes, as reported in Tab. 2 for one of the prototypes. All the variables are measured every 1 minute and gathered together in a database. The monitoring system is based on a NI LabView software reading and recording data from the Sun Saver MPPT and Seneca data acquisition system.

Different ventilation machine consumption profiles were applied to test the energy matching performance of each mock-up. Initially, occupancy profiles and related VM hourly profiles were generated for different room occupancies (1, 2 or 4 people), usage (bedroom or living room) and IAQ level (category II or III). These profiles were used as input to simulate the energy matching performance of the three mock-ups under the laboratory conditions. These simulations were done with an ad-hoc developed tool programmed in Phyton (Lovati, et al., 2017), that assesses the energy balance between the PV production and the consumption of the VM with a battery at hourly time steps. One of the outputs was the actual VM working hourly profile, considering that some moments the PV-battery system could not supply the required power to run the ventilation device. These profiles were used as inputs to a TRNSYS model to predict the indoor CO_2 concentrations reached by the actual VM working profiles and therefore the potential discomfort situations. Based on such simulation results, arbitrary threshold of discomfort hours of max 25% of occupied hours with CO_2 concentration above 1750 ppm, and VM Working Hours Rate (WHR), i.e. ratio between the actual VM working hours and the due ones as defined in the theoretical profiles, of min 80%, were used to select the VM profiles to be implemented for each mock-up. Fig. 5 shows the profiles chosen for each mock-up, as well as their main predicted KPIs. SWB with PV in sill and overhang were tested with a VM profile defined for a bedroom, so working only during the night at a constant medium speed. SWB with vertical PV was tested to cover a more demanding profile, i.e. for a living room. In this case, the VM is active during the day and disactivated at night, increasing its speed in the evening when the maximum occupancy is foreseen.

Tab. 2: SWB performance test measurements for mock-up 3 (BIPV vertical)

TARGET	MEASUREMENT	MEASURED BY		SENSOR POSITION
		SENSOR	DATA ACQUISITION	
1. Weather	Solar irradiance	Pyranometer Kipp & Zonen CMP11	Seneca Z-8TC-1	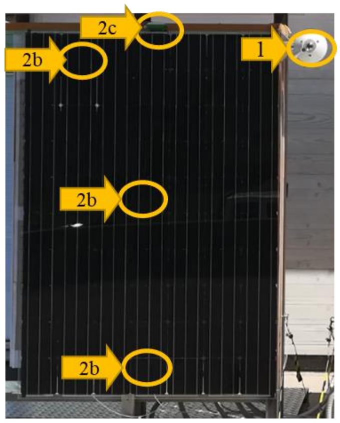
2. PV	a) Electrical parameters: I, V	Built in MPPT	SunSaver MPPT 15L	
	b) Temp. PV (x3)	PT100	Seneca Z-4RTD2	
	c) Temp. air behind PV	EE16	Seneca Z-8AI	
3. Battery	a) Electrical parameters: I, V, Charge state	Built in MPPT	SunSaver MPPT 15L	
	b) Temp. battery	PT1000	SunSaver MPPT 15L	
4. VM	Electrical parameters: I, V, Load state	Built in MPPT	SunSaver MPPT 15L	
5. Air	Temp. air inside the box	EE16	Seneca Z-8AI	

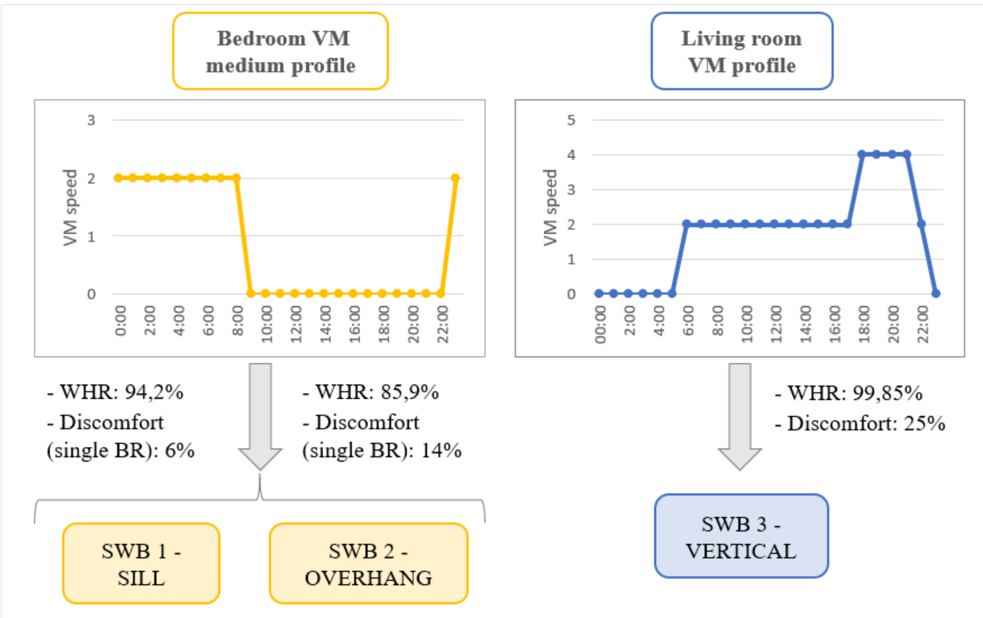

Fig. 5: Ventilation machine profiles applied to each Solar Window Block configuration and their corresponding predicted performance in terms of Working Hours Rate and Discomfort hours

2.4. Design adaptation

Often the development of a new technology sees continuous design correction and adaptation due to several problems and issues that comes up along the innovative development process. Hence, a further step in the SWB validation process was the design adaptation. Starting from the preliminary design output described in (Andaloro, et al., 2018), the SWB design adaptation process was carried out through the following phases.

(i) Executive design: the detailed drawings of the window block, the components, their dimensions and the main "boundary limits" were carefully analyzed. Specifically, the components' position into the wooden box was studied to define their interfaces. Moreover, energy matching simulations were performed to predict the SWB performance under the real demo case conditions (location, orientation and components features).

(ii) Electrical design scheme and fire protection: these issues arose during the demo case design and deeply modified the components' position into the SWB wooden box, highlighting the need of the operational temperature test (section 2.2). In particular, the MPPT, protection fuses and batteries needed a "fire protected" area to decrease the fire risk working on the air ventilation flow scheme and non-combustible materials.

(iii) Operation & Maintenance analysis: the need for frequent maintenance on the VM, such as filter exchange or cleaning, and the possible system restart due to system stop or unexpected problems, was investigated and affected the internal wooden structure design.

(iv) Trial Window installation: A key aspect of the final SWB design validation was the installation of a "trial window". Just one complete SWB was manufactured and installed in the Italian demo carefully following all the installation steps, checking the interferences between the SWB and the existing wall and between each component. The demo implementation was done for a residential building in Florence (Italy), characterized by 12 apartments and 51 windows.

Fig. 6 illustrates the overall design adaptation process with the timeline that starts from the concept idea till the executive design and manufacturing. The manufactured elements (in yellow), together with the test campaign and Demo design adaptation (light grey) were useful to collect valuable information and apply them in the design, since they were developed mostly in parallel.

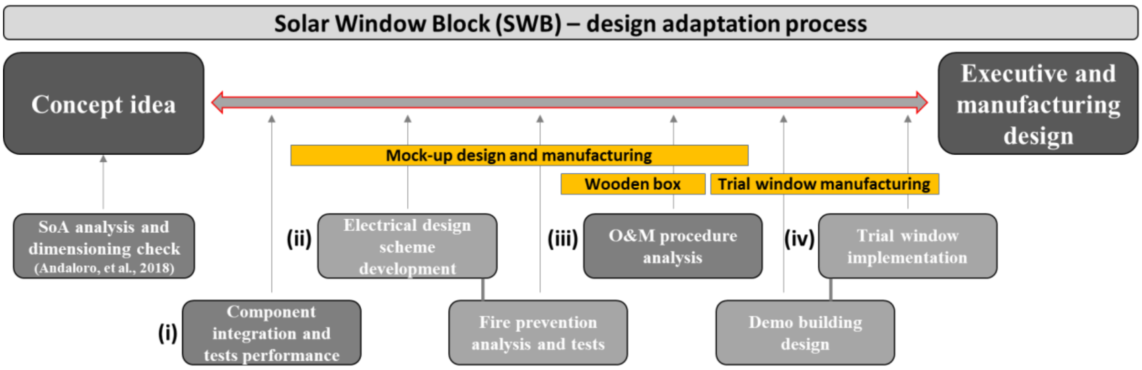

Fig. 6: SWB design adaptation process

3. Results and discussion

3.1. Operational temperature tests

Initially, the operational temperature tests served to verify the real battery capacity and define the optimal control strategy and its main parameters. Thanks to these tests, the battery voltage values corresponding to the main State of Charge points shown in Fig. 4 were identified as follows: 20% SoC = 25.4V, 80% SoC = 27.2V and 95% SoC = 28.6V.

With regard to the temperatures measured, Tab. 3 gathers the maximum registered temperatures in each component and the test scenario under which they occurred. As resulted from these data, batteries reached 31°C, while the MPPT and DC/DC converter are the most heated up components, (46.6°C and 44.3°C respectively).

This demonstrated the crucial importance of the ventilation grids, as well as their positioning below and above these components to enhance their cooling through natural ventilation. The heat generated by the electrical equipment resulted in heating up the air inside the box. In the worst case, the box air temperature increased of around 6°C, with a room temperature of 25°C and ventilation grids closed.

Tab. 3: Maximum measured temperatures during operational temperature tests

Measurement	Internal Air – close to components	Internal Air – close to outlet grid	Battery	MPPT – surface	MPPT – Internal Heatsink	DC/DC
Max. measured temperature*	30.8°C	28.2°C	31°C	46.6°C	53°C	44.3°C
Max. allowed temperature**	-	-	~ 70°C	~ 60°C	~ 80°C	~ 70°C
Related test conditions	Max power Max load Closed holes	Max power No load Open holes	Max power No load Open holes	Max power Max load Closed holes	Max power Max load Closed holes	Max power Max load Closed holes

* Tests performed in a controlled environmental temperature of 25°C
** Information from data sheet of each component

As can be seen in Tab. 3, the operational temperature tests showed proper functioning and standard heating of the system, reaching temperatures in the wooden compartment within acceptable ranges in all scenarios. The maximum temperatures reached in all the electrical components were below the maximum allowed temperatures, even in the most demanding theoretical cases, with maximum power input, maximum ventilation fan speed and ventilation grids closed.

In order to see the effect of the different test scenarios in one of the measured temperatures, Fig. 7 gathers the internal air temperature evolution under the most representative and extreme test conditions. It shows that when testing the system in a more realistic scenario (section 2.2), such as variable power input profile and box ventilation grids open, the temperatures reached were lower than the maximum ones reported in Tab. 3.

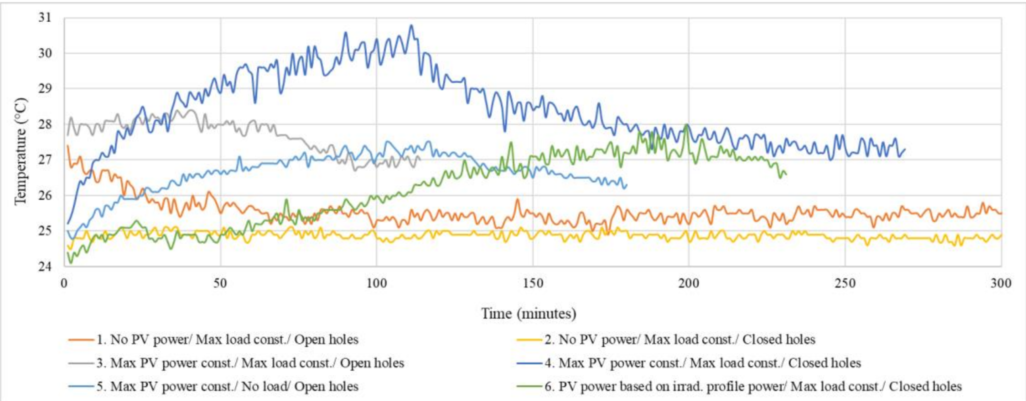

Fig. 7: Internal air temperature evolution during the different test scenarios

As can be seen in Fig. 7, the main condition affecting the heating is the power input. The highest temperatures are reached when the maximum constant PV power is applied during the complete charge of the battery, and load is demanding power at the same time (max air temp. 30.8°C). In a real case following the sun irradiance profile, where is not possible to have a constant PV maximum power, the charge of the batteries is performed in a slower pace generating less heat in the MPPT and thus in the surrounding air inside the box (max temp. 28°C). Besides, in these conditions, the cooling effect of the natural ventilation is significant, reducing the max air temp in more than 2°C. However, when the battery is only being discharged with the ventilation machine consumption, almost no heating occurs, and the effect of the natural ventilation is negligible.

3.2. Solar Window Block performance tests

The main result of the SWB performance tests is the capability of each SWB configuration to match the energy demand of the ventilation machine profile with the energy provided by the PV-battery system. This capability has been assessed based on the VM working time rate.

As shown in Tab. 4, throughout July and August 2020, SWB configurations with PV in sill (1) and vertical (3) were able to cover the 100% of the time the VM demand. However, the SWB with PV in overhang position (2) covered the 91.7% of the time the load. The difference in the VM demand coverage between the different configurations is due to the PV-battery system design of each of them. The PV module of SWB 2 is made of amorphous silicon technology (Tab. 1), which has a lower efficiency (6%), while the other two configurations use crystalline silicone (eff. 15%). As seen in Tab. 4, the VM demand coverage rates are higher in the test results than in the simulations, although following the same trend (SWB 2 with the lowest value). This is reasonable taken into account that the simulated results covered the whole year performance, while the test results only covered two summer months.

Tab. 4: Summary of SWB performance results

KEY PERFORMANCE INDICATOR	SWB 1 – BIPV SILL	SWB 2 – BIPV OVERHANG	SWB 3 – VERTICAL BIPV
VM Working Rate (test result*)	100 %	91.7 %	100 %
VM Working Rate (simulation result**)	94.2 %	85.9 %	99.85 %
Efficiency of the system (total energy consumed by VM / total energy generated by PV)	57.6%	61.5%	84.7%
Max PV surface average temperature reached	78.3 °C	69.1 °C	67.8 °C
*Indicator measured for July and August in minute time steps			
**Indicator calculated for the whole year in hour time steps			

Another interesting parameter reported in Tab. 4 is the ratio between the energy consumed by the VM and the energy generated by the PV, which allowed to understand the efficiency of the whole electric system. First of all, to better understand this value it is important to bear in mind that the MPPT adjusts the PV operation point in the I-V curve and therefore the generation, based on the demand of the VM and battery at each moment. Apart from that, this efficiency parameter takes into account the efficiency of the MPPT, battery charging and discharging and the partial self-consumption. That said, SWB 3 presents an efficiency of almost 85%, while SWB 2 configuration 62 % and SWB 1 configuration 58 %. SWB 3 higher efficiency can be explained because the load matches the generation in real time, so there is some direct self-consumption, avoiding the passage through the battery with the corresponding higher efficiency. Besides, the higher generation and consumption powers of this case fit better the MPPT optimal efficiency conditions. In the other two cases, with a bedroom VM profile, the efficiency is lower because the load does not match the generation, so the VM is always taking energy from the battery, working thus in a less efficient way. Finally, the booster required in SWB 1 to increase the voltage has a lower efficiency than the MPPT present in the other configurations, so making this version the less efficient one.

Tab. 4 also gathers the maximum temperatures reached in the rear surface of the PV modules. SWB with PV in sill was the one reaching the highest temperatures, around 78°C, due to its almost horizontal orientation and consequent reception of more direct irradiation during the summer months. SWB with vertical PV reached the lowest temperatures, around 68°C, due to its vertical position and consequent lack of reception of direct irradiation during the summer months. Besides, the VM working schedule of this latter case is demanding energy during the day, thus making the PV work while it is receiving the radiation and consequently dissipate part of the heat received when converting the radiation in electricity. In the cases with bedroom VM profile, the energy demand occurs at night, so during the day might be times in which the PV is not working if the battery already full, and consequently not dissipating part of that heat with the electricity generation.

Fig. 8 shows the evolution of the PV power generation, the VM power consumption and the battery voltage along a clear sky day of July 2020. SWB 1 configuration shows a continuous discharging of battery during the night hours, when the VM is demanding energy. While during the day the PV is producing up to 47W (56Wp) and charging the battery. In the evening when the irradiance is lower, the battery starts to discharge at a slower pace due to the inherent consumption of the system, and in a higher pace once the VM is activated at night. SWB 2 covers the same VM profile as in the previous case, but two significant differences in its performance can be appreciated. Firstly, the maximum PV production hardly reaches 22W (31Wp). Secondly, the lower capacity battery of this system results in reaching the maximum charge around 15:00 and the consequent stop in the PV production followed by the battery voltage relaxation. SWB 3, instead, presents a completely different trend due to the different VM demand profile. During the night there is no load consumption, just the inherent one of the system. During the morning the PV is producing electricity up to 109W (291Wp), which is used to charge the battery and feed the VM. Around 13:00 the battery reaches its maximum state of charge and therefore the PV production is reduced to the same amount of power that the VM is demanding, occurring direct self-consumption. In the evening when the PV availability is low, the VM starts again taking the electricity from the battery until the night when is switched off.

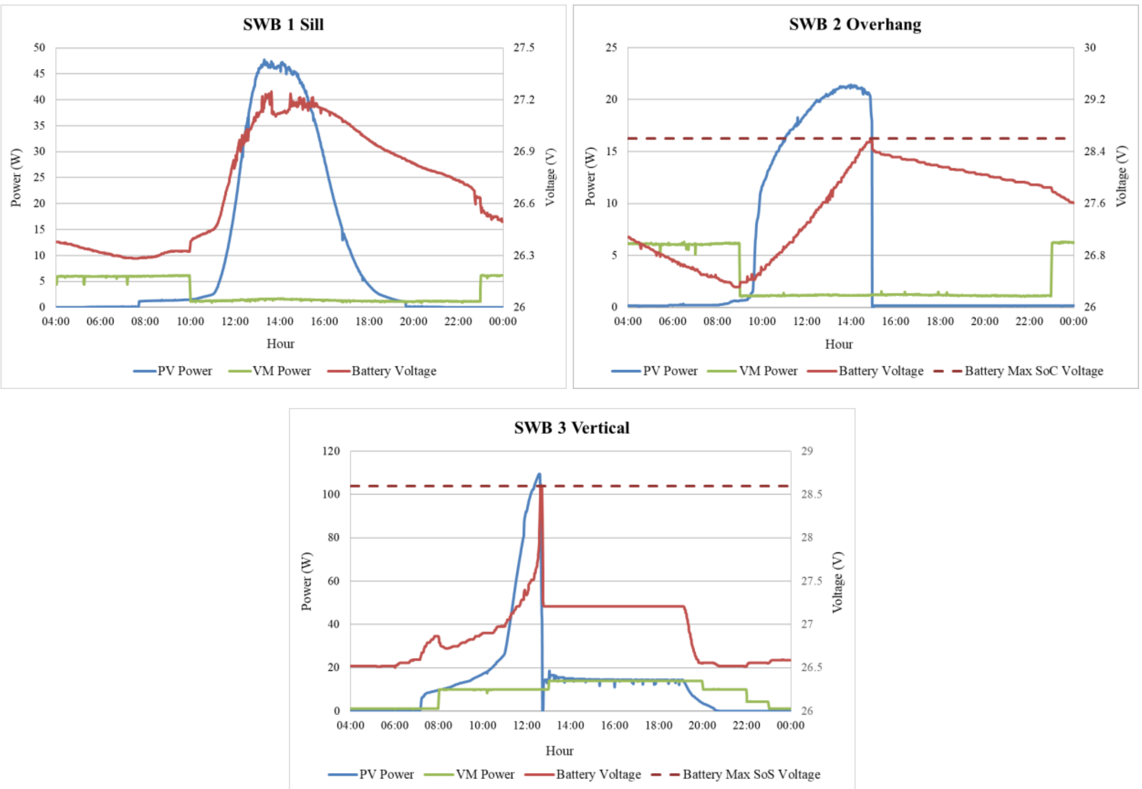

Fig. 8: Evolution of PV power, battery voltage and VM power along one clear sky day of July 2020: SWB 1, SWB 2 and SWB 3

3.3. Design adaptation

Thanks to the information collected from the mock-ups manufacturing and the testing campaign, together with the feedback from demo owners, the SWB design was adapted to answer to the arisen issues and allow its implementation in the real demo building. The main improvements resulting from the whole process (Fig. 6) are summarized below.

(i) Adaptation 1: Optimized SWB components integration and interfaces design. The VM, batteries, MPPT DC/DC converter and fuses were located in an optimized position based on a dedicated substructure, allowing a quick and safe connection among all the electrical components.

(ii) Adaptation 2: Fire resistant electrical compartment and natural air ventilation flow scheme. A specific fire resistance compartment for batteries was selected and installed in the wooden box. MPPT, DC/DC converter and fuses were located in the wooden box with further protection to avoid unexpected users touch or interferences. All the internal compartment was covered with non-flammable material and the holes for the natural ventilation were positioned in correspondence to the batteries, MPPT and the DC/DC converter (as explained in section 3.1) to allow an homogeneous and adequate natural ventilation.

(iii) Adaptation 3: Operation & Maintenance. The VM was positioned allowing an easy filter exchange without interfering with the electrical components foreseeing a series of openings and doors. The batteries' compartment, as well as all the rest of the electrical components were located in order to avoid final-user accidental interaction. Moreover, the rest of electrical components was positioned in a quick accessible part of the wooden box to allow a fast check from the electrician and a quick restart of the system. Every component was mechanically fixed avoiding glues to facilitate its removal.

(iv) Adaptation 4: Step-by-step installation procedure definition. As final step of the design and implementation phases, a detailed step-by-step installation procedure was elaborated easing all future installations by different companies (knowledge transfer), also providing some critical aspects and recommendation to avoid undesirable errors. The "trial window" concept was proposed as a further mandatory validation step to be introduced between the mock-up realization and the whole SWBs implementation. This new approach was positively evaluated from all the technology providers and the demo owner because it brought to light valuable feedback that allowed further improvement and optimization to the executive and detailed design of the system.

The whole design adaptation process, as described in Fig. 9, from the preliminary component integration to the executive design, sets the basis to validate the SWB design for its implementation in a real demo case building.

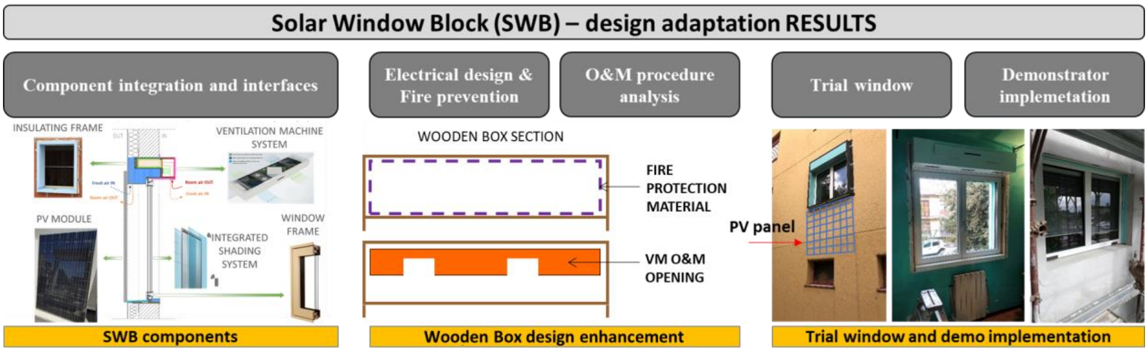

Fig. 9: SWB design adaptation results

4. Conclusions

The SWB testing and adaptation processes described in this paper allowed to validate the SWB design, focusing on its proper functioning and actual performance, as well as contributed to optimize the SWB detailed design.

Thanks to the operational temperature tests, the appropriate functioning of the electrical system of the SWB was verified under more demanding conditions than real ones. Although in all cases the temperatures reached were within the acceptable range, the importance of allowing a proper natural ventilation through the wooden box was demonstrated and therefore applied in the SWB design.

The energy matching performance tests verified the correct operation of the system in its off-grid setup and underlined the different performances achieved by each SWB configuration. The solution with the vertical BIPV showed higher efficiency, higher energy matching capability and consequent better autonomous functioning. This case also showed a proper coverage of the ventilation machine profile of a living room with 4 people, guaranteeing an acceptable indoor air exchange. The sill and overhang BIPV configurations could not guarantee the total ventilation machine working hours for a living room case, but could match appropriately a bedroom ventilation profile, specially the configuration with the PV in sill. However, a longer test data collection is required to get a better overview of the SWB performance along the year and, in fact, is already ongoing. Besides these testing, also the monitoring data from the implemented SWB in the demo site will contribute to better understand the actual performance of the system under real conditions and different location and orientations.

Regarding the SWB design adaptation a new detailed SWB configuration was achieved, which integrated the meaningful inputs gathered during the different prototypes manufacturing process, testing campaign and trial window installation process. Thanks to that, the SWB design was validated as a valuable, flexible, and robust option for the building retrofit in terms of enhanced performance and comfort.

5. Acknowledgments

This work has received funding within the H2020 project Energy Matching under grant agreement Nº 768766. Authors kindly acknowledge the technology providers involved in the SWB development process, Eurofinestra (Giovanni Toniato) for providing schematic design, for the manufacturing of all the mock-ups, for technical know-how and its transfer on installation procedures; Pellini (Luca Papaiz) for providing details on the shading system and its control strategy, Onyx Solar (Jose Maria Jimenez) for providing detailed technical data for the different PV configurations, for the manufacturing of the PV modules for the 3 mock-ups; Tulipps (Eugene Widlak) and Plastica (Gerard Berenschot) for providing details on the PV mounting substructure, click & go and U rails system respectively; CASA S.p.A. for the electrical component scheme and useful feedback on the installation procedure and components integration. We also acknowledge Thesan and Gruppo Savio for providing technical installation details related to the ventilation unit. Authors also acknowledge Annalisa Andaloro, Annamaria Belleri, Giuseppe De Michele, David Moser, Laura Maturi, Marco Lovati, Jennifer Adami, Mattia Dallapiccola from EURAC research for supporting the simulation work during the SWB development process.

6. References

Andaloro, A, Avesani, S, Belleri, A & Machado, M, 2018, ‘Adaptive window block for residential use: optimization of energy efficiency and user´s comfort’, *FACADE2018 Adaptive! Adaptive Facade Network Conference,* Luzern, Switzerland, 26-27 November.

Andaloro, A, Minguez, L & Avesani, S, 2020, ‘Active and energy autonomous window: renewable energy integration through design for manufacturing and assembly’, *Façade Tectonics 2020 World Congress*, Los Angeles, United States, 5-27 August.

DIRECTIVE (EU) 2018/844 OF THE EUROPEAN PARLIAMENT AND OF THE COUNCIL of 30 May 2018 amending Directive 2010/31/EU on the energy performance of buildings and Directive 2012/27/EU on energy efficiency

DIRECTIVE 2012/27/EU OF THE EUROPEAN PARLIAMENT AND OF THE COUNCIL of 25 October 2012 on energy efficiency, amending Directives 2009/125/EC and 2010/30/EU and repealing Directives 2004/8/EC and 2006/32/EC

Lovati, M, Albatici, R, Maturi, L & Moser, D, 2017, ‘Effect of module orientation and batteries on performance of building integrated photovoltaic systems’ *33rd European Photovoltaic Solar Energy Conference and Exhibition,* Amsterdam, Netherlands, 25-29 September.

THE ROLE OF RENEWABLE ENERGY TECHNOLOGIES IN THE ENERGY RENOVATION OF RESIDENTIAL BUILDINGS

Chiara Dipasquale[1], Elena Bee[1] and Roberto Fedrizzi[1]

[1] Institute for Renewable Energy - Eurac Research, Bolzano (Italy)

Abstract

The high share of energy consumption of the residential sector and the low renovation rate of existing buildings move through the need of finding solutions that facilitate the retrofit process. Common heating and cooling systems are often not adequate to the building as consequence energy plant operation is not efficient and running costs are high, or renovation works result intrusive and tenants or dwelling owners obstruct their execution.

The here presented study investigates retrofit solutions packages applied to different multi-family house typologies located through Europe. Intervention on the envelope follows the actual national minimum requirements for energy efficiency, efficient heating and cooling systems are recommended for the different building typologies and renewable energies technologies are considered for contributing to the reduction of energy consumption. Energy performance of the retrofit packages, energy savings and running costs are assessed through dynamic simulations for all the studied cases.

Keywords: Renewable energy, building renovation

1. Introduction

The well-known share of energy consumption due to residential buildings and the high percentage of European buildings built before 1990 require the promotion of massive energy renovation actions of the existing building stock. However, this process attempts to spread due to high investment cost, low acceptance of the owners or tenants, non-clear economic, energy and comfort advantages, design effort, intervention works in occupied buildings and definition of the retrofit solution.

Some of these barriers can be overcame by selecting the most appropriate solution for the building typology, avoiding components oversizing and knowing expected energy and economic savings. Commonly, retrofit solutions are constituted by standard layouts and one generation unit that simplifies the installation and management of the whole system, but does not exploit renewable energies neither optimizes the system functioning. Moreover, a standard configuration usually implies components oversizing and consequently high installation and running costs, non-efficient system operation and users discomfort.

Indications on suitable retrofit solutions for specific building typologies, with expected energy savings and operation costs would help and therefore foster the renovation rate. The study presented in the following analyses retrofit packages for four representative building typologies of multi-family houses located in four locations throughout Europe. The retrofit solutions investigate interventions on the envelope following the current national indications of envelope performance, three heating and cooling (H&C) system layouts coupled with renewable energy technologies (solar thermal collectors and photovoltaic PV system). A database of model-based results collects energy performance of the studied cases, calculated through dynamic simulations where the buildings with the proposed renovation packages are modeled and simulated in the four reference locations.

doi:10.18086/eurosun.2020.01.08 Available at http://proceedings.ises.org

2. Methodology

2.1. Approach

The approach adopted in this study exploits dynamic energy simulations of buildings with integrated HVAC systems pre (pre-RS) and post (post-RS) renovation to evaluate the impact of refurbishment in terms of energy, environmental and economic indicators.

The developed methodology consists of:

- definition of the reference locations, each representing a typical European climate typology based on Heating Degree Days (HDD) (Custom Degree Day Data, http://www.degreedays.net);
- definition of reference buildings and HVAC system pre intervention (pre-RSs);
- definition of retrofit packages (RPs) to be applied to each pre-RS, including envelope insulation, windows replacement, heating and cooling system efficiency improvement and adoption of renewable energy sources;

2.2. Reference locations

The following presented scenarios are simulated in the typical climatic conditions (typical meteorological year) of four European locations. Each reference climate refers to a country and typical weather conditions of a city are used for the dynamic simulations. Reference locations differ each other of around 500 HDD in order to cover main part of European climates. Table 1 summarizes the four reference climates, with the corresponding country used for building characteristics and national requirements, and the related city for the weather conditions. The fourth column of the table reports the HDD of that city calculated on 18°C basis for the last 3 years (2017-2019). The fifth column shows the average external temperature over the year which characterize the climate.

Table 1: Reference climatic conditions and heating degree days

Reference climate	Country	City	Heating Degree Days	Average temperature [°C]
Continental	Germany	Stuttgart	2902	9
Oceanic	United Kingdom	London	2452	12
Southern Dry	Spain	Madrid	1993	14
Mediterranean	Italy	Rome	1400	16

2.3 Reference buildings and HVAC systems (pre-RSs)

The reference buildings are multi-family houses built between 1980-1990, because 70% of European existing buildings belong to this period (Birchall, 2006) and are still not renovated, which implies a large potential of decarbonization of the residential sector.

In order to consider different buildings shapes, which directly impact on the heating and cooling demands, four building typologies are used with different surface over volume ratio (S/V). The four reference building typologies are: low-rise (LRMF), high-rise (HRMF), small (SMFH) and large (LMFH) multi-family houses. Figure 1 shows a view of the 3D model for each of the considered building typology. Table 2 summarizes the reference buildings geometric characteristics and the HVAC system type in the pre-RS. The four typologies differ for the number of floors, the horizontal development and the total heated area. The shape factors (S/V ratio) ranges from 0.15 for the high-rise building, which despite its height has a compact shape, to 0.45 for the small building.

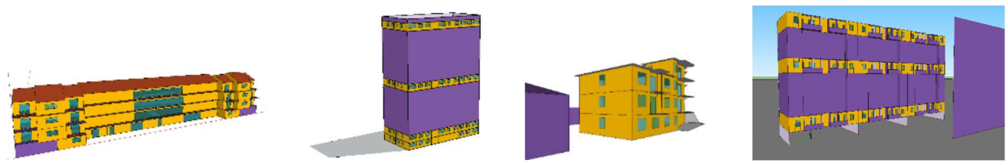

LRMF HRMF SMFH LMFH

Fig. 1: Reference buildings 3D model view

Table 2: Reference buildings geometric characteristics and HVAC systems (pre-RS)

Building type	Number of floors	Dwell. per floor	Total area	S/V ratio	HVAC –heating (pre-RS)	HVAC –cooling (pre-RS)	HVAC – DHW (pre-RS)
LRMF	4	15	4055	0.34	Decentralized gas boiler (η_{eff} = 0.80)	Split units (EER = 2.5)	Decentralized gas boiler (η_{eff} = 0.80)
HRMF	17	6	7140	0.15	Centralized gas boiler (η_{eff} = 0.80)	Split units (EER = 2.5)	Centralized gas boiler (η_{eff} = 0.80)
SMFH	4	2	712	0.45	Centralized gas boiler (η_{eff} = 0.80)	Split units (EER = 2.5)	Decentralized electric boilers (η_{eff} = 0.85)
LMFH	8	10	7120	0.27	Centralized gas boiler (η_{eff} = 0.80)	Split units (EER = 2.5)	Decentralized electric boilers (η_{eff} = 0.85)

2.4. Retrofit packages

As previously mentioned, each retrofit package is composed by the intervention on the envelope, the HVAC replacement and the adoption of renewable energy technologies.

The intervention on the envelope are aimed at reducing the building demands by improving the envelope performance. The thermal transmittance of the envelope elements in the pre-RS are referred to buildings built between 1980 and 1990. Walls construction changes depending on the location. These values refer to the study conducted during the FP7 project iNSPiRe (Dipasquale et al., 2019). In the post-RS the thermal transmittance are in agreement with the national requirements of the considered location/country for new and renovated buildings. More info in the refence. Since each location is representative of a climate (see next paragraph), Table 3 summarizes the thermal transmittance associated to each climate, both in the pre-RS and in the post-RS.

Table 3: Reference buildings geometric characteristics and HVAC systems

	Pre-RS				Post-RS			
Climate	U_{wall} [W/m²K]	U_{roof} [W/m²K]	U_{ground} [W/m²K]	$U_{windows}$ [W/m²K]	U_{wall} [W/m²K]	U_{roof} [W/m²K]	U_{ground} [W/m²K]	$U_{windows}$ [W/m²K]
Continental	0.65	0.42	0.69	2.92	0.25	0.19	0.23	1.10
Oceanic	0.76	0.59	1.07	4.36	0.18	0.13	0.13	1.40
Mediterranean	1.00	1.24	1.51	4.03	0.29	0.26	0.34	2.00
Southern Dry	1.56	1.33	1.07	3.49	0.41	0.35	0.65	1.80

The replacement of the existing HVAC system is aimed at improving the energy efficiency, limiting/avoiding the use of fossil fuels, and improving the comfort condition of the occupants (including air quality). In all the cases the solutions adopted are mainly based on heat pumps (aerothermal or geothermal). However, very different system layout, distribution schemes, emission devices, and control strategies are adopted depending on the application feasibility and building typology. The HVAC systems configurations are described in Table 4 and are referred to as retrofit solution 1, 2 and 3 (RS1, RS2, RS3). The combination of a building typology with the HVAC system is based on choices that consider the feasibility of the installation (centralized vs decentralized systems) or whose application gives some results that can be extended to similar cases. For further details on the HVAC solutions and the control strategies, please refer to BuildHeat, 2020.

Depending on the building typology and available building external surfaces (roof or external walls oriented to South, East or West), each renovation solution is coupled with a photovoltaic (PV) system only or a solar thermal collectors (STC) system too. PV covers part of the electricity used by heat pumps or auxiliary devices while STC provide a share of Domestic Hot Water (DHW) production. The size of the adopted PV and STC systems is shown in Table 5.

Table 4: Reference buildings geometric characteristics and HVAC systems

Retrofit solution	Main generation	Heating/ cooling emission system	Mechanical ventilation	Solar technologies
RS1	Decentralized air-to-air heat pumps + DHW production	Full-air system	Included in the heating/cooling system with heat recovery	PV
RS2	Decentralized brine to water heat-pumps	Radiators	-	PV
RS3	Centralized air-to-water heat pump	Fan-coils	Decentralized cross flow units with heat recovery	PV+STC

Table 5: Solar technologies installations

Scenario	PV	STC
LRMF+ RS1	55.4 kWp (12% vertical, 88% at 30°)	-
HRMF + RS2	48 kWp (50% vertical, 50% at 30°)	-
SMFH + RS3	10.8 kWp – 10°	37 collectors vertical, south facing
LMFH + RS3	54 kW kWp – 10°	37 collectors vertical, south facing

3. Results

Each combination of reference building plus retrofit solution has been evaluated in each climate for a total number of 16 post-RSs. The impact of each intervention of a retrofit package (envelope insulation, HVAC replacement and adoption of renewable sources) with respect to the case pre intervention pre-RS has been evaluated separately. Considerations on all the cases together and therefore looking at the impact of the climate, the building typology and the adopted solution are also carried out and below reported. For this last analysis, primary energy use (PE) and seasonal performance factor (SPF) were used as key performance indicators.

For each of the 16 cases, in addition to PE reduction, the presence of PV and STC is evaluated in terms of PV share (share of the total electricity consumption covered by the PV) and solar thermal (ST) contribution (share of the DHW thermal demand covered with STC). The economic performance is evaluated in terms of operative cost in a typical year and it also considers the compensation for the surplus PV electricity fed into the grid. All the comparisons and assessment of energy savings, unless otherwise specified, are calculated with respect to the reference case.

In this paper, only part of the results of the presented study is reported. In particular, Mediterranean (MED) and Continental (CON) climates are reported as example of a southern and northern climate, while all the details can be found in BuildHeat 2020. Figures 2 and 3, referred to the MED and the CON climates respectively, show the primary energy consumption in the reference case (first column), PE if intervention on the envelope and HVAC system are implemented (second column) and the total PE consumption when also PV and STC are implemented (third column). PE is divided by energy use: space heating, space cooling, DHW demand and ventilation. On the right axis, it is possible to read the PV self-consumption and STC contribution. Despite the variety of building typologies and renovation solutions and the climates, we can note as the upgrading of envelope thermal characteristics to the current requirements and the use of more efficient HVAC systems can reduce primary energy consumption in a range of 60%-65% with respect to the case pre renovation. Only one exception is HRMF building typology that is characterized by a large number of apartments with only one external surface and located in an intermediate floor. As a consequence, an intervention on the envelope is effective in reducing heating demand, but not for cooling demand. However, the covering of this load with a heat pump allows to register a reduction of PE consumption in order of 25% in the Mediterranean climate where cooling demand is higher and 50% in a northern climate. To additionally increase these savings, renewable energies can give a contribution depending on the installation surface availability and control logics adopted for managing energy production.

In the Mediterranean climate the PV self-consumption on yearly basis amounts to 33% in the LRMF+RS1 scenario, 15% in both HRMF+RS2 and SMFH+RS3 scenarios and 38% in LMFH+RS3 scenario. In the Continental climate the PV self-consumption is 27% in LRMF+RS1 scenario, 12% in HRMF+RS2, 11% in SMFH+RS3 scenario, and 28% in LMFH+RS3 scenario. The increase of PV self-consumption in the warmer climates is due to the more frequent match between the consumption and the PV production, which, in turn, is mainly due to the larger consumption for cooling.

Solar thermal collectors contribute for 28% and 11% of the building total heating production (in the Mediterranean and the Continental climates, respectively) in the SMFH+RS3 scenario and for 5% and 2% in the LMFH+RS3 scenario. The very low ST contribution in the SMFH+RS3 scenario is due to the small south oriented surface where STC is installed corresponding to the surface for 1/5 of the dwellings, whereas the contribution is calculated with respect to the whole building.

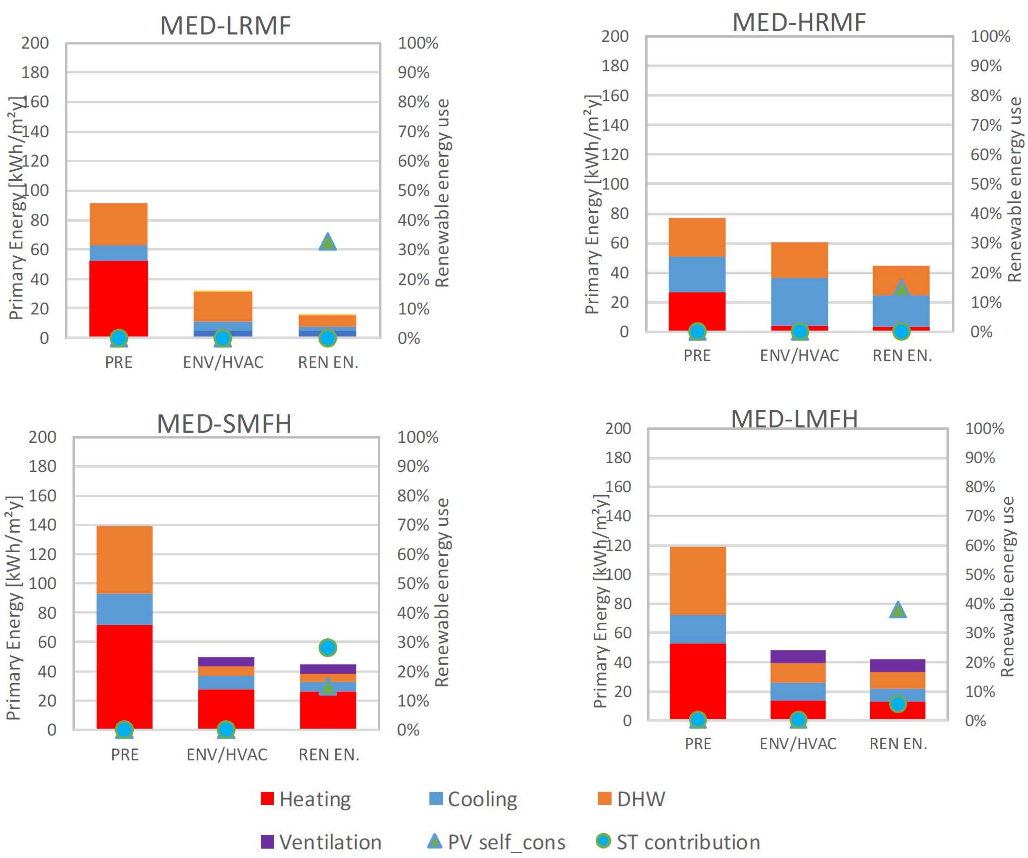

Fig. 2: Primary energy decrease for each intervention and by energy use, PV self-consumption and STC contribution in the Mediterranean climate

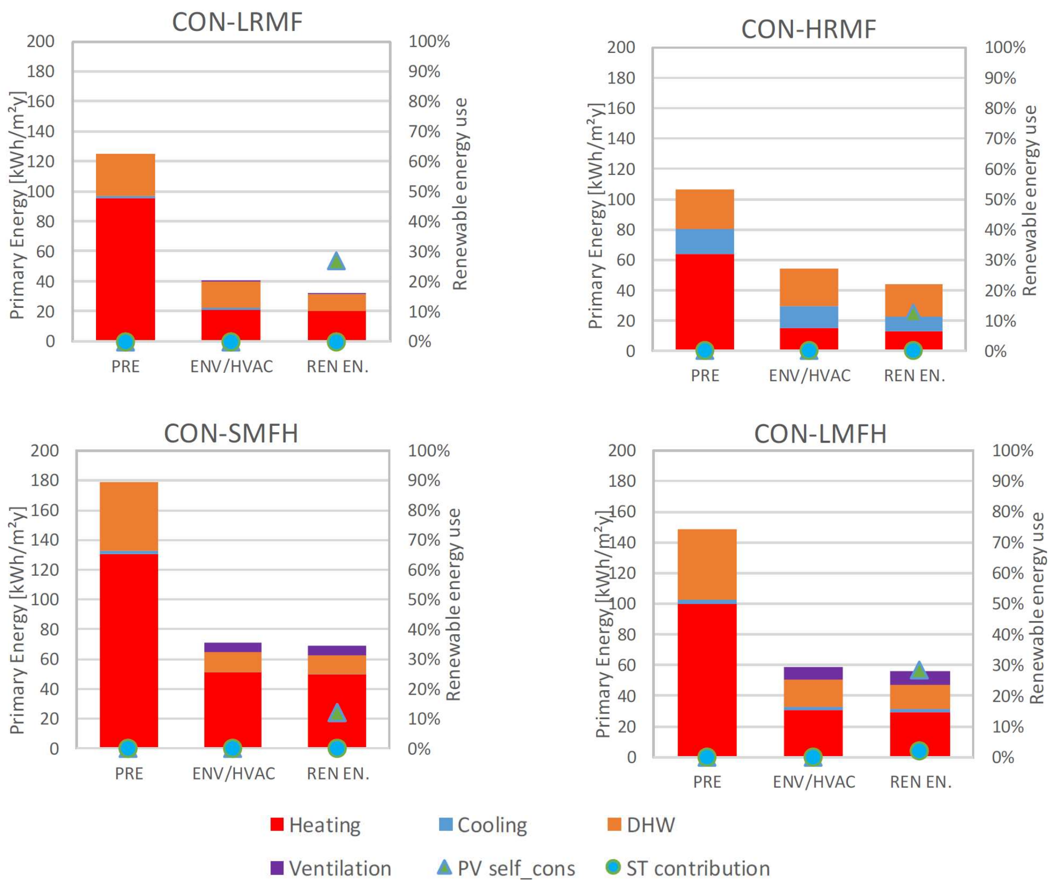

Fig. 3: Primary energy decrease for each intervention and by energy use, PV self-consumption and STC contribution in the Continental climate

Comparing all the results for the four analysed climates, Figure 4 shows PE consumption of the reference case pre-RS in very light green, the PE consumption with intervention on the envelope (light green) and replacement of the HVAC system (green) and with the use of renewable energy too (dark green). Depending on the amount of installed PV or STC, the adopted control strategy, the building typology, HVAC system adopted and climates, PE consumption for post-RS ranges between 18 up to 62 kWh/m²·y with the main cases below 50 kWh/m²·y. Due to the building shape, SMFHs result in higher heating demands and therefore higher PE consumption.

The energy efficiency of the system has been evaluated by considering the Seasonal Performance Factor for each use (space heating, cooling; DHW) and for the whole system. This indicator takes into account all the system losses and auxiliary consumption and it is calculated as the ratio between thermal energy provided to the user for covering its load and electricity consumed for that purpose. The seasonal performance factors (SPF) of the HVAC systems adopted in the renovations range between 2.7 and 7 depending on the climate and RS. Looking at the total SPF of Figure 5, the highest values are found in RS1 because of the use of a decentralized heat pump, together with heat recovery, air recirculation and PV system. Centralized systems (RS3) have a total SPF in a range of 2.7-2.8 in the coldest climates and 3.1-3.4 in the warmest ones as thermal losses have a higher weight on the total SPF. The decentralized system with ground source heat pumps shows SPFs for the whole system around 3-3.5 throughout the climates as temperature at source side is more favourable than external temperatures and slightly differ from one climate to the other. With regard to the single uses (heating, cooling and DHW), the lowest system performance occurs for DHW production in RS2, as the load side working temperature of the machines implies lower COPs. Improvement of SPF for DHW can be achieved by integrating DHW production with a solar thermal system or exploiting waste heat from cooling production (i.e. RS3) or coupling an electrical resistance that exploits excess PV production (i.e. RS1). The zero value for SPF refers to a case where there is no cooling demand.

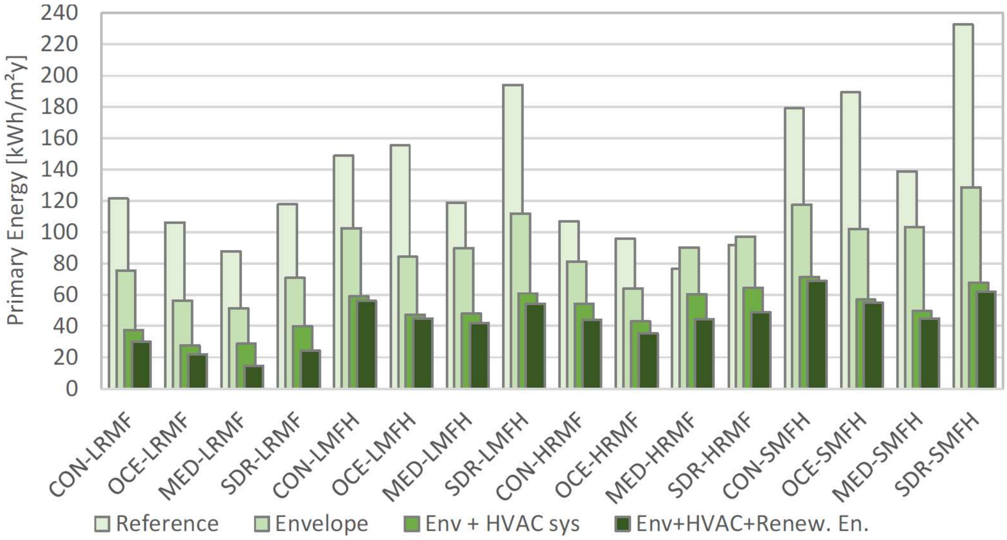

Fig. 4: Primary energy consumption of the pre-RS (Reference) and after the envelope renovation (Envelope), the replacement of the HVAC system (Env. + HVAC sys.) and the use of renewable sources (Env. + HVAC sys. + Renew. En.).

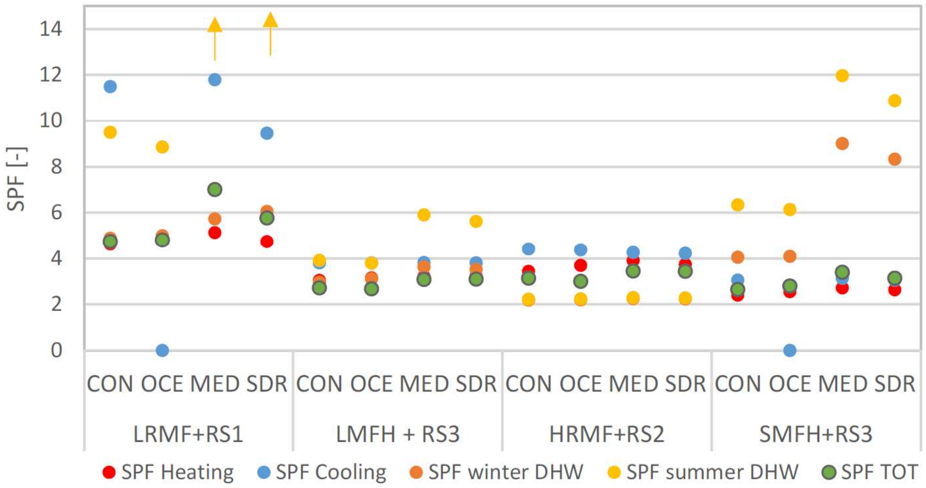

Fig. 5: Seasonal Performance Factors (SPF) for each energy use and for each of the analyzed case

The impact of solar energy on the total energy consumption is very different among the analyzed cases, due to the variety of building loads, solar field typology (PV/ST), sizing, and orientation. Focusing on the PV systems, which are present in all the considered scenarios, Figure 6 shows the total production for each case divided into self-consumed energy (red), and energy fed into the grid (yellow). The energy required from the grid (grey), is also shown. The electric energy is divided by the heated floor area to allow the comparison between different cases.

Looking at the red/yellow columns, self-consumed energy with respect to the total PV production is around 25-35% in LRMF case, between 30-40% in LMFH, between 35-50% in HRMF and between 10-20% in SMFH.

The highest values of PV share (electric energy from PV over the total consumed electric energy) are observed for the LRMF thanks to the improved control strategy that exploits PV surplus production for DHW uses. This emphasizes the importance of such algorithms for enhancing the use of solar energy. In the other cases, PV share ranges between 3% for the northern climates with centralized system and 27% in the southern climates with decentralized systems. This is in line with results in Bee et al., 2019, where, even with a larger PV area with respect to the floor area, the highest PV share obtained among different European climates without specific control strategy and without electric storage is 40%.

By comparing the LMFH and the SMFH, which are renovated with the same retrofit solution (RS3), a small difference in the PV share can be noticed being higher in LMFHs despite the lower PV installed area over heated area. This can be explained by the lower load distribution over the PV production hours that occurs in a small MFH with respect to a large one, which reduces the match of the total load and PV production. Consequently, the SMFH result the building typology with the highest amount of energy from the grid per m^2 of floor area.

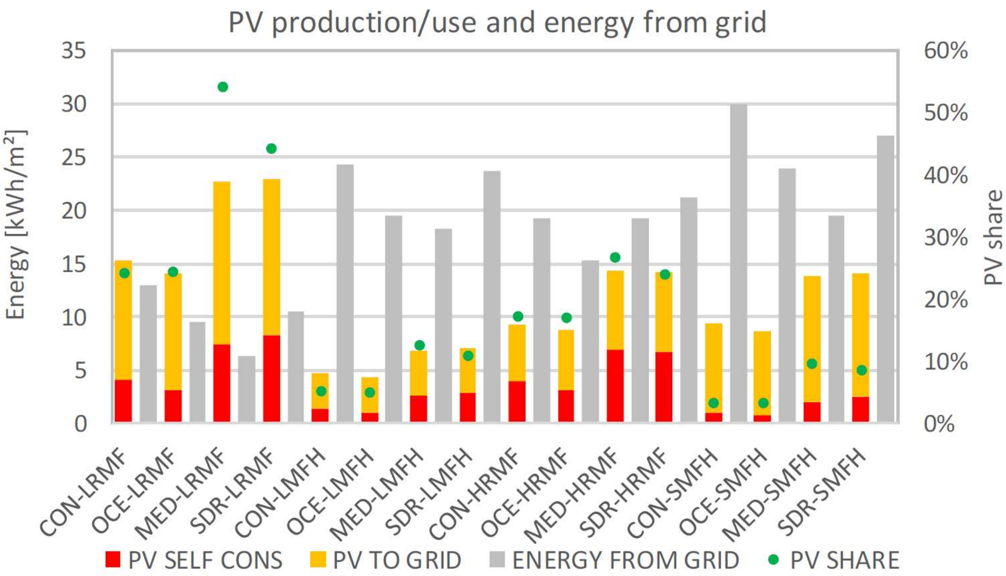

Fig. 6: Comparison of PV share, self-consumed energy, energy fed into the grid and energy taken from the grid, for each of the analyzed case

The annual operating costs of each pre-RS and post-RS are calculated based on the cost of energy (natural gas and electricity) in the four considered countries. Depending on the analyzed case, a specific cost of electricity or gas has been assumed, according to the values given by Eurostat (2019). Table 6 summarizes the adopted values.

In the post-RSs, there is a surplus of electric energy which is not directly used (yellow bar in Figure 6) but is fed into the grid. Each country applies (or could not) a different policy for selling energy fed into the grid with different prices. In this regard, the European scenario is quite complex and not uniform (Banja et al., 2017; Fruhmann and Tuerk, 2014). For this reason, we have analysed three scenarios that consider a different compensation of the surplus energy. First scenario assumes that surplus energy is bought at same cost as energy from the grid; in the second scenario, surplus energy is paid half of the energy from grid while in the third scenario surplus energy is bought at zero cost, so considering as it came from PV production.

In the following, total operating costs (C_{tot}) in the post-RS are calculated in these three different conditions, which involve different economical compensations, on an annual basis, for the surplus energy fed into the grid ($E_{to\ grid}$):

a. Scenario 1: no support scheme is applied: $C_{tot} = E_{fromgrid} \cdot P_p$

b. Scenario 2: compensation at 50% of the purchase price (P_p): $C_{tot} = E_{from\ grid} \cdot P_p - E_{to\ grid} \cdot 0.5\ P_p$

c. Scenario 3: compensation at 100% of the purchase price (P_p): $C_{tot} = E_{from\ grid} \cdot P_p - E_{to\ grid} \cdot P_p$

Where $E_{fromgrid}$ is quantity of electricity taken from grid; the P_p is the purchase price that is the unitary price of energy in the reference countries (Table 6); E_{togrid} is surplus energy fed into the grid and re-used by the building.

Table 6: Unitary prices of energy in the reference countries

		Germany	United Kingdom	Italy	Spain
Electricity	€/kWh	0.3088	0.2122	0.2301	0.2403
Gas	€/kWh	0.0632	0.0493	0.0769	0.0736

The results are shown in Figure 7 in terms of operating cost per m^2 of building floor area. The grey column represents operating costs of the pre-RS, the green column refers to the operating costs post-RS without any compensation policy (condition a), in the blue column the operating costs are calculated with the simplified net-metering scheme with conditions b and the orange with conditions c. Looking at all the analysed cases and considering the first scenario (green column), annual cost reduction from pre-RS to post-RS ranges from 22% to 78% thanks to the improvement of the building envelope, of the HVAC system efficiency and of the renewable energy use. By applying a scenario b, the further saving ranges from 7% in the Continental climate with the LMFH to the 100% in the Mediterranean climate with the LRMF building (complete compensation of the purchased electricity) as this solution already foresaw very low electric consumption. By applying scenario c, additional costs savings can be achieved, from 15-20% in the LMFH up to 40% in HRMF and 60% in SMFH in the Mediterranean climate. Under condition c, annual costs for heating and cooling uses in multi-family houses lies below 5 €/kWh for almost all the cases, with exception of two cases in the Continental climate where building loads are higher and PV production lower and unitary cost of energy is quite high.

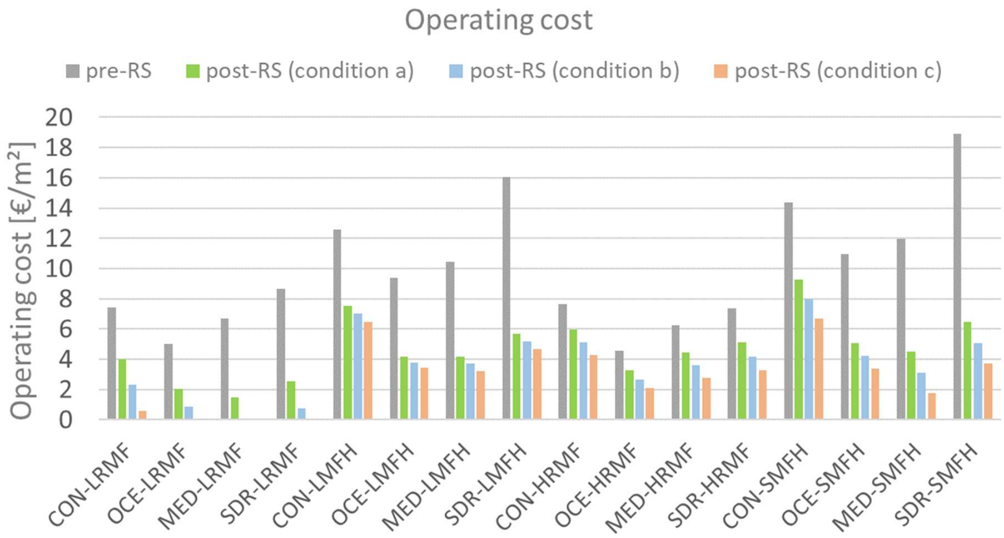

Fig. 7: Operating costs in the pre-RS and in the post-RS with different compensation schemes for the electricity.

4. Conclusions

In this study, a set of renovation measures for multi-family houses are analysed, considering a variety of building typologies, retrofit solutions, and climates. The results from the dynamic simulations prove that the adopted interventions can lead to a significant primary energy reduction in all the climates, while improving the comfort condition for the occupants. The impact of the solar energy technologies on the primary energy reduction is small if compared to the contribution of the envelope renovation and the HVAC replacement, but contributes on the PE consumption of the different uses in the order of 5% for DHW up to 20-30% for space cooling and 40% where PV use is optimized with specific control strategies. As a consequence, renewable energy contribution becomes key especially in those cases where cooling demand is not negligible.

Better exploitation of renewable energy use can be achieved by implementing control strategies that maximize the match between energy production and energy consumption and reduce the surplus of energy fed into the grid. This aspect is also highlighted by an analysis on the operative costs that shows as a support scheme based on the net-metering can lead to the complete compensation of the cost for the electricity purchase where total electricity consumption is close to the overall PV production or to additional savings on the operative costs of an average of 30-40% depending on the electricity use and PV production. Despite the economic analysis conducted does not focus on the renovation investment cost and payback time, a significant reduction of the annual operating cost in all the scenarios shows the profitability of the intervention.

5. Acknowledgments

The research leading to these results has received funding from the European Union's Horizon 2020 research and innovation programme under the project BuildHeat Standardised approaches and products for the systemic retrofit of residential BUILDings, focusing on HEATing and cooling consumption attenuations, Grant Agreement No. 680658.

6. References

Appendice A Allegato I DM 26/6/2015, 2015. Descrizione dell'edificio di riferimento e parametri di verifica. https://www.anit.it/wp-content/uploads/2018/03/miniGuidaANIT_gennaio2018.pdf

Banja M., Jégard M., Monforti-Ferrario F., Dallemand J.-F., Taylor N., Motola V., Sikkema R., 2017. Renewables in the EU: the support framework towards a single energy market. https://e3p.jrc.ec.europa.eu/sites/default/files/documents/publications/kjna29100enn.pdf

Bee, E., Prada, A., Baggio, P., Psimopoulos E., 2019. Air-source heat pump and photovoltaic systems for residential heating and cooling: Potential of self-consumption in different European climates. Build. Simul. 12, 453–463. https://doi.org/10.1007/s12273-018-0501-5

Birchall S., Gustafsson M., Wallis I., Dipasquale C., Bellini A., Fedrizzi R., 2016. Survey and simulation of energy use in the European building stock. Proceedings of the 12th REHVA World Congress CLIMA

BuildHeat project, 2020. EC H2020 Grant Agreement No. 680658. D4.5 Retrofit protocols. https://zenodo.org/record/3734970#.X0S7x-gzY2w

Codigo técnico de la edificación. Guía de aplicación DB HE, 2019. Gobierno de España, https://www.codigotecnico.org/pdf/GuiasyOtros/Guia_aplicacion_DBHE2019.pdf

Custom Degree Day Data, website http://www.degreedays.net

Dipasquale C., Fedrizzi R., Bellini A., Gustafsson M., Ochs F., Bales C., 2019. Database of energy, environmental and economic indicators of renovation packages for European residential buildings. Energy and Building, Vol. 203. https://doi.org/10.1016/j.enbuild.2019.1094

Energieeinsparverordnung - EnEV 2014 / EnEV ab 2016 https://www.enev-online.com/enev_2014_volltext/index.htm

Eurostat, 2019. Electricity prices (including taxes) for household consumers, first half 2019. Eurostat statistics Explained, https://ec.europa.eu/eurostat/statistics-explained/index.php/Electricity_price_statistics

Eurostat, 2019. Natural gas prices (including taxes) for household consumers, first half 2019. Eurostat statistics Explained, https://ec.europa.eu/eurostat/statistics-explained/index.php/Natural_gas_price_statistics

Fruhmann C., Tuerk A., 2014. Renewable Energy Support Policies in Europe. Climate Policy Info Hub, 3 November 2014. http://climatepolicyinfohub.eu/renewable-energy-support-policies-europe

The Future Homes Standard, 2019. Consultation on changes to Part L (conservation of fuel and power) and Part F (ventilation) of the Building Regulations for new buildings. Ministry of Housing Communities and Local Government. https://assets.publishing.service.gov.uk/government/uploads/system/uploads/attachment_data/file/852605/Future_Homes_Standard_2019_Consultation.pdf

Facade Integrated PV applications uptake in Non-domestic Buildings: A Sensitivity Analysis of Multi-criteria Performance Analysis

Nilmini Weerasinghe[1] and Rebecca Jing Yang[1]

RMIT University, 124 Latrobe Street, Melbourne, VIC, 3000 Australia

Abstract

Integration of PV modules into the building envelope is obviously the paradigm shift in the building industry. PV modules with a greater degree of architectural appealing and facade requirements are slowly acknowledged. With the growing concerns of this technology, many more developments are introduced to eliminate the current obstacles. Besides, the system performances continuously shift due to various uncertainties in the industry, causing diverse decision choices. Therefore, this paper aims to investigate the potential uncertainties that alter the performances of the systems. Environmental aspect, architectural suitability and economic benefits are observed the most concerning performances of systems and are quantified using LCOE, NPV/kW and DPP, material offset and CO_2 emission savings. The sensitivity analysis is conducted on four uncertainties recognized in industry such as capital cost, electricity conversion efficiency, conventional facade material cost and financial incentives. Assessment is conducted for the thirty-six facade integrated PV systems in Australia, North America and Europe with the limited to non-domestic buildings. It is noticeable that decisions should not be compromised by looking only at single decision criteria. The results revealed that the influence of capital cost, financial incentives and conventional building material values are substantial that electricity conversion efficiency. The projects reveal favourable economic performances even with the absence of financial supports by taking consideration of both direct and indirect benefits. It is promising to replace conventional building materials with the PV modules. Learning from the current experiences would be the ideal solution to guide future directions on research, investment decisions and policy makings

Keywords: façade integrated systems, multi-criteria performance, sensitivity analysis, decision making

1. Introduction

Photovoltaic (PV) technologies are being recognised as the most promising application to generate green electricity. Unlike other PV applications, Building Integrated PV (BIPV) can be applied to various parts of the building structure such as walls, roofs, shades, windows and balustrades depending on the electricity generation capacity (Attoye et al., 2017). It is a decentralised energy technology that produces not only green energy but also performs as a building material (Osseweijer et al., 2018). PV modules being endorsing aesthetic appealing of buildings, growing attention is cultivated on facade integrated systems in the building sector. This further boosted with the development of high-rise buildings that are taller than wider, particularly in urban dense. A substantial untapped area is opened to harvest solar energy generating a significant share of the building energy demand by integrating PV into the envelope (Shirazi et al., 2019). However, there is a vast refusal to facade integrated system due to the number of reasons such as lack of awareness, poor performances, underestimating benefits, resistance to change, insufficient standards and technical complexities (Curtius, 2018;Attoye et al., 2017;Osseweijer et al., 2018). Architects, builders and building owners still worried about the performance of systems and its appropriateness as a conventional facade material technology developing massive barrier for the deployment (Attoye et al., 2017;Curtius, 2018). However, a limited number of facade integrated PV systems of architecturally pleasing and high-performance executes globally. Disseminating the performances of such system helps on rapid deployment.

The previous studies discussed a variety of performances of systems using real case information or simulations on a different scale. Environmental aspect, architectural suitability and economic benefits are observed the most involved performances for the choice of the system (Attoye et al., 2017;Curtius, 2018;IEA-PVPS, 2018). It is noticed that these performances continuously shift due to the uncertainties in the external and internal environment. The industry reforms by introducing innovative technologies cater to architectural fit, high energy efficiency and methods such as prefabricated systems (Attoye et al., 2017;IEA-PVPS, 2018). The policies are implemented cross value chain in domestic markets (Zhang et al., 2018). Accordingly, the steady growth of new technologies is forecasted almost achieving the best performance of such systems (Erika et al., 2018). Therefore,

doi:10.18086/eurosun.2020.01.09 Available at http://proceedings.ises.org

it is imperative to inform the effect of uncertainties on multiple performances. Therefore. this study aims to educate the influence of uncertainties on various performances of the system with the use of existing facade integrated systems across countries. Learning from the recent experiences would be the ideal solution to guide future directions on research, investment decisions and policy makings. The findings help on elevating the confidence level on system updates as the assessment is purely based on the real case information. A few studies used such a considerable number of real data in different regions to understand future investment directions and deployment strategies. The scope of this paper is limited to assess the performance of systems commissioned between year 2009 – 2018 in non-nondomestic buildings in western countries. Thereby, thirty-six projects in Australia, Europe and North America are assessed in terms of three performance aspects namely economic, environmental and structural value using five parameters net present value (NPV/kW), discounted payback period (DPP), levelized cost of energy (LCOE), material offset (MF) and CO_2 emission saving. A sensitivity analysis is conducted on most common uncertainty factors of capital cost, electricity conversion efficiency, material cost and financial incentives by creating a range of scenarios to understand their impacts on system performances. The research outcome is a practical reference for multiple stakeholder cross value chain to establish on their proposals on facades integrated PV systems.

2. Multi-criteria Performances

Integration of PV modules into the building facades provide multiple benefits despite the clean energy generation. PV facades are conventionally made up as walls, glazing, claddings and other external structures such as lovers and balconies (Attoye et al., 2017). Multiple performances are obviously the key decision criteria for such system uptake. The previous studies conducted numerous assessment using various parameters to inform the performance of facade system and enhance the confidence in the acceptance of such technology. Attoye et al. (2017) classified performances as economic, environmental and design-related benefits. Economic benefits are capital cost associated savings and environmental benefits are greenhouse gas emission savings. Some the design-related benefits are daylights, aesthetic quality and sun protection (Attoye et al., 2017). The performance of thermal control, aesthetic and daylighting functions are attracted by the practitioners (Attoye et al., 2017;Zhang et al., 2018). It is noted that various parameters are used to quantify these performances. The most studies employed NPV, LCOE, DPP, internal rate of return (IRR) and capital cost to assess the economic performances (Sorgato et al., 2018;Gholami et al., 2019;Arnaout et al., 2019). Environmental benefits are assessed in terms of lifetime energy pack periods or CO_2 emission savings (Zhang et al., 2018). The cost of conventional building materials with the BIPV module are compared to identify the net benefits of the structural suitability of new technology (IEA-PVPS, 2018;Bonomo et al., 2017). With the consent of multiple parameters, this study employed five parameters that investigate the performance of economic, energy, environmental, and structural value of the facade integrated PV applications. They are LCOE, NPV and DPP as economic aspects, material offset as structural value and CO_2 emission savings as environmental aspects. The below describes these metrics.

LCOE: Levelized cost of energy represents a cost of energy generation throughout the lifespan (Shirazi et al., 2019;Wang et al., 2011). The mathematical LCOE model symbolises the ratio of total lifecycle cost over total lifetime output energy and unit is cost/kWh. This is more explainable than cost/kW which ignores the lifetime performances (Wang et al., 2011). LCOE is generally compared with retail electricity price (Zhang et al., 2018). The studies used various cost parameters in LCOE analysis. The intension of this assessment is to elaborate on the lifetime cost aspects of facades integrated systems with the presence of both direct and indirect costs. Thereby, The lifecycle costs are included as capital cost, material replacement cost, maintenance and operation cost, salvage value, incentives and inverter replacement cost (Wang et al., 2011;Corti et al., 2020;Gholami et al., 2019;Weerasinghe and Yang, 2020). The capital cost represents the cost of modules, balance of system (BOS), installation, and procurement that spent at the initial investment (Wang et al., 2011). Material displacement is a benefit acquired due to the replacement of PV with conventional building materials. This benefit is added to reflects the performance of PV modules as a building material. The idea is embedded in the calculations by various researchers believing different aspects such as 1) Gholami et al. (2019) deducted the equivalent material cost from the project investment cost to described the total investment cost 2) Corti et al. (2020) used incremental cost considering offset of material cost to module cost. The financial incentives that received at the initial and following years are added as a benefit in the calculation. The operation and maintenance cost is an annual cost spent on services, performance monitoring and other maintenance. Inverter replacements are performed every ten years

(Sorgato et al., 2018;Yang and Carre, 2017). The salvage value refers to the value of the systems at the end of project life (Shahsavar and Khanmohammadi, 2020). Time value of money is indicted, and real interest rate is used in the calculation. The lifetime energy performance is identified using annual electricity generation over time with the inclusion of annual energy degradation rate.

NPV: Net present value is the most popular economic parameters in investment decisions. NPV denotes the net economic value of the project that deducts lifecycle costs from lifecycle incomes (Gholami et al., 2019). Lifecycle cost identified in LCOE is used as capital cost, material displacement cost, lifecycle maintenance cost and replacement cost, salvage value and incentives. Lifecycle incomes are two types namely energy bill offset and revenue by selling electricity to the national grid (Wu et al., 2018;Yang and Carre, 2017;Bonomo et al., 2017). The energy bill offset is the value of the amount of electricity consumed from the system which is a deduction from the national supply. This is valued at the rate of retail electricity price. The national electricity price fluctuation is counted in the calculation(Yang and Carre, 2017). The excess electricity sell to the national grid is identified and monetised using Feed-in-Tariff (FIT) to obtain its economic benefits.

Discounted Payback Period (DPP): Discounted payback period refers to recovery periods of initial investment which is a significant parameter of decision making (Wu et al., 2018). The lifecycle costs are deducted from the lifecycle incomes annually to identify the period that fully pays off the cost (Sorgato et al., 2018). The same cost and income components used for the NPV is applied to DPP. The lifecycle cost parameters are capital cost, annual maintenance cost, inverter replacement cost, material displacement and lifecycle incomes are energy bill offset and excess grid supply. The short payback period is always promising in the investment.

Material Offset: Material offset is identical to the structural value of the system. Judging that value signifies the characteristics of materials such as aesthetic appearance, colour pattern, transparency and building requirements, cost of both PV modules and building materials are compared to identify the significant benefit of the replacement. The suggested formula is the deduction of the cost of equivalent conventional facade material with the total cost of the PV system. Unit is cost/m^2. The cost of installation is assumed as similar in both materials. Positive value signifies the benefits as BIPV is cheaper than facade materials.

CO_2 Emission Savings: This metric is used to explain the investors' commitment to sustainability and environmental aspects. Lifetime energy payback period and greenhouse gas emissions rate that blend both embodied and operational energy are the most common parameters identifying environmental preference. Due to the complexity of identifying projects specific embodied energy in multiple projects, the operational energy is taken into consideration. Thereby, CO_2 emission savings is calculated as a ration of electricity generation to total building demand as a percentage value.

The immense effort is being put forward to enhance the aesthetic value of modules along with satisfying building material requirements over the years. The new technologies that provide more esthetic appearances are well accepted by the users (Sánchez-Pantoja et al., 2018). Further, increasing module efficiency that leads to improving the electricity conversion efficiency facilitated to enhance the performance of systems to a great degree. However, architectural design objectives such as daylight, visual impact sometimes can be compromised with the energy performances and maximum output of the modules (Attoye et al., 2017). Decreasing cost of modules and other subsystems leads to accelerate the system uptake as the capital cost is the most contributing factor in the deployment (Curtius, 2018). The government policies addressing each stakeholder have proved rapid growth in different economics (Zhang et al., 2018). Recent years there is a technology advancement for cost reductions and improving system efficiencies. Further, colour, pattern texture and integration methods such as prefabrication, low maintenance cost are launched as a result of technology developments (Arnaout et al., 2019). Poor performances, cost, government incentives are some of the critical drivers of implementation of systems. The factors are subjected to uncertainties caused by the changes in future conditions. It seems that capital cost, electricity conversion efficiency, financial incentives and traditional material value are highly volatile in the industry. Therefore, these factors are selected to test in this paper. These are uncertainties in the market, technology development and policy aspects.

3. Real Case Information

The paper aims to understand the influence of uncertainties on the performance of facade integrated applications. Initially, a data of façade integrated PV projects are gathered from publicly available records such as websites

(Onyx Solar, 2016), databases (SUPSI/ISAAC, 2013;Eurac, 2013), articles (IEA-PVPS, 2018), books and journal articles (Maturi and Adami, 2018)). The project-specific data including, capital cost, annual energy generation, building energy demand, module area, system capacity, material displacement value, rebate, salvage value, inverter replacement cost, FIT, discount rate, electricity price are required performing the calculations. The projects that provide most of the data are selected in the analysis. Annual energy generation, system capacity, module technologies and area are confirmed data for project selection. When data are unavailable, approximate values are taken places. The capital cost is unavailable in nine projects and value is allocated considering 1) 1.2% of construction cost (IEA-PVPS, 2018) and 2) referring similar projects by location, technology and year. The total building energy demand is unfound in five projects where it is assumed 5% of self-sufficiency for pilot BIPV projects. Due to unavailability of data, the standard cost is applied for few parameters like 1) operation and maintenance cost as 1% of capital cost (Sorgato et al., 2018), 2) inverter replacements as 10% of capital cost and assume constant (Sorgato et al., 2018;Yang and Carre, 2017), 3) salvage value is 5% of the capital cost (Shahsavar and Khanmohammadi, 2020), 4) lifespan as thirty years (Wang et al., 2011) and 5) annual electricity degradation as 0.5% (James et al., 2011). The equivalent building material of façade systems is identified as a curtain wall (Aluminium frame with glass) and balustrade with tough glass for balconies. The average cost of curtain wall for Australia, North America and Europe are 897, 1056 and 1272 AUD/m^2(Weerasinghe and Yang, 2020;Rawlinsons, 2018;Spon's, 2018;RSMeans, 2018). All values are charged to the project commissioned year. Also, the project-specific information such as electricity prices, FIT and discount factors are gathered by the project commissioned year from the publicly available information such as Worldbank (2020), TradingEconomics (2020), PORDATA (2020), PVTECH (2020).

Details of the solar facade projects employed this analysis are illustrated in Figure 1, which is grouped based on various characteristics of the applications. The research consisted of thirty-six projects and thirty-three projects are facades that replaced curtain wall, rain screen, double skin facade and three projects are balconies. Only six projects received financial incentives where three projects are fully funded and the remaining projects received 45%, 30% and 48% of capital cost as a rebate. The location of the projects is groped based on Australia, North America, and Europe. Most projects are in Europe (thirty-one) while four and one projects located in North America and Australia. Systems are categorised on the type of buildings namely commercial, educational and apartment buildings. There are sixteen, seven and thirteen of them, respectively. Moreover, twenty-four projects installed at the initial stage and remaining twelve projects are attached in refurbishment stage of the building. Pie chart showed the commissioned year of the projects as the projects implemented from 2009 to 2020 is selected for the assessments. The capacity of the projects ranges between 5 to 700 kW. The modules of facade applications are made of different technology and transparency levels. The modules of twenty-five projects used c-Si technology while eight and three projects are made of a-Si and CIGS technology.

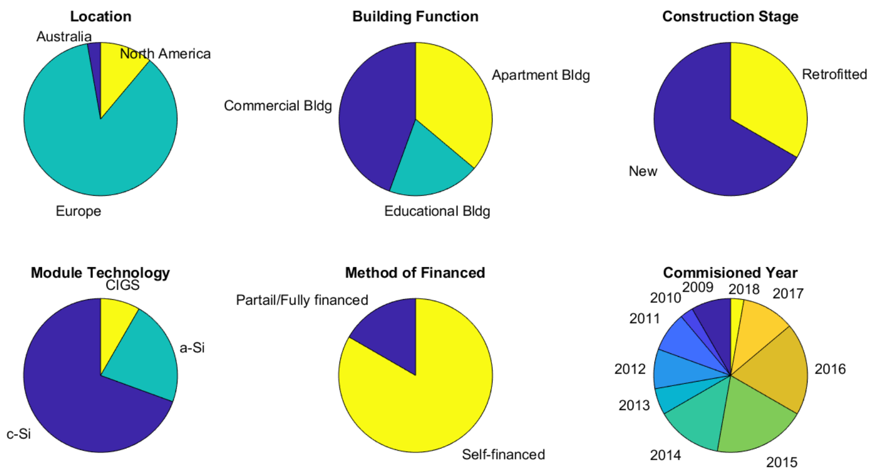

Figure 1: Details of Facade Integrated Systems

4. Sensitivity Analysis

Sensitivity analysis is typically used to assess the uncertainties of model output that are derived from a variety of inputs (Shirazi et al., 2019). This study aims to ascertain the influence of uncertainty factors on five performances. The analysis is conducted keeping thirty-six case as the base case and change selected input parameter to a wide scale that range from minimum to maximum possible values. The median value of the projects is then imported in each scenario to understand the effect of parameters on the performances. MATLAB application is employed to execute the calculations. The below section describes the uncertainty factor.

Capital cost: Capital cost is the most crucial information for investment decisions as the decisions are sometimes made on just looking at it only. The capital cost represents the total cost of the system, including hardware cost (BIPV modules, inverters, and mounting system etc.) and labour, installation and another relevant cost that incurred at the initial stage. BIPV modules stand for a major share of capital cost. However, the cost of solar facade is often debated in many studies. According to BuildUp (2019), the capital cost of opaque and semitransparent façades are approximately 850 and 550 €/m^2 in Europe. The capital cost of the cohort is ranged between 272 to 2,382 AUD/m^2 which is a wide range with an average price of 886 AUD/m^2. The authors highlighted that distribution of capital cost is in an acceptable content which is sometimes lower than someone of the conventional materials. The cost of the modules depends on diverse characteristics such as transparency, patterns, colour, shape and technology (Erika et al., 2018). Aesthetically appearances with high-performance modules are obviously expensive than standard facade applications. Further, inverter and battery display significant cost share in the capital cost and change parallel to the module cost. According to BuildUp (2019), the capital cost is expected to decreases over time. Considering the uncertainties in the capital cost, a wide range that distributes between -80% to +100% of the base value is developed to perform the sensitivity analysis.

Electricity conversion efficiency: Electricity conversion efficiency is an electricity generation capacity of the systems. Amount of electricity generation is an important decision criterion particular in the urban dense(Shirazi et al., 2019). Electricity conversion efficiency depends on the solar irradiation levels based on location and orientation combined with hardware performances (Zhang et al., 2018). The efficiency of the module technology works an essential contribution. It is noted that high transparency levels, colour and patterns may lower the system efficiency (Erika et al., 2018). Currently, three types of module technologies are recognised namely 1) crystalline technologies 2) thin film and 3) innovative technologies (Zhang et al., 2018). The power efficiencies of these technologies are between 4% to 25% (Zhang et al., 2018;Joseph et al., 2019). High energy efficiency with architectural and aesthetically suitable modules are the future of this industry. Impact of energy efficiencies on five performances is identified in this sensitivity analysis. Due to the availability of the information, the conversion efficiency is defined in annual electricity generation of systems. The base value is changed between -80% to +100% of base value devising worst case to best case scenarios. A diverse annual final yield is observed in current projects and they spread between 98 to 1,110 kWh/kW.

Conventional material prices: Investment of active solar facade is judged by comparing standard facade materials. Multiple facade materials by various colour, materials, appearance and performances can substitute the PV modules. The current façade integrated systems are compared with the average value of the curtain wall. According to SUPSI (2015), the expenses of the curtain wall are between 500 -1100 €/m^2 and the cost of high standard stone cladding are 300 - 600 €/m^2 in Europe. The depending on the material used for the comparison, a variety of benefits can be achieved. Therefore, looking at multiple disparities between a conventional material princess, a range of values are assigned to determine the effect of costs on five performances. The lowest value represents -80% of base value and the highest value is double of the base value (+100%) of selected facade materials. This enables to resolve the effect of multiple building materials on system performances.

Financial incentives: Many incentive schemes, particularly from the government, are being announced for renewable applications. The government's supports for investments observed the rapid growth of this technology (Zhang et al., 2018). Various policies are implemented targeting multiple stakeholders in the value chain to promote domestic distribution. Cash incentives for initial investments, FIT for long term benefits, loan schemes and other policies are some of them. This study considers the cash incentives given to the building owners or investors. The effect of financial aids for initial investments on five decision performances is estimated in the sensitivity analysis. A range is developed as self-financed to fully funded projects. The sensitivity analysis ignored the current rebate to develop hypothetical cases identifying the effect of the different share of capital costs as financial incentives.

5. Results and Discussion

The data distribution of real cases and the uncertainty of capital cost, electricity conversion efficiency, material offset, and financial incentives on system performances are described in this section.

5.1 Multi-criteria Performances of Systems

Figure 2 portrayed the distribution of five performance criteria of thirty-six facade integrated PV systems. As showed in Figure 2 (a), most of LCOEs are distributed between 0.15 (negative) - 0.25 AUD/kWh with the average value of 0.1 (negative) AUD/kWh. The average electricity rate (0.2347 AUD/kWh) is higher than most of LCOEs. This suggested that the cost of electricity production of PV facades is cheaper than to national production. Further, half of the projects possess negative LCOE indicating that lifecycle incomes diminish the cost. This is a positive indication of the performance of the systems. NPV/kW is observed a range in the box plot as most lie between 938 (negative) to 5319 AUD/kW with the median value of 3,515 AUD/kW. Although optimistic performances are noticed, few extreme worst and best projects are also underlined in the cohort. The distribution of DPP is

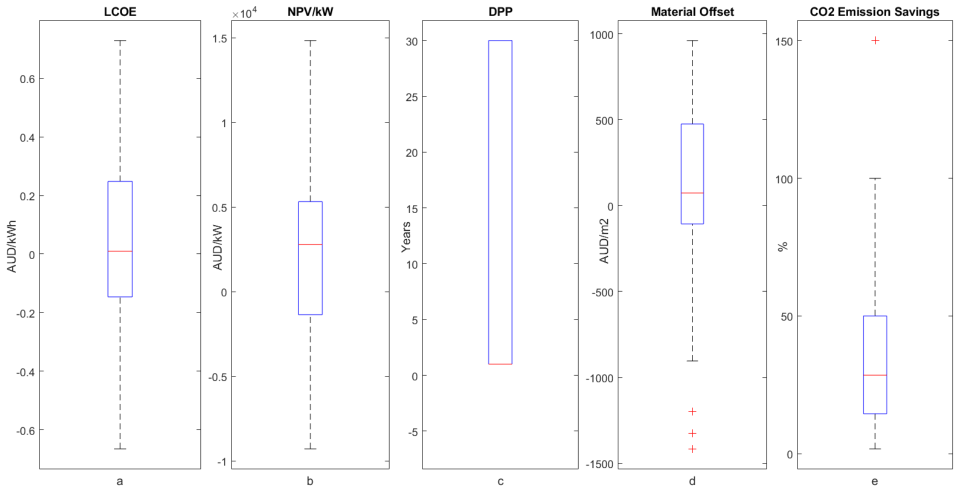

extended between one year to thirty years considering the project lifecycle. However, the majority sit in the shortest payback period. This emphasised that facade integrated systems are feasible in terms of DPP. Most of the material offset values are scattered between (104) (negative) to 475 AUD/m^2. The average material offset is a positive indicating that in most cases, the cost of the traditional facade is expensive than BIPV. The distribution of CO_2 emission is scattered between 14% to 50% with a median of 28% in the box plot. This implies that most projects consume PV electricity for less than half of the building demand. However, few projects display high self-sufficient percentage. Overall performance of five parameters showed positive indications for many of the façade systems. This can be drawn that much of the facade integrated systems are favourable in relation to energy, environment, and structural value performances under the current condition. Next, sensitivity analysis is performed employing these values as base cases to estimate the influence of driving factors on system performances. The results are discussed below.

Figure 2: Multi-criteria Performances

5.2 Levelized Cost of Energy (LCOE)

Levelized cost of energy (LCOE) signifies the cost of electricity generation over the lifespan, which is generally compared with the retail electricity prices. The electricity prices of the projects are between 0.1310 – 0.4013 AUD/kWh. LCOE is compared with median electricity price: 0.24 AUD/kWh. Electricity prices are varied upon the project commission year and the country. The average electricity prices based on region Australia, North America and Europe are as sequentially 0.258, 0.234 and 0.148 AUD/kWh. It seems that Australia shows the highest electricity prices and North America is the lowest. Figure 3 depicted the distribution of LCOEs of selected uncertainty factors. It appears that LCOEs increases with the surge of capital cost. Declining trends of LCOE is shown with the rise of financial incentives, energy conversion efficiency and conventional material cost.

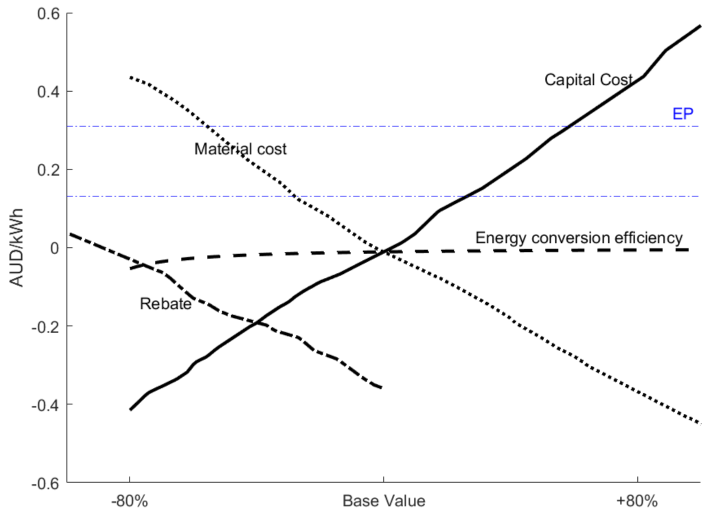

Figure 3: Distribution of Levelized Cost of Energy

LCOE distribution in capital cost is observed a significant move indicating 0.0054 AUD/kWh per 1% unit of change. The adverse LCOE is identified when the capital cost is beyond 1,309 AUD/$m^{2,}$ representing 48% increase to the base value. It implies that capital cost more than 1,309 AUD/m^2 triggered an adverse performance. Negative LCOE is identified with the fall of the capital costs. As discussed above, negative LCOE represented an income source where lifecycle cost is recovered from the benefits. The maximum capital cost to achieve negative LCOE performances is 902 AUD/m^2. Projects are more favourable after this point. Energy conversion efficiency noticed a slight growth of LCOE with increasing values. The variance of annual energy generation is within the acceptable levels as it is lower the marginal electricity prices. LCOE varied by 0.0002 AUD/kWh for 1 % of change of annual energy generation. The trend of LCOE remains less than the average electricity price during the variance of energy generation between -80% to +100% of the base value.

The diverse share of financial aids on investments displays a decreasing trend of LCOE. LCOE is 0.035 AUD/kWh without any financial supports which is lower than the electricity rate indicating favourable performances. Financial aid for complete reimbursement is the most favourable performances resulting in negative LCOE of 0.35 AUD/kWh. The slope of the results represents 0.004 AUD/kWh for a one % share of capital cost reimbursement. LCOE lies in satisfactory performance region, which is less than electricity price whatever the financial aids. This suggested that the projects are feasible with respect to LCOE in the absence of financial incentives. The increasing cost of conventional façade materials demonstrated a decreasing trend of LCOE. It is noted that 0.005 AUD/kWh of LCOE with the 1% unit of variances. It seems that favourable LCOE achieved with the substitute of conventional materials which are higher than 587 AUD/m^2. The negative LCOE is noticed after 1,066 AUD/m^2 of the cost of the traditional materials.

According to Figure 3, capital cost represented a substantial influence and electricity conversion efficiency resulted in the least effect on LCOE. The second effect is observed in traditional facade material trend, which closes to the capital cost. However, material cost represents a positive relationship while the capital cost is otherwise with LCOE.

5.3 Net Present Value/kW

NPV/kW described in terms of benefit per system capacity for the comparison due to the various capacities of projects in the cohort. Figure 4 illustrates the distribution of NPV/kW across the variance of capital cost, electricity conversion efficiency, rebate and conventional material cost. Electricity conversion efficiency, rebate and material cost is noticed a positive relationship while capital cost represents a reverse connection with NPV. The trends dispersed between a wide range of AUD/kW.

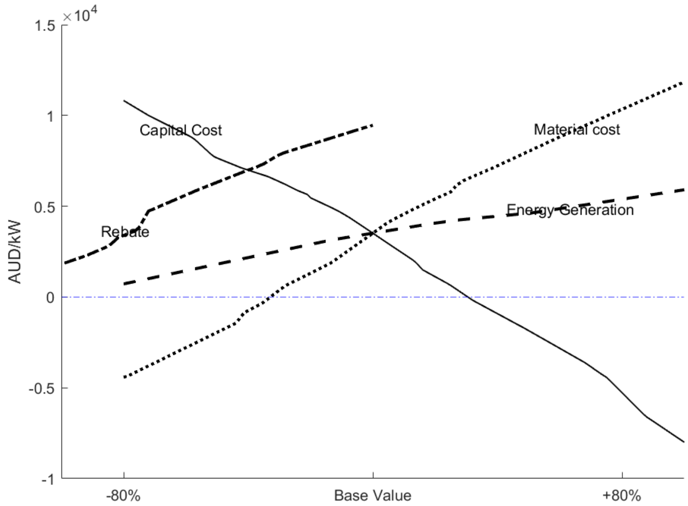

Figure 4: Distribution of Net Present Value /kW

The declining trend is observed in capital cost variation which is about 102 AUD/kW fall for 1% of the unit increase. The drop obviously increases the performances of NPV/kW. The average capital cost is 885 AUD/m^2 in the cohort. The results revealed that capital cost more than 1,150 AUD/m^2 (+30% base value) results in negative NPV/kW performances. The variance of electricity conversion efficiency displays an upward trend. According to Figure 4, the current efficiency is acceptable to attain positive NPV/kW of most of the projects while increasing values elevate the NPV/kW. It is spotted an NPV/kW of 28 AUD/kW for the unit change of electricity conversion efficiency. Further, the self-financed projects receive favourable performances which are about 1,866 AUD/kW. With the increasing share of financial aids, the projects reach substantial positive NPV/kW. Averagely, fully financed projects achieve NPV/kW of 9,667 AUD/kW. This resulted that projects promise positive NPV/kW without financial supports when both direct and indirect benefits are counted. Conventional material prices correspond to a significant effect in the NPV. It fluctuates over 93 AUD/kW for 1% change. The material prices less than 766 AUD/m^2 (-33%) indicated an unfavourable NPV/kW performance. This implies that traditional façade material replacement is encouraging if it is over 766 AUD/m^2. According to the results, the most considerable effect is observed in the capital cost, whereas the material cost, rebate and electricity conversion efficiency affect NPV/kW consequently.

5.4 Discounted Payback Period

DPP described the investment recovery period which is the most concerning factor on decisions. Figure 5 illustrated the distribution of DPP along with the four uncertainty factors. DPP is calculated to the 30 years of lifespan. Figure 5 indicated that inverse relationship of capital cost and positive relationships with electricity conversion efficiency, rebate and material values with the DPP. An increasing capital cost adversely influenced the discount factor as lower capital cost always create short DPP. Having a one-year payback period is A reward as the cost is recovered within the first. The capital cost which is beyond 1,150 AUD/m^2 is adverse as the project received lengthier payback periods. It seems that electricity conversion received minimal force on the payback period. With the lowest annual energy generation, 25 years of DPP is achieved. This is feasible as it is less than the project life. The one-year payback period remains during the change in energy generation efficiency. According to Figure 5, DPP is constant during the change of financial aids. This indicates that with or without financial aids, the projects can still achieve a short payback period. The distribution of the payback period in material offset is significant. The results revealed that a minimum of 766 AUD/m^2 material value is essential to achieve a one-year payback period. Expensive building materials offer a positive performance of DPP.

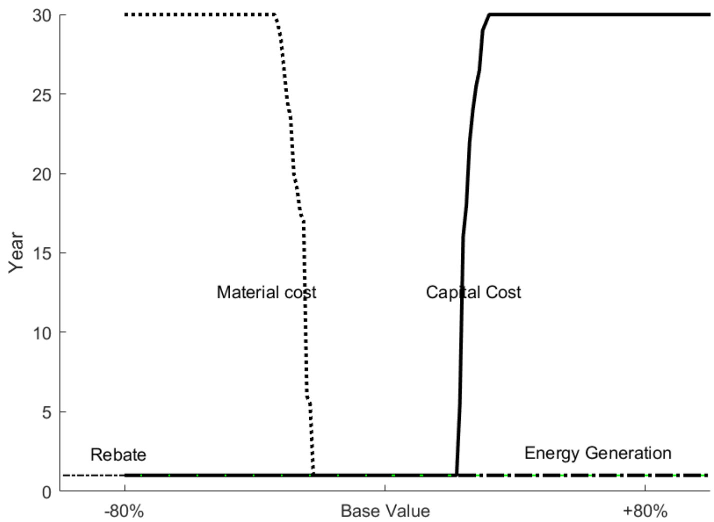

Figure 5: Distribution of Discounted Payback Period

5.5 Material Offset

Material offset value described a comparison of facade materials with BIPV modules. The positive value is a profit to the investor as the cost of systems is less than the equivalent building material. Figure 6 depicted the result of capital cost, rebate, electricity conversion efficiency and material cost on material offset values. Material offset distribute between 700 (negative) to 1,200 AUD/m^2 for building material variance of -80% to +100% of base value. The capital cost and material cost observed a considerable variance, while rebate and electricity conversion is negligible. Rebate and electricity conversion efficiencies are unrelated to the structural aspects of the building materials.

Further, increasing capital cost represents adverse performances while conventional material cost factor is otherwise. The capital cost is observed 8.7 AUD/m^2 variance of the material offset. The fall of material offset with the rising capital cost is noticed in Figure 6. The material offset value is unfavourable after the capital cost of

1,035 AUD/m^2 (+17%). This indicates that too expensive systems are a detriment to use.

The distribution of material cost over the conventional facade materials noted an upward trend. It is revealed that

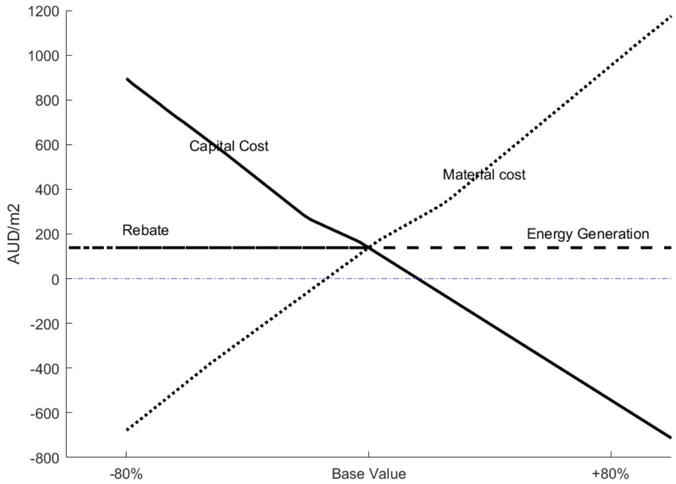

Figure 6: Distribution of Material Offset

increasing values of traditional material of facade increase more positive material offset performances. For examples, the replacement of expensive building material cost with BIPV modules is always beneficial. The material offset of 11 AUD/m^2 is received with 1% change of conventional materials. As indicated in Figure 6, the cost of conventional building materials which are less than 944 AUD/m^2 is adverse. The highest effect is recognised in the facade cost instead of capital cost.

5.6 CO_2 Emission Savings

CO_2 emission saving is an indication of sustainability criteria on decision making. The parameter represents the ratio of total electricity generation to building energy demand. The high value defined self-consumption building as consuming more electricity from the BIPV systems while feeding excess to the national grid. Figure 7 represents the variance of driving factors on CO_2 emission savings. As indicated, only electricity conversion efficiency influences CO_2 emission savings while others are irrelevant. The distribution of CO_2 emission savings is 15% to 56%, with an average of 30%. It is observed an upward trend of CO_2 emission savings for the variance of electricity efficiency. Increasing efficiency improves the amount of electricity generation, which is eventually expanding CO_2 emission savings. This offset the conventional electricity requirements implying environmental benefit aspects. It is identified 0.28% variance of CO_2 emission savings with the electricity conversion efficiency.

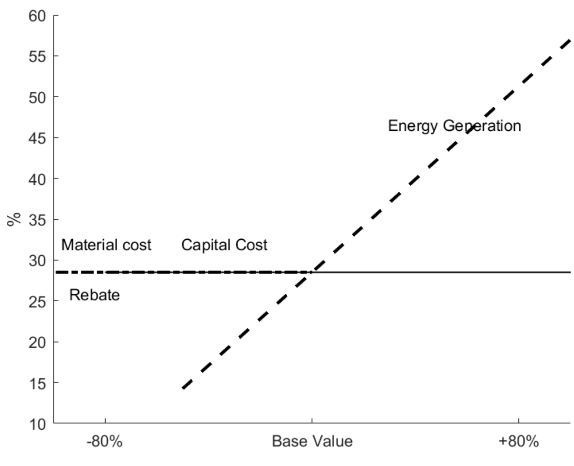

Figure 7: Distribution of CO_2 Emission Savings

6. Conclusions

Facade integrated PV systems promise the great degree of aesthetically appealing designs in the buildings to generate a significant share of building energy demand. It is an opportunity to construct renewable energy with no land use and less infrastructure using the untapped area of building facades. Yet, the architects, building owners and other building professionals doubt on the performance of such systems creating publicly unacceptable technology. Many developments are being emerged in the industry during the recent past escalating performance of systems. Due to the volatility in this market, uncertainties could govern diverse decision choices for practitioners. The study attempts to inform the influences of uncertainties on system performance that lead to the decision of system uptake. The sensitivity analysis is conducted contemplating possible circumstance execute in the industry. The results revealed that the performances of façade integrated PV systems are diverse. The effectiveness of BIPV performances are based on the balance of multiple criteria. It is noticeable that decisions should not be compromised by looking only at single decision criteria. The interesting results of sensitivity analysis are the influence of capital cost, financial incentives and building material values are substantial compared to electricity conversion efficiency. The capital cost more than 1,300 AUD/m^2, 1150 AUD/$m^{2,}$ 1035 AUD/m^2 showed adverse LCOE, NPV/kW and DPP and material offset performances respectively. Increasing the energy efficiency of modules improve the performance of all kind except building materials. The projects reveal favourable economic performances even with the absence of financial supports due to the taking to consideration of both direct and indirect benefits are counted. It is favourable to replace conventional building materials with the PV modules. This study is limited to investigate only four uncertainties, although multiple drivers could affect the performance of the systems. Further, only five performances are developed due to the availability of information on existing projects. Therefore, the outcome of this study lies within a limited scope.

With the increasing development of buildings in the urban dense and attention of sustainability technologies, façade integrated systems will have a massive demand among the building sector. Hence, technology developments are unstoppable in this industry, providing high-performance applications. It is forecasted many more uncertainties in this industry. This study offers a practical reference to expand the BIPV uptake in different economies by looking at the significant effect of the key uncertainties on decision criteria or multiple performances of systems.

7. References

Arnaout, M. A., Go, Y. I. & Saqaff, A. 2019. Pilot study on building-integrated PV: Technical assessment and economic analysis. *International Journal of Energy Research,* n/a.

Attoye, D. E., Aoul, K. a. T. & Hassan, A. 2017. A Review on Building Integrated Photovoltaic Façade Customization Potentials. *Sustainability,* 9**,** 1-24.

Bonomo, P., Frontini, F., De Berardinis, P. & Donsante, I. 2017. BIPV: building envelope solutions in a multi-criteria approach. A method for assessing life-cycle costs in the early design phase. *Advances in Building Energy Research,* 11**,** 104-129.

Buildup. 2019. *Overview: Building integrated photovoltaics (BIPV) as a viable option among renewables* [Online]. Available: https://www.buildup.eu/en/news/overview-building-integrated-photovoltaics-bipv-viable-option-among-renewables.

Corti, P., Capannolo, L., Bonomo, P., De Berardinis, P. & Frontini, F. 2020. Comparative Analysis of BIPV Solutions to Define Energy and Cost-Effectiveness in a Case Study. *Energies,* 13**,** 3827.

Curtius, H. C. 2018. The adoption of building-integrated photovoltaics: barriers and facilitators. *Renewable Energy,* 126**,** 783-790.

Erika, S., Pierluigi, B. & Francesco, F. 2018. *Active BIPV Glass Facades: Current Trends of Innovation* [Online]. Glass on Web. Available: https://www.glassonweb.com/article/active-bipv-glass-facades-current-trends-innovation.

Eurac Research. 2013. *BIPV projects*. Institute For Renewable Energy, Available: https://bipv.eurac.edu/en.

Gholami, H., Rostvik, H. N. & Müller-Eie, D. 2019. Holistic economic analysis of building integrated photovoltaics (BIPV) system: Case studies evaluation. *Energy and Buildings,* 203**,** 109461.

IEA-PVPS 2018. Transition towards Sound BIPV Business Models. International Energy Agency

Joseph, B., Pogrebnaya, T. & Kichonge, B. 2019. Semitransparent Building-Integrated Photovoltaic: Review on Energy Performance, Challenges, and Future Potential. *International Journal of Photoenergy,* 2019**,** 5214150.

Maturi, L. & Adami, J. 2018. Case Studies. *Building Integrated Photovoltaic (BIPV) in Trentino Alto Adige.* Cham: Springer International Publishing.

Osseweijer, F. J. W., Van Den Hurk, L. B. P., Teunissen, E. J. H. M. & Van Sark, W. G. J. H. M. 2018. A comparative review of building integrated photovoltaics ecosystems in selected European countries. *Renewable and Sustainable Energy Reviews,* 90**,** 1027-1040.

PORDATA. 2020. *Electricity prices for domestic and industrial users (PPS)* [Online]. Available: https://www.pordata.pt/DB/Europa/Ambiente+de+Consulta/Tabela [Accessed].

PVTECH. 2020. *Tariffs* [Online]. Available: https://www.pv-tech.org/tariffs/list.

Rawlinsons, Q. S. 2018. *Rawlinsons Australian Construction Handbook 2020,* Perth, AUSTRALIA, Rawlinsons Publishing.

Rsmeans 2018. *Commercial Renovation Cost Data,* America, Construction Publishers and Consultants.

Sánchez-Pantoja, N., Vidal, R. & Pastor, M. C. 2018. Aesthetic perception of photovoltaic integration within new proposals for ecological architecture. *Sustainable Cities and Society,* 39**,** 203-214.

Shahsavar, A. & Khanmohammadi, S. 2020. Energy and economic evaluation and multicriteria optimization of different arrangements of integrated photovoltaic thermal and heat recovery wheel system. *International Journal of Energy Research,* 44**,** 1488-1505.

Shirazi, A. M., Zomorodian, Z. S. & Tahsildoost, M. 2019. Techno-economic BIPV evaluation method in urban areas. *Renewable Energy,* 143**,** 1235-1246.

Sorgato, M. J., Schneider, K. & Rüther, R. 2018. Technical and economic evaluation of thin-film CdTe building-integrated photovoltaics (BIPV) replacing façade and rooftop materials in office buildings in a warm and sunny climate. *Renewable Energy,* 118**,** 84-98.

Spon's Architects 2018. *Spon's Architects' and Builders' Price*, Taylor & Francis. https://books.google.com.au/books?id=h_GsBAAAQBAJ>

SUPSI 2015. Building Integrated Photovoltaics. Swiss BIPV Competence Centre, Switzerland.

Supsi/Isaac 2013. BIPV Examples. Available: http://www.bipv.ch/

James. T, Alan, G., Michae, W., Robert, M. & Sean, O. 2011. Building-Integrated Photovoltaics (BIPV) in the Residential Sector: An Analysis of Installed Rooftop System Prices. USA: National Renewable Energy Laboratory

Tradingeconomics. 2020. *Real interest rate* [Online]. Available: https://tradingeconomics.com [Accessed].

Wang, Z., Ai, Q., Xie, D. & Jiang, C. A Research on Shading and LCOE of Building Integrated Photovoltaic. 2011 Asia-Pacific Power and Energy Engineering Conference, 25-28 March. 1-4.

Weerasinghe, N. & Yang, R. J. 2020. Modelling economic viability of facade-integrated photovoltaic applications in non-domestic buildings *Asia Pacific Solar Research Conference.* Canberra,.

Worldbank. 2020. *Real interest rate* [Online]. Available: https://data.worldbank.org/indicator/FR.INR.RINR.

Wu, Y.-W., Wen, M.-H. D., Young, L.-M. & Hsu, I. T. 2018. LCA-Based Economic Benefit Analysis for Building Integrated Photovoltaic (BIPV) Façades: A Case Study in Taiwan. *International Journal of Green Energy,* 15**,** 8-12.

Yang, R. J. & Carre, A. 2017. Design, Simulation, and Assessment of BIPV: A Student Accommodation Building in Australia. *International Conference on Sustainable Infrastructure 2017* p187-200.

Zhang, T., Wang, M. & Yang, H. 2018. A Review of the Energy Performance and Life-Cycle Assessment of Building-Integrated Photovoltaic (BIPV) Systems. *Energies,* 11**,** 3157.

OPV-Façades – Students design concepts of multi-functional solar façades

Roland Krippner[1] and Fabian Flade[2]

[1] Nuremburg Tech – Technische Hochschule Nürnberg Georg Simon Ohm, Faculty of Architecture, Nuremburg (Germany)

[2] Bavarian Association for the Promotion of Solar Energy – Solarenergieförderverein Bayern e. V., Munich (Germany)

Abstract

In the field of building integrated photovoltaics (BIPV), thin-film PV modules or films with organic solar cells (OPV) in particular also represent new solutions, especially when it comes to requirements for flexible module sizes and geometries. These potentials have not yet been exploited enough for further developments.

In the context of a course with master students of the Faculty of Architecture of the Nuremburg Tech in the summer semester 2018, a solar façade was planned for this innovative technology at the former ZAE office and research building in Erlangen as a beacon project and research object, which provides sun and glare protection for the interior and functions as a visible sign of advanced energy research. This eye-catcher is intended to demonstrate how a fully functional yet aesthetically pleasing construction can be realised.

In the end, the concepts developed did not always meet the requirement of planning a solar façade with simple means, but in the occupation with interesting references and their adaptation, the designs show consistently functional and aesthetically appealing solutions for a striking sign of advanced energy research.

Keywords: OPV, printed PV, BIPV, PV façades, solar architecture

1. Introduction

Decentralized energy supply is of crucial importance for sustainable architecture and urban planning. For a 100 percent renewable energy supply in Central Europe, solar activation of the building envelope plays a major role. Particularly in connection with the various approaches and activities such as the „Plus Energy House“, „Energy Efficiency House Plus“, „Active Solar House“ and the implementation of the European Directive on the Energy Performance of Buildings (from 2019 / 2021), the issue of the integration of photovoltaic (PV) modules in building envelopes is of central importance in construction - especially for future-oriented façade designs.

2. Façades and solar technology

The use of solar technology in façades is often very limited, especially in dense urban structures. The solar yields are also reduced by up to 40 percent compared to optimally aligned south-facing roofs. Nevertheless, there are a number of reasons to consider the use of photovoltaics in façades as well. For example, if the roof surfaces of multi-storey buildings are unfavourably exposed, too small or unsuitable in terms of layout and surface area. Last but not least, solar technology also expands the design repertoire and can become a symbol for the use of renewable energies in façades.

Examples from the past decades impressively demonstrate that PV modules can be installed in almost any façade construction. [1] Multiple use is also considered a major advantage of photovoltaics; a particularly conclusive approach to overlapping functions is the use as sun protection. Both shading elements and PV systems work effectively when they are optimally aligned with the sun. The sun protection can be effectively increased with photovoltaics if these shutters are installed in front of the building and can be tracked.

doi:10.18086/eurosun.2020.01.10 Available at http://proceedings.ises.org

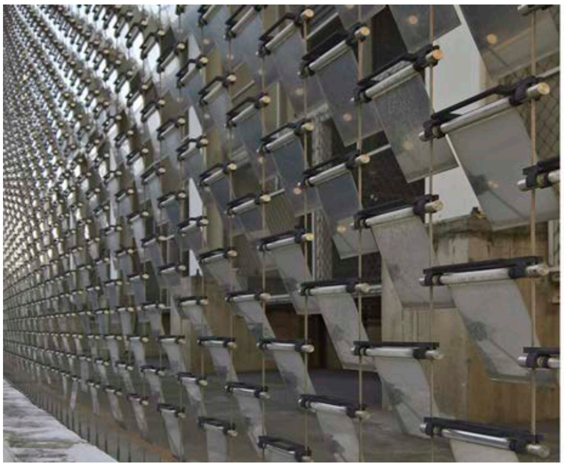

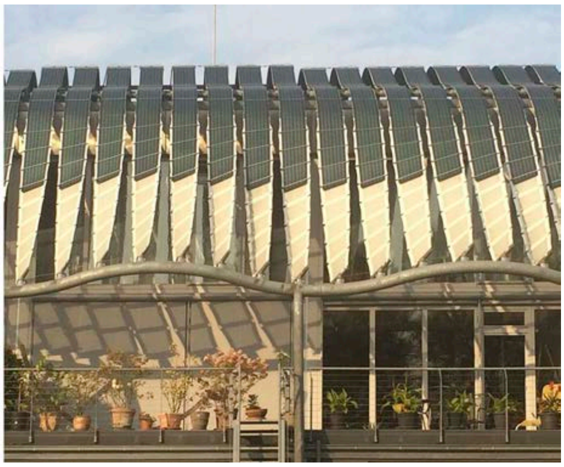

Fig. 1: Wind Arbor, Ned Kahn Studios (Photo: Christoph J. Brabec)
Fig. 2: Soft House, Kennedy & Violich Architecture (Photo: Roland Krippner)

3. Adaptive façades

Over the past decades, façades have developed from static systems to structures with a large number of different movable and controllable components. These should be able to react (automatically) to changing climatic factors under the site-specific conditions. The expansion from the pure, monofunctional protective functions of the façade to a variety of control functions plays an important role, especially in the area of energy management and thermal and visual comfort. [2] On the material side, lightweight construction materials, such as new textile composite construction methods, renewable raw materials and bio-based plastics as well as organic photovoltaics (OPV) enable promising developments.

One variant in this context are kinetic façades, where the use of moving elements also produces novel aesthetic effects. In recent years, Californian artist Ned Kahn has realized a number of projects in which he translates natural phenomena like the wind or sun rays into simple but fascinating constructions with constantly changing appearance, e. g. “Wind Arbor“, Hotel Marina Bay Sands (2011) in Singapore. (Fig. 1)

4. Flexible modules and OPV

Despite the numerous positive examples, architects continue to cite the lack of openness to adaptation with regard to formats, surface effects and colouring, especially of crystalline PV modules, as an obstacle to more intensive involvement with photovoltaics.

When it comes to requirements for flexible module sizes and geometries, thin-film PV modules or films with organic solar cells (OPV) in particular also represent new solutions, such as the SwissTech Convention Centre (2012) in Lausanne by Richter Dahl Rocha & Associés Architectes SA or the Smart Material House / Soft House (2013) by Kennedy & Violich Architecture from Boston, completed as part of the Hamburg IBA. (Fig. 2) Both façades show two different approaches to the use of (O)PV. On the one hand, it is used on or in rigid carrier materials, and on the other, flexible solutions are found in foil/rope net or membrane constructions.

At a company headquarters in Dresden (2014), blue semi-transparent foil strips are inserted into horizontally formatted laminated glass panes in two rows one above the other, while at the Duisport (2018) the solar foils are mounted vertically, three strips of equal width per panel, on the metal façade. Although this makes the warehouse „the world‘s largest façade installation with organic photovoltaics“ [3], in terms of design the approach falls far short of the solutions implemented by Friedrich Ernst von Garnier in the hot strip slitting line of ThyssenKrupp Stahl AG in Duisburg-Beeckerwerth (2002). HHS planners + architects from Kassel are gluing the OPV films directly to the thermal insulation composite system on the gable façade of apartment buildings dating from the 1950s in Frankfurt/Main. Conceptually, the vertically arranged sheets vary in terms of colour (green and red tones) and width as well as design as single or double elements, which at least creates a certain appealing variance with the barcode type arrangement. [4]

In the smart / BASF solar gate for the IAA 2011 in Frankfurt/Main the OPV foils were arranged under a massive polygonal steel girder by means of a tensioned cable construction, which nevertheless leads to a filigree solution. For the German pavilion at EXPO 2015 in Milan, Schmidhuber Brand Experience created a series of shade-giving solar trees with various hexagonal OPV „leaves“. Here as well as at the Peace and Security Building of the African Union (2016) in Addis Ababa, where square modules in a pixel-like arrangement under a glass dome replicate the African continent, new approaches in the area of sun protection devices and/or roofing for the light and flexible modules are becoming visible.

In connection with numerous ingenious and several artistic façade constructions, there is a pool of architectural reference projects here, which has so far been made far too little useable for further developments in the field of building-integrated photovoltaics (BIPV).

5. OPV façade for the ZAE building in Erlangen

Organic photovoltaic modules and printing processes for their manufacture in a roll-to-roll process are being developed by the former Bavarian Center for Applied Energy Research (ZAE Bayern). [5]

In the context of a course with master students of the Faculty of Architecture of the Nuremberg Tech in the summer semester 2018 [6], a solar façade was planned for this innovative technology at the front section of the ZAE in Erlangen (Fig. 3), which on the one hand provides sun and glare protection for the interior, and on the other hand functions as a visible sign of advanced energy research. This eyecatcher should demonstrate how a fully functional and yet aesthetically pleasing construction can be realized (with simple means).

The ZAE building is located at the western entrance to the southern campus of the Friedrich-Alexander-University of Erlangen-Nuremberg. The L-shaped structure is three-storeyed and oriented to the northeast/southwest. The building forms the access area. Due to clearance areas and the entrance to the underground car park, the two-storey front section tapers in the northwest and is indented in the southeast.

On the ground floor there is a meeting room and on the upper floor a lounge. To the east, both rooms have extensive glazing in posts and mullions construction (grey), which is inserted between the reinforced concrete structure (pillars and ceiling slabs). The adjoining solid exterior walls are designed with a thermal insulation composite system, which is also contrasted in colour (red) with the glazing area.

In these structural conditions resulted the constructional constraints for the load transfer, which can take place not only in the massive walls of the corridor/staircase (three-storey part of the front section) but also, and above all, in the floor slabs. With regard to the foundation, access to the underground car park had to be guaranteed.

Fig. 3: ZAE-Bayern / Office and research building (2011), architekturbüro fischer + partner (Photo: Tobias Stubhan)

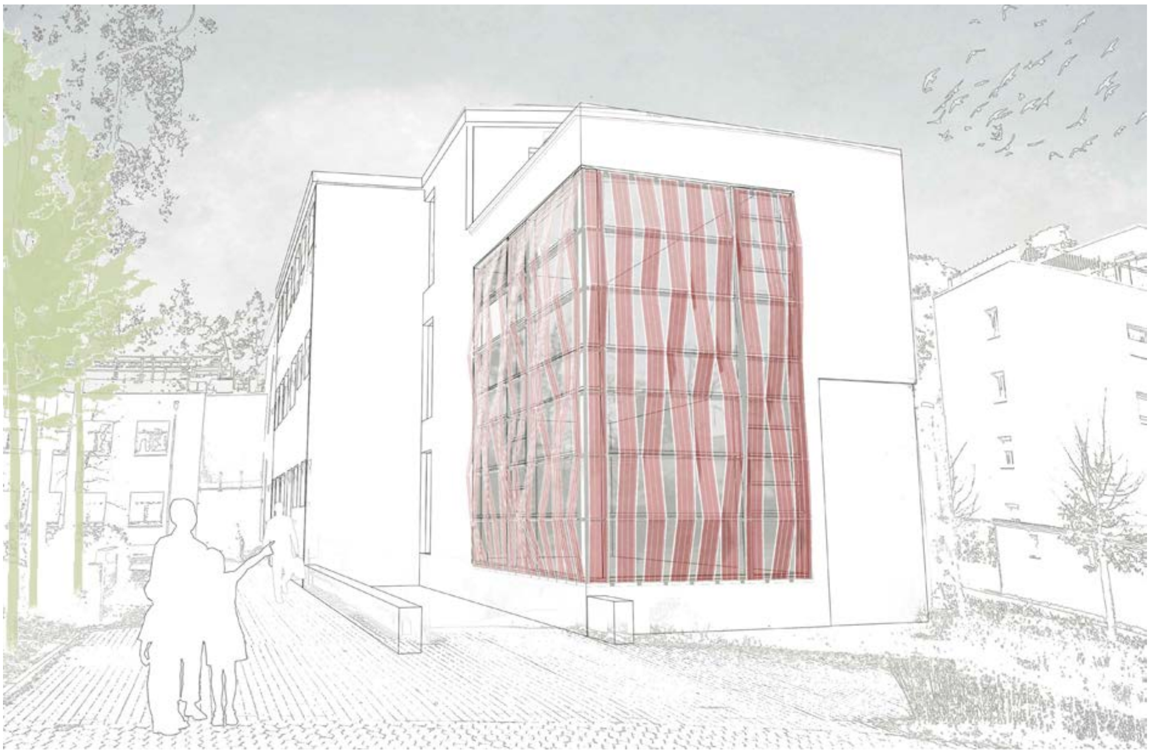

Fig. 4: Moritz Bachmann and Sven Vorliczky, rendering

6. The projects

A number of differences can be identified in the constructional design as well as in the façade structures. [7]

Essential parameters are:

- Structure
- Position to the building and façade area
- Supporting material
- Module design

With regard to the overall structural appearance, a simplified distinction can be made between band-like and planar/point-like solutions, which are designed to be flat or spatial. In terms of design, systems with flat or curved supports/primary and secondary beams or rope net and frame structures with secondary support structure can be found.

For the design, the position in relation to the building is an important requirement, especially since the exit to the underground car park makes the foundation of the structure difficult. Therefore, solutions can be found which are arranged parallel, directly on the existing façade, and designs in which the supporting structure is transmitted at a distance on the boundary wall of the underground car park exit. With regard to the covering of the façade area, concepts have been chosen that form the construction with two to three storeys in the southeast, while others also include the northeast façade in order to give the construction a certain visibility in the context of the access area to the university campus. Partial roofing in the area of the flat roof is also proposed.

In most projects, a plastic foil is used as a carrier material in which the OPV modules are encapsulated and thus additionally protected from the weather. Some solutions use rope nets or membranes in addition to rod-shaped steel profiles. In the module design, there are also strip and planar/point-like solutions that sound out the design potential of the OPV. In all projects, the aim was to make it as easy as possible to exchange the OPV modules with regard to the façade construction as a research object and test facility.

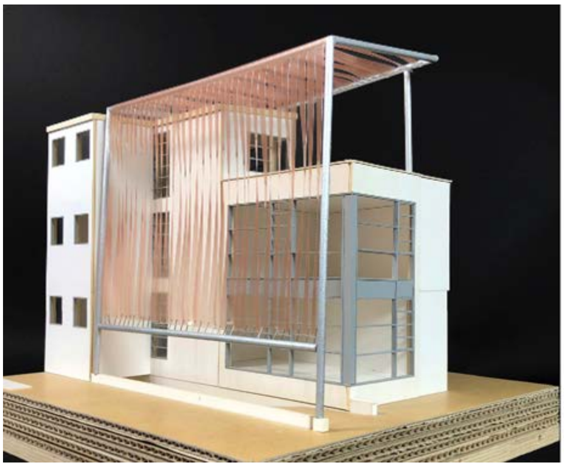
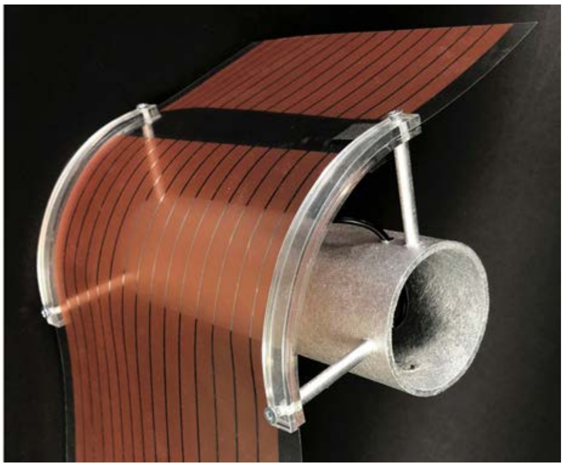

Fig. 5: Daniel Huuck and Alexis Lode, modell 1:50, model 1:2

6.1 Linear façade structures

Within the band-like concepts, Moritz Bachmann and Sven Vorliczky position the OPV façade in the area of the mullion and framed glazing façade. The solar foils are vertically mounted over the two storeys in the south- and the northeast. The substructure of square hollow profiles, which follows the structure of the existing façade, is fixed to the façade mullions at certain points. Based on the motif "rays of light from different points of the compass", different high and low points are distributed over the surface, which move the solar foils against each other in the area of the mullions. This results in different expansions for a view from the inside, which nevertheless provide sufficient sun protection. Integrated, opening frames allow access to the windows. (Fig. 4)

In contrast, Daniel Huuck and Alexis Lode move away their construction "Beyond" from the façade level. In doing so, they refer to the edges of the building and create the largest possible PV generator area. From the base point, the sheets are stretched over spacers (Fig. 5) in the plane of the parapet up to the edge beam of the roofing to also indicate the performance of the solar foils over the length. At end points, the sheets can be rotated 90° out of the plane. This allows partial tracking of the OPV modules and creates different viewing angles. To simplify the rotation, the paths are grouped in 5 areas. The partial roofing opens up additional possibilities of perception of the OPV in the overhead area.

Benedikt Buchmüller and Quirin Stammler extend the framework over two floors, but it is clearly extended beyond the alignment of the building. The length is determined on the one hand by the shading of the north-east façade, on the other hand the external effect is increased, as the OPV façade is thus also perceptible from the north. In addition, an "inviting gesture" to the main entrance is created and the access to the underground car park is separated from the pedestrian access. The tracks of the solar foils are fixed at the height of the floor ceiling and can be rotated by 45° in both directions by means of two movable holding points. (Fig. 6)

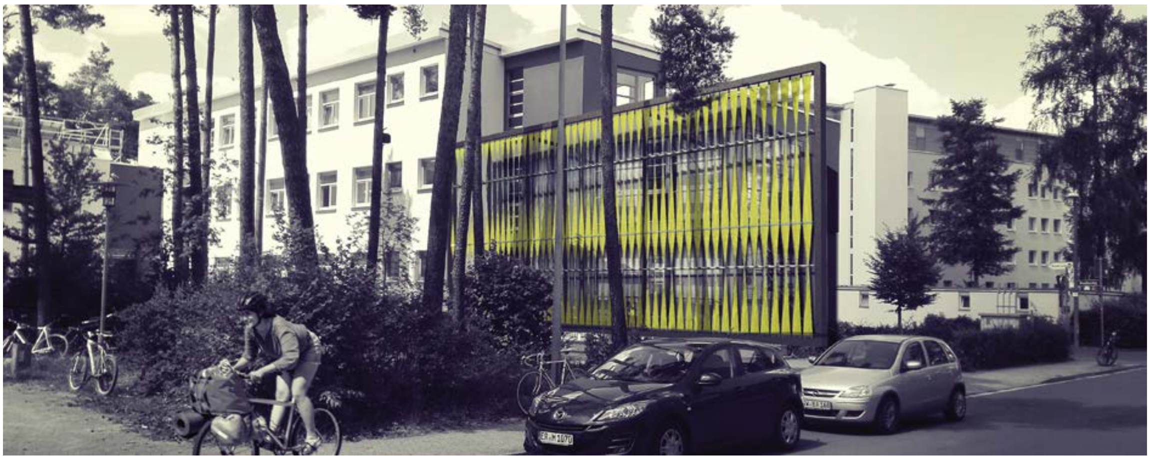

Fig. 6: Benedikt Buchmüller and Quirin Stammler, rendering

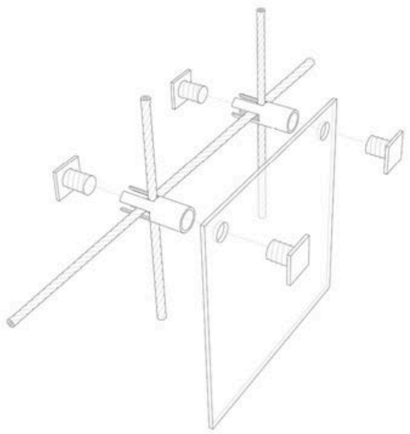


Fig. 7: Peter Simon and Benedikt Zarschizky, drawing and rendering

In the “Square“ concept by Peter Simon and Benedikt Zarschizky, the primary construction forms a square frame that ends at the height of the attic of the three-storey main building. An orthogonal cable net is stretched between the edge beams, to which the OPV modules are fixed in vertical stripes. Different square surfaces are generated with colour variations, which create a nuanced internal division. (Fig. 7)

Marjhonelly Concepcion and Nicole Polster chose a different approach, because they lay the solar films as horizontal strips around the three façades of the front section. Their “copper coil“ concept refers to the ZAE Bayern logo “as a significant symbol of energy research“. Horizontal sliding shutters, also fitted with OPVs, can be installed in front of the glazing on both floors to adjust the use of daylight and visibility as required. To stabilise the sheets, they are held in position field by field by springs on tensioning ropes. (Fig. 8)

6.2 Planar / point-like façade structures

The “squameus“ concept by Julia Credé and Astrid Pümmerlein was inspired by the roofing of a terrace at the AA School of Architecture in London. Two curved girders are placed at an angle in front of the south-west façade and run across the flat roof terrace. Folded plastic foils with integrated OPV modules are attached to the diamond-shaped stainless steel cable net stretched between them. The OPV modules are arranged closer and closer to the roof. (Fig. 9)

Fig. 8: Marjhonelly Concepcion and Nicole Polster, rendering

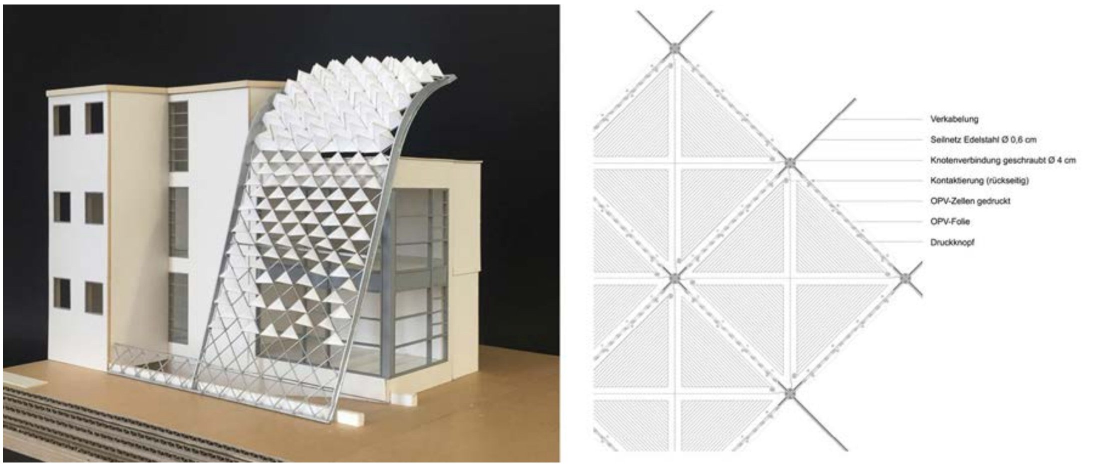

Fig. 9: Julia Credé and Astrid Pümmerlein, model 1:50, detail 1:5

The reference for Gözde Gürbüzler and Lisa Stapf is another realized project. The façades of the extension of the King Fahad National Library in Riyadh (2014) form a spatial zone of curtain-type, three-dimensionally shaped fibreglass membranes, equally elegant construction and efficient sun protection. For the ZAE building, this approach is varied in such a way that the membrane façade to the south-east is formed at a lesser depth, while to the north-east the aim is to create a three-dimensional spatial effect. The OPV modules are placed in horizontal strips on the sun sails, which are clearly spaced in the field of vision in terms of density. (Fig. 10)

The team of Antonia Bader, Stefanie Matthäi and Dominic Weinstein presents the post and beam construction with vertical steel tubes in a half façade grid, on which triangular frames are arranged offset to each other and rotated by 45° from the plane, which also creates a spatially attractive effect. (Fig. 11)

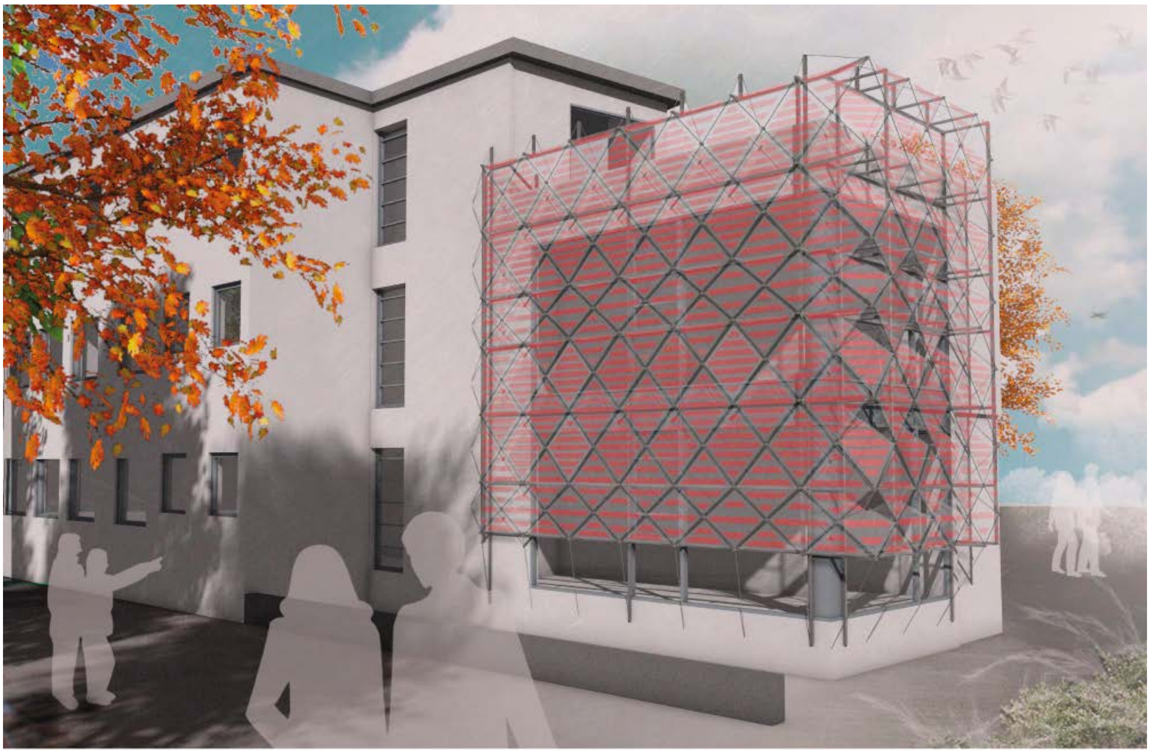

Fig. 10: Gözde Gürbüzler and Lisa Stapf, rendering

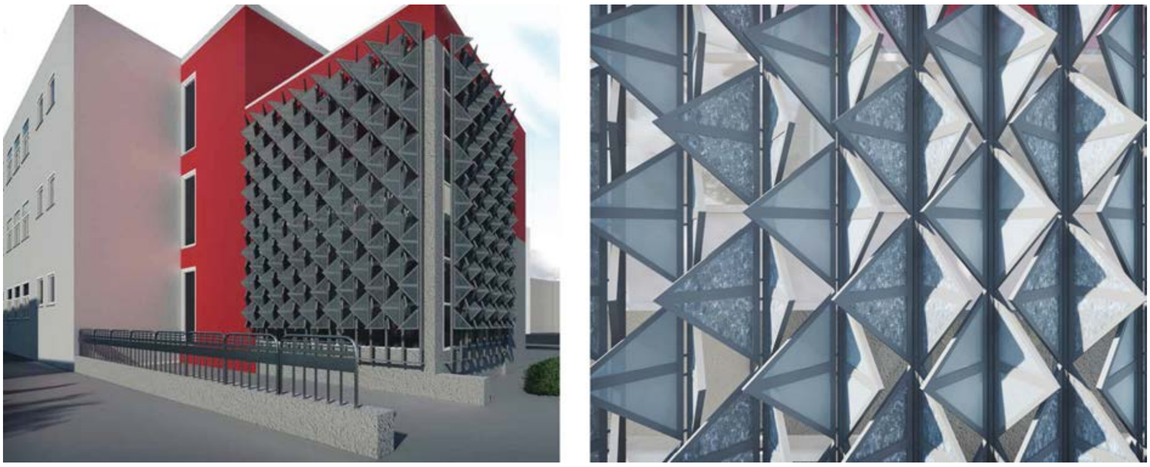

Fig. 11: Antonia Bader, Stefanie Matthäi and Dominic Weinstein, renderimgs

Robert Braun and Theresa Ketisch also position the OPV screen directly on the existing front section, but lay the frame construction with a square grid completely over the two façade areas. Three different sizes of the OPV modules (45 x 45 cm, 60 x 60 cm, 75 x 75 cm), which are suspended over the diagonal, are a response to the different requirements in the façade zones. (Fig. 12)

Tessa Distler and Merve Tufan in turn divide their construction, which is put in front to the south-east façade as a three-storey structure, into nine almost square sections. The horizontal cables of the hexagonal netting in front of it are also covered with hexagonal foils, each with three diamond-shaped OPV modules. (Fig. 13)

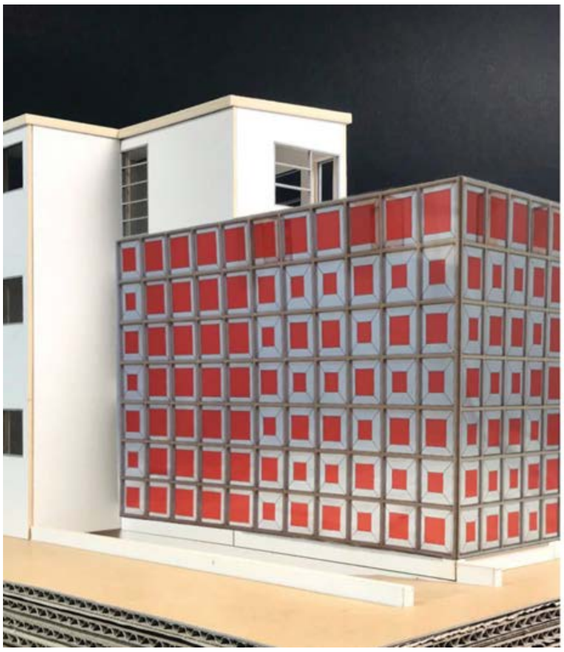

Fig. 12: Robert Braun and Therese Ketisch, model 1:50

Fig. 13: Tessa Distler and Merve Tufan, rendering

Fig. 14: Lisa Prokein and Lisa Schreiber, model 1:50

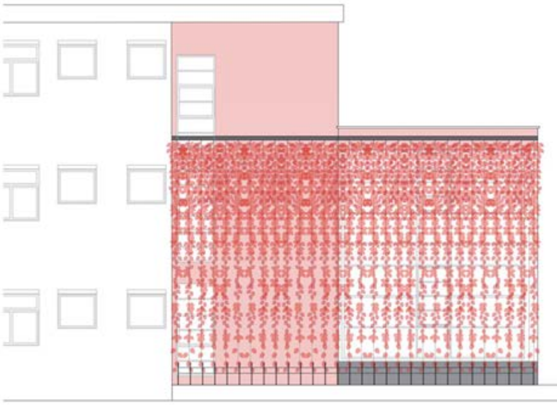

Figure 15: Giulia Rudloff and Katarina Sokac, drawing

Leaf-like structures show the projects of Lisa Prokein and Lisa Schreiber as well as Giulia Rudloff and Katarina Sokac. In the former, a fine net of vertical steel profiles is attached to the supporting structure, on which folded solar foils in six different sizes are alternately fixed, which additionally creates a shimmering appearance through variation in the arrangement. (Fig. 14)

In their "Plug-in Leaf" concept, Rudloff and Sokac stretch steel cables between the wall of the underground car park exit and a beam which rests on brackets at parapet height on the eastern corner of the front section. Three differently abstracted formats (based on leaves of oak, Norway maple (Fig. 15/16), hornbeam) are attached to these by means of thin, slightly bent metal tubing, which also includes the cable duct. In addition to the rotation of the surface between the base and the top of the construction, a very small but "natural" solution is created in the interplay of light and shadow, with advantages when replacing the modules.

Free forms, which are placed between the heterogeneous parts of the building, are chosen by two teams. Simone Baiz and Josefine Raab stretch a cable net construction over the south-east and north-east façades, in the meshes of which square modules of varying density are inserted. (Fig. 17)

In contrast, Kevin Beierlein and Fabian Holzer place a supporting structure with repeatedly spatially curved edge beams in front of the two façades of the head building. A plastic film is streched between them, curved in the same and opposite directions, as a carrier material for diamond-shaped OPV modules. (Fig. 18)

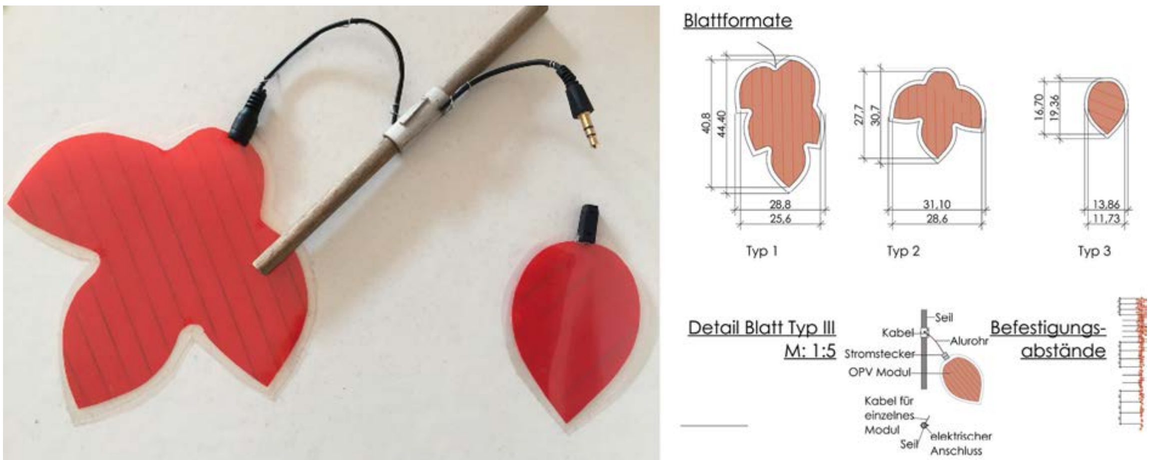

Fig. 16: Giulia Rudloff and Katarina Sokac, model 1:2, drawing (leaf sizes, detail leaf type III, fixing distances)

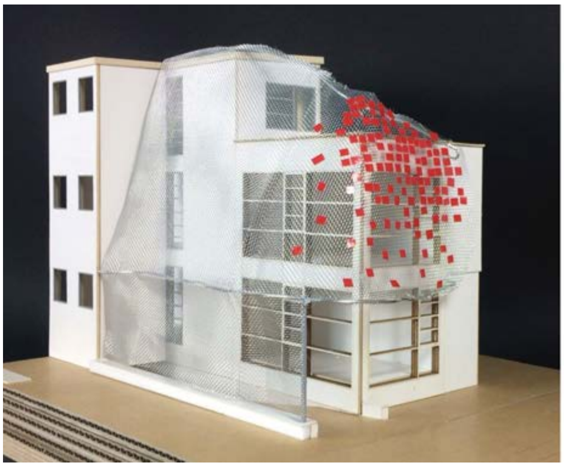

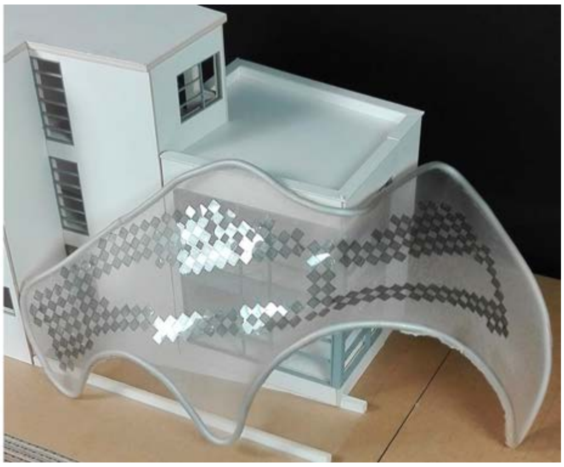

Fig. 17: Simone Baiz and Josefine Raab, model 1:50 Fig. 18: Kevin Beierlein and Fabian Holzer, model 1:50

7. (Interim) Conclusion

Considering the search for quality standards and competent decision-makers in the field of building-integrated photovoltaics (BIPV), architects – and planners – are primarily called upon to develop new solutions. This still means that the profession has to deal much more with the “progress in technology and science for an integral, future-oriented and resource-saving building“ (Helmut C. Schulitz) [9].

With regard to Generation Y or Z, it is not only in the face of student strikes for the climate said, that “concern for the environment is politicized“ and “sustainability is modern“.[10] Therefore, students play an important role to interest architects in the multifunctional and design potential of photovoltaics. Even if topics such as BIPV continue to receive little attention in the curricula of architecture faculties, seminars such as “OPV Façade for the ZAE Building in Erlangen“ show how curiosity and creativity can be successfully activated. [11]

In the end, the concepts developed did not always meet the requirement of planning a solar façade as a lighthouse project and research object with simple means, but in the occupation with interesting references and their adaptation, the designs, which also include in-depth structural engineering, show consistently functional and aesthetically appealing solutions for a striking sign of advanced energy research.

Students teams

Moritz Bachmann, Sven Vorliczky / Antonia Bader, Stefanie Matthäi, Dominic Weinstein / Simone Baiz, Josefine Raab / Kevin Beierlein, Fabian Holzer / Robert Braun, Theresa Ketisch / Benedikt Buchmüller, Quirin Stammler / Marjhonelly Concepcion, Nicole Polster / Julia Credé, Astrid Pümmerlein / Tessa Distler, Merve Tufan / Gözde Gürbüzler, Lisa Stapf / Daniel Huuck, Alexis Lode / Lisa Prokein, Lisa Schreiber / Giulia Rudloff, Katarina Sokac / Peter Simon, Benedikt Zarschizky

8. References

[1] See competition „Architectural Award Building-Integrated Solar Technology“. https://www.sev-bayern.de <07.08.2020>, Krippner, R., 2017. Building Integrated Solar Technology. Detail green books. Munich. Solar Energy, in: Herzog, T., Krippner, R., Lang, W., 2017 (2nd edition). Façade Construction Manual. Munich, pp. 294-321 and Krippner, R., 2015. Energietechnik und Baukultur gehen Hand in Hand. In: B+B Bauen im Bestand, pp. 10–14

[2] See Manipulators, in: Herzog, T., Krippner, R., Lang, W., 2017 (2nd edition). Façade Construction Manual. Munich, pp. 266-293 and Krippner, R., 2005. (Gebäude-)Hüllen – zwischen bewußtem Nutzerverhalten und intelligenter Technik. In: Beton + Fertigteil Jahrbuch. Wiesbaden, pp. 50-54

[3] https://www.heliatek.com/blog/worlds-largest-facade-installed-with-organic-photovoltaics-in-the-port-of-duisburg/ <07.08.2020>

[4] https://www.hhs.ag/projects.html?projekt=aktiv-stadthaus-im-bestand-frankfurt&typologie= <07.08.2020>

[5] https://www.encn.de/en/research/renewable-energies/printed-photovoltaik <07.08.2020>

[6] MA-Modul Vertiefung 2 Technik „Material und Energie“: OPV-Fassade für ZAE-Gebäude in Erlangen. The seminar has been accompanied by Dr. Hans-Joachim Egelhaaf (Energie Campus Nürnberg / ZAE Bayern) and Dr.-Ing. Alexander Hentschel (Dr. Kreutz und Partner, Nuremberg).

[7] Meanwhile Helmholtz Institute Erlangen-Nürnberg for Renewable Energy (HI ERN). http://www.hi-ern.de/hi-ern/EN/home.html <07.08.2020>

[8] See exhibition: OPV-Fassade für das ZAE-Gebäude in Erlangen. Studentische Entwürfe [SS 2018, LV: MA-2200 Seminar „Material und Energie“]. Editors: Roland Krippner; Fabian Flade. Nuremburg Tech, Faculty of architecture, field of teaching Construction and Technology, Nuremberg, 2019.

[9| Schulitz, H. C., Form follows performance. 2010. In: Schulitz: Form follows performance / Leistungsform. Schulitz Architekten, Works 1995-2010. Basel [et al.], p. 9

[10] Stremmel, Jan: Alles Klima. In: Süddeutsche Zeitung, Nr. 40, 16./17.02.2019, p. 45

[11] The students have been awarded 2nd prize at the Innovationspreis Erneuerbare Energien 2018 of the Frank Seuling Stiftung (https://www.th-nuernberg.de/news/innovationspreis-erneuerbare-e/ <07.08.2020>

Cleanvelope – Students concepts of refurbishment with solar energy and façade greening

Roland Krippner[1] and Fabian Flade[2]

[1] Nuremburg Tech – Technische Hochschule Nürnberg Georg Simon Ohm, Faculty of Architecture, Nuremburg (Germany)

[2] Bavarian Association for the Promotion of Solar Energy – Solarenergieförderverein Bayern e. V., Munich (Germany)

Abstract

A task of the future, with regard to the social challenges of the transformation of the energy system and the adaption to the climate change, is to upgrade the energy efficiency of old buildings. The EU has set itself the goal of making the building stock almost climate-neutral by 2050. A forward-looking approach is to combine building greening techniques and photovoltaics (PV), as a number of synergy effects can be expected here.

A seminar in the master‘s programme at the Faculty of Architecture of Nuremburg Tech in summer semester 2019 examined how buildings can be upgraded between the conflicting priorities of building culture, renovation, solar technology and building greening. Using the example of the “Nordring“ quarter (12 multi-storey residential buildings built in 1959) in Nuremburg, renovation concepts with building greenery and photovoltaics were developed, which, in addition to a design upgrade, demonstrate that both strategies complement each other effectively. In 20 projects, different approaches, from cautious intervention to strong transformation, were developed and constructively deepened. The results show an enormous potential for upgrading of the building environment and housing stock.

Keywords: BIPV, PV façades, solar architecture, building greening

1. Introduction

The climate change requires new concepts in architecture and urban planning. A central task is the energy efficiency of old buildings. The EU has set itself the goal of making the building stock almost climate-neutral by 2050. A forward-looking approach is to combine building greening techniques and photovoltaics (PV), as a number of synergy effects can be expected here.

Plants are an ideal natural design element for an ecological envelope concept. In recent years, green façades and green walls have been used more and more in the construction of modern energy-efficient buildings. [1] Due to adiabatic cooling processes, plants can also be used as natural air-conditioning systems in urban and building planning. In doing so, they fulfil a variety of other functions, such as natural air filtering of fine dust, absorption of carbon dioxide, noise reduction, etc. [2] In addition, temperatures on façade surfaces can be significantly reduced.

Façades are becoming increasingly important for solar activation of the building envelope, especially in an urban context, because, among other things, the roof surfaces of multi-storey buildings are often no longer sufficient for the integration of solar technology. Thermal solar collectors and PV modules are also important elements of solar construction and are now regarded as self-evident components of energy-efficient buildings and advanced envelope constructions. [3]

The combination of building greening and photovoltaics not only has positive effects for the design, both strategies can also complement each other functionally. Crystalline PV modules in particular react sensitively to temperature increases, i.e. the cooler the installation, the more efficiently solar electricity can be produced. Especially in the summer months, when there is a lot of solar radiation, a green environment can enable a better performance of photovoltaics.

doi:10.18086/eurosun.2020.01.11 Available at http://proceedings.ises.org


Fig. 1: Aerial view of the "Nordring" quarter (Source: wbg) / Fig. 2: Model of the "Nordring" quarter (Photo: Michael Pfisterer)

The combination of green walls and PV is not a new field of work for architects, as this combination has already been considered in competitions and has also been implemented in buildings in isolated cases. [4] In the context of a seminar in the master's programme at summer semester 2019 [5] it was now examined how buildings can be upgraded between the conflicting priorities of building culture, renovation, solar technology and buildimg greening. Using the example of quarter „Nordring" (12 multi-storey residential buildings from 1959) in Nuremberg (Fig. 1), renovation concepts were developed, which, in addition to a design upgrade, show that building greening and photovoltaics complement each other effectively. In 20 projects, different approaches, from cautious intervention to strong transformation, were developed and constructively deepened. The results show an enormous potential for the upgrading of the building environment and housing stock.

2. The projects

All refurbishment concepts are based on the approach of improving the thermal properties of the building envelope. In the area of the façade, the existing outer wall was often energetically upgraded with additional thermal insulation layers in ventilated curtain wall constructions, cladding material wood and/or wood-based materials. The opening sizes and formats of the windows have been partially or completely changed and additional (semi-)transparent shells have been placed in front of the balconies or new loggias have been proposed for the thermal improvement of the open areas close to the dwellings. The roofs were generally increased in height to provide solutions for the increased demand for apartments, especially in urban areas, by means of structural densification.

2.1 Linear buildings with north-south orientation

The buildings Gerngrosstraße 30 as well as Nordring 127 - 131 and Nordring 133 + 135 are three-storey buildings with undeveloped pitched roofs. They have a north-south orientation. The façades of the residential buildings, which are organized as two-winged structures, feature regular arrangements of single and double-wing windows; Gerngrosstraße 30 and Nordring 127 - 131 have balconies to the south. In addition to structural similarities, the location of Nordring 127 - 131 and Nordring 133 + 135 brings greater demands on the refurbishment concepts for noise protection.

The two works on the building at Gerngrosstrasse 30 already show typical refurbishment strategies using solar technology (photovoltaics) and building greening as examples. Tobias Moninger and Julia Spreng remove the existing roof and provide a "balcony shelf" as a horizontal extension for the entire south side. The modular extension with differentiation in room height ends with the front edge of the balconies. The vertical extension is

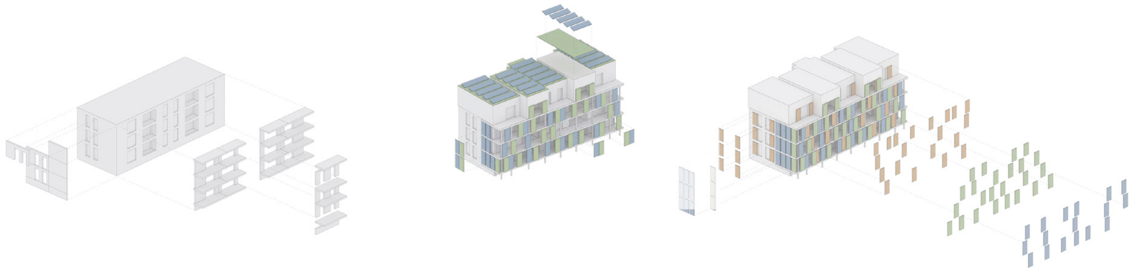

Fig. 3: Tobias Moninger and Julia Spreng, isometric drawing

clearly visible with the wooden sheathing opposite the thermal insulation composite system. To the south, a multi-layered façade is proposed, in which sun protection, green walls (climbing plants in troughs) and PV panels (monocrystalline cells) are arranged in high-form façade modules. The plants also take over functions of sun and privacy protection. The flat roof is greened and equipped with south-facing photovoltaics.

In addition to new thermally separated loggias in the area of the demolished balconies, Yazan Doudieh and Hendrik Sell propose a full-area building greening with climbing plants, whose circumferential gutters restructure the building floor-by-floor. As an energy envelope, the partially two-storey solid wood extension with pitched roof is in the area of the opaque surfaces completely equipped with frameless PV modules (anthracite-coloured, non visible monocrystalline cells) in a curtain-type, rear-ventilated construction.

In their project “Green Prospects“ (Nordring 127-131), Gabriel Barklam and Martin Riemann replace the existing pitched roof by a single-storey extension and place in front of the south side a four-storey structure with largely identical solid wood modules. Loggias (with horizontal PV and wooden sliding shutters) with open areas (vegetable beds and climbing plants) are created for each apartment. Large-scale PV modules are arranged above the new green roof. This approach pursues a homogeneous appearance with the multi-layered new spatial zone, in which old and new are no longer legible.

Fig. 4: Tobias Moninger and Julia Spreng, elevation 1:20

Fig. 4: Yazan Doudieh and Henrik Sell, rendering

Sevil Demirkol and Muhammet Mustafa Salihoglu follow a similar concept. Vertical frames, with integrated plant boxes at the new balconies, are placed in front of the south side. In the area of the opaque wall surfaces, climbing plants and PV modules are arranged alternately. To enhance the open space close to the building, a noise protection wall made of wooden frame elements is proposed. The existing pitched roof remains a temperature buffer; the south side is designed as a fully integrated PV generator.

In the neighbouring building (Nordring 133+135) at the east, David Honke and Max Kellermann as well as Annika Leiter and Sonja Silano focus on a single-storey noise protection wall. In the former, wooden pavilions serve as visual and noise protection. They collect energy and allow green common areas shielded from the street to the south. The single-storey extension with the wooden cladding, in conjunction with alternately arranged loggias, clearly marks the vertical and horizontal expansion. The building greening close to the apartments is reduced to potted plants in the loggias.

At Leiter and Silano, the noise barrier with a green wall to the street, also improves the quality of the air, while spatial domains differentiate the common area. In addition to occasional wooden modules arranged in front of the living rooms with potted plants, generous, greened loggias are offered in the addition of another storey. The south-facing sloping roof area is used entirely for solar power generation.

Fig. 5: Gabriel Barklam and Martin Riemann, rendering / Fig. 6: Model buildings Nordring 127 – 135 (Photo: Michael Pfisterer)

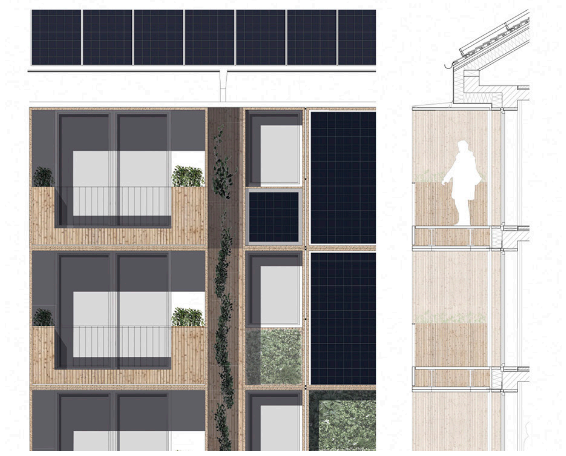

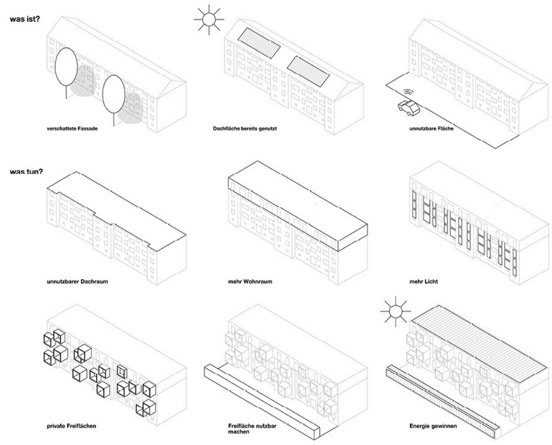

Fig. 7: Sevil Demirkol and Muhammet Mustafa Salihoglu, rendering / Fig. 8: David Honke and Max Kellermann, concept

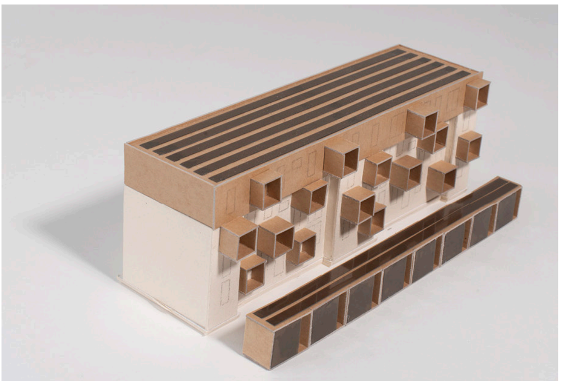

Fig. 9: David Honke and Max Kellermann, model 1:50 / Fig. 10: Annika Leiter and Sonja Silano, model1:50

2.2 Linear buildings with east-west orientation

The buildings at Nordring 137-155 and Schopenhauerstraße 32-36 are four-storey linear buildings with pitched roofs, also not developed, which are arranged east-west. The building sections, each of which is organised as a two-span structure, differ slightly in the length of the buildings and in the access.

For Nordring 137-139, Federica Cimino and Diana Rolof propose an extension with a pitched roof. While the east façade is given a new cladding of vertical wooden boards, in the west a balcony zone that changes floor by floor is placed in front of the living rooms. The building greening is placed on the south side and also serves as a horizontal end to the open space. On the gable wall in the north, ten façade modules with moss are arranged in five horizontal bands. On the south side, PV modules arranged in the same design add to the roof system.

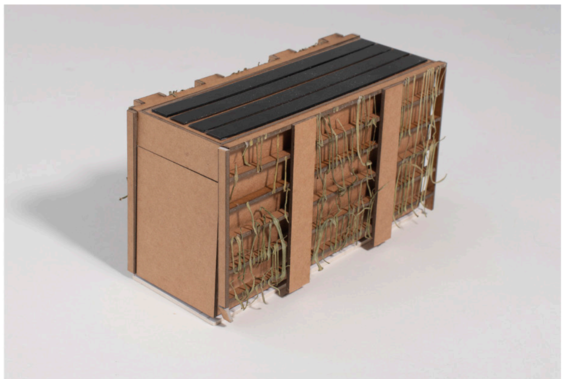

Fig. 11: Federica Cimino and Diana Rolof , model 1:50 / Fig. 12: Hüseyna Koc and Melek Sakanci, model 1:50

Fig. 13: Models Nordring 137 – 153 (Photo: Michael Pfisterer)

In the neighbouring building Nordring 141-143, the vertical extension is carried out via a single-storey addition with a flat roof. Hüseyna Koc and Melek Sakanci leave the narrow sides largely untreated, but present the east and west façades with a spatial structure over the entire surface. In addition to the living spaces, room modules are proposed as loggias, which penetrate the level of the metal mesh as a climbing aid. The building greening is done via plant boxes on each floor. The new flat roof is fully equipped with east-west oriented PV modules.

At the linear building located to the east, Franziska Kopf and Lisa Schubothe react on the basis of sun position studies and existing trees with horizontal extensions mirrored over the diagonal. Thus, the northern apartments get a thermal buffer zone in the east, the southern apartments in the west. The new pitched roof has an additional gallery level in the area of the ridge. As an extension of the roof, the glazed areas of the conservatories with greening are fitted with semi-transparent PV modules; the opaque roof surfaces and the upper third of the south wall are fitted with anthracite, monocrystalline PV shingles mounted over the corner.

Marius Sperger and Sarah Strohbach envisage extensions of the living spaces for Nordring 149-151 both in the east and west. The balconies will alternate in the supporting structure floor by floor. While on the gable sides and along the posts ground-based climbing plants grow upwards, plant troughs and raised beds for planting vegetables are provided in the area of the balconies. The two roof areas are fully equipped with a roof integrated PV generator.

Marco Burger and Johannes Poerschke do not see any vertical extension for Nordring 153-155. The existing roof space is retained as a thermal buffer. The outer wall will have a wooden façade with vertical sheathing all around and spatial expansion is planned on both long sides. Mobile plant gutters with climbing plant trellis

Fig. 14: Marco Burger and Johannes Poersche, rendering / Fig. 15: Carmen Dieterich and Franziska Kühn, model 1:50

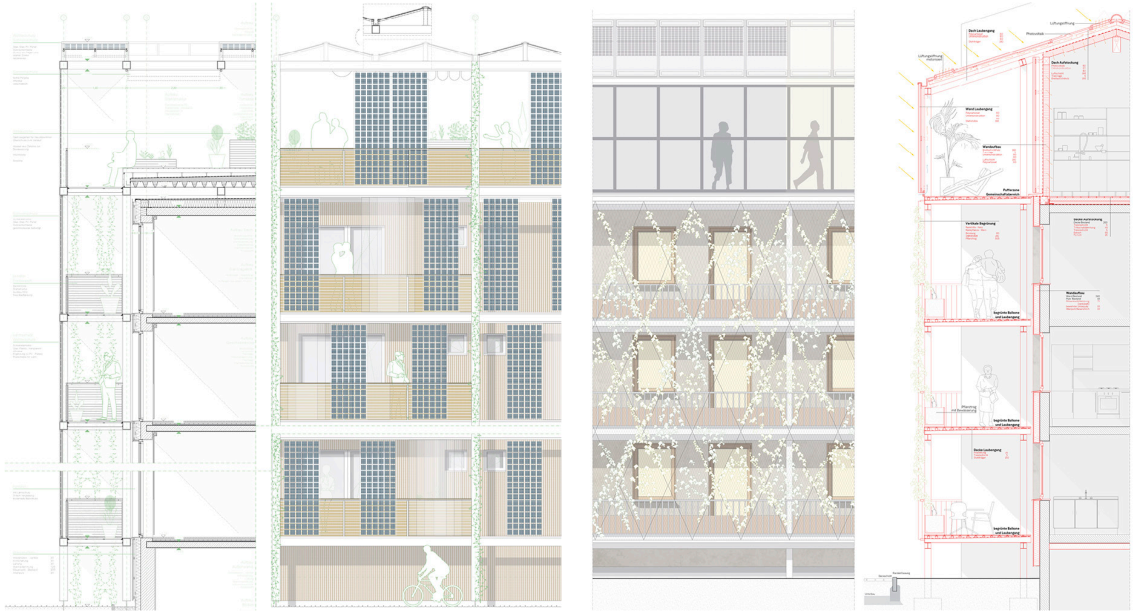

Fig. 16: Eva Grotter and Marie Christine Häußler, section 1:20 / Fig. 17: Julia Hager and Daniel Jäger, section 1:20

are arranged in sections at floor level as movable sun and sight protection. The upper end is formed by vacuum tube collectors. The roof area is divided into smaller fields of double-rowed rooftop PV systems. The concept is supplemented by a rainwater management system. For noise protection, between the multi-family dwellings a building made of prefabricated concrete elements is proposed, whose south-facing sloping roof surface is on the one hand a PV generator, while the upper third ends with a planting box for the green projecting wall.

A new aspect is introduced by Sandra Keß and Charlotte Strohbach at Schopenhauerstraße 32-36 with their „Bee Green“ renovation concept: urban biodiversity with beekeeping. A part of the roof area of the extension will be used for beekeeping, the rest for solar thermal energy. On the ground floor, the students propose a public use, including a „honey café“. The horizontal extension in the east and in the west will take place from the 1st floor on. The end is formed by alternating green areas on each floor (climbing plants in boxes) and PV panels, which are mounted at the edge of the roof as protection against the weather. In front of the brick façade on the gable side in the south, a large cable net trellis extends the green façade.

Carmen Dieterich and Franziska Kühn call their approach for the same building “invasive to the maximum“. In addition to the horizontal extension, a narrow zone with window seats in the east, deep balconies in the west, the living space is significantly increased with a complete storey plus extended pitched roof. Troughs for plants shrubs are integrated into the structure placed in front, made of prefabricated reinforced concrete elements. The extended roof and the south façade are fully covered with anthracite CIS thin-film modules.

2.3 Residential buildings

The two flat-roofed buildings in the east of the quarter, Nordring 159 (five-storey) and Gerngrosstrasse 32 (three-storey), located in the north-east along Otto-Geßler-Strasse, differ in the organisation and development of the living spaces. Both buildings were originally designed as 1-room flats and were accessible via a courtyard-side access balcony, Nordring 159 in the north and Gerngrosstraße 32 in the west. At the end of the 1980s, the building was redesigned by merging rooms into 4-room flats."

With their “active building skin“ concept, Eva Grotter and Marie Christine Häußler house Nordring 159 with a new steel structure on the long sides and above the single-storey addition. This construction replaces the existing access balcony in the north and takes up the private living space extension in the south. Semi-transparent PV modules serve as privacy and sun protection in the area of the balconies; while potted plants are largely provided there, self-climbing plants grow upwards along the columns. In contrast, one funds large areas of façade greening in the north along the access balcony. Above the top floor, a multifaceted roof garden is created, especially for growing vegetables. As protection against the weather, photovoltaics are arranged in a flat east-west orientation over partial areas.

The approach of Fatemeh Sedrehneshin and Vanessa van Zoest is also characterised by a strong transformation. A steel construction is placed in front of he long sides in the south (balconies) and north (new arcade). The spandrel areas and the prismatic triangular surfaces connecting the floors and inclined to each other are alternately covered with greenery and photovoltaics. Due to their spatially layered arrangement, certain synergies are created and the concept shows a dynamic façade design. Instead of adding a storey, it is proposed to create an indented roof garden.

Eslam Mohamed Ahmed and Felix Prommersberger also replace the access balcony in the north with a thermally separated support structure and place glazed balconies with PV parapets in front of the living areas. In contrast to this clear horizontal arrangement, the areas in front of the former kitchen windows are designed as vertical zones for climbing plants. The new flat roof is designed as a PV generator with east-west modules covering the entire surface.

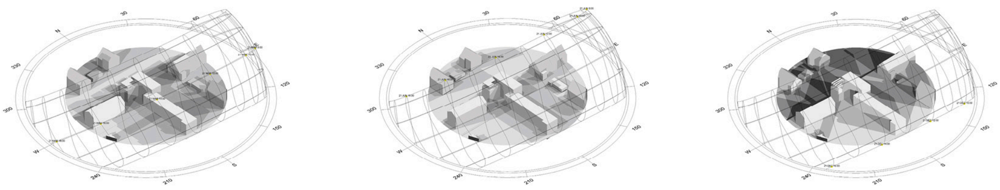

Fig. 18: Philipp Oebius and Tina Zahl, shadowing analyses

The two concepts for the building at Gerngrosstrasse 32 address further variations. In addition to adding another storey to the three-storey building, Philipp Oebius and Tina Zahl propose a spatial extension along Gerngrosstrasse as a urban redensification following extensive shadowing analyses. In addition to further additional living space, a "photovoltaic roof garden" [6] with an intensively planted terrace will be created on level 4. A pergola made of solid structural timber with south-facing sheds and semi-transparent PV modules will provide shade and generate solar power. In the existing building, plant troughs are arranged on the ceiling level all the way around from the first floor and east-west oriented PV modules are arranged on the extensively greened flat roof.

Julia Hager and Daniel Jäger extend the pergola with balcony areas and complete the building with an additional attic storey, whose western façade flushly covers the new outdoor areas. The special feature of the glulam attic storey is that its entire enveloping surfaces are designed with polycarbonate multiwall sheets as air collectors.

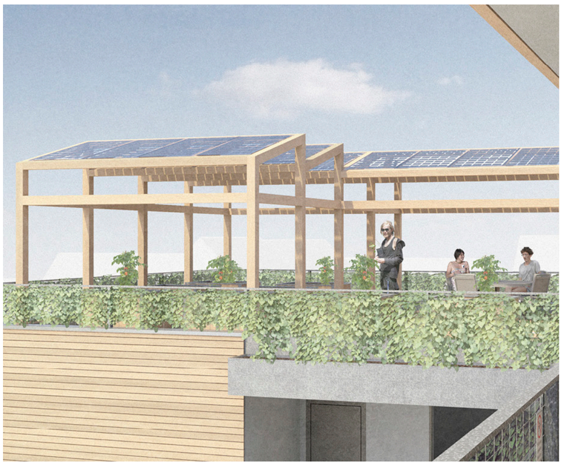 

Fig. 19: Philipp Oebius and Tina Zahl, rendering / Fig. 20 Julia Hager and Daniel Jäger, model 1:50 (Photo: Michael Pfisterer)

Fig. 21: Giulia Seltmann and Moritz von Frankenberg-Carbon, rendering

To the west, a thermal buffer zone is placed in front of the outer wall as a common area. While on the east façade vertically tensioned wire ropes serve as a climbing aid, in the west the wire ropes are arranged diagonally in front of the building-high metal wire mesh. On the sloping roof surfaces, PV modules are positioned in areas below the ventilation openings on the ridge.

2.4 Point blocks

The two buildings, which were erected south of the road, form a special structural form. They are five-storey point houses with an H-shaped ground plan. Nordring 142 is set back somewhat from the alignment of the street and to the east of it Nordring 144. The buildings have two very different façades. On the east and west sides there are perforated façades with plaster surfaces (in the planning permission, a slab grid is still visible), while in the north and south, wall panes are designed as fair-faced brickwork, which only have openings with the vertical row of kitchen windows in the area of the "constriction".

Giulia Seltmann and Moritz von Frankenberg-Carbon leave the wall panes at north ring 144 as a characteristic feature and propose an internal insulation. The building will be raised by one storey and a scaffolding construction with balconies will be placed in front of the east and west façades. Narrow channels for climbing plants are fixed at ceiling level, with horizontal PV sliding elements in front of them as privacy and sun protection. In the area of the attic, semi-transparent PV modules provide weather protection. Additional balconies are provided in the recesses at a distance from the staircase. The flat roof is extensively greened with PV modules arranged in east-west sections.

The square kitchen windows in the wall panels form the dimensional reference for Irene Bauer's renovation concept for the Nordring 142 building. She is developing a kind of modular system with four different elements made of fibre concrete. Their geometry has been chosen in such a way that even the basic module has sound insulation functions. The other modules contain sun protection, a green wall, a dust filter, and finally photovoltaics for electricity generation. These are arranged differently depending on requirements and exposure and are presented as a self-supporting structure to the insulated exterior walls. In the recesses in the area of the staircase, common areas close to the apartments with climbing plants arranged floor by floor are proposed as filter layer. Above the existing, undeveloped top floor a roof garden is created, framed by a pergola and zoned into communal and play areas with space for raised beds for urban gardening.

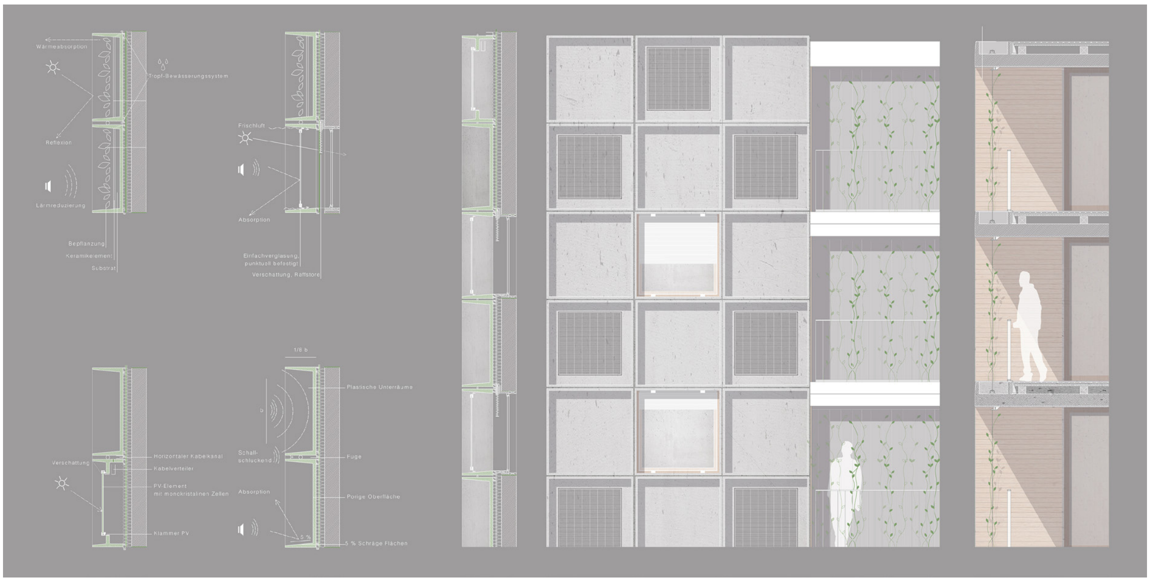

Fig. 22: Irene Bauer, vertical section and elevation 1:20

3. (Interim) Conclusion

The students proposed different renovation strategies for the buildings. In the concepts with building greening and solar technology, the use of wood and wood-based materials for energetic refurbishment is often the alternative to the common thermal insulation composite system. The use of plants and photovoltaics differs in the façade and roof area. In some of the projects, supplementary noise protection structures are proposed for upgrading and expansion.

In the façades, building greening and PV are often functionally separated. Climbing plants are used in gutters arranged floor by floor. The advantages of radiation permeability are specifically used for privacy and sun protection. In connection with the newly created open areas close to the apartments (balconies and glazed loggias), there are also approaches that allow the cultivation of herbs with raised beds. In the ecological building envelope concepts, the plants function primarily as an atmospheric design element, without neglecting their function as natural air conditioning.

Combinations largely refer to extensively greened flat roofs with flat-sloping PV modules. This shows that, taking into account the basic requirements of both systems, functioning, integrated solutions can be implemented. In some projects, the top of the building becomes a PV roof garden with an intensively planted terrace, which connects urban gardening with common areas.

In the case of photovoltaics, in some examples solar thermal technology is used, in the façade (semi-transparent) modules in the parapet and as storey-high visual and sun protection elements are installed. Particularly in multi-storey residential construction, vertical building surfaces are becoming increasingly important for solar activation, as the roof surfaces are often no longer sufficient for the integration of solar technology.

Conceptually, references to well-known implementations, such as wagnis4 in Munich (2012-2014) by A2architekten Freising with FreiRaumArchitekten Regensburg, can be seen. At the same time, there are also references to advanced concepts such as Günter Pfeifer‘s “cybernetic planning“ [7] with large-area air collectors or independent approaches to a modular system with small modules. One work proposes a change of use on the ground floor and combines biodiversity with urban beekeeping.

The solutions developed in the course of a seminar in the master‘s programme open up the possibility of integrating current topics of the social challenges of energy system transformation and climate adaptation into architecture teaching, and last but not least a fruitful knowledge and technology transfer to relevant research activities in the field of teaching “construction and technology“ [8].

Students teams

Gabriel Barklam, Martin Riemann / Irene Bauer / Marco Burger, Johannes Poerschke / Federica Cimino, Diana Rolof / Sevil Demirkol, Muhammet M. Salihoglu / Carmen Dieterich, Franziska Kühn / Yazan Doudieh, Hendrik Sell / Eva Grotter, Marie Christine Häußler / Julia Hager, Daniel Jäger / David Honke, Max Kellermann / Sandra Keß, Charlotte Strohbach / Hüseyna Koc, Melek Sakanci / Franziska Kopf, Lisa Schubothe / Annika Leiter, Sonja Silano / Eslam Mohamed Samir, Florian Prommersberger / Tobias Moninger, Julia Spreng / Philipp Oebius, Tina Zahl / Faterneh Sedrehneshin, Vanessa van Zoest / Giulia Seltmann, Moritz von Frankenberg-Carbon / Sarah Strohbach, Markus Sperger

4. References

[1] Herzog, T., Krippner, R., Lang, W., 2017 (2nd edition). Façade Construction Manual. Edition Detail, Munich, pp. 336-341 and Krippner, R., 2013. Innovative Fassadenlösungen für energieeffiziente Gebäude. in: 19. Internationales Holzbau-Forum. “Aus der Praxis - Für die Praxis”, Biel/Bienne, pp. 1-11, 7f.

[2] Pfoser, N., Jenner, N., Henrich, J., Heusinger, J., Weber, S., 2013. Gebäude Begrünung Energie. Potenziale und Wechselwirkungen. Forschungsbericht. Darmstadt, pp. 16-19.

[3] Krippner, R., 2017. Building Integrated Solar Technology. Architektur. Detail green books. Munich, pp. 64-71 and Herzog, T., Krippner, R., Lang, W., 2017 (2nd edition), Façade Construction Manual. Edition Detail, Munich, pp. 294-321.

[4] Bott, B., Krippner, R., Fuchs, H., 2017. Fassadenbegrünung und Photovoltaik in der Bestandssanierung am Beispiel des Verwaltungsbaus von SUN. In: 9. Forum “Bauwerkintegrierte Photovoltaik”. Regensburg, pp. 111-118 and https://smartcity.wien.gv.at/site/en/50-green-houses/ <07.19.2020>

[5] MA-Modul Vertiefung 2 Technik „Material und Energie“: Cleanvelope – Sanierungskonzepte mit Solartechnik und Gebäudebegrünung (Nürnberg “Nordring”). The seminar has been accompanied by Dr.-Ing. Claudia Hemmerle and M.Sc. Elisabeth Faßbender (Technische Universität München, Fakultät für Architektur, Lehrstuhl für Gebäudetechnologie und klimagerechtes Bauen.

[6] https://smartcity.wien.gv.at/site/en/photovoltaic-roof-garden/ <02.03.2020>

[7] Pfeifer, G., 2016. Kybernetische Architektur. Freiburg i.Br.

[8] „EnOB: GreenFaBS: Einsatz von Grünfassaden zur Reduzierung des Kühlbedarfs fassadenintegrierter dezentraler Gebäudetechnik (02/2019-01/2021). https://www.enargus.de/pub/bscw.cgi/?op=enargus.eps2&q=Technische%20Hochschule%20Nürnberg%20Georg%20Simon%20Ohm&v=10&s=7&id=1050391 <07.19.2020>

EVALUATING THE SOLAR POTENTIAL OF ROOFTOPS ON CAMPUS SAN JOAQUÍN, SANTIAGO – CHILE USING OPENSOURCE GIS

Redlich Garcia[1], Jesús Polo[2]

[1] Pontificia Universidad Católica de Chile, Santiago (Chile)

[2] Centro de Investigaciones Energéticas, Medioambientales, y Tecnológicas (CIEMAT), Madrid (España)

Abstract

Over recent years, photovoltaic systems have become increasingly popular for the installation on buildings' rooftops. Due to the increasing demand for electricity through Photovoltaic (PV) systems, it is necessary to evaluate the solar potential on roofs in the first place. Since from these values, it is possible to analyze which rooftops are suitable for the installation of photovoltaic systems to produce the maximum electrical energy but estimate the actual solar potential for applications in the dense urban environment is a difficult mission. In this work, the solar potential in roofs is calculated in Santiago de Chile using opensource GIS. The Global Horizontal Irradiance (GHI) used for this analysis was taken from the Solar Laboratory of Pontificia Universidad Católica de Chile. The other components of radiation: Direct Normal Irradiance (DNI) and Diffuse Horizontal Irradiance (DHI) were obtained although of the BRL model for Santiago de Chile. Using the method of Sandia National Laboratory, a typical meteorological year (TMY) was built to handle like input in the process of calculation of the solar potential on the rooftops. A Digital Surface Model (DSM) is used to describe urban geometry. Another sensitivity analysis done in this research was with the albedo, where it was changed in 6 values assuming that exist several buildings with different materials around of building chosen as the case of study. The methodology was validated against measurements made on-site, showing a slight overestimation in the winter months compared to the summer months. An albedo sensitivity analysis was also performed, in which it is evident that the increase of the estimated radiation in the rooftops is linear. Still, the differences in the rise between albedos 0.2 and 0.4 tend to remain constant, therefore, because the compactness effect is relatively meaningless, to use very high albedos.

Keywords: Solar Potential Estimations, GIS, Digital Surface Model, Albedo, Typical Meteorological Year.

1. Introduction

Nowadays, renewable energies are continued growth, as fossil fuels are always more expensive and difficult to find. Furthermore, the latest environmental disasters caused by oil drilling and transportation have further focused the attention of the whole world on the risks connected to fossil fuels. In the last June, the Norilsk diesel oil spill is an ongoing industrial disaster near Norilsk, Krasnoyarsk Krai, Russia. A fuel storage tank at Norilsk-Taimyr Energy's Thermal Power Plant No. 3 (owned by Nornickel) collapsed, inundating local rivers with up to 17,500 tonnes of diesel oil

doi:10.18086/eurosun.2020.01.12 Available at http://proceedings.ises.org

(Ilyushina 2020), is a clear example. In the last years, many attempts have been made to control and avoid environmental disaster due to fossil fuels, but it has been in vain. One of the most attractive renewable energy is solar energy. Solar energy is a renewable energy source that can be converted into electrical energy using the Photovoltaics (PV) effect or thermal process. Considering the photovoltaic solar energy conversion, the Building Integrated Photovoltaic systems (BiPV) is an excellent technology for the energy market. In Chile, this field of energy is taking importance because there are optimal conditions in the Atacama Desert. However, in the field of urban environments is just beginning to work.

The complex urban environment with varying building block densities and even more so building elevations, combined with limited available construction data about the existing building stock, are the main reason for the difficulties emerging in the effort to assess solar potential. The solar energy potential of roofs on the urban level has been a significant support of renewable energy strategies action plans on urban or on an even broader level. The rooftops were the first surfaces to explorers when PV decided into an urban environment. However, this process is highly unsuitable for the estimation of solar potential over a broader region with thousands of rooftops. An automated approach is necessary for larger areas. Such methods produce results that are then displayed using a web-based Geographic Information System (GIS) application, which allows users to overview solar potential estimation for their buildings' rooftops (Brumen *et al.* 2014).

However, great efforts are usually made in search of low manufacturing cost by technology research (Socorro García-Cascales *et al.* 2012). To promote the utilization efficiency of solar energy is necessary to evaluate solar energy potential and analyze its distribution over urban areas and satisfy as much urban energy demand as possible (Li *et al.* 2016).

Many authors have worked in solar potential in cities, and they have used diverse methods to estimate de solar radiation in rooftop or facades. (Hachem *et al.* 2011) chose two-story single housing units as case studies to investigate the effects of roof shapes on solar energy potential. Yet these initial studies are often limited to self-shadowing in the built environment. To address the spatial factors, geographic information system (GIS) techniques are also frequently incorporated in the estimation. (Ordóñez *et al.* 2010). Through digital maps produced by Google Earth, they determined the solar potential for the installation of grid-connected photovoltaic systems on rooftops in Andalusia. (Tereci *et al.* 2009) applied LiDAR (Light Detection and Ranging) data to build a Digital Surface Model (DSM), determining the annual solar potential for identified building roofs in combination with ALK map data and GIS software. (Redweik *et al.* 2013) proposed a solar radiation method based on the r.sun radiation model developed by (Suri *et al.* 2007) and incorporated this in the open-source GRASS GIS. The results revealed that the potential of building facades is lower than the roofs, although they usually have large areas.

The objective of this paper is the estimation of the solar potential of rooftops in Campus San Joaquín, Santiago - Chile using opensource GIS, and the incidence of the radiation of albedo in the estimated radiation is analyzed. The first part of the paper present the methodology used with the opensource GIS: QGIS and the SEBE (Solar Energy Building Structures) (Lindberg *et al.* 2015) model although of Complement UMEP from QGIS, including the solar radiation as an input although of TMY built of Sandia National Laboratory (Serpil Yilmaz and Ismail Ekmekci 2017), and the features about Digital Surface Model (DSM) followed by an evaluation of the solar potential of rooftops in Santiago de Chile. Finally, the incidence of radiation of albedo is evaluated.

2. Methodology

2.1. Model

The assessment of the solar potential of rooftops is based on the model of (Lindberg *et al.* 2015), SEBE (Solar Energy on Building Structures), which is in the Urban Multi-scale Environmental Predictor (UMEP) complement of the open-source computer software QGIS.

2.2. Input Data.

The irradiation data used as input in the UMEP complement is a Typical Meteorological Year (TMY). It was built with hourly Global Horizontal Irradiation (GHI) data measured at the solar energy laboratory at the Pontificia Universidad Católica de Chile, San Joaquín campus. The Sandia National Laboratory method (Finkelstein and Schafer 1971) was used for building the TMY.

As well as the geographic location of the area (latitude, longitude, and altitude) and the time zone are obtained from the same Laboratory, whilst the data of the horizontal diffuse irradiance (DHI), the direct normal irradiance (DNI), were obtained through the BRL estimation model (Rojas *et al.* 2019). The digital surface model (DSM) was obtained through photogrammetry with a resolution of 1 m, and a dimension of 280 m x 395 m.

2.3. Typical Meteorological Year (TMY) and Irradiation data.

The Sandia method has been used for constructing the TMYs, which is based upon the Finkelstein-Schafer (FS) statistic for selecting the single month candidates (Finkelstein and Schafer 1971). The FS statistic for a meteorological variable X to be considered in the TMY is defined as,

$$FS_X(y,m) = \frac{1}{N}\sum_{i=1}^{N}\left|CDF_m(X_i) - CDF_{y,m}(X_i)\right| \qquad \text{(eq. 1)}$$

where CDF_m is the long-term cumulative distribution function of daily values of variable X for month m, $CDF_{y,m}$ is the short-term (corresponding to year y) cumulative distribution function of daily values of X, and N is the number of bins. The month candidate is corresponding to the minimum value of the weighted sum (WS) of FS statistics corresponding to each meteorological variable considered.

$$WS(y,m) = \sum_{X=1}^{M} W_X\ FS_X(y,m) \qquad \text{(eq. 2)}$$

Where W_X is the relative weight of the variable X, and M is the number of variables involved.

The data used as input for the analysis is obtained in the following way. In essence, the GHI is derived from the measurements obtained from the solar Laboratory of the Pontificia Universidad Católica de Chile, the rest of the components (DNI and DHI) are obtained from the BRL model of diffuse radiation prediction, applied for Santiago de Chile (Rojas *et al.* 2019). Using the eq. 3:

$$d = \frac{1}{1+e^{-6.274+7.6266k_t-0.0398AST-0.0178\alpha+2.606K_t+2.3392\psi}} \qquad \text{(eq. 3)}$$

Where k_t is hourly clearness index, AST is solar time, α solar altitude angle, K_t daily clearness index, and ψ is persistence.

2.4. Calculation of radiation in rooftops

In Fig. 1 shows the workflow of the calculation of the solar potential of rooftops. Firstly, we have the measured hourly GHI, then the BRL model is applied (García et al. 2017), and the artificial series of DHI and DNI are obtained. After that, the Sandia National Laboratory method is applied to build the TMY. The digital surface model (DSM) is made from photos taken from Google Earth and using the technique of photogrammetry to obtain a three-dimensional model, which in this case will be considered only the roofs of the DSM. Already with this data, we proceed to use the UMEP plug-in of the open-source software QGIS: the SEBE method. In this part of the process, factors such as wall height, wall aspect, the view factor are calculated from the DSM provided, and the value of albedo is introduced. The result of this process is the energy in the rooftops indicated in the MDS; they are superimposed in an OpenStreetMaps template, which coincides with the MDS since it is georeferenced according to the Universal Transversal Mercator (UTM) coordinates of the place under study.

The area of study is Campus San Joaquin, Santiago - Chile can be seen in the map obtained from OpenStreetMaps in Fig. 2. Consequently, the output of this methodology consists of several maps for roofs of total irradiance, annuals, monthly, or daily.

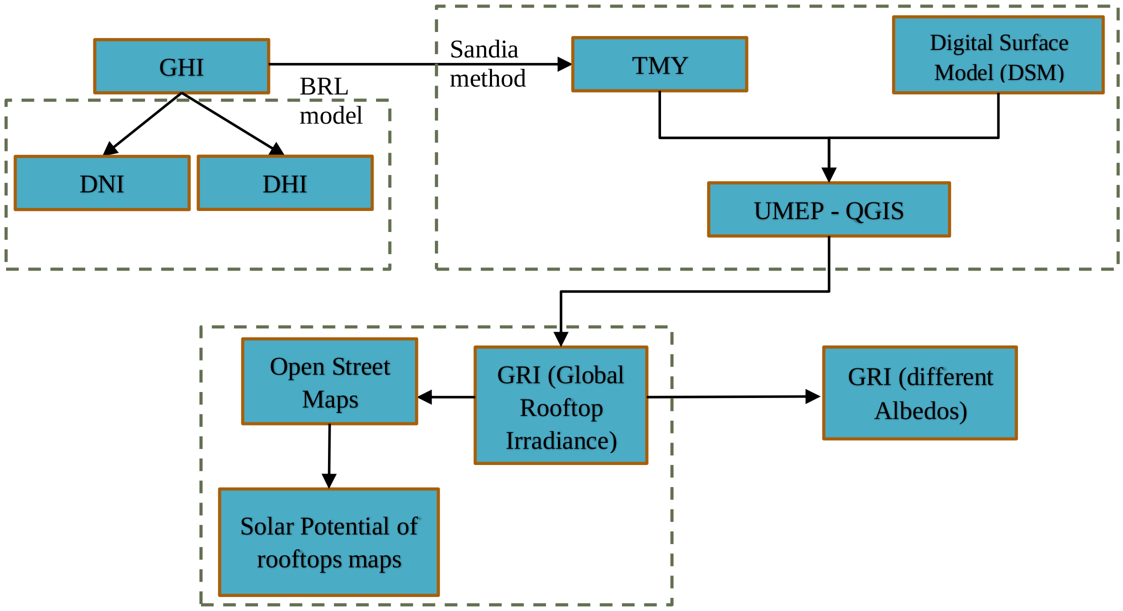

Fig. 1. Methodology to estimate solar potential on Campus San Joaquín, Santiago - Chile

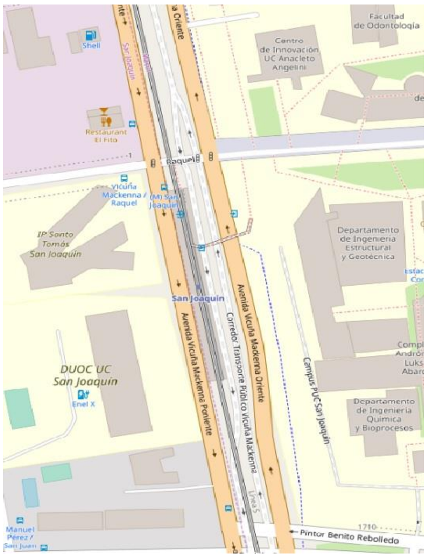

Fig. 2. Map from OpenStreetMaps of Campus San Joaquín, Santiago - Chile

3. Results

The results are shown below in Fig. 3 is the total monthly energy of two characteristic months such as January (summer) and June (winter), on the roofs of buildings on the San Joaquin campus, Santiago - Chile. It can be observed how the radiation on the rooftops tends to be uniform despite the different heights that each building has as well as it is remarkable that the selected urban environment is very open to the field of obstacles. Similarly, due to compacity, we can observe a slight change in the pattern of radiation. Even though not all the buildings were taken into account, it should be noted that the QGIS considers all the buildings, since the MDS has the information of all the heights present in the selected area.

In Fig. 4 shows the annual solar radiation over this study. As expected, this figure clearly illustrates that irradiation levels of building roofs are usually much higher when compared with ground surfaces. The study area is 280 m x 395 m, and the annual total solar energy reaches 1800 kWh/m^2/year. Moreover, this is compared with the global horizontal irradiation measured in Fig. 5, although the differences between estimated and observed values are slightly more than 4% for the first three months, the differences for winter months relatively high, and the average value is 43%.

In general line, we can see an overestimate of the estimated solar potential on the roofs concerning the incident radiation measured. It is due to the overlap of some buildings in others (Brito *et al.* 2019).

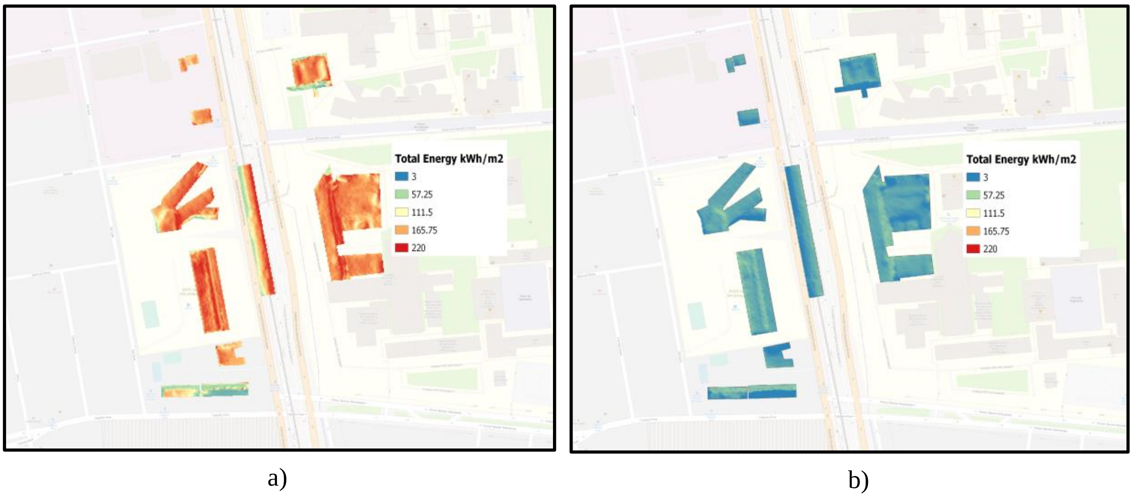

Fig. 3. Monthly Solar Potential on the rooftops. a) January, b) June

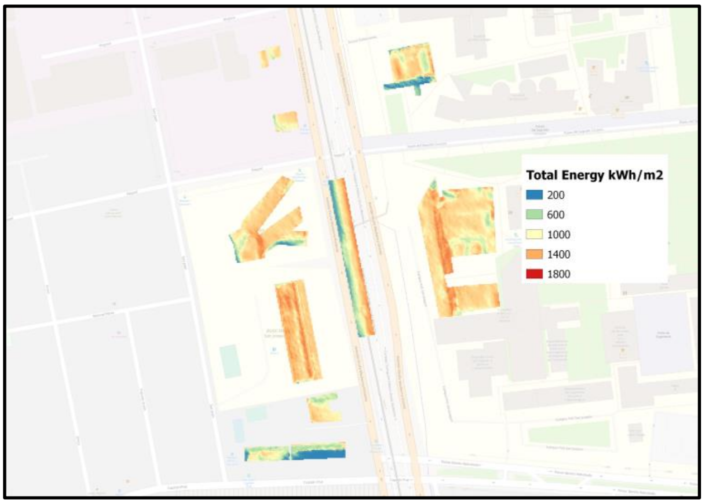

Fig. 4. Annual Solar Potential on Campus San Joaquín, Santiago - Chile

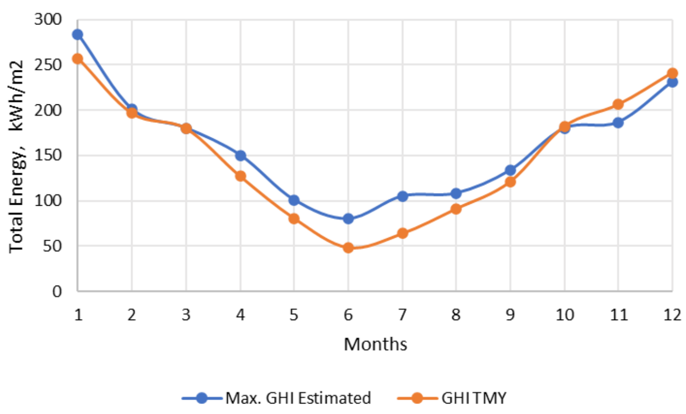

Fig. 5. Comparison GHI from TMY, and GHI on rooftops

Quantifying the graph of Fig. 5, we can see Tab. 1 in which we realize that the average quadratic error is 20 kWh/m^2. This value, in annual energy, does not have a greater incidence, we would be talking about an error of approximately 14%, which is evident in the winter months, but this is due to the effects of shadows by buildings close to each other.

Tab. 1. Metrics Errors for evaluating Solar Potential in rooftops

RMSE	20.9 kWh/m^2
NRMSE	14%

4. Sensitivity analysis of albedo radiation

One of the factors affecting the calculation of radiation in urban environments is reflected radiation, in which the albedo is the main factor, depending on the surfaces surrounding the buildings under study. In the case of roofs, the incidence of albedo only depends on higher buildings with very distinct wall surfaces. To have an idea of the construction materials found in urban environments, Tab. 2 is shown, where the albedo value and the emissivity of each material are also shown.

Tab. 2. The albedos of various materials.

Material	Albedo	Emissivity
Concrete	0.3	0.94
Red Brick	0.3	0.90
Building Brick	-	-
Concrete tiles	-	0.63
Wood (Freshly planed)	0.4	0.90
White paper	0.75	0.95
Tar paper	0.05	0.93
White Plaster	0.93	0.91
Bright galvanized iron	0.35	0.13
Bright aluminium foil	0.85	0.04
White pigment	0.85	0.96
Grey pigment	0.03	0.87
Green pigment	0.73	0.95
White paint on aluminium	0.80	0.91
Black paint on aluminium	0.04	0.88
Aluminium paint	0.80	0.27-0.67

Gravel	0.72	0.28
Sand	0.24	0.76

Surface material with a high albedo index (reflectivity) to solar radiation reduces the amount of energy absorbed through building envelopes and urban structures and keep their surfaces cooler. Materials with high emissivities are good emitters of long-wave energy and readily release the energy that has been absorbed as short-wave radiation (Asimakopoulos *et al.* 2011).

In our case, we used albedo values between 0.1 and 0.6 to exemplify that the buildings were surrounded by other structures that are made of various construction materials that often exist in today's urban environments. In Fig. 6, the behavior of the total radiation is observed as it tends to increase linearly. The differences in the increase of the annual solar potential estimated with albedos between 0.2 and 0.4 trends to be constant. When the albedo tends to be less than 0.2, the radiation no longer experiences any change but remains constant.

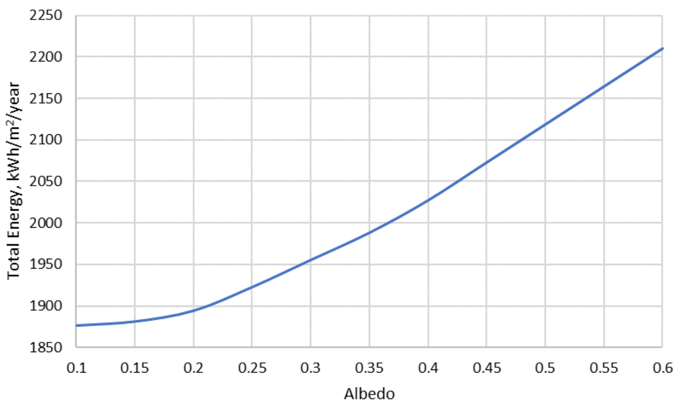

Fig. 6. Solar potential of rooftops with different albedo values

5. Conclusions

In this paper, we have described a methodology for estimating solar potential on roofs through an open-source computer tool QGIS. The Solar Energy on Building Envelopes (SEBE) model for the estimation of short-wave irradiance on roofs is a UMEP add-on to the QGIS computer software. It is classified as a 2.5-dimensional model and makes use of digital surface models to calculate solar radiation. Our digital surface model was obtained through a process called photogrammetry based on satellite photos taken from Google Earth. To get a detailed description of the forcing conditions, the model uses a TMY built through the Sandia National Laboratory methodology using as a basis the measured global horizontal irradiation, diffuse, and direct normal radiation estimated through the BRL model. The methodology was validated against measurements made on-site, showing a slight overestimation in the winter months compared to the summer months. However, this error is mostly due to the effect of compactness of the studied area. An albedo sensitivity analysis was also performed, in which it is evident that the increase of the estimated radiation in the rooftops is linear. Still, the differences in the rise between albedos 0.2 and 0.4 tend to remain constant, therefore, because the compactness effect is relatively meaningless, to use very high albedos.

6. Acknowledgments

Redlich García would like to thank the Chilean National Commission for Scientific and Technological Research (CONICYT) for his doctoral scholarship as per the CONICYT PHCA/DoctoradoNacional/21171766, and CIEMAT for the opportunity to do my international internships.

7. References

Asimakopoulos, D.N., Asimakopoulos, V.D., Chrisomallidou, N., Klitsikas, N., Mangold, D., Michel, P., Santamouris, M. and Tsangrassoulis, A. 2011. *Energy and Climate in the Urban Built Environment* Santamouris, M. (ed.). Routledge, New York.

Brito, M.C., Redweik, P., Catita, C., Freitas, S. and Santos, M. 2019. 3D solar potential in the urban environment: A case study in lisbon. *Energies* 12.

Brumen, M., Lukač, N. and Žalik, B. 2014. GIS Application for Solar Potential Estimation on Buildings Roofs. *... on Building and Exploring Web Based ...* Brumen, M.: 1–6.

Finkelstein, J.M. and Schafer, R.E. 1971. Improved goodness-of-fit tests. *Biometrika* 58: 641–645.

Hachem, C., Athienitis, A. and Fazio, P. 2011. Parametric investigation of geometric form effects on solar potential of housing units. *Solar Energy* 85: 1864–1877.

Ilyushina, M. 2020. Putin declares emergency over 20,000 ton diesel spill. *CNN*: 1.

Li, Y., Ding, D., Liu, C. and Wang, C. 2016. A pixel-based approach to estimation of solar energy potential on building roofs. *Energy and Buildings* 129: 563–573.

Lindberg, F., Jonsson, P., Honjo, T. and Wästberg, D. 2015. Solar energy on building envelopes - 3D modelling in a 2D environment. *Solar Energy* 115: 369–378.

Ordóñez, J., Jadraque, E., Alegre, J. and Martínez, G. 2010. Analysis of the photovoltaic solar energy capacity of residential rooftops in Andalusia (Spain). *Renewable and Sustainable Energy Reviews* 14: 2122–2130.

Redweik, P., Catita, C. and Brito, M. 2013. Solar energy potential on roofs and facades in an urban landscape. *Solar Energy* 97: 332–341.

Rojas, R.G., Alvarado, N., Boland, J., Escobar, R. and Castillejo-Cuberos, A. 2019. Diffuse fraction estimation using the BRL model and relationship of predictors under Chilean, Costa Rican and Australian climatic conditions. *Renewable Energy* 136: 1091–1106.

Serpil Yilmaz and Ismail Ekmekci. 2017. The Generation of Typical Meteorological Year and Climatic Database of Turkey for the Energy Analysis of Buildings. *Journal of Environmental Science and Engineering A* 6.

Socorro García-Cascales, M., Teresa Lamata, M. and Miguel Sánchez-Lozano, J. 2012. Evaluation of photovoltaic cells in a multi-criteria decision making process. *Annals of Operations Research* 199: 373–391.

Suri, M., Huld, T., Dunlop, E.D. and Ossenbrink, H. 2007. Potential of Solar electricitygeneration in the European Union member states and candidate countries (Suri 2007).pdf. *Solar Energy* 81: 1295–1305.

Tereci, A., Schneider, D., Kesten, D., Strzalka, A. and Eicker, U. 2009. Energy saving potential and economical analysis of solar systems in the urban quarter scharnhauser park. *29th ISES Biennial Solar World Congress 2009, ISES 2009* 2: 1814–1822.

Cooling Potential of Solar-Ice Systems in Multi-Family Buildings

Mattia Battaglia, Jeremias Schmidli, Maike Schubert and Daniel Carbonell

Institut für Solartechnik (SPF), Ostschweizer Fachhochschule (OST),
CH-8640 Rapperswil, Switzerland

Abstract

Solar-ice systems are an emerging technology to provide renewable heat. Storing the ice that is generated during the heating season until summer can help to cover the increasing cooling demand in residential buildings. The potential of this approach is analyzed based on dynamic yearly system simulations in TRNSYS. Two different control strategies are discussed for three different locations in Switzerland. The results demonstrate that a passive cooling approach can provide cooling that is sufficient for a well insulated multi-family building in Zurich with little additional costs. To increase the cooling potential of the system, the heat pump operation for domestic hot water preparation can be used during the summer months.

Keywords: ice storage, solar heating and cooling, system simulation

Nomenclature

A_{coll}	collector area	V_{ice}	ice storage volume
Q_{sc}	space cooling energy	$Q^{heat,pri}_{ice-storage}$	heat from primary loop to ice storage
$Q^{gains}_{ice-storage}$	heat gains ice storage wall	$Q^{cool,pri}_{ice-storage}$	cold from primary loop to ice storage
$Q^{losses}_{ice-storage}$	heat losses ice storage wall	Q^{acum}_{ice}	ice storage total accumulated cooling energy
Q_{dhw}	domestic hot water demand	Q^{loss}_{circ}	circulation losses
Q_{sh}	space heating demand	Q_{sc}	space cooling demand
$Q_{ice-storage,walls}$	total energy transfer walls	Q_{col}	solar collector gains
$El_{Hp,comp}$	el. consumption heat pump	$El^{Aux}_{Tes,sh}$	el. consumption auxiliary heater sh
$El^{Aux}_{Tes,dhw}$	el. consumption auxiliary heater dhw	SPF	system performance factor

doi:10.18086/eurosun.2020.01.13 Available at http://proceedings.ises.org

1. Introduction

Ice storages are a well proven technology for cooling applications where their main role consists in peak shaving of cooling loads at noon or in providing high cooling power for industrial processes. On the other hand, an ice storage can also be used for solar heating applications which is a promising way to increase the share of renewable energy in buildings. It has been demonstrated that the system can reach a yearly average performance that is comparable to ground source systems by making use of the latent heat that is released during icing as a source for the heat pump (Abrahamsson et al., 1981, Carbonell et al., 2016b). In future climate scenarios, increased cooling demand during summer will lead to increased stress in energy supply systems (Jakubcionis and Carlsson, 2017). Therefore, new approaches for energy efficient cooling are needed. In this study, it is analyzed if the ice produced in the ice storage of a solar-ice system during the heating season can be stored during spring and used for cooling during summer with minimal additional energy consumption.

2. Solar ice-system system concept

The solar-ice system investigated has been subject of several experimental and modelling studies (Carbonell et al., 2016a, 2014). This study builds on a recent publication in which different hydraulic layouts of the system were tested for their performance to meet the demand of a multi-family building (Carbonell et al., 2019). To provide solar-ice systems the cooling functionality, the ice produced in the heating season is stored for later use in the cooling season. Thus, the ice storage can not serve as a heat sink for the evaporator during this period. Therefore, the system layout needs to provide a connection of the solar collector to the heat pump. For the simulations described in this report, the archetype that is shown in Figure 1 was used. In this variant of a solar-ice system, the heat of the solar collector can be delivered to three different heat sinks: to the thermal energy storages, to the evaporator of the heat pump or to the ice storage.

The physical layout that was simulated is shown in Figure 2. The only renewable heat source of the system is the solar collector field, that with first priority delivers heat to the heat pump evaporator in winter periods. If the outlet temperature of the solar collector is high enough, the solar thermal energy is used to charge the domestic hot water storage and with second priority the space heating storage. If the source temperature provided by the solar collector drops below the minimal evaporator input temperature, the collector operation is stopped and the heat pump runs completely using the ice storage. The domestic hot water is delivered by an external heat exchanger unit. On the demand side of the external domestic hot water heat exchanger, fast availability of hot water during tapping is guaranteed by a circulation loop. In time steps with no tapping, a second double port is used in the domestic hot water storage tank to account for the higher return temperatures of the circulation loop.

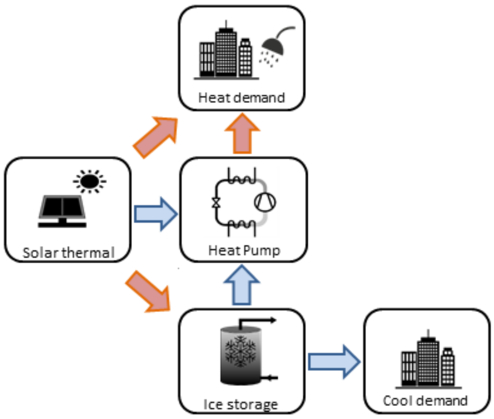

Fig. 1: Simplified solar-ice system concept.

In order to use the solar-ice system for cooling during summer, two different control strategies have been analyzed. They both extend a base solar-ice control that was described in detail in Philippen et al. (2015) for the particular case of thermal-deicing and in Carbonell et al. (2017a) without the deicing functionality. Since cooling exhibits high peak power during summer, large heat exchanger areas are necessary in the system. Therefore, for this double purpose system, a system without deicing is considered in which the heat exchangers cover the whole storage volume. During normal heating operation the control has the following three priorities

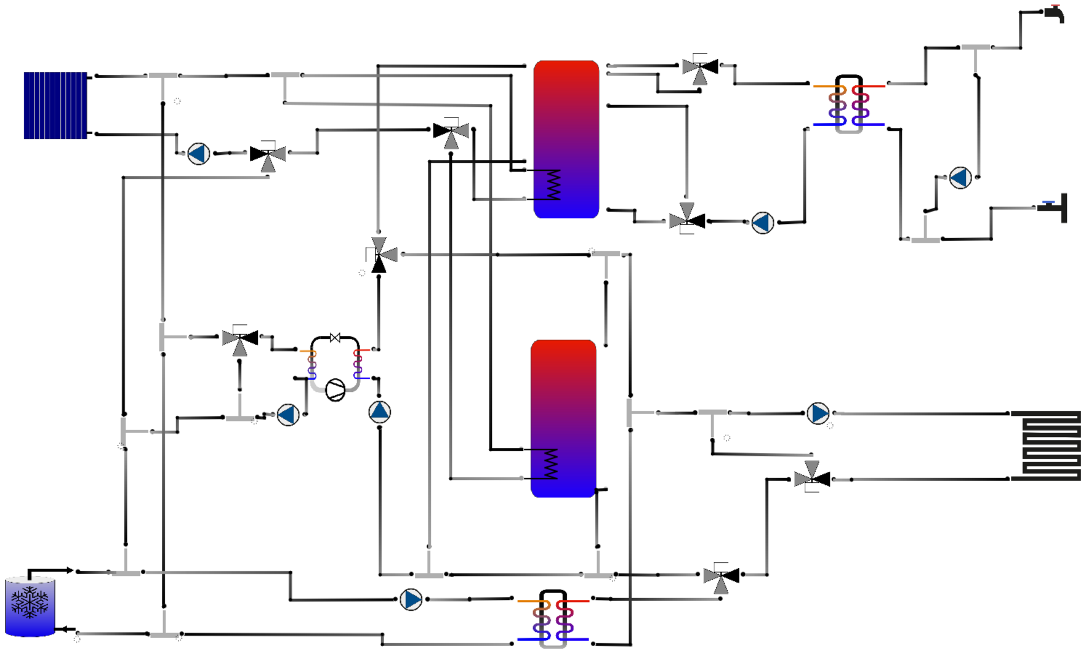

Fig. 2: Hydraulic scheme of the simulation.

1. Use the solar heat for direct charging of the domestic hot water storage.
2. Use the solar heat for direct charging of the space heating storage (only during heating season).
3. Switching on the heat pump when needed to provide the heat demand with the solar collectors as the main heat source.
4. Operate the heat pump with the ice storage as the main heat source in case of too low source temperatures of the solar collectors.
5. Use the low-grade solar heat to load/regenerate the ice storage.

The cooling was added to the control by avoiding active regeneration of the ice storage below an ice fraction of 50 % from March to September to preserve the ice in the latent storage. Some ice melting from the maximum ice fraction of 80 % to 50 % was included to still enable heat extraction in case of high heating demand during March and April.

The first cooling strategy is the **passive cooling** mode. In this approach, no additional changes besides the stopping of the ice storage charging in spring are present. The goal of this strategy is to cover as much demand as possible by simply storing the ice in the ice storage from the heating period to the cooling period. This approach will have only little influence on the SPF of the heating system but the total amount of cooling capacity will be strictly limited to the ice storage volume and the heat gains from the ground during spring.

Since for many applications, the passive cooling approach will not be able to cover the cooling demand, the cooling by a heat pump in DHW mode was added as a second control strategy. In this mode, in addition to the changes described for the first mode, the direct charging of the domestic hot water storage tank by solar collectors is completely suppressed during the summer months. In fact, solar collectors are not used at all during summer months, not even as a heat source for the heat pump to provide the DHW demands. This forces the heat pump to extract heat from the ice storage during the preparation of domestic hot water which will add more cooling capacity to the system. However, this will result in a decreased overall system efficiency SPF_{SHP+} since the heat pump will run in time periods where solar collectors could cover the DHW demand more energetically efficient.

2.1. Performance indicators

The main performance indicator for the systems is the System Performance Factor calculated as described in Malenkovic et al. (2012):

$$SPF_{SHP+} = \frac{Q_{DHW} + Q_{SH}}{P_{el,T}} = \frac{Q_D}{P_{el,T}} \tag{1}$$

Q is the yearly heat demand and $P_{el,T}$ the yearly electricity consumption of the heating system. The subscripts SHP, DHW, SH and D stand for solar and heat pump, domestic hot water, space heating, and total demand respectively.

The yearly electricity consumption is calculated as:

$$P_{el,T} = P_{el,pu} + P_{el,hp} + P_{el,cu} + P_{el,back-up} + P_{el,pen} \tag{2}$$

where the subscripts pu, hp, cu, aux and pen refer to circulation pumps, heat pump, control unit, back-up and penalties respectively. The symbol "+" in the SHP+ from Eq. 1 refers to the consideration of the heat distribution circulating pump in the electricity consumption. Therefore, the system performance indicator used in this work includes all circulation pumps of the system and also all thermal losses/gains from storages and piping. Penalties for not providing the heating demand at the desired comfort temperature are calculated according to Haller et al. (2012). $P_{el,back-up}$ is the energy used from the direct electric back-up system. This back-up is implemented with two electrical rods for DHW and SH in the storage. The back-up is switched on when the temperature of the brine at the inlet of the evaporator drops below $-8\,°C$. This is the case when the ice storage is at its maximum allowed ice fraction and the energy gained in the collector field is not sufficient (night or foggy times with low ambient temperatures).

3. Simulation model

The simulations were done in TRNSYS 17 (Klein et al., 2010) using the open source python framework pytrnsys (Carbonell et al., 2020). The pytrnsys framework allows the fast and efficient simulation and processing of parametric runs by splitting the TRNSYS dck file into component specific ddck files. The simulation timestep was set to 2 minutes in all simulations. In total 14 months starting from July were simulated to ensure correct initialization of the ice storage. The results were taken from the last 12 months of the simulation starting in September.

3.1. Weather data and building model

The building simulated is the reference multi-family building MFB30 (Iturralde et al., 2019). The building represents a typical swiss multi-family building with 6 flats and high insulation standard. For the study of the cooling potential three locations in Switzerland with different characteristics were included. Zurich represents the climatic conditions of the densely populated Swiss midlands with medium heating demand and low cooling demand. The city of Geneva is included as an example of slightly warmer climatic conditions with medium heating demand and medium cooling demand. The location of Locarno in the Swiss south has reduced heating demand and increased cooling demand compared to other Swiss cities while still being in a heating dominant region. The heating set point temperature was at 21 °C and the cooling set point temperature at 24 °C. The

Tab. 1: Heating and cooling demand of the MFB30 building in the three cities.

Month	Zurich (SMA)		Geneva (GVE)		Locarno (OTL)		DHW
	Heat (kWh)	Cold (kWh)	Heat (kWh)	Cold (kWh)	Heat (kWh)	Cold (kWh)	(kWh)
Jan	6741	0	5858	0	5328	0	1581
Feb	5281	0	4554	0	3104	0	1347
Mar	3521	0	2097	0	1221	0	1406
Apr	4845	0	3862	0	2767	0	1460
May	1919	0	1287	0	550	60	1535
Jun	65	604	0	1092	0	2137	1460
Jul	0	1198	0	2663	0	2985	1351
Aug	0	712	0	1879	0	3582	1577
Sept	1074	0	507	0	0	0	1363
Oct	1906	0	741	0	251	0	1558
Nov	4458	0	3943	0	2995	0	1398
Dec	6373	0	5649	0	5028	0	1525
Total	36187	2514	28501	5634	21247	8764	17564

summary of the resulting demands of the three different locations can be found in Table 1.

3.2. Ice Storage Model

The ice storage model used is described in detail in Carbonell et al. (2018). For the simulations a capillary mat model was used. The distance between the capillary mats was set to 10 cm. The distances between the capillary pipes in the mat was assumed to be 3 cm according to products available on the market. The total ice storage volume was set relative to the yearly heating and domestic hot water demand expressed in MWh. Values in the range of $0.5\,\mathrm{m^3/MWh}$ to $1\,\mathrm{m^3/MWh}$ were investigated that were found to lead to systems that are economically competitive compared to ground source heat pump systems(Carbonell et al., 2017b). The ice storage was assumed to have a quadratic layout and a height of 2.5 m.

Furthermore, it was assumed that the ice storage is buried in the ground next to the building. The ice storage is insulated with a foam of heat conductivity $0.041\,\mathrm{W/(mK)}$ and thickness 5 cm resulting in a U-value of $0.82\,\mathrm{W/(m^2K)}$. The ground model and the used parametrization is described in detail in Carbonell et al. (2016b).

4. Results

As a base case, a system dimensioned to economically and energetically compete to ground source systems has been simulated (Carbonell et al., 2017b). The ice storage volume was set to $0.5\,\mathrm{m^3/MWh}$ which in the location of Zurich resulted in a total volume of $27\,\mathrm{m^3}$. The collector area was set to $1.75\,\mathrm{m^2/MWh}$ which led to a size of 93 $\mathrm{m^2}$. The overall heat balance of the passive cooling system in the location of Zurich is shown in Figure 3. The heat sources of the system are the collector gains Q_{col}, the electricity consumption of the heat pump $El_{\mathrm{Hp,comp}}$ as well as the auxiliary heaters in the space heating tank $El^{\mathrm{Aux}}_{\mathrm{Tes,sh}}$ and the domestic hot water tank $El^{\mathrm{Aux}}_{\mathrm{Tes,dhw}}$. The heat sinks of the system are the domestic hot water demand Q_{dhw}, the space heating demand Q_{sh} and the circulation losses $Q^{\mathrm{loss}}_{\mathrm{circ}}$. Depending on the average state of the ice storage in a month, the accumulated heat $Q^{\mathrm{acum,\,sens+lat}}_{\mathrm{ice-storage}}$ and the heat transfer through the ice storage wall $Q_{\mathrm{ice-storage,walls}}$ can have positive or negative monthly values. In Fig. 3 the pipe and the losses of the thermal storage have been omitted as they have only a minor effect on the yearly scale. The results show, that with the chosen system size the ice storage starts to be fully iced in January and the electric backup has to provide some of the heat during the winter months. This is a result of the sizing concept that aims to reduce the cost of the solar ice system and to make it economically more attractive while reaching $SPF_{\mathrm{SHP+}}$ in the range of ground source heat pumps.

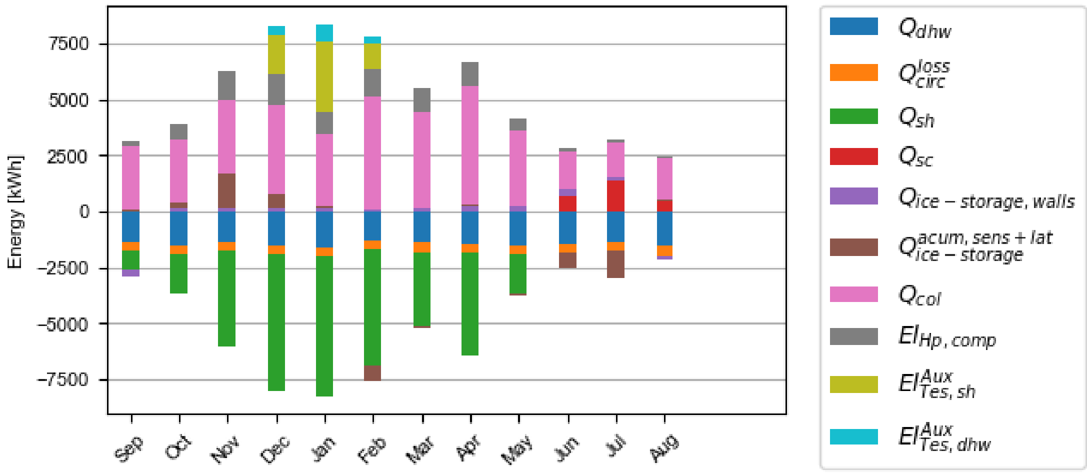

Fig. 3: Heat balance of the passive cooling system in Zurich.

4.1. *Passive cooling*

In order to analyze in detail the cooling potential of the passive control approach, the corresponding energy balance of the ice storage is shown in Figure 4. The balance involves the cold $Q_{sc}^{extracted}$ delivered by the ice storage to the space cooling system, the heat gains and losses through the ice storage wall $Q_{walls}^{gains/losses}$, the heat and cold delivered to the ice storage by the solar collector and the heat pump $Q_{col}^{delivered}/Q_{hp}^{extracted}$ as well as the cooling energy accumulated in the ice storage $Q^{acum, sens+lat}$. Figure 4 shows the monthly cumulative values starting from September. The total amount of heat extracted from the ice storage between September and January adds up to 2526 kWh. While this exceeds the total cooling demand of 2514 kWh in Zurich, not all energy is kept during spring. In the months between February and May 674 kWh of cooling energy in the ice storage are lost due to natural melting by heat gains from the ground. In addition, a warm period is present in late February in the weather data that was used for Zurich. Since the used cooling control stops normal operation to prevent melting not before the beginning of March this leads to some active regeneration of the ice storage. Part of the losses in stored ice capacity are compensated by some additional heat that is extracted during spring due to the heat pump operation, mostly for space heating.

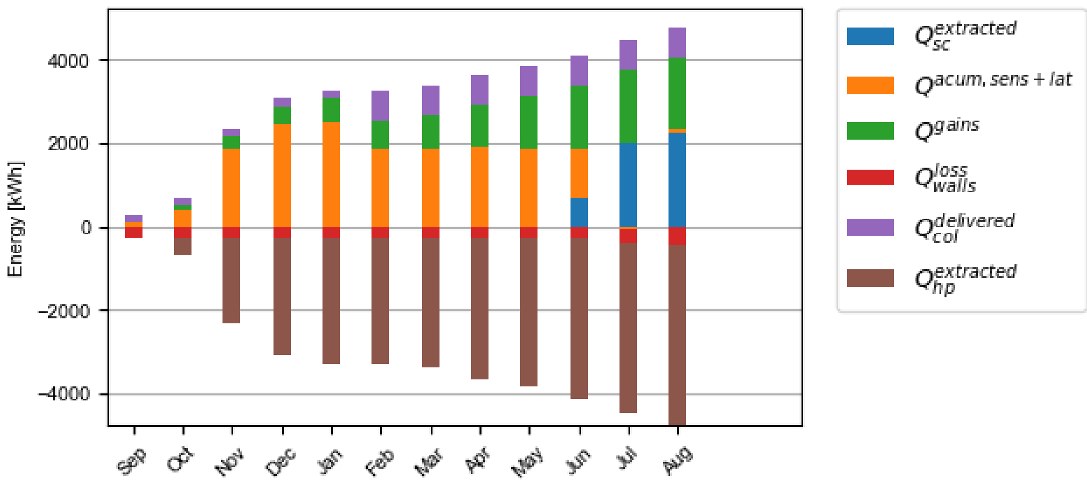

Fig. 4: Heat balance on the ice-storage of the passive cooling system in Zurich.

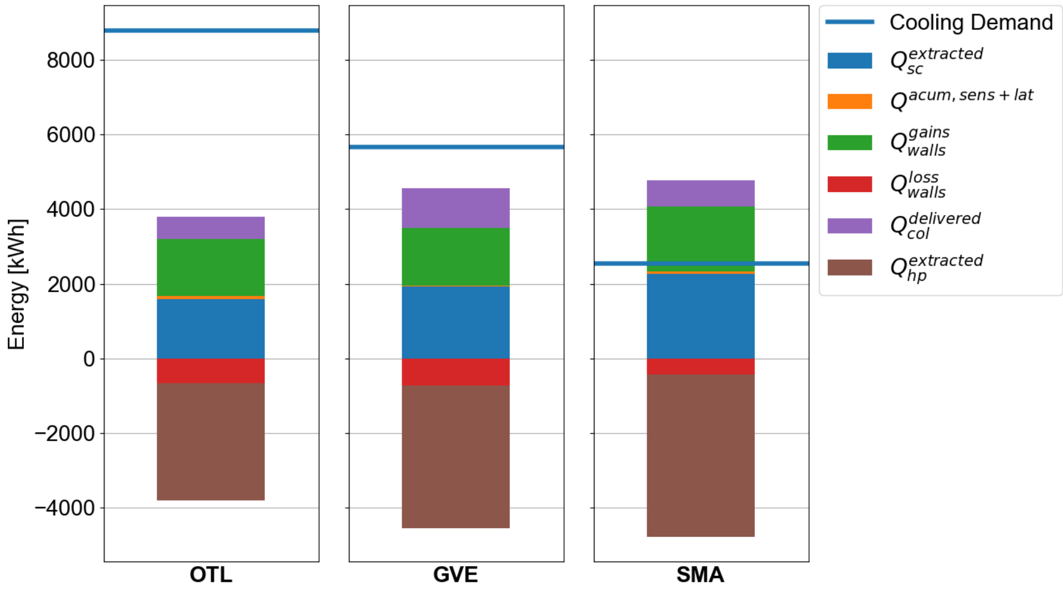

Fig. 5: Final cumulative heat balance after one year of the passive cooling strategy in Zurich (SMA,V_{ice}=26.6 m^3, A_{col}=93.1 m^2), Geneva (GVE,V_{ice}=22.8 m^3), A_{col}=79.6 m^2) and Locarno (OTL,V_{ice}=19.1 m^3, A_{col}=67.0 m^2).

Tab. 2: Summary of provided cooling energy and corresponding SPFs for the simulated system variants.

Strategy	V_{ice}	A_{col}	Zurich (SMA)		Geneva (GVE)		Locarno (OTL)	
			Cold	SPF_{SHP+}	Cold	SPF_{SHP+}	Cold	SPF_{SHP+}
	m^3/MWh	m^2/MWh	kWh	-	kWh	-	kWh	-
No Cooling	0.5	1.75	-	3.3	-	4.3	-	5.6
Passive Cooling	0.5	1.75	2485	3.2	2133	4.1	1797	5.4
Passive Cooling	1.0	1.5	2730	3.3	3633	4.4	3267	5.2
Cooling-By-Hp	0.5	1.75	2916	3.0	4635	3.8	5141	4.8

In Figure 5, the cumulated monthly balance results for one completed year are shown for different locations. The overall results shows that the passive cooling approach is approximately able to provide the defined cooling demand in Zurich but not the higher cooling demands in Locarno (OTL) and Geneva (GVE). The total cooling energy delivered by the system in Locarno and Geneva is even lower than that of Zurich due to the lower ice storage volume used. Notice that ice storage volume is sized with respect to the heating demand and this is lower in Geneva and Locarno compared to Zurich. The effect of the passive cooling strategy on the yearly SPF of the system is given in Table 2. The results confirm that the passive cooling does not affect the SPF significantly, showing deviations from the system without cooling of below 5 %.

Since the cooling potential in the passive cooling approach is limited by the ice volume in the end of the heating season, a larger ice storage volume of 1 m^3/MWh in combination with a reduced collector area of 1.5 m^2/MWh has been investigated. The results of the simulations are shown in Figure 6. It can be seen that increasing the storage size while reducing the collector area can significantly increase the cooling potential of the system. However, in the case of Locarno, the decreased collector area had a negative influence on the SPF_{SHP+}. Notice that the reduction of the collector field is proposed to keep the installation cost similar when increasing the ice storage with the added benefit of being able to provide more cooling demand for *free*.

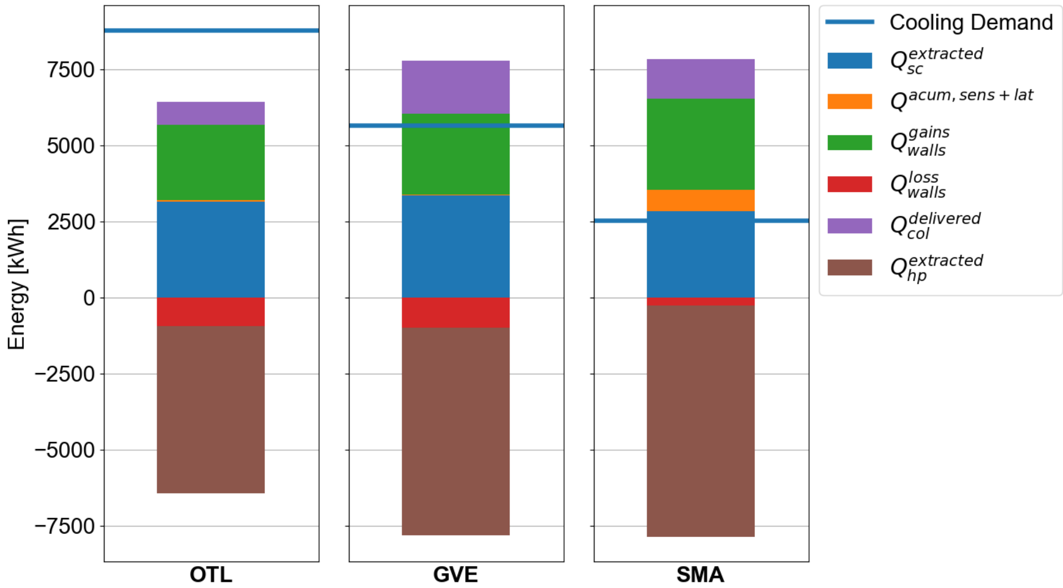

Fig. 6: Final cumulative heat balance after one year of the passive cooling strategy using an ice storage volume of $1.0\,\mathrm{m}^3/\mathrm{MWh}$ **and a collector area of** $1.5\,\mathrm{m}^2/\mathrm{MWh}$ **in Zurich** $(\mathrm{SMA}, \mathrm{V}_{\mathrm{ice}} = 53.2\,\mathrm{m}^3, \mathrm{A}_{\mathrm{col}} = 79.8\,\mathrm{m}^2)$**, Geneva** $(\mathrm{GVE}, \mathrm{V}_{\mathrm{ice}} = 45.5\,\mathrm{m}^3, \mathrm{A}_{\mathrm{col}} = 68.3\,\mathrm{m}^2)$ **and Locarno** $(\mathrm{OTL}, \mathrm{V}_{\mathrm{ice}} = 38.2\,\mathrm{m}^3, \mathrm{A}_{\mathrm{col}} = 57.4\,\mathrm{m}^2)$

4.2. Cooling by heat pump in domestic hot water mode

The comparison of the results for the three different locations with the cooling by the heat pump in domestic hot water strategy are shown in Figure 7. The simulations show that the cooling energy provided in Geneva and Locarno is increased by 2503 kWh and 3344 kWh respectively. These results correspond well to the total amount of domestic hot water demand during the cooling season of 5484 kWh which, in combination with the heat pump coefficient of performance map, sets an upper limit to the potential increase of available cooling energy compared to the passive cooling case.

The increased use of the heat pump for domestic hot water preparation reduces the overall system performance of the heating system as can be seen in Table 2. The decrease in SPF now exceeds 10 % in all locations as can be seen in Table 2.

5. Conclusions

The presented system simulations demonstrate the general potential of the solar-ice system for cooling application. Using an economically feasible dimensioning of the system, sufficient cooling can be provided for location with low demand like Zurich by simply stopping the active melting of the ice during spring. This approach has the advantage of not reducing the $\mathrm{SPF}_{\mathrm{SHP+}}$ of the heating system significantly as well as affording minimal additional costs for implementation.

A passive cooling approach is not sufficient to cover the demand in locations with higher cooling demand such as Geneva or Locarno. If the ice storage volume is defined according to the heating demand, the lower ice capacity available from heating in a warmer climate does not help to deal with higher cooling demand during summer. Some optimization can be made by increasing the ice storage volume and enhancing the heat extraction of the heat pump during the heating season. However, this measures also lead to additional costs and it would have to be evaluated if such systems would be economically competitive.

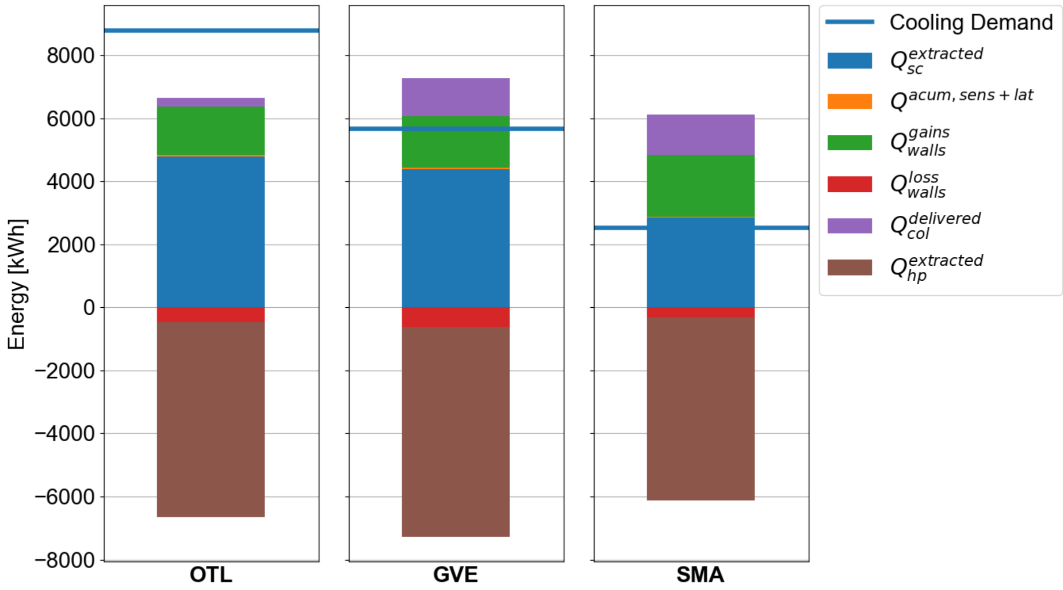

Fig. 7: Final cumulative heat balance after one year of the Cooling-By-Hp strategy using an ice storage volume of $0.5\,\mathrm{m}^3/\mathrm{MWh}$ **and a collector area of** $1.75\,\mathrm{m}^2/\mathrm{MWh}$ **in Zurich** ($\mathrm{SMA}, V_{ice} = 26.6\,\mathrm{m}^3, A_{col} = 93.1\,\mathrm{m}^2$)**, Geneva** ($\mathrm{GVE}, V_{ice} = 22.8\,\mathrm{m}^3, A_{col} = 79.6\,\mathrm{m}^2$) **and Locarno** ($\mathrm{OTL}, V_{ice} = 19.1\ \mathrm{m}^3, A_{col} = 67.0\ \mathrm{m}^2$)

By using the cold of the heat pump evaporator during the summer months, the cooling potential of the system can be more than doubled. Since the heat pump replaces freely available heat from the solar collector, such an approach leads to a decreased $\mathrm{SPF}_{\mathrm{SHP+}}$ of the system. Whether such an approach is economically beneficial will largely depend on the case-to-case basis and should be considered in future works.

Acknowledgments

The authors would like to thank the Swiss Federal Office of Energy (SFOE) for the financing support received under the project BigIce.

References

Abrahamsson, T., Jonson, S., Lagerkvist, K.O., 1981. Heat from solar energy and air with storage in water and ice, The Bramhult project in Boras: design, building, and performance evaluation of a Swedish solar energy and heat pump system for six detached houses. Swedish Council for Building Research in Stockholm, Sweden.

Carbonell, D., Battaglia, M., Daniel, D.P., Haller, M.Y., 2017a. Ice-Ex - Heat Exchanger Analyses for Ice Storages in Solar and Heat Pump Applications. Institut für Solartechnik SPF for Swiss Federal Office of Energy (SFOE), Research Programme Solar Heat and Heat Storage, CH-3003 Bern.

Carbonell, D., Battaglia, M., Philippen, D., Haller, M., 2018. Numerical and experimental evaluation of ice storages with ice on capillary mat heat exchangers for solar-ice systems. International Journal of Refrigeration 88, 383 – 401.

Carbonell, D., Battaglia, M., Schmidli, J., Schubert, M., Neugebauer, M., 2020. pytrnsys. `https://github.com/dcarbonellsanchez/pytrnsys`.

Carbonell, D., Granzotto, M., Battaglia, M., Philippen, D., Haller, M.Y., 2016a. Experimental investigations of heat exchangers in ice storages for combined solar and heat pump systems., in: 11^{th} ISES EuroSun Conference, International Solar Energy Society (ISES), Palma (Mallorca), Spain.

Carbonell, D., Philippen, D., Battaglia, M., Haller, M.Y., 2017b. Cost energetic analyses of ice storage heat exchangers in solar-ice systems, in: ISES Conference Proceedings. International Conference on Solar Heating and Cooling for Buildings and Industry (SHC 2017), Abu Dhabi, United Arab Emirates.

Carbonell, D., Philippen, D., Granzotto, M., Haller, M.Y., Frank, E., 2014. Simulation of combined solar thermal, heat pump, ice storage and waste water heat recovery systems. Design criteria and parametric studies., in: Proceedings of EuroSun, International Solar Energy Society (ISES), Aix les Bains, France.

Carbonell, D., Philippen, D., Haller, M.Y., 2016b. Modeling of an ice storage buried in the ground for solar heating applications. Validations with one year of monitored data from a pilot plant. Solar Energy 125, 398–414.

Carbonell, D., Schmidli, J., Philippen, D., Haller, M., 2019. Solar-ice systems for multi-family buildings: hydraulics and weather data analysis. E3S Web of Conferences 111, 01013.

Haller, M.Y., Dott, R., Ruschenburg, J., Ochs, F., Bony, J., 2012. The reference framework for system simulation of the IEA SHC Task44/HPP Annex 38: Part A : General simulation boundary conditions. Technical Report IEA-SHC Task44 Subtask C.

Iturralde, J., Alonso, L., Carrera, A., Salom, J., Battaglia, M., Carbonell, D., 2019. Energy demands for multi-family buildings in different climatic zones. Deliverable D1.1 of H2020 TRI-HP (www.tri-hp-eu). https://doi.org/10.5281/zenodo.3763249 .

Jakubcionis, M., Carlsson, J., 2017. Estimation of European Union residential sector space cooling potential. Energy Policy 101, 225–235.

Klein et al., 2010. TRNSYS 17: A Transient System Simulation Program, Solar Energy Laboratory. Technical Report. University of Wisconsin, Madison, USA, http://sel.me.wisc.edu/trnsys.

Malenkovic, I., Eicher, S., Bony, J., 2012. Definition of main system boundaries and performance figures for reporting on SHP systems. IEA-SHC Task44 Subtask B.

Philippen, D., Carbonell, D., Granzotto, M., Zenhäusern, D., Haller, M.Y., Brunold, S., 2015. High-Ice - System development for high solar thermal gains with ice storage and heat pump. Institut für Solartechnik SPF for Swiss Federal Office of Energy (SFOE), Research Programme Solar Heat and Heat Storage, CH-3003 Bern.

Solar Steel Sandwich Panels for Industrial and Commercial Buildings: System Simulations and Potential Analysis

Finn Weiland, Maik Kirchner, Fabian Hüsing, Federico Giovannetti

Institute for Solar Energy Research in Hamelin (ISFH), Emmerthal (Germany)

Abstract

Building integration can improve the architectural and aesthetical quality of solar installations and reduce their cost. The development and performance assessment of solar steel sandwich panels for the use in industrial and commercial buildings have been already demonstrated in previous works. The present paper analyses the behavior of the panels for the assistance of ground-coupled heat pump systems by means of simulations with TRNSYS, focusing on the energetic regeneration of the geothermal source. The results show that the combination with solar panels can slightly improve the energy performance of well-designed systems (+5%), but significantly affects the efficiency of systems with undersized borehole heat exchangers. Solar regeneration enables to reduce the length or the number of the boreholes by 25 % to 30 % and the area necessary for their installation up to 80 %.

Keywords: heat pump system, solar collector, solar regeneration, building integration, sandwich panel

1. Introduction

The research project "Building-integrated solar steel sandwich elements for industrial and commercial buildings with a mineral wool core" aims at the solar thermal use of sandwich façades to supply heat to non-residential buildings. Steel sandwich panels are well-established components for the cost-effective manufacturing of functional envelopes in commercial and industrial buildings. They can be adapted for the active use of solar energy by integrating suitable heat exchangers between the front cladding and the insulating core, as already shown in previous works (Fig. 1, left). Weiland et al. (2019) show the performance potential of different absorber geometries in FEM simulation studies validated by measurements. On the basis of these results, large-format prototypes with heat exchangers consisting of meander tube registers with heat transfer plates were manufactured in the project. The performance of first demonstrators has been determined by means of indoor and outdoor measurements (ISO 9806, 2018). For large-sized prototypes (2 m²) with a grey coating (solar absorptance = 0.865, according to ISO 9050) and 70% activation of the total surface we reported zero-loss thermal efficiencies η_0 up to 0.56. Calculations based on validated FEM-models (Fig. 1, bottom right) estimate maximum values up to 75%.

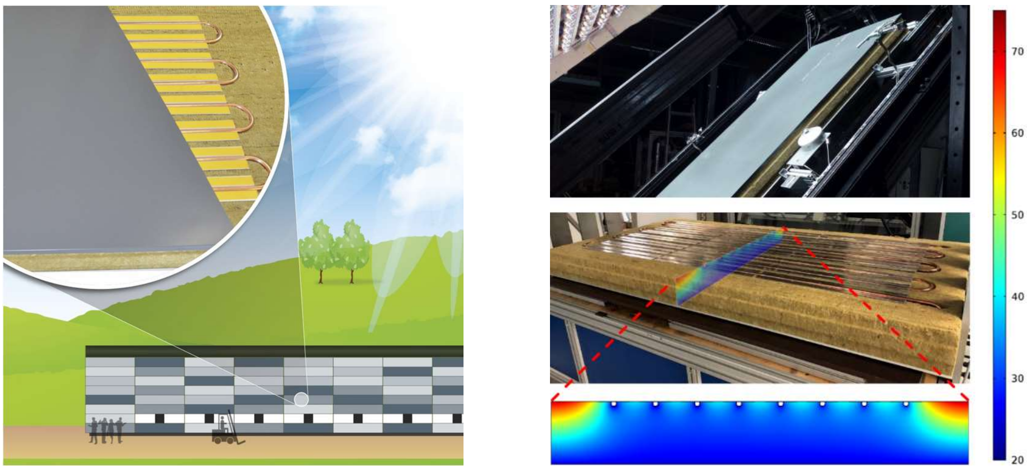

Fig. 1: Exemplary visualization of building integrated solar panels with detail of the developed prototype (left) and a prototype in the sun simulator (top right), with a temperature field of the validated FEM simulations (in degrees Celsius) (bottom right).

doi:10.18086/eurosun.2020.01.14 Available at http://proceedings.ises.org

The aim of the simulation studies presented in this paper is to investigate the behavior of the developed sandwich panels in systems and their potential for supplying heat to industrial and commercial buildings. The solar-activated panels correspond in their design to uncovered thermal collectors and have a relatively high heat loss coefficient. They supply heat mainly at ambient temperature level (< 40° C) and are thus optimally suited for combination with ground-coupled heat pump systems. The focus of the work is on their combination with brine-to-water heat pumps and on their potential to regenerate the geothermal source. The regeneration not only offers the opportunity to increase the efficiency and robustness of the systems, but is also a prerequisite for ensuring their sustainable operation. For regeneration, various measures can be considered, with solar thermal energy being a reasonable and proven option. Extensive studies on this topic have already been carried out in previous works (Bertram et al., 2014; Hadorn, 2015; Persdorf et al., 2015).

2. Boundary conditions of the Simulation studies

The simulations are carried out with the software TRNSYS. The transient system simulation software TRNSYS (version 17) is mainly used for the modelling of multi-zone buildings and heating systems in dynamic annual simulations (Transsolar Energietechnik, 2012). The following section describes the boundary conditions of the simulations, parameter variations and sensitivity analyses.

2.1. Heat demand: Building model and usage profiles

The thermal energy is provided for an exemplary building with a floor area of 900 m², which is heated by an industrial floor heating system. The basic dimensions are shown in figure 3. The specifications of the outer shell are described in Feldmann et al. (2014) and are adapted to the requirements of the current energy saving directive (EnEV, 2016). Decisive for the selection of components is the maximum value of the heat transfer coefficient for non-residential buildings. Relevant are the key figures for enclosing building components such as exterior walls and roofs (U = 0.35 W/m²K). Accordingly, construction-relevant, marketable steel sandwich elements with a mineral wool core and an insulation thickness of 120 mm were selected. The natural lighting of the building is provided by a 50 m long ridge light band.

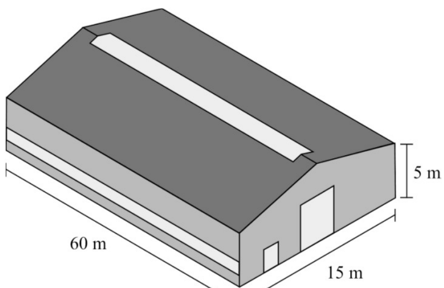

Fig. 2: Schematic representation (left) and supporting structure (right) of the investigated building

The reference document for the energy evaluation of buildings is the DIN V 18599 (2018), which specifies compliance with the energy requirements according to EnEV and takes into account compliance with the EEWärmeG (2008). Oschatz et al. (2015) provide a good overview of the requirements for non-residential buildings in this context. There are essentially three activity levels for activities in commercial and industrial buildings and associated minimum requirements for the target room temperature and the minimum air change rate. The requirements for the room temperature are also defined by the technical workplace regulation (BAuA, 2018). The scenarios used in the simulations are chosen in accordance with the relevant standards. For the studies in this paper, a scenario for a production hall heated to 19 °C target temperature is selected. Within the building, a two-shift operation with light work (standing or walking) with internal gains of 39 W/m² for duration of occupancy is simulated. The provision of hot drinking water is not considered due to the varying loads in commercial and industrial scenarios. Besides a continuous natural infiltration of 0.14 h^{-1}, an air exchange rate through ventilation of 0.60 h^{-1} is assumed when the building is occupied. The internal gains are calculated according to DIN V 18599 over an average occupancy density. The resulting heat demand for the location Zurich (Meteonorm, 2015) is 82.9 MWh/a, which corresponds to a specific heat demand of 92.1 kWh/(m²a). The floor heating is designed for a flow temperature of 35 °C, a return flow temperature of 30 °C and has a specific heating power of 57 W/m². 600 m² of the floor area are activated, which corresponds to a total heating power of 34.2 kW.

2.2. System configuration

In order to demonstrate the effects of the solar use of steel sandwich façades, we have defined two heat pump systems for comparison. The main reference system is a brine-water heat pump system (55.8 kW at B0/W35, COP = 4.81), in which borehole heat exchanger (a field of geothermal probes) serves as a heat source for the heat pump. In the case of solar regeneration, this reference system is extended by a field of solar-activated steel sandwich elements on the south façade of the building. In addition, the results are compared with an air-to-water heat pump system (65.1 kW at A2/W35, COP = 3.60), where the ambient air serves as heat source for the heat pump. In each system, a buffer tank is connected between the heat pump and the underfloor heating system to avoid frequent clocking and thus minimize the number of heat pump starts. The storage tank is also used in practice with air-water heat pumps to provide the necessary energy for defrosting. For the sake of simplicity, these defrosting operations are not taken into account in the simulations. The three systems are schematically shown without the buffer storage tanks in Figure 3:

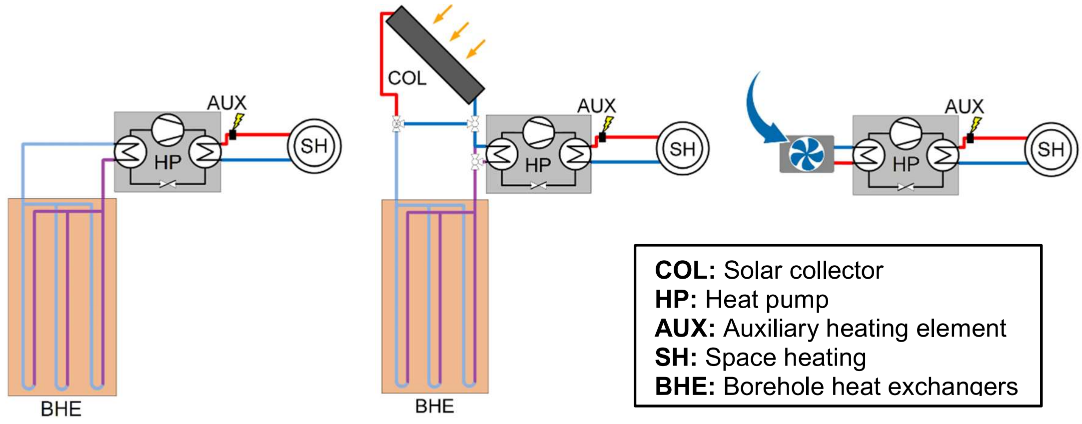

Fig. 3: Schematic representation of the system configurations examined: Brine-water heat pump with borehole heat exchanger without (left) and with solar thermal regeneration (middle) and air-to-water heat pump (right)

The regeneration of the borehole heat exchanger takes place as soon as the outlet temperature of the collector field exceeds the outlet temperature of the borehole field by 5 K. The collector circuit comes to a standstill again when the collector outlet temperature falls below the outlet temperature of the borehole heat exchanger.

2.3. Heat pump source: Geothermal borehole heat exchanger

The source of the heat pump system consists of a field of geothermal probes, each 100 m long. The upper 2 m are thermally insulated (frost protection) and the rest is effectively used for heat exchange with the ground. The probes are arranged in a rectangular area with a distance of 10 m each. The number of probes is set as a simulation parameter to investigate the influence of the size of the field on the system performance. The number and arrangement of the probes shown in the following table are selected for the simulation study:

Tab. 1: Investigated number and arrangement of the boreholes in the probe field in the parameter study

Quantity	Arrangement	Total length	Surface area
6	2 x 3	600 m	200 m²
9	3 x 3	900 m	400 m²
12	3 x 4	1200 m	600 m²
16	4 x 4	1600 m	900 m²

For the soil properties, a normal to poor subsoil with a thermal conductivity of λ = 1.52 W/(m*K) is assumed in accordance with VDI 6440-2 (2019), which corresponds to a heat extraction rate of 35 W/m. In order to ensure a sustainable operation of the borehole heat exchanger, the simulation period is set to 25 years and the minimum inlet temperature of the probe field was limited to -3 °C in order to avoid frost conditions in the filling material (SIA, 2010). In addition, the inlet temperature in the case of solar regeneration is limited to a maximum of 25 °C in order to meet the sustainability criteria.

2.3. Solar activated steel sandwich panels

The characteristic values of the sandwich collectors used in the simulations correspond to the characteristic values of a prototype measured in the sun simulator according to ISO 9806 (2018). The conversion factor η_0 is 53.3 % and the absorption coefficient α is 86.5 % (RAL 7012). The linear loss coefficient b_1 is 8.9 W/(m²K) and the wind-dependent coefficients b_2 and b_u are 1.37 J/(m³K) and 0.057 s/m respectively (Weiland et al., 2019). The efficiency η of the collector can be calculated with these characteristic values, depending on the wind speed v. The efficiency also depends on the temperature difference between ambient and fluid temperature T_{fl} - T_a, divided by the standardized irradiance E_N. This term is also called $Tm*$.

$$\eta = \eta_0 * (1 - b_u * v) - (b_1 + b_2 * v) * \frac{T_{fl} - T_a}{E_N} \qquad \text{(eq. 1)}$$

When calculating the normalized irradiance E_N, the radiant heat losses are taken into account or compensated for if the sky temperature deviates from the ambient temperature. The collector characteristic curves are shown in Figure 4 for three different wind speeds.

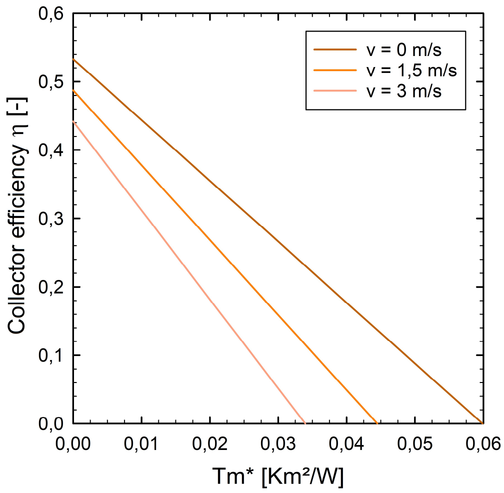

Fig. 4: Efficiency curve of the collector at different wind speeds

The effective capacity c_{eff} of the collector is calculated according to ISO 9806 (2018) and is 16.5 kJ/(m²K). In a parameter study, the area of the solar-activated façade is varied between 60 m² and 120 m². In a further parameter study, the solar absorptance of the cover shell is varied to take into account the influence of differently colored surfaces. In addition to the color RAL 7012 (α = 86.5 %), the following grey shades commonly used for commercial building envelopes are considered: RAL 9006 (α = 52.8 %), RAL 9007 (α = 76.2 %), and RAL 7016 (α = 91.3 %). The collector characteristics correspondent to these color variations are calculated with a stationary collector model developed at ISFH (Föste, 2013).

2.3. Evaluation criteria

The energy evaluation is based on the Seasonal Performance Factor (SPF) calculated at the end of the simulation period (25 years of operation). The selected evaluation boundary is decisive for this criterion. In the frame of the IEA TASK 44, Malenković et al. (2013) give an overview of the different evaluation boundaries and their suitability for the comparison of different heat supply systems with heat pumps. The SHP+ boundary covers all electrical consumers of the heat supply system so that different supply systems can be compared very well with each other at identical load profiles and temperatures. The system annual performance factor SPF_{SHP+} is therefore selected for our assessment. It is defined as the ratio of the heat provided by the room heating Q_{RH} to the total electrical work W_{total} required. This consists of the respective work of the heat pump W_{WP}, of the circulation pumps W_{CP}, of the electrical heater W_{EH} and the auxiliary energy W_{Aux}:

$$SPF_{SHP+} = \frac{Q_{RH}}{W_{total}} = \frac{Q_{RH}}{W_{HP} + W_{CP} + W_{EH} + W_{Aux}} \qquad \text{(eq. 2)}$$

Another decisive factor for the efficiency of the system is the bivalence point, the minimum inlet temperature of the ground heat exchanger fluid. Since it is limited to -3 °C, an electrical heater takes over the heat supply if this temperature falls below this value.

3. Results of the energetic analysis

The results show that the ground-coupled systems achieve a very high efficiency. For example with a probe length of 1200 m, the SPF_{SHP+} slightly improves from 4.50 (reference system) to 4.74 by regenerating the borehole heat exchanger with solar-thermally activated sandwich elements. The significantly greater effect, however, is achieved with a tightly dimensioned geothermal heat source due to the possibility of reducing the borehole length. By using 120 m² sandwich elements, the length can be reduced by 25 % to 30 % with the same energetic performance. To illustrate these results, Figure 5 shows the SPF_{SHP+} (left) and the minimum fluid inlet temperature (right) after an operating time of 25 years:

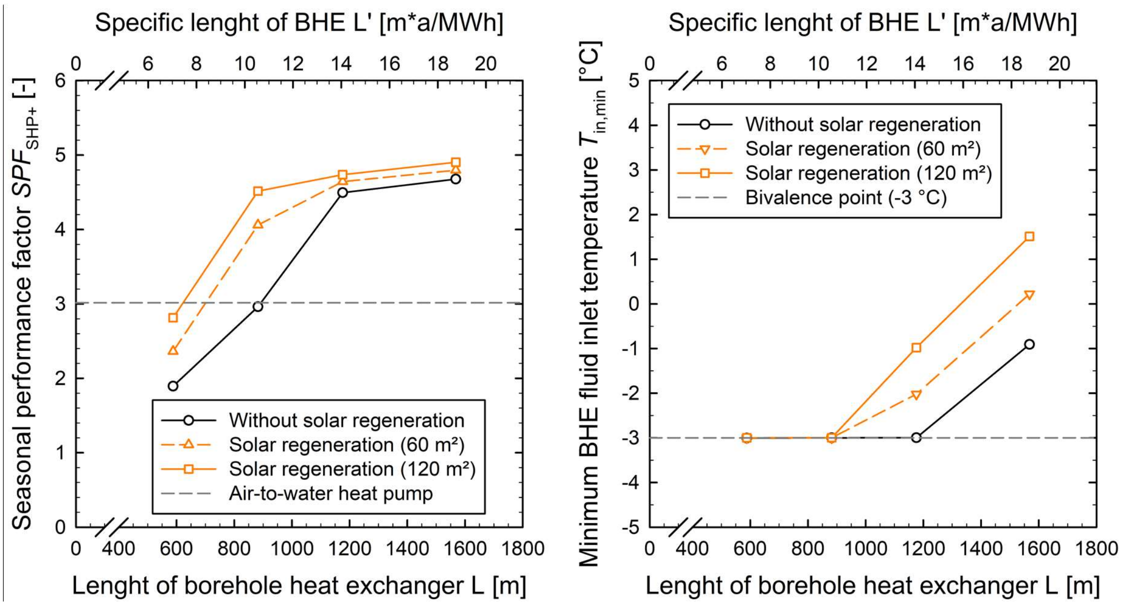

Fig. 5: Seasonal performance factor (left) and minimum fluid inlet temperature into the probe field after 25 years of operation.

The results with an air-to-water heat pump as the heat generator show that this simpler system is about 35% less efficient and thus consumes 35% more electricity than the ground-couple one. Furthermore, the seasonal differences in the efficiency are significantly higher than that. Accordingly, if the source of the heat supply is a geothermal probe field instead of ambient air, up to 100 tons of CO_2 can be saved over a period of 25 years. Solar regeneration not only enables a reduction of length or number of the borehole heat exchangers, but also generally ensures a more sustainable operation of the system. For this purpose, comparative temperature cross sections of probe fields with 12 probes resulting from the TRNSYS simulations are shown in Figure 6.

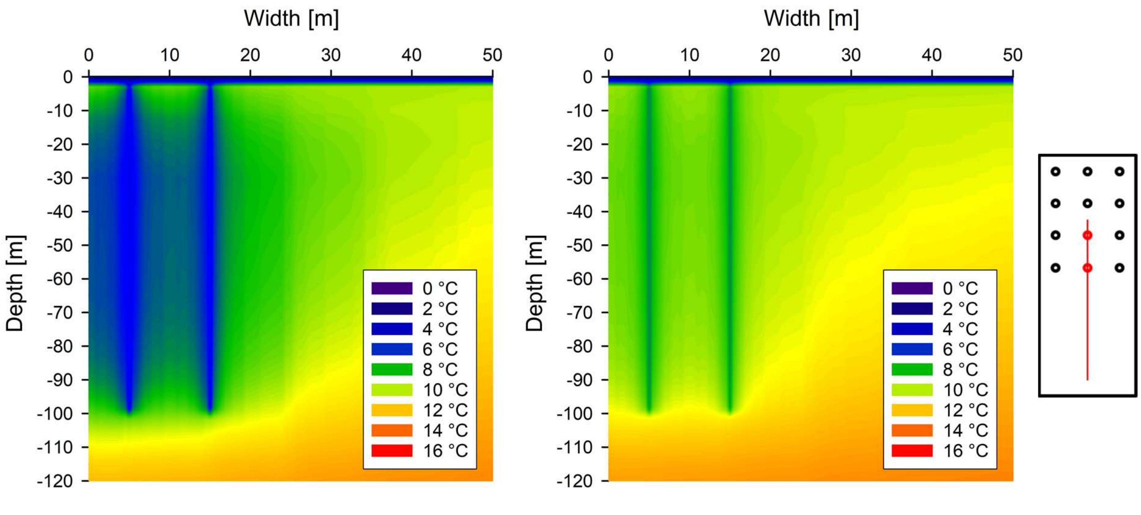

Fig. 6: Vertical temperature cross sections of probe fields with 12 probes after an operating time of 25 years (31. December): without solar regeneration (left) and with solar regeneration (120 m² collector surface, right). Shown are the two probes highlighted in the schematic on the far right.

In contrast to the reference system, the temperature in the ground is not influenced so strongly in the long term in case of solar regeneration: the soil cools down more slowly and a stationary level is reached after only a few years. Without regeneration the ground continues to cool down even after 25 years of operation. At the same time, the robustness of the system can be increased by solar regeneration, especially for undersized borehole heat exchangers. These results are also in line with the findings of previous ISFH projects (Bertram et al., 2014) and further studies, e.g. by Persdorf et al. (2015). Additional simulations show that the probe spacing can be halved in case of solar regeneration without compromising the system performance, since regeneration significantly reduces the mutual interaction between the probes. Figure 7 compares the change of the seasonal performance factor over the operating time of 25 years for different distances of the probes in the field with and without solar regeneration. On the left side a field with 9 probes and on the right side one with 16 probes.

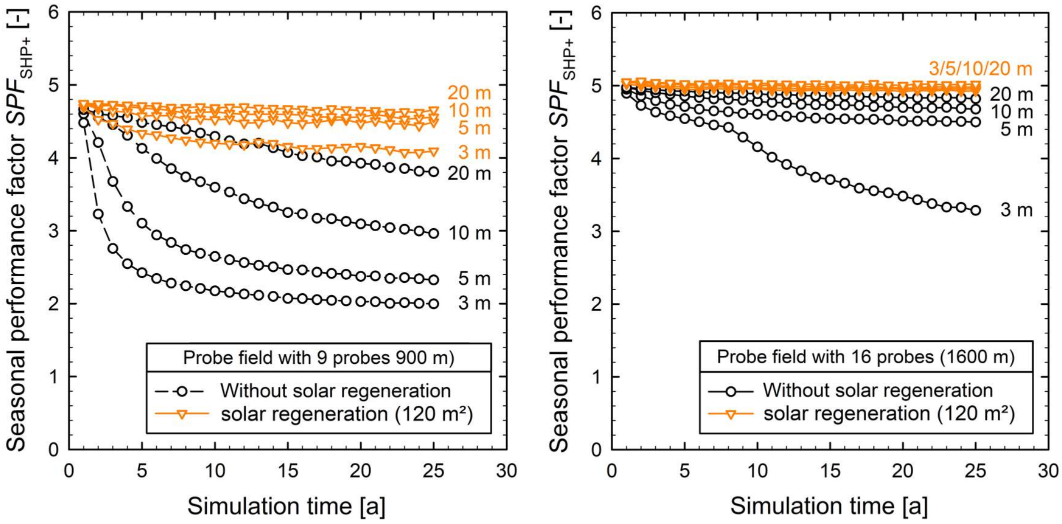

Fig. 7: Change of the seasonal performance factor over the operating time of 25 years for different distances of the probes in the field with and without solar regeneration: A probe field with 9 probes (left) and a probe field with 16 probes (right)

The efficiency of the system with solar regeneration is not significantly affected by reducing the distance from 10 m to 5 m, even with tightly dimensioned probe fields (9 probes). The required surface area of the field can therefore be significantly reduced by saving probes or probe length and reducing the distance between the probes. For the described system, for example, the required surface area for the probe field can be reduced from 900 m² (16 probes; 10 m distance) to 150 m² (12 probes; 5 m distance). This comes with the same efficiency and higher robustness, and corresponds to an area reduction of 83.3%. The effect significantly extends the range of applications of efficient heat pump systems with borehole heat exchangers, which usually require a lot of space. Another possible application for solar regeneration with steel sandwich elements is the replacement of an old heat pump with a more efficient new unit. Here, the existing geothermal heat source may be undersized, so that regeneration through the solar panels offers the possibility to keep the existing plant operational.

The results of the variation of the solar absorptance (52.8 % to 91.3 %) of cover plates with different colors are shown in Figure 8. A low absorptance only has an impact in undersized systems. With a large collector surface (120 m²), only the lightest shade of gray (RAL 9006) leads to a minor reduction in efficiency. This means that different colors with higher absorptance, such as dark blue, dark green, dark red, dark gray and black, can be used for the solar panels without significantly affecting the system performance, thus ensuring architects a very high degree of design freedom.

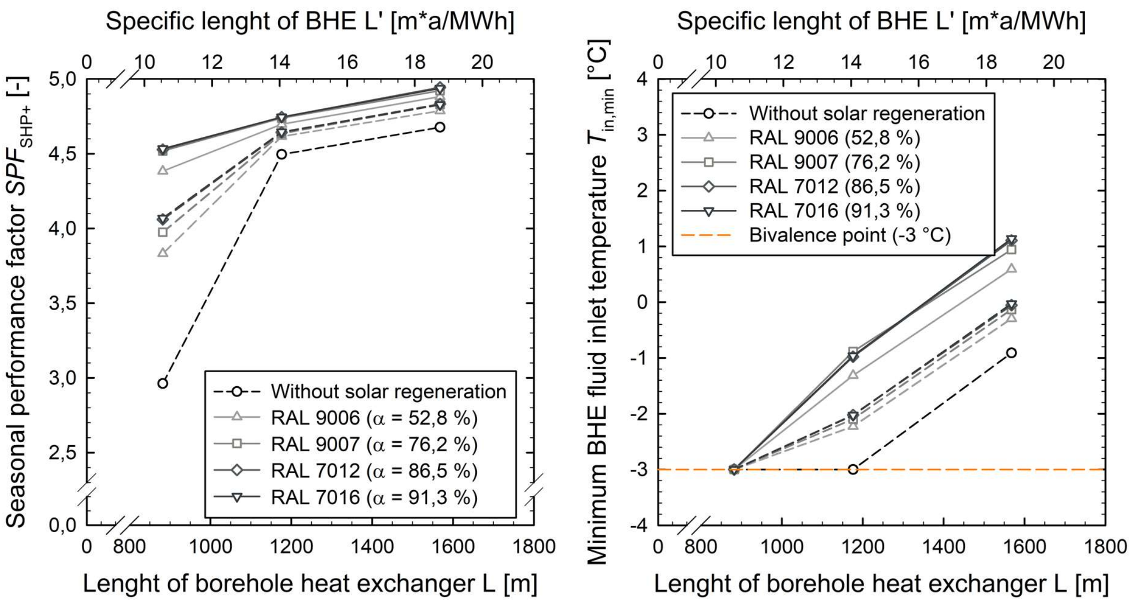

Fig. 8: Seasonal performance factor (left) and minimum fluid inlet temperature into the probe field for modules with different solar absorptance and collector surfaces of 60 m² (striated) and 120 m² (continuous), after an operating time of 25 years

4. Cost analysis

The economic evaluation of the systems is based on a simplified approach of the levelized cost of heat (LCoH) methodology, as defined by Louvet et al. (2018). Corporate taxes, an annual depreciation or any residual values are not taken into account. The discount rate is set to 0% and no subsidies are used. This simplifies the formula for the heat production costs as follows:

$$LCoH = \frac{I_0 + \sum_{t=1}^{T} C_t}{\sum_{t=1}^{T} E_t} \qquad \text{(eq. 3)}$$

- $LCoH$: levelized cost of heat [€/kWh]
- I_0: initial investment [€]
- C_t: yearly operation and maintenance costs [€]
- E_t: yearly energy consumption [kWh]
- t: year
- T: evaluation period in years

The annual maintenance M_t and the annual operation costs O_t are summarized in the running costs C_t:

$$C_t = O_t + M_t \qquad \text{(eq. 4)}$$

These two costs are calculated and handled separately for the following studies.

4.1. Boundary conditions

The investment costs of the investigated systems are shown in Table 2. All costs are calculated without value added tax and are based on estimates and mean values from offers obtained from manufacturer and planner.

Tab. 2: Investment costs of the two reference systems and the system with solar regeneration

Probe length	600 m	900 m	1200 m	1600 m
System configuration	**Investment costs**			
Reference HP+ BHE	70 000 €	87 500 €	105 000 €	128 500 €
Reference air-to-water HP	45 000 €			
Solar regeneration 120 m²	77 000 €	94 500 €	112 000 €	135 500 €

It is noticeable that the investment costs for the probe field are a large part of the investment costs. For the annual maintenance costs, a conservative value is determined in accordance with VDI 2067 (2012), which corresponds to 3% of the respective investment costs. The electricity price, which is decisive for the operation-related costs, is assumed to be 22.2 €ct/kWh with an annual price increase of 3%. These values correspond to the current price level for smaller businesses with an annual electricity demand of up to 100,000 kWh and an average price change rate of the last 10 years. The evaluation period is set to 25 years, analogously to the system simulations. The lifetime of the main components is approximately in this range. A replacement of hydraulic pumps is included in the maintenance costs. Shorter evaluation periods, which are common in industrial and commercial applications, enormously favor the investment-friendly system with an air-to-water heat pump.

4.2 Results

The estimation for all three investigated systems comes to comparable levelized cost of heat for a borehole heat exchanger with a length of 1200 m (12 probes) (see Figure 9, left). The use of solar-thermally activated sandwich elements can save approx. 10,000 € in investment costs. This result is achieved by saving 25 to 30% of the borehole heat exchangers and, at the same time, making an additional investment in the solar façade. The reference system with an air-to-water heat pump is significantly less expensive in investment, but has similarly high cost of heat due to the higher power consumption during operation and the associated electricity costs. The levelized cost of heat in €ct/kWh are shown in Figure 9 on the left side. A more detailed breakdown of the investment, maintenance and operating costs for selected scenarios is shown on the right side of the figure. The graph illustrates clearly that a higher investment is associated with a higher efficiency of the system and thus lower operating costs.

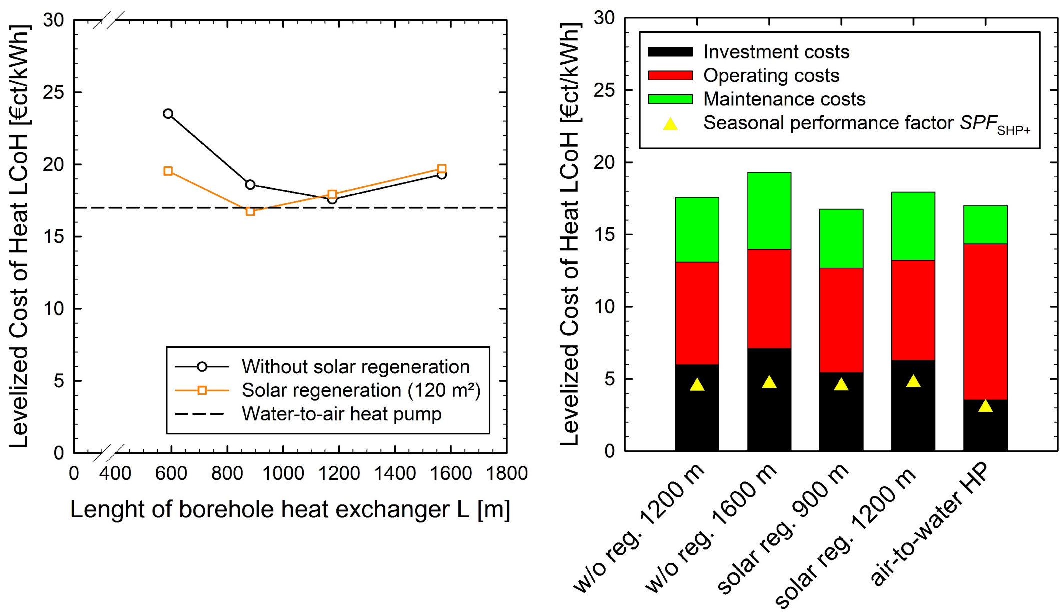

Fig. 9: Levelized cost of heat in €ct/kWh (left) and detailed representation of the individual cost parameters (right)

These results are not fully reliable due to uncertainties regarding the investment costs and the development of electricity prices. Therefore, we carried out a sensitivity analysis to investigate which parameters influence the levelized cost of heat to what extent. Figure 10 shows the impact of individual cost parameters for a ground-coupled heat pump system with solar regeneration (left) and a system with an air-to-water heat pump (right).

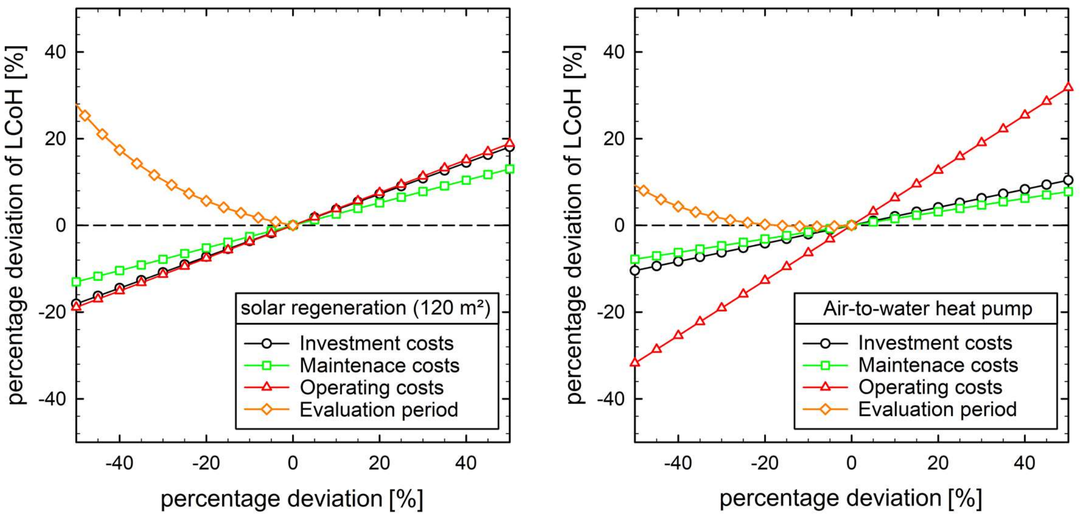

Fig. 9: Influence of individual cost parameters and the evaluation period on the levelized costs of heat for the system with 1200 m solar regenerated borehole heat exchangers (left) and the air-to-water heat pump system (right)

The individual cost parameters have a very different influence on the two systems, as expected. Due to the different investment costs, the evaluation period has a much larger impact on the ground-coupled system. The air-to-water heat pump system, on the other hand, is mainly influenced by the operation costs.

5. Summary

This paper presents the behavior of solar-activated steel sandwich elements in low-temperature heat supply systems with ground-coupled heat pumps for commercial and industrial applications. The simulation results show that by using the solar energy gained from façades to regenerate the borehole heat exchanger, the length or the number of the boreholes can be reduced by 25 % to 30 %. In addition, the distance between the individual probes can be significantly reduced. Thus more than 80 % of the required area of the probe field can be saved. Regeneration can also ensure a more sustainable operation of the systems and make them more robust against insufficient dimensioning. When planning solar-thermally activated steel sandwich façades, a great design freedom is given with regards to the color of the panels. The selection of color shades with a solar absorptance above 76 % is enough to ensure the maximum efficiency of solar regeneration. Besides different shades of grey, also red, green or blue coatings can thus be taken into consideration by architects.

The levelized cost of heat of the solar-assisted system are comparable to those of the reference systems. However, the use of steel sandwich elements can slightly reduce the investment by reducing the size of the geothermal heat exchanger. The respective costs of a reference system with an air-to-water heat pump are also in the same range. But this comes with 30% less efficiency and therefore more electricity is required to cover the heat demand.

6. Acknowledgement

The AiF research project "Building-integrated solar steel sandwich elements with mineral wool core for industrial and commercial construction“ underlying this publication is funded by the state of Lower Saxony and the Federal Ministry of Economic Affairs and Energy under the reference number 19520N following a decision of the German Bundestag. The work is carried out in cooperation with the Dortmund University of Applied Sciences and Arts, Department of Architecture and Metal Construction and the Research Association for Steel Application (FOSTA). The authors thank for the support as well as for the fruitful cooperation with the project partners. The responsibility for the content of this publication lies exclusively with the authors.

7. References

BAuA, 2018. Technical rules for workplaces – room temperature - ASR A3.5, 2010, modified 2018

Bertram, E., 2014. Solar Assisted Heat Pump Systems with Ground Heat Exchanger – Simulation Studies in: Energy Procedia Vol. 48, pp 505-514

DIN, 2018. DIN V 18599:2018-12, Energy efficiency of buildings - Calculation of the net, final and primary energy demand for heating, cooling, ventilation, domestic hot water and lighting. Beuth Verlag, Berlin

EEWärmeG, 2008. Renewable Energies Heating Act. Beuth Verlag, Berlin

EnEV, 2016. EnEV 2014, Energy Saving Directive, status as of 2016

Feldmann, M., Kuhnhenne, M., Pyschny, D., Brieden, M., Hachul, H., Bach, J., Rößling, H., Rexroth, S., Deininger, F., Morana, R., Görner, R., Ummenhofer, T., Misiek, T., Krüger, H., Fauth C., 2014. Mehrdimensionale energieoptimierte Gebäudehüllen in Stahlleichtbauweise für den Industrie- und Gewerbebau, final report of the AiF project P880 / IGF-Nr. 16936. Düsseldorf

Föste, S., 2013. Flachkollektor mit selektiv beschichteter Zweischeibenverglasung, thesis (in german). Hannover

Hadorn, J.-C., 2015. Solar and Heat Pump Systems for Residential Buildings. Final report, IEA SHC TASK 44. Ernst & Sohn, Berlin

ISO, 2018. ISO 9806:2018-04. Solar energy – Solar thermal collectors – Test methods, German version. Beuth Verlag, Berlin

Louvet, Y., Fischer, S., Furbo, S., Giovannetti, F., Mauthner, F., Mugnier, D., Philippen, D., 2018. Guideline for levelized cost of heat (LCOH) calculations for solar thermal applications. Info sheet A.2, IEA SHC TASK 44

Malenković, I., Pärisch, P., Eicher, S., Bony, J., Hartl, M., 2013. Definition of Main System Boundaries and Performance Figures for Reporting on SHP Systems. Technical report, IEA SHC TASK 54

Meteonorm, 2015. Handbook Part I & II (Version 7.1), Bern

Oschatz, B., Rosenkranz, J., Weber, K., 2015. Leitfaden zur Planung neuer Hallengebäude nach Energieeinsparverordnung EnEV 2014 und Erneuerbare-Energien-Wärmegesetz 2011. Figawa, Köln

Persdorf, P., Ruesch, F., Haller, M. Y., 2015. RegenOpt, final report. Zürich

SIA, 2010. SIA 384/6:2010, Erdwärmesonden. Zürich

Transsolar Energietechnik, 2012. TRNSYS Version 17.01

VDI, 2012. VDI 2067-1:2012-09, Economic efficiency of building installations - Fundamentals and economic calculation. Beuth Verlag, Berlin

VDI, 2019. VDI 4640-2:2019-06, Thermal use of the underground - ground source heat pump systems. Beuth Verlag, Berlin

Weiland, F., Kirchner, M., Rensinghoff, V., Giovannetti, F., Kastner, O., Ridder, D., Tekinbas, Y., Hachul, H., 2019. Performance assessment of solar thermally activated steel sandwich panels with mineral wool core for industrial and commercial buildings. J. Phys. Conf. Ser. 1343 012098

02. Solar Assisted District Heating and Cooling

German cities towards 100 % renewable energy – Heat Hub Hennigsdorf

Magdalena Berberich, Dirk Mangold

Solites, Steinbeis Research Institute for Solar and Sustainable Thermal Energy Systems, Stuttgart (Germany)

Abstract

The Heat Hub Hennigsdorf is a lighthouse example how cities can contribute to the German energy transition to renewable energies ("Energiewende") by setting binding targets themselves and decarbonizing their heat supply together with local stakeholders. The municipal utilities of Hennigsdorf aims at a district heating with 100 % renewable and CO_2-neutral heat in 2025 for its yearly heat demand of 120 GWh/a. Until the year 2022, the share of CO_2-neutral heat in the district heating will be increased from 50 to 84 %. To reach this target, different decentralized and renewable heat sources are on the way to be integrated into the district heating net. Biomass driven combined heat and power plants are already used to about 50 % of the annual heat load. To be able to operate the district heating with fluctuating industrial waste and solar thermal heat, the entire network has to be developed to a Heat Hub by integrating two heat storages of 1 000 and 22 000 m³. This is one of the largest funded research and demonstration projects of the German Federal Ministry for Economic Affairs and Energy (BMWi) in the field of heating networks and a model for the decarbonization of existing district heating supplies (Gintars, 2018).

Keywords: Renewable district heating, decarbonization, heat transition, solar thermal, industrial waste heat

1. Introduction

The decarbonization of the heat supply is one important pillar for the German energy transition to renewable energies ("Energiewende"). The strategy aims to reduce greenhouse gas emissions by 80 % in 2050 compared to 1990 levels. The heating area has a share of approx. 54 % of final energy consumption. Of this alone, approx. 27 % points on the final energy consumption for space heating. At the same time, the heating transition also represents an opportunity for Germany as a highly industrialized country, as it offers the possibility of generating added value to German companies. Energy efficiency and the increased use of renewable energies and waste heat creates innovations, new business models and jobs in future markets. According to the principle "Efficiency First!" the heat demand is to be significantly reduced by improving energy efficiency in the building and industrial sector as well as in trade and commerce and the remaining demand is to be covered by renewable energy sources. Even with ambitious expansion paths for renewable energies in the heating sector, it will not be possible to completely cover today's heating requirements with renewable energies. (BMWi, Energieeffizienz in Zahlen, 2019)

2. Solar Thermal as an Option not only for Cities

District heating (DH) is a great option to increase the overall energy efficiency in urban areas and an important platform to increase the share of renewable and fossil-free energies in the heat supply. Solar thermal energy from large-scale solar thermal collector areas is one possible heat source for sustainable DH, as it is emission-free, available everywhere and offers stable operating costs for decades (Epp & Oropeza, 2019). By the end of 2019, in Germany 37 solar district heating (SDH) systems were in operation with a total gross collector area of about 69 900 m² (Geiger, et al., 2020). The system sizes range from 99 m² to 8 300 m² with an average collector area of 1 890 m². With the installation of a 14 800 m² solar collector field integrated in the district heating system of the city of Ludwigsburg, the biggest SDH plant went in operation in spring 2020 (Stadtwerke Ludwigsburg, 2020). In the German SDH market, flat plate collectors are mainly used, but evacuated tube collectors have a relatively high share of 34 % of installed collector area. For SDH systems, typical values for temperatures are 70-110 °C in supply and 40-80 °C in return flow (Tschopp, et al., 2020).

Characteristic for the German market is a broad variety of applications. SDH applications range from small villages

doi:10.18086/eurosun.2020.02.01 Available at http://proceedings.ises.org

and rural areas, to SDH for districts and SDH for cities and urban centers. In cities and urban areas, the main heat producers are usually combined heat and power plants, heating plants, waste incineration or industrial waste heat. Depending on the system size and efficiency of the solar thermal plant, solar heat production costs below 50 €/MWh can be reached without incentives (Berberich & Mangold, 2017).

Solar thermal projects are often realized in bioenergy villages ("Bioenergiedorf"). The combination of wood chip boilers and solar thermal plants turned out to be one successful system for an efficient heat supply, the bioenergy village Büsingen is a good example (Solites, 2013). The projects are usually initiated by citizens, who cooperate with the municipality, local craftsmen, building companies and consulting engineers. Oftentimes, the citizens set up a registered cooperative to manage the energy supply and distribution, which has the aim of long-term favorable prices instead of short-term profit maximization. Furthermore, it allows a high degree of co-determination and limited liability risks.

Another typical business strategy for large-scale solar thermal systems in Germany is the change from fossil fuels to renewable energies in DH systems. Especially for DH networks with a relatively high thermal load, a solar thermal system can directly feed into the network without additional storage system. This allows for a cheap heat production but only for limited solar fraction of the entire heat demand of the DH network. One regulatory reason for this effort is the reduction of the primary energy factor of the DH network due to solar thermal integration. With a reduced primary energy factor, new customers meet the legal requirements for using renewable energies in new buildings by connecting to the DH network (BMWi, Erneuerbare-Energien-Wärmegesetz - EEWärmeG, 2018). Furthermore, DH companies as well as industries benefit from long-term cost stability of solar heat.

3. Development of the Heat Hub

Climate protection through decarbonization of the heat supply and the development of a sustainable supply system for the citizens are the main motivators for the Heat Hub Hennigsdorf. With the decision to transform their heat supply to 100 % CO_2-neutral heat until 2025, the city of Hennigsdorf is a pioneer of the energy transition in Germany. The DH of Hennigsdorf is a typical existing DH network of a mid-sized-town with 26 000 inhabitants, northwest of the German capital Berlin. A specialty of the heating network Hennigsdorf is its far geographic expansion from north to south, see Figure 1. The first boiler house was built in the mid-1960s, which heated some blocks of flats and commercial buildings with raw lignite (Stadtwerke Hennigsdorf, 2020). The city and the DH grew over the years and raw lignite was replaced by anthracite coal, heating oil and finally natural gas. About 80 % of the city are now provided with DH from seven central heating plants. The DH system is operated with 85 to 108 °C in supply and 60 °C in return flow and can currently be combined to form an entire network, but in some operating cases, it is separated into two to four sections.

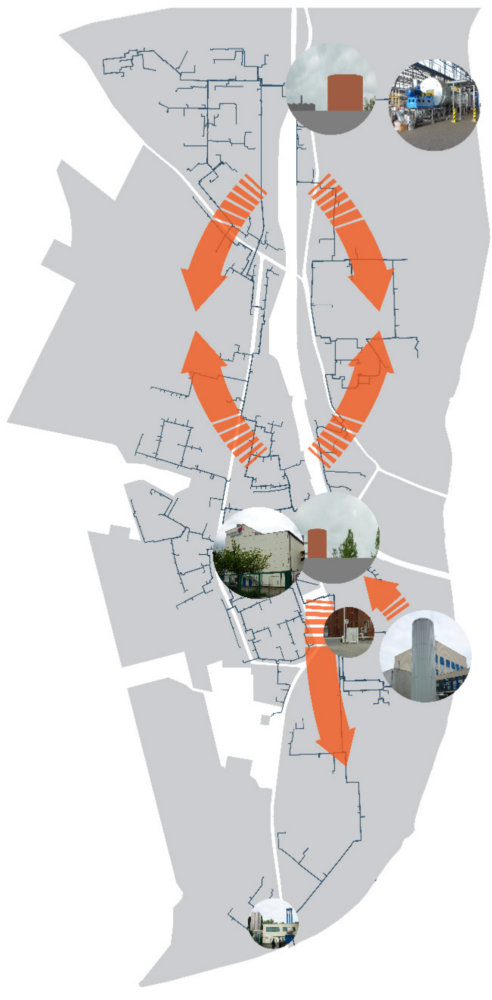

Figure 1: Overview of the city area and the heating plants (Solites)

Since 2006 the overall strategy of the city of Hennigsdorf and their utilities is to reinvest in CO_2-neutral heat production technologies. To legally separate the district heating network and the heat generation, a new municipal project company (KPG GmbH & Co. KG) was founded and the utilities began to sell its heating plants to this company. In first steps in 2009 and 2012, a woodchip combined heat and power (CHP) plant with Organic Rankine Cycle (ORC) technology and a biogas CHP were realized by the project company. At the same time, the different subnetworks of the district heating were linked and combined to one entire network. Nowadays, about half of the overall heat demand is provided by these two plants with renewable heat (Stadtwerke Hennigsdorf, 2018).

In 2015 a climate protection strategy was decided by the municipal council, which is geared to the climate protection plan 2050 of the German Federal Government aiming at a greenhouse gas neutrality of all sectors (Stadtwerke Hennigsdorf, 2018). Until 2022 the share of fossil-free heat in the DH Hennigsdorf is to be increased to more than 80 % as an intermediate step. The completion of 100 % of CO_2-neutrality is planned to be reached in 2025 (Stadtwerke Hennigsdorf, 2019).

A well-rehearsed local project team of the project company KPG, the utilities Stadtwerke Hennigsdorf, the planning company Tetra Ingenieure GmbH and project management company Ruppin Consult GmbH is completed by the research institute Solites that has comprehensive experience in consulting and realizing innovative systems like the Heat Hub Hennigsdorf. This team is supported by the management board of the utilities and the municipal council that are willing to make strong decisions for reaching their self set goals.

In a first project phase in 2016 and 2017, the project team created an overall concept for the heat supply:

- Use of waste heat from the local steelworks (implemented in 2019)
- Increase of solar thermal heat production (3 000 m² central and smaller areas decentral)
- Use of power-to-heat from renewable surplus electricity (project WindNODE)
- Realization of existing optimization potentials in the customer systems
- Realization of existing optimization potentials in the district heating network
- Dismantling of old systems that are fired with fossil oil or anthracite
- Construction of a multifunctional heat storage with 22 000 m³ and a buffer storage with 1 000 m³ of water volume
- Adaptions of the existing district heating routes to the Heat Hub
- Development and realization of a smart superior control system for the entire Heat Hub together with a comprehensive integration of sensors and actors within the district heating network

The project Heat Hub is attached to another one that regards a CO_2-neutral electricity production by wind mills in the region around the city (WindNODE, 2020). The WindNODE project, in which a total of more than 70 partners from business, science and industry from Thuringia to Mecklenburg-Western Pomerania are involved, researches possible solutions for the system integration of renewable energies. The use of storage technologies and flexible control of power consumption should enable to keep the necessary expansion of the electricity grid as low as possible while still integrating an increasing share of renewable energies into the supply system. In Brandenburg, six projects are being carried out as part of the WindNODE joint project, including the sub-project Power-to-Heat (PtH) in district heating to make the load more flexible in the power grid. WindNODE is part of the “Smart Energy Showcase - Digital Agenda for the Energy Transition” (SINTEG) funding program of the German Federal Ministry for Economic Affairs and Energy.

In addition to the implementation of numerous measures in the district heating network of Hennigsdorf like described above, the construction of a Power-to-Heat (PtH) system of 5 MW_{el} is an additional technology for achieving a CO_2-neutral heat supply.

In order to create the necessary flexibility between the deviating demand of the heating network and the different heat generations from the heating plants, the industrial waste heat recovery and the solar thermal plants, the two heat storages will be used. The PtH plant shall than use corresponding price signals from a newly generated marketing platform in times of regenerative surplus electricity to use the electricity in the heating network and thus further reduce heat generation based on conventional energy sources. Currently a PtH-system cannot be operated economically, due to German legal framework conditions.

4. Implementation of the Heat Hub

Since 2017 the project team is working in the second project phase to plan and realize the measures described above. Some of the main construction sites and already realized sub-projects are shown and described in this section.

In early summer 2019, the waste heat from the steelworks was successfully integrated in the district heating. Behind the heat exchanger in Figure 2, a walking beam furnace heats up steel billets with several gas burners. The exhaust gas leaves the furnace at a temperature of up to 500 °C and the waste heat is transferred in the tube bundle heat exchanger to the water circuit with a target temperature of 95 °C. The heat exchanger has a nominal output of

7.5 MW_{th}. Current measurement data show that even a bit more than 8 MW thermal power can be supplied. The operation of the waste heat recovery depends strongly on the dynamics of the walking beam furnace, which is a challenge for the regulation of the exhaust gas heat exchanger and the water cycle.

A great success of the project is that the utilities of Hennigsdorf were able to conclude a contract with the operator of the steelworks H.E.S. for the long-term use of the waste heat from the steelworks. Not every industrial partner is willing to do this what makes the use of industrial waste heat often quite difficult. If further heat sources in the steelworks can be used for heat recovery in the future, the use of waste heat could be expanded. The heat pipeline from the steelworks to the connection in the DH network has already been designed to double the heat transport.

Figure 2: Heat exchanger subsystem to use industrial waste heat from steelworks (picture: Solites, 17.06.2020)

To transport the heat from the steelworks to the DH, a heat pipeline of about 800 m length and a new heating plant "Nord 2" were built. “Nord 2” includes two peak load gas fired boilers and the pumps for supplying the heat to the DH. The heat pipeline from the heating plant “Nord 2” to the existing district heating net had to tunnel under the railway line, which was a particular challenge and took a few months for approval (Figure 3). Renovation and optimization work is also being carried out in other areas of the DH. Since with the industrial waste heat a main heat source will be integrated at the northern end of the heating network, the heat must be transported to the network areas with the highest heat consumption (network area “Zentrum” in the middle of the city, see also Figure 1). Therefore an additional third connection pipeline was built between the heating plant “Nord 2” and the area “Zentrum” and is planned to go into operation in autumn 2020. This solution is more economical but hydraulically more sensible than replacing the existing pipelines with a larger pipe diameter.

Another major task is the installation and programming of the monitoring system, which measures data on temperatures, heat quantities, flow rates and pressures in all heating plants of the entire system and saves them every 1 minute. The measurement concept provides for the measurement data to be forwarded from the panel PCs in the individual heating plants to a superior control system, where the data is visualized and saved for further processing. Additional data lines have to be laid for this and the superior control technology has been being installed and programmed. These tasks are currently in progress together with the construction sites in the heating plants. In the industrial waste heat plant area, its connection to the heating network and in the new heating plant “Nord 2”, the data from around 80 measuring points are captured, processed and saved to be evaluated by the plant operator, Stadtwerke Hennigsdorf, in order to optimize the operation. An overall scientific evaluation of the system is carried out by Solites.

Figure 3: Installation of the heat pipeline to tunnel under the rail trail (picture: Solites, 16.05.2019)

In early summer 2020, the first thermal energy storage with 1 000 m³ water volume went into operation and is used to optimize the operation of the biomass CHP plant in times with medium and low heat demand (Figure 4). It was built as a steel tank by welding the individual bent steel sheets together. The bottom and lid are built with dished bottoms so that the tank can withstand the over pressure of 5 bar of the DH network due to the direct integration of the storage in the kind of a hydraulic switch. For the integration of the new heat storage into the existing heating plant “Zentrum”, extensive renovation work was carried out in this heating plant. In the future, the storage facility is to be supplemented by a power-to-heat system so that excess electrical energy from renewable sources is converted into heat and stored for use in the DH network.

Figure 4: Buffer tank storage under construction (left) and finished (right) (pictures: Solites, 08.01.2020 and 16.06.2020)

For the expansion of the solar thermal heat generation, the replacement of the roof-integrated solar thermal collectors on the residential buildings of the “Cohn’s Quarter” began in autumn 2019 and will be finished in autumn 2020. A total of five roofs are equipped with solar collectors, the total collector area is 854 m² (Figure 5).

The wooden frames of the collectors integrated into the roof 18 years ago had reached their lifespan. The structural requirements, the stipulations of the design statutes for the "Cohn's Quarter" and the economic constraints posed major challenges for the development of the renovation concept for the solar roofs and the solar system technology in the basements of the houses. Since the today's solar thermal industry do not offer a sufficient number of providers with coherent concepts for maintaining the roof integration, a sheet metal roof is now being built after the existing collectors have been dismantled, on which the collectors are mounted. A detailed pre-planning enabled a cost-effective installation of the collector surfaces.

Figure 5: Replacement of formerly roof-integrated collectors on the roof of one out of five multifamily houses with large-scale solar thermal collectors on newly built sheet metal roof (picture: Solites, 17.06.2020)

Apart from the ongoing construction sites, the project team is currently working intensively on the superior control strategy for the overall system.

5. The Heat Hub

The challenges that give the Heat Hub Hennigsdorf its name lie in the integration of various decentralized fossil-free heat sources in an existing district heating network under economic conditions. For an overview of the system see Figure 6. The target is to minimize the use of fossil energy in the overall DH in the future and to enable the Heat Hub Hennigsdorf to be operated automatically. From the year 2025, the gas boilers should no longer be used. Thus even any reheating of fossil-free energy sources that deliver a supply temperature that is lower than the set supply temperature should be avoided. This is important, because the supply temperature of the biomass CHP is limited to 90 °C and the supply temperature of the waste heat depends on the dynamics of the walking beam furnace with a target temperature of 95 °C, while the supply temperature of the DH is set to 95 °C in winter. A reliably functioning of the temperature stratifications in the heat storages is therefore essential for the functioning of the Heat Hub. Then, the entire DH network must always be operated in one overall system. On the one hand this enables the heat transfer between the biomass CHP, the buffer storage in the heating plant "Zentrum" and the multifunctional heat storage near the heating plant "Nord 2" and on the other hand it secures the necessary supply temperature in the DH network. Since the transport capacity between the two storages is limited, they must be actively charged and discharged in addition to their function as hydraulic switches. It is important at what time the thermal storages are charged and discharged. For example, the operation of the biomass CHP is optimized with the network buffer storage. When the buffer storage is fully loaded, it must be decided whether the biomass CHP is modulated to lower output with lower efficiency or whether heat is transferred to the multifunctional heat storage.

A superior control system is required for such kind of system optimization, based on the current operation and the boundary conditions of all heating plants. The individual heat sources and generators are still operated by the local controls, which transfer selected measurement data and parameters to the superior network control level. The sequence of the heat generators and the charging and discharging of the heat storages is also determined by economic criteria (order of heat sources).

For the development of the superior control concept, the results of the hydraulic calculations of the DH network by the project partner Tetra Ingenieure were taken into account, which gave hydraulic limitations of the heat transfer ratios visible in individual network sections. Based on these results, Solites carried out numerical simulations with the simulation software TRNSYS. These show what shares the individual heat generators have in the overall heat supply and how these shares depend on the selected control parameters. By interacting the results of the network hydraulic simulations and the TRNSYS simulations, a comprehensive examination and optimization of the overall heat supply system for the entire DH system is possible.

A complete automation of the control processes asks for the consideration of all necessary operating cases during the planning process, what is very extensive. From the perspective of the utilities of Hennigsdorf, the decision to transfer heat between the heat storages will initially remain a manual process that is initiated by the operating personnel and not automatically by the superior control. For an automated control, further construction measures for the implementation of the control technology, renewal of the local control of the heating plant “Zentrum”, the lines for the data transmission, acquisition of further necessary measurement data and the visualization of the measuring points are necessary. According to the current planning status, this work should be carried out step by step and completed in 2023 or 2024 depending on the progress of the construction and the programming work.

An automated superior control is demanding, but also efficient compared to manual control by the operating staff. The measured data on industrial waste heat generation over the summer of 2020 and especially in the 2020/2021 heating period will provide important information in order to be able to plan and implement further automation steps.

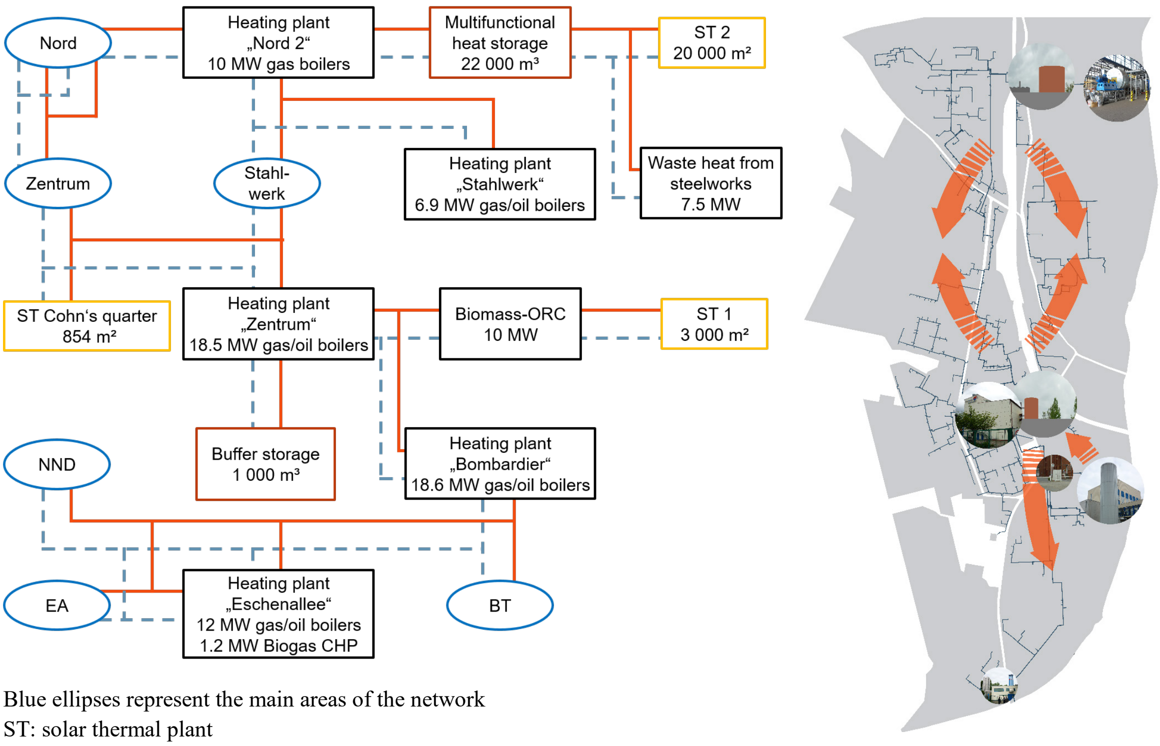

Blue ellipses represent the main areas of the network
ST: solar thermal plant

Figure 6: Simplified hydraulic scheme of the DH Hennigsdorf with thermal capacities (left) and overview of the city area (right)

In order to verify the concept of the Heat Hub Hennigsdorf from the first project phase with the new findings from the measurement data of the operation of the already realized subsystems, Solites again carried out TRNSYS simulations, but now based on actual monitoring data of the industrial waste heat generation, the connecting pipeline and the new built heating central “Nord 2”. Therefore Solites had to evaluate the available monitoring data in detail to derive as best as possible characteristic courses of industrial waste heat supply. Charactersistic means here that the measurement data also show realistic operation in the future after the construction of the multifunctional heat storage. Then the industrial waste heat exchanger is expected to operate much more evenly, as the heat can then always be delivered to the storage. Currently, the waste heat is being supplied by the heating plant “Nord 2” directly to the DH, which cannot always take the possible entire heat output of the industrial waste heat recovery.

The TRNSYS simulations were carried out in a time step of 10 minutes over 3 years. The results of the third year are evaluated and shown here. This means that the storage volume at the beginning of the third year has a realistic temperature distribution. The simulations targeted on the volume of the multifunctional heat storage that fits best to the system regarding the amount of fossil energy reduction and at the same time the resulting overall system economics. Several storage volumes between 500 and 100 000 m³ were simulated for three different waste heat profiles that are based on the evaluation of the measurement data as described above. As this paper gives an overview of the whole project Heat Hub Hennigsdorf, all the details of the measurement data analysis and simulation results cannot be shown here.

For waste heat profile 1, the measured data was used directly that results in a yearly waste heat potential of 16 GWh/a.

In the waste heat profile 2 the monitoring data have been corrected to the target values of the flow and return temperatures specified for the upcoming system with a realized multifunctional heat storage (flow temperature of 90 ... 95 °C and return temperature of 61 °C). To approach future operation conditions, the measured mass flow from the waste heat recovery was compressed and shifted upwards, to achieve a more uniform system operation, which is expected with the realized multifunctional heat storage. This results in a waste heat potential of 37 GWh/a.

For waste heat profile 3, the mass flow from profile 2 was condensed further resulting in a waste heat potential of 42 GWh/a.

The simulation results for the share of fossil-free heat in relation to the total heat generation of the entire Hennigsdorf DH and the number of storage cycles per year are shown in Figure 7 over the storage volume for waste heat profile 3. The entire Hennigsdorf DH comprises all heating plants and a yearly heat production of 125 GWh/a. In Figure 5, each cross shows the simulation of one storage volume. The proportion of fossil-free heat increases from 73 to almost 82 %. From a storage volume of 15 000 m³, 80 % fossil-free heat can be used. A maximum is not reached up to 100 000 m³.

With waste heat profile 1, i.e. the current measurement data, a share of fossil-free heat between almost 65 and 66% can be achieved. As the analysis of the measurement data shows, the temporary hydraulic switch, which instead of the future multifunctional heat storage decouples between the waste heat circuit and the circuit in “Nord 2” leads to a reduction in the usable amount of heat in the waste heat exchanger. With the more realistic waste heat profile 2, the proportion of fossil-free heat increases considerably to 71 to almost 80 %, whereby the 80 % can only be achieved with a storage volume of 100 000 m³.

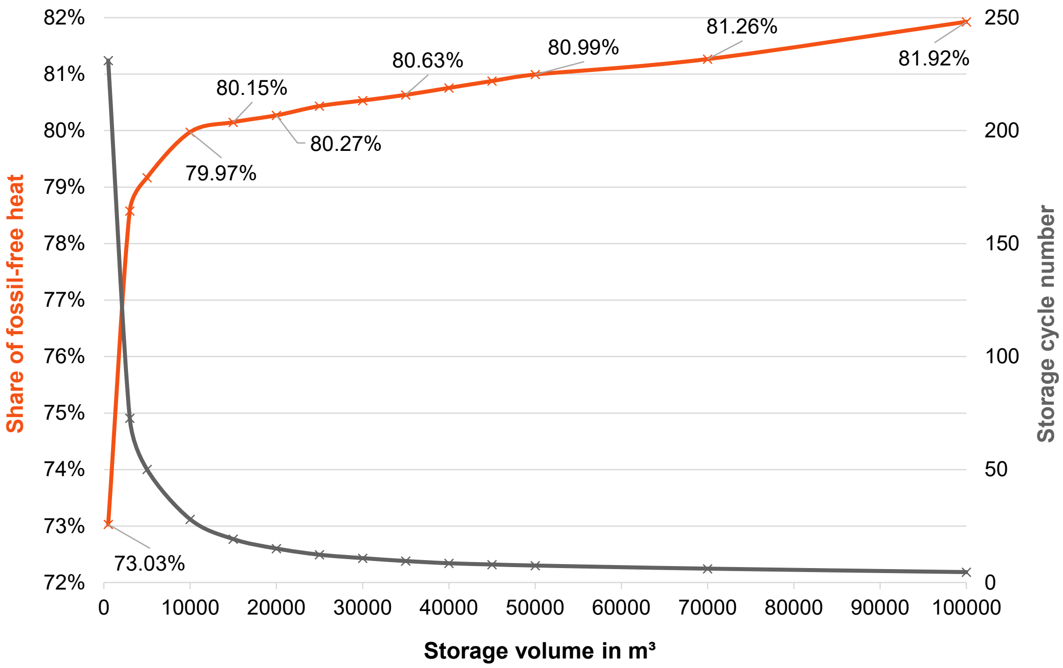

Figure 7: Share of fossil-free heat for the entire DH system and storage cycle number per year over heat storage volume of the multifunctional heat storage for the Heat Hub Hennigsdorf (TRNSYS simulations)

With waste heat profile 3 and 20 000 m³ storage volume, Figure 8 shows the monthly balance of the heat production as an example. The theoretically usable amount of waste heat is roughly the same in every month (except for a 3-week break in operation in August). In the summer months, the amount of waste heat that can be used, is mainly influenced by the storage volume. The output of the biomass CHP is also reduced in the summer months by the superior system control. The internal energy change of the multifunctional heat storage indicates that the storage has a higher energy content at the end of the month than at the beginning of the month (wide column, e.g. in April), or that the storage tank has a lower energy content at the end of the month than at the beginning of the month (narrow column, e.g. in August).

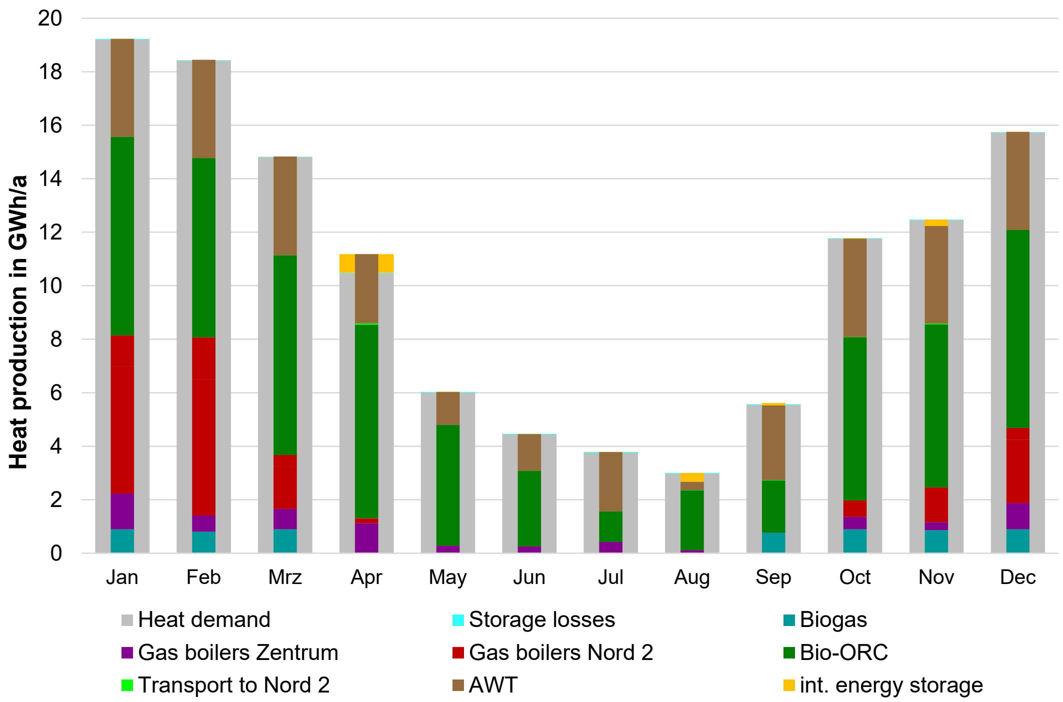

Figure 8: Monthly balance of heat production and the heat demand of the entire DH system Hennigsdorf (TRNSYS simulation with 20 000 m³ storage volume, waste heat profile 3)

The detailed view of ten temperature sensors in the multifunctional heat storage (evenly distributed over the height, T800 above and T890 below) shows that the storage volume is mainly heated in the upper layers in the winter months and is charged through to the lowest storage layer between April and September, see Figure 9. In order to achieve an optimal use of the available waste heat, the storage management and the regulation of the subsystem waste heat to "Nord 2" must follow the dynamics, especially of the waste heat supply and in the summer months.

The extensive simulations with TRNSYS show that in addition to the choosen volume of the multifunctional heat storage, the waste heat supply from the steelworks in particular has a decisive influence on the storage volume that is necessary for a fossil-free share of 80 % of the heat generation. In project phase 1, a usable amount of waste heat of 40 GWh/a was assumed with moderate supply dynamics and thus an initial volume of the multifunctional heat storage was determined to be 22 000 m³. The simulation results now show that when using the measurement data that is now available - taking into account the fact that the current operation cannot correspond to an operation with multifunctional heat storage - even a slightly smaller heat storage volume for the goal of a fossil-free share of heat generation of 80 % is sufficient. The optimal storage volume depends on the amount of waste heat available. The superior control system (with manual or automated decisions) will also have a significant impact on the operation of the multifunctional heat storage. In which dimension the multifunctional heat storage will be planned and built will be decided in the next months, accompanied by further TRNSYS simulations.

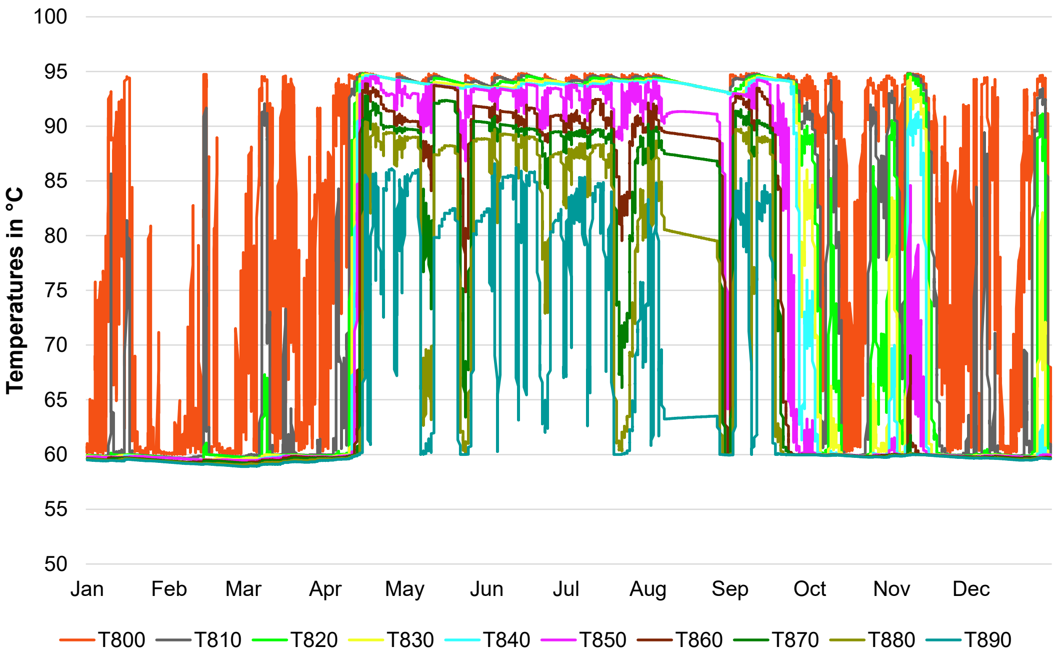

Figure 9: Temperatures inside the multifunctional heat storage over one year (TRNSYS simulation with 20 000 m³ storage volume, waste heat profile 3)

Also the superior control concept will be further developed and optimized with the help of further analyzes of the measurement data and of TRNSYS simulations. For example, the operation of the biomass CHP can be better adapted to the waste heat supply in the summer months. How the waste heat supply will develop in the future and how the walking beam furnace is operated are very important information for the control of the Heat Hub Hennigsdorf. However, these can hardly be predicted and therefore always remain an unknown variable to which the control of the overall system must react.

6. Outlook

As described in this paper, a lot of work has already been carried out, from conception to numerical and hydraulic simulations, planning, installations and construction work. There are still many tasks to be done before the city of Hennigsdorf actually has a CO_2-free heat supply. The planning of the multifunctional heat storage system is currently underway and the construction is due to be completed in 2022. In addition, a ground-mounted solar thermal collector area with 3 000 m² will be built in 2021 and the superior control system will be adapted step by step to the growing system.

Although a bunch of innovations is in the Heat Hub Hennigsdorf, until now main bottle necks were raised by the state-of-the-art and existing laws like the cost for using surplus renewable electricity of wind mills, the tunneling of a railway, project coordination with a very lot of different companies etc. Additionally, financing of this big project by a mid-sized utilities is a challenge due to risk assessment of the banks. Therefore, different subsidy schemes were combined: funding of innovative technologies by the German Federal Ministry for Economic Affairs and Energy with 3.8 Mio. Euro and credits from the Reconstruction Loan Corporation.

To achieve a 100 % fossil-free heat supply in 2025, additional heat sources will be necessary. An area for a further 20 000 m² of solar thermal collectors and the construction of two PtH systems in the heating plants "Nord 2" and "Zentrum" are possible options.

The example of Hennigsdorf shows how cities can contribute to the decarbonisation of the heat supply by setting binding targets themselves and implementing them together with their utilities. The European target of 100 % fossil-free heat supply in cities will only be reached if there are pioneers who dare to start - like Hennigsdorf!

7. References

Berberich, M., & Mangold, D. (2017). Solar district heating in Europe: supplying renewable zero-emission heat. in Proceedings of IEA SHC, Abu Dhabi, UAE.

BMWi. (2018). Erneuerbare-Energien-Wärmegesetz - EEWärmeG.

BMWi. (2019). Energieeffizienz in Zahlen. Berlin: BMWi.

Epp, B., & Oropeza, M. (2019). Solar Heat for Cities - the sustainable solution for district heating. IEA SHC Task 55.

Geiger, P., Pauschinger, T., Sandrock, M., Maaß, C., Westholm, H., Stehle, M., . . . Böhnisch, H. (2020, December). SolnetBW II - Solare Wärmenetze für Baden-Württemberg. Stuttgart.

Gintars, D. (2018). BINE Projektinfo: District heating network becomes heat hub. Retrieved April 15, 2020, from http://www.bine.info/en/publications/projektinfos/publikation/fernwaermenetz-wird-zur-waermedrehscheibe/das-netz-als-waermedrehscheibe/

Solites. (2013). SDHplus Bioenergy villages Germany. Stuttgart: Solites.

Stadtwerke Hennigsdorf. (2018, December). Auf dem Weg zur CO2-neutralen Fernwärmeversorgung in der Stadt Hennigsdorf. Hennigsdorf, Germany.

Stadtwerke Hennigsdorf. (2020, March). Energie Kundenjournal der Stadtwerke Hennigsdorf. Hennigsdorf, Germany.

Stadtwerke Ludwigsburg. (2020). Kommunales Klimaschutz-Modellprojekt SolarHeatGrid. Retrieved February 17, 2020, from https://www.swlb.de/solar-heat-grid

Tschopp, D., Tian, Z., Berberich, M., Fan, J., Perers, B., & Furbo, S. (2020). Large-scale solar thermal systems in leading countries: A review and comparative study of Denmark, China, Germany and Austria. Retrieved from https://doi.org/10.1016/j.apenergy.2020.114997

WindNODE. (2020, 8 20). Das Schaufenster für intelligente Energie im Nordosten WindNODE. Retrieved from www.windnode.de

Supported by:

Federal Ministry
for Economic Affairs
and Energy

on the basis of a decision
by the German Bundestag

The project "Renewable district heating 2020 – the multifunctional district heating network as a heat hub" has received funding from the German Ministry for Economic Affairs and Energy on the basis of a decision by the German Bundestag.

The sole responsibility for the content of this publication lies with the authors. It does not necessarily reflect the opinion of the funding organizations. Neither the funding organizations nor the authors are responsible for any use that may be made of the information contained therein.

Designing District Heating Systems for an Improved Economic Efficiency: A Case Study of a Renewable Rural District Heating Network

Johannes Zipplies, Isabelle Best, Janybek Orozaliev and Klaus Vajen

University of Kassel, Institute of Thermal Engineering,
Kurt-Wolters-Straße 3, 34109 Kassel (Germany), solar@uni-kassel.de

Abstract

In the design phase of district heating networks many parameters that determine the economic efficiency of the network must be chosen. This contribution investigates the economic effects of the choice of the piping system (single or twin pipes), the maximum specific pressure drop, and the return temperature for a rural district heating network. The economic analysis takes costs for network construction and maintenance, heat losses and pump energy into account. The results show that the design variant using twin pipes, pipe dimensioning to 250 Pa/m and network temperatures of 80 °C flow and 45 °C return is most cost efficient, with heat distribution costs of 3.7 €ct/kWh. This is a cost reduction of 20 % in comparison to the reference variant with single pipes, pipe dimensioning to 120 Pa/m and network temperatures of 80 °C flow and 60 °C return.

Keywords: district heating network, design, dimensioning, heat distribution costs

1. Introduction

District heating networks (DHN) are a key technology to integrate renewable heat sources such as solar, biomass, waste heat or combined heat and power generation into future sustainable heat supply systems. While urban areas have high heat demand densities which are favorable for the economic efficiency of DHN, achieving reasonable heat distribution costs in rural areas is a challenge.

During the planning phase of a DHN, many parameters that strongly influence its future economic performance are determined. Of high importance are the choice of the piping type and the network temperatures. Another essential factor are the individual diameters of the pipes, that are usually determined by choosing a maximum specific pressure drop that is allowed at design conditions. In the literature, many different recommendations for the choice of the maximum specific pressure drop can be found, ranging from 100 Pa/m up to above 300 Pa/m (Best et al., 2018). In this contribution, an optimized design for a DHN in a rural area is developed considering these parameters.

2. Case Study

The DHN investigated here is currently in the planning phase. The heat will be generated from wood chips (wood scrap material) in the base load and from biogas, using highly flexible combined heat and power units that will be operated such that they help balance fluctuating renewables. Thus, the heat generation is fully renewable and has additional positive effects for the integration of renewables into the electricity sector.

The DHN shall supply a small village (90 household connections) and a large public property with heat (see fig. 1). The total trench length is about 6 km, while the linear heat density of 730 kWh/(m·a) is rather low. The local conditions entail long transport pipes from the heat supply unit to the village and the public property that make up about half of the total trench length.

doi:10.18086/eurosun.2020.02.02 Available at http://proceedings.ises.org

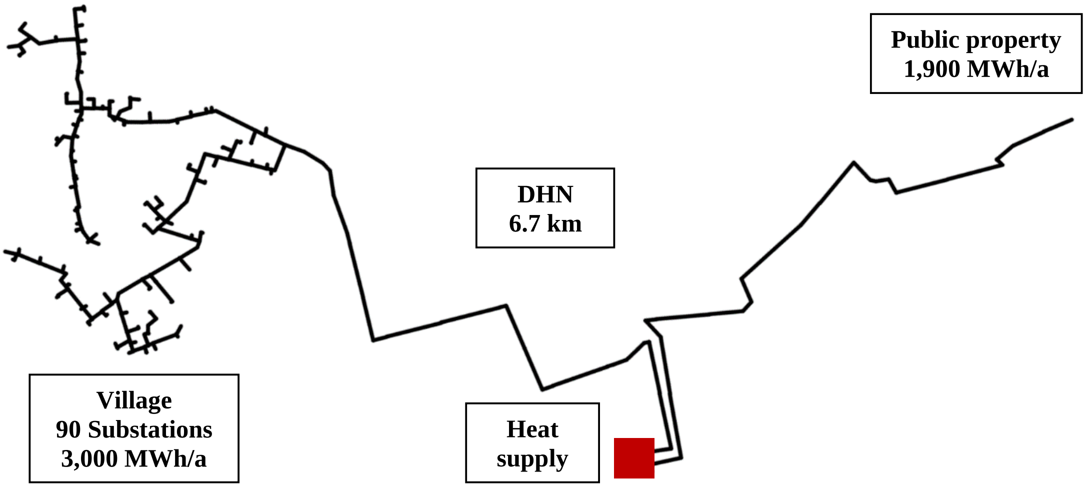

Fig. 1: The rural DHN. Two transport pipes, each about 1.4 km, connect the heat supply unit with the village (90 substations) and the large public property.

The heat customers in the village are single-family and small multi-family buildings, among which only a few have been constructed recently, so that the building stock exhibits a high specific heat demand of 150 kWh/(m^2·a) on average. In the village, the network shall be operated year-round, while the summer heat demand of the public property will be met locally, so that this transport pipe can be shut down for three months.

3. Methods

3.1. Calculation of the maximum heat power

The design process of the DHN starts with determining the maximum heat load that may occur. From another project, detailed calculations of the heat load of the residential buildings in the village, that take heat losses through the building envelope and solar gains into account, are available. Based on these load profiles, the maximum heat load at an ambient temperature of -12 °C (standard ambient temperature for heat load calculations in this area according to Deutsches Institut für Normung e.V., 2008) is calculated.

The additional heat power to provide domestic hot water is included according to the German standard DIN 4708 (Deutsches Institut für Normung e.V., 1994). For this calculation, information about the number of inhabitants and living space is used and a domestic hot water preparation with a storage volume of 30 l/person is assumed.

For each of the 90 residential buildings, maximum heat powers ranging from 8 kW to 41 kW that sum up to 1.54 MW are determined. The public property has a maximum heat power of 2.14 MW, so that in total, a maximum heat power of 3.7 MW must be provided by the DHN.

3.2. Simultaneity

Not all heat customers need the maximum heat power at the same instant, so that the maximum instantaneous heat load for the DHN is less than the sum of all individual maximum heat loads. This effect is described by the simultaneity factor, that can be determined according to equation 1 and is restricted to values from 0 to 1.

$$f_{\mathrm{sim}} = \frac{\max_t\left(\sum_{i=1}^{N} \dot{Q}_i(t)\right)}{\sum_{i=1}^{N} \max_t\left(\dot{Q}_i(t)\right)} \qquad \text{(eq. 1)}$$

with:

f_{sim}	Simultaneity factor
N	Total number of heat customers
$\dot{Q}_i(t)$	Heat power of the customer i at time t

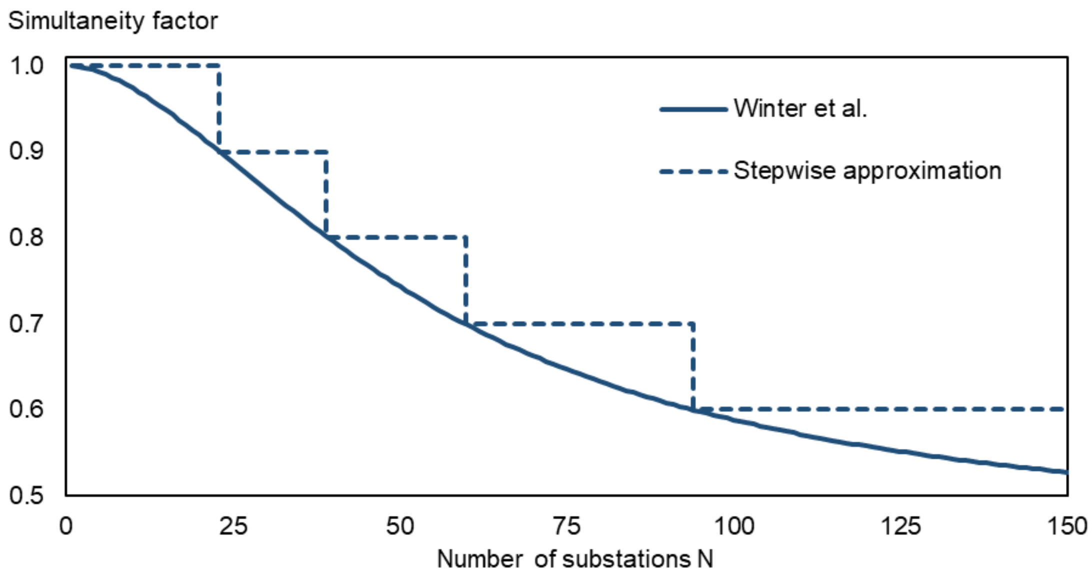

Fig. 2: Empirical simultaneity factor (Winter et al., 2001).

In the literature, various approaches to calculate the simultaneity factor with respect to the total number of customers N can be found. In this contribution, an empirical formula is used, that has been determined using a large data base from DHNs with a customer composition similar to this case study (Winter et al., 2001). This simultaneity factor is calculated as a stepwise approximation (steps of 0.1) in the design process of the network (see fig. 2). When determining the diameter of a pipe segment, the simultaneity factor according to the number of substations N downstream the pipe segment is used to adapt the maximum power that the respective pipe segment shall meet.

3.3. Design variants

In total, five different design variants are considered. All of them use pipes with insulation series 3 (the particular specification is according to Isoplus “konti” pipes, according to Koidl, 2016) in order to limit heat losses to a minimum despite the rather low linear heat density of the DHN. Furthermore, a design flow temperature of 80 °C is chosen for all design variants.

The reference design variant uses single pipes that are designed with a maximum specific pressure drop of 120 Pa/m and a return temperature of 60 °C, without taking simultaneity factors into account. The return temperature of 60 °C is a high return temperature, that must be expected for customers with unsatisfactory secondary installations (no hydraulic balancing, inefficient domestic hot water preparation and storage).

The following design variants change these parameters step-by-step, whereby from one to the other the parameter is chosen, for which the best relation of benefit to effort is anticipated. In this way, twin pipes, a high maximum specific pressure drop of 250 Pa/m, a return temperature of 45 °C and the consideration of simultaneity factors are investigated.

3.4. Pipe dimensioning

The dimensioning of the pipe network is carried out with a thermo-hydraulic model in the commercial software STANET® (Fischer-Uhrig, 2019). First, a detailed model of the DHN is built and parametrized, that represents the piping route including all house lead-in pipes.

For each variant, volume flow rates at maximum load conditions are determined for every pipe segment in consideration of the maximum heat loads of the substations, design temperatures of the network and, if applicable, the simultaneity factors. Then every pipe segment’s diameter is determined, such that its specific pressure drop is only just below the maximum specific pressure drop (120 Pa/m or 250 Pa/m). At this, the pressure loss calculation takes individual points of flow resistance into account using a generalized estimation based on the length and the diameter of the pipe segment. This dimensioning procedure is carried out iteratively, as changes in pipe diameters entail minor changes in flow temperatures at the substations. A stable result is reached after no more than three iterations.

3.5. Determination of heat losses and pump energy demand

For each variant, heat losses and pump energy demand for a whole year are determined using thermo-hydraulic simulations. The precalculated heat load profiles for each customer are available at a resolution of one hour. Additionally, load profiles for domestic hot water are generated for each substation individually using the DHWcalc tool (Jordan et al., 2017). The effects of secondary installations (time shifts, losses) are neglected at this stage. The total load profile for all loads is split into two parts, first for the heating season (mid of September until mid of June) and second for the summer period, when the network section to the public properties will be shut down, so that this period must be considered separately. In fig. 3 the load duration curves (sorted hourly load values) for both periods are depicted. To limit the effort for simulations and calculations to a reasonable extent, the load duration curves are classified into six (heating season) and three (summer) load classes, each with a constant power and a suitable duration, that represent the load duration curves, as shown in fig. 3. Instead of simulating the whole year in hourly resolution, these representative load states are simulated, and the results are extrapolated according to the respective duration of each load class.

These nine representative load states are simulated for each design variant using the thermo-hydraulic model in STANET® to determine heat losses of the DHN as well as volume flow rates and differential pressures of the network pumps. The heat loss calculation includes the interaction between flow and return pipe of twin pipes in a simplified way: The heat loss coefficients for the twin pipes are set according to heat flows at typical temperatures (75 °C flow / 50 °C return / 10 °C soil temperature), which results in low heat losses from return pipes, as they gain some heat from the flow pipes. In the simulations, as a simplification, a constant return temperature according to the design variant (60 °C or 45 °C) is assumed at the consumer substations. However, the variable flow temperature is 70 °C in summer and rises linearly to 80 °C, while ambient temperatures fall from 15 °C to -10 °C.

The electric power consumption of the pump motor is calculated from volume flow rate, differential pressure, and the total pump efficiency (including motor efficiency) according to equation 2.

$$P_{\text{pump}} = \frac{\dot{V}\,\Delta p}{\eta_{\text{pump,tot}}} \qquad \text{(eq. 2)}$$

where

P_{pump}	electric power consumption of the pump motor
$\dot{V}$	volume flow rate
Δp	differential pressure
$\eta_{\text{pump,tot}}$	total pump efficiency (including motor efficiency)

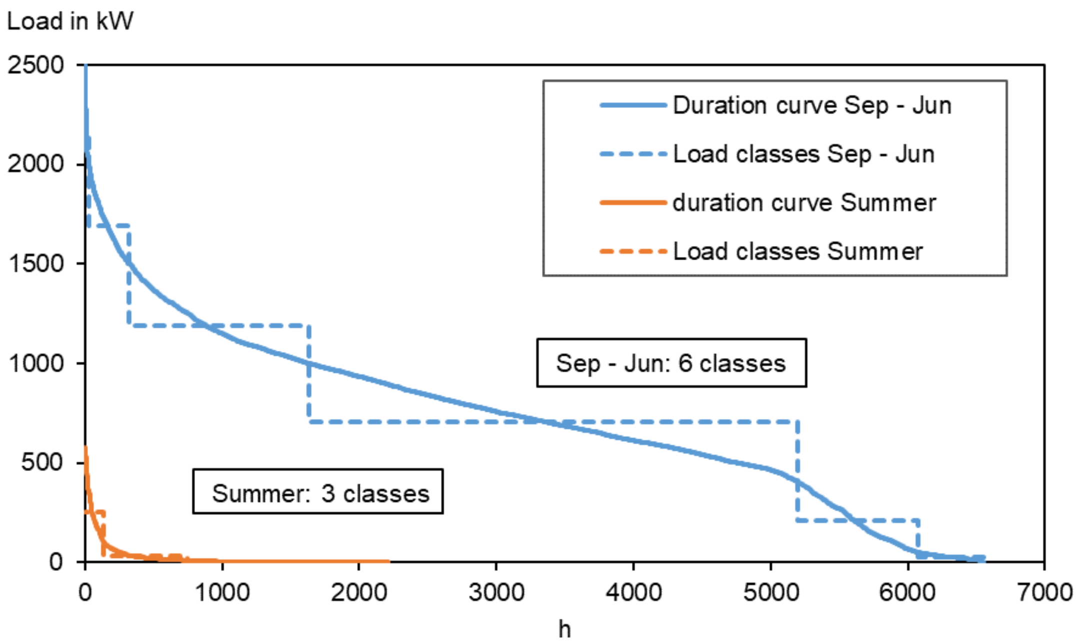

Fig. 3: Load duration curves for heating season (mid of September until mid of June) and the representative load classes.

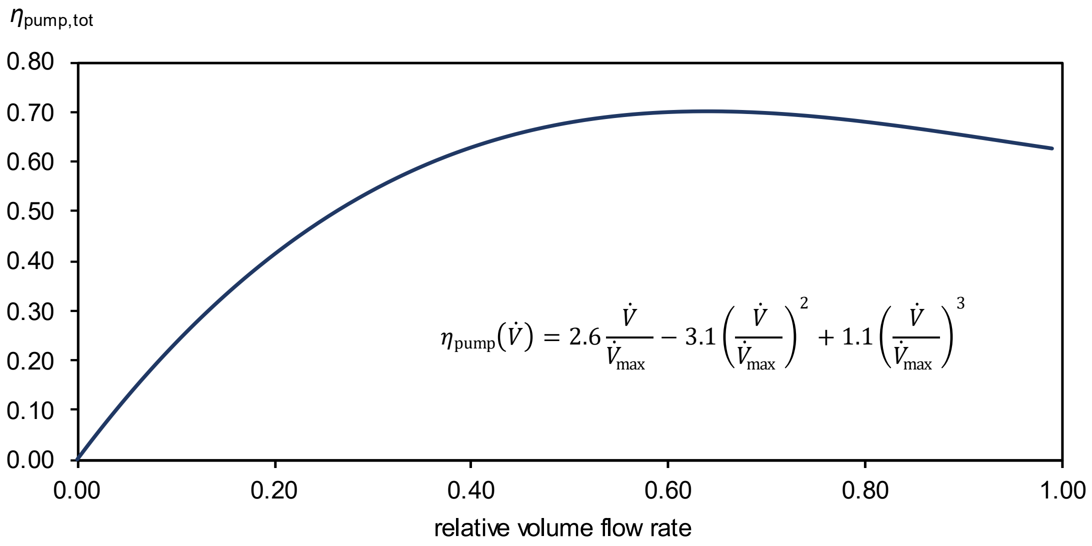

Fig. 4: Assumed total pump efficiency as a function of relative volume flow rate.

The total pump efficiency depends on the type of the pump and in general depends on the volume flow rate. In this contribution, the generic approximation for the total pump efficiency depicted in fig. 4 is used. It shows a very low total pump efficiency at low volume flow rates, reaches a maximum of 70 % at medium and high volume flow rates and finally drops slightly towards maximum pump capacity. The speed of the pump is controlled so that a minimum differential pressure of 0.6 bar at the consumer substations is maintained. In this case study, only a single pump is assumed. In cases where several pumps with different capacities are installed, high pump efficiencies even during low load perios are possible by using the smaller pump, which reduces the electricity consumption of the pumps.

Based on the values for pump and heat loss power for each representative load state, annual values are extrapolated according to the duration of each state.

3.6. Calculation of heat distribution costs

Based on the results of the previous steps, the heat distribution costs per delivered heat are calculated, whereby construction and maintenance of the DHN including substations, costs for heat losses and costs for pump energy are included.

The network construction costs for each pipe segment are calculated according to a cost approach that specifies costs for each pipe depending on the its diameter and the ground condition (green area or paved surface, see fig. 5) (Manderfeld et al., 2008).

The costs include the pipe itself, ground works, pipe installation and restoration of the ground surface. It is assumed, that the network costs for single and twin pipes do not differ significantly from each other (Manderfeld et al., 2008). The transport pipes will be laid in green areas, whereas the distribution pipes in the village will be laid in streets, so that costs for paved surfaces apply.

The heat distribution costs are determined via a dynamic economic analysis as an annuity, which is finally divided by the annual heat delivery, to ensure the comparability of the results. The important parameters of the economic analysis are summarized in table 1. The values are taken from the literature or are chosen by the DHN operator of the case study, as indicated in the table. Subsidies, price increase and inflation are excluded from the economic analysis.

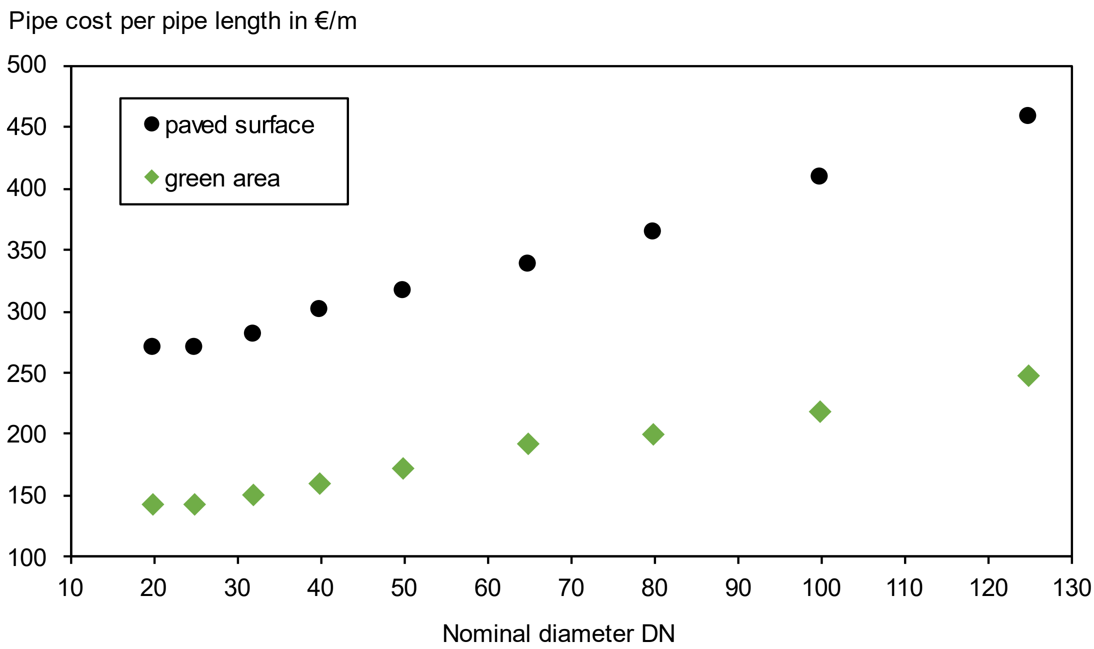

Fig. 5: Pipe costs per meter trench depending on nominal diameter and ground condition including construction costs and pipe material costs (Manderfeld et al., 2008).

Table 1: Parameters of the economic analysis

Parameter	Value	Taken from
Cost per substation	3,600 €	Stuible et al., 2016
Interest rate	2 %	DHN operator
Service life pipes	30 a	Große et al., 2017
Service life substations & pump	20 a	Große et al., 2017
Planning costs	14 % of CAPEX	HOAI (Bundesministerium für Wirtschaft und Energie (BMWi), 2013)
Operation & maintenance network	1 % of CAPEX p.a.	Große et al., 2017
Operation & maintenance substations	3 % of CAPEX p.a.	VDI 2067 (VDI-Gesellschaft Bauen und Gebäudetechnik (GBG), 2012)
Price for heat supply	45 €/MWh	DHN operator
Price for pump electricity	170 €/MWh	DHN operator

4. Results

All results are given in table 2 and the specific heat distribution costs of the different design variants of the DHN are presented in figure 6. Variant 1 uses twin pipes instead of single pipes. In addition, variant 2 is designed with a maximum specific pressure drop of 250 Pa/m instead of 120 Pa/m. As a next step, a return temperature of 45 °C instead of 60 °C is assumed for variant 3. This may require larger heat exchangers and an improved control in the substations and additional improvements of the secondary installations such as hydraulic balancing and an efficient domestic hot water preparation. These potential additional costs for these measures are not included in the economic analysis. Finally, simultaneity factors are included in the design process of the pipe segments in variant 4.

Table 2: Results of the design process and economic analysis for the DHN

Parameter	Unit	Reference	V1	V2	V3	V4
Design criteria						
Piping type	-	single	**twin**	**twin**	**twin**	**twin**
Δp_{max}	Pa/m	120	120	**250**	**250**	**250**
T_{flow} / T_{return}	°C	80 / 60	80 / 60	80 / 60	80 / **45**	80 / **45**
Simultaneity	-	none	none	none	none	**included**
Selected parameters						
Network volume	m^3	140	138	103	65	53
Pressure rating	-	PN6	PN6	PN10	PN10	PN16
Heat losses	% *)	19.5	10.7	10.1	9.3	9.1
Pump energy	% *)	0.30	0.32	0.49	0.42	0.79
				*) in relation to the annual heat input into the DHN		
Heat distribution costs						
Network costs	€ct/kWh	3.40	3.39	3.27	3.12	3.08
Heat loss costs	€ct/kWh	1.09	0.54	0.51	0.46	0.45
Pumping costs	€ct/kWh	0.06	0.06	0.09	0.08	0.15

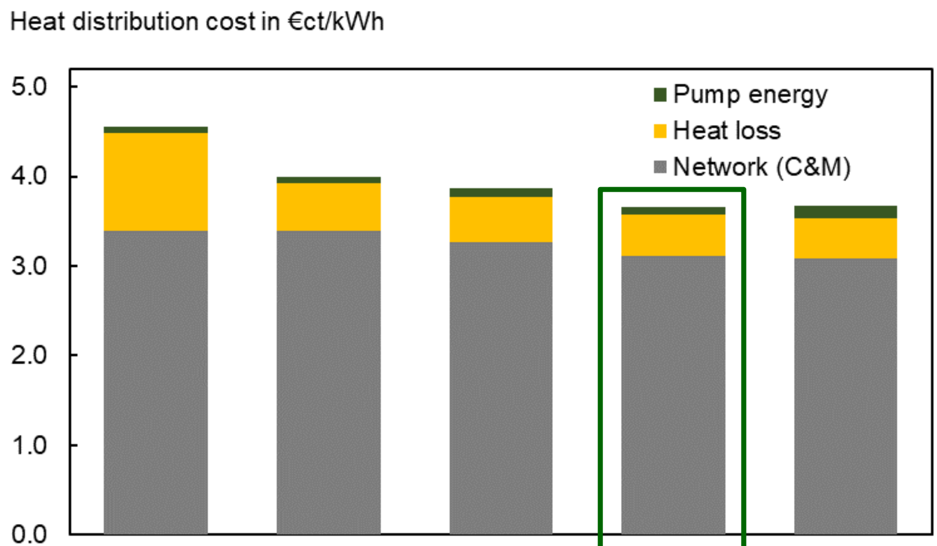

Parameter	Reference	V1	V2	V3	V4
Piping type	single	**twin**	**twin**	**twin**	**twin**
Δp_{max} in Pa/m	120	120	**250**	**250**	**250**
T_{flow} / T_{return} in °C	80 / 60	80 / 60	80 / 60	80 / **45**	80 / **45**
Simultaneity	none	none	none	none	**included**

Fig. 6: Specific heat distribution costs of the design variants, separated into cost for the network (construction and maintenance of all components, including substations and pumps), for heat losses, and for the pump energy.

The results show that the costs for the network infrastructure (construction and maintenance) dominate for all design variants. The costs for heat losses are substantially lower while costs for pumping energy form the smallest portion.

The reference variant has high heat losses of 19.5 % of the heat input into the DHN. Its specific heat distribution costs are 4.55 €ct/kWh (in relation to the delivered heat). By using twin pipes in variant 1, the heat losses are reduced to 10.7 %. The heat distribution costs decrease by 0.56 €ct/kWh, which is almost exclusively an effect of the reduced heat losses.

Variant 2 has smaller pipe diameters (the network volume is reduced by about 25 %) due to the higher specific pressure drop that is used in the design process. In consequence, the heat distribution costs are reduced by another 0.12 €ct/kWh, which is mainly due to reduced investments for the pipe construction, while a minor increase of pump energy costs is compensated by an equal reduction of heat loss costs. This variant entails higher pressures in the network, so that a pressure rating of PN10 instead of PN6 is required for the components.

As a next step, a reduced return temperature of 45 °C instead of 60 °C is assumed for variant 3. This leads to reduced volume flow rates in the network allowing for thinner pipes, which in total leads to a reduction of the network volume by another 25 %. The total heat distribution costs show a further decrease by 0.19 €ct/kWh, which is mainly attributed to reduced costs for the network itself, while heat loss and pump energy costs decrease as well. It should be noted that this result is based on the assumption, that the reduced return temperatures can be reached during the whole year, which limits the comparability of the variants 3 and 4 with the previous design variants. However, the result shows, that when designing DHNs, the lowest possible return temperature should be aimed for and implemented, as this is favorable for all three cost components.

Including simultaneity factors in the design process of variant 4 leads to a substantial rise in pump energy costs, that are not fully compensated by reduced network and heat loss costs. This variant requires a pressure rating of PN16 for all network components.

Overall, variant 3 with twin pipes, a pipe dimensioning at 250 Pa/m and network temperatures of 80 °C supply and 45 °C return temperature is the most cost-effective solution. Compared to the reference variant, the heat distribution costs are reduced by 20 %.

5. Discussion

5.1. Additional efforts for the design variants

The design variants 1 to 4 entail individual extra efforts, that cannot be clearly quantified and that highly depend on the respective local conditions. This paragraph discusses these extra efforts in detail.

Twin pipes, as used for variants 1 to 4 may under certain circumstances lead to increased complexity of the installation, because it is more difficult to circumvent unexpected underground obstacles with this pipe system. Thus, additional bends and additional labour and expenses may be needed. The risk of this factor mainly depends on how many other underground installations will be found along the network route – and how much is known about them in advance. In very unfavourable cases, the additional effort may even lead to a situation, where for distinct areas of the DHN single pipes should be preferred to twin pipes.

The design with higher specific pressure drops entails an equivalent increase in network pressures. While the reference variant and variant 1 may be built with a pressure rating of PN6, variant 2 and 3 require PN10 and variant 4 even needs PN16. Typically, pipes and substations have at least a PN10 pressure rating (compare Koidl, 2016 and YADOS GmbH, 2016). However, components with PN16 pressure rating may entail additional costs, that could not be quantified in this work due to a lack of adequate information in the literature. In general, it is recommendable not to exceed pressure ratings by a little and rather stay within PN10 for small DHNs.

Assuming reduced return temperatures of 45 °C in the design process (variants 3 and 4) requires improvements of the secondary installations of the customers. In particular, hydraulic balancing of the heating system has to be undertaken and outdated components for domestic hot water preparation should be replaced by efficient technologies. The costs for these measures are not included in this work, as they strongly depend on the individual situation of the customer installations and cannot be reliably quantified. Furthermore, these measures lead to other positive effects: For example, hydraulic balancing substantially improves the comfort in the building (no over- and underheating), which may already justify the costs.

5.2. Transferability of the methods and results

The methods to optimally design rural DHNs described in this work can be transferred to other case studies, provided that the required data is available. The results of the case study may be transferred to other cases, if the essential parameters of the DHN (e.g. linear heat density, size of the network) and of the economic analysis (especially interest rate, heat and electricity prices) roughly coincide.

In particular, the result that twin pipes yield a substantial cost reduction due to reduced heat losses is robust and can be transferred to other small rural DHNs. Furthermore, it is generally recommendable to design small rural DHNs with a rather high specific pressure drop of about 250 Pa/m, even if the exact optimal value is subject to the costs for heat, electricity, and network construction of the individual case. In addition, striving for low return temperatures in the design phase of the network certainly leads to a cost reduction for the DHN, because all cost components decrease with decreasing return temperatures. The exact value that can be reached in the respective case however depends on the effort, that the customers must undertake to maintain this temperature in operation.

In this case study, considering simultaneity factors in the design process has not proven favorable. This result cannot be transferred to small rural DHNs in general, it rather is a consequence of the special network structure of the case study with very long transport pipes. Considering simultaneity factors leads to a change of pipe diameters by one step along the whole length of the transport pipe which entails a doubling of pressure losses in the thermo-hydraulic simulations. In contrast, for DHNs with a heat supply unit within the area of heat demand, considering simultaneity factors in the design process may be favorable. Therefore, the design method using simultaneity factors has been described in detail, so that it can be used and evaluated in other cases.

6. Summary

This contribution describes the design process of a small rural DHN and compares five design variants by a dynamic economic analysis based on results from thermo-hydraulic simulations.

Overall, a network design using twin pipes, a pipe dimensioning at 250 Pa/m and network temperatures of 80 °C flow and 45 °C return temperature is the most cost-effective solution, with heat distribution costs of 3.7 €ct/kWh. Compared to the reference variant with single pipes, pipe dimensioning at 120 Pa/m and network temperatures of 80 °C / 60 °C (flow / return), the heat distribution costs are reduced by 20 %.

In general, the common pipe dimensioning with a maximum specific pressure drop of about 100 Pa/m is not cost-optimal for small DHN. Instead, higher for the maximum specific pressure drop should be used. Furthermore, the results show that rural DHN should be designed with twin pipes and lowest-possible return temperatures to reach optimal heat distribution costs.

7. Acknowledgments

This contribution is based upon the work conducted within the SINTEG project Csells funded by the German Federal Ministry for Economic Affairs and Energy (grant number 03SIN119).

8. References

Best, I., Orozaliev, J., Vajen, K., 2018. Impact of Different Design Guidelines on the Total Distribution Costs of 4th Generation District Heating Networks. Energy Procedia 149, 151–160.

Bundesministerium für Wirtschaft und Energie (BMWi), 2013. Verordnung über die Honorare für Architekten und Ingenieurleistungen (Honorarordnung für Architekten und Ingenieure - HOAI). Beuth Verlag GmbH. https://www.hoai.de/online/HOAI_2013/HOAI_2013.php.

Deutsches Institut für Normung e.V., 1994. DIN 4708 Central heat-water-installations. Part 2: Rules for the determination of the water-heat-demand in dwelling-houses. Beuth Verlag GmbH, Berlin.

Deutsches Institut für Normung e.V., 2008. DIN 12831 Heizungsanlagen in Gebäuden - Verfahren zur Berechnung der Norm-Heizlast - Nationaler Anhang NA. Beuth Verlag GmbH.

Fischer-Uhrig, F., 2019. STANET. Netzberechnung. Ingenieurbüro Fischer-Uhrig, Berlin.

Große, R., Christopher, B., Stefan, W., Geyer, R., Robbi, S., 2017. Long term (2050) projections of techno-economic performance of large-scale heating and cooling in the EU. External study performed by ILF Consulting Engineers Austria GmbH, and AIT Austrian Institute of Technology GmbH for the Joint Research Centre. EUR28859.

Jordan, U., Vajen, K., Braas, H., 2017. Handbuch DHWcalc. Version 2.02b (März 2017). Institut für Thermische Energietechnik; Fachgebiet Solar und Anlagentechnik, Kassel.

Koidl, C., 2016. Kapitel 2 - Starre Verbundsysteme, in: isoplus Fernwärmetechnik (Ed.), Planungshandbuch.

Manderfeld, M., Jentsch, A., Pohlig, A., Dötsch, C., Richter, S., Bohn, K., 2008. Abschlussbericht Forschungsvorhaben Fernwärme in der Fläche RDH (Rural District Heating) . Ermittlung des Fernwärmepotentials unter Berücksichtigung der neuester Verlegeverfahren und unterschiedlicher Energiedargebote in der Fläche der Bundesrepublik Deutschland. Accessed 18.12.17.

Stuible, A., Zech, D., Wülbeck, H.-F., Sperber, E., Nast, M., Hartmann, H., Reisinger, K., Budig, C., Orozaliev, J., Pag, F., Vajen, K., Erler, R., Janczik, S., Kaltschmitt, M., Niederberger, M., 2016. Evaluierung von Einzelmaßnahmen zur Nutzung erneuerbarer Energien im Wärmemarkt (Marktanreizprogramm) für den Zeitraum 2012 bis 2014. Evaluierung des Förderjahres 2014.

VDI-Gesellschaft Bauen und Gebäudetechnik (GBG), 2012. VDI 2067 Blatt 1 - Wirtschaftlichkeit gebäudetechnischer Anlagen. Grundlagen und Kostenberechnung, Düsseldorf, 44 pp.

Winter, W., Haslauer, T., Obernberger, I., 2001. Untersuchungen der Gleichzeitigkeit in kleinen und mittleren Nahwärmenetzen. Euro Heat & Power (9, 10).

YADOS GmbH, 2016. Standardisierte Wärmeübergabestation YADO|GIRO, Hoyerswerda. www.yados.de/pdf-katalog/yado-giro. Accessed 23 April 2020.

EnRSim - A simple calculation tool for renewable based heating networks plant

Nicolas Lamaison[1], Mathieu Vallée[1], Jean-François Robin[1], Christine Delord[2], Romain Genet[3] and Cédric Paulus[1]

[1] CEA LITEN, Grenoble (France)

[2] INES PFE, Le Bourget du Lac (France)

[3] INDDIGO, Chambéry (France)

Abstract

Renewable-based production plants for District Heating Networks (DHN) should be deployed massively in the coming years. The present document introduces to the community a new pre-feasibility study tool, ENRSIM, to simulate such plants. That business-oriented tool allows the simulation of plants with up to 3 different units with an optional thermal storage. The plant model is implemented in Dymola and controlled using field-based expert laws using a co-simulation platform. Computation is performed over 1 year at a time step of 1 hour and takes about 1 minute on a standard laptop. An example including solar, biomass, gas and storage is here presented highlighting the type of results obtained. The example is extended to predictive control highlighting that the latter associated to MILP programming leads to optimal interactions between the components. A minimal increase of 4.3% in renewable energy content and 77% in biomass boiler startups was obtained using predictive control as opposed to field based expert laws.

Keywords: Simplified simulation tool, DHN, Renewable-based production plants, Predictive Control, MILP

1. Introduction and tool features

Due to their ability to distribute large amount of renewable energy, District Heating Networks (DHN) are expected to exhibit a considerable development in the coming years in France (DGEC France, 2019). In that context, the appropriate sizing of the renewable-based production units in accordance to the other production units becomes a prime objective. Traditional sizing methods are static and combine the demand monotone together with linear cost characteristic to obtain a break-even diagram (Frederiksen and Werner, 2013). The latter results in a piling of the heat generators on the demand monotone as a function of their profitability zones, which depend on their hours of operation. Another solution is to use dynamic tools (such as EnergyPRO®) and successive calculations.

The ENRSIM software, introduced by the present paper and cofounded by the French Renewable Energy Agency (ADEME), aims at providing such a simple dynamic tool for multi-renewable based DHN plants simulations, particularly for the integration of solar energy and storage. It targets mostly engineering offices and collectivities. It is available in French and English. The user can simulate up to 3 generators in the following list: Solar thermal, Biomass boiler, Gas boiler, CHP and Heat pump. Daily storage common to all generators and dedicated daily storage for each solar field can be setup. Finally, various configurations (serial and parallel) can be simulated. As the tool focuses on solar thermal, many parameters are available for the solar plant while the other heat units have a limited number of parameters.

Operational performances of complex energy systems can be significantly underestimated when rule-based (expert laws) control is used (Giraud et al., 2017). Thus, appropriate sizing of storage capabilities is sub-optimal when using tools based on such rules. The reasons are: i) they do not consider a time horizon compatible with the storage time constant and ii) they pre-assume specific utilization of the storage. Thus, an extension of the EnRSim calculation core to predictive control associated to Mixed Integer Linear Programming (MILP) is here presented on a case study.

The present paper is organized as follows: presentation of the EnRSim tool architecture in Section 2, a tool demo through a case study in Section 3, an extension of the case study with the introduction of predictive control in Section 4 and conclusions and perspectives in Section 5.

doi:10.18086/eurosun.2020.02.03 Available at http://proceedings.ises.org

2. Tool architecture and description

2.1. Overall architecture

Fig. 1 presents the tool architecture including a graphical user interface, pre-processing modules, the calculation core and post-processing modules. The tool performs a 1-year simulation at a time step of 1 hour. The following paragraphs give details on the pre-processing modules, calculation core and post-processing modules while the next section presents snapshot of the graphical user interface through a case study.

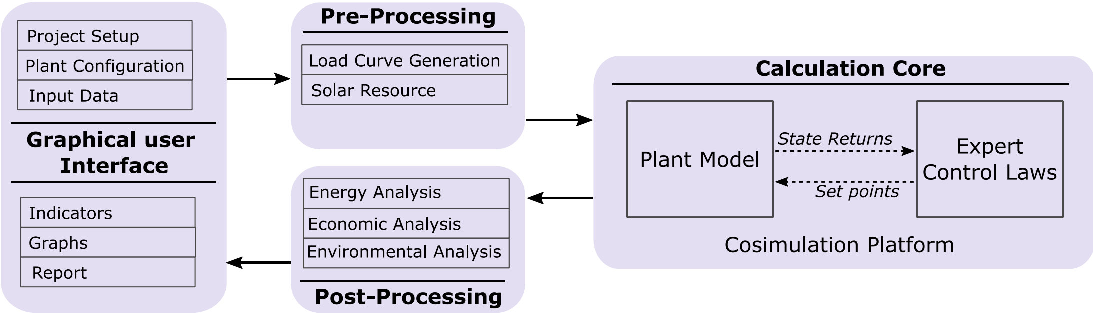

Fig. 1: Overall EnRSim tool architecture

2.2. Pre-processing modules

The first pre-processing module, referred as 'Load Curve Generation' in Fig. 1, calculates the hourly aggregated DHN heat demand and associated departure/return temperatures based on user input monthly overall heat demands. To do so, the module i) first, distributes the monthly loads among monthly losses, domestic hot water (DHW) and space heating and ii) second, allocates the calculated monthly contribution for each 1 hour time step. For both steps, the module uses the user chosen hourly ambient temperature profile together with assumptions on i) heating laws for the network temperatures, ii) yearly heat loss, iii) cold water mains temperature, iv) normed monthly distribution of DHW load, v) DHW production temperature and simultaneity factor, vi) normed daily distribution of DHW and space heating loads. The methodology implemented in this module was previously validated using real DHN data (Provent et al., 2013). It is worth mentioning that the user can also use his own load curve.

The second pre-processing module, referred as 'Solar Resource' in Fig. 1, treats the user input solar resource with i) tilt and ii) solar masks correction. The former transforms the user input horizontal direct and diffuse irradiation into the associated tilted contributions. The latter accounts for external and array shading, whose validations are respectively shown in Fig. 2 and Fig. 3 for the direct part of the irradiation (diffuse part not shown). Both figures present the value of the correction factor along the year (time step of 1 hour) in a plan Elevation vs Azimuth. For the external shading, Fig. 2 clearly shows that the external correction factor $f_{dir,e}$ is 0 (i.e. incoming irradiation is fully shaded) when the sun is below the external mask while it is 1 (i.e. no shading) when above. Regarding array shading (Fig. 3), simulations with type 56 of TRNSYS® were performed for fixed solar azimuth values (vertical lines with triangle markers on Fig. 3), which allowed validating the results obtained with the 'Solar Resource' module for the array shading correction factor $f_{dir,a}$ (circle markers).

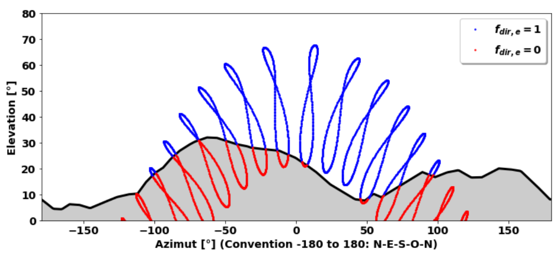

Fig. 2: 'Solar Resource' module external shading validation

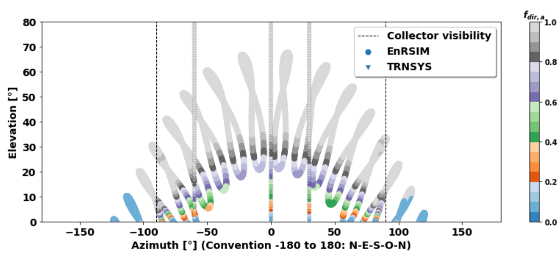

Fig. 3: 'Solar Resource' module array shading validation

2.3. Plant Model

The plant model is programmed using the Modelica language and implemented within Dymola®. It uses production unit and storage models from the in-house 'DistrictHeating' library (Giraud et al., 2015). Fig. 4 shows a schematic of the model implemented. It is meant to be generic, i.e. the goal is to have a single model capable of managing a large majority of the current configurations or ones that look promising going forward for a heating network thermal plant. In this thermal heating plant model, we find 5 potential generators in parallel (Biomass, Cogeneration, Heat Pump, Gas and Solar), 3 potential generators in series upstream (Cogeneration, Heat Pump, Solar), 1 potential common storage and 1 back-up generator whose aim is to satisfy the load curve in all circumstances. Both solar fields also include a dedicated storage. For each of the block embedded, steady-state mass balance and dynamic energy balance are solved. Further details are provided in Appendix.

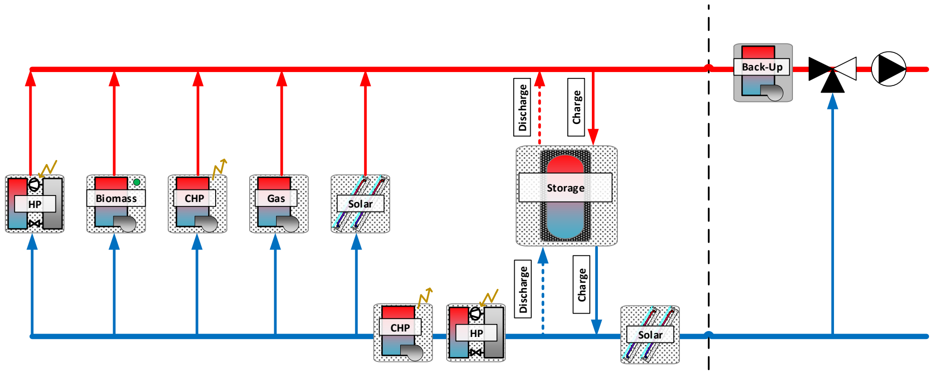

Fig. 4: Schematic of the generic calculation core plant model

The Modelica-based plant model is encapsulated using FMI standard (FMI development group, 2014) and embedded into the in-house co-simulation platform PEGASE (Vallée et al., 2019) where it is operated aside a controller module containing the expert laws. Fig. 1 illustrates the interaction between the plant model and the controller.

2.4. Expert Control Laws

The EnRSim tool is based on predefined control laws. The parameters of each unit for the control laws are i) the calendar availability (A), ii) the priority (P), iii) the minimum and maximum thermal power (P_{min}/P_{max}), and iv) the maximum outlet temperature ($T_{o,max}$). Depending on the plant configuration (2 units in parallel and 1 unit in upstream serial, 3 in parallel, 2 in serial, etc.) , the control laws are different. Fig. 5 presents the expert law logic for 2 units in parallel. Each branch leads to a set of thermal power and mass flow rate set points for both generators. Startup and shutoff are handled within this logic diagram.

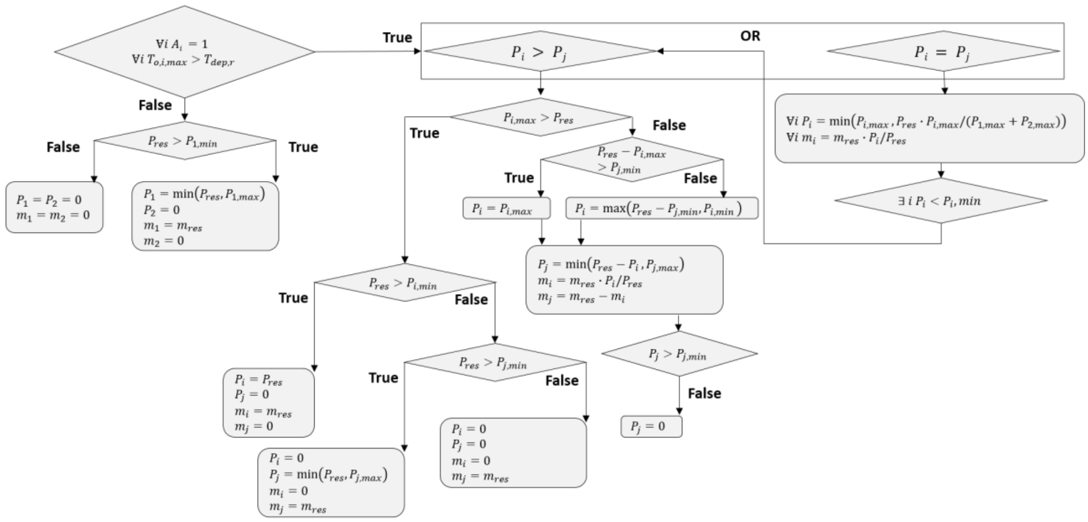

Fig. 5: Example of expert law control for 2 units in parallel

Another set of control laws exist for the common storage (shown in Fig. 4). For the latter, the user can choose between 'Charging' or 'Discharging' priority. For both priorities, charge and discharge modes are controlled differently, as shown in Fig. 6, depending on the storage state of charge (τ) and the level of thermal power of each generator (P_i). To summarize, charging priority prevents frequent start and stop of generators while discharging priority favors storage discharge during peak demand events.

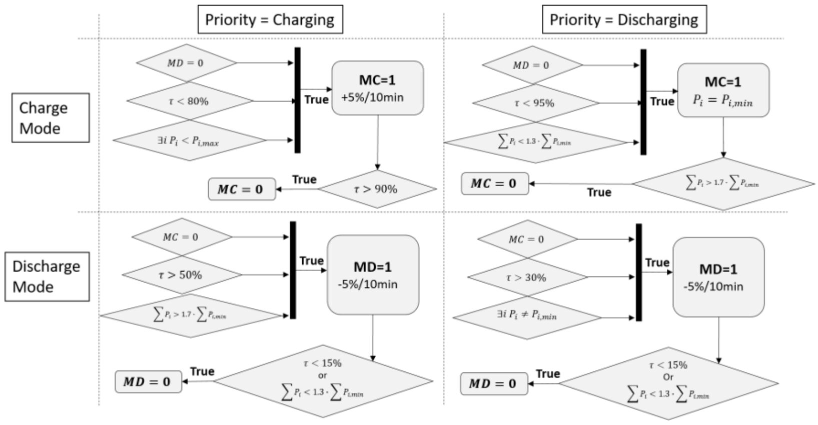

Fig. 6: Common storage expert control laws

2.5. Post-processing modules

The tool includes three post-processing modules that respectively calculate economic (e.g. Levelized Cost of Heat), energetic (e.g. Solar fraction), technical (e.g. number of startups) and environmental indicators (e.g. CO2 emissions and renewable energy ratio).

3. Case study

This section introduces the case study addressed in the present paper. The case study is first used to present snapshot of the tool graphical user interface (see section 3). Second, it is used to compare expert control and predictive control (see section 4).

3.1. Presentation

The architecture chosen for the present case study is shown in Fig. 7, which is a snapshot of the plant configuration tab of the tool graphical user interface (GUI). This architecture represents a typical problem of solar thermal integration into district heating network production plants already equipped with a biomass boiler. In such a case, the biomass boiler generally operates as base load generator during the heating season and is stopped during summer because of minimum load technical constraint. In summer, the gas boiler thus ensures the entire load. In order to increase the summer renewable energy share, solar thermal seems to be an attractive solution.

However, this solution is problematic during mid-season when the biomass is still operating. Indeed, the solar thermal production during sunny days of the mid-season may push the biomass boiler close to its technical minimal load and sometimes even to stoppage. The latter leads to significant operational difficulties and generally results unwantedly in an increase of gas share in the production mix. The use of a storage can reduce this behavior. However, its sizing and control operation represent tedious tasks.

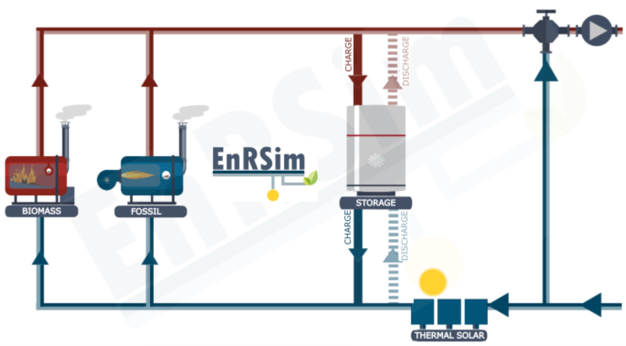

Fig. 7: Plant Configuration Tab

For the present case study, the solar field has an upwind serial position with respect to the biomass boiler, gas boiler and storage, as seen in Fig. 7. With this location, the solar field is not affected by possible higher temperature coming from the storage during charging phase. However, the solar field does not have access to the common storage and must then be equipped with a dedicated storage (not shown on Fig. 7). In this position, the common storage is thus useful to the biomass boiler operation only.

Lyon (France) was chosen as the location of the production plant. From weather data from MeteoNorm®, the ‘Load Curve Generation’ pre-processing module (see section 2) constructed the load curves, whose GUI snapshots are shown in Fig. 8 and Fig. 9, respectively for the thermal power monotone and the hourly DHN temperature variations.

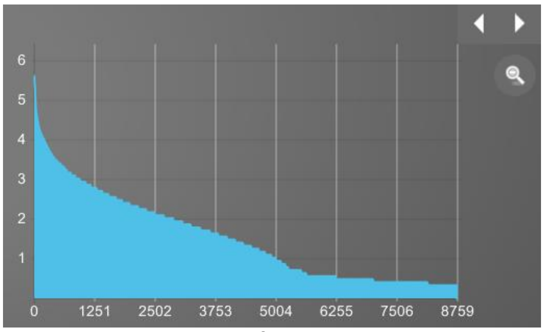

Fig. 8: Monotone of the load curve (MW)

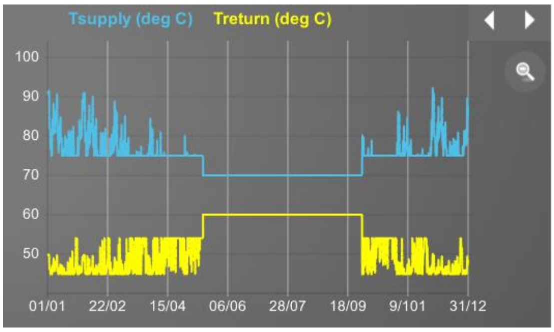

Fig. 9: Generated Load Curve (Temperatures)

The base sizing considered for this production plant is as follows:

- Common storage : 400m^3 (about 22MWh for the DHN operational temperatures, see Fig. 9) ;
- Solar field: 150 solar collectors of about 15m² each of transparent area whose characteristics are typical of large collectors designed for district heating applications. The solar collectors azimuth and tilt are respectively 0° and 30°. As explained beforehand, a solar field dedicated storage of 100m^3 is also considered, the storage operating as an interface between the solar field and the network return pipe;
- The biomass boiler nominal power is 4.5MW with a minimum to maximum power ratio of 30%. The biomass is stopped during summer season (from 15th of May to 1st of October).

The solar thermal field is operated at constant primary (solar collectors) and secondary (between heat exchanger to storage) flow rates. The latter is set to induce a 20K temperature increase throughout the field at the field nominal power ($700 \cdot A_{solar,field}$ with $A_{solar,field}$ $[m^2]$ the total solar field transparent area). The flow rate from the DHN through the storage depends on the temperature level in the storage. When the latter is below the return temperature of the DHN, the flow rate is set to zero. When it is above the DHN return temperature but below the DHN departure temperature, it is set equal to the DHN flow rate. Finally, if it is above the departure temperature, flow mixing is performed as shown in Equation (1).

$$\dot{m}_{sol} = \dot{m}_{DHN} \cdot \frac{T_{dep,DHN} - T_{ret,DHN}}{T_{high,stock} - T_{ret,DHN}} \quad (1)$$

With $\dot{m}_{sol}$ $[kg/s]$ and $\dot{m}_{DHN}$ $[kg/s]$ the flow rates respectively through the solar dedicated storage and the DHN, and $T_{dep,DHN}$, $T_{ret,DHN}$ and $T_{high,stock}$ the DHN departure, DHN return and top solar dedicated storage temperatures.

3.2. GUI results

Fig. 10 and Fig. 11 present snapshots of the GUI results visualization panel with respectively a zoom of the hourly production trajectories and the monthly energy mix. In addition to those results, the GUI provides a set of indicators and alerts regarding undesired results (solar field overheating, high number of generator startups, etc.). Finally, the user can generate an automatic report with an extra set of graphs.

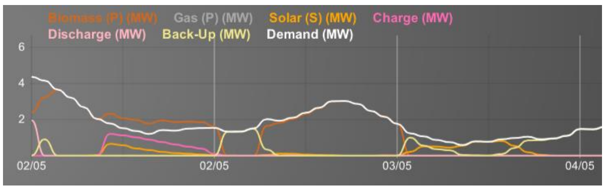

Fig. 10: Production trajectories

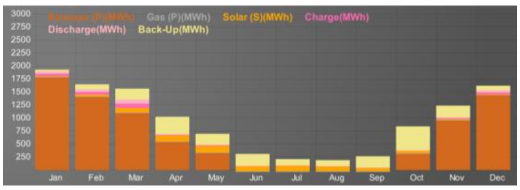
Fig. 11: Monthly Energy Mix

For the base sizing of the case study, the results listed in the GUI are an energy mix composed of 74.2% biomass, 9.8% solar and 16.0% gas. The number of biomass startup is however very high (177) and the tool thus gives an alert. At this point, it is worth mentioning that number of startup includes both cold and warm startup. While the former represents switch off of the generator for a long period of time, the latter represents short switched off periods. For the biomass boiler, it means that it does not produce for the DHN but its combustion chamber is kept at nominal temperature.

Further results will be shown in the next section, which will compare various sizing but also various control laws.

4. Sizing influence and extension to predictive control

The present section will deal with simulations of the case study for various sizing of the biomass boiler. In addition, we will show the influence on the sizing of the substitution of expert laws by predictive control.

4.1. Principles of predictive control

During the sizing stage, representative boundary conditions (weather, loads, etc.) over a given temporal horizon are generally supposed. Accounting for the knowledge of this boundary conditions in the future $(t > t_{now})$ when taking an operation decision at time t_{now} gives a predictive rather than reactive characteristic to the controller. The principle of predictive control is thus to benefit from previsions on boundary conditions by evaluating their impact on the future states of the system and including this knowledge in the calculation of next operational set points.

Accounting for the knowledge of the future boundary conditions using an expert law (i.e. rule-based) approach can be very complex to formulate and is generally sub optimal. Another solution is to use a mathematics-based approach in which the physic of the production plant is described in a simplified manner within a mixed integer linear programing (MILP) framework. The latter allows accounting for system-based constraints (mass and energy balances) together with technical constraints (power levels, ramps, etc.) in the calculation of the control trajectories while certifying an optimal of an objective function (generally the cost) with respect to the constraints defined. The combination of predictive control and MILP is referred from now on as optimal control.

The general MILP formulation is shown in Equation (2). The objective is to find the vector of decision variables $\boldsymbol{x}^T = (\boldsymbol{x_1}, \dots \boldsymbol{x_j}, \boldsymbol{x_{j+1}}, \dots, \boldsymbol{x_n})$ solution of the problem of Equation (2), $\boldsymbol{x}$ being composed of continuous $(1, \dots, j)$ and integer $(j+1, \dots, n)$ variables.

$$\min_{x} f_{cost} = c^T.\boldsymbol{x}$$
$$with \begin{cases} LHS \leq A.\boldsymbol{x} \leq RHS \\ l_b \leq \boldsymbol{x} \leq u_b \end{cases} \tag{2}$$

where c [n] is a vector of cost, A[m x n], LHS[m] and RHS[m] are respectively the matrix and vectors of linear constraints, and l_b [n] and u_b [n] are respectively the lower and upper bounds vector for the decision variables.

Fig. 12 presents the modifications operated to EnRSim calculation core (see Fig. 1) in order to integrate optimal control as a replacement of expert law reactive control. The modifications are two folds:

i) The new temporal scheme with consideration of the boundary conditions over the horizon t to $t + future$. It is worth mentioning here that $future$ means a given number of time steps (48 for the present case study). The latter allows having a tractable MILP problem that can be solved rapidly. In order to perform a simulation, we perform an optimization over the next 48 hours at every time step of 1 hour. That temporal scheme is referred as receding horizon with the end of the $future$ number of time steps getting closer and closer to the end of the year at each simulation. The PEGASE co-simulation platform (Vallée et al., 2019) which embeds the calculation core has native receding horizon capabilities.

ii) The replacement of the rule-based reactive control block by the optimal block whose equations are described in next section.

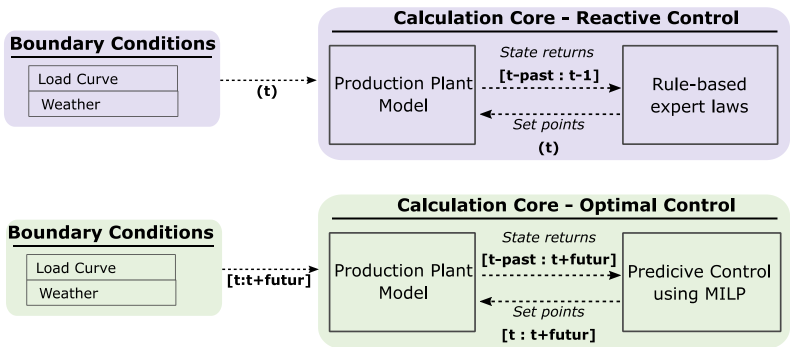

Fig. 12: Extension of EnRSim calculation core to optimal control

4.2. MILP model

The different models used for the MILP formulation of the case study are now described. In the following equations, the bold variables represent optimisation variables, i.e. the ones constituting the $\boldsymbol{x}$ vector from equation (2).

Equation (3) : System energy balance

In the energy balance of Equation (3), the thermal power of he biomass boiler $\left(\boldsymbol{P^{bio}}(t)\right)$, gas boiler $\left(\boldsymbol{P^{gas}}(t)\right)$, and charge/discharge ($\boldsymbol{P^{st}_{charge}}(t)$ and $\boldsymbol{P^{st}_{discharge}}(t)$) of the storage are optimization variables. The total demand (P_{load}) is a boundary condition while the solar production (P^{sol}), calculated by the plant production model at each time step of the future horizon, is an input data.

$$\boldsymbol{P^{bio}}(t) + \boldsymbol{P^{gas}}(t) + \boldsymbol{P^{st}_{décharge}}(t) + P^{sol}(t) = \boldsymbol{P^{st}_{charge}}(t) + P_{load}(t) \tag{3}$$

Equation (4) : Heat generators power levels constraints

Equation (4) is used for both the biomass and gas boilers. r^i represent the ratio betwenn the minimum and nominal power P^i_{max} of generator 'i' (30% and 0% respectively for the biomass and gas boiler). $\boldsymbol{P^i}(t)$ is the thermal power of generator 'i' and $\boldsymbol{Y^i}(t)$ represent the state ON (1) or OFF (0) of generator 'i'.

$$r^i * P^i_{max} * \boldsymbol{Y^i}(t) \le \boldsymbol{P^i}(t) \le P^i_{max} * \boldsymbol{Y^i}(t) \tag{4}$$

Equations (5) and (6) : Heat generators startup constraints

In order to be representative and avoid unrealistic heat generators startup at high frequency, it is necessary to constrain it by introducing a new intermediate variable $\boldsymbol{X^i}(t)$. The latter is 1 when the generator is started and 0 the rest of the time, as shown in Equation (5). Equation (6) is then used to set the value of $\boldsymbol{X^i}(t)$. However, the latter equation does not set the value of $\boldsymbol{X^i}(t)$ when $\boldsymbol{Y^i}(t-1) = \boldsymbol{Y^i}(t) = 1$, i.e. when the generator is ON and stays ON (a very frequent situation). In this situation, we want the value of $\boldsymbol{X^i}(t)$ to be 0. Introducing startup costs in the objective function (see Equation (12)) will force the optimizer to use $\boldsymbol{X^i}(t) = 0$ in this situation.

$$\boldsymbol{X^i}(t) = \begin{cases} 1\ if\ \boldsymbol{Y^i}(t-1) = 0\ and\ \boldsymbol{Y^i}(t) = 1 \\ 0\ however \end{cases} \tag{5}$$

$$\boldsymbol{Y^i}(t) - \boldsymbol{Y^i}(t-1) \le \boldsymbol{X^i}(t) \le \boldsymbol{Y^i}(t) \tag{6}$$

Equations (7) to (11): Storage model

Equation (7) present the energy balance of the storage with $\boldsymbol{P}$ $[W]$ and $\boldsymbol{E}$ $[J]$ respectively the power and energy, Δt[s] the time step, K_{loss} $[s^{-1}]$ the heat loss coefficient and the indices 'ch' and 'disch' for charge and discharge. Equation (8) sets equal the storage energy at time $t = 0$ and $t = t_{future}$, which corresponds to the end of the future horizon considered by the optimal control. Equations (9) and (10) represent the thermal power limit (P^{st}_{max}) for the charge and discharge with $\boldsymbol{Y^{st}}$ a binary variable forcing the storage to be either charging or discharging but never both at the same time. Finally, Equation (11) limits the maximum of energy E^{st}_{max} that the storage can handle.

$$\frac{\boldsymbol{E^{st}(t) - E^{st}(t-1)}}{\Delta t} = \boldsymbol{P^{st}_{ch}(t)} - \boldsymbol{P^{st}_{disch}(t)} - K_{loss} * \boldsymbol{E^{st}(t)} \tag{7}$$

$$\boldsymbol{E_{st}(t = 0) = E_{st}(t = N \cdot \Delta t)} \tag{8}$$

$$0 \le \boldsymbol{P^{st}_{ch}(t)} \le P^{st}_{max} * \left(1 - \boldsymbol{Y^{st}(t)}\right) \tag{9}$$

$$0 \le \boldsymbol{P^{st}_{dech}(t)} \le P^{st}_{max} * \boldsymbol{Y^{st}(t)} \tag{10}$$

$$0 \le \boldsymbol{E^{st}(t)} \le E^{st}_{max} \tag{11}$$

Equation (12): Objective function

The objective function for the MILP model is shown in Equation (12). The latter is composed of startup c^i_{dem} and production c^i_{prod} costs for each generator 'i'. The variable Hor is the number of time steps of the horizon considered and N_{equ} is the number of generator (2 in the present case study). The starting costs of the biomass boiler are here considered 3 times higher than the gas boiler ones.

$$f_{cout} = c_{dem} + c_{prod} = \sum_{t=1}^{Hor}\sum_{i=1}^{N_{equ}} c_{dem}^{i} * \boldsymbol{X^i}(t) + \sum_{t=1}^{Hor}\sum_{i=1}^{N_{equ}} c_{prod}^{i} * \boldsymbol{P^i}(t) * \Delta t \tag{12}$$

The MILP model has been implemented using an in-house library. At each time step, the MILP model is solved using Cplex (IBM ILOG, 2015).

4.3. Results

Fig. 13 presents a synthesis of the results obtained for the case study (biomass boiler, gas boiler, storage and solar thermal field, see Section 3). The biomass nominal power is varied from 2 to 6MW while the rest of the parameters and sizing are kept fixed. Rules-based (expert law) and optimal control are compared. The results are shown in a plan Yearly gas share =f(number of biomass startup). The number of full storage cycles (i.e. ratio of the yearly integral of charged power over maximum storage energy) is also shown with a color scale.

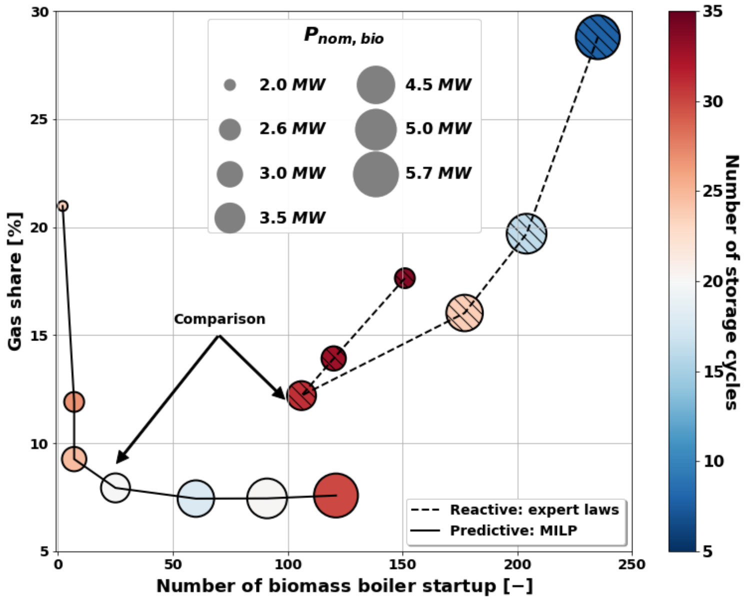

Fig. 13: Gas share as a function of number of biomass boiler startup for various size of biomass boiler – Expert laws vs predictive control

The main conclusions to draw from Fig. 13 are the following:

- For all the cases, the optimal control allow limiting both the gas share and the number of biomass startup with respect to the expert laws;
- The obtained results are much more sensitive to the biomass boiler sizing in the case of the expert laws;
- The expert law control presents an optimum with respect to the 2 indicators (for $P_{nom}^{bio} = 3.5MW$) while the predictive control presents a Pareto front, i.e. for each point of the curve, there is no other point for which both indicators are better. This fact highlights clearly that optimal control reaches control optimality for each design;
- For the expert laws, the increase of biomass startup below a sizing of 3.5MW is due to the static laws presented in section 2. Indeed, the storage discharge is stopped based on the power level at a given time instant and a margin with respect to the minimum power. The latter gives a smaller margin when the minimum power of the biomass is smaller. The solar production being the same, this margin is not sufficient anymore to prevent a stoppage of the biomass boiler, i.e. storage discharge is too significant;
- Finally, the non-adaptive feature of the expert laws leads to a monotonic storage cycles variations when the biomass boiler sizing is decreased. Contrarily, the adaptive feature of the optimal control modify its storage behavior as a function of the biomass boiler sizing, leading to non-monotonic storage cycles evolution.

Thus, Fig. 13 shows clearly a strong inter-dependency between the sizing optimization and the expert law parametrization. However, using optimal control allows focusing on the optimization of the sizing with respect to a set of indicators without having to readjust for each sizing the parameters of the controller. The 2 systems pointed out by an arrow on Fig. 13 are now studied with more details (Pmax/Pmin = 3.5MW/1.05MW).

Fig. 14 and Fig. 15 presents the daily averaged monotone of the demand together with the associated energy mix respectively for expert law and predictive control. The striking result here is the better storage usage during the critical periods, i.e. during winter peaks and mid-season solar intermittency, when using predictive control. The latter leads to an extra gas usage when using expert laws during these critical periods.

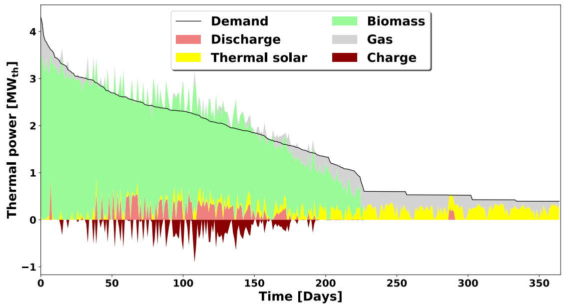

Fig. 14: Daily averaged monotone of the demand and energy mix for expert laws control ($P_{nom}^{bio} = 3.5MW$)

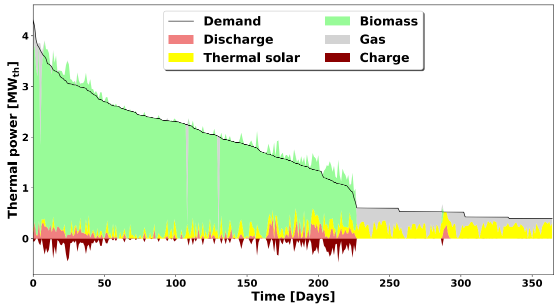

Fig. 15: Daily averaged monotone of the demand and energy mix for predictive control ($P_{nom}^{bio} = 3.5MW$)

In view of this advantageous storage behavior with optimal control, the energy mix is more virtuous, as shown in Tab. 1 with 4.3% increase in renewable energy content of the production. Additionally, the number of biomass startup is reduced by 77%. It is worth noticing here that, when looking at Fig. 13, those values represent the lower boundaries of the benefit we can obtain with optimal control. Thanks to optimal control, the initial willingness, which was increasing the renewable energy share in summer by integrating solar thermal, can thus be achieved without introducing control issues during mid-season.

It is worth mentioning here that we have performed our analysis with a fixed solar thermal field and common storage size with only a variation of the biomass boiler size. A different approach with a fixed biomass boiler size but varying solar field size would have led to a larger solar field using optimal control for the same set of indicators.

Tab. 1 : Energy mix and number of biomass boiler startup obtained for the sizing $P_{nom}^{bio} = 3.5MW$

	Expert Laws	Optimal Control
Biomass [%]	78.0	82.3
Thermal solar [%]	9.8	9.8
Gas [%]	12.2	7.9
Renewable Energy Content [%]	87.8	92.1
Number of biomass boiler startup [-]	106	25

A closer look on the operational differences between the 2 control modes is presented in Fig. 16 and Fig. 17. The figures highlight 5 days of operation early May, i.e. mid-season, respectively for expert laws and predictive control. Both the energy mix and the storage level are shown on the 2 graphs. Interestingly, the storage is much more active when using expert laws with an overall very high storage level. However, the expert laws are i) unable to discharge the storage to avoid using gas during the first demand peak above the nominal biomass boiler power and ii) unable to charge the storage during the solar production toward the end of the week, leading to undesired biomass stoppages. Optimal control however leads to no gas consumption during these 5 days of operation. It is also worth noting that in this control mode the charge and discharge phases are arranged so that heat does not stay too long in the storage. The latter is due to Equation (7) and the heat loss associated to high level of energy is the storage. The optimizer will always try to limit them.

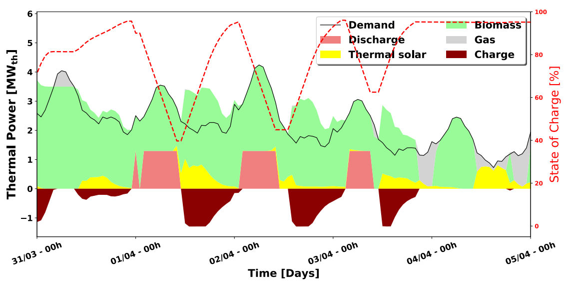

Fig. 16: Detailed hourly results for 5 days in April and expert laws control ($P_{nom}^{bio} = 3.5MW$)

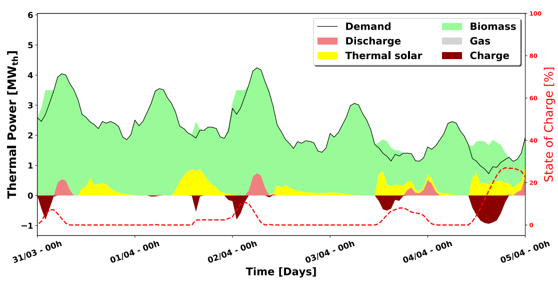

Fig. 17: Detailed hourly results for 5 days in April and predictive control ($P_{nom}^{bio} = 3.5MW$)

5. Conclusion and perspectives

The present paper introduced the EnRSim tool, a simulator of renewable-based production plants using field-based expert laws. That tool aims at helping professionals to size the units in the pre-feasibility stage. The tool is composed of i) pre-processing modules calculating the DHN load and the solar resource corrections, ii) a calculation core based on a co-simulation platform including a model of the production plant and a rule-based control module, iii) post-processing modules for energetic, economic and environmental calculations, iv) a user friendly graphical user interface, and v) an automatic report generation engine. Up to three generators among biomass boiler, solar thermal, heat pump, cogeneration and gas boiler can be simulated in various configuration (serial and parallel) with or without storage. Yearly simulations are performed at a time step of 1 hour in about 1 minute on an office laptop computer. A case study using biomass boiler, solar thermal field, gas boiler and storage showed the type of results obtained, i.e. production trajectories and key performance indicators. Since summer 2020, the tool including expert law control is available for download in French and English for free.

The EnRSim calculation core was then modified by replacing the expert law control block with optimal control (predictive control with MILP model and receding horizon). The paper then shows how optimal control can be used in a sizing stage. The same case study as for the tool demo was extended to various biomass boiler sizing and tested under optimal and expert law controls. In summary, the advantage of predictive control combined to MILP is that the interactions between the components of the production plant are not predefined and are rather calculated optimally and at each time step. The latter allows the controller to be adaptive and led for the case study to a minimal 4.3% increase in renewable energy content and 77% reduction in biomass boiler startup. With such an approach, the full potential of a storage can thus be accounted for in sizing stage. More specifically, it is shown here that for the MILP, the storage handles more properly both the peak heat demands in winter and the potential short biomass startup/shutoff cycles in mid-season. There is obviously the possibility of improving both the expert law and its parameters. Better results, but not better than the MILP (for which optimality is proven), should be obtained at the price of a time-consuming iteration process to find the right set of parameters, which itself depends on the sizing and thus require an update for each sizing.

The extension of EnRSim calculation core to predictive control will allow evaluating more profitably additional configuration combining biomass, solar thermal and storage, especially those for which the common storage can also be used by the solar field, as done in many existing installations.

6. Acknowledgments

The authors wish to thank ADEME, the French Renewable Energy Agency, for its co-funding for the EnRSim project. The EnRSIM tool is available for download at the following link: **https://enrsim.ines-solaire.org.**

7. References

FMI development group, 2014. Functional Mock-up Interface for Model Exchange and Co-Simulation 2014. [WWW Document]. Httpsfmi-Stand.-Dev. URL (accessed 3.25.20).

Frederiksen, S., Werner, S., 2013. District Heating and Cooling. Professional Pub Serv.

Giraud, L., Bavière, R., Vallée, M., Paulus, C., 2015. Presentation, Validation and Application of the DistrictHeating Modelica Library. Versailles, France, p. 10. https://doi.org/10.3384/ecp1511879

Giraud, L., Merabet, M., Baviere, R., Vallée, M., 2017. Optimal control of district heating systems using dynamic simulation and mixed integer linear programming, in: Proceedings of the 12th International Modelica Conference, Prague, Czech Republic, May 15-17, 2017. Linköping University Electronic Press, pp. 141–150.

IBM ILOG, 2015. IBM ILOG CPLEX Optimization Studio V12.7.0 documentation.

Provent, A.-S., Guillot, B., Renaude, F., Dumas, J., Genet, R., Martins, M., Le Denn, A., 2013. Smart Grid Solaire Thermique: Rapport d'étude sur les réseaux de chaleur existants et les réseaux adaptés aux Eco-quartiers (No. 1.1.1). ADEME.

Vallée, M., Bavière, R., Seguin, V., Vuillerme, V., Lamaison, N., Descamps, M., Aurousseau, A., 2019. An efficient co-simulation and control approach to tackle complex multi-domain energetic systems: concepts and applications of the PEGASE platform. Presented at the ECOS conference, Wroclaw, Poland.

Appendix: Details of the dynamic plant models

Biomass, Gas and CHP

From the point of view of the core calculation, biomass, gas and cogeneration generators are modelled in the same way. It is important to note that in this model, we consider only the power injected in the heat transfer fluid. The difference in yield between these generators is calculated in the post-processing. Another difference between these models is in the user's settings.The energy balance for this model of generator is presented in equation (13) below.

$$\left((\rho.cp.V)_f + C_{bo}\right).\frac{dT_{out}}{dt} = P_{bo} - \dot{m}_f.cp.(T_{out} - T_{in}) - G.(T_{moy} - T_{ext}) \tag{13}$$

Where ρ $[kg.m^{-3}]$ is the density of the heat transfer fluid, cp $[J.kg^{-1}.K^{-1}]$ the heat transfer fluid's specific thermal capacity, V $[m^3]$ the internal volume of the combustion chamber $[m^3]$, C_{bo} $[J.K^{-1}]$ the boiler's thermal capacity, P_{bo} $[W]$ the power transferred to the fluid by the boiler, $\dot{m}_f$ $[kg.s^{-1}]$ the flow of the heat transfer fluid, T_{out} $[K]$ and T_{in} $[K]$ the respective inlet and outlet temperatures, T_{moy} $[K]$ the heat transfer fluid's mean temperature in the boiler, T_{ext} $[K]$ the room temperature in the boiler room and G $[W.K^{-1}]$ an overall thermal loss coefficient.

If these generators are installed in parallel, the settings sent by the control unit are the power and the flow. If the generators are installed in series (cogeneration), the setting sent by the control unit is only the power.

Heat pump

The energy balances for the heat pump model are presented in Equations (14), (15) and (16). The COP (coefficient of performance) laws are explained in Equation (17) and (18).

$$\rho.cp.V_{hot}.\frac{dT_{hot}^{out}}{dt} = -Q_{hot} - \dot{m}_{f,hot}.cp.\left(T_{hot}^{out} - T_{hot}^{in}\right) \tag{14}$$

$$\rho.cp.V_{cold}.\frac{dT_{cold}^{out}}{dt} = -Q_{cold} - \dot{m}_{f,cold}.cp.\left(T_{cold}^{out} - T_{cold}^{in}\right) \tag{15}$$

$$W + Q_{hot} + Q_{cold} = 0 \tag{16}$$

$$COP_{global} = -\frac{Q_{hot}}{W} \tag{17}$$

$$COP_{global} = K_{degrad}.Coeff_{carnot}.\frac{T_{hot}^{out}}{T_{hot}^{out} - T_{cold}^{out}} \tag{18}$$

Where V_{hot} $[m^3]$ and $V_{cold}[m^3]$ are respectively the volumes of heat transfer fluid on the hot side (condenser) and cold side (evaporator) of the heat pump, T_{hot}^{out} $[K]$ and T_{cold}^{out} $[K]$ the outlet temperatures on the hot and cold side respectively, T_{hot}^{in} $[K]$ and T_{cold}^{in} $[K]$ the inlet temperatures on the hot and cold side respectively, $\dot{m}_{f,hot}$ $[kg.s^{-1}]$ and $\dot{m}_{f,cold}$ $[kg.s^{-1}]$ the respective flows on the heat network and cold source sides in the heat pump, Q_{hot} $[W]$ and Q_{cold} $[W]$ the thermal power transferred to the fluid on the hot and cold side respectively, W $[W]$the electrical power of the heat pump compressor, COP_{global} $[-]$ the heat pump's coefficient of performance, $Coeff_{carnot}$ a coefficient representing the heat pump's performance relative to a Carnot efficiency (set from the man-machine interface) and K_{degrad} $[-]$ a linear coefficient of degradation of the COP between 0 and 1 between a heating capacity of 0 and a minimum heating capacity (given by the man-machine interface) $Q_{hot,min}$ $[W]$.

If the generator is installed in parallel, the instructions sent by the control unit are the power and the flow. If the generator is installed in series, the instruction sent by the control unit is only the power.

Storage

The storage system's stratification is considered. It is therefore discretized in N_{seg} segments (see Fig. 18). The storage has an input/output port at the top and an input/output port at the bottom for the charge/discharge modes respectively.

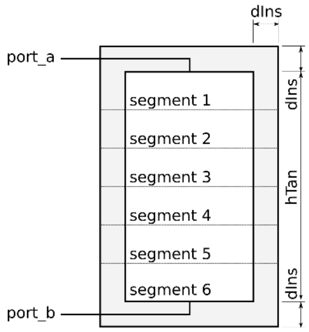

Fig. 18: Schematic of the stratified storage model

The distributed model of this sensible storage is presented in Equation (19) for each segment 'i'.

$$Q_{top,i} + Q_{bot,i} + Q_{pertes,i} = \rho . cp . V_i . \frac{dT_{out,i}}{dt} + \dot{m}_{f,st} . cp . \left(T_{out,i} - T_{out,i-1}\right) \quad (19)$$

Where $Q_{top,i}$ $[W]$ and $Q_{bot,i}$ $[W]$ are the thermal exchanges at the top and bottom terminals of the element considered. These thermal powers take into account i) the axial conduction between the different fluid elements, ii) the thermal loss through convection at the top and bottom of the storage and iii) an automatic destratification term if a cold element should be above a hot element. $Q_{pertes,i}$ $[W]$ represents the thermal loss of segment 'i' through its lateral surface, $\dot{m}_{f,st}$ $[kg.s^{-1}]$ is the flow of fluid in the storage. Lastly, V_i, $T_{out,i}$ and $T_{out,i-1}$ respectively represent the volume, the outlet temperature of segment 'i' and the outlet temperature of element 'i-1'.

Depending on how the storage is used, it is important that the $\dot{m}_{f,st}$ sign varies (positive for discharging and negative for loading). For this storage, the instruction sent by the control unit is the through flow $\dot{m}_{f,st}$.

<u>Solar field</u>

The energy balance in this element is presented in the Equations (20) and (21) below.

$$C \frac{dT_m}{dt} = A_{field}(\eta_0 G_T - a_1(T_m - T_a) - a_2(T_m - T_a)^2) + \dot{m}_{sol} cp (T_{in} - T_{out}) \quad (20)$$

$$G_T = I_b K_b + I_d K_d \quad (21)$$

Where C $[J.kg^{-1}]$ is the total capacity of the panel (fluid and structure), T_m $[K]$, T_{in} $[K]$, T_{out} $[K]$ and T_a $[K]$ the mean inlet, outlet and exterior temperatures, A_{field} $[m^2]$ the area of the field considered, η_0 $[-]$, a_1 $[-]$ and a_2 $[-]$ respectively the optic effectiveness and the coefficient of first order and second order thermal losses, $\dot{m}_{sol}$ $[kg.s^{-1}]$ the solar exchanger's secondary flow (network side), cp $[J.kg^{-1}.K^{-1}]$ the specific thermal capacity of the heat transfer fluid, $I_b[W \cdot m^{-2}]$ and $I_d[W \cdot m^{-2}]$ respectively the direct and diffuse irradiation in the collector tilt, and $K_b[-]$ and $K_d[-]$ the incidence angle modifiers respectively for the direct and diffuse radiations.

The modelling of the exchanger is done through a constant thermal conductance. The inertia and the thermal losses in the field's pipes are taken into account through thermal capacities and conductance. The modelling of the solar storage is similar to that used for the common storage system.

For the installation of this field in parallel and in series, the instruction sent by the control unit is the flow going through the specific storage.

Smart Urban Energy Concept: Integration of Heat Pumps, PV, Cogeneration, and District Heating in existing Multi-Family Buildings

Manuel Lämmle[1], Stefan Hess[2], and Sebastian Herkel[1]

[1] Fraunhofer Institute for Solar Energy Systems (ISE), Freiburg (Germany)

[2] Department of Sustainable Systems Engineering - INATECH, Albert-Ludwigs-Universität Freiburg (Germany)

Abstract

An innovative urban energy concept for a German district with five existing multi-family buildings integrates photovoltaics, heat pumps, and cogeneration units in a district heating grid for an energy-efficient and economic heat and electricity supply. Simulation results show the synergies of a smart integration of proven technologies: by means of optimized component dimensioning, a suitable hydraulic design and smart control strategies, the CO_2 emissions can be reduced by 52 %. At the same time, the district concept is economically viable showing a positive annual turnover.

The energy system will be implemented in 2020, followed by a scientific monitoring and evaluation of the performance. If the monitoring data confirm the promising simulation results, the energy concept can serve as a model for energy-efficient and economic renovation of similar districts.

Keywords: *heat pumps, smart grid, district heating, energy management, CO2 reduction,*

1. Introduction and motivation

The energetic renovation of existing multi-family buildings is a central challenge for decarbonizing the building sector. Heat pumps are a promising renewable heating technology with low CO_2 emissions if powered by renewable electricity. However, the implementation in multi-family houses faces technical (temperature levels, availability of heat sources, renewable power supply) and economic challenges.

An innovative urban energy concept is developed, implemented and monitored for a cluster of five multi-family houses within the project "Smart District Karlsruhe-Durlach". The five buildings were constructed in the 1960s and comprise 175 apartments and a total heated floor area of 11.603 m². The buildings have already been insulated and renovated in 1995, and thus reach a relatively low specific heating demand of 53 kWh/m²/y. The heat demand for space heating and hot water is currently covered by gas boilers, while electricity is supplied by the power grid, resulting in a large CO_2 footprint.

Figure 1: Photo of the building (left, © Stefan Hess, INATECH) and the district (right, © Google Earth, Map data: Google, GeoBasis-DE/BKG)

The central objectives of the new energy supply concept are:

1) Reduction of CO_2 emissions by 50 %
2) Demonstrate the application of heat pump technologies in existing multi-family houses
3) Smart integration of proven technologies, connected by a central energy management system for optimized

doi:10.18086/eurosun.2020.02.04 Available at http://proceedings.ises.org

operation

4) Implement an energy efficient and economically viable concept, which allows for scaling and transfer to similar districts

This paper details the smart urban energy concept, which will be implemented in Karlsruhe-Durlach, with a focus on the energy management system and preliminary simulation results.

2. Smart integration of PV, Heat pumps and CHP

A multitude of different supply concepts and component dimensions were simulated with a specifically developed simulation tool. The optimization model varied the topology (i.e. the integration points of heat pumps and CHP, and the size of the district heating network) and the components dimensions (installed power of PV, HP, CHP, boiler and heat storages) within the given boundary conditions. The underlying optimization objectives were:

- Minimize CO_2 emissions from gas and electricity import, assuming CO_2 emission factors for electricity and for natural gas. CO_2 emissions are minimized by reducing the imports of natural gas and electricity and by increasing the export of electricity.
- Maximize annual earnings before interest and taxes (EBIT) for the contractor considering costs for investment, maintenance, gas and electricity imports and exports. The internal cost structure and the current German regulative situation with EEG tariffs and CHP and tenant bonuses were considered. EBIT is maximized by low investment and low operational costs.

Next to simulation results and the corresponding energy balance, the German regulatory boundary conditions (EEG, KWKG, Mieterstrommodell, BMWi 2017) and local restrictions (crossing of street, limited space in basements, design of new heating plant) were considered.

Based on these considerations, the final energy concept shown in Figure 2 will be realized and implemented until the end of 2020:

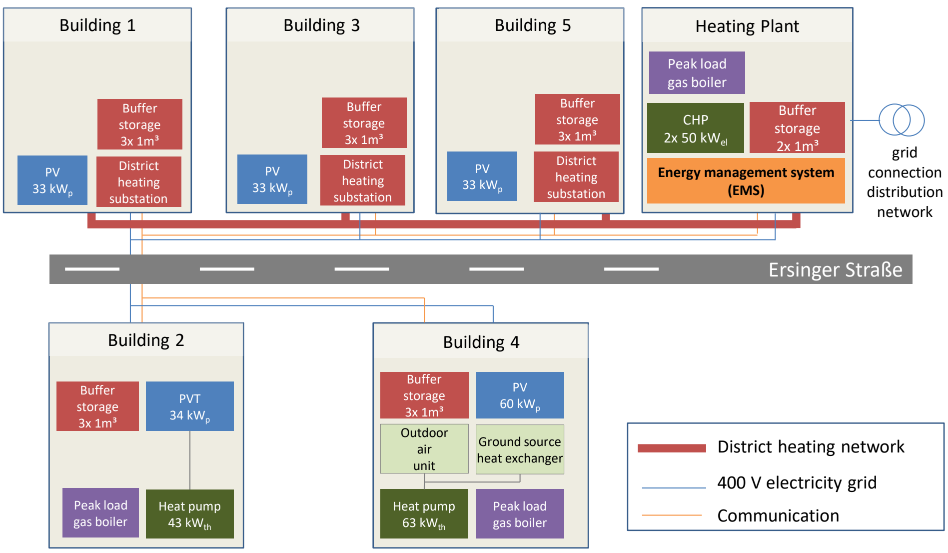

Figure 2: Energy supply system for the smart energy district Karlsruhe-Durlach

PV modules are installed on all five buildings with a total power of 194 kW_p. Optimization results for the energy concept showed, that large PV capacities are beneficial under both economic and energy efficiency considerations due to low levelized costs of electricity and low carbon intensity. However, owing to legislative regulations, the installed power is limited to 100 kW_p per year. The PV arrays will therefore be installed in two stages.

Two decentral heat pumps supply heat to building 2 and 4 with a thermal power of 43kW_{th} and 63 kW_{th}. The heat pumps use innovative low temperature sources, which specifically address the challenge of limited heat sources in urban areas (Hess et al., 2019). Heat pump 1 in building 2 is coupled to hybrid photovoltaic/thermal PVT collectors with a total area of 200 m². Uncovered PVT collectors with enhanced heat transfer of ambient energy through a finned heat exchanger at the rear side (Leibfried et al., 2019) are used as the sole source for the heat pump with a thermal power of 43 kW_{th}. Heat pump 2 in building 4 uses a dual heat source with intelligent control and hydraulics.

Compared to a single-source heat pump, only 50 % of ground source heat exchanger is required. The remaining thermal power is supplied by an air-to-water heat exchanger. It is expected to achieve a seasonal performance factor similar to a ground-source heat pump while investment costs are in the range of an air-source heat pump (Günther and Obermann, 2019). Low supply temperatures on the heating distribution side are achieved by hydronic balanced heating systems, a selected exchange of 10 % of all radiators in the apartments (Lämmle et al., 2019), and an ultrafiltration unit in the drinking water circulation which filters Legionellae mechanically.

Three buildings are connected to a district heating network, which is powered by a heating plant outside of building 5. Two combined heat and power unit (CHP) fueled by natural gas CHP units, each with a power of 50 kW_{el}/86 kW_{th}, supply heat to the district heating network and generate electricity for the district and heat pumps. These CHP units will also be commissioned in two stages owing to more beneficial feed-in-tariffs for smaller CHP plants in Germany. A new heating plant will be designed and constructed for this purposes, as the space is the basement was neither sufficient for a central solution with the heating plant integrated in the basement, nor a decentral solution with distributed CHPs. A two pipe district heating network will distribute the heat from the heating plant to the substations in each building.

All heat generator units (heat pumps and CHPs) have peak load gas boilers as auxiliary heating backup. Buffer storages are included in all buildings and in the heating plant to allow for a flexible operation of CHP and heat pumps. On the electrical side, the heating plant is equipped with a transformation station to benefit from lower import and export prices for electricity from the grid.

3. Energy management system

The new energy concept intelligently combines proven technologies to achieve energy-efficiency, a low CO_2 footprint and an economic business case for the energy contractor. This is also achieved by the smart operation of the heat pump and the CHP with the objective to optimize energy-efficiency and economics.

A local electricity grid connects all five buildings for this purpose. Thus, electricity from PV and CHP can be utilized locally by the heat pumps for power-to-heat applications. Moreover, the PV modules also supply tenants and households with locally generated electricity within the so-called “Mieterstrommodell”. Within this legislative framework, tenants can benefit from a local PV plant by lower electricity tariffs while the operator receives a small bonus per kWh of PV electricity sold to the households. However, the “Mieterstrommodell” is only applicable to PV and not to CHPs and all tenants can decide freely whether to participate or not.

Nonetheless, the local electricity grid enables an enhanced energy management. The target for the optimization is the maximization of self-consumption and self-sufficiency and thus economic profitability. For this purpose both cogeneration units in the heating plant and both heat pumps are connected to the central energy management system. Depending on the generated PV power and heat and power demand in the households, the energy management (Figure 3) system requests the operation of CHP or heat pump:

- The CHP units preferably operate in periods of high local electricity demand, as sum of electricity demand of households and heat pumps minus the PV power.
- The heat pumps preferably operate in periods of excess electricity, as sum of electricity from PV and CHP minus the electricity demand of households. For further flexibility, the heat pumps can be operated in discrete power stages with optional heating rod operation.

Hence, the energy management optimizes the operation of heat pumps and CHP for an optimized utilization of the intermittent generation of PV electricity, which ultimately leads to a maximized self-consumption and self-sufficiency and thus to an improved economic profitability and lower CO_2 footprint.

Next to rule-based heuristic control strategies, a more sophisticated model predictive control (MPC) approach will be developed, implemented and tested. The MPC approach considers weather and PV forecast, the current states of charge of the thermal storages, and models future heat and power demand with a neural-network trained demand prediction model. It is expected that the sophisticated MPC approach further optimizes self-consumption and self-sufficiency.

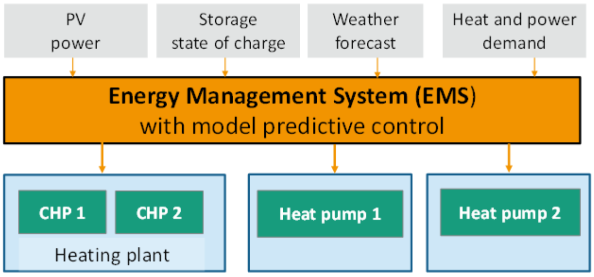

Figure 3: Functional structure of the energy management system with model predictive control strategies

Additionally, the energy management system integrates the following functions:

- Management level: monitoring, data storage, reporting, evaluation of performance
- Automatization level: control of heating plant and the district heating network
- Fault detection and diagnostics: implementation and testing of algorithms based on artificial intelligence

Thus, the smart integration of the basic technologies via the energy management system allows for an efficient and economic operation by optimizing self-consumption and self-sufficiency of PV and CHP electricity.

4. Simulated performance of the smart district

The energetic, economic and ecologic performance of the district was simulated with a specifically developed simulation tool for designing energy concepts for buildings and districts with a focus on energy management and integration of heat pumps in district heating networks.

Figure 4 illustrates the annual energy balance for the employed technologies and the energy flows between each component.

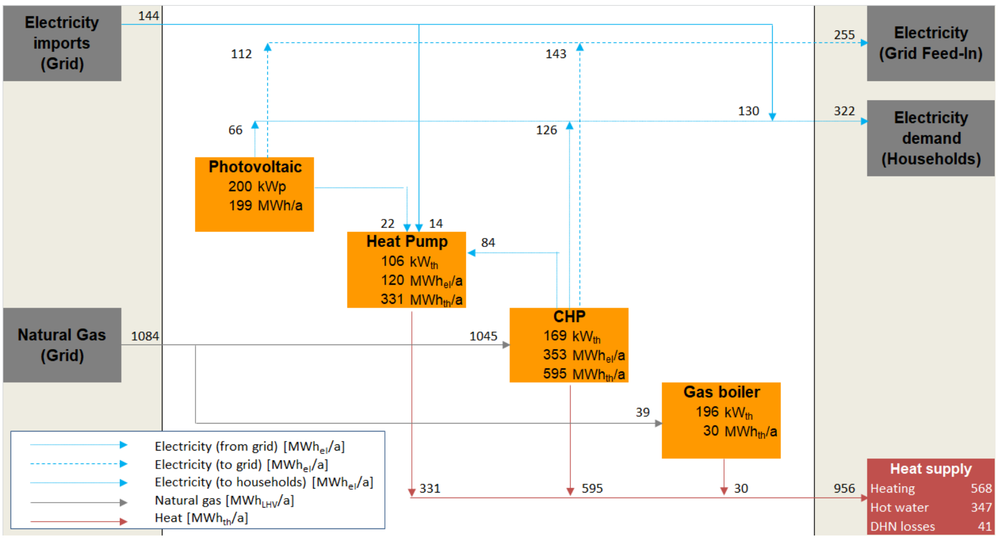

Figure 4: Annual energy flows of the smart energy district.

The simulation with the aforementioned components and topography yields the following key performance indicators:

The energy balance indicates an electrical self-sufficiency of the district of 67 %, i.e. two thirds of the electricity demand of households and the heat pump is generated locally by PV and the CHP. The heat pumps even achieve a self-sufficiency rate of 88 %. With regards to self-consumption, 44 % of the PV electricity and 59 % of the CHP electricity is consumed within the district.

Using German CO_2 emission factors for natural gas (227 g_{CO2eq}/kWh) and for electricity imports and exports (403 g_{CO2eq}/kWh, estimated electricity mix of 2020, Fritsche and Greß (2019)), the total CO_2 footprint is reduced by 52 % compared to the previous energy concept with grid electricity and decentral heat from gas boilers. Thereof, the heat supply is decarbonized by the heat pumps, which utilize ambient low temperature heat from air, sun, and ground, and low-carbon electricity from PV and CHP. The electricity generated from both PV and CHP achieves a significantly lower CO_2 intensity compared to electricity from the grid. Hence, PV and CHP yield a reduction of the CO_2 intensity for the electricity supply of the district.

With regards to the economic performance, the evaluation of investment and operation costs shows that the energy system achieves a similar economic performance as the current energy system. This allows for a profitable business case for the contractor and similar or even lower costs of energy for the tenants.

5. Conclusion and outlook

The energetic renovation of existing multi-family buildings is a central challenge for decarbonizing the building sector. The presented energy concept combines PV, heat pumps and cogeneration units for an energy-efficient supply of heat and electricity to a district with existing multi-family houses. The simulation results illustrate the synergies of integrating PV, HP and CHP in district heating grids: the smart combination of all three technologies allows a good balance between high economic profitability, energy efficiency and a low CO_2-footprint.

This is due to an optimized sizing of components, specific hydraulic design and a smart control strategy. The energy management system preferably operates the heat pump with excess PV or CHP electricity, and operates the CHP in periods with a high electricity demand. Thus, electrical self-sufficiency and self-consumption are improved and grid imports are reduced.

In 2020, the presented energy concept will be implemented in the district, followed by a period of optimization of operation, where the model predictive control strategies will be implemented and tests. Moreover, the performance of the buildings and the overall district will be monitored. If the promising simulation results can be verified by field tests, the energy concept can serve as a model for the energetic renovation of other districts.

6. Acknowledgments

This work was funded by BMWi (Germany Ministry of Economic Affairs) based on a resolution of the German Bundestag within the project “SQ-Durlach”, grant number 03ET1590B. The authors are grateful for this support and like to thank the project partner Karlsruher Energieservice GmbH and the implementing companies for the fruitful cooperation.

7. References

Fritsche, U., Greß, H.-W., 2019. Der nichterneuerbare kumulierte Energieverbrauch und THG-Emissionen des deutschen Strommix im Jahr 2018 sowie Ausblicke auf 2020 bis 2050: Bericht für die HEA - Fachgemeinschaft für effiziente Energieanwendung e.V. IINAS - Institut für Nachhaltigkeitsanalaysen und -strategien GmbH.

Günther, D., Obermann, S., 2019. HEAVEN: Modulierende Sole-Wärmepumpe mit Mehrquellensystem und dezentrale Lüftungsanlagen. Poster, Low-Ex im Bestand.

Hess, S., Vollmer, R., Wapler, J., Kleinstück, M., Bongs, C., Henning, H.-M., 2019. Ambient Heat Source Availability for Low-Ex Heating of Multi-Family Buildings. Proceedings of the ISES Solar World Congress, 04.11.2019 - 07.11.2019, Santiago, Chile, 1–12. https://doi.org/10.18086/swc.2019.10.01.

Lämmle, M., Wapler, J., Kropp, M., Hess, S., Hahn, D., David, G., Herkel, S., 2019. Gezielter Heizkörper-Austausch in Wärmepumpenheizungsanlagen. DKV-Tagung 2019, Ulm, AA IV.16, Deutscher Kälte- und Klimatechnischer Verein.

Leibfried, U., Fischer, S., Asenbeck, S., 2019. PVT-Wärmepumpensystem SOLINK - Systemvalidierung und zwei Jahre Praxiserfahrung. Symposium Thermische Solarenergie Bad Staffelstein.

Using existing infrastructure to transform urban district heating systems to renewable energy supply

Ulrich Trabert, Isabelle Best, Weena Bergstraesser, Oleg Kusyy, Janybek Orozaliev, Klaus Vajen

University of Kassel, Institute of Thermal Engineering, Kassel (Germany)

Abstract

In this case study the integration of a river water heat pump at an existing combined heat and power plant was examined with the aim to achieve a 50 % renewable cover ratio in the district heating system of an urban district. Three different concepts were designed in line with the requirements of the German subsidy program "Wärmenetzsysteme 4.0". Furthermore, the integration of decentralized solar thermal rooftop systems was analyzed regarding the suitable rooftops in the district and the potential feed-in into the district heating system. A focus of the conducted dynamic 15-year simulation with the software energyPRO is on electricity market price induced heat production. The relevant components include the operation of the heat pump and a storage, but also additional combined heat and power and power-to-heat units. The heat supply concepts are compared in terms of operational characteristics and economic efficiency.

Keywords: Urban district heating, transformation process, river water heat pump, decentralized solar thermal systems, levelized cost of heat

Abbreviations:

CHP	Combined heat and power	LCoH	Levelized cost of heat
COP	Coefficient of performance	PtH	Power-to-heat
DH	District heating	SPF	Seasonal performance factor
FLH	Full load hours	TTES	Tank thermal energy storage

1. Introduction

Urban district heating (DH) systems in Germany today are usually large 2nd or 3rd generation networks with more than 100 km route length and supply temperatures in the range of 90 °C up to 120 °C (Frederiksen and Werner, 2017; Schweikardt et al., 2012). An important first step to transform those networks to 4th generation DH systems is the reduction of network temperatures to promote the efficient integration of renewable energies. To initiate this transformation process, it can be beneficial to implement subnetworks in the most suitable areas of a large heating network for a smooth transition to smart thermal energy systems. According to AGFW e.V. (2019), 80 % of the heat distributed via heating networks in 2018 was produced in combined heat and power (CHP) processes. With coal and gas fired power plants phasing out of operation in the next decades, new use cases need to be developed for the existing infrastructure. Those sites bear the potential to advance the interaction between the heat and electricity sector. The shift from a sole production site to a more flexible operation as a prosumer supports the integration of renewable energies into the electricity grid by reducing the required electrical storage capacity. At the same time, the exploitation of environmental heat by heat pumps requires electricity. A common feature of centralized CHP plants located close to cities are river water cooling systems. The associated infrastructure and permissions for river water usage enable an easy integration of environmental heat into urban DH systems. In this paper a techno-economic analyses of three different concepts for this use case is conducted with a focus on electricity market price induced heat production.

2. Case study

This case study is about a district in the center of a German city with an existing DH network. The framework for the investigation is given by the German subsidy program "Wärmenetzsysteme 4.0" (heating network systems 4.0) according to BAFA (2020). The program is aimed at promoting the development of new smart thermal energy

doi:10.18086/eurosun.2020.02.05 Available at http://proceedings.ises.org

networks, but also at transforming existing DH networks. The key requirement of the program is that at least 50 % of the heat supply is to be covered by renewable energies.

2.1 Boundary conditions of the urban district

The district is a densely populated area with mostly multi-family houses, but also some commerce and industry. More than 70 % of the building stock connected to the DH network has been built before the year 1960 and more than 40 % even before 1918. The mean specific heat demand of the residential buildings is around 100 kWh/(m²·a), including space heating and domestic hot water. In total, the residential heat demand amounts to 29.2 GWh/a, while the non-residential heat demand is about 8.6 GWh/a. It is expected that the heat demand of the current customers will decrease due to renovation measures and rising mean ambient temperatures. Nevertheless, the district bears sufficient potential for new heating network connections. It is assumed that the reduction in heat demand is continually compensated through customer acquisition in the future. In addition, a nearby new housing development with around 12.8 GWh/a heat demand is supposed to be connected to the DH network until 2030. This leads to the heat demand scenario depicted in Fig. 1.

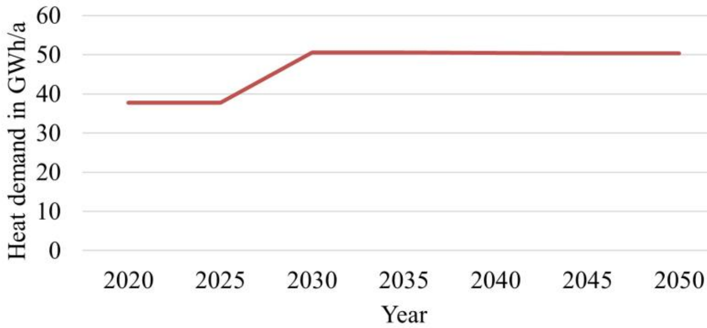

Fig. 1 Heat demand development from 2020 to 2050

There is one main supply line of the heating network leading into the district, which is the only connection of the district to the main heat supplier, the CHP power plant. This juncture can be used to create a subnetwork with lower operating temperatures compared to the high temperature primary network. At the same time, the CHP power plant is located next to a river. The route length of the subnetwork is around 15.2 km, so that the linear heat demand density is 2.5 MWh/(m_{route}·a) today. Due to the mentioned extensions of the grid in the heat demand scenario, the linear heat density decreases to 2.2 MWh/(m_{route}·a) until the year 2038.

2.2 Integration of a river water heat pump

The highest potential for renewable heat in the district bears the development of environmental heat of the adjacent river. The river temperature drops to values between 0 and 10 °C in winter, while in summer it can rise to just over 20 °C. The river heat is therefore available at a just sufficient temperature level to be used by a heat pump and fed into the subnetwork of the district. The necessary river water extraction points already exist at the CHP plant site including the corresponding permit to use the river water for CHP cooling. In this context, the river temperature may be increased by up to 3 K to a maximum of 28 °C. After consultation with the utility, no major obstacles are to be expected for an extension of this permit for heating purposes. Cooling the currently maximum permissible volume flow by only 2 K corresponds to a thermal capacity of 50 MW.

A schematic diagram of the integration concept at the CHP plant site is depicted in Fig. 2. Part of the volume flow of the river water is redirected through a shell-and-tube heat exchanger. The river water heat is then transferred to an intermediate cycle (70 % water, 30 % glycol) to prevent contact between the refrigerant of the heat pump and the river water. In the case at hand suitable refrigerants are ammonia (R717) and hydrofluorolefins (HFOs), which are both characterized through very low global warming potentials. Within the case study ammonia was chosen as refrigerant due to its higher efficiency compared to HFOs according to Jesper et al. (2021). As the temperature lift ranges from 53 K in the summer up to 86 K in the winter, it is also more efficient to use a two-stage heat pump. The seasonal performance factor (SPF) estimated for this use case with a method developed by Jesper et al. (2021) is 2.3 for a single-stage versus 3.0 for a two-stage system. The heat pump is connected to a tank thermal energy storage (TTES), that can be charged with up to 90 °C. When the heat load of the subnetwork exceeds the maximum heat output of the TTES, the residual load is covered by the primary DH network through a district substation. In this case a smart control strategy is to be developed that maximizes the efficiency of the heat pump by setting the optimized volume flows and supply temperatures of the heat pump and the post-heating with the district substation.

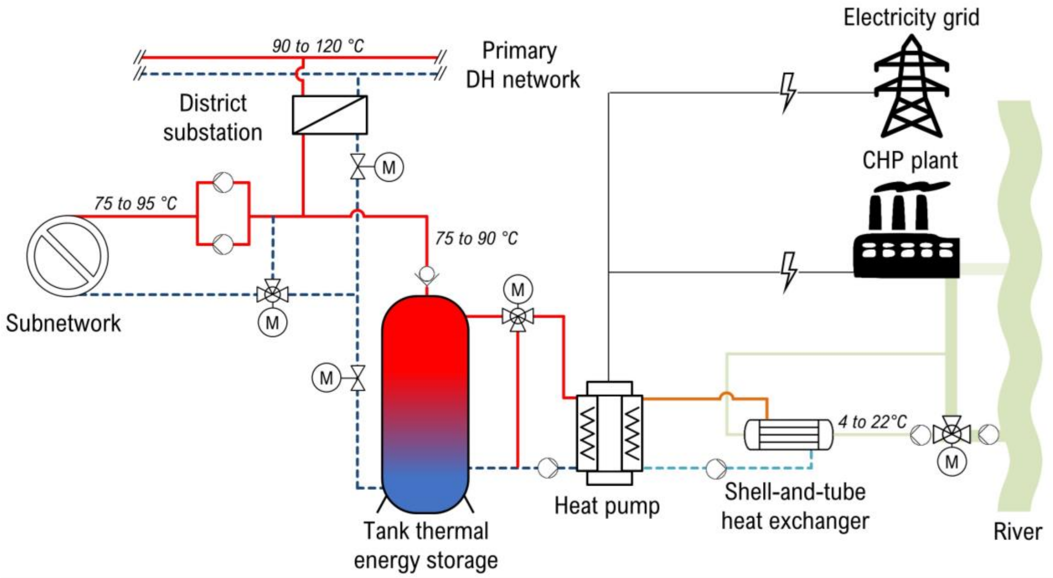

Fig. 2: Integration of a river water heat pump (schematic diagram)

2.3 Potential for solar thermal heat

The lack of open spaces in the district only leaves the option of decentralized rooftop systems in terms of solar thermal heat. According to Heymann et al. (2019) the minimum collector area of solar thermal systems feeding into the DH network should be 200 m² due to the complexity as well as high investment and operating costs. To determine the total potential collector area in the district, large rooftops were analyzed systematically with the help of the city's solar map and 3D-scans of the buildings. After applying the exclusion criteria of a minimum collector area of 200 m² per system and a minimum collector area of 350 m² per building complex, a total potential of 8,300 m² could be identified. Nevertheless, the feasibility of the systems is strongly dependent on individual local conditions, so that those buildings with the highest implementation probability were selected by the utility according to Tab. 1. The final selection amounts to a total collector area of 4,841 m².

Tab. 1: Potential collector areas of solar thermal rooftop systems

ID	Inclination	Orientation*	Collector Area
01	0°	+30°	504 m²
02	0°	-15°	525 m²
03	0°	-2°, 0°	463 m²
04	30°	-90°	848 m²
05	0°	+10°	384 m²
06	0°	-15°	1590 m²
07	0°	-15°	526 m²
* -90° = East; 0° = South; +90° = West			

2.4 Heat supply concepts

Within the case study the following three concepts are compared regarding operational characteristics and economic efficiency (see Fig. 3). The core element to achieve the required cover ratio of 50 % renewable energies in all three concepts is the river water heat pump in combination with a TTES. In all cases the primary network covers the residual load and serves as a backup but is hydraulically separated from the subnetwork through a district substation. In Concept II, the heat pump is complemented by the decentralized solar thermal rooftop systems, that feed directly into the supply line of the grid using individual feed-in stations. Concept III consists of additional CHP and Power-to-Heat (PtH) units to account for the sector coupling aspects of heat production.

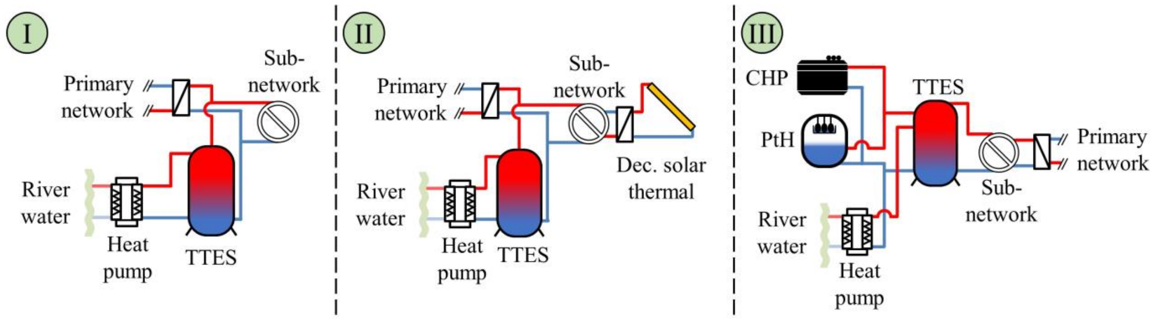

Fig. 3 Schematic diagrams of three heat supply concepts

The heat production components are designed to still reach a 50 % renewable cover ratio in the year 2030, when the peak in heat demand is expected. The resulting dimensions are shown in Tab. 2.

Tab. 2: Component dimensions

Component	Concept I	Concept II	Concept III
Heat pump	4.7 MW_{th}	4.7 MW_{th}	6.2 MW_{th}
Solar thermal systems	-	4,841 m²	-
CHP unit	-	-	7.12 MW_{th}; 7.2 MW_{el}
PtH unit	-	-	2.2 MW_{th}
Storage	600 m³	600 m³	7000 m³

It must be noted that although there are additional decentralized solar thermal systems in Concept II, the heat pump needs the same heat output as in Concept I. This is resulting from the sole availability of solar heat during low heat load periods in summer, while the contribution of the heat pump in winter is decisive to reach the desired renewable cover ratio. In Concept III, a goal of the design is to achieve a very flexible heat production with a focus on electricity market prices. The CHP unit is designed to only operate 3,000 full load hours per year, but it still partially displaces renewable heat when electricity prices are high. In turn, the heat pump requires a larger heat output for periods with low electricity prices to reach the same desired renewable cover ratio as in Concept I and II. While the smaller storages in Concept I and II are short-term storages to shift daily summer loads, the much larger storage volume in Concept III is driven by a minimum requirement in the subsidy program in combination with CHP units.

2.5 Framework for the economic comparison of the heat supply concepts

The relevant expenses for the economic comparison include investments, fuel costs as well as maintenance and service costs for the respective components mentioned in section 2.4. On these grounds the Levelized Cost of Heat (LCoH) for each concept is calculated. According to Baez and Larriba Martinez (2015) LCoH is "the constant and theoretical cost of generating one kWh of heat, which is equal to the discounted expenses incurred throughout the lifetime of the investment" and is determined following equation 1. The required input variables are discussed in the following.

$$LCoH = \frac{I+\sum_{t=1}^{T}\frac{C_t-S_t-RV}{(1+i)^t}}{\sum_{t=1}^{T}\frac{E_t}{(1+i)^t}} \qquad \text{(eq. 1)}$$

$LCoH$	Levelized Cost of Heat [€/MWh]	S_t	Revenue from operation [€]
I	Investment costs [€]	RV	Residual value [€]
T	Assessment period [-]	i	Discount rate [%]
t	Year [-]	E_t	Produced heat [MWh]
C_t	Operating costs [€]		

The assessment period (T) is 15 years and equals the simulation period (see section 3.1). The investment costs (I) for the components are shown as specific values in Tab. 3. The program "Wärmenetzsysteme 4.0" grants a 30 % subsidy on the investments. Hence, the total investment is lowest in Concept I with 2.25 M€, about 4.93 M€ in Concept II due to the additional solar thermal systems and 8.74 M€ in Concept III, where the most and largest components are planned.

Tab. 3: Specific turn-key investment costs

Component	Specific investment costs			Reference
	Concept I	Concept II	Concept III	
Heat pump	578 €/kW_{th}	578 €/kW_{th}	558 €/kW_{th}	Manufacturer information; Große et al. (2017); Wolf (2017)
Solar thermal systems	-	790 €/m²	-	Heymann et al. (2019)
PtH unit	-	-	180 €/kW_{th}	Große et al. (2017)
CHP unit	-	-	654 €/kW_{el}	Klein et al. (2014)
Storage	830 €/m³	830 €/m³	561 €/m³	Große et al. (2017)

The operating costs (C_t) include the fuel costs, but also costs for maintenance and service. The fuel costs are determined with the results of dynamic simulations (see section 3) and prognoses for specific costs of electricity and natural gas. The prognoses were provided by the utility and are based on energy market models by the company Prognos AG. Thus, the mean electricity spot market price ranges from 58.3 €/MWh in the year 2024 up to 72.8 €/MWh in 2038. It is assumed that the heat pump is driven by self-generated electricity from the CHP plant. Therefore, the lost revenue from a potential electricity feed-in is considered as electricity costs. Additionally, German legislation requires 40 % of the renewable energy levy to be paid for self-generated electricity consumption in this case. The levy is expected to be at 58.9 €/MWh in the year 2024 and decreases to 13.6 €/MWh until 2038. The forecasted natural gas price is at 39.1 €/MWh in 2024 and increases to 47.2 €/MWh until 2038. This already includes a tax on CO_2-emissions, which is assumed to be at 45 €/t_{CO2} in 2024 and increases to 68 €/t_{CO2} in 2038. The costs for maintenance and service of the components are assumed according to the references listed in Tab. 3. The revenue from operation (S_t) is only relevant in Concept III, where the fed-in electricity of the CHP unit is remunerated according to electricity spot market prices. It is assumed that the storages and the solar thermal systems have a useful life of 25 years, which exceeds the assessment period. Therefore, their residual value (RV) is taken into consideration for calculating the LCoH. This is not relevant for the heat pump, the CHP and the PtH unit, as a useful life of 15 years is assumed for those components. The discount rate (i) was chosen at 8 %. Finally, the heat (E_t) that is produced by the new components is considered.

3. Simulation of heat production

As a focus of the concept comparison is on electricity market price induced heat production, the software energyPRO is used to simulate long-term operation of the components on an hourly basis. The software enables a simple integration of time series, including a prognosis of electricity spot market prices, weather data (ambient temperature, river temperature, soil temperature) and its respective expected developments in the future. The heat production components are prioritized for every timestep with the time series as boundary conditions. The software uses an analytical optimization method to find the best solution for meeting the heat demand while utilizing the available storage capacity. In contrast, the complexity of decentralized solar thermal systems feeding into a DH system cannot be modelled in energyPRO. Therefore, the software Polysun is used to simulate the solar thermal feed-in and is afterwards transmitted to energyPRO as a time series.

3.1 Boundary conditions of the energyPRO model

The most important boundary conditions for the simulation of heat production are laid out in the following. The simulation period is 15 years starting from the year 2024 until 2038. A corresponding prognosis for ambient temperatures was generated with the software Meteonorm. Based on the correlation between historical ambient temperature and river temperature at the CHP plant site, a prognosis for the river temperature was modelled. Furthermore, the supply and return temperature of the subnetwork of the DH system were implemented as a function of ambient temperature (see Fig. 4). The depicted supply temperature curve reflects a mean temperature decrease of 19 K compared to the supply temperature of the primary network.

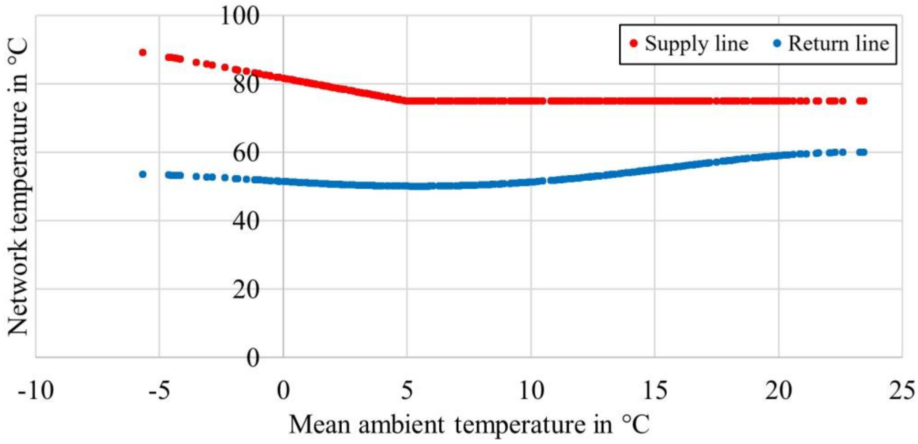

Fig. 4: Network operating temperatures

The temperature difference between supply line of the subnetwork and the river is crucial to predict the efficiency of the heat pump. For this purpose, a method by Jesper et al. (2021) was applied, that enables to estimate the coefficient of performance (COP) as a function of temperature lift between heat source and heat sink of the heat pump. The hourly prediction of the COP was then considered as a boundary condition in the simulation model and for the calculation of electricity costs. It is assumed that the electricity for the heat pump as well as the electricity export of the CHP unit is directly traded at a spot market. The relevant long-term time series of hourly electricity spot market prices is retrieved from the prognosis mentioned in section 2.5.

The simulation model considers the hourly heat load curves for all customers as well as network losses. The annual heat demand was allocated to the days of the year depending on mean ambient temperatures of the reference year 2020. The allocation relies on standard load profiles according to Hellwig (2003) and the respective further development by Hinterstocker et al. (2015). The used profiles correspond to residential and non-residential buildings. Measurements of the actual heat load in the district were used to create hourly profiles from the allocated daily heat demands. The resulting heat load profiles for the residential and non-residential buildings connected to the subnetwork can be seen in Fig. 5. Additionally, the load profile for the network losses was modelled using the heat transfer coefficient area product (UA-value) of the heating network and the difference between network and soil temperature. Due to the lowered supply temperatures in the subnetwork, it is assumed that the heat losses are reduced from 14.5 % to 12.3 % of the heat feed-in.

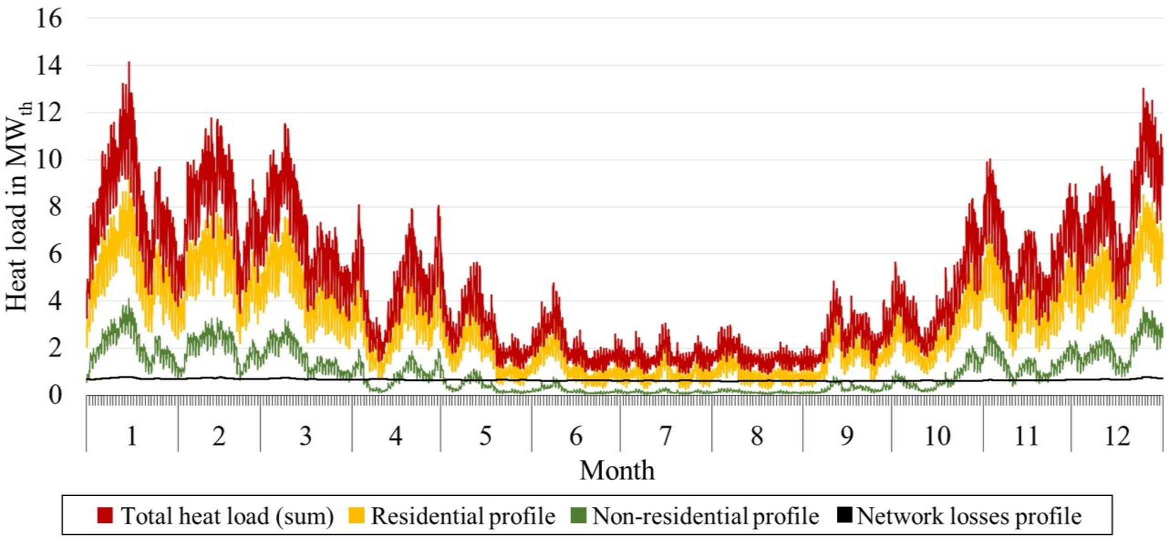

Fig. 5: Hourly total heat load and consumption profiles as course of the year

3.2 Simulation of solar thermal feed-in

The software Polysun offers a model template to simulate the direct feed-in of solar thermal systems into the supply line of DH networks. The model was adapted to the given use case using the configuration guidelines described by Schäfer et al. (2015). Seven representative models were configured with respect to the identified potential systems in section 2.3. This includes collector area, pipe lengths, orientation, inclination, shading, and temperatures. CPC vacuum tube collectors were chosen as collector type. The operation of the representative models was then scaled to the total potential collector area. The resulting annual profile can be seen in Fig. 6. The total potential solar thermal feed-in amounts to 1,824 MWh/a. With a collector area of only 4,841 m² the expected excess heat, that would require a storage, is only 2,4 % of the total feed-in. Furthermore, it can be observed that due to row shading and higher supply temperatures (> 80°C) in winter, there is almost no feed-in from November until February. The specific yields of the seven representative systems range from 336 to 391 kWh/m²·a. A subsequent thermohydraulic simulation of the heating network, that was conducted by the utility, verified the feasibility of the solar thermal feed-in.

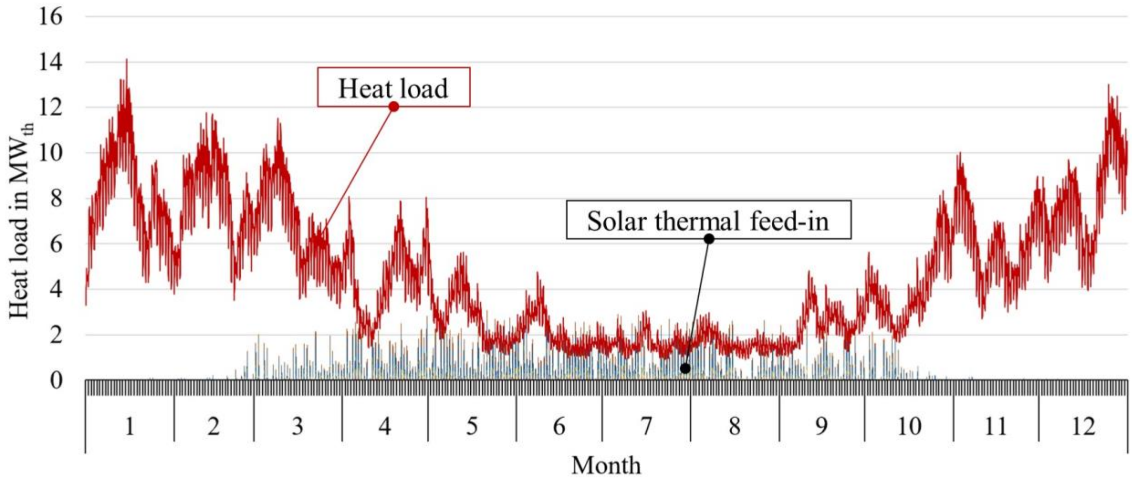

Fig. 6: Hourly solar thermal feed-in and total heat load as course of the year

3.3 Simulation results

The resulting key figures of the energyPRO simulation are shown as mean values of the 15-year simulation period in Tab. 4. The desired renewable cover ratio of a minimum of 50 % is reached in all three concepts throughout the entire simulation period. The additional solar thermal heat in Concept II leads to a slightly lower cover ratio of the heat pump compared to Concept I. With an additional CHP unit in Concept III, the primary network only covers the peak loads with a cover ratio of 5.7 %. The PtH unit just covers 0.5 % due to a limitation in the operation strategy to run at negative electricity market prices. As a result of the larger heat pump and storage in Concept III, a more flexible operation of the heat pump can be seen. The full load hours (FLH) are significantly lower than in Concept I and II. The seasonal performance factor (SPF) is almost identical in all cases. In the course of a year, the coefficient of performance (COP) can get as low as 2.50 in winter, while it reaches up to 3.45 during the summer. Even though the storage in Concept III is almost 12-times larger than in Concept I and II, the storage cycles still indicate an acceptable utilization.

Tab. 4: Concept comparison - Simulation results

Key figure		**Concept I**	**Concept II**	**Concept III**
Cover ratio	*Heat pump*	53.4 %	50.9 %	54.7 %
	Solar thermal	-	3.3 %	-
	PtH unit	-	-	0.5 %
	CHP unit	-	-	39.1 %
	Primary network	46.6 %	45.8 %	5.7 %
FLH heat pump		6,120 h/a	5,828 h/a	4758 h/a
SPF heat pump		3.05	3.04	3.04
FLH CHP unit		-	-	2961
Storage cycles		225 cycles/a	233 cycles/a	59 cycles/a

4. Opportunities for sector coupling

In the following the three heat supply concepts are analyzed regarding their electricity market price induced operation. For this purpose, mean daily operations within the 15-year simulation period are shown in Fig. 7 to Fig. 11. The possibility to adapt the heat production according to electricity market prices is strongly dependent on the month of the year. In the summer, when the heat load is driven by domestic hot water demand and reaches only 15 to 20 % of the winter load, the heat pump is much more flexible to run at low market prices and utilize the storage.

In July (see Fig. 7 to Fig. 9), the mean electricity market price shows a significant dip around noon. This can be traced back to the feed-in of a large amount of solar PV-systems in Germany, that usually peaks around noon. The mean operation of the heat pump in Concept I (see Fig. 7) adapts to this dip and loads the storage (blue/yellow shaded bars) around noon. The same is true for the operation during the night, although the market price does not drop as much here. This indicates that the heat output of the heat pump and storage size limit the flexible operation.

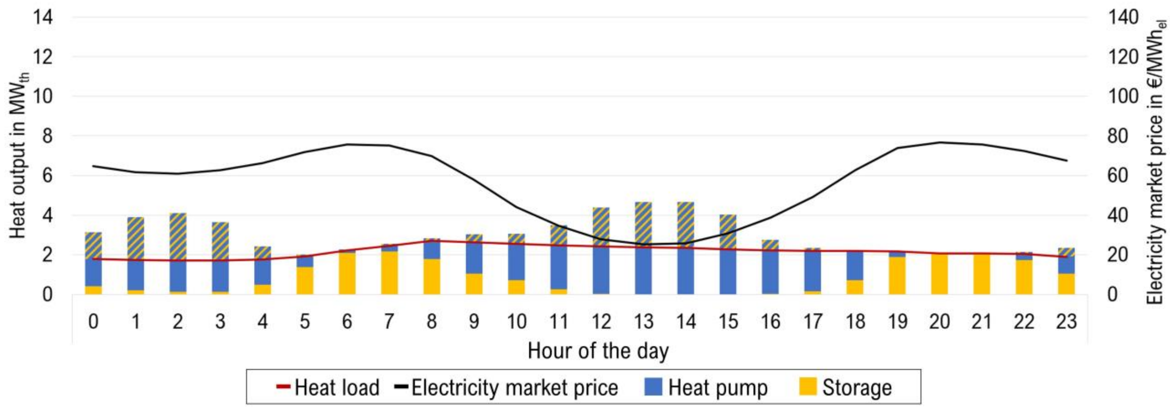

Fig. 7: Concept I - Mean daily operation in July

In Concept II, the additional solar thermal heat primarily reduces the heat pump operation at low market prices and high COPs in the summer (see Fig. 8), as their feed-in profile is almost identical to that of solar PV-systems into the electricity grid. The solar thermal peak is slightly before noon because most of the identified potential collector areas in section 2.3 are oriented to the east or southeast.

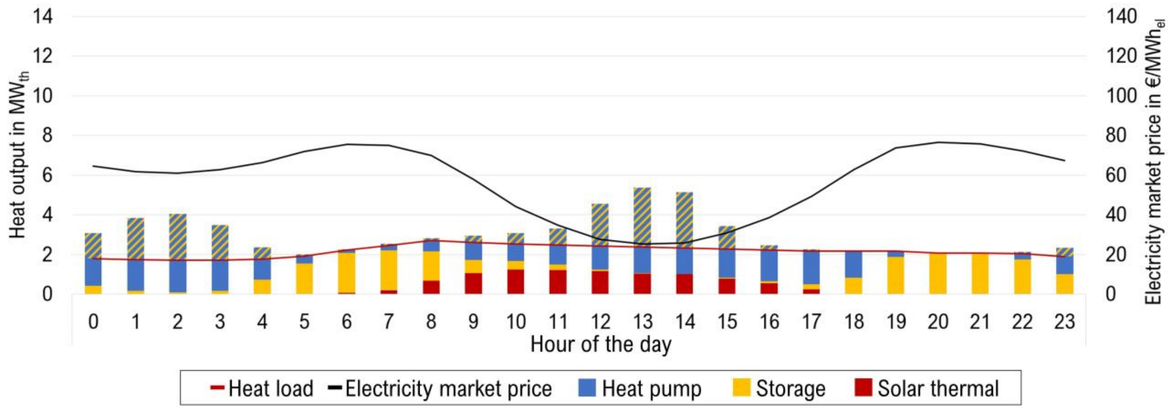

Fig. 8: Concept II - Mean daily operation in July

In contrast to Concept I and II, the combination of a larger heat pump and storage in Concept III enables a more extensive utilization of the market price dip around noon. Even the operation at night is at a minimum here (see Fig. 9).

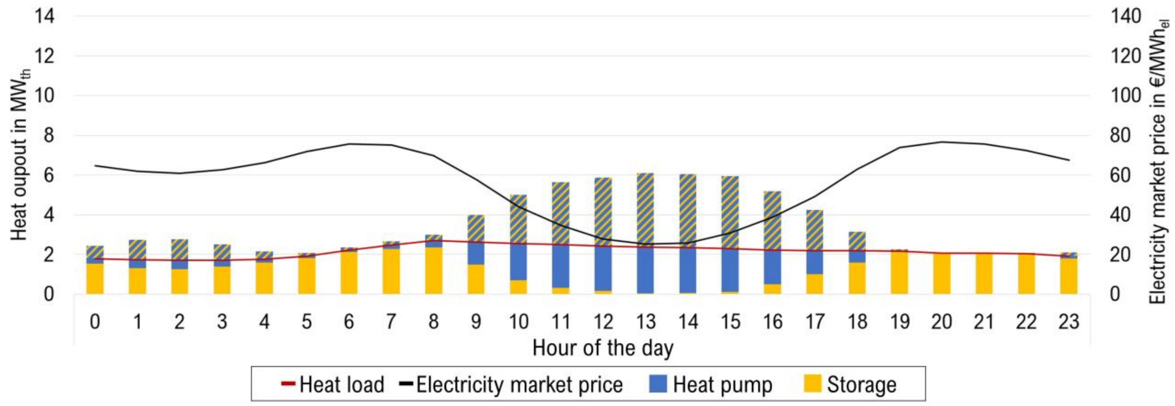

Fig. 9: Concept III - Mean daily operation in July

In Fig. 10 the mean daily operation of Concept III in October is shown as an example for the transitional periods. The mean daily course of the electricity market price is now characterized by a morning and evening peak, while the dip at noon caused by solar PV feed-in declines.

The heat load of the heating network in the spring and fall is about twice as high as in the summer due to additional space heating demand. Therefore, the flexibility of the systems decreases especially in Concepts I and II. Nevertheless, the mean daily profiles show, that an operation of the heat pump during the morning and evening market price peaks is still prevented to the extent possible. As depicted in Fig. 10, this operational characteristic can particularly be seen in Concept III. Additionally, the CHP unit supports this operation by following the opposite course of the heat pump producing heat and electricity when market prices are high.

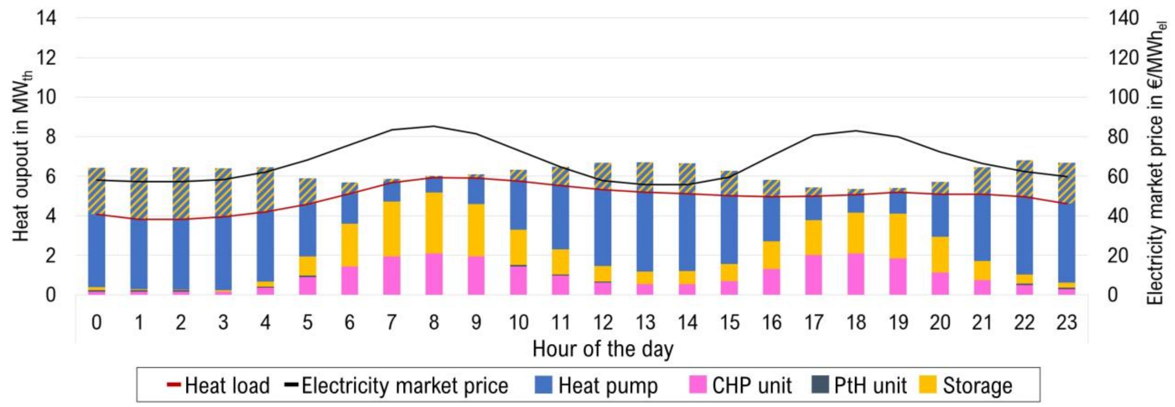

Fig. 10: Concept III - Mean daily operation in October

When the heat load is reaching its maximum in winter, the flexibility of the systems declines. As shown in Fig. 11, the mean electricity market price in January is characterized by low prices at night as well as the morning and evening peaks. In Concept III, the CHP unit still feeds in most during those peaks, but the operation of the heat pump does not seem to be affected by the market price anymore. In that context it must be noted that the mean heat output of the heat pump in January is significantly lower at only 2 to 3 MW_{th} compared to the maximum of 6.2 MW_{th} during the summer. This effect is caused by periods with very low river temperatures below 4 °C. During those periods, the heat pump cannot operate at all due to technical limitations, so that the mean heat output decreases.

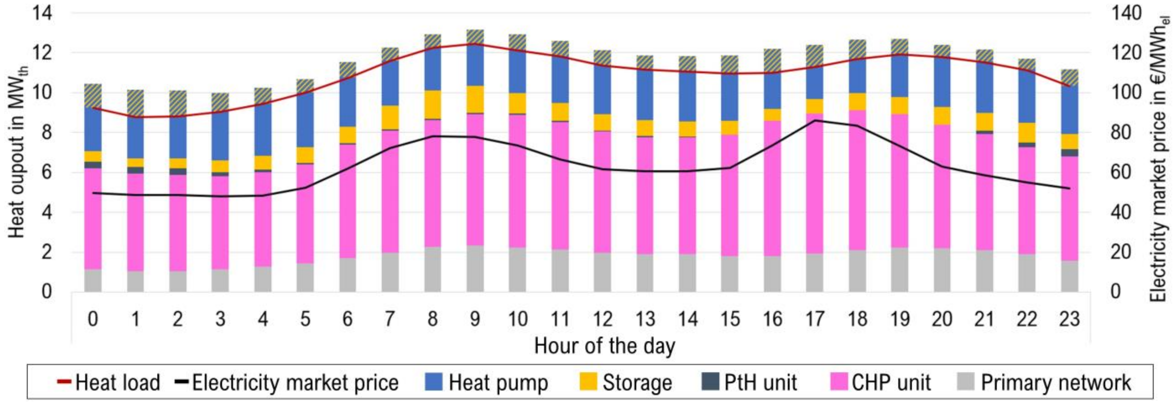

Fig. 11: Concept III - Mean daily operation in January

As a key figure to summarize and reflect on the conducted analysis, the mean deviation (d) of the consumption and feed-in of electricity from mean market price ($\bar{c}_{el,market}$) is considered. It is calculated according to equation 2 and 3 with the cost of electricity ($C_{el,HP}$) and the electricity consumption ($E_{el,HP}$) of the heat pump, respectively the revenue ($S_{el,CHP}$) and the exported electricity ($E_{el,CHP}$) of the CHP unit.

$$d_{consumption} = \left(\frac{\frac{C_{el,HP}}{E_{el,HP}}}{\bar{c}_{el,market}} - 1 \right) * 100\% \qquad \text{(eq. 2)}$$

$$d_{feed-in} = \left(\frac{\frac{S_{el,CHP}}{E_{el,CHP}}}{\bar{c}_{el,market}} - 1 \right) * 100\% \qquad \text{(eq. 3)}$$

$d_{consumption}$	Mean deviation of the consumption of electricity from mean market price [%]
$d_{feed-in}$	Mean deviation of the feed-in of electricity from mean market price [%]
$C_{el,HP}$	Cost of electricity for the heat pump [€]
$E_{el,HP}$	Electricity consumption of the heat pump [MWh$_{el}$]
$S_{el,CHP}$	Revenue from feed-in of electricity of the CHP unit [€]
$E_{el,CHP}$	Exported electricity of the CHP unit [MWh$_{el}$]
$\bar{c}_{el,market}$	Mean electricity market price [-]

The deviation concerning the electricity consumption of the heat pump is quite low in Concept I with -3.5 % and Concept II with -2.7 %. The slightly lower deviation in Concept II is consistent with the observations made in Fig. 8. The more flexible operation in Concept III leads to a significant deviation of -15.5 %. This shows that a flexible operation in transitional periods is necessary to achieve significantly lower market prices for electricity consumption. The same applies to the feed-in of electricity by the CHP unit in Concept III, which is even at +23.6 %.

5. Economic comparison of heat supply concepts

The LCoH for the three concepts are depicted in Fig. 12. The corresponding economic framework conditions are laid out in section 2.5. The lowest LCoH are achieved in Concept I with 36.7 €/MWh. Here, electricity costs account for the largest share with 68 %, while the investment for the heat pump and the storage is only 25 % of the total. The LCoH in Concept II is 45.8 €/MWh and therefore almost 25 % higher than in Concept I. The largest cost component is still the electricity for the heat pump with 52 % of the LCoH. Despite that the share of the investment costs for the decentralized solar thermal system is 19 % of the LCoH and therefore causes the significant deviation from Concept I. Considering that the solar thermal systems only achieve a cover ratio of 3.3 %, an economic efficiency is not given. The flexible electricity market price induced operation in Concept III leads to lower shares of the electricity costs, but also for natural gas for the CHP unit as revenue from electricity feed-in is generated. Nevertheless, this is not reflected in the LCoH of 44.6 €/MWh, which are 21.5 % higher than in Concept I due to the high total investment volume for additional components. In this context the requirement for the large storage volume in the subsidy program in connection with CHP units must be noted.

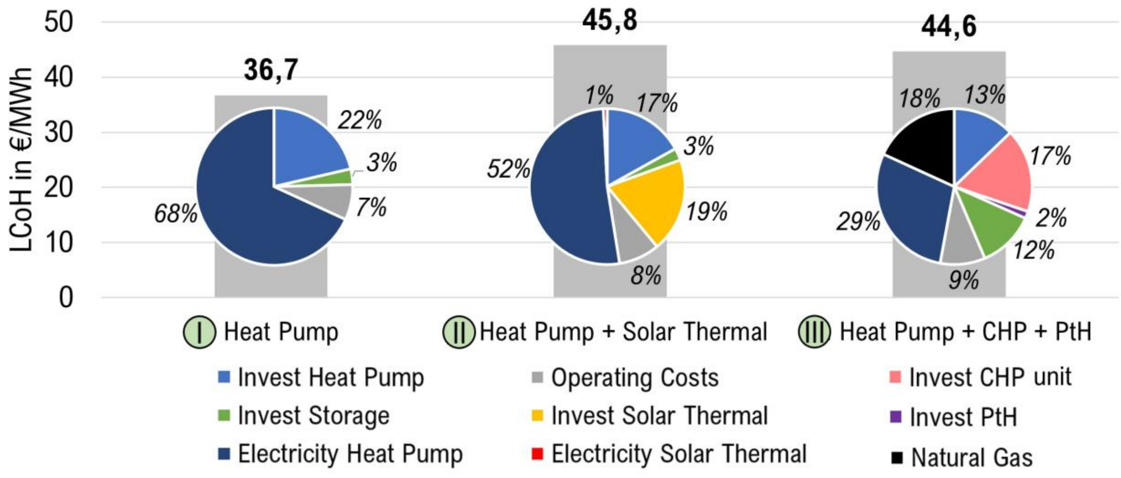

Fig. 12: Concept comparison - Levelized Cost of Heat (LCoH)

6. Discussion

In this paper, the integration of a river water heat pump at an existing CHP plant site was illustrated and analyzed in terms of technical and economic aspects. In a densely populated area this presents an excellent opportunity for the decarbonization of urban DH systems. In addition, the shown concept can be scaled by extending the heat pump feed-in to the primary DH network, as only 5 % of the theoretically available heat flow from the river was considered in the case study. Three different heat supply concepts were designed combining the river water heat pump with decentralized solar thermal rooftop systems as well as a CHP and PtH unit. 15-year dynamic simulations were used to investigate how the shown use case can support the energy system transformation process by aligning heat production with electricity spot market prices. As the prognosis for market prices is heavily dependent on external conditions, further investigations with different scenarios for the development of the electricity sector should be conducted. In that context the framework for heat pumps operated with net electricity plays an important role. The economic efficiency of very flexible heat production systems could be further improved if the cost of electricity bears even more flexible price components like grid usage charges and system services.

The conducted case study shows that the system with the least components to meet the 50 % renewable cover ratio is the most cost efficient with the underlying subsidy program “Wärmenetzsysteme 4.0” (BAFA, 2020). The integration of decentralized solar thermal systems is cost intensive, which leads to the conclusion that the potential for large on-ground collector fields should be exploited first. It is important to keep in mind that the goal of 50 % renewable cover ratio is only an intermediate milestone to an all renewable scenario. In this light, the shown Concept III gives an outlook on how green fuels could be used in smaller decentralized CHP units in the future.

7. References

AGFW e.V., 2019. AGFW-Hauptbericht 2018. AGFW e.V., Frankfurt am Main, Germany.

Baez, M. J., Larriba Martinez, T., 2015: Technical Report on the Elaboration of a Cost Estimation Methodology. Work Package 3 – Estimating RHC energy costs. Creara. Madrid, Spain.

BAFA, 2020. Modellvorhaben Wärmenetzsysteme 4.0. https://www.bafa.de/DE/Energie/Energieeffizienz/Waermenetze/waermenetze_node.html;jsessionid=59C35C9BB1737E484CC479F94B8C1571.1_cid381. Accessed 31 August 2020. Bundesamt für Wirtschaft und Ausfuhrkontrolle, Eschborn, Germany.

Frederiksen, S., Werner, S., 2017. District heating and Cooling, first ed. Studentlitteratur, Lund, Sweden.

Große R, Christopher B, Stefan W, Geyer R, Robbi S, 2017. Long term (2050) projections of techno-economic performance of large-scale heating and cooling in the EU: external study performed by ILF Consulting Engineers Austria GmbH and AIT Austrian Institute of Technology GmbH for the Joint Research Centre. Publications Office of the European Union, Luxembourg.

Hellwig, M., 2003. Entwicklung und Anwendung parametrisierter Standard-Lastprofile. Institute of Power Engineering. Dissertation. TU Munich, Munich, Germany.

Heymann, M., Rosemann, T., Rühling, K., Hoppe, S., Wudenka, E., Hafner, B., 2019. Kostenreduktionspotential beim Ausbau der Solarisierung von Fernwärmenetzen durch Standardisierung. TU Dresden and Viessmann Werke GmbH & Co. KG. Dresden, Allendorf, Germany.

Hinterstocker, M., Eberl, B., v. Roon, S., 2015. Weiterentwicklung des Standardlastprofilverfahrens Gas. Forschungsgesellschaft für Energiewirtschaft mbH (FfE), München, Germany.

Jesper, M., Schlosser, F., Pag, F., Walmsley, T.G., Schmitt, B., Vajen, K., 2021. Large-scale heat pumps: Uptake and performance modelling of market-available devices. Renewable and Sustainable Energy Reviews. 137, 110646.

Klein, C., Rozanski, K., Gailfuß, M., Kukuk, J. Beck, T., 2014. BHKW-Kenndaten 2014/2015. Module, Anbieter, Kosten. ASUE Arbeitsgemeinschaft für sparsamen und umweltfreundlichen Energieverbrauch e.V., Berlin, Germany.

Schäfer, K., Mangold, D., Pauschinger, T., 2015. DEZENTRAL – Dezentrale Einspeisung in Nah- und Fernwärmesysteme unter besonderer Berücksichtigung der Solarthermie. Teilbericht des Verbundpartners Solites. Forschungsbericht zum Forschungsvorhaben 03ET1039C. Steinbeis Forschungsinstitut für solare und zukunftsfähige thermische Energiesysteme, Stuttgart, Germany.

Schweikardt, S., Didycz, M., Engelsing, F., Wacker, K., 2012. Sektoruntersuchung Fernwärme. Bundeskartellamt, Bonn, Germany.

Wolf, S., 2017. Integration von Wärmepumpen in industrielle Produktionssysteme. Institute of Energy Economics and Rational Energy Use. Dissertation. University of Stuttgart, Stuttgart, Germany.

Measurement Results of a District Heating System with Decentralized Incorporated Solar Thermal Energy for an Energy, Cost Effective and Electricity Grid Favorable Intermitting Operation

Axel Oliva[1], Youmi Kim[1], Manuel Lämmle[1], Sebastian Herkel[1], Alexander Ripka[2] and Christoph Gebele[2]

[1] Fraunhofer Institute for Solar Energy Systems ISE, Freiburg i.Br. (Germany)

[2] Badenova Wärmeplus GmbH & Co. KG, Freiburg i.Br. (Germany)

Abstract

An overall measurement analysis of a district heating system with distributed decentralized solar thermal systems is given for the period of in total one year. Due to the solar thermal yield of each building supply system the district heating system results in an intermitting operation especially during summer period of time. By implementing intelligent operation modes developed by Elci (2018) and Elci et al. (2015) DH supply of each building connection unit are to harmonize over time to enlarge periods of intermitting operation of the DHN especially by taking periods of a high share of PV in the electricity grid into account. Focus in the analysis carried out is put to energy efficiency and temperature levels of each building supply system and it is shown that the energetic design key data are met. Operational performance instead is related on the analyzed high return temperatures of the systems due to hydraulic unbalanced issues and is therefore away from the expected based on the concepts for energy and cost efficient operation modes by Elci (2018) and Elci et al. (2015).

Keywords: decentralized solar district heating system, economic optimal operation, decentralized feed-in, intermitting district heating operation modes, Freiburg-Gutleutmatten

1. Introduction

During the course of an inner-city development the housing estate with 500 apartments, a heated floor area of 40.000 m² in a development area of 82.000 m² and a heat demand of 2.900 MWh/a is being realized. Within the frame of this project decentralized solar thermal systems are installed in each building and will be integrated in a heat supply concept based on a combined heat and power (CHP) district heating (DH) system. The idea is that during periods with high irradiation in summer heat demand is covered by solar thermal systems and during winter by the CHP unit. The assumption is that this kind of design and operation management will be constructive to supply an urban area on a medium and long-term perspective. Central objectives of the project are to implement a concept for the operation management and to derive general rules for comparable urban areas. This will be carried out considering the ongoing massive transformation process of the overall energy system.

2. Demonstration site of “Freiburg Gutleutmatten” and its realization

In this concept, the total heat demand is covered by 38 decentralized solar thermal units including its decentralized storages and the heat produced by the central CHP unit and boiler. The total area of collectors amounts to 2.000 m² (1.400 kW_{th}) and the specific storage volume is approximately 80 litres/$m^2_{aperture}$. It is expected that this leads to a total heat coverage of about 30 % and enable a self-sustaining supply by solar thermal for long periods during summer. The remaining heat demand is supplied by the central CHP unit and boiler. The heat losses of the network (1.540 m) are designed to about 260 MWh/a where the reduced operation time is not taken into account. The aim is to reduce the distribution losses by more than 30 %.

2.1. Objectives of the project

Firstly, the role of solar thermal technology in supplying heat to urban areas is evaluated. This is done by considering prospective conditions of the energy business. The focal point is thereby put on an integral consideration of power and heat consumption and the corresponding supply network systems. Secondly, an innovative and economically promising solution is demonstrated for investors, for the operator and finally for the clients in the integration of solar thermal technology to take the district heating network (DHN) for

doi:10.18086/eurosun.2020.02.06 Available at http://proceedings.ises.org

some periods of time during summer out of operation. The approach is a decentralized implementation of solar thermal into the supply systems of each connection unit to deactivate the CHP operated district heating network for time periods with high irradiation and hence a high fraction of photovoltaics in the electricity grid. During these periods the operation of the CHP is expected to be uneconomical due to the low corresponding feed in tariff.

2.2. Basic features

2.2.1. Key data

The urban development area has the key data as shown in Table 1. It is characterized by a wide variety of system sizes and architectural feature that is due to the fact that the development planning intents to cover a wide range of individual aspects and each property has different ownerships.

Table 1: Basic design values for heat supply of the district of Freiburg-Gutleutmatten

Urban scale of area:	81.500 m²
Accommodation units:	525 (1 ... 42)
Heated floor area:	40.000 m² (3 to 9 floors)
Total heat demand: (~10 % losses DH)	2.900 MWh/a
DHW and circulation:	30 kWh/m²$_{hf}$
Specific heating demand:	35 kWh/m²$_{hf}$
Supply- / Return temp.:	75 °C / 40 °C
Trench length:	1.540 m
Building DH substations:	38 (5 kW$_{th}$ … 100 kW$_{th}$)
ST-system:	2.200 m² (7 m² … 145 m²)
Specific area of ST:	0.05 m²$_{Aap}$/m²$_{hf}$
Specific ST yield:	17.5 kWh/m²$_{hf}$
Solar thermal fraction:	30 %

Due to the scientific focus of operation periods in summer, the size of solar thermal systems installed in each unit is demonstrated in Figure 1. Systems with heat transfer stations at each apartment (HTS) are indicated separately as well as systems with vacuum tube collectors instead of flat-plate collectors.

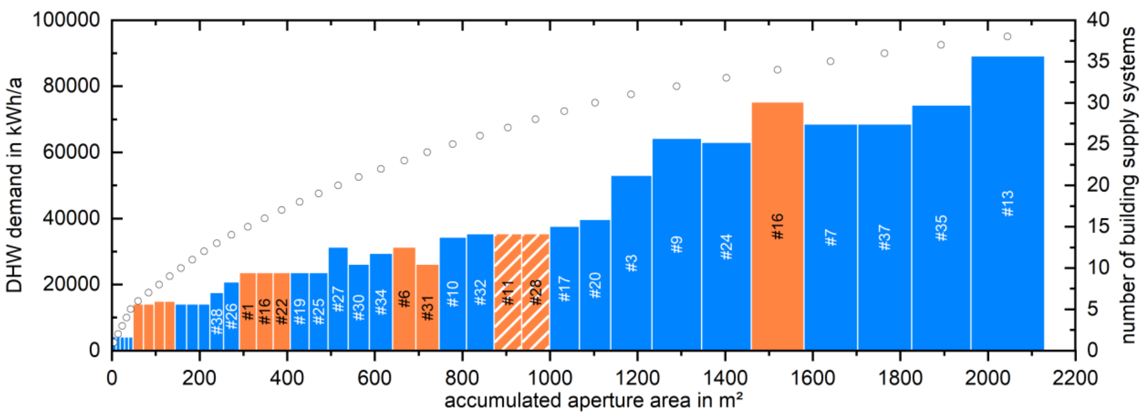

Figure 1: Dimensioning of all building supply systems regarding aperture area and the related DHW demand. Bars in orange stand for decentralized DHW systems with apartment heat transfer stations, crosshatched bars stand for evacuated tube collector systems.

The high range of dimensioning of the resulting connection units becomes clear. The hydraulic layout of the DHN and the related aperture areas of the DH connection units are shown in Figure 2.

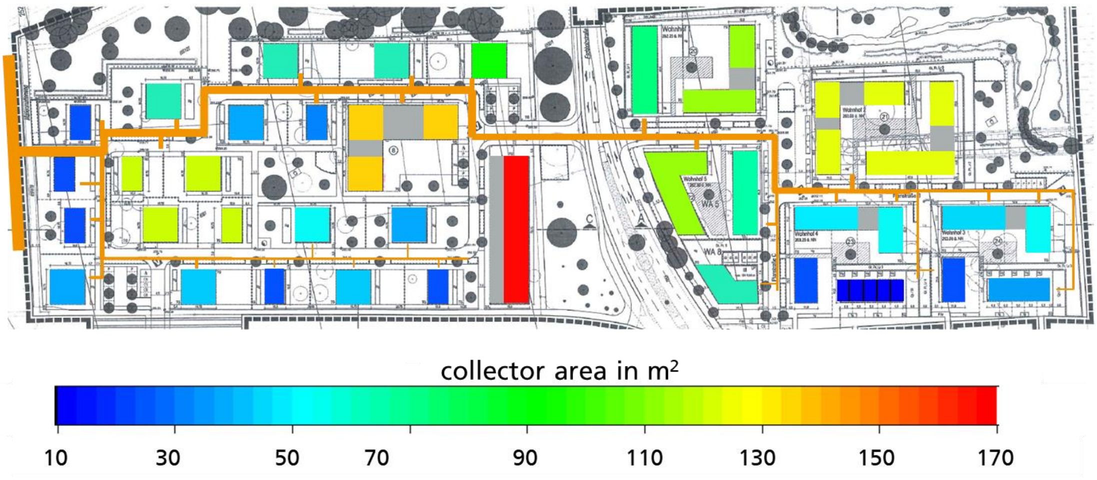

Figure 2: Distribution of aperture area related to the hydraulic distribution system of DH in "Freiburg-Gutleutmatten"

Special attention has to be put on the detached houses connected at the end of the DHN, because those units are the smallest in size and are at the point that is the farthest way from the feed-in point of the DHN.

2.2.2. System layout

The following Figure 3 illustrates the basic system layout for a general decentralized heat supply system for the case of heat supply from a) the DHN or b) from the ST system. The scientific investment includes standard pumps for the decentralized ST-feed as option for smart DHN operation modes described in Elci 2018 and Elci et al. 2015 (compare Figure 4).

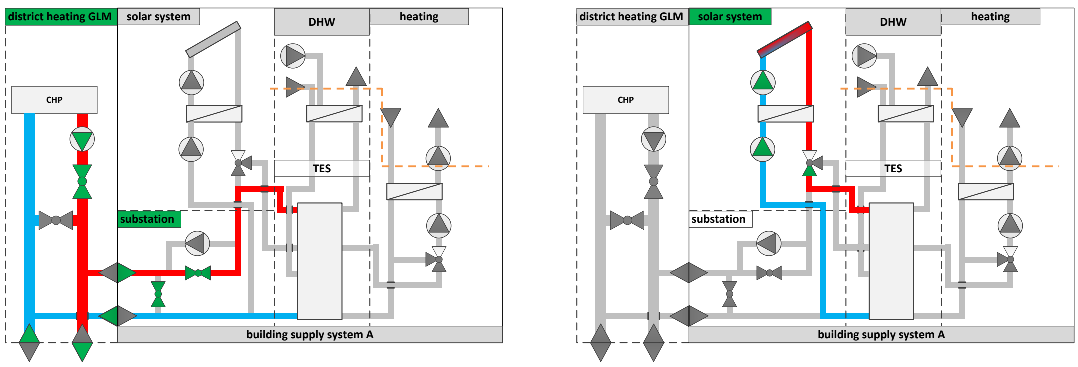

a) Heat supply from DHN **b) Heat supply from decentralized ST system**

Figure 3: Basic hydraulic layout of a DH connection unit for one building including the solar thermal system. The boundary for the investment of the heat supplying company does include the hot water storage tanks as well as the solar-thermal system and is indicated by the orange dashed line.

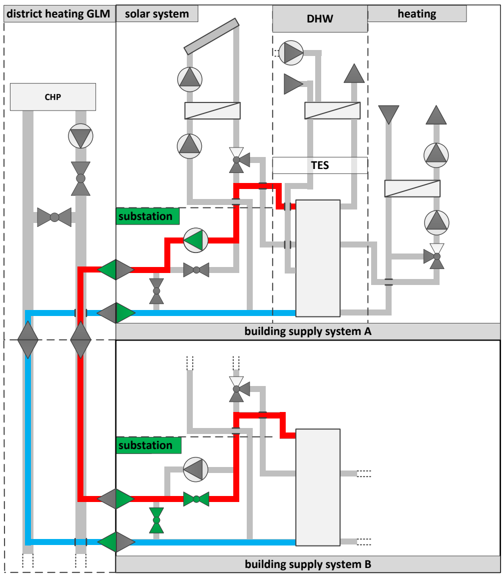

Figure 4: Decentralized ST-feed in for cooperation modes of neighbored connection units described in Elci 2018 and Elci et al. 2015.

In the district of "Freiburg-Gutleutmatten" the heat supply system for each building is quite unique due to the fact of separate ownership. Basically, three different hydraulic schemes have been installed. These different layouts result in three different general measurement schemes (Table 2):

- Scheme 1: Decentralized apartment heat transfer stations with two piping distribution system, one heat meter at load side
- Scheme 2: Centralized DHW preparation with two separate heat meters for distribution of DHW including circulation and another for distribution of space heating
- Scheme 3: Centralized DHW preparation with three separate heat meters for distribution of DHW, circulation and distribution of space heating

Table 2: Measurement schemes in district of "Freiburg-Gutleutmatten" for different DH connection units and the resulting installation of heat meters

System measurement scheme	DHW	Circulation	Space heating	Total load side
1				×
2	×		×	×
3	×	×	×	×

2.3. Realization process

The construction started in 2016 by taking the first solar-thermal system in operation and is still an ongoing process. By August 2020 one solar thermal system has not yet been commissioned, and another one has just been taken in operation. Several typical operational optimizations have been carried out to that point of time. The following issues are most significant:

- It has been observed that the dynamics of solar thermal system are much higher than the dynamics the system control is able to handle. Especially the temperature measurement at the collector field has caused a lot of work for optimization. At the moment the collector fields are driven by a method used by vacuum tube collectors to ensure that the temperature sensors constantly reads correct values
- The ability of data transmission and dynamic parametrization of the installed controller is far from the demanded possibilities.

- The volume flows for primary and secondary circuits of the solar thermal system used are not balanced efficiently.
- Some valves used to get stuck so that they had to be replaced.

3. Heat balances and energy efficiency

In the first step, energy balances for the entire district heating network are shown. In the second step, analysis is done for the system of DH connection units.

3.1. District heating

The heat balance for the entire district is analyzed with the restriction of ongoing work in progress at the site.

3.1.1. Heat balances for entire district

The entire heat transferred to the district heating network Q_{DHN} is at 2 311 MWh in the period of 15th August 2019 to 14th August 2020. There was a period of missing measurement data from 27th January 2020 to 1st March 2020. For this period, missing values are interpolated based on the average slope of the adjacent missing period. This value puts against the sum of all heat meters of the DH connection units $\sum Q_{DHN,CU,i}$ of 2,101 MWh. Here, there existed several small missing data periods as well. For this period, data interpolation has fulfilled as well. Heat losses of DHN $Q_{DHN,loss}$ during that period of time account to 210 MWh. This means relative losses of 9.07 %. Furthermore, the solar thermal yield over all systems $\sum Q_{ST,i}$ achieved a value of 686 MWh. The sum of all heat meters that account for distribution supply of DHW, circulation and space heating of the building supply system as useful supplied heat output to the distribution system of the connected building $\sum Q_{bui,cons,i}$ amounts to 2,440 MWh. When taking that value into account, including the losses of the building supply systems $\sum Q_{bui,loss,i}$ of 131 MWh and the losses of the DHN $Q_{DHN,loss}$ and putting the transferred heat of district heating against Q_{DHN}, a solar thermal fraction $f_{sol,DH}$ of 17 % is being calculated based on equation 1 for the entire district heating system. Resulting from the heat balance, the heat losses of building supply system $\sum Q_{bui,loss,i}$ are calculated. The balance and the corresponding losses are shown in Figure 5.

$$f_{sol,DH} = 1 - \frac{Q_{DHN}}{\sum Q_{\mathrm{bui,cons,i}} + \sum Q_{\mathrm{bui,loss,i}} + Q_{\mathrm{DHN,loss}}} \quad \text{(eq. 1)}$$

$$Q_{bui,cons,i} = Q_{DHW} + Q_{circ} + Q_{SH} \quad \text{(eq. 2)}$$

where Q_{DHW} is domestic hot water, Q_{circ} is circulation losses of DHW distribution and Q_{SH} is space heating.

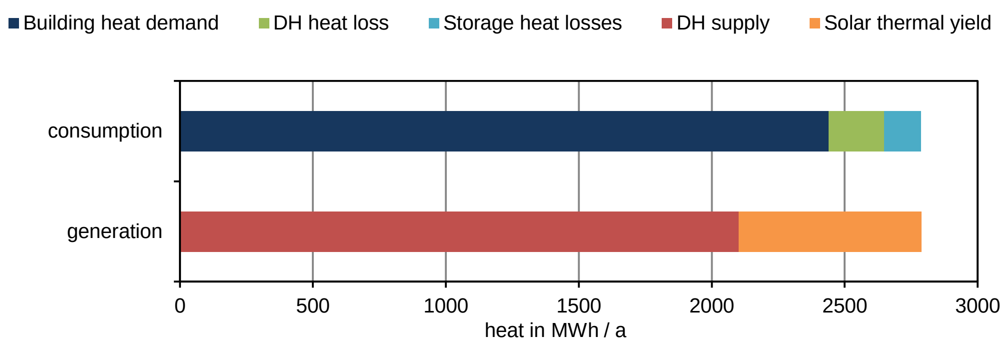

Figure 5: Heat balance for the heat supplying systems and heat consumption systems in the district of "Freiburg-Gutleutmatten" for the period of 15th August 2019 to 14th August 2020

3.1.2. Daily mean power and temperatures at district heating substation system

The daily mean of the power at district heating substation system and the sum of the power of the DH connection units are shown in the Figure 6. The plot is not in order of time but is sorted by the order of the power at district heating substation system. Any day with missing point is excluded. The maximum value of the daily mean power at district heating substation system is at 848 kW. Due to heat losses in the DH network the power at DH level is mostly larger than the sum value of DH connection units. Some exceptional cases seem to be caused by outliers or unexpected malfunctions from supply side considering the supply temperature. The area under the line can be interpreted as a heat in kWh. Therefore, the area between the green and blue line is expected loss for the district heating system. For the entire period, the supply temperature maintains similar values with an average of 70.7 °C while the return temperature shows a trend having low temperatures when power is high. That is due to the fact of too high volume flows at low loads at the DH primary side and indicates hydraulic unbalanced systems.

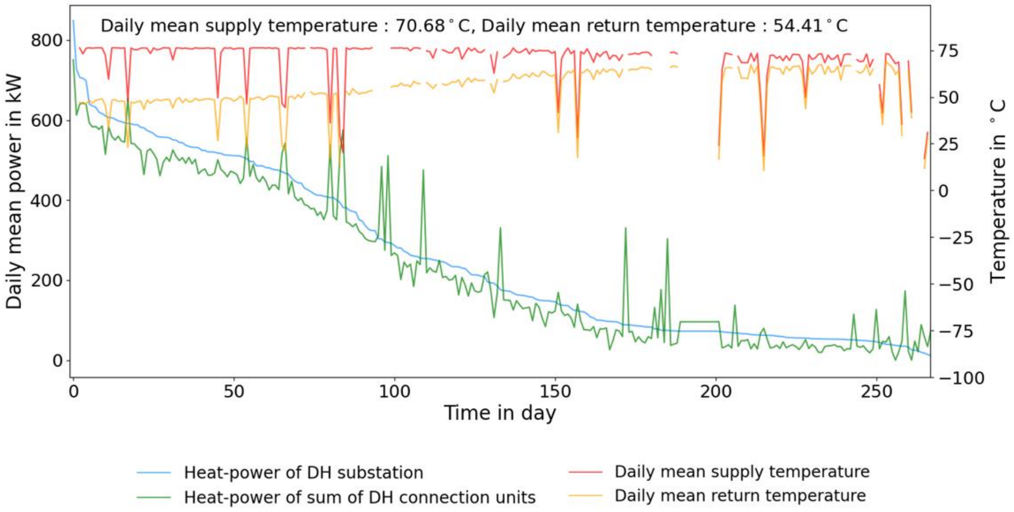

Figure 6: Daily mean for heat and power at district heating system of "Freiburg-Gutleutmatten"

3.2. DH connection units and building heat supply systems

In this chapter, the connection units and its related building heat supply systems are analyzed. The distribution of heat supplies (solar thermal and district heating), heat consumptions for various usages (DHW and circulation and space heating), return flow temperatures and solar thermal fraction are plotted altogether in Figure 7 and Figure 8. Each bar represents each DH connection unit and those are in ascendant order of corresponding floor area. The heat values are calculated as kWh per square meter of heated floor area of each DH connection units. Figure 8 shows the average values for one year of 15th August 2019 to 14th August 2020. Figure 7 shows the seasonal representations with July 2020 in Figure 7a and January 2020 in Figure 7b.

3.2.1. Total heating supply to the distribution system of the building heat supply systems

The demand for domestic hot water was designed at 15 kWh/(m^2_{hfa} a) considering each connection unit. Circulation losses were taken into account with another 15 kWh/(m^2_{hfa} a). In Figure 7a, monthly values for the period of July 2020 are shown, where space heating operation is supposed not to occur due to the related ambient temperatures. By that it becomes clear that design and measured values do not differ much from each other.

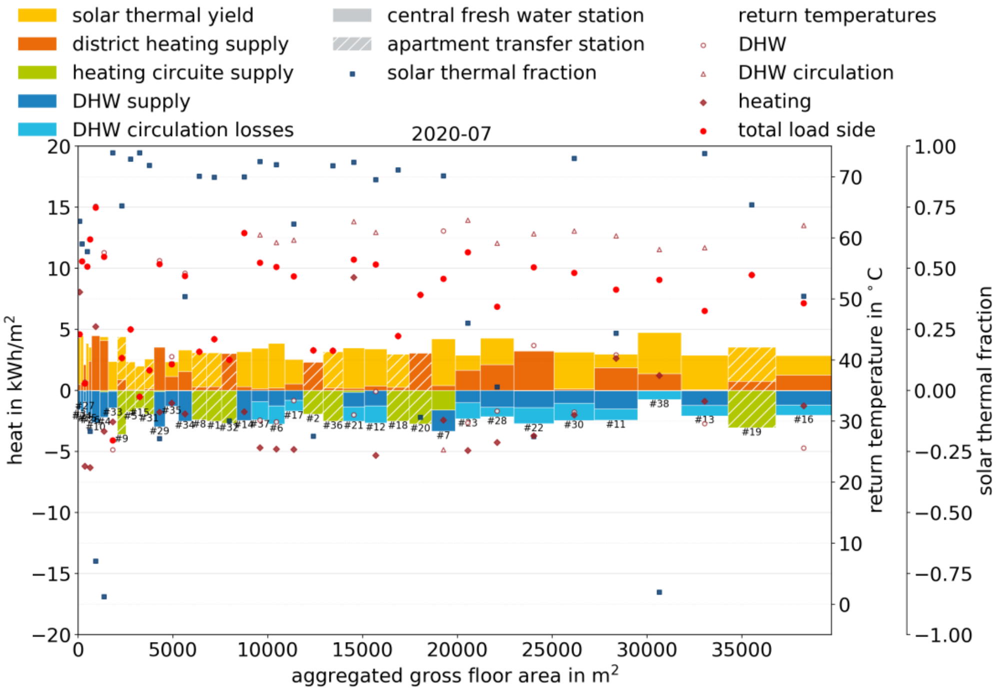

a) Summer (July 2020)

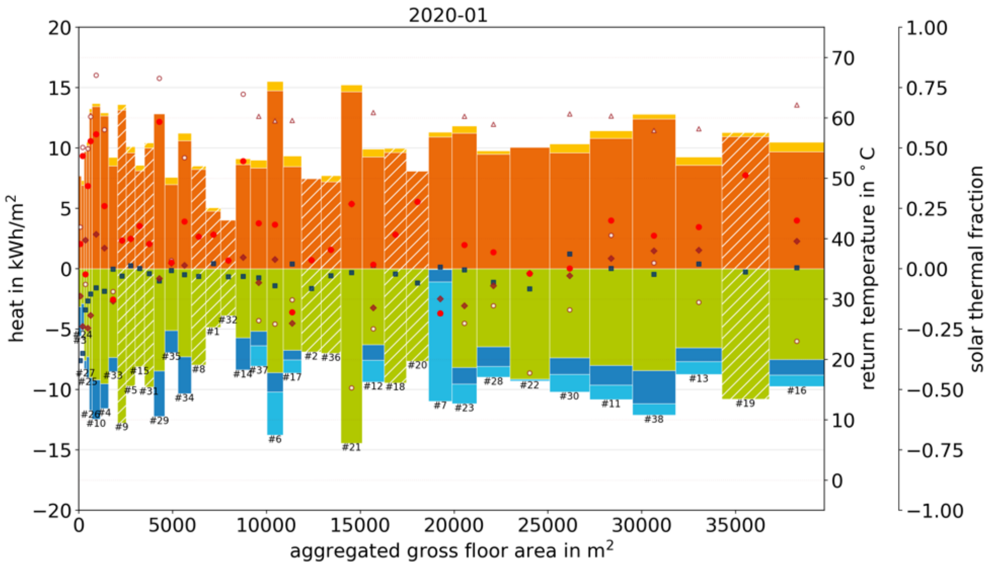

b) Winter (January 2020)

Figure 7: Specific heat supply and consumption, return flow temperatures and solar thermal fraction for each unit for summer (July 2020) and winter (January 2020) period. The specific heat is calculated based on floor area. Each building is represented as a bar

The heat demand for space heating was designed to 35 kWh/(m²$_{hfa}$ a). Regarding the thermal insulation standard KfW-Effizienzhaus 55 (EnEV2014) has been applied under additional requirements of the city of Freiburg i.Br. Thereby heat recovery from ventilation was not a mandatory feature. It can be shown that during the period of 15th August 2019 to 14th August 2020 heat demand is in a range of 33.4 kWh/(m²$_{hfa}$ a) to 85.4 kWh/(m²$_{hfa}$ a) at a mean of 57.7 kWh/(m²$_{hfa}$ a).

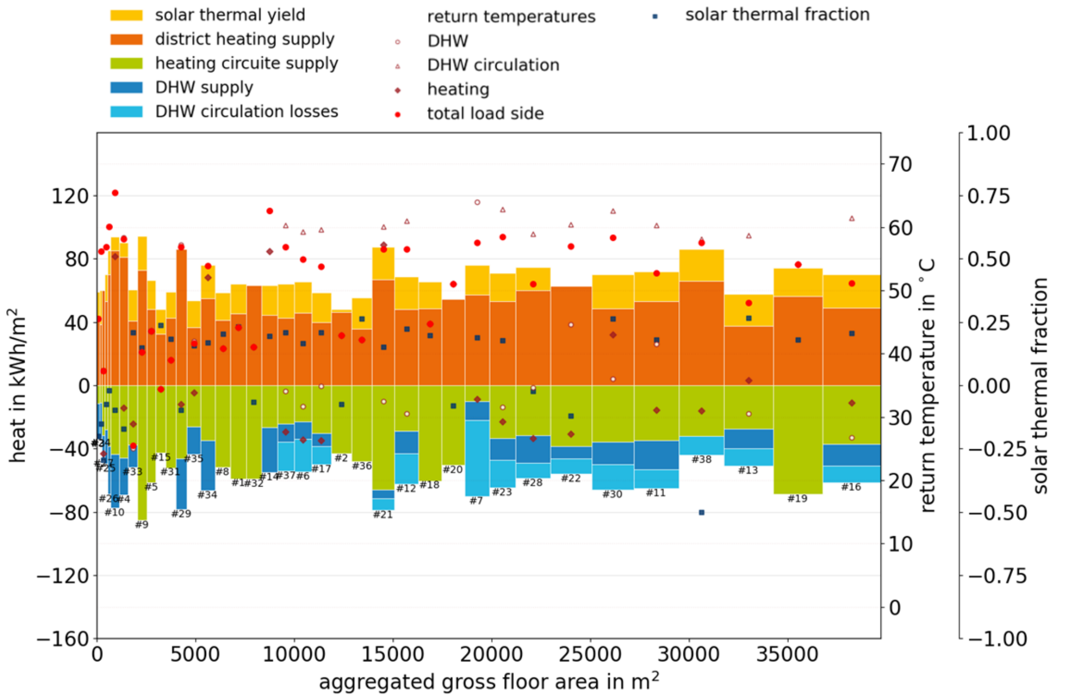

Figure 8: Specific heat supplies and consumptions, return flow temperatures and solar thermal fraction for each unit for one year. The specific heat is calculated based on floor area. Each building is represented as a bar ascendant ordered by the floor area

3.2.2. Solar thermal yield

The same analysis is carried out for the solar thermal yield corresponding to each connection unit. Solar thermal yield has been designed to 350 kWh/(m^2_{Aap} a) by taking 0.05 m^2_{Aap}/m_{hfa} into account. The real installation differs regarding area especially for those two connection units where evacuated tube collectors have been installed instead of flat plate collectors. These systems were designed with 0.036 m^2_{Aap}/m_{hfa}. This means a specific solar thermal yield of 1/3 higher is expected compared to flat plate collectors. The range for the measured yield is in between 8.8 kWh/(m^2_{hfa} a) and 21.5 kWh/(m^2_{hfa} a) with a mean value over all connection units of 18.1 kWh/(m^2_{hfa} a).

3.2.3. Solar thermal fraction

The solar thermal fraction $f_{sol,DH}$ has already been stated for the entire DHN in equation 1. The same relation can be used for each DH connection unit in the district as following equation 3.

$$f_{sol,i} = 1 - \frac{Q_{DHN,i}}{Q_{bui,cons,i}} \qquad \text{(eq. 3)}$$

Looking at Figure 7 it becomes obvious that some systems run on elevated temperatures at the set point temperature sensor of the hot water storage tank and additionally on a high level of effective operating return temperature. This leads to even negative values for f_{sol} for 14 out of 38 systems examined in the stated period of time.

For seasonal comparison, the solar thermal fractions in summer are much higher than the ones in winter as we can clearly see in Figure 8a and 8b. In summer, the heat supply as well as the demand are already very low which would be expected to be no space heating demand any more. Furthermore, the absolute contribution of solar thermal high caused by high solar irradiation. Those factors are resulting larger than 75% of solar thermal fraction for most of buildings. Meanwhile during the winter, both heat supply and demand are increased by two to three times. Most contributions are coming from the space heating expressed as green color. As a result the solar fraction is dramatically decreased.

3.2.4. Temperatures of distribution systems of the building supply systems

As shown in Figure 7 and Figure 8, four categorized return flow temperatures are analysed as below.

- Return flow temperature of distribution for DHW supply ($T_{\mathrm{DHW,ret}}$)
- Return flow temperature of circulation for DHW supply ($T_{\mathrm{DHW,cir,ret}}$)
- Return flow temperature of distribution of space heating supply ($T_{\mathrm{SH,ret}}$)
- Effective return flow temperature of overall consumption circuits of the building supply systems ($T_{\mathrm{load,ret}}$)

For the following analysis it is important to keep in mind the measurement schemes stated in Table 2 that does indicate the hydraulic circuits related to that temperatures.

$T_{\mathrm{DHW,ret}}$ can be observed for the measurement schemes of Type 3 of Table 2. Considering Figure 8 most significant are some quite high values of T_{DHW} at values of more than 40 °C at #22 and close to it in #11. It can be shown that most heat meters detect temperatures in a range of 20 °C to 30 °C.

Considering again measurement schemes of Type 3 of Table 2 temperature of circulation flows can be taken into account as well. Remarkable high temperatures $T_{\mathrm{DHW,circ,ret}}$ can be analysed. Especially in some smaller dimensioned systems this temperature can reach values of about 65 °C. This means that there is no temperature difference of the set-point temperature for DHW preparation and the return flow temperature of DHW circulation. It can be stated that circulation return flow temperatures are far from energy efficient operation.

The operative temperature of return flow for space heating supply $T_{\mathrm{SH,ret}}$ can be analysed for Type 3 and Type 2 of Table 2. By looking at Figure 8 it is shown that this temperature is in a range of about 25 °C to 35 °C. That is about in the expected range due to the fact that most of these buildings include radiator heating systems as well. But also very small buildings like #29 and #35 show quite high temperatures although floor heating systems are installed.

Finally the effective total load operative return temperature for the demonstrated period of one year in Figure 8 can be examined by considering $T_{\mathrm{load,ret}}$. For that value quite a high level is shown at a range of about 60 °C. The analysed values seem to represent quite a contemporary standard DHN system without any measures for energy efficiency.

The return temperatures for DHW, circulation and for some extend space heating can be also compared in different seasons as shown in Figure 7a and Figure 7b. Overall, these DHW related temperatures are basically not related to seasonal effects. In Type 1 of Table 2 the temperatures are effected of the space heating system and so show the characteristics of higher values during summer period of time than during winter periods, where the space heating system does dominate the energy consumption by lower return temperatures.

3.2.5. Temperatures of hot water storage tanks

The hourly mean temperatures of the top of the hot water storage tanks of each DH connection unit can be examined in Figure 9. It becomes obvious that some systems operate at temperatures over the set point of the hot water storage tank sensor for quite long periods of time and others do not do so and so depend on heat supply of the DHN. By that, a shift of solar thermal energy by solar thermal feed in seems to be an attractive option to reduce standard heat supply by DHN as much as possible.

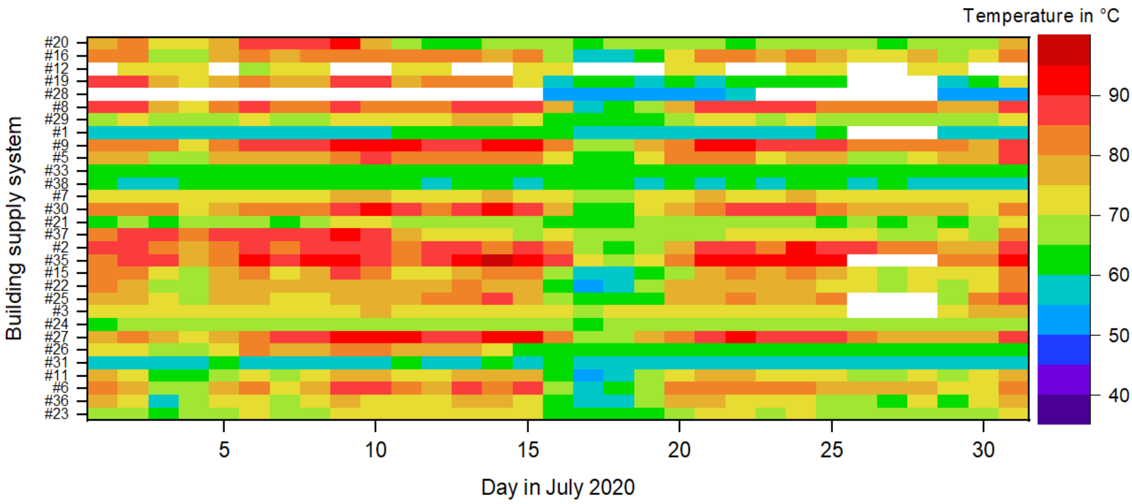

Figure 9: Daily mean temperatures at the set point sensor for district heating supply of the hot water storage tanks of each connection unit for the period of July 2020

4. Intermitting operation of the district heating network

In this section, the heat demand of each building supply system through the connection unit to the DHN is analyzed. In the following Figure 10, the heat demand for the month of July in 2020 is visualized in a time step of 15 minutes. Missing data occurred constantly over all systems and is grey colored.

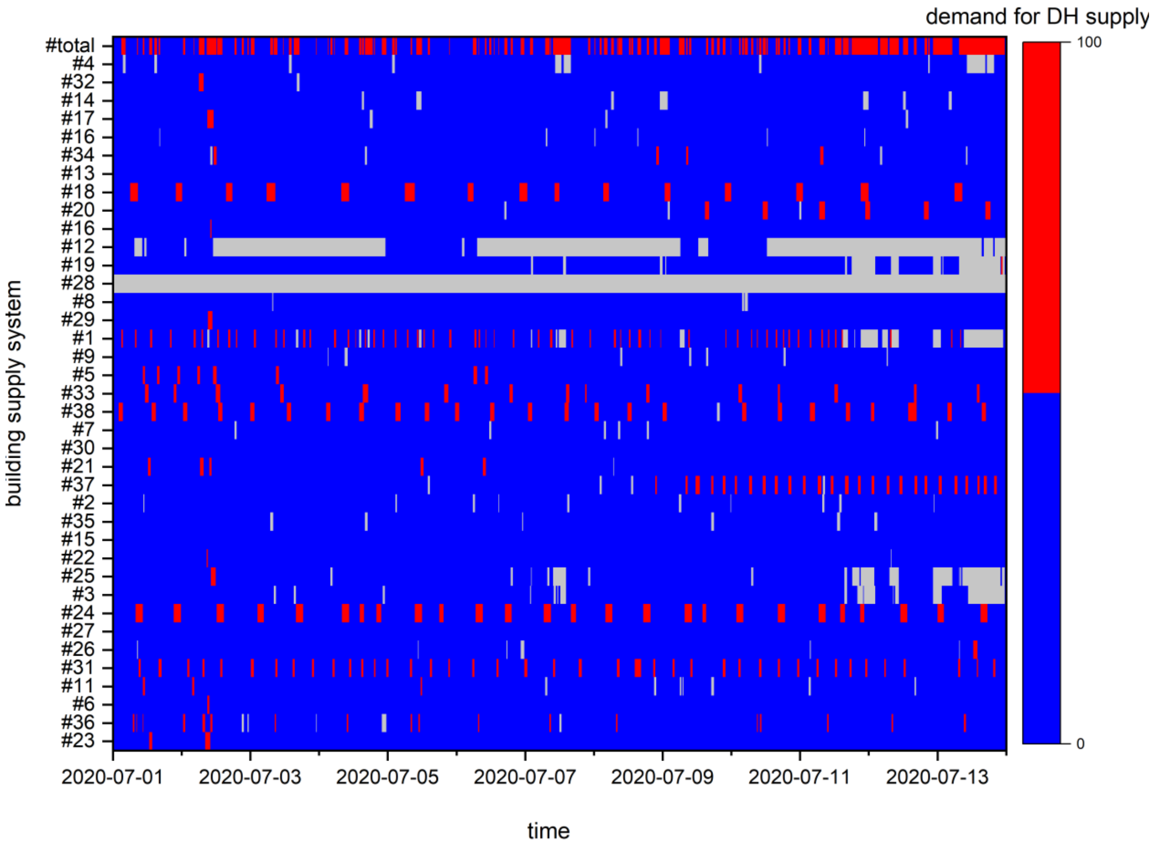

Figure 10: Demand of each building supply system for DH supply in the month of July of 2020 in time steps of 15 min. Heat demand is in red, missing data in grey and no demand for DH supply in blue color. For the consideration of #total the connection units of the

It becomes clear that there are only small periods of time where all building supply systems have no DHN heat demand. Furthermore, missing data at least two of the 38 building supply system (#12 and #28) affects the analysis significantly. In addition, it has to be considered that in the related period of time, three solar thermal systems were not in operation (#18, #24, #28). With the assumption, that the “nan” values have a heat demand (red), 1.5 % of the entire time of that period has to be considered without heat demand of the entire building supply systems connected to DHN. This is a reasonably low number. By taking the three systems out of the analysis and eliminating the two systems with missing data, the result changes to 25 % of time. For that consideration the fictive value “#total” is shown in the graph by its resulting development over time.

5. Conclusions and outlook

The DHN and 38 building supply systems meet in general the energy design parameters ($Q_{\mathrm{DHN,loss}}$ = 9 %, Q_{ST} = 340 kWh/m²$_{\mathrm{Aap}}$, $Q_{\mathrm{bui,cons}}$ = 56 kWh/m²$_{\mathrm{hfa}}$). Due to the large range of dimensioning and different ownership of the 38 building supply systems, it is challenging to establish a district wide standard of concept of control and hydraulic layout. The installation processes and the operation are therefore considered as quite “unhandy”. This is resulting in a reasonable energy efficiency ($\bar{T}_{\mathrm{bui,DHN,return}}$ = 46°C) and the effective solar thermal yields do not achieve the optimum temperature levels as originally designed.

Typical malfunctions are caused by hydraulic components (e.g. stuck valves), the sensor system (e.g. temperature measurement), data transmissions and insufficient and not adequate standard control algorithms. Thereby they seem not to be appropriate to be integrated in recent “standard” digital processes.

Around 50 % of the building supply systems do not operate as designed with regards to its “temperature efficiency”. This results in more operation time of the DHN during summer than expected (e.g. only 25 % time with intermitting operation in July 2020).

The “solar thermal feed in” to support neighboring supply systems and to obtain a more robust DH system regarding DH supply will be taken into operation in a scientific approach by implementing both rule based control and model predictive control algorithms. This sophisticated approach, however, currently suffers from “real world” implementation issues. Results of that will be shown in further future analysis.

The future research will focus on increasing the robustness of the digital systems and to gather further insights into the dynamics of the related hydraulic systems. A centrally managed, digitalized control may increase the robustness of the hydraulic system as demonstrated in the concept developed (Elci, 2018; Oliva et al.,2019).

To achieve this, more research on how to transfer “real world” hydraulic installations into digitalized systems has to be conducted. The challenges should focused along the entire system starting from measurement equipment, hydraulic components, software solutions, data transmission, treatment methods to data analysis and visualization algorithms. Therefore, more insights into the characterization of components and dynamics of hydraulic systems have to be gathered to establish robust MPC or rule based control methods.

Acknowledgments

The project has been partially funded by the German Federal Ministry of Economic and Energy and Badenova Wärmeplus GmbH und Co. KG. The authors take responsibility for the stated issues.

References

Elci, Mehmet (2018): Smarte und Dezentrale Solare Fernwärme. Dissertation. Fraunhofer Verlag.

Elci, Mehmet (2018): Wärmeverteilnetz und Verfahren zur Wärmeverteilung. Deutschland Patent DE102017201197A1.

Oliva, Axel; Herkel, Sebastian; Elci, Mehment; Hemling, Sebastian; Wapler, Sebastian; Ripka, Alexander (2019): EnWiSol. Soarthermie in der städtischen Energieversorgung – Energiewirtschaftliche Analyse und Demonstrationsvorhaben „Freiburg-Gutleutmatten“. http://publica.fraunhofer.de/documents/N-549554.html.

Analysis of Heat Pumps Operated by Solar Photovoltaic Systems for District Heating Systems in Lithuania

Rokas Valancius[1], Rao Martand Singh[2], Andrius Jurelionis[1] and Jurgita Cerneckiene[1]

[1] Kaunas University of Technology, Faculty of Civil Engineering and Architecture, Kaunas (Lithuania)

[2] Norwegian University of Science and Technology, Trondheim (Norway)

Abstract

More than half of all buildings in Lithuania are heated through the district heating systems. Biofuel, natural gas, oil and coal are the most popular fuels, and the usage of waste from incineration is growing rapidly. In smaller towns, boiler houses fired by coal or peat run the district heating systems

Although the use of biofuels and gas is efficient, considered somewhat clean, and inexpensive but the use of polluting fossil fuels raises many questions. It poses a big challenge how a heat production system can be cost effective, low maintenance and environmentally friendly.

This study aims to review and analyse the possibilities of using geothermal energy via heat pumps, and solar photovoltaic systems for heat production in district heating systems in Lithuania.

Keywords: renewable energy, photovoltaic systems, heat pumps, geothermal energy, district heating, energy prices

1. Introduction

Renewable energy segment has continued to grow worldwide in recent years, alongside increasing global energy consumption, decreasing investment in many renewable energy sources, and declining global fossil fuel prices. Furthermore, in a lot of countries, the fluctuating price of fossil fuels has had a serious impact on energy security. Several alternative resources can provide clean, continuous, and renewable energy, such as solar, wind, biomass, hydro, and geothermal energy. Many studies showed that photovoltaic systems (PV) have become the cheapest source of electrical power [PV Magazine 2017; Forbes 2019, DW 2020]. The efficiency of heat pumps increased in last years and price dropped at the same time. Geothermal technologies for heating and cooling grids is still on the development phase, but some studies and demonstration projects showed promising results [Bernati 2016; Think Geoenergy 2020].

Lithuania is a country in the Baltic region of Europe, with an area of 65300 km^2 and a population of 2.8 million. More than 53 % of all buildings in Lithuania are heated through the district heating systems. Biofuel, natural gas or oil are the most popular fuels, and the usage of waste incineration is growing rapidly (see Fig. 1). In smaller towns, there are boiler houses fired by coal or peat [LSTA 2020]. Lithuanian district heating (DH) networks can be classified as conventional network grids with temperatures range in the order of 60–120 °C.

Photovoltaic market blossomed in Lithuania only in 2013. Small-scale solar photovoltaic systems became more attractive after the national energy distribution operator offered the possibility of electrical energy ‘storage’ in the grid after 2015. Only in recent years, photovoltaic system prices have dropped significantly, and a subsidy system for renewable energy sources in single-family buildings, public buildings, factories, etc. has been started [Valancius et al. 2018a].

In 2020, the prices of natural gas for citizens in Lithuania varied from 0.28 to 0.47 €/m^3, depending on the total consumption per calendar year. Electricity prices currently vary from 0.095 to 0.149 €/kWh for households depending on the selected tariff [Ignitis 2020].

doi:10.18086/eurosun.2020.02.07 Available at http://proceedings.ises.org

This study aims to review and analyse the possibilities of using heat pumps, geothermal energy, and solar photovoltaic systems for heat production in district heating systems in Lithuania.

2. Review of Lithuanian District Heating Market

The year 1939 could be entitled as the start of the DH in Lithuania when the power station with 3 “Gebrueder Wagner” steam boilers of the total 2 MW (3 t/h) power was installed to supply thermal energy for a hospital complex in Kaunas City – Kaunas Clinics. The WW II interrupted the development of the sector and the next big installation occurred only in 1947 when it started to supply steam for the paper factory from the nearby Petrašiūnai power station (Kaunas). During period 1949-1955 other stations in the biggest cities of Lithuania (Vilnius, Klaipėda, Šiauliai, Panevėžys) started to work catering both industrial and residential building demands. The speed of the development of DH systems in Lithuania or supplied energy quantity reached its peaks within the period 1967-1990. The total length of the DH network was almost 3000 km in 2017. [LSTA 2020]

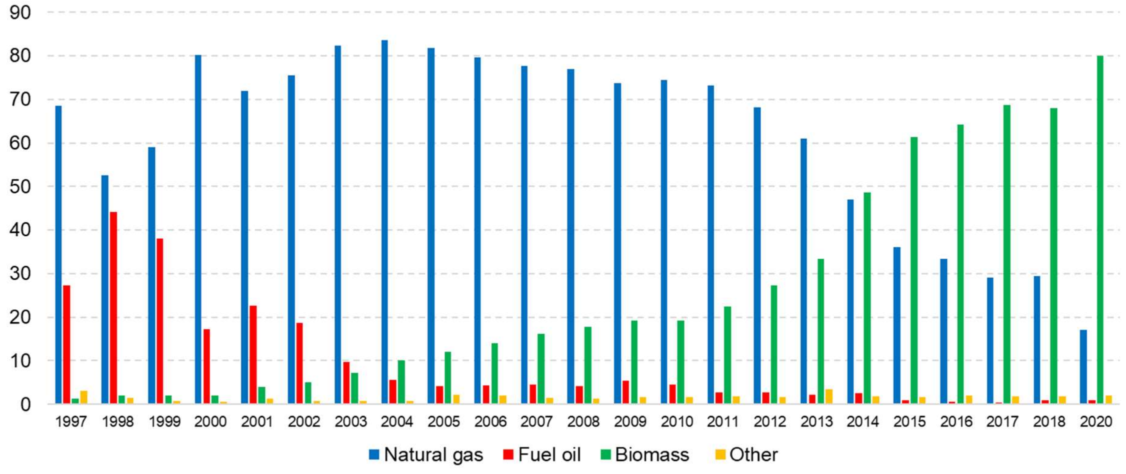

Fig. 1: The structure of fuel in DH production; 1997 – 2020 [LSTA 2020]

According to the statistics of 2017, the annual thermal energy production in DH plants was about 9000 GWh with an installed capacity of approximately 7700 MW. A difficult but also promising period for the DH sector was after Lithuania regained independence from the Soviet Union in 1990. The fossil fuel (gas and oil) prices increased severely but at the same time, all modern worldwide renewable technologies became available. The biggest challenges were to decrease the share of fossil fuel to ensure energy independence for the country and to decrease heat losses in pipeline systems that were relatively high when compared with modern European countries.

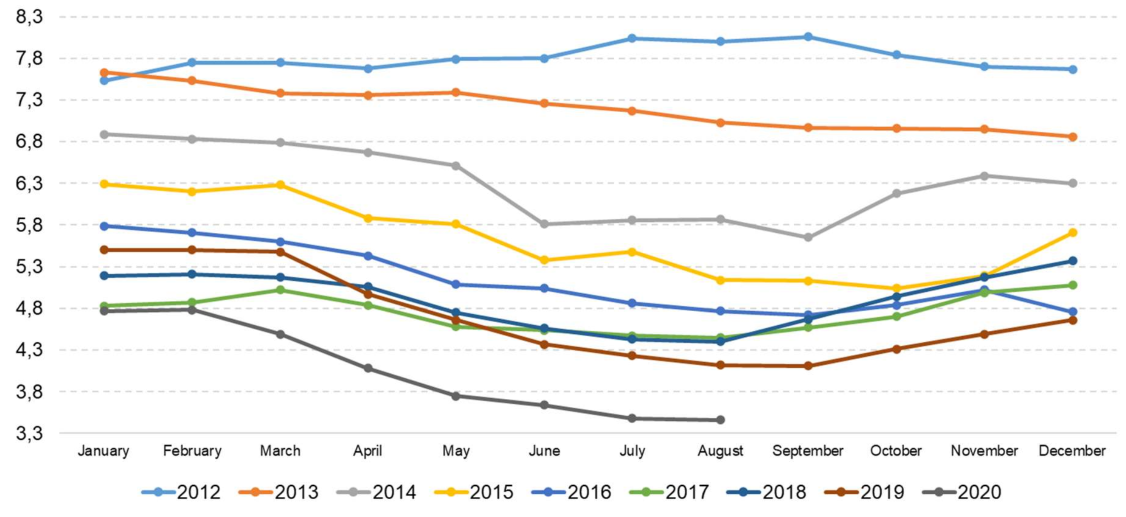

Fig. 2: Thermal energy supplied to DH prices in Lithuania ct/kWh (VAT excluded); 2012-2020 [ENMIN 2020]

Fig. 1 indicates that the oil share started to decrease but natural gas still was the main fuel for quite a long period. Now the most important energy source in the Lithuania DH sector is biomass.

Another technical challenge that still has the potential to be mitigated is the thermal energy transition losses in the DH network. Lithuania, between 1996-2018, decreased it twice to 15% but still didn't reached the heat losses of the modern Western European countries which consist of approx. 10% [Andrews et al. 2012].

The main consumers of the DH in Lithuania are apartment residents (72%), public building users (14%), and private business sector (14%), but apartment residents that make up the greater part sometimes cause payment problems for DH suppliers [ENMIN 2020]. DH systems service about 76% of buildings in the cities or 53% of buildings in the country totally [REGULA 2020]. The price of DH energy supplied for a final user depends on the exact supplier and fluctuates a little during different months but had a tendency to decrease during the recent years (see Fig. 2).

3. PV Systems, Heat Pumps and Geothermal Energy for District Heating Systems in Lithuania

3.1. PV Market in Lithuania

Large-scale solar photovoltaic systems only blossomed in 2013 due to a very good purchase price. Small-scale (up to 10 kW) solar photovoltaic systems became more attractive after the national energy distribution operator offered the possibility of electrical energy 'storage' in the grid after 2015. Only in recent years, photovoltaic system prices have dropped significantly, and a subsidy system has been started [Valancius et al. 2018].

The cost of solar modules and the installation of solar photovoltaic systems has dropped significantly in recent years, and efficiency has increased. At the begging of 2020, the price of small (up to 10 kWp) domestic rooftop PV system in Lithuania has dropped to 780-1000 EUR/kWp. Since 2015 legal entities can install solar photovoltaic systems with a two-sided metering system. It is not allowed for the installed capacity of a solar photovoltaic system to exceed the permissible power consumption set for the facility.

During 2020 the record amount of 9 million EUR is planned for the subsidies to PV systems. The record subsidies in the amount of 4.5 million EUR are planned for the installation of remote solar PV systems or the purchase of the part in solar PV parks. Also, 4.5 million EUR will be allocated to solar PV systems in single-family houses. The compensation for 1 kW of installed solar PV capacity is 323 EUR [APVA 2020].

Also, the compensation in the amount of 100 % of installation cost can be received for schools, hospitals, and other public buildings. Only a feasibility study and a design for the building of a solar PV system have to be prepared on their own expenses. According to the promotional measures for industrial facilities, there is a possibility to receive the support from 30 to 80 % of investments for sustainable resources equipment [APVA 2020]

Some studies and calculations showed that if the state (government) support has been received the payback period of a solar PV in a single-family house varies from 4 to 7 years. The payback period for larger facilities is from 3 to 6 years [LSEA 2020; Valancius et al. 2018]. The payback period depends mainly on the proper selection of the system, the cost of installation and equipment chosen.

The fact that solar power plants can already fully compete with traditional energy sources is also evident by the rapidly growing number of solar power plants in Lithuania, as well as the ongoing tenders for the design and installation of new solar power plants.

More than 1800 new clients were connected between May and November of 2019, in comparison between the years 2015 and 2018 only about 1100 new connections were made. From 2016 to 2020 the number of consumers who produced energy increased from 248 to more than 3000. This number is increasing every week by an average of 80 new producing consumers [ENMIN 2020a].

Thus, the synthesis of a heat pump and a solar photovoltaic system can be an efficient, economical, and environmentally friendly way of producing heat has already been proven in small single-family home systems [Valancius et al. 2018a; Valancius et al. 2019].

3.2. Heat Pumps Market in Lithuania

Heat pumps (HP) have been finding their way into the Lithuanian market since the beginning of the 21st century, and currently, there are many good practice examples in the country, especially in the residential and public sectors. The financial confidence of households has led to increased acquisition of relatively more expensive and yet easier to maintain systems. Growing housing completions also helped the market to boost the usage of HPs. Price decrease and stimulating economic factors pushed up the market growth [Valancius et al. 2019].

A heat pump use is economically advantageous in Lithuania, and the market share of these systems is growing. Studies have reported seasonal performance factor (SPF) ranges within 1.8 and 5.6. The lower SPF values are typically attributed to air source heat pumps (ASHPs), whereas the higher efficiency is achieved by ground or water source heat pump systems [Valancius et al. 2019].

Costs of heating and other energy needs for buildings are the most important factors that influence the renewable energy market. It is evident that in most cases the growth of these markets depends upon subsidies. In Lithuania, limited subsidy systems and funds for renewable energy installations existed since 2005. Depending on a project, it is possible to apply for a subsidy covering from 40% to 100% of initial costs. For example, it is possible to get a subsidy of up to 50% for a single-family building, up to 40% for a multifamily building, and up to 100% for hospitals.

About 8938 units of different HPs were sold in 2017 in Lithuania [Valancius et al. 2019]. It shows that HPs have become the most popular choice within newly constructed, single-family residential buildings and their owners. Current trends indicate that HPs are also slowly replacing gas and solid fuel boilers, as well as district heating in existing buildings. Compared to previous years the sales of HPs in 2017 increased significantly. This growth can be attributed to increased efficiency and reduced capital expenses for ASHP installations. On the other hand, the price reduction of solar photovoltaic systems and new storage technologies helped to grow, not only installations of solar photovoltaic systems, but HPs as well.

The main factor hindering market growth in Lithuania is the high initial cost of these HPs. The payback period of HP systems in most cases is too long to ensure the stable growth of HP applications without governmental grants. Despite the long payback period, the market of HP systems is slowly growing, and the trend continues towards larger HP systems in multifamily buildings, hospitals, hotels, and other large complexes due to support from the EU and other funds [Valancius et al. 2019].

3.3. Geothermal Energy in Lithuania

Researches on the use of geothermal energy in Lithuania started more than 30 years ago. Reviewed geological and geophysical data showed that there is a geothermal anomaly of high energy potential at greater depths in Western Lithuania (see Fig. 3). Its uniqueness is clearly shown by the heat flow indicators: in the background of the surrounding geothermal field of intensity 40–50 mW/m^2, the intensity of the anomalous field of Western Lithuania is 90–100 mW/m^2. The surveys showed that geothermal waters in the south-western part of Lithuania lie at a depth of about 1,200 m, and their temperature reaches about 50 degrees [LGA 2020; Visegrad Post 2016].

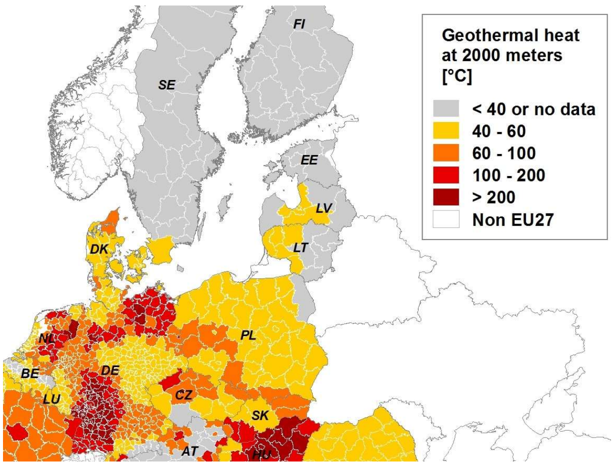

Fig. 3: Geothermal heat at 2000 meters depth [Halmstad and Aalborg Universities 2013]

The cost-effective temperature of about 150ºC, which can be directly used for heating buildings, is found in Lithuania in crystalline bedrock. The minimum depth is in the southern part of Western Lithuania and on the southern coast, where the 150ºC isotherm is 4.3-4.5 km deep. In other areas of Western Lithuania, this temperature is deeper - from 5 km (eg in Klaipėda) to 6 km. For comparison, in the eastern part of Lithuania, its depth reaches 7-8 km [LGA 2020].

3.3.1. First Geothermal Plant in Baltic States

Klaipėda Geothermal Power Plant - was the first geothermal heating power plant in the Baltic States. The construction was commenced in 1997. The project was supported by the Danish Environment Agency and the World Environment Fund, also a loan was received from the World Bank. Klaipėda Geothermal Power Plant operated 4 wells. The pumps pumped 38°C heat geothermal water from a Devonian layer at a depth of 1135 meters. Up to 700 m^3 of water could be obtained from the two wells per hour, however, the ground took back only 450 m^3 of water. In summer, the plant supplied heat to about half of Klaipėda, in winter it produced enough energy for about 10% of the city. The capacity of the geothermal power plant was 10-35 MW. Geothermal loop flow rate - 160–210 m^3/h [LGA 2020].

It was not easy for a state-owned company to introduce new technologies and promoting ecological ideas to gain a foothold in the energy market. Suppliers of traditional heat sources were reluctant to let competitors in. With the start of the operation of the geothermal power plant, the operation load in traditional boilers decreased and fossil fuels were burnt less. Although this power plant is a good example of how geothermal water can be used to solve heating problems, however, the most appropriate management model for the company that would help to reconcile two goals of expanding alternative energy sources and ensuring their economic viability were difficult to achieve. Without price regulation, it was difficult for a loss-making company to repay its loans in the first year. The managers of the company managing the power plant had offered to use part of pumped water for other purposes as well - for medical treatment, fish breeding, road irrigation, and heating of swimming pools.

The company's operations were suspended in 2017, the main reasons for which were high liabilities of the company and a fall in the cost of energy production from traditional energy sources. Investors who were willing to lease this heating company were sought and could not be found. At the beginning of 2019, the company was declared bankrupt. The geothermal power plant is currently conserved and is not monitored. It is not clear whether and how much it would cost to revive the operation of the geothermal power plant.

3.3.2. The Possibilities of Geothermal Energy Usage in Vilkaviškis City

At the beginning of the 21st century, it was proposed to build a power plant in Vilkaviškis and use these waters for heating of the district's apartments and houses, medical therapy, and other purposes. The German company Geothermie Neubrandenburg was interested in the possibility of building a geothermal water power plant in Vilkaviškis. They invested 100 thousand marks in this project. It was estimated that the construction of the power plant should cost about 11 million dollars, and that money could pay for itself in 5 to 10 years. However, after failing to find funding for this project, it was not launched.

In 2009-2010, the possibility of constructing a power plant was floated again. It was planned to build a 7.5 MW geothermal power plant that would significantly reduce the area's carbon footprint. This power plant was supposed to cost 6.3 million EUR and to be built by 2017 but the real work did not start.

Once again, in 2015 it was returned to the ideas of the project implementation. The German company Geothermie Neubrandenburg visited Lithuania again and offered to continue cooperation and seek funding sources.

After receiving the support from the leaders of Vilkaviškis district, at the beginning of this year, it was returned to the ideas of using geothermal energy for heating buildings, hot water preparation, and medical purposes. Whether the project will not be stopped again the time will show.

4. Application Possibilities, Perspectives and Limitations

The use of PV systems and heat pumps in heating networks has good prospects in Lithuania and other countries. Such systems, where the electricity produced by PV can be used for the energy-requiring heat pump, have already found application in single-family homes and other small or medium-sized systems (see Fig. 4).

The required high temperatures of heat carrier is one of the main technical factors limiting the application of geothermal energy and heat pumps in district heating networks in Lithuania. The temperature, depending on the district heating network, the season, and the ambient air temperatures, varies from approximately 60 to 120 degrees. In most cases, it is technically difficult for heat pumps to reach such temperatures, or they do not operate as efficiently as in low-temperature heating systems. The transfer of heating networks in large cities to lower temperatures would be complicated, due to existing traditional heating systems and energy inefficient buildings. However, a reduction of heat carrier temperatures would be possible in small district heating systems by renovating heat supply networks, as well as home heating and hot water systems.

Another factor that impedes the installation of geothermal energy and heat pumps in district heating networks is the relatively low cost of heat produced and supplied in most Lithuanian cities. Especially in cities where heat is produced by burning biofuels.

Also, large initial investments compared to other heat production methods (e.g. burning gas or biofuels) are not attractive to investors. While on the other hand heat pumps and geothermal heating systems have some of the lowest operating and maintenance costs.

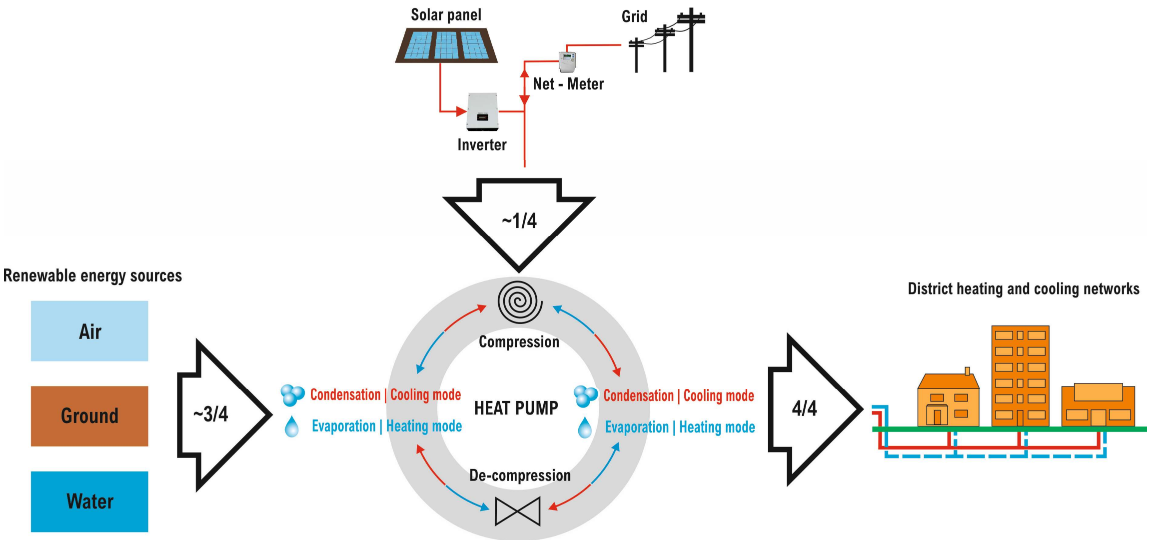

Fig. 4: The principal scheme of a heat pump operated by a PV system for district heating and cooling networks

Though attempts have been made to evaluate the use of geothermal energy and heat pumps in district heating systems, none of the projects have been implemented. In recent years, several studies and calculations have been carried out on how to use absorption heat pumps to raise the temperature of the return heat carrier, several such projects have already reached the design stage.

Although the installation of geothermal energy, heat pumps, and solar PV systems in district heating networks is promising, however presently heat production and supply companies have used the support to invest only in the installation of solar PV systems up to 500 kW to cover electricity needs.

5. Discussions and Conclusions

The high temperature required for heat supply is the main disadvantage of the efficient use of heat pumps. The reduction of temperature of the supplied heat carrier is an important issue for the efficient use of HPs in district heating networks.

The cost of PV systems has fallen rapidly in recent years and different subsidy systems were launched in Lithuania. However, the installation of solar PV systems to satisfy the needs of district heating networks has started recently.

Although the use of combinations of geothermal technologies, heat pumps, and solar photovoltaic systems in district heating systems is promising, this technology is not yet comparable to traditional energy sources, especially when it comes to the price of kWh of energy produced. This was also shown by the example of Klaipėda Geothermal Power Plant as well as in the implementation of other projects.

The state (government) support for the installation of such systems is essential for this technology to spread faster in Lithuania. Also, some good demonstration examples would help to reveal the advantages of this technology for heat producers and suppliers.

6. Acknowledgments

This article is based upon work from COST Action CA18219 Research network for including geothermal technologies into decarbonized heating and cooling grids, supported by COST (European Cooperation in Science and Technology).

7. References

Andrews, D., Riekkola, A. K., Tzimas, E, Serpa, J., Carlsson, J., Pardo-Garcia, N., Papaioannou, I. Background Report on EU-27 district heating and cooling potentials, barriers, best practice and measures of promotion, 2012. ISBN 978-92-79-23882-6

Bernati, R. Deep geothermal energy for heating and cooling. Renewable Heating and Cooling 2016, 67-88. https://doi.org/10.1016/B978-1-78242-213-6.00004-7

APVA 2020. Lietuvos Respublikos aplinkos ministerijos. Aplinkos projektų valdymo agentūra. [accessed 14 June 2020]. Available from Internet: https://www.apva.lt/naujienos/

DW 2020. Falling solar panel prices spell sunny future for clean energy [accessed 3 June 2020]. Available from Internet: https://www.dw.com/en/cheap-solar-energy-prices-explained/a-53590607

ENMIN 2020. Lietuvos Respublikos energetikos ministerija [accessed 25 June 2020]. Available from Internet: http://enmin.lrv.lt/uploads/enmin/documents/files/Nacionaline%20energetines%20nepriklausomybes%20strategija_2018_LT.pdf

ENMIN 2020a. Lietuvos Respublikos energetikos ministerija [accessed 25 June 2020]. Available from Internet: https://enmin.lrv.lt/lt/veiklos-sritys-3/atsinaujinantys-energijos-istekliai/elektros-energija-gaminantys-vartotojai

Ignitis 2020. Ignitis [accessed 2 Juli 2020]. Available from Internet: https://ignitis.lt/lt/elektros-kainos

Forbes 2019. Renewable Energy Is Now The Cheapest Option - Even Without Subsidies [accessed 3 June 2020]. Available from Internet: https://www.forbes.com/sites/jamesellsmoor/2019/06/15/renewable-energy-is-now-the-cheapest-option-even-without-subsidies/#1049df175a6b

LGA 2020. Lietuvos geotermijos asociacija [accessed 3 July 2020]. Available from Internet: http://www.geotermijosasociacija.lt/dokumentai

LSEA 2020. Lietuvos saulės energetikos asociacija [accessed 25 June 2020]. Available from Internet: http://www.lsea.lt/lt/naujienos/aktuali-informacija/saules-elektrine-namu-ukyje-ka-daryti-ir-kiek-tai-uztrunka

LSTA 2020. Lietuvos šilumos tiekėjų asociacija [accessed 23 Juli 2020]. Available from Internet: https://lsta.lt/

REGULA 2020. Valstybinė energetikos reguliavimo tarnyba. [accessed 25 June 2020]. Available from Internet: http://www.regula.lt/Puslapiai/naujienos/2020-metai/2020-rugpjutis/rugpjucio-silumos-kainos-kilovatvalandes-kaina-mazesne.aspx

PV Magazine 2019. Solar on course to become the world's cheapest source of energy within the next 10 years. [accessed 3 Juni 2020]. Available from Internet: https://www.pv-magazine.com/2017/01/03/solar-on-course-to-become-the-worlds-cheapest-source-of-energy-within-the-next-10-years/

Think Geoenergy 2020. Munich targeting geothermal district heating for 560,000 households [accessed 3 June 2020]. Available from Internet: https://www.thinkgeoenergy.com/munich-targeting-geothermal-district-heating-for-560000-households/

Valancius, R., Cerneckiene, J., Vaiciunas, J., Jurelionis, A., Fokaides, P. 2018. Solar Thermal Systems vs. Photovoltaic Systems. Case study: Single Family Building in Lithuania. EuroSun 2018 Conference Proceedings. https://doi:10.18086/eurosun2018.01.11

Valancius, R., Mutiari A., Singh A., Alexander, C., De La Cruz, D. A., E del Pozo Jr., F., 2018a. Solar Photovoltaic Systems in the Built Environment: Today Trends and Future Challenges. Journal of Sustainable Architecture and Civil Engineering. 23(2), 2018a. https://doi.org/10.5755/j01.sace.23.2.21268

Valancius, R., Singh, R.M., Jurelionis, A., Vaiciunas, J. A Review of Heat Pump Systems and Applications in Cold Climates: Evidence from Lithuania. Energies 2019, 12, 4331. https://doi.org/10.3390/en12224331

Visegrad Post 2016. Geothermal Energy: Massive Potential Under Exploited in the V4 [accessed 6 July 2020]. Available from Internet: https://visegradpost.com/en/2016/10/19/geothermal-energy-massive-potential-under-exploited-in-the-v4/

Solar Cooling for the Sunbelt Regions – a new IEA SHC Task

Daniel Neyer[1,2] and Uli Jakob[3]

[1] Neyer Brainworks GmbH, Bludenz (Austria)

[2] University of Innsbruck, Innsbruck (Austria)

[3] Dr. Jakob energy research GmbH & Co. KG, Weinstadt (Germany)

Abstract

In 2016, air-conditioning accounted for nearly 20% of the total electricity demand in buildings worldwide and is growing faster than any other energy consumption in buildings. The lion's share of the projected growth in energy use for space cooling comes from emerging economies. This Solar Cooling initiative in cooperation with SHC TCP and MI IC7 is focusing on innovations for affordable, safe and reliable Solar Cooling systems for the Sunbelt regions. The innovation is the adaptation of existing concepts/technologies to the Sunbelt regions using solar energy, either solar thermal or solar PV.

The importance of the topic is reflected by the high number of interested entities and their feedback to the workplan and its specific content. Although the IEA SHC Task 65 started in July 2020 several ongoing R&D and demo projects of can be put forward in connection to different activities. This paper introduces the IEA SHC Task 65 and its main content, highlights the ongoing research projects and aims to attract a larger audience to get part of the initiative.

Keywords: Solar thermal cooling, PV cooling, sunbelt regions, IEA SHC Task 65, MI IC7

1. Introduction

Global energy demand is growing, although its growth rate is less than in the past. Nevertheless, by 2040 an increase of 30% is projected by OECD (2017). Nowadays air-conditioning accounts for nearly 20% of the total electricity demand in buildings worldwide and is growing faster than any other consumption in buildings (OECD/IEA 2018). The undisputed rationales for the increase are global economic and population growth and thus rising standards of living. Growth in the demand of cooling is especially driven by countries with high temperatures. Three emerging countries (India, China, Indonesia) contribute to more than half of the annual growth rates. Additionally, the efficiency of the air-conditioners varies considerably. The most common systems run at half of the available efficiency (OECD/IEA 2018). If measures are not taken to counteract this increase, the space cooling demand could triple by 2050. With the increase in demand the increase in the cost of electricity and summer brownouts can be considered, which have been attributed to the large number of conventional air conditioning systems running on electricity. As the number of traditional vapor compression chillers grow so do greenhouse gas emissions, both from direct leakage of high GWP refrigerant, such as HFCs, and from indirect emissions related to fossil fuel derived electricity consumption.

Solar air-conditioning is intuitively a good combination, because the demand for air-conditioning correlates quite well with the availability of the sun. The hotter and sunnier the day, the more air-conditioning is required. Interest in solar air-conditioning has grown steadily over the last years. A survey has estimated the number of worldwide installations at nearly 1,350 systems (Mugnier and Jakob 2015). Solar air-conditioning can be achieved by either driving a vapor compression air-conditioner with electricity produced by solar photovoltaic cells or by driving a thermal chiller with solar thermal heat. The knowhow capitalized in OECD countries (Europe, US, Australia, etc.) on solar cooling technology (both thermal and PV) is already very great, but very few efforts have been made to adapt and transfer this knowhow to Sunbelt countries such as Africa, MENA, Asian countries, which are all dynamic emerging economies They are also part of the global increase in demand for air conditioning (AC), where solar cooling could play an important role, as these are all highly irradiated regions of the world. Therefore, the

doi:10.18086/eurosun.2020.02.08 Available at http://proceedings.ises.org

present Task 65 is aiming to develop innovations for affordable, safe and reliable cooling systems for the sunbelt regions worldwide (sunny and hot climates, between the 20th and 40th degrees of latitude in the northern and southern hemisphere). It should cover the small to large size segment of cooling and air conditioning (between 2 kW_c and 5,000 kW_c). The implementation/adaptation of components and systems for the different boundary conditions is forced by cooperation with industry and with support of target countries like UAE, India, etc. through Mission Innovation (MI) Innovation Challenge “Affordable Heating and Cooling of Buildings” (IC7).

2. Sunbelt regions

The Sunbelt countries can be grouped in sunny, hot-arid or hot- humid climates between the 20th and 40th degrees of latitude in the northern and southern hemisphere. According to the climate classification of Köppen-Geiger (Geiger 1954) the range is between Group A (tropical climates), Group B (dry climates) and Group C (temperate climates). A world map which shows the countries inside or touching the Sunbelt on the northern and southern hemisphere is shown in Figure 1. Overall 84 countries can be accounted to the Sunbelt. Table 1 lists all these countries.

Tab. 1: List of countries inside or touching the Sunbelt

Afghanistan	Dominican Republic	Madagascar	Saudi Arabia
Albania	Egypt	Mali	South Africa South Korea
Algeria	Eritrea	Malta	Spain
Argentina	Greece	Mauritania	Swaziland
Armenia	Guatemala	Mexico	Syria
Australia	Haiti	Morocco	Taiwan
Azerbaijan	India	Mozambique	Tajikistan
Bahrain	Iran	Namibia	Thailand
Bangladesh	Iraq	Nepal	The Bahamas
Belize	Israel	New Caledonia	Tunisia
Belize	Italy	New Zealand	Turkey
Bolivia	Jamaica	Niger	Turkmenistan
Botswana	Japan	North Korea	United Arab Emirates
Brazil	Jordan	North Sudan	United States of America
Bhutan	Jordan, West	Oman	Uruguay
Burma	Kuwait	Pakistan	Uzbekistan
Chad	Kyrgyzstan	Paraguay	Vanuatu
Chile	Laos	Philippines	Vietnam
China	Lebanon	Portugal	Western Sahara
Cuba	Lesotho	Puerto Rico	Yemen
Cyprus	Libya	Qatar	Zimbabwe

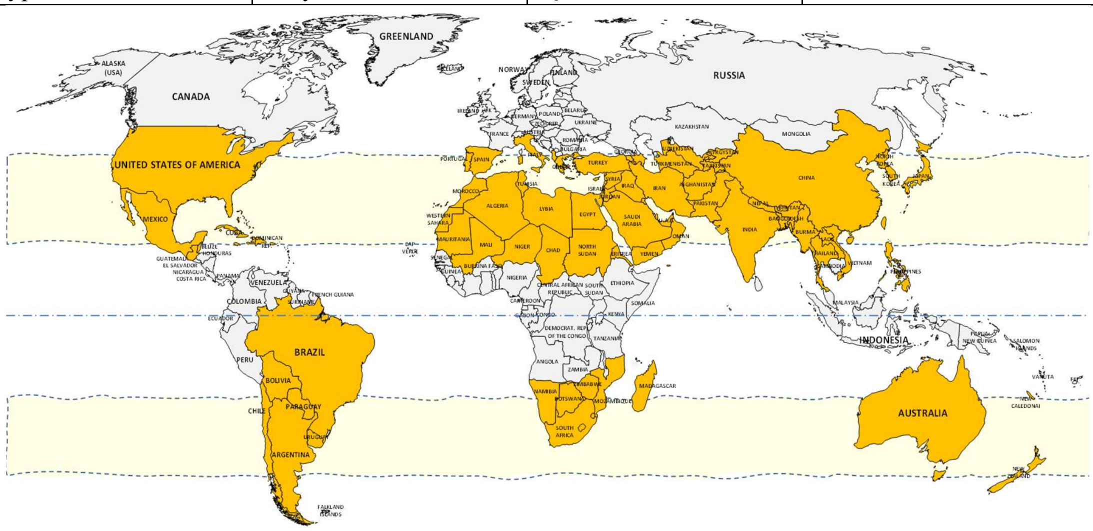

Fig. 1: Countries inside or touching the Sunbelt on northern and southern hemisphere

3. History of previous IEA SHC Tasks on Solar Cooling

Solar thermal/photovoltaic driven heating and cooling systems are belonging to the IEA SHC Strategic Plan Key Technologies (IEA SHC 2009, 2014, 2018), because they have the potential to cover much of the rising demand for air-conditioning by solar energy. The R&D projects of the recent decades, as well as the IEA Solar Heating and Cooling program tasks show the major technical and economic burden. The overall target of all these tasks and the solar heating and cooling program is to encourage a strong and sustainable market.

Initial work is completed in **IEA SHC Task 25** (Henning 1999) dealing with improvement of market conditions, promotion of primary energy and electricity peak reduction and the identification of promising technologies for solar (thermal) air conditioning.

Building on these results, **IEA SHC Task 38** (Henning 2006) is sub-divided into small and large-scale systems. On the one hand, market surveys are conducted to point out the availability and performance of components (Reinholdt et al. 2010) but also the modelling of these components is conducted in detail (Beccali et al. 2003; Bongs et al. 2010; Bourdoukan et al. 2009; Marletta et al. 2010). On the other hand, an initial comprehensive monitoring procedure (Napolitano et al. 2010) is established, existing systems are analysed accordingly (Thür et al. 2010; Jaehnig and Thür 2011) and main learnings are summarized (Preisler et al. 2011). A comprehensive life cycle assessment of solar cooling systems is applied to four case studies (Beccali et al. 2010) outlining not only the detailed energetic and environmental advantages of the solar applications, but also a database of main components for further investigation. In general, the lack of (technical and economic) performance at component and especially at system level (electrical performance, system losses, etc.) are documented in detail.

Thus, the follow up **IEA SHC Task 48** (Mugnier 2011) focuses on quality at component and system level, as well as on market support measures. Different components such as pumps (Helm et al. 2015), collectors (Calderoni 2015), chillers (Melograno et al. 2015) and heat rejection units (Fedrizzi et al. 2014) are analysed and their influence at system level is illustrated. Followed by methods of system characterization (Menegon and Fedrizzi 2015) and assessment criteria for technical and economic performance (Neyer et al. 2015) best practice solutions are identified (Selke and Frein 2015) and design guidelines (Mugnier et al. 2017b) are documented accordingly. Promising system efficiency and economic competitive solutions are found, and policy advice is formulated to further stimulate the market. Beside the solar thermal system solutions, PV driven solutions are entering the R&D of solar cooling.

The latest **IEA SHC Task 53** (Mugnier 2014) on new generation solar heating and cooling focuses on both, solar thermal and photovoltaic supported systems, best practice solutions and on performance, benchmarking and assessment. A comprehensive overview of commercially available existing but also new products is given by Mugnier et al. (2017a). Ongoing not yet published work focuses on new system configurations, storage concepts, life cycle analysis (LCA) and techno-ecological comparisons as well as the technical and economical assessment (Neyer et al. 2016) of the new systems.

4. Objectives of new IEA SHC Task 65

The key objective of this Task 65 is to adapt, verify and promote solar cooling as an affordable and reliable solution in the rising cooling demand across Sunbelt countries. The (existing) technologies need to be adapted to the specific boundaries and analysed and optimized in terms of investment and operating cost and their environmental impact (e.g. solar fraction) as well as compared and benchmarked on a unified level against reference technologies on a life cycle cost bases.

Solar cooling should become a reliable part of the future cooling supply in Sunbelt regions. After completion of the Task 65 the following should be achieved:

- Increase the audience and attention on solar cooling solutions through the combination of MI IC7 and IEA SHC activities and the entire stakeholders.
- Provide a platform for the transfer and exchange of know-how and experiences from OECD countries, already having long experiences in solar cooling, towards Sunbelt countries (e.g. Africa, MENA, Asia, …) and vice versa.

- Support the development of solar cooling technologies on component and system level adapted for the boundary conditions of Sunbelt (tropical, arid, etc.) that are affordable, safe and reliable in the medium to large scale (2 kW-5,000 kW) capacities
- Adapt existing technology, economic and financial analyses tools to assess and compare economic and financial viability of different cooling options with a life-cycle cost-benefit analyses (LCCBA) model.
- Apply the LCCBA framework to assess case studies and use cases from subtasks A and B to draw conclusions and recommendations for solar cooling technology and market development and policy design.
- Pre-assess ‘bankability’ of solar cooling investments with financial KPIs.
- Find boundary conditions (technical/economic) under which solar cooling is competitive against fossil driven systems and different renewable solutions.
- Establishing of a technical and economic data base to provide a standardized assessment of demo (or simulated) use-cases.
- Accelerate the market creation and development through communication and dissemination activities.

5. Task Structure

The Subtask structure is oriented to welcome MI IC7 projects and identified action areas and to support the market creation in Sunbelt regions. The structure is open for all technologies/ components of solar cooling, creating a path from idea to action in the promising market. Existing/new technologies need to be adapted to the boundary conditions of the Sunbelt regions, innovation on system level and demonstration cases create best practice examples, which are analysed with a uniformed method and database adding up to the necessary pool of knowledge to push outreaching dissemination activities (Figure 2).

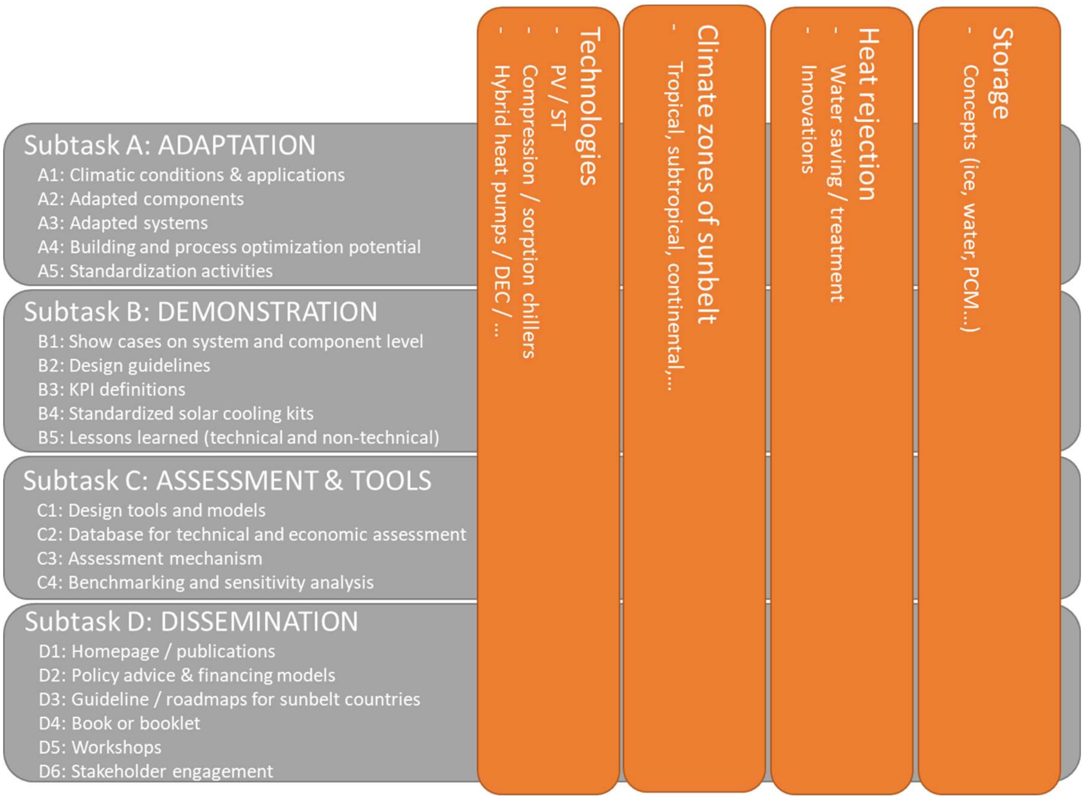

Fig. 2: IEA SHC Task 65 Subtask structure

5.1 Specific objectives of Subtask A

- Deliver a base for market studies for certain components and solar cooling systems
- Document the commercially available equipment compatible with PV electricity supply as well as solar thermal cooling equipment
- Get to know R&D entities / manufacturer working on solar cooling components and systems and their expected technology development, especially according to the key point of climatic adaptation efforts
- Document and show different possibilities of storages on hot / cold side or any other state
- Evaluate the economic potential of adaption to certain climates and application, especially when they can be simplified on component and system level
- Map the technical and economic potential for solar cooling of building / process optimization under different climates and national standards

5.2 Specific objectives of Subtask B

- Update and transfer procedures for measuring the performance of the solar cooling systems and to communicate existing monitoring procedure for field tests or demo projects
- Define and select technical and economic key performance factors for the different stakeholders in the entire project phases
- Documentation of the demonstration plant and their achieved technical and economic KPIs
- Analyse potential technical issues on monitored systems and create lessons learned for the specific climactic conditions
- Report selected pest practise examples of solar cooling in sunbelt countries

5.3 Specific objectives of Subtask C

- Collection of supporting decision tools for technical, economic and financial analyses with different levels of detail from simple pre-study tools to sophisticated dynamic simulation models
- Adapt existing technology, economic and financial analyses tools to assess and compare economic and financial viability of different cooling options with a life-cycle cost-benefit analyses (LCCBA) model
- Apply LCCBA framework to assess case studies and use cases from subtask A and B to draw conclusions and recommendations for solar cooling technology and market development and policy design
- Decision support in various phases of a project cycle from initial project ideas, comparison of technology options to detailed investment grade calculation up to optimization of the operation phase based on case studies and use cases from subtasks A and B
- Analyse the economic and environmental potentials of innovative technical concepts across the sunbelt boundary conditions
- Pre-assess ‘bankability’ of solar cooling investments with financial KPIs
- Analyse and report the technical and economic performance of demonstration plant and selected best practise example of Subtask B.

5.4 Specific objectives of Subtask D

- Establish communication structure with stakeholders
- Disseminate the task results on national and international level
- Provide efficient communication tools such as brochures/guidelines/Roadmaps/Book
- Collect and structure evidence for policymakers of the sunbelt countries
- Stimulate innovation through the communication of shortcomings

6. Acknowledgments

This work has partially received funding from the German Federal Ministry for Economic Affairs and Energy (BMWi / PtJ) under grant agreement No. FKZ 03ETW024B (SorptionTakeOff).

7. References

Beccali, M.; Butera, F.; Guanella, R.; Adhikari, R. S. (2003): Simplified models for the performance evaluation of desiccant wheel dehumidification. In Int. J. Energy Res. 27 (1), pp. 17–29. DOI: 10.1002/er.856.

Beccali, M.; Cellura, M.; Ardente, F.; Longo, S.; Nocke, B.; Finocchiaro, P. et al. (2010): Lif Cycle Assessment of Solar Cooling Systems. A technical report of subtask D, Activity D3. Edited by SHC Solar Heating & Cooling Programme.

Bongs, C.; Dalibard, A.; Kohlenbach, P.; Marc, O. Gurruchaga, I.; Tsekouras, P. (2010): Simulation Tools for Solar Cooling Systems – Comparison for a Virtual Chilled Water System. In D. Chwieduk, W. Streicher, W. Weiss (Eds.): Proceedings of the EuroSun 2010 Conference. EuroSun 2010. Graz, Austria, 28.09.2010 - 01.10.2010. Freiburg, Germany: International Solar Energy Society, pp. 1–8.

Bourdoukan, P.; Wiemken, E.; Kohlenbach, P.; Wurtz, E.; Moser, H.; Morgenstern, A. et al. (2009): Description of simulation tools used in solar cooling. New developments in simulation tools and models and their validation. Edited by SHC Solar Heating & Cooling Programme.

Calderoni, M. (2015): State of the art on new collectors& characterization. IEA SHC Task 48. Edited by SHC Solar Heating & Cooling Programme.

Fedrizzi, R.; Vittoriosi, A.; Romeli, D.; D'Antoni, M.; Fugmann, H.; Nienborg, B. et al. (2014): Heat Rejection Systems for solar cooling. Edited by SHC Solar Heating & Cooling Programme.

Geiger, R. (1954): Klassifikation der Klimate nach W. Köppen. Landolt-Börnstein – Zahlenwerte und Funktionen Landolt-Börnstein – Zahlenwerte und Funktionen aus Physik, Chemie, Astronomie, Geophysik und Technik, alte Serie. pp. 603-607. Edited by Springer.

Helm, M.; Preisler, A.; Neyer, D.; Thür, A.; Sire, R.; Safarik, M. et al. (2015): Pumps Efficiency and Adaptability. IEA SHC Task 48. Edited by SHC Solar Heating & Cooling Programme.

Henning, H.-M. (1999): Solar Assisted Air Conditioning of Buildings - IEA SHC Task 25. Edited by SHC Solar Heating & Cooling Programme. Available online at http://task25.iea-shc.org/, checked on 2/5/2018.

Henning, Hans-Martin (2006): IEA SHC Task 38. Solar Air Conditioning and Refrigeration. Edited by SHC Solar Heating & Cooling Programme. Germany. Available online at http://task38.iea-shc.org/, checked on 2/5/2018.

IEA SHC, T. ExCoC.P. (2009): IEA SHC Strategic Plan 2009-2013. Edited by SHC Solar Heating & Cooling Programme. Available online at http://www.iea-shc.org/Data/Sites/1/documents/strategicplan/SHC_Strategic_Plan.pdf, checked on 1/15/2018.

IEA SHC, T. ExCoC.P. (2014): Solar Heating and Cooling Programme, Strategic Plan 2014-2018. Edited by SHC Solar Heating & Cooling Programme. Available online at https://www.iea-shc.org/Data/Sites/1/documents/strategicplan/shc-strategic-plan-2014-2018.pdf, checked on 10/9/2019.

IEA SHC, T. ExCoC.P. (2018): IEA SHC TCP, Strategic Work Plan 2019 - 2024. Edited by SHC Solar Heating & Cooling Programme. Available online at https://www.iea-shc.org/Data/Sites/1/media/documents/members-area/shc_tcp-strategic_plan_2019-2024-final-aug_2018.pdf, checked on 10/9/2019.

Jaehnig, D.; Thür, A. (2011): Monitoring Results. IEA SHC Task 38. Edited by SHC Solar Heating & Cooling Programme.

Jakob, U.; Kiedaisch, F. (2019) Analysis of a solar hybrid cooling system for industrial applications, SWC 2019-SHC 2019, doi:10.18086/swc.2019.55.07.

Marletta, Luigi; Bongs, C.; Bourdoukan, P.; Evola, G.; Joubert, P.; Moser, H. et al. (2010): Exergy Analysis of Solar Cooling Systems. Edited by SHC Solar Heating & Cooling Programme.

Melograno, P.; Vasta, S.; B., F.; Fedrizzi, R.; Doell, J. (2015): Chiller Characterization. IEA SHC Task 48. Edited by SHC Solar Heating & Cooling Programme.

Menegon, Diego; Fedrizzi, Roberto (2015): Reprot on system characterization in the laboratory. IEA SHC Task 48. Edited by SHC Solar Heating & Cooling Programme.

Mugnier, D. (2011): Quality Assurance & Support Measures for Solar Cooling Systems - IEA SHC Task 48. Edited by SHC Solar Heating & Cooling Programme. Available online at http://task48.iea-shc.org/, checked on 2/5/2018.

Mugnier, D. (2014): New Generation Solar Cooling & Heating Systems (PV or solar thermally driven systems). IEA SHC Task 53. Edited by SHC Solar Heating & Cooling Programme. Available online at http://task53.iea-shc.org/, checked on 1/15/2018.

Mugnier, D.; Jakob, U. (2015): Status of solar cooling in the World. Markets and available products. In WIREs Energy Environ 4 (3), pp. 229–234. DOI: 10.1002/wene.132.

Mugnier, D.; Mopty, A.; Rennhofer, M.; Selke, T. (2017a): State of the art of new generation commercially available products. Edited by SHC Solar Heating & Cooling Programme.

Mugnier, D.; Neyer, D.; White, S. D. (Eds.) (2017b): The Solar Cooling Design Guide - Case Studies of Successful Solar Air Conditioning Design. Berlin, Germany: Wilhelm Ernst & Sohn

Napolitano, A.; Sparber, W.; Thür, A.; Finocchiaro, P.; Nocke, B. (2010): Monitoring Procedure for Solar Cooling Systems, A joint technical report of subtask A and B. International Energy Agency, Solar Heating and Cooling Program, IEA SHC Task 38.

Neyer, Daniel; Neyer, Jacqueline; Thür, Alexander; Fedrizzi, Roberto; Vittoriosi, Alice (2015): Collection of criteria to quantify the quality and cost. Final Deliverable. International Energy Agency.

Neyer, Daniel; Neyer, Jacqueline; Stadler, Katharina; Thür, Alexander (2016): Energy-Economy-Ecology-Evaluation Tool, T53E4-Tool, Tool Description and introductory Manual. Deliverable C3-1, IEA SHC Task 53. International Energy Agency.

Neyer, D.; et al. (2019) Solar Heating and Cooling in hot and humid climates – sol.e.h.² Project Introduction, SWC 2019-SHC 2019, paper ID 10400.

OECD (2017): World Energy Outlook 2017. Paris: OECD Publishing. Available online at https://ebookcentral.proquest.com/lib/gbv/detail.action?docID=5160837.

OECD/IEA (2018): The Future of Cooling. Opportunities for energy efficient air conditioning. Edited by IEA Publications, International Energy Agency.

Preisler, A.; Jaehnig, D.; LeDenn, A.; Jakob, U.; Olsacher, N.; Focke, H. et al. (2011): Installation, Operation and Maintenance Guidelines for Pre Engineered Systems. Edited by SHC Solar Heating & Cooling Programme.

Reinholdt, Lars; Moser, H.; Podesser, E.; Mugnier, D.; Schnider, P.; Nunez, T.; Kuehn, A. (2010): Heat Rejection. Edited by SHC Solar Heating & Cooling Programme.

Roumpedakis, T.; et al. (2019) Performance results of a solar adsorption cooling and heating unit, SWC 2019-SHC 2019, paper ID 11465

Selke, T.; Frein, A. (2015): Collection of Good Practices for DEC design and installation. Edited by SHC Solar Heating & Cooling Programme.

Thür, Alexander; Jaehnig, Dagmar; Núñez, Thomas; Wiemken, Edo; Helm, Martin; Mugnier, Daniel et al. (2010): Monitoring Program of Small Scale Solar Heating and Cooling Systems Within IEA-SHC Task 38 – Procedure and First Results. In D. Chwieduk, W. Streicher, W. Weiss (Eds.): Proceedings of the EuroSun 2010 Conference. EuroSun 2010. Graz, Austria, 28.09.2010 - 01.10.2010. Freiburg, Germany: International Solar Energy Society, pp. 1–8.

Desiccant Based Evaporative Air Condition System for Hot and Humid Climate

Muhammad Ehsan Ullah Kayani [1], Syed Shan E Haider Zaidi [1], Tashfeen Ali Ahmed [1], Usama Ishaq [1], Muhammad Ahmad [1], Roha Ashfaq [1], Hafiz M. Abd-ur-Rehman [1,*]

[1] School of Mechanical & Manufacturing Engineering, National University of Sciences & Technology, H-12 Campus, Islamabad, Pakistan.

* Corresponding author: abd-ur-rehman_@hotmail.com

Abstract

Conventional air conditioning system fails to provide comfort conditions in humid areas. Moreover, the refrigerants used in the conventional air conditioning system not only contribute to the ozone layer depletion in stratosphere but also directly lead to global warming when released in the atmosphere. Desiccant based evaporative cooling system has the potential to be an environmentally friendly alternative to conventional air conditioning system. The objective of this work is to design and develop a solid desiccant based evaporative cooling system for hot and humid environment. The system consists of a radial blade solid desiccant wheel for the extraction of the moisture from the air, a combination of direct and indirect evaporative coolers to lower the temperature of air, and solar air heater to provide the regeneration heat for desiccant wheel. Results indicate that human comfort zone can be achieved in hot and humid conditions using the proposed solar regenerated desiccant based evaporative cooling system with 70% less energy as compared to its counter vapor compression air conditioning systems.

Keywords: desiccant wheel, solar air conditioning, silica gel, evaporative cooler

1. Introduction

The rapidly increasing energy consumption along with its adverse effect on the environment is the most threatening concern of present time(Abd-Ur-Rehman and Al-Sulaiman, 2016, 2014). Buildings are major consumer of the primary energy production and most of the energy is utilized for the purpose of cooling and heating (Abd-ur-Rehman et al., 2018; Abd-Ur-Rehman and Shakir, 2016). The widely used method to condition air is the vapor compression refrigeration method. Providing the comfort conditions to the people not only means to control the sensible load capacity (temperature control) but also the latent load capacity (humidity control). In order to control latent load, the conventional vapor compression system uses the process of condensation to condense the water vapors on the coils when the air is cooled below its dew point temperature and then reheated again up to the required supply conditions. Normally the vapor compression cycle is working on 0.75 sensible heat ratio means 75% of the capacity is used in controlling the sensible loading while remaining 25% of the capacity is used in controlling the latent loading. So, it will provide the comfort conditions when the sensible heat ratio is greater than 0.75 (Mujahid Rafique et al., 2015). The sensible heat ratio in hot and humid areas is found to be less than 0.75. In order to condition air in such areas the conventional vapor compression system can be used but it will require a large amount of electrical energy. Moreover, the excess use of vapor compression system has affected the environment in a harmful way. The ozone layer has depleted because of the chlorofluorocarbons used in a vapor compression air conditioning (VAC) system.

An alternative to the VAC systems is required that can use renewable energy. Evaporative cooling, one of the oldest methods, is one technique to meet cooling demand of the building by utilizing evaporative cooling effect, with less power requirements, about one fourth to that of the VAC systems. Evaporative cooling is a simple, cost effective, and environment friendly technique for space cooling. The evaporative coolers are best fit for temperature control when air humidity is low. While for both temperature and humidity control in hot and humid climate, the effectiveness of the evaporative cooler drops remarkably. Therefore, it is used along with some other dehumidification system. One way to achieve comfort conditions for hot and humid climate is through indirect evaporative coolers. However, the efficiency of indirect evaporative cooler is only around 60-70%. A desiccant dehumidifier, whose purpose is to removes the moisture from the process air, can be used in conjunction with a VAC system, to allow the cooling system to function effectively. Such a system is called, hybrid desiccant cooling system. The use of hybrid desiccant cooling system can not only control the latent load but also reduce running costs and power consumption.

doi:10.18086/eurosun.2020.02.09 Available at http://proceedings.ises.org

The new technology of desiccant based evaporative cooling consists of two components i.e., a desiccant for the moisture removal and an evaporative cooler (Direct or Indirect) for reducing temperature. It significantly reduces the consumption of the electrical energy compared to the conventional vapor compression cycle (Mujahid Rafique et al., 2015). It provides more economical, cleaner and accessible air conditioning. The working mechanism of the system is such that when the hot and humid air enters in the system (ventilated or recirculated), its moisture is extracted by the desiccant. When the moisture is absorbed from this process air, its temperature further rises. The temperature is then lowered by using heat exchangers. For a continuous system, the moisture absorbed by the desiccant should be extracted (regenerated) out from it so that it is able to absorb more moisture from the process air. There is certain temperature needed to regenerate this desiccant that can be done by electric heater, waste heat, or solar energy. The main focus of the experiment is to determine effectiveness of radial desiccant wheel in terms of moisture removal, regeneration requirement and pressure drop but a complete system comprising of fans, coolers and solar air collector is established to evaluate its strength for air conditioning purposes. Table 1 shows the comparison between vapor compression, evaporative cooling, and desiccant based evaporative cooling techniques.

Tab.1: Comparison between vapor compression, evaporative cooling, and desiccant based evaporative cooling techniques.

	Vapor compression system	Evaporative cooling system	Desiccant based evaporative cooling system
Description	Controls latent load by cooling the air below its dew point. The conditions where latent load is overwhelming, its energy consumption is greatly increased. Leakage of refrigerants are harmful to environment and atmosphere.	Direct Evaporative Coolers with operational efficiency 85% and Indirect with efficiency of 60-70%. Perform well for sensible cooling. Ineffective in controlling latent load in hot and humid environment.	Desiccant controls latent load and evaporative coolers control sensible load. Water and air are used as working medium. Regeneration of desiccant using solar air heater substantially decreases the electricity requirements.
Cost of Operation	High	Low	Low
Investment Cost	High	Low	Medium
Energy Source	High grade energy, e.g., Electricity	Low grade energy, e.g., Solar energy, Waste heat	Low grade energy, e.g., Solar energy, Waste heat
Latent Load Control	Accurate	Low	Accurate
Sensible Load Control	Accurate	Accurate	Accurate
Green House Gas emissions	High	Low	Low
Cooling Medium	Refrigerants	Water	Water

2. Proposed design & Experiment

The proposed design of desiccant based evaporative cooling uses a radial blades desiccant wheel to experience lower pressure drop in comparison to honeycomb structure. Figure 1 shows the radial blade wheel and its comparison with honeycomb structure. (D. O'Connor, J. K. Calautit, and B. R. Hughes, 2016).

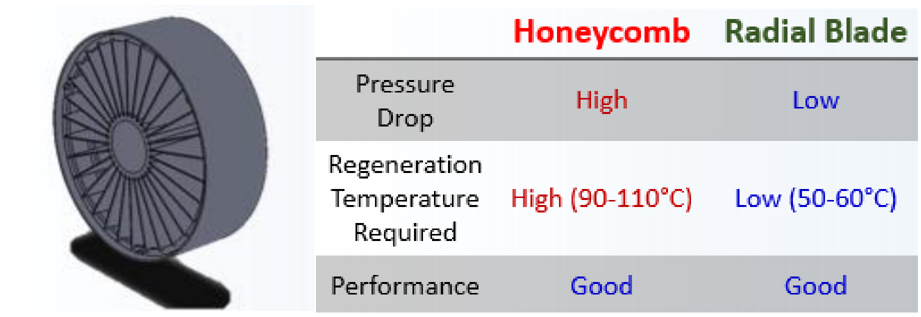

	Honeycomb	Radial Blade
Pressure Drop	High	Low
Regeneration Temperature Required	High (90-110°C)	Low (50-60°C)
Performance	Good	Good

Fig. 1: Radial blades desiccant wheel and its comparison with honeycomb matrix desiccant wheel.

The radial blades are coated with silica gel as a solid desiccant material to absorb moisture. The use of solid desiccant material is advantageous in comparison to liquid desiccant as the later has phenomenon of carry over i.e., travelling of the liquid desiccant through the air to the conditioned space which is harmful for the human. Moreover, the regeneration method used in the liquid desiccant system is comparatively complex (Rafique et al., 2016). Table 2 defines the specifications of the radial desiccant wheel.

Tab. 2: Specifications of Desiccant Wheel

Number of blades	30
Blade Length	110 mm
Blade Width	100 mm
Desiccant Wheel Diameter	300 mm
Weight	3 kg

The schematic diagram and 3-D design of the proposed desiccant based evaporative air conditioning system is shown in figure 2 and figure 3 respectively. The actual prototype is exactly similar to figure 3. Prototype is divided into two air passageways. One carries the hot air from solar air collector for regeneration of desiccant wheel while the second is dehumidified through the wheel and cooled through set of coolers. Aluminum V-Corrugated plate solar air collector is used with a surface area of $1m^2$. The energy consumption of the system (fans, water pump & motor for rotation of desiccant wheel) is 80 Watts. Humid ambient air at 1 enters the processing side of desiccant wheel that consist of radial blades instead of conventionally used honeycomb structure. After dehumidification, temperature of process air increases due to adsorption. Process air is sensibly cooled between state point 2 and 3 by finned tube heat exchanger. It is further cooled between state point 3 and 4 by evaporative cooler before entering to the room. The water from evaporative cooler is first pumped to the heat exchanger and then passes onto the cooling pads. This is done because water after evaporation is cooler. Ambient air at 5 enters the solar air heater where its temperature is increased by solar radiations. This high temperature air at 6 is them passed from desiccant wheel to remove the moisture and exist at point 7 to atmosphere.

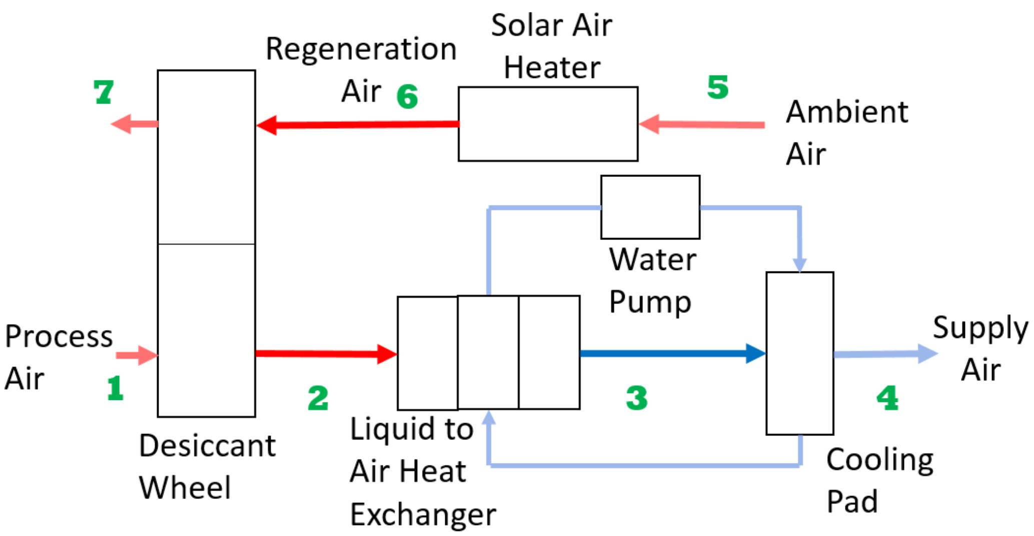

Fig. 2: Schematic diagram of the proposed desiccant based evaporative cooling system.

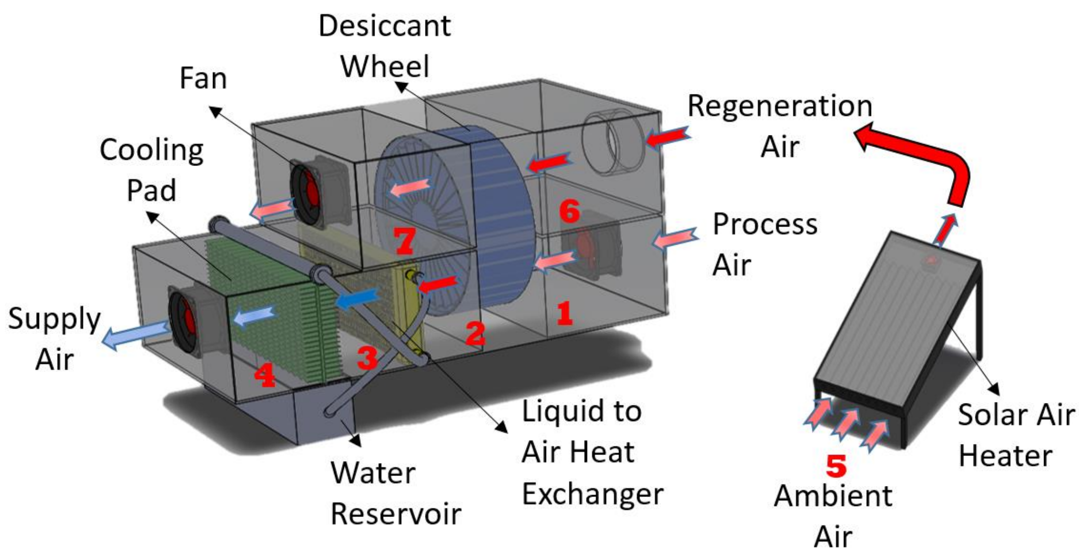

Fig. 3: 3-D diagram of the developed prototype of desiccant based evaporative cooling system.

3. Results and Discussion

The readings for this experiment were taken half an hour after the system was turned on so constant values can be obtained without any fluctuations. Rotation speed for desiccant wheel was kept at 35 Revolutions per hour. The pressure drop in radial desiccant wheel lies in the range of 2 – 10 Pascal depending on number and geometry of blades in the wheel (D. O'Connor, J. K. Calautit, and B. R. Hughes, 2016). The moisture removal in the radial blade desiccant wheel was 11 g/kg of dry air at 35 ˚C dry bulb temp and 65 % relative humidity of inlet process air. The states in table 3 are same as mentioned in figure 3.

Tab. 3: Experimental results of temperature and humidity

State	Temperature (°C)	Relative Humidity (%)	Specific Humidity (g/kg)
Process Air (mass flow rate = 0.035 kg/s)			
1	35	65	23.5
2	45	20	12
3	35	35	12
4	26	75	16
Regenerative Air (mass flow rate = 0.04 kg/s)			
5	35	65	23.5
6	55	23	23.5
7	42	66	35

The point 1 on the psychometric chart figure (4) indicate the ambient air conditions (35 C temperature with 65 % relative humidity) at the inlet of the desiccant based evaporative cooling system. As the ambient air pass through the radial blade desiccant wheel, its moisture is reduced to 20 % but its temperature is increased to 45 ˚C due to dehumidification as shown by point 2 on the psychometric chart. The dehumidified air is then passed through the indirect air-water heat exchanger that reduce its temperature to 35 ˚C without adding moisture in it as shown by point 3 on the psychometric chart. The air is further cooled using cooling pads that acts as an evaporative cooler to reduce the temperature of air and the moisture content increase due to the direct contact of air with water. The point 4 on psychometric chart represents the supply air temperature of 26 ˚C with 75 % relative humidity that is very close to the human comfort zone in summer region defined by ISO standards (ISO/EN 7730) and shown in figure 4 and 6.

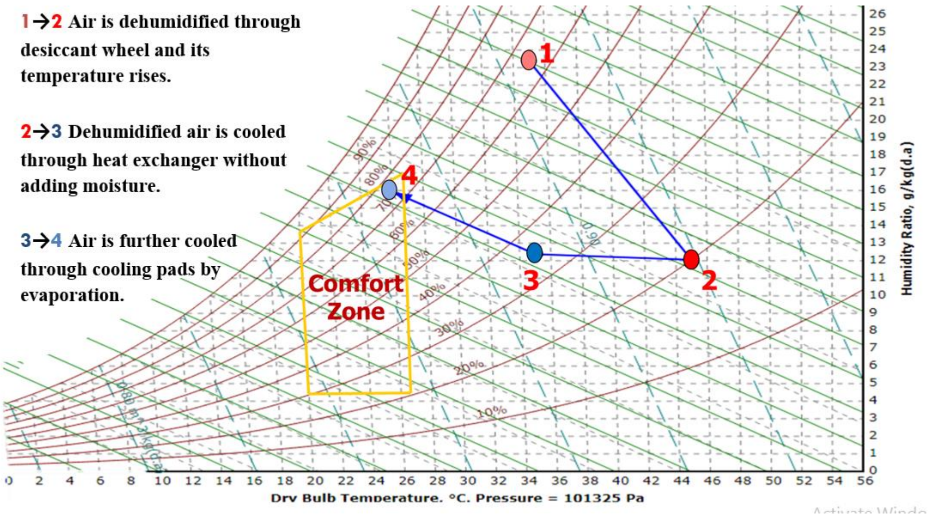

Fig. 4: Psychometric chart showing the temperature and humidity at different locations of the desiccant based evaporative air conditioning system.

The enthalpy difference between state 1 and 4 is 29 kJ/kg. Using mass flow rate, the cooling load comes out to be approximately 1kW. Energy Efficiency Ratio = (Cooling output in BTU/h)/Energy Consumption in Watts

Energy Efficiency Ratio = 3412/80

Energy Efficiency Ratio = 42

Energy efficiency ratio of Vapor Compression Air Conditioners is in the range of 10 – 12 which proves that Desiccant based evaporative coolers can save up to 70 % energy.

The point 5 on the psychometric chart (figure 5) indicate the ambient air conditions (35 ˚C temperature with 65 % relative humidity) at the inlet of the solar air collector. As air passes through solar air heater, its temperature rises but specific humidity remains constant as shown by point 6 on psychometric chart. Finally, this heated air passes through desiccant wheel to regenerate it, lowering its temperature and increasing the humidity content as evident from point 7 on chart.

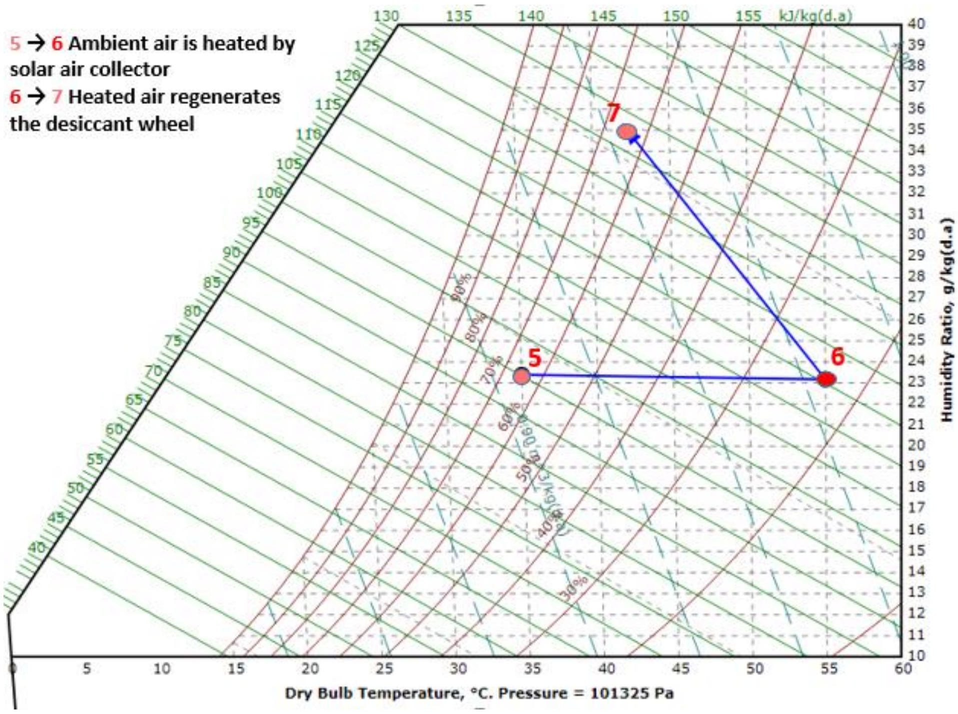

Fig. 5: Psychometric chart showing the temperature and humidity of regenerative air.

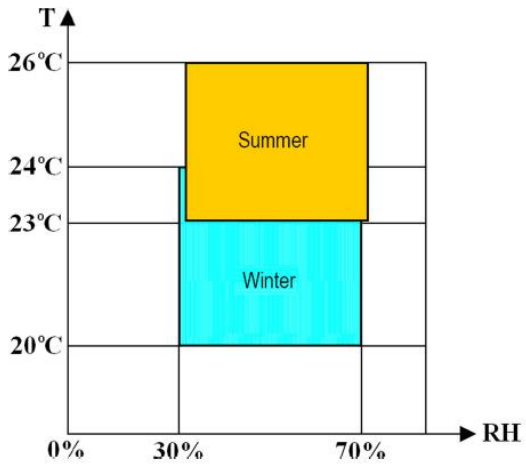

Fig. 6: ISO/EN 7730 chart depicting human thermal comfort conditions (ISO, 2005).

These experimental results needed comparison with industrially manufactured honeycomb desiccant wheel so NOVEL Aire Simulator was used. This software produces practical results corresponding to various inlet conditions across honeycomb desiccant wheels. (Model: WSG 250 x 200) was selected because it was in closest resemblance to the prototype radial desiccant wheel. These desiccant wheels have a lower limit on regeneration temperature so temperature lower than 66 ˚C could not be used for regeneration. Rest of the inlet conditions are mentioned in figure 7.

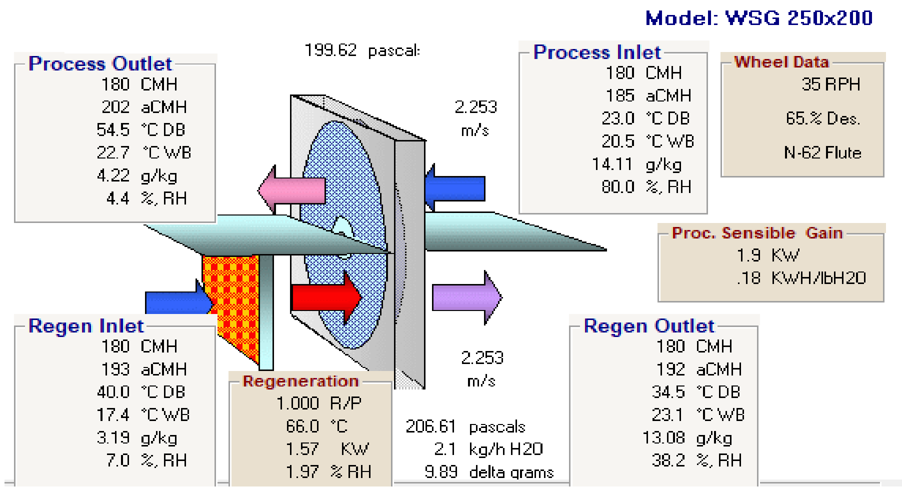

Fig. 7: The NOVEL Aire Technology simulator interface along with inlet and outlet parameters.

It is to be noted that moisture removal rate is almost 10 g/kg of dry air which is less as compared to radial desiccant wheel even with higher regeneration temperature. Secondly the massive pressure drop across the wheel will increase the overall energy consumption of the system.

4. Conclusion and Future Work

A prototype of solar regenerated desiccant based evaporative cooling system is design and tested for hot and humid environment. The radial blades desiccant wheel requires lower regeneration temperatures, experience lower pressure drop in comparison to honeycomb structure matrix and the tested system consumes around 70 % less energy as compared to vapor compression air conditioning systems. However, the system needs further improvement to fully satisfy the human comfort zone. One of the major issues that reduces the efficiency of the cooling process in the system is the carryover of the warm regenerative air when the blades move from the regeneration side to the process side. This warm air is mixed with the process air and increases its temperature. Consequently, the overall cooling effect of the system is reduced. Therefore, the design needs further improvement to avoid the mixing of regeneration and process air.

5. Acknowledgments

The authors acknowledge the anonymous reviewers for providing valuable suggestions.

6. References

Abd-Ur-Rehman, H.M., Al-Sulaiman, F.A., 2016. Optimum selection of solar water heating (SWH) systems based on their comparative techno-economic feasibility study for the domestic sector of Saudi Arabia. Renew. Sustain. Energy Rev. https://doi.org/10.1016/j.rser.2016.04.047

Abd-Ur-Rehman, H.M., Al-Sulaiman, F.A., 2014. Techno-economic evaluation of different types of solar collectors for water heating application in domestic sector of Saudi Arabia, in: IREC 2014 - 5th International Renewable Energy Congress. IEEE Computer Society. https://doi.org/10.1109/IREC.2014.6826977

Abd-ur-Rehman, H.M., Al-Sulaiman, F.A., Mehmood, A., Shakir, S., Umer, M., 2018. The potential of energy savings and the prospects of cleaner energy production by solar energy integration in the residential buildings of Saudi Arabia. J. Clean. Prod. 183, 1122–1130. https://doi.org/10.1016/j.jclepro.2018.02.187

Abd-Ur-Rehman, H.M., Shakir, S., 2016. ENERGY CONSERVATION OPPERTUNITIES AND SOLAR ENERGY INTEGRATION PROSPECTS IN THE RESIDENTIAL SECTOR OF KSA. pp. 11–14. https://doi.org/10.18086/eurosun.2016.11.01

ISO, 2005. ISO 7730: Ergonomics of the thermal environment Analytical determination and interpretation of thermal comfort using calculation of the PMV and PPD indices and local thermal comfort criteria. Management 3, 605–615. https://doi.org/10.1016/j.soildyn.2004.11.005

Mujahid Rafique, M., Gandhidasan, P., Rehman, S., Al-Hadhrami, L.M., 2015. A review on desiccant based evaporative cooling systems. Renew. Sustain. Energy Rev. https://doi.org/10.1016/j.rser.2015.01.051

Rafique, M.M., Gandhidasan, P., Bahaidarah, H.M.S., 2016. Liquid desiccant materials and dehumidifiers - A review [WWW Document]. Renew. Sustain. Energy Rev. https://doi.org/10.1016/j.rser.2015.11.061

Renewable-Energy-Driven Heat Pumps for Districts to Reduce Primary Energy Demand

Elisabeth Schneider[1], Tobias Ohrdes[1], Ann-Kathrin Fries[2], Michael Knoop[3], Oliver Bast[3], Joachim Behnisch[4]

[1] Institute for Solar Energy Research Hamelin, Emmerthal

[2] Institute of Electrical Power Engineering and Energy Systems TU Clausthal, Clausthal

[3] STIEBEL ELTRON GmbH & CO. KG, Holzminden

[4] Energieservice Westfalen Weser GmbH, Kirchlengern

Abstract

Renewably driven heat pumps (HP) have considerable potential for primary energy savings in districts. Using measurement data of an existing district, this article shows the potential of a renewable heat supply using heat pumps. A simulation model for heat pump districts is presented, which has been validated by measured data. Using this model, heat pump control strategies in combination with different supply concepts are developed and examined by simulation. The results show that a renewable coverage of up to 80% can be achieved by using suitable heat pump operation strategies in combination with local photovoltaic (PV) and wind power (WP) as well as battery storages with 6 kWh capacity per building. It is also possible to increase the share of renewable energy to a complete satisfaction of demand. For the scenario considered, this would require a four times higher renewable energy production than the annual demand in the district and a battery capacity of 30 kWh per household.

Keywords: Heat pump, Control strategies, Renewable Energy Prediction, Sector Coupling, District.

1. Introduction

The renewable energy (RE) supply of buildings and districts is an important condition for reducing CO2 emissions. While 45% of electricity in Germany (Fraunhofer ISE, 2019) is generated from renewable energies, the heating sector lags far behind. In private households, 83% of the final energy is used for space heating and domestic hot water (AG Energiebilanzen, 2019a) produced with a renewable heat share of currently only 14% (AG Energiebilanzen, 2019b).

Heat pumps are considered as key technology for the energy transition in the heating sector, since they offer a large potential for reducing CO2 emissions. This potential can be exploited if the electricity for heat pumps is simultaneously covered by renewable energies from wind power and photovoltaic systems. In order to bring supply and demand into line and thus relieve the strain on electrical grids, coordinated operation of heat pumps in districts could be beneficial. Within the framework of the research project "Wind-Solar-Heat Pump Urban District”, a model is being developed that calculates the power and heat requirements in the district on a detailed building level and determines the power flows in the electrical distribution network dynamically over the course of the year. The model enables the evaluation of operating strategies for heat pumps with regard to relieving the load on the electrical distribution networks and reducing the primary energy demand in the district.

doi:10.18086/eurosun.2020.02.10 Available at http://proceedings.ises.org

2. Measurements in real districts

Within the framework of the research project, measurements of electricity and heat consumption are carried out in two districts. One of these districts is the solar district at Ohrberg near Hamelin in Lower Saxony (Germany). It was built around the year 2000 and contains 70 low-energy single-family houses with a specific heat demand of about 45-50 kWh/m²/a (Toelle et al., 2002). All buildings are equipped with water-water-heat pumps connected to a cold local heating network. The cold local heating network is a special feature of this district: it provides an approximately constant source temperature of 12 °C for the heat pumps throughout the year.

In order to make detailed statements about the power consumption of heat pumps and households, more than half of all buildings were equipped with measuring instruments. The electrical power consumption of heat pumps as well as all household loads of these building are recorded in intervals of 10 seconds. In addition, local photovoltaic systems, the local network transformer and the cold local heating network are equipped with measuring instruments. Weather data such as ambient temperature and solar irradiation as well as data from local wind power plants complete the entire energy monitoring of the district.

3. District model

In order to analyze heat pump districts and determine optimization potentials, a simulation model for heat and electricity in the district was developed within the project. The model enables all important components of the building energy supply to be described with their dynamic behavior for each building separately. The building models are integrated into an electrical distribution network at district level. The district simulation is carried out in steps of one minute for any period of time. For this purpose, measured weather data, measured household load profiles and domestic hot water (DHW) profiles generated with "DHWcalc" (Jordan and Vajen, 2017) are used as input. A constant heat pump source temperature of 12 °C is assumed to represent the heating network. No thermal or hydraulic model for the heating network is used. The simulation is used to determine heat load profiles of the individual buildings and the electrical load on the local network transformer. Under dynamic conditions, control strategies at building and district level can be investigated and evaluated for different district structures and building energy systems.

3.1. Building Model

Simplified component models are used to represent the individual buildings and their respective supply system. The models are based on or derived from scientifically recognized models or validated using the TRNSYS simulation program. The individual component models are briefly presented below:

The thermal building model is represented by a node model consisting of RC elements. For this purpose, the two-node building model according to Koene et al. (2014) was extended by two additional nodes for the heating system. The building model is based on a few parameters such as thermal building capacity, thermal resistances of the building envelope and for ventilation and heat gains, which are either determined from building physics data or determined from measurement data using an automated procedure (Schneider et al., 2019).

The thermal model for storage tanks for DHW and heating system were also created based on a few RC elements and validated using TRNSYS type 340 (Drück, 2006). As a reasonable compromise between model accuracy and computational effort, we model the storage tank with four nodes. In addition to direct loading and unloading, it also allows the use of a simplified modeled internal heat exchanger.

The heat pump is modeled following the TRNSYS type 401. The model is based on biquadratic polynomials, which represent the steady-state operating conditions of the heat pump. In addition cycling losses due to heating-up and cooling down processes are modeled via PT1 elements. For air-source heat pumps, de-icing losses are also taken into account (Wetter and Afjei, 1996). The model can be used to represent both fixed-speed and inverter-controlled heat pumps.

For modeling the PV system, the incident angle reflection losses of the module are considered using the approach of the American Society of Heating, Refrigeration and Air Conditioning (1977). Considering the PV module temperature according to G. Tamizhmani et al. (2003), the DC power is calculated. The thermal inertia of the modules is taken into account using a PT1 element. The conversion efficiency of the PV inverter is calculated using the "PerMod" model of HTW Berlin (Weniger et al., 2019).

The battery storage is also modeled using the “PerMod" model from HTW-Berlin (Weniger et al., 2019). This takes into account conversion losses of the power electronics, standby losses, battery losses and static and dynamic control deviations.

The power of the wind turbines is calculated using the characteristics of a 2 kW generator with a hub height of about 100 m.

The models were validated using measurement data from the Ohrberg district.

3.2. Energy Management

The operation of all components is controlled in an energy management module. This enables the implementation of control strategies (CS) at building and district level. The following operating strategies are examined:

1. Decentralized heat demand-driven control strategy (CS 1)

The heat pump starts heating as soon as the temperature in the DHW storage or heating tank falls below the defined lower temperature limit. It stops heating when the upper temperature limit is reached. The heating storage tank heats the building to a setpoint temperature which is also specified. If a battery storage exists, it operates with regard to the electrical house connection point in order to minimize the load transferred to or from the grid. If wind energy is considered for RE production, it is also be included in the battery control strategy.

2. Decentralized control strategy optimized for RE coverage based on forecasts (CS 2)

The following forecasts are generated:

- PV and wind energy forecasts based on ideal weather forecasts,
- ideal forecasts of electrical household loads,
- ideal forecasts of the DHW and of the building heating energy demand, assumed as basis for the prediction of the storage temperatures and the electrical demand of the heat pump.

Based on these forecasts, the temperature limits of the thermal storages as well as the room set temperature of the building are controlled flexibly: First of all, the non-shiftable electrical household loads are subtracted from the renewable energy production. If, as shown in Figure 1, no or insufficient RE is available for heat supply, but a sufficient amount of RE is expected in the near future, the upper and lower temperature limits (T_U and T_L) of the thermal storages are shifted downwards ($T_{U\ new}$ and $T_{L\ new}$), as well as the setpoint room temperature of the building. Because even lower temperature values are permitted for a short time, the system avoids the use of grid power for heating and uses the predicted RE yield for powering the heat pump. The optimal temperature shift was determined by previous simulations in order to maximize renewable coverage. The temperature reduction was chosen in such a way that no significant restrictions in comfort occur for the building temperature or the DHW.

If a surplus of RE is available, as shown in Figure 2, shortly before the end of the predicted surplus, the temperature limits of the storage tanks and the building temperature are shifted upwards ($T_{U\ new}$ and $T_{L\ new}$), so that the surplus of RE energy is stored as heat. Outside the heating period, the heating storage tank is not charged, therefore only the DHW storage tank is available.

If a battery storage exists, it operates similar to CS 1, in order to minimize the load transfer at the house connection point.

3. Central control strategy optimized for RE coverage based on forecasts (CS 3)

The central RE consumption-optimized control strategy at district level is similar to the decentralized RE consumption-optimized operation strategy at building level and uses the same forecasts, with the difference that the energy balances are considered at district level and not at building level. If there is currently no or too little renewable energy available for heat supply and if the forecast renewable energy production is sufficient to cover the entire district demand, the temperature limits of the thermal storages and buildings are reduced here as well. If sufficient renewable energy generation is predicted, the heat pumps of the buildings with the currently lowest temperatures are successively put into operation according to a calculated demand ranking, until the total capacity of the heat pumps almost corresponds to the available renewable energy generation.

All battery storages operate with regard to the local grid transformer, in order to minimize the load transfer for the whole district. All decentralized existing batteries are synchronously charged or discharged. In terms of energy balance, this is identical to a large central district battery storage.

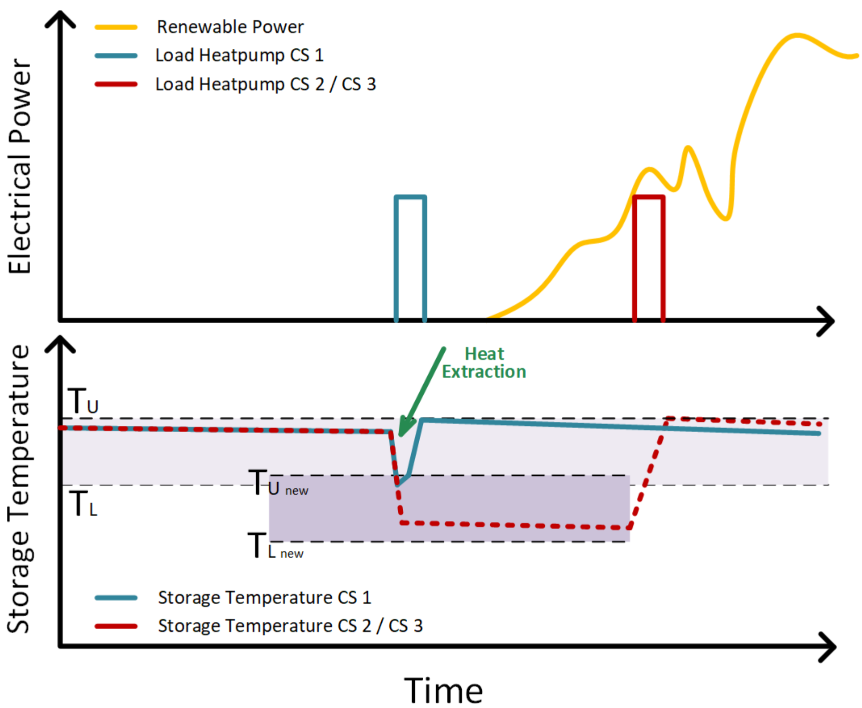

Figure 1: Schematic illustration of reducing the storage temperature limits in CS 2 and CS 3 in case of soon expected EE-production

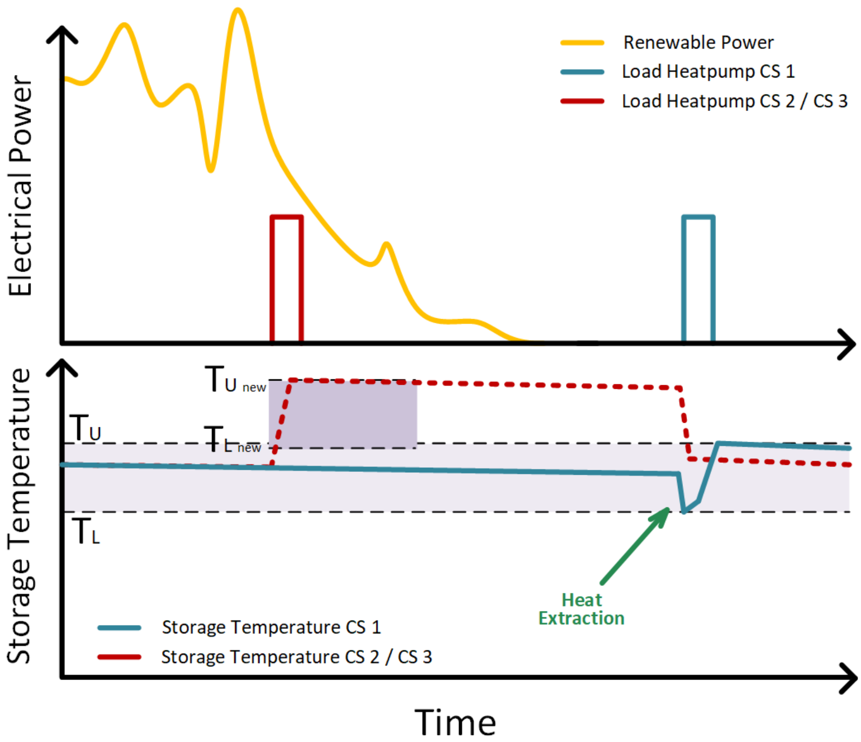

Figure 2: Schematic illustration of increasing the storage temperature limits in CS 2 and CS 3 in case of an energy surplus

4. Scenarios for a renewable district supply

Based on the district model, different supply scenarios are examined. First of all, the supply of RE is analyzed for the monitored Ohrberg settlement. With a heat demand controlled HP control strategy (CS 1) without battery storage, the generation power of PV and wind energy is varied. Figure 3 shows the RE coverage rates for different nominal powers of PV and wind power plants.

The graph shows that with a RE production to energy consumption ratio of 1:1 (energy demand coverage with locally produced renewable energy is 100% in the annual balance), a maximum RE coverage of 32% can be achieved with PV supply alone. If only wind energy is used instead of PV, a maximum degree of coverage of 50% can be achieved. By combining both energy sources, a degree of coverage of up to 56% is possible. The maximum RE coverage can be obtained with a PV-to-wind nominal power between 1:1 and 1:2. The RE coverage rate can be further increased by increasing the RE production/consumption ratio.

Using the developed district model, the potentials of building energy systems and their energy management for RE supply can be evaluated. The basis for the following results is again the district structure as it is found in the district at Ohrberg. In six scenarios, the building energy technology is successively supplemented with additional components, such as energy management for heat pump or battery storage. For the installation of renewable energies it is assumed that the available roof areas of the buildings are covered either with 4.2 kWp PV systems each or with 2.1 kWp PV systems, if combined with 1.4 kW wind energy. The capacities are chosen in such a way that approximately as much energy is generated by RE per year as is consumed in all buildings. The dimensions of the individual components are in the range of those normally found in households.

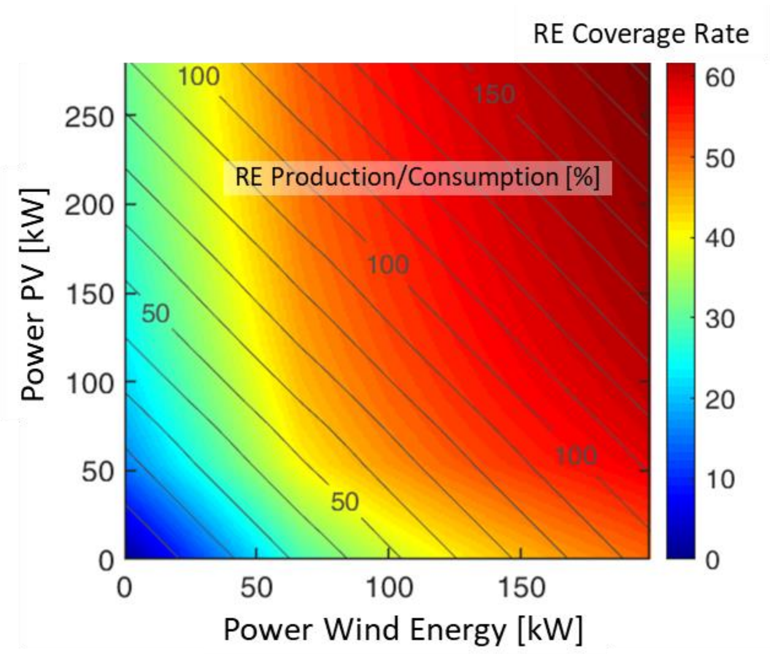

Figure 3: RE coverage depending on nominal PV and wind power

The results of the following six scenarios are shown in Figure 4. It should be noted that the renewable coverage refers only to the electrical energy. A total energy consideration, which also includes the regenerative environmental energy used by the heat pumps, would result in an even slightly higher share of renewable coverage.

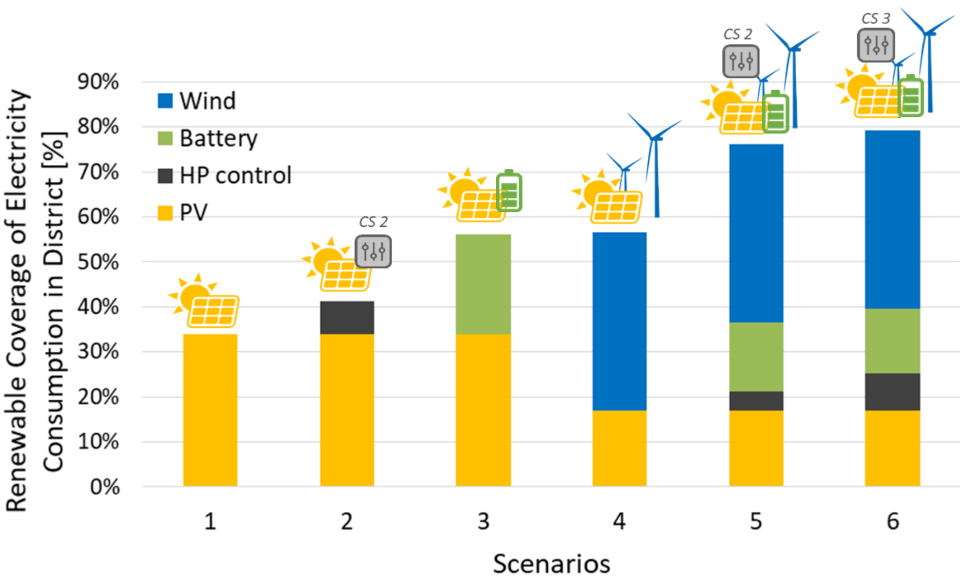

Figure 4: Renewable coverage of electricity consumption in the district for various scenarios with a ratio of renewable energy production to consumption of approx. 1

1. In scenario 1, each building is equipped with a PV system with a size of 4.2 kWp. The HPs are operating on a heat demand basis (CS 1). This results in a renewable coverage of 33% at district level.
2. In scenario 2, the HPs are operating RE consumption-optimized, taking into account the PV systems and based on forecasts at building level (CS 2). This increases the renewable share of coverage to 41%.
3. In scenario 3, the PV systems are each extended by a 6.3 kWh battery storage. Here, the heat demand-driven operation strategy (CS 1) is applied again. The renewable share of coverage is increased to 56%.
4. In Scenario 4, using the heat demand-based operation strategy (CS 1), 2.1 kWp PV and 1.4 kW wind energy are assumed for each building. This already achieves a coverage of 57% without using a battery storage.
5. In scenario 5 all extensions of the previous scenarios are combined. Based on forecasts at building level, the RE consumption-optimized operation strategy (CS 2) is applied. In this way, local renewable coverage rates of 76 % are possible.
6. Scenario 6 is identical to scenario 5 except for the operation strategy, which uses the renewable energy consumption-optimized operation strategy at district level based on forecasts (CS 3). This way, renewable coverage shares of almost 80% are possible.

The results show that the coverage rate of a PV system can be increased by 24% just by using a RE consumption-optimized HP operation strategy, i.e. by shifting the HP operating times. Furthermore, the combination of PV (2.1 kWp) and wind energy (1.4 kW) without battery storage achieves approximately identical RE coverage rates as the PV system (4.2 kWp) in combination with a battery storage (6.3 kWh). This is due to the high simultaneity between wind energy and heat pump utilization, especially in the winter months. Furthermore, it also shows that PV and wind energy complement each other well for the heating requirements of residential buildings during the course of the year. Moreover, it can be seen that a centralized district control is preferable to a decentralized approach, since it allows additional balancing of power between different buildings and through load prioritization a higher amount of RE can be used.

The following section examines which measures are necessary to achieve almost 100% renewable energy supply in the district with scenario 6. For this purpose, the installed PV and wind energy power capacities are scaled in simulations, so that in addition to the 1:1 ratio of RE generation to consumption, ratios of 2:1 and 4:1 are also considered. Additionally, the battery storage sizes are varied. Figure 5 shows the RE coverage rates achieved for the different parameter combinations.

The results show that 100% RE coverage is possible for the scenario considered here with a generation/consumption ratio of four and a battery storage capacity of 30 kWh/building. A battery capacity of 30 kWh per building is quite conceivable if it is assumed that in the future, for example, batteries from electric vehicles will also be included in energy management. With double renewable energy generation and the same battery size, a renewable energy coverage of 97% is already achieved, and with the reference renewable energy generation a renewable energy coverage of 85%. Thus, a significant increase in RE generation capacity would lead to much higher investment cost but relatively little gain in RE coverage.

In general, it should be noted that the limitation of RE coverage is caused by individual low-wind phases in winter, when there is a high demand for heating energy and little PV yield is generated anyway. The achievable annual RE coverage is therefore particularly dependent on the winter weather. Consequently, the presented results are to be evaluated taking into account the specific weather data used.

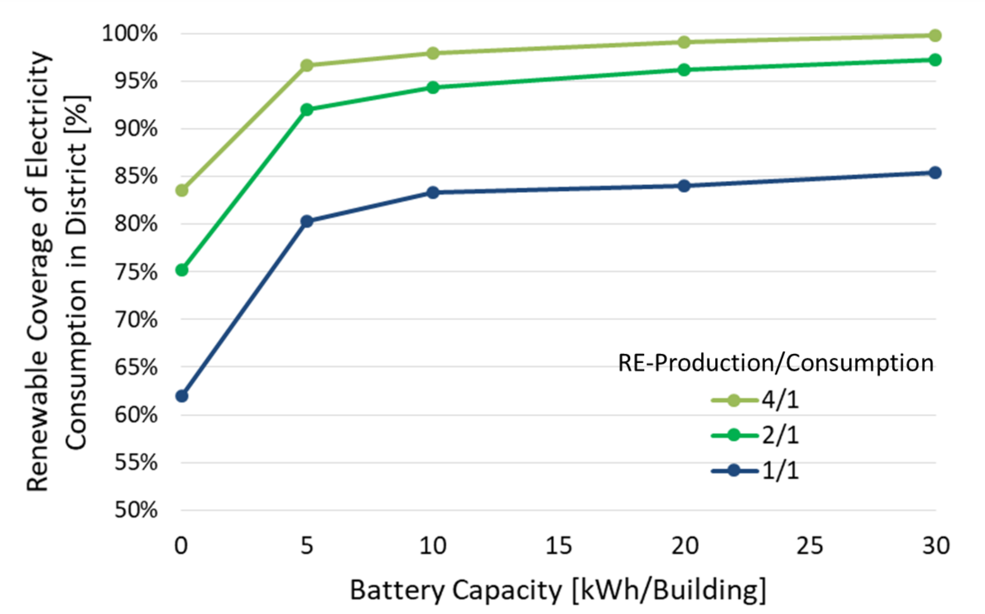

Figure 5: Renewable coverage in the district for supply scenarios with scaled RE generation and different battery storage capacities

5. Summary and outlook

A district model was developed that can simulate the electricity and heat demand over the course of a year. This offers the possibility to evaluate different supply concepts and operating strategies in districts. At first, supply scenarios were considered whose energy production is equivalent to the annual demand in the district. The results show that for an existing PV system an increase of the PV coverage in the building of 24% is possible, just by the use of low-investment measures such as energy management with intelligent heat pump control and weather forecasting. It is also shown that control strategies on district level are more efficient than on building level. For the considered scenario with local PV and wind power and battery storages with 6 kWh per building a central control strategy leads to an increase of 4% of RE coverage in district. Altogether with this RE supply quantity, RE coverage rates up to 80% can be reached in district.

An increase in the degree of coverage up to 95% is possible by doubling the renewable energy production and the battery capacity. For a full renewable supply, a quadrupling of the renewable energy generation and a 30 kWh battery capacity per building are necessary. A reduction in the required renewable energy production capacity would be conceivable if other types of consumers were included in the district balance, e.g. from trade and industry, that have different electrical load profiles and can also provide waste heat for heating residential buildings.

Furthermore, the described forecast-based HP operation strategies can be optimized by means of mathematical optimization methods and with regard to further objective functions. Besides the renewable coverage, objective criterions such as primary energy demand, CO2 emissions or fluctuating exchange prices of electricity are also of interest.

6. Acknowledgement

The research work on which this publication is based was carried out in the frame of the joint project "Wind-Solar-Heat Pump Urban District", with funds of the Federal Ministry for Economic Affairs and Energy under the reference number 03ET1444A based on a resolution of the German Federal Parliament and supported by the Lower Saxony Ministry of Science and Culture. The authors are grateful for the support. The responsibility for the content of this publication lies exclusively with the authors.

7. References

AG Energiebilanzen e.V., 2019 a. Anwendungsbilanzen für die Endenergiesektoren in Deutschland in den Jahren 2013 bis 2017. Berlin.

AG Energiebilanzen e.V., 2019 b. Auswertungstabellen zur Energiebilanz Deutschland. Berlin.

American Society of Heating Refrigeration and Air Conditioning, 1977. ASHRAE standard 93-77. New York.

Drück, H., 2006. MULTIPORT Store - Model for TRNSYS. Institut für Thermodynamik und Wärmetechnik (ITW) Universität Stuttgart.

Fraunhofer ISE. Energy Charts. [Online]. Available: https://energy-charts.de. [Accessed: 26-Nov-2019].

Jordan, U., Vajen, K., 2017. DHWcalc. Universität Kassel, Institut für Thermische Energietechnik, Kassel.

Koene, F.G.H., Bakker, L.G., Lanceta, D., Narmsara, S., 2014. Simplified Building Model of District. BauSIM 2014, Aachen.

Schneider, E., Littwin, M., Knoop, M., Pärisch, P., Kastner, O., Ohrdes, T, 2019. Entwicklung und messwertbasierte Parametrierung eines vereinfachten Gebäudemodells für die Quartiersmodellierung. Symposium Solarthermie und innovative Wärmesysteme 2019, Bad Staffelstein.

Tamizhmani, G., Ji, L., Tang, Y., Petacci, L., Osterwald, C., 2003. Photovoltaic Module Thermal / Wind Performance : Long -Term Monitoring and Model Development For Energy Rating. NCPV Sol. Progr. Rev. Meet., pp. 936–939.

Toelle, L., Otto J., Christoffers, D. D., 2002. Qualitätssicherung mit Informations- und Beratungskampagne bei der Realisierung einer Solarsiedlung. Emmerthal.

Weniger, J., Tjaden, T., Orth, N., Maier, S., 2019. Performance Simulation Model for PV-Battery Systems (PerMod) [Online]. Available: https://pvspeicher.htw-berlin.de/permod/. [Accessed: 08-Nov-2019].

Wetter, M., Afjei, T., 1996. TRNSYS Type – Compressor heat pump including frost and cycle losses, Version 1.1. Zentralschweizerisches Technikum Luzern.

03. Solar Heat for Industrial Processes

Assessment of Process Heating and Cooling Demand for Solar System Installation at Typical Industries in Ethiopia

Yacob G. Hiben[1, 2], Mulu B. Kahsay[1], Johan Lauwart[2]

[1] Thermal and Energy Systems Chair, School of Mechanical and Industrial Engineering, Mekelle University, Mekelle (Ethiopia)

[2] Department of Electronics and Information Systems, Faculty of Engineering and Architecture, Ghent University, Ghent-Zwijnaarde (Belgium)

Abstract

Several measures that bring about structural change in the economy of Ethiopia have been taken to achieve the overall goal of the industrial development strategy. However, the substantial share of fossil fuels and electricity requirement has been increased the burden on the trade balance of the imported petroleum volume and the Ethiopian power system. With this, considerable attention is being given for the energy that can be met alternatively using solar radiation which might be quite effective and economically competitive to the conventional systems as most regions in the country experience a more or less good intensity and uniform solar radiation. The development of an economically feasible and energy-efficient solar system requires validation through studies. Hence, the assessment of heating and cooling potential to identify the load profile which is non-existent mostly is necessary. Looking into the majority of solar industrial processes operating worldwide and the industrial sector development in Ethiopia, a survey has been made of two target industries (leather and soft drinks). The load profile results for the case studies at Sheba Leather Industry P.L.C. and MOHA Soft Drinks S.C showed a considerable demand for hot water at temperatures approximately equal to 35-55 ^{0}C and 60-85 ^{0}C respectively. The corresponding energy needed to heat the amount of water per day is estimated to be 10 GJ and 54 GJ. There is also a significant cold water-glycol solution demand at a temperature approximately equal to 4 ^{0}C with a corresponding estimated daily cooling capacity of 21 GJ in MOHA. These relevant results and the identified daily, weekly, and annual load profile will have significant importance for cost-effective energy substitution and conservation measures.

Keywords: Industrial process, Heating, Cooling, Demand, Ethiopia

1. Introduction

As a developing country, the overall goal of the industrial development strategy in Ethiopia is to bring about structural change in the economy. It is aimed at increasing the GDP share of the industry sector specifically increasing the share of the manufacturing sub-sector (MoI, 2017). With this objective, the government has taken several measures including establishing industrial zones, furnishing the industrial estates with necessary infrastructures (e.g. roads, power, telecommunication, and water), and organizing a responsible organ entrusted with the task of promoting and regulating this activity. The manufacturing sector is characterized by a high concentration of a limited range of light manufacturing activities such as leather, food and beverage, textile, non-metallic, and furniture. The leather and food and beverage products with experienced reordered rankings have been on the top for the last 15 years. Moreover, policymakers have been doing their relentless efforts to promote these industries over the last decade. The industrial facilities are concentrated around the federal and regional capitals and primarily serve the domestic market (Gebreeyesus, 2013; Encyclopedia, 2013).

The industrial productions are supplied by different process streams which absorb heat (cold streams) and release heat (hot streams). Thermal and electrical energy are commonly utilized in the plants to supply the heating and cooling effects (Schweiger et al., 2015; Vannoni et al., 2008). At a global level, the use of fossil fuels is reported as the primary source of energy to meet industrial sector energy demand (Solomon, 1983). Likewise, the in-country electricity consumption was distributed as industrial (37%), residential (37%), and commercial (26%). The volume of petroleum imports mainly used in the transport and industry sector has been growing rapidly (8% annually and higher) over the past ten years (Energypedia, 2013; FDRE, 2013). Thus, considerable attention is being given for the industrial processes that can be met alternatively using solar energy since most regions in the country experience a more or less uniform solar radiation (5 to 7 kWh/m² for 5 to 8 hours) that might be quite effective and economically competitive with conventional heating and cooling systems (UNEP, 2015; REEP, n.d.).

doi:10.18086/eurosun.2020.03.01 Available at http://proceedings.ises.org

Acceptance and dissemination of solar industrial process heating and cooling systems depend on their performance in industrial applications as the same directly affects their economic feasibility. Performance of the systems depend on several parameters such as available solar radiation, climatic conditions at the location of use, characteristics of solar collector used, and required process heating and cooling conditions (delivery temperatures, pressures, and mass flow rate, etc.) (von Storch et al., 2016; Mekhilef et al., 2011; Andersen and Furbo, 2009; Adsten et al., 2002; Rabl, 1981). It is, therefore, crucial to conduct a comprehensive feasibility study of solar energy for industrial processing. As such, quantifying the industrial heating and cooling demand within the plant under full operation is important. In short, the assessment is designed to determine where, when, why, and how heating and cooling is being used.

Many studies dealing with the performance assessment of solar industrial heating process (SIHP) systems have been reported in studies involving low temperature and intermediate temperature systems that could be easily provided by currently commercially available and marketed solar thermal technologies. The amount of thermal energy required in most of the industrial processes is below 250 °C (Ratismith et al., 2017; Ruud Kempener, 2014; ESTIF, 2006; Kalogirou, 2003). From the low-temperature systems, the effect of varying thermal energy demand due to different working patterns on the performance has been analyzed (Thabit and Stark, 1986). In this analysis, it was found that on clear sunny days, 95% of the thermal energy demand can be met with solar energy-based systems. For instance, the performance assessment details of a solar hot water generating system in an Australian food processing industry have been reported in the literature (Proctor and Morse, 1977). From the estimates obtained in the study, it was concluded that about 50% of the total heat demand of the industry that is required between 40 and 60 °C temperatures, could be supplied with available solar collector technologies. In another paper, a study for the application of non-concentrating collectors for the food industry in Germany is presented. In particular, the planning of four solar thermal systems producing process heat for a large and a small brewery, a malt factory, and a dairy are presented. In the breweries, the washing machines for returned bottles were chosen as a suitable process to be fed by solar energy; in the dairy, the spray-dryers for milk and whey powder production; and in the malt factory, the wither and kiln processes. Up to 400 kWh/m^2 per annum were delivered from the solar collectors, depending on the type of collector (Kalogirou and Soteris, 2003). The use of solar energy to drive thermal powered cooling is also used as an alternative to the conventional systems. Most of the solar cooling systems are based on single-effect absorption chillers (which are more commercially developed). Flat-plate collectors or evacuated tube collectors are usually operated at temperatures around 85 ^{0}C to 95 ^{0}C for this purpose (Jaiswal et al., 2016; Allouhi et al., 2015; Lu et al., 2013; Luo et al., 2007; Luo et al., 2006).

Studies dealing with investigations of the economic viability of solar hot water and cooling systems have also reported. For instance, the system's economic viability for the soft drinks and vegetable oil industry in Khartoum (Sudan) was carried out (Ibrahim et al., 1990). The results presented that the solar energy systems have significant potential in industrial processes and substantial life-cycle savings can be achieved. In different case studies carried out in Greece (Karagiorgas et al., 2001), economic evaluation of SIHP systems with conventional fossil fuel-based systems have been made. In this analysis, eight successful applications of solar thermal systems have been identified. The outcomes of the study revealed that due to the increase in the price of liquid fuels, SIHP systems shall become cost-effective. Similarly, the case studies on the adoption of SIHP in the industries in Turkey and Pakistan confirmed the economic viability of SIHP for low temperature (60 to 80 °C) requirements (Muneer et al., 2006; Proctor and Morse, 1977). Abdulateef et al. (Abdulateef et al., 2011) also reported the economic performance of a non-concentrated solar-driven NH_3-H_2O absorption cooling system. As the collector area increases, the solar savings also increase until reaching the optimum collector area. But when the collector area is further increased, though the fuel savings continue to increase, the solar savings are decreased due to the excessive installation costs.

Looking into the majority of the projects on solar industrial process heat plants operating worldwide and the industrial sector development in Ethiopia, this paper investigates the potential in two target industries by case studies at Sheba Leather Industry (SLI) and MOHA Soft Drinks – Mekelle plant (MSD). The study data from these factories represents well the majority of the industries in the group. The study was made during regular operation of the factories and includes identifying: (i) current technologies and source of energy for heating and cooling, (ii) processes demanding hot and cold streams, (iii) working temperature and consumption level of the processes, and (iv) variability of the processes. The outputs of the study will have significant importance in terms of proper identification of daily, weekly, and annual load profiles useful for cost-effective implementation of the solar energy system thereby minimization of the uncertain conventional energy prices and environmental impacts.

2. Materials and Methods

2.1. Description of Target Industries

Leather industries play an important role in processing a by-product or waste from the meat industry, namely the skins and hides into the leather in different mechanical and chemical processing steps such as tanning and re-tanning. The soft drinks industry processes sugar, carbonated water, and other flavors to form soda in different mechanical and chemical processing steps such as washing, sugar dissolving, mixing, and filling. These processes use a large quantity of water and energy in which the quantities vary depending on the specific processes operated, the equipment used, and management practices. The use of old and new technologies also leads to a wide variation in water and energy consumption.

Ethiopia’s leather and soft drinks industry is witnessing rapid growth, as many domestic and multinational firms are being engaged in the production for domestic and global markets. There are around 30 tanneries processing skins and hides to different types of finished leather. The total wet-end installed capacity amounted to around 275 million square feet per year. Ethiopia’s largest livestock population around 58 million cattle (the largest in Africa and 6^{th} in the world), 29 million sheep (3^{rd} in Africa and 10^{th} in the world), and 30 million goats (3^{rd} in Africa and 8^{th} in the world) also represents a largely untapped market. The Ethiopian beverages industry profiles 16 companies including the eight operating units under MOHA which dominates Ethiopia's multi-million dollar carbonated soft drinks market, with a market share of approximately 52%. A population of more than 100 million people also represents a largely untapped consumer market and growing demand for carbonated soft drinks.

In this paper, the typical leather and soft drinks factories in Northern Ethiopia, Tigray region are assessed for the case studies. SLI is located at Wukro city 822 km and MSD is located at Mekelle city 780 km far from the capital Addis Ababa. In SLI, wet-blue processing involves the processing of raw skins and hides into a product called Crust, a stable product that cannot rot and is an internationally traded commodity. The production line in MSD is designed to bottle the processed soda in 330 milliliters bottles in the form of Pepsi-Cola, Miranda, and 7Up.

2.2. Description of Target Utilities

Currently, a considerable amount of fuel, electricity, and water are utilized every year by the utilities and processing units for heating and cooling purposes. The industrial processing units use boilers to produce steam (the vaporized state of water). This contains heat energy and transfers that energy into a variety of processes in the industries. Similarly, chillers are used to produce cold which absorbs energy from a variety of hot stream processes. The general production and distribution flow of steam and cold media is shown in Figure 1.

Fig. 1: General production and distribution flow of steam and cold media

The boiler in SLI and MSD is essentially a cylindrical shape closed vessel inside which water is stored. Basic parts of the boiler are burner, combustion chamber, and heat exchanger. The fuel is stored in fuel tanks. The pressurized fuel is burnt in a furnace and hot gases are produced. These hot gases come in contact with water vessels to transfer their heat to the water and consequently, steam is produced in the boiler. Accumulator or steam head is used for distributing steam that is produced in the boiler to the sections in which the pressure is reduced. Some steam/water is lost through leakages and other losses, so the water recycled into the boiler feed tanks or economizer after steam has been condensed is less in amount and this requires adding more make-up water at a specific interval. Steam flash from the boiler is used to pre-heat the condensate and make-up water in the feed water tank before it is fed into the boilers for reducing fuel consumption. For that matter, solar water heaters to pre-heat the make-up water and condensate return is identified as one option to reduce steam flash and fuel needed.

The refrigeration cycle in MSD chiller starts with a low-temperature and low-pressure (1 ^{0}C, 3.5 bar) gas, ammonia (NH_3) as a refrigerant entering the compressor (45 kW) where it is compressed to high-temperature and high-pressure gas (36 ^{0}C, 13 bar) entering the condenser to reject heat. In the evaporator, heat from the process water-glycol solution boils the refrigerant, which changes it from a high-pressure gas to a low-pressure gas and chills the water-glycol solution supplied to the processes. This cold fluid removes heat from the processes and the warm fluid returns to the chiller. For that matter, one option to reduce compressor power needed would be to use solar water heaters for absorption type refrigeration.

2.3. Description of Target Processes

The heating and cooling processes of the industries are represented by a high share of heat demand in the low to medium temperature range and cooling capacity. In SLI, typical process hot water consumption during production includes tanning and re-tanning of skins and hides. In MSD, typical process hot water and cold water-glycol solution consumption during production include case washing, bottle washing, syrup preparation, and cleaning in the place (CIP).

The wet-blue processed in SLI use hot water and chemicals in two steps. In these stages, hot water is prepared in separate tanks in two ways (1) using the steam condensates from the drying processes in the finishing section for the skin line and (2) using dry steam from the boiler using plate type heat exchanger for the hide line. Finally, hot water is supplied to the tanning and re-tanning drums at the required amount and temperatures. The skin process has two functional drums (3, 000 Liters each) for tanning and five drums (900 Liters each and 2, 000 Liters each) for two stages re-tanning. The hide process has three functional drums (3, 500 Liters each) for tanning and four drums (900 Liters each and 1, 500 Liters each) for two stages re-tanning.

The case and bottle washers use make-up water, steam, and caustic soda to wash the cases and bottles. The washer's nominal performance is mainly dependent on the carbonate content of the caustic. The create washer has once chamber for soaking. The bottle washer has one pre-wash section, two chambers for soaking with different concentrations, and three rinsing sections. These steps are done in the washing machine which consists of a series of tanks and sprays nozzles. There is no direct contact of steam and the bottles in the washing process, except that heat is passed through tube type heat exchanger made of stainless steel in three tanks. When the steam loses heat to the water, it condenses and goes back to the boiler feed water tank or economizer through a return pipe. The freshwater consumption to the sections is on average 12 m^3/hr.

Sugar is dissolved for the preparation of simple syrup (a mixture of hot water and sugar). The sugar dissolver has a motor mounted on it that drives the agitator, to ensure uniform distribution of heat. The water (3, 200 Liters per batch) is heated by steam passing through a steam jacket in between the walls of the cylinder. When the steam loses heat to the water, it condenses and is let out of the steam jacket through a pipe at the lower end of the cylinder. The condensate from the sugar dissolver goes back to the boiler feedwater tank or economizer. Sugar is poured in the heated water, to ensure the sugar dissolves the mixture is allowed to wait for some time. Once the mixture (simple syrup) is prepared, it is cooled while flowing to the final syrup tank in the double heat exchanger. The first step is to exchange heat with cold water from a cooling tower and the second step is to exchange heat with cold water-glycol solution from the chiller. A pumping system (17 m^3/hr) circulates the water-glycol solution from the chiller to the process.

The syrup can be referred to as final syrup when it is at the prescribed volume for the final batch size prepared after adding the beverage base ingredients and topping up with the treated water. This final syrup is ready in the blending tanks for use in the filling and bottling line, provided that it passed all the required quality control tests. Once the mixture (Soda) is prepared in the mixer, it is also cooled while flowing to the filler using a cold water-glycol solution from the chiller. A pumping system (35 m^3/hr) circulates the water-glycol solution from the chiller to the process.

The CIP tanks (10, 000 Liters hot caustic and 10, 000 Liters hot water) is used for cleaning the pipes and the tanks in the manufacturing processes. The water used in CIP is heated using steam and a heat exchanger. The hot water is circulated in the tank according to the changeover matrix for 3-step and 5-step cleaning.

2.4. Data Collection and Processing

Data collection was made within the scope from the identified utilities and processes for the hot and cold streams. Primary data was collected through field visits and measurements in the utilities and processes within the factories. Secondary data was collected from existing recorded data, monthly utility bills, and invoices for delivered energy and fuel, process manual, machine catalog, and literature. The collected data are analyzed to get energy demand and load profiles. A spreadsheet was used to create a database and analyze data.

A detailed material and heat balance with their corresponding assumptions were conducted to evaluate missed data using (1) and (2) (Amiri, 2012):

$$m_{in} = m_{out} \; or \; \rho v_{in} = \rho v_{out} \tag{1}$$

$$Q_{net} = m_1 C_p(\Delta T_1) - m_2 C_p(\Delta T_2) \; = \; m_1(\Delta h_1) - m_2(\Delta h_2) \tag{2}$$

Primary energy consumption is estimated from equation (3):

$$Energy\ Demand = \frac{\rho v C_p (T_{set\ pt} - T_{supply})}{\eta} \quad (3)$$

Fluid properties can be found from property tables or the property equations in Table 1.

Tab. 1: Property equations for liquid water (273.2 K – 600 K) and atmospheric pressure (Zografos et al., 1987)

Equation	Dimension
$\rho = -3.0115 * 10^{-6} T_{av}{}^{3} + 9.6272 * 10^{-4} T_{av}{}^{2} - 0.11052 T_{av} + 1022.4$	kgm^{-3}
$C_p = 1.7850 * 10^{-7} T_{av}{}^{3} - 1.9149 * 10^{-4} T_{av}{}^{2} + 6.7953 * 10^{-2} T_{av} - 3.7559$	$kJkg^{-1}K^{-1}$

Where m is fluid mass flow, ρ is the fluid density, v is fluid volume, C_P is fluid specific heat, T is fluid temperature, h is fluid enthalpy, and η is efficiency.

For continuous processes, hourly basis data were separated according to each hour average production and consumption of the processes obtained from equation (4):

$$consumption\ per\ hour = production\ per\ hour * consumption\ per\ product$$

$$consumption\ per\ hour = \frac{daily\ consumption}{daily\ processing\ time\ in\ hour} \quad (4)$$

For non-continuous (batch) processes, hourly basis data were separated according to an estimated demand of the processes and the schedule which lasts obtained from equation (5):

$$consumption\ per\ hour = \frac{consumption\ per\ batch}{process\ time\ schedule\ in\ hour}, process\ time\ schedule < 1$$

$$consumption\ per\ hour = consumption\ per\ batch, process\ time\ schedule \geq 1 \text{ and first hour} \quad (5)$$

$$consumption\ per\ hour = 0, process\ time\ schedule \geq 1 \text{ and not the first hour}$$

3. Results and Discussion

3.1. Capacity and Availability

The capacity and availability of the factories and processes are summarized in Table 2.

Tab. 2: Capacity and availability of the factories and processes

Description	SLI	MSD
Production capacity	→ 6, 000 pcs of skin/day → 600 pcs of hides/day	→ 36, 000 bottles/h
Running time	→ 16 h/day in two shifts from 6:00 am to 10:00 pm. → Alternate 6 and 5 days a week. → No work during holidays and machine unavailability.	→ 16 h/day in two shifts from 6:00 am to 10:00 pm. → 6 days a week. → No work during holidays, machine unavailability, annual planned maintenance.
Availability	→ 95.84%	→ 82.6%
Actual annual processing	→ 98, 691.3 m^2 Skin → 223, 026.6 m^2 Hide	→ 101 million bottles

3.2. Heating and Cooling Utilities and Consumptions

Essential data on the base heating and cooling utilities can be seen in Table 3.

Tab. 3: Heating and cooling utilities technical and operations data

Industry	SLI	MSD	
Type	Brox Boiler	MINGAZZNI Boiler	HANSA Chiller
Model	SYK100	CEI EN 60439-1	TIWK AP 2 V300 1180
Energy source	Furnace oil	Diesel Fuel	Electricity
Heating value	44 MJ/kg	45 MJ/kg	-

Sp. gravity	0.95 kg/l	0.86 kg/l	-
Cost	16.55 Birr/l	18.30 Birr/l	-
Material out	Steam	Steam	Cold water-glycol solution
Material in	Feedwater	Feedwater	Hot water-glycol solution
Capacity	4000 kg/hr	350 - 4000 kg/hr	393 kW, 55 m^3/hr
T_{out} , P_{out}	100 – 195 ^{0}C, 1 – 10 bar	100 – 190 ^{0}C, 5 - 11bar	4 ^{0}C, 1.5 bar
T_{in}, P_{in}	75 – 85 ^{0}C, 1 - 7 bar	80 – 85 ^{0}C, 5 - 7 bar	11 ^{0}C, 1.5 bar
Efficiency	83%	84%	4.4 COP
Operation schedule	7:00 am - 6:00 pm (11 hrs/day)	7:00 am - 9:00 pm (15 hrs/day)	7:00 am - 8:00 pm (14 hrs/day)
Variability	Continuous with variable load	Continuous with variable load	Continuous with variable load
Output energy consumption	0.029 l/kg	0.0235 l/kg	0.029 kJ/m^3
Production output consumption	2264 kg/hr	2929.26 kg/hr	47.14 m^3/hr
Production loss	2%	2%	-
Production energy consumption	0.35 l/m^2	0.0042 l/bottle	0.0014 kJ/bottle
Production energy cost	5.77 Birr/m^2	0.076 Birr/bottle	0.023 Birr/bottle

3.3. Processes Heating and Cooling Profiles

Most of the processes heating and cooling systems are indirect heating using heat exchangers and cooling coils except the direct heating by the steam flash for the feed water and use of condensate return for SLI skin processing. The heat exchangers have approximately an effectiveness of 0.9. The supply temperatures of make-up and recycled or condensate water are between 22-24 ^{0}C and 70-80 ^{0}C respectively. The water-glycol solution is supplied at 11 ^{0}C. Each process has specific requirements such as water quantity, setpoint temperature, and period of usage. Table 4 provides brief information regarding the processes unit operations considered.

Tab. 4: Working conditions for each industrial process

Industry	Unit operation	Load profile			
		Daily water supply (m^3)	**Setpoint Temp. (^{0}C)**	**Period (hrs)**	**Energy Demand (GJ)**
SLI	Skin tanning	24	35	4 (1 pm - 5 pm)	1.48
	Skin re-tanning	22.50	40	4 (7 am - 10 am, 4 pm - 5 pm)	2.02
		10	50	1 (11 am – 12 am)	1.46
	Hide tanning	21	40	2 (1 pm – 3 pm)	1.88
	Hide re-tanning	18	45	4 (7 am - 10 am, 4 pm – 5 pm)	2.12
		6	55	1 (11 am – 12 am)	1.04
	Feedwater pre-heating	15	80	11 (7 am – 6 pm)	4.70
	(Make-up, Condensate)	10	80	11 (7 am – 6 pm)	3.24
MSD	Create washing	70	40	12 (7 am – 7 pm)	6.28
	Bottle soaking 1	68	75	12 (7 am – 7 pm)	2.01
	Bottle soaking 2	68	80	12 (7 am – 7 pm)	19.36
	Bottle hot water tank	10	60	12 (7 am – 7 pm)	21.24
	Sugar dissolving	9.6	80	3 (7 am – 8 am, 11 am – 12 pm, 4 pm – 5 pm)	2.99
	CIP	20	85	1 (8 pm – 9 pm)	2.21
	Feedwater pre-heating	0.83	85	14 (7 am – 9 pm)	0.28
	(Make-up, Condensate)	41.33	85	14 (7 am – 9 pm)	3.41
	Water-glycol cooling	650	4	12 (7 am – 7 pm)	21.1

The volume of water needed for each process has been determined using the manufacturing characteristics and the recognized standards. The approximate hot water consumption for each factory was: (a) SLI processes, 101.5 m^3/day; (b) MSD processes, 245.6 m^3/day; (c) SLI feedwater, 25.3 m^3/day; and (d) MSD feedwater, 42.2 m^3/day.

The approximate cold water-glycol solution consumption for SMD was 522 m^3/day. The energy needed to heat the amount of water per day is estimated: (a) SLI processes, 10 GJ; (b) MSD processes, 54.1 GJ; (c) SLI feedwater, 7.94 GJ; and (d) MSD feedwater, 3.69 GJ. The approximate daily cooling capacity is estimated at 21.1 GJ. A quasi-repeated hourly load profile for the working days and weeks in a year is illustrated in Figure.2.

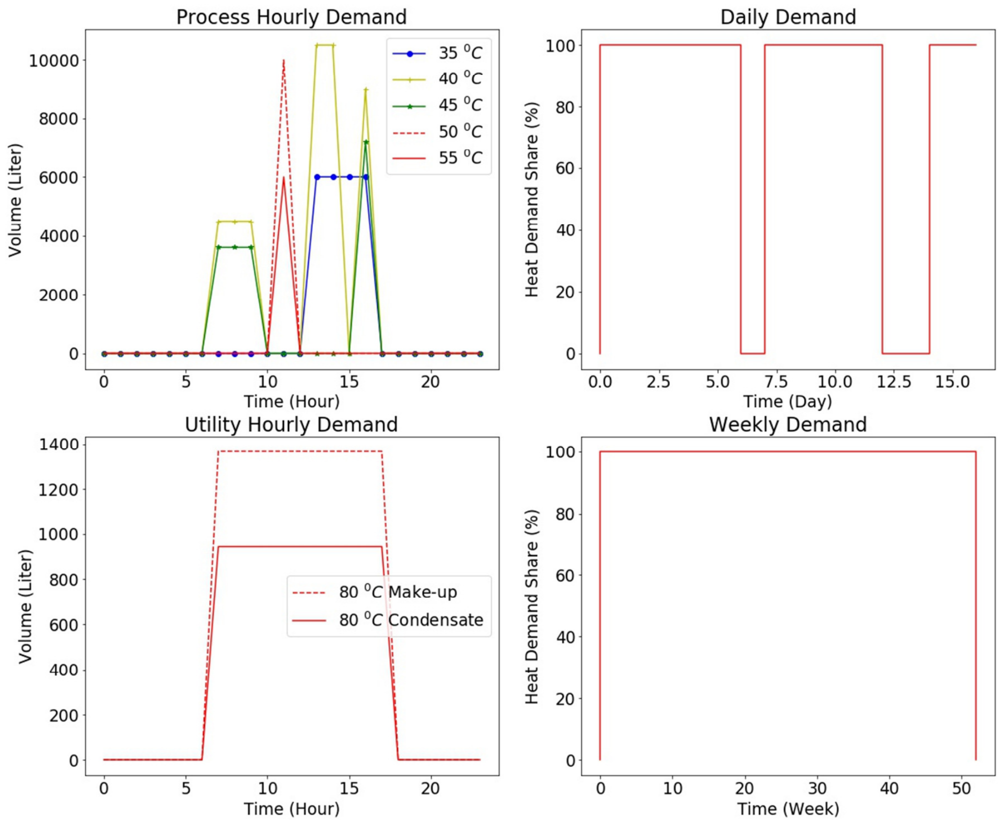

(a)

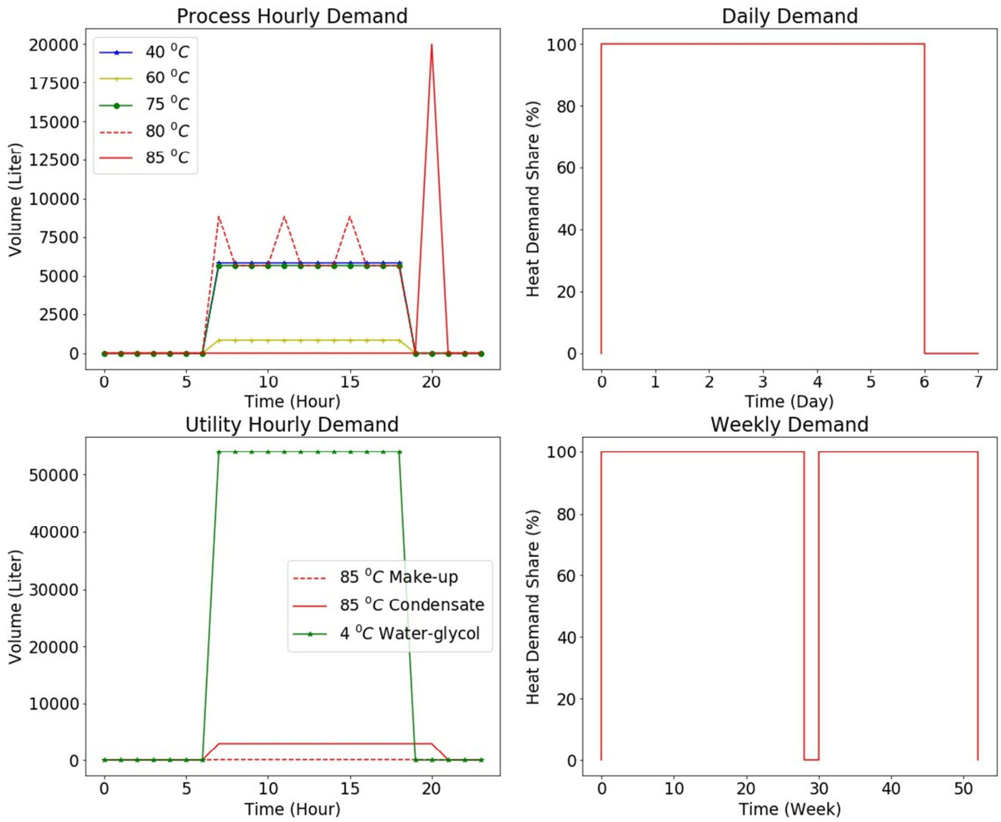

(b)

Fig. 2: Load profiles (a) Processes and feedwater heating in SLI, (b) Processes, feedwater heating, and water-glycol cooling in MSD

This proper identification of daily consumption was one of the objectives of the study and it is important information for system sizing. All the factories mainly process their products during the day time as shown in Figure 2 (a and b). During the night there is no hot water demand since the companies are only working from 6:00 am to 10:00 pm (two shifts). In SLI, there is no demand for alternate one or two days at weekends (Figure 2a). In MSD, there is no demand at weekends and during the 29 and 30 weeks of a year (Figure 2b).

Figure 2 illustrates the hourly hot water demands averaged during the days for SLI and MSD. As shown in Figure 2a, the demand at the leather factory is intermittent at some interval of hours. It indicates that the peak demand reaching 10, 000 liters per hour at a temperature of 40 ^{0}C is around noon, which is an advantage for storage size reduction of solar energy application. Figure 2b shows the demand at the soft drinks factory is nearly uniform with batch processes for sugar dissolving and CIP at some interval of hours. Large hot water consumption reaching 5,000 liters per hour at a temperature of 80 ^{0}C is continuously required during the day. The peak demand reaching 20, 000 liters per hour at a temperature of 85 ^{0}C is mostly around evening when all the production equipment is cleaned before closing time. Similarly, uniform consumption during working hours is shown in Figure 2 (a and b) to pre-heat feedwater and cool the water-glycol solution.

4. Conclusion

The heating and cooling potential assessment in SLI and MSD were conducted to quantify the requirements of the processes for identifying potential intervention areas for solar thermal integration. Based on the assessment performed, SLI works in two shifts with alternate five or six days a week all over the year and SMD works in two shifts with six days a week all over the year except for two weeks planned maintenance period. Discontinuous (batch) load profiles of the hot water demand for tanning and re-tanning processes in SLI as well as sugar dissolving and cleaning of production equipment in MSD are identified. During working hours, there is a high demand for hot water around noon in SLI and in MSD, though there is always a certain demand for cleaning water, there is a very high demand mostly when all the production equipment is cleaned before closing time. Besides, the continuous load profile of the washing processes is being part of the production in MSD. Constant boiler feedwater heating as well as water-glycol solution cooling are also identified as energy-intensive processes for possible solar thermal integration. Such a reliable knowledge of the process parameters (mass flows, temperature levels, load profile, etc.) are pre-conditions to plan and design a reliable and economical solar thermal system.

5. Acknowledgments

The authors would like to acknowledge CoE in REWiSE project for the funds to the Ph.D. study leading to this article.

6. References

Abdulateef, J., Alghoul, M., Zaharim, A., Sopian, K. Bin, 2011. Economic analysis of combined solar-assisted ejector absorption refrigeration system.

Adsten, M., Perers, B., Wäckelgård, E., 2002. The influence of climate and location on collector performance. Renewable Energy 25, 499–509. https://doi.org/10.1016/S0960-1481(01)00091-X

Allouhi, A., Kousksou, T., Jamil, A., Bruel, P., Mourad, Y., Zeraouli, Y., 2015. Solar driven cooling systems: An updated review. Renewable and Sustainable Energy Reviews. https://doi.org/10.1016/j.rser.2014.12.014

Amiri, M., 2012. Fundamentals of Thermodynamics, in: Introduction to Thermodynamics of Mechanical Fatigue. pp. 11–27. https://doi.org/10.1201/b12725-3

Andersen, E., Furbo, S., 2009. Theoretical variations of the thermal performance of different solar collectors and solar combi systems as function of the varying yearly weather conditions in Denmark. Solar Energy 83, 552–565. https://doi.org/10.1016/j.solener.2008.10.009

Encyclopedia, 2013. Industry - Ethiopia - future, sector [WWW Document]. URL https://www.nationsencyclopedia.com/Africa/Ethiopia-INDUSTRY.html (accessed 4.9.19).

Energypedia, 2013. Ethiopia Energy Situation - energypedia.info [WWW Document]. URL https://energypedia.info/wiki/Ethiopia_Energy_Situation (accessed 4.8.19).

ESTIF, 2006. European Solar Thermal Industry Federation [WWW Document]. URL http://www.estif.org/fileadmin/estif/content/policies/downloads/D23-solar-industrial-process-heat.pdf (accessed 3.18.19).

FDRE, F.D.R. of E.M. of W.I. and E., 2013. Updated Rapid Assessment and Gap Analysis on Sustainable Energy for All [WWW Document]. URL https://www.se4all-africa.org/fileadmin/uploads/se4all/Documents/Country_RAGAs/MWH_-_Updated-Rapid_Gap_Analysis.pdf (accessed 4.8.19).

Gebreeyesus, M., 2013. Industrial Policy and Development in Ethiopia: Evolution and Current Performance. WIDER Working Paper.

Ibrahim, O.M., Ghoneim, A.A., Halabi, O.A., Kamil, A., 1990. Solar industrial process heat potential in Khartoum, Sudan. Solar & Wind Technology 7, 649–654. https://doi.org/10.1016/0741-983X(90)90039-5

Jaiswal, A.K., Mitra, S., Dutta, P., Srinivasan, K., Srinivasa Murthy, S., 2016. Influence of cycle time and collector area on solar driven adsorption chillers. Solar Energy 136, 450–459. https://doi.org/10.1016/j.solener.2016.07.023

Kalogirou, S., 2003. The potential of solar industrial process heat applications. Applied Energy 76, 337–361. https://doi.org/10.1016/S0306-2619(02)00176-9

Kalogirou, Soteris, 2003. The potential of solar industrial process heat applications. Applied Energy 76, 337–361.

Karagiorgas, M., Botzios, A., Tsoutsos, T., 2001. Industrial solar thermal applications in Greece: Economic evaluation, quality requirements and case studies. Renewable and Sustainable Energy Reviews 5, 157–173. https://doi.org/10.1016/S1364-0321(00)00012-5

Lu, Z.S., Wang, R.Z., Xia, Z.Z., Lu, X.R., Yang, C.B., Ma, Y.C., Ma, G.B., 2013. Study of a novel solar adsorption cooling system and a solar absorption cooling system with new CPC collectors. Renewable Energy 50, 299–306. https://doi.org/10.1016/J.RENENE.2012.07.001

Luo, H.L., Dai, Y.J., Wang, R.Z., Wu, J.Y., Xu, Y.X., Shen, J.M., 2006. Experimental investigation of a solar adsorption chiller used for grain depot cooling. Applied Thermal Engineering 26, 1218–1225. https://doi.org/10.1016/J.APPLTHERMALENG.2005.10.036

Luo, H.L., Wang, R.Z., Dai, Y.J., Wu, J.Y., Shen, J.M., Zhang, B.B., 2007. An efficient solar-powered adsorption chiller and its application in low-temperature grain storage. Solar Energy 81, 607–613.

https://doi.org/10.1016/J.SOLENER.2006.09.001

Mekhilef, S., Saidur, R., Safari, A., 2011. A review on solar energy use in industries. Renewable and Sustainable Energy Reviews. https://doi.org/10.1016/j.rser.2010.12.018

MoI, 2017. Investment Opportunity in Manufacturing Industry Investment Research, Monitoring and Support Directorate 1–34.

Muneer, T., Maubleu, S., Asif, M., 2006. Prospects of solar water heating for textile industry in Pakistan. Renewable and Sustainable Energy Reviews 10, 1–23. https://doi.org/10.1016/J.RSER.2004.07.003

Proctor, D., Morse, R.N., 1977. Solar energy for the Australian food processing industry. Solar Energy 19, 63–72. https://doi.org/10.1016/0038-092X(77)90089-5

Rabl, A., 1981. Yearly average performance of the principal solar collector types. Solar Energy 27, 215–233. https://doi.org/10.1016/0038-092X(81)90123-7

Ratismith, W., Favre, Y., Canaff, M., Briggs, J., 2017. A non-tracking concentrating collector for solar thermal applications. Applied Energy 200, 39–46. https://doi.org/10.1016/j.apenergy.2017.05.044

REEP, n.d. Ethiopia Infrastructure, Power & Energy Investment Summit 2014 | REEEP [WWW Document]. URL https://www.reeep.org/events/ethiopia-infrastructure-power-energy-investment-summit-2014 (accessed 4.8.19).

Ruud Kempener, 2014. IEA-ETSAP and IRENA Solar Heat for Industrial Processes ENERGY TECHNOLOGY SYSTEMS ANALYSIS PROGRAMME.

Schweiger, H., Mendes, J.F., Carvalho, M.J., Hennecke, K., Krüger, D., 2015. Solar heat for industrial processes, in: Advances in Solar Energy: An Annual Review of Research and Development in Renewable Energy Technologies. pp. 216–260. https://doi.org/10.4324/9781315793221-14

Solomon, J., 1983. PROCESS HEATING. Chemical Engineer (London) 24–26.

Thabit, S.S., Stark, J., 1986. Effects of working patterns on solar generated heat in UK industry. Applied Energy 22, 165–186. https://doi.org/10.1016/0306-2619(86)90001-2

UNEP, 2015. Etiopia: Energy profile, Total energy production,Total energy consumption and Production.

Vannoni, C., Battisti, R., Drigo, S., 2008. Task 33/IV-Potential for Solar Heat in Industrial Processes Potential for Solar Heat in Industrial Processes Task 33/IV-Potential for Solar Heat in Industrial Processes.

von Storch, H., Roeb, M., Stadler, H., Sattler, C., Bardow, A., Hoffschmidt, B., 2016. On the assessment of renewable industrial processes: Case study for solar co-production of methanol and power. Applied Energy 183, 121–132. https://doi.org/10.1016/j.apenergy.2016.08.141

Zografos, A.I., Martin, W.A., Sunderland, J.E., 1987. Equations of properties as a function of temperature for seven fluids. Computer Methods in Applied Mechanics and Engineering 61, 177–187. https://doi.org/10.1016/0045-7825(87)90003-X

Real-Time Multiobjective Optimization in Solar Membrane Distillation Processes

María M. Lozano[1], Juan D. Gil[1], Lidia Roca[2], Manuel Berenguel[1], Manuel Pérez[1], Robin De Keyser[3]

[1]Centro Mixto Ciesol, ceiA3, Universidad de Almería, Almería (Spain)
[2]CIEMAT-Plataforma Solar de Almería, Tabernas (Spain)
[3]DySC research group on Dynamical Systems and Control, Ghent University, Ghent (Belgium)

Abstract

Solar Membrane Distillation (SMD) technology is a promising separation method that uses low-grade solar energy as power source. Despite this technology has not been industrially implemented yet, it is in an advanced phase of maturity so that current research works are mainly focused on the development of suitable operating strategies to improve the Membrane Distillation (MD) modules performance. The intermittent and unpredictable behavior of solar energy as well as the hybrid nature of SMD plants make the development of real-time operating strategies essential. Accordingly, this paper proposes a real-time multiobjective optimization method based on the combination of a state machine and a Nonlinear Model Predictive Control (NMPC) technique for the maximization of the distillate production and the thermal efficiency of the plant, two of the major impediments preventing the commercialization of SMD facilities. Simulation results and a comparison with a manual operating strategy are provided to evidence the benefits achieved with the proposed technique.

Keywords: Solar desalination, Process control, Dynamic simulation, Solar thermal energy, Thermal storage.

1. Introduction

Water demand is increasing steadily due to the growth of the population and the associated socio-economic development of industrial and agricultural activities. In addition, climate change and contamination are aggravating the water problem worldwide so that, some studies report that around 5.7 billion people (around 60 % of the world population) can suffer from water scarcity in 2050 (WWAP, 2018). Taking into account this panorama, desalination methods are getting more and more attention as a way to enhance water supply options in arid or semi-arid areas. However, although desalination stands out as one of the most effective solutions, irresponsible and intensive use of this technology can cause severe environmental problems due to the high energy consumption of current desalination technologies. This problem is even more significant if one considers that only around 1 % of total desalination facilities currently in operation are powered with renewable energy (Ghaffour et al., 2014). Therefore, it is necessary to improve the combination between conventional desalination methods and renewable energies and to explore alternative methods that present better characteristics to be combined with these renewable sources.

In the line of the search for substitute desalination methods, one of the main techniques that is gaining interest in recent decades is the MD technology. MD is a thermally driven separation technique that requires a low operating temperature (between 60-85 ºC). This fact makes the case for combining MD processes with low-grade solar energy, forming sustainable plants that reduce the carbon footprint (Zaragoza et al. 2014). Moreover, the simplicity of the process and its tolerance to both, small-scale decentralized use and intermittent operation, make MD technology one of the most appropriate methods to develop stand-alone desalination plants to be implemented in isolated areas with small-medium water needs and good availability of solar irradiance, as island regions. In fact, this is one of the most favorable applications of MD technology since other desalination techniques significantly increase costs at downscale (Guillén-Burrieza et al. 2015) and normally require on-grid power. Nevertheless, to fully commercialize MD technology, both the design of the modules and the operating strategies must be improved to increase the thermal efficiency and distillate production of MD modules, which are the two of the main drawbacks so far.

doi:10.18086/eurosun.2020.03.02 Available at http://proceedings.ises.org

Since the emergence of MD technology in 1963, research efforts have been focused on the search of new membranes and designs of MD modules. These investigations have caused a significant progress in terms of thermal energy as MD modules have gone from an initial thermal consumption of 810 kWh/m^3 (Guillén-Burrieza et al. 2011) to current consumptions of around 49 kWh/m^3 (Andrés-Mañas et al. 2020). That is why MD technology is in a new phase of development in which other research addressing the optimal operation of MD modules, especially when they are coupled with solar energy, are arising (Gil et al. 2020). From the point of view of the operation, the main difficulties presented in these plants appear as a result of their hybrid nature. SMD plants include solar fields and thermal storage devices requiring proper management techniques in real-time according to the thermal storage state, the level of irradiance and operating necessities (i.e., water needs); which is difficult and laborious to perform manually. As a consequence, not long ago, the interest in the application of control and real-time optimization techniques in these kinds of plants has grown (Thomas et al., 2017). For example, in Refs. (Chang et al., 2010; Porrazo et al., 2013) control methods based on ON/OFF controllers or Proportional, Integral and Derivative (PID) controllers aimed at temperature regulation were proposed. These kinds of methods provide adequate strategies to improve the dispatchability of SMD plants, dealing with their hybrid nature and allowing the operators to maintain a desired operating temperature in the MD module. However, they do not consider improving the thermal efficiency and the distillate production of the MD module, the two main metrics used to evaluate its performance. More recently, advanced control strategies based on the Model Predictive Control (MPC) technique have been proposed which are tasked with improving the aforementioned metrics separately (Gil et al., 2018a; Bendevis et al., 2020; Guo et al., 2020). The problem is that to increase the distillate production and thermal efficiency converse operating conditions are required in the feed flow rate of the MD module. Thus, the works referenced above only consider mono-objective optimization problems responsible for improving only one of the metrics in real-time. To the authors' knowledge, there are no works in the literature addressing this multiobjective optimization problem in real-time; what can be fundamental to the proper industrialization of the MD technology.

Based on the above issues, this paper proposes a real-time multiobjective optimization method to improve in real-time both the distillate production and the thermal efficiency. The developed algorithm is composed by two main parts. First, following the ideas presented in our previous work (Gil et al., 2018a), a state machine tasked with selecting the adequate operating mode of the facility is used to deal with the hybrid nature of the plant. Second, an NMPC technique that calculates optimal control actions in real-time according to the operating mode and operating conditions is used to improve the desired objectives. Several simulation tests using a validated model of a real pilot plant located at Plataforma Solar de Almería (PSA) have been carried out from which the benefits of the designed control architecture are demonstrated.

2. System description

In this work, a real pilot plant located at PSA (www.psa.es) has been used as reference to perform the simulation analysis. The schematic diagram of the facility is presented in Fig. 1.

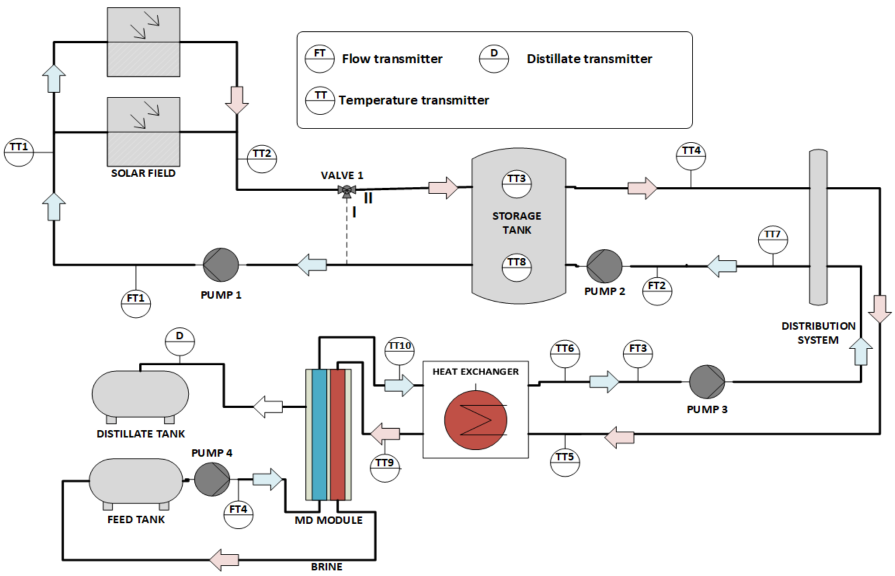

Fig. 1: Schematic diagram of the SMD plant at PSA.

In this facility, the thermal power demanded by the MD unit is provided through a solar thermal field composed of flat-plate collectors, with a total surface area of 22.8 m^2 and a nominal capacity of 7 kW_{th}.This solar field is directly coupled to a thermal storage tank with a capacity of 1500 L. Then, a distribution system is available that connects with a heat exchanger in charge of giving the thermal power to the MD module. The facility is fully monitored and controlled by a Supervisory Control and Data Acquisition (SCADA) system. Tab. 1 of the appendix summarizes the main variables of interest for this work. Please note that a complete description of the plant as well as of the MD module used in this work can be found in (Zaragoza et al. 2014; Gil et al., 2018a) and (Gil et al., 2018b) respectively.

3. System modelling

This section shows an overview of the model of the SMD plant used in both the simulation tests and the predictive control strategy. It should be noted that the whole model was already presented and validated in (Gil et al., 2018a; 2018b).

First, the solar field was modelled by means of a lumped-parameter model given by:

$$A_{sf}\rho c_p \frac{d\mathrm{TT2(t)}}{dt} = \beta \mathrm{I(t)} - \frac{H_1}{L_{eq}}\left(\bar{T}(t) - \mathrm{T}_a(t)\right) - c_p \dot{m}_{eq}(t)\frac{\mathrm{TT2}(t) - \mathrm{TT1}(t)}{L_{eq}}, \quad \text{(eq. 1)}$$

where:

$$L_{eq} = L_a n_{cs}, \quad \text{(eq. 2)}$$

$$\dot{m}_{eq}(t) = \frac{\mathrm{FT1}(t)\rho}{c_1}, \quad \text{(eq. 3)}$$

$$\bar{T}(t) = \frac{\mathrm{TT1}(t) + \mathrm{TT2}(t)}{2}. \quad \text{(eq. 4)}$$

Second, the inlet solar field temperature was characterized by using a static mass balance:

$$\mathrm{TT1}(t) = \mathrm{TT2}(t)\frac{\mathrm{V1}(t)}{100} + \mathrm{TT8}(t)\left(1 - \frac{\mathrm{V1}(t)}{100}\right). \quad \text{(eq. 5)}$$

Third, the storage tank was modelled by using a two-nodes stratified dynamical model which can be described as follows:

$$\frac{d\mathrm{TT3(t)}}{dt} = \frac{1}{\rho V_1}\left(\dot{m}_{sf}(t)\mathrm{TT2}(t) + \dot{m}_{ds}(t)\mathrm{TT8}(t) - \dot{m}_{sf}(t)\mathrm{TT3}(t) - \dot{m}_{ds}(t)\mathrm{TT3}(t) - \frac{H_2(\mathrm{TT3}(t) - \mathrm{T}_a(t))}{c_p}\right), \quad \text{(eq. 6)}$$

$$\frac{d\mathrm{TT8(t)}}{dt} = \frac{1}{\rho V_1}\left(\dot{m}_{sf}(t)\mathrm{TT3}(t) + \dot{m}_{ds}(t)\mathrm{TT7}(t) - \dot{m}_{sf}(t)\mathrm{TT8}(t) - \dot{m}_{ds}(t)\mathrm{TT8}(t) - \frac{H_3(\mathrm{TT8}(t) - \mathrm{T}_a(t))}{c_p}\right), \quad \text{(eq. 7)}$$

where:

$$\dot{m}_{sf}(t) = \frac{\mathrm{FT1}(t)\frac{\mathrm{V1}(t)}{100}\rho}{c_2}, \quad \text{(eq. 8)}$$

$$\dot{m}_{sf}(t) = \frac{\mathrm{FT2}(t)\rho}{c_2}. \quad \text{(eq. 9)}$$

Fourth, the temperatures at both sides of the heat exchanger were adjusted by using a first principles-based static model:

$$\mathrm{TT6}(t) = \mathrm{TT5}(t) - \eta_1\left(\mathrm{TT5}(t) - \mathrm{TT9}(t)\right), \quad \text{(eq. 10)}$$

$$\mathrm{TT10}(t) = \mathrm{TT9}(t) - \eta_2\left(\mathrm{TT5}(t) - \mathrm{TT6}(t)\right), \quad \text{(eq. 11)}$$

where:

$$\eta_1 = \frac{1-e^{\theta}}{1-\frac{\dot{m}_{he}(t)c_p}{\dot{m}_{MD}(t)c_{p,sw}}e^{\theta}}, \qquad \text{(eq. 12)}$$

$$\eta_2 = \frac{\dot{m}_{he}(t)c_p}{\dot{m}_{MD}(t)c_{p,sw}}, \qquad \text{(eq. 13)}$$

$$\theta = \alpha A_{he}\left(\frac{1}{\dot{m}_{he}(t)c_p} - \frac{1}{\dot{m}_{MD}(t)c_{p,sw}}\right). \qquad \text{(eq. 14)}$$

Finally, the MD module was modelled by using an Artificial Neural Network (ANN) model described and validated in (Gil et al., 2018b). This model provides the value of the distillate production (D) and Specific Thermal Energy Consumption (STEC) according to the value of the evaporator channel inlet temperature of the MD module (TT9), the feed water flow rate (FT4), and the operating conditions of the feed water in terms of temperature and salinity. These two lasts are considered constants in this work assuming typical mean values of the Mediterranean Sea, 20 ºC and 35 g/L respectively. Therefore, the ANN model can be generically described as:

$$\mathrm{D}(t) = f(\mathrm{TT9}(t), \mathrm{FT4}(t)), \qquad \text{(eq. 15)}$$

$$\mathrm{STEC}(t) = f(\mathrm{TT9}(t), \mathrm{FT4}(t)), \qquad \text{(eq. 16)}$$

where $f(\cdot)$ is a function of its arguments given by the ANN model.

It should be remarked that all the constants and parameters involved in the model as well as their units and values are presented in Tab. 2 of the Appendix.

4. Real-time operating strategy

As stated before, one of the main operating problems of MD systems consists of maximizing their distillate production and thermal efficiency in real-time, particularly when they are powered with solar energy. To address this issue, in this paper, a control system is proposed (see Fig. 2) composed of two main parts: i) a state machine and ii) an NMPC controller based on the Nonlinear Extended Prediction Self-Adaptative Control (NEPSAC) algorithm (De Keyser, 2003).

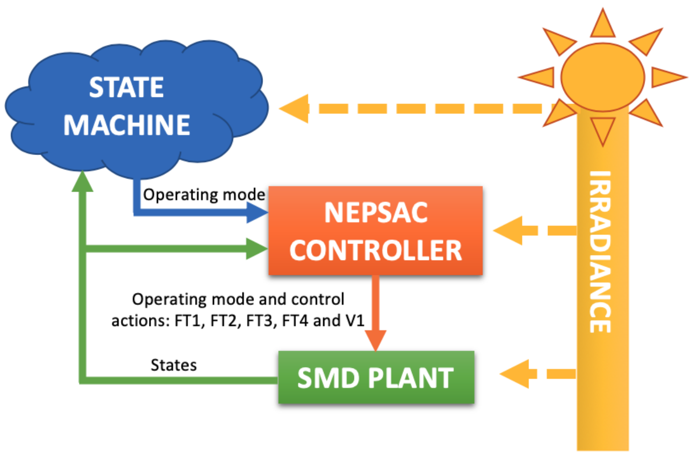

Fig. 2: Schematic diagram of the control system.

On the one hand, the state machine is responsible for dealing with the hybrid nature of the SMD plant. Thus, it receives the states of the real plant and the external operating conditions, i.e. global irradiance, and decides the most appropriate operating mode according to a designed rule-based system. On the other hand, the NEPSAC controller computes the optimal control signals, i.e. FT1, FT2, FT3, FT4, and V1, based on the selected operating mode, the operating conditions and the plant states; trying to maximize the distillate production and thermal efficiency of the MD module. It should be pointed out that the control problem changes in each of the operating modes since not all the variables are involved in all the operating modes. Also, in some of them, the MD module is not in operation, so the objectives of the optimization problem also differ from the aforementioned ones. In what follows, the design of the two blocks is presented.

4.1. State machine

Three different operating modes have been differentiated for the SMD plant:

- **Mode 1:** This mode is used to heat the storage tank. The MD module cannot be operated under 60 ºC since it is not economically profitable (Gil et al., 2018a). So, if the tank is unloaded in terms of thermal energy, the solar field is used to heat the tank fast until reaching the required operating temperature by the MD module. The rules for selecting this operating mode are: TT1≤TT2, $I \geq I_{th}$, and $TT3 \leq T_{th}$, where I_{th} and T_{th} are the threshold values of global irradiance and temperature in the tank required to turn on the solar field and MD module respectively, which are calculated as presented in (Gil et al., 2018a). In this operating mode, the control variables used by the NMPC controller are FT1 and V1, and the main objective is to increase the temperature in the upper part of the tank.

- **Mode 2:** In this mode, the solar field feeds the storage tank, which, in turn, is used to power the MD module. The rules used for selecting this mode are: TT1≤TT2, $I \geq I_{th}$, and $TT3 \geq T_{th}$. In this case, the whole facility is in operation so that the control variables are FT1, FT2, FT3, FT4, and V1. However, different objectives can be differentiated for the optimal operation of the facility as increasing the temperature in the upper part of the tank and the one at the inlet of the heat exchanger, and increasing the distillate production and thermal efficiency of the MD module.

- **Mode 3:** This mode is used when the level of irradiance is low so that the solar field cannot be operated, but there is still enough thermal energy in the tank to operate the MD module. Here, the rules used are: TT1≥TT2, $I \leq I_{th}$, and $TT3 \geq T_{th}$. In this mode, the control problem is simplified in comparison with the previous one being the control variables FT2, FT3, and FT4, and the objectives to increase the temperature at the inlet of the heat exchanger and to increase the distillate production and thermal efficiency of it.

Fig. 3 shows the flow that can occur among the different operating modes. Please note that, in the figure, mode 0 refers to an operating mode in which the SMD facility is turned off as none of the rules mentioned above are satisfied. Finally, it should be remarked that the rules are cheeked with mean values of the last ten minutes instead of using instantaneous ones thus avoiding chattering problems. Also, bumpless transfer mechanisms are used for switching among the different modes.

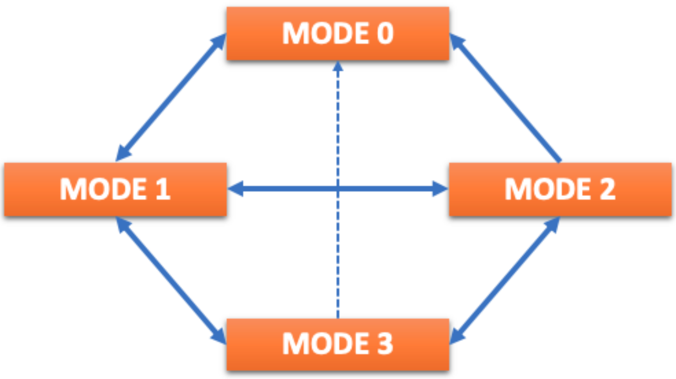

Fig. 3: Connections among operating modes.

4.2. NEPSAC controller

4.2.1. NEPSAC overview

Among the different MPC techniques, the NEPSAC (De Keyser, 2003) control strategy has been selected in this research work due to its favourable characteristics when dealing with nonlinear systems such as the whole model of the SMD plant used in this work. As other MPC strategies, the NEPSAC controller is based on the following three issues: i) the use of a model of the system at hand to predict the outputs along a determined prediction horizon, ii) minimization of an objective function to calculate the future control signals, and iii) the use of a receding horizon strategy so that at each sampling time the first control signal is sent to the real system whereas the rest of the calculated sequence is rejected. The main difference among the different MPC techniques is the model used to represent the system and the disturbances. The NEPSAC algorithm is based on the Extended Prediction Self-Adaptive Control (EPSAC) technique proposed in (De Keyser, 2003), in which the model output $x(t)$ can be described as:

$$x(t) = f(x(t-1), x(t-2), \dots, u(t-1), u(t-2), \dots), \qquad \text{(eq. 17)}$$

where $f(\cdot)$ can be a linear or a nonlinear function and $u(t)$ is the control input. Thus, the generic model used in this algorithm can be posed as:

$$y(t) = x(t) + n(t), \qquad \text{(eq. 18)}$$

where $y(t)$ denotes the output of the system, $x(t)$ represents the model output and $n(t)$ is the model/process disturbance. In this work, $n(t)$ is calculated to remove the steady state error between the predictions and the real measured values:

$$n(t) = \frac{1}{1-q^{-1}} e(t), \qquad \text{(eq. 19)}$$

being $e(t)$ the error and q^{-1} the backward shift operator.

Therefore, using the generic model in eq.18, the outputs along the prediction horizon can be computed as:

$$y(t+k|t) = x(t+k|t) + n(t+k|t), \qquad \text{(eq. 20)}$$

for $k= N_1, \dots, N_2$ being N_1 and N_2 the minimum and maximum prediction horizons. Thus, the predictions of the process outputs are calculated using the measurements available at sampling time t, i.e., past outputs $[y(t), y(t-1), \dots.]$ and past inputs $[u(t-1), u(t-2), \dots.]$, and the value of the future control inputs $[u(t|t), u(t+1|t), \dots.]$. Taking into account this last statement, eq. 20 can be rewritten as:

$$y(t+k|t) = y_{base}(t+k|t) + y_{opt}(t+k|t), \qquad \text{(eq. 21)}$$

where $y_{base}(t+k|t)$ contains the effect of past inputs, the influence of a pre-specified future base control sequence $u_{base}(t+k|t)$, and the future predicted behaviour of disturbances $n(t+k|t)$. $y_{opt}(t+k|t)$ is related to the effect of the optimal control actions $\delta u(t|t), \dots, \delta u(t+N_u-1|t)$, where N_u is the control horizon and $\delta u(t+k|t) = u(t+k|t) - u_{base}(t+k|t)$. This optimized output can be computed as:

$$y_{opt}(t+k|t) = h_k \delta u(t|t) + h_{k-1}\delta u(t+1|t) + \cdots g_{k-N_u+1}\delta u(t+N_u-1|t), \qquad \text{(eq. 22)}$$

where $h_1, \dots, h_{N_2}$ and $g_1, \dots, g_{N_2}$ are the unit impulse response and step response coefficients respectively. By expressing eq. 21 and eq. 22 on a matrix way, the MPC formulation emerges:

$$\mathbf{Y} = \overline{\mathbf{Y}} + \mathbf{GU}, \qquad \text{(eq. 23)}$$

where:

$$\mathbf{Y} = [y(t+N_1|t), \dots, y(t+N_2|t)]^T, \qquad \text{(eq. 24)}$$

$$\overline{\mathbf{Y}} = [y_{base}(t+N_1|t), \dots, y_{base}(t+N_2|t)]^T, \qquad \text{(eq. 25)}$$

$$\mathbf{U} = [\delta u(t|t), \dots, \delta u(t+N_u-1|t)]^T, \qquad \text{(eq. 26)}$$

$$\mathbf{G} = \begin{bmatrix} h_{N_1} & h_{N_1-1} & h_{N_1-2} & \cdots & g_{N_1-N_u+1} \\ h_{N_1+1} & h_{N_1} & h_{N_1-1} & \cdots & g_{N_1-N_u+2} \\ \cdots & \cdots & \cdots & \cdots & \cdots \\ h_{N_2} & h_{N_2-1} & h_{N_2-2} & \cdots & g_{N_2-N_u+1} \end{bmatrix}. \qquad \text{(eq. 27)}$$

Once the model to calculate the predictions is obtained the control signals can be directly computed by minimizing a given objective function; as long as the function in eq. 17 be linear. It should be pointed out that, the calculation of the predictions in the form expressed in eq. 21 involves the use of the superposition principle, which does not hold in nonlinear systems. In this way, the strategy presented above is only valid from a practical point of view when a nonlinear function in eq. 17 is used. Thus, by selecting an appropriate $\boldsymbol{u_{base}}$, the term $\boldsymbol{y_{opt}}$ in eq. 21 can gradually be zero in an iterative way. This then becomes the optimal solution as the superposition principle is no longer involved. This procedure is given by the following algorithm:

1. Initialize $u_{base}(t+1|t)$ at the optimal value computed in the previous sampling time.
2. Calculate matrix **G** using the nonlinear model in eq. 17 to obtain eq. 27. To do that, a unit impulse or step must be injected to the model in eq. 17 around the current operating trajectory.
3. Calculate $\delta u(t+k|t)$ for $k=0 \dots N_u-1$ by minimizing the given objective function and obtain the resulting control signals $u(t+k|t) = u_{base}(t+1|t)+\delta u(t+k|t)$ for $k=0 \dots N_u-1$.
4. Return to step 3 by taking the calculated $u(t+k|t)$ as the new set of $u_{base}(t+1|t)$.
5. Stop when $u_{base}(t+1|t)$ converges to the optimal value, which is that the difference between the value of $u_{base}(t+1|t)$ among two consecutive iterations is close to 0 or lower than a given tolerance.

4.2.2. NEPSAC applied to the SMD plant

The SMD plant can be classified as a Multiple Input Multiple Output (MIMO) system taking into account the different control variables, i.e., FT1, V1, FT2, FT3 and FT4, and the system outputs of interest to perform an optimal operation of the plant, i.e., TT3, TT9, D, and STEC. In this way, by following the NEPSAC technique described above, the predictions in this MIMO system can be calculated as:

$$\begin{bmatrix}\mathbf{Y_{TT3}}\\ \mathbf{Y_{TT9}}\\ \mathbf{Y_{D}}\\ \mathbf{Y_{STEC}}\end{bmatrix}=\begin{bmatrix}\mathbf{\overline{Y}_{TT3}}\\ \mathbf{\overline{Y}_{TT9}}\\ \mathbf{\overline{Y}_{D}}\\ \mathbf{\overline{Y}_{STEC}}\end{bmatrix}+\begin{bmatrix}\mathbf{G_{FT1}^{TT3}} & \mathbf{G_{V1}^{TT3}} & \mathbf{G_{FT2}^{TT3}} & \mathbf{G_{FT4}^{TT3}}\\ \mathbf{G_{FT1}^{TT9}} & \mathbf{G_{V1}^{TT9}} & \mathbf{G_{FT2}^{TT9}} & \mathbf{G_{FT4}^{TT9}}\\ \mathbf{G_{FT1}^{D}} & \mathbf{G_{V1}^{D}} & \mathbf{G_{FT2}^{D}} & \mathbf{G_{FT4}^{D}}\\ \mathbf{G_{FT1}^{STEC}} & \mathbf{G_{V1}^{STEC}} & \mathbf{G_{FT2}^{STEC}} & \mathbf{G_{FT4}^{STEC}}\end{bmatrix}\cdot\begin{bmatrix}\mathbf{U_{FT1}}\\ \mathbf{U_{V1}}\\ \mathbf{U_{FT2}}\\ \mathbf{U_{FT4}}\end{bmatrix}, \qquad \text{(eq. 28)}$$

where vectors $\mathbf{Y_i}$, $\mathbf{\overline{Y}_i}$, $\mathbf{U_i}$ are arranged in the form presented in eqs. 24, 25 and 26 respectively, and matrix $\mathbf{G_i^j}$ in the way showed in eq. 27. Please note that FT3 has not been included in eq. 28 as it must be operated at the same level as FT4 in order to achieve maximum heat transfer in the heat exchanger (Gil et al., 2018a). It should also be pointed out that not all the control variables are physically related to all the system outputs. For example, the feed flow rate in the MD module (FT4) does not affect to the temperature in the storage tank (see Fig. 1). Thus, some of the terms can be removed from eq. 28 simplifying the calculations at each sampling time:

$$\begin{bmatrix}\mathbf{Y_{TT3}}\\ \mathbf{Y_{TT9}}\\ \mathbf{Y_{D}}\\ \mathbf{Y_{STEC}}\end{bmatrix}=\begin{bmatrix}\mathbf{\overline{Y}_{TT3}}\\ \mathbf{\overline{Y}_{TT9}}\\ \mathbf{\overline{Y}_{D}}\\ \mathbf{\overline{Y}_{STEC}}\end{bmatrix}+\begin{bmatrix}\mathbf{G_{FT1}^{TT3}} & \mathbf{G_{V1}^{TT3}} & \mathbf{0} & \mathbf{0}\\ \mathbf{0} & \mathbf{0} & \mathbf{G_{FT2}^{TT9}} & \mathbf{0}\\ \mathbf{0} & \mathbf{0} & \mathbf{0} & \mathbf{G_{FT4}^{D}}\\ \mathbf{0} & \mathbf{0} & \mathbf{0} & \mathbf{G_{FT4}^{STEC}}\end{bmatrix}\cdot\begin{bmatrix}\mathbf{U_{FT1}}\\ \mathbf{U_{V1}}\\ \mathbf{U_{FT2}}\\ \mathbf{U_{FT4}}\end{bmatrix}. \qquad \text{(eq. 29)}$$

Moreover, although eq. 29 is the general expression used to model the whole SMD plant, this function is also adapted to each of the operating modes of the plant, according to the variables involved in them. For instance, in mode 1, only the prediction of the temperature in the upper part of the tank ($\mathbf{Y_{TT3}}$) must be considered, as the rest of the plant is turned off. In mode 2, the whole function in eq. 29 must be used as the entire plant is in operation. Finally, in mode 3, the prediction of the temperature in the upper part of the tank ($\mathbf{Y_{TT3}}$) can be removed as the solar field is turned off. Therefore, at each sampling time, the NEPSAC controller receives the selected operating mode by the state machine, as presented in Fig. 2, and computes only the necessary terms of the matrix, thus reducing the computing time requirements.

The last step in the NEPSAC technique is to formulate the objective functions used to calculate the optimal control actions in each of the operating modes. These functions can be posed according to the objectives described in section 4.1. Besides, due to the physical relationship among input and output variables (see eq. 29) and due to the arrangement of the real facility (see Fig. 1), we can decouple the whole optimization problem into two different ones: one to calculate the optimal control signals related to the solar field circuit (FT1, V1, FT2), and another one to calculate the control signal related to the MD module (FT4). In the first case, the objective is to maximize the temperature in the upper part of the tank and the temperature at the inlet of the heat exchanger, so the objective function can be formulated as:

$$J_1 = -\sum_{k=1}^{N_2} y_{TT3}(t+k|t) - \sum_{k=1}^{N_2} y_{TT9}(t+k|t). \quad \text{(eq. 30)}$$

This cost function is used in the three operating modes of the plant, but it is adapted to each of them. In mode 1, only the first term in the function is taken into account, in mode 2, both terms are considered, and in mode 3, only the second term is used. Secondly, for the MD module, the objective is to maximize its distillate production and thermal efficiency. As commented before, these two variables require contrary operating conditions in the feed flow rate (FT4) so the following multiobjective optimization problem can be cast:

$$\begin{bmatrix} J_2 \\ J_3 \end{bmatrix} = \begin{bmatrix} \sum_{k=1}^{N_2} y_{STEC}(t+k|t) \\ -\sum_{k=1}^{N_2} y_D(t+k|t) \end{bmatrix}. \quad \text{(eq. 31)}$$

It should be remarked that both optimization problems are subjected to some constraints related to the physical limits of actuators and the operating constraints:

$$\begin{aligned} &7.5 \text{ L/min} \leq \text{FT1} \leq 20 \text{ L/min}, \\ &0\ \% \leq \text{V1} \leq 100\ \%, \\ &15 \text{ L/min} \leq \text{FT1} \leq 22 \text{ L/min}, \\ &6.66 \text{ L/h} \leq \text{FT4} \leq 10 \text{ L/h}, \\ &\text{TT2} \leq 100\ ^{\circ}\text{C}. \end{aligned} \quad \text{(eq. 32)}$$

5. Results and discussion

A wide variety of simulations using the nonlinear dynamical model presented in section 3 and real meteorological data from PSA were performed. The simulations were carried out using MATLAB 2019b software and its optimization toolbox. Specifically, the *fmincon* algorithm was used to solve the optimization problem in eq. 30 and the *paretosearch* algorithm to work out the one in eq. 31 (MATLAB, 2019). The sampling time of the control strategy was 5 min according to the system dynamics (Gil et al., 2018a). The prediction and control horizon were fixed at $N_1 = 1$, $N_2 = 10$, $N_u = 1$, which were chosen after exhaustive simulations until obtaining the desired closed loop response and following traditional recommendations in MPC techniques, i.e, $N_u \ll N_2$. In the following subsections the main results obtained are analyzed.

5.1. Multiobjective optimization problem: Pareto front.

Before analyzing the performance of the control algorithm during typical operating days, it is important to visualize the Pareto front obtained at each sampling time in the mutiobjective optimization problem in eq. 31, as well as to establish the selection of the optimal operating point. The Pareto front can be observed in Fig. 4.

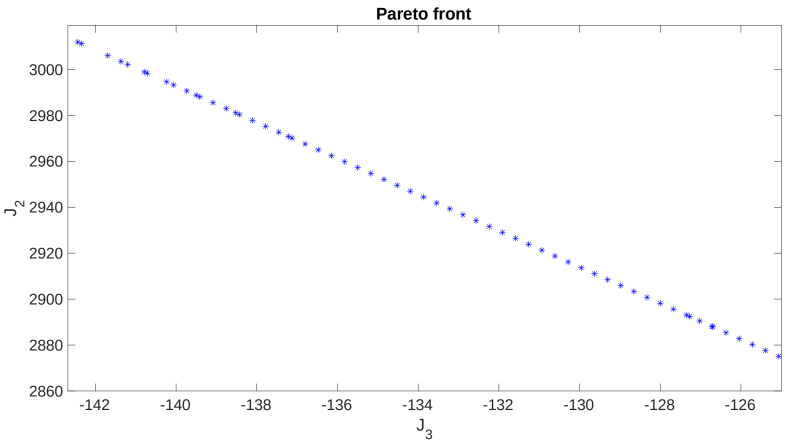

Fig. 4: Pareto front obtained in a single sampling time.

In this case, the Pareto front is composed of 60 points representing the different optimal points that can be adopted to maximize the thermal efficiency and the distillate production of the MD module. In this work, the middle point has been used as optimal solution, which represents the tradeoff solution among the two objectives. However, it should be commented that in real cases, the solution must be chosen according to the operating requirements, i.e., a given water demand.

5.2. Simulation results

In this subsection, the results obtained during a week operating the facility are presented. The simulation results are shown in Fig. 5. In this figure, the first graph (a) shows the irradiance conditions. Please note that the week chosen includes sunny and cloudy days thus increasing the reliability of the obtained results. The second graph (b) presents the temperatures of the SMD plant. The third one (c) includes the specific thermal consumption (STEC) and distillate production of the MD module. The fourth one (d) presents the control actions associated with each of the pumps of the SMD plant whereas the fifth one (e) shows the valve 1 aperture. The last one (f) includes the selected operating mode by the state machine.

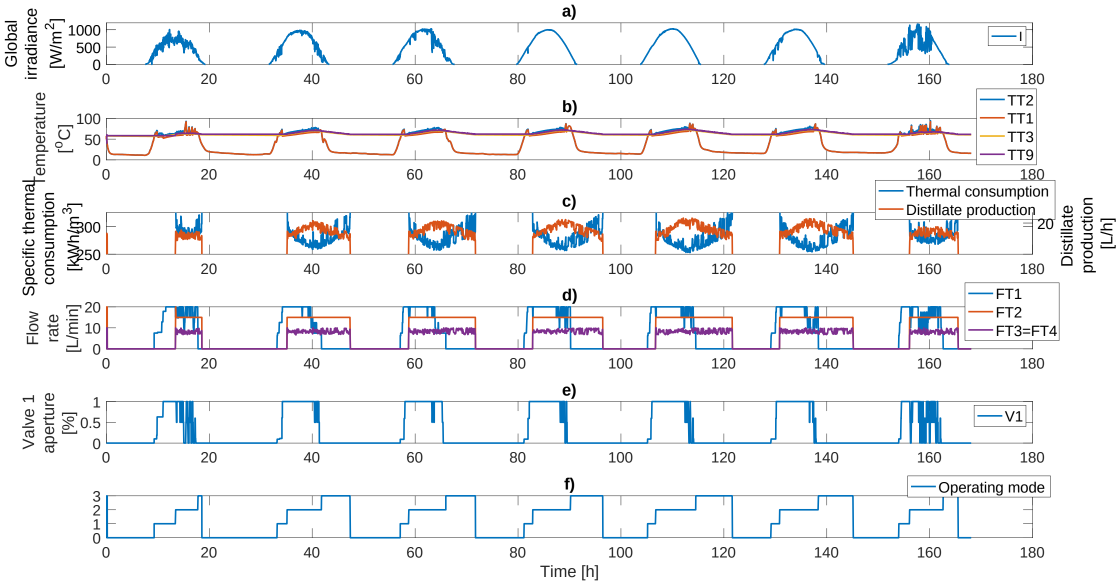

Fig. 5: Simulation results.

In general terms, it can be observed how in all the days the procedure is similar. The operation starts in mode 1 until reaching the required operating point in the storage tank to turn on the MD module. Then, the plant operates in mode 2 until the level of irradiance is low, preventing to load the storage tank. At this point, the state machine selects mode 3 and it maintains this operating mode until the tank is discharged in terms of thermal energy. It should be pointed out that the time during which the SMD plant operates in mode 3 depends on the irradiance conditions of each day. It can also be seen how the NEPSAC controller selects the optimal control actions in each of the operating modes according to the established objectives.

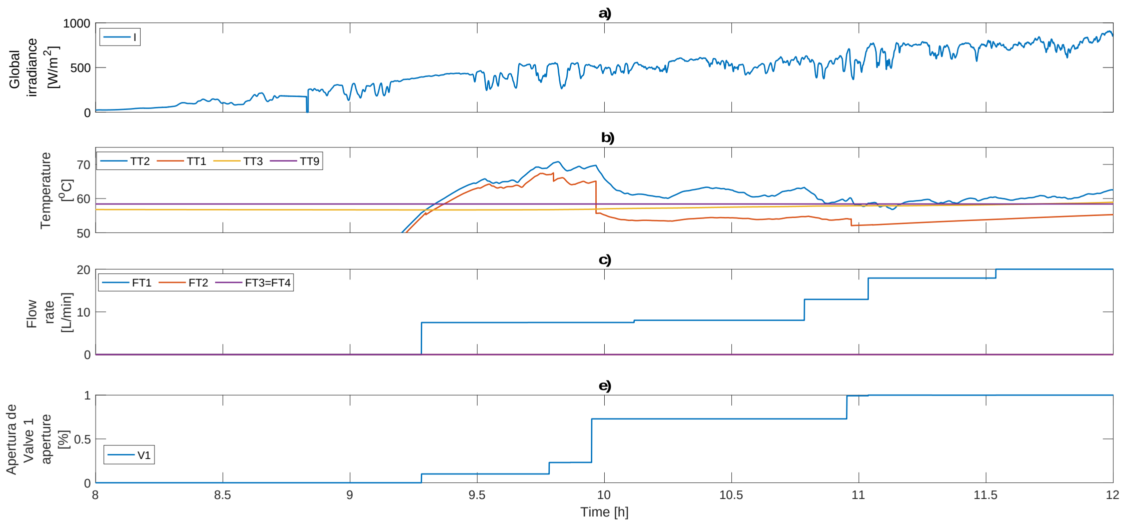

Fig. 6: Results of the first operating day when the state machine selects mode 1.

To highlight the performance of the NEPSAC controller, Fig. 6 presents the beginning of the first operating day when the state machine chooses the operating mode 1. Please remember that in this mode the objective is to heat the tank fast, which is to increment the temperature at the top of the storage tank. In this way, it can be seen how the NEPSAC controller manages the valve 1 (V1) aperture and the solar field flow rate (FT1) to achieve this. Specifically, it gradually opens valve 1 towards the tank in a controlled way (see Fig. 6-d), pulling out cold fluid from the lower part of the tank, warming it by using the solar field, and inserting it by the upper part of the tank. Also, it regulates the flow rate (see Fig. 6-c) according to the operating conditions in terms of temperature (see Fig. 6-b) and global irradiance (see Fig. 6-a), preventing to load the tank with cold fluid (see Fig. 6-b).

5.3. Comparison with a manual operation

In order to demonstrate the good performance of the designed control strategy, the results presented in Fig. 5 were compared to those obtained in a manual operation. In the manual operation, the state machine was used with the same rules presented in section 4.1 but maintaining the actuators operating in a fixed point, which was selected following the ones usually used by the operators of the real facility at PSA.

Thus, three different metrics were selected to perform the comparison: i) the mean STEC of the whole simulation test, ii) the total distillate production, and iii) the number of operating hours of the MD module. The results showed how the thermal efficiency could be improved by 4 %, the total distillate production by 29 %, and the number of operating hours of the MD module by 16 %. Similar results can be found in different simulation scenarios.

6. Conclusions

This paper proposes an optimal operating strategy to improve the thermal efficiency and distillate production of a Solar Membrane Distillation plant in real-time. The operating strategy is based on a control structure composed of a state machine and an NMPC strategy based on the NEPSAC algorithm. The following conclusions can be drawn from the obtained results:

1. The proposed control technique has resulted in a powerful tool to optimally manage the SMD plant with different irradiance conditions.
2. The obtained metrics improved those of a manual operation. For example, the distillate production can be improved by up to 29 % whereas the specific thermal energy consumption by up to 4 %. These improvements could mean significant advanced towards the commercialization of the technology.

7. Acknowledgments

This work has been financed by the MICROPROD-SOLAR project of the Spanish State Research Agency (ref. PCI2019-103378), which supports the CYTED program call for Strategic Projects on distributed generation, renewable energies and microgrids in Strategic Enclaves of Latin America. Juan D. Gil acknowledges the financial assistance of the University of Almería through its Research and Transfer Plan.

8. References

Andrés-Mañas, J. A., Ruiz-Aguirre, A., Acién, F. G., Zaragoza, G., 2020. Performance increase of membrane distillation pilot scale modules operating in vacuum-enhanced air-gap configuration. Desalination, 475, 114202.

Bendevis, P., Karam, A., Laleg-Kirati, T. M., 2020. Optimal model-free control of solar thermal membrane distillation system. Computers & Chemical Engineering, 133, 106622.

Chang, H., Wang, G. B., Chen, Y. H., Li, C. C., Chang, C. L., 2010. Modeling and optimization of a solar driven membrane distillation desalination system. Renewable Energy, 35(12), 2714-2722.

De Keyser, R., 2003. Model Based Predictive Control. Invited Chapter in UNESCO Encyclopaedia of Life Support Systems Article contribution 6.43. 16.1.

Ghaffour, N., Lattemann, S., Missimer, T., Ng, K. C., Sinha, S., Amy, G., 2014. Renewable energy-driven innovative energy-efficient desalination technologies. Applied Energy, 136, 1155-1165.

Gil, J. D., Roca, L., Ruiz-Aguirre, A., Zaragoza, G., Berenguel, M., 2018a. Optimal operation of a solar membrane distillation pilot plant via nonlinear model predictive control. Computers & Chemical Engineering, 109, 151-165.

Gil, J. D., Ruiz-Aguirre, A., Roca, L., Zaragoza, G., Berenguel, M, 2018b. Prediction models to analyse the performance of a commercial-scale membrane distillation unit for desalting brines from RO plants. Desalination, 445, 15-28.

Gil, J.D., Roca, L., Berenguel, M. 2020. Modelling and automatic control in solar membrane distillation: Fundamentals and proposals for its technological development. Revista Iberoamericana de Automática e Informática Industrial (In press). https://doi.org/10.4995/riai.2020.13122

Guillén-Burrieza, E., Blanco, J., Zaragoza, G., Alarcón, D. C., Palenzuela, P., Ibarra, M., Gernjak, W., 2011. Experimental analysis of an air gap membrane distillation solar desalination pilot system. Journal of Membrane Science, 379(1-2), 386-396.

Guillén-Burrieza, E., Alarcón-Padilla, D. C., Palenzuela, P., Zaragoza, G., 2015. Techno-economic assessment of a pilot-scale plant for solar desalination based on existing plate and frame MD technology. Desalination, 374, 70-80.

Guo, X., Albalawi, F., Laleg-Kirati, T. M., 2020. Observer-based economic model predictive control for direct contact membrane distillation. Chemical Engineering Research and Design, 156, 86-99.

MATLAB, 2019. MATLAB optimization toolbox release 2019b. Natick, MA, USA: The MathWorks.

Porrazzo, R., Cipollina, A., Galluzzo, M., Micale, G., 2013. A neural network-based optimizing control system for a seawater-desalination solar-powered membrane distillation unit. Computers & Chemical Engineering, 54, 79-96.

Thomas, N., Mavukkandy, M. O., Loutatidou, S., Arafat, H. A., 2017. Membrane distillation research & implementation: Lessons from the past five decades. Separation and Purification Technology, 189, 108-127.

Zaragoza, G., Ruiz-Aguirre, A., Guillén-Burrieza, E., 2014. Efficiency in the use of solar thermal energy of small membrane desalination systems for decentralized water production. Applied Energy, 130, 491-499.

WWAP, 2018. The United Nations World Water Development Report 2018: Nature-based Solutions for Water. Paris, UNESCO.

Appendix: Variables, Units and Symbols

Table 1: Variables of interest monitored in the SMD facility at PSA.

Description	Symbol	Unit
Distillate production	D	L/h
Solar field flow rate	FT1	L/min
Distribution system flow rate	FT2	L/min
Heat exchanger flow rate	FT3	L/min
Feed water flow rate	FT4	L/h
Global irradiance	I	W/m^2
Ambient temperature	T_a	ºC
Inlet solar field temperature	TT1	ºC
Outlet solar field temperature	TT2	ºC
Temperature at the top of the storage tank	TT3	ºC
Inlet distribution system temperature	TT4	ºC
Inlet heat exchanger temperature, hot side	TT5	ºC
Outlet heat exchanger temperature, hot side	TT6	ºC
Outlet distribution system temperature	TT7	ºC
Temperature at the bottom of the storage tank	TT8	ºC
Outlet heat exchanger temperature, cold side	TT9	ºC
Inlet heat exchanger temperature, cold side	TT10	ºC
Valve 1 aperture	V1	%

Table 2: Symbols and constants used in the model of the SMD plant.

Description	Symbol	Unit
Heat exchanger area	A_{he}	1.65 m^2
Cross-section area of one fluid inside the flat-plate collector	A_{sf}	$1.539 \cdot 10^{-4}$ m^2
Conversion factor to account for connections, number of modules and unit conversion	c_1	$108 \cdot 10^4$ s L/(min m^3)
Conversion factor	c_2	$6 \cdot 10^4$ s L/(min m^3)
Specific heat capacity of water	c_p	J/(kg ºC)
Specific heat capacity of sea water	$c_{p.sw}$	J/(kg ºC)
Solar field global thermal losses coefficient	H_1	5.88 J/(s ºC)
Tank thermal losses coefficient, upper part	H_2	3.6 J/(s ºC)
Tank thermal losses coefficient, lower part	H_3	3.8 J/(s ºC)
Collector absorber tube length	L_a	1.95 m
Equivalent absorber tube length	L_{eq}	m
Distribution system mass flow rate	$\dot{m}_{ds}$	kg/s
Equivalent solar field mass flow rate	$\dot{m}_{eq}$	kg/s
Heat exchanger mass flow rate	$\dot{m}_{he}$	kg/s
Membrane distillation module mass flow rate	$\dot{m}_{MD}$	kg/s
Solar field mass flow rate	$\dot{m}_{sf}$	kg/s
Number of series connections in a collector group	n_{cs}	5
Equivalent absorber tube mean temperature	$\bar{T}$	ºC
Volume, first stratification	V_1	0.75 m^3
Volume, second stratification	V_2	0.75 m^3
Heat exchanger heat transfer coefficient	α	670.80 W/(m^2 K)
Irradiance model parameter	β	0.11 m
Heat exchanger auxiliary factor 1	η_1	-
Heat exchanger auxiliary factor 2	η_2	-
Heat exchanger auxiliary factor 3	θ	-
Demineralized water density	ρ	kg/m^3

Table 3: Symbols and constants used in the formulation of the control system.

Description	Symbol	Unit
Error between the model output and the real system output	$e(\cdot)$	-
Step response coefficient	g	-
Matrix of unit impulse and step response coefficients	$\mathbf{G}$	-
Unit impulse response coefficient	h	-
Value of global irradiance necessary to turn on the solar field	I_{th}	W/m^2
Model/process disturbance	$n(\cdot)$	-
Minimum prediction horizon	N_1	-
Maximum prediction horizon	N_2	-
Control horizon	N_u	-
Backward shift operator	q^{-1}	-
Value of temperature necessary to turn on the MD module	T_{th}	ºC
Control input	$u(\cdot)$	-
Base control sequence	$u_{base}(\cdot)$	-
Vector of control actions	$\mathbf{U}$	-
Model output	$x(\cdot)$	-
Output of the system	$y(\cdot)$	-
Variable containing the effect of past inputs and outputs and predicted disturbances	$y_{base}(\cdot)$	-
Variable containing the effect of the optimized control actions	$y_{opt}(\cdot)$	-
Vector of system outputs	$\mathbf{Y}$	-
Vector of y_{base}	$\bar{\mathbf{Y}}$	-
Control action increment	δu	-

A Novel Effluent Evaporation System for Industrial Applications

Puneet Saini[1,2], Prakash Bhalekar[1], Jubin Kumaran[2]
[1] Quadsun solar solutions, Gurugram (India)
[2] Energy Technology, Dalarna University, Falun (Sweden)

Abstract

This paper presents the design, working principle, and field performance data of a novel effluent/brine evaporation system developed and commercialised by Quadsun solar solutions, India. The developed evaporator aims to address the challenges with existing evaporation technologies to reduce the land area requirement and heat consumption for brine evaporation while minimising the system operational cost. The developed evaporator system works on a data-driven control strategy where the effect of constraints on the evaporation rate is non-linear, and the objective function is set to minimise the electricity consumption of the system. The optimisation of the evaporation rate in the system control volume is achieved by variation of a) mass flow rate of brine, b) wind speed over the evaporation surface and c) contact area between brine and air. The system performance results are presented for an installed site located in Northern India for a testing period of 64 days. The results are further compared with a solar pond evaporation system using an analytical model. The result shows that the proposed evaporator has an average specific evaporation rate (SER) of 0.48 $L/(h \cdot m^2)$, which is 3.8 times higher compared to SER for the solar pond for the same meteorological conditions. Furthermore, the compactness of the proposed evaporator design results in significant land savings compared to the pond evaporation system.

Keywords: Evaporation, quadsun, brine management, solar pond, solar evaporation.

---

1. INTRODUCTION

“Industrial effluent” is the wastewater generated by various industries as an undesirable by-product. The old practices to get rid of the effluent such as draining of effluent into natural water bodies, and deep injection into the ground has posed a severe threat to the ecosystem. The consequences of these unsustainable practices are severely reflected in a water-stressed country such as India. The major sources of water pollution are concentrated among highly water-intensive industries such as leather, textile, chemical, mining, steel, sugar, and paper industry (Murthy and Dasgupta, 1985). It is estimated that only 40 % of the industrial effluent is treated from these industries and rest 60 % of untreated effluents ended into the ecosystem (Rajaram and Das. 2008). The problem can be realized on a larger scale in certain regions such as Tiruppur (Tamil Nadu) and Kanpur (Uttar Pradesh) with a strong presence of the textile and leather industry. These regions are affected by wastewater to an extent that resulted in the drinking of groundwater and soil cultivation nearly impossible (Furn, 2004). The effect of untreated water has enabled the infusion of toxic elements such as Lead, Mercury, and Zinc in the domestic water supply.

Global research organisations and national governments put a lot of efforts to develop sustainable solutions to curb this problem. Solar heating and cooling program of IEA initiated task 62 in the year 2018 with a focus on the use of sustainable energy sources such as solar energy for industrial wastewater treatment (IEA SHC task 62, 2018). Realizing the severity of the problem, the government of India in the year 2015 issued a draft notification on the amendment of rules on standards for effluent from the textile industry. The amendment proposed to install zero liquid discharge (ZLD) systems in all textile processing units (Grönwall and Jonsson, 2017). ZLD is based on the reduce-reuse-recycle principle, which recycles the wastewater by chemical treatment and therefore allows the reuse of treated water (Lee et al., 2007). In a ZLD system achieved using reverse osmosis (R.O), wastewater is passed thru R.O membranes at high pressure. The permeate is recycled as input water, whereas R.O rejects (brine effluents) undergoes reject management cycles using mechanical evaporation and crystallization where salt is recovered from the brine effluents (Grönwall and Jonsson, 2017b).

doi:10.18086/eurosun.2020.03.03 Available at http://proceedings.ises.org

The R.O reject can be also be transported to the common effluent treatment plants set up by the local pollution control bodies or industrial clusters.

Achieving ZLD is an energy-intensive process and most of the energy is consumed in the electrical and thermal form. Thermal energy is usually consumed in the form of steam during evaporation in reject management systems which can employ a multi-effect evaporator, falling film evaporator, evaporation by spraying, etc. Reject management (evaporation and crystallization) can cost almost 50 % of the total ZLD cost. Moreover, the high operational cost forced the industries to bypass these systems to protect their profits and resulted in the use of unsustainable practices such as drainage of wastewater in rivers. However, strong enforcement by the state pollution control agencies results in closure of various industrial units due to the non-adherence to the treatment standards. This enforcement attracted a lot of interest to develop a cost-effective brine effluent management system to lower down the capital and operational cost (Narayanan, 2015). Therefore, this paper presents a novel wastewater evaporator for R.O rejects, developed and patented by Quadsun solar solutions in India (Quadsun, 2020). The design of the evaporator is intended to address the major challenge faced with existing evaporation techniques such as high temperature and pressure requirements, high electricity consumption, and high operational costs. The developed evaporator can be used in combination with solar heat, which can further lower down the operational costs. The working methodology of the evaporator is presented along with various integration schemes. Moreover, the field performance of the evaporator from one of the installed sites is also presented and compared with a solar pond evaporation system. The next section presents the overview of various technologies used for evaporation, followed by the proposed system description. Lastly, field performance, conclusions, and uncertainties are presented.

2. LITERATURE REVIEW

Most of the evaporation techniques used in the industries consist of:

- Thermal evaporation system: Multi-effect evaporator (MEE), multi-stage flash (MSF) evaporator, and falling film evaporator.
- Mechanical evaporation system: Mechanical vapor recompression, evaporation ponds with sprinklers.
- Solar pond.

Currently, MEE is widely popular in industries having an in-house effluent treatment plant. MEE is used in combination with a crystallizer or agitated thin film dryers to dry out the salt from the brine. These systems required steam input at a temperature above 120 °C and 3 bar pressure (Nafey, 2006). The vapor from one stage of the evaporator is used as a heat source for the subsequent stage (called effects) and this results in the better utilisation of input steam. The number of effects is an optimisation between an increase in capital cost and energy savings due to the additional effect. The overall operational cost of MEE can range from 50-300 Rs/kL (0.5-3.5 €/kL) of evaporated brine, depending on the number of effects and type of fuel used to generate the steam.

Evaporation ponds are characterized as a wide-open area exposed to solar irradiation and filled with brine water which is to be evaporated. These ponds are easy to construct and operate with minimal mechanical and operator inputs. These ponds are widely used in arid and semi-arid regions as the meteorological conditions are favorable for evaporation. The evaporation rate using this method is dependent on the local weather conditions and can vary from 1-6 mm/day from a solar pond having a surface area of 1 m^2. The major concern with this method is the low evaporation rate and large area requirement. Furthermore, the failure of the protective lining in these ponds can results in the seepage of brine into the ground, which poses a severe threat to groundwater.

A number of studies are available which deals with evaporation enhancement of solar ponds using solar thermal collectors. Sampathakar et. al (2001) tested an evaporation system consist of solar flat plate collectors (FPC) and brine sprinkler system. The FPC is used to increase the brine temperature by 3 °C and nozzles of various diameters are used to sprinkle brine on the evaporation pond. The rate of evaporation observed from the system is 14 mm/(day.m^2), which was 2-3 times more than the natural evaporation system. However, the author realized the problem with drifting of the sprinkled brine into the air during the experimentation. In another similar study by Reilly (2009), a solar evaporation pond of 20,000 m^2 surface area was integrated with a 100 m^2 FPC system and long-term performance was monitored for Melbourne climatic conditions. Results show a mean evaporation enhancement ratio (EER) of 1.52 compared to the natural evaporation. Philip et. al (2013) presented a solar and wind-aided cross flow evaporator for RO reject management, as an alternative to conventional evaporator systems. In the proposed arrangement, the brine drips from an elevated tank on a vertical hanging cloth. The wind flow across the cloth results in mass and energy transfer and cause brine evaporation. The author reported a strong increase (13 folds) in the evaporation rate compared to conventional ponds. However, no information on the operational cost and durability of clothes under high brine concentration is provided. Guitierrez et. al (1993) studied the effect of floating aluminium fins in various orientations to analyse the increased evaporation area due to the fins. The experiments carried on small-scale prototype results in 20 % more evaporation using perpendicular fin arrangement compared to the natural evaporation. Kannan and Rao (2000) carried a detailed experimental parametric study to analyse the effect of various parameters such as air temperature, wind velocity, salt bath temperature, and salt concentration on the evaporation rate. The results are compared with the Sherwood and Pigford model to verify the effect of controlling parameters. The author concluded a good match in experimental and predicted results derived from the model. Moreover, brine input temperature was identified as the strongest influencing parameter to increase the evaporation. Based on the literature survey, the following controllable parameters were used in the developed evaporator to increase the evaporation rate:

- Increase in the brine temperature.
- Increase in wind speed on the evaporating surface
- Increase in the contact area between brine and air.

The proposed evaporator in this paper makes use of the above 3 parameters, along with a stringent control strategy for optimizing the thermal mass of brine and wind speed over the evaporating surface to maximise the evaporation rate and minimising the required energy input. The control of these parameters results in a significant increase in the evaporation rate which further results in lower operational costs.

3 SYSTEM DESCRIPTION

3.1 Working principle

The working principle of the developed evaporator is based on maintaining a certain set of conditions in the evaporator control volume predicted and optimised by a data-driven control strategy. The control unit of the evaporator plays a central role to optimise the system operation. The input to the control unit is provided by measurements of meteorological and energy parameters as defined in Table 1. The control unit uses these parameters to calculate the evaporation rate using artificial neural network (ANN) trained with experimental data. Using ANN model, several sets of simulation runs are carried over a wide range of control parameters such as the mass flow rate of brine, wind speed, and injection velocity.

Tab. 1: Parameters used for the evaporator control system

Parameter type	Control parameter	Instrument
Controllable input parameters	Mass of feed brine	Variable speed pump and controller
	Wind speed on the evaporator surface	Variable-speed fan and controller
	Contact area b/w air and water surface	Injection velocity and spray angle
Meteorological parameters	Ambient temperature	Temperature sensor
	Relative humidity at the inlet of the evaporator	Hygrometer
	Relative humidity at the outlet of the evaporator	
	Wind speed	Anemometer
	Global horizontal irradiation	Pyranometer

Energy parameters	Solar collector efficiency	Controller (only in case of the solar hybrid evaporator)
	Energy in the storage tank	Temperature sensor and level sensor
	Brine concentration	Digital TDS meter

As the aim is to reduce the operational electricity consumption, the model with a minimum value of specific fan power consumption (kWh/m^3) is selected. The output of the control system is a new set of input parameter values that are communicated to the interface devices to vary mass flow rate, wind speed, and injection velocity of effluent. The framework for the evaporation control system is shown in Figure 1. The evaporator also has various safety features and a remote management system to identify and resolve any issue during the operational period to ensure system reliability.

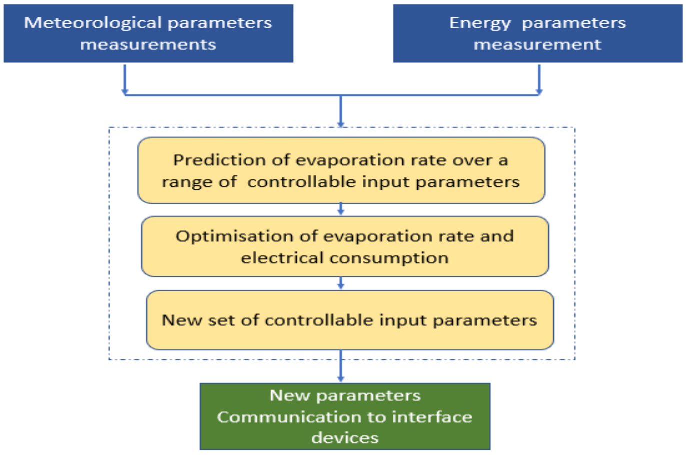

Fig. 1: Framework of the evaporator control system

3.2. System components

The evaporator can be seen as a stacked version of the solar pond, where several evaporating surfaces (pans) are placed on top of each other, resulting in significant footprint savings. An evaporation unit is a combination of various sub-modules (pan, fan, and injection sub-modules) integrated and working in synchronization with the control system. The schematic of the evaporator with various components is shown in Figure 2.

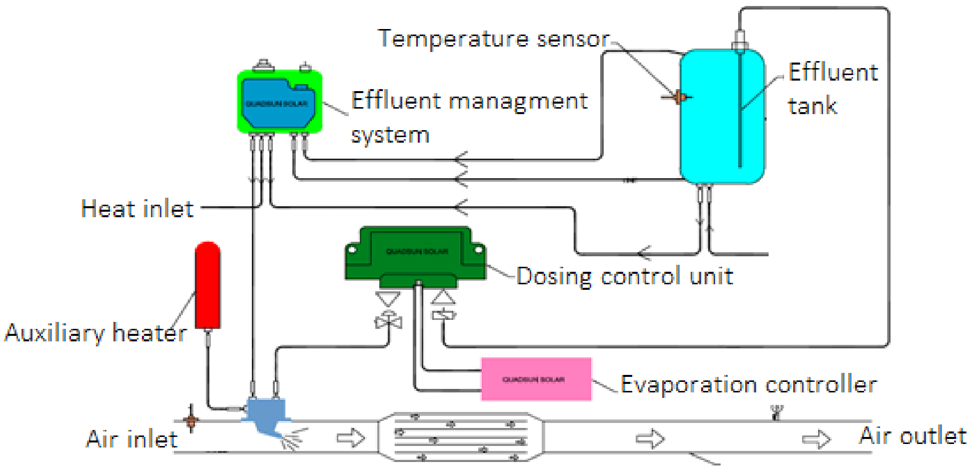

Fig. 2: Schematic of the developed evaporator

A carefully designed pattern on the surface of the pan allows the uniform spreading of the sprinkled brine and also increase the contact area between brine and air stream. The gap between the pan surfaces is optimised to maximise the surface wind speed while preventing the drifting of brine into the air stream. The fan and injection sub-modules work in conjunction with the evaporator controller to assure a set of input data conditions governed by the control algorithm. The evaporator has a peak capacity of 2500 litres per day (LPD) under defined climatic conditions of input brine temperature > 40 ºC, ambient temperature >20 ºC, relative humidity < 70 %). The capacity of the evaporator is optimised to assure the scalability of the unit for larger installations while minimising the installation time and logistic issues. The key design specifications of the evaporator are shown in Table 2 and the exploded view of the various components is shown in Figure 3.

Tab. 2: Design specification of the evaporator

Unit capacity	2500	LPD
Hours of operation	20	Hours/day
Input brine TDS range	0 - 300000	mg/L
Brine temperature range	20- 90	ºC
Electricity consumption	25-35	kWh/day
Thermal energy requirement	160-180	kWh/day
Footprint area	4	m^2

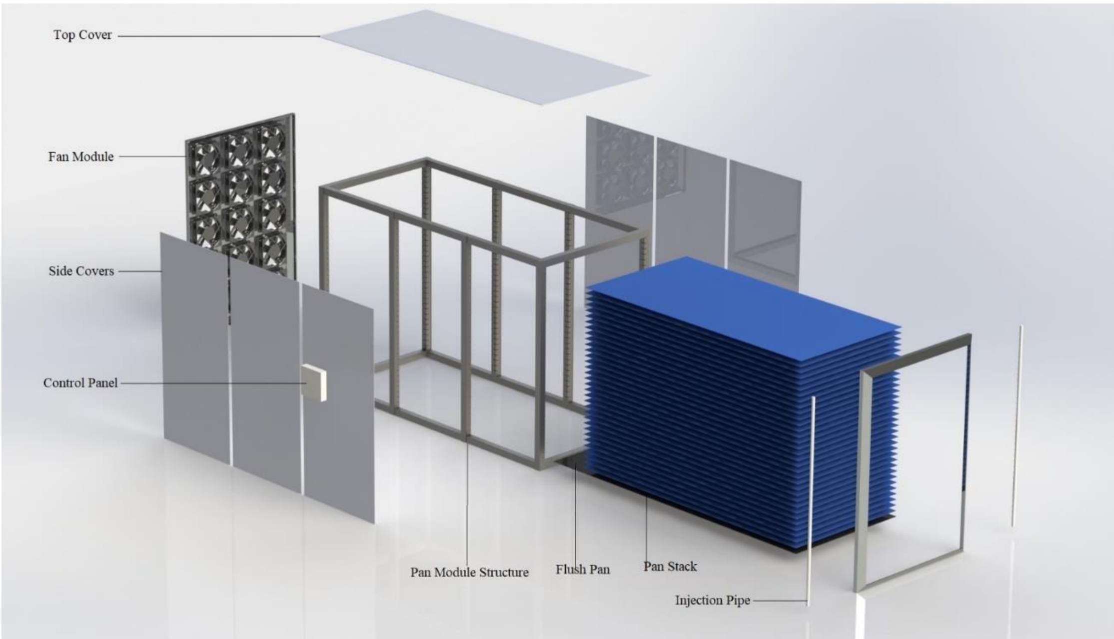

Fig 3: Exploded view of the evaporator

To achieve a higher evaporation capacity, several modules are integrated with a parallel arrangement. The system is designed to evaporate a wide variety of R.O reject (brine) with TDS up to 300,000 mg/L.

3.3. Integration

The brine to be evaporated is stored in an insulated storage tank. The brine in the tank can be heated using multiple sources such as solar thermal collectors, condensate return from the boiler system, or waste heat from various processes. The maximum allowable storage temperature is 95 ºC due to material constraints in the evaporator. The working cycle of the evaporator is as below :

- Brine is sprinkled on pan modules by an injection system to create a thin layer of fluid over the pan surface area. The quantity and frequency of the injection are decided by the control system.

- The thin layer of hot brine is evaporated by the air flowing over the pan surface. The wind speed over the surface is varied by the control module.
- The injection process continues as per the design control strategy until the flush cycle is triggered.
- The flush cycle drains the high TDS brine from the pan into another holding tank.
- This loop is continued until a drying cycle is triggered, and the brine injection on the pans in stopped.
- The drying cycle results in salt precipitation over the entire pan surface.
- Once the salt is formed on the pans, a semi-automatic scrapping process recovers the salt to start with the next cycle.

The higher wind speed on the evaporator surface along with control of injection brine quantity and contact area results in optimum conditions to achieve a high evaporation rate. The evaporator unit can also be used as a "concentrator" without the requirement for salt precipitation. This arrangement is of particular interest while retrofitting the evaporator unit in the existing brine management system to lower down the operational cost. The intended purpose of the evaporator in this configuration is to increase the concentration of the input brine and therefore reducing its volume, before feeding it to the existing MEE or MVR system. This results in lower operational costs due to fewer operating hours of the existing evaporation system. The working cycle in this configuration is similar to "salt precipitation" configuration except that the drying cycle is bypassed. The framework for both integration schemes is shown in Figure 4.

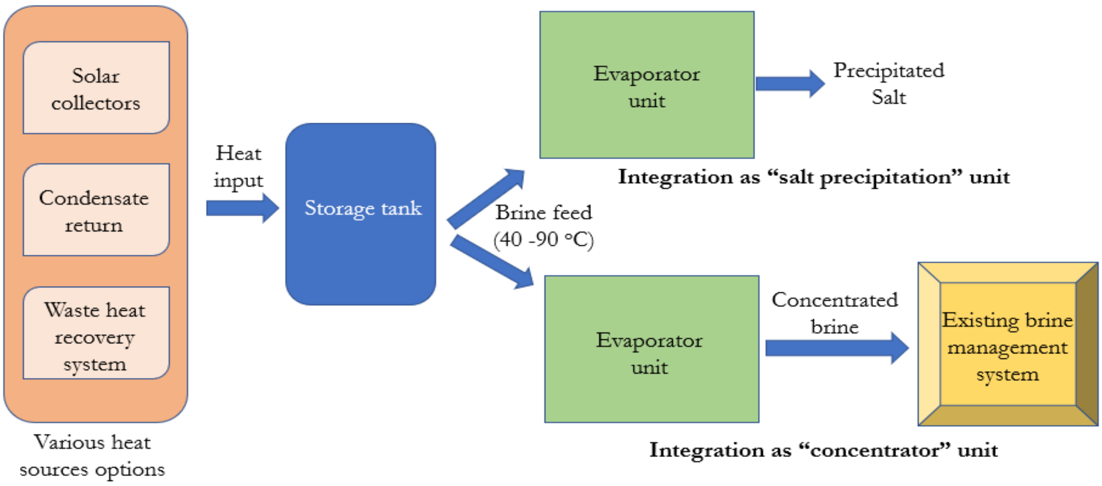

Fig. 4: Various integration schemes for proposed evaporator

3.4 Analytical model for pond evaporation

In this paper, the performance of the proposed evaporator is compared with a solar pond evaporation system. Standard Penman equation (Penman, 1948) is used to determine water evaporation from open water sources. However, to determine the evaporation rate from salt solutions, the standard Penman equation was modified to account for the reduced vapour pressure of the saltwater mixture. For this study, an analytical model based on modified Penman's equation is used to calculate the evaporation rate for solar ponds (Akridge, 2008), as expressed in Equation 1.

$$\lambda E = \frac{\Delta}{(\Delta+\gamma)} R_n + \frac{\gamma}{(\Delta+\gamma)} f(u)(e_s - e) \qquad \text{(eq. 1)}$$

Where, E is the evaporation rate from salt solution (mm/day), λ is the latent heat of vaporization (MJ/kg), Δ is the gradient of the vapour pressure-temperature curve (kPa °C^{-1}), γ is the psychometric constant (kPa °C^{-1}), R_n is the net solar radiation (MJ m^{-2} day^{-1}), $f(u)$ is a function of wind speed and e_s and e are the saturation vapour pressure of water and ambient vapour pressure (kPa), respectively. The latent heat of vaporization λ is a function of temperature and is expresses using Equation 2.

$$\lambda = 2.501 - 0.002361 * T \qquad \text{(eq. 2)}$$

where T is ambient temperature (^oC). The saturation vapour pressure e_s is modified by introducing a factor a_w to reflect the reduction in saturation vapour pressure when salts are dissolved, and shown in Equation 3.

$$e_s = 0.6108 * a_w * e^{\frac{17.27*T}{237.3+T}} \qquad \text{(eq. 3)}$$

a_w is the activity coefficient of water as per Equation 4.

$$a_w = -0.0011m^2 - 0.0319m + 1 \qquad \text{(eq. 4)}$$

Where m is the concentration of brine expressed as molarity. The gradient of saturation vapour pressure-temperature function Δ is calculated as per Equation 5

$$\Delta = \frac{4098 e_s}{(237.3+T)^2} \qquad \text{(eq. 5)}$$

The psychometric constant γ is calculated as per Equation 6.

$$\gamma = 0.000655 * 101.3 * \left(\frac{293-0.0065z}{293}\right)^{5.26} \qquad \text{(eq. 6)}$$

where z is the altitude above sea level (m). The vapour pressure e can be obtained from the relative humidity H_r (%) using Equation 7.

$$e = \frac{H_r e_s}{100} \qquad \text{(eq. 7)}$$

For an exposed evaporation surface, the wind function f(u) is obtained using Equation 8.

$$\text{f(u)} = 6.43(1 + 0.536U_2) \qquad \text{(eq. 8)}$$

where U_2 is the wind speed (m/s). Akridge validated the model by comparing the results of the modified Penman equation by comparing the evaporation rate from salt ponds in Chinese and Mexican climatic conditions (William, 2002; Chiang,1976)

3.5 Key performance indicators

The KPIs in this study are defined to evaluate evaporator performance and to establish a comparison with pond evaporation. The following KPIs are used in this paper for results and discussions on system modus operandi. Specific evaporation rate (SER): This represents the volume of water evaporated per unit evaporation surface area in one hour, shown in Equation 9.

$$SER = \frac{v}{A_e \cdot N} \qquad \text{(eq. 9)}$$

Where, $v, A_e, and\ N$ represents volume of water evaporated (litres), evaporation surface area in (m^2), and the number of operational hours respectively. It is important to realise the potential land savings benefits of the proposed evaporator system compared to pond evaporation. To account for this, a footprint area specific evaporation rate (SER_{fp}) is used, and calculated using Equation 10.

$$SER_{fp} = \frac{v}{A_{fp} \cdot N} \qquad \text{(eq. 10)}$$

Where, A_{fp} represents the footprint area of the evaporation system.

4. PERFORMANCE RESULTS

The product was commercialized in the year 2018 and is currently installed in various industries across India. Performance data from one of the installed site is presented in this section, and results are compared with the pond evaporation system. The installed site is located in Gurugram, Haryana (28.25° N, 76.96° E), which is classified as a humid subtropical climatic zone. The installed system is used to evaporate the brine from the effluent treatment plant having a TDS concentration of 100000 mg/L. The evaporator unit consists of 40 pans with a total evaporation surface area of 60 m^2. The footprint area of the installed system is 4 m^2. In the tested arrangement, the brine feed to the evaporator is given at ambient water temperature without any external heating provision. The exclusion of the heating source is chosen to have a fair comparison with the pond evaporation system. The measured parameters along with a list of instruments are given in Table 3. The data logging interval for all parameters in 1 minute. The irradiation for the test site is obtained from weather data station located 10 km from the test site.

Tab. 3: List of measurement parameters and instrument details

S.No	Parameter	Instrument	Model No	Range	Resolution	Accuracy	Logging time
1	Temperatures (Ambient/Brine)	Temperature sensor	PT100	(-200 to 800 ºC)	0.001 ºC	0.015	1 minute
2	Wind speed	Anemometer	HTC AVM 07	0.8 to 30 m/s	0.01 m/s	±2 %	1 minute
3	Relative humidity	Hygrometer	RHT10	0 to 100 %	0.1% RH	±3 %	1 minute
4	Global horizontal irradiation	Extracted from a calibrated weather station					1 minute

Testing is performed for 64 days from April to June 2019. The testing setup is shown in Figure 5. The average ambient temperature, wind speed, and R.H value for the tested period are 30.4 ºC, 1.4 m/s, and 43.2 % respectively, and the daily variation for these parameters is shown in Figure 6.

Fig. 5: Overview of the testing setup

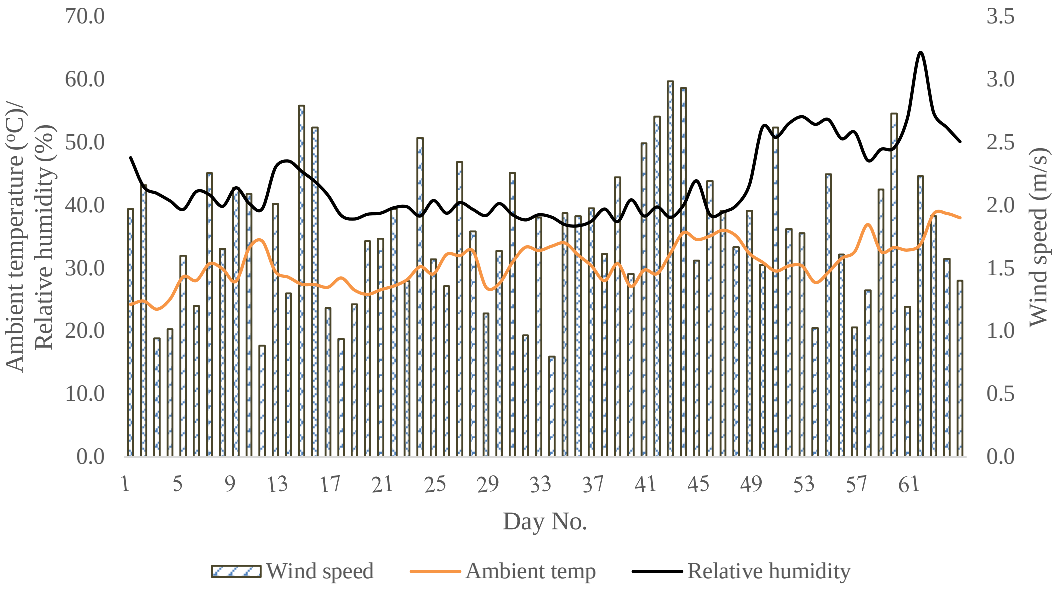

Fig. 6: Daily variation in meteorological parameter

Measurements show that the total quantity of brine evaporated during the testing period is 35.9 m^3, with total system operational hours of 1233. The analysis shows that the hourly average evaporation rate is 29.1 L/h, SER is 0.48 L/(h·m^2), and SER_{fp} is 7.29 L/(h·m^2). The variation in evaporated brine quantity per day is shown in Figure 7.

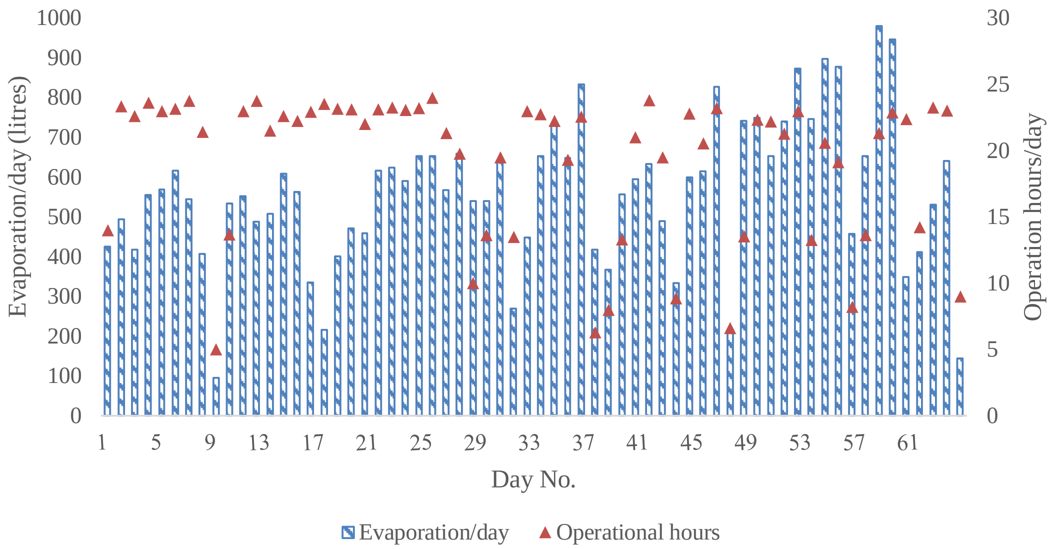

Fig. 7: Variation of evaporation quantity per day

The results show a strong effect of relative humidity and ambient temperature on the evaporation rate as shown in Figure 8. As expected, SER is higher at high ambient temperature and lower relative humidity conditions. However, the evaporation rate is dependent on a complex interplay of meteorological parameters and operating condition, and justify the higher evaporation rate for some point despite low ambient temperature and higher relative humidity conditions.

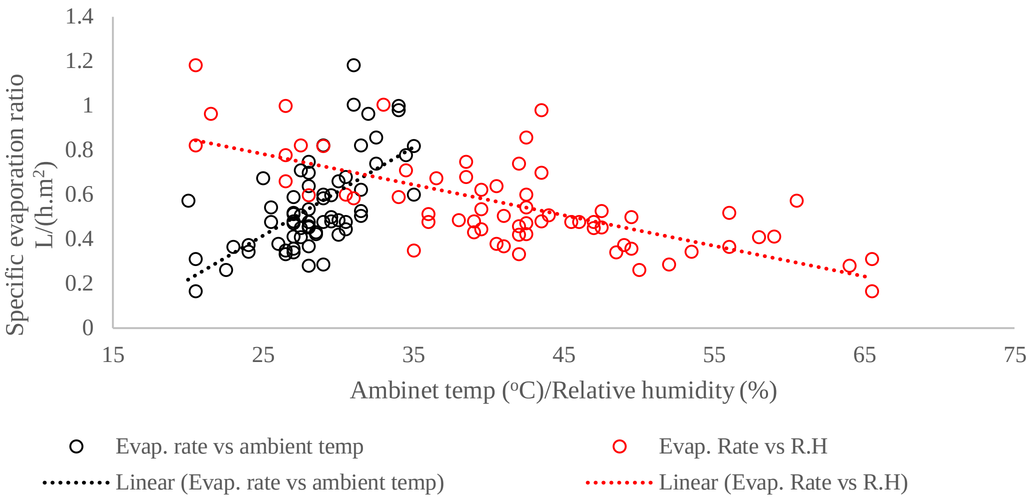

Fig. 8: Effect of R.H and ambient temperature on Specific evaporation ratio

In the proposed evaporation system, electricity is consumed by fans, water pumps, and electronic components of the control system. The average electricity consumption of fans and the water pump is measured at 19.2 kWh/m^3. The operational cost of evaporation with the proposed system is 0.15 Rs/L (1.7 €/m^3) calculated at an electricity price of 8 Rs./kWh (91 €/MWh), and Rs. to € conversion rate of 0.0113.

The performance results are compared with a hypothetical evaporation pond using an analytical model as explained in sub-section 3.4. Pond surface area is assumed at 60 m^2, which is equal to the total evaporation surface area in the proposed evaporator. The footprint area for the pond is assumed the same as its surface area i.e. 60 m^2. R.H data used in the analytical model is derived from a separate hygrometer installed in an open area to avoid uncertainties due to the localised humidity zone near Quadsun evaporator. The irradiation data is obtained from ground-based weather stations near the test site. The average daily GHI for the testing period 6.7 kWh/m^2 and the daily variation in GHI is shown in Figure 9.

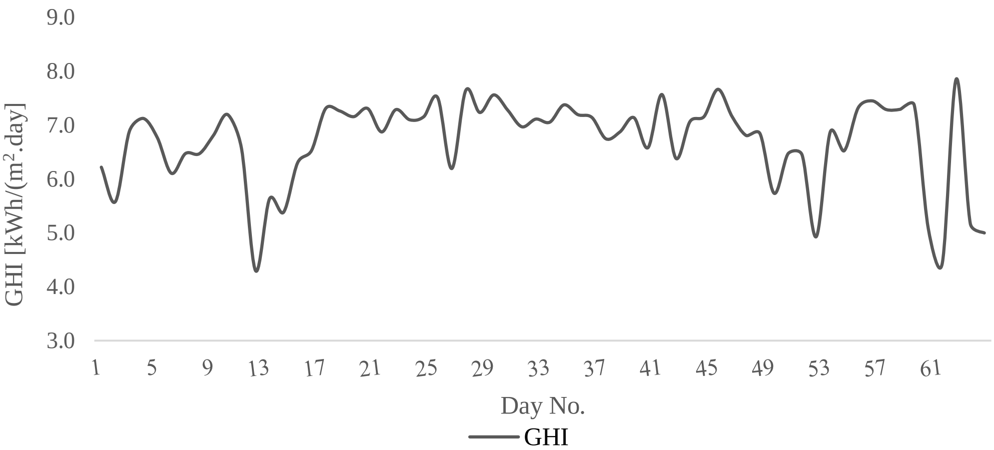

Fig. 9: Daily variation in global horizontal irradiation during the testing period

The pond model predicts the average evaporation of 3.1 L/(day·m^2), with a peak value of 4.5 L/(day·m^2). The model results match well with measurements from a real pond detailed in Sampathakar et. al (2001). The simulation results show a total evaporation of 9.4 m^3 evaluated for the same operational hours as QS evaporator (1233 hours). The hourly average evaporation rate for 60 m^2 pond surface area is calculated at 7.6 L/h, with SER and SER_{fp} of 0.12 L/(h·m^2). The results show that the proposed evaporator has a 3.8 times higher SER compared to the pond evaporator. Furthermore, the designed evaporator can be imagined as a stacked version of pond evaporator, which leads to significant land savings for end-users. Analysis reveals that SER_{fp} for QS evaporator is 57 times higher compared to the pond evaporator. This is because the proposed evaporator requires nearly 4 m^2 footprint area for 60 m^2 evaporation surface area. The comparison of cumulative evaporation and SER is shown in Figure 10.

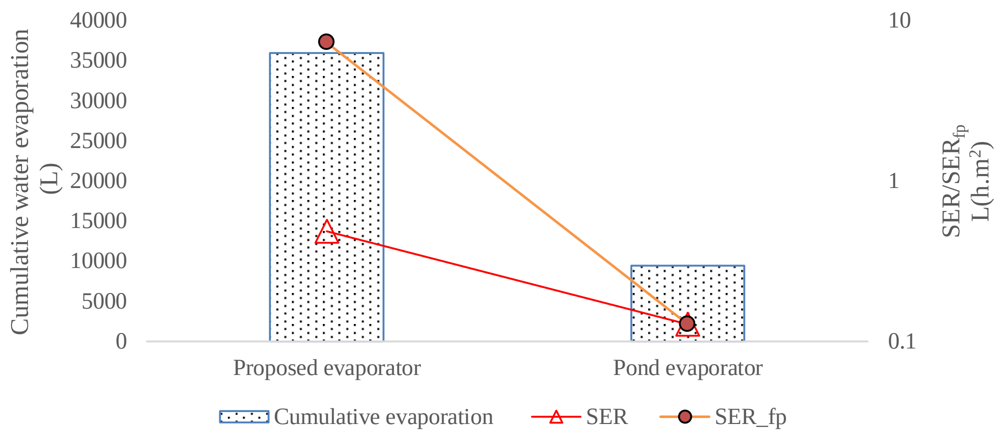

Fig. 10: Comparison of total evaporation and specific evaporation ratio

5 LIMITATIONS

The data analysis is detailed in approach however limited to only one climatic context. System performance will have significant seasonal variation, and thus needs evaluation. The data for rainy days is omitted from the analysis. To have a fair comparison, the operational hours of the pond evaporation is considered equal to the proposed evaporator. In reality, the pond system will evaporate for 24 hours daily as there are no mechanical/electrical components involved. During rainy seasons, rainwater can accumulate in these ponds and most industries have no provision of covering these ponds. This can have a negative impact on evaporation however, this effect is not considered in this study. Future work can include a detailed economic analysis along with land savings potential.

6 DISCUSSION

An evaporator unit is developed, and the field-testing results for the Northern Indian climatic context is presented. The developed evaporator aims to address the challenges of existing evaporation systems by minimizing the operational cost, land area requirement, heat, and electricity consumption of the system. The stringent control strategy is based on data-driven optimisation which keeps the system electricity consumption to a minimum while maximizing the evaporation rate. The testing data over 64 days is presented, which results in an average evaporation rate of 0.48 L/(h·m^2). The system has a footprint area of 4 m^2 and evaporates about 36 m^3 of brine in 64 days with total operational hours of 1233. The operational cost of evaporation is evaluated at 0.15 Rs./L, which is about 4 times less than the conventional brine management systems. A comparison with the pond evaporation system reveals significant improvement in the evaporation rate with the proposed evaporator design. The SER for the proposed evaporator is 3.8x higher achieved at 15x less footprint area. The evaporator holds tremendous potential and can be integrated with solar heat and PV to provide a complete sustainable solution to industries.

REFERENCES

Akridge, D. Glen, Methods for calculating brine evaporation rates during salt production, Journal of Archaelogical Science 35, 1453-1462, 2008

Furn, K, 2004. Effects of dyeing and bleaching industries on the area around the Orathupalayam Dam in Southern India (Dissertation). Institutionen för geovetenskaper, Uppsala. Retrieved from http://urn.kb.se/resolve?urn=urn:nbn:se:uu:diva-88862

Grönwall,J., Jonsson,A., 2017. Regulating Effluents From India's Textile Sector: New Commands and Compliance Monitoring for Zero Liquid Discharge, Stockholm International Water Institute.

Grönwall,J., and Jonsson,A.C., 2017b. The Impact of 'zero' coming into fashion: Zero Liquid Discharge uptake and socio-technical transitions in Tirupur. Water Alternatives 10(2): 602-624.

Gutierrez, O., 1993. Effect of Wetted Floating Fins on Water-Atmosphere Heat Exchange. *Journal of Energy Engineering*, 119(1), pp.32-42.

IEA solar heating and cooling program. 2018. Solar energy in industrial water and waste water treatment [online]. Avilable www.task62.iea-shc.org [Accessed : 25-July-2020]

Kannan,S.,and Rao,G., 2000. A study of the design of solar evaporation pan, Indian Journal of Chemical Technology 7(6):326-331

Lee, K., Arnot, T., and Mattia, D., 2011. A review of reverse osmosis membrane materials for desalination—Development to date and future potential. *Journal of Membrane Science*, 370(1-2), pp.1-22.

Murty, M N., and Dasgupta, Ajit, K.,1985. Economic Evaluation of Water Pollution Abatement: A Case Study of Paper and Pulp Industry in India. Indian Economic Review.20 (2), 1985 .231-267.

Nafey, A., Fath, H. and Mabrouk, A., 2006. Thermo-economic investigation of multi effect evaporation (MEE) and hybrid multi effect evaporation—multi stage flash (MEE-MSF) systems. *Desalination*, 201(1-3), pp.241-254.

Narayanan,S., 2015. Tirupur dyeing units told to close *Down To Earth*. Available: https://www.downtoearth.org.in/news/tirupur-dyeing-units-told-to-close-33025. [Accessed: 06-Aug-2020].

Penman, H.L., Natural Evaporation from open water, bare soil, and grass. Proceedings of the Royal Society Series A 193, 120-145, 1948

Philip, L., Reddy, K., Kumar, B., Bhallamudi, S. and Kannan, A., 2013. Performance evaluation of a solar and wind aided cross-flow evaporator for RO reject management. *Desalination*, 317, pp.1-10.

Quadsun Solar, 2020. Presenting the future of solar energy. [Online]. Available: http://quadsunsolar.com/. [Accessed: 06-Aug-2020].

Rajaram, T. and Das, A., 2008. Water pollution by industrial effluents in India: Discharge scenarios and case for participatory ecosystem specific local regulation. *Futures*, 40(1), pp.56-69.

Reilly,D.,2009. Evaporation Enhancement from Evaporation Ponds Using Collector Plate Units. School of Civil, Environmental and Chemical Engineering Science, Engineering and Technology Portfolio, RMIT University, Australia.

Sampathkumar,S., and viswanathan,m., 2001. Accelerated evaporation of saline streams in solar pans. Regional program for pollution control in tanning industries in South East Asia, UNIDO.

Williams, E., Salt production in the coastal area of Michoacan, Mexico. Ancient Mesoamerica 13, 237-253, 2002.

Chiang. T.C., The production of salt in China, 1644 – 1911. Annals of the Associations of American Geographers 66, 516 – 530, 1976.

Performance enhancement of a chimney operated passive solar dryer

Gedion Habtay[1], Janos Buzas[2] and István Farkas[2]

[1]Mechanical Engineering Doctoral School Szent István University, Páter K. u. 1., Gödöllő, H-2100 Hungary

[2]Department of Physics and Process Control, Szent István University Páter K. u. 1., Gödöllő, H-2100, Hungary

Abstract

This paper presents a performance evaluation of a passive solar dryer by a chimney effect experimentally. In this study, three different configurations of solar dryers have been proposed: two passive dryers (Case-1 and Case-2) and an active dryer (Case-3), one of the passive dryer with a chimney (Case-2) and the other without a chimney (Case-1). The energy and exergy efficiencies have been determined for the proposed solar dryers, and comparisons were made with one another. It also presents the effect of temperature rise and airflow rate. Thermocouples were placed to different locations along the solar dryer to collect temperature data for experimental analysis. The energy efficiency varied from 3% to 7% for Case-1, from 20% to 26% for Case-2, and from 21% to 42% for Case-3, while the exergy efficiency changed between 2% and 12% for all cases. The highest exergy efficiency was achieved by Case-1. The results revealed that a chimney dryer improved the airflow rate to a maximum of 0.71 $m.s^{-1}$ while a dryer without a chimney was 0.3 $m.s^{-1}$. Moreover, this paper found that energy efficiency increased with the airflow rate, whereas exergy efficiency decreased.

Key-words. Chimney effect, dryer, energy and exergy, solar air heater, solar radiation, temperature rise.

1. Introduction

Solar energy is fundamentally an inexhaustible source and capable of meeting some of the world's future energy needs. It is the most promising unconventional energy to contribute to low temperature applications like solar dryers and it is mainly dependent on location, availability of radiation, weather and time (Jain et al., 2017). Solar dryer is the oldest crop drying method that uses radiation from the sun as an input source. It is one of the energy intensive methods in which a large amount of energy is used to convert the moisture of the product into its vapour in the agricultural processing industry. The purpose of solar dryer is to reduce the water content of the products to the required moisture level to prevent the spoilage of the products (Belessiotis and Delyannis, 2011; El Hage et al., 2018).

The performance of solar dryers is determined by many factors such as the nature of dryers, intensity of solar radiation, ambient condition, drying rate, etc. (Mustayen et al., 2015). Solar dryers are broadly classified into natural convection dryers and forced convection dryers based on the mode of airflow. The air movement in natural convection is due to the buoyancy effect. This type of dryer normally operates inefficiently because the air circulation is poor (Ekechukwu and Norton, 1997). This results in higher temperature in the drying chamber which leads to burning of the product. The problem can be combated by using a properly designed chimney which can increase the air flow through the drying system (Habtay et al., 2019 and Afriyie et al., 2009).

The chimney effect has been studied in the past, but very few previous experiments have been considered in terms of enhanced convection. Senadeera and Kalugalage (2004) suggested that a chimney with polyethylene has a higher efficiency than the GI sheet metal chimney. In order to obtain a higher air flow rate in the drying system, the chimney should be heated so that mean air temperature in the chimney is higher than the ambient temperature. The effect of the chimney on the thermal performance of the solar air collectors has not been fully investigated experimentally.

Various researchers have experimentally performed exergy analysis of solar air collectors in addition to energy analysis (Benli, 2013; Esen, 2008). Exergy analysis estimates the efficient use of solar radiant energy and is used

doi:10.18086/eurosun.2020.03.04 Available at http://proceedings.ises.org

to improve the efficiency of a thermal system. Bouadila et al. (2014) studied the energy and exergy efficiency on solar air collectors experimentally using the equations of the first and second laws of thermodynamics. Their result showed that the daily average energy and exergy efficiencies were 40% and 22%, and it was also found that the collector outlet temperature is affected by the airflow velocity.

This study is concerned with investigating the effect of chimney on the thermal performance of the solar air collector of an indirect solar dryer experimentally under the no-load condition and using the equations of the first and second laws of thermodynamics. Three cases were tested in this study: Case-1: passive solar dryer without chimney; Case-2: same as Case-1 but with chimney; Case-3: active solar dryer. In addition, the comparison between a natural and an active solar dryer is investigated based on the presence of a chimney in a natural solar dryer.

2. Materials and Methods

The experimental study has been carried out in the Solar Laboratory of Szent István University, Gödöllő, Hungary. The latitude and longitude of the site are 47°35'24'' N and 19°21'36'' E, respectively. Solar insolation, ambient temperature, inlet airflow velocity, and temperatures at specific locations on the solar dryer were measured and recorded on 25 and 27 of September 2019. The duration of the measurement is from 10:00 to 15:00. The system has a height of 4.20 m and consists of a cylindrical chimney, a drying chamber, and a solar air collector. An appropriate chimney length has been considered to ensure thermally fully developed conditions at the chimney exit. The chimney was made up of plastic (PVC) pipe painted with matt black on its outer surface and installed at the exit end of the drying chamber. The characterization of the airflow inside the dryer included the determination of the meteorological and flow conditions.

2.1. Experiment set-up

The parameters to be measured for this study include collector inlet and outlet air temperatures, chimney outlet and ambient temperatures, airflow velocity at the collector inlet, and solar irradiation intensity on the collector surface. The experimental set-up is shown in Fig. 1.

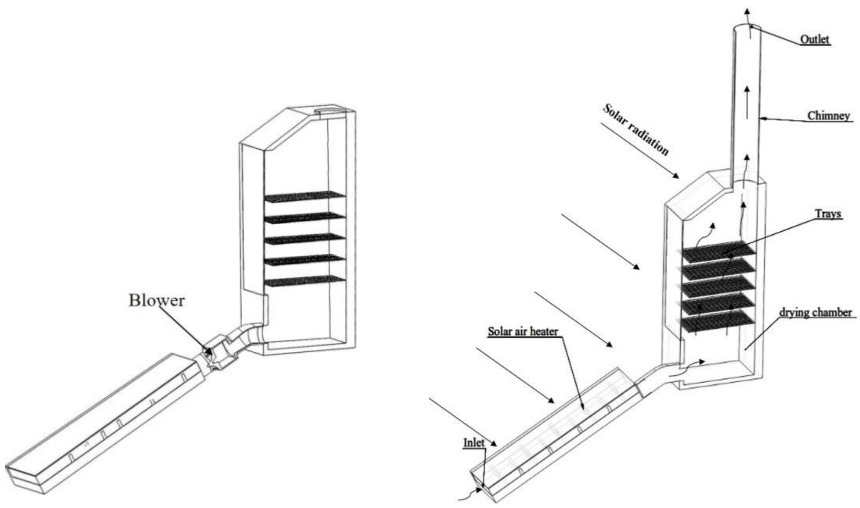

Fig. 1: Sectional view of a forced and natural convection solar dryers

The measuring devices used in this study are listed in Table 1. Temperatures were measured using the K-type thermocouple at different locations on the solar dryer. Each thermocouple was installed in the data logger and recorded automatically. The global solar radiation on the collector was measured using a pyranometer, with the sensor connected to the interface ADAMS 4018, which converts a digital signal in the data acquisition system. The air velocity at the collector inlet was measured using a digital handheld anemometer with an accuracy of ±0.3%.

Tab. 1: Apparatus used for data measurement

Instruments	Company, Country	Specification
Pyranometer	CM-11, Kipp & Zonen, Italy	Max: 4000 W m^{-2}
Thermocouple	8CH temperature data logger (KRIDA electronics), Latvia	-55 °C to 125 °C
Handheld anemometer	EC-MR 330 Eurochron GmbH, Germany	0 to 30 m s^{-2}

2.2. Energy and exergy analysis

The first and second laws of thermodynamics were used to investigate the energy and exergy efficiency of the solar air collector. The energy efficiency of the solar air collector is defined based on the first law of thermodynamics:

$$\eta_i = \frac{Q_u}{IA_c}. \qquad \text{(eq. 1)}$$

The useful energy gain for the presented system is calculated as follows:

$$Q_u = \dot{m}C_p(T_o - T_i), \qquad \text{(eq. 2)}$$

where,

Q_u (W) is the useful energy gain

I (W m^{-2}) is solar radiation intensity

A_c (m^2) is the collector area

$\dot{m}$ (kg.s^{-1}) is the mass flow rate at the collector inlet

C_p (J kg^{-1} K^{-1}) is the specific heat capacity of air

T_i and T_o (K) are the collector inlet and outlet air temperature

The exergy efficiency can be calculated on the basis of the second law of thermodynamics as the ratio of the exergy absorbed by the moving air to the exergy of the solar radiation on the collector:

$$\eta_{ii} = \frac{Ex_u}{Ex_{in}}. \qquad \text{(eq. 3)}$$

The useful exergy gain by air in the collector is defined as:

$$\mathrm{Ex_u} = \dot{m}\left[\mathrm{C_p}(\mathrm{T_o} - \mathrm{T_i}) - \mathrm{T_a}\left(\mathrm{C_v}\mathrm{Ln}\left(\frac{\mathrm{T_o}}{\mathrm{T_i}}\right) - \mathrm{RLn}\left(\frac{\rho_o}{\rho_i}\right)\right)\right] \qquad \text{(eq. 4)}$$

and the input exergy of the sun radiation is defined as (Bahrehmand et al., 2015):

$$\mathrm{Ex_{in}} = \left(1 + \frac{1}{3}\left(\frac{\mathrm{T_a}}{\mathrm{T_s}}\right)^4 - \frac{4\mathrm{T_a}}{3\mathrm{T_s}}\right)\mathrm{IA_c}\ , \qquad \text{(eq. 5)}$$

where,

η_{ii} (%) is the exergy efficiency of the collector

Ex_u(W) is the actual exergy delivered to the air

Ex_{in}(W) is the input exergy of the sun radiation

R (287 $J.kg^{-1}.K^{-1}$) is universal gas constant

ρ_i and ρ_o ($kg.m^{-3}$) are the air density

Ta (K) is the temperature of the ambient

Ts (K) is the temperature of the sun, 5600 K is assumed.

3. Results and Discussion

In this study, three different solar dryer arrangements were investigated experimentally. The energy and exergy efficiency of three different configurations were calculated directly from the data of each study case. The experimental results are presented in the form of graphs describing solar insolation, temperature rise through the collector, airflow velocity, energy efficiency and exergy efficiency as a function of time of day.

3.1. Airflow velocity and dry air temperature

The variation of airflow velocity at the collector inlet, dry air temperature at the chimney outlet (for Case-2) and at the drying chamber outlet (Case-1) as a function of time are shown in Fig. 2. During the experiments, the drying air temperature for Case-2 ranged from 29 to 51°C, and drying air temperature for Case-1 ranged from 46 to 57°C. The trend of temperature variations was similar for both cases. The variation in air temperature is mainly due to the occurrence of incident radiation on the dryer surface.

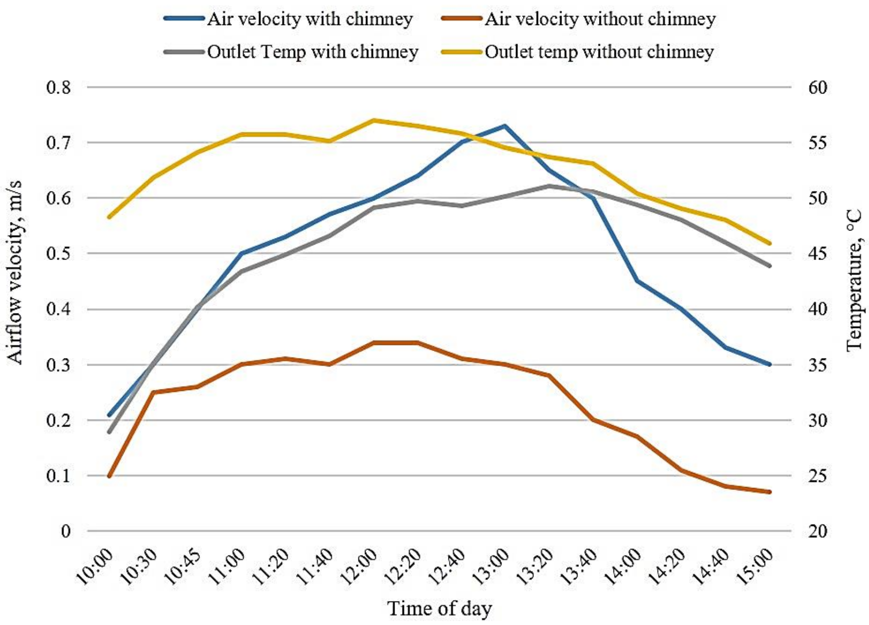

Fig. 2: Comparison of airflow and outlet temperature of a solar dryer with and without a chimney

The velocity of the flowing air was measured at the collector inlet. Fig.2 shows the recorded value of airflow velocity as a function of time. The airflow velocity for Case-1 was about 0.3 $m. s^{-1}$ while Case-2 obtained 0.7 $m. s^{-1}$. This increased airflow velocity showed that the passive solar dryer with a chimney (Case-2) was able to provide 60% more airflow than the one without a chimney (Case-1) under similar climatic conditions. The result can be explained by the fact that the airflow increases with the presence of the chimney. Chen and Qu (2014) made a similar observation. The airflow rate is mainly affected by the chimney height and the temperature difference between the average air temperature in the chimney and the ambient temperature. Fig. 2 also shows almost the same pattern in air temperature and velocity across dryer systems.

3.2 Temperature rise and solar radiation intensity at solar air collector

Fig. 3 (a-c) shows the variation of flowing air temperature at the inlet and outlet of the solar air heater and the solar radiation intensity measured during the experimental days. The values of solar radiation change in the range of 560 W m^{-2} and 950 W m^{-2} and reach the maximum at noon time. The inlet and outlet temperatures varied almost linearly with the incident solar radiation. Case-1 had a higher temperature rise than Case-3 and no significant difference with Case-2. As known, at lower air flow rate the air have more time to get hot inside the collector. It can also be seen that the average clearness index for Case-1, Case-2, and Case-3 are 0.49, 0.50, and 0.64 respectively. The clearness index is defined as the ratio of daily radiation to extraterrestrial radiation for the day (Duffie and Beckman, 2013). It indicates the clearer days (higher clearness indexes correspond to clearer days). The variation of temperature rises for Case-1, Case-2, and Case-3 are 9 to 23 °C, 7 to 18 °C, and 4 to 8 °C, respectively.

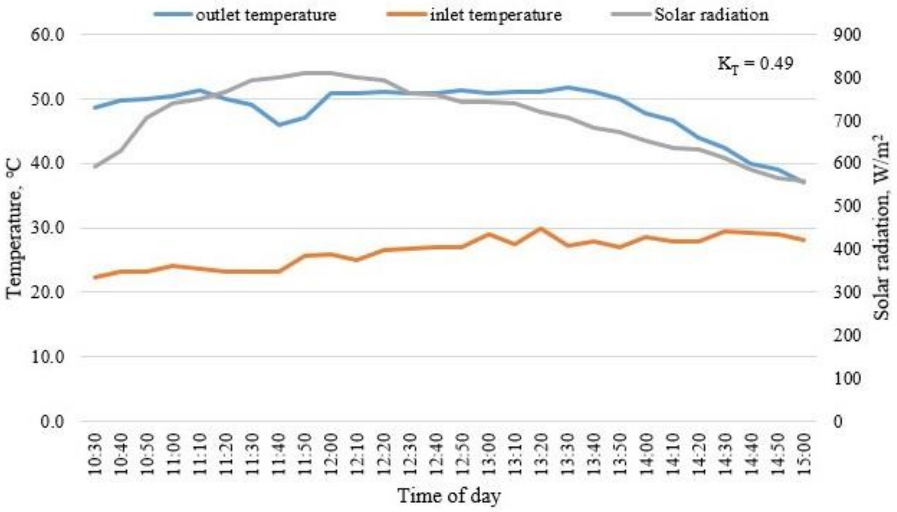

(a)

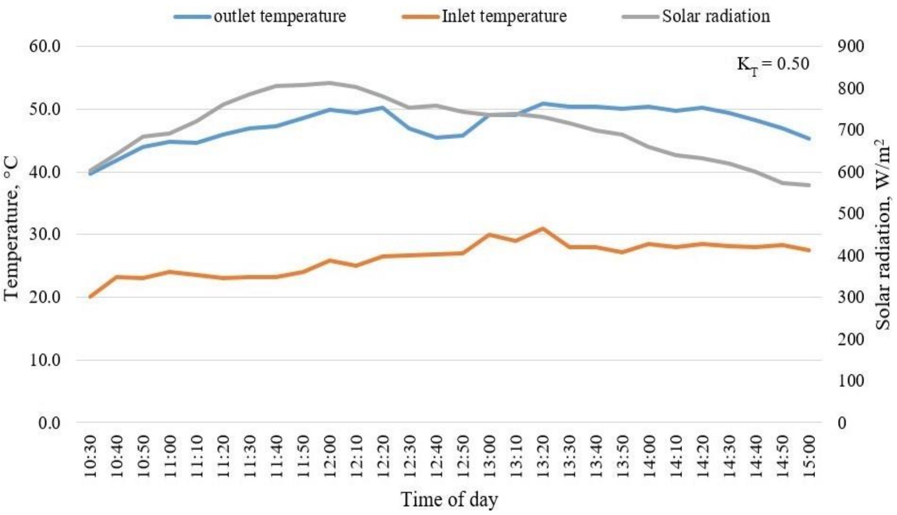

(b)

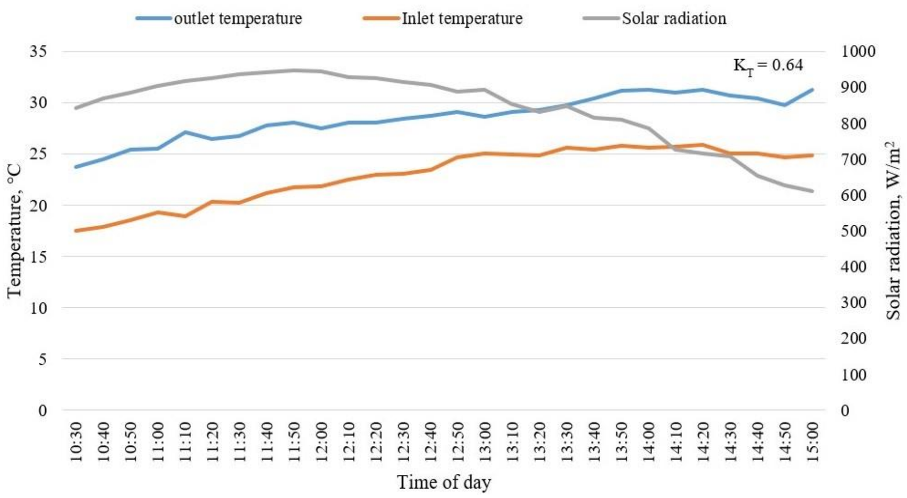

(c)

Fig. 3: Collector inlet and outlet temperatures and solar radiation: (a) Case 1; (b) Case 2; and (c) Case 3

3.3 Energy and exergy efficiencies of the collector

A plot of computed (using Eq. 1 and Eq.2) hourly energy and exergy efficiency curve of the collector for the three Cases (1-3) is shown in Fig. 4. Fig. 4(a) presents the energy efficiency of the collector. The efficiency varies between 3% and 7% for Case-1, between 20% and 26% for Case-2, and between 21% and 42% for Case-3. The highest energy efficiency was found for Case-3, whereas the lowest values were obtained for the dryer without a chimney (Case-1). This can be explained that airflow rate is very high in active solar dryer. The range of variation of the resulting values is due to variations of climatic conditions. The energy efficiency for Case-3 is higher, around 83.6% and 26% by comparing Case-1 and Case-2, respectively. The result show that a negative relationship between energy efficiency and temperature rise was observed. The trends of the daily exergy efficiency in all the cases were similar.

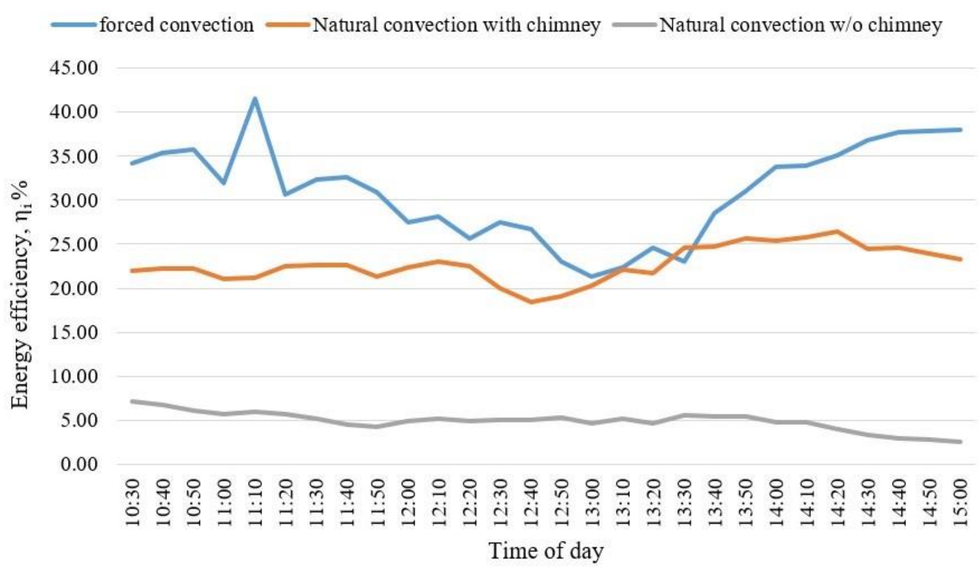

(a)

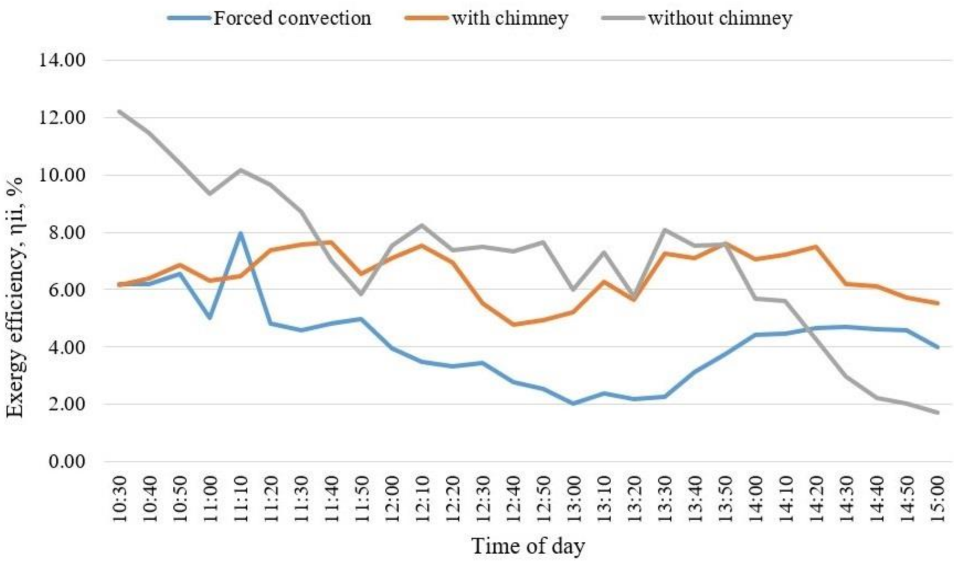

(b)

Fig. 4: The instantaneous energy and exergy efficiencies

The exergy efficiency on the collector, based on the three configurations, against the time of day is presented in Fig. 4(b). Solar dryer without chimney (Case-1) was obtained the highest exergy efficiency in comparison with active solar dryer due to low airflow rate occurred in this dryer. The values of exergy efficiency computed using Eq. (2) varies from 2 % to 12% in Case-1, from 5% to 8% in Case-2, and from 2% to 8% in Case-3. The variation of the efficiency value of chimney solar dryer and active solar dryer was similar. The exergy efficiency order of the three configurations was determined as dryer without a chimney, dryer with a chimney, and active solar dryer. It was observed that by lowering the airflow rate the exergy efficiency increased linearly. Table-2 presents the summary results of average daily energy and exergy gain together with energy and exergy efficiency. The highest total energy gain was obtained by the active solar dryer and followed by a chimney dryer. When compared as a percentage of the daily exergy gain, it was clearly seen that Case-2 had a higher percentage of exergy gain than Case-3. However, energy efficiency of Case-2 had a lower value than that of Case-3. As known, the air flow rate is the most significant parameter in evaluating a solar air collector's thermal efficiency.

Tab. 2: Average daily energy and exergy efficiency

Type	Energy gain (kJ)	Exergy gain (kJ)	Energy efficiency %	Exergy efficiency %
Case-1	358.2	479	5.01	7.16
Case-2	1628.2	438.64	22.62	6.56
Case-3	2615.21	332.33	30.52	4.17

4. Conclusions

Main conclusions derived from the results of the present study as follows:

- The highest energy efficiency of the collector was achieved by the active solar dryer, whereas the lowest values were obtained for passive solar dryer without a chimney.
- The performance of a passive solar dryer can be enhanced by the chimney.
- The energy efficiency depends significantly on the solar radiation and air flow rate.
- The values of energy efficiency varied from 3% to 26% for passive solar dryer and from 21% to 42% for active solar dryer.
- The exergy efficiency of the collector under passive solar dryer without a chimney was found high in

this study.

- Energy efficiency is not sufficient to evaluate the performance of the dryer system. Exergy efficiency is a reciprocal of energy efficiency.
- This study will be beneficial to the interested researcher in the performance improvement of the passive solar dyers.

5. Acknowledgments

This work was supported by the Stipendium Hungaricum Programme and by the Doctoral School of Mechanical engineering, Szent István University, Gödöllő, Hungary.

6. References

Afriyie, J.K., Nazha, M.A., Rajakaruna, H., Forson, F.K., 2009. Experimental investigations of a chimney-dependent solar crop dryer. Renew. Energy 34, 217-222. https://doi.org/10.1016/j.renene.2008.04.010

Bahrehmand, D., Ameri M., Gholampour, M., 2015. Energy and Exergy Analysis of different Solar Air Collector Systems with Forced Convection. *Renew. Energy*, 83, 1119-1130.

Belessiotis, V., Delyannis, E., 2011. Solar drying. Sol. Energy 85, 1665–1691. https://doi.org/10.1016/j.solener.2009.10.001

Benli, H., 2013. Experimentally derived efficiency and exergy analysis of a new solar air heater having different surface shapes. Renew. Energy, 50, 58-67.

Bouadila, S., Lazaar, M., Skouri, S., Kooli, S. and Farhat, A., 2014. Energy and exergy analysis of a new solar air heater with latent storage energy. Int. J. of Hydrogen Energy, *39*(27), 15266-15274.

Chen, w., Qu, M., 2014. Analysis of the heat transfer and airflow in solar chimney drying system with porous absorber. Renew. Energy 63, 511–518. https://doi.org/10.1016/j.renene.2013.10.006

Duffie, J., Beckman, W., 2013. Solar Engineering of Thermal Processes, Fourth ed, John Wiley & Sons, New Jersey.

Ekechukwu, O.V., Norton, B., 1997. Design and measured performance of a solar chimney for natural-circulation solar energy dryers. Renew. Energy. 10, 81–90. https://doi.org/10.1016/0960-1481(96)00005-5

El Hage, H., Herez, A., Ramadan, M., Bazzi, H., Khaled, M., 2018. An investigation on solar drying: A review with economic and environmental assessment. Energy 157, 815-829. https://doi.org/10.1016/j.energy.2018.05.197

Esen, H., 2008. Experimental energy and exergy analysis of a double-flow solar air heater having different obstacles on absorber plates. Building and Environ. *43*(6), 1046-1054.

Habtay G., Buzás J., Farkas I., 2019. Mathematical modelling of cylindrical chimney effect in solar dyer, Hungarian Agricultural Engineering 36, 69-74. http://doi.org/10.17676/HAE.2019.36.69

Jain, S.K., Agrawal, G.D., Mishra, R., 2017. Review on thermal performance enhancement of solar air heater using artificial roughness. Intr. Conference on Technological Advancements in Power and Energy (TAP Energy), 1-6. DOI: 10.1109/TAPENERGY.2017.8397248

Mustayen, A.G., Rahman, M.M., Mekhilef, S., Saidur, R., 2015. Performance evaluation of a solar powered air dryer for white oyster mushroom drying. Int. J. of Green Energy. 12, 1113-1121. https://doi.org/10.1080/15435075.2014.891221

Senadeera, W., Kalugalage,I., 2004. Performance evaluation of an affordable solar dryer for drying crops. In proceeding of the Biennial conference of the Society for Engineering in Agriculture, Australia, 1-7.

Hybrid Solar Heat Generation Modelling and Cases

Parthiv Kurup[1], Sertaç Akar[1], Josh McTigue[1] and Matt Boyd[1]

[1] National Renewable Energy Laboratory, Golden, Colorado (USA)

Abstract

Renewable thermal energy systems (RTES) harness renewable energy sources to provide services for space heating and cooling, district heating, domestic hot water, and industrial process heat (IPH). The use of low-pressure steam generated by the combustion of fossil fuels is common today to provide process heat for industrial facilities. Solar IPH (SIPH) technologies could economically replace the steam or heat needs at many industrial sites by providing high-temperature pressurized hot water, a heat transfer fluid (HTF) such as synthetic-oil, or direct steam (Kurup and Turchi, 2015). RTES could be hybridized with technology options or combined with the existing heat supply (e.g. fuels), to give options for targeted IPH application and the reduction of fuel consumption. This work has tested hybrid system modelling approaches. Initial results show when a natural gas (NG) burner that feeds an IPH application of 300°C, has both air and NG streams pre-heated with a solar field/RTES exit temperature of 180°C (via an HTF), a 13% NG offset is possible. NG offsets reach up to 26%, when the RTES exit temperatures are at 300°C for a given annual capacity factor of 24%. This can be even higher with addition of thermal energy storage (TES).

Keywords: Solar Industrial Process Heat (SIPH), Hybrid System Modeling, System Advisor Model (SAM), RTES

1. Introduction

In 2017 the International Energy Agency (IEA) estimated that 32% of total global energy is consumed by industry. Of that, it was found that 74% of the total industrial energy is used for industrial process heat (IPH). It should be noted that 90% of the IPH provided comes from fuels such as coal, NG and oil (Philibert, 2017). Varying fuel prices, along with calls to divest from fossil fuels, creates a strong incentive to switch to renewable heat solutions in industry, but currently renewably sourced heat, including biomass, represents only 10% of the global heat demand (IEA, 2018). At the time of writing, only one country (Denmark) had a 100% renewable heat target, compared to 57 countries with 100% renewable electricity targets (REN21, 2020). Denmark is also the only country to have a 100% final energy target to be met by renewables (REN21, 2020). Buildings and industrial thermal energy applications require different temperature ranges, quantities, and rates of thermal energy (Schoeneberger et al., 2020). Hybrid solutions and thermal energy storage (TES) will be important for the dispatch of heat, at optimal times needed by the demand side of the buildings and industrial applications. Denmark is a prime example where hybrid renewable thermal energy system (RTES) solutions are being deployed and are cost competitive with the current regional NG costs in Denmark. A hybrid RTES in Tårs, Denmark, that combines flat plate collectors (FPCs) and concentrating solar power (CSP) parabolic trough collectors (PTCs) coupled in series, with water storage has been operational since 2015 (Perers et al., 2016). This hybrid RTES connects to the existing gas fired district heating system and can meet approximately 30% of the town's annual district heating needs (Aalborg CSP, 2015; Putz and Epp, 2019). It is worth noting the hybrid RTES for the town of 840 households, had an estimated levelized cost of heat (LCOH) of approximately €30/megawatt hour thermal (MWh_{th}) or USD $\$33/MWh_{th}$ [as of 29th Nov. 2019 (X-Rates, 2020)], compared to €62/MWh_{th} ($\$68/MWh_{th}$ as of 29th Nov. 2019) for the average heat cost from the existing gas boilers (Putz and Epp, 2019). As can be seen, the LCOH of a hybrid RTES system even in latitudes such as Denmark, can be competitive with the costs of operations from NG, given sufficient solar thermal yield and high enough gas prices.

The National Renewable Energy Laboratory (NREL) System Advisor Model (SAM) is a well-established tool for modeling solar heat systems (Wagner and Gilman, 2011). Solar water heating (SWH) with glazed and evacuated tube FPCs, Linear Fresnel Collectors (LFCs), and PTCs can already be modeled to evaluate the thermal yield. SAM's CSP models for IPH can use PTC and LFC technologies, that can either deliver heat to an HTF, or directly via direct steam generation (DSG). The HTF for the CSP process heat module can be molten salt, synthetic oil, or pressurized steam. To note, no SIPH plants where molten salt as the HTF have been found to date, and as such this is not considered viable yet for industry. The SWH and CSP annual thermal outputs can be post-processed with existing financial models from the SAM to calculate financial metrics such as the LCOH and net present

doi:10.18086/eurosun.2020.03.05 Available at http://proceedings.ises.org

value (NPV), though for the highlighted cases studies, detailed economic evaluation is outside of the current scope of this paper. Currently, the public version of SAM (2020.2.29) can do single system modelling very well but it is not yet capable of hybrid RTES modelling at different temperatures or combining technologies such as FPCs and CSP. For this paper and work, SAM 2020.2.29 has been used for the CSP process heat modules (NREL, 2020a).

2. Methodology

We have developed an initial framework and a variety of approaches to hybrid system modeling for RTES at different temperatures or combinations of technologies. This framework is detailed in a paper expected to be published through SolarPACES 2020, while this paper focuses on some of the main results from the modelling scenarios. Initial models to test key hybrid systems are designed based on commercially available solar heat technologies such as FPCs, LFCs and PTCs, which are suitable for integration with TES and conventional NG burners on industrial sites. As highlighted in Morocco, modelling studies have been undertaken looking at the use of LFCs which act as a pre-heat to an air stream entering an industrial NG burner (Laadel et al., 2018), where the modelling was done using the EBSILON Professional software. In this context, we used SAM, MATLAB, and the IPSEpro thermal process modeling software. The results from the three scenarios highlighted in this paper are:

- FPCs and PTCs with TES (using a synthetic oil)
- Constant and variable temperature PTCs with an HTF and NG burner
- DSG LFCs and Phase Change Material (PCM) storage

The first case scenario, using the separate SAM modules, is designed to pre-heat the HTF (Therminol-VP1) through the FPC system, and then send it to a PTC solar field coupled to the TES with an exit temperature of 300°C, which is more in line with medium temperature IPH applications. The IPH application could use the heated synthetic oil to heat a process or generate steam for a desired application.

The second case scenario, modelled in IPSEpro, uses a constant and varied solar field/RTES exit temperature (via an HTF) to provide heat to an air and/or fuel streams, that supply an existing NG burner system. This is expected to be suitable for hybridization of existing industrial systems that use NG burners today.

The third case scenario uses an array of DSG LFCs coupled with TES, which uses a PCM to improve the system's flexibility and capacity factor. The annual thermal output from SAM of individual heat generation models can be post-processed and combined with existing dispatch models for IPH and TES. PCMs store energy in the latent heat of the phase change and can thus achieve relatively high energy densities (Sharan et al., 2019).

3. Results

3.1. FPCs and PTCs with TES

The first scenario uses process heat modules that exist separately within SAM, i.e. the SWH, and the parabolic trough heat modules. The hybrid system is also combined with a TES. For this paper, the heated fluid exiting the PTCs can be used to either heat a process or generate steam for a desired application (Figure 1). The key innovation in this hybrid model is then to combine the modules for the hybrid RTES energy generation model. Note, the financials are not included currently in this hybrid model. This scenario is designed to pre-heat the HTF through an FPC system to an intermediate temperature, and then send it to a PTC system to reach the higher process heat temperature. This hybrid RTES is an existing and commercially operating system (e.g. the 6.8MW_{th} site in Tårs, Denmark), where the FPCs heat unpressurized water to approximately 75 °C, and the heated water is sent to the PTCs, where the exit temperature of the water is 98 °C (Aalborg CSP, 2015; Putz and Epp, 2019). This paper's scenario though allows for a high temperature HTF instead of an unpressurized water, and the concept is more suited for IPH application.

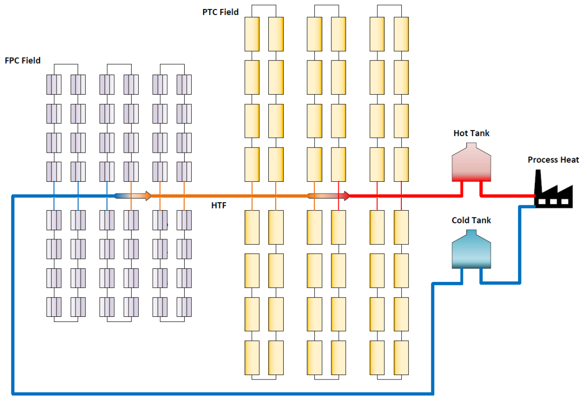

Figure 1 Schematic for Hybrid FPC and PTC model with TES for process heat application. (The relative size of the FPC and PTC system varies by IPH application and the land availability)

The hybrid FPC and PTC plant is sized according to the desired process heating power, temperature, hours of thermal storage, mass flow constraints and the nominal temperature into and out of the FPC field. The sizing procedure is similar to the sizing of a regular PTC-only plant: the heating power dictates the total size of the field, the process heat temperature dictates the number of PTCs in series, and the mass flow constraints of the PTCs dictate the number of subfields. However, with the hybrid plant, the PTC field is sized using a higher inlet temperature, resulting in fewer PTCs in series.

For this analysis, the FPC field is and sized according to the design mass flow, the relatively constant process heat, cold outlet temperature, and the target intermediate FPC outlet/PTC inlet design temperature. Note, this is an example FPC collector which can operate with the needed pressure from the available and pre-built SWH collectors for modelling which are available in SAM 20.2.29 (NREL, 2020a). A single HTF (Therminol VP-1) flows from the FPC field directly to the PTC field. The design mass flow is dictated by the design plant power and temperature, and in turn determines the number of FPCs in parallel. The temperature rise from the cold inlet to the intermediate temperature determines the number of FPCs in series. This sizing is performed at a constant standard ambient temperature and irradiance; however, since the FPCs are stationary and experience a range of cosine losses throughout the day and seasons, the intermediate temperature is always changing.

The PTC field is made up of troughs with 6m aperture width, and 80mm receivers. Again, this is an available selectable collector in the SAM parabolic trough process heat module, others are also available (NREL, 2020a). This variable intermediate temperature requires that the plant controller be more sophisticated than that for a regular PTC or regular FPC plant. The controller is similar to that for a PTC-only plant where the mass flow through the entire system regulates the outlet temperature. The PTCs are also still used to provide a high-temperature limit control via defocusing or pointing away from the sun. However, model convergence for this hybrid plant requires more algorithmic logic as the PTCs cannot as easily predict their inlet temperature iteration to iteration.

For this simulation, the default or base case TES sizing was for 8hrs of storage, to cover ramp-downs in the evening and ramp-ups in the morning. Both the FPCs and the PTCs are sized such that $5MW_{th}$ is delivered at the process heat sink or PTC to process heat exchanger (HX) via the Therminol VP-1. This is with a solar multiple of approximately 1.9. Table 1 shows the key assumptions and solar field sizes for this scenario. As can be seen, the FPCs have a solar field area of 918 m^2 and the PTCs a single loop aperture area of 2,624 m^2 with 8 actual loops. The system design is a test case to prove the operation of the hybrid model and it is not optimized to scale the solar field area for PTC. The ongoing work is focusing on optimization and dispatch modeling to scale down the PTC solar field area.

Table 1 Key assumptions and solar field sizes for FPCs and PTCs with TES scenario

Parameter	FPCs	PTCs
Collector Type	Heliodyne Gobi 400	SkyFuel SkyTrough (80mm)
HTF	Therminol VP-1	Therminol VP-1
Solar Field (m^2)	918	20,992
Design Inlet Temperature (°C)	27	150
Design Outlet Temperature (°C)	150	300

The SAM hybrid model produces hourly simulations for a specific location based on the annual typical meteorological year (TMY) file, which includes the hourly ambient temperature and the direct normal irradiation (DNI). In this scenario, the location of the simulated site is Lancaster, California, which has an annual average DNI of 7.93 kWh/m^2/day (NREL, 2020a). Note, the SAM tool can input TMY or weather files for simulations across the world, and for the United States the National Solar Radiation Database (NSRDB) has been used (NREL, 2020b).

The FPCs can potentially work with Therminol VP-1 which allows to use the same HTF in the PTC field. To give a sense of the overall impact of the hybrid RTES, annual simulations at hourly timesteps were performed. Figure 2 shows the annual profile of the heat sink inlet temperature, PTC inlet temperature, and the FPC exit temperature over a 24-hour period. It is important to highlight, that while there are minor differences between the PTC outlet and the process load HX inlet (e.g. due to thermal losses in the piping from the PTC solar field and the HX inlet), over the year it can be considered effectively the same. The variable PTC inlet temperature (i.e. the fluid temperature from the FPCs) is shown in orange in the top plot in Figure 2, in addition to the cold tank temperature (blue), hot tank temperature (green) and the heat sink inlet temperature (maroon). On average the output temperature from the FPCs during the peak time of the in the day is around 210 °C. This significant temperature increase of the FPC inlet allows the PTCs to then raise the HTF temperature to 285 °C (Figure 2). The heat sink inlet varies during most of the day, especially dropping significantly during the nighttime. Addition of TES increases the thermal output after daylight hours and provides constant inlet temperature of 27 °C to the FPC field.

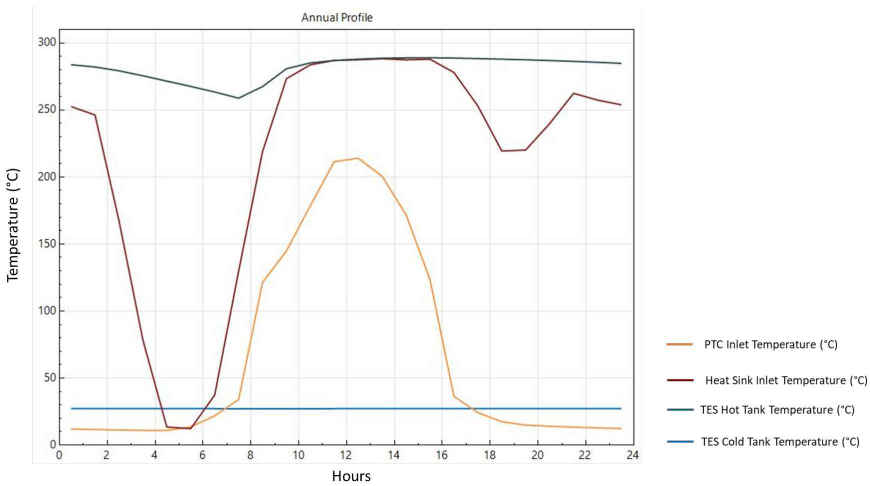

Figure 2 Annual average daily temperature profile of hybrid FPC + PTC + TES system with 8 hours of storage. Orange curve: variable PTC inlet temperature; maroon curve: heat sink inlet temperature or temperature delivered from the hybrid RTES; green curve: hot tank temperature; and blue curve cold tank temperature or inlet temperature to FPC system)

To highlight the difference between operating the hybrid RTES with 8hrs of TES and without storage, Figure 3 shows the impact of the storage on the temperature of the heated fluid delivered to the process load HX. The blue line represents the direct PTC output with no storage, and the red line shows the difference in daily generation for the 8hr storage situation, which is the base case for this scenario. As seen, the TES increases the energy delivered to the HX.

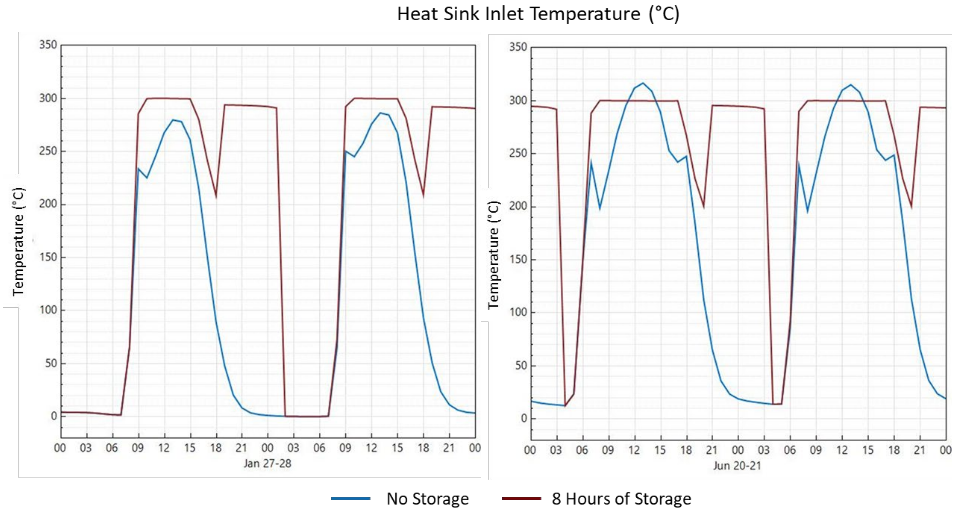

Figure 3 Temperature delivered to process heat form the hybrid FPC-PTC-TES system for typical days in January and June (blue curve represents TES off case, red curve represents 8 hours of TES case)

Figure 3 left shows the hourly simulation results of the process HX inlet temperature for 2 days in January (20th and 21st) as representative winter days, and Figure 3 right shows 2 days in June (20th and 21st) as representative summer days based on the TMY file. As seen, the key effects of storage increase the temperature delivered to the process HX to nearly the same temperatures as during the day when the PTCs are operating. The storage (8hrs) for winter and summer have similar effects, and on average extend the number of hours of delivering nearly 300 °C heat by approximately 6-8hrs. Without storage it is clear that the PTCs send heated fluid at much more variable temperature, as the heated fluid temperature is coupled to the extent of solar radiation available in the day. Delivered heat is suitable for a range of industrial processes such as; precipitation of primary metals, distillation of plastics and drying of chemicals which require around 300 °C process heat (Schoeneberger et al., 2020)

A parametric analysis for this scenario has been performed, where the numbers of hours of storage were varied. Table 2 shows the variation of the capacity factor, and the resulting impact on the annual net generation by changing the hours of storage in comparison to the base case of 8hrs.

Table 2 Parametric analysis showing the change in system annual capacity factor and annual net energy generation for various TES hours (*base case for thermal storage hours)

Thermal Storage (hours)	Capacity Factor (%)	Annual Net Energy Generation (MWh)	Change in net generation from 8hrs case (%)	Thermal Energy Stored in Charging State (MWth)
0	33 %	14,262	-52 %	0
2	46 %	20,287	-32 %	3,381
4	54 %	23,542	-21 %	6,815
8*	68 %	29,770	0 %	13,346
12	80 %	35,255	18 %	19,087

As seen in Table 2, increasing storage has a significant impact on the net annual generation of the combined solar fields, and that at 8hrs of storage the hybrid RTES can operate with a capacity factor of approximately 68% in Lancaster, California. When the storage is increased to 12hrs, the net generation increases by 18%, similarly if the storage is decreased to 4hrs, the net generation decreases by 21%, both compared to the 8hrs base case.

3.2. Constant and variable temperature solar field PTCs with an HTF and NG burner

As highlighted, scenario two in this paper is the use of PTCs with a liquid HTF providing heat input into the air and NG streams that feed a constant load NG combustor that provides heat for an IPH application at 1,000 °C or 300 °C. The HTF can be used to pre-heat the NG stream, the airstream entering the NG burner, or both. This scenario is a potential near term representation of what industrial sites could utilize to hybridize their current existing system with a renewable thermal input and as such reduce fuel consumption. To develop this hybrid RTES model, the first stage was to simulate a constant solar field outlet temperature, and then develop it further where a variable temperature PTC solar field is used instead of a constant exit temperature.

The first test case of this scenario, the heated HTF (Therminol VP-1, a commonly used synthetic oil in CSP electricity generation plants) is set at a constant 250 °C exit temperature from the solar field/RTES (e.g. with PTCs) and the air feed flow rate is set at 50 kg/s. Effectively the RTES exit temperature is constant through the year. As mentioned for the high temperature IPH application, the outlet of the NG burner that feeds the IPH application is 1,000 °C. IPSEpro software is used to calculate heat balances, enthalpies, and simulate processes for the HX and NG burner. Figure 4 shows the base case NG burner without solar heating (A) and constant temperature solar field heating of the NG and air streams (B) prior to input into the NG combustor for 1,000 °C process heat application.

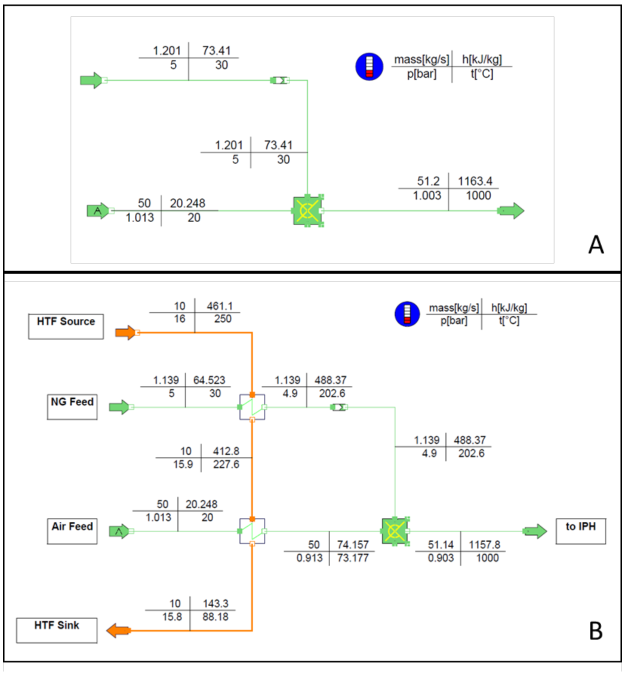

Figure 4 Constant temperature solar field and NG combustor for 1,000 °C process heat application, the air feed flow rate is set at 50 kg/s. (A: base case NG burner without solar heating, B: solar heating for both NG and air streams)

The constant temperature HTF, can heat the NG and air stream separately, or as in Figure 4 both streams. Table 3 shows the impact of the heat input into the NG stream, the air stream and then both. The biggest single impact is when the heated fluid from the solar field heats the air stream prior to entering the NG combustor, where due to the increased enthalpy of the air, slightly less gas is required (5% less) to reach the 1,000 °C air temperature needed for the IPH application. Note, due to the 1.2 kg/s of NG and 50 kg/s of air for the base case, most of the energy from the HTF is used for the NG heating. When the NG and air streams entering the NG burner are both heated to 203 °C and 72 °C respectively through two separate HXs, it is possible to reduce NG consumption by approximately 5% compared to the base case where no renewable heat is added (Table 3). This analysis has not done optimization of the delta temperature rise across the air and NG HXs highlighted in Figure 4.

Table 3. Summary of results from constant solar field and NG hybrid system models for 1000 °C process heat application with 50 kg/s air inlet mass flow to the NG burner.

Heating from solar field	No heating	NG only	Air only	NG and Air
NG burner air feed temperature (°C)	20	20	78	72
NG burner gas feed temperature (°C)	30	202	30	203
NG mass flow (kg/s)	1.201	1.199	1.145	1.139
Change in NG mass flow (%)	**0.0 %**	**- 0.1 %**	**- 4.7 %**	**- 5.1 %**

In second test case (medium IPH temperature), the exit temperature of the solar field/RTES is set as 180 °C, the air feed flow rate is set at 50 kg/s and the outlet of the NG burner that feeds the IPH application is now 300 °C. Note, due to the reduction in the IPH temperature (i.e. 300 °C instead of 1,000 °C), 0.3.01 kg/s of NG is needed compared to 1.2 kg/s. When the NG and air streams entering the NG burner are heated to 161 °C and 58 °C respectively through two separate HXs, it is possible to reduce NG consumption by approximately 13% compared to the base case where no renewable heat is added (Table 4).

Table 4 Summary of results from constant solar field and NG hybrid system models for 300 °C process heat application with 50 kg/s air inlet mass flow to the NG burner

Heating from solar field	No Heating	NG only	Air only	NG and Air
NG burner air feed temperature (°C)	20	20	59	58
NG burner gas feed temperature (°C)	30	166	30	161
NG mass flow (kg/s)	0.301	0.299	0.274	0.262
Change in NG mass flow (%)	**0.0 %**	**- 0.3 %**	**- 9.0 %**	**- 13.0 %**

In third case, a fully operational PTC system has been modelled with a variable HTF temperature. The PTC system is designed to operate with a 24% capacity factor (approximately 2,076 hours of annual full load operation) and providing a maximum outlet temperature between 180 °C and 300 °C. Figure 5 shows the process flow diagram of the variable temperature PTC solar field and NG burner model where both the NG and air streams are heated.

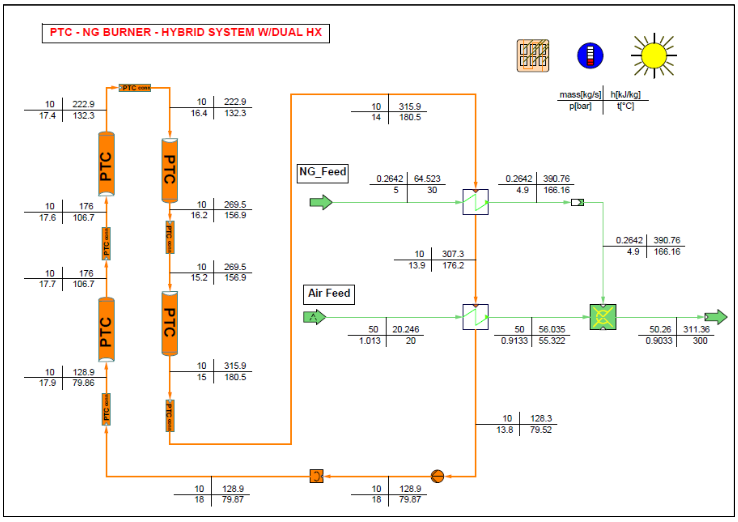

Figure 5 Variable temperature PTC and NG combustor for 300 °C process heat application, and air feed flow rate is set at 50 kg/s

Table 5 shows the progression of having the PTC outlet temperature increase from 180 °C to 300 °C, when the capacity factor is 24%. The reduction in NG mass flow can be as high as 26% when the HTF reaches 300 °C and offsets the NG consumption of the burner (Table 5). To note, this result is valid for a capacity factor of about 24%, and the model does not include TES and so the reduction of NG occurs within the sunlight hours of the day (8-9 hours). As seen, when the PTC solar field exit temperature is closely aligned to the process temperature (i.e. 300 °C) compared to 1000 °C, a greater amount of NG can be offset (-26% compared to -14%).

Table 5 Change in NG mass flow with respect to variable temperature HTF from PTC system for 300 °C process heat application with 50 kg/s air inlet mass flow to the NG burner

Heating from solar field	No Heating	180 °C	200 °C	250 °C	300 °C
NG mass flow (kg/s)	0.301	0.262	0.256	0.242	0.223
Change in NG mass flow (%)	0.0 %	-13 %	- 15 %	- 19 %	- 26 %

3.3. DSG LFCs with PCM storage

The third scenario uses DSG LFCs coupled with TES to improve the system's flexibility and capacity factor. PCMs are chosen as the storage medium as they have relatively high energy densities. PCMs store energy in the latent heat of the phase change are well suited for integration with systems that use steam as the working fluid since both media go through a phase change allowing the temperature profiles to be matched which improves the effectiveness of heat transfer (Sharan et al., 2019).

The DSG LFC system is designed for 1 MW_{th} capacity with a solar multiple of 1.2 and target steam quality of 0.75. Single loop aperture area is calculated as 3,081 m^2 which generates actual thermal output leaving in steam up to 2.11 MW_{th} . The PCM TES size adjusted to maintain the thermal output correspondingly.

The DSG LFC system is modelled with SAM which evaluates the annual performance of the solar system. The annual performance of the DSG SAM module has been compared and validated to an operating DSG LFC solar field (Kurup et al., 2017). The annual thermal yield from the DSG LFC solar field is 3,470 MWh_{th} in Tucson, Arizona, without storage. When the solar multiple is increased to 2, and a TES of 6hrs is added, the thermal yield can increase by 60%, and thereby increasing the capacity factor.

The steam properties such as temperature, mass flow rate and steam quality are calculated for each hour of the year depending on the available solar resource. Figure 6 shows the annual average daily temperature profile and field average outlet steam quality of the DGS LFC system. As seen in Figure 6, during the day the DSG LFC produces on average approximately a stable 270 °C steam output (red curve) during daylight, at a quality of approximately 60%.

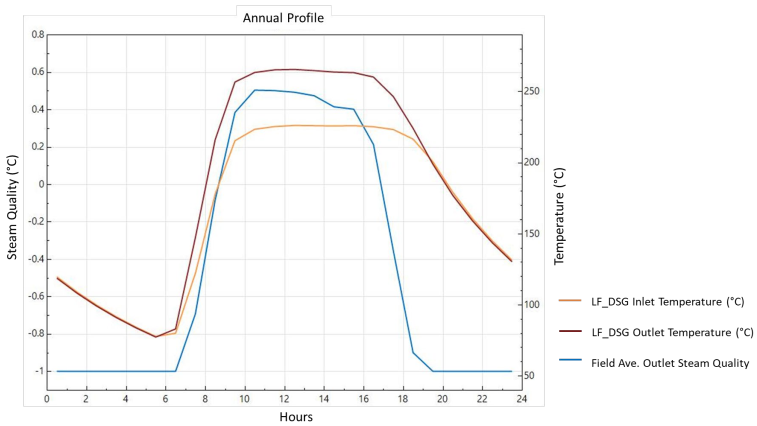

Figure 6 Annual average daily temperature profile and field average outlet steam quality of LF-DGS system. Orange curve: LF-DSG inlet temperature, maroon curve: LF-DSG outlet temperature, and blue curve field average outlet steam quality)

Figure 7 shows the hourly steam mass flow from the DSG LFC solar field for a typical week in January and July (blue and orange respectively). As seen, the steam output in winter compared to summer days is approximately 50% less (i.e. mass flow of 0.8 kg/s compared to 1.6 kg/s). Figure 7 also shows how the steam output from the solar field is impacted by transients (e.g., weather events and cloud passage), where the steam output e.g., on day 9 in winter drops significantly. Similarly, the weather event and reduction of steam output drops to nearly 0 and increases again once the clouds have passed on day 10 in July.

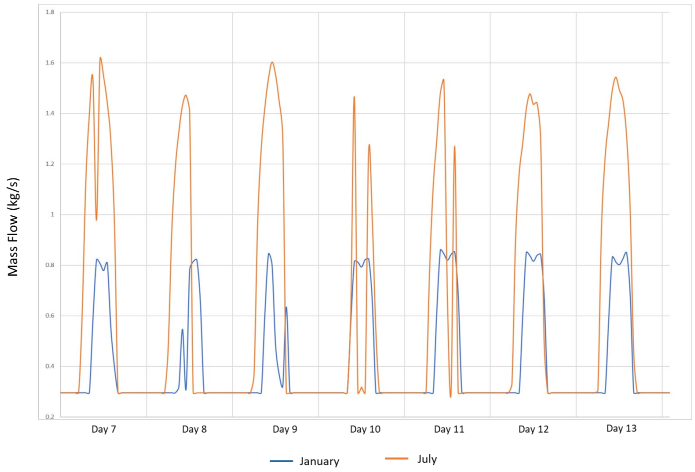

Figure 7 Hourly steam mass flow from DSG-LF solar field for a typical week in January and July

This thermal output is then used to determine the charging and discharging behavior of the TES system. The PCM-TES is modelled in MATLAB following prior NREL work (Sharan et al., 2019), albeit with several adaptations to capture the varying heat transfer coefficients of condensing and evaporating steam. Steam travels through steel pipes which are surrounded by the PCM, as illustrated in Figure 8. Numerous tubes are bundled together into large 'tanks' to store the required quantity of energy.

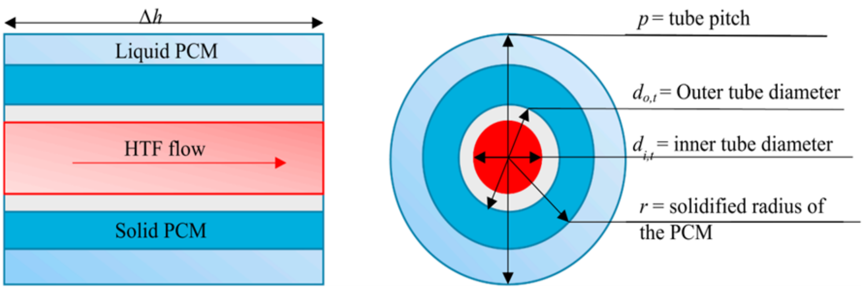

Figure 8 Schematic diagram of a shell-and-tube PCM thermal storage system (Sharan et al., 2019)

The system is operated assuming that the load requires a constant power input which is delivered by steam. The DSG system generates steam, and if the produced power exceeds the load's requirement then the excess steam passes through the TES thereby storing energy. When the solar resource reduces below the power requirements, the storage is discharged. In this example, it is assumed that the load has a power requirement of 1 MW_{th} at a steam temperature of 240 °C. The DSG LFC must generate steam at a higher temperature than this, so that the steam produced by the PCM meets the 240 °C requirement. In this example, the DSG LFC produces steam at 5 bar, corresponding to a temperature of 270 °C. Sodium formate is chosen as the PCM and this material has a phase change temperature of 258 °C (see Table 6). The discharging steam is generated at a pressure of 35 bar, which corresponds to a discharging temperature of 243 °C. Thus, the melted PCM is sufficiently hot to generate the required temperature of steam.

Table 6: Properties of the PCM sodium formate

Parameter	Unit	Property
Melting point	°C	258
Density	kg/m^3	1,920
Heat capacity	kJ/kgK	1.216
Latent heat	kJ/kg	245

Figure 9 and Figure 10 show the effect of the solar field and thermal storage size for several days of operation during the summer and winter. Results are shown for systems with a solar multiple of 2 and 4 with storage durations of 6 and 12 hours. The figures show the power produced at each hour by the DSG LFC, as well as the power that charges (negative) or discharges the storage (positive). The power that is then sent to the load is also shown. For a solar multiple of 2 with 6 hours of storage, solar energy is rarely stored during the winter. During the summer energy is stored, but the storage is too small so that later in the afternoon solar energy cannot be stored and too much power is sent to the load (and may be curtailed). Increasing the storage duration to 12 hours means that solar energy is not dumped and that the load can be supplied with power for most of the night.

Increasing the solar multiple to 4 enables the system to provide power to load for a large proportion of the time during the winter. During the summer large quantities of power are curtailed with only six hours of storage. With a storage duration of 12 hours, power can be delivered continuously in the summer. Interestingly, the storage is not fully discharged during the first evening. As a result, the storage cannot store all the excess energy during the second day and some of this energy is dumped (or sent to the load). However, even this very large system is unable to provide power continuously in the winter and an auxiliary power supply is required.

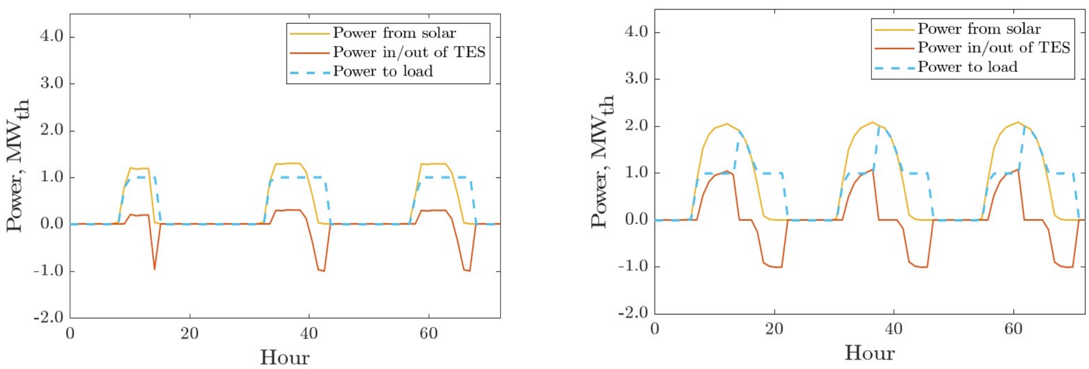

Figure 9 Thermal powers in DSG-TES system. Solar multiple = 2, thermal storage duration = 6 hours. (left) February (right) June

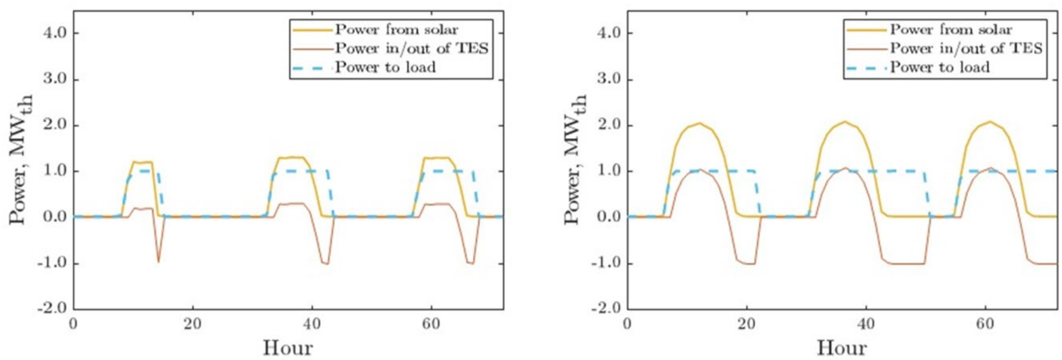

Figure 10 Thermal powers in DSG-TES system. Solar multiple = 2, thermal storage duration = 12 hours. (left) February (right) June

4. Discussions and Future Work

This paper has created and modified existing energy generation tools such as the SAM, to develop 3 main hybrid RTES models for the delivery of renewable heat to IPH applications. To begin to generate results, code modifications and hybrid RTES models have been developed and require further testing and refinement.

4.1. FPCs and PTCs with TES

The benefit of this hybrid system for district heating and potentially industrial applications, is that it can potentially reduce the plant cost relative to a PTC-only plant having the same output specifications if, for example, the same HTF can be utilized in the FPCs and the PTCs. Also, the FPCs are more efficient at lower temperatures (e.g. less than 100 °C) and the PTCs are more efficient above this and the PTCs allow for an overheat protection if needed. The lower temperature heating can be achieved by cheaper FPCs, while the higher temperature heating outside the range of the FPCs is accomplished by the PTCs.

Future work for the FPC-PTC-TES hybrid case scenario and modelling efforts include:

- Use of different HTFs like mineral oil or unpressurized water (i.e. similar to the Tårs plant)
- If the collector characteristics can be modelled, use of a smaller PTC (e.g. aperture width of 2m), that is designed for SIPH application instead of a 6m aperture trough designed for CSP electricity generation
- Connecting the FPC field to the PTC field by a HX for better pressure, TES dispatch and temperature control. Also optimizing the field sizing between the FPCs and PTCs.
- Additional SAM user interface for FPC module selection and modifications
- Adding more capital cost estimates for both FPC and PTC system and improving the SAM financial models to reflect a real hybrid case project economics
- Potentially releasing the hybrid add-on to the SAM public version e.g. with validation

This hybrid RTES model has shown that the utilization of Therminol VP-1 through the FPC and PTC solar fields as a single working fluid is feasible. This is not currently done in industry but was undertaken to create a working hybrid model. For further model developments, we aim to also create a version of this hybrid RTES where the solar fields are separated such that unpressurized water/glycol runs in the FPC field, and with a HX coupling to the PTC field which operates Therminol-VP1. This would then allow the use of unpressurized fluids, smaller volumes of Therminol VP-1 and TES tanks, and therefore potential cost savings for the system integration. This needs to be investigated.

It is expected that while this could be an effective solution, the economics are unclear and require further work to determine the benefit. Further work is needed to compare a pressurized system (if possible) compared to one with Therminol VP-1. With improvements and continued development of the FPC-PTC-TES model, the aim will be to validate the thermal yields, operation modes, and TES dispatch with real operating plants such as the Tårs plant, with weather files for Denmark and for the U.S.

4.2. Constant and variable temperature solar field PTCs with an HTF and NG burner

The hypothetical scenario was to test hybrid modelling and potential impacts. As such a real IPH application will have further refinement e.g. specific temperatures for the process. The results of the constant solar field PTCs with HTF and NG burner showed only a 5% offset due to the temperature difference between the process temperature (1,000 °C) and the solar field outlet temperature (250 °C), for a 50 kg/s air flow to the NG combustor. As mentioned, this is for the situation where the NG flow into the combustor without renewable heat is 1.2 kg/s compared to 50 kg/s of air, as such most of the temperature rise was seen in the NG stream rather than the air stream. Optimization of the delta temperature rise across the air stream HX and NG HXs will need to be investigated to highlight the best NG offset. For the 1000 °C case of scenario two, this basically shows that with today's technology, solar fields can offset a limited amount of NG consumption for an energy intense process application. The optimization in the future will show whether the NG offset can be increased, for example by increasing the heat delivered to the air stream.

For the medium temperature process heat case (300 °C) and the solar field outlet temperature of 180 °C, with a 50 kg/s airflow into the combustor, the NG offset could increase up to 13%. However, when the PTCs exit temperature is raised to 300 °C, the offset of NG consumption is expected to be 26%, for a given annual capacity factor of 24%. This system, without TES, can only provide heat during daylight hours. When TES is added e.g. 4-8hrs, the capacity factor can be increased to approximately 50% based on the DNI conditions. This would provide is a significant financial saving. This is a hypothetical study to show the functionally of a hybrid RTES integrated to the NG burner, which requires optimization based on heat demand and air flow to the process. The economic analysis would also highlight aspects such as NPV and payback if for example the costs of the hybrid RTES are identified, to then determine the LCOH as found in other analysis (Kurup and Turchi, 2019).

SIPH could be used to meet high temperature applications (i.e. 1,000 °C) in the longer term, where CSP towers are utilized. For example, CSP towers with particles that are directly heated are already showing promising test results at 965 °C (DLR, 2018). Similarly, air towers are reporting greater than 1,000 °C with on-sun tests (Heliogen, 2020). Therefore, future SAM modules with the CSP Tower could be adjusted for SIPH where the powerblock is removed.

As a future work, economic analysis is expected to be conducted to optimize the RTES in a cost-effective hybrid scenario. Other alternative scenarios including TES addition to the PTC system, co-operation of PTC and NG burner to provide heat to process in two separate heat streams, and waste heat recovery with a recuperator after NG burner will also be analyzed to compare effectiveness of use of hybridization and systems costs. We are also planning to add an optimized dispatch model to the variable temperature solar field PTCs with an HTF and NG burner using hourly DNI data as an input and providing hourly thermal output to maximizing the NG offset.

4.3. DSG-LFCs with PCM storage

A solar thermal system that is designed to produce the required power at the peak solar insolation is defined as having a solar multiple of 1. Since this modelled system requires a power of 1 MW_{th} is delivered continuously, a solar field with a solar multiple of 1 would produce less than 1 MW_{th} for most of the year. Thus, the solar field must be oversized compared to this design point. For example, a system with a solar multiple of 2 would be twice the size of the nominal design (Figure 11). For applications which require power continuously the solar multiple is typically quite large between 3 and 4. This means that during peak daytime hours, most of the solar energy that is generated is stored in the TES. For example, the solar field may generate 4 MW_{th} of which 3 MW_{th} passes through the thermal storage. However, during the night, the storage only discharges at a rate of 1 MW_{th} – i.e. the mass flow rate of steam during charge is approximately three times higher than during discharge (the actual mass flow rates are slightly different to this since the heat transfer coefficient differs during condensation and boiling of steam). This is for future work.

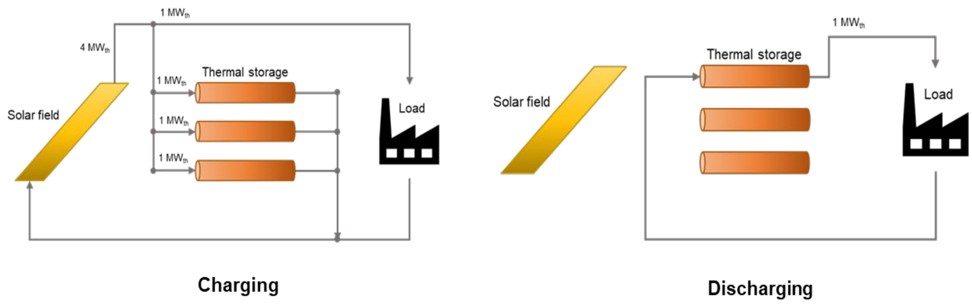

Figure 11: Schematic of a DSG-TES system with multiple PCM storage tanks. (left) Charging. All storage tanks are charged simultaneously, and the load is also powered by the solar resource. (right) Discharging. Solar energy is not available, and the storage tanks discharge one at a time to provide power to the load.

Key design variables for these systems are the sizing of the solar field and the thermal storage. The solar multiple should be large enough that the load is supplied with the required power throughout the night, even on low solar days. The reduced solar availability in the winter requires extremely large and uneconomical solar fields and an auxiliary power supply is necessary. The thermal storage should be large to store all the excess energy from the solar field otherwise the excess energy will be dumped. The storage system should also be designed to charge and discharge at the required power ratings. The sizing of the solar field, thermal storage, and auxiliary power supply is an interconnected problem, which requires the economics of the application to be considered to find the optimal configuration.

Ideally, the storage system should be charged and discharged at a similar rate. Charging and discharging at very different rates reduces the storage efficiency. For example, Figure 12 illustrates the performance of a tank that is designed to be charged at 3 MW_{th}. As can be seen, the steam enters the tank with a quality of 0.6 and is fully condensed by the exit of the storage. The tank is then discharged at a third of the rate (1 MW_{th}), as illustrated in Figure 12. Due to the lower mass flow rate, the saturated water at the inlet boils about halfway along the pipe. Thus, most of the heat transfer occurs in the inlet section of the pipe and the PCM solidifies here first, whilst still being liquid in the rest of the pipe. As time progresses, the solid-liquid front in the PCM gradually moves axially along the pipe. The discontinuities and uneven shapes can be explained by significant changes in the overall heat transfer coefficient, which varies substantially as steam goes from saturated water to saturated steam and goes through nucleation-dominated and convection-dominated boiling processes.

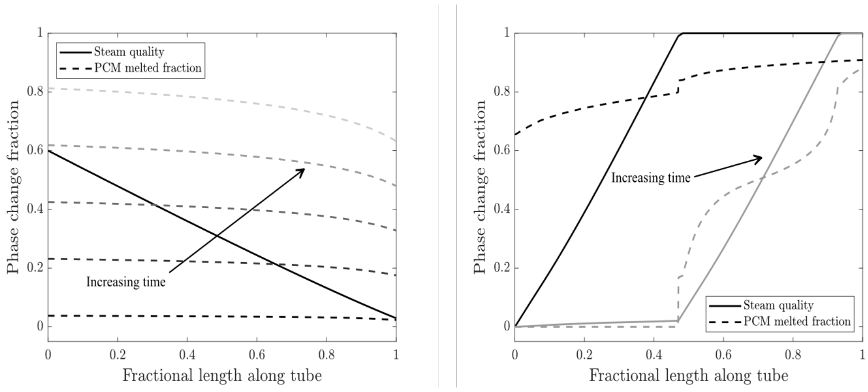

Figure 12 Phase change fraction along the length of the PCM-TES during charge (left) and discharge (right).

It is preferable for the PCM to solidify and melt uniformly along the length of the pipe. In order to achieve this, the thermal storage is discretized into several tanks. The system is designed so that the charging and discharging rates of each tank are approximately equal. For the example above, the system charges at 3 MW_{th} with all tanks being charged simultaneously – i.e. each tank is charged at 1 MW_{th}. During discharge, the tanks are then discharged one at a time at a rate of 1 MW_{th}. This ensures that the PCM melts and solidifies almost uniformly along the length of the tank, and thereby improves the TES efficiency under the wide range of scenarios required by realistic load cycles.

The choice of PCM allows the TES to closely match the process steam temperature. Sodium formate has a melting temperature of 258 °C, latent heat of 245 kJ/kg, heat capacity of 1.2 kJ/kg-K and a unit cost of $0.4/kg (Sharan et al., 2019). Other available PCMs that could be suitable for a similar industrial application are sodium nitrate ($0.8/kg), sodium nitrate-potassium nitrate ($0.8/kg) and lithium nitrate ($8.4/kg). Lithium nitrate can be an alternative to sodium formate, which has a similar melting point of 253 °C, latent heat of 200 kJ/kg and heat capacity of 1.5 kJ/kg-K. However, the cost difference makes it very unlikely to be used. Based on both process temperature and cost of material, sodium formate is an attractive option for the process temperature of 240 °C at 35 bars.

5. Acknowledgments

NREL does not endorse the companies specified in this paper, and any mention is strictly for research purposes only. This work was authored in part by the National Renewable Energy Laboratory, operated by Alliance for Sustainable Energy, LLC, for the U.S. Department of Energy (DOE) under Contract No. DE-AC36-08GO28308. Funding provided by the U.S. Department of Energy Office of Energy Efficiency and Renewable Energy's Office of Strategic Programs and Solar Energy Technologies Office. The views expressed herein do not necessarily represent the views of the DOE or the U.S. Government. The U.S. Government retains and the publisher, by accepting the article for publication, acknowledges that the U.S. Government retains a nonexclusive, paid up, irrevocable, worldwide license to publish or reproduce the published form of this work, or allow others to do so, for U.S. Government purposes.

6. References

Aalborg CSP, 2015. 6.8MWth Solar District Heating System in Taars, Denmark. https://www.aalborgcsp.com/projects/68mwth-solar-district-heating-system-in-taars-denmark/ (accessed 3.25.20).

DLR, 2018. DLR's new solar receiver CentRec® exceeds 900 degrees Celsius target in the Jülich Solar Power Tower. German Aerospace Center.

Heliogen, 2020. Heliogen - Replacing Fuels with Sunlight https://heliogen.com/ (accessed 8.24.20).

Kurup, P., Parikh, A., Möllenkamp, J., Beikircher, T., Samoli, A., Turchi, C., 2017. SAM process heat model development and validation: liquid-htf trough and direct steam generation linear focus systems, in: ISES Solar World Congress 2017. Presented at the IEA SHC International Conference on Solar Heating and Cooling for Buildings and Industry, International Solar Energy Society, Abu Dhabi, United Arab Emirates. https://doi.org/doi:10.18086/swc.2017.26.06

Kurup, P., Turchi, C., 2019. Case Study of a Californian Brewery to Potentially Use Concentrating Solar Power for Renewable Heat Generation, in: IEA SHC International Conference on Solar Heating and Cooling for Buildings and Industry 2019. Presented at the ISES Solar World Congress 2019, International Solar Energy Soceity, Santiago, Chile. https://doi.org/10.18086/swc.2019.12.07

Laadel, N.E., Mouaky, A., Agalit, H., Bennouna, E.G., 2018. Solar Heat Integration in Rotational Molding Process: Case Study, in: Proceedings of EuroSun 2018. Presented at the ISES EuroSun 2018 Conference, International Solar Energy Society, Rapperswil, Switzerland, pp. 1–11. https://doi.org/10.18086/eurosun2018.08.05

NREL, 2020a. Download - System Advisor Model (SAM). https://sam.nrel.gov/download.html (accessed 8.7.20).

NREL, 2020b. NSRDB: National Solar Radiation Database. https://nsrdb.nrel.gov/ (accessed 8.19.20).

Putz, S., Epp, B., 2019. Solar Heat for Cities - The Sustainable Solution for District Heating.

REN21, 2020. Renewables 2020 Global Status Report. Renewable Energy Network for the 21st Century, Paris, France.

Schoeneberger, C.A., McMillan, C.A., Kurup, P., Akar, S., Margolis, R., Masanet, E., 2020. Solar for industrial process heat: A review of technologies, analysis approaches, and potential applications in the United States. Energy 206, 118083. https://doi.org/10.1016/j.energy.2020.118083

Sharan, P., Turchi, C., Kurup, P., 2019. Optimal design of phase change material storage for steam production using annual simulation. Solar Energy 185, 494–507. https://doi.org/10.1016/j.solener.2019.04.077

X-Rates, 2020. EUR Historical Exchange Rates (Euro) - 2019-11-29 https://www.x-rates.com/historical/?from=EUR&amount=30&date=2019-11-29 (accessed 8.15.20).

Industrial Turbo-Assisted Direct Solar Air Heater Using Linear Fresnel Concentrating Collectors

Antonio Famiglietti[1], Antonio Lecuona-Neumann[1], Mohammad Rahjoo[1] and José Nogueira-Goriba[2]

1 Universidad Carlos III de Madrid, Departamento de Ingenieria Termica y de Fluidos, Grupo ITEA, Leganés (Spain),

2 Universidad de Castilla La Mancha, Campus de Excelencia Internacional en Energia y Medioambiente, Escuela de Ingenieria Industrial y Aeroespacial, Toledo (Spain)

Abstract

Among the solar technologies nowadays considered as renewable energy sources for industrial processes, concentrating solar collectors are receiving growing attention due to their capability of providing heat at higher temperatures than other solar collectors. This study focuses on the application of linear Fresnel collectors to directly produce hot air in the medium temperature range 150 °C - 400 °C for industrial processes, aiming at low cost. An innovative layout is proposed. Air is used as heat transfer fluid inside the solar receiver, a low-cost commercial turbocharger is used to compress ambient air through the plant, extracting from the solar source the required pumping power with the attached turbine, minimizing auxiliary energy consumption. A *turbo-assisted direct solar air heater* of medium-scale size is designed and simulated along representative days of a typical meteorological year, in order to assess the concept, its performances and relevant technical aspects. The study confirms its technical feasibility either in summer and winter season for the selected location (Madrid, Spain). The system provides an hot air stream between 300°C and 400°C without external energy consumption for pumping, avoiding the receiver tube overheating.

Solar Air Heater, Solar Heat for Industrial Processes, SHIP, Concentrating Solar Heat, Linear Fresnel collector

1. Introduction

Industry accounts for 38% of the final energy consumption worldwide (International Energy Agency 2018). The large thermal energy demand for industrial processes covers a broad range of temperatures, customarily: the low-temperature range T < 150 °C, the medium temperature range 150 °C < T < 400 °C, and the high-temperature range T > 400 °C. (Sharma et al. 2017) states that 60% of industrial energy heat demand is between 30 and 250 °C. Most of exiting Solar Heat for Industrial Processes, SHIP, installation are in the low-temperature range where flat plate collectors FPCs or evacuated tubes collectors ETCs can be used (Mekhilef, Saidur, and Safari 2011). Concentrating solar heat CSH can be provided at higher temperatures using parabolic trough collectors PTCs or linear Fresnel collectors LFCs. Industrial CSH existing plants are reported in (Sharma et al. 2017) as well as in (SHIP Database). PTC, and with a lesser extend LFC, are used for steam production, industrial refrigeration coupled with absorption chillers, water heating and process heating. Almost all of them use liquid heat carrying fluids.

Industrial processes using air as a heat-supplying fluid are widespread. Among them, drying and air preheating are high energy-demanding processes, common to several industrial sectors, as food and beverage, chemical, pulp and paper, residues and wastewater treatments, among others. Temperature requirements vary with the specific application, from low to medium temperature ranges. For such applications, this study evaluates a novel open circuit to atmosphere OCA direct solar air heater. It provides hot air up to 350 °C using off-the-shelf concentrating collectors. The herewith studied technology avoids the cost, weight, hurdle, environmental impact, and risks of liquid heat-carrying liquids. Moreover, it avoids the use of heat exchangers.

2. Turbo-assisted direct solar air heater

The *Turbo-assisted direct air heater*, T-SAH, is a unique technology (Lecuona-Neumann 2016) able to heat ambient air up to the medium temperature range using concentrating solar collectors, as linear Fresnel collector

doi:10.18086/eurosun.2020.03.06 Available at http://proceedings.ises.org

LFC, or Parabolic Trough collector PTC, not requiring the use of conventional heat transfer fluid HTF (e.g., thermal oil, water, …) and an heat exchanger HX for heat delivery, improving the flexibility and safety, besides to reduce cost.

Due to its physical properties, air at ambient conditions is not appropriate as a heat carrier. Internal heat transfer rate occurring between the solar receiver wall and the internal airflow is modest compared to other HTFs, and as a result, the wall over-temperature is high. The relatively low air density and specific heat capacity turn into high mean flow velocities required to limit the outlet temperature. This is necessary to avoid receiver wall overheating, especially under high solar heat flux conditions, (i.e., large collector aperture and length, and/or high solar irradiance). The pumping power required to overcome the total pressure drops across the receiver and piping can be in the same order of magnitude of the captured solar power, which comes from high auxiliary energy consumption.

In the proposed layout, Fig.1, an automotive turbocharger is used to alleviate or eliminate these drawbacks and even convert them into an advantage. Ambient air is pressurized before entering the collector using a compressor *c*. Compressing power is recovered by the attached expander *e* after heating. For a given mass flow rate required to remove heat from the receiver, the increase in density obtained thanks to compression translates into lower the mean velocities, minimizing the pressure drop across the receiver and the pumping power required, in spite of the increase of temperature through the compressor. The compressor and the turbine expander are mechanically coupled as in a Brayton cycle configuration. Since no net mechanical work is expected to be extracted at the shaft, an automotive turbocharger is used. If there is mechanical power left, it will be in the outlet flow.

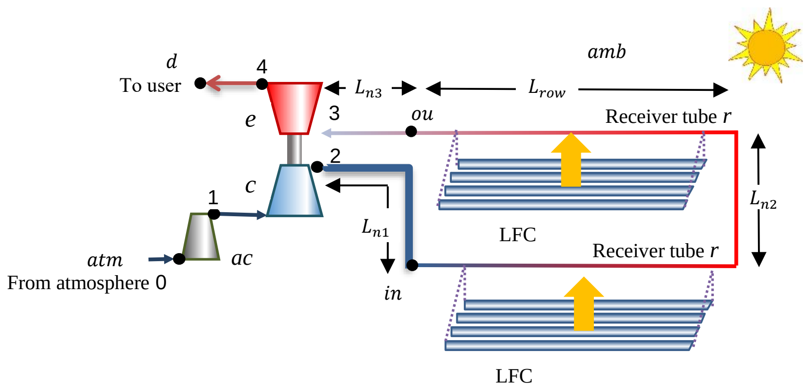

Fig. 1: Turbo-assisted direct solar air heater concept using LFCs, $n_s = 2$ and $n_p = 1$.

As long as turbocharger freewheeling is achieved, no external power is needed to pump air throughout the collector, since the turbine can drive the compressor, providing the compressing and the pumping power required. An auxiliary compressor can supply the pumping power during starting transient, cloudy transients, as well as for control purposes, avoiding overheating. Air exits the turbine at 300 - 400 °C. (Famiglietti et al. 2020) presents a generic theoretical investigation on the proposed layout, including numerical modeling, critical parameters and performance assessment.

According to the mentioned layout, a small to the medium-scale facility has been modeled and simulated in the present work. A solar field has been configured combining commercial LFCs in parallel and series layout in order to suitably match with a specific turbocharger. The single LFC module is $L_m = 5.28$ long, having an aperture of $W_a = 5$ m and a reflective surface of $A_m = 26.40$ m^2. A series of $n_s = 6$ modules are aligned to obtain a U-loop, while $n_p = 4$ U-loops are connected in parallel to the single turbocharger. The U-loop length is a good compromise between the need to capture enough solar power to produce useful outlet temperatures and the need to keep small pressure drops across the loop. Additionally, too short series would result in relatively high optical end losses at the collector rows extremities. 4 U-loops in parallel guarantee enough mass flow rate, matching the operative range of increased size turbochargers, which results in high-performance. The solar field axis N-S oriented, results in an overall capturing surface of 633.6 m^2, which is a small/medium scale plant suitable for industrial applications.

3. Numerical model

The LFCs field has been modeled using the peak optical efficiency $\eta_{op0} = 0.63$ given by the manufacturer (Solatom, n.d.), applying the incident angle modifiers $IAM_T\langle\theta_T\rangle$ and $IAM_L\langle\theta_L\rangle$ for taking into account the optical losses related to transversal and longitudinal components of sun rays incidence angle (Karathanasis 2019). The solar power incident at the collector tube axis $\dot{Q}_s$ results as in eq. (1).

$$\dot{Q}_s = G_{bn} IAM_T\langle\theta_T\rangle IAM_L\langle\theta_L\rangle \eta_{op0} W_a L_m n_s n_p \qquad \text{(eq.1)}$$

Optical end losses, due to the concentrated radiation impacting out of the tube length are taken into account through the end losses factor $f_{end}\langle\theta_L\rangle = \dot{Q}_r/\dot{Q}_s$, (Heimsath et al. 2014) being $\dot{Q}_r$ the net solar power impacting on the solar receiver tube.

A steady-state model of receiver tube is obtained using the heat removal factor F_R and efficiency factor F' as proposed by (Duffie, Beckman, and McGowan 1985), for what the useful power transferred to air across the tube length L becomes $\dot{Q}_u$, which is used to heat the air flow rate $\dot{m}$:

$$\dot{Q}_u = F_R L P_{ex}[\dot{q}_s - U_L(T_{in} - T_{amb})] = \dot{m}(c_{p,ou}T_{ou,t} - c_{p,in}T_{in,t}) \qquad \text{(eq.2)}$$

$$F_R\langle\dot{m}\rangle = \frac{\dot{m}c_p}{LP_{ex}U_L}\left[1 - \exp\left(-\frac{LF'P_{ex}U_L}{\dot{m}c_p}\right)\right]; \qquad F' = \frac{1}{1 + \frac{U_L P_{ex}}{h_a P}} \qquad \text{(eq.3)}$$

The solar heat flux is obtained from eq.(1) as $\dot{q}_s = G_{bn} IAM_T\langle\theta_T\rangle IAM_L\langle\theta_L\rangle \eta_{op0} W_a P_{ex}^{-1}$, being P_{ex} and P the external and internal tube perimeters, U_L the heat transfer coefficient from the tube wall to ambient, $T_{in,t}$ and $T_{ou,t}$ are the stagnation temperatures at the tube inlet and outlet respectively, h_a is the internal wall to air heat transfer coefficient. The value of U_L for any tube wall temperature is obtained from the thermal losses test performed by (Burkholder and Kutscher 2008) on a usual evacuated tube with an external diameter $D_{ex} =$ 0.07 m, equipped with selective coating. Discretization is applied to the overall receiver length to increase accuracy.

A turbocharger model is due to computing the system. Under steady-state conditions, the turbine and the compressor, which are connected by the shared shaft, hold the mechanical balance when eq. (4) is verified. This means that the power generated by air expansion through the turbine $\dot{W}_e$ is able to drive the compressor that consumes the power $\dot{W}_c$, considering a mechanical efficiency at the shaft η_m. Under this condition, the turbocharger run at the constant rotational speed n_T without external auxiliary energy consumption. For the proposed layout, it means that the compressor is able to pump air through the solar field without consuming external energy, thus in autonomous mode, while at the turbine outlet airflow holds the medium temperature range, useful for industrial usage in thermal processes.

$$\dot{W}_e\eta_m - \dot{W}_c = \dot{W}_{net} = 0 \qquad \text{(eq. 4)}$$

According to the cycle points reported in Fig. 1, the compressor and turbine powers can be obtained from isoentropic total to total efficiencies η_e and η_c, pressure ratios $\pi_c = \frac{p_{2t}}{p_{1t}}$ and $\pi_e = \frac{p_{3t}}{p_{4t}}$, and inlet stagnation temperatures T_{1t} and T_{3t} , respectively for the compressor eq. (5) and the turbine eq. (6), where $\gamma = c_p/c_v$.

$$\dot{W}_c = \dot{m}c_{p,c}T_{1t}\left(\pi_c^{\frac{\gamma_c - 1}{\gamma_c}} - 1\right)\eta_c^{-1} \qquad \text{(eq. 5)}$$

$$\dot{W}_e = \dot{m}c_{p,e}T_{3t}\left[1 - \pi_e^{-\frac{\gamma_e - 1}{\gamma_e}}\right]\eta_e \qquad \text{(eq. 6)}$$

The total temperature at the receiver tube inlet results from eq. (7). Air is available for usage at turbine exit temperature T_{4t}, as in eq. (8).

$$T_{2t} = T_{1t}\left[1 + \left(\pi_c^{\frac{\gamma_c - 1}{\gamma_c}} - 1\right)\eta_c^{-1}\right] \qquad \text{(eq. 7)}$$

$$T_{4t} = T_{3t}\left[1 - \eta_e(1 - \pi_e^{-\frac{\gamma_e - 1}{\gamma_e}})\right] \qquad \text{(eq. 8)}$$

Compressor performance can be described using two relations $\pi_c = \pi_c\langle \dot{m}, T_{in}, n_T\rangle$ and $\eta_c = \eta_c\langle \dot{m}, T_{in}, n_T\rangle$, which can be extrapolated from compressor performance maps provided by the manufacturers, (Guzzella and Onder 2010). Following the same approach, the relation $\dot{m}\langle\pi_e\rangle$ for the turbine is extrapolated from the map given by the manufacturer. A turbine efficiency model $\eta_e\langle n_T, \pi_e\rangle$ is implemented following (Guzzella and Onder 2010). The turbomachines performance model, together with the collector and receiver model above described, enables to determine the operative point for the system under steady-state conditions, according to solar position and irradiance at given ambient conditions. Autonomous operations, or freewheeling, is achieved when eq. (4) is verified. On the other hand, the receiver tube thermal limit indicated at 600 °C by most manufacturers should not be overcome. A good matching between the solar field and the turbocharger can be obtained by selecting the suitable turbocharger size among the available models on the market, so that the limited operating range of compressor and turbine, indicated by their performance maps, fits the solar power variation along the day and the year.

4. Results

The *turbo-assisted solar air heater* herewith proposed has been simulated on typical representative days of the year, extracted from the Typical Meteorological Year TMY (Habte et al. 2017) for the location of Madrid (Spain).

Fig.2 reports performances during a typical summer day with a clear sky in July. In Fig 2(a) direct solar normal irradiance G_{bn} is shown across true solar time TST, together with incident angle modifiers and the optical end losses factor f_{end}, as they determine the solar power at the receiver tube $\dot{Q}_r$. It can be noted that either f_{end} and IAM_L reaches values close to unity due to the high sun elevation at midday in summer. It follows that the end losses $\dot{Q}_{fend} = \dot{Q}_s - \dot{Q}_r = \dot{Q}_s(1 - f_{end})$ are moderate, in spite of the relatively short collector rows, as reported in Fig. 2(b). $\dot{Q}_s$ and $\dot{Q}_r$ are also reported, as well as the power delivered to the user $\dot{Q}_a = (T_4 c_{p,a} - T_{amb} c_{p,amb})\dot{m}$. Thermal losses from the receiver tubes as well as connection pipes L_{n1}, L_{n2}, L_{n3} are estimated as $\dot{Q}_L = \dot{Q}_r - \dot{Q}_a$. The solar power available during the day on an equivalent solar field surface normal to sunrays $\dot{Q}_{bn} = G_{bn} L_m W_a n_s n_p$ is reported. It can be noted that the system is not operating during the overall daylight time interval, since it is shut off during the first and the last hours of the day when the solar power is low. In fact, under low irradiance conditions is not possible to find freewheeling. This is mainly due to the compressor operating range not yielding enough efficiency at very low mass flow rates, as it is required at low irradiance conditions. A load factor $LF = \dot{q}_s/\dot{q}_{s,max}$ can be defined as the ratio between the solar heat flux at the receiver and its maximum value expected across the year, with $\dot{q}_{s,max} = 13{,}500\ \mathrm{Wm^{-2}}$. Below a certain load factor, the system does not operate in autonomous mode and is considered as shut off in the present simulation. The threshold load factor LF_{th} resulted in being around 0.3 for the turbocharger and solar field layout considered. The load factor is reported in Fig 2(b).

Fig.2 (c) shows the temperature of the main points of the circuit, as indicated in Fig.1. Outlet compressor temperature is affected by the compression ratio, eq. (7), and varies across the day, reaching 150 °C as maximum. T_3 results from the power gained $\dot{Q}_u$, eq. (2), across the receiver tube by the airflow. It must be high enough to provide the required power at the turbine but ensuring that the maximum wall temperature allowed $T_{w,max}$ is not overcome. Wall temperature corresponding to the tube end T_{w3} is reported, confirming that $T_{w3} < T_{w,max} = 600$ °C. Surprisingly, the air temperature at the turbine outlet delivered to the user T_4 shows a relatively flat profile along the operating hours, between 350 °C and 380 °C. This can be considered very favourable. The mass flow rate varies across the day between $0.3\ \mathrm{kg/s}$ and $0.65\ \mathrm{kg/s}$, according to the turbocharger maps. In fact, the variation of solar power affects the inlet turbine temperature, hence the provided $\dot{W}_e$, bringing the turbocharger to modify its operating point. Higher solar power leads the turbocharger to operate at higher speeds, hence with higher mass flow rates and pressure ratios, Fig.2 (c)-(d). Isoentropic efficiencies, also reported, keep close to the maximum values across the operating hours. Turbocharger speed is reported in terms of corrected speed $n_{c,cor} = n_T\sqrt{T_{c,ref}T_1^{-1}}$, with $T_{c,ref} = 302.6$ K over the maximum $n_{c,cor}^{max} = 87{,}986$ rpm for the selected turbocharger, being $n_{c,cor}^{min} = 27{,}960$ rpm.

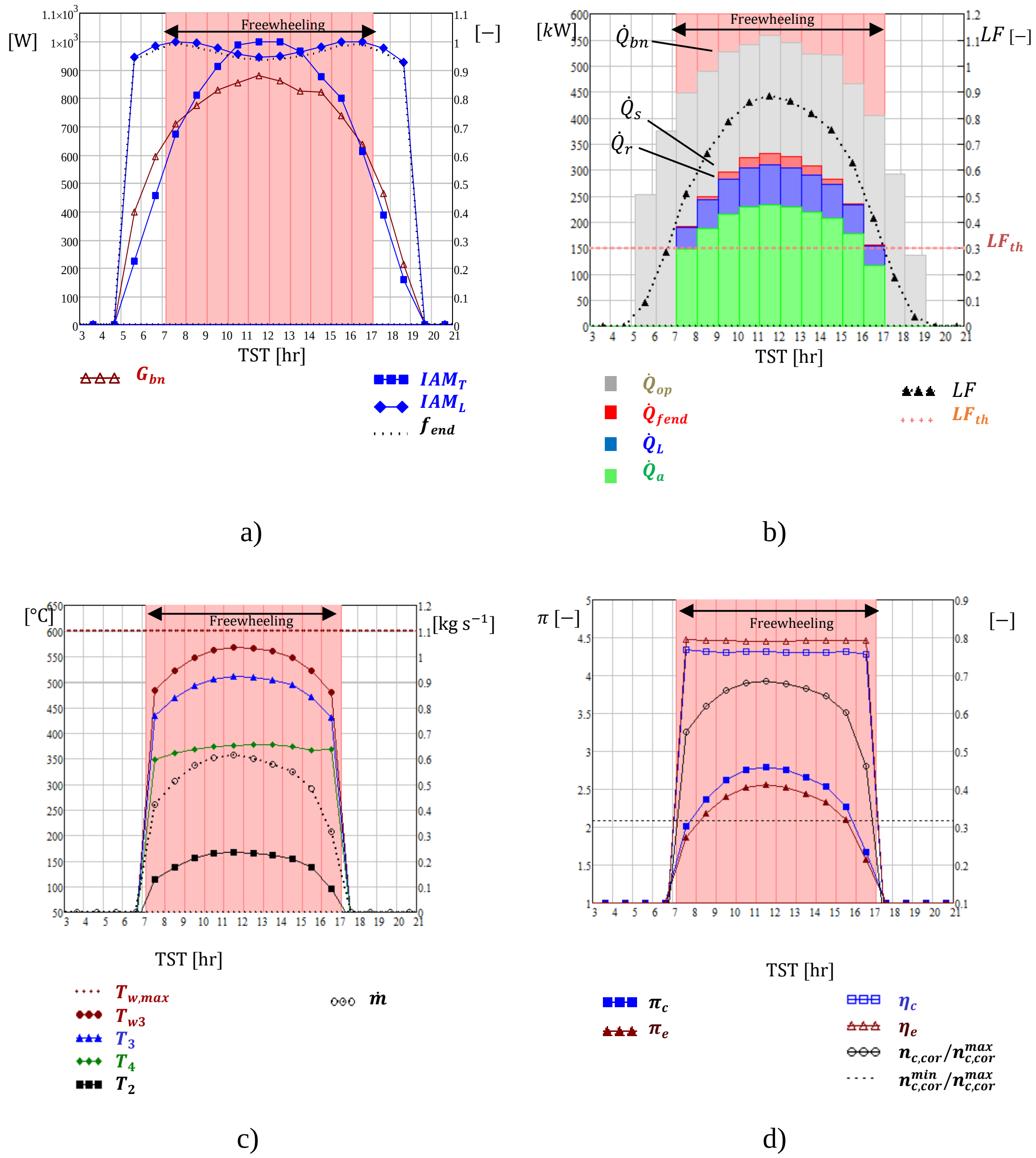

Fig.2 Performance in a clear summer day, Madrid (Spain).

Performances during a typical day with clear sky in March are representative of the intermediate seasons, Fig.3. The lower sun elevation results in lower optical efficiency, being the incident angle modifier lower than in the summer case. End losses are also more significant. The load factor, Fig.3(b) is lower than LF_{th} either in the morning and afternoon. Operative hours are reduced with respect to the summer case, but the system can produce hot air in the central hours of the day. On the other hand, the output air temperature remains higher than 300 °C, fulfilling the scope of medium temperature heat production, Fig.3(c).

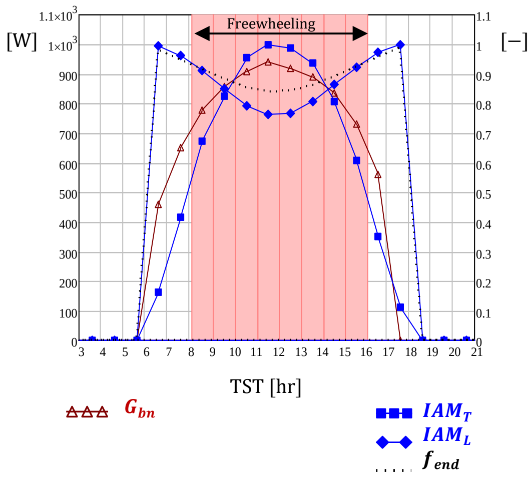

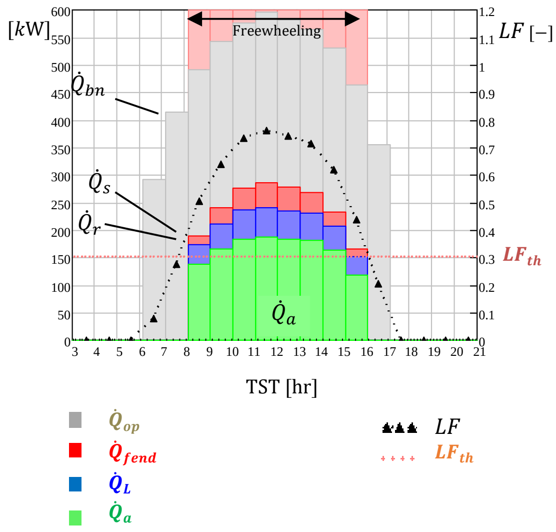

a) b)

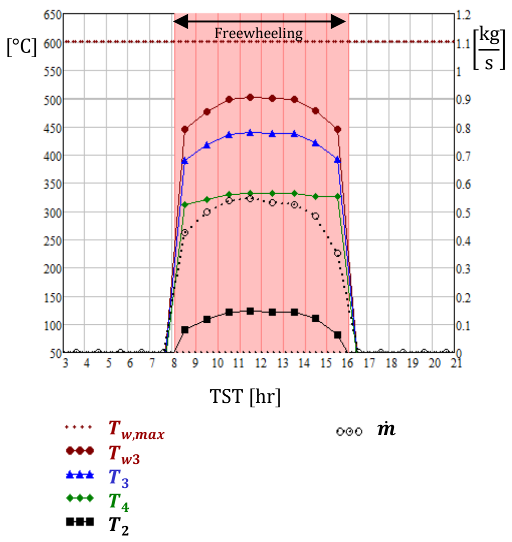

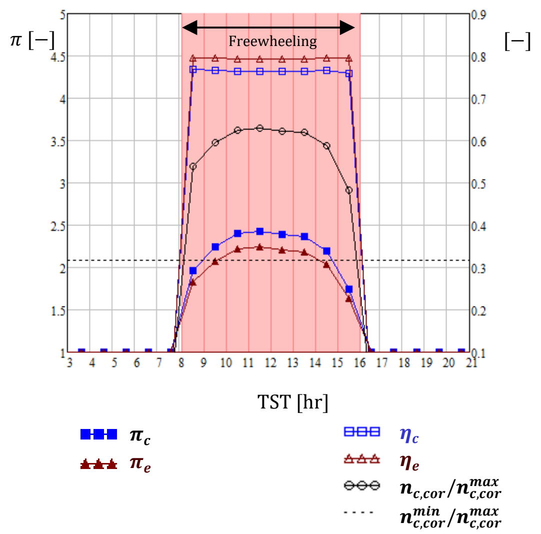

c) d)

Fig.3 Performance in a clear spring day, Madrid (Spain).

In addition to the above numerical experiments, the behavior of the T-SAH is investigated for a typical winter day of December, with a clear sky. Fig. 4 depicts the performances. It can be noted as the optical efficiency is reduced due to lower IAM_L and f_{end}, with respect to the previous cases. As indicated in Fig.4(b), only for a few hours of the day, the load factor overcomes the threshold value, and the system operates in freewheeling. The power delivered is modest while the optical end losses increase in relative terms. The delivered airflow holds a temperature above 300 °C, although the mass flow rate is modest, as well as the pressure ratios, Fig. 4(c).

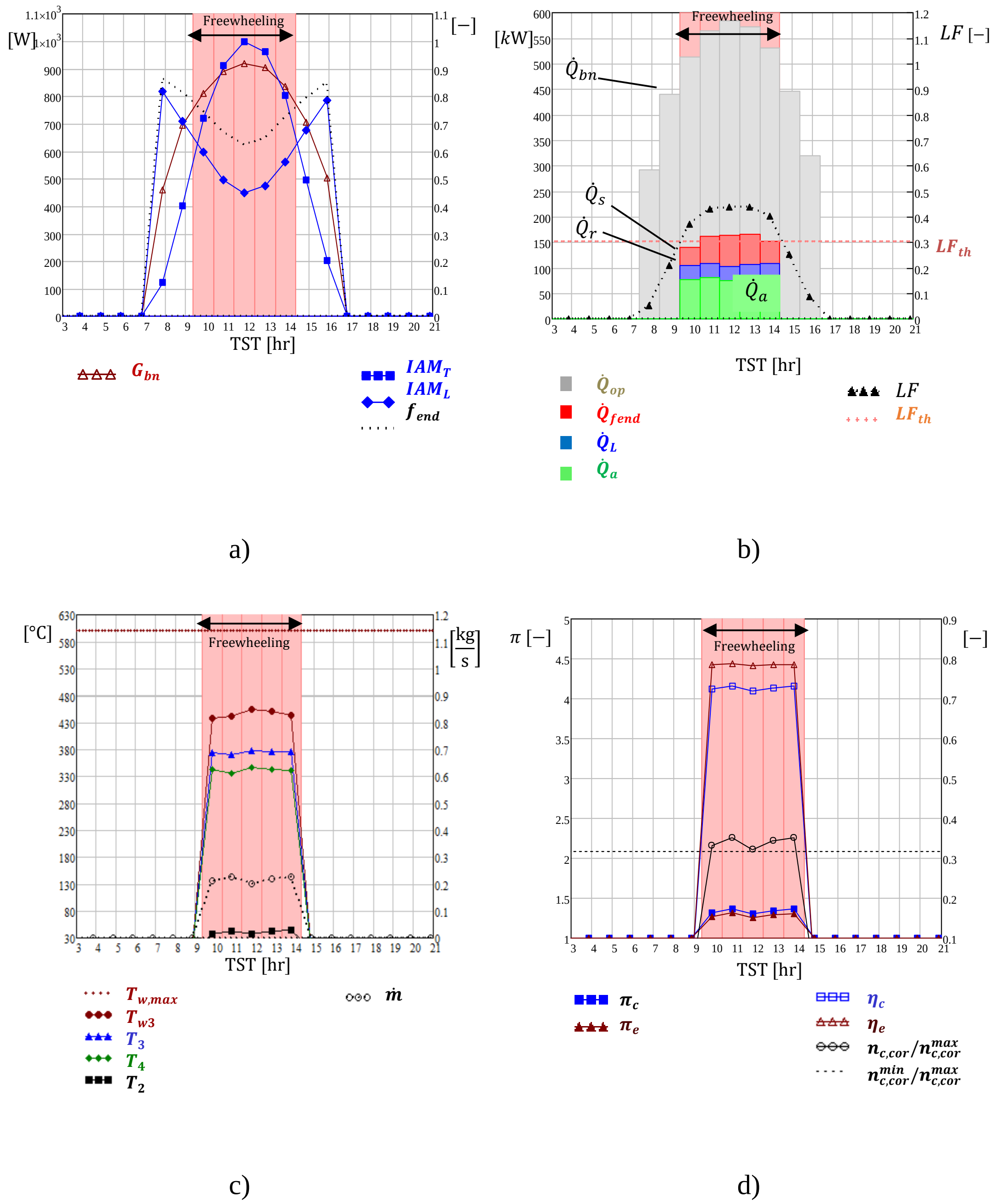

Fig. 4 Performances during a typical winter clear day.

The cases above analyzed show that the T-SAH, without any backup or boost power, can operate during the whole year. However, a drop both in the delivered power and in daily operating hours occur from summer to winter season. During cloudy days the system would have a discontinued operation. The reason is that under low irradiance conditions, the turbocharger is not able to work in freewheeling, and the T-SAH must be considered shut off in the present simulation. Improvements are possible for these shut off conditions. One is straightforward; the turbocharger can be bypassed from the circuit. Then the air is pumped using the auxiliary compressor (Fig.1). This allows producing solar hot air, although consuming auxiliary energy for pumping, which is expected to be low due to the low solar power and low mass flow rate involved. In addition, the integration with external renewable energy sources can be considered, as well as a thermal storage unit.

5. Conclusions

An innovative solar air heater using concentrating Linear Fresnel collectors for industrial application has been presented and analysed in this study. The turbo-assisted solar air heater has been numerically simulated through a steady-state model. This allows to investigate the behaviour of a medium scale facility under a variety of conditions and to identify the relevant design and optimization parameters. The model obtained computes the operational state of the system and hot air production at any hour of the typical meteorological year from a given location.

The results confirm the technical feasibility and interest of the concept. The simulation run for representative clear days shows the main features of the system, indicating that the use of a turbocharger allows obtaining a remarkable steady temperature profile for the delivered airflow during the sunny hours of the day, without consuming external energy for pumping.

The T-SAH facilities so configured can provide hot air between 300 °C and 400 °C during summer, winter and intermediate season of the year for the selected location of Madrid (Spain) with a continental Mediterranean climate. The study offers a platform for demonstration plants design paving the way to more low carbon industries.

6. Numenclature

Latin

A	Aperture surface area [m^2]
ac	Auxiliary compressor
c_p	Air specific heat capacity [J kg^{-1} ℃$^{-1}$]
D	Inner diameter of the receiver tube [m]
F'	Collector efficiency factor [-]
F_R	Collector heat removal factor [-]
f	Darcy friction coefficient [-]. f Function
f_{end}	Optical end losses factor [-]
G_{bn}	Normal beam irradiance [W m^{-2}]
h_a	Air heat transfer coefficient [W m^{-2} ℃$^{-1}$]
IAM	Incidence angle modifier [-]
k	Thermal conductivity [W m^{-1} ℃$^{-1}$]
L	Length [m]
LF	Load factor $\dot{q}_s/\dot{q}_{s,peak}$
$\dot{m}$	Air mass flow rate [kg s^{-1}]
n	Rotating speed [rpm]
n_p	Number parallel U-loops
n_s	Number of modules in series in a U-loop
P	Receiver tube cross-section perimeter [m]
Pr	Prandtl number [-]
p	Pressure [Pa]
$\dot{Q}$	Thermal power [W]
Q	Thermal energy [J]
$\dot{q}_s$	Concentrated solar irradiance [W m^{-2}]
$\dot{q}_u$	Thermal power flux to air [W m^{-2}]
Re	Reynolds number [-]
T	Temperature [K, °C]
TST	True solar time [hr]
U_L	Thermal losses coefficient receiver [Wm^{-2} K^{-1}]
$\dot{W}$	Power [W]
W_a	Rectangular aperture total width [m]

Greek

γ	Isentropic exponent [-]
ρ	Density [kg m^{-3}]
η_{op0}	Maximum optical efficiency [-]
η_m	Mechanical efficiency of turbocharger [-]
η	Total to total isentropic efficiency [-]
π	Pressure ratio [-]

Subscripts

$_a$	Air
$_{amb}$	Ambient
$_{atm}$	Atmospheric
$_{bn}$	Normal beams
$_c$	Compression. Compressor
$_e$	Expansion. Turbine
$_{ex}$	Receiver tube external surface
$_{fend}$	End optical losses factor
$_{in}$	Inlet
$_{ou}$	Outlet
$_t$	Stagnation variable
$_{th}$	Threshold
$_{tot}$	Total
$_T$	Turbocharger
$_w$	Wall
$_0$	Inlet from atmosphere
$_1$	Compressor inlet
$_2$	Compressor outlet
$_3$	Turbine inlet
$_4$	Turbine outlet

Superscripts

^{min}	Minimum
^{max}	Maximum

Acronyms

ETC	Evacuated Tube Collector
CSH	Concentrating Solar Heat
HTF	Heat Transfer Fluid
IAM	Incident Angle Modifier
LFC	Linear Fresnel collector
PTC	Parabolic Trough Collector
SAH	Solar Air Heater
SHC	Solar Heating Collectors
SHIP	Solar Heat for Industrial Processes

Others

$\langle\ \rangle$	Functional dependence

θ_L	Longitudinal angle [rad]
θ_T	Transversal angle [rad]

7. References

Burkholder, F, and C Kutscher. 2008. "Heat-Loss Testing of Solel's UVAC3 Parabolic Trough Receiver." *NREL Technical Report* TP-550-423 (January): 19.

Duffie, John A., William A. Beckman, and Jon McGowan. 1985. *Solar Engineering of Thermal Processes*. *American Journal of Physics*. Vol. 53. https://doi.org/10.1119/1.14178.

Famiglietti, A., A. Lecuona-Neumann, J. Nogueira, and M. Rahjoo. 2020. "Direct Solar Production of Medium Temperature Hot Air for Industrial Applications in Linear Concentrating Solar Collectors Using an Open Brayton Cycle. Viability Analysis." *Applied Thermal Engineering* 169. https://doi.org/10.1016/j.applthermaleng.2020.114914.

Guzzella, Lino, and Christopher H. Onder. 2010. *Introduction to Modeling and Control of Internal Combustion Engine Systems*. https://doi.org/10.1007/978-3-642-10775-7.

Habte, Aron, Thomas Stoffel, Richard Perez, Daryl Myers, Christian Gueymard, Philippe Blanc, and Stefan Wilbert. 2017. "*Best Practices Handbook for the Collection and Use of Solar Resource Data for Solar Energy Applications: Second Edition.*" NREL, no. December 2017: 2.1-2.22. www.nrel.gov/publications.

Heimsath, A., G. Bern, D. Van Rooyen, and P. Nitz. 2014. "Quantifying Optical Loss Factors of Small Linear Concentrating Collectors for Process Heat Application." *Energy Procedia* 48 (March 2016): 77–86. https://doi.org/10.1016/j.egypro.2014.02.010.

International Energy Agency. 2018. "KEY WORLD ENERGY STATISTICS 2019."

Karathanasis, Stavros. 2019. *Linear Fresnel Reflector Systems for Solar Radiation Concentration*. *Linear Fresnel Reflector Systems for Solar Radiation Concentration*. https://doi.org/10.1007/978-3-030-05279-9.

Lecuona-Neumann, A. 2016. *Secadero solar*. Patented in Spain P201630068, issued in 2016.

Mekhilef, S., R. Saidur, and A. Safari. 2011. "A Review on Solar Energy Use in Industries." *Renewable and Sustainable Energy Reviews* 15 (4): 1777–90. https://doi.org/10.1016/j.rser.2010.12.018.

Sharma, Ashish K., Chandan Sharma, Subhash C. Mullick, and Tara C. Kandpal. 2017. "Solar Industrial Process Heating: A Review." *Renewable and Sustainable Energy Reviews* 78 (December 2016): 124–37. https://doi.org/10.1016/j.rser.2017.04.079.

"SHIP Database." n.d. http://ship-plants.info/.

Solatom. n.d. "SOLAR STEAM FOR INDUSTRIAL PROCESSES." http://www.solatom.com/.

COST REDUCTION BY COMBINING SOLAR THERMAL TECHNOLOGIES FOR A DISPATCHABLE STEAM GENERATION

Mr. Nicolas Ürlings[1], Mr. Shishir Uppangala[1], Mr. Stelios Constantinou[2],

[1] protarget AG, Zeissstr. 5, 50859 Cologne, Germany

[2] KEAN soft drinks Ltd., P.O. BOX 50300, 3603-Limassol

Abstract

Compound Parabolic Concentrator's (CPC) are usually not associated with the production of steam, as with the required high operating temperature to produce steam the thermal losses of the CPC are predominant. In this paper a system is presented to include a CPC solar field into the solar thermal generation of steam for a process heat consumer. The presented system includes a Parabolic Trough Collector (PTC) field to generate steam at 188°C/11barg. The CPC system is used to pre-heat the feed water to 95°C. This combined solar system is built by the protarget AG in Cyprus, Limassol at the premises of KEAN soft drinks Ltd. to provide heat for the orange juice production. In this paper it is shown how both technologies, the CPC system with 225m² collector gross area and the PTC system with 283m² collector gross area, are integrated in the same industrial process. The consumption of process heat at this specific application starts early in the morning with no sunshine available. Therefore, an arrangement including a Thermal Energy Storage (TES) for each of the technologies is found. The operating behaviour of both technologies contributing to the same energy consumer is presented. The innovation of combining these two technologies promises a cost reduction; therefore, a detailed economic analysis is shown and the cost reduction potential is explained. The economic calculation is indicating an advantage of the combined system instead of a solely PTC system. The PTC only system generated the steam at ca. +2.5% of the cost compared to a combined system considering a 1.25MW nominal thermal power application built in Limassol, Cyprus. This paper validates the benchmark calculation and how a variation of the installed system size will impact the cost reduction.

Keywords: Parabolic Trough Collector, PTC, Compound Parabolic Concentrator, CPC, Thermal Energy Storage, TES, process heat, cost reduction

1. Introduction

As part of the European "Green Deal", the European Commission proposed on the 4th of March 2020 the first European Climate Law to formulate the 2050 climate-neutrality target – to realize this mark an economy with net-zero greenhouse gas emissions is required. A net-zero emission is defining that all man-made greenhouse gas emissions must be absorbed from the atmosphere via natural and artificial sinks. The Climate Law underlines the EU's commitment to the global climate action under the Paris agreement. The objective of the Paris agreement is to keep the global temperature increase to below 2°C and pursue efforts to keep it to 1.5°C.

To realize these temperature targets the introduction and establishment of renewable energies in all energy consuming sectors from the power sector to industry, mobility, buildings and agriculture is required. To facilitate and accelerate the elemental shift to a clean energy economy several measures have to be taken. These measures are made of political stimulations on different levels (policies, subsidies, legislation, etc.) as well as intensified technical research and development to reduce the costs of renewable energy systems itself. The Members of the European Union agreed in July 2020 on contributing to the goals of the European Green Deal and that 30% of the overall 1.8 trillion € budget will be assigned to climate related investments.

In 2017, the transport sector accounted for 28% of total final energy consumption in Europe. This sector is followed by the residential sector with (24 %), the industrial sector with 24% and others like commercial and public services with equally 24%. The industrial sector itself consumes ca. 66% of its energy in the form of heat. Of this heat consumption only a fraction off ca. 0.1% is supplied by solar thermal systems. The highest fraction of the heat consumption is covered by burning natural gas, followed by coal and oil products (International Energy Agency, 2017).

The market of solar thermal energy in the industry is still untapped, indicating the great and wide potential of possible applications. Solar thermal solutions may be a key factor realizing the European "Green Deal".

doi:10.18086/eurosun.2020.03.07 Available at http://proceedings.ises.org

The distribution of the Global Horizontal Irradiance (GHI) within Europe indicates that especially for countries in the south of Europe solar thermal technologies are showing a potentially high energy yield. In addition to the solar resource, solar thermal energy is of special interest to the industry, if prices for fossil fuels are high (as it is the case for instance in Cyprus). The dependence on the import of petroleum products can be observed in the majority of European countries. A typical imported fuel used by the industry is Light Fuel Oil (LFO). This is also the fuel used by KEAN to fire the conventional steam boiler.

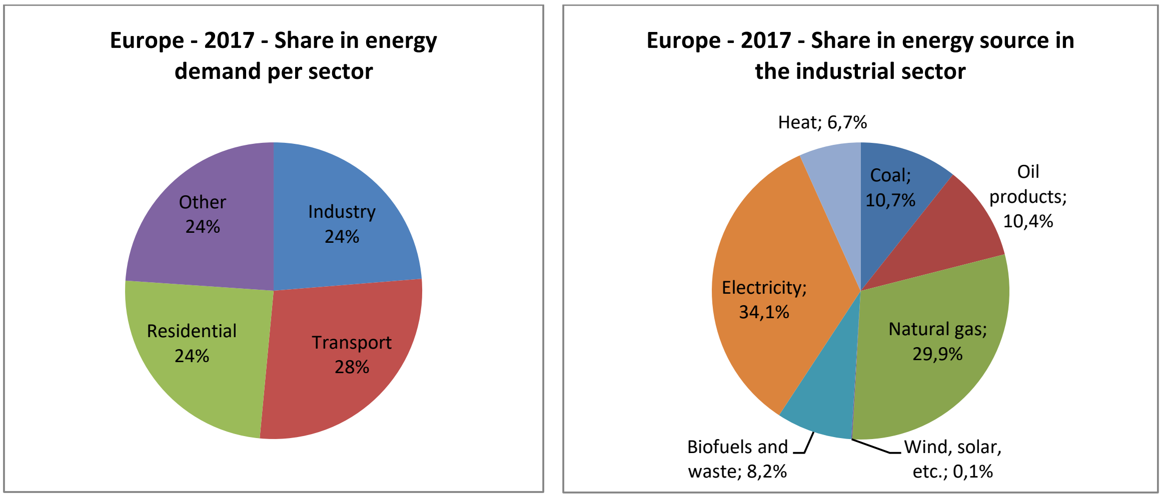

Fig. 1: Share in Europe's total energy demand in 2017 indicating the energy sources of the industrial sector (IEA, 2017)

Research and development on solar thermal systems is carried out for many years. Allot of studies and projects are aiming to reduce the levelized cost of heat, for instance of the steam generated for an industrial consumer. The result of lower steam cost of a solar thermal system is resulting in a reduced Return on Invest (RoI). The development presented in this paper is an integral solar thermal system consisting of a combination of two solar technologies. The aim of this concept is to apply both systems at the optimal operation point and therefore reduce the total investment cost by maintaining at the same time the energy yield compared to a single system. In order to make solar thermal technologies more attractive to the industry, Thermal Energy Storage solutions are further developed as well. The application of a TES may have an additional positive impact on the RoI as dumping of solar thermal energy can be reduced and energy can be made available when it is required by the consumer, thus decoupled from the availability of sunshine.

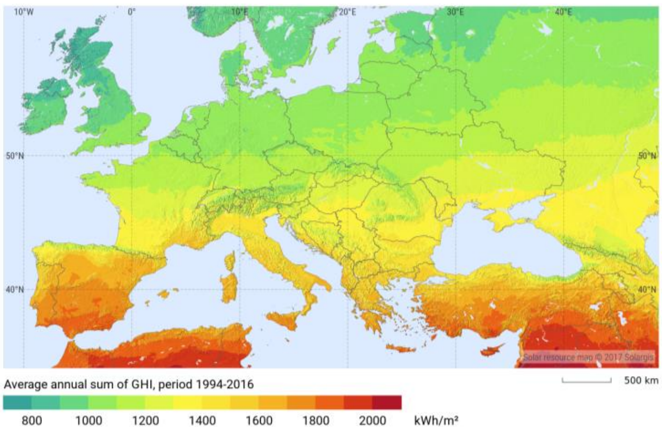

Fig. 2: Global Horizontal Irradiation in Europe (Average of 1994-2016) (Solar resource map © 2019 Solargis, 2020)

The characteristics of the two combined solar technologies are explained in this paper. The efficiency under different operation temperatures is shown for both technologies. The TES chosen in each of the systems is described and the key parameters are given. In order to combine the two technologies and make use of their optimum operational range, the consumer side has to be considered to adapt the technologies to the requirements of the present process. To understand the heat supplying process of the application certain measurements are executed to identify the consumption and operation pattern. In addition, the optimal integration point of the consumer has to be identified. This pre-design procedure and its results are described in this paper.

The realized system and the parameters are given in this paper. It is shown how a CPC feed water heating system is sized. A layout of the entire system displaying the conventional and the solar thermal energy sources is given.

The reduction of the cost of generated steam by means of solar thermal power is the content of the presented work. Therefore, an economic analysis is calculating the benefit of combining the two solar thermal technologies. The investment cost for the low temperature (CPC) and the high temperature (PTC) solar thermal systems are included, as well as the maintenance and operational costs. The specific costs of the different TES are built-in the economic model as well.

Fig. 3: A picture showing both technologies at KEAN (CPC foreground and PTC in the background) ©protarget AG

2. Methodology to integrate the technologies

The purpose of the solar thermal systems is to generate process heat and save conventional energy resources (in this case Light Fuel Oil consumed by a conventional steam boiler). After examination of the conventional steam generation system of the industrial consumer the most suitable integration point has been identified.

2.1 Measurement campaign

During the pre-design study an ultrasonic water flow meter has been installed to exactly determine the amount and time of the feed water is supplied into the conventional steam boiler. By the results of the measurement and the identification of the operation pattern throughout the day, it was found that the low temperature collectors can be used to heat up the feed water of the conventional steam generator. Nevertheless, the operation pattern showed that a TES is required based on the amount of water required during times with no sunshine available (basically early in the morning during the beginning of the production).

One pattern of the feed water supply the measurements underlined is that in the beginning of the production at 4:00AM local time a high amount of feed water is pumped into the steam boiler. After examining the level gauge of the steam boiler, it was found that during the night the water in the boiler cools down to an extent resulting in a substantially reduced volume of the water in the steam boiler. The feed water pump of the steam boiler is triggered by the water level switch of the steam boiler and as the steam boiler is switched on in the morning a high amount of water at low temperatures (ambient temperatures) is pumped into the boiler till the set water level is reached. This effect causes the steam boiler to heat up very slowly in the morning as a huge amount of cold water is within the steam boiler. The measurement values shown in Figure 4 are reflecting an average day in September. Especially in the time of the juice extraction between February and April the amount of required feed water i.e. steam is much higher.

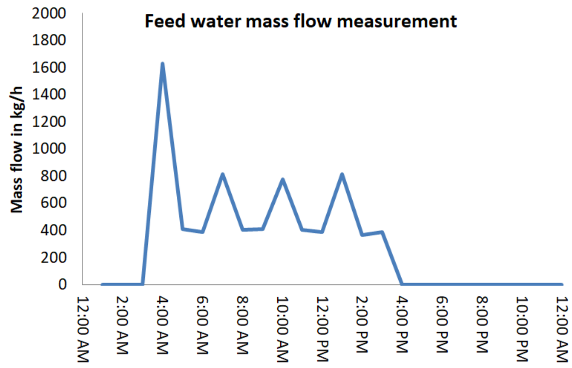

Fig. 4: Graph indicating the mass flow of the feed water into the existing steam boiler

2.2 Energy integration

Under energy integration it is understood how a CPC solar field could contribute to the steam generation of an industrial process heat consumer. Considering the Enthalpy-Temperature (h-T) correlation of water at the process pressure of 10barg the steam generating process can be explained. The enthalpy of the feed water at KEAN is in average about 25°C (depending on the amount of condensate return it can go up to ca. 40°C). Condensate return can be taken into account when the system is already in operation, but is not being observed during start-up or after cooldown phases. The enthalpy of water at 25°C is 104.8kJ/kg and it is 398.0kJ/kg at 95°C. The resulting difference when heating water from 25°C to 95°C is 293.2kJ/kg. Converting water from 25°C directly into steam at 10barg (184°C) takes 2675.8kJ/kg. The share of heating the water to 95°C is about 11% of the total energy required for this process. This energy can be delivered by the CPC system and the share is independent on the amount of power actually required. This calculation with the exemplary process parameters for the KEAN factory shows that the CPC system can be seized individually from a PTC field.

2.3 Technical integration

As described under the Deliverable B2: Integration Guideline from the IEA SHC Task 49 (Muster, 2015) the integration of solar thermal energy can be divided between the integration on supply level and the integration on process level. The CPC system is applied on the supply level by heating the feed water. The PTC system integration point is for the KEAN case on the process level. The PTC system has been built close to the tetra pack line of the KEAN factory and the load profile of the tetra pack line is assuring a very complete usage of the PTC generated steam. In the schematic layout in Fig. 5 the integration of both systems at KEAN can be seen. The higher the rated power of the PTC plant in comparison to the total amount of required power of the plant the more advantageous it is to integrate on the supply level to allow for more flexibility. Feed water is heated only for the conventional steam boiler in the KEAN.

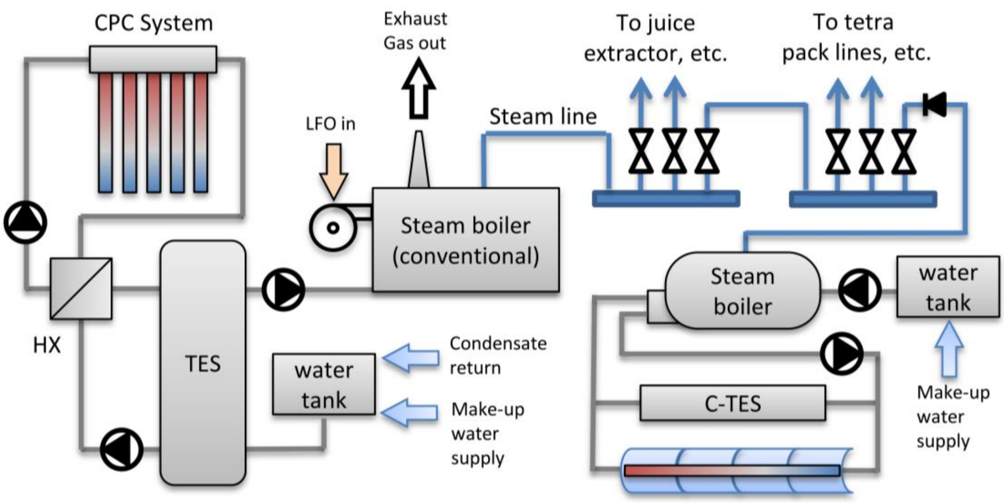

Fig. 5: Schematic layout of the combined solar system and conventional boiler

3. System description

The company protarget AG has developed and installed a system of a combination of a PTC and a CPC solar field to lower the overall cost. It is suitable for any industrial steam consumer, but in this case providing solar thermal generated steam for an orange juice factory. Therefore, the application can be categorized into the following industry sector definitions C10.3 - Processing and preserving of fruit and vegetables or alternatively C11 – Manufacture of beverages. Worldwide only 39 solar systems can be counted falling into these two sectors (SHIP, 2020). By means of this number it can be seen that the introduction of solar thermal energies into this industry sector has just begun and further effort is required to provide this huge sector with the existing solutions. The individual solar thermal systems are described in this section giving the key parameters.

Fig. 6: Aerial view of the CPC and PTC combined system, ©protarget AG

3.1 PTC system

The Parabolic Trough Collector system at KEAN involves a two-row parabolic trough collector loop. The aperture of the collector is of about 3 metres and the row length is of ca. 48m. The gross area of the PTC is in total about 283m². A two-module Concrete Thermal Energy Storage (C-TES) and a fairly standard kettle-type steam boiler for steam generation are the other main components of the system. The parts are shown and denominated in Fig. 5. The two-module C-TES and the steam boiler including the oil handling unit like pumps and expansion vessels are placed within shipping containers (as it may be seen in the aerial view in Fig. 6). The so-called control container including the steam boiler and the system technology has been fully manufactured in the workshop of the protarget AG in Cologne and is designed for a simple connection without mayor interventions on site. Considering Fig. 6 the size and localization of the parabolic trough collector system at the KEAN factory can be estimated as well. The Heat Transfer Fluid for this system is of HELISOL® XA silicone oil from WACKER Chemie AG. This fluid can be heated up to 425°C and is fairly new on the market. At the KEAN factory, steam is required early in the morning when the production starts, in this case the CTES is discharged and the stored energy is used to produce steam. The C-TES is partly charged in the afternoons and fully charged on weekends when the factory is closed. This operation mode allows the PTC system to produce steam at about 11barg/188°C (slightly above the 10barg of the conventional steam boiler) early in the morning when no sunshine is available. The rated capacity of the C-TES is about 640kWh. Further information about the PTC plant can be found in various publications (Sattler, 2018/2019).

3.2 CPC system

The CPC system is installed on a roof with east-west orientation and an elevation of about 17.2°. The solar field is therefore split into two independent operating circuits with separate pumps. The indirect heated thermocline storage of a capacity of about 400kWh is providing energy in the early morning at the start of the production and at times with bad weather conditions. The employed CPC collector consists of 18 vacuum tubes with a highly selective absorber layer and is of a gross area of 3.41m². 66 Collectors have been installed forming a solar field gross area of 225m². As a working fluid demineralized water is used without additives like glycol.

The split in an east and west oriented solar field as shown in Fig. 6 provides an even solar thermal energy distribution throughout the day. The CPC system is operated at a temperature at the exit of the solar field of about 100°C. This provides that the TES is charged with water up to 95°C. In this order, the at atmospheric pressure operated TES stores the energy at the maximum possible temperature avoiding the generation of steam within the storage itself.

3.3 Operation characteristics

In the following section the operating behaviour of both technologies contributing to the same energy consumer are shown and explained. In Fig. 7 the feed water heating of the CPC System is shown and at the same time the steam generation from the PTC system. This figure is given to demonstrate the feasibility of the concept of having two solar technologies within the same process heat network, where “SF” stands for solar field.

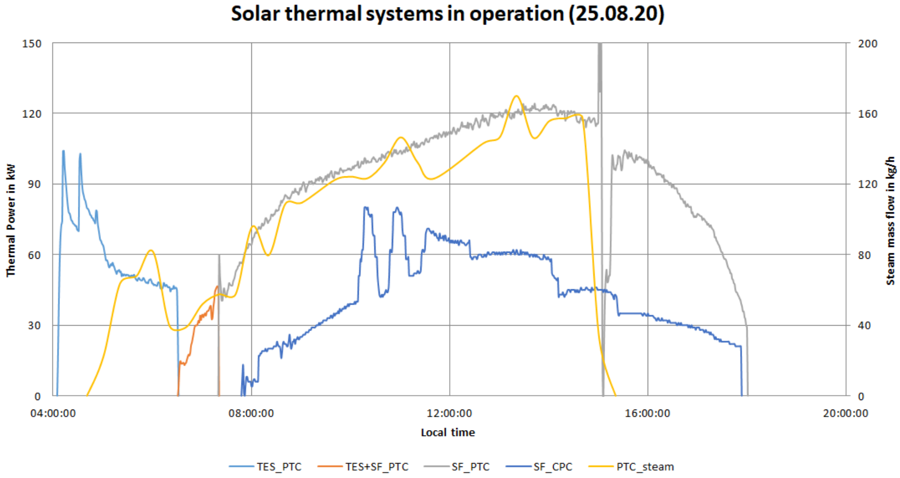

Fig. 7: Operational curves for PTC and CPC

It has been observed during operation that the conventional steam boiler is quickly (about 1.5 hours sooner than without a CPC pre heater) heated up and at the desired temperature, thus ready to produce steam. This effect is explained by the introduction of the hot water from the feed water thermocline TES in the morning into the steam boiler instead of cold water. Considering the water volume required in the boiler in the morning this makes a significant difference of the temperature of the water in the steam boiler at the beginning of the start-up procedure. The plant still begins the start-up phase at 4am, but the production of the beverages can be ramped up earlier as steam is available earlier. This results in theory in a higher production volume per day and therefore is a benefit in terms of efficiency of the production process of the beverages itself.

3.4 Efficiency comparison

The thermal efficiency curves of the two applied technologies are shown in Fig. 8. The thermal efficiency decreases with an increasing mean temperature in the collector. The given Curves are based on a Direct Normal Irradiance (DNI) of 850W/m² and a Diffuse Horizontal Irradiance (DHI) of 150W/m². The efficiency decrease of the PTC at higher temperatures is smaller than the pronounced efficiency drop of the CPC.

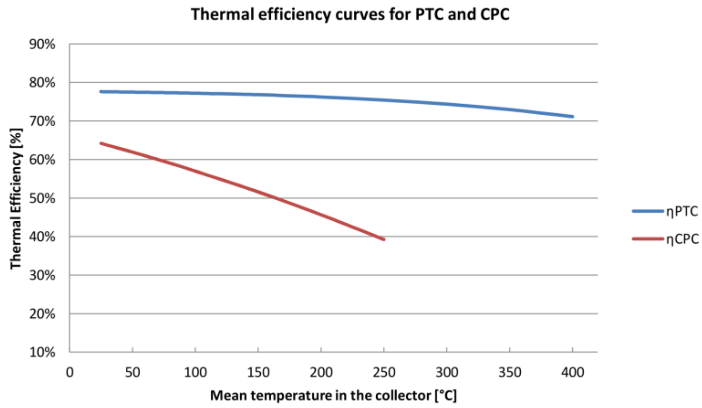

Fig. 8: Thermal efficiency curves for PTC and CPC

4. Economic analysis and cost reduction potential

To expose the cost reduction potential of applying both presented technologies in one system a holistic approach is chosen. This means, besides the specific investment cost of both of the technologies the specific investment of the Thermal Energy Storage and the specific maintenance and operation costs have to be considered. A CPC System can be mounted on a roof as executed at the presented system; therefore, land cost can be saved and the system can be installed very close to the conventional steam boiler to minimize piping losses (and cost). Nevertheless, land costs are not considered in this study as the variance on possible sites is too high to pic a representative value. A CPC solar field may also be installed on the ground under certain conditions and therefore also create land cost as a PTC system. In order to combine both technologies, the adequate solar field size has to be found for both. The approach followed in this paper is based on the calculations shown in Chapter 2 “Methodology to integrate the technologies” under Subchapter 2.2 “Energy integration”. The concept basically applies that the feed water heating demand of up to 95°C is about 11% of the total energy demand to produce steam to the required parameters. Therefore, a simple, but yet meaningful economic analysis is to compare a solar field with 10 Solar Collector Assemblies (SCA) of a PTC with a solar field of 9 SCA of a PTC and a CPC solar field with 120 collectors. This system design is set for the benchmark calculation to demonstrate the cost reduction potential. In the graph shown in Fig. 9 the system design philosophy is visualized. In can be seen that both system arrangements are resulting in a similar amount of energy generated, namely 3144 MWh/a for the PTC system only and 3200 MWh/a for the combined system. The question answered in this paper is which arrangement generates energy to better overall costs.

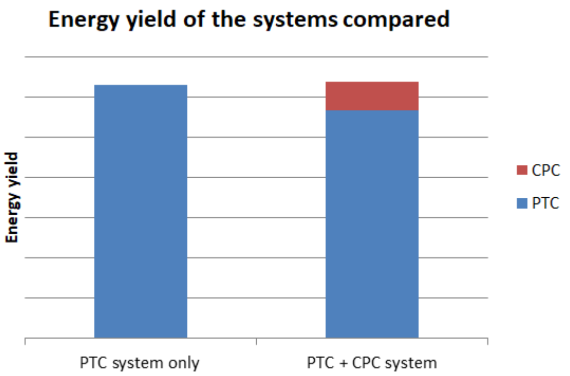

Fig. 9: Energy yield of the systems compared

The specific investment cost of a low temperature thermocline storage is calculated with 10,000€/MWh capacity. In comparison, the specific cost of storing energy at temperature levels up to 425°C in a C-TES are located at 50,000€/MWh capacity for the defined storage size. The sizing of the two TES is done similarly then the sizing of the solar field design philosophy resulting in a C-TES capacity of 4.3MWh and a 0.55MWh capacity for the feed water thermocline TES. Accordingly, the storage capacity for the PTC only system is 4.85MWh (C-TES). The total investment cost of both systems is very similar, namely 1.455.740€ for the purely PTC system and 1.464.216€ for the combined system. The specific operation and maintenance cost (€/kWh per annum) of a CPC system are at 0.001€/kWh$_{th}$ and therefore around a third of the specific cost of a PTC system with 0.0035€/kWh$_{th}$.

The economic analysis is based on an interest rate of 5% and a lifetime of both technologies of 25years. As a reference site to determine the solar resource and environmental conditions, the location of the present combined system at Limassol, Cyprus is defined.

4.1 Results

The cost for the thermal energy generated by the combined system of the CPC and PTC is about 0.0242€/kWh$_{th}$. For the PTC only system the cost of the generated thermal energy is 0.0248€/kWh$_{th}$. Considering the given steam parameter at the defined application the cost of steam is 18.00€/ton of steam (CPC and PTC) and 18.44€/ton of steam (PTC only). This analysis shows that the energy cost of a PTC system only for the specified benchmark is about 2.5% higher than a combined system of CPC and PTC.

4.2 Discussion

A CPC system includes lower specific cost for the collector, the TES and the maintenance and operation. Nevertheless, a CPC collector is less efficient in terms of optical and thermal efficiency and harvests less energy throughout the day as it is a non-tracking collector. On the other side a CPC collector is able to make use of DHI and converts it into thermal energy. With the economic calculation it was found that considering the current status with the given efficiencies, costs and properties of both technologies a combination is sensible and demonstrates a cost reduction. The system arrangements both result in very similar investment cost with 0.5% more investment cost for the combined system. The combined system produces about 1.7% more energy and shows a noticeable reduction in overall maintenance costs of 7.1%.

The presented analysis is limited by the weather conditions on the specific site. For other sites with different values for the DNI, DHI and ambient temperature, the cost difference of the systems may shape different. Especially a higher share in DHI of the GHI as found in India for instance may be even more advantageous for the combined system. For countries with lower ambient temperature throughout the year the thermal yield of the CPC would be reduced and impacting the cost reduction potential. For the applied system size the specific investment cost for a CPC are already settled down to a degree where the reduction from the economy of scale is minor. On the other hand, the difference of 9 or 10 SCA of a PTC in terms of the specific investment is considerable. For a system with increased capacity for instance with 36 SCA of PTC + 480 CPC and 40 SCA of PTC the cost reduction becomes less due to the noticeable drop of the specific investment cost of the PTC.

5. Conclusion

Under the specified conditions the combination of the CPC and PTC technology results in a reduced cost of the generated thermal energy. With the operational combined system at the KEAN juice factory the feasibility of integrating both technologies into one industrial heat consumer is demonstrated and verified. Both technologies are operating with a Thermal Energy Storage to supply the energy when requested by the consumer. The presented development makes a solar process heat system economically more attractive and may contribute to cover a higher share of the industrial heat demand by solar thermal power than currently observed.

6. Acknowledgments

The protarget AG and project authors would like to express their sincere gratitude for the confidence given by everyone involved and the fruitful collaboration within this project. Especially the ongoing support and contribution of KEAN soft drinks Ltd. and their employees made this project being a great success.

7. References

International Energy Agency (IEA), Europe's Energy Statistics 2017, online tables www.iea.org/statistics/ (last access 07.08.2020)

Solargis, Solar resource maps of Europe Solar resource map © 2019 Solargis https://solargis.com/maps-and-gis-data/download/europe (last access 07.08.2020)

Muster, Hassine, Helmke, Heß, Krummenacher, Schmitt, Schnitzer, 2015, Deliverable B2: Integration Guideline from the IEA SHC Task 49, https://task49.iea-shc.org/ (last access 07.08.2020)

Database for applications of solar heat integration in industrial processes - SHIP, 2020, http://ship-plants.info/

J. C. Sattler et al., "Dynamic Simulation Model of a Parabolic Trough Collector System with Concrete Thermal Energy Storage for Process Steam Generation", SolarPACES and AIP Conference Proceedings (2018)

J. C. Sattler et al., "Dynamic Simulation Tool for a Performance Evaluation and Sensitivity Study of a Parabolic Trough Collector System with Concrete Thermal Energy Storage", SolarPACES and AIP Conference Proceedings (2019)

J. C. Sattler et al., "Operational Experience and Behaviour of a Parabolic Trough Collector System with Concrete Thermal Energy Storage for Process Steam Generation in Cyprus" SolarPACES and AIP Conference Proceedings (2019)

INTEGRATED PLATFORM FOR ROOFTOP INSTALLATIONS OF FRESNEL COLLECTORS FOR SOLAR PROCESS HEAT GENERATION

Irapua Santos Ribeiro[1], Andreas Burger[1], Stephan Scherer[1] and Luís Miguel Braga[2]

[1] Industrial Solar GmbH, Freiburg (Germany)

[2] RAR – Refinarias de Açúcar Reunidas S.A., Porto (Portugal)

Abstract

The heat demand represents 74% of the total industrial energy demand worldwide (Solar-Payback, 2018). Solar process heat can supply a great share of this demand and provide process heat with diverse solar technologies such as the Fresnel collector. As industrial customers typically have limited ground availability, the rooftops are often the only option for the solar field installation, as represented in the project SHIP2FAIR. This article explains the main constraints for the installation of Fresnel collectors on rooftops and a novel concept of integrated lightweight platform walkways along the collector structure, overcoming a common hurdle of integration onto uneven roofs in industrial buildings. The article also presents a case study from an installation at a sugar refinery in Portugal.

Keywords: *solar process heat; linear Fresnel collector; industrial rooftop installation, solar energy, ship2fair*

1. Introduction

The share of energy demand in the industrial sector represents approximately 1/3 of the global energy demand (heat and electricity), of which about 74% is used for heating (Solar-Payback, 2018). Solar process heat technologies are already mature and can cover a large share of this demand, but it is often constrained by area availability. This is particularly challenging for concentrating technologies that have typically higher static and dynamic loads per foot point than non-concentrating technologies, as these have a higher amount of footpoints per collector area. Nevertheless, even non-concentrating solar collectors have their development delayed due to high roof integration costs (Juanicó, 2008).

Furthermore, linear concentrating technologies, such as the Fresnel collector, which is already proven on rooftops installations, still face two important constraints:

- The need of longer strings for reducing optical losses.
- Required even platforms for cost-efficient installation and maintenance activities, such as cleaning.

While roof areas are usually not used or interesting for other purposes, available ground areas are often reserved for a potential factory expansion and usually evaluated with a ground price that adds up to the overall costs of the solar system. In many cases, the available installation ground is far from the hydraulic integration points which leads to additional system costs, pressure head, and thermal losses.

Although efforts to integrate small-scale Fresnel collectors onto roofs have been attempted in the past, industrial-scale roof integration remains a main challenge and only a limited number of successful cases can be found in the literature (Sultana, Morrison, & Rosengarten, 2011). As an example of such constraints, at the SHIP2FAIR project (Solar Heat for Industrial Process towards Food and Agro Industries commitment in Renewables), three out of four demo sites are planned as rooftop installations using different solar thermal technologies, including the Fresnel collectors. The project aims to foster the integration and promote the use of solar process heat in industrial processes for the agro-food industry.

This paper presents the main features of a linear Fresnel collector and its installation characteristics, challenges, and possibilities in a variety of roof types. The proposed solution in this paper simplifies the building-integration of the Fresnel solar concentrators by using a design approach that integrates lightweight and cost-efficient walkways directly into the structure of the collector. In the end, a case study from one of the SHIP2FAIR demo sites at a sugar factory is discussed and further conclusions are drawn.

doi:10.18086/eurosun.2020.03.08 Available at http://proceedings.ises.org

2. Material and methods

Solar process heat generation using Fresnel collectors

A linear Fresnel collector is a concentrating solar technology that uses multiple primary mirrors to focus the sunlight onto an absorber. The modular LF-11 collector was designed to address the so-far untapped market potential previously described. Figure 1 below shows three LF-11 modules with main components and dimensions. The uniaxially tracked primary mirrors (a) and the secondary reflector (c) focus the irradiation onto an absorber tube (b). The heat is absorbed by the flowing fluid and transferred to the industrial production processes. The technology is suitable for generating heat at up to 400 °C and pressures up to 120 bars.

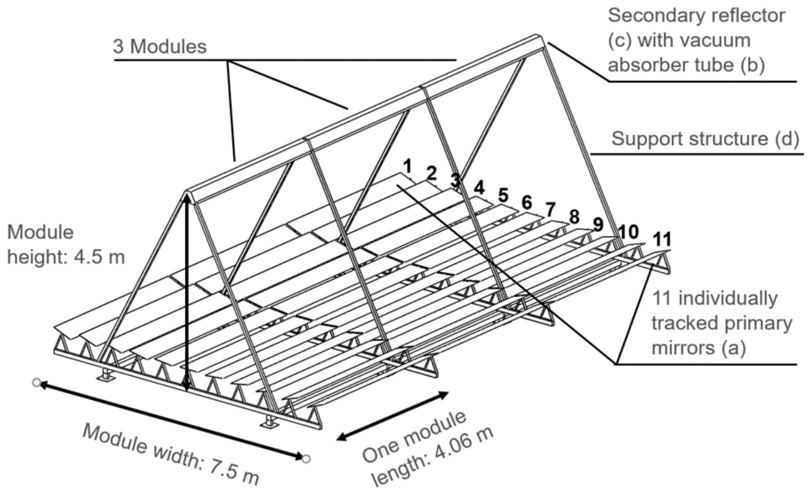

Figure 1 - Main characteristics of the LF-11 Fresnel Collector

The lightweight and modular structure (d) in combination with the high heat gain per installed area are designed for rooftop installations in industrial and utility facilities. The system generates steam directly (Mokhtar, et al., 2015) and can also be operated with different heat transfer fluids such as pressurised water and thermal oil. The solar process heat system can be integrated into customer's grids in various ways:

- Direct integration into steam grids.
- Direct or indirect integration into water or thermal oil heat grids.
- Indirect integration with a heat exchanger to heat any type of process.

Roof integration of Fresnel collectors

The LF-11 collector has been optimized for rooftop installations throughout several advancement steps. The collector design is optimized for high ground usage factor, low specific weight, low wind resistance during operation, and extremely low wind resistance during standby, as depicted in Figure 2.

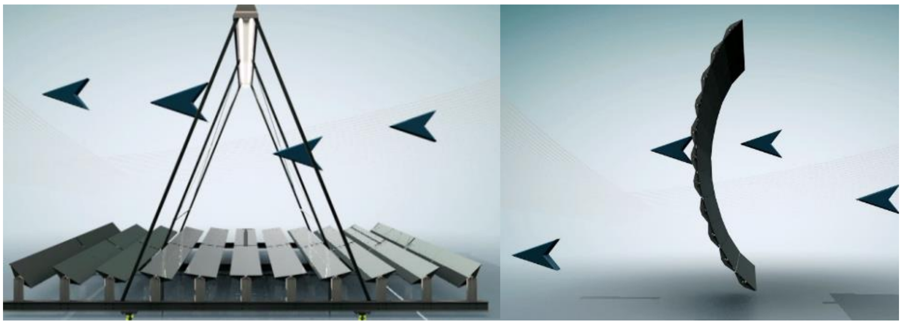

Figure 2 - Wind resistance of Linear Fresnel Collector (LFC) and Parabolic Trough Collector (PTC)

Another characteristic of the LF-11 is the simple building interface, which is a result of the extensive development of the collector design. A full collector string can be carried by only two horizontal I-beams or two rows of foundation points as shown in the red arrows from Figure 3 below:

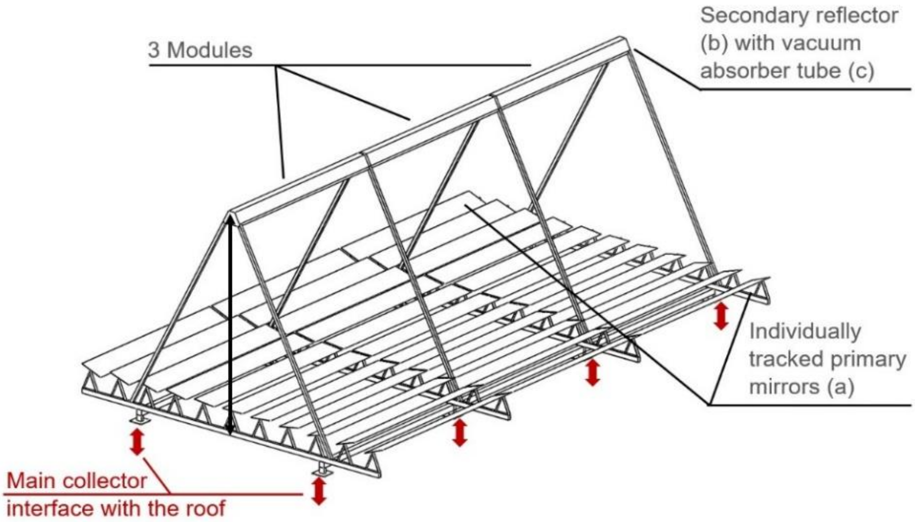

Figure 3 - LF-11 roof interface

From the LF-11 projects implemented so far by Industrial Solar, approximately 25% were assembled on the ground, whereas all others were rooftop installations. Less than 20% of the projects needed an additional walking platform, although the trend towards more rooftop projects with obstacles in their accessibility increases, as the examples of the two demo sites planned within the SHIP2FAIR project, with both projects requiring this additional accessibility effort.

The simplified collector to building interface of only two beams per collector string can be applied for buildings where the roof surface is suitable as walkways for construction and maintenance accessibility. For roofs requiring additional platforms due to the roof inclination or non-accessibility, many additional structural beams are required to carry the walkway platform resulting in a significant increase in the implementation costs and overall weight.

In order to overcome this issue, a simplified design that integrates lightweight walkways directly into the structure of the Fresnel collector is now presented. In this case, the cost-efficient solution uses walkways that are carried by the existing structure of the LF-11 collector. The main advantage is the avoidance of additional structural beams to carry the substructure. The number of interfaces to the customer's roof is thereby reduced, while weight and cost can be minimized. Typically, both the cost and weight of the required substructure can be reduced by more than 50% and the platform installation simplified and standardized for lowering installation efforts, time, and costs.

The basic configuration places these integrated platforms for maintenance purposes between each second longitudinal mirror row to access them from one side.

The walkways have combined skirting to increase safety. A walkway can also be realized along one side of the collector with a similar design. If needed, closed platforms at one or both ends of each collector string can also be realized using different profile designs, as shown in Figure 4, which allows a flat platform layout.

Figure 4 – Different structural profile designs for integrated platforms

Figure 5 below shows a configuration with standard paths inside the collector, one additional path outside the collector in a longitudinal direction, as well as a short platform at the end of the collector for easy access. Handrails, fencing, and other structural details are not shown but are foreseen to be incorporated in the integrated platform design.

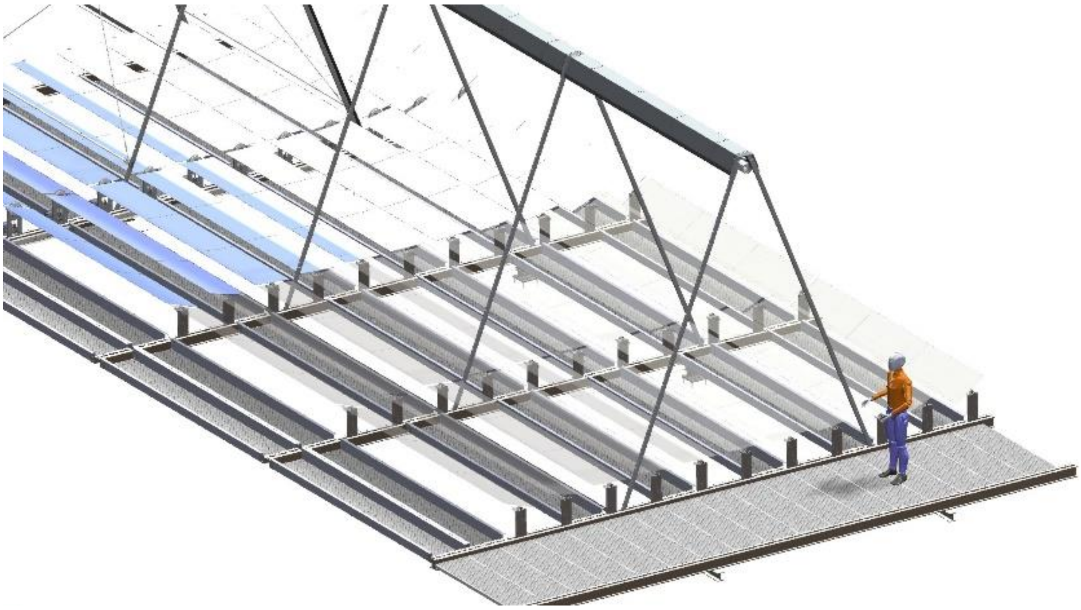

Figure 5 - Schematic configuration around a collector string

Different integration configurations can be designed to permit integration on different roof types and system layouts and to fulfil accessibility requirements depending on the size of the solar field.

In order to identify the suitable roof integration designs and to find the optimized number of walkways, several concepts were studied, as shown in Table 1 below. Concepts A - H show transversal views of the collector strings, whereas concepts I and J show longitudinal views. For each concept, there is an indication of the suitability and comments for the combination of different roof types and collector field design.

Table 1 - Rooftop collector field design concepts

Concept	Schematic collector field design	Suitability	Comments
A	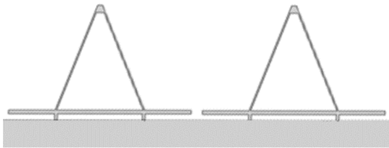	Ideal	Easy access, no walking platforms needed.
B	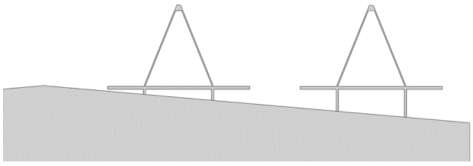	Adequate	For mirror rows with > 50 cm from the roof surface, integrated walkway platforms are required.
C	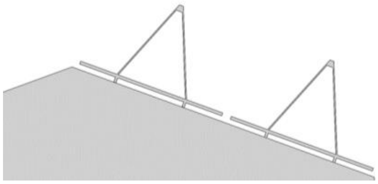	Unsuitable	Transversal collector inclination is unsuitable.
D	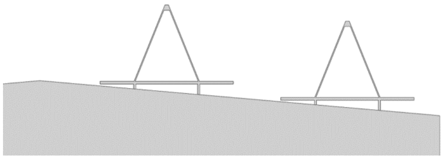	Adequate	In direct steam systems, extra hydraulic components are required to compensate for height offset. For mirror rows with > 50 cm from the roof surface, integrated walkway platforms are required.
E	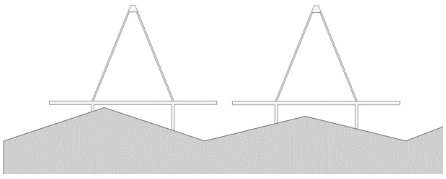	Adequate	For mirror rows with > 50 cm from the roof surface, integrated walkway platforms are required.
F	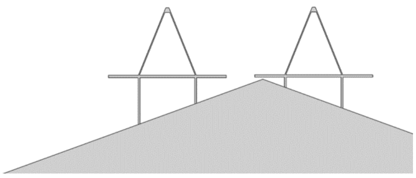	Adequate	For mirror rows with > 50 cm from the roof surface, integrated walkway platforms are required.
G	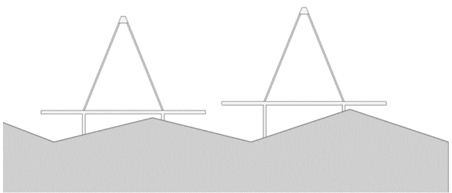	Adequate	In direct steam systems, extra hydraulic components are required to compensate for height offset. For mirror rows with > 50 cm from the roof surface, integrated walkway platforms are required.
H	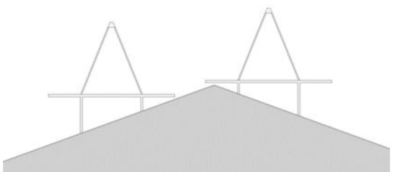	Adequate	In direct steam systems, extra hydraulic components are required to compensate for height offset. For mirror rows with > 50 cm from the roof surface,

			integrated walkway platforms are required.
I	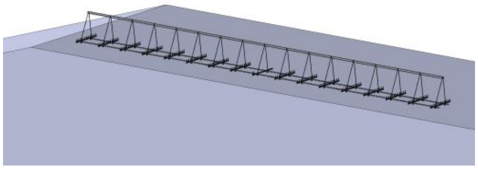	Unsuitable	Longitudinal collector inclination is unsuitable.
J	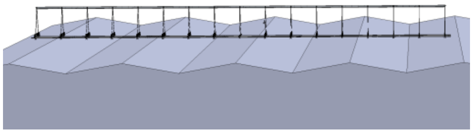	Ideal	For mirror rows with > 50 cm from the roof surface, integrated walkway platforms are required.

For inclined roofs, part of the mirror rows is accessible from the roof level while others need additional walkways. The main design criteria are to permit easy access at the level of primary mirrors from the walkways and/or roof, as seen in Figure 6, which shows a transversal view of the LF-11 collector with the main dimensions.

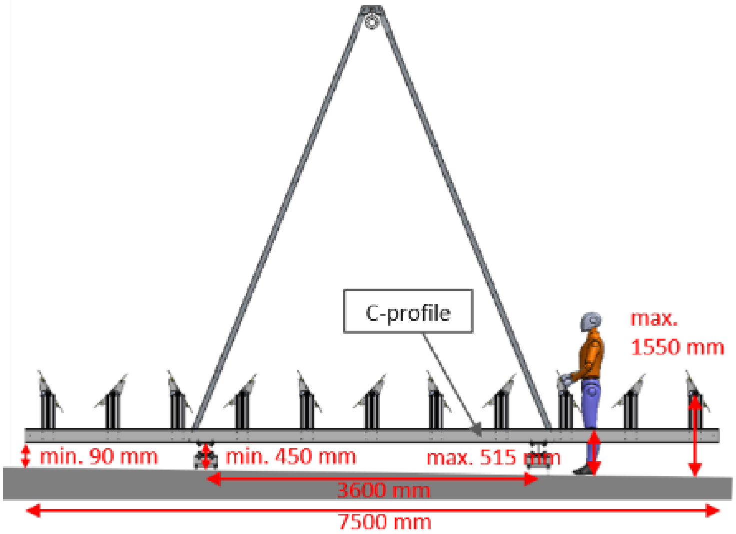

Figure 6 - LF-11 collector structural dimensions for access design

Table 2 below presents the design criteria of a minimum number of walking platforms inside the collector field depending on the inclination of the tilted roof.

Table 2 - Required number of walkways depending on roof inclination

Roof inclination	Platform walkways inside collector field	Platform walkways outside collector field	Extension of beams required	Total no. of platform walkways
1°	0	-	-	0
2°	2	-	-	2
3…6°	3	-	-	3
7 °	3	1	-	4
8°…15°	4	1	yes	5
> 15°	5	1-2	yes	6-7

- For flat roofs up to a maximum 1°, no platforms are needed: the height above structural elements is still low enough to access the field as indicated in Figure 6.
- For 2°, two walking platforms would be sufficient, whereas for systems of 7° four paths are needed.
- At angles higher than 15°, the maximum number of five walking platforms are needed inside the solar collector, as well as one or two at the longitudinal sides of the collector.

3. Case study

Reference case

In 2017 Industrial Solar realized a Fresnel project for direct steam generation with a collector layout of 3 x 19 LF-11 modules. The collector field was constructed over an inclined sandwich panel roof – a typical roof type for industrial buildings. The accesses between collector strings and in between mirror rows were built using standard grating covering the whole collector area including walkways around the collector. For the standard grating, specific weight of 22 kg/m² is assumed.

In addition to the longitudinal I-beams required for the LF-11 collector, as indicated in blue in Figure 7, several other beams were required to carry the grating platform.

This platform is considered as a reference case to evaluate the weight reduction potential which can be reached with the integrated platforms.

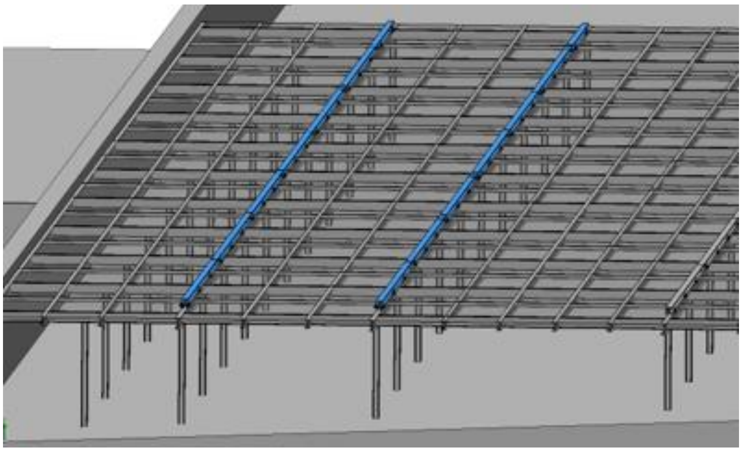

Figure 7 Structural beams for the Fresnel collector (blue) and support structure to carry a standard grating

RAR Project – SHIP2FAIR demo site

RAR (Refinarias de Açúcar Reunidas) is one of the partners in the SHIP2FAIR project that will receive a solar process heat system designed with the LF-11 collectors. The sugar refinery is located in the centre of Porto (Portugal). The available roof area is very limited with only about 1000 m², which requires a high space efficiency from the solar collector and optimisation of the overall substructure needed. The roof has an inclination of 14° and its surface is only partially accessible. The characteristic lightweight structure of the roof requires the reduction of the total weight.

The RAR demo site follows the concept of roof integration type "D", as shown in Figure 8. The two collector strings in parallel are aligned with different levels and require additional walking platforms for installation and maintenance accessibility.

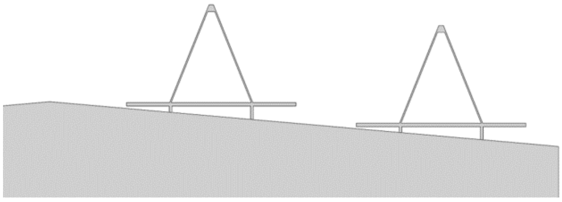

Figure 8 - Roof integration concept type "D" for two LF-11 collector strings

The weight reduction potential has been evaluated in two different integrated platform layouts: (i) fully covered collector area including side walkways at all outer sides, and (ii) reduced integrated platform layout with minimum walkways required to ensure accessibility to all mirror rows.

The evaluation showed that the main benefits of the integrated platforms result in the fact, that the new platforms need fewer substructure beams but can stay only with the two main longitudinal beams per collector string. Moreover, the skirting of the integrated platforms gives the opportunity of a partial platform layout which strongly reduces the platform weight.

- In the case of the full collector area covered by integrated platforms, the weight of platforms including support beams can be reduced by approx. 36 % in comparison to the reference case.
- For the reduced integrated platform layout with partial walkways in functional sections, the weight of the platforms including the required substructure can be reduced by approx. 66%.

4. Conclusion

The large demand for process heat opens a wide range of opportunities for concentrating solar collectors, that are available for a wide range of temperatures and heat transfer fluids. However, a suitable installation area is an important limiting factor that hampers the potential for solar process heat projects. With the characteristics of a high ground usage factor, low specific weight, low wind resistance, and a simple building interface, the LF-11 Fresnel collector overcome part of the hurdles and is optimized for roof installations. Nevertheless, many roofs require additional walkway platforms which add weight, cost, and complexity during installation.

With the main objectives of demonstrating and validating demo systems at industrial sites and promoting solar process heat projects during their whole life cycle, the SHIP2FAIR project brings together industrial customers and technology providers to find cost-efficient solutions and reduce complexity in order to complete successful systems.

This paper presented and discussed the potential of a new integrated platform design that uses the existing collector structure as a support for the platform and can be assembled in a variety of rooftop integration concepts. A weight comparison for a case study shows that the weight for the platform including the additionally required substructure can be reduced by up to 66%.

The weight reduction combined with a simplification of installation is expected to have an essential effect on the overall platform and substructure cost. For future projects, this can be further investigated in detail using different concepts in order to address each project characteristics and limitation, in order to unlock the large market potential of carbon-neutral solar process heat.

5. Acknowledgments

The project received funding from European Union’s Horizon 2020 research and innovation program under the grant agreement No 792276- Solar Heat for Industrial Process towards Food and Agro Industries Commitment in Renewables (SHIP2FAIR).

6. References

Juanicó, L. (2008). A New Design of Low-Cost Roof-Integrated Solar Collector for Household Heating and Cooling. *Proceedings of ISES World Congress 2007 (Vol. I – Vol. V).* Berlin, Heidelberg: Springer.

Mokhtar, M., Berger, M., Zahler, C., Krüger, D., Schenk, H., & Stieglitz, R. (2015). Direct Steam Generation for Process Heat using Fresnel Collectors. *Int. J. of Thermal & Environmental Engineering*, 3-9.

Solar-Payback. (2018). *Global Heat Demand in Industry*. Retrieved from Solar Payback: https://www.solar-payback.com/potential/

Sultana, T., Morrison, G. L., & Rosengarten, G. (2011). Thermal performance of a roof integrated solar microconcentrating collector. *AuSES Solar Conference.* Canberra, Australia.

Decarbonization of industrial processes: technologies, applications and perspectives of low-temperature solar heat (80-150°C)

Bartali R.[1], Christodoulaki R.[2], Drosou V. [2], Baker D.[3], Svaizer P.[1], Alarcon-Padilla D.[4], Osório T.[5], Kramer W.[6], Bolognese M.[1], Prattico L.[1], Viesi D.[1], Roca L.[4], Guillen E.[7], Fluch J.[7] , Bayer O.[3], Pinarli D.[3], Erdogan S.[3], Brunner C.[7], Cavada R.[1], Bonizzi A.[1], Cimatti A.[1], Zanetti A.[1] and Crema L.[1]

1) Fondazione Bruno Kessler, Applied Research in Energy Systems, Via Sommarive 18, 38123, Trento Italy
2) CRES, Centre for Renewable Energy Sources and Savings, 19klm Marathonos av, 19009, Athens, Greece.
3) Middle East Technical University, Center for Solar Energy Research and Applications, Ankara, Turkey.
4) CIEMAT-Plataforma Solar de Almería, Ctra. de Senés km 4.5, 04200 Tabernas (Almería), Spain.
5) University of Evora - Renewable Energies Chair, Solar Concentrators Testing Platform, Herdade da Mitra - Valverde, 7000-083 Nossa Senhora da Tourega, Portugal.
6) Fraunhofer Institute for Solar Energy Systems, Heidenhofstrasse 11, 79110 Freiburg, Germany.
7) AEE – Institute for Sustainable Technologies, Feldgasse 19, 8200 Gleisdorf, Austria.

Summary

Low-temperature (80-150°C) solar collectors guarantee a very high efficiency (up to 60%) in the conversion of solar radiation into useful thermal energy. Moreover, solar thermal technologies are already reliable solutions, relatively cheap and widely available in the market. For that reason, solar collectors operating at low temperatures are among the most important sustainable technologies that can reduce the fossil fuel consumption of industrial processes and their corresponding carbon footprint. Unfortunately, Solar Heat for Industrial Processes (SHIP) is still mostly unused for several reasons, e.g., not easy identification of the appropriate applications (e.g., cleaning processes, drying, desalination) or lack of knowledge of the potential environmental and economic benefit of the use of SHIP technologies. For that reason, this work includes i) an overview of solar technologies for low/medium -temperature SHIP (80-150°C) ii) results obtained on the innovative design of the mirrors used in evacuated receiver tube by means of a variation in the shape of its internal reflector iii) estimation of CO_2 saving using a solar field based on evacuated tube collector (ETC). The work also includes a comparison of the standard ETC solar plant with an ETC solar plant embedded with reflectors with innovative shape.

Keywords: ETC, new reflectors, predictive simulation tools, advanced control systems, solar process heat, decarbonization

1. Introduction

More than 30 billion tons of CO_2 are released into the atmosphere every year, and this is causing climate change (Jackson *et al.*, 2018). For this reason, nowadays, it is necessary to organise large-scale decarbonization of energy processes (Gao *et al.*, 2018). Solar thermal energy is an alternative energy source to fossil fuels, it is already available, and it does not produce CO_2. The industrial sector consumes approximately 29% of the

doi:10.18086/eurosun.2020.03.09 Available at http://proceedings.ises.org

world's total energy consumption, which is more energy than any other end-use sector (Bolognese, Viesi, *et al.*, 2020). This value in Europe is 22.8% of which heat demand is 71% (Valencia *et al.*, 2017). The use of alternative sustainable and carbon-free technologies for the generation of thermal energy is now a compulsory choice. Solar heat has enormous potential for thermal applications but is still mostly unused, for industrial processes. In the industrial field, more than 30% of processes work in a temperature range from 60 - 150°C. For these reasons, the development of systems able to efficiently transform solar energy into heat is crucial for many industrial applications such as drying process, desalination, distillation, pasteurization and many others (Platzer, 2015). Heat production using solar energy is based on photo-thermal conversion; the photo-thermal effect is produced by a) photoexcitation due to absorption of solar photons using an optical absorber surface (black surface), b) energy release by photons to the absorber surface (heat production) and c) transfer of the produced heat using a thermodynamic fluid (Fudholi and Sopian, 2019)(Atkinson *et al.*, 2015)(Gao *et al.*, 2018). The efficiency of the photon-thermal conversion, at low temperatures (80-150°C) in particular, is very high, up to 60%, (Papadimitratos, Sobhansarbandi and Pozdin, 2016) (Wäckelgård *et al.*, 2015,). For this reason, this kind of conversion is one of the most efficient methods to convert solar energy into usable energy. The solar collectors are devices that are able to use the photo-thermal conversion in an effective manner by reducing infrared losses using appropriate optical-structural configurations. Furthermore, the solar collectors, assembled as a solar plant, are able to efficiently transport the heat produced by a solar collector a to specific thermal processes, e.g., industrial processes. Currently, the industrial sector is responsible for approximately 22.8% of Europe's total energy consumption, 71% of which is heat (Valencia *et al.*, 2017). The extensive use of fossil fuels in the industrial sector produces billions of tons of carbon dioxide (CO_2) each year, contributing to climate change. Solar heat can mitigate this problem, especially considering that in the industrial sector, more than 30% of processes work within a temperature range of 60-150°C. Unfortunately, Solar Heat for Industrial Processes (SHIP) is still mostly unused for several reasons e.g. not easy identification of the appropriate applications (e.g. cleaning processes, drying, desalination or integration in existing supply systems.), problem related on space occupation, or lacking knowledge of the great techno-economical potentials of SHIP. For this reason, in this paper includes first a brief overview of available solar technologies and applications for low/medium-temperature SHIP (80-150°C). In the second part we reported the results obtained using evacuated receiver tube with internal reflector with different shape, where we observed, and potential improve of optical performance of solar collector. Finally, taking into account the performance of solar collector we estimate the potential CO_2 emission reduction, in a agro-food industry. Moreover, we compared the performance of a solar field and a solar field with enhanced optical performance, considering the result obtained in the second part.

1.1 Overview of solar technologies for low temperature heat for industrial processes

The importance of and interest in solar energy is not new; for instance, one of the first methods to preserve food was through drying by exposing the food to natural ventilation and solar radiation. Taylor and Hayashi (2007) reported that in ancient times, pieces of meat were dried and preserved by people living around the Don River in southern Moscow (9000 BC). Solar saltworks were common in the Greek and Roman ages, such as the Salina di Trapani or Salina di Ostia. Solar drying using the sun has also been used for several centuries for many other foods, including fish and grapes. Nowdays many applications and scientific works are dedicated to solar technologies, e.g water heating(Ekechukwu and Norton, 1999)(Pangavhane and Sawhney, 2002). Heat production using solar energy is based on photo-thermal conversion. The photoexcitation can be observed in inorganic materials, such as noble metals and semiconductors, as well as in organic materials such as carbon-based materials, dyes and conjugated polymers. The efficiency of photon-thermal conversion, particularly at low temperatures, is remarkably high (>60 %). The main component of a solar thermal system is the solar collector. Solar thermal collectors capture the sunrays and convert the solar radiation into thermal energy that is then transferred to a working fluid termed Heat Transfer Fluid (HTF). The HTF can be air, steam or liquid such as water, glycol, diathermic oil, molten salt or ethanol (Kalogirou, 2009). Tracking the sun allows the design of concentration systems with reduced acceptance angles, in comparison with stationary systems, to achieve higher efficiency at higher working temperatures., but with an increase of the cost of a solar field. In the Tab 1 we reported some applications of solar thermal collectors in the industrial processes. For low temperature applications (80 -150 °C) the most suitable technologies are stationary collectors like flat plate collectors (FPC), evacuated tube collectors (ETC) compound parabolic collectors (CPC) and Flat evacuated collectors (FEC) thanks to their excellent efficiencies at low temperatures (80-120 °C), simplicity of installation and low cost. Small-scale sizing of Linear Fresnel Reflector (LFR) and Parabolic Trough Collector (PTC) are used in particular when temperatures required for industrial processes are higher than 120 °C. Parabolic Dish (PD) and Solar Tower (ST) are used when concentration ratio and high temperature is needed, for instance, for the thermochemical reaction or for production of solar thermal electricity (STE) ('Concentrating Solar Power', 2012).

Tab 1: Examples of type of solar collectors used in different sectors, for various processes and the typical temperature of solar loop.

Sector Industrial	Process	Solar Collectors types	Process temperature C°	Reference
Automotive	Paint application	ETC	90	(Hisan *et al.*, 2018)
Chemical Pharmaceutical	Cleaning Process Drying Water treatments	FPC	55	(Hisan *et al.*, 2018)(Mehrdadi *et al.*, 2007)
Mining	Galvanic Bath	ETC	60-80	(Hisan *et al.*, 2018)
Metal	Circulation	PTC	95	(Hisan *et al.*, 2018)
Food & Beverage	Pasta production Drying of vegetables Milk pasteurization Pasteurization Sterilization Drying of agriculture water sludge	LFR FPC FPC PTC PD	100-150 30°-80° 66°-118° 90-110° 55°-100°	(A. Buscemi, D. Panno, G. Ciulla, M. Beccali, 2018)(Bolognese, Viesi, *et al.*, 2020) (Fudholi and Sopian, 2019) (Panchal, Patel and Chaudhary, 2018) (Rawlins and Asgcroft, 2013) (Salim, 2018)
Water treatment	Disinfection of Contaminated water Desalination	CPC FPC CPC	80 70 60-90	(Vidal and DÃ-az, 2000) (Alarcón *et al.*, 2005)

As reported in table 1 there are already several examples of study and applications of solar heat in industrial processes, and many of these examples are related directly or indirectly to food and beverage sector. For this reason one of the main interesting sector of SHIP technologies is the food and beverage sector where several processes required heat at relative low temperature (80°C-150°C) such a: drying, pasteurization, washing and sterilization (Lauterbach *et al.*, 2012). For this range of the temperature the evacuated collectors show and good thermo-optical performance and low cost. The improvement of the performance of this collector, in any case can promote the reduction of the CO_2 emission and a reduction of the capital cost of the solar field. For these reasons we studied the optical performance improvement induced by internal reflectors in evacuated tube collectors.

2. Evaluation of the optical efficiency of an evacuated receiver tube with internal reflector of different shapes.

In this paragraph we studied an evacuated tube collector ETC made by parallel evacuated glass tubes. Each evacuated tube consists of two tubes, the inner and outer. We considered the configuration with the outer tube is a transparent glass tube and the inner is can be made of copper applied with a selective coating, (this is the typical configuration for direct flow evacuated tube). Solar irradiation passes through the transparent outer tube, and it is absorbed by the inner tube. To minimize heat losses, the annular space between these two tubes is kept in a vacuum (M.A. Sabiha, R. Saidur, S. Mekhilef, 2015). According to many researchers, ETCs have considerably higher performance than flat plate solar collectors since they can collect a higher share of both direct and diffuse radiation during the day. In the literature, many studies have discussed the optical and thermal properties of the evacuated tube collectors. Back in 1974, Winston (Winston, 1974) studied a novel collector with a trough-like reflecting wall light channel with a concentration factor of 10 without diurnal tracking of the sun. One year later (Winston, 1975), they further proposed the use of a receiver for maximizing the concentrating radiation, having different cross-sections; circular, oval and fin. Rabl (Rabl, 1976) compared a variety of solar concentrators in terms of concentration ratio, acceptance angle, sensitivity to mirror errors, size of reflector area and average number of reflections, leading to a design method for maximum concentration. Rabl's next study (A. Rabl, 1976) presented the equations of the convective and radiative heat transfer and the performance of a collector with compound parabolic concentrator CPC. Lately, Telesa et al. (M. Telesa, K. Ismail, 2019) investigated the optical and thermal performance of a new ETC with and without solar tracking system, by building and validating a numerical code that calculated the effect of tilt angle, reflectivity, vacuum quality and eccentricity of the absorber. Mao et al. (C. Mao, M. Li, N. Li, M. Shan, 2019) studied theoretically and experimentally the positioning of an external reflector in an all-glass ETC. Unfortunately, there is limited research work regarding the optical design aspects in evacuated tube collectors with internal reflectors and even fewer on the geometry of the internal reflector. This work discusses the impact of the different geometries of the internal reflector on the optical efficiency of the evacuated tube collector. The receiver tube considered in the present study addresses the medium temperature applications, 100-250^{o}C, and consists of an evacuated tube, inside which an absorber tube that hosts the thermal fluid is placed. A reflector is also placed inside the evacuated tube and underneath the absorber tube, in order to provide concentration and thus, to increase the optical efficiency.

2.1 Mirror shapes for ETCs receiver tubes

ETC receivers can differ in their design in terms of materials and geometries (Felinski and Sekret, 2017). The solar receiver under investigation consists of an evacuated glass tube with an absorber tube inside and a reflector underneath the absorber. The solar radiation that penetrates the glass tube either hits the absorber directly or hits the surface of the reflector, and it is then reflected to the absorber's surface. In the surface of the absorber tube, the solar energy is absorbed and converted into heat which is then transferred to the heat transfer medium that flows inside the absorber. This section describes the research work implemented for direct flow receivers. The use of a reflector sheet inside the receiver tube, instead of outside, is the central concept, since it enables a performance enhancement and simultaneously, it addresses the durability and modularity issues that are common in this type of collectors. Also, it allows the use of higher reflectivity aluminium reflectors that cannot be used outdoor in open air. The four different configurations of internal reflectors that have been studied are shown below (Fig. *1*).

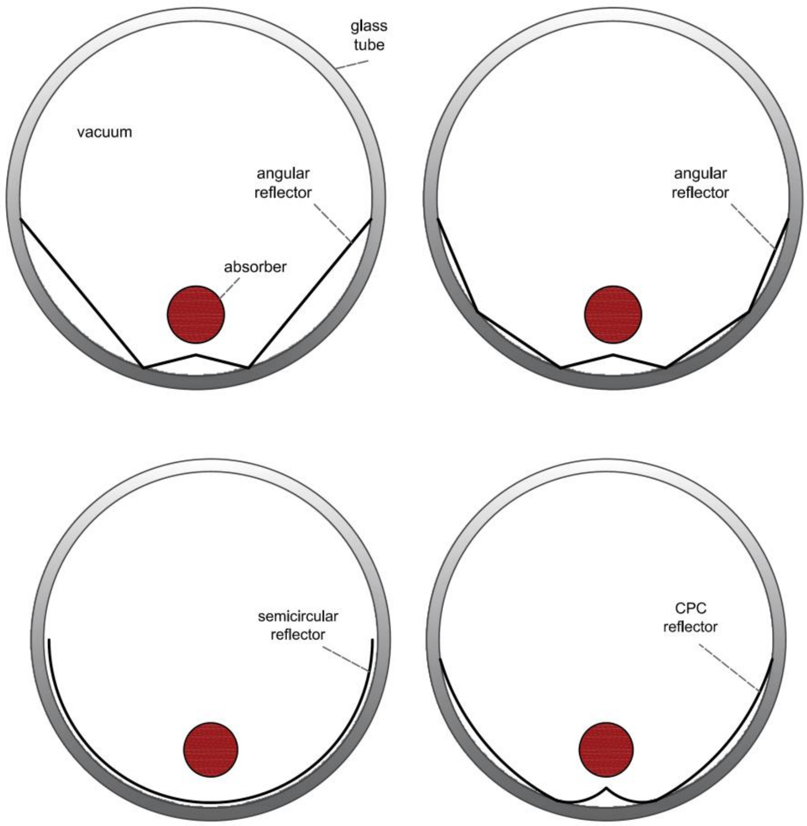

Fig. 1: Different configurations of internal ETC reflectors, from left to right: 4-sided angular, 6-sided angular, semi-circular and compound parabolic (base scenario).

The studied configurations include the most used Compound Parabolic Concentrator CPC (base scenario), the less used Semi-Circular (SC) concentrator and two simpler configurations; the 4-sided and 6-sided angular reflectors (hereafter defined as W4 and W6), (***Fig. 1***). These simple designs are studied because they are considered as simple approaches to the SC and CPC reflectors, but with an expected lower production cost due to the absence of curves. Initially, a theoretical, fully developed CPC curve was built and simulated in order to evaluate the accuracy of the results. *Tab.* **2** shows the input variables for the theoretical fully developed CPC curve and the CPC base scenario. The solar conditions set are: Sunshape type: Pillbox; irradiance: 1000W/m^2; theta$_{Max}$: 0.00465 rad (circumsolar ratio). The simulation results for the fully developed curve showed an intercept factor of 0.998, and therefore, the accuracy of the developed model is considered acceptable.

Tab. 2: Technical characteristics of ETC-CPC under investigation and for the fully developed CPC curve.

Parameter	ETC-CPC	Fully developed curve	Unit
Outer diameter of glass	0.1	not applicable	m
Inner diameter of the glass	0.093	not applicable	m
Outer diameter of absorber	0.015	0.015	m
Inner radius of CPC curve	0.0075	0.0105	m
Outer radius of CPC curve	0.0105	0.0105	m
Acceptance angle	20	20	deg
Truncation angle	0	0	deg
Truncation height	0.025	not applicable	m
Reflectivity	0.95	1	-
Length of tube	1	1	m
Aperture area	0.1…	0.193	m^2
Direct Normal Irradiance	1000	1000	W/m^2
Power received on the absorber surface	84.9	192.7	W
Efficiency	84.9	99.8	%

The dimensions used for the 4-sided angular reflector are: sides length 0.0506 m and 0.0143 m and the respective internal angles are 116^o and 208^o. The 6-sided angular reflector: sides length 0.0263 m, 0.0265 m and 0.0143 m and the respective internal angles are 147^o, 132^o and 208^o. The diameter of the semi-circular reflector is 0.09 m.

2.2 Description of the Ray Tracing simulation model

The optical analysis is implemented through the development of an optical simulation model in Tonatiuh ray-tracing software (Christodoulaki, Tsekouras P. and Drosou, 2019) (*Tonatiuh software*). Tonatiuh is an open-source Monte Carlo ray tracer software for the optical simulation of solar concentrating systems and it was selected due to its high accuracy and adaptability to model modifications. Once the geometry and the materials of the solar receiver are inserted, Tonatiuh simulates the system's optical behaviour, under different solar conditions. These conditions are characterized by the Sun position in the sky, which define the main direction of the incoming direct solar radiation, and the direct solar irradiance, which defines the amount of radiant power per unit area normal to the main direction of the incoming solar radiation associated with that radiation.

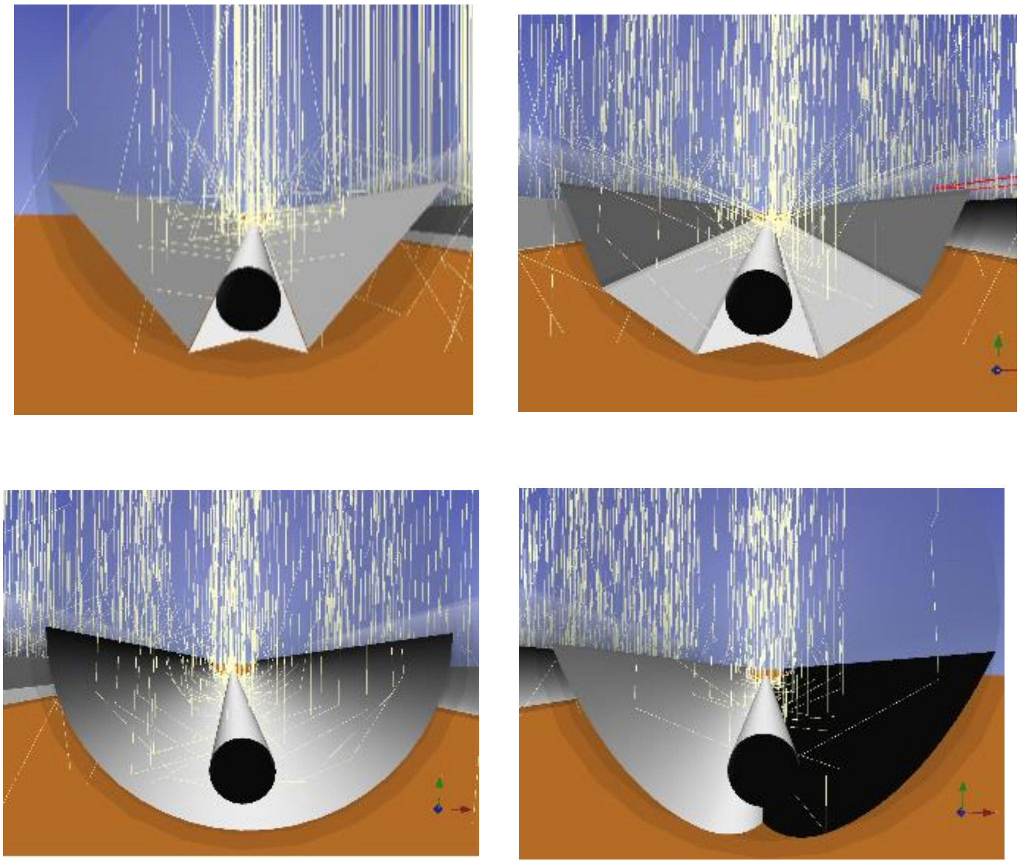

Fig. 2: Ray tracing figure of the four different evacuated tube receivers, under 90° Sun elevation. From left to right: 4-sided angular, 6-sided angular, semi-circular and compound parabolic reflector.

The ray-tracing analysis shows that the CPC reflector outperforms in terms of ray concentration, followed by the SC reflector, as shown in ***Fig. 2***. The high optical efficiency of the CPC is expected (power production >85W) since CPC is the ideal optics. At the same time though, this design incorporates some construction complexities, since the exact CPC shape has to be tailored for each specific pipe geometry (depending on the diameter of evacuated tube, on its position inside the absorber, and the dimension of the absorber tube) and its curvature is continuously varied. Regarding the simpler design of the 4-sided and 6-sided angular reflectors, the raytracing reveals that many rays escape from these tubes, ***Fig. 2***. Their poor performances were expected since they both have a simpler geometry than the SC and CPC reflectors.

2.3 Results of the optical analysis

Following the model's development, simulations with varying sun position (i.e., elevation and azimuth) were performed to generate the Incidence Angle Modifier (IAM) curve for each receiver. Additionally, the power production from each receiver under different sun positions was also calculated. Fig. 3 shows the power production (W) and presents the Incidence Angle Modifier curve for all receivers considered and for Sun incidence angles from 0° to 60°. It can be seen that for small angles of incidence, from 0° to 15°, the CPC reflector outperforms. The second-best option in terms of optical performance would be the SC reflector, as it presents two crucial features: its power production is more even for all the incidence angles considered, and its power production is higher than that of the CPC for incidence angles higher than 15°. At this point, it should be noted that the CPC reflector has the most significant variation of power production under different Sun elevations (i.e., 81W at 10° but 41W at 20^0), whereas the SC reflector has the most even power production. Moreover, the 6-sided angular reflector has slightly better performance than the 4-sided one for incidence angles up to 30°. Finally, for incidence angles higher than 40°, the SC reflector has a clear advantage over the other three (CPC, 6 sided and 4 sided), in which the presence of the reflector seems insignificant since all three tubes have almost the same performance.

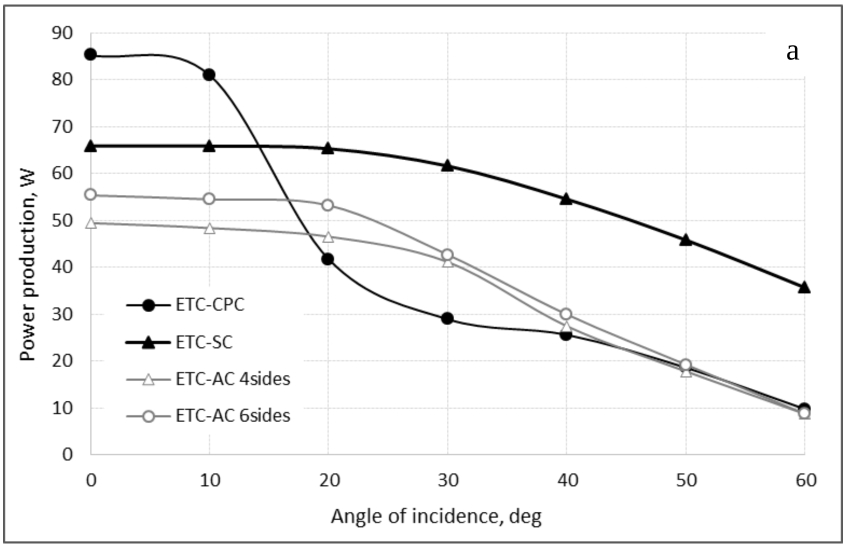

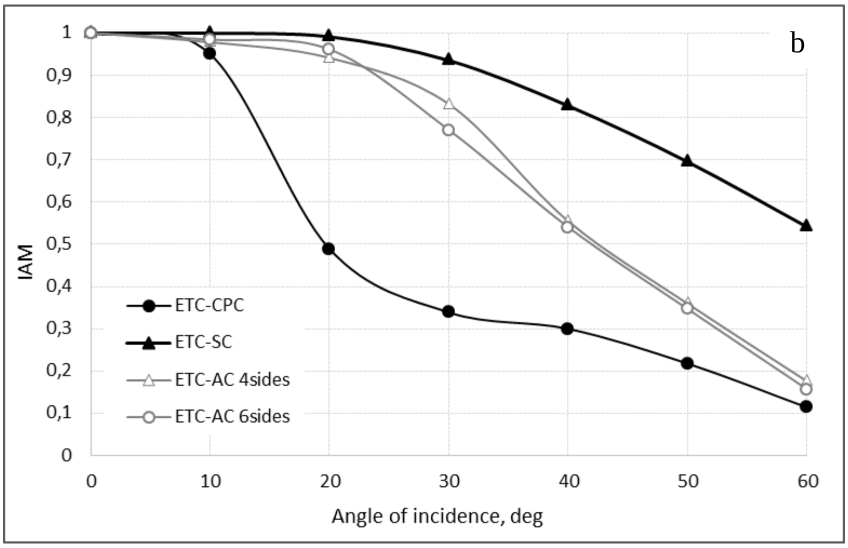

Fig. 3 Power production (W) of the four different evacuated tube receivers for various sun incidence angles (a). Right: IAM curve of the four different evacuated tube receivers for various sun incidence angles (b).

The results of the optical analysis show that the receiver with the SC internal reflector has a competitive performance towards the CPC reflector and could act as an alternative option, under specific circumstances, as shown in Fig. 3. The reflector as an internal component of an ETC-CPC collector has been tested on an ad-hoc test bench hereafter called ETC-Test bench; a modular prototype that simulates an evacuate pipe has been realized at lab scale. The modular test bench is composed of a glass vacuum chamber with Viton seal (simulate the external glass of ETC), a black receiver connected with an aluminium cover, a metallic holder with O-ring seal for glass, a connection to the vacuum sensor and vacuum pump and a connection for the venting (nitrogen or air). The glass cylinder has an internal diameter of 15.8 cm, which allows the easy insertion of mirrors with different shapes.

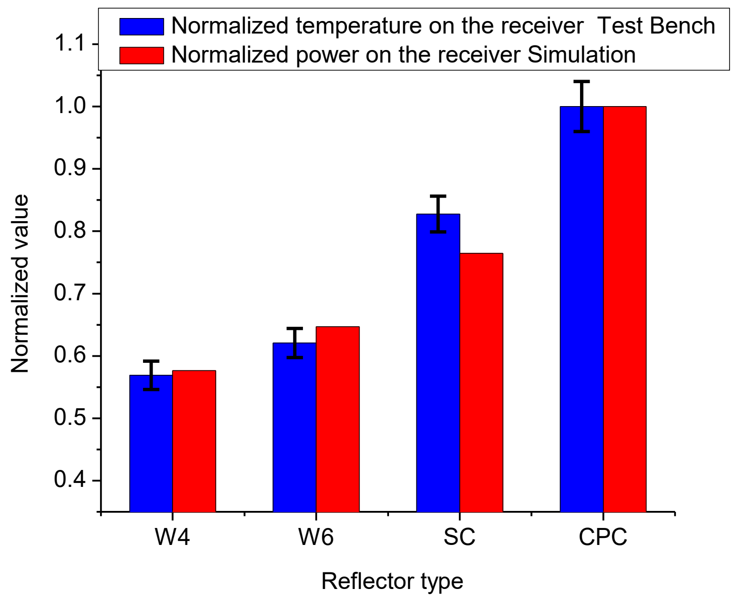

Fig. 4. Comparison of the result obtained in the test bench and obtained by simulation

A solar illuminator of 900W/m^2 was used in the ETC-Test bench. Temperatures were recorded by thermocouples on the surface of the receiver. The reflectors with the different shapes have been tested in the test bench (W4, W6, SC, and CPC). The normalized temperature recorded has been compared with normalized power on receiver estimated by simulations, Fig. 4. The results show a similar trend indicating a good correlation between the simulations and experimental results. The experimental results show the mirror with CPC profile has better performance (normal illumination) as predicted by the simulation. The experimental improvement in terms of the temperature of CPC mirror with respect to the circular mirror was >10%.

3. Decarbonization of industrial processes using SHIP technologies

The use of solar heat in industrial processes leads to a reduced consumption of fossil fuels and consequently to a lower emission of tons of CO_2 per year. To understand the reduction of emission of CO_2 , the yearly thermal energy production of solar thermal field was estimated. (Bolognese, Grigiante and Crema, 2019) (Koffi *et al.*, 2017)(Bolognese, Crema, *et al.*, 2020). In particular, the drying process in a food and beverage industrial sector was considered (Food an beverage processes) (Brunetti *et al.*, 2015)(Migliori *et al.*, 2005). In the calculation, an industry "virtually" located in Rome, with a space availability of a 1000 m^2 (≈ 32*32 m) and a yearly thermal energy consumption of about 700 MWh/year, was considered. In order to avoid self-shading phenomena, the number of conventional ETC solar collectors is 174, resulting from the inclination of the panels, their size and their south-facing orientation (Bolognese, Viesi, *et al.*, 2020). The hourly data of solar radiation and environmental temperature of the TMY by PVGIS (*PVGIS*) were used. Moreover, in order to calculate the longitudinal e transversal components of incidence angle modifier, the apparent motion of the sun is calculated on an hourly basis considering the right geographical position of the location. The calculation of useful thermal power has been hourly calculated as follows:

$$Q_{sf} = A_g\, GHI\left[K_{\theta_l} K_{\theta_t} c_0 - a_1(T_{es} - T_{env}) - a_2(T_{es} - T_{env})^2\right] \qquad \text{(eq. 1)}$$

in which A_g is the total net surface of the solar field, K_{θ_l} and K_{θ_t} are the components of the incidence angle modifier that depends on geographical location (Morin *et al.*, 2012; A. Buscemi, D. Panno, G. Ciulla, M. Beccali, 2018), T_{env} is the environmental temperature, GHI is the hourly solar global horizontal radiation c_0,

a_1 and a_2 are the coefficients used for the calculation of efficiency and T_{es} is the industrial process temperature. Assuming a continuous day time heat load profile and a typical process temperature in the range from 137 °C, the yearly thermal energy production of the conventional solar field is 314 MWh/year. The CO_2 saved has been calculated considering the natural gas as conventinal fuel to produce thermal energy and considering a gas standard emission factor of 0.202 tCO2/MWh (Brigitte Koffi and Cerutti, 2017) .The results show that a ETC solar field of 1000 m^2 shows excellent performanc , in fact it can avoid the emission of a huge amount of CO_2 70 ton /years. Moreover, the ETC solar field performance, considering improvements induced by the increased efficiency of the optics, reported in the paragraph 2, (hereafter ETC-CPC, internal mirror improvement of optical proprieties of 10%) was calculated. With these enhancements, the thermal energy production resulted of 345 MWh/year. In this case we estimate that the solar field can avoid that emission of 77tons of CO_2.peryear. The payback time for each set-up was in first approximation estimated. The payback time can be estimate considering the total capital expenditure (CAPEX) and Operating and maintenance costs (OPEX). The CAPEX has been calculated considering an average price per unit of the gross occupied area of 110 €/m^2 (Luca Prattico, et.al. 2018) and a number of additional costs due to the installation and equipment necessary for piping and, operating and maintenance costs (OPEX) for this type of collector were considered as a percentage of total CAPEX (i.e. 20%). Moreover, in the evaluation of payback time we considered a) the incentives available in Italy for sustainable energies *Conto Termico 2.0* (Energetici, 2016). b) cost of fossil fuel taking into account increase in fossil fuel costs (about 1.5 % per year) for 25 years (solar field lifetime). The results are reported in table 3. In the first approximation, in 25 years there is a potential saving in economic terms of about 300 K€ for the solar field while considering the solar field with improved optics is possible to save 330 K€. Therefore, the payback time of approximately 6 years and avoids the emission of 70 tons of CO_2 per year. While the payback time of for solar field with the innovative optics is approximately 5.5 years with the avoiding of 77 tons of CO_2 per year as summarized in Table 3.

Tab. 3: Environmental/Economic impact

Ex. Rome (Italy)	Solar fraction	Saved CO_2	Payback time
Solar Field ETC	45	70 ton per year	≈6
Solar Field ETC-CPC optimized optics	50	77 ton per year	≈5.5

4. Conclusion

This work includes i) an overview of solar technologies for low/medium -temperature SHIP (80-150°C) ii) results obtained on the mirrors with innovative shape used in evacuated receiver tube iii) estimation of CO_2 saving using a solar field based on evacuated tube collector. As a summary, the food and beverage sector are one of the most interesting sectors for the SHIP technologies, in particular for the evacuated collectors. For this reason, we studied how to improve optical performance in ETC. The results on mirrors show that internal mirror with CPC design in ETC collector allows a sensible improved on optical performance (10%). Considering the performance of evacuated collector, we calculated CO_2 saving in a industry in a food and beverage secto.We observed that a solar field-based on ETC of 1000m^2 is already able to reduce remarkably the CO_2 emissions of industrial processes. We estimated a reduction of CO_2 emission of 70 tons per years. While considering the solar field with optimized optics a saving of 77 ton per years is possible.

5. Acknowledgements

This research work was implemented in the framework of the EU H2020 LCE-33-2016 (RIA) project INSHIP Integrating National Research Agendas on Solar Heat for Industrial Processes, GA 731287, duration 01.01.2017 – 31.12.2020, *https://www.inship.eu/*

6. References

A. Buscemi, D. Panno, G. Ciulla, M. Beccali, V. L. B. (2018) 'Concrete thermal energy storage for linear Fresnel collectors; exploiting the South Mediterranean's solar potential for agrifood processes', *Energy Conver. Manag*, 166(719–734).

A. Rabl (1976) 'Optical and thermal properties of compound parabolic concentrators', *Solar Energy*, 18, pp. 497–511.

Alarcón, D. *et al.* (2005) 'Design and setup of hybrid solar seawater desalination system: the AQUASOL project', *ISES Solar World Congress*, (May 2014).

Atkinson, C. *et al.* (2015) 'Coatings for concentrating solar systems – A review', *Renewable and Sustainable Energy Reviews*. Elsevier, 45, pp. 113–122. doi: 10.1016/j.rser.2015.01.015.

Bolognese, M., Viesi, D., *et al.* (2020) 'Modeling study for low-carbon industrial processes integrating solar thermal technologies . A case study in the Italian Alps : The Felicetti Pasta Factory', *Solar Energy*. Elsevier Ltd, 208(August), pp. 548–558. doi: 10.1016/j.solener.2020.07.091.

Bolognese, M., Crema, L., *et al.* (2020) 'Solar Thermal Technologies for Low-Carbon Industrial Processes: Dynamic Modelling, Techno-Economic Analysis and Environmental Impact', *Proceedings*, 58(1), p. 14. doi: 10.3390/wef-06911.

Bolognese, M., Grigiante, M. and Crema, L. (2019) *Studio di ingegnerizzazione per processi industriali a bassa emissione carbonica con l'utilizzo di tecnologie solari termiche.Caso studio:pastificio Felicetti,*. Dipartimento di Ingegneria Civile, Ambientale, Università di Trento.

Brunetti, L. *et al.* (2015) 'for fresh pasta process m m er ci al us e on ly on er', XLVI, pp. 167–171. doi: 10.4081/jae.2015.478.

C. Mao, M. Li, N. Li, M. Shan, X. Y. (2019) 'Mathematical model development and optimal design of the horizontal all-glass evacuated tube solar collectors integrated with bottom mirror reflectors for solar energy harvesting', *Applied Energy*, 238, pp. 54–68.

Christodoulaki, R., Tsekouras P. and Drosou, V. (2019) 'Optical analysis of an evacuated tube collector with built-in compound parabolic concentrator for process heat applications', in *SBE19 Thessaloniki Sustainability in the built environment for climate change mitigation*.

'Concentrating Solar Power' (2012) *Irena working Paper*, 1(2).

Ekechukwu, O. V. and Norton, B. (1999) 'Review of solar-energy drying systems II: An overview of solar drying technology', *Energy Conversion and Management*. doi: 10.1016/S0196-8904(98)00093-4.

Energetici, G. S. (2016) *Incentivazione della produzione di energia termica da impianti a fonti rinnovabili ed interventi di efficienza energetica di piccole dimensioni. REGOLE APPLICATIVE DEL D.M. 16 FEBBRAIO 2016*.

Felinski, P. and Sekret, R. (2017) 'Effect of PCM application inside an evacuated tube collector on the thermal performance of a domestic hot water system', *Energy and Buildings*, 152, pp. 558–557.

Fudholi, A. and Sopian, K. (2019) 'A review of solar air fl at plate collector for drying application', *Renewable and Sustainable Energy Reviews*. Elsevier Ltd, 102(November 2018), pp. 333–345. doi: 10.1016/j.rser.2018.12.032.

Gao, M. *et al.* (2018) 'Solar Absorber Material and System Designs for Photothermal Water Vaporization towards Clean Water and Energy Production Energy & Environmental Science Solar absorber material and system designs for water and energy production', *Energy & Environmental Science*. Royal Society of Chemistry, (July). doi: 10.1039/c8ee01146j.

Hisan, S. *et al.* (2018) 'Solar Process Heat in Industrial Systems- A Global Review', *Renew. Sustain. Energy Rev.*, 82, pp. 2270–2286.

Jackson, R. B. *et al.* (2018) 'Global energy growth is outpacing decarbonization Global energy growth is outpacing decarbonization', *Environmental Research Letters*. IOP Publishing, 13, p. 120401.

Kalogirou, S. A. (2009) *Solar Energy Engineering, Processes and systems.* Edited by A. Press. Elsevier.
Koffi, B. *et al.* (2017) *Covenant of Mayors for Climate and Energy: Default emission factors for local emission inventories*.

Lauterbach, C. *et al.* (2012) 'The potential of solar heat for industrial processes in Germany', *Renewable and Sustainable Energy Reviews*. Elsevier, 16(7), pp. 5121–5130. doi: 10.1016/j.rser.2012.04.032.

Luca Prattico, L. T. (no date) 'Performance assessment of a solar-powered organic rankine cycle for combined heat and power generation in small size rural applications. .', *E. S.*

M. Telesa, K. Ismail, A. A. (2019) 'A new version of a low concentration evacuated tube solar collector: Optical and thermal investigation', *Solar Energy*, 180, pp. 324–339.

M.A. Sabiha, R. Saidur, S. Mekhilef, O. M. (2015) 'Progress and latest developments of evacuated tube solar collectors', *Renew. Sustain. Energy Rev.*, 51, pp. 1038–1054.

Mehrdadi, N. *et al.* (2007) 'Aplication of Solar Energy for Drying of Sludge from Pharmaceutical Industrial Waste Water and Probable Reuse', *Int. J. Environ. Res. 1(1):42-48*, 1(1), pp. 42–48.

Migliori, M. *et al.* (2005) 'Modelling of high quality pasta drying : quality indices and industrial application q', *Journal of food engineering*, 71, pp. 242–251. doi: 10.1016/j.jfoodeng.2004.11.004.

Morin, G. *et al.* (2012) 'Comparison of Linear Fresnel and Parabolic Trough Collector power plants', *Solar Energy*. Elsevier {BV}, 86(1), pp. 1–12. doi: 10.1016/j.solener.2011.06.020.

Panchal, H., Patel, J. and Chaudhary, S. (2018) 'A Comprehensive Review of Solar Milk Pasteurization System', *Journal of Solar Energy Engineering, Transactions of the ASME*, 140(1), pp. 1–8. doi: 10.1115/1.4038505.

Pangavhane, D. R. and Sawhney, R. L. (2002) 'Review of research and development work on solar dryers for grape drying', *Energy Conversion and Management*. doi: 10.1016/S0196-8904(01)00006-1.

Papadimitratos, A., Sobhansarbandi, S. and Pozdin, V. (2016) 'ScienceDirect', *SOLAR ENERGY.* Elsevier Ltd, 129(October 2017), pp. 10–19. doi: 10.1016/j.solener.2015.12.040.

Platzer, W. (2015) 'Potential studies on solar process heat worldwide, Deliverable C5', *IEA SHC Task 49*, p. 17.

PVGIS (2019). Available at: https://re.jrc.ec.europa.eu/pvg_tools/en/#MR.

Rabl, A. (1976) 'Comparison of Solar Concentrators', *Solar Energy*, 18(93–111).

Rawlins, J. and Asgcroft, M. (2013) 'Small-scale Concentrated Solar Power A review of current activity and potential to accelerate deployment', *Carbon Trust*, 1(March), pp. 1–44.

Salim, R. D. (2018) 'Manufacturing Procedure of a Hybrid Design of Solar Collector (Sterilization and Water Heating) by Solar and Electrical Energy', *ICOASE 2018 - International Conference on Advanced Science and Engineering*. IEEE, (October 2018), pp. 353–356. doi: 10.1109/ICOASE.2018.8548807.

Tonatiuh software (no date). Available at: http://iat-cener.github.io/tonatiuh/.

Valencia, G. *et al.* (2017) 'Energy Saving in Industrial Process Based on the Equivalent Production Method to Calculate Energy Performance Indicators Energy Saving in Industrial Process Based on the Equivalent Production Method to Calculate Energy Performance Indicators', *Chemical Engineering Transactios*, 57(September), pp. 709–715. doi: 10.3303/CET1757119.

Vidal, A. and DÃ-az, A. I. (2000) 'High-Performance, Low-Cost Solar Collectors for Disinfection of Contaminated Water', *Water Environment Research*, 72(3), pp. 271–276. doi: 10.2307/25045375.

Wäckelgård, E. *et al.* (2015) 'Solar Energy Materials & Solar Cells Development of W – SiO 2 and Nb – TiO 2 solar absorber coatings for combined heat and power systems at intermediate operation temperatures', *Solar Energy Materials and Solar Cells*. Elsevier, 133, pp. 180–193. doi: 10.1016/j.solmat.2014.10.022.

Winston, R. (1974) 'Principles of solar concentrators of a novel design', *Sol. Energy*, 16(2), pp. 89–95.

Winston, R. (1975) 'Principles of Cylindrical Concentrators for Solar Energy', *Solar Energy*, 17, pp. 255–258.

BILLY SOLAR: SCALABLE AND COST-EFFECTIVE SOLAR HEATING UNITS FOR INDUSTRY

Mercedes H. Rittmann-Frank[1], Florian Ruesch[1], Andreas Häberle[1]

[1] SPF Institut für Solartechnik, OST Ostschweizer Fachhochschule, Oberseestr. 10, CH-8640 Rapperswil (Switzerland)

Abstract

Here we present preliminary results of the Billy Solar project, which pursues the goal of developing a fully configured and modular scalable solar heating system for industrial use at different production sites and for different processes. For this purpose, a "one size fits all" concept will be developed based on simulation together with collector manufacturers, software developers, application partners from industry and research institutes. The system consists primarily of solar thermal collectors and a heat storage. As an alternative to solar thermal, photovoltaics combined with heat pumps or possibly a combination of both approaches are investigated. Based on this, financing models are derived.

Keywords:solar process heat, modular, load profiles

1. Introduction

An increasing number of industrial companies are reducing their CO_2 footprint by using heat from solar energy. Although the number of solar thermal systems for generating solar process heat more than quadrupled from 120 to 500 between 2012 and 2016 worldwide [1] the potential for solar process heat is still almost untapped. Most of these solar heating systems are the result of tailor-made individual planning, which makes them less attractive for industrial companies. The objective of the Billy Solar project is to boost the deployment of solar heat in industry and give an alternative approach to the traditional planning, where solar thermal installations in industry require literally months of project planning and energy calculations and a lot of experience with such systems. Often, the cost of planning and the complex integration scheme challenges the project. Until now solar process heat systems have been designed for specific requirements for each type of costumer making it expensive and thus limiting its desirable extensive deployment. Thus in Billy Solar we investigate a more standardised approach by the development of an adaptable modular system and the analysis of the energy demand of various industries.

For this purpose a "one size fits all" concept will be developed based on system simulations. This concept will be applied to different sites with various process heat demands. Because the heating system is not tailor-made, there will be deviations from the ideal configuration at a single integration site. The big advantage, however, is that the high planning effort for each individual integration is eliminated and a system can be put together in which all components fit together ideally and which is composed of modular units. A unit consists primarily of a solar thermal system with storage. As an alternative to solar thermal energy, photovoltaics combined with heat pumps or a combination of both approaches will be investigated as well. Based on this, financing models will be derived.

2. Method

For the development of the modular heat units, typical industrial load profiles are first identified by:

1. classification according to energy consumption per process, process requirements (temperature, load profile, storage possibilities), specification of the energy supply network, connection to district heating, options for waste heat utilization

2. data extraction from existing data from energy flow and pinch analyses.

Based on this typical load profiles and their specifications (temperature, pressure, medium, load profile, etc.), modular units (solar thermal, photovoltaic and heat pump) for the provision of a certain amount of heat are developed simulation-based with the software Polysun. These units consist of a basic unit and allow easy

doi:10.18086/eurosun.2020.03.10 Available at http://proceedings.ises.org

upscaling. For this purpose, the Polysun tool will be extended to map complex industrial boundary conditions.

Finally, the costs of the overall system will be examined and worked out on the basis of various scenarios and business models in cooperation with the various interest groups (collector manufacturers, industrial partners, energy suppliers, etc.).

3. Preliminary Results

By examining energy consumption data, temperature levels and other data from pinch analyses collected for various companies and sites by the project partner HSLU, several recurring heat sink profiles could be identified, e.g. from galvanizing and painting basins.
In addition, questionnaires were prepared which allow for a rough energetic analysis and give relevant information on process level, which is important for the development of the heat units and for possible energetic efficiency measures. The questionnaire is based on the freely-available Solind Tool [2]. These questionnaires were completed for seven different production sites of Emmi, the biggest dairy in Switzerland.

Various recurring processes were identified as suitable heat sinks for a standardized solar thermal integration (e.g. cleaning, pasteurization). Furthermore, the Polysun software has been extended in such way that complex industrial profiles and their heat consumption can be integrated relatively easily. By means of simulations the parameters of the systems (type of collector technology, collector field area, volume of the heat storage tank, irradiation and process heat consumption) were varied and the system was optimized according to energetic and economic aspects (system, integration and installation costs). The simulations carried out in the examined industrial plants and processes result in different solar fractions depending on the varied parameters. For the design of the optimal solar thermal system, the system costs play a decisive role in addition to the solar heat yield. Here the term "optimal" solar thermal system describes the most economical combination of collector field size and storage volume with the lowest system costs per energy unit produced. The system costs refer to solar collectors including all components in the collector circuit (collector, elevation, pipes, pumps, heat exchanger, accessories, etc.) up to the heat exchanger for the heat transfer from the solar circuit to the heat supply circuit of the company as well as the installation. Different cost functions were used to define the system costs depending on collector technology and storage volume and are based on offers for large-scale systems from various research projects and for the heat storage tanks on price lists from manufacturers [3] [4].

With the help of these cost functions, the simulated solar heat yield from the simulation study can be assigned and the levelized cost of heat (LCoH) can be determined for the simulated version. To calculate the LCoH, the definition of the heat price according to IEA SHC Task 54 in Formula 1 was used.

Formula 1: Calculation of the Levelized Cost of Heat (LCoH) in CHF/MWh

$$LCoH = \frac{I_{Sol} + \sum_{t=1}^{T} \frac{C_{t,Sol}}{(1+r)^t} - S_{Sol}}{\sum_{t=1}^{T} \frac{E_{t,Sol}}{(1+r)^t}}$$

$I_{sol} = Total\ investment\ cost$ $\qquad$ $r = Tax\ rate\ in\ \%$

$C_t = annual\ operation\ cost$ $\qquad$ $T = amortisation\ time\ in\ year$

$E_t = annual\ solar\ yield\ in\ MWh$ $\qquad$ $S_{sol} = Subsidy$

By means of linear interpolation between the simulated collector field sizes and heat storage volumes from the simulation study, profitability matrices can be presented for the operations and processes (Figure 1). The solar heat production costs have been calculated over a period of 25 years at an interest rate of 3% and without ongoing operating costs. The representation with color coding of the lowest solar heat prices of an enterprise makes it possible to identify the suitable combination sizes from collector field size and storage volume. As an example, Figure 1 shows the profitability matrix for the LCoH for a company in Switzerland using flat plate collectors to provide process heat up to 80°C.

	LCoH CHF/ MWh																									
	Storage size [m3]																									
Collector field [m2]	0	10	20	30	40	50	60	70	80	90	100	110	120	130	140	150	160	170	180	190	200	210	220	230	240	250
100	185.2	119.9	127.9	135.7	143.3	150.9	149.6	148.5	147.6	146.7	145.9															
200	170.5	115.1	116.2	117.3	118.3	119.3	120.1	120.8	121.5	122.2	122.8															
300	160.6	110.1	108.9	107.7	106.6	105.7	106.7	107.7	108.7	109.7	110.6															
400	153.5	106.1	103.6	101.4	99.4	97.6	98.7	99.7	100.8	101.8	102.8															
500	148.0	102.7	99.6	96.9	94.3	92.0	93.1	94.1	95.1	96.2	97.1															
600	146.1	104.3	100.8	97.6	94.7	92.1	92.6	93.1	93.6	94.0	94.5															
700	144.3	105.1	101.3	97.8	94.7	91.9	91.9	92.0	92.1	92.1	92.2															
800	142.4	105.5	101.4	97.8	94.4	91.4	91.2	90.9	90.6	90.4	90.2															
900	140.6	105.6	101.4	97.5	94.0	90.9	90.4	89.8	**89.3**	**88.8**	**88.4**															
1000	139.0	105.5	101.1	97.1	93.6	90.3	**89.5**	**88.8**	**88.1**	**87.4**	**86.8**	**88.3**	**89.8**	91.3	92.9	94.5	95.2	95.9	96.6	97.3	98.0	98.9	99.8	100.8	101.7	102.6
1100	141.5	110.0	105.1	100.8	96.8	93.2	92.3	91.5	90.7	89.9	**89.1**	90.4	91.8	93.1	94.5	95.8	96.5	97.1	97.7	98.3	98.9	99.7	100.5	101.3	102.1	102.8
1200	143.5	114.1	108.8	104.0	99.7	95.9	94.8	93.9	92.9	92.0	91.1	92.3	93.5	94.6	95.8	97.0	97.5	98.1	98.6	99.1	99.6	100.3	101.0	101.6	102.3	103.0
1300	145.2	117.8	112.0	106.9	102.3	98.2	97.1	96.0	94.9	93.9	92.9	93.9	94.9	95.9	96.9	98.0	98.4	98.9	99.3	99.7	100.2	100.8	101.3	101.9	102.5	103.0
1400	146.6	121.2	115.0	109.5	104.7	100.3	99.0	97.8	96.7	95.6	94.5	95.4	96.2	97.1	97.9	98.8	99.1	99.5	99.9	100.3	100.6	101.1	101.6	102.1	102.5	103.0
1500	147.8	124.2	117.7	111.9	106.8	102.1	100.8	99.5	98.3	97.1	95.9	96.6	97.3	98.0	98.7	99.4	99.8	100.1	100.4	100.7	101.0	101.4	101.8	102.2	102.5	102.9
1600	148.7	127.1	120.2	114.1	108.7	103.8	102.4	101.0	99.7	98.4	97.2	97.8	98.3	98.9	99.5	100.0	100.3	100.5	100.8	101.0	101.2	101.6	101.9	102.2	102.5	102.8
1700	149.5	129.6	122.4	116.0	110.4	105.3	103.8	102.4	101.0	99.6	98.3	98.8	99.2	99.6	100.1	100.5	100.7	100.9	101.1	101.2	101.4	101.7	101.9	102.2	102.4	102.6
1800	150.2	132.0	124.5	117.8	112.0	106.7	105.1	103.6	102.1	100.7	99.3	99.6	100.0	100.3	100.6	100.9	101.0	101.2	101.3	101.4	101.6	101.7	101.9	102.1	102.3	102.4
1900	150.7	134.2	126.4	119.5	113.4	108.0	106.3	104.7	103.1	101.6	100.2	100.4	100.6	100.8	101.0	101.2	101.3	101.4	101.5	101.6	101.6	101.8	101.9	102.0	102.1	102.2
2000	151.2	136.2	128.1	121.0	114.7	109.1	107.3	105.6	104.0	102.5	101.0	101.1	101.2	101.3	101.4	101.5	101.5	101.6	101.6	101.6	101.7	101.7	101.8	101.9	101.9	102.0
2100	151.5	138.1	129.7	122.3	115.9	110.1	108.3	106.5	104.9	103.3	101.8	101.8	101.7	101.7	101.7	101.7	101.7	101.7	101.7	101.7	101.7	101.7	101.7	101.7	101.7	101.7
2200	151.8	139.8	131.2	123.6	116.9	111.0	109.2	107.4	105.6	104.0	102.4	102.3	102.2	102.1	102.0	101.8	101.8	101.8	101.7	101.7	101.7	101.6	101.6	101.5	101.5	101.5
2300	152.0	141.4	132.5	124.8	117.9	111.9	109.9	108.1	106.3	104.6	103.0	102.8	102.6	102.4	102.2	102.0	101.9	101.8	101.8	101.7	101.6	101.5	101.5	101.4	101.3	101.2
2400	152.2	142.9	133.8	125.8	118.8	112.7	110.7	108.8	106.9	105.2	103.6	103.2	102.9	102.7	102.4	102.1	102.0	101.9	101.8	101.7	101.6	101.4	101.3	101.2	101.0	100.9
2500	152.3	144.3	134.9	126.8	119.7	113.4	111.3	109.4	107.5	105.7	104.0	103.6	103.3	102.9	102.5	102.1	102.0	101.9	101.7	101.6	101.5	101.3	101.1	101.0	100.8	100.6
2600	155.9	147.4	137.7	129.3	122.0	115.5	113.3	111.3	109.4	107.5	105.7	105.3	105.0	104.6	104.2	103.8	103.7	103.5	103.4	103.2	103.1	102.9	102.7	102.5	102.4	102.2
2700	159.5	150.4	140.4	131.8	124.2	117.5	115.3	113.2	111.1	109.2	107.3	107.0	106.6	106.2	105.8	105.5	105.3	105.1	105.0	104.8	104.6	104.4	104.2	104.0	103.9	103.7
2800	163.0	153.3	143.0	134.1	126.3	119.5	117.2	114.9	112.8	110.8	108.9	108.5	108.2	107.8	107.4	107.1	106.9	106.7	106.5	106.3	106.1	105.9	105.7	105.5	105.3	105.1
2900	166.3	156.1	145.6	136.4	128.4	121.4	119.0	116.7	114.5	112.4	110.4	110.0	109.7	109.3	108.9	108.6	108.4	108.2	108.0	107.7	107.5	107.3	107.1	106.9	106.7	106.5
3000	169.6	158.9	148.0	138.6	130.4	123.2	120.7	118.3	116.1	113.9	111.8	111.5	111.1	110.8	110.4	110.1	109.8	109.6	109.4	109.1	108.9	108.7	108.5	108.2	108.0	107.8
3100	172.9	161.5	150.4	140.8	132.4	125.0	122.4	119.9	117.6	115.4	113.2	112.9	112.5	112.2	111.8	111.5	111.2	111.0	110.7	110.5	110.3	110.0	109.8	109.5	109.3	109.1
3200	176.0	164.1	152.7	142.8	134.2	126.7	124.0	121.5	119.1	116.8	114.6	114.2	113.9	113.5	113.2	112.8	112.6	112.3	112.0	111.8	111.5	111.3	111.0	110.8	110.6	110.3
3300	179.1	166.6	154.9	144.8	136.1	128.4	125.6	123.0	120.5	118.1	115.9	115.5	115.2	114.8	114.5	114.2	113.9	113.6	113.3	113.0	112.8	112.5	112.3	112.0	111.8	111.5
3400	182.1	169.0	157.1	146.8	137.8	130.0	127.1	124.4	121.8	119.4	117.1	116.7	116.4	116.1	115.8	115.4	115.1	114.8	114.5	114.3	114.0	113.7	113.4	113.2	112.9	112.7
3500	185.0	171.4	159.2	148.7	139.5	131.5	128.6	125.8	123.2	120.7	118.3	117.9	117.6	117.3	117.0	116.7	116.4	116.0	115.7	115.4	115.1	114.9	114.6	114.3	114.1	113.8
3600	187.9	173.7	161.2	150.5	141.2	133.0	130.0	127.1	124.4	121.9	119.4	119.1	118.8	118.5	118.2	117.9	117.5	117.2	116.9	116.6	116.2	116.0	115.7	115.4	115.1	114.9
3700	190.7	175.9	163.2	152.2	142.8	134.5	131.4	128.4	125.7	123.0	120.5	120.2	119.9	119.6	119.3	119.0	118.7	118.3	118.0	117.7	117.3	117.0	116.8	116.5	116.2	115.9
3800	193.4	178.1	165.1	154.0	144.3	135.9	132.7	129.7	126.9	124.2	121.6	121.3	121.0	120.7	120.4	120.1	119.8	119.4	119.1	118.7	118.4	118.1	117.8	117.5	117.2	116.9
3900	196.1	180.2	167.0	155.6	145.8	137.2	134.0	130.9	128.0	125.3	122.6	122.3	122.1	121.8	121.5	121.2	120.8	120.5	120.1	119.7	119.4	119.1	118.8	118.5	118.2	117.9
4000	198.7	182.3	168.8	157.3	147.3	138.5	135.2	132.1	129.1	126.3	123.6	123.3	123.1	122.8	122.5	122.2	121.9	121.5	121.1	120.7	120.4	120.0	119.7	119.4	119.2	118.9

Figure 1: Example for a LCoH matrix for a solar process heat field with flat plate collectors. Here the solar process heat system is simulated with different collector field sizes and storage volumes with color coding from the highest heat prices in red to the lowest in green

Figure 1 shows that the economically most promising range for this exemplary case study begins with a collector field size of 2500 m^2 and a storage volume of 80-90 m^3 upwards. The lowest solar heat price of 83.7 CHF/MWh is achieved for this example a large collector field size of 5'000 m^2 and a heat storage tank volume of 250m^3. This results indicates, that bigger systems lead to lower prices, however this limit was set in this project due to the space restrictions in the company.

The LCoH matrix was calculated for all investigated companies and production sites. This resulted in a first estimation for the dimensioning of a smallest standard module for industrial solar thermal systems, which has a collector field area of 100 m² and a hot water storage tank with 10 m³. These interim results have to be confirmed and refined in the course of the project. Figure 2 shows the investigated industrial sites, their heat consumption and average required process temperature. The color-coded area indicates a range for the heat production costs for the optimal size of the solar unit (collector area and storage tank). In the BillySolar project different economic scenarios were calculated, here in Fig. 2 the heat price is shown without and including operating costs. On the one hand, it can be seen that the heat price is inversely related to the total energy consumption of the company. Furthermore, a tendency to increased solar heat prices for higher process temperatures can be identified. This is caused by a decreasing solar yield for higher operation temperatures of the solar collectors.

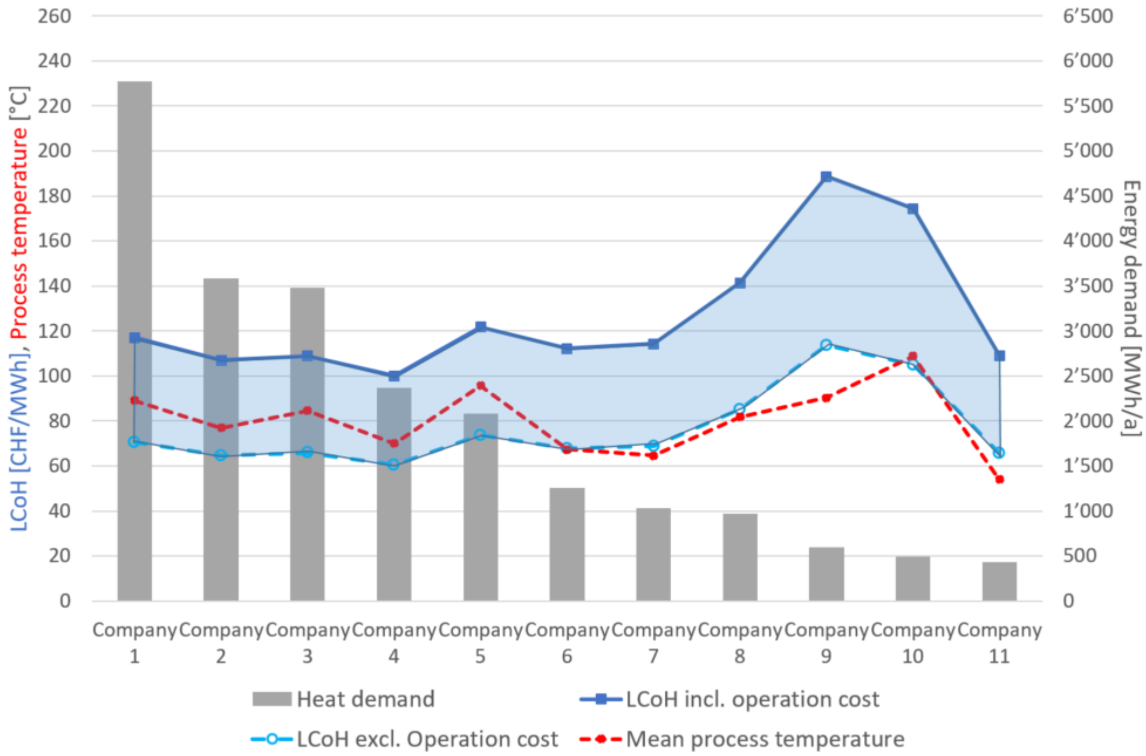

Figure 2 Heat price for vacuum tube collector unit (blue area between solid and dashed line, left axis) according to energy demand (grey bars, right axis) and process temperature (red dashed line, left axis)

4. Outlook

The next step is to investigate a photovoltaic heat pump (PV-HP) unit with different heat sources (outside air, waste heat) for the previously investigated industrial sites and compare it with the solar thermal (ST) units. A system based on PV-HP will in most cases not be operated independently from the power grid. Therefore, a system design can only be made in connection with economic parameters (especially the feed-in and purchase tariffs for electricity at the respective site). From comparison studies between the technologies, scenarios and optimal conditions it will be determined in which case either the use of solar thermal energy, a PV-HP system or a combination of these technologies is more advantageous for the industrial end user.

Furthermore, the interaction of several units during upscaling and their combination (ST supplemented with PV-HP, possibly also integration of waste heat into the smallest unit), based on concrete process data, will be investigated by means of simulations. In this process, the combination and dimensioning of components (ST and PV-WP, if necessary, additional waste heat, district heating) will be coordinated and optimized.

Finally, possible financing options will be considered. Currently, the financing of solar process heat plants in Switzerland is done through general construction financing, there are no special programs or project financing. Since solar plants are planned individually for the use at the respective location, the financing of existing plants is also individually tailored to the respective owner. The conditions are to be improved by standardizing the units, easy dismantling and a broad customer structure connected to heating networks. Against this background, models involving industry as prosumer as well as contracting and leasing models are to be investigated.

References

[1] "Solarwirtschaft," [Online]. Available: https://www.solarwirtschaft.de/presse/pressemeldungen/pressemeldungen-im-detail/news/neue-internetseite-zeigt-vorteile-von-industrieller-prozesswaerme-in-drei-sprachen.html..

[2] S. I. f. Solartechnik, “SPF Solind Tool,” 2019. [Online]. Available: https://www.spf.ch/index.php?id=19086.

[3] B. M. e. al, “Deliverable B2: Integration Guideline,” IEA SHC Task 49 SolarPaces Annex IV, 2015, 2015.

[4] I. M. u. F. Ruesch, “Machbarkeit solarunterstützter Wärmenetze im Kanton St.Gallen,” Bundesamt für Energie BFE, 2017.

Water Sludge Drying: Modelling of a Solar Thermal Plant for a Solar Vacuum Dryer

Ruben Bartali[1], Özgur Bayer[2], Deniz Pınarlı[2], Selin Erdoğan[2], Michele Bolognese[1], Derek Baker[2], Luca Pratticò[1,3] and Luigi Crema[1]

[1] Fondazione Bruno Kessler, Applied Research on Energy System Unit, Via Sommarive, 18, 38123, Trento, Italy

[2] Middle East Technical University, Mechanical Engineering Department, 06800, Ankara, Turkey

[3] "Sapienza" University of Rome, Via Eudossiana 18, Rome, Italy

The use of dryers that operate at pressures below atmospheric can be a smart technological solution to allow better matching between commercial solar collectors and solar drying applications. At atmospheric pressure, water boils at 100°C, while at 500 mbar, 200 mbar, and 100 mbar water boils at 81.5°C, 60.5°C, and 45.6 °C, respectively. For instance, for Evacuated Tube Collectors (ETC) it is challenging to provide a constant heat at temperatures higher than 90°C. Furthermore, the tuning of the boiling temperature allows a better adaptation of the solar heat provided by a solar plant to the heat required for water sludge drying. To understand the technical feasibility of a Vacuum Solar dryer for water sludge, two solar plants with two types of solar collectors with water as the working fluid were modelled: i) ETC ii) parabolic trough collector (PTC). The modelling and design of a vacuum dryer for the drying of water sludges is presented. The results reveal that a light vacuum can improve the performance in terms of the solar fraction of the solar dryer for both ETC and PTC solar fields.

Keywords: ETC, PTC, solar vacuum dryer, predictive simulation tools, decarbonization

1. Introduction

Solar-thermal driven dryers (i.e. *solar dryers*) are a potentially attractive technology for a wide range of industrial sectors including chemical, food and beverage, plastic, and metallurgical (Hisan *et al.*, no date). Until 2018, approximately 75% of solar dryer articles published in the literature are dedicated to the agro-food sector (e.g. drying of fruit and vegetables), while the other articles are mainly devoted to drying processes for timber and other forest products, water waste, heat pumps, carpet production, and natural rubber (Goh *et al.*, 2011)(Bekkioui *et al.*, 2011) (Fuller, 2002)(Bal, Satya and Naik, 2010). One key parameter when assessing the feasibility for powering an industrial drying process using solar thermal is the temperature required by the drying processes (Hisan *et al.*, no date). The temperature of the drying process allows the proper choice of solar collector, the heat transfer fluid (HTF), and heat exchanger. In the agro-food sector, solar dryers are widely used because the temperatures required for drying processes are typically relatively low (e.g. 40-70°C) and easy to reach using commercially-available, inexpensive and efficient collectors such as flat-plate liquid collectors, air collectors, and greenhouses. Drying cabinets typically work in the temperature range of 60°C to 80°C, and usually, in this range, the use of an evacuated tube collector with water as the heat transfer fluid is the appropriate choice (Prakash and Kumar, 2014). On the other hand, for applications such as paper drying, and drying a finished product, the temperature required is often higher than 100°C or 200°C and the collector used in this kind of application can be a parabolic trough collector (PTC) or evacuated flat plate collector. Moreover, in this range of temperature, pressurized water and thermal oil are typical heat transfer fluids.

doi:10.18086/eurosun.2020.03.11 Available at http://proceedings.ises.org

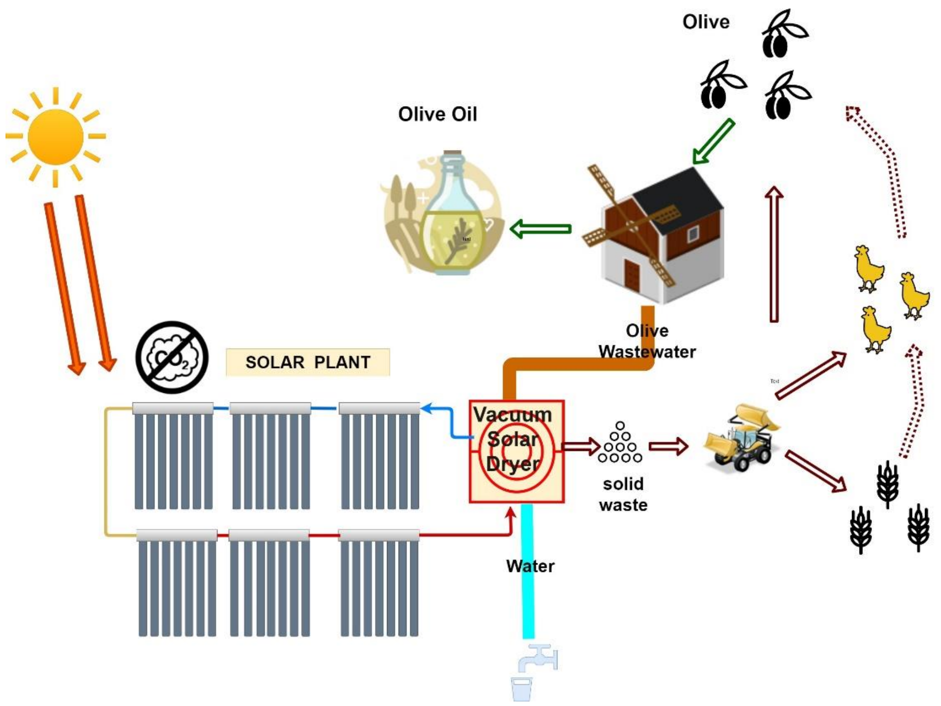

Fig. 1. Sketch of a solar plant for solar drying of Olive water sludge, the solid waste can be also valorized in other agro-food cycles (Dermeche *et al.*, 2013)(Encinar *et al.*, 2008) .

One of the most attractive emerging sectors for solar drying is waste water treatment, such as pharmaceutical wastewater. Another interesting application is the drying of microalgae used for instance in biofuel production (Gouveia *et al.*, 2016)(Villagracia *et al.*, 2016). In all these applications to promote the use of solar energies, it is very important to provide in an efficient mode the heat from the solar field to the dryer. Vacuum technologies can be useful to optimize the performances of the solar collector in the solar drying sector. Water, in fact, boils at 100°C at atmospheric pressure, but the reduction of pressure decreases the boiling temperature and can be a smart technological solution to allow the thermal matching of commercial solar collectors with solar drying applications. For instance, for Evacuated Tube Collectors (ETCs) providing a constant heat at temperatures higher than 90° is challenging, while using Parabolic Trough Collectors (PTCs) maintaining temperatures higher than 100°C is much easier. But the PTC technology requires sophisticated optics, a tracking system, and the installation is more complex. Therefore, to amortize the investment it is very important to maximize the use of the heat provided by the solar field. For this reason, in this work, we study the solar field with a vacuum dryer system used to treat olive water sludge (Wu *et al.*, 2010) (Bennamoun, 2012). A schematic of the overall system is presented in Fig. 1. In this work, a solar dryer with a maximum power of 280 kW has been analyzed. The solar dryer under study uses vacuum technology to reduce the boiling temperature of the water sludge to be dried. Two solar plants with two different solar collector models were modelled, to understand the benefits of a solar dryer.

- Vacuum Solar dryer with ETC and water as the HTF;
- Vacuum Solar dryer with PTC and water as the HTF.

For both simulations, we considered a common vacuum solar dryer. In the first part of this work, the design of the solar vacuum dryer and solar field is reported. In the second part, the modelling results obtained for the ETC and PTC solar fields are reported and compared.

2. Methods

2.1 Design of the Vacuum solar Dryer

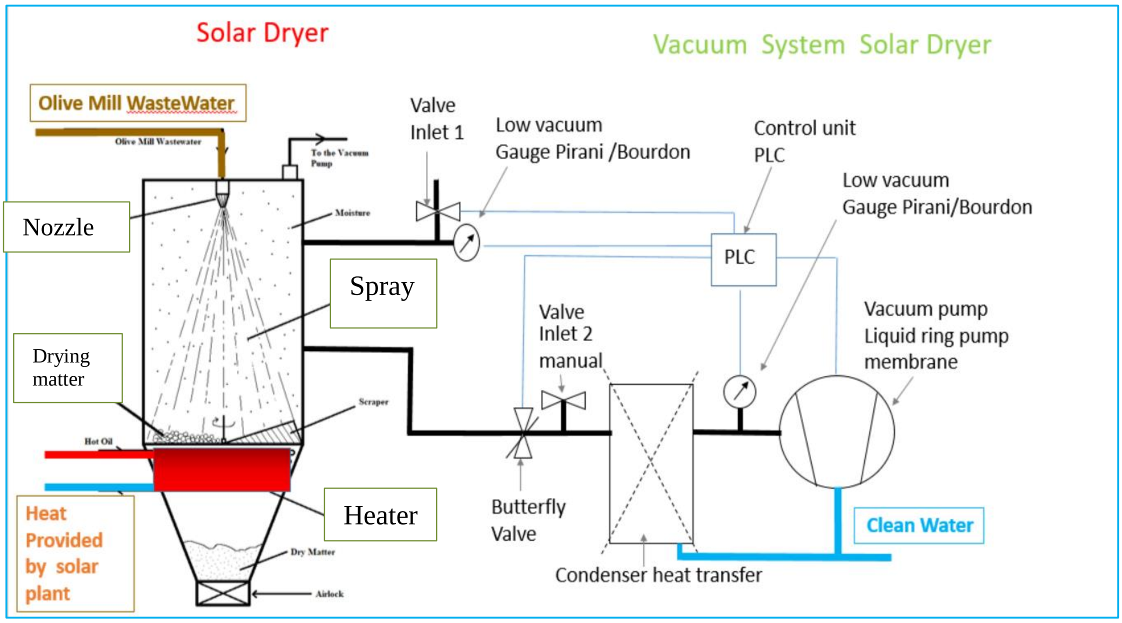

Fig. 2 Design of solar dryer with the vacuum system

The design of the solar vacuum dryer is depicted Fig. 2, and it is composed of a vacuum chamber and a vacuum system. The vacuum system design contains a pumped line and a venting (inlet) line. For this kind of vacuum Pirani or Bourdon sensors can be used, and the vacuum pumping speed (that allows the control of the vacuum pressure in the dryer) can be controlled by a butterfly valve. The vacuum can be generated using a liquid ring vacuum pump or a membrane pump. The vacuum system can be controlled by the Programmable Logic Controller (PLC). One of the most critical techno-economical parameters in the design of a vacuum system is the thickness of the wall of the vacuum chamber; if the wall is too thin, the external pressure will deform the dryer apparatus (collapse) and if the thickness is too thick, the weight and the cost of the apparatus can be too high. The thickness of the wall strongly depends on the volume of the vacuum tank. The volume of the tank has been dimensioned to ensure on the one hand the complete evaporation of the liquid and on the other hand to avoid a deformation induced by external pressure. Droplet diameter size coming out of the spray dryer was assumed as 1 mm and required vacancy around the droplet was found as 5 times of droplet size. Considering: i) the amount of wastewater that should be dried per second, ii) droplet speed and vacancy to droplet ratio, and iii) the structural problem induced by the vacuum (wall thickness), a cylindrical dryer tank with 61 cm diameter and 1-meter height with a spraying angle of 33,9° has been considered. The wall thickness was found as a minimum value of 2 mm with stress and fracture analyses (eq. 1). Aluminium was selected as the tank material and its technical characteristics are presented in Table 1.

Table 1:Technical characteristics of aluminium

Yield stress of aluminium	0.78 MPa
K_{IC}(Critical Stress Intensity Factor)	24 $MPa.m^{1/2}$
Possible crack size	1mm
Vacuum Pressure	100 mbar

$$Wall\ Thickness = (Vacuum\ Pressure * Tank\ Radius)/(Safety\ Factor * Yield\ Stress) \qquad \text{(eq.1)}$$

The vacuum dryer has been designed with a vacuum system which can reach a vacuum pressure of 100 mbar which corresponds to 45.8 °C of water boiling temperature. Using this vacuum pressure, the system presents lower power input need, which was found as 216 kW.

In solar vacuum dryers two strategies can be used to adjust the heat power at the output. The first performs a variation of mass flow rate. The second is obtained through a variation of boiling temperature:

1) Arranging vacuum pressure inside the tank so that the boiling temperature of water changes. At 500 mbar, the boiling temperature is 81.5°C whereas at 200 mbar, it is 60.5°C. With higher vacuum, less energy is required to heat up the sprayed mill wastewater to the boiling temperature. It is therefore possible to adjust the pressure according to the availability of solar radiation, during the day, to ensure greater uniformity of thermal energy production.
2) Adjusting the mass flow rate of mill wastewater through the spray nozzle. The system is capable of drying more material when the solar energy input is higher.

Based on the average amount of olive processed per year, a daily average production was calculated as 0.83 tons per day. Moreover, the amount of wastewater produced was calculated assuming 5% of wastewater in solid matter and remained part in water (average value). The required flow rate of wastewater is calculated as:

$$\dot{m}_w = \frac{daily\ wastewater\ outcome}{daily\ PTC\ working\ hours} \quad \text{(eq.2)}$$

All these calculations were embedded in Visual Basic (VB) code such that if any of these parameters needs to be changed, new size outputs are provided by a button running with this code.

PARAMETERS	
Olive [tones/year]	300
Mill water / oil [m^3/ton]	1
days per year	93
Solid Ratio Percentage [%]	5
Solar Energy Hours (7.00-19.00)	12
Density of water	958,35
hfg of water [kJ/kg]	2493
Droplet size [mm]	1
Droplet speed [m/s]	0,1
Height of dryer [m]	1
Vacancy radius/particle radius	5
Vacuum Pressure [mbar]	200
Yield Strength [Mpa]	0,78
Kıc of material [Mpa*m^1/2]	24
Safety Factor	4
Crack length [cm]	1
Temperature of mill water	25
Cp of water	4,2199
Evaporation Temp (Temp inside vacuum)	60,5

OUTPUTS		
Volume flow rate of mill water (through nozzle) [L/min]	4,675	L/min
Required Power	196,317	kW
Number of Droplets	186012,340	
Minimum volume needed in dryer for the droplet area	0,097	m^3
Radius of cylindrical design	0,305	m
Spray Angle	33,920	degrees
Wall Thickness	1,955	mm

Düğme 3

Fig. 3 Picture of VBA interface

The VB routine was designed to model the characteristics of the solar vacuum dryer. The code takes as inputs the constant sludge flow rate of the production line and the vacuum pressure provided by the system. A medium-sized factory that processes 300 tons of olives per year was considered. The total thermal power (P) required for the drying process is estimated as Equation 3. Two periods are considered for building Equation 3: the total amount of power needed to bring all of the mill water to the boiling temperature of water for the present vacuum condition and to evaporate the water portion of the whole fluid. :

$$P = \dot{m}_w . c_p . \left(T_{evap,p} - T_w\right) + \dot{m}_w . \rho_w . h_{fg} \quad \text{(eq.3)}$$

where
$\dot{m}_w$: Mass flow rate of mill wastewater (or the fluid which will be dried) flowing through nozzle [kg s^{-1}]
c_p : Specific heat capacity of mill wastewater [J kg^{-1} °C^{-1}]
T_w : Temperature of mill wastewater coming from nozzle to the tank [°C]
$T_{evap,p}$: Evaporation/ boiling temperature of water at provided vacuum pressure [°C]
ρ_w : ratio of water in mill wastewater [mass of water/mass of mill wastewater]
h_{fg} : specific enthalpy of evaporation of water [kJ kg^{-1}]

$\dot{m}_w$ correspond to a value of about 0,0745 kg/s when Equation 2 is used with the average amount of olive processed per year for a middle-sized factory consideration. It is the total amount of fluid (mill water) which should be brought to the boiling temperature. After the whole fluid reaches that temperature, only the water portion should be evaporated which corresponds to the $\dot{m}_w$x ρ_w where ρ_w (the ratio of water in mill water) is

95%. T_w is the first temperature of mill water before entering the drying cycle and assumed as 25°C. $T_{evap,p}$, h_{fg} and c_p values are dependent on the temperature and pressure values inside the tank, therefore changeable. The corresponding values for each temperature and pressure variation are tabulated in a separate Excel sheet and the “VLOOKUP” formulas in “Parameters” table pulls the right value for the inputted vacuum pressure from these tables, then pastes to the related cell in the “Parameters” Table seen in Figure 3. For instance, for a vacuum pressure of 200mbar, $T_{evap,p}$, $c_p$and h_{fg} values are pulled. Pulled values for 200mbar are $T_{evap,p}$=60.5°C, c_p =4.1816 kJ/kg K and h_{fg}= 2358.5 kJ/kg. Required power input is 196.317 kW for that case. When the vacuum pressure is increased to 500mbar, $T_{evap,p}$ becomes 81.5°C, and corresponding values to that temperature are: c_p =4.2199 kJ/kgK and h_{fg}= 2302.3 kJ/kg. Required power input for that case is 188.400 kW.

2.2 Modelling of solar field

Considering the features of the solar dryer described above, the solar field has been modelled employing either the PTC or ETC. The PTC field with north-south axis tracking is connected to a thermal storage unit in which the HTF acts as the storage medium. While the HTF is being circulated through the absorber pipe of PTC by a pump, it absorbs concentrated solar irradiation. The flow in the absorber pipe is considered as uniform, incompressible, single-phase flow with constant properties. A 1-D transient thermal model is employed to obtain the HTF temperature as a function of time and location along the absorber pipe. Neglecting axial conduction, the energy equation is given as follows:

$$\frac{\partial T}{\partial t}(x,t) + u\frac{\partial T}{\partial x}(x,t) = \frac{q_{abs} - q_{loss,col}}{L\rho A c_p} \qquad \text{(eq.4)}$$

Where u is the flow velocity, q_{abs} is the absorbed solar heat, q_{loss} is the heat loss to environment from the collector, L is the collector length, ρ is the HTF density, A is the cross-sectional area of receiver pipe and c_p is the specific heat of the HTF. c_p is assumed to be constant due to its small variation with temperature. Assuming constant collector efficiency, q_{abs} is calculated by the following equation:

$$q_{abs} = \eta_0\ (GII)\ A_{aperture} \qquad \text{(eq. 5)}$$

Where η_0 is the average collector efficiency and GII is the global inclined irradiance. An overall heat transfer coefficient is determined to estimate the convective heat loss to the ambient air. Neglecting radiative losses, q_{loss} is calculated as follows:

$$q_{loss,col} = U_{col}\ A_{p,col}\ (T_{avg,col} - T_{amb}) \qquad \text{(eq. 6)}$$

The Partial Derivative Equations (PDE), eq. (4), is solved numerically using the finite volume method (FVM). Assuming the HTF is completely mixed in the storage tank, lumped tank model is employed to obtain the storage HTF temperature. The collector field outlet temperature is imposed as a boundary condition to the lumped tank model as follows:

$$V_{tank}\ \rho c_p \frac{dT_{tank}}{dt} = \dot{m} c_p \left(T_{col,out} - T_{col,in}\right) - q_{loss,tank} - q_{load} \qquad \text{(eq. 7)}$$

where V_{tank} is the storage tank volume, T_{tank} is the storage HTF temperature, $\dot{m}$ is the mass flow rate of HTF through the receiver pipe of PTC, $T_{col,in}$ and $T_{col,out}$ are collector inlet and outlet temperatures, respectively. $q_{loss,tank}$ is the heat loss to the environment from the storage tank, it is calculated in a similar manner to eq. 6. q_{load} is the process heat load on the solar thermal system that is used to boil olive mill waste water. Then, the flow rate of waste-water that can be boiled using solar heat can be calculated as:

$$\dot{m_w} = \frac{q_{load}}{h_{fg}} \qquad \text{(eq. 8)}$$

where $\dot{m_w}$ is the maximum flow rate of olive mill waste-water that can be boiled using solar heat and h_{fg} is the latent heat of boiling of water under vacuum pressure. Although h_{fg} slightly increases with decreasing pressure, vacuuming the drying chamber is still beneficial due to the lower temperature requirement of the drying process. In addition, reduced boiling temperature results in increased temperature difference which enhances heat transfer from HTF to olive mill wastewater.

For ETC solar field we considered a solar plant of 514 m^2 composed of 150 collectors, the solar plant uses pressurized water as the HTF. The empirical technical data about optical efficiency (a_0) and heat losses of 1st and 2nd order (c_1, c_2) of the commercial ETC used, are presented in the Table 2(Bolognese *et al.*, 2020)

Tab. 2: Coefficients of efficiency and heat losses

$a_0(W/m^2)$	$c_1(W/m^2K)$	$c_2(W/m^2K^2)$
0.718	0.974	0.005

Moreover, the overall efficiency η depends on the longitudinal and transversal Incidence Angle Modifiers (K_l, K_t) which are necessary to calculate the effective efficiency η.

$$\eta = K_l K_t\, a_0 - c_1 \frac{(T_* - T_{ext})}{GHI} - c_2 \frac{(T_* - T_{ext})^2}{GHI} \qquad \text{(eq. 6)}$$

Here T_* is the average temperature of solar collectors $\left(T_* = \frac{T_{in}+T_{out}}{2}\right)$ and T_{ext} is the environmental temperature. In order to analyse the dynamic transient behaviour of a solar field composed of ETC the commercial dynamic simulation software Dymola - Dassault Systems (Dassault Systèmes, 2017)with the *Thermocycle* library (Desideri *et al.*, 2018) were used. In the dynamic simulation, the mass flow rate and recirculation loop are controlled by two proportional integrative (PI) controllers using the outlet hot water tank temperature as measurement point and the temperature of 90 °C as the set point. If the temperature does not reach 90 °C, the flow rate decreases while the recirculation valve opens. The configuration of the solar field consists of 15 solar collectors in parallel and 10 solar collectors in series.
PVGIS (*PVGIS*) has been used as the source for the solar radiation data from a Typical Meteorological Year (TMY). In particular, the Global Horizontal Irradiation (GHI) has been taken for 21-23 June, in Rome (Lat: 41.895°, Long: 12.485°).

3. Modelling results

To understand the technical feasibility of a solar dryer, two solar plants with two kinds of solar collector were modelled:

i) *Vacuum Solar dryer with ETC collector and water as the working fluid*
ii) Vacuum Solar dryer with PTC collector and water as the working fluid

The performance of solar dryers was calculated for 21-23 June considering Rome as the location of the plant. The area of collectors for both the solar fields are similar and limited around 500m^2. The collector areas are slightly underpowered, (in particular, ETC) to understand the impact of the vacuum dryer technology. For the ETC solar field, we considered a tank with a storage capacity of 1 m^3 while for PTC solar field, a storage tank of 6 m^3 is assumed. Tab reports a summary of the main characteristic of the solar plant structure used to obtain the different performances in the modelling of the solar vacuum dryer.

Tab. 3: Summary of the main characteristic of the solar plant structure used to obtain the best performance in the modelling of the solar vacuum dryer.

	Total Collector Area [m^2]	N Collector Series / Parallel	Storage Capacity [m^3]	Temp. Range [°C]	Avg. working hours per day		
					[1000 mbar / No vacuum]	[500 mbar]	[200 mbar]
ETC	514	10/15	1	90-60	0	3.94	9.08
PTC	480	12/10	6	80-120	9.82	10.97	12.29

Fig. 4 shows the temperature of the working fluid (red) and the temperature of water in the tank (blue). The days of the 21st-23rd of June were considered (72 hours) for the ETC solar field. We remark, as the energy source which turns the drying cycle is solar powered (therefore not stable during the day) the system should be adaptive to the power input; for instance, arranging the vacuum pressure inside the solar drying tank. For instance, if there is a low power input to the system (temporarily cloudy), the vacuum pressure can be reduced to reduce the boiling temperature of the water, making it easier to dry the water sludge. Even if ETC solar field is underpowered (limited field area), thanks to the good efficiency of ETC, the maximum temperature reached at atmospheric pressure by the working fluid is relatively high 85°C; but not enough to obtain effective boiling of the water at ambient pressure (considering this solar dryer). While the estimated boiling temperatures at different vacuum pressures, 500mbar and 200mbar, are 81.5°C and 60.5°C, respectively (highlighted as horizontal lines in Fig. 4). Considering these boiling temperatures, we have estimated the average hours per day where the dryer is effectively fed by the solar field (see Tab).

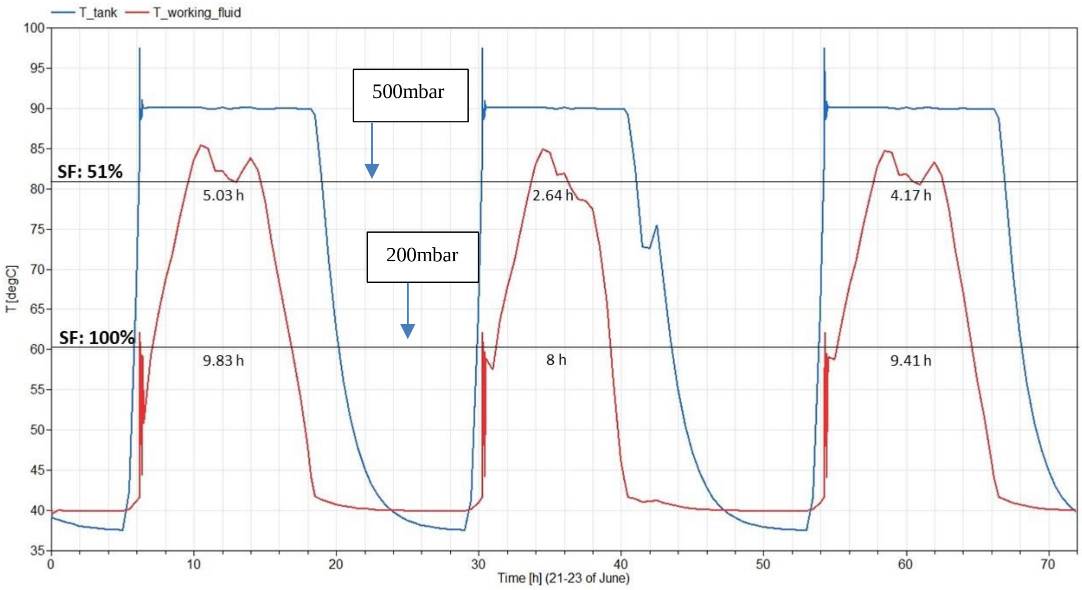

Fig. 4: Distributions of temperatures of Storage Tank and Working fluid are reported along 72 hours, from 21st to 23rd of June in Rome. Two black horizontal lines highlight the necessary temperatures to feed the solar dryer at 500 mbar or 200 mbar. The hours of actual feed of the solar dryer for the different vacuum conditions are also reported.

The ETC results show that with a pressure of 500 mbar, it is possible to cover the thermal energy demand of the drying processes for around 4 hours per day; while at 200 mbar, it covers more than 8 hours per day. If a more complex and expensive pumping system is employed, the pressure can be furtherly decreased to 100 mbar, and the ETC's can cover the energy demand for more than 10 hours. The simulation of the PTC solar field using the same conditions of the solar radiation revealed that at atmospheric pressure it is possible to cover the thermal energy demand of the drying processes for around 9.82 hours per day; (81.8% solar fraction); while at the pressure (inside the solar dryer) of 500 mbar, is possible to reach a solar fraction of 91.4% for 10.97 hours on an average day in June. By simulation, it is also found that increasing the mass flow rate from 1.5 kg/s to 3.0 kg/s allows to decrease the heat losses and to increase the solar fraction from 89.7% to 91.4% (considering this solar dryer). As a summary, we observed that in the ETC solar field with limited gross area, without vacuum, it is not possible to dry the water sludges using this solar dryer, while it is possible for several hours using a vacuum pressure of 500 mbar (estimated solar fraction around 50%). For the PTC solar field, using this solar dryer, the solar fraction at ambient conditions is around 81.8% but with a vacuum pressure of 500mbar, it is possible to reach a value of 91.4 % (leads to a solar fraction increase of 12%). With both solar thermal technologies, ETC and PTC, it is possible to cover a solar fraction of 100% using a vacuum pressure of 200 mbar. The simulation results show that using a relatively small depression in the solar dryer pressure (500-200 mbar) allows an increase in both kinds of systems, ETC and PTC. We remark that at this range of vacuum pressure (rough vacuum) the vacuum system does not require expensive, sophisticated pumps or sensors such as turbomolecular pumps or thermionic sensors. Therefore, the cost of a solar vacuum dryer could be quite affordable for industrial applications

4. Acknowledgements

This research work was implemented in the framework of the EU H2020 LCE-33-2016 (RIA) project INSHIP Integrating National Research Agendas on Solar Heat for Industrial Processes, GA 731287, duration 01.01.2017 – 31.12.2020, *https://www.inship.eu/*

5. References

Bal, L. M., Satya, S. and Naik, S. N. (2010) 'Solar dryer with thermal energy storage systems for drying agricultural food products : A review Solar dryer with thermal energy storage systems for drying agricultural food products : A review', *Renewable and Sustainable Energy Reviews*. Elsevier Ltd, 14(8), pp. 2298–2314. doi: 10.1016/j.rser.2010.04.014.

Bekkioui, N. *et al.* (2011) 'Solar drying of pine lumber: Verification of a mathematical model', *Maderas. Ciencia y tecnología*, 13(1), pp. 29–40. doi: 10.4067/S0718-221X2011000100003.

Bennamoun, L. (2012) 'Solar drying of wastewater sludge: A review', *Renewable and Sustainable Energy Reviews*, pp. 1061–1073. doi: 10.1016/j.rser.2011.10.005.

Bolognese, M. *et al.* (2020) 'Modeling study for low-carbon industrial processes integrating solar thermal technologies . A case study in the Italian Alps : The Felicetti Pasta Factory', *Solar Energy*. Elsevier Ltd, 208(August), pp. 548–558. doi: 10.1016/j.solener.2020.07.091.

Dassault Systèmes (2017) *Dymola Systems Engineering*. Available at: https://www.3ds.com.

Dermeche, S. *et al.* (2013) 'Olive mill wastes: Biochemical characterizations and valorization strategies', *Process Biochemistry*. Elsevier Ltd, 48(10), pp. 1532–1552. doi: 10.1016/j.procbio.2013.07.010.

Desideri, A. *et al.* (2018) 'Steady-state and dynamic validation of a parabolic trough collector model using the ThermoCycle Modelica library', *Solar Energy*, 174, pp. 866–877. doi: 10.1016/j.solener.2018.08.026.

Encinar, J. M. *et al.* (2008) 'Pyrolysis and catalytic steam gasification of olive oil waste in two stages', *Renewable Energy and Power Quality Journal*, 1(6), pp. 697–702. doi: 10.24084/repqj06.415.

Fuller, R. J. (2002) 'NATURAL CONVECTION SOLAR DRYER WITH BIOMASS BACK-UP HEATER', 72(1), pp. 75–83.

Goh, L. J. *et al.* (2011) 'Review of heat pump systems for drying application', 15, pp. 4788–4796. doi: 10.1016/j.rser.2011.07.072.

Gouveia, L. *et al.* (2016) 'Microalgae biomass production using wastewater: Treatment and costs. Scale-up considerations.', *Algal Research*. Elsevier B.V., 16(June), pp. 167–176. doi: 10.1016/j.algal.2016.03.010.

Hisan, S. *et al.* (no date) 'Solar Process Heat in Industrial Systems- A Global Review', pp. 1–20.

Prakash, O. and Kumar, A. (2014) 'Solar greenhouse drying: A review', *Renewable and Sustainable Energy Reviews*. doi: 10.1016/j.rser.2013.08.084.

PVGIS (2020). Available at: https://ec.europa.eu/jrc/en/pvgis (Accessed: 31 May 2020).

Villagracia, A. R. C. *et al.* (2016) 'Microwave drying characteristics of microalgae (Chlorella vulgaris) for biofuel production', *Clean Technologies and Environmental Policy*. Springer Berlin Heidelberg, 18(8), pp. 2441–2451. doi: 10.1007/s10098-016-1169-0.

Wu, X. H. *et al.* (2010) 'Dewatering and Drying in Mineral Processing Industry : Potential for Innovation', *Drying Technology: An International Journal*, 28, pp. 834–842. doi: 10.1080/07373937.2010.490485.

04. Domestic Hot Water and Space Heating

PHOTOVOLTAIC HEAT PUMP SYSTEM FOR RENOVATED BUILDINGS – MEASURES FOR INCREASED EFFICIENCY

Andreas Heinz[1], Christian Gaber[1], Robert Haberl[2], Michel Y. Haller[2], Joachim Kalkgruber[3] and Rüdiger Schober[3]

[1] Institute of Thermal Engineering (IWT), Graz University of Technology, 8010 Graz (Austria)

[2] SPF Institute for Solar Technology, Eastern Switzerland University of Applied Sciences (OST), Rapperswil (Switzerland)

[3] SOLARFOCUS GmbH, St.Ulrich/Steyr (Austria)

Abstract

In this paper we describe the development and analysis of a hybrid heating system for space heating and domestic hot water that is designed to enable an energy-efficient supply of renovated residential buildings with an existing radiator heating system, requiring high flow temperatures. The system consists of a dedicated air-to-water heat pump using the natural refrigerant R290 (Propane), a thermal energy storage, a photovoltaic system and an advanced control. The development is done with the objective of a reduction of the system's electrical energy consumption from the grid by 25 % compared to a defined reference system. Detailed system simulations in TRNSYS were performed to evaluate the effect of different measures concerning the heat pump cycle, the storage tank and the control for a renovated reference single family house. The results show that with a combination of all considered measures a reduction of the grid consumption by 32 % compared to the reference system is possible with a PV size of 10 kWp. With 5 kWp still a reduction of 25 % can be achieved.

Keywords: Air-to-water heat pump, photovoltaic, self-sufficiency

1 Introduction

The building sector plays a central role in achieving energy and climate policy objectives all over Europe. In Austria more than one third of the final energy consumption is used to provide space heating, domestic hot water and cooling in residential and service buildings. With a construction rate of new buildings of only about 1-2 % per year, the greatest energy saving potential lies with existing buildings in need of renovation. Around 1.5 million of the 2 million buildings in Austria fall into the single-family or two-family house category, providing a large potential for savings. With regard to the construction periods, the highest potential lies with buildings built between 1961 and 1980, since about one third of the entire Austrian building stock was constructed in this period (Amtmann, 2010).

Thermal renovation together with the replacement of inefficient, fossil fuel based heating systems provides a large potential for energy savings. Air-to-water heat pumps are in principle an attractive alternative heating system for such buildings due to relatively low investment costs and simple installation. However, this solution is often not implemented due to the heat emission system, which usually consists of radiators, that are often not replaced during a renovation because of cost reasons. Therefore, relatively high supply temperatures are required, which limits the efficiency of the heat pump (HP).

In the last years the demand for solutions enabling a high self-consumption of electricity from PV plants has strongly increased due to the decrease of feed-in tariffs for electricity from photovoltaic (PV) systems and as possibility for stabilizing the electricity grid. Strategies for increasing PV self-consumption for heating systems with heat pumps have recently been analyzed with system simulations in (Battaglia et al., 2017) for an air source heat pump, in (Thür et al., 2018) for a ground source heat pump system, and in (Toradmal et al., 2018) for an air- and ground source heat pump, all of them reporting promising results.

In this paper we describe and analyze a hybrid heating system for space heating and domestic hot water that is

doi:10.18086/eurosun.2020.04.01 Available at http://proceedings.ises.org

developed in the ongoing research project "HybridHeat4San". The system is designed to enable an energy-efficient supply of renovated residential buildings with an existing radiator heating system, requiring high flow temperatures. A reduction of the overall electricity consumption is achieved by an efficient air-source heat pump and an optimized integration of a water combi storage tank (combistore). The HP is coupled to a PV system with the aim to reduce the electricity consumed from the grid by targeted operation of the compressor with PV electricity using an intelligent control strategy.

The described system is analyzed using detailed system simulations in TRNSYS 17 (2014) and results are compared to a defined reference system using a set of performance indicators. Different control strategies are evaluated concerning the fulfillment of the project objective, which is to reach a reduction of electricity consumption from the grid of 25 % compared to the reference system. The influence of the PV size on performance figures and the operational (electricity) costs is analyzed.

2 Boundary conditions and assumptions

2.1 Building, climate and domestic hot water

A single-family house with a heated floor area of 185 m² was defined as the reference building (Fig. 1) in two variants concerning the thermal insulation standard and was modelled in the simulation software TRNSYS 17:

- Before renovation
- After renovation (usual renovation)

The wall structures were chosen on the basis of building typologies for Austria defined in the European project TABULA (Tabula, 2018). The starting point was a building of the age class 1960-1981 with the according wall structures as defined in TABULA, which defines the variant "before renovation". For the "after renovation" scenario, a "usual renovation", like it is defined in TABULA with according wall structures, was used.

All assumptions regarding the air exchange (incl. additional window ventilation in summer) and the shading of the building were taken from the reference building model of the IEA SHC Task 44 (Dott et al., 2013). The software "Load Profile Generator" (2018), which was developed as part of a dissertation at Chemnitz University of Technology (Pflugradt, 2016), was used for the internal heat gains from devices and lighting as well as from persons present in the building. Load profiles were created for a household with four persons (both parents working, two school-aged children) stored as a template in the software. For the heat gains by devices and for the presence of persons, a separate load file for the TRNSYS simulation was created.

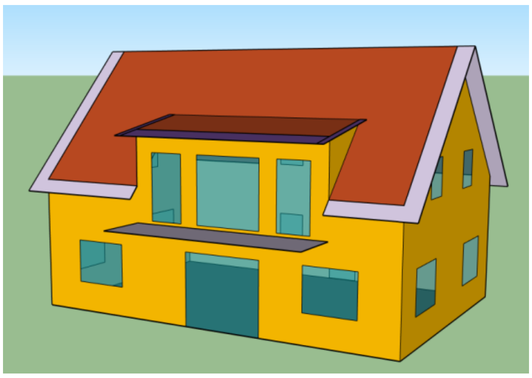

Fig. 1: Reference single family building

The resulting load profile for devices and lighting was created with a resolution of one minute and results in electrical gains totaling 16.4 kWh/m².a. The same profile is also assumed for the consumption of household electricity with a total of 3058 kWh/a. For the persons present, a sensitive heat output of 60 W per person and a latent heat output of 40 W were assumed according to ISO 7730.

As climate data set a "Test Reference Year", as described in (Bales et al., 2012), for the city of Zurich is used. The annual average of the outdoor temperature is 9.1 °C, the solar radiation on a 45° inclined surface facing south sums up to 1306 kWh/(m².a) and to 1111 kWh/(m².a) on the horizontal.

Assuming a room set temperature of 22 °C the simulations resulted in a space heating demand of 38 670 kWh and a heat load of 15.4 kW for the building before renovation and 12 212 kWh/a and 7 kW after renovation. For all the simulations shown in this work the renovated building scenario was used.

The tap profile for domestic hot water (DHW) was taken from the FP7 project MacSheep (Bales et al., 2012). The profile was created with the DHW_{calc} software (Jordan and Vajen, 2012) and has a total heat demand of 3038 kWh.

2.2 Heat emission system

For the heat emission system, radiators with a radiator exponent n=1.3 were assumed. For the “before renovation” scenario, a flow temperature t_{fl}=90 °C and a return temperature t_{ret}=70 °C were assumed for the heating load $\dot{Q}_{100}$ in the design point (design ambient temperature -11 °C), which was still common for heating systems built in the 1960s and 70s according to (Biberacher, 2010) and (Schramek and Recknagel, 2007). For the "after renovation" scenario, the necessary t_{fl} and t_{ret} were determined for the reduced heating load of the renovated building assuming constant heating surfaces. Thus, at - 11 °C, the flow temperature is 58 °C and the return temperature 48.9 °C (see Fig. 2).

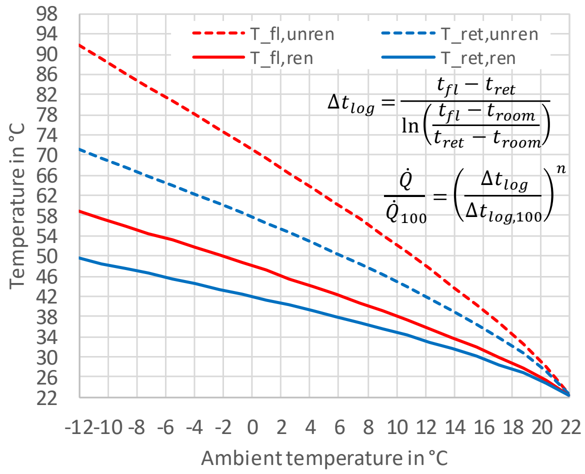

Fig. 2: Flow and return temperatures for the renovated (ren) and unrenovated (unren) building scenario

2.3 Hydraulic system layout

Regarding the system layout, two different variants were assumed. The first step in the project was to define a reference system that represented the current state of the art of HP systems available from the industrial partner in the project. This system was used as a basis for comparison to evaluate different measures of improvement for the System developed in the project (System B).

System A, depicted in Fig. 3, was used as the reference system. Here the DHW is heated in a hot water tank with a volume of 300 liters, which is charged via an internal heat exchanger. A buffer tank with a volume of 200 liters is connected in parallel to the heat emission system.

The air-source heat pump can charge one of the two storage tanks at a time, switching over via 3-way valves. The buffer storage tank is connected to the heat pump in parallel with the heating circuit. This means that when the heat pump charges the storage tank, part of the volume flow available in the heat pump circuit flows through the heating circuit. The proportion depends on the current flow rate in the heating circuit, which in turn depends on the current position of the three-way valve and the flow rate through the radiators.

For the heat losses of the storage tanks, it was assumed that the buffer tank has a heat loss value UA of 1.67 W/K and the hot water tank of 1.53 W/K, which corresponds to energy efficiency class C or B according to (EC, 2013).

System B, which was used as the basis for the system development within the project, is shown Fig.4. The air-source HP is connected to a storage tank with a volume of 1000 liters. The heat losses of the tank were assumed with efficiency class B according to (EC, 2013). Compared to the reference system the volume is larger, in order to provide storage capacity for the control strategies to increase PV self-consumption by targeted operation of the compressor to overcharge the storage (see section 2.7).

Using three-way-valves, the heat pump can charge either the DHW zone of the tank via the two connections on the top or the space heating zone via the lower connections. The storage tank is connected to the heat pump in parallel to the space heating system. This means, when the store is being charged for space heating by the heat pump, some of the flow will go via the space heating distribution loop and the rest will go through the store. As in the reference system, the proportions depend on the current operating conditions (current flow) of the space heating loop. DHW preparation is done via a freshwater station (external plate heat exchanger) to a temperature of 45 °C.

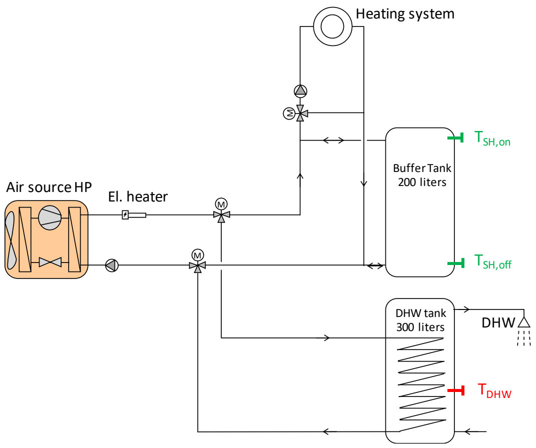

Fig. 3: Hydraulic layout of the reference heating system (System A)

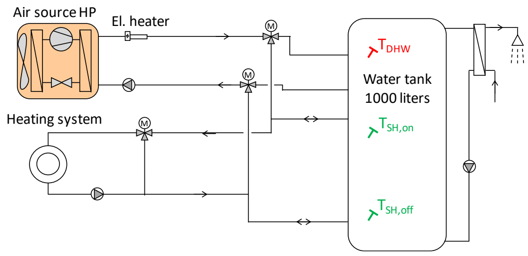

Fig. 4: Hydraulic layout of the developed heating system with combistore (System B)

2.4 Heat pump

The heat pumps of the two systems were modelled with the semi-physical HP model Type 887, which was developed by IWT and SPF (described in (Dott et al., 2013) and (Hengel et al., 2014)). The model is based on an iterative calculation of the refrigerant cycle using the thermodynamic properties of the used refrigerant. Start/stop losses and defrosting losses are considered. Detailed compressor performance data of real compressors was used, depending on the evaporation, condensation temperature and the compressor speed. The operational limits of the compressors were taken into account (max. condensation and min. evaporation temperature depending on the compressor speed).

Tab. 1: COP of the R410A HP model used for the reference system in comparison to test results from (NTB Buchs, 2018)

	A7/W35-30	A-10/W35	A-7/W34	A2/W35	A7/W27	A7/W55-47	A-10/W55	A-7/W52	A2/W42	A7/W36
Model HP Reference System	**4.52**	**2.72**	**3.02**	**3.77**	**5.48**	**2.95**	**2.04**	**2.26**	**3.24**	**4.34**
Test results Avg.	**4.71**	**2.62**	**2.80**	**3.76**	**5.60**	**2.83**	**1.94**	**2.14**	**3.19**	**4.56**
Test results Max.	5.10	3.20	3.30	4.30	6.70	3.30	2.30	2.40	3.80	5.10
Test results Min.	4.10	2.30	2.40	3.10	4.60	2.20	1.70	1.90	2.70	4.00
Deviation from test results Avg. in %	**-4.1**	**3.7**	**8.0**	**0.1**	**-2.1**	**4.1**	**5.2**	**5.8**	**1.5**	**-4.8**
Deviation from test results Max. in %	-11.4	-15.1	-8.3	-12.4	-18.2	-10.7	-11.3	-5.6	-14.8	-14.9
Deviation from test results Min. in %	10.2	18.2	26.0	21.5	19.2	33.9	20.1	19.2	19.9	8.5

For the reference system (**System A**) an air-to-water HP with a standard cycle (see Fig. 5) with accumulator and R410A as refrigerant was assumed. A speed controlled compressor with a speed range is 22 – 100 % used. The parameterized heat pump model results in a thermal capacity of 7.7 kW and a COP of 2.72 at the operating conditions A-10W35 and 10.8 kW and COP 3.39 at A2W35, both at full compressor speed.

Simulation results with the parameterized model were compared with test results for air-source heat pumps from a HP test center (NTB Buchs, 2018). An average of the COP results of all tested units with the refrigerant R410A and a heat output of up to 15 kW was determined for different operating conditions. In Table 1, the COP values resulting from simulations are compared with those of the test results. It can be seen that for all considered operating points, the simulation results are between the best and worst test results and mostly higher than average.

For **System B** a heat pump cycle with the natural refrigerant R290 (propane) was used. Propane offers superior properties especially concerning the compressor discharge temperature, which enables higher condensation temperatures and generally wider operational limits of the compressor. This offers advantages for the here discussed system with high flow temperatures and especially for the coupling with PV and overcharging to higher temperatures. The compressor used for this HP has a speed range of 17 to 100 %.

Additionally, a subcooler is used in the refrigerant cycle, which offers advantages concerning the COP, especially if the temperature difference on the heat sink side is large, as it is in the case of a radiator heating system. An exemplary operating point is shown in Fig. 5 in a temperature-enthalpy diagram for a standard cycle and a cycle with additional subcooler. Simulations have shown that the subcooler improves the COP compared to a standard HP cycle without any subcooling by 4-7 % over the whole range of operating conditions.

A prototype of this HP was built by the industrial partner and measurements were carried out in the climate chamber of IWT. In total 50 different steady-state operating conditions[1] were measured, including defrosting cycles and an analysis of start/stop losses. The HP model used for the simulations of System B was parameterized using these measurements. The parameterized model results in a thermal capacity of 7.6 kW and a COP of 2.92 at the operating conditions A-10W35 and 10.2 kW and COP 3.82 at A2W35, both at full compressor speed.

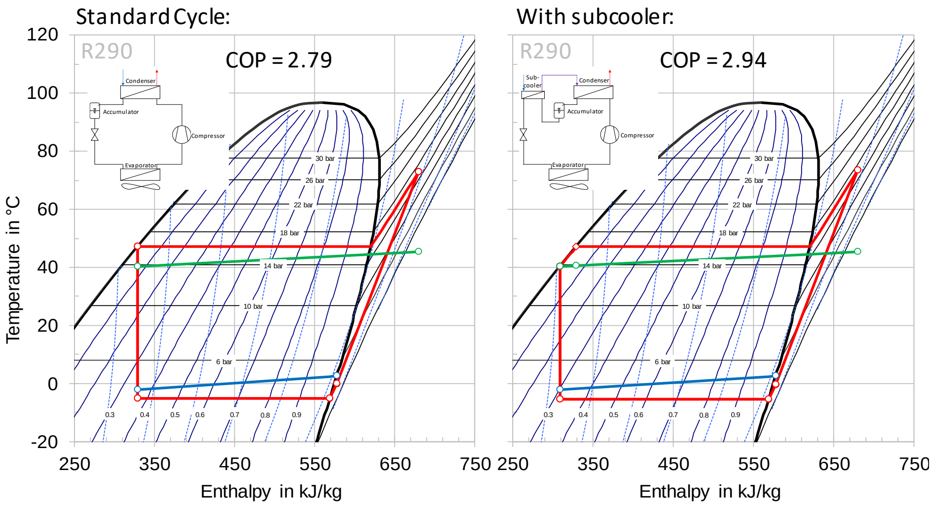

Fig. 5: T/h-diagram of an exemplary heat pump cycle with R290 @ A2W45 without (left) and with (right) subcooler

2.5 Storage tank

The combistore used in System B was optimized concerning the position of the inlets and outlets and of the temperature sensors by means of system simulations based on an initial configuration. For this purpose, the individual connection heights and sensor positions were varied in a large number of annual simulations within a certain range until and an optimum was found with regard to energy consumption.

Installations in the storage tank for efficient handling of the high volume flow rates of a heat pump to avoid inlet jet mixing were designed and selected using CFD simulations by the project partner SPF. The CFD simulations were carried out to find a suitable design for these diffusers. A total of 9 different geometries were simulated and their stratification behavior examined with simulations of both, hot water charging as well as the charging and discharging of the space heating zone.

The storage that was designed with the help of simulations was then tested on the test bench of SPF in dynamic operation, including the fresh water module for DHW preparation. A test method to measure the stratification efficiency as key performance indicator was used (Haller et al. 2018, Haller et al. 2019). The laboratory test is based on a 24-hour cycle, where realistic and dynamic charging and discharging is applied according to boundary conditions of real weather data of a day in the year. This work and the CFD optimization is described in detail in a second contribution to the EUROSUN 2020 conference by Haberl et al. (2020).

Based on the results of the 24-hour test the simulation models used for the annual TRNSYS simulations were parameterized. The storage tank was simulated using the one-dimensional multi-node model Type 340 (Drück, 2006), the fresh water module using Type 805 (Haller, 2007).

2.6 Photovoltaic system

For the photovoltaic panels the parameters of polycrystalline modules were used. The PV array was modelled using Type94a, based on the four-parameter equivalent circuit model (TRNSYS 17, 2014). The PV yield was calculated in every time step depending on the current solar radiation (diffuse and beam) and its incident angle

[1] Compressor speed range: 1700 to 7200 rpm,
heat source (air) temperatures: -10 to 12 °C,
heat sink temperatures: 35 to 65 °C

onto the PV panels. The efficiency of the inverter was assumed to be 0.94. In the basic variant of the system a PV size of 10 kWp is used, which is about the maximum that can be placed on the available roof area. A variation of the PV size is discussed later in the results section.

2.7 Control strategies

Concerning the control of the system three strategies are analyzed and compared:

- **Standard**: This is the basic control strategy that was used in System A and B for charging the storage tank(s). PV is only used by the heat pump if it is in operation by coincidence, when PV electricity is available. Charging of the DHW zone of the tank by the heat pump is started, if T_{DHW} < 45 °C (sensor position in Fig. 3 and Fig. 4) and is stopped, when T_{DHW} > 55 °C. The space heating zone is charged, if $T_{SH,on} < T_{fl}$ and stopped when $T_{SH,off} > T_{fl}$+2K, where T_{fl} is the flow temperature depending on the ambient temperature (Fig. 2).
- **PV$_{Store}$**: In this strategy, that was applied for System B in order to increase self-consumption and self-sufficiency (see section 3), the heat pump is used to overcharge the storage tank, when enough excess PV electricity is available. Whenever the available PV electricity exceeds the current household electricity demand by 0.7 kW the system is switched to "overcharging mode". This means that the DHW and space heating zone of the combistore are both heated to higher temperatures compared to strategy "Standard". Due to the operational limits of the compressor, overheating is done dependent on the ambient temperature (T_{amb}) to max. 60 °C when T_{amb} > 5 °C and to 55 °C if $T_{amb} \leq$ 5 °C. In this mode, the speed of the compressor is adapted in order to match the electricity consumption of the heat pump to the available PV excess electricity ($P_{el,PV,exc}$, Eq.1). Overcharging is stopped when either the storage temperature reaches the temperature limit or PV excess drops below 0.6 kW.
- **PV$_{Store}$ & PV$_{Troom}$**: For System B in addition to "PV$_{Store}$" the strategy "PV$_{Troom}$" makes use of the thermal inertia of the building structure. If the "overcharging mode" is active as described above, the set room temperature is increased by +0.5 K and otherwise decreased by -0.5 K, starting from the standard value of 22 °C. The basic idea is to shift heat generation into times with PV yield and to store heat in the building structure.

3 Performance figures

In order to enable a comparison of the analyzed variants of the system and the control the following performance figures were defined, all of them on an annual basis. The electricity consumption for the considered heating system ($W_{el,sys}$, Eq. 2) was calculated including the HP, pumps and the electrical heater. The energy that has to be drawn from the grid was determined both for the heating system ($W_{el,sys,grid}$, Eq. 3) and the whole building ($W_{el,grid}$, Eq. 4), including household (hh) electricity. This was done based on the time-step of one minute that was used in all simulations.

Three seasonal performance factors were determined. SPF_{HP} describes the performance of the HP as a component. The whole heating system was considered with SPF_{sys}, where only useful energy delivered for space heating (SH) and DHW was considered and the total electricity consumption of the system. Only taking into account the system's electricity consumption from the grid results in $SPF_{sys,PV}$.

The self-sufficiency ratio is the fraction of the electricity consumption that can be covered by PV and was calculated on the level of the heating system (SSR_{sys}) and for the whole building (SSR_{tot}) including household electricity. The fraction of PV electricity that is consumed on-site is expressed by the self-consumption ratio (SCR).

$$P_{el,PV,exc} = max\left(\left(P_{el,PV} - P_{el,hh}\right), 0\right) \qquad \text{Eq. 1}$$

$$W_{el,sys} = \int \left(P_{el,HP} + P_{el,pumps} + P_{el,heater}\right) dt \qquad \text{Eq. 2}$$

$$W_{el,sys,grid} = \int max\left(\left(P_{el,sys} - P_{el,PV,exc}\right), 0\right) dt \qquad \text{Eq. 3}$$

$$W_{el,grid} = \int max\left(\left(P_{el,sys} + P_{el,hh} - P_{el,PV}\right), 0\right) dt \qquad \text{Eq. 4}$$

$$W_{el,feedin} = \int max\left((P_{el,PV,exc} - P_{el,sys}),0\right) dt \qquad \text{Eq. 5}$$

$$SPF_{HP} = \frac{\int \dot{Q}_{cond} dt}{W_{el,HP}} \qquad \text{Eq. 6}$$

$$SPF_{sys} = \frac{\int (\dot{Q}_{SH} + \dot{Q}_{DHW}) dt}{W_{el,sys}} \qquad \text{Eq. 7}$$

$$SPF_{sys,PV} = \frac{\int (\dot{Q}_{SH} + \dot{Q}_{DHW}) dt}{W_{el,sys,grid}} \qquad \text{Eq. 8}$$

$$SSR_{sys} = 1 - \frac{W_{el,sys,grid}}{W_{el,sys}} \qquad \text{Eq. 9}$$

$$SSR_{tot} = 1 - \frac{W_{el,grid}}{W_{el,sys} + W_{el,hh}} \qquad \text{Eq. 10}$$

$$SCR = 1 - \frac{W_{el,feedin}}{W_{el,PV}} \qquad \text{Eq. 11}$$

$$Net\ el. Costs = W_{el,grid}\ c_{Purchase} - W_{el,feedin}\ c_{feedin} \qquad \text{Eq. 12}$$

The net electricity costs (Eq. 12) were calculated considering the total electricity consumption from the grid including household electricity ($W_{el,grid}$) and the amount of PV electricity sold to the grid ($W_{el,feedin}$). For the results shown in this paper an electricity purchase price $c_{purchase}$ of 0.18 €/kWh was assumed and a feed-in tariff c_{feedin} of 0.05 €/kWh, which currently are typical values in Austria.

4 Results and discussion

The simulation results are summarized in Table 2 for the systems A and B in form of the defined performance figures. System A, which was simulated only with the control strategy "Standard", was used as the reference case within the project with the objective of saving 25 % of electricity drawn from the grid ($W_{el,sys,grid}$). Simulations for System B were carried out with the three control strategies described in section 2.7.

Tab. 2: Performance figures for the simulated systems and control variants, difference compared to the reference system (System A) is indicated in brackets

System		System A (Reference system)	System B		
Control		**Standard**	**Standard**	**PV_{Store}**	**PV_{Store} & PV_{Troom}**
$W_{el,sys}$	kWh/a	6726	5919 (-12.0 %)	6367 (-5.3 %)	6242 (-7.2 %)
$W_{el,sys,grid}$	kWh/a	5807	5032 (-13.3 %)	4359 (-24.9 %)	3964 (-31.7 %)
$W_{el,grid}$	kWh/a	7902	7127 (-9.8 %)	6454 (-18.3 %)	6059 (-23.3 %)
$W_{el,feedin}$	kWh/a	6877	6909 (+0.5 %)	5788 (-15.8 %)	5518 (-19.8 %)
SPF_{HP}	-	2.71	2.99 (+10.6 %)	2.86 (+5.6 %)	2.90 (+7.2 %)
SPF_{sys}	-	2.27	2.57 (+13.2 %)	2.39 (+5.3 %)	2.43 (+6.8 %)
$SPF_{sys,PV}$	-	2.63	3.02 (+14.9 %)	3.49 (+32.8 %)	3.82 (+45.2 %)
SSR_{sys}	-	0.19	0.21 (+7.1 %)	0.32 (+63.9 %)	0.35 (+81.1 %)
SSR_{tot}	-	0.14	0.15 (+9.6 %)	0.32 (+131 %)	0.36 (+167 %)
SCR	-	0.21	0.21 (-1.7 %)	0.34 (+57.9 %)	0.37 (+72.2 %)
Net el. Costs	€/a	1078	937 (-13.1 %)	872 (-19.1 %)	815 (-24.5 %)

Applying the control "Standard" both for System A and System B shows that the improved HP and storage setup results in a reduction of the system electricity consumption ($W_{el,sys}$) of 12 % and that 13 % less electricity has to be drawn from the grid ($W_{el,sys,grid}$). Detailed energy balances of the heating system for the simulated variants are shown in Fig. 6. Compared to the reference, system SPF_{HP} is increased by 10 % (Table 2) due to better overall efficiency of the R290 cycle with the subcooler, although the HP losses of the prototype configuration are higher than what was assumed for the HP of the reference system (Fig. 6). Storage losses are reduced by about 200 kWh despite of the two times larger volume, due to slightly better insulation and better surface area to volume ratio of one large store compared to two small ones.

Electrical energy balances including household electricity are shown in Fig. 7. A fraction of 31 % of the household electricity can be covered by PV in all considered variants. This is independent of the used control strategies, as they only influence the heating system and not the household electricity consumption.

With the control "Standard" and the assumed PV size of 10 kWp, a system self-sufficiency ratio SSR_{sys} of 19 % is achieved for System A, whereas System B reaches 21 %. This is mainly due to the lower energy consumption $W_{el,sys}$. The net electricity costs are 13 % lower for System B compared to System A due to lower electricity consumption from and slightly higher feed-in into the grid.

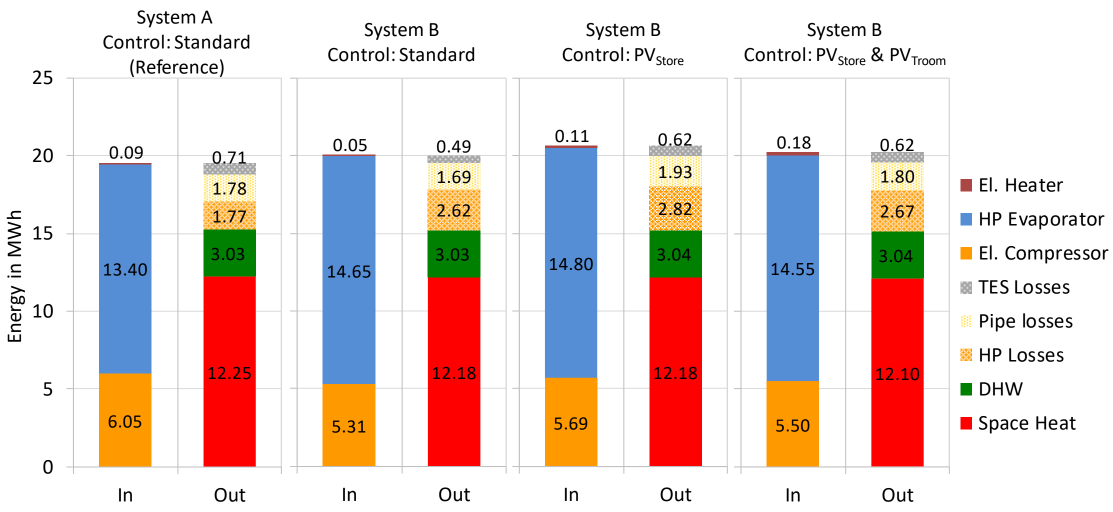

Fig. 6: Energy balance for System A and System B with different control strategies; Energy flow into the system is shown on the left (In), energy consumption and losses on the right (Out)

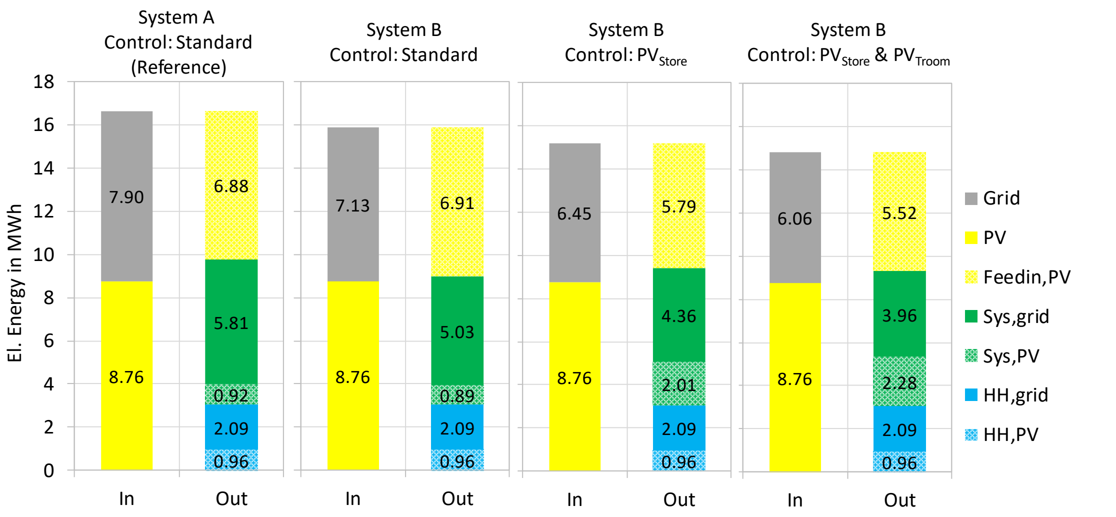

Fig. 7: Electrical energy balance for System A and System B with different control strategies

Applying control strategy "PV_{Store}" to System B results in a reduction of SPF_{HP} and increased electricity consumption of the system $W_{el,sys}$. This is due to the HP being increasingly operated with higher condensation temperatures, when overheating of the store is performed in times of available PV electricity and higher heat losses from the store and from the pipes. However, SSR_{sys} is increased to 32 %, and $W_{el,sys,grid}$ is reduced by 13 % compared to System B with the control "Standard" and by almost 25 % compared to the reference system. This means that according to the simulation results the project objective of 25 % lower grid electricity can already be reached with System B and this control strategy.

SCR is increased from 21 to 34 %, as PV feed-in into the grid is reduced by about 1100 kWh compared to strategy "Standard". Actually, grid feed-in is reduced more than grid consumption, which is a result of the higher overall electricity consumption due to overcharging of the store. However, with the assumed feed-in tariff of 0.05 €/kWh compared to a consumption price of 0.18 €/kWh the net el. costs are reduced by 65 €/a.

If the strategy "PV_{Troom}" is applied additionally, grid consumption $W_{el,sys,grid}$ can be further reduced to 3964 kWh and the self-sufficiency ratio SSR_{sys} is increased to 36 %. So the variation of the room temperature of only ± 0.5 K causes an additional decrease of grid consumption of 9 % compared to "PV_{Store}". Concerning the overall project objective a reduction of $W_{el,sys,grid}$ of about 32 % is possible compared to the reference system by applying both "PV_{Store}" and "PV_{Troom}". Compared to "PV_{Store}" electricity costs are reduced by another 57 €/a.

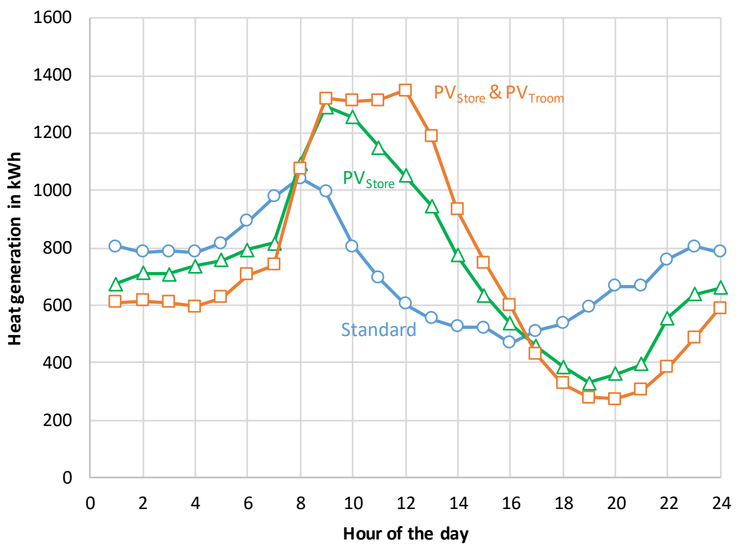

Fig. 8: Annual sum of heat generated by the HP at hours of the day with different control strategies

Both applied control strategies cause a shift of HP operation into times, where PV electricity is available, which naturally results in a shift from night to day. This can be seen in Fig. 8, which shows the annual sum of heat generated by the HP at different hours of the day for the three used strategies. On the one hand, this shift means that the HP tends to be operated with higher evaporation temperatures, as the ambient temperature is higher during the day than in the night and early morning hours. On the other hand, overcharging of the store causes higher condensation temperatures, which in the end leads to a lower SPF_{HP} compared to the strategy "Standard".

An interesting aspect about strategy "PV_{Troom}" is that the space heating demand remains almost unchanged compared to the other strategies (Fig. 6), although an adaptation of the room temperature depending on available PV excess electricity is done. The reason is that the adaption in both directions (± 0.5 K) causes the room temperature to be on average very similar to strategy "Standard". This is shown in Fig. 9 with hourly average values of the room temperature and annual duration curves of the room temperature for both strategies. Concerning thermal comfort a room temperature variation in this range should not be a problem.

A simulation variant that was carried out with only increasing the set room temperature in times of available PV (+ 1 K) showed that this also decreases the grid consumption, but to a much lower extent. This is due to an increase of the space heating demand and therefore also the overall system electricity consumption. Due to the increased consumption a larger fraction of PV electricity is consumed on site and a smaller fraction is fed into the grid. This also causes disadvantages concerning the net electricity costs compared to the here used strategy PV_{Troom}.

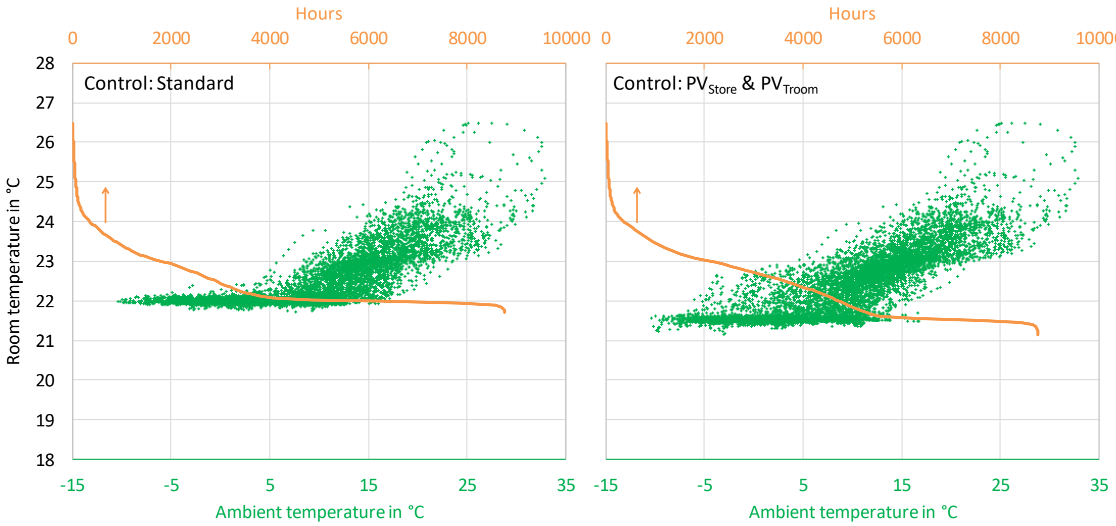

Fig. 9: Room temperatures (hourly averages) as function of the ambient temperature and annual duration curve of the room temperature for System B with the control strategies "Standard" and "PV$_{Store}$, PV$_{Troom}$"

All results presented up to here apply to the initially assumed PV capacity of 10 kWp. With this size the self-consumption ratio SCR is 37 %, so a large fraction of the PV electricity is fed into the grid. Now it would be interesting to see how the results change when a smaller PV system is used. Thus, the PV size was varied between 1 and 10 kWp to analyze the influence. The results are shown in Fig. 10 for System B with the control strategies "Standard" and "PV$_{Store}$ & PV$_{Troom}$". As expected, $W_{el,sys,grid}$ and $W_{el,grid}$ increase with decreasing PV size, while $W_{el,feedin}$ decreases. However, the increase of grid consumption is much lower than the decrease of feed-in. For example, if the PV system is changed from 10 to 5 kWh, $W_{el,grid}$ increases by 620 kWh, while $W_{el,feedin}$ decreases by 3740 kWh (strategy "PV$_{Store}$ & PV$_{Troom}$").

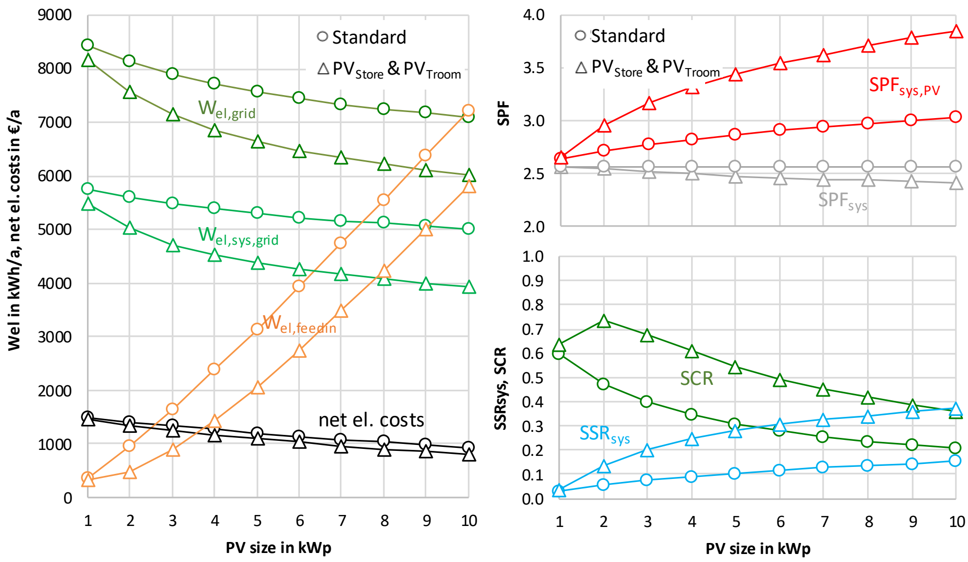

Fig. 10: Influence of the PV size on the system performance for System B with the control strategies "Standard" and "PV$_{Store}$ & PV$_{Troom}$"

Decreasing the PV size results in a reduction of $SPF_{sys,PV}$, but an increase of SPF_{sys}. The latter is because a larger amount of available PV electricity leads to increased overcharging of the store and therefore higher overall electricity consumption. For strategy "Standard" SPF_{sys} is independent of the PV size, as here HP and PV are operated "in parallel" without interaction.

The self-consumption ratio SCR increases with decreasing PV size, with a maximum of 74 % at 2 kWp. With the smallest size of 1 kWp, SCR decreases, which is mostly due to the criterion for switching on the PV overcharging (see section 2.7), which is hardly reached with this very small size. The maximum self-sufficiency ratio SSR_{sys} of 37 % is achieved with the largest PV size, but in this case with a SCR of only 36 %.

5 Conclusions and Outlook

The results of the performed analysis show that a hybrid system combining an air-source heat pump with PV is a possibility to significantly reduce the electricity consumption and the operative costs of the considered heating system in a renovated building with high supply temperatures and a heating demand (space heating and DHW) of about 15200 kWh.

With the shown combination of a dedicated HP, optimized integration of a combistore and targeted operation of the HP with electricity from a 10 kWp PV system, a reduction of the electricity consumption from the grid of 32 % compared to a reference system with the same PV size is possible. If only electricity from the grid is considered, the system seasonal performance factor ($SPF_{sys,PV}$) is 3.8, which is in the range of a ground source HP in combination with a low-temperature heating system.

Using a heat pump in combination with a low-temperature heating system should of course always be preferred and could achieve even better overall results if combined with PV. However, current market practice shows that existing high-temperature systems are often not replaced during renovations and here a combination with PV is an attractive solution to significantly save energy, CO_2 emissions and costs.

The net electricity costs (considering also PV electricity sold to the grid) of the proposed system are 264 €/a lower than for the reference system, assuming an electricity purchase price of 0.18 €/kWh and a feed-in tariff of 0.05 €/kWh. Compared to the reference system without any PV the cost savings are 946 €/a. Assuming investment costs for a PV system in the range of 1300 to 1700 €/kWp the PV installation should pay off well within the lifetime.

One noteworthy aspect about the results is that the project objective of 25 % reduction of grid consumption of the system can easily be achieved also with a smaller PV size. With only 5 kWp -24.8 % are possible compared to the reference system, for which a PV size of 10 kWp was assumed. Compared to a reference system without any PV the reduction is 35 %. A smaller size could be especially interesting due to the larger fraction of electricity consumed on-site, as feed-in tariffs are likely to further decrease in the future.

The main components of the proposed system have already been tested in the laboratory of IWT (heat pump) and SPF (storage tank), whereby the results of these measurements were considered in the parametrization of the used simulation models. The complete hybrid heating system is currently assembled at SPF in Rapperswil, where it will be tested in a 6-day Hardware-in-the-Loop system test, which enables an extrapolation to annual results. The aim of this test is to confirm the results of the simulation work carried out within the project and the calculated performance figures.

6 Acknowledgments

The project “HybridHeat4San” is funded by the Austrian Climate and Energy Fund and is carried out as part of the Energy Research Program 2016.

7 References

Amtmann M. (2010): ‘Scientific Report D6.9: Reference buildings - The Austrian building typology, A classification of the Austrian residential building stock. IEE - Intelligent Energy Europe.’ Österreichische Energieagentur – Austrian Energy Agency, 2010.

Bales C., Heinz A., and Haller M. (2012): ‘Deliverable 7.1 - Definition of Boundary Conditions, FP7 project MacSheep (grant agreement 282825)’, 2012.

Battaglia M., Haberl R., Bamberger E., Haller M. (2017): ‘Increased self-consumption and grid flexibility of PV and heat pump systems with thermal and electrical storage’, Energy Procedia, vol. 135, pp. 358–366, Oct. 2017.

Biberacher M. (2010): ‘Räumliche Modelle als Entscheidungsgrundlage für die Inwertsetzung regional verfügbarer Energiepotenziale zur CO_2-neutralen Deckung des lokalen Wärmebedarfs’, 2010.

Dott R., Haller M. Y., Ruschenburg J., Ochs F., Bony J., 2013: 'The reference framework for system simulations of the IEA SHC Task 44/HPP Annex 38 Part B: buildings and space heat load', International Energy Agency, 2013.

Dott R., Afjei T., Genkinger A., Dalibard A., Carbonell D., Consul R., Heinz A., Haller M., Witzig A., Facão J. (2013): Models of sub-components and validation for the IEA SHC Task 44/HPP Annex 38 Part C: heat pump models. International Energy Agency, A technical report of subtask C Deliverable C 2.

Drück H. (2006): „MULTIPORT Store-Model for TRNSYS, Type340. Version 1.99F, March 2006". 2006.

EC (2013): 'Commission Delegated Regulation (EU) No 812/2013 of 18 February 2013 supplementing Directive 2010/30/EU of the European parliament and of the Council with regard to the energy labelling of water heaters, hot water storage tanks and packages of water heater and solar device'. 06-Sep-2013; https://eur-lex.europa.eu/legal-content/DE/TXT/PDF/?uri=OJ:L:2013:239:FULL&from=DE.

Haberl R., Schmidli J., Heinz A., Kalkgruber J. & Haller M.Y. (2020): A Combi Storage for Combination with Heat Pumps - From Simulations to the Test Bench Results. In: Proc. of the EuroSun 2020 Conference, Athens, Greece.

Haller H. (2007): 'Type 805: DHW heat exchanger, Version 1.1', SPF Institute for Solar Technology, 2007

Haller M.Y., Haberl R, Persdorf P, Reber A. (2018): Stratification Efficiency of Thermal Energy Storage Systems – A new KPI based on Dynamic Hardware in the Loop Testing - Part I: Test Procedure. Energy Procedia 2018;155:188–208. https://doi.org/10.1016/j.egypro.2018.11.056.

Haller MY, Haberl R, Reber A. (2019): Stratification efficiency of thermal energy storage systems – A new KPI based on dynamic hardware in the loop testing - Part II: Test results. Energy and Buildings 2019;202:109366. https://doi.org/10.1016/j.enbuild.2019.109366.

Hengel F., Heinz A., Rieberer R. (2014): Analysis of an air source heat pump system with speed controlled compressor and vapor injection; in: 11th IEA Heat Pump Conference., pp. 1–15.

Jordan U., Vajen K. (2012): 'DHWcalc - Tool for the Generation of Domestic Hot Water (DHW) Profiles on a Statistical Basis'. Universität Kassel, Institut für Thermische Energietechnik, 2012.

LoadProfileGenerator (2018). [Online]. Available: http://www.loadprofilegenerator.de/. [Accessed: 07-Mar-2018].

NTB Buchs (2018): Prüfresulate Wärmepumpen; NTB Buchs, Institut für Energiesysteme IES - Wärmepumpen Testzentrum WPZ. Available online: https://www.ntb.ch/fue/institute/ies/wpz/pruefresultate-waermepumpen/. [accessed: 06-Feb-2018].

Pflugradt N. D. (2016): 'Modellierung von Wasser- und Energieverbräuchen in Haushalten', Dissertation, Technische Universität Chemnitz, 2016.

Schramek E. R., Recknagel H. (2007): "Taschenbuch für Heizung + Klimatechnik 07/08". Oldenbourg Industrieverlag, ISBN 10: 3-8356-3104-7, 2007

Tabula (2018): 'TABULA WebTool'. [Online]. Available: http://webtool.building-typology.eu/?c=all#bm. [Accessed: 31-Jan-2018].

Thür A., Calabrese T., Streicher W. (2018): 'Smart grid and PV driven ground heat pump as thermal battery in small buildings for optimized electricity consumption', Solar Energy, vol. 174, pp. 273–285, Nov. 2018.

Toradmal A., Kemmler T., Thomas B. (2018): 'Boosting the share of onsite PV-electricity utilization by optimized scheduling of a heat pump using buildings thermal inertia', Applied Thermal Engineering, vol. 137, pp. 248–258, Jun. 2018.

TRNSYS (2014): „TRNSYS 17: a Transient System Simulation Program, Volume 4: Mathematical Reference. Solar Energy Laboratory, University of Wisconsin-Madison". 2014.

TRNSYS 17 (2014): „TRNSYS 17: a Transient System Simulation Program, Volume 4: Mathematical Reference. Solar Energy Laboratory, University of Wisconsin-Madison". 2014.

Fault Detection for Solar Thermal Systems - Overall System Evaluation or Component-Oriented Approach

Christoph Schmelzer[1], Matthias Georgii[1], Janybek Orozaliev[1] and Klaus Vajen[1]

[1] Institute of Thermal Engineering, University of Kassel, Kassel (Germany)

Abstract

The paper at hand describes an FSC-based method to automatically assess the performance of a solar combi system. The impact of both inexpensive and improved sensor equipment on the detection accuracy is investigated, capabilities and limitations of this approach are discussed. Advantages and disadvantages of this overall system evaluation are compared to those of the standard fault detection system by means of a component-oriented approach.

Keywords: Solar heating, yield control, function control, monitoring, fault detection

1. Overall System Evaluation – FSC-based approach

This section gives a short overview of the Fractional Solar Consumption (FSC) in application to assessing the performance of a solar combi system. More details on the capabilities and limitations of this approach can be found in (Schmelzer et. al. 2018, Georgii et. al. 2019).

The overall system evaluation is based on FSC, which was developed in IEA SHC task 26 to compare solar combi systems with different system designs at different locations in Europe (Letz, 2002). The underlying principle is illustrated in fig. 1: to determine the maximum solar fraction, the usable solar radiation (orange dashed area) is divided by the reference demand (green + orange dashed area). The usable solar radiation is calculated by comparing the radiation on the collector plane and the measured heat demand (with estimated storage losses), taking into account that solar excess radiation in summer cannot be used.

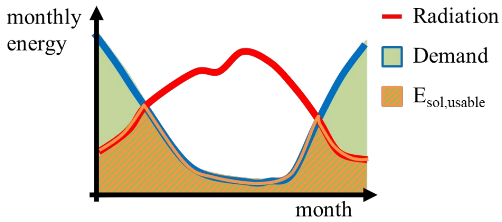

Fig. 1: Comparison of monthly energy demand and solar radiation to determine the maximum usable solar energy for a specific building, dhw demand, collector area, slope and tilt (Letz, 2002)

FSC does not depend on any system design aspects (except the collector area), but on the total irradiation on the collector plane and the demand. Therefore, it describes the energetic boundary conditions for the system. To calculate FSC, the heat demand for domestic hot water Q_{dhw} (incl. circulation) and space heating Q_{sh} must be measured. Since the storage in solar heating systems is larger compared to a reference system, the storage losses for the reference $Q_{loss,ref}$ are estimated using eq. 1. The equation considers a storage size of 75 % of the daily dhw draw-off.

$$Q_{loss,ref} = 0.16\frac{\mathrm{W}}{\mathrm{K}}\sqrt{0.75 \cdot \left(\frac{1}{\mathrm{d}}\right)^{-1} \cdot V_{dhw,daily}} \cdot (52.5 - 15)\mathrm{K} \cdot \Delta t \qquad \text{(eq. 1)}$$

With these losses, the reference energy E_{ref} can be calculated as follows:

$$E_{ref} = Q_{dhw} + Q_{sh} + Q_{loss,ref}. \qquad \text{(eq. 2)}$$

As described above, the usable solar energy is calculated as sum of monthly minima of the irradiation on the collector plane $(A_{col} \cdot H_{t,m})$ and the heat demand E_{ref} for the whole year:

$$E_{sol,usable} = \sum_{m=1}^{12} \min\left[\left(A_{col} \cdot H_{t,m}\right), E_{ref,m}\right]. \qquad \text{(eq. 3)}$$

The FSC is then calculated by dividing the usable solar energy by the reference energy demand:

$$FSC = \frac{E_{sol,usable}}{E_{ref}}. \qquad \text{(eq. 4)}$$

doi:10.18086/eurosun.2020.04.02 Available at http://proceedings.ises.org

There are some minor differences to the standard calculation approach described in (Letz, 2002). For simplicity, no boiler efficiencies were taken into account. In eqs. 2-4 only delivered energies are considered.

To assess the systems performance, another key figure describing the actual system behaviour is needed. In the following, this is done by a slightly adjusted definition of the fractional solar savings f_{sav}. Normally, boiler efficiencies and a (simulated) reference for the auxiliary energy are required to calculate f_{sav}. By assuming that the boiler efficiencies are almost the same and estimating the storage losses according to eq. 1, f_{sav} can be calculated as follows:

$$f_{sav} = 1 - \frac{Q_{aux,delivered}}{E_{ref}} . \qquad \text{(eq. 5)}$$

In (Letz, 2002) quadratic correlations are used to describe the relation between the expected f_{sav} (for fault free systems) and FSC. In the present approach power functions are chosen (see eq. 6), which enable the correction of several influential parameters (Georgii et. al. 2009).

$$f_{sav,expected} = e^{c_0} \cdot (FSC)^{c_{FSC}} \cdot (X_1)^{c_1} \cdot (X_2)^{c_2} \cdot (X_3)^{c_3} \cdot \ldots \qquad \text{(eq. 6)}$$

The underlying system simulations and the subsequent analysis showed that the following parameter must be considered for a reliable prediction of f_{sav}:

- Share of Q_{dhw} in $E_{sol,usable}$
- Ratio of auxiliary heated storage volume to daily dhw draw-off
- UA-value of the storage
- Specific storage volume (l/m^2_{coll})
- Boiler setpoint temperature

With the described set of formulas, the systems performance can be assessed automatically by calculating the measured energy savings $f_{sav,measured}$ (eq. 5) and comparing them to the expected savings $f_{sav,expected}$ for the fault-free system operation, using eq. 6. Fig. 2 illustrates the general principle.

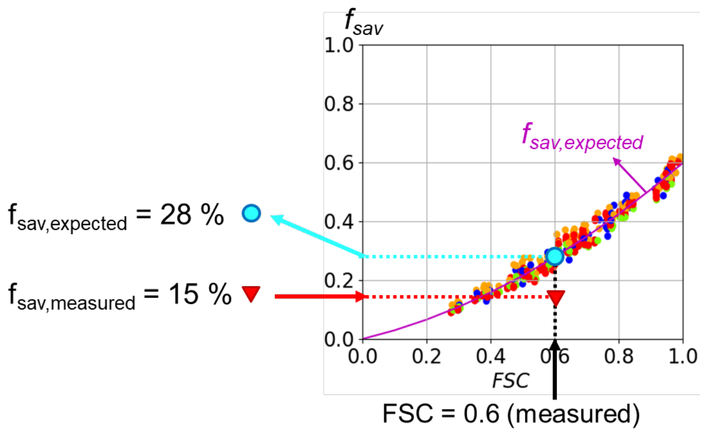

Fig. 2: System assessment with FSC – 1. Calculate $f_{sav,measured}$ with measured auxiliary energy – 2. Calculate $f_{sav,expected}$ using FSC correlations

Thus, the performance indicator PI can be calculated:

$$PI = \frac{f_{sav,measured}}{f_{sav,expected}} . \qquad \text{(eq. 7)}$$

With this easy-to-understand key figure, the system performance can directly be evaluated. The performance indicator can theoretically detect any fault with a significant impact on the solar energy yield.

2. Impact of measurement uncertainties on detection accuracy of FSC-based overall system evaluation

2.1 Methodology – Monte Carlo Analysis

To estimate the impact of different sensor equipment on the accuracy of the key figures and calculate respective uncertainties, a Monte Carlo Analysis (MCA) was performed. To do so, sensor data, previously modelled by simulations, was used as the true value of each sensor and then uncertainties were added as follows.

In the first step, the systematic sensor uncertainties u_{sys} are chosen normally distributed and independent of each other. The standard deviation for the normal distribution σ is set to be a half of the measurement uncertainty of the respective sensor (X):

$$\sigma = \frac{u_{X,sys}}{2}. \qquad \text{(eq. 8)}$$

This approach ensures that 95.5 % of the selected uncertainties lie within the specified limits. Conversely, this also means that 4.5 % of the measurement errors exceed the limits and show larger deviations. As an example, fig. 3 illustrates three different fixed systematic errors for a sensor measuring temperature or temperature difference. The 2σ range [-0.8K, 0.8K] is marked in magenta. Three specific systematic uncertainties each fixed for one calculation run, are depicted by blue, green and cyan arrows. The mean of the normal distribution is chosen at 0 K, meaning that randomly chosen uncertainties are most likely much smaller than the specified limit. However, there is a small probability of 4.5%, that the randomly chosen value exceeds the 2σ range, e.g. the cyan arrow in fig. 3. At the end of step one, each signal gets shifted by its offset (fig. 4, left).

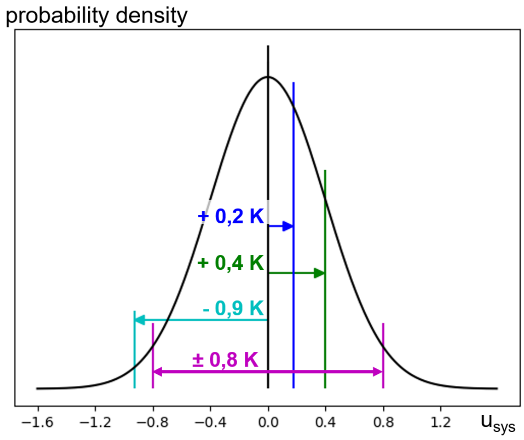

Fig. 3: MCA – Exemplary selection of systematic uncertainties for temperature or temperature difference measurement

In the second step, normally distributed stochastic noise is applied to the data (with a standard deviation equal to half of the maximum error of each sensor and the mean value equal to zero), see fig. 4, right.

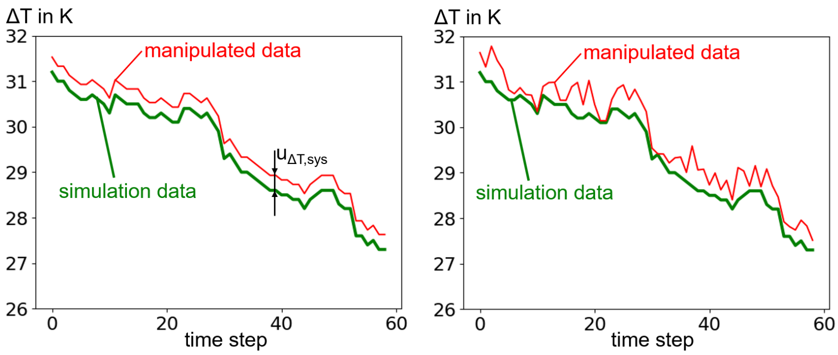

Fig. 4: MCA – Exemplary selection of systematic uncertainty (shift on the left) and stochastic noise (on the right) for a temperature difference

Finally, the monthly energies and key figures are calculated using sensor data manipulated in two previous steps.

To obtain reliable probability distributions for the system key figures, it is required by the MCA to repeat these three steps very often (in this paper n = 1,000 times). In this way, a large number of randomly selected systematic uncertainties is taken into account. From the distributions 68 % and 95.5 % quantiles can be derived, which can be used as a measure for the resulting uncertainties for f_{sav} and FSC. In the following, the 95.5 % quantiles are used.

2.2 Impact of inexpensive sensor equipment on detection accuracy

Since the additional costs are crucial for the implementation of a fault detection system, first step was to investigate the impact of an inexpensive reference measurement equipment on the fault detection accuracy. The reference sensor equipment consists of the following sensors:

- Temperature sensors: Class B
- Flow measurement: Vortex Sensors (accuracy ± 5 % RD)
- Radiation: Estimated via satellite data

Fig. 5 illustrates the resulting uncertainties for f_{sav} and FSC for one example system and their impact on the detection accuracy of the system evaluation. The black circle shows the actual f_{sav}-FSC-value for one specific combi system in Germany with a collector area of 20 m². As displayed by the red error bars, the key figures cannot be determined very precisely. The actual f_{sav} = 34 % and FSC = 66 % can only be roughly estimated due to inaccuracy of the sensor equipment at the following ranges: f_{sav} = (22..46) %, FSC = (57..75) %.

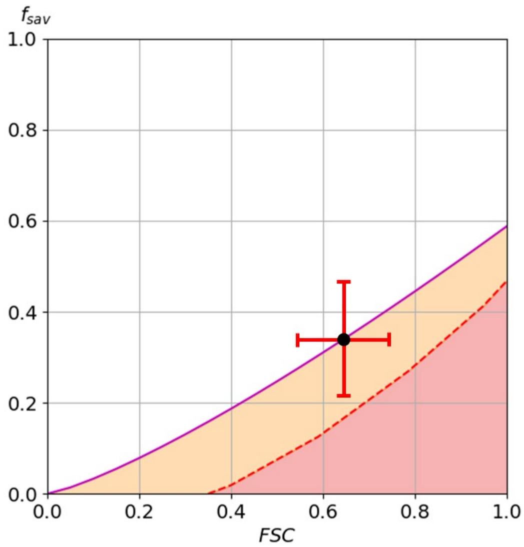

Fig. 5: Impact of inexpensive sensor equipment on detection accuracy

Moreover, the uncertainties have a strong impact on the detection accuracy and on the informative value of the system assessment. The orange area in fig. 5 illustrates the resulting uncertainties for the correlation. The dotted red line shows the minimum f_{sav} for systems with this measurement equipment, that still might be close to the theoretical correlation. Only if the measured f_{sav} lies within the red area it is certain, that there must be a fault in the system causing a detectable reduced energy yield. This also means that the fault detection is not possible where the red area is zero. Thus, for the inexpensive sensor equipment, the detection is only applicable for systems with f_{sav} > 18 % or an FSC > 35 %.

2.3 Cost-efficient measurement equipment

To reduce measurement uncertainties and therewith enhance detection accuracy, a cost-efficient solution must be found. Based on an extensive market research, costs for different sensors were identified (end user prices for Germany incl. VAT and installation). Then, each sensor was improved separately and the effect on f_{sav} and FSC was analysed. In this way, the most influential sensors can be determined and reasonable sensor combinations for improving the detection accuracy identified. A detailed analysis of the effects of single sensors on the measured heat quantities in each loop can be found in (Schmelzer et. al. 2019). Fig. 6 shows the resulting costs and uncertainties. On the y-axis the improved uncertainties of f_{sav} and FSC are divided by the uncertainty of the reference sensor equipment, see 2.2. On the x-axis costs of different sensor improvements are shown. Starting with the reference sensor equipment at total costs of approx. 1,000€, the first step is replacing the temperature sensors in the auxiliary and space heating loops by class AA sensors. In the second step, additionally, the dhw temperature sensors are improved to class AA sensors, water meters are placed in aux and sh loop and a radiation sensor is installed. Steps 3, 4 and 5 show the additional impact of heat meters in different loops.

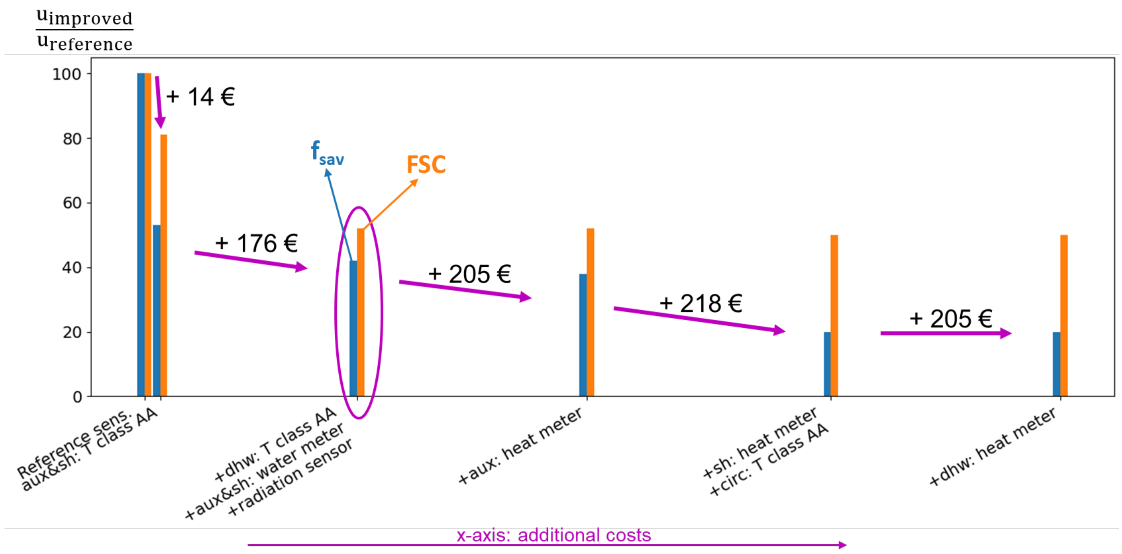

Fig. 6: Costs for improving sensor accuracy and impact on uncertainty of resulting key figures f_{sav} and FSC

As fig.6 illustrates, the first two steps have the largest impact on uncertainty of both key figures, while still being reasonably priced. For additional 190 €, the uncertainties of f_{sav} and FSC can be reduced by 60 % and 50 %, respectively. In the further steps it can be seen that a heat meter in the auxiliary loop does not reduce the uncertainties noticeably, but a heat meter in the space heating loop has a significant impact on the accuracy of f_{sav}. Since the heat meter price (incl. installation) is about 200 €, application of heat meters is not considered in the following. To show the impact of an improved sensor equipment, the second step is chosen as the improved set of sensors (magenta ellipse in fig.6, improved: T class AA in aux, sh and dhw loops; water meter in aux and sh loops; radiation sensor).

2.4 Impact of improved sensor equipment

Fig. 7 illustrates the impact of the improved sensors on the uncertainty ranges for f_{sav} and FSC (green error bars) compared to the inexpensive reference equipment (red error bars). With the improved sensors the resulting uncertainty ranges of the example system are reduced significantly: The actual values of f_{sav} = 34 % and FSC = 66 % can be estimated at the following ranges: f_{sav} = (30..38) %, FSC = (61..71) %.

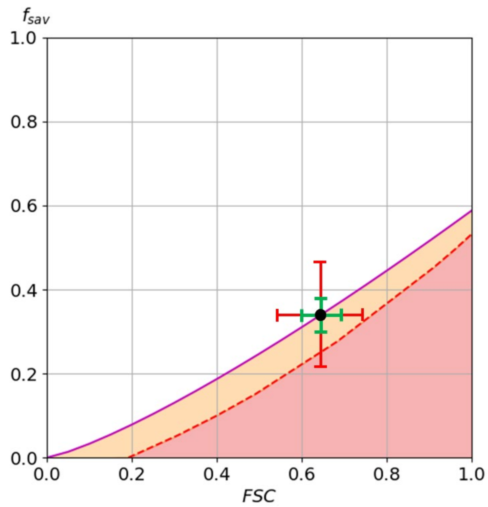

Fig. 7: Impact of improved sensor equipment on detection accuracy

The uncertainty range for the system assessment is also significantly reduced by this improvement. As fig. 7 shows, the yellow area is much narrower compared to the reference (see fig. 5). This means that the fault detection is possible for systems with a mean or predicted f_{sav} > 10 % and FSC > 20 %. Thus, the fault detection is applicable for a much wider variety of combi systems. Tab. 1 summarises the results of different sensor equipment.

Tab. 1: Impact of inexpensive and improved sensor equipment on system assessment

	Additional costs (approx.)	Uncertainty range of f_{sav} and FSC for example system	No assessment for systems with a mean f_{sav} or FSC if
Reference sens. equipment	1,000 €	f_{sav} = (34 ± 12) % FSC = (65 ± 8) %	f_{sav} < 18 % FSC < 35 %
Improved sens. equipment	1,200 €	f_{sav} = (34 ± 4) % FSC = (65 ± 5) %	f_{sav} < 10 % FSC < 20 %

3. Component-Oriented Approach

Instead of aiming at the most universal and powerful fault indicator, another approach is to make use of the already existing measurement equipment and to investigate, which information regarding the functionality of the STS can be derived. Often, this approach focuses on the assessment of single components rather than on the evaluation of the whole system. Fig. 8 shows a stepwise approach for an algorithm-based, component-oriented fault detection. In the first step, measured values are combined to generate features, e.g. a flow sensor can be used to calculate the feature "loop in operation" if the measured flow is above a specified threshold. If a feature or a combination of features reveal unusual or unexpected behaviour, a symptom is generated. E.g. if the temperatures in the solar loop are very high during operation. In the last step, faults in the system can be diagnosed or at least narrowed down by analysing the occurring symptoms.

Fig. 8: Stepwise approach for an algorithm-based, component-oriented fault detection

To develop algorithms for a specific fault, first the suspicious system behaviour (symptom) which points to this fault must be identified. On this basis, different detection paths can be investigated and tested with measured or simulated data. Depending on the required sensors, paths with low or no additional costs can be identified. E.g., if the pump in the solar loop stops working, this could easily be detected with a flow sensor, which, however, is usually not installed in small STS. One symptom related to this fault is, that no temperature difference between flow and return side is expected, even when the operation conditions are met (fig. 9). The operation conditions can be checked by the controller's pump signal (feature in magenta). The feature in cyan is an indicator for pump operation generated by using the flow and return temperatures only. In this STS, a valve in the solar loop was closed between 18th and 21st May 2016 to simulate a pump failure. As fig. 9 shows, the described symptom is reliably reported (green/red) on the days where the pump failure is simulated.

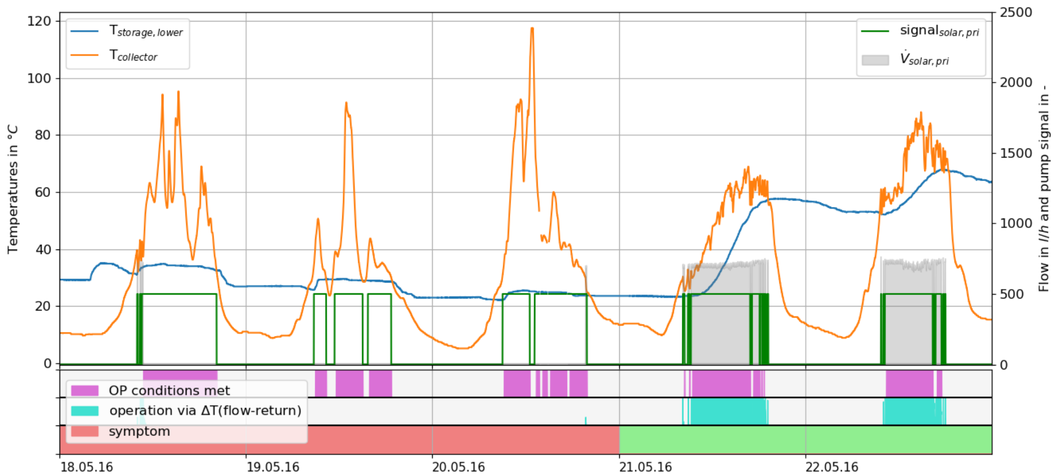

Fig. 9: Features and symptom for a pump failure detection, using controller signal and temperatures

4. Conclusion and comparison

The capabilities and limitations of the discussed approaches are summarised and compared in Tab. 2. On the one hand, the main advantage of the FSC-based overall system evaluation is its comprehensibility and, at the same time, simplicity of the PI indicator: the output describes the whole system and it can be understood without any background knowledge. Moreover, this approach automatically detects faults whenever the fractional solar savings f_{sav} are significantly reduced. Therefore, so the approach is reliable and automatically rates faulty states according to their impact on the energy savings, thus avoiding "unimportant" faults. On the other hand, the approach is only applicable for larger combi systems and has high additional costs of about 1,200 € because of the required precise measurement equipment. The FSC-based system assessment does not provide information on the possible cause for the reduced f_{sav}, and since 12 months of data are required to calculate the key figures, the reaction time is rather slow.

The component-oriented approach on the contrary addresses exactly these challenges. It is applicable for basically any system and reacts directly to faults that can be detected by available measurement equipment at no additional costs. Since the algorithms must be designed for specific faults or symptoms (suspicious system behaviour), the informative value of the output is much higher. However, often a component's behaviour must be derived indirectly, taking into account its interactions with other components. Hence, the prior information is required or (implicit) assumptions have to be made about a component's surrounding, i.e. to which other components it is linked, and which other signals are available. This means that it is much effort to take into account many different possibilities for both the surroundings of a component and the available measurement equipment, even when looking at just one fault or symptom. This has a negative impact on the level of automation and the comprehensibility of the delivered output. Instead of a single intuitive key figure, the different algorithms generate symptoms and create warnings if the system behaves unusually. These messages have to be "manually" analysed by the user or by sophisticated subsequent algorithms which still have to be developed. Additionally, it must be noted, that the capabilities and limitations for the algorithm-based approach significantly depend on the existing or planned measurement equipment. Starting with basic equipment at no additional costs, only few algorithms will be applicable and, thus, few faults detectable. If an extensive system assessment is to be implemented, the additional costs will increase.

Tab. 2: Comparison of Overall System Evaluation and Component-Oriented Approach

	Overall System Evaluation (FSC-based approach)	**Component-oriented approach (algorithm-based)**
Easy to understand	+	-
Reliable (no false alarms)	+	-
Automated	+	+
Low costs	-	+
Informative (what is wrong)	-	+
Applicable for any system	-	+
Response time	-	+

For larger solar combi systems, application of both approaches is recommended. In this way the assessment can benefit from the additional information and the fast response time of the algorithm-based approach on the one hand, and from the automated rating of the energetic impact of any fault on the other hand. For smaller solar assisted heating systems and other applications, the component-oriented, algorithm-based approach is still the only applicable option and should hence be considered early in the planning phase. It can be very beneficial, if additional (inexpensive) sensors are implemented in strategic places to enable the applicability of as many algorithms as possible.

Acknowledgments

We would like to thank the German Federal Ministry for Economic Affairs and Energy BMWi (FKZ 0325870A) and the PtJ, our scientific partners CEA INES, IGTE Stuttgart, and our project partners Bosch, Enertracting, RESOL, SOLVIS, Vaillant, Viessmann, and WILO.

References

Letz, T., 2002. Validation and background information on the FSC procedure. A Report of IEA SHC Task 26 – Solar Combisystems. URL: https://task26.iea-shc.org/Data/Sites/1/publications/task26-b-dc_procedure.pdf (last accessed 29.08.2020)

Georgii M., Schmelzer C., Kusyy O., Orozaliev J., Vajen K., 2019. Zur Verbesserung der Abschätzung der Leistungsfähigkeit thermischer Solaranlagen mittels FSC-Korrelationen. Proc. Symposium Solarthermie, Bad Staffelstein, 21.05.-23.05.2019

Schmelzer C., Georgii M., Kusyy O., Orozaliev J., Vajen K., 2018. Towards Automated Continuous Performance Benchmarking of DHW and Combi Systems. Proc. EuroSun, Rapperswil, Switzerland, 10.09.-13.09.2018. doi:10.18086/eurosun2018.01.10, URL: http://proceedings.ises.org/paper/eurosun2018/eurosun2018-0019-Schmelzer.pdf (last accessed 31.08.2020)

Schmelzer C., Georgii M., Kusyy O., Orozaliev J., Vajen K., 2019. Auswirkungen von Messunsicherheiten auf die Genauigkeit der Ermittlung von Wärmemengen in solarunterstützten Wärmeversorgungssystemen. Proc. Symposium Solarthermie, Bad Staffelstein, 21.05.-23.05.2019

A Parametric Study on the Feasibility of Solar-thermal Space Heating and Hot Water Preparation under Cold Climates in Central Asian Rural Areas

Kedar Mehta[1], Mathias Ehrenwirth[1], Christoph Trinkl[1], Wilfried Zörner[1] and Rick Greenough[2]

[1] Institute of new Energy Systems, Technische Hochschule Ingolstadt (Germany)

[2] Institute of Energy and Sustainable Development, De Montfort University, Leicester (UK)

Abstract

A large part of the Kyrgyz territory is covered by mountain ranges which result in extremely cold winter periods. The cold climatic conditions of Kyrgyzstan define heating as an essential need for Kyrgyz people. The majority of the residential buildings are constructed with poor thermal insulation or none at all, which yields high energy consumption in buildings to maintain thermal comfort. Especially in rural households, the heat demand is usually covered by solid fuels (i.e. wood, branches, coal and other solid fuels) burned in traditional stoves / boilers. The intensive use of solid fuels contributes to indoor and outdoor air pollution. Hence, there is a substantial need to provide sustainable and adequate heating services for residential buildings, particularly for the rural population. In response to this, the presented research article describes an investigation of solar resources to support space heating and domestic hot water preparation for single-family homes in rural Kyrgyzstan. Besides that, it identifies the thermal performance of typical single-family houses by considering local boundary conditions such as cold climate, high-altitude and routine behavior of the inhabitants. The determination of fuel savings by implementing solar-thermal domestic heating systems helps to explain the positive impacts on the environment. The investigation shows a significant solar-thermal energy potential available for domestic space heating and hot water preparation in Kyrgyzstan.

Keywords: cold climate, building, solar-thermal energy, space heating, domestic hot water

1. Introduction

The Kyrgyz Republic (Kyrgyzstan) is the former Soviet Union country located along the eastern edge of Central Asia, surrounded by Kazakhstan on the north, Uzbekistan on the west and southwest, Tajikistan on the southwest and China on the east (Fig. 1). It is a landlocked country with a population of 6.3 million people. The majority of the Kyrgyz population (66 %) lives in rural areas; in the foothills and mountain areas (NSC, 2018b). The Tien Shan mountain range occupies more than 85 % of the Kyrgyz territory and almost 90 % of the Kyrgyz territory is located 1,500 meters above sea level (NSC, 2018b).

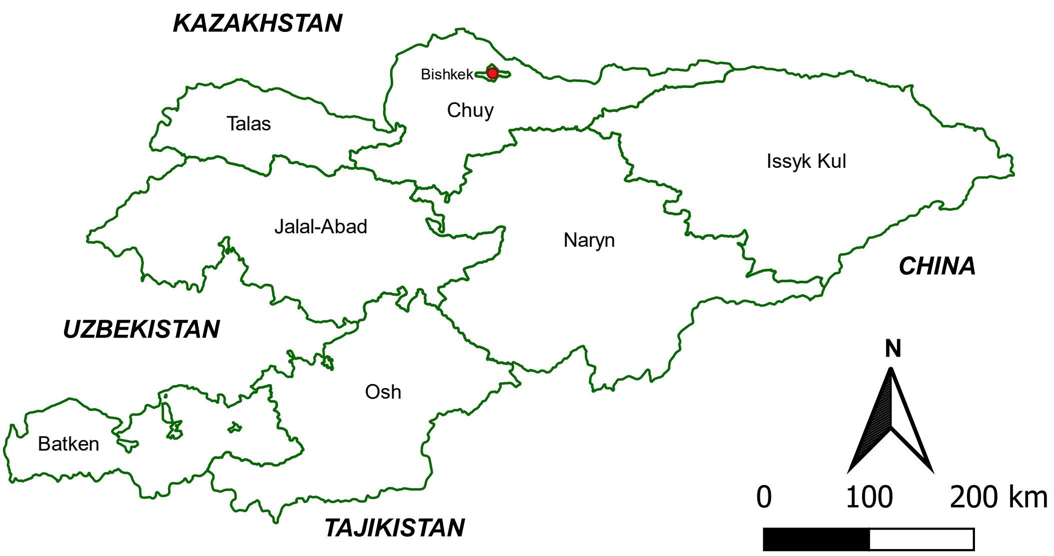

Fig. 1 Regional map of Kyrgyzstan

doi:10.18086/eurosun.2020.04.03 Available at http://proceedings.ises.org

A large part of the Kyrgyz territory is covered by mountain ranges with extremely cold winters with the temperatures ranging between about -4 °C to -6 °C in the lowlands and -25 °C to -30 °C in the mountainous valleys (Bergström and Johannessen, 2014). The cold climate is responsible for the long heating period of about six to nine months in the country. Hence, domestic heating is an essential need for the Kyrgyz population. The main three climatic zones of Kyrgyzstan are listed in Tab. 1 and are characterized by their approximate length of a heating season.

Tab. 1 Climatic zones of Kyrgyzstan (data according to Balabanyan (2015))

Region of Kyrgyzstan	Average outdoor air temperature during winter	Heating season length [days]	Heating Degree Days
Osh and Jalalabat	+1.4 ºC	135	2,240
Bishkek and Talas, Kara-Balta, Tokmok and cities in the Chui valley	-1.0 ºC	160	3,040
Naryn province, south-eastern areas of Issyk-Kul province	-6.9 ºC	197	4,905

The rural settlements in Kyrgyzstan are situated far away from major energy production centers and main economic centers, therefore they are less likely to have access to communal services such as connection to a district heating system, piped water into dwelling and sewage system. Further to this, most of the residential buildings in Kyrgyzstan were constructed during the Soviet era. Typical village houses in Kyrgyzstan are either built with poor insulation or even completely without insulation (Haab, 2017). Hence, residential buildings require a considerable amount of energy for space heating. Commonly, the high domestic heat demand is usually covered by solid fuels. Due to the lack of energy supply, the rural Kyrgyz population is forced to extract the energy they require from their surrounding environment. The cold weather conditions yield higher fuel consumption to meet domestic heat demand in rural areas of Kyrgyzstan.

The heavy reliance on natural resources by local people makes Kyrgyzstan most vulnerable to climate change among Central Asian regions (UNICEF, 2017). Furthermore, overuse of non-sustainable solid fuels is not favorable from both a health and an environmental point of view. On the other hand, the country has significant untapped renewable energy resources (UNDP, 2014). Therefore, this research paper aims to investigate the potential of the various renewable resources as well as how to meet the energy demand for domestic space heating and domestic hot water preparation of single-family houses in rural Kyrgyzstan with the available renewable energy resources.

2. Energy landscape of Kyrgyzstan

2.1 Current energy situation

The long-range of mountains results in a great number of glaciers and permanent snow in the country. Thus, abundant hydro resources are a keystone profile of Kyrgyzstan. The enormous water resources are used for 80 % of the total electrical power production by different small hydropower plants in Kyrgyzstan (Gassner et al., 2017). Access to electricity through the national grid is nearly universal in Kyrgyzstan, covering 99.8 % of rural and urban households (Gassner et al., 2017). The price of grid-supplied electricity in Kyrgyzstan is approximately 0.01 USD / kWh, which is the lowest electricity price in Central Asia (Gassner et al., 2017).

However, electricity is not a reliable source of energy for heating and is not preferred by the rural population. During winter, the river flow decreases, leading to reduced power production. The users experience frequent interruptions in the supply of electricity as well as fluctuations in voltage because of reduced power production in winter (FAO, 2016; IEC, 2018). Low-income, rural and mountainous households reportedly experience interruptions in electricity services weekly (FAO, 2016). Many rural households, especially in mountainous areas, do not have a permanent source of income because job opportunities are scarce. To increase their energy security, villagers collect heating fuel or purchase and store it whenever they have the financial capacity (Bakashova et al., 2013).

To survive with inconsistent energy supply as well as poverty, rural communities often switch to solid fuels to maintain thermal comfort of their houses. Access to the district heating (DH) networks is limited to urban areas, but even here they supply heat to only about 19 % of the urban population (Balabanyan, 2015). Close to 73 % of rural households are intensively using non-sustainable biomass or coal burned in traditional stoves / boilers for space heating (Balabanyan, 2015).

Rural households use a variety of solid fuels to meet domestic heat demand. Most rural families prefer to use coal or wood and less frequently animal dung. The on-site household survey revealed that during the heating period (October to March), a typical rural Kyrgyz household (with a floor area of ~ 100 m^2) consumes 2 to 5 tonnes of coal, 1.5 to 3m^3 of firewood and 1 to 2 truck of cow dung to maintain the thermal comfort in the house. People fulfil their primary need for warmth and this induces overuse of firewood, which is one of the major reasons for deforestation. Additionally, non-sustainable solid fuel use contributes to indoor and outdoor air pollution in Kyrgyzstan (World Bank and Factfish, 2015a, 2015b).

2.2 Renewable energy in Kyrgyzstan

Among various renewable energy resources, only hydro energy plays a significant role in the Kyrgyz energy sector. Besides the abundant hydro resources, Kyrgyzstan is blessed with good potential of solar, wind and biomass energy (UNDP, 2014). It is estimated that the country's total renewable energy potential of approximately 270 GW can replace up to 51 % of energy consumption in the country (Asian Development Bank, 2016). Due to the low and non-cost-effective-electricity tariffs and the strength of hydropower, other renewable energy sources are mainly untapped in Kyrgyzstan. Tab. 2 captures the estimated technical potential of renewable energy sources in the Kyrgyz Republic (UNDP, 2014).

Tab. 2 Technical potential of renewable energy (RE) sources in Kyrgyzstan (data according to UNDP (2014))

Type	Solar PV	Wind	Small hydro	Biomass
Technical Potential for Installed RE Capacity in MW	267,000	1,500	1,800	200
Installed renewable electricity capacity 2012 in MW	0	0	41.4	0

Kyrgyzstan is located in the Northern hemisphere between 39° and 43° latitude. Therefore, the high-altitude characteristic is responsible for more than 300 solar days in a year (Kampakis, 2015). The sunshine duration for Kyrgyzstan is between 2,100 to 2,900 hours annually (Kampakis, 2015; Baybagyshov and Degembaeva, 2019). As the altitude of the country is not uniform, the availability of solar irradiation deviates according to the individual location of the region. Though, the annual average solar irradiation of the country ranges between 1,500-1,600 kWh/m^2, which is almost 60 % higher as compared to Germany (World Bank, 2017). Fig. 2 illustrates the global horizontal irradiation of the Kyrgyz Republic. Nevertheless, the utilization of solar energy in Kyrgyzstan is barely developed.

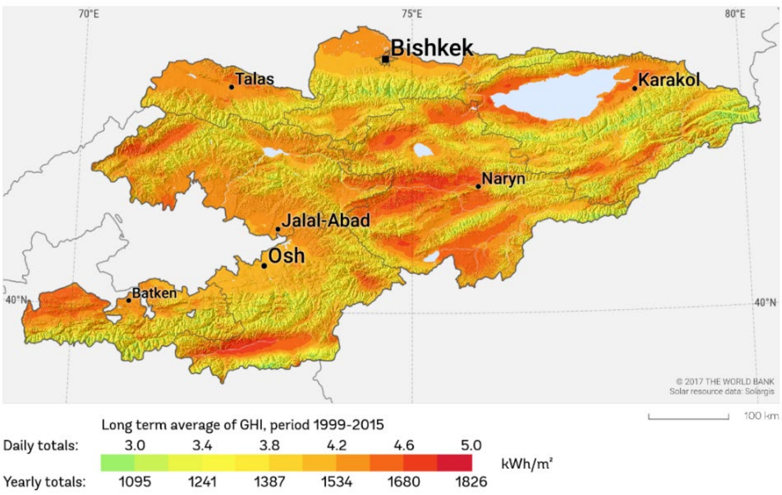

Fig. 2 Global Horizontal Irradiation of Kyrgyzstan (World Bank, 2017)

Out of the other available untapped renewable energy resources, solar energy is considered as one of the most promising energy sources. Kelpšaitė et al. (2018) draw attention to the usage of solar photovoltaic (PV) and mentioned that solar PV is more suitable for the public sector or to install mini-grid power plants. Most Kyrgyz households are connected to the national grid. Thus, the application of photovoltaic energy is an option for the service sector where PV panels could be used in public and commercial buildings to reduce the burden on the national grid. Kyrgyzstan has also drawn on its rich resources of silicon to develop PV manufacturing units. To date, solar power deployment in Kyrgyzstan has taken place either in the form of pilot projects or mini off-grid installations.

The high-altitude characteristic, significant solar irradiation and abundant sunshine hours also underline the potential of solar-thermal energy which can be utilized for sustainable heat energy supply (Abidov et al., 2020). However, there are very limited studies available that focus on solar thermal assisted heat supply systems and their usage in Kyrgyzstan. The technical potential and feasibility of a solar-thermal system for the domestic space heating system and domestic hot water preparation remain unclear for the rural regions of Kyrgyzstan. Hence, untapped solar thermal energy is considered in the presented article to provide a sustainable heat supply for domestic space heating and hot water preparation. Naryn, a rural region of Kyrgyzstan is chosen as a location for feasibility study.

3. Energy demand modelling

To integrate solar thermal energy for a single-family house heating system in Naryn (Kyrgyzstan), it is necessary to identify an annual heat load of a typical rural house. It is also necessary to identify the characteristics of rural Kyrgyz houses in order to describe the thermal operation of a single-family house.

3.1 Profile of rural Kyrgyz houses

There are approximately 1.8 million dwellings in Kyrgyzstan. Due to the higher population in rural areas, the number of houses is greater there than in urban areas (NSC, 2018a). Most rural houses are self-built and therefore do not use advanced construction materials with good insulating qualities (Haab, 2017). Because of the self-build construction process, building codes are seldom considered while constructing rural houses. Fig. 3 represents typical residential buildings in rural Kyrgyzstan.

Fig. 3 Typical rural Kyrgyz houses with natural walls and open gable roof

The field survey indicates that typical rural houses are built with clay and straw or adobe, which are commonly traditional building construction materials in the Kyrgyz countryside. The self-made bricks for building walls are formed by a mixture of clay and straw. Kyrgyz households are generally large, with more than four people on average and an average living area of 90 m^2 – 100 m^2. The majority of rural households were built in the Soviet era. The age of the residential buildings, poor housing conditions and the absence of proper thermal insulation result in high heat demand and low thermal comfort in Kyrgyz houses. To save money on heating fuels, rural households usually occupy only one room for heating and close down the rest of the house in winter, which results in indoor air pollution and is responsible for health issues (Balabanyan, 2015).

To determine the annual space heat demand of a rural Kyrgyz house, a building model was developed in *EnergyPlus* (NREL, 2019). *EnergyPlus* calculated the required thermal load of the house by calculating the heat losses through the building envelope considering the local climate. The general building information and building sketch are shown in Fig. 4.

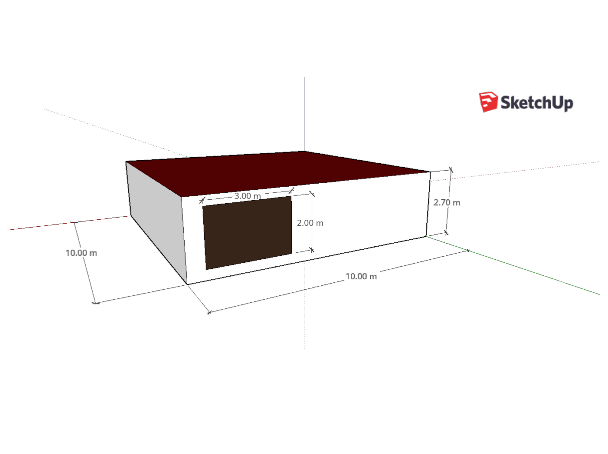

Living area	100 m²
Building orientation	North
Building location	Naryn, Kyrgyzstan
Number of thermal zones	1 (single zone)
Number of windows	2 (East and West Wall)
Dimensions of window	6 m² (3m x 2m)
People occupancy	4 people
Heating set point	20 °C
Lighting level	1,000 Watt

Fig. 4 Building description

Due to a lack of information about building typology and building codes in Kyrgyzstan, the building model was developed from data found in the literature study. The construction of the opaque elements (walls, floor, and roof) is described in Tab. 3.

Tab. 3 Thermal properties of building envelope (data according to (UNECE, 2010; Botpaev et al., 2013; Haab, 2017))

Assembly	Layer	Thickness [m]	Density [kg/m³]	Conductivity [W/(mK)]	Capacity [kJ/(kgK)]	U-value [W/(m²K)]
Celling and Roof	Roof tile	0.02	2,200	0.96	0.92	1.6
	Plywood	0.035	300	0.081	2.50	
External walls	Plaster outside	0.03	1,800	0.76	0.84	1.1
	Brick	0.38	1,600	0.58	0.84	
	Plaster inside	0.03	1,800	0.76	0.84	
Floor	Pinewood	0.03	600	0.13	1.70	1.7
	Plaster	0.05	1,800	0.76	0.84	
	Concrete slab	0.22	2,500	1.92	1.13	
Window	Glass	0.006	-	0.90	-	3.6
	Air	0.003	-	-	-	
	Glass	0.006	-	0.90	-	

The standard schedule of house occupancy and lighting for a single-family house was adopted from the *EnergyPlus* dataset to consider internal gain by the inhabitants and lighting (NREL, 2019). Tab. 4 describes the occupancy and house lighting profile as fractions of present persons.

Tab. 4 Daily occupancy profile and daily electrical gains in a fraction of present persons (data according to NREL (2019))

Time	Until 6:00	Until 7:00	Until 8:00	Until 12:00	Until 13:00	Until 16:00	Until 17:00	Until 18:00	Until 24:00
Occupancy	1	0.1	0.5	1	0.5	1	0.5	0.1	1
Lighting	0.05	0.2	1	1	1	1	1	0.5	0.05

3.2 Heat demand for space heating and domestic hot water

In order to maintain 20 °C in the living area of the described rural Naryn house, the annual heat demand was determined in *EnergyPlus*. The obtained annual specific heat demand by simulation of a single-family house in rural Kyrgyzstan for space heating is 327.19 kWh/m^2. Fig. 5 represents the detailed space heating demand profile of the reference building (simulation results).

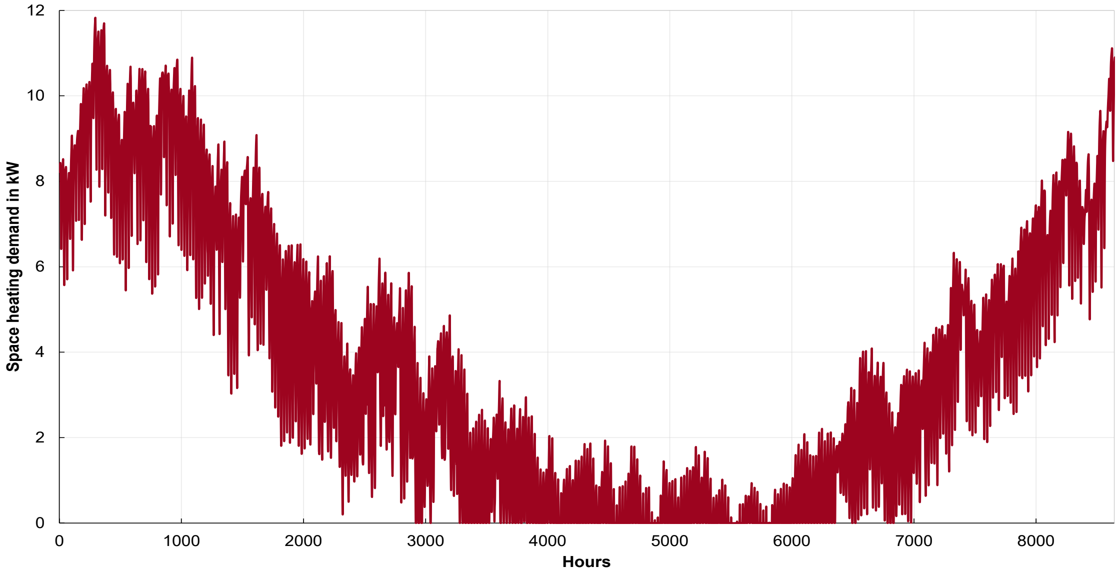

Fig. 5 Annual space heating load Q_SH of the reference building

To maintain thermal comfort throughout the heating season, a considerable amount of energy is required for space heating, since the building is uninsulated as well as Naryn region holds the coldest winter among Kyrgyz regions. However, the annual building energy consumption for heating in Kyrgyzstan (and other Central Asian countries) is at 240-360 kWh/m^2, which is more than two times higher than average European levels (100-120 kWh/m^2 (Bergström and Johannessen, 2014; Kerimray et al., 2017)) due to its climatic patterns.

Despite the abundance of available hydro resources, the water supply structure is not yet fully developed in Kyrgyzstan. Hence, only 15 % of rural households have a connection with piped water. As a result, only 4 % of rural homes have an indoor shower room (FAO, 2016). Therefore, it is difficult to estimate domestic hot water consumption in a single-family rural house. To consider domestic hot water consumption in the investigation, the European tapping standard for domestic hot water demand (Load profile L) was considered for the simulation (EN 13203-2:2015). Fig. 6 represents the tapping cycle to consider the energy demand of domestic hot water preparation. The selected tapping cycle features 24 tappings (draw-offs) for various uses including shower, floor cleaning, household cleaning as well as dishwashing. To maintain a room ambient temperature of 20 °C throughout the heating season, a considerable amount of energy is required. On the other hand, the demand for DHW is constant over the year according to European tapping standard. The daily energy demand for domestic hot water is 11.65 kWh/d.

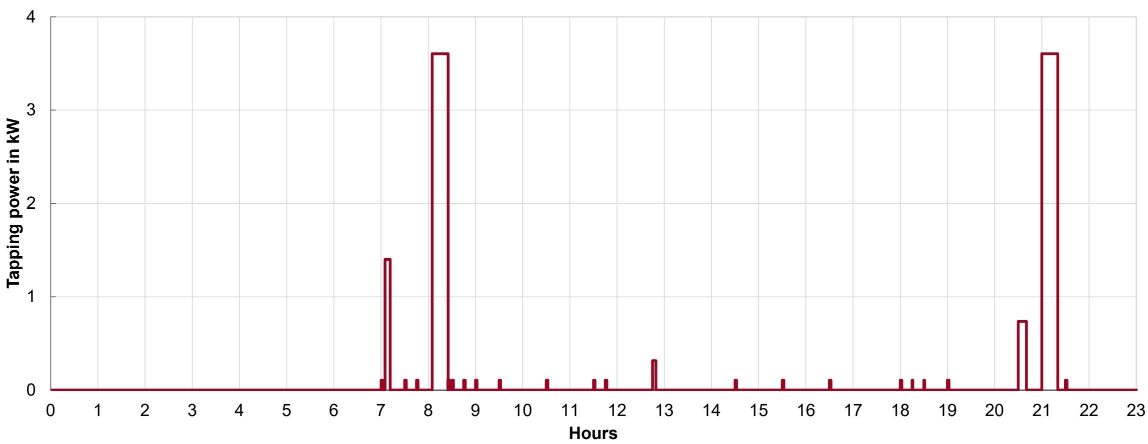

Fig. 6 Daily constant Domestic Hot Water (DHW) consumption Q_DHW of the reference building (EN 13203-2:2015)

4. Energy supply modeling

To meet the total heat load of the single-family house (space heating & domestic hot water), a suitable solar-thermal heat supply was developed in MATLAB / Simulink using the CARNOT toolbox (CARNOT Toolbox, 2010). The characteristic heat load profile of the house serves as an input to the system simulation model.

4.1 Energy supply on household level

For cold climatic regions (especially in winter), the sunlight period is short compared to summer. Furthermore, losses at the solar collector are higher (Mori and Kawamura, 2014). Therefore, without a large storage, a solar thermal system cannot produce enough energy to satisfy the total heat load of the house. Therefore, the solar thermal operated house heating system must be complemented by an auxiliary back-up heating system.

The key aim of the research paper is to identify the residential energy demand trend in case of space heating DHW demand by considering a worst-case scenario (old and uninsulated building in an extremely cold climate) in Kyrgyzstan and design a sufficiently suitable energy supply model to meet that demand. Fig. 7 represents the energy supply system (i.e. non-ideal / non-optimised solar combi system), which need to be properly designed / optimised before implementation. It has been noted that the reference house is uninsulated and therefore it requires more energy to maintain thermal comfort inside the house. Hence, the space heating demand has a high fraction of the total heat demand. While it was assumed that the house has daily constant hot water energy demand according to the European Tapping cycle which has a negligible portion of total heat demand.

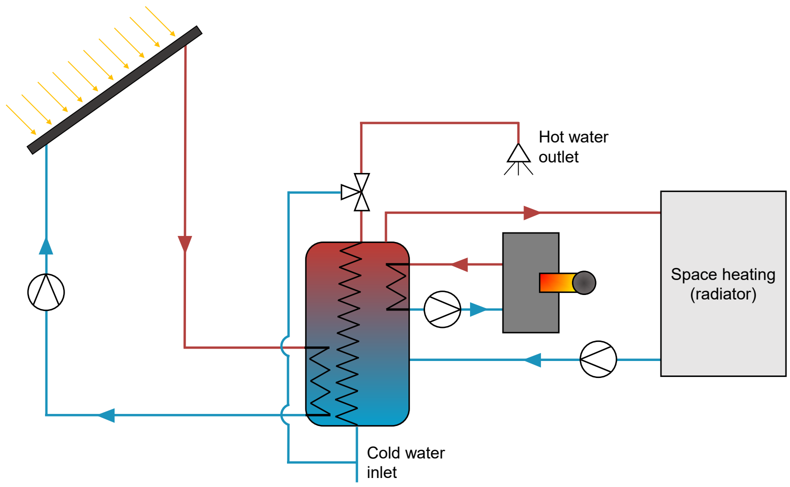

Fig. 7 Energy system layout

To assess the technical performance of solar-thermal system design options for heat supply of the single-family house, a parametric study was conducted. The size of the collector array and the size of the thermal storage tank was varied in a parametric study. The volume of storage tank has been varied with a step size of 100 liters from 100 l to 1,000 l. Similarly, the number of collectors (2m² per collector) has been increased in a step size of 2, from 2 to 20 collectors. Thus, for each combination of storage volume and number of collectors, simulations have been performed, in total 100 simulations. The key technical input parameters for the simulation model are mentioned in Tab. 5.

Tab. 5 Key technical input parameters for the simulation model

Annual global solar irradiation of location	1,694.5 kWh/m^2
Average ambient temperature of location	4.70 °C
Maximum ambient temperature	32.3 °C
Minimum ambient temperature	-26.4 °C
Annual space heating demand Q_SH (radiator)	32,719 kWh
Annual domestic hot water demand Q_DHW	4,554 kWh
Area of solar-thermal collector	2 m^2
Initial temperature of collector	20 °C
Collector tilt angle to horizontal	30 °
Capacity of auxiliary heating	15 kW

4.2 Simulation results and technical assessment of parametric study

To evaluate the system size options and identify the suitable combination of storage tank volume and solar collector area the solar heat production fraction was calculated by eq.1. The calculation of heat production ratio characterizes the contribution of solar energy for each combination which is presented in Fig. 8.

$$Heat\ production\ ratio\ r = \frac{Heat\ generation\ by\ solar\ collector\ array\ Q\_sol\ (kWh)}{Heat\ generation\ by\ auxiliary\ heater\ Q\_aux\ (kWh)} \quad \text{eq.1}$$

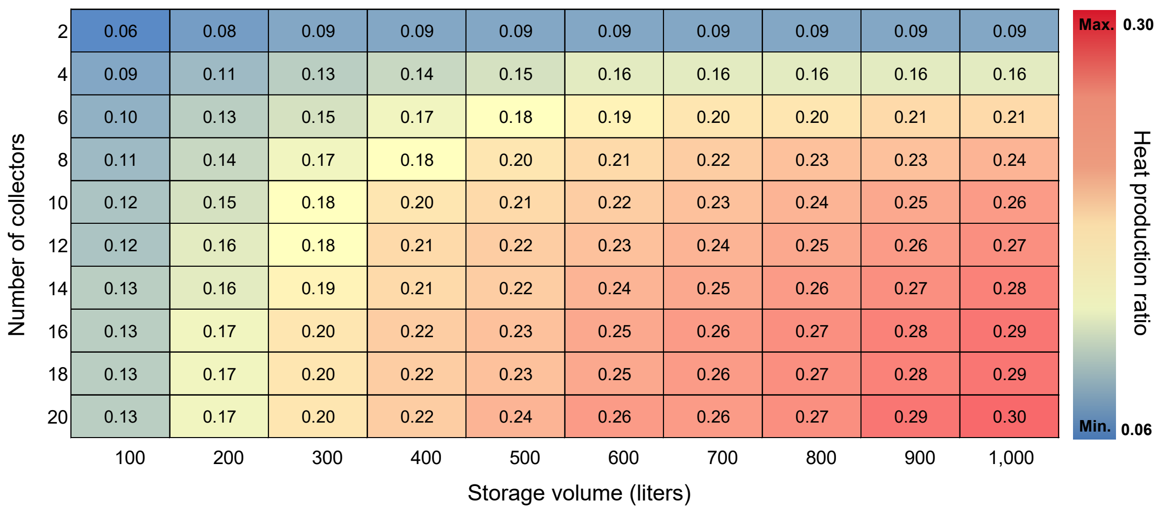

Fig. 8 Heat production ratio by solar collector array

It can be evaluated from Fig. 8 that the minimum heat production ratio by solar energy is 0.06 and a maximum heat production contribution by solar is 0.30, thus the evaluated system designs can contribute between 6 % to a maximum of 30 % total heat production. For suitable size selection, three cases were selected and analyzed:

- Case 1: 15 % heat production by solar
- Case 2: 20 % heat production by solar
- Case 3: 25 % heat production by solar

To evaluate the possible solutions for the selected three cases, several combinations of the number of solar collectors and respective storage volume are available which is presented in Fig. 9.

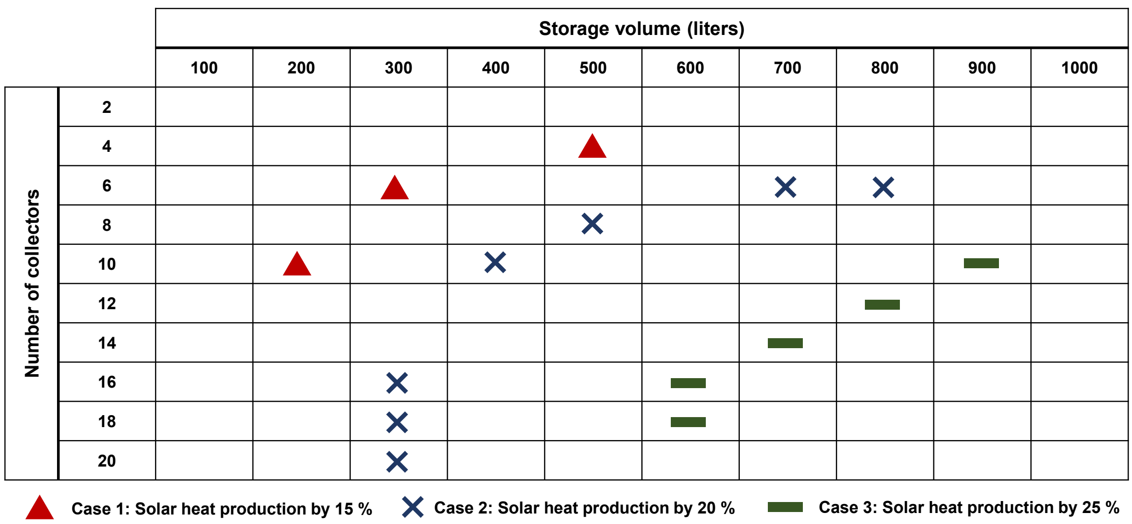

Fig. 9 Characterization of selected three cases with respect to storage volume and number of collectors

It can be examined from Fig. 9 for 15 %, 20 % and 25 % share of solar heat production, comparatively reliable options are available. Naturally, a larger storage tank contains a higher capacity to store more thermal energy. However, the increment of storage size results in higher heat loss through a storage tank (Li et al., 2015; Sarbu and

Sebarchievici, 2018). Generally, the volume of hot water storage systems ranges between 200 l to 500 l especially for single-family house energy supply systems (Çomaklı et al., 2012; Cygas and Tollazzi, 2014). Larger hot water storage tanks are commonly used for seasonal storage of solar thermal heat in combination with small district heating (Sarbu and Sebarchievici, 2018). In addition, greater collector area causes a high investment cost.

Therefore, in terms of reducing the usage of non-sustainable solid fuels for house heating, the parametric study results to select the energy system which can generate 20 % solar heat. It is examined from Fig. 9 that with the selection of moderate storage volume (500 l) and 8 solar thermal collectors, 20 % of solar heat production can be achieved, and Fig. 10 represented the detailed simulation results for that combination.

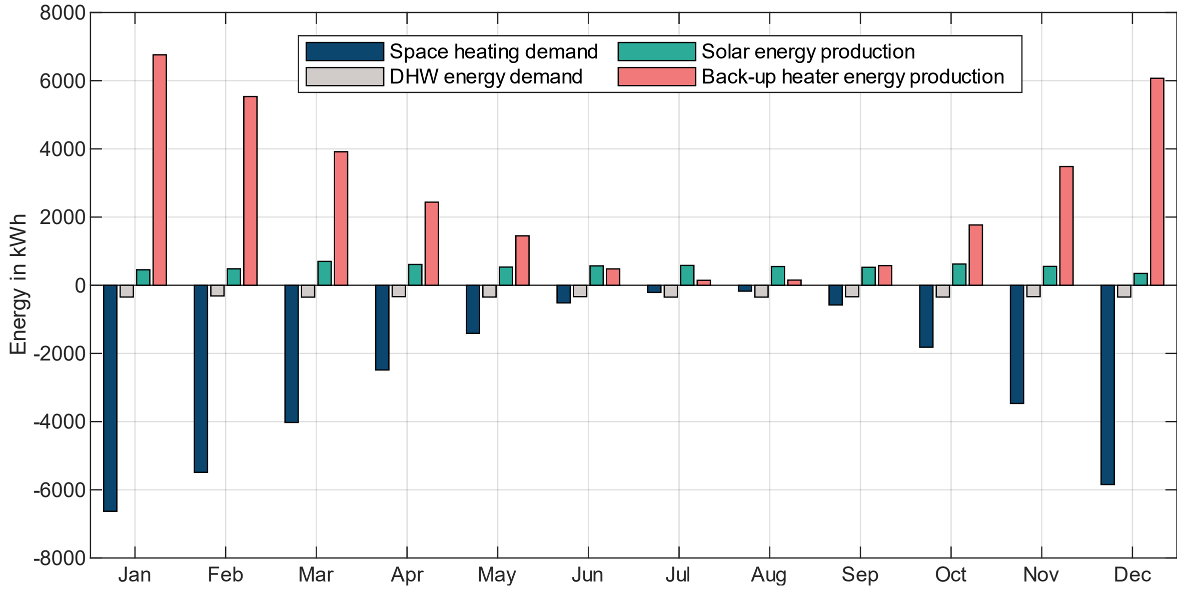

Fig. 10 Monthly energy production and consumption

To produce 20 % renewable heat, eight solar flat-plate collectors each with an area of two square meters are considered in the simulation system. The highest monthly energy production from solar is around 700 kWh in March and the lowest energy production is around 345 kWh in December (Fig. 10). As solar energy is not prominent and the production of solar energy could not meet the desired heat load for space heating and domestic hot water, auxiliary heating system works as a back-up heating system. To identify that energy-saving, a house heating energy system solely based on fossil fuel has been simulated. It is calculated that a 20 % contribution of solar heat production in the energy system helps to reduce around 6,000 kWh annual secondary energy demand generated by non-sustainable solid fuels.

5. Conclusion

The extremely cold winters of Kyrgyzstan are translated into high heat demand to maintain thermal comfort in the house. Especially in rural Kyrgyzstan, the high demand is typically covered by crude and inefficient heating systems that use non–sustainable solid fuels. The usage of such fuels is not favorable in terms of health and environmental concerns. Hence, there is a substantial need to provide sustainable and adequate heating services for residential buildings, particularly for the rural population. The presented research article deals with the identification of available solar-thermal resources to cover the energy demand for space heating and hot water preparation for a single-family house in rural Kyrgyzstan.

The presented research article offers a wide range of solar-thermal system sizes options by performing a parametric study by considering the different number of solar collectors and sizes of the thermal storage tank. The results indicate that the integration of 20 % solar heat production to the modeled house can be helpful to reduce around 6,000 kWh of heat energy annually, which is produced by non-sustainable solid fuels. The lack of information about rural building construction, Kyrgyz building code as well as occupant behavior, the presented research considered several assumptions for hot water consumption profile, a few building assemblies based on available literature. Further to this, the energy supply system was designed to evaluate the preliminary feasibility of the involvement of solar thermal collectors. The energy system should be optimised and improved as a future scope of research as this article adopted a non-ideal / non-optimised technical setup for the feasibility study.

The investigation identified that in reality, other than the cold climatic conditions of the country, the poor thermal insulation of houses is majorly responsible for high heat demand. Improved thermal insulation could have a significant positive effect on reducing overall heat energy consumption, living conditions and the indoor air temperature. Further to this, some of the major obstacles to use solar thermal-energy in Kyrgyzstan are lack of basic information, lack of skills / training to operate the energy system, as well as extreme poverty in rural Kyrgyzstan.

In general, the assessment shows that from a technical point of view, solar-thermal energy is a suitable solution for space heating and domestic hot water preparation under the given climatic and building infrastructure conditions. The presented information in the research articles reveals the technical potential of solar-thermal energy in Kyrgyzstan which opens the doors for investors to invest in the field of renewable heating and can bring solar-thermal energy in Kyrgyzstan.

6. Acknowledgments

The work presented in this paper was funded by the Federal Ministry of Education and Research (BMBF) of the Federal Republic of Germany within the CLIENT II funding programme (International Partnerships for Sustainable Innovations) for the project “ÖkoFlussPlan” (Project ID 01LZ1802A-F). The overall aim of ÖkoFlussPlan is to preserve the alluvial forests along the Naryn river and to implement sustainable energy solutions for the local population.

7. References

Abidov, A., Ryspaev, T., Satybaldyev, A., Gorbacheva, A., 2020. Comparative Analysis of Some Types of Renewable Energy Sources.

Asian Development Bank, 2016. Study for a Power Sector Financing Road Map within Central Asia Regional Economic Cooperation. Kyrgyz Republic. Mobilizing Financing for Priority Projects. https://www.carecprogram.org/uploads/CAREC_TA8727_CountryReport_KyrgyzRepublic.pdf. Accessed 15 January 2020.

Bakashova, A., Jorritsma, F., Choitonbaeva, A., Wendland, C., 2013. Opportunities to Stimulate Local Economies through Sustainable Innovations for Home Comfort. Gender-sensitive feasibility study for rural areas in Issyk Kul and Naryn. Women in Europe for a Common Future (WECF). www.wecf.eu/download/2013/June/HOMECOMFORTstudy.pdf. Accessed 20 March 2019.

Balabanyan, A., 2015. Keeping warm: Urban heating options in the Kyrgyz Republic. Summary report (English). The World Bank Group, Washington, DC. http://documents.worldbank.org/curated/en/555021468011161504/pdf/97409-WP-P133058-Box391503B-PUBLIC-Heating-Assessment-for-Kyrgyz-P133058-Final.pdf. Accessed 27 November 2018.

Baybagyshov, E., Degembaeva, N., 2019. Analysis of usage of the renewable energy in Kyrgyzstan. IOP Conf. Ser.: Earth Environ. Sci. 249, 12021.

Bergström, S., Johannessen, F., 2014. Sustainable housing in Kyrgyzstan. Investigation of two multi- apartment buildings in Bishkek. The Department of Energy Sciences. Lund University, Faculty of Engineering, Lund. http://www.ees.energy.lth.se/fileadmin/ees/Publikationer/Ex5297-Bergstrom_Johannessen.pdf. Accessed 18 February 2020.

Botpaev, R., Orozaliev, J., Vajen, K., 2013. Economically optimal level of thermal insulation for single-family houses in Kyrgyzstan. https://www.uni-kassel.de/maschinenbau/fileadmin/datas/fb15/110912_Paper_Thermal_Insulation_for_single-family_houses_in_Kyrgyzstan_rb.pdf. Accessed 20 December 2018.

CARNOT Toolbox, 2010. CARNOT. Solar-Institut Juelich.

Çomaklı, K., Çakır, U., Kaya, M., Bakirci, K., 2012. The relation of collector and storage tank size in solar heating systems. Energy Conversion and Management 63, 112–117.

Cygas, D., Tollazzi, T. (Eds.), 2014. The 9th International Conference "Environmental Engineering 2014". Vilnius Gediminas Technical University Press “Technika” 2014, Vilnius, Lithuania.

EN 13203-2:2015. Gasbeheizte Geräte für die sanitäre Warmwasserbereitung für den Hausgebrauch –. Teil 2:

Bewertung des Energieverbrauchs, Berlin (Germany). https://www.din.de/de/mitwirken/normenausschuesse/nagas/entwuerfe/wdc-beuth:din21:279694799. Accessed 12 July 2020.

FAO, 2016. National gender profile of agricultural and rural livelihoods - Kyrgyz Republic. Country gender assessment series. Food and Agriculture Organization of the United Nations, Ankara (Turkey). http://www.fao.org/3/a-i5763e.pdf. Accessed 20 August 2020.

Gassner, K.B., Rosenthal, N., Hankinson, D.J., 2017. Analysis of the Kyrgyz Republic’s energy sector. Final Report. World Bank energy and extractives global practice ECA region. The Public Private Infrastructure Advisory Facility. https://openknowledge.worldbank.org/handle/10986/29045. Accessed 20 September 2018.

Haab, E., 2017. Energy profiles for Kyrgyz mountain villages as a basis for a targeted energy strategy development of a survey method and pilot run in Jergetal. Bachelor thesis, Wädenswil.

IEC, 2018. In-Depth Review of the Energy Efficiency Policy of the Kyrgyz Republic. Energy Charter Protocol on Energy Efficiency and Related Environmental Aspects. Energy Charter Secretariat, Brussels (Belgiumt). https://energycharter.org/fileadmin/DocumentsMedia/IDEER/IDEER-KyrgyzstanEN2018.pdf. Accessed 21 April 2020.

Kampakis, A., 2015. Divesting From Fossil Fuels in Central Asia. Factors affecting Renewable Energy Transition in Kazakhstan, Kyrgyzstan, Tajikistan. Research Project. ERM Masters Program 2014-2015, Amsterdam.

Kelpšaitė, J., Mooldijk, S., Brückmann, R., Blajin, C., Goldmann, A., Hirning, J., Torliene, L., 2018. Analysis of the potential and market entry barriers to solar power projects in Kyrgyzstan. ZMVI6-2517AA0554. eclareon GmbH, Berlin (Germany).

Kerimray, A., Miglio, R.D., Solorzano, L.R., Gallachóir, B.Ó., 2017. Household Energy Consumption and Energy Poverty in Kazakhstan IAEE Energy Forum 26, 31–34.

Li, T., Liu, Y., Wang, D., Shang, K., Liu, J., 2015. Optimization Analysis on Storage Tank Volume in Solar Heating System. Procedia Engineering 121, 1356–1364.

Mori, T., Kawamura, A., 2014. Design of Solar Water Heating System for Detached House in Cold Climate Area. Energy Procedia 48, 1393–1400.

NREL, 2019. EnergyPlus. U.S. Department of Energy.

NSC, 2018a. 1.05.02.12 Livestock and bird population by category of households in Kyrgyz Republic. National Statistical Committee of the Kyrgyz Republic. http://www.stat.kg/en/statistics/selskoe-hozyajstvo/.

NSC, 2018b. National Statistical Committee of the Kyrgyz Republic. Kyrgyzstan. Brief statistical handbook. Annual publication, Bishkek (Kyrgyzstan). http://www.stat.kg/media/publicationarchive/16db2910-6b8d-48f9-80b9-45b7ac3347bd.pdf. Accessed 22 August 2020.

Sarbu, I., Sebarchievici, C., 2018. A Comprehensive Review of Thermal Energy Storage. Sustainability 10 (2), 191.

UNDP, 2014. Renewable energy snapshot: Kyrgyzstan. http://www.eurasia.undp.org/content/dam/rbec/docs/Kyrgyzstan.pdf. Accessed 25 July 2020.

UNECE, 2010. Country profiles on the housing sector. Kyrgyzstan ECE/HBP/157. Country profiles on the housing sector, Geneva (Switzerland). http://www.unece.org/fileadmin/DAM/hlm/documents/Publications/cp.kyrgyzstan.e.pdf. Accessed 10 January 2019.

UNICEF, 2017. Climate Analysis for Children in Kyrgyzstan. Working Paper. United Nations International Children's Emergency Fund. https://www.unicef.org/kyrgyzstan/media/1526/file/Kyrgyzstan%20Climate%20Landscape%20Analysis%20for%20Children.pdf%20.pdf. Accessed 28 December 2019.

World Bank, 2017. Solar resource maps of Kyrgyz Republic. Photovoltaic Electricity Potential. Solar resource data: Solargis. https://data.worldbank.org/indicator/SI.POV.NAHC?locations=KG. Accessed 25 July 2020.

World Bank and Factfish, 2015a. Kyrgyzstan: CO2 emissions from solid fuel consumption (kt). http://www.factfish.com/statistic-country/kyrgyzstan/co2%20emissions%20from%20solid%20fuel%20consumption. Accessed 17 July 2020.

World Bank and Factfish, 2015b. Kyrgyzstan: Forest area (sq. km). http://www.factfish.com/statistic-country/kyrgyzstan/forest%20area. Accessed 17 July 2020.

Impact of Locally Available Thermal Insulation Structures on Space Heating Demand of High-altitude Rural Buildings: A Case Study of Kyrgyzstan

Kedar Mehta[1], Mathias Ehrenwirth[1], Christoph Trinkl[1], Wilfried Zörner[1] and Rick Greenough[2]

[1] Institute of new Energy Systems, Technische Hochschule Ingolstadt (Germany)

[2] Institute of Energy and Sustainable Development, De Montfort University, Leicester (UK)

Abstract

Kyrgyzstan is a high-altitude mountainous country situated in a cold climatic zone. The age of the residential buildings, poor housing conditions and the absence of proper thermal insulation result in high heat demand and low thermal comfort in Kyrgyz houses. To maintain thermal comfort, the rural residents use traditional heating stoves to burn solid fuels during the winter months. Overconsumption of natural resources is mainly responsible for deforestation, as well as indoor and outdoor air pollution. Implementation of building thermal insulation is considered as one of the potential measures for energy conservation. In regards to this, the presented research proposes the various thermal insulation structures developed from the locally available natural materials. Further to this, it identifies the effectiveness of various thermal insulation structures on the annual space heating demand of a high-altitude single-family house located in rural Kyrgyzstan. The results show that the insulation parameter helps to save a considerable amount of space heating demand by up to 30 % in the case of existing houses and up to 70 % for newly built houses in rural Kyrgyzstan.

Keywords: Domestic space heating, energy efficiency, cold climate, high-altitude, thermal insulation

1. Introduction

The Kyrgyz Republic is a landlocked country located in northeastern Central Asia between two major mountain systems, the Tian Shan and the Pamir with a population of around 6.3 million (NSC, 2018). Approximately 94 % of the Kyrgyz Republic's territory is located at altitudes higher than 1,000 meters and almost 40 % at higher than 3,000 meters above sea level (NSC, 2018). Hence, the Kyrgyz climate is characterized as sharp continental with a long and harsh winter. The variety of average surface temperatures is directly related to the country's territorial arrangement and therefore it ranges from 10 °C in the areas at an altitude lower than 1,000 meters to -5 °C in the areas at an altitude higher than 3,000 meters. Average low winter temperatures can reach below -20 °C in high elevations, while average summer high temperatures are in the high teens to low twenties across the country (USAID, 2018). On the other hand, the average annual temperature is around 2 °C for the entire country. Fig. 1 represents the map of Kyrgyzstan as well as the map of the country's Köppen climate classification.

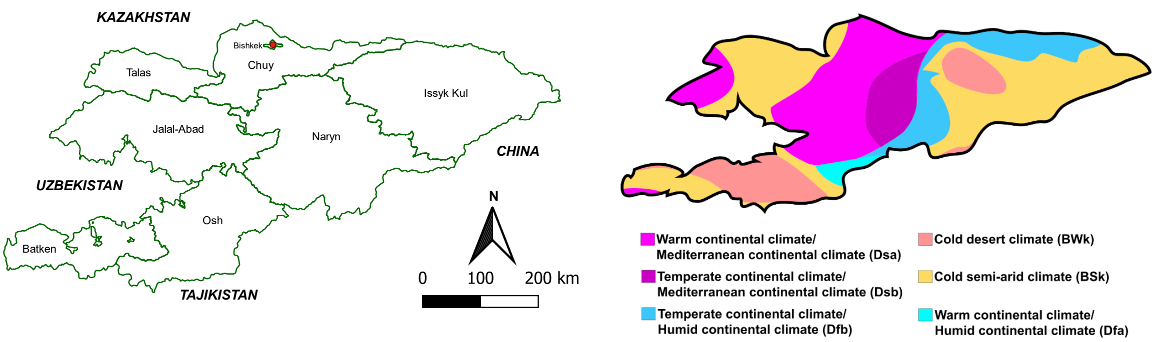

Fig. 1 Regional map of Kyrgyzstan (left) and its map of Köppen climate classification (right) (Köppen and Geiger, 2016)

The cold and extended winters in the country define house heating as a key primary need for Kyrgyz people. The buildings situated at high-altitude regions of Kyrgyzstan face a supplementary challenge because most of the energy is required for space heating rather than cooking. The higher the altitude, the longer and colder the winters will be and the more house heating is required (Wiedemann et al., 2012). Therefore, the residential sector is the highest energy-consuming sector in Kyrgyzstan (IEA, 2017).

doi:10.18086/eurosun.2020.04.04 Available at http://proceedings.ises.org

Almost all housing stock in Kyrgyzstan was constructed during the Soviet period roughly 35-60 years ago without proper construction materials, which leads to high heat demand, particularly in rural regions where almost 66 % of the Kyrgyz population lives (UNICEF, 2013; NSC, 2018). While the connection to the district heating system is limited to the capital city and other urban areas, almost 80 % of households resort to individual traditional heating solutions fueled by non-sustainable solid fuels (i.e. coal, firewood, wood branches, cow-dung etc.) (World Bank, 2020). To meet high heat demand and maintain thermal comfort in the house, rural people depend on the available natural resources. The existence of many uninsulated buildings, especially in rural Kyrgyzstan, has focused growing attention on the subject of building thermal insulation.

There is a need to identify suitable thermal insulation methods for residential buildings, particularly for high-altitude rural areas. Few researchers have addressed the problem and proved that the introduction of artificial insulation structures plays a vital role to reduce the space heating demand. However, by considering the local boundary conditions such as intense poverty and limited income of rural houses, the presented research article investigates the impact of insulation structures on Kyrgyz buildings, which are developed from the locally available sustainable insulation materials to make such insulation economically feasible.

2. Profile of rural Kyrgyz buildings

2.1 An overview of traditional building structures

Due to the mountainous nature of the Kyrgyz territory, less than 20 % of the country is suitable for comfortable living. Therefore, most of the building stock (about 85 %) is concentrated in a comparatively small area as rural settlements, or urban clusters (UNFCC, 2017). The building traditions vary in different parts of Kyrgyzstan. Both residential and public buildings are characterized by low energy efficiency due to the age of the building stock, inadequate maintenance and the absence of proper thermal insulation. However, rural buildings in Kyrgyzstan are dominated by traditional construction techniques with conventional building materials such as earth, cob, adobe, stone and raw bricks. Most of the rural houses do not use construction materials with good insulating qualities for building construction (MEI, 2013). Further to this, building codes are not enforced adequately to rural households (UNECE, 2018).

The living space / floor area of the typical Kyrgyz house varies between 90 m^2 to 110 m^2 and is used by around four to five people on average. From a field visit to Ak-Tal (a high-altitude rural community situated in Naryn region), it was found that a typical rural house has an earthen floor with a layer of natural stone and / or concrete for the stability of the foundation as a first layer. The floor is built with a thickness of 0.25 m to 0.50 m usually without thermal insulation. The walls are commonly built with soil or adobe bricks with a thickness of 0.35 m to 0.50 m with no additional thermal insulation. However, the rural house walls are finished by a thin layer of lime plaster. Furthermore, the construction of a ceiling is similar to the floor, which consists of wooden boards and open space under the roof. The ceiling usually has a thin layer of clay-straw plaster to reduce the heat transfer through the ceiling. Rural buildings in Kyrgyzstan are generally built with wooden beam ceiling covered by a gable roof to protect the ceiling from the weather, especially snowfall and rainfall. Fig. 2 represents some typical traditional rural Kyrgyz houses.

Fig. 2 Typical rural Kyrgyz houses in the Ak-Tal region

Because of the inappropriate building structures, the energy consumption per square meter in Kyrgyzstan is almost 3-5 times higher compared to European countries (UNICEF, 2013). Kerimray et al. (2017) and Bergström and Johannessen (2014) also mentioned that the annual building energy consumption for heating in Kyrgyzstan (and other Central Asian countries) ranges between 240 and 360 kWh/m^2, which is more than two times higher than the average European level. During winter, high-altitude regions need a considerable amount of energy, when the air temperature falls below zero during the heating period (October to March). The challenging climate patterns as well as traditional building structures are responsible for a high space heating demand in high-altitude rural settlements in Kyrgyzstan.

2.2 Potential of energy savings in Kyrgyzstan

The conditions of poor building infrastructure represent a huge potential for energy savings in Kyrgyzstan. According to the *Mountain Societies Research Institute*, up to almost 60 % of heat losses can be saved by introducing the proper thermal insulation measures to rural buildings (Hall, 2018). Thermography is one of the most convenient ways to diagnose and monitor the heat transfer of a building. Hence, a thermographic analysis was performed in typical Kyrgyz households for the presented research work. The thermal images of some rural Kyrgyz houses are exemplarily shown in Fig. 3.

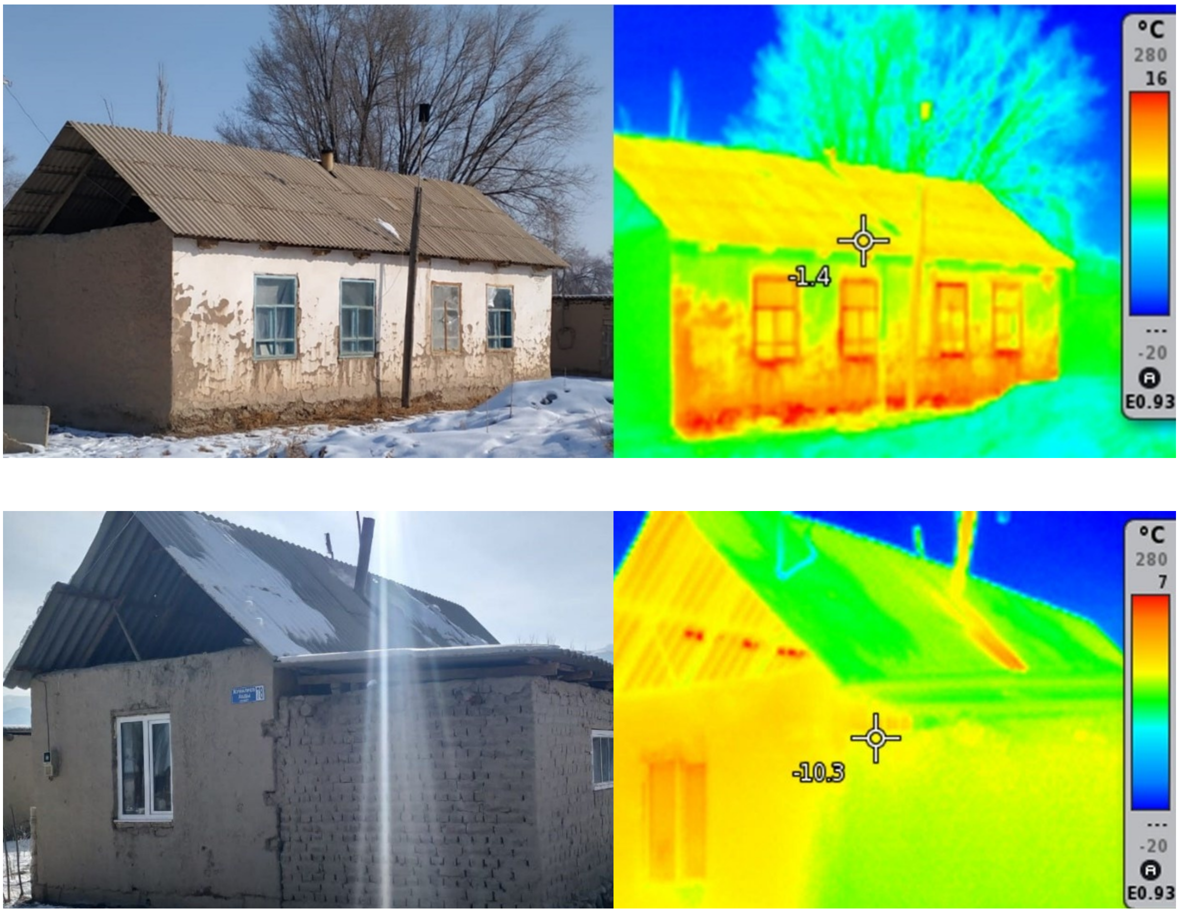

Fig. 3 Thermal images of uninsulated Kyrgyz houses in Ak-Tal region during the heating season

In the Kyrgyz Republic, access to reliable and affordable heating is mandatory because of the sharp and freezing winters. Because of the absence of heating solutions such as district heating in rural areas, nearly three-quarters of rural households use traditional stoves or boilers burning non-sustainable solid fuels to maintain thermal comfort in the house (Balabanyan, 2015; World Bank, 2020).

It was assessed from the on-site visit that during the winter period (from October to March), based on the availability of heating fuels and financial capabilities, the average rural family needs to use 2 to 4 tons of coal, 1.5 to 3 m³ of firewood and 1 to 2 truckloads of cow dung to maintain thermal comfort in the house. The high consumption of solid fuels promotes indoor and outdoor air pollution. Therefore, improving energy efficiency for rural houses is a vital factor in reducing the space heating demand.

3. Potential of natural insulation materials in Kyrgyzstan

Kyrgyzstan's poverty level remains high with a Human Development Index (HDI) ranking of 122 out of 195 countries and 26.5 % of the population living below the national poverty line (World Bank, 2016; UNDP, 2018). The village population is heavily dependent on the agriculture sector for their livelihood (FAO, 2016). The agriculture sector is the mainstay of the Kyrgyz economy and it covers 20 % of the total GDP and engages 48 % of the total human resources (FAO, 2016).

The land used for agricultural production accounts for almost 55 % of Kyrgyz's total land area. The primary use of this land is for agriculture and pasture for livestock (mainly sheep, goats, and cattle), which is the traditional vocation of the Kyrgyz people. The active agriculture sector features a high number of livestock and the use of animal husbandry. Due to the specific geographical conditions of the country, most of the farms are located in mountainous regions at high altitudes. However, the cold climates and snowfall in the mountain regions slow down the agricultural activity during the winter in Kyrgyzstan. Agriculture is mostly reliant on climatic patterns and weather conditions as well as in most cases being vulnerable to environmental changes. Therefore, the rural population struggles to generate a constant income from their occupation in agriculture. This is one of the reasons for the higher poverty rate in rural Kyrgyzstan (Sagynbekova, 2017). Due to unstable income sources and intense poverty in rural Kyrgyzstan, the application of thermal insulation to their homes is not considered practical by most rural householders (Hall, 2018).

On the contrary, the active agricultural sector in combination with a considerable amount of livestock reveals a great potential of natural and sustainable materials, which can be utilized as thermal insulation for rural Kyrgyz houses. Furthermore, the geographical location of Kyrgyzstan allows the import of modern insulation materials from neighboring countries (i.e. China and Russia). Therefore, besides natural insulation materials, the assessment identified the availability and countable suppliers of modern insulation materials in Kyrgyzstan (KyrSEFF, 2018). Fig. 4 represents information on the classification of widely available insulation materials in Kyrgyzstan.

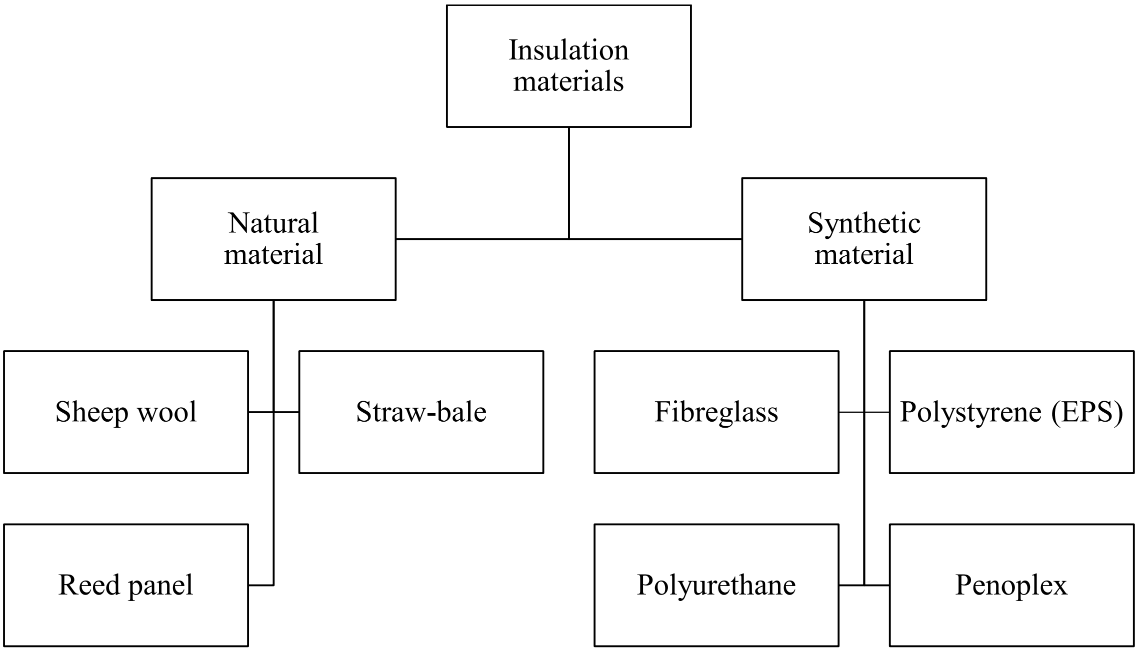

Fig. 4 Classification of widely available building insulation materials in Kyrgyzstan

The thermal properties of insulation materials as well as the minimum recommended thickness of natural and synthetic materials are mentioned by several institutes and organizations working in Kyrgyzstan to improve energy efficiency standards. The suggested values with the range of average thermal conductivity are mentioned in Tab. 1. The use of specified materials is not widespread in Kyrgyzstan because of the lack of knowledge and limited income sources of rural people.

Tab. 1 Comparative analysis of the thermal performance of natural insulation materials and synthetic materials (data according to CEEBA, 2011; Aditya et al., 2017; UNIDO, 2017; KyrSEFF, 2018; Polonets, 2019)

Type	Material	Thermal conductivity in W/(m·K)	Recommended minimum thickness in mm		
			Walls	Floor	Roof
Natural material	Sheep wool	0.038 - 0.054	60	60	100
	Straw-bale	0.028 - 0.030	40	40	100
	Reed panel	0.055 - 0.070	90	90	150
Synthetic material	Fiberglass	0.030 - 0.040	-	-	-
	Polystyrene (EPS)	0.038 - 0.042	50	50	100
	Polyurethane	0.021 - 0.038	30	30	80
	Penoplex	0.028	30	30	60

4. Comparative analysis of insulation structures on space heating demand

4.1 Application of thermal insulation in rural Kyrgyz houses

The assessment identified that both natural and synthetic insulation materials are available in Kyrgyzstan. Synthetic materials are mainly available in urban areas but are not easily accessible in rural areas. Furthermore, synthetic materials (generally industry processed) are expensive and – due to the poverty of rural Kyrgyz people – not affordable for a typical villager. There is therefore an urgent need to develop affordable insulation methods based on natural resources, which are widely and locally available in rural Kyrgyzstan to reduce the over usage of non-sustainable solid fuels. Hence, this research article considers the natural insulation materials in Tab.1 to develop insulation methods and to assess their effectiveness in reducing the space heating demand.

In general practice, it is a strategic approach to insulate a building from main components, including walls, doors and windows, where heat transfer predominantly takes place (Aditya et al., 2017). However, traditional buildings in Kyrgyzstan have different characteristics, such as an open space between ceiling and roof, natural walls as well as an uninsulated or poorly insulated floor and ceiling. Therefore, this research article considers the typical vernacular architecture of Kyrgyzstan and different classified categories for insulation application as mentioned in Tab. 2.

Tab. 2 Details of various cases of application of thermal insulation for investigation

Case studies for investigation	Case 1	Case 2	Case 3
	Closing of open roof from both sides (roof cover)	Insulation of existing rural houses	Insulation of new house construction
Roof cover	✓	-	-
Wall insulation	-	✓	✓
Floor insulation	-	-	✓
Ceiling insulation	-	✓	✓

4.2 Development of simulation models and results for different cases

The investigation recommended the various thermal insulation approaches using the available sustainable materials and their effects on the overall thermal load of a rural house. To evaluate the impact of various insulation methods, a high-altitude single-family house, situated in rural Kyrgyzstan was modeled and its thermal load was calculated in *EnergyPlus* (NREL, 2019). The uninsulated house model was later modified by the application of thermal insulation methods to investigate the different cases mentioned in Tab. 2. To identify the influence of the thermal insulation, the improved heat demand of an insulated house was compared with the heat demand of an uninsulated house.

- Uninsulated house

The typical uninsulated rural Kyrgyz house was modelled in *EnergyPlus* based on the author's observations and interviews with rural Kyrgyz people living in the rural Naryn region. The selected single-family house was designed without any thermal insulation and provided 100 m² of living area with a single thermal zone. The orientation of the house was assigned to the northern hemisphere. Two windows were considered, one in the eastern wall and one in the western wall, each with an area of 6 m^2, in order to maximize solar gains. To achieve and maintain thermal comfort in the reference house, the heating set point of the house was considered to be 20 °C. The construction of the opaque elements (walls, floor, and ceiling) is described in Tab. 3.

Tab. 3 Assigned data set to *EnergyPlus* for construction of buildings elements

Assembly	Layer	Thickness [m]	Conductivity [W/(mK)]	Density [kg/m³]	Capacity [kJ/(kgK)]	U-value [W/(m²K)]
Wooden beam ceiling with gable roof	Clay-straw mixture	0.03	0.10	300	0.90	0.86
	Spruce wood	0.08	0.13	450	1,60	
External walls	Lime render	0.02	0.87	1,400	1.00	1.13
	Adobe brick	0.40	0.58	1,600	0.84	
	Lime render	0.02	0.87	1,400	1.00	
Floor	Spruce wood	0.05	0.13	450	1.60	1.48
	Concrete slab	0.25	2.00	2,400	0.95	
Window	Glass	0.006	0.90	-	-	3.6
	Air	0.003	-	-	-	
	Glass	0.006	0.90	-	-	

The heat demand of the reference house was calculated in *EnergyPlus* by considering the heat losses through different building components (i.e. walls, floor and ceiling), local climate, occupant's behavior, internal gains, external solar gains etc. To simulate the open roof space in *EnergyPlus*, the reference house with an open roof space was developed as a rectangular-shaped single node model, where the exterior ceiling which was not exposed to solar irradiation but to convection by the wind. Fig. 5 represents the obtained monthly space heating demand of the specified reference house with the monthly average temperature. The annual specific heat demand of single-family houses in rural Kyrgyzstan for space heating is 302 kWh/m^2 which is validated with the available literature (Bergström and Johannessen, 2014; Kerimray et al., 2017).

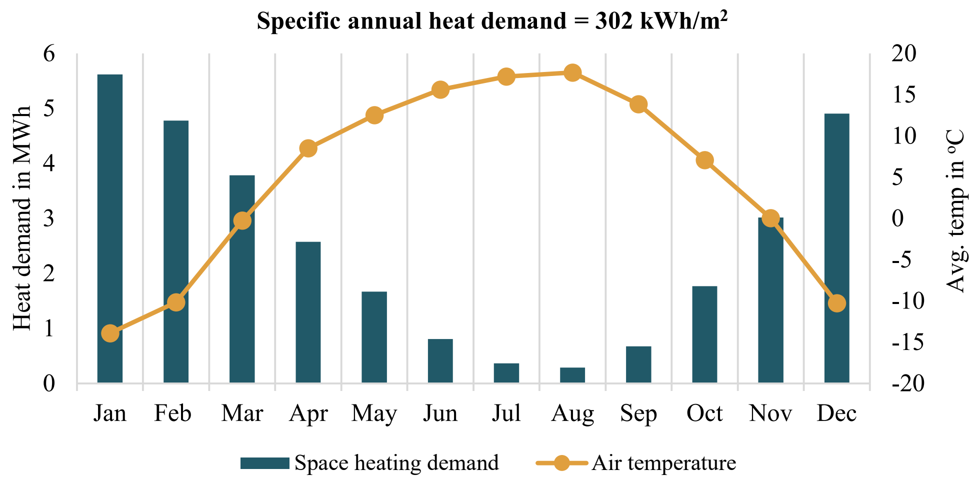

Fig. 5 Monthly space heating demand of reference (uninsulated) building and average ambient temperature of location

- Case 1: Closing of open roof from both sides (roof cover)

In the older and cheaply constructed houses, the metal roof is placed on the wooden beam ceiling. However, because of the concentrated poverty in rural areas and traditional building construction methods, the gable roof usually is not covered at either end, which creates an open space between the ceiling and gable roof (see Fig. 2). This is a prevalent practice for low-income Kyrgyz households. Naturally, the open space induces a considerable amount of heat loss during windy days. The closing of the open roof of typical buildings can be helpful to reduce the thermal load of the house. Therefore, in the presented article, this case was considered as case 1 by covering the roof to investigate its impact on the thermal load of the reference building.

To investigate case 1, the open roof of an uninsulated house was covered with a thick layer of spruce wood (0.05 m) from both sides in order to prevent air leakage through the uncovered space between the ceiling and roof. This case was modelled without any additional application of insulation materials. The result of case 1 is presented in Tab. 4, which outlines the heat demand comparison of the reference uninsulated house with an open and a closed roof.

Tab. 4 Comparison of specific annual heat demand for case 1

Uninsulated house with open roof	Uninsulated house with closed roof
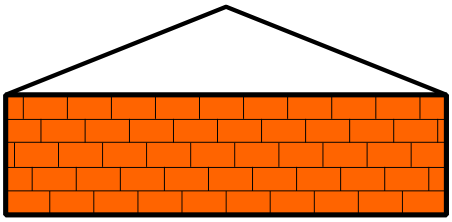	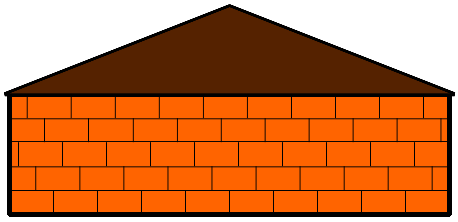
Specific annual heat demand = 302 kWh / m^2	Specific annual heat demand = 243 kWh / m^2

- Case 2: Insulation of existing rural houses

A potential way to improve energy efficiency standards of the existing traditional rural buildings will be to apply insulation layers on the exterior walls as well as on ceiling. Therefore, for case 2, an existing house was modelled and simulated by the application of different insulation structures on walls and ceiling.

- Case 3: Insulation of new house construction

This case was designed and investigated for considering a new house under construction where the opportunity is available to insulate building walls, floor and ceiling. The selected house was insulated with natural insulation materials on the walls, floor and ceiling. The schematic of insulation structures for case 2 and case 3 is shown in Tab. 5.

Tab. 5 Schematic of insulation structures with the different natural insulation materials for walls, ceiling and floor

(= Adobe brick, = Lime render, = Ceiling spruce wood, = Concrete slab, = Floor spruce wood, = clay-straw mixture, = Sheep wool, = Straw-bale, =Reed panel)

	Uninsulated assembly	Sheep wool assembly	Straw-bale assembly	Reed panel assembly
Wall	≈ 0.40 m of adobe brick with a thin layer of lime render	Insulation thickness 0.06 m	Insulation thickness 0.04 m	Insulation thickness 0.09 m
	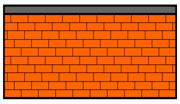	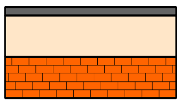	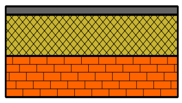	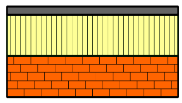
Ceiling	≈ 0.15 m of spruce wood with the thin layer clay-straw mixture	Insulation thickness 0.10 m	Insulation thickness 0.10 m	Insulation thickness 0.15 m
	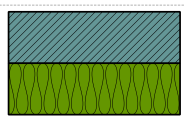	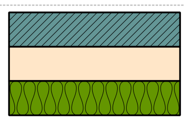	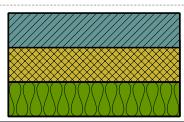	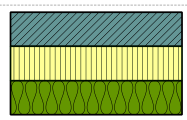
Floor	≈ 0.25 m of a concrete slab with a thin layer of spruce wood	Insulation thickness 0.06 m	Insulation thickness 0.06 m	Insulation thickness 0.06 m
	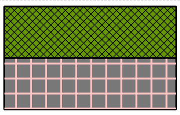	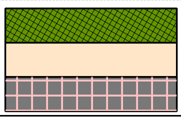	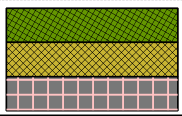	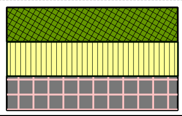

The results of thermal insulation and its impact on space heating demand were compared with the space heating demand of a traditional rural house (uninsulated) to outline the influence of insulation measures. The results of case 2 and case 3 are presented in Tab. 6 and Tab. 7 respectively.

Tab. 6 Effectiveness of various insulation structures on space heating demand (case 2: Insulation of existing rural

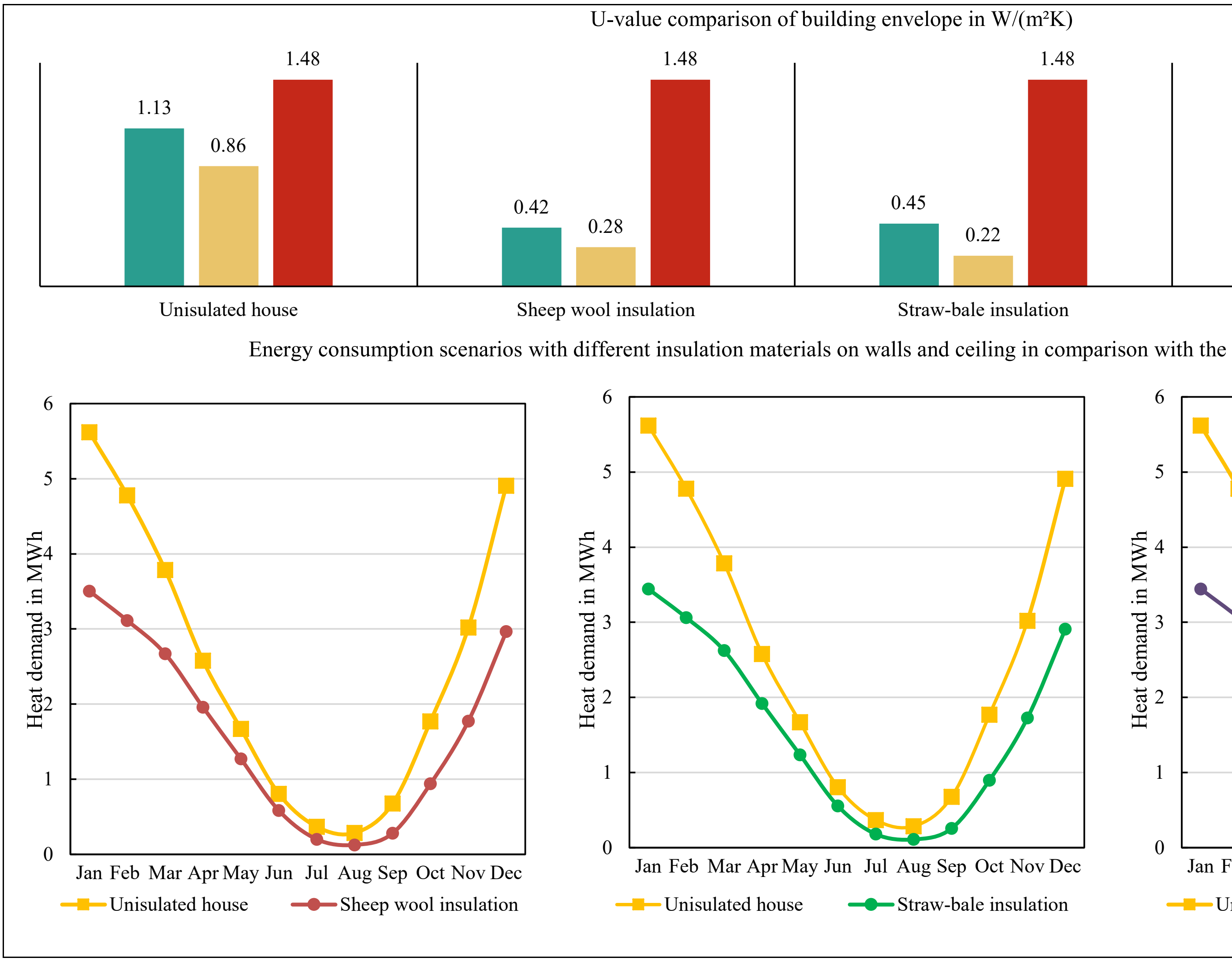

Tab. 7 Effectiveness of various insulation structures on space heating demand (case 3: Insulation of new house cons

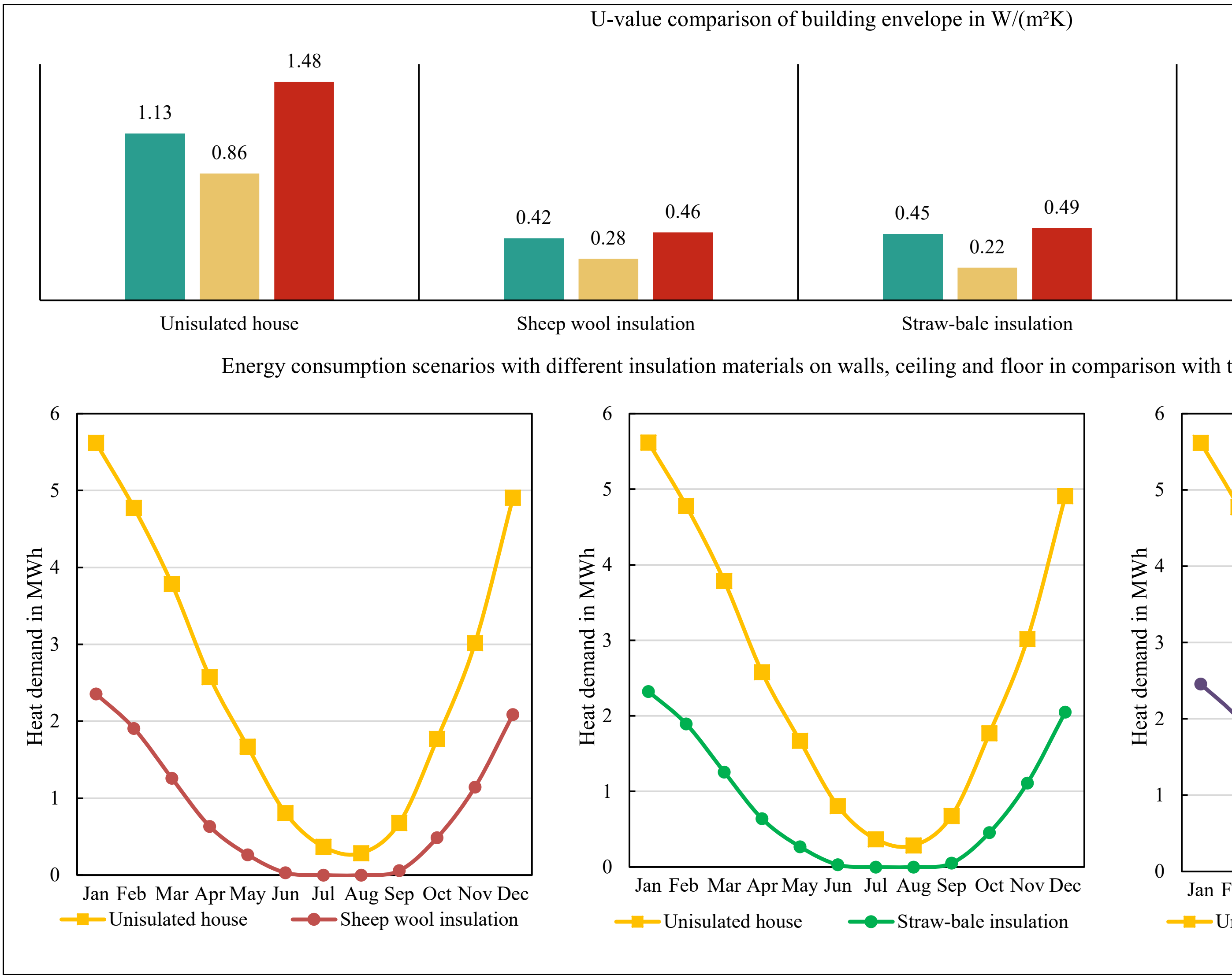

To summaries the effectiveness of different design concepts, the specific annual heat demand of various cases is presented in Tab. 8.

Tab. 8 Summary of results of comparative analysis of insulation structures on space heating demand

Insulation type	Insulation condition				Specific annual heat demand in kWh/m²
	Roof cover	Walls	Ceiling	Floor	
Uninsulated house	-	-	-	-	302
	✓	-	-	-	243
Sheep wool insulation	-	✓	✓	-	193
	-	✓	✓	✓	102
Straw-bale insulation	**-**	**✓**	**✓**	**-**	**189**
	-	**✓**	**✓**	**✓**	**100**
Reed panel insulation	-	✓	✓	-	197
	-	✓	✓	✓	107

It can be observed from the results that depending on the insulation type in combination with insulation parameters, a considerable amount of heat demand can be reduced while maintaining comfort levels. The investigation identified that covering the open sides of the roof raises the opportunity to decrease the specific heat demand by up to 20 %. The insulation application to walls and ceiling can save up to 100 kWh/year of heat demand in existing vernacular Kyrgyz buildings. Furthermore, the consideration of good insulation layers to walls, ceiling and floor (in case of new building construction) means that about 200 kWh/year of thermal energy can be reduced per square meter. It can be seen from Tab. 8 that the straw-bale insulation structures have a substantially better effect on reducing space heating demand than other methods.

The natural materials mentioned in the study are locally available. Existing low-income rural households can adopt the presented idea to insulate their houses to reduce the space heating demand. Naturally, the reduction of thermal load can substantially reduce their heating fuel expenditure. The proposed investigation also suggested the sequence to insulate rural Kyrgyz house from derived results. Application of insulation layers to walls and ceiling can make a significant influence on heat demand and heating costs can be reduced by 10 to 30% according to house size and building construction quality. Also, according to future financial capability, one can introduce roof cover to the insulated house to reduce the heat leakages from open space, which can help to cut down the heating expenses up to 40 to 50 %.

5. Conclusions

The cold climate and high-altitude characteristics of Kyrgyzstan are experienced as a long and harsh winter period. The old and traditional buildings without any thermal insulation aggravate the high space heating demand in Kyrgyz houses, especially in rural regions. This high thermal demand of the house is principally met by the considerable use of non-sustainable solid fuels. The overuse of solid fuels, especially their combustion in inefficient traditional heating stoves exposes rural Kyrgyz people to indoor and outdoor air pollution. Appropriate thermal insulation is necessary to reduce the high space heating demand in rural Kyrgyzstan. However, because of the widespread and deep poverty as well as the lack of awareness in rural Kyrgyzstan, insulation measures are seldomly considered during building construction. Therefore, the presented research article has considered locally available natural and sustainable materials for the investigation, to make the insulation structures economically feasible.

Three widely available natural insulation materials of sheep wool, straw-bale and reed panel were chosen to design insulation structures. Various case studies were performed by considering local boundary conditions to conduct the investigation. The results of the assessment highlighted that the thermal insulation measures can substantially reduce the heat demand by up to 30 % in the case of existing houses and up to 70 % for new houses in rural Kyrgyzstan, which will help to reduce a considerable amount of non-sustainable solid fuel use. The presented study was performed by considering the minimum recommended thickness suggested by local organizations. One can perform the study to identify the optimum level of thickness and feasibility study from the economic point of view.

6. Acknowledgments

The work presented in this paper was funded by the Federal Ministry of Education and Research (BMBF) of the Federal Republic of Germany within the CLIENT II funding programme International Partnerships for Sustainable Innovations under the project “ÖkoFlussPlan” (Project ID 01LZ1802A-F). The overall aim of ÖkoFlussPlan is to preserve the alluvial forests along the Naryn river and to implement sustainable energy solutions for the local population.

7. References

Aditya, L., Mahlia, T.M.I., Rismanchi, B., Ng, H.M., Hasan, M.H., Metselaar, H.S.C., Muraza, O., Aditiya, H.B., 2017. A review on insulation materials for energy conservation in buildings. Renewable and Sustainable Energy Reviews 73, 1352–1365.

Balabanyan, A., 2015. Keeping warm: Urban heating options in the Kyrgyz Republic. Summary report (English). The World Bank Group, Washington, DC. http://documents.worldbank.org/curated/en/555021468011161504/pdf/97409-WP-P133058-Box391503B-PUBLIC-Heating-Assessment-for-Kyrgyz-P133058-Final.pdf. Accessed 27 April 2020.

Bergström, S., Johannessen, F., 2014. Sustainable housing in Kyrgyzstan. Investigation of two multi- apartment buildings in Bishkek. The Department of Energy Sciences. Lund University, Faculty of Engineering, Lund. http://www.ees.energy.lth.se/fileadmin/ees/Publikationer/Ex5297-Bergstrom_Johannessen.pdf. Accessed 18 February 2020.

FAO, 2016. National gender profile of agricultural and rural livelihoods - Kyrgyz Republic. Country gender assessment series. Food and Agriculture Organization of the United Nations, Ankara (Turkey). http://www.fao.org/3/a-i5763e.pdf. Accessed 20 July 2020.

Hall, K., 2018. Supporting energy efficiency and renewables uptake in rural communities in mountainous Kyrgyzstan. Mountain Societies Research Institute, Bishkek (Kyrgyzstan).

IEA, 2017. Total primary energy supply (TPES) by source. https://www.iea.org/data-and-statistics?country=KYRGYZSTAN&fuel=Energy%20supply&indicator=Total%20primary%20energy%20supply%20(TPES)%20by%20source.

Kerimray, A., Miglio, R.D., Solorzano, L.R., Gallachóir, B.Ó., 2017. Household Energy Consumption and Energy Poverty in Kazakhstan IAEE Energy Forum 26, 31–34.

Köppen, Geiger, 2016. Kyrgyzstan map of Köppen climate classification. https://commons.wikimedia.org/wiki/File:Kyrgyzstan_map_of_K%C3%B6ppen_climate_classification.svg.

KyrSEFF, 2018. РУКОВОДСТВО для монтажников. Sustainable Energy Fund of Kyrgyzstan, Bishkek (Kyrgyzstan).

MEI, 2013. Microfinancing household insulation and heating measures in Kyrgyzstan. An Assessment Study by MicroEnergy International for Deutsche Gesellschaft für Internationale Zusammenarbeit GmbH. MicroEnergy International, Berlin (Germany). https://eba.klink.asia/klink/ccf9ca/download. Accessed 25 January 2019.

NREL, 2019. EnergyPlus. U.S. Department of Energy.

NSC, 2018. National Statistical Committee of the Kyrgyz Republic. Kyrgyzstan. Brief statistical handbook. Annual publication, Bishkek (Kyrgyzstan). http://www.stat.kg/media/publicationarchive/16db2910-6b8d-48f9-80b9-45b7ac3347bd.pdf. Accessed 10 August 2020.

Polonets, L., 2019. РУКОВОДСТВО для монтажников. Energy Centre Bratislava and CAMP Alatoo, Bratislava (Slovakia).

Sagynbekova, L., 2017. Environment, Rural Livelihoods, and Labor Migration. A Case Study in Central Kyrgyzstan. Mountain Research and Development 37 (4), 456–463.

UNDP, 2018. Latest Human Development Index (HDI) ranking. http://hdr.undp.org/en/2018-update. Accessed 24 February 2020.

UNECE, 2018. Mapping of Existing Energy Efficiency Standards and Technologies in Buildings in the UNECE Region, Geneva (Switzerland). https://www.unece.org/fileadmin/DAM/hlm/Meetings/2018/09_05-

07_St._Petersburg/EE_Standards_in_Buildings_full_version.ENG.pdf.

UNFCC, 2017. Third National Communication of the Kyrgyz Republic under the UN Framework Convention on Climate Change, Bishkek (Kyrgyzstan). https://unfccc.int/sites/default/files/resource/NC3_Kyrgyzstan_English_24Jan2017.pdf.

UNICEF, 2013. Improving Energy Efficiency in Buildings. United Nations Development Programme. https://www.kg.undp.org/content/kyrgyzstan/en/home/operations/projects/sustainable_development/energy-efficiency-buildings.html.

UNIDO, 2017. Thermal Insulation. Propoerties and apllications in housing. United Nations Industrial Development Organization, Vienna (Austria).

USAID, 2018. Climate risk profile. Kyrgyz Republic. https://www.climatelinks.org/sites/default/files/asset/document/2018_USAID-CCIS-Project_Climate-Risk-Profile-Kyrgyz-Republic.pdf.pdf.

Wiedemann, C., Salzmann, S., Mirshakarov, I., Volkmer, H., 2012. Thermal Insulation in High Mountainous Regions. Mountain Research and Development 32 (3), 294–303.

World Bank, 2016. Kyrgyzstan: Poverty headcount ratio at national poverty lines (% of population). https://data.worldbank.org/indicator/SI.POV.NAHC?locations=KG. Accessed 15 August 2020.

World Bank, 2020. Fueling Kyrgyzstan’s Transition to Clean Household Heating Solutions. The World Bank Group, Washington, DC.

DESIGN AND MONITORING OF A SOLAR THERMAL, PV AND HEAT PUMP SYSTEM

Georgios Dermentzis[1,2], Fabian Ochs[1] and Nicola Franzoi[1]

[1] University of Innsbruck, Innsbruck (Austria)

[2] Aristotle University of Thessaloniki, Thessaloniki (Greece)

Abstract

Two new, residential, and high-performance buildings were constructed in Innsbruck, Austria (with cold winters and mild summers) aiming to achieve net-zero energy building (NZEB) standard. The design was supported by the Passive House design tool PHPP. A groundwater heat pump, solar thermal collectors, photovoltaic panels (PV), and heat recovery ventilation units were installed. On one building a solar thermal system of 74 m^2 and a PV system of 52.5 m^2 and in the other building a PV system of 99.8 m^2 were installed. Four years of monitoring data are available. In this study, a monthly comparison between the monitoring data and the design values (PHPP) is presented concerning the performance of solar thermal, PV, and the heat pump. In addition, the efficiency of the solar thermal system is compared against the one of PV driven heat pump system, and the direct exploitation of onsite electricity generation is analyzed.

Keywords: solar thermal, PV, heat pump, in-situ monitoring, PHPP, NZEB

1. Introduction

The recast of the European building directive (Directive 2010/31/EU, 2010) defined the path to nearly zero energy buildings (nZEB). Three aspects are addressed: (a) new buildings will have a very high-energy performance, (b) the remaining very low energy demand will be provided to a very significant share by renewable energies, and (c) cost-optimal levels for minimum energy performance are requested.

Hence, the aim of the EPBD recast was the minimization of the residual energy demand and CO_2-emissions, while economics should be considered. Thus, future buildings should have a very high-energy performance, such as Passive Houses, and should be operated e.g. with a heat pump together with a significant amount of energy from cost-effective renewable energy sources (PV and/or solar thermal).

As Ochs et al. (2017) described, the definition of nZEB varies among the different EU member countries, while net-zero energy buildings (NZEB) is the building with an annual balance between the electricity from and to the grid. Several studies about nZEB (Ascione et al., 2016; Attia et al., 2013; Becchio et al., 2015; Deng et al., 2014; Kneifel and Webb, 2016; Tsalikis and Martinopoulos, 2015) and NZEB (Attia et al., 2017; Goggins et al., 2016; Guillén-Lambea et al., 2017; Kurnitski et al., 2011; Lu et al., 2017; Paiho et al., 2017; Santoli et al., 2014) can be found in the literature. However, the implementation of the EPBD is far less ambitious in some of the European member countries (BPIE, 2016). The more important is it to demonstrate best practice examples and highlight non-renewable primary energy and CO_2-savings.

A dominating concept to reach the zero-energy balance over an annual period for an nZEB and NZEB is the combination of solar PV systems and heat pumps. In the IEA HPT Annex 49 (A49, n.d.), a follow-up of Annex 40, heat pump integration options for nZEBs are investigated as well as the design and control for heat pumps in nZEB and the integration into energy systems. Solar thermal can be relevant as it is technically and economically less challenging to store heat compared to the storage of electricity. Storage is relevant to reduce the remaining electricity usage in winter, which has generally a higher fossil (and/or nuclear) share. Hence, nZEBs should be evaluated considering the time of electricity usage from the grid.

“NZEB” as a goal can be a misleading concept, since an optimization for net-zero may lead to one-story buildings because reaching the net-zero balance is more difficult compared to a multi-story building (with smaller roof and façade area related to the treated area). However, MFHs, which are more compact, are favorable from the overall energetic and macro-economic point of view, compare also (Feist, 2014).

In this paper, the results of the monitoring of four seasons are highlighted and the monitored energy

doi:10.18086/eurosun.2020.04.05 Available at http://proceedings.ises.org

performance is compared to the designed one based on a steady-state calculation using the Passivhaus Planning Package (PHPP). The focus is on solar thermal, PV, and heat pump. The present study enhances the discussion about the design and evaluation of NZEBs using solar energy with a monitoring example from central Europe.

2. Concept

Two residential Passive House buildings were constructed in Innsbruck, Austria. The two multi-family houses consist of 26 apartments - 16 in the north building and 10 in the south building. In this project, the goal was to reach the NZEB standard, which was defined as the annual balance between the electricity consumed for heating (space heating and domestic hot water) and ventilation (excluding household appliances), and the electricity produced by renewable sources. Fig. 1 presents a simplified hydraulic scheme of the heating system. A two-stage groundwater source heat pump with a power of 58 kW (at W10/W35) including a desuperheater was used. The available roof space of the north building was covered by a solar thermal system with 74 m^2 and PV with 52.5 m^2 (8.5 kWp). An additional PV system of 99.8 m2 (16 kWp) was placed on the roof of the south building. The ventilation units were centralized (three in total) including heat recovery. In combination with floor heating and a heat exchanger in each flat for domestic hot water (DHW), a four-pipe distribution system was used to minimize the distribution losses; two pipes for the DHW (flow temperature of 52°C) and two pipes for the space heating (with flow temperature of 35°C). Therefore, stratification was obtained in the 6000 liter storage to improve energy performance, since the heat pump can operate at a low sink temperature for supplying space heating.

Through a simulation study, the share of PV (max 19 KWp) and solar thermal collectors (ST) was varied to determine the maximum possible energy yield considering PV and ST system efficiencies including heat pump performance and distribution losses (Tab. 1). The optimal design (from an energetic point of view) was found to be 74 m² ST and correspondingly 53 m² PV on the north roof (Ochs et al., 2014).

During the final design process and the construction of the two buildings, some parameters changed concerning the original planning. The floor heating flow temperature is 30 °C (30/26 °C instead of 28/24 °C) and the DHW flow temperature is 55 °C. A 3-pipe system with a common return pipe of floor heating and DHW was installed instead of the initially proposed 4-pipe system.

Tab. 1: Characteristic data of the two buildings NHT Vögelebichl according to the design (Ochs et al., 2014)

	North building	South building
Number of Flats	16	10
Treated area	1269.8 m²	818.8 m²
Designed Heating Demand (PHPP)	13.5 kWh/(m² a)	17.0 kWh/(m² a)
Designed Heating Load (PHPP)	12.0 W/m²	13.9 W/m²
PV size	8.5 kWp	16 kWp
Solar Thermal (ST)	50 m² (ca. 35 % of roof area)	-
Buffer storage	6000 Liters	

A detailed monitoring system was installed consisting of 58 temperature sensors, 12 humidity sensors, 2 pressure sensors, 37 signals (e.g. controllers, valves, pumps, etc.), 22 heat meters, 7 electricity meters, and 2 volume flow meters. The focus was on energy performance. The thermal comfort of the south building is monitored, too. The operation of a monitoring system has started in November 2015, thus, monitoring data of four years are available.

During the design phase of the project, PHPP (Feist, 1998) was used as an energy calculation tool. PHPP uses monthly energy balance (ISO, 2008) with a detailed description of the building envelope including thermal bridges, ventilation, DHW (incl. distribution losses), etc., and also includes the prediction of the performance of air or ground-coupled heat pumps using an improved bin method. It includes an algorithm to predict the use of solar thermal energy. In addition, it calculates the electricity produced by a PV system. Finally, it is cross-validated against measured data and simulation results.

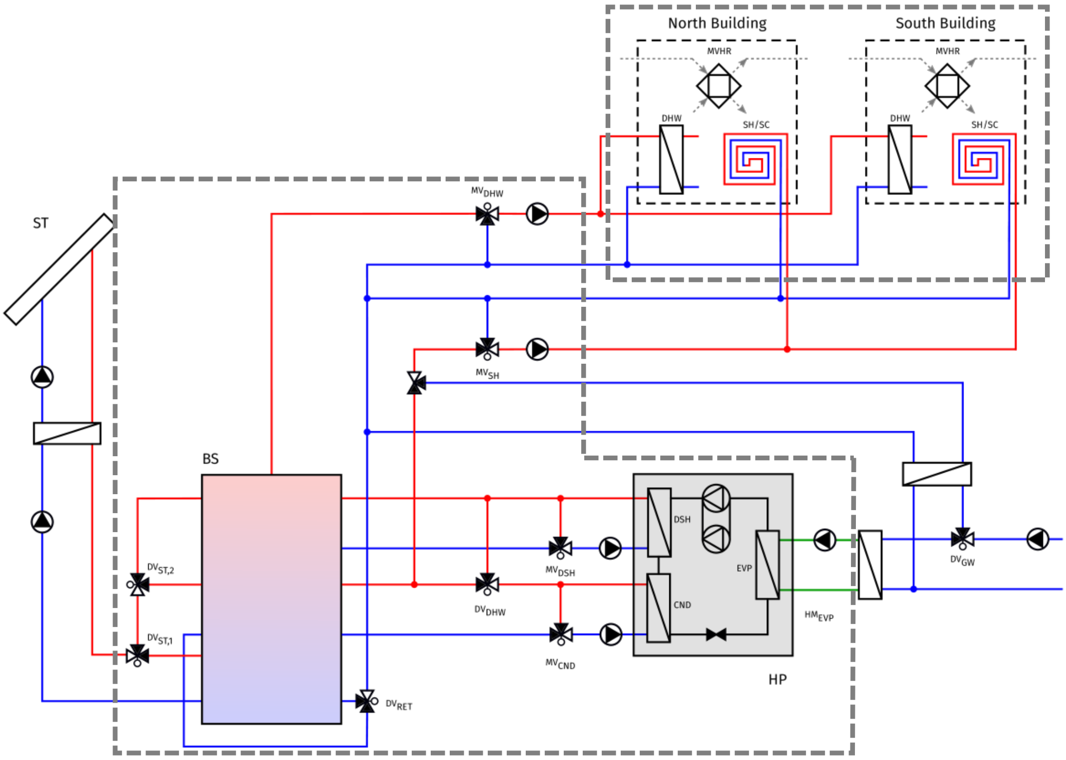

Fig. 1: Simplified hydraulic scheme with Solar Collectors (SC), Buffer Storage (BS), 2-stage ground-water heat pump (HP) with desuperheating (DSH) in heating mode with floor heating and decentral heat exchanger for domestic hot water (DHW) supply (Franzoi, 2020)

3. Design and monitoring results

3.1. Solar thermal

In Fig. 2, the monthly thermal energy production of the ST system is depicted. The bars show the monitoring values of the four years, and the lines, the calculated values in PHPP. Two cases are presented using PHPP: the ‘design’ one that corresponds to the values during the design phase, and the ‘calibrated’ one in which the heating and DHW demands are calibrated to the monitoring data (this has been done since the algorithm for the ST production depends on the heating and DHW demand, which is an input). It can be observed that the ‘PHPP design’ is on the safe side compared to the monitoring results, especially during the summer months. However, ‘PHPP calibrated’ is in a good agreement with the monitoring data, e.g. in 2018, PHPP calculated 12% less energy compared to the measured one.

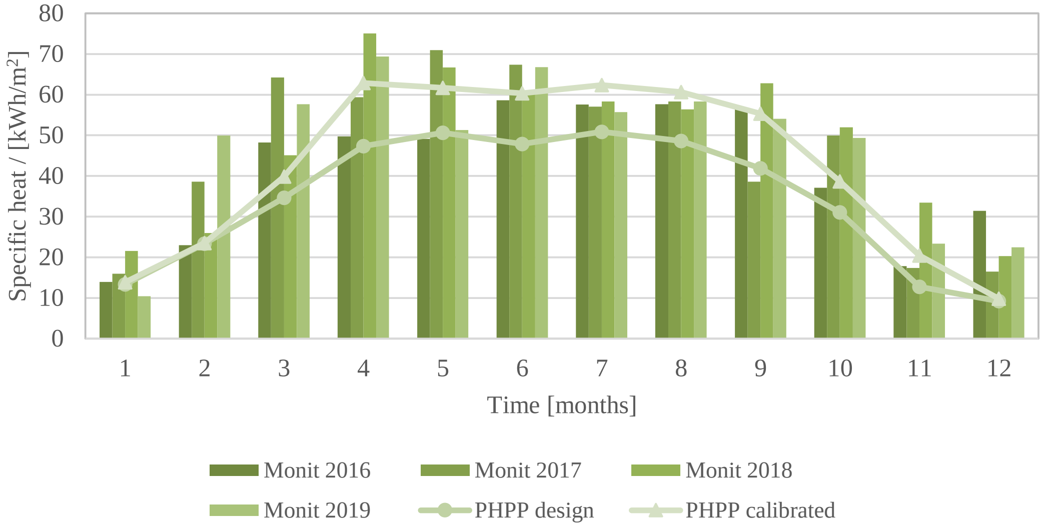

Fig. 2: Thermal energy produced by the solar collectors (ST) from 4 monitoring years and the predicted one by PHPP (once the original design values and once with calibrated heating and DHW demand).

Fig. 3 shows the 'PHPP calibrated' values of the ST versus the minimum, average, and maximum monthly monitoring values. PHPP is close to the minimum values from October to March and close to the average values in the rest months. Thus, PHPP has higher accuracy in summer months (with high ST production) and slightly underestimation in winter months (with low ST production).

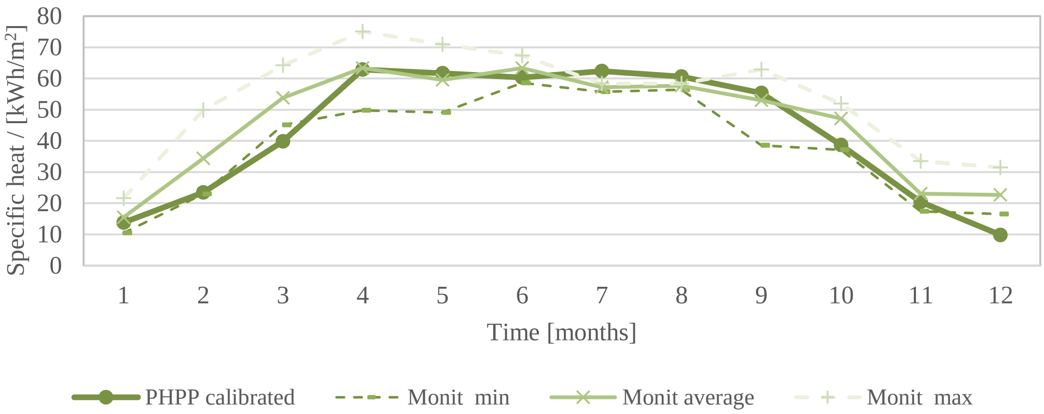

Fig. 3: Comparison of monthly ST production between PHPP and 4 years of monitoring data.

3.2. PV System

The monitored and predicted monthly electricity yield of the PV system is presented in Fig. 4, and in annual values in Tab. 2. PHPP underestimates the PV production in the non-winter months. On an annual basis, PHPP predicted 26% to 35% less electricity production than measured.

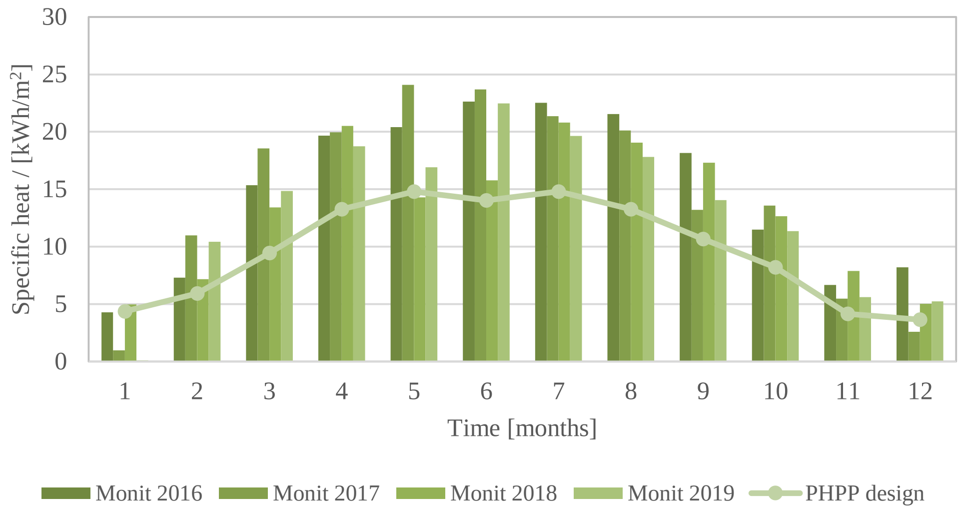

Fig. 4: Monthly measured (of the four monitoring years) PV yield and design PV yield in PHPP.

Tab. 2: Annual comparison of the measured (of the four monitoring years) and designed PV yield

Year	**Design [kWh m^{-2}]**	**Monitoring [kWh m^{-2}]**	**Difference [%]**
2016	117	178	35%
2017		175	33%
2018		159	27%
2019		157	26%

3.3. Solar thermal versus PV driven heat pump

Fig. 5 shows the comparison for the supplied heat of the ST and PV driven heat pump for the 4th year of monitoring (2019). The monthly PV electricity is multiplied with the monthly seasonal performance factor of the heat pump (SPF_HP) and then it is compared to the ST produced heat. The ST production is higher than the heat delivered by the PV driven heat pump in every month. The difference seems to be lower in winter months. In annual values, ST produces 28 % more heat. It is important to note that storage losses were excluded in this comparison.

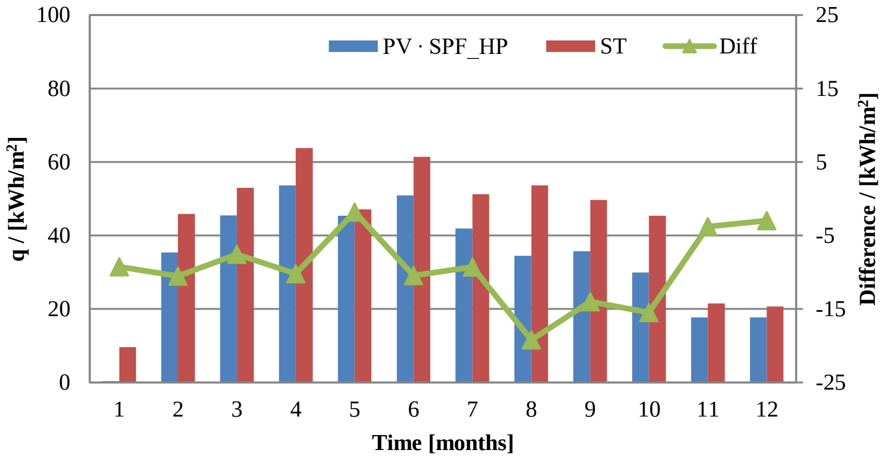

Fig. 5: Thermal energy supplied by PV driven heat pump (HP) and ST per installed square meter of each system (PV and ST). The produced electricity from PV is multiplied with the monthly SPF of the heat pump (including the HP related pumps). Monitoring results of the year 2019

The annual comparison between ST and PV driven heat pump is presented in Fig. 6. Overall, ST is preferable from the energy point of view, since it produces from 6% to 36% more heat compared to the PV driven heat pump. Notice that in 2018 there was a failure of the inverter on the north building, therefore the PV yield is significantly lower than the other years.

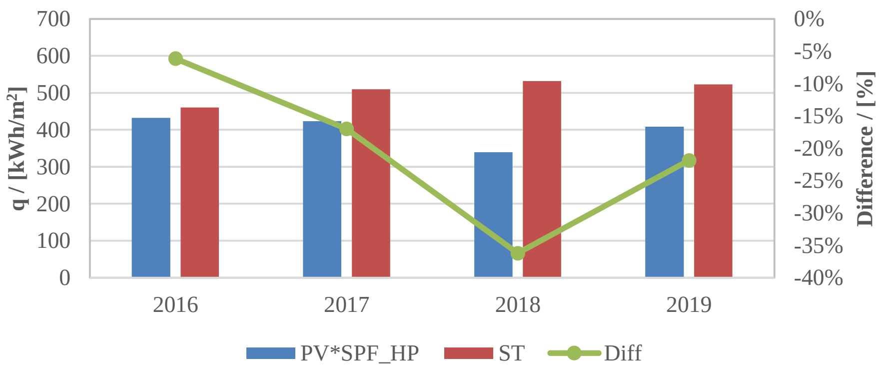

Fig. 6: Monitoring results of four years. Thermal energy supplied by PV driven HP and ST per installed square meter of each system (PV and ST). The produced electricity from PV is multiplied with the monthly SPF of the heat pump (including the HP related circulation pumps).

4. PV supply and load cover factors

4.1 HP and PV evaluation with PHPP

Within Task 56 ("IEA SHC Task 56/ Building Integrated Solar Envelope Systems, International Energy Agency,"), a new worksheet (add-on) for PHPP was developed to calculate the monthly electricity consumption of a heat pump having as input the annual electricity consumption from PHPP 'HP' sheet, and the monthly photovoltaic (PV) self-consumption (Ochs et al., 2020). The annual electricity consumption of the heat pump is distributed to the months based on the Carnot method in a post-processing step. This is performed separately, once for the use of a heat pump for space heating and once for domestic hot water preparation. Furthermore, the use of a solar thermal system in combination with the heat pump is possible.

As an outcome, the calculation of supply (SCF) and load cover factors (LCF) is possible. The supply (SCF) and load cover factors (LCF) indicate the direct utilization of the onsite electricity generation. The SCF is the ratio of self-consumed energy to the onsite generation energy, therefore representing the percentage of supplied energy directly consumed onsite. The equation representing the SCF is

$$\mathrm{SCF} = \frac{\int \dot{W}_{sc} dt}{\int \dot{W}_{PV} dt} \qquad \text{(eq. 1)}$$

where $\dot{W}_{sc}$ is the self-consumed power and $\dot{W}_{PV}$ is the PV generated power.

The LCF represents the fraction of the total consumed energy that is directly provided by the onsite generators being defined as the ratio of the self-consumed energy to the total energy consumption.

$$\mathrm{LCF} = \frac{\int \dot{W}_{sc} dt}{\int \dot{W}_{C} dt} \qquad \text{(eq. 2)}$$

where $\dot{W}_C$ is the total consumed power.

4.2 Supply cover factors (SCF) and load cover factors (LCF) in the case study

The SCF and LCF for the heating and non-heating seasons of 2019 and the estimated SCF and LCF of 2018 are reported in Tab. 3. The total energy consumption is considered for the calculation of SCF and LCF. It includes the electric energy needed by the HVAC (from monitoring) and the energy used for the household appliances. As appliances were not monitored, an optimistic annual consumption of 1500 kWh/a per flat is used as annual appliances energy consumption. As a load profile, the average electric energy consumption of 74 residential buildings in Germany was used as reported in Tjaden et al. (2015).

Fig. 7 presents the electricity consumption of the heat pump and the auxiliaries as well as the electricity produced by the PV in 2019. There is a surplus in the summer months, but in winter, the coverage of the consumed electricity by PV is insignificant.

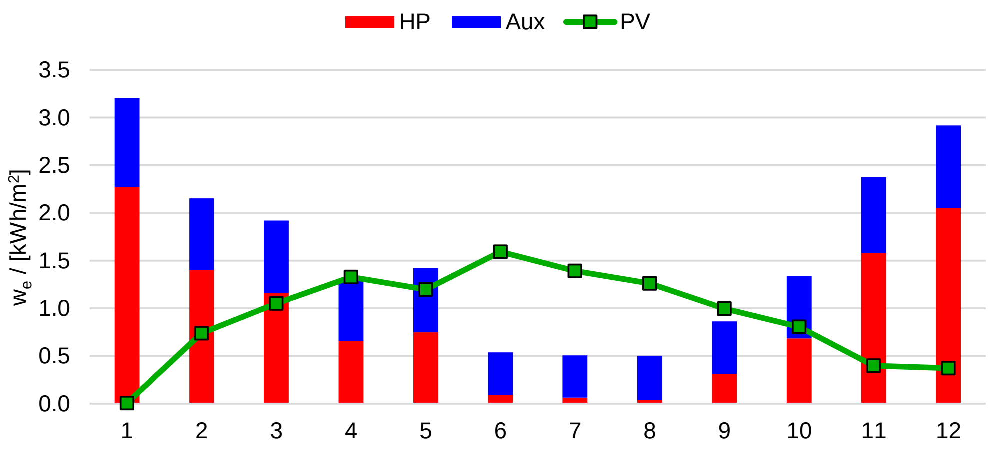

Fig. 7: *Monthly electricity consumption by the HP and the auxiliaries, and PV electricity yield in 2019* (*Final report IEA HPT Annex 49 Task 3, Field monitoring in nZEB*, 2020)

SCF and LCF can be evaluated from the monitoring data for 2019, while data gaps in the monitoring in 2017 and 2018 do not allow for a complete calculation of the actual self-consumption. However, for 2018 it is possible to estimate the self-consumption by simulating the power profile of the PVs. Therefore, a model of the PVs was realized in Simulink using the CARNOT library, and parametrized to the monitoring data of 2019, leading to a relative error between the predicted and measured energy of 6%, with the simulation model slightly overestimating the onsite generation. The measured and simulated PV energy yield relative error in 2018 is 8%. Being the estimated energy generation overestimated, the resulting factors for 2018 might be slightly overestimated, too.

Fig. 8 shows the total power and PV generated power profiles for a winter and summer day in 2019, with a shaded area representing the self-consumed energy. During the summer day, it can be noticed that the power consumption is on average lower than the winter day as a consequence of almost no heat pump operation (the DHW demand is covered mostly by ST). In both cases, the peak power generation is not exploited completely, suggesting that a battery or a control strategy properly programmed could improve the self-consumption.

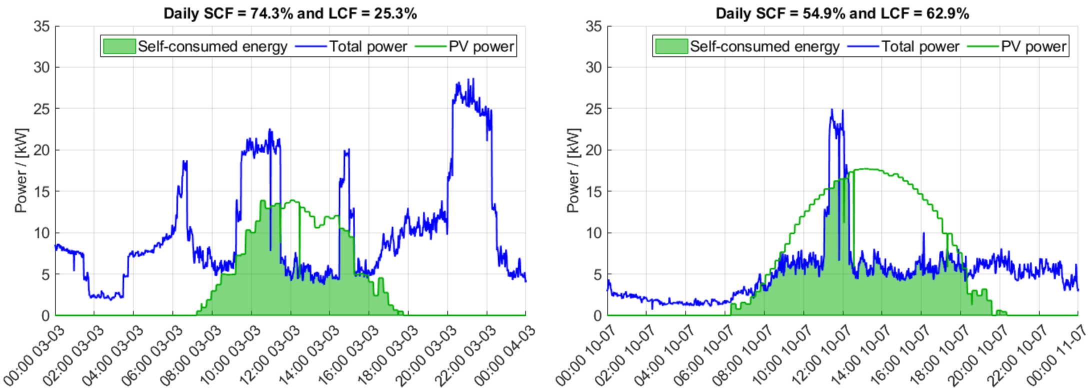

Fig. 8: Left: power profile for a day in the heating season, Right: power profile for a day in the non-heating season, in both figures the share that is self-consumed, is highlighted.

Tab. 3: Load (LCF) and supply cover factor (SCF) in 2019 for the heating and non-heating season and annual

	Heating season		Non-heating season		Annual	
	SCF	**LCF**	**SCF**	**LCF**	**SCF**	**LCF**
2018	84%	13%	62%	40%	67%	24%
2019	84%	6%	60%	31%	64%	18%

The LCF is between 18 % and 24 % (lower in 2019 because of the higher overall consumption) on an annual basis but is only 6 % to 13 % during the heating season, highlighting once more the small contribution of the PV during this season. The SCF is on average 66 % on an annual basis, meaning that throughout the year at least two-third of the generated energy is consumed onsite. Due to the lower consumption during the non-heating season, the SCF results slightly lower than the average and the LCF is significantly higher.

5. Conclusions

The design and monitoring results of a solar thermal, PV, and heat pump system are presented in this paper. The comparison between PHPP and monitoring data showed good agreement in the case of solar thermal energy. PHPP underestimated the PV electricity production, especially in summer months. The solar thermal system produced from 6% to 36% more thermal energy compared to a PV driven heat pump (the monthly PV yield was multiplied to the monthly seasonal performance factor of the heat pump) on an annual basis.

Furthermore, the add-on worksheet in PHPP that calculates among others the supply and load cover factors of PV and heat pump systems (including solar thermal is possible) is presented. The monitoring data analysis showed a load cover factor of 18% and a supply cover factor of 64% in 2019.

6. Acknowledgment

This project is financially supported by Neue Heimat Tirol (NHT), Innsbruck, Austria. Building design optimization, PHPP calculations, and PH certification were done by PHI Innsbruck. The financial supports from the Austrian Ministry for Transport, Innovation, and Technology, and the Austrian Research Promotion Agency (FFG) through the IEA Research Cooperation (IEA HPT Annex 49) to this work are gratefully acknowledged.

7. References

A49, n.d. IEA HPT Annex 49 [www Document]. URL http://heatpumpingtechnologies.org/annex49/

Ascione, F., Bianco, N., Böttcher, O., Kaltenbrunner, R., Vanoli, G.P., 2016. Net zero-energy buildings in Germany: Design, model calibration and lessons learned from a case-study in Berlin. Energy and Buildings 133, 688–710. https://doi.org/10.1016/j.enbuild.2016.10.019

Attia, S., De Herde, A., Gratia, E., Hensen, J.L.M., 2013. Achieving informed decision-making for net zero energy buildings design using building performance simulation tools. Building Simulation 6, 3–21. https://doi.org/10.1007/s12273-013-0105-z

Attia, S., Eleftheriou, P., Xeni, F., Morlot, R., Ménézo, C., Kostopoulos, V., Betsi, M., Kalaitzoglou, I., Pagliano, L., Cellura, M., Almeida, M., Ferreira, M., Baracu, T., Badescu, V., Crutescu, R., Hidalgo-Betanzos, J.M., 2017. Overview and future challenges of nearly zero energy buildings (nZEB) design in Southern Europe. Energy and Buildings 155, 439–458. https://doi.org/10.1016/j.enbuild.2017.09.043

Becchio, C., Dabbene, P., Fabrizio, E., Monetti, V., Filippi, M., 2015. Cost optimality assessment of a single family house: Building and technical systems solutions for the nZEB target. Energy and Buildings 90, 173–187. https://doi.org/10.1016/j.enbuild.2014.12.050

BPIE, 2016. Nearly Zero Energy Buildings in Europe, Energy. Brussels,Belgium.

Deng, S., Wang, R.Z., Dai, Y.J., 2014. How to evaluate performance of net zero energy building – A literature research. Energy 71, 1–16. https://doi.org/10.1016/j.energy.2014.05.007

Directive 2010/31/EU, 2010. Directive 2010/31/EU of the European Parliament and of the Council of 19 May 2010 on the energy performance of buildings. The European Parliament and the Council of the European Union. Official Journal of European Union L153, 13–35. https://doi.org/10.3000/17252555.L_2010.153.eng

Feist, W., 2014. Passive House - the next decade, in: Passive House Institute (Ed.), 18th International Passive House Conference. Aachen, Germany, pp. 635–658.

Feist, W., 1998. PHPP - Passive House Planning Package [WWW Document]. URL http://passiv.de/en/04_phpp/04_phpp.htm (accessed 4.18.17).

Final report IEA HPT Annex 49 Task 3, Field monitoring in nZEB, 2020.

Franzoi, N., 2020. Simulation Based Optimization of a Heating System in a High-Performance Building. Master Thesis. Free University of Bozen-Bolzano and University of Trento.

Goggins, J., Moran, P., Armstrong, A., Hajdukiewicz, M., 2016. Lifecycle environmental and economic performance of nearly zero energy buildings (NZEB) in Ireland. Energy and Buildings 116, 622–637. https://doi.org/10.1016/j.enbuild.2016.01.016

Guillén-Lambea, S., Rodríguez-Soria, B., Marín, J.M., 2017. Comfort settings and energy demand for residential nZEB in warm climates. Applied Energy 202, 471–486. https://doi.org/10.1016/j.apenergy.2017.05.163

IEA SHC Task 56/ Building Integrated Solar Envelope Systems, International Energy Agency [WWW Document], n.d. URL https://task56.iea-shc.org/

ISO, 2008. ISO 13790. Energy performance of buildings - Calculation of energy use for space heating and cooling.

Kneifel, J., Webb, D., 2016. Predicting energy performance of a net-zero energy building: A statistical approach. Applied Energy 178, 468–483. https://doi.org/10.1016/j.apenergy.2016.06.013

Kurnitski, J., Saari, A., Kalamees, T., Vuolle, M., Niemelä, J., Tark, T., 2011. Cost optimal and nearly zero (nZEB) energy performance calculations for residential buildings with REHVA definition for nZEB national implementation. Energy and Buildings 43, 3279–3288. https://doi.org/10.1016/j.enbuild.2011.08.033

Lu, Y., Wang, S., Yan, C., Huang, Z., 2017. Robust optimal design of renewable energy system in nearly/net zero energy buildings under uncertainties. Applied Energy 187, 62–71. https://doi.org/10.1016/j.apenergy.2016.11.042

Ochs, F., Dermentzis, G., Feist, W., 2014. Minimization of the Residual Energy Demand of Multi-storey Passive Houses – Energetic and Economic Analysis of Solar Thermal and PV in Combination with a Heat Pump. Energy Procedia 48, 1124–1133. https://doi.org/10.1016/j.egypro.2014.02.127

Ochs, F., Dermentzis, G., Ksiezyk, A., 2017. Simulation and Monitoring Results of two MFHs in PH Standard with Heat Pump, Solar Thermal and PV, in: Solar Heating Conference 2017. Abu Dhabi, UAE.

Ochs, F., Dermentzis, G., Magni, M., 2020. PHPP vs. dynamic simulation – prediction of PV-self-consumption with the PHPP, in: 24th International Passive House Conference.

Paiho, S., Pulakka, S., Knuuti, A., 2017. Life-cycle cost analyses of heat pump concepts for Finnish new nearly zero energy residential buildings. Energy and Buildings 150, 396–402. https://doi.org/10.1016/j.enbuild.2017.06.034

Santoli, L. de, Mancini, F., Rossetti, S., 2014. The energy sustainability of Palazzo Italia at EXPO 2015: Analysis of an nZEB building. Energy and Buildings 82, 534–539. https://doi.org/10.1016/j.enbuild.2014.07.057

Tjaden, T., Bergner, J., Weniger, J., Quaschning, V., 2015. Representative electrical load profiles of residential buildings in Germany with a temporal resolution of one second, Dataset, HTW Berlin - University of Applied Sciences Research. https://doi.org/10.13140/RG.2.1.5112.0080

Tsalikis, G., Martinopoulos, G., 2015. Solar energy systems potential for nearly net zero energy residential buildings. Solar Energy 115, 743–756. https://doi.org/10.1016/j.solener.2015.03.037

Parameter study of four different instantaneous water heaters in a solar assisted multi-family-house with TRNSYS

Peter Pärisch, Christoph Büttner, Jonas Keuler, Carsten Lampe, and Federico Giovannetti

Institute for Solar Energy Research (ISFH), 31860 Emmerthal (Germany)

Abstract

The use of instantaneous water heaters avoids heating of the complete storage to 60 °C, which is necessary to fulfill hygienic requirements. This allows temperature sensitive renewable heat supply systems, like solar thermal or heat pumps, to decarbonize the heat demand in bivalent systems. Technical properties of the instantaneous water heater (IWH), like the specific heat transfer rate *UA* and switching time of the return flow diverter, have been derived from a market survey and lab tests. A suitable setting/choice of these properties can increase the solar thermal yield, improve the temperature stratification and may reduce the maximum required temperature in the upper part of the storage. This allows a solar thermal collector to substitute more fossil fuels and to reduce more effectively CO_2-emissions. A parametric study with a DHW supply system of a multi-family house with 8 apartments reveals that the CO_2-savings by solar thermal heat are highly sensitive to these technical properties. They range from (35 % up to 46 %).

Keywords: instantaneous water heater, legionella, solar thermal, UA-value, return diverter, TRNSYS simulation, efficiency

1. Introduction

In Germany, the final energy consumption per capita is about 30 MWh/a, equivalent to a total amount of 9000 PJ/a, and almost unchanged in the last 10 years (cf. Fig. 1).

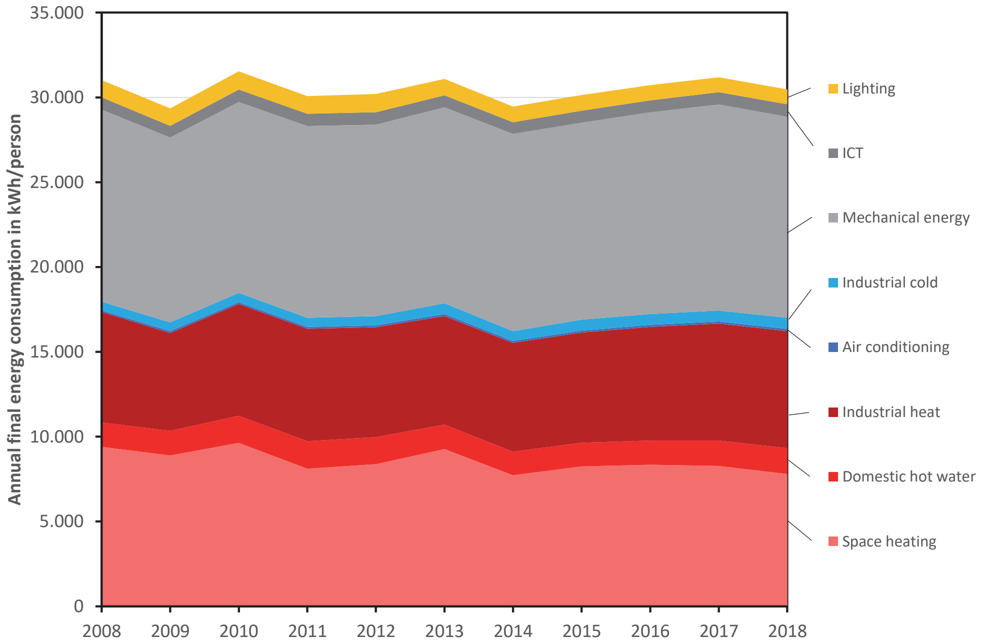

Fig. 1: German final energy consumption of the years 2008-2018 for different application sectors (data from AGEB e.V. (2019))

doi:10.18086/eurosun.2020.04.06 Available at http://proceedings.ises.org

Slightly more than half of the final energy consumption (FEC) is accounted for by the heating sector as a whole and almost a third of the FEC is related to space heating and potable hot water in the residential sector. The consumption of space heating is slowly declining due to renovation activities and climate change. Roughly 5 % of the FEC is accounted for by the heating of drinking water, which after all generates around 36 mil. tons of CO_2. The residential sector accounts for the largest share, 3.9 % (cf. Fig. 2). According to surveys conducted by the statistical offices of the federal and state governments, the residential sector in 2018 consists of around 60 % multi-family houses and 40 % single-family houses (Statistisches Bundesamt, 2019).

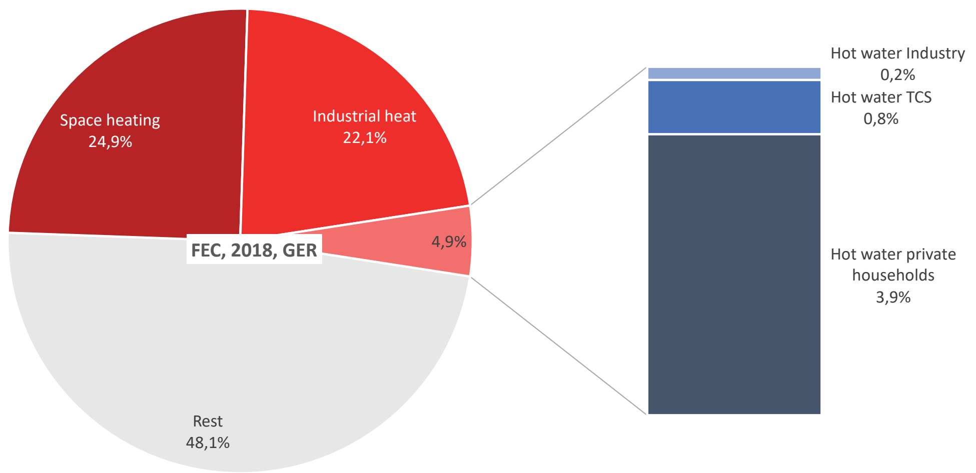

Fig. 2: Distribution of the German final energy consumption 2018 for different sectors and analysis of the domestic hot water sector (data from AGEB e.V. (2019))

The modernization and renewal of the building stock is not only accompanied by a declining share of energy for space heating, but also by a reduction in the temperatures required for heating. The heating of domestic hot water is coming into focus, not least because it determines the necessary temperature level of the heat generator. As a result, the heating of drinking water - especially in large-scale facilities - is an obstacle for temperature-sensitive heat pumps, solar thermal energy and heating networks based on renewable energies.

This paper presents the German Standards for the operation of domestic hot water heaters (DHW heaters) resulting from drinking water hygiene. Central instantaneous water heaters (short: IWH) are regarded as one solution for dissolving or reducing the obstacles. Due to the lack of product and test standards, a comparability of IWH with regard to important technical properties is not given. On the basis of a parameter study in TRNSYS the influence of these technical properties on the energy efficiency of a typical apartment building is investigated.

2. Hygienic regulations

Drinking water is not sterile, but contains (in low concentration) naturally occurring bacteria, including the genus Legionella. Based on projections, Legionella bacteria cause about 15,000 - 30,000 pneumonia cases in Germany every year (von Baum et al., 2008), of which about 15 % are fatal. They can multiply to a critical number in domestic hot water installations if the generally accepted codes of practice are disregarded, and can enter the lungs in droplets. The purpose of the regulations is to prevent this (TrinkwV, 2018) and there are a number of standards and guidelines that specify the generally accepted codes of practice (DVGW W551, 2004; DIN EN 806-2, 2005; DIN 1988-200, 2012; VDI/DVGW 6023, 2013). An essential parameter for the reproduction of the legionella is the water temperature (Brundrett, 1992), but also (stagnation) time, nutrient supply and turbulence in the pipe have an influence (Kistemann and Bausch, 2019).

The normative requirements for the hygienic operation of drinking water heaters currently differentiate between large and small systems or central and decentral systems (see Table 1).

According to DVGW worksheet W551 (DVGW W551, 2004) and DVGW-information no. 90 (DVGW, 2017), small systems are systems in detached and semi-detached houses as well as drinking water installations in which the content of the DHW storage is less than 400 l and the respective pipe volume to each tapping point is less than 3 l. Reducing the outlet temperature of the domestic water heater (abbreviation: PWH = potable water hot) below 60 °C is only permissible in small systems. In this case, a minimum of 50 °C is recommended. A circulation line is required from a pipeline volume of 3 l to the most distant tapping point. Its return temperature (PWH-C) must not drop below 55 °C.

(DIN 1988-200, 2012) distinguishes between central and decentral water heaters and introduces water exchange as the criterion for a tolerated temperature reduction at the outlet of central domestic water heaters. If the entire content of the domestic hot water installation is replaced within three days, the temperature may be reduced by up to 10 K. This could be achieved, for example, with looped-through ring installations with automatic rinsing systems. For decentral water heater, which correspond to small systems, the PWH temperature may be 50 °C or even below dependent on the pipe content.

The temperature of the domestic cold water (abbreviation PWC = potable water cold) may not exceed 25 °C (VDI/DVGW 6023, 2013).

Table 1: Overview of the two German Standards regarding the operation of drink water installations

	DVGW W551:2004		**DIN 1988-200:2012**	
	Small system	**Large system**	**Central WH**	**Decentral WH**
Outlet temperature of water heater (PWH-temperature)	- Recommendation: ≥ 50 °C[1]	60 °C	≥ 60 °C (≥ 50 °C, if water exchange within 3 days)	≥ 50 °C (< 50 °C, if pipe content ≤ 3 l)
Preheating stages of bivalent storage water heater	1 x per day 60 °C, if storage volume ≥ 400 l	1 x per day 60 °C		
Circulation	Mandatory, if pipe content > 3 l	Mandatory	Mandatory, if pipe content >3 l	- (unless pipe content >3 l)

[1] with mandatory possibility to heat up to 60 °C

Central instantaneous water heaters enable domestic hot water (DHW) installations with low volumes of hot drinking water. The frequent water exchange shifts the hygienic problem of bacterial proliferation to the biofilm inside the pipes, drinking cold water and stagnant water in pipes. A so far only hypothetical reduction of the hot drinking water temperature would have the following beneficial effects on these hygiene parameters:

- reduced risk of warming potable cold water due to less heat losses
- increased flow velocity in the hot drinking water pipe due to different mixing ratio at the tap
- more frequent exchange of hot drinking water

The beneficial effect of a reduced operating temperature on the energy consumption of generation, storage and piping system is obvious. Nevertheless, the set temperature from the IWH is 60 °C in this parametric study.

Independently of a hypothetic temperature reduction, IWH with buffer storage catalyze the decarbonization of large DHW installations combined with solar thermal energy (or heat pumps). The colder preheating stage of the buffer storage leads to a higher efficiency of these temperature-sensitive heat generators.

Decisive for the economic efficiency and acceptance of such a modernization are high-quality IWH and good planning. Unfortunately, the market is characterized on the supplier side by a lack of transparency regarding the relevant technical features of the instantaneous water heaters and on the planner side by ignorance regarding loads and dimensioning. Ruesch and Frank (2011) and Lampe and Bölter (2017) have started a standardization process for IWH without circulation and this paper aims at contributing to the definition of efficiency properties of IWHs for large DHW installations.

3. Simulation boundary conditions

Fig. 3 illustrates the investigated heat supply system using the example of an apartment building, (Mercker and Arnold, 2017) with 8 apartments and a heated living area of 520 m², which was mapped in TRNSYS 17. A central IWH supplies the taps and the circulation with heat from a buffer storage tank heated bivalent by a solar thermal system and a gas boiler.

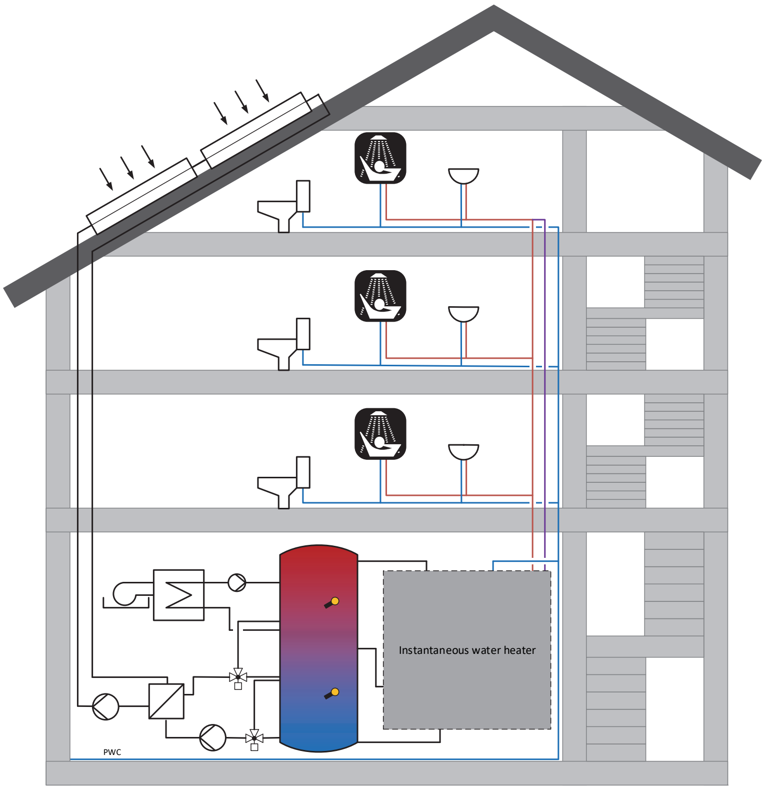

Fig. 3: Schematic of the investigated DHW-system of a multi-family house

The condensing gas boiler is controlled by a normal thermostatic control with a temperature sensor in the storage, whereby the temperature sensor is located centrally between the supply and return pipe. For the gas boiler, the switch-on temperature is 65 °C and the switch-off temperature 70 °C. Both parameters, coupled together with a fix 5 K difference, are part of a minimization algorithm, which also accounts for DHW penalties (see below).

The solar thermal system is simulated with Type 832 with a constant collector area of 32 m², which corresponds to 4 m² per apartment as recommended by Mercker and Arnold (2017). The external plate heat exchanger comprises an UA-value of 120 W/K per m² collector area according to VDI 6002-1 (2014). The controller activates the primary pump if the difference between collector temperature and storage temperature (midway between flow and return of lower solar section) exceeds 15 K and stops it if it falls below 5 K. The secondary pump starts if the heat exchanger inlet temperature on the primary side exceeds the storage temperature by 7 K. Both pumps stop if the temperature difference of primary heat exchanger inlet and storage drops below 3 K. On the primary and secondary side, the capacity flows are adapted to each other. The operating mode of the pumps is low-flow with 20 l/(m²·h). The maximum storage tank temperature is 95 °C, from which only the secondary pump is switched-off. The primary pump is switched-off if a collector temperature above 130 °C occurs to account for the evaporation temperature. The solar flow can either load the upper or lower storage tank section depending on the temperatures. To load the upper solar section the secondary outlet temperature has to exceed this section temperature (midway between flow and return).The two heat generators are operated in bivalent-parallel mode, i.e. there is no communication, for example to suppress auxiliary heating.

The gas boiler is simulated with the Type 204 developed at ISFH from Glembin et al. (2013). The modulating condensing gas boiler has a heat output of 28.5 kW at 60 °C inlet temperature. Other important parameters are: minimum degree of modulation 28 %, water content 7.3 l.

The buffer tank with a volume of 1600 l is simulated with Type 340 (Drück, 2006). It has a height of 1.8 m and the relative connection heights for boiler flow pipe are 80 %, for boiler return pipe 60 %, for solar flow pipe 45 % (lower) and 65 % (upper), for solar return pipe 5 %(lower) and 45 % (upper), for IWH flow pipe 100 %, for IWH return pipe 0 %, for IWH return pipe in circulation mode 50 %. The storage tank losses amount to about 10 kWh/d.

DHWcalc version 2.02b was used for the definition of the tapping profile (resolution 1 min) of the assumed building with 8 apartments (Jordan et al., 2019). The daily draw-off volume of 440 l at 60/10 °C corresponds to 12-16 persons. The summer holidays are taken into account. See Pärisch et al. (2020) for a frequency distribution of the tap load profile and a comparison to measured values. The peak output approximately 80 kW (≙23 l/min at 60/10 °C) allows using IWH for single and two-family houses also for this multi-family house.

We assume thermostatic mixing valves at the apartments with a set temperature of 45 °C and recalculate the tapping flow rate $\dot{V}_{tap}$ on the basis of the DHWcalc file. The flow rate through the instantaneous water heater $\dot{V}_{IWH}$ is modified for different temperatures leaving the pipe $\vartheta_{\text{pipe,out}}$.

$$\dot{V}_{IWH} = \dot{V}_{tap} \cdot \frac{\vartheta_{tap,45°C} - \vartheta_{PWC}}{\vartheta_{pipe,out} - \vartheta_{PWC}} \qquad \textbf{eq. 1}$$

If either the water temperature leaving the pipe $\vartheta_{\text{pipe,out}}$ drops below 44 °C or the water temperature leaving IWH drops below 60 °C for more than 0.15 h, the simulation is stopped. In this way the DHW penalties are minimized and the lowest set temperature for the gas boiler of upper storage is found.

The heat loss rate in circulation mode results from a pipe length of 48 m of uninsulated pipe (assumption for existing buildings) of around 1070 W. The volume flow rate of circulation is 160 l/h, so that the return flow temperature does not fall below 55 °C in steady-state operation. To simplify matters, we assume that the circulation volume flow is zero during tapping events.

Simulation time step is 2 s. We adjusted the minimum draw-off duration in DHWcalc to 1 min (smallest possible value). As most tapping events for hand washing are less than 1 min in real buildings, we assume that DHWcalc underestimates the amount of small tapping events. On the other hand, most heat demand occurs for showering and bathing. Therefore, we estimate that our results will slightly underestimate the importance of return diversion.

4. Investigated parameters

Technical properties of the IWH, that are largely inaccessible to the specialist planner and installer and thus are not comparable, can influence the profitability of partially regenerative heat supply systems, their efficiency and the CO_2 savings achieved.

In the following investigation, TRNSYS 17 is used to simulate the essential technical features of IWHs and their energetic relevance for an exemplary large domestic hot water installation. Based on a market survey of electronic IWHs, four types of modules are identified. These hydraulic variants of the IWH are shown in simplified form in Table 2.

Table 2: Schematics for the investigated IWH

I Standard Electronically controlled instantaneous water heaters normally use a modulating circulating pump. Some manufacturers use a 3-way valve to modulate the thermal power. These products with small UA-values are typically installed in small systems without circulation. 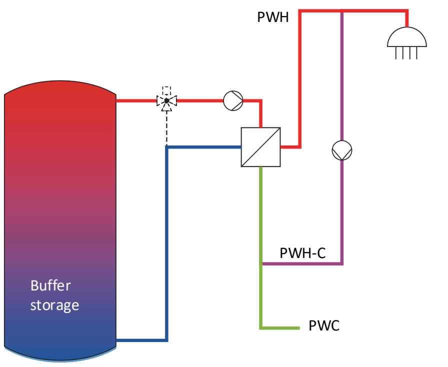	II Standard with return flow diverter With circulation, a return flow diverter is often used to improve the temperature stratification. Shown here is a 3-way switching valve with a specific actuating time. It is varied between 2 s and 50 s. A switching time below 2 s can be achieved by using two pumps in the two return flows, for example. UA-values are higher than for I. 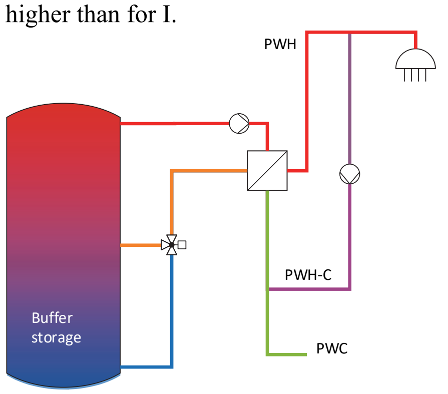
III Standard with circulation heat exchanger in parallel Some products use a separate heat exchanger for circulation. With this parallel connection, the circulation heat exchanger and the associated pump can be optimised for the small volume flows. Switching time is below 2 s and UA-values are slightly higher than for II. 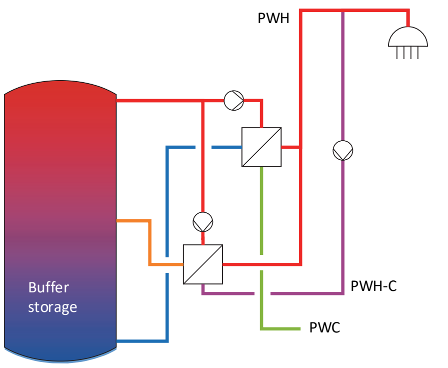	IV Standard with circulation heat exchanger in series Alternatively, it is conceivable to connect two heat exchangers in series. This enables particularly good cooling during tapping operation and highest UA-values. Switching time is also below 2 s. 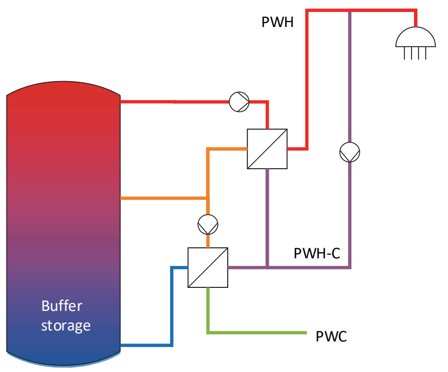

The IWHs vary in switching time between circulation and tapping mode and the specific heat transfer rate, which is abbreviated as *UA* (note that this is not only a heat exchanger property, but rather a property of the IWH). They influence the three most important quality measures of IWH with regard to thermal energy efficiency, which are visualized in Fig. 4 using a module based on concept II. This generic IWH is used in TRNSYS to model all four types of modules.

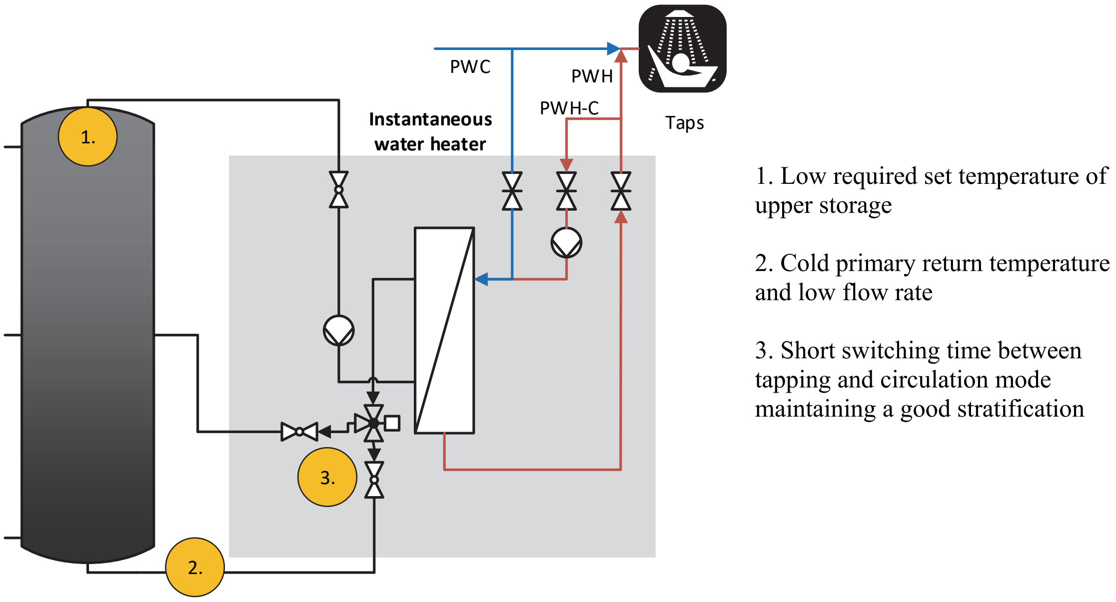

Fig. 4: Generic instantaneous water heater model for simulating large DHW-systems with three quality measures

A low required set temperature of the upper storage (**point 1**) to fulfill the demand is decisive for high solar fraction (or heat pump fraction) and low thermal losses. The required temperature difference between heating water inlet and domestic hot water outlet is not only a heat exchanger property, but also dependent from the whole module hydraulics.

Cold return temperatures on the primary side (**point 2**) improve the efficiency of all heat generators, including condensing boilers, and reduce temperature mixing in the storage by reducing the flow velocity at the tank connections.

In pure circulation mode (PWH-C), the secondary inlet temperature to the central IWH is 55 °C, so that the primary-side return flow is connected to the buffer tank in middle height to maintain temperature stratification. During tapping, the cold water temperature (PWC) dominates, so that the 3-way reversing valve switches the primary return flow to the lower storage tank section. A short actuating time (**point 3**) is essential to maintain the temperature stratification.

The specific heat transfer rates (*UA*-values) of the IWH modules are approximated and classified according to our laboratory measurements with following equations.

$$UA = f_\vartheta \cdot \left(-3\frac{W/K}{(l/min)^2} \cdot \dot{V}_{sec}^{\ 2} + 295\frac{W/K}{l/min} \cdot \dot{V}_{sec}\right) \cdot f \qquad \textbf{eq. 2}$$

$$\text{with } f_\vartheta = \left(1.0395 - 0.008 \cdot \left(\vartheta_{P,in} - 60°C\right)\right) \qquad \textbf{eq. 3}$$

The temperature correction factor f_ϑ is only defined for primary inlet temperatures $\vartheta_{P,in}$ between 60 and 90 °C. The tapping flow rate on the secondary side $\dot{V}_{sec}$ is in l/min and the specific heat transfer rate (UA) is in W/K. Via the factor f different powerful concepts of the IWH modules are simulated. f is varied between 1.0 and 2.5.

Fig. 5 compares the variation range of the UA value according to eq. 2 with six different measured stations at 70 °C or 90 °C primary inlet temperature, 60 °C domestic hot water temperature and 10 °C cold water temperature. A factor f = 1.0 to 1.5 represents a standard station for a small system according to concept I, whose performance is sufficient for the multi-family house tapping profile. Three different products Ia, Ib and Ic are shown here. The factor f = 1.5 to 2.0 represents large modules for multi-family houses according to concept II or III. The factor f = 2.5 stands for particularly efficient heat exchangers or concept IV with two heat exchangers connected in series. It is important to emphasize that the measured IWHs are only random samples and the following study is not a weighting of station concepts but of properties. Basically, each IWH module concept has the potential to achieve the same properties but at different costs.

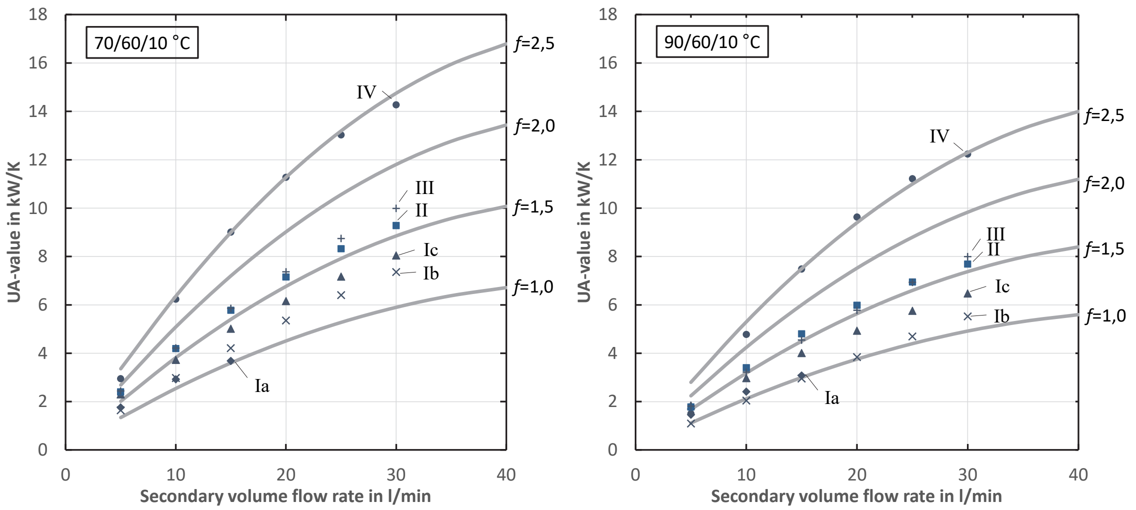

Fig. 5: Comparison of different measured UA-values (points) of six different IWH at 70 °C/60 °C/10 °C (left) or 90/60/10 °C (right) with eq. 2 with different factors *f* (lines)

The *UA* value in circulation mode or the *UA* value of the circulation heat exchanger is constant and set to 500 W/K due to the small volume flows and high temperatures.

The actuating time (t_{RL}) of the primary return between the lower and middle section of storage is modelled with Type 84 (moving average) between 2 s, 18 s, 34 s and 50 s. Table 3 shows the varied parameters. The set temperature of the gas boiler for the upper storage volume is part of a minimization search.

Table 3: Overview of the varied parameters in the simulation

Factor *f* for UA	Changeover time t_{RL}	Circulation heat loss rate	Set temperature of upper storage
1,0	2 s	1,07 kW	Find minimum ()
1,5	18 s		
2,0	34 s		
2,5	50 s		
	Always bottom		

5. Results

As main evaluation parameter, the CO_2 savings (cf. eq. 4) are compared to a reference system, which is the standard IWH concept I without return diverter with a factor *f* of 1 of the *UA* value. To simplify matters, only the solar thermal system is switched off in the simulation. The tank size and connection heights of the gas boiler remain unchanged. The lower part of the storage tank heats up to 55 °C because of circulation mode. The set temperature in upper part is minimized with respect to DHW penalties, as well. It is 70 °C.

$$f_{sav,CO2} = 1 - \frac{\left(Q_{Gas} \cdot f_{Gas,CO2} + W_{el} \cdot f_{el,CO2}\right)}{\left(Q_{Gas} \cdot f_{Gas,CO2} + W_{el} \cdot f_{el,CO2}\right)_{ref}} \qquad \textbf{eq. 4}$$

The gas consumption Q_{Gas} and the electricity consumption W_{el} are multiplied with their corresponding emission factors. The CO_2 emission factors of the German electricity mix and natural gas change with the system boundaries (including or excluding upstream emissions) and time (especially for electricity). Taking into account upstream emissions and other greenhouse gases, according to a forecast of IINAS the emission factors for electricity in 2020 are $f_{el,CO2}$=403 gCO_2-eq/kWh_{el} (Fritsche and Greß, 2019) and $f_{Gas,CO2}$=250 gCO_2-eq/kWh_{Gas} for natural gas (Fritsche, 2016). As solar heat has a very low electricity consumption, we neglect its influence.

Comparing the bivalent system with the reference system (see Fig. 6 left), the CO_2 savings are highly dependent on IWH properties (35 to 46 %).

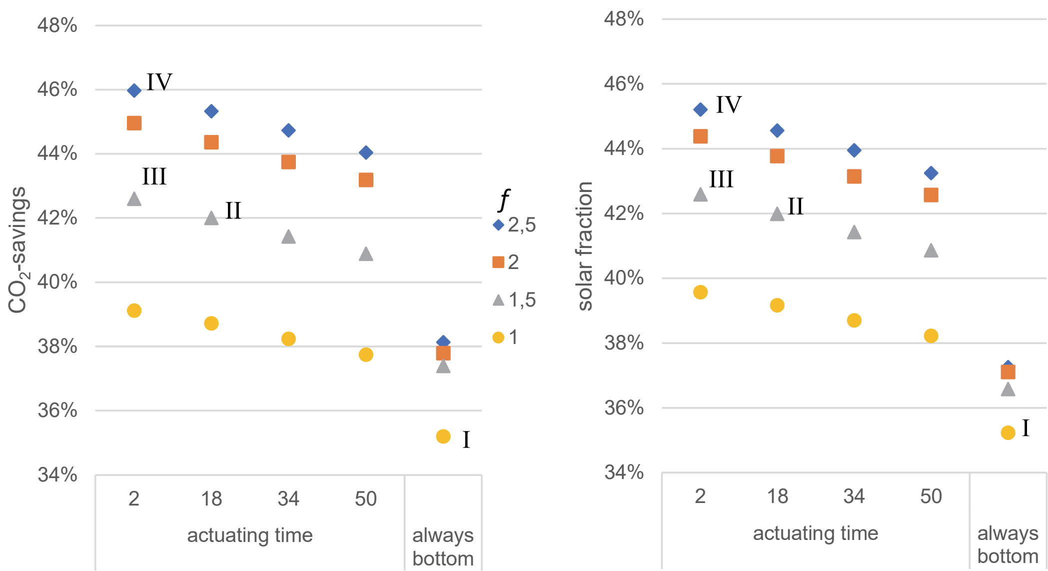

Fig. 6: Influence of actuating time and specific heat capacity *UA* on CO_2 savings (left) and solar fraction (right) compared to the reference system (I, II, III and IV acc. to Table 2)

The results clearly show that a switch between lower and middle storage section feed-in is beneficial in terms of CO_2-savings. A simple IWH designed for single family houses with always bottom storage feed-in (I) can supply the multi-family house without penalty, but achieves the lowest CO_2-savings of 35 %. Here, a higher specific heat transfer rate UA improves the results only by 3 %-abs. With return diverter the influence of the specific heat transfer rate (factor f) increases. Here, f improves the results by 6-7 %-points. Additionally, a fast return flow diversion, e. g. using two pumps or fast diverter valves, results in 4 %-abs better results compared to always bottom. Thus, the IWH concept IV reaches the highest CO_2-savings of 46 %. Note: when considering the fuel costs (not shown), this is exactly the same values.

To analyze the effects further, the solar fraction f_{sol} is calculated as well according to eq. 5. Solar thermal heat Q_{sol} and the heat from the condensing boiler Q_{Boiler} are heat inputs to the storage. f_{sol} is an indicator for low storage temperatures at the bottom part and for good stratification during discharging.

$$f_{sol} = \frac{Q_{sol}}{Q_{Boiler} + Q_{sol}} \qquad \textbf{eq. 5}$$

Fig. 6 (right) shows clearly, that the sensitivity of CO_2-savings with regards to the IWH properties comes mainly from the sensitivity of the solar fraction. All values are roughly 1 %-abs lower than the fractional CO_2-savings, which depends on the reduced storage and boiler losses. Thus, all the conclusions presented above are applicable to this figure. The solar fraction rises due to higher solar collector yields and lower upper set temperatures of the gas boiler.

These set temperatures, which have been minimized as explained above, are depicted in Fig. 7 over the factor f for the heat transfer rate. Note: Besides of stochastic fluctuations there is no significant influence of actuating time on minimum set temperature. However, efficient heat exchangers reduce the set temperature for the gas boiler of the upper storage by 5-6 K. The set temperature for the heater of upper storage part $T_{Set,HE} = 64.5\ °C$ for factor $f = 1$ can be significantly reduced down to 59 °C for concept IV.

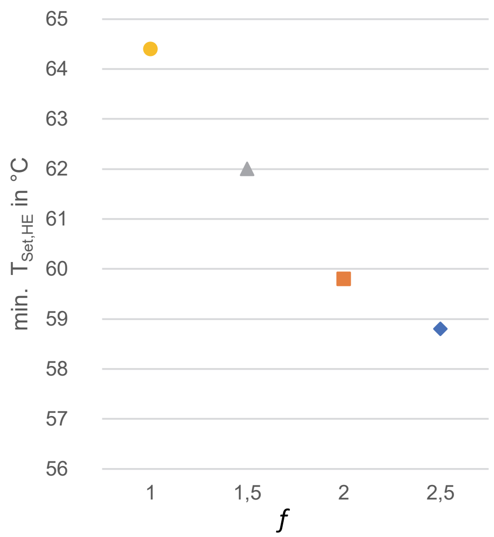

Fig. 7: Influence of the factor *f* of the IWH on minimum set temperature of upper storage

6. Summary

As the efficiency standard of buildings becomes more restrictive, the heating of domestic hot water is increasingly coming into focus, as it determines the minimum temperature level of the heat supply systems. Bivalent heat supply systems with IWH are a suitable means to decarbonize the heat demand in large domestic water installations. IWH are helpful because they create a cold preheating volume in the buffer storage tank, which enables the efficient integration of regenerative heat generators such as solar thermal systems and heat pumps.

In a parameter study, four different IWH concepts are investigated in an exemplary bivalent heat supply system with gas boiler and solar thermal collector for an apartment building. The specific heat transfer rate *UA* and the actuating time of the return flow diverter have a significant influence on the efficiency of the solar thermal system. The annual CO_2-savings increases from 35 % to over 46 % with higher *UA* and shorter actuating time of the return diverter. While a return flow diverter increases the solar yield and the CO_2-savings, it does hardly influence the minimum set temperature of the upper storage. To lower this temperature, a good specific heat transfer rate is beneficial.

However, if a two return system is available, it is advantageous if it is fast, so that the cold returns can be fed to the preheating section as quickly as possible. Hence, the transferability of the results to other bivalent heat supply systems with other operating strategies has to be investigated in more detail in future works.

7. Acknowledgement

The authors are grateful for the support of the Federal State of Lower Saxony and responsible for the content.

8. References

AGEB e.V. (Ed.), 2019. Anwendungsbilanzen zur Energiebilanz Deutschland Endenergieverbrauch nach Energieträgern und Anwendungszwecken.

Brundrett, G.W., 1992. Legionella and building services. Butterworth Heinemann, Oxford [England] ; Boston.

DIN 1988-200, 2012. Technische Regeln für Trinkwasser-Installationen - Teil 200: Installation Typ A (geschlossenes System) - Planung, Bauteile, Apparate, Werkstoffe.

DIN EN 806-2, 2005. Technische Regeln für Trinkwasser-Installationen - Teil 2: Planung.

Drück, H., 2006. Mathematische Modellierung und experimentelle Prüfung von Warmwasserspeichern für Solaranlagen (Dissertation). Universität Stuttgart, Stuttgart, Deutschland.

DVGW (Ed.), 2017. DVGW-Information Wasser Nr. 90.

DVGW W551 (Ed.), 2004. Trinkwassererwärmungs- und Trinkwasserleitungsanlagen - Technische Maßnahmen zur Verminderung des Legionellenwachstums - Planung, Errichtung, Betrieb und Sanierung von Trinkwasser-Installationen.

Fritsche, U., 2016. Globales Emissions-Modell integrierter Systeme (GEMIS): CO2-Faktoren - wie werden sie ermittelt? Wie sehen die aktuellen Faktoren aus?

Fritsche, U., Greß, H.-W., 2019. Der nichterneuerbare kumulierte Energieverbrauch und THG-Emissionen des deutschen Strommix im Jahr 2018 sowie Ausblicke auf 2020 bis 2050 (Bericht für die HEA - Fachgemeinschaft für effiziente Energieanwendung e.V.). IINAS Internationales Institut für Nachhaltigkeitsanalysen und -strategien GmbH.

Glembin, J., Bertram, E., Rockendorf, G., Steinweg, J., 2013. A New Easy-to-Parameterize Boiler Model for Dynamic Simulations. ASHRAE Transactions 2013 119, 270–292.

Jordan, U., Braas, H., Best, I., Orozaliev, J., Vajen, K., Kassel, U., 2019. DHWcalc Update 2.02: Programm zur Generierung von Trinkwasser-Zapfprofilen auf statistischer Basis. Presented at the Symposium Solarthermie und innovative Wärmesysteme, Conexio GmbH, Kloster Banz, Bad Staffelstein, p. 14.

Kistemann, T., Bausch, K., 2019. Prozessziel Trinkwassergüte: Trinkwassergüte – Energieeffizienz - Digitalisierung, in: Gebäudetechnik Als Strukturgeber Für Bau- Und Betriebsprozesse. Springer Vieweg, Berlin, Germany, pp. 91–166. https://doi.org/10.1007/978-3-662-58157-5_2

Lampe, C., Bölter, M., 2017. Charakterisierung neuer Komponenten in der Heizungstechnik: Frischwasser- und Wohnungsstationen (Schlussbericht No. 03FS14029). Institut für Solarenergieforschung Hameln GmbH, Emmerthal, Deutschland.

Mercker, O., Arnold, O., 2017. Ansätze zur Reduktion der konventionell erzeugten Wärmeverteilverluste in solar unterstützten Mehrfamilienhäusern (Schlussbericht No. 03ET1194A). Institut für Solarenergieforschung Hameln GmbH, Emmerthal, Deutschland.

Pärisch, P., Büttner, C., Keuler, J., Chhugani, B., Lampe, C., 2020. Warum sind Frischwasserstationen wichtig für die Dekarbonisierung großer Trinkwasserinstallationen?, in: Tagungsunterlagen des Online-Symposiums Solarthermie und innovative Wärmesysteme. Presented at the Solarthermie und innovative Wärmesysteme, pp. 533–548.

Ruesch, F., Frank, E., 2011. Untersuchung und Bewertung angepasster Lösungen zur Trinkwarmwasserbereitstellung. Entwiclung einer Testprozedur für Frischwassermodule (Abschlussbericht No. BFE-Projektnummer 102955). Bundesamt für Energie, Schweiz, Rapperswil, Schweiz.

Statistisches Bundesamt (Ed.), 2019. Wohnen in Deutschland. Zusatzprogramm des Mikrozensus 2018.

TrinkwV, 2018. Verordnung über die Qualität von Wasser für den menschlichen Gebrauch - Trinkwasserverordnung in der Fassung der Bekanntmachung vom 10. März 2016 (BGBl. I S. 459), die zuletzt durch Artikel 1 der Verordnung vom 3. Januar 2018 (BGBl. I S. 99) geändert worden ist.

VDI 6002-1, 2014. Solare Trinkwassererwärmung - Allgemeine Grundlagen, Systemtechnik und Anwendung im Wohnungsbau.

VDI/DVGW 6023, 2013. Hygiene in Trinkwasser-Installationen - Anforderungen an Planung, Ausführung, Betrieb und Instandhaltung.

von Baum, H., Ewig, S., Marre, R., Suttorp, N., Gonschior, S., Welte, T., Lück, C., Competence Network for Community Acquired Pneumonia Study Group, 2008. Community-Acquired Legionella Pneumonia: New Insights from the German Competence Network for Community Acquired Pneumonia. Clinical Infectious Diseases 46, 1356–1364. https://doi.org/10.1086/586741

FOUR INNOVATIVE SOLAR COUPLED HEAT PUMP SOLUTIONS FOR BUILDING HEATING AND COOLING

David Chèze[1], Alessandra Cuneo[2], Carlo Macciò[2], Matteo Porta[2], Giuseppe Dino[3], Andrea Frazzica[3] and Andrea Gabaldón[4]

[1] Univ Grenoble Alpes, CEA, LITEN, INES, F-38000 Grenoble (France)

[2] RINA Consulting, Genova (Italy)

[3] CNR ITAE, Messina (Italy)

[4] CARTIF, Valladolid (Spain)

Abstract

Despite the huge primary energy consumption associated with heating and cooling (H&C) demand in EU building stock, the share of installed renewable H&C solutions is still marginal (i.e. 5%). In order to speed up a transition towards the widespread application of renewable H&C in buildings, innovative solutions are designed to compete against traditional solutions. SunHorizon project aims to demonstrate the potential for a user-friendly and cost-effective solution based on an optimized design and combination of commercial innovative solar technologies (thermal or/and PV) and Heat Pumps (HP). This paper presents how different technologies (two solar panels, three HPs and thermal storage) have been coupled in four different Technology Packages (TPs) to satisfy H&C demand of both residential and tertiary buildings. Preliminary thermo-economic TRNSYS simulation results are presented about four demo sites in Latvia, Germany and Spain, to demonstrate such innovative solutions able to cover up to 80% of H&C demand with a reduction of greenhouse gas (GHG) emissions up to 70%.

Keywords: solar panels, heat pumps, heating and cooling, buildings, electricity self-consumption, grid feed-in

1. Introduction

Buildings are responsible for 41% of EU energy consumption and H&C equals 55% of the total EU energy demand (ODYSSEE, 2018). This demand is mostly met by fossil fuels, with natural gas having the main share, while renewable energy sources (RES) remain marginal (5%). However, according to the EC’s H&C Strategy, the H&C sector still accounts for 59% of total EU gas consumption, and almost half of EU's buildings have boilers with an efficiency rate below 60% (IEA. 2018). Nevertheless, RES are becoming increasingly common and socially accepted. Therefore, to speed up a transition towards RES-based H&C in buildings, innovative solutions are designed to compete against traditional solutions with equivalent or lower investment costs and payback times, while guaranteeing similar or better levels of comfort. Both residential and tertiary new buildings types are expected to become highly efficient. Currently, solar panels and Heat Pump (HP) are the most common and socially accepted RES Based H&C solutions. Bringing together existing and mature HP and solar technologies guarantees a simple energy system nevertheless efforts are still required to refine their coupling, as they are used to be designed and operated separately. Solar and HP can form an integrated solution with several key advantages: high RES share and energy efficiency, low electricity and primary-energy demand, low GHG/CO_2 emission. HP are well suited to low-temperature needs as for well-insulated residential and tertiary buildings. In parallel solar thermal and PV reduces also the thermal and electricity demand in non-renovated envelopes. The current work is performed in the context of the SunHorizon project (H2020 Project GA818329) which objective is to analyze the performance of building-integrated solar and HPs solution specifics and their individual challenges towards saving Non-Renewable Primary energy (PEnren) via increased Renewable Energy Ratio (RER), cost reduction (optimized size, installation cost reduction etc.) and reliability (lifetime and reduced maintenance). Innovative components as the BH20 unique thermal compressor heat pump from BOOSTHEAT (BH), the Hybrid adsorption/compression chiller from FAHRENHEIT (FAHR), the high-vacuum flat thermal panels from TVP

Selection and/or peer review under responsibility of Scientific Committee
doi:10.18086/eurosun.2020.04.07 Available at http://proceedings.ises.org

SOLAR (TVP) and the hybrid PVT panels from DualSun (DS) are integrated in four TPs including thermal energy water storage from RATIOTHERM (RT) and A-/B- WHP (reversible Air/Brine source to Water HP) from BDR THERMEA (BDR). Details on each specific technology could be found in SunHorizon website. Each TP aims at covering space heating (SH), domestic hot water (DHW) and/or space cooling (SC) demand of eight different demo sites (small and large residential buildings as well as tertiary buildings) across EU climates, local energy mix and costs in Germany, Spain, Belgium and Latvia (CEA et al., 2020). A quick outlook of the composition of the four TPs and the demo sites locations is illustrated in Tab. 1. In Section 2, the key aspects of the preliminary design and TRNSYS modelling with respect to TP1, TP2, TP3, TP4, in particular experience in the elaboration of compliant control rules between the manufacturers of the solar and HP system parts has been presented. Then, Section 3 essentially emphasizes noticeable characteristics and the respective estimated energy and costs savings through the analysis of the simulation results, referring to Key Performance Indicators (KPI) commonly used in solar and HP contexts (CARTIF et al., 2019).

Tab. 1: Technology packages

heat pumps \ solar panels	**Hybrid PVT DUALSUN**	**High-vacuum flat thermal TVP SOLAR**
Thermal compressor HP BOOSTHEAT	TP2: Mixed solar-assisted / parallel integration in Riga (Latvia)	TP1: Parallel integration in Berlin (Germany)
Hybrid adsorption/compression cascade chiller FAHRENHEIT		TP3: Solar -driven thermal chiller in Sant Cugat (Spain)
Reversible Air-water to water HP BDR THERMEA	TP4: Parallel integration in Madrid (Spain)	

2. SunHorizon technologies architecture and modelling

2.1 TP1 development and modelling

The challenge of TP1 is to combine each other the TVP solar panels, BH HP and RT thermal storage separate technologies and controllers, while meeting each manufacturer objectives and pursuing replication perspective within SunHorizon and beyond in the future. Fig.1 shows the hydraulic layout agreed by the manufacturers that ensures parallel operation of TVP and BH on the SH and DHW demand. It enables direct use of TVP heat at possibly high temperature above the cold return line from the radiator space heating SH circuit, and DHW solar preheating from accumulated solar heat in RT tank, before BH20 gas burner ensures water is heated up to the desired temperature. It also mutualizes one outdoor fan coil to operate the BH20 unit during the heating season and to dissipate excess heat from the TVP collector. Apart from the new component for BH thermal compressor heat pump BH20, existing TRNSYS components have been used in the TP1 assembly system model. It runs annual simulation at 3 minutes time step to investigate dynamic component interactions and usual solar combisytem control rules summarized in Tab.2.

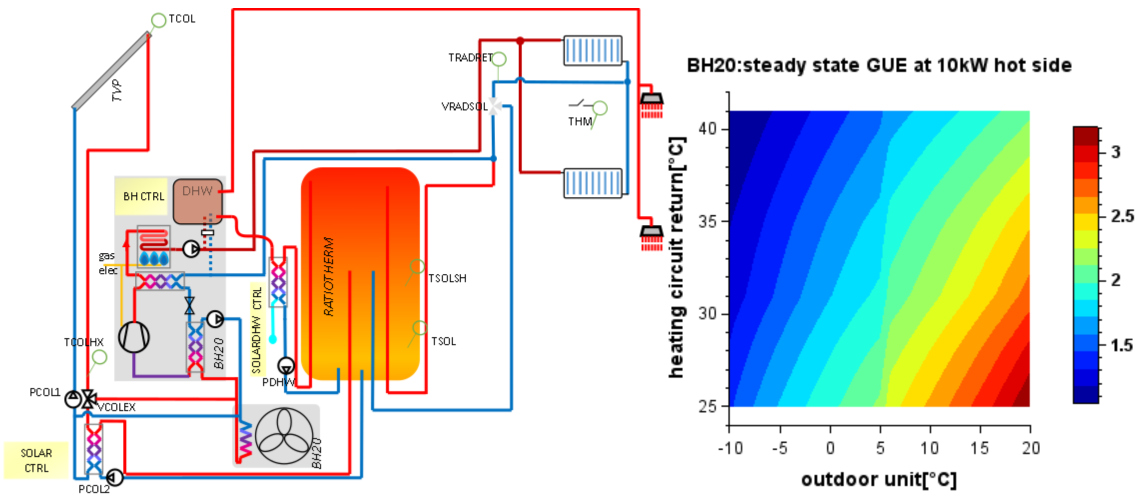

Fig. 1 TP1 concept for simulation and BH20 core Gas Utilization Efficiency (GUE)

Solar circuit: The quasi-dynamic solar thermal collector model Type 832 maintained by SPF (Haller et al. 2012) is selected for the solar flat panels performance modelling. The Type 832 parameters for TVP thermal panels are set regarding the coefficients from EN ISO 9806 terminology $\eta_{0,b}$ = 0.737; c1 = 0.504 W/(m².K); c2 =0.006 W/(m².K²); c3, c4, c6 =0 / Kd= 0.957. Default flat plate coefficients are assumed for IAM b0=0.18 and thermal capacitance 7000 J/K.m². The collector tilt is 60° to match the slope of the roof in Berlin demo site and to reduce the overheating risk in summer when possible no DHW consumption during holidays. The solar tank is Type 340 model (Drück, 2006), the solar brine/water and DHW solar pre-heating heat exchangers are Type 5 models.

SH and DHW, heat demand models: The reference building connected to the TP1 is an historical house (beginning XXth century) renovated in 2006, 284 m² living area occupied by 7 peoples in three levels and thermal zones, under Berlin climate, modelled by multi-zone building TYPE56. The DHWcalc software (Jordan et al. 2005) was used to generate a synthetic yearly profile that matches the overall annual estimated consumption with realistic distribution of the consumption, statistical day-to-day variations. The configuration is reflecting a multifamily building, split into 2 households and average total daily consumption 300L at 45°C.

BH20 model: The BH unit is including the thermal gas fired compressor CO_2 heat pump and the conventional condensing gas burner for DHW preparation (also used as backup of thermodynamic cycle on space heating complementary capacity request). The model is mainly relying on user Type 5837 and simulates the physical behavior including internal controller (extern sensors/actuators management) and issues performance outputs in steady state under the variable operating conditions: temperature at the cold (-10/20°C) and hot (30/55°C in SH, 10/85°C in DHW) sides of the heat pump, full or part load operation request (25-100% nominal capacity 20kW in SH operation). The performance outputs rely on continuous interpolation of the performance tables shared by BH from internal tests of the BH20 unit in space heating operation, shown in Fig. 1 (left). The maximum BH20 capacity parameter is variable from the 20kW nominal capacity. The BH20 unit is linked to an outdoor fan coil, modelled by Type 91 heat air/brine exchanger. The air flow rate is controlled by Type5837 SFan 0-100% output fan speed signal that is adjusting the nominal air flow rate to the current heat demand. The electricity consumption of the fan is approximated as a parabolic curve depending on the requested air flow-sfan signal, fitted from the BH20 manufacturer data. On the other hand, the BH Type 5837 is connected to a 65L DHW cylindrical insulated tank modelled by Type 340.

Tab. 2 TP1 overall control strategy

TVP solar thermal supply	PCOL1 and PCOL2 are flowing solar heat into solar tank when TCOL is 5K higher than the tank bottom temperature TSOL. When RT max temperature is 85°C and TVP max outlet temperature is 120°C, outdoor fan coil, diverter VCOLEX and solar pump PCOL1 are dissipating excess solar heat.
DHW	DHW heat exchanger is heating first from solar tank the sanitary cold water, assuming tank side flow identical to the water draw then it flows into the Boosheat backup heated DHW tank.
Space heating	SH radiator demand signal and flow are raised by thermostat THM with 20°C setpoint, differential controller with +1K deadband (radiator circuit heating curve with 70°C at -12°C and 40°C at 15°C). VRADSOL diverter is switching the return flow from radiator circuit to the solar pre-heating tank when the mid-tank temperature is 5K above otherwise the solar tank is bypassed.
BoostHeat	CO_2 thermodynamic cycle activated for space heating with support of auxiliary gas burner to ensure the heating curve flow temperature up to 20kW. The DHW boostheat tank set point temperature is 55°C, heated up by auxiliary gas burner.

2.2 TP2 development and modelling

The second TP is focused in the combination of BH HP with hybrid-PVT panels from DualSun together with a stratified thermal storage manufacturer by RT to be installed in a small residential building in Riga. The building is a privately owned single-family residential house built in 2013, with a heated area of 234.8 m2 distributed into two floors. The existing system (Gas boiler) will be integrated with the new system as a back-up service (e.g. during first operational tests, etc.). A model of the SunHorizon system has been produced in TRNSYS 18 in order to preliminary assess its performance.

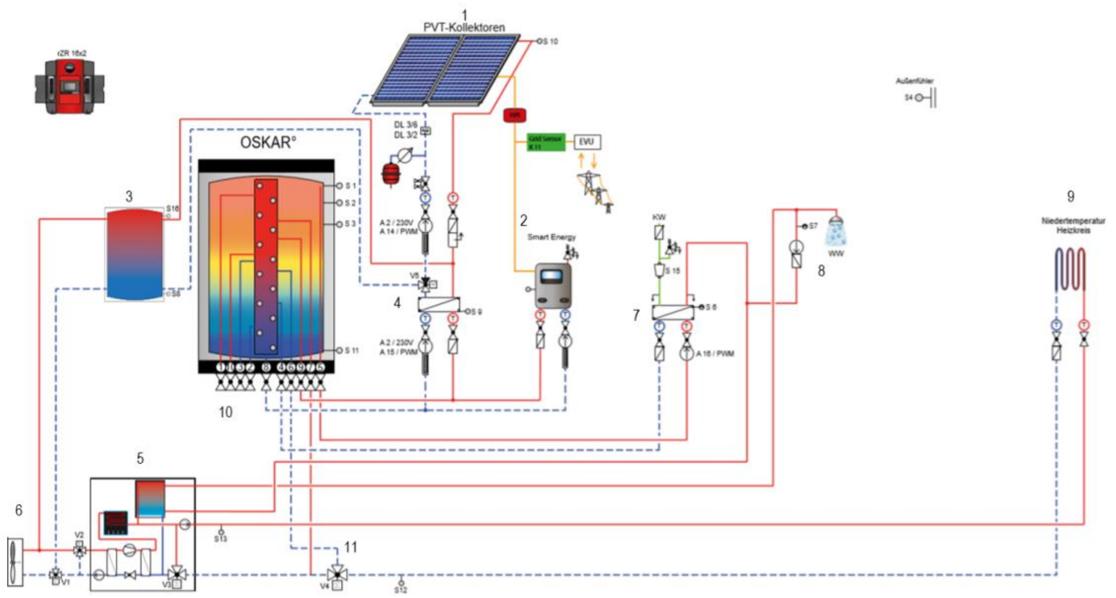

Fig. 2 – TP2 Schematics for Riga demosite

The Fig. 2 shows the SunHorizon TP2 schematics. Next, a description of the devised concept is presented according to the control strategy description in Tab. 2. The DualSun PVT panels (1) can heat up the stratified tank provided by RT (10) through a direct heat exchanger (4) when the outlet temperature from PVT panels is higher than the RT tank (S3). When the temperature is lower, a three ways valve is switched to connect the PVT panels to the glycol tank (3) in order to run the evaporator of the BH heat pump unit (5). PV production from (1) is mainly used to cover electricity demand from the building. When the electrical production exceeds the building's demand, then the smart energy electrical heater (2) can be used to heat up the RT tank (10) till the maximum temperature set for the tank is reached. This way, electricity is almost always self-consumed. The evaporator of the BH unit can be driven by (1)+(3) or by an outdoor dry cooler (6). BH unit heats up the flow in two phases. First, the water is heated up in the condenser (up to 50º). Second, if the desired temperature is higher than the condenser outlet, a secondary burner heats up the flow up to 70ºC. DHW demand will be preheated by heat exchanger (7) with the RT tank and later will flow to the DHW tank inside the BH unit to be heated up by the BH unit (5). The radiator stream will be preheated first with the RT tank through a three-way valve (11), and then by the BH unit (5). The BH unit is modelled in TRNSYS in a similar way as in TP1. DualSun PVT panels are modelled in TRNSYS using Type 816, which constitutes a dedicated simulation module with a nominal photovoltaic power of 310W and coefficients from EN ISO 9806 terminology of $\eta_{0,b} = 0.559$; c1 = 15.8 W/(m².K); c2 =0 W/(m².K²); c3, c4, c6 =0. The baseline consumption of the building has been evaluated considering weather profile and users profiles. The users' profiles in terms of DHW, space heating and electricity consumption has been modelled using CRESTmodel (McKenna and Thomson, 2016) and calibrated according to the total annual consumption derived from the bills.

Heating circuit: When the temperature of the RT tank at the center-bottom position within the tank is higher than the temperature of the return heating circuit, the water is preheated at the RT Tank. A mixing valve is used to control the supply temperature of the radiator according to the selected set point taking into account the return temperature. The two radiatiors are connected to the primary heating circuit, since they work with the same water temperature. The pump flow rate is fixed and is equal to the sum of the flow rate of two radiator. Then to provide the right flow rate to the radiators, two diverters are used.

Hot water circuit: The DHW is first preheated with the RT through a HX and later, it is streamed to the BH dedicated tank. The BH tank is maintained at a given temperature (e.g. 60ºC), in order to ensure the DHW supply temperature requested by the final users. The BH DHW tank is heated by the BH unit, which stops to provide heat to the radiators and heat up the tank. When the tank is heated the BH unit return to provide heat to the radiators. When providing heat to the DHW tank, the BH types turns into the control mode 2, that means that has a behaviour equal to a traditional condensing boiler of 18kW.

Solar circuit: The solar circuit is activated when the solar irradiation is higher than 540 kJ/hr/m2 and the outlet temperature of DualSun panels is higher than the glycol tank temperature or the RT tank temperature. The heating of the RT tank has the priority. When the outlet temperature is lower than the bottom temperature of the tank, the flow is then switched towards the glycole tank. Due to the local legislation in Latvia, the maximum allowed installed installed capacity of a micro generator used for net metering is 11.1 kW, limiting though the maximum number of panels at 35 (10.9 kWp).

Tab. 2 Control strategies

DualSun thermal supply	DualSun supply RT if DualSun outlet temperature is >= RT temperature + 5 °C DualSun supply Glycol Tank if DualSun outlet temperature is < RT temperature + 5°C and > Glycol Tank temperature.
RT Tank	RT max temperature: 80°C RT Preheating circuit is activated if the return temperature from the emission system is <= RT temperature - 2°C
Electricity management	Electricity is self-consumed if demand and production are simultaneous. Electricity surplus is supplied to the grid until the total surplus produced reaches the post retrofit electricity consumption. Electricity is provided to smart energy heater once the maximum surplus which can be supplied to the grid is reached.
Evaporator of BH	The BH's evaporator can be driven by an outdoor drycooler or the glycol loop connected to the DualSun panels. Whenever the glycol tank temperature is higher than the outdoor air temperature, the use of the glycol tank as evaporator is prioritized (if BH system is required).

2.3 TP3 development and modelling

TP3 illustrated in Fig. 3 will be installed in a tertiary building (civic center) located in Sant Cugat del Vallès (Spain), built in 2006. The heating and cooling installation of the existing system is based on Reversible air to water heat pump: 93.6 kW (nominal cooling capacity) –96.3 kW (nominal heating capacity) and Air handling unit (AHU): 110 kW (cooling capacity) –67.78 kW (heating capacity). The conditioned area and volume are respectively 816 m^2 and 3400 m^3. A simulation of actual and future HVAC plant was performed by means of two different software: First, the IESVE simulation is run to obtain the heating and cooling (H/C) loads from the building model, then its results are used as input for H/C system plant simulated in TRNSYS18. The TP3 system was modelled in TRNSYS by considering the datasheet of each installed equipment. The AHU was modelled component by component, while the heat pump was modelled by a calculator that implements equation obtained from a statistical analysis of operating data declared in the official datasheet. The non-linear polynomial eq. 1 correlates operating temperatures with real performances of the components.

$$\mathrm{f}(\mathrm{T}_{air}, \mathrm{T}_{water\_out}) = \mathrm{p00} + \mathrm{p10} * \mathrm{T}_{air} + \mathrm{p01} * \mathrm{T}_{\mathrm{water\_out}} + \mathrm{p20} * {T_{air}}^2 + \mathrm{p11} * \mathrm{T}_{air} * \mathrm{T}_{water\_out} \quad \text{(eq. 1)}$$

The TP3 system will be integrated with the existing HVAC; TVP panel, FAHR hybrid adsorption chiller and RT stratified tank will be integrated, the new system will be connected in series upstream to the existing heat pump (Fig. 3), the existing primary pump will be changed with a variable speed one. The only heat source is the solar one, TVP panel will produce as much thermal energy as possible with a maximum temperature range between 70°C and 100°C. During winter, the hot water produced by TVP panels will support the existing plant and is directly delivered to the existing heat pump, in summer it supplies the FAHR thermally driven chiller. FAHR Hybrid Chiller (HC) consists of two components: a vapour compression water to water chiller and an adsorption one, they are connected in parallel to a cold buffer tank and then to the existing chiller. The nominal cooling power are 50 kW for the vapour compression chiller and 20 kW for the sorption one. TVP panel surface is 220 m^2 south oriented (azimuth=0) and tilted 30°, the volume of stratified storage is 10 m^3.

As for the existing reversible HP, the Hybrid Chiller (HC) was modelled by implementing performance equations. The compression unit was modelled through a performance equation analogous to eq. 1. For the sorption unit a linear model that considers the three operating temperatures (HT-high temperature, MT-recooling temperature, LT-cooling temperature) was implemented. Source data were provided by FAHR and converted in a statistical correlation. In this case the temperatures of water inlet inside the machine were considered, the correlation was calculated both for cooling power and COP.

$$\mathrm{f}(\mathrm{HT}_{in}, \mathrm{MT}_{in}, \mathrm{LT}_{in},) = \mathrm{I} + \mathrm{a} * \mathrm{HT}_{in} + \mathrm{b} * \mathrm{MT}_{\mathrm{in}} + \mathrm{c} * \mathrm{LT}_{in} \quad \text{(eq. 2)}$$

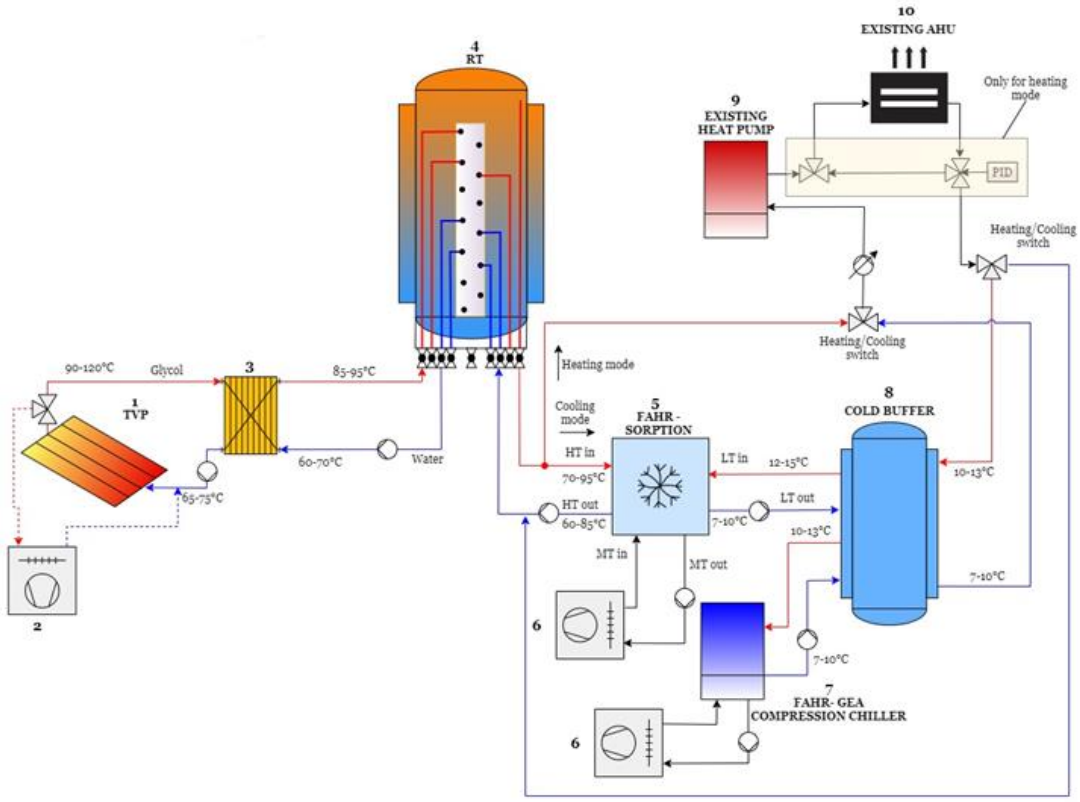

Fig. 3 Integration between existing system and SunHorizon TP3

In Tab. 3, the control strategy considers the behavior of the existing plant deduced from the preliminary data retrieved from the existing monitoring system.

Tab. 3 Control strategy for the existing system

Component	Signal logic
AHU fan (type 662)	Aquastat controller based on indoor air temperature setpoint and daily schedule (6:00-22:00) : T setpoint 25°C (Cooling mode) – 21°C (Heating mode)
AHU control dump	40% recirculation air ratio (fixed by demo site owners)
pump (type 654)	Signal pump=1 following daily schedule (6:00-22:00)
Existing HP (eq. 1)	HP 4 power levels: 0% - 37% - 63% - 100%. PID controller based on temperature setpoint of HP water outlet: 40°C for heating and 7°C for cooling

A summary of control strategy for each component of the TP3 is reported in Tab. 4. The general controls implemented in the existing HVAC system is only changed regarding the primary pump.

Tab. 4 control strategy for SunHorizon model

Component	Control description
TVP temperature control	Type 539 (TVP solar panel), configured to internally vary the flowrate aiming at 95°C outlet setpoint temperature
Safety diverter valve	Aquastat controller based on TVP water outlet temperature (setpoint 100°C).
HC Dry Cooler settings	Dry cooler types 511, configured to modulate fan speed aiming at 25°C outlet fluid temperature
HC Sorption unit	Aquastat controller based on temperature inlet of sorption chiller (setpoint 8°C)

HC Compression unit	Chiller 2 power levels: 50% and 100%. PID controller based on temperature outlet from the chiller (setpoint 7°C)
Tempering valve – AHU hydronic loop (heating operation)	The tempering valve mixes the hot water delivered by TVP panel with return warm water from AHU coil during winter operation whenever TVP production is higher than hot water AHU inlet set point (40°C)
Primary pump (variable speed)	60%-100% signal, the intensity of signal is proportional to the difference between the temperature of water outlet from AHU coils and the setpoint

2.4 TP4 development and modelling

TP4 couples BDR HPs with DualSun PVT is shown in Fig. 4 applied in Madrid demo case, and consists of DualSun PVT panels (1) driving the evaporator of a Brine Water HP (BWHP) (3), an Air Water HP as back-up (6) and two storage tanks from RT: one for space heating and space cooling demand(4), and another one for DHW demand(5). The solar driven heat pump allows to store the solar energy in RT tanks via the BWHP as well as producing PV electric energy to drive both HP and cover partially the electrical demand of the building. A small glycol buffer (2) is installed between the BWHP and PVT collectors to de-couple the flow rates. The AWHP one includes an electric resistance (2x6kW) to have the possibility to perform thermal shock as legionella preventive control – in case of need.

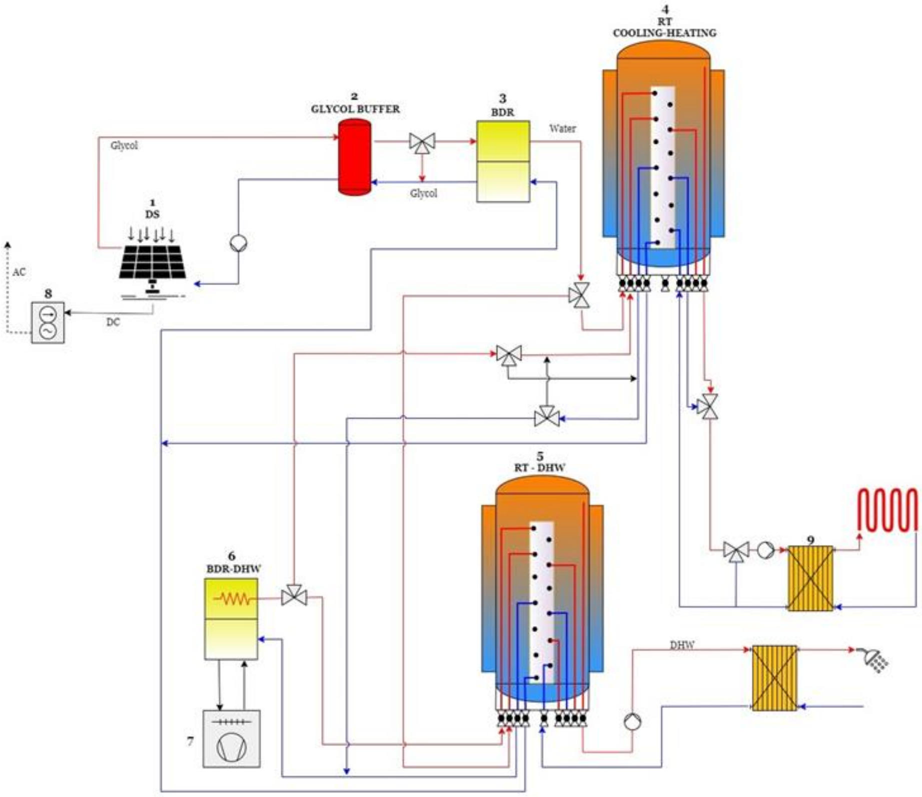

Fig. 4 Integration between existing system and SunHorizon TP4

Modelling approach: In TRNSYS the DualSun PVT panels are modelled using Type 816, using the same coefficients as in TP2. The collector tilt is set to 35º, to optimize the thermal and PV production in Madrid. The small glycol buffer is modelled using Type4a with default values and a volume of 0.2m3. BWHP is modelled using Type 927 using the performance map of GSHP 9 TR-E model from BDR, which has a capacity of 9 kW and a COP of 3.42 (B0/W45, EN14511). The temperature at the entrance of the BWHP is limited to a maximum of 35ºC and minimum of -15ºC with Type 953 (tempering valve) for safety reasons. The AWHP is modelled using 941 using the performance map from HP HPI Evolution model 27 TR-2 from BDR, which has a capacity of 24.4kW and COP 3.94 (A7/W35, EN14511). Heat pump flow rates are designed to supply a temperature difference of 5ºC, whereas the solar loop flow rate is set to 60 kg/h·m2. The building where TP4 is applied consists of a retrofitted social housing building in Madrid. The building demand is estimated using Design Builder resulting in a space heating and space cooling demand of 31.8 kWh/m2 and 9.36 kWh/m2, respectively. Fancoils are modelled using Type 91 to heat or cool the air of the Type 56 building. DHW consumption is estimated in 122 kWh/person using CREST software demand. As baseline case, DHW and SH is provided by a boiler with an efficiency of 80% and cooling is satisfied with individual splits with an EER of 2.5.

Control strategy: The DualSun solar thermal loop is switch on whenever the temperature at the outlet of the solar collector is five degrees greater than the bottom temperature of the buffer tank, whereas the HP’s operation depends on its efficiencies. HP efficiencies are modelled with empirical equations depending on the supply and evaporator’s temperature. Tab. 5 control modes are modelled in MATLAB and coupled with TRNSYS via Type155, to assess the efficiency every 5 minutes and switch on the heat pump with the highest efficiency whenever there is DHW, SH or SC request. When there are two demand requests, DHW is supplied with the HP with the highest efficiency. To avoid reversing the mode of the BWHP too many times, the cooling reverse mode is only switched on whenever there is an excess of PV production and no DHW request. When the maximum or minimum temperature at the inlets of the HPs are reached, the control signal is disabled. The MATLAB program takes into account the different operation modes in the different seasons and DHW is always prioritized (See Tab. 5). DHW or SH is requested whenever the top tank temperature is lower than the setpoint temperature (50ºC and 45ºC, respectively). SC is requested whenever the bottom tank temperature is higher than the cooling setpoint temperature (15ºC).

Tab. 5 Control Modes in TP4 for selection of HP supply types to meet the thermal demand types

	Only AWHP on	**Only BWHP on**	**Both on**
DHW request	Mode 1b	Mode 2b	Mode 3b: AWHP>DHW, BWHP>SH
SH request (heating season)	Mode 1a (heating)	Mode 2a (heating)	Mode 3a: BWHP>DHW, AWHP>SH
SC request (cooling season)	Mode 1a (cooling)	Mode 2a (cooling). Only if excess of PV production and no DHW request	Mode 3a: BWHP>DHW, AWHP>SC

3. Results and discussion

3.1 TP1 results

The parametric study for the preliminary sizing from simulations of solar field and tank regarding the non-renewable energy and Customer Bill Reduction (CBR) savings is balanced by the amount of solar heat dissipated, since the impact of the solar field overheating protection emerged from industry partners and demo site responsible discussions. The Fig. 5 shows a turning point around 800L solar tank volume for both CBR costs and 10% limit-dissipated heat curves that mostly selected the TP1 configuration as 10 m² TVP solar panels, 0.8 m^3 RT tank and 20kW BH unit. The Tab. 6 shows its performance results, considering the existing heating system is gas boiler and SDHW with assumed solar fraction of 50%, consuming 37.2 MWh PE, that means 2.1k€ costs and 7.4 tons $CO_{2,eq}$ emissions per year. The 63% TVP solar useful heat efficiency outperforms by 30% its traditional flat plate competitor (same area) that leads to 3% extra PE savings. The integration of solar thermal TVP and RT tank from BH20 single unit is increasing from 25 to 36% the $f_{sav,PEnren}$ and the GUE from 130 to 132%, mostly by reducing the share of high temperature DHW demand in total BH20 heat supply.

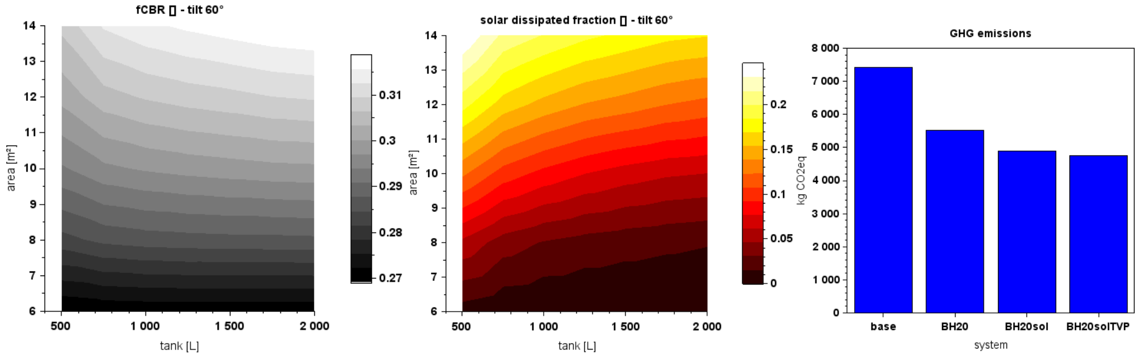

Fig. 5 Analysis of bill reduction (left), overheating (mid) and system configuration effect (right)

Tab. 6 Estimated annual KPIs for TP1 in Berlin demo site

$\eta_{TVP,53°C}^{gross}$	$f_{sol,th}$	$dTtank$	GUE	RER	$f_{sav,PEnren}$	$f_{sav,GHG}$	f_{CBR}
63%	14%	34K	132%	31%	36%	36%	30%

3.2 TP2 results

The simulation has been performed considering 35 maximum number of panels (58m²) and an heat pump of 20kW to be installed and varying the dimension of the storage to understand the optimum situation that allow to have a balanced energy savings reduction and customer bill reduction. To calculate the energy cost, the discount obtained on the electricity price thanks to the net metering has been considered: the extra electricity produced and not self-consumed, can be supplied to the grid. Based on a yearly calculation, a discount of 35% on the energy price is considered for an amount of energy equal to the extra energy supplied. This amount cannot exceed the yearly electricity consumption. From the Fig. 6, the KPIs about reducing energy consumption, greenhouse gases emissions and energy cost show that the tank size has a limited effect (~ 1-2 %) on savings, either fsav or fCBR (39% is about 745€). An on-going optimization of the set of control parameters is aiming to improve further these KPIs.

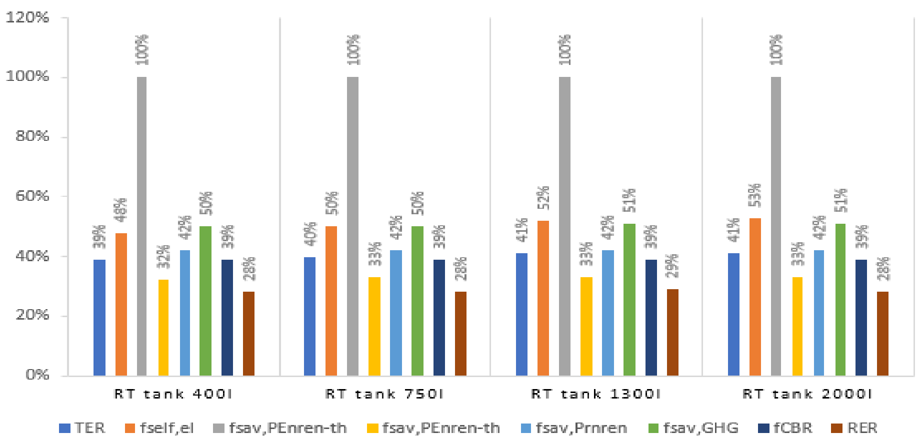

Fig. 6 Simulated performance of TP2 configurations in Riga demo case

Tab. 7 Simulated performance of TP2 selected 1300L configuration in Riga demo case.

$f_{self,el}$	TER	GUE	RER	$f_{sav,PEnren-el}$	$f_{sav,PEnren-th}$	$f_{sav,PEnren}$	$f_{sav,GHG}$	f_{CBR}
52%	41%	125%	29%	100%	33%	42%	51%	39%

3.3 TP3 results

As detailed in CEA et al. 2020, a tailored hourly weather file for the year 2019 relying on interpolation from

Athenium Analytics (an iScan service provided in IESVE) and Meteonorm files was developed to account for realistic user demand in both simulations (building and system). Several analyses performed before the simulation addressed a first sizing of the main components, then, the simulation results assessed the optimal compromise between theoretical optimal size and technical issues. The main technical matters are related to the optimal coupling between solar production and sorption demand, the configuration of hybrid chiller and its consequent sizing, the correct coupling between existing system and TP installation. The hybrid chiller consists in parallel connection of 50 kW vapor compression module and 20 kW sorption unit (nominal cooling power). TVP panel surface is 220 m^2 south oriented and tilted 30°, the volume of stratified storage is 10 m^3. The main result from Tab. 8 is the reduction of 33.4% of electrical energy consumption and fsol-sh solar fraction in heating season close to one. During summer the hybrid chiller covers the 57.7% of cooling energy supply with an increase of energy efficiency and energy saving (Fig.7). Moreover, the sorption unit supplies cooling energy with a very high efficiency due to its low electrical demand and to its renewable source for driving power. The hybrid chiller coupled with a renewable energy source (TVP) let to achieve one of the main goal of Sunhorizon project regarding 33% PEnren savings and 52% renewable energy ratio. The control strategy of hybrid system plays a crucial role to balance the sorption and vapour compression cooling production. Tab. 4 shows different temperature set point for each unit in order to maximise the sorption production and the solar energy supply. The investigation of additional sorption modules installation shown severe increase of auxiliaries' electricity consumption, not balanced by enhanced cooling power. In the sizing of TVP solar field, it shows an overproduction that can't be stored beyond the tank maximum safety temperature, therefore it is dissipated. To minimize the solar energy waste two ways were investigated: reduce the solar field area or increase the stratification tank volume. The first way is not suitable because of the significant decrease of sorption cooling production, from the second, arises technical troubles regarding the installation and not significant benefits in terms of energy storage. The solar energy wasted during summer amounts to 31.9% of production, in winter is 24.1%; during the periods in which there is no heating or cooling demand the solar energy production must be fully wasted since there are no DHW load. Tab. 6 reports the main KPIs estimated for TP3 in Sant Cugat where the relative values are referring to absolute values of PESnren 43994 kWh, GHGsav 7825 $kgCO_{2,}eq$ and CBR 5270€. Furthermore, TP3 achieved better indoor comfort conditions than the existing H/C system by reducing the HCI from 817 to 83 K.h and CCI from 1748 to 1360 K.h.

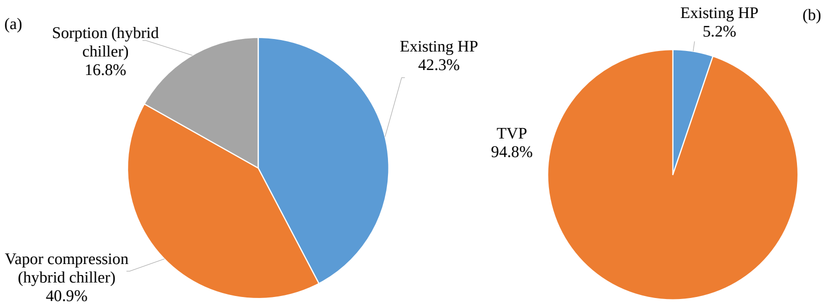

Fig. 7: Source distribution for cooling (a) and heating (b) energy supply

Tab. 8 TP3 main annual KPIs

$\eta^{gross}_{TVP,76°C}$	$f_{sol,th}$	$f_{sol,sh}$	$SEER$	RER	$f_{sav,PE_{nren}}$	$f_{sav,GHG}$	f_{CBR}
0.51	18.27	0.95	6.9	52%	33.4%	33.4%	33.4%

3.4 TP4 results

A parametric study is performed to size the system components, varying the volume of the RT tanks, slope of the DualSun PVT modules and setpoint temperatures. From the main results illustrated in Fig. 8, the system is not sensible with the variation of the volume of the RT tank, but as the volume increases the primary energy savings increases slightly. The lower the tilt inclination, the lower the PV production and the system achieved more PEnren savings between 35-45º (there is not significant variation between this two). By increasing the DHW setpoint to 60ºC in the tank, the savings are reduced in 2.5% points, while by moving the position of the monitored temperature to the middle-top tank (a relative height of 0.7), the savings are reduced in 0.5% (more energy is charged in the tank). By increasing the capacity of the DHW tank, the primary energy savings increase 0.1% as well as the RER. The same happens by increasing the capacity of the SH/SC tank. Nevertheless, due to space limitation in the technical room, the capacity of both tanks are limited to a height of 1.5 meters and a capacity of 1.3 m^3, and 1m3 respectively, in order to ensure stratification. Furthermore, the current control strategy is compared with a temperature-dependent control strategy that does not consider the efficiencies of the BDR HPs (reference case vs. simpler control in Fig. 7). This simple strategy switches on the BWHP whenever the solar field is warm enough. The minimum working temperature of the BWHP is -15ºC and this control strategy does not allow the BWHP to work when the sun is gone. As a result, during winter time the AWHP is mainly used, increasing the electricity consumption in nearly 1800kWh/year. With a control strategy that allows to compare the efficiency of both HPs, results in 11% more primary energy savings and higher solar thermal production (as the DualSun PVT panels work as evaporator when the sun is gone). This leads to make use of 82.3% of the heat provided by the PVT panels and, by means of the BWHP, provide 66.9% of the heat needed in the system. The optimal cases are obtained with bigger tanks, but due to space limitations option 5 (100 kg/h·panel) with the efficiency-dependent control is chosen, with the following parameters: a flow rate in the DualSun panels of 100 kg/h·panel, solar tilt of 35º, volumes of 0.2 m3 for the buffer tank, 1.3m3 for the DHW tank, and 1 m3 for SH tank, with a DHW setpoint of 50ºC and the position of the sensor at the top of the tank (in heating mode).

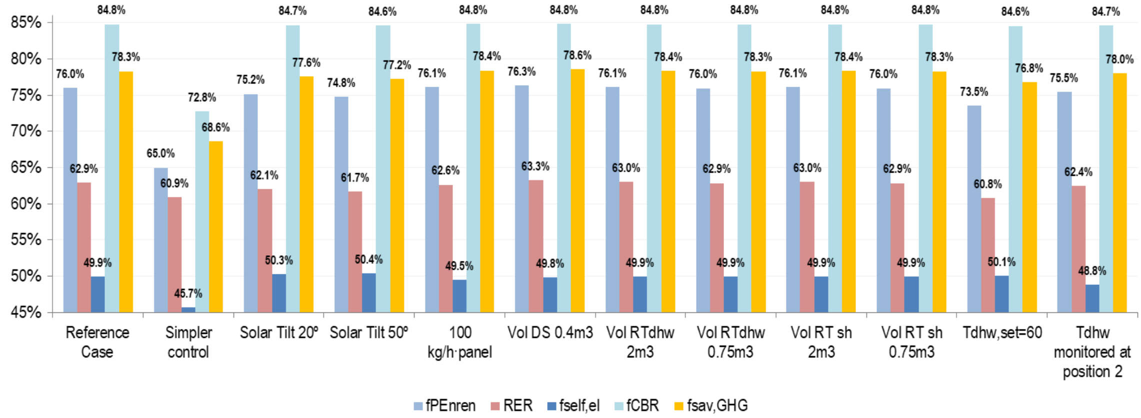

Fig. 8 Parametric Study for TP4-1 in Madrid demo site

The estimated TP4 annual KPIs are shown in Tab.9 where the savings are compared to the mostly gas-fueled baseline in Madrid demo case. Considering only AWHP supply for heating and cooling without PVT-driven-BWHP, the simulation estimates 41.3 MWh PEnren consumption, SCOP=2.7 and SEER=4.3. It means the DualSun solar PVT integration with BDR BWHP in TP4 would reach $f_{sav,PEnren}$ =54% and increased SCOP=3.59 compared to AWHP alone since it runs as support in heating mode .

Tab. 9 Estimated annual KPIs for TP4-1 in Madrid demo site

$\eta^{gross}_{DS,18°C}$	$f_{sol,th}$	$\eta^{gross}_{DS,el}$	$f_{self,el}$	TER	$dT_{tank,DHW}$	$dT_{tank,SH/SC}$	RER	$f_{sav,PE_{nren}}$	$f_{sav,GHG}$	f_{CBR}[1]
20.3%	66.9%	16.4%	49.5%	1.2	16K	2K	62.6%	76.1%	70.3%	84.8%

4. Conclusion

The current work managed simulation studies about design and sizing of HP, thermal storage, solar collectors that allow for selecting four appropriate configurations of the TPs for their respective demo sites: small residential building in Berlin, Germany (TP1), small residential building in Riga, Latvia (TP2), tertiary civic center in Saint Cugat, Spain (TP3) and large social-housing apartment in Madrid, Spain (TP4) with annual savings results in terms of non-renewable primary energy consumption, GHG emissions and operating costs. In parallel, other configurations of the four TPs have been selected similarly to end up with the preliminary definition of eight SunHorizon demo pilots. The annual savings are ranging from 33 to 70 % regarding GHG emissions, from 30 to 85% regarding the operation costs. It depends in a large extent on the demo site localization and existing system and verifies the expectation that the larger solar panels area, the higher the savings up to a limit, as illustrated in

[1] Most of the savings are obtained by removing the gas contract from the dwellings.

Fig. 5 for TP1. For the TP1, TP3 solar thermal systems, it emphasizes the requirement of excess solar heat dissipation in building context with summer fluctuating heat load, that is facing in the other hand to the urban heat island reduction issue, whenever no detrimental operation cost effects were detected. It shows also rather flat optimal tank size for all TPs, mostly ending with selection of smallest tank in the range to lower the installation costs.

The previous descriptions of control and the simulations analysis showed that evolutions from original single component approach are required by HP controller manufacturer to run efficiently the systems. Indeed, it's the flexible device connected to stable energy network to ensure that the end-user temperature demand is satisfied, to look carefully to the solar REN source state and storage, to optimize overall energy savings sometimes against its pure own performance, or require to run HP internal pump to flow solar in heating circuit, while still considering hardware safety temperature limitation (bypass valve mostly required).

These system models and simulation results are being used for the design of specific tests following the semi-virtual approach (Chèze et al., 2018) and to compare with the test results before installing the TPs on-site in 2021. The TRNSYS dynamic simulation models are currently used for the development of advanced control to be demonstrated in Riga and Sant Cugat sites. They will be run again at the end of the demonstration phase for the comparison with the performance monitoring data and the estimation of the savings, and in replication and exploitation case studies where the TPs may compete each other's or against single HP or PV+HP. Beyond project end, these models are the basis of either in-depth system model development with interested industrial partners or simplified system model for sizing tool.

5. Acknowledgments

The SunHorizon Project has received funding from the European Union's Horizon 2020 Research and Innovation Programme under Grant Agreement N. 818329.

6. References

CARTIF, CEA, CNR ITAE, Checkwatt, RINA-Consulting, BDR THERMEA, Ratiotherm, Fahrenheit, Dualsun, Boostheat, TVPsolar, Exergy, EMVS, VEOLIA, AJSCV, Riga University, GRE-Liège, 2019. KPIs assessment based methodology (Public report No. D2.4), SunHorizon no. 818329. INEA, EC, http://www.SunHorizon-project.eu/wp-content/uploads/2019/12/D2.4-KPI-assessment.pdf. (last access 24/07/2020)

CEA, RINA-Consulting, Schneider Electric, Boostheat, CNR ITAE, CARTIF, AJSCV, GRE-Liège, BDR THERMEA, VEOLIA, Riga University, EMVS, 2020. Report on baseline and boundary conditions of SunHorizon demo sites, including monitoring aspects (Public report No. D6.1), SunHorizon no. 818329. INEA, EC, http://www.SunHorizon-project.eu/wp-content/uploads/2020/07/D6.1-demo-energy-audit.pdf. (last access 24/07/2020)

Chèze, D., Lamaison, N., Breitenbach, P., Fuligni, F., 2018. Comparative dynamic performance tests of two real technology packages for buildings heating system retrofit. EuroSun 2018. doi:10.18086/eurosun2018.01.07

Drück, Harald. 2006. Stratified fluid storage tank with four internal heat exchangers, ten connections for direct charge and discharge and an internal electrical heater -Type 340. TRNSYS. ITW Stuttgart: Transsolar.

H2020 Innovation Action GA818329, http://www.SunHorizon-project.eu/ (last access 24/07/2020)

Haller, Michel, Bengt Perers, Chris Bales, Janne Paavilainen, Antoine Dalibard, Stefan Fischer, and Erik Bertram. 2012. TRNSYS Type832v5.00 Dynamic Collector Model.

Jordan, U., Vajen, K., Kassel, U., 2005. DHWcalc: Program to generate domestic hot water profiles with statistical means for user defined conditions, ISES Solar World Congress, Orlando (US), p. 6.

IEA. 2018. Global Energy and CO2 Status Report 2017

McKenna, E., Thomson, M., 2016. High-resolution stochastic integrated thermal–electrical domestic demand model. Applied Energy 165, 445–461. https://doi.org/10.1016/j.apenergy.2015.12.089

ODYSSEE, 2018. Energy efficiency trends in buildings

Modelling of Inverter Heat Pumps in TRNSYS

Fabian Hüsing[1] and Peter Pärisch[1]

[1] Institute for Solar Energy Research Hamelin (ISFH)

Abstract

Validated simulation models are important for the development of advanced system design and control strategies. In this contribution we present an approach to model inverter heat pumps by combination of multiple single speed models in TRNSYS. Performance data of a brine/water heat pump is determined by experimental investigations for three levels of inverter frequency. Deviation in efficiency is observed at source temperatures above 10 °C, with lower inverter frequencies reaching higher coefficients of performance. Each level of inverter frequency is modelled with one instance of TRNSYS Type 401. To validate the modelling approach, we use experimental data of load variations. Relative deviations show an overestimation of heat transferred at condenser of $\Delta Q_{cond,rel} = 3.7\,\%$ and electric energy used at compressor of $\Delta P_{el,rel} = 2\,\%$ in the simulation Overall, the approach is able to represent the operational behavior of an inverter heat pump and can be suggested for system control strategy development by means of simulations.

Keywords: inverter heat pump, performance data, TRNSYS model, experimental validation

1. Introduction

Scenarios for an efficient and feasible transformation towards a fully renewable energy supply system identify electric compression heat pumps (hereafter HP) as a key technology (Bründlinger et al. 2018, Gebert et al. 2018, Henning & Palzer 2013). This assessment is based on several characteristic features. HP contribute to an integrated energy supply by linking the electricity and heat sectors. Efficient heat generation as well as opportunities for connection of thermal storage capacity and demand management are important in this context. Furthermore, HP operate at a decentralized level, as they gain a high percentage of the heat they provide in their vicinity. Therefore, use of HP contributes to an even allocation of energy processing units.

Inverter heat pumps are able to modify their heat output and demand for electric power by changing the rotational speed of the compressor and aperture of expansion valves. Therefore, they add an important degree of freedom regarding optimized control of heat pump systems. Especially systems with generation of electricity on site and/or complex heat source designs are expected to benefit from optimized control strategies.

In development and optimization of system design and control strategies numeric simulations are an established tool. To evaluate the potentials of inverter heat pumps in differently configured heating systems, it is crucial to use component models validated with experimental data.

2. Experiment and Simulation

In this contribution we present experimental investigations performed on a commercially available heat pump and propose an approach to model inverter heat pumps in TRNSYS (Klein et al. 2010). For detailed analysis a dynamic load cycle is measured and used for validation of the proposed modelling approach.

Identification of heat pump parameters

Performance data for the HP is determined under steady state operation conditions. A brine/water HP (hereafter BWHP) is tested for the parameter set described in Table 1 based on the procedure defined in parts 2 and 3 of DIN EN 14511 standard. The aim is to identify performance data for a wide range of evaporator inlet and condenser outlet temperatures ($T_{evap,in}$ and $T_{cond,out}$) at different partial loads (inverter frequencies).

doi:10.18086/eurosun.2020.04.08 Available at http://proceedings.ises.org

Table 1: Brine/Water HP - parameter set tested

$T_{evap,in}$	$T_{cond,out}$	f
°C	°C	Hz
-5	35	30
0		
5	45	60
10		
15	55	90
20		

Figure 1 depicts a schematic of the experimental setup used for the investigation. A fluid circuit with a resistance heater is connected to the evaporator of the BHWP to operate as a heat source. The source circuit is filled with brine. The condenser of the BHWP is connected to a fluid circuit filled with water, operating as a heat sink. The sink circuit is coupled to a chilled water distributing network over a heat exchanger and includes a resistance heater. The setup allows heat supply at the source circuit and heat extraction and supply at the sink circuit and therefore, control of inlet temperatures at evaporator and condenser. Heat source and sink temperatures at the inlet and outlet of the evaporator and condenser are measured with calibrated Pt100 immersion temperature sensor couples (uncertainty of measurement: ±0.10 K for temperature, ±0.04 K for temperature difference). Mass flows through the evaporator and condenser are measured with Coriolis mass flow meters (uncertainty of measurement: ±0.17 %). Electrical power at the BWHP compressor is measured with a power analyzer (uncertainty of measurement: ±0.47 %).

Steady state operation conditions (deviations of state variables smaller than defined in Table 4 of DIN EN 14511:2013 Part 3) are captured over thirty minutes at a measurement interval of six seconds for each combination of parameters in Table 1. For each combination of inverter frequency and condenser outlet temperature, mass flows in evaporator and condenser circuits ($\dot{m}_{cond}$ und $\dot{m}_{evap}$) are determined at nominal conditions given in Tables 7, 8 and 9 of DIN EN 14511:2013 Part 2, which define evaporator and condenser in- and outlet temperatures. All other evaporator inlet temperature levels are tested at same mass flows for given combinations of inverter frequency and condenser outlet temperature, resulting in different evaporator outlet and condenser inlet temperatures.

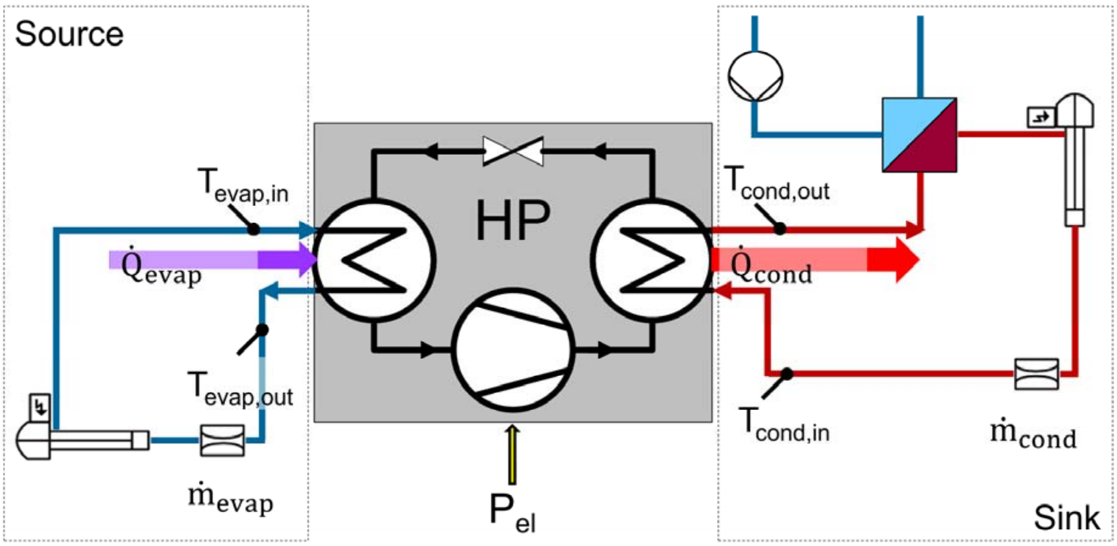

Figure 1: Schematic testing environment for experimental investigation

The heat flux transferred at the condenser is calculated according to Equation (1).

$$\dot{Q}_{cond} = \dot{m}_{cond} * c_p * (T_{cond,out} - T_{cond,in}) \quad \text{(Equation. 1)}$$

$\dot{Q}_{cond}$ = heat flux transferred to sink circuit at condenser; $\dot{m}_{cond}$ = mass flow at condenser; c_p = specific heat capacity; $T_{cond,in}$ = condenser inlet temperature; $T_{cond,out}$ = condenser outlet temperature

In Figure 2 the condenser heat flux is plotted against the evaporator inlet temperature for different condenser outlet temperatures and inverter frequencies. The inverter frequency is distinguished by color (green ≙ 30 Hz, blue ≙ 60 Hz and orange ≙ 90Hz). Darker shades correspond to higher temperatures at the condenser outlet. At 30 Hz inverter frequency and a condenser outlet temperature of 55 °C, steady state conditions are not reached.

The condenser heat flux increases with inverter frequency and source temperature. For most of the data, higher heating powers are reached at lower condenser outlet temperatures. Heating powers between 1.6 kW and 9.5 kW are recorded. At an inverter frequency of 90 Hz the heating power shows weaker increase at evaporator inlet temperatures above 10 °C for condenser outlet temperatures of 35 °C and 45 °C.

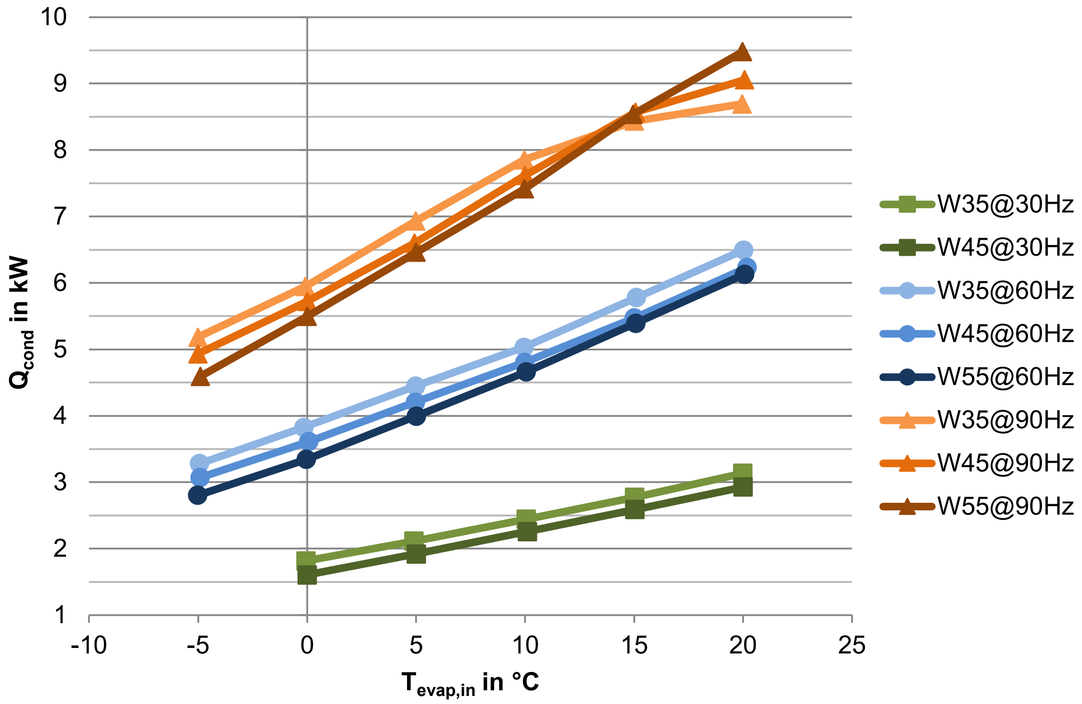

Figure 2: Condenser heat flux over source temperature

The coefficient of performance (COP) is calculated according to Equation (2). In contrast to DIN EN 14511:2013, no electric power for pumps or controller are considered. This is due to the fact, that these components are individually considered in TRNSYS simulations and are thus not needed for parameterization of the model.

$$COP = \frac{\sum_{\tau} \dot{Q}_{cond}}{\sum_{\tau} P_{el}} \quad \text{(Equation 2)}$$

COP = coefficient of performance; P_{el} = electrical power of the BWHP compressor; τ = time period of stationary measurement

Figure 3 depicts the COP as function of the evaporator inlet temperature for different condenser outlet temperatures and inverter frequencies. The coloring is analog to Figure 2. Determined COP reach values from 2.47 to 8.86. In general, higher COP are achieved at higher evaporator inlet temperatures. In the following the influence of the inverter frequency is discussed at a condenser outlet temperature of 35 °C (upper three graphs). At low evaporator inlet temperatures small differences in COP are observed. With increasing evaporator inlet temperature, larger differences occur. At evaporator inlet temperatures above 10 °C, the increase of COP at 90 Hz shows a decreasing trend, while at 60 Hz linear and at 30 Hz exponential increase is observed. This leads to a large divergence in COP at the highest source temperature ($COP_{B20W35@30Hz}$ = 8.86 versus $COP_{B20W35@90Hz}$ = 5.33).

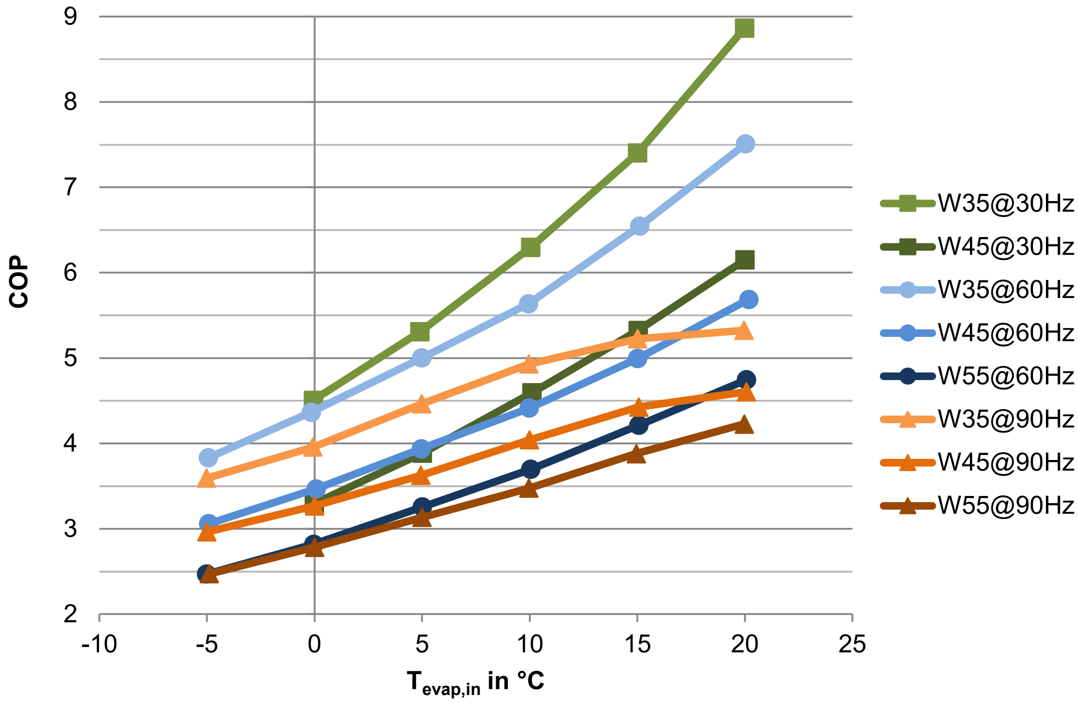

Figure 3: Coefficient of performance (COP) over source temperature

Modelling approach

To reproduce the performance of a HP at various inverter frequencies a TRNSYS model is developed. TRNSYS Type 401 (Afjei & Winter, 1997), which calculates the condenser heat flux and electric power based on the evaporator inlet and condenser outlet temperatures by a biquadratic polynomial, is used. We choose the approach to combine multiple instances of Type 401, first presented in (Hüsing et al. 2018). Each instance of Type 401 is parameterized with polynomial coefficients derived from the performance data at one inverter frequency, thus modelling one load level. Outputs for all load levels are simultaneously calculated throughout the simulations. To obtain the conditions for a given inverter frequency, linear interpolation between results of adjacent load levels is implemented.

For the BWHP three instances of Type 401 are used to calculate results for operation at 30, 60 and 90 Hz inverter frequency. In Figure 4 the structure of the model in TRNSYS simulation studio is shown. Input variables, either from data files or a surrounding system simulation, supplied to all three instances are evaporator and condenser inlet temperatures as well as mass flows. Each instance calculates its output variables. The most important output variables are evaporator and condenser powers and outlet temperatures, as well as compressor power. The output variables are connected to the Equation block "HP_Output", where the interpolation, based on the inverter frequency is performed. The inverter frequency is supplied to the "HP_Output" equation block and may be derived from measurement data or obtained using different control strategies.

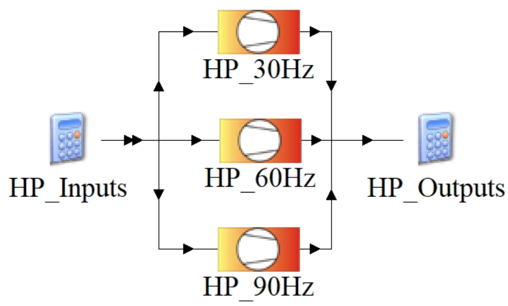

Figure 4: Structure of inverter heat pump model in TRNSYS Simulation Studio

The heat capacity of the heat pump condenser is important for accurate modelling of dynamic operation (Mercker et al. 2014). In Type 401 it is regarded via time constants for heating up and cooling down (Afjei & Winter, 1997). For the presented model we assume, that the time constant for cooling down ($\tau_{cooling} = 45$ s) is not influenced by inverter frequency. We assume the time constant for heating up to be inversely proportional to inverter frequency, as the heat flow is nearly proportional to the inverter frequency and the total heat capacity does not change. The time constants are calculated according to Equation (3), with $\tau_{heating}(f_{ref}) = 30$ s at $f_{ref} = 90\ Hz$.

$$\tau_{heating}(f) = \frac{f_{ref}}{f} * \tau_{heating}(f_{ref}) \qquad \text{(Equation 3)}$$

$\tau_{heating}(f)$ = inverter frequency dependent time constant for heating thermal inertia of the condenser; f = inverter frequency; $\tau_{heating}(f_{ref})$ = time constant for heating at reference inverter frequency

Temperatures and heating rates for all partial loads and the interpolated results can be monitored by online plotters throughout the simulation. The proposed approach allows the replacement of single component HP models in existing system simulation models by connections to the "HP_Input" and "HP_Output" blocks.

Validation against experimental data

To validate the modelling approach, we use data from experiments with load variations. The experiment is carried out in the setup described above and shown in Figure 1. At set points for the evaporator inlet ($T_{evap,in}$ = 10 °C) and condenser outlet temperature ($T_{cond,out}$ = 45 °C), the inverter frequency is varied in steps of 60; 75; 90; 80 Hz. Corresponding to each variation in inverter frequency, the condenser outlet temperature changes. After reaching steady state, the condenser inlet temperature is adjusted to reach a condenser outlet temperature $T_{cond,out}$ = 45 °C. Thus, intervals of with small variation of condenser temperatures (± 2 K) are recorded. In Figure 5 temporal progress of inverter frequency during the experiment is depicted.

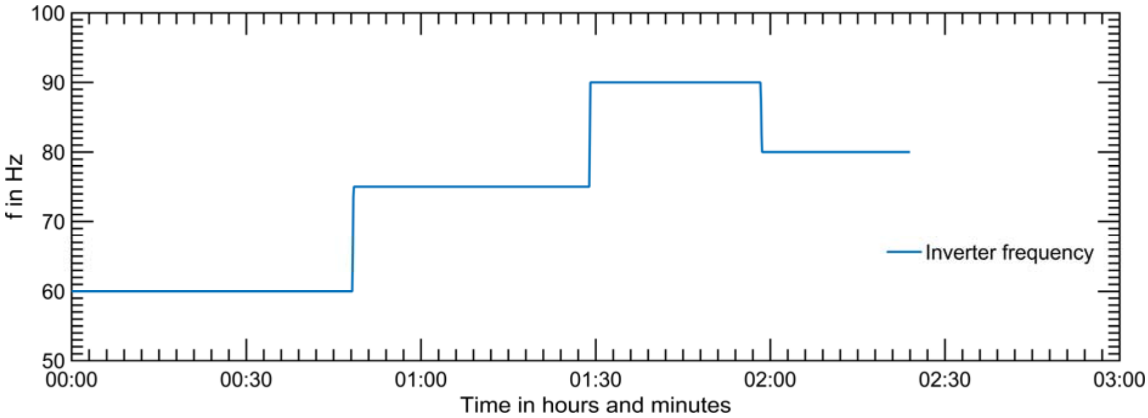

Figure 5: Temporal progression of inverter frequency

We use the modelling approach described in the previous paragraph to simulate the load variations. Therefore, measured data for evaporator and condenser inlet temperatures and mass flows, as well as the inverter frequency are supplied to the model. Throughout the simulation temporal progresses of evaporator and condenser outlet temperatures and heat fluxes as well as electric power at the compressor are recorded in a data file. Subsequently the simulation outputs are compared to the measured data, to assess the accuracy of the modelling approach.

In Figure 6 temperatures are plotted against time. Due to the larger deviations in outlet temperatures at the beginning of the simulation, induced by initial conditions, the first two minutes are not considered for the subsequent analysis. The upper plot shows the evaporator inlet temperature and the measured as well as simulated evaporator outlet temperature. The temporal progress shows good agreement for the simulated evaporator outlet temperature. Maximum deviation of -0.89 K is observed, while a mean deviation of -0.06 K is achieved. The lower plot shows the condenser inlet temperature and the measured as well as the simulated condenser outlet temperatures. Mean deviation of 0.07 K and maximum deviation of 1.78 K are slightly larger than those at the evaporator. Still a good agreement in temporal progress can be confirmed.

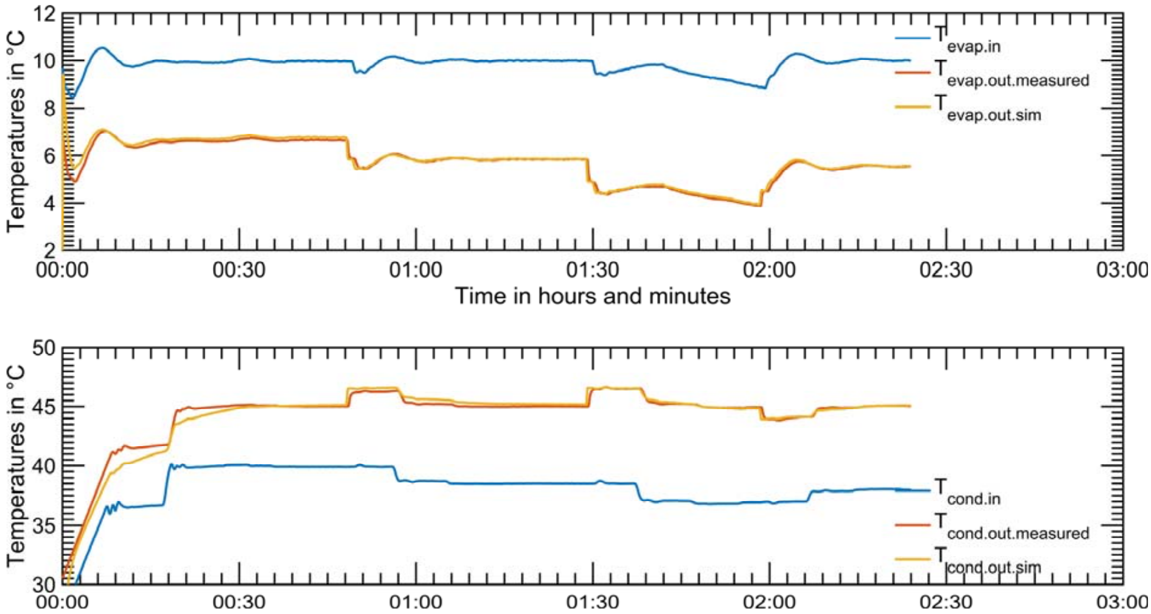

Figure 6: Measured and simulated evaporator and condenser temperatures over time

In Figure 7 the flows of heat at condenser (top) and electric power (bottom) are plotted against the time. While the levels of condenser heat flux are well represented in the simulation, single fluctuations which occurred during the measurement are not reproduced by the simulation model. These fluctuations can be attributed to unevenly distribution of temperatures and thermal inertia of the heat carrier in the sink circuit. As the distribution of heat capacity of the heat carrier is not modelled (only one temperature node for the circuit in Type 401) further extensions are needed for a more accurate representation. In the time interval shortly after changes in inverter frequency, we observe that the temperatures and heat flux changes are more directly in the simulation than in the measurement. This is attributed to a change in condenser outlet temperature, which in reality is delayed by the thermal inertia of the condenser. Because in simulation all load levels are computed in parallel, the change in inverter frequency shows immediate effect on the interpolated output variables.

The temporal progress of electric power shows good agreement between measurement and simulation. Integral quantities for heat transferred at condenser and electric energy used at compressor are calculated according to Equations (4) and (5) for measured and simulated data.

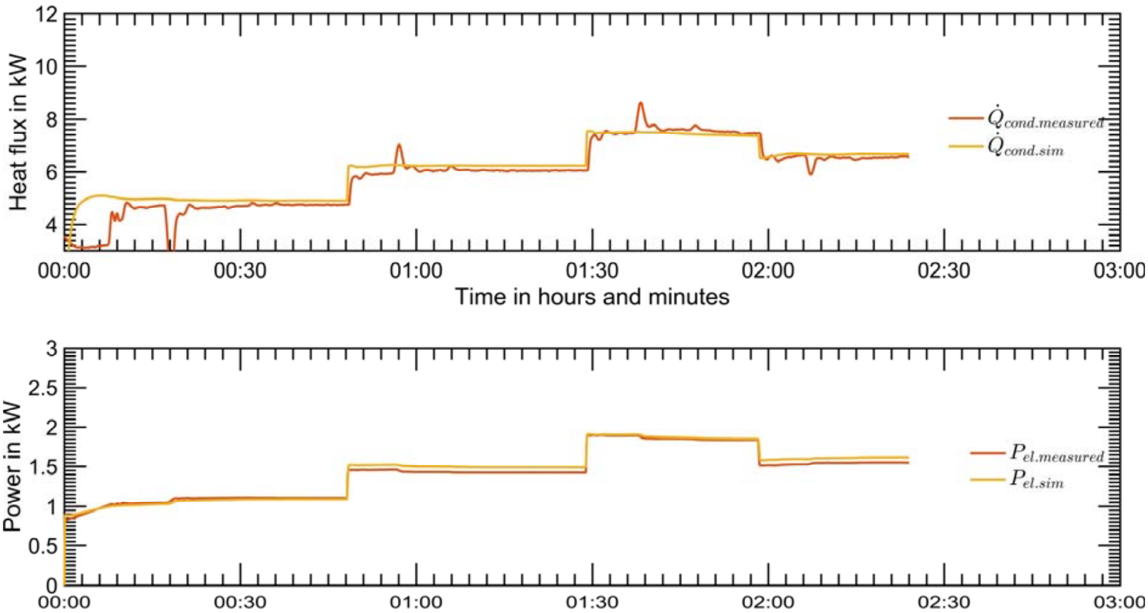

Figure 7: Measured and simulated heat fluxes and powers over time

$Q_{cond} = \sum_{\tau} \dot{Q}_{cond} * \Delta\tau$ (Equation 4)

Q_{cond} = heat energy transferred to the sink circuit at condenser; $\dot{Q}_{cond}$ = heat flux transferred to the sink circuit at condenser; τ = time period of the measurement; $\Delta\tau$ = time interval of the measurement

$W_{el} = \sum_{\tau} P_{el} * \Delta\tau$ (Equation 5)

W_{el} = electric energy used at compressor; P_{el} = electric power used at compressor; τ = time period of measurement; $\Delta\tau$ = time interval of the measurement

Amounts of heat transferred at condenser are $Q_{cond,measured} = 14.11\ kWh$ and $Q_{cond,SIM} = 14.64\ kWh$, respectively. For the electric energy used at the compressor $P_{el,measured} = 3.40\ kWh$ and $P_{el,SIM} = 3.47\ kWh$ result. Relative deviations are calculated according to Equation (6) and show an overestimation of heat $\Delta Q_{cond,rel} = 3.7\ \%$ and $\Delta P_{el,rel} = 2\ \%$ in the simulation. Hence, the performance of the BWHP is overestimated by $\Delta COP = 3.1\ \%$.

$\Delta E_{rel} = \frac{(E_{sim} - E_{measured})}{E_{measured}}$ (Equation 6)

ΔE_{rel} = relative deviation in energy between measurement and simulation; E_{sim} = simulated energy quantity (Q_{cond} or W_{el}); $E_{measured}$ = measured energy quantity

3. Discussion

Performance data of a BWHP is successfully determined by experimental investigation. The data shows large influence of inverter frequency on efficiency. Especially at higher source temperatures (above 10 °C) the operation at lower inverter frequencies induces significantly higher coefficients of performance. Therefore, selection of inverter frequency is a crucial factor for the control of heat pump systems. We expect especially solar assisted HP systems (solar heat sources - high source temperatures and/or solar electricity – demand management) with inverter heat pumps to benefit from sophisticated control strategies.

A trend to decreasing heating power at high source temperatures and maximum inverter frequency is observed. This may be attributed to one of the inner components of the HP (compressor, expansion valve, heat exchangers) reaching a physical limit. More detailed analysis of the inner cycle could provide better insight.

An approach to model inverter heat pumps by use of multiple instances of TRNSYS Type 401 is presented. In best-case this would allow to model inverter HP by performance data available from certified testing (e.g. DIN EN 14825:2018).

The validation concerning frequency variation and small temperature variations at the operating point B10W45 shows good agreement in temporal progress of the decisive variables (outlet temperatures and energy fluxes). Relative deviations of energy quantities are below 4 %. The deviation corresponds well with modelling of single speed heat pump without mass flow correction (Pärisch et al. 2014).

Larger deviations are observed shortly after changes of inverter frequency or inlet temperature. This emphasizes the importance of the thermal inertia of the condenser (heat up time constant), which is not yet a part of performance data provided by certified testing. The presented approach is not able to model effects of thermal inertia in cases of temperature changes resulting from inverter frequency modification.

Overall the approach is able to represent the operational behavior of inverter heat pumps. Therefore, it can be used for system control strategy development by means of simulations.

4. Outlook

Our current work aims at validating the modeling approach with a broader range of boundary conditions, such as lower inverter frequencies and temperature variation over larger ranges.

In ongoing research, the presented approach is applied to model an air/water HP. Experimental investigations are carried out at a new modular heat pump test facility at ISFH. The new facility is designed to enable heat pump testing at wider ranges of temperatures and mass flows than the setup used for the investigations in this contribution.

5. Acknowledgments

The presented works result from research projects funded by the state of Lower Saxony and the European Union (contract no. ZW 6-85037507) as well as the German Federal Ministry of Economy and Energy (contract no. 03ET1275A). The authors are grateful for the support of their work. The content of this publication is the sole responsibility of the authors.

Special appreciation is also expressed to Ms. Marie Kreye, who largely contributed to the presented results in the frame of her bachelor thesis.

6. References

Afjei, T. and Wetter, M. 1997. Compressor Heat Pump Including Frost and Cacle Losses, Version 1.1 Model Description and Implenmenting into TRNSYS, Zentralschweizerisches Technikum Luzern, Horw

Bründlinger T., König J. E., Frank O., Gründig D., Jugel C., Kraft P., Krieger O., Mischinger S., Prein P., Seidl H., Siegemund S., Stolte C., Teichmann M., Willke J., Wolke M. 2018. dena-Leitstudie Integrierte Energiewende – Ergebnisbericht und Handlungsempfehlungen, Herausgeber: Deutsche Energie-Agentur GmbH (dena), Berlin

DIN EN 14511:2013-12, Air conditioners, liquid chilling packages and heat pumps for space heating and cooling and process chillers, with electrically driven compressors – Parts 2 and 3, German version EN 14511:2013, Beuth Verlag, Berlin, 2013

DIN EN 14825:2019-07, Air conditioners, liquid chilling packages and heat pumps, with electrically driven compressors, for space heating and cooling - Testing and rating at part load conditions and calculation of seasonal performance; German version EN 14825:2018, Beuth Verlag, Berlin, 2019

Gebert P., Herhold P., Burchard J., Schönberger S., Rechenmacher F. Kirchner A., Kemmler A. and Wünsch M. 2018. Klimapfade für Deutschland – Study by Boston Consulting Group and Prognos on behalf of the Bundesverband der Deutschen Industrie (BDI) e.V., Berlin

Henning H.-M. and Palzer A. 2013. Energiesystem Deutschland 2050, Fraunhofer-Institut für Solare Energiesysteme ISE, Freiburg

Hüsing F., Mercker O., Hirsch H., Kuntz D., Walker-Hertkorn S., Sabel M. 2018. Horizontal ground heat exchangers and solar collectors as optimized bivalent heat source for highly efficient heat pump systems, Final report (german language), Institut für Solarenergieforschung, Hameln, https://doi.org/10.2314/GBV:1047633868

Mercker, O., Pärisch, P. and Rockendorf G. 2014. Taktverhalten von Sole/Wasser-Wärmepumpen – Messung der thermischen Zeitkonstanten und ihre Bedeutung für die Jahresarbeitszahl, Proceedings of BauSIM 2014 - Fifth German-Austrian IBPSA Conference, RWTH Aachen University, Aachen

Pärisch P., Mercker O., Warmuth J., Tepe R., Bertram E., Rockendorf G. 2014. Investigation and model validation of a ground-coupled heat pump for the combination with solar collectors; in Applied Thermal Energy Volume 62, Issue 2 (2014) P. 375-381, Elsevier, München

Klein S.A., et al., 2010. TRNSYS 17. A Transient System Simulation Program, Solar Energy Laboratory, University of Wisconsin, Madison, USA, http://sel.me.wisc.edu/trnsys

05. PV and PVT Systems for Buildings and Industry

Innovative Coupling of PVT Collectors with Electric-Driven Heat Pumps for Sustainable Buildings

George Meramveliotakis[1], George Kosmadakis[1], Achileas Krikas[1], João Gomes[2,3] and Marika Pilou[1]

[1] Thermal Hydraulics and Multiphase Flow Laboratory, National Centre for Scientific Research "Demokritos", Agia Paraskevi (Greece)

[2] Department of Building Engineering, Energy Systems and Sustainability Science, University of Gävle, Gävle (Sweden)

[3] Research Department, MG Sustainable Engineering AB, Uppsala (Sweden)

Abstract

An innovative renewable-energy based system is examined for covering the heating and cooling demand in residential buildings. This system adopts an alternative solar-assisted heat pump configuration, developed around its two main components: the PVT collectors and a dual-source heat pump. The heat produced by the collectors can be either used directly for covering the heating needs or stored in a buffer tank for supplying the heat pump with low-temperature heat, exploiting all solar heat and operating the heat pump with an elevated performance for a longer period during the day. Once the stored heat in the buffer tank is discharged, the heat pump is supplied by ambient heat. The same configuration can also operate at cooling mode during summer, with the heat pump reversing its operation. The current work examines the main system parameters, in order to evaluate its performance for covering a large share of the building's energy needs.

Keywords: PVT collectors, dual-source heat pump, buildings, cooling and heating demand, domestic hot water

1. Introduction

Solar energy applications in buildings are increasing with many of them based on solar thermal collectors, photovoltaic (PV) panels or, in more advanced systems, hybrid photovoltaic-thermal (PVT) collectors (Buker and Riffat, 2016). At the same time, the use of domestic heat pumps for heating and cooling is rising (Guo and Goumba, 2018), because of their capacity to meet the buildings' energy demand, especially when they are supplied with low-temperature heat of up to 25 ºC (Naranjo-Mendoza et al., 2019). The integration of the two above energy systems, i.e. solar-assisted heat pumps (SAHPs), results in maximum solar energy utilization and enhances the performance of the individual components, (Kim et al., 2018).

The main functionality of the integrated system is to either provide the required heat to the users directly from the solar collectors when the temperature is high enough or supply the heat pump with heat at low-temperature to increase its coefficient of performance (COP). A wide variety of thermal coupling methods exists, such as with direct or indirect heat transfer from the collector, aiming to improve the combined efficiency. Another concept that does not rely on the solar-assistance principal is the PV plus heat pump, which requires less piping and connections (Wang et al., 2020), with the main focus being placed on reducing the electricity consumption from the grid.

Based on the above general principles of combining either solar thermal collectors or PV panels with heat pumps, an alternative design is proposed here, based on the use of PVT collectors that produce simultaneously heat and electricity (Vaishak and Bhale, 2019). All the PVT heat production can be exploited in such coupling, even if it is at low-temperature and not used directly, but rather supplying the heat pump for greatly increasing its performance (Fine et al., 2017). The concept is realized here with:

- The use of standard water tanks to store either heating or cooling to cover the building energy demand,

doi:10.18086/eurosun.2020.05.01 Available at http://proceedings.ises.org

aiming to decouple to some extent the consumption from the production.

- The heat supply of the heat pump from either low-temperature water or ambient air, resulting to a dual-source unit, with the selection based on the maximum performance.

The integrated system is described in Section 2, where the main components and functions are presented, while the numerical model for its annual simulation based on typical building energy demand is presented in Section 3. Section 4 presents the main results of the system operation and performance during a winter and a summer day, as well as during a whole year for a multi-family residential building located in Athens (Greece). Finally, the conclusions of this study and the further steps are highlighted in Section 5.

2. System description

2.1 Overall layout

The main system components are the PVT collectors for producing heat and electricity and the dual-source (air or water) heat pump for heating and cooling. The system is intended for a multi-family residential building with the same concept also applicable in other types of buildings, such as single-family houses and offices after some modifications. The heating and cooling modes are illustrated in Fig. 1, along with the main system components and their connections.

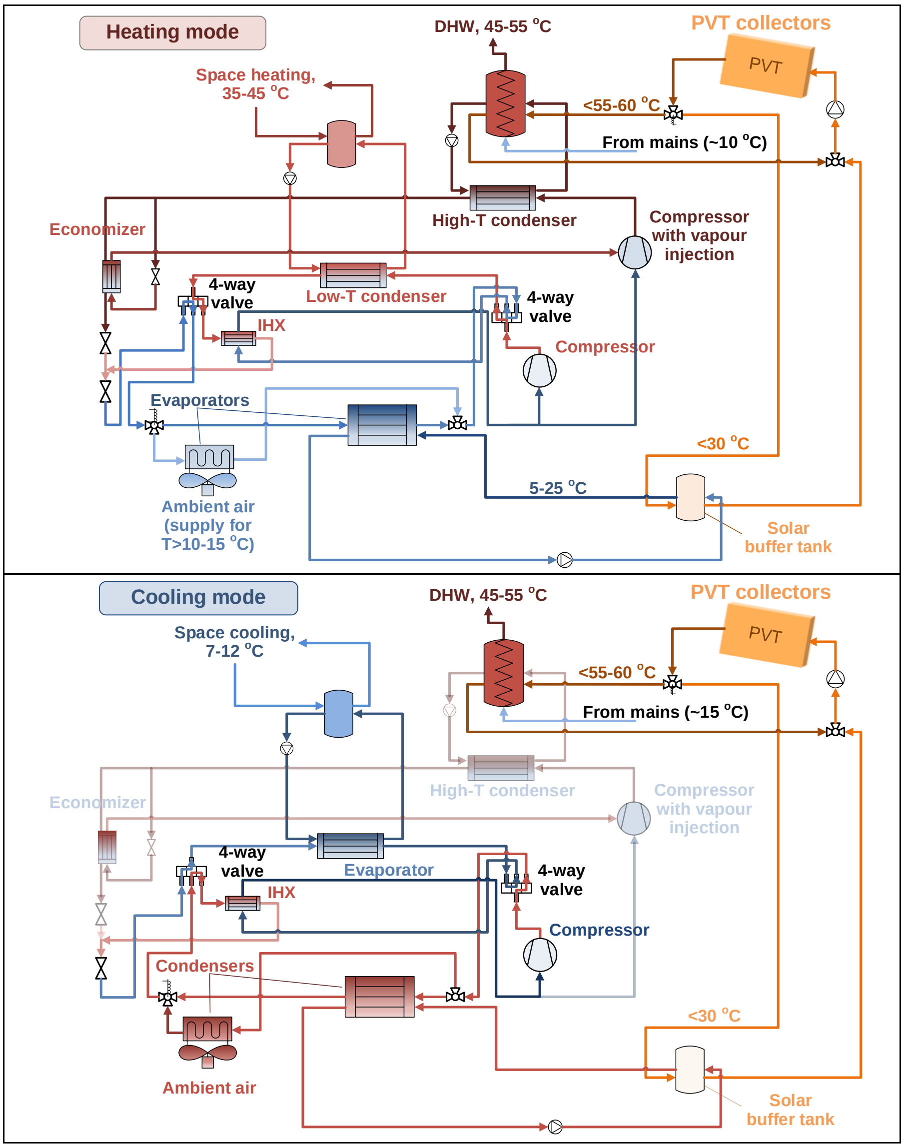

Fig. 1: System operation at heating mode (top) and at cooling mode (bottom), including the main system components

The electrical-driven heat pump is two-stage with the compressors placed in parallel. The high-temperature stage produces heat for domestic hot water (DHW) and is equipped with an economizer with vapour injection in the compressor. The low-temperature stage produces either space heating or space cooling and includes a subcooler (an internal heat exchanger – IHX) for increasing the COP. This configuration has been selected among many that have been examined (e.g. with in-series or parallel compressors, intercoolers, economizers) and showed the highest COP. Moreover, it can produce both heating and DHW at the same time.

For reversing the heat pump operation from heating to cooling mode and vice versa, two 4-way valves are included. One valve is the standard one placed at the compressor discharge, while the second one is necessary due to the presence of the subcooler at the outlet of the low-temperature condenser. The system operation for both the heating and cooling seasons is described next.

2.2 Heating season

For time intervals with adequate solar irradiation, the heat produced by the PVT collectors is of high enough temperature, over 45 °C, and charges the main water tank that is used for covering the building's domestic hot water (DHW) needs. Alternatively, when the solar radiation is low, the temperature of this heat is reduced and usually cannot be exploited by the main water tank. In the proposed system, this heat is stored in another tank (the "solar buffer tank") for supplying the evaporator of the heat pump and thus greatly increasing its COP to over 3.5-4 for DHW production at 55 °C (directed to the main tank) and space heating at 45 °C.

When the solar buffer is completely discharged and the temperature of the stored water drops below 5 °C, the heat pump switches its heat supply to ambient air. This flexibility is further enhanced with the presence of another buffer tank that stores the produced heat for the space heating needs, and decouples to some extent the time of heating demand with the heat pump operation, and thus reduce the electricity demand from the grid.

2.3 Cooling season

The system operation is simplified during the cooling season, since the heat produced by the PVT collectors is primarily stored in the main tank for covering the hot water needs of the building. At the same time, the solar buffer tank is always kept charged with a stored water temperature up to 25 °C, since usually there is an excess of solar heat production during summer. The purpose of storing heat also in the solar buffer tank is to allow a high heat pump performance for DHW production, in case the direct use of the collectors for charging the main water tank is not adequate. This is the case of a very high DHW demand.

However, the main function of the heat pump during the summer period is to deliver the space cooling at 7 °C, which is stored in the same buffer tank as space heating (heating is not used during this period). The reversing of the heat pump operation is necessary and no simultaneous production of DHW and space cooling is possible, always giving priority to the DHW. The effective cooling is provided in the evaporator, while the cycle rejects heat to the ambient through the air-cooled condenser.

3. Description of the numerical model

3.1 Overview

The complete system model has been developed in the Engineering Equation Solver – EES environment (Klein, 2020), and simulates the system operation during the average day of each month, using as input the energy demand, with the separate model of the latter described later. The system model is based on the modeling of its individual components, which are described next.

3.2 Heat pump

The two-stage heat pump uses a refrigerant with an ultra-low global warming potential (GWP). Two screened refrigerants have been examined that fulfill this, R1234yf and R1234ze(E), with the latter bringing a higher COP by up to 10-15% and a much higher heating capacity. Therefore, R1234ze(E) has been finally selected, with all simulations presented here relying on this HFO refrigerant.

As described previously, the heat pump has two separate condensers, one delivering heat for DHW production up to 55 °C and the other for space heating at 45 °C. At cooling mode, the cycle is reversed and only the low-temperature compressor operates rejecting heat to the ambient, as indicated in Fig. 1.

The heat pump modeling is based on a validated thermodynamic model developed in EES software (Kosmadakis and Neofytou, 2019), enriched to account for the finned-tube heat exchanger (HEX) and the compressor model, with the latter based on a semi-hermetic screw compressor of Bitzer with a displacement of 140 m^3/h at 50 Hz. The resulting heating capacity is 30 and 60 kW for DHW and space heating respectively.

Various simulation runs have been conducted leading to the sizing of the main components (e.g. the plate HEXs, air-fan). Once sizing was specified, the heat pump operation has been examined for variable heat source and sink temperatures. The results have been processed and used in a regression analysis for developing correlations of the key parameters, COP and heating/cooling production. These correlations are given as polynomials of the hot and cold side temperatures to allow a straightforward integration in the overall EES system model.

3.3 PVT collector

The PVT collector features an asymmetric low-concentration stationary reflector design, with a total size of 2.31 × 0.955 m. The thermal and electrical capacity is 1250 and 250 W respectively at standard conditions. A tilt of 30° is considered. The heat production per m^2 of the collector (P_{th}) is given by Eq. (1).

$$P_{th} = P_{th,exp} - P_{th,loss} \quad (1)$$

where $P_{th,exp}$ is the exploitable thermal power and $P_{th,loss}$ is the thermal loss of the collector given by suitable equation which takes into consideration thermal loss characteristics of the PVT panels.

According to the manufacturer, the exploitable thermal power per m^2 is given by Eq. (2).

$$P_{th,exp} = n_{th,b} \cdot I_{b,T} \cdot IAM_{th} + n_{th,d} \cdot (I_{d,T} + I_{refl,T}) \quad (2)$$

where $I_{b,T}$, $I_{d,T}$, $I_{ref,T}$ are the hourly beam, diffuse and reflective radiation components on the tilted collector surface, $n_{th,b}$ and $n_{th,d}$ are the thermal efficiency coefficients that correspond to heat acquisition by beam and diffuse radiations respectively, and IAM_{th} is the thermal incidence angle modifier.

The electrical production per m^2 of the collector is given by Eq. (3).

$$P_{el} = \left[n_{el,b} \cdot \left(I_{b,T}\right) \cdot IAM_{el} + n_{el,d} \cdot \left(I_{d,T} + I_{refl,T}\right)\right] \cdot [1 - a_{el}(T_m - T_{stc})] \quad (3)$$

where T_{stc} is the temperature at standard test conditions equal to 25 °C, $n_{el,b}$ and $n_{el,d}$ are the electrical efficiency coefficients that correspond to electrical production by beam and diffuse radiation components, a_{el} is the temperature loss coefficient, and IAM_{el} is the electrical incidence angle modifier.

Further details of the collector with its performance parameters and modelling features are provided by Bernando et al., 2013 and Gomes et al., 2014.

3.4 Water tanks

The system model is supplemented with two different types of water tanks (see Fig. 1): main water tank and buffer water tank. The main water tank is supplied with heat directly from the PVT collectors at elevated temperature for producing hot water. In case this is not enough, the heat pump delivers the remaining heat to this tank. Stratification is needed to store as much as thermal energy while having high temperature differences in the inlet/outlet water flows (Rahman et al., 2016). Moreover, the mains water inlet has a very low temperature, favoring the stratified temperature distribution. Thus, an immersed heat exchanger is included, in which the tap water is circulated. The main water tank is modeled by splitting the tank in a finite number of 1-D volumes across the axis of equal height (Panaras et al., 2013) and applying energy balance in each volume. Heat transfer occurs between the volumes and between the volumes and the immersed heat exchanger. Ambient heat losses are calculated from each volume separately, according to its temperature and surface in contact with the tank walls.

There are two buffer tanks with their main functions as follows:

1. The solar buffer tank for storing the low-temperature heat produced by the collectors for supplying the

heat pump.

2. The space buffer tank for storing hot/chilled water for supplying the building's space heating/cooling network during the winter/summer season respectively, connected to the condenser/evaporator of the heat pump.

The modeling approach of the above two tanks is simple, since their temperature range is limited, usually by about ±10 °C, with a small variation between the inlet/outlet temperature of the water flows. This makes it possible to model these tanks as a single-volume tank, assuming the same water temperature within the whole tank (Panaras et al., 2013). This temperature is calculated based on the heat source and sink, as well as on the heat losses to the ambient through an unsteady energy balance equation.

3.5 Heating and cooling demand profiles

The complete system model considers a typical heating and cooling demand of a multi-family residential building. Heating includes both space heating and DHW. The space heating and cooling demand profile is estimated by an in-house code developed in Python exclusively for that purpose. The aforementioned calculations are based on thermal zones (one for each floor), thermostat preferences, building specifications (e.g. surface area and U values of the walls), solar heat gains and internal gains from occupants, according to Hoogsteen et al., 2016 and ASHRAE Handbook, 2017. A smart thermostat approach is introduced into the code, for restricting the sharp increase of space heating and cooling demand at peak hours, and thus smooth the profiles, indicating a realistic handling of the building loads. Furthermore, it is considered that the temperature in each floor is stabilized to a certain value, when occupants are absent. Calculation of the necessary thermal loads to keep the indoor air temperature to the set-point temperature, allowing a variation of ±1 K, is based on distinguishing between heating and cooling seasons. The necessary weather data to perform the calculations are the annual solar irradiation components and ambient temperature, with the former obtained from TRNSYS software (Klein et al., 2005).

A small multi-family building with five 100-m^2 well-insulated apartments is considered. Moreover, each apartment occupies a whole floor and hosts a family composed of two adults and two children. The weather data of Athens, Greece, are used for the calculations with a time-step of 10 minutes.

A typical daily space heating and cooling profile is shown in Fig. 2 during a winter (1st of January) and a summer day (1st of July) respectively, together with the internal heat gain that also includes the solar gain. The peak of the heat gain is higher during winter, since a larger amount of solar radiation reaches the glazing of the building.

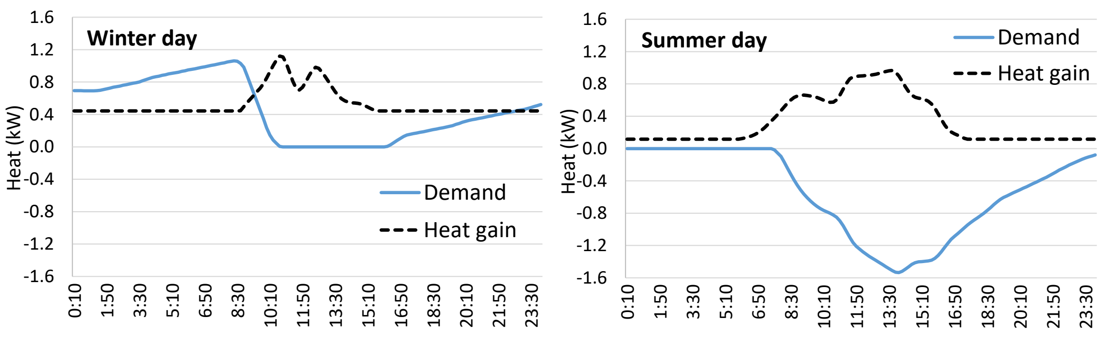

Fig. 2: Space heating and cooling demand and heat gain profile of each apartment during a winter day (left) and a summer day (right) in Athens, Greece

The specific energy demand of this building is about 100 kWh/m^2, divided into 59.45 kWh/m^2 for space heating and 40.34 kWh/m^2 for space cooling.

The DHW profile required by the model is calculated according to EN16147:2017 standard for water-heaters, hot water storage appliances and water heating systems (EU Regulation No 814/2013). The standard defines a 24-h measurement tapping cycle with its total thermal energy content of almost 12 kWh per apartment and per day, corresponding to the "L" profile. This profile is shown in Fig. 3, with the same used for all days of the year.

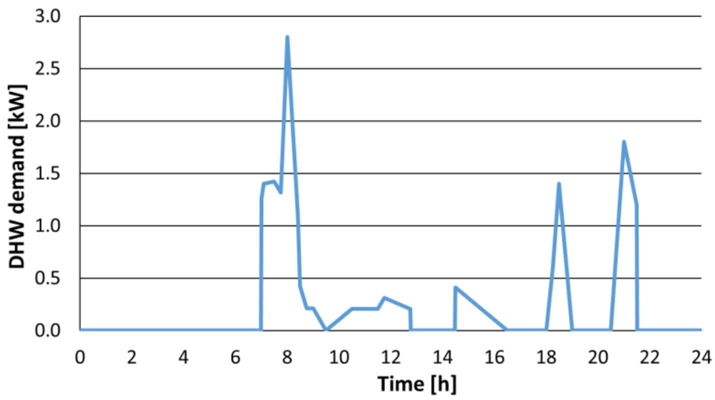

Fig. 3: DHW profile ("L") during the day, according to the standard EN16147:2017

This profile is included in the EES code, and in combination with the heating and cooling needs define the overall demand for the building energy system simulation.

4. Results and discussion

The main results are related to the energy production potential and the temporal performance of the main components. Since the PVT surface has an important role on the system performance, mostly for heating, its effect will be also examined. The results are initially presented for the reference case with a PVT surface of 50 m^2 for a residential building with 5 apartments for a typical day in January (winter) and July (summer) in Athens, Greece.

4.1 Winter day

The heat pump configuration is flexible, allowing the simultaneous operation of both compressors for the production for both space heating and DHW. This is clearly depicted in Fig. 4 during the winter day.

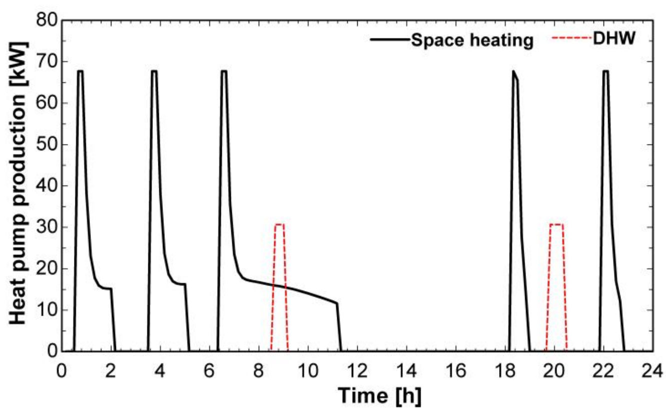

Fig. 4: Heat pump production for space heating and DHW during the winter day

The volume of the space heating buffer tank is 2 m^3, which is large enough to avoid the frequent switch-on of the heat pump. During this typical winter day, the heat pump operates five times for space heating production, mostly during the night and early in the morning, to increase the temperature of the space buffer tank to 45 ^oC. On the other hand, the production of 30 kW for DHW is needed only twice per day for charging the main water tank, closely following the demand profile of Fig. 3.

The charging process is shown in Fig. 5 through the average temperature of the stored water in all three tanks (main, space heating buffer, and solar buffer). The average temperature of the main tank is divided into the temperature of its upper part (heat supplied by the heat pump) and to its lower part (heat supplied by the PVT collectors).

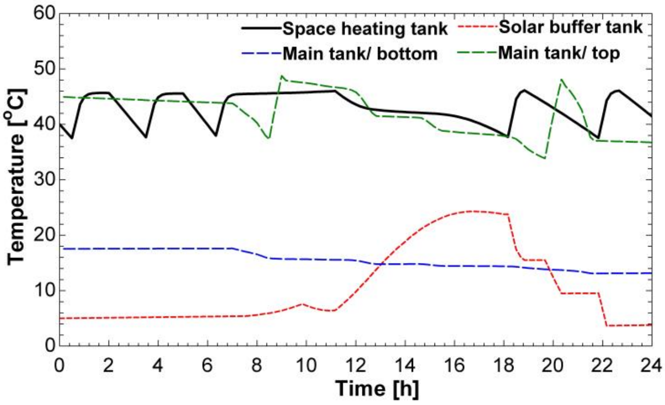

Fig. 5: Average temperature of the water tanks (main tank divided into top and bottom parts) during the winter day

The temperature of the space heating buffer tank ranges between 40 and 45 °C, with the lower limit defined as the minimum to engage the heat pump operation. From 11:30 to 18:00 all space heating demand is covered by the stored thermal energy of the water, gradually reducing its temperature, without the need to operate the heat pump during this period.

The water of the main tank at the top part is kept at elevated temperature the whole day, showing some fluctuations, according to the DHW demand and the heat pump operation. The bottom part remains at a low temperature, since the PVT collectors supply a very small amount of heat to the main tank during this day. The rest is directed to the solar buffer tank, with its temperature always kept within the range of 5-25 °C. When the minimum threshold of 5 °C is reached, the heat pump switches its heat source to the ambient air. Moreover, the water temperature in this tank reaches 25 °C late in the afternoon, after being charged during the whole day, allowing for a very efficient heat pump operation, as shown in Fig. 6, in which the COP is presented along with the electricity consumption of the heat pump.

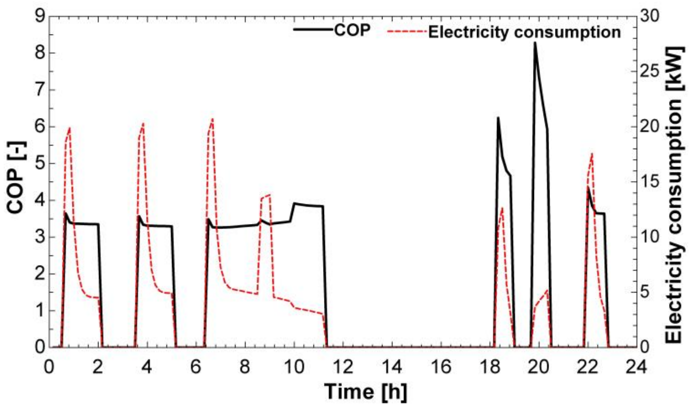

Fig. 6: COP and electricity consumption of the heat pump during the winter day

The COP is in the range of 3.5-4 from midnight until noon, but increases significantly in the evening to 5-6 due to the elevated solar buffer tank temperature at the same period (see Fig. 5). As a result, the demand for electricity is reduced to values below 17 kW between 18:00 and 23:00, whereas between 00:00 and 11:00 is up to 20 kW.

4.2 Summer day

During summer, the space buffer tank (see Fig. 1) is used to store chilled water. Heat is extracted from this tank to keep it at a low temperature, with the lowest limit set to 7 °C, which is the standard for space cooling appliances with water (e.g. fan coils). Figure 7 shows the heat pump operation to reduce the temperature of this tank, as well as to charge the main tank for covering the DHW loads for a typical summer day. Simultaneous operation at these two modes is not possible, as described previously.

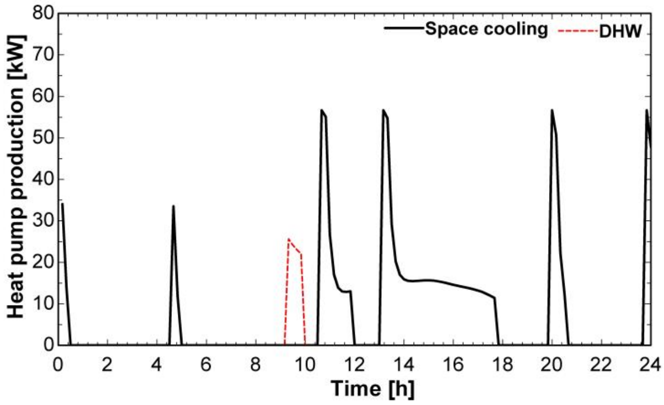

Fig. 7: Heat pump production for space cooling and DHW during the summer day

The heat pump operates five times during the summer day, with a long operation during noon and afternoon, when cooling loads of the building are higher (see Fig. 2). During start-up, the maximum cooling capacity of about 55 kW is observed due to the high temperature difference (inlet/outlet) of the water at the condenser side. Moreover, the largest fraction of DHW demand is directly supplied by the PVT collectors, heating up the main water tank (its bottom part). This results to the operation of the heat pump for DHW production only once during this day with a duration of about 50 minutes. The evolution of the water tank temperatures as the result of the charging by the heat pump is shown in Fig. 8.

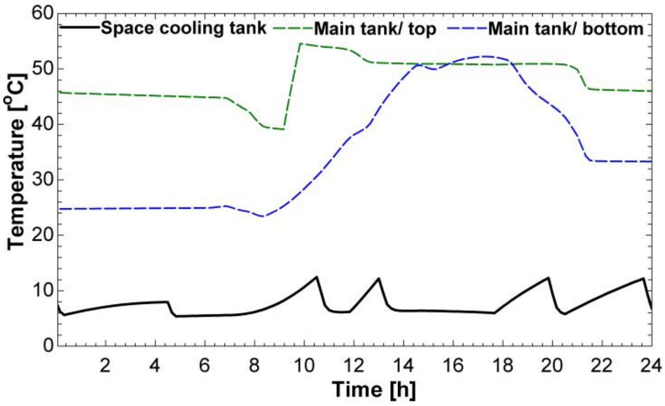

Fig. 8: Average temperature of the water tanks (main tank divided into top and bottom parts) during the summer day

The heat pump starts operating, when the temperature of the space cooling buffer tank approaches the upper 12 ^oC threshold, which takes place at around noon, due to the high cooling loads. In this mode, the heat sink at the condenser side of the heat pump is the ambient air.

Moreover, the water temperature at the main tank is mostly charged by the PVT collectors, since its temperature at the bottom part is adequate for heating the mains water for most of the hours during the summer day. The heat pump operates for DHW production only early in the morning, when the PVT heat production is very small and not adequate to ensure a high enough temperature for the DHW flow. The result is the rapid increase of the average water temperature at the upper part of the main tank to over 50 ^oC, which is kept at such temperature level until the evening.

The heat pump for DHW production operates with a high COP in the range of 6-7, since it is supplied with the heat of the ambient air, whose temperature is about 30 ^oC at noon. This is shown in Fig. 9, together with the electricity consumption for both DHW and space cooling production.

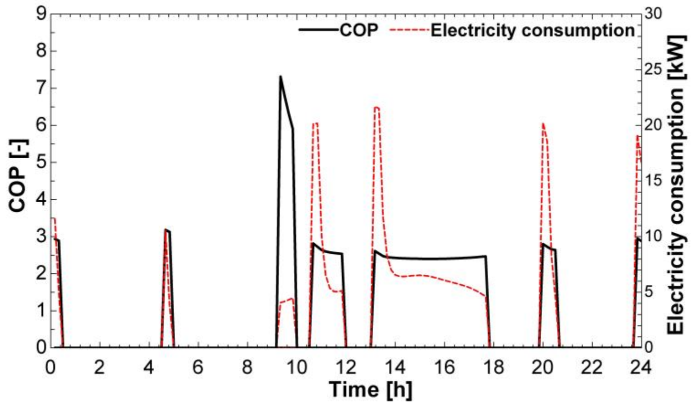

Fig. 9: COP and electricity consumption of the heat pump during the summer day

The COP for space cooling production is always kept in the range of 2.7-3.1 during the summer day. The COP for cooling is reduced during the noon-afternoon hours, when the ambient temperature shows the maximum values during the day, whereas early in the morning the performance is improved, reaching a COP of 3.1 and an electricity consumption of 10 kW.

4.3 Comparison of winter and summer system operation

The main performance indicators are presented in Table 1 during the winter and summer day. These indicators are related to both the heat pump and the PVT collectors and they are averaged during the two days.

Table 1: Performance indicators during the winter and summer day

Indicator (daily averaged)	Winter day	Summer day
COP for space heating (-)	3.66	-
COP for DHW (-)	4.25	6.61
COP for space cooling (-)	-	2.84
Space heating production (kWh)	313.6	-
DHW production by the heat pump (kWh)	47.07	18.29
Space cooling production (kWh)	-	149.2
Heat pump electricity consumption (kWh)	76.73	55.73
PVT electricity efficiency (%)	5.52	4.57
PVT thermal efficiency (%)	35.18	21.61
PVT electricity production (kWh)	7.96	16.33
PVT heat production (kWh)	50.75	77.21

The heat pump operates with a higher COP for DHW production by 55%, during summer, since its heat source has an elevated temperature during this period, which enhances its performance. On the other hand, the COP for space cooling is similar to standard heat pumps, since the unit relies on ambient air for rejecting the condenser heat. Moreover, the PVT collectors show a higher electrical and thermal efficiency during winter, due to the reduced working temperatures, which is beneficial for their performance. This is more pronounced for the thermal efficiency, which is increased by 63% compared to the operation during the summer day, while the electrical efficiency is less sensitive to the water temperature of the collectors.

4.4 Annual system performance

The annual system performance has been also examined, with the average COP of the heat pump during each month of the year shown in Fig. 10.

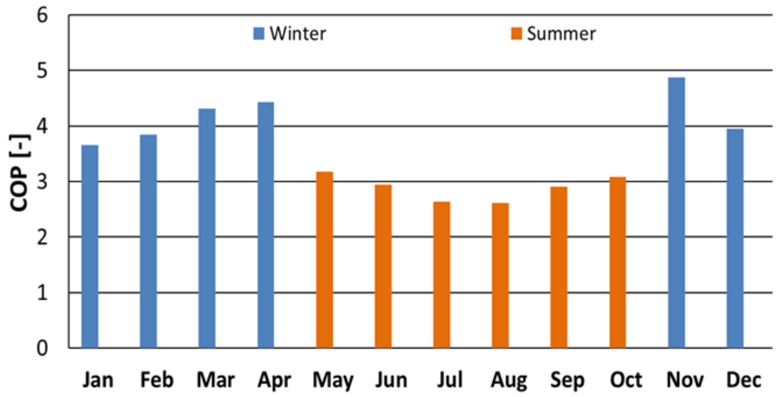

Fig. 10: Average COP of the heat pump during each month

The average COP for heating is lower than 4 during the winter months (December to February), while it is increased over 4 in spring and autumn, as a direct result of higher ambient temperature and availability of solar radiation. During the cooling period, when the space cooling production from the heat pump is much higher than the DHW production, the COP shows its lowest values during July and August, which are the hottest months of the year, while it increases to about 3 during May and October.

The results of a similar analysis concerning the electrical and thermal efficiency of the PVT collectors during each month are presented in Fig. 11.

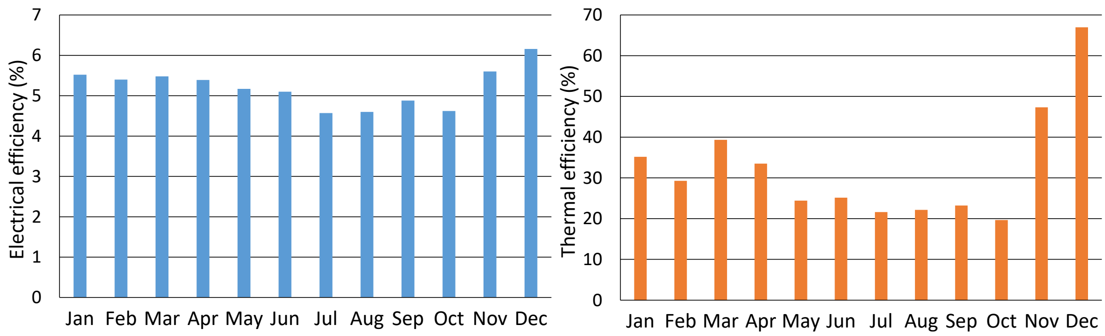

Fig. 11: Electrical (left) and thermal efficiency (right) of the PVT collectors during each month

Both electrical and thermal efficiency are increased during the winter period, when the PVT collectors operate for charging the solar buffer tank, with their temperature always kept below 25-30 ^{o}C. The highest performance is observed in December with an electrical efficiency exceeding 6%, while the average is about 5%. The highest thermal efficiency of the PVT collectors of 46% is also reached during this month, since the ambient temperature is still not very low with many moments producing heat at low temperature for supplying the solar buffer tank. Both these aspects favor the performance of the PVT collectors.

4.5 Effect of the PVT surface

The final part of this work examines the effect of the PVT surface on the overall system performance. The case presented previously relies on a PVT surface of 50 m^2 and reaches a maximum water temperature of 70 ^{o}C in the main tank during summer. Therefore, it is possible to increase the PVT surface to even 100 m^2 and still avoid over-heating, reaching a maximum tank temperature of 95 ^{o}C. By doing so, the system performance is improved mostly during winter with a higher heat production, with a positive impact on the COP of the heat pump. Moreover, the electricity production of the collectors is increased, but still the electricity consumption of the heat pump is always higher, and thus defining the net electricity consumption at system-level, which provides their difference.

The annually averaged performance indicators of the examined system are presented in Table 2 for a variable PVT collectors' surface.

Table 2: Performance indicators for different PVT collectors' surfaces

Indicator (annually averaged)	PVT collectors' surface (m^2)		
	20	**50**	**100**
COP for space heating (-)	4.03	4.13	4.21
COP for DHW (-)	5.70	5.75	5.77
COP for space cooling (-)	2.89		
Net electricity consumption (MWh)	16.44	13.65	9.53
PVT electrical efficiency (%)	5.36	5.20	5.03
PVT thermal efficiency (%)	37.99	31.77	24.63

The increase of the PVT surface from 20 m^2 to 100 m^2 improves the COP for space heating by 5%, while the COP for DHW shows a minor increase and remains practically the same. During summer, the heat pump uses only ambient air for cooling production, which does not depend on the PVT surface and therefore it is exactly the same. Finally, the efficiency of the PVT collectors is reduced, when a larger surface is used, due to the higher working temperatures, and this is especially obvious on the thermal efficiency, which reduces even below 25% in case a 100 m^2 PVT surface is used.

5. Conclusions

A flexible solar-based system for heating and cooling is proposed, with the dual-source heat pump being capable to select the source that maximizes its performance. The system performance greatly increases with the use of the PVT collectors that operate with a higher electric and thermal efficiency especially during winter, when their high-temperature operation is avoided.

During winter, the exploitation of the low-temperature heat produced by the PVT collectors allows the heat pump to operate with a high COP for both space heating and DHW production, and at the same time the PVT efficiency reaches higher values. On the other hand during summer, the solar-assistance mode of the heat pump introduces a minor improvement, only for DHW production, since the cooling demand is much higher than the DHW needs, for the weather data of Athens, Greece.

The next steps of this work are to conduct tests on an improved version of the PVT collector and on the flexible heat pump, and examine the system performance under a larger range of scenarios and cases, such as for other locations in Europe (e.g. with higher heating and no cooling needs), and for different building types including buildings without DHW needs (e.g. office buildings). Finally, a significant improvement of the system configuration will be the addition of a ground heat exchanger (e.g. borehole thermal energy storage) as an additional potential heat source for the heat pump, resulting to a multi-source configuration, expected to offer significant performance improvement for cooling production during summer.

6. Acknowledgments

This work has been performed within the RES4BUILD project (Renewables for clean energy buildings in a future power system) – Horizon 2020 program, Grant Agreement no. 814865.

7. References

ASHRAE, ASHRAE Handbook, 2017. Fundamentals. SI edition. Ashrae, USA.

Bernardo, R., et al., 2013. Measurements of the electrical incidence angle modifiers of an asymmetrical photovoltaic/thermal compound parabolic concentrating-collector. Engineering, 5(01), p.37.

Buker, M.S. and Riffat, S.B., 2016. Solar assisted heat pump systems for low temperature water heating applications: A systematic review. Renewable and Sustainable Energy Reviews, 55, pp.399-413.

EU Regulation No 814/2013 of 2 August 2013 implementing Directive 2009/125/EC of the European

Parliament and of the Council with regard to ecodesign requirements for water heaters and hot water storage tanks; https://eur-lex.europa.eu/eli/reg/2013/814/2017-01-09 (accessed on 16/07/2020).

Fine, J.P., Friedman, J. and Dworkin, S.B., 2017. Detailed modeling of a novel photovoltaic thermal cascade heat pump domestic water heating system. Renewable Energy, 101, pp.500-513.

Gomes, J., Diwan, L., Bernardo, R. and Karlsson, B., 2014. Minimizing the impact of shading at oblique solar angles in a fully enclosed asymmetric concentrating PVT collector. In Energy Procedia (Vol. 57, pp. 2176-2185).

Guo, X. and Goumba, A.P., 2018. Air source heat pump for domestic hot water supply: Performance comparison between individual and building scale installations. Energy, 164, pp.794-802.

Hoogsteen, G., Molderink, A., Hurink, J.L. and Smit, G.J., 2016, April. Generation of flexible domestic load profiles to evaluate demand side management approaches. In 2016 IEEE International Energy Conference (ENERGYCON) (pp. 1-6). IEEE.

Kim, T., Choi, B.I., Han, Y.S. and Do, K.H., 2018. A comparative investigation of solar-assisted heat pumps with solar thermal collectors for a hot water supply system. Energy Conversion and Management, 172, pp.472-484.

Klein, S.A. et al., 2005. TRNSYS 16: A Transient System Simulation Program, Solar Energy Laboratory, University of Wisconsin, Madison, USA, http://sel.me.wisc.edu/trnsys.

Klein, S.A., 2020. Engineering Equation Solver-EES, Version 10.834, Academic Professional.

Kosmadakis, G. and Neofytou, P., 2019. Investigating the effect of nanorefrigerants on a heat pump performance and cost-effectiveness. Thermal Science and Engineering Progress, 13, p.100371.

Naranjo-Mendoza, C., Oyinlola, M.A., Wright, A.J. and Greenough, R.M., 2019. Experimental study of a domestic solar-assisted ground source heat pump with seasonal underground thermal energy storage through shallow boreholes. Applied Thermal Engineering, 162, p.114218.

Panaras, G., Mathioulakis, E. and Belessiotis, V., 2013. Investigation of the performance of a combined solar thermal heat pump hot water system. Solar Energy, 93, pp.169-182.

Rahman, A., Smith, A.D. and Fumo, N., 2016. Performance modeling and parametric study of a stratified water thermal storage tank. Applied Thermal Engineering, 100, pp.668-679.

Vaishak, S. and Bhale, P.V., 2019. Photovoltaic/thermal-solar assisted heat pump system: Current status and future prospects. Solar Energy, 189, pp.268-284.

Wang, X., Xia, L., Bales, C., Zhang, X., Copertaro, B., Pan, S. and Wu, J., 2020. A systematic review of recent air source heat pump (ASHP) systems assisted by solar thermal, photovoltaic and photovoltaic/thermal sources. Renewable Energy, 146, pp.2472-248.

Performance assessment of an LCPV/T solar hybrid plant for a wellness center building in Mexico

Iván P. Acosta-Pazmiño[1], Carlos I. Rivera-Solorio[1] and Miguel A. Gijón-Rivera[2]

[1] Tecnologico de Monterrey, Escuela de Ingeniería y Ciencias, Ave. Eugenio Garza Sada 2501, Monterrey (Mexico)

[2] Tecnologico de Monterrey, Escuela de Ingeniería y Ciencias, Vía Atlixcáyotl 2301, Reserva Territorial Atlixcáyotl, Puebla (Mexico)

Abstract

Buildings are responsible for almost half of the worldwide final energy consumption. A large amount of this energy is produced by fossil fuels. Solar energy can effectively produce the thermal and electric energy consumed by buildings, using hybrid photovoltaic/thermal (PV/T) technologies. This document presents a performance evaluation of a hybrid low concentrating PV/T (LCPV/T) plant operating in a student health and wellness center building on a college campus in Mexico. The hybrid solar plant consists of 144 parabolic trough-based collectors with a hybridized receptor that includes c-Si PV cells. The results showed that the solar field could cover up to 91% of the hot water demand of the building during the summer season and 32% during the winter period. The peak thermal and electric power were 190 kW and 37.6 kW, respectively. The hybrid system could annually save USD 7,185, accounting for heat (natural gas boiler), and electricity generation. Nevertheless, the payback period was 17.37 years, which was mainly caused by a reduced natural gas price in Monterrey, Mexico. Finally, an annual reduction of 97.9 metric tons of CO_2 emissions was reached.

Keywords: Solar energy, hybrid collectors, LCPV/T, dynamic evaluation, buildings, Mexico.

1. Introduction

In 2018, about 55% of the world's population lived in urban areas. This portion is projected to grow to 68% by 2050 (United Nations, 2019). Most of these people will probably allocate in buildings due to urban development and land limitations in most of the cities. Buildings are responsible for almost half of the worldwide final energy consumption, which is mainly produced by fossil fuels. Solar energy is a vast and renewable primary energy source that can effectively and efficiently produce the electrical and thermal energy consumed by buildings. Hybrid solar photovoltaic/thermal (PV/T) collectors can produce thermal and electrical energy simultaneously, reducing the area required for installation in comparison with stand-alone photovoltaics and thermal collectors. This characteristic is particularly convenient for buildings due to limited roof available area and energy profiles consumption, both thermal and electrical.

There have been several studies regarding the performance evaluation of PV/T plants. For instance, Sotehi et al., 2016 developed a theoretical approach of a Net Zero Energy Building (NZEB) using hybrid PV/T solar collectors in Ouargla City. They found that is possible to cover the domestic hot water demands of the building with the hybrid technology coupled with passive solar architecture to reduce energy consumption. Moreover, the electricity produced could cover the annual needs for air conditioning, lighting, and household equipment. Fuentes et al., 2018 performed an experimental evaluation between hybrid PV/T and simple PV systems intended for Building Integrated PV (BIPV). They concluded that the PV/T system did not present higher electrical efficiencies than simple PV as expected due to the active cooling mechanism. However, the combined thermal and electrical efficiencies reached 80% and 19% for the exergy efficiency. Yang et al., 2019 simulated a low-concentrating PV/T triple-generation system for hot water, power, and cooling. The results showed that the hybrid system could generate hot water at 45°C - 90°C, with an electrical efficiency of the PV cells of 10%, and a COP above 0.5 for the lithium-bromide absorption chiller.

Herrando et al., 2019 performed an evaluation of a 1.68 MWp solar combined cooling, heating, and power (S-CCHP) system based on hybrid photovoltaic/thermal (PV/T) collectors for a University Campus in Bari, Italy. The hybrid plant can satisfy 20.9%, 55.1%, and 16.3% of the space-heating, cooling, and electrical demands of the campus. The techno-economic performance evaluation resulted in a 16.7 years payback time. Wang et al.,

doi:10.18086/eurosun.2020.05.02 Available at http://proceedings.ises.org

2019 developed a techno-economic assessment of hybrid PV/T systems and compared them with conventional solar-energy systems; PV and evacuated tubes collectors. They found that the PV/T system surpassed other conventional ones in terms of energy production, supplying with 82.3% and 51.3 % of the electric and thermal building demand, respectively. However, PV presented the lowest payback period (9.4 years) and the lowest levelized cost of energy (LCOE) of 0.089 €/kWh.

The literature review showed that most of the performance evaluations of PV/T plants for building applications have been performed mainly in Europe and Asia. Consequently, there is a lack of information and knowledge about the potential of this technology in Latin America, despite that most of the increase in energy consumption in buildings is expected to occur in emerging economies. Moreover, the levels of insolation that reach most of the Mexican territory, like Monterrey, increase the potential of using solar technologies to produce heat and power.

This document presents a dynamic performance evaluation of an LCPV/T plant for a student health and wellness center building in Monterrey, Mexico. The study is based on transient simulations developed in TRNSYS software. Thermal and electrical energy yields of the plant are evaluated, along with the other operational variables, such as thermal and electrical peak power, and temperature profiles. An economic evaluation of the solar hybrid plant in terms of estimating the final cost of the system, the annual savings due to fuel and electricity consumption reduction, and the payback time of the investment is also approached. Moreover, the environmental impact due to the displacement of Natural gas is evaluated in terms of CO_2 emissions.

2. Methodology

The evaluation of the LCPV/T plant was performed in the TRNSYS software environment. The hybrid plant consists of 144 hybrid collectors, 12 rows of 12 collectors each, that cover a total roof area of 1281 m^2. The hybrid collectors are based on a small-sized parabolic trough with a triangular receptor that has attached c-Si back-contact solar cells, on the sides of the receiver that collect concentrated sunlight. The hot water produced by the plant will be used to cover part of the thermal demands of the building; domestic hot water (DHW) and pool heating. While the electrical production is just considered to be additional energy input to the building electricity consumption, which will be accounted for monetary and environmental gains. A simplified process diagram of the simulated system is presented in Fig 1. Energy Plus Weather (EPW) files were used to simulate a typical meteorological year in the studied location.

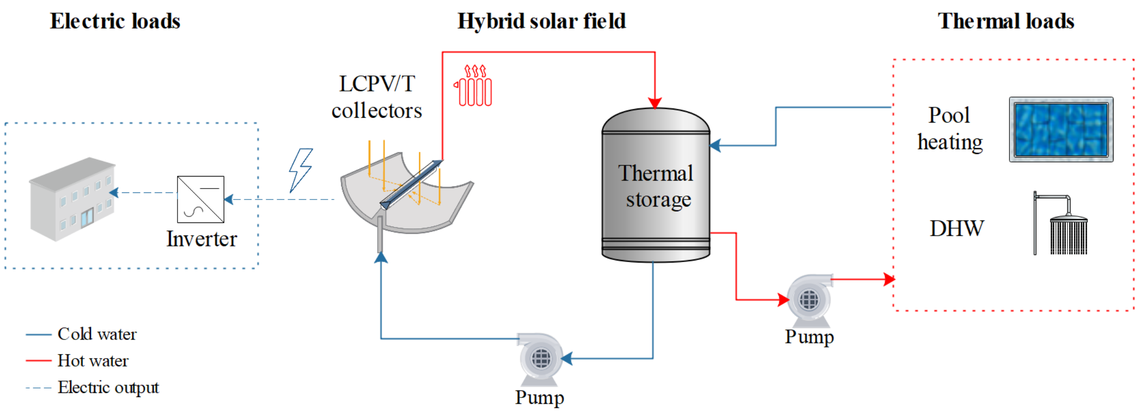

Fig. 1. Hybrid solar heat&power system configuration.

The hybrid collector was modeled using a modified version of Type 50f that considers the incidence angle modifier of the system. Type 50f is a component developed to model concentrating hybrid solar collectors where the thermal losses are a function of the wind velocity and collector temperature. As we proposed in this study, type 50f was modified to include the incidence angle modifier of the system $K(\theta)$ to model the concentrating collector. Moreover, the thermal performance parameters, such as the contact resistance between PV cells and absorber R_c, heat transfer coefficient between the duct and the heat transfer fluid $U_{Abs_{Fluid}}$, and the heat transfer coefficient for thermal losses of the collector U_L, were obtained using a one-dimensional steady-state model of the hybrid collector, previously developed by (Acosta P., 2016). The principal equations to calculate the thermal and electric performance of the hybrid LCPV/T collector are presented in eq.1– eq.6. The most important inputs of the simulation model are presented in Table 1.

Useful thermal output (Duffie and Beckman, 2013):

$$\dot{Q}_u = F_R A_a \left[S - \frac{A_r}{A_a} U_L (T_i - T_{amb})\right] \quad \text{(eq. 1)}$$

Collector heat removal factor (Florschuetz, 1979):

$$F_R = \frac{\dot{m}\, cp}{U_L} [1 - \exp\,(-U_L F' / \dot{m}\, cp)] \quad \text{(eq. 2)}$$

Collector efficiency factor (Duffie and Beckman, 2013):

$$F' = \left(1 + \frac{U_L}{U_{Abs_{Fluid}}}\right) \quad \text{(eq. 3)}$$

Heat loss coefficient (Duffie and Beckman, 2013):

$$U_L = \frac{Q_{Loss}}{A_r (T_r - T_{amb})} \quad \text{(eq. 4)}$$

Incidence angle modifier (Gaul and Rabl, 1980):

$$K(\theta) = 1 - b_o \left(\frac{1}{cos(\theta)} - 1\right) \quad \text{(eq. 5)}$$

Electric output (Florschuetz, 1979):

$$P_e = \frac{A_a\, S\, \eta_{PV}}{\alpha} \sqrt{\left\{1 - \frac{\eta_{PV_r}\, K_T}{\eta_{PV}} \left[F_R (T_i - T_a) + \frac{S}{U_L} (1 - F_R)\right]\right\}} \quad \text{(eq. 6)}$$

The parameter b_o, which shapes the curvature of the function presented in eq. 5, was taken from the value obtained by (Bernardo et al., 2011).

Table 1. Inputs of the simulation model in TRNSYS.

Feature	Value
Process and solar field	
Daily hot water demand	30 m^3
Temperature demand	55℃
Solar field azimuth	16.6
Thermal storage capacity	30 m^3
Heat demand	94.4 kW
Hybrid collector	
Optical efficiency, η_{0A}	0.601
Concentration ratio	14.8
Internal heat transfer coefficient, $U_{Abs_{Fluid}}$	3838 W/m^2K
Heat loss coefficient, U_L	2.77 W/m^2 K
Temperature coefficient, K_T	0.33 %/K
Energy prices	
Natural Gas	3.13 USD $/GJ
Electricity (average commercial tariff)	0.064 USD $/kWh

The annual heat and electricity production of the hybrid solar plant is calculated with the following relations:

Thermal energy yield:

$$Q_u = \int \dot{Q_u} dt \qquad \text{(eq. 7)}$$

Electrical energy yield:

$$E_{el} = \int P_e dt \qquad \text{(eq. 8)}$$

The annual monetary savings caused by onsite energy generation, both thermal (Q_u) and electrical (E_{el}), were calculated with eq. 9-14. For the thermal part, the calculation was based on obtaining how much fuel (F) is needed in order to produce the same amount of heat that the hybrid solar plant generates. The efficiency considered for the boiler was $\eta_b = 60\%$, which is the average efficiency of a low load natural gas boiler (IEA International Energy Agency, 2010). To determine the monetary savings (C_F) of the displacement of natural gas, the local price (FP) of Natural gas was considered, Table 1. For electricity generation savings (C_E), the average efficiency of a DC-AC conversion ($\eta_e = 95\%$) as well as a local tariff (EP) for commercial electricity service were considered to calculate the cost savings due to electricity generation (M_E). The total annual cost savings (C_s) is determined with eq. 14.

$$Q_F = \frac{Q_u}{\eta_b} \qquad \text{(eq. 9)}$$

$$F = \frac{Q_F}{\left(C_{LHV_f}\right)} \qquad \text{(eq. 10)}$$

$$E = E_{el} \cdot \eta_e \qquad \text{(eq. 11)}$$

$$C_F = FP \cdot Q_F \qquad \text{(eq. 12)}$$

$$C_E = EP \cdot E \qquad \text{(eq. 13)}$$

$$C_s = C_F + C_E - C_{O\&M} \qquad \text{(eq. 14)}$$

The CO_2e emissions abatement potential is estimated using the emissions factors for natural gas boiler combustion and electricity generation determined by the Intergovernmental Panel on Climate Change (IPCC) in 2006. For Natural gas combustion, the emissions factor is 0.2 kgCO_2e/kWh, whilst for electricity generation the emissions factor is 0.45 kgCO_2e/kWh.

The total hybrid plant cost (C_o) was estimated from eq. 15 (Kalogirou, 2009), considering the cost breakdown presented in Table 2, and the payback time (PBT) of the plant was calculated considering an average inflation rate (i_F) of 10%, a local discount rate (d) of 5%, and an annual energy production derate of 0.5%. The cash flow for each year are calculated independently for the fuel and electricity cost savings and taking into account the time value of money.

$$PBT = \frac{ln\left[\frac{C_o(i_F - d)}{C_s} + 1\right]}{ln\left(\frac{1 + i_F}{1 + d}\right)} \qquad \text{(eq. 15)}$$

Table 2. Cost breakdown of the LCPV/T plant.

Component	Cost
Parabolic trough collectors, USD	$209.7 \cdot A_{LCPVT}$
Hybrid receiver, USD	$0.2 \cdot C_{LCPVT}$
Water tank, USD (Wang et al., 2020)	$0.874 \cdot V_T(l) + 763.5$

Inverter, USD/kW	200
Pump, USD (Wang et al., 2020)	$500(P_{pump}/300)^{0.25}$
Piping*, USD (Wang et al., 2020)	$(0.897 + 0.21D_{pipe}) \cdot L_{pipe}$
Controller, USD	600
Installation cost, USD (Wang et al., 2020)	$0.2 \cdot$ Total component cost
Annual O&M cost, USD (Wang et al., 2020)	$0.005 \cdot$ Total component cost

* D_{pipe} in [mm] and L_{pipe} in [m]

3. Results

The monthly thermal and electric yield and the solar fraction of the hybrid LCPV/T plant are presented in **Fig. 2**. It could be noticed that the proposed solar plant can achieve a solar fraction as high as 91% during the summer season. Conversely, during winter the hybrid plant supplied 32% of the building's hot water demand. Q load represents the total hot water demand for a specified period of time (monthly, annually). Q useful is the thermal energy produced by the hybrid solar plant that can be consumed by the building. Q aux is the heat produced by a natural gas-fired boiler to cover the total hot water demand of the building. E useful is the electricity produced by the hybrid plant. **Fig. 3** presents the energy yield of the solar field on an annual basis. The hybrid plant produced 55% of the annual hot water demand of the studied building. Moreover, an additional 45.7 MWh of electricity is produced. This represents an important gain that will reduce the grid electricity consumption of the building, hence produce additional monetary savings and CO_2e emissions abatement.

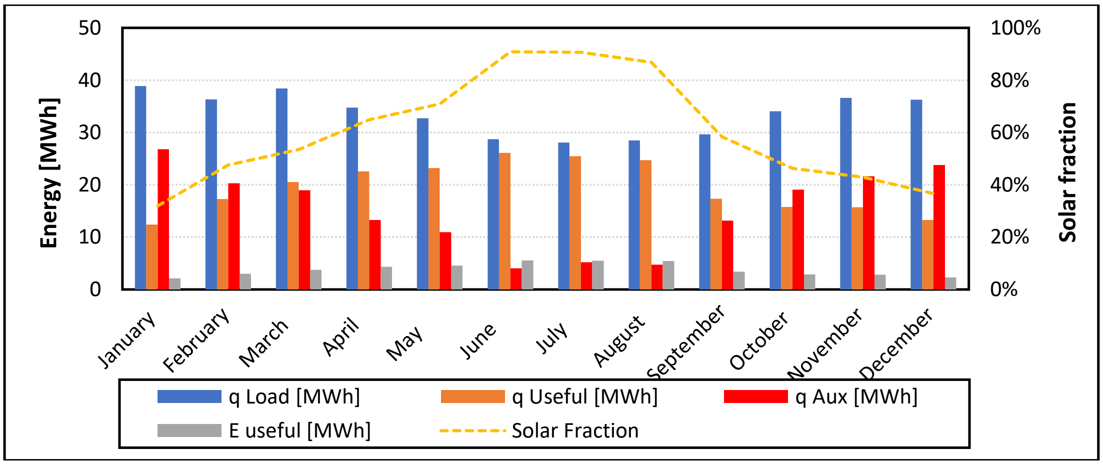

Fig. 2: Solar hybrid plant monthly energy yield and solar fraction.

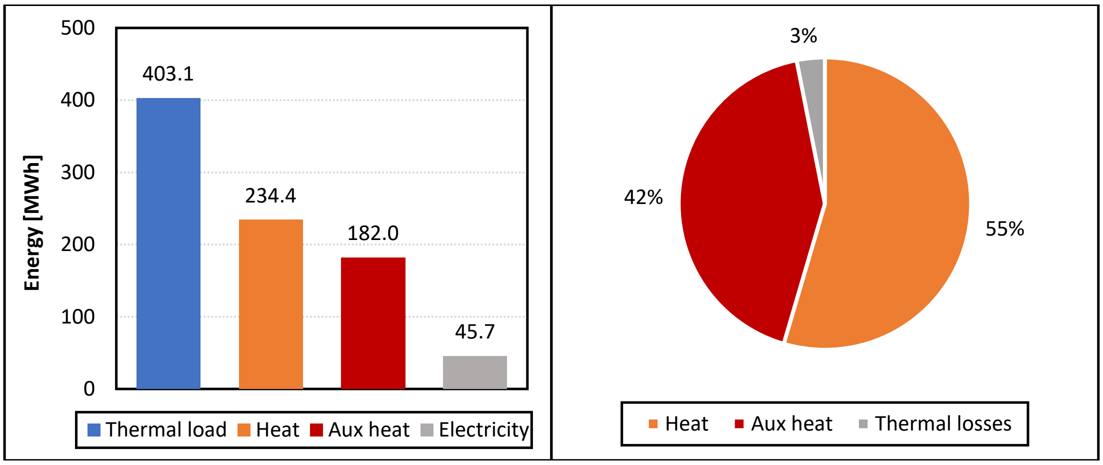

Fig. 3: Annual energy yield (left), and share of hot water demand (right).

Regarding the hot water temperature produced by the solar hybrid field considering a constant heat demand of 94.4kW, during summer the maximum recorded water outlet temperature was 60°C, while in winter was 40°C,

Fig. 4. The peak values for the thermal and electrical power, during a typical summer day, were 190 kW and 37.6 kW, respectively, **Fig. 5**.

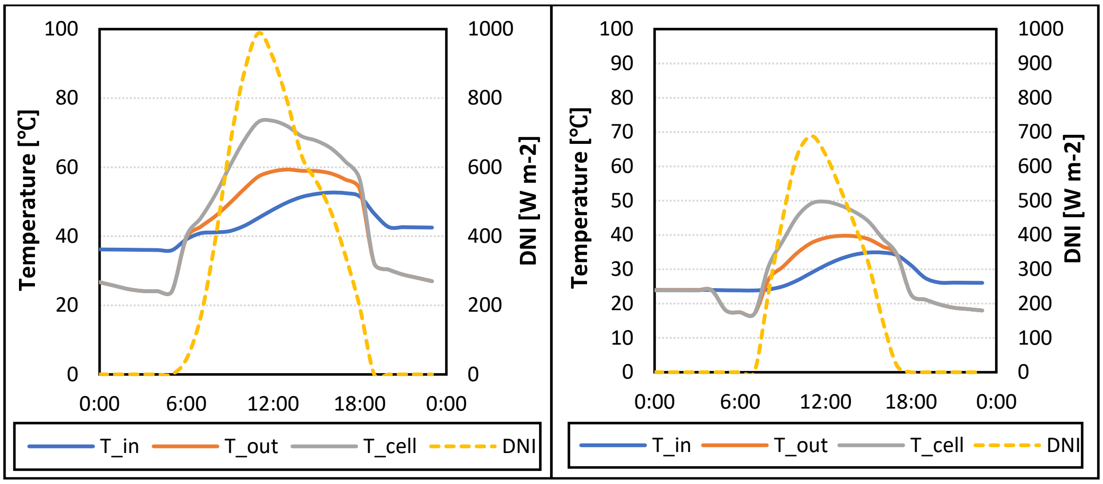

Fig. 4: Temperature profile and DNI during summer (left), and winter (right) typical days.

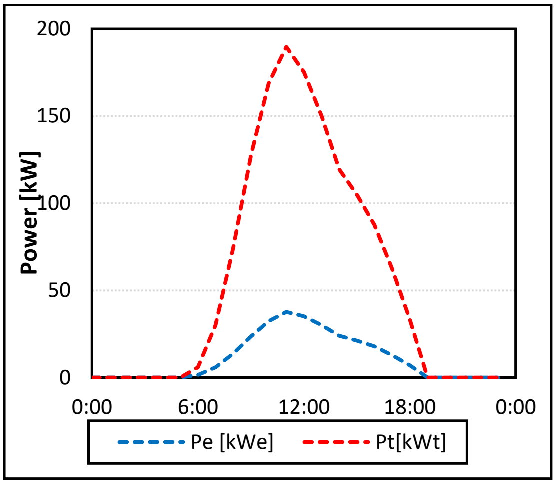

Fig. 5: Thermal and electrical peak power during a summer typical day.

The monetary and environmental benefits of the clean energy production of the hybrid solar plant are presented in **Fig. 6**. It could be noticed that the hybrid plant can annually generate USD 7,185 of monetary savings, accounting for heat and electricity generation. Moreover, the annual reduction of CO_2e emissions can reach 97.9 metric tons, of which the majority, i.e., 80% (78.14 tons) is associated with the displacement of natural gas for heat generation. This is equivalent to take out of the streets nearly 21 passenger vehicles every year (United States Environmental Protection Agency, 2020). If we consider a 25 years lifespan of the hybrid plant, its application into the wellness center can avoid the emission of 2,446 metric tons of CO_2e. The total initial cost of the hybrid plant is estimated to be $178,657 USD, and the payback period obtained is 17.37 years. The electricity price to natural gas price ratio obtained is 5.68, which clearly shows a remarkably low price of natural gas, despite the electricity tariff is also lower in comparison with other regions. This price ratio is 16.4% greater than the highest reported by (Wang et al., 2020), which was 4.88 (Italy). Better economic performance of hybrid plants is achieved when the energetics price ratio is closer than one.

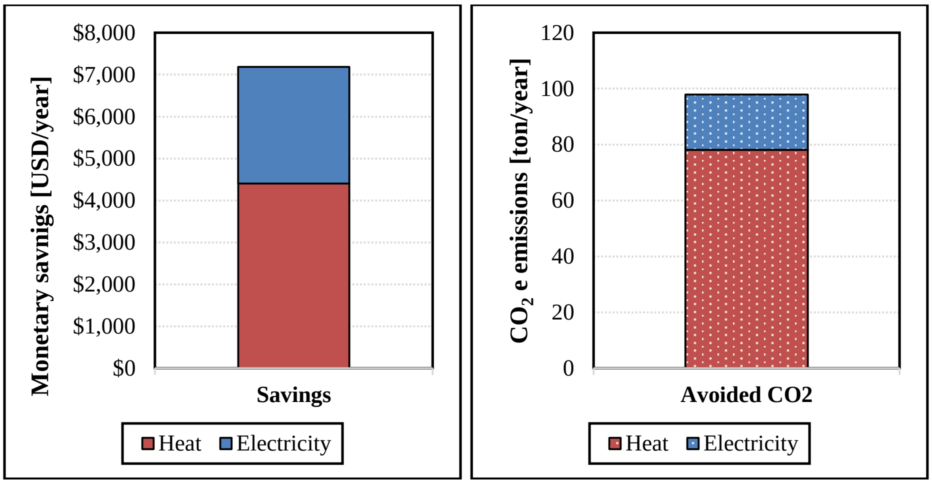

Fig. 6: Annual monetary savings (left) and avoided CO_2 emissions (right).

4. Discussion

The performance of a solar hybrid plant in a student health and wellness center building on a university college in Monterrey was studied. Results show that the thermal demand, by means of domestic hot water and pool heating, can be partially covered by the proposed solar hybrid system. During the summer season, the solar fraction can achieve values of up to 91%, which is possible due to the increased solar resource available, and the reduced thermal losses caused by higher ambient temperature during this season. On the other hand, during winter, only 32% of thermal demand is covered by the solar hybrid plant, due to lower available insolation and ambient temperatures.

The thermal storage capacity allows that the solar field water outlet temperatures remain relatively low, even during high solar resource days. This is particularly important to keep the temperature of the hybrid collectors low enough to preserve electricity production. The physics of LCPV/T collectors, like the one evaluated in this document, provokes that the electric and thermal systems of the collector are thermally-coupled, which means that an increase in the receptor temperature will result in a temperature rise in the PV module attached to the hybrid receptor, hence a reduction in solar to electricity conversion. Another relevant operational characteristic that helps maintaining the temperature of the hybrid receptor under acceptable ranges is a constant hot water demand, which is common in wellness center buildings were the hot water demand is relatively constant throughout the year, due to the consumption of hot water for pool heating, showers, and faucets.

Regarding the economic analysis, it could be noticed that the hybrid plant system is a costly alternative for heat and power generation, that offers a payback time of nearly 17 years, which is long in comparison with other clean energy generation systems that may present payback periods between 3-8 years. The long payback period is mainly caused by the low local price of natural gas in Monterrey, and with a lower outcome, by the subsidized electrical commercial tariff scheme in Mexico. The price ratio of electricity and natural gas should be lower (<2.0) in order to achieve greater monetary savings. Further efforts should be made in order to reduce the total component and installation cost of the proposed hybrid technology in order to achieve more competitive costs in comparison with conventional technologies. Moreover, higher fuel prices and local incentives would make the proposed technology more attractive for investment. It is important to mention that if the economic performance of the proposed plant is not the decision-maker, from the environmental perspective, hybrid solar technology has an excellent CO_2 emission reduction potential, achieving, in this case, a specific reduction of 76.4 $kgCO_2e$ per square meter of the required installation area. Both the economic and environmental impact of the proposed hybrid plant can have a more significant effect when the thermal generation displaces other fuels like Diesel, Fuel Oil, or LPG.

5. Acknowledgments

The authors express their acknowledgments to the Consejo Nacional de Ciencia y Tecnología (CONACYT) and the Secretaría de Energía (SENER) for making this work possible. The research has been supported under the Energy Sustainability Grants / Project No 291590.

6. References

Acosta P., I.P., 2016. Caracterización y evaluación de un sistema híbrido fotovoltaico/térmico basado en un concentrador parabólico lineal. Tecnológico de Monterrey.

Bernardo, L.R., Perers, B., Håkansson, H., Karlsson, B., 2011. Performance evaluation of low concentrating photovoltaic/thermal systems: A case study from Sweden. Sol. Energy 85, 1499–1510. https://doi.org/10.1016/j.solener.2011.04.006

Duffie, J.A., Beckman, W.A., 2013. Solar engineering of thermal processes. Wiley.

Florschuetz, L.W., 1979. Extension of the Hottel-Whillier model to the analysis of combined photovoltaic/thermal flat plate collectors. Sol. Energy 22, 361–366. https://doi.org/10.1016/0038-092X(79)90190-7

Fuentes, M., Vivar, M., de la Casa, J., Aguilera, J., 2018. An experimental comparison between commercial hybrid PV-T and simple PV systems intended for BIPV. Renew. Sustain. Energy Rev. 93, 110–120. https://doi.org/10.1016/j.rser.2018.05.021

Gaul, H., Rabl, A., 1980. Incidence-Angle Modifier and Average Optical Efficiency of Parabolic Trough Collectors. J. Sol. Energy Eng. 102, 16–21. https://doi.org/10.1115/1.3266115

Herrando, M., Pantaleo, A.M., Wang, K., Markides, C.N., 2019. Solar combined cooling, heating and power systems based on hybrid PVT, PV or solar-thermal collectors for building applications. Renew. Energy 143, 637–647. https://doi.org/10.1016/j.renene.2019.05.004

IEA International Energy Agency, 2010. Industrial Combustion Boilers, Industrial Combustion Testing - Energy Technology Systems Analysis Programme. https://doi.org/10.1201/ebk1420085280

Kalogirou, S.A., 2009. Solar Energy Engineering, Solar Energy Engineering. https://doi.org/10.1016/B978-0-12-374501-9.00009-1

Sotehi, O., Chaker, A., Maalouf, C., 2016. Hybrid PV/T water solar collector for net zero energy building and fresh water production: A theoretical approach. Desalination 385, 1–11. https://doi.org/10.1016/j.desal.2016.01.034

United Nations, 2019. World Urbanization Prospects The 2018 Revision, Demographic Research. New York. https://doi.org/10.4054/demres.2005.12.9

United States Environmental Protection Agency, 2020. Greenhouse Gas Equivalencies Calculator [WWW Document]. URL https://www.epa.gov/energy/greenhouse-gas-equivalencies-calculator (accessed 8.4.20).

Wang, K., Herrando, M., Pantaleo, A.M., Markides, C.N., 2019. Technoeconomic assessments of hybrid photovoltaic-thermal vs. conventional solar-energy systems: Case studies in heat and power provision to sports centres. Appl. Energy 254, 113657. https://doi.org/10.1016/j.apenergy.2019.113657

Wang, K., Pantaleo, A.M., Herrando, M., Faccia, M., Pesmazoglou, I., Franchetti, B.M., Markides, C.N., 2020. Spectral-splitting hybrid PV-thermal (PVT) systems for combined heat and power provision to dairy farms. Renew. Energy 159, 1047–1065. https://doi.org/10.1016/j.renene.2020.05.120

Yang, L., Heng, Z., Haiping, C., Han, Y., Fei, Y., 2019. Simulating and experimental research on a low-concentrating PV/T triple-generation system. Energy Convers. Manag. 199, 111942. https://doi.org/10.1016/j.enconman.2019.111942

ASSESSING THE LONG-TERM PERFORMANCE DEGRADATION OF PV MODULES IN THE SUB-SAHARAN ENVIRONMENT

Divine Atsu[1], Istvan Seres[2] and Istvan Farkas[2]

[1]Mechanical Engineering Doctoral School Szent István University, Páter K. u. 1., Gödöllő, H-2100 Hungary

[2]Department of Physics and Process Control, Szent István University Páter K. u. 1., Gödöllő, H-2100, Hungary

Abstract

This experimental study evaluates the long-term performance and degradation of solar PV modules exposed to the tropical climate of the sub-Saharan. The methods employed for the assessment are Visual inspection, I-V curve characterization, and thermal evaluation by IR imaging. In determining the state of the bypass diodes, the process of partial shading was applied. After thirteen (13) years of exposure in actual outdoor operation, modules showed a reduction in short circuit current (I_{sc}), from 7% to 16.4%, with an average drop of 11.7% compared with the nameplate values. The decline in open-circuit voltage (V_{oc}) ranges from 11.4% to 17.1% with an average reduction of 14.8%. Reduction in Fill Factor (FF) ranges from 11.3% to 24.2%, and a power loss is of 34.5% to 41.4%. EVA browning was the most severe and widespread defect observed through the visual analysis of the modules.

Keywords: PV system, performance, reliability, tropical climate, characterization,

1. Introduction

The market share of solar PV in the power industry has experienced unmatched growth in the past years as a result of its potential as a feasible alternative for fossil fuels. Solar PV has seen increases in both the utility-scale and small scall applications as a result of the continuous drop in cost. As of 2019, the total global capacity stood at 646.8 GW, which about 21.3% change over the previous year's capacity. The yearly additions of Solar PV have also been unprecedented. The new installations in solar PV for 2019 alone amounted to 137.5 GW, which is 34.3% higher than 2018's additions (Powerweb, 2020). The growth experienced in this area is as a result of the favourable policies by various governments and international organizations, and the attractive investment environments that exist in different countries coupled with the rising cost of conventional energy sources and their negative environmental impacts. The increasing growth is, however, not without the challenges of reliability and degradation encountered on-site.

Consistent performance evaluation of solar modules under different climatic conditions will help curb site-specific reliability issues and further enhance its acceptance and growth. Warranty for the non-failure of solar modules given by most manufacturers is for 25 years which provides the assurance of 80% power output for the given time (Vázquez and Rey-Stolle, 2008). However, the reliability of solar modules is dependent on conditions present at the location of operation controlled by factors such as radiation levels, temperature, humidity wind speed and ultraviolet radiation (Rahman et al., 2015).

To further guarantee the reliable performance of PV modules, they are passed through rigorous testing requirements as prescribed by the IEC standards (IEC, 2016). This includes the accelerated ageing test to reveal any design and manufacturing lapses (Jordan and Kurtz, 2013). The factors that lead to failure of solar modules in operation include corrosion, light-induced degradation, break-in contacts, crack cells encapsulant discolouration, delamination, diode failure, hotspots and broken interconnects (Chamberlin, 2011).

Before PV modules are certified for commercial use, they are taken through rigorous test procedures according to regional and international standards such as the EN, IEC, ANSI standards. These test procedures are intended to reveal design and manufacturing defects which are capable of initiating the early failure and degradation of PV modules than anticipated whiles in operation. Recently, the accelerated ageing test has been incorporated in the qualifications which have led to the improvement of PV technology over the past few decades. However, not all

doi:10.18086/eurosun.2020.05.03 Available at http://proceedings.ises.org

failure and degradation modes PV modules that take place whiles in operation in different climates are revealed by the abovementioned tests. It is thus a deliberate approach to investigate the issues that arise under outdoor operating conditions (Sharma and Chandel, 2003). The long-lasting and durability PV modules in operation are dependent on the failure and degradation modes controlled by factors like solar irradiation, humidity, ambient temperature ultraviolet intensity (UV) and wind. Other factors that influence the degradation are the defects that occur during the production process, transportation and installation (Rahman et al., 2015)

Several studies have been conducted in different locations to assess the degradation rate of varying PV technologies as shown by (Chamberlin, 2011 Jordan and Kurtz, 2013). However, data available on module performance and reliability assessment for the Tropical sub-Saharan climate, which experiences relatively severe environmental conditions, is negligibly small (Rajput et al., 2016).

2. Materials and Methods

The system under study is located in Koforidua in the Eastern Region of Ghana and situated on the coordinates 6.062545 *N*, -0.266001 W at an elevation of 173 m above sea level. According to the Köppen-Geiger climate classification, its climate is as ‘Aw’ which is savanna with dry winter (Merkel, 2019). The annual average temperature and rainfall figures for the location are 25.9 °C and about 1407 mm, respectively, as shown in Fig. 1. The average yearly horizontal radiation of the site is 1,733.75 kW h m^{-2} Yr^{-1} with average daily irradiation of 4.75 kW h m^{-2} d^{-1}. The average monthly humidity values for the site range from 76.5 - 88.3%. Minimum and maximum wind speed are 2.40 and 4.19 ms^{-1}, respectively. The dry season and the wet seasons are the two major seasons experienced in Koforidua. The dry season usually starts from December and ends in March while the wet season starts from April to November.

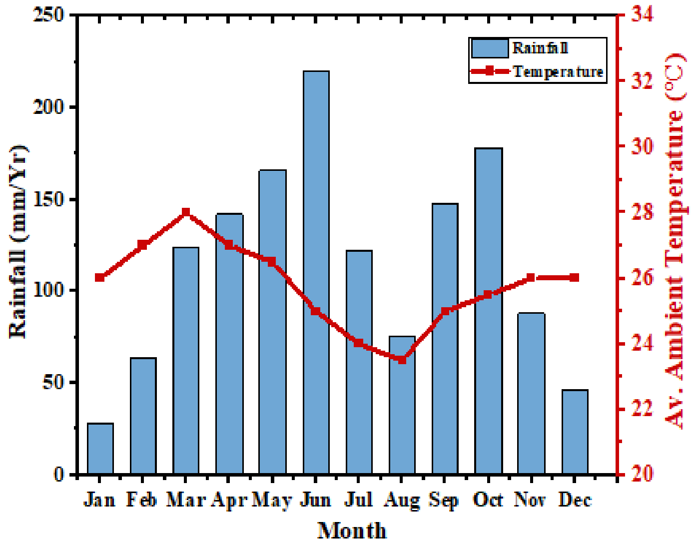

Fig 1: Rainfall pattern and the ambient temperature of the site (Merkel, 2019)

The system for study, an off-grid PV system was installed in 2007, at the student entrepreneurial centre for the training of students and also as a backup for the power requirements of the centre. The system is a ground-mount system with the modules fixed on a structure made of aluminium angle bars and bolted onto metal bars, as shown in figure 2.

Fig. 2: Picture of the installed system

The installation consists of four monocrystalline modules with specifications presented in Table 1. The modules have been certified according to the standards of CE Europe, TÜV and ESTI. The manufacturer's warranty provided is 25 years for 80 % power output.

Tab. 1: Specification of the PV module at STC given by the manufacturer

Parameters	Value
Maximum power (P_{max})	50Wp
Short circuit current (I_{sc})	3.16A
Open circuit voltage (Voc)	21.6V
Voltage at Pmax (V_{mp})	17.60V
Current at Pmax (I_{mp})	2.9A
NOCT	43±2°
Power tolerance	±10%

The methods employed for the analysis include Visual inspection, I-V curve characterization and thermal evaluation by IR imaging were used for the assessment of the modules (Atsu et al., 2020). The process of partial shading of modules was applied to assess the state of the bypass diodes. The uniform translation procedure developed by the Joint Research Centre of the EC is adopted for the translation procedure.

The modules were electrically isolated from each other during the experimentation. The parameters of the modules obtained by employing the EKO MP–170 I-V curve plotter under the experimental conditions. The curve plotter has an accuracy of (± 1% for 10 –1000 V) for Voltage (V_{dc}) and (± 1% for 0.1 – 10 *A*) for current (I_{dc}). Solar irradiation was measured at the plane of the array using the Kimo solarimeter LSL 200 (resolution *1* Wm^{-2}, accuracy *5%).* The Voltcraft infrared thermometer *(IR260 – 8S)* having a measuring range of *-30 to 260 ℃ (± 2 ℃)*, resolution and emissivity of *0.1 ℃* and *0.95* respectively was used to measure the temperature of the modules. Infrared (IR) images were obtained using the (NEC Avio H2640) camera with the following specifications: Accuracy of ± *2% or* ± *2* °C, Spectral range, *8-13 μm*, temperature range, *−40 to 500 °C,* and emissivity of *0.1–1.00.* Quantitative analysis of the captured IR images was performed with the aid of the Report Generator Lite software. The experiment was conducted on a bright sunny day in order to obtain the corresponding results at STC devoid of significant variations which would have occurred at low levels of solar irradiation (Priya et al., 2015).

The translation procedure developed by the Joint Research Centre of the European Commission was used for the translation of experimental data to standard test condition (STC) values. It is a convenient and straightforward method that can be used without applying specific parameters determined under specified conditions of temperature and irradiation. This procedure has a translation accuracy of 4% that is achieved under one experimental measurement (IEA-PVP, 2014).

The following default values were applied: temperature coefficient of I_{sc} (α)= 0.0045, temperature coefficient of V_{oc} (b) =0.06 and irradiance correction factor (a)= 0.06. These default values are valid for crystalline silicon modules. These values are valid for crystalline silicon modules. Equations 1 to 4 provide the procedure for translation of the parameters of the PV modules in operation without determining any specified constants at predetermined ambient and irradiation conditions which are not achievable with modules in real operation (Quansah et al., 2017).

$$I_{sc,2} = I_{sc,1}[1 + \alpha(T_2 - T_1)]\frac{G_2}{G_1} \quad \text{(eq. 1)}$$

$$V_{oc,2} = V_{oc,1}\left[1 + aIn\frac{G_2}{G_1} + b(T_2 - T_1)\right] \quad \text{(eq. 2)}$$

$$I_2 = I_1\left(\frac{I_{sc,2}}{I_{sc,1}}\right) \quad \text{(eq. 3)}$$

$$V_2 = V_1 + (V_{oc,2} - V_{oc,1}) + R_s\,(I_1 - I_2) \quad \text{(eq. 4)}$$

3. Results and Discussion

3.1. Visual Inspection

Visual inspection is the quickest and less intricate process for detecting defects and failures in solar modules (Oliveira et al., 2017). The most suitable period for performing the visual inspection on solar modules is under the illumination of about 1000 lux and applies to defects detectable with the unaided eye (Priya et al., 2015). The experimental measurement and the visual inspection of the PV modules were conducted at irradiation levels close to 1000 W/m2. Table 2 presents the results of the visual inspection.

Tab. 2: Results of the visual inspection

PV module component	Observation/remark	Image
Front of PV module	Shows no sign of delamination, or browning. Glass still feels smooth. Except for accumulated dirt in the lower end and the edges.	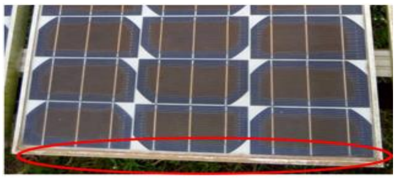
PV cells	All cells uncracked and not broken. Each cell shows some level of discoloration of encapsulant (>70%). EVA discoloration was observed in all the modules.	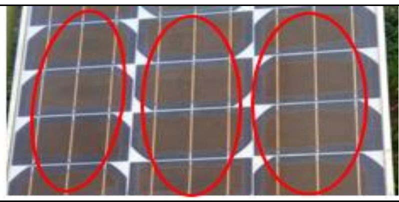
Cell metallization	Shows no sign of burns or having been oxidized except for browning or colouration of cell interconnects ribbons.	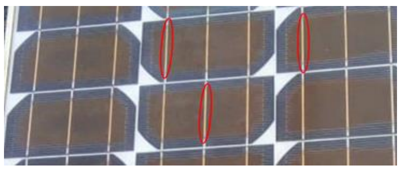
Junction box	Intact and all well closed but corrosion observed at portions when opened. This was seen in the junction boxes for all four modules at similar spots. This may be due to moisture ingress. It can also be as a result of the material used which may have a high affinity for water vapour	

	Evidence of bad wiring was observed. (Module wire touching conducting components within the box). This may lead to internal arcing in the box. This was seen for only module 4. This could be a result of students' activities on the system.	
Module frame	Well intact with no scratches or broken parts and not askew. Some discoloration as a result of the accumulation of dirt and water mostly at the bottom half of the module.	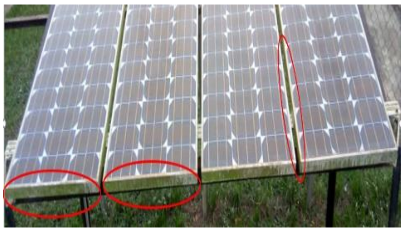

The IEC 61215 standard for degradation requires only total irradiation of *15 kWh/m²* of UV energy. Hence, under real operation conditions, PV modules have the potential of degradation of *5%* or more, and EVA browning just under UV irradiation of *150 kWh/m²* or more (Oliveira et al., 2017). With the annual radiation levels of the site being *1,733.75 kWh/m²*, there is a high possibility of browning of the modules. Table 2 shows the prevalent rate of browning of EVA, covering about 70% of each cell surface. EVA browning is directly proportional to the Ultraviolet (UV) light, leading to transmittance loss and decline in the performance output. Other defects detected are the browning of the interconnect metallization and the corrosion of metal portions in the junction box.

3.2. Degradation rates

Conversion of measured module parameters to the corresponding values at standard test conditions (STC) was carried out using the JRC method. Module 2 recorded the highest Isc of 2.94 A compared to the nameplate value. Module 1 recorded the lowest Isc of 2.6 A. The average Isc for the array was 2.78 A, with the average decline in Isc, determined as 11.7%. Module 1 had the highest reduction of 16.4% in Isc and the lowest drop of 7% was observed for module 2, as illustrated in Figure 3. The annual average decline in Isc is 0.98%.

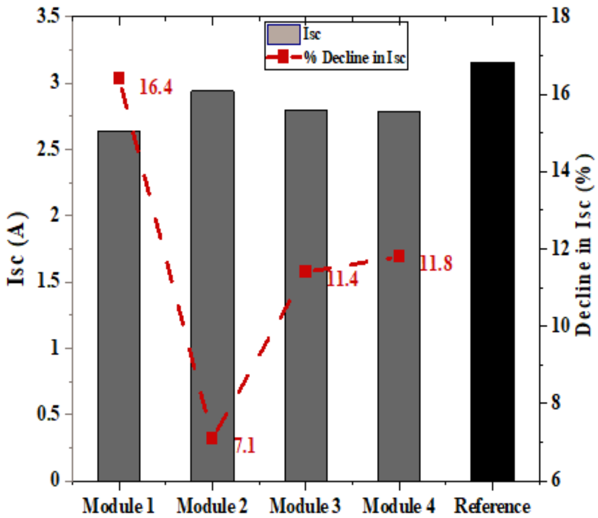

Fig. 3: Short circuit current at STC

The mean Voc for the array was found to be 18.4 V which is 14.8% less than the manufacturer's value of 21.6 V, as shown in figure 3. Module recorded the highest Voc of 19.4 V, and the least Voc of 17.91 V was determined for module 3, with a percentage decline of 17.1%. The average degradation in Voc is 14.8% which indicates an annual decrease in Voc of 1.23%.

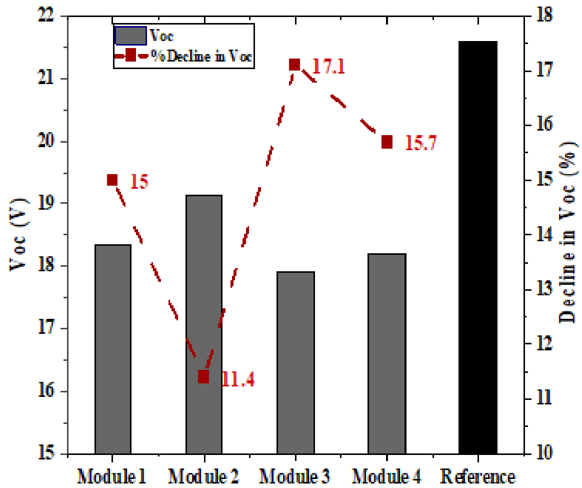

Fig. 4: Open-circuit voltage at STC

The average fill factor at STC determined for the array is 60.05. The highest decline in fill factor of 24.2% was determined for module 3, while the least drop of 11.3% is recorded by module 1, as illustrated by figure 5. The average decline in FF is 18.0%. This presents an annual mean reduction in FF to be 1.5%.

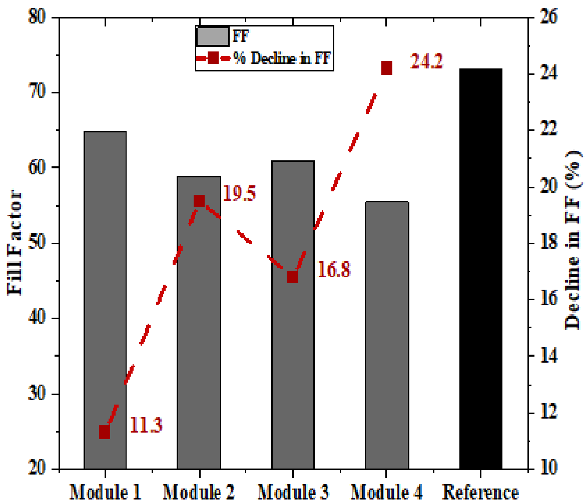

Fig. 5: Fill factor at STC

The average power output determined for the modules was 30.86 *W*. The highest and lowest power of 32.72 *Wp* and 29.3 *Wp* were determined for modules 2 and 3, respectively. A significant decline in the power output of 41.4% was recorded by module 3. The lowest drop was found to be 34.6% for module 2, as presented by figure 6. The average reduction in the nominal power for the array was 38.3% which indicates an average annual decline of 3.19% for the 12 years in operation.

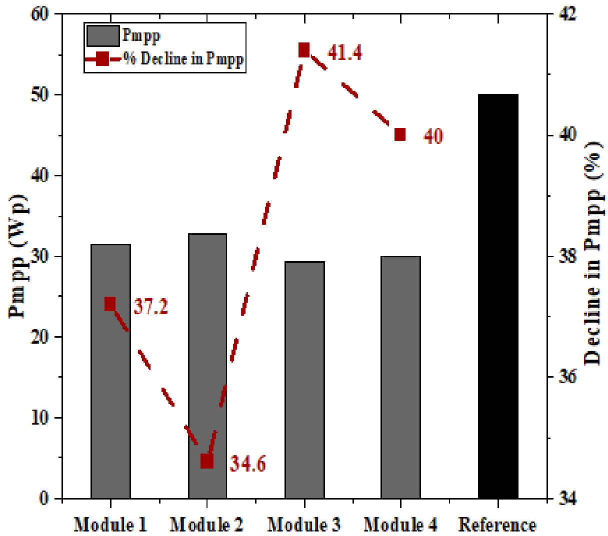

Fig. 6: Nominal power at STC

According to (Köntges, M. et al., 2017), the sequence of the impact of the failure modes is the potential induced degradation, failure of bypass diodes and discoloration of the EVA. This is because there are not appropriate tests yet approved for these failure mechanisms. It is therefore not unexpected the evidence of high degradation levels of the modules with proofs of acute EVA discoloration and bypass diode failures. As it is corroborated by (Munoz et al., 2011), the degree of discoloration of EVA determines the change in the transmittance of the light reaching the solar cells. Thus, the decrease in the power generated.

3.3. Temperature measurement

The method of thermography was applied to determine the trend of the operating temperatures of the modules for the period of the experiment. The report lite software was used to perform the quantitative analysis of the captured IR images. The total surface area of the modules was used during the process. Results show that module 3 had the highest temperature of 59.5 °C whiles the lowest temperature of 45.9 °C was recorded for module 4. The highest mean temperature of 56.3 °C was obtained by module 1, with module 4 recording the least mean temperature of 52.4 °C. Modules 2 and 3 had average temperatures of 55.3 °C and 55.03 °C, respectively, whereas module 4 had the most significant temperature dissimilarity of 10.7 °C, as well as the lowest mean temperature. Module 3, 2 and 1 respectively recorded temperature dissimilarity of 10.0, 6.5 and 4.2 °C. The determined standard deviation values are 1.5905, 2.8557, 3.8676, and 4.7545 for modules 1, 2, 3 and 4, respectively. The average temperatures were 56.28, 55.25, 55.03 and 52.38 for modules 1, 2, 3 and 4, respectively, as illustrated in figure 7. The temperature variations experienced by the four modules are as a result of the varying absorption rates of solar radiation caused by the non-uniform discoloration of EVA in each module. The uneven discoloration of the modules also causes dissimilar electrical defects which lead to mismatch losses and consequently causing the modules to generate different temperatures on their surfaces.

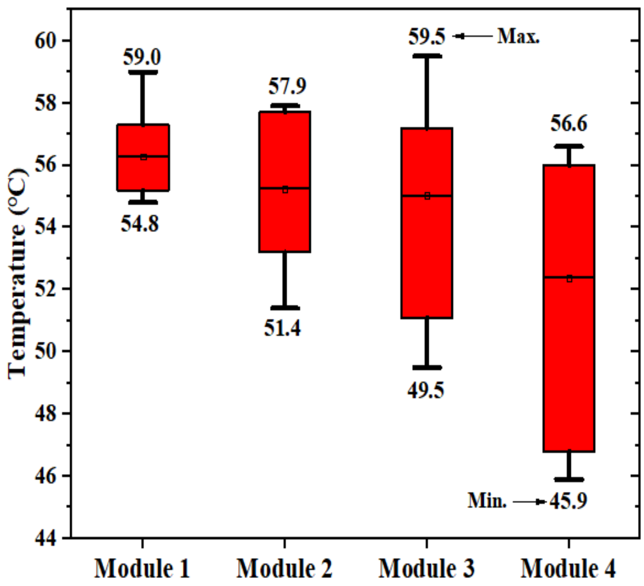

Fig. 7: Temperature distribution of modules

3.4. Bypass diode test

The state of the bypass diodes was assessed by applying the partial shading method. Each module was partially shaded using an opaque object; one at a time and the characteristic I-V and P-V curves traced. In the scenario of a malfunctioning bypass diode, there is a decline in the flow of current in the shaded string of cells as they are not protected. However, in the case of modules having functioning diodes, the decline in current is transformed into inflection points. The results show that the curve outputs deviate from the standard I-V curves with a significant drop in current to the extent of being negligible, as shown in figure 8. The I-V curves and P-V curves under partial shading conditions for all four modules are similar to figure 8 in magnitude and shape. The voltage of all studied modules, however, remained unaffected. This indicates an open circuit performance for the modules; a state in which an insignificant amount of current or no current flows through the circuit. This condition may be the result of defective bypass diodes or soldering disconnection between the bypass diode and the metal contact inside the junction box.

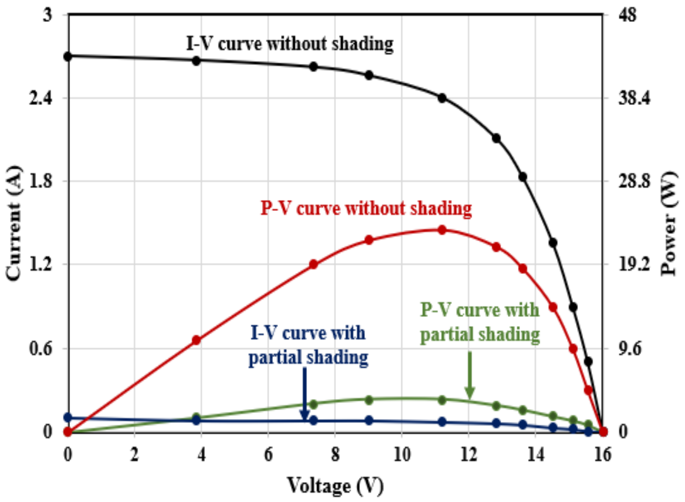

Fig. 8: Characteristic I-V, P-V curves (unshaded and partially shaded) for module 4

4. Conclusion

On-site performance evaluation of PV modules aims to reveal the degradation and failure modes influenced by climate-specific factors. The results of such studies help to enhance the reliability of PV modules by increasing the service life of PV systems.

In this current study, the degradation rates and failure modes of a 12-year-old ground mount off-grid solar PV modules installed in the harsh weather conditions of the sub-Saharan was investigated. It was revealed that the decline in the nominal power ranges from 34.6% to 41.4% with an average decrease of 3.19% per year. In comparison with the nameplate module characteristics of a nominal power 50 Wp, Isc 3.16 A, Voc 21.6, the decline in the experimental values were 7.1 to 16.4% for Isc, 11.4 to 17.1% for Voc and 11.3 to 24.2% for the FF. All four modules had their bypass diodes malfunctioned and exhibited widespread EVA discoloration, covering about 70% of the total surface area of each module. The thermography analysis revealed temperature dissimilarities ranging from 4.2 to 10.7 ºC. This study provides more insights into the diverse impacts of different environments on the long term performance of PV modules.

5. Acknowledgement

This work was supported by the Stipendium Hungaricum Programme and the Mechanical Engineering Doctoral School, Szent István University, Gödöllő, Hungary.

6. References

Powerweb (2020). http://www.fi-powerweb.com/Renewable-Energy.html (accessed: 01/08/2020)

Atsu D., Seres I., Farkas I. 2020. Thermal behaviour analysis of different solar PV modules via thermographic imaging, Journal of Renewable and Sustainable Energy, Vol. 12, No. 1:013503, 1-8.

Chamberlin, C.E., Rocheleau, M.A., Marshall, M.W., Lehman, P.A. Comparison of PV module performance before and after 11 and 20 years of field exposure. Proceedings of the 37th IEEE photovoltaic specialists conference; 2011.

IEC 61215-1-1:2016, Terrestrial photovoltaic (PV) modules - Design qualification and type approval - Part 1-1: Special requirements for testing of crystalline silicon photovoltaic (PV) modules.

Jordan, D.C., Kurtz, S.R., 2013. Photovoltaic degradation rates-an analytical review. Prog. in Phot: Res. and Appl. 21, pp. 12–29.

Rahman, M.M., Hasanuzzaman, M., Rahim, N.A., 2015. Effects of Various Parameters on PV Module Power and Efficiency. Ener. Conv. and Mgt. 103, 348 – 358.

Vázquez, M., Rey-Stolle, I., 2008. Photovoltaic module reliability model based on field degradation studies. Prog. in Phot: Res. and Appl. 16, 419–433.

Merkel, A. 2019. Weather of Koforidua. https://en.climate-data.org/africa/ghana/eastern-region/koforidua-52344/ [accessed: 20/12/19].

Sharma, V., Chandel, S. S., 2013. Performance and degradation analysis for long term reliability of solar photovoltaic systems: A review. Renewable and Sustainable Energy Reviews, 27, 753–767.

Rajput, P., Tiwari, G. N., Sastry, O. S., Bora, B., Sharma, V., 2016. Degradation of monocrystalline photovoltaic modules after 22 years of outdoor exposure in the composite climate of India, Sol. Energy. 135, 786–795. https://doi.org/10.1016/j.solener.2016.06.047.

Priya, S. S., Sastry, O. S., Bora, B., Kumar, A., 2015. Comparison of curve correction procedure of current and voltage as per IEC 60891 for thin-film technology. 2015 IEEE 42nd Photovolt. Spec. Conf. PVSC, 2015. https://doi.org/10.1109/PVSC.2015.7355843.

IEA-PVPS. Review of Failures of Photovoltaic Modules; OECD/IEA: Paris, France, 2014.

Quansah, D., Adaramola, M., Takyi, G., Edwin, I., 2017. Reliability and Degradation of Solar PV Modules—Case Study of 19-Year-Old Polycrystalline Modules in Ghana. Technologies, 5(2), 22.

Oliveira, M. C. C. de., Diniz, A. S. A. C., Viana, M. M., Lins, V. D. F. C., 2017. The causes and effects of degradation of encapsulant ethylene vinyl acetate copolymer (EVA) in crystalline silicon photovoltaic modules: A review. Renewable and Sustainable Energy Reviews, 81, 2299-2317.

Köntges, M. et al.: Assessment of Photovoltaic Failures in the field. IEA PVPS Task 13, Subtask 3, 2017.

Munoz, M. A., Alonso-García, M. C., Vela, N., Chenlo, F., 2011. Early degradation of silicon PV modules and guaranty conditions. Solar Energy, 85(9), 2264–2274.

Digital mapping of techno-economic performance of a water-based solar photovoltaic/thermal (PVT) system for buildings over large geographical cities

Santhan Reddy Penaka[1,4], Puneet Kumar Saini[2], Xingxing Zhang[1], Alejandro del Amo[3]

[1] Dalarna University, Falun (Sweden)

[2] Uppsala University, Uppsala (Sweden)

[3] Abora Solar, Zaragoza (Spain)

[4] Penaka Solar AB, Borlänge (Sweden)

Abstract

Solar photovoltaic thermal (PVT) is an emerging technology, capable of producing electrical and thermal energy using a single collector. However, to achieve larger market penetration for this technology, it is imperative to have an understanding of the energetic performance for different climatic conditions and the economic performance under various financial scenarios. This paper thus presents a techno-economic evaluation of a typical water based PVT system for electricity and domestic hot water applications in 85 locations worldwide. The simulations are performed using a validated tool with one-hour time step for output. The thermal performance of the collector is evaluated using energy utilization ratio as efficiency as key performance indicators, which are further visualized by the digital mapping approach. The economic performance is assessed using net present value and payback period under two financial scenarios: (1) total system cost as a capital investment in the first year; (2) only 25 % of total system cost is a capital investment and remaining 75 % investment is considered with financing period with certain interest rate. The results show that such a PVT system has better energy performance for the locations with a low annual ambient temperature and vice versa. Furthermore, it is seen that the system boundaries, such as load profile, hot water storage volume, etc., can have a significant effect on the annual energy production of the system. Economic analysis indicates that the average net present values per unit collector area are 1800 € and 2200 € respectively among the 85 cities for financial model 1 and financial model 2. Nevertheless, from the payback period point of view, financial model 1 is recommended for the locations with high interest rate. The study is helpful to set an understanding of general factors influencing the techno-economic performance of PVT systems.

Keywords: PVT, Water-based PVT, Techno-economic analysis, Digital mapping

1. Introduction

1.1 Background and existing studies

The concept of "electrify everything" considers solar energy as a key renewable technology with an aim of de-carbonization of domestic heating demand (Jia, Alva and Fang, 2019). The rapid growth in Photovoltaic (PV) installation capacity from the last few years has further strengthen the importance of PV as the main driver of renewable transformation. (Joshi and Dhoble, 2018). PV remains an interesting subject area for many researchers, global leaders, and manufacturers because of its reliability, sustainability, ease of installation, and economic feasibility (Al-Waeli *et al.*, 2017). However, the concurrence of heat/electricity demand and limited roof area in domestic dwellings does require technologies, which can generate energy efficiently in both thermal and electrical form. Therefore, there is a huge potential for well-designed systems by combining both solar PV and solar thermal technologies. A relatively new commercialized concept of solar photovoltaic/thermal (PVT) technology can achieve such a goal by generating both electrical and thermal energy together using a single panel (Gu *et al.*, 2018). Realizing its importance, the Solar Heating and Cooling Program (SHC) of the International Energy Agency (IEA) has initiated the task 60 for PVT applications and solutions to HVAC systems in buildings ('PVT systems IEA SHC 60 - Annex 180504.pdf', no date). The task is active from January 2018 and has built a huge knowledge base around PVT systems for its use in domestic and industrial applications.

PVT system can be categorized in several ways, however, the most common is based on heat-transfer medium (air based/liquid based) used in the PVT collector (Zhang *et al.*, 2012). The liquid based types are dominating the current PVT market in terms of the number of installations due to high efficiency, and ease of integration in existing hydronic systems (Ramschak, 2020). In a standard liquid based PVT collector, the heat carrier is usually

doi:10.18086/eurosun.2020.05.04 Available at http://proceedings.ises.org

water or brine mixture, which is allowed to circulate in a heat exchanger behind the PV cells. The circulation results in a heat transfer through the back sheet of the module, which raises the fluid temperature enough to use for various applications such as hot water, swimming pool heating etc. From a technical perspective, PVT technology is well developed and it can be coupled with various energy systems. For instance, it can go hand-in-hand with the emerging awareness of heat pump technology with/without borehole storage ('IEA-SHC-Task60-Highlights-2019.pdf', no date). However, the main barriers currently in PVT development and deployment are lack of testing standards, uncertain financial incentives, and business models across different regions in a niche market. Therefore, the business potential of PVT solution is not fully explored, although it can be a very efficient solution for domestic and industrial heating requirements.

However, most of the existing techno-economic studies focused on a single climate, with a straightforward economic-financial analysis. Furthermore, complicated procedures or individual software are used to estimate the performance of PVT collectors, where it lacks a comprehensive simulation of PVT techno-economic performance through a common tool over a large geographic area, aiming for application feasibility and business potentials. Besides, many studies have reported solar energy resource potential on buildings at different spatial scales using digital mapping methods, such as digital numerical maps (Jung, Han and Kim, 2019), digital surface model (Oh and Park, 2018), satellite imageries and geographic information systems [25, 26], multi-scale uncertainty-aware ranking of different urban locations (Peronato *et al.*, 2018), which provide direct evaluations for solar application, leading to robust planning decisions. Nevertheless, no study is found yet for mapping of techno-economic performance of PVT systems.

As a result, this paper aims to fill these research gaps by utilizing a validated simulation tool to perform a comprehensive techno-economic performance simulation for a wide range of cities. The results are further analyzed and visualized using a digital numerical mapping approach to set a comparison among various regions.

1.2 Aim and objectives

This study aims at simulation and mapping of the energetic and economic indicators of a typical PVT system over different regions, to establish a digital performance database for various key performance indicators (KPI). The economic feasibility of the PVT collector is obtained and compared under various financial scenario models. The data obtained from simulations are used to establish a simple correlation between variables affecting the PVT system.

The main objectives of this paper are to:

- Assess the thermal and electrical performance of a typical PVT system [6] in 85 locations across the World using a validated simulation tool.
- Evaluate the economic performance using NPV and payback period using two financial scenarios.
- Analysis and visualization of energy and economic performance.

The significance of this paper lies in (1) understanding of typical PVT components behavior at system level, (2) mapping of the collector energetic and economic performance at different climatic conditions across the world. This research results would reflect the concrete developments to this subject area and helps the promotion of the potential markets, e.g. discovering the economic feasibility of the PVT system, and feasible financial solutions to the PVT system in different regions. This paper evaluates the related business benefits of a typical PVT system, which would help to develop a database as repository of PVT performances in different regions and contexts. The research results will be useful for researchers, planners, and policy-makers to further evaluate PVT potentials in a net-zero/positive energy district towards energy surplus and climate neutrality.

2. System description and research methodology

This paper focus on a typical PVT collector developed by a Spanish manufacturer named Abora solar. The collector is market available and more than 5700 m^2 of the gross collector is installed for a broad range of applications. The collector is a covered PVT type with an additional layer of glass on the top of the collector (in addition to a glass layer for PV cells) to reduce the heat convection losses. The rated power of the collector is 365 W at Standard Testing Conditions (STC), with a collector area of 1.96 m^2 consisting of 72 mono-crystalline cells. The main specifications and characteristics of analysed PVT collector are shown in

Table 1.

Table 1. Specifications and characteristics of the modelled PVT collector

Parameter	Description
Length * width * thickness	1970 * 995 * 107 mm
Gross collector area	1.96 m^2
Number of PV cells	72
Cell type	Mono-crystalline
Rated power	365 Wp
Electric efficiency at STC conditions	17 %
Thermal efficiency at STC conditions	70 %
Temperature coefficient of PV	-0.41 % /˚C
Thermal efficiency at zero mean temperature	0.7
Coefficient of thermal losses, a_1	5.98 $W/m^2 \cdot K$
Coefficient of thermal losses, a_2	0.021 $W/m^2 \cdot K^2$
Internal water volume	1.78Litres

2.1 Research methodology

The simulation is carried using a validated tool developed by the manufacturer of the studied PVT collector. The "*Abora hybrid simulation tool*" (*Contact*, no date) was used to map the performance across 85 cities shown in Fig 1. The cities were chosen based on population density and geographical coordinates in different countries to represent a large market potential in these regions. The simulation tool accepts a wide range of design and financial input parameters, e.g. location and weather resources, electrical and thermal demands, local energy tariffs, specific storage volume, PVT panel and installation parameters, interest rate, and financing period, etc. The performance model used in the tool for evaluation of PVT performance is validated in [24], where a heat pump system integrated with 25 PVT modules was monitored, and measurements were also compared with the dynamic simulation model built in TRNSYS for Zaragoza, Spain.

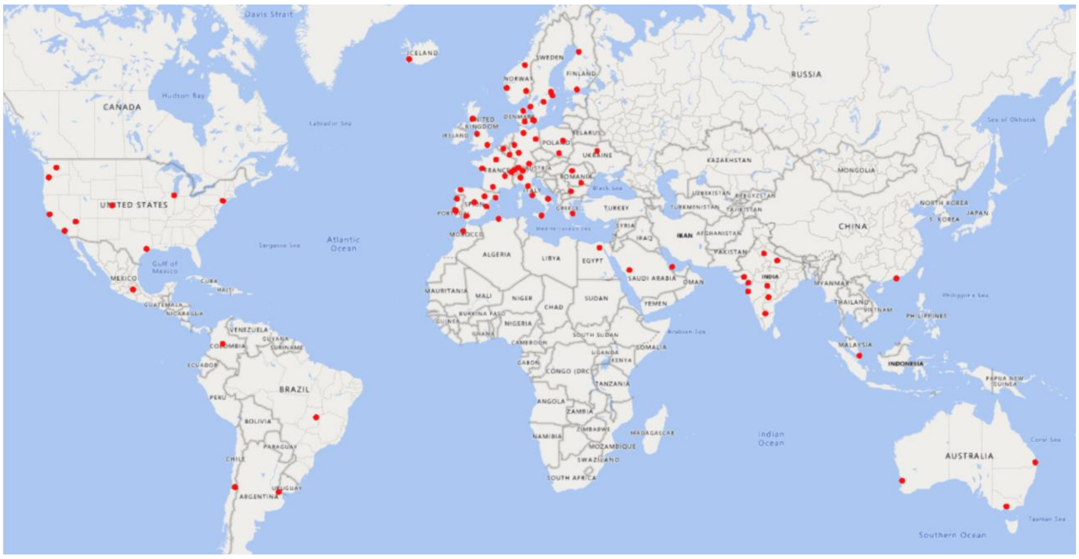

Fig 1. The simulated locations for techno-economic analysis

This paper further applies the digital numerical map approach based on heat maps to visualize the performance of various indicators across simulated locations. The simulation results for all locations are exported to Microsoft Excel for calculations of energy efficiency (*Microsoft Excel, Spreadsheet Software, Excel Free Trial*, no date). After then, the results are visualized using QGIS tool, which provides a heat map rendering to design a point layer data with a kernel density estimation processing algorithm (*Welcome to the QGIS project!*, no date). Initially, a parametric study of components at the system level is considered according to the operation flow of the simulation tool indicated in the flow chart shown in Fig. 2. Then, the simulations are carried with defined boundary conditions and the results are represented subsequently as monthly electrical and thermal performances, energy savings, economic parameters, such as NPV, payback period.

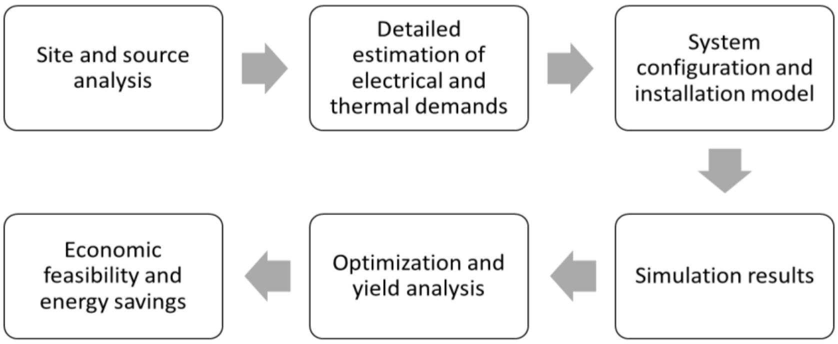

Fig. 2. Operation flow of the simulation tool

This paper also considers the economic performance of the collector in two different financial models, which are described below:

- Model 1: The total system cost is invested in the first year.
- Model 2: Only 25 % of total system cost is a capital investment and the remaining 75 % investment is considered with the financing period with a certain interest rate.

The boundary conditions for the analysis is shown in **Table 2**.

Table 2. Boundary conditions for the simulation tool

Parameter	Description
Type of application	Single-family house
Type of demand	Electricity demand, and Thermal demand for DHW,
Auxiliary system	Electrical heater
Auxiliary system energy price	This has been selected for the appropriate location
No. of people in house	5
DHW temperature	60 ºC
Collector model	aH72SK
No. of collectors	1
Specific volume capacity	80 liters/m^2
Inclination	These were selected optimally based on a parametric study for maximum energy production.
Type of mounting structure	Tilted
Type of inverter	Single-phase inverter
Annual maintenance cost	Assumed that no maintenance is required for a single collector to reduce uncertainties.
Electricity and combustible price increment	6 % per year is assumed for all the locations
System lifetime	25 years
Interest rate	Selected appropriately for each location

Initially, the energy performance of the PVT system is simulated in 85 different locations using the simulation tool. In order to discover and compare the collector energy performance in different locations, the thermal demand is maintained the same in all selected locations. Therefore, the simulated system considers a single PVT collector (1.96 m^2), for a single-family house application with 5 people, for the same demand, and the same tank volume for all locations. These assumptions provide a common system boundary to understand the effect of climatic variables and financing parameters on collector performance. Two types of demands are considered as DHW and electricity use in the building. In the electricity model, no price difference in self-consumed and exported power to the grid is considered. In the thermal system configuration, the auxiliary source for the house is the electricity grid with appropriate energy prices for every location. The generated DHW by the collector is utilized for household purposes using a storage tank connected to the auxiliary system which will deliver demand at the desired temperature of 60 °C**.** For each location, the installed tilt and azimuth angles are taken optimally based on higher collector production. The specific volume capacity is assumed 80 liters/m^2 for all the locations which is equivalent to total 150 liters of storage tank capacity.

In the proposed simplified energy system, PVT collector is directly connected to the tank without any internal or external heat exchanger. The cold water from the tank enters the PVT module, exchange heat from the absorber, and hot water is fed to the top of the tank. The DHW cold water enters at bottom of the tank, and hot water leaves from top of the tank for DHW supply in building. The DHW distribution system and associated heat losses are not considered in the analysis. The maximum DHW supply temperature is set at 60 ºC, and an electric auxiliary heater is provisioned in the tank for periods when the energy from PVT modules is not enough to meet the DHW load. Electric heater starts and stops at the determined dead band to optimize energy consumption, while maintaining the fixed supply DHW temperature. During the periods when tank temperature exceeds the set limit, the energy from PVT modules is fed to a heat sink (air/water heat exchanger), and this spilled energy from the collector is not counted as part of useful energy output.

In the electrical system configuration, the generated DC power will be converted to the AC power using an inverter. Then, it is utilized by household purposes and the remaining will be sent to the electricity grid, whereas the excess electricity demand is taken from the grid connection. As the tilt angle of the PVT collector is a key parameter that will also decide the collector production, a preliminary parametric study is carried for each location to determine the optimal tilt angle for maximum annual collector production.

The total system cost is determined using variables such a module cost, system components cost, annual operation, and maintenance cost. The electricity and auxiliary energy price escalation is assumed 6 % per year for all the locations. The payback time and NPV are estimated by considering a reference system using an electric heater.

The economic performance of the collector in two different financial models is evaluated based:

- Model 1: The total system cost is invested in the first year,
- Model 2: The total system cost is paid for 7 years with a certain variable interest rate with every location.

3. Results and Discussion

3.1 Energy performance evaluation of PVT panel

3.1.1 Collector thermal production

The simulated results are visualised using geo-spatial maps, as they provide a clear indication for the understanding of regional trends for thermal and electrical output despite large data sets. Fig. 3 shows the variation in the thermal output of the collector.

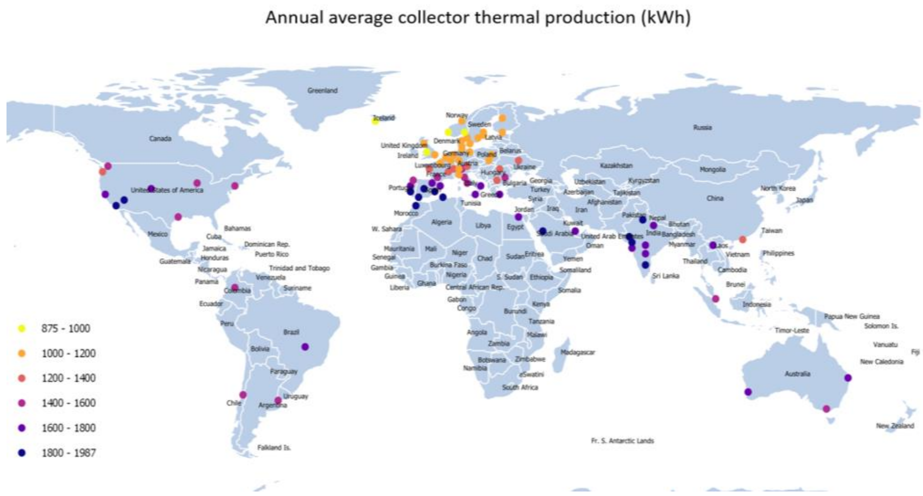

Fig. 3. Annual average collector thermal performance

The general trend shows that thermal output is higher in countries with higher irradiation such as Saudi Arabia, Algeria, Morocco, Brazil, Mexico, India, etc., with annual thermal production above 1800 kWh (area-specific output 918 kWh/m^2) due to high GHI and ambient temperatures. The lower band of average collector production can be seen in Reykjavik, Iceland and for some locations in Norway with a specific output of 475 kWh/m^2 and 500 kWh/m^2 respectively. Similar thermal output is obtained for locations in counties such as Sweden, Finland, United Kingdom, Denmark, etc., with less than 510 kWh/m^2 annual production. The collector shows better performance in countries, such as Spain, Portugal, and Australia with collector production of above 1600 kWh (816 kWh/ m^2).

3.1.2 Collector electrical production

Fig. 4 represents the electrical performance of the collector, which shows similar trends as thermal output. For locations in countries with high GHI such as Saudi Arabia, Algeria, Morocco, Brazil, India, etc have generation above 500 kWh, and peak value in Saudi Arabia with 540 kWh. The electrical production is much less in Iceland with 266 kWh due to less available GHI, And the collector lower than 300 kWh in locations, such as Sweden, Finland, Denmark, Poland, United Kingdom, etc., The collector performed slightly better in Spain, Portugal, and Australia with more than 400 kWh annually. However, it shows there is no significant difference in thermal and electrical production trends. Furthermore, a correlation of collector electrical production with GHI and ambient temperature is developed based on all monthly points from all chosen locations and a positive correlation is realized as shown in Fig. 5. A large variation in electrical output for similar values of ambient temperature can be observed, which again shows that GHI is the critical parameter governing the electrical output of the collector.

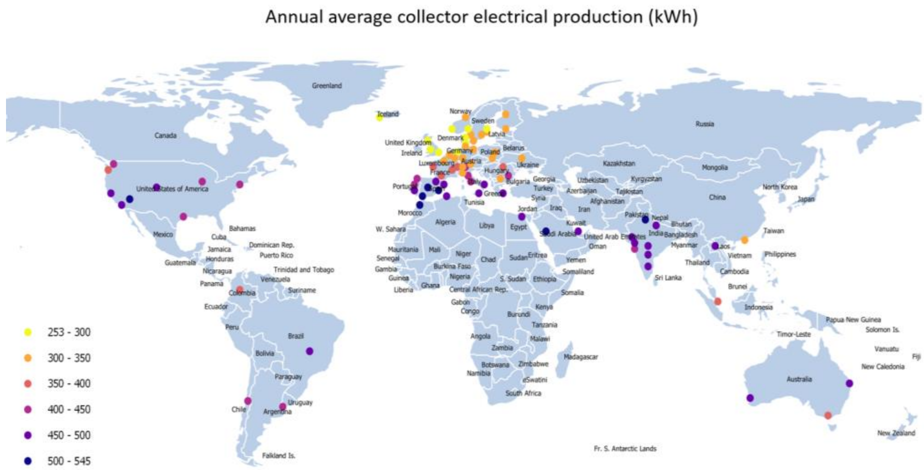

Fig. 4. Annual average collector electrical performance

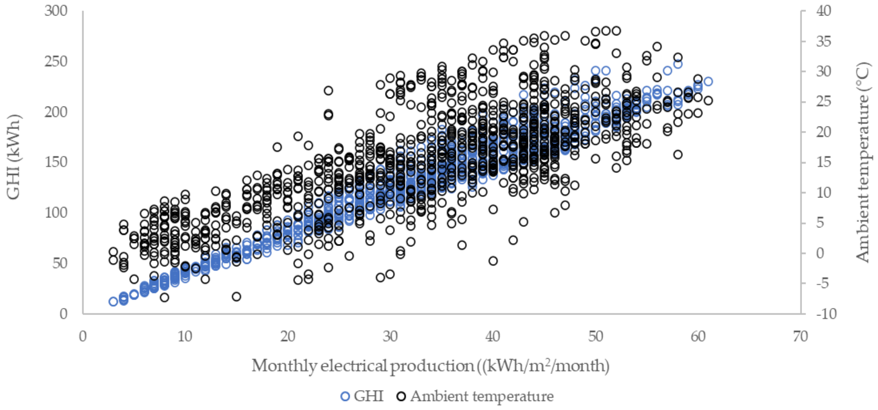

Fig. 5. Correlation of collector electrical production with Global Horizontal Irradiation (GHI) and ambient temperature

3.1.3 Collector energy utilization ratio

The energy utilization ratio of the collector for various locations is shown in Fig. 6. The correlation trends between energy utilization ratio and annual average ambient temperature are shown in Fig. 7 with consideration of all selected 85 geographical locations to derive a possible trend between the parameters.

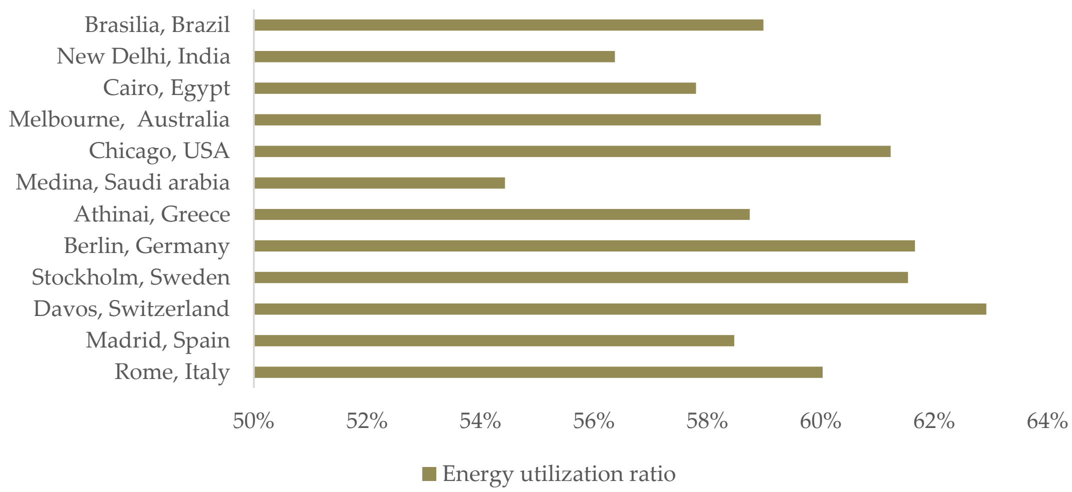

Fig. 6. Collector energy utilization ratio

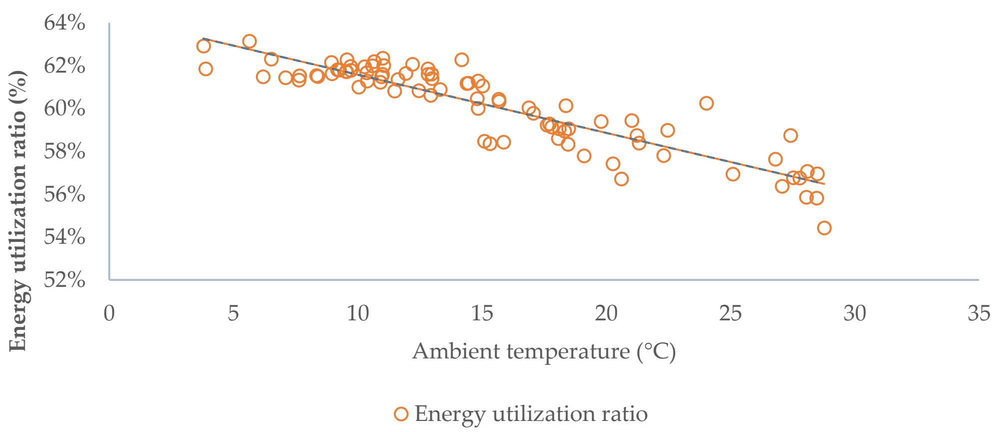

Fig. 7. Correlation of Energy utilization ratio with the annual average ambient temperature

Some locations show interesting results of system boundaries on PVT collector performance. This can be realized by comparing the energy utilization ratio for Medina (high irradiation) and Davos (low irradiation location). The energy utilization for Davos (63 %) is higher compare to Medina (52.5 %), even though the absolute value of total energy output is higher for Medina (2506 kWh), compared to Davos (1988 kWh). This is because the load demand for Medina is comparably lower, while the other system design parameters remain the same (collector area, tank volume, etc.), which resulted in higher average tank temp, and thus lower collector efficiency for Medina. Results show that the total thermal demand for every location is varying depending on the ambient temperature. It is because of the temperature difference between the annual average ambient temperature of each location and desired water temperature (assumed 60°C), which has to be covered by the collector thermal production

4.2.1 Collector economic performance in Financing model 1

This financing model scenario has assumed that the total cost of the system is invested in the first year of the system period. As the total system cost will be invested in the first year, no interest rate is not considered. Fig. 8 is the digital representation of NPV potential per unit collector area with financial model 1 in all 85 geographical cities across the World and Fig. 9 shows the NPV potential per unit collector area in geographical cities in the European continent.

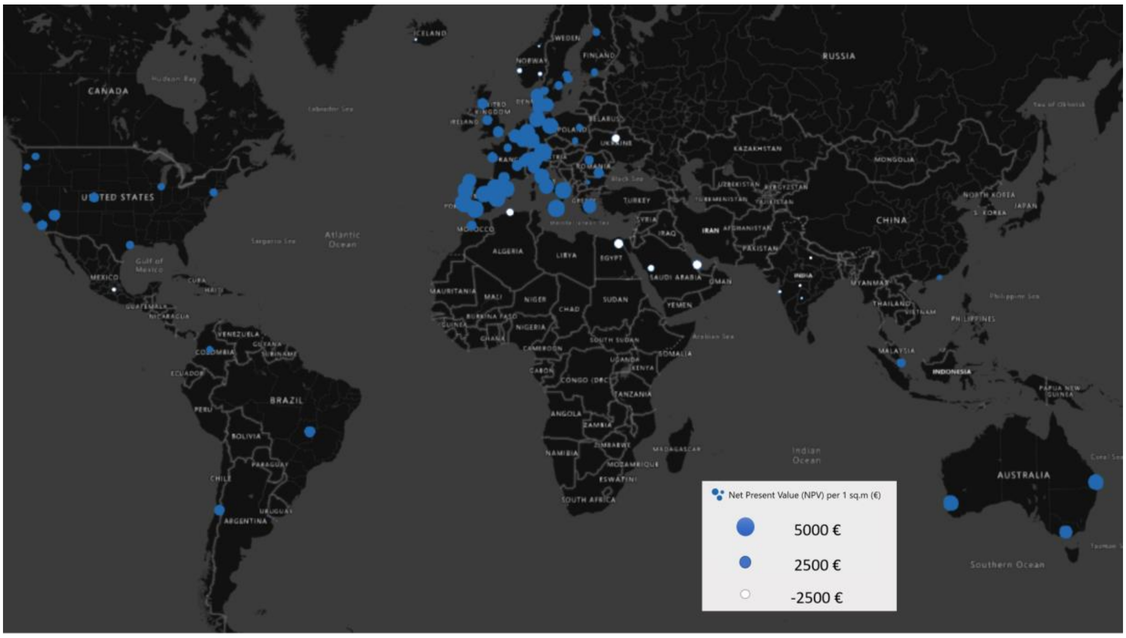

Fig. 8. NPV potential per unit collector area for financing model 1

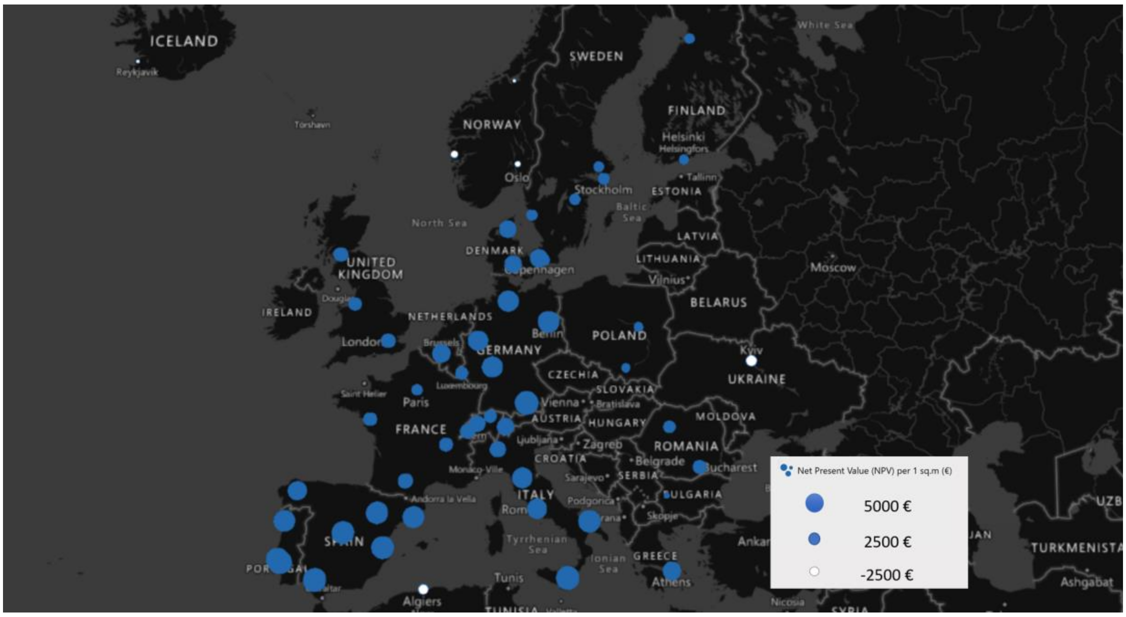

Fig. 9. NPV potential per unit collector area in Europe for financing model 1

The cities with larger dots represent the high NPV potential and cities with smaller dot size represents the least NPV potential. The cities Catania and Munich have the highest potential of 5140 € and 5348 € respectively, followed by Bari, Lisbon, Setubal, Sevilla, Valencia, Zaragoza, Madrid and Berlin cities has potentially more than 4500 € per unit collector area. This is due to their high available GHI and electricity grid price, so the energy savings are high in these locations which reflected in huge NPV potential for this system. Although cities, such as Oslo, Bergen, Reykjavik, etc., with relatively less electricity grid price, resulted in negative NPV due to lower available GHI. The cities with high collector production such as Medina, Algeria, Cairo have shown negative NPV potential due to a very less electricity grid price which eventually showed fewer energy savings.

The NPV potential in all 85 simulated cities has been selected divided and segmented for the appropriate countries to define the NPV range per unit collector area of each country as shown in Fig. 10. A large variation in NPV can be seen in few countries, such as Italy, Portugal, due to variability in GHI for simulated locations. However, a smaller variation is identified in countries such as China, Argentina, Brazil, etc., this is because only one city has been simulated in this paper, which is part of the key uncertainty.

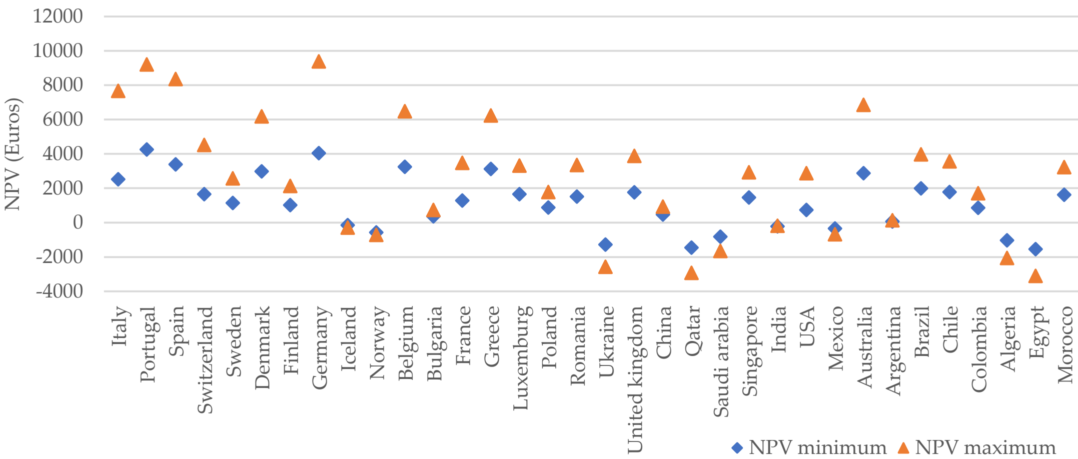

Fig. 10. Country-wise NPV potential per unit collector area for financial model 1

Fig. 11 shows the payback period of this PVT system for a single-family house of 5 people in several countries based on financial model 1. The results show that the total system cost will be returned in the first 10 years in countries, such as Australia, Belgium, Denmark, Germany, Greece, Italy, Portugal, Spain, Switzerland, etc. This is due to high collector production and high electricity grid price. Although countries such as Algeria, Saudi Arabia, Egypt have the highest collector production, the grid price is comparatively lower, which reflects the payback period of more than 20 years.

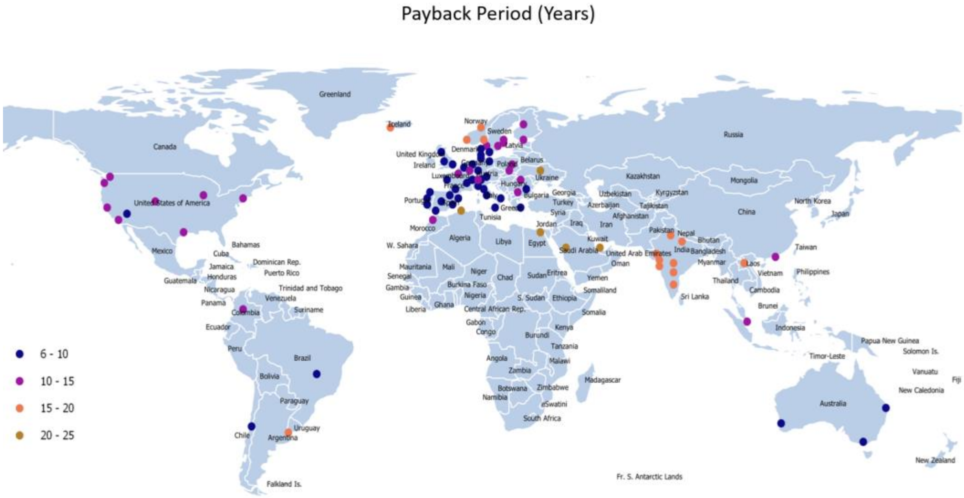

Fig. 11. Country-wise average payback period of the PVT collector system

4.2.2 Collector economic performance in financing model 2

This financing model has been analyzed by assuming that 75 % of total system cost is paid within a financing period of 7 years with a certain interest rate and the remaining 25 % of total system cost is invested in the first year without any interest rate. The NPV potential per unit collector area with financing model 2 in 85 geographical cities across the world is shown in Fig. 12 and NPV potential per unit collector area in a specific European continent is shown in Fig. 13.

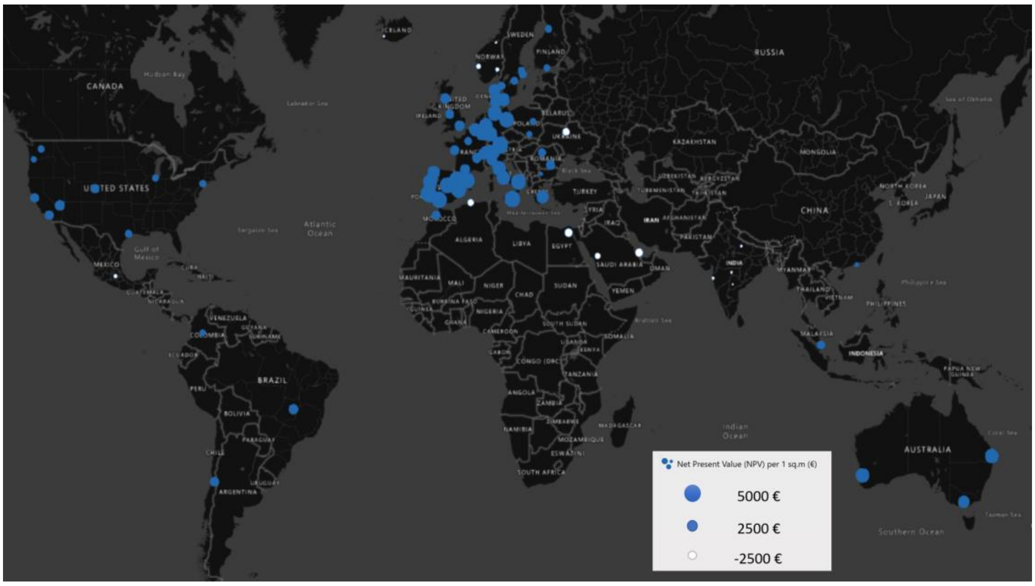

Fig. 12. NPV potential per unit collector area for financing model 2

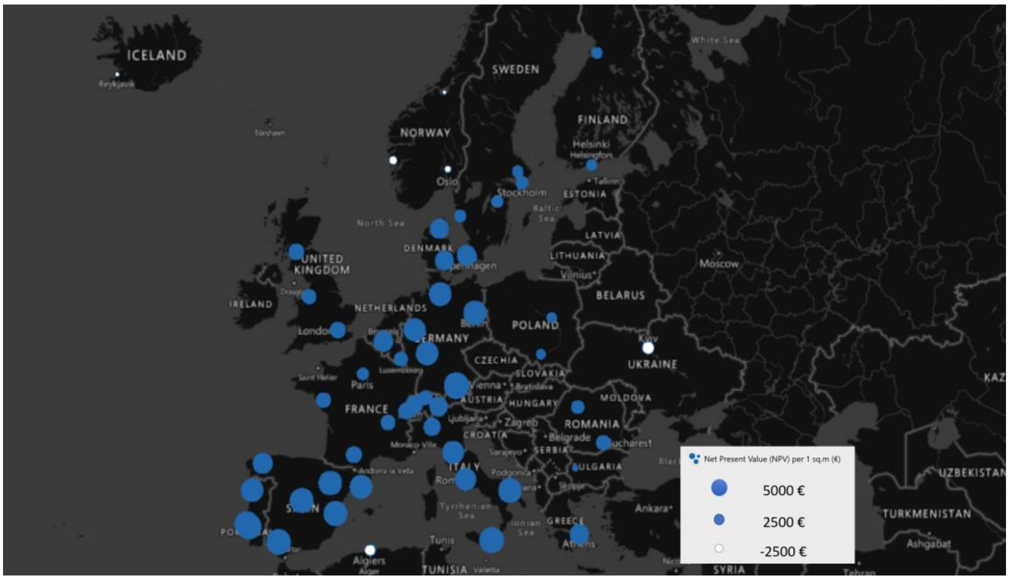

Fig. 13. NPV potential per unit collector area in Europe for financing model 2

The cities with larger dots represent the high NPV potential and cities with smaller dots represent the lower NPV potential. The cities performed high NPV potential in financing model 1, such as Catania and Munich, which has shown improved NPV of 5140 € and 5348 € respectively because of Zero interest rates in those countries. This is because if the interest rate is zero, the user needs to pay the part of system cost in later years, and the present value of this investment will be lower due to the time value of money. This will reduce the accumulated investment and thus higher NPV. However, if the interest rate is high, the extra amount paid due to high interest in later years, which will overweigh the advantage due to the time value of money and it will decrease the overall NPV. Therefore, Financial model 1 is recommended for countries with high interest rate to maximize the NPV, and minimize the payback. Whereas, financial model 2 is recommended for counties with zero or lower interest rates to maximize the NPV. The effect of NPV change due to financial model 2 compare to model 1 is shown in Fig. 14. As expected, the countries with high interest rate have shown a negative effect on NPV and countries with less and zero interest rates has shown better NPV potential, such as USA, Australia and most of the European countries. However, due to high interest rate of 38 % in Argentina, a huge negative impact is identified with this financing model 2.

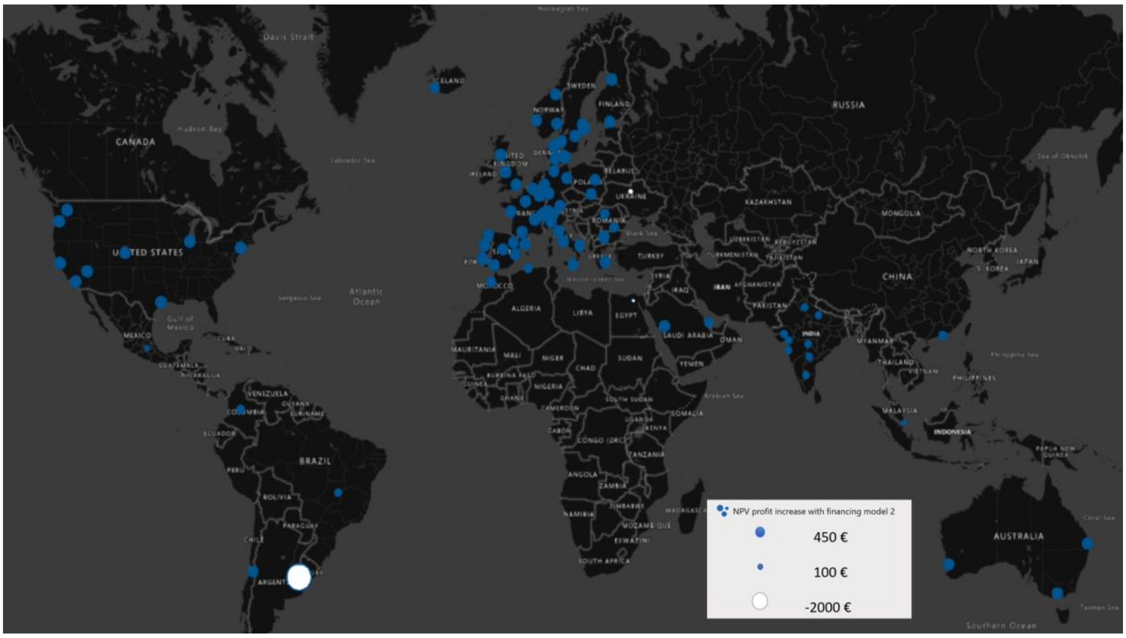

Fig. 14. NPV profit increase with financing model 2

4. Conclusions

The performance of an energy system consists of a PVT collector performance and storage tank is evaluated for 85 locations across a large cities. The optimal tilt angle of PVT collector, load demand, and electricity prices are chosen appropriately for each simulated location. The results show that the major parameter influencing the PVT performance is GHI, and results derived a strong linear correlation between collector output and GHI. The other factor influencing energetic performance is ambient temperature, source, and load water temperatures. The energetic utilization ratio is dependent on total thermal demand and specific volume ratio (v/a ratio), as it can have a major influence on the fluid temperature in the storage tank, and thus collector total production. The electrical production by PVT collector is higher in high ambient temperature locations. The highest and lowest energy utilization ratio of the collector is recorded in Reykjavik, Iceland (63 %), and Medina, Saudi Arabia (54 %) respectively. Most importantly, the results show that the higher energetic output does not guarantee high economic feasibility. There are several factors such as electricity price, interest rate, and selection of financial model which can highly affect the economic feasibility of PVT collector. The average NPV per unit collector area of 85 geographical cities for financial model 1 and financial model 2 is 1886 € and 2221 € respectively. The NPV and payback period analysis of the PVT system has shown positive results for the cities, which have high collector production and high electricity grid price reflecting high energy savings. However, the financing model 1 is highly recommended for the locations with high interest rates and financial model 2 is beneficial for the locations with less interest rates. This paper offers potential insight into the promotion of the PVT market in different regions.

Author Contributions: S.R. Penaka works on simulation, analysis, and writing. X. Zhang contributes on supervision, concept development, structuring, and writing. P.K. Saini contributes to simulation. A.d. Amo dedicates to simulation and analysis.

Funding: This research received funding from the Germany-Sweden joint project: ‘Product and process development for the preparing and realization of complete buildings of various types of use using energy efficient, partially energy independent lightweight construction solutions, ENSECO’.

Acknowledgments: The authors acknowledge the useful gains from the IEA SHC task 60.

Conflicts of Interest: The authors declare no conflict of interest.

References

1. Al-Waeli, A. H. A. *et al.* (2017) ‘Photovoltaic/Thermal (PV/T) systems: Status and future prospects’, *Renewable and Sustainable Energy Reviews*, 77, pp. 109–130. doi: 10.1016/j.rser.2017.03.126.

2. Bremer, M. *et al.* (2016) ‘A new multi-scale 3D-GIS-approach for the assessment and dissemination of solar income of digital city models’, *Computers, Environment and Urban Systems*, 57, pp. 144–154. doi: 10.1016/j.compenvurbsys.2016.02.007.

3. *Contact* (no date) *Abora Solar*. Available at: https://abora-solar.com/en/contact/ (Accessed: 29 November 2019).

4. Gu, Y. *et al.* (2018) ‘Techno-economic analysis of a solar photovoltaic/thermal (PV/T) concentrator for building application in Sweden using Monte Carlo method’, *Energy Conversion and Management*, 165, pp. 8–24. doi: 10.1016/j.enconman.2018.03.043.

5. ‘IEA-SHC-Task60-Highlights-2019.pdf’ (no date). Available at: https://task60.iea-shc.org/Data/Sites/1/publications/IEA-SHC-Task60-Highlights-2019.pdf (Accessed: 10 June 2020).

6. Jia, Y., Alva, G. and Fang, G. (2019) ‘Development and applications of photovoltaic–thermal systems: A review’, *Renewable and Sustainable Energy Reviews*, 102, pp. 249–265. doi: 10.1016/j.rser.2018.12.030.

7. Joshi, S. S. and Dhoble, A. S. (2018) ‘Photovoltaic -Thermal systems (PVT): Technology review and future trends’, *Renewable and Sustainable Energy Reviews*, 92, pp. 848–882. doi: 10.1016/j.rser.2018.04.067.

8. Jung, J., Han, S. and Kim, B. (2019) 'Digital numerical map-oriented estimation of solar energy potential for site selection of photovoltaic solar panels on national highway slopes', *Applied Energy*, 242, pp. 57–68. doi: 10.1016/j.apenergy.2019.03.101.

9. *Microsoft Excel, Spreadsheet Software, Excel Free Trial* (no date). Available at: https://www.microsoft.com/en-ww/microsoft-365/excel (Accessed: 29 July 2020).

10. Mishra, T. *et al.* (2020) 'Assessment of solar power potential in a hill state of India using remote sensing and Geographic Information System', *Remote Sensing Applications: Society and Environment*, p. 100370. doi: 10.1016/j.rsase.2020.100370.

11. Oh, M. and Park, H.-D. (2018) 'A new algorithm using a pyramid dataset for calculating shadowing in solar potential mapping', *Renewable Energy*, 126, pp. 465–474. doi: 10.1016/j.renene.2018.03.068.

12. Peronato, G. *et al.* (2018) 'A toolkit for multi-scale mapping of the solar energy-generation potential of buildings in urban environments under uncertainty', *Solar Energy*, 173, pp. 861–874. doi: 10.1016/j.solener.2018.08.017.

13. 'PVT systems IEA SHC 60 - Annex 180504.pdf' (no date). Available at: http://task60.iea-shc.org/Data/Sites/1/publications/PVT%20systems%20IEA%20SHC%2060%20-%20Annex%20180504.pdf (Accessed: 25 November 2019).

14. Ramschak, T. (2020) */ieashc-task60-2020-0001*. IEA SHC Task 60. doi: 10.18777/ieashc-task60-2020-0001.

15. *Welcome to the QGIS project!* (no date). Available at: https://qgis.org/en/site/ (Accessed: 29 July 2020).

16. Zhang, X. *et al.* (2012) 'Review of R&D progress and practical application of the solar photovoltaic/thermal (PV/T) technologies', *Renewable and Sustainable Energy Reviews*, 16(1), pp. 599–617. doi: 10.1016/j.rser.2011.08.026.

PHOTOVOLTAIC SELF-CONSUMPTION IN ELECTRIC VEHICLE CHARGING STATIONS

E. Alcover[*] , R. Pujol-Nadal[†*], J. L. Rosselló, M. Roca, V. Martínez-Moll[†*], B. Mas, V. Canals[†*]

University of Balearic Islands (UIB), Department of Physics, Palma of Majorca 07122, Spain

[†]:Energy Engineering Group (GREEn)

Summary

The present work addresses the energy and economic impact that the incorporation of photovoltaic self-consumption (PV) in its form of surpluses received under compensation, within the framework of RD244 / 2019, will entail in public car parks that provide electric vehicle (EV) charging services. Presenting the different methodologies developed and integrated into a tool in charge of: statistically planning the number of parking spaces required for a given level of EV penetration based on historical data on individualized parking billing, estimating the energy demand related to charging at one-minute intervals statistically simulating a representative EV mobile fleet, and estimating the generation of a grid-connected photovoltaic installation taking into account different generation limiting effects (shadows, fouling plates, effect of ambient temperature, inverter performance). Finally, the billing module is described for facilities with an access rate of 3.0A under the self-consumption modality with compensated surpluses. Specifically, two photovoltaic generation scenarios are analyzed by installing a different number of PV canopies equipped with double charging points in mode 3 in a car park located in the center of Palma de Mallorca, taking into account the evolution of the levels penetration rate for the next 5 years. The results show how with low EV penetrations, such as 2.35%, the increases in demand and energy billing are relevant, reaching 45.82% and 34.39% respectively. While the different PV self-consumption scenarios will lead to significant reductions in the energy term and in the amount of the energy bill, reaching 29.74% and 20.08% respectively.

Keywords: Photovoltaics; Self-consumption; Pluggable electric vehicle; Monte Carlo method; Artificial intelligence

1. Introduction

The transport sector represents 25% of world energy consumption, with oil and other liquid fuels being the main energy sources related to this sector, responsible for CO_2 and other greenhouse gas (GHG) emissions (EIA, 2016). In order to reduce the pollution generated by this sector, a lot of countries are looking toward a substitution of the internal combustion vehicles for more environmentally friendly alternatives (Amini et al., 2016), as the pluggable electric vehicle (PEV), that seems to be more respectful with the environment and presents lower operational costs (Tulpule et al., 2013). In this framework, it is essential that the public sector take the initiative in the deployment of a charging infrastructure for PEV, thus promoting the PEV adoption by consumers. In turn, the objective of reducing to zero the emissions in 2050 in the EU (EU, 2020) will accelerate the energy transition that will involve massive penetration of renewable sources, mainly of solar PV origin in urban areas. In this scenario, the PEV charging can help the power-grid to maintain the balance between supply and demand; which will allow a greater penetration of renewable energies (Fattori et al., 2014). This work analyzes the energy and economic benefit related to the incorporation of photovoltaic self-consumption in public parking lots to cope with the PEV load.

In the context of the ongoing energy transition that will lead to the massive penetration of renewable sources, mainly photovoltaic (PV) in urban areas related to self-consumption. Where PV generation is characterized by a non-dispatchable and time-varying power supply, while EV load demand is characterized by controllable loads and energy storage capacity, with which it makes sense to combine the load of the EV with PV generation (Nunes

doi:10.18086/eurosun.2020.05.05 Available at http://proceedings.ises.org

et al., 2015). In turn, the production of energy from PV origin could also allow a greater penetration of electric vehicles, as it does not lead to a significant increase in net demand if EVs are charged from PV. Although its integration must be carried out with great care so as not to compromise the stability of the electrical network (Poullikkas, 2015; Romo & Micheloud, 2015), related to the variability of PV generation (Nunes et al., 2016) and the increase in specific demand that the load of the EV

Also, EV car parks equipped with photovoltaic solar energy can be deployed on the surface in practically any place that has a basic electrical infrastructure, such as: shopping centers, train and bus stations, universities, public and private car parks... Being the typical infrastructure of the EV solar charging stations composed by a battery parking, covered by solar panels of about 12-15m^2, supported in the air by metal or wooden structures. Under this structure, there are located the different charging stations for electric vehicles. Its usual arrangement being that of groups of two rows of parallel parking spaces separated by a circulation road in between (Amini et al., 2017)

The present work analyzes the energy and economic benefit that the incorporation of photovoltaic generation in self-consumption modality with ex-surplus beneficiaries receiving compensation (Ecológica, 2019), included in RD244 / 2019 recently approved in Spain, on the demand for EV charging located in public car parks. For this, a numerical tool has been developed to plan the needs of new charging infrastructures and the energy impact that these will entail on the base demand of the different public car parks. To this tool, separate estimation modules for photovoltaic generation and estimation of energy billing in self-consumption mode with surpluses received for compensation have been incorporated for this work.

2. Evolution of EV penetration

In order to have a forecast of the EV energy demand, it is essential to have a forecast of the evolution of the incorporation of the electric vehicle in the mobile fleet, with a horizon of at least 5 years to establish priorities and horizons in the development of EV charging infrastructures and their associated energy impact. For this, it has been chosen to predict the evolution of the penetration of the electric vehicle in the mobile park of the Balearic Islands from historical data on annual car registrations / sales nationwide. The EV penetration has been forecasted for the next 5 years (2019-2023) from the historical series of monthly electric vehicle sales and through a Box-Jenkins statistical model of the AutoRegressive Integrated Moving Average (ARIMA) family, implemented on MATLAB®, specifically for forecasting time series based on past observations of the own series and previous forecasting errors. The model, expressed as ARIMA (p, d, q), is defined by the parameters p, d, q, where p determines the auto regressive non-stationary coefficient (AR) order, d determines the non-stationary integrative term (I) order and q defines the moving average term (MA) order. Mathematically, the model is expressed as:

$$Y_t = \left(\Phi_0 + \sum_{i=1}^{p} \Phi_i \Delta^d Y_{t-1}\right) + \left(Y_t - \Delta^d Y_t\right) + \left(\epsilon_t - \sum_{i=1}^{q} \theta_i \epsilon_{t-1}\right) \quad \text{(eq. 1)}$$

Where "d" corresponds to the number of differences or derivatives to make to convert the input time series into stationary, the terms $\phi_1,\ldots,\phi_p$ are the coefficients of the autoregressive part of the model, the terms $\theta_1,\ldots,\theta_p$ are the coefficients of the moving averages part of the model, ϕ_o is a constant, ε_t is the error term, and $\Delta Y_t = Y_t\text{-}Y_{t-1}$ represents the remainder between the output value of the time series at time t and the previous instant t-1.

Specifically, the model implemented is a Seasonal AutoRegressive Integrated Moving Average (SARIMA), because of its capability of incorporating the effect of the seasonality of the EV sales throughout the year in the model. Once the time series has been analyzed and its basic components identified, a model has been implemented with $\phi_o = 0$, a number of differences d=1 in order to convert the time series into stationary, a term of the non-seasonal moving average of order q=1, and finally a seasonal term of period 12 (months) and unit order of the Seasonal Moving Average SMA = 1, period that corresponds to one year. The results of the forecast of the monthly sales of EV + PHEV have been integrated annually in order to estimate the annual sales for the next 5 years, which are presented in **Table 1**.

The evolution of the electric mobility in the Balearic Islands follows the same characteristics that the mean of Spain, then the main source of historical data used in this work is the national sales of electric vehicles that can be extrapolated to the local behavior. Three main data sources has been used, the first one is the monthly time series of EV and PHEV registrations, at national level, for the period from 01/01/2014 to 31/12/2019, obtained from Instituto de Estudio de Automoción (IDEAUTO) (*Instituto de Estudio de Automoción (IDEAUTO)*, n.d.); the second one is the historical data of EVs monthly sales at national level and the historical data of the passenger car fleet at the Balearic Islands, obtained from the *Direccion General de Trafico* (DGT) (Dirección General de Trafico (DGT), 2019) and the third one is EV sales time series at national level for the period from 01/01/2014 to 31/12/2019, provided by the Spanish Association of Automobile Manufacturers and Trucks (ANFAC) (ANFAC, 2020).

Table 1. Forecasted EV penetration for the period (2019-2023) at the Balearic Islands

YEAR	EV in circulation at the Balearic Islands	Penetration of the EV in the passenger car fleet
2019	1.817	0.28%
2020	3.117	0.47%
2021	5.331	0.81%
2022	9.100	1.38%
2023	15.516	2.35%

In order to have a reliable model, we need to know which are the main models that conform the Balearic Islads fleet. For that, the models of the fleet are going to be approximated as the 11 more sold vehicles in Spain, 6 pure electric vehicles and 5 plug-in hybrid vehicles, obtained from the IDEAUTO database, and with the penetration percentage stablished according to the actual national electric vehicle fleet. In such way, the percentage between BEV and PHEV would be 62.83% and 38.17% respectively, conforming a fleet with almost the same distribution than the real one (62.19% and 37.81%).

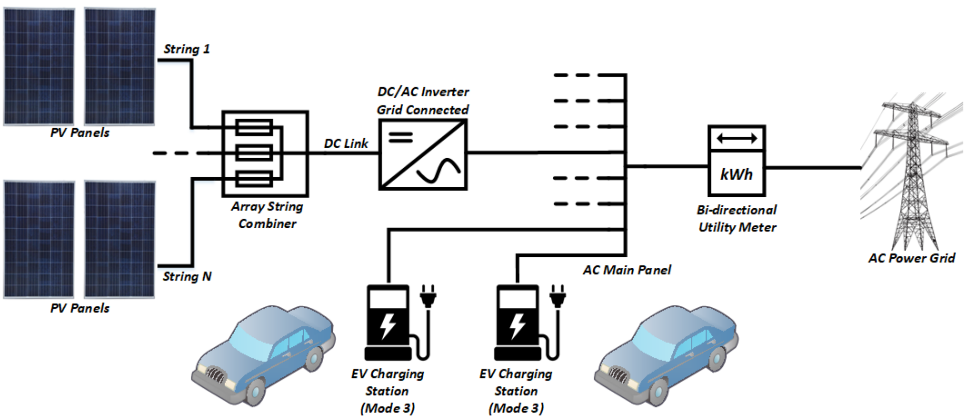

Fig 1. Grid-connected PV generation system architecture to support EV charging.

3. Methodology

The methodology in charge of planning the charging infrastructures and estimating their energy demand presented in this work has focused on analyzing the demand for normal / slow and semi-fast AC load in mode 3 of EVs in a load power range of [2.3-22kW] in car parks. publics in rotation regime, for a relatively low range of EV penetration levels [0-2.35%]. It is supported by 8 sub-modules that implement specific parts of the developed methodology and it implements a Montecarlo algorithm at its core, which will perform a minute-by-minute simulation of parking for a time series of 10 repetitions of the reference year (2017).

3.1. Analysis and Modelling of Parking Occupancy

The first module, the analysis and modeling of parking occupancy module, is in charge of adjusting the statistical distribution of the parking periods and the diagram of average occupancy for the parking, for two annual periods (high and low season), from the historical billing information of the studied parking. In order to know the distribution of the parking periods, the histogram of the parking durations for intervals of 10 minutes in a range of [0, 2000] minutes is constructed, thus eliminating atypical parking periods. Whose shape perfectly follows a continuous distribution like Weibull's We(x, λ, k).

$$f(x;\lambda,k) = \begin{cases} \frac{k}{\lambda}\left(\frac{x}{\lambda}\right)^{k-1} e^{-\left(\frac{x}{\lambda}\right)^{k}} & x \geq 0 \\ 0 & x < 0 \end{cases} \quad \text{(eq. 2)}$$

The two parameters that determine the shape of the Weibull distribution are the form parameter (k) and the scaling parameter of the distribution (λ), and are determined by applying a least squares method to the obtained histogram of the input data. After determining the parking periods distribution, the modulus obtains the hourly mean occupancy from the mean number of vehicles that start and end their parking each hour in a determined period.

3.2. Load Demand Curves Generator

The load demand curve generator module is in charge of generating the charging curves of the batteries of the vehicles of the local EV fleet. Specifically, the methodology developed aims to emulate the demand associated with battery charging, using a two-stage function. A first section at constant nominal power and a second one at variable power that will decrease exponentially. The characteristics of the local EV fleet is loaded from an external file that details, for each of the 11 (5 pure electric and 6 plug-in hybrids) EV conforming the fleet, the main characteristics: the absolute percentage of penetration of the model in the fleet, the useful energy of the battery, the charging time and the nominal charging power of the vehicle, in addition to other parameters.

3.3. EV Occupancy Generator

The third module determines the occupancy of the EV from the penetration value of the EV in the mobile park and from the data on the average hourly occupancy of the car park, which will provide the average number of entrances / parking lots of vehicles for all time intervals of the evaluation period. First it generates uniformly distributed random number U(0,1) that determines if the entering vehicle is electric or not, then, for each EV entering in the parking, three new random numbers will be generated. The first one U(1,60) determines the entering minute, the second, that follows a Weibull distribution, will randomly set the duration of the parking characteristic of the parking; and the third one, U(0,1) will determine the EV model that has accessed the parking.

3.4. Photovoltaic Generation

The photovoltaic generation module will calculate the energy generated by the PV installation from the meteorological data provided by the *Agencia Estatal de Meteorología* (*AEMET*, n.d.), specifically, the hourly data for global horizontal solar irradiance (DGI), diffuse horizontal solar irradiance (DHI), normal direct irradiance (DNI) and ambient temperature. From the solar position, calculated using the algorithm of the Solar Platform of Almería (PSA) (Blanco-Muriel et al., 2001), and the hourly means of irradiance applying geometric methods, the diffuse irradiance (IDif), the direct irradiance (ID) and the global irradiance that will get to a given photovoltaic panel can be determined. Finally, in order to determine the electrical power P_{AC} delivered by the inverter to the grid, the NRW PVWatts model (Dobos, 2014) was chosen, which proposes for the estimation of the inverter performance an empirical function scaled according to the nominal efficiency of the PV inverter.

3.5. Hourly Base Demand Generator

In order to know the total energy demand of the parking it is necessary to know the parking base demand and the real EV demand. The first, the power demand of the public parking lot is usually related to the lightning and ventilation systems. In this case, as the parking is located on the surface, there is no ventilation and the base demand will be lower than in other public parking lots. The methodology used to evaluate the hourly mean base demand is based on the historical invoices of the parking. This task is performed loading an external file (.csv) with the billing of the last years, that contains all the information of the historical invoices for an access toll 3.0A (P_{Cont}≥15kW @400V_{AC}).

3.6. Real Occupation and Energy Demand Generator

The real occupation and energy demand generator sub-modulus determines the energy demand of the EV charging points from the minute by minute occupation previously generated, taken into account the limitation of vehicles that can be charging at the same time.

3.7. Demand Integrator

It is responsible for integrating the energy demand of energy companies in four-hour periods and hours, for subsequent analysis and evaluation of electricity billing. Where the quarter hourly is needed in order to determine the contribution of the maximeter to the power term[kW], while the hourly demand will be used for determining the contribution to the energy term[kWh]; both related to the energetic billing.

3.8. Energy Billing

Finally, the last module is in charge of calculating the monthly energy bill (Ministerio de Industria Energía y Turismo, 2014) for a 3.0A access toll, a typical typology for public parking lots. It is a billing system that always uses hourly discrimination in three periods: P1 (Peak), P2 (Plan) and P3 (Valley); and each period corresponds to a daily time slot where the cost of energy and contracted power is different. The rates integrated in the tool are presented in **Table 2**, which also include the equipment rental term (€ 414.72 / year), the electricity tax (5.11%) and VAT (21%)

Table 2. Access toll 3.0A

Rate / Power Range	[€] Power Term P1	[€] Power Term P2	[€] Power Term P3	[€] Power Term P1	[€] Power Term P2	[€] Power Term P3
Fare 1 / 15 a 30 kW	41,95	25,17	16,78	0,1272	0,1141	0,0853

4. Results

The proposed methodology has been applied to a public parking lot located in the center of Palma de Mallorca, facing northwest; where their 83 parking spaces are operated in a rotation regime from Monday to Saturday with a schedule from 7 a.m. to 10 p.m. In turn, the car park has a 15kW contract for the three billing periods, and an annual energy consumption of about 8,000 kWh.

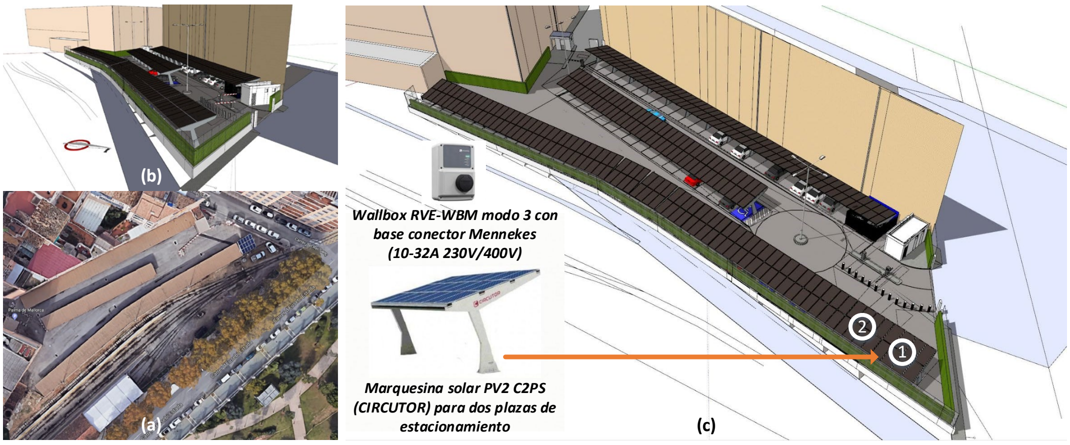

Fig 2. a: Parking location. b: Orientation of the car park. c: Description and location of the solar canopies.

4.1. Planning the Load Infrastructure

Before performing any energetic or economical analysis it is necessary to plan the needed infrastructures for the studied parking. For that, the number of recharging points and number of EV parking lots needed for covering the P_{99} and $P_{99.6}$ percentiles of EV parking attempts which will be given with the EV penetration levels for the next 5 years. A scan be shown in **Fig 3**, either for the percentile P_{99} and the $P_{99.6}$ two parking spaces for EV recharge will be required.

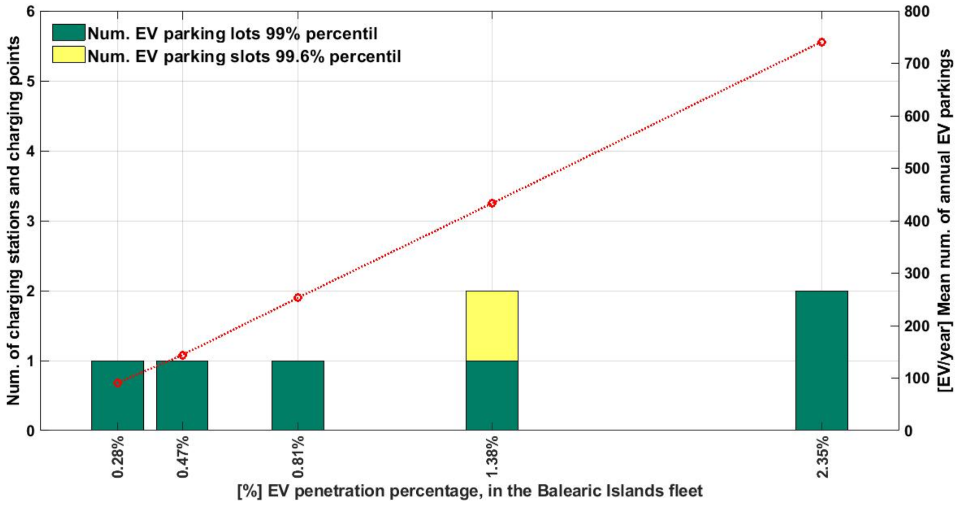

Fig 3. Planning of EV charging stations and spaces requirements

In turn, the two scenarios proposed for photovoltaic generation will consist of the installation of 1 or 2 PV2 canopies from the manufacturer Circutor, the specifications of which are presented in **Table 3**, as shown in Fig. 3c. Both scenarios meet the requirements for parking spaces and charging stations for the period analyzed.

Table 3. Parameters associated with the two PV self-consumption scenarios

Scenario	Num. Modules PV (270 Wp)	[kWp] Power PV	Num. Inversors x [kW] PNominal	Num. lots / Núm. Charging points mode 3
1: 1 x Canopy PV2-2	15	4,05	1 x 3,70	2 / 1
2: 2 x Canopy PV2-2	30	8,10	1 x 7	4 / 2

4.2. Energetic Analysis

Once determined the number of recharging points installed in the parking, the methodology proceeds to estimate the base energy demand of the car park combined with that associated with EV charging based on the penetration level established annually, in minute-by-minute intervals. Then, this energy demand is integrated into quarter-hour periods and schedules that will serve as reference energy demand, for subsequent analysis. The obtained results show that the total energy demand (P1 + P2 + P3) will increase in just 5 years by 45.82%. In turn, if we analyze the increase of energy demand for the three different billing periods, the current energy demand in period P1 (18-22h) will increase by [36-39%], that of period P2 (8-18h and 22-24h) by [79-82%], while that of period P3 (00-08h) will remain practically unchanged. The results on the period P3 is because the parking lot is closed from 10 p.m. to 7 a.m. Next, the methodology estimates the energy demand incorporating the two PV self-consumption scenarios for the different levels of EV penetration; thus, obtaining the combined energy demands by billing period (quarter-hours and hours), and their respective P_{99} percentiles and demand peaks.

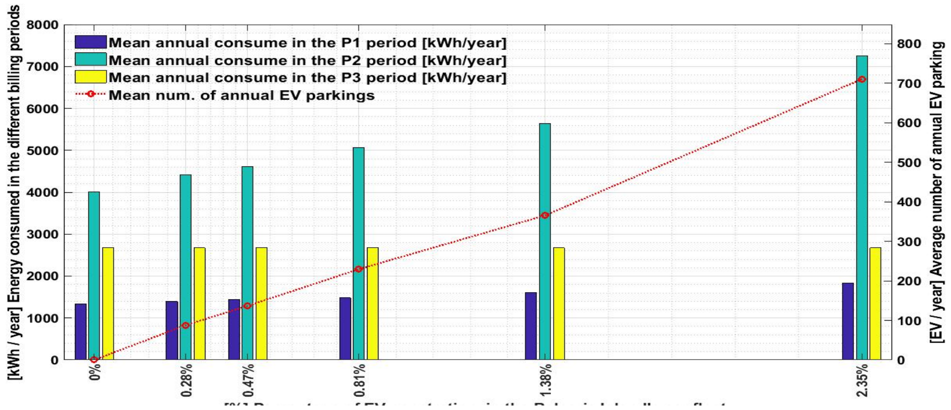

Fig 4. Impact of the penetration of electric vehicles on energy demand, for the different billing periods.

Next, the methodology estimates the energy demand incorporating the two PV self-consumption scenarios for the different levels of EV penetration; thus, obtaining the combined energy demands by billing period (quarter-hours and hours), and their respective P_{99} percentiles and demand peaks. In order to facilitate the interpretation of the results obtained, the demands for the different scenarios of EV penetration and PV self-consumption are presented in **Table 4** as a percentage with respect to the base demand of the reference year 2017 for this car park.

Table 4. Energy demand of the car park for the different PV self-consumption scenarios

Without PV/ VE penetration	(2017) 0%	(2019) 0,28%	(2020) 0,47%	(2021) 0,81%	(2022) 1,38%	(2023) 2,35%
Num. Parking lots / Charging stations	0/0	1/1	1/1	1/1	1/1	2/2
Annual Dem. P1 [kWh]	1.337	4,92%	7,95%	13,14%	20,64%	36,81%
Annual Dem. P2 [kWh]	4.011	9,42%	15,42%	26,44%	40,54%	79,34%
Annual Dem. P3 [kWh]	2.674	0%	0%	0%	0%	0,04%
Total Annual Dem [kWh]	8.022	5,53%	9,03%	15,41%	23,71%	45,82%
P99 Quarter-hourly Dem. [kWh]	0	1,69	4,60	6,20	7,52	9,88
Peak Quarter-hourly Dem. [kWh]	0	5,42	7,52	8,28	10,13	14,39
P99 Hourly Dem. [kWh]	0	2,85	4,20	4,99	6,39	8,28
[Scenario 1]: 1 x Canopy PV2-2 → (4,05 kWp)						
Annual Dem. P1 [kWh]	1.337	3,43%	6,65%	9,72%	19,44%	36,61%
Anual Dem. P2 [kWh]	4.011	-38,31%	-33,96%	-23,87%	-11,34%	24,59%
Anual Dem. P3 [kWh]	2.674	0,00%	0,00%	0,00%	0,00%	0,00%
Anual Dem. Total [kWh]	8.022	-18,67%	-15,96%	-10,40%	-2,52%	18,31%
P99 Quarter-hourly Dem. [kWh]	0	1,32	3,22	4,80	6,57	9,10
Peak Quarter-hourly Dem. [kWh]	0	4,86	5,98	7,52	9,44	13,67
P99 Hourly Dem. [kWh]	0	2,15	3,22	4,40	5,41	7,66
[Scenario 2]: 2 x Canopy PV2-2 → (8,10 kWp)						
Annual Dem. P1 [kWh]	1.337	3,60%	5,55%	10,26%	19,14%	39,05%
Anual Dem. P2 [kWh]	4.011	-43,50%	-39,65%	-31,91%	-21,83%	6,82%
Anual Dem. P3 [kWh]	2.674	0,00%	0,00%	0,00%	0,00%	0,00%
Anual Dem. Total [kWh]	8.022	-21,24%	-18,98%	-14,33%	-7,81%	9,83%

P99 Quarter-hourly Dem. [kWh]	0	0,92	2,38	4,60	6,19	8,28
Peak Quarter-hourly Dem. [kWh]	0	4,37	5,40	7,52	8,28	12,34
P99 Hourly Dem. [kWh]	0	1,44	2,70	4,03	4,88	7,32

The results presented clearly show how the incorporation of PV generation in a self-consumption regime has a beneficial effect, reducing the global energy demand. The first scenario (1x PV canopy (4.05 kWp)) analyzed shows a reduction in the average demand of 25.81% for PEV penetration levels in the range [0, 2.35%], while for second scenario (2xPV canopy (8.10 kWp)) this reduction reaches 29.74%.

4.3. Economic Analysis

From the information linked to the access tariff that the car park has contracted and the energy demands obtained in the previous section, the billing sub-module has been used to determine the annual amount of energy billing (adding the monthly billings from the car park). To facilitate the subsequent analysis of the energy costs evaluated for the different EV penetration levels and shown in **Table 5**, it has been chosen to present the energy amounts broken down in euros for the scenario without PV contribution; while the PV self-consumption scenarios are presented as a percentage with respect to the energy costs of the year 2017, taken as a reference.

Table 5. Energy billing associated with the energy demand of the car park for PV self-consumption scenarios

Without PV/ VE penetration	**(2017) 0%**	**(2019) 0,28%**	**(2020) 0,47%**	**(2021) 0,81%**	**(2022) 1,38%**	**(2023) 2,35%**
ΔEnergy Term [%]	855,99€	6,01%	9,16%	15,57%	25,59%	51,33%
ΔPower Term [%]	1.258,52€	4,65%	6,59%	9,08%	13,60%	33,66%
Invoice amount [€/year]	3.191,18	3.330,95	3.396,40	3.506,01	3.687,42	4.288,72
ΔAnnual invoice amount [%]	0	4,38%	6,43%	9,87%	15,55%	34,39%
[Scenario 1]: 1 x Canopy PV2-2 → (4,05 kWp)						
ΔEnergy Term [%]	855,99€	-30,16%	-27,21%	-21,27%	-11,79%	12,30%
ΔPower Term [%]	1.258,52€	3,11%	4,82%	7,09%	11,26%	29,99%
Invoice amount [€/year]	3.191,18	2.923,31	2.982,63	3.083,46	3.252,99	3.814,22
ΔInvoice amount [%]	0	-8,39%	-6,54%	-3,38%	1,94%	19,52%
Surplus Amount [€/year]	0	86,58	85,58	83,46	80,93	73,26
Amount of Energy given away [€/year]	0	0	0	0	0	0
[Scenario 2]: 2 x Canopy PV2-2 → (8,10 kWp)						
ΔEnergy Term [%]	855,99€	-50,19%	-47,18%	-41,16%	-33,58%	-13,25%
ΔPower Term [%]	1.258,52€	2,64%	3,08%	7,02%	10,39%	25,85%
Invoice amount [€/year]	3.191,18	2.716,22	2.755,70	2.883,65	3.019,29	3.486,08
ΔInvoice amount [%]	0	-14,88%	-13,65%	-9,64%	-5,39%	9,24%
Surplus Amount [€/year]	0	236,51	232,82	228,57	221,84	204,92
Amount of Energy given away [€/year]	0	0	0	0	0	0

It should be noted that savings are concentrated in the P2 period (08-18h). In turn, in the P1 period (18h-22h) the solar contribution can only slightly contain the increase in demand. Meanwhile, the economic analysis shows how small PEV penetration rates will lead to significant increases in the energy bill. A PEV penetration of 2.35% will lead to an increase of 34.39% of the energy bill. At the same time, the PV self-consumption of 4.05kWp reached the saving average of 13.25% of the energy bill for the different levels of PEV, while the PV self-consumption of 8.10kWp the savings grew to 20.08%.

The reduction in demand comes from self-consumption, that is, from the subtraction of instantaneous power demand with that generated for each instant of time While surpluses, generated energy that cannot be self-consumed instantly, cannot be discounted from the global energy demand for a specific billing period in accordance with RD244 / 2019, as if it happens with the net balance in other countries from the EU.

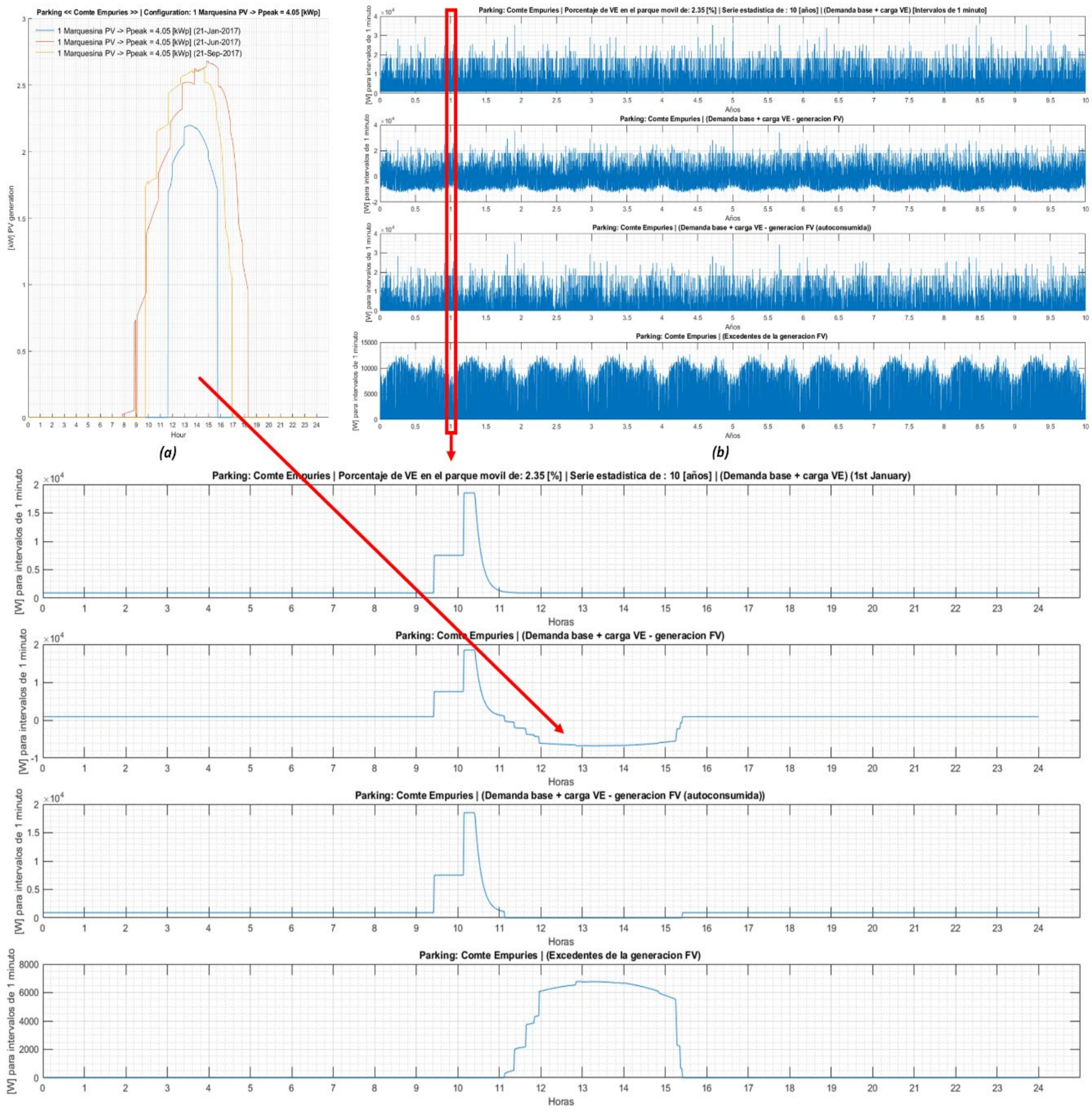

Fig. 3: a) Minute by minute generation of the 4,05 KWp PV installation, for different dates. b) Demands and generations minute by minute for a penetration of 2.35% of the EV, and scenario of self-consumption PV.

5. Conclusions

This work has presented a methodology to plan the PEV charging infrastructure and estimate its associated energy demand. The results show how PV self-consumption is an effective mechanism to mitigate the increase in the cost of the energy bill, essentially impacting the energy term, at least for the current PEV levels of penetration. Where the PV self-consumption of 4.05kWp has achieved an average demand reduction of 25.81% for the different levels of EV penetration, while the PV self-consumption of 8.10kWp has achieved an average demand reduction of 29, 74%. Concentrating most of the savings in the period from 8 am to 6 pm, where PV generation is concentrated. In turn, the results show that the most interesting self-consumption scenario, for a car park with a small base demand as is the case, is the one made up of only one PV canopy (4.05kWp). This is due to the fact that the self-consumption modality with surpluses under compensation, included in RD244 / 2019, is focused on direct self-consumption, penalizing generation surpluses through an asymmetric compensation of generation against demand.

6. Acknowledgements

This work was supported in part by the Spanish Ministry of Economic Affairs and Digital Transformation (MINECO) and the EU with Regional European Development Founds under Grant TEC2017-84877-R.

7. References

AEMET. (n.d.). www.aemet.es

Amini, M. H., Boroojeni, K. G., Jian Wang, C., Nejadpak, A., Iyengar, S. S., & Karabasoglu, O. (2016). Effect of electric vehicle parking lots' charging demand as dispatchable loads on power systems loss. *IEEE International Conference on Electro Information Technology*, *2016-August*, 499–503. https://doi.org/10.1109/EIT.2016.7535291

Amini, M. H., Moghaddam, M. P., & Karabasoglu, O. (2017). Simultaneous allocation of electric vehicles' parking lots and distributed renewable resources in smart power distribution networks. *Sustainable Cities and Society*, *28*, 332–342. https://doi.org/10.1016/j.scs.2016.10.006

ANFAC. (2020). *Informe anual ANFAC 2019*.

Blanco-Muriel, M., Alarcón-Padilla, D. C., López-Moratalla, T., & Lara-Coira, M. (2001). Computing the solar vector. *Solar Energy*, *70*(5), 431–441. https://doi.org/10.1016/S0038-092X(00)00156-0

Dirección General de Trafico (DGT). (2019). *Parque de vehículos - Tablas Auxiliares Anuario - 2019*.

Dobos, A. (2014). *PVWatts Version 5 Manual*. https://doi.org/10.2172/1158421

Ecológica, M. para la T. (2019). Real Decreto 244/2019. *Boe*, *90*, 68–71. https://www.boe.es/buscar/pdf/2019/BOE-A-2019-5089-consolidado.pdf

EIA. (2016). International Energy Outlook 2016. *Office of Integrated and International Energy Analysis*, *1*(May), 1–244. https://doi.org/DOE/EIA-0383(2013)

EU. (2020). A European Green Deal. *European Commission - European Commission*, *December 2019*. https://ec.europa.eu/info/strategy/priorities-2019-2024/european-green-deal_en

Fattori, F., Anglani, N., & Muliere, G. (2014). Combining photovoltaic energy with electric vehicles, smart charging and vehicle-to-grid. *Solar Energy*, *110*, 438–451. https://doi.org/10.1016/j.solener.2014.09.034

Instituto de Estudio de Automoción (IDEAUTO). (n.d.). https://www.ideauto.com/

Ministerio de Industria Energía y Turismo. (2014). *Resolución de 23 de mayo de 2014, de la Dirección General de Política Energética y Minas, por la que se establece el contenido mínimo y el modelo de factura de electricidad.* https://www.boe.es/buscar/pdf/2014/BOE-A-2014-5655-consolidado.pdf

Nunes, P., Farias, T., & Brito, M. C. (2015). Day charging electric vehicles with excess solar electricity for a sustainable energy system. *Energy*, *80*, 263–274. https://doi.org/10.1016/J.ENERGY.2014.11.069

Nunes, P., Figueiredo, R., & Brito, M. C. (2016). The use of parking lots to solar-charge electric vehicles.

Renewable and Sustainable Energy Reviews, *66*, 679–693. https://doi.org/10.1016/j.rser.2016.08.015

Poullikkas, A. (2015). Sustainable options for electric vehicle technologies. *Renewable and Sustainable Energy Reviews*, *41*, 1277–1287. https://doi.org/10.1016/j.rser.2014.09.016

Romo, R., & Micheloud, O. (2015). Power quality of actual grids with plug-in electric vehicles in presence of renewables and micro-grids. *Renewable and Sustainable Energy Reviews*, *46*, 189–200. https://doi.org/10.1016/j.rser.2015.02.014

Tulpule, P. J., Marano, V., Yurkovich, S., & Rizzoni, G. (2013). Economic and environmental impacts of a PV powered workplace parking garage charging station. *Applied Energy*, *108*, 323–332. https://doi.org/10.1016/J.APENERGY.2013.02.068

Performance Evaluation of a Hybrid PVT Solar Installation with Phase Change Material

Dr. Raquel Simón-Allué[1], Dr. Adriana Coca-Ortegón[1], Raúl Villén[1], Dr. Isabel Guedea[1]

[1] EndeF Engineering SL, Zaragoza (Spain)

Abstract

This paper evaluates the energy performance of an innovative solar installation composed of photovoltaic-thermal panels (PVT), half of which contain a layer of phase change material (PCM) within the panel. The main objective for the PCM inclusion is to provide an extra cooling effect to the PV laminate, as well as to take advantage of the excess heat produced during the hours of maximum sunshine and reallocate it at the end of the day. The solar circuit is completed with a stratified storage tank specially developed to work with multi-energy source while maximizing heat exploitation at low temperatures. The installation is located in the south of Spain and was designed in the frame of the European LowUP project (http://lowup-h2020.eu/) to provide electricity and heat to an office building. This work presents the analysis of the solar field during several months of operation.

Keywords: Solar energy, Photovoltaic-thermal (PVT), Phase change material, Field measurements

1. Introduction

Despite the effort of scientist, engineers, authorities and involved entities to improve the integration and efficiency of renewable systems, their contribution to final energy consumption remains low. According to statistics, only the 29.9% of the EU-28's total production of primary energy is from renewable energy sources (Eurostat, 2019) and it has fallen to 19.3% when the global world production is analyzed (REN21, 2017). If we focus on sectors, renewable energy met less than 14% in buildings and 14.5% of total energy demand industrial uses (REN21, 2020). In buildings in particular, more than three-quarters of the global final energy demand was for heating and cooling end uses, which remain largely fossil-fuel based. If we take into account the last restrictions (European Commission, 2019), an integrated approach for advancing both renewables and energy efficiency remains crucial.

In this frame, solar energy has a key role to play, as one of the most promising alternatives due to the abundant, inexhaustible and clean nature of the sun (Parida et al., 2011). As indicated in the last Global Status Report (REN21, 2020), solar energy was, together with wind, the renewable energy with the greatest projection in the energy market due to the decrease kWh cost. In the case of solar photovoltaics (PV), the market increased in a 12% in 2019, reaching to record figures, and experienced strong growth in the share of rooftop PV systems. However, solar energy still have some limitations, mainly related to low cell efficiencies, real economic profitability or government policies (Kabir et al., 2018; Karakaya and Sriwannawit, 2015). Further efforts are needed to achieve a better exploitation of solar energy and enable us its use it in new applications.

One way to improve the solar performance is to combine thermal and photovoltaic technologies on the same module, known as PVT panels (Besheer et al., 2016; Chow et al., 2012). The PVT collectors can generate both electricity and low-grade thermal energy during the daytime and have been widely studied during last decade (Aste et al., 2015; Buonomano et al., 2016; Jonas et al., 2019). Their relevance was pointed out by the International Energy Agency through the Task 60 of the Solar Heating & Cooling Programme (IEA-SCH, 2020), dedicated to PVT Systems and applications.

Due the mismatch between solar resource and heating demand, other relevant component in the solar systems is the energy storage technology. In the case of solar thermal installations, the most common options are Sensible Thermal Energy Storage Technologies (TES), using water storage tanks (Dincer and Rosen, 2011; Fertahi et al., 2018). Among the options used to improve the performance of this technology are the development of super-insulations, and the design of stratifier elements in order to reduce the mixing of fluids with different temperature levels (Andersen et al., 2007; Fertahi et al., 2018; Göppert et al., 2009; IEA, 2014).

An additional improvement is presented here through the addition of phase change material (PCM) within the PVT module. As widely known, phase change material (PCM) first absorbs sensible heat and when it reaches to

doi:10.18086/eurosun.2020.05.06 Available at http://proceedings.ises.org

its melting temperature, it absorbs latent heat. When the temperature goes down, it recovers the initial state while releases the heat stored. In the case of PVT solar collectors, it presents the twofold benefit of absorbing the excessive heat and reducing the PV working temperature.

Numerous works have focused on the benefits of PCM and solar combination from experimental (Islam et al., 2016; Mahamudul et al., 2016) to numerical point of view (Huang et al., 2007; Sarwar et al., 2011), mostly applied to separated thermal or PV panels. However, its integration on PVT collectors is scarcer, and just a few focus on the experimental behavior of PVT with PCM directly inserted (Browne et al., 2015; Preet et al., 2017; Yang et al., 2018), all of them related lab-testing experiments on traditional PVT collectors. To the author´s knowledge, there is a lack of studies about real installations working with PVT-PCM, which is exactly the goal of this work.

With a view to expanding this scope, this work presents the solar on-site performance of a demonstration plant which incorporates a novel PVT-PCM panel and a stratified storage tank with specific flow management to work with multi-energy source. The PVT-PCM collector was particularly developed for this purpose and placed next to the same model without PCM to evaluate the improvement derived from the PCM insertion. This installation works under real environmental conditions to provide electricity and cover heating needs from an office building.

2. Description of the installation

This installation takes part of one of the four demonstration plants developed within the framework of the LowUP project (“LowUP,” 2020), with the aim of developing low temperature heat supply systems (30-35ºC) generated by renewable energy sources and use of wastewater. This particular solar installation is located in Seville, south of Spain, with the main objective of providing electricity and heat for heating (low temperature radiant floor) to an office building.

Solar field is composed by 40 photovoltaic-thermal (PVT) panels distributed in eight benches of five panels, and separated in two parallel lines (see Fig. 1): one with 20 plain PVT panels (Line w/o PCM) and second with 20 PVT panels with a layer of phase-change material (PCM) inserted (Line w/ PCM). Panels are hydraulically connected in parallel via Tichelmann loop. All panels are installed facing south (0º) with a tilt of 45º, to intensify the energy production in winter.

Fig. 1: Physical arrangement of the solar field (left) and stratified storage tank (right).

The entire plant is originally designed to operate with several low temperature sources (LTS: solar field, sewage water) and low temperature loads (LTL: radiant floor, dry cooler). However, to better analyze the contribution of the solar components, only one source (solar field) and one load (radiant floor) have been studied.

2.1. PVT collectors and PCM

The internal configuration of PVT panels was developed in the first age of the project, where their design was selected from several options. Due to the extreme climate of Seville and the low temperature needed for the supply, all PVT panels are unglazed. They incorporate a 60-cell 275W polycrystalline PV module (A_G=1.65 m^2, A_{PV}=1.56 m^2), together with an aluminum absorber through which the exchange fluid flows. In the case of the PVT-PCM line, panels incorporate a layer of PCM in direct contact with the heat absorber to remove the surplus heat. All panels are closed with a 25-mm layer of insulation and a metal rear sheet.

The initial objective of the inclusion of PCM was to control the excess of heat generated in the PVT, limit the maximum temperature of the PV and store the heat generated with a temperature higher than the required for the thermal load (40ºC). Thus, the melting range selected for this application was 48ºC, greater than other PCMs found in literature for solar applications (Atkin and Farid, 2015; Hasan et al., 2010; Ma et al., 2015).

The PCM used for this application was inorganic, a salt hydrate type C48 from ClimSEL™ line (Fig. 2, melting temperature point: 48°C, melting latent heat:180 kJ/kg and density: 1300 kg/m3) (ClimSel C48, 2017). In order to prevent hybrid collector units from possible PCM leaks during the liquid state, PCM was added to the panel in individual packages covered by an external aluminium foil enclosure. Each pouch contained 0.5 kg of PCM and had a dimension of 125x300x10 mm. A total of 32 PCM packages (16 kg) were located inside each PVT panel, between the heat absorber and the insulation, forming a grid of 4x8 PCM elements. The result was a 10 mm PCM layer covering more than 80% of the absorber surface, where the heat is transferred by conduction, from the heat fluid to the PCM or vice versa.

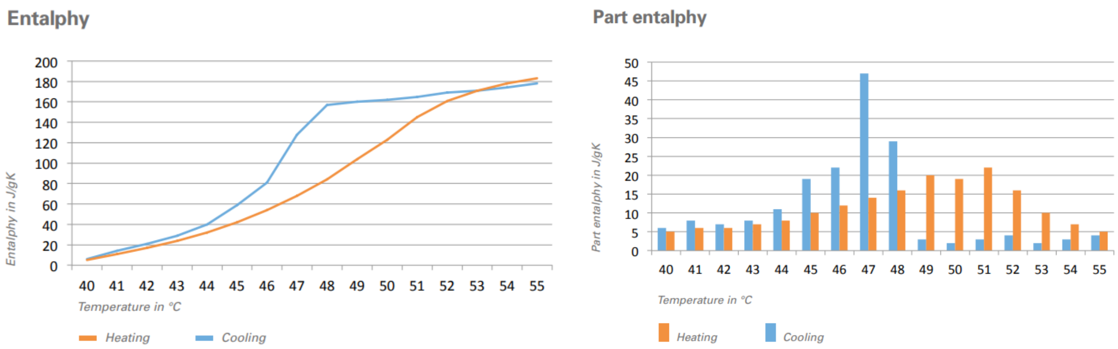

Fig. 2: Enthalpy and partial enthalpy absorbed and released by the PCM according to datasheet (ClimSel C48, 2017). Performance during melting (orange) and during crystallization (blue).

A redesign of the PVT assembly was also carried out to minimize the panel size, reduce labor time and facilitate the installation process. Further information about the manufacturing process and experimental testing of the PVT panels can be found in Simón-Allué et al. 2019.

2.1. Stratified storage tank

Due to the characteristics of the installation, with several low temperature sources (LTS) and low temperature loads (LTL), a particular thermal water storage tank was developed within the framework of the project, with a total volume of 6630l. The tank includes different stratifying elements, which contribute to not mixing fluids at different temperatures, thus improving the energy and exergetic efficiency of the installation. These stratifying elements are the following: a stratification column for a low temperature heat source (LTS), in this case, solar energy (Fig. 3 (a)); a second stratification column; which receives the return of a low temperature thermal load (LTL), in this case, the radiant floor from the office building (Fig. 3 (b)); and finally, two horizontal diffusers, designed to distribute the heat coming from a second low-temperature heat source, in this case a heat pump (Fig. 3 (c)).

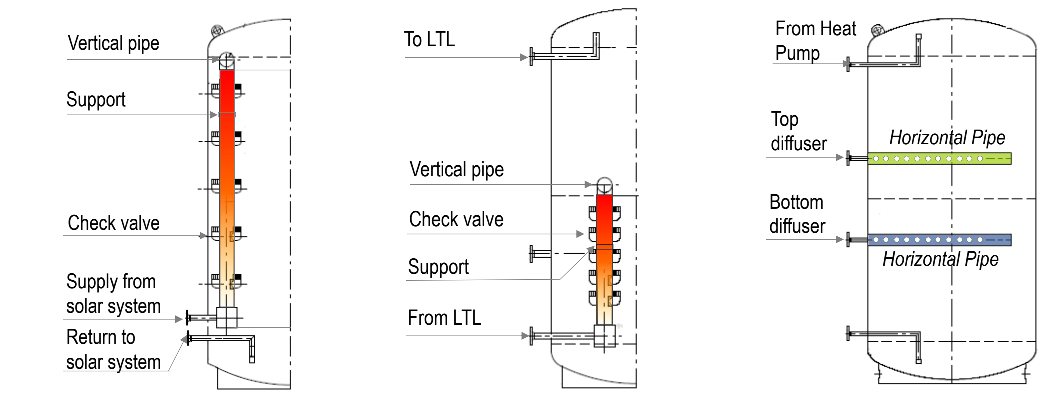

(a) Stratifying column for Low Temperature Source (LTS) *(b) Stratifying column for Low Temperature Load (LTL)* *(c) Horizontal diffusers*

Fig. 3: Stratified elements inside of thermal water tank.

The stratification columns consist of a collector tube, placed in a vertical position inside the thermal storage tank, with a set of check valves installed along the column. These valves cause a low-pressure drop in the system and regulate their state (open/close) with regard to the pressure difference between inside and outside of the collector, thus allowing the fluid to be introduced the tank according to the temperature level.

In order to monitor the tank-stratification, a total of 12 temperature sensors, type PT100, were installed inside the tank, distributed vertically.

2.2. Other components

Electrical circuit accounts on a three-phase 10 kW solar inverter, from the SMA Sunny Tripower line. Besides, the hydraulic circuit is completed with a heat sink (Inditer ATS-391 32 kW) to evacuate heat in case of necessity, two expansion vessels (20L each) to absorb expansion of the fluid and a circulating pump (Wilo Stratus DN 40 1/16).

Solar field is equipped with a complete list of sensors to favor monitoring of the energy generation, including temperature sensors, pressure valves, flow meters and electrical gauge. A weather station is also included with a pyranometer and anemometer to measure solar radiation and air velocity on field.

Additional temperature sensors are included in the inlet and outlet of each bench and inside panels with and without PCM, to better assess the PCM performance during operation. In the case of panels without PCM, three temperature probes are located between the heat absorber and the rear insulation, at the bottom (next to the inlet), middle and top (next to the outlet) of the panel. In the case of panels with PCM, three probes are located between the heat absorber and PCM packages at the bottom (next to the inlet), middle and top (next to the outlet) of the panel, and two more between PCM packages and back insulation at the bottom (next to the inlet) and top (next to the outlet) of the panel.

3. Testing conditions

The installation has been running during the summer months of Spain, corresponding to May to August. For this study, two working modes have been analysed, with and without heating loads. In both working modes, solar field operates by transferring heat to the stratified storage tank.

- Mode #1: solar field + stratified tank, operating with heating loads

In this mode two cases are analysed: when the heating load (HL) is produced during the daylight, matching the solar generation, and when the HL is produced at the end of the day, displaced from the solar generation.

- Mode #2: solar field + stratified tank, operating without heating loads

In this mode three cases are analysed, depending on the temperature storage tank at the beginning of the day. Since there is no thermal load applied to the storage tank, the starting temperature of the water storage directly modifies the operation of the solar field. Thus, three cases are studied considering cold tank (T_m ~25ºC), warm tank (T_m ~42ºC) and hot tank (T_m ~52ºC),

The control of the installation is performed based on the fluid temperature in the outlet of the solar field. Since the plant is designed to provide heat for heating purposes, specifically a low temperature radiant floor which operates below 40ºC, the solar field is regulated to provide an outlet fluid temperature of 45ºC. When the solar circuit is under this value, the pump reduces the rate flow in steps up to reach the minimum flow (25% of the nominal flow) in order to increase the outlet temperature of the panels. When the solar circuit is above this temperature, the pump increases the rate flow up to reach the nominal flow. The nominal flow value considered in the solar circuit is 40 l/(h·m2), which makes a total of 1.250 l/h per line (with and without PCM).

All tests have been performed on days with clear sky, under similar environmental conditions.

4. Performance indicators

To evaluate and compare the performance of each line (with and without PCM) when working in the two operating modes (with and without heating loads), we have calculated several performance indicators here described.

4.1. PVT collectors

Both thermal and electrical daily power production are quantified. However, in order to avoid deviations resulting from small variations of the solar irradiance, thermal and electrical efficiencies are used to compare results on different cases.

The thermal power (in Watts) generated by each line is calculated based on the fluid flow rate ($\dot{m}_{line}$) and the thermal gap of the fluid in its path through the 20 collectors of each line (eq. 1). Then, the instantaneous thermal efficiency is calculated considering the irradiation on the collector plane (in W/m2) and the total solar surface of the line ($A_{G,TOT} = A_G \cdot 20$ panels) (eq. 2).

$$\dot{Q}_{th} = \dot{m}_{line} \cdot c_f \cdot \Delta T \qquad \text{eq. 1}$$

$$\eta_{th} = \frac{\dot{Q}_{th}}{(A_{G,TOT} \cdot G)} \qquad \text{eq. 2}$$

Following same procedure, instantaneous electrical efficiency is calculated based on the instantaneous electrical output (P_e) and the total photovoltaic surface of the line ($A_{PV,TOT} = A_{PV} \cdot 20$ panels) (eq. 3).

$$\eta_{PV} = \frac{P_e}{(A_{PV,TOT} \cdot G)} \qquad \text{eq. 3}$$

Total PVT efficiency of each line is calculated through the direct addition of the thermal and electrical efficiencies, given by eq. 4, where ζ is the blanketing factor, corresponding to the quotient between the photovoltaic and the gross area of the PVT, $\zeta = A_{PV}/A_G$ (Huang et al., 2001; Yang et al., 2018). For these panels, ζ takes the value of 0,945.

$$\eta_{TOT,line} = \eta_{th,line} + \zeta \cdot \eta_{e,line} \qquad \text{eq. 4}$$

Total amount of thermal (Q) and electrical energy (E) generated during the day by each line are also calculated based on the power and the daily operation time for the thermal and electrical circuit, respectively. Then, daily efficiencies are calculated as indicated in eq. 5 and eq. 6, being I the total radiation incident on each line during the whole day.

$$\overline{\eta_{th}} = Q/I \qquad \text{eq. 5}$$

$$\overline{\eta_{PV}} = E/I \qquad \text{eq. 6}$$

4.2. Storage indicators

The potential of the PCM is directly related to the temperature reached inside the PVT collectors. In order to be able to compare both cases, two parameters are calculated.

First, the total amount of heat released by the PCM (Q_{PCM}) is calculated based on the difference between the thermal energy generated in the line with and without PCM, measured when the solar field is lowering temperature and starts working below 48ºC (Fig. 2, melting PCM point). This time period varies from each case.

The melting factor (estimation of the amount of PCM melted based on the energy released) is calculated as indicates in eq. 7, where LH is the latent heat of the PCM (180 kJ/kg) and QTY_{PCM} the amount of PCM inserted in the PCM line (320kg).

$$MF_{PCM} = \frac{Q_{PCM}}{(LH \cdot QTY_{PCM})} = \frac{(Q_{PCM\ line} - Q_{PVT\ line})_{blw\ 48^{o}C}}{(LH \cdot QTY_{PCM})} \qquad \text{eq. 7}$$

The tank-stratification is evaluated during the charging process, through the vertical temperature profile evolution, obtained from the 12 temperature sensors installed inside the tank. During this charging process, the maximum temperature difference inside the tank ($\Delta T_{ST,\ MAX}$) is calculated according to eq. 8.

$$\Delta T_{ST,MAX} = T_{top} - T_{bottom} \qquad \text{eq. 8}$$

Other complementary stratification indicators, based on variables such us, Moment of Energy (M), calculated for each layer inside of tank (Andersen, 2007, p. 1220), are outside the scope of this paper.

5. Results & discussion

Environmental conditions of the different testing days are gathered in Tab. 1. In order to focus on the most relevant time period, average values have been calculated from data registered from 11 to 6 pm, which matches the time slot with maximum solar radiation. In this table, average data corresponding to the solar irradiance on the collector plane (G_m), environmental temperature (Ta_m) and wind speed on collector plane (Wind SP_m) are presented.

Tab. 1: Average values (from 11 to 6 pm) of environmental conditions given on testing days.

Mode	Case	G_m (W/m2)	Ta_m (ºC)	Wind SP_m (m/s)
#1	HL 2 to 8 pm	698	29,3	0,82
	HL 7 pm to midnight	682	33,0	0,95
#2	Cold Tank	687	26,2	0,77
	Warm Tank	710	31,1	1,64
	Hot Tank	709	35,7	1,02

Mean values of solar irradiance seem to be slightly low considering the high solar radiation of the south of Spain. However, it should be remarked the G_m value is calculated on the collector plane, with in this case it has a tilt of 45º. This angle is 8º over the latitude of Seville (37º) and was selected to emphasize the power generation during winter, but that entails a lowering of the radiation received on the plane during the summer. With this in mind, G_m values are logical.

5.1. Mode #1: Solar field with heating load

Daily profile of power generation and instantaneous efficiencies when the installation is working with heating loads during the daylight are presented in Fig. 4. On the left vertical axis, this figure shows the thermal (continuous lines) and electrical power (double line) for lines with (dark purple) and without PCM (green) as well as the solar radiation incident over each 20-panels line. On the right vertical axis, the figure includes total efficiencies calculated as indicated in eq. 4. To complete the information, temperature daily profiles are also provided in Fig. 5, showing temperature data at the inlet and outlet of each line (left) and inside the storage tank (right).

Based on these figures, the inclusion of PCM inside the panels leads to an increase in the thermal and electrical power during the day. At the beginning of the day (up to 12pm), the thermal generation of the line with PCM remains slightly lower than the line without, due to the inertia provoked by the PCM consumes part of the heat generated by heating the PCM instead of the fluid. After midday, the solar field begins to provide heat to the storage tank and increases the gap between inlet/outlet temperatures of solar collectors. At 2 pm, the heating load starts to remove heat from the lower layers of the storage tank. Since the thermal loads are not much higher than the solar generation, the higher layers of the tank continue to accumulate solar heat, favoring stratification. The maximum gap found in the storage tank during the charging process rises up to 13ºC. In the solar circuit, the fluid reaches temperatures of 50ºC in the outlet of the collector, which allows us to assume that the layer of PCM in contact with the heat absorber has started to melt.

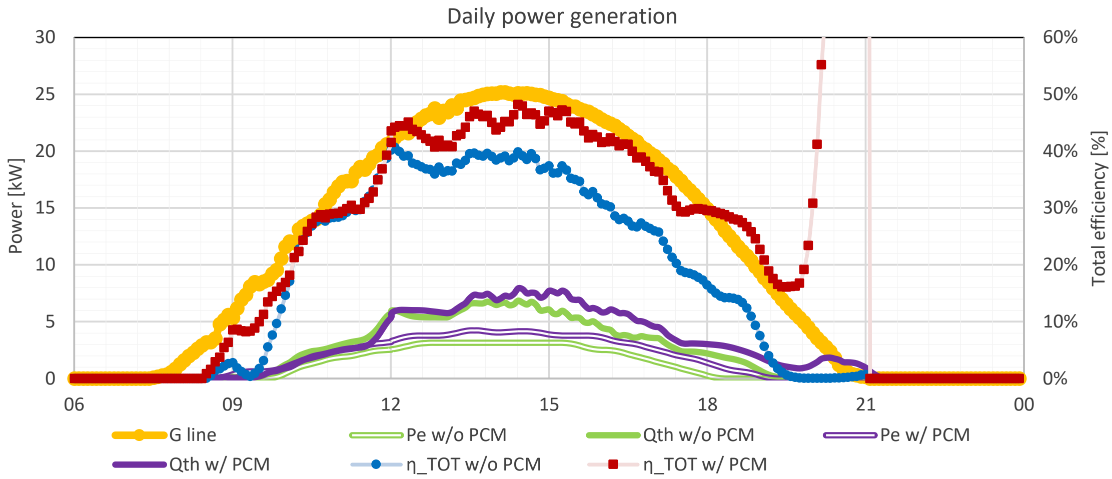

Fig. 4: Power generation and total efficiency daily profile in Mode #1, heating load from 2pm to 8 pm.

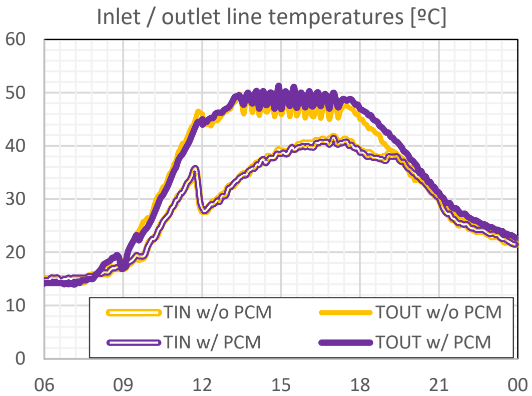

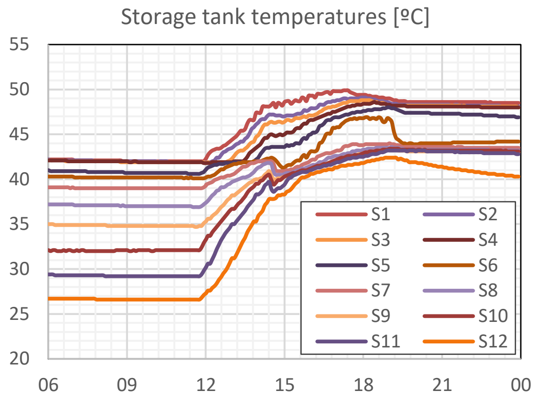

Fig. 5: Temperature daily profile in the inlet/outlet lines (left) and storage stratification (right) in Mode #1, heating load from 2pm to 8 pm.

Instant efficiencies reflect the pattern followed by the thermal and electrical power generation, showing a higher value for the line with PCM than the line without. At the end of the day, it is noticeable a peak on the efficiency of the PCM line, due to the late thermal energy produced in this line at the end of the day. This thermal power is not resulting from the sun radiation, but from the heat stored in the PCM, so it has no sense to relate it directly to the solar radiation. These efficiency values are not considered in the study.

Contrary to expectations, the use of PCM does not lead to a reduction of the operating fluid temperature, which keep quite similar in both lines (Fig. 5, left). However, higher electrical efficiencies are found in the PCM line versus the plain PVT line, which indicates a significant difference on the cell temperature (around 0.5% each ºC, according to literature). At this point, it should be remarked that the operating temperature is measured based on the fluid temperatures, but not the PV cell temperatures, which are substantially lower.

Our assumption is that the inclusion of PCM favors the heat transmission from the PV laminate to the heat absorber and the PCM layer, making the PV cell work in a lower temperature and transferring more heat to the fluid. This better transmission (made by conduction) may be the result of adding one more metallic layer to which the heat passes, or that the assembly of the components within the PVT with PCM has been carried out with higher pressure in the manufacturing phase (to include an extra layer of 10mm into the same space) that maximizes the contact. The consequence of this better heat transmission would be the reduction of the PV temperature but the increase on the PCM layer, which would result in a similar operating temperature of the fluid. This assumption may explain the increase on the instantaneous thermal and electrical efficiencies for the line with PCM.

When similar heating load is scheduled during the evening, the system works as there was no heating load during daylight, and heat generated in the solar field is only stored in the tank. In this case, the stratification capacity of the tank keeps very limited due to the continuous charging process and the maximum temperature gap between top and bottom layers round 5ºC (see Fig. 6, right).

Since the system is not able to evacuate heat up to 7pm, both the tank and the solar circuit work in a higher operating temperature (Fig. 6, left), which provokes a greater amount of PCM melted. The PCM releases the energy stored when the solar circuit starts lowering temperature at the end of the day, coinciding in time with the activation of the heating load, which makes it possible to make use of the heat generated. As a result, the thermal improvement provoked by this case is higher than others.

The addition of PCM causes an improvement of around 4% in the PV performance and between 2 to 9% in the thermal performance, for cases with daily or evening heating load.

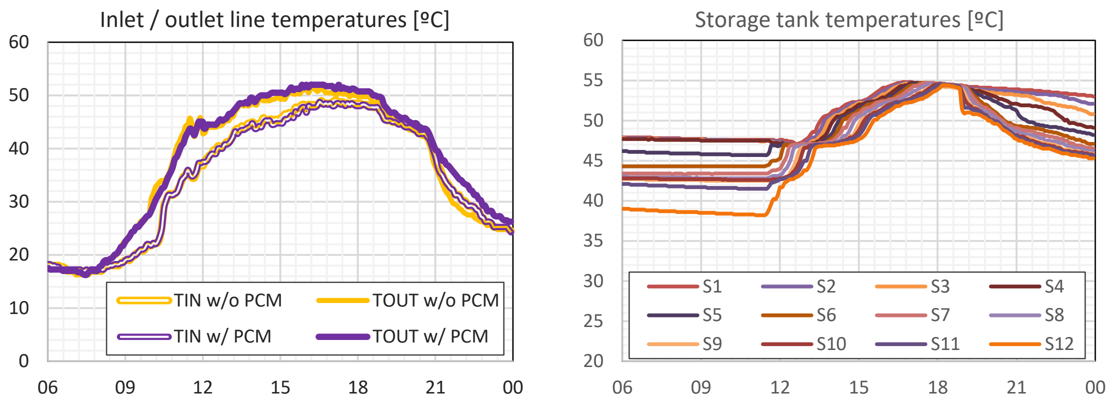

Fig. 6: Temperature daily profile in the inlet/outlet lines (left) and storage stratification (right) in Mode #1, heating loads from 7 pm to midnight.

Tab. 2: Main performance values for Mode #1, when the heating load is produced during the daylight (from 2pm to 8pm) and during the evening (from 7pm to midnight).

Heating load	Line	$T_{op,m}$ (11 – 6 pm)	$\eta_{th,m}$ (11 – 6 pm)	$\eta_{PV,m}$ (11 – 6 pm)	$\Delta T_{ST,MAX}$	$\overline{\eta_{th}}$	$\overline{\eta_{PV}}$	MF_{PCM}
2 pm to 8 pm	w/o PCM	41.3	21.8 %	11.1 %	13ºC	20.3 %	11.3 %	-
	w/ PCM	41.6	25.0 %	15.2 %		24.6 %	14.4 %	23%
7 pm to midnight	w/o PCM	45.9	22.3 %	10.0 %	5 ºC	22.5 %	10.2 %	-
	w/ PCM	45.8	28.9 %	14.4 %		31.4 %	13.7 %	35%

5.2. Mode #2: Solar field without heating load

When there are no thermal loads during the day, the capacity of the thermal tank to store heat becomes paramount, which is directly dependent on the storage temperature at the beginning of the test. Therefore, comparison at different storage temperatures is included. Main performance data are collected in Tab. 3.

When the starting temperature of the storage tank is low (below operating temperature of the solar circuit), the tank capacity to store energy is high, as it is also the temperature gap between inlet and outlet in the solar field (Fig. 7, left). However, to reach the objective temperature, the system needs to work with lower fluid flow, so the thermal generation is limited. The great stratification capacity of the tank is very visible here, reaching to maximum temperature difference inside the tank of 17ºC (Fig. 7, right).

In this case, thermal and electrical efficiencies (see Tab. 3) are similar to those values found in Mode #1, with daily heating load. This happens because the storage tank is able to store all the heat generated by the solar field, so the absence of load is not noticeable.

When the storage tank is heated, it becomes more difficult for the tank to store all the heat generated in the solar field. The stratification capacity of the tank is minimal and all the layers end with the same temperature (Fig. 8). This forces the solar circuit to operate at a higher temperature, which reduces general efficiencies but increases the amount of PCM melted during the day, intensifying its effect at the end of the day. At this point, the storage capacity of the PCM becomes more relevant.

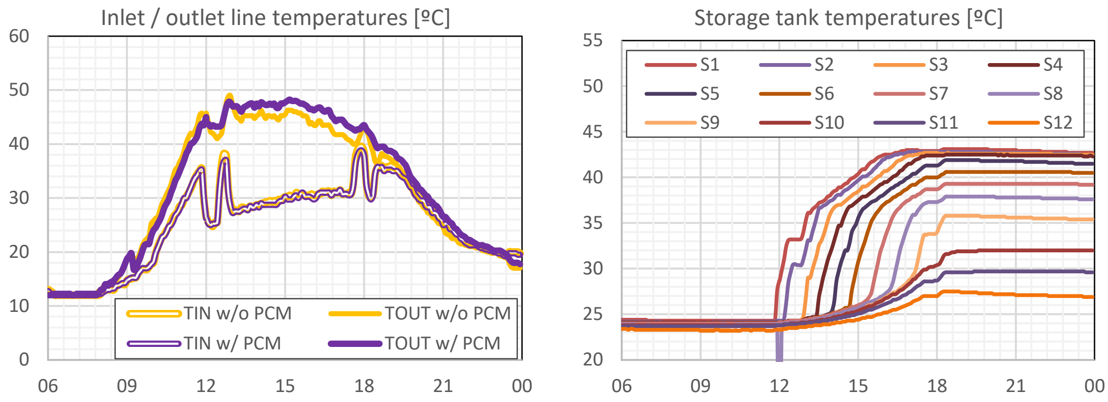

Fig. 7: Temperature daily profile in the inlet/outlet lines (left) and storage stratification (right) in Mode #2, cold tank.

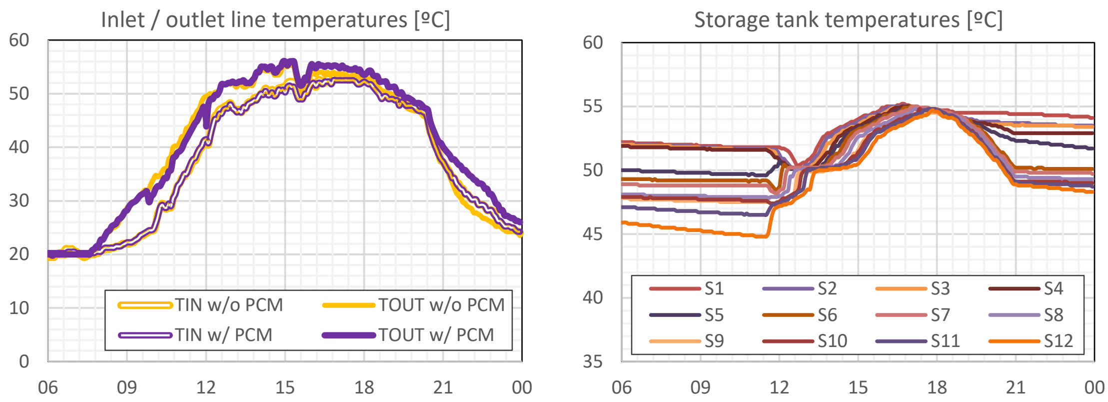

Fig. 8: Temperature daily profile in the inlet/outlet lines (left) and storage stratification (right) in Mode #2, hot tank.

Tab. 3: Main performance values for Mode #2, without heating loads.

Case	Line	Tm (11 – 6 pm)	$\eta_{th,m}$ (11 – 6 pm)	$\eta_{PV,m}$ (11 – 6 pm)	$\Delta T_{ST,MAX}$	$\overline{\eta_{th}}$	$\overline{\eta_{PV}}$	MF_{PCM}
Cold Tank	w/o PCM	37.2	21.8 %	11.9 %	17.3	20.3 %	11.9 %	-
	w/ PCM	37.7	24.9 %	15.3 %		23.7 %	14.3 %	12%
Warm Tank	w/o PCM	43.4	19.3 %	10.3 %	4.4	18.0 %	9.8 %	-
	w/ PCM	43.4	28.6 %	14.3 %		27.9 %	13.3 %	31%
Hot Tank	w/o PCM	49.9	16.5 %	9.3 %	4.1	15.3 %	9.3 %	-
	w/ PCM	49.9	23.0 %	13.7 %		25.8 %	12.8 %	56%

If we compare lines without PCM, the instantaneous thermal and electrical efficiencies decrease while the internal tank temperature and therefore, the operating temperature of the solar circuit increases (see Tab. 3). The same is true for the daily efficiencies and the electrical side of PCM line.

However, if we compare thermal performance of lines with PCM the analysis goes more complicated. When the tank is cold, the inlet temperature of the solar circuit is cooler than other cases, so as the medium temperature of the PVT+PCM collectors. This provokes that only a small part of the PCM is melted and the effect in the thermal generation remains low. When the tank is warm, however, the effect of the PCM gains importance while the operation temperature is still not very high. As a consequence, the instantaneous efficiency increases, as well as the daily one, which takes into account the thermal generation at the end of the day. When the tank is too hot, as in the third case, the amount of PCM melted is maximum, but the high operating temperature of the solar circuit decreases the thermal performance versus the other two cases. The daily thermal efficiency $\overline{\eta_{th}}$ still remains higher than in the case of cold tank, because it takes into account the energy stored in the PCM melted and released at the end of the day.

The addition of PCM entails an improvement of around 4% in the PV performance and between 3 to 10% in the thermal performance, for cold to hot tank cases, respectively.

6. Conclusions

From the data exposed in this work, we can obtain several main conclusions.

- The use of PCM did not lead to a reduction on the fluid temperature, contrary to that exposed in literature. It may be explained because the PCM used in this case has a melting point (48ºC) much higher than other studies (ranged between 20-30ºC), and then the PVT solar field is not able to work for a long time over this temperature to provoked a reduction in the operating temperature.
- However, the addition of PCM provokes significant improvements in the thermal and electrical performance of the solar circuit, with direct influence not only in the energy generated at the end of the day, but also in the instantaneous efficiencies. This efficiency improvement may be explained due to a better heat transmission from the PV cell to the to the heat absorber and the PCM layer, which would reduce the PV cell temperature but increase the PCM layer, resulting in similar fluid temperatures. This improvement is more noticeable when the solar circuit works in a higher temperature, since more amount of PCM is activated.
- The sensitive thermal storage tank helps to properly manage low-temperature heat sources, such as solar energy from PVT collectors. When the demand takes place throughout the day, as is usual in offices, the stratification of the tank is maintained and allows a better use of the energy produced. When the demand takes place at the end of the day, the stratification is lower, but the tank reaches higher temperatures, storing more thermal energy for its later.
- The great volume of the storage tank, as well as the stratification capacity, hinders the absence of heating demand and allows the solar circuit to operate with acceptable efficiencies, comparable to those obtained with heat evacuation. In case of high temperature, this storage capacity of the tank is endorsed by the storage capability of the PCM.

Although further analysis is recommended to fully address and quantify the benefits of PCM in a PVT solar installation, this work provides reliable data of a PVT+PCM installation working under real conditions where the addition of PCM showed an undeniable improvement. Further studies are needed to evaluate the goodness of the installation in other climate conditions (winter) or different points of view (economical, environmental).

7. Acknowledgments

This work takes part of the LowUp project (*LOW valued energy sources UPgrading for buildings and industry uses)* which has received funding from the European Union's Horizon 2020 Research and Innovation Program under Grant Agreement n°723930.

8. References

Andersen, E., Furbo, S., Fan, J., 2007. Multilayer fabric stratification pipes for solar tanks. Sol. Energy 81, 1219–1226. https://doi.org/10.1016/j.solener.2007.01.008

Aste, N., Leonforte, F., Del Pero, C., 2015. Design, modeling and performance monitoring of a photovoltaic-thermal (PVT) water collector. Sol. Energy 112, 85–99. https://doi.org/10.1016/j.solener.2014.11.025

Atkin, P., Farid, M.M., 2015. Improving the efficiency of photovoltaic cells using PCM infused graphite and aluminium fins. Sol. Energy 114, 217–228. https://doi.org/10.1016/j.solener.2015.01.037

Besheer, A.H., Smyth, M., Zacharopoulos, A., Mondol, J., Pugsley, A., 2016. Review on recent approaches for hybrid PV/T solar technology. Int. J. Energy Res. 40, 2038–2053. https://doi.org/10.1002/er.3567

Browne, M.C., Lawlor, K., Kelly, A., Norton, B., Cormack, S.J.M., 2015. Indoor Characterisation of a Photovoltaic/ Thermal Phase Change Material System. Energy Procedia 70, 163–171. https://doi.org/10.1016/j.egypro.2015.02.112

Buonomano, A., Calise, F., Vicidomini, M., 2016. Design, simulation and experimental investigation of a solar system based on PV panels and PVT collectors. Energies 9, 1–17. https://doi.org/10.3390/en9070497

Chow, T.T., Tiwari, G.N., Menezo, C., 2012. Hybrid solar: A review on photovoltaic and thermal power integration. Int. J. Photoenergy 2012. https://doi.org/10.1155/2012/307287

ClimSel C48, 2017. Product specification sheet.

Dincer, I., Rosen, M.A., 2011. Thermal energy storage. Systems and applications, 2nd ed. Wiley. A John Wiley and Sons, Ltd., UK.

European Commission, 2019. European Green Deal, EU Climate Action. Belgium. https://doi.org/10.1017/CBO9781107415324.004

Eurostat, 2019. Energy, Transport and environment statistics. 2019 edition. Luxembourg. https://doi.org/10.2785/660147

Fertahi, S. ed D., Jamil, A., Benbassou, A., 2018. Review on Solar Thermal Stratified Storage Tanks (STSST): Insight on stratification studies and efficiency indicators. Sol. Energy 176, 126–145. https://doi.org/10.1016/j.solener.2018.10.028

Göppert, S., Lohse, R., Urbaneck, T., Schirmer, U., Platzer, B., Steinert, P., 2009. New computation method for stratification pipes of solar storage tanks. Sol. Energy 83, 1578–1587. https://doi.org/10.1016/j.solener.2009.05.007

Hasan, A., Mccormack, S.J., Huang, M.J., Norton, B., 2010. Evaluation of phase change materials for thermal regulation enhancement of building integrated photovoltaics. Sol. Energy 84, 1601–1612. https://doi.org/10.1016/j.solener.2010.06.010

Huang, B.J., Lin, T.H., Hung, W.C., Sun, F.S., 2001. Performance evaluation of solar photovoltaic / thermal systems. Sol. Energy 70, 443–448. https://doi.org/10.1016/S0038-092X(00)00153-5

Huang, M.J., Eames, P.C., Norton, B., 2007. Comparison of Predictions Made Using a New 3D Phase Change Material Thermal Control Model with Experimental Measurements and Predictions Made Using a Validated 2D Model. Heat Transf. Eng. 28, 31–37. https://doi.org/10.1080/01457630600985634

IEA-SCH, 2020. Task 60 [WWW Document]. PVT Syst. Appl. PVT Collect. New Solut. HVAC Syst. URL https://task60.iea-shc.org/ (accessed 11.8.20).

IEA, 2014. Technology Roadmap Energy Storage. https://doi.org/10.1007/springerreference_7300

Islam, M.M., Pandey, A.K., Hasanuzzaman, M., Rahim, N.A., 2016. Recent progresses and achievements in photovoltaic-phase change material technology: A review with special treatment on photovoltaic thermal-phase change material systems. Energy Convers. Manag. 126, 177–204. https://doi.org/10.1016/j.enconman.2016.07.075

Jonas, D., Lämmle, M., Theis, D., Schneider, S., Frey, G., 2019. Performance modeling of PVT collectors: Implementation, validation and parameter identification approach using TRNSYS. Sol. Energy 193, 51–64. https://doi.org/10.1016/j.solener.2019.09.047

Kabir, E., Kumar, P., Kumar, S., Adelodun, A.A., Kim, K.H., 2018. Solar energy: Potential and future prospects. Renew. Sustain. Energy Rev. 82, 894–900. https://doi.org/10.1016/j.rser.2017.09.094

Karakaya, E., Sriwannawit, P., 2015. Barriers to the adoption of photovoltaic systems: The state of the art. Renew. Sustain. Energy Rev. 49, 60–66. https://doi.org/10.1016/j.rser.2015.04.058

LowUP [WWW Document], 2020. . Low valued energy sources Upgrad. Build. Ind. uses. URL http://lowup-h2020.eu/ (accessed 8.12.20).

Ma, T., Yang, H., Zhang, Y., Lu, L., Wang, X., 2015. Using phase change materials in photovoltaic systems for thermal regulation and electrical efficiency improvement: A review and outlook. Renew. Sustain. Energy Rev. 43, 1273–1284. https://doi.org/10.1016/j.rser.2014.12.003

Mahamudul, H., Rahman, M., Metselaar, H.S.C., Mekhilef, S., Shezan, S.A., Sohel, R., Bin, S., Karim, A., Nur, W., Badiuzaman, I., 2016. Temperature Regulation of Photovoltaic Module Using Phase Change Material : A Numerical Analysis and Experimental Investigation. Int. J. Photoenergy 1–8.

Parida, B., Iniyan, S., Goic, R., 2011. A review of solar photovoltaic technologies. Renew. Sustain. Energy Rev. 15, 1625–1636. https://doi.org/10.1016/j.rser.2010.11.032

Preet, S., Bhushan, B., Mahajan, T., 2017. Experimental investigation of water based photovoltaic/thermal (PV/T) system with and without phase change material (PCM). Sol. Energy 155, 1104–1120. https://doi.org/10.1016/j.solener.2017.07.040

REN21, 2020. Renewables 2020 Global Status Report, Renewable Energy Policy Network for the Century 21. Paris, France.

REN21, 2017. Renewables 2017: Global Status Report, Renewable Energy Policy Network for the Century 21. Paris.

Sarwar, J., Mccormack, S., Huang, M.J., Norton, B., Engineering, E., 2011. Experimental Validation of CFD modelling for thermal regulation of Photovoltaic Panels using Phase Change Material, in: International Conference for Sustainable Energy Storage. Belfast, Ireland, pp. 21–24.

Simón-Allué, R., Guedea, I., Villén, R., Brun, G., 2019. Experimental study of Phase Change Material influence on different models of Photovoltaic-Thermal collectors. Sol. Energy 190, 1–9. https://doi.org/10.1016/j.solener.2019.08.005

Yang, X., Sun, L., Yuan, Y., Zhao, X., Cao, X., 2018. Experimental investigation on performance comparison of PV/T-PCM system and PV/T system. Renew. Energy 119, 152–159. https://doi.org/10.1016/j.renene.2017.11.094

Design Concepts for a Spectral Splitting CPVT Receiver

Alois Resch[1] and Robert Höller[1]

[1] University of Applied Sciences Upper Austria, Stelzhamerstrasse 23, 4600 Wels, Austria

Abstract

The technology of combined photovoltaic and solar thermal energy conversion (PVT) can have certain advantages compared to separate solar systems, if the corresponding PVT collectors are utilized in proper applications. However, if the considered heat sink requires temperatures beyond 100°C, the conventional PVT collector would not be suitable anymore, as thermal absorber and PV cells are thermally coupled in typical PVT systems. This would lead to an undesired temperature level in the PV part that makes the electrical energy conversion highly inefficient. This discrepancy between the optimum operating temperatures of the thermal and the electrical part becomes even more significant for concentrating PVT (CPVT) collectors. The approach of Spectral Splitting can provide a possible solution for this challenge. The basic principle is to split the solar spectrum into several wavelength ranges and impinge the PV cells only with the specific spectral range of highest conversion efficiency. The remaining parts of the spectrum are absorbed in the thermal receiver part and directly transformed into heat. Thermal decoupling between electrical and thermal receiver parts supports both the thermal and the electrical conversion efficiency. This presented paper describes the development of novel design concepts for the implementation of Spectral Splitting in a CPVT receiver for a linear Fresnel collector. A quantitative assessment revealed two favorable designs with different PV technologies that will be used for further investigations.

Keywords: Concentrating solar, Spectral Splitting, CPVT, Fresnel collector

1. Introduction

PVT collectors combine both solar technologies Photovoltaics (PV) and solar thermal energy conversion (ST) in one single device. In most of the current PVT concepts, the PV cells are thermally coupled to a thermal absorber that extracts a part of the cells´ waste heat, which is transferred to a thermal storage or a heat sink by the hydraulic system. If operated in the optimum temperature range, PVT collectors can provide several advantages compared to separated systems, like an increased PV-yield due to the reduced average temperature of the PV cells, increased total energy yield per m² of roof area and reduced installation costs. On the other hand, the essential thermal coupling between the two systems implicates the challenge that conventional PVT collectors are hardly suitable for heat applications with a temperature demand above approx. 80°C. The PV cells work very inefficiently in this temperature range and some constructive parts like the cell encapsulation or the back sheet reach their specification limits (Zenhäusern, 2017).

If PVT collectors shall be applicable to support thermal industrial processes with temperature requirements above 100°C, concentration of the solar irradiance is essentially needed. However, a thermally coupled construction like the conventional PVT collectors is not sensible for this case, due the above-mentioned discrepancy between the PV efficiency and the thermal output temperature. Nevertheless, the concept of Spectral Splitting can provide an approach to work on this technical challenge.

2. The Concept of Spectral Splitting

The central idea of Spectral Splitting is to irradiate on the PV cells in a PVT collector only a selected range of the solar spectrum that can be converted into electricity with maximum efficiency. This is the segment of wavelengths where the spectral response SR (resp. the external quantum efficiency EQE) of a PV cell reaches its maximum, meaning that the incident photons have suitable energy in order to generate electron-hole-pairs efficiently, e.g. without causing relevant heat losses within the cell due to thermalization. The remaining parts of the spectrum containing photons with less-suitable energy for the electricity generation are converted into thermal energy directly. On the one hand, this is the infrared range (IR) of the spectrum, where the photon energy does not exceed the bandgap energy of the PV. On the other hand, the photons´ energy in the ultraviolet

doi:10.18086/eurosun.2020.05.07 Available at http://proceedings.ises.org

range (UV) is far beyond the bandgap energy so that it can only be converted partly into electricity. Figure 1 illustrates this described wavelength separation for an exemplary configuration, where the spectrum in the range of 700 nm to 1100 nm is transmitted to crystalline Silicon (c-Si) PV cells, while all other parts of the incident solar irradiance are converted into heat by a thermal absorber. The ASTM G173-03 Reference Spectrum, AM1.5, receiving surface at 37° tilt, published by NREL (no date) is used in this figure. The SR curve of c-Si is an exemplary one and was extracted from Quaschning (2011).

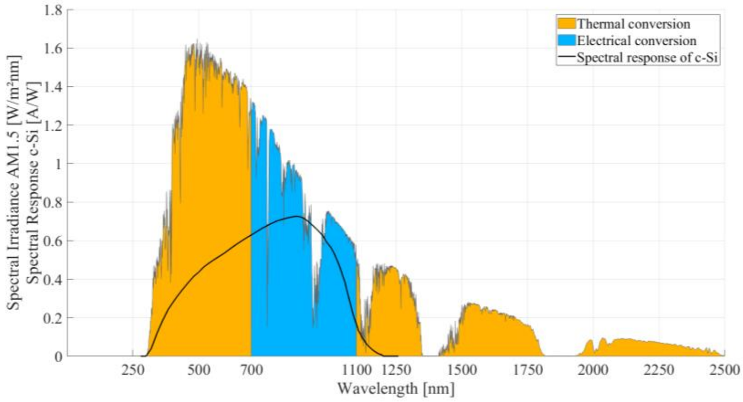

Fig. 1: Wavelength separation in an exemplary Spectral Splitting configuration

Imenes and Mills (2004) described the Spectral Splitting concept and provided a thorough review of different constructive approaches that significantly depend on the considered concentration system as well. However, the research work presented in this paper only focuses on the development of a compact CPVT receiver for a linear concentrating Fresnel collector in order to deepen already gained experience in this field during previous projects (Everett et al., 2012; Resch, 2012; Hangweirer et al., 2015; Reinbrech et al., 2016). Furthermore, the final developed receiver concept will be realized as a prototype and tested on an existing Fresnel mirror field.

The principal implementation of the considered Spectral Splitting concept can be explained by a schematic illustration from Everett et al. (2012), see Figure 2. The incident sunlight (red arrow) is reflected by the Fresnel mirrors and enters the thermal part of the compact receiver, realized as a glass fluid channel. An absorptive filter is implemented in the fluid channel and represents the “thermal absorber” with specified spectral characteristic. The spectral transmittance of the filter shows a steep rise from ideally 0% to 100% at a selectable wavelength, e.g. at 700 nm. Hence, the short wavelengths between 280 nm and 700 nm are absorbed by the filter and converted into heat, while the spectral range > 700 nm is directed further upwards to the PV cells. The absorptive filter is fully immersed in heat transfer fluid that transports the generated heat to any storage or heat sink. Furthermore, applicable fluids like water or propylene glycol (Resch, 2012) also provide an essential spectral property, as its transmittance for the passing irradiance decreases significantly for wavelengths > 1100 nm. Therefore, only the spectral range between 700 nm and 1100 nm reaches the PV cells, where it can generate electricity with maximum efficiency (SR resp. EQE). All other wavelengths are converted into heat, either in the absorptive filter or in the heat transfer fluid directly.

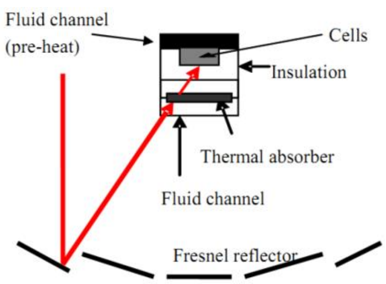

Fig. 2: Schematic assembly of the beam splitting receiver concept (Everett et al., 2012)

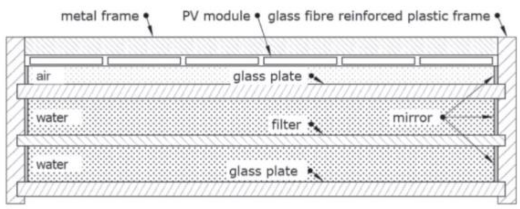

Fig. 3: Cross section of a Spectral Splitting CPVT receiver proposed by Hangweirer et al. (2015)

Hangweirer et al. (2015) proposed a construction for a compact Spectral Splitting CPVT receiver as it is depicted in Figure 3. Following the concept of Everett et al. (2012), it consists of an absorptive filter implemented in a glass fluid channel with rectangular cross section. The PV cells are spatially separated from the thermal receiver part by an air volume in order to improve thermal decoupling.

Stanley et al. (2016) contributed substantial results in this research field, as they also performed experimental work with the developed compact Spectral Splitting receiver. In this case, circular cross section was chosen for the thermal receiver part by using a glass tube that contains the absorptive filter. This approach appears to provide improved durability for prototyping and experimental investigations, e.g. due to higher pressure resistance of a circular tube compared to a rectangular fluid channel.

These described research results were used as a basis for further developing the compact Spectral Splitting receiver concept. The following section 3 summarizes the receiver design phase.

3. Novel CPVT Receiver Design Concepts

3.1 Objectives and approach for designing new CPVT receiver configurations

The principal way of implementing the method of Spectral Splitting within this project is restricted to a compact construction of the receiver, as described above. Moreover, the following requirements for the CPVT receiver had to be considered during the design phase:

- Aperture width of the receiver sufficient for existing Fresnel mirror field
- Operating temperature range up to 200°C
- Heat transfer medium only in liquid phase
- Solid absorption filter with selectable characteristic
- Covering glass for thermal receiver to reduce losses
- Crystalline Silicon or thin-film PV technology for the electrical receiver
- Material availability for building a receiver prototype with an approximate length of 2 m
- Durability for experimental work
- Limited budget for material costs

High importance was attached to the aspect of practical realizability and economic feasibility, because the following prototyping and experimental phase are seen as significantly relevant for the final outcomes of the entire project. Therefore, the receiver designs were kept as simple as possible, but fulfilling the requirements above. The aspect of production costs was taken into account in terms of respecting the limited budget for the receiver material. Although it is important on the long hand to develop low-cost solutions, as the economic competitiveness is always a key indicator for new components, there was no special emphasis on reducing the costs for the receiver within this design phase. At this stage of the development, the focus lays on the technical feasibility and the functional demonstration of the Spectral Splitting concept. Cost optimization is seen as a subsequent step towards a possible product development, which is not an aim of the project described in this paper.

3.2 Optical modelling of the Fresnel mirror field

Before starting the development of different receiver designs, it was necessary to calculate the expected width of the focus image on the receiver incidence plane. On the one hand, this depends on the geometric arrangement of the mirrors (mirror width, number of mirrors, gap between the mirrors…), which is given in this case by an existing Fresnel mirror field with a length of 5.8 m and a total width of 2.3 m, see Figure 4. A number of 28 mirrors are mounted in parallel with a width of 70 mm each, all mechanically interconnected by one central control rod. On the other hand, the mounting height of the receiver has significant influence on the focus image width. If the mounting height is small, internal shading of the Fresnel mirrors reduces the optical performance of the collector, the focus image on the receiver incidence plane is wide and therefore the concentration ratio (CR) is low. By contrast, a big mounting height results in higher mechanical effort and higher optical losses due to inaccuracies of the mirror planes and the tracking system. Basing on experience with the thermal version of the Fresnel collector, a receiver mounting height of 1.5 m above the mirror mounting plane was chosen for performing a two-dimensional (2D) optical modelling of the planned arrangement.

Fig. 4: Fresnel mirror field available for experimental work

The 2D optical modelling was done in MATLAB™ in order to obtain several performance parameters of the Fresnel system like the concentration ratio CR, the optical losses by internal shading, and the width of the focus image or the distribution of irradiance on the receiver incidence plane. This model is not restricted to the specific Fresnel mirror field considered in this project, but it can be parametrized to any kind of linear Fresnel mirror system. It calculates the performance parameters mentioned above in dependence on the elevation angle of the sun, although only the transversal mode is considered yet. An extension of the model to include also the longitudinal mode is planned for the following project phases.

Figure 5 depicts the shading simulation for an elevation angle of 30°. The orange lines represent the incident solar beams, and the red dashed lines illustrate the reflected beams. A schematic receiver is assumed as a rectangular cross section in light green. The following four internal shading mechanisms are considered in this model:

- Mirror self-shading: The incident radiation on one mirror can cause shade on the following mirror.
- Mirror backwards shading: The reflected beams of one mirror can be partly blocked by the previous mirror.
- Receiver shading: The receiver itself can cause shade on the mirror field.
- Frame shading: The frame of the mirror field construction can shade mirrors at the edge.

All of these shading mechanisms are strongly depending on the elevation angle of the sun. Therefore, the simulation was performed stepwise for elevation angles between 5° and 90°, calculating all four shading mechanisms for each mirror.

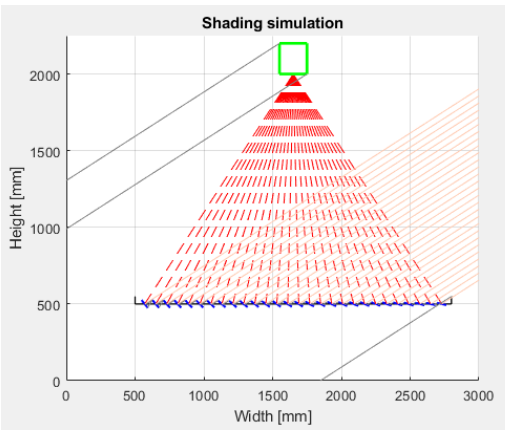

Fig. 5: Modelling of internal shading (elevation angle 30°)

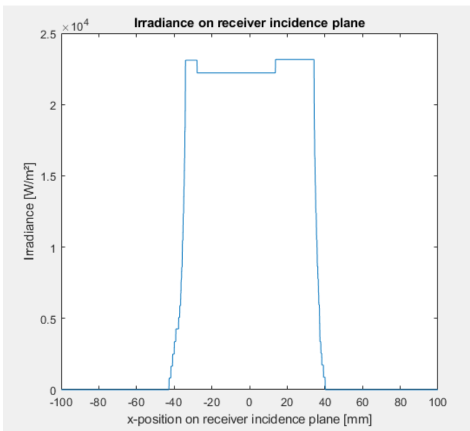

Fig. 6: Resulting irradiance distribution on receiver incidence plane (elevation angle 68°)

For the receiver design phase, it was most important to derive the expected maximum width of the focus image on the receiver incidence plane, as this is a crucial information for constructing the aperture of the receiver accordingly. The width of the focus image and the received irradiance are highly influenced by the internal shading in the mirror field and therefore depend on the elevation angle as well. The optical modelling with varying elevation angles reveals that the maximum width of the focus image is expected to be 83 mm at an elevation angle of 68°. Figure 6 illustrates this step of the simulation and shows the distribution of irradiance along the x-position on the receiver input plane. The maximum irradiance at this elevation angle is calculated with 23.1 kW/m². The stepped reduction of irradiance between x = - 28 mm and x = + 14 mm is caused by the receiver shading.

3.3 Development of novel CPVT receiver designs

Basing on these simulation results, the required aperture width was chosen to be 100 mm in order to provide some tolerance for possible inaccuracies like in the tracking system or in the alignment of the mirrors. Seven different receiver designs have been developed taking into account the requirements mentioned at the beginning of this section. Five of the designs are constructed to use crystalline Silicon (c-Si) PV cells, and two design proposals are developed using thin-film PV technology. The necessity of an additional cooling circuit for the remaining waste heat of the PV cells has to be clarified by the subsequent thermal modelling. Therefore, each receiver design consists of one version with backside cooling tubes for the PV and another version without backside cooling. The absorption filter is implemented in one to three inner glass tubes with different dimensions and arrangements. Common for all design proposals is an enveloping outer glass tube, providing an air gap to the inner glass tube(s) that serves on the one hand as thermal decoupling to the PV cells and on the other hand as thermal insulation for the hot fluid, in order to reduce convection losses to ambient air. The following Table 1 summarizes all developed receiver designs in both versions with and without backside cooling and describes the most important attributes of each design proposal. The cross sections of all constructions are illustrated.

Tab. 1: Overview of developed designs for a compact CPVT receiver

Receiver designs with backside cooling of PV	Receiver designs without backside cooling of PV	Description of designs
Design #1		
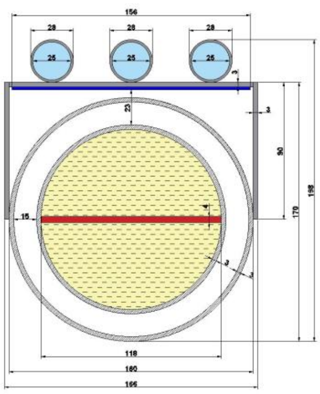	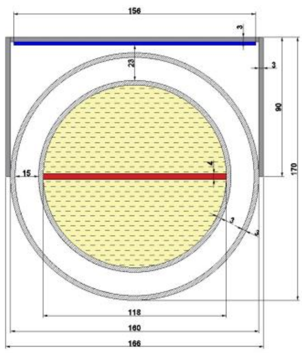	c-Si PV with a width of 156 mm (8”) One central inner glass tube → difficult stability due to the weight of the fluid One absorption filter with a width of 118 mm → high costs expected Distance between hot fluid and PV: 23 mm

Design #2

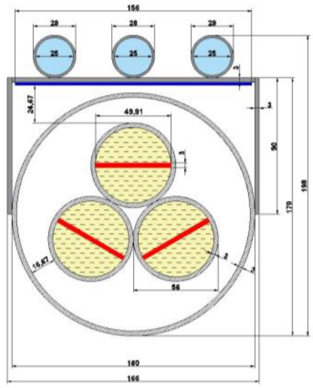

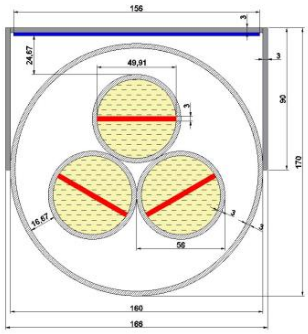

c-Si PV with a width of 156 mm (8")

Three inner glass tubes → good stability expected

Three absorption filters with a width of 50 mm → acceptable costs expected

Overlapping of the glass tubes economically inefficient

Distance between hot fluid and PV: 25 mm

Design #3

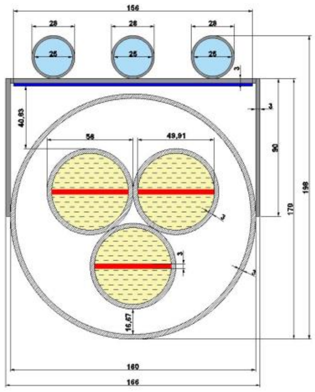

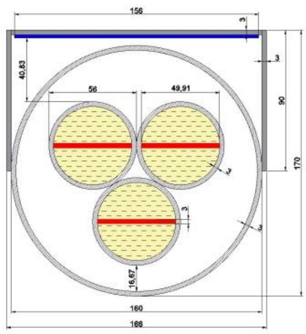

c-Si PV with a width of 156 mm (8")

Three inner glass tubes → good stability expected

Three absorption filters with a width of 50 mm → acceptable costs expected

Overlapping of the glass tubes economically inefficient

Distance between hot fluid and PV: 41 mm

Design #4

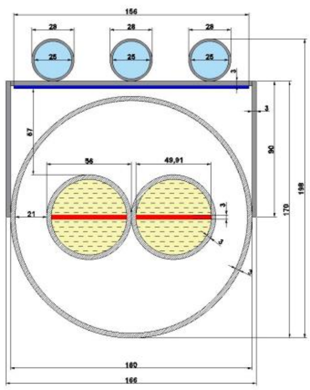

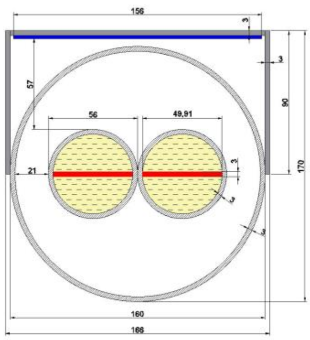

c-Si PV with a width of 156 mm (8")

Two inner glass tubes → good stability expected

Two absorption filters with a width of 50 mm → reduced costs

No overlapping of inner glass tubes

Large gap between inner and outer glass tubes

Distance between hot fluid and PV: 57 mm

Design #5

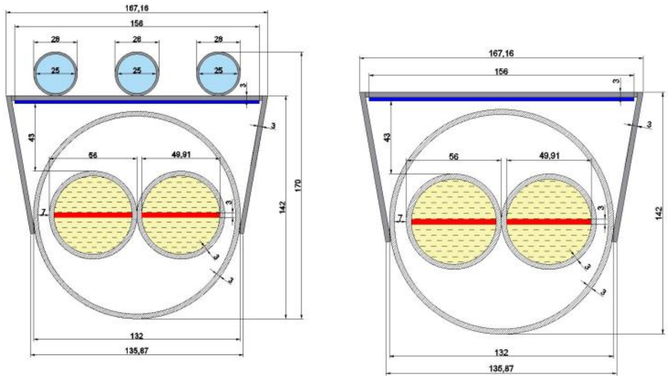

c-Si PV with a width of 156 mm (8")

Two inner glass tubes

Two absorption filters with a width of 50 mm

Reduced gap between inner and outer glass tubes

Skewed walls of receiver housing → more effort for assembly

Distance between hot fluid and PV: 43 mm

Design #6

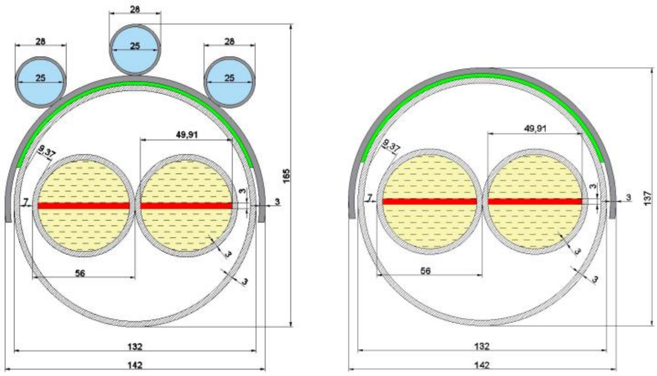

Thin-film PV bended over outer glass tube

Two inner glass tubes

Two absorption filters with a width of 50 mm

Half-shell as receiver housing → low costs and low assembly effort expected

Minimum distance between hot fluid and PV: 9 mm

Design #7

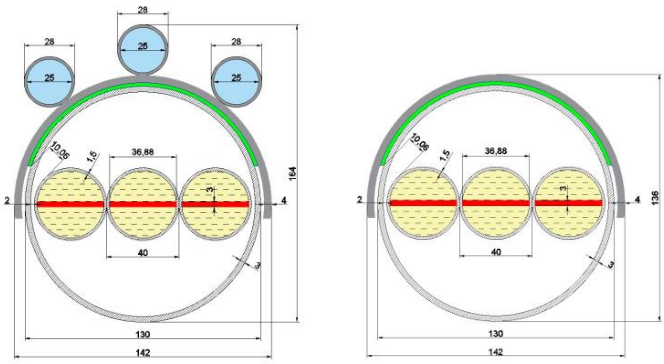

Thin-film PV bended over outer glass tube

Three inner glass tubes → improved stability, but higher assembly effort

Three absorption filters with a width of 37 mm

Half-shell as receiver housing → low costs and low assembly effort expected

Minimum distance between hot fluid and PV: 10 mm

3.4 Qualitative assessment of developed receiver concepts

The subsequent task in the project will be a thorough modelling of the compact CPVT receiver in terms of optical, thermal and hydraulic behaviour. As this cannot be done with all developed receiver concepts due to limitations of time and budget, a qualitative assessment was applied in order to select the best concept for further investigations.

This assessment contained technical criteria as well as aspects regarding the planned experimental realization of the receiver.

The following technical criteria have been considered for each receiver design:

- Pressure resistance of the thermal receiver part
- Heat transfer from the absorption filter to the fluid
- Weight of the thermal receiver part
- Heat transfer between thermal and electrical receiver part
- Absorption losses on the inner side walls of the receiver housing
- Inhomogeneous cross section and therefore inhomogeneous distribution of irradiance within the receiver
- Temperature control of PV cells
- Reflection losses due to multiple optical interfaces
- Relation between filter width and receiver aperture width

With respect to the planned prototyping and experimental work with the receiver, several more criteria have been evaluated for the receiver designs:

- Availability of the PV cells, the absorption filter and the glass tubes
- Costs of material
- Location and accessibility of the suppliers

Each criterion has been evaluated for each receiver design by assigning a grade of 1 to 5. An evaluation of "1" represents the positive compliance of the criterion, whereas "5" indicates a severe deficit of the respective design in the considered aspect. The assessment was done separately for the technical and the experimental criteria.

Table 2 depicts the evaluation matrix of the technical criteria. Each receiver design number is listed twice, one time for the variant with backside cooling of the PV and one time without, indicated by the additional *. The arithmetic average in the bottom row represents the result of the technical assessment.

Tab. 2: Assessment of receiver designs by technical criteria

Technical criteria	Receiver design #													
	1	1*	2	2*	3	3*	4	4*	5	5*	6	6*	7	7*
Pressure resistance thermal receiver part	3	3	2	2	2	2	2	2	2	2	2	2	1	1
Heat transfer absorption filter to fluid	3	3	2	2	2	2	2	2	2	2	2	2	1	1
Weight of the thermal receiver part	5	5	4	4	4	4	3	3	2	2	2	2	1	1
Heat transfer thermal to electr. receiver part	4	4	4	4	3	3	1	1	2	2	3	3	3	3
Absorpt. losses on inner side walls	3	3	3	3	3	3	3	3	2	2	1	1	1	1
Inhomogeneous distribution of irradiance	2	2	2	2	2	2	2	2	3	3	1	1	1	1
Temperature control of PV cells	1	5	1	5	1	5	1	5	1	5	1	5	1	5
Reflection losses due to multiple interfaces	2	2	4	4	4	4	2	2	2	2	2	2	2	2
Relation filter width - receiver aperture	2	2	4	4	3	3	4	4	2	2	2	2	1	1
Average	**2.8**	**3.2**	**2.9**	**3.3**	**2.7**	**3.1**	**2.2**	**2.7**	**2.0**	**2.4**	**1.8**	**2.2**	**1.3**	**1.8**

Similarly, the experimental criteria were evaluated, as shown in Table 3.

Tab. 3: Assessment of receiver designs by experimental criteria

Experimental criteria	Design #													
	1	1*	2	2*	3	3*	4	4*	5	5*	6	6*	7	7*
Availability of PV cells	2	2	2	2	2	2	2	2	2	2	3	3	3	3
Availability of absorption filter	4	4	2	2	2	2	2	2	2	2	2	2	1	1
Availability of glass tubes	1	1	1	1	1	1	1	1	1	1	1	1	1	1
Costs of material	3	3	2	2	2	2	2	2	2	2	2	2	1	1
Location and accessibility of suppliers	1	1	1	1	1	1	1	1	1	1	1	1	1	1
Average	**2.2**	**2.2**	**1.6**	**1.6**	**1.6**	**1.6**	**1.6**	**1.6**	**1.6**	**1.6**	**1.8**	**1.8**	**1.4**	**1.4**

The results of the technical and the experimental evaluation were merged by calculating the average values for each receiver design. Table 4 presents the final results of the assessment.

Tab. 4: Final assessment of receiver designs

	Design #													
	1	1*	2	2*	3	3*	4	4*	5	5*	6	6*	7	7*
Results of technical assessment	2.8	3.2	2.9	3.3	2.7	3.1	2.2	2.7	2.0	2.4	1.8	2.2	1.3	1.8
Results of experimental assessment	2.2	2.2	1.6	1.6	1.6	1.6	1.6	1.6	1.6	1.6	1.8	1.8	1.4	1.4
Final average	**2.5**	**2.7**	**2.2**	**2.5**	**2.1**	**2.4**	**1.9**	**2.1**	**1.8**	**2.0**	**1.8**	**2.0**	**1.4**	**1.6**

This performed qualitative assessment did not yield any decision about the two considered PV technologies. Further quantitative investigations will have to point out, if c-Si or thin-film PV will be more feasible for the planned CPVT receiver. Therefore, the best receiver designs for each PV technology were chosen for the further work. In case of c-Si technology, the design #5 with backside cooling obtained the best evaluation, and design #7 with backside cooling was assessed to be the most promising solution for thin-film PV. The following sub-section describes the two final receiver design concepts in detail.

3.5 Final receiver designs for further investigation

The CPVT receiver design concepts that are illustrated as cross sections in Figures 7 and 8 obtained the best evaluation during the qualitative assessment process. Both of them appear to be technically feasible, according to the criteria mentioned above. Moreover, the design proposals are expected to be realizable as a prototype of 2 m length in order to fulfil the experimental tasks of this project.

The thermal part of the receiver is designed similarly for both proposals. The key component is the absorption filter (illustrated in red) that is implemented in the inner glass tubes with an inner diameter of 50 mm (design #5) resp. 37 mm (design #7). Therefore, the total width of the absorption filter will be 100 mm resp. 111 mm, as it was the requirement, given by the optical simulation of the expected focus image width. The outer glass tube with an outer diameter of 132 mm (design #5) resp. 130 mm (design #7) serves as an insulating envelope for the inner parts, as its air volume reduces heat transfer to the ambient air and to the PV cells as well.

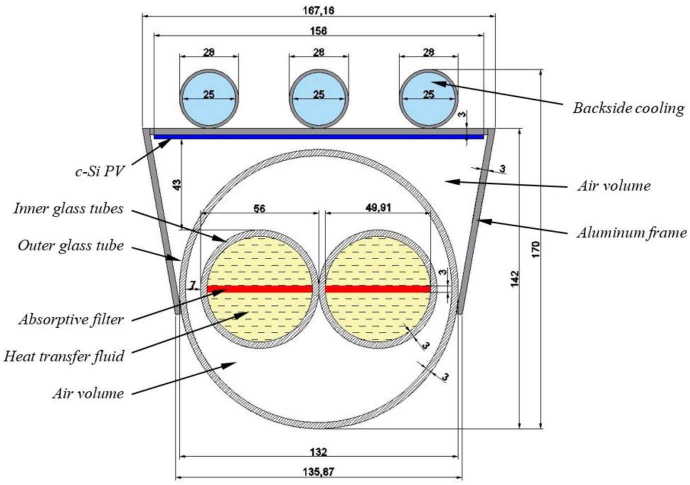

Fig. 7: Cross section of CPVT receiver design #5 with c-Si PV technology

The electrical part of the receiver is constructed differently for the two design proposals. If c-Si PV technology will be implemented, the arrangement could be chosen as illustrated by the cross section in Figure 7. The PV cells (colored in dark blue) are positioned above the thermal receiver with a distance of 43 mm to the hot surface of the inner tubes. Thermal modelling will reveal the effect of this thermal decoupling between the thermal and electrical receiver part. The backside cooling pipes are intended to provide a possibility of maintaining the temperature of the PV cells, in case this is required for the experimental work with the prototype. The total width of this receiver design is mainly given by the width of the PV part, which was chosen with 156 mm, as this corresponds to a standard PV cell size (8-inch wafer). In this way, 12 PV cells in a row could be connected to one string, without further treatment of the cells itself (e.g. cutting to any other size). Skewed sidewalls of the Aluminum receiver housing are necessary, but raising the effort for assembling. The planar construction of the PV cells results in an inhomogeneous air volume between the outer glass tube and the PV layer, that is expected to lead to a less-than-ideal distribution of irradiance, e.g. due to reflections on the sidewalls. By contrast, the second design proposal in Figure 8 utilizes bendable thin-film PV technology, colored in green. This arrangement can be advantageous in terms of internal irradiance distribution as well as in terms of total compactness of the receiver, because dead volumes are reduced.

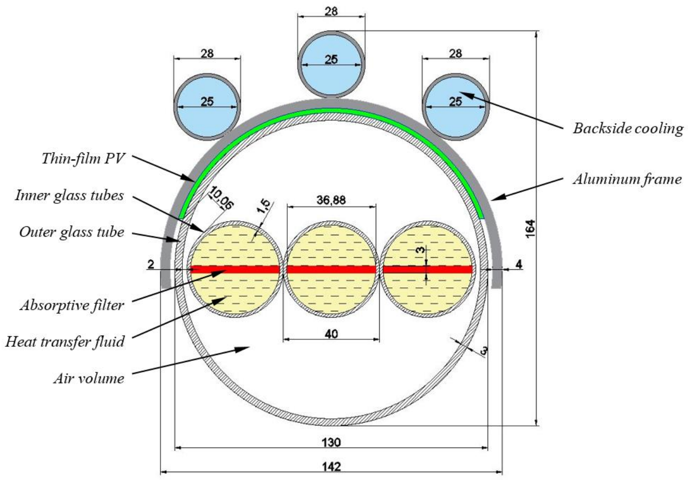

Fig. 8: Cross section of CPVT receiver design #7 with thin-film PV technology

The thin-film PV layer in design #7 is directly attached to the outer glass tube and backwards covered by a half-shell aluminum housing. Backside cooling pipes are planned as in design #5 and can be even more important in this configuration, as the geometrical distance between the hot surface of the inner tubes and the PV varies between 10 mm and 37 mm.

4. Further Investigations and Outlook

The two receiver designs described above will be the basis for further development steps. These will firstly involve a detailed modelling phase:

- Enhancement of the optical mirror field modelling in terms of integrating both transversal and longitudinal modes
- Modelling of the irradiance distribution within the receiver
- Modelling of the Spectral Splitting effect including an optimization of the absorption filter characteristic
- Thermal and hydraulic modelling of the entire receiver
- Calculation of electrical and thermal characteristic values

This modelling phase will yield quantitative results regarding the specified requirements and will point out the potential for possible improvements in the receiver designs. Furthermore, it will deliver a comparison of the two considered PV technologies, which is of high importance in order to take a subsequent decision about the receiver design to be used for prototyping.

In parallel to the modelling phase, material investigation needs to be performed. This includes:

- Thermal life-time validation and UV exposure tests of candidate fluids and absorption filters
- Spectral transmission measurements with candidate fluids, glass tubes and absorption filters
- Spectral response measurements with the considered PV cells

The final stage of the project consists of the prototyping phase, where the developed compact CPVT receiver will be assembled with a length of 2 m and installed on the existing Fresnel mirror field. Optical, electrical and thermal performance measurements of this novel CPVT collector under real conditions will reveal, if the theoretical results can be confirmed by experimental data.

5. Acknowledgments

The described work is carried out within the project ENTHYRE, which is funded by the government of Upper Austria (Land Oberösterreich) in the frame of the “Dissertationsprogramm der FH OÖ”.

6. References

Everett, V., Wu, Y., Resch, A., Ebert, M., Vivar, M., Thomsen, E., Harvey, J., Scott, P., Greaves, M., Tanner, A., Blakers, A., 2012. Towards an innovative spectral-splitting hybrid PV-T micro-concentrator. Proceedings of the 8th international conference on concentrating photovoltaic systems, American Institute of Physics, Vol. 1477, pp. 230-234

Hangweirer, M., Höller, R., Schneider, H., 2015. Design and analysis of a novel concentrated photovoltaic–thermal receiver concept. Japanese Journal of Applied Physics, Vol. 54, pp. 08KE01 1-8

Imenes A., Mills, D., 2004. Spectral beam splitting technology for increased conversion efficiency in solar concentrating systems: a review. Solar Energy Materials and Solar Cells, Vol. 84, pp. 19–69.

NREL, no date. ASTM G-173-03 tables. Available at: https://www.nrel.gov/grid/solar-resource/spectra-am1.5.html; accessed: 6th of November 2019

Quaschning, V., 2011. Regenerative Energiesysteme | Technologie – Berechnung – Simulation, 7th ed. Hanser, München

Reinbrech, R., Höller, R., Schneider, H., 2016. Integration of Spectral Splitting in a CPV-T Receiver Concept. Proceedings of the EU PVSEC 2016, Munich

Resch, A., 2012. Implementation of Spectral Splitting in a Hybrid Concentrator Photovoltaic and Thermal

Solar Collector. Master Thesis, University of Applied Sciences Upper Austria, Wels

Stanley, C., Mojiri, A., Rahat, M., Blakers, A., Rosengarten, G., 2016. Performance testing of a spectral beam splitting hybrid PVT solar receiver for linear concentrators. Applied Energy. 168, 303–313.

Zenhäusern, D., Bamberger, E., Baggenstos, A., 2017. PVT Wrap-Up | Energiesysteme mit Photovoltaisch-Thermischen Solarkollektoren

The Concept of Zero-Emission Cooling

Alois Resch[1] and Harald Dehner[1]

[1] University of Applied Sciences Upper Austria, Stelzhamerstrasse 23, 4600 Wels, Austria

Abstract

Cooling demand in residential and industrial applications causes a tremendous consumption of electrical energy due to the conventional technology of compression chillers. Furthermore, future scenarios depict a significant increase of the cooling demand for the year 2050, so that 16% of the entire global electricity consumption is originated by the cooling sector by then, with the consequence of emitting enormous amounts of CO_2 emissions. Therefore, renewable and emission-free solutions for satisfying the worldwide cooling demand are highly important. The concept of "Zero-Emission Cooling" proposed in this paper considers the combination of an adsorption chiller and a double-glazed PVT collector in order to generate emission-free cold. The chiller under investigation already starts to work at a driving temperature of 55°C, and the double-glazing of the PVT collector makes it capable of providing temperatures up to 80°C more efficiently than others. The electrical output of the collector supplies all electric components and provides excess energy to be fed into the grid. The performed investigation showed that the concept basically works from the technical point of view, although a big collector area is required in order to provide enough driving power for the chiller. Most of the produced electrical energy can be fed into the grid, as only 13% are required to supply the internal electric consumers.

Keywords: Cooling demand, solar cooling, PVT collector, emission-free cooling

1. Introduction

Cooling demand is growing drastically all over the world, both in the residential sector and in commercial applications. The global cooling output capacity (measured in GW) has almost tripled between the years 1990 and 2016, leading to an electricity demand of around 2,000 TWh respectively nearly 10% of the global total electricity consumption in 2016. Moreover, the cooling sector has a severe impact on the electricity network, as this huge number of electrically driven chillers are more and more contributing to peak load within the grids (OECD/IEA, 2018).

Solar thermal cooling systems provide an efficient and renewable alternative to electrically driven cooling devices. As the thermal driving power for sorption chillers is taken from the sun, electricity from the grid is only necessary to drive pumps and valves, making it possible to reduce the electric energy demand by around 80% compared to conventional compression chillers. A number of 1800 solar cooling systems have been in operation in the year 2018 with cooling capacities up to the MW-range (Weiss and Spörk-Dür, 2019).

Scenarios of the further development of the cooling sector pointed out that for the year 2050 the electrical energy demand will triple to an amount of around 6,200 TWh, causing 16% of the total global electricity demand by then (OECD/IEA, 2018). With respect to the climate crisis, this increasing energy demand for cooling applications should not be accepted. Renewable cooling solutions must be pushed forward to achieve faster and deeper market penetration.

The concept of "Zero-Emission Cooling" discussed in this paper can provide such a renewable way for covering the cooling demand of residential or office buildings. The intention of this concept is to supply an adsorption chiller not only thermally by a solar thermal collector, as it is done by the established technology of solar cooling, but also electrically by the combination with a PVT-collector. In this way, the energy demand from conventional sources like fossil fuels or the electrical grid and therefore the corresponding greenhouse gas emissions could be reduced to zero.

Research activities in this field of solar combined cooling, heating and power systems (S-CCHP) have achieved promising results (e.g. Herrando et al., 2019). One of the research outcomes so far is the fact that on the one

doi:10.18086/eurosun.2020.05.08 Available at http://proceedings.ises.org

hand sorption chillers need a certain driving temperature in the range of 70°C upwards in order to reach a reasonable coefficient of performance (COP). On the other hand, most of the available non-concentrating PVT-collectors are designed to reach optimal performance in low-temperature applications, but show considerable efficiency reduction at temperature differences above 50 K to ambient air (Zenhäusern et al., 2017). Therefore, the central aim of this presented work is to analyze a novel configuration of components for providing an S-CCHP system that can have the potential to be more competitive to conventional cooling technologies. Analysis was done theoretically and experimentally.

2. System configuration and pre-dimensioning of components

This section describes the configuration of the considered S-CCHP system and summarizes the performed pre-dimensioning of the relevant components.

2.1 System configuration

The S-CCHP under investigation is illustrated schematically in Figure 1 below. The PVT collector field supplies its thermal power via the high-temperature (HT) storage tank to the HT-circuit of the adsorption chiller ($\dot{Q}_{HT}$). The HT storage tank is required to compensate fluctuations of the solar energy delivery as well as of the energy demand from the chiller. The cooling load is represented by an office building. The thermal power extracted from the building is transferred to the low-temperature (LT) storage tank that is connected to the LT circuit of the chiller. Similarly as on the HT side, also this tank serves as a hydraulic compensator for occurring fluctuations in the available cooling power $\dot{Q}_{LT}$. The entire thermal power $\dot{Q}_{MT}$ is released to ambient air by the heat rejection tower.

The electrical power P_{el} generated by the PVT collector field is used to supply all electric components of the system like pumps, fans, valves, control units, sensors and so on. If excess energy occurs, it can be fed into the grid.

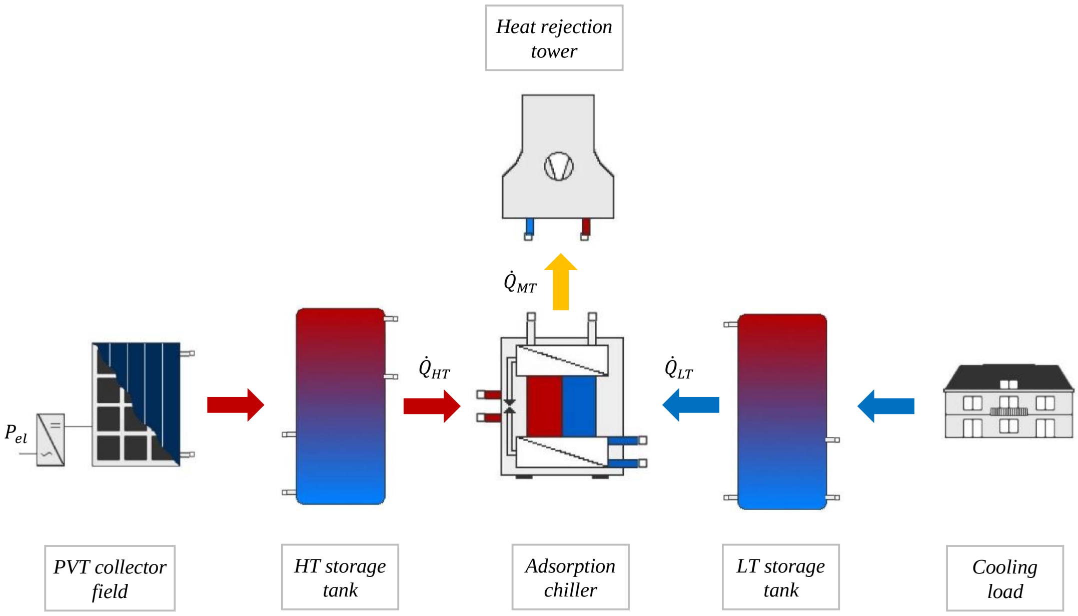

Fig. 1: Schematic overview of the system configuration

The considered PVT collector *Solar One* from the Austrian supplier 3F Solar Technologies GmbH and is a water-driven and covered type of flat plate PVT, see Figure 2. The reason why it was chosen for this described investigation is its double glazing construction with Argon filling that provides improved suitability for applications with higher temperature demand due to reduced heat losses via the front side of the collector. The thermal performance curve of the PVT collector was measured by the Austrian Institute of Technology in 2016. It is displayed in the following Figure 3 (AIT, 2016).

Fig. 2: View of the Solar One PVT collector (3F Solar, 2020)

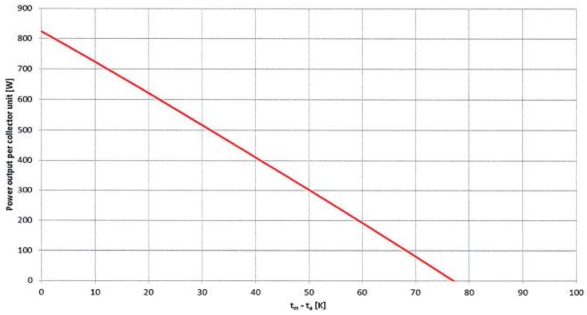

Fig. 3: Thermal performance curve of the Solar One PVT collector; G = 1000 W/m², ambient air velocity = 3 m/s (AIT, 2016)

Other relevant technical information of the PVT collector (3F Solar, 2018):

- Gross area: 1.696 m²
- 60 mono-crystalline Silicon cells
- Nominal electrical power (STC-conditions): 290 Wp
- Maximum thermal power (EN ISO 9806): 825 W

As mentioned above, the double-glazed construction of the PVT collector promises to be more suitable for higher temperature demand that is usually given by sorption chillers. On the other hand, the specific a**d**sorption chiller considered for this analyzed configuration was chosen because it can be operated with relatively low temperature in the HT circuit, compared to a**b**sorption systems. Hence, the combination of these two key components could have the potential to be more efficient in technical and economic issues than other configurations.

The adsorption chiller used for this investigation is the type *eCoo 10* from the German supplier Fahrenheit. It consists of two evacuated process chambers containing Silicagel as the active sorption material. Most relevant technical information from the datasheet (Fahrenheit, 2019) is listed as follows:

- Nominal cooling power: 16.7 kW @ HT = 85°C, MT = 24°C, LT = 19°C
- Maximum COP: 0.65
- Nominal volume flows: $\dot{V}_{HT}$ = 2.5 m³/h, $\dot{V}_{MT}$ = 5.1 m³/h, $\dot{V}_{LT}$ = 2.9 m³/h
- Electrical power demand: 800 W
- Minimum HT temperature to start operation: 55°C

Besides its suitability in terms of temperature requirement, the Fahrenheit chiller was also chosen for this investigation because it is installed in one of the laboratories of the University of Applied Sciences Upper Austria. Therefore, the theoretical work could be supported by experimental tasks, e.g. measurement of the COP under different operating conditions, see also section 3.

2.2 Pre-dimensioning of components

As the size of the adsorption chiller was already given by the available Fahrenheit system, a pre-dimensioning of the PVT collector field and the storages could be done. This first level of system dimensioning did not claim to yield exact numbers for all steps of calculation, but to have basic information of the components´ size in order to be able to start detailed system simulations more efficiently.

PVT collector field

The first dimensioning for the collector field was done basing on the nominal operating point of the chiller, which is characterized by the nominal cooling load of 16.7 kW at 85°C of driving temperature and a COP of 0.65.

The COP is defined as follows:

$$COP = \frac{\dot{Q}_{LT}}{\dot{Q}_{HT}} \quad \text{(eq. 1)}$$

$\dot{Q}_{LT}$ is the cooling power available in the low-temperature (LT) circuit, and $\dot{Q}_{HT}$ is the required driving power that has to be supplied to the high-temperature (HT) circuit of the chiller.

$\dot{Q}_{HT}$ for the given adsorption chiller is:

$$\dot{Q}_{HT} = \frac{\dot{Q}_{LT}}{COP} = \frac{16.7\ kW}{0.65} = 25.7\ kW \quad \text{(eq. 2)}$$

Furthermore, $\dot{Q}_{HT}$ can be used to calculate the temperature difference in the HT-circuit of the chiller:

$$\dot{Q}_{HT} = \dot{m}_{HT} * c_p * \Delta\vartheta_{HT} = \dot{m}_{HT} * c_p * (\vartheta_{HT,in} - \vartheta_{HT,out}) \quad \text{(eq. 3)}$$

$$\Delta\vartheta_{HT} = \frac{\dot{Q}_{HT}}{\dot{V}_{HT} * \rho * c_p} = \frac{25.7\ kW}{2.5\frac{m^3}{h} * 972\ \frac{kg}{m^3} * 4.196\frac{kJ}{kg * K} * 3600^{-1}\frac{h}{s}} = 9.07\ K \quad \text{(eq. 4)}$$

$\dot{V}_{HT}$ is the required volume flow in the HT-circuit, specified by the supplier. Density ρ and specific heat capacity c_p of water were taken for an expected mean temperature of 80°C (Böckh and Wetzel, 2009, p. 234).

The input temperature of the HT-circuit $\vartheta_{HT,in}$ is defined with 85°C in the nominal operating point. Therefore, the output temperature of the HT-circuit $\vartheta_{HT,out}$ can be calculated:

$$\vartheta_{HT,out} = \vartheta_{HT,in} - \Delta\vartheta_{HT} = 85°C - 9.07\ K = 75.93°C \approx 76°C \quad \text{(eq. 5)}$$

Considering the simplified approach that the HT-circuit of the chiller is directly connected to the PVT collector field without any losses, the temperatures $\vartheta_{HT,in}$ and $\vartheta_{HT,out}$ also occur as input and output temperatures of the collector field $\vartheta_{C,in}$ and $\vartheta_{C,out}$. The average collector temperature $\vartheta_{C,mean}$ is calculated as follows:

$$\vartheta_{C,mean} = \frac{\vartheta_{C,in} + \vartheta_{C,out}}{2} = \frac{76°C + 85°C}{2} = 80.5°C \quad \text{(eq. 6)}$$

The efficiency of any solar thermal collector is generally described by the following equation (Quaschning, 2011, p. 111):

$$\eta_C = \eta_0 - \frac{c_1}{E} * (\vartheta_{C,mean} - \vartheta_a) - \frac{c_2}{E} * (\vartheta_{C,mean} - \vartheta_a)^2 \quad \text{(eq. 7)}$$

The optical efficiency η_0, the linear loss coefficient c_1 and the quadratic loss coefficient c_2 for this specific PVT collector are available in the report of its thermal performance test (AIT, 2016). If the irradiance E is chosen with 1000 W/m² and the ambient air temperature ϑ_a with 35°C, the collector efficiency for this operating point of supplying the adsorption chiller can be calculated to:

$$\eta_C = 0.487 - \frac{5.881\ \frac{W}{m^2 * K}}{1000\ \frac{W}{m^2}} * (80.5°C - 35°C) - \frac{0.006\ \frac{W}{m^2 * K^2}}{1000\ \frac{W}{m^2}} * (80.5°C - 35°C)^2 = 0.207 \quad \text{(eq. 8)}$$

Hence, the thermal efficiency of the considered PVT collector at this specific application is 20.7%, corresponding to deliver a thermal power $\dot{Q}_C$ of 207 W_{th} per m² collector area at an irradiance of 1000 W/m². The total area of the required collector field is therefore:

$$A_{C,tot} = \frac{\dot{Q}_{HT}}{\dot{Q}_C} = \frac{25.7\ kW}{0.207\ \frac{kW}{m^2}} = 124.2\ m^2 \approx 124\ m^2 \qquad \text{(eq. 9)}$$

The field of PVT collectors needs a size of 124 m² in order to supply the adsorption chiller with the required thermal power and temperature in the nominal operating point. As the gross area of one collector is specified with 1.696 m², the total number of necessary collectors is 74.

The nominal electrical power output per collector P_{STC} at standard test conditions STC (1000 W/m², AM1.5, 25°C) is 290 W_p (3F Solar, 2018). The PVT collector is equipped with mono-crystalline PV cells that show a typical temperature coefficient c_T in terms of output power of -0.4 to -0.5%/K (Mertens, 2018, p. 104). Assuming that the PV cells are reaching the same temperature of 80°C as the thermal absorber while powering the adsorption chiller, the expected electrical output power $P_{C,nom}$ per collector at this nominal operating condition is:

$$P_{C,nom} = P_{STC} * (1 + c_T * \Delta\vartheta) = 290\ W * (1 - 0.0045 * 55\ K) = 218.2\ W \qquad \text{(eq. 10)}$$

The entire collector field consisting of 74 collectors provides a nominal electrical power $P_{F,nom}$ of:

$$P_{F,nom} = P_{C,nom} * 74 = 16.15\ kW \qquad \text{(eq. 11)}$$

Storages

As illustrated in Figure 1, the cooling system includes two storage tanks, one on the HT side of the chiller and another one on the LT side. The HT storage tank has the purpose to work as a hydraulic compensator, because the heat demand from the chiller is fluctuating due to the internal sorption process and the intermittent operation of the sorption chambers (SOLAIR, 2009, p. 75). On the other hand, it serves as an energy storage for cases of temporal mismatch between solar irradiance (e.g. due to clouds) and cooling demand. For pre-dimensioning the HT storage tank for the considered system, it was defined that the tank should be able to bridge a "dark" time span t_{dark} of 2 hours without solar input. Furthermore, a temperature drop $\Delta\vartheta_{St,HT}$ of 10 K (from 85°C to 75°C) in the tank during this period of discharging was defined to be acceptable. These definitions were used to calculate the required energy $Q_{St,HT}$ to be stored in the tank:

$$Q_{St,HT} = \dot{Q}_{HT} * t_{dark} = 25.7\ kW * 2\ h = 51.4\ kWh \qquad \text{(eq. 12)}$$

The necessary volume of the HT storage tank $V_{St,HT}$ is the following:

$$V_{St,HT} = \frac{Q_{St,HT}}{\rho * c_p * \Delta\vartheta_{St,HT}} = \frac{51.4\ kWh}{972\ \frac{kg}{m^3} * 4.196\ \frac{kJ}{kg * K} * 3600^{-1}\ \frac{h}{s} * 10\ K} = 4.54\ m^3 \qquad \text{(eq. 13)}$$

The storage tank on the LT side of the adsorption chiller was not intended to fulfil any energy storage purpose as this is already covered by the HT storage tank. The LT tank should only serve as a hydraulic compensator to buffer the fluctuating generation of cooling power by the chiller. The typical cycle duration for switching the operation of the two adsorption process chambers was assumed to be between 10 and 15 min. Therefore, the LT storage tank was dimensioned to buffer a cycle time t_{cycle} of 15 min. Within this time span, the temperature in the tank should not rise beyond 24°C, leading to a temperature difference $\Delta\vartheta_{St,LT}$ of 5 K in reference to the nominal temperature of 19°C. Using these assumptions, the energy to be stored in the LT storage tank can be calculated:

$$Q_{St,LT} = \dot{Q}_{LT} * t_{cycle} = 16.7\ kW * 0.25\ h = 4.18\ kWh \qquad \text{(eq. 14)}$$

The necessary volume of the LT storage tank $V_{St,LT}$ is:

$$V_{St,LT} = \frac{Q_{St,LT}}{\rho * c_p * \Delta\vartheta_{St,LT}} = \frac{4.18\ kWh}{998\ \frac{kg}{m^3} * 4.183\ \frac{kJ}{kg * K} * 3600^{-1}\ \frac{h}{s} * 5\ K} = 0.721\ m^3 \qquad \text{(eq. 15)}$$

Density ρ and specific heat capacity c_p for equation 15 were taken from Böckh and Wetzel (2009, p. 234) for an average water temperature of 22°C.

Heat rejection tower

The extracted heat from the cooling load $\dot{Q}_{LT}$ and the driving heat of the chiller $\dot{Q}_{HT}$ has to be released into ambient air by the mid-temperature (MT) circuit of the chiller. The corresponding rejection heat $\dot{Q}_{MT}$ is calculated for the nominal operating:

$$\dot{Q}_{MT} = \dot{Q}_{HT} + \dot{Q}_{LT} = 25.7\ kW + 16.7\ kW = 42.4\ kW \qquad \text{(eq. 16)}$$

The supplier Fahrenheit also provides heat rejection systems for their chillers. For this case, the hybrid heat rejection tower *eRec 20 | 58 WV* was chosen, because it has a nominal rejection power of 58 kW. The electrical power demand is specified with 1.08 kW (Fahrenheit, 2020).

2.3 Summary of the system configuration

The pre-dimensioned system for realizing the concept of Zero-Emission Cooling can be summarized as follows:

The PVT collector field needs a size of 124 m² in order to generate the required HT-power of 25.7 kW_{th} at 85°C. Corresponding to the specified operation point for a COP of 0.65 according to the chiller´s datasheet, the system can provide a cooling power of 16.7 kW.

An electrical power of 16.2 kW_{el} will be generated by the collector field, if the PV cells are operated at a temperature of 80°C. The heat rejection tower and the electric components within the chiller require a total electrical power of around 2 kW_{el}, leading to an excess power of 14 kW_{el} that can be delivered to the grid.

The thermal storages are estimated to have a required volume of 4.5 m³ for the HT side and 0.7 m³ for the LT circuit. The cooling load is not specified, but it is assumed to be a small office building or a family house with a cooling demand suitable for the capability of the considered adsorption chiller.

3. Laboratory measurements

The University of Applied Sciences Upper Austria operates a modular heat engineering laboratory that was developed to investigate a wide range of thermal processes with a temperature range of up to 200°C (Resch and Kraft, 2016). Thermal cooling is one of the operating modes of this laboratory. Therefore, a Fahrenheit adsorption chiller *eCoo 10* is installed that can be driven by various heat sources like solar thermal collectors, a biomass kettle or a tempering device. A buffer storage tank with a volume of 1000 liters emulates the cooling load for the chiller. Figure 4 provides a view of this lab arrangement. Heat rejection is either done via a wet cooling tower on the roof-top (see Figure 5) or via an internal waste heat cooling circuit that is connected to a water basin with 80 m³ of volume and a constant temperature of 12°C.

Fig. 4: Adsorption chiller Fahrenheit *eCoo 10* and the emulated cooling load at the heat engineering laboratory

Fig. 5: Wet cooling tower on the roof-top of the University of Applied Sciences Upper Austria

In reference to the described concept of Zero-Emission Cooling, this laboratory configuration was used to obtain experimental data of the adsorption chiller. The chiller was driven in different operation conditions in order to measure the thermal power in its three hydraulic circuits (HT, MT and LT) and to determine the corresponding COP. The mass flows are measured by electromagnetic flow sensors *KROHNE OPTIFLUX 6300* with an accuracy of +/- 0.5% of measured value (MV). The sensors for measuring the inlet and outlet temperatures are PT100 1/10 DIN class B with an accuracy of +/- 0.065 K of MV (@ 70°C). The HT-circuit of the chiller was supplied by a tempering device *Huber Unistat 530 W* in combination with a 1000 liters buffer storage tank in order to ensure constant inlet temperature for the chiller. The heat rejection was done by the internal waste heat cooling circuit, but combined with a bypass valve for controlling the MT inlet temperature. Similarly, the LT inlet temperature is controlled by bypassing the cooling load partly.

18 different operating conditions were investigated during this laboratory measurement with HT-temperatures between 55°C and 85°C, MT-temperatures between 20°C and 40°C and LT-temperatures between 15°C and 30°C. The volume flows were constantly set to $\dot{V}_{HT}$ = 2.5 m³/h, $\dot{V}_{MT}$ = 5.1 m³/h, $\dot{V}_{LT}$ = 2.9 m³/h according to the specified nominal operating point. The following Figure 6 illustrates an extract of the measurement sequence at the operating point with HT/MT/LT = 80°C/30°C/25°C. Inlet and outlet temperatures of the three circuits HT, MT and LT are given. The obvious fluctuations of all temperatures is caused by the cyclic operation of the two internal adsorption chambers and are typical for this kind of chiller. Remarkable is the cycle time of 7 min, which is below the assumption that was used to do the pre-dimensioning of the LT storage (see sub-section 2.2).

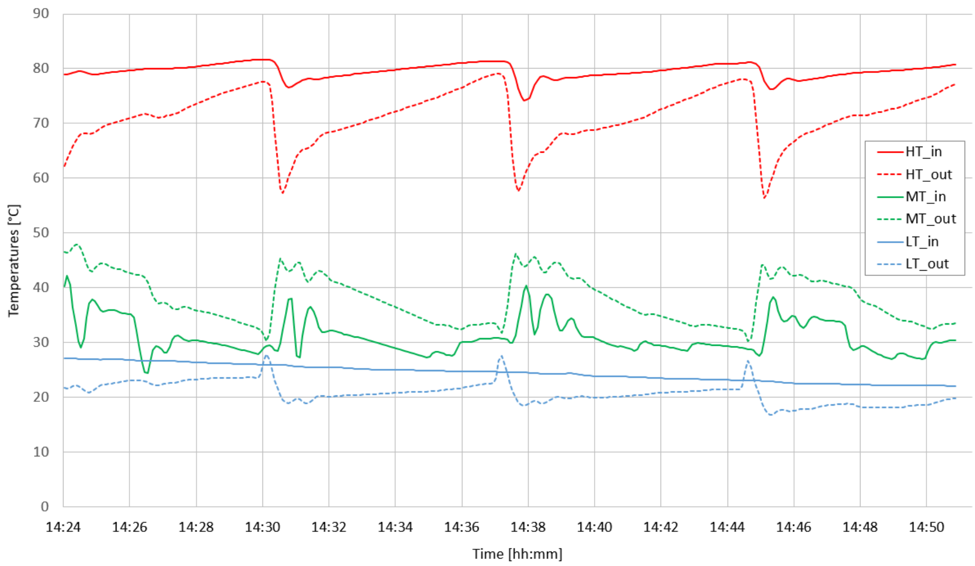

Fig. 6: Measured temperatures of the Fahrenheit adsorption chiller eCoo 10 at HT/MT/LT = 80°C/30°C/25°C

The results of the calculation of thermal powers averaged for the displayed time span are the following:

$\dot{Q}_{HT}$ = 24.15 kW, $\dot{Q}_{MT}$ = 41.34 kW, $\dot{Q}_{LT}$ = 12.19 kW

The COP for this specific operating point can be calculated according to Equation 1:

$$COP = \frac{\dot{Q}_{LT}}{\dot{Q}_{HT}} = \frac{12.19\ kW}{24.15\ kW} = 0.505$$

This COP at HT/MT/LT = 80°C/30°C/25°C was the maximum performance that could be achieved during the conduction of laboratory measurements. The averaged value of COP over these considered 18 operating points covering a wide temperature range was calculated with 0.41.

4. Simulation of the Zero-Emission Cooling concept

Basing on the results of the pre-dimensioning, the Zero-Emission Cooling system concept was realised in the simulation software POLYSUN, according to Figure 1. The available model for the PVT collector was parameterized with the conversion efficiency coefficients taken from the report of its thermal performance test (AIT, 2016). The Fahrenheit chiller was represented by the general model of a sorption chiller available in POLYSUN. The parameters for specifying the performance of the chiller were taken from the results of the laboratory measurements. The cooling load was defined to be an office building with a total floor space of 300 m² and a specific cooling power demand of 25 W/m². The total cooling power demand results to 7.5 kW, which is less than 50% of the chiller´s cooling capacity of 16.7 kW. The location of this installation was chosen with the city of Wels in Austria.

Figure 7 depicts the annual simulation of room temperature in the considered building as well as the resulting deficit of cooling power. The top chart describes the situation without cooling in order to obtain the maximum expected room temperature, which would be 32.5°C in this case. The bottom chart includes the proposed cooling system with 124 m² of PVT collectors and the adsorption chiller *eCoo 10*. The room temperature setpoint was 22°C, and the operation of the chiller was limited to the time span between beginning of April and end of August.

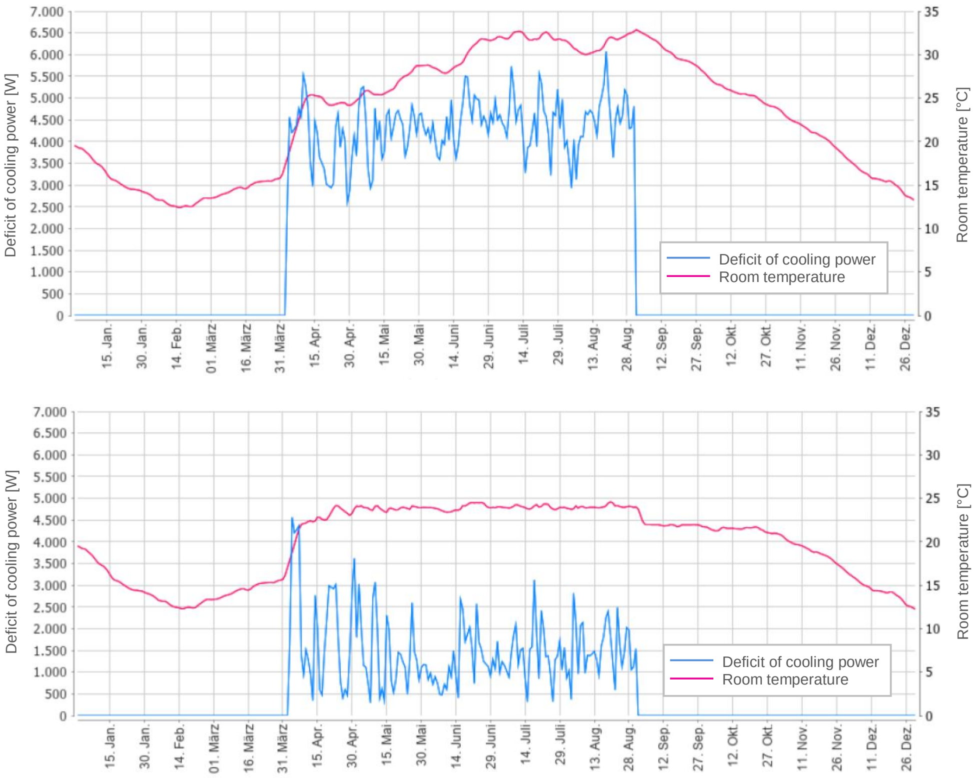

Fig. 7: Simulation of room temperature without cooling (top) and with proposed cooling system (bottom)

The resulting room temperature during summer with activated cooling system was around 24°C, meaning that the setpoint could not be reached. In terms of cooling power it can be observed that the maximum demand is simulated to 6 kW in case of deactivated cooling. On the same day, the deficit of cooling power in case of activated cooling is still 2.5 kW, resulting in an effective cooling power of the chiller of 3.5 kW. This performance result is not satisfying compared to the nominal chiller power of 16.7 kW. First analysis of the simulation details shows that the PVT collector field hardly reaches the required output temperature of 85°C and therefore the chiller cannot run on optimal COPs. Deeper investigation of these results and an extension of the simulation has to be done in order to improve the thermal performance of this proposed Zero-Emission Cooling concept.

5. Summary of results

The results obtained so far during the investigation of the described concept of Zero-Emission Cooling can be summarized as follows:

- The pre-dimensioning of the entire system was done basing on a COP of the chiller of 0.65. The laboratory measurements of the chiller performance revealed that this assumption was too optimistic, as the average measured COP over the entire temperature range was 0.41. The COP of 0.65 given by the supplier´s datasheet is the maximum possible one under optimum conditions, which should not be used for considering system configurations with PVT collectors.
- Experimental work with the chiller during the laboratory measurements confirmed its robustness against changing hydraulic and thermal conditions. As promised by the datasheet, the chiller starts to work at driving temperatures above 55°C, which makes it attractive to be combined with low-temperature heat sources. Although, a low COP has to be accepted at such a low driving temperature.
- The considered PVT collector is constructed with double-glazing in order to reduce heat losses via the front side and therefore to be capable of providing higher temperatures. Nevertheless, the efficiency of the collector at a temperature difference of 45 K to ambient air is reduced to 20.7%. This leads to the high demand of 124 m² collector area in order to be able to generate the required 25.7 kW_{th} at 80°C mean temperature.
- First simulations of the system for the location of Wels point out that the defined room temperature in the considered office building cannot be maintained completely. A deficit of cooling power occurs, although the cooling load of the building is less than 50% of the chiller´s cooling capacity. An explanation for this issue can be that the chiller does not run in the range of high COP due to the limited driving temperature delivered by the PVT collector field.
- The electrical energy output of the PVT collector field of 16 kW_{el} can only be used partly by the cooling system itself. The electric components of the chiller and the heat rejection tower have a combined power demand of 2 kW, which corresponds to 13% of the power produced by the collectors.

6. Conclusions and outlook

The concept of Zero-Emission Cooling as part of the solar combined cooling, heating and power systems (S-CCHP) provides an interesting approach for directing the worldwide cooling sector towards an emission-free and renewable future. The technology of adsorption chillers is a robust and mature alternative to the conventional cooling systems using compression chillers. The combination with double-glazed PVT collectors is possible, although it requires substantial collector areas in order to be capable of generating enough thermal power at reasonable temperatures. Coincidently, large areas of PVT collectors produce significantly more electrical power than needed by the cooling system.

Deeper investigation in terms of the following issues could reveal potential for improving the considered cooling concept:

- Enlargement of the simulation: optimization of control strategies, location-dependent aspects, variation of cooling loads
- Comparison with separated solar systems: Solar thermal collector field for supplying the chiller thermally and optimized number of PV modules to supply all electrical consumers
- Ecologic and economic assessment in comparison to conventional cooling systems
- Enlargement of the system in terms of utilizing the solar heat of the PVT collectors also for supporting hot water generation and space heating
- Implementation of hydraulic solutions to use the rejected heat for soil regeneration, swimming pool heating or pre-heating for hot water generation and space heating

7. Acknowledgments

This project is financed by research subsidies granted by the government of Upper Austria. Further acknowledgments are dedicated to the following students of the University of Applied Sciences Upper Austria for contributing to this project: Theresa Laister, Manuel Raschhofer, Daniel Schnauer, Alija Spahic, Marcel Urich and Christian Wagner.

8. References

3F Solar Technologies GmbH, 2018. Solar One Hybridkollektor Produktdatenblatt. Vienna

3F Solar Technologies GmbH, 2020. Solar One Hybridkollektor. Available at: https://www.3f-solar.at/3f-hybridkollektor/; accessed: 24 July 2020

AIT – Austrian Institute of Technology, 2016. Report of thermal performance testing | PVT collector Solar One from manufacturer 3F Solar Technologies GmbH. AIT, Vienna

Böckh, P. v., Wetzel, T., 2009. Wärmeübertragung | Grundlagen und Praxis, third ed. Springer, Berlin

Fahrenheit GmbH, 2019. Technische Daten und Montageanleitung (TDI) für eCoo 10. München

Fahrenheit GmbH, 2020. Rückkühler: Effizient, hygienisch, freikühlfähig. Available at: https://download.fahrenheit.cool/Deutsch/Datenbl%C3%A4tter/Zubeh%C3%B6r/FAHRENHEIT_Technische_Daten_R%C3%BCckk%C3%BChler_2018.pdf; accessed: 27 August 2020

Herrando, M., Pantaleo, A. M., Wang, K., Markides, C. N., 2019. Solar combined cooling, heating and power systems based on hybrid PVT, PV or solar-thermal collectors for building applications. Renewable Energy, Vol. 143, pp. 637-647

Mertens, K., 2018. Photovoltaik | Lehrbuch zu Grundlagen, Technologie und Praxis, 4th ed. Hanser, München

OECD/IEA, 2018. The Future of Cooling - Opportunities for energy efficient air conditioning, edited by IEA Publications, International Energy Agency.

Quaschning, V., 2011. Regenerative Energiesysteme | Technologie – Berechnung – Simulation, 7th ed. Hanser, München

Resch, A., Kraft, R., 2016. Industrial Integration of Mid-Temperature Solar Heat – First Experiences and Measurement Results. Conference Proceedings Eurosun 2016, Palma de Mallorca. doi:10.18086/eurosun.2016.02.11

SOLAIR, 2009. Requirements on the design and configuration of small and medium sized solar air-conditioning applications. Available at: www.solair-project.eu; accessed: 28 July 2020

Weiss, W., Spörk-Dür, M., 2019. Solar Heat Worldwide – Global Market Development and Trends in 2018 | Detailed Market Figures 2017.

Zenhäusern, D., Bamberger, E., Baggenstos, A., 2017. PVT Wrap-Up | Energiesysteme mit Photovoltaisch-Thermischen Solarkollektoren

Mathematical Modelling of Power to heat Strategies to support Sector Coupling

Nayrana Daborer-Prado[1], Alois Resch[1]

[1] University of Applied Sciences Upper Austria, Energy Research Group ASIC, Wels, Austria

Abstract

Sector coupling refers to the idea of interconnecting the energy consuming sectors like buildings (heating and cooling), mobility, gas and industry with the electricity-producing sector. Among several sector coupling strategies, power to heat (P2H) poses as one of the most necessary ones, since heating and cooling accounts for 51% of the final energy demand in the world, and only 10% of it is provided by renewable sources (REN21, 2019). In this work, different P2H systems and applications, namely a residential and an industrial application were investigated and the total energy produced by them was stored in water tanks for a later on use. Based on those results, it could be determined which one of the systems analyzed provided the best solution in terms of energy conversion in comparison with each other. Furthermore, in order to provide a general idea of the greenhouse gas emissions avoided, the amount of CO_2 and fossil fuel savings was computed and presented in the results section. The mathematical modelling of the all systems was created using MATLAB/Simulink™, and their results are displayed in this work.

Keywords: Power to heat, Sector coupling, Mathematical modelling

1. Introduction

Power to heat (P2H) technologies have proven themselves as a reliable ally when it comes to balance the energy grid and promote the use of the surplus energy produced by the renewable systems during peak moments. As it is well known, among several advantages, one of the principal ones is the ability of providing grid stabilization by shaving the peak energy and supporting the balance of the asymmetric load. This is done by avoiding the shutdown of solar power stations or wind turbines during grid overload moments and using this extra energy to run the P2H systems, which will then, convert this electrical energy into heat.

When considering the implementation of a renewable energy power plant it is important to consider, not only the amount of energy that can be produced by it, but also the amount of CO_2 emissions that can be avoided. It is notorious that the carbon dioxide and other greenhouse gases emissions are responsible for the increase in the planet's temperature by nearly 1°C since the Industrial revolution, and that those gases come mainly from human activity. That is the reason why in the last decade, several climate policies to reduce these emissions were developed and why several subsidies were created for the construction and implementation of renewable power plants all over the world (Ritchie, Rosesr, 2017).

Based on those subsidies, in the last few years, the installation of clean renewable electrical energy and heat generation systems became progressively accessible not only to the average homeowners but also for the industries. This has a positive impact because in most developing countries the industries accounts for more than a third of total final energy consumption, and up to eighty percent of this sector's energy is used to produce heat (process heat for high or low temperature applications). Therefore, there is an increasing necessity for the industries to make use of cleaner sources of electricity and heat (Wohlgemuth, Monga, 2008).

In this work, different ways of implementing power to heat systems were analyzed, namely a residential and an industrial application, and simulations were performed using the software MATLAB/Simulink ™. One of the goals of this work is to evaluate the amount of energy that can be produced by the systems and which quantity of it can be converted into heat and stored in a water tank, fulfilling this way the integration concept of the sector coupling. A second objective is to determine which one of the systems analyzed provide the best solution in terms of energy conversion in comparison with each other, as well as avoided fossil fuel use and avoided CO_2 emissions to the environment.

doi:10.18086/eurosun.2020.05.09 Available at http://proceedings.ises.org

2. Methodology

In order to provide a comprehensive investigation about the power to heat implementation possibilities, two types of applications were compared. As previously mentioned, the first type was a residential application and the second type an industrial application. It is important to note that all the systems used in the simulations here performed were extracted from the CARNOT block-set in MATLAB (Solar Institut Juelich, 2018) and some of them were modified according to the goals of the project. In the following sections, the structure, major components and configuration of each of these systems will be presented, in parenthesis, next to the name of each component, one can find the corresponding name of the Simulink block in the CARNOT block-set.

2.1. Residential application

For this application, the domestic hot water generation for a single-family house was examined and a comparison between a conventional solar thermal system and a power to heat strategy was investigated. For both systems, it was considered that three people lived in the house and that the amount of water used per person was around 50 liters (l) per day, totalizing a Domestic Hot Water (DHW) use of 150 l of per day. With the purpose of meeting these criteria, a water tank containing 400 l of water was used as storage system and a water taping scheme was created to regulate the consumption behavior of the household. Concerning the tapping system, it was developed to tap the water from the tank three times per day, namely at 7:00, 13:00 and 19:00 o'clock, with the tapping in the morning and in the evening lasting twice as long as the tapping at noon and all of them summing up 150 l of water by the end of the day. In the next sections, the characteristics of both systems will be discussed.

2.1.1. Photovoltaic system plus electric heater

Regarding the P2H system, the approach considered was a photovoltaic system plus an electric heater. The basic components used in this simulation were photovoltaic panels (PV) with 4.2 kWp power *(PV Module simple)*, an electric element *(Electric Heating)* and a water storage tank *(Storage Type 2)* containing 400 l of water. In this arrangement, the PV was used to provide electricity to the electric element that was immersed in the water storage tank and installed in a height equivalent to 25% of the tank total height, counting from the bottom to the top. Regarding the tank, it is arranged in a standing position and starts with a temperature of 65 ºC.

For backup purposes, an additional electric element system was installed in the tank (at around 70% of the tank total height), this being powered by the grid energy.

2.1.2. Solar thermal collectors plus water storage tank

As it is well known, the solar thermal water system is not part of the power to heat systems category, nevertheless, it was here included in order to provide a source of reference to the study. The basic components used for this system were a water storage tank *(Storage Type 2)*, with the same characteristics as the previous one (400 l and initial temperature of 65 ºC) and a solar thermal collector system (ST) *(Solar Thermal Collector ISO 9806)*, which is directly connected to the tank. For auxiliary purposes, a water pump *(Pump Constant)* was also included, which pumps the water from the tank back to the solar collector. In order to keep all the systems comparable, a thermal collector size of 6 m² was chosen. Using the well-established conversion factor of 0.7 kW/m² (Weiss, Spörk-Dür, 2019), this corresponds to an output power of 4.2 kW_{th}, equal to the PV system mentioned above, which presents an area of about 28 m², (assuming an efficiency of 15%).

Alike the previous system, in this arrangement, for backup purposes, an additional electric element system *(Electric Heating)* was installed inside of the tank (at around 70% of the tank total height), this also being powered by the grid energy.

2.2. Industrial application

For this application, the generation of hot water for any industrial demand was analyzed and a comparison between two distinct power to heat strategies was investigated. For both systems, a water storage tank with 50 m^3 was used and the goal was to keep water temperatures between 60 ºC and 95 ºC inside of the tank during the whole year. As well as in the previous application, a water use profile was also developed for this arrangement, but in this case, instead of tapping water only three times during the day, the water was constantly drawn from the tank between 7:00 and 17:00 o'clock and used in the industry processes. Considering that, a constant amount of 100 kW was constantly being drawn from the tank, after the ten hours of operation a total of 1000 kWh was consumed per day in this system. The characteristics of both systems are discussed below.

2.2.1. Photovoltaic plus electric heater

The basic components used in this simulation were photovoltaic panels (PV) *(PV Module simple)* with 200 kWp output power, an electric element *(Electric Heating)* and a water storage tank *(Storage Type 2)* containing 50 m^3 of water. In this arrangement, the PV was, again, used to provide electricity to the electric element that was immersed in the water storage tank and installed in a height equivalent to 25% of the tank total height, counting from the bottom to the top. Essentially, this system is a scaled up version of the photovoltaic system used previously for the residential application.

This design also presents an electric element installed in the upper part of the water tank, working as a backup heater.

2.2.2. Photovoltaic plus heat pump

The basic components included in this arrangement were a water/water heat pump with 200 kW electric power, a photovoltaic system and a water storage tank. For the sake of comparability, the same photovoltaic system *(PV Module simple)* with 200 kWp power and water tank *(Storage Type 2)* with 50 m^3 of water, stating at 65 ºC, used in the previous system, were implemented in this arrangement. Water pumps *(Pump Constant)* and an inverter *(Inverter)* were also included in order to complete the connections between the main components. An electric element *(Electric Heating)* was also installed in the upper part of the tank to operate as a backup heating system. In this system, the PV system is used to provide energy to the heat pump, which transfers heat to the water tank, additionally, the temperature of the water coming from the ground heat source to the heat pump is always around 10 °C.

3. Simulation Results

3.1. Residential application results

This section aims to compare the pure thermal system described in Section 2.1.2, with the system using a power to heat strategy described in Section 2.1.1. In order to provide a broader view of the systems functionality, an annual and a daily comparison of both systems was performed. It is also important to notice that, the weather files used for all simulations here performed, come from a region in West Germany.

<u>Daily comparison:</u> For this comparison, two different days with distinct weather conditions, one in summer and the other in winter were chosen and the water temperature obtained throughout the tank was measured. In order to allow a better observation of the temperatures inside of the water tank, the same was divided into ten nodes being Node 1 on the very bottom and Node 10 on the top, which can be seen on the top part of the Figure 1 and Figure 2 below.

Since, for the photovoltaic plus electric heater system, the heating element was installed in the second node, it is possible to observe that when the water tapping occurs, the temperature on the bottom of the tank decreases, while the temperature for the other nodes do not change so much. This happens due to the difference in density between hot and cold water, as it is known, hot water has a smaller density than the cold water and is carried to the upper parts of the tank. At the end of the day, a bigger difference between the layers can be noticed, with the bottom layers colder than the top ones.

Regarding the solar thermal system, the heat exchange zone between the solar collector and the water tank is located in the bottom of the tank and therefore, a similar behavior as in the previous system can be detected. In this arrangement, it is also possible to notice that when the tapping occurs, the temperature of water inside the tank starts to change and at the end of the day, a greater difference between the layers can be seen.

It is also important to highlight that a temperature limit of 95 °C was set in tank in order to avoid water temperatures higher than 100 °C. Consequently, during some days with high solar radiation (normally in summer) when the water temperature in the tank reaches the limit, no more energy is transferred from the photovoltaic or solar thermal system into the tank.

Figure 1 and Figure 2 display the behavior presented during a sunny summer day. In this case, the solar thermal and the photovoltaic system present similar results, nevertheless, one can notice that between the first and second tapping, in the photovoltaic system the temperatures between the different nodes is basically the same, while in the solar thermal system there is already a small variation amid the temperatures.

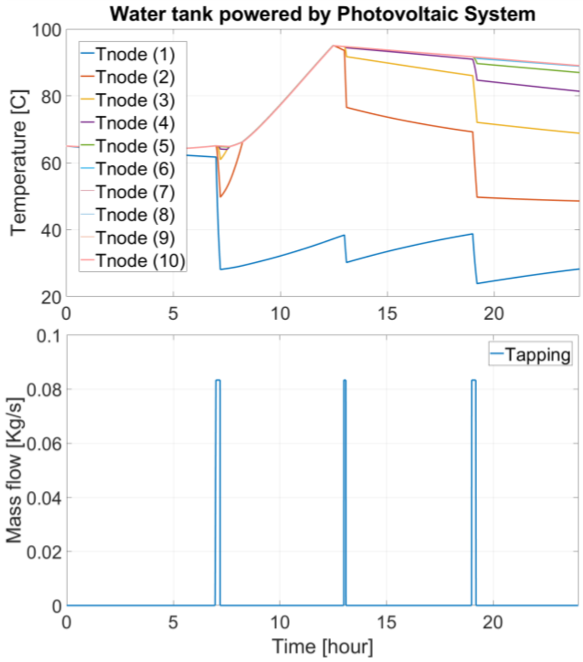

Figure 1: Final temperature in water tank with PV system (top) and tapping mass flow (bottom) in a summer day

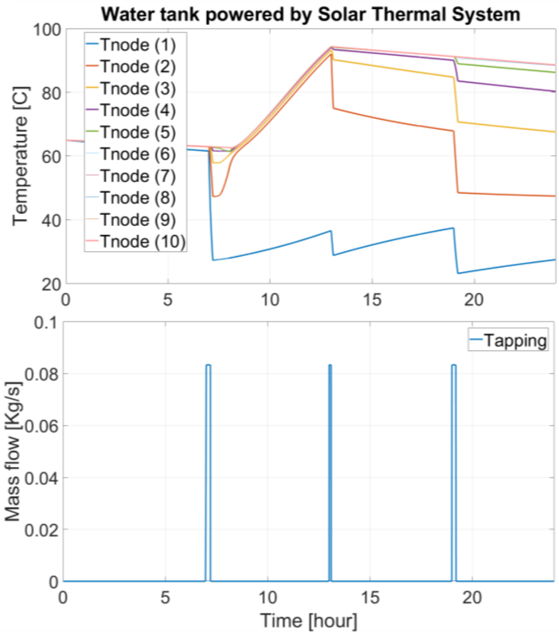

Figure 2: Final temperature in water tank with ST system (top) and tapping mass flow (bottom) in a summer day

With respect to the winter day, Figure 3 and Figure 4 display how the systems behave with such weather conditions. For the photovoltaic arrangement, it is possible to see that in the middle of the day the temperature in the middle nodes of the tank increase a bit and that at around 19:00 o'clock, when the last tapping occurs, the last node increases its temperature suddenly, which happens because the backup electric heater started to function. As formerly explained, a backup heater was installed in the upper part of the tank in all systems and it was set to start operation when the water temperature around it decreased below 60 °C.

Concerning the solar thermal system, the temperature in the tank decreases throughout the day and at 16:00 and 19:00 o'clock it is possible to see an increase in the temperature of the top nodes, which again happens because the backup heater started to function, when the temperature reached levels below 60 °C.

By the end of this day, the PV system could provide almost 60 % of the energy needed to maintain the tank temperature at 60 °C, while the ST system did not deliver any energy to tank and had to use the backup heater, with energy coming from the grid. The reason behind this behavior is that, in a day with low irradiation or an overcasted day, the PV system can still produce a certain amount of energy to power up the electric heater, while, for the ST system, the amount of irradiation available is not enough to achieve high temperatures in the collectors, which therefore do not deliver any energy to the tank requiring then, the backup heater.

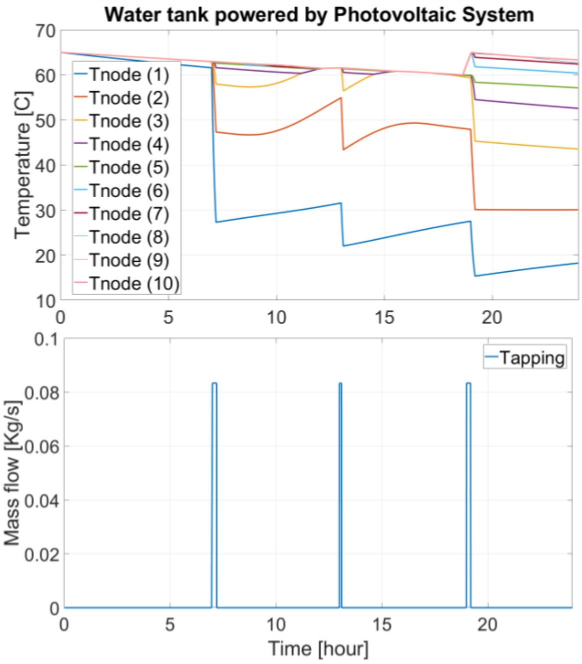

Figure 3: Final temperature in water tank with PV system (top) and tapping mass flow (bottom) in a winter day

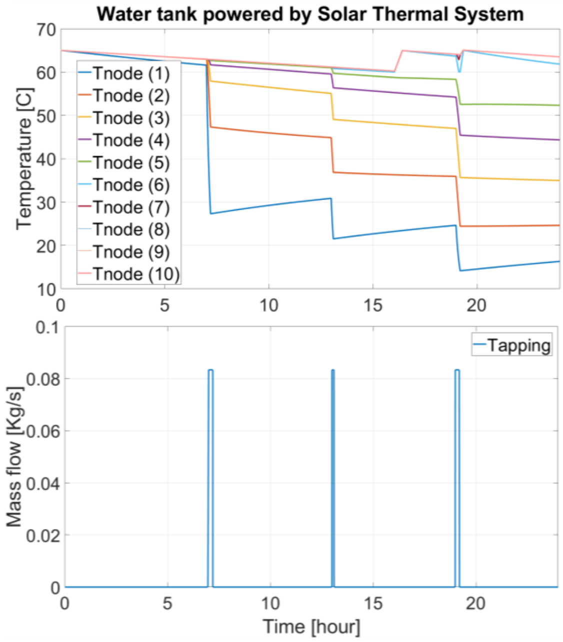

Figure 4: Final temperature in water tank with PV system (top) and tapping mass flow (bottom) in a winter day

<u>Annual comparison:</u> For this comparison, the annual behavior of both systems was analyzed. Here the focus was to calculate the total solar fraction supplied by the systems and also the avoided fossil fuel use and the avoided CO_2 emissions.

Figure 5 and Figure 6 display the total annual amount of energy produced by the solar thermal and the photovoltaic system, respectively, as well as the amount of energy needed from the grid during the year. One can perceive that in Figure 5, the final difference between the grid consumption and the ST system production is smaller than the difference between the PV system production and the grid consumption displayed in Figure 6. This indicates that the photovoltaic system needed less energy coming from the grid during the year than the solar thermal arrangement. In both pictures, during the periods with better weather conditions, from around day 100 till day 300 (sunnier days with reduced amount of clouds), it is possible to observe that the Grid need slightly increase in the ST simulation, while for the PV system, the energy needed from the grid basically does not change during this time. Therefore, during this time the photovoltaic system was able to provide all the energy needed to keep the temperature inside the water tank at the desired levels without using any backup power coming from the grid. While, on the other hand, the solar thermal system needed some backup coming from the grid.

- Solar fraction

Regarding the solar fraction, the total amount of energy needed to keep the water tank at the desired temperature was computed and the percentage coming from the grid and from the heating system was calculated. As it was expected, the photovoltaic system performed better and presented a higher solar fraction than the solar thermal arrangement.

For the solar thermal system, the solar fraction represents 66.5 % coming from the collectors and 33.5 % of the total energy coming from the grid. While for the photovoltaic system, 80.9 % from the total energy was provided by the PV panels, while only 19.1 % of the energy had to be consumed from the grid.

- Avoided fossil fuel use and CO_2 emissions

In order to calculate the amount of CO_2 equivalent of the technologies here presented, a report from energy and environmental research published by the government of Austria, which is based on the European Network Transmission System Operator for Electricity (ENTSO-E), was used as reference (Biermayr et al., 2020). Based on the total production of the solar thermal system per year, which was 2160 kWh and using the CO_2 equivalent emission coefficient of 434.7 gCO_{2equi}/kWh, it was possible to determine that the amount of 939 kilograms of CO_2 were spared by the use of this system. This is also equivalent to CO_2 emissions from 355 liters of diesel that could be spared by the use of this technology (Valsecchi et al., 2009).

With respect to the photovoltaic system, the annual production was around 2800 kWh, based on this value and using the same reference previously employed, the amount of CO_2 emissions avoided was determined as 1217 kilograms of CO_2 (Biermayr et al., 2020). This is also equivalent to CO_2 emissions from 460 liters of diesel that could be spared (Valsecchi et al., 2009). It is important to notice that this section focus on the CO_2 emission that could be spared by the use of the technologies here described and that do not take into account the CO_2 emissions during the manufacturing and recycling processes.

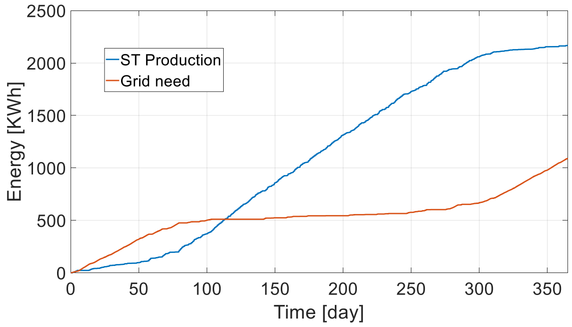

Figure 5: Yearly solar thermal energy production versus energy needed from grid

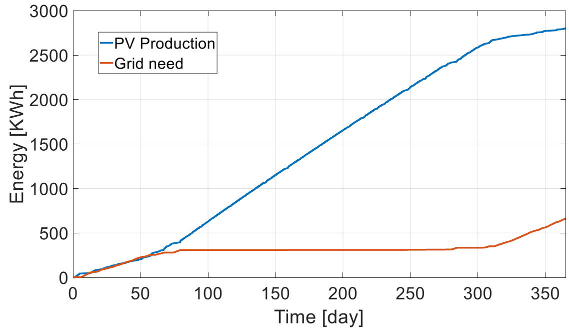

Figure 6: Yearly photovoltaic energy production versus energy needed from grid

3.2. Industrial application results

This section aims to compare the applications of the two different power to heat strategies discussed in sections 2.2.1 and 2.2.2, a photovoltaic system connected to an electric element and a photovoltaic system connected to a heat pump, respectively. The same strategy used for the residential application was also implemented for the industrial application, hence, in order to provide a broader view of the systems functionality, a daily and an annual comparison of both systems was performed. It is also important to notice that, the same weather files, from a region in West Germany, formerly used in the simulations, were also implemented here. Both systems have the purpose of keeping the water tank at the desired temperature in order for it, to be able to provide enough hot water to run distinct industrial processes.

Daily comparison: For this comparison, once more, two different days with distinct weather conditions, one in summer and the other in winter were chosen and the water temperature obtained throughout the tank was measured. For the industrial application, as well as in the previous application, in order to allow a better observation of the temperatures inside of the water tank, the same was divided into ten nodes, being Node 1 on the bottom and Node 10 on the top, which can be seen on the top part of the Figure 7 and Figure 8 below.

It is also important to emphasize that, also for this application, a temperature limit of 95 °C was set in the tank in order to avoid water temperatures higher than 100 °C. Therefore, during some days with high solar radiation when the water temperature in the tank reaches the limit, no more energy is transferred from the photovoltaic or heat pump system into the tank.

In Figure 7, it is possible to see the difference between the node temperatures as soon as the tapping starts and the PV system starts delivering energy to tank. As earlier mentioned, the photovoltaic system presents an electric element installed in the bottom of the storage tank, consequently, the temperatures from the second node upwards increase and the temperature of the bottom node continues to decrease. One can also notice that immediately after the tapping ceases, the temperatures inside the storage stop changing and remain the same until the end of the day.

Regarding the heat pump system, the heat exchange zone was installed on the bottom of the tank and when the heat pump operates all the nodes above the heating zone have their temperature increased as well. Across the day, the heat pump is turned on and off a few times, which leads to this peak behavior that can be observed in Figure 8. Also in this system, when the tapping stops, the temperature inside of the tank do not change anymore and remain the same until the end of the day.

When comparing both figures one can recognize that for the heat pump system the water temperature inside of the water tank reaches higher values than the ones achieved in the photovoltaic plus electric heater arrangement. However, in Figure 7, all the energy used could be provided by the system, while in Figure 8, part of the energy had to be provided by the grid, in order to power up the heat pump.

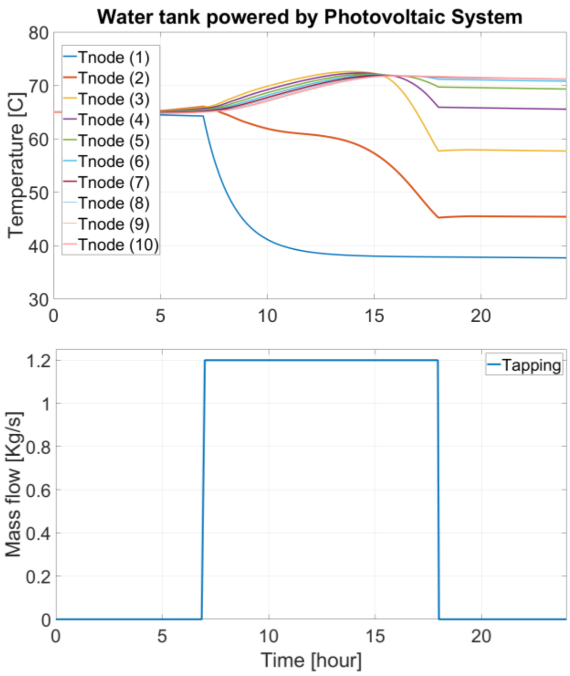

Figure 7: Final temperature in water tank with PV system (top) and tapping mass flow (bottom) in a summer day

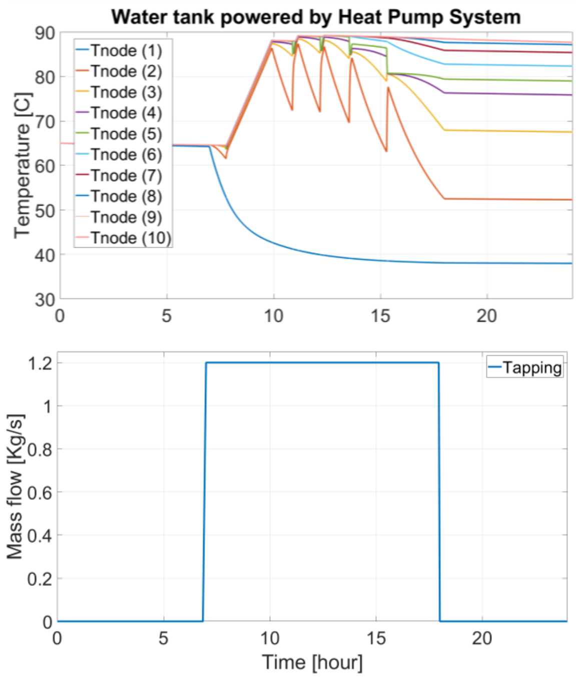

Figure 8: Final temperature in water tank with HP system (top) and tapping mass flow (bottom) in a summer day

Regarding the winter day, as earlier mentioned, in the photovoltaic system, a backup heating element was installed in the upper part of the tank, and should start operating when the temperature around it reaches values below 60 °C. Figure 9 presents the behavior of the photovoltaic arrangement in this day, and it is possible to observe that throughout this time, the temperature in the bottom layers of the tank decrease when the tapping begins. However, as soon as the temperature around the backup heater sensor reaches the set value (60°C), it starts operating and the temperature in the upper nodes increase.

With respect to the heat pump system, Figure 10 displays its performance in this winter day. It is possible to recognize the similarity between the peak behavior presented here and in Figure 8. In the winter day, however, the heat pump is turned on and off more often and the temperatures reached by the system are lower than the ones reached during summer, which was already expected. Once more, when the tapping in the system ceases the temperature of all nodes inside of the tank remain the same until the end of the day.

When comparing both systems, it is possible to notice that, the end temperatures inside of the tank differ considerably by the end of the day, in Figure 9 one can see that basically half of the tank has temperatures between 40 °C and 50°C, while in Figure 10, only the bottom node presents a lower temperature and all the other nodes have temperatures greater than 58 °C. Despite that, in order to keep the temperature at the desired level (60°C) both of them needed to consume energy from the grid. As predicted, the amount consumed was much bigger for the photovoltaic plus electric element arrangement than for the heat pump system.

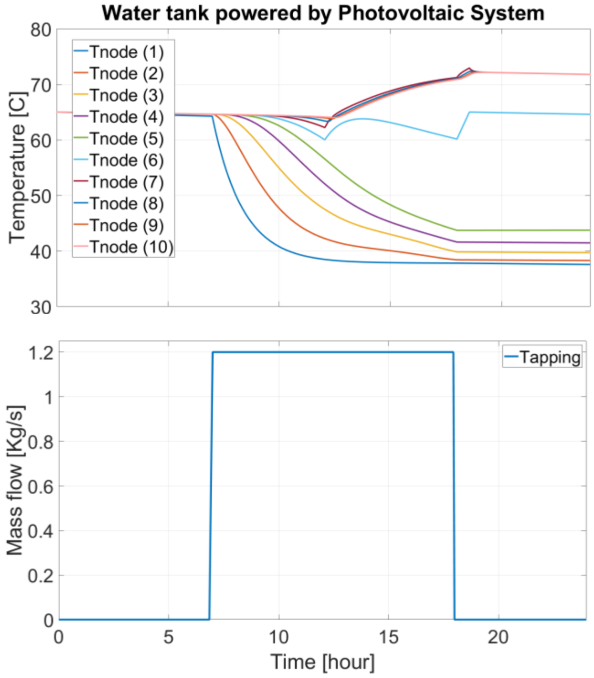

Figure 9: Final temperature in water tank with PV system (top) and tapping mass flow (bottom) in a winter day

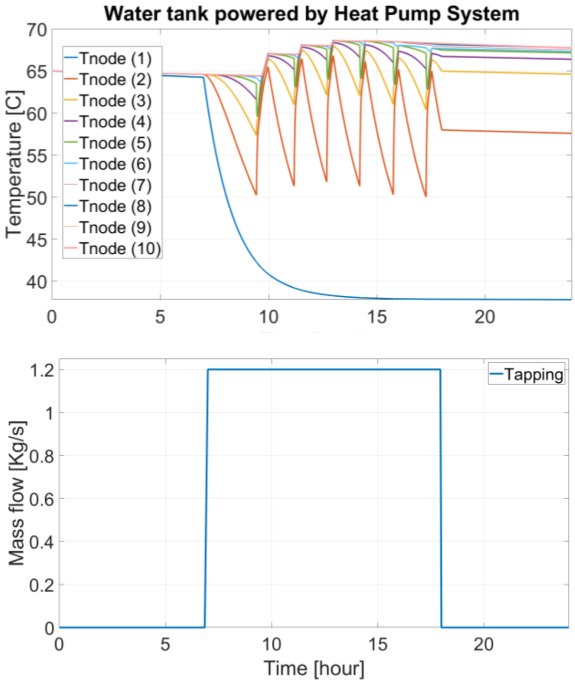

Figure 10: Final temperature in water tank with PV system (top) and tapping mass flow (bottom) in a winter day

Annual comparison: For both systems, it was observed if it was possible to maintain the desired temperature inside of the tank during the time while the tapping was occurring and how much extra power coming from the grid would need to be consumed to reach this goal in a yearly perspective. This section also focused on calculating the total renewable fraction supplied by the systems and also the avoided fossil fuel use and the avoided CO_2 emissions.

In Figure 11, the total amount of energy produced by the photovoltaic system to power the electric element during an entire year can be observed, as well as the total energy consumed from the grid in the same period. It can be noticed that, from around day 100 until day 300 (usually, sunnier days with reduced amount of clouds), the amount of Grid need (red line), present a small increase when compared to the periods in the begin and end of the year (winter days, usually with lower solar irradiation). Nevertheless, by the end of the year, the total amount needed from the grid was higher than what could be provided by the PV system.

Regarding the heat pump system, Figure 12 displays the total amount of energy consumed from the grid (red line) and the amount of energy provided by the renewable sources (photovoltaic plus heat source) to the tank. One can notice that this S shape behavior present in the previous picture during the summer months, for the grid energy, cannot be seen in Figure 12. This means that during this time, a higher amount of energy from the grid was consumed to power up the heat pump system than what was needed to power the electric element inside of the tank in the previous system.

When comparing both figures, it is possible to notice that the final amount of energy needed from the grid is far larger for the PV plus electric element system (232 MWh) than what is needed for the photovoltaic plus heat pump system (124 MWh). This happens due to the extra heat source energy that comes from the ground and is used as heat source by the heat pump, decreasing the amount of energy that this system needs to consume from the grid to keep the temperature inside the storage at the desired level.

- Renewable fraction

The renewable fraction corresponds, in this case, to the amount of energy that is being provided by the renewable sources in the systems here presented (photovoltaic and ground source). Not only for the photovoltaic plus electric element system, but also for the photovoltaic plus heat pump arrangement, the total amount of energy needed to keep the water tank at the desired temperature, was computed and the percentage coming from the grid and from the heating system was calculated. Concerning the industrial application, the photovoltaic plus heat pump system had a better performance than the photovoltaic plus electric element system and, therefore, presents a higher solar fraction.

For the PV plus electric element system, the solar fraction represents 45.7 % coming from the PV panels and 54.3% of the total energy coming from the grid. While for the PV plus heat pump system, 71.6 % from the total energy was provided by the PV panels and ground source, while 28.4 % of the energy had to be consumed from the grid.

- Avoided fossil fuel and CO2 emission

Based on the total production of the photovoltaic plus electric system per year, which was 196.2 MWh and using once more the CO_2 equivalent emission coefficient of 434.7 gCO_{2equi}/kWh, it was possible to determine that the amount of 83.5 tons of CO_2 were spared by the use of this system (Biermayr et al., 2020). This is also equivalent to the CO_2 emissions from 32 cubic meters of diesel (Valsecchi et al., 2009).

With respect to the PV plus heat pump system, the total annual production was 313 MWh, based on this value and using the same CO_2 equivalent emission coefficient of 434.7 gCO_{2equi}/kWh, it could be determined that the amount of CO_2 emissions avoided was 136 tons of CO_2 (Biermayr et al., 2020). This is equivalent to the CO_2 emissions from 51.5 cubic meters of diesel that could be spared (Valsecchi et al., 2009). As mentioned in the previous section, the focus of this investigation, is on the CO_2 emission that could be spared by the use of the technologies here described and do not take into account the CO_2 emissions during the manufacturing and recycling processes of these components.

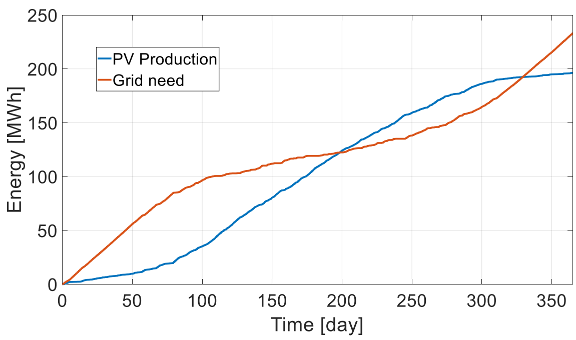

Figure 11: Yearly large scale photovoltaic energy production versus energy needed from grid

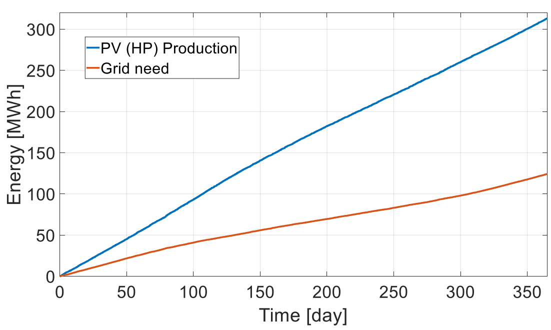

Figure 12: Yearly large scale photovoltaic energy production to heat pump versus energy needed from grid

4. Conclusions

In conclusion, this work could demonstrate that, first, the modelling of Power to Heat systems can be done utilizing MATLAB/Simulink ™ and that its results look reliable. Second, the models developed can be used not only for residential applications, but also in an industrial scale.

As previously discussed, one of the major goals of this work was to analyze different applications of P2H technologies and state if they are reasonable systems to be implemented in a sector coupling project. By the end of this study, it is clear that when it comes to integrate the energy coming from the renewable sources into the storage systems, all the different applications here proposed, presented a good outcome and that the bigger part of the energy generated could be incorporated into the storage systems. However, it was also possible to notice that some systems performed better than others did.

Regarding the household application, the solar thermal and the photovoltaic systems presented a satisfactory solar fraction when considering the annual simulation, having the photovoltaic arrangement a better performance (80.9% solar fraction) than the solar thermal structure (66.5%). This suggests that, both systems can be installed in a household with no further problems and that the habitants would have enough Domestic Hot Water throughout the year at the desired temperature.

Concerning the industrial application, it could be observed that the photovoltaic plus heat pump and the photovoltaic plus electric element systems showed a good performance. However, as it was expected, the solar fraction achieved in the annual simulation by the PV plus heat pump system was better (71.6%) than the one of the PV plus electric element arrangement (45.7%). Based on that it is possible to affirm that the photovoltaic system connected to the electric element immersed in the water tank not only performed better in the residential application, but also presented satisfactory results the industrial application and should definitely, be taken into consideration when considering a P2H strategy for a Sector Coupling project.

It also should be noted that, the use of any of the applications here discussed leads to CO_2 emissions savings and that, as previously presented, up to 136 tons of CO_2 could be spared, when using, for example, the PV plus heat pump system in the industrial application. This is important because these are times when, not only the CO_2 emissions of all energy systems should be taken in consideration but also how much fossil fuel use can be avoided by its implementation.

Factors like solar collector prices, photovoltaic panels' prices and investment capital for an eventual renovation of the heating system in the household or in the hot water cycle in an industrial plant can make one system be a better investment than the other but these were topics not explored in this work.

Finally, it is also important to remark that the weather file used in the simulations has a huge influence in the final results of the systems. In this work, as previously mentioned, the weather files used come from a location in West Germany, which presents a high amount of overcasted days throughout the year, which, therefore, decreases the amount of energy that can be delivered not only by the solar thermal system but also by the photovoltaic system. Choosing a location on the southern hemisphere or in places with a higher amount of sunny days throughout the year will lead to a higher solar fraction for all the systems here discussed and therefore a better performance.

5. Acknowledgments

This project is financed by research subsidies granted by the government of Upper Austria.

6. References

REN21, 2019. Renewables 2019 Global Status Report. Paris, REN21 Secretariat

Ritchie H., Rosesr M, 2017. CO2 and Greenhouse gas emissions. Last revised August 2020, accessed on 28/08/2020, URL (https://ourworldindata.org/co2-and-other-greenhouse-gas-emissions)

Wohlgemuth N., Monga P., 2008. Renewable Energy for Industrial Applications in Developing Countries. In: Goswami D.Y., Zhao Y. (eds) Proceedings of ISES World Congress 2007 (Vol. I – Vol. V). Springer, Berlin, Heidelberg. https://doi.org/10.1007/978-3-540-75997-3_593

Solar Institut Juelich. 2018. CARNOT Toolbox. Matlab/Simulink R2018a.

Weiss W., Spörk-Dür, M, 2019. Solar Heat Worldwide. AEE INTEC.

Biermayr, P., Dißauer, C., Eberl, M., Enigl, M., Fechner, H., Fürnsinn, B., Jaksch-Fliegenschnee, M., Leonhartsberger, K., Moidl, S., Prem, E., Schmidl, C., Strasser, C., Weiss, W., Wittmann, M., Wonisch, P., Wopienka, E. 2020. Innovative Energietechnologien in Österreich Marktentwicklung 2019. Wien: Bundesministeriums für Klimaschutz, Umwelt, Energie, Mobilität, Innovation und Technologie (BMK).

Valsecchi C., ten Brink P., Bassi S., Withana S., Lewis M., Best A., Oosterhuis F., Dias Soares C., Rogers-Ganter H., Kaphengst T. 2009. Environmentally Harmful Subsidies: Identification and Assessment, Final report for the European Commission's DG Environment, November 2009. Annex 5: Subsidy level indicators for the case studies. Accessed on 18/12/2020, URL (https://ec.europa.eu/environment/enveco/taxation/pdf/Annex%205%20-%20Calculations%20from%20the%20case%20studies.pdf)

Solar Assisted Heat Pump Systems Based on Hybrid PVT Collectors for the Provision of Hot Water, Cooling and Electricity in Buildings

María Herrando[1], Adriana Coca-Ortegón[2], Isabel Guedea[2] and Norberto Fueyo

[1] Fluid Mechanics Group, School of Engineering and Architecture University of Zaragoza, Zaragoza (Spain)

[2] EndeF Engineering S.L., Zaragoza (Spain)

Abstract

This work aims to assess the techno-economic performance of solar hybrid PVT collectors integrated via thermal storage tanks with an air-to-water reversible vapour-compression (rev-VC) unit. Real weather data along with the actual heating, cooling and electricity demands of an industrial building are inputs to the transient model. Different configurations are analysed varying the number of PVT collectors and the storage tanks' volumes. Radiative cooling of the PVT collectors is also considered to satisfy the cooling demand. The results show that the proposed systems have the potential to cover 19.2% to 46.5% of the cooling demand through radiative cooling, depending on the number of PVT collectors, thus decreasing the electricity consumed by the rev-VC. All the analysed configurations can also cover >60% of the demand for heat at 60ºC and between 31.7% to 48.5% of the electricity demand of the analysed building. The systems have a payback time of <10 years. The selected system, consisting of 16 PVT collectors (26.1 m^2) and 2 tanks of 350 L each one, is currently being manufactured and will be tested under real weather conditions from middle September 2020.

Keywords: hybrid PVT collector, energy modelling, heat pump, payback time, radiative cooling

1. Introduction

Heating and cooling (H/C) is the largest energy-consuming application in Europe, responsible for 51% of the total final energy demand (580 Mtoe) (European Union, 2018). Most of the demand is for space heating (52%) process heating (30%) and water heating (10%), with space cooling demand being still limited but fast-growing. Buildings are the main consumers of H/C: 45% of the energy for H/C is used in the residential sector, 37% in industry and 18% in services (European Commission, 2016). However, the share of renewable energy (RES) for H/C in 2016 was only 19.1% (European Union, 2018). Thus, the development and implementation of RES for building H/C are essential for displacing fossil-fuel utilisation, reducing emissions and increasing the share of RES. Solar heating and cooling (SHC) technologies appear as an attractive decarbonisation alternative, as they can provide both heating and cooling.

In recent years, hybrid photovoltaic-thermal (PVT) collectors are gaining increasing attention both in research and in applications, as they combine the output of photovoltaic (PV) and solar thermal systems from the same aperture area: they generate both electricity and useful heat simultaneously (Herrando et al., 2019b), with higher overall efficiency than the separate systems (Das et al., 2018; Joshi and Dhoble, 2018). Further, the integration of PVT collectors with H/C technologies allows the simultaneous generation of hot water, cooling and electricity, and thus has the potential to cover a significant fraction of the energy demands of buildings (Herrando et al., 2019a). The relevance and potential of PVT collectors and their integration with other components to obtain new solutions in HVAC systems are confirmed with the creation of Task 60 of PVT systems of the SHC programme of the IEA (IEA, 2018). However, most of the research in the literature focuses on SHC technologies that use solar thermal collectors (Ge et al., 2018) for solar cooling (Leonzio, 2017; Montagnino, 2017), or PV panels integrated into solar assisted heat pump (SAHP) systems for solar heating (Bellos et al., 2016; Thygesen and Karlsson, 2014; Vaishak and Bhale, 2019).

This research proposes solar combined cooling, heating and power (S-CCHP) systems based on PVT collectors to help decarbonising industrial buildings. The aim here is to analyse the techno-economic performance of several S-CCHP system configurations and select the system size to build a pilot plant that will provide cooling, heating and power to an industrial building. To this end, a transient model is developed that features PVT collectors,

doi:10.18086/eurosun.2020.05.10 Available at http://proceedings.ises.org

thermal storage and an air-to-water (a-w) reversible vapour-compression (rev-VC) unit (also known as solar-assisted heat pump, SAHP).

2. Methodology

The proposed S-CCHP systems are modelled in dynamic simulation software, TRNSYS (Klein, 2016), where the real heating, cooling and electricity demands of an industrial building located in Zaragoza (Spain) are used as inputs to the model to undertake transient simulations with a 15-min time-step for a period of one year. The existing scenario of energy demand and supply is considered to estimate the annual cost savings with the proposed systems, considering current utility prices. The systems' payback time is also estimated.

2.1. Energy demand of the industrial building

The industrial building consists of two main areas: the manufacturing area and the office area. The manufacturing area includes lighting and different electrically powered devices and equipment. This area also demands hot water at 60 ºC for the shower section. The office area has a demand for heating and cooling, which are currently satisfied by an air-to-air reversible vapour compression unit, powered by electricity. This area also includes lighting and other small electrical devices (e.g. computers, printers, etc.).

Table 1 presents the real energy demand of the industrial building, including heat at 60ºC, space heating or low-temperature heat (30-35ºC), cooling (18-23ºC) and electricity consumption (for lighting and other electrical devices). The total annual electricity consumption in the industrial building is 24,566 kWh, of which 11,728 kWh (48%) corresponds to the thermal energy demand. Specifically, the largest thermal energy demand is cooling, accounting for 39%, followed by low-temperature heat and heat at 60 ºC demands (35% and 26% respectively).

Tab. 1: Annual energy demands and their corresponding energy consumptions for the industrial building under study.

Description	Heat at 60ºC ($Q_{H60,dem}$)	Low-temperature heat ($Q_{lth,dem}$)	Cooling ($Q_{Cool,dem}$)	Electricity ($E_{El,dem}$)
Schedule	Mon - Fri (8-18h)	Mon - Fri (8-18h)	Mon - Fri (8-18h)	Baseload (24 h/day) + Higher consumption Mon - Fri (8-18h)
Temperature (ºC)	60	30-35	7 a 12	
Annual demand (kWh/year)	2,998	9,772	9,193	12,548
Existing system	Electrical heater	Air-to-air heat pump		-
Current system efficiency	0.98	2.36	2.03	-
Annual consumption (kWh/year)	3,060	4,140	4,528	12,548

2.2 Solar Combined Cooling Heating and Power System

The S-CCHP system consists of PVT collectors, an a-w rev-VC unit and two parallel storage tanks, the hot-water tank to satisfy heat at 60 °C and the inertia tank to satisfy low-temperature heating or cooling demands. Depending on the tanks' temperature and the PVT collectors' temperature, the thermal output of the PVT collectors is directed to one of the two tanks through an active closed-loop system with a bypass valve controlled by a differential temperature controller (Figure 1). When there is cooling demand, water circulates through the PVT collectors at night to cool the water in the inertia tank (radiative cooling). In both heating and cooling modes, the a-w rev-VC unit acts as an auxiliary heater/cooler, to reach the set-point temperatures of the building's thermal demand. The rev-VC unit is electrically powered by the PVT collectors, and the PVT electrical output not consumed by the rev-VC unit is used to match the industry's electricity demand. The main system components (PVT collectors, storage tanks, rev-VC unit) are implemented in the model modifying the corresponding types to match the real characteristics and performance of the commercial units.

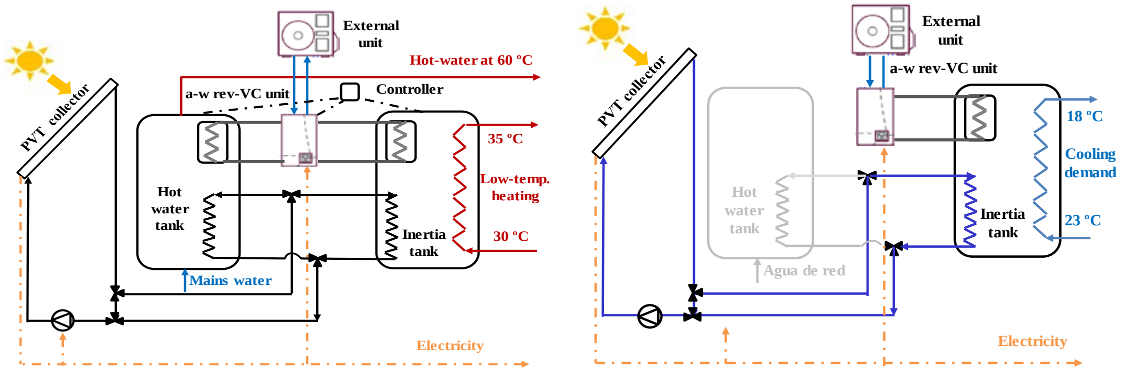

Fig. 1: Schematic diagrams of the S-CCHP systems in (left) heating mode and (right) cooling mode.

PVT collector

The ECOVOLT collector (uncovered, 300 W_p, 1.63 m^2 aperture area) is used in this work (EndeF, 2017). Type 50d is modified and adjusted to match the thermal efficiency (η_{th}) and the electrical efficiency (η_e) curves provided by the manufacturer (see Eqs. (1-3)). PVT collectors are connected in parallel so as flow-rate, inlet and outlet water temperatures all the same in all of them. A constant flow-rate of 50 l/h is used in both PVT collectors (Herrando et al., 2018a).

$$\eta_{th} = 0.472 - 9.5 \cdot T_r \quad \text{(eq. 1)}$$

$$T_r = \frac{(T_{fm} - T_a)}{I_t} \quad \text{(eq. 2)}$$

$$\eta_e = 0.1844 \cdot \left(1 - 0.0039 \cdot \left(T_{PV} - T_{ref}\right)\right) \quad \text{(eq. 3)}$$

where T_r is the reduced temperature, I_t (W/m^2) is the total global solar irradiance on the surface at a tilted angle, T_{fm} is the mean fluid temperature, T_a is the ambient temperature, T_{PV} is the PV cell temperature and T_{ref} is 25 °C (value given by the manufacturer).

Stratified water storage tanks

The tanks are modelled using a stratified water storage tank of constant fluid mass (Type 534), considering six fully mixed equal-volume segments that divide the cylinder along its vertical axis. In the hot-water tank, preheated water for heat at 60 °C demand is supplied via a port at the top of the tank, and water is refilled by mains water from the bottom node. One immersed heat exchanger connected to the PVT collector array runs from the middle (n=3) to the bottom of the tank (n=6), and another one connected with the a-w VC unit runs from the top (n=1) to the next node (n=2) to heat the water inside the tank to the set-point temperature (see Fig. 1 left). The stratified inertia tank that satisfies the low-temperature heating also has two immersed heat exchangers connected with the PVT collector array (from n=3 to n=6) and with the a-w VC unit (from n=1 to n=2), and a third immersed heat exchanger that heats the water for low-temperature heating, or cools the water for cooling, depending on the operation mode, in a closed-loop. The cooling demand is satisfied through this second storage tank, with the a-w VC unit working in cooling mode and the PVT collector array working at night. The storage tanks' volumes are varied through the variation of the V_t/A_{cT} ratio, where V_t is the tank volume (L) and A_{cT} is the total solar collector area (m^2). The size of the solar immersed heat exchanger coils also varies with the tank size through the variation of the tank height.

rev-VC unit

The reversible Vapour-Compression (VC) unit acts as an auxiliary heating/cooling. The unit is modelled using Type 941, and the data files (performance data) are modified to fit the real performance of the rev-VC unit (e.g. temperatures, COP, electricity consumption) provided by the manufacturer. Based on the thermal energy demands of the industrial building, the Yutaki S6 model (RWM-6.0) from Hitachi is selected (Hitachi), with a nominal thermal power of 16 kW for heating and 13.7 kW for cooling.

2.3 Key Performance Indicators

A set of Key Performance Indicators (KPIs) are defined to analyse the different solar configurations considered in this work, based on a report of Subtask D of Task 60 (IEA, 2018):

- Thermal energy yield per m^2 (Q_{PVT}, kWh/m^2): thermal energy output of the PVT collectors per m^2
- Electrical energy yield (E_{PVT}, kWh/m^2): electricity output of the PVT collectors per m^2
- Solar fractions: defined as the energy demand covered divided by the total energy demand: Solar thermal fraction of heat at 60ºC ($f_{s,H60}$), low-temperature heat ($f_{s,lth}$), radiative cooling ($f_{s,c-r}$), solar electrical fraction of cooling ($f_{s,c-e}$) and electricity demand ($f_{s,e}$).
- Investment cost (C_0, €/m^2): estimated from price lists available from solar retailers in the EU (Barilla Solar, 2017; Viridian Solar, 2017; Wagner Renewable, 2017). The cost of the storage tank is estimated using a correlation based on market prices of existing tanks across a range of storage volumes (Herrando et al., 2018b). The total installation costs are also considered. The main costs are associated with the vapour compression unit (42%) and the PVT collectors and support structures (27%).
- Payback time (*PBT*, years): defined as the period of time required to recover the investment cost (Herrando et al., 2018b; Kalogirou, 2014), is estimated:

$$PBT = \frac{ln\left[\frac{C_0\cdot(i_F-d)}{AS}+1\right]}{ln\left(\frac{1+i_F}{1+d}\right)} \quad \text{(eq. 4)}$$

where d is the discount rate (5%) (International Energy Agency (IEA), 2010; Kim et al., 2012) and i_F is the fuel inflation rate (3.5%) (Herrando et al., 2019a). The annual savings (*AS*) refer to the difference between the current annual costs that the industrial building incurs to cover all the energy demand (e.g. business as usual scenario, AC_{bau}), and the annual costs that the building would incur to cover all the energy demand if the proposed solar system was installed (AC_{ss}):

$$AS = AC_{bau} - AC_{ss} \quad \text{(eq. 5)}$$

$$AC_{bau} = E_{El,dem}\cdot c_e + \frac{Q_{H60,dem}}{COP}\cdot c_e + \frac{Q_{lth,dem}}{COP}\cdot c_e + \frac{Q_{Cool,dem}}{COP}\cdot c_e \quad \text{(eq. 6)}$$

$$AC_{ss} = E_{grid}\cdot c_e + E_{exc}\cdot s_e \quad \text{(eq. 7)}$$

where $E_{El,dem}$ refers to the electricity demand of the factory, $Q_{H60,dem}$ is the demand of heat at 60 °C, $Q_{lth,dem}$ is the low-temperature heat demand, $Q_{Cool,dem}$ is the cooling demand, E_{grid} is the electricity demand that cannot be covered by the proposed solar system and thus should be imported from the grid, E_{exc} is the electricity excess exported to the grid and imported later on via net metering, c_e is the electricity price (0.244 €/kWh) and s_e is electricity price for the net metering option (0.122 €/kWh).

3. Results and discussion

Initial validation was undertaken at the component level. For the PVT collectors, the electrical efficiency curve obtained in the simulation is within 2% of the respective efficiency provided by the manufacturer, while the thermal efficiency is within 5%, except for T_r > 0.045. However these high T_r values are for T_{in} > 70 °C; and uncovered PVT collectors are not usually operated at temperatures higher than 70 °C, because thermal losses at these temperatures are larger than thermal gains, and therefore water is cooled, rather than heated, in the collector. The performance of the rev-VC unit was validated with the manufacturers' data, integrated into the TRNSYS type.

3.1 Sensitivity Analysis

A series of sensitivity analyses were undertaken to optimise the system's performance and minimise the system's payback time. The modified parameters were the number of PVT collectors with the corresponding solar collector area (A_{cT}), and the sizes of the storage tanks, including the volume of the hot-water tank (V_{t1}) and the volume of the inertia tank (V_{t2}). Table 2 summarises the parameters' values as well as the main results for the different analysed cases.

The priority given for the electricity generated by the PVT collectors is to cover: 1) electricity consumed by the rev-VC for cooling ($E_{Cool.rVC}$), 2) electricity demand ($E_{El.dem}$), 3) electricity consumed by the rev-VC for low-temperature heat ($E_{lth,rVC}$), 4) electricity consumed by the rev-VC for heat at 60 °C ($E_{H60,rVC}$).

Tab. 2: Summary of analysed cases and annual energy results for the studied industrial building.

Variable	Analysed Cases					
	C1	**C2**	**C3**	**C4**	**C5**	**C6**
Nº PVT collectors **(-)**	16	16	16	30	30	30
A_{cT} (m^2)	26.1	26.1	26.1	48.9	48.9	48.9
V_{t1} (L)	350	600	950	500	500	500
V_{t2} (L)	350	350	350	500	1000	1500
V_t=V_{t1}+V_{t2} (L)	700	950	1400	1000	1500	2000
V_{t1} /A_{cT} (L/m^2)	13.4	23.0	36.4	10.2	10.2	10.2
V_{t2} /A_{cT} (L/m^2)	13.4	13.4	13.4	10.2	20.4	30.7
V_t /A_{cT} (L/m^2)	26.8	36.4	49.8	20.5	30.7	40.9
$T_{max,t1}$ (°C)	71.7	70.1	64.8	72.4	72.4	72.4
$T_{max,t2}$ (°C)	41.8	41.7	41.7	41.5	40.8	40.7
Q_{PVT} (kWh/m^2)	101.6	104.9	117.5	69.2	71.6	72.8
E_{PVT} (kWh/m^2)	242.2	242.4	242.7	241.5	241.6	241.6
$f_{s,H60}$ (%)	60.4%	63.7%	60.9%	68.3%	68.1%	68.4%
$f_{s,lth}$ (%)	4.6%	4.4%	4.1%	7.5%	8.7%	9.3%
$f_{s,c-r}$ (%)	13.5%	13.5%	13.5%	19.2%	34.9%	46.5%
$f_{s,c-e}$ (%)	49.5%	49.6%	48.6%	94.5%	95.4%	94.8%
$f_{s,e}$ (%)	31.7%	31.7%	31.7%	48.2%	48.5%	48.5%
C_0 (€/m^2)	850	858	870	656	665	674
PBT **(years)**	8.7	8.9	8.9	9.4	9.6	9.7

The results show that, for the same number of PVT collectors, increasing the hot-water tank volume (cases C1-C3) leads to larger thermal energy yield per m^2 (Q_{PVT}), which is attributed to the larger thermal storage capacity per m^2 (V_{t1} /A_{cT}). Similarly, increasing the inertia tank volume (C4-C6) also leads to larger thermal energy yield per m^2, for the same reason (larger V_{t2} /A_{cT} in this case). However, the thermal energy yield per m^2 is lower for the cases with more PVT collectors, because of the lower total thermal storage capacity m^2 (V_t /A_{cT}) and the consequently higher tank temperature, as shown in Table 2. The water that passes through the PVT collectors is hotter and thus the collectors work at a lower thermal efficiency.

The solar thermal fraction of heat at 60ºC ($f_{s,H60}$) is larger in cases C4 to C6 due to the higher temperature of the hot-water tank, and the larger number of PVT collectors (larger A_{cT}) and thermal storage capacity (V_t). Similarly, the solar thermal fraction of low-temperature heat ($f_{s,lth}$) and the solar thermal fraction of the radiative cooling ($f_{s,c-r}$) are larger as the inertia tank volume (V_{t2}) increases, as expected. It is observed that the latter ($f_{s,c-r}$) considerably increases with the size of this tank, increasing from 19.2% to 46.5% when the inertia tank volume (V_{t2}) is tripled.

The solar electrical fraction of cooling ($f_{s,c-e}$) considerably increases with the number of PVT collectors (cases C4 to C6), as more electricity is generated and thus a larger percentage of the electricity consumed by the rev-VC unit for cooling is covered, with values between 94.5% and 94.8%. The solar electricity fraction of electricity demand ($f_{s,e}$) also increases with the number of PVT collectors, but al less extent, from 31.7% to 48.5% (see cases C4 to C6). The reason attributed is the priorities set within the system, as first the electricity consumed by the rev-VC unit for cooling is covered, and then the excess is used to cover the electricity demand of the building (lighting and other devices).

The system's payback time is larger for the systems with 30 PVT collectors, despite the lower investment cost per m^2 (cases C4 to C6). The main reason attributed to this is the more profitable use of the electricity generated by the PVT collectors. As the number of PVT collectors increases, there is more excess electricity, that is, a larger fraction of the electricity generated cannot be instantaneously used to cover the demand, and thus it has to be exported to the grid, and imported later on when there is more demand than generation. However, the price at which the electricity exported and imported later on is lower than the electricity price (half in this case, as shown in Section 2.3), so larger economic savings are achieved when the electricity is directly used in the building.

Based on these results, the component dimensions of case C1 are selected to build the pilot plant: 16 PVT collectors, with a total solar PVT area of 26.1 m^2; tank volumes, V_{t1} and V_{t2}, of 350 L each one, which implies a total accumulation volume of 700 L, and a ratio V_t / A_{cT} of 26.8. The following section shows the transient results obtained for this case (C1).

3.2 Transient Results of the selected S-CCHP system

This section presents the results of the selected configuration during nine consecutive days in summer (when there is cooling demand) and in winter (when there is low-temperature heat demand).

Figure 2 shows that at night (when there is no solar irradiance, yellow continuous line), the water temperature at the outlet of the PVT collectors drops (dark-red dashed-dotted line). When it is below the water temperature at the bottom of the inertia tank (orange dotted line), the water enters the immersed heat exchanger to cool down the inertia tank. Thanks to this, it is observed that a part of the cooling demand (dashed purple line) can be covered with the radiative cooling (violet continuous line).

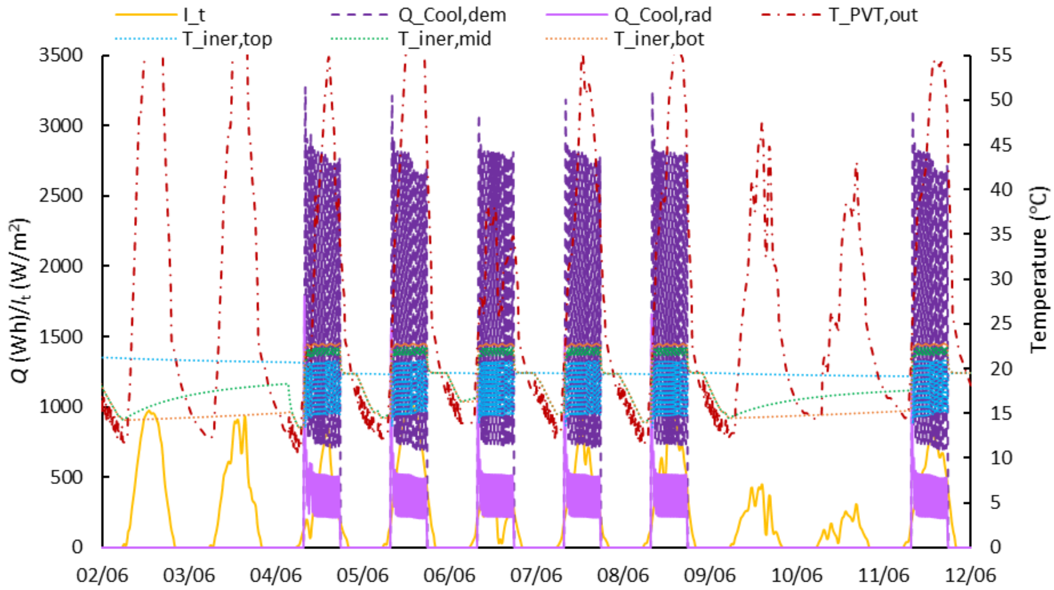

Fig. 2: Total solar irradiance at tilted angle (I_t), cooling demand ($Q_{Cool,dem}$), cooling demand covered with radiative cooling ($Q_{Cool,rad}$), PVT water output temperature ($T_{PVT,out}$), water temperature at the top of the inertia tank ($T_{iner,top}$), water temperature at the middle of the inertia tank ($T_{iner,mid}$), and water temperature at the bottom of the inertia tank ($T_{iner,bot}$) during 2-11 June.

The cooling demand not covered with the radiative cooling is satisfied by the rev-VC unit, which cools down the inertia tank to the required temperature. The electricity consumed by this unit is shown in Figure 3 (dark-blue dotted line, $E_{Cool.rVC}$), as well as the electricity instantaneously covered (light-blue continuous line, $E_{Cool.cov}$) with the PVT electrical output (red continuous line). It is observed that on sunny days, a considerable amount of the energy consumed by the rev-VC for cooling is instantaneously covered, as it occurs during the days when solar irradiance is high (yellow continuous line). The rest of the electricity is used to cover the electricity demand of the industry (dashed purple line). It is observed that during the first weekend (first two days of Figure 3) when there is no cooling demand, all the electricity demand of the industry is covered (violet continuous line). Instead, due to the low irradiance levels during the second weekend (yellow continuous line), the electricity demand is only partially covered.

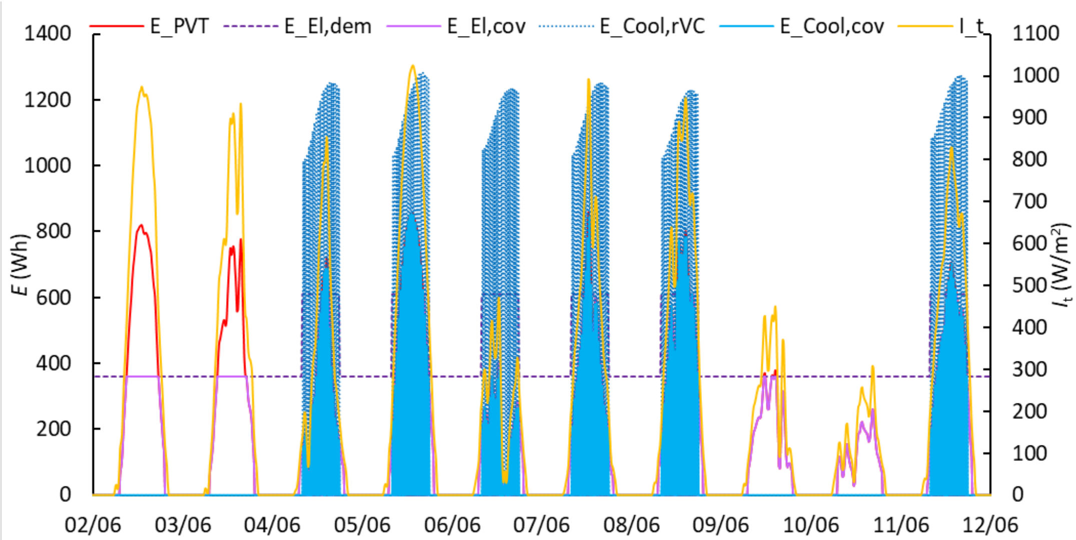

Fig. 3: Total electricity generated (E_{PVT}), electricity demand ($E_{El.dem}$), electricity demand instantaneously covered ($E_{El,cov}$), electricity consumed by the rev-VC for cooling ($E_{Cool.rVC}$), electricity consumed by the rev-VC for cooling instantaneously covered ($E_{Cool.cov}$), and total solar irradiance at tilted angle (I_t) during 2-11 June.

Figure 4 shows the low-temperature heat demand (dashed purple line, $Q_{lth,dem}$), along with the part covered by the PVT thermal output (violet continuous line, $Q_{lth,cov}$). The system gives priority to heat the water in the inertia tank until 40 °C, thus, during the first weekend, when there are not heating demands, water from the PVT collectors heats the inertia tank until it reaches 40 °C (see dark-red and green dotted lines). Afterwards, early in the morning, part of the low-temperature heat demand is covered with the PVT thermal output. The rest of the demand is covered by the rev-VC unit (see Figure 6), which heats the water at the top of the tank (dark-red dotted line).

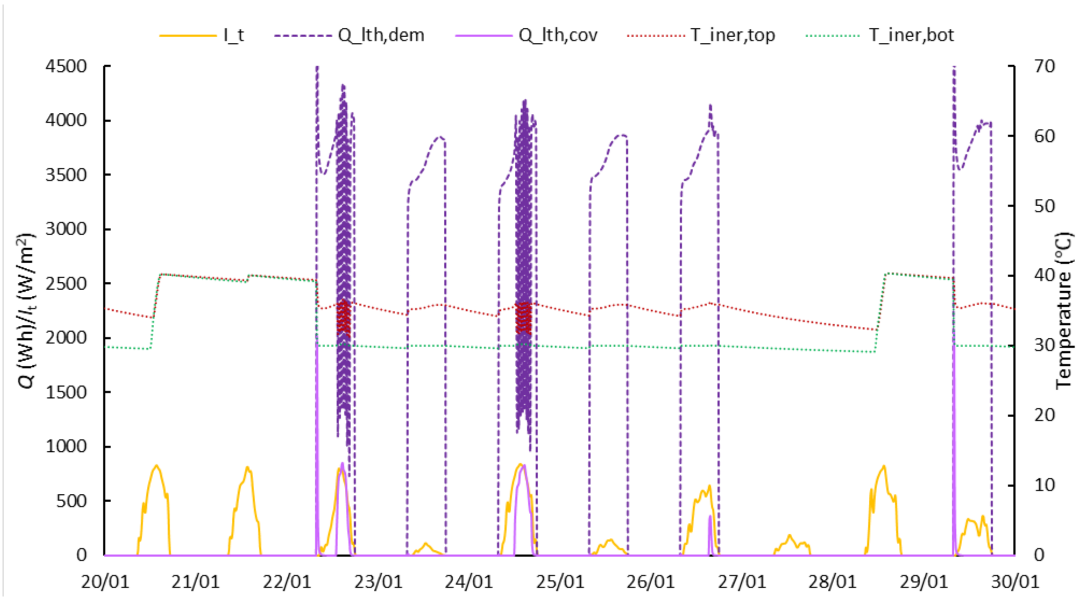

Fig. 4: Total solar irradiance at tilted angle (I_t), low-temperature heat demand ($Q_{lth,dem}$), low-temperature heat demand covered ($Q_{lth,cov}$), water temperature at the top of the inertia tank ($T_{iner,top}$) and water temperature at the bottom of the inertia tank ($T_{iner,bot}$) during 20-29 January.

As shown in Figure 5, the demand for heat at 60 °C (dark-blue dotted line, $Q_{H60,dem}$) is constant from Monday to Friday at working hours. The PVT thermal output heats the water in the hot-water tank after the inertia tank reaches 40 °C, increasing the water temperature (red dashed-dotted line), so part of the demand of heat at 60 °C is covered (light-blue continuous line). The rest of the demand is covered by the rev-VC unit, which heats the water at the top of the tank until it reaches the set-point (red dashed-dotted line).

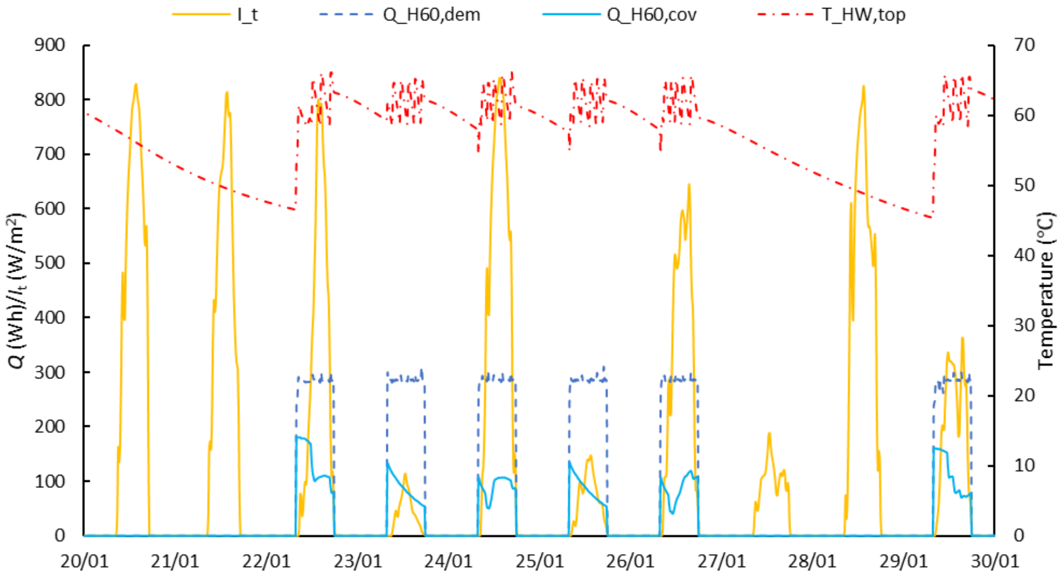

Fig. 5: Total solar irradiance at tilted angle (I_t), demand of heat at 60 °C ($Q_{H60,dem}$), demand of heat at 60 °C covered ($Q_{H60,cov}$low-temperature heat demand covered ($Q_{lth,cov}$), and water temperature at the top of the hot-water tank ($T_{HW,top}$), during 20-29 January.

The heating demands not covered with the PVT thermal output are satisfied by the rev-VC unit, which heats the tanks to the required temperatures. The electricity consumed by this unit for low-temperature heat (dark-blue dotted line, $E_{lth,rVC}$) is shown in Figure 6 and for heat at 60 °C (dashed purple line, $E_{H60,rVC}$) is shown in Figure 7. Figure 6 shows that during the week, the days with a large PVT electrical output (red continuous line), due to high irradiance levels (yellow continuous line), that is, 22[nd] and 24[th] of January, part of the low-temperature heat demand is instantaneously covered by the PVT electrical output (light-blue continuous line, $E_{lth,cov}$). However, the rest of the days, with a lower electricity generation, only a limited amount of the low-temperature heat demand is instantaneously covered.

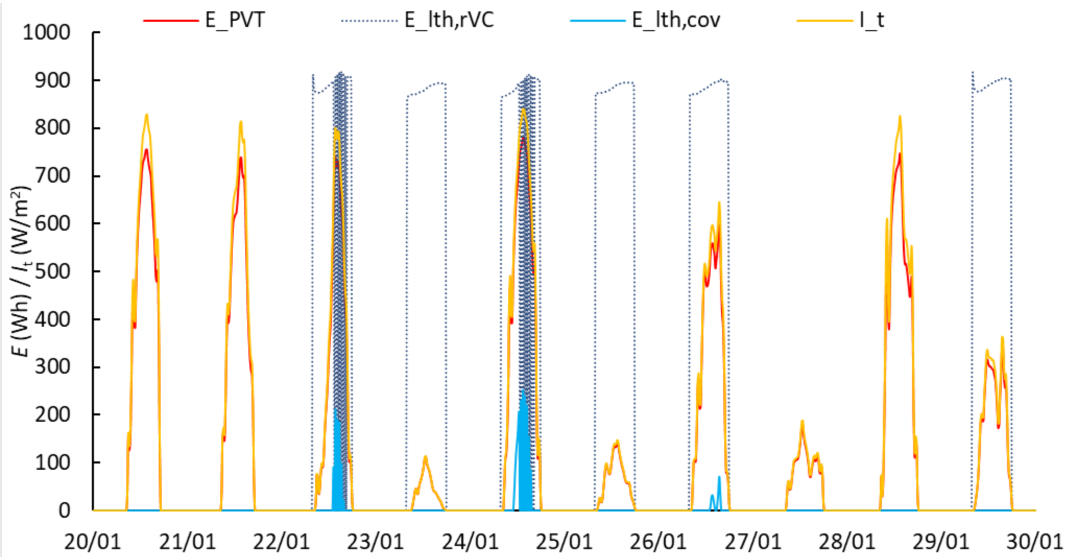

Fig. 6: Total electricity generated (E_{PVT}), electricity consumed by the rev-VC for low-temperature heat ($E_{lth,rVC}$), electricity consumed by the rev-VC for low-temperature heat instantaneously covered ($E_{lth.cov}$), and total solar irradiance at tilted angle during 20-29 January.

Figure 7 shows that only a very limited amount of the electricity consumed by the rev-VC unit for heat at 60 ℃ (dashed purple line, $E_{H60,rVC}$) is instantaneously covered by the PVT electrical output, negligible during the days shown here (violet continuous line, $E_{H60,cov}$). This is attributed to the priorities given within the system, as the electricity consumed by the rev-VC for heat at 60 ℃ is the last one to be satisfied, as explained in Section 3.1.

It is observed that during the first weekend there is a considerable excess of electricity (dashed-dotted green line) which is fed into the grid, to be imported later on to cover the electricity consumed during the night. The reason is the large PVT electrical output (red continuous line) due to the high irradiance levels (yellow continuous line), along with the fact that during the weekend there are no heating and cooling demands. Conversely, the low irradiance levels of the first day of the second weekend (27th Jan) lead to low electricity generation and thus there is no electricity surplus.

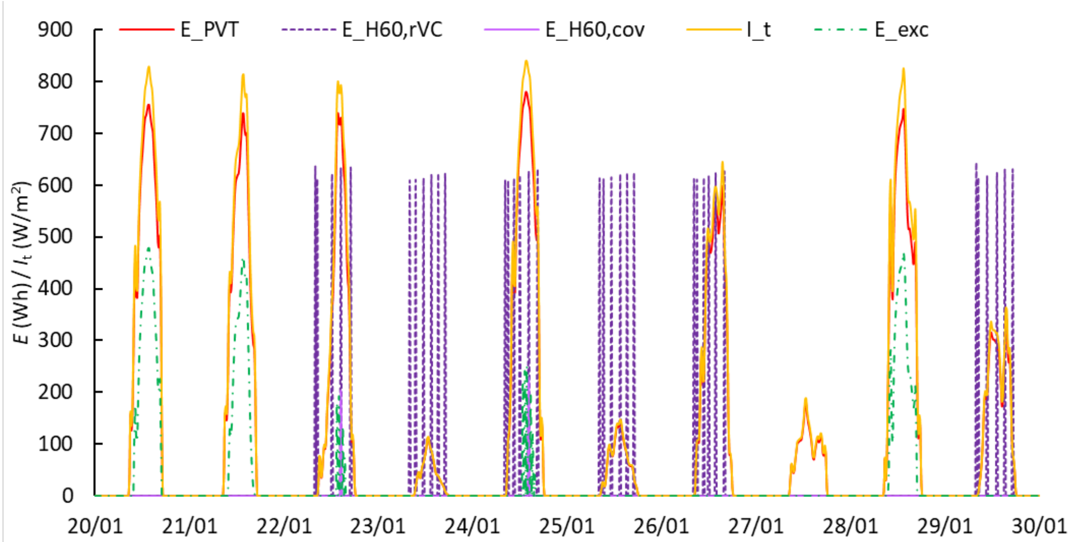

Fig. 7: Total electricity generated (E_{PVT}), electricity consumed by the rev-VC for heat at 60 ℃ ($E_{H60,rVC}$), electricity consumed by the rev-VC for heat at 60 ℃ instantaneously covered ($E_{H60,cov}$), electricity surplus fed into the grid (E_{exc}) and total solar irradiance at tilted angle during 20-29 January.

4. Conclusions

This paper presents the techno-economic performance of several S-CCHP system configurations that feature PVT collectors, thermal storage and an air-to-water (a-w) reversible vapour-compression (rev-VC) unit, for cooling, heating and power provision to an industrial building. The real heating, cooling and electricity demands of an industrial building located in Zaragoza (Spain) are used as inputs to the transient model developed.

In the proposed systems, the PVT thermal output is used to heat the water of two parallel storage tanks, one that provides heat at 60ºC (hot-water tank) and another one that satisfies low-temperature heat in winter and cooling in summer (inertia tank). In summer, water circulates at night through the PVT collectors to cool the water in the inertia tank (radiative cooling). The PVT electrical output is to used cover the electricity demand as well as the electricity consumed by the rev-VC to provide the rest of the cooling, low-temperature heat and heat at 60 ℃ demands.

The results show that the S-CCHP systems have the potential to cover 19.2% to 46.5% of the cooling demand with radiative cooling, depending on the number of PVT collectors, decreasing the electricity consumed by the rev-VC unit. Of the latter, ~50% and ~95% can be covered with the PVT electrical output, with 16 and 30 PVT collectors respectively. All the analysed configurations can also cover >60% of the demand for heat at 60ºC and between 31.7% to 48.5% of the electricity demand (lighting and other devices) of the analysed building.

The economic analysis shows that the lower price at which the electricity exported is imported later on compared to the electricity price (half in this case) influences the profitability of the system. As a consequence, lower economic savings are achieved as the electricity directly used in the building decreases, that is, as the electricity excess increases. Still, all the proposed configurations have a payback time of <10 years. The selected S-CCHP system configuration, 16 PVT collectors (26.1 m^2) and 2 tanks of 350 L each one, is currently being manufactured and will be tested under real weather conditions from middle September 2020.

5. Acknowledgements

This work was undertaken in the framework of 3GSol project, funded under the Retos-Colaboración 2017 Programme, National R&D and Innovation Plan, by the Spanish Government, Ministry of Science, Innovation and Universities and cofunded by the EU, through the European Regional Development Fund (ERDF) [grant number RTC-2017-6026-3].

6. References

Barilla Solar, 2017. Wholesale Solar Thermal Supplies Barilla Solar http://www.barillasolar.co.uk/ (accessed 7.19.17).

Bellos, E., Tzivanidis, C., Moschos, K., Antonopoulos, K.A., 2016. Energetic and financial evaluation of solar assisted heat pump space heating systems. Energy Convers. Manag. 120, 306–319. https://doi.org/10.1016/J.ENCONMAN.2016.05.004

Das, D., Kalita, P., Roy, O., 2018. Flat plate hybrid photovoltaic- thermal (PV/T) system: A review on design and development. Renew. Sustain. Energy Rev. 84, 111–130. https://doi.org/10.1016/j.rser.2018.01.002

EndeF, 2017. Endef - Energy, Development and Future. http://endef.com (accessed 2.10.17).

European Commission, 2016. An EU strategy on heating and cooling. Communication from the Commission to the European Parliament, the Council, the European Economic and Social Committee and the Committee of the Regions.

European Union, 2018. Energy in figures – Statistical pocketbook.

Ge, T.S., Wang, R.Z., Xu, Z.Y., Pan, Q.W., Du, S., Chen, X.M., Ma, T., Wu, X.N., Sun, X.L., Chen, J.F., 2018. Solar heating and cooling: Present and future development. Renew. Energy 126, 1126–1140. https://doi.org/10.1016/J.RENENE.2017.06.081

Herrando, M., Pantaleo, A.M., Wang, K., Markides, C.N., 2019a. Solar combined cooling, heating and power systems based on hybrid PVT, PV or solar-thermal collectors for building applications. Renew. Energy 143, 637–647. https://doi.org/10.1016/j.renene.2019.05.004

Herrando, M., Ramos, A., Freeman, J., Zabalza, I., Markides, C.N., 2018a. Technoeconomic modelling and optimisation of solar combined heat and power systems based on flat-box PVT collectors for domestic applications. Energy Convers. Manag. 175, 67–85. https://doi.org/10.1016/j.enconman.2018.07.045

Herrando, M., Ramos, A., Zabalza, I., 2018b. Cost competitiveness of a novel PVT-based solar combined heating and power system: Influence of economic parameters and financial incentives. Energy Convers. Manag. 166, 758–770. https://doi.org/10.1016/j.enconman.2018.04.005

Herrando, M., Ramos, A., Zabalza, I., Markides, C.N., 2019b. A comprehensive assessment of alternative absorber-exchanger designs for hybrid PVT-water collectors. Appl. Energy 235, 1583–1602. https://doi.org/10.1016/J.APENERGY.2018.11.024

Hitachi, YUTAKI S COMBI. https://www.hitachiaircon.es/gamas/aerotermia/yutaki-s-combi (accessed 20.8.20).

IEA, 2018. Task 60: PVT Systems: Application of PVT Collectors and New Solutions in HVAC Systems, Solar Heating and Cooling Programme.

International Energy Agency (IEA), 2010. Projected Costs of Generating Electricity.

Joshi, S.S., Dhoble, A.S., 2018. Photovoltaic -Thermal systems (PVT): Technology review and future trends. Renew. Sustain. Energy Rev. 92, 848–882. https://doi.org/10.1016/j.rser.2018.04.067

Kalogirou, S.A., 2014. Solar energy engineering: processes and systems, Second Edi. ed. Academic Press. https://doi.org/10.1016/B978-0-12-374501-9.00014-5

Kim, Y., Thu, K., Kaur, H., Singh, C., Choon, K., 2012. Thermal analysis and performance optimization of a solar hot water plant with economic evaluation. Sol. Energy 86, 1378–1395. https://doi.org/10.1016/j.solener.2012.01.030

Klein, S.A., 2016. TRNSYS 18: A Transient System Simulation Program.

Leonzio, G., 2017. Solar systems integrated with absorption heat pumps and thermal energy storages: state of art. Renew. Sustain. Energy Rev. 70, 492–505. https://doi.org/10.1016/J.RSER.2016.11.117

Montagnino, F.M., 2017. Solar cooling technologies. Design, application and performance of existing projects. Sol. Energy 154, 144–157. https://doi.org/10.1016/J.SOLENER.2017.01.033

Thygesen, R., Karlsson, B., 2014. Simulation and analysis of a solar assisted heat pump system with two different storage types for high levels of PV electricity self-consumption. Sol. Energy 103, 19–27. https://doi.org/10.1016/j.solener.2014.02.013

Vaishak, S., Bhale, P. V., 2019. Photovoltaic/thermal-solar assisted heat pump system: Current status and future prospects. Sol. Energy 189, 268–284. https://doi.org/10.1016/j.solener.2019.07.051

Viridian Solar, 2017. The Pod - Solar Water Heating Simplified. http://www.viridiansolar.co.uk/solar-products-solar-heating-with-combi-pod.html (accessed 7.19.17).

Wagner Renewable, 2017. Home Page - Wagner Renewables Ltd. http://www.wagnersolarshop.com/ (accessed 7.19.17).

High Market Potential Applications for PVT with Heat Pumps

Nelson Sommerfeldt, Francisco Beltran and Hatef Madani

KTH Royal Institute of Technology, Stockholm (Sweden)

Abstract

Within the heat pump sector, there are applications where photovoltaic/thermal (PVT) collectors can offer greater value with lower investment costs than the current alternatives. The first is ground source heat pumps (GSHP) with under dimensioned boreholes. The second is a solar source heat pump (SSHP) where the PVT collectors are a replacement for the traditional air heat exchanger in an air source heat pump (ASHP). Complete systems models for a multi-family house are simulated in TRNSYS to determine seasonal performance factors (SPF), which are then compared technically and economically to each respective alternative. A 156 m^2 PVT array is capable of improving the SPF of a degraded GSHP by 30%, the same gains as drilling additional boreholes but at a lower cost. The SSHP with a 235 m^2 PVT array can reach an SPF of 2.6, comparable to the performance of an ASHP, but has the cost of a GSHP. Already today, PVT can economically compete with borehole drilling for GSHP and the SSHP concept shows enough market potential to warrant investment and development towards broader adoption.

Keywords: PV/thermal, Solar Hybrid, Solar Heat Pump, TRNSYS

1. Introduction

Relative to solar thermal (ST) and photovoltaics (PV), the market penetration of PV/thermal (PVT) hybrid collectors has been extremely limited (Weiss and Spörk-Dür, 2019). Recent cost reductions in photovoltaic (PV) modules have made PVT collectors more interesting economically, particularly when combined with heat pumps in a series configuration (Sommerfeldt and Madani, 2016). Previous studies have found that the primary benefit of adding PVT collectors to ground source heat pumps (GSHP) in a series/regenerative configuration has been the reduction of required borehole length (Bertram et al., 2012; Emmi et al., 2015; Eslami-nejad et al., 2009). While savings can be made on the borehole drilling, the high cost of the PVT systems currently make PV-only systems more economically interesting for new installations (Sommerfeldt and Madani, 2019). However, with strategies for reduced collector costs due to standardization and scaling (Thür et al., 2018) and the projected growth of the European heat pump market (EHPA, 2019), unglazed PVT can find interesting market opportunities.

One such possibility is the future GSHP retrofit market. After 20 years of heat extraction, the temperature in ground heat exchangers (GHE) is reduced, which is typically designed into the original system. However, when it is time to replace the heat pump with a new, more efficient unit, the higher efficiency combined with the already degraded boreholes means the GHE will be undersized. The traditional solution would be to increase the size of the GHE, assuming the necessary land area is available and the owner is accepting of damage to their garden. PVT offers an alternative that could be cost effective, reduces impact on the property, and increases renewable energy utilization in the building. Markets with a longer history of GSHP installation, like Austria, Sweden, and Switzerland, are starting to grapple with the retrofit issue, and the increased installations of GSHP in the 2010’s means that many other European countries will come to the same challenges in 10-15 years (EHPA, 2019).

Another potential application are solar sourced heat pumps (SSHP) as a replacement for air source heat pumps (ASHP). ASHP are far more common than GSHP due to their lower costs and ease of installation, however the need for a noisy heat exchanger on the building’s exterior is a drawback. PVT could replace this heat exchanger and provide energy to the heat pump from both the sun and air. A recent study demonstrated the

doi:10.18086/eurosun.2020.05.11 Available at http://proceedings.ises.org

potential for insulated PVT collectors to meet winter loads at -10 °C, concluding that the system concept showed promise but should use uninsulated collectors to improve heat transfer between the air and working fluid (Schmidt et al., 2018). A further improvement could be forced convection on the rear side of the PVT so long as the fan speeds are not so high that they produce the same noise problems as ASHP. The resulting system could be a more aesthetically attractive and quieter alternative to ASHP, which has a much larger market potential than GSHP and would help build the scale PVT needs to achieve the necessary cost reductions.

2. Objective and Methodology

This is a market feasibility study with the aim of identifying low-barrier entry points for PVT collectors as an integral part of heat pump systems. This is achieved by benchmarking technical performance with traditional solutions and comparing the initial investment costs. Two applications are investigated; PVT in support of older GSHPs with degraded boreholes and PVT in a SSHP configuration. Focus is on the Nordic market, which has the highest per capita rate of heat pump installations in Europe (EHPA, 2019), with climate and economic boundary conditions from Stockholm, Sweden.

For the GSHP renovation test, the borehole length is reduced by 60% from a standard design and simulated for 10 years, resulting in the reduced ground temperatures and high backup heater use typical of older heat pumps. At this point, PVT arrays or additional boreholes are added and the simulation continued for another 10 years. For the SSHP test, the same variable speed heat pump model is used but with a bypass around the boreholes. Modifications to the PVT collector are tested towards the goal of increasing heat transfer with the air, such as increasing surface area of the heat exchanger and introducing forced convection. Simulation of the fans is done by increasing the convection coefficient on the rear side of the PVT in conjunction with multiple fan speeds and air velocities.

The technical performance for both tests are demonstrated with seasonal performance factor (SPF_{4+}), given by Equation 1 and includes: total space heat (Q_{sh}) and domestic hot water (Q_{dhw}) demand of the building, electricity supply to the compressor (E_{hp}), and parasitic loads [circulations pumps for source ($E_{p,src}$) and sink ($E_{p,snk}$) loops, supporting heater for the heat pump (E_{bb}) and the hot water tank ($E_{b,dhw}$), the PVT circulation pump ($E_{p,pvt}$), and the PVT fans ($E_{f,pvt}$)].

$$SPF_{4+} = \frac{Q_{sh} + Q_{dhw}}{E_{hp} + E_{p,src} + E_{p,snk} + E_{bb} + E_{b,dhw} + E_{p,pvt} + E_{f,pvt}} \quad \text{(eq. 1)}$$

3. Model Description

The exploratory nature of this study drives an approach that is adopted from previous work, requiring minimal model development while meeting the objectives. Simulations are performed with a full solar heat pump model in TRNSYS17 (Klein et al., 2009), shown in Fig. 1, which includes a multi-zone building, ground source heat pump, boreholes, and PVT collectors integrated in series. A full description of the TRNSYS model and economic assumptions can be found in (Sommerfeldt and Madani, 2019) and is therefore only briefly described here with a focus on modifications specific to the study. It is worth noting however that all costs are reported without VAT or local subsidies, and that prices are taken from the 2019 Swedish market and converted into Euros with a 10:1 ratio.

3.1 System Model

The target building is a typical multi-family house located in Stockholm, requiring 125 kWh m^{-2} yr^{-1} of space heating and 38 kWh m^{-2} yr^{-1} of domestic hot water. The high level of space heating is common among buildings from the 1980's and earlier without energy efficiency retrofits. The same 88 kW, variable speed, brine-to-water heat pump is applied in both cases. The maximum PVT array size is 144 collectors, equaling 235 m^2 and 40 kW_p and are connected in series via a plate heat exchanger as shown in Fig. 1. The borehole circuit includes a bypass valve where the boreholes can be removed from the circuit. The bypass is only used for isolating the PVT to create a SSHP configuration, as is not part of a control strategy with GSHP.

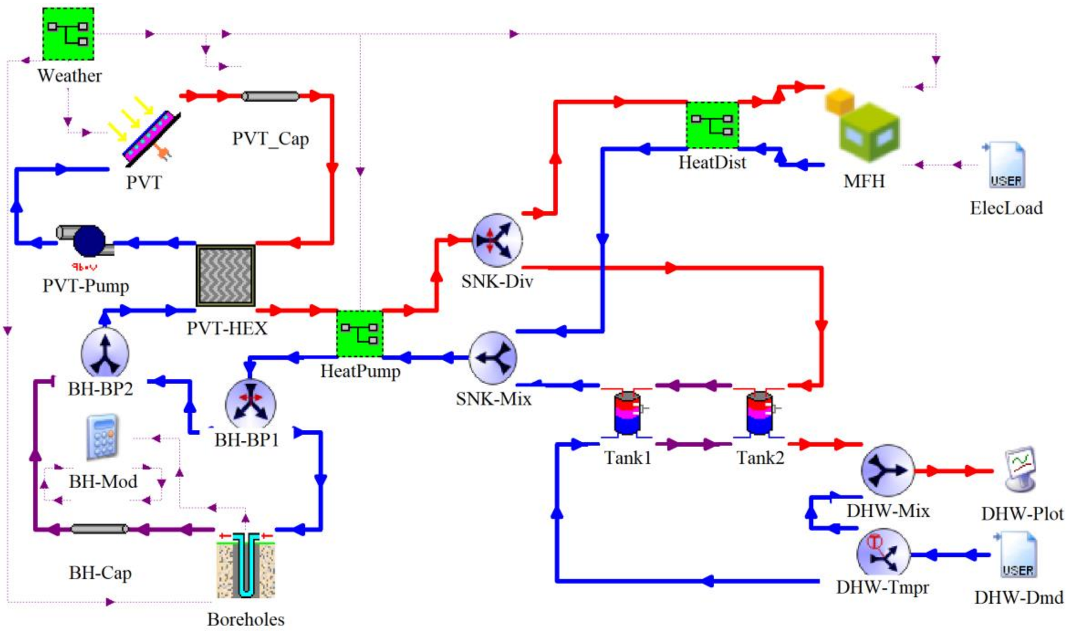

Fig. 1: TRNSYS model representing the GSHP and SSHP systems

3.2 Borehole Fields

Type 557a, based on the Duct Storage Model (Hellström, 1989), is used to model the borehole field with fluid capacity and residency modeled using a modified version of the method proposed by Pärisch et al. (2015). The model assumes equidistant spacing between boreholes (triangular pattern) inside of a cylindrical volume. This approach makes parametric studies inside TRNSYS convenient and has been shown to perform well against g-function based models with rectangular drilling patterns (Fossa and Minchio, 2013; Spitler et al., 2009).

The baseline borehole field is sized using a modified ASHRAE approach (Rolando et al., 2015) and has a total length of 3600 m (12 boreholes, 300 m deep, 20 m spacing). The reduced field removes seven of the 12 holes for a total length of 1500 m, but maintains the 300 m depth and 20 m spacing.

In cases where additional boreholes are drilled, the reduced field is simulated for 10 years. The next 10-year simulation is prepared with the full 12 boreholes, but is precooled until the average soil temperature at the center of the soil volume matches the final temperature from the first 10 years. The main limitation to this approach is the inability to control the undisturbed ground temperature in the soil volume that contains new boreholes. A temperature gradient does exist in the precooled soil volume, however it is unknown to what degree this would match a real world temperatures of soil around an existing borehole field. Given the scope is limited to economic feasibility, the uncertainty in soil temperatures is assumed to be within acceptable limits.

3.3 PVT Collectors

The PVT collectors are simulated using Type 560, a theoretical model allowing customized geometry and external convection coefficient. The baseline design is based on a tested and validated prototype fin-and-tube PVT collector (Sommerfeldt and Ollas, 2017). This model is applied to the GSHP and SSHP systems, but the SSHP application also makes three modifications aimed at increasing heat exchange with the air:

1. Increasing the tube count to represent a wetted-absorber design.
2. Increasing the external convection coefficient to represent forced convection with fans.
3. Increasing the internal convection coefficient to represent changes to heat exchanger geometry.

A wetted absorber design increases the heat exchange area of the collector fluid with the PV cells and air. Type 560 is based on the Hottel and Whillier model (Duffie and Beckman, 2013; Hottel and Whillier, 1955) derivation of solar collector performance, meaning that it is limited to fin-and-tube designs. To model a wetted absorber, it is possible to use many small tubes such that the fins become almost non-existent, which produces comparable results to a 1D model (Pressiani et al., 2016). With 240 tubes at 0.002 m diameter, the cross-sectional area of the tubes remains similar to the current design. The fins also become 0.002 m thereby representing a 50% wetted absorber. Since an actual collector design has not be realized yet, this is assumed to be a reasonable design assumption given that there are box-channel designs currently on the market with greater contact areas between the fluid and the absorber.

There has been extensive work reviewing convection coefficients related to wind, and Sartori (2006) summarized the models most relevant to solar collectors, i.e. forced air flow across flat surfaces. The conclusions produced three equations considering wind velocity and swept length for laminar, mixed, and turbulent flows. This study assumes turbulent flow for the backside of the collector, and is determined with Equation 2. Equivalent air speeds of 6 and 12 m/s are tested with a PVT collector length of 1.6 m, corresponding to convection coefficients of 21.9 and 38.1 W m^{-2} K^{-1}. The forced convection is only applied when the heat pump is operating. When not applied, natural convection with a coefficient of 6.0 W m^{-2} K^{-1} is assumed.

$$h_c = 5.75 V^{0.8} L^{-0.2} \quad \text{(eq. 2)}$$

4. Results and Discussion

4.1 Drilling and PVT

Figure 2 shows the development of SPF_4 in the GSHP over the 20-year simulation. The baseline system has a 20-year average SPF_{4+} of 3.3, which is expected for an older building with high power and heating supply temperatures. The reduced boreholes require considerable backup heater use, resulting in an SPF_{4+} that starts at 2.9 in year one and falls to 2.3 in year 10 as the surround soil cools. When the PVT array is added, backup heater use is reduced and within four years, the boreholes reach steady state. Three array sizes are tested, 48, 96 and 144 PVT collectors, with steady state SPF_{4+} of 2.8, 2.9 and 2.9, respectively. Drilling 2100 m of additional borehole in year 10 has a similar resulting SPF_{4+} of 2.9. This result suggests that from a technical perspective, PVT collectors could provide a similar benefit to an undersized GHE as additional drilling.

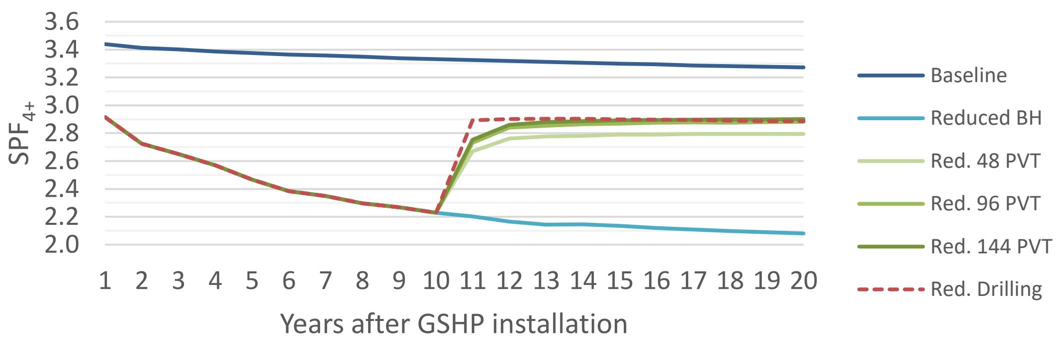

Fig. 2: SPF_4 of the degraded GSHP with PVT added in Year 10

A regression model of borehole costs derived from a survey of Swedish drillers suggests that the cost of drilling a new borehole field can be estimated at 20 € m^{-1} of total length (Mazzotti et al., 2018) with an additional 10 € m^{-1} for piping materials and commissioning. Therefore, the additional 2100 m of borehole in this system would cost €63k, assuming there are no additional costs associated with expanding the existing system. By comparison, the 48, 96, and 144 PVT collector systems would cost approximately €40k, €70k, and €100k, respectively. This is particularly noteworthy given that a 96-collector system can deliver nearly identical technical performance as the drilling for only 10% higher cost. It then has the additional benefits of not disturbing the land with drilling equipment, stabilizing borehole temperatures from further degradation, and generating renewable electricity worth approximately €15k over its 30-year lifetime.

Given that the Swedish market conditions can be characterized by low drilling and electricity prices, these results can be interpreted as somewhat conservative. For example, drilling prices up to 100 € m^{-1} have been applied to other European markets (Helpin et al., 2011), which makes PVT a far better economic choice. Higher electricity prices and generally stronger solar resources will also lead to a higher value of PV generation, further improving the economic conditions.

4.2 SSHP

The SSHP system uses 144 PVT collectors considering four designs;

- Baseline: the original PVT collector design with six runners without forced convection
- Abs: the modified PVT design with wetted absorber, without forced convection
- Low: the modified PVT design with 6 m/s forced convection
- High: the modified PVT design with 12 m/s forced convection

The results in Figure 3 show that the design changes dramatically improve SPF_{4+} up to 2.6. The largest improvements however come from the heat exchanger modification and the introduction of forced convection, whereas increasing fan speeds have diminishing returns. These results are comparable to other indirect SSHP studies in cold climates, suggesting the system is operating correctly (Chu and Cruickshank, 2014).

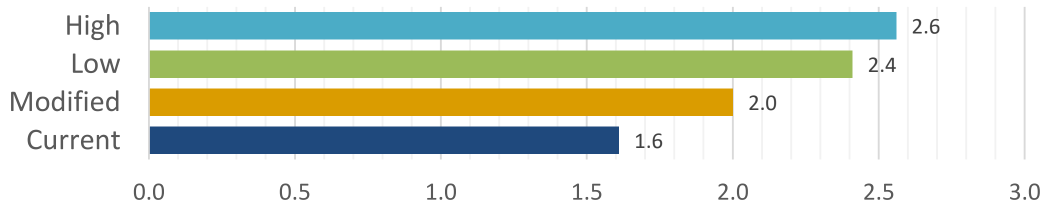

Fig. 3: SPF_{4+} of the SSHP with multiple PVT designs

The improvements in SPF are primarily due to the reduced reliance on direct electric backup heaters, a function of the increased power and energy supplied by the PVT. Figure 4 shows the specific annual thermal energy captured from the PVT array for each design. The baseline system already has relatively high thermal production from the PVT collectors at 485 kWh m^{-2} yr^{-1} due to the low operating temperatures. Production increases by 40% with the heat exchanger modification, and a further 23% with low fan speeds. Here also it can be seen that increasing fan speed has marginal benefits for energy capture, however it could be more critical for peak power.

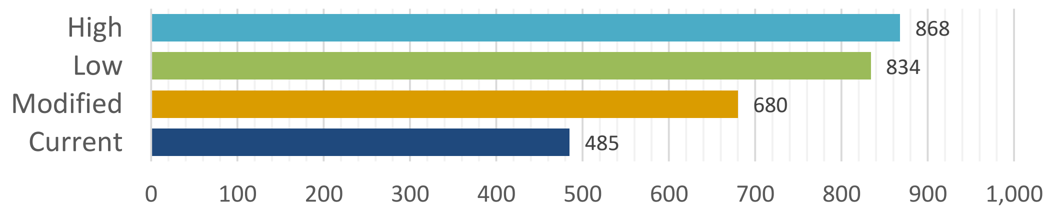

Fig. 4: Specific thermal production (kWh m^{-2} yr^{-1}) of the multiple PVT designs in an SSHP system

SPF values between 1.5 – 3.0 are common for air-to-water heat pumps in a Nordic climate, suggesting a SSHP could be a competitive alternative (Stignor and Walfridson, 2019). The market price for a newly installed ASHP are generally 1150 €/kW (Swedish Refrigeration and Heat Pump Association, 2018) and PV for residential buildings 1300 €/kW (Lindahl et al., 2019), meaning a comparable solution using traditional ASHP would cost approximately €153k. The marginal cost for a PVT system (on top of PV-only) is approximately €60k, making the total cost similar to a GSHP rather than ASHP (Swedish Refrigeration and Heat Pump Association, 2018).

Although not directly comparable on cost with ASHP, PVT provides the potential benefit of little to no fan noise like a GSHP. The main limitation is the low SPF, however it is challenging to say exactly how air or solar sourced heat pumps would perform in an older multifamily house since there are very few examples. There are even modern GSHP installations in Sweden with an SPF_{4+} of 2.7 (Gervind et al., 2016), suggesting that the low values could be a function of high temperature radiators rather than the concept as a whole.

A notable omission from the SSHP results are defrosting losses, which can be as much as 10% in ASHP (Stignor and Walfridson, 2019). Initial experimental results suggest that a PVT sourced system would require much less defrosting due to the solar radiation and if there were no forced convection (Schmidt et al., 2018). Quantification of annual performance and defrosting behavior is certainly needed in future analysis.

5. Conclusions and Future Work

Two applications for PVT integration with heat pumps have been described that have similar or lower investment costs than comparable alternatives while providing additional non-economic value. For GSHP, PVT offers a lower cost alternative to drilling additional boreholes in existing systems, which is likely to be a growing challenge as GSHP markets mature. The target buildings should be those with older heat pumps that are nearing replacement with a more efficient unit, or poorly designed systems that are relying too much on the direct electric backup heater. SSHP may be able to eliminate loud heat exchangers, but they do so at GSHP prices and ASHP performance. SSHP could be viable for customers willing to pay for the increased comfort and technological novelty, however these would likely be traditional "early adopters." More development work is needed to reduce PVT costs if they are to be directly cost competitive with ASHP.

Several companies in Sweden have started to install PVT collectors on degraded boreholes, and while the systems are monitored there lacks enough data to do a full borehole or systems model validation. The difficulty of modeling a complex thermal gradient in a systems tool like TRNSYS means that either more complex modeling and/or improved quality and quantity of monitored systems is needed to validate the preliminary findings here.

As demonstrated with previous studies (Herrando et al., 2019), the increase in PVT heat exchanger area will increase heat transfer rates, suggesting a wetted absorber designs (such as the flax box) should be pursued over additional fin-and-tube development. The addition of forced convection to PVT collectors also shows potential in increasing heat capture from the air in SSHP systems. The target characteristics used here can be guidelines for future design work, however much more detailed modeling is necessary. At the systems level, additional work is needed in the characterization of SSHP systems, for example empirical SPF values, control optimization, and defrosting losses. Since much of the potential for cost reductions rely on high-volume manufacturing processes, feasibility studies in additional climates and markets are also needed to quantify the broader market potential for PVT heat pumps at a European or global level and critical for scalability.

6. Acknowledgements

This study is funded by Mistra Innovation (project no. MI23.1), for which the authors are grateful.

7. References

Bertram, E., Glembin, J., Rockendorf, G., 2012. Unglazed PVT collectors as additional heat source in heat pump systems with borehole heat exchanger. Energy Procedia 30, 414–423. https://doi.org/10.1016/j.egypro.2012.11.049

Chu, J., Cruickshank, C.A., 2014. Solar-Assisted Heat Pump Systems: A Review of Existing Studies and Their Applicability to the Canadian Residential Sector. J. Sol. Energy Eng. 136, 041013. https://doi.org/10.1115/1.4027735

Duffie, J.A., Beckman, W.A., 2013. Solar Engineering of Thermal Processes, Fourth. ed. John Wiley & Sons, Inc., Hoboken, NJ.

EHPA, 2019. European Heat Pump Market and Statistics Report 2019. Brussels.

Emmi, G., Zarrella, A., De Carli, M., Galgaro, A., 2015. An analysis of solar assisted ground source heat pumps in cold climates. Energy Convers. Manag. 106, 660–675. https://doi.org/10.1016/j.enconman.2015.10.016

Eslami-nejad, P., Langlois, A., Chapuis, S., Bernier, M., Faraj, W., 2009. Solar Heat Injection Into Boreholes, in: 4th Canadian Solar Buildings Conference, Toronto, June 25-27, 2009. Toronto, pp. 237–246.

Fossa, M., Minchio, F., 2013. The effect of borefield geometry and ground thermal load profile on hourly thermal response of geothermal heat pump systems. Energy 51, 323–329. https://doi.org/10.1016/j.energy.2012.12.043

Gervind, P., Benson, J., Jardeby, Å., Nordman, R., 2016. Solhybrid och bergvärme- Förnybart med ny systemlösning (2016:01).

Hellström, G., 1989. Duct Ground Heat Storage Model - Manual for Computer Code. Department of

Mathematical Physics, University of Lund, Sweden.

Helpin, V., Kummert, M., Cauret, O., 2011. Experimental and simulation study of hybrid ground source heat pump systems with unglazed solar collectors for french office buildings. Proc. Build. Simul. 2011 12th Conf. Int. Build. Perform. Simul. Assoc. 2957–2964.

Herrando, M., Ramos, A., Zabalza, I., Markides, C.N., 2019. A comprehensive assessment of alternative absorber-exchanger designs for hybrid PVT-water collectors. Appl. Energy 235, 1583–1602. https://doi.org/10.1016/j.apenergy.2018.11.024

Hottel, H.C., Whillier, A., 1955. Evaluation of flat-plate solar collector performance, in: Transcript of the Conference on the Use of Solar Energy, The Scientific Basis, Vol. II, Part 1, Section A. University of Arizona Press, Tucson, Arizona, pp. 74–104.

Klein, S., Beckman, W.A., Mitchell, J., Duffie, J.A., Freeman, T., 2009. TRNSYS 17, A Transient System Simulation Program.

Lindahl, J., Stoltz, C., Oller-Westerberg, A., Berard, J., 2019. National Survey Report of PV Power Applications in Sweden 2018.

Mazzotti, W., Acuña, J., Lazzarotto, A., Palm, B., 2018. Deep Boreholes for Ground-Source Heat Pump - Effsys Expand Final Report.

Pärisch, P., Mercker, O., Oberdorfer, P., Bertram, E., Tepe, R., Rockendorf, G., 2015. Short-term experiments with borehole heat exchangers and model validation in TRNSYS. Renew. Energy 74, 471–477. https://doi.org/10.1016/j.renene.2014.07.052

Pressiani, M., Sommerfeldt, N., Madani, H., 2016. Investigation of PV/Thermal Collector Models for Use With Ground Source Heat Pumps in Transient Simulations, in: Proceedings of the ISES Eurosun 2016 Conference. ISES, Palma de Mallorca, Spain, pp. 1305–1316. https://doi.org/10.18086/eurosun.2016.08.19

Rolando, D., Acuna, J., Fossa, M., 2015. A Web Application for Geothermal Borefield Design. World Geotherm. Congr. 2015 19–25.

Sartori, E., 2006. Convection coefficient equations for forced air flow over flat surfaces. Sol. Energy 80, 1063–1071. https://doi.org/10.1016/j.solener.2005.11.001

Schmidt, C., Schäfer, A., Kramer, K., 2018. Single source “solar thermal” heat pump for residential heat supply: Performance with an array of unglazed PVT collectors, in: 12th ISES Eurosun Conference. Rapperswil, Switzerland.

Sommerfeldt, N., Madani, H., 2019. In-depth techno-economic analysis of PV/Thermal plus ground source heat pump systems for multi-family houses in a heating dominated climate. Sol. Energy 190, 44–62. https://doi.org/10.1016/J.SOLENER.2019.07.080

Sommerfeldt, N., Madani, H., 2016. Review of Solar PV/Thermal Plus Ground Source Heat Pump Systems for European Multi-Family Houses, in: 11th ISES Eurosun Conference. Palma de Mallorca, Spain, pp. 1382–1393. https://doi.org/10.18086/eurosun.2016.08.15

Sommerfeldt, N., Ollas, P., 2017. Reverse Engineering Prototype Solar PV / Thermal Collector Properties from Empirical Data for Use in TRNSYS Type 560, in: Proc. of the ISES Solar World Congress 2017. ISES, Abu Dhabi, pp. 1121–1132. https://doi.org/10.18086/swc.2017.18.11

Spitler, J., Cullin, J., Bernier, M., Kummert, M., Cui, P., Liu, X., Lee, E., Fisher, D., 2009. Preliminary intermodel comparison of ground heat exchanger simulation models, in: Proceedings of 11th International Conference on Thermal Energy Storage. Stockholm, Sweden.

Stignor, C.H., Walfridson, T., 2019. Nordsyn study on air-to-water heat pumps in humid Nordic climate (TemaNord 2019:502). https://doi.org/10.6027/TN2019-502

Swedish Refrigeration and Heat Pump Association, 2018. PULSEN 2018 - The industry more positive than ever! [WWW Document]. URL https://skvp.se/aktuellt-o-opinion/statistik/pulsen/2018-eng (accessed 6.1.18).

Thür, A., Giovannetti, F., Fischer, S., 2018. Improvements Developed during the IEA SHC Task 54 [WWW Document]. URL http://task54.iea-shc.org/Data/Sites/1/publications/ISEC-2018-Presentation-Task54-Thuer.pdf (accessed 10.30.18).

Weiss, W., Spörk-Dür, M., 2019. Solar Heat Worldwide. IEA Solar Heating and Cooling Programme.

PV power operation of a solar driven cooling compressor cluster

Battery charging level controlled PV electric energy self-consumption

Omlin L.[1], Voirol A.[1], Gantenbein P.[1], Daguenet X.[1], Haeberle A.[1], Bosshard A.[2] and Guentert P.[3]

[1] SPF Institute for Solar Technology, Eastern Switzerland University of Applied Sciences (OST), Rapperswil

[2] Leutwyler Kühlanlagen AG, CH-8344 Bäretswil (Switzerland)

[3] pg-consult guentert, Colmarerstrasse 14, CH-4055 Basel (Switzerland)

Abstract

A 24 V (voltage) DC driven cooling compressor cluster of two parallel compressors of ($Comp_1$) 1.6 kW_p and ($Comp_2$) 2.5 kW_p cooling power was integrated in a simple cold distribution system for room cooling. A battery and a sensible cold storage allow room cooling in periods of no solar irradiation. The cold distribution is performed through capillary tubes in a cubic duct. The air flow in the duct is sustained through gravitational force i.e. natural convection. To start one of compressors of the cluster the requirement of the min. DC power from the PV field is at least 30 %-50 % of the maximum electric power needed. The compressor cluster operation is battery charging level controlled. A coincidence of available PV power and compressor cluster electric power consumption is in most of the time reached. But at high battery charging level (>75% of max. level) and low PV power the coincidence is interrupted by a switch on of the second compressor to discharge the battery to a level range of 65 % -75 %. Nevertheless a 90 % direct self-consumption of the PV electric energy is reached by the solar compressor cooling system.

Keywords: Cooling cluster, PV solar driven DC compressor, battery level control, natural air convection.

1. Introduction

The cooling demand in the buildings sector will increase in the future and thus the growth of the cooling market is expected. There are many reasons for an increasing building room temperature, such as the growing number of electronic devices, the increased use of large glass facades in the buildings. Due to the climatic changes the share of commercial and residential buildings equipped with cooling systems is expected to increase continuously. To cover the cooling demand in buildings with the available converted solar energy is a sustainable option and has the big advantage of the timely coincidence (IEA SHC Task 53). Fig. 1 shows a close coincidence of solar irradiation, ambient temperature and room air temperature in an office building in Rapperswil (Switzerland). The coupling of a Photovoltaic (PV) field with an electrically driven compressor cooling machine is the concept of solar electric based room air-conditioning (Chen et al. 2020, Liu et al. 2017). PV electrically driven heating and cooling components such as vapour compression heat pumps, chillers or reversible heat pumps in connection with heat and/or cold storages are attractive and sustainable options for the energy supply in buildings. And in case of heating/cooling demand out of solar irradiance a battery can cover the demand if the system is not grid connected. To reduce system costs for example Han et al. 2019 presented a system with impedance matching control strategy without battery i.e. PV direct feed of the compressor. The components comprising a PV electric driven cooling system are market available and the PV market dynamics leads to cost reductions of up to 10 % every year for PV modules. However, still only a few complete system solutions which use photovoltaics for DC driven compressor clusters with a high direct self-consumption are available on the market (Liu et al. 2017).

In this experimental study, the setup of a small scale PV solar cooling system with a DC driven compressor cluster is shown and measurement results are discussed.

doi:10.18086/eurosun.2020.05.12 Available at http://proceedings.ises.org

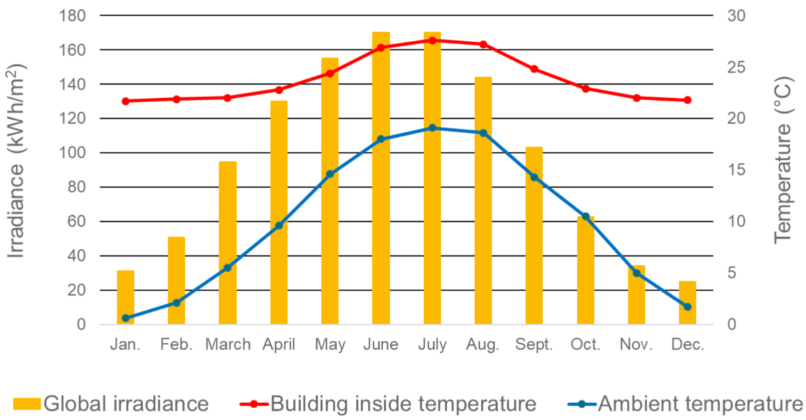

Fig. 1: Weather data and building room temperature: Global solar irradiance, ambient temperature (Meteotest) and the simulated room temperature without cooling of an office building in Rapperswil (Switzerland). A correlation of the temperature curves can be seen and solar irradiation is one of the reasons.

2. Cooling system, system control and data acquisition

An off grid PV driven cooling system (Fig. 2) for room cooling was built in the laboratory. The system consist of a PV field, a DC compressor cluster (two compressors in parallel) which produces the cold energy, a sensible cold storage for shifting the gained cold energy from the day into the night, a battery, and a cold distribution sub-system with two cubic ducts containing capillary tubes. The air flow in the ducts is sustained through gravitational force i.e. natural convection. The battery supplies the DC compressor cluster during short time PV power interruptions due to clouds and to run the cold distribution pump P1 (Fig. 2) during night time i.e. during time of no solar irradiation. In Tab. 1 a summary of the system components, their number in the system and a description is given.

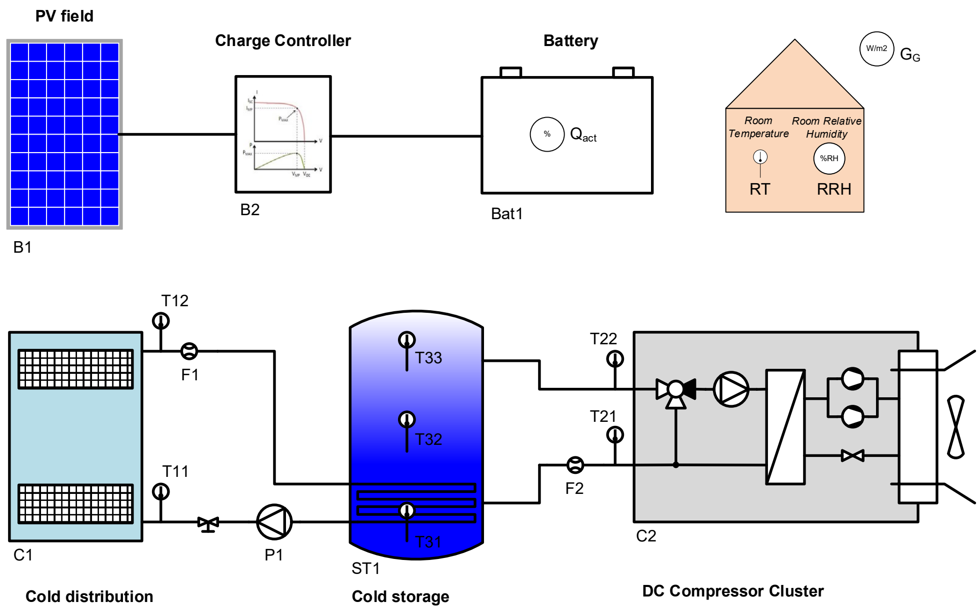

Fig. 2: Schematic of the system: PV field B1, MPP Battery charge controller B2 and Battery Bat1 (above) and cold distribution C1, sensible storage ST1 and DC compressor cluster C2 (below).

Tab. 1: System components

Component	Type and manufacturer	number in the system	Description and parameter
DC compressor cluster (C2)	2 Sierra compressors in parallel (Leutwyler AG)	1	0.5 kW – 6 kW cooling power (modulated)
PV field (B1)	Sky module 270 Wp (Meyer Burger)	6	1.4 kWp (@ STC) [1]
Cold storage (ST1)	Sensible storage TPSK 500 (NIBE)	1	477 liter of water
Battery (Bat1)	Sun power VR M 135/12Volt (Hoppecke)	2	111 Ah / C10 serial connection for 24 V
MPPT battery charge controller (B2)	VT80 (STUDER INNOTEC SA)	1	2500 W
Cold distribution (C1)	cooling shaft (1 x 2 x 0.2 m^3) (Solarfreeze)	2	1 - 4 kW cooling power (16 °C/20 °C; 32 °C / 80 % r.H.)[2]
Distribution pump (P1)	24 VDC solar pump (unknown)	1	800 l/h (max.), Δp 5 m, 22 W
Data acquisition DAQ	LabVIEW® (National Instruments)	1	Own programmed GUI, Computer and I/O hardware

One of the aims of the performed work is a high PV direct self-consumtion, which means, at a defined battery status S, a close to zero I_{Bat} (0 A) current to or from the battery (Fig. 4). And so, to achieve the highest possible direct self-consumption, the current I_{CM} to the cooling cluster has to be close or equal to the current I_{PV} from the PV flied. The measured charging level Q_{Bat} (% of fully charged battery) and battery current I_{Bat} are used as the two input variables for the system control to determine Y_{KM} as the current control output signal (4..20 mA) to the cooling machine. The system control unit regulates the cooling cluster machine (the cooling system) in such a case, that nearly no battery current I_{Bat} is flowing i.e. the current I_{PV} is close to or equal to the current I_{CM}. All the available PV power is used directly in the cooling machine, without temporary storage in the battery.

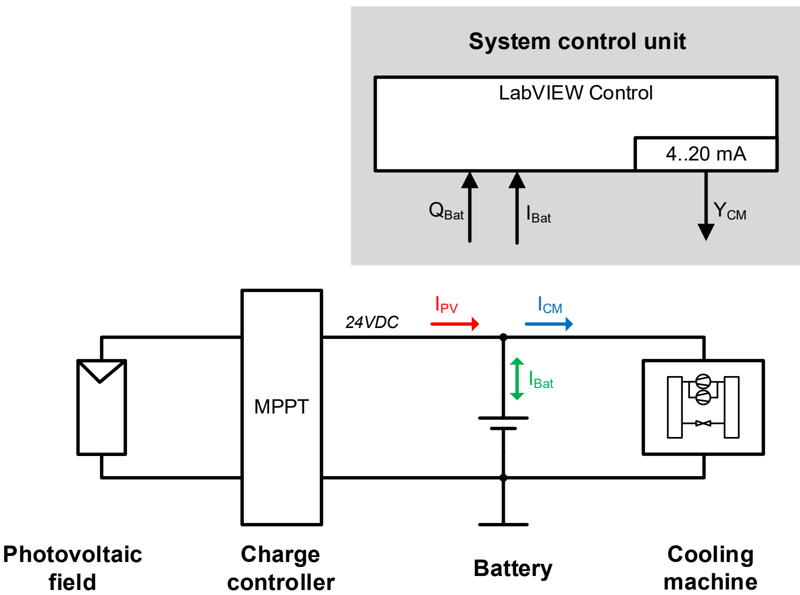

Fig. 4: Schematic of the electric part of the system and the system control unit (PV field current I_{PV}, current to the cooling compressor cluster I_{CM}, current to or from the battery I_{Bat}, battery charging level Q_{Bat}, compressor cluster control current Y_{CM}).

[1] The total peak power of the PV field at standard test conditions (STC) is 1.4 kWp. Due to ageing of the (2nd class) PV modules, the power of the PV field is reduced compared to the initial (new) efficiency indicated in the data sheet.
[2] Cooling fluid temperature inlet to and outlet of the cooling duct capillary tubes heat exchanger, climatic chamber air temperature and relative air humidity.

In case of no solar irradiation and to have an operation of the compressor cluster and/or the cooling fluid pump P1 an arbitrary minimum charging level Q_{Bat_min} of the battery has to be available. This charging level limit is determined according the expected cooling demand after sun set and has the state of charge level SOC = 65 % of maximum of the battery. Due to the behavior (programming) of the solar charge controller, which limits the maximum charge current (I_{PV}) when a certain State of Charge (SOC) level (SOC > 80 %) is reached, it's necessary to keep the SOC of the battery on a lower level, below 75 % of maximum. Summarized, the system control unit keeps the battery level in a range of 65 % - 75 % which corresponds to the battery status S = Okay. Tab. 2 gives a connecting relation of the battery status S, state of charge SOC and the compressor cluster control of the speed n.

There are three battery status S which the battery can assume depending on the SOC. If the battery reaches the battery status "High", the compressor cluster runs at maximum power and thus is reduces the battery level down to the "Okay" range of 65 % - 75 %. And vice versa, if the battery reaches the battery status "Low", the compressor cluster is turned off to charge the battery (from the PV field) up the "Okay" level.

Tab. 2: Control status of the battery

Battery Status S	State of charge SOC	Compressor cluster control
"Low"	< 65 %	"Minimum power, turned off" Comp1(n=0) & Comp2(n=0)
"Okay"	65 % - 75 %	"Controlled power ($I_{PV} = I_{CM}$)" Comp1(n) & Comp2(n)
"High"	> 75 %	"Maximum power" Comp1(n=max) & Comp2(n=max)

The compressor cooling cluster is realized with two parallel compressors of (Comp1) 1.6 kWp and (Comp2) 2.5 kWp cooling power. Both compressors are speed controlled with a minimum switch-on electric power of at least 30 % to 50 % of maximum power. The control of the compressor cluster can be sectioned in three control phases, these are A, B and C. Tab. 2 shows the description and the running status of each compressor and Fig. 5 illustrates this.

Tab. 2: Control phases (time range) of the compressor cluster in operation (Fig. 5)

Phase	Compressor 1	Compressor 2	Description
A	Comp1(n)	Comp2(n=standby)	Comp1 is running in the speed controlled power range but there is not enough energy from the PV field to run Comp2 as well (Comp2 = standby).
B	Comp1(n=max)	Comp2(n=standby)	Comp1 is running on maximum power Comp2 is in standby.
C	Comp1(n=max)	Comp2(n)	Comp1 runs at maximum speed and Comp2 runs at speed controlled range (following the available PV power) .

Fig. 5 shows a theoretical example of the electrical power consumption phases of the compressor cluster. In the control phase A and C the PV power matches the compressor cluster electric power. In phase A compressor 1 (Comp1) runs in a power controlled range, Comp2 is off, and in phase C Comp1 runs at maximum power while compressor 2 (Comp2) runs in a power controlled range. In the control phase B Comp 1 is running on maximum power and the difference to the PV field power is feed into the battery. Comp2 starts (or stops at the end of the day) at the transition from phase B to phase C (transition of phase C to phase B) at a power level 1/3 of its maximum electric power (consumption). In this theoretical example the battery status S is "Okay" for the whole day.

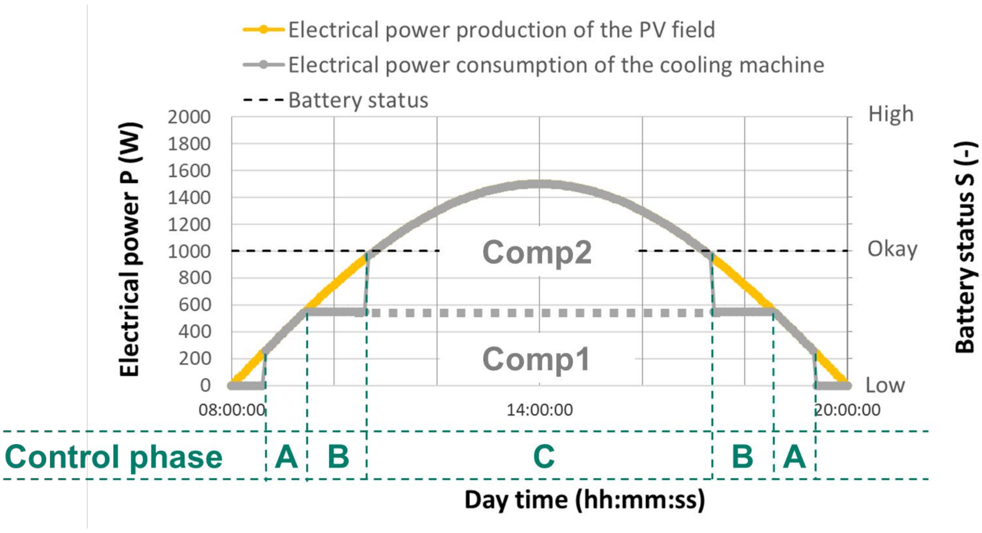

Fig. 5: Performance curve of the cooling cluster: Electrical power production P of the PV field (yellow) and a theoretical possible power consumption curve of the cooling cluster of two compressors (grey) at a sunny day. On the second vertical axis the battery control status S is shown.

3. Measurement results

Fig. 6 and 7 are showing measurement results acquired at the 27th of May from 08:00 o'clock in the morning till 20:00 o'clock in the evening. The compressor cluster is running from 09:00 o'clock until almost 19:00 o'clock in different control phases.

The power consumption of the cooling machine is not congruent with the power production of the PV field. There are many broad peaks during the control phase B, which can be explained by a battery status induced battery discharging (Figure 7) and a running of Comp2. In phase C many negative power spikes of the compressor cluster are visible. These spikes are not finally investigated. We assume that they stem from over temperature and over-pressure compressor cluster turnoffs.

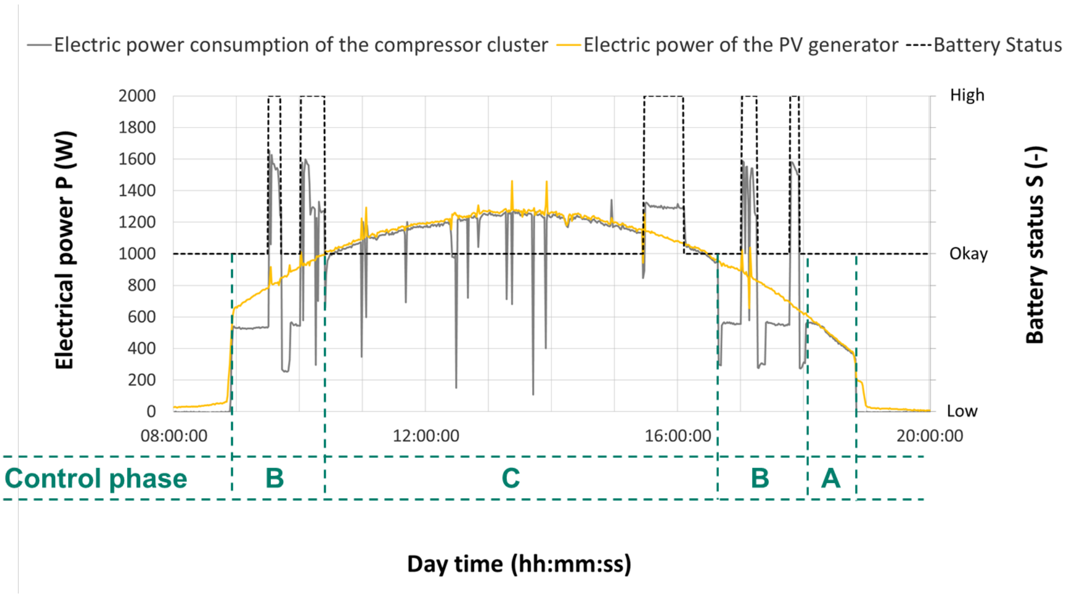

Fig. 6: Measurement results at the sunny 27th of May 2020: The yellow curve shows the PV power production. The grey curve shows the power consumption of the compressor cluster and the dashed grey curve the battery status S.

At the beginning of the first control phase B, when the battery status S is "Okay", we can see that a positive battery current is charging the battery. This leads to an increasing battery SOC until the battery status S changes from "Okay" to "High". After both compressors of the cluster are switched on a negative battery current flows out of the battery and into the compressor cluster. The battery status turns back to "Okay". During the control phase A and C the battery current is controlled to zero with many spikes in phase C. This spikes, which are charching the battery, are the reason for the battery discharging phase in the time range of 15:30 o' clock and 16:10 o'clock.. In times where the battery current I_{Bat} is zero (0) the electric current from the PV field I_{PV} is equal the electric current I_{CM} to the compressor cluster.

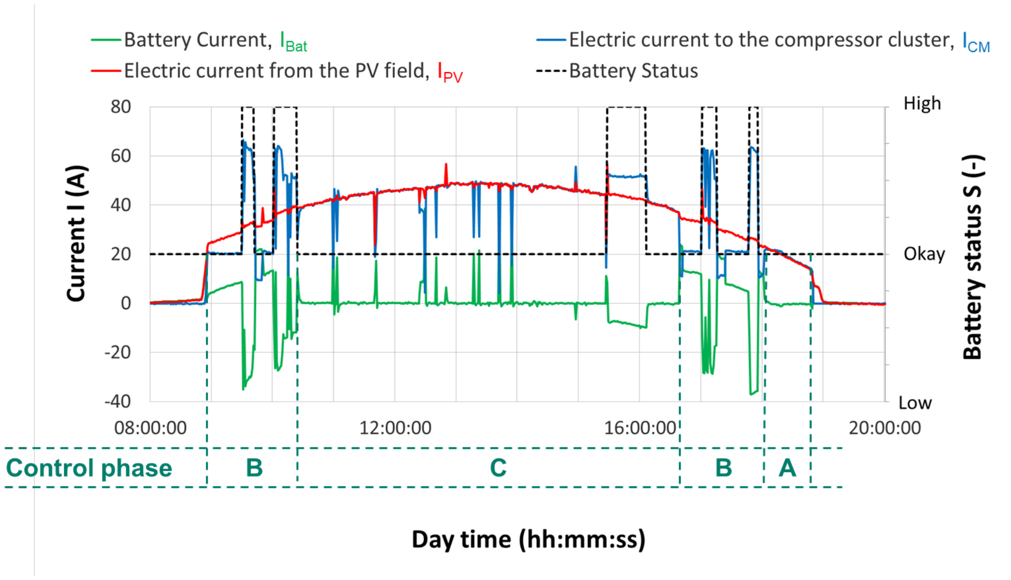

Fig. 7: Electrical currents I and battery status S: Electric current from the PV field (red), electric current to the cooling compressor cluster (blue) and controlled battery current (green) in function of time. In the case of 100 % of direct self-consumption the battery current is zero. The battery status S shows the charging level of the battery – where "Okay" for S can be set arbitrarily.

4. Discussion and Outlook

A solar electric cooling system with a DC driven compressor cluster was set up and measurements were performed. With the battery (storage) to supply the cooling fluid pump with electric energy and the sensible cold storage the option for room air-cooling in times of no solar irradiation is available. The results show electric power peaks during operation (i.e. current peaks) due to battery discharging and compressor over-temperature and overpressure reasons. Most of the operation time, a coincidence of electric current from the PV field and electric current to the compressor cluster was observed. A PV energy self-consumption higher than 90 % was reached.

The operation has to be optimized towards a higher direct self-consumption, through the avoidance of peaks in the electric current, with a better system control program (and adjusting battery size and charging level S "Ok"). A scaling for a pilot system with a power up to several 10 kW – is aimed in the future. And with the help of a numerical model the battery size (Ah) and battery status S (-) will be better adjusted to the systems needs.

5. Acknowledgments

Financial support of Eastern Switzerland University of Applied Sciences (OST) and Innosuisse funding is highly acknowledged.

6. References

IEA SHC Task 53, Mugnier D. operating agent, https://task53.iea-shc.org/publications (27.08.2020).

Chen Y., Liu Y., Liu J., Luo X., Wang D., Wang Y., Lui J., Design and adaptability of photovoltaic air conditioning system based on office buildings. Solar Energy, Volume 202, 15 May 2020, Pages 17-24.

Liu Z., Li a., Wang Q., Chi Y., Zhang L., Performance study of a quasi grid-connected photovoltaic powered DC air conditioner in a hot summer zone. Applied Thermal Engineering, Volume 121, 5 July 2017, Pages 1102-1110.

Han Y., Li Ming, Wang Y., Li G., Ma X., Wang R., Wang L., Impedance matching control strategy for a solar cooling system driven by distributed photovoltaics. Energy 168 (2019) 953 – 965.

Model Validation and Performance Assessment of Unglazed Photovoltaic-Thermal Collectors with Heat Pump Systems

Bharat Chhugani, Peter Pärisch, Maik Kirchner, Matthias Littwin,

Carsten Lampe and Federico Giovannetti

Institute for Solar Energy Research Hamelin (ISFH), 31860 Emmerthal (Germany)

Abstract

PVT collectors convert solar radiation into both useful heat and electricity. Therefore, with the same PV area more solar energy could be harvested. The work investigates a novel unglazed liquid-based PVT collectors as a single source in a heat pump system for the energy supply of a single-family house. In this hybrid collector, the PV panel is thermally coupled with a specially designed brine-to-air heat exchanger on backside, which enables to gain energy from the sun and ambient air. Therefore, this novel collector is validated with the PVT collector model in TRNSYS for varying weather conditions based on the measurement results from our test facility and presented in the paper. The comparison shows good agreement, despite the missing reproduction of icing and detailed condensation processes in the simulation type. Based on this model, the impact of a PVT-heat pump system is further investigated by yearly dynamic simulations in TRNSYS for space heating, domestic hot water and defrosting of PVT. The results show that the seasonal performance factor of the PVT to HP system can reach 3.18 with the PVT area of only 20 m². The seasonal performance factor including self-consumed PV fraction for the heating system reaches 3.49 with the same collector area and without any additional battery storage.

Keywords: Photovoltaic-Thermal (PVT) collector, TRNSYS Simulation, heat pump system

1. Introduction and methodology

Photovoltaic - Thermal (PVT) collectors are a combination of a solar thermal collector and a photovoltaic module in a single component, which simultaneously generates power and heat from the same area. Therefore, PVT can maximise the fraction of renewable energy source utilisation. Nowadays, commonly available liquid-based PVT collectors are unglazed PVT collector (WISC), glazed PVT collector, concentrating PVT collector (CPVT) (Lämmle 2018). Unglazed PVT collectors are beneficial for operation near ambient temperatures particularly because of high heat transfer to ambient air even in times of low radiation (Lämmle 2018). Among all three collector types, unglazed PVT collectors are widely popular in the northern European market also as an additional heat source for heat pumps (Bertram et al. 2011; Hüsing et al. 2018).

In the presented research work, unglazed SOLINK PVT collectors have been comprehensively investigated. This PVT collector concept has been developed by the company Consolar Solare Energiesysteme GmbH, Karlsruhe Institute of Technology (KIT), and Triple Solar B.V. (Leibfried et al. 2017) and is shown in Figure 1. The PVT collector is thermally coupled with a fin-tube heat exchanger on the backside of PV. The fin surface area is 10 times larger than the PV area in each module, which increases the use of energy from the sun and ambient air and hence the PVT collector works as a good environmental heat exchanger. In addition to convective heat gains in times of low irradiation particularly in winters or nights, condensation heat gains, as well as heat gains through the phase change to frost occur on larger fins surfaces, which improves the thermal collector output and makes it suitable for working as a sole heat source of a heat pump. Therefore, this unglazed PVT offers a promising alternative to conventional geothermal sources of brine-water heat pumps as well as to an air-water heat pump.

doi:10.18086/eurosun.2020.05.13 Available at http://proceedings.ises.org

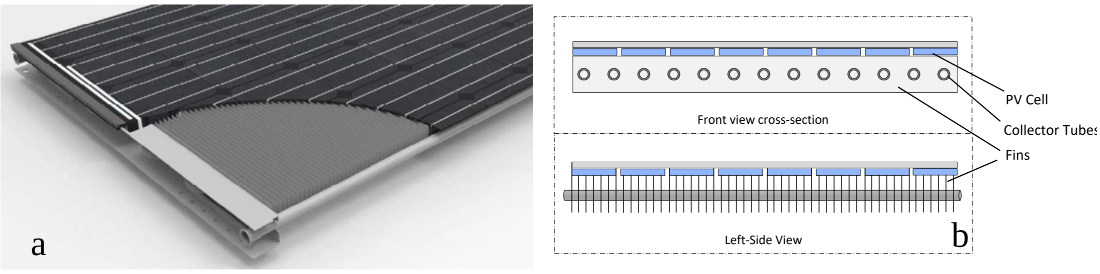

Fig. 1: (a) Sectional view of the PVT collector: the fin tube heat exchanger on the backside of the surface (Leibfried 2018), (b) Schematic diagram of PVT Collector

Within the scope of the research project “TwinPower”, nine south-facing PVT Modules with the area of ~18 m² (in Figure 2 right) have been installed and monitored at the test roof of ISFH. Additionally, nine standard PV modules have also been monitored for the direct comparison of the electrical performance of thermally cooled PVT and non-cooled PV modules. The PV module field is shown in Figure 2 (left).

Fig. 2: Module test fields at the ISFH (left: PV module field; right: PVT field)

Both modules have identical PV cells, and their electrical characteristics under Standard Test Conditions (STC) are shown in table 2.

Tab. 1: Electrical characteristic data of the investigated PVT collector (STC)

Pmax (Wp)	**Electrical Efficiency (ηel)**	**Open circuit voltage (Voc)**	**Short circuit current (Isc)**	**Maximum power voltage (Vmp)**	**Maximum power current (Imp)**	**Power temperature coefficient**
340 W	17.5 %	48.0 V	9.45 A	37.6 V	9.05 A	- 0.39 %/K

The thermal efficiency of this PVT collector was determined by means of outdoor measurements at IGTE (University of Stuttgart) according to the Standard ISO 9806:2013 as part of a Solar Keymark certification. Table 2 shows the thermal collector parameters for this single module test. Additional investigations of the collector have been carried out at ISFH and extensively presented in (Giovannetti et al. 2019; Lampe et al. 2019), The authors analysed the performance of a collector field under real environmental conditions. The correspondent results are presented in Table 3.

Tab. 2: Thermal collector parameter of single PVT module according to Solar Keymark Test (Giovannetti et al. 2019)

Thermal collector parameters (MPP)	
η0,b (collector efficiency)	0.468
c1 (heat loss coefficient in W/m²K)	22.99
c3 (wind dependence heat loss coefficient in J/m³K)	7.57
c4 (sky temperature dependence of the heat loss coefficient)	0.434
c5 (collector capacity in kJ/m²K)	26.05
c6 (wind dependence conversion factor in s/m)	0.067

Additionally, a PVT heat pump system has also been investigated in a Hardware-in-the-Loop (HiL) real-time test environment. In HiL tests, the energy source (PVT collectors), the heat pump (HP) and the thermal buffer storage operate in real-time as hardware. A TRNSYS co-simulation calculates the space heating demand (SH) of the building and the test facility emulates the energy sinks for domestic hot water (DHW) and space heating (SH). Results of the HiL measurement are briefly presented in (Chhugani et al. 2020). The goal there was to analyse and evaluate the system for the energy supply of a single-family house under dynamic weather conditions. The results showed a good system efficiency (average daily performance factor 3.3) when PVT collectors are directly coupled with the heat pump as a sole heat source. According to these first tests, the PVT assisted HP could be a promising alternative to an air-source heat pump.

In the presented investigation, data from the PVT measurements have been used for validation of the TRNSYS type 203 (Stegmann. et al. 2011). Type 203 is based on parameters resulting from standard test procedures of the thermal and electrical characteristic curve. It was developed by ISFH and successfully validated for the use with ground-coupled heat pump systems. The new validation methodology is shown in Figure 3. The type calculates the simulated collector outlet temperature, thermal and electrical collector yield and the condensation gains. However, the condensation gains are only calculated from the front surface of the collector, which might lead to some uncertainty in case of SOLINK PVT collector because of its unique construction with fins on the rear side. The influence of icing, precipitation, and wind direction, which are expected to play a relevant role, can cause deviation in simulation output.

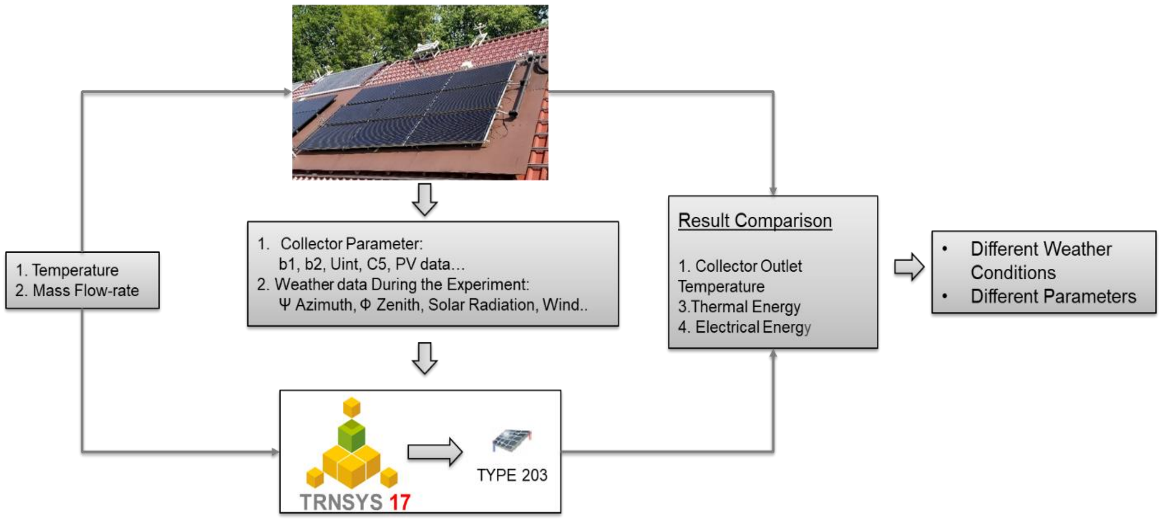

Fig. 3: PVT validation methodology

In order to validate the model, meteorological and energetic data of the collector are measured at ISFH with one-second time steps, which includes collector in- and outlet temperatures, flow rate, longwave irradiance, air velocity, global and diffuse irradiance, ambient air temperature, and humidity. In the end, all measured and calculated data are fed into the simulation and compared with real outputs. For the PVT validation, different collector parameter sets have been investigated. Firstly, the Solar Keymark parameters, which result from the single collector test. The second parameter set was determined from the PVT collector field test at ISFH, as explained in (Giovannetti et al. 2019; Lampe et al. 2019). Both parameter sets are summarised in Table 3. The results show that the overall heat transfer coefficient *U*-value $(U = c_1 + c_3 \cdot wind)$ of the PVT field is reduced by about 20 % compared to the *U*-value determined from the single panel. The reduction is caused largely by the different wind exposure of the collector and the high sensitivity of the collector design (finned heat exchanger). Both parameter sets have been used in the simulation/validation and compared with measured outputs.

In contrast to the ISO 9806:2013, type 203 requires the thermal collector parameter determined according to the test standard EN 12975. Hence, the values of the Solar Keymark datasheet are converted according to the following equations (1 to 5). Table 3 also shows the performance parameters of an additional reference PVT module, which was developed by ISFH and used for comparison with the SOLINK PVT in yearly system simulations (chapter 3).

$$c_1 = b_1 \qquad \text{(eq. 1)}$$

$$c_3 = b_2 \qquad \text{(eq. 2)}$$

$$c_4 = \eta_{0,\text{hem}} \cdot \frac{\varepsilon}{\alpha} \qquad \text{(eq. 3)}$$

$$c_6 = \eta_{0,\text{hem}} \cdot b_u \qquad \text{(eq. 4)}$$

$$\eta_{0,\text{hem}} = \eta_{0,\text{b}} \cdot K_\text{b}(\Theta) \cdot \frac{Gb}{G} + \eta_{0,\text{b}} \cdot Kd \cdot \frac{Gb}{G} \qquad \text{(eq. 5)}$$

Where ε is hemispherical emittance, α is solar absorptance, Gb is direct solar irradiance for beam irradiance, Kd is incidence angle modifier for diffuse radiation, θ is the angle of incidence.

Tab. 3: Thermal collector parameters used in PVT validation and system simulation

Thermal Collector Parameters (MPP)	Solar Keymark Test Parameter	ISFH -Field Test Parameter	Reference PVT module (ISFH)
η0,b (Zero-loss efficiency based on beam irradiance)	0.468	0.532	0.661
b1 (Heat loss coefficient in W/m²K)	22.99	19.08	12.47
b2 (Wind dependence heat loss coefficient in J/m³K)	7.57	3.69	3.71
bu (Wind dependence conversion factor in s/m)	0.144	0.126	0.079
collector capacity in kJ/m²K	26.05	26.05	15.00

2. PVT model validation

2.1 Validation under winter conditions

In general, simulated and measured results of thermal energy output are expected to show good agreement because the simulation model uses the collector parameters determined from the collector tests. The first validation is performed for winter measurement with Solar Keymark test parameter over a total measuring period of 50 hours, from 7th to 9th January 2019 and is shown in Figure 4.

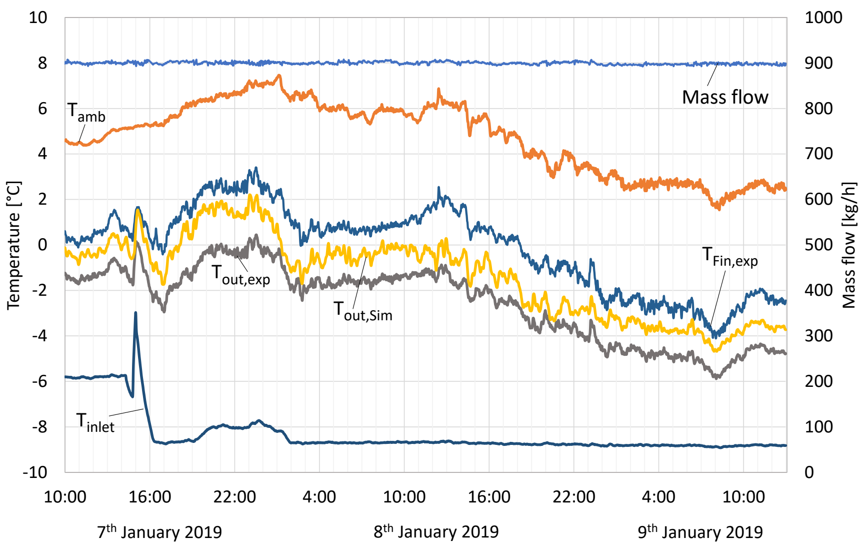

Fig. 4: Comparison of type 203 and measurements based on “Solar Keymark test parameters” for winter measurements

In Figure 4, the left axis shows ambient temperature (T_amb), collector inlet temperature (T_inlet), measured collector outlet temperature (T_out,exp), simulated collector outlet temperature (T_out,sim), measured collector fin temperature during the experiment (T_Fin,exp) and on the right axis mass flow rate in collector field. The results clearly show a significant deviation between the measured and simulated collector outlet temperature. The simulated outlet temperature is always higher than the measured output. Thus, the thermal performance, which is proportional to the temperature difference (T_out – T_inlet), is overestimated by the simulation model. This is caused by the higher heat loss coefficient exhibited by a single module compared to a larger collector field, due to the already mentioned different impact of ambient temperature and wind on the two configurations. In the PVT field, collectors are paced together, so that wind turbulence and velocity in the air gap between the roof and the field by nearby PVT modules are reduced. Both effects can be easily seen from table 3, where the value of b_2 from the field measurement is reduced by approx. factor 2 compared to the single module parameter and b_1 is roughly 20 % lower. Consequently, during the first validation attempt, the simulated thermal energy output was 20.2 % higher than the measured output over the considered time. Solar Keymark test parameters are thus not suitable to simulate PVT fields with SOLINK-collectors.

Further validation was performed by using the field test parameters. The simulation results are shown in Figure 5. The simulated outlet temperature shows good agreement with the measured value, and total thermal energy outputs during the considered time period were 14.8 kWh/m² simulated vs 15.8 kWh/m² measured. The slight deviation can be attributed to the following reasons: firstly, a wind direction effect on the heat loss coefficient because of the special finned heat exchanger of the SOLINK PVT. If the wind flows along the fin planes, the factor b_2 will increase and vice versa if the wind direction is perpendicular to the planes. Secondly, further disregarded meteorological influences, such as precipitation. Non-negligible thermal power can be exchanged between the unglazed solar collector and the rainwater. The rainwater temperature is very difficult to define according to climatic conditions, and this effect is comprehensively presented in (Bunea et al. 2015). And during the experiment, measured rainfall was 0.8, 10.7 and 0.3 litre/m² on 7th, 8th, 9th January respectively. Thirdly, missing condensation gains calculation from the backside of fins surface in the type. The condensation gains in type 203 are calculated only from the front side of the collector, and in the investigated field maximum condensation gains occur through the fins, which is not possible to simulate within this type. Condensation effect occurs if the surface temperature (T_Fin,exp) is below dew point and above frost point (between 0 °C to -3 °C). As fin temperature and dew point fall below the frost point, the correspondent heat transfer mechanism cannot be reproduced by the model as well.

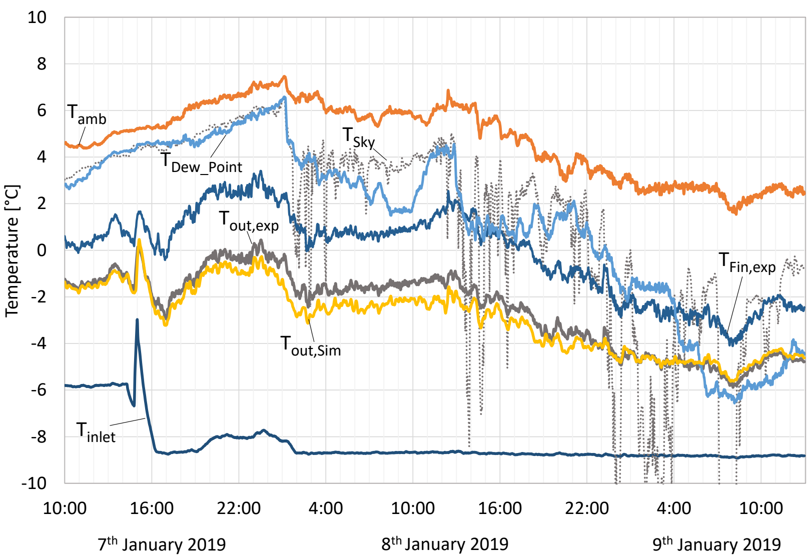

Fig. 5: Comparison of type 203 and measurements based on “ISFH - Field Test parameter” winter measurements

In the next phase, the PVT collector has been tested under frost and ice formation; the experiments and validations were carried out with PVT inlet temperatures below -10 °C for almost 34 hours. During the experiment, ice formation on the fins surface on the rear side of PVT was observed. Figure 6 shows this process at three different times. The first picture shows the collector before ice formation, the second picture shows ice formation during the daytime, and the last one shows ice formation during nighttime. The timing of the respective pictures are represented with arrows in Figure 7, which displays the course of the relevant temperatures during experiments and simulations.

Fig. 6: Ice formation under the PVT collector field (back side of the PVT – fins surface)

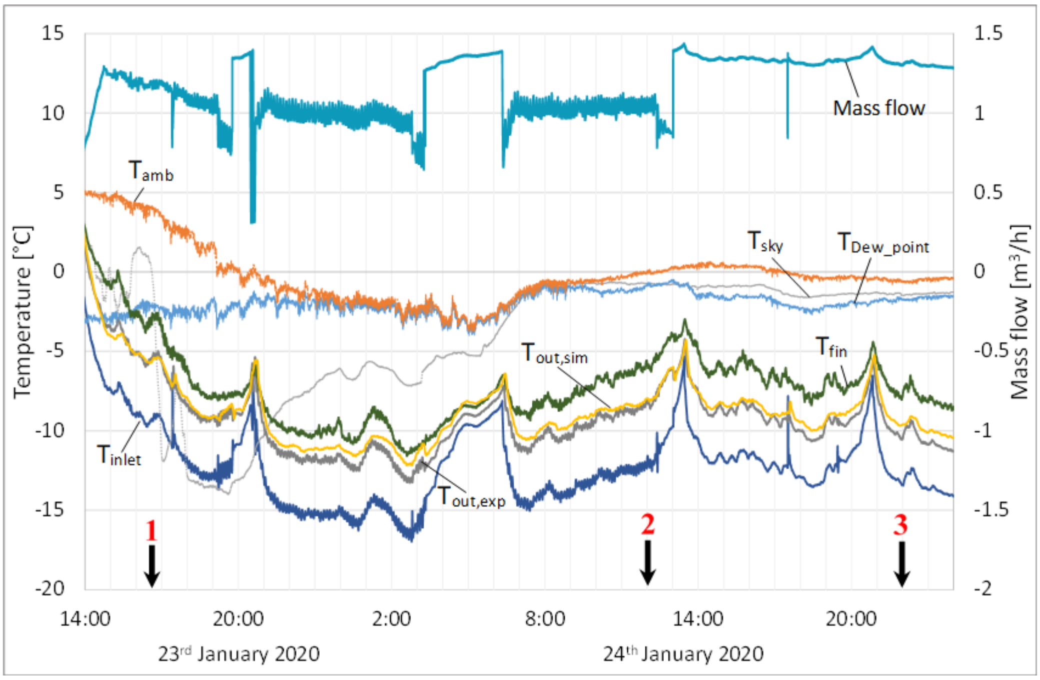

Fig. 7: Comparison of type 203 and measurements during ice formation on the PVT collector field

Quantitative comparison of simulations and measurement before ice formation (until arrow 1), shows only slight difference in thermal output (measurement: 0.87 kWh/m² vs simulation: 0.85 kWh/m²). After the ice formation on the collector (after point 1), stronger deviations are observed, and the simulated output is higher than measured values (measurement: 6.03 kWh/m² vs simulation: 7.12 kWh/m²). The most probable explanation for this deviation is an overestimation of convective gains (b_1 and b_2). The ice formation on the collector field is hindering the heat transport from ambient to the collector. On the other hand, the negative effect on heat loss because of the ice formation is not implemented in the model. However, this model error only occurs, when PVT is operating under extreme conditions (no defrosting of PVT, heat pump running continuously, no direct sunshine). Usually, this takes place only in few extreme winter days, and this is not the typical instance. In the simulation, this effect can be reduced by regularly defrosting of PVT collector, which is realistic and reduces the model errors. Therefore, in the yearly simulations PVT defrosting is also implemented.

2.2 Validation under summer conditions:

The type 203 has also been validated for summer weather conditions with using the ISFH field parameter set, over a total measuring period of 40 hours. The results are shown in Figure 8 (thermal output) and Figure 9 (electrical output). As illustrated in Figure 8, the measured thermal output is reproduced very well by the model. However, the cooling energy during the night (02:00 to 06:00) shows some inconsistency, which is to some extent to be attributed to the special collector design and has to be addressed in future work for cooling applications.

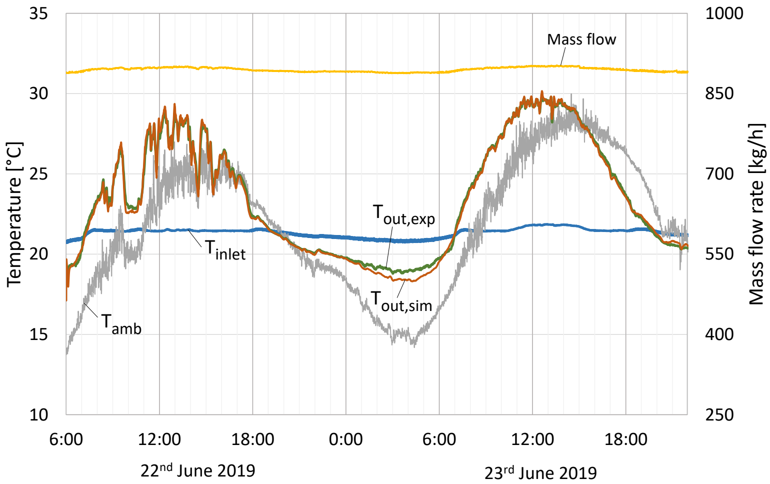

Fig. 8: Comparison of type 203 and measurements during summer measurements

During the same experiment, PVT electrical output from collectors is also compared with simulations. The electrical power shows excellent agreement with a deviation of approx. 2 %, the total electrical output measurement 2.38 kWh/m² to simulation 2.34 kWh/m². The slight difference between simulation and experiment power might be affected by the different estimation of the cell temperature because of the additional collector passive cooling with fins in the PVT field, which is not considered by the model.

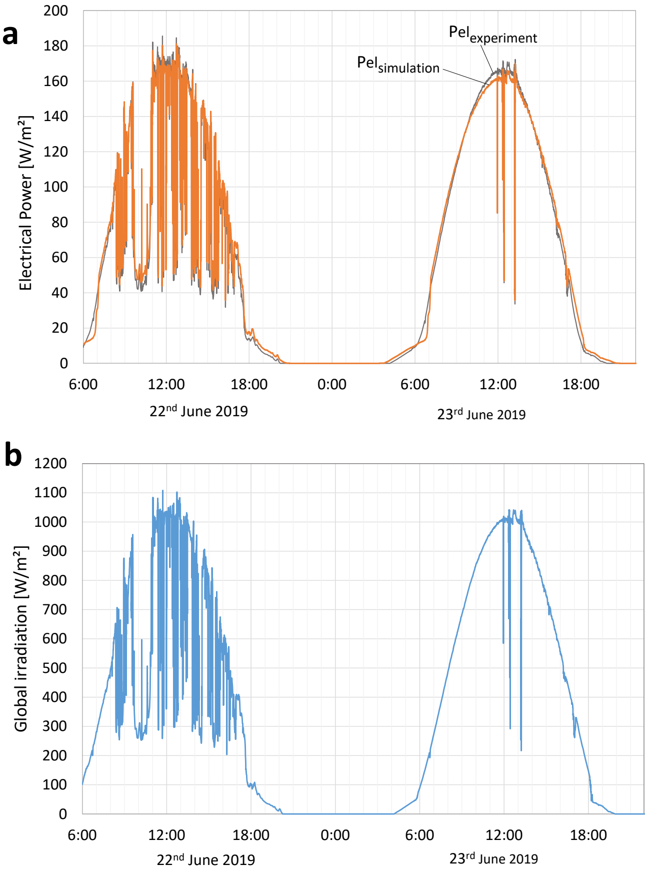

Fig. 9: Validation of type 203: (a) Electrical output during summer measurements (b) Measured global radiation near the collector plane

To conclude, it can be assumed that the simulation with type 203 model works well even for the SOLINK collector if collector parameter set from the field measurement is used. Besides, it is also expected that type 203 can be used in simulations with PVT coupled heat pump systems if icing and condensation gains do not play a relevant role during operation. For a more general implementation, the existing model needs to be extended in order to reproduce these additional effects. In the following section, the influence of the PVT on the heat pump system is explained by means of yearly simulations.

3. System simulation

PVT coupled HP system has been simulated with the dynamic simulation software TRNSYS (Transient System Simulation Program) to calculate the energy supply of a single-family house. Figure 10 illustrates the simulated thermal and electrical system. The system consists of PVT-modules as a sole heat source of the heat pump, thermal buffer storage at the sink side for domestic hot water preparation via instantaneous water heater and for space heating of the building. To avoid ice formation on/under the PVT field, a defrosting function is implemented in the yearly simulations, and the necessary heat is directly supplied by the storage via an external heat exchanger. The PVT-system with a DC/AC-inverter supplies electric energy to the heat pump system at first priority.

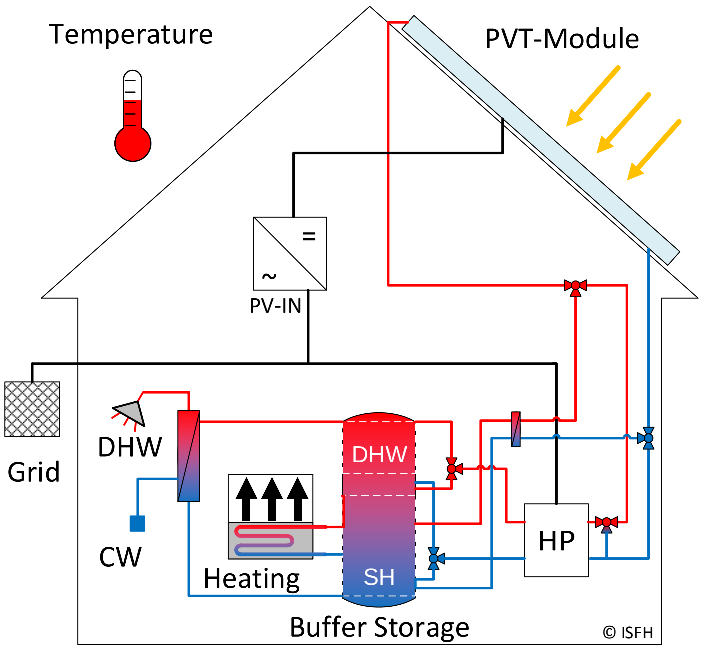

Fig. 10: Simulation system overview

The building model used in the investigations is the Single Family House (SFH45) based on IEA SHC, Task 44 / HPP Annex 38. The detailed description of the boundary conditions, load profiles and building components have been published within IEA Task 44 (Dott et al. 2013; Haller et al. 2013). SFH45 was developed in such a way that it can represent the heat demand and hot water demand of a new building with a good thermal insulated building envelope. An overview of the main simulation parameters is presented in Table 4. The tapping profile has been derived from DIN EN 16147 with an energy demand of approx. 5.8 kWh/d. The total flow of 145 litres/d with an average cold-water temperature of 10 °C is assumed and hot water is tapped at 45 °C. The required amount of heat for defrosting depends on the PVT design. Defrosting heat is taken from the storage via a heat exchanger, which increases the energy demand of the system. The defrosting demand was approx. 390 kWh/a for the collector field (PVT area 20 m²).

In the simulation, a brine-water inverter heat pump (HP) has been used with thermal power of 9.1 kW and the COP of 4.13 by B0/W35 at 75 % of compressor speed. This heat pump has been designed to operate with PVT collectors as a single heat source for low-temperature heating systems; therefore, the heat pump can work down to the minimum inlet temperature of -15 °C and maximum of 30 °C at the evaporator side. Moreover, the heat pump has a backup electrical heater of 8 kW. For modelling TRNSYS type 401 was used.

Tab. 4. Description of the main simulation parameters

Description	Value
Location	Zurich (Switzerland)
Building size	140 m² (Floor area)
Heat demand for space heating	SFH45 ≈ 48 kWh/(m²·a) (Floor heating)
Domestic hot water demand	2141 kWh/a (at 45 °C)
PVT collector (type 203)	1 m² to 60 m²
Thermal storage tank (type 340)	560 liter
T ambient average	9.9 °C
Irradiation on collector (diff + dir)	1276 kWh/(m²·a)

For the evaluation of the system, the seasonal performance factors (SPF) with different system boundaries have been used. These indicators are explained below in eq. 6 to 8 together with the square view (Figure 11).

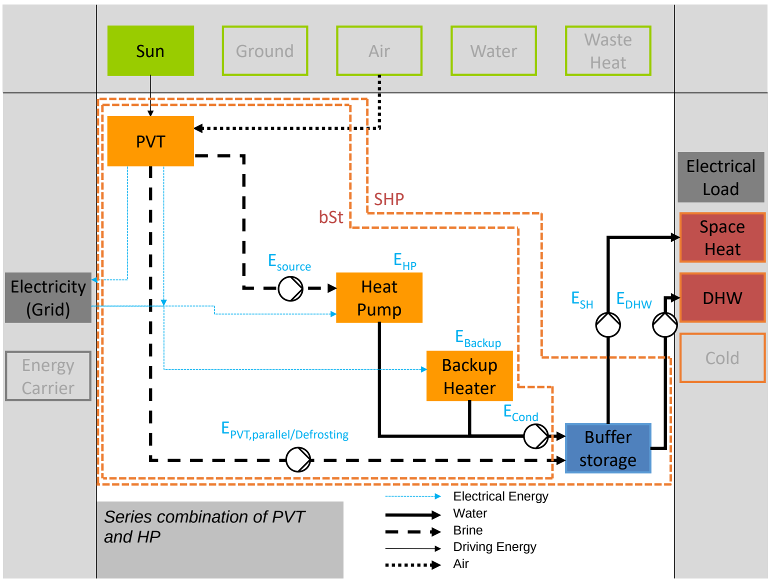

Fig. 11: System square view with different system boundary

First indicator SPF_{bSt} (before storage), is the ratio between amounts of heat supplied by the condenser ($\dot{Q}_{Condenser}$), backup heater ($\dot{Q}_{Aux}$) and energy delivered for defrosting and PVT direct loading energy ($\dot{Q}_{Defrosting/PVT,parallel}$) divided by the electrical energy provided within this boundary. $\dot{E}_{HP}$ is electrical energy of the heat pump compressor, $\dot{E}_{source+Cond}$ is pumps energy of the source and sink side, $\dot{E}_{Aux}$ is heater electrical energy and $\dot{E}_{PVT,parallel}$ is pump energy for defrosting or PVT direct.

The second indicator is the SPF_{SHP} of the system. It defines the ratio between amounts of heat delivered by the system (SH, DHW) to the electrical energy consumed over a specified period. Moreover, to make a system comparable with other systems, in SHP boundary, the electrical consumption of the heating and the water circulation pump of the building is not included in the system calculation. The index is defined according to IEA Task - 44 SHP boundary conditions (Malenković et al. 2012). In contrast to the SPF_{SHP} boundary, the next performance indicator $SPF_{SHP}^{(\mathrm{Grid})}$ represents self-consumed PVT electricity in SHP boundary (without battery storage) and is explained in eq. 8.

$$SPF_{bSt} = \frac{\int (\dot{Q}_{Condenser} + \dot{Q}_{Aux} + \dot{Q}_{Defrosting/PVT,parallel})\, dt}{\int (\dot{E}_{HP} + \dot{E}_{source+Cond} + \dot{E}_{Aux} + \dot{E}_{PVT,parallel})\, dt} \qquad (eq.\ 6)$$

$$SPF_{SHP} = \frac{\int (\dot{Q}_{SH} + \dot{Q}_{DHW})\, dt}{\int (\dot{E}_{HP} + \dot{E}_{source+Cond} + \dot{E}_{Aux} + \dot{E}_{PVT,parallel})\, dt} \qquad (eq.\ 7)$$

$$SPF_{SHP}^{(Grid)} = \frac{\int (\dot{Q}_{SH} + \dot{Q}_{DHW})\, dt}{\int (\dot{E}_{HP} + \dot{E}_{source+Cond} + \dot{E}_{Aux} + \dot{E}_{PVT,parallel} - \dot{E}_{PVT})\, dt} \qquad (eq.\ 8)$$

In order to investigate the impact of PVT on system performance, two different PVT collectors have been compared: the SOLINK collector (field parameter set) and a reference PVT collector (Table 3). As the heat pump plays a crucial role in PVT coupled heat pump systems, especially when PVT has been designed to be used as a single heat source; therefore two different bivalence temperatures for the heat pump have been simulated. The bivalence temperature of a heat pump indicates that if the evaporator inlet temperature drops below the threshold, the electric heater is turned on, and the heat pump compressor stops. In the simulation, bivalence temperatures -15 °C and -10 °C were used. The bivalence temperature variations give an idea of the importance of selecting a proper heat pump because commonly market available heat pumps have a bivalence point up to -10 °C.

Figure 12 illustrates seasonal performance factors depending on the different collector area. For the SOLINK PVT with an area of 20 m² and an inverter heat pump (bivalence of -15 °C), the achieved SPF_{SHP} is 3.18. To achieve the same performance factor with the reference PVT collector, almost 30 m² PVT area is required.

On the other hand, with same collector but commonly available heat pump (bivalence of -10 °C), the seasonal performance factor of the system decreases significantly, which is due to the additional use of an auxiliary heater. Approx. 40 m² of SOLINK PVT collector is required to reach SPF_{SHP} of 3.18, and with the reference PVT even 50 m² area is not enough to get the SPF of more than 3.1.

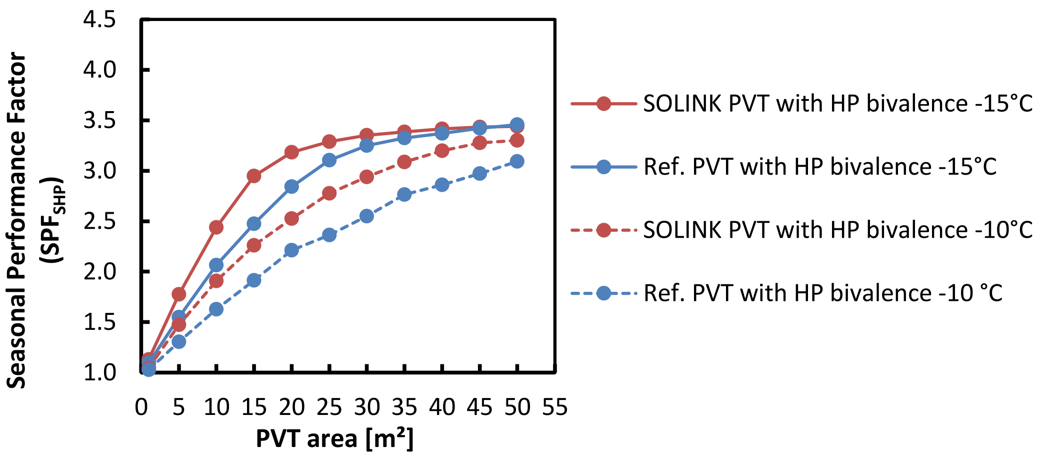

Fig. 12: Seasonal performance factor (SHP) as a function of the PVT collector area from 1 to 50 m², for two different collectors and different bivalence points of the heat pump

Often PVT manufacturers tend to use the system performance factor including self-consumed PV electrical energy ($SPF_{SHP}^{(grid)}$). However, one has to pay attention to the priority of electricity consumptions, the household electricity profile or heat pump or the control strategy. Furthermore, this performance factor gives the PV electricity the same weightage as the electricity demand, which is not valid due to feed-in tariffs. In our case the $SPF_{SHP}^{(grid)}$ amounts to 3.49 with same 20 m² and increases gradually with the PVT area. No battery storage and no household electrical consumption are considered. Figure 13 compares the three different performance factors.

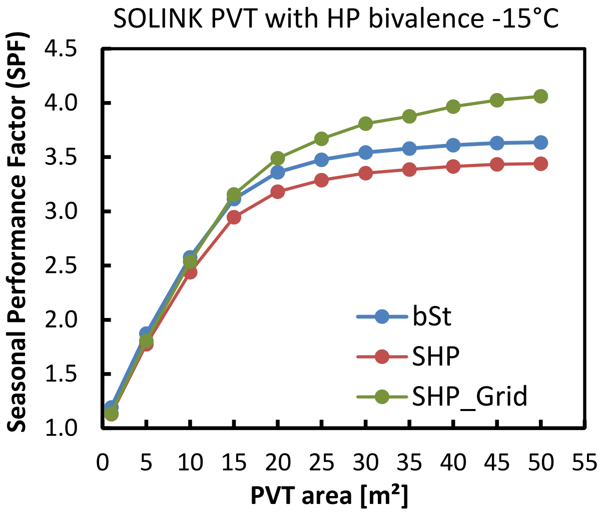

Fig. 13: Overview of three different Seasonal performance factor with the variation of the SOLINK PVT area from 1 to 50 m²

4. Conclusion

In the frame of a research project, investigations have been carried out on the SOLINK PVT collector with finned tube heat exchanger by means of experiments and simulations. The special construction of the PVT increases the convective heat transfer from the environment, and thus the collector acts as an excellent environmental heat exchanger. In the investigation, the PVT model type 203 is compared in TRNSYS with the measurement data. The result shows a very good agreement with collector parameters determined from field measurement at ISFH. The deviation is caused by the special design of the PVT with fins, which enhances convective heat transfer and condensation gains as well as by ice formation, which is not considered by the model and requires further development. Based on this model, PVT assisted heat supply systems have been investigated in TRNSYS for the energy supply of the single-family house (SFH45).

With the help of yearly system simulations, two main effects have been identified: efficient PVT panels (in our case SOLINK) can significantly improve the system performances and require fewer PVT panels compared to the reference PVT to get the same SPF. With the PVT area of 20 m², seasonal performance factors SPF_{SHP} and $SPF_{SHP}^{(\mathrm{Grid})}$ of 3.18 and 3.49 were achieved respectively for the location Zurich with cold winters and warm summers. In the assessment of PVT for heat pumps, much better results can be achieved by selecting an appropriate heat pump. In our case a lower bivalence temperature from -10 °C to -15 °C, can reduce the required PVT area by 50 % from 40 m² to 20 m², to get the same SPF.

Overall, when the investigated PVT collectors are directly coupled with the heat pump as a sole heat source, the achieved system efficiency is good and can be used as an alternative to an air source heat pump. Besides, by considering PV electrical generation (self-consumed), the system performance factor can be significantly increased. Moreover, in the simulation, the system has been investigated with a simple, demand-oriented system control strategy, and by changing to a more complex, PV oriented control strategy higher performance is expected.

5. Acknowledgements

The presented work and the results are part of the research project “TwinPower - 0325867B” and “integraTE - 03EGB0023C”, which are funded by the German Federal Ministry for Economic Affairs and Energy (BMWi), and supported by the Lower Saxony Ministry of Science and Culture. The authors are grateful for the support and responsible for the content of the publication.

6. References

Bertram, E.; Kirchner, M.; Rockendorf, G.; Stegmann, M., (2011), Solarthermie2000plus: Solare Gebäudewärmeversorgung mit unverglasten photovoltaisch-thermischen Kollektoren, Erdsonden und Wärmepumpen für 100% Deckungsanteil. Kurzbezeichnung: BiSolar-WP, Förderkennzeichen: 0325952B.

Bunea, M.; Perers, B.; Eicher, S.; Hildbrand, C.; Bony, J.; Citherlet, S., (2015), Mathematical modelling of unglazed solar collectors under extreme operating conditions. In: *Solar Energy* 118, S. 547–561. DOI: 10.1016/j.solener.2015.06.012.

Chhugani, B.; Kirchner, M.; Littwin, M.; Lampe, C.; Giovannetti, F.; Pärisch, P., (2020). Investigation of Photovoltaic-Thermal (PVT) collector for direct coupling with Heat Pumps: Hardware in the Loop (HiL) and TRNSYS Simulations. 8th IBPSA Building Simulation Conference for Germany and Austria, BauSim2020.

Dott, R.; Haller, M. Y.; Ruschenburg, J.; Ochs, F.; Bony, J., (2013), The Reference Framework for System Simulations of the IEA SHC Task 44 / HPP Annex 38. Part B: Buildings and Space Heat Load, A technical report of subtask C Report C1 Part B.

Giovannetti, F.; Lampe, C.; Kirchner, M.; Littwin, M.; Asenbeck, S.; Fischer, S., (2019). Experimental Investigations on Photovoltaic-Thermal Arrays Designed for the Use as Heat Pump Source. IEA SHC International Conference on Solar Heating and Cooling for Buildings and Industry, Santiago, Chile.

Haller, M. Y.; Dott, R.; Ruschenburg, J.; Ochs, F.; Bony, J., (2013), The Reference Framework for System Simulations of the IEA SHC Task 44 / HPP Annex 38. Part B: Buildings and Space Heat Load, A technical report of subtask C Report C1 Part A.

Hüsing, F.; Mercker, O.; Hirsch, H., (2018), Erdwärmekollektoren und Sonnenkollektoren als optimierte bivalente Quelle für hocheffiziente Wärmepumpensysteme. Kurzbezeichnung: „Terra-Solar-Quelle“, Förderkennzeichen: 03ET1275.

Lämmle, M., (2018), Thermisches Management PVT Kollektoren. Dissertation: Development and modelling of highly efficient glazed, flat plate PVT collectors with low-emissivity coatings and overheating protection.

Lampe, C.; Kirchner, M.; Littwin, M.; Giovannetti, F.; Asenbeck, S.; Fischer, S., (2019), Experimentelle Untersuchungen an Testfeldern mit SOLINK-photovoltaisch-thermischen Kollektoren. Symposium Solarthermie und Innovative Wärmesysteme, 21-23 May 2019. Bad Staffelstein, Germany.

Littwin, M.; Chhugani, B.; Lampe, C.; Kirchner, M.; Giovannetti, F.; Pärisch, P., (2019), PVT-Systeme: Hardware-in-the-loop Tests und TRNSYS Jahressimulationen. Online Symposium Solarthermie und Innovative Wärmesysteme, 12-14 May 2020. Bad Staffelstein, Germany.

Leibfried, U.; Wagner, A.; Abdul-Zahra, A., (2017), Hocheffiziente, auf intelligenter Verknüpfung von PVT- und Wärmepumpentechnik basierende Wärmeversorgung für Gebäudebestand und Neubau. Schlussbericht zum Förderprojekt SOLINK, Aktenzeichen: 33226/01.

Malenković, I.; Pärisch, P.; Eicher, S.; Bony, J.; Hartl, M., (2012), Definition of Main System Boundaries and Performance Figures for Reporting on SHP Systems, Deliverable B1, IEA SHC Task 44/ HPP Annex 38.

The European Commission Policy towards the Key Enabling Technology in Photovoltaics - the Perovskite Solar Cell and its Urban Applications Potential for Buildings

A. Rządkowska

European Solar Network, Bruges, Belgium

Institute of International Studies, University of Wrocław, Wrocław, Poland

E-mail: agnieszka.rzadkowska@eusolarnet.org

Abstract

The paper covers European Commission policy on the emerging solar cell technology based on perovskites. As perovskite photovoltaics was identified as one of just 12 Key Enabling Technologies (KETs) for the European Union to be able to achieve and sustain global technological supremacy, it is considered a strategic area for the European development. Perovskite solar cells demonstrated spectacular growth of efficiencies from 2.6% back in 2006 up to 25% (in pure perovskites) and ca. 30% (in tandem) in 2020. The competition is fierce internationally (with Asian companies investing strongly in pilot production lines) but Europe has secured a forward position with early undertaken R&D and has a chance to successfully secure a leading position in this technological international race in PV and more generally in renewables, repositioning itself in global value chains after over a decade of surrendering the field in PV modules production. Perovskite solar cells are becoming very attractive for commercialization (especially for smart buildings) not only due to cheap costs of fabrication (full printing in roll-to-roll configurations) but also due to material properties (semi-transparent and elastic thin-films).

Key words: European Union, European Commission, policy, PV, perovskite, solar cells, buildings

1. Introduction

At the end of 2017 the European Commission concluded a study on the Key Enabling Technologies (KETs) for the EU to achieve technological global supremacy (Dervojeda et al. 2017). A total of only 12 promising KETs were identified across many industry sectors as technologies that hold potential to assure through further development that the EU will stay ahead of the international competition. One of just 12 identified KETs was a perovskite solar cell, a very cheap and universal thin-film emerging class of SCs, strongly developed in the EU in the recent years.

The promising KETs based technologies were identified as growing in such an intensity to guarantee a strong potential for the EU to lead globally, scaling impacts in terms of economy and jobs - may be thus considered as strategic for the further EU development. This is where the EC policy, particularly enabling high quality R&D is strongly pronounced. The European Commission granted PV R&D funding amounted to over 500M Euro vastly increasing from below of 100M Euro back in 2015 (Jaeger-Waldau, 2019). The PV prices drop enabling economic forces to drive energy transition are directly due to exponential nature of efficiencies growth observed throughout the last half of a century. 47 years of data prove that each time the installed PV power capacity doubled, the price fell by 28% (Wang, 2018). This progress was mostly driven by development of the traditional p-type wafer Si cells representing until 2017 over 90% of the market. Yet this domination is nearing to an end with emerging new PV technologies, especially very cheap and universal thin-film solar cells based on perovskite. Perovskite SCs undergo strong R&D that has resulted in lifting their efficiencies from only 2% back in 2006 to over 25% for single-junction perovskite cells in 2020. Four-years old market forecasts for perovskite SC devices estimated reaching $214 million value in 2025, but this figure is already considered underestimated, with expected surpassing Euro 1B when the technology is mass-produced.

doi:10.18086/eurosun.2020.05.14 Available at http://proceedings.ises.org

2. Perovskite Solar Cell

Perovskite solar cells which can be relatively easily chemically synthesized are currently considered as one of the most promising and economically viable base materials for mass-scale commercial PV. In contrast to traditional p-n junction semiconductor solar cells (like Si cells), perovskite cells (considered third generation solar cells, or qualified as one of the most important emerging PV technology) are soluble in many different types of solvents and remain semi-transparent after crystallization in very thin layers. As such, perovskite SCs may be easily ink-jet or screen printed in simple roll-to-roll processes or even sprayed onto large surfaces similarly like ordinary paints that when activated with chemically induced crystallization process create untra-thin-film layers (below 1 μm) also relatively easily further integrated in elastic perovskite SC device. Those properties make the perovskite cells significantly cheaper in fabrication and very well suited to mass-output market uptake and vast applications (such as so called energy smart buildings elevations coverings of variety of geometries, semitransparent windows, roofs coverings, outdoor furniture, vehicles or even clothing external surfaces that may produce enough power from the sunlight to e.g. charge a personal mobile device). The same properties make these cells specially interesting for advanced space applications in replacing of the sturdy and heavy panels with in-orbit printed (from the liquid solvents containers) flexible and large-surface sheets of thin-film solar modules or coverings for objects in space, even facilitating the planned future self-sustained missions to the Moon or Mars. Perovskites may be a game changer not only due to its excellent efficiency/cost ratio (nearing 0,014 Euro/kWh) but also due to key properties of semi-transparency and elasticity allowing bending and forming in different shapes and surfaces coverings. As buildings are estimated to account for over 40% of the energy demand, building-integrated solar cells are primary application for PV. Perovskite in contrast to sturdy Si panels offer simple whole-surface coverings techniques including aspects such as architectural freedom and so called smart windows with tunable semitransparency. Thus the potential for perovskite thin-film modules to cover roofs, facades and glass is already beginning to be commercially addressed by construction companies (like e.g. Skanska partnering with Saule Technologies commercializing perovskites cells in a mass production lines launched in March 2020). Futher technological developments (especially in plasmonic efficiencies enhancements by inclusion of metallic nano-structures) yet even more increases the potential of this emerging photovoltaic technology.

Following chapters study the progress of this KET and the EU policy support towards it.

3. Perovskite Solar Cell Technological Challenges and Perspectives

A perovskite solar cell utilizes a perovskite structured compound (i.e. material with the same crystal structure as the $CaTiO_3$ – calcium titanium oxide, originally discovered in 1839 and named after Russian mineralogist Lev Perovski), most commonly a hybrid organic-inorganic lead or inorganic tin halide-based material. It represents an emerging class of thin-film photovoltaic cells. Perovskites are efficient at absorbing light and transporting charges which are the key material properties for producing electricity from the sunlight. The main problem of the perovskite solar cells are lower efficiencies in applications-required chemically stable solar cell device configurations that might be greatly improved with optimized metalization in form of nano-particles inclusions and plasmonic energy mediation effects (Schaadt et al. 2005, Lim et al. 2007, Jeng et al. 2015, Matheu et al. 2008, Losurdo et al. 2009, Luo et al. 2014, Pillai et al. 2007, Stuart and Hall 1998, Pillai et al. 2006, Jacak et al. 2016, 2018, 2020). This concept was proven specifically in perovskites in the initial experimental trials (Zhang et al. 2013, Yao et al. 2019, Wu et al. 2016) with a surprisingly strong magnitude of the plasmonic efficiency enhancement observed for perovskite (well beyond magnitudes in traditional p-n junction solar cells) but is not yet understood in terms of physical mechanisms involved and not described in physical models, nor developed commercially. Current R&D initiatives focus on mastering and employing a very strong plasmon photovoltaic enhancement in metalized perovskite solar cells in order to commercialize it on a wide scale. This among others requires development of a microscopic quantum mechanical model of the new channel of plasmon mediated enhancement of the PV effect in perovskites (Laska et al. 2020) which was confirmed in the recent experiments (Zhang et al. 2013, Yao et al. 2019, Wu et al. 2016), taking into account that perovskite SCs hold a strategic potential for the EU, which managed to secure in the recent years a very strong position in terms of global competition in this area. The lacking quantum description of the nano-plasmonic perovskite photovoltaic effect enhancement is deemed to enable its technological optimization and further development towards devices designs, industrial production processes and market-ready metalized perovskite solar cells of highly increased efficiencies. A strong increase of the perovskite SCs efficiencies (the experimental record is 40% relative increase due to metalization as achieved experimentally by Wu et al. 2016) is most probably due to the reduction of the exciton binding energy, but not of plasmon induced strengthening of photon absorption known from the p-n junction solar cells (like the metalized Si cells). On the technological side, nanoparticles are embedded in the perovskite compounds close to the interface with the electron or hole absorber in the architecture of a hybrid chemical perovskite cell. Such cells operate in a different manner than conventional p-n junction cells, resulting in a different type of the plasmonic PV effect, which, however, is surprisingly strong.

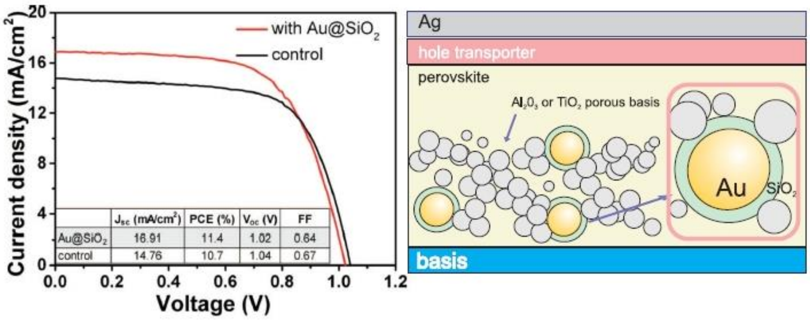

Fig.1. The I-V characteristics of the perovskite cell with porous Al_2O_3 basis filled with Au@SiO_2 core-shell nanoparticles after experiment (Zhang et al. 2013); a strong increase of the photo-current is noticeable with simultaneous lowering of the voltage; (right panel) the scheme of location of dielectric coated core-shell gold nanoparticles.

The R&D plans are to scientifically explain this effect enabling its further technological development by applying various quantum techniques, including the Fermi golden rule to the coupling of the dipole near-field-zone (lower distance than the wavelength) radiation of surface plasmons in nanoparticles to the band electrons in a nearby semiconductor. The research plans involves simultaneously both components of this effect, i.e. optical (the one in p-n junction cells and resolving itself mainly to a photon absorption growth) and electrical (the newly discovered in perovskite cells apparently beyond absorption) ones in a common general microscopic model, allowing for the parameter optimization in a technological fine-tuning towards the innovative products development. The objective of the research in this domain is thus to commercialize the new technology of plasmon enhanced metalized perovskite solar cells, allowing for commercialization of the initially proven feasibility of relative increasing of the perovskite SCs efficiencies in a magnitude of 40%, depending on the particularities of the solar cell design towards harnessing the investigated technology and prepare the perovskite metalized solar cells in terms of prototype devices to be introduced to the market. This research objective holds a potential to support novel breakthrough in a general PV uptake due to an improved cost/efficiency ratios and practical advantages of the thin-film and elastic perovskite solar cells devices with efficiencies significantly exceeding current state of the art (with cost nearing towards 0,009 Euro per kWh from the current value of ca. 0,015 Euro per kWh achieved in 2020).

The objective of technologically mastering particularities of the new plasmon effect in the perovskite SCs is of a major significance as the efficiency of these cells without any metallic components has been lifted from 2% (2006) and 3.8% (2009) to 25.3% (2019) and circa 30% (in tandem) and its further increase (up to 40% relative increase as proven in trial experiments) due to metalization is highly impressive and carries with itself very significant market potential for a mainstream proliferation of PV (very realistic at the mentioned above target energy production unitary costs).

Cheap and relatively simple low-temperature chemical technology of perovskite cell production, the possibility to produce ultra-thin plastic panels in a roll-to-roll processing including ink-jet or screen printing and covering arbitrary substrates (windows, walls, tiles) with thin elastic cells, indicate that perovskite cells might become a default choice for many application sectors as the future mass industry PV solution. Recent advances in durability enhancement of perovskite SCs are also encouraging and motivating interest in metalization of these cells. As mentioned in 2019 NASA announced the beginning of trials using ultra-thin perovskite panels ink-jet printed in space and transported on e.g. to the Moon or Mars in liquid form instead of the conventional large and heavy PV panels. This is considered additionally feasible as the main destructive factors temporarily degrading perovskite cells, such as humidity and oxygen, are not present in space or on the Moon.

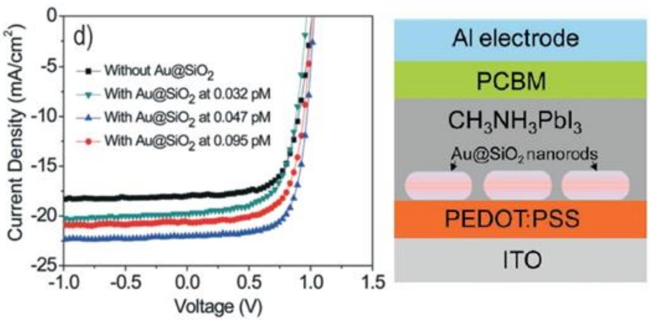

Fig.2. The I-V characteristics of the perovskite solar cell metalized with gold code-shell nanorods (right panel) embedded at the interface between the PEDOT:PSS later and the perovskite later, after the experiment (Wu et al. 2016).

Therefore, the lasting metalization of perovskite cells would provide an important contribution to optimize their efficiencies and also to accommodate the spectral characteristic of final cells to a different solar radiation spectrum in various circumstances beyond Earth’s atmosphere. Identification and technological fine-tuning of the microscopic mechanism of both the branches of the plasmon PV effect in perovskites is of major significance for development of the plasmonic enhanced photovoltaics.

4. European Commission Policy in Support of the Perovskite PV R&D

The Horizon 2020 Work Programme 2018-2020 in its Section 10. defines major research directions towards achieving a goal of building a low-carbon, climate resilient future for Europe with secure, clean and efficient energy. Upon these directions Research and Innovation actions calls have been planned focusing on novel technologies on renewable energy. The scope of these efforts resolve to achieving climate neutrality in the energy sector with securing economically justified energy sources with minimized environmental signatures.

The perovskite solar cells R&D directly adheres to the main measures as defined in scope of the revised H2020 Work Programme. The perovskite SC R&D aims at progress in cheaper and more performant renewable energy generation technologies in domain of PV, as well as in supporting increase of the renewable energy innovations market-uptake for solidifying an already pronounced capacity of the European Union in this area. The relevant H2020 calls focus on the efforts in research activities aimed at identifying and harnessing solar energy breakthroughs that will feed the innovation cycle and become the basis of the next generation of the EU photovoltaic technologies. The Work Programme requires that the R&D contributes to implementing priorities for strengthening of the EU leadership in renewables articulated in the Communication for Accelerating Clean Energy Innovation – European Commission COM(2016) 763. This communication points that further accelerating the transition to low-carbon competitive economy is both an urgent necessity and at the same time a tremendous opportunity for Europe being also a central challenge of our time, while taking into account pollution impacts and the global warming. As the EU is well placed to lead in the clean energy transition it also holds a strong technological position in this domain. In recent decades Europe was leading global efforts to fight climate change and was a driving force in developing renewables. As further pronounced in the Clean Energy for All Europeans – European Commission COM(2016) 860, innovation in renewable energy is one of the key areas where action can be strengthened by current technological position of the EU on a global scene with synergies achieved in successful proposals implementation results, assumed to support jobs, growth and industrial investment in Europe. The impact of the perovskite SC R&D as one of the EU KETs thus addresses global competitiveness of the EU in regard to photovoltaics.

The Energy Union policy set out on the basis of the above mentioned European Commission communicated standpoints in particular address the two following goals: 1) putting energy efficiency first and 2) achieving global leadership in renewable energies. The EC has estimated that in order to reach the EU's 2030 climate and energy targets, about €379 billion investments are needed annually over the 2020-2030 period (with €27 billion devoted to public and private research annually) with significant shares targeted at the further development of PV.

It should be however stressed that photovoltaic industry in the EU experienced significant problems with employment reductions in the recent decade due to industrial PV production downfalls in Europe resulting from overseas market competition, mainly from Asia (and in particular China). The Chinese competitors are reported (cf. European Commission funded study by Dervojeda et al. 2017) to be actively supported by the local government using multiple means, such as special tax exemptions, access to low interest investment, direct subsidies to sell the products on the EU and US markets below their production costs, IP looting, etc. targeted at reaching a global economic domination on the market of PV devices and enjoying the benefits coming from such position, enabling also increasing the technological edge. Furthermore, Chinese PV advancing production processes and technologies are usually associated with a considerable environmental pollution levels, much beyond the norms accepted in Europe. As stipulated by European Commission, in the current situation the main direction to re-establish a fair play competition with Asian players in a domain of emerging PV technologies is by providing stimulatory and widely-scaled R&D funding in Europe, developing many possible directions simultaneously to possibly create a strong synergy between European technologies. The technology planned for R&D in perovskite PV holds such a potential with its universal character, enabling to enhance almost all types of perovskite SC fabrication techniques with initially proven as impressive relative efficiencies increases (in relative improvement of up to even 40% as demonstrated Wu et al. 2016).

Also the market-enabled impact is pronounced in the revised Work Programme of the H2020 priorities in regard to photovoltaics. Emerging and new PV technologies including perovskite cells are specially promoted on the level of Research and Innovation actions in H2020 Work Programme, with the priorities involving maximising industry engagement in development and commercialization activities of the researched renewable energy technologies. The European Commission has e.g. recognized a goal – cf. European Commission Decision C(2020)4029, 2020 – in the H2020 program to overcome the short-term orientation of industry and engage it in activities with a longer-term focus (at least 3-5 years ahead), which is also well aligned with the investigated R&D in metalized perovskite SCs nano-plasmonic efficiencies enhancements.

In general we all realize that the depletion of fossil fuels and global warming resulting from the use of these traditional energy sources reveals the need to focus on renewable and clean energy sources. This is especially underlined by the so called European Green Deal policy in the new appointment of the European Commission that continues the same direction with however a new impetus and yet even stronger focus of the renewable energy strategic significance for the problems related to climate changes and the fossil fuels caused pollution and its social and economic impacts. As renewable and clean energy, photovoltaics have secured its position as one of the most promising and dynamically developing sustainable and clean energy source. Since the production of first modern solar modules in 1954 in Bell Labs, many types of solar cells have been developed and successfully commercialized. Solar cell technologies advances are usually connected to new achievements in theoretical and experimental studies in the domain of light absorbing materials. In the recent decades, a huge effort has been focused on enabling new PV materials to produce high quality SCs with increasing efficiencies in converting sunlight to electric energy at decreasing costs.

The perovskite PV research has therefore a strongly applicative and prospective character of commercial significance which directly responds to the expectations outlined in the relevant section of the H2020 Work Programme. The main expected contribution of this research domain is targeted at the reduction of the solar power costs with PV efficiencies enhancements and the objectives straightforwardly support the Strategic Targets of the H2020 Work Programme in its corresponding scope. Additionally the H2020 WP sets emphasis on including international cooperation opportunities whenever relevant to the proposal and the domain, in particular in the context of the Mission Innovation Challenges. This is widely addressed in the present cooperation in the EU scale within this PV R&D domain with a lasting partnership between the partners, who already cooperated in numerous research endeavours, including recent years lasting cooperation in the H2020 EU COST program MultiScale Solar (http://multiscalesolar.eu). The corresponding RIA H2020 calls expect bottom-up proposals addressing any renewable technology currently in the early phases of research which is the topic that our proposal focuses on. The current research of the metalized perovskite PV technology is between TRL 1/2 to TRL 4/5. As with the programmed H2020 Work Programme requirements, the expected impact of research must be based on the concept already proven, which ist he case, and further developed to contribute to accelerating and reducing the cost of the next generation of sustainable renewable energy generation. It should also directly advance the knowledge and scientific proofs of the technological feasibility of the plasmonically enhanced perovskite SCs, including environmental, social and economic benefits from this technology. This research area also demonstrates the required contribution for establishing a European innovation base and supporting a sustainable renewable energy system. Yet even more importantly the impact of the researched metalized perovskite SCs hold a potential to provide a real breakthrough in applied photovoltaics in general, facilitating its major market uptake, as a combination of cheaply produced (yet low energy-efficient in stable chemical configurations) perovskite cells with advanced quantumly enabled plasmonic efficiency improvements by metallic nano-modification (that as validated are able to enhance the efficiency by even 40% relative growth). This holds a strong potential for overall PV proliferation as a mainstream electricity source in multitude of everyday applications.

Currently, the most commonly developed inorganic (synthesizable with chemical crystallization techniques convenient for mass production and ink-jet/screen printing) perovskite solar cells are $CsPbI_3$, $CsPbI_2Br$ $CsPbIBr_2$ and $CsPbBr_3$. The $CsPbI_3$ with a narrow band (of 1.73eV) is one of best candidates for harvesting solar energy. The CsBp perovskite solar cells show the best performance among inorganic cells (Ho-Baillie et al. 2019), yet its black phase (α-$CsPbI_3$) suffers from notorious instability at room temperature, causing rapid degradation to the so called yellow phase (δ-$CsPbI_3$) of poor-efficiency (Sutton et al. 2016, Hu et al. 2017, Eperon et al. 2015, Luo et al. 2016, Akkerman et al. 2015, Stoumpos et al. 2013). There are thus many challenges in the fabrication of stable cells devices. Incorporation of bromide ions into Cs perovskites in place of iodide ions to form $CsPbBr_3$ is currently considered the most promising alternative for improving phase stability, but its large band gap (2.25 eV) limits light collection thus reducing the cell efficiency (Li et al. 2018, Liu et al. 2019). Recently much effort has been put into the development of completely inorganic cells to improve phase stability, which is its main limitation and the results are promising. Within those efforts over the few past years, multiple companies and researchers have reported new efficiency records in area of perovskite SCs.

The current record for perovskite SC efficiency is 29.1% from Helmholtz-Zentrum Berlin achieved in January 2020 which is a result directly competing with much more complicated and expensive to produce GaAs thin-film SCs. However this result was achieved for the tandem perovskite/Si configuration. Before this in June 2018 Oxford PV announced that it had developed 27.3% perovskite-silicon tandem device (in December 2018 the same company announced a 28% world performance record for tandem Si perovskite cells), so there is a steady growth of circa 1% annually.

For multi-junction tandem configurations the Shockley-Queisser limit can be overcome and advanced (yet much more complex to fabricate and expensive as well as less practical in terms of flexibility) SCs of these type will be characterized with further-on increasing efficiencies. On the other hand for single junction perovskite cells the upper limit is the Shockley-Queisser limit, theoretically accepted for perovskite SCs at the level of circa 31% (Sha et al. 2015), which is close to the theoretical SQ limit of 32% for single junction Si-based solar cells and 33% achievable by GaAs cells. The current record for laboratory achieved single-junction perovskite cell efficiency is circa 25% first approached in September 2019 by Korea Research Institute of Chemical Technology (KRICT) and MIT cooperation and later on surpassed with 25,2% by University of Korea (however in unstable regime precluding a practical device as of yet). For market applicable perovskite cells (or whole modules) the achievable efficiencies are however much lower. In Japan, in July 2018, Toshiba and NEDO cooperation announced similar 703 cm^2 perovskite module with a stable performance at 11.7%. In Europe, in April 2018, the EU Solliance Project announced its most effective perovskite module of 144 cm^2 and stable efficiency of 13.8%. In July 2018 Chinese Microquanta announced a new record for the mini perovskite commercial module at 17.3% (the module module contained 7 cells and had an area of only 17 cm^2). In October 2019, the company achieved a record conversion rate of 14.24% for a large perovskite solar module of 800 cm). Each cell in the module has an efficiency of 14.5%. More recently, in September 2019, Solliance and the American company MiaSolé announced another achievement: 23% energy conversion efficiency in a flexible tandem solar cell: an upper flexible translucent perovskite solar cell with an indium and gallium selenium lower flexible cell (CIGS).

In April 2020 Saule Technologies in Poland secured funding to launch mass production of stable ink-jet printed perovskite modules (following few years long large scale investment for R&D) with efficiency slightly surpassing 10%, but with relatively large surfaces of $1m^2$. The technology of metalized perovskite improvement by nano-plasmonic effects mediating energy transfer in a newly discovered exciton channel beyond the currently known mechanisms in standard p-n junction solar cells has highly universal character in terms of applications to improve the practically achieved efficiencies in stable perovskite chemical configurations to support reaching the objectives set out in H2020 WP. This technology is easily scaled from a PV cell level to a complete SC module. The main property of this technology, enables metallic nanoparticles inclusions into the liquid screen printing of the solar cell upon a process of perovskite chemically induced crystallization after screen-printing takes place. This allows to fabricate metalized perovskite cells in a roll-to-roll approach conditioned by the scale of the printing device. The efforts are thus focusing on research and prototypes development and testing on the level of cells and modules with a goal to obtain a universal efficiency increase, stability and large-scale manufacturability for thin film PV that will be competitive with existing commercial perovskite PV technologies at a very low cost of modification of the production processes addressing the novel PV technology requirements as defined in the H2020 Work Programme. The results of the research are aimed at supporting European Union in improving its position in global competition for the efficient thin-film solar cells research and economically viable convenient mass production techniques supporting goals of the WP and the European Strategic Energy Technology Plan (SET Plan - https://ec.europa.eu/energy/en/topics/technology-and-innovation/strategic-energy-technology-plan).

In terms of Key Performance Indicators (in connection to the SET-Plan) the research objectives aim at overcoming the economic barrier in PV cost/efficiency ratio that currently withhold solar energy transition. The R&D efforts hence address the issue on how to optimize metalization of perovskite cells and how to design and produce such devices, including also a challenging question on space-applications (i.e. addressing different spectra of solar radiation). This research domain also enhances knowledge diffusion in the EU increasing innovation capacity in the low-carbon economy sector and integrating advanced research capabilities upon a prospective PV technology. Growing share of Renewable Energy Sources represents a strong contribution to the COP21 objectives and United Nations Sustainable Development Goals (IEA 2018, IRENA 2018). In 2018, the renewable energy share in the EU represented 17.5% of total energy consumption with increasing share of PV (amounting 4% share – Eurostat 2019). The PV energy is positioned to soon dominate RES and slowly starts to challenge fossil fuels in the recent years in many sectors due to increasing ratios of efficiency per cost, continuously brought up by the new solar cells technologies (IRENA 2018). In 2020 PV may have already finally become the cheapest source of the electrical energy in general (cf. Qatar General Electricity & Water Corporation, 2020).

The PV energy, as an already top effective renewable energy source, is deemed to become in the near future a mainstream economically viable option for ensuring carbon-free and ubiquitous electricity source to our civilization. One of main problems of modern solar cells is the robust design of PV panels which are limited in scope of their possible applications. The much more universal SC technology of flexible perovskites that can be integrated on any surfaces (including window tiles, surface coverings of any objects or devices, including electronics, cars, clothing, etc.) is on the other hand hampered by lower efficiencies. The research objectives thus focus on understanding and improving perovskite SCs efficiencies by plasmonic enhancement due to metalization, thus not only ensuring high efficiencies but also pushing economically viable thin-film elastic SC devices towards the market. This addresses applicable research with goals in commercialization of the new technology, including such critical issues as devices designs, production costs, operational reliability and durability. The significance of the researched metalized perovskite PV technology in domain of renewables can be well compared to other competing technologies, such as CSP (Concentrated Solar Power, with lensing designed to collect solar radiation in heat) as targeted in further development by the European Strategic Energy Technology Plan.

The SET Plan has established strategic targets for CSP development, of which the first target is *"More than 40% reduction of energy costs by 2020, reaching a price <0.10 €/kWh".* The target CSP unitary price of SET-

Plan is thus greater by 1 order of magnitude in comparison to the unitary price of PV energy generation that current research plans in the scope of plasmonically enabled perovskite solar cell pursue: i.e. values of 0.01 Euro/kWh and below. This research adheres to the H2020 Work Programme in contributing to the development of the next generation of highly efficient and flexible-structure solar cells based on plasmonically activated metalized perovskites, thus focusing on potential cost-effective solutions enabling further proliferation of PV energy, as well as renewables in general to support decarbonization and sustained development. It pursues optimizing of the the perovskite SC technology by researching innovation of plasmonic enhancement due to metallic nano-modifications with contributions of quantum effects on the verge of frontier of basic science. This R&D domain involves fundamental study to provide clear scientific description of not yet fully understood core physical mechanisms involved in the proven effect to be able to optimize and later bring this technology from a prototype stage towards the commercial product, scaling its market potential and competitiveness upon ongoing fine-tuning of the product designs and its reliability.

5. Summary and Conclusions Regarding Future Prospects of Perovskite PV

At the summary the author would like to stress the role of the the Perovskite Solar Cell as the EU Key Enabling Technology. As stipulated in the introductory chapter at the end of 2017 the European Union in its study on Key Enabling Technologies for achieving technological global supremacy for the EU has identified only a total of 12 promising KETs among all technologies as the ones holding potential for the EU to assure through further development that the EU industry in those KETs respective areas will stay ahead of international competition. In energy context the Perovskite Solar Cell was defined as the KET for the EU, mainly due to the EU’s secured leading position in this technology as well as due to high efficiency/cost ratio (ca. 0,014 Euro/kWh) and other key properties such as semi-transparency or elasticity supporting wide applications of this PV technology.

As buildings are estimated to account for over 40% of the energy demand in the EU, building-integrated solar cells are the primary application for PV. Perovskite in contrast to sturdy Si panels offer simple whole-surface coverings techniques including aspects such as architectural freedom. The advantages of the Perovskite Solar Cells are primarily due to the elastic thin-film PV technology being easily and cheaply ink-jet or screen printed in simple roll-to-roll processes or even sprayed onto large surfaces similarly like paints that when activated with chemically induced crystallization process make thin-film layers (thickness below 1 μm).

These devices are thus well suited to mass-output market uptake and vast applications (such as energy smart buildings elevations coverings of variety of diff. geometries, semitransparent or smart windows, roofs coverings, outdoor furniture, vehicles or even clothing external surfaces that produce enough power to charge a phone).

Skanska partnering with Saule now commercialize Perovskite SCs in newly developed buildings as large area elevations and windows coverings. Perovskite eff. rose rapidly from just 2% in 2006 to 25.3% in 2020 and up to 30% in tandem, however have stability / durability problems at higher efficiencies (are currently stable at ca. 15% eff.) Therefore the R&D initiatives are needed in this emerging PV technology domain.

In May 2019 the Cost of Ownership of just 0.20 EUR/Watt-peak was proven achievable for single-junction pure perovskites modules prototypes by CHEOPS project (cheops-project.eu). Other research initiatives (including e.g. the 2020 PLASMPERCELL H2020 proposal, involving scientific partnership of European Solar Network - Belgium, National Centre for Scientific Research - France, Technical University of Clausthal, Friedrich Schiller University Jena, International Solar Energy Research Center Konstanz - Germany, University of Rome Tor Vergata - Italy, Aristotle University of Thessaloniki and Organic Electronics Technologies - Greece, PlasmaSolaris - Poland, Endüstriyel Elektrik - Turkey and the University of Belgrade - Serbia and with the present paper's author holding the role of the coordinator of the consortium on behalf of the European Solar Network) targeted R&D in the perovskite SCs efficiency increases with up to 40% relative increase proven achievable due to the nano-plasmonic enhancements (inclusion of metallic nano-particles).

A relative growth of about 40% as already demonstrated means that if one has a cheap and stable perovskite SC production technology at just circa 15% efficiency one can releatively easily grow this efficiency to circa 21% with similar chemical morphology and stability of the original cell employing quantum processes of plasmonic energy transfer mediation (noble metals or TMN nanoparticles). This with a very marginal additional cost of few % (in materials, cell fabrication, module assembly, installation, etc.) diminishes the Cost of Ownership towards values of 0.15 - 0.14 EUR/Wp.

This is an example of the perovskite PV R&D direction that is well aligned with the EU's PV research support priorities and policies (involving the KET, following priorities set out in the SET Plan, including maximizing the efficiency/cost ratios), pronouncing perovskite SCs KET role for the EU.

6. References

Akkerman, Q.A. et al., 2015. Tuning the optical properties of cesium lead halide perovskite nanocrystals by anion exchange reactions, J. Am. Chem. Soc., 137, pp. 10276-10281, 10.1021/jacs.5b05602

Dervojeda, K., Lengton, M., Koonstra, A., 2017. Perovskite Solar Cells, Report on promising KETs, KETs Observatory Phase II, EASME/COSME, European Commission

Eperon, G.E., Paternò, G.M., Sutton, R.J., Zampetti, A., Haghighirad, A.A., Cacialli, F., Snaith, H.J., 2015. Inorganic caesium lead iodide perovskite solar cells, J. Mater. Chem. A, 3, pp. 19688-19695, 10.1039/C5TA06398A

European Commission, 2020. Strategic Energy Technology Plan, 2014-2020, https://ec.europa.eu/energy/en/topics/technology-and-innovation/strategic-energy-technology-plan

European Commission COM(2016) 763

European Commission COM(2016) 860

European Commission Decision C(2020)4029, 2020. Horizon 2020, Work Programme 2018 - 2020

Eurostat, 2019. https://ec.europa.eu/eurostat/statistics-explained/index.php/Renewable_energy_statistics

Ho-Baillie, A., Zhang, M., Lau, C.F.J., Ma, F.-J., Huang, S., 2019. Untapped potentials of inorganic metal halide perovskite solar cells, Joule, 3, pp. 938-955, 10.1016/j.joule.2019.02.002

Hu, Y., Bai, F., Liu, X., Ji, Q., Miao, X., Qiu, T., Zhang, S., 2017. Bismuth incorporation stabilized α-$CsPbI_3$ for fully inorganic perovskite solar cells, ACS Energy Lett., 2, pp. 2219-2227, 10.1021/acsenergylett.7b00508

International Energy Agency, 2018. Market Report Series: Renewables 2018 - English ES

IRENA, 2018. Global Energy Transformation. A roadmap to 2050, Microscopy Research and Technique

Jacak, W., 2020. Quantum nano-plasmonics, first edition, Cambridge University Press

Jacak, J., Jacak, W., 2018. "Plasmon-induced enhancement of efficiency of solar cells modified by metallic nano-particles: Material dependence", J. Appl. Phys. 124, https://doi.org/10.1063/1.5040014, p. 073107

Jacak, W., Popko, E., Henrykowski, A., Zielony, E., Luka, G., Pietruszka, R., Witkowski, B., Wachnicki, L., Godlewski, M., Chang, L.-B., Jeng, M.-J., 2016. "On the size dependence and the spatial range for the plasmon effect in photovoltaic efficiency enhancement", Sol. Energy Mater. Sol. Cells 147, p. 1

Jaeger-Waldau, A., 2019. PV Status Report, Joint Research Centre, Publications Office of the European Union, Luxembourg

Jeng, M.-J., Zih-Y, C., Xiao, Y.-L., Chang, L.-B., Ao, J., Sun, Y., Popko, E., Jacak, W., Chow, L., 2015. "The efficiency enhancement of silicon and CIGS solar cells by the incorporation of metal nanoparticles", Materials 8, p. 6761

Laska, M., Krzemińska, Z., Kluczyk-Korch, K., Schaadt, D., Popko, E., Jacak, W.A., Jacak, J.E., 2020. Metallization of solar cells, exciton channel of plasmon photovoltaic effect in perovskite cells, Nano Energy

Li, H. et al., 2018. Interface engineering using a perovskite derivative phase for efficient and stable $CsPbBr_3$ solar cells, J. Mater. Chem. A, 6, pp. 14255-14261, 10.1039/c8ta03811b

Lim, S. et al., 2007. "Photocurrent spectroscopy of optical absorption enhancement in silicon photodiodes via scattering from surface plasmon polaritons in gold nanoparticles", Journal of Applied Physics 101(10), p. 104309

Liu, X. et al., 2019. Boosting the efficiency of carbon-based planar $CsPbBr_3$ perovskite solar cells by a modified multistep spin-coating technique and interface engineering, Nano Energy, 56, pp. 184-195, 10.1016/j.nanoen.2018.11.053

Losurdo, M. et al., 2009. “Enhanced absorption in Au nanoparticles/a-Si:H/c-Si heterojunction solar cells exploiting au surface plasmon resonance”, Sol. Energy Mater. Sol. Cells 93, p. 1749

Luo, P., Xia, W., Zhou, S., Sun, L., Cheng, J., Xu, C., Lu, Y., 2016. Solvent engineering for ambient-air-processed, phase-stable CsPbI3 in perovskite solar cells, J. Phys. Chem. Lett., 7, pp. 3603-3608, 10.1021/acs.jpclett.6b01576

Luo, L., Xie, C., Wang, X., Yu, Y., Wu, C., Hu, H., Zhou, K., Zhang, X., Jie, J., 2014. “Surface plasmon resonance enhanced highly efficient planar silicon solar cell”, Nano Energy 9, pp. 112–120

Matheu, P., Lim, S., Derkacs, D., McPheeters, C., Yu, E., 2008. “Metal and dielectric nanoparticle scattering for improved optical absorption in photovoltaic devices”, Applied Physics Letters 93(11), p. 113108

Pillai, S., Catchpole, K., Trupke, T., Green, M., 2007. “Surface plasmon enhanced silicon solar cells”, Journal of Applied Physics 101(9), p. 093105

Pillai, S., Catchpole, K., Trupke, T., Zhang, G., Zhao, J., Green, M. A., 2006. “Enhanced emission from Si-based light-emitting diodes using surface plasmons”, Appl. Phys. Lett. 88, p. 161102

Sha, W.E.I., Ren, X., Chen, L., Choy, W.C.H., 2015. The Efficiency Limit of CH3NH3PbI3 Perovskite Solar Cells, Appl. Phys. Lett. 106, 221104

Schaadt, D. M., Feng, B., Yu, E. T., 2005. “Enhanced semiconductor optical absorption via surface plasmon excitation in metal nanoparticles”, Appl. Phys. Lett. 86, p. 063106

Stoumpos, C.C. et al., 2013. Semiconducting tin and lead iodide perovskites with organic cations: phase transitions, high mobilities, and near-infrared photoluminescent properties, Inorg. Chem., 52, pp. 9019-9038, 10.1021/ic401215x

Stuart, H. R., Hall, D. G., 1998. “Island size effect in nanoparticles photodetectors”, Appl. Phys. Lett. 73, p. 3815

Sutton, R.J., Eperon, G.E., Miranda, L., Parrott, E.S., Kamino, B.A., Patel, J.B., Hörantner, M.T., Johnston, M.B., Haghighirad, A.A., Moore, D.T., Snaith, H.J., 2016. Bandgap-tunable cesium lead halide perovskites with high thermal stability for efficient solar cells, Adv. Energy Mater., 6, p. 1502458, 10.1002/aenm.201502458

Qatar General Electricity & Water Corporation, 2020. Kahramaa and Siraj Energy Sign Agreements for Al-Kharsaah Solar PV Power Plant

Wang, 2018. Solar modules to get even cheaper and more efficient, Bloomberg New Energy Finance

Wu, R., Yang, B., Zhang, C., Huang, Y., Cui, Y., Liu, P., Zhou, C., Hao, Y., Gao, Y., Yang, J., 2016. “Prominent efficiency enhancement in perovskite solar cells employing silica-coated gold nanorods”, J. of Phys. Chem. C 120, p. 6996

Yao, K. et al., 2019. “Plasmonic metal nanoparticles with core-bishell structure for high-performance organic and perovskite solar cells”, ACS Nano 13, p. 5397

Zhang, W., Saliba, M., Stranks, S., Sun, Y., Shi, X., Wiesner, U., Snaith, H., 2013. “Enhancement of perovskite-based solar cells employing core-shell metal nanoparticles”, Nano Lett. 13(9), p. 4505

An innovative plant integrating PVT and geothermal reversible heat pump for heating and cooling in residential applications

Marco Pellegrini[1], Giovanni Chiappa[2] and Matteo Chiappa[2]

[1] Department of Industrial Engineering, University of Bologna, Forlì (Italy)

[2] HDEMIA Srl, Merate (Italy)

Abstract

Many new technologies and projects are currently being undertaken worldwide to assist in the reduction of fossil fuel consumption. Significant progress has been made so far, and one promising solution moving towards a low-carbon heating and cooling energy production in buildings is in the combined generation of renewable electricity and heat based on photovoltaic thermal collectors (PVT). In several European countries the PVT market is picking up speed. The possible applications for PVT-collectors are very varied and range from e.g. swimming pool heating to solar heat for industrial processes, but many of the already installed PVT systems have been applied to cover thermal and electrical energy demand at residential scale. The paper aims to show the results achieved in the power, heating and cooling production by a PVT plant integrated with geothermal reversible heat pump. The paper includes a description of the technology, the performance measured in a first installation and a preliminary economic assessment.

Keywords: PVT, geothermal heat pump, solar heating and cooling, energy efficiency.

1. Introduction

Cities are fundamental in the world's transition to a low-carbon economy, since cities account for about 65% of global energy use and about 70% of man-made carbon emissions. While many cities have so far focused primarily on energy efficiency, the next step towards an urban sustainable energy system will require a significant increase in the use of renewable energy. Renewables can bring tremendous benefits to cities, including cleaner air, modern services and improved living spaces, and have huge impacts on several sectors, from buildings to transport, from lighting to industry.

Photovoltaic (PV) modules and solar thermal collectors are being installed in residential buildings and in some industrial utilities to respectively produce electrical and thermal energy. Both technologies have been widely applied and demonstrated to be reliable and effective (Weiss and Spork-Dur, 2020). Photovoltaic thermal (PVT) collectors can be considered as an hybrid technology combining PV and solar thermal components into a single module to simultaneously generate electricity and heat. The integration of PV and solar thermal technology in one device enhances solar energy conversion efficiency and also achieves optimized use of surfaces. Different kinds of PVT collectors have been tested in different locations, therefore a wide literature exists (Joshi and Dhoble, 2018).

PVT market is a niche market if compared with solar thermal and PV; nevertheless, by the end of 2018 more than 1 million m^2 of PVT collectors were installed in over 25 countries (Weiss and Spork-Dur, 2020): in the European market, France is the leader with an installed collector area of 484,587 m^2 followed by Germany with 112,326 m^2 and the Netherlands with 32,127 m^2. In Italy, Spain and Switzerland, collector areas range between 10,000 m^2 and 15,000 m^2. Indeed, the Italian market already showed a great interest in PVT collectors since 2010-2012, when a local increasing of both PVT collectors manufacturers and sales were observed as well as a growing interest from the research field (Aste et al., 2014; Bianchini et al., 2017). Nevertheless, at the time PVT collectors were not cost competitive with PV modules and/or solar thermal collectors and not reliable enough. Now, the market is demonstrating a growing interest in the technology, especially in combination with other renewables. In fact, the non-availability and unpredictability of solar source all the time throughout the year has led to research in the area

doi:10.18086/eurosun.2020.05.15 Available at http://proceedings.ises.org

of solar hybrid renewable energy systems (HRESs). In the past few years, a lot of research has taken place in the design, optimization, operation and control of HRESs (Rekioua,2020). In particular, the integration of PVT with several geothermal systems have been explored, like PVT and heat pumps with borehole heat exchangers (Bertram et al., 2011; Yao et al., 2020) or PVT and open-loop ground source heat pumps (Pellegrini et al., 2019; Hoekstra et al., 2020). Since PVT collectors can be substantially classified into systems that are designed to optimize the heat production or the power production, several combinations of PVT, heat pumps and geothermal for renewable power, heating and cooling generation in buildings can be found in literature.

The paper aims to introduce a novel hybrid renewable energy system, called "Geosolzero", able to cover power, space heating and cooling and domestic hot water (DHW) demand of a single-family house. This system consists of two arrays of PV modules and PVT collectors integrated with a geothermal reversible heat pump. The novelty of the system is related to i) the optimization of power production of PVT collectors and ii) the patented design of the ground plate heat exchangers. The paper includes a description of the plant, the performance measured in a first single-family house installation in Northern Italy and a preliminary economic assessment. Geosolzero plant has been included in the list of representative PVT worldwide plants mapped by the IEA SHC Task 60 "Application of PVT collectors" (Ramschack et al., 2020).

2. Description of the plant

The Geosolzero system has been firstly installed in 2016 in a renovated single-family house in Suello (Italy). The town of Suello is located in the North of Italy, close to the lake of Annone, which is 50 km from Milan. Suello is about 300 meters above sea level and it is characterized by 2,460 heating degrees days and a mean annual solar radiation of about 1,400 kWh/m^2. The building is certified as Class A+ and has an area of about 250 m^2 that is thermally controlled by a HVAC system (in Figure 1 an extract of the executive project of the building).

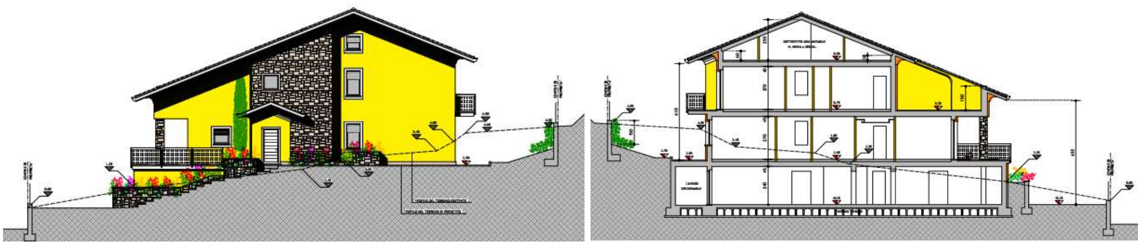

Fig. 1: The executive project of the single-family house in Suello.

The Geosolzero system includes a reversible heat pump, two storage tanks (one for hot/cold water and one for DHW, both with a capacity of 0.3 m^3), 16 unglazed PVT collectors, 16 PV modules and two patented ground plate heat exchangers PVT collectors coolant fluid is a mixture of water and glycol (30%). PV modules and PVT collectors are installed on the house roof. More in detail, the PVT collectors are Solink HBK250850 with a total collector area of 26.08 m^2 and 4 kW peak electrical output. PVT collectors are oriented to the South with an inclination angle of 35°. The PV modules are installed with the same orientation and comprises modules of the same PVT type, i.e. though without heat absorbers (26.08 m^2 and 4 kW peak). Information about PVT collectors (both electric and thermal) and PV modules (only electric) are summarized in Table 1. The electric power produced by both PVT collectors and PV modules is converted into alternating current via one ABB Trio inverter (model 8.5) with two MPPT strings.

Tab. 1: Main electric and thermal characteristics of the PVT collectors (Solink HBK250850). Thermal characteristics are referred to the aperture area.

Electric characteristics	
Electric power at STC conditions	250 W (±3%)
Aperture area	1.570 m x 0.920 m
NOCT	44°C

MPP voltage	29.2 V
MPP current	8.45 A
Open circuit voltage	37.6 V
Short circuit current	8.91 A
Power loss thermal coefficient	-0.44%/°C
Thermal characteristics	
Max stagnation temperature	83°C
Nominal thermal power	849 W (±1.6%)
Peak thermal efficiency	49.1%
Linear coefficient of thermal dispersion a1	10.04 W/m^{2}K
Quadratic coefficient of thermal dispersion a2	0.000 W/m^{2}K^2
Time constant C	147 s
Thermal capacity K	31.4 kJ/K
Max coolant flowrate per module	0.12 m^3/h

In the summer (Figure 2 the building is cooled through the reversible heat pump, which is electrically driven by the PVT collectors and PV modules, while the condenser is connected to one ground plate heat exchanger. PVT collectors are cooled by another twin ground plate heat exchange. Heat pump and PVT collectors circuits are disconnected since manual valves on the lines are closed.

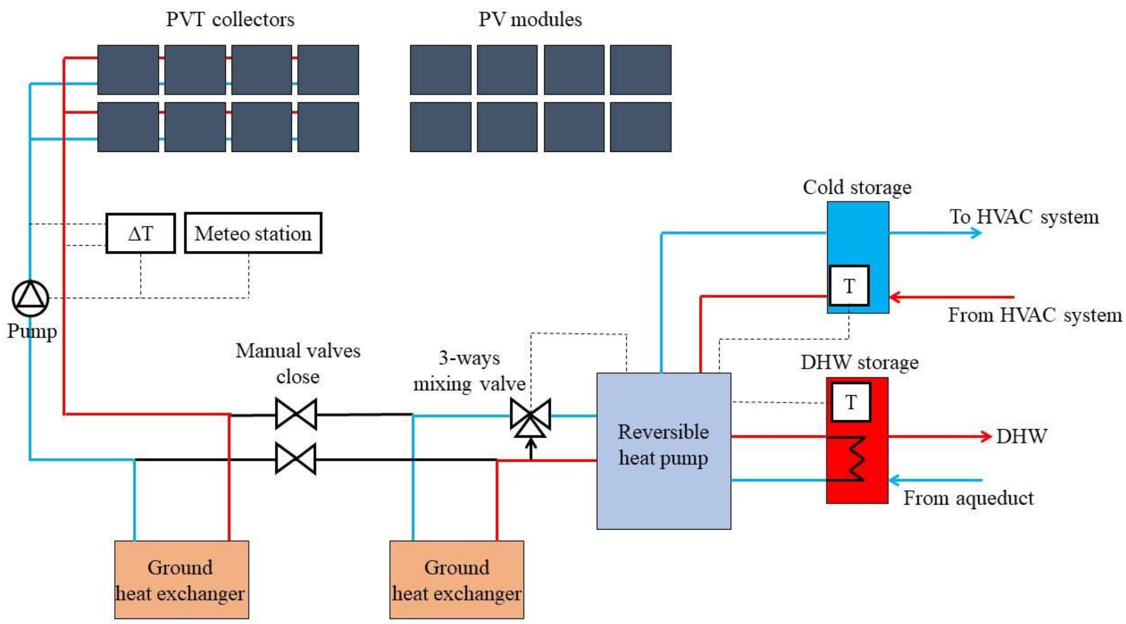

Fig. 2: P&ID of the system and hot/cold flowrate in summertime operation.

In the winter (Figure 3), the manual valves are open and the heat produced by PVT collectors is used on the evaporator side of the heat pump, together with the heat extracted by the ground. In both seasons the production of DHW is directly managed by the reversible heat pump control unit: when DHW is required by the user, an internal 3-ways valve gives priority to the production of DHW in both summer or winter time. The heating and cooling supply system is depicted accordingly to (Jonas, 2019) in the simplified form in Figure 4.

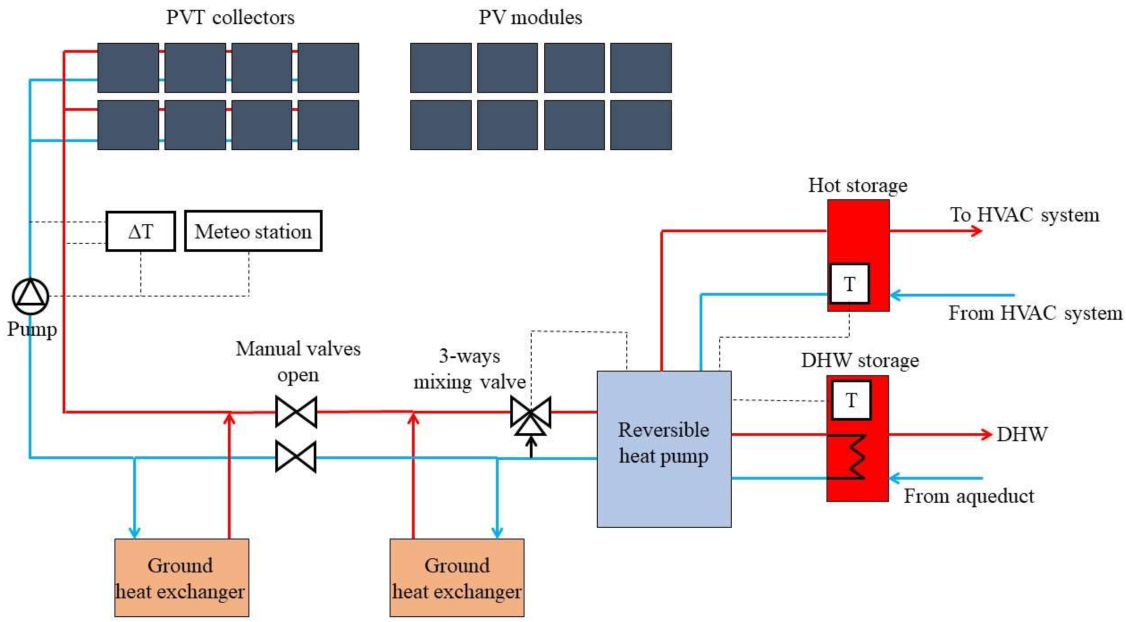

Fig. 3: P&ID of the system and hot/cold flowrate in wintertime operation,

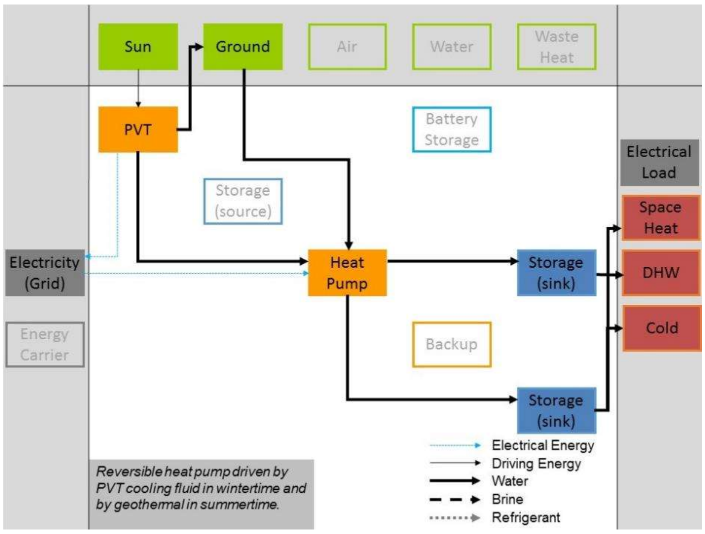

Fig. 4: Visualization of the integrated PVT plant.

The characteristics of the reversible heat pump are summarized in Table 2, while the information about the ground plate heat exchangers are in Table 3. In particular, the ground plate heat exchangers have been designed by HDEMIA for the integration in the plant concept as a further renewable source/sink able to integrate or compensate the energy contribution coming from the PVT collectors.

Tab. 2: Main electric and thermal characteristics of the reversible heat pump installed in the plant.

Main characteristics	
Manufacturer	ENEREN
Model	ENX012HL
Refrigerant	R410A

Size	0.803 m x 0.606 m x 1.247 m
Cooling operation (chiller) @ condenser 30÷35°C	
Cooled fluid temperature @evaporator	7÷12°C
Cooling power	2.50÷10.10
Power consumption (including internal pumps)	0.50÷2.60
EER	5.19÷3.91
Heating operation (heat pump) @ evaporator 0÷-3°C	
Heated fluid temperature @condenser	30÷35°C
Heating power	2.30÷9.90
Power consumption (including internal pumps)	0.40÷2.30
COP	5.25÷4.32
Heating operation (heat pump) @ evaporator 10÷5°C	
Heated fluid temperature @condenser	30÷35°C
Heating power	3.00÷12.80
Power consumption (including internal pumps)	0.40÷2.40
COP	7.04÷5.22
DHW production @evaporator 10÷5°C	
DHW @condenser	50÷55°C
Heating power	2.70÷11.50
Power consumption (including internal pumps)	0.70÷3.40
COP	3.74÷3.35

Tab. 3: Main characteristics of the ground heat exchangers.

Plate size	1.500 m x 0.750 m
Plate weight	6.5 kg
Number of plates	6 per heat exchanger
Installation depth	Under 5 m
Max fluid flowrate per plate	0.3 m^3/h
Plate material	Anodised aluminium with protective coating in PVC

The coolant flowrate through the PVT collectors is guaranteed by a pump (Grundfos SOLAR PML 25-145) and it is controlled by a solar thermal differential temperature unit (PAW SC3.6). Therefore, the control strategy of the PVT cooling system is based on keeping constant the temperature difference between PVT arrays inlet and outlet through the control of the coolant flowrate. The operation of the reversible heat pump is controlled by its own control unit: in particular, the reversible heat pump control unit manages i) the 3-way mixing valve that optimizes the inlet temperature from the heat source/sink and ii) all the inverters installed on refrigerant compressor and fluid pumps motors to optimize the differential temperatures in the heat exchangers through flow rate control on the evaporator and condenser sides. As mentioned before, the reversible heat pump control unit also manages the DHW production. A Siemens RLU220 controller has been installed for the monitoring and control of the whole plant, including temperature monitoring (via Siemens QAD22 temperature sensors) in the hot/cold water and DHW storages. The control logic has not been implemented yet due to the difficulties in integrating the control units of the PVT coolant circulating pump and of the reversible heat pump (SHC IEA, 2014).

The advantage in the adoption of the described ground configuration is that the geothermal closed-loop is realized with a compact and easy to install device (i.e. the ground plate heat exchanger) that can be applied with relatively low cost also in existing buildings. In fact, in comparison with the proposed solution, the realization of close-loop systems usually requires larger area for horizontal borehole heat exchangers or greater depth for vertical borehole heat exchangers (Rees, 2016). Another option is the integration of PVT collectors with open-loop geothermal systems, i.e. the direct use of groundwater as heat source or sink, but with higher investment and maintenance and operation costs (Rees, 2016). Nevertheless, the application of HDEMIA ground heat exchangers can concentrate the heat exchange in a relatively small volume, and so the risk of local thermal short circuit may be expected.

3. Techno-economic assessment

Based on the building executive project, the users yearly energy demand was calculated in 26.89 kWh/m^2 for space heating, 5.36 kWh/m^2 for space cooling and 467 kWh el for DHW production. Over the years the system has been monitored to evaluate its performances and the real behavior of the users.

The mean yearly energy demand for space heating results as about 11,750 kWh (i.e. 47.00 kWh/m^2 per year, that is 75% more than expected). The difference between calculated and measured energy consumption for space heating is due by the users behavior, since the rooms' set points for space heating were found to be set at temperature much higher than the standard 20°C in wintertime. The whole energy demand is covered by the heat pump, since the plant has no thermal auxiliaries (i.e. natural gas or electric boilers). Therefore, the design of the plant results in a good capacity to cover also heating peak requests higher than expected. The mean yearly energy demand for space cooling results as about 1,408 kWh (i.e. 5.63 kWh/m^2 per year, that is 5% more than calculated). In that case, the user needs are in good agreement with the expected energy consumption. The energy demand for DHW production has been estimated on the basis of heat pump operation while no space heating or cooling demand was present. The mean yearly consumption of DHW has been estimated in 512 kWh el per year, once again in good agreement with the design forecasts.

The seasonal COP of the heat pump in winter (including DHW production) has been assessed in 4.04, while the EER of the reversible heat pump in summer (including DHW production) has been assessed in 3.93. COP and EER have been both computed by considering as system boundary the reversible heat pump. Further investigations, including a revamping of the monitoring system, would be necessary to evaluate the plant performances at extended boundaries.

The PVT plant has a mean yearly energy production of about 5,200 kWh el (DC side) plus 16,320 kWh th. While the electric energy produced is used to power the heat pump all over the year, only a small amount of the heat produced by the PVT plant is directly used for the users, i.e. less than 10% (1,438 kWh th), via the heat pump. Nevertheless, the amount of heat sunk in the ground in the summertime has beneficial effects on the heat pump operation at the beginning of the winter season, but this contribution is not easy to assess without a proper monitoring system. The rest of the heat (over 90%) produced by the PVT collectors is sunk in the ground. Therefore, the logic of the plant is to optimize PVT power production through collectors cooling at relatively low temperatures, while penalizing the heat recovery. The final result is that the PVT plant power production over the year is able to cover space heating and cooling and DHW demands. In fact, while the power demands for space heating, space cooling and DHW production are, respectively, 2,908 kWh, 358 kWh and 512 kWh, with a total amount of 3,778 kWh per year, the PVT plant alone is able to produce about 4,992 kWh (including inverter efficiency). Hence, the electricity produced every year by the PVT plant exceeds the reversible heat pump consumption. Nevertheless, since the power consumption and power production is not contemporary, and there is no electric storage in the building, based on the monthly energy bills the electricity self-sufficiency fraction of the system can be estimated in 25%.

Due to the characteristic of the plant installed in Suello, it is possible to compare the seasonal electric performances of the PVT collectors and the same PV modules, i.e. PVT collectors with and without active cooling. It is interesting to note how PVT collectors are able to produce up to 10% more than the PV plant, thus maximizing solar power production when needed. Another interesting finding resulted from the plant operation is the implementation of a control strategy which has been implemented as “ground night cooling”, i.e. the use of PVT collectors during the night to cool down the ground when consecutive summer days with high air temperature peaks are registered. This strategy, which is beneficial for the reversible heat pump operation and EER, may need further investigation to evaluate how the night coolant circulation may affect the seasonal efficiency of the whole system.

The investment cost of the whole system is about 39,000 € (VAT excluded), while yearly operation and maintenance costs can be estimated in not more than 1% of the initial investment. The so-called “levelised cost of energy” (LCOEn) generated by the system can be expressed as in Equation 1:

$$LCOEn = \frac{I_0+\sum_{t=1}^{T=25}\left(OM_t-E_{PVT}^{El}\cdot P_{el}\right)\cdot(1+r)^{-t}}{\sum_{t=1}^{T=25}\left(Q_{sys}+C_{sys}+Q_{DHW}\right)\cdot(1+r)^{-t}} \qquad \text{(eq. 1)}$$

where: I_0 is the initial investment (not including the PV modules); OM_t are operation and maintenance costs in the year; $E^{El}{}_{PVT}$ is the electric energy produced by the PVT and sold to the grid; P_{el} is the price at which the electric energy produced by the PVT is sold; Q_{sys} and C_{sys} are, respectively, the heat and cold delivered to the end-users; Q_{DHW} is the DHW production; t is the year, with a whole period of analysis of 20 years; r is the discount rate. Table 4 summarizes the main parameters considered in the economic assessment. It should be noted that i) the selling price considers the “net metering” option that is available in Italy for PV or PVT installations under 20 kW p and ii) the initial investment do not take into account the 50% tax credit that is available for such a kind of investment in Italy.

Tab. 4: Economic parameters considered in the economic assessment.

Parameter	Symbol	Value
Initial investment	I_0	39,000 €
Period analysis	T	20 years
Yearly operation and maintenance cost	OM_t	390 €/year
Yearly electric energy sold to the grid	$E^{El}{}_{PVT}$	1,700 kWh/year
Electric energy selling price	P_{el}	0.09 €/kWh
Yearly heat delivered to the user	Q_{sys}	11,750 kWh/year
Yearly cooling energy delivered to the user	C_{sys}	1,408 kWh/year
Yearly DHW delivered to the user	Q_{DHW}	2,040 kWh/year
Discount rate	r	4%

The LCOEn of the system described in the paper is 0.20 €/kWh: the LCOEn is reduced to 0.11 €/kWh if the tax credit is considered. Since heat, cold and electricity are generally not considered to have the same value per unit of energy, it would be useful to define the levelised costs of the different energy forms separately. Nevertheless, the allocation (splitting) of the total costs to the different energy contributions is to some extent a matter of convention. Therefore, the authors preferred to compute the whole LCOEn to be compared with other heating/cooling options in the same boundary conditions or application.

4. Conclusions

The paper shows the results of 3 years of operation of an innovative plant for building heating and cooling. The plant includes 16 PVT collectors, a reversible heat pump, two storage tanks and two ground heat exchangers. The plant control strategy is dedicated to the optimization of the PV operation to maximize the power output of the plant. The plant demonstrated to be effective in satisfying the energy demand coming from the users. Further optimizations are possible to increase the seasonal COP/EER through a more sophisticated control system which should integrate together the solar circulating pump and the heat pump control units.

5. References

Aste, N., del Pero, C., Leonforte, F., 2014. Water flat plate PV–thermal collectors: A review. Sol. Energ. 102, 98-115. https://doi.org/10.1016/j.solener.2014.01.025

Bertram, E., Stegmann, M., Rockendorf, G., 2011. Heat Pump Systems with Borehole Heat Exchanger and Unglazed PVT-Collector. Proceedings of the Solar World Conference 2011. https://doi:10.18086/swc.2011.26.02

Bianchini, A., Guzzini, A., Pellegrini, M., Saccani, C., 2017. Photovoltaic/thermal (PV/T) solar system: experimental measurements, performance analysis and economic assessment. Renew. Energ. 111, 543-555. https://doi.org/10.1016/j.renene.2017.04.051

Hoekstra, N., Pellegrini, M., Bloemendal, M., Spaak, G., Andreu Gallego, A., Rodriguez Comins, J., Grotenhuis, T., Picone, S., Murrell, A.J., Steeman, H.J., Verrone, A., Doornenbal, P., Christophersen, M., Bennedsen, L., Henssen, M., Moinier, S., Saccani, C., 2020. Increasing market opportunities for renewable energy technologies with innovations in aquifer thermal energy storage. Sci. Total Environ. 709, 136142. https://doi.org/10.1016/j.scitotenv.2019.136142

Jonas, D., 2019. Visualization of energy flows in PVT systems. https://doi.org/10.18777/ieashc-task60-2019-0001

Joshi , S.S., Dhoble, A.S., 2018. Photovoltaic-Thermal systems (PVT): Technology review and future trends. Renew. Sust. Energ. Rev. 92, 848-882. https://doi.org/10.1016/j.rser.2018.04.067

Pellegrini, M., Hoekstra, N., Bloemendal, M., Andreu Gallego, A., Rodriguez Comins, J., Grotenhuis, T., Mazzoni, M., Picone, S., Murrell, A.J., Steeman, H.J., Spaak, G., 2019. Low carbon heating and cooling by combining various technologies with Aquifer Thermal Energy Storage. Sci. Total Environ. 665, 1-10. https://doi.org/10.1016/j.scitotenv.2019.01.135

Ramschak, T., Baggenstos, A., Mellor, A., Gagliano, A., Corino, C., Zenhäusern, D., Cabral, D., Ryan, G., Guedea, I., Brottier, L., Ruoff, U., Schubert, M., Lämmle, M., Pellegrini, M., Dannemand, M., Cañada, M., Radisch, N., Pokorny, N., 2020. Existing PVT Systems and Solutions. https://doi.org/10.18777/ieashc-task60-2020-0001

Rees, S.J., 2016. Advances in Ground-Source Heat Pump Systems, first ed. Woodhead Publishing, Sawston. https://doi.org/10.1016/C2014-0-03840-3

Rekioua, D., 2020. Hybrid Renewable Energy Systems Overview. In: Hybrid Renewable Energy Systems. Green Energy and Technology. Springer, Cham. https://doi.org/10.1007

SHC IEA, 2014. Solar and Heat Pump Systems, Position Paper, Task 44/Annex 38 Solar and Heat Pump Systems.

Weiss, W., Spork-Dur, M., 2020. Solar Heat Worldwide.

Yao, J., Liu, W., Zhang, L., Tian, B., Dai, Y., Huang, M., 2020. Performance analysis of a residential heating system using borehole heat exchanger coupled with solar assisted PV/T heat pump. Renew. Energ. 160, 160-175. https://doi.org/10.1016/j.renene.2020.06.101

An optimization approach to control the energy flows in renewable energy communities

Gerald Steinmaurer[1]

[1] FH OOE Forschungs & Entwicklungs GmbH, Wels (Austria)

Abstract

Energy communities are new concepts in the European legislation, where it is possible to produce, store and also sell (renewable) energy via the public grid. Participants of such communities can then sell a surplus of Photovoltaic energy to their neighbors and all players can then economically benefit from this energy exchange. This exchange must be coordinated within the energy community and can be seen as a typical optimization task in order to minimize the costs of all players respectively to maximize the benefit of every participant.

Key-words: Energy communities, optimization, photovoltaics, storage systems, optimal power flow

1. Introduction

An energy community is a new concept in the European legislation ("winter package") and will be an essential parts of the new energy distribution system [*EE-RL 2018*]. Within these communities, renewable energy will be exchanged beyond household or company borders and every participant of such a community is allowed to produce, sell, buy or store energy. This paper shows a method to coordinate the energy flows within such a community in order to maximize the benefit of each participant and to distribute the savings of the partners in an energy community in a fair way.

To establish energy communities, possible participants would like to benefit from this energy cooperation. These advantages are almost always linked to monetary benefits. Such a benefit in general can be a reduced or even waived grid charges for exchanged energy or simply a reduced purchase price for (renewable) excess power from e.g. a photovoltaic plant from the neighbour.

In the future, the energy exchange in energy communities must be controlled in order to maximize the benefit for the participants. The control of optimal power flow within such an energy community is typically a static and straightforward task. The consideration of storage units changes the problem into a dynamical one [*Steinmaurer*].

For measurement purposes and energy billing, the purchased and supplied electrical energy is discretized in time intervals of 15min. Therefor it makes sense to consider the problem of energy flow coordination in an energy community as a discrete optimization task.

2. Participants of energy communities

2.1 Definition of energy flows in an energy community

In this work, each participant of a renewable energy community has the following properties, according to Figure 1. The states x_1 ... x_8 are power values of this player in the community and describe the energy flow situation. State x_5 refers to the state of charge of the storage unit. Arrows indicate possible energy flow directions,like load and PV production, costs for energy purchase (x_1) as well as remuneration for feed-in (x_2) are assumed to be known.

doi:10.18086/eurosun.2020.05.16 Available at http://proceedings.ises.org

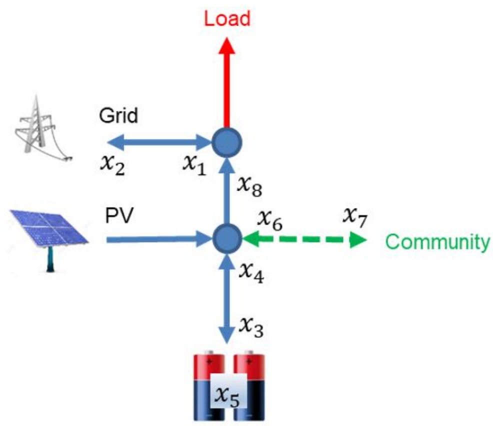

Figure 1: Structure of energy flow optimization of one single participant in an energy community. States xi consider power flow at every time instant

Every Energy community consist of N participants with properties of Figure 1. Renewable energy is considered to be exchanged via the public grid - but with different fees and costs (so the states x_6 and x_7 are necessary).

The energy exchange will be calculated at discrete time instants $m, m = 1, \ldots, M$.

The usage of Figure 1 directly leads to the following energy balance equations for each participant n and at every time instant m with a discretization interval time T

$$x_{1,n,m} - x_{2,n,m} + x_{8,n,m} = P_{load,n,m} \qquad \text{(eq. 1)}$$

$$-x_{3,n,m} + x_{4,n,m} + x_{6,n,m} - x_{7,n,m} + x_{8,n,m} = P_{PV,n,m} \qquad \text{(eq. 2)}$$

The change of the charge level $(x_{5,n,m} - x_{5,n,m-1})$ of the storage of a participant n between time instant m and $(m-1)$ can be calculated as

$$-\eta_{ch,n} x_{3,n,m} + \frac{1}{\eta_{dis,n}} x_{4,n,m} + T\left(x_{5,n,m} - x_{5,n,m-1}\right) = 0 \qquad \text{(eq. 3)}$$

whereas $\eta_{ch,n}$, $\eta_{dis,n}$ are charging respectively discharging efficiencies of the storage unit of participant n and T the duration of the discrete time instants.

Within the energy community it is necessary, that the sum of the exchanged energy of all participants is balanced at every time instant m, i.e.

$$\sum_{n=1}^{N} x_{6,n,m} - x_{7,n,m} = 0, \quad m = 1..M \qquad \text{(eq. 4)}$$

The costs for participant n in the time instant m can be calculated as

$$\tilde{c}_{n,m} = c_{1,n} x_{1,n,m} - c_{2,n} x_{2,n,m} + c_{6,n} x_{6,n,m} - c_{7,n} x_{7,n,m} \qquad \text{(eq. 5)}$$

whereas

$c_{1,n}$ costs for grid purchase of particiant n

$c_{2,n}$ feed-in tariff of particiant n

$c_{6,n}$; $c_{7,n}$ costs respectively feed-in tariff for the community exchange

All this aspects lead in general to an enormous number of equations, so it makes sense to group and simplify the formal description.

3. Formulation of a linear optimization task

The 8 states for participant n in the time instant m can be collected in an vector $\tilde{\boldsymbol{x}}_{n,m}$

$$\tilde{\boldsymbol{x}}_{n,m}^T = [x_{1,n,m} \quad x_{2,n,m} \quad x_{3,n,m} \quad x_{4,n,m} \quad x_{5,n,m} \quad x_{6,n,m} \quad x_{7,n,m} \quad x_{8,n,m}] \qquad \text{(eq. 6)}$$

In order to simplify the description, (eq.1) to (eq.3) are then

$$\tilde{\boldsymbol{A}}_{n,m}\, \tilde{\boldsymbol{x}}_{n,m}^T = \tilde{\boldsymbol{b}}_{n,m} \qquad \text{(eq. 7)}$$

$$\tilde{\boldsymbol{A}}_{n,m} = \begin{bmatrix} 1 & -1 & 0 & 0 & 0 & 0 & 0 & 1 \\ 1 & 0 & -1 & 1 & 0 & 1 & -1 & 1 \\ 0 & 0 & -\eta_{ch,n} & \frac{1}{\eta_{dis,n}} & T & 0 & 0 & 0 \end{bmatrix} \qquad \text{(eq. 8)}$$

$$\tilde{\boldsymbol{b}}^{\boldsymbol{T}}{}_{n,m} = [P_{load,n,m} \quad P_{PV,n,m} \quad 0] \qquad \text{(eq. 9)}$$

The costs for participant n in the time instant m depend only on the states 1, 2, 6 and 7

$$\tilde{\boldsymbol{c}}_n\, \tilde{\boldsymbol{x}}_{n,m}^T \qquad \text{(eq. 10)}$$

with

$$\tilde{\boldsymbol{c}}_n = [c_{1,n} \quad -c_{2,n} \quad 0 \quad 0 \quad 0 \quad c_{6,n} \quad -c_{7,n} \quad 0] \qquad \text{(eq. 11)}$$

The problem of this energy flow coordination is to find an optimal state vector $\boldsymbol{x}$

$$\boldsymbol{x} = [\,[\tilde{\boldsymbol{x}}_{1,1}^T \quad \dots \quad \tilde{\boldsymbol{x}}_{n,1}^T] \quad [\tilde{\boldsymbol{x}}_{1,2}^T \quad \dots \quad \tilde{\boldsymbol{x}}_{n,2}^T] \quad \dots \quad [\tilde{\boldsymbol{x}}_{1,m}^T \quad \dots \quad \tilde{\boldsymbol{x}}_{n,m}^T]\,] \qquad \text{(eq. 12)}$$

to minimize $\boldsymbol{c}^T\boldsymbol{x}$ with

$$\boldsymbol{c} = [\,[\tilde{c}_{1,1} \quad \dots \quad \tilde{c}_{n,1}] \quad [\tilde{c}_{1,2} \quad \dots \quad \tilde{c}_{n,2}] \quad \dots \quad [\tilde{c}_{1,m} \quad \dots \quad \tilde{c}_{n,m}]\,] \qquad \text{(eq. 13)}$$

and fulfilling the boundary conditions. The overall energy flow coordination problem considering all time instants an every participating partner leads then to an a linear programming procedure []

$$\min_{\boldsymbol{x}} \boldsymbol{c}^T\boldsymbol{x} \qquad \text{(eq. 14)}$$

$$\boldsymbol{A}_{eq}\boldsymbol{x} = \boldsymbol{b}_{eq}$$

$$\boldsymbol{x}_{lb} \le \boldsymbol{x} \le \boldsymbol{x}_{ub}$$

considering equality constraints $\boldsymbol{A}_{eq}\boldsymbol{x} = \boldsymbol{b}_{eq}$ ((eq. 1) to (eq. 4)) and inequality constraints $\boldsymbol{x}_{lb} \le \boldsymbol{x} \le \boldsymbol{x}_{ub}$ (e.g. maximum and minimum power, storage limitations, …).

4. Test cases

The objective function to be minimized for this task ($\boldsymbol{c}^T\boldsymbol{x}$) is the sum of all costs of each participant in the considered time interval (power purchase costs, reduced by feed-in remuneration). Within this work a sampling time of 1 h is used.

In order to test the optimization task and examine the resulting energy flows, test cases with participants with different properties (with or without PV, storage existing or not, load profiles, tariff situation, ..:) are examined for a sunny day with significant PV production. The individual parameters of 4 candidates (participant P1 – P4) to attend an energy community are listed up in Tab. 1. The monetary difference between $c_{6,n}$ and $c_{7,n}$ is used to cover fees for using the public grid.

The last line of Tab.1 shows the costs of each participant without attendance at the community for this exemplary single day, which are the result of purchased and supplied energy, considering the associated costs. The Fig 1 show the load and PV production data for this day. The overall costs of all participants sum up to 271.33 €.

Tab. 1: Parameters of participants of an energy community

Participant		P1	P2	P3	P4
Grid Purchase costs $c_{1,n}$	$\frac{€Cent}{kWh}$	10.5	10.5	12	15
Grid Feed-in tariff $c_{2,n}$	$\frac{€Cent}{kWh}$	5			
Community purchase $c_{6,n}$	$\frac{€Cent}{kWh}$	8			
Community feed-in $c_{7,n}$	$\frac{€Cent}{kWh}$	7			
Storage size	kWh	-	-	100	-
Costs on exemplary day	€	103.95	34.15	14.73	118.50
Summed Costs	€	271.33			

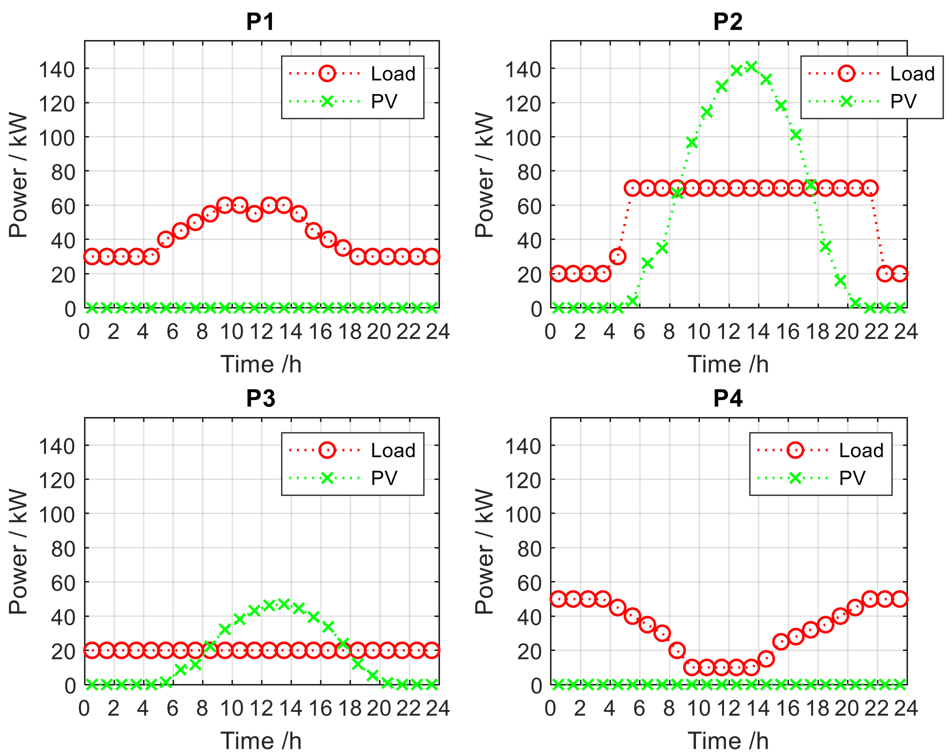

Fig. 1: Load and PV power of participants P1 to P4 on the exemplary day

4.1 Case 1: Energy community with P1 and P2

The first case study combines the participants P1 and P2, which form a quite reasonable community: P1 is a pure consumer and P2 offers energy excess from the photovoltaic plant during this sunny day. P1 pays 8 $€Cent/kWh$ for the purchased energy (which is less than from the grid) and P2 sells the energy at a higher price than the feed-in tariff. The resulting optimized time history of this simply energy exchange is shown in Fig. 2, where the third subplot shows, that excess energy from P2 is sold to P1. Since no storage unit is built in, the state of charge (SOC) is equal to zero. The problem of this test case is converted into a linear optimization task (eq. 14) and solved with the standard software MATLAB.

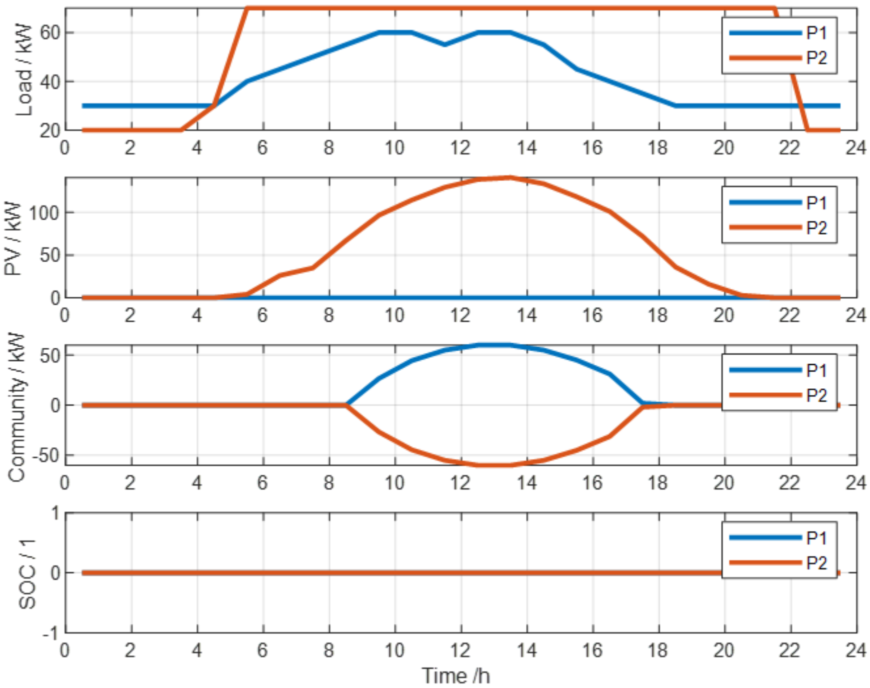

Fig. 2: First: Load profile of P1 and P2; Second: PV production; Third: Exchanged energy in the community, Fourth: State of Charge

4.2 Case 2: Energy community with P1, P2 and P3

The second case study combines the participants P1, P2 and P3, where in contrast to case study 1 with P3 an additional PV-energy provider with an integrated storage unit is part of the community. The necessary additional boundary condition for the charge level of the store of P3 is set to 50% at the beginning and at the end of the exemplary day to yield comparable results. The solution of the optimization procedure (eq. 14) results in a time behaviour according to Fig. 3

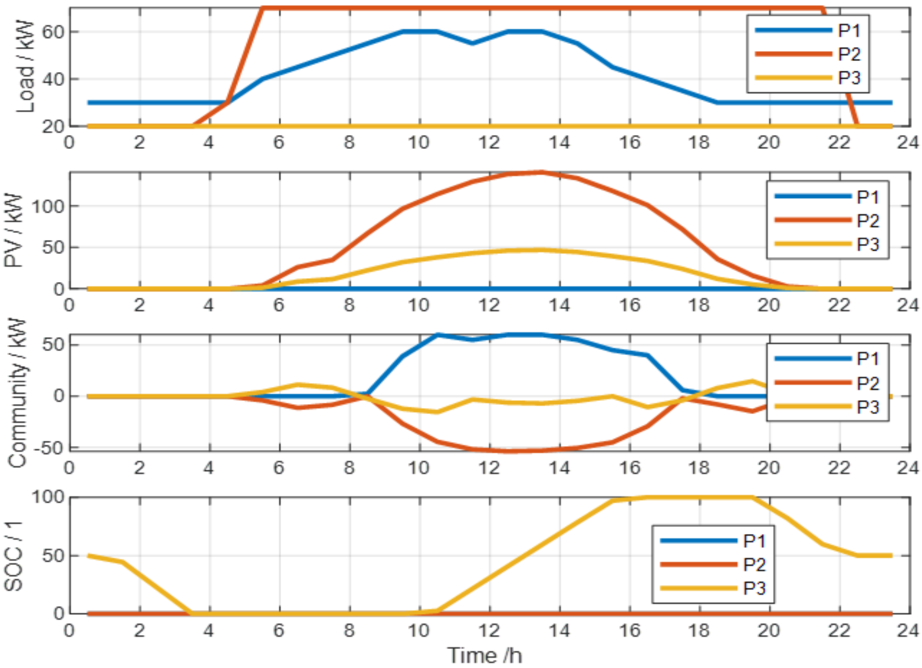

Fig. 3: Results of the optimization of an energy community with P1, P2 and P3

4.3 Case 3: Energy community with P1, P2, P3 and P4

In the third test case, an additional pure consumer (P4) was included. The combination of all four participants yields to an optimized time behaviour of Fig. 4.

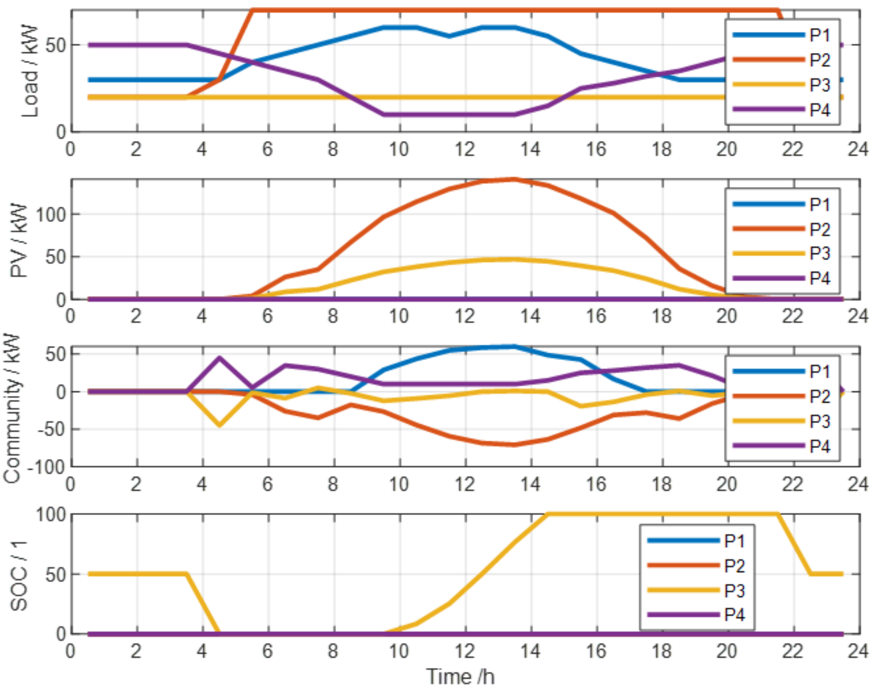

Fig. 4: Results of the optimization of an energy community with four participants

4.4 Analysis of the test cases

The goal of each optimization procedure according to (eq. 14) is the minimization of the sum of costs (also considering revenues for selling energy to the grid or to community partners), such that boundary conditions are satisfied. The reduction of individual costs for each participant is not a primary objective. Tab. 2 shows the resulting costs and the changes of costs (“savings”) for the test cases. It is obvious, that the savings for the community are growing (to be precise: do not decrease) with an increasing number of participants, but the individual savings of the attendees are not balanced. The worst case happens for P3 in the optimized energy community with four participants, where P3 has a disadvantage of 3.78€ for attending the community.

Tab. 2: Results cost for each participant in every test case and the saving in comparison to the individual costs without being part of an energy community

			P1	**P2**	**P3**	**P4**	**Sum**
Individual cost without energy community		€	103.95	34.15	14.73	118.50	271.33
Test Case 1 P1&P2	Savings through community	€	9.48	7.59	-	-	17.07
Test Case P1&P2&P3	Savings through community	€	10.57	5.41	3.28	-	19.25
Test Case 3 P1&P2&P3&P4	Savings through community	€	10.56	5.41	**-3.78**	27.31	34.99

5. Consequences of the test cases results

Analysing the resulting cost structure of the optimized energy communities offers the situation that the overall costs are minimized. The major drawback of this optimization results is, that not every participant in this community benefit in the same extend. It can happen, that someone even pays more for the energy (P3 in test case 3) as without the community and others benefit above average. Such an unfair distribution of economic savings will not lead to a long-term collaboration within the renewable energy community.

In order to find a fair distribution of the community benefits, two possible solutions are presented.

5.1 Limitation of individual benefits of the participants

To avoid economic drawbacks of participants in the energy community, an additional boundary condition can be integrated into the optimization task: each participant must at least benefit to a specified extend. This lead to an optimization task with an additional inequality boundary conditions (eq. 15). Tab 3 shows the results with this additional “minimum savings” for the test cases 3 of chapter 4.3 with all four participants.

$$\min_{\boldsymbol{x}} \boldsymbol{c}^T \boldsymbol{x} \quad \text{(eq. 15)}$$

$$\boldsymbol{A}_{eq}\boldsymbol{x} = \boldsymbol{b}_{eq}$$

$$\boldsymbol{A}_{ineq}x \leq \boldsymbol{b}_{ineq}$$

$$\boldsymbol{x}_{lb} \leq \boldsymbol{x} \leq \boldsymbol{x}_{ub}$$

Tab. 3: Consideration of limiting the individual benefits of participants,
***) No solution found for minimum savings of 10€**

		Minimum savings	**P1**	**P2**	**P3**	**P4**	**Sum of savings**
Savings	€	Not considered	10.56	5.41	-3.78	27.31	34.99
Savings	€	≥ 0 (no individual losses)	8.87	2.58	0	22.03	33.49
Savings	€	≥ 3	8.87	3	3	16.48	31.35
Saving*)	€	≥ 10	-	-	-	-	-

5.2 Assessment of the individual contribution to the energy community
The results of chapter 5.1 show, that the limitation of drawbacks or the demand for an minimum benefits reduces the overall savings of the community. In order to gain the maximum benefits, an operation without limitations (like in test case 3) can be carried out and then the community savings are distributed among the participants. This leads to the problem of determining the importance of each participants with respect to the community. Should everyone get the same share of the savings?

To assess the contribution of each participant, the following procedure is used:

1) Run the optimization without limiting the benefits (like test case 3 in chapter 4.3)

2) Exclude single partners from the community and calculate the resulting optimal costs of this reduced community.

The achieved savings (Tab. 4) can be used as an indicator for the importance of each participant. For the test case 3 from chapter 4.3 it turns out, that excluding P2 reduces the savings from 34.99€ to 10.04€ - P2 is the most important participant on this day in the considered renewable energy community.

Tab. 4: Assessment of the individual contribution to the energy community

	Savings	**Resulting Assessment**
Community without **P1**	19.04 €	
Community without **P2**	10.04 €	P2 is the MSP – most significant participant
Community without **P3**	29.79 €	P3 is the LSP – least significant participant
Community without **P4**	19.25 €	
Community with **all participants**	34.99 €	

6. Acknowledgments

This project is financed by research subsidies granted by the government of Upper Austria, Project: "Methodenentwicklung für Energieflussoptinmierung".

7. References

EE-RL 2018: Directive (EU) 2018/2001 of the European Parliament and of the Council of 11 December 2018 on the promotion of the use of energy from renewable sources.

Steinmaurer Gerald: "Optimale Steuerung von Leistungsquellen mit Zwischenspeicher", VDI-Verlag, ISBN-Nr.: 978-3-18-513008-3, 2007.

06. Solar Thermal Collectors and Solar Loop Components

COMBINING RADIATIVE COLLECTOR AND EMITTER WITH COMPRESSION HEAT PUMP: NUMERICAL ANALYSIS

Roger Vilà, Marc Garcia, Marc Medrano, Ingrid Martorell, Albert Castell

Sustainable Energy, Machinery and Buildings (SEMB) Research Group, INSPIRES Research Centre, Universitat de Lleida, Pere de Cabrera s/n, 25001 Lleida

Summary

A Radiative Collector and Emitter (RCE) is a technology which combines solar collection and radiative cooling to provide both heat and cold from renewable sources. Solar collection uses radiation coming from the Sun to heat up a fluid, while radiative cooling takes advantage of the atmospheric window to emit thermal radiation to the sky with no interference with the atmosphere to cool down a fluid. However, temperatures achieved by radiative cooling are not always suitable for cooling applications. Combining the RCE with a compression heat pump (HP) can improve the coefficient of performance (COP) of the heat pump by using a colder heat sink for the condenser, the cold produced by the RCE. A numerical analysis using TRNSYS is done to determine the improvements in the COP of the HP when combined with an RCE. Results show an increase of the COP of both the heat pump and the whole system when combined with the RCE. The COP of the heat pump is the one with a higher increase, from 2.5-3.5 to 3.5-5.

Keywords: radiative cooling, heat pump, coefficient of performance, numerical simulation

1. Introduction

In the last decades, climate change and global warming have become a major concern for society. The energetic model, based on fossil fuels, is one of the main contributors to these problems. In order to address them, governments have promoted energy savings policies (Directive 2010/31/EU) as well as renewable energy implementation (Directive 2009/28/EC). One of the main consumers of energy is the building sector, which consumes around one-third of the global worldwide energy consumption (https://www.iea.org/topics/buildings). Moreover, in terms of pollution in Europe, the commercial, institutional and households sector is the largest contributor to Benzo[a]pyrene (BaP), primary particulate matter (PM), Carbon monoxide (CO) and Black carbon (BC), and it also contributes to Non-methane volatile organic compound (NMVOC), Cadmium (Cd), Sulphur oxides (SO_X), Nickel (Ni), and Nitrogen oxides (NO_X) emissions (European Environment Agency).

Renewable energies are becoming more important every day. While technologies such solar thermal collection are mature technologies able to produce hot water and are already introduced in the market, there is no renewable technology with such development in terms of cooling potential. Radiative cooling is a technology with the potential of producing cold water from a renewable source by emitting thermal energy to the sky (Vall and Castell, 2017) through the infrared atmospheric window. Although this technology has been previously studied, the main focus has been placed in analysing the infrared atmospheric window and the atmospheric infrared radiation (Bell et al., 1960). However, its development has not reached the market yet.

The combination of radiative cooling with other renewable technologies could foster its development and implementation in the market. A Radiative Collector and Emitter (RCE) is a technology which combines solar collection and radiative cooling to provide both heat and cold from renewable sources. While solar collection uses radiation coming from the Sun to heat up a fluid, radiative cooling takes advantage of the atmospheric window transparency in the 7-14 µm range to emit thermal radiation to the sky with no interference with the atmosphere to cool down a fluid.

This concept was first proposed by Vall et al. (Vall et al., 2018), determining its potential in terms of energy production and demand coverage of different buildings under different weather conditions, and demonstrating its suitability for certain building typologies and climates. However, temperature levels and integration with the building system were not studied. The concept was based on an adaptive cover, which could adapt its optical properties to perform both functionalities: solar collection and radiative cooling. This adaptive cover was a sliding cover composed of two materials, one for each functionality (glass for solar collection and polyethylene for radiative cooling).

doi:10.18086/eurosun.2020.06.01 Available at http://proceedings.ises.org

Compression heat pumps (HP) are widely used for heat and cold production in buildings, being the main cooling system worldwide. Although heat pumps are considered as a renewable energy source depending on their seasonal performance (Directive 2009/28/EC), the efficiency of HP depends dramatically on the temperature level of the heat sink, which usually is the ambient air. The fact that HP usually operate under hot weather conditions, and during the hottest hours of the day, raises the temperature level of the heat sink, thus reducing its coefficient of performance (COP). The combination of HP with RCE could improve the COP of the system by using the cold produced by the RCE at nighttime as a heat sink for the HP operating at daytime.

This study presents a numerical analysis of the combination of HP with RCE in order to determine the potential improvements in the COP of the system.

2. Methodology

A numerical model of the RCE is published in the literature (Vall et al., 2020). This model, developed as TRNSYS type, simulates the behavior of an RCE device, and was validated with experimental results.

The model is based on the energy balance between the RCE and the ambient air and the sky, in order to determine the net heat flux entering or leaving the RCE (Fig. 1). The RCE is discretized in different nodes based on an electric analogy in a one-dimension approach (1D) in order to reduce the computation time. However, some 2D effects are introduced into the model based on detailed simulations performed on Comsol Multiphysics (Vall et al., 2020).

The equivalent resistance network of the model is shown in Fig. 2. There is one temperature node for the screen (c), the RCE surface (1), the pipe (2) and its internal (outlet) fluid (w2), and the back insulation (3). The fluid enters the pipe at temperature T_{w1}.

The relations between the nodes are based on basic heat transfer equations. Each node has a thermal capacity and each relation between nodes is represented by a thermal resistance. The thermal resistance between the fluid at the outlet of the pipe (node w2) and a fictitious node (w1) which represents the fluid at the inlet of the pipe is used to introduce a second dimension required in the model to determine the heat flux between the inlet and the outlet of the pipe. Thus, this node has no capacitance, and can be considered as an input to the model.

The radiation balance is done for 4 different wavelength ranges (0-4 µm, 4-7 µm, 7-14 µm and >14 µm). The model also allows using 2 different cover materials. These two functionalities allow the RCE model to distinguish between radiation for different wavelength, with special interest in the atmospheric window (7-14 µm) to simulate the double functionality solar collector – radiative cooler.

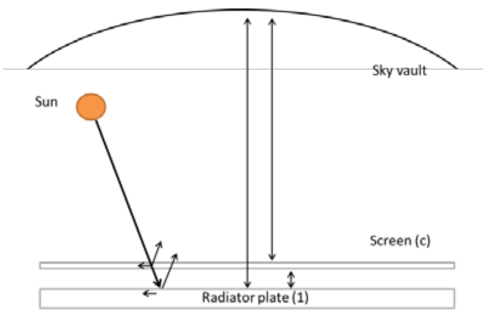

Fig. 1 Global energy balance scheme (Vall et al., 2020).

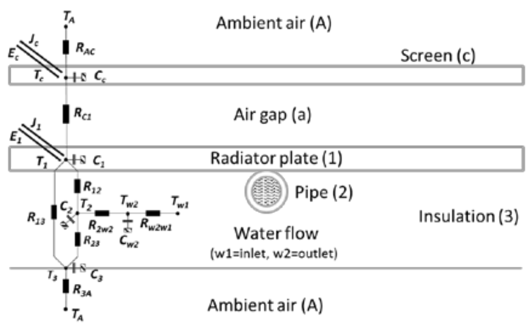

Fig. 2. Scheme of the 1D resistance-capacitance model (Vall et al., 2020).

This model has been used in this study, combined with a heat pump (Type 927 from TRNSYS TESS library, which simulates a water-water heat pump of 2 kW of power with variable COP).

The RCE field (10 RCE devices of 2 m^2 connected in parallel) produces heat during the day, which is stored in a hot water tank (1 m^3, using Type 156 which simulates a water tank with an internal coil heat exchanger) for later use as domestic hot water (DHW). Similarly, it produces cold during the night, which is stored in a cold water tank (0.15 m^3, using Type 158 which simulates a water tank with no internal heat exchanger), which will be used as a heat sink for the condenser of the HP during the day. The HP absorbs heat from the cooling tank (0.25 m^3 using Type 158, where heat from the building is rejected by the cooling distribution system) and releases it to the cold water tank. An air-water heat exchanger (Type 5c from TRNSYS) is coupled to the cold water tank from the RCE field. The HP is releasing the heat absorbed from the cooling demand at this tank, thus increasing its temperature. The heat exchanger dissipates this heat to the ambient air during daytime to avoid overheating. A conceptual scheme of the installation is presented in Fig. 3.

A thermostat (Type 2b) is used to set the outlet temperature of the HP to keep the cooling tank at a temperature below 10 ºC. The flow rate passing through the RCE field is simulated using Type 110, a variable flow pump. Based on previous experience, for solar collection mode the flow rate is set to 170 kg/h, while for radiative cooling mode the flow rate is set to 72 kg/h.

To control the operation mode, which determines the flow rate and the position of the adaptive cover, a new type was developed. The RCE field operates under solar collection mode during daytime if solar radiation is higher than 100 W/m^2, and at night operates under radiative cooling mode if the net radiation balance in the radiator is higher than 25 W/m^2. Otherwise, the RCE field is stopped. To determine daytime and nighttime hours, the average sunrise and sunset time for each month is used.

The demand of hot and cold water is simulated using Type 14b (Replacement water) and Type 14e (Mains temperature). For cold water, the demand simulates that of an office during summer months. Thus, 100 kg/h of cooling water are used during the hottest hours of the day (from 13:00 to 17:00). This water returns to the cooling tank at a temperature of 20 ºC. For hot water, the demand is not focused on any specific application, but on consuming the energy stored and discharging the tank. Thus, a flow rate of 100 kg/h is used during the night (from 21:00 to 7:00) to cool down the tank. The water returns to the tank at a temperature of 20 ºC.

The COP of such system is compared to that of a heat pump alone covering the same cooling demand (Fig. 3).

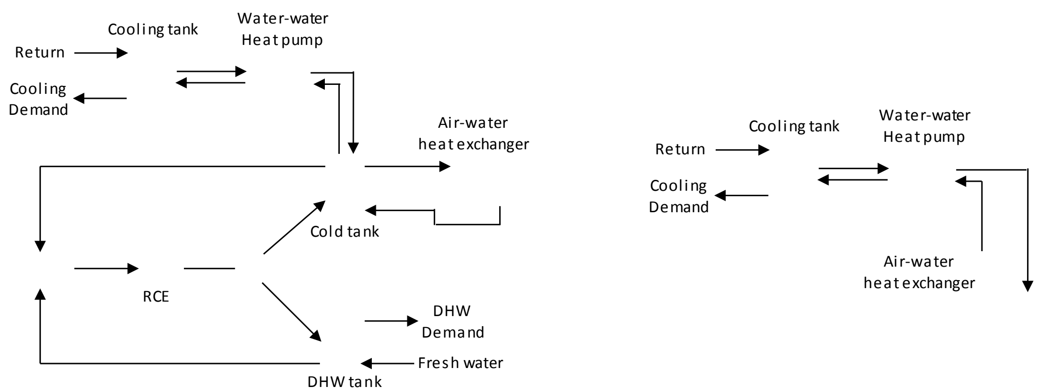

Fig. 3. Conceptual scheme of the RCE combined with a HP (left), and the HP alone (right).

Simulations have been performed for the hottest months of the year, when both DHW and cooling are required. Thus, the months considered are June, July, August, and September. The weather data is extracted from the EnergyPlus weather file for Lleida (Catalonia, Spain), using Type 15-3 of TRNSYS. An additional processing of the data is required to determine the horizontal infrared radiation, which is not provided by the weather file. For such calculations the methodology proposed by EnergyPlus has been used (Eq. 1 and Eq. 2), using the ambient temperature (T_{ambient}), the dew point temperature (T_{dp}), and the opaque sky cover (N) taken from the EnergyPlus weather data file for Lleida.

$$IR_{radiation} = sky_{emissivity} \cdot \sigma \cdot T_{ambient}^4 \qquad \text{Eq. 1}$$

$$sky_{emissivity} = \left(0.787 + 0.764 \cdot ln\left(\frac{T_{dp}}{273}\right)\right) \cdot (1 + 0.0224N - 0.0035N^2 + 0.00028N^3) \qquad \text{Eq. 2}$$

Where:

$sky_{emissivity}: Sky\ emissivity\ [-]$

$T_{dp}: Dew\ point\ temperature\ [K]$

$N: Opaque\ sky\ cover\ [-]$

$IR_{radiation}: Horizontal\ Infrared\ Radiation\ \left[\frac{W}{m^2}\right]$

$\sigma: Stefan - Boltzmann\ constant \left[5.6704 \cdot 10^{-8}\ \frac{W}{m^2 \cdot K^4}\right]$

$T_{ambient}$: $Ambient\ temperature\ [K]$

Simulations were performed using a time step of 5 minutes. The main parameters analyzed are the power generated by the RCE ($\dot{Q}_{RCE}$, Eq. 3), and the coefficient of performance of the heat pump (COP_{BC}, Eq. 4) and the whole system (COP_{syst}, Eq. 5).

The thermal power generated by the RCE is determined as:

$$\dot{Q}_{RCE} = \dot{m} \cdot Cp \cdot (T_{in} - T_{out}) \qquad \text{Eq. 3}$$

Where:

$\dot{Q}_{RCE}$: power generated by the RCE field [W]

$\dot{m}$: mass flow rate circulating through the RCE field [kg/s]

Cp : specific heat of the fluid circulating through the RCE field [J/kg·K]

T_{in} : inlet temperature of the fluid at the RCE field [K]

T_{out} : outlet temperature of the fluid at the RCE field [K]

The COP of the heat pump is determined as:

$$COP_{BC} = \frac{\dot{Q}_{BC}}{\dot{W}_{e,BC}} \qquad \text{Eq. 4}$$

Where:

COP_{BC} is the COP of the heat pump [-]

$\dot{Q}_{BC}$ is the power generated by the heat pump [W]

$\dot{W}_{e,BC}$ is the electric consumption of the heat pump [W]

The COP of the whole system is determined as:

$$COP_{sist} = \frac{\dot{Q}_{BC}}{\dot{W}_{e,sist}} \qquad \text{Eq. 5}$$

Where:

COP_{syst} is the COP of the whole system [-]

$\dot{Q}_{BC}$ is the power generated by the heat pump [W]

$\dot{W}_{e,sist}$ is the electric consumption of the whole system [W]

3. Results and discussion

Fig. 4 shows the daily average power per surface unit of RCE for both solar collection and radiative cooling modes for the RCE+HP circuit. Results show that the cooling power of the RCE is one order of magnitude lower than the heating power, following the proportion of available solar radiation to available radiative cooling potential.

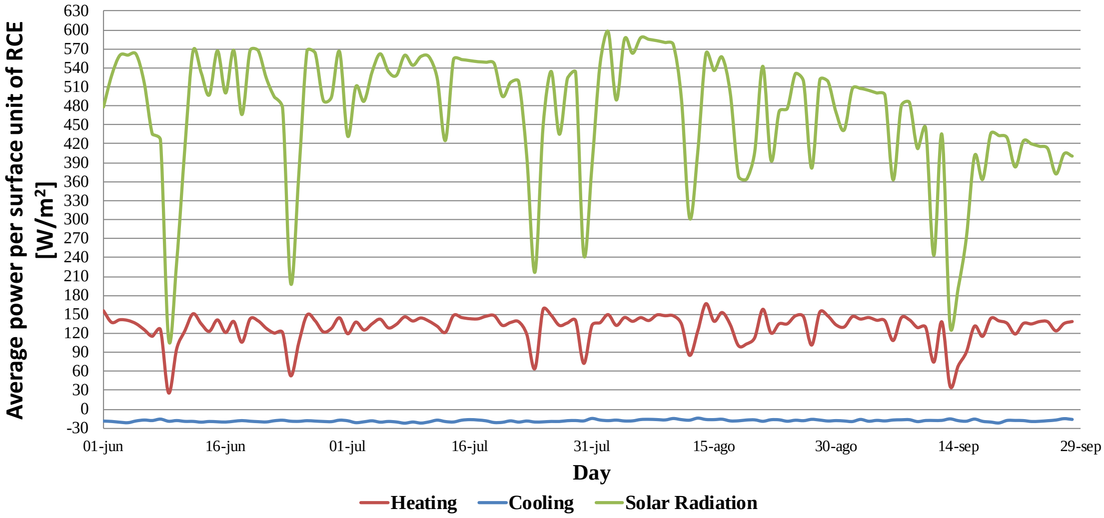

Fig. 4. Daily average power per surface unit of RCE in the RCE+HP circuit.

Fig. 5 shows the average temperature difference between the outlet RCE water temperature and the ambient temperature for the RCE+HP circuit for the month of July. During solar collection mode, temperature differences up to 45ºC are achieved, while during radiative cooling mode, up to 5ºC sub-ambient temperatures are achieved.

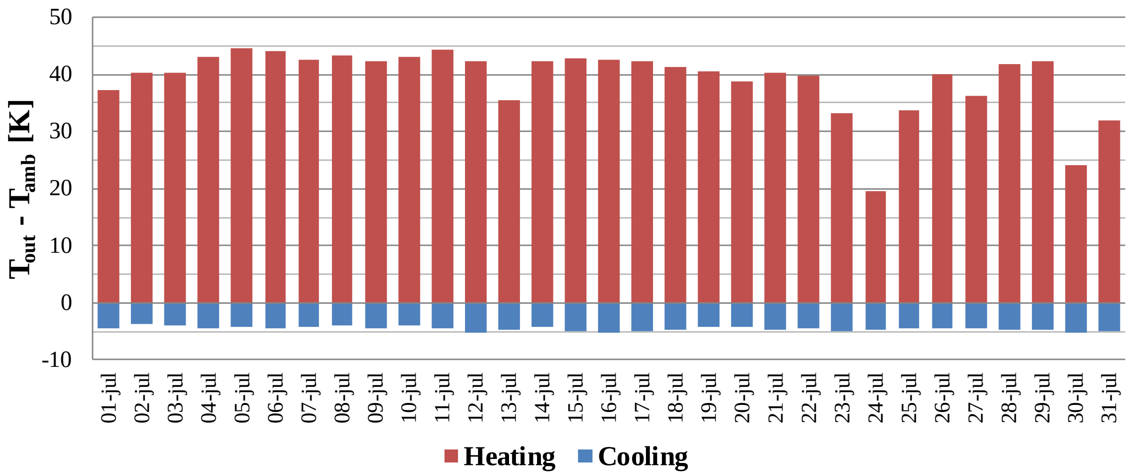

Fig. 5. Average temperature difference between the outlet RCE water temperature and the ambient temperature for the RCE+HP circuit for the month of July.

A comparison of the COP of the heat pump for both cases is presented in Fig. 6 for the month of July. Results show that the COP of the heat pump is significantly improved by its combination with the RCE. While the COP of the heat pump when operating alone ranges from 2.5 to 3.5 depending on the day, the COP of the heat pump when operating in combination with the RCE ranges from 3.5 to 5.

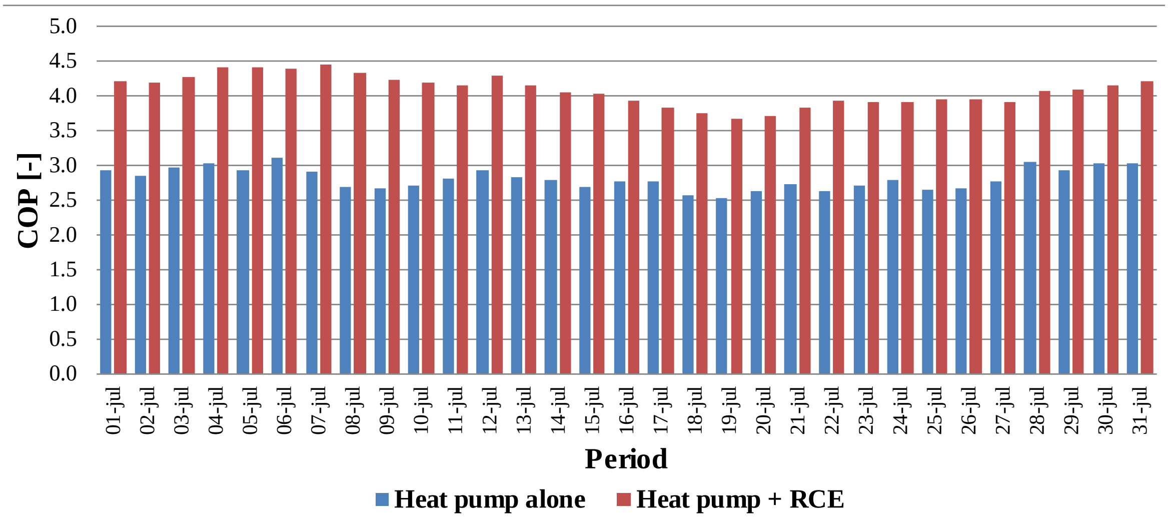

Fig. 6. Comparison of the COP of the heat pump when operating the heat pump alone and the heat pump in combination with the RCE for the month of July.

On the other hand, when the COP of the whole system is considered (taking into account all the energy consumptions needed for the pumps and heat exchanger), the improvements are significantly reduced. While the COP of the system with the heat pump operating alone ranges from 2 to 3, the one for the system with the heat pump operating in combination with the RCE ranges from 2.5 to 3. A comparison of the COP of the system for both cases is presented in Fig. 7 for the month of July.

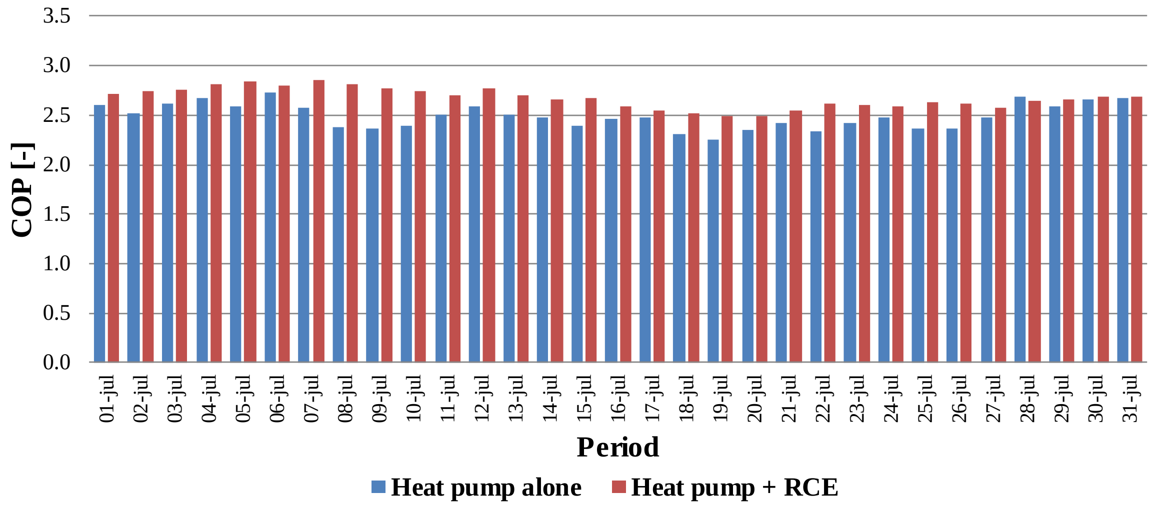

Fig. 7. Comparison of the COP of the whole system when operating the heat pump alone and the heat pump in combination with the RCE for the month of July.

4. Conclusions

By means of numerical simulation it has been demonstrated that the use of an RCE device can achieve both hot water production during daytime and sub-ambient temperatures during nighttime for the hottest months of the year. However, the average power is one order of magnitude higher for hot water generation than for cold water generation, following the proportion of available solar radiation to available radiative cooling potential.

The increase of the coefficient of performance of the heat pump and the whole system when combined with the RCE has been analyzed numerically. The results show that the combination of the HP with the RCE increases the COP for both the heat pump and the whole system. This increase is more significant when considering the heat pump (from 2.5-3.5 to 3.5-5), and it is reduced when considering the whole system (from 2-3 to 2.5-3) due to the energy use for auxiliary equipment. Thus, the use of pumps and the heat exchanger must be optimized in order to maximize the increase of the COP of the system.

5. Acknowledgements

The work was partially funded by the Catalan Government under grant agreement (2017 SGR 659), the Spanish government under grant agreement RTI2018-097669-A-I00 (Ministerio de Ciencia, Innovación y Universidades), and Fundación Iberdrola España under project “Desarrollo y evaluación de un equipo para producción combinada de frío y calor mediante refrigeración radiante y captación solar”.

6. References

European Parliament. Directive 2010/31/EU of the European Parliament and of the Council of 19 May 2010 on the energy performance of buildings. J Eur Union 2010; 153:13–35.

European Parliament. Directive 2009/28/EC of the European Parliament and of the Council of 23 April 2009 on the promotion of the use of energy from renewable sources and amending and subsequently repealing. Directives 2001/77/EC and 2003/30/EC. J Eur Union 2009; 140:16–62. http://dx.doi.org/10.3000/17252555.L_2009.140.eng.

https://www.iea.org/topics/buildings (accessed 7.29.20).

European Environment Agency. Report No 10/2019 Air quality in Europe — 2019 report. doi:10.2800/822355.

Vall, S., Castell, A., 2017. Radiative cooling as low-grade energy source: A literature review, Renewable and Sustainable Energy Reviews 77, 803–820. http://dx.doi.org/10.1016/j.rser.2017.04.010

Bell, E., Eisner, L., Young, J., Oetjen, R., 1960. Spectral-radiance of sky and terrain at wavelengths between 1 and 20 microns. II. Sky measurements. J Opt Soc Am 50, 1313–1320. http://dx.doi.org/10.1364/JOSA.50.001313.

Vall, S., Castell, A., Medrano, M., 2018. Energy Savings Potential of a Novel Radiative Cooling and Solar Thermal Collection Concept in Buildings for Various World Climates, Energy Technol. 6, 2200–2209. https://doi.org/10.1002/ente.201800164

Vall, S., Johannes, K., David, D., Castell, A., 2020. A new flat-plate radiative cooling and solar collector numerical model: Evaluation and metamodeling, Energy 202, 117750. https://doi.org/10.1016/j.energy.2020.117750

European Commission. Decision of 1 March 2013 (2013/114/EU) establishing the guidelines for Member States on calculating renewable energy from heat pumps from different heat pump technologies pursuant to Article 5 of Directive 2009/28/EC of the European Parliament and of the. J Eur Union 2013; 62:27–35.

Transmittance analysis for materials suitable as radiative cooling windshield and aging study for polyethylene

Carrobé A, Martorell I, Solé C and Castell A

Sustainable Energy, Machinery and Buildings (SEMB) Research Group, INSPIRES Research Centre, Universitat de Lleida, Lleida (Spain)

Abstract

Nowadays space conditioning with renewable energy is one of the highest challenges of our society. Solar collection is a suitable source of energy for domestic hot water and space heating, but there is no green source to cool the spaces during hot periods or for hot climates. Radiative cooling seems to be a feasible solution for it. Elsewhere the Radiative Cooler Emitter (RCE) is presented, a device with an adaptive cover concept that combines both functionalities: solar collection during daytime and radiative cooling during nighttime. In this study, the solar and IR transmittances are analyzed for five samples: polycarbonate, methacrylate, and three commercial samples of low density polyethylene (LDPE): 17 μm, 50 μm and 200 μm). The aging of 50 μm low density polyethylene film is also studied during two months of environmental exposure in a RCE prototype (summer 2019). Presence of double bonds and C=O groups are detected, which implies a degradation of the polyethylene during the experimental campaign.

Keywords: radiative cooling, polyethylene aging, renewables, experimental analysis, solar transmittance

1. Introduction

In the EU, 40% of the total energy consumption is located in buildings, specifically in space conditioning and domestic hot water (DHW) (European Commission, "Energy performance of buildings directive."). When analyzing the energy consumption in buildings, the Eurostat (European Commission, n.d.) determines that 64.1 % of the total consumption in buildings is dedicated to space heating, 14.8 % to DHW, and 0.3 % to space cooling.

Solar collection is nowadays the most convenient source of renewable energy for domestic hot water, but there is no proper renewable source of energy for space cooling. Elsewhere a new device called Radiative Cooler Emitter (RCE) is presented (Vall, 2020). This equipment combines solar collection during daytime and radiative cooling during nighttime, thanks to an adaptive cover concept.

Radiative cooling uses the sky as a heat sink, benefiting from its effective temperature, which is much lower than ambient temperature (lower than 0 ºC or even −10 ºC (Bell, 1960)). Energy can be dissipated to the sky taking advantage of the infrared atmospheric window (7–14 μm). This window allows infrared radiation to pass directly to outer space without intermediate absorption and re-emission in the atmosphere. Heat dissipation is produced by long wave radiation (thermal radiation) from a surface to the sky.

Before designing and building the RCE, the materials involved in the device should be studied. The glass used in solar collectors blocks infrared radiation and it is not useful for radiative cooling. This is why as said previously an adaptive cover concept is defined. This adaptive cover counts with two different materials: one for solar collection during daytime and another for night radiative cooling. Glass, already widely used in solar collectors, is selected as the material for the solar collection function. The main characteristic that the night radiative cooling material must meet is a high transmission in the long wavelength IR spectrum. Specifically, high values of transmittance in the atmospheric window (7–14 μm)

doi:10.18086/eurosun.2020.06.02 Available at http://proceedings.ises.org

during the whole operation lifetime. High solar transmittance is also desirable for maintaining the same solar collection efficiency. Materials found after bibliography review are basically polymeric materials (Tsilingiris, 2003, Xu et al., 2018, Fu et al., 2019, Liu et al., 2019) , non-polymeric materials such as zinc crystals (Bosi et al., 2014, Chen et al., 2016, Laatioui et al., 2018), and cadmium sheets (Benlattar et al., 2006), and chromic materials (Hjortsberg and Granqvist, 1981).

Among these non-plastic candidate materials, crystals have the advantage of having greater resistance to external environmental conditions. However, the high costs of these crystals, and the impossibility of producing them in adequate dimensions for the RCE, make them unfeasible. On the other hand, there is very little bibliography referring to cadmium sheets for radiant cooling applications and the last reference is from 2006. Finally, it should be noticed that chromic materials have very interesting properties as adaptive covers, but further fundamental material research must still be done. Thus, all these materials have been discarded as possible candidates and the material chosen for the adaptive cover will be a plastic. Plastics have less resistance to external environmental conditions, but they can be produced in adequate dimensions and cost, and have been used in previous studies of radiative cooling. According to the literature, polyethylene film is mostly used as cover for radiative cooling. However, polyethylene suffers degradation during exposure time, losing elasticity and deformation capacity, manifested in the appearance of carbonyl groups (Carrasco, 2001).

The objective of this paper is to analyze the solar and IR transmittance of different plastics to determine their suitability for radiative cooling applications. Since the RCE will be exposed to external weather conditions, materials degradation during lifetime is relevant. This is why an aging study for polyethylene is also performed.

2. Methodology

To accomplish with the objectives of the study, the methodology is divided into two parts. First, a transmittance analysis of five possible material samples to be used as adaptive covers of the RCE. These materials should not block the solar collection and must allow the IR radiation from the RCE to cross to the atmosphere. The second part consists of analyzing the aging of the material with the best performance in the transmittance analysis.

The selection of the plastics has considered three different commercial plastics as methacrylate, polycarbonate and polyethylene. Polyethylene is the plastic widely used in radiative cooling applications and this is why three LDPE polyethylene samples with different thickness have been chosen: 17 μm LDPE (transparent film for kitchen use), 50 μm LDPE (transparent film for industrial use), and 200 μm LDPE (greenhouse cover). In order to study the optical behavior of these materials, spectroscopic analysis to cover wavelengths from 200 nm to 15300 nm are performed. For the UV-Vis study, a UV Analytikjena Specord 2010 (190-1100 nm) with a resolution of 1 nm was used; for the near infrared area (NIR) the Foss NDS XDS Rapid Content Analyzer spectrophotometer (400-2500 nm, 62 scans) was used. Each continuous spectrum of the NIR region was recorded in a rectangular cell (15 cm x 3.5 cm) and 62 scans of each sample were performed, covering the wavelength range between 800 and 2500 nm. Although the NIR spectra comprise the visible area (between 400 and 800 nm) only the NIR data between 800 and 2500 nm were used, since the reference capsule absorbs more than the samples. Finally, the analysis by FT-IR spectroscopy (Fourier Transform-Infrared) was carried out with a Jasco FT-IR 6300 series equipment with ATR diamond / ZnSe accessory and TGS detector. Each spectrum is recorded with 64 scans, in the 2500-15384 nm range and with a resolution of 4 cm^{-1}.

The second part of the study is to analyze the behavior of the plastic which performs better in the transmittance test in experimental real conditions. In other words, in contact with the environment and mounted on the RCE prototype. During the experimentation in summer 2019, the plastic was exposed to atmospheric conditions, during a period of 2 months. The plastic was covered by the glass of the solar collector during the day and uncovered at night. A visual inspection of the plastic detected changes in the material due to the variation of temperature and solar radiation. The changes observed are irregular since there are areas that do not present changes, other areas of the film with dark color and regions where the plastic loses firmness. To study the degradation of the plastic, an aging experiment was designed using three samples of the selected plastic: (1) brand new plastic (NEW). This is a plastic that has not been installed in the RCE, (2) plastic exposed 2 months and with visual degradation detection –either dark color, firmness lost or both- (OLD 1), and (3) plastic exposed 2 months but without visual degradation detection (OLD 2). After the two months exposure, three samples of each category were analyzed in UV-Vis and FT-IR using the same equipment described previously. Three repetitions of each sample were performed, which means that a total of 18 spectra were analyzed.

3. Results

3.1. Transmittance analysis of plastics

Figure 1 shows the UV-Vis, NIR and FT-IR (with ATR mode) spectra for the five plastics studied:

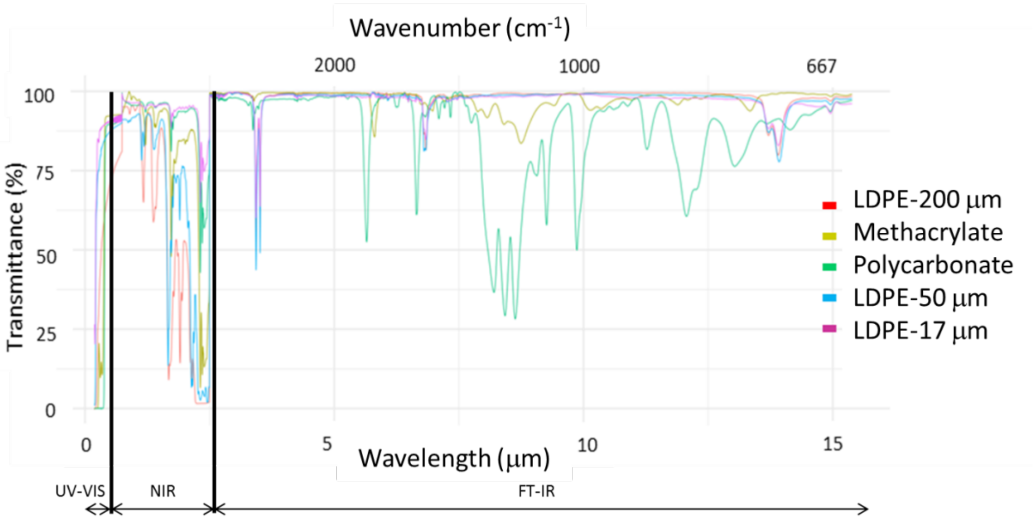

Figure 1. UV-Vis, NIR and FT-IR in ATR mode spectra for the five candidates.

Although the complete spectra for the five plastic materials are presented in Figure 1, it is important to highlight here that for the RCE application, the transmittance regions of interest are the UV-Vis, during the solar collection, and the large IR (FT-IR), during the radiant cooling process. In particular, for the RCE application high transmittance values in the UV-Vis and FT-IR regions are desired in order to allow both solar collection and radiative cooling.

First, looking at the UV-Vis spectrum region it is observed that the transmittance behavior is similar for all plastics. However, when analyzing the transmittance behavior in detail it is detected that transmittance values for greenhouse plastic are 10 % lower. The NIR spectra show that in the near infrared area each material has a different behavior and no common pattern is observed. Finally, when observing the FT-IR spectra, it is seen that absorbance bands (peaks) for the five materials are basically in the same regions, which confirms that all of them belong to the plastics family. However, the intensity of the absorbance bands is different and this will determine the average transmittance values of each material in the FT-IR spectrum. From Figure 1 it is seen that polycarbonate and methacrylate have a very different behavior from the polyethylene samples. It is also important to note that the three polyethylene samples show the absorption bands at the same wavelengths, confirming that the three materials are polyethylene. No significant differences are observed between these three materials in Figure 1.

Next, and in order to determine which of these plastics, from the optical properties point of view, is the best for the radiative cooling application a comparison in the atmospheric window is done. Figure 2 shows transmittance values for the five samples between 7 and 14 µm.

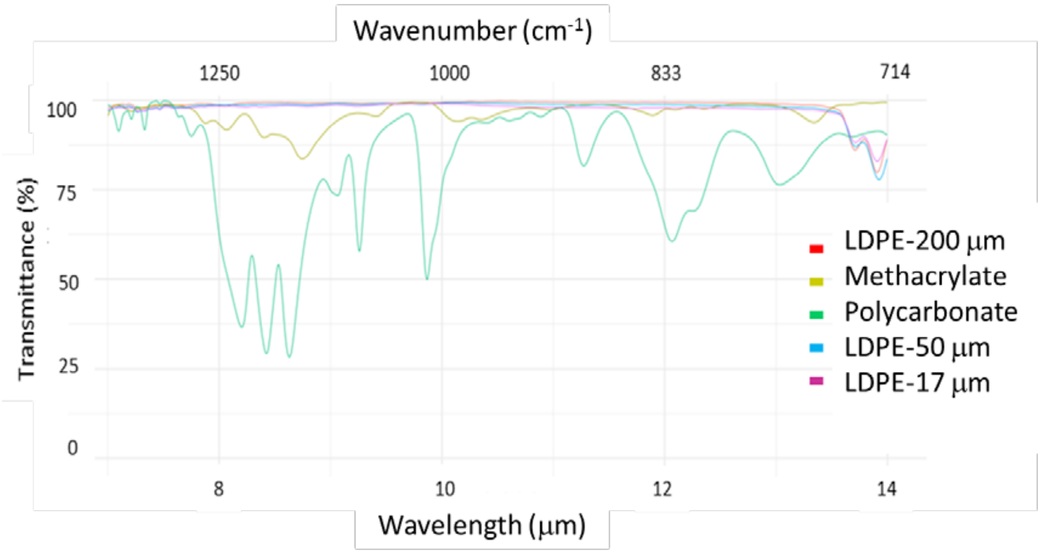

Figure 2. FT-IR in ATR mode spectra for the five candidates in the atmospheric window.

From Figure 2 it is seen that polycarbonate is the material that shows the largest absorption bands in the atmospheric window. In addition, these bands are wide, which translates into significantly lower average transmittance values. Thus, polycarbonate can be quickly discarded as a candidate material for the RCE cover. Methacrylate also shows more absorption bands in the atmospheric window than the polyethylene samples and it is also excluded as a candidate material for the RCE application. The other three samples present, on the one hand, a fairly constant behavior, without the presence of significant peaks, and on the other hand, higher transmittance values than methacrylate and polycarbonate. Thus, no significant differences between the three polyethylene candidates are observed in Figure 2.

At this point, the 17 µm LDPE is discarded due to its fragility, considering that the prototype will be located outside. 50 µm LDPE (transparent film) and 200 µm LDPE (greenhouse cover) have a very similar behavior in the atmospheric window. 50 µm LDPE transparent film is finally chosen for two reasons. First, because similar thickness have been used in the radiative cooling application bibliography and offers high values of transmittance in the atmospheric window, and second, because in the UV-Vis region the transmittance average value of the polyethylene is 10 % higher than the one shown by 200 µm LDPE (greenhouse cover). Thus, the cover material selected for the RCE is a polyethylene (PE) in the form of a flexible film 0.5 mm thick.

In order to characterize the material, the main spectral signals present in the 50 µm LDPE in the long infrared zone are determined. For this, three new polyethylene samples are selected and repetitions of three spectra are performed for each sample. The equipment used is the Jasco FT-IR 6300 series with ATR diamond / ZnSe accessory and TGS detector. Each spectrum is recorded with 64 scans and with a resolution of 4 cm^{-1}. Figure 3 shows that all the most intense bands of the FT-IR spectrum correspond to polyethylene, with no other chemical compound. No differences are observed between the nine spectra of the polyethylene either. It is confirmed that the polyethylene selected is a low density polyethylene since an absorption band at 1377 cm^{-1} is detected. The typical absorption bands of polyethylene are: 2915 cm^{-1} asymmetric CH_2 stretching, 2848 cm^{-1} symmetric CH_2 stretching, 1471 cm^{-1} CH_2 bending, 1377 cm^{-1} symmetric CH_3 bending, 1302 cm^{-1} twisting vibration and 719 cm^{-1} CH_2 rocking.

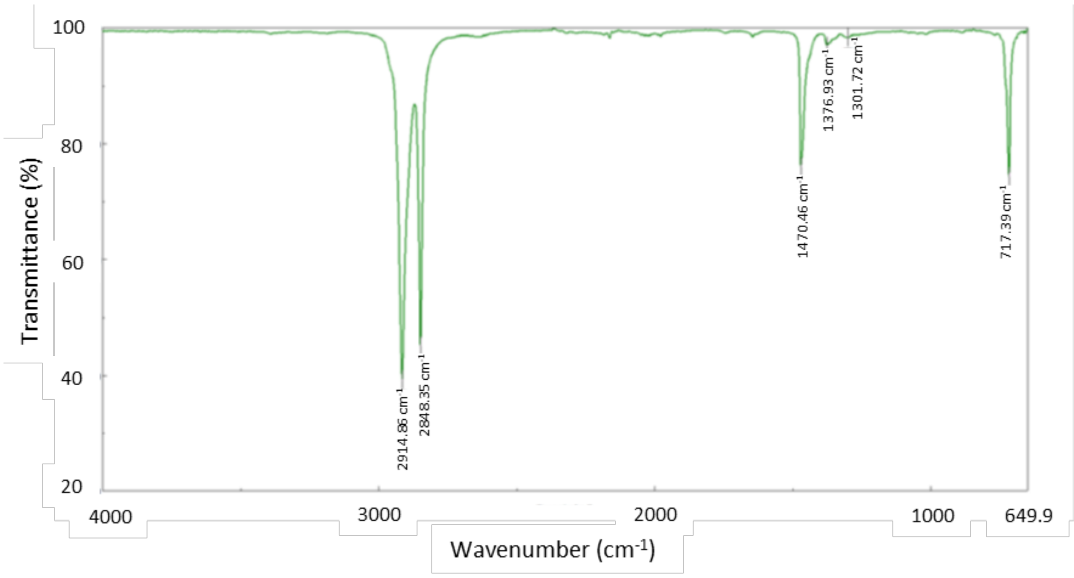

Figure 3. FT-IR using ATR mode for the 50 μm LDPE selected for radiative cooling application.

In order to determine the average transmittance of the candidate material in the atmospheric window, a FT-IR spectrum is carried out in Transmission mode using a FT-IR Thermo Nicolet is50 equipment with a DTGS detector and KBr beam splitter with a resolution of 4 cm^{-1}. The transmission spectrum obtained with 64 scans of the 50 μm thick polyethylene is shown in Figure 4. The average transmittance of this polyethylene in the atmospheric window (7-14 μm) is 80,69 %, a value very similar to literature (Hu et. al. 2015).

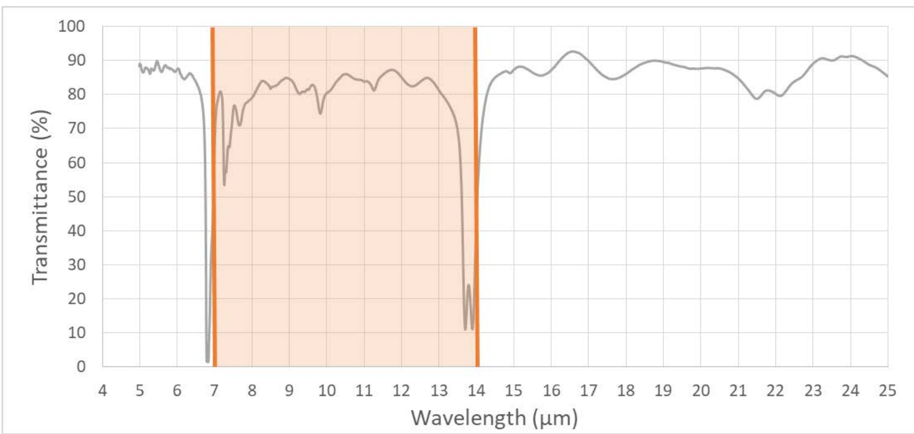

Figure 4. FT-IR spectrum in Transmission mode of the 50 μm polyethylene. The atmospheric window is shadowed.

3.2. Aging study for polyethylene

The next step is to study the 50 μm polyethylene behavior under experimental conditions in the RCE. To do so, a RCE prototype was designed and constructed using a solar collector. The glass screen of the solar collector was removed to install the 50 μm polyethylene film. Once the polyethylene was located, the glass was placed at the original place. The prototype works collecting the sun during daytime and once the day is over, the cover glass is removed and the plastic enables the radiative cooling mode. Experiments were performed during two months in summer 2019.

As explained in the introduction section of this paper, a total of nine 50 μm polyethylene samples were studied. Three samples correspond to the NEW polyethylene, the one that has not been exposed to external conditions, three more samples were selected for the part of the plastic that showed visual degradation (OLD 1) and three more for the part that did not show visual degradation (OLD 2). In order to determine the polyethylene degradation process spectrophotometric analysis in UV-Vis and FT-IR are conducted in the same equipment mentioned above (Figures 5 and 6, respectively).

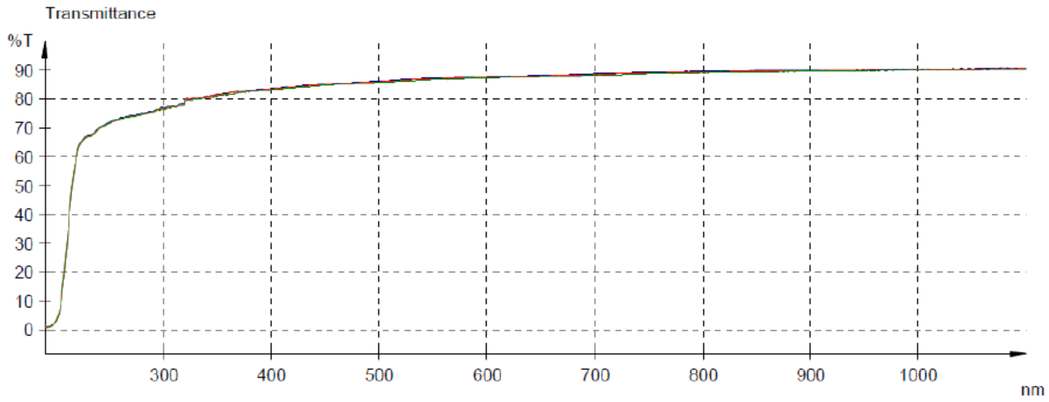

(a) NEW

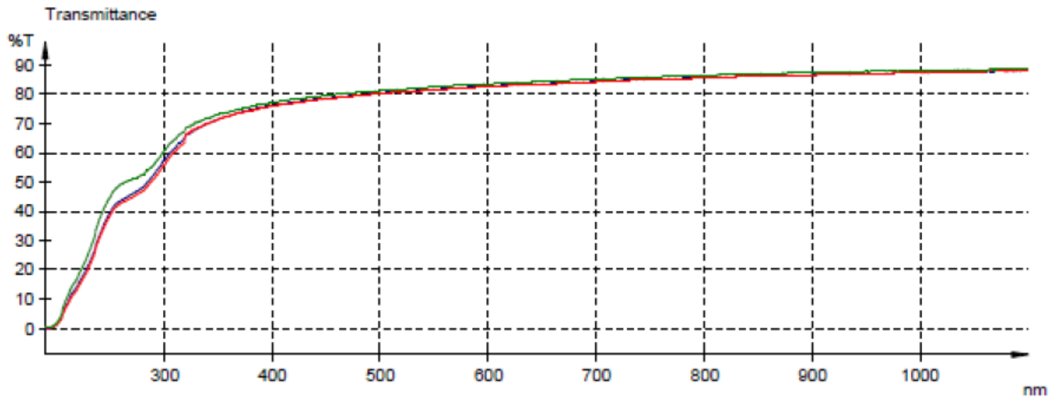

(b) OLD 1

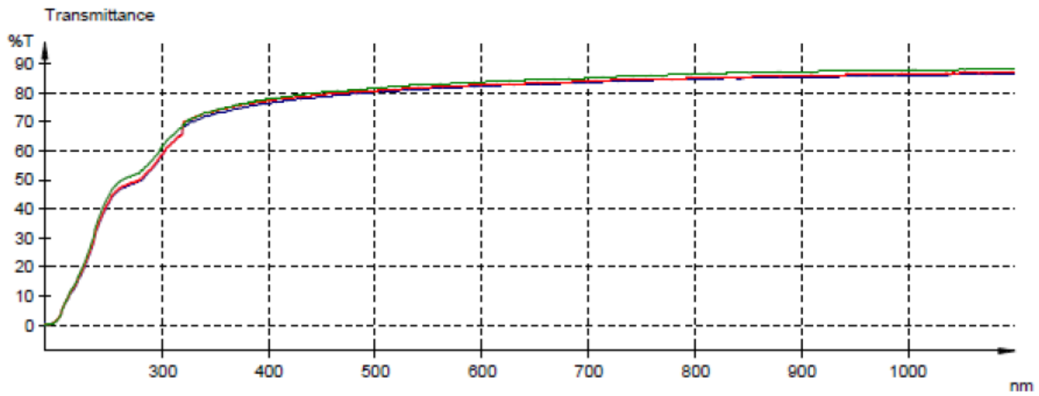

(c) OLD 2

Figure 5. UV-Vis spectra of the 50 μm polyethylene.

Looking at Figure 5 it is seen that no significant differences for the three samples of each category (NEW, OLD 1, and OLD 2) exist. However, when looking at the transmittance values between 200 and 550 nm, samples OLD 1 and OLD 2 show lower transmittance values that the NEW samples. These results indicate the appearance of double bonds in the plastic due to environmental exposition and C-H bonds degradation.

Figure 6 presents the FT-IR spectra for the NEW, OLD 1 and OLD 2 samples. In this case, a comparison of the average spectra for the NEW, OLD 1 and OLD 2 samples is presented in order to compare the absorbance bands positions and intensity. From Figure 6 it can be concluded that the descriptive absorbance bands of low density polyethylene do not disappear after the environmental exposition. However, new absorbance bands are present in the OLD 1 and OLD 2 samples.

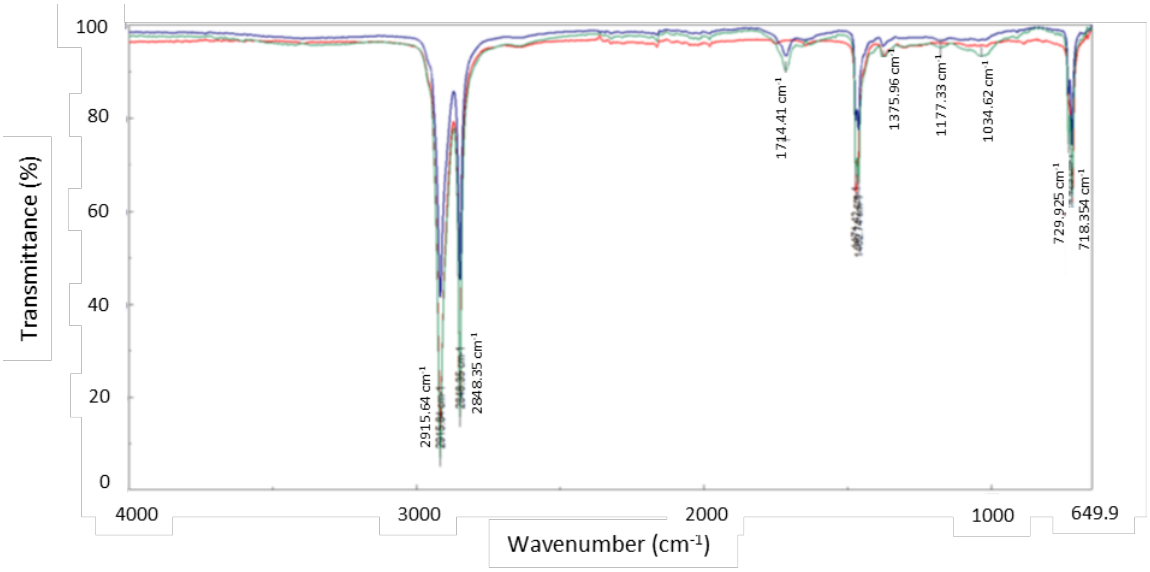

Figure 6. FT-IR spectra of the 50 μm polyethylene: NEW (red), OLD 1 (green) and OLD 2 (blue).

In order to study the new bands, the FT-IR spectra for the NEW, OLD 1 and OLD 2 polyethylene samples in the atmospheric window is presented in Figure 7.

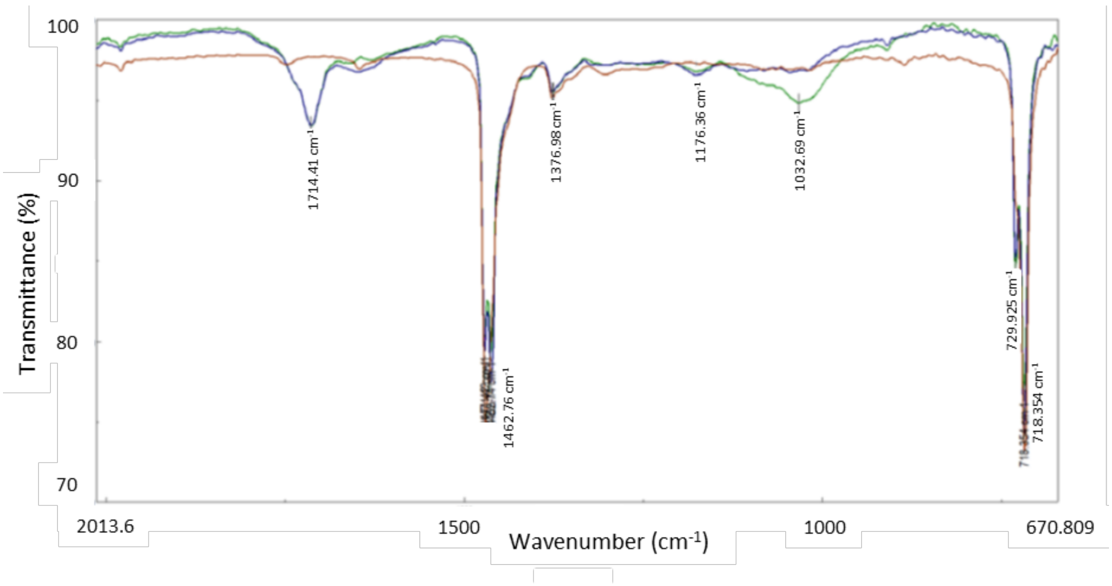

Figure 7. FT-IR spectra of the 50 μm polyethylene in the atmospheric window: NEW (brown, OLD 1 (green) and OLD 2 (blue).

The main differences that have been detected between the three 50 μm thick polyethylene samples are the increase in the signal around 1035 and 1177 cm^{-1}, especially in the OLD 1 sample. The 1035 cm^{-1} area corresponds to the absorption frequency of CO bonds. A new signal also appears at 1714 cm^{-1}, corresponding to the absorption of C = O bonds, which seems to indicate a degradation of polyethylene through an oxidative process. It is important to note that no formation of hydroxyl groups is observed (broad bands around 3200-2550 cm^{-1}).

On the other hand and when doing a detailed analysis of the absorbance bands, it is also detected that the 1470 cm^{-1} signal has shifted to 1471 cm^{-1} and a new band has appeared at 1462 cm^{-1}. Also the 718 cm^{-1} signal has shifted to 717 cm^{-1} and a new signal has appeared at 730 cm^{-1}. All this is possibly due to changes in the polymeric structure of polyethylene, but specific tests should be performed in order to identify with precision the nature of these polymeric structure changes.

To know the degree of chemical degradation, the carbonyl and vinyl indices have been calculated, as in Albertsson et al. (1987) and Muthukumar et al. (2014). The vinyl index is a measure of the concentration of double bonds and the carbonyl index is a measure of the concentration of carbonyl groups. To calculate the vinyl index, the area between 1680-1583 cm^{-1} has been integrated and divided by the area 1511-1417 cm^{-1}. For the calculation of the carbonyl index, the area between 1640-1804 cm^{-1} has been integrated and divided by the area 1511-1417 cm^{-1}. The areas have been calculated with the program of the FT-IR team of the Servei Científico-Tècnic of the UdL "Spectra analysis" with the conditions "two-point base" and "add under baseline". Table 1 shows the results.

Tab. 1. Vinyl and carbonyl average indices and standard deviations (SD) of 50 μm polyethylene NEW, OLD 1 and OLD 2.

	Vynil index (average)	SD	Carbonyl index (average)	SD
NEW	0.04	0.01	0.02	0.00
OLD 1	0.02	0.00	0.36	0.07
OLD 2	0.06	0.04	0.44	0.11

The results in Table 1 show a clear increase in the carbonyl index between the NEW sample (0.02) and the OLD 1 (0.36) and OLD 2 samples (0.44). These values corroborate the oxidative process detected with the FT-IR spectra. On the other hand, the values of the vinyl index seem to indicate that there is no clear increase trend of double bonds during the two months of exposure of the 50 μm thick polyethylene in the RCE equipment.

Finally, the average transmittances in the atmospheric window for OLD 1 and OLD 2 are 80.39 % and 79.89 %, respectively. A decrease of only 0.3% respect the NEW sample is observed for OLD 1 and a decrease of 0.8 % respect the NEW one is observed for OLD 2.

4. Conclusions

After performing transmittance analysis (UV-Vis and FT-IR) of five plastics candidates (polycarbonate, methacrylate, 17 μm LDPE, 50 μm LDPE, and 200 μm LDPE) for the RCE prototype, a 50 μm low density polyethylene has been selected for being the plastic with higher transmittance. The average transmittance in the atmospheric window (7-14 μm) of the 50 μm low density polyethylene, calculated using FT-IR in Transmission mode, is 80.7 %.

A 2 months aging study has proved that the chemical structure of the polyethylene changes by the fact that the plastic is placed on the RCE prototype and exposed to outdoor environmental conditions. FT-IR analyses show that new functional groups appear indicating oxidative processes. Although double bonds and carbonyl groups detected in the polyethylene after the two months exposure, indicate a change in the structure, transmittance decreases only by 0.3 % for OLD 1 and by 0.8 % for OLD 2, compared to the NEW polyethylene sample. These results show a stable behavior of the transmittance for polyethylene.

5. Acknowledgments

The work was partially funded by the Spanish government under grant agreement RTI2018-097669-AI00 (Ministerio de Ciencia, Innovación y Universidades) and by Fundación Iberdrola España under project “Desarrollo y evaluación de un equipo para producción combinada de frío y calor mediante refrigeración radiante y captación solar”. The authors would like to thank Generalitat de Catalunya for the project grant given to their research group (2017 SGR 659). Ariadna Carrobé would like to thank the Secretaria d’Universitats i Recerca del Departament d’Empresa i Coneixement de la Generalitat de Catalunya for its research fellowship.

6. References

Bell, E.E., Eisner, L., Young, J., Oetjen, R.A, 1960. Spectral-Radiance of Sky and Terrain at Wavelengths between 1and 20 Microns. II. Sky Measurements. J. Opt. Soc. Am., 50, 1313–1320.

Benlattar M., Oualim E. M., Harmouchi M., Mouhsen A., Belafhal A., 2006, “Radiative properties of cadmium telluride thin film as radiative cooling materials,” Opt. Commun., vol. 256, no. 1–3, pp. 10–15, 2005, doi: 10.1016/j.optcom.2005.06.033.

Bosi, S.G., Bathgate, S.N., Mills, D.R., 2014. At last! A durable convection cover for atmospheric window radiative cooling applications. Presented at the Energy Procedia, pp. 1997–2004. https://doi.org/10.1016/j.egypro.2014.10.064

Carrasco, F., Pagés, P., Pascual, S., Colom, X., 2001. Artificial aging of high-density polyethylene by ultraviolet irradiation. European Polymer J., 37 (7): 1457-1464.

Chen, Z., Zhu, L., Raman, A., Fan, S., 2016. Radiative cooling to deep sub-freezing temperatures through a 24-h day–night cycle. Nature Communications 7, 13729. https://doi.org/10.1038/ncomms13729

European Comission, “Energy performance of buildings directive.” https://ec.europa.eu/energy/en/topics/energy-efficiency/energy-performance-of-buildings/energy-performance-buildings-directive#documents (accessed Jan. 23, 2018).

Eurostat, “Energy consumption in households,” May 2019. https://ec.europa.eu/eurostat/statistics-explained/index.php?title=Energy_consumption_in_households#Use_of_energy_products_in_households_by_purpose.

Fu, Y., Yang, J., Su, Y.S., Du, W., Ma, Y.G., 2019. Daytime passive radiative cooler using porous alumina. Solar Energy Materials and Solar Cells 191, 50–54. https://doi.org/10.1016/j.solmat.2018.10.027

Hjortsberg, A., Granqvist, C.G., 1981. Radiative cooling with selectively emitting ethylene gas. Applied Physics Letters 39, 507–509. https://doi.org/10.1063/1.92783

Hu, M., Pei, G., Li, L., Zheng, R., Li, J., Ji, Jie, 2015. Theoretical and Experimental Study of Spectral SelectivitySurface for Both Solar Heating and Radiative Cooling. Int. J. of Photoenergy.

Laatioui, S., Benlattar, M., Mazroui, M., Saadouni, K., 2018. Zinc monochalcogenide thin films ZnX (X = S, Se, Te) as radiative cooling materials. Optik 166, 24–30. https://doi.org/10.1016/j.ijleo.2018.04.004

Liu, C., Wu, Y., Wang, B., Zhao, C.Y., Bao, H., 2019. Effect of atmospheric water vapor on radiative cooling performance of different surfaces. Solar Energy 183, 218–225. https://doi.org/10.1016/j.solener.2019.03.011

Tsilingiris, P.T., 2003. Comparative evaluation of the infrared transmission of polymer films. Energy Conversion and Management 44, 2839–2856. https://doi.org/10.1016/S0196-8904(03)00066-9

Vall, S., Medrano, M., Solé, C., Castell, C, 2020. Combined Radiative Cooling and Solar Thermal Collection: Experimental Proof of Concept, Energies, 13 (4), 893-905.

Xu, Z., Li, N., Liu, D., Huang, X., Wang, J., Wu, W., Zhang, H., Liu, H., Zhang, Z., Zhong, M., 2018. A new crystal Mg11(HPO3)8(OH)6 for daytime radiative cooling. Solar Energy Materials and Solar Cells 185, 536–541. https://doi.org/10.1016/j.solmat.2018.06.012

Experimental Study of a Combined Solar Heating and Radiative Cooling Device with an Adaptive Cover

Ariadna Carrobé, Marc Medrano, Cristian Solé, Ingrid Martorell, Lidia Rincón, Albert Castell

Sustainable Energy, Machinery and Buildings (SEMB) Research Group, INSPIRES Research Centre, Universitat de Lleida, Pere de Cabrera s/n, 25001 Lleida (Spain)

Abstract

Nowadays, climate change impact is becoming more important in our daylife and the use of renewable energy sources to cover the space conditioning and Domestic Hot Water (DHW) demands is growing every year. In this study, a new device that works with renewable energies and combines two different concepts, radiative cooling and thermal solar collection, is presented. The device is called Radiative Collector and Emitter (RCE) and it consists of a modified solar collector based on an adaptive cover. The absorber is covered by a polyethylene film and the glass of the solar collector is removed during the night to allow the radiative cooling effect. Due to this adaptive cover, during daytime the greenhouse effect is allowed because of the glass cover, favoring the solar collection; and during nighttime, radiative cooling is allowed through the polyethylene film in the same device. The adaptive cover allows the different properties of the materials to be used according to its mode of operation. This equipment has been experimentally tested during summertime 2019, in the University of Lleida, where the climate corresponds to a Semi-Arid Climate (BSk according to Köppen and Geiger climate classification). Results show that the RCE performs similarly to a solar collector during the day, with average heating values of 573.69 W/m^2, and is able to provide extra cooling at night, at an average cooling rate of 15.57 W/m^2.

Keywords: radiative cooling, solar thermal collection, renewable energy, adaptive cover, experimental setup

1. Introduction

The effects of climate change are becoming more dangerous and destructive day after day. The building stock is responsible for 40% of our energy consumption and 36% of all CO_2 emissions in the EU (European Commission, n.d.). Special efforts are being made in renovating the current building stock by energy efficiency means as well as considering the deployment of renewables (*UE 2018/844*, 2018). The use of renewable energy sources to cover space conditioning and DHW demands seems more likely over the years. While solar thermal energy can cover building heating and DHW demands (Kristin et al., 2016), there is not a technology with such potential and development for space cooling yet.

Alternatively, radiative cooling is a renewable cooling technology that uses the sky as a heat sink, benefiting from its effective temperature, which is much lower than ambient temperature. Energy can be dissipated to the sky taking advantage of the infrared atmospheric window (7–14 μm). This window allows infrared radiation to pass directly to outer space without intermediate absorption and re-emission in the atmosphere (Vall et al., 2020). The research for cover materials that allow this heat exchange to the atmosphere is focused on polymers, and the most common material tested and analyzed is polyethylene.

Most of the initial research conducted in this topic is related with the use of this technology, radiative cooling, during nighttime, because during daytime the power of solar radiation is higher than the net power of radiative cooling. However, recently some authors (Bhatia et al., 2018; Feng et al., 2019; Nilsson and Niklasson, 1995; Pech-May and Retsch, 2020; Yalçın et al., 2020) also studied the potential of radiative cooling during daytime. Some authors suggest that when combining the daytime solar heat collection and the nighttime radiative cooling, an extra overall power can be achieved with this combined system (Vall et al., 2020).

The main objective of this study is to analyze experimentally the combination of solar collection and radiative

doi:10.18086/eurosun.2020.06.03 Available at http://proceedings.ises.org

cooling in the same equipment. This equipment is called Radiative Collector and Emitter (RCE) and it relies on an adaptive cover using different optical properties for each functionality. This is, when the RCE works as a solar collector a high spectral transmittance in the solar radiation band and a very low spectral transmittance in the infrared band is required. On the other hand, during radiative cooling mode high spectral transmittance values in the atmospheric window wavelengths are required.

2. Experimental setup

The experimental setup consisted of a Radiative Collector and Emitter (RCE), two water tanks (the hot water tank has a heating coil), a heat exchanger, instrumentation and the control and data acquisition systems.

A sketch of the experimental setup is presented in Figure 1:

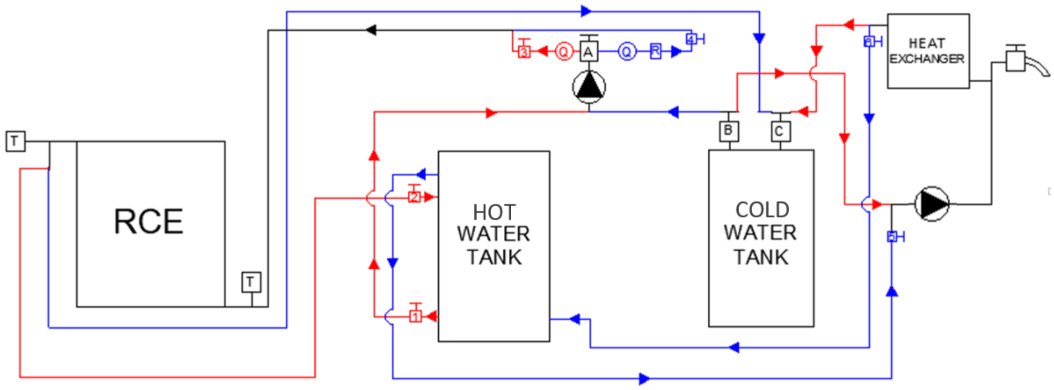

Figure 1: Sketch of the experimental setup. In red is colored the solar collection mode and in blue the radiative cooling mode.

Figure 1 presents the water flow coloured according to the mode and the direction of the flow. During solar collection mode (daytime, in red colour) water leaves the heating coil from the hot water tank (150 L) and passes through the pump and the Badger Meter flow meter. Directly water goes to the RCE device where temperature increases due to solar radiation and goes back to the heating coil to heat up the hot water tank. Meanwhile the water from the cold water tank (50 L), which has been cooled during nighttime, enters the water-air heat exchanger to increase its temperature until it reaches the exterior temperature, simulating a cooling demand.

During radiative cooling mode (night-time, blue) water leaves the cold water tank and passes through the pump and the Schmidt Mess flow meter entering the RCE to decrease its temperature due to radiative cooling. From the RCE it goes back to the cold water tank decreasing the temperature of the water in this tank. Meanwhile the water from the hot water tank, which has been heated during daytime, passes through the water-air heat exchanger decreasing its temperature to the exterior temperature, simulating a DHW demand.

To develop the RCE, a solar collector model BAXI SOL200, 2 m x 1 m x 80 mm, was modified. In this solar collector, the glass screen has been removed and the surface of the radiator has been painted with black paint in order to reduce the IR reflection of the absorber, as it is shown in Figure 2. These thermal images were taken with a thermal camera FLIR E6.

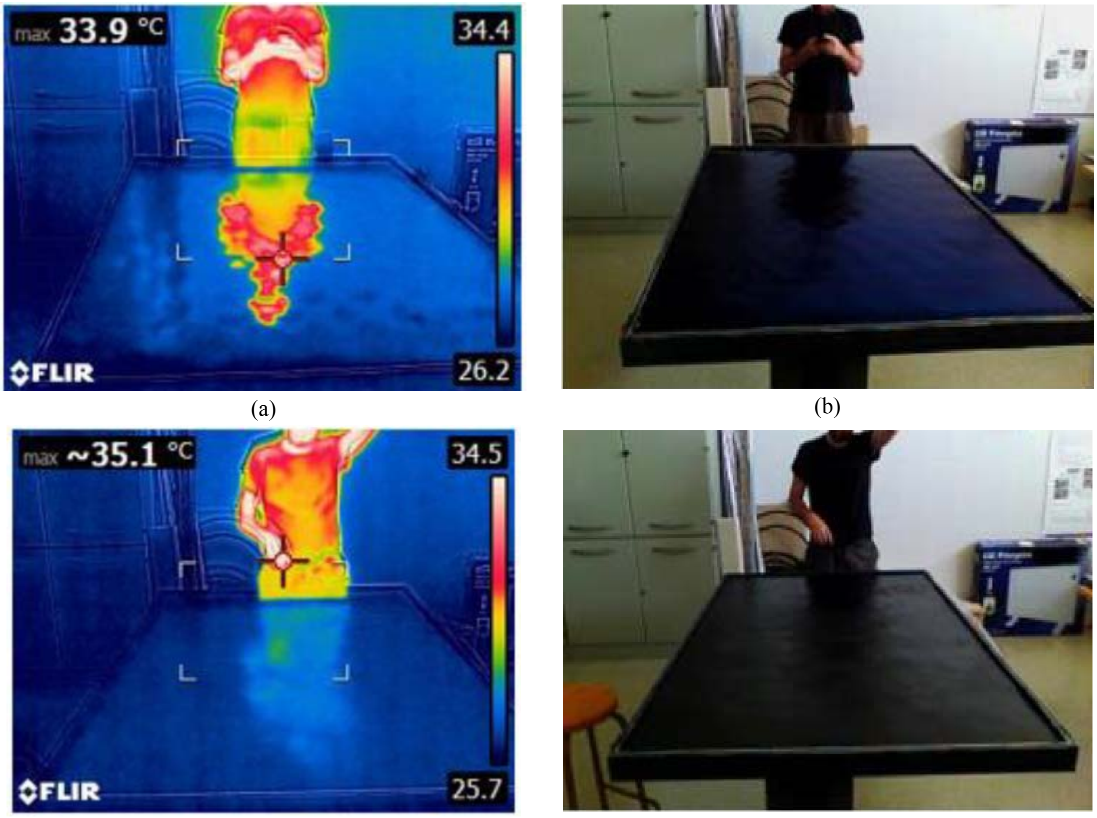

(a) (b)

(c) (d)

Figure 2: Above, there are the thermal camera (a) and the real (b) pictures of the normal absorber with selective surface, below there are the same pictures (c-d), taken with the absorber surface painted in black.

As Figure 2 shows, the absorber reduced the IR reflection after painting the surface with black paint. On the right pictures it is observed the color difference of the absorber: in (b) the absorber is dark blue whilst in (d), the absorber is completely black. The effect of having or not a selective surface in the absorber is observed on the left pictures where in (a) the IR reflection of the person is perfectly recorded by the thermal camera, whilst in (c) the reflection is almost non-existent.

To cover the absorber, the glass surface has been replaced by a 0.5 mm thick polyethylene film. To maintain the polyethylene film straight and prevent the film from bending, nylon ropes have been added every 15 cm in both directions of the collector, the long margin and the small one, as presented in the following Figure 3. This action was taken based on our experience with a previous prototype (Vall et al., 2020).

Figure 3: Nylon mesh located on the absorber in order to maintain straight the polyethylene film.

The transparent glass cover taken from the original solar collector is surrounded by an aluminium frame and four small wheels (Ø 15 cm, plastic 3D printed) are located in the shorter sides of the frame, two per each side. In the absorber, two long aluminium guides are attached in the shorter side. These guides are for the transparent glass to slide along them depending on the function mode. During day-time, the RCE is in solar collection mode, so the glass cover will be placed on top of the RCE; during night-time the glass cover will be removed and slid to the side. Thus the RCE will only have the polyethylene film as a cover for the radiative cooling.

Figure 4: RCE device with the glass cover sliding over the aluminium guides.

The experimental station is located in Lleida, where the climate is considered Semi-Arid (BSk) according to Köppen and Geiger classification and the data recorded are:

- The solar radiation, measured using a solar meter, model SMART SMP6 (2.5% accuracy).
- The external air temperature and relative humidity, using an Elektronik EE210 sensor (± 0.1 % uncertainty).
- The incoming infrared radiation with a pyrgeometer, model LP PIRG 01-DeltaOhm (5% accuracy).

In addition, the RCE device and the installation itself was monitored with the following equipment:

- The inlet and outlet temperatures of the water in the RCE were measured with platinum resistance thermometer Pt100 type 1/10 B DIIN. Accuracy at 20 °C: ±0.04°C.
- The water flow rate depends on the operating mode, so two flow meters were installed because the flow rates are very different between modes. To reduce the flow rate a restrictor valve is installed in the night mode circuit. For solar collection mode a Badger Meter-Primo Advanced (0.25% accuracy) is used whereas during the radiative cooling mode a Schmidt Mess-SDNC 503 GA-20 (4% accuracy) monitored the night flow.
- The acquisition data equipment consisted of a data logger model DIN DL-01-CPU, connected to the adapter data logger-computer model AC-250. The computer software to compile the data was STEP TCS-01. All data were registered and recorded at a time-frequency resolution of 1 min.

3. Methodology

The experimentation was performed during 6 weeks in summer 2019 in the University of Lleida (Spain). It was annotated daily in a field notebook the visual weather and sky conditions.

The results were analyzed weekly, corresponding to the following dates:

- 1st week: from 11th to 14th July, 2019
- 2nd week: from 15th to 21st July, 2019
- 3rd week: from 22nd to 28th July, 2019
- 4th week: from 29th July to 4th August, 2019
- 5th week from 5th to 11th August, 2019
- 6th week: from 12th to 16th August, 2019

It is important to highlight that data corresponding to the first week of analysis were only used to adjust the operation of the experimental facility and confirm that all the equipment was working properly.

According to the operational mode the flow range is set up as 0.8 L/min for radiative cooling mode and 1.8 L/min for solar collection mode.

Since the glass had to be slid manually and also the configuration of the valves to drive the fluid throughout the experimental set up was manual, a schedule for changing the modes was defined. Between 8 and 9 AM, the RCE would be set to the solar collection mode and the glass will be on top of the absorber; and between 8 – 9 PM, the RCE would start operation in the radiative cooling mode, so the glass will be slid aside to allow the refrigeration of the fluid. Transition modes of 2 h, between 7:30-9:30 AM and 7:30-9:30 PM were considered and experimental data for these periods were neglected to avoid transient unstable data. Thus, every day is defined as 10 h of solar collection mode (9:30 AM - 7:30 PM) and 10 h of radiative cooling mode (9:30 PM - 7:30 AM).

Mean values were calculated every 30 minutes for all the monitored parameters in order to analyze the behavior of the prototype.

Based on the measured solar radiation and IR sky radiation, days and nights were classified as clear or cloudy. This classification is based on a solar radiation and IR sky radiation ratio calculated respect to its maximum, taking 1000 W/m^2 for the solar radiation and 494 W/m^2 for the IR sky radiation.

The average power produced by the RCE, both during the solar collection mode and the radiative cooling mode, is calculated following this equation:

$$Power = \rho * C_p * \nu * \Delta T_{RCE} \quad \text{(eq. 1)}$$

Where:

ρ: Fluid density [km/m^3]

C_p: Specific heat of the fluid [KJ/kg·K]

ν: Volumetric flow taken from the flow meter located in the installation [m^3/s].

ΔT_{RCE}: Temperature difference of the fluid between the inlet and outlet point of the RCE [K].

4. Results and discussion

According to the previous section classification, in the following Figure 4, it is presented the daily average solar radiation ratio and IR radiation ratio, which were obtained dividing the daily average radiation considered (solar or IR) by the maximum radiations mentioned above.

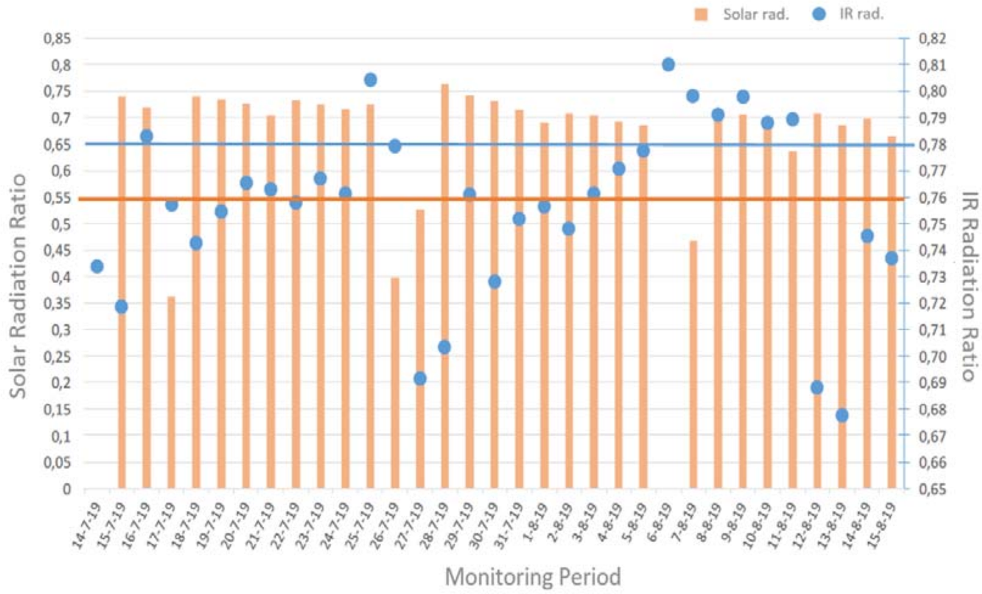

Figure 5: Average solar and IR radiation ratio in daily basis. In orange the solar radiation ratio and in blue the night radiation ratio. The horizontal lines correspond to the threshold to classify a day/night as clear or cloudy. The blue dot placed in day 14th July, 2019 corresponds to the night of 14th-15th July, 2019.

Observing the solar radiation ratio orange bars, most of the days are around 0.7 except for 4 (17th, 26th, 27th July and 7th August). From the experimentation notebook it is known that on 17th and 26th of July it was raining and the sky was completely cloudy during all day. Thus, for the sake of classifying the days in a simple and easy way and without any aim of generalizing this classification outside this paper, a solar radiation threshold of 0.55 is defined, so the days with higher ratio are considered clear and the days below this ratio cloudy.

Looking at the IR radiation blue dots, it is observed that they present lower oscillation than solar irradiation ratios. Note that the two highest values of radiation ratio nights are associated to days with very low solar radiation ratios (cloudy days). Assuming that it is reasonable that the night previous to a cloudy day has been a cloudy night as well, and knowing by theory that high humidity and high cloud cover is associated to higher sky IR radiation values and lower radiative cooling potential, it is taken the lowest IR radiation ratio corresponding to the previous night of cloudy day (26th - 27th July) as reference value to classify in a binary way the night cloudiness. This value corresponds to 0.78. Again, this classification is specific to this experimentation and should not be applied in other contexts.

Therefore, from all the monitoring period, the cloudy days were 17th, 26th, 27th July and 7th August, 2019; and the cloudy nights were 16th, 25th, 26th July and from 6th to 11th August. The rest of the monitoring period was considered clear days and nights.

From Figure 6 to Figure 9 the average daily values of the RCE power, using the eq. 1 previously presented, external temperature and outlet RCE temperature are presented for the four different sky conditions defined above: clear day, cloudy day, clear night and cloudy night along the 5 weeks of experimental testing.

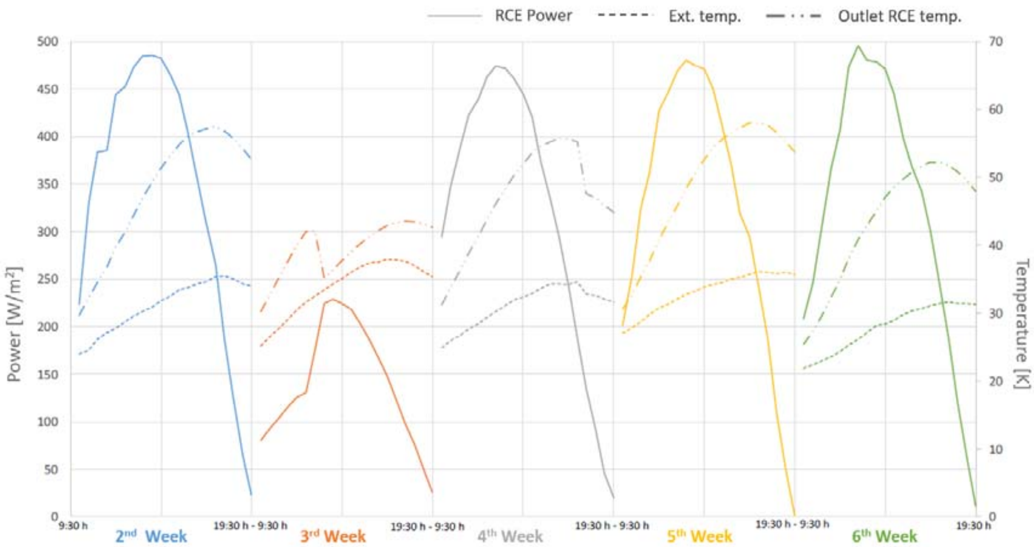

Figure 6: Average clear day corresponding to the experimental week.

In Figure 6, it is observed an average day evolution considering the average values of the clear days corresponding to each experimental week. The first week is not considered as explained in previous sections. During the 3rd week, the RCE was covered during daytime, although the facility was still operating in normal collection mode to prevent overheating. This effect is shown in Figure 6, when the 3rd week results show the lowest RCE power production. Apart from this 3rd week, the behavior of all three parameters presented (RCE power, external temperature and outlet RCE temperature) are almost the same. The continuous line corresponding to the RCE power reaches almost 500 W/m^2 each day, having the highest point during midday, around 1 PM. As expected, water from the RCE keeps increasing its temperature during the day, achieving its maximum of about 56 ºC around 5:30 PM, represented with the dot-dot-dash line. This outlet RCE temperature has the same tendency as the exterior temperature represented with the small dots line.

Figure 7: Average cloudy day corresponding to the experimental week.

During the monitoring period and according to our criteria, only four days were considered cloudy. Those days correspond to the 2nd week (17th of July), 3rd week (26th and 27th of July) and 5th week (7th of August). To present the results similar to the clear days, in the above Figure 7 are presented the weeks corresponding to the cloudy days, but in this case there is only one cloudy day for the 2nd and 5th week, and the average of two cloudy days in the 3rd week. In the case of cloudy days the behavior between weeks is also similar, but not as smooth as during clear days. Different RCE power peaks are recorded which might correspond to clear or less cloudy periods of time during the day. As it happened in the clear days, the outlet RCE temperature is increasing during the day having its maximum between 40-50 ºC around 5:30 PM. In this case the exterior temperature remains quite stable around 30 ºC.

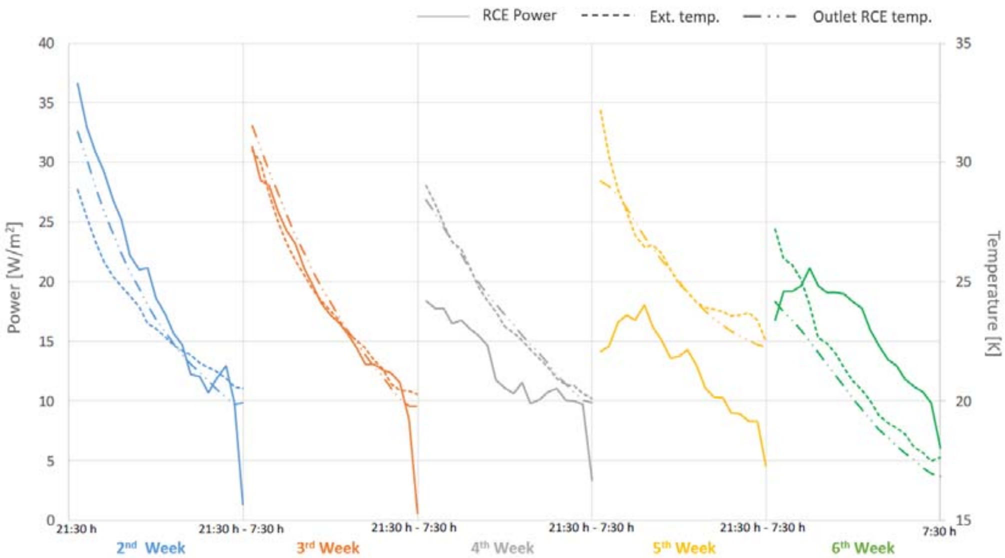

Figure 8: Average clear night corresponding to the experimental week.

In Figure 8 is presented the clear night behavior of a typical night for the five weeks of experimental tests. As it happened during the analysis of clear days, the evolution of the temperatures and the RCE power is similar for all weeks. As the external temperature is decreasing during the night, the RCE power is also decreasing having higher values at the beginning of the night, at 9:30 PM. This RCE power values decrease from 30 - 35 W/m^2 for the 2nd and 3rd weeks, and from 17 – 20 W/m^2 for the 4th, 5th and 6th weeks to 10 W/m^2 before sunrise at 7 AM. From 3:30 AM the outlet temperature of the RCE is lower than the exterior temperature (22 ºC) and it remains below it until the sunrise when the radiative cooling mode is over, except from the 6th week when the outlet RCE temperature is all the time under the external temperature. This subambient cooling temperature goes up to 3ºC below the external temperature. As it is observed in Figure 8, the RCE power decreases during the experimentation period, obtaining lower RCE powers for the 4th and 5th weeks of experiments than the 1st and 2nd weeks. This decreasing power might be caused by the aging and deterioration of the PE film but also due to the dust accumulated on it. Thus, before the last week of experiments, the film was cleaned with an electrostatic towel and an increase of 3 W/m^2 in the RCE power was registered. However, cleaning the polyethylene film was not enough for obtaining the RCE power results of the first weeks of experiments.

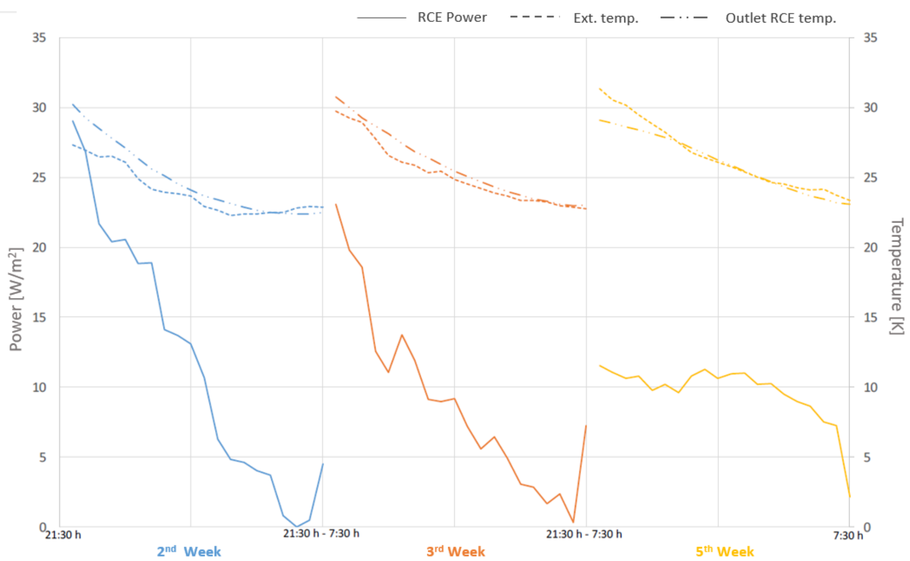

Figure 9: Average cloudy night corresponding to the experimental week.

In the above Figure 9, the average cloudy nights considered following our criteria described before, are presented according to the corresponding week: 16th of July (2nd week), 25th and 26th of July (3rd week) and from 6th to 11th of August (5th week). The behavior of the RCE is almost the same throughout the weeks monitored. As it happened during clear nights, the RCE power is decreasing during the night as the external and the outlet RCE temperature, which are very similar during all the night, are also decreasing. This effect occurs because the radiative cooling power depends on the surface temperature of the absorber, which is decreasing during the night. It has been recorded subambient cooling temperatures for the outlet RCE temperature around 6 AM during 2nd and 3rd week, and a bit before (around 3:30 AM) for the 5th week, as it happened for the clear nights.

Table 1 shows average and maximum values for the temperature difference between the outlet of the RCE and the external temperature and the thermal power obtained depending on the sky condition.

Tab. 1: Average and maximum values for the temperature difference in the RCE and thermal RCE power .

	Solar collection mode		**Radiative cooling mode**	
	Clear day	**Cloudy day**	**Clear night**	**Cloudy night**
Average ΔT (ºC)	16.93	5.86	- 1.1	-0.6
Max. ΔT (ºC)	22.53	9.57	-3.04	-2.21
Average RCE power (W/m^2)	573.69	385.22	-15.57	-9.73
Max. RCE power (W/m^2)	865.27	696.02	-36.60	-29.03

To calculate the average and the maximum temperature difference, it has been considered only the values during the period when a subambient cooling temperature has been registered in the RCE.

The results show similar behavior according to the sky conditions. During clear sky condition, the RCE power obtained is higher for solar radiation and radiative cooling collection. The same happens with the average and maximum subambient cooling temperature, obtaining higher values for clear sky condition.

For clear days the average RCE power is 573.69 W/m^2, having its maximum around midday with a value of 865.27 W/m^2, and the outlet temperature is about 17 ºC higher than the external temperature which rises up to 37 ºC.

During cloudy days the RCE power obtained is much lower, having a maximum value of 696.02 W/m^2 and average of 385.22 W/m^2 The outlet temperature of the RCE is also lower, increasing just an average of 5.86 ºC and a maximum of 9.57 ºC from the external temperature which does not exceed 32 ºC.

Regarding the radiative cooling analysis, comparing the results with the solar collection mode, those are much lower. For clear nights, the maximum RCE power is -36.60 W/m^2, and the average power obtained is -15.57 W/m^2. The outlet RCE temperature is under the ambient temperature an average of -1.1 ºC and a maximum of -3.04 ºC.

For the cloudy nights, when the sky infrared radiation is higher, the results are even lower. The average value of the RCE power on cloudy nights is about 10 W/m^2 with maximum values of 29 W/m^2 for the first two weeks analyzed. The average difference between the outlet RCE temperature and the external temperature is -0.6 ºC, having the maximum difference in the last week of experiments obtaining a difference of -2.21 ºC.

As expected, the results for the collection mode are much higher than the radiative cooling mode. The average thermal RCE power is almost 37 times higher during solar collection mode.

5. Conclusions

The RCE is a possible solution for space conditioning. The concept of combining solar collection and radiative cooling in a single prototype is possible and it produces similar solar collection power with an additional radiative cooling power during night time. During solar collection mode higher power is achieved than during radiative cooling mode. Although radiative cooling may not be, nowadays, the solution for space cooling, it can complement conventional cooling systems, reducing the emissions since it is a renewable energy.

The results from the monitoring period presented in this study demonstrate the potential of the Radiative Cooler and Emitter concept to produce hot water during daytime and cool water below room temperature during night time with a single equipment.

Another result from the experimentation is the negative effect of the dust and dirt accumulation on the cover of the RCE. After the 5th week of experiments, the polyethylene and the glass cover have been thoroughly cleaned and better results are obtained in the last week of experiments, with a significant performance improvement for the radiative cooling mode during clear days, despite the deterioration of the polyethylene film.

More research on the adaptive cover, the use of other materials and the PE aging is needed. With a more resistant material to the weather conditions and better optical characteristics (high transmittance in the atmospheric window) the deterioration observed during this experimentation will not appear or it will take longer, and higher values for the radiative cooling power will be achieved.

6. Acknowledgment

The work was partially funded by the Spanish government under grant agreement RTI2018-097669-AI00 (Ministerio de Ciencia, Innovación y Universidades) and by Fundación Iberdrola España under project “Desarrollo y evaluación de un equipo para producción combinada de frío y calor mediante refrigeración radiante y captación solar”. The authors would like to thank Generalitat de Catalunya for the project grant given to their research group (2017 SGR 659). Ariadna Carrobé would like to thank the Secretaria d’Universitats i Recerca del Departament d’Empresa i Coneixement de la Generalitat de Catalunya for its research fellowship. The authors would like to thank Ginesta Jové Artal for her final degree project.

7. References

Bhatia, B., Leroy, A., Shen, Y., Zhao, L., Gianello, M., Li, D., Gu, T., Hu, J., Soljačić, M., Wang, E.N., 2018. Passive directional sub-ambient daytime radiative cooling. Nature Communications 9, 5001. https://doi.org/10.1038/s41467-018-07293-9

European Commission, n.d. Energy efficiency in buildings [WWW Document]. European Commission - European Commission. URL https://ec.europa.eu/info/news/focus-energy-efficiency-buildings-2020-feb-17_en (accessed 7.22.20).

Feng, J., Santamouris, M., Shah, K.W., Ranzi, G., 2019. Thermal analysis in daytime radiative cooling. IOP Conference Series: Materials Science and Engineering 609, 072064. https://doi.org/10.1088/1757-899X/609/7/072064

Kristin, S., Sverrisson, F., Appavou, F., Brown, A., Epp, B., Ledreiter, A., 2016. Renewables 2016 Global Status Report. Paris, France.

Nilsson, T.M.J., Niklasson, G.A., 1995. Radiative cooling during the day: simulations and experiments on pigmented polyethylene cover foils. Solar Energy Materials and Solar Cells 37, 93–118. https://doi.org/10.1016/0927-0248(94)00200-2

Pech-May, N.W., Retsch, M., 2020. Tunable daytime passive radiative cooling based on a broadband angle selective low-pass filter. Nanoscale Adv. 2, 249–255. https://doi.org/10.1039/C9NA00557A

UE 2018/844, 2018. , 156.

Vall, S., Medrano, M., Solé, C., Castell, A., 2020. Combined Radiative Cooling and Solar Thermal Collection: Experimental Proof of Concept. Energies 13, 893. https://doi.org/10.3390/en13040893

Yalçın, R.A., Blandre, E., Joulain, K., Drévillon, J., 2020. Daytime radiative cooling with silica fiber network. Solar Energy Materials and Solar Cells 206, 110320. https://doi.org/10.1016/j.solmat.2019.110320

Optimal Characteristics of an Adaptive Windshield for a Solar Collector and Radiative Cooling Combined System

Roger Vilà, Ingrid Martorell, Marc Medrano, Albert Castell

Sustainable Energy, Machinery and Buildings (SEMB) Research Group, INSPIRES Research Centre, Universitat de Lleida, Pere de Cabrera s/n, 25001 Lleida (Spain)

Abstract

Radiative cooling is a promising technology for space cooling which can be combined with solar heating applications, enabling the production of both energy demands –heat during daytime and cold during nighttime– in a single device; reducing the non-renewable primary energy consumption for space conditioning and domestic hot water. An adaptive cover allows a mode switch, enabling heat or cold production, by combining materials with suitable optical properties for each mode. Another effect derived from the usage of covers is the reduction of convective heat losses, enhancing the performance of the device. Glass covers have been used in solar heating applications; polyethylene has been widely proposed in radiative cooling applications while zinc-based compounds are transparent enough to solar and infrared radiation in the atmospheric window to be used in RCE applications. Smart materials show tunability of properties of radiative surfaces but upon this time, they have not been used as covers neither in radiative cooling applications, nor in combined radiative cooling and solar heating applications.

Keywords: Radiative cooling, solar thermal collection, renewable energy, adaptive cover, convection reduction

1. Introduction

Radiative cooling is a process by which a surface reduces its temperature by emitting thermal radiation towards the outer space, taking advantage of the infrared atmospheric window transparency in the 7-14 µm range (Vall and Castell, 2017). Under clear sky conditions radiation to the outer space is maximized. Radiative coolers can be combined with solar heating applications, thus enabling the combined production of both energy demands – heat during daytime and cold in nighttime– in a single device (Vall et al., 2018). The authors named this device *Radiative Collector and Emitter* (RCE). For the sake of simplicity, this paper also refers to it as RCE.

RCE is presented as a green alternative which may reduce the dependence to non-renewable energy consumption for space conditioning and domestic hot water obtention.

One of the main drawbacks of radiative coolers is the low cooling rates they operate in: between 20-80 W/m^2 on average, with peak values of 120 W/m^2 (Vall et al., 2018). Ambient conditions and optical properties of materials play a role to determine the total performance of these devices. In the last years new metamaterials and photonic crystals have been developed with optimum selective emissivity/absorptance. They have been used as a proof-of-concept of radiative coolers' emitting surfaces (Ko et al., 2018) which allow daytime radiative cooling. These materials present a repeated structure of a size smaller than light; when the wavelengths interact with this structure the material shows properties which cannot be found in nature. However, as these selective surfaces reflect solar radiation, they are not suitable for heating production during the day.

Net cooling is also influenced by conduction and convection heat energy gains. In order to achieve higher cooling rates, the use of convective barriers has been proposed, enabling to cool surfaces below ambient temperature. In solar heating applications, glass has been used as a cover which enables the greenhouse effect of the solar collector and reduces convective heat exchanges. To combine solar heating and radiative cooling functionalities in a single device, an adaptive cover needs to be developed. This cover needs to be transparent to solar radiation and opaque to long-wave radiation during collection mode, and transparent to long-wave radiation during radiative cooling mode. This cover, also named windshield, has to withstand the exposition to climatological conditions: wind, tearing, rain-water (Gentle et al., 2013), snow, degradation due to UV exposition and also the presence of animals (birds and insects) which can damage the structure.

doi:10.18086/eurosun.2020.06.04 Available at http://proceedings.ises.org

This field has not been investigated as deeply as the emitting surfaces. In this work the advantages and limitations of a cover for RCE systems will be analyzed, and a literature search of similar existing solutions and materials offering the suitable optical properties in the two modes of operation will be presented and discussed.

2. Cover materials

2.1. Smart Materials

Smart materials are the most appealing solution for the fabrication of an adaptive RCE cover, as the double functionality can be achieved using only one material, which can modify their optical properties in response to external stimuli. These smart materials must show high transmittance in the solar wavelengths and low transmittance in the atmospheric window during the solar collection mode while, during the radiative cooling mode, the transmittance in the atmospheric window should be high.

The use of smart materials on emitting surfaces has been studied in RC applications. According to Kort-Kamp's models, vanadium dioxide (VO_2) (a thermochromic material) arranged in a photonic structure could achieve a reduction of surface temperature. Compared to ambient temperature, it was a 6°C reduction of the surface temperature under ~ 100 W/m^2 cooling rates. Based on a H_2SO_4-doped polyaniline films device, Xu et al. (Xu et al., 2020) achieved changes of emissivity of 0.4 in the 8-14 µm range -atmospheric window- allowing radiative cooling under low voltage.

Confining emitting infrared gases in the air gap between the emitting/absorbing surface and the infrared-transparent convective cover, selective radiative cooling can be achieved. Spectrometry techniques found that ethylene, ethyl oxide and ammonia (Hjortsberg and Granqvist, 1981; Lushiku et al., 1984; Lushiku and Granqvist, 1982) are three gases which - in the presence of low humidity - show high emissivity in the atmospheric window wavelengths (8-14 µm). In an experiment with ethylene gas, under daytime conditions, authors measured a drop of 10ºC with respect to the environment (Hjortsberg and Granqvist, 1981).

2.2. Polymeric covers

Polymers have been the most widely used materials in the manufacture of covers in radiative cooling applications. Optimal polymers in these applications must have a high transmittance in the infrared range, thus allowing the passage of infrared thermal radiation, while separating the emitting surface from the outside and diminishing unfavorable convection exchanges.

According to Tsilingiris (Tsilingiris, 2003), who studied the applicability of ten different polymers in radiative thermal applications, the most suitable polymers were polypropylene and polyethylene as they had a higher transmittance in the infrared range; while fiberglass, kapton and mylar showed the lowest transmittance coefficients not being suitable in radiative cooling applications.

Both for its high availability, cost, and for its optical properties, polyethylene has been the most widely used material in the manufacture of covers. In thin foils, these polymers exhibit an almost ideal transparency (Bartoli et al., 1977). In recent times several authors have used this polymer as a windscreen in both nocturnal radiative cooling and daytime radiative cooling applications (Fu et al., 2019; Xu et al., 2018). As an example, Zhao et al. (Zhao et al., 2019) circulated water under a metamaterial emitting surface covered with a polyethylene windshield, achieving a temperature difference of 10 °C between water and the environment. Polyethylene in the form of an aerogel has also been studied. This material had a high transmissivity in the infrared but a high reflectance in the solar range, making it not optimal in combined applications of RCE (Leroy et al., 2019).

Polyethylene has also been used in combined solar heating and radiative cooling applications (Hu et al., 2018; Long et al., 2019). Matsuta et al. (Matsuta et al., 1987) achieved maximum values of 610 W/m^2 in collection mode and 51 W/m^2 in radiative mode. Without the effect of a glass cover, the efficiency of the solar collection - with circulating water in pipes - decreases to 26.8 - 40.7% when combined with radiative cooling (Hu et al., 2019). Vall et al. (Vall et al., 2018, 2020) proposed a double mobile cover, called adaptive cover, of glass and polyethylene: during the collection mode both materials act as cover while during the radiative cooling mode only polyethylene is present. This configuration presented a main drawback as this sliding mechanism occupies two times the surface of the emitter. Another configuration was proposed using polyethylene film covering a porous cooling material with near-unity infrared emissivity in the 8-14µm range achieving radiative cooling on one side of the device. The other side is configured to achieve solar heating; switching of modes was done with a rotating shaft (Liu et al., 2020).

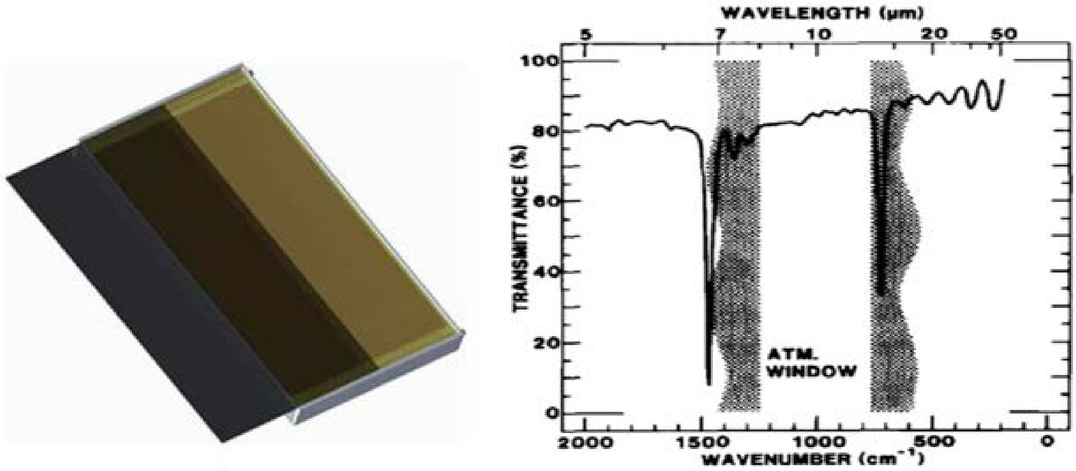

Fig 1. (Left) Sliding adaptive cover: during daytime solar collection the glass cover slides to the top of the absorbing surface and slides off the surface during nightime radiative cooling mode *(Vall et al., 2018)*. **(Right)** Transmittance of 30 µm thick polyethylene's foil *(Nilsson et al., 1985)*.

Other polymers studied were 0.0127 mm thick films of fluorinated ethylene propylene (better known for its commercial name Teflon) (Johnson, 1975), which offered an infrared transmittance of 0.7, and polyester (Orel et al., 1993). Table 1 summarizes the transmittances of these polymeric covers.

Tab.1. Polymeric covers' transmittances

Cover material	Reference	Thickness	τ_{atm}	τ_{sol}	Commentary
Teflon	(Johnson, 1975)	127 µm	~ 0.7	-	-
PE	(Raman et al., 2014)	12.5 µm	-	-	-
PE	(Hu et al., 2015, 2016a, 2018)	20 µm	0.83	0.85	-
PE	(Hu et al., 2016b)	6 µm	0.87	0.89	-
PE	(Hu et al., 2020, 2019)	6 µm	0.87	0.89	-
PE	(Zhao et al., 2019)	-	High	High	-
PE	(Ao et al., 2019)	20 µm	-	-	-
PE	(Liu et al., 2019)	-	-	-	-
PE	(Matsuta et al., 1987b)	30 µm	0.86	0.85	-
PE	(Tsilingiris, 2003)	130 µm	0.79	-	-
PE	(Tsilingiris, 2003)	50 µm	0.88	0.87	-
PE	(Xu et al., 2018)	-	-	-	-
PE	(Fu et al., 2019)	50 µm	-	-	-
PE	(Al-Nimr et al., 1998)	40 µm	High	-	-
PE	(Ali et al., 1998)	50 µm	0.72 0.69 0.57 0.42	-	New film 5 days exposition 30 days exposition 100 days exposition
PE	(Hamza H. Ali et al., 1995)	50 µm	0.74**¡Error! Marca**	-	-

			dor no defini do.		
PE	(Nwaji et al., 2020)	1 µm	0.92	-	-
PE	(Gentle et al., 2013)	Ø150 µm	0.872	-	Fibermesh cover
PE	(Nilsson et al., 1985)	30 µm	0.85	-	-
PE	(Bhatia et al., 2018)	-	0.92	<0.45	-
PE aerogel	(Leroy et al., 2019)	6 mm	0.80	0.11	-
Polyester	(Orel et al., 1993)	50 µm	High	-	-
Polycarbonate	(Tsilingiris, 2003)	1.22 mm	0.06	-	-
Kapton	(Tsilingiris, 2003)	130 µm	0.08	-	-
Mylar	(Tsilingiris, 2003)	130 µm	0.05	-	-
PP	(Tsilingiris, 2003)	130 µm	0.50	-	-
Plexiglass	(Tsilingiris, 2003)	1.52 mm	0.01	-	-
Vinyl	(Tsilingiris, 2003)	125 µm	0.21	-	-
Fiberglass	(Tsilingiris, 2003)	960 µm	0.04	-	-

Polymeric covers have mechanical drawbacks when used as long-lasting covers. These covers are exposed to inclement weather conditions as well as the presence of animals that may end up affecting the structure of this element. Increasing the thickness to deal with this problem does not turn out to be an efficient solution. Ali et al. (Ali et al., 1998; Hamza H. Ali et al., 1995) studied that the increase in thickness has a negative effect on the transmittance of polyethylene and as a consequence, on the overall performance of radiative cooling: when it increased from 25 µm to 50 µm, the performance worsened by 8.6%.

New polymeric structures were also investigated. Nilsson et al (Nilsson et al., 1985) proposed a V-shapped arrangement of three layers of corrugated polyethylene. They obtained an infrared transmissivity close to film configurations but its thicker structure could provide – although it has not been studied - a higher structural rigidity. Gentle et al. (Gentle et al., 2013), for their part, proposed a polymer mesh made of PE fibers of 150 µm diameter that would provide a transparency of 87% and an expected lifespan of 5 years.

Aging due to continuous exposure to outdoors' condition also has a negative effect on the transmittance of polyethylene. Under the climatic conditions of Assiut (Egypt), a 50 µm polyethylene film dropped its transmittance from 0.72 to 0.42 after 100 days of outdoor exposure; the radiative cooling performance decreased by 33.3% (Ali et al., 1998).

2.3. Non-polymeric covers

Zinc crystals are presented as a possible alternative to polymeric coatings. For the purpose of designing a durable convective cover for radiative cooling applications, Bosi et al. (Bosi et al., 2014) identified ZnS crystals as a promising material which, with a thickness of 4 mm, had a transmittance in the atmospheric window of 0.64.

The infrared transmittances of ZnS crystals, as well as ZnTe and ZnSe, lie between 0.66 and 0.77 and in the solar range, transmittances fall between 0.61-0.66 (Laatioui et al., 2018). They can be thought of as transparent enough to be used in combined solar heating and radiative cooling (RCE) applications. These materials were also used in radiative cooling daytime applications: Chen et al. (Chen et al., 2016) achieved a record decrease of 42ºC below ambient of the surface temperature with a complex system consisting on a highly selective emitter covered with a ZnSe cover to minimize solar radiation and supported by a vacuum chamber which minimizes parasitic conductive and convective losses.

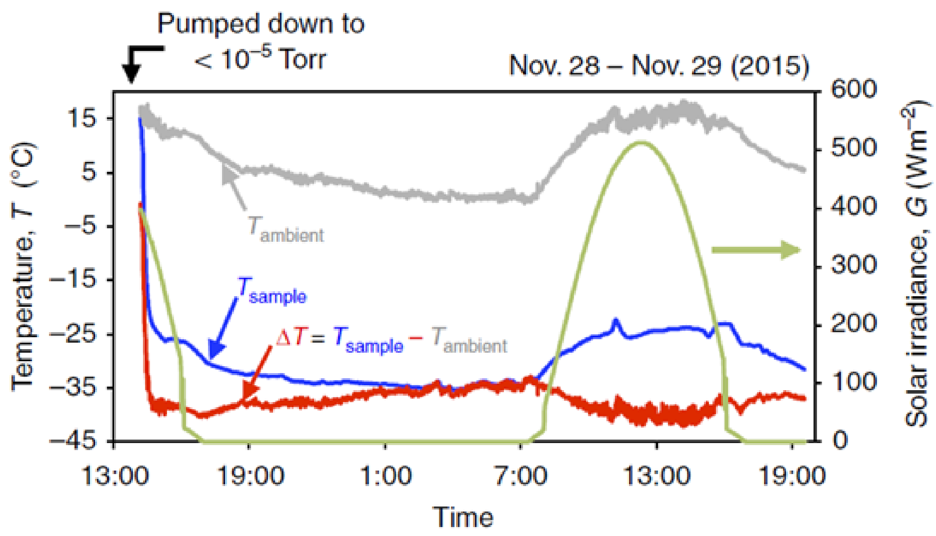

Fig 2. A large temperature reduction below ambient was achieved through radiative cooling in a 24-h day–night cycle in a device which combined a selective emitter, a zinc crystal cover and a vacuum chamber *(Chen et al., 2016).*

The disadvantage of zinc crystals is their high cost. To our knowledge, these crystals are used in commercial applications for thermographic cameras. These crystals are sold in small sizes buttons (Ø 5cm) and their cost is around 500€. Table 2 summarizes the optical properties of zinc-based covers.

Tab. 2. Optical properties of zinc crystal covers

Cover material	Reference	Thickness	τ_{atm}	τ_{sol}	ρ_{atm}	ρ_{sol}	α_{atm}	α_{sol}
ZnS	(Bosi et al., 2014)	4 mm	0.64	-	-	-	-	-
ZnS	(Bathgate and Bosi, 2011)	4 mm	0.64	-	-	-	-	-
ZnS	(Laatioui et al., 2018)	1 mm	0.77	0.66	0.12	0.21	0.11	0.13
ZnSe	(Bathgate and Bosi, 2011)	7.1 mm	0.7	-	-	-	-	-
ZnSe	(Chen et al., 2016)	-	0.87	-	-	-	-	-
ZnSe	(Laatioui et al., 2018)	1 mm	0.71	0.65	0.17	0.20	0.12	0.15
ZnTe	(Laatioui et al., 2018)	1 mm	0.66	0.61	0.21	0.22	0.13	0.17

Cadmium-based films (CdS and CdTe) are another possibility for radiative cooling applications as they presented an average transmittance between 0.61 and 0.8 in the range of the atmospheric window. These materials, however, had a low transmittance and a high absorbance in the solar range. At first glance it seems to be an unsuitable material for RCE applications but RCE designs can be thought of in which the cadmium film acts as an absorber during the solar capture mode and as a convective screen during the radiative cooling mode.

3. Discussion

The most attractive solution are smart materials with the ability to switch their optical properties as a result of external stimuli (temperature, electricity or gas presence) and, although they have been used as radiative surfaces in radiative cooling researches, in the literature it has not been found yet any use in the construction of convection covers for combined radiative cooling and solar heating.

To date, there is no proof-of-concept of non-polymeric coatings in RCE applications. However, as we have seen, the optical characteristics seem to indicate that the presented non-polymeric materials could become possible materials in RCE applications. Same as happened with polymeric covers, in order to obtain better performances in the solar collection mode, these should be combined with glass covers.

Current existing solutions involve the use of materials transparent to radiation in the solar band and in the atmospheric window, which reduces the performance during solar collection. The other proposed solution is the combination of these materials with glass screens during the solar collection mode. This solution, however, implies more complex RCE designs with greater space availability requirements.

Among the transparent materials for both solar and infrared radiation in the atmospheric window are polymers, with polyethylene as the most used material in radiative cooling, and zinc-based crystals, which have better mechanical properties than polymers at the expense of worse optical properties and a higher cost.

4. Conclusions

In this paper we have presented the optical properties that a convective cover (or windshields) must have in order to achieve the best performance of a combined diurnal solar collector and nocturnal radiative cooler (RCE).

After reviewing the existing literature, it can be pointed that much of the effort has been put on developing surfaces that maximize the absorbed or emitted radiation, whereas little research has been conducted on new covers that minimize convective exchanges. So far there is no definitive material for this type of covers. This results points towards a new line of research in the field of radiative cooling.

5. Acknowledgments

The work was partially funded by the Catalan Government under grant agreement (2017 SGR 659), and the Spanish government under grant agreement RTI2018-097669-A-I00 (Ministerio de Ciencia, Innovación y Universidades).

6. References

Ali, A.H.H., Saito, H., Taha, I.M.S., Kishinami, K., Ismail, I.M., 1998. Effect of aging, thickness and color on both the radiative properties of polyethylene films and performance of the nocturnal cooling unit. Energy Conversion and Management 39, 87–93. https://doi.org/10.1016/S0196-8904(96)00174-4

Al-Nimr, M.A., Kodah, Z., Nassar, B., 1998. A theoretical and experimental investigation of a radiative cooling system. Solar Energy 63, 367–373. https://doi.org/10.1016/S0038-092X(98)00098-X

Ao, X., Hu, M., Zhao, B., Chen, N., Pei, G., Zou, C., 2019. Preliminary experimental study of a specular and a diffuse surface for daytime radiative cooling. Solar Energy Materials and Solar Cells 191, 290–296. https://doi.org/10.1016/j.solmat.2018.11.032

Bathgate, S.N., Bosi, S.G., 2011. A robust convection cover material for selective radiative cooling applications. Solar Energy Materials and Solar Cells 95, 2778–2785. https://doi.org/10.1016/j.solmat.2011.05.027

Bhatia, B., Leroy, A., Shen, Y., Zhao, L., Gianello, M., Li, D., Gu, T., Hu, J., Soljačić, M., Wang, E.N., 2018. Passive directional sub-ambient daytime radiative cooling. Nature Communications 9, 5001. https://doi.org/10.1038/s41467-018-07293-9

Bosi, S.G., Bathgate, S.N., Mills, D.R., 2014. At last! A durable convection cover for atmospheric window radiative cooling applications. Presented at the Energy Procedia, pp. 1997–2004. https://doi.org/10.1016/j.egypro.2014.10.064

Chen, Z., Zhu, L., Raman, A., Fan, S., 2016. Radiative cooling to deep sub-freezing temperatures through a 24-h day–night cycle. Nature Communications 7, 13729. https://doi.org/10.1038/ncomms13729

Fu, Y., Yang, J., Su, Y.S., Du, W., Ma, Y.G., 2019. Daytime passive radiative cooler using porous alumina. Solar Energy Materials and Solar Cells 191, 50–54. https://doi.org/10.1016/j.solmat.2018.10.027

Gentle, A.R., Dybdal, K.L., Smith, G.B., 2013. Polymeric mesh for durable infra-red transparent convection shields: Applications in cool roofs and sky cooling. Solar Energy Materials and Solar Cells 115, 79–85. https://doi.org/10.1016/j.solmat.2013.03.001

Hamza H. Ali, A., Taha, I.M.S., Ismail, I.M., 1995. Cooling of water flowing through a night sky radiator. Solar Energy 55, 235–253. https://doi.org/10.1016/0038-092X(95)00030-U

Hjortsberg, A., Granqvist, C.G., 1981. Radiative cooling with selectively emitting ethylene gas. Applied Physics Letters 39, 507–509. https://doi.org/10.1063/1.92783

Hu, M., Pei, G., Li, L., Zheng, R., Li, J., Ji, J., 2015. Theoretical and Experimental Study of Spectral Selectivity Surface for Both Solar Heating and Radiative Cooling. International Journal of Photoenergy 2015, 1–9. https://doi.org/10.1155/2015/807875

Hu, M., Pei, G., Wang, Q., Li, J., Wang, Y., Ji, J., 2016a. Field test and preliminary analysis of a combined diurnal solar heating and nocturnal radiative cooling system. Applied Energy 179, 899–908. https://doi.org/10.1016/j.apenergy.2016.07.066

Hu, M., Zhao, B., Ao, X., Chen, N., Cao, J., Wang, Q., Su, Y., Pei, G., 2020. Feasibility research on a double-covered hybrid photo-thermal and radiative sky cooling module. Solar Energy 197, 332–343. https://doi.org/10.1016/j.solener.2020.01.022

Hu, M., Zhao, B., Ao, X., Feng, J., Cao, J., Su, Y., Pei, G., 2019. Experimental study on a hybrid photo-thermal and radiative cooling collector using black acrylic paint as the panel coating. Renewable Energy 139, 1217–1226. https://doi.org/10.1016/j.renene.2019.03.013

Hu, M., Zhao, B., Ao, X., Su, Y., Pei, G., 2018. Numerical study and experimental validation of a combined diurnal solar heating and nocturnal radiative cooling collector. Applied Thermal Engineering 145, 1–13. https://doi.org/10.1016/j.applthermaleng.2018.08.097

Hu, M., Zhao, B., li, J., Wang, Y., Pei, G., 2016b. Preliminary thermal analysis of a combined photovoltaic-photothermic-nocturnal radiative cooling system. Energy. https://doi.org/10.1016/j.energy.2017.03.075

Johnson, T.E., 1975. Radiation cooling of structures with infrared transparent wind screens. Solar Energy 17, 173–178. https://doi.org/10.1016/0038-092X(75)90056-0

Ko, B., Lee, D., Badloe, T., Rho, J., 2018. Metamaterial-Based Radiative Cooling: Towards Energy-Free All-Day Cooling. Energies 12, 89. https://doi.org/10.3390/en12010089

Laatioui, S., Benlattar, M., Mazroui, M., Saadouni, K., 2018. Zinc monochalcogenide thin films ZnX (X = S, Se, Te) as radiative cooling materials. Optik 166, 24–30. https://doi.org/10.1016/j.ijleo.2018.04.004

Leroy, A., Bhatia, B., Kelsall, C.C., Castillejo-Cuberos, A., Di Capua H., M., Zhao, L., Zhang, L., Guzman, A.M., Wang, E.N., 2019. High-performance subambient radiative cooling enabled by optically selective and thermally insulating polyethylene aerogel. Sci. Adv. 5, eaat9480. https://doi.org/10.1126/sciadv.aat9480

Liu, C., Wu, Y., Wang, B., Zhao, C.Y., Bao, H., 2019. Effect of atmospheric water vapor on radiative cooling performance of different surfaces. Solar Energy 183, 218–225. https://doi.org/10.1016/j.solener.2019.03.011

Long, L., Yang, Y., Wang, L., 2019. Simultaneously enhanced solar absorption and radiative cooling with thin silica micro-grating coatings for silicon solar cells. Solar Energy Materials and Solar Cells 197, 19–24. https://doi.org/10.1016/j.solmat.2019.04.006

Lushiku, E.M., Eriksson, T.S., Hjortsberg, A., Granqvist, C.G., 1984. Radiative cooling to low temperatures with selectively infrared-emitting gases. Solar & Wind Technology 1, 115–121. https://doi.org/10.1016/0741-983X(84)90013-4

Lushiku, E.M., Granqvist, C.G., 1982. Radiative cooling with selectively infrared-emitting gases. Journal of Applied Physics 53, 5526–5530. https://doi.org/10.1364/AO.23.001835

Matsuta, M., Terada, S., Ito, H., 1987a. Solar Heating and radiative cooling using a solar collector-sky radiator with a spectrally selective surface. Solar Energy 39, 183–186.

Matsuta, M., Terada, S., Ito, H., 1987b. Solar Heating and radiative cooling using a solar collector-sky radiator with a spectrally selective surface. Solar Energy 39, 183–186.

Nilsson, N.A., Eriksson, T.S., Granqvist, C.G., 1985. Infrared-transparent convection shields for radiative cooling: Initial results on corrugated polyethylene foils. Solar Energy Materials 12, 327–333. https://doi.org/10.1016/0165-1633(85)90002-4

Nwaji, G.N., Okoronkwo, C.A., Ogueke, N.V., Anyanwu, E.E., 2020. Investigation of a hybrid solar collector/nocturnal radiator for water heating/cooling in selected Nigerian cities. Renewable Energy 145, 2561–2574. https://doi.org/10.1016/j.renene.2019.07.144

Orel, B., Klanjsek Gunde, M., Krainer, A., 1993. Radiative Cooling Efficiency of White Pigmented Paints. Solar Energy 50, 477–482.

Raman, A.P., Anoma, M.A., Zhu, L., Rephaeli, E., Fan, S., 2014. Passive radiative cooling below ambient air temperature under direct sunlight. Nature 515, 540–544. https://doi.org/10.1038/nature13883

Tsilingiris, P.T., 2003. Comparative evaluation of the infrared transmission of polymer films. Energy Conversion and Management 44, 2839–2856. https://doi.org/10.1016/S0196-8904(03)00066-9

Vall, S., Castell, A., 2017. Radiative cooling as low-grade energy source: A literature review. Renewable and Sustainable Energy Reviews 77, 803–820. https://doi.org/10.1016/j.rser.2017.04.010

Vall, S., Castell, A., Medrano, M., 2018. Energy Savings Potential of a Novel Radiative Cooling and Solar Thermal Collection Concept in Buildings for Various World Climates. Energy Technol. 6, 2200–2209. https://doi.org/10.1002/ente.201800164

Xu, G., Zhang, L., Wang, B., Chen, X., Dou, S., Pan, M., Ren, F., Li, X., Li, Y., 2020. A visible-to-infrared broadband flexible electrochromic device based polyaniline for simultaneously variable optical and thermal management. Solar Energy Materials and Solar Cells 208, 110356. https://doi.org/10.1016/j.solmat.2019.110356

Xu, Z., Li, N., Liu, D., Huang, X., Wang, J., Wu, W., Zhang, H., Liu, H., Zhang, Z., Zhong, M., 2018. A new crystal Mg11(HPO3)8(OH)6 for daytime radiative cooling. Solar Energy Materials and Solar Cells 185, 536–541. https://doi.org/10.1016/j.solmat.2018.06.012

Zhao, B., Hu, M., Ao, X., Huang, X., Ren, X., Pei, G., 2019. Conventional photovoltaic panel for nocturnal radiative cooling and preliminary performance analysis. Energy 175, 677–686. https://doi.org/10.1016/j.energy.2019.03.106

ENERGY ASSESSMENT OF FAÇADE-INTEGRATED SOLAR THERMAL COLLECTORS IN MULTI-FLOOR BUILDINGS

Paolo Bonato[1] and Roberto Fedrizzi[1]

[1]Eurac Research, Institute for Renewable Energy, Bolzano (Italy)

Abstract

The aim of this work is to assess the energy performance of solar thermal collectors integrated in the façade of residential and tertiary multi-story buildings. Here, the collected solar heat collected is exploited to cover a share of the space heating and hot water preparation thermal loads, replacing the use of a traditional fossil fuel-based generation system. The assessment is carried out with the use of dynamic energy simulations based on the TRNSYS software, where a thermal zone is appropriately characterized to model the modular unit composing the perimetral zones of the studied building types. The scope of the paper includes a parametrical analysis for three characteristic European climates (Mediterranean climate, Continental climate and Nordic climate), two specific water storage volumes and two facade designs. Based on the studied scenarios, it is concluded that façade-integrated solar thermal collectors applied to hotels, hospitals and dorms can well exploit the locally available solar irradiation and reach interesting solar yields and solar fractions, whereas office buildings show a poor matching at higher latitudes.

Keywords: BIST, solar thermal, dynamic simulations, TRNSYS.

1. Introduction

Over the last years, the integration of solar technologies into the buildings' envelope has gained traction, becoming a viable option for building designers and a business opportunity for the industry. Research projects and international networks such as IEA SHC Task 56 [1] and Cost Action 1403 [2] have studied the issue from the economical, technological and energy perspectives, with the aim to develop and promote solutions close to market. In the current panorama, the building-integrated photovoltaics sector counts for a wide range of products offered in a variety of installation typologies, shapes and colors, and the elaboration of the standard EN 50583 [3] was a significant step toward a progressive development of the industry. Conversely, the market penetration of constructive solutions integrating solar thermal collectors in the envelope remains scarce, even though the solution holds a great potential in applications that show a good matching between solar availability and heat demand, due to the high solar radiation-to-heat conversion efficiencies of thermal collectors.

In this sense, buildings such as hotels, dorms or long-term care wings of hospitals are characterized by high thermal loads that are largely connected to hot water preparation and thus do not show large seasonal variations. These applications could then represent a great opportunity for the use of solar thermal collectors. Tall multi-floor buildings, however, do not usually offer roof areas adequate for solar thermal installations with good load coverages, as the limited roof surface is often devoted to the installation of technical equipment such as air handling units, chimneys, antennas, dry coolers, façade cleaning equipment etc. On the contrary, facades offer plenty of available surfaces for solar installations, but in fact they are rarely exploited for this scope, even when the solar exposure is favorable and the external shading is negligible.

In literature, a few studies tackle the topic of the façade-integration of solar thermal collectors in multi-story buildings. Hegarty et al. explored the application of building-integrated solar thermal collectors in a number of building types, focusing however only on the hot water preparation thermal load and limiting the investigation to the climate of Dublin. In his study, Hegarty concludes that there is a case for façade integrated solar thermal collectors as a result of limited roof spaces, especially for high rise buildings with high hot water consumption [4]. Giovanardi investigated the integration of unglazed solar thermal collectors in the façade of a hotel and a multifamily residential building [5]. Sánchez-Barroso et al. studied the use of solar thermal

doi:10.18086/eurosun.2020.06.05 Available at http://proceedings.ises.org

collectors for hot water preparation in hospitals in the Spanish region, reporting very interesting payback time values (4.7 years) [6]. His study focused on roof installations, but the conclusions are very encouraging to explore other ways of integrating solar thermal collectors when roof surfaces are not available. In this context, the aim of this paper is to assess the energy performance of façade-integrated solar thermal collectors applied to energy-intensive multi-story buildings such as hotels, dorms and hospitals by quantifying the share of the thermal load (including both space heating and hot water preparation) that can be covered with solar thermal energy in a variety of climates. Additionally, the case of office buildings is considered for comparison purposes.

To reach this goal, thermal loads and solar heat production are estimated by numerical models developed with a dynamic energy simulation software (TRNSYS). Here, the most simple and modular units composing the perimetral zones of the studied building typologies (a hotel room, a dorm room, a long-term care wing of a hospital and an office cell) are characterized with literature values with concerns to infiltration, ventilation, hot water load etc. Annual energy simulations are performed for a range of European climates (Rome, Stuttgart and Stockholm) and relevant key performance indicators such as annual solar yield, solar fraction and annual useful energy demand are calculated to assess the performance of the technological solution.

In the next section, methodology and simulation models are described with focus on the energy system and the thermal zone, so to provide the reader with a better comprehension of the outcomes of the assessment. In section three, the key performance indicators are illustrated, and the numerical results of the energy simulations are reported and discussed. The paper concludes highlighting the main results with an outlook to future work.

2. Methodology and simulation model

The assessment of the facade-integrated solar thermal solution is carried out for four building typologies (hotel, hospital, dorm and office rooms) via annual energy simulations performed with the use of the software TRNSYS. In the simulation environment, a numerical model is developed to represent the thermal zone and the components of the energy system including solar thermal collectors, piping and a water storage.

More in detail, the thermal load is assessed considering the hot water preparation load and the space heating demand of the perimetral areas of a floor of the building, neglecting common areas and technical spaces. To further simplify the modelling approach and the computation load, it is assumed that the perimetral area of the floor is divided into multiple identical spaces (or rooms), which are taken as the modular elements of the building structure. The space heating load is then composed around the load of a single-room reference zone tested in the simulation software for different azimuthal orientations, considering the blueprint of the floor shown in Figure 2. The space heating water loop is connected to a floor-based central water storage and delivers to the rooms the amount of heating power that maintains the convective air temperature at the setpoint. The hot water preparation load is accounted as a heat withdrawal from the water storage.

Figure 1 shows a 3-dimensional view of the modelled thermal zone and Table 1 lists its main characteristics and relevant features.

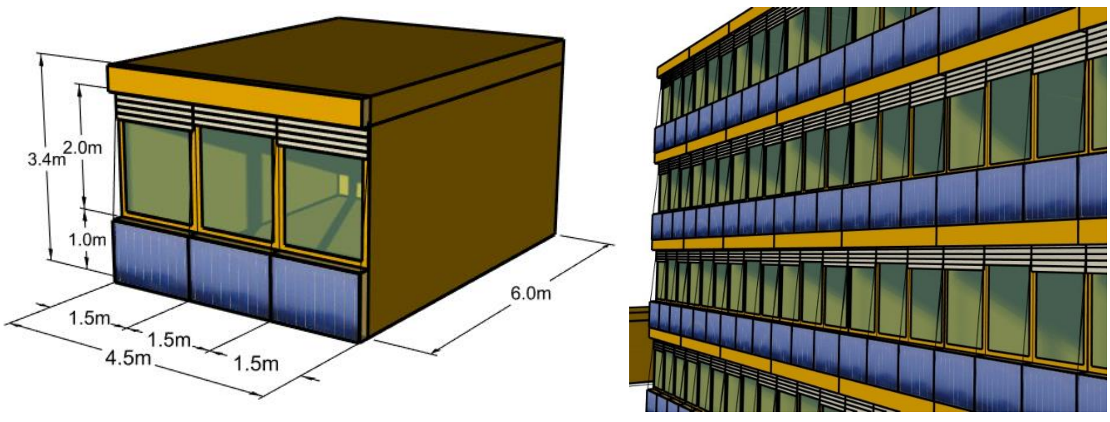

Fig. 1: 3D rendering of the thermal zone (left) and the building facade (right) – Window-to-wall ratio = 60%

Tab. 1: Thermal and optical properties of the external wall

Building assemblies			
g-value (glass)	Stockholm	0.63	
	Stuttgart	0.59	
	Rome	0.33	
U-value (glass)	Stockholm	0.81	W/(m²K)
	Stuttgart	1.29	W/(m²K)
	Rome	1.40	W/(m²K)
U-value (window frame)		1.18	W/(m²K)
U-value (opaque)		0.25	W/(m²K)
Window-to-wall ratio (incl. frame)		45 to 60	%

Tab. 2: Boundary conditions and characterization of the reference thermal zone

	Hotel room	**Hospital room**	**Dorm room**	**Office room**	
Geometry and occupancy					
Floor area	27				m²
Gross air volume	81				m³
Full-occupancy rate	2				p/room
Crowding index	0.07				p/m²
Ventilation and infiltrations					
Design ventilation rate (during occupancy)	11				L/(s·p)
Heat recovery efficiency [7]	70				%
Infiltration rate	0.15				1/h
Movable solar shading system					
Shading factor (when activated)	70				%
Beam radiation threshold for shadings activation	150				W/m²
Internal gains [7]					
Human presence – Latent heat gain	0.08				kg/(h·p)
Human presence – Sensible heat gain	70				W/p
Usage hours per day	16.0	24.0	17.0	11.0	h/day
Full occupancy hours per day	12.2	24.0	14.0	7.2	h/day
Day off per week	0	0	0	2	day/week
Appliances – peak power	8.0	4.0	8.0	7.0	W/m²
Appliances – standby consumption	0.8	0.4	0.8	0.7	W/m²
Artificial lighting – peak power	2.7	4.5	2.7	11.6	W/m²
Contemporaneity factor	70	80	80	80	%
Thermal demand					
Hot water demand (at 60°C) [7]	40	60	35	3	l/(day·p)
Tap water temperature [7]	10				°C
Space heating set point temperature	21				°C
Energy generation, storage and distribution					
Average efficiency of gas boiler	85				%
Insulation thickness of pipes (λ = 0.04 W/m/K)	3 (pipes), 15 (storage)				cm
Length of the pipes	109 (solar loop), 207 (heating loop)				m
Water content of the storage	40 to 70				l/m²

It is assumed that flat solar thermal collectors are installed into the lower opaque section of each of the three 1.5 m wide modules composing the façade of all rooms facing South. The solar collectors integrated in the facade of single rooms are connected in series whereas the circuits of different rooms are connected in parallel, as shown in Figure 2. The solar heat is delivered to a floor-based water storage and partly replaces the use of a back-up heat generation system (gas boiler) that is connected in parallel to the same storage. Two solar collector sizes are considered, thus leading to designs of the façade showing different window-to-wall ratios (WWR). Geometries and thermal properties of the solar thermal collectors are reported below in Table 3.

Tab. 3: Geometries and thermal properties of the flat solar thermal collectors

	WWR	Gross area (1x collector)	Aperture area (1x collector)	Gross area (per room)	Slope	Eta0	a1	a2	Back-Insulation
Size #1	45 %	2.25 m^2	2.00 m^2	6.75 m^2	90°	0.79	3.979	0.014	70 mm Rockwool
Size #2	60 %	1.50 m^2	1.34 m^2	4.50 m^2					

The simulation model features a thermal link between façade module and solar collector, meaning that the presence of the solar thermal collector influences the thermal load of the zone and vice-versa. It is assumed that the solar thermal collectors are installed on the South-façade of the building and that the external shading is negligible.

It is assumed that the reference floor has an overall area of about 500 m^2 and that the width-to-depth ratio is equal to 2:1, as illustrated in Figure 2. Table 4 reports relevant data on the geometry of the floor and on the solar thermal collectors' field.

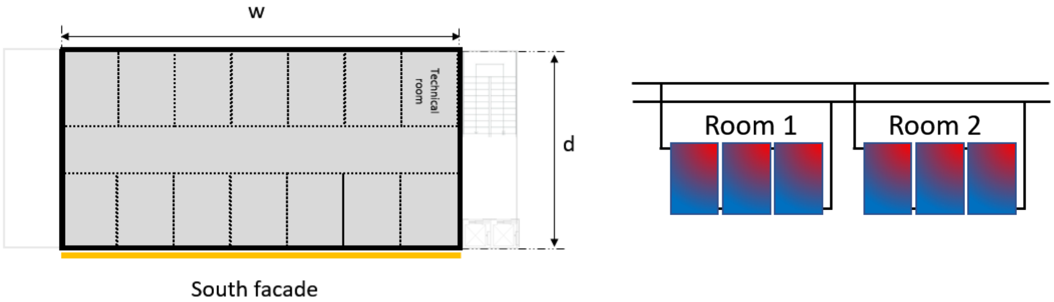

Fig. 2: Floor design (left) - top view, width (w) and depth (d) of the floor highlighted, Hydraulic connections (right)

Tab. 4: Geometry of the reference floor and the solar thermal collectors' field

	Solar collectors' area per floor	Solar collectors' area / Total façade area	South façade area per floor	Total façade area per floor	Floor area (w x d)	Rooms area / Floor area
WWR = 45%	47.3 m^2	15 %	107 m^2	321 m^2	496 m^2	71%
WWR = 60%	31.5 m^2	10 %				

To widen the scope of the paper and investigate the performance of the solution in a variety of contexts, the energy analysis is conducted for three representative European locations, that is Rome (Italy) for the Mediterranean climate, Stuttgart (Germany) for the Continental climate and Stockholm (Sweden) for the Nordic climate [8]. The weather dataset used in the energy simulations is generated using the database Meteonorm 7 and contains hourly values of meteorological parameters such as ambient air temperature, humidity and solar radiation for a one-year period. For comparison purposes, Figure 3 and Table 5 show a selection of annual meteorological parameters for the three locations.

Tab. 5: Annual meteorological data for the three locations (Rome, Stuttgart and Stockholm) – Global irradiation on the horizontal ($H_{0°}$), Global irradiation on a vertical South-facing surface ($H_{90°,S}$), Average ambient temperature ($T_{a,av}$) and Heating Degree Days (HDD)

		Rome	Stuttgart	Stockholm
$H_{0°}$	kWh/(m^2·y)	1637	1105	954
$H_{90°,S}$	kWh/(m^2·y)	1267	899	900
$T_{a,av}$	°C	15.8	9.9	7.8
$HDD_{12,20}$	Kd	1355	3220	3998

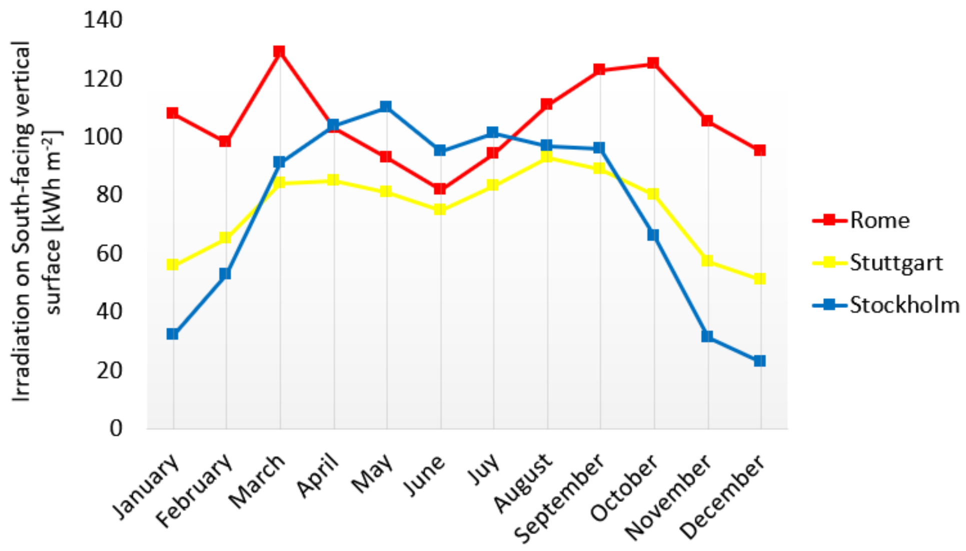

Fig. 3: Monthly irradiation on a vertical South-facing surface for the three locations (Rome in red, Stuttgart in yellow and Stockholm in blue)

Finally, a parameter that can significantly influence the energy performance of solar thermal systems is the size of the water tank, with larger volumes usually corresponding to better solar yields. To quantify this effect on the overall performances, two storage sizes are considered corresponding to 40 and 70 liters of water per square meter of solar thermal collectors' area. To summarize, Table 5 lists the parameters investigated in this study. Such factors are evaluated in a full-factorial combination, for a total of 48 different scenarios.

Tab. 5: List of the parameters considered in the study

Climate	Building type	WWR	Tank size
Rome Stuttgart Stockholm	Hotel Hospital Dorm Office	45% 60%	40 l/m^2 70 l/m^2

3. Results and discussion

The key performance indicators considered for the energy assessment are the annual solar yield, the solar fraction, the annual thermal load, the energy contributions to the water storage and the utility bill savings. All quantities are expressed per square meter of floor area unless stated otherwise. The results of the energy assessment are reported in Table 6 and discussed below.

- The annual solar yield is the solar energy harvested by the solar collectors over the course of one year per square meter of collector's gross area.
- The solar fraction is the share of thermal energy generated by the solar thermal collectors' field.
- The annual thermal load is the thermal energy for space heating and hot water preparation made available to users by the energy system over the course of one year.
- The annual energy contributions to the storage are the thermal energy inputs of back-up system and solar collectors' field to the water storage over the course of one year. Their sum is higher than the annual thermal load since storage and distribution heat losses are also accounted.
- The energy bill saving is the monetary saving achieved over the course of one year thanks to the solar thermal collectors. The saving is calculated against a set of baseline scenarios where the solar collectors are not implemented. The bill is calculated assuming an energy price of 0.10 euro/kWh for gas and 0.20 euro/kWh for electricity, and accounts for the consumption of auxiliaries (circulation pumps). Possible subsidies to renewable energy generation are not included.

Tab. 6: Results of the energy assessment for four building typologies (hotels, hospital, dorm and offices), three locations (Rome, Stuttgart and Stockholm), two window-to-wall ratios (45% and 60%) and two tank sizes (40 l/m² and 70 l/m²)

Scenario				**Energy assessment results**							
	Climate	WWR	Tank Size	Annual solar yield	Solar fraction	Space heating thermal load	Hot water prep. thermal load	Total thermal load	Heat generated by gas boiler to tank	Heat generated by solar field to tank	Annual energy bill saving
		%	l/m²	kWh/m²	%	kWh/m²	kWh/m²	kWh/m²	kWh/m²	kWh/m²	€/year
HOTEL	Rome	45	40	414	74%	6.5	31.1	37.6	12.8	36.2	1999
			70	436	78%	6.5	31.1	37.6	11.1	38.4	2096
		60	40	487	59%	7.5	31.1	38.6	20.7	28.6	1599
			70	520	63%	7.5	31.1	38.6	18.8	30.8	1713
	Stuttgart	45	40	282	40%	20.0	31.1	51.1	37.1	25.0	1386
			70	301	43%	20.0	31.1	51.1	35.6	26.9	1472
		60	40	322	30%	22.5	31.1	53.7	45.0	19.1	1072
			70	346	32%	22.5	31.1	53.7	43.6	20.8	1156
	Stockholm	45	40	259	34%	25.2	31.1	56.3	44.6	22.9	1261
			70	278	36%	25.2	31.1	56.3	43.2	24.7	1341
		60	40	304	26%	28.0	31.1	59.1	51.7	18.0	1004
			70	326	28%	28.0	31.1	59.1	50.4	19.5	1081
HOSPITAL	Rome	45	40	508	68%	4.2	53.4	57.6	22.4	45.7	2594
			70	533	71%	4.2	53.4	57.6	20.2	48.4	2725
		60	40	582	52%	5.2	53.4	58.6	33.4	35.3	2018
			70	608	54%	5.2	53.4	58.6	31.8	37.2	2112
	Stuttgart	45	40	339	38%	17.7	53.4	71.0	50.9	30.9	1750
			70	359	41%	17.7	53.4	71.1	49.1	33.0	1854
		60	40	382	28%	20.4	53.4	73.8	60.7	23.4	1336
			70	403	30%	20.4	53.4	73.8	59.4	24.9	1414
	Stockholm	45	40	321	34%	22.3	53.4	75.7	57.4	29.1	1651
			70	341	36%	22.3	53.4	75.7	55.7	31.1	1749
		60	40	365	26%	25.3	53.4	78.6	66.7	22.3	1276
			70	386	27%	25.3	53.4	78.7	65.4	23.8	1353
DORM	Rome	45	40	411	77%	4.8	31.1	36.0	11.1	36.0	1989
			70	433	80%	4.8	31.1	36.0	9.5	38.1	2082
		60	40	486	61%	5.8	31.1	37.0	19.0	28.5	1595
			70	519	65%	5.8	31.1	37.0	17.0	30.8	1711
	Stuttgart	45	40	282	42%	18.0	31.1	49.1	35.1	25.0	1382
			70	301	44%	18.0	31.1	49.1	33.6	26.9	1471
		60	40	322	31%	20.6	31.1	51.8	43.1	19.2	1073
			70	346	33%	20.6	31.1	51.8	41.7	20.8	1155
	Stockholm	45	40	259	35%	23.0	31.1	54.1	42.3	22.9	1260
			70	278	37%	23.0	31.1	54.1	41.0	24.7	1340
		60	40	304	27%	25.9	31.1	57.0	49.6	18.0	1003
			70	326	29%	25.9	31.1	57.0	48.2	19.6	1081
OFFICE	Rome	45	40	184	88%	2.6	1.9	4.5	1.5	14.5	682
			70	199	92%	2.6	1.9	4.5	1.0	15.9	712
		60	40	247	73%	3.5	1.9	5.4	3.5	12.9	627
			70	266	77%	3.5	1.9	5.4	2.8	14.1	663
	Stuttgart	45	40	139	37%	11.2	1.9	13.1	13.4	11.4	536
			70	155	41%	11.2	1.9	13.1	12.5	12.9	586
		60	40	165	25%	13.9	1.9	15.8	18.0	8.8	421
			70	181	28%	13.9	1.9	15.8	17.3	9.9	458
	Stockholm	45	40	117	25%	13.9	1.9	15.8	18.0	9.5	431
			70	129	27%	13.9	1.9	15.8	17.5	10.7	460
		60	40	137	17%	16.9	1.9	18.8	22.6	7.2	329
			70	152	18%	16.9	1.9	18.8	22.2	8.2	357

The energy assessment shows that building type and climate greatly impact on the thermal demand in terms of overall load and composition. Conversely, the size of the water storage has no influence, and the use of different window-to-wall ratios affects only the space heating demand with limited effects on the total thermal load As expected, higher space heating loads are found for higher window-to-wall ratios and colder climates, despite the use of progressively more insulating glazing at higher latitudes. The total thermal load increases with the latitude and is general significantly higher for hotels, dorms and hospitals. For these building types, the annual hot water preparation heat represents the largest share of the total load (especially in the climate of Rome), and ranges from 31.1 kWh/m^2 in hotels and dorms to 53.4 kWh/m^2 in hospitals. In offices, the hot water preparation load represents instead the lowest share of the thermal demand and accounts for only 1.9 kWh/m^2. As exemplification, Figure 4 shows the annual thermal load for a number of building typologies and climates.

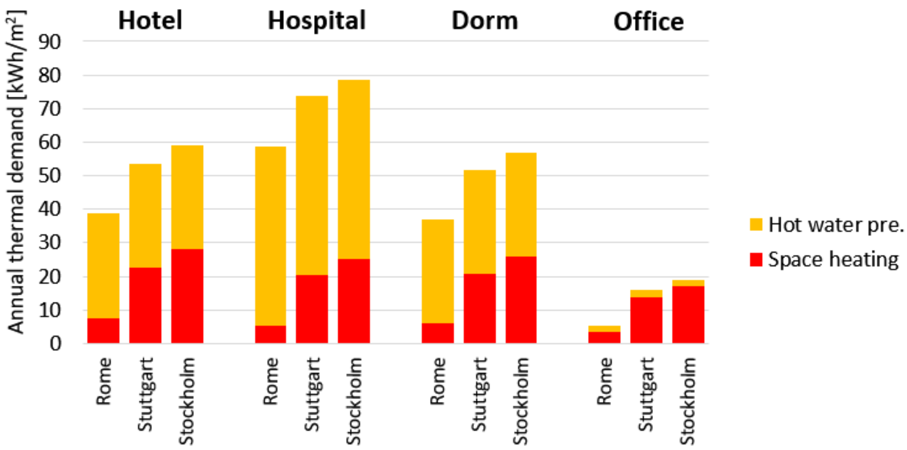

Fig. 4: Space heating and hot water preparation load for four building typologies (hotel, hospital, dorm, office) and three climates (Rome, Stuttgart, Stockholm) for WWR = 60%

Concerning the performance of the solar thermal field, it is observed that high solar coverage factors can be achieved in Rome (solar fractions ranging from 52% to 92%), whereas worse performance are reached in Stuttgart (from 25% to 44%) and Stockholm (from 17% to 37%). This is connected the availability of solar irradiation as already shown in Figure 3 and Table 5, and points to the obvious conclusion that solar systems perform better where the is abundance of solar resource. Looking at the solar yield figures, it is noticed that the building typology has a very high impact, and that even in harsher climates solar thermal collectors can have interesting solar yields in hotels, dorms and hospitals. This is because, as already seen, in these building types a large share of the thermal load is connected to hot water preparation, which shows only slight seasonal variations. It follows that in these localities it is still possible to generate valuable solar heat during summertime, when solar irradiation is not lacking and solar angles are not unfavorable as at lower latitudes. Office buildings, however, cannot exploit this opportunity, being most of their heat demand connected to space heating, which is required during wintertime.

The use of larger solar fields leads to higher solar fractions and a higher solar energy input to the storage. This growth is, however, less than proportional to the increase of the solar field area: increasing the collectors' surface of +50% (from case WWR = 60% to case WWR = 45%) leads to an increase of the solar fraction indicator ranging from 8% to 17% and of the solar field energy output from 13% to 32%, depending on climate and building typology. The reason is that larger solar fields can harvest more solar energy being the capture surface larger, but smaller solar fields are in fact exploited more intensively, as it can be clearly seen comparing the solar yield values. Given their lower energy output, smaller solar thermal systems tend indeed to work more hours with better working conditions due to the lower temperature level of the thermal system.

In all studied scenarios, the use of larger water storages enhances the solar performances of the energy system, with improvements that depend on building type and climate. For the same solar heating gain, higher water volumes allow to work with lower temperatures levels with resulting lower thermal losses in the solar pipe loop and thermal collectors. The total thermal losses through the storage mantle, however, might be higher due to the larger heat dispersing surface of the tank. Moreover, more solar heat can be stored before reaching the maximum temperature limits of the storage, thus promoting a better exploitation of the solar resource and reducing the number of stagnation hours. Furthermore, the higher thermal capacity also improves the capability of the system to store solar energy when available and meet the thermal demand when the solar irradiation levels are low or during nighttime. In the studied scenarios, it is observed that larger storages lead to higher solar fractions with improvements ranging from 1.3% to almost 5%, and better solar yields. More specifically, the largest increases of solar yield are achieved in climates with higher solar availability, for scenarios where the storage was already lower in size because of the smaller solar collectors field (that is WWR = 60%), and for specific building typologies (hotels, hospital, dorm).

As already discussed, the building typology has a substantial impact on the performances of the solar field. The best figures are achieved by the hospital building typology, with solar yields ranging between 321 kWh/m^2 and 608 kWh/m^2. The energy bill savings are also very significant, and range between 1276 euro/year and 2725 euro/year. Hotel and dorms show similar load profiles for both space heating and hot water preparation. The energy figures and the solar performances are also very close, with solar yields ranging from 259 kWh/m^2 to 520 kWh/m^2, and energy bill savings between 1003 euro/year and 2096 euro/year. Office buildings can also reach interesting solar coverages, with values in the same range as for the other building typologies. The solar yields, however, are much lower and range between 117 kWh/m^2 and 266 kWh/m^2, with energy bill savings ranging between 329 euro/year and 712 euro/year. For the office scenarios, a high number of stagnation hours is observed during summer in all climates but still the solar fraction figures remain low in Stuttgart and Stockholm. This is a clear indication that at higher latitudes the asynchrony of solar availability and thermal load throughout the year is a critical issue for solar thermal systems applied to office buildings. In the climate of Rome, instead, the solar irradiation on the South façade does not vary significantly from summer to winter, and thus a simple solution to increase solar yield and reduce overheating hours as well as the investment costs could be downsizing the solar field under 31.5 m^2 of solar collectors' area per floor, which is the lowest value tested in this study. It can be concluded that solar thermal applications such as the one proposed have a larger potential when applied to hospitals, hotels and dorms, whereas the application in office buildings should be carefully considered, especially at higher latitudes.

4. Conclusions

Based on the analyzed building and climate, one of the preliminary conclusion is that the integration of solar thermal systems into the façade of high rise buildings such as hotels, dorms and hospitals lead to interesting performances in terms of solar coverage of the thermal load and energy savings. The effects of climate and availability of solar radiation were quantified, and although the solar performances at higher latitudes are worse compared to the ones obtained in Southern locations, the possibility of covering high hot water load during summertime and mid-seasons represents a good opportunity for solar thermal systems. On the contrary, the thermal load of office buildings is primarily related to space heating and thus greatly vary during the year. This can be a critical issue at higher latitudes due to the low solar irradiation during the winter months. It was verified that larger solar fields allow to harvest solar energy, but that the increase is less proportional to the increment of solar field. For a +50% solar collectors' surface increase, an increment of the solar energy output between 13% and 32% was found depending on climate and building typology. Larger water storages consent to improve the solar yield and solar coverage, but such improvement tough not negligible remains limited to a maximum of +5% in the studied cases.

Future studies could investigate the economics of the proposed solutions, comparing estimated energy savings to the investment and maintenance costs of the solution over the lifetime of the façade. In addition, it could be interesting to compare the profitability of façade-integrated photovoltaics as alternative or complementary solution to a solar thermal field for the climates and building typologies considered in this study.

5. References

[1] IEA SHC Task 56, «Building Integrated Solar Envelope Systems for HVAC and Lighting,» 2016. [website]. Available: http://task56.iea-shc.org/.

[2] COST Action TU 1403, «Adaptive Facades Network» [website]. Available: http://tu1403.eu/.

[3] EN 50583, «Photovoltaics In Buildings-Part 1: BIPV Modules» and «Photovoltaics In Buildings-Part 2: BIPV Systems» , 2016

[4] O'Hegarty, R., Kinnane, O., & McCormack, S. (2014). A case for facade integrated solar thermal systems. In Energy Procedia: International Conference on Solar Heating and Cooling for Buildings and Industry, SHC 2014, (Vol. 70, pp. 103-110). Elsevier. DOI: 10.1016/j.egypro.2015.02.104

[5] Giovanardi, A., Integrated solar thermal façade component for building energy retrofit, PhD thesis, Eurac Research and Università degli Studi di Trento, 2012.

[6] Sánchez-Barroso, G., González-Domínguez, J., García-Sanz-Calcedo, J., (2020). Potential Savings in DHW Facilities through the Use of Solar Thermal Energy in the Hospitals of Extremadura (Spain). International Journal of Environmental Research and Public Health, 17, 2658. DOI: 10.3390/ijerph17082658

[7] SIA Zurich. SIA 2024:2015: Raumnutzungsdaten für die Energie- und Gebäudetechnik. SNR 592024:2015, 2015.

[8] Kuhn, T. E., Fath, K., Bales, C., Gustafsson, M., Nouvel, R., Fedrizzi, R., D2.3 RES availability survey and boundary conditions for simulations, FP7 Inspire project, 2014.

Experimental evaluation of stagnation-safe flat plate collectors with heat pipes for domestic hot water preparation in thermosiphon systems

Bert Schiebler, Dennis Walentin, Julian Schumann and Federico Giovannetti

Institut für Solarenergieforschung Hameln (ISFH), Am Ohrberg 1, 31860 Emmerthal (Germany)

Abstract

Overheating in thermosiphon systems, which represent the dominating solar thermal technology worldwide and are often installed in regions with water scarcity, can lead to significant water losses and to failures of the safety valve. The paper analyses the behavior of a prototype thermosiphon system, provided with a novel flat plate collector, by comparing it with a conventional system based on experimental investigations. The novel collector is equipped with specially designed heat pipes, offering an intrinsically safe solution to limit the stagnation load in the heat tank up to a desired temperature. The results of the performance tests according to ISO 9459-5 show, that the prototype system can achieve similar solar yields as the standard system (-2% to -4%, depending on the location). Stagnation measurements report a maximum temperature of 96 °C in the heat tank of the prototype. The conventional system reaches temperatures above 100 °C, which leads to a pressure increase of 3.4 bar.

Keywords: thermosiphon systems; flat plate collectors; heat pipes; stagnation, overheating protection

1. Introduction

Thermosiphon systems (TSS) dominate the solar thermal market, representing more than 75 % of the total and about 90 % of the new installations worldwide (Weiss et al. 2019). Thus, the development of efficient and cost-effective thermosiphon systems based on heat pipes has a huge potential. Heat pipes are already well-established in evacuated tubular collectors as devices to transfer the heat from the absorber plate to the solar circuit or to the hot water tank. Flat plate collectors with heat pipes, on the contrary, have only been realized within research projects so far (Jack et al. 2014).

In TSS, heat pipes offer a simple system hydraulics and enable the thermal decoupling of the absorber from the heat tank. On the basis of the so-called dry-out limit - an inherent physical effect of heat pipes - the cyclic process and respectively the heat transfer can be suppressed above a certain temperature, by choosing suitable design parameters (type and quantity of the heat carrier). For TSS the reference temperature is set below 100 °C in order to prevent boiling and the loss of water by the safety valve in case of continued overheating. It must be considered that these systems are often operated at locations where drinking water is a scarce resource. Moreover, in regions with calcareous water, a frequent opening of the safety valve at high temperatures often leads to its failure (Zörner et al. 2010). In contrast to commercially available TSS, which are already offered with cooling and safety solutions (Wagner 2014), the use of heat pipes offers a simple, cost-effective and at the same time intrinsically safe way of limiting the temperature.

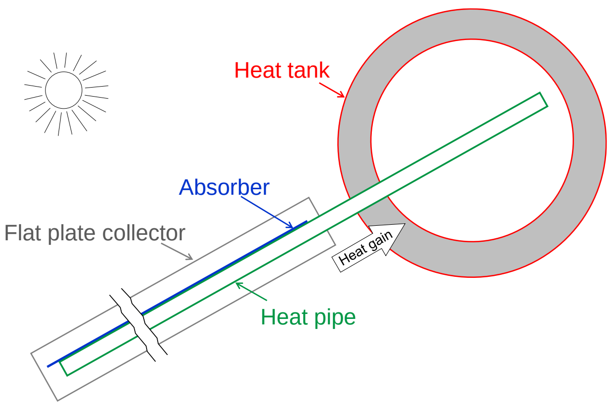

Figure 1: Section of a TSS with heat pipe in the heat flow path between the absorber plate and the domestic hot water tank

doi:10.18086/eurosun.2020.06.06 Available at http://proceedings.ises.org

2. Experimental investigation of the system behavior

2.1. Experimental setup

For a holistic assessment, we carry out comparative experimental investigations on a prototype and a standard system. The standard system is used as reference and features a classical double circuit (closed loop System) with a common flat plate collector and a double shell tank (see Figure 2, left). Thus, the natural circulation of the collector circuit fluid only runs through the outer jacket of the heat tank. The prototype system exhibits a flat plate collector with novel aluminum heat pipes. These are metallically connected to the absorber along the evaporator section and their condenser project into the heat tank (see Figure 2, right). A water-glycol mixture as well as a complex double shell heat tank are not necessary in this case. Both TSS have a collector gross area of 2 m² and a tank volume of 200 l, which represents a usual dimension for such solar thermal water heaters in Mediterranean locations. Further specifications of collectors and heat pipes are given in Table 2 (see Appendix). Figure 2 shows the standard system (a) and the heat pipe system (b) during tests at ISFH.

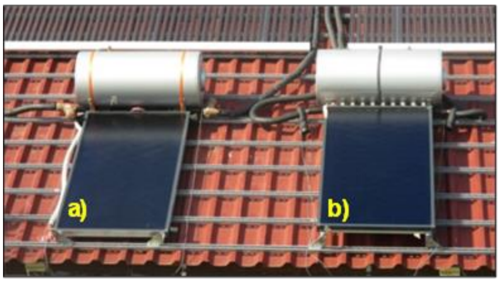

Figure 2: Experimental outdoor facility: a) standard and b) heat pipe TSS

To carry out dynamic system tests (DST), we installed a test setup according to (ISO 9459-5 2007), which can emulate hot water taps under software control (see Figure 3, left). Using suitable sensors, the energy balance around the heat tank can be determined and the system yield as well as the system performance can be specified. In addition, we installed further sensors for temperature and pressure measurement at the heat tank to evaluate the thermal loads during stagnation periods. Furthermore, we use a bypass with a pump for conditioning the heat tank by an electric heater up to high temperatures as shown in Figure 3 right. This procedure is exclusively intended to initiate stagnation sequences.

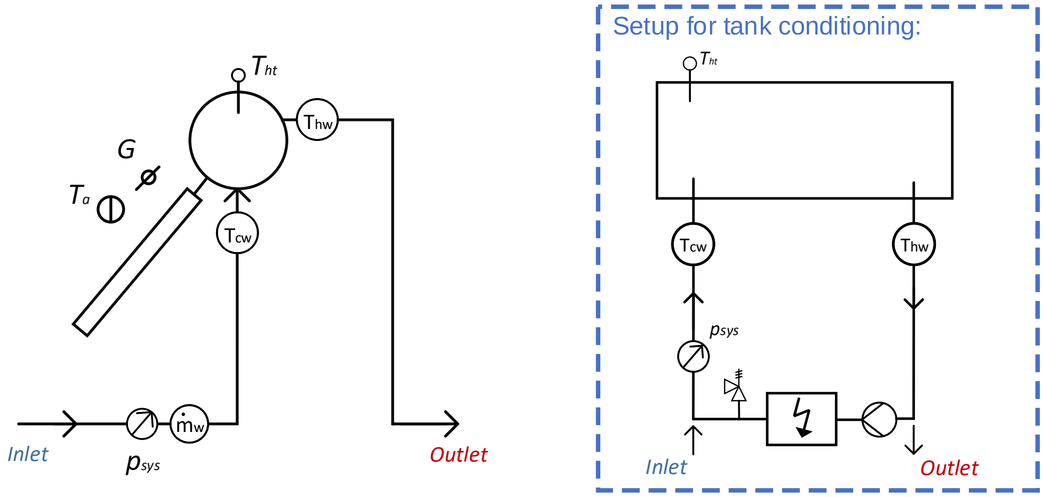

G	Global radiation	T_{cw}	Inlet temperature heat tank
T_a	Ambient temperature	T_{hw}	Outlet temperature heat tank
p_{sys}	System pressure	T_{ht}	Heat tank temperature
$\dot{m}_w$	Mass flow rate		

Figure 3: Test setup and measurement devices for dynamic system tests with TSS according to ISO 9459-5 (left) as well as for conditioning the heat tank before stagnation sequences (right)

2.2. DST System parameters

The aim of the DST procedure is to determine the performance of complete solar thermal systems under real conditions. The system is investigated under characteristic operating conditions by setting defined test sequences. Each sequence represents a separate period of measurement and needs several days. These data can be used in a system simulation to determine the annual yield. The identified model parameters of both systems are shown in Table 1.

Tab. 1: Identified model parameters of the dynamic system testing procedure for both the standard system (a) and the heat pipe system (b)

Parameters	Symbol	Unit	Standard (a)	Heat Pipe (b)
Effective collector loop area	A_C*	m²	1.05	1.04
Heat-loss coefficient of the collector loop	u_C	$Wm^{-2}K^{-1}$	4.76	5.43
Heat-loss rate of the store	U_S	WK^{-1}	2.21	1.94
Heat capacity of the heat tank	C_S	MJK^{-1}	0.79	0.77
Fraction of the store heated by the auxiliary heater	f_{aux}	-	-	-
Draw-off mixing parameter	D_L	-	0.055	0.036
Collector loop stratification parameter	S_C	-	0.015	0.019

We can see that the effective collector area A_C* of both systems differs only slightly. The real collector area and the optical properties of both collectors are identical, so that the values for A_C* are directly comparable. According to (Spirkl 1990), A_C* can be used to draw conclusions about the conversion factor η_0 and thus the quality of the thermal connection of the solar absorber to the heat tank. The value for the heat pipe system (b) is approx. 1 % lower, so that we can conclude that the heat transport capacity of both systems is almost equal. The effective heat loss coefficient u_C describes the sum of the thermal losses occurring in the collector circuit. Based on the measurement results, we found a loss coefficient of 5.4 W/m²K for the heat pipe system (b), which is about 0.7 W/m²K higher compared to the standard system (a). This effect is probably caused by the heat pipe-based temperature limitation, which can minimally affect the collector performance at high operating temperatures. However, we cannot clearly analyze these effects due to its compact design as a thermosiphon system. In addition, we can see that the heat loss rate of the heat tank U_S is correspondingly higher in the standard system (a). Both heat tanks are identical in volume and dimensions of the drinking water part (ratio of diameter and width), whereby a double shell tank is used in the standard system (a). Thus, the heat input due to natural circulation of the collector circuit fluid through the outer jacket. In the prototype system (b), the heat is transferred directly to the inner part of tank by the heat pipes, whereby the outer jacket is not used. The air filled outer jacket of (b) can lead to lower heat losses and thus to lower values of U_S. The heat tank capacity C_S of both systems differ only minimally, but this may also be due to the uncertainty of the procedure of parameter identification based on individual measurement data sets. The proportion of the auxiliary volume f_{aux} is typically > 75 % for thermosiphon systems, which are usually equipped with an electric heating rod. According to (ISO 9459-5 2007), the auxiliary heating must be deactivated during the tests and the parameter f_{aux} is not considered. The parameter D_L describes the demixing of the heat tank during tapping and S_C the stratification at the heat tank due to the input by the solar loop. Both parameters are in a similar range so that it will not be further discussed here. Because some parameters, especially u_C and U_S, are not completely independent of each other, it is advisable to consider the entire parameters in the context of a long-term prediction and quantify the total system performance instead.

2.3. System performance in operation mode

The system performance is expressed by the annual yield and was determined by operating the two systems according to the DST procedure described in (ISO 9459-5 2007). The results depend on the tapping rates and on the climatic conditions of the considered locations. In general, the differences between standard (a) and heat pipe (b) system are almost negligible for small tapping rates and increase with higher heat demands, as shown in Figure 4. The solar yield of the heat pipe system is reduced by a maximum of 5 % compared to the standard system. In Athens, representing a typical climate for TSS, the deviations in annual yield ranges between 2 and 3 %. This confirms the result of the parameters consideration in section 2.2, that both systems are almost on the same performance level.

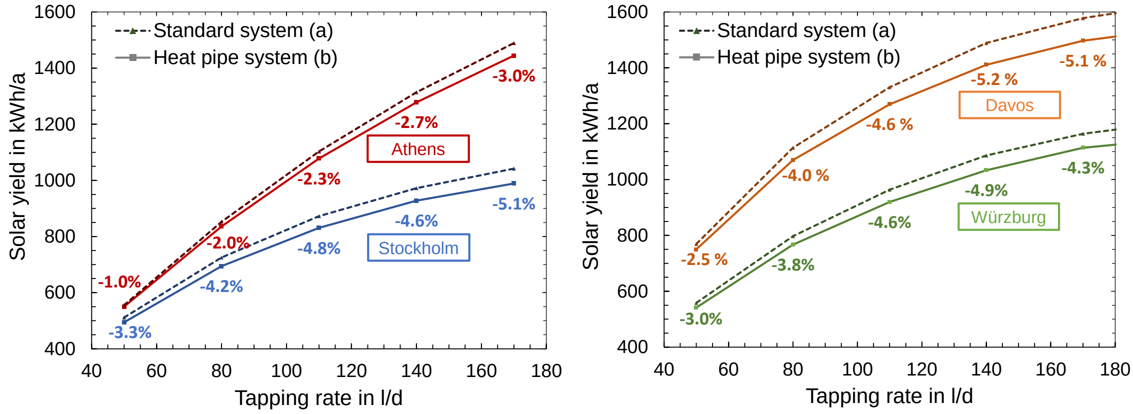

Figure 4: Solar yield of the standard system (a) and the heat pipe system (b) for all considered locations against the tapping rate

Figure 5 shows the energy balances of both systems for all considered locations at a typical tapping rate of 80 l/d. The annual hot water demand represents the sum of solar yield and auxiliary energy demand. Depending on the location, the solar yield of the heat pipe system (b) is between 17 kWh/a (Athens) and 44 kWh/a (Davos) lower, which leads to a corresponding increase in the auxiliary energy demand. Compared to the standard system (a), the maximum relative reduction of solar yield occurs in Stockholm with 4.2 %. In Athens, on the other hand, the relative deviation in solar yield is only 2 %. The deviation of the system results may be mainly due to the difference of the parameters A_C* and u_C. However, under consideration of the uncertainty of the DST method of about 5 % (Visser et al. 1997) the deviations of the prototype system can be negligible.

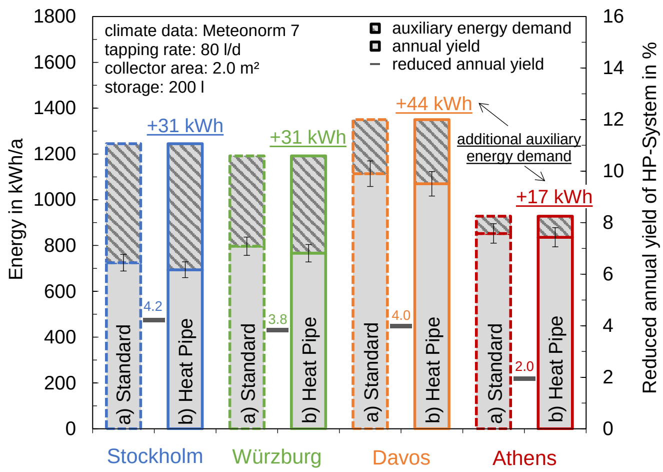

Figure 5: Annual energy balances of the standard system (a) and the heat pipes system (b) for all considered locations at a tapping rate of 80 l/d

2.4. Stagnation mode

In addition to the behavior in operation mode, we also investigate the case of stagnation using a suitable test procedure. For that, we electrically warm up both heat tanks to a temperature level of > 95 °C on a sunny day and mixed up the heat tank volume by the pump. After conditioning the heat tank, we adjust the system overpressure to about the same level (1 bar) and leave both systems exposed to the solar irradiation. This procedure should imitate several days of standstill, i.e. no tapping from the heat tank, at full solar irradiation.

Figure 6 shows the corresponding temperature and pressure curves for such a stagnation sequence. The heat tank temperature of the heat pipe system (b) remains almost constant after the conditioning procedure and amounts to a maximum temperature of 96 °C, while the absorber temperature rises to 188 °C. This results in a temperature gradient of approx. 90 K between the solar absorber and the heat tank due to the heat pipe-based power shut-off. In the standard system (a), the heat tank temperature increases to a maximum of 109 °C, which initially only means a 13 K higher thermal load compared to the heat pipe system (b). However, when looking at the system over pressure, there is a significantly pressure increase in the standard system of approx. 3.7 bar as consequence of the further increasing heat tank temperature. In contrast, the pressure in the heat pipe system remains almost unchanged.

Beforehand we expected a higher thermal load in the standard system. This can be explained by the meteorological conditions of the outdoor measurements at the ISFH. We further assumed that higher stagnation loads occur at southern European or North African locations with higher solar irradiation and higher ambient temperature. However, it should be noted that with a 3 bar safety valve or a higher outlet pressure (2 – 4 bar), which often corresponds to the pressure in drinking water systems, the safety valve would have opened several times and drinking water would have been lost.

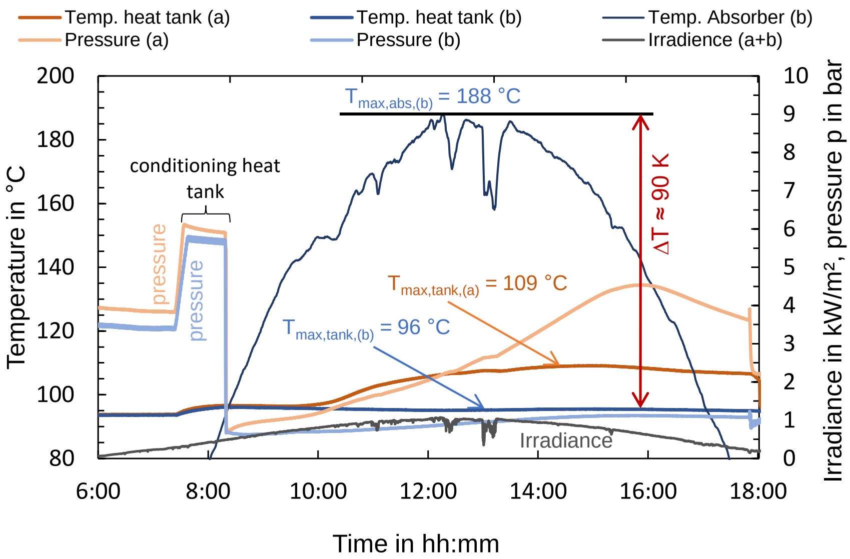

Figure 6: Temperatures and system overpressure of the standard system (a) and the heat pipe system (b) during a stagnation period at the ISFH test field

3. Cost reductions

Figure 7 shows the expected investment costs of a heat pipe system in relation to a standard system (without safety solution). The heat pipe system corresponds as far as possible to the prototype-tested version in the previous sections. We initially assumed that the costs for the collector with absorber-heat pipe solution do not differ from the standard case. According to the statement of the manufacturer, it can be expected that the additional effort for the aluminum heat pipes production can be compensated by the complete substitution of the expensive copper piping of the standard collector. A significant saving compared to state-of-the-art systems is estimated at the collector hydraulic, because the solar circuit is no longer necessary due to the use of heat pipes. Thus, a hydraulic circuit between collector and heat tank are not required. This also eliminates the costs of the solar fluid (water-glycol mixture). In addition, the costs of the drinking water tank can decrease, as a double shell tank can be replaced by a simple tank with connections for the heat pipes, which is easy to manufacture for the tank producer. Due to the elimination of collector piping, the installation procedure will be much easier. However, the additional effort to install the collector to the heat tank (inserting and sealing the heat pipes in the heat tank) will compensate this advantage. Thus, no change in the installation procedure is supposed. Overall, a cost-saving potential of about 15 % can be expected for the heat pipe-based system in terms of investment costs.

In practice, TSS with overheating protection leads to a significantly lower frequency of faults and failures. This is the reason for systems with appropriate safety solutions, which are already being offered today (Wagner 2014). The heat pipe collector automatically leads to a temperature limitation because of the thermo-physical effects inside the heat pipe, which are independent of additional mechanical components and completely intrinsically safe. In contrast, conventional safety solutions are usually based on complex cooling or compensation systems.

Compared to such systems, heat pipe based TSS can be much more cost-effective. Compared to TSS without temperature limitation, further advantages are possible due to the possible longer service life of some components as well as lower maintenance and service costs. Currently, neither any concrete data nor experience reports are available. Within the framework of planned demonstration systems, these expectations are to be checked in practice.

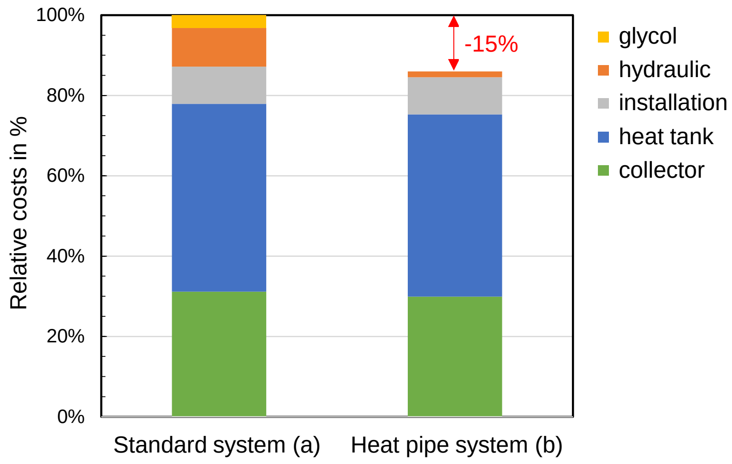

Figure 7: Expected investment costs (components and installation) of a novel heat pipe based TSS in comparison to a comparable standard system

4. Conclusion and outlook

We investigated the performance of a novel thermosiphon system with a heat pipe-based flat plate collector using dynamic system tests (DST). That prototype system achieved almost the same system performance as a comparable standard system. Depending on the location, the solar yield of the heat pipe system is less than 5 % for common domestic hot water loads. For the climate of Athens, representative for most TSS-typical locations, the solar yield is only 2 % below that of the standard system.

In addition to the system performance, we investigated the stagnation behavior using appropriate test sequences. For this, we emulated the standstill of the systems (no hot water tapping for several days) at the ISFH test field. The results show that the maximum heat tank temperature in the heat pipe system can be limited intrinsically safe to 96 °C, whereas the maximum heat tank temperature in the standard system was measured at 109 °C. We had previously been expected higher temperatures for the standard system. However, the temperature increase of 13 K results in a corresponding pressure increase. The maximum system pressure is about 3.4 bar higher than in the heat pipe system. Depending on the mains pressure, such an increase can lead to continuous triggering of the safety valve. Depending on the availability of drinking water, this means on the one hand the loss of a valuable resource. On the other hand, a permanent opening of the safety valve at high temperatures leads to leaks and ultimately to its failure (especially in regions with calcareous water). It is to be expected that this problem can be reduced by limiting the further overheating of the heat tank, even if it is only 10 – 20 K. Unfortunately, concrete data and experience reports from thermosiphon systems at locations with high solar irradiation are difficult to obtain.

An estimation of the component costs shows that the main advantages of heat pipe based thermosiphon systems result from the much simpler system hydraulic. Overall, the considered heat-pipe system is expected to have 15 % lower investment costs compared to the state of the art. In prospective activities, the heat pipe systems need to prove in real system operation so that statements on lifetime and maintenance costs are determined.

5. Acknowledgments

The two projects "Cost effective and reliable solar systems with novel heat pipe collectors" (reference number 0325550A-C) and “Development and demonstration of innovative, stagnation safe solar thermal systems with heat-pipes collectors” (reference number 03ETW005A-C) underlying this publication were funded by the state of Lower Saxony and the German Federal Ministry of Economy and Energy, following a decision of the German Parliament. The investigations are carried out in cooperation with the companies KBB Kollektorbau GmbH, NARVA Lichtquellen GmbH & Co. KG and AKOTEC Produktionsgesellschaft mbH.

The authors are grateful for the support. The responsibility for the content of this publication lies with the authors.

6. References

ISO 9459-5, 2007: System performance characterization by means of whole-system tests and computer simulation. Beuth Verlag, Berlin

Jack S., Parzefall J., Luttmann T., Giovannetti F., 2014. Flat plate aluminium heat pipe collector with inherently limited stagnation temperature. Energy Procedia 48 p. 105-113

Schiebler B., Weiland F., Giovannetti F., 2017. Experimental evaluation of evacuated tube collectors with heat pipes to avoid stagnation loads in a domestic hot water system, ISES SWC-Conference, 29 October -03 November 2017, Abu Dhabi, Conference proceedings p. 2117-2126

Spirkl W., 1990. Dynamische Vermessung von Solaranlagen zur Warmwasserbereitung, VDI-Fortschrittberichte, Reihe 6: Energieerzeugung Nr. 241

Spirkl W., 1997. Dynamic System Testing Program Manual, InSitu Scientific Software

TÜV-Rheinland, 2014. Solar KEYMARK Certificate Licence Number 011-7S471 R. DIN CERTCO, Berlin

Visser H., 1997. Dynamic Testing of Active Solar Heating Systems, Final Report of the IEA SHC – Task 14 Dynamic Component and System Testing Subtask Software

Wagner & Co, 2014: SECUterm 160 P / 200 P / 300 P, Thermosiphon-System zur Freiaufstellung, Technical information / Installation instruction

Weiss W., Spörk-Dür M., 2019: Global Market Development and Trends in 2018, Detailed Market Figures 2017. Solar Heat Worldwide

Zörner W., Brandmayer S., 2010: Forschungsvorhaben – Optimierte Thermosiphon-Solaranlagen: Schaffung wissenschaftlicher Grundlagen und Entwicklung einer marktangepassten, seriennahen Prototyp-Anlage. Final report (AZ: 25027-24/2), Ingolstadt

7. Appendix

7.1. Specifications of the collectors and heat pipes

Tab. 2: Specific collector / heat pipe parameter for the standard system (a) and the heat pipe system (b)

Parameter	Standard (a)	Heat Pipe (b)
Heat pipe evaporator length	-	1.850 m
Heat pipe transport zone length	-	0.172 m
Heat pipe condenser length	-	0.287 m
Heat pipe diameter (evaporator)	-	0.008 m
Heat pipe diameter (condenser)	-	0.008 m
Number of heat pipes per collector	-	10
Heat pipe heat carrier fluid	-	Butane (3.74 g)
Maximum temperature heat pipe process	-	107 °C
Aperture area collector	1.83 m²	1.83 m²
Cross area collector	2.02 m²	2.02 m²
Heat tank volume	200 l	200 l

Electrodeposited and Sputtered Selective Coatings for Solar-to-Thermal Energy Conversion

Lizama-Tzec F.[1], Pérez-Espinoza R.[2], Vega-Poot A.[1], Herrera-Zamora D.[1], Becerril-González J.[1], Cetina-Dorantes M.[1], Rodriguez-Gattorno G.[1], Ares-Muzio O.[1], García-Valladares O.[3], Oskam G.[1]

[1]Departamento de Física Aplicada, Centro de Investigación y de Estudios Avanzados del IPN, Mérida, Yucatán, México.

[2]Módulo Solar S.A. de C.V., Calle 23 Este No. 3, Col. CIVAC, 62578, Jiutepec, Morelos, México.

[3]Instituto de Energías Renovables de la Universidad Nacional Autónoma de México (IER-UNAM), Privada Xochicalco s/n, 62580, Temixco, Morelos, México.

Abstract

In this work, we report on the deposition and characterization of selective coatings for solar-to-thermal energy conversion systems for applications of low to medium temperatures. Both sputtering and electrodeposition were used to deposit the layers of typical multilayer coatings. The completely electrodeposited selective films consist of an infrared reflecting nickel interlayer on stainless steel, and a black nickel solar absorber material. An alumina/molybdenum/alumina (AMA) multilayer absorber material was deposited by sputtering on stainless steel and copper with electrodeposited nickel (Cu/Ni). The optical properties of the films were studied as a function of the thermal treatment and were compared with similar selective coatings with sputtered alumina as antireflective coating. The films were thermally treated and characterized by reflectance spectroscopy, FESEM, DSC, XRD, profilometry and Raman measurements. Finally, we report on the scale-up of these films, and the results obtained on individual fin collectors showed that our selective coatings exhibit a performance close to the benchmark coating in the market.

Keywords: Electrodeposition, Sputter deposition, Solar-to-Thermal Energy Conversion,

1. Introduction

Selective coatings for solar thermal applications are usually obtained by sputtering or electrodeposition (Wackelgard, Ewa; Hultmark, 1998), (Wäckelgard, 1998), (Gogna and Chopra, 1979), (Nunes et al., 2018), (Manson and Brendel, 1982), (Patel et al., 1985), (Abbas, 2000), and a wide range of systems has been reported (Boström et al., 2004), (Boström et al., 2007), (Khatibani and Rozati, 2016). However, there are still many systems left to explore, in particular when combining sputter-deposited layers with electrodeposited layers in a single system. Also, within both the electrodeposition and sputter deposition methods, there are still many variables that may be evaluated to improve performance. The current market for selective coatings is dominated by coatings obtained by PVD (physical vapor deposition), but several companies that use electroplating are gradually obtaining a part of the market (Berner, 2016). Currently no company combines the advantages of electroplating with PVD technologies to have better coatings. In this work, we evaluated the performance and feasibility of obtaining a deposit based on electrodeposition of selective coatings and the application of antireflective coating by sputtering on stainless steel and copper, both for smaller area and for industrial size substrates. We have obtained selective coatings on copper and stainless steel and evaluated their optical properties and thermal stability. The main motivation is to determine the most suitable synthesis conditions for the scale-up towards functional pieces. The pieces have been applied in a single fin collector system, and the several coatings have been evaluated and compared against commercial Cu-TiNOX coating.

doi:10.18086/eurosun.2020.06.07 Available at http://proceedings.ises.org

2. Experimental

For the films obtained by electroplating, a potentiostat-galvanostat Gamry Reference 3000 was used, employing stainless steel (AISI 304) pieces of 0.04 m x 0.06 m as substrate. The stainless steel was used to study the thermal performance of the black nickel absorber film. The stainless steel substrate was initially treated with a nickel strike bath under the conditions previously reported (Lizama-Tzec et al., 2014). The selective coating electrodeposition procedure for the bright nickel film was from a modified Watts bath at -50 A m^{-2} and the black nickel film was electrodeposited from a plating bath based on $NiCl_2$ and NaCl. The films were obtained by applying two pulses of 60 s at -26 A m^{-2} and 90 s at -14 A m^{-2}. The electrodeposition area was 0.0016 m^2. After black nickel electrodeposition, a thin film of 300 nm alumina was applied. For the deposition of alumina, the RF sputtering technique was used at 280 W; the chamber was evacuated to 1.3 x 10^{-3} Pa and an argon atmosphere was employed. Magnetron guns with targets of alumina were used to deposit the alumina coatings. The AMA deposition process was optimized on borosilicate glass (2.6 cm x 7.6 cm x 1 mm) and after that applied to stainless steel. These coatings are composed of 3 layers: Al_2O_3-Mo-Al_2O_3 from top to bottom. The alumina films (90 nm) and the Mo intermediate layer (10 nm) were deposited using RF-sputtering at 0.93 Pa of argon pressure and a power of 280 W. The samples were subjected to thermal treatment processes in a muffle furnace (Thermo Scientific, model FB1315M), consisting in one heating cycle for the stainless steel samples at 250 ºC for 200 hours at a heating ramp of 0.16 ºC s^{-1} for substrates. The selective coatings were obtained under the conditions and treatments listed in Table 1.

Tab. 1: Methods used for the preparation and thermal treatments of selective coatings prepared on this work.

Sample	Current Density (A m^{-2})	Time (s)	Treatment Temperature (ºC)	Time (h)
SS/Ni/NB	-26/-14	60/90	N/A	N/A
SS/Ni/NB thermally treated	-26/-14	60/90	250	200
SS/Ni/NB/Alumina	-26/-14	60/90	N/A	N/A
SS/Ni/NB/Alumina-thermally treated	-26/-14	60/90	250	200
SS/AMA	N/A	N/A	400	2

The selective coatings were characterized by relative total reflectance spectroscopy (Shimadzu Corporation, 2013) using a UV-Vis spectrophotometer (Avantes, model Avaspec 2048, in the wavelength range: 0.3 to 2.5 µm), and an infrared spectrometer (Avantes, model Avaspec-Nir 256-2.5), both with an integrating sphere (Avantes, model 50-Ls-HAL). For the UV-VIS-NIR measurements, the AVANTES WS-2 white reflective tile, consisting of a white, diffuse, high-grade PTFE material, was used as the reference. The reflectance spectra obtained in the range of 2.5 to 15 µm was obtained with an FTIR spectrometer (Perkin Elmer, Frontier NIR/MIR model), equipped with an integrating sphere (PICO, Integrat IR model), and a gold standard was used as the reference. The solar absorptance was determined by weighting the reflection spectrum against the solar radiation spectrum ASTM G173-0329, using equation (1). To approximate the thermal emittance at maximum real operating conditions of the devices, the emittance was calculated using T= 250 ºC in equation (2). To determine the thermal emittance, the reflection of the coatings was measured by weighting the reflection spectrum against the blackbody radiation at 250 ºC. The corresponding equations are:

$$\alpha = \frac{\int_{0.3}^{2.5} I_{SUN}(\lambda)\,[1-\rho(\lambda)]d\lambda}{\int_{0.3}^{2.5} I_{SUN}(\lambda)} \qquad \text{(eq. 1)}$$

$$\varepsilon = \frac{\int_{2.5}^{15} I_b(\lambda)\,[1-\rho(\lambda)]d\lambda}{\int_{2.5}^{15} I_b(\lambda)} \quad \text{(eq. 2)}$$

where $\rho(\lambda)$ is the wavelength dependent reflectance, and the black body radiation as a function of wavelength and temperature is given by $I_b(\lambda, T) = c_1/\left\{\lambda^5\left[e^{\left(\frac{c_2}{\lambda T}\right)} - 1\right]\right\}$ with c_1 = 3.743x10^{-16} W m^2 and c_2 = 1.4387x10^{-2} m K.

The wavelength limits in the integral are chosen according to our experimental capabilities. The electrodeposited films were studied by field emission scanning electron microscopy (FESEM) (JEOL JSM-7600F), X-ray diffraction (XRD) was performed using a Siemens D-5000 for the analysis of the selective film and for the analysis of the black nickel powder, a Bruker D8-Advance with a Bragg-Brentano geometry was used. Both use monochromatic Cu-Kα radiation (λ = 1.5418 Å). To study the oxidation process at distinct temperatures in the black nickel film and to differentiate from the bright nickel underlayer, the black nickel films were electrodeposited directly on stainless steel at the same conditions as for SS/Ni/NB films. The black nickel film average thickness before and after thermal treatments were 290±10 nm and 260±10 nm respectively, the sampling area was 5 x 10^{-5} m^2. The film thickness was measured with profilometry using a KLA-Tencor D-120. The thickness of the alumina films was 300±10 nm.

Black nickel powder was also analyzed to determine the effects of interaction between the substrate and black nickel under thermal treatment. Black nickel powder was obtained by scraping the material off the SS substrate with electrodeposited black nickel film. The powders were further characterized using differential scanning calorimetry (DSC) using a TA Instruments, Discovery TGA series. The samples were heated in air at temperature range of 25 °C to 500 °C.

Raman spectroscopy measurements were performed at room temperature (25 °C) using 488 nm and 633 nm laser light (1 x 10^{-3} W) in a confocal Raman spectrophotometer (Alpha 300, WiTec) for excitation in a back-scattering geometry. The confocal microscope with a 50X objective on a triple spectrometer was operated in the subtractive mode. It was equipped with a detector illuminated by backlighting; the Raman signal was calibrated with a Si reference. The measurements were performed in three points on each sample, and generally the characteristics observed in each spectrum were independent of location.

The scale-up was achieved by using the experimental conditions for the films obtained on 0.0016 m^2 SS samples and using a steel electrochemical plating cell covered with an anticorrosion ceramic coating of 2 m long, 0.36 m wide, and 0.3 m high. The counter electrodes consisted of nickel rounds in titanium baskets and the current was applied with a power supply. In the case of copper fins, the nickel strike film was not applied. The tube and sheet of the copper fins were welded by ultrasound. The size of the sheet of copper fins was 1.9 m long and 0.107 m wide. The sputtering chamber used for the deposition of alumina on 0.0016 m^2 samples was also used to deposit alumina and AMA coatings on electrodeposited nickel-coated copper fins. The chamber was provided with lateral side arms of 2 m to house the copper fins and contains a system for moving the pieces. Alumina and molybdenum magnetrons of suitable size were used.

3. Results

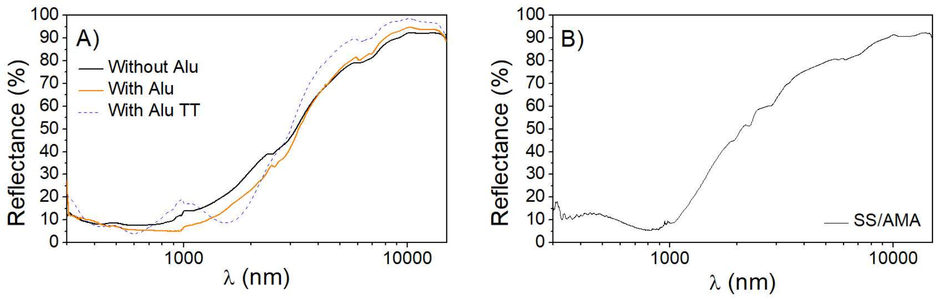

Fig. 1: A) Reflectance spectra for electrodeposited SS/Ni/NB with sputtered alumina with thermal treatment (TT) at 250 °C for 200 hours. B) Reflectance spectrum for SS/AMA.

The Figure 1 A) shows the reflectance spectra for electrodeposited Ni/NB on stainless steel substrates with alumina before and after thermal treatment. In the graph it is possible to observe that the absorptance increased when the alumina was present as shown in Table 2. After the thermal treatment, between 300 nm to 2500 nm some interference peaks appear related with the coupling between the refractive indices of the black nickel and the alumina. The thermal emittance decreased related with the increase of the slope in the infrared range; this could be explained by the recrystallization of the bright nickel interlayer after the thermal treatment. Figure 1 B) shows the reflectance curve for the sputtered AMA coating on stainless steel. The graph for the thermally treated sample at 250 ºC was superimposed with the as-deposited film, showing the thermal stability of this coating at the treatment temperature.

Tab. 2: Optical values calculated with equations 1 and 2 for the deposited selective coatings before and after the thermal treatment.

	α 0.3-2.5 μm (%)	ε at 250 °C 2.5-15 μm (%)	Alumina (Alu) thickness (nm)	AMA thickness Alu/Mo/Alu (nm)	Spectral selectivity $S=\alpha-0.5\varepsilon$ (%)
SS/Ni/NB	88 ± 1	16 ± 1			80 ± 1.4
SS/Ni/NB	92 ± 1	16 ± 1	300		84 ± 1.4
SS/Ni/NB TT	90 ± 1	10 ± 1	300		85 ± 1.4
SS/AMA	89 ± 1	10 ± 1		90-10-90	84 ± 1.4
SS/AMA TT	89 ± 1	10 ± 1			84 ± 1.4

In the reflectance graph for the thermal treated samples several bands were observed, which can be attributed to interference effects or effects of interdiffusion substrate components towards the absorber film. In order to try to explain the observed changes in reflectance for the films with alumina, DSC measurements were performed. Figure 2 A) shows the DSC measurement for the black nickel powder. From 250 ºC to 300 ºC a shoulder can be observed related with $Ni(OH)_2$ crystallization to NiO. From 342 ºC to 450 ºC another exothermic shoulder can be observed related to Ni oxidation in the black nickel film. The above observations can be correlated with X-ray diffraction results in Figure 2 B). The measurement for the powder that was not treated shows reflections for Ni metal. For the sample treated at 250 ºC, an additional reflection related with NiO is observed. After thermal treatment at 350 ºC the peaks for metallic nickel decrease and the peaks for NiO become more intense.

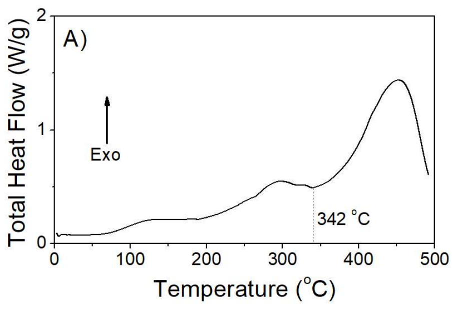

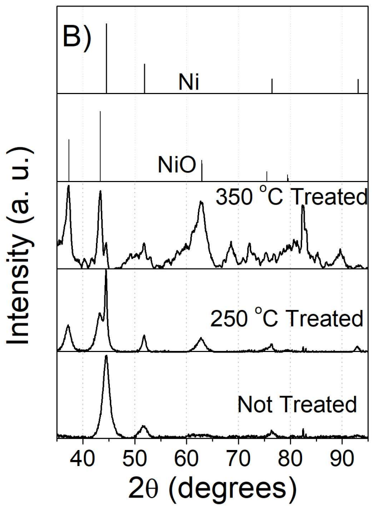

Fig. 2: A) DSC measurements for black nickel powder. B) XRD measurements for black nickel powders obtained from electrodeposited films. The reference pattern for NiO was according to the International Centre for Diffraction Data (ICDD) Powder Diffraction File PDF 073-1559, and for Ni was the PDF pattern 004-0850.

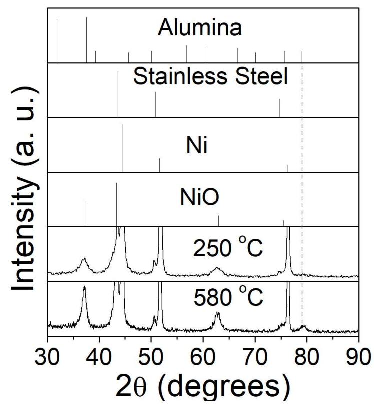

Fig. 3: XRD measurements for SS/Ni/NB with alumina after thermal treatment at 250 °C and 580 °C. Diffraction peaks of stainless steel were found according to the International Centre for Diffraction Data (ICDD) Powder Diffraction File (PDF) PDF 33-0397, The reference pattern for NiO was the PDF 073-1559, for Ni was the PDF pattern 004-0850 and the alumina PDF pattern was 047-7292.

The X-ray diffraction patterns for the SS/Ni/NB/Alu films only show peaks related with bright nickel and stainless steel. The thermally treated samples only show peaks for nickel, stainless steel, and nickel oxide, indicating that the alumina deposited was amorphous and that the thermal treatment at 250 ºC did not crystallize the film. For the sample treated at 580 ºC peaks for alumina were detected indicated with a dotted line in Figure 3.

Figure 4 shows the SEM images of the electrodeposited films before and after thermal treatment. In Figure 4 A) the nanostructured porous morphology of black nickel film is observed; it is formed by nanoflakes vertically oriented to the substrate. In Figure 4 B) it is possible to observe that the nanoflakes are composed of smaller spherical aggregates, but the morphology does not change after thermal treatment. Figure 4 C) shows the morphology of the sample covered with alumina after treatment at 250 ºC: the samples were covered without cracks or voids and the nanoflakes were completely covered with alumina. In the film with 300 nm alumina a homogeneous and compact morphology exists.

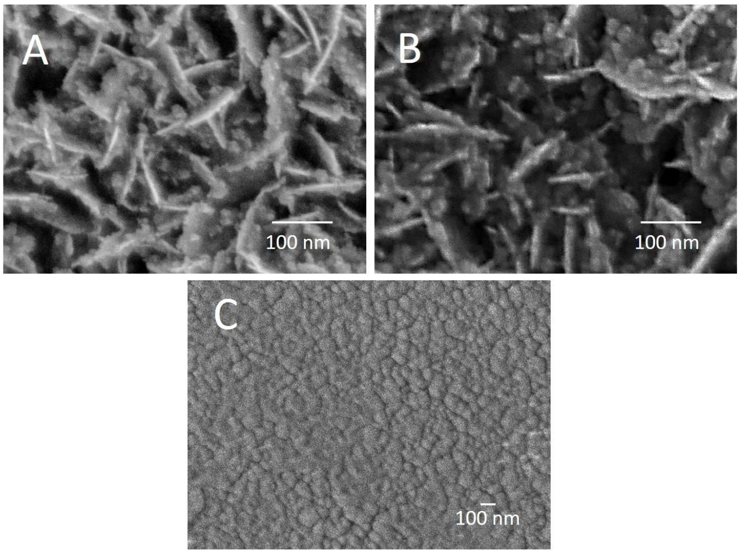

Fig. 4: SEM images for black nickel films: A) without thermal treatment; B) after thermal treatment; and C) alumina film on top of SS/Ni/NB after thermal treatment at 250 ºC.

With the intention to corroborate that after the treatment at 250 ºC the components of the substrate did not diffuse towards the absorber surface; RAMAN measurements were performed. Figure 5 shows the reference spectra of NiO, $Ni(OH)_2$ and NiOOH. The NiO and NiOOH spectra were taken of the RRUFF data base and the $Ni(OH)_2$ spectrum was obtained from an electrodeposited film on stainless steel. From 400 cm^{-1} to 650 cm^{-1} overlapping shoulders can be observed in the two samples, both with and without thermal treatment. For the sample after treatment at 250 ºC, it was found that the shoulders at 1390 cm^{-1} and 1610 cm^{-1} disappear, in concordance with the DSC measurements that showed that at this temperature $Ni(OH)_2$ crystallizes. This measurement emphasizes the thermal stability of the films at this temperature and shows that components from the substrate do not diffuse towards the absorber film.

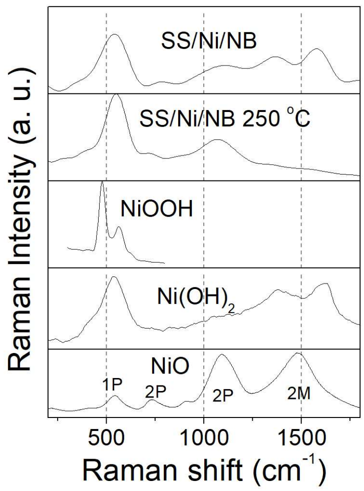

Fig. 5: Raman measurements for black nickel films with and without thermal treatment.

Once the characteristics of black nickel and AMA films were studied on stainless steel, we proceeded to build and evaluate solar collectors with copper fins coated with Ni/NB/Alu, and fins with electrodeposited nickel and sputtered AMA. The collectors were evaluated according the Mexican standard NMX-ES-001-NORMEX-2005 (“NORMA NMX-ES-001-NORMEX-2005, Energía solar – rendimiento térmico y funcionalidad de colectores solares para calentamiento de agua – método de pruebas y etiquetado,” 2005).

The stagnation temperature is known to be less than 200 ºC for these devices so the results obtained on stainless steel for SS/Ni/NB/Alu and SS/AMA coatings are representative for these systems on copper. In addition, the stability of selective coatings on copper was previously studied (Estrella-Gutiérrez et al., 2016). We found that at 200 ºC the bright nickel act as diffusive barrier to copper atoms. The performance of the fins was compared with the Cu-TiNOX. The Cu-TiNOX is a benchmark selective coating in the market. The thermal efficiency of built solar collectors with electrodeposited/sputtered fins was calculated from equation 3 where ṁ is the mass flow of water (kg s^{-1}), C is the specific heat of water (4186 J kg^{-1} K^{-1}), G is the solar irradiance (W m^{-2}), A is the collector aperture area (m^2). The results are shown in Table 3.

$$\eta = \frac{\dot{m}C\,(T_{out} - T_{in})}{GA} = \frac{Q_u}{GA}$$ (eq. 3)

Tab. 3: Results of the characterization of single-fin collectors; the aperture area of the collectors was 0.43 m^2. The transmittance (τ) of the collector glass was 0.85±0.01. A = 0.2 m^2

Fin	T_{in} (ºC)	T_{out} (ºC)	Solar Irradiance (W m^{-2})	ΔT (ºC)	Q_u (W)	η (%)	α (%)	ε (%)	Optical efficiency (ατ)
Cu/Ni/NB/Alu	64.3	67.0	1029.5	2.8	84	40	88.5±0.1	11.2±0.1	0.752
Cu/Ni/AMA	67.2	69.9	864.0	2.6	84	48	89.0±0.1	8.0±0.1	0.756
Cu/TiNOX	63.7	66.5	1013.2	2.8	92	45	92.0±0.1	6.0±0.1	0.782

From Table 3 it can be observed that the performance of the fins with AMA was higher than for the TiNOX fin, and the fin with alumina shows a similar efficiency value. The theorical optical efficiency was calculated as ατ. The results show that the experimental efficiency of the solar collectors is not only a function of the optical properties related with the highest theoretical optical efficiency. Instead, the difference between the trends observed for the optical and experimental efficiencies illustrate that additional factors play a role.

4. Conclusions

Selective coatings obtained by sputtering and electroplating show promising optical properties after thermal treatment, and both processes were scaled-up towards solar collectors. The performance of individual fin collectors with Cu/Ni/BN covered with alumina and the Cu/Ni/AMA coatings was found to be close to the benchmark selective coating. XRD and DSC measurements showed the temperature range of thermal stability of black nickel powder. From the experimental result we can conclude that the use of mixed techniques was promising for the preparation of selective coatings with excellent thermal performance.

5. Acknowledgments

The authors are grateful for the financial support received from the Institute of Renewable Energies (IER-UNAM), through the Mexican Center for Innovation in Solar Energy (CeMIE-Sol), within the framework of the 2013-02 Call, of the CONACYT SECTORIAL FUND -SENER-ENERGY SUSTAINABILITY, within the Strategic Projects 69, 18 and 81, through which it was possible to develop research and support the training of human resources at the postgraduate level. We also gratefully acknowledge the help of Willian Cauich, Beatriz Heredia, Dora Huerta, Daniel Aguilar, and José Bante-Guerra by the characterization of the materials, and the National Laboratory for the Study of Nano and Biomaterials (LANNBIO) for the use of the equipment.

6. References

Abbas, A., 2000. Solchrome solar selective coatings - an effective way for solar water heaters globally. Renew. energy 19, 145–154. https://doi.org/10.1016/S0960-1481(99)00028-2.

Berner, J., 2016. Manufacturers of thin coatings need to have a thick skin. Sun Wind Energy 4, 38–41.

Boström, T., Westin, G., Wäckelgård, E., 2007. Optimization of a solution-chemically derived solar absorbing spectrally selective surface. Sol. Energy Mater. Sol. Cells 91, 38–43. https://doi.org/10.1016/j.solmat.2006.07.002.

Boström, T.K., Wäckelgård, E., Westin, G., 2004. Anti-reflection coatings for solution-chemically derived nickel - Alumina solar absorbers. Sol. Energy Mater. Sol. Cells 84, 183–191. https://doi.org/10.1016/j.solmat.2003.12.015.

Estrella-Gutiérrez, M.A., Lizama-Tzec, F.I., Arés-Muzio, O., Oskam, G., 2016. Influence of a metallic nickel interlayer on the performance of solar absorber coatings based on black nickel electrodeposited onto copper. Electrochim. Acta 213, 460–468. https://doi.org/10.1016/j.electacta.2016.07.125.

Gogna, P.K., Chopra, K.L., 1979. Selective black nickel coatings on zinc surfaces by chemical conversion. Sol. Energy 23, 405–408. https://doi.org/10.1016/0038-092X(79)90148-8.

Khatibani, A.B., Rozati, S.M., 2016. Spray pyrolytically grown NiAlOx cermets for solar thermal selective absorbers: Spectral properties and thermal stability. Bull. Mater. Sci. 39, 97–107. https://doi.org/10.1007/s12034-015-1146-y.

Lizama-Tzec, F.I., Macías, J.D., Estrella-Gutiérrez, M.A., Cahue-López, A.C., Arés, O., de Coss, R., Alvarado-Gil, J.J., Oskam, G., 2014. Electrodeposition and characterization of nanostructured black nickel selective absorber coatings for solarthermal energy conversion. J. Mater. Sci. Mater. Electron. https://doi.org/10.1007/s10854-014-2195-5

Manson, J.J., Brendel, T.A., 1982. Maxorb -a new selective surface on nickel. SPIE 324, 139–145.

NORMA NMX-ES-001-NORMEX-2005, Energía solar – rendimiento térmico y funcionalidad de colectores solares para calentamiento de agua – método de pruebas y etiquetado, 2005. . Secr. Energ. 1–65.

Nunes, R.A.X., Costa, V.C., Sade, W., Araújo, F.R., Silvaa, G.M., 2018. Selective surfaces of black chromium for use in solar absorbers. Mater. Res. 21. https://doi.org/10.1590/1980-5373-mr-2017-0556.

Patel, S.N., Inal, O.T., Singh, A.J., Scherer, A., 1985. Optimization and thermal degradation study of black nickel solar collector coatings. Sol. Energy Mater. 11, 381–399. https://doi.org/10.1016/0165-1633(85)90010-3

Shimadzu Corporation, 2013. C101-E127 UV Talk Letter 12, 1–12.

Wackelgard, Ewa; Hultmark, G., 1998. Industrially sputtered solar absorber surface. Sol. Energy Mater. Sol. Cells 54, 165–170. https://doi.org/DOI: 10.1016/S0927-0248(98)00067-1.

Wäckelgard, E., 1998. Characterization of black nickel solar absorber coatings electroplated in a nickel chlorine aqueous solution. Sol. Enegy Mater. Sol. Cells 56, 35–44.

Optimized Design of the Insulating Gas Layer in Solar Thermal Collectors

Pascal Leibbrandt, Thomas Schabbach

Institut für Regenerative Energietechnik, University of Applied Sciences Nordhausen (Germany)

Summary

The aim of the investigations shown here is to further investigate the convective heat losses in insulation gas layers. These investigations are relevant for the design of the thickness of the insulation gas layer, as this is a main factor influencing the reduction of convective losses. The example used here of the solar glass collector is an extension of the insulating glass collector. The studies on the solar glass collector led to the results shown here, too. In recent studies based on CFD simulations and experimental measurements, deviations from the standard calculation approach by Hollands (1976) are identified and corrected with a correction function. The results shown here apply this correction function to the dimensioning of the thickness of the insulation gas layer. The convective heat transfer coefficient in the gas layer differs up to approx. 30% regarding Hollands (1976).

Keywords: Heat Transfer, Convective Heat Transfer, Conductive / Quasi-Conductive Regime, Calculation Approach, Insulating Glass, Solar Collector, Glass Cavity, Correction Function

1. Problem Definition

To guarantee an optimal collector efficiency, the convective front loss through the insulating gas layer is investigated. The gas volume, filled with insulating gas or air has a length L_{20}, a width B_{20} and a thickness s_{20}, see fig. 1. The resulting aspect ratio is $AR = AR_{20} = L_{20}/s_{20}$.

The most used approach to calculate the convective heat transfer was investigated by Hollands (1976) using an aspect ratio of AR = 48. The boundary conditions / assumptions are also: isothermal glass surface temperatures $T_{11}(x, y)$ and $T_{33}(x, y)$, respectively T_{13} and T_{31}, a gas layer pressure p_{20} and a tilt angle φ.

Other research also dealt with experimental and theoretical approaches to the determination of the convective heat transfer coefficient in gas layers. Especially Bartelsen (1993) and Föste (2013) showed that measured data from flat-plate collectors led to higher heat transfer coefficients about 10% regarding to Hollands (1976). Measurements by Föste (2013) on isolating glass collector showed a deviation up to 32%. Yiqin (1991) also investigated mean differences up to 10% in the heat transfer. Eismann (2015) presents analytically derived correction parameter, which was adapted to non-isothermal boundary conditions and highly selective coatings. Own results of the authors Leibbrandt (2016), Leibbrandt (2017) and Leibbrandt (2018) describe recent CFD simulations that deal with the topic and reveal new findings. The aim of the investigations presented here is to determine the convective heat transfer coefficient $h_{20,c}$ in the gas layer between the surfaces (13) and (31), see fig. 1.

doi:10.18086/eurosun.2020.06.08 Available at http://proceedings.ises.org

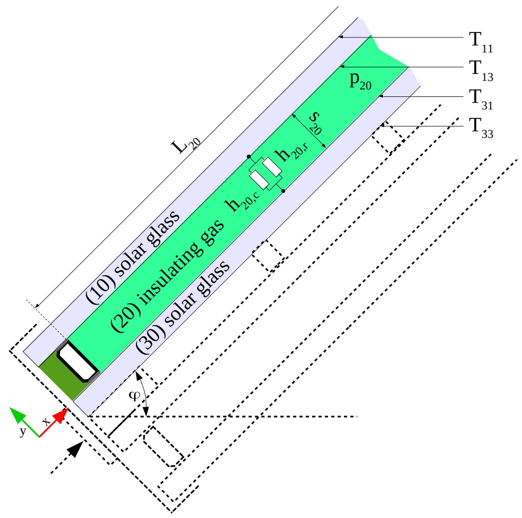

Fig. 1: Geometry and boundary conditions

2. Heat transfer in enclosed Insulating Gas Layers heated from below

The heat losses at the front of the collector are largely determined by internal free convection and radiation. The heat transfer flow is

$$\dot{Q} = A_{20} \cdot h_{20} \cdot (T_{31} - T_{13}) \qquad \text{(eq. 1)}$$

With the area $A_{20} = L_{20} \cdot B_{20}$. The total heat transfer coefficient h_{20} consists of the shares for the convective heat transfer coefficient $h_{20,c}$ and the radiative heat transfer coefficient $h_{20,r}$. It is

$$h_{20} = h_{20,c} + h_{20,r} \qquad \text{(eq. 2)}$$

The convective heat transfer coefficient $h_{20,c}$ is calculated from the Nusselt number Nu, which is specified for free convection from eq. 3 with the Rayleigh number Ra,

$$Nu = Nu(Ra) \qquad \text{(eq. 3)}$$

Hollands (1976) developed the following eq. from experimental measurements. The eq. is split in three parts, depending on the Rayleigh number considered in the problem. The part […]+ activates the terms in brackets for different Rayleigh numbers regimes. It is $[\dots]^+ = (|[\dots]| + [\dots])/2$.

$$Nu = 1 + 1.44 \cdot A \cdot [B]^+ + [C]^+ \qquad \text{(eq. 4)}$$

With:

$$A = 1 - \frac{1708 \cdot (\sin(1.8 \cdot \varphi))^{\frac{1}{6}}}{Ra \cdot \cos(\varphi)} \quad B = 1 - \frac{1708}{Ra \cdot \cos(\varphi)} \quad C = \left(\frac{Ra \cdot \cos(\varphi)}{5830}\right)^{\frac{1}{3}} - 1 \qquad \text{(eq. 5)}$$

With the factors B and C the modified Rayleigh number $Ra^* = Ra \cdot \cos(\varphi)$. This is necessary because the flow must be characterized into three flow regimes:

- At lower Rayleigh numbers ($Ra^* < 1708$) the conductive behavior dominates, since the flow velocities are very small. This flow regime is called quasi-conductive regime.
- With increasing Rayleigh numbers ($1708 < Ra^* < 5830$) the flow velocity increases and a monocellular basic flow develops: The gas particles rise at the hot underside, are deflected in the head area of the gas volume and sink again at the cold upper side. In this range of Rayleigh numbers the regime is called monocellular flow or post-conductive.

- With an even higher Rayleigh number ($Ra^* > 5830$) the monocellular flow decays into a multicellular flow with several convection rolls. Flow reversals now also takes place within the gas volume. This flow type is called multicellular flow regime.

To ensure a low heat transfer coefficient in the gas layer and thus a good collector efficiency due to low heat losses, the distance s_{20} should be designed in the way that $Ra^* = 1708$ where the insulating effect of the gas is at its maximum, the convective behavior and thus the heat transfer coefficient are minimum.

In eq. 4 and 5, this point is equal to $B = C = 0$ and $Ra^* = 1708$. For that state with $Ra^* < 1708$ and $Nu = 1$ all present approaches including Hollands (1976) use $Nu = 1$ just from theory without any measurements.

For the conductive regime ($Ra^* < 1708$), Hollands (1976) assumes $Nu = 1$, which corresponds to the case of pure heat conduction. However, pure heat conduction would only occur if the heat flow field is one-dimensional and a stagnant fluid is assumed. But as soon as the heat flow field deviates from the ideal one-dimensional case or as soon as also flow velocities occur in the gas layer $Nu > 1$ should be assumed.

Based on previous CFD simulations further influencing parameters are identified for determining the convective heat transfer coefficient in the gas layer. The experimental setup according Hollands (1976) was simulated in a 3D CFD simulation to validate the used physical models and the discretization. Simplified preliminary CFD investigations are carried out to analyze the flow phenomena in the gas layer. Thus, it is possible to investigate the varirty of parameters such as boundary conditions and geometric parameters. With the CFD simulations, it is shown that the heat transfer coefficient depends on the geometry and boundary conditions. This results for different AR in a variation of the Nusselt number. Beside the results for $Ra^* > 1708$, the CFD simulations also show a dependency $Nu(AR)$ for $Ra^* < 1708$. Also the assumption that $Nu > 1$ cloud be proven for $Ra^* < 1708$ with this CFD simulations.

3. Experimental Investigations

For experimental investigation, insulating glazings with the following design are measured in a test facility according to DIN 12664 (2001). The three insulating glazings examined have the basic dimensions of 500 x 500 mm. The construction of the insulating glazings consists of a 4 mm single-pane safety glass (ESG) pane, the insulating gas layer (here argon) between the panes and a further 4 mm ESG pane. The edge seal consists of an aluminium spacer with butyl as the primary seal and a secondary seal made of thiokol. Under consideration of the size of the spacer (10 mm) the resulting length of the gas layer is 480 mm. The layer thicknesses in the experiment (10.0, 8.0, 6.0 mm) can be adjusted by different thicknesses of the spacer. The resulting aspect ratios AR are 48.0, 60.0 and 80.0.

In the test facility for thermal conductivity measurements according to DIN 12664 (2001) a one-dimensional constant and uniform heat flow density is generated for plane shaped homogeneous sample bodies (here insulating glazings) with plane, plane-parallel surfaces. The test device therefore consists of a central measuring section (evaluation area) in which the measurement is carried out and a surrounding protection ring (guarded hot plate setup). After setting a stationary state in the measurement section, the heat flow density is calculated from the measurement of the heat flow and the evaluation area through which the heat flow passes. The temperature difference between the surfaces of the insulating glass is measured with temperature sensors on the surface of the insulating glass.

As boundary conditions for the experiment, the insulating glass mean temperatures is 20.0, 40.0, 60.0, and 80.0 °C at temperature difference of 20 K for each set. The measurement is carried out for tilt angles of 0, 20, 40 and 60°.

The convective heat transfer coefficient $h_{20,c}$ is calculated with the overall thermal resistance of the insulating glass and under consideration of the thermal resistances of the glass panes and the radiative heat transfer coefficient $h_{20,r}$. The resulting deviations between $h_{20,c}$ and the heat transfer coefficient according to Hollands (1976) h_{Holl} lead to the following correction function regarding *Nu* (for 48 ≤ AR ≤ 80 and $Ra^* < 1708$).

$$D = D_2 \cdot AR^2 + D_1 \cdot AR + D_0 \quad \text{(eq. 6)}$$

With: $D_2 = 1.292\ 10^{-4}$, $D_1 = -2.283\ 10^{-2}$ and $D_0 = 2.035$

This leads to the proposal of a corrective term **D** for eq. 7. **D** should just be used for $Ra^* < 1708$ and is only experimental proved for $48 < AR < 80$. The resulting adapted equation is now:

$$Nu = 1 + \boldsymbol{D} + 1.44 \cdot A \cdot [B]^{+} + [C]^{+} \qquad \text{(eq. 7)}$$

Simplified 2D simulations with the boundary conditions analogous to the measurements confirm the measurement results and the dependence of the heat transfer coefficient on the aspect ratio. Further deviations can also be determined from the simulations for other aspect ratios. As the aspect ratio increases, the layer becomes specifically thinner and the viscous effects dominate over the buoyancy forces. The ratio between buoyancy and viscosity within the fluid changes. This results in lower flow velocities within the layer, which means that the heat transfer is more influenced by conduction than by convection. The heat transfer coefficient and the corresponding Nusselt number Nu thus increases for lower aspect ratio AR due to higher mean flow velocities u.

$$AR \downarrow \rightarrow\ u \uparrow \rightarrow Nu\ \uparrow$$

Tab. 1: Overview simplified 2D simulations

φ	40°	40°	40°
T_{13} / T_{31}	70 / 90 °C	70 / 90 °C	70 / 90 °C
AR	48	60	80
Nu	1.27	1.16	1.04
u_{max}	17.87 mm/s	10.77 mm/s	5.72 mm/s
Velocity Field	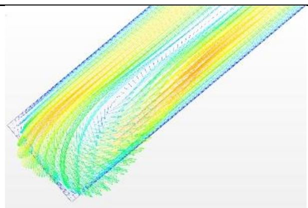	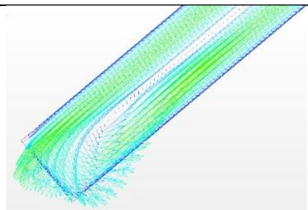	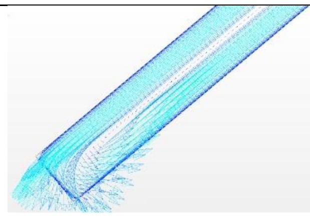
	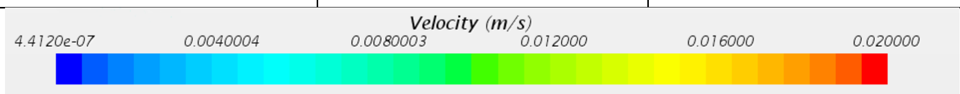		

4. Results

The propagated correction function and optimized design of the insulating glass layer (here thickness s_{20}) is done here for two operation points. The use of the correction function leads just to a small change in the insulation layer thickness but shows an even higher convective heat transfer coefficient in the range of approx. +30% for small AR and approx. +10% for large AR and $Ra^* < 1708$.

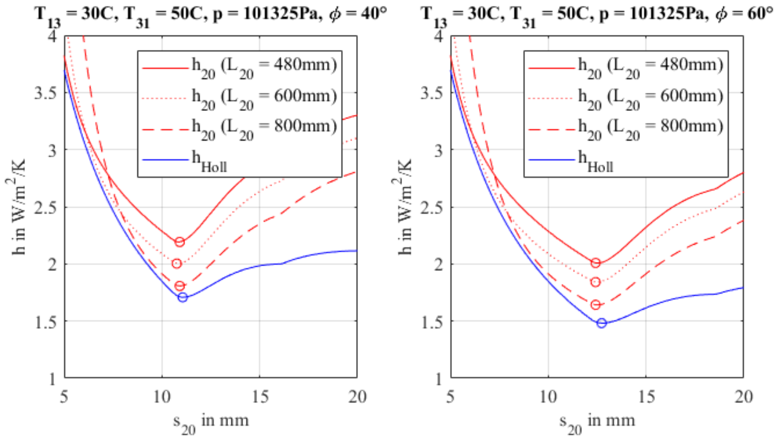

Fig. 2: Heat transfer coefficients in gas layer with correction function

These changes in the investigated field of $Ra^* < 1708$ do not lead to a significant change in the design of flat-plate or insulating glass collectors, but must be taken into account in the collector and system simulation.

5. References

Bartelsen, Janßen, Rockendorf, 1993. Heat Transfer by Natural Convection in the Air Gap of Flat Plate Collectors. Proceedings ISES Solar World Congress, pp. 267-273, Budapest, Ungarn

Eismann, 2015. Accurate analytical modeling of at plate solar collectors: Extended correlation for convective heat loss across the air gap between absorber and cover plate. Solar Energy 122, 1214 – 1224

DIN 12664, 2001. Wärmetechnisches Verhalten von Baustoffen und Bauprodukten. Bestimmung des Wärmedurchlasswiderstandes nach dem Verfahren mit dem Plattengerät und dem Wärmestrommessplatten-Gerät – Trockene und feuchte Produkte mit mittlerem und niedrigem Wärmedurchlasswiderstand. Deutsche Fassung EN 12664:2001. Berlin

Föste, 2013. Flachkollektor mit selektiv beschichteter Zweischeibenverglasung. Dissertation, Gottfried Wilhelm Leibniz Universität Hannover

Hollands, Unny, Raithby, Konicek, 1976. Free Convective Heat Transfer Across Inclined Air Layers. J. Heat Transfer 98(2), 189-193

Leibbrandt, Schabbach, Dölz, Rhein, 2016. CFD-Untersuchungen zu konvektiven Wärmeverlusten in Scheibenzwischenräumen mit großem Seitenverhältnis. 26. OTTI Symposium Thermische Solarenergie, Bad Staffelstein

Leibbrandt, Schabbach, Dölz, Rhein, 2017. Experimental and CDF Optimization on Flow and Heat Transfer to a Solar Flat-Plate Glass Collector. Solar World Proceedings ISES Solar World Congress, Abu Dhabi

Leibbrandt, Schabbach, Dölz, Rhein, 2018. Untersuchungsergebnisse zur Strömung und Wärmeübertragung im Nurglaskollektor. 28. OTTI Symposium Thermische Solarenergie, Bad Staffelstein

Yiqin et al., 1991. Measured Top Heat Loss Coefficients for Flat Plate Collectors with Inner Teflon Covers. Proceedings of the Biennial Congress of the International Solar Energy Society, Denver, Colorado

Micro-Mirror Concentrator System

Alexopoulos Spiros Orestis[1], Argiriou Athanassios[2], Dokouzis Alexandros Panagiotis[2], Dümmler Andreas[1], Göttsche Joachim [1], Kosmopoulos Georgios[2], Panagopoulos Orestis[2]

[1] Solar Institut Julich, Jülich of Aachen University of Applied Sciences (Germany)

[2] Physics Department, University of Patras, Patras (Greece)

Abstract

As part of the research project SCoSCo an innovative collector concept was developed by the consortium of the ScoSco project, namely University Patras, Solar-Institut Jülich, Calpak S.A., Hilger GmbH and Heliokon GmbH. The objective of the project is to develop a concentrating collector that could be easily integrated in buildings; therefore, a concentrating solar collector with fixed mirror was found to be an interesting approach.

The state-of-the-art methods for the generation of solar process heat use different concepts like tracking Fresnel mirrors or parabolic troughs. The proposed concept is innovative and presents advantages in cost- and life-cycle assessments. It can also be integrated in buildings very easily. The scientific findings answer for example the question of the geometric configuration of the concentrator and the optimal receiver type.

Keywords: Solar Process Heat, Concentrating Collector, Raytracing, Mirror Array

1. Introduction

In the past decades, several approaches of solar process heat collectors were developed (Weiss, 2008). Most approaches use single tracking axis linear concentrators (parabolic trough or Fresnel). The moving primary aperture area of tracking trough collectors prohibit an easy integration into buildings. On the contrary, linear Fresnel collectors can be easily installed on flat roofs. In order to achieve high performance, precise tracking is necessary. Typically, evacuated receiver tubes must be used to reach high conversion efficiency at medium operating temperatures (150 - 200 °C). Due to the costly components, solar process heat at these temperatures is still relatively expensive.

2. The mirror-array approach

As part of the Germano-Hellenic bilateral research project SCoSCo an innovative collector concept was developed with the objective to design and test a concentrating collector that could be easily integrated in buildings; therefore, a concentrating solar collector with fixed mirror was found to be an interesting approach. Within the scope of the project in order to reduce costs, a concentrating collector with a simple flat-plate receiver is proposed. The optical concentrator consists of an array of mirror facets placed in a box that protects the mirrors from wind loads and dirt. The innovative micro mirror box system has a built-in tracking mechanism, but the whole system is fixed. The solar concentrator consists of an array of mirror facets preconfigured to form a focal point at approximately 1.5 m. During tracking all mirrors move simultaneously in a coupled double - axis mode, in order to maintain the system in focus along the sun path. The mirrors and the corresponding mechanical system are housed inside a glass-covered casing like that of a flat-plate collector, as seen in Fig 1. The mirror module is installed at a fixed position. Therefore, this concept can be considered as fixed-mirror solar concentrator (FMSC) or Fresnel dish concentrator.

Selection and/or peer review under responsibility of Scientific Committee
doi:10.18086/eurosun.2020.06.09 Available at http://proceedings.ises.org

Fig. 1: Mirror-Box Concentrator with Receiver

The receiver can be a relatively small flat-plate collector, optimized for high-intensity solar irradiance and higher temperatures (e.g. using AR-coated iron-free glass cover, thicker absorber sheet, closer fluid channels, high-temperature resisting materials and insulation).

This concept presents the following advantages:

• The point-focusing feature allows high concentration values of ~50 even with relatively large optical and tracking errors of about ± 10 mrad.

• Instead of expensive receiver tubes, a small non-evacuated flat-plate receiver can be used.

• A patent of micro-mirror systems was filed by SIJ/DLR in 2006 (Sauerborn, 2008). A prototype developed for CSP applications was already designed (see Fig. 1).

• It is an innovative concept that has not yet been analysed and tested and no research results regarding its performance were found in the literature.

3. Optical performance analysis

Raytracing models were created with the COMSOL (Fig.2) and Tonatiuh software tools. These calculations allow the specification of the number of mirrors, their dimensions, and their gap width. All (rectangular and flat) mirror facets are arranged so that their centres are positioned on a regular grid on a flat plane. The size and position of the receiver can be modified. It always faces the centre of the mirror array. Its position can only be modified in form of a rotation around the mirror array y-axis.

The alignment of the mirrors is defined by the method "create_FMA" in which all mirror facets are adjusted to reflect incoming light from each mirror facet centre to the receiver centre if the incidence angle is normal to the array plane. The adjustment angles are different for each mirror facet. This 2-axis rotation is carried out in two steps, first a rotation around the y axis pivoted at the facet centre, second a rotation around the x axis pivoted at the facet centre. The order matters in two aspects: firstly, the angular adjustments have to be calculated differently if the order of rotations is reversed, secondly, it affects the facet orientation (in the sense of its rotation around its facet normal).

Similar considerations have to be done with respect to the tracking angles. They are directly related to the arrangement of the cardanic bearings of the mirror facets, which consist of an outer (fixed) bearing and an inner one fixed to the rotating outer one. The COMSOL model assumes an inner bearing that allows rotation around the y axis and an outer (fixed) bearing with x-axis rotation (see appendix B for the code of this alignment). The tracking angles are the same for each mirror facet.

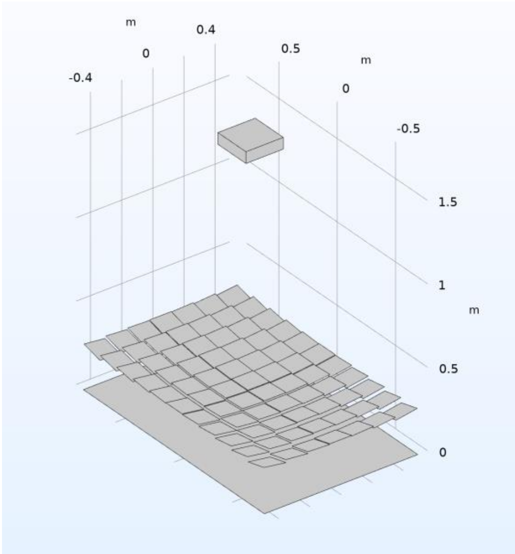

Fig. 2: View of the raytracing elements of the micro-mirror system 7x11

The optical errors of tracking, alignment and mirror surface quality are combined in one parameter “opticalError” which is used to create a random cone of reflected rays with normal distribution. The sigma value of this distribution is set to “opticalError”. The angular ray distribution of the sun disk is also implemented on the mirror surfaces and combined with the optical error calculation. In order to implement this, the equations of the surface reflection at the element “wall_1” had to be modified accordingly. The principle of raytracing model and the reflected rays are shown in Fig. 3.

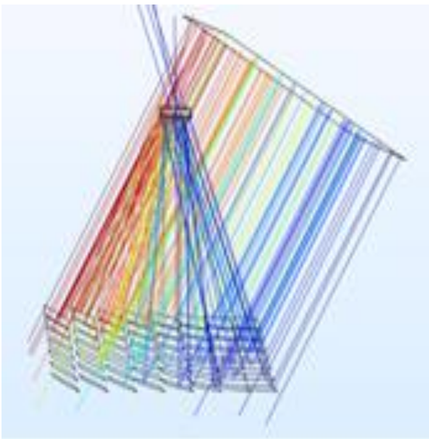

Fig. 3: Raytracing simulation of mirror-array system

Raytracing simulation allows the calculation of the intensity distribution on the receiver (see Fig.4).

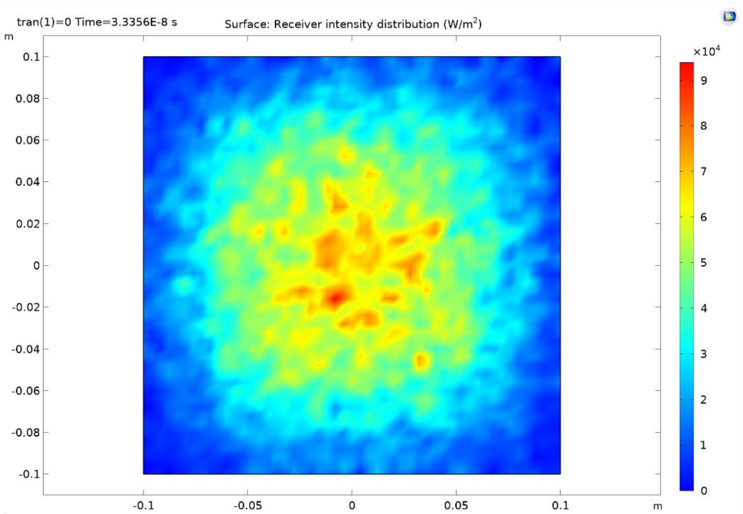

Fig. 4: Resulting intensity distribution on the receiver due to focusing with the mirror box

As a key result, the optical intercept factor γ was determined as a function of the angles of incidence (Table 3).

Table 1: Intercept data from COMSOL simulations of Table 3, left: transversal, right longitudinal variation of incidence angle (100,000 rays).

θ_{trans}	γ		θ_{long}	γ
0	0.883		0	0.883
15	0.887		15	0.898
30	0.886		30	0.926
45	0.795		45	0.916
60	0.653		60	0.836
75	0.482		75	0.698

The relatively low intercept factor γ of 88.3 % at 0° (normal) incidence is due to the gap between the mirror facets and the relatively large optical error of ± 7 mrad. If the error is increased to ± 10 mrad the intercept at normal incidence decreases to 0.833.

For the optimization of the collector parameters the thermal efficiency of the whole system was supposed to be > 50 % at the design point (normal incidence, 250 °C collector temperature). This goal can be achieved with the following parameters:

Table 2: Collector parameters allowing a thermal efficiency > 50 % at the design point

Mirror reflectivity	ρ_m	0.9
Mirror glass cover transmittance	τ_m	0.92
Absorber absorptance	α_a	0.92
Receiver window transmittance	τ_w	0.95
Collector efficiency factor	F'_c	0.97

The optical efficiency η_o can be calculated from these parameters as

$\eta_o = F'_c \cdot \gamma \cdot \rho_m \cdot (\tau_m)^2 \cdot \alpha_a \cdot \tau_w$.

The overall collector efficiency is calculated as

$$\eta = \eta_o - F_c' \cdot U_L \frac{(T_m - T_U)}{G_{DNI}}$$

with T_m the average collector fluid temperature, T_U the ambient temperature, G_{DNI} the direct beam radiation intensity, and $U_L = a_1 + a_2 \cdot (T_m - T_U)$ the overall thermal loss coefficient.

Table 3: Ray tracing parameters allowing a concentration ratio of c=38

mirrorWidthX	0.14	M	Width of the mirror in the x-direction
mirrorWidthY	0.14	M	Width of the mirror in y-direction
gapX	0.0015	M	gap between mirrors in x-direction
gapY	0.0015	M	gap between mirrors in y-direction
focalLength	1.4	M	Focal length of the mirror array and distance of receiver from array centre
numMirX	7		number of mirrors in the x-direction
numMirY	11		number of mirrors in the y-direction
ref	1		mirror reflectivity
opticalError	7×10^{-3}		optical error normal random distribution
sundisk	4.65×10^{-3}		sun disk uniform random distribution
rec_width	0.2	M	receiver width
rec_length	0.2	M	receiver length

The overall optimization of parameters is also limited by the practical limitations of the size of the cover glass, which should not exceed a width of about 1 m.

In order to cross-check our calculations, the Tonatiuh software was used. Tonatiuh is an open source Monte Carlo ray-tracing software developed specifically for solar power plants. A model with the dimensions in and optical characteristics described in Table 3 was used as input. The intercept factor was calculated as a function of the incidence angle and similar results with COMSOL were obtained. The intensity distribution on the absorber surface patterns were also similar for both software.

4. Thermal Performance Analysis

Figure 5 shows the complete model of the solar collector system for the calculation of annual energy yield with Matlab Simulink Carnot toolbox. The Carnot program combines the easy-to-use graphical environment of Simulink with the powerful algorithms and differential equation solvers of MATLAB for the application of solar thermal system simulation (Wemhöner et. al 2000). The thermal loss parameters of the receiver were assumed to be a_1 = 6.28 W/m²/K and a_2 = 0.005 W/m²/K.

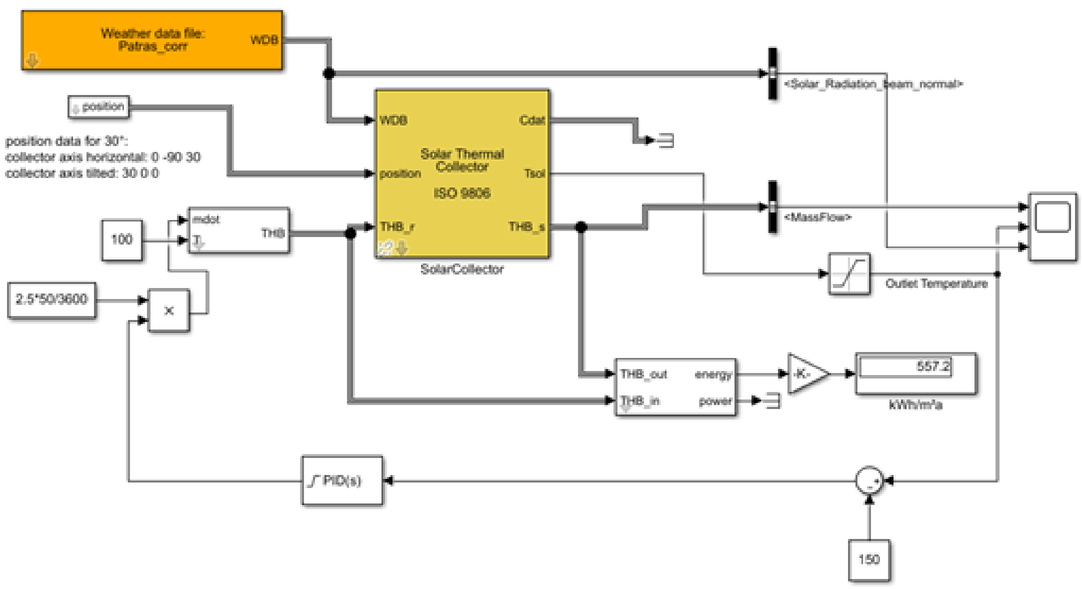

Fig. 5: Annual Energy Yield Simulation (Carnot Toolbox (CARNOT, 2019)

A sensor is connected to the solar collector to measure the mass flow of the heat transfer fluid and the output temperature. The sum block calculates the temperature difference between the set point value (150°C) and the actual value of the outlet temperature of the solar collector measured by the sensor. Since there are fluctuations in solar radiation throughout the day, the temperature difference is fed into the PID Controller to control the mass flow of the heat transfer fluid inside of the collector and keeping the outlet temperature of the solar collector at 150 °C with a constant inlet temperature of 100 °C.

The input and output of the THB of the solar collector is connected to a block called Energy Meter. The Energy Meter block calculates the annual solar yield of the system by measuring the temperature of the inlet and outlet of the solar collector and the volumetric flow rate of the heat transfer medium. The function of the gain block is to convert the energy in J to $\frac{kWh}{m^2a}$.

The annual energy yield for this concept is 793 kWh/m²a at Patras (weather data 2016) for the case with ± 7 mrad error and 750 kWh/m²a for the case with ± 10 mrad error, respectively.

5. Modification of the Incidence Angle to simplify the box construction

In addition, a series of simulations were performed using MATLAB/Simulink/Carnot (2019) to calculate the performance with different IAM functions, in which the IAM was set to zero above angles of incidence varying between 20° and 45° (transversal) and between 40° and 70° (longitudinal). Thus, the effect of restricting the angular range can be explored. For very large angles of incidence the energy of the reflected rays does not have a big influence on the annual energy yield; therefore, the construction of the mirror box, especially the movement of the mirrors, can be simplified. Through the limited angle, the mounting pins can be constructed shorter and because of that the height and the width of the box is even smaller. Nevertheless, it is very important that the Energy Yield is bigger than 700 kWh/m²a, and in the following steps the incidence angle was varied to find out the optimum.

The simulation results illustrated in Fig. 6 show that it is possible to "cut-off" the incidence angle. With the full range of rays in the longitudinal direction and the variation in the transversal direction it appears that it is possible only to consider the rays with an incidence angle ± 40°; this leads to an annual energy yield of 741.8 kWh/m²a. For the longitudinal direction with the full range of transversal rays, it is possible to stop the simulation at ± 60° with the annual energy yield of 716.6 kWh/m²a. The combination of both gives as a simplification optimum at the transversal ±45° and at the longitudinal ±60°. In this case the annual energy yield is 709.8 kWh/m²a.

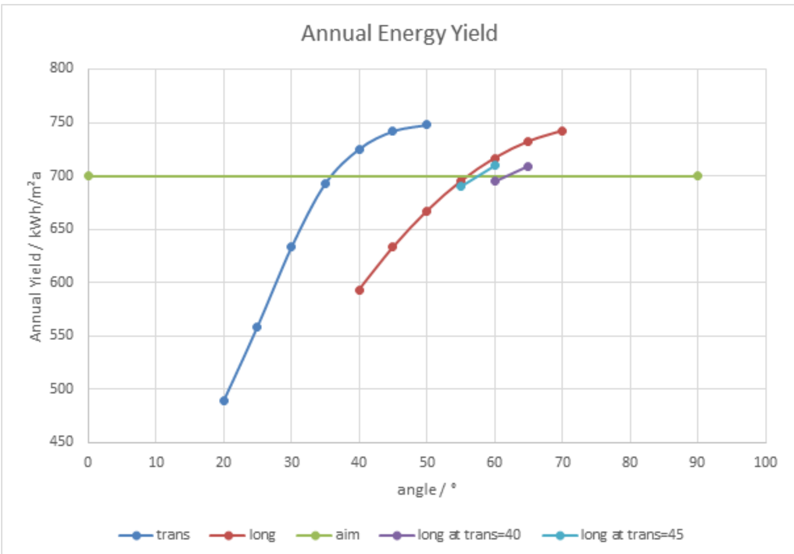

Fig. 6: Annual Energy Yield with variation of incidence angle (longitudinal and transversal) at which the IAM is set to zero (±10 mrad case)

The result of that simulation showed that the mirrors only have to move by ± 22.5° in the transversal and ± 30° in the longitudinal direction.

From these limits, the pin length L and the distance D from the point of rotation to the box edge can be derived as shown in Figure 7 and Figure 8:

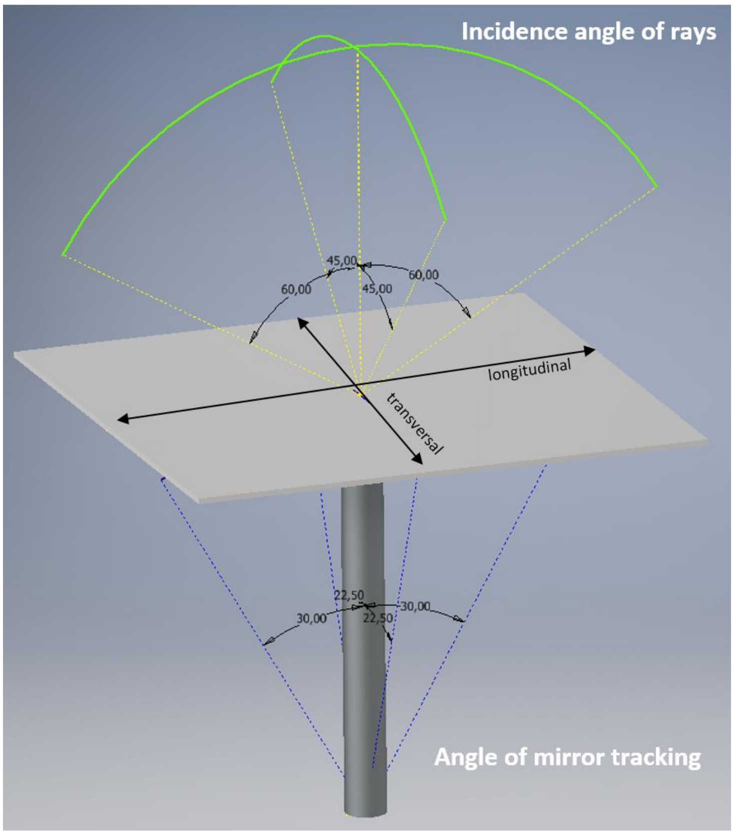

Fig. 7: Sketch of mirror tracking path (yellow: angles of incidence, blue: pin/mirror movement)

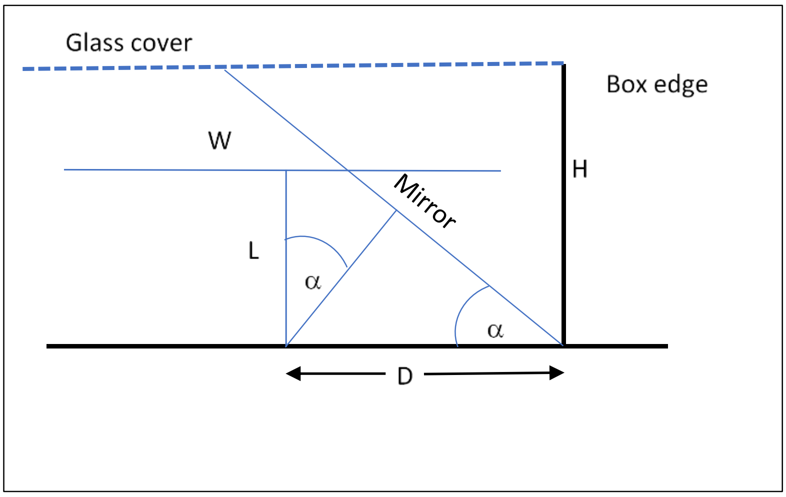

Fig. 8: Sketch of the calculation of Length and angles for pin movement

With the given angular restrictions and the mirror width W = 14 cm, the following dimensions can be realized:

L = 5 cm, D = 10 cm, and H = 8 cm.

6. Conclusion

A concentrating collector with a simple flat-plate receiver is proposed. The proposed concept is innovative and presents advantages in cost and life-cycle assessments. Optical simulations were performed using COMSOL and Tonatiuh software, yielding similar and satisfactory results. The expected energy yield can be up to about 800 kWh/m^2a under the weather conditions of Patras, Greece using standard optical components. Further improvements are possible by using AR glazing for the glass cover of the mirror array, higher absorber, or mirror quality. A cost-benefit analysis of these material properties will have to be carried out. The new collector design can also be integrated in buildings very easily. On our next steps, two identical prototypes will be assembled and tested experimentally in Jülich, Germany and Patras, Greece, in order to study the proposed system's behaviour under outdoor conditions for both climate zones. Technical details of the tracking system, as well as operating problems and impacts on the overall system cost is confidential at this point but will be published as soon as the experimental testing is complete.

7. Acknowledgments

This project was co-funded by the German Federal Ministry of Education and Research and the Hellenic Secretariat for Research and Technology (SCOSCO project) in the framework of the Greek-German co-operation.

8. References

CARNOT Toolbox Ver. 7.0 for MATLAB/Simulink R2018b, Solar-Institut Juelich.

Tonatiuh Ver. 2.2.4 https://iat-cener.github.io/tonatiuh/, Creative Commons Attribution-Noncommercial-Share Alike 3.0 Unported License

Sauerborn, M., Göttsche, J., Hoffschmidt, B., Schmitz, S., Rebholz, C., Ifland, D., Ansorge, F., Buck, R., Teufel, E., 2008. Test of a Mini-Mirror Array for Solar Concentrating Systems, EUROSUN 2008, Lisbon, Portugal.

C. Wemhöner, B. Hafner, K. Schwarzer: Simulation of solar thermal systems with Carnot blockset in the einvironment Matlab Simulink, Eurosun 2000

Weiss, W., Rommel, M., 2008. Process heat collectors. State of the Art within Task 33. International Energy Agency.

07. Thermal Storage

EuroSun 2020
EXPERIMENTAL ANALYSIS OF LATENT THERMAL ENERGY STORAGE CHARGING AND DISCHARGING

Mateo Kirincic, Anica Trp, Kristian Lenic, Fran Torbarina

University of Rijeka, Faculty of Engineering, Department of Thermodynamics and Energy Engineering, Vukovarska 58, 51000 Rijeka, Croatia

Summary

Experimental investigation of latent thermal energy storage (LTES) charging and discharging has been performed. The LTES unit is a shell-and tube type tank with water as the heat transfer fluid (HTF), which flows through the tubes, and technical grade paraffin RT 25 as the phase change material (PCM), filling the shell side. The total of 19 longitudinally finned tubes are arranged concentrically in the tank. A set of 30 thermocouples have been placed at various radial and axial positions on the PCM side for monitoring transient temperature variations during charging and discharging processes. Timewise temperature variations of PCM during charging and discharging, for different HTF inlet temperatures, have been presented. Stored and released thermal energy have been calculated and analyzed.

Key words: latent thermal energy storage, experimental research, charging and discharging.

1. Introduction

Due to increase in both global economy and population, the need for continuous energy supply has been steadily growing. Fossil fuels have been used as a principal energy source for most of the last century. However, these fuels emit compounds which are harmful to the environment and increase global warming. More sustainable technologies are needed to maintain both stable economic growth and healthier environment. One of the renewable technologies in domestic and industrial applications is the storage of thermal energy provided by solar radiation during the day, and its release during the night (Jegadheeswaran, 2009). Thermal energy can be stored in the form of sensible heat, latent heat or thermochemical energy. In a latent thermal energy storage (LTES), the thermal energy acquired by solar collectors is carried by heat transfer fluid (HTF) and stored inside a phase change material (PCM) during charging period (melting) and released during discharging period (solidification), using PCM's latent heat to store and release additional energy. Since most organic PCMs exhibit low thermal conductivity (which is about 0.2 W/mK (Khan et al., 2016)), various heat transfer enhancement techniques have been suggested and investigated. The most common one is the use of extended surfaces (fins) and their geometry characteristics so placement inside the LTES can greatly increase heat transfer in both charging and discharging processes. Fins are implemented in various LTES geometries, e.g. double pipe, triplex tube and shell-and tube configurations, the latter of which is the most used (Al-Abidi et al., 2012).

Ezan et al. (2011) performed an experimental investigation of the thermal performance of shell and tube LTES during charging and discharging cycles with water as HTF. Storage capacity of the system was calculated for different operating and geometry conditions; HTF inlet temperature and flow rate, shell diameter and thermal conductivity of the tube material. It was concluded that the dominant heat transfer mechanism during melting is natural convection, and conduction during solidification. The effect of HTF inlet temperature on thermal performance is greater than the effect of HTF flow rate. Akgun et al. (2007) experimentally assessed charging and discharging processes in a vertical shell-and-tube heat exchanger. They observed that melting time was significantly decreased by increasing the HTF inlet temperature. Khan and Khan (2017) experimentally investigated the discharging cycles of paraffin in a shell-and-tube LTES with longitudinal fins. They studied the influence of HTF inlet temperature and flow rate. Increasing the HTF inlet temperature and flow rate

doi:10.18086/eurosun.2020.07.01 Available at http://proceedings.ises.org

resulted in lower thermal resistance caused by solidified paraffin. Hosseini et al. (2012) experimentally investigated the charging process in horizontal shell-and-tube LTES. They observed the highest temperature values are present in the uppermost region due to natural convection. Additionally, by increasing the HTF inlet temperature from 70 to 80 °C, the total melting time is reduced by 37%. Kabbara et al. (2016) experimentally investigated the discharging process of dodecanoic acid in a vertical shell-and-tube LTES with rectangular fins. They reported that discharge power was slightly improved by increasing the HTF flow rate. Lohrasbi et al. (2017) comparatively examined the thermal performance of PCM in vertical-shell-and-tube configurations with no fins, optimized circular fins and longitudinal fins. It was reported that the phase transition rate for optimized circular fins and longitudinal fins were 3.55 and 4.28 times higher as compared to no fins orientation, respectively. Agyenim et al. (2009) experimentally investigated the influence of radial and longitudinal fins on thermal performance in a shell-and-tube LTES with erythritol as PCM. It was reported that cumulative thermal energy discharge for no fins, radial fins and longitudinal fins were 4977.8 kJ, 7293.1 kJ and 8813.1 kJ, respectively. Similarly, Caron-Soupart et al. (2016) experimentally investigated the phase change behavior of paraffin RT 35 HC in shell-and-tube with three configurations: no fins, radial fins and longitudinal fins. They observed that longitudinal fins had resulted in greater temperature gradient and thermal power when compared to cases with radial fins or without fins. Agarwal and Sarviya (2016) designed and studied the shell-and-tube type LTES for solar dryer, with paraffin used as PCM, and air as HTF. Heat transfer characteristics of the system have been evaluated during charging and discharging processes. They studied the effects of flow rate and temperature of HTF on the charging and discharging process in LTES, obtaining temperature distributions along the radial and longitudinal directions. Thermal performance of the system was evaluated in terms of cumulative charged and discharged energy.

As seen from the literature, longitudinal fins are an effective means for enhancing thermal performance during both charging and discharging processes. This investigation presents an experimental analysis of charging and discharging processes in the shell-and-tube type LTES with external longitudinal fins. It aims to investigate the influence of HTF inlet temperature on charging and discharging processes. A series of measurements have been carried out in order to assess the LTES' thermal performance. Based on measurement data, stored and released thermal energy have been calculated. Results can be used in further investigations in modeling and optimization of heat transfer in LTES, as well as modeling and optimization of thermal systems which include this type of storage tanks.

2. Experimental setup

2.1. System description and LTES tank

Experimental setup consists of a LTES tank, 49 kW water-water heat pump, hot and cold water tanks, thermostatic mixing valve as well as circulation pumps in the condenser-hot tank circuit, evaporator-cold tank circuit and working tank-test unit circuit. Working tank is hot tank during charging, and cold tank during discharging processes investigations. The investigated LTES is designed and constructed shell-and-tube type tank, vertically oriented and consisted of 19 concentric aluminum tubes, each containing eight equidistant longitudinal fins with 66 mm length and 2 mm width, offset by an angle of 45°. The tubes are made of aluminum and their inner and outer diameters are 25 and 30 mm, respectively. Outer diameter of the tank is 950 mm, while its height is 1500 mm. To reduce heat losses through the shell, it has been insulated with 25 mm of expanded rubber foam. The LTES tank, tube configuration and single longitudinally finned tube are shown in Fig. 1.

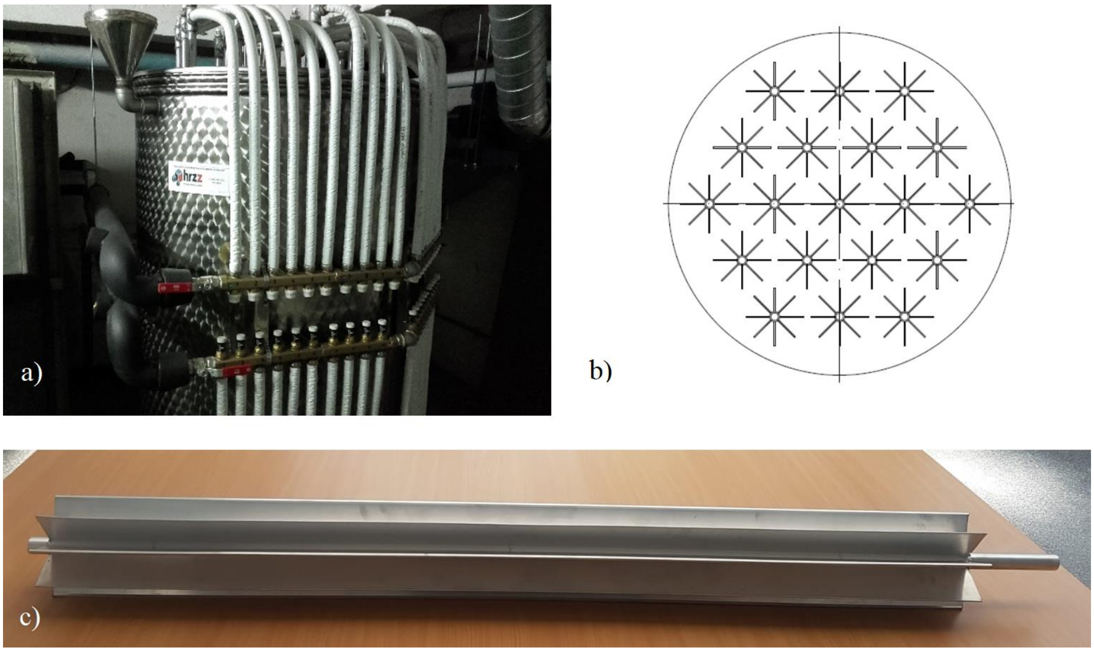

Fig. 1. Latent thermal energy storage tank (a), configuration of tubes and fins inside the tank (b), longitudinally finned tube (c)

Water, which flows through the tubes, enters the tank at the top and serves as the heat transfer fluid. 760 kg of Rubitherm's RT 25 paraffin is used as PCM and fills the shell side of the tank. Thermal and physical properties of RT 25 paraffin are given in Table 1.

Table 1. Thermal and physical properties of RT 25 (Rubitherm GmbH, 2018)

Melting/solidification temperature range	22-26 °C
Latent heat	170 kJ/kg
Thermal conductivity	0.2 W/mK
Specific heat capacity	2 kJ/kgK
Density solid/liquid	880/760 kg/m^3
Kinematic viscosity (liquid)	4.7 mm^2/s

2.2. Experimental procedure

Measurements have been performed in the Laboratory for thermal measurements at University of Rijeka, Faculty of Engineering. A total of 30 K-type thermocouples have been placed in PCM at axial and radial positions, in order to monitor the transient temperature changes during charging and discharging processes. Their axial and radial positions, around one tube in the tube arrangement, regarding to the water inlet position and tube center, are shown in Fig. 2 in top and cross section views, and in Table 2, where nomenclature of the thermocouples has been provided. Two additional thermocouples have been placed at the HTF inlet and outlet of the LTES.

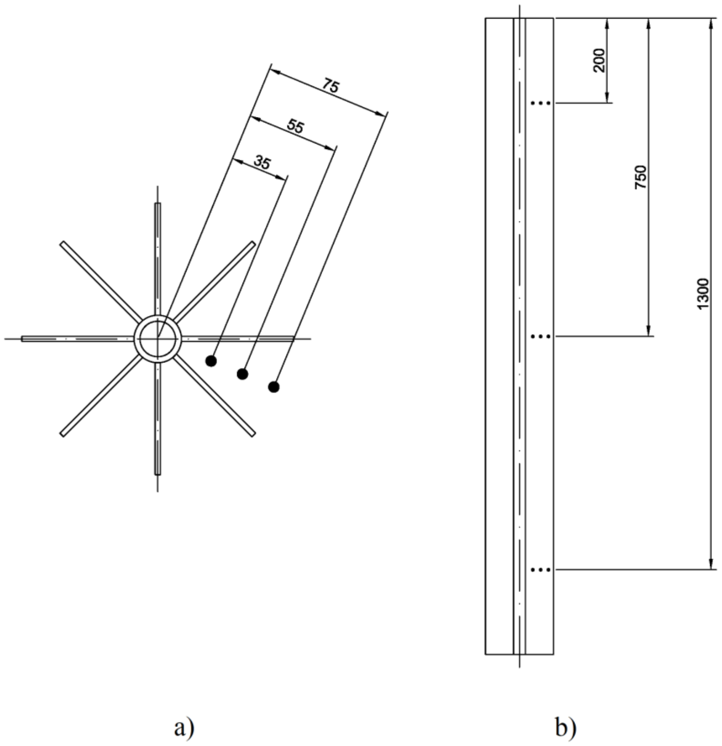

Fig. 2. Thermocouples position on the paraffin-side of the LTES, top view (a), cross section view (b)

Table 2. Axial and radial positions of thermocouples inside the LTES

Thermocouple no.	1	2	3	4	5	6	7	8	9
Axial position (m)	0.2	0.2	0.2	0.75	0.75	0.75	1.3	1.3	1.3
Radial position (m)	0.035	0.055	0.075	0.035	0.055	0.075	0.035	0.055	0.075

Data acquisition system, linked with personal computer, and the software LabView were used to acquire and store measurements into a file (Fig. 3). Temperatures were measured and stored every 10 seconds. Initial conditions were defined by uniform temperature distribution throughout the PCM, below melting point in charging investigations, and above melting point in discharging investigations.

Fig. 3. Data acquisition system linked with personal computer

Mass flow rate of HTF was constant, controlled by working tank-test unit circulation pump. Constant HTF inlet temperature was controlled by three-way valve. Flow and temperature control system is shown in Fig. 4. When all thermocouples had shown temperatures above the melting point during charging analyses or below melting point for discharging analyses, the experiment was completed.

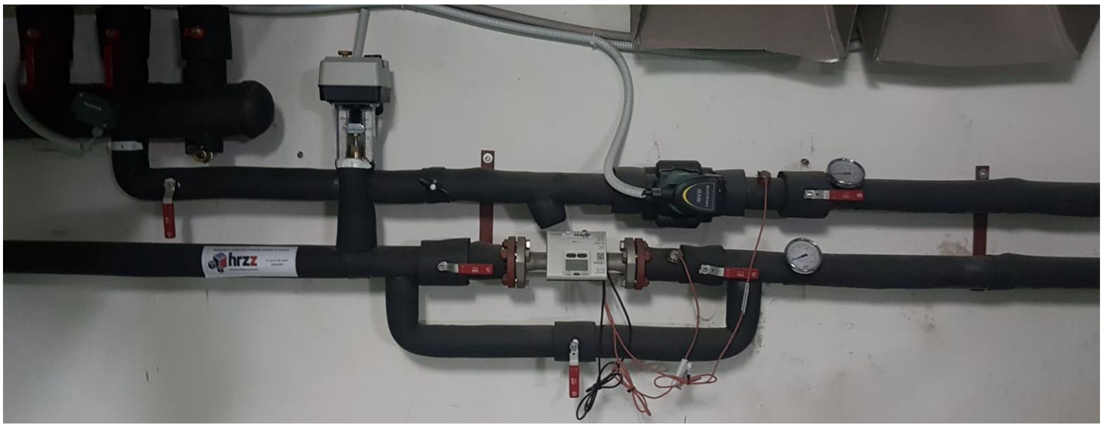

Fig. 4. Flow and temperature control system

3. Results and discussion

Temperature variations of PCM have been analyzed for various HTF inlet temperatures. In charging processes, the HTF inlet temperatures varied from 37 to 42 °C, and in discharging processes, those varied from 7 to 13 °C. Flow rate was 620 l/h for all analyzed cases, in both charging and discharging processes.

3.1. Charging processes

Transient PCM temperature variations in LTES, for different HTF inlet temperatures, during charging at axial position 0.75 m and radial position 0.035 m (position 4) are presented in Fig. 5. It can be noted that melting is not isothermal, and occurs in a temperature range, between 18 and 25 °C. This is due to natural convection-governed melting process. Conduction is dominant only in the solid phase, and as liquid layer of molten PCM grows, natural convection begins to take over as the dominant heat transfer mechanism. As the liquid layer grows, natural convection becomes more intense. As PCM is completely melted, i.e. when the temperature has reached 25 °C, a rise in temperature can be observed, indicating sensible heat transfer in completely molten liquid PCM, governed predominantly by natural convection. As seen from Fig. 5, shorter melting time is achieved for the HTF inlet temperatures 40 and 42 °C, while melting time for HTF inlet temperature 37 °C is considerably longer. Transient temperature variations of PCM for different radial positions at axial position 0.2 m (positions 1, 2 and 3) for HTF inlet temperature 37 °C are presented in Fig. 6.

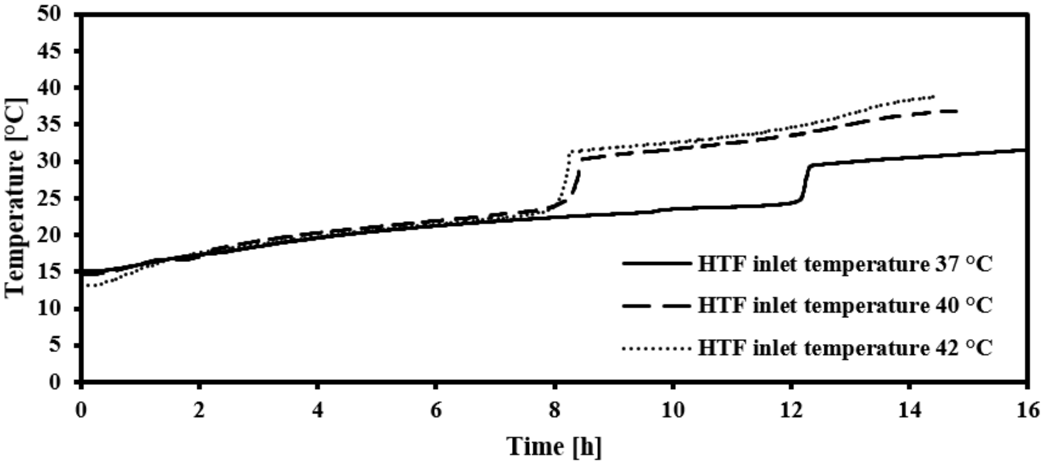

Fig. 5. Experimentally acquired transient PCM temperature variations inside the LTES at position x = 0.75 m, r = 0.035 m (position 4) during charging processes with different HTF inlet temperatures

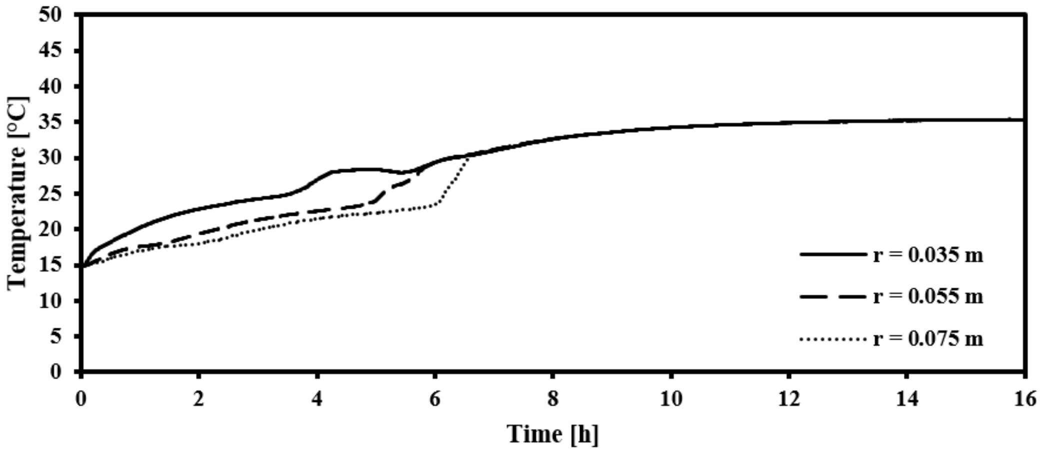

Fig. 6. Transient PCM temperature variations inside the LTES during charging with HTF inlet temperature 37 °C, at axial position x = 0.2 m and for different radial positions (positions 1, 2 and 3)

It can be observed that melting process is faster at smaller radius i.e. smaller distance from the tube. In comparison with Fig. 5, can be observed that melting process is significantly faster in the top-most section of the LTES (x = 0.2 m), due to rising of lighter liquid PCM particles, i.e. stronger influence of natural convection. Additionally, HTF temperature is the largest in that region, since HTF enters into the LTES at the top, also intensifying heat transfer.

3.2. Discharging processes

Transient PCM temperature variations in LTES, for different HTF inlet temperatures, during discharging at axial position 0.2 m and radial position 0.035 m (position 1) are presented in Fig. 7. It can be seen that, unlike melting processes, solidification processes are nearly isothermal, occurring at 25 °C. It is also observed that discharging process can be divided into three parts; cooling of liquid PCM, with natural convection present only at the beginning and diminishing as the process goes on, followed by nearly isothermal conduction-dominated solidification, and finally, cooling of the solid PCM, once the solidification process is complete. The shortest discharging time is achieved for the lowest HTF inlet temperature, 7 °C.

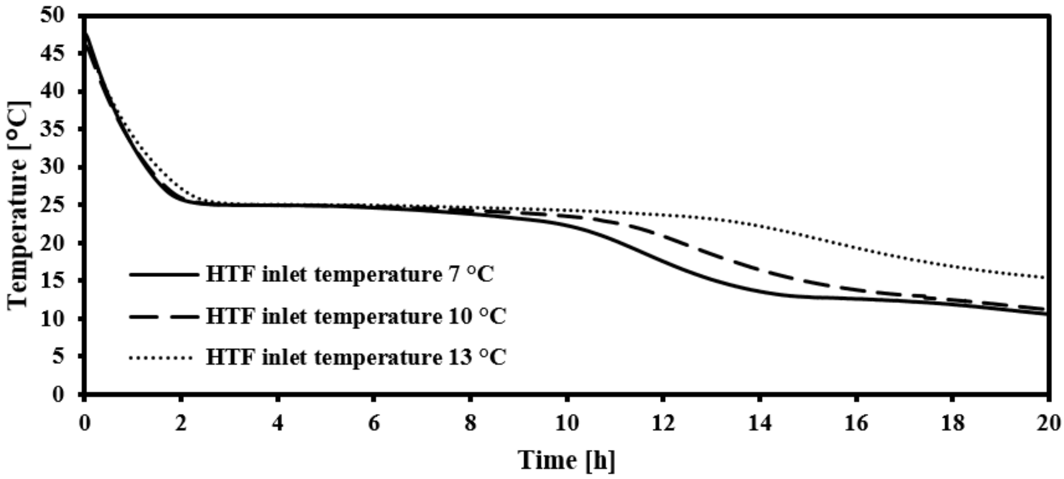

Fig. 7. Experimentally acquired transient PCM temperature variations inside the LTES at position x = 0.2 m, r = 0.035 m (position 1) during discharging processes with different HTF inlet temperatures

Transient PCM temperature variations for various radial positions at axial position 0.75 m (positions 4, 5 and 6) and for HTF inlet temperature 7 °C are presented in Fig. 8. Comparing with Fig. 7 can be observed that lower measurement positions, further from the HTF inlet, have longer solidification times than higher positions.

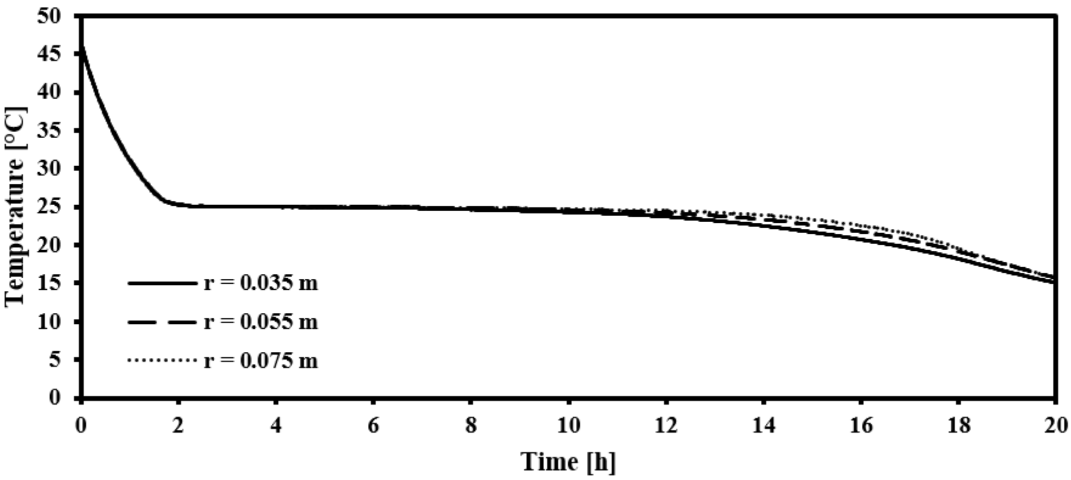

Fig. 8. Transient PCM temperature variations inside the LTES during discharging with HTF inlet temperature 7 °C, at axial position x = 0.75 m and for different radial positions (positions 4, 5 and 6)

Furthermore, comparing with previous figures, it can also be observed that discharging processes are noticeably slower than charging processes, due to lack of natural convection during solidification and increasingly higher thermal resistance provided by solidified PCM.

3.3. Stored thermal energy

In order to obtain LTES heat storing capability, as well as to validate performed measurements, cumulative amounts of thermal energy on HTF and PCM sides, for both charging and discharging processes, have been calculated according to the equation:

$$Q = \sum_{i}^{n} \dot{V}_{HTF} \cdot \rho_{HTF} \cdot c_{HTF} \cdot (t_{in,HTF} - t_{out,HTF}) \cdot \Delta\tau = m_{PCM} \cdot L + \sum_{i}^{n} m_{PCM} \cdot c_{PCM} \cdot (\bar{t}_{PCM} - \bar{t}_{PCM}^{0}) \qquad \text{(eq. 1)}$$

Amounts of thermal energy stored in LTES during charging and released during discharging, for different HTF inlet temperatures, are represented in Fig. 9.

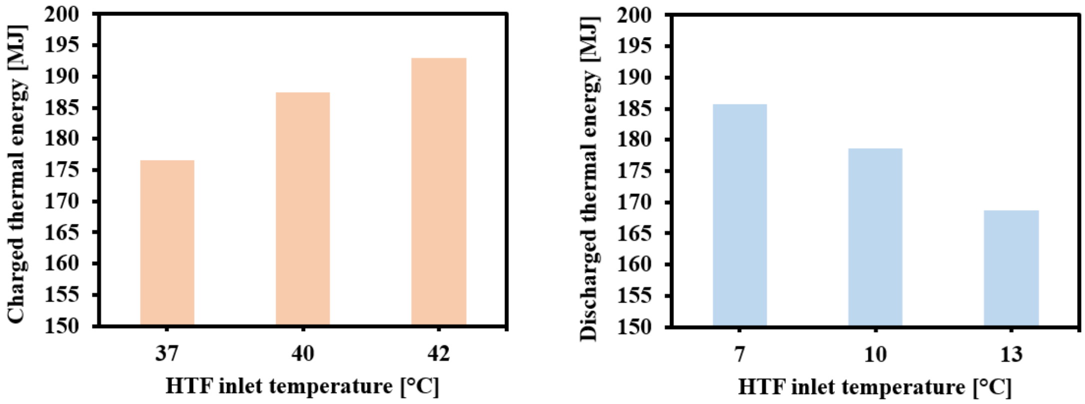

Fig. 9. Comparison of stored thermal energy during charging and released thermal energy during discharging

As seen from Fig. 9, the highest amount of stored thermal energy (193.1 MJ) during charging analyses is achieved for the highest HTF inlet temperature, 42 °C. The highest amount of released thermal energy (185.7 MJ) in discharging analyses is obtained for the lowest HTF inlet temperature, 7 °C.

4. Conclusion

Influence of HTF inlet temperature on charging and discharging processes inside a vertically oriented shell-and-tube type LTES with longitudinal fins has been experimentally analyzed. It can be observed that charging and discharging processes are the shortest for highest and lowest HTF inlet temperatures, respectively. Also, natural convection is the dominant heat transfer mechanism in charging processes, and is negligible in discharging processes, which are conduction-governed. Amounts of stored and released thermal energy for analyzed processes have been calculated. Obtained results can be used in further analyses and numerical modeling of heat transfer in the longitudinally-finned LTES, as well as modeling of thermal systems incorporating this type of LTES tank.

List of symbols

m_{PCM} – PCM mass [kg]

L – PCM latent heat [kJ/kg]

c_{PCM} – PCM specific heat capacity [kJ/kgK]

$\bar{t}_{PCM}$ – PCM average temperature in current measurement timestep [°C]

$\bar{t}_{PCM}^{0}$ – PCM average temperature in previous measurement timestep [°C]

$\dot{V}_{HTF}$ – HTF volume flow rate [m^3/s]

ρ_{HTF} – HTF density [kg/m^3]

c_{HTF} – HTF specific heat capacity [kJ/kgK]

$t_{in,HTF}$ – HTF inlet temperature in current measurement timestep [°C]

$t_{out,HTF}$ – HTF outlet temperature in current measurement timestep [°C]

$\Delta\tau$ – measurement interval (timestep) [s]

Acknowledgement

This work has been supported in part by Croatian Science Foundation under the project HEXENER (IP-2016-06-4095) and in part by the University of Rijeka under the project number „uniri-tehnic-18-69“.

References

Agarwal, A., Sarviya, R.M., “An experimental investigation of shell and tube latent heat storage for solar dryer using paraffin wax as heat storage material”, Engineering Science and Technology, an International Journal, 19(1), 619-631, 2016.

Agyenim, F., Eames, P., Smyth, M., “A comparison of heat transfer enhancement in a medium temperature thermal energy storage heat exchanger using fins”, Solar Energy, 83, 1509-20, 2009.

Akgun, M., Aydın, O., Kaygusuz, K., “Experimental study on melting/solidification characteristics of a paraffin as PCM”, Energy Conversion and Management, 48(2), 669-678, 2007.

Al-Abidi, A.A, Mat, S., Sopian, K., Sulaiman, M.Y., Lim, C.H., Abdulrahman, T.H., “Review of thermal energy storage for air conditioning system”, Renewable and Sustainable Energy Reviews, 16(8), 5802-19, 2012.

Caron-Soupart, A., Fourmigué, J-F., Marty, P., Couturier, R., “Performance analysis of thermal energy storage systems using phase change material”, Applied Thermal Engineering, 98, 1286-96, 2016.

Ezan, M.A., Ozdogan, M., Erek, A., “Experimental study on charging and discharging periods of water in a latent heat storage unit”, International Journal of Thermal Sciences, 50, 2205-19, 2011.

Hosseini, M.J., Ranjbar, A.A., Sedighi, K., Rahimi, M., “A combined experimental and computational study on the melting behavior of a medium temperature phase change storage material inside shell and tube heat exchanger”, International Communications in Heat and Mass Transfer, 9(39), 1416-24, 2012.

Jegadheeswaran, S.P.S., “Performance enhancement in latent heat thermal storage system: a review,” Renewable and Sustainable Energy, 9(13), 2225-44, 2009.

Kabbara, M., Groulx, D., Joseph, A., “Experimental investigations of a latent heat energy storage unit using finned tubes”, Applied Thermal Engineering, 101, 601-11, 2016.

Khan Z., Khan Z., Ghafoor A., “A review of performance enhancement of PCM based latent heat storage system within the context of materials, thermal stability and compatibility”, Energy Conversion and Management, 115, 132-58, 2016.

Khan, Z., Khan, Z.A., “An experimental investigation of discharge/solidification cycle of paraffin in novel shell and tube with longitudinal fins based latent heat storage system”, Energy Conversion and Management, 154, 157-167, 2017.

Lohrasbi, S., Gorji-Bandpy M., Ganji, D.D., “Thermal penetration depth enhancement in latent heat thermal energy storage system in the presence of heat pipe based on both charging and discharging processes”, Energy Conversion and Management, 148, 646-67, 2017.

Rubitherm GmbH, RT 25 data sheet, 2018.

Exergetic performance of medium temperature metallic solder based cascaded PCM thermal energy storage systems during charging

Ashmore Mawire[1], Chidiebere Ekwomadu[1] and Adedamola Shobo[2]

[1]Department of Physics and Electronics, North West University (Mafikeng Campus), Private Bag X2046, Mmabatho 2735, South Africa

[2] Department of Mathematics, Science and Sports Education, University of Namibia, Private Bag 5507, Oshakati, Namibia

Abstract

Metallic phase change materials are attractive candidates for use in thermal energy storage systems, but their high cost per unit volume may prohibit their usage. To reduce the cost, some volume of metallic phase change materials may be replaced with other cheaper phase change materials. Three packed bed cascaded latent heat thermal energy storage (LHTES) systems for medium temperature applications are experimentally evaluated and compared to a single phase change material (PCM) packed bed LHTES of eutectic solder capsules from a charging exergetic rate perspective. Cascaded system 1 comprises of eutectic solder PCM capsules at the top, and erythritol PCM capsules at the bottom in equal storage volumes. Cascaded system 2 consists of eutectic solder PCM capsules at the top and adipic acid PCM capsules at the bottom in equal storage volumes. Cascaded system 3 consists of three PCM capsule layers of eutectic solder at the top, adipic acid in the middle, and erythritol at the bottom in equal storage volumes. Cascaded system 3, the 3 PCM cascaded system shows higher exergy charging rates because of the release of latent heat in 3 phase change transitions. Its thermal performance is, however, comparable to cascaded system 2 with adipic acid at the bottom of the storage tank. The charging times for cascaded system 2 and cascaded system 3 are also shorter as compared to the other storage systems suggesting a better charging performance. The single PCM shows the lowest exergy charging rate at the lowest flowrate but its performance improved to be better than that of cascaded system 1 with an increase in the flowrate.

Keywords: Adipic acid, Charging exergy rates, Cascaded latent heat thermal energy storage, Erythritol, Eutectic solder, Packed bed

1. Introduction

Metallic phase change materials (PCMs) have been suggested for use in latent heat thermal energy storage (LHTES) systems which are useful to address the mismatch between solar energy supply and demand [1]. Solar energy may be utilized for domestic applications like water heating and cooking. Metallic PCMs are particularly attractive due to their high thermal conductivities, high latent heat per unit volume, low vapor pressure, good thermal cycling stability and negligible degrees of sub-cooling [2-6].

The usage of metallic PCMs in practical thermal energy storage (TES) systems may be hampered by their high cost per unit joule of energy storable/deliverable. Cascading different PCMs with different melting temperatures in single/multiple TES tanks has been suggested by a recent comprehensive review as a method that increases the effectiveness of latent heat storage systems [7]. Moreover, including other cheaper PCMs with a metallic PCM in a cascaded configuration in a TES tank has the potential to lower the cost of the overall system. Numerous past studies have investigated different configurations of cascaded LHTES systems from various perspectives, and for different proposed temperature applications as reported in [7]. Studies on packed bed cascaded latent heat storage configurations which are simpler and more efficient are rather limited especially for medium temperature applications [8-13].

doi:10.18086/eurosun.2020.07.02 Available at http://proceedings.ises.org

While numerous previous studies have investigated the optimization of the performance of cascaded LHTES systems from a broad range of parameters for low and high temperatures, a limited number of the systems have been designed for medium temperature applications (100 - 300 ºC). Hence, the objective of this study is to investigate the charging performance of a packed bed LHTES, using a metallic PCM and two organic PCMs, for medium temperature applications. The idea is to combine the advantage of the high thermal conductivity of the metallic PCM with that of the cheapness of the organic PCMs as well as their high latent heats of fusion. Sunflower Oil will be utilized as the heat transfer fluid (HTF) as it has been reported to possess good heat transfer and good stratification properties in a TES tank [14]. The use of vegetable oils such as Sunflower Oil for domestic heating needs is particularly attractive due to their environmental friendliness, cheapness, availability and good thermal reliability within the medium temperature range as highlighted by Mawire [15], Hoffmann et al. [16] and by Hossain et al. [17] in their recent studies.

The eutectic solder, Sn63/Pb37, used in this study has recently been reported to be a good metallic PCM for medium temperature TES applications [18]. In another recent study, a packed bed TES system with the encapsulated eutectic solder alone showed promising thermal performance [19]. In another related study, the performance of the eutectic solder packed bed TES system was compared with a similar TES system incorporating both encapsulated solder cascaded and encapsulated erythritol in a 50:50 ratio in the TES tank [20]. The cascaded TES system generally showed better overall efficiencies at high temperatures and at high HTF flow rates. The performances of three similar packed bed TES systems containing erythritol, eutectic solder and adipic acid, respectively, were compared recently in [21], and the results obtained showed reasonably good performance for these three PCMs. The aim of this comparative study is to compare the performances of the TES systems investigated in [20] with one in which erythritol is replaced by adipic acid and another one comprising of three PCMs cascaded in equal layers in the same TES tank. This is in a bid to obtain an efficient TES system for medium temperature applications in terms of both thermal performance and cost. The exergetic performance is considered in this paper since it gives a true reflection of the quality of the energy stored accounting for heat losses when compared to the energetic performance.

2. Experimental method and procedure

Figure 1 shows schematic diagrams of the four TES configurations considered in this study.

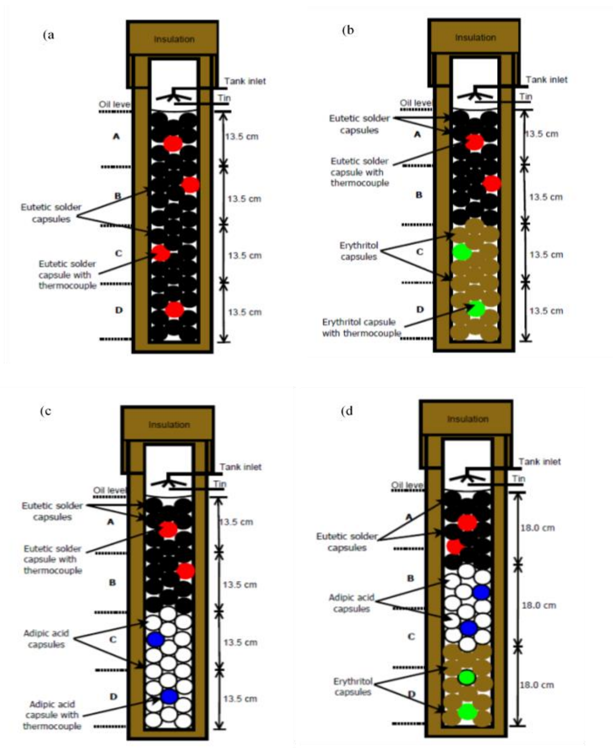

Figure 1: Schematic diagrams of the four storage systems: (a) the single PCM system, (b) cascaded system 1, (c) cascaded system 2 and (d) cascaded system 3.

The single PCM system (a) is composed of 42 eutectic solder (Sn63/Pb37) capsules with four capsules having thermocouples to monitor the PCM temperature, one placed at each of the four levels (A-D). Cascaded TES 1 (b) comprises of 21 eutectic solder PCM capsules at the top and 21 erythritol PCM capsules at the bottom. Two capsules of each PCM have thermocouples to monitor the PCM temperatures at levels A-D. Cascaded TES 2 consists of 21 eutectic solder PCM capsules at the top, and 21 adipic acid PCM capsules at the bottom. Also, two capsules of each PCM have thermocouples to monitor the PCM temperatures at levels A-D. Cascaded system 3 consists of three PCM capsule layers of eutectic solder at the top (14 capsules), adipic acid in the middle (14 capsules) and erythritol at the bottom (14 capsules).

Similar pre-fabricated spherical aluminum capsules, each with a diameter of 0.05 m and a wall thickness of 0.001 m were used for encapsulating the PCMs in this study. Each PCM was melted and then poured into the capsules. Forty-two capsules were filled with eutectic solder (Sn63/Pb37), twenty-one with erythritol, and another twenty-one with adipic acid. Each capsule was filled up to about 80 % of the total volume with liquid PCM to allow for thermal expansion.

Table 1: Thermo-physical properties of the three PCMs used in this study.

Property	Erythritol	Adipic Acid	Eutectic Solder (Sn63Pb37)
Melting Temperature (ºC)	118.4 - 122.0 [22]	151.5-153.0 [24]	183 [26]
Specific Heat Capacity (kJ/kgK)	1.38 (20 ºC) [23] 2.76 (140ºC)	1.59 (20 ºC) [24] 2.26 (150 ºC)	0.21 (30 ºC) [27]
Phase change enthalpy (kJ/kg)	310.6 [22]	238.5 [24]	52.1 [26]
Density (kg/m^3)	1480 (20º C) [23] 1300 (140º C)	1360 (20 ºC) [24] 1093 (163 ºC)	8400 [28]
Thermal conductivity (W/m K)	0.733 (20º C) [23] 0.326 (140º C)	0.16 (150 ºC) [25]	50 [27]
Average mass of PCM in a capsule (g)	64.02	60.03	364.03

Thermo-physical properties of erythritol, adipic acid and the eutectic solder as obtained from open literature are presented in Table 1. The average mass of erythritol in the capsules was almost similar to the average mass of adipic acid in the capsules. The eutectic solder has the largest mass of PCM inside the capsules due its higher density. Erythritol possesses the largest phase change enthalpy, while the eutectic solder has the least. The thermal conductivity of the solder is the highest, while adipic acid shows the lowest thermal conductivity.

The basic experimental setup is shown in Figure 2, and a more detailed description of the setup may be found in our previous studies [20, 21]. The experimental setup consists of an insulated, cylindrical aluminium TES tank whose contents may be any of the configurations depicted in Figure 1. Charging occurs when valves 3, 5 and 7 are open. The electrical heater (f) with embedded oil circulating copper spiral coils heats up the oil which is pumped through the flow pipes to the top of the TES tank (a). The heating power and the maximum temperature of the heating unit is controlled by a temperature controller (g). Charging of the TES system is terminated when the average bottom fluid temperature TD (average of T41, T42, T43) is 190 ºC for the single PCM system to ensure that the bottom PCM is melted since the melting temperature of the eutectic solder is 183 ºC.

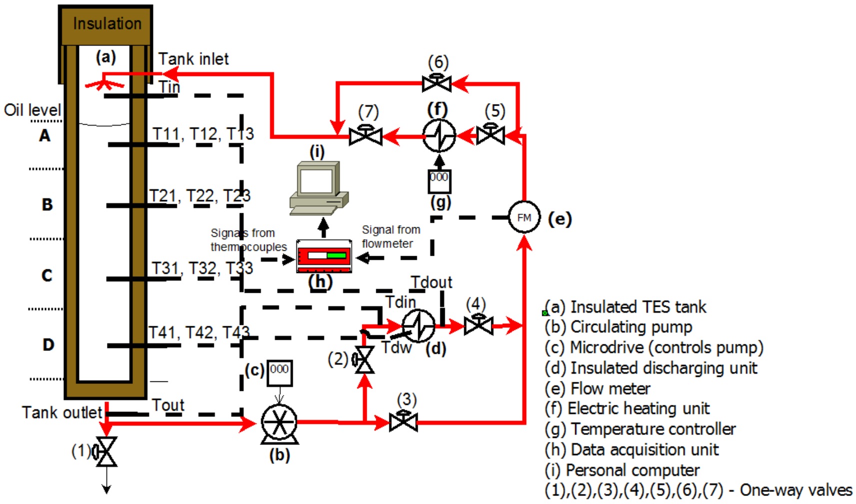

Figure 2: Experimental setup to characterize the four TES systems during charging.

For the cascaded systems, charging is terminated when the average bottom temperature is 180 °C to ensure the flashpoints of the bottom PCMs (erythritol and adipic acid) are not reached. The flash point temperatures of adipic acid and erythritol are about 196 °C and 209 °C, respectively. To investigate the effects of the HTF flowrate on the charging characteristics, the maximum heater temperature was set to 280 °C. The three different charging flowrates used were 4 ml/s, 6 ml/s and 8 ml/s , respectively. These are referred to low, medium and high charging flowrates in this study. The desired HTF flowrate was regulated via the micro-drive (c) which regulated the pumping power of the circulating pump (b).

3. Exergy analysis

The charging exergy rate which signifies the quality of the energy stored is expressed as [29, 30]:

$$\dot{E}_{XCH} = \rho_{av} c_{av} \dot{V}_{ch} \left[(T_{chin} - T_{chout}) - T_{amb} \ln\left(\frac{T_{chin}}{T_{chout}}\right) \right] \quad (1)$$

where T_{amb} is the ambient temperature. The average variation of the density and the specific heat capacity of the HTF with temperature is given as [15]:

$$\rho_{av}\ (kg/m^3) = 930.62 - 0.65 T_{av} \quad (2)$$

and

$$c_{av}\ (J/kgK) = 2115.0 + 3.13 T_{av} \quad (3)$$

where T_{av} is the average of the inlet and outlet HTF temperatures.

4. Results and discussion

Figure 3 shows average charging HTF temperature profiles for the four TES systems with the low charging flowrate of 4 ml/s. T_{Chin} is the charging inlet temperature at the top of the storage tank, T_A to T_D are the average HTF temperatures at the four different sections of the TES tanks (taken from the top to the bottom), T_{Chout} is the outlet charging temperature from the bottom of the TES tanks, and T_{amb} is the ambient temperature in the laboratory. The commencement of the phase change processes for the different PCMs in the tanks are pointed out by the arrows on the plots.

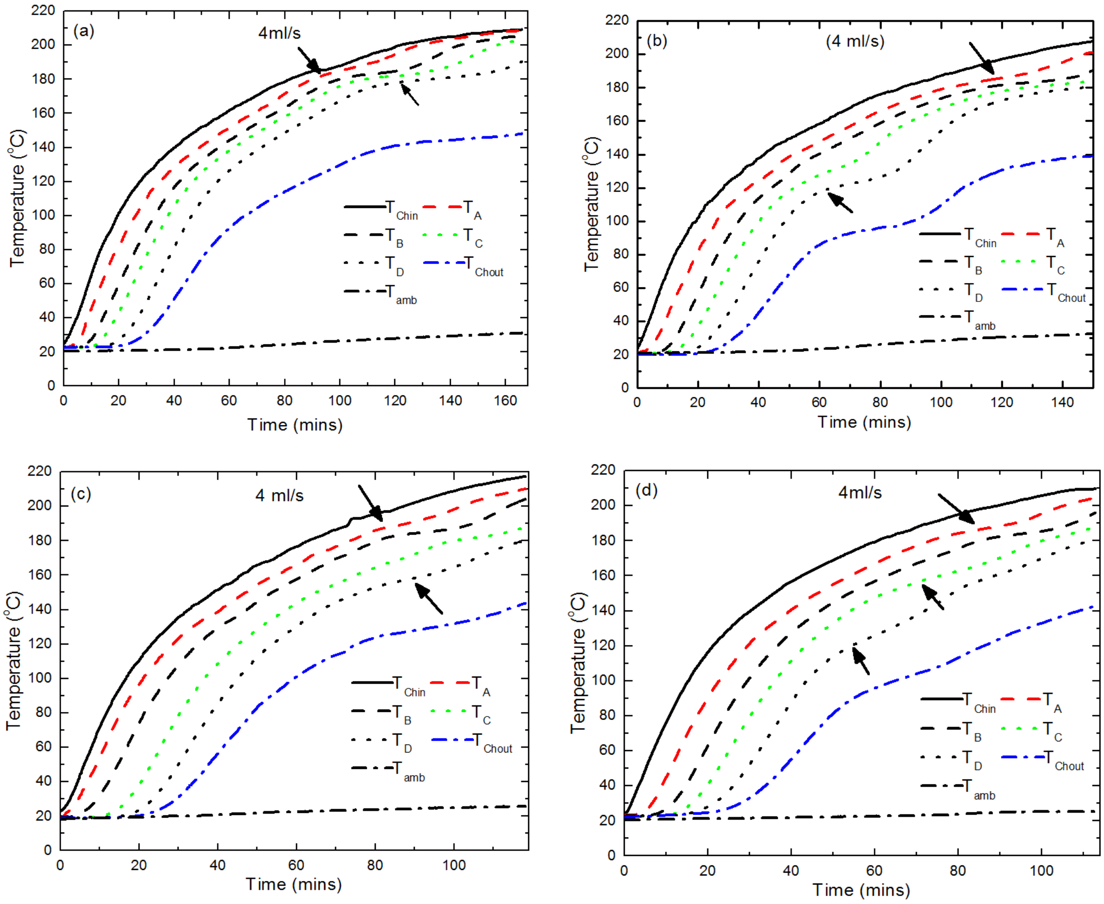

Figure 3: Average charging temperature profiles at a heater set temperature of 280 °C using a low flowrate of 4 ml/s for (a) a single PCM system, (b) cascaded system 1, (c) cascaded system 2 and (d) cascaded system 3.

The single PCM TES tank shows the longest charging time of around 170 mins due to the larger thermal mass of metallic PCMs in the tank. Cascaded TES 1 with erythritol capsules at the bottom shows a charging time longer than the other cascaded TES systems, due to the lower melting temperature of erythritol which is 120 °C. The phase change process at the bottom thus occurs earlier and for a longer duration as compared to the other cascaded systems making the bottom limiting temperature to be approached later. One possible explanation is the low thermal conductivity of erythritol in the liquid phase which slows down heat transfer in the liquid phase. The charging time for cascaded TES 1 is comparable to that of single PCM system whereas the charging times of cascaded TES 2 and cascaded TES 3 containing adipic acid are considerably shorter and comparable. The cascaded TES 3 (with the three PCMs) charges up in the shortest duration of about 112 mins. It seems the slightly lower thermal mass of adipic in the liquid phase for cascaded TES 2 and cascaded TES 3 has an effect of lowering the charging time even if the thermal conductivity is lower for adipic acid compared to erythritol.

In terms of the charging phase change transitions, the single PCM shows phase change transitions which commence from the top to bottom since charging occurs from the top to the bottom. In contrast to this behaviour, the cascaded systems with lower meting temperature PCMs at the bottom, show phase change transitions that commence from the bottom lower temperature PCMs to the upper high melting temperature PCMs at the top. The most pronounced phase change transitions at the bottom are seen with cascaded TES 1 consisting of eutectic solder and erythritol. This is probably due to the larger phase change enthalpy of erythritol compared to the other PCMs.

Exergy rate profiles of the TES systems are presented in Figure 4. For the low charging flowrate (Figure 5 (a)), cascaded system 3 shows the highest exergy rate values from around 30 mins to 90 mins as compared to the other TES systems. This is due to the larger degree of thermal stratification during this period induced by the phase change transitions of adipic acid and erythritol during this period. The exergy rate of each TES is seen to increase at steady rates as T_{chin} increases. The rates at which the exergy accumulates in each of the TES system is, however, seen to slow down as T_{chin} approaches a steady state maximum value induced by the set heater temperature, Cascaded TES 2 shows the second best thermal performance in terms of the exergy rate values for the low flowrate, and its exergy rate values become greater than those of cascaded TES 3 after 90 mins of charging. This is possibly due to the earlier phase change of the eutectic solder at section B of the storage tank as compared to the PCM at the same section of cascaded TES 3. Cascaded TES 1 shows the third best thermal performance in terms of useful energy at the low flowrate. The single PCM system possessed the lowest rates of exergy accumulation due to the high phase change temperature of the solder. Exergy rate values range from 0 W to about 225 W. The highest exergy values at the end of charging processes are seen with cascaded TES 2, followed by cascaded TES 3, cascaded TES 1 and lastly by the single PCM system.

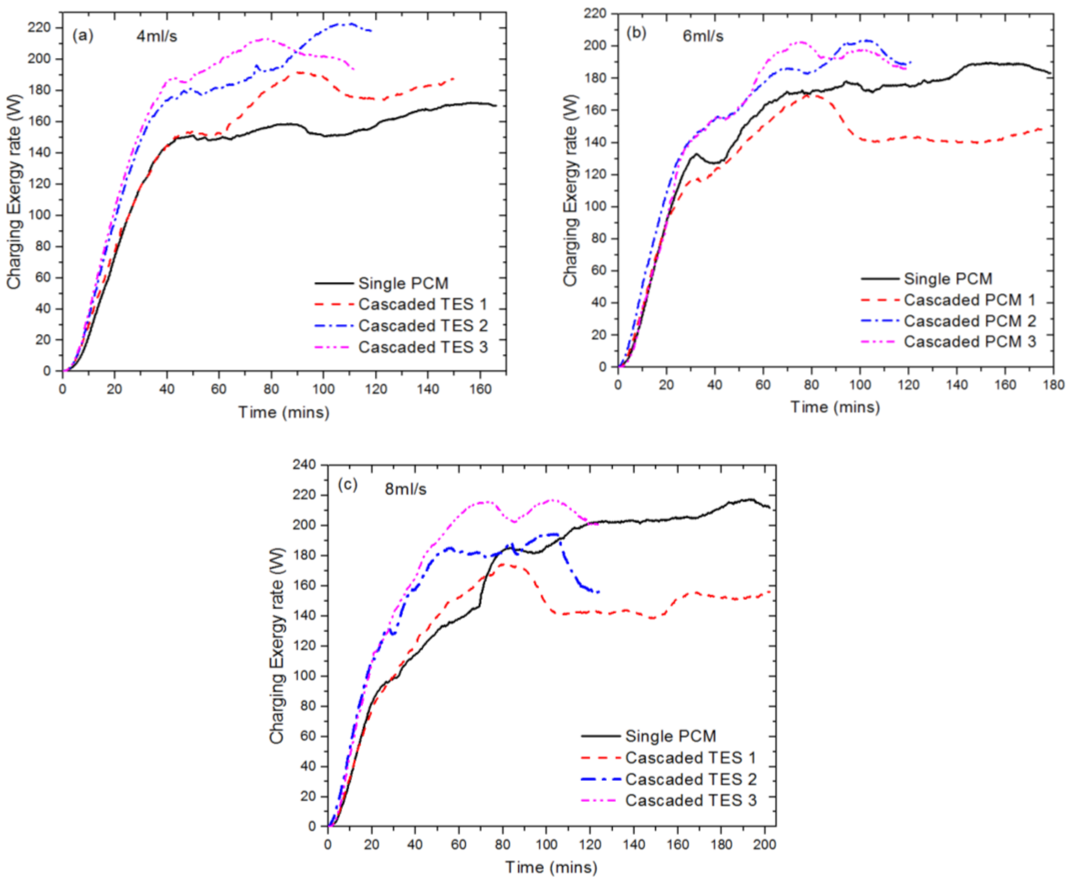

Figure 4: The time-wise variation in the charging exergy rate profiles at (a) low, (b) medium and (c) high HTF flowrate for the four TES systems

With the medium flowrate, cascaded TES 2 shows the higher initial exergy rate values as compared to the other TES systems possibly due to the lower thermal conductivity and slightly larger thermal mass effect. However, after about 20 mins, the rate of exergy accumulation of cascaded TES 3 increases to be similar to that of cascaded TES 2. About the same time, the exergy rate of the single PCM system also overshoots that of cascaded TES 1. Cascaded system 1 shows the worst thermal performance in terms of the exergy rates at this flowrate.

At the highest flowrate, cascaded TES 3 and cascaded TES 2 show similar exergy rates until about 25 mins when the former can be seen to accumulate exergy at greater rates than the latter. After about 100 mins, the exergy accumulation rate for cascaded TES 2 begins to degrade. The single PCM system can be observed to steadily increase in its exergy accumulation rate, and it eventually becomes the best from about 120 mins until the end of charging. Cascaded TES 1 can be observed to be the poorest performer in terms of exergy accumulation rate at the high flowrate. The peak exergy accumulation rates of cascaded systems 1 - 3 can be seen to generally reduce as the HTF’s flowrate is increased, whereas those of the single PCM system increase suggesting an exergy accumulation rate improvement with an increase in the flowrate.

5. Conclusion

Experimental exergy charging characteristics of four medium temperature packed bed latent heat thermal energy storage systems using Sunflower Oil as the heat transfer fluid have been compared and presented. Cascaded TES 3, the 3 PCM cascaded system showed higher exergy charging rates because of the release of latent heat in 3 phase change transitions. Its thermal performance was comparable to cascaded TES 2 with adipic acid at the bottom of the storage tank. The charging times for cascaded TES 2 and cascaded TES 3 are also shorter when compared to the other storage systems suggesting a better charging performance. The single PCM showed the lowest exergy charging rate at the lowest flowrate but its performance improved to better than that of cascaded TES 1 with an increase in the flowrate. This suggests that performance improvement in cascaded TES systems depends on the melting temperature of PCM since the lower melting temperature PCM in cascaded TES 1 showed poorer exergetic performance in some instances compared to the single PCM system.

References

[1] Fernández AI, Barreneche C, Belusko M, Segarra M, Bruno F, Cabeza LF. Considerations for the use of metal alloys as phase change materials for high temperature applications. Solar Energy Materials and Solar Cells 2017; 171: 275–81.

[2] Ma F, Zheng P. Investigation on the performance of a high-temperature packed bed latent heat thermal energy storage system using Al-Si alloy. Energy Conversion and Management 2017; 150: 500–14.

[3] Fukahori R, Nomura T, Zhu C, Sheng N, Okinaka N, Akiyama T. Macro-encapsulation of metallic phase change material using cylindrical-type ceramic containers for high-temperature thermal energy storage. Applied Energy 2016; 170: 324–28.

[4] Kotzé JP, von Backström TW, Erens PJ. Simulation and testing of a latent heat thermal energy storage unit with metallic phase change material. Energy Procedia 2014; 49: 860 – 69.

[5] Wang X, Liu J, Zhang Y, Di H, Jiang Y. Experimental research on a kind of novel high temperature phase change storage heater. Energy Conversion and Management 2006; 47: 2211–22.

[6] Zhang G, Li J, Chen Y, Xiang H, Ma B, Xu Z, Ma X. Encapsulation of copper-based phase change materials for high temperature thermal energy storage. Solar Energy Materials & Solar Cells 2014; 128: 131–37.

[7] Lakshmi Narasimhan N. Assessment of latent heat thermal storage systems operating with multiple phase change materials. Journal of Energy Storage 2019; 23: 442–55.

[8] Yang L, Zhang XS. Performance of a new packed bed using stratified phase change capsules. International Journal of Low-Carbon Technologies 2012; 7: 208–14.

[9] Mao Q, Zhang Y. Thermal energy storage performance of a three-PCM cascade tank in a high-temperature packed bed system. Renewable Energy 2020; 152: 110–19.

[10] Cheng X, Zhai X. Thermal performance analysis and optimization of a cascaded packed bed cool thermal energy storage unit using multiple phase change materials. Applied Energy 2018; 215: 566–76

[11] Cheng X, Zhai X. Thermal performance analysis of a cascaded cold storage unit using multiple PCMs. Energy 2018; 143: 448–57.

[12] Adebiyi GA, Hodge BK, Steele WG, Jalalzadeh-Azar A, Nsofor EC. Computer simulation of a high-temperature thermal energy storage system employing multiple families of phase-change storage materials. Journal of Energy Resources and Technology 1996; 118: 102–11.

[13] Aldoss TK, Rahman MM. Comparison between the single-PCM and multi-PCM thermal energy storage design. Energy Conversion and Management 2014; 83: 79–87.

[14] Mawire A, Taole S, Phori A. Performance comparison of thermal energy storage oils for solar cookers during charging. Applied Thermal Engineering 2014; 73: 1321–29.

[15] Mawire A. Performance of Sunflower Performance of Sunflower Oil as a sensible heat storage medium for domestic applications. Journal of Energy Storage 2016; 5: 1–9.

[16] Hoffmann JF, Vaitilingom G, Henry JF, Chirtoc M, Olives R, Goetz V, et al. Temperature dependence of thermophysical and rheological properties of seven vegetable oils in view of their use as heat transfer fluids in concentrated solar plants. Solar Energy Materials and Solar Cells 2018; 178: 129-38.

[17] Hossain AK, Davies A. Plant oils as fuels for compression ignition engines: A technical review and life-cycle analysis. Renewable Energy 2010; 35: 1–13.

[18] Mawire A, Lentswe KA, Shobo A. Performance comparison of four spherically encapsulated phase change materials for medium temperature domestic applications. Journal of Energy Storage 2019; 23: 469–79.

[19] Mawire A, Lefenya TM, Ekwomadu CS, Lentswe KA, Shobo AB. Performance of a medium temperature eutectic solder packed bed latent heat storage system for domestic applications. Journal of Energy Storage 2020; 28: 101294.

[20] Mawire A, Ekwomadu CS, Lafenya TM, Shobo A. Performance comparison of two metallic eutectic solder based medium-temperature domestic thermal energy storage systems. Energy 2020; 194: 116828.

[21] Mawire A, Lefenya TM, Ekwomadu CS, Lentswe KA, Shobo AB. Performance comparison of medium temperature domestic packed bed latent heat storage systems. Renewable Energy 2020; 23: 1897–1906.

[22] Shobo AB, Mawire A. Experimental comparison of the thermal performances of acetanilide, meso-erythritol and an In-Sn alloy in similar spherical capsules. Applied Thermal Engineering 2017; 124: 871–82.

[23] Agyenim F, Eames P, Smyth M. Heat transfer enhancement in medium temperature thermal energy storage system using a multitube heat transfer array. Renewable Energy 2010; 35: 198-207.

[24] Adipure Datasheet 2018. http://adi-pure.invista.com/e-trolley/page_11546/index.html (accessed 05.04.2020).

[25] Yaws, C. L. (1995). Handbook of Thermal Conductivity. Volume 3. Organic Compounds C8 to C28. Houston, TX: Gulf Publishing Company.

[26] Morando C, Fornaro O, Garbellini O, Palacio H. Thermal properties of Sn-based solder alloys. Journal of Material Science: Materials in Electronics 2014; 25: 3440–47.

[27] Wu YK, Lin KL, Salami B. Specific Heat Capacities of Sn-Zn-Based Solders and Sn-Ag-Cu Solders Measured Using Differential Scanning Calorimetry. Journal of Electronic Materials 2009; 38: 227–30.

[28] Sn63Pb37 RA Solder Wire 4880-4888 Technical Data Sheet 2018. https://images-na.ssl-images-amazon.com/images/I/81h+ZhgF19L.pdf (accessed 05.04.2020).

[29] Alam TE. Experimental investigation of encapsulated phase change materials for thermal energy storage. PhD Thesis 2015, University of South Florida, USA.

[30] Jegadheeswaran S, Pohekar SD, Kousksou T. Exergy based performance evaluation of latent heat thermal storage system: a review, Renewable and Sustainable Energy Reviews 2010;14: 2580–95.

Packed-bed Thermocline Testing Facility with Air as HTF for Sensible Thermal Energy Storage

Elisa Alonso[1], Esther Rojas[1] and Rocío Bayón[1]

[1] Thermal Storage and Solar Fuels Unit, PSA-CIEMAT Madrid (Spain)

Abstract

Sensible heat from CSP plants or other energy sources can be stored in one-single tank storage system that performs by creating a thermocline between a cold and hot zone. The Thermal Storage Group of CIEMAT has available a testing facility for packed-bed thermocline TES, named ALTAYR, suitable for operating in a wide range of temperatures and flowrates, different solid materials and charge and discharge modes. Such facility is useful for forecasting the behavior of industrial thermocline tanks, especially when it is combined with mathematical models able to count for scale aspects, as well as for different material assessment. In this work, different experimental tests operating with ALTAYR under different conditions are presented. Two types of pebbles have been employed as filler materials and their storage capacity has been compared. The temperatures in both solid and air have been measured independently using four different experimental methodologies to differentiate between them. However, it appears to be no measurable difference. The tank wall thermal conductivity has been obtained from one long duration experimental test in order to characterize the tank and be able to calculate thermal losses through the wall.

Keywords: Thermal Energy Storage, Packed-bed Thermocline, Sensible Heat, CSP

1. Introduction

A CSP plant can include large thermal energy storage (TES), and thanks to it the electricity supply is possible for extended periods, even at night-time and it is not affected by short term variations due to clouds occurrence during the sunny time. This advantage over other renewable which does not count with storage of large capacity (wind and PV) provides high flexibility and dispatchability to CSP and makes it the key to have a renewable energy mix (Islam et al., 2018). Currently, the mainstream TES solutions are based on sensible heat storage (SHS) and use a molten salt mixture that are stored in a two tanks system, one tank devoted to hot salt and another to cold salt. However, compared to this system, an only one thermocline tank is about 35% cheaper (Gil et al., 2010). A thermocline tank usually contains a solid filler that occupy most of the total volume and, thus, contribute to reduce the global cost of the system. As fillers, cheap and locally available materials are normally employed. Natural materials such as sand or different kind of stones are common (Schlipf et al.,2014). They form a packed-bed through which a liquid or gas flows. This work focuses in an air-rock packed bed able to operate at maximum temperature over 700ºC. In a system of such characteristics and according to most of literature references, it is expected to find significant differences between air and solid temperature (Bayón and Rojas, 2013). Using the facility available at CIEMAT, named, ALTAYR, experimental methodologies have been devised and put in practice with the objective to differentially measure solid and air temperature. The general performance of the packed-bed tank has been also analyzed. The relevance of a deep understanding on this storage prototype behavior stands on the need of employing it as an experimental tool to: 1) study the effects of the main parameters which will be critical for an industrial-scale thermocline tank design, 2) validate numerical models developed to allow the analysis of a wide range of operation conditions, 3) study the goodness of different materials as storage media.

2. Experimental Facility

ALTAYR´s main component is a cylindrical tank with a bed height of 0.5 m (tank height 0.72 m) and 0.5 m in inner diameter. It consists of a metal casing with a ceramic inner wall, separated by an insultation layer. On and under the cylindrical main body there are two additional conical bodies coinciding with the air inlet and outlet. Working in charge mode, the hot air is heated by a set of electrical resistances. It flows to the tank thanks to a blower and a flowmeter -with a valve- that propel the atmospheric air toward the resistances container and

doi:10.18086/eurosun.2020.07.03 Available at http://proceedings.ises.org

following to the tank. Air temperature is set by using a control system configured in a control board. Temperature from ambient to more than 1000 ºC can be set and achieved by the resistances, although in this work the goal has been established in 700 ºC. The hot air crosses the tank from the top to the bottom and exists through the lower pipe, which, after a certain path, leads to outside.

The tank is provided with a fair number of thermocouples for temperature monitoring. In the rock-bed, temperature is measured at 9 different heights and 4 radiuses. Moreover, the temperature on the outer wall of the tank is measured at 10 heights and 5 angular positions and the air temperature at the inlet and outlet is also measured.

To modify the working mode to discharge, the pipes connections can be exchanged so that the tube coming from the blower would enter through the base of the tank and the hot air would exit through the top and would been ejected.

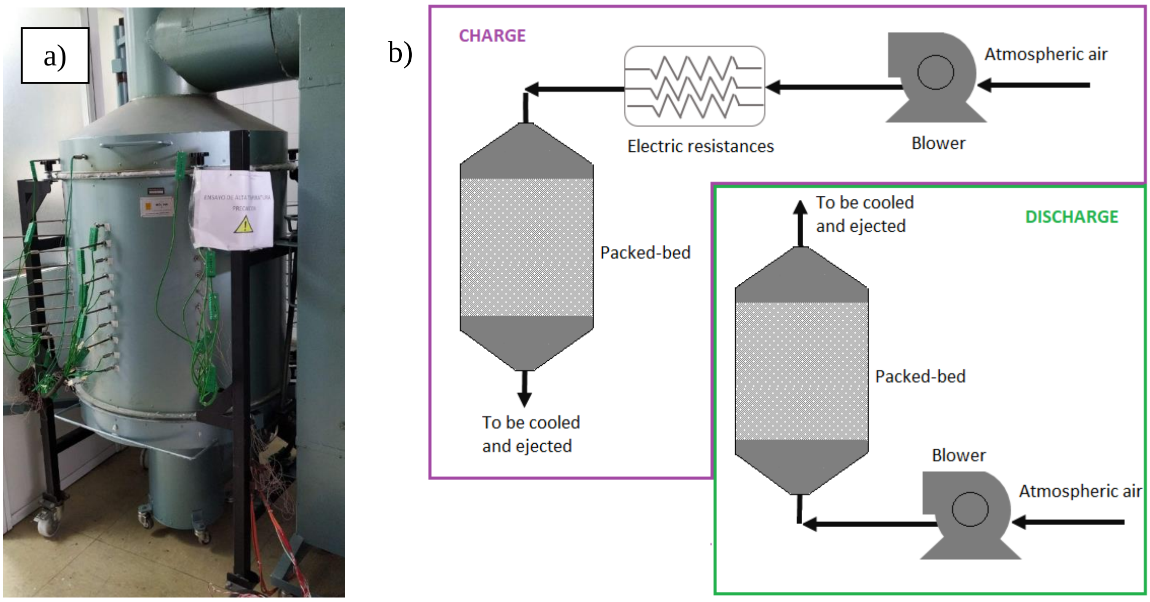

Fig. 1: a) Picture of ALTAYR packed-bed tank. b) Schematic of the main components of the experimental facility when working in charge and discharge modes.

3. Filler Characteristics

Two economic types of pebbles, easily reachable through gardening products suppliers, were purchased to be employed as filler materials. They are showed in Fig. 2 once they had been placed inside the tank. Composition of pebbles in filler 1 is not informed by the provider, who offer the material as “white boulder”. The mechanic resistance of the pebbles was noted to be low since they broke under light pressure. Filler 2 composition was specified by the provider as mainly SiO_2, with unknown purity. The porosity was obtained experimentally by measuring the water volume that fits on 0.1 m^2 of pebbles.

Tab. 1: Main properties of the two filler materials.

Property	Filler 1	Filler 2
Composition	Unknown	Mainly silica
Color	White	Beige
Size (mm)	12/25	14/22
Density (kg/m^3)	1790	1780
Porosity	0.37	0.31

Fig. 2: Two kind of fillers employed for the experimental tests.

4. Experimental tests

The tank was filled with around 150 kg of pebbles. Experimentation consisted in a set of tests of charge and discharge processes performed for each of the two filler materials. Threshold temperature during charge was stablished by setting up the air stream temperature in values between 300º C and 700 ºC. Discharge tests were started after ending charge and manually changing the tubing connections to lead the cold air at room temperature enter through the tank bottom. Air mass flowrates between 50 and 100 kg/h were employed for the different tests. The electric energy consumption to heat up the air was also accounted by means of a consumption meter. Figure 3 shows a detailed representation on the thermocouples position along the tank height and radius. Red and grey lines and dots correspond to thermocouples at alternate levels that are introduced inside the packed bed, touching the pebbles but completely surrounded by air. The temperature values they record are more likely the air temperature. Green lines and dots, instead, represent particular thermocouples that measure temperature inside the rocks for which one the following procedures has been applied:

- A: Taking a thermocouple provided with a rigid, metallic sheath, one of the stones was pierced to make a hole with around the same diameter than the sheath (6 mm) and about 5 mm in depth. The thermocouple was then inserted into the hole. This strategy was employed with filler 1 because filler 2 rocks could not be easily mechanized and broke when holes of 6 mm in diameter were tried.

- B: Taking a flexible, 0.5 mm in diameter thermocouple, it is inserted into a natural, small hole existing in a pebble. This strategy was employed with filler 2.

- C: A hole of around 3-4 mm in diameter was made in a stone. The hole was then filled with ceramic fiber and a flexible, 0.5 mm in diameter thermocouple was pricked. This strategy was employed with rocks of filler 2, which did not endure holes of 6 mm in diameter, but they did of smaller diameter.

- D: The front of a thermocouple provided with a rigid, metallic sheath was put in contact with a flat face of a stone. Avoiding the contact surface, the end of the thermocouple and the stone were covered by high temperature refractory cement that rapidly hardened.

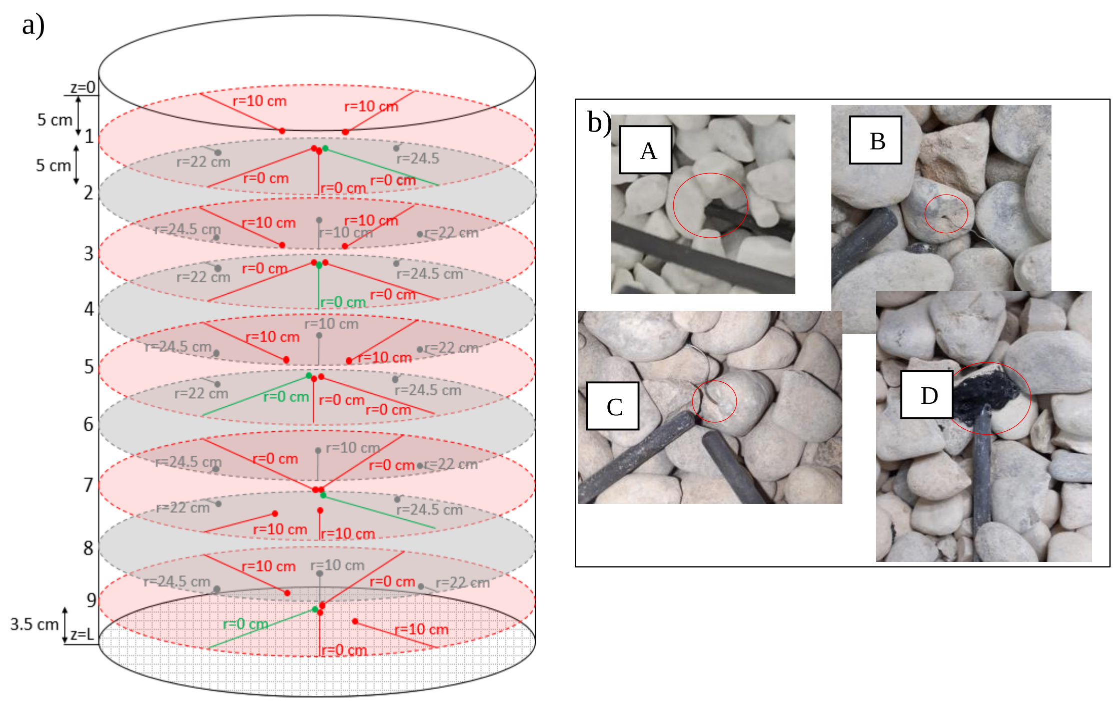

Fig. 3: a) Schematic of the thermocline tank where the positions of thermocouples have been indicated by height levels, radius and angles. b) Images of the thermocouples devoted to measure the solid temperature according to four different procedures described above.

5. Results

5.1. General performance

Figure 4 shows two experimental cases of charge performed for filler 1 (a and c) and discharge performed for filler 2 (b and d) using ALTAYR facility-. For -each one, data have been represented in both temperature versus time, as directly recorded by the data logger and- temperature versus tank height to appreciate the time evolution of the thermocline.

Temperature data were recorded along the time as presented in Fig. 4 a) and c). Temperature curves correspond to thermocouples placed in the middle of the cylindrical tank, being the upper one that of maximum temperature and the lower one that of minimum. z values corresponding to the position of each thermocouple are 0, 0.05, 0.15, 0.25, 0.35 and 0.45 m. b) and d) correspond to the same cases but the thermocline formation along height is represented. During the experimental work, it was clearly observed that required time to charge and discharge is strongly influenced by the type of filler, the range of temperatures and the air mass flowrate. Next sections deepen in the effect of these parameters. The initial temperature of discharge case is not constant due to the facility requires manual actuation to change the working mode. That means that the experimenter employs a certain time to switch off the blower and the heater, to start a new data recording program and to change the position of two heavy tubes. The upper limit of the selected operation parameters range, that is, threshold temperature of 700ºC and flowrate of 100 kg/h were unsuccessfully achieved, because the heater needs to work at its limit of power and thus, reaching the temperature set point delays too much. Then, such a combination of parameters was avoided.

Charge data of temperature-time could be analyzed by fitting the experimental curves to an algebraic sigmoid function as previously reported in (Bayón and Rojas, 2018). For each tank position (zc), this curve fitting leads to a value of time (tc) that corresponds to the sigmoid inflection point. In this way, plotting zc vs. its corresponding tc it is obtained a linear variation whose slope is the thermocline velocity vTC. For the test of Figure 4 a) the thermocline velocity is $3.89 \cdot 10^{-5}$ m/s.

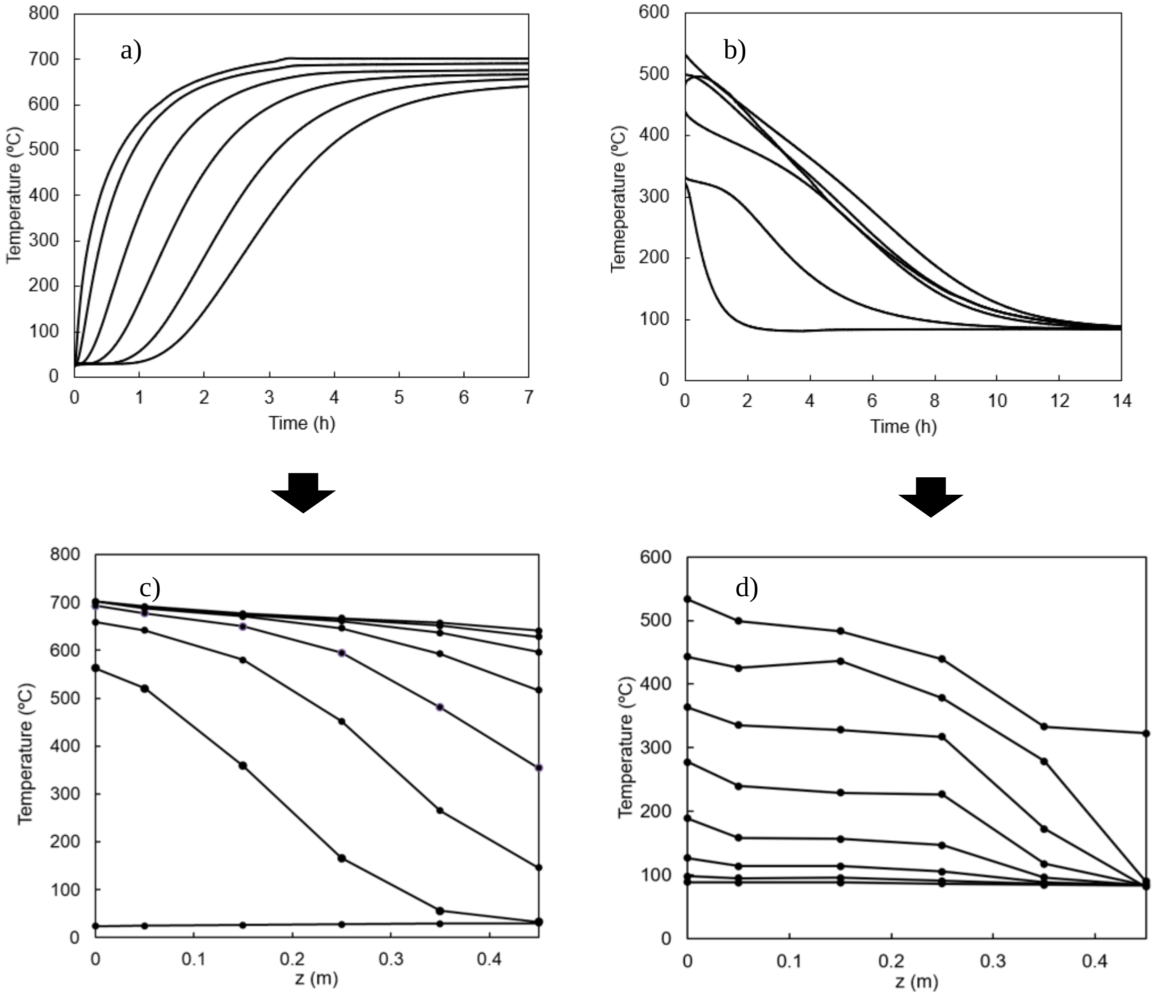

Fig. 4: Temperature distribution in two experimental case: a) and c): charge, maximum temperature 700 ºC, air flowrate 80 kg/h. b) and d)): discharge, maximum temperature 600 ºC, air flowrate 50 kg/h. Note that origin in z coordinate is considered in the top of the tank. The time gap between lines is 1 h for Fig. 4 c) and 2 h for Fig. 4 d), being the first one time equal to 0.

In energy storage systems, charge and discharge efficiencies are usually selected as performance indicators (Hoffmann et al., 2017). Their utility to assess the storage system is relevant when it is integrated in a plant that operates under determinate conditions to which the storage must be adapted. In those cases, the storage system performs charge and discharge cycles between two given threshold temperatures. Here, an instantaneous overall efficiency of the whole packed-bed facility has been calculated as the ratio between the stored energy and the supplied energy, which is globally accounted by the electricity consumption meter.

$$\eta_{overall} = \frac{m \cdot C_p (T_b - T_i)}{E_e} \qquad \text{(eq. 1)}$$

Figure 5 a) shows the overall facility efficiency evolution throughout a test with maximum temperature of 300ºC and a duration of 22 h. The packed-bed material was filler 2, mainly composed of silica, and which specific heat can be approximated to that of quartzite, that is, 840 J/kg·K (Gautan and Saini, 2020). Maximum efficiency takes place after around 6 hours of heating, being 6.8 %. The higher the maximum temperature, the higher the efficiency. For instance, in the case of the experiment represented in Fig. 9 (filler 2, 6 hours of heating with a threshold temperature of 700ºC) the maximum efficiency reaches 15.7% and takes place after 5.6 hours of heating (Figure 5 b)).

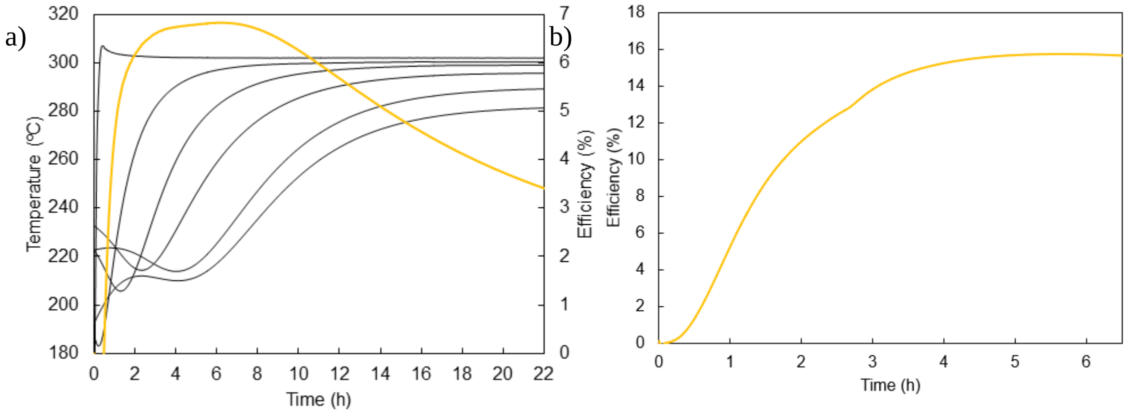

Fig. 5: Two examples of the overall facility efficiency. a) Test with filler 2, maximum temperature of 300ºC, duration of 22 h. Black lines show the temperature evolution in different tank heights (0, 0.05, 0.15, 0.25, 0.35 and 0.45) b) Test with filler 2, maximum temperature of 700ºC, duration of 6 h. Figure 4 b) corresponds to the temperature evolution represented by red curves in Fig. 9.

5.2. Solid and air temperature

The temperature differences between solid and air is not high enough to be evaluated by means of any of the measurement strategies applied in this work. In Fig.6 four examples of comparison of solid and air temperatures are showed. Each one of the described methods have been employed to difference them, which have been measured at the same height and radius. As observed, the differences between solid and air temperature is not higher than the own error between the two measurements of air temperature taken by two equal thermocouples placed together.

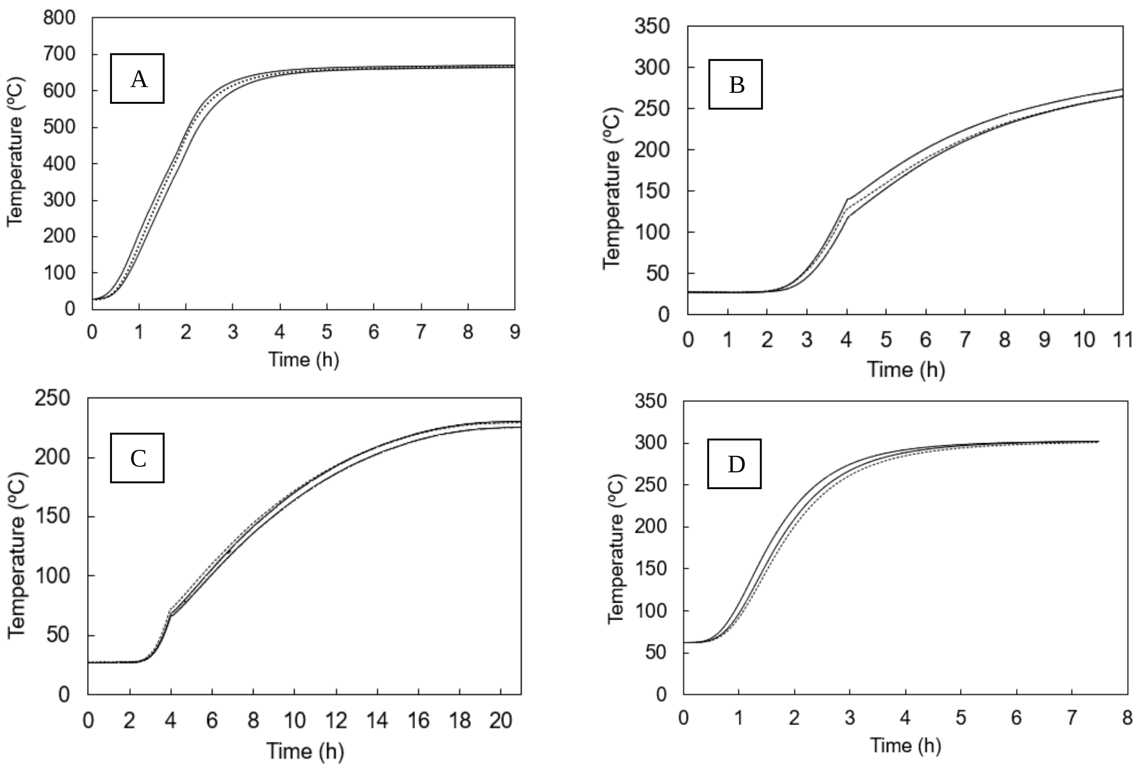

Fig. 5: A result example of each strategy to differentiate solid temperature from air one. Each letter corresponds to the case indicated in section 4.

5.3. Air mass flowrate influence in the thermocline behaviour

It is expected the air flowrate introduced in the tank, which directly affects the interstitial air velocity, modifies the velocity of the thermocline. Figure 7 is devoted to show this effect. The thermoclines of four experimental cases, which operation conditions are indicated in Tab. 2, are represented for 8 hours of charge and temporal gaps of 1 hour. 8 hours is enough time to completely charge the tank when the maximum temperature is 300 in both cases although the charge is faster for a flowrate of 100 kg/h. In this case, the tank is also practically charged after 7 hours. When the maximum temperature is higher, as observed in cases A and B, the required time to charge de tank is obviously higher as well. However, comparing cases A and B it is clearly observed how the higher the air flowrate, the faster the progression of the thermocline. More than visually, the thermocline behaviour can be compared with accuracy by calculating the vTC according to Bayón and Rojas, 2018, and as explained above. The corresponding values have been included for each case in the last column of Tab. 2.

Tab.2. Operational conditions of the cases showed in Fig. 6.

Case	Filler	T_{max} (ºC)	Air flowrate (kg/h)	vTC (m/s)
A	1	700	50	$3.15 \cdot 10^{-5}$
B	1	700	80	$3.89 \cdot 10^{-5}$
C	1	300	80	$7.41 \cdot 10^{-5}$
D	1	300	100	$8.09 \cdot 10^{-5}$

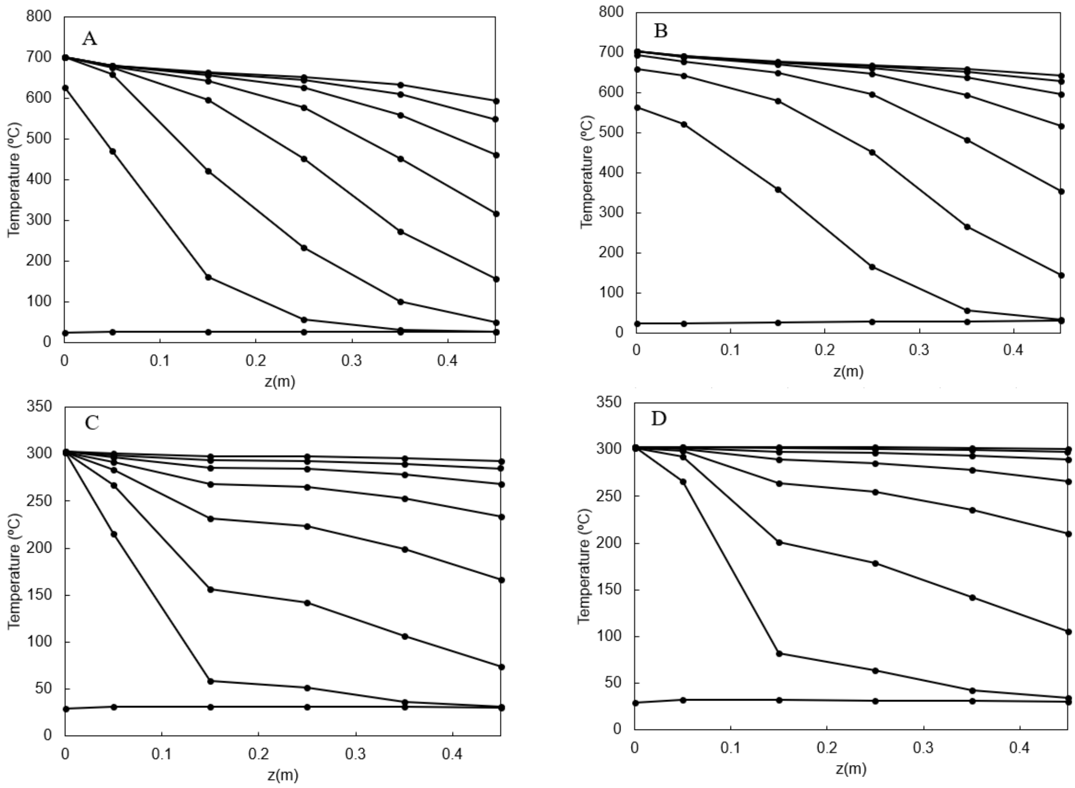

Fig. 7: Thermocline formation and evolution for maximum temperature 700 ºC and 2 values of air flow mass and for maximum temperature 300 ºC and 2 values of air flow mass (see Tab. 2) . The time gap between lines is 1 h, being the first one time equal to 0.

5.4. Wall heat transfer coefficient

The experimental case reported in Fig. 4 a) was retained to calculate global heat transfer coefficient through the tank wall. In that experiment, due to its long duration, stationary thermal conditions were achieved both in the packed-bed and the external wall (see Fig. 8). Known the air flowrate and the values of temperature, an energy balance applied to the tank can be expressed as follows:

$$\dot{m_{air}} Cp_{air}(T_{in} - T_{out}) = \frac{2\pi k_{wall} L (T_{wall,int} - T_{wall,ext})}{ln\frac{r_{ext}}{r_{int}}} \qquad \text{(eq. 2)}$$

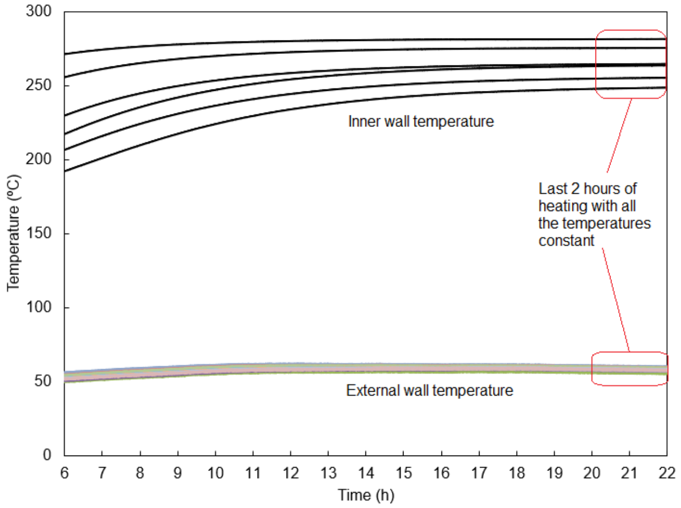

Fig. 8: Experimental case with maximum temperature 300 ºC and 50 kg/h of air flowrate used to calculate the global heat transfer coefficient of the tank wall. The figure focuses on the region where temperatures

According to eq. 2 k_{wall}, which corresponds to the global conductivity involving all the wall layers is 0.4 W/m·K.

Once known k_{wall}, thermal losses can be calculated during the experiments. For comparative purposes, three different cases have been represented. Table 3 shows the operational conditions of each one.

Tab.3. Operational conditions of the cases showed in Fig. 8.

Case	Filler	T_{max} (ºC)	Air flowrate (kg/h)
A (blue)	1	700	50
B (yellow)	2	300	50
C (green)	2	300	100

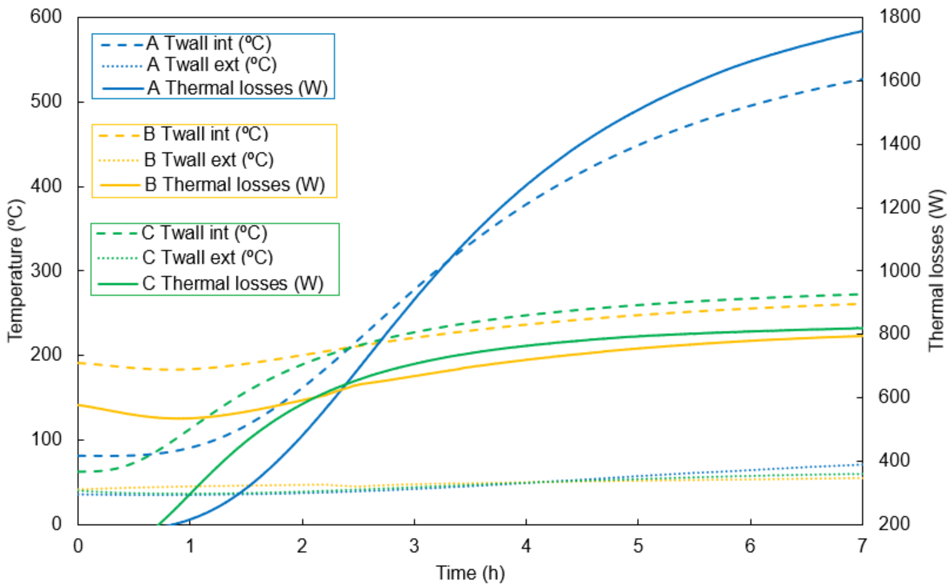

Fig. 9: Inner wall and external wall temperatures and thermal losses through the tank wall calculated for three different experimental cases defined in Tab. 3.

Moreover, known the electric consumption to heat up the air, and neglecting the losses to convert electricity into heat, the thermal losses in the heater and along the tube from heater to tank are also calculated, which, for this experimental test, results of 174.8 W.

5.5. Comparison between the two fillers

By comparing two tests under similar operational conditions, each one using one type of filler, the first observed result is the higher storage capacity of filler 2, probably due to its higher specific heat. They are represented in Fig.10. Both tests consumed 78±2 kWh_e for 6 hours of heating, with a T_{in} set in 700 ºC and a flowrate of 50 kg/h. As observed in Figure 9 filler 1, represented in green, achieved much higher average temperature than filler 2, in red. Thermal losses thorough the tank wall are lower in the case of filler 2. In other words, the total thermal capacity of the storage system with filler 1 is much closer to be completed than with filler 2 after 6 hours of heating. Ensayed et al. (1988) defined the Bed Storage Factor (BSF) as the ratio of energy stored in the bed at a moment of time to the maximum possible energy storage in the bed:

$$BSF = \frac{m \cdot C_p(T_b - T_i)}{m \cdot C_p(T_{max} - T_i)} \qquad \text{(eq. 3)}$$

where T_{max} is the maximum temperature of air inlet, T_i is the initial temperature of the bed and T_b is the average bed temperature achieved in the considered time. Such a definition is equivalent to the capacity ratio found in (Hänchen et al. ,2011). Since thermocouples placed in the packed bed are equidistant, T_b can be calculated as the direct average temperature of the 5 measured values after 6 hours, excluding T1 that corresponds to the air inlet temperature and it is taken above the packed-bed in the air stream. T6 is taken inside the bed at its bottom, but the values are so close to the air outlet temperature that both curves overlap in Fig. 9. T2 to T6 are the values measured by the thermocouples distributed downstream in the tank. According to Eq. 3 BSF is 0.89 for filler 1 and 0.49 for filler 2. Neglecting differences in thermal losses for rapid estimation purposes, the total storage capacity is around 1.8 times higher with filler 2, as schematically represented by the blue rectangles in Fig. 9. The whole rectangles would represent the total capacity for each case and the blue area would correspond to the full fraction after 6 hours according to the graphed experiments. vTC for both cases have been also calculated and their values are $3.145 \cdot 10^{-5}$ m/s for filler 1 and $3.097 \cdot 10^{-5}$ m/s for filler 2.

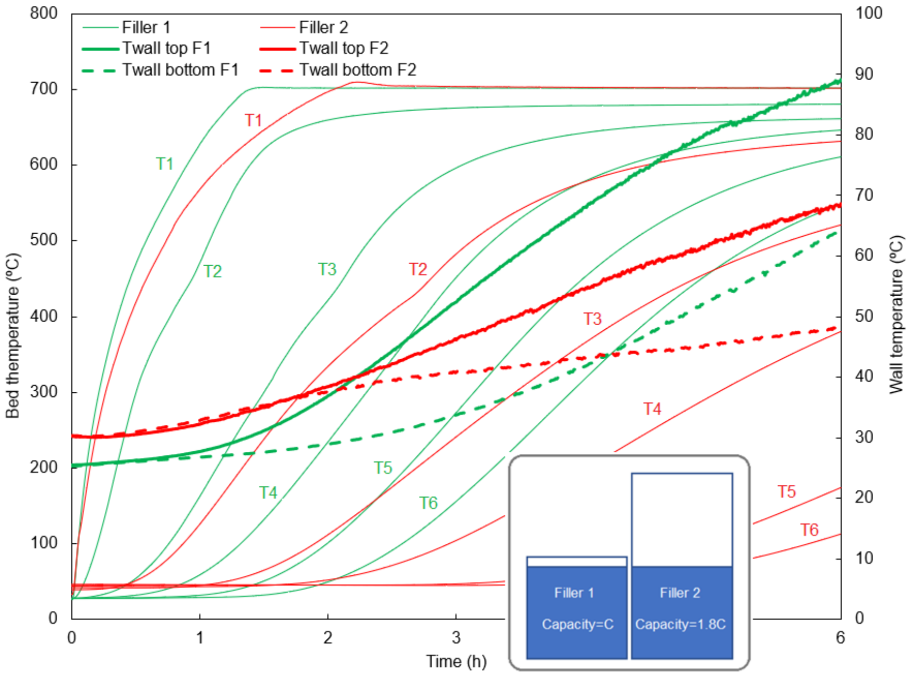

Fig. 10: Comparison between the performance of the storage system using two types of fillers. Charging tests with mass flowrate 50 kg/h and maximum temperature 700 ºC.

Considering a constant C_p of filler 2 of 840 J/kgK (as reported in Gautan and Saini, 2020 for quartzite), the maximum theoretical storage capacity of the system containing filler 2 would be 84 MJ and containing filler 1 47 MJ.

6. Conclusions

ALTAYR tank protype was assessed as a tool for air-solid thermocline studies. Two different filler materials were tested and the second one, which composition is basically SiO_2, presented storage capacity around 1.8 times the first tested material. The tank is useful to measure thermocline velocities under different working conditions, as it is able to operate in a large range of temperature and air flowrates. It was probed how thermocline velocity increases with air flowrate and decreases with maximum set temperature in charge experiments. The global conductivity of the tank wall, including all the layers, was calculated by means of a steady state experiment in which inner and external wall temperature maintained constant. Its value is 0.4 W/m·K. Four strategies to discriminate solid and air temperature were tried. However, the temperature differences between solid and air was not high enough to be evaluated by means of any of the measurement methods applied in this work. Instead, the differences between solid and air temperature was not higher than the own experimental error.

7. Acknowledgments

The authors wish to thank "Comunidad de Madrid" for its support to the ACES2030-CM project (S2018/EMT-4319) through the Program of R&D activities between research groups in Technologies 2018, co-financed by European Structural Funds.

8. References

Bayón, R., Rojas, E. 2013. Simulation of thermocline storage for solar thermal power plants: From dimensionless results to prototypes and real-size tanks. Int. J. Heat Mass Transf. 60, 713–721.

Bayón, R., Rojas, E. 2018. Analysis of packed-bed thermocline storage tank performance by means of a new analytical function. AIP Conf. Proc. 2033, 090002.

Elsayed, M.M., Megahed, I.E., El-Refaee, M. M. 1988. Experimental testing of fluidized bed thermal storage. Sol. Wind Tech. 5, 15–25.

Gautam, A., Saini, R.P. 2020. A review on sensible heat based packed bed solar thermal energy storage system for low temperature applications. Sol. Energy. 207, 937–956.

Gil A., Medrano M., Martorell I., Lázaro A., Dolado, P., Zalba B., Cabeza L. 2010. State of the art on high temperature thermal energy storage for power generation. Part 1—Concepts, materials and modellization. Renew. Sustain. Energy Rev. 14, 31–55. Ç

Hänchen, M., Brückner, S., Steinfeld, A. 2010. High-temperature thermal storage using a packed bed of rocks- Heat transfer analysis and experimental validation. App. Th. Eng. 31, 1798–1806.

Hoffmann, J. F., Fasquelle, T., Goetz, V., Py, X. 2017. Experimental and numerical investigation of a thermocline thermal energy storage tank. App. Th. Eng. 114, 896–904.

Islam M.T., Huda N., Abdullah A.B, Saidur R. 2018. A comprehensive review of state-of-the-art concentrating solar power (CSP) technologies: Current status and research trends. Renew. Sustain. Energy Rev. 91, 987–1018.

Schlipf, D., Schicktanz, P., Maier, H, Schneider, G. 2015.Using sand and other small grained materials as heat storage medium in a packed bed HTTESS. Energy Procedia. 69, 1029–1038.

Thermodynamic Analysis of a Cascaded Latent Heat Store in a Pumped Thermal Electricity Storage System

Yao Zhao[1,2], Christos N. Markides[2] and Changying Zhao[1]

[1] Institute of Engineering Thermophysics, School of Mechanical Engineering, Shanghai Jiao Tong University, Shanghai (China)

[2] Clean Energy Processes (CEP) Laboratory, Department of Chemical Engineering, Imperial College London, London (United Kingdom)

Abstract

In this paper, the feasibility of replacing sensible-heat, packed-bed stores with cascaded latent-heat stores in pumped thermal electricity storage systems is explored through thermodynamic optimization based on exergy and entropy generation. The effects of the total stage number and of the *NTU* on the temperature distributions, energy, exergy and entropy generation in each stage, and over the cascaded store during the heat charging and discharging processes are discussed. The optimal outlet and melting temperatures of each stage during the heat charging process are both found to follow a geometric progression along the length of the store. It is found that the first few storage stages play a more important role in terms of overall heat transfer, exergy storage and release in both the heat charging and discharging processes. During the heat charging process, the total exergy storage rate increases and approaches its maximum, while the total entropy generation rate decreases and stabilizes as the total stage number and *NTU* increase. During the heat discharging process, the total heat transfer and total exergy release rates both increase as the total stage number and *NTU* increase, while the total entropy generation rate decreases. The highest roundtrip energy and exergy efficiencies are 94%-98% and 88%-95% for the investigated *NTU*s, respectively. The highest roundtrip energy and exergy efficiencies are 73%-98% and 60%-95% for the investigated total stage numbers.

Keywords: cascaded store, entropy generation, exergy, latent heat storage, pumped thermal electricity storage

1. Introduction

Renewable energy technologies are increasingly used for power generation, and with many of them having unpredictable (fluctuating and intermittent) generation characteristics, an increasing interest has grown in large-scale electrical energy storage solutions (Gür, 2018). Currently, three commercial large-scale electrical energy storage technologies are available at varying technology readiness levels (TRLs): pumped hydroelectric storage (PHS), compressed air energy storage (CAES) and flow batteries, all of which can offer power delivery rates over 1 MW and storage capacities over 1 MWh at the same time (Benato and Stoppato, 2018; Gür, 2018). However, PHS and CAES are both limited by geographical restrictions that arise from their operating principles and are key to their deployment, while flow batteries suffer from the poor lifetime and the high capital costs. Pumped thermal electricity storage (PTES) is regarded as a promising alternative large-scale electricity storage technology because it is neither subjected to geographical restrictions, nor subjected to lifetime and cost disadvantages in the way flow batteries are (Desrues et al., 2010). In PTES, excess electricity is used during charging to create a temperature difference between hot and cold stores. At a later time, when this is required, this temperature difference is used to drive a thermodynamic cycle to generate electricity during discharging, with a theoretical roundtrip efficiency of 100% (Steinmann, 2017).

In general, according to the selected thermodynamic cycle and working fluid, PTES technology can be divided into systems based on the Joule-Brayton cycle (Georgiou et al., 2018; McTigue et al., 2015; White et al., 2013), those based on the transcritical CO_2 cycle (Mercangöz et al., 2012; Morandin et al., 2012a, b; Morandin et al., 2013), and those based on the water-steam Rankine cycle (Jockenhöfer et al., 2018; Steinmann, 2017; Steinmann, 2014). In Joule-Brayton-cycle PTES systems, argon is often chosen as the working fluid and packed-bed tanks are recommended as the stores. White (2011) analysed the thermodynamic losses in the sensible-heat, packed-bed reservoirs of a PTES system and discussed their performance dependence on geometrical design parameters (e.g., pebble size) and operating conditions (e.g., temperatures). In a follow-up publication, White et al. (2014) further emphasized the links between wave propagation and thermodynamic losses in such sensible-heat packed-bed stores.

doi:10.18086/eurosun.2020.07.04 Available at http://proceedings.ises.org

However, packed-bed stores, and especially hot stores which operate at higher pressures, require high-strength materials to make the tanks withstand the pressures within the system, which increases their costs significantly. In this context, cascaded latent heat stores are an option for replacing packed-bed stores for the following reasons: (1) they alleviate the need for pressurized storage tanks; (2) they can have higher energy densities and smaller sizes; and (3) they have the potential to have lower costs if their smaller size can be exploited.

In this work, the feasibility of a cascaded latent-heat store as the hot store in a PTES system is explored from a thermodynamic perspective. The effects of the total stage number and *NTU* on the heat transfer, exergy storage/release and entropy generation rates in each stage and in the cascaded store are investigated during both the heat charging and discharging processes, and the resulting roundtrip energy and exergy efficiencies are reported.

2. Model description

2.1 Physical model

Figure 1 (a) shows a simplified PTES system layout with its four main components: a compressor, an expander and two thermal (hot and cold) stores. In this system, Joule-Brayton cycle and reverse Joule-Brayton cycle are used to realize the electricity charging and discharging processes. A Joule-Brayton cycle when using argon as the working fluid during charging is shown in the *T*-*s* diagram in Fig. 1 (b), which consists of a compression process (4→1), an expansion process (2→3) and two heat transfer processes (hot storage: 1→2, and cold storage: 3→4). The operating conditions during charging, along with relevant thermophysical properties are listed in Table 1.

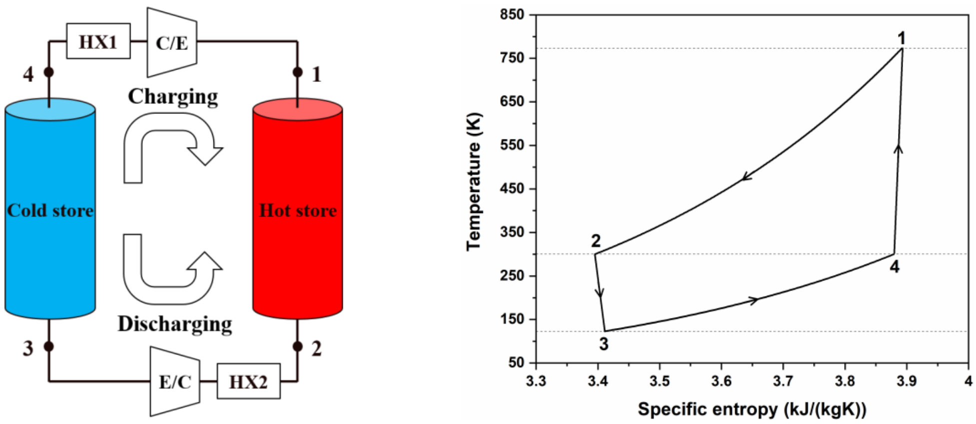

(a) Layout of a PTES system **(b) *T*-*s* diagram of a typical cycle during charging**

Fig. 1: Pumped thermal electricity storage: (a) Layout, and (b) thermodynamic cycle

Tab. 1: Operation conditions and thermophysical properties

Parameter	Unit	Value
Inlet temperature of hot store/outlet temperature of compressor, T_1	K	773
Outlet temperature of hot store/inlet temperature of expander, T_2	K	300
Inlet temperature of cold store/outlet temperature of expander, T_3	K	123
Outlet temperature of cold store/inlet temperature of compressor, T_4	K	300
Pressure in hot store, p_1 and p_2	bar	10
Pressure in cold store, p_3 and p_4	bar	1
Environmental temperature, T_e	K	293.15
Mass flow rate of argon, $\dot{m}$	kg/s	12.5
Specific heat capacity of argon, c_p	J/(kg K)	524.4

A cascaded latent-heat store used as the hot store in a PTES system is considered in this work, as shown in Fig. 2. Multiple phase change materials (PCMs) are used in this store, which are arranged according to their melting temperatures along the length of the store. A heat transfer fluid flows through the PCMs in order to perform the heat storage and release processes. In Fig. 2, $T_{m,i}$, $T_{c,i}$ and $T_{d,n-i+1}$ are the melting temperature and the HTF outlet temperatures in the i^{th} store/stage during charging and discharging, respectively. Some assumptions are made in order to simplify the physical problem: (1) temperature difference inside PCMs is neglected; (2) sensible heat of PCMs is also neglected compare with latent heat; (3) temperature distribution in the direction normal to the flow direction is neglected; (4) thermophysical properties of PCMs and HTF are constant; and (5) $T_{m,i} \geq T_e$; (6) $Q_{c,i} \geq Q_{d,i}$. Here, the HTF inlet and outlet temperatures during heat charging are fixed at 773 K and 300 K, respectively. The HTF inlet temperature during heat discharging is 293.15 K, which is equal to the environmental temperature.

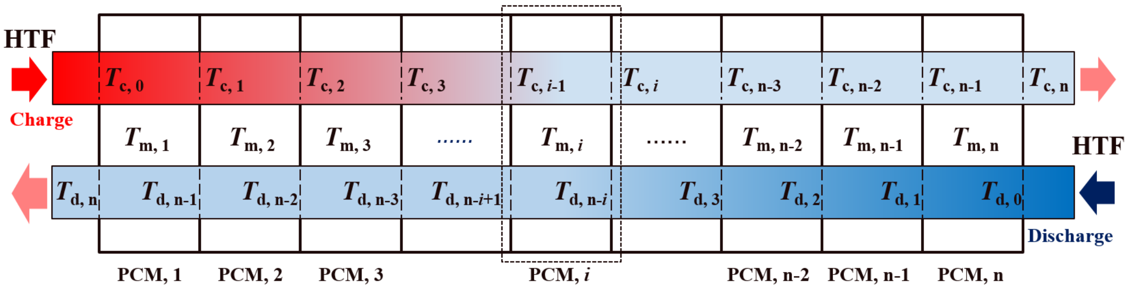

Fig. 2: Schematic diagram of a cascaded latent-heat store

2.2 Mathematical model

In the i^{th} stage during the heat charging process, the heat transfer rate is:

$$\dot{Q}_{c,i} = c_p \dot{m}\left(T_{c,i-1}-T_{c,i}\right) = U_i A_i \left\{\left(T_{c,i-1}-T_{c,i}\right)/\ln\left[\left(T_{c,i-1}-T_{m,i}\right)/\left(T_{c,i}-T_{m,i}\right)\right]\right\} \quad \text{(eq. 1)}$$

where U_i and A_i are the heat transfer coefficient and the heat exchange area, respectively.

The NTU in the i^{th} stage is defined as:

$$NTU = \left(U_i A_i\right)/\left(c_p \dot{m}\right) = \ln\left[\left(T_{c,i-1}-T_{m,i}\right)/\left(T_{c,i}-T_{m,i}\right)\right] \quad \text{(eq. 2)}$$

Then the melting temperature in the i^{th} stage can be obtained:

$$T_{m,i} = \left(C_i T_{c,i} - T_{c,i-1}\right)/\left(C_i - 1\right) \quad \text{(eq. 3)}$$

where $C_i = e^{NTU}$. To simplify the problem, the NTU in each stage is considered to be equal, so $C_i = C$.

The exergy storage rate can be calculated as:

$$\dot{E}x_{c,i} = \dot{Q}_{c,i}\left(1 - T_e/T_{m,i}\right) \quad \text{(eq. 4)}$$

The entropy generation rate can be expressed as:

$$\dot{S}_{g,c,i} = \Delta\dot{S}_{c,i} - \dot{S}_{f,c,i} - \left(s_{c,i-1} - s_{c,i}\right)\dot{m} = c_p \dot{m}\left[\ln\left(T_{c,i}/T_{c,i-1}\right) + \left(T_{c,i-1}-T_{c,i}\right)/T_{m,i}\right] \quad \text{(eq. 5)}$$

where $\Delta\dot{S}_{c,i}$ is the entropy accumulation rate, $\dot{S}_{f,c,i}$ the entropy transfer rate, and $s_{c,i-1}$ and $s_{c,i}$ the specific entropy at the inlet and outlet.

For the cascaded latent heat store, the total exergy storage and total entropy generation rate during the heat charging process are given as:

$$\dot{E}x_{c,total} = \sum_{i=1}^{n} \dot{E}x_{c,i} = \sum_{i=1}^{n}\left[\dot{Q}_{c,i}\left(1 - T_e/T_{m,i}\right)\right] \quad \text{(eq. 6)}$$

$$\dot{S}_{g,c,total} = \sum_{i=1}^{n} \dot{S}_{g,c,i} = c_p \dot{m} \sum_{i=1}^{n}\left[\ln\left(T_{c,i}/T_{c,i-1}\right) + \left(T_{c,i-1}-T_{c,i}\right)/T_{m,i}\right] \quad \text{(eq. 7)}$$

Thermodynamic optimization is performed based on the maximization of total exergy storage rate and the minimization of total entropy generation rate, respectively.

First, to maximize the total exergy storage rate, the following expressions should be satisfied:

$$\frac{\partial \dot{E}x_{\mathrm{c,total}}}{\partial T_{\mathrm{c},i}}=\begin{cases} c_{\mathrm{p}}\dot{m}T_{\mathrm{e}}\left(C-1\right)^2\left[T_{\mathrm{c},i\text{-}1}\Big/\left(CT_{\mathrm{c},i}-T_{\mathrm{c},i\text{-}1}\right)^2-T_{\mathrm{c},i+1}\Big/\left(CT_{\mathrm{c},i+1}-T_{\mathrm{c},i}\right)^2\right]=0, & 1\le i\le \mathrm{n}\text{-}1 \\ c_{\mathrm{p}}\dot{m}\left[\left(C-1\right)^2 T_{\mathrm{e}}T_{\mathrm{c,n\text{-}1}}\Big/\left(CT_{\mathrm{c,n}}-T_{\mathrm{c,n\text{-}1}}\right)^2-1\right]=0, & i=\mathrm{n}\end{cases} \quad \text{(eq. 8)}$$

$$\frac{\partial^2 \dot{E}x_{\mathrm{c,total}}}{\partial T_{\mathrm{c},i}{}^2}<0 \quad \text{(eq. 9)}$$

Second, the minimization of the total entropy generation rate must be carried out using the total heat transfer rate θ as a constraint. A new function is established based on the Lagrange multiplier method as shown below:

$$G\left(T_{\mathrm{c},1},T_{\mathrm{c},2},\cdots T_{\mathrm{c},i}\cdots,T_{\mathrm{c,n\text{-}1}},T_{\mathrm{c,n}},\delta\right)=\dot{S}_{\mathrm{g,c,total}}+\delta\left(\dot{Q}_{\mathrm{c,total}}-\theta\right) \quad \text{(eq. 10)}$$

The following relations should be satisfied:

$$\frac{\partial G}{\partial T_{\mathrm{c},i}}=\begin{cases} c_{\mathrm{p}}\dot{m}\left(C-1\right)^2\left[-T_{\mathrm{c},i\text{-}1}\Big/\left(CT_{\mathrm{c},i}-T_{\mathrm{c},i\text{-}1}\right)^2+T_{\mathrm{c},i+1}\Big/\left(CT_{\mathrm{c},i+1}-T_{\mathrm{c},i}\right)^2\right]=0, & 1\le i\le \mathrm{n}\text{-}1 \\ c_{\mathrm{p}}\dot{m}\left[1/T_{\mathrm{c},i}-\left(C-1\right)^2 T_{\mathrm{c},i\text{-}1}\Big/\left(CT_{\mathrm{c},i}-T_{\mathrm{c},i\text{-}1}\right)^2-\delta\right]=0, & i=\mathrm{n}\end{cases} \quad \text{(eq. 11)}$$

$$\frac{\partial G}{\partial \delta}=c_{\mathrm{p}}\dot{m}\left(T_{\mathrm{c},0}-T_{\mathrm{c,n}}\right)-\theta=0 \quad \text{(eq. 12)}$$

$$\frac{\partial^2 G}{\partial T_{\mathrm{c},i}{}^2}>0 \quad \text{(eq. 13)}$$

$$\frac{\partial^2 G}{\partial \delta^2}>0 \quad \text{(eq. 14)}$$

By solving eqs. 8-9 and eqs. 11-14, the same analytical solution to the outlet temperature of the i^{th} stage during the heat charging process, $T_{\mathrm{c},i}$, exists for the above two optimization problems based on exergy and entropy generation:

$$T_{\mathrm{c},i,\mathrm{opt}}=T_{\mathrm{c},0}\left(T_{\mathrm{c,n,opt}}/T_{\mathrm{c},0}\right)^{i/\mathrm{n}}=T_{\mathrm{c},0}\left[1-\theta\Big/\left(c_{\mathrm{p}}\dot{m}T_{\mathrm{c},0}\right)\right]^{i/\mathrm{n}} \quad \text{(eq. 15)}$$

Eq. 15 shows that the optimal outlet temperatures of the stages are in a geometric progression, which means the following relations are satisfied:

$$T_{\mathrm{c,n,opt}}/T_{\mathrm{c,n\text{-}1,opt}}=T_{\mathrm{c,n\text{-}1,opt}}/T_{\mathrm{c,n\text{-}2,opt}}=\cdots=T_{\mathrm{c},i,\mathrm{opt}}/T_{\mathrm{c},i\text{-}1,\mathrm{opt}}=\cdots=T_{\mathrm{c,2,opt}}/T_{\mathrm{c,1,opt}}=T_{\mathrm{c,1,opt}}/T_{\mathrm{c},0}=q,\quad 1\le i\le \mathrm{n} \quad \text{(eq. 16)}$$

where q is the common ratio of the geometric progression. Then the optimal melting temperatures of the i^{th} stage are obtained together with eq. 3 as follows:

$$T_{\mathrm{m},i,\mathrm{opt}}=\left(CT_{\mathrm{c},i,\mathrm{opt}}-T_{\mathrm{c},i\text{-}1,\mathrm{opt}}\right)/\left(C-1\right)=\left(CT_{\mathrm{c},0}q^i-T_{\mathrm{c},0}q^{i-1}\right)/\left(C-1\right)=T_{\mathrm{c},0}q^{i-1}\left(Cq-1\right)/\left(C-1\right) \quad \text{(eq. 17)}$$

Eq. 17 shows that the optimal melting temperatures of the stages are also in a geometric progression with a common ratio of q.

In the heat discharging process, the melting temperature in each stage is the same with those of the heat charging process. For the i^{th} stage, the outlet temperature is calculated as:

$$T_{\mathrm{d,n}\text{-}i+1}=\frac{C-1}{C}T_{\mathrm{m},i,\mathrm{opt}}+\frac{1}{C}T_{\mathrm{d,n}\text{-}i}=\frac{C-1}{C}T_{\mathrm{m},i,\mathrm{opt}}+\sum_{j=2}^{\mathrm{n}\text{-}i+1}\frac{C-1}{C^j}T_{\mathrm{m},i+j\text{-}1,\mathrm{opt}}+\frac{1}{C^{\mathrm{n}\text{-}i+1}}T_{\mathrm{d},0} \quad \text{(eq. 18)}$$

The heat transfer rate, exergy release rate and entropy generation rate are written as:

$$\dot{Q}_{\mathrm{d},i}=c_{\mathrm{p}}\dot{m}\left(T_{\mathrm{d,n}\text{-}i+1}-T_{\mathrm{d,n}\text{-}i}\right) \quad \text{(eq. 19)}$$

$$\dot{E}x_{\mathrm{d},i}=c_{\mathrm{p}}\dot{m}\left[T_{\mathrm{d,n}\text{-}i+1}-T_{\mathrm{d,n}\text{-}i}-T_{\mathrm{e}}\ln\left(T_{\mathrm{d,n}\text{-}i+1}/T_{\mathrm{d,n}\text{-}i}\right)\right] \quad \text{(eq. 20)}$$

$$\dot{S}_{\mathrm{g,d},i}=c_{\mathrm{p}}\dot{m}\left[\left(T_{\mathrm{d,n}\text{-}i}-T_{\mathrm{d,n}\text{-}i+1}\right)/T_{\mathrm{m},i}-\ln\left(T_{\mathrm{d,n}\text{-}i}/T_{\mathrm{d,n}\text{-}i+1}\right)\right] \quad \text{(eq. 21)}$$

Then the total heat transfer rate, total exergy release rate and total entropy generation rate are obtained:

$$\dot{Q}_{\mathrm{d,total}}=\sum_{i=1}^{\mathrm{n}}\dot{Q}_{\mathrm{d},i} \quad \text{(eq. 22)}$$

$$\dot{E}x_{\mathrm{d,total}} = \sum_{i=1}^{n} \dot{E}x_{\mathrm{d},i} \quad \text{(eq. 23)}$$

$$\dot{S}_{\mathrm{g,d,total}} = \sum_{i=1}^{n} \dot{S}_{\mathrm{g,d},i} \quad \text{(eq. 24)}$$

3. Results and discussion

3.1. Heat charging process

Figure 3 shows the melting/outlet temperatures, heat transfer rate, exergy storage rate and entropy generation rate in each stage when the total stage number is 4, 8 and 12, respectively, and *NTU* is 3. As shown in Fig. 3 (a), melting/outlet temperatures both decrease along the HTF flow direction. In Fig. 3 (b) and (c), both heat transfer rates and exergy storage rates also decrease along the HTF direction. The decreased heat transfer rate is caused by the smaller difference between melting temperatures and outlet temperatures in each stage. The smaller temperature difference, together with the lower melting temperature further makes the exergy storage rate decrease along the HTF flow direction. The stages close to the inlet play a more important role in heat transfer and exergy storage. The entropy generation rates in each stage are equal to each other, indicating the same thermodynamic irreversibility. As for the effect of total stage number, it is observed that larger total stage number could widen the range of melting/outlet temperatures, meaning more heat sources at different grades for the subsequent use. Larger total stage number could also cause the distribution of heat transfer rates and exergy storage rates in each stage to be more uniform, thus making full use of the heat storage capacity in each stage. The entropy generation rate in each stage tends to be lower for a larger total stage number.

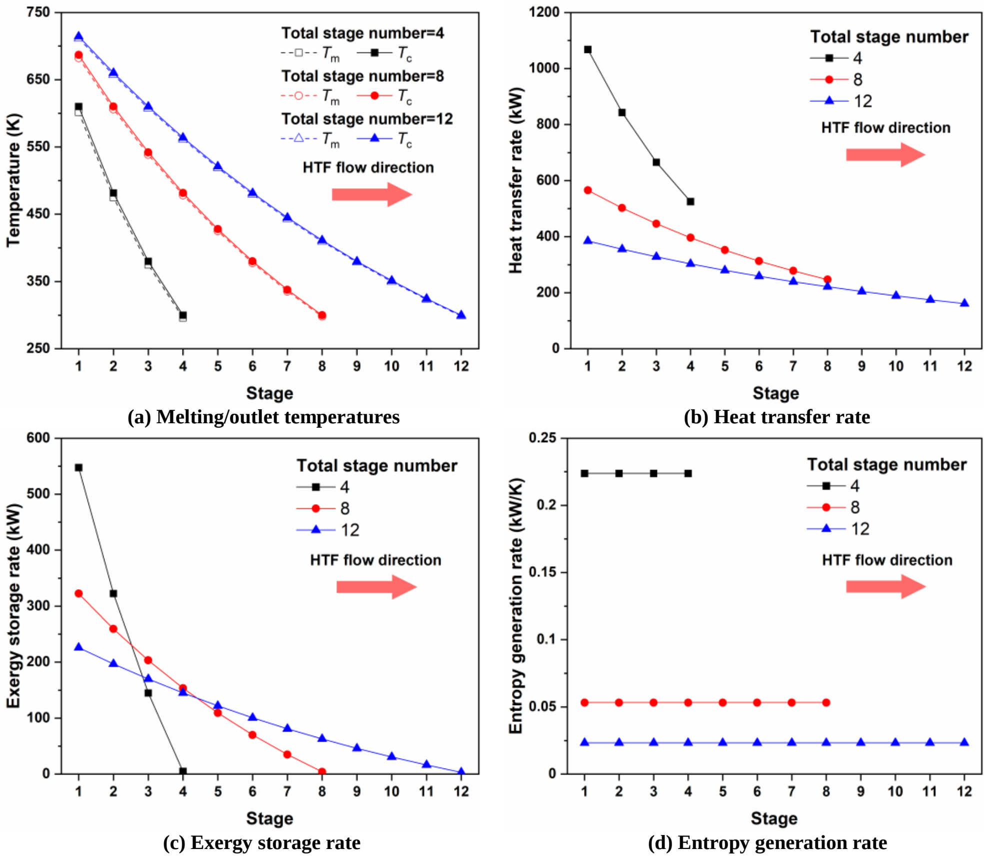

Fig. 3: Effect of total stage number on the thermodynamic performance in each stage

Figure 4 shows the effect of total stage number on the total exergy storage rate and total entropy generation rate of the latent heat store when *NTU* is 0.8, 1, 2, 3, 4 and 5, respectively. The total exergy transfer rate is 1.28 MW, as shown in Fig. 4 (a). As the total stage number increases, the total exergy storage rates increase and approach the total exergy transfer rate, indicating higher exergy storage efficiencies. When the total stage number increases to a critical number, the enhancement of exergy storage rate tends to be weaker, meaning that it is unnecessary to add more stages beyond the critical number from a thermodynamic view. The total entropy generation rates decrease and approach a certain small value with the total stage number, indicating the thermodynamic irreversibility could be significantly reduced by adding certain stages. It is also shown that at *NTU*s of 0.8, 1, 2, 3 and 4, the thermodynamic parameters are neglected when the total stage number is smaller than certain value. If the heat transfer inside the stage is not strong enough, the optimal melting temperatures of the last few stages may be lower than the environmental temperature, especially for small total stage numbers, which causes the stored exergy not to be heat exergy.

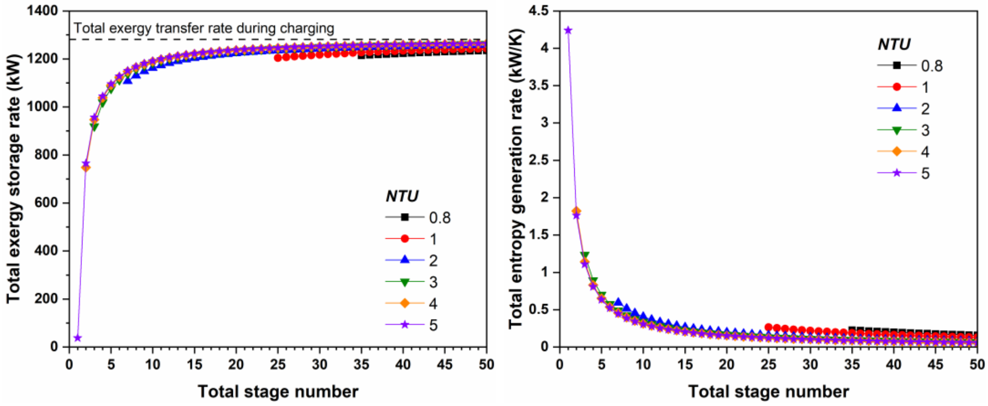

(a) Total exergy storage rate **(b) Total entropy generation rate**

Fig. 4: Effect of total stage number on the thermodynamic performance of the cascaded latent heat store

Figure 5 shows the melting/outlet temperatures, heat transfer rate, exergy storage rate and entropy generation rate in each stage when *NTU* is 1.2, 2.4 and 3.6, respectively and the total stage number is 20. For different *NTU*s, the outlet temperatures in each stage are the same due to the fixed inlet and outlet temperatures of the latent heat store, which further leads to the same heat transfer rates in each stage, as shown in Fig. 5 (a) and (b). As *NTU* increases, the melting temperatures in each stage tend to be raised and closer to the outlet temperature in each stage, because it is no longer necessary to maintain a large temperature difference for heat transfer. Then larger *NTU*s further improve the exergy storage rate and reduce the entropy generation rate in each stage, as shown in Fig. 5 (c) and (d).

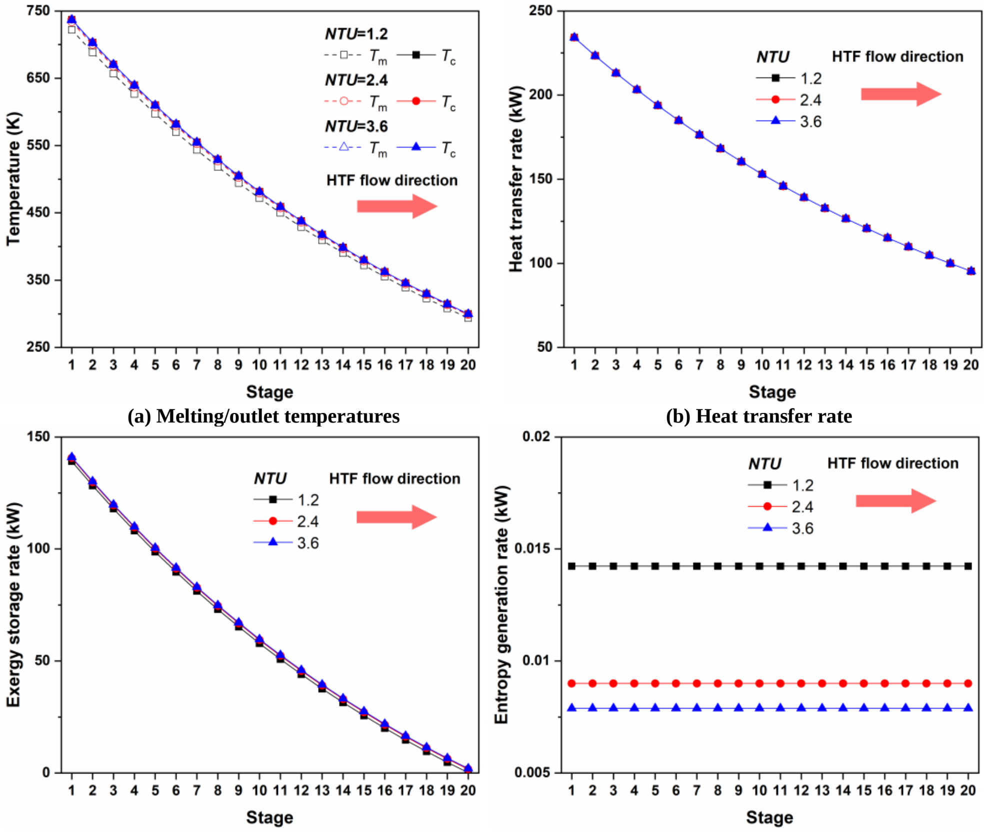

(a) Melting/outlet temperatures **(b) Heat transfer rate**

(c) Exergy storage rate **(d) Entropy generation rate**

Fig. 5: Effect of *NTU* on the thermodynamic performance in each stage

Figure 6 shows the effect of *NTU* on the total exergy storage rate and total entropy generation rate of the latent heat store when total storage number is 50, 40, 30, 20, 10 and 5, respectively. The total exergy transfer rate is also 1.28 MW. As *NTU* increases, the total exergy storage rates increase and then the enhancement effect tends to be weak, meaning that it is unnecessary to increase *NTU* beyond the critical number from a thermodynamic view. However, the maximum total exergy storage rates are raised for larger total stage numbers. The total entropy generation rates decrease and approach different certain small values with *NTU*, indicating the thermodynamic irreversibility could be significantly reduced by increasing *NTU*. It is shown that at low *NTU*s, the thermodynamic parameters are also neglected due to the optimal melting temperatures lower than the environmental temperature in the last few stages.

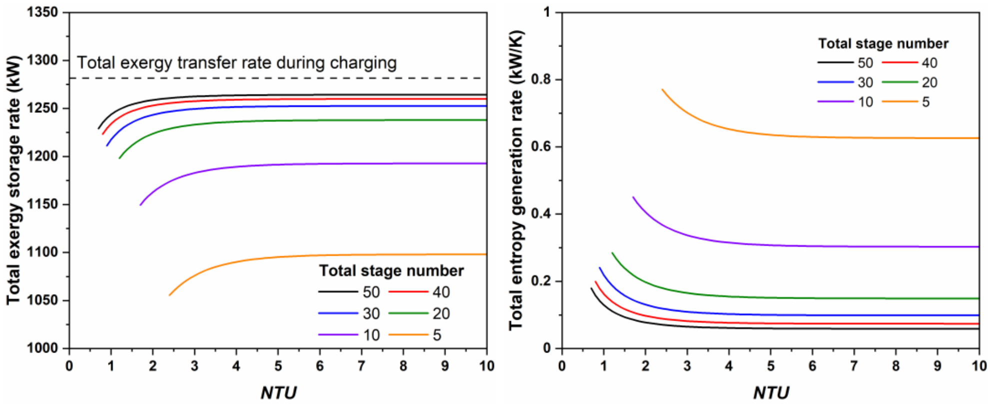

(a) Total exergy storage rate **(b) Total entropy generation rate**

Fig. 6: Effect of *NTU* on the thermodynamic performance of the cascaded latent heat store

3.2. Heat discharging process

Figure 7 shows the melting/outlet temperatures, heat transfer rate, exergy release rate and entropy generation rate in each stage when the total stage number is 4, 8 and 12, respectively, and *NTU* is 3. As shown in Fig. 7 (a), melting temperatures are the same with those of the heat charging process and outlet temperatures increase along the HTF flow direction. In Fig. 7 (b) and (c), both heat transfer rates and exergy release rates also increase along the HTF direction. The stages close to the inlet of the heat charging process also play a more important role in heat transfer and exergy release. Different from the heat charging process, entropy generation rates in each stage increase and then be stable, indicating the thermodynamic irreversibility in the last few stages is relatively low. As for the effect of total stage number, larger total stage numbers could significantly raise the outlet temperatures, meaning higher grades. Larger total stage number could also cause the distribution of heat transfer rates and exergy release rates in each stage to be more uniform. The entropy generation rates in the last few stages are affected by the HTF inlet temperature during discharging, but the average entropy generation rate in each stage tends to be lower for a larger total stage number.

Figure 8 shows the effect of total stage number on the total heat transfer rate, total exergy storage rate and total entropy generation rate of the latent heat store when *NTU* is 0.8, 1, 2, 3, 4 and 5, respectively. The total energy transfer rate and total exergy transfer rate during charging are 3.10 MW and 1.28 MW, respectively, as reference values. At *NTU*s of 0.8, 1, 2, 3 and 4, the thermodynamic parameters are neglected when the total stage number is smaller than certain value due to the corresponding melting temperatures lower than the environmental temperature. Moreover, considering the energy balance between the charging and discharging processes, the thermodynamic parameters in some last few stages are also neglected. As the total stage number increases, the total heat transfer rates and total exergy storage rates both increase. The highest roundtrip energy efficiencies are 94%, 95%, 97%, 98%, 98% and 98%, while the highest roundtrip exergy efficiencies reach 88%, 90%, 94%, 95%, 95% and 95% for *NTU*s of 0.8, 1, 2, 3, 4 and 5, respectively. The total entropy generation rates decrease with the total stage number, indicating the thermodynamic irreversibility could be significantly reduced by adding certain stages. When total stage number is 1, the entropy generation rate for *NTU* of 5 are close to zero due to the small differences between HTF temperatures and melting temperatures.

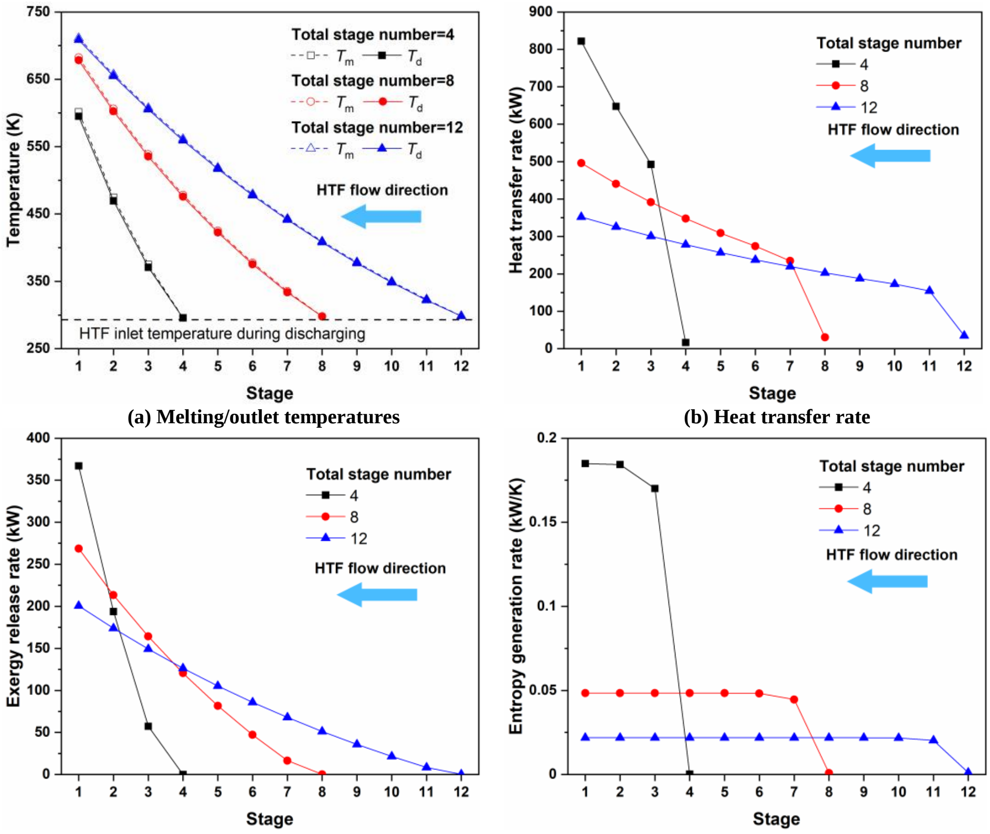

(a) Melting/outlet temperatures (b) Heat transfer rate

(c) Exergy release rate (d) Entropy generation rate

Fig. 7: Effect of total stage number on the thermodynamic performance in each stage

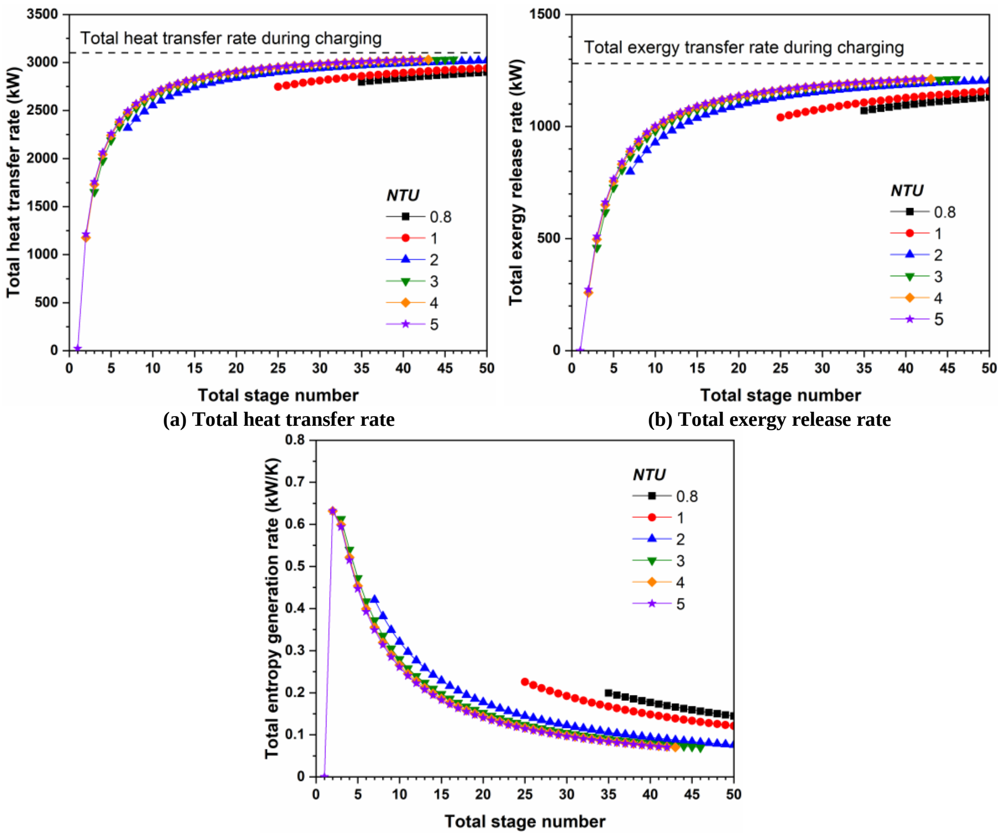

(a) Total heat transfer rate (b) Total exergy release rate

(c) Total entropy generation rate

Fig. 8: Effect of total stage number on the thermodynamic performance of the cascaded latent heat store

Figure 9 shows the melting/outlet temperatures, heat transfer rate, exergy release rate and entropy generation rate in each stage when *NTU* is 1.2, 2.4 and 3.6, respectively and the total stage number is 20. Melting temperatures are also the same with those of the heat charging process. As *NTU* increases, the outlet temperatures in each stage tend to be raised and closer to the melting temperatures in each stage. Larger *NTU*s further improve the heat transfer rate and exergy release rate in each stage. As for the entropy generation rate, the last few stages are also affected by the HTF inlet temperature during discharging, but the average entropy generation rate in each stage tends to be lower for a larger *NTU*.

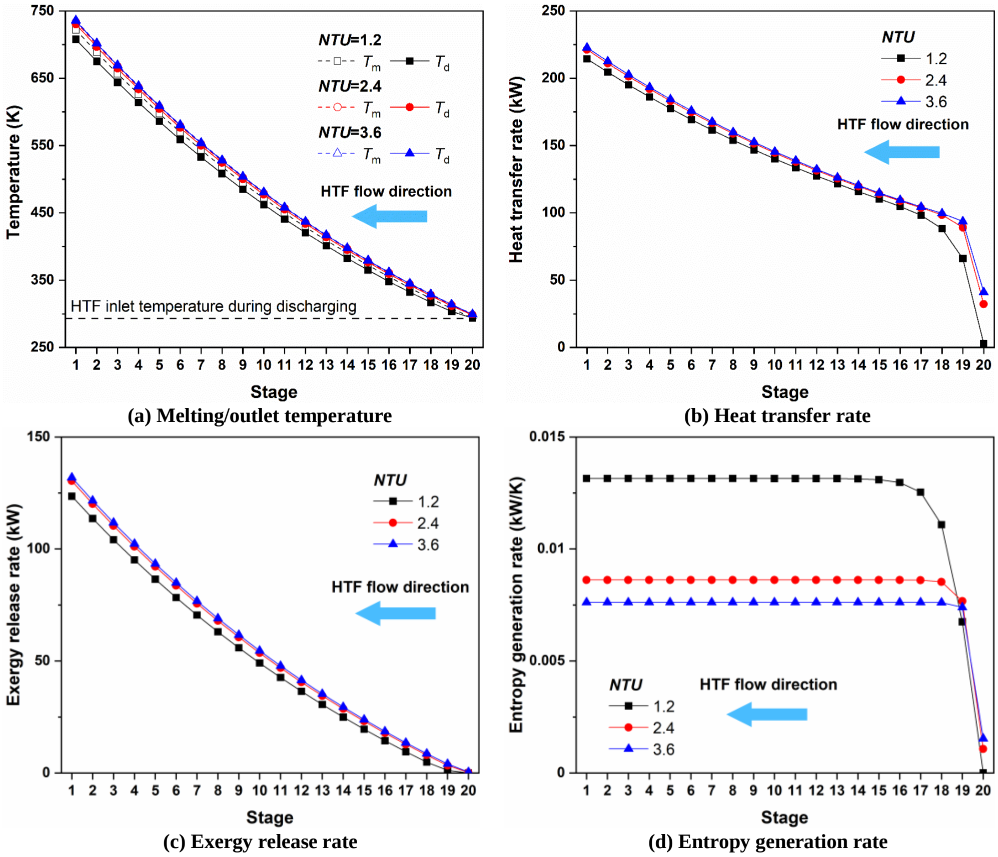

Fig. 9: Effect of *NTU* on the thermodynamic performance in each stage

Figure 10 shows the effect of the *NTU* on the total heat transfer rate, the total exergy storage rate and the total entropy generation rate of the latent heat store when total storage number is 50, 40, 30, 20, 10 and 5, respectively. The total energy transfer rate and total exergy transfer rate during charging are 3.10 MW and 1.28 MW, respectively, as reference values. For total stage number of 50, the total heat transfer rates and total exergy release rates increase with *NTU*, while for total stage number of 40, 30, 20, 10 and 5, the total heat transfer rates and total exergy release rates increase with *NTU* and then stabilize. The highest roundtrip energy efficiencies are 98%, 98%, 96%, 94%, 87% and 73%, while the highest roundtrip exergy efficiencies reach 95%, 94%, 92%, 89%, 79% and 60% for total stage numbers of 50, 40, 30, 20, 10 and 5, respectively. The total entropy generation rates decrease with *NTU*, indicating thermodynamic irreversibility could be significantly reduced by increasing *NTU*. For *NTU*s of 40, 30, 20, 10 and 5, the total entropy generation rates finally stabilize, meaning that thermodynamic irreversibility could not be further reduced beyond a certain *NTU*.

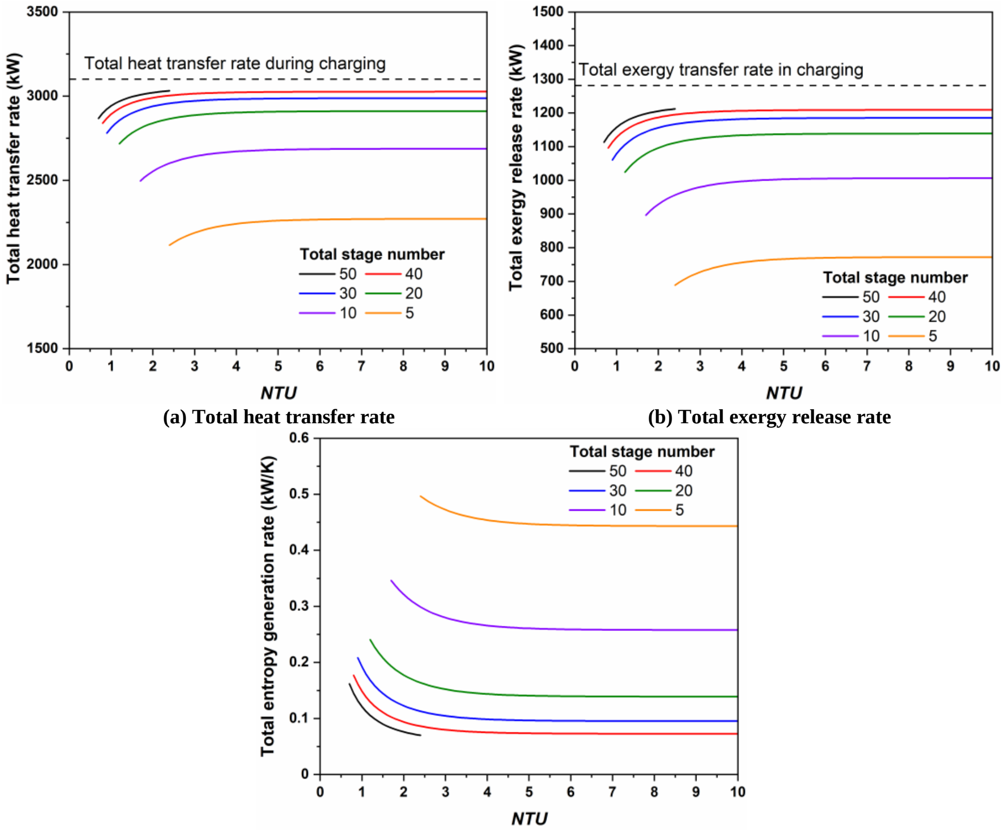

(a) Total heat transfer rate

(b) Total exergy release rate

(c) Total entropy generation rate

Fig. 10: Effect of *NTU* on the thermodynamic performance of the cascaded latent heat store

4. Conclusions

The thermodynamic feasibility of cascaded latent-heat stores in pumped thermal electricity storage (PTES) systems was explored through exergy and entropy generation optimization. The effects of the total stage number and *NTU* on the temperature distributions, energy, exergy and entropy generation in each stage and over the cascaded store during heat charging and discharging were discussed.

The optimal outlet and melting temperatures in each stage during the heat charging process are found to follow a geometric progression along the length of the store. The first few storage stages play a more important role in heat transfer, exergy storage and release during both the heat charging and discharging processes.

A larger total stage number can widen the range of melting/outlet temperatures and cause the distribution of heat transfer rates and exergy storage/release rates in each stage to be more uniform. In the heat charging process, the entropy generation rate in each stage tends to be lower for a larger stage number, while in the heat discharging process, the entropy generation rates in the last few stages are affected by the HTF inlet temperature. In the heat charging process, the total exergy storage rate increases while the total entropy generation rate decreases as the total stage number increases up to a critical number, meaning that it is unnecessary to add more stages beyond the critical number from a thermodynamic perspective. In the heat discharging process, the total heat transfer rates and total exergy storage rates both increase, and the total entropy generation rates decrease as the total stage number increases. The highest roundtrip energy efficiencies range from 94% to 98%, while the highest roundtrip exergy efficiencies range from 88% to 95% for the presently investigated cases, respectively.

As the *NTU* increases, the outlet and melting temperatures in each stage tend to approach each other and the exergy storage/release rates are improved. In the heat discharging process, the heat transfer rates in each stage also increase with the *NTU*. In the heat charging process, the entropy generation rate in each stage tends to be lower for a larger *NTU*, while in the heat discharging process, the entropy generation rates in the last few stages are also affected by the HTF inlet temperature. In the heat charging process, the total exergy storage rates increase and the total entropy generation rates decrease as the *NTU* increases until a certain value. For fewer total stages, any enhancement of the thermodynamic performance of the store by increasing the *NTU* decreases. In the discharging process, the total heat transfer rates and total exergy release rates increase, and the total entropy generation rates decrease with the *NTU*. The highest roundtrip energy efficiencies range from 73% to 98%, while the highest roundtrip exergy efficiencies range from 60% to 95% for the presently investigated cases, respectively.

5. Acknowledgments

This work was supported by the National Natural Science Foundation of China (Grant No. 51906150). It was also supported by the UK Engineering and Physical Sciences Research Council (EPSRC) [grant numbers EP/P004709/1, EP/R045518/1, and EP/S032622/1]. Data supporting this publication can be obtained on request from cep-lab@imperial.ac.uk.

6. References

Benato, A., Stoppato, A., 2018. Pumped Thermal Electricity Storage: A technology overview. Thermal Science and Engineering Progress 6, 301-315.

Desrues, T., Ruer, J., Marty, P., Fourmigué, J.F., 2010. A thermal energy storage process for large scale electric applications. Applied Thermal Engineering 30(5), 425-432.

Georgiou, S., Shah, N., Markides, C.N., 2018. A thermo-economic analysis and comparison of pumped-thermal and liquid-air electricity storage systems. Applied Energy 226, 1119-1133.

Gür, T.M., 2018. Review of electrical energy storage technologies, materials and systems: challenges and prospects for large-scale grid storage. Energy & Environmental Science 11(10), 2696-2767.

Jockenhöfer, H., Steinmann, W.-D., Bauer, D., 2018. Detailed numerical investigation of a pumped thermal energy storage with low temperature heat integration. Energy 145, 665-676.

McTigue, J.D., White, A.J., Markides, C.N., 2015. Parametric studies and optimisation of pumped thermal electricity storage. Applied Energy 137, 800-811.

Mercangöz, M., Hemrle, J., Kaufmann, L., Z'Graggen, A., Ohler, C., 2012. Electrothermal energy storage with transcritical CO2 cycles. Energy 45(1), 407-415.

Morandin, M., Maréchal, F., Mercangöz, M., Buchter, F., 2012a. Conceptual design of a thermo-electrical energy storage system based on heat integration of thermodynamic cycles – Part A: Methodology and base case. Energy 45(1), 375-385.

Morandin, M., Maréchal, F., Mercangöz, M., Buchter, F., 2012b. Conceptual design of a thermo-electrical energy storage system based on heat integration of thermodynamic cycles – Part B: Alternative system configurations. Energy 45(1), 386-396.

Morandin, M., Mercangöz, M., Hemrle, J., Maréchal, F., Favrat, D., 2013. Thermoeconomic design optimization of a thermo-electric energy storage system based on transcritical CO2 cycles. Energy 58, 571-587.

Steinmann, W.-D., 2017. Thermo-mechanical concepts for bulk energy storage. Renewable and Sustainable Energy Reviews 75, 205-219.

Steinmann, W.D., 2014. The CHEST (Compressed Heat Energy STorage) concept for facility scale thermo mechanical energy storage. Energy 69, 543-552.

White, A., McTigue, J., Markides, C., 2014. Wave propagation and thermodynamic losses in packed-bed thermal reservoirs for energy storage. Applied Energy 130, 648-657.

White, A., Parks, G., Markides, C.N., 2013. Thermodynamic analysis of pumped thermal electricity storage. Applied Thermal Engineering 53(2), 291-298.

White, A.J., 2011. Loss analysis of thermal reservoirs for electrical energy storage schemes. Applied Energy 88(11), 4150-4159.

Comparative Study of Phase Change Material Characterization Methods

Maxime Thonon[1], Yasmine Lalau[2], Enghok Leang[3], Erwin Franquet[2], Gilles Fraisse[1], Stéphane Gibout[2], Laurent Zalewski[3]

[1] Univ. Savoie Mont Blanc, CNRS, LOCIE, 73000 Chambéry, France

[2] Universite de Pau et des Pays de l'Adour, E2S UPPA, LaTEP, Pau, France

[3] Laboratoire de Génie Civil et géo-Environnement, Université d'Artois, ULR 4515, F-62400 Béthune, France

Abstract

Modeling latent heat thermal energy storage systems is mostly achieved by implementing the enthalpy curve of the phase change material (PCM) into a numerical model. Then, the accuracy of the model depends on the accuracy of the enthalpy curve. The objective of this study is to compare the enthalpy curve obtained with four different characterization methods. Two methods are based on differential scanning calorimeter (DSC) experiments with dynamic and step modes. By modeling an experimental set-up, which contains a greater mass of PCM than with DSC, the two other methods use inverse methods to identify the analytical model describing the phase change process. Paraffin RT58, a PCM suitable for domestic hot water (DHW) storage, is selected for this study. Results highlight the same enthalpy difference for each method between 20°C and 65°C. Even if the end of the phase change process is described slightly differently for the two DSC methods than for the two inverse methods, results are mainly similar and all methods give a correct description of the phase change process. Conclusions are only relevant for the studied PCM, which does not undergo supercooling.

Keywords: PCM, Characterization, Enthalpy curve, DSC, Inverse method

Nomenclature

Latin letters

C_{eff}	**Effective heat capacity**, $\mathrm{J.kg^{-1}.K^{-1}}$
C_p	**Specific heat capacity**, $\mathrm{J.kg^{-1}.K^{-1}}$
f	**Liquid fraction**
H	**Enthalpy**, $\mathrm{J.kg^{-1}}$
L	**Latent heat**, $\mathrm{kJ.kg^{-1}}$
m	**Mass**, kg
T	**Temperature**, K
t	**Time**, s

Greek letters

Δt	**Time step**, s
ϵ	**Coefficient of latent heat repartition**
ϕ	**Heat flux**, W
λ	**Thermal conductivity**, $\mathrm{W.m^{-1}.K^{-1}}$
ρ	**Density**, $\mathrm{kg.m^{-3}}$
σ	**Coefficient of analytical model**

Subscripts

L	**Liquid**
PC	**Phase change**
S	**Solid**
Tot	**Total**

Exponent

Exp	**Experimental**

doi:10.18086/eurosun.2020.07.05 Available at http://proceedings.ises.org

Hx	Heat exchanger
Num	Numerical
PCM	Phase change material
$PMMA$	Poly(methyl methacrylate)
$Sens$	Sensible heat

1. Introduction

Latent heat thermal energy storage (LHTES) systems seem promising to store heat with a high energetic density, and PCM are already used in various applications (Sharma et al., 2009). A correct sizing of a LHTES system requires both an accurate modeling of the phase change process and an accurate identification of the PCM properties. As shown by (Dolado et al., 2012), a rather slight uncertainty on the phase change temperature leads to a high uncertainty on the heat exchange during charging and discharging process.

PCM characterization with DSC is the most common method to obtain both the PCM properties and the enthalpy curve describing the phase change process. Supercooling apart, the enthalpy curve of a PCM must be unique and only dependent on the temperature according to (Dumas et al., 2014). However, the heating rate and the mass of the PCM sample might influence the results as observed by (Lazaro et al., 2013).

The identification of PCM properties and the phase change dynamic might also be achieved by inverse method. An analytical formulation of the thermodynamic state of the PCM, depending only on the temperature, is used in a numerical model representing the experimental set-up. The parameters involved in the analytical model are then identified with an optimization algorithm to fit the numerical heat flux with the experimental, used as a reference. The inverse method might be performed on experimental results coming from DSC experiments (Franquet et al., 2012) or from a heat flux bench (Tittelein et al., 2015).

The PCM selected for this study is RT58, a paraffin manufactured by Rubitherm. This PCM is suitable for DHW storage with a phase change temperature around 58°C and no supercooling phenomenon. The objective of this study is to compare four PCM characterization methods. Two of them rely on DSC experiments, one with dynamic mode and the other with step mode. The two others characterization method are based on inverse methods with a global identification or an energy balance identification.

2. Differential scanning calorimeter characterization

2.1. Dynamic mode

PCM characterization by DSC with dynamic mode consists in monitoring the heat flux exchanged between a sample of few milligrams of PCM and its surrounding. Figure 1 illustrates the principle of DSC characterization with the dynamic mode for heating and cooling experiments. The enthalpy curve is obtained by plotting the exchanged heat in function of the temperature applied to the sample. As mentioned before, the heating and cooling rate might influence the results as the sample temperature is not exactly equal to the heat source temperature during the phase change. Indeed, the PCMs for LHTES are selected for their high thermal storage capacity, and most of them tend to have low thermal conductivity: that results in internal temperature gradient during their thermal characterisation. The sample temperature being measured on its external surface, this temperature will be overestimated during heating and underestimated during cooling. Thus, the true sample temperature should be enclosed by the heating and cooling curves. The challenge is then to find the appropriate temperature rate that minimize the difference between heating and cooling measurements. A low speed would minimize the sample thermal gradient but should not lead to an important signal-to-noise ratio that would increase the error in enthalpy variation estimation. One can note that it is impossible to determine for PCMs with high supercooling degree.

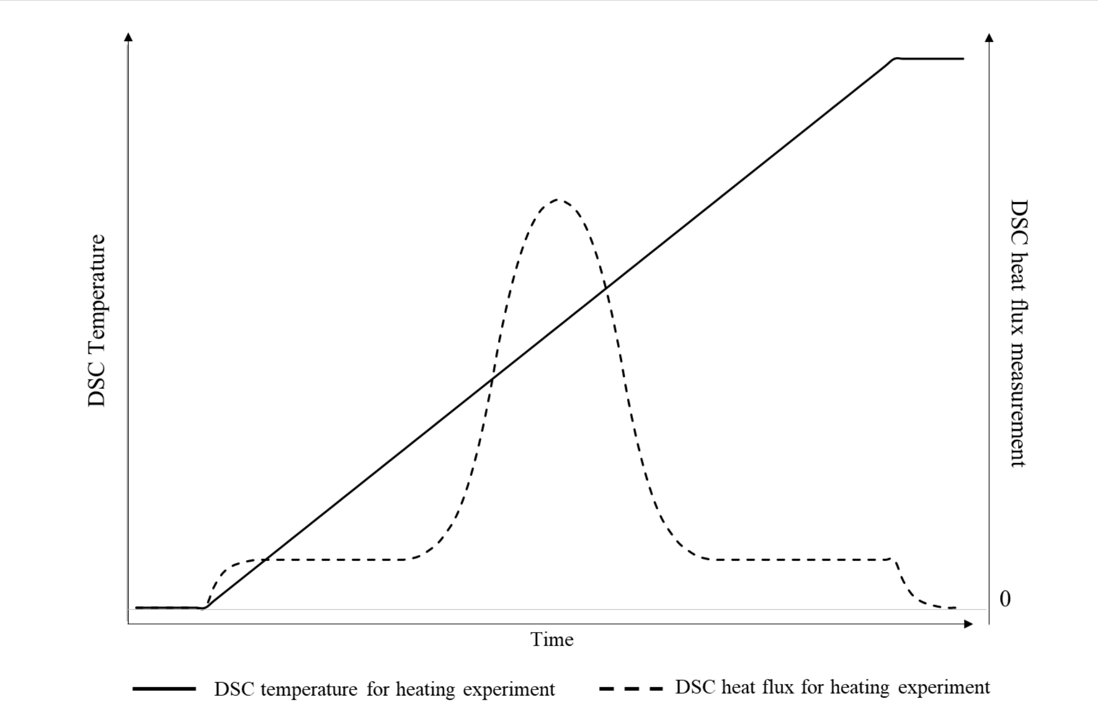

Fig. 1: Principe of DSC characterization with the dynamic mode

For RT58, this rate is reached for heating and cooling rate of 0.5 $K.min^{-1}$. Even if the difference between the heating and cooling curve is at its minimum for this rate, the two curves do not completely match one another. The average value between the enthalpy curve of heating and cooling is then selected to obtain the enthalpy curve of RT58 by DSC on dynamic mode.

2.2. Step mode

The DSC step mode consists of setting small temperatures step to heat the PCM sample, waiting for thermal equilibrium between each step identified by a signal returning to zero. Figure 2 illustrates the principle of DSC characterization with the step mode. The energy exchanged between two steps is monitored by plotting the flux along the temperature for each step, forming a peak which area is proportional to the heat absorbed by the sample. Then, the enthalpy curve may be built from this data by plotting the energy absorbed by the sample for each temperature step. Compared to the dynamic mode, the step mode overcomes the rate influence and is less dependent to the mass of the sample. However, the experimental characterization requires a longer duration as the thermal equilibrium has to be reached before applying the next temperature step. The temperature difference between two steps is also a parameter which might influence the results (Gibout et al., 2017). A too high temperature step leads to an inaccurate representation of the phase change process as the heat flux peak is not clearly identified. On the contrary, the energy exchanged between small temperature steps might be too low to be correctly monitored by the heat flux sensor compared to the heat flux noise. Temperature steps of 1K are selected in this study as it allows an accurate representation of the thermodynamic state of RT58 while having a short experiment and no influence of the heat flux noise on the measurements. The same heating rate of 0.5 $K.min^{-1}$ than in dynamic mode is set.

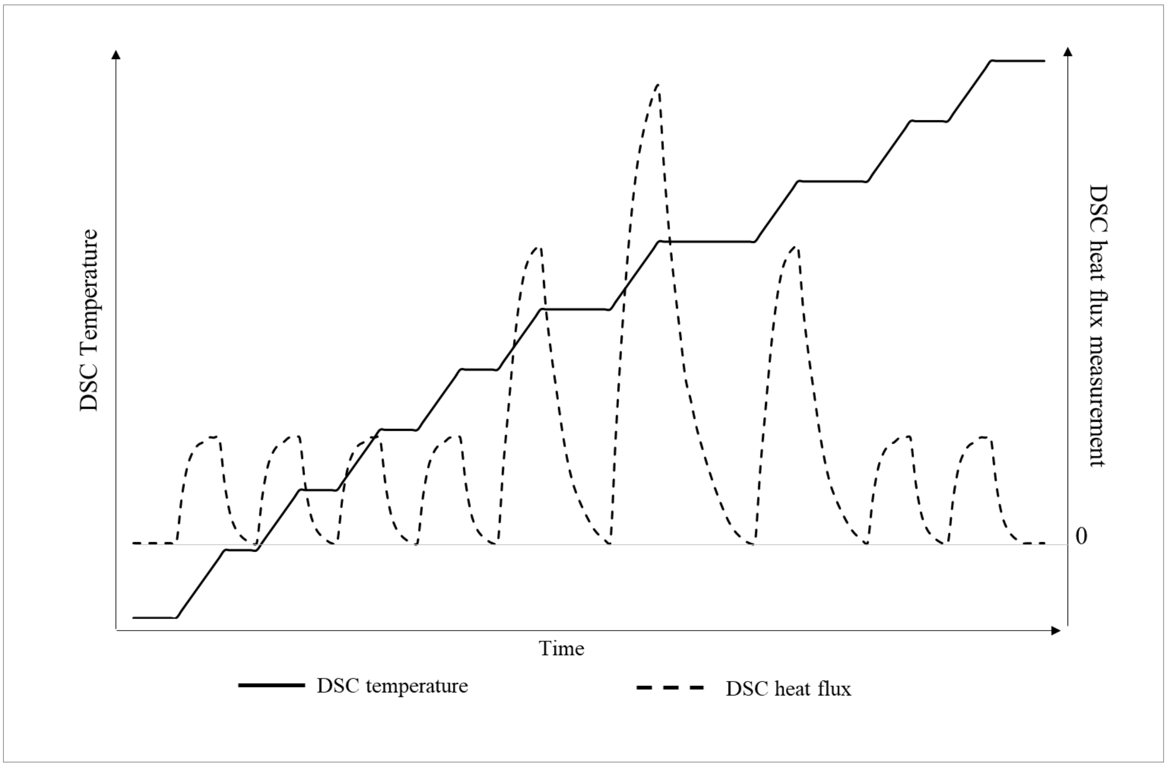

Fig. 2: Principe of DSC characterization with the step mode

3. Inverse method characterizations

3.1. Experimental set-up

The experimental apparatus is a heat flux bench, similar to the one used by (Younsi et al., 2011) and it is detailed in figure 3. The PCM is contained inside a rectangular polymethyl methacrylate (PMMA) brick heated or cooled by two heat exchangers. The PMMA brick measures $210 * 140 * 20$ mm with a wall thickness of 4 mm and contains a mass of 215g of RT58. The heat fluxes and temperatures between the two heat exchangers and the sample are measured by heat fluxmeters on each side of the PMMA brick. The fluxmeters sensitivity is $117\ \mu V.Wm^{-2}$ with an accuracy of 3%. A T-type thermocouple, calibrated at 0.1°C, is also inserted inside the PCM to monitor the variation of the PCM temperature, which is not equivalent to the heat exchangers temperature. The heat transfers within the PCM can be considered in 1D as the lateral sides of the PMMA brick are insulated and the sample width is small compared to the heated surfaces. Heating and cooling ramp of 18h are applied by the heat exchangers to the sample between 20°C and 70°C

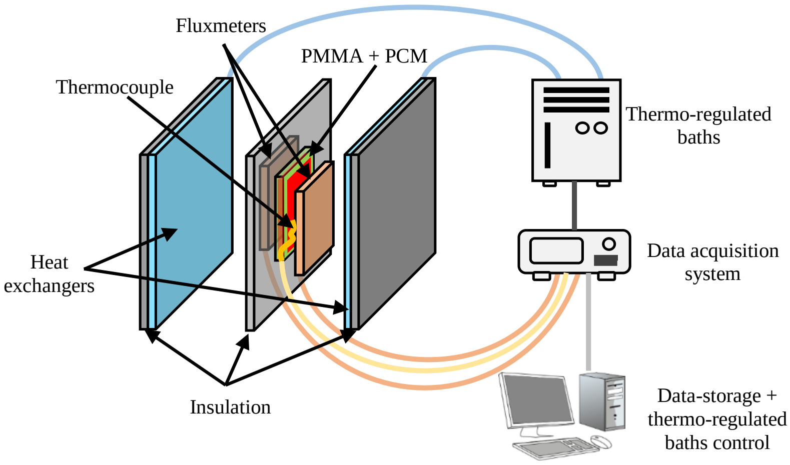

Fig. 3: Experimental apparatus of the heat flux bench

3.2. Modelling of the set-up

The heat flux bench is modelled in 1D by finite difference method with Python programming language. The PCM is discretized in 10 nodes and the boundary conditions of the system are the temperatures applied by the heat exchangers on each side of the sample.

The analytical equation chosen to describe the evolution of the thermodynamic state of the PCM in function of temperature can either be formulated according to the liquid fraction $f(T)$, the effective heat capacity $C_{eff}(T)$ or the enthalpy $H(T)$ as shown with equation 1. Considering only heat transfers by conduction, the equation governing the phase change problem is detailed by equation 2.

$$C_{eff}(T) = \frac{dH(T)}{dT} = Cp_S + (Cp_L - Cp_S)\ \times f(T) + L \times \frac{df(T)}{dT} \qquad \text{(eq. 1)}$$

$$\frac{\partial T}{\partial t} = \frac{\lambda}{\rho\, C_{eff}(T)} \nabla^2 T \qquad \text{(eq. 2)}$$

In this study, the analytical model selected describes the evolution of the liquid fraction based on the derivative of an asymmetrical Gaussian function as shown by equation 3. Temperature T_{PC} corresponds to the steepest slope on the liquid fraction curve, which is equivalent to the highest effective heat capacity. Temperature T_S refers to the highest temperature where the PCM is fully solid and temperature T_L to the lowest temperature where the PCM is fully liquid. Coefficients σ_S (equation 4) and σ_L (equation 5) ensure a liquid fraction close to 0 at T_S and to 1 at T_L.

$$f(T) = \begin{cases} \dfrac{\sigma_S}{\sigma_S + \sigma_L}\left[erf\left(\dfrac{T - T_{PC}}{\sigma_S}\right) + 1\right] & T \le T_{PC} \\ \dfrac{1}{\sigma_S + \sigma_L}\left[\sigma_L \times erf\left(\dfrac{T - T_{PC}}{\sigma_L}\right) + \sigma_S\right] & T > T_{PC} \end{cases} \qquad \text{(eq. 3)}$$

$$\sigma_S = \frac{\sqrt{2}}{4}(T_{PC} - T_S) \qquad \text{(eq. 4)}$$

$$\sigma_L = \frac{\sqrt{2}}{4}(T_L - T_{PC}) \qquad \text{(eq. 5)}$$

If two heat flux peaks are observed experimentally, equation 1 evolves to equation 6 in order to improve the accuracy of the analytical model. The two heat flux peaks are assumed to be related to two distinct materials, A and B, composing the PCM. The evolution of the liquid fraction of each material, $f_A(T)$ and $f_B(T)$, are supposed independent and the contribution to the total latent heat of the PCM for each material is represented by L_A and L_B. Assuming that specific latent heats of material A and B are equivalent, the total liquid fraction $f_{Tot}(T)$ of the PCM is obtained with a coefficient of latent heat repartition $\epsilon = L_A/(L_A + L_B)$ to weight liquid fraction $f_A(T)$ and $f_B(T)$ by ϵ and $(1 - \epsilon)$, respectively.

$$C_{eff}(T) = Cp_S + (Cp_L - Cp_S) \times f_{Tot}(T) + L_A \times \frac{df_A(T)}{dT} + L_B \times \frac{df_B(T)}{dT} \qquad \text{(eq. 6)}$$

3.3. Inverse method principle

The aim of identification by inverse method is to determine unknown parameters involved in the numerical model, such as PCM properties in our case, to fit the numerical results with the experimental ones, which are used as references. The experimental heating and cooling rates are used as input in the numerical model, the output being the numerical heat flux which is compared to the experimental one monitored by the heat fluxmeter sensors. The fitness between the numerical and experimental results is evaluated with the least square approach. Particle swarm optimization (PSO) algorithm is used to perform the inverse method and identify the best set of parameters with the following parametrization: swarmsize=50, particle velocity=0.6, search away particle best known solution=0.7, search away swarm best known solution=0.3.

The main limitation of inverse methods is the convergence as it is not guaranteed that the identified set of parameters is the global solution and not a local solution. The best way to reach convergence is to properly parametrize the optimization algorithm and to reduce the number of parameters to identify.

3.4. Global inverse method

The global identification by inverse method is achieved in three steps. First, the liquid density of the PCM is measured by weighting, right after filling the PMMA brick with the liquid PCM at 70°C. Once fully solid at 20°C, the solid density is obtained by measuring the height difference of the PCM in the PMMA brick compared to liquid state.

The second step consists in performing an inverse method to identify the solid and liquid specific heat capacities and thermal conductivities. Experiments on fully solid and liquid PCM are used as references to identify these parameters.

The third step identifies the latent heat and the parameters involved in the analytical model, to describe the thermodynamic state of the PCM, with a second inverse method. The experiment with heating and cooling ramp of 18h between 20°C and 70°C is selected as reference for the inverse method. Slow heat and cooling ramps make it easier for the PSO algorithm to identify the PCM properties and the phase transition is more distinct than for fast heating and cooling ramps.

3.5. Energy balance inverse method

In the energy balance inverse method, compared to global inverse method, the latent heat and the specific heat capacities of the PCM are identified altogether by energy balance equations on the experimental results. The contribution of sensible heat and latent heat to the total heat flux exchanged by the PCM are presented on figure 4. As shown by equation 7 and equation 8, the solid and liquid specific heat capacities are determined by dividing the sensible heat exchanged on fully solid and liquid state by the temperature range where the PCM is fully solid and liquid respectively. Then, the latent heat (equation 12) is obtained by removing the sensible heats of both the PMMA brick (equation 10) and the PCM (equation 11) to the total heat exchanged by the PCM (Equation 11) during the heating and cooling process. This fourth step, with energy balance identification, is added between step I and II of global inverse method. Then, only the thermal conductivities have to be identified in the first inverse method, and the latent heat is removed to the set of parameters to identify in the second inverse method. Table 1 summarizes the identification process of the global inverse method, detailed in the previous section, and the energy balance method, detailed in this section. Table 2 detailed the PCM properties obtained after performing the global inverse method and the energy balance inverse method.

$$Cp_S = \frac{\left(\sum_{t_0}^{t_1} \phi^{Exp} \times \Delta t\right) - m^{PMMA} \times Cp^{PMMA} \times (T_1^{Hx} - T_0^{Hx})}{m^{PCM}(T_1^{Hx} - T_0^{Hx})} \quad \text{(eq. 7)}$$

$$Cp_L = \frac{\left(\sum_{t_2}^{t_3} \phi^{Exp} \times \Delta t\right) - m^{PMMA} \times Cp^{PMMA} \times (T_3^{Hx} - T_2^{Hx})}{m^{PCM}(T_3^{Hx} - T_2^{Hx})} \quad \text{(eq. 8)}$$

$$E^{Tot} = \sum_{t_0}^{t_3} \phi^{Exp} \times \Delta t \quad \text{(eq. 9)}$$

$$E^{PMMA} = Cp^{PMMA} m^{PMMA} (T_3^{Hx} - T_0^{Hx}) \quad \text{(eq. 10)}$$

$$E^{Sens} = m^{PCM} \left(Cp_S (T_1^{Hx} - T_0^{Hx}) + \frac{Cp_L + Cp_S}{2} (T_2^{Hx} - T_1^{Hx}) + Cp_L (T_3^{Hx} - T_2^{Hx}) \right) \quad \text{(eq. 11)}$$

$$L = \frac{E^{Tot} - E^{PMMA} - E^{Sens}}{m^{PCM}} \quad \text{(eq. 12)}$$

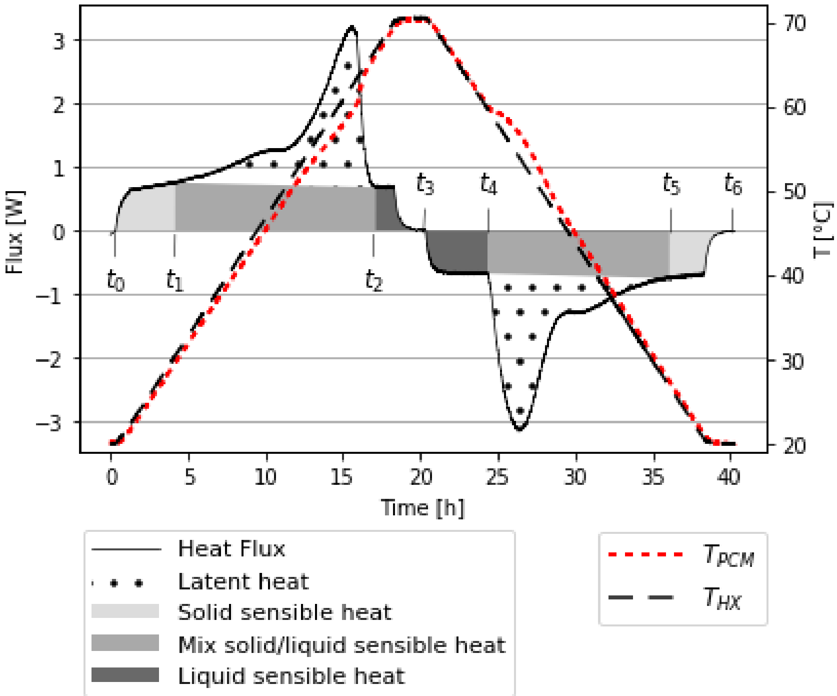

Fig. 4: Contribution of sensible heat and latent heat to the total heat exchanged by the PCM

Tab. 1: Identification process of PCM properties for global inverse method and energy balance inverse method

PCM properties	Global inverse method	Energy balance inverse method
ρ_S, ρ_L	Experimental weighting (step I)	Experimental weighting (step I)
Cp_S, Cp_L	Inverse Method I (step II)	Energy balance (step II)
λ_S, λ_L	Inverse Method I (step II)	Inverse Method I (step III)
L	Inverse Method II (step III)	Energy balance (step II)
$\epsilon, T_{S\,A}, T_{PC\,A}, T_{L\,A}, T_{S\,B}, T_{PC\,B}, T_{L\,B}$	Inverse Method II (step III)	Inverse Method II (step IV)

Adding a fourth step to the identification process present two main advantages. First, it ensures an equivalent energy balance between the experimental and numerical results as the specific heat capacities and the latent heat are identified directly on experimental results. Secondly, fewer parameters have to be identified on inverse method I and II, which means a faster optimization time to converge to the global solution.

4. Results

Before comparing results from DSC experiments and inverse methods, the accuracy of the global inverse method and the energy balance inverse method has to be checked. As shown by figure 5 and figure 6, both global inverse method and energy balance inverse method represent correctly the evolution of the temperature and the heat flux, the main heat flux peak being around 59°C and the secondary one around 45°C. The selected analytical model combined to the modelling of two materials A and B is then relevant to model paraffin RT58. The difference between the two methods seems minimal but, when having a closer look at the evolution of the error between numerical and experimental results with figure 7, a slightly better accuracy is observed for the global inverse method. This was expected as the latent heat is identified with the global inverse method to fit the experimental and numerical heat flux curves, and then perform better than for the energy balance inverse method where the latent heat is fixed by experimental results.

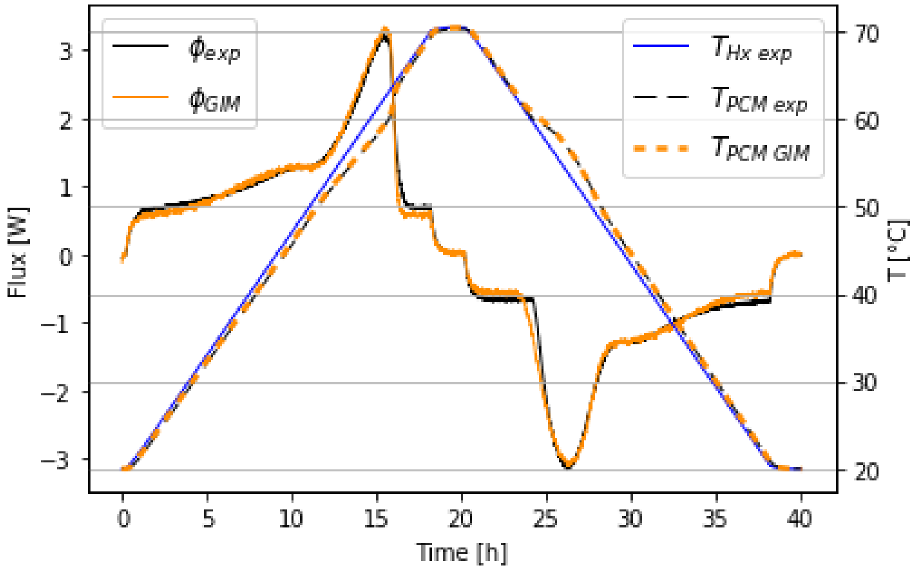

Fig. 5: Comparison between experimental and numerical heat flux and temperature for the global inverse method (GIM)

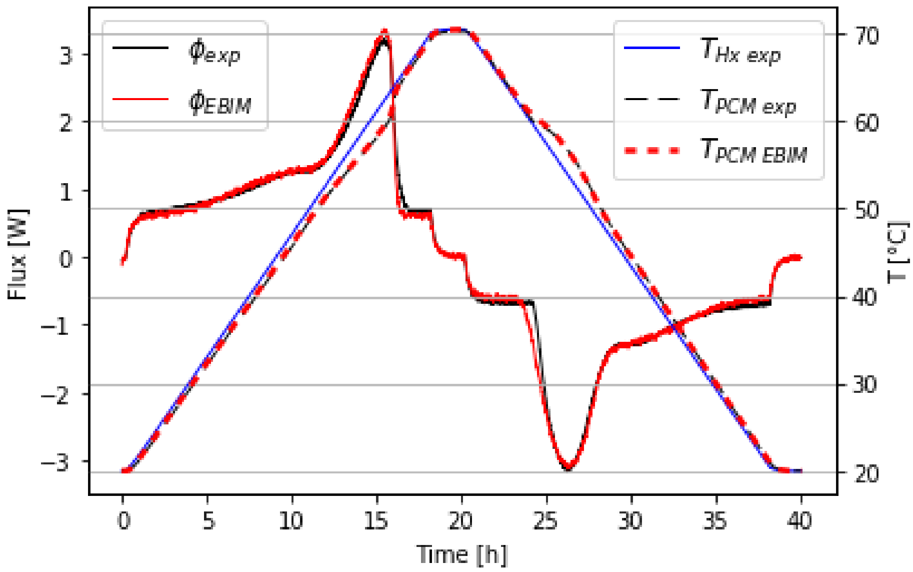

Fig. 6: Comparison between experimental and numerical heat flux and temperature for the energy balance inverse method (EBIM)

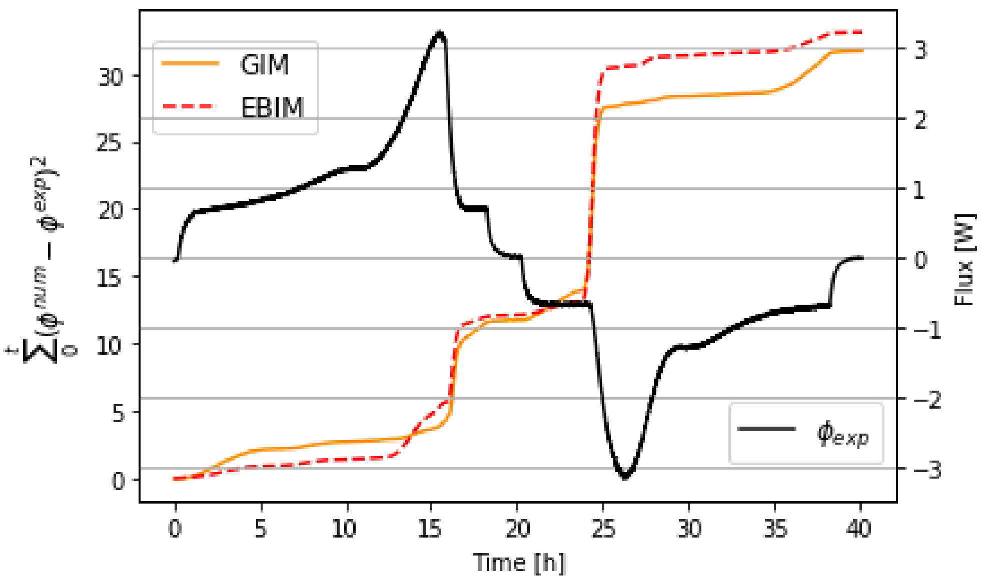

Fig. 7: Evolution of the quadratic error between experimental and numerical heat flux for the global inverse method (GIM) and the energy balance inverse method (EBIM)

The enthalpy curves obtained with each method are presented figure 8. All four characterization methods lead to almost the same enthalpy curve in overall. The final enthalpy value only differs by 3.3% between the highest one, the energy balance inverse method, and the lowest one, the DSC dynamic mode. The scale difference between the DSC sample and the brick sample used in the heat flux bench does not influence the enthalpy curve. The results from DSC dynamic mode are almost equivalent than those from step mode, implying that heating and cooling rate of 0.5 $K.min^{-1}$ is appropriate for the characterization of RT58. As shown by table 2, differences between PCM properties identified by the two inverse methods are minimal and therefore leads to an almost equivalent enthalpy curve. Eventually, each method seems appropriate to identify the enthalpy curve or RT58. The modelling of complete melting and solidification will hardly change from one method to another.

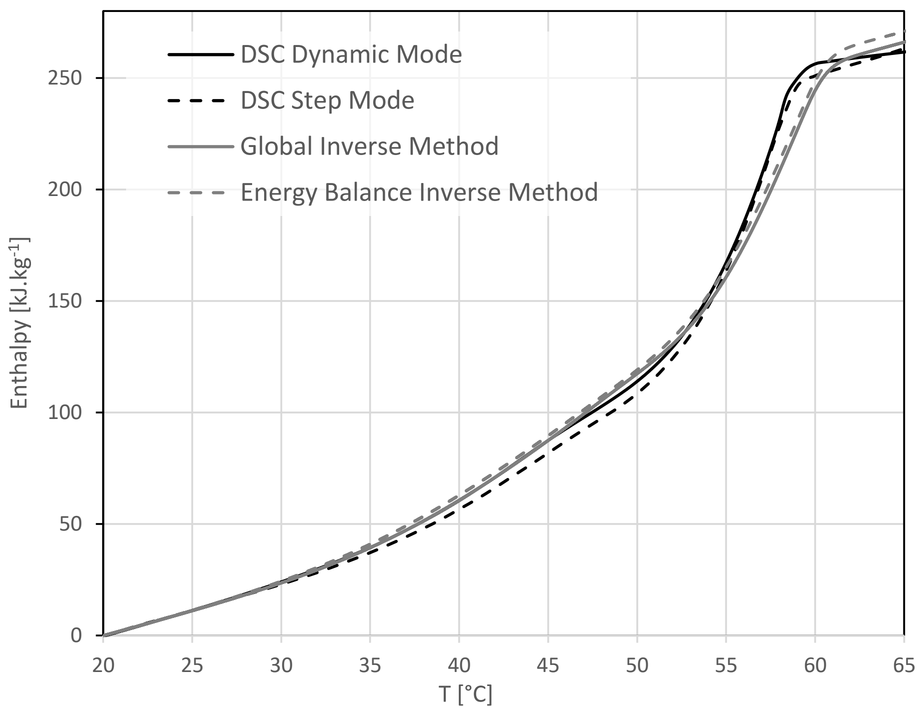

Fig. 8: Enthalpy curve of paraffin RT58 obtained with the four characterization methods tested (from reference set at zero at 20°C)

Tab. 2: PCM properties identified with global inverse method (GIM) and energy balance inverse method (EBIM)

PCM properties	Unit	GIM	EBIM
ρ_S	$kg.m^{-3}$	880	880
ρ_L	$kg.m^{-3}$	808	808
Cp_S	$J.kg^{-1}.K^{-1}$	1925	2112
Cp_L	$J.kg^{-1}.K^{-1}$	1975	2100
λ_S	$W.m^{-1}.K^{-1}$	0.198	0.206
λ_L	$W.m^{-1}.K^{-1}$	0.241	0.237
L	$kJ.kg^{-1}$	177.2	172.4
ϵ	-	0.32	0.30
$T_{S\,A}$	°C	10.0	9.7
$T_{PC\,A}$	°C	45.4	45.4
$T_{L\,A}$	°C	60.2	59.8.
$T_{S\,B}$	°C	40.6	39.6
$T_{PC\,B}$	°C	59.3	59.3
$T_{L\,B}$	°C	63.6	63.7

However, small differences still exist between the different characterization methods, especially between DSC and inverse methods. Indeed, the two DSC methods and the two inverse methods give a slightly different evaluation of the end of the phase change process. The liquid state seems to be fully reached at 59.5°C for the two inverse methods and at 60.5°C for the DSC methods. It results in a maximal enthalpy difference of 25 $kJ.kg^{-1}$ at 59°C, which might lead to different numerical performances, particularly for partial phase change around 57-60°C.

5. Conclusion

To conclude, four characterization methods have been tested to determine the enthalpy curve of RT58, two based on DSC methods with dynamic mode and step mode, the other two relying on a numerical model to identify the PCM properties with a global inverse method or an energy balance inverse method. Results are mainly similar for each method with an equivalent heat exchanged. The phase change dynamic on the phase change temperature range is however slightly different between the two DSC methods and the two inverse methods. Modelling of complete phase change will be almost not influenced, but the modelling of partial phase change might be slightly different. The equivalence between the four characterization methods is only relevant for the considered PCM RT58 and cannot be withdrawn to other PCM.

6. Acknowledgments

This study takes part in the EUROPA project funded by the ANR (French National Research Agency).

7. References

Dolado, P., Mazo, J., Lázaro, A., Marín, J.M., Zalba, B., 2012. Experimental validation of a theoretical model: Uncertainty propagation analysis to a PCM-air thermal energy storage unit. Energy and Buildings 45, 124–131. https://doi.org/10.1016/j.enbuild.2011.10.055

Dumas, J.-P., Gibout, S., Zalewski, L., Johannes, K., Franquet, E., Lassue, S., Bédécarrats, J.-P., Tittelein, P., Kuznik, F., 2014. Interpretation of calorimetry experiments to characterise phase change materials. International Journal of Thermal Sciences 78, 48–55. https://doi.org/10.1016/j.ijthermalsci.2013.11.014

Franquet, E., Gibout, S., Bédécarrats, J.-P., Haillot, D., Dumas, J.-P., 2012. Inverse method for the identification of the enthalpy of phase change materials from calorimetry experiments. Thermochimica Acta 546, 61–80. https://doi.org/10.1016/j.tca.2012.07.015

Gibout, S., Molina, S., Haillot, D., Franquet, E., 2017. Méthode STEP : Caractérisation de La Précision et Conditions Optimales d’analyse. In XIIIe Colloque interuniversitaire franco-québécois sur la Thermique des Systèmes énergétiques (CIFQ).

Lazaro, A., Peñalosa, C., Solé, A., Diarce, G., Haussmann, T., Fois, M., Zalba, B., Gshwander, S., Cabeza, L.F., 2013. Intercomparative tests on phase change materials characterisation with differential scanning calorimeter. Applied Energy 109, 415–420. https://doi.org/10.1016/j.apenergy.2012.11.045

Sharma, A., Tyagi, V.V., Chen, C.R., Buddhi, D., 2009. Review on thermal energy storage with phase change materials and applications. Renewable and Sustainable Energy Reviews 13, 318–345. https://doi.org/10.1016/j.rser.2007.10.005

Tittelein, P., Gibout, S., Franquet, E., Zalewski, L., Defer, D., 2015. Identification of Thermal Properties and Thermodynamic Model for a Cement Mortar Containing PCM by Using Inverse Method. Energy Procedia 78, 1696–1701. https://doi.org/10.1016/j.egypro.2015.11.265

Younsi, Z., Zalewski, L., Lassue, S., Rousse, D.R., Joulin, A., 2011. A Novel Technique for Experimental Thermophysical Characterization of Phase-Change Materials. International Journal of Thermophysics 32, 674–692. https://doi.org/10.1007/s10765-010-0900-z

ADVANCES IN MODELING AND EVALUATION OF LARGE-SCALE HOT WATER TANKS AND PITS IN RENEWABLE-BASED DISTRICT HEATING

Abdulrahman Dahash[1], Fabian Ochs[1] and Alice Tosatto[1]

[1] Unit of Energy Efficient Buildings/Department of Structural Engineering and Material Sciences/University of Innsbruck, Innsbruck (Austria)

Abstract

Large-scale seasonal thermal energy storage (TES) emerges as a promising component in the future renewable-based district heating (R-DH) systems whereby large shares of renewables are being integrated. To enable such storage systems with large volumes to fulfill the seasonal tasks with high technical efficiency at cost-optimal level, they should be thoroughly examined, properly designed and planned. Thus, simulation-driven assessments are crucial to investigate these systems in order to avoid high capital cost with performance below expectations. While detailed finite-element simulations inspect multi-physical aspects (e.g. conduction, convection, mass transfer), dynamic simulation and pre-design tools are inevitably needed to capture the system's energy flows. Consequently, this work reports and reviews the development of a wide variety of numerical models and their validation for advanced TES applications.

Keywords: Hot water tank, buried pit, numerical modeling and simulation, renewable-based district heating, seasonal thermal energy storage, co-simulation approaches.

1. Introduction

To properly phase-out the conventional fuels (e.g. natural gas) and pave the way toward the decarbonization of the heating sector, alternative substitutes have to be accordingly addressed. Thus, the integration of alternative energy resources (e.g. solar energy, geothermal, industrial waste heat) found its place favorably in district heating (DH) systems whereby the share of renewables is gradually increasing forming the so-called renewables-based district heating (R-DH) systems (Ochs et al., 2019). Yet, it is important to mention that the renewables are often subject to a major pitfall as they seasonally and daily fluctuate leading to the intermittency by which heat might be available when it is not required. Thus, the integration of renewables might alter the overall national energy scheme (Dahash et al., 2019a) and some risks might appear (e.g. security of supply is violated). Hence, large-scale seasonal thermal energy storage (STES) plays a key role in R-DH systems as it is capable to bridge the gap between the renewables' availability and heat demand eliminating the mismatch (Dahash et al., 2019a).

Accordingly, it is held that a large-scale and long-term TES enables a more flexible integration of renewables in DH systems and, as a result, has benefits in terms of lower fossil fuels consumption, higher primary energy savings and lower CO_2 emissions. Yet, the high capital cost associated to STES is frequently seen as a major downside. Together with the space availability, complex planning layout and the presence of groundwater tables, these are the set of major challenges in STES domain to be tackled among others (Dahash et al., 2019a). Thus, simulation-based analyses are perfectly suited to the planning phase of such large-scale systems since its construction is considered a complex process.

2. Challenges in Planning and Construction of Seasonal TES

To select properly the design, geometry and construction type for a large-scale seasonal TES, a great number of inputs (hydro- geological factors, system characteristics, thermal losses, investment cost, etc.) have to be repetitively evaluated until a compromise between the technical performance and the economic feasible investment is found (Dahash et al., 2019a).

Fig. 1 schematically demonstrates the role of the most significant parameters influencing the construction of buried TES. Therein, the different players are classified into different categories and accordingly assigned

doi:10.18086/eurosun.2020.07.06 Available at http://proceedings.ises.org

following their impact on the desired type of the storage. Firstly, the site's ground conditions (e.g. soil excavation) have a direct impact on the capital cost, whereas the indirect impact is seen as it influences the construction type. The site has a further impact on the TES geometry (maximum available surface, maximum depth, etc.) when considering the static loads (e.g. pressure forces) implied on TES. Next, the application (e.g. heat-supply system) into which the TES is being integrated is strongly influenced by the storage duration (buffer or long-term TES) through the number of charging cycles from an operational point of view. This influence has in return an impact on the construction type of the TES, which subsequently influences the capital costs and, therefore, the cycle number has also an impact on the capital costs. Thereby, it is difficult to determine the optimum type of TES and its corresponding construction without the aid of numerical simulations and profound reliable key performance indicators (Ochs et al., 2015a).

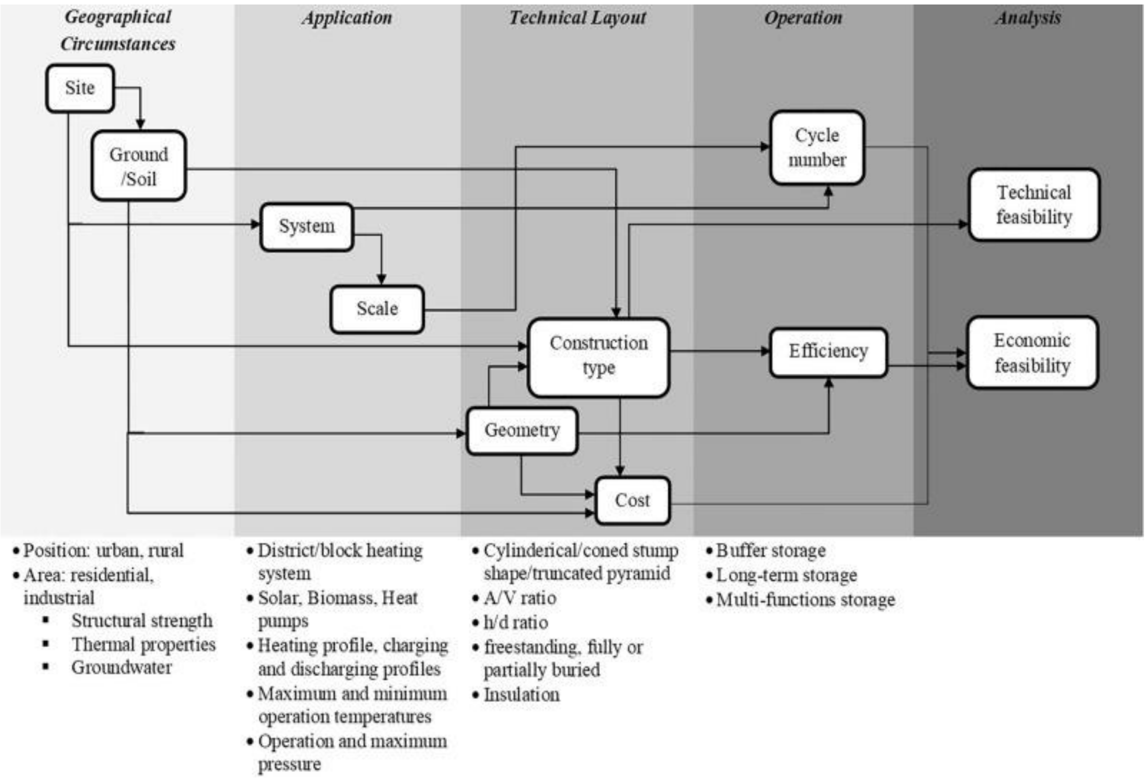

Fig. 1: Schematic representation of the most influencing parameters on the construction of large-scale underground TES and its economic feasibility (reproduced from (Dahash et al., 2019a)).

Further, the construction type has an impact on the heat-supply system efficiency as well on the TES. For instance, Ochs et al. (2019) compared the efficiency of two TES geometries (i.e. conical pit and cylindrical tank) under the same set of boundary conditions concluding that the tank outperforms the other option. Then, the efficiency affects the economic feasibility and, subsequently, the TES geometry disturbs the economic feasibility as the tank is often seen the most-costly option for STES. Thus, in the framework of an international project entitled "Giga-Scale Thermal Energy Storage for Renewable Districts" (giga_TES, 2019), an ultimate milestone is to set the planning guidelines and tools for different TES construction types (i.e. tanks, conical pits, pyramid pit) under different boundary conditions (e.g. groundwater existence/flow). It is held that such guidelines will help the engineers and researchers later to understand better which construction type is perfectly suited to the given tasks and can withstand the different challenges. Thus, the project also investigates a number of simulation tools for the modeling of large-scale seasonal TES with different operation parameters and boundary conditions.

3. Modeling and Simulation of Large-Scale Seasonal TES

The interconnections between the different categories shown in Fig. 1 highlight the importance of TES simulations. Besides, the construction of large-scale TES systems tends to be costly and, therefore, this inevitably demonstrates the significance of TES modeling to guarantee the economic feasibility and the effective planning layout for the system. As a result, modeling process suits ideally to these tasks and helps in understanding the operation of these systems, which permits in producing the optimal planning and later developing them. Consequently, it is remarkable that TES modeling simulations can be categorized into a wide range of levels following the goal of the investigation. Hence, TES modeling undergoes a systematic process in which the goals are pre-design, detailed design, technology integration, evaluation and optimization.

Fig. 2 reveals the TES modeling process hierarchy whereby at the early phase of TES construction a pre-design tool is frequently used for the planning phase and, then, details are consecutively included in the model until it reaches a detailed model. Next, the TES undergoes a technology investigation as it is integrated within an energy system (e.g. DH system). Accordingly, the TES technology is thoroughly evaluated and the outputs are post-processed resulting into some optimization proposals (e.g. material development, optimal construction type, optimum insulation thickness and DH operation control strategies). Meanwhile, it is important to keep in mind that there exist three factors strongly influencing the computation time: level of detail (pre-design, detailed), number of components (technology integration) and simulated time (daily, multi annual). These players might dramatically alter the computation time as shown in Fig. 3. In order to optimally select the right level, the aim of analysis should be beforehand defined.

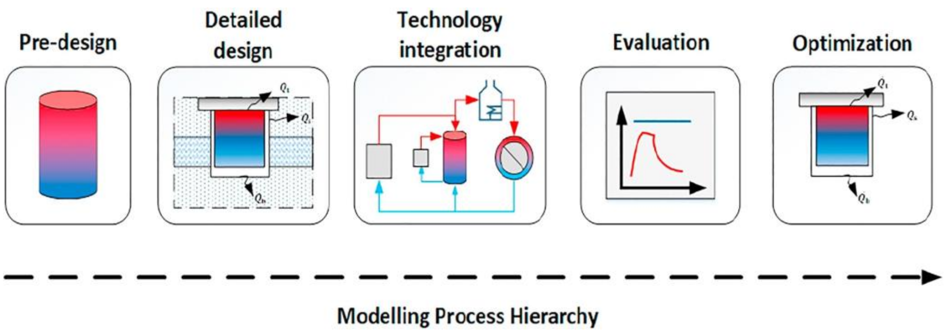

Fig. 2: An exemplary hierarchy for modeling process of large-scale TES in DH systems (reproduced from (Dahash et al., 2019a)).

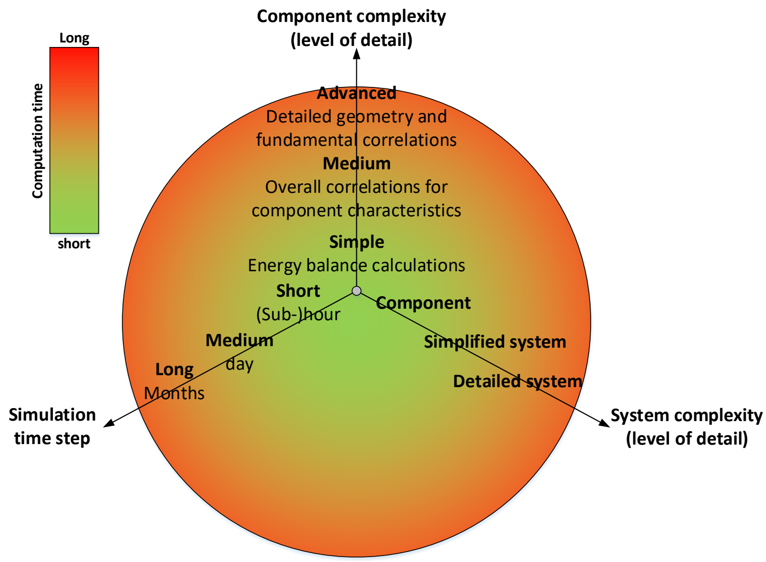

Fig. 3: Computation time for TES simulations.

For the pre-design level, some prototyping tools are used to give a glimpse on the TES and its integration and these tools produce preliminary performance indicators. Out of these tools, an online solar district heating (SDH) tool can be used for the preliminary cost-benefit analysis (Solites, 2013). This tool supports both centralized and decentralized SDH systems. Within "*giga_TES*" project, a pre-design tool is developed using Microsoft Excel and is known as "Load Profile Generator" (O'Donovan, 2019). It is as a simple monthly-balance tool that simulates TES with a 3-nodes model neglecting thermal losses to the environment.

Given the complexity seen when modeling the thermo-hydraulic behavior (stratification, buoyancy, etc.) of large-scale TES systems, a wide range of tools is usually used in modeling TES systems. Such tools are commonly categorized into three types: (a) energy system simulation (ESS) that involves tools like Modelica/Dymola, TRNSYS, Matlab/Simulink, (b) building physics envelope heat and mass transfer tools such as WUFI Pro and Delphin, and (c) computational fluid dynamics (CFD) such as ANSYS Fluent, OpenFOAM and COMSOL Multiphysics (which is also used for building envelope heat and mass transfer).

Accordingly, it is crucial to point out that different discretization schemes are used in simulation tools. Herein, the discretization of the spatial domain is executed using either finite element method (FEM), finite difference method (FDM) or finite volume method (FVM). Besides, the level of detail profoundly depends on the model's dimensionality. For instance, highly-detailed models require 3-D representation and as the level of detail becomes less required, then the model can be reduced to 1-D model.

ESS tools (e.g. Modelica/Dymola) often employ FDM as discretization fashion for models represented as 0-D or 1-D. Yet, it is possible to develop 2-D models in such tools but the computation time might exceed the limits. On the other hand, CFD tools (e.g. ANSYS Fluent) require exact representation for the investigated case and, thus, 2-D or 3-D representation become more important. In order to carry out accurate CFD predications, CFD models are often discretized in FVM or FEM fashion. Further, heat transfer problems call the necessity for accurate domain representation and the utilization of FEM. For example, the TES surrounding soil can be developed in COMSOL Multiphysics as an axisymmetric 2-D model that is discretized in a FEM fashion. Accordingly, this section reports the most common techniques used in modeling TES based on the component level (detailed), TES level, system level and the coupling of all.

3.1 Component-level modeling

Herein, it is strongly significant to emphasize the term "component-level" modeling. This arises from the fact that, for example, the domains (cover, liner, insulation, groundwater and surrounding soil) shown in Fig. 4 can be all together realized in one single model forming a stand-alone component-level model that represents the TES envelope domain with its insulation, charging/discharging devices and surroundings domains. Otherwise, the term also encompasses that each single domain (e.g. insulation) can be developed individually in one component-level model, which is later coupled to another component-level model (e.g. fluid domain) and, therefore, the result is a compact model that encompasses two or more component-level models. Whereas the term system-level modeling (the following subsection) stands for the process in which TES is treated as an energy system integrated into a larger energy system and, thus, system-level is widely custom for the overall energy system.

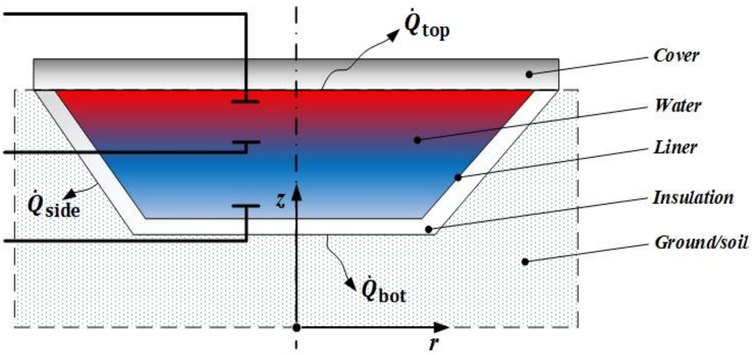

Fig. 4: An exemplary 2-D representation of an underground shallow pit with the different domains (Dahash et al., 2020a).

In component-level category, the TES is systematically modeled; subsequently, producing a detailed model. Accordingly, a numerical modeling approach has been broadly employed for component level modeling because it enables the inclusion of a comprehensive range of physics, sketches the desired geometry of the TES component and allows the integration of the surroundings' heat transfer (mainly the one between the soil and the TES). Therefore, CFD is used in which the models are exact representations of the actual component geometry in a discretized fashion. Besides, all transport mechanisms (e.g. moisture transfer in TES envelope) occurring in reality can be considered in CFD models.

Numerical modeling of hot water tanks has been extensively paid a great attention in the literature. Nevertheless, there were little efforts made for modeling large-scale hot water tanks numerically, especially in the case of underground tanks. For instance, Panthalookaran et al. (2008) developed numerical computational fluid dynamic (CFD) models ideally suited for specific tasks (i.e. charging/discharging modes). The models were calibrated against measured data from two buried TES tanks in Germany. One of the tanks is installed in Hannover–Kronsberg with a volume of 2750 m^3, whilst the other is the underground TES in Friedrichshafen–Wiggenhausen with a volume of appx. 12,000 m^3. The models were used to develop a new characterization method for performance evaluation of various boundary designs during standby mode in large-scale stratified TES (Panthalookaran et al., 2011). Other than those, it is challenging to find other published CFD models that are valid for large-scale underground storage tanks.

On the other hand, the numerical modeling of large-scale pit TES has been lately investigated in the literature. For instance, Chang et al. (2017a) presents a CFD model for a PTES component with transient conditions. Therein, the transient natural convection in a PTES is examined and, subsequently, the mechanism of temperature stratification driven by buoyancy phenomenon is reported. Additionally, the model was validated with experimental data from in-situ test rig with a lab-scale. Later, the model was used to evaluate the thermal performance of a PTES for different key characteristic parameters (Chang et al., 2017b). Therein, it was observed a degradation in stratification degree, which was strongly attributed to the decrease in the PTES depth and, thus, less thermal efficiency. Another conclusion was that PTES thermal efficiency drastically decreases as the slope angle becomes smaller (Chang et al., 2017a). It can be concluded that as the depth decreases with a decrease in slope angle, the upper and lower perimeters of storage increase resulting in unfavorable values of aspect ratio (H/d). Furthermore, Fan et al. (2017) investigated numerically and experimentally the thermal behavior of the seasonal water pit heat storage (a total volume of 75,000 m^3) in Marstal solar heating plant (Denmark) by means of a CFD model for short simulation periods. In this model, the interaction between the heat storage and the ground itself is also included.

Moreover, Urbaneck (2004) investigated the thermal behavior for a gravel-water pit TES in Chemnitz, Germany by means of CFD simulations for short simulation periods. Therein, the pit model was validated and, then, a parametric study was performed to determine the effective thermal conductivity of gravel-water medium. Also, the effects seen during charging/discharging modes were examined and explained by means of this CFD simulation. It is observed that large-scale and flat vortices occurred during water exchange (charging/discharging) and they existed for several hours after the exchange process.

Despite the detailed outcomes revealed by CFD models, CFD simulations inevitably call a necessity for large computation efforts as their simulations demand the solution for a set of partial differential equations (PDE) to provide the corresponding physical values (e.g. temperature, pressure, humidity, velocity etc.) and, Accordingly, great computation efforts are required for large-scale seasonal TES for (multi-) annual system simulations, which is currently not feasible and probably not in the near future (Ochs et al., 2009a). Hence, CFD simulations were perfectly tailored for investigations during TES standby mode or short-term operation. Furthermore, another drawback of CFD models is that any slight change in geometry is related with a complex numerical mesh generation. Consequently, assumptions are frequently set for a number of inputs (e.g. material properties and boundary conditions) in simulation studies. These assumptions produce, in fact, a positive notable reduction in the computation efforts forming the so-called “coarse models” (Ochs, 2009b).

Coarse models simplify the geometry investigated and, subsequently, do not depict the exact thermal hydraulic behavior resulting into inaccurate account for the thermal losses (Ochs, 2009b). Regardless of these shortcomings, there have been quite extensive work to develop dynamic models for large-scale underground TES systems in different simulation environments. For instance, several coarse models are applicable for large-scale TES systems in TRNSYS simulation environments (Schmidt et al., 2018a). Those coarse models, however, consider one-dimensional flow inside TES (FDM or plug flow). One of these coarse models is the XST-model (type 342) that simulates buried cylindrical water tanks (Raab et al. 2005). Another model is the so-called ICEPIT-model (type 343), which represents buried gravel-water pit TES (Hornberger, 1998). It is worthy to mention that ICEPIT-model outperforms XST-model because it permits simulating several shapes (i.e. cylindrical geometries and truncated cones), whilst the XST-model simulates only cylindrical geometries (Ochs, 2015b). In addition, ICEPIT-model is able to use water as storage medium instead of gravel-water, which makes this model more advantageous than XST model. Moreover, there exist other tank models (e.g. type 534, type 4) in TRNSYS environment. Yet, it is often argued whether type 534 and type 4 are perfectly capable to represent large-scale STES. On a brighter note, Li et al. (2019) examined the influence of 3 control strategies on the overall performance of an S-DH system equipped with a 3000 m^3 pit TES using the model type 534 to represent PTES. Compared to types 342 and 343, TES model type 534 demands an individual ground model when TES is buried.

Ochs (2009b) compared both models (i.e. type 342, type 343) using experimental data for large-scale underground TES and, subsequently, he concluded that both models provide comparable results but they are not sufficiently flexible with respect to geometry and, subsequently, they may not accurately depict the heat and moisture transfer. This is because both models employ FD method for modeling the heat conduction in the ground, whereas it is important to use FEM for complex geometries.

Furthermore, the engineering consulting company (*Thermal Energy System Specialists (TESS)*) established a 3-D model for STES simulations with different cross-sections based on a special request from the Danish STES planning company (PlanEnergi), which owns the copyrights of this model. It is noteworthy to mention that this model is a segmental 3-D model in which only a quarter of the STES is computed, whilst symmetry planes are assigned for the remaining STES domain in order to reduce the computation efforts. In this context, Klöck (2018) carried out the calibration of this model with different cross-sections (e.g. circular or rectangular) against measured data from Dronninglund pit storage (Schmidt and Sørensen, 2018b).

Hence, it is essential to develop dynamic models (FD models) for underground tank TES that can be effectively coupled to other models (FE models) that examine more in-depth the heat transfer and fluid flow in the surrounding ground, which facilitates more accurate simulation results (Ochs, 2014, 2015b). In this context, Dahash et al. developed a numerical multi-physics TES model as part of "*giga_TES*" project. The model is developed in COMSOL Multiphysics® and capable to capture the different geometrical options (e.g. tank, cone, pyramid) as shown in Fig. 5. It is noteworthy to mention that COMSOL Multiphysics interprets the system of partial differential equations via FEM and solves it via advanced numerical methods.

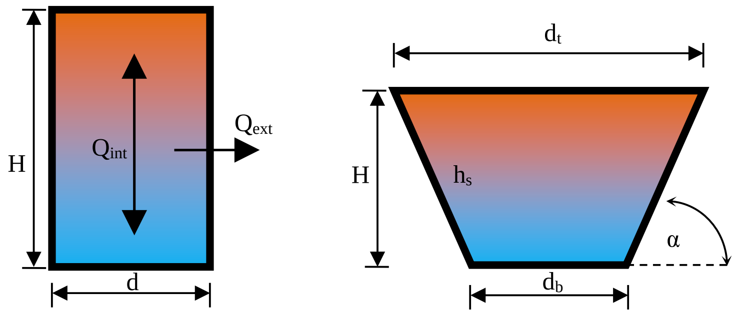

Fig. 5: Geometry of a seasonal thermal energy storage with internal and external losses: (a) tank, (b) pit (Dahash et al., 2020a).

3.2 Validation of the developed component-level model

In order to gain trust in the results of a transient model, it is important to compare the model results against measured data. Thus, the Dronninglund pit TES in Denmark was chosen as a case study for validating the developed model in COMSOL Multiphysics (Sørensen and Schmidt, 2018). This pit TES has a volume of approximately 60,000 m^3 and presented in Fig. 4. Thus, Table 1 provides an overall energy balance for the Dronninglund PTES in which a comparison between simulated (cone PTES, pyramid PTES) and measured energy is revealed.

In Table 1, the pyramid PTES is a 3-D numerical model and corresponds exactly to the Dronninglund PTES from a geometric point of view, whilst the cone PTES is an axisymmetric 2-D model and represents the adaptation of Dronninglund into a conical geometry. Concerning the charging/discharging energy, the model "pyramid PTES" provides results slightly closer to measurements than those of the cone, whereas the simulated outcome for the change in internal energy (dQ) deviates in both cases by 2 MWh. Given a deviation lower than 3 % for both models in comparison to the measurements, it is held that both models are reliable. Further information concerning the developed model and its validation can be found in (Dahash et al., 2020a).

Fig. 6 depicts the breakdown of charging/discharging energy for the Dronninglund PTES in which the simulated monthly energy is compared to that of the measurement. Therein, the positive values stand for energy charged into PTES, whereas the negative values represent the energy discharged out of PTES. Apparently, the error is below 2 % over most of the year 2015. However, this is not true for November of the simulated year as a remarkable error in the charging energy is observed for both models. It is held that this error is primarily originated due to the low measured charging energy during November against which any small difference between the measured and simulated values might lead to an apparent error.

Table 1: Simulated and measured energy flows for Dronninglund PTES (reproduced from (Dahash et al., 2020a)).

	Charging Energy	Discharging Energy	Internal Energy	Thermal Losses				Efficiency	
	Q_{ch}	Q_{dis}	dQ	Q_{top}	Q_{side}	Q_{bot}	Q_{loss}	η_I	η_{II}
	[MWh]	[MWh]	[MWh]	[MWh]				[-]	
Measurements	12 760	11 982	-497	786	-	-	1275	0.9	0.76
Pyramid PTES	12 743	11 966	-499	787	481	9	1276	0.9	0.76
ε [%]	0.13	0.13	0.4	0.13	-	-	0.1	0	0
Cone PTES	12 741	11 962	-495	788	478	9	1274	0.9	0.76
ε [%]	0.15	0.17	0.4	0.25	-	-	0.1	0	0

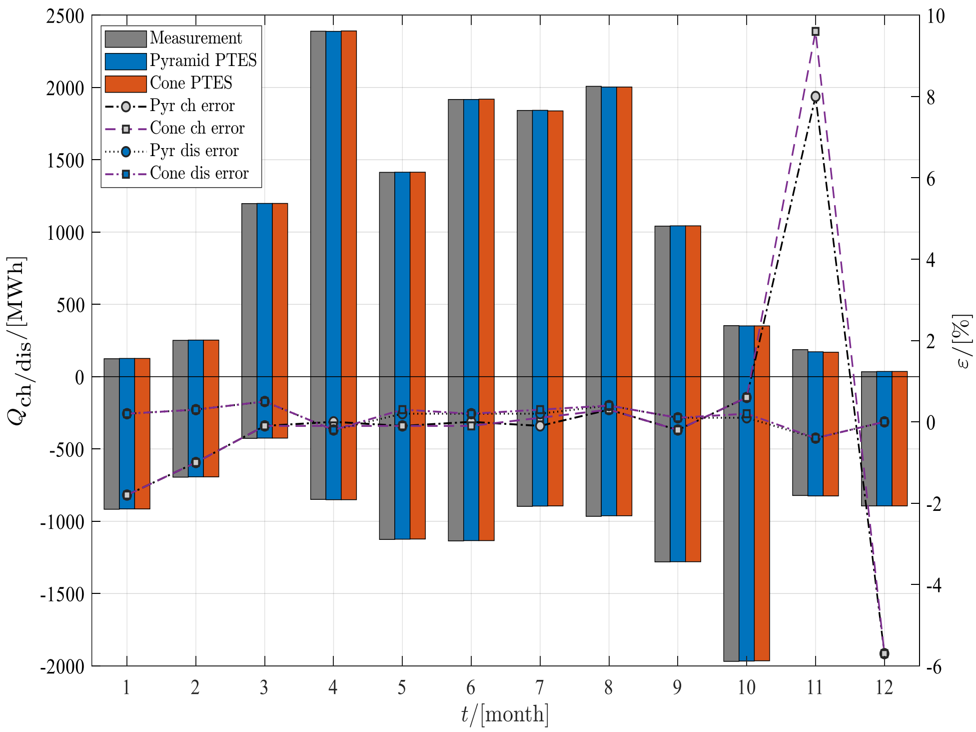

Fig. 6: Breakdown of simulated charged (+)/discharged (-) energy into/from PTES compared to the measurement in the year 2015 (reproduced from (Dahash et al., 2020a)).

Fig. 7 proves a remarkable matching between both simulated and measured PTES temperature for an array of heights from 16 m down to 0.5 m. Inevitably, it reveals that PTES reached a maximum temperature of around 89°C during summer (starting from day 230 to day 280). Throughout this period, PTES functioned as a short-term storage. Whereas for the period (60 – 180 days), PTES was into operation as multi-functional storage.

It is worthy to mention that the existence of groundwater in TES surroundings might eventually lead to higher thermal losses and, accordingly, higher temperatures in the ground. Therefore, it is of high importance to include the groundwater existence in the TES modeling. Thus, Dahash et al. (2019b) further extended the aforementioned developed model further to include the groundwater. The inclusion of groundwater aspect was validated against FEFLOW (Diersch, 2014), which is a well-established FE tool for groundwater simulations.

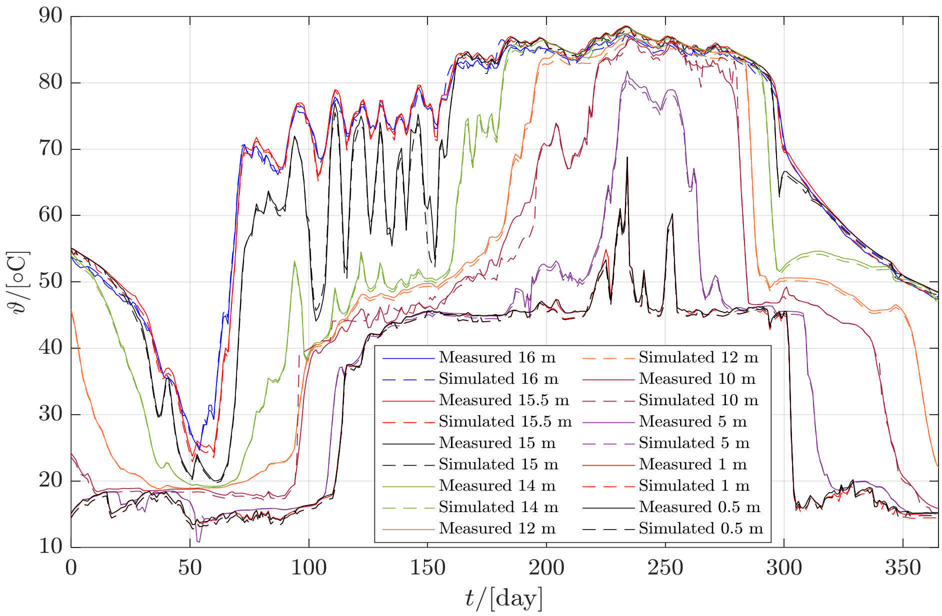

Fig. 7: Development of PTES simulated and measured temperatures in the year 2015 with hourly resolution (reproduced from (Dahash et al., 2020a)).

3.3 System-Level Modeling and Efforts to Couple System-Level Model with Component-Level Model

Numerical modeling tools (e.g. COMSOL Multiphysics) can accurately deliver robust analyses of buried TES and, subsequently, profound insights that enable optimizing the stores for an efficient design and operation. Yet, ESS tools are commonly used for system-level modeling in order to reduce the computation efforts. Such tools are TRNSYS, EnergyPlus, Modelica/Dymola, Matlab/Simulink and others. Compared to other ESS tools, TRNSYS is frequently seen as the widely-used tool when modeling buried water TES as its TES models can be easily coupled to buildings, heating plants and other components in a system level and also due its modular nature for adding further new components (Crawley et al., 2008). Nevertheless, there exist attempts to seek the modeling of buried TES in other environments. For instance, Ochs (2014) presents a dynamic FD model that is able to represent various construction shapes (cylinder, cone) for underground hot water TES in Matlab/Simulink environment.

Further, a dynamic model for a solar DH system with a seasonal TES was presented in (Kubiński and Szabłowski, 2019). The dynamic model was developed in Aspen HYSYS software to represent the S-DH systems in Vojens, Denmark. Given the fact that this tool offers only cylindrical tanks, the PTES installation in Vojens was approximated to a tank with same upper circumference and volume of the actual TES. Another drawback in the tank model is that it is a fully-mixed component and, thus, to tackle this challenge different tank elements were connected in series to develop a stratified tank. It is important to mention that the proposed modelling approach led to results significantly differ from the actual installation.

In an attempt to condense the computational efforts, van der Heijde et al. (2019a) utilized time aggregation algorithms (i.e. representative days) to represent an S-DH system equipped with a seasonal TES. It was revealed that the algorithm is computationally cheaper by 10-30 times when compared to simulations without aggregation. Yet, it was concluded that the minimum required number of representative days was not obtained. On a brighter note, the algorithm was recently used to determine the optimal design and control of a fictional district energy system of the city of Genk, Belgium (van Der Heijde et al., 2019b).

In Modelica/Dymola, there exist a number of TES components that are used for investigation purposes. For instance, there exist different configurations of TES in Modelica Buildings library (Wetter et al., 2014) such as: TES with internal heat exchanger, TES without heat exchanger and others. These models were validated in different research studies. Yet, these models were limited to small-scale TES (residential buildings TES with ~ 1 m^3 up 3 m^3). Thus, different system-level TES components are developed for large-scale TES in Modelica/Dymola tool within the framework of giga_TES project and they are being investigated for calibration purposes. Yet, these models are characterized with a major shortcoming as they are capable to only represent tanks. In this context, Dahash et al. (2020b) presented the development of Modelica buildings library TES models for large-scale TES simulations. Further, the work developed a 2-D soil domain using FD discretization in order to simulate underground large-scale TES. The model was cross-validated against the aforementioned COMSOL model and, then, used for TES design optimization.

Given the importance of accurate multiphysics in modeling underground TES, and the less computation efforts seen by ESS tools, it is quite often to integrate a component-level model into a system-level model. This steers the efforts to couple ESS tools (e.g. TRNSYS) with accurate multiphysics tools (e.g. COMSOL Multiphysics) forming the so-called (ESS-HAM) or (ESS-hygrothermal) coupling (Ferroukhi et al., 2017 and van Belleghem et al., 2011). This approach delivers detailed performance analysis for the energy system (e.g. TES) with simulation of heat, moisture and air (HAM) transfer and, subsequently, it provides comprehensive modeling of the envelope domain (e.g. TES wall, insulation and liner) (Cóstola et al., 2009).

Accordingly, Fig. 8 shows an exemplary overview for a co-simulation process in which a detailed TES model is developed in a multiphysics tool and coupled to an ESS tool. In this process, the TES model consists of TES envelope domain with fluid domain. The calculation procedure used for the multiphysics tool could be identical or different to that used in an ESS tool. This schematic overview represents a possible co-simulation platform used for a large-scale TES system that is buried in the ground.

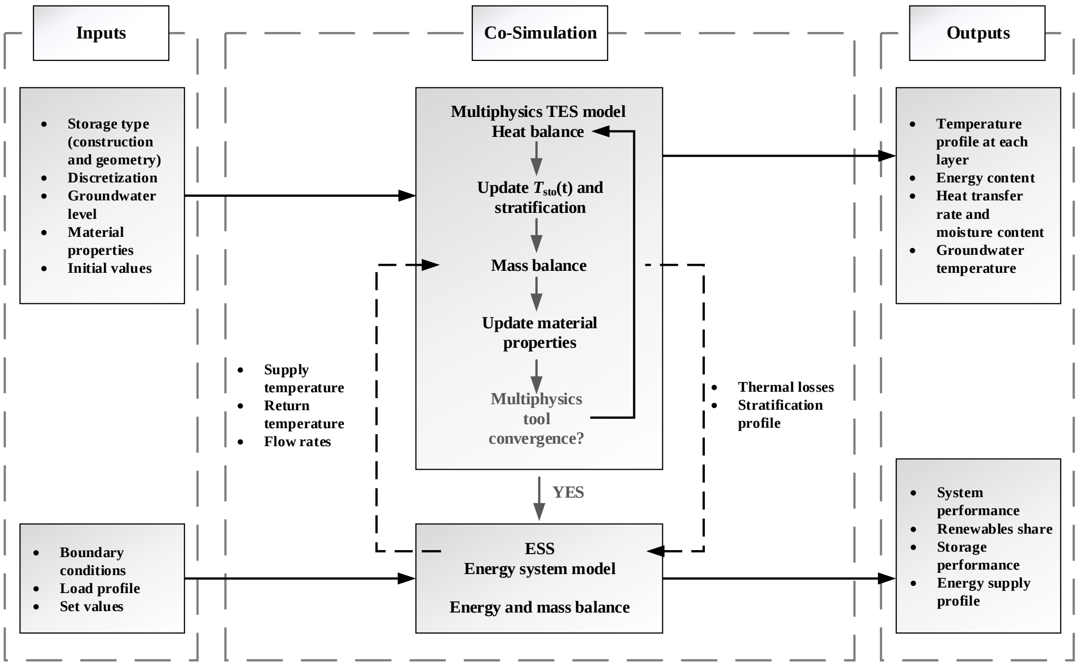

Fig. 8: An exemplary schematic overview for a co-simulation platform for developing a large-scale buried TES (reproduced from (Dahash et al., 2019a)).

Material properties, groundwater level, discretization mode, storage type and initial values are all together given as inputs to the multiphysics tool, whereas boundary conditions, load profiles (e.g. heat load, supply and return temperature, flowrates) and set values are inputs for ESS tool. The co-simulation process starts at a time step (t) with running the simulation for the TES model in multiphysics tool and, then, the values (thermal losses and stratification profile) are extracted and transferred to ESS tool. Next, ESS tool runs the simulation for the overall energy system considering accurate thermal losses and temperature profiles for TES. Thus, the ESS tool computes accurate values for the energy system and, then, it exchanges temperatures (supply and return), flowrates and load profiles with the multiphysics tool. Therefore, in the next time step (t+1) the multiphysics tool is able to compute again the values and exchanges it with ESS tool. This process is repeated for a required investigation time (e.g. 5 years) and, later, each model delivers different outputs. For the multiphysics tool, the outputs are temperature and energy content at each layer, moisture transfer rate to the surroundings and groundwater temperature. Whereas the outputs for ESS tool are renewables share, system and storage performance and energy supply profile.

Inevitably, it is important to pinpoint that the co-simulation process given in Fig. 8 is an example for a possible coupling between an ESS tool and a multiphysics one and the process is not necessarily limited to those. Other possible co-simulations can be set up between different tools and following different algorithms. Another experience, for example also not limited, is the co-simulation between a CFD tool (e.g. ANSYS Fluent) and a multiphysics tool. In such a coupling, the fluid domain (i.e. water) and the thermo-hydraulic behavior (e.g. stratification, buoyancy) are fully developed in the CFD tool, whereas the TES envelope (e.g. walls, insulation and liners) are implemented in a multiphysics tool. This process also produces valuable analysis regarding the heat transfer performance between the fluid and envelope domains. Therefore, it is highly recommended to underline the goal of co-simulation so that the tools that serve the required goal can be short listed.

Additionally, another successful proposal for co-simulation environments is the TISC suite, which makes possible to couple some simulation tools. This software package succeeds in connecting a numerical modelling tool (i.e. COMSOL Multiphysics) with ESS tool (i.e. Modelica/Dymola) and it consists of a simulation package and control package and, therefore, this makes it possible to run simulation for three or more partial simulations (TLK-Thermo GmbH, 2019). Another successful technique is the functional mock-up interface (FMI) tool, which is a standard option for supporting dynamic model exchange and co-simulation (Blochwitz et al., 2011). Besides, building controls virtual test bed (BCVTB) is also sometimes experienced for coupling different simulation tools enabling a co-simulation environment. This software environment permits, additionally, to couple the simulation tools with existing hardware (Wetter and Haves, 2008).

Yet, it is noteworthy to highlight the gap seen between the two levels of modeling in spite of the few aforementioned studies. Hence, it is remarkably important to create a well-established linking platform for large-scale underground water stores detailed models coupled into energy system simulation tools, rather than standing-alone models (either detailed or coarse models).

4. Conclusion

Seasonal thermal energy storage systems are prominent elements for renewable-based district heating systems. Yet, the large volumes and the corresponding investment costs are key obstacles that hold this technology from being experimentally examined. Therefore, simulation-driven assessments are crucial to investigate these systems. Accordingly, this work reported the recent advances in modeling of large-scale TES. The work illustrated the TES modeling hierarchy process as it is categorized into: pre-design, detailed design, technology integration, evaluation and optimization. The work reported the different models used in each step of the modeling process hierarchy.

Further, the work documented a synopsis of research studies highlighting the advantages and pitfalls of the existing TES models. Thus, the work reported the TES modeling development within the international project (Giga_TES). A component-level TES model was implemented in COMSOL Multiphysics and validated against measured data from Dronninglund pit TES in Denmark. The numerical model was further extended to include the groundwater aspects in order to permit the inspection of groundwater influence on TES operation. Moreover, the work discussed the development of different coarse models that are appropriate for system simulations in Modelica/Dymola. Yet, the major downside of the coarse models is that they are capable to represent tanks only. Thus, future work will focus on further development of Modelica/Dymola TES models to represent other TES geometries (e.g. cone, pyramid).

5. Acknowledgments

This project is financed by the Austrian “Klima- und Energiefonds” and performed in the frame of the program “Energieforschung”. It is part of the Austrian flagship research project “Giga-Scale Thermal Energy Storage for Renewable Districts” (giga_TES, Project Nr.: 860949). Therefore, the authors wish to acknowledge the financial support for this work.

6. References

Blochwitz, T., Otter, M., Arnold, M., Bausch, C., Clauß, C., Elmqvist, H., Junghanns, A., Mauss, J., Monteiro, M., Neidhold, T., Neumerkel, D., Olsson, H., Peetz, J.-V., Wolf, S., 2011. *The Functional Mockup Interface for Tool independent Exchange of Simulation Models.* Dresden, Germany, Linköping University Electronic Press, Linköpings universitet, pp. 105-114.

Chang, C., Nie, B., Leng, G., Li, C., She, X., Peng, X., Deng, J., 2017. Influences of the key characteristic parameters on the thermal performance of a water pit seasonal thermal storage. *Energy Procedia,* Volume 142, pp. 495-500.

Chang, C., Wu, Z., Navarro, H., Li, C., Leng, G., Li, X., Yang, M., Wang, Z., Ding, Y., 2017. Comparative study of the transient natural convection in an underground water pit thermal storage. *Applied Energy,* Volume 208, pp. 1162-1173.

Cóstola, D., Blocken, B., Hensen, J., 2009. *External Coupling Between BES and HAM Programs for Whole-Building Simulation.* Glasgow, Scotland, s.n., pp. 316-323.

Crawley, D. B., Hand, J. W., Kummert, M., Griffith, B. T., 2008. Contrasting the capabilities of building energy performance simulation programs. *Building and Environment*, 43(4), pp. 661-673.

Dahash, A., Bianchi Janetti, M., Ochs, F., 2019b. *Numerical analysis and evaluation of large-scale hot water tanks and pits in district heating systems.* Rome (Italy), 02-04 September 2019, s.n., pp. 1692-1699.

Dahash, A., Ochs, F, Bianchi Janetti, M., Streicher, W., 2019a. Advances in seasonal thermal energy storage for solar district heating applications: A critical review on large-scale hot-water tank and pit thermal energy storage systems. *Applied Energy,* Volume 239, pp. 296-315.

Dahash, A., Ochs, F., Tosatto, A., Streicher, W., 2020a. Toward Efficient Numerical Modeling and Analysis of Large-Scale Thermal Energy Storage for Renewable District Heating Systems. *Applied Energy,* pp. (Submitted - Under Review).

Dahash, A., Ochs, F., Tosatto, A., 2020b. *Simulation-Based Design Optimization of Large-Scale Seasonal Thermal Energy Storage in Renewables-Based District Heating Systems.* Graz, Austria, IBPSA.

Diersch, H.-J. G., 2014. *FEFLOW – Finite element modeling of flow, mass and heat transport in porous and fractured media.* Berlin : Springer.

Fan, J., Huang, J., Chatzidiakos, A., Furbo, S., 2017. *Experimental and theoretic investigations of thermal behavior of a seasonal water pit heat storage.* Abu Dhabi, United Arab Emirates, s.n.

Ferroukhi, M.-Y., Belarbi, R., Limam, K., Bosschaerts, W., 2017. Experimental validation of a HAM-BES co-simulation approach. *Energy Procedia,* Volume 139, pp. 517-523.

Giga_TES, 2019. *"Giga-Scale Thermal Energy Storage for Renewable Districts".* [Online] Available at: https://gigates.at/

Hornberger, M., 1998. *Solar unterstützte Heizung und Kühlung von Gebäuden.* Stuttgart(Institüt für Thermodynamik und Wärmetechnik (ITW), Universität Stuttgart): Forschungsberichte des Deutschen Kälte- und Klimatechnischen Vereins, Nr. 47.

Klöck, M., 2018. *Validierung eines Simulationsmodells für solare Fernwärmeversorgungen mit saisonalem Erdbecken-Wärmespeicher,* Reutlingen: Hochschule Reutlingen, Steinbeis Forschungsinstitut für solare und zukunftsfähige thermische Energiesysteme.

Kubiński, K., Szabłowski, L., 2019. Dynamic model of solar heating plant with seasonal thermal energy storage. *Renewable Energy,* Volume 145, pp. 2025-2033.

Li, X., Wang, Z., Li, J., Yang, M., Yuan, G., Bai, Y., Chen, L., Xu, T., Gilmanova, A., 2019. Comparison of control strategies for a solar heating system with underground pit seasonal storage in the non-heating season. *Journal of Energy Storage,* Volume 26.

O'Donovan, K., 2019. *Load Profile Generator Tool,* s.l.: AEE INTEC.

Ochs, F., Dahash, A., Tosatto, A., Bianchi Janetti, M., 2019. Techno-economic planning and construction of cost-effective large-scale hot water thermal energy storage for Renewable District heating systems. *Renewable Energy,* Volume 150, pp. 1165-1177.

Ochs, F., Heidemann, W., Müller-Steinhagen, H., 2009a. *Modeling Large-Scale Seasonal Thermal Energy Stores.* Stockholm, Sweden, s.n.

Ochs, F., 2009b. *Modelling Large-Scale Thermal Energy Stores, Ph.D. Dissertation.* Stuttgart: Shaker Verlag.

Ochs, F., 2014. *Large-Scale Thermal Energy Stores in District Heating Systems – Simulation Based Optimization.* Aix-les-Bains, France, International Solar Energy Society (ISES).

Ochs, F., Zottl, A., Lauermann, M., Schranzhofer, H., Halmdienst, C., Reiterer, D., 2015a. *Store4Grid: Optimierte Erdbecken-Wärmespeicher für Wärmenetze,* s.l.: Klima- und Energiefonds.

Ochs, F., 2015b. *Simulation Based Optimization of Pit and Tank Thermal Energy Storage for Solar District Heating Systems.* Toulouse, France, s.n.

Panthalookaran, V., El-Amin, M. F., Heidemann, W., Müller-Steinhagen, H., 2008. Calibrated models for simulation of stratified hot water heat stores. *International Journal of Energy Research,* 32(7).

Panthalookaran, V., Heidemann, W., Müller-Steinhagen, H., 2011. The Effects of Boundary Design on the Efficiency of Large-Scale Hot Water Heat Stores. *Journal of Solar Energy Engineering,* 133(4).

Raab, S., Mangold, D., Müller-Steinhagen, H., 2005. Validation of a computer model for solar assisted district heating systems with seasonal hot water heat store. *Solar Energy,* 79(5), pp. 531-543.

Schmidt, T., Pauschinger, T., Sørensen, P. A., Snijders, A., Djebbar, R., Boulter, R., Thornton, J., 2018a. Design Aspects for Large-scale Pit and Aquifer Thermal Energy Storage for District Heating and Cooling. *Energy Procedia,* Volume 149, pp. 585-594.

Schmidt, T., Sørensen, P. A., 2018b. *Monitoring Results from Large Scale Heat Storages for District Heating in Denmark.* Adana, Turkey, s.n.

Solites, 2013. *SDH Online-Calculator.* [Online] Available at: http://www.sdh-online.solites.de/ [Accessed 15 August 2020].

Sørensen, P. A., Schmidt, T., 2018. *Design and Construction of Large Scale Heat Storages for District Heating in Denmark.* Adana, Turkey, s.n.

TLK-Thermo GmbH, 2019. *TISC Suite – Software package for coupling simulation tools.* [Online] Available at: https://www.tlk-thermo.com/index.php/en/software-products/tisc-suite [Accessed 15 August 2020].

Urbaneck, T., 2004. *Berechnung des thermischen Verhaltens von Kies-Wasser-Speichern, Ph.D. Dissertation,* Aachen: Shaker Verlag.

van Belleghem, M., Steeman, M., Willockx, A., Janssens, A., De Paepe, M., 2011. Benchmark experiments for moisture transfer modelling in air and porous materials. *Building and Environment,* 46(4), pp. 884-898.

van der Heijde, B., Vandermeulen, A., Salenbien, R., Helsen, L., 2019a. Representative days selection for district energy system optimisation: a solar district heating system with seasonal storage. *Applied Energy,* Volume 248, pp. 79-94.

van der Heijde, B., Vandermeulen, A., Salenbien, R., Helsen, L., 2019b. Integrated Optimal Design and Control of Fourth Generation District Heating Networks with Thermal Energy Storage. *Energies,* 12(14).

Wetter, M., Haves, P., 2008. *A Modular Building Controls Virtual Test Bed for the Integration of Heterogeneous Systems.* Berkeley, CA, USA, International Building Performance Simulation Association, p. 69–76.

Wetter, M., Zuo, W., Nouidui, T.S., Pang, X., 2014. Modelica Buildings library. *Journal of Building Performance Simulation,* 7(4), pp. 253-270.

A COMBI STORAGE FOR COMBINATION WITH HEAT PUMPS – FROM SIMULATIONS TO THE TEST BENCH RESULTS

Robert Haberl[1], Jeremias Schmidli[1], Andreas Heinz[2], Joachim Kalkgruber[3] and Michel Y. Haller[1]

[1] SPF Institute for Solar Technology, Eastern Switzerland University of Applied Sciences (OST), Rapperswil (Switzerland)

[2] Institute of Thermal Engineering (IWT), Graz University of Technology, 8010 Graz (Austria)

[3] SOLARFOCUS GmbH, St.Ulrich/Steyr (Austria)

Abstract

In this work the development and testing of a combi storage tank for the combination with a heat pump is described. The appropriate size and segmentation of the storage in different zones was determined with simulations in TRNSYS. Installations in the storage tank for efficient handling of the high volume flow rates of a heat pump were designed and selected using CFD simulations. Finally, the finished storage tank was tested to determine its stratification efficiency, demonstrating its good stratification properties. The storage tank performs very well with a stratification efficiency of 84 % at system level. The separation of the temperature ranges for hot water preparation in the storage tank above and the space-heating zone remains intact even when charged with the high mass flow rate of 2570 kg/h. As a result, the heat pump can be operated with a low supply temperature (the power weighted average supply temperature of the heat pump was 33 °C) and thus at a favorable operating point with high efficiency.

Keywords: Combistore, heat pump, stratification efficiency, CFD simulations, measurement, hardware-in-the-Loop

1. Introduction

The thermal refurbishment of existing buildings together with the replacement of inefficient, fossil fuel based heating systems provides a large potential for energy savings. Heat pumps are an attractive alternative heating system. Thermal energy storages (TES) are used widely for the storage of heat for domestic hot water (DHW) and space heating. Increased storage volumes are installed when fluctuating renewable energies are introduced into the system, such as heat from solar thermal installations or from the combination of photovoltaics (PV) and heat pumps with special control for the increase of PV self-consumption.

However, when this kind of storage is used in combination with a heat pump, the temperature stratification of the storage is a decisive factor for the overall efficiency and thus for the consumed final energy of the system. This paper presents the development of a combi storage tank, which was part of a larger project called "HybridHeat4San". In this project a hybrid heating system for space heating and domestic hot water was designed, which enables an energy-efficient supply of renovated residential buildings with an existing radiator heating system.

2. Zoning of the storage tank and simulation of the diffusors at the inlet

Basis for the system development within the project is a hydraulic layout with a combined storage tank (combistore) for domestic hot water (DHW) preparation and space heating. An air-source heat pump is connected to the combistore. It uses three-way-valves to charge either the DHW zone of the tank via the two connections on the top or the space heating zone via the two lower connections. The space heating system is supplied from the heat pump connections to the space heating zone of the storage via two T-pieces. This arrangement reduces the mass flow rate over the storage tank during space heating operation. DHW is provided by a DHW heat exchanger (external plate heat exchanger) with a temperature of 45 °C at its secondary outlet. Fig. 1 shows the hydraulic scheme, including the system boundaries for the subsequent measurement of the storage system.

doi:10.18086/eurosun.2020.07.07 Available at http://proceedings.ises.org

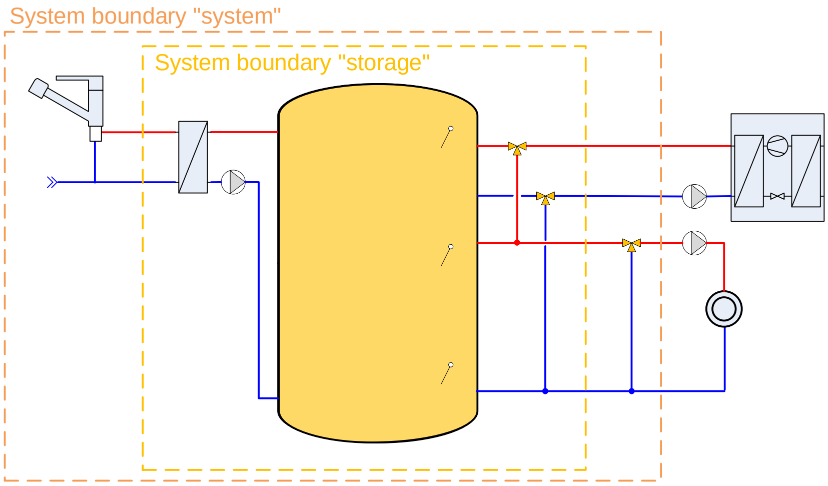

Fig. 1: Hydraulic scheme of the storage system, including the system boundaries for the subsequent measurement.

For a storage tank used in combination with a heat pump, the thermal stratification is of particular importance, since the efficiency of the heat pump depends on the temperature at which it has to provide heat. Three main processes deteriorate stratification and therefore increase the electricity consumption of the heat pump:

- Heat conduction and thermal diffusion processes in the storage medium and in the material of the containment and internal objects such as heat exchangers,
- plume entrainment caused by buoyant fluid movements, and
- inlet jet mixing caused by the kinetic energy and turbulences from direct charging.

In the basic configuration, a combistore with a volume of 1000 l was assumed, whose data was provided by the industrial partner. As a first step, the position of the inlets and outlets and the temperature sensors on the storage tank were optimized using system simulations. For this purpose, the individual connection heights and sensor positions were varied within a certain range in a large number of annual simulations, thus finding an optimum in terms of energy consumption of the overall system. These simulations were carried out with the program TRNSYS. In the simulation, the multiport store model from Drück & Pauschinger (2006) with a vertical node count of 100 was used. The mixing processes caused by inlet jet mixing in the storage tank were not represented by the model. Plume entrainment (which is only represented in the model in an idealized way) is avoided by the appropriate selection of the inlet positions.

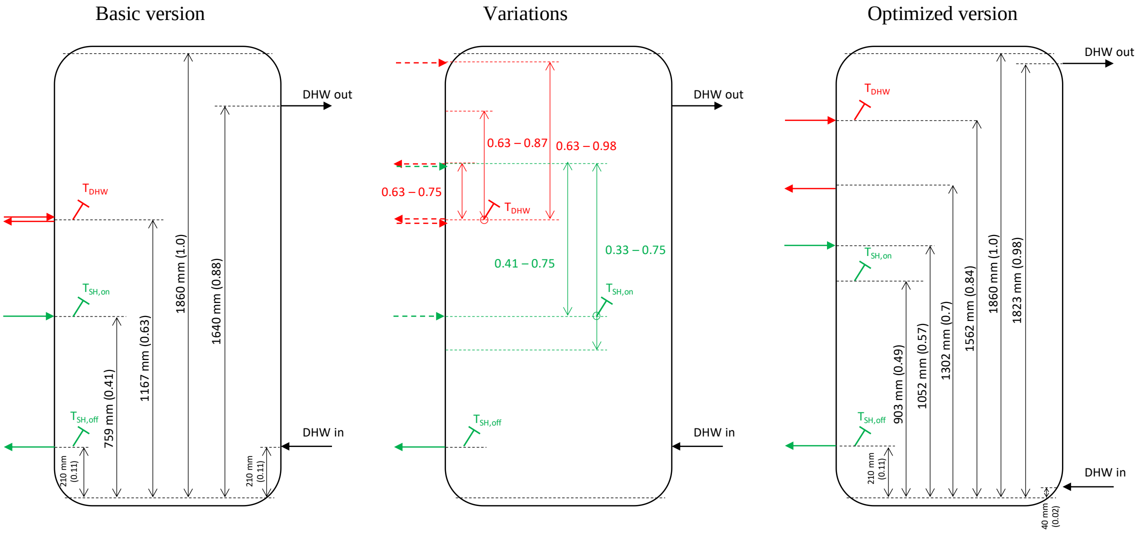

Fig. 2: Optimization of storage tank connections and sensor positions (left: original configuration or basic version, middle: variation ranges, right: optimized variant).

In the simulations of the overall system, the optimized connection configuration leads to a reduction of the system electric energy consumption by 4 % compared to the initial situation (Fig. 2 left). A detailed description of the simulation model and the boundary conditions can be found in a second contribution to the EuroSun 2020 conference in Heinz et al. (2020), entitled "Photovoltaic Heat Pump System for Renovated Buildings – Measures for Increased Efficiency". As already shown in the work of Gwerder et al. (2016), the geometry of the storage tank inlets has a very large effect on the stratification efficiency and the conservation of exergy in the storage tank, especially at high charging volume flow rates, as they occur with heat pumps. This is particularly important for operation with a heat pump, because a loss of exergy (or production of entropy) in the storage tank inevitably leads to a lower COP of the heat pump during charging and thus to higher electricity consumption of the system (compare Haller et al. 2019).

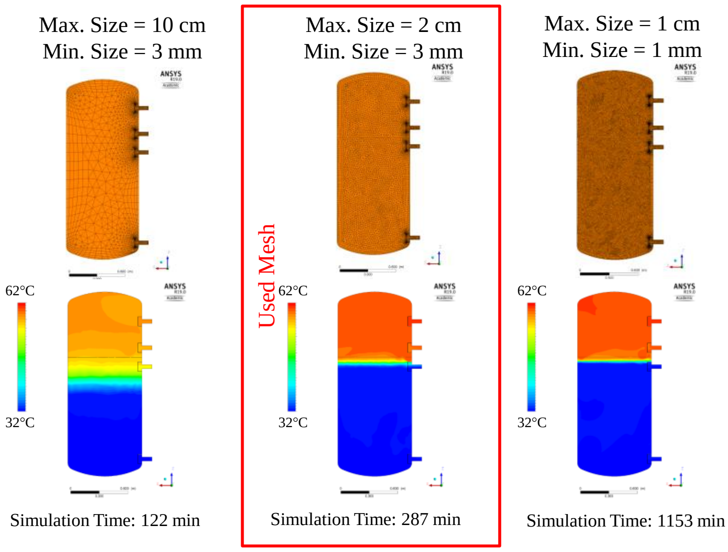

Fig. 3: Overview mesh study. Simulation type: DHW charging.

CFD simulations with ANSYS CFX 19.1 were carried out to determine a suitable inlet geometry, respectively a diffuser. The Scale-Adaptive Shear-Stress-Transport-Model was used as turbulence model. The influence of the mesh was first determined by a mesh study and a meaningful grid size for the simulation was determined. Fig. 3 shows an overview of the mesh study: The thermocline in the storage tank during the process of DHW charging was examined after 20 minutes of time with an inlet mass flow rate of 2750 kg/h for a diffusor design that ensures a velocity into the bulk storage volume of < 0.1 m/s. Different tetrahedron meshes were used. The figure shows good correspondence between the results of the simulations shown in the middle (max./min. size of 20/3 mm) and on the right (max./min. size of 10/1 mm), and the meshing shown in the middle was chosen. Subsequently, charging and discharging processes of both the DHW zone and the space heating zone of the storage tank were simulated with different diffuser geometries. The diffusor design was intended to keep the mixing inside the storage tank as low as possible despite the high volume flow rates. Nine different diffuser geometries were simulated and their stratification behavior examined: Five different variants of a baffle plate and/or a division into flow channels, three different geometries that can be folded from one sheet metal and fixed to the storage wall by spot welding and one variant with a perforated plate at the inlet to the storage volume. Special attention was paid to the charging of the space heating zone, as the upper part of the storage tank is reserved for the storage of heat for DHW at much higher temperatures and should not be influenced negatively (i.e. the temperature in this region should not decrease) during this process. Fig. 4 shows exemplary the temperature distribution in the storage tank after 7 min. of space heat charging, for various diffusor geometries. Each of the shown simulations started with the same temperature of 50 °C in the upper part of the storage tank above the separating plate.

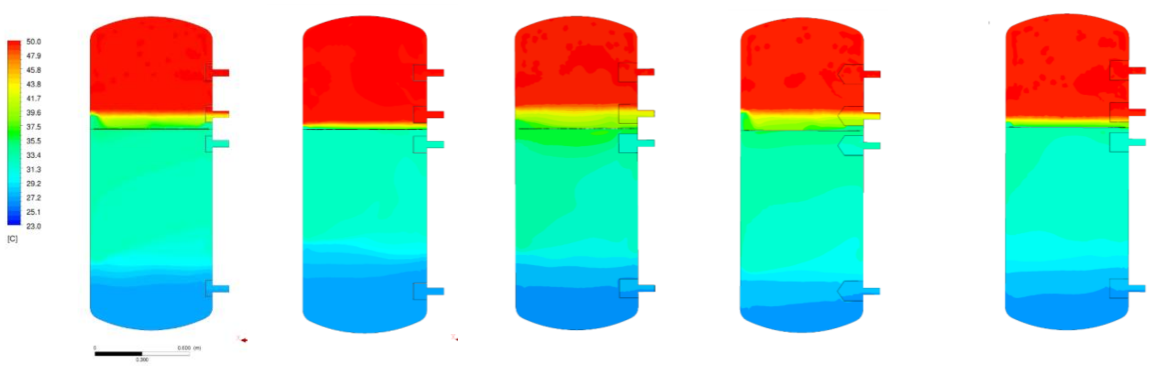

Fig. 4: Temperature distribution in the storage tank after 7 min. space heat charging simulated by CFD, for various inlet diffusors; each simulation started with the same temperature of 50 °C in the upper part of the storage tank.

The inlet geometry that was finally chosen meets the recommendations defined in Gwerder et al. (2016):

- The Reynolds number of the flow at the entrance should be below a certain value, i.e. less than 3000–7000, velocities should be below 0.1 m/s as suggested by Jenni (2000), and possibly even lower for larger inlet diameters and larger mass flow rates.
- The flow has to be sufficiently developed, requiring a minimal entrance length of 3 - 4 times the hydraulic diameter after a change of cross section or flow direction.

According to the geometries and dimensions determined with the help of various simulations, a storage tank was produced by the company Solarfocus and sent to the Institute for Solar Technology SPF for testing.

3. Measurement of stratification efficiency

3.1 Test method

A test method to measure the stratification efficiency as key performance indicator was used. The Concise Cycle Test (CCT) method follows the hardware-in-the-loop concept: The storage, including the hydraulics for charging and discharging (compare Fig. 1), is installed on the test bench. The test bench emulates the thermal load as well as a heat pump to provide heat according to the actual temperature in the storage tank. A predefined 24 h load profile for DHW and space heat demand is used and repeated several times in succession (compare Haller et al. 2018).

The space heating load of the test day is 42.5 kWh at a constant outside temperature of 2.5 °C. Fig. 5 shows the continuous target value for space heating. The test bench emulates both the heating circuit pump and the heating circuit mixer. The return temperature is determined and emulated based on the supply temperature, which is derived from the temperature delivered by the storage and the hydraulics, in combination with the current target heating power and heat transfer rate to the heated room. The target supply temperature for the space heating system remains constant at 30 °C during the test. To successfully complete a test, the supply temperature must be high enough for delivery of heat to a room with 20 °C temperature and a given floor heating system with its heat transfer capacity, and the average supply temperature during the test must be higher than 30 °C. The daily DHW demand is 9.45 kWh, corresponding to a consumption of 232 l at a cold water temperature of 10 °C and a hot water temperature of 45 °C.

To emulate the heat pump, a model of a non-power-controlled air-to-water heat pump with a nominal power of 15 kW at A7/W35 was used. The mass flow rate in the heat pump emulation is set to 2570 kg/h, which corresponds to a temperature spread of 5 K for the nominal heating capacity.

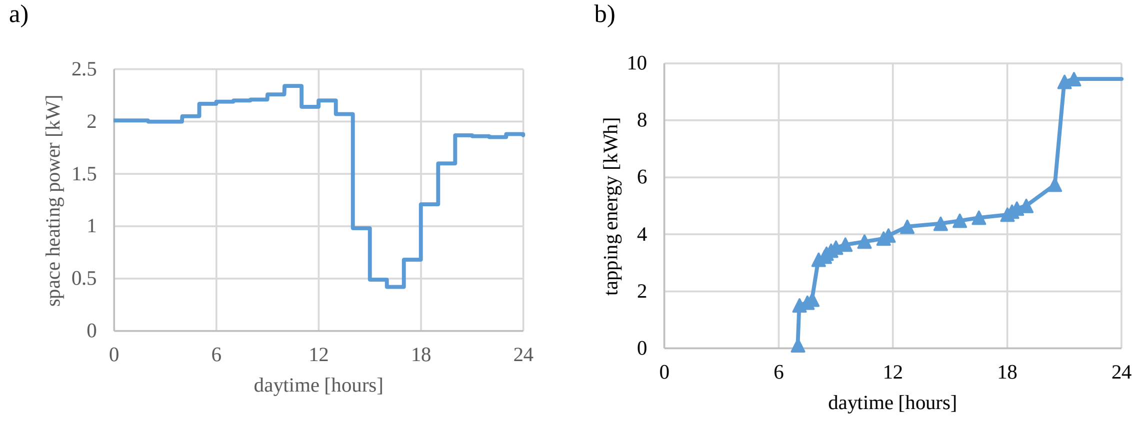

Fig. 5: Space heating load (a) and DHW profile (b) of the test cycle.

The test method is based on the fact, that mixing of fluids with different temperatures results in (measurable) entropy production. The method thus uses the second law of thermodynamics by measuring the irreversible entropy production of storage systems ($\Delta S_{irr,exp}$) during realistic operation. From the entropy production measured during the test cycle, the stratification efficiency (ζ_{str}) is determined as a dimensionless quantity. For this purpose, the measured entropy production is set in relation to the entropy production of a completely mixed storage unit ($\Delta S_{irr,mix}$)[1]:

$$\zeta_{str} = 1 - \frac{\Delta S_{irr,exp}}{\Delta S_{irr,mix}} \quad \textbf{(eq. 1)}$$

The stratification efficiency thus describes how well the storage tank "does its job" compared to a completely mixed storage tank (worst case). A perfectly stratified system[2] would achieve a stratification efficiency of 100 %. A completely mixed storage 0 %. The method is described in detail in Haller et al. (2018, 2019).

Not only stratification processes in the storage tank are relevant for the stratification efficiency, but also mixing processes and heat transfer in the hydraulic system for charging and discharging the storage tank. Therefore, external heat exchangers, such as for DHW preparation, the additional pumps provided for this purpose and the corresponding hydraulics are also included in the system boundary. In Fig. 1, different boundaries for the balancing are drawn, whereby the boundary "system" describes the decisive variable.

3.2 Test results

During the stratification efficiency test, the heat pump is switched on and off according to the temperature in the storage tank. Fig. 6 shows the positions of the sensors used for this. The selected set-point temperatures are shown in Table 1, whereby it should be noted that hot water production was limited to two time windows per day (from 2:00 to 4:00 and from 16:00 to 18:00). The target temperature set in the DHW heat exchanger was 47 °C. This allowed a DHW temperature of 45 °C to be guaranteed at all times.

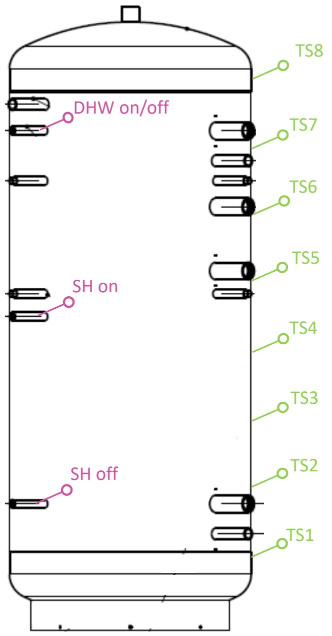

Fig. 6: Storage tank including the hydraulics on the test bench (left) and the positions of temperature sensors for the control of the heat pump (DHW on/off, SH on/off) as well as the positions of the temperature sensors, which were fixed equidistantly to the tank wall with a sensor tape for monitoring purposes (right).

[1] The worst case is a completely mixed storage tank, which must always be charged with the maximum supply temperature of the heat pump of 55 °C.
[2] A perfectly stratified system is not physically possible, so the result of the measurement will always be less than 100 %.

Table 1: Set-point temperatures (for control of the heat pump).

DHW on	°C	47
DHW off	°C	51
SH on	°C	25
SH off	°C	27

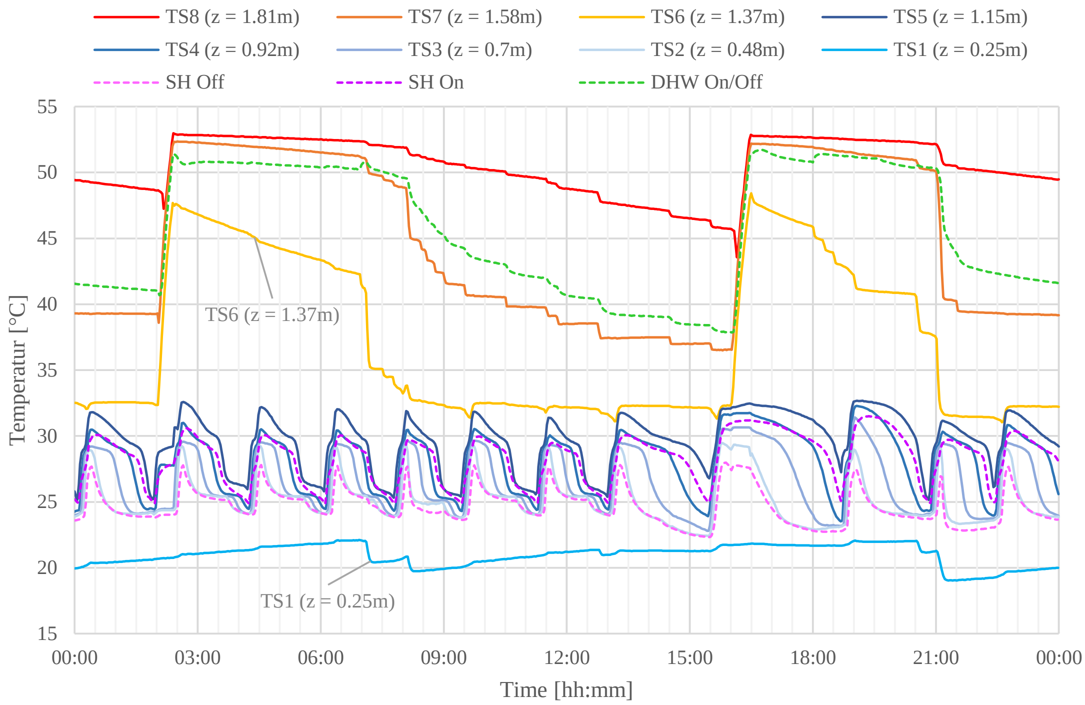

Fig. 7: Temperatures during the measurement. In addition to the contact sensors TS1 to TS8 on the storage tank wall that were used for monitoring only, the temperatures for controlling the heat pump for hot water (WW) and space heating (RH) are also shown.

Fig. 7 shows the temperature curves during the 24-h test cycle. These show a good separation of the DHW zone from the space heating zone. During the charging of the DHW zone at 2:00 and 16:00, the temperatures in the lower part remain unaffected. Also during the charging of the space heating zone, only sensor TS6 close to the interface between the two zones is influenced slightly.

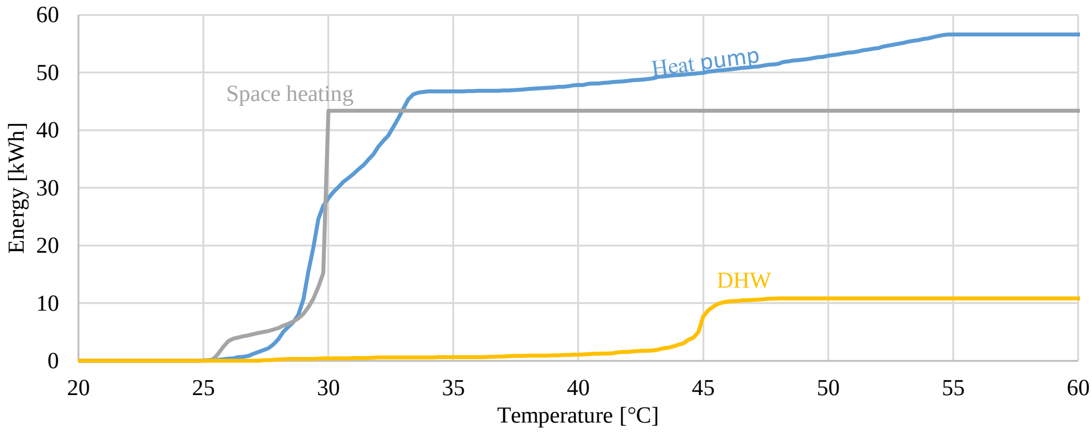

Fig. 8: Energy temperature diagram of the measurement.

Fig. 8 shows an energy-temperature diagram of the measurement. In this diagram, the energy supplied to the system from the heat pump as well as the energy supplied by the system for space heating and hot water are sorted according to their supply temperature. The sharp edge for the space heating curve results from the fact that the mixing to the target flow temperature of 30 °C was not done with a mixer installed in real life, but was calculated by the test bench software. It can be seen that approx. 47 kWh were delivered by the heat pump with a supply temperature below 34 °C, i.e. slightly more than was necessary to cover the space heating demand. The reason for this is the preheating of the hot water supply in the lower part of the storage tank. The shown line of the heat supply by the heat pump shows a bend in the area of the heat supply for the space heating. Up to a flow temperature of 30 °C the flow temperature remains constant over a longer period of time. During this time the thermocline in the storage tank is pushed down. Once the space heating zone has been completely charged, the return temperature rises and so does the flow temperature shown. Only with the second cycle the temperature is raised to the required temperature.

The energy balances and the entropy produced in the storage system are shown in Table 2 and Table 3. In each test, the 24-hour test cycle is repeated without interruption until the results of three consecutive test cycles are practically identical. This report shows the average values from the last three consecutive test cycles. The stratification efficiency is reflected in the measured entropy production in the system (Table 3). This should be as low as possible for a good stratification efficiency.

Table 2: Results of the stratification test – energy balance in kWh.

Heat pump (total heat)	55.32
Heat pump (heat in DHW-mode)	9.38
Space Heating	42.22
DHW (above 40 °C)	9.45
DHW (below 40 °C) [(a)]	1.37
Storage change [(b)]	0.26
Losses	2.05

[(a)] When tapping DHW, the heat is only defined as useful heat when 40 °C is reached.

[(b)] Difference in the energy content of the storage tank at the beginning and end of the 24 h test cycle (identical energy content is desired).

Table 3: Results of the stratification test - entropy production in the storage system in kJ/K. Low values mean good stratification and exergy conservation.

Within the storage tank	7.52
In the hydraulics	1.11
Total	8.64
Total Entropy production of a fully mixed storage tank	54.00

From the entropy balance, the stratification efficiency is calculated for the balance boundary already described (see Fig. 1):

- "Storage": For the storage tank with all internal and external heat exchangers and the hydraulics for charging and discharging. This key figure provides information about the stratification behavior of the storage tank including the loading hydraulics and heat exchangers.
- "System": For the storage system including discharge hydraulics. This figure also takes into account the entropy production in the mixing valves for space heating and hot water ("balance limit system").

The difference between the two figures provides information about the influence of the integration of the storage tank into the system and the control of the charging and discharging. The numbers are shown in Table 4 together with the repeatability of the results[1].

The DHW ratio is the ratio of the amount of heat supplied by the heat pump in DHW mode to the actual DHW drawn from the storage tank. This figure gives an important indication for the quality of the separation of the different zones for hot water and space heating in the storage tank and is therefore a good indicator for the storage concept and management. The aim should be to achieve the lowest possible value for the hot water ratio[2].

[1] Specified by twofold standard deviation of the mean value from three successive measurements.

[2] Assuming that the water in the lower part of the storage tank is preheated to the temperature of the space heating system, the amount of heat supplied by the heat pump for hot water should not exceed the amount of heat drawn from the storage tank.

Table 4: Stratification efficiency and DHW ratio.

Stratification efficiency storage (%)	**86.07**
Twofold standard deviation (%)	0.11
Stratification efficiency system (%)	**84.01**
Twofold standard deviation (%)	0.02
DHW ratio (-)	**0.87**
Twofold standard deviation (%)	1.34

Table 5 shows the power weighted average temperatures of heat input and heat output. The average supply temperature of the heat pump is determined according to eq. 2. The average temperatures for the heat output are determined in the same way.

$$\overline{T_{HP,flow}} = \frac{\sum(T_{HP,flow,i} \cdot \dot{Q}_{HP,i})}{\sum \dot{Q}_{HP,i}} \quad \textbf{(eq. 2)}$$

Table 5: Average flow temperatures of the heat input and heat output, weighted according to output.

Heat input	
Heat pump [°C]	33.1
Heat output	
Space heating [°C]	30.4
DHW [°C]	43.5

Fig. 9 shows the stratification efficiency (green) of the system. It also shows the loss of stratification efficiency, which is due to entropy production in the storage including discharging heat exchanger (dark grey) or in the hydraulic system, i.e. DHW and space heating mixing valve that reduce the supply to the temperatures that were actually needed (light grey).

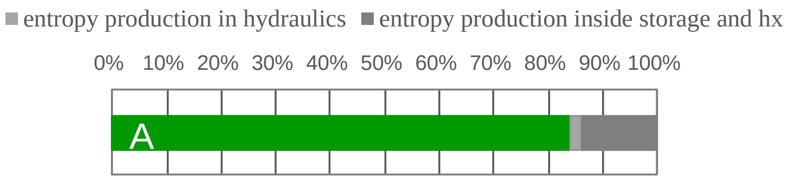

Fig. 9: Stratification efficiency and stratification losses of the storage system.

4. Comparison of simulations with measurement

After completion of the stratification test with the combined storage tank, the same test cycle was applied to the simulation model of the storage tank in TRNSYS. Fig. 10 shows the temperature curves obtained from measurements as well as from simulations. It can be seen that the storage temperatures during charging by the heat pump for hot water as well as for space heating match quite well between measurements and simulations. A difference can be seen especially in the discharging of the storage tank through the DHW heat exchanger: The temperatures in the upper part of the storage tank remain high for a longer time in the simulation than in the real measurement. The temperature in the lowest section of the storage tank is lower in the simulation than in the measurement.

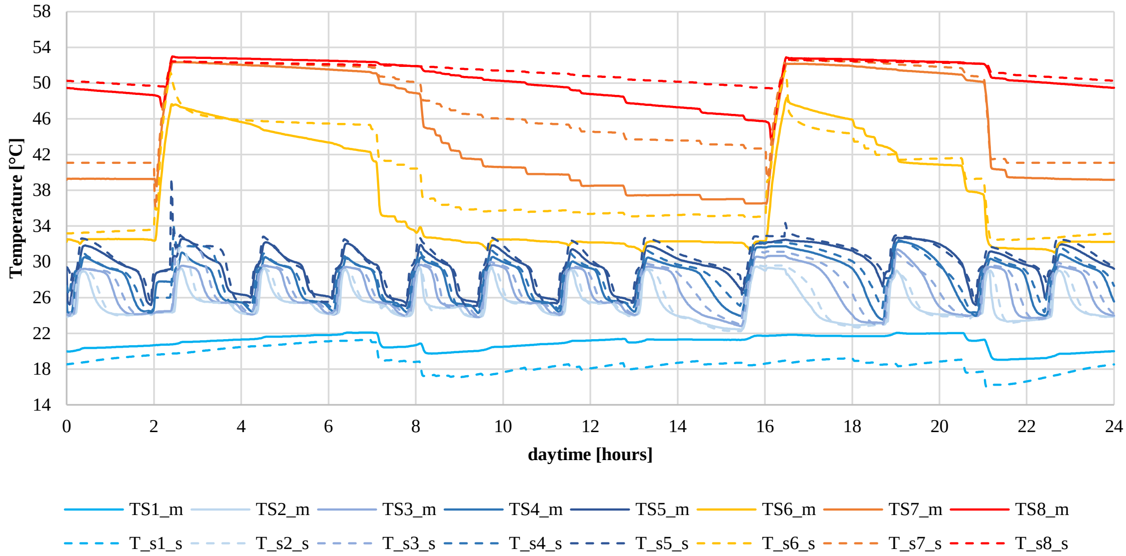

Fig. 10: Comparison of simulated (_s) and measured (_m) temperatures of the combistore, with the initial parameters of the simulation.

In order to achieve a better agreement of the simulations with the measurements, a few parameters in the DHW heat exchanger and its hydraulic integration had to be adjusted. The target temperature of the DHW heat exchanger was adjusted to 47 °C according to the real measurement, the pipe length between the DHW heat exchanger and the storage tank was increased to 1.5 m instead of 0.5 m and the UA-Value of the DHW heat exchanger was reduced by 20 %. Due to these small adjustments a much better agreement of the simulation with the measured data was achieved, which is shown in Fig. 11.

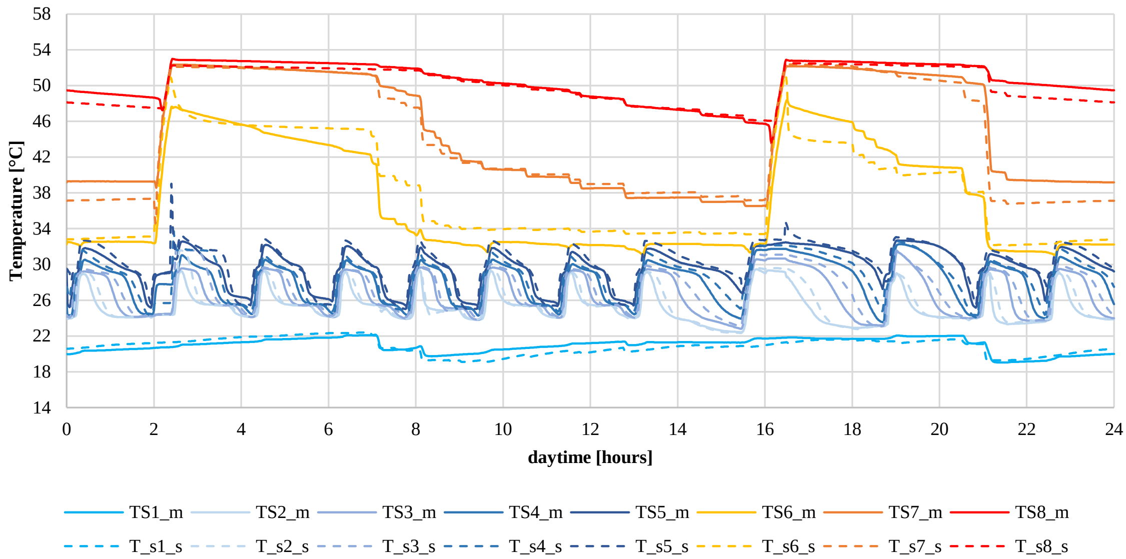

Fig. 11: Comparison of simulated (_s) and measured (_m) temperatures of the combistore after adaption of the simulation parameters of the DHW heat exchanger and its hydraulic connections.

6. Summary

In this work the development and testing of a combistore for the combination with a heat pump is described. The appropriate size and segmentation of the storage in different zones was determined with simulations in TRNSYS, using a storage model that cannot simulate mixing processes due to high flow velocities (inlet jet mixing) but takes into account the effects of incorrect positioning of the connections. An optimization of the connection heights led to a 4 % reduction in energy consumption in the simulations.

With the help of CFD simulations in ANSYS CFX, a diffuser design was developed which calms the incoming flow to such an extent that an existing thermocline in the storage tank is not destroyed even at mass flows of 2750 kg/h.

The stratification efficiency of the combistore developed in this way was then measured. For this purpose, the storage tank, including the hydraulics for charging and discharging and a DHW heat exchanger, was installed on the test rig. The test method follows the hardware-in-the-loop and concise cycle test concepts: The test bench emulates the charging and discharging processes according to a predefined 24-hour load profile and the actual temperature in the storage tank. During this dynamic and realistic operation, the entropy generated within the storage system is determined. By comparing the measured entropy with the entropy production of a fully mixed storage tank, the stratification efficiency can then be determined on a scale from 0 % (fully mixed) to 100 % (ideally stratified).

The storage tank performs very well with a stratification efficiency of 84 % at system level when charged by a 15 kW heat pump with a flow rate of 2570 kg/h. The separation of the temperature zones for hot water preparation above and the space heating zone below remains intact even when the storage is charged with the high mass flow rate mentioned above. As a result, the heat pump can be operated with a low supply temperature (the power weighted average supply temperature of the heat pump was 33 °C) and thus at a favorable operating point, with high efficiency. The ratio of the amount of heat supplied by the heat pump in hot water mode to the actual hot water drawn from the storage tank was 0.87 - a further indication of good separation of the different temperature zones in the storage tank.

A comparison of the measured data from the stratification test with the TRNSYS simulation model shows that the mixing in the storage tank (due to the incoming volume flow) is prevented so well that an exact image of the storage tank can be simulated even with a simulation model, which cannot represent inlet jet mixing processes. In order to closely match the measured temperatures of the storage tank with simulations, only adjustments of the integration of the DHW heat exchanger were necessary.

7. Acknowledgements

The project "HybridHeat4San" is funded by the Austrian Climate and Energy Fund and is carried out as part of the Energy Research Program 2016.

8. References

Drück, H. & Pauschinger, D., 2006. *MULTIPORT Store-Model, Type, 2006*. http://www.trnsys.de/download/en/ts_type_340_en.pdf.

Gwerder, C., Lötscher, L., et al., 2016. *Horizontal Inlets of Water Storage Tanks With Low Disturbance of Stratification*. Journal of Solar Energy Engineering, 138(5), p.051011–051019.

Haller, M.Y., Haberl, R., Persdorf, P. & Reber, A., 2018. *Stratification Efficiency of Thermal Energy Storage Systems – A new KPI based on Dynamic Hardware in the Loop Testing - Part I: Test Procedure*. Energy Procedia, 155, p.188–208.

Haller, M.Y., Haberl, R. & Reber, A., 2019. *Stratification Efficiency of Thermal Energy Storage Systems – A new KPI based on Dynamic Hardware in the Loop Testing - Part II: Test Results*. Energy and Buildings, 202, p.Article 109366.

Heinz, A., Gaber, C., Haberl, R., Haller, M.Y., Kalkgruber, J. & Schober, R., 2020. *Photovoltaic Heat Pump System for Renovated Buildings - Measures for Increased Efficiency*. In: Proceedings of EuroSun 2020, Athens, Greece.

Jenni, J., 2000. *Speicher in Theorie und Praxis. Jenni Energietechnik AG, Oberburg bei Burgdorf*.

Thermal Energy storage capacity on different types of zeolites

Oscar Seco Calvo[1], Helena López Moreno[1], Rafael Olmedo Mezcua[1]andJosé Antonio Ferrer Tevar[1]

[1] Energy Department, Energy Efficiency in Buildings Unit, CIEMAT www.ciemat.es, Madrid (Spain)

Abstract

In this study, the quality and thermal storage capacity of different types of zeolites have been analysed. The main objective of this work is to evaluate the thermal storage capacity of different types of zeolites exposed to hydrothermal control, resulting in an assessment of their thermal storage potential, based on the cationic exchange inside their cells.

Different lab experiments have been carried out, in which the behaviour of each sample has been evaluated under different conditions of drying (muffle, stove and desiccators) and operation, defining the thermal storage capacity for the different cases. A specific prototype has been designed for this purpose, which consists in different specific reactors for each zeolite type, including a sample storage chamber. "ThermaCAM SC660 Wes (TC)" results obtained for the different zeolites at different conditions, reveal high cationic exchange capacity for all types of zeolites. Drying and cooling conditions in the absence of humidity have been seen to influence results in a high extent, as well as the adequate design of the reactor, to provide effective air friction with the zeolite sample.

Keywords:Heat Transfer, Building Envelope, Thermal Comfort, Buildings, gaseous emissions, physical-chemical characterization, Thermal, CAM

1. Introduction

The need for energy saving in different fields of research has become increasingly important and has reached many different sectors. Among these ones, energy conservation in buildings is of high interest for all countries, including those situated in warm climates. This aim can be achieved not only by developing new building materials, but also with the implementation of new uses for existing materials from other applications, such as the case of the zeolites, presented in this research.

Another potential advantage is the zeolite avoids possible toxic pollutants of the heat systems and keep this heat, so the air wasted in these systems can be cleaner and of better quality.

2. Evaluation capacity of thermal storage

One of the best applications for these systems where residual energy is stored is the supply of peak energy demands in buildings. The mechanism involved consists in the activation of zeolites by using thermal energy waste of industrial processes and storing it in the absence of humidity (Mugnier and V. Goetz, 2011). This energy can also be stocked and transported where the heat is needed.

This study is the first part of a project where the capacity of thermal storage for zeolites has been evaluated by means of laboratory scale experiments.

2.1. Zeolite material: Mineral & synthetic

Nowadays, in the marketplace it can easily find the natural zeolite. It is a product that comes directly from the stone quarry and one of the common uses is for buildings and construction. In this study, the properties of this type of zeolite have been studied and compared with the synthetic zeolite type. On the contrary, the synthetic one is not commonly found in the market, so the production of this material would be increased if some

doi:10.18086/eurosun.2020.07.08 Available at http://proceedings.ises.org

application for the industry would be developed.

Materials selected include different sieves of both Natural Zeolite and Synthetic Zeolite. Natural Zeolite is a natural rock with high porosity and cation exchange capacity, selective absorption and reversible hydration. Synthetic Zeolites are a porous material with different properties and wide use in multiple sectors, such as an additive from water treatment plants, soil additives, cleaning products and even cosmetic synthesis. For the analysis, it is used and compared a mineral zeolite type and three synthetic zeolite types (4A,13x pellets and 13x spheres) (Zeochem).

The process that is searched in this research is to employ the cationic exchange for this kind of material to apply in thermal storage, using one of these two phases of the any zeolite material. The dry phase is named *activated*, because it is the one that you can use to extract the energy in heat form (S.Z. Xu , R.Z. Wang 2019).

The laboratory process to dry the material is divided in three steps. The first one consists in using the powerful laboratory muffle furnaces that are available for temperatures up to 1.000 °C in a small cell. After different tests to check the necessary strength to apply in any zeolites tested, it has been observed that in any case with less than 0,1 kg of sample, 40 minutes at 465ºC is enough energy to dehydrate completely the zeolite. The next step is to place the sample in oven at 110ºC for one day and it is finally stored in a vacuum desiccator for further analysis. The most important consideration in this process is the absence of air or humidity in the room. At this moment, the sample is ready for thermal heat capacity analysis in the reactor prototype.

2.2. Lab experiment: Reactor design

To check the thermal storage capacity of different types of zeolites, it´s needed to create different reactor prototypes. In this case, two reactors have been designed for both the natural and the synthetic zeolites. First of all, the design needs to be simulated by computer, and make it equal in flow proportionally for a both prototypes.

The sample is encapsulated in a cell and located in the middle position of a tube of about two meters length, according to the weight and volume of each zeolite type (S.Z. Xu,, Lemingtona 2018). Image 1 shows a ventilation equipment corresponding to the reactor diameter. The rest of the equipment is always the same in all experiments; with an air inlet and outlet where different temperatures and air speeds are recorded according to ambient conditions of outside temperature, pressure and humidity values. At the same time, temporal evolution is monitored by a thermographic (Hauer, 200) recording equipment of video and photographic model "ThermaCAM SC660 Wes (TC)" (accuracy ±1°C or ±1% of reading in a limited temperature range, ±2°C or ±2% of reading with thermal sensitivity NETD <30 mK @ +30°C), anemometers of air velocity / airflow transmitter Kimo instrument CTV 200 (accuracy air velocity from 0 to 3 m/s : ±3% of reading ±0,03 m/s / accuracy temperature ±0,5% of reading ±0,3°C), Kestrel 3000 environmental meter (accuracy ±3% of reading or ±0.1 m/s / ±1ºC) and a Fluke IR thermometer is use to check inside and outside ambient conditions of the prototype (Zhang, 2000) and verifications of the rest of equipment.

By means of these prototypes it has been possible to test different experimental conditions, as the reactor allows to control in real time different parameters as the ambient temperature and the air humidity, as the input sample it´s taken from a controlled flow of air through the first part of the reactor (Boer, R., et al. 2004) (Image 1).

2.3. Results Storage capacity

In the present figures (Figure 1, Figure 2, Figure 3 and Figure 4), the most representative results of the conducted experiments in the prototype reactor for the different zeolites types are shown. Red and blue lines show air temperature and air velocity evolution along the time, indicating the temperature and air velocity between the incoming air for ambient and the air once it passed through zeolite chamber (Núñez, 2001). In any cases the red line presents a high of temperature respect the blue one, checking the thermal storage capacity of the zeolites (S. Hongois, F. Kuznik 2014).

The amount to charge the zeolite cell reactor was near 1 kg in the case of the natural one, while for the synthetic zeolite less than 0,1 kg was necessary (Kakiuchi, et al. 2004). If the amount of the sample in the chamber would be reduced under these values, it would not work as outside air has almost the same temperature than the incoming ambient air.

By analyzing Figure 1, for the natural zeolite in stones form up to 8 cm size, it can be checked how this kind of zeolite works properly and the temperature of the whole reactor is seen to be increased by the heat conduction (Visscher et al. 2004). One of the objectives of this study consisted in collecting the heat coming from the chamber in the outside part of the reactor.

The comparisons of the results are shown in Figure 1 (5ºC for 6`), Figure 2 (10ºC for 20`), Figure 3 (8ºC for 25`) and Figure 4 (8ºC for 30`) for the different Zeolite types.

With regards to the synthetic zeolite, the results presented here are the most representative obtained from the analysis of three different types of Zeolite, comparing their morphology (Annerand Holl,2003) and structure.

From Figure 2 and Figure 3, it can be checked that for the Zeolite in Spheres 13x and Zeolite in Spheres 4A, in spite of having the same shape the behavior is improved when using the 13x molecular sieves. In the last case temperature is increased 8ºC for 25 minutes while for the 4A it increases up to 10ºC at the beginning, but the heating time is seen to be lower.

Finally, Figure 3 and Figure 4, show different shapes of the same zeolite type. It can be observed that in pellets shape, temperature is increased 8ºC for 30 minutes. This is the major time registered for all experiments developed and the results are replicable in different ambient condition for this kind of synthetic zeolite, but the air friction with sphere zeolite is bigger. Image 2 and Image 3 are the same picture with different camera lens. Image 2 shows, for the Zeolite 13x Sieves Pellets, that the reactor keeps cool, except in the chamber and the heated air is perfectly leaded up to the outside part of the prototype. When spheres type is employed, same results are obtained, but the air friction is better and more stable heat conduction to the outside part of the prototype.

3. Tables, figures, equations, and lists

3.1. Figures

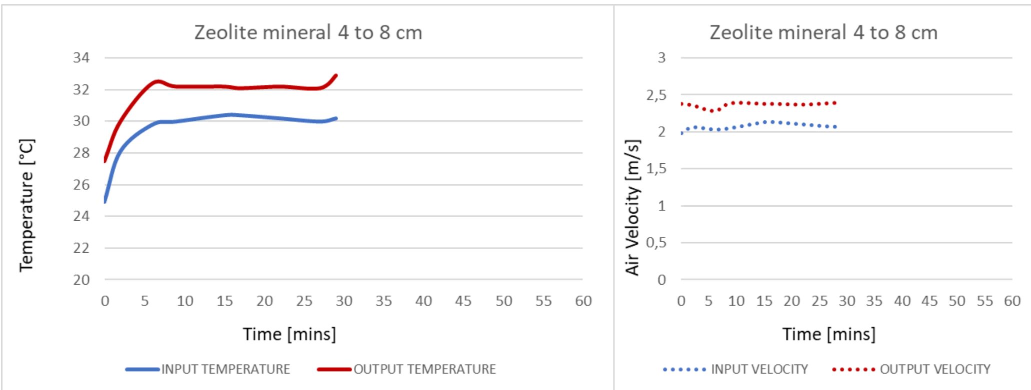

Figure 1: Zeolite mineral. 4 to 8 cm

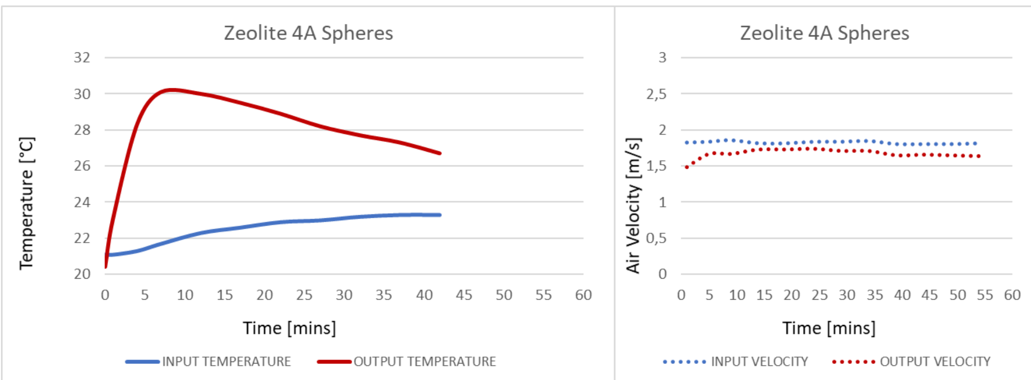

Figure 2: Zeolite 4A Spheres

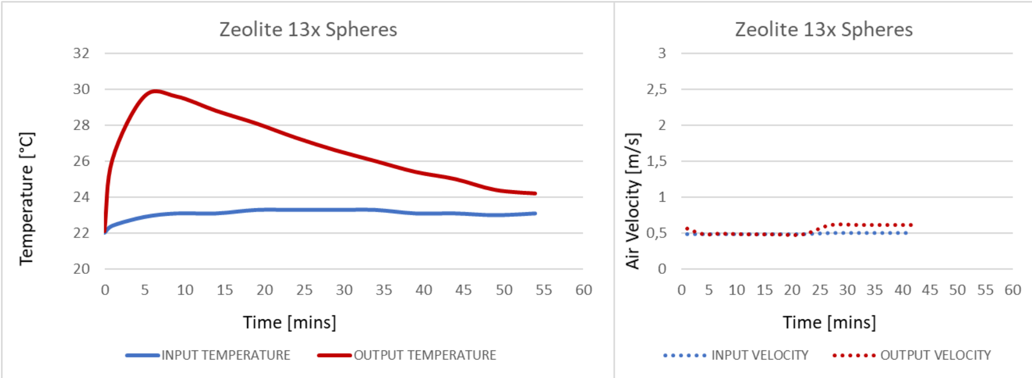

Figure 3: Zeolite 13x Spheres

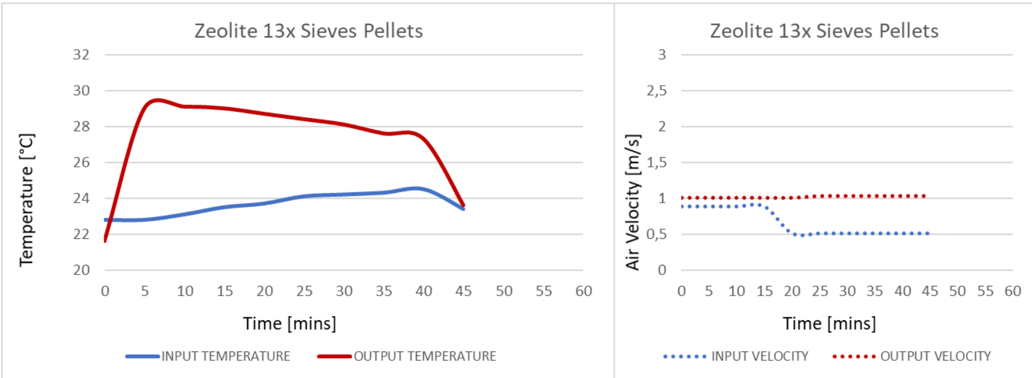

Figure4: Zeolite 13x Sieves Pellets

3.2. Images

Image 1: Lab experiment, reactor designs for different ambient condition

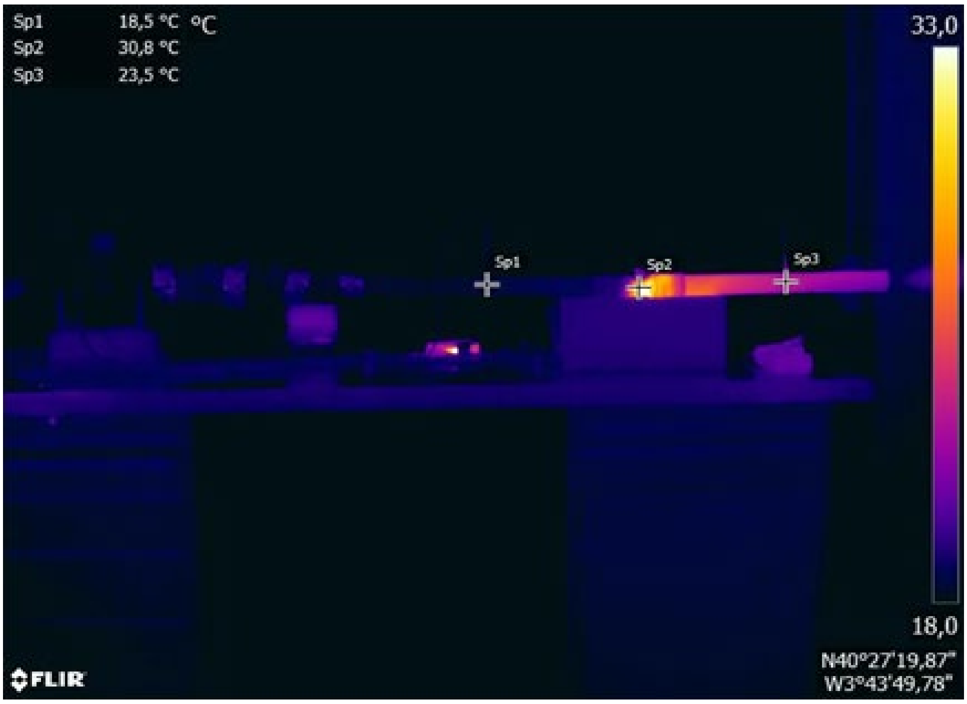

Image 2: IR vision for Zeolite 13x Sieves Pellets

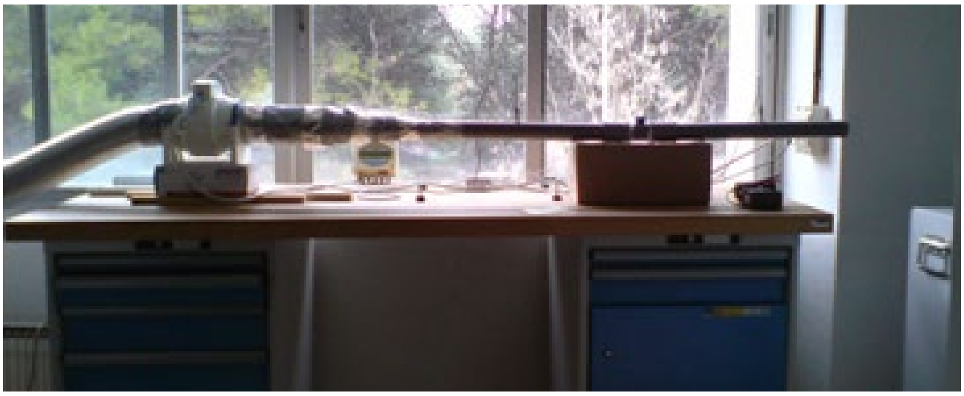

Image 3: Normal vision for Zeolite 13x Sieves Pellets

3. Conclusions

This study demonstrates that a high cationic exchange capacity for all types of zeolites is evaluated.

Natural zeolite needs more mass to take advantage of the cationic exchange's energy and the reactor system loses part of this energy by heat conduction.

In the heat test, the Zeolite 13 x test has the best results of the empirical campaing rising its temperature at 8 degrees Celsius for 25 minutes and during this time the rising is close to this 8ºC in every moment. In addition, the Zeolite 13 x spheres has a better result of material degradation.

The micro calorimetry experiments reveal that the energy level is maintained over more than seven charge/discharge cycles without any degradation of quality and reliability.

The reactor design is the key for a good air friction and to a proper energy saving produced by the zeolite.

Zeolite 13x exhibits the best results for all experimental tests carried out, keeping its temperature for a long time and the sphere shape can provide an effective air friction. Thus, Zeolite 13x Spheres has been selected to be employed in scaling up projects.

4. Acknowledgments

I would like to thank my supervisor, Dr Ferrer Tevar and the rest of the team "Research unit of Energy Efficiency in Buildings" in CIEMAT, for providing guidance and feedback throughout this project.

5. References

European Commission (2018): SET-Plan ACTION n°3.2 Implementation Plan – Europe to become a global role model in integrated, innovative solutions for the planning, deployment, and replication of Positive Energy Districts. European Commission, Brussels.

IEA-EBC (2018): IEA Energy in Buildings and Communities Programme Strategic Plan 2019-2024. International Energy Agency, Paris.

S.Z. Xu,, Lemingtona, R.Z. Wang,, L.W. Wang, J. Zhub. A zeolite 13X/magnesium sulfate–water sorption thermal energy storage device for domestic heating. Energy Conversion and Management 171 (2018) 98–109

S.Z. Xu , R.Z. Wang , L.W. Wang , J. Zhu Performance characterizations and thermodynamic analysis of magnesium sulfate-impregnated zeolite 13X and activated alumina composite sorbents for thermal energy storage.. Energy 167 (2019) 889-901

S. Hongois, F. Kuznik, Ph. Stevens, J.-J. Roux Developement and characterisation of a new MgSO4-zeolite composite for long-term thermal energy storage.. HAL Id: hal-00683965 on 9 Jun 2014

Anner, N and S. Holl, Solicon as energy carrier – facts and perspectives, Proceedings of ECOS, Copenhagen, June/July 2003.

Boer, R., et al. Solid Sorption Cooling with Integrated Storage: The SWEAT Prototype. in Proc. International Conference on Heat Powered Cycles, HPC 2004. 2004. Larnaca, Cyprus. http://www.ecn.nl/docs/library/report/2004/rx04080.pdf

HauerA., Thermochemical Energy Storage in Open Sorption Systems – Temperature Lift, Coefficient of Performance and Energy Density. TERRASTOCK 2000, Proceedings of the 8th International Conference on Thermal Energy Storage, Stuttgart Germany, August 2000.

KakiuchiH., et al. Novel zeolite adsorbents and their application for AHP and Desiccant system, Presented at the IEA-Annex 17 Meeting in Beijing, 2004

Mugnier D. and GoetzV.Energy storage comparison of sorption systems for cooling and refrigeration. Solar Energy, Vol. 71 No. 1, pp. 47-55, 2001.

NúñezT., CharakterisierunguzndBewertung von AdsorbentienfürWärmetransformationsanwendungen, PhD Dissertation, University of Freiburg, 2001 www.freidok.uni-freiburg.de/volltexte/335/pdf/DissertationNunez.pdf

Visscher K., et al. (2004) ECN Report ECN-C--04-074: Compactechemischeseizoenopslag van zonnewarmte; Eindrapportage, ECN, Petten, Holland.http://www.ecn.nl/library/reports/2004/c04074.html. ECN-C--04-074.

Zeochen, www.zeochem.comTSDS-0014/V1/PKH230713. Access August 2020

ZhangL. Z., Design and testing of an automobile waste heat adsorption cooling system. Applied Thermal Engineering 20 (2000) 103-114.

A Novel State of Charge Sensor Concept for Thermochemical Heat Storage

Harald Kirchsteiger[1] and Patrick Kefer[1]

[1]Research Group ASiC, University of Applied Sciences Upper Austria, Wels, Austria

Abstract

A functional prototype of a state of charge sensor for a solid sorption thermochemical heat storage was developed. The sensor concept is based on detecting the relative change of permittivity when water vapour adsorbs on the surface of the sorptive material. This is done by measuring the capacitance of a capacitor where the sorptive material is utilized as dielectric. We were considering Zeolite and Silica gel in the experimental validation of the sensor concept. The experiments showed a strong correlation between the measured capacity and the weight of the material which indicates the saturation with water, both in the adsorption and in the desorption stage. Several consecutive experiments proved the repeatability of the measurements which subsequently could be used to identify a sensor calibration function in order to relate the capacitance with the state of charge.

Keywords: Sorption thermal energy storage, solid adsorption

1. Introduction

Storage of heat is essential in industry as well as in domestic homes and can be realized through many different technological pathways. Sorption thermal storage methods and materials are a very active area of research (Aydin et al. 2015) and are often utilized in combination with solar energy production. The concept of storing surplus solar energy during summertime and using it in wintertime for e.g. space heating is referred to as seasonal storage (Scapino et al. 2017). Various different process types of thermochemical sorption energy storages for seasonal storage are compared against each other in (Fumey et al. 2019). The main process technologies can be subdivided into open and closed systems (Bott et al. 2019) depending on whether the thermochemical material is operating at atmospheric pressure or is contained inside of a vacuum chamber. Another distinction can be made whether the sorption material is continuously transported while reacting (Zettl et al. 2014, Zettl and Kirchsteiger 2018) or is stationary in a fixed bed reactor (Mette et al. 2014) without material movement. In this work, our prototype state of charge sensor is evaluated on an open process with a fixed bed.

There is a whole variety of material combinations where the thermochemical effect of storing and releasing energy through adsorption of a fluid (called *adsorbate*) on a solid material (called *adsorbent*) is utilized (Shmroukh et al. 2015). From a process handling point of view, the combinations of Zeolite or SilicaGel as adsorbent and water vapor as adsorbate are frequently used because the temperatures are in a reasonable range, there are no hazardous chemicals involved and the materials are relatively cheap. Those are the reasons why those combinations are considered in this study as well.

The basic and simplified working principle of an open solid sorption storage using the material combination zeolite and water vapor is shown in Fig. 1: When charging, a flow of hot and dry air dries the sorptive material, removing the adsorbed water atoms from the pores. This process is called *desorption*. The dried out material stores heat at low temperatures without losses as long as it does not get in contact with water vapor. For discharging, water vapor needs to be provided to the sorptive material where the water atoms adsorb in the pores thereby releasing large amounts of energy in the form of heat. This process is called *adsorption*. The whole process is repeatable without losses, although the hydrothermal stability of the zeolite powder or beads decreases with usage (Fischer et al. 2018). A more detailed process description can be found e.g. in (Do 1998).

doi:10.18086/eurosun.2020.07.09 Available at http://proceedings.ises.org

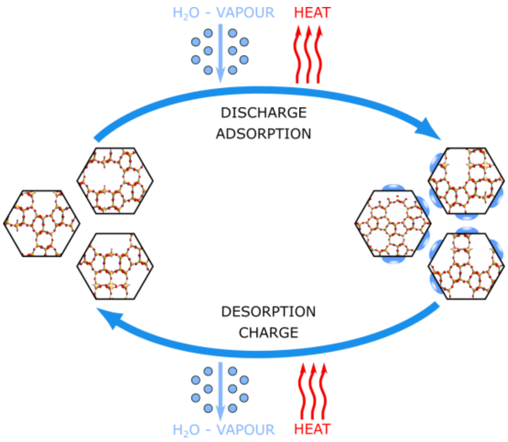

Fig. 1: Sorption working principle (the hexagons indicate Zeolite molecules)

Sorption thermal storage devices can play a significant role in future renewable energy system for domestic homes. Their efficient use requires advancements in materials science (development of adsorbents with high storage energy density), in process engineering (system layout, efficient material transportation, avoid mechanical stress to the adsorbents), and in overall process control (temperature regulation and humidity control). From the control point of view, sensors are required to measure the current state of charge of the system. The importance of sensing the state of charge has already been recognized in the battery storage community a long time ago (How et al. 2019). Recently, the phase change material (PCM) storage community focuses on state of charge sensors as well (Steinmaurer et al. 2014, Barz et al. 2018).

Currently, no specific sensors to measure or estimate the state of charge of sorption storages or sorptive material are available. Experimental prototype solutions were presented in (Luoma et al. 2017) where infrared spectroscopy was used to analyze the reflected light from specifically prepared zeolite tabs and conclude on the water content in the material. Besides physical measurement principles, there is the alternative option to employ software sensors which make use of mathematical models. In (Scapino et al. 2019) such a concept was introduced using neural networks, however, the method was only tested on datasets generated with another model (of higher complexity) but not on real data.

In this paper, an experimentally validated proof of concept sensor based on measuring the relative change in permittivity is described. We consider zeolite and silica gel in the form of small beads with a diameter between 2 and 5 mm and water vapor as adsorbate. A specific lab setup was designed to experimentally validate the sensor concept both in adsorption and in desorption mode.

2. Methods

The physical principle used to detect the water content of the sorption material is the difference in relative permittivity of water (Andryieuski et al. 2015) and the adsorbent. The relative permittivity of water up to 1 GHz is in the range of 50-90 (see Fig. 2) whereas the permittivity of sorption material is typically in the single digits. In (Zheng et al. 2013) it is stated that a direct correlation of adsorbed amount of water and the dielectric constant of the material is existent.

If sorption material is utilized as dielectric of a capacitor, the capacity is directly correlated to the relative permittivity of the material. The voltage V, i.e. the difference in the potential, is defined as the line integral across an electric field E. In a one-dimensional point of view (for plate-type capacitors) this is

$$V = \int E(z)dz = \int \frac{\sigma(z)}{\epsilon_0 \epsilon_r} dz \qquad (2.1)$$

where ε_0 is the permittivity of vacuum, ε_r is the relative permittivity of the material used as dielectric of the capacitor and σ is the charge density. The capacity C is then given as:

$$C = \frac{Q}{V(Q)} \qquad (2.2)$$

where Q denotes the electrical charge. Since most capacity measurement techniques work with transient input signals (rectangular or sine), the frequency range must be considered in order to get good sensitivity for the measurement i.e. higher values for the relative permittivity. As Fig. 2 shows, signals below approximately 1 GHz will be suitable in that regard.

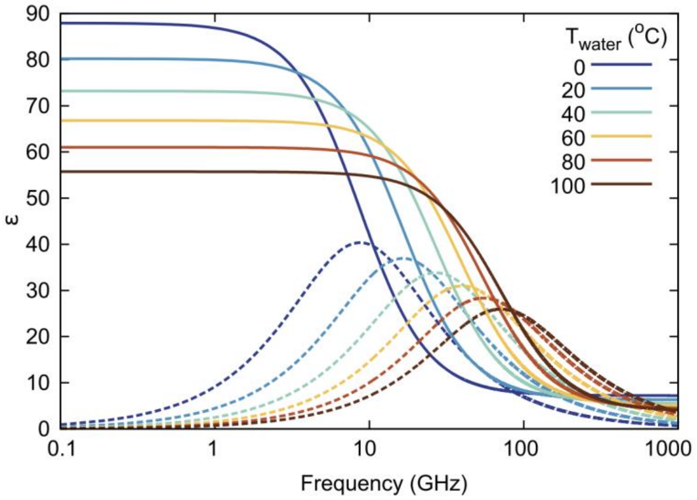

Fig. 2: relative permittivity of water (Andryieuski et al 2015)

3. Sensor prototype and lab setup

The conceptual lab setup to validate the experimental prototype is shown in Fig. 3. The main components are a radial fan, an electrical heater, the measurement capacitance filled with sorptive material, a scale and a flexible hose connection between the part resting on the scale and the rest of the setup.

The actual realization of this concept in a lab-scale prototype is shown in Fig. 4 and was described in detail in (Bin Azman et al. 2020). The capacitance filled with sorptive material is made out of two concentric copper cylinders with diameters of 90mm and 60mm respectively. The air supply shown in the lower left part of Fig. 4 can be controlled with respect to temperature and air mass flow. The selectable temperature range is between ambient and a maximum of 300°C which enables to perform an efficient desorption while the material is inside of the storage. The air flow through the storage is continuously adjustable with a radial fan which sucks in ambient air. For process monitoring, temperature sensors and humidity sensors are installed at the outlet of the air stream after the storage.

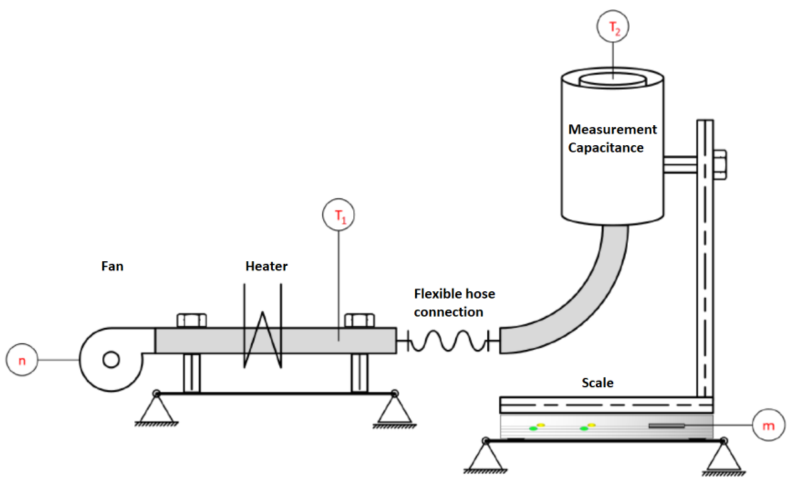

Fig. 3: Schematic of the entire experimental setup

The capacitance itself is evaluated with an oscillator circuit made out of a parallel connection of a known capacitance C and an inductance L that results in a resonance frequency

$$f_R = \frac{1}{2\pi\sqrt{LC}} \tag{3.1}$$

Connecting the unknown capacitance C_X of the storage in parallel to C results in a modified resonance frequency

$$f_R' = \frac{1}{2\pi\sqrt{L(C + C_X)}} \tag{3.2}$$

Based on those two frequencies and the known values of the components, the unknown capacity is evaluated:

$$C_X = \left(\frac{f_R}{f_R'} - 1\right) C \tag{3.3}$$

The whole setup is resting on a lab scale with a resolution of 0.05g, which continuously measures the weight. This weight measurement serves as a reference value for the unknown state of charge of the material since an adsorption or desorption of water vapor is directly reflected in the weight. The measurement capacitance cylinder is filled with approximately 500g material.

All measurements were cyclically recorded with an Almemo (Ahlborn Mess- und Regelungstechnik GmbH, Holzkirchen, Germany) data logging device connected to a standard desktop PC running MATLAB/Simulink (MathWorks, Natick, MA) which was used to implement the control loops for the temperature and fan speed.

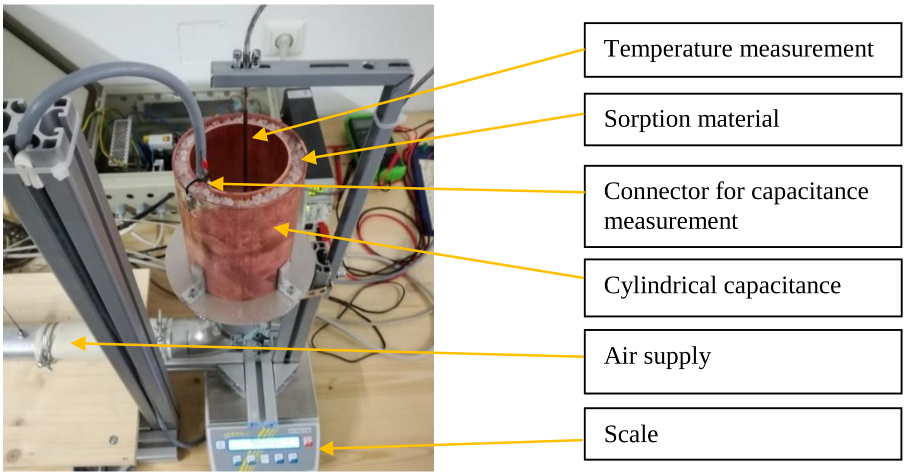

Fig. 4: Experimental setup used to validate the sensor concept

4. Evaluation Procedure and Results

In this section, we present the measurement results of the prototype capacitive sorption sensor evaluated on a fixed bed reactor using Zeolite and SilicaGel. The results are subdivided in adsorption and desorption results for both materials.

The measurement procedure started with filling the measurement cylinder (inside and annulus) with approximately 500g material with an initially unknown charge with water vapor. Then, the heater was set to a temperature of 300°C in the case of zeolite (180°C in the case of Silicagel) in order to achieve a desorption. The desorption stage was held until the weight did not change significantly anymore which was after around one hour. Subsequently, the temperature was set to 20°C (for both material types), effectively switching off the heater, and running into an adsorption stage. The switch from desorption to adsorption is not instantaneously, since the measurement cylinder and pipe connections initially need to cool down from the high desorption temperatures. The adsorption stage was again held until the weight did not increase significantly anymore which was after around two hours. This cycle of desorption and adsorption was repeated for five times in order to analyze the repeatability and reliability of the prototype sensor concept.

The measurement results of one such cycle for zeolite are shown in Fig. 5. On the left side is the desorption stage and on the right side the adsorption. Those two stages follow each other immediately, however, there is a small time gap in the measurements due to saving the data and restarting the measurement hardware. The desorption figure to the left shows that the 300°C air temperature after the heater leads to a temperature of approximately 200°C at the outlet of the storage which is high enough to enable a significant desorption. The activity of the sorptive material can be monitored by the relative humidity of the outlet air stream: initially (between 0 and 5 minutes) large absolute quantities of water vapour are released (note that in this period the temperature is already increasing up to almost 100°C). Later on, the released water vapour diminishes and eventually reaches a steady state which depends on the desorption temperature and the partial pressure of H_2O of the surrounding air. From the bottom graphs in Fig. 5 it already becomes evident that the weight measurement and the proposed capacity measurement are highly correlated. From the top graph on the right side of Fig. 5 the cool down phase of the equipment can be observed between 0 and approximately 5 minutes. Additionally, heat is actively produced by the zeolite because of the supply with humid air at ambient temperature. All measurements were done in January 2018, during Wintertime in Austria where there is a typical relative humidity of ambient air of approximately 30% and an ambient temperature of approximately 22° indoors. This low humidity is the reason why the desorption part of the experiment takes relatively long and would be much faster if larger amounts of water vapour would be provided. This does, however, not affect the validation of the sensor principle in any way.

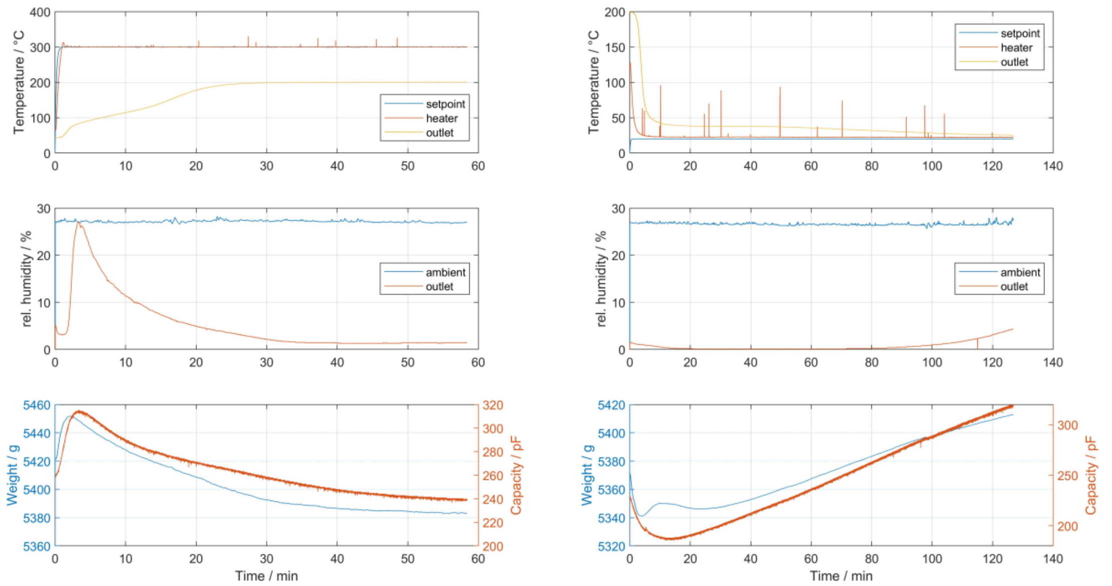

Fig. 5: One cycle of zeolite desorption (left) followed by adsorption (right)

To better evaluate the connection between the measured capacitance and the weight, they were plotted against each other as shown in Fig. 6 for Zeolite and Fig. 7 for Silica gel. Under the assumption that the weight is an indicator for the state of charge of the material, an ideal sensor would result in a straight line in those graphs providing a linear relationship between the sensed quantity and the reference value. In the case of zeolite adsorption such a linear relationship indeed occurs, however, in the case of zeolite desorption the resulting graph is only piecewise linear consisting roughly of a combination of two linear functions. For silica gel the relationship is following a polynomial shape for adsorption (see Fig. 7) and is linear in a large range for desorption followed by a slightly steeper increase for higher masses, i.e. higher state of charge.

5. Discussion and Conclusion

From the results presented in the previous section, the general conclusion is that the measured capacitance is a good indicator of the material weight, which in turn is directly connected with the state of charge. Therefore, the hypothesis of using a capacitance measurement as substitute for the state of charge of the material proves to be true. For the piecewise linear and polynomial relationship, a simple sensor calibration function needs to be developed and implemented in the sensor hardware. Such a sensor calibration function seems to be a possible approach since the non-linear behavior could be reproduced within small margins in five independent experiments.

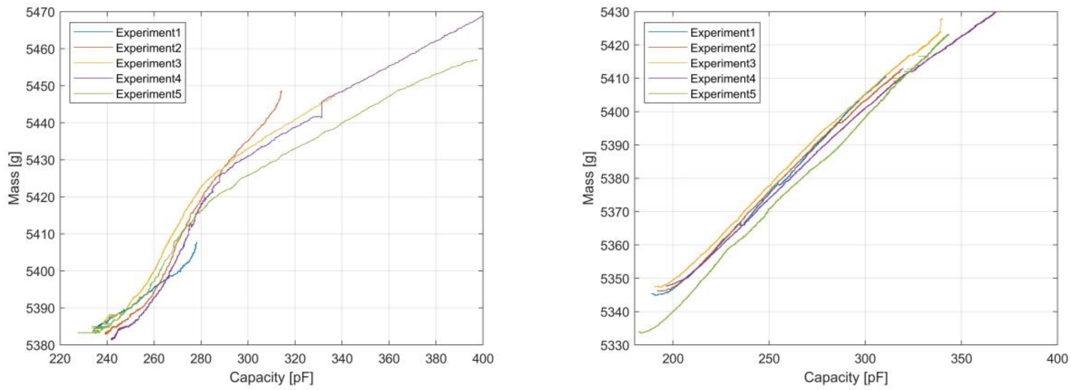

Fig. 6: Zeolite desorption (left) and adsorption (right)

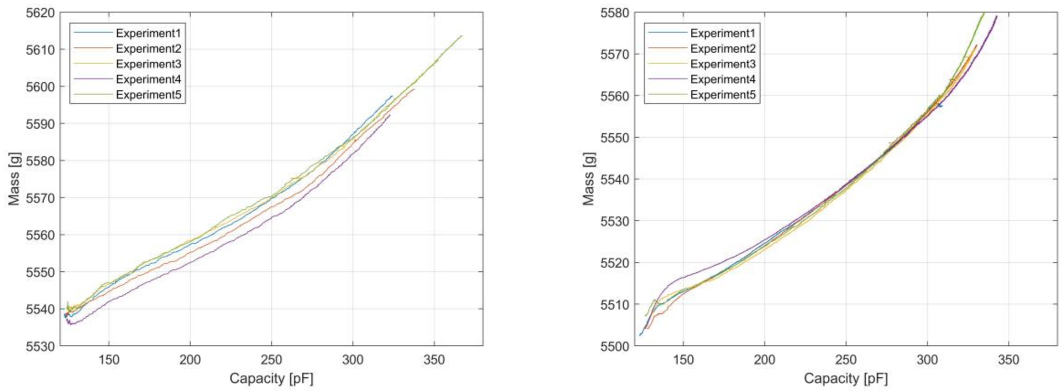

Fig. 7: Silica gel desorption (left) and adsorption (right)

The results presented prove the general validity of a concept of a state of charge sensor based on a capacitance measurement, however, several issues need further investigation:

- In the current prototype, the sensor itself is the storage. In future applications, especially for large scale storages, it should be aimed for to miniaturize the sensor.
- Miniaturized sensors based on the proposed concept could be placed at several locations inside a large scale storage providing a distributed information of the state of charge, similar to Li-ion batteries where the state of charge of individual cells is monitored and an overall state of charge is calculated.
- The sensor reading is by construction an average of the state of charge of the whole material inside the active area of the capacitance. Making the capacitance smaller could lead to a higher variance.
- A miniaturized sensor leads to smaller values of the capacity, which makes the evaluation more difficult.
- The sensor prototype was already tested on a moving bed reactor where material is continuously passing through the capacitance; however, this also needs further investigation.

None of those issues seems to be jeopardizing the general concept, thus we are working to expand the possibilities and accuracy of the current prototype.

6. Acknowledgments

This project is financed by research subsidies granted by the government of Upper Austria. We would like to thank Alyna Ong Ching Wuie and Sulaiman Bin Azman for carrying out lab experiments and preparation of selected figures.

7. References

A. Andryieuski, S. M. Kuznetsova, S. V. Zhukovsky, Y. S. Kivshar, and A. V. Lavrinenko, 2015. Water: Promising Opportunities For Tunable All-dielectric Electromagnetic Metamaterials, Sci Rep, vol. 5, no. 1, p. 13535, doi: 10/gg8qv2.

Devrim Aydin, Sean P. Casey, Saffa Riffat, 2015. The latest advancements on thermochemical heat storage systems. J. of Renewable and Sustainable Energy Reviews 41, 356-367.

T. Barz, D. Seliger, K. Marx, A. Sommer, S. F. Walter, H. G. Bock, S. Körkel, 2018. State and state of charge estimation for a latent heat storage. Control Engineering Practice 72, 151-166.

S. Bin Azman, N. Daborer-Prado, H. Kirchsteiger, 2020. Aufbau, Inbetriebnahme und Modellierung eines Sorptionsprüfstandes im Labormaßstab. 16. Symposium Energieinnovationen, 12. – 14.02.2020 Graz, Austria.

C. Bott, I. Dressel, P. Bayer, 2019. State-of-technology review of water-based closed seasonal thermal energy storage systems. J. of Renewable and Sustainable Energy Reviews 113, 109241.

D. D. Do, 1998. Adsorption Analysis: Equilibria and Kinetics. Imperial College Press, London.

F. Fischer, W. Lutz, J.C. Buhl, E. Laevemann, 2018. Insights into the hydrothermal stability of zeolite 13X. Microporous and Mesoporous Materials. Vol. 262, 258-268

B. Fumey, R. Weber, L. Baldini, 2015. Sorption based long-term thermal energy storage – Process classification and analysis of performance limitations: A review. J. of Renewable and Sustainable Energy Reviews 111, 57-74.

D. N. T. How, M. A. Hannan, M. S. Hossain Lipu, Pin Jern Ker, 2019. State of Charge Estimation for Lithium-Ion Batteries Using Model-Based and Data-Driven Methods: A Review. IEEE Access vol.7 136116-136136

Pekka Luoma, Petra Müller, Harald Kirchsteiger, Patrick Kefer, Markus Brandstetter, 2017. Feasibility of Next Generation Infrared Microspectrometers Demonstrated on Characterization of Zeolite Materials. Proceedings of the 4th European Conference on Process Analytics and Control Technology EuroPACT2017.

B. Mette, H. Kerskes, H. Drück, 2014. Experimental and numerical investigations of different reactor concepts for thermochemical energy storage. Energy Procedia 57, 2380-2389.

L. Scapino, H. A. Zondag, J. Van Bael, J. Diriken, C. C. M. Rindt, 2017. Energy density and storage capacity cost comparison of conceptual solid and liquid sorption seasonal heat storage systems for low-temperature space heating. J. of Renewable and Sustainable Energy Reviews 76, 13104-1331.

L. Scapino, H. A. Zondag, J. Diriken, C. C. M. Rindt, J. Van Bael. 2019. Modeling the performance of a sorption thermal energy storage reactor using artificial neural networks. Applied Energy. Vol. 253, 113525.

Ahmed N. Shmroukh, Ahmed Hamza H. Ali, Shinichi Ookawara, 2015. Adsorption working pairs for adsorption cooling chillers: A review based on adsorption capacity and environmental impact. J. of Renewable and Sustainable Energy Reviews 50, 445-456.

G. Steinmaurer, M. Krupa, P. Kefer, 2014. Development of sensors for measuring the enthalpy of PCM storage systems. Energy Procedia 48, 440-446.

Bernhard Zettl, Gerald Englmair, Gerald Steinmaurer, 2014. Development of a revolving drum reactor for open-sorption heat storage processes. Applied Thermal Engineering 70, 42-49.

Bernhard Zettl and Harald Kirchsteiger, 2018. An open sorption heat storage application. Proceedings of the International Sustainable Energy Conference, Graz, Austria. p.605-611.

Zheng, Y., Meyer, G., Lanagan, M., Agrawal, D., Cheng, J., 2013. A study of water sorption effects on the microwave dielectric properties of calcium chloride/silica gel composites. Materials Letters 95, 157–159. https://doi.org/10/f4rw43

Assessing the Long-Term Stability of Fatty Acids for Latent Heat Storage by Studying their Thermal Degradation Kinetics

Rocío Bayón[1], Aristides Bonanos[2] and Esther Rojas[1]

[1] CIEMAT-PSA, Madrid (Spain)

[2] The Cyprus Institute, Nicosia (Cyprus)

Abstract

The thermal degradation kinetics of lauric acid has been studied with the aim of assessing its long-term stability and performance as a latent heat storage medium for low temperature applications. For this purpose, dynamic thermogravimetric (TG) measurements were carried out under different gas atmospheres (N_2 and air) and at various heating rates. The kinetic analysis of TG curves assuming a zero-order evaporation process led to activation energy values very close to the evaporation enthalpy although the simulated dα/dT curves could not reproduce the ones experimentally obtained. On the other hand, the analysis of TG measurements with a model-free isoconversional method has shown that the activation energy significantly varies with the degree of conversion. All these results indicate that thermal degradation of lauric acid is a multi-step process whose single-step mechanisms have to be identified. A deconvolution analysis of dα/dT curves was performed by using Fraser-Suzuki functions so that two single-step reaction mechanisms were proposed: the first associated with the evaporation with an activation energy value of 83±8 kJ/mol, while the other may be related to the emission of volatile compounds. The activation energy value of the second mechanism is lower when lauric acid is heated up in air, which may indicate that O_2 is involved in the reaction. The calculated TG curves, assuming the occurrence of these two mechanisms, fit very well to the corresponding experimental curves. Isothermal degradation curves have been calculated by considering both mechanisms and, according to them, lauric acid should totally disappear after 30 days if it is kept under N_2 at 5 ºC above its melting temperature. However preliminary isothermal test in an oven with small samples (in the range of few grams) disagree with those predictions. Hence further isothermal experiments under conditions closer to the real service ones are required in order obtain reliable isothermal degradation curves and assess long-term stability of lauric acid.

Keywords: PCM, lauric acid, TG measurements, kinetic analysis, multi-step processes

1. Introduction

Phase change materials (PCM) with melting temperatures (T_m) between 30 ºC and 70 °C are of particular interest for solar thermal energy storage in the low-temperature range. One of the most critical issues when choosing a PCM for a certain storage application is its long-term performance, which is normally assessed through melting/freezing cycles. However, if a PCM undergoes some kind of degradation after melting due to a chemical reaction or phase segregation, it will be hindered during the freezing period. Hence this kind of tests is not sufficient for validating the successful life-performance of a PCM. Another way to assess long-term stability of PCMs is to carry out kinetic studies of possible degradation processes (Bayón and Rojas, 2019). If a PCM undergoes degradation due to the occurrence of chemical reactions in liquid state, thermogravimetric (TG) measurements can be used for determining the kinetics of such reactions (Vyazovkin et al. 2011). The starting point for the kinetic analysis of TG measurements is the equation which defines the reaction rate:

$$\frac{d\alpha}{dt} = Ae^{\left(\frac{-E}{RT}\right)}f(\alpha) \qquad \text{(eq. 1)}$$

where α is the degree of conversion at a certain time, calculated from TG experimental data and normally expressed in mass loss percentage ($\alpha = 1 - TG(\%)/100$). A, E and R are the frequency factor, the activation energy and the molar gas constant, all present in the Arrhenius law for the reaction rate constant and *f(α)* is a function whose form depends on the mathematical model describing the reaction mechanism. In a dynamic TG

doi:10.18086/eurosun.2020.07.10 Available at http://proceedings.ises.org

measurement performed at constant heating rate $\beta = \frac{dT}{dt}$, (eq. 1) becomes:

$$\frac{d\alpha}{dT} = \frac{Af(\alpha)e^{-E/RT}}{\beta} \quad \text{(eq. 2)}$$

This equation corresponds to the slope of the TG curve in each point, in other words to the dTG (=derivative) curve obtained during the experiments but expressed in terms of α. Therefore, by integrating (eq. 2), the equation of TG curve (α vs. T) can be calculated:

$$\int_0^\alpha \frac{d\alpha}{f(\alpha)} = g(\alpha) = \frac{A}{\beta}\int_{T_0}^{T} e^{-E/RT}dT = \frac{AE}{\beta R}p\left(\frac{E}{RT}\right) \quad \text{(eq. 3)}$$

Similarly to *f(α)*, the *g(α)* function depends on the model used to describe the reaction mechanism (Vyazovkin et al. 2011) whereas *p(E/RT)* is the temperature integral (Doyle, 1961). Since this integral cannot be calculated explicitly, either numerical methods or analytical approximations have been proposed by different authors (Órfão, 2007) for its evaluation.

The aim of any kinetic analysis is to obtain the kinetic triplet: *E*, *A* and *f(α)*. This can be accomplished by applying either model-fitting methods or model-free isoconversional methods (Vyazovkin et al. 2011). If the reaction mechanism is unknown, the activation energy, *E*, can be estimated with any of the most accurate isoconversional methods (Coats and Redfern, 1964; Akahira and Sunose, 1971; Miura and Maki, 1998). Once the activation energy is obtained, the frequency factor, *A*, and the reaction mechanism, *f(α)*, must also be determined. If the process under study obeys single-step kinetics, meaning that *E* does not vary significantly with α, several methods can be used for obtaining both *A* and *f(α)* or *g(α)*: Kissinger method (Kissinger, 1957), Coats-Redfern method with discriminating approach (Coats and Redfern, 1964) or the method of master plots (Vyazovkin et al. 2011) are some examples.

Conversely, for multi-step processes, the *E* calculated with the isoconversional methods is expected to change with α due to the different relative contributions of each single-step to the overall reaction rate. The occurrence of multi-step processes can also be detected if the dTG curve does not present a unique maximum for the reaction rate but is composed of a series of peaks, which may or may not overlap. In this case, each reaction mechanism or step should be somehow separated and analyzed independently. One way to separate overlapping rate peaks is to perform a deconvolution analysis by using mathematical functions that have peak shapes (Vyazovkin et al. 2020). Since the rate peaks of single-step reactions generally exhibit asymmetric shapes, one of the most commonly used function for deconvoluting dTG curves is the Fraser-Suzuki function (Fraser and Suzuki, 1969; Rusch and Lelieur, 1973). Many examples can be found in the literature in relation to the use of Fraser-Suzuki (*FS*) functions in the kinetic analysis of TG measurements of different kinds of materials (Perejón et al., 2011; Cheng et al., 2015; Stankovic et al., 2018). Once the single-step processes have been identified, the kinetic triplet for each reaction mechanism can be obtained by applying any of the above mentioned methods (Kissinger, 1957; Coats and Redfern, 1964; Vyazovkin et al. 2011).

Fatty acids, either pure or their mixtures, are among the PCM whose melting temperature is in the range of 30 ºC to 70 ºC. Some previous studies of various fatty acids have demonstrated that their thermal properties (i.e. melting temperature and enthalpy) do not significantly change after up to 3000 consecutive melting/freezing cycles (Kahwaji, 2017). However, up to now, no degradation studies from the kinetic point of view have been carried out for these PCMs. Hence long-term performance of fatty acids as latent storage materials is still not fully assessed.

Being aware of this problem, in the Thermal Storage Unit of CIEMAT-PSA we aim to study the degradation kinetics of various straight-chain fatty acids normally used as PCM. In this work we present the results obtained up to now for dodecanoic acid ($C_{11}H_{23}$-COOH), also known as lauric acid with a melting temperature of T_m=45 ºC. For this purpose, dynamic thermogravimetric (TG) measurements have been performed with different heating rates under either N_2 or air. The analysis of TG results by a model-free isoconversional method has shown an important variation of the activation energy with conversion, which supports the occurrence of multi-step processes. Hence deconvolution of dTG curves has been performed for separating the single-step reaction processes and obtaining the corresponding Arrhenius parameters together with the possible reaction mechanisms. Finally the TG curves have been simulated and compared with the experimental ones and the isothermal degradation curves have been calculated and discussed.

2. Experimental

The lauric acid used in this work had >98% purity and was supplied by Sigma-Aldrich. Dynamic thermogravimetric (TG) analysis was performed in a TGA Q500 apparatus from TA Instruments®. TG measurements were carried out for samples of 10-12 mg with heating rates, β, ranging from 1 ºC/min to 20 ºC/min under either N_2 or air atmosphere at 90 ml/min. The results of TG analysis are mass-loss percentage curves TG (%) and the corresponding derivative curves dTG (%/K) expressed as a function of temperature one for each heating rate, β. Examples of both sets of curves are displayed in Fig. 1 for the case of lauric acid measured under N_2 atmosphere.

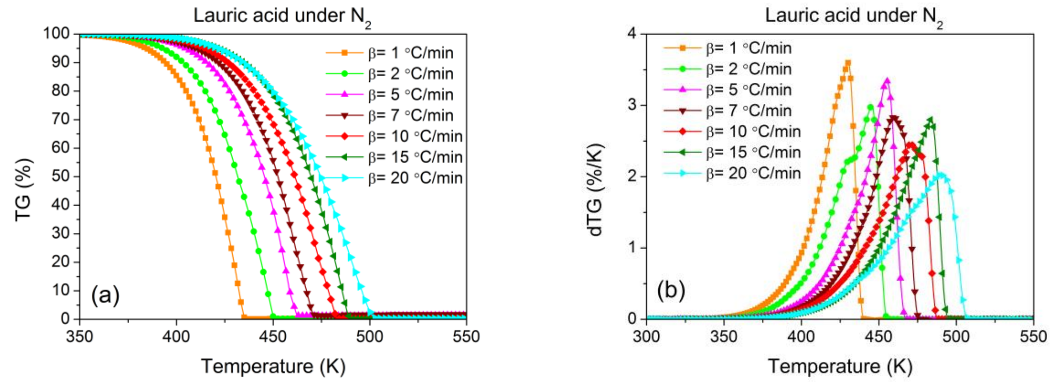

Fig. 1. Experimental TG (%) (a) and dTG (%/K) (b) curves obtained for lauric acid under N_2.

3. Results and discussion

3.1. Estimation of the activation energy, *E*

In principle, straight-chain fatty acids are expected to undergo evaporation upon heating. According to the literature (Penner, 1952), evaporation can be considered as a zero-order mechanism (F0) for which $f(\alpha)=1$, so that (eq. 2) expressed in logarithmic form becomes:

$$\ln\frac{d\alpha}{dT} = \ln\frac{A}{\beta} - \frac{E}{RT} \qquad \text{(eq. 4)}$$

By this linear plot, both the activation energy and the pre-exponential factor can be calculated directly from dTG curve expressed in terms of α. Shen and Alexander already studied the evaporation kinetics of various fatty acids by applying (eq. 4) to dTG curves measured under N_2 (100 ml/min) at 2 ºC/min (Shen and Alexander, 1999). They took the curve at the lowest heating rate because in suchcases the system is expected to be closer to the thermodynamic equilibrium (Arias et al., 2009). In order to compare with their results, we also applied this method to our dTG curves measured at 2 ºC/min under both N_2 and air (90 ml/min) atmospheres. The *E* and *logA* values reported by Shen and Alexander are recorded in Table 1 together with the corresponding values obtained in this work. For the activation energy, our values are slightly higher than the obtained by these authors but in any case, they are still quite close to the evaporation enthalpy calculated from Clausius-Clapeyron and Antoine equations (ΔH_{evap}=82.92 kJ/mol) (Shen and Alexander, 1999). This supports the fact that evaporation of lauric acid is occurring. As for the *logA*, our values seem to be slightly lower than the one reported by Shen and Alexander if min^{-1} units are assumed for *A*. However, the results cannot be compared since these authors do not give information about the corresponding units of *A*.

Table 1. Arrhenius parameters (E and logA) obtained by Shen and Alexander, 1999 and in this work by assuming a zero-order evaporation process for lauric acid under N_2 and air.

Ref.	*Atmosphere*	*E (kJ/mol)*	*logA*
Shen and Alexander, 1999	N_2	81.98	9.72 (-)
This work	N_2	83.10	8.96 (min^{-1}) or 7.18 (s^{-1})
This work	air	83.80	9.08 (min^{-1}) or 7.30 (s^{-1})

By using this method we also calculated the Arrhenius parameters for the dTG curve measured under both N_2 and air at β=1 ºC/min, the lowest heating rate in our set of experiments. In Fig. 2 (a) and (b) the corresponding linear plots of (eq. 4) are displayed for such rate together with the values of E and $logA$ (min^{-1}) obtained. As we can see, the linear fitting is very good for the curves measured under both atmospheres.

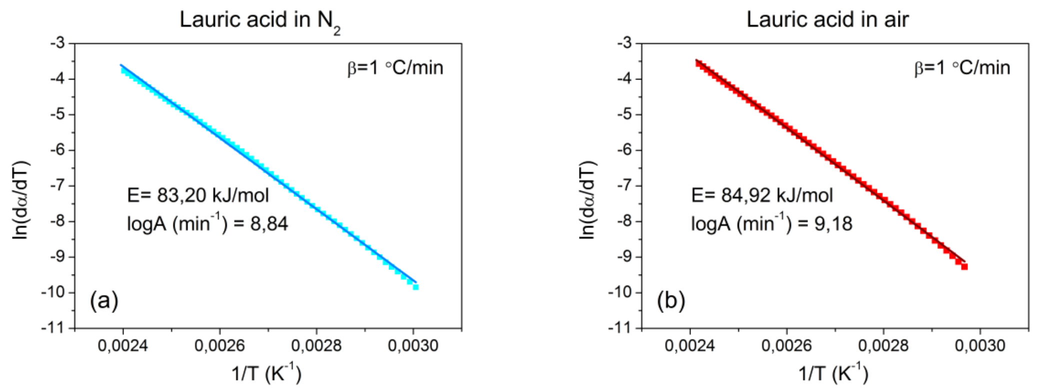

Fig. 2. Linear plot of (eq. 4) for dTG curve of lauric acid at β=1ºC/min under both N_2 (a) and air (b).

The dTG curves have been simulated with (eq. 2) by assuming a zero-order mechanism ($f(\alpha)$=1) and taking the Arrhenius parameters obtained for β=1 ºC/min. In Fig. 3 the resulting dTG curves have been compared with the experimental ones for lauric acid under N_2 at β=1 ºC/min and β=20 ºC/min (a) and under air at β=1 ºC/min and β=15 ºC/min (b). For both atmospheres we can see that the simulated dTG curves for low heating rates fit quite well the experimental data. However, for high heating rates, the simulated curves do not represent the thermal behavior of lauric acid. Hence, this indicates that in addition to vaporization, other degradation mechanisms are taking place when lauric acid is heated.

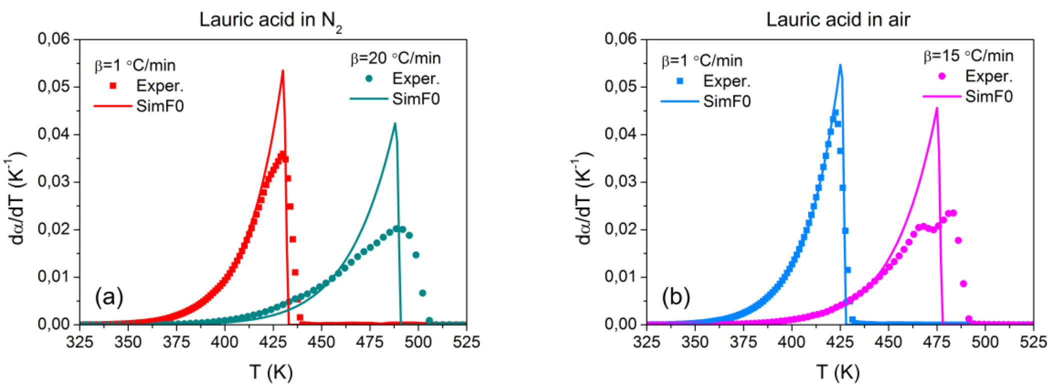

Fig. 3 Simulation of dTG curves for f(α)=1 and the Arrhenius parameters of Fig. 2 and comparison with the experimental data of lauric acid under N_2 at β= 1ºC/min and β= 20 ºC/min (a) and under air at β= 1ºC/min and β= 15 ºC/min (b).

In order to improve the kinetic analysis of TG measurements, a model-free isoconversional method was applied. This kind of methods allows estimating the activation energy as a function of α without choosing any model, $f(\alpha)$, for the reaction mechanism. The basic assumption of these methods is that the reaction rate at constant extent of conversion, α, depends only on temperature, so that constant E values can be expected. Some of the most accurate isoconversional methods (Coats and Redfern, 1964; Akahira and Sunose, 1971; Miura and Maki, 1998) are based on linear expressions like:

$$\ln\frac{\beta}{T^2} = Constant\ -\frac{E}{RT} \qquad \text{(eq. 5)}$$

From a set of TG curves obtained at different heating rates and taking the temperatures at which a certain degree of conversion occurs, the activation energy can be obtained from the slope of the linear plot of (eq. 5). Fig. 4 (a) shows $\ln(\beta/T^2)\ vs. 1/T$ plot and the corresponding linear fit for TG measurements of lauric acid under N_2 and air at α=0.5. By using the same procedure, the activation energy was calculated for other conversion values and the results are displayed in Fig. 4 (b) together with the E values obtained from the linear fits of Fig. 2. We can clearly see that E varies significantly with α not only for the case of lauric acid under N_2 but also for the case of air atmosphere. On the other hand, comparing with the E values obtained from the plot of (eq. 4) (see Fig. 2), strong differences are observed. For the case of lauric acid under N_2, as we move towards high conversion degrees, E values approach a constant value very close to the one obtained with (eq. 4) and hence to the evaporation enthalpy. Similar behavior was observed by other authors for caprylic acid (Arias et al., 2009). However, for the case of lauric acid under air, the variation of E with α not only does not approach a constant value but decreases almost linearly as conversion increases. Moreover, in Fig. 4 we can see that E is well below the value obtained from the plot of (eq. 4) for the case of lauric acid under air.

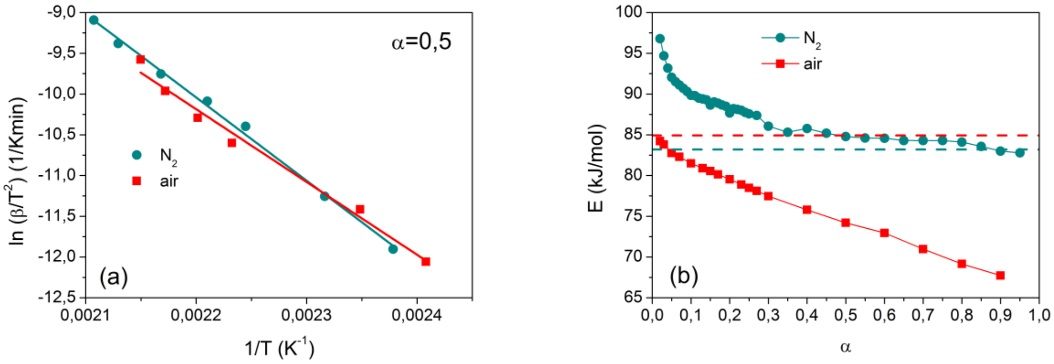

Fig. 4. ***ln(β/T²)*** **vs.** ***1/T*** **plot (a) and** ***E*** **vs** ***α*** **plot (b) for TG measurements under N_2 and air performed for lauric acid.**

The discrepancies in the results depending on the kinetic analysis method applied together with the variation of E with α, seem to indicate that a single-step reaction mechanism cannot be assumed for the thermal degradation of this acid. Actually, if we have a closer look to the dTG curves lauric acid under N_2 (Fig. 1(b)), we can see that they could be composed by two or more overlapped peaks. In our opinion, apart from evaporation, other additional reactions leading to volatile compounds may happen during the heating of lauric acid. Moreover, the fact that E values are lower in air than in N_2, seem to indicate that the presence of oxygen leads to different reactions that may accelerate the degradation process.

3.2. Deconvolution of dTG curves using Fraser-Suzuki functions

If a chemical reaction does not proceed in a single-step mechanism, a previous separation of the possible reaction processes should be carried out. A said above, this separation can be done by performing a deconvolution analysis of the dTG curves expressed in terms of conversion ($d\alpha/dT$) by means of Fraser-Suzuki (*FS*) functions. If these functions are used in normalized form (i.e. the area under the curve is equal to 1), we can assume that each curve corresponds to an independent single-step reaction mechanism. The normalized *FS* function has the following mathematical expression:

$$\frac{d\alpha}{dT} = \left[\frac{2}{w}\exp\left(-\frac{s^2}{4\ln 2}\right)\left(\frac{ln2}{\pi}\right)^{1/2}\right]\exp\left\{-\frac{ln2}{s^2}\left[\ln(1+2s\frac{T-p}{w})\right]^2\right\} \qquad \text{(eq. 6)}$$

It contains three parameters: the peak-maximum position, p, the half-height width, w, and the asymmetry factor, s. Deconvolution can be done with two or more FS_n curves, each one with a certain contribution factor, C_n, to the final curve. This means that, in addition to the three parameters of each curve, the contribution factors must be included in the fitting process to the experimental $d\alpha/dT$ curves, which can be calculated as:

$$\left[\frac{d\alpha}{dT}\right]_\beta = \sum_1^n C_i * FS_i\,(p_i, w_i, s_i) \;\; where \; \sum C_i = 1 \;\; and \;\; 0 < C_i < 1 \qquad \text{(eq. 7)}$$

If no restrictions are imposed to the parameters of (eq. 7), many combinations of FS_i and C_i may lead to good deconvolution results and it may happen that in the end it is not be possible to associate the obtained *FS* curves to any reaction mechanism. In order to overcome this issue, $d\alpha/dT$ curves were constructed from (eq. 2) for different reaction mechanisms (i.e., $f(\alpha)$ expressions) (Vyazovkin et al. 2011), various heating rates, β, and generic values of E and A. The resulting curves were fitted to the normalized Fraser-Suzuki function and the relationship between *FS* parameters (p, w and s) and the kinetic parameters ($f(\alpha)$, E, A and β) was analyzed. The details of this study are out of the scope of this paper and will be reported in another work still under preparation. The main conclusion of that study was that the asymmetry factor, *s*, depends only on the reaction mechanism, *f(α)*, remaining almost constant for any value of *E*, *A* and *β*. This means that specific values of *s* can be first checked for the FS_n functions used in the deconvolution in order to see which ones could lead to the best fitting. Moreover since we assume that each FS_n curve corresponds to a certain reaction mechanism, each curve should have not only the same *s* but also the same contribution factor C_n for all the heating velocities. This procedure requires the previous selection of a reaction mechanism through *f(α)* but it also reduces the freedom of the FS_n parameters and C_n making the deconvolution process more effective. The deconvolution of *dα/dT* curves was done with MATALB® software by using a self-made code.

The *dα/dT* curves of lauric acid measured under either N_2 or air, could be deconvolved by using only two *FS* curves. Different values of *s* were checked for each curve and it was concluded that the best fitting was achieved for s_1= -0.67 and s_2= between -0.35 and -0.38. The value of s_1 can be associated to a 1/2-order model (F05) while the values of s_2 can be associated to Avrami-Erofeev models (A2, A3 and A4) (Vyazovkin et al. 2011). In Table 2, the mathematical expressions of *f(α)* and *f'(α)* (to be used in Kissinger method) have been recorded together with the associated values of the *s* parameter in *FS* function.

Table 2. Mathematical expressions of *f(α)* and *f'(α)* with the associated values of s parameter of *FS* function.

Model ID	$f(\alpha)$	$f'(\alpha) = df(\alpha)/\alpha$	s
F05	$(1-\alpha)^{1/2}$	$-1/2(1-\alpha)^{-1/2}$	-0.67
An (2, 3, 4)	$n(1-\alpha)[-\ln(1-\alpha)]^{1/n}$	$-n[-\ln(1-\alpha)]^{(n-1)/n} + (n-1)[-\ln(1-\alpha)]^{-1/n2}$	[-0.35, -0.38]

The results of *dα/dT* curve deconvolution with two *FS* curves are displayed in Fig. 5 for lauric acid under N_2 at *β*= 1 ºC/min and 20 ºC/min (a) and under air at *β*= 2 ºC/min and 15 ºC/min (b). In N_2 atmosphere the contribution coefficients are 0.55 for FS_1 and 0.45 for FS_2 while, in air atmosphere, the contributions are 0.6 and 0.4 respectively. As we can see, the curves used in the deconvolution fit quite well the experimental *dα/dT* curves in the whole range of heating rates.

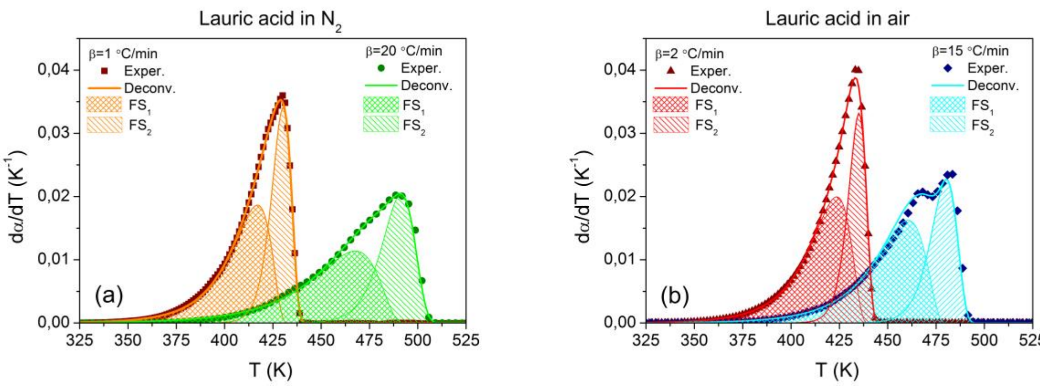

Fig. 5. Deconvolution results of *dα/dT* curves for lauric acid. Under N_2 at β= 1 ºC/min and 20 ºC/min (a) and under air at β= 2 ºC/min and 15 ºC/min (b).

3.3. Application of Kissinger method for calculating the Arrhenius parameters: *E* and log*A*

The *FS* curves resulting from the deconvolution process can be then treated as *dα/dT* curves associated to single-step reaction mechanisms. Moreover, since the deconvolution has been done by assuming some specific mechanisms, *f(α)*, the method of Kissinger (Kissinger, 1957) can be applied for obtaining the Arrhenius parameters. This method is derived from (eq. 1) under the condition of maximum reaction rate: $d^2\alpha/d\,t^2 = 0$ so that:

$$\frac{E\beta}{T_m^2} = -Af'(\alpha_m)e^{\left(\frac{-E}{RT_m}\right)} \qquad \text{(eq. 8)}$$

Where $f'(\alpha_m) = \left[\frac{df(\alpha)}{d\alpha}\right]_{T_m}$ and the subscript *m* denotes the values related to the maximum.

After simple rearrangement, (eq. 8) is transformed into the Kissinger equation:

$$\ln\left(\frac{\beta}{T_m^2}\right) = \ln\left[-\frac{AR}{E}f'(\alpha_m)\right] - \frac{E}{RT_m} \quad \text{(eq. 9)}$$

If the mathematical expression of $f(\alpha)$ is known, $f'(\alpha_m)$ can be calculated (see Table 2) and the frequency factor, A, obtained from the intercept of the liner plot since E is given by the slope. It must be pointed out that although it seems that the left hand terms of (eq. 5) and (eq. 9) are the same, they are not because they are derived from different assumptions. Actually the Kissinger method yields a reliable estimation of E only if α_m does not vary significantly with β. This happens for many reaction models (Braun and Burnham, 1987; Cheng et al., 1993) but not for all models. Hence the independence of α_m with β has to be checked before applying this method. In our case, α_m remained constant for all the values of β for both sets of FS curves (see Table 3), so that we could apply the Kissinger method for obtaining the Arrhenius parameters of each single-step reaction mechanism.

The Kissinger plots of both FS_1 and FS_2 sets of curves for lauric acid under N_2 and air are displayed Fig. 6 (a) and (b) respectively. From the slope of the linear plots, E was calculated for each single-step reaction mechanism. For calculating the pre-exponential factor, A, from the intercept of the linear fit, the $f'(\alpha)$ associated to the expected reaction mechanism must be taken. For the case of FS_2 curves, the $f'(\alpha)$ associated to three Avrami-Erofeev mechanisms were checked and the corresponding A values were calculated. In order to determine which Avrami-Erofeev mechanism was the most appropriate, $d\alpha/dT$ curves were simulated for each of them using (eq. 2) and the Arrhenius parameters obtained with Kissinger method. These curves were compared with the FS_2 curves so that the most appropriate mechanism could be established. In the end the Avrami-Erofeev mechanism that better fitter FS_2 set of curves was the A3 for the case of lauric acid under N_2 and the A4 for the case of lauric acid under air (see Table 3).

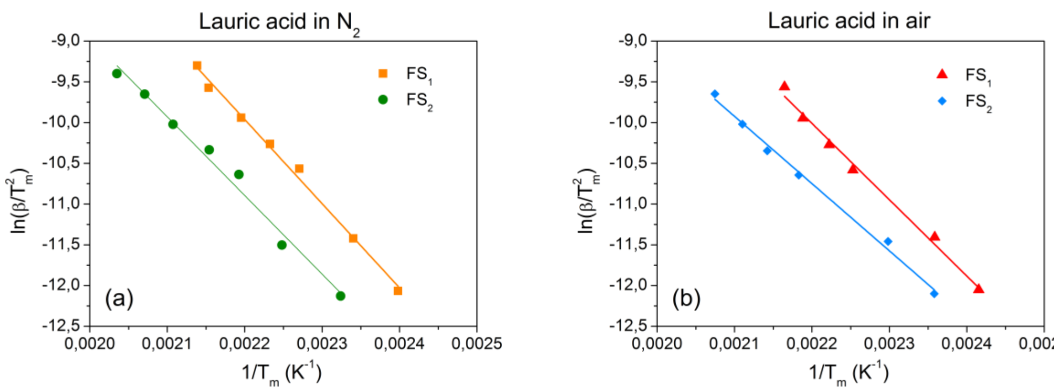

Fig. 6. Kissinger plots of the FS curves obtained in the deconvolution of experimental dα/dT curves for lauric acid under N_2 (a) and air (b) atmospheres.

Once the kind of Avrami-Erofeev model was identified, both deconvolutions and Kissinger plots were further refined. The final values of the Arrhenius parameters E and $logA$ (min^{-1}) are the ones recorded in Table 3. In terms of activation energy, the values obtained with the Kissinger method are in the range of the ones displayed in the E vs. α plots of Fig. 4 (b), being lower for lauric acid under air than for lauric acid under N_2.

Table 3. Contribution coefficient and Arrhenius parameters obtained by Kissinger method for the two reaction mechanisms proposed for the thermal degradation of lauric acid under N_2 and under air.

Atmosphere	FS_n curve	C_n	Model ID	E (kJ/mol)	α_m	$logA$ (min^{-1})
N_2	FS_1	0.55	F05	85.9±1	0.715	9.59
N_2	FS_2	0.45	A3	80.2±1	0.620	8.51
air	FS_1	0.6	F05	77.8 ±1	0.715	8.60
air	FS_2	0.4	A4	68.6±1	0.620	7.15

In principle, the F05 mechanisms identified in the thermal degradation of lauric acid for FS_1 could be associated to the evaporation process, since $d\alpha/dT$ curves calculated with (eq. 2) for both zero-order and 1/2-order mechanism with the same Arrhenius parameters are quite coincident in the temperature range below the maximum rate. As for the activation energies recorded in Table 3 associated to the F05 mechanism, they are both different from the values obtained from the plot of (eq. 4). However, if we take into account that 10% error in the activation energy is quite reasonable in any kinetic analysis (Vyazovkin et al. 2011), we can assume that FS_1 curves can be associated to the evaporation of lauric acid which can be represented by a 1/2-order mechanism with E=83±8 kJ/mol. In order to support this assumption, $d\alpha/dT$ curves were constructed by using (eq. 2) for 1/2-order mechanism, $f(\alpha) = (1-\alpha)^{1/2}$, with the Arrhenius parameters recorded in Table 3 for both N_2 and air atmospheres at various heating rates and then fitted to single *FS* functions. The variation of the parameter p (i. e. peak-maximum position) with the heating rate, β, for both atmospheres is displayed in Fig. 7. The values of p parameter corresponding to the FS_1 curves resulting from the deconvolution of the experimental $d\alpha/dT$ curves have been included as well. As we can observe, the values of p are not very different for the F05 curves simulated with the Arrhenius parameters either for the case of N_2 or for the case of air. Moreover the p values of the FS_1 curves resulting from the deconvolution process are also very close the values obtained for the simulated F05 curves.

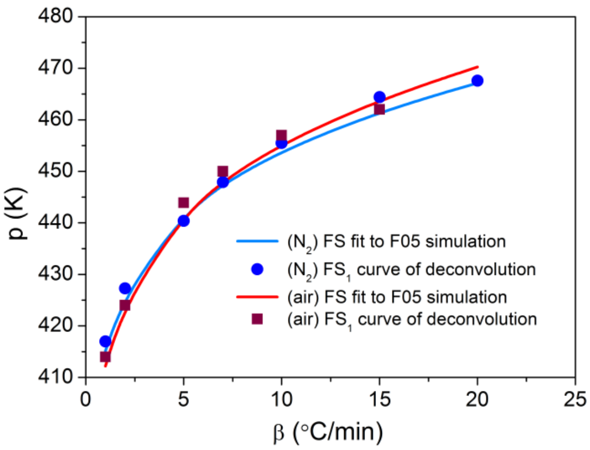

Fig. 7. Plot of p vs. β for FS curves resulting from the fitting of F05 curves and the deconvolution of experimental $d\alpha/dT$ curves of lauric acid under N_2 and air.

For the case of FS_2 curves, Avrami-Erofeev mechanism (A3) is associated to three dimensional nucleation processes and the A4 to a four dimensional nucleation. Since we do not have information about the reaction products we cannot propose possible reactions processes that can be related to any Avrami-Erofeev mechanism. In order to elucidate the reactions that my occur during thermal degradation of lauric acid, TG measurements with the analysis of the evolved gases would be required, especially in the case of the measurements under air since this is the most conventional atmosphere in which PCM operate when they are implemented in latent heat storage modules.

3.3. Construction of α vs. T curves

Once the kinetic triplet is determined, (eq. 3) can be used for constructing the α vs. T curves at different heating velocities and comparing them with the experimental TG curves. In Fig. 8 some of these curves are displayed for the case of lauric acid under N_2 (a) (β=1, 5, 20 ºC/min) and under air (b) (β=2, 5, 15 ºC/min). In both cases we can see that the calculated curves fit very well the experimental curves for all the heating velocities.

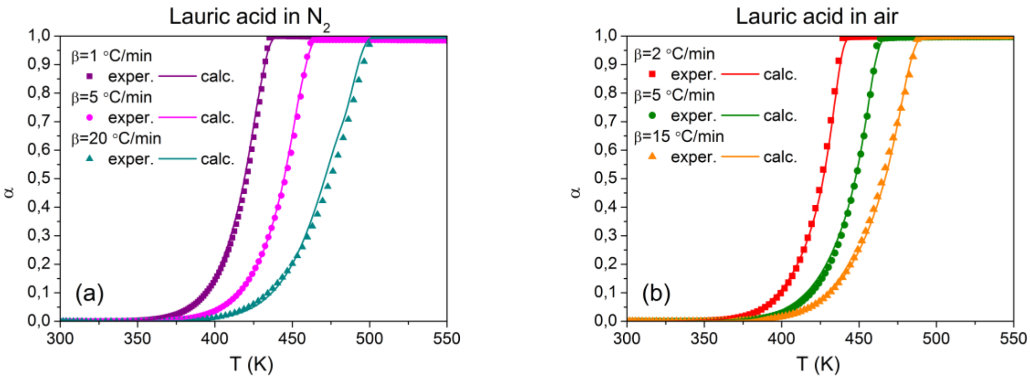

Fig. 8. Calculated α vs. T curves for lauric acid under N_2 (a) and air (b) at various heating velocities, β. Comparison with the experimental TG curves expressed in terms of α.

3.4. Construction of the isothermal degradation curves

Isothermal degradation or ageing time curves can be constructed by rearranging (eq. 1) and integrating at constant temperature:

$$\int_0^t dt = \frac{1}{Ae^{\left(\frac{-E}{RT}\right)}} \int_0^\alpha \frac{d\alpha}{f(\alpha)} \qquad \text{(eq. 10)}$$

$$t = \frac{g(\alpha)}{Ae^{\left(\frac{-E}{RT}\right)}} \qquad \text{(eq. 11)}$$

Hence from the expression of the *g(α)* function we can obtain the relationship between the ageing time, *t*, and the corresponding conversion, *α*. Here, *g(α)* is a combination of two independent mechanisms, each of them with their corresponding Arrhenius parameters and contribution to the whole conversion. Therefore the curve of (eq. 11) must also contain the contribution of the independent mechanisms. The *g(α)* expressions associated to the mechanisms proposed for the thermal degradation of lauric acid are displayed in Table 4.

Table 4. Mathematical expressions of *g(α)* for the reaction mechanisms proposed for lauric acid thermal degradation.

Model ID	$g(\alpha)$
F05	$\frac{1-(1-\alpha)^{0.5}}{0.5}$
A3	$[-\ln(1-\alpha)]^{1/3}$
A4	$[-\ln(1-\alpha)]^{1/4}$

The isothermal degradation curves calculated for lauric acid under N_2 and under air at both 50ºC (T_m+5 ºC) and 55 ºC (T_m+10 ºC) are displayed in Fig. 9. As we can see, lauric acid degrades faster under air than under N_2, which is not surprising since the activation energies for this acid in air are lower. However, according to these curves, even if lauric acid is kept under N_2 at 50 ºC (i.e., 5 ºC above the melting temperature), its mass should have disappeared from the container in less than one month. In order to check these predictions, some preliminary isothermal tests with samples in the range of grams have been performed in an oven at 50ºC under air and no variation of sample mass has been observed for several weeks. Actually since evaporation (and gas emission) is a surface phenomenon, it is reasonable to assume that the rate of loss of molecules from a given volume is not only proportional to the sample mass but also to the molecules exposed on the surface (Penner, 1952). Hence, if sample mass is very low and vapor molecules are removed by a carrier, which is the case of TG measurements that are always performed under a gas flow, evaporation and gas emission processes will be faster and so will be the mass loss. This indicates that the kinetic analysis of TG measurements must be complemented with experiments inside an oven under isothermal conditions with samples of larger mass. This should allow extrapolating the degradation processes to the real operation conditions and hence obtaining more reliable isothermal degradation curves.

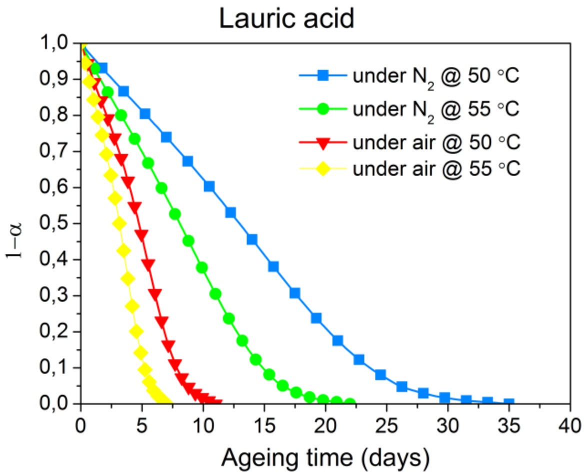

Fig. 9. Isothermal degradation curves for lauric acid under N_2 and under air at both 50ºC (T_m+5 ºC) and 55 ºC (T_m+10 ºC).

4. Conclusions and future actions

In this work, the kinetic analysis of TG measurements under both N_2 and air atmospheres has been carried out for lauric acid, a straight-chain fatty acid normally used as a PCM for latent heat storage in low temperature applications. In a first approach, Arrhenius parameters were calculated assuming a zero-order evaporation process with the resulting activation energy very close to the evaporation enthalpy. However the experimental $d\alpha/dT$ curves could not be simulated by only considering the evaporation of lauric acid. By using a model-free isoconversional method we found that the activation energy varied significantly with the conversion so that a multi-step processes should be assumed for lauric acid thermal degradation. From a deconvolution analysis of $d\alpha/dT$ curves two single-step reaction mechanisms could be proposed. One of the mechanisms was associated to the evaporation since its activation energy was within 10% error range of the evaporation enthalpy. The other mechanism could be related to the evolution of volatile compounds but the corresponding reaction paths are still undetermined. Since the activation energy value of this second mechanism was lower when lauric acid was heated up in air, it is very likely that O_2 is involved in the process. According to the isothermal degradation curves, it is expected that lauric acid totally disappears after 30 days when kept under N_2 at 5 ºC above its melting temperature. However, the long-term non-stability of lauric acid cannot be confirmed yet since some preliminary isothermal experiments inside an oven have shown that it does not behave as predicted by these curves. As part of future actions, we can say that the kinetic analysis would be improved if evolved gases were analyzed since this would help identifying which reactions are taking place apart from evaporation. Moreover chemical changes without gas emission could happen as well. Keeping in mind that assessing the long-term stability is our goal, isothermal experiments in oven with larger amounts of sample are necessary for obtaining isothermal degradation curves that are more reliable and representative of the degradation processes occurring under real operation conditions. The same kind of kinetic analysis should be carried out for the rest of fatty acids we have considered as PCM for latent heat storage in low-temperature applications.

5. Acknowledgments

This work has been supported by Comunidad de Madrid and European Structural Funds through ACES2030 Project (S2018/EM-4319) and by European Union's Horizon H2020 Research and Innovation Programme through SFERA III Project (GA Nº 823802).

6. References

Arias, S., Prieto, M. M., Ramajo, R., Espina, A., García, J. R., 2009. Model free kinetics applied to the evaporation of caprylic acid. J. Therm. Anal. Calorim. 98, 457-462.

Akahira, T., Sunose, T., 1971. Method of determining activation deterioration constant of electrical insulating materials. Res. Report Chiba Inst. Technol. (Sci. Technol.) 16, 22–31.

Bayón, R., Rojas, E., 2019. Development of a new methodology for validating thermal storage media: Application to phase change materials. Int. J. Energy Res. 43, 6521-6541.

Braun, R. L., Burnham, A. K., 1987. Analysis of chemical reaction kinetics using a distribution of activation energies and simpler models. Energy Fuels 1, 153-161.

Cheng, D., Gao, X., Dollimore, D., 1993. A generalized from of the Kissinger equation. Thermochim. Acta 215, 109-117.

Cheng, Z., Wu, W., Ji, P., Zhou, X., Liu, R., Cai, J., 2015. Applicatility of Fraser-Suzuki function in kinetic analysis of DAEM processes and lingnocellulosic biomass pyrolysis process. J. Therm. Anal. .Calorim. 119, 1429-1438.

Coats, W., Redfern, J. P., 1964. Kinetic parameters from thermogravimetric data. Nature 201, 68.

Doyle, C. C., 1961. Kinetic analysis of thermogravimetric data. J. Appl. Polym. Sci. 5 (15), 285-292.

Fraser, R. D. B., Suzuki, E., 1969. Resolution of overlapping bands: functions for simulating band shapes. Anal. Chem. 41(1), 37-39.

Güneş, M., Güneş, S., 1999. The influences of various parameters on the numerical solution of nonisothermal DAEM equation. Thermochim. Acta 336, 73-96.

Kahwaji, S., Johnson, M. B., Kheirabadi, A. C., Groulx, D., White, M. A., 2017. Fatty acids and related phase change materials for reliable thermal energy storage at moderate temperatures. Sol. Energy Mater. Sol. Cells. 167, 109-120.

Kissinger, H. E,, 1957. Reaction kinetics in differential thermal analyisis. Anal. Chem. 29, 1702-1706.

Miura, K., Maki, T., 1998. A simple method for estimating f(E) and k0(E) in the distributed activation energy model. Energy Fuels 12(5), 864-869.

Órfão, J., 2007 Review and evaluation of the approximations to the temperature integral. AICHE J. 31 (11), 2905-2915.

Penner, S. S., 1952. On the kinetics of evaporation. J. Phys. Chem. 56(4), 475-479

Perejón, A., Sáncez-Jiménez, P. E., Criado J. M., Pérz-Maqueda, L. A., 2011. Kinetica of complex solid-state reactions. A new deconvolution procedure. J. Phys. Chem. B 115, 1780-1791.

Rusch, P. F., Lelieur, J. P., 1973. Analytical moments of skewed gaussian distribution functions. Anal. Chem. 45(8), 1541-1543.

Shen, L., Alexander, K. S., 1999. A thermal analysis of long chain fatty acids. Thermochim. Acta 340-341, 271-278.

Stankovic, B., Jovanovic, J., Adnadjevic, B., 2018. Application of the Suzuki–Fraser function in modelling the non-isothermal dehydroxylation kinetics of fullerol. React. Kinet. Mech. Cat. 123 (2), 421-438.

Vyazovkin, S., Burnham, A. K.,Criado, J. M., Pérez-Maqueda, L. A., Popescu, C., Sbirrazzouli, N., 2011. ICTAC Kinetics Committee recommendations for performing kinetic computations on thermal analysis data. Thermochim. Acta 520, 1-19.

Vyazovkin, S., Burnham, A. K., Favergeon, L., Koga, N., Moukhina, E., Pérez-Maqueda, L. A., Sbirrazzouli, N., 2020. ICTAC Kinetics Committee recommendations for analysis of multi-step kinetics. Thermochim. Acta 689, 178597

Desorption characteristics of a lab-scale tube-bundle heat and mass transfer unit

Xavier Daguenet[1], Loris Laib[1], Paul Gantenbein[1], Fabio Lichtensteiger[1] and Andreas Haeberle[1]

[1]SPF Institute for Solar Technology, HSR University of Applied Sciences Rapperswil, Rapperswil (Switzerland)

Abstract

Thermal energy storages tackle the load shift and can balance the availability of supply and demand. Types of storages are sensible, latent and thermo-chemical. The selection of the storage materials – and thus the storage type - is one of the key tasks and depends on the time length of energy storage as well as on power and capacity demand. Because of their high potential energy density and thus their low volume, absorption storages are under investigation. Regarding their heat and mass transfer coefficient for charging and discharging, tube-bundles are an option to form falling films and keep the flexibility of multiuse as absorber, desorber, evaporator and condenser. In this paper, the application of a tube-bundle heat and mass exchangers (HMX) and its characteristics in the charging process step for liquid sorbate i.e. desorption of water (vapor) is presented. The sorbent-sorbate combination is aqueous sodium hydroxide and a concentration difference of 20 wt.% is aimed to reach a high energy storage density. The characterization of different HMX versions in desorption modus are presented in this paper. Even if the best performing HMX versions are not the same in absorption and in desorption modus, it was found that some adaptations could lead to a HMX working decently in both modus.

Keywords: Sorption thermal storage, desorption, tube-bundle, heat and mass transfer.

1. Introduction

Storing energy is essential in energy systems to equalize demand and supply or for power peak cutting. The shift load can be from short term up to long-term of seasons (from summer to winter). With the restriction of low available room – or the prerequisite of using as low volume for the storage unit as possible and as much as needed – thermo-chemical materials are favored. This is because of the potential high volumetric energy storage density (N'Tsoukpoe et al. 2009). In addition, the energy storage is loss less as long the system is not in operation. Absorption based thermal energy storages are widely under research with one focus of long-term i.e. seasonal application (IEA SHC Task 58 ECES Annex 33). One key component of the absorption storage is the power unit, which operates under sub-atmospheric pressure conditions. Tube-bundles used in the power unit as heat and mass exchangers keep the flexibility of multiuse as absorber, desorber, evaporator and condenser (Thome n.d.; Daguenet-Frick et al. 2015). In the proposed paper we present experimental results of the desorption process step i.e. the charging of the storage with aqueous sodium lye as the sorbent and water vapor as the sorbate.

2. Laboratory test rig and investigated HMX

To assess different kind of HMX, a 1 kW closed sorption thermal energy storage system was engineered and in-house built at SPF (Daguenet-Frick et al. 2018). This laboratory test rig is shown on Fig. 1. Associated is a CAD view of the facility with description of its main components as well as the fluid flow paths.

doi:10.18086/eurosun.2020.07.11 Available at http://proceedings.ises.org

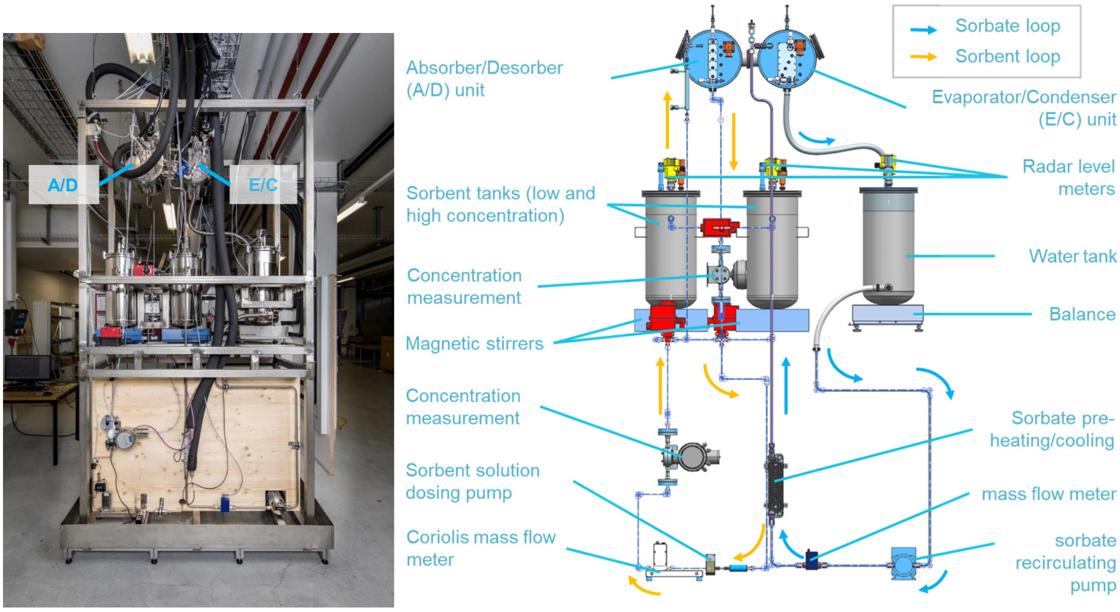

Fig.1: Picture of the laboratory test rig at SPF (left) and associated components description as well as fluid flow paths (CAD view, right).

On Fig. 2, an exploded view, the Absorber/Desorber (A/D) can be distinguished from the Evaporator/Condenser (E/C) HMX. To avoid limitations, this E/C unit was designed large enough, with an active length of the heat and mass exchanger of 300 mm, and to have the A/D as the object of investigation.

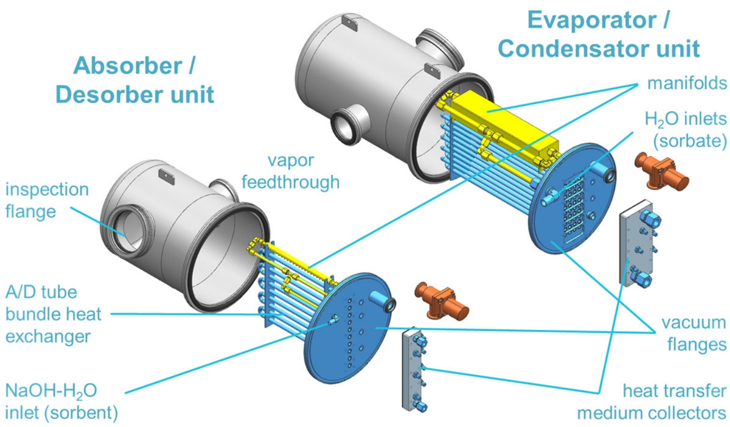

Fig. 2: Detailed view of the A/D and E/C units as well as the smooth heat exchanger tube bundles (exploded CAD view).

For the A/D HMX, different tube designs were used in the experiments, to compare the influence of the enlarged heat exchanger area on the wetting performance. In fact, the wetting behavior of the tube is strongly influenced by the sorbent surface tension, tube surface structure and material. A structured tube surface is favored to increase the interface of the falling liquid sorbent to the sorbate vapor for a high mass transfer rate in the future HMX of the power unit. These HMX serve as absorber and desorber in the lab-scale test rig operating with NaOH-H_2O as sorbent. Tube-bundles with different tube surface structures were retained and implemented in the HMX design as pointed out by Fig. 3. Smooth surface tube bundle (6 and 10 tubes) constitute the reference HMX. These references HMX are compared to a ten-tube textured surface HMX as well as to two six-tube HMX whose tubes are wrapped by a metallic mesh. Two versions of this mesh-wrapped HMX were designed and manufactured (Fig. 3, right).

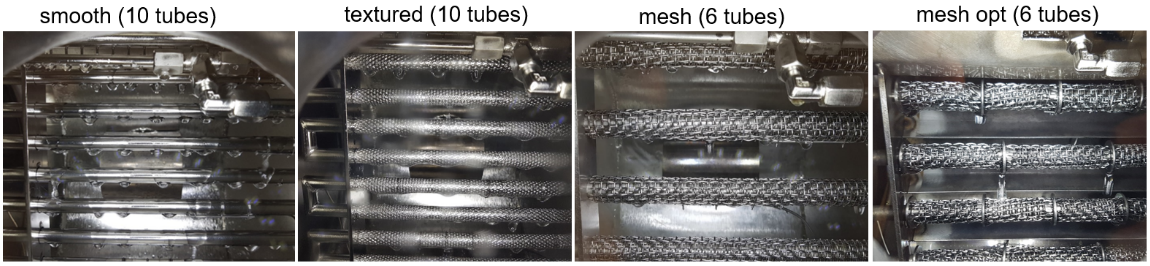

Fig. 3: Tube-bundle types in the power unit of the lab-scale energy storage setup.

In Fig. 4 the HMX second version for optimized absorption process (the limiting process), is shown in detail. Thanks to CCD imaging technologies applied to the former measurement campaigns, wetting aspects were considered for its design:

- Circular washers are placed on the tubes, displaced from one tube row to the next underneath and at equal distances. This arrangement is chosen to enable a good fluid distribution all over the tube bundle. In fact, without washers, a fluid coalescence to liquid sorbent columns were noticed, leading to a bad sorbent distribution on the tubes and thus to lower heat and mass exchanges on the bottom tubes of the HMX.
- Bended washers were placed at the outer (left and right) end of the tubes to avoid sodium hydroxide to flow along the HMX left and right (reinforcement) baffles.
- Deflectors were added to limit the fluid losses during the desorption process. In fact, the metallic mesh enables to enhance the fluid/gas contact area during the absorption process. But during the desorption process it retains the liquid sodium hydroxide close to the tube surface due to the capillarity effects of the mesh – leading to a higher "artificial" hydrostatic pressure. This leads to a higher necessary boiling temperature (vapor pressure) for evaporation on the tube and the triggering of a sparkling phenomenon (local overheating). The sparkling is linked to fluid losses and thus to bad desorption performances.
- The temperature difference (varying between 19 K and 55 K) between the HTF (Heat Transfer Fluid) temperature at the inlet of the absorber ($T_{iad}(1)$) and the condenser ($T_{iec}(1)$) as well as the sodium lye volume flow rate (36 ml/min and 67 ml/min) were used as the main independent variables.

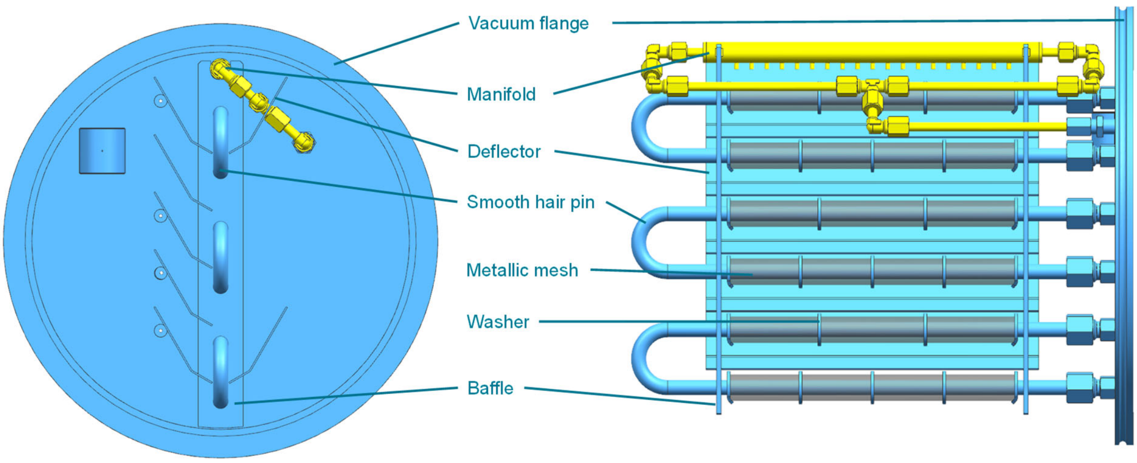

Fig. 4: CAD back- (left) and side- (right) view of the optimized six-tube HMX with washers and deflectors.

For an optical monitoring of the sodium hydroxide flow pattern, three deflectors were removed on the right side of the HMX (Fig. 3, left). For the side view (Fig. 3 right), all deflectors on the right side were hide from the drawing to simplify the understanding.

3. Results

From a series of measurements that were carried out, results of the desorption process (the storage charging) are presented in this section. For all desorption experiments the sodium hydroxide enters through a manifold, is evenly distributed on the tube bundle and has an initial concentration of 30 wt.% (NaOH in the aqueous lye). During the desorption process, water is evaporated out of the sorbent sodium hydroxide falling along the HMX tube bundle and the concentration is increased. The temperature difference between the A/D and E/C unit constitutes the one independent variable of the desorption process, as it causes a pressure difference - driving force - leading to the vapour transport from the desorber to the condenser unit. The lye volume flow rate was used as the second independent variable.

Fig. 5 depicts the influence of this temperature difference for different HMX geometries on the effective exchanged power Φ (measured on the HTF side, left graph) as well as on the concentration difference between the outlet and the inlet of the desorber (Fig. 4, right). For this measurement campaigns, the inlet HTF temperature of the A/D HMX $T_{iad}(1)$ varies between 43 °C and 80 °C. The other parameters are taken constant: inlet sodium hydroxide concentration *wtad(11)* = 30 wt.%, inlet sodium hydroxide volume flow rate *vead* = 67 ml/min, heat transfer fluid (HTF) volume flow rate on the desorber side *viad* = 85 l/h, water recirculation flow rate on the condenser side *veec* = 100 l/h, HTF volume flow rate on the condenser side *viec* = 200 l/h and associated inlet temperature $T_{iec}(1)$ = 25 °C.

Generally, the power exchanged during the desorption process increases with increasing temperature difference between the (unified) absorber-desorber (A/D) and (unified) evaporator-condenser (E/C) unit. This behaviour is contrary to the results of the absorption measurements where the driving force of the process (the pressure difference) decreases by higher temperature differences.

As a first conclusion, the HMX with textured tubes performs significantly better (in terms of exchanged power as well as concentration difference) than the smooth reference HMX in both desorption and absorption modus. However, with the higher inlet sodium hydroxide volume flow rate of 67 ml/min, a concentration difference of maximum 10 wt.% was reached with the textured tubes and by a temperature difference of 55 K). This is only half of the aimed concentration difference of 20 wt.%. In the desorption modus, the geometries with meshes had a lower performance than the reference HMX. In fact, these meshed geometries were optimised for the absorption modus. However, the performances of the optimised mesh geometry HMX are significantly improved (about 10 %) in comparison to the initial mesh HMX. This effect is attributed to the deflectors, which limit the losses of sodium hydroxide due to the sparkling phenomenon described in former paragraph.

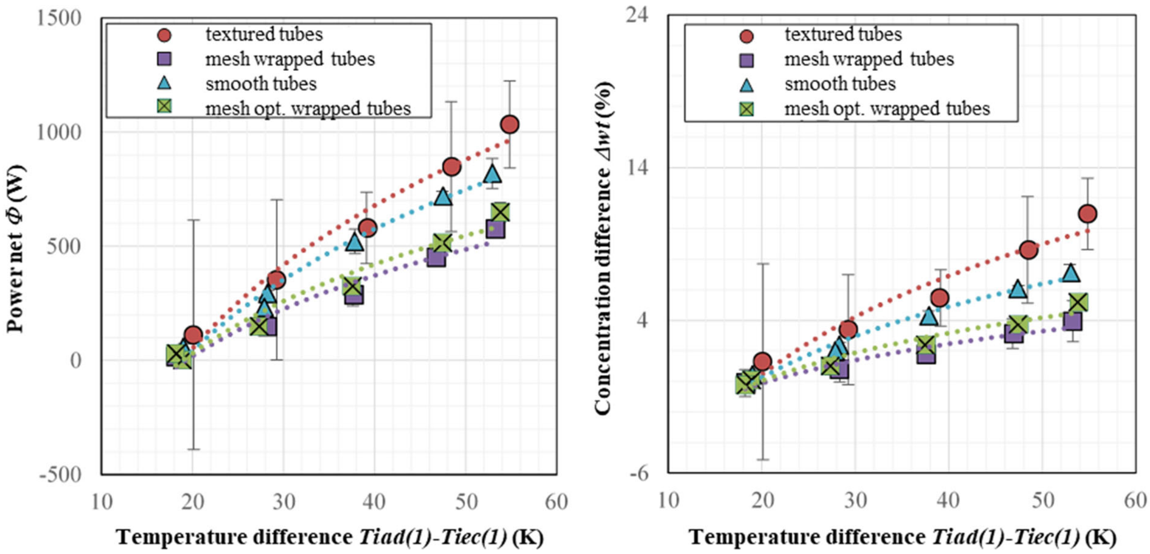

Fig. 5: Power Φ (W) and concentration difference Δwt (%) in function of the temperature difference between the desorber and the condenser unit for different kind of desorber HMX.

Figure 5 shows the influence of the sodium hydroxide volume flow rates (36 compared to 67 ml/min). The desorption power Φ (left) and the absolute difference in sodium lye concentration Δwt (right) are plotted in function of the desorber to condenser temperature difference (triangle dots for *vead* = 36 mL/min, square dots for *vead* = 67 mL/min) for the smooth reference HMX as well as for the optimised mesh HMX. As for the former measurement campaign, the temperature of the cooling circuit (condenser) was kept constant at 25 °C whereas the temperature of the heating circuit (HTF inside the tubes of the desorber) was stepwise increased from 43 °C to 80 °C.

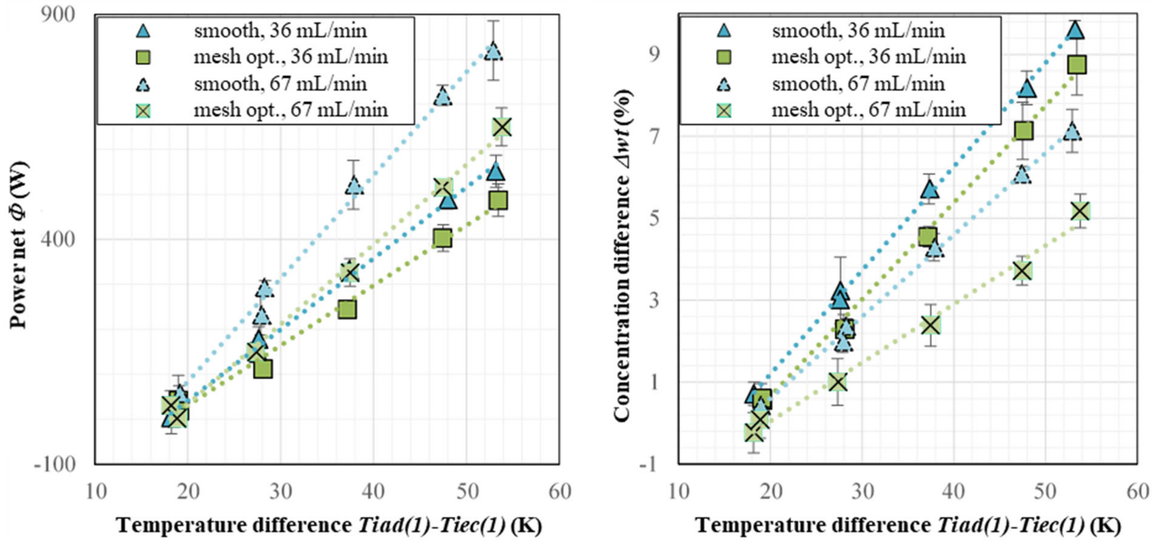

Fig. 6: Power Φ (W) and concentration difference Δwt (wt.%) in function of the temperature difference between the desorber and the condenser unit for two sodium hydroxide mass flow rates *vead* as well as for smooth and optimized desorber HMX.

If the sodium hydroxide volume flow is increased a higher desorption power can be measured. However, at low temperature differences, the desorption power does not increase much with the higher flow as in this case the pressure difference seems to limit the desorption power. Furthermore, for a given temperature difference, a lower sodium hydroxide volume flow rate enables to increase the concentration difference between the inlet and the outlet of the HMX. This enhancement is quite significant for the optimised mesh HMX (more than 50 % of relative improvement) than for the smooth HMX (about 20 % compared to smooth tubes without mesh). In a same way, the sodium hydroxide volume flow has less influence on the optimised mesh HMX than on the smooth one. The explanation for both phenomenon is certainly that the surface wetting as well as the fluid distribution are better (and less dependent on the volume flow rate) for the optimised mesh HMX than for the smooth one.

As a summary of this part, it was shown that, even if the component is optimised for the absorption process, some behaviours concerning the HMX operation are similar in the absorption and in the desorption process (wetting and fluid distribution for example). Furthermore, by taking into account some behaviours specific to the desorption process (sparkling phenomenon for example), the HMX can be optimised to get good performances in both absorption and desorption modes as a compromise.

4. Post processing

In order to figure out the heat losses of such a seasonal storage, it was decided to calculate from the measurements its efficiency in both absorption and desorption modus. In fact, contrary to regular storages, for this kind of storage the losses are not spread over time (the educts are stored and can be maintained indefinitely without losses) but occur during the conversion processes. For the desorption process, the simplified efficiency is calculated as given by eq. 1:

$$\eta_{simplified,desorption} = \frac{\Phi_{net} - \Phi_{DT}}{\Phi_{net}} \qquad \text{(eq. 1)}$$

with Φ_{net} the net power matching with the power delivered by the desorber to the HTF and Φ_{DT} matching with the power that is lost due to the preheating (temperature rise) of the sodium hydroxide within the A/D HMX. Part of this energy may be gained by adding a recovery heat exchanger to the system (preheating of the sodium hydroxide entering the absorber/desorber).

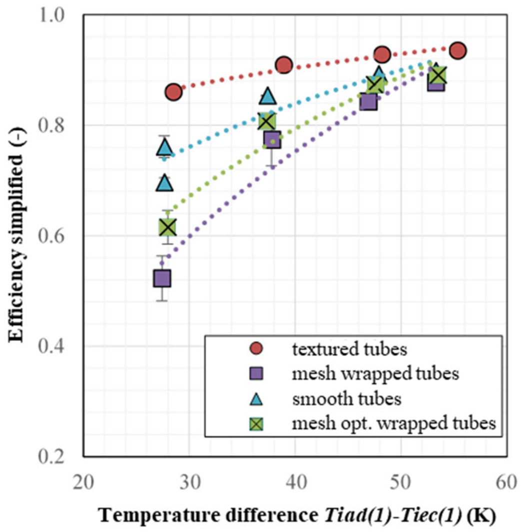

Fig. 7: Efficiency of the desorption process at *vead* = 36 ml/min of sodium hydroxide volume flow.

Fig. 7 depicts the evolution of the efficiency of the desorption at a sodium hydroxide volume flow rate of 36 mL/min for different temperature differences and various HMX design units. At low temperature differences (inlet HTF temperature of the A/D HMX $T_{iad}(1)$ of about 55 °C), the HMX with textured tubes performs the best followed by the reference HMX with smooth tubes and then the optimized mesh version (itself better than the standard mesh HMX). Nevertheless, at higher temperature (inlet HTF temperature of the A/D HMX $T_{iad}(1)$ higher than 70 °C) - which will also be the working boundary conditions as high concentration differences are pursued as seen in previous section - the differences are narrowing and the efficiency of all HMX is about 90 %.

By combining the efficiency of both absorption and desorption processes, an overall efficiency in the range of 80 % can be expected. This efficiency, already quite high, has surely potential to be increased: additional heat recovery exchanger, better ratio exchanged energy (proportional to the unit volume) vs. heat losses (proportional to the unit surface) for installation larger than 1 kW, possible improvement of the insulation…

5. Conclusion and Outlook

As a conclusion, thermal energy storage tackles a load shifting i.e. the mismatch of energy supply and demand. To fulfil this task, absorption storages are envisaged to be an high energy density alternative to sensible storages. In fact, apart from the operation (conversion process has a given efficiency) absorption storage are loss less as long as they are not in operation. With chosen design, an overall efficiency of at least 80 % can be expected. De facto, tube-bundles for falling film formation keep the simplicity and flexibility to be used in the thermal energy storage power unit, enabling to combine the desorber and the absorber function in a same physical component. A further development and improvement (additive manufacturing for example) is necessary to reach the aimed concentration difference. The combination of the absorption and desorption process steps will enable to save costs and space for the commercial version of the thermochemical heat storage.

6. Acknowledgments

We gratefully acknowledge the support from the Swiss Federal Office of Energy (SFOE) as well as the support from Innosuisse – Swiss Innovation Agency in the frame of the Swiss Competence Center for Energy Research.

7. References

Daguenet-Frick, X., Dudita, M., Omlin, L. & Gantenbein, P., 2018. Seasonal Thermal Energy Storage with Aqueous Sodium Hydroxide – Development and Measurements on the Heat and Mass Exchangers. Energy Procedia, 155, p.286–294.

Daguenet-Frick, X., Gantenbein, P., Frank, E., Fumey, B. & Weber, R., 2015. Development of a numerical model for the reaction zone design of an aqueous sodium hydroxide seasonal thermal energy storage. Solar Energy, 121, p.17–30.
N'Tsoukpoe, K.E., Liu, H., Le Pierrès, N. & Luo, L., 2009. A review on long-term sorption solar energy storage. Renewable and Sustainable Energy Reviews, 13(9), p.2385–2396.
Thome, J.R., Wolverine Engineering Data Book III, 2010th ed. Wolverine Tube, inc.

Appendix: Abbreviations and symbols

Table 1: Table of abbreviations and symbols

Quantity	Symbol	Unit
absorber/desorber	*A/D*	-
charge-coupled device	*CCD*	-
computer-aided design	*CAD*	-
concentration difference	Δwt	wt.%
efficiency	η	-
evaporator/condenser	*E/C*	-
heat and mass exchanger	*HMX*	-
heat transfer fluid	*HTF*	-
HTF volume flow rate in the A/D HMX	*viad*	l/h
inlet HTF temperature of the A/D HMX	$T_{iad}(1)$	°C
inlet HTF temperature of the E/C HMX	$T_{iec}(1)$	°C
inlet sodium hydroxide concentration	*wtad(11)*	wt.%
inlet sodium hydroxide volume flow rate	*vead*	l/h
net power	Φ_{net}	W
optimised	*opt.*	-
power	Φ	W
power linked with the fluid preheating	Φ_{DT}	W
temperature difference (independent parameter)	$T_{iad}(1)\text{-}T_{iec}(1)$	K
HTF volume flow rate in the E/C HMX	*viec*	l/h
water recirculation flow rate in the E/C HMX	*veec*	l/h

08. Testing & Certification

Soiling Effect in a Central Receiver Solar Plant under Real Outdoor Conditions

Alejandro Martinez[1], Iván Bravo[1], Ricardo Conceição[1,2], José González-Aguilar[1] and Manuel Romero[1]

[1] High Temperature Processes Unit, IMDEA Energy, Móstoles (Spain)

[2] Institute of Earth Sciences, Évora (Portugal)

Abstract

Reflectance loss is assessed on heliostats of the very-high concentration solar tower facility located in Móstoles, near Madrid, Spain. This region is characterized by an annual direct normal irradiance availability around 1,900 kWh/m^2, which makes it economic viable for concentrating solar power (CSP) plants. Moreover, its location nearby a highly populated area and one of the busiest highways in Spain, introduces additional features relevant in soiling analyses. The reflectance loss was measured with a Condor reflectometer on thirteen single-facet heliostats, in which nine of them are in different locations of the solar field and tilted 10º south, while four of them are side by side with different tilt angles, also turned in the same direction. The aim is to evaluate the soiling effect in an urban environment, to assess the soiling ratio and rates through the solar field, and to identify possible stow positions to reduce the soiling effect.

Keywords: Soiling, CSP, Urban Environment

1. Introduction

Particle deposition and its effect onto the optical properties in solar technologies, such as scattering and absorption (Vivar et al., 2010), have been a widely studied subject, due to its negative influence on the performance of solar power plants. Soiling decreases the transmittance and specular reflectance of surfaces, which reduces the power output of any solar energy plant. Literature in this area have been reported since the 40s of XX century (Hottel and Woertz, 1942) and have progressively evolved by introducing new techniques and developments (Pulipaka and Kumar, 2016; Sayyah et al., 2017).

Soiling effect has been widely analyzed in photovoltaics (PV) (Gostein et al., 2015; Piedra et al., 2018; You et al., 2018) stimulated by the low price of PV modules, particularly after Chinese PV production enters into the global market, and due to cheap instrumentation to measure soiling on this technology. On the other hand, soling research in concentrating solar technologies (CST) highlights a significant impact of soiling when compared with PV, because the lower acceptance angles (Bellmann et al., 2020). Current research points out that soiling can reduce the reflectance about 10% per month, even for low soiling regimes locations (Conceição et al., 2018a), and can be as high as 40% or more per month in high soiling regimes places, such as near deserts (Bouaddi et al., 2017; Merrouni et al., 2017). Moreover, besides lowering the transmittance and reflectance of glass and mirrors, it increases the operation & maintenance (O&M) costs by increases the need to clean the solar plants.

This work addresses a preliminary analysis on soiling effect in central receiver CST in an urban environment, which is extremely interesting, since reflectance related loss studies are most of the times performed near desert areas, which are characterized by high dust concentration, or in rural areas. Nevertheless, this region is located near one the largest metropoles in Spain, Madrid, and one the busiest Spanish highways, which can also be an important factor to contributing to soiling effect. For the authors' best knowledge, this study is the first ever made for the region of Móstoles, Madrid, Spain.

The paper structure is as follows: Section 2 describes the methodology used, as well as, the layout of the solar field and the selected heliostats; Section 3 includes the results for selected heliostats tilted 10º turned south, spread around the solar field, as well as, an analysis regarding four heliostats located side by side with different tilt angles;

doi:10.18086/eurosun.2020.08.01 Available at http://proceedings.ises.org

Section 4 includes an analysis regarding the soiling effect in different areas of the same heliostat; Section 5 includes a brief summary of the results and discussion.

2. Methodology

The experiment was performed at the Very-High Concentration Solar Tower (VHCST) facility (Romero et al., 2017, Martínez-Hernández et al., 2020) placed at IMDEA Energy premises in Móstoles, near Madrid. This location has a climate classified as Csa, with hot dry summers and a wet season (September to May) with rainfall events more pronounced towards the end of the year. The VHCST facility has 169 3 m^2 single-facet heliostats, see Fig. 1, that concentrate the solar radiation into a solar reactor, located at the top of the solar tower. Measurements were performed using a Condor reflectometer, developed by Abengoa Solar, on thirteen mirrors, as shown in Fig. 1. Nine heliostats were kept tilted 10º (marked by red rectangles in Fig. 1) and four were tilted 0º, 15º, 30º and 45º, respectively (marked by a green rectangle in Fig. 1), all facing south. Location of the nine heliostats was chosen to analyze the soiling variation throughout the solar field. Having four heliostats side by side, but with different slopes, allows to understand the effect of the tilt angle, which can modify soiling removal due to dew formation and rainfall events.

Each heliostat facet was measured on five different spots: top left, top right, center, bottom left and bottom right. This was performed to determine soiling distribution on the mirror surface, because soiling deposition, due to the heliostat curvature, can be higher in some areas compared to others. The measurements were performed with a Condor reflectometer, which has a resolution of ±0.001, a repeatability of ±0.002 reflectance units with 95% confidence, an accuracy of ±0.002 reflectance units [1], and the (half) acceptance aperture is 204 mrad, see Fig. 2.

Fig. 1: (Left) Scheme of the Solar field layout, with the row number marked on the left side, as well as, the heliostat number in each row, and selected heliostats to assess the soiling effect on the reflectance. Red squares indicate the heliostats that were left tilted 10º, while the green ones indicate the 0, 15, 30 and 45º tilted heliostats, from left to right, respectively; and (right) Real image, taken from the top of the Solar Tower at IMDEA Energy, Madrid, Spain.

Fig. 2: Condor reflectometer, developed by Abengoa Solar, with the VHCST on the background.

The soiling ratio, i.e., the relative reflectance loss the original clean value, was calculated as follows:

- The parameter λ is the reflectance measured with soiling, and λ_0 is the reflectance in clean state of each of the five measured locations in each mirror.
- All the measurements for each location within the same mirror, are normalized for the clean value, the maximum possible achievable reflectance, which corresponds to the $\frac{\lambda}{\lambda_0}$ term.
- Then the mean of the five ratios is calculated, which is denominated $\bar{R} = \frac{\lambda}{\lambda_0}$.
- In order to calculate the Soiling Ratio, the mean of the five ratios is subtracted to one, $1 - \bar{R}$.
- Finally, the Soiling ratio in percentage, is given by:

$$SR = (1 - \bar{R}) \times 100 \qquad \text{(eq. 1)}$$

3. Results

3.1 Fixed Tilt Positions

In Fig. 3, it is shown the soiling ratio between January 14th and March 12th. The solar field was cleaned on February 5th and February 27th, which are marked as black vertical lines in the plot. The soiling ratio throughout the solar field is always lower than 2%, which means that the selected heliostats undergo a similar behavior in terms of reflectance loss. This can be due to the small size (507 m^2) and compactness of the solar field. The SR achieves its highest value after January 20th, when a massive transport of dust from Sahara Desert reached the region of Madrid, as illustrated in Fig. 4. This will be analyzed in detail next.

Soiling rates were calculated assuming a linear function of time in those periods between heavy rainfall events when soiling tendency is to increase. These periods, named P1, P2 and P3, are identified with red dashed vertical lines in Fig. 3. The period P1 corresponds to the interval between January 20th and 23th with presence of aerosols composed of Saharan desert dust, P2 is the period between the two mirror cleanings of the solar field, and P3 comprises the period between a rain event and the latest measurements before the lockdown due to covid-19 pandemic begun.

In Table 1, the fitted soiling rates and the corresponding coefficient of determination, r^2, are given for each period, P1, P2 and P3.

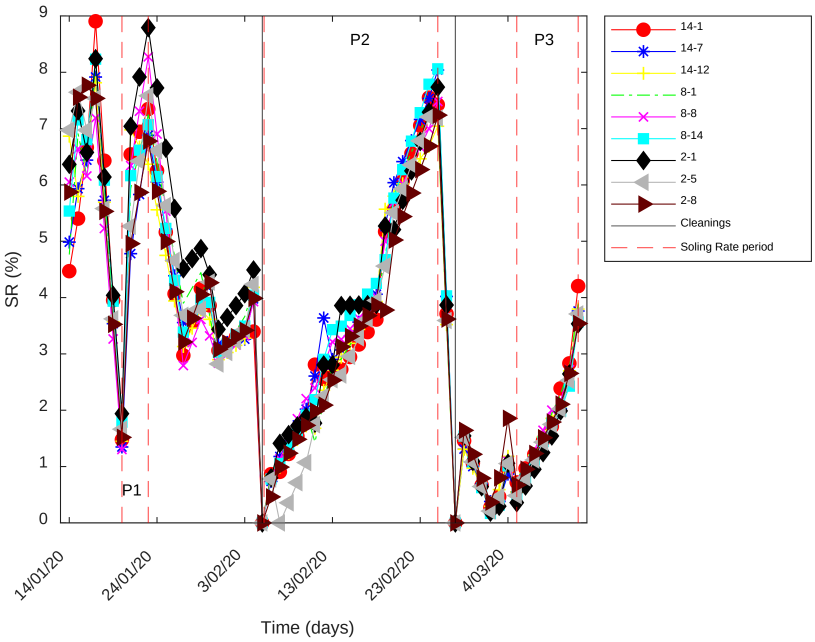

Fig. 3: Soiling ratio from January to March with the manual cleanings marked in solid grey lines and the periods (P1, P2 and P3), for which the soiling rates have been calculated.

Table 1: Soiling rates for periods with increasing soiling ratio.

Heliostat id.	***ΔSR (%)*** (P1) | (P2) | (P3)	***r^2*** (P1) | (P2) | (P3)
14-1	1.80 | 0.34 | 0.45	0.71 | 0.95 | 0.89
14-7	1.77 | 0.38 | 0.41	0.90 | 0.96 | 0.92
14-12	1.45 | 0.35 | 0.41	0.51 | 0.97 | 0.93
8-1	1.79 | 0.37 | 0.42	0.79 | 0.96 | 0.95
8-8	2.19 | 0.35 | 0.40	0.83 | 0.98 | 0.96
8-14	1.63 | 0.38 | 0.39	0.74 | 0.98 | 0.94
2-1	2.14 | 0.35 | 0.42	0.81 | 0.97 | 0.95
2-5	1.90 | 0.39 | 0.41	0.91 | 0.97 | 0.93
2-8	1.67 | 0.34 | 0.37	0.88 | 0.98 | 0.94

As expected, the period P1 has the highest soiling rate, because of the fast dust accumulation and the lowest coefficient of determination compared with periods P2 and P3. The dust deposition occurred rapidly, because of the Saharan desert dust event, and did not follow a constant pace. Consequently, the soiling rate was not well-described by a linear function. In Figure 4, it is illustrated the atmospheric dust forecast provided by the Barcelona Supercomputing Center (BSC) on January 21st and 23rd. The maps point to a massive amount of dust being blown from the Sahara Desert into southern Europe, mainly Spain and Portugal. The forecasted dust load for the region of Móstoles, Madrid, is the highest possible, ≥ 4 g/m^2.

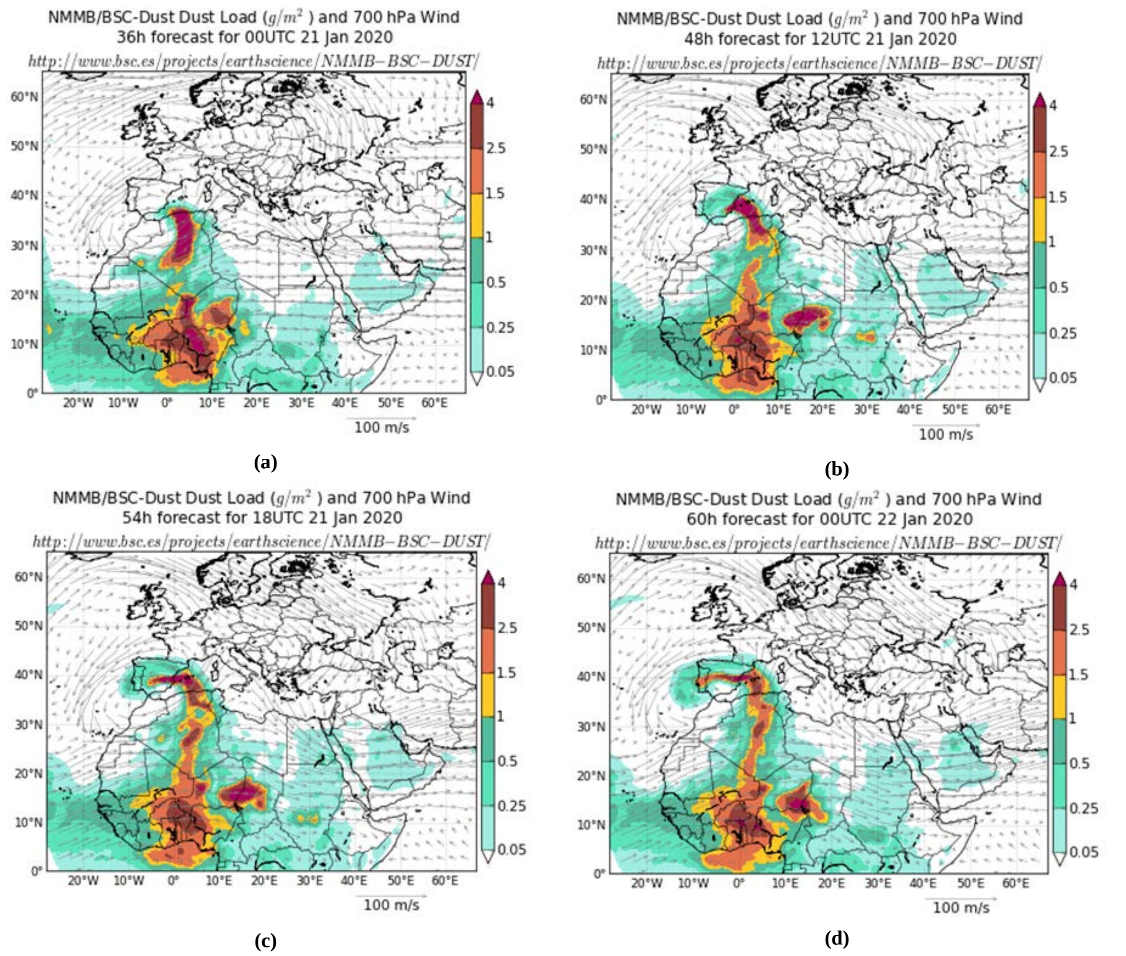

Fig. 4: BSC dust load forecasts: a) for January 21st at 00 UTC; b) for January 21st at 12 UTC; c) for January 21st at 18 UTC; d) for January 22nd at 00 UTC.

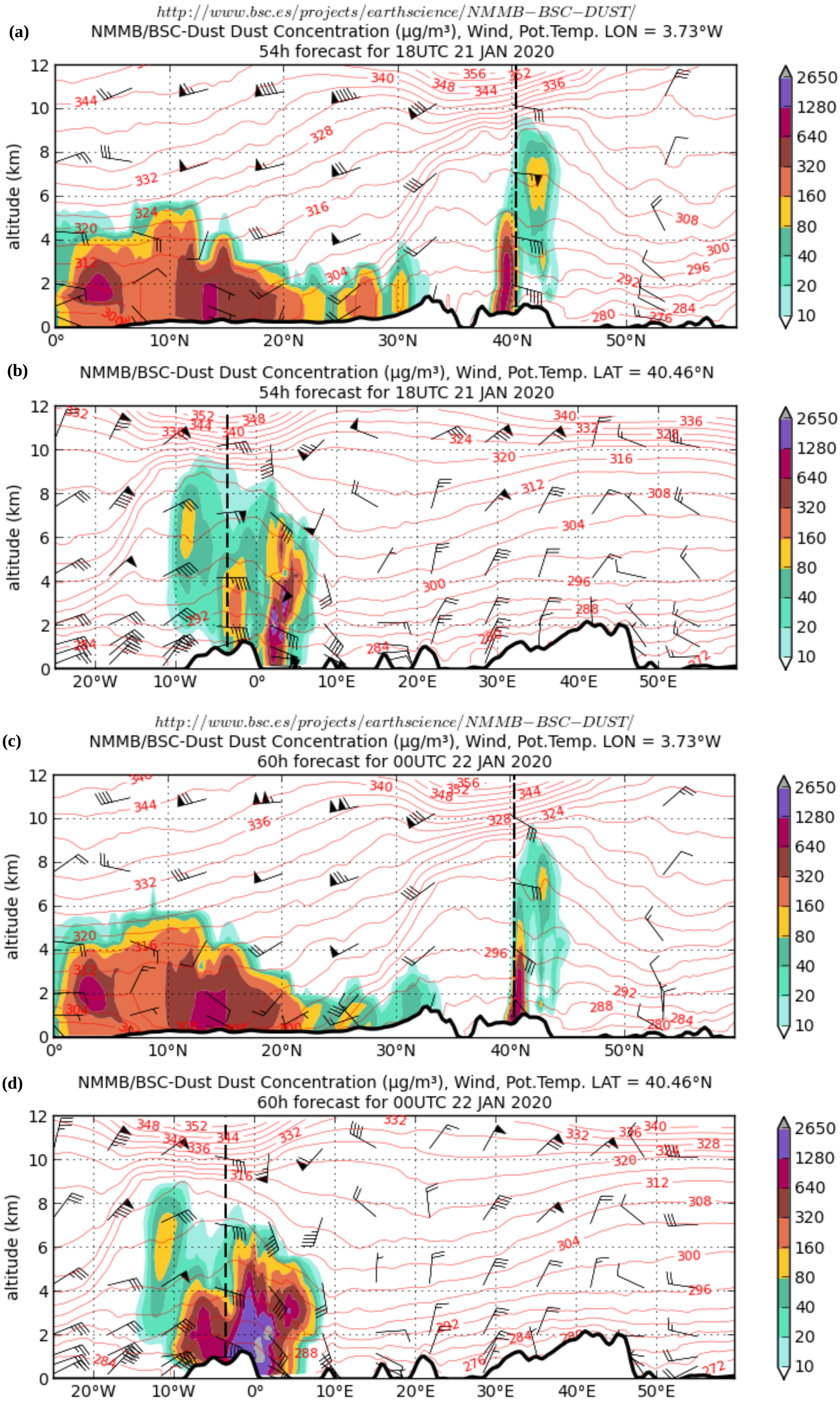

Fig. 5: BSC dust concentration forecast: (a) N-S vertical profile on January 21st; (b) W-E vertical profile on January 21st; (c) N-S vertical profile on January 22nd; and (d) W-E vertical profile on January 22nd.

Thus, based on the forecasts and on the data retrieved, it is assumed that the long-range transport of Saharan desert dust is responsible for the soiling rates between 1.45%/day to 2.19%/day for P1, the highest detected during the measurement campaign.

Moreover, on the IMDEA Energy facilities coordinates, 40.339ºN, 3.88ºW, it can be seen on Fig. 5, that the dust plume was forecasted to be suspended between 0 to 4 km, which corresponds to altitudes from where particles can easily be deposited onto surfaces on the ground. Besides this, high dust concentrations, between 640 to 2,650 μ/m^3 were forecasted for both vertical profiles.

Besides P1, from the beginning of the measurements until the solar field was first cleaned, on February 5th, this period was characterized by unstable weather conditions, with several rainfall events and possible dew formation. This also influenced soiling deposition, resuspension and removal from the heliostats, which resulted in a soiling ratio with an irregular shaped evolution.

Regarding the period P2, which basically includes all the period from the first to the second solar field cleaning, these might be the characteristic soiling rates for winter, excluding special events (such as the long-range transport of Saharan desert dust), which range between 0.34%/day to 0.39%/day. Moreover, the r^2 is close to 1.00, which indicates that the reflectance loss due to soiling during P2 is well-described by linear behavior. During this period, there was not rainfall events, which contributed to the linear increase of the soiling ratio.

The period P3, which includes the end of February and two weeks of March, also presents a soiling rate with a linear behavior, but lower correlation in comparison to P2. However, the soiling rates are higher than on P2, with values ranging from 0.37%/day to 0.47%/day. This effect is probably due to the atmospheric pollen concentration, which tends to be higher on March then on February (Subiza et al., 1995). Pollen, together with the background atmospheric particle concentration that exists every day, can increase soiling related losses (Conceição et al., 2018b). Unfortunately, due to the covid-19 lockdown, it was not possible to continue reflectance measurements during spring, but it is expected that the soiling rates can be higher than the ones obtained here, mainly on April and May.

3.2. Variable Tilted Positions

This section emphasizes the effect of the tilt angle on the reflectance loss of four mirrors selected on the same row, Fig. 6.

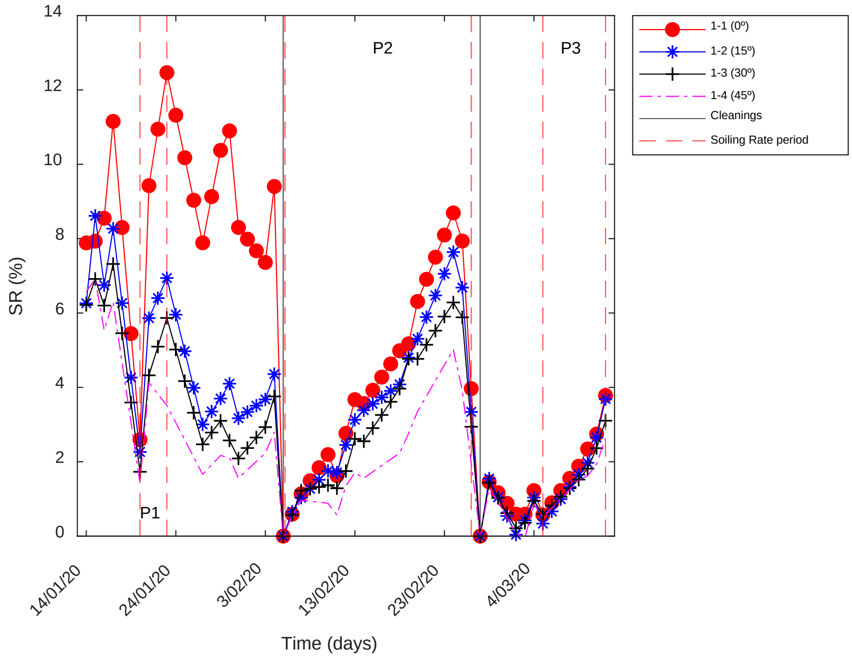

Fig. 6: Soiling ratio from January to March, for the tilt angle experiment, with the manual cleanings marked in solid grey lines and the periods (P1, P2 and P3), for which the soiling rates have been calculated.

It can be clearly seen the effect of the tilt angle when the long-range transport of Saharan desert dust happened. The horizontal heliostat reached almost 13% reflectance loss, during P1, with respect to the reference state (clean surface), whereas the 15º one reached around 6.5%. Since, according to the BSC dust forecasts, the deposition was wet, therefore it is normal to have such difference, which are about half on these two mirrors. Moreover, the higher the tilt angle, the lesser the soiling effect. It should be noted that due to the fact that deposition was in part due to light rain (that brought the dust down from the atmosphere) and because of the high tilt angle of the surface, the 45º heliostat did not get too much soiled. Instead, it got cleaned before the other mirrors, because water was able to slip from the surface, dragging particle with it.

Table 2: Soiling rates for periods with increasing soiling ratio, for the tilt angle experiment.

Heliostat id.	***ΔSR (%/day)*** **(P1) | (P2) | (P3)**	***r^2*** **(P1) | (P2) | (P3)**
1-1 (0º)	3.11 | 0.42 | 0.42	0.85 | 0.98 | 0.96
1-2 (15º)	1.46 | 0.36 | 0.44	0.79 | 0.98 | 0.94
1-3 (30º)	1.32 | 0.31 | 0.33	0.90 | 0.98 | 0.94
1-4 (45º)	0.60 | 0.22 | 0.27	0.40| 0.90 | 0.96

Moreover, it can be seen in Table 2 that during P2, both the 1-1 (0º) and the 1-2 (15º) have soiling rates similar to heliostats shown in Table 1. This is because the ones in Table 1 were tilted 10º. The significant differences appear on the 1-3 (30º) and 1-4 (45º) heliostats. Namely the heliostat with less soiling, regardless of the period, is the one tilted 45º, with extremely low soiling rates, around 0.22%/day to 0.27%/day. This is indeed the position less prone to soiling, and highest probability to be efficiently cleaned by rainfall, and it should be used for the resting position for the solar field. This probably can reduce the reflectance loss during winter and avoid some cleanings, therefore spending less capital during this season. Moreover, during this season, there were not many rainfall events, and one can assume that, if it rains more frequently during this period, and if the 45º position is used, it might be possible to not clean the solar field from January to March, and still maintain a reflectance loss under 10% , which should be enough for any experiments to be performed at the solar tower without any problem.

3.3. Intra-mirror Variation

It is important to understand how the mirror tilt is correlated with the soiling deposition, within different areas within the same mirror. For that, the data corresponding to the four heliostats tilted is used and compared. The mean of the standard deviation of the five measured positions for each heliostat, for the entire measuring campaign, was calculated and it is shown on Fig. 7.

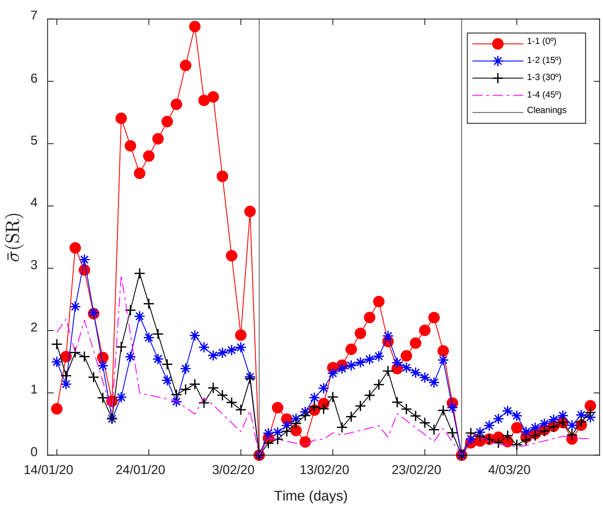

Fig. 7: Mean of the standard deviation for the five positions measure in each of the four tilted heliostats.

As it can be seen, the highest standard deviations are seen for the horizontal heliostat (0º), and the trend detected is that the soiling deposits (or is washed) in a more homogenous way, with higher tilt angles. Moreover, data analysis, not shown here, demonstrates that the most critical soiling areas within the mirror are the center and the bottom part. The center accumulation is and due to low tilt angles, because water from rainfall will accumulate there until it dries, leaving a pool of dust, see Fig. 8, and because the fact that the surface is curved. The bottom particle accumulation, is due to the fact that the tilt angle may not be enough for water to completely slip away from the heliostats' surface. This creates a small water layer at the bottom edge of the heliostats' surface, and when it dries, it leaves that area of the heliostat soiled. It should be noted that sometimes the accumulation will not be at the center of the heliostat, but will be a little moved, due to the fact that the surface is not perfectly curved and the heliostat is not perfectly tilted south.

Fig. 8: Soiling accumulation near the center part of a heliostat due to low tilt angle resting position, and soiling accumulation on the bottom part of the surface.

This means that higher tilt angles are important not only to reduce soiling effect, as seen in the previous sections, which is a direct consequence of less particle deposition at such high slopes, and the fact that is easier from rainfall to clean the surface, but it is also important to maintain a higher degree of soiling deposition homogeneity. This homogeneity can be advantageous: from a cleaning point of view, it can probably be easier to clean and do it faster on a surface that does not have localized and hard bounded soiling in multiple layers; from an optical point of view, it might be the case that non-homogenous soiling deposition, for instance in the center of the heliostat, and considering that its surface is not perfectly curved, can reduce and modify the flux map at the target, resulting in a lower performance.

4. Conclusions

A soiling campaign was recorded from January to March 2020 on the heliostats of the VHCST located at IMDEA Energy in Mostoles, Madrid, Spain. Regarding soiling assessment, 9 heliostats, tilted 10º, were used. It was seen that the soiling effect is similar for different positions of the solar field, which can be due to the fact that the area occupied by the solar field is small. It was also detected that for this part of the year, from January to March, that soiling effect can reduce reflectance around 10% or more, depending on the tilt angle. More specifically it was seen that during January, the soiling ratio reached its highest value, which was due to a long-range transport of Saharan desert dust. During February, due to the lack of rainfall events, the soiling ratio behaved in a linear fashion, which is in line with results obtained in other studies. The soiling rate, which already include part of March, shows higher values than the one of February, which can be due to the higher atmospheric pollen concentration.

Therefore, it is concluded, from the measured data, that soiling can be a problem in this region, because the high soiling rates, even though it is not located near a desert, especially considering the season. Moreover, long-range transport of Saharan desert dust can reach this location, which can increase very rapidly the reflectance loss.

Future work will imply a longer solar campaign, including the dry season, to characterize what type of soiling deposits in the location, to characterize seasonal and annual trends of the soiling effect, to compare soiling rates between different seasons, and to study possible cleaning scenarios and schedules.

5. Acknowledgments

The data and/or images from the (NMMB/BSC-Dust or BSC-DREAM8b) model, operated by the Barcelona Supercomputing Center (http://www.bsc.es/ess/bsc-dust-daily-forecast/) is acknowledge. This project has received funding from the European Union's Horizon 2020 research and innovation programme under grant agreement Nº 823802 (SFERA III). The authors wish to thank to “Comunidad de Madrid” and European Structural Funds for their financial support to ACES2030-CM project (S2018/EMT-4319). AMH also acknowledge support from the Community of Madrid (Spain) through the Young Employment Program (PEJD-2017-PRE/AMB-4951).

6. References

Bellmann, P., Silva, H.G., Wolfertstetter, F., Conceicao, R., 2020. Comparative modelling of optical soiling losses for CSP and PV devices in regard to gravimetric density. Sol. Energy 197, 229–237.

Bouaddi, S., Ihlal, A., Fernández-García, A., 2017. Comparative analysis of soiling of CSP mirror materials in arid zones. Renew. Energy 101, 437–449. https://doi.org/10.1016/j.renene.2016.08.067

Conceição, R., Silva, H.G., Collares-Pereira, M., 2018a. CSP mirror soiling characterization and modeling. Sol. Energy Mater. Sol. Cells 185. https://doi.org/10.1016/j.solmat.2018.05.035

Conceição, R., Silva, H.G., Mirão, J., Collares-Pereira, M., 2018b. Organic Soiling : The Role of Pollen in PV Module Performance Degradation. Energies Special Ed, 1–13. https://doi.org/10.3390/en11020294

Gostein, M., Duster, T., Thuman, C., 2015. Accurately measuring PV soiling losses with soiling station employing module power measurements. 2015 IEEE 42nd Photovolt. Spec. Conf. PVSC 2015 3–7. https://doi.org/10.1109/PVSC.2015.7355993

Martínez-Hernández, A., Gonzalo, I.B., Romero, M., González-Aguilar, J., 2020. Drift analysis in tilt-roll heliostats. Solar Energy 211, 1170-1183. https://doi.org/10.1016/j.solener.2020.10.057

Merrouni, A.A., Mezrhab, A., Ghennioui, A., Naimi, Z., 2017. Measurement, comparison and monitoring of solar mirror’s specular reflectivity using two different Reflectometers. Energy Procedia 119, 433–445. https://doi.org/10.1016/j.egypro.2017.07.045

Piedra, P.G., Llanza, L.R., Moosmüller, H., 2018. Optical losses of photovoltaic modules due to mineral dust deposition: Experimental measurements and theoretical modeling. Sol. Energy 164, 160–173. https://doi.org/10.1016/j.solener.2018.02.030

Pulipaka, S., Kumar, R., 2016. Power prediction of soiled PV module with neural networks using hybrid data clustering and division techniques. Sol. Energy 133, 485–500. https://doi.org/10.1016/j.solener.2016.04.004

Romero, M., González-Aguilar, J., Luque, S., 2017. Ultra-modular 500m2 heliostat field for high flux/high temperature solar-driven processes. AIP Conf. Proc. 1850. https://doi.org/10.1063/1.4984387

Sayyah, A., Eriksen, R.S., Horenstein, M.N., Mazumder, M.K., 2017. Performance Analysis of Electrodynamic Screens Based on Residual Particle Size Distribution. IEEE J. Photovoltaics 7, 221–229. https://doi.org/10.1109/JPHOTOV.2016.2617088

Vivar, M., Herrero, R., Antón, I., Martínez-Moreno, F., Moretón, R., Sala, G., Blakers, A.W., Smeltink, J., 2010. Effect of soiling in CPV systems. Sol. Energy 84, 1327–1335. https://doi.org/10.1016/j.solener.2010.03.031

You, S., Lim, Y.J., Dai, Y., Wang, C.H., 2018. On the temporal modelling of solar photovoltaic soiling: Energy and economic impacts in seven cities. Appl. Energy 228, 1136–1146. https://doi.org/10.1016/j.apenergy.2018.07.020

A NEW FACILITY FOR TESTING LINE–FOCUS CONCENTRATING SOLAR COLLECTORS FOR PROCESS HEAT APPLICATIONS

Luis M. Domínguez–López[1], Loreto Valenzuela[1] and Eduardo Zarza[1]

[1] CIEMAT – Plataforma Solar de Almería, Senés Road, km 4, E04200 Tabernas (Spain)

Abstract

This article describes the characteristics and design aspects considered in the definition and construction of an experimental facility for testing tracking solar collectors of small size adequate for supplying thermal energy in the medium temperature range (between 100 to 250 ºC). Manufacturers of tracking solar thermal collectors need to test and to know the real performance parameters of their new designs, and the potential customer needs to have the solar collectors certificated according to standard test methods as ISO 9806:2017.

The test facility presented in this paper will meet all these needs because it fulfills the pressure, temperature, heat transfer fluid and flowrate requirements; both to evaluate the designs, and to certify the expected real performance. Additionally, this test facility will also be useful to evaluate components for hydraulic circuits of solar process heat applications up to 250 ºC.

Keywords: solar thermal systems, solar collector testing, optical–thermal performance, pressurized hot water, solar process heat applications, solar heat in industrial processes (SHIP), balance of plant

1. Introduction

The Plataforma Solar de Almería[1] (PSA), belonging to the Spanish Centro de Investigaciones Energéticas Medioambientales y Tecnológicas (CIEMAT), has two test facilities for testing commercial parabolic trough collectors:

- The first parabolic through collector (PTC) test loop was built at PSA in 1996. It was engineered for PTC testing up to 75 meters long, East–West oriented. This facility was used for more than fifteen years with several PTC prototypes, which were installed in successive years, reaching three different collectors in parallel.
- It became necessary to approach a new test facility due to the previous test loop reached its maximum capacity, so the second test loop was built in 2015, the Parabolic Trough Test Loop (PTTL), with capacity to operate in two solar fields simultaneously: one solar field for East–West oriented PTC prototypes up to 150 m long, and another solar field for North–South oriented PTC suitable for complete collector loops up to 600 m long (León et al, 2014).

Both test facilities were designed for large–sized PTCs using silicon–based thermal oil as heat transfer fluid up to 400 ºC of outlet temperature, and focused to large commercial PTC solar fields for electricity generation. But they are not adequate for testing small–sized collectors due to requirements regarding flowrate and pressure testing conditions.

Because the use of solar energy for the supply of thermal energy to industrial processes is a market which growth expectations are high (IEA, 2012), it has been decided to build a new experimental facility, suitable for the testing of medium temperature (100–250 °C) solar thermal collectors. Any type of line–focus tracking solar collector, either PTCs or linear Fresnel type, can be tested, including new prototypes (Pulido Iparraguirre et al, 2019) and components for the hydraulic circuit.

[1] www.psa.es

doi:10.18086/eurosun.2020.08.02 Available at http://proceedings.ises.org

For these applications of solar heat in industrial processes (SHIP) is more usual to use water instead of thermal or synthetic oils (heat transfer fluids, HTF), the temperature is lower, and the pressure higher, because of the different fluid, water. So, for this type of PTC, smaller, with lower capacity and with different HTF, is necessary to undertake a new facility with these features.

At PSA there have been some previous projects focused on the design, construction and evaluation of small–sized PTCs. In particular, for the CAPSOL project it was erected a small facility for the testing of two prototypes of small–sized PTCs using pressurized hot water up to 220 °C (Fernández–García et al, 2018). However, that facility is already out of work. The previous PSA's experience in the CAPSOL project and the most recent experience in the testing of large–sized collectors (Valenzuela et al, 2014) have been considered in the design of this new facility.

Although the PSA has several laboratories for testing the optical performance and reliability of components (e.g. mirrors, receiver tubes, etc.); finally, any new design of solar collector requires the testing of a complete prototype in real outdoor conditions.

2. General overview

2.1 Commercial PTCs

Many industrial processes need thermal energy in the temperature range from 60 ºC to 220 ºC, some others exceptionally up to 260 ºC (Kalogirou, 2002). The application of this range of process temperature is suitable both for direct heating, as well as for solar cooling, power generation with Organic Rankine Cycle and desalination.

There is a wide variety of commercial tracking solar collectors, with a wide range of characteristics. After the review of the main commercial collectors, that was carried out in the framework of the European project STAGE–STE[2], a compromise solution can be reached for their features, that could be summarized as follows:

- Aperture width: up to 3 meters.
- Aperture length: from 2 to 5 meters, some of them up to 20 meters.
- Temperature: from 130 ºC to 230 ºC.
- Thermal power delivered per unit: from 2 to 16 kW, some of them up to 150 kW.

2.2 Standards for testing

The test facility presented in this article will fulfill the current standards for solar thermal collectors testing (Fernández–García et al, 2018): ASTM E905–87:2013, SRCC 600 2014–17:2015 and ISO 9806:2017. The standard EN 12975–2:2006 is already withdrawn and substituted by ISO 9806:2017. All parameters will be measured with the required accuracy.

The most restrictive required uncertainty of cited above standards for each parameter are shown in the Table 1, together with the uncertainty available in the installation.

Tab. 1: Most restrictive required accuracy of the standard, and accuracy available in the new PSA's test facility

Parameter	Standard	PSA's test facility
Mass flowrate	≤ 1.0 % (all standards)	0.1 %
Inlet water temperature	≤ 0.2 ºC (ISO 9806:2017)	±0.1 ºC to 0.525 ºC (0 ºC to 250 ºC)
Differential water temperature	< 0.05 ºC (ISO 9806:2017)	±0.2 ºC to 1.05 ºC (0 ºC to 250 ºC)

[2] www.stage–ste.eu

2.3 Water vs silicon based HTF

The use of water as HTF has some advantages over thermal or synthetic oils. Water is environmental friendly and the facilities do not need ATEX requirements, which are required when thermal oils are used. On the other hand, the installations need to be designed for higher pressure, that is affordable by existing commercial equipment if very high temperatures are not reached (up to 220 ºC to 250 ºC). So, water is more suitable for these type of collectors.

3. Test facility features

The main features of the new solar collectors' test facility are the following:

- Heat transfer fluid: pressurized hot water (environmental friendly fluid).
- Operation manometric pressure: up to 4.2 MPa.
- Operation temperature: up to 250 ºC.
- Operation flowrate: from 0.05 to 0.5 $kg \cdot s^{-1}$.
- Expected size of the solar collectors tested: up to 25 m^2 per collector unit.
- Material used for the hydraulic circuit: stainless steel.
- Field length: up to 40 m, in both orientations: East–West and North–South.
- Cooling system capacity: up to 150 kWt, depending on the operating conditions.
- Uncertainty of flowrate measurement: better than 1.0 %.
- Uncertainty of inlet/outlet water temperature: ±0.1 ºC to 0.525 ºC (0 ºC to 250 ºC)

4. New facility description

The design of this new test facility is defined both by the operating conditions to carry out the testing (Fernández–García, 2018), and by the restrictions included in the certification standards: ISO 9806:2017 and ASTM E905–87:2013. Because of that, the instrumentation chosen is the best of state of the art, for fulfilling the measurements uncertainty restrictions in the certification standards.

Two orientations for the collector field are possible: East–West for determining the optical and thermal performance in reduced test periods thanks to the possibility to have different incidence angles during the same testing day, and North–South for determining the thermal performance in commercial configuration. The facility has all the necessary elements: feed water system, heating system, cooling system, instrumentation and control system, auxiliaries, etc.

The balance of plant (BoP) is the installation around the solar collector with the capacity of feeding it with water at the fixed temperature, pressure and flowrate for testing, and with the cooling ability to dissipate the thermal energy generated in the solar collector in the air cooler before the water returns to the feed water tank. An auxiliary heating system is included as well for pre–conditioning the feeding water temperature to the solar collector system. In addition, both the design of the installation itself and the control system must be able of keeping the operating conditions in steady state.

The first important feature in this project is the used material, that is stainless steel AISI 304 or better in all parts in contact with the water, to avoid corrosion problems linked to the use of carbon steel.

The maximum operating temperature of 250 ºC corresponds to the collector outlet temperature. It is usually in this type of facility that the admissible maximum temperature in the rest of the installation is lower than the maximum temperature, but in this facility, the design temperature in overall part of the installation is 250 ºC, or even higher in almost all mechanical equipment.

This maximum temperature involves the maximum pressure required in the whole installation. Likewise, the maximum allowable working pressure of the installation is at least of 4.8 MPa (manometric). In order to fulfill the operating conditions, it was selected the Class 600 of the standard ASME B16.34 and ASME B16.5 instead of the standard DIN EN 1092–1, because of the rating PN63 does not fulfill for all of stainless steels, and the rating PN100 is well above for the requirements.

A simplified scheme of the BoP of this experimental testing facility is shown in the Figure 1.

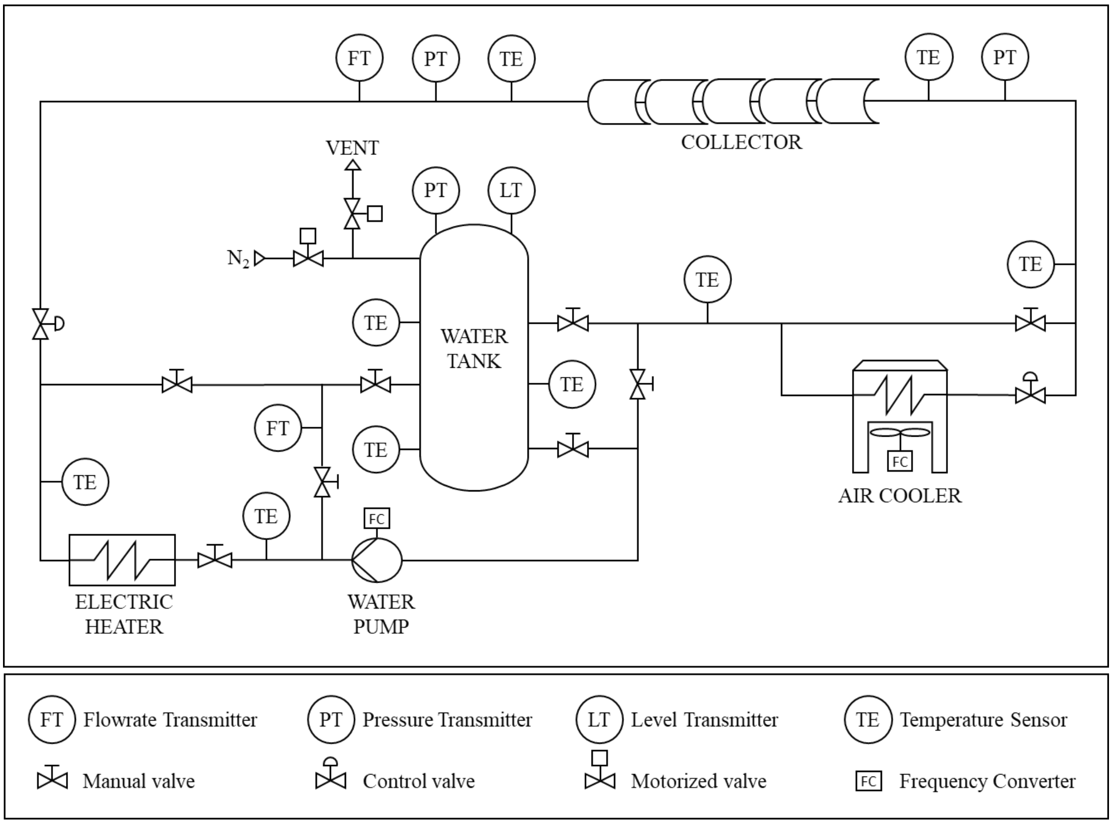

Fig.1: Simplified scheme of the new PSA's experimental facility for testing line–focus tracking solar collectors

4.1. General layout

The general layout of the test facility has enough field area around to install solar collectors in both directions (North–South and East–West) as shown in the layout of Figure 2.

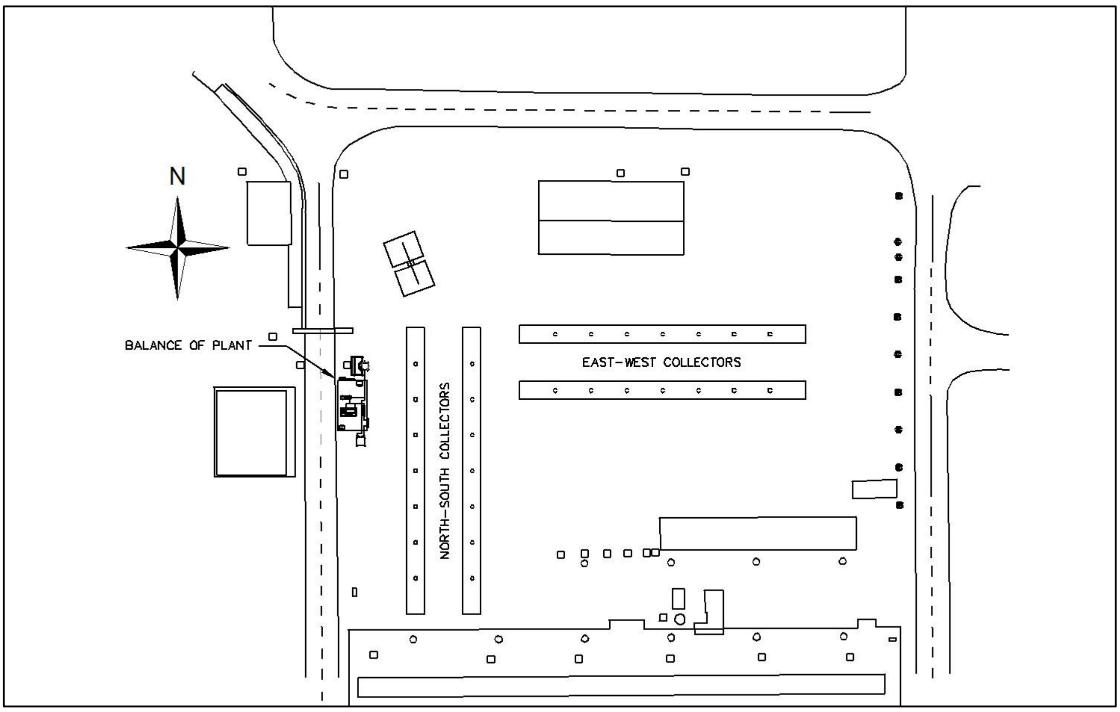

Fig.2: General layout of the new PSA's test facility

The location of the main equipment of the BoP is shown in the Figure 3. There is a reserve area for the future installation of an air condenser in the case of direct steam generation solar collector field will be tested.

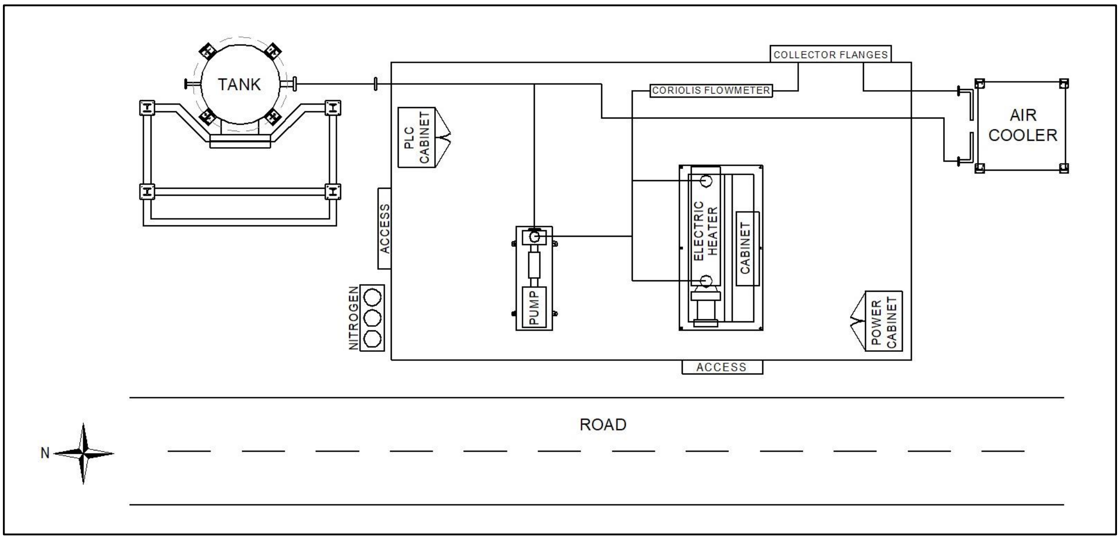

Fig.3: BoP layout with the main equipment

4.2 Water tank

The volume of the tank is 3000 l, which is enough to contain more than 2000 l of water, and so, with the capacity to maintain the feeding condition to the solar collector at least for one hour at the maximum flowrate of 1800 $l \cdot s^{-1}$. The tank is installed in vertical position, with a diameter around 1 m and a height of 3.5 m.

The tank has three inlet/outlet flanges, with one reserve flange, to configure it as needed. These flanges are bigger than corresponding pipe for allowing the insertion of different types of diffuser inside, so the tank could be configured as expansion tank, feed tank, or even with stratification of temperature to keep the outlet temperature nearly constant. With this target, the temperature is measured in three different levels. The nether outlet flange is lateral and not at the bottom, to avoid vortex formation and possible deposition of particles.

A nitrogen pressurization system is connected to the top, with two motorized on/off valves for feeding nitrogen and for venting, respectively. In this way, the overall installation keeps pressurized.

The maximum allowable working pressure (MAWP) of this component is 50 MPa at 280 ºC.

4.3 Water pump

Due to its tough working conditions a water pump with higher capacity than required has been chosen, because of that a recirculation pipe is needed. The pump is centrifugal and the coupling is magnetic. An additional cooling system is not required.

The water pump can work up to 280 ºC, with a maximum pressure in the discharge of 4.8 MPa.

4.4 Electric heater

The electric heater is installed in line (not in the water tank, like in the original installation CAPSOL). Although this situation of the electric heater complicates the installation, it provides more operation capacities for testing, and it can be operated in two different ways:

- fine regulation of the temperature, both in the inlet and the outlet of the solar collector, with the aim of compensating the small heat losses in the piping.
- preheat the overall water of the installation up to the temperature set point to start the testing.

A pressure switch, a level switch and a resistance temperature switch are installed to guarantee a safe operation. The MAWP of the electric heater is 50 MPa at 280 ºC.

The heating power is 24 kWt, that is regulated with thyristors in the overall range in the own electric cabinet. This power allows to preheat the installation and the 2000 l of water in 20 hours, from 25 to 225 ºC, and a thermal increase of 11.5 ºC with the maximum testing flowrate of 0.5 $kg \cdot s^{-1}$.

4.5 Air Cooler

The capacity of the air cooler was selected as a compromise solution, since the cooling capacity increases quickly with the inlet water temperature. Finally, the cooling power of the air cooler is from 50 kWt to 300 kWt with inlet water temperature of 75 ºC and 250 ºC respectively, taking in account an ambient temperature of 40 ºC.

The manifolds are assembled with flanges and pipes of a diameter of one inch, while the internal pipes have a diameter of half inch, with aluminum fins.

A frequency converter connected to the fan electric motor is used to regulate the outlet water temperature in the low temperature range, while in the upper temperature range is necessary a control valve in the bypass of the air cooler to limit the water flow to be cooled and limit the air cooler performance.

The MAWP of the air cooler is 50 MPa at 280 ºC.

4.6 Piping and valves

As mentioned above, the Class 600 of ASME was selected for valves and flanges. Some valves have higher Class for supply reasons. Different types of valves have been selected to be tested for this type of installation, and then, make the installation itself to have experimental characteristics.

The pipe was selected with Schedule 10S for pipe of one inch, and 40S for pipe of two inches; mainly for reasons of mechanical strength rather than hydrostatic pressure required.

The entire installation will be insulated with stone wool with thickness from 40 mm (piping) to 100 mm (water tank, electric heater).

4.7 Instrumentation and control system

The instrumentation complies with the requirements of the testing standards. The instruments involved directly in the collector performance measurements have the best accuracy available in the state of the art of the instrumentation manufacturers.

A Coriolis flowmeter has been selected, with an accuracy of 0.1% in full measuring range from 0.05 $kg \cdot s^{-1}$ to 0.5 $kg \cdot s^{-1}$; this instrument measures as well the volumetric flowrate, the pressure and the density.

For water inlet/outlet temperature measurements, resistance temperature detector (RTD) type Pt100 have been selected, with Class AA (IEC 60751), and 4–wire connection, that is the best state or the art. Even in this case, the accuracy is from ±0.1 ºC to 0.525 ºC, not enough to fulfill the standard ISO 9806. The PSA is working for improving the uncertainty in the differential temperature measurement through the collector for fulfilling the standard requirement.

For the rest of the installation thermocouples Type T with Class 1 have been selected (IEC 60584–1), with an accuracy from ±0.5 ºC to ±1.0 ºC depending on the measured temperature; and a vortex flowmeter for measuring the recirculation flowrate with an accuracy of ±0.75 %. All the pressure transmitters have a very high accuracy of ±0.0275 bar.

The ambient conditions (direct solar irradiance, ambient temperature, wind speed and direction) are measured with existing equipment from a neighbor test facility. Direct solar irradiance is measured with a pyrheliometer model CH1 by Kipp&Zonen (Valenzuela et al., 2014). The direct normal irradiance measurement has an average instrumental error of ±10 $W \cdot m^2$.

The main automatic control loops are the following:

- Inlet or outlet water temperature by regulation of the heating power in the electric heater.
- Flowrate through the solar collector by regulation with the frequency converter for speed regulation of the water pump, and with a control valve for fine regulation.

- Return water temperature to the tank by regulation with the frequency converter for speed regulation of the air cooler fan, and with a control valve of the bypass for the high range of temperature.
- Gas phase of nitrogen in the upper tank by actuation of both motorized valves of nitrogen and vent.

The control system has some safety interlocks for avoiding unsafe operations of the installation. A PLC cabinet will be installed on site in the installation, and the SCADA system will be installed at the control room. The power and PLC cabinets will be installed in opposite corners for avoiding electrical interferences between them (as shown in Figure 3).

The wiring will be conventional with 2–wire for 4–20 mA signal and power supply, with communication protocol HART. Others instruments have communication protocol MODBUS. As mentioned above, ATEX version is not required.

Although the instruments are calibrated on factory, all instruments can be re–calibrated in the own PSA's electronic laboratories.

Currently, the basic engineering of the project, P&ID, technical specifications and purchasing of the water pump, expansion tank, electric heater, air cooler, manual valves and instrumentation have been completed. And the following tasks are under execution: piping flexibility and temperature expansion studies with AutoPIPE, (as shown in Figure 4), erection specification and isometric drawings, foundation technical specification, and electrical and PLC cabinets specification.

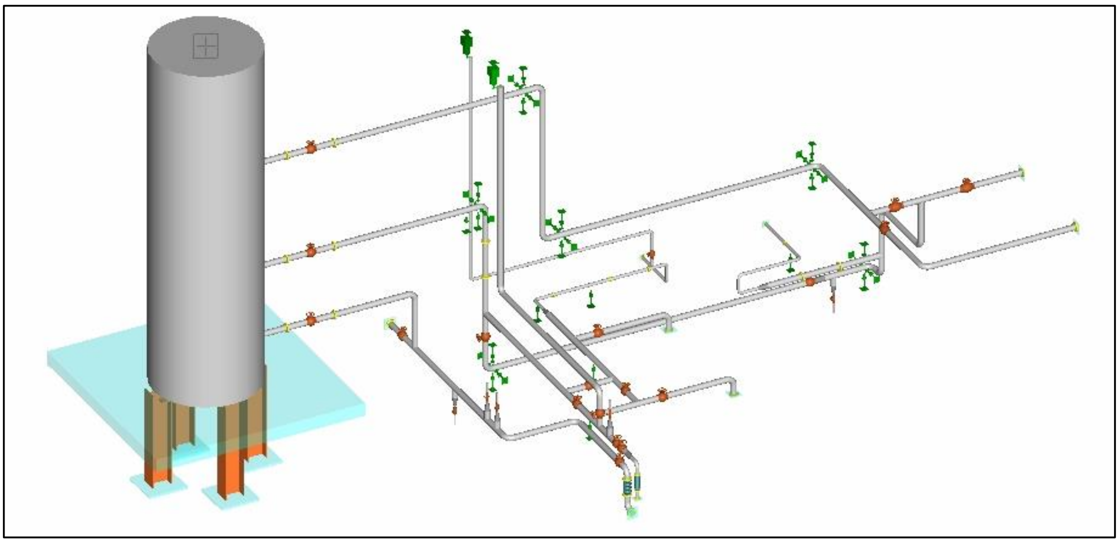

Fig.4: Exemplary scheme of flexibility and temperature expansion studies with AutoPIPE of the BoP of the new test facility

5. Operation modes and testing procedure

The operation modes of the installation are the following:

- Filling and emptying the installation with water.
- Pre–heating the installation.
- Cooling the installation.
- Feeding the solar collector for testing.

Since the collectors can be placed in both North–South and East–West orientation, two types of tests can be carried out on them:

- Optical and thermal performance testing of collector, in East–West orientation.
- Thermal performance of collector in commercial North–South orientation.

The new test facility also allows the testing of new BoP equipment (small thermal energy storage units, heat exchangers, micro–turbines, etc.) designed for SHIP applications. Since it is expected to have several collector units installed on site, solar thermal energy produced can be used to test new equipment for industrial heat applications.

6. Conclusions

This installation provides the PSA with a new test facility to carry out optical and thermal performance testing, in both testing and commercial collectors orientation, for a complete evaluation of any small–sized line–focus solar collector designed for solar heat in industrial processes, both from the point of view of testing and improving the manufacturers' designs, as well as for certification of the performance of the equipment that has reached the commercial distribution.

7. Acknowledgments

The authors thank to the collaboration agreement SolarNOVAII (ICTS–2017–03–CIEMAT–04) that was signed between the Spanish Administration and CIEMAT, with support from European Union FEDER program, that devoted some funds to this new facility; and to SOLTERMIN project, funded from Spanish Ministry of Economy, Industry and Competitiveness (Ref. ENE2017–83973–R).

8. References

ASME B16.34–2004. Valves–flanged, threaded and welding end.

ASME B16.5–2003. Pipe flanges and flanged fittings.

ASTM E905–87:2013. Standard Test Method for Determining Thermal Performance of Tracking Concentrating Solar Collectors.

DIN EN 1092–1:2018. Flanges and their joints – Circular flanges for pipes, valves, fittings and accessories, PN designated – Part 1: Steel flanges.

Fernández–García, A., Valenzuela, L., Zarza, E., Rojas, E., Pérez, M., Hernández–Escobedo, Q., Manzano–Agugliaro, F. 2018. SMALL–SIZED parabolic–trough solar collectors: Development of a test loop and evaluation of testing conditions. Energy 152, 401–415.

IEA–International Energy Agency. 2012. Technology roadmap. Solar heating and cooling.

IEC 60584–1:2013. Thermocouples – Part 1: EMF specifications and tolerances.

IEC 60751:2008. Industrial platinum resistance thermometers and platinum temperature sensors.

ISO 9806:2017. Solar energy – Solar thermal collectors – Test methods.

Kalogirou, S. 2003. The potential of solar industrial process heat applications. Applied Energy 76, 337–361.

León, J., Clavero, J., Valenzuela, L., Zarza, E., García, G. 2014. PTTL–A life–size test loop for parabolic trough collectors. SolarPACES 2013. Energy Procedia 49, 136–144.

Pulido Iparraguirre, D., Serrano–Aguilera, J. J., Valenzuela, L., Fernández–García, A. 2016. Optimizing design of a Linear Fresnel Reflector for process heat supply. Conference Proceedings of Eurosun 2016, Palma de Mallorca, Spain, 11-14 October 2016. https://doi.org/10.18086/eurosun.2016.02.21.

UNE–EN 12975–2:2006. Thermal solar systems and components – Solar collectors – Part 2: Test methods

Valenzuela, L., López–Martín, R., Zarza, E. 2014. Optical and thermal performance of large–size parabolic–trough solar collectors from outdoor experiments: A test method and a case study. Energy 70, 456–464.

OVERVIEW ON EUROPEAN STANDARDS AND CERTIFICATION ISSUES FOR SOLAR THERMAL SYSTEMS

Vassiliki Drosou[1], Andreas Bohren[2]

[1]Solar Thermal Systems Department, Center for Renewable Energy Sources and Saving, Pikermi, Athens 19009 (Greece)

[2]SPF Institute for Solar technology, Oberseestrase 10, 8640 Rapperswil (Switzerland)

Abstract

European Standards can be used to enhance safety and performance, improve energy efficiency, and protect consumers, workers and the environment. They complement European and national policies, and make it easier for businesses and other actors to respect relevant legislation. European Standardization is a key instrument for consolidating the Single Market and facilitating cross-border trade – within Europe and also with the rest of the world. Furthermore, “Keymark” is the voluntary European certification mark demonstrating conformity with European Standards. In the last years solar installations have advanced to standard house equipment, attracting also the attention of the European legislators. Solar products, as all products, must meet certain essential requirements related to health, safety and environment before they can be placed on the European market. These requirements are defined by the European Union directives, which are adopted by each member country as national legislation. Several directives offer considerable support to the development of the solar market. Furthermore public subsidies are allocated by states/communities provided that the product is certified under a proper certification scheme. The scope of this work is to present an overview of European standards for solar thermal systems and components, to update on the Solar Keymark quality label, as well as to discuss on relevant legislative issues as “Energy Labelling” and “Energy Performance in Buildings Directive” in relation with solar thermal systems. Future trends and needs for standardization are also discussed and highlighted.

Keywords: Type your keywords here, separated by commas,

1. Introduction

Solar energy is a form of renewable energy which can be converted into useful thermal or electrical energy for use in the residential, commercial and industrial sector. The conversion of solar energy in thermal energy is made with the use of solar thermal systems. The main component of a solar thermal system is solar thermal collector. Solar thermal collectors may be classified in two categories: with or without sun tracking mechanism. Sun tracking mechanism is used to adjust the collector orientation in a sun-following solar collector system. For low-medium temperature applications are usually used solar thermal collectors where all the parts of the collector system are stationary. Solar thermal collectors with solar radiation concentration are used for medium and high temperature applications. Solar concentration is the re-direction of solar radiation to enhance the irradiance received by the absorber or the receiver. Concentrating solar thermal systems use mirrors or lenses with tracking systems to focus a large area of sunlight onto a smaller area.

Solar thermal systems may produce fluid of low ($T < 100\ ^{\circ}C$), medium ($100\ ^{\circ}C < T < 400\ ^{\circ}C$) and high ($T > 400\ ^{\circ}C$) temperatures that can be used directly or be transformed into other forms of energy as mechanical, electrical and chemical.

The most common applications of solar thermal systems are:

- Sanitary hot water production
- Hot air production for space heating and drying

doi:10.18086/eurosun.2020.08.03 Available at http://proceedings.ises.org

- District heating
- Space heating / cooling
- Solar desalination
- Industrial process heat
- Electricity production

Solar heat thermal systems must be clearly distinguished from two other renewable energy technologies using the sun directly – Photovoltaic and Concentrated Solar Power – both of which provide electricity, while solar heat thermal systems produce heat that conveyed to a heat transfer medium – usually a liquid but also air in the case of air collectors. The heated medium is used either directly (to heat tap water for example) or indirectly by means of a heat exchanger which transfers the heat to its final destination (for instance in space heating or industrial process heat).

Most of the solar heat systems in use today are related to low-temperature heat demand in buildings: providing hot water and space heating. The solar heat can be produced on-site for individual houses or delivered via a district heating network. For industrial processes, solar heat systems are well suited for generating low temperature heat up to 150°C. There are well-known applications of solar heat in breweries, mining, agriculture (crops drying) or textile sector. (SHE-ESTIF, 2020). The global cumulated solar heat thermal capacity in operation at the end of 2019 was 479 GWth (684 million square meters), the vast majority of which is installed in China and Europe. The corresponding annual solar thermal energy yield amounted to 389 TWh, which correlates to savings of 41.9 million tons of oil and 135.1 million tons of CO_2 (IEA, 2020).

European Standardization plays an important role in the development and consolidation of the European Single Market. The fact that each European Standard is recognized across the whole of Europe, and automatically becomes the national standard in 34 European countries, makes it much easier for businesses to sell their goods or services to customers throughout the European Single Market. Innovation needs standardization and that standards are essential for market uptake of innovative products and services since they provide a strong long term platform for further innovation.

Standards provide opportunities for:

- Transfer of innovative know-how to the market
- Dissemination of research results (Subtasks A, B and C)
- Opportunity to network
- Helping access to public procurement markets
- Comparability & interoperability: measurements, quality indicators, test methods
- Reassurance for European consumers
- Faster and easier access to markets

Standardization supports economic activity, boosts productivity, increases trade within the European Single Market and allows businesses of all sizes to access markets around the world. Recent studies highlight the positive relationship between the use of standards and economic growth, labour productivity, and the ability of companies to export their products. Standardization is supported by specific policy context, as:

- the Innovation Union, 2010: “Standards play an important role for innovation”,
- the Standardization Regulation, 1025/2012: “Standards can help to bridge the gap between research and marketable products or services”,
- Horizon 2020 “Contribute to European competitiveness through support to the standardisation process and standards”
- the Single Market Communication 550/2015 “Standards are crucial for innovation and progress in the Single Market: they increase safety, interoperability and competition and help remove trade barriers”.

Standardization is not the same as legislation. Standards are developed through a process of collaboration among stakeholders and they are approved and published by recognized standardization bodies. Regulations and other types of legislation are adopted by governments at national or regional level, or by supranational and/or inter-governmental organizations such as the European Union. Moreover, the use of standards is voluntary whereas regulations are legally enforceable. Standards can facilitate compliance with legislation. The relationship between standardization and legislation at European level has been developed in accordance with the so-called 'New Approach' to technical harmonization and standards, which was introduced in 1985. Additionally there are European Commission's standardization requests, the so-called European "Mandates". Mandates are the mechanism by which the European Commission (EC) and the secretariat of the European Free Trade Association (EFTA) request the European Standardization Organizations (ESOs) to develop and adopt European standards in support of European policies and legislation.

European standards are the basis for the "Solar Keymark", the European quality mark for all solar thermal products. The Solar Keymark is a voluntary third-party certification mark for solar thermal products, owned by CEN/CENELEC. Every certified product is in full conformity with the relevant European standards and fulfills additional requirements to assure constant quality. This level of quality is maintained by initial type testing and by regular check of the products and their production sites by independent inspectors. Consumers and authorities can fully rely on the certified products. The "Solar Keymark" is the basis for most European supporting schemes and it is also increasingly recognized or adapted worldwide.

This research work is focused on standardization, certification and legislative issues in European level related to solar thermal systems and their components.

2. European standardization on solar thermal systems

Standards are documents that set out specifications and other technical information with regard to various kinds of products, materials, services and processes. The European Committee for Standardization is called CEN. CEN is one of three European Standardization Organizations (together with CENELEC and ETSI) that have been officially recognized by the European Union and by the European Free Trade Association (EFTA) as being responsible for developing and defining voluntary standards at European level.

The Members of CEN are the National Standardization Bodies (NSBs) of 34 European countries – including all the member states of the European Union (EU) and other countries that are part of the European Single Market. CEN works with its Members to develop and define European Standards in response to specific needs that have been identified by businesses and other users of standards.

European Standards (ENs) are developed by teams of experts who have particular knowledge of the specific sector or topic that is being addressed. The members of Technical Committees (TCs) as well as sub-committees and Working Groups (WGs) are nominated by the national standardization organizations. Each NSB that is part of the CEN system is obliged to adopt each EN as a national standard and make it available to customers in their country. They also have to withdraw any existing national standard that conflicts with the new EN. Therefore, one EN becomes the national standard in all 34 countries covered by CEN Members. Moreover, many ENs are also adopted as identical national standards by CEN Affiliates, which are the NSBs of 17 neighboring countries, and by NSBs in other countries around the world.

The ENs published by CEN are developed by experts, established by consensus and adopted by the Members of CEN. It is important to note that the use of standards is voluntary, and so there is no legal obligation to apply them. Around 30% of the ENs published by CEN have been developed in response to specific requests (standardization mandates) issued by the European Commission. Many of these standards are known as 'harmonized standards'. They enable businesses to ensure that their products or services comply with essential requirements that have been set out in European legislation (EU Directives). In such cases, we can say that the standard provides 'presumption of conformity' with the essential requirements of the relevant legislation (CEN, 2020).

CEN develops via its technical committee on CEN TC 312 “Thermal solar systems and components” the European Standards for solar thermal systems. CEN/TC312 is engaged in the standardization of thermal solar systems and their associated components. Its main scope is the preparation of ENs and other CEN products, to cover Preparation of European Standards to cover terminology, general requirements, characteristics, test methods, conformity evaluation and labelling of thermal solar systems and components.

CEN/TC312 was created after a request of the European Solar Industry Federation (ESIF) to CEN. Afterwards, a liaison between CEN/TC312 and European Solar Thermal Industry Federation (ESTIF) was established. Moreover CEN/TC312 works in close liaison status with the International committee for solar energy ISO/TC 180 "Solar energy" under Vienna Agreement, for producing EN ISO standard.

The main focus of CEN/TC312 is to ensure homogenous testing procedures for solar thermal systems and components. The standards and specifications of CEN/TC312 are required by a large number of different parties. These include manufacturers of solar thermal collectors, systems and components, manufacturers of solar water heater stores and combisystems and appropriate control equipment, national authorities, energy service companies, engineers and consumers. CEN/TC312 has elaborated a set of products (ENs) in the solar thermal energy field including solar collectors, factory made systems, solar energy vocabulary, custom built systems as well as collectors' components and materials.

Currently the published standards under the responsibility of CEN TC312 are as shown in Tab.1.

Tab.1 CEN TC312 published standards

Reference	Title
EN ISO 9488:1999	Solar energy - Vocabulary (ISO 9488:1999)
EN 12975-1:2006+A1:2010	Thermal solar systems and components - Solar collectors - Part 1: General requirements
EN ISO 22975-3:2014	Solar energy - Collector components and materials - Part 3: Absorber surface durability (ISO 22975-3:2014)
EN ISO 22975-1:2016	Solar energy - Collector components and materials - Part 1: Evacuated tubes - Durability and performance (ISO 22975-1:2016)
EN ISO 22975-2:2016	Solar energy - Collector components and materials - Part 2: Heat-pipes for solar thermal application - Durability and performance (ISO 22975-2:2016)
EN 12976-1:2017	Thermal solar systems and components - Factory made systems - Part 1: General requirements
EN ISO 9806:2017	Solar energy - Solar thermal collectors - Test methods (ISO 9806:2017)
EN 12977-2:2018	Thermal solar systems and components - Custom built systems - Part 2: Test methods for solar water heaters and combisystems
EN 12977-4:2018	Thermal solar systems and components - Custom built systems - Part 4: Performance test methods for solar combistores
EN 12977-5:2018	Thermal solar systems and components - Custom built systems - Part 5: Performance test methods for control equipment
EN 12977-1:2018	Thermal solar systems and components - Custom built systems - Part 1: General requirements for solar water heaters and combisystems
EN 12977-3:2018	Thermal solar systems and components - Custom built systems - Part 3: Performance test methods for solar water heater stores
EN 12976-2:2019	Thermal solar systems and components - Factory made systems - Part 2: Test methods

The standards under development (not published) under the responsibility of CEN TC312 are as shown in Tab. 2.

Tab.2 CEN TC312 standards under development

Reference	Title
FprEN 12975	Solar collectors - General requirements
FprEN 12976-1:2018	Thermal solar systems and components - Factory made systems - Part 1: General requirements
prEN ISO 9488	Solar energy - Vocabulary (ISO/DIS 9488:2020)

3. European certification on solar thermal systems

In the 1990s the solar thermal market in Europe started to grow considerably, in part due to financial support programs in various countries. The European market grew quickly from 250.000 kWth to over 800.000 kWth of newly installed capacity per year. Many companies started exporting their products into other European markets but found hurdles in the form of different requirements in the incentive programmes, which became an obstacle to market entry. As a result, if a company wanted to sell one collector to different countries in Europe, it had to undergo several different tests and gain additional certificates and approvals. This process was extremely complicated, expensive and cumbersome and hindered the development of solar thermal in Europe and the growth of solar thermal manufacturers.

In 2003 ESTIF and major testing institutes formulated the Solar Keymark Scheme rules as a unified and simple solution in order to get solar thermal products recognized all over Europe. This work was done on the framework of an EU co-financed project running from 2000 until 2003: Solar Keymark I (ALTENER - Solar Keymark - AL/2000/144). This work was followed up by Solar Keymark II (EU-IEE (Solar Keymark II - EIE/05/052/SI2.420194). After these two projects the Solar Keymark was the most successful Keymark scheme and more than two thirds of the collectors sold had the Solar Keymark. Testing, inspection and certification were now organized into a single streamlined process and was recognised by authorities all over Europe.

The Solar Keymark is a voluntary third-party certification mark for solar thermal products, demonstrating to end-users that a product conforms to the relevant European standards and fulfills additional requirements. The Solar Keymark logo is shown in Fig.1.

Fig.1 The Solar Keymark logo

Every certified product is in full conformity with the relevant European standards and fulfills additional requirements to assure constant quality. This level of quality is maintained by initial type testing and by regular check of the products and their production sites by independent inspectors. Consumers and authorities can fully rely on the certified products. The Solar Keymark aims at reducing trade barriers and promotes the use of high quality solar thermal products in the European market and beyond. It is used in Europe and increasingly recognized worldwide. The Solar Keymark is a CEN/CENELEC European mark scheme, dedicated to:

•Solar thermal collectors,

•Solar thermal systems, storages and controllers.

The Solar Keymark is the main quality label for solar thermal products and is widely spread across the European market and beyond. The Solar Keymark is not the same as CE-mark. The Solar Keymark is a voluntary quality label and CE-mark just attests that the product fulfills minimum legal requirements according to specific European Directives.

A Solar Keymark can only be issued by an empowered "certification body" after the product has been tested by an accredited testing laboratory. The certification bodies are empowered by the CEN Certification Board (CCB). The certification body is the organization responsible for awarding Solar Keymark certificates and the testing laboratory is the organization responsible for all the testing. Solar Keymark certification it is essential that the product tested is a sample taken randomly from the current production or stock by an independent inspector. Furthermore, the production and Quality Management System as implemented at the factory will be checked by an independent inspector on site or under remote factory inspection procedure. Currently it is allowed also collector efficiency tests in a real-life environment. In this aspect it is possible to create efficiency curves and to calculate all values required for a Solar Keymark Certificate by using only the results gained from field-testing. Large flat plate or on-site built vacuum tube collectors, as is typical of solar district heating, benefit from this new option.

The Solar Keymark certification process in order to obtain the Solar Keymark is shown in Fig.2.

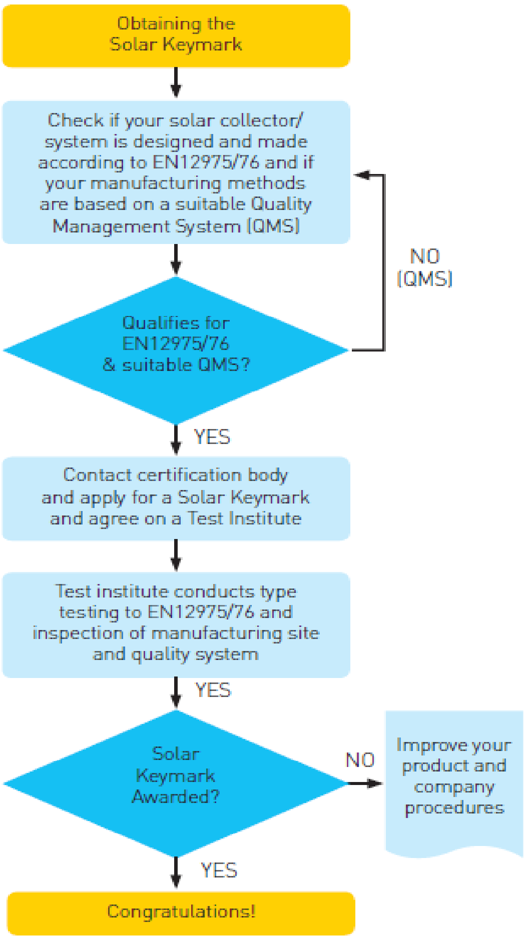

Fig.2 The certification process in order to obtain the Solar Keymark

Currently, 1358 Solar Keymark licenses are granted from which 1109 are attributed to solar thermal collectors, 237 to factory made and custom built solar thermal systems and 12 are attributed to solar water heater and solar combistores and controllers (Solar Keymark, 2020).

4. European Legislation on solar thermal systems

The EU legislation on Ecodesign and Energy Labelling aim at improving the energy efficiency of products, and providing information on product's efficiency to consumers. It helps orientating the choices of informed consumers, and eliminate the least performing products from the market, contributing to the EU's 2020 energy efficiency objective.

The Ecodesign Directive provides consistent EU-wide rules for improving the environmental performance of products, such as household appliances, information and communication technologies or engineering. The Directive sets out minimum mandatory requirements for the energy efficiency of these products. The Energy Labelling Directive complements those Ecodesign requirements with obligations regarding consumer information, namely by the use of energy labels indicating the efficiency of the product or package, besides additional relevant information to the market and consumers.

More specifically EU Directive 92/75/EC established an energy consumption labelling scheme. The directive was implemented by several other directives thus most white goods, light bulb packaging and cars must have an EU Energy Label clearly displayed when offered for sale or rent. The energy efficiency of the appliance is rated in terms of a set of energy efficiency classes from A to G on the label, A being the most energy efficient, G the least efficient. The labels also give other useful information to the customer as they choose between various models. The information should also be given in catalogues and included by internet retailers on their websites.

In an attempt to keep up with advances in energy efficiency, A+, A++ and A+++ grades were later introduced for various products; since 2010, a new type of label exists that makes use of pictograms rather than words, to allow manufacturers to use a single label for products sold in different countries. The labelling and eco-design obligations for heaters (LOT1) and water heaters (LOT2) came into force on the 26th September 2015. Directive 92/75/EC was replaced by Directive 2010/30/EU and was again replaced by Regulation 2017/1369/EU from 1 August 2017. Updated labelling requirements are expected to enter into force in 2021.

The Commission Regulation (EU) No 813/2013 (Ecodesign regulation) and the Commission Delegated Regulation (EU) No 811/2013 (Energy labelling regulation) regulate domestic space and combination heaters. Water heaters by the Commission Regulation (EU) No 814/2013 (Ecodesign regulation) and Commission Delegated Regulation (EU) No 812/2013 (Energy labelling regulation). Solar thermal systems and collectors are falling under these regulations. The main purpose of the regulations is to visualize the primary energy consumption of different appliances for different applications. Not only to inform the consumers, but also to provide a legislative tool for continuous reduction of the emissions. The European mechanism for reducing the energy consumptions and CO_2 emissions is a step-by–step increase of the minimum energy class for the products brought to market. Every few years these minimum requirements are adjusted depending the current situation and the available technologies.

The energy labels are separated into at least four categories:

- The appliance's details: according to each appliance, specific details, of the model and its materials.
- Energy class: a colour code associated to a letter (from A to G) that gives an idea of the appliance's electrical consumption.
- Consumption, efficiency, capacity, etc.: this section gives information according to appliance type.
- Noise: the noise emitted by the appliance in decibels.

From 1st January 2019 the registration of space and water heating products in the European Product Registry for Energy Labelling (EPREL) database is compulsory. In this database have to be registered:

- all new products,
- all products placed in the market before the end of 2018 within a 6 month period
- products covered by a delegated act under Energy Labelling regulations
- “solar devices” and other components of a package
- packages, if placed in the market as a package by the manufacturer.

Solar thermal devices are heat generators that can supply up most of water heating needs and supply considerable part of the space heating. They are 100% CO_2 free heating technology, low life cycle costs, high recyclability of materials. Additionally they do not consume energy, hence cannot be applied any product label except for solar water heater, thus the thermosiphon systems with immersion electric heater.

In contrast to most of the traditional systems such as heat pumps, oil or gas boilers, solar thermal systems are more complex as they usually cannot provide the annual energy demand on their own. Solar thermal systems are usually used together with other appliances. To consider this, the regulations introduced the so-called package label, where the energy efficiency of combinations of heating appliance have to be computed. Of course, such energy efficiency can be computed using dedicated simulation tools considering all specifications of the appliances. For the purpose of legislation it is however not practicable to use such simulation tools. It is therefore mandatory to develop and introduce simple methods such that the efficiency of a system can be computed with simple tools while still providing sufficient correctness of the results. For bigger companies (system houses) offering all parts of a system, simplification is not relevant as they can provide the calculations tools easily for the whole scope of their products. Simplification is however essential for SME who are often combining different appliances from different suppliers. It is common use to mix and install collectors, storages and heat pumps from different suppliers into one system. It is therefore relevant that energy efficiency can be determined with some very simple calculation steps or with a simple tool. The methods that are currently defined in the regulations have shown to be too confusing so that they are not usable. Some studies have also shown that the reliability of the results is not yet satisfactory. The reliability of the results is essential as the energy labelling regulation requires also market surveillance. Products have to be taken form the market and their labelling has to be checked by independent laboratories. To prevent from legal problems it is therefore essential that the calculation methods are unambiguous and reliable.

The current methods have shown to underestimate the performance of solar thermal systems, as they are considered as supplementary heaters contributing with a fixed ratio to the annual energy load. In reality, solar thermal systems easily cover during the summer months the whole energy demand. During the rest of the year, they provide energy anytime the sun is available. The solar thermal system must therefore be considered as primary heater providing CO_2 free energy whenever sun is available. The backup heater or supplementary heater has to provide energy only in the case when solar energy is not sufficiently available. Even if the annual contribution of the backup heater is bigger than the solar contribution it is therefore essential to consider solar thermal as primary energy source.

As an alternative to the current calculation methods, ESTIF has developed the so-called simplified method, which is based on the Gross Solar Yield (GSY) of the collector. The main idea of using the Gross Yield is to base the calculation on the available energy provided by the collector. Using a dedicated simple calculation method the seasonality of the availability is taken into account. In the calculation basis of the method the heat loss of a C-class storage tank with a volume appropriate for the Gross Yield is already considered overall. Thus no storage data are necessary for the calculation. A better or worse label class of the storage tank than the reference class C has a small influence on the result and to keep the method simple it is therefore not taken into account. Moreover there is no need for a detailed consideration of the storage as there are already existing separate requirements for its energy efficiency and it has to be labeled anyway. It is then assumed that the system planner is competent enough to select an appropriate storage type and size. The method proposed by ESTIF will provide simple lookup tables where depending on the number of collectors and the load profile a so called solar device efficiency is determined independently from the backup heater. By multiplying with the energy efficiency of the backup heater, the overall system efficiency is then easily calculated. This simplified method is not only providing a more realistic rating of solar thermal, it is also much more reliable than the current method as it is based on the Gross Solar Yield. This Gross Solar Yield is part of the standard Solar Keymark datasheet and is available for all certified collectors in Europe with very high reliability. As outlined above, this is an important asset in view of the coming market surveillance activities. Main advantage of the proposed method is that it is independent of the backup heater. Thus the same method applies for all backup appliances, meaning that it will be applicable to any future energy providing system, but also for retro-labelling existing systems.

Currently it is available the final version of the review study on Ecodesign and Energy Label regulations for Boilers (Lot 1) and Water Heaters (Lot 2) as it was elaborated by Solar Heat Europe association and other solar experts and presented to European Commission and consultants. All details and preparatory studies are public available at https://www.ecoboiler-review.eu/ and https://www.ecohotwater-review.eu/.

In addition to the Ecodesign and Energy labelling regulations, solar thermal collectors also fall under the construction product regulation CPR (Council Directive 89/106/EEC). As for any other building products it is expected also for heating appliances installed in and on the building that some basic safety requirements are fulfilled and that specific performance are declared. For solar thermal systems this concerns mainly the collector installed on the building. The requirements with respect to safety and the methodology to provide the declarations of performance are defined in harmonized European standards. The most critical performances that must be declared for a collector are the mechanical resistance to climatic loads (wind, snow, …) and the fire safety classification. Other requirements such as the declaration of the thermal performance, the sound level, the electric safety etc. are easy to be declared for solar thermal collectors. The regulation furthermore requires that a dedicated quality management system must be operational in the production of the collectors to be sure that the declared performance are always guaranteed. Most of these requirements, except for fire safety, are already covered by the Solar Keymark scheme, which is based on the European standards. The main difference between a conventional standard and a harmonized standard are the non-technical constraints: The harmonized standard is a legally binding document and not a technical document issued by a private organization. In the current framework, it is therefore very challenging to elaborate a harmonized standard. For the standard EN 12975, which is intended to become a harmonized collector standard under CPR, the de-harmonization is currently in discussion to de-block the pending revision.

5. Future trends

It is a fact that almost 40% of EU's overall energy consumption accounts to domestic heating systems for hot water production and space heating. These systems are becoming more and more hybrid systems including different technologies using intelligent and interacting controllers. New technologies such as home batteries or other applications such as domestic cooling will further accentuate this development.

The standardization of all these appliances is up to now predominately based on individual single appliance testing under well-defined stable boundary conditions. This individual approach induced a series of evident problems. Additionally, the series of standards in the framework of the energy performance of buildings (e.g. EN 15316) is addressing combined / hybrid systems, although limited to the overall effect on the building energy performance and lacking accurate methods for the complex control strategies and interactions. The European Energy labelling and Eco-design (Lot 1 and Lot 2), approach the hybrid issue with the so called 'Package label', that is practical for its purpose, but lacks the desired accuracy one would expect from a product standard. Moreover, adding new appliances to an existing system cannot be handled in an appropriate manner. Due to the lack of fitting appropriate standards for hybrid systems ErP regulations lack options for adequate surveillance activities.

There is a clear need for a new generation of energy standards aimed at hybrid systems at the level of product standards; accurate, product performance comparison, harmonized reference conditions and practical in its implementation. In this aspect it is evident that there is a need for the elaboration and development of a new generation of standards for hybrid systems.

One other aspect is related to a new International Energy Agency (IEA) Task for solar heat for industrial processes, namely "Solar Process Heat - IEA Joint SHC Task 64/ SolarPACES Task IV" has already been activated in order to help solar technologies be and also be recognized as a reliable part of process heat supply systems. In this Task is included a dedicated Subtask D „Standardization and Certification" in order to implement the necessary actions for the enforcement of solar process heat competitiveness through support to the standardization and certification issues.

Concluding, legislation in Europe is increasingly putting a significant requirement of testing and paper-work on solar market but on the same time offers a common European wide legislation framework and supports the penetration of the market by solar systems. Through the Solar Keymark certification scheme, cross border barriers are reduced. A set of sound ENs for solar thermal systems exists, supporting both legislation and certification and a well-functioning mechanism is available for the constant development of standards to keep up with new legal issues and needs.

6. References

CEN https://www.cen.eu/ (date of access: 18/08/2020)

IEA-SHC (2020) '*IEA Solar heating and cooling programme - Solar heat worldwide Global Market Development and Trends in 2019 – Detailed Market Figures 2018'*. Weiss, W., Spörk-Dür, M. https://www.iea-shc.org/solar-heat-worldwide (accessed 18/08/2020)

SHE-ESTIF, 2020 http://solarheateurope.eu/about-solar-heat/solar-heat-what-is-it/ (date of access: 18/08/2020)

Solar Keymark http://www.estif.org/solarkeymarknew/ (date of access: 18/08/2020)

https://www.ecoboiler-review.eu/ (date of access: 18/08/2020)

https://www.ecohotwater-review.eu/ (date of access: 18/08/2020)

09. Solar Resource and Energy Meteorology

Radiative Cooling Potential Maps for Spain

Roger Vilà, Lídia Rincón, Marc Medrano, Albert Castell

Sustainable Energy, Machinery and Buildings (SEMB) Research Group, INSPIRES Research Centre, Universitat de Lleida, Pere de Cabrera s/n, 25001 Lleida (Spain)

Abstract

Radiative cooling is a novel technology which provides cooling power by emitting thermal radiation using the sky as a heat sink. Under proper conditions, net radiative cooling power of an ideal surface can be expressed as the difference between the emitted longwave radiation of a black surface minus the infrared radiation emitted by the atmosphere and absorbed by the surface. This atmospheric radiation depends on the local conditions. A continuous map of the radiative cooling potential in Spain has been prepared using two interpolation methods: Inversed Distance Weighted (IDW) and Kriging. The results obtained showed an average cooling potential of 55-60 W/m^2. Climate change, under different IPCC scenarios, do not have a big impact in the average capacity to do radiative cooling in Spain.

Keywords: radiative cooling, cooling potential, renewable energy, spatial interpolation, climate change

1. Introduction

The contribution of the greenhouse gases to climate change, as a result of the human activity, has reached a consensus among the scientific community. Global environmental awareness is currently increasing among society; this concern is reflected in public policies such as the Project Europe 2030 (*Project Europe 2030*, 2010). In the European Union, consumption in buildings accounts for 40% of the total energy demand and 36% of CO_2 emissions (European Comission, n.d.). In residential buildings this energy is mostly used for space conditioning purposes and domestic hot water (DHW). In this context, the share of renewable energies only accounts for 17.5%.

Radiative cooling is a novel, renewable and clean technology for space cooling. Radiative cooling is the process by which a surface -named radiative cooler- cools down by emitting thermal radiation towards the outer space taking advantage of the infrared atmospheric window transparency in the 7-14 µm range (Vall and Castell, 2017).

Under nighttime conditions, in the absence of solar radiation, radiative cooling power of a radiative cooler, at temperature T_s, can be expressed as eq. 1. The first term of the equation refers to the infrared energy radiated by the surface, the second term corresponds to the infrared radiation emitted by the atmosphere and absorbed by the surface, q_{cond} and q_{conv} are non-radiative heat exchanges. The emittance (ε_s) of ideal surfaces is equal to one, maximizing radiative cooling, if the surface is assumed to work at ambient temperature it can be expressed as eq. 2. If a radiative cooler is designed to work at ambient temperature, convective and conductive heat exchanges are minimized and radiative power is expressed as eq. 3 (Chang and Zhang, 2019).

$$q_c(T_s) = \varepsilon_s \sigma T_s^4 - \varepsilon_s \varepsilon_{sky} \sigma T_a^4 - q_{cond} - q_{conv} \quad [W/m^2] \qquad \text{(eq. 1)}$$

$$q_{c,ideal}(T_a) = \sigma T_a^4 (1 - \varepsilon_{sky}) - q_{cond} - q_{conv} \quad [W/m^2] \qquad \text{(eq. 2)}$$

$$q_{c,ideal}(T_a) = \sigma T_a^4 (1 - \varepsilon_{sky}) \quad [W/m^2] \qquad \text{(eq. 3)}$$

Infrared radiation from the atmosphere depends on the local conditions. As a consequence, radiative cooling potential varies between zones. Up until this time, it doesn't exist, in European countries, a source of field values of radiative cooling potential based on the location. Prediction of radiative cooling potential in different areas could become an aid to drive public policies on the usage of renewable energies.

Based on statistical models, and using available meteorological data for small group of points, the prediction of radiative cooling potential can be obtained for a whole region or country. Chang and Zhang (Chang and Zhang, 2019) modeled incoming infrared radiation in China and studied the radiative cooling potential using Kriging interpolation. Li et al. (Li et al., 2019) used Inverse Distance Weighting (IDW) interpolation to generate radiative cooling potential maps in USA. In this study we used both geostatistical methodologies to predict radiative cooling maps in Spain in order to discover what is the maximum potential of radiative cooling in Spain and which are the regions that have more potential. This study is complemented with the exploration of the evolution of radiative

doi:10.18086/eurosun.2020.09.01 Available at http://proceedings.ises.org

cooling potential in Spain under the context of climate change.

2. Methods

2.1. Data Acquisition

Climate data was obtained from the Meteonorm database. Meteonorm is a software used in energy simulation of buildings and solar applications that combines global meteorological data, space interpolations and stochastic weather generation (Remund et al., 2019).

The data obtained corresponded to the period 1991-2010 and each point in the sample contained hourly weather data for each day in a year. These data included ambient temperature, T_a and long-wave radiation from the atmosphere, q_{atm}, used in the calculation of radiative cooling. The sample was made up of data from 63 points in Spain. The number of points, 63, was determined by the total of points available in Metonorm, of which 52 belonged to the peninsular region, 3 to the Balearic Islands and 8 to the Canary Islands.

The evolution of the nocturnal potential of radiative cooling in the context of climate change was also studied using Meteonorm's data based on the emission scenarios presented in the fourth IPCC assessment report. The fifth assessment report presented new scenarios, the SRC scenarios; however, the fourth IPCC scenarios were chosen as for the SRC scenarios data was only available for big urban areas, which would have meant a very small dataset. For the Fourth Assessment Report (AR-4) based scenarios, data was available in all of the 63 points. Data was obtained from the three different scenarios available in Meteonorm: B1 (low emissions), A1B (middle emission) and A2 (high emission) (Solomon et al., 2007). Data from 2020 to 2050 maintained the same structure described above.

2.2. Data Preparation

Data preprocessing and data cleaning, as well as the statistical analysis and spatial predictions, were done with Rstudio version 1.3.

In order to obtain the nighttime radiative cooling (RC) potential, once the cleaning was performed, night values of the dataset were filtered. The maximum RC potential for each hour was calculated using the eq. 4. At each point of the sample the mean was calculated to know the annual average value of the radiative cooling potential.

$$q_{c,ideal}(T_a) = \sigma T_a^4 - q_{atm}\ [W/m^2] \qquad \text{(eq. 4)}$$

Some authors affirm that one requirement for Kriging is a normal distribution of the data (Hengl, n.d.), being necessary a transformation of the data in case it is not followed. Other authors say that there is no guarantee that doing this pre-transformation will result in better biased estimators (Villatoro et al., 2008). It was verified, using a Chi-Squared and a Shapiro-Wilk tests, that the data followed a normal distribution.

2.3. Interpolation models and validations

Two interpolation models have been used to predict the potential in Spain: Inverse Distance Weighting (IDW) and Kriging.

IDW is a deterministic model which assumes that close points are more correlated than others, and the influence of sample points to an unknown point decreases with a power of the distance. IDW estimator is computed as (Li et al., 2019):

$$\hat{z}(s_0) = \frac{\sum_i^N w(s_i)\cdot z(s_i)}{\sum_i^N w(s_i)} \qquad \text{(eq. 5)}$$

Where $\hat{z}(s_0)$ is the predicted value at a point s_0, $z(s_i)$ is the sample value at station s_i, N is the number of sample points and $w(s_i)$ is the weight of station $s_i$which is defined as the Euclidean distance to a p power.

$$w(s_i) = \|s_i - s_0\|^{-p} \qquad \text{(eq. 6)}$$

Kriging is a stochastic model based on the covariance of the sample point (Scheuerer et al., 2013) where predictions at an unknown point are a weighted linear combination of values at known points. Same as the IDW, it assumes that the points closer to the point of study have the greatest influence on the prediction, having a greater autocorrelation; while with distant points it becomes independent. The main difference is that in Kriging weights are not only based on this distance but they are also chosen to ensure an unbiased model and a minimum variance, adding complexity to the model. The quantification of these weights is achieved through the use of variograms. In the case study, theoretical variograms were adjusted to the data so that the error was minimal. The variogram is defined as the variance of the difference between field values at two locations (Hengl, n.d.):

$$\gamma(h) = \frac{1}{2} E\left[\left(z(s_i) - z(s_i + h)\right)^2\right]$$

Where $\gamma(h)$ is the theoretical variogram, $z(s_i)$ is the value of the target variable and $z(s_i + h)$ is the value of neighboring points at distance h.

Predictions were made in both models at a total of 296.197 new points. In order to assess the fit of the models, Leave-one-out cross-validation (LOOCV) was applied. LOOCV makes predictions at points in the sample using all data except that of the point in question; the process is repeated for all points in the sample. The differences between the predicted values and the observed values were then compared and the coefficients of determination (R^2) and root-mean-square deviation (RMSD) were computed.

3. Results and discussion

3.1. IDW and Kriging. Interpolation: 1991-2010 period.

Fig. 1 shows the spatial prediction maps of annual nocturnal radiative cooling potential for Spain. In both models, spatial distribution can be divided into a central area and the Canary Islands with the highest potential, the Mediterranean coast - south and east - with medium potential and the North Atlantic and Cantabrian area with the lowest potential in conjunction with the Balearic Islands.

Both models predict similar average annual values. The results of the Kriging model are slightly higher: the average night-time potential across the country is 59.89 W/m^2 while the IDW model predicts an average of 58.89 W/m^2. The maximum and minimum values of the Kriging interpolator are 70.88 W/m^2 and 45.6 W/m^2, respectively, while for the IDW model, these values are 70.82 W/m^2 and 45.4 W/m^2.

Cross-validation analyzed the goodness of each of the models. R^2 of the Kriging model is 0.71 and the RMSE is 3.05 W/m^2. In the case of IDW, it has a slightly worse performance: the value of R^2 is 0.61 and the RMSD is equal to 3.64 W/m^2.

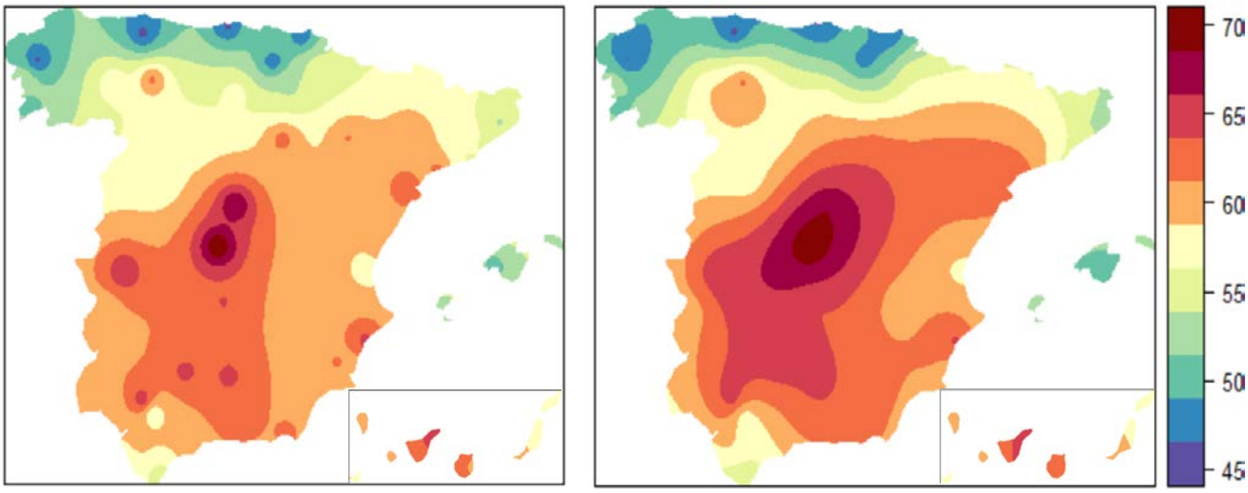

Fig. 1. Map of distribution of anual average nighttime radiative cooling potential [W/m^2] . Two models have been used IDW (left) and Kriging (right).

It is also noteworthy the phenomenon known as "bull's eyes" that appears on the map of the IDW model, represented by unrealistic circular patterns around the area of influence of the sampling points. The Kriging map, on the other hand, presents smoother transitions that pick up the variability of the different points.

3.2. IPCC scenarios. Prediction of radiative cooling evolution.

IPCC scenarios have been interpolated using the Kriging model. They predict a drop of radiative cooling potential with respect to 1991-2010 results. Maps show that the potential of the regions to produce radiative cooling does not vary between 2020 and 2050 (Fig. 2, Fig. 3, Fig. 4), remaining almost constant. For example, the average potential in 2020 within the A1B scenario is 55.67 W/m^2 while in 2050 it is 55.64 W/m^2. In this scenario the maximum and minimum values were 61.43 W/m^2 and 49.46 W/m^2 in 2020 and, 61.60 W/m^2 and 44.46 W/m^2 in 2050. Table 1 lists these summary metrics for the different scenarios. It can be seen that the results converge in the three scenarios, with no significant differences among them. Two main regions can be distinguished: one with higher potential formed by the central regions, the south-west, north-east and the Canary Islands; and the other region, with lower potential, formed by the north, the east and south-east coast and the Balearic Islands.

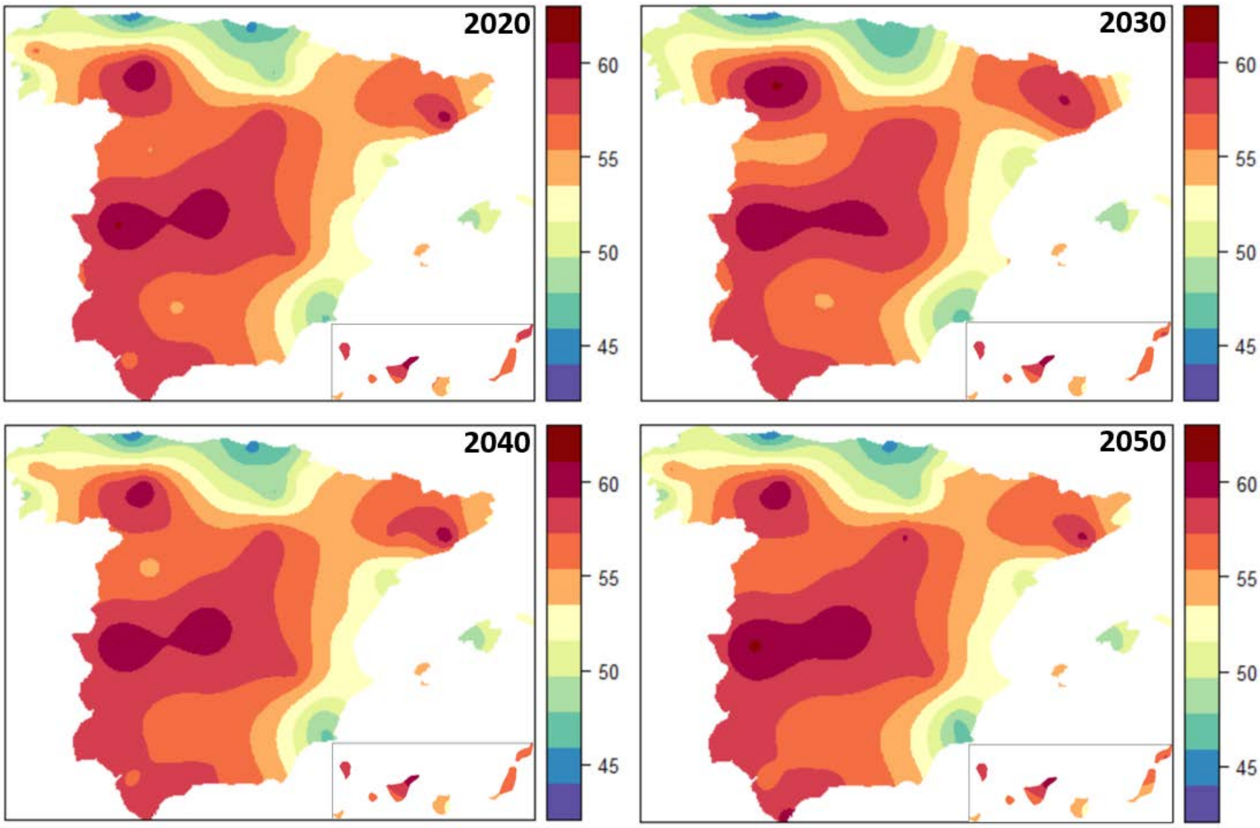

Fig. 2. Map of predictions of nighttime radiative cooling potential [W/m^2] for the period 2020-2050 based on the scenario A1B from the IPCC.

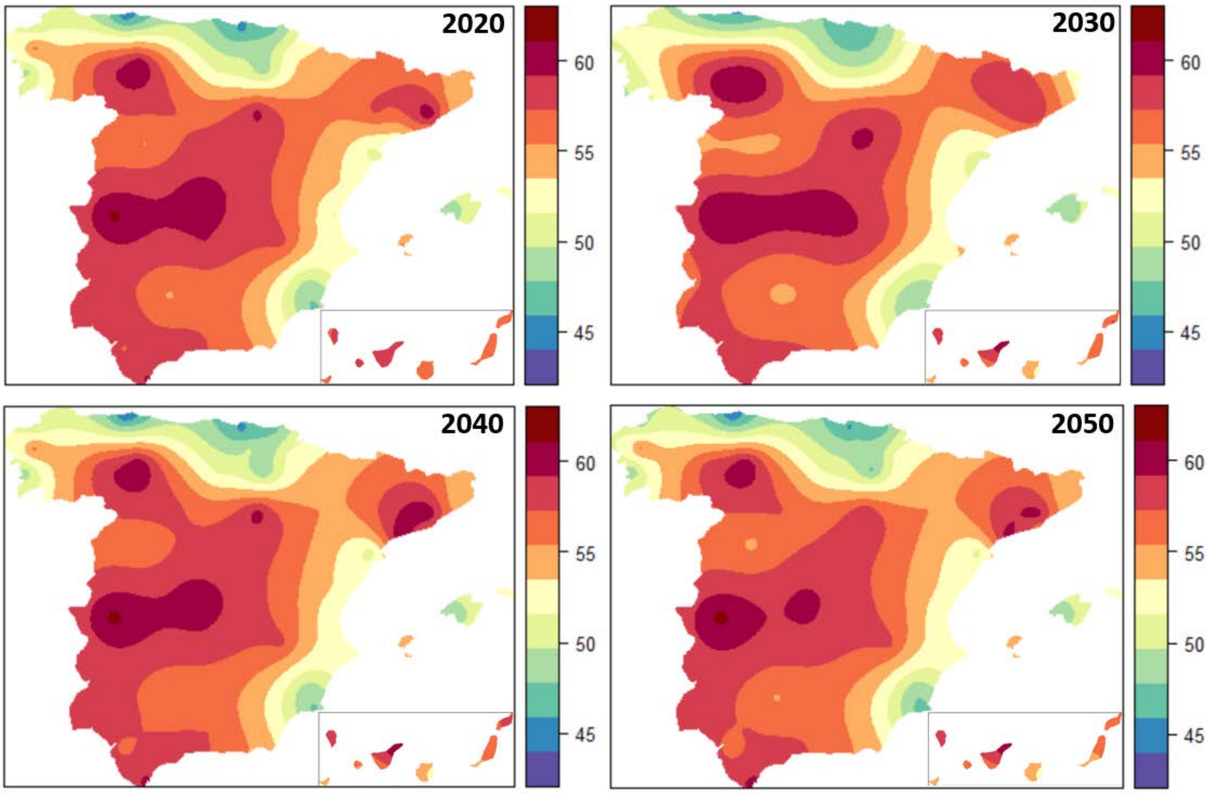

Fig. 3. Map of predictions of nighttime radiative cooling potential [W/m^2] for the period 2020-2050 based on the scenario A2 from the IPCC.

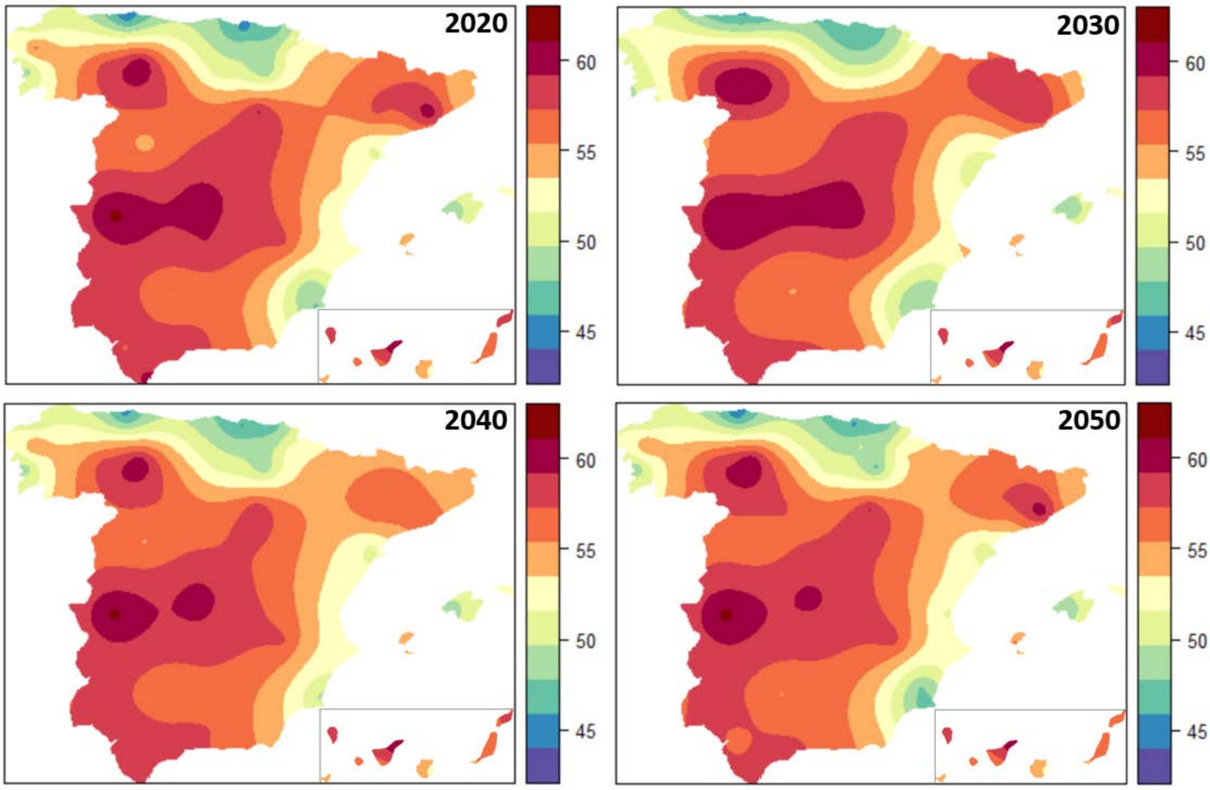

Fig. 4. Map of predictions of nighttime radiative cooling potential [W/m^2] for the period 2020-2050 based on the scenario B1 from the IPCC.

Tab. 1. *Summary metrics of the prediction models*

Year	Scenario	Min	Max	Average	R^2	RMSD
2020		44.46	61.43	55.67	0.60	2.83
2030	A1B	44.76	61.16	55.53	0.61	2.84
2040		44.36	61.21	55.61	0.63	2.75
2050		44.49	61.60	55.64	0.62	2.81
2020		44.74	61.62	55.90	0.63	2.77
2030	A2	45.45	60.69	55.59	0.60	2.84
2040		44.29	61.75	55.83	0.59	2.96
2050		44.55	61.77	55.64	0.60	2.89
2020		44.30	61.73	55.78	0.61	2.85
2030	B1	45.56	60.95	55.77	0.60	2.90
2040		45.17	61.68	55.69	0.47	3.28
2050		44.43	61.71	55.50	0.60	2.88

From the sample values, in both A1B and A2 scenarios, temperature increases over 1°C while this increase is less than 0.5°C in the B1 scenario. As a result of this increase in temperature (Fig. 5), the infrared radiation emitted by the radiative cooler slightly increases. The infrared radiation from the atmosphere –and absorbed by the radiative cooler– also increases (Fig. 6), compensating this radiation emitted by the radiative cooler due to the surface temperature. As a result of this balance, the average radiative cooling remains constant throughout the studied years (Fig. 7).

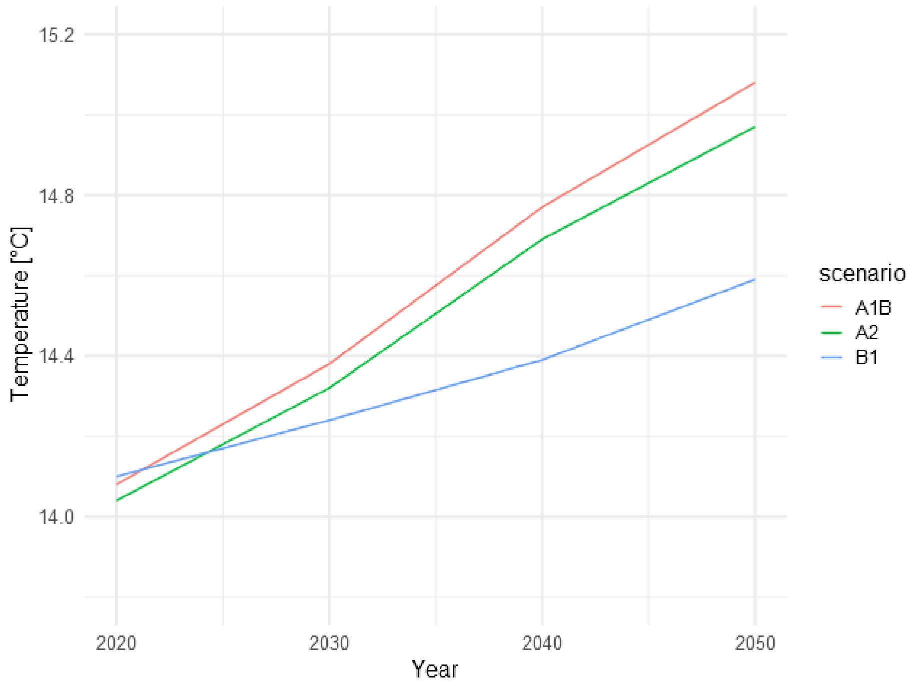

Fig. 5. Evolution of the mean surface temperature for different IPCC scenarios.

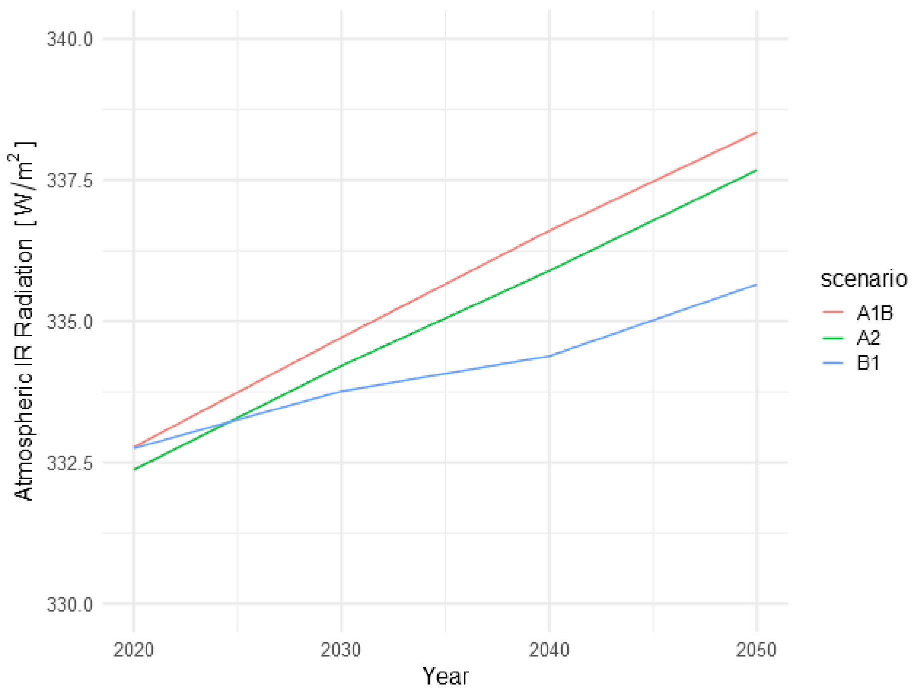

Fig. 6. Evolution of the infrared radiation coming from atmosphere and absorbed by the emitting surface for different IPCC scenarios.

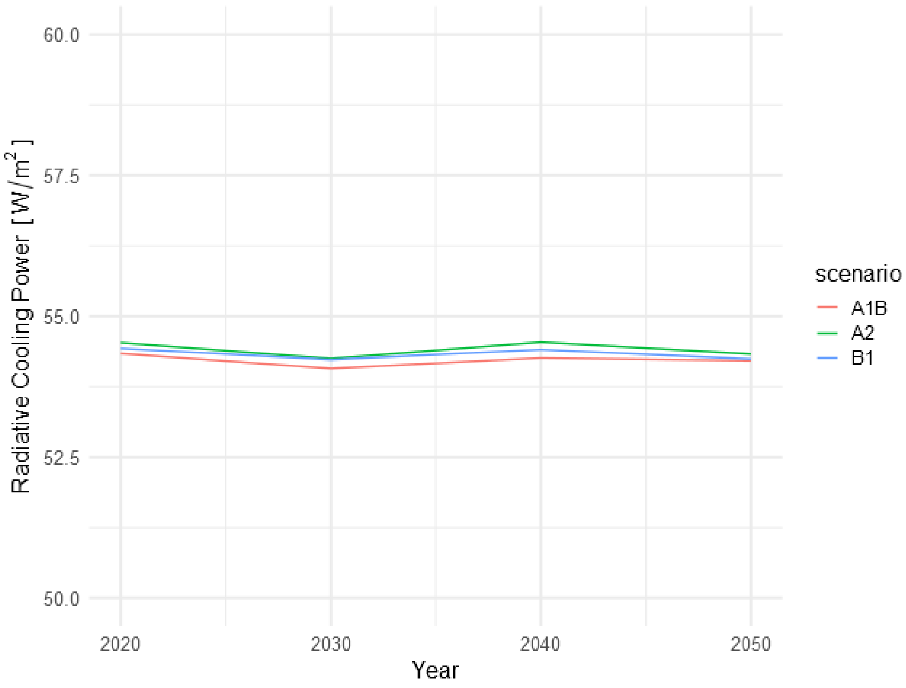

Fig. 7. The evolution of the net radiative cooling power, computed as the difference between the emitted radiation and the absorbed radiation from the atmosphere, remains constant under different IPCC scenarios.

4. Conclusions

This work has presented the nocturnal potential in Spain of a renewable technology for cold production: radiative cooling. To determine this potential two interpolation models have been used: IDW and Kriging. The results show that the average annual capacity for surfaces that behave like an ideal black body is around 58-60 W/m^2; the actual case will remain below these estimations. Radiative cooling potential depends on the location The most favorable areas for radiative cooling are the central regions and the Canary Islands, while the north and the Balearic Islands have lower predictions. Of the two models used, the Kriging model appears to be a better model than the IDW. In IDW, source points have a strong influence on the final predictions showing, in the maps, unrealistic patterns around them; in Kriging, predictions present smoother transition.

Predictions of the evolution of the potential have also been made based on different emission scenarios from the fourth IPCC report. Under these scenarios, the average annual night potential is slightly reduced to 55-56 W/m^2. These scenarios predict a temperature rise of 0.49°C, in the most favorable scenario, and 1°C in the most unfavorable between 2020 and 2050. An increase in ambient temperature does not mean an increase in potential as it is balanced out by an increase in long-wave atmospheric radiation.

All three scenarios have converged to similar radiative cooling nocturnal values. Despite the slight reduction in potential, climate change does not have a significant impact on the average capacity for radiative cooling in Spain. In these scenarios the northern region of the country is distinguished from the rest of the country.

5. Acknowledgments

The work was partially funded by the Spanish government under grant agreement RTI2018-097669-AI00 (Ministerio de Ciencia, Innovación y Universidades). The authors would like to thank Generalitat de Catalunya for the project grant given to their research group (2017 SGR 659).

6. References

Chang, K., Zhang, Q., 2019. Modeling of downward longwave radiation and radiative cooling potential in China. Journal of Renewable and Sustainable Energy 11, 066501. https://doi.org/10.1063/1.5117319

European Comission, n.d. Energy performance of buildings directive. URL https://ec.europa.eu/energy/en/topics/energy-efficiency/energy-performance-of-buildings/energy-performance-buildings-directive#documents (accessed 1.23.18).

Hengl, T., n.d. A Practical Guide to Geostatistical Mapping 165.

Li, M., Peterson, H.B., Coimbra, C.F.M., 2019. Radiative cooling resource maps for the contiguous United States. Journal of Renewable and Sustainable Energy 11, 036501. https://doi.org/10.1063/1.5094510

Project Europe 2030: challenges and opportunities : a report to the European Council by the Reflection Group on the Future of the EU 2030, 2010. . Publications Office of the European Union, Luxemburg.

Remund, J., Müller, S., Kunz, S., Huguenin-Landl, B., Studer, C., Cattin, R., 2019. Meteonorm. Meteotest, Switzerland.

Scheuerer, M., Schaback, R., Schlather, M., 2013. Interpolation of spatial data – A stochastic or a deterministic problem? Eur. J. Appl. Math 24, 601–629. https://doi.org/10.1017/S0956792513000016

Solomon, S., Intergovernmental Panel on Climate Change, Intergovernmental Panel on Climate Change (Eds.), 2007. Climate change 2007: the physical science basis: contribution of Working Group I to the Fourth Assessment Report of the Intergovernmental Panel on Climate Change. Cambridge University Press, Cambridge ; New York.

Vall, S., Castell, A., 2017. Radiative cooling as low-grade energy source: A literature review. Renewable and Sustainable Energy Reviews 77, 803–820. https://doi.org/10.1016/j.rser.2017.04.010

Villatoro, M., Henríquez, C., Sancho, F., 2008. Comparación de los interpoladores IDW y Kriging en la variación espacial de pH, Ca, CICE y P del suelo. Agronomía Costarricense 12.

Photosynthetically Active Radiation Monitoring Network in Spain

Ana A. Navarro[1], Rita X. Valenzuela[1], Ousmane Wane[1,2], Francisco Ferrera-Cobos[1,3], Luis F. Zarzalejo[1], Jose M. Vindel[1], Guillermo Díaz[4] and Jose M. Franco-Valiente[4]

[1] CIEMAT, Madrid (Spain)

[2] CIB-CSIC, Madrid (Spain)

[3] E.T.S.I. Agronómica, Alimentaria y de Biosistemas, Universidad Politécnica de Madrid, Madrid (Spain)

[4] CETA-CIEMAT, Trujillo (Spain)

Abstract

The main objective is the development of a network of measurement, modeling, database and web services of photosynthetically active radiation (PAR) over mainland Spain.

Keywords: photosynthetically active radiation, PAR, measurement network

1. Introduction

Photosynthetically Active Radiation (PAR) includes wavelengths between 400-700 nm of the solar spectrum. This portion of solar irradiance can be used by plants, algae, and cyanobacteria to fix inorganic carbon in the form of organic carbon throughout photosynthesis.

Unfortunately, only a few radiometric stations can provide PAR measurements on the ground and it is often calculated as a constant ratio of the broadband solar radiation. However, the ratio between PAR and Global Horizontal Irradiance (GHI) is not constant, depends on climatic characteristics, aerosol presence, etc of each location (Ferrera-Cobos et al., 2020a, 2020b).

PAR is of interest in many applications, such as biomass for energy, assessment of energy balance in ecosystems, or crop production for food. Related to water assessment, it may be interesting for monitoring and detection of harmful algae blooms and also in the study of the productivity of microalgae in wastewater treatment for a small population. One of these applications is explored in ALGATEC-CM project, which addresses the technical and economic difficulties that hinder the full industrial implementation of microalgae. One of the objectives of this project is the assessment of the PAR resource in the Madrid region and modeling the best conditions of PAR irradiance and temperature for the growth of microalgae.

The main outcome of this project is filling this absence of measurements, recording measurements of PAR on mainland Spain and providing access to them through a web page. This communication describes the main features of the PAR network and details of its implementation.

doi:10.18086/eurosun.2020.09.02 Available at http://proceedings.ises.org

Fig. 1: PAR stations in all Peninsular Spain. In red the stations of the Madrid region

2. PAR Network

The Photosynthetically Active Radiation network consists of twelve stations across Spain located in Lugo (Galicia), Villaviciosa (Asturias), Vitoria (País Vasco), Zaragoza (Aragón), Soria and Salamanca (Castilla León), Albacete (Castilla la Mancha), Córdoba and Almería (Andalucía), Aranjuez, Buitrago and Alameda del Valle (Madrid) as illustrated by Fig. 1.

2.1. Selection of the specific sites for PAR stations

The most representative sites to place the stations were selected using cluster analysis. Estimations of the Spectral Resolved Irradiance product (Muller et al., 2009; Müller et al., 2013) provided by CM-SAF over mainland Spain were used, this product includes the bands of the solar spectrum divided according to the absorption coefficient of different gases, named Kato bands (Kato et al., 1999, Wandji et al., 2015). The PAR estimations were obtained using the bands between 400 nm to 700 nm, whereas GHI estimations needed all the bands corresponding to the whole solar spectrum.

The representative variable was the clearness PAR index, kt_{PAR}, which is similar to the clearness index, kt. In this case, it is defined as the ratio between PAR reaching the Earth’s surface and extraterrestrial PAR. After performing the clustering analysis, two regions were obtained: one covering the north of Spain, with some small areas in the second one, that covers the rest of the territory. This division reflects the main climatic characteristics of Spain. Details of the algorithm performed can be found in a previous study (Vindel et al., 2018).

2.2. Network instrumentation and installation

Once the optimal locations were known, the objective was focused on detecting the suitable sites, with clear land and secure places. Several contacts were established with different entities that had the infrastructures and space to install the PAR stations.

Previous to the installation, the horizon was determined using HORIcatcher software. The HORIcatcher (HORICatcher, 2020) consists of a digital camera with a fisheye mirror that works with the Meteonorm software. The software tool allows users to describe horizon obstacles, sunshine duration, and sun exposure reduced by obstacles like trees, houses, or mountains throughout the year.

The basic configuration of stations is described in Table 1.

Tab. 1: Equipment for PAR network

Instrument type	Manufacter / model	Measurement
Data Logger	HOBO / RX3000	Data acquisition
Data Logger	Campbell / CR1000	Data acquisition
Pyranometer	Kipp & Zonen / CM21	GHI
Silicon pyranometer	Apogee / SP-110-SS	GHI
Quantum PAR sensor	Eko / ML-020P	PAR
Quantum PAR sensor	Apogee / SQ-110/120	PAR
Temperature/Relative humidity sensor	Vaisala / HMP45A	T/H
Temperature/Relative humidity sensor	ONSET / S-THB-M002	T/H

All instruments were calibrated before installation by the manufacturers, however, an intercomparison campaign was carried out to verify that all sensors are analogous and in consequence their measurements are reliable. All radiometers were assembled and programmed according to the supplier's instructions and were subsequently monitored. The analysis of the data obtained during the intercomparison campaign concluded that none of them showed significant deviations and that, therefore, all sensors were suitable to be displayed in the network.

The network comprises twelve stations distributed across mainland Spain (Table 2). They were installed according to the characteristics of the places, four stations were installed in a portable tripod (Buitrago, Córdoba, Lugo, and Salamanca), three of them in a stainless-steel and galvanized pole (Albacete, Zaragoza, Vitoria, Villaviciosa) and two are in CIEMAT facilities at Plataforma Solar de Almería (PSA) and Centro de Desarrollo de Energías Renovables, CEDER-CIEMAT in Soria. Nine of the stations are fully autonomous by using GSM network and solar power as an energy supplier, the other two are connected to our local area network.

The PAR network measures continuously with a sampling frequency of 1 min for all variables. An automated data collection protocol was defined to collect the recordings from each station at a centralized server located in Centro Extremeño de Tecnologías Avanzadas (CETA-CIEMAT). Thus, the established configuration allows a daily generation of data files for each station. The recorded variables (PAR, GHI, Temperature, Humidity, and Dew Point) are dumped automatically to the central server via FTP.

The database includes the register of all metadata such as location, sensors, or calibrations. Also an upgrade of procedures is in progress, this will allow to determine and store information related to timestamp, such as quality controls, missing data detection, and verification that record data are within acceptable range limits.

Tab. 2: Localization of all PAR stations.

Station ID	Latitude	Longitude	Height (m)	Climate type	Operational
Albacete	39.042	-2.082	696	Continental Mediterranean	26/03/2019
Aranjuez	40.074	-3.524	505	Continental Mediterranean	11/02/2020
Buitrago	40.992	-3.654	996	Mountain	10/01/2020

Córdoba	37.857	-4.803	106	Continental Mediterranean	27/03/2020
Lugo	42.995	-7.541	495	Oceanic	15/04/2019
Salamanca	40.798	-5.715	290	Continental Mediterranean	13/03/2019
Villaviciosa	43.476	-5.441	662	Oceanic	13/05/2019
Vitoria	42.854	-2.622	525	Oceanic	08/04/2019
Zaragoza	41.727	-0.814	243	Continental Mediterranean	18/03/2019
CEDER-CIEMAT	41.601	-2.508	1051	Continental Mediterranean	15/07/2015
PSA-CIEMAT	37.092	-2.364	400	Standard Mediterranean	21/01/2016
Alameda	40.915	-3.844	1115	Mountain	Scheduled in Sept. 2020

3. Working in progress

PAR may be of interest in several applications, as it has been mentioned before, such as the convenience of using microalgae for wastewater treatment for small communities. The Solar Radiation Group for Energetic Applications (CIEMAT) is currently collaborating in the project *Development of Advanced Microalgae Technologies for a Circular Economy (ALGATEC),* where is participating in an analysis of a methodology for identifying suitable sites to locate High Rate Algae Pond (HRAP) in the Madrid region. HRAP is a low-cost wastewater treatment system designed to achieve secondary wastewater treatment and biomass production from algae. The algae supply the oxygen demand for the bacterial degradation of organic matter, and the bacteria excrete mineral compounds that provide nutrition to the algae. Biogas self-consumption generated from the anaerobic digestion of the sludge (algae and bacteria) produced in the wastewater treatment may help to reduce the energy consumption of the whole plant. The knowledge of microalgae productivity under different climatic conditions can help to carry out an economic feasibility analysis of the system. Fig 2, display, as an example, one of the station ensembles and the results of the conventional regression and ANN models obtained in PSA-CIEMAT station.

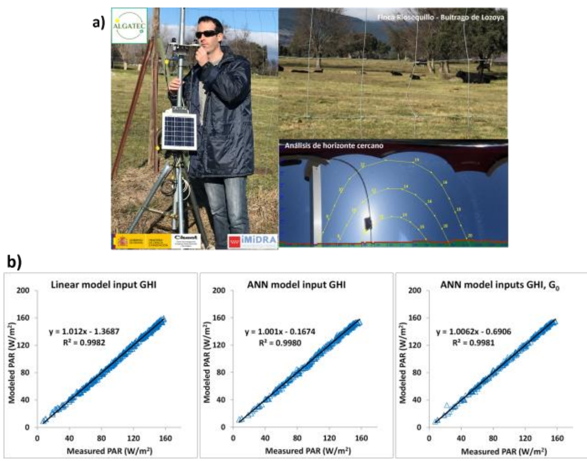

Fig 2. a) Drawn horizon line and Buitrago station assembly, b) Models' validation on PSA station

The ALGATEC project handles three measuring stations that belong to the PAR network described before, implemented in the Madrid region, which are, Aranjuez, Buitrago, and Alameda, the latest not installed yet because of COVID pandemic management difficulties. These measurements will be used to obtain a *Representative Meteorological Week* per quarter, as a concept similar to the *Representative Solar Year* (RSY) for thermoelectric solar plants, to carry out a long-term study of the meteorological variables, which electricity production estimations depend on. The study reflects the variability and the most probable statistical representation in the long-term of the climatology of the location, taking into account the variables considered. Therefore, this concept is transferred to the evaluation of sites for HRAP systems to study the influence of weather conditions in the Madrid region; the long-term behavior of some important meteorological variables for the growth of microalgae in the wastewater system plant is studied, considering that the rest of the necessary growth parameters are enough and in optimal concentration, and depending only on the climate of the location

There are measurement stations providing PAR and other variables, for each cluster resulting from applying the previously explained methodology based on the kt_{PAR}. Therefore PAR estimations from satellite imagery (CM-SAF, EUMESAT) can be adjusted with the data from each of the measurement stations in each cluster. As a result, PAR values will be more accurate. For this, it is necessary at least one-year of data in the sites of Buitrago, Aranjuez, and Alameda stations to do the adjustment.

4. Conclusion

The design, installation, and operation of twelve PAR stations monitoring network have been described in this communication. The PAR network will provide good quality data and aims to grow, facilitate and promote the work of all researchers interested in exploring knowledge of PAR radiation as an energy source, as well as any other studies that need PAR measurements to be developed, as applications on wastewater treatment by microalgae.

5. Acknowledgments

We gratefully acknowledge funding for this research from the Autonomous Community of Madrid, Spain and co-financed by the FEDER “A way of making Europe” ALGATEC-CM (P2018/BAA-4532), Spanish Ministry of Economic and Competitiveness (CGL2016-79284-P AEI/FEDER/UE) and the governments of Ibero-American countries in the framework of CYTED-IberoAmerican Programme on Science and Technology for Development (Red RENUWAL P320RT0005 CYTED). We also gratefully acknowledge the technicians of Escola Politécnica Superior de Lugo – USC, Instituto Vasco de Investigación y Desarrollo Agrario – NEIKER, Estación Experimental de Aula Dei – CSIC), Centro Hispanoluso de Investigaciones Agrarias – CIALE – USAL, Instituto Técnico Agronómico Provincial –ITAP and Instituto Andaluz de Investigación y Formación Agraria, Pesquera, Alimentaria y de la Producción Ecológica – IFAPA, Instituto Madrileño de Investigación y Desarrollo Rural, Agrario y Alimentario – Finca Riosequillo and Finca La Chimenea – IMIDRA in maintaining these sites through the duration of this study. F. F-C. was supported by pre-doctoral contract funding from Spanish Ministry of Economic and Competitiveness (BES-2017-082043).

6. References

Ferrera-Cobos, F., Vindel, J.M., Valenzuela, R.X., González, J.A., 2020a. Models for estimating daily photosynthetically active radiation in oceanic and mediterranean climates and their improvement by site adaptation techniques. Adv Space Res 65, 1894–1909. https://doi.org/10.1016/j.asr.2020.01.018

Ferrera-Cobos, F., Vindel, J.M., Valenzuela, R.X., González, J.A., 2020b. Analysis of Spatial and Temporal Variability of the PAR/GHI Ratio and PAR Modeling Based on Two Satellite Estimates. Remote Sens 12, 1262. https://doi.org/10.3390/rs12081262

HORICatcher, 2019. HORIcatcher product at meteonorm website. URL: https://meteonorm.com/produkt/horicatcher. accessed 01 April 2020.

Kato, S., et al. 1999. The k-distribution method and correlated-k approximation for a shortwave radiative transfer model. J. Quantitative Spectroscopy and Radiative Transfer 62, 109–121.

Mueller, R.W., et al. 2009. The CM-SAF operational scheme for the satellite-based retrieval of solar surface irradiance - A LUT based eigenvector hybrid approach. Remote Sensing of Environment 113, 1012–1024.

Müller, R., Behrendt, T. 2013. Algorithm Theoretical Baseline Document: Spectrally Resolved Solar Surface Irradiance SRI. doi:10.5676/EUMETSAT_SAF_CM/CLAAS/V001

Vindel J.M., et al., 2018. Methodology for optimizing a photosynthetically active radiation monitoring network from satellite-derived estimations: A case study over mainland Spain. Atmos. Res. 212, 227–239. https://doi.org/10.1016/j.atmosres.2018.05.010

Wandji, W., et al. 2015. Estimating the photosynthetically active radiation under clear skies by means of a new approach. Adv. Sci. Res. 12, 5–10.

Evaluation of weather conditions in urban climate studies over different Madrid neighbourhoods: Influence of urban morphologies on the microclimate

Helena López Moreno[1,2], Emanuela Giancola[1], María Nuria Sánchez Egido[1], José Antonio Ferrer Tevar[1] and Silvia Soutullo Castro[1]

[1] Department of Energy, Energy Efficiency in Buildings Unit of CIEMAT, Madrid (Spain)

[2] Construction and Architectural Technology, Department of UPM, Madrid (Spain)

Abstract

Urban microscale data is crucial in the evaluation of a wide range of engineering applications. However, it is observed an outdated climate data files and an undetailed boundary conditions within the urban environment, triggering variations between real and simulated energy data. This fact is proved through the analysis of two accessible weather files (EPW and CTE) and an updated experimental climate datafile (EXP10). Then, there are characterized the albedo (α), the emissivity (ε), the sky view factor (SVF) and the Mean Radiant Temperature (MRT) for three representative urban structures, considered notable variables for the outdoor energy assessment.

The EXP10 data are warmer, drier and have intense and longer radiation than EPW and CTE files, showing an increase MRT values for all cases. Some MRT variations are also found between urban typologies. Dense-medium-rise areas with limited green-tree zones (DS_Usera) present a low-medium emissivity and SVF, being the MRT higher during the night. On the contrary, sprawl-high-rise areas with medium green-tree zones (OB_Cañorroto) have a high albedo SVF, graphing the lowest MRT during the night. Although tree crowed areas reduce the MRT along the day, they could increase these values during the night because of the possible low SVF in their canopy as it is shown in sprawl-low-rise areas with large green-tree zones (SH_Viso).

Keywords: climate change, boundary conditions, urban microclimate, urban typology, mean radiant temperature

1. Introduction

As a response to the growing urbanization, numerous neighbourhoods with different density and several building structures have been built around the cities. These neighbourhoods are characterized by a large number of low-rise to high-rise structures and autonomous buildings with different layouts/forms (Sharifi 2019), different geometries and public/private open spaces (Wang et al. 2016). The result of these changes in the physical characteristics of cities is an urban microclimate characterized by a set of twisted climatic conditions with multiple levels of humidity, temperature, and wind speed that prevails in an urban area (Jhaldiyal et al. 2018). It is generally accepted that urban microclimate conditions have major impacts on the variations of local weather variables (air temperature, wind flow, shortwave/longwave radiation etc.) (Javanroodi and Nik 2020). These facts impact on air pollution patterns (Castaldo et al. 2017), building's energy performance (Soutullo et al. 2020; Sánchez et al. 2020), urban health (Linares, n.d.), thermal comfort (Lai et al. 2019), as well as the development of daily activities.

Climate change makes cities even more vulnerable to these urban microclimatic variations. In addition to the global rise of temperatures, it is expected extreme weather events more intense, frequent and long (IPCC, 2018). In an increasingly urbanized world, where most of the half of the population live in urban areas, it is crucial to define an accurate climate change adaptation plan to ensure the development of activities and health´s quality. According to the Agenda 2030, this framework must be based on sustainable principles, considering both humans and other living beings. However, some shortcomings seem to limit the development of resilient cities. A lack of updated climate files and an undetailed knowledge of the climate variation within the urban structures could cut down the effectiveness of frameworks designed to face the new climate scenarios.

To this end, this article proposes a methodology to quantify the incidence of macroscale climate conditions on

doi:10.18086/eurosun.2020.09.03 Available at http://proceedings.ises.org

urban structures by calculating different urban typologies through dynamic simulations. The main objectives proposed of this paper are: a) Quantify differences and climate trends for widely used climate data and an updated experimental climate data. b) Analyse different urban characteristics in the city and their influence in the urban microclimate. c) Study the diverse urban boundary conditions and their impact on the main microclimate variables.

2. From macroscale climate conditions to microscale urban climate

Urban structures modify the local climate conditions (macro level) within the city (micro level), changing the energy balances. This effect is known as urban microclimate and it is due to the substitution of the natural layer to buildings and paved surfaces. The urban microclimate variability can be assessed transforming the macroscale climate to urban microclimate through the local climate files, urban characteristics and their boundary conditions.

2.1. Climate files

The weather of a region is obtained from the treatment of the climatic variables registered by meteorological stations over long periods of time. There are multiple global climate classifications. Köppen-Geiger is one of the most known, however many of them only provide a general idea of the local climate but do not consider relevant factors for a specific location as the orography, green areas, mass of water, soil characteristics or the wind or insolation profiles. A common method to summarize the local weather conditions is the typical meteorological year (TMY), that must be based on long term weather variables records (at least 10 years), to ensure the natural climate cycles. Depending on the study, there are diverse methodologies to assess the TMY, varying the weight factor of the meteorological variables (Zarzalejo et al. 1995; Soutullo et al. 2020; 2017). Representative days or periods can be also useful to study the seasonal climate behaviour.

The urban or buildings energy simulation software, use the TMY files to feed their calculations. The EPW files are used by the Energy+ software or the MET files developed by the Spanish Building Code (CTE) for their standard simulation tool. Nonetheless, the use of these easily available files for the urban quantifications lead to high levels of uncertainties. These files are usually outdated despising the global warming. In addition, these files are commonly based on weather recording stations located out of the city, not considering the specific boundary conditions and the urban microclimate effect that modifies the local weather conditions in the city.

Updated climate data files from recent long-term experimental monitored campaigns should be considered integrating the climate change and its direct impact on our environment. Annual and seasonal averages of relevant meteorological variables should be assessed but also identify extreme weather events. Temperature and solar global radiation as well as relative humidity and wind are usually analysed.

2.2. Urban characteristics

Built environments present a varied range of buildings characteristics, materials properties or urban distributions, as a result of the evolution needs in the city´s growth. The urban aspects are linked to a specific period as the use of materials or constructive systems. Beyond this, flowering urban theories about how to understand the city or the socioeconomic conditions of the citizens had influence in the urban environment and its transformation. Examples of these facts are the role that have green or pedestrian areas of different neighbourhoods compared to the private vehicle, or the housing design for workers compared to higher-income population.

To gather the differences between urban conditions, it is used urban typologies classifications. They define the common parameters that group certain ways of designing and building. Through them, the global behaviour of an area could be estimated effectively. In addition, their top-down approach from an intermediate scale allows us to analyse common trends that are not generally considered in administrative divisions or at the building level.

Some urban classifications are developed based on urban indicators through the aerial image's analysis covering wide world´s areas. Corine Land Cover Classification (CLC), the Urban Atlas project or the Local Climate Zones (LCZ) (Stewart and Oke 2012) classify the areas in predefined categories, giving an urban pattern idea. On the other hand, more detailed urban classification methods are carried out specifically to a city or a region, considering the local urban conditions, codes, normative, culture or uses. The city of Madrid has different urban designation as the Regional Direction of the Spanish Cadastre (RDSC), the Statistical Institute of the Madrid Community (SIMC) or the General Urban Planning Plan (GUPP). Finally, World Urban Database and Access Portal Tools (WUDAP) try to combine both classification types over different approach levels.

2.3. Boundary conditions of urban environments

The boundary conditions are a key factor in the physical behaviour modifying its climate environment. Some of European roadmaps as the Strategic Energy Technology plan (SET-Plan, 2018), point out the necessity to assess these boundary conditions deeply in order to ensure an optimized integration of an energy transition framework.

Their role it is crucial in the meteorological variables as temperature, humidity, wind and radiation values. They depend on a combination of factors as the albedo (α) and emissivity (ε) that refer to the material characteristics, while the Sky View Factor (SVF) is related to the morphology conditions. The albedo depends on the reflection capacity of the material and it is related to the colour and surface characteristics. The emissivity is defined as the capacity of surface materials to emit the heat as thermal radiation. The proportion of visible sky above a certain observation point determines the Sky View Factor. In urban areas, these factors are the result of the human activity and must be controlled in order to not reach more extreme climates conditions in urban areas, optimizing the distribution of the city network. The influences of the most significant variables in the city are:

- *Soil:* The colour, composition, porosity, thermal inertia, etc., impact on the climatology of the area modifying reflected solar radiation, thermal gradient or air quality.
- *Water:* The presence of water may act as a temperature stabilizer through evaporative exchanges.
- *Vegetation:* Plants notably affects shading factors, thermal gradients, moisture content and air quality.
- *Wind circulation:* The speed and direction of wind is strongly influenced by the orography, the water masses, etc., modifying the sensation of thermal comfort.
- *Urban environment:* Buildings, infrastructures or human activity have a dominant influence on the climate conditions of the city. The modification of the urban climate conditions depends on numerous factors such as the construction materials (absorptivity or reflection), the presence of green areas (elements of shade and humidity), the height of the buildings (solar accessibility or air circulation) or the conditioning systems (heat pumps, air conditioners, etc).

2.4. Microclimatic conditions, variability within the urban structure

The most influential meteorological variables on the urban microclimate are temperature and solar radiation. These variables regulate most of the urban energy exchanges, so their intensity, variability or hourly distribution are determining factors, influenced by the boundary conditions (Shahrestani et al. 2015). They are the main factors of the widely studied Urban Heat Island (UHI), that implies a global rise of temperatures in the built environment as a consequence of human influence (Oke T.R. 1982). However, other meteorological variables should be considered. The air humidity determines the use of different passive thermal conditioning strategies as evaporative and dehumidification cooling. The correct consideration of the preferential wind flows and the adequate distributions of urban structures are crucial to define urban areas with optimum thermal comfort and air quality.

Regarding the thermal comfort and consequently the urban health and the development of daily activities, other variables as the Mean Radian Temperature (MRT) represent a determinant factor. It is defined as the uniform temperature of an imaginary room in which the radiant heat transfer from the human body is equal to that carried out in a non-uniform real room. MRT depends on the heat emitted by the surrounding materials and it cannot be obtained directly. The MRT´s calculation is based on measures as the globe temperature (Tg) or six directions method (Marino, Nucara, and Polimeni 2018). However, the complex and limiting process, lead to the use of energy simulation tools as Envimet, Trnsys, Star CCM+ or SkyHelios, commonly used for the energy simulation.

3. Case of study: city of Madrid

The methodology proposed starts with the creation of a climate file, adapted to the current climate trends through a long-term experimental campaign (EPX10). The EXP10 data and two representative climate files (EPW and CTE) have been used to analyse the climate trends. Secondly, representative urban morphologies have been selected, studying their morphological and material properties. Thirdly, the interactions between urban morphology characteristics and weather variables of experimental and representative climate files have been assessed. Variations of albedo (α), emissivity (ε), Sky View Factor (SVF) and Mean Radian Temperature (MRT) at the urban microscale are studied for these urban morphologies by dynamic simulations. Finally, the city of Madrid is selected as a case of study. It is chosen by its urban complexity and its morphological and material diversity. In addition, Madrid is the biggest city in Spain, with diverse activities and socioeconomic profiles.

3.1. Quantifying the climatic trends

Madrid is characterized by temperate climate with dry hot summers and mild cool winters. It is classified as hot-summer Mediterranean climate in Köppen-Geiger classification; however as it is explained in section 2.1 this is a regional global classification that doesn't consider local deviations due to urban factors.

To quantify the urban energy performance representative meteorological years are needed. Two free available representative meteorological years of Madrid are used in this study: CTE and EPW. The CTE climate data is provided by the Spanish Ministry to obtain the certification of the energy performance of buildings (CTE 2015). The representative file EPW is provided by the Energy Plus website (EnergyPlus n.d.) and created by ASHRAE for energy calculations using the international weather format IWEC.

These files do not represent the climate change, so long-time series of meteorological measurements of the last years are recommended. To quantify the climate trends registered in Madrid during the last decade, an experimental campaign of 10 years (EXP10) has been carried out by CIEMAT (Sánchez et al. 2020)

3.1.1. Climate file comparisons (representative vs experimental climate files)

The comparison between the long-term experimental climatic file (EXP10) and the representative meteorological years (EPW and CTE), gives an idea of how the climate patterns have changed during the last years due to climate change. To this end, climate biases from using different data files have been done. Based on hourly data, it has been compared the mean values of the main meteorological variables through the annual mean values and the annual means of the standard deviations. Table 1 highlights the differences and similarities between them.

Both the mean temperature and solar radiation increase in the experimental database, as opposed to the observed decrease in the relative humidity. Therefore, an increasing trend has been observed over time towards warmer and drier climates. On the contrary, the value of the standard deviation remains similar in all the databases. In conclusion, historical-synthetic weather data show major differences from current real climate scenario that can be explained as a result of global climate warming effects.

Table 1. Main meteorological variables (annual mean and annual mean standard deviation values) for EPW, CTE and EXP

Climate data	EPW	CTE	EXP-10
Annual air temperature (Ta) + standard deviation (°C)	14.3 ± 8.6	13.6 ± 8.6	15.8 ± 8.2
Annual relative humidity (RH) + standard deviation (%)	62 ± 21.5	58 ± 16.6	51 ± 18.2
Annual global solar radiation (G) + standard deviation (kWh/m^2)	185 ± 235	178 ± 262	188± 256

The Box and Whisker methodology (Petruccelli et al. 1999) has been applied to identify trends, variances, symmetry and extreme values of the three climate files studied. A box plot has been created and represented in Figure 1 to evaluate the annual distribution of temperature (left side), relative humidity (middle side) and global solar radiation (right side). In these graphs the brown bars represent the EPW file, the red bars represent the CTE file and the blue bars represent the EXP10 file. The bottom and the top of this box represent the 25 and 75 percentiles respectively while the middle line represents the median value of the data series and the cross indicates the mean values. The extreme values have been calculated considering the inter-quartile range (IQR), the absolute difference between the 25 and 75 percentiles. Outliers values (out of the 1,5*IQR) are not represented.

Attending to the temperature values similar IQR is obtained for the CTE and EPW files (between 7°-20°C) being slightly higher for the EXP10 file (9°-22°C). The extreme values both upper and lower are higher for EPW and CTE, however, in the EXP10 database the median temperature is more centred with respect to the 1st and 3rd quartiles and the mean temperature is higher for EXP10 file (15.8°C) than EPW and CTE (14.3°C and 13.6°C).

The median relative humidity registered for the EXP10 file (51%) is lower than the other two files (62-58%). The IQR values for the EXP10 files are the lowest, reaching minimum extreme values. EPW files present the highest variability as is shown in its IQR and extreme values.

The annual median global solar radiation varies from 177W/m^2 (CTE file) to 188 W/m^2 (EXP10 file). The IQR and extreme values are slightly higher for the EXP10 files.

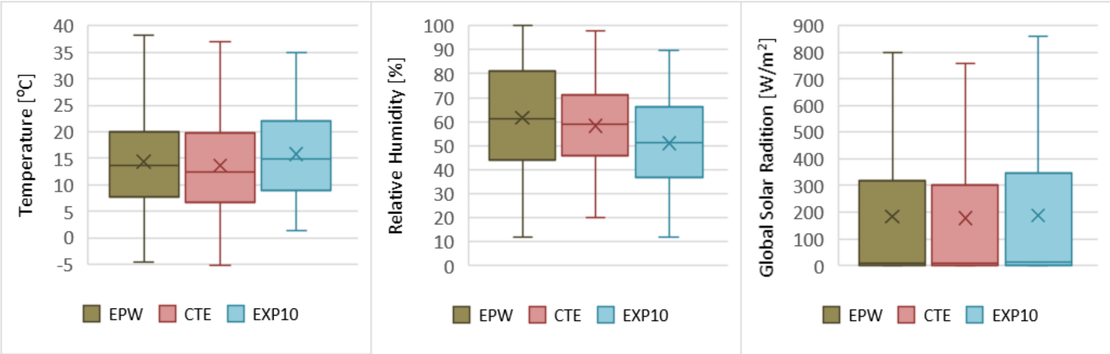

Figure 1. Annual statistical behaviour of temperature, relative humidity and solar global radiation registered by the representative file EPW (brown bars), representative file CTE (red bars) and experimental file EPX10 (blue bars).

3.1.2. Summer and winter representative days

The hourly climatic evolution throughout a representative day of a specific period allows identifying the quantity of the extreme values and when they take place. One winter and one summer typical days are calculated using the Hall methodology. This method calculates the absolute difference between daily and seasonal variables with the Filkenstein-Schafer statistics. The most representative day is selected as the minimal value of the weighted sum. The microclimatic variables have been weighted by the PASCOOL method (Soutullo et al. 2017). The summer representative day (SRD) and winter representative day (WRD) of each climate data file is shown in Table 2.

Table 2. Seasonal typical days obtained for the three climate files studied

Climate files	EXP10	EPW	CTE
Summer Representative Day (SRD)	25 July	15 August	5 August
Winter Representative Day (WRD)	29 January	3 February	30 December

Figure 2 graphs the summer and winter air temperature (Ta), relative humidity (RH) and global solar radiation (G) for the EPW (brown lines), CTE (red lines) and EXP10 files (blue lines).

The EXP10 climate file presents higher temperatures for the SRD and WRD. This fact it is especially significant for the SRD, where the EXP10 file has approximately 5°C above the EPW and CTE along the day. Generally, the SRD values are between 15°C to 35 °C. For the WRD the values of air temperature for the EXP10 are similar to the CTE and something lower for EPW. For the WRD the lowest Ta value is -3°C and the highest value is 11°C.

On the contrary, the humidity records for the EPX10 climate data is approximately 20% lower than EPW for the SRD, with values from 76-26 % for all climate files. The EXP10 data file for the WRD is slightly higher than the CTE climate file, but lower than the EPW data. The humidity variations range from 55-95% for the WRD.

Although the global solar radiation values are very similar for all climate data, the EXP10 file reaches slightly lower maximum values for the SRD. The maximum global solar incidence values are between 800 to 900 kW/m^2, while for the WRD the maximum values range from 300 to 400 kW/m^2.

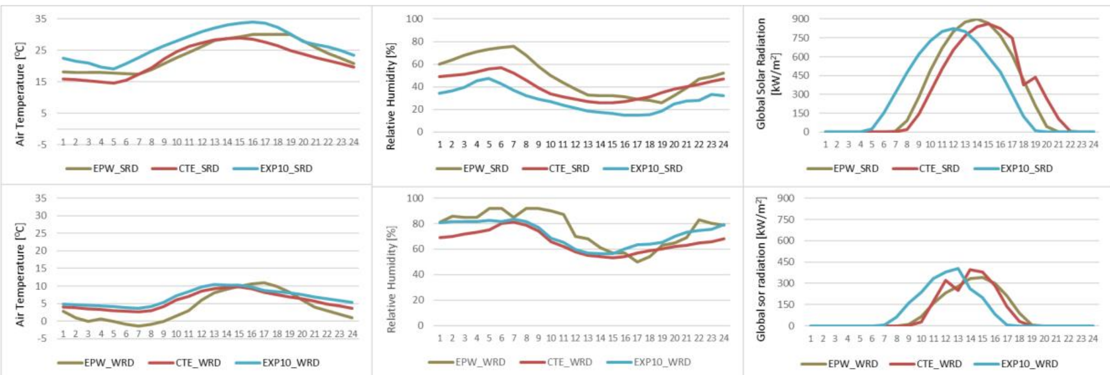

Figure 2. Meteorological values (Ta, RH and G) for summer and winter representative days for EPW, CTE and EXP10 files

All the graphs present small temporal deviations. This is due to the recording method and the generation of the representative meteorological year. CTE and EXP10 files are in solar data, while EPW data is in local time without considering daylight saving time. Also, the CTE records include an offset according to the equation of time.

3.1.3. Climate trends

To quantify the variability of the weather registered in Madrid during the last decade, climate indices have been calculated annually and seasonally for the CTE, EPW and EXP10 databases (Table 3). These indices have been provided by the European Climate Assessment & Dataset (ECA&D project).

The annual climate indexes are focused on the evaluation of the heat and cold trends. Generally, is found an increase of warm scenarios for the EXP10 climate data comparing to the EPW and CTE files, with higher maximum and minimum temperatures (SU and TR index). EPW is characterized by the highest temperature variability as it is graphed before (Figure 1). On the other hand, the seasonal indices are considered for the sunshine, humidity and wind tendencies. The sum of daily hours (SS) is the highest for the EXP10 file for summer and winter representative days and no significant differences exist between EPW and CTE climate files. The mean daily humidity (RH) is lowest in the SRD for the EXP10 database in summer, but the RH index is medium for the winter season. Finally, the FG index, associated to the mean wind velocity, present extreme values for the EPW and the CTE climate files, while the EXP10 data file has medium values for the summer and winter season.

Table 3. Annual and daily climate indices obtained for the EPW, CTE and EXP10 climate files.

Index type	Annual Climate Index. Definition		EPW		CTE		EXP10	
HEAT	ETR	Extreme temperature range considering daily maximum and minimum temperatures	45		42		33	
	SU	Number of days with daily maximum temperature above 25 °C	111		100		129	
	TR	Number of days with daily minimum temperature above 20 °C	8		19		29	
COLD	FD	Number of days with daily minimum temperature below 0 °C	0		2		0	
Index type	**Seasonal Climate Index. Definition**		**EPW**		**CTE**		**EXP10**	
			SRD	**WRD**	**SRD**	**WRD**	**SRD**	**WRD**
SUNSHINE	SS	Sum of daily sunshine duration in hours	15	11	15	10	19	14
HUMIDITY	RH	Mean daily relative humidity	49	76	40	66	28	72
WIND	FG	Mean daily wind strength	2,4	0,4	1,1	2,4	1,6	1,5

3.2. Urban properties of the representative neighbourhoods

In order to quantify differences between the urban typologies and their boundary conditions for a further urban microclimatic study, three representative neighbourhoods have been analysed. through the Statistical Institute of the Community of Madrid (SICM) classification. The SICM has been selected to be the most updated and tailored for this study. It revels the urban patterns according to Madrid´s urban evolution by 8 residential urban typologies. The three selected neighbourhoods are Usera, Cañorroto and El Viso, that belongs respectively to Developed settlements (DS), Open blocks (OB) and Single/semi-detached house (SH). They have been chosen because of their significant differences in their urban patterns and their representativeness within the city.

The Figure 3 shows these significant differences between DS_Usera (blue), OB_Cañorroto (green) and SH_El Viso (orange) through the urban distributions (left), urban materials (center) and building density and high (right).

The DS_Usera neighbourhood is characterized by having most of its public space destined to roads (30%) and the residential space for built areas (62%). Consequently, the main materials found in DS_Usera are asphalt and plaster. This area has a high density (about 3500 residential buildings/km^2) with a mean height of 9 m.

The public space (no residential) of the OB_Cañorroto neighbourhood is equally divided between roads and green areas (26 and 27 % respectively) while the private zones (residential) are occupied mainly by pavement (26%) and then by building area (16%). These facts mean that the material distribution in this urban typology is balanced between asphalt, concrete and grass; plaster surfaces are slightly lower. The building density is low (about 1500 residential buildings/km^2), however the buildings are taller (mean high of 12 m).

The no residential areas for the SH_Viso zone are employed mostly for roads in the (30%). The residential surfaces are occupied mainly by gardens, the printed building area and less notably by pavements (29, 26 and 8% respectively). The material surfaces are mostly grass, asphalt and plaster, being less representative the concreate. The quantity of buildings per surface are low (1700 residential buildings/km^2) with a low mean height (9 m).

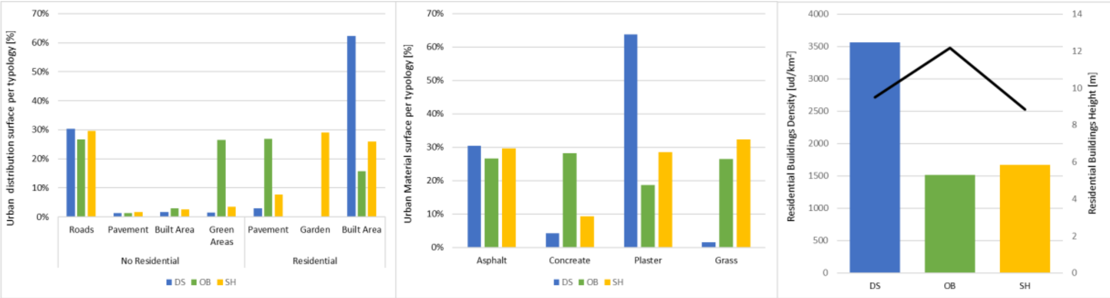

Figure 3. Mean urban characteristics for DS_Usera (blue columns), OB_Cañorroto (green columns) and SH_El Viso (orange columns). Urban distributions (left), urban materials (center) and building density and high (right).

For a better understanding of the urban typologies, their spatial distribution is represented in the Figure 4. It shows the diversity within neighbourhoods for the urban materials (1st row) building high and trees (2nd row) and urban perspective (3rd row). As it is described before DS_Usera is based on compacted-medium rise buildings with limited green and tree areas. OB_Cañorroto is defined by sprawl-high rise buildings with large public green areas and medium tree quantity. SH_Viso is identified by sprawl-low rise building with large private green and tree areas.

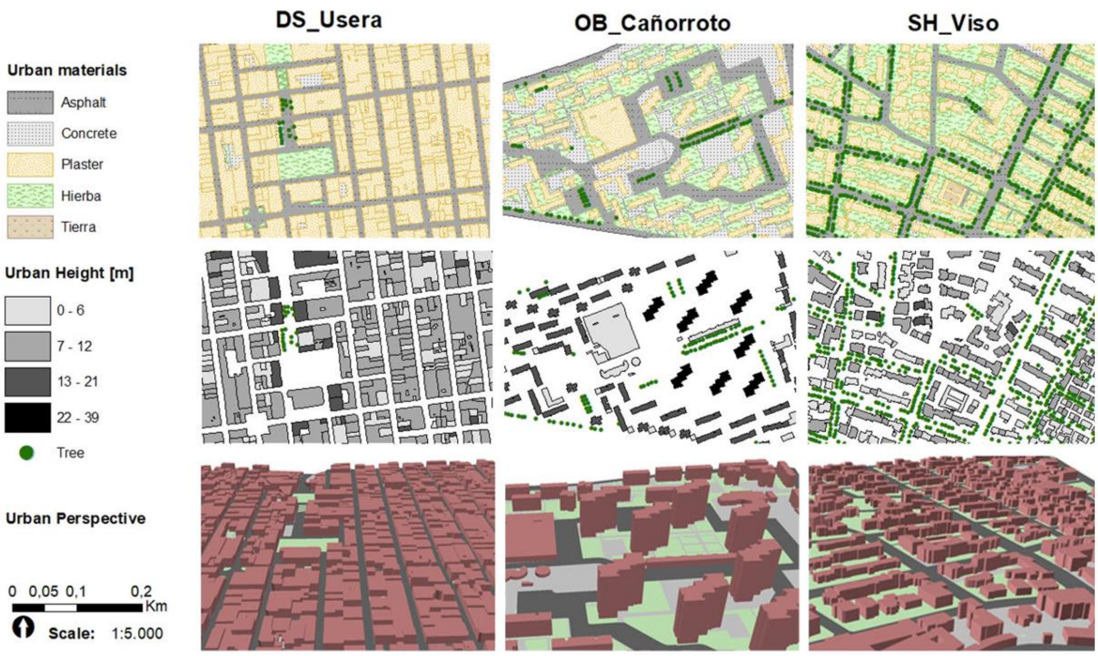

Figure 4. Spatial distribution of the urban characteristics for DS_Usera (left), OB_Cañorroto (center) and SH_El Viso (right). Urban materials (1st row) building high and trees (2nd row) and urban perspective (3rd row).

3.3. Simulation of boundary conditions and microclimate variables

The deep knowledge of the boundary conditions and the urban microclimate behaviour of the representative urban typologies are enabled through the SkyHelios Pro software (Fröhlich and Matzarakis 2018). It is a dynamic simulation program focused on the urban climate study that allows the calculation and visualization of continuous results for each point of a complex area. As each urban typology is gathered by their common urban morphologies and material patterns, they should have similar boundary conditions and urban climate behaviour.

The program has been fed in each studied neighbourhood by a) Hourly urban meteorological variables Ta, RH, Wv and G for the EPW, CTE and EXP10 climate files. b) Urban morphology through 3D representation and its material properties and trees (Table 4) through a Geographic Information System (GIS). Each urban model contains a 5 x 5 m calculation grid at the height of 1.1 m for each representative location to assess the variations during 24 hours for a summer and winter typical day. The grid´s pixels indicates the mean values for the 5 x 5 m area, being the total calculated points 25872 for DS_Usera, 7254 for OB_Cañorroto and 14536 for SH_El Viso.

Table 4. Material properties for the urban simulation

Material	Asphalt	Concrete	Plaster	Grass	Tree
Albedo	0.13	0.23	0.30	0.23	0.20
Emissivity	0.95	0.80	0.92	0.93	0.98
Transparency	1.00	1.00	1.00	1.00	0.90

3.3.1. Boundary conditions of the representative urban typologies

As it is shown in the Figure 5, the boundary conditions are assessed by the albedo (α), the emissivity (ε) and the sky view factor (SVF) for the representative urban typologies. The figure´s rows represent the spatial distribution of the albedo, the emissivity and the sky view factor values for the representative neighbourhoods (in columns). On the right side it is graphed the mean (strong colour) and the standard deviation (light colour). All the values are calculated for outdoor areas, not considering the buildings zones.

The Developed Settlements (DS_Usera) typology presents medium values of albedo (0.304 ± 0.003), low emissivity (0.923 ± 0.003) and a low-medium sky view factor (0.458 ± 0.162). This numbers are related to a high presence of buildings (plaster) and a lack of green areas and trees. The SVF values are explained by the relation between the width of the street and the buildings height. Slightly morphological and material variations are found, reflected in the low standard deviation for all studied variables.

The Open blocks (OB_Cañorroto) neighbourhood has high values of albedo (0.305 ± 0.006), medium emissivity (0.926 ± 0.007) and high sky view factor (0.566 ± 0.1654). The equal materials distributions can be associated to the no significant albedo and emissivity properties and standard deviation, that only change in the center of the spatial representation due to the tree’s presence. The open spaces between buildings rise the SVF.

The Single-semidetached Houses (SH_Viso) have a low albedo (0.301 ± 0.007), high emissivity (0.936 ± 0.012) and a medium sky view factor (0.497 ± 0.168). The high presence of grass and tress is linked to this albedo and emissivity. The mix of tree and no tree areas trigger a higher values variability (standard deviation). Although the relationship between high buildings and width street is low, the street trees blocks the sky visibility (SVF)

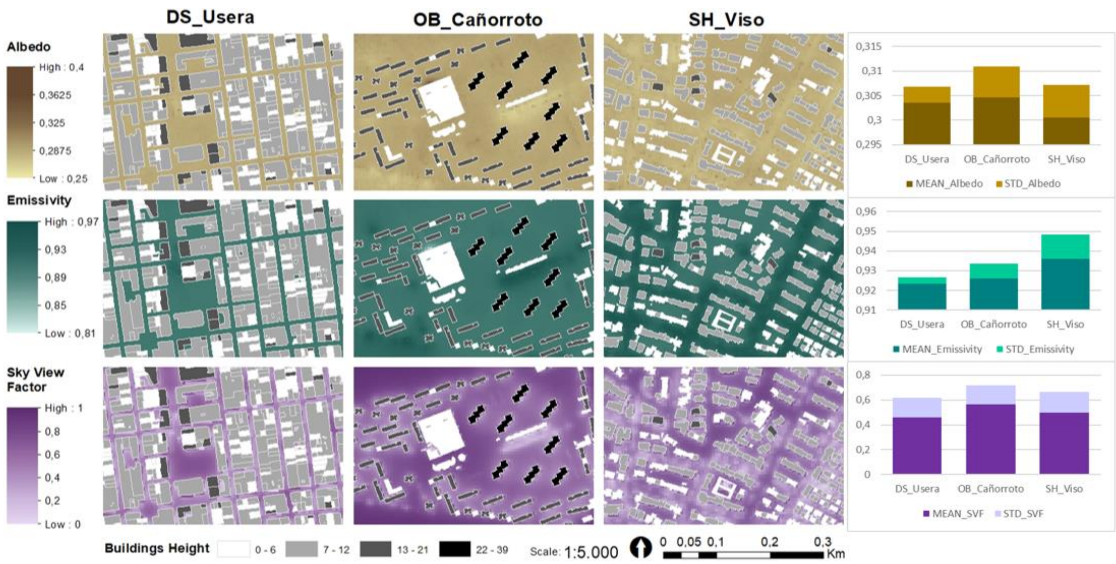

Figure 5. Spatial distribution mean and standard deviation of the boundary conditions for DS_Usera (left), OB_Cañorroto (center) and SH_El Viso (right). Albedo (1st row), emissivity (2nd row) and sky view factor (3rd row).

3.3.2. *Microclimatic variables, Mean Radiant Temperature (MRT) of representative urban typologies*

The behaviour of the Mean Radiant Temperature (MRT) within the urban structures is selected as a relevant microclimate variable because it is crucial in the thermal urban comfort evaluation. The hourly MRT is simulated for the whole representative typologies and the different climate data for the SRD and the WRD. The Figure 6 represents the SRD and WRD hourly MRT for the climate files EPW (stripped line), CTE (dotted line) and EXP10 (simple line) separately for each urban typology. The hourly TMR values refer to the hourly mean of TMR for the whole neighbourhood´s outdoor areas, not considering the buildings areas.

For all urban typologies the MRT values present a high variability between day and night for both SRD and WRD, being even more significant in summer (higher than 50 ºC). The records for the SRD go from 8.6 to 13.3 ºC during the night (no solar radiation) but raising to the highest values about 14:00 pm (local hour) with values from 56.20 to 62.35 ºC. In winter, similar behaviour is found but lower values are obtained. The TMR values for the WRD on the night range from -10.14 to -2.36 ºC; in the afternoon are achieved records from 22.49 to 31.20 ºC.

Relevant differences are found for the experimental climate data (EXP10) being for almost all urban typologies higher than the available TMY data (EPW and CTE). This significant pattern is more relevant for the SRD with upper approximated higher values of 4 to 6 ºC throughout the day.

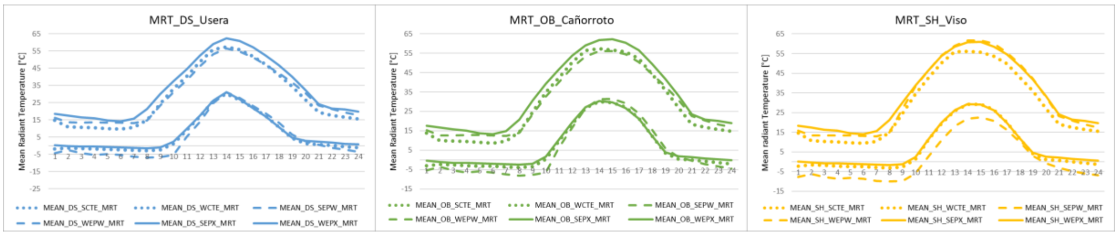

Figure 6. Hourly MRT for EWP, CTE and EXP10 climate data for DS_Usera (left), OB_Cañorroto (center) and SH_Viso (right)

With the aim of quantifying the differences between urban typologies, it is represented in the Figure 7.a the hourly MRT values for the SRD and WRD for the experimental climate data (EXP10). The widely range of MRT during the night and day, difficult the comparison between urban typologies. In that sense, it is graphed for the conducted values of the EXP10 climate data the gradient between the mean hourly MRT for all urban typologies within a representative day and the simulated hourly MRT for each urban typology. The Figure 7.b represents the ΔMRT values for the SRD (upper) and WRD (bottom).

For both SRD and WRD it is observed during the night high values of MRT for DS_Usera, followed by SH_Viso and OB_Cañorroto. During the day these records are inverted being lower for Developed Settlements (DS) and higher for Open Blocks (OB) and Single/semidetached houses (SH), except the central hours of the day. At this time of the day, the only shadowed areas are found under the tree canopy due to the vertical solar radiation. This fact shows the highest MRT values for DS zones followed by OB and SH neighbourhoods.

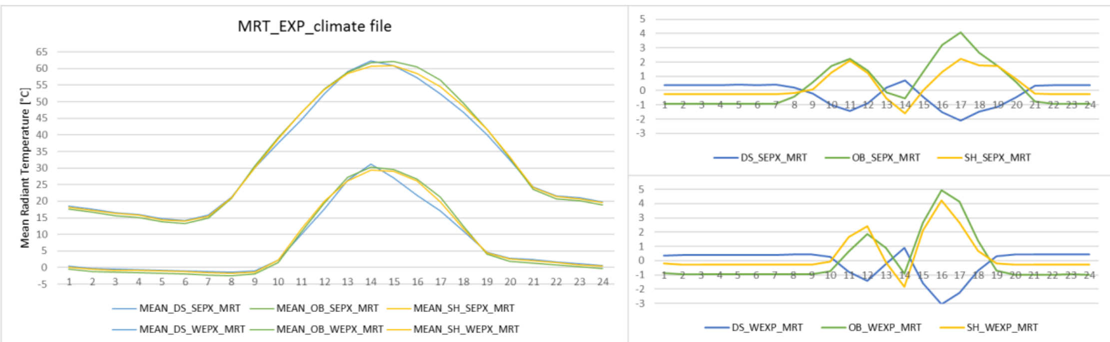

Figure 7. MRT associated values for EXP10 climate data for DS_Usera, OB_Cañorroto and SH_Viso. a) Hourly MRT values for SRD and WRD. b) MRT gradient for SRD (upper) and WRD (bottom)

Finally, a spatial representation of the MRT for the representative typologies is developed in order to study the variability within the urban structure. Using the SRD and WRD of the EXP10 climate file, Figure 8 represents a daily MRT behaviour for DS_Usera, OB_Cañorroto and SH_Viso at different hours. These daytimes belong to the night, hours after the sunrise, central day hours and hours before the sunset.

The spatial image of the Figure 8 shows the influence of the solar radiation in MRT values because of the urban morphologies and materials. Although the intensity of the MRT is higher and longer for the SRD both SRD and WRD behaviours are analogous. During the night the MRT values are the lowest and similar for all the zones, only a slightly higher records are found in below the tree surfaces. In the first hours of the day (8:00 - 10:00) the sun radiation start introducing in the urban structure. At that point, the cool areas found during the nigh are still cold, but a flip behaviour starts warming rising up the TMR values. The increase velocity of the TMR depends on the capacity of sun rays to penetrate in the city (no shadow areas and a high value of SVF foster this process), the albedo of surfaces (low albedos foster the process) and the emissivity of materials (low emissivity foster this process). In the central hours of the day (14:00) most of surfaces achieve the highest MRT values, only reduced by the trees or building tiny shadow areas. Low sky view factors, low albedos, and low emissivities increase the TMR in the noon time. Finally, during the sunset (17:00 - 19:00) the TMR records become to decline. At this moment surfaces with a high shadow level, high sky view factor, high albedo and high emissivity carry out this process faster and having the lowest TMR records during the night.

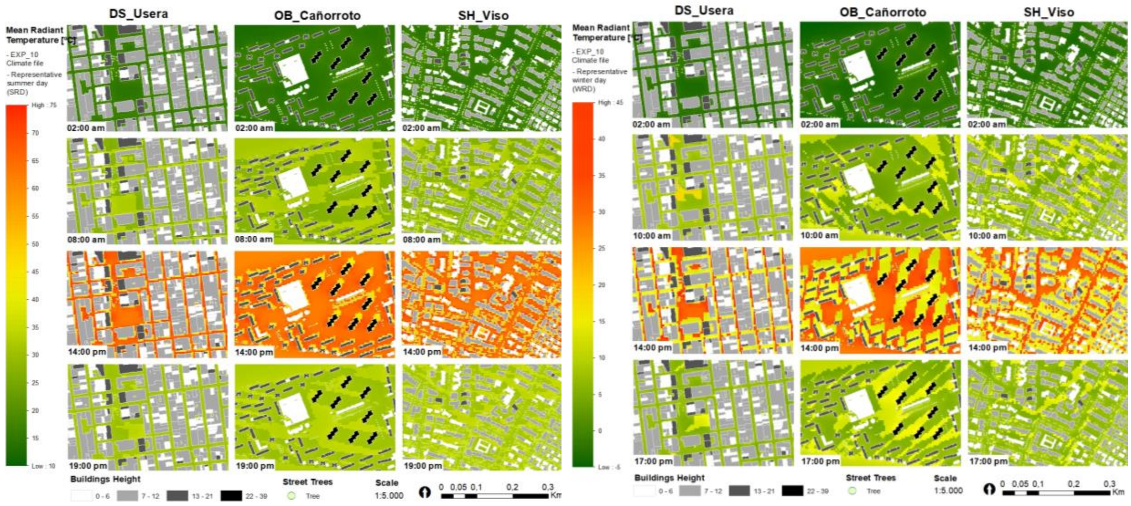

Figure 8. Spatial distribution of the MRT for the EXP10 data file for DS_Usera, OB_Cañorroto and SH_Viso. Daily behaviour for the SRD at 2.00, 8:00, 14:00 and 19:00 (left). Daily behaviour for the WRD at 2:00, 10:00, 14:00 and 17:00 (right)

4. Conclusions

This paper presents an approach to transform the macroscale climate conditions to microscale urban climate in order to aboard the warming and drier scenarios in cities due to the climate change and the urban microclimate effects. The city of Madrid is selected as a case of study, because of its morphologies and materials diversity.

To study the climate change effect in the city an updated experimental climate data file based on 10 years records data (EXP10) have been compared with two free available and representative climate files widely used (EPW and CTE) through different methodologies for the main meteorological variables. In addition, to obtain a better seasonal study the summer and winter representative days (SRD and WRD) have been calculated for all data files and the climate trends are studied by different climate indices. For all cases, the EXP10 data file shows approximately 2ºC warmer, a 10 % dryer values and a higher and longer solar radiation than the representative climate files (EPW and CTE). This comparison evidence the climate change tendencies and an urgent need to update the climate files used worldwide by simulation software (Energy+ is fed by EPW files) or normative applications (Spanish energy certification tools used by CTE files).

Then, the urban microclimate effect has been evaluated though the simulation of the boundary conditions and microclimatic variables by the SkyHelios Pro software for the previous climate data and different structures within the city. Three urban structures associated to prototype neighbourhoods have been selected by considering the most significant differences between urban structures and their relevant representativeness in the urban context. The selected urban typologies are: a) Developed Settlements (DS_Usera), dense-medium-rise areas with limited green or tree zones. b) Open blocks (OB_Cañorroto), sprawl-high-rise areas with public green zones and a medium ratio of trees. c) Single/semidetached Houses (SH_Viso), sprawl-low-rise areas with mainly private large green or tree zones. For all typologies, the roads (asphalt) represent between a third and a quarter of the total area.

The boundary conditions depend on the built environment characteristics. Because of this, the urban morphology and materials are assessed. The distribution of the buildings and trees are related to the sky view factor (SVF). Compacted and tree crowded areas have a lower value than sprawl and limit tree areas. The most significance material variations seem to belong to the green surfaces and more specifically to the tree area, characterized by low albedo (α) and high emissivity (ε). According to these properties the urban typologies present: a) DS_usera: SVF= low-medium, α=medium and ε =low. b) OB_Cañorroto: SVF=high, α=high and ε =medium. c) SH_Viso: SVF=medium, α=low and ε =high.

The influence of the boundary conditions in the microclimatic variables is proved by the Mean Radiant Temperature (MRT). The hourly MRT values have been generated for all climate data bases and urban typologies in the SRD and WRD. Low MRT values are graphed when there is no sunshine presence and they rise up to the highest values in the central hours of the day, when the solar radiation is maximum. A high MRT variability is found for SRD and WRD with differences between 40-50ºC during the night and day. The experimental data file (EXP10) has the highest records in all cases, being even more intense in summer with 4 - 6 ºC higher that EPW and CTE data, showing the impact of the climate change in energy simulations.

Regarding the hourly the TMR values between urban typologies, slightly differences are shown meanly during the night for summer and winter time. The DS_Usera TMR graphs a modest upper value throughout the night, followed by the SH_Viso records and the lowest values are for the OB_Cañorroto typology. This effect is associated to a low emissivity of the DS_Usera materials and a medium value of SVF (dense-medium-rise areas with limited green or tree zones), fostering that the absorbed heat during the day is emitted along the night finding some traps in this process because the urban structure. During the day this observed behaviour is thinly flipped, for the DS_Usera area, because of the structure shadows, except in the central hours, where only the tree shadows reduce the MRT. On the contrary, OB_Cañorroto due to their high albedo and medium emissivity materials and a high SVF value, present the lowest values during the night (sprawl-high-rise areas with public green zones and a medium ratio of trees). It should to be highlighted that although tree areas reduce the MRT values during the day because of their shadow and high emissivity, they also reduce notably the SVF, concentrating the heat in their canopy and increasing the MRT during the night, as it is occurred in the SH_Viso area. MRT differences could be even more notably if the neighbourhoods were simulated with real meteorological variables, instead of having a single climate data file for all typologies.

Suitable climate data considering the climate change and the boundary conditions and their influence in the microclimate variations within the city, should be recognize for further analysis. An updated and realistic microclimate behaviour will be decisive for future resilient strategies in urban environments fostering the habitability and wellbeing in public outdoor spaces, especially in most vulnerable neighbourhoods.

5. References

Castaldo, Veronica Lucia, Anna Laura Pisello, Ilaria Pigliautile, Cristina Piselli, and Franco Cotana. 2017. “Microclimate and Air Quality Investigation in Historic Hilly Urban Areas: Experimental and Numerical Investigation in Central Italy.” *Sustainable Cities and Society* 33 (September 2016): 27–44. https://doi.org/10.1016/j.scs.2017.05.017.

CTE. 2015. “Índice Objeto Clima de Referencia Climas de Referencia En Soporte Informático (MET).”

ECA&D “European Climate Assessment & Dataset.” n.d. Accessed May 5, 2020. https://www.ecad.eu/.

EnergyPlus. n.d. “Weather Data Sources | EnergyPlus.” Accessed August 26, 2020. https://energyplus.net/weather/sources.

Fröhlich, D., and Andreas Matzarakis. 2018. “SkyHelios - A Model for the Rapid Calculation of Spatially Resolved Micro Scale Climate Factors.” https://www.urbanclimate.net/skyhelios/.

IPCC 2018. “IPCC, 2018: Global Warming of 1.5°C.” https://www.ipcc.ch/sr15

Javanroodi, Kavan, and Vahid M. Nik. 2020. “Interactions between Extreme Climate and Urban Morphology:

Investigating the Evolution of Extreme Wind Speeds from Mesoscale to Microscale." *Urban Climate* 31 (May 2019): 100544. https://doi.org/10.1016/j.uclim.2019.100544.

Jhaldiyal, Alok, Kshama Gupta, Prasun Kumar Gupta, Praveen Thakur, and Pramod Kumar. 2018. "Urban Morphology Extractor: A Spatial Tool for Characterizing Urban Morphology." *Urban Climate* 24 (July 2017): 237–46. https://doi.org/10.1016/j.uclim.2018.04.003.

Lai, Dayi, Wenyu Liu, Tingting Gan, Kuixing Liu, and Qingyan Chen. 2019. "A Review of Mitigating Strategies to Improve the Thermal Environment and Thermal Comfort in Urban Outdoor Spaces." *Science of the Total Environment* 661: 337–53. https://doi.org/10.1016/j.scitotenv.2019.01.062.

Linares, Cristina. n.d. "Cambio Climático y Salud: Impacto de Olas de Calor y de Frío." https://www.miteco.gob.es/es/ceneam/grupos-de-trabajo-y-seminarios/respuestas-desde-la-educacion-y-la-comunicacion-al-cambio-climatico/2-cristina-linares-cc-salud_tcm30-486764.pdf.

Marino, Concettina, Antonino Nucara, and Erika Polimeni. 2018. "Outdoor Mean Radiant Temperature Estimation : Is the Black-Globe Thermometer Method a Feasible Course of Action ?," no. February 2019. https://doi.org/10.1109/EEEIC.2018.8493714.

Oke T.R. 1982. "The Energetic Basis of the Urban Heat Island." *Royal Meteorological Society* 108. https://rmets.onlinelibrary.wiley.com/doi/abs/10.1002/qj.49710845502.

Petruccelli, J.D., B. Nandram, and M. Chen. 1999. "Prentice Hall." *Applied Statistics for Engineers and Scientists, Prentice Hall Nueva Jersey*.

Sánchez, M. N., S. Soutullo, R. Olmedo, D. Bravo, S. Castaño, and M. J. Jiménez. 2020. "An Experimental Methodology to Assess the Climate Impact on the Energy Performance of Buildings: A Ten-Year Evaluation in Temperate and Cold Desert Areas." *Applied Energy* 264 (February): 114730. https://doi.org/10.1016/j.apenergy.2020.114730.

SET-Plan Working Group. 2018. "Europe to Become a Global Role Model in Integrated, Innovative Solutions for the Planning, Deployment, and Replication of Positive Energy Districts." *SET-Plan Action No 3.2 Implementation Plan*, no. June: 1–72. https://setis.ec.europa.eu/system/files/setplan_smartcities_implementationplan.pdf.

Shahrestani, Mehdi, Runming Yao, Zhiwen Luo, Erdal Turkbeyler, and Hywel Davies. 2015. "A Field Study of Urban Microclimates in London." *Renewable Energy* 73: 3–9. https://doi.org/10.1016/j.renene.2014.05.061.

Sharifi, Ayyoob. 2019. *Resilient Urban Forms: A Macro-Scale Analysis*. *Cities*. Vol. 85. https://doi.org/10.1016/j.cities.2018.11.023.

SICM "Statistical Institute of the Community of Madrid." n.d. Nomecalles - Nomenclator y Callejero de La Comunidad de Madrid. Accessed August 26, 2020. https://www.madrid.org/nomecalles/.

Soutullo, S., E. Giancola, M. J. Jiménez, J. A. Ferrer, and M. N. Sánchez. 2020. "How Climate Trends Impact on the Thermal Performance of a Typical Residential Building in Madrid." *Energies* 13 (1). https://doi.org/10.3390/en13010237.

Soutullo, S., M. N. Sánchez, R. Enríquez, M. J. Jimenez, and M. R. Heras. 2017. "Empirical Estimation of the Climatic Representativeness in Two Different Areas: Desert and Mediterranean Climates." *Energy Procedia* 122: 829–34. https://doi.org/10.1016/j.egypro.2017.07.415.

Stewart, I. D., and T. R. Oke. 2012. "Local Climate Zones for Urban Temperature Studies." *Bulletin of the American Meteorological Society* 93 (12): 1879–1900. https://doi.org/10.1175/BAMS-D-11-00019.1.

Wang, Zhi Hua, Xiaoxi Zhao, Jiachuan Yang, and Jiyun Song. 2016. "Cooling and Energy Saving Potentials of Shade Trees and Urban Lawns in a Desert City." *Applied Energy* 161 (January): 437–44. https://doi.org/10.1016/j.apenergy.2015.10.047.

Zarzalejo, Luis, Felix Tellez, Elena Palomo del Barrio, and M R Heras. 1995. "Creation of Typical Meteorological Years (TMY) for Southern Spanish Cities." In *International Symposium Passive Cooling of Buildings*.

Solar Irradiance (Global, Direct and Diffuse) Quality Control Methodologies Review: Application to Time Series Measured At LES/LNEG, Lisboa, Portugal

Filipe Marques[1], Soraia Páscoa[1], Maria João Carvalho[1] and João P. Cardoso[1]

[1] Laboratório Nacional de Energia e Geologia, I.P., Lisboa (Portugal)

Abstract

Solar irradiance spatial and temporal quantification is essential to the development, implementation, and operation of solar systems, being used throughout a solar project lifecycle. It is crucial to have good quality data measured in meteorological and radiometric ground stations in order to enable the calibration and validation of irradiance models and data series. The Solar Energy laboratory at LNEG operates a meteorological station gathering relevant parameters to characterize the solar irradiation profile for the city of Lisbon in Portugal. This work presents and compares the application of different methodologies used for quality control of solar irradiance measurements. Three methods - the CIE (1994) / Muneer and Fairooz (2002), the QCRad and the IEC - were tested against two synthetic data sets: a clear-sky year and a typical meteorological year randomly and uniformly infused with errors. IEC showed to have limitation regarding the extreme value criteria for beam normal irradiance and CIE for the diffuse horizontal irradiance. The QCRad presented the best performance, with total sensitivity above 80% and maximum specificity. This method was applied to the measured data of LES-LNEG between 2014 and 2018. Most of the detected errors were detected during the coherence test stage, having a higher prevalence between 2015 and mid-2016, highlighting the need to modify the diffuse horizontal irradiance measuring system.

Keywords: solar irradiance, meteorological data, quality control

1. Introduction

Solar irradiance spatial and temporal quantification is essential to the development, implementation and operation of solar systems, being used throughout a solar project lifecycle (Sengupta et al., 2017): selection of installation location; solar systems' performance estimation and viability evaluation during the planning, financing and plant dimensioning stages; performance evaluation during commissioning and throughout the life of the solar system; production forecasting and operation planning.

Different types of meteorological data series can be used for the above purposes: data series from ground station measurements; data series obtained from satellite information; data series generated from stochastic models based on statistical information. However, even for the last two cases it is crucial to have data measured at meteorological and radiometric ground stations to enable the calibration and validation of models and data series.

The measurement of solar irradiance entails several uncertainty and error sources that need to be taken into consideration when building the data sets. Thus, it is necessary to have quality control procedures in place when treating and assembling raw irradiance date into data sets, otherwise the irradiance data will not be suitable for use in the aforementioned processes. Several methodologies have been proposed (see section 3) but to the authors' best knowledge there is a lack of systematic inter-methodology comparisons.

The Solar Energy Laboratory (LES) from the National Laboratory for Energy and Geology, I.P. (LNEG) measures and gathers meteorological data at the Lumiar campus in Lisbon, Portugal, within the scope of its research and solar collector testing activities. This information is used to characterize the solar irradiation profile for the city of Lisbon. Currently the data quality control was performed guarantying the calibration of the equipment on annual or biennial frequency and by graphical representation of the radiation components in order to identify inconsistencies In order to implement an automated quality control method, a comparison between three well known quality control methods was performed and is presented in this work. The comparison was performed for synthetic irradiance data for a typical meteorological year and a clear sky year for the city of Lisbon. Based on the comparison results, a method was selected and applied to the irradiance data acquired in LES between 2015 and November 2018.

doi:10.18086/eurosun.2020.09.04 Available at http://proceedings.ises.org

2. Equipment characteristics - associated uncertainties and problems

When performing irradiation measurements errors can arise from various sources: intrinsic characteristics of the equipment used; problems in the operation of that equipment; processing of the results. Some of these errors are systematic while others are random in their nature. Some of these errors will persist even after careful debugging of the installation and its operational proceedings. The creation of irradiance data sets for solar applications requires the detection and correction of the data entries affected by them.

2.1. Equipment characteristics and associated uncertainty

Equipment measurement uncertainty usually arise from sensors and their construction (Muneer and Fairooz, 2002) or the tracking system. Choosing an adequate sensor is fundamental to avoid this type of errors. This uncertainty is dependent on equipment characteristics which are summarized, for pyrheliometers, in Table 7.2 and for pyranometers, in Table 7.4, of the WMO Guide, nº 8 (WMO, 2018). These characteristics are response time, zero offset, resolution, stability, temperature response, non-linearity, spectral sensitivity and tilt response.

For each of these characteristics it is well defined the admissible uncertainty values for high and good quality in the case of pyrheliometers and for high, good or moderate quality in the case of pyranometers. If these are verified it is possible to consider an achievable uncertainty with 95% confidence level for hourly values as given in Table 1.

Tab. 1: Achievable uncertainty with 95% confidence level for hourly values.

Pyrheliometers		Pyranometers	
High quality	0.7 %	**High quality**	3 %
Good quality	1.5 %	**Good quality**	8 %
		Moderate quality	20 %

The usual classification of pyrheliometers and pyranometers, according to the ISO 9060:1990 standard (ISO, 1990), is secondary standard, first class and second class. It is assumed that these correspond respectively to high, good and moderate quality equipment.

2.2. Operation errors

The referred classification can only be considered, according the WMO Guide, No.8 (volume 1, chapter 7), 2018, if the equipment is used by well trained personnel and follow adequate quality control procedures. Incorrect positioning, operation, or maintenance of the equipment may result in the errors listed in Table 2 below (Muneer and Fairooz 2002, Yournes et al. 2005). Sometimes limitations of operation produce this type of errors, and knowledge of them is important to understand the measured data and implement adequate measures of mitigation.

Tab. 2: Types of errors that arise from the handling the equipment (adapted from Muneer and Fairooz 2002, Yournes et al. 2005).

Error Type	Description	Mitigation
Shading caused by building structures	The presence of structures like building and trees in the way of radiation.	Positioning the equipment in a place sufficiently away from any structure. It is a systematic error that can be detected in its prevalence in the data. It can be mitigated through data imputation techniques.
Incorrect sensor levelling	The uncertainty of sensor levelling adds additional uncertainty to measures and calculations.	Performing an accurate levelling of the sensor. It is a systematic error. When identified, it can be corrected in the data.
Electrical fields in the vicinity of cables	Electrical fields may distort the signal flowing in weakly shielded cable and cause misreadings at the registry.	Protecting cables from strong electric fields. Buying cables with proper electromagnetic radiation shielding.

Mechanical Loading of Cables	Mechanical loading on cables connecting the irradiance sensor to the datalogger may result in signal damage due to piezoelectric effects. There is internal generation of electrical charge in response to the applied mechanical stress, which can cause noise in the data, usually observed as unusually high values of irradiance measurement.	Protecting the cables from mechanical loading risk. Not having cables in zones where objects are deposited or passageways where loads flow. It may be systematic in nature or occasional. The occasional mechanical loading can be identified by the "spikes" observed in the registered data.
Surface obstruction	The presence of dust, snow, dew, water-droplets, bird droppings, etc. on the sensor coverture obstructs the irradiation arriving to the sensor. Weather conditions and ambient conditions may result in some obstruction to the path of the radiation, causing misreads of the current irradiation.	Cleaning regularly the sensor coverture, especially in times where there is an increased risk of surface obstruction.
Complete or partial shade-ring misalignment	The misalignment of the shade-ring may allow some beam irradiation to hit the sensor.	Accurate alignment of the shade ring.
Station or equipment shut-down	Either for maintenance, for repair, lack of operator or due to unfortunate circumstances, the equipment or the station may have to shutdown, pause or function in temporary malfunction.	The observation of the measurements' unidentified errors or omissions is needed to identify and correct the cause. Data imputation may minimize the problems and omissions in the data.

3. Quality control procedures

LNEG-LES automatic quality control process starts with the filtration and treatment of measurements that may present anomalies related with incorrect operation of measuring equipment, data acquisition and data storage (e.g.: blank entries, not a number entries, etc.). This is followed by a frequency analysis of the data sampling period, where measurement gaps or periods between sequential data points are identified and corrected, without modification of the measurement values. Finally, the coherence of the measured value is checked.

Several quality control procedures are available in the literature, e.g.: NREL (1993), CIE (1994), Long and Dutton (2002), Muneer and Fairooz (2002), Yournes et al. (2005), Shi and Long (2008), Journée and Bertrand (2011), IEC (2017). In this work three well known procedures were selected for comparison in order to evaluate the best option to implement within LNEG-LES automatic procedure:

- **CIE**: The first 2 levels of tests proposed by the International Commission on Illumination, CIE (1994), as described by Yournes et al. (2005), plus an extra step proposed by Muneer and Fairooz (2002);
- **QC Rad:** (V2.0) by Long and Dutton (2002), used by the Baseline Surface Radiation Network (BSRN), the National Surface Radiation Budget Network for Atmospheric Research (SUFRAD), and others (Shi and Long 2008);
- **IEC**: the methodology for the creation of annual solar radiation data series presented in IEC TS 62862-1-2:2017 Solar thermal electric plants - Part 1-2: General - Creation of annual solar radiation data set for solar thermal electric (STE) plant simulation.

Each methodology considers different thresholds for the validity of the analysis:

- **CIE** notes that automatic testing should not be performed when the solar elevation is less than 4º (zenith angles larger than 96º) and when the global irradiance G_h is less than 20 W/m^2 - Yournes et al. (2005) increases to less than 7º;
- **QC Rad** considers null the terms in its equations that calculate the horizontal component of the irradiance for zenith angles larger than 90º and restricts the validity of the tests to air temperatures between 170K and 350K;

- **IEC** does not mention limitations to the application of the method.

In general, measurement coherence control is performed in three stages applied in the following order: 1 - evaluation of the measurements' physical feasibility; 2 - evaluation of rare occurrence values; 3 - evaluation of the irradiance measurements' coherence. However, different methodologies may include additional tests.

QC Rad and IEC follow the standard order of steps 1, then 2, then 3. CIE follows a different order: 1, then 3, then 2.

It should be noted that quality control methodologies do not attempt to correct values, but only to signal and/or discard those that are unreliable. If a measurement does not pass a test in a given stage, it is considered to not having passed the quality control and does not continues to be evaluated by following tests/stages.

3.1 Physical feasibility

The first stage identifies values in the data that are not physically possible, therefore filtering large measurement errors. Each of the 3 irradiance variables are tested to check of they are within the limits listed in Table 3.

Tab. 3: Parameters for assessment of physically possible values.

Quantity	Method	Lower Limit [Wm^{-2}]	Higher Limit [Wm^{-2}]
Global horizontal irradiance (G_h)	IEC	0	G_{sc}
	QC Rad	-4	$G_{SC}/AU^2 \times 1.5 \times (cos\,\theta_z)^{1.2} + 100$
	CIE	0	$G_{o,h} \times 1.2$
	CIE modified by Yournes et al. (2005)	0	$G_{o,h}$
Diffuse horizontal irradiance ($G_{d,h}$)	IEC	0	$G_h + 10$
	QC Rad	-4	$G_{SC}/AU^2 \times 0.95 \times (cos\,\theta_z)^{1.2} + 50$
	CIE	0	$G_{o,h} \times 0.8$
	CIE modified by Yournes et al. (2005)	0	G_h
Direct Normal irradiance ($G_{b,n}$)	IEC	0	G_{sc}
	QC Rad	-4	G_{SC}/AU^2
	CIE	0	G_o

CIE and IEC assumes a solar constant with the value *1367 W m^{-2}*, while QCRad assumes a slightly larger solar constant: *1368 W m^{-2}*.

3.2 Extremely rare values

The second stage identifies extremely rare values in the data, further restricting the interval of accepted values. It is physically possible for the irradiance to be outside this interval for very short periods of time or extremely rare situations. However, it is advisable to filter these values when building representative data sets or for calculations.

Tab. 4: Parameters for evaluation of extremely rare possible values.

Quantity	Method	Lower Limit [Wm^{-2}]	Higher Limit [Wm^{-2}]
Global horizontal irradiance (G_h)	IEC	0	G_{SC}, $if\ \theta_z < 80^o$ $G_h + 0.56 \times (\theta_z - 93.9)^2$, $if\ \theta_z \geq 80^o$
	QC Rad	-2	$G_{SC}/AU^2 \times 1.2 \times (cos\,\theta_z)^{1.2} + 50$
	CIE	0	$G_{h,CS}$
Diffuse horizontal irradiance ($G_{d,h}$)	IEC	0	1000 W m^{-2}
	QC Rad	-2	$G_{SC}/AU^2 \times 0.75 \times (cos\,\theta_z)^{1.2} + 30$
	CIE	$G_{d,h,CS}$	$G_{d,h,OC}$
Direct normal irradiance ($G_{b,n}$)	IEC	0	$G_{sc}\,\varepsilon_0\,0.9^m$
	QC Rad	-2	$G_{SC}/AU^2 \times 0.95 \times (cos\,\theta_z)^{0.2} + 10$
	CIE	—	—

This step was added to the CIE method by Muneer and Fayred (2002) and compares the diffuse and global horizontal irradiances to the values of the extreme conditions calculated with Page's models for very clear and heavily overcast skies. For the clear-sky, the same values of the respective series were used.

3.3 Coherence evaluation

The three irradiance values under consideration (G_h, $G_{d,h}$ and $G_{b,n}$) are physically related to each other, thus, the third step of the procedure checks for deviations to the physical relationships between the irradiance measurements (Table 5). In the table $r = G_h / (G_{d,h} + G_{b,h})$.

Tab. 5: Parameters for evaluation of the irradiance values' coherence.

Physical relationship	Method	Lower Limit [W m^{-2}]	Higher Limit [W m^{-2}]
$G_h - (G_{d,h} + G_{b,h})$	IEC	-80	80
	QC Rad	$(1-r)\,G_h$, with $0.92 < r < 1.08$ for $\theta_z < 75^o$; $0.85 < r < 1.15$ for $93^o > \theta_z > 75^o$; and $G_{d,h} + G_{b,h} > 50$	
	CIE	$(1-r)\,G_h$, with $0.85 < r < 1.15$	
$G_{d,h}/G_h$	QC Rad	—	1.05 for $\theta_z < 75^o$; 1.10 for $93^o > \theta_z > 75^o$; and $G_{d,h} + G_{b,h} > 50$
	CIE	—	1.10

4. Methodology

The direct comparison of the application of the three methods to measured data does not allow for a proper comparison of the methods performance since it is not possible to ascertain if each method is identifying true errors or not, i.e., it is not possible to compare the number of false positives (data entries that are correct but are identified as errors), false negatives (data entries that have an error but are identified as correct) and correct error identifications for each method.

Thus, to make a performance comparison of the aforementioned methods, it was decided to apply the methods to synthetic data series (where all entries were correct) modified by the insertion of deliberate errors. Afterwards, the method with better results was applied to a measured data set consisting of irradiance values measured at the LNEG-LES meteorological station between 2015 and 2018.

4.1 Generation of reference data

Two synthetic data sets were generated using the software Meteonorm v7.1 for the LNEG-LES location in Lisbon (38,774º N, 9,178º W, 184 m above mean sea level). Each data set presents hourly irradiance data (global and diffuse in the horizontal plane and beam normal). The first corresponds to a typical meteorological year (TMY) while the second was generated using a clear sky model (CS).

For each data set, synthetic errors were added to 25% of the entries, chosen randomly and uniformly from the whole. These entries were further divided randomly into 4 groups with identical size. The first group is intended for errors affecting the three irradiance variables simultaneously (e.g., sources of errors related to the measurement instant and affecting all irradiance variables at the same time), the second group is intended for errors affecting each irradiance variable at different times (e.g., sources of errors related to the measurement equipment), and the third and fourth groups are intended for errors affecting simultaneously two irradiance variables. Finally, each of these groups was divided into five sets each corresponding to one of the following factors, 1.5, 2, 5, 10 or 100, multiplied by the original value. The synthetic errors added to a portion of the data in this analysis are therefore relative errors, where the multiplication factor represents the power gain on the final measurement due to additional noise power (e.g., can be equal to 1 plus the inverse of the signal to noise ratio, the ratio of the signal power to the background noise power), thus encompassing multiple different possible sources of errors. Each data set ended up having a total of 40% entries with at least one error in one of the measured variables. Figure 1 shows an example of 2 annual plots for each data set of the location of the errors affecting the Global Horizontal Irradiance, where the uniform temporal dispersion of those errors is clearly visible.

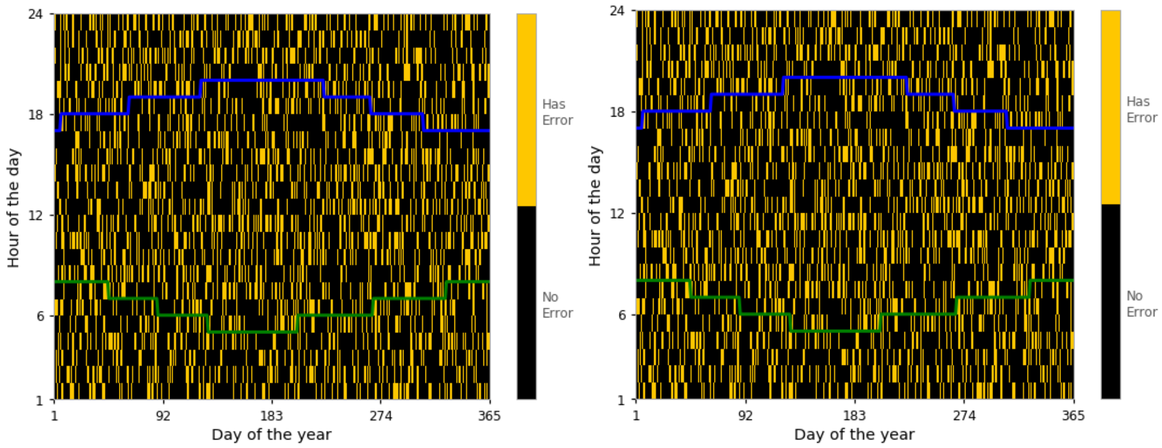

Fig. 1: Annual plots of the errors' location in reference data sets. Left is the CS data and right is the TMY data (green line – civil dawn; blue line – civil twilight).

4.2 Radiometric data measurement

The meteorological station operated by LES is equipped with instruments and a data acquisition system to measure all solar radiation components – direct normal irradiance (DNI) and global and diffuse irradiance in the horizontal plane – and ambient dry bulb temperature. The measurements are performed with data acquisition rates of at least one measurement per minute. The existing equipment are listed in Table 6 and are subject to periodic calibration, annual- for the pyranometers and biennial for the pyrheliometer.

Tab. 6: Measuring equipment used at LES' meteorological station.

Direct solar irradiance	Pyrheliometer Kipp & Zonen CHP1
Global solar irradiance	Pyranometer Kipp & Zonen CM6B
Diffuse solar irradiance	Pyranometer Kipp & Zonen CM6B with shading ring until May 2016 and shading sphere since June 2016
Ambient temperature	Resistance temperature detector (platinum resistance) with four wire reading

A data set was created consisting of all the irradiance data measured between 2015 and October 2018.

4.3 Comparative analysis

Three methods were selected for the comparison: IEC, QC Rad and CIE with the extra step proposed by Muneer and Fairooz (2002). The application of the three methods to the synthetic data series was analyzed in terms of the number and ratio of true positives and false positives, i.e., correct entries signaled as error.

Moreover, the sensitivity and specificity of each method was computed (Shreffler and Huecker 2020). The method sensitivity corresponds to the ratio between the number of true positives and the number of errors in the data set. The method specificity corresponds to the ratio between the number of true negatives and the number of correct entries in the data set. The positive likelihood ratio - ratio between the method sensitivity and the specificity complement - was also computed (Shreffler and Huecker 2020).

5. Results

5.1 Comparison of the different methods

Figure 2 shows that all three methods have a high sensitivity, i.e., they detect a significant share of the synthetic errors (true positives) – it should be noticed that night values have been excluded from the total number. The QC Rad has the most constant performance of the three across all irradiance values, with sensitivities between 75% and 92% for both data sets. The CIE method has a sensitivity around that of the QC Rad for the CS data set. However, for the TMY data set, it presents a higher sensitivity for the diffuse horizontal irradiances, with almost all errors detected, and consequently presents a very high number of total true positives. On the other hand, the IEC method presents a better sensitivity for the beam normal irradiance in the CS data set resulting in an excellent total sensitivity, however the same does not happen for the TMY data set. It has a slightly lower sensitivity for the diffuse irradiance errors but slightly higher for the beam irradiance.

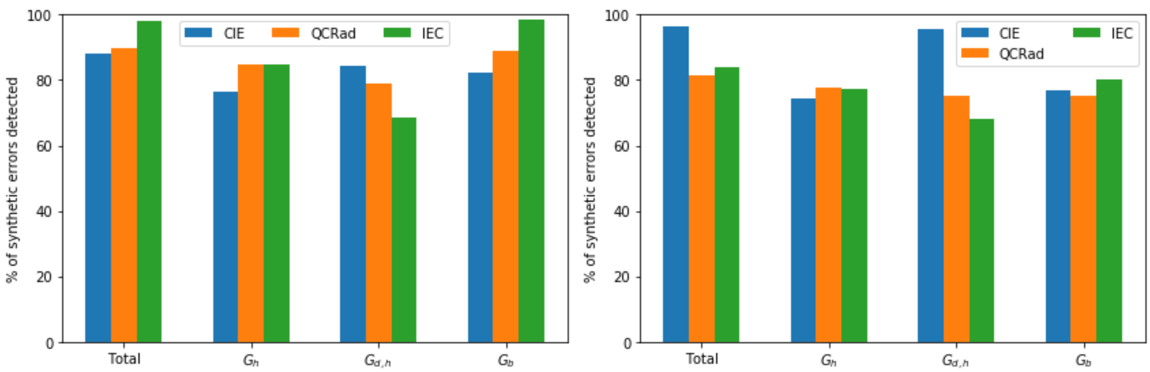

Fig. 2: Plot of the sensitivity of the tests on the two data sets: left is the CS, and right is the TMY. Results for the total of the entries with at least one error in one of the variables, and for each variable.

However, some methods detected a large amount of false errors (i.e., false positives). The IEC presents the highest sensitivity for the beam normal irradiance, but it also has the lowest specificity for that variable, with 40% of false positives detection for the TMY data set and 82% for the CS data set (see Figure 3). This is an indication that one of the stages is signaling an excessive amount of errors, generating false positives. Figure 4 shows that the IEC method is signaling an excessive amount of errors due to violation of the extreme values criteria. When analyzed together, figure 2 and 4 clearly shows there is a problem with the higher limit criteria set for the bean normal irradiance for the IEC method.

Similarly, the very large sensitivity on testing the diffuse horizontal irradiance of the CIE for the TMY data set is matched by a very low specificity. This is due mostly to the last stage of the tests, the extremely rare values test. Perhaps the use of Page model is not adequate to this location. Naturally, when testing the CS data set, the problem is substantially reduced.

The QCRad, on the other hand, presents an impeccable specificity: with zero false positives, i.e., specificity of 1. The specificity less than one for the specific variables is due to the third quality control stage flagging an error as a result of a true error in one of the other variables.

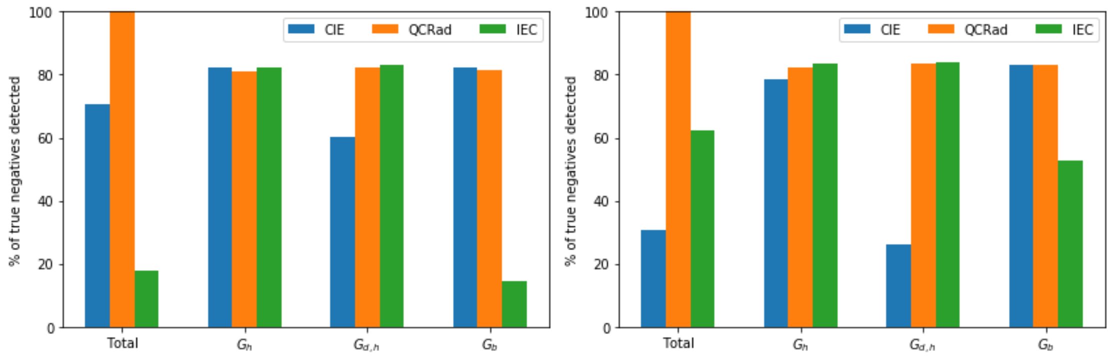

Fig. 3: Plot of the specificity of the tests on the two data sets: left is the CS, and right is the TMY. Results for the total of the entries with all true values detected in the variables, and for each variable.

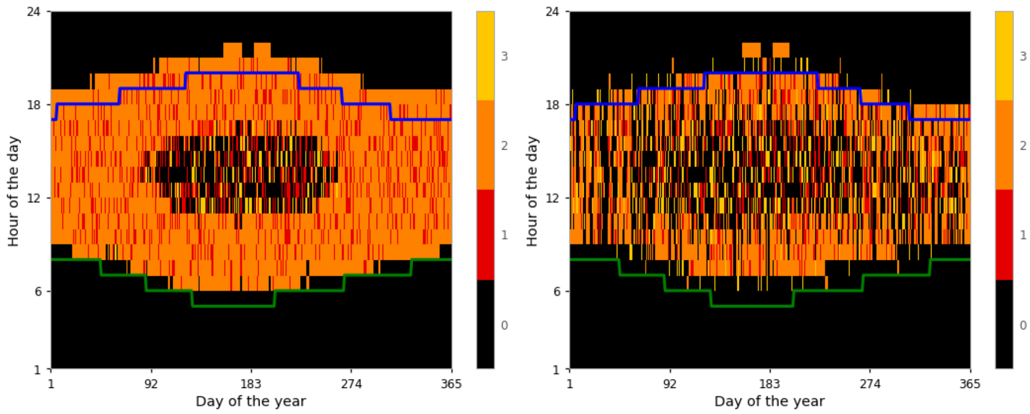

Fig. 4: Annual plot for the quality control of the direct normal irradiance for the IEC method: left is the CS, and right is the TMY. The numbers correspond to the error detection stage, where 0 is no detection. The green line represents the civil dawn and the blue line the civil twilight.

To compare the value of performing each test, the positive likelihood ratio was calculated (see Figure 5). As expected from the observations above, performing the QC Rad quality control on the synthetic data sets yielded the largest value by far, only detecting true errors. The issues with CIE and IEC are clearly reflected in Figure 5 – lowest likelihood for CIE when looking at diffuse irradiance and lowest likelihood for IEC when looking at beam normal irradiance.

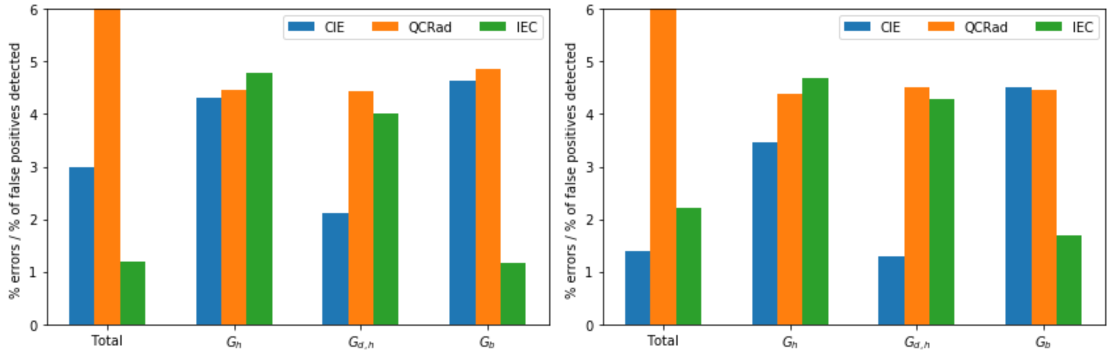

Fig. 5: Plot of the positive likelihood of the tests on the two data sets: left is the CS, and right is the TMY. Results for the total of the entries with at least one error in one of the variables, and for each variable.

In face of this results, the QCRad method which presents very good sensitivity values with perfect specificity (resulting in the highest positive likelihood ratio) was chosen for quality testing the LES data set with real measures.

5.2 Application to measured data

The test detected around 10% of possible errors in the measured data. Figure 6 shows that the number of errors detected is larger for 2015 and decreases afterwards, being substantially lower for 2017 and 2018.

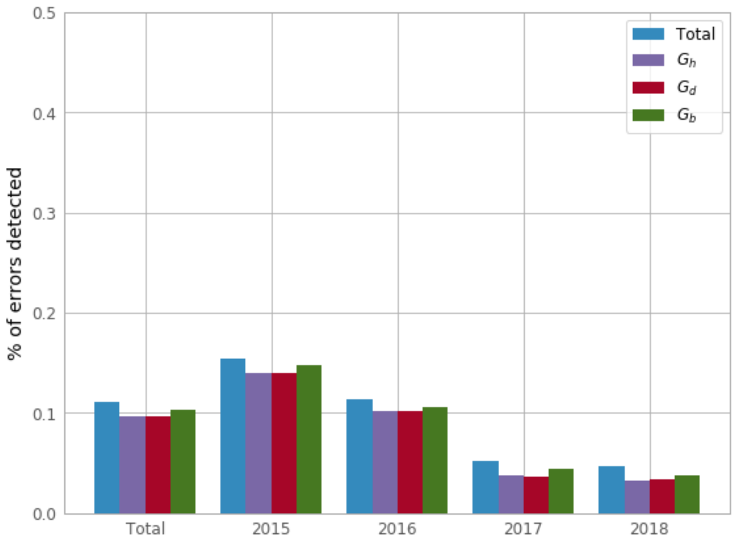

Fig. 6: Plot of the percentage of errors detected in the data for different years.

Figure 7 reveals the time location of the flagged measures and the test stage that flagged it. There are some stage 1 errors signaled for very small angles, but most errors are due to the coherence test. The yearly difference is likely due to a modification to the shading of the pyranometer used to measure diffuse horizontal irradiance, and signal the need to apply a shade-ring correction factor the 2015 and 2016 data.

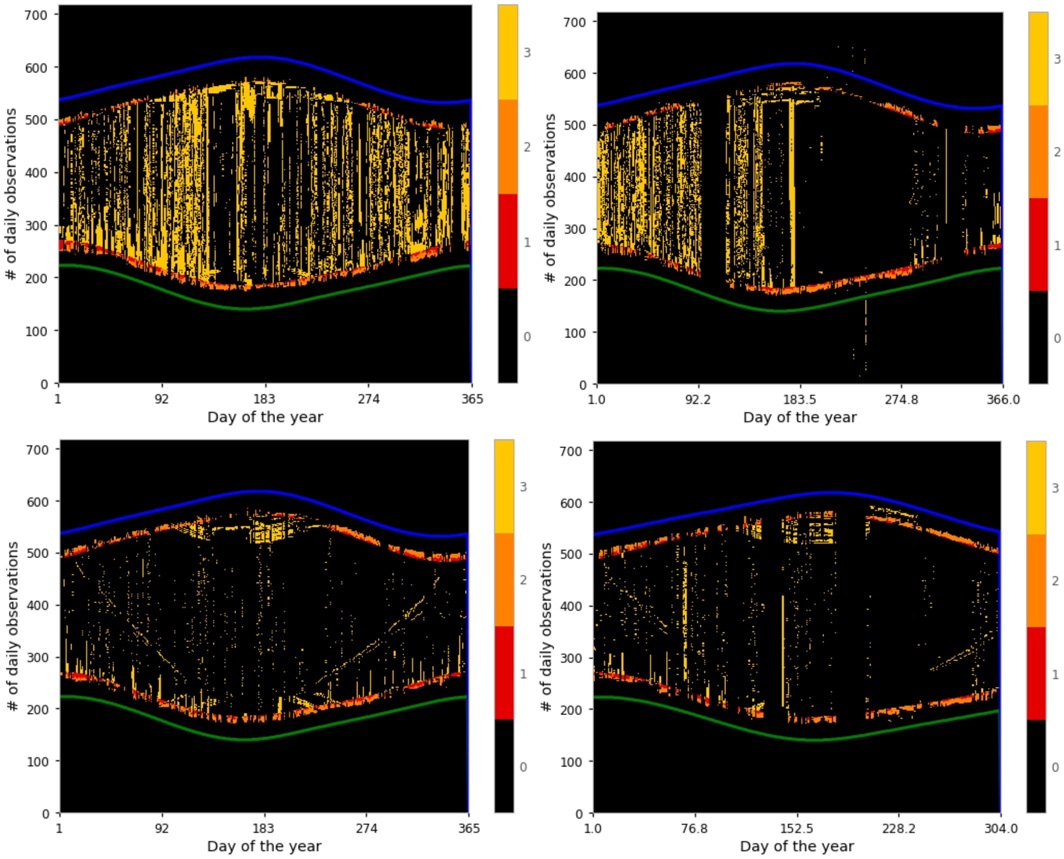

Fig. 7: Annual plot of the quality control results for the LES-LNEG global horizontal irradiance data. From the left upper corner to the right lower corner: 2015, 2016, 2017, 2018. The numbers correspond to the error detection stage, where 0 is no detection. The green line represents the civil dawn and the blue line the civil twilight.

6. Conclusions

Three irradiance data quality testing methods - the CIE(1994)/Muneer and Fairooz (2002), the QCRad and the IEC - were tested against two synthetic data sets: clear-sky and typical mean year randomly and uniformly infused with errors.

All tests had a sensitivity value from 68% to 98%. The QCRad presented the best performance, with sensitivities between 75% and 92% and maximum specificity. The other methods have a performance close to that, but present problems in some of the testing stages. The CIE method presents a problem when detecting errors for the diffuse horizontal irradiances due to an excess of error detection (false positives) originated by its extreme values criteria. The IEC method presents a problem when detecting errors for beam normal irradiance due to an excess of error detection generated by the application of its extreme values criteria.

Thus, it is advisable to review the extreme criteria for the diffuse horizontal irradiance in the case of the CIE method and for the beam normal irradiance in the case of the IEC method.

The QCRad quality control method was applied to the measured data of LES-LNEG between 2015 and 2018. It proved efficient in detecting irradiance measurement errors matching deficiencies previously identified during the regular operation of the meteorological station. For example, it detected errors due to the shading ring that are in accordance with the change of the apparatus to one that is more precise: the shading sphere, proving to be able to signal the need to apply a correction factor to the data.

7. Acknowledments

This work has been co-funded by the INTERREG V-A Spain-Portugal (POCTEP) Programme 2014-2020 through Project SECASOL (0029_SECASOL_5_E).

This work is part of the activities of the Infrastructure Project “INIESC - Infraestrutura Nacional de Investigação em Energia Solar de Concentração” (ALT20-03-0145-FEDER-022113), supported by national funds through

FCT/MCTES (PIDDAC) and co-funded by the European Regional Development Fund through the Alentejo and Lisbon Regional Operational Programmes.

8. References

Guide to Instruments and Methods of Observation, Volume I – Measurement of Meteorological Variables, 2018 edition, World Meteorological Organization, ISBN 978-92-63-10008-5

International Commission on Illumination (CIE), 1994. Guide to recommended practice of daylight measurements. Report no. CIE-108. Wein, Austria

International Electrotechnical Comission (IEC), 2017. Solar thermal electric plants – Part 1-2: General -Creation of annual solar radiation data set for solar thermal electric (STE) plant simulation, IEC TS 62862-1-2:2017. Geneva, Switzerland

International Organization for Standardization (ISO), 1990. Solar energy – Specification and classification of instruments for measuring hemispherical solar and direct solar radiation, ISO 9060:1990. Geneva, Switzerland

Journée, M. and Bertrand, C., 2011. Quality control of solar radiation data within the RMIB solar measurements network. Solar Energy, 85, pp. 72-86, 10.1016/j.solener.2010.10.021

Long, C.N., Dutton, E.G., 2002. BSRN Global Network recommended QC tests, V2.0. BSRN Technical Report.

Long, C.N., Shi, Y., 2008. An Automated Quality Assessment and Control Algorithm for Surface

Muneer, T., Fairooz, F., 2002. Quality control of solar radiation and sunshine measurements – lessons learnt from processing worldwide databases. Building Serv. Eng. Res. Technol. 23,3, 151–166.

NREL, 1993. Users Manual for SERI QC Software - Assessing the Quality of Solar Radiation Data, Technical Report. National Renewable Energy Laboratory (NREL), Golden, CO. Available from: http://www.nrel.gov/docs/legosti/old/5608.pdf

Radiation Measurements. The Open Atmospheric Science Journal, 2008, 2, 23-37.

Sengupta, M., Habte, A., Gueymard, C., Wilbert, S., Renné, D., Stoffel, T., 2017. Best Practices Handbook for the Collection and Use of Solar Resource Data for Solar Energy Applications: Second Edition. Technical Report NREL/TP-5D00-68886. National Renewable Energy Laboratory, Golden.

Shreffler J, Huecker MR. Diagnostic Testing Accuracy: Sensitivity, Specificity, Predictive Values and Likelihood Ratios. [Updated 2020 Apr 20]. In: StatPearls [Internet]. Treasure Island (FL): StatPearls Publishing; 2020 Jan-. Available from: https://www.ncbi.nlm.nih.gov/books/NBK557491/

Younes, S., Claywell, R., Muneer, T., 2005. Energy. 30, 1533-1549.

9. Nomenclature

Name or quantity	Symbol	Unit
Air mass	m	-
Angle	θ	º
Astronomical unit	AU	AU
Baseline Surface Radiation Network	BSRN	
International Commission on Illumination	CIE	
International Electrotechnical Comission	IEC	
Irradiance, global irradiance	G	W m^{-2}
Sun-earth distance correction	ε_0	

Subscript	Symbol
Adjusted	a
Beam (direct)	b
Clear-Sky Model	CS
Diffuse	d
Horizontal	h
Outside atmosphere	o
Overcast model	OC
Solar	s
Solar constant	SC
Zenith	z

10. Solar Education

The challenges of Solar Energy in Saudi Arabia and The Desert areas

Raghad ALamro[1,2]

[1] UTokyo, Tokyo (Japan)

[2] UQU, Makkah (Saudi Arabia)

Abstract

Saudi Arabia, the epicenter of the global oil industry, has been showing keen interest in solar energy in recent years. In addition to the plentiful availability of empty stretches of desert that may accommodate infrastructure for solar power projects, however, there are many obstacles and problems facing solar energy and solar panels in climate conditions such as high temperatures, dust, and humidity because they will create many challenges and opportunities. So, these are effects on photovoltaic plants and Concentrated Solar Power (CSP) plants. The purpose of this study is to present a review of the available solutions to these challenges and discuss these solutions, and I will draw my own conclusion.

Keywords: temperature effect, dust effect, humidity effect, photovoltaic, PCM, Self-Cleaning

---

1. Introduction

Saudi Arabia has one of the world's highest solar irradiation in the world, estimated at approximately 2,200 thermal kWh of solar radiation per m2. The country is strategically located near the Sun Belt. Energy from photovoltaic (PV) could be an obvious excellent alternative energy source for Saudi Arabia since it is sunny and has one of the highest direct normal irradiation (DNI) resources in the world. There are many obstacles and problems facing solar energy and solar panels in environmental factors such as high temperatures, dust and humidity.[1]

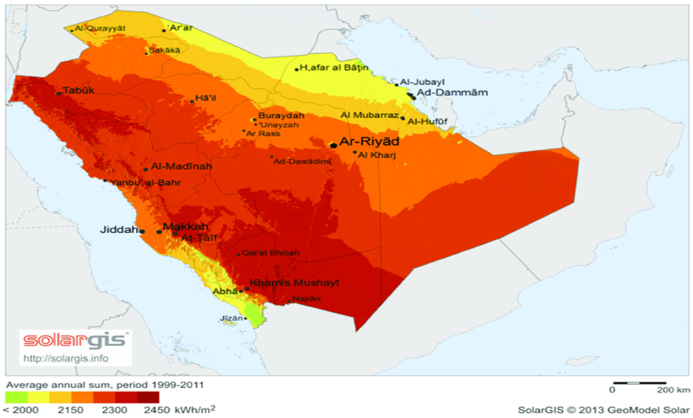

Fig.1: solar irradiation in Saudi Arabia

doi:10.18086/eurosun.2020.10.01 Available at http://proceedings.ises.org

2. photovoltaics: Background

When light hits the surface of materials, it might be reflected, transmitted or absorbed mostly converting the photon energy to heat. However, some materials have the characteristic of converting the energy of incident photons into electricity.[12]

A large majority of solar cells are made from silicon. When silicon absorbs sunlight, the energy from the sun excites some of the cell's electrons into a mobile state where they are free to move around the entire cell. However, in solar cells, there is a separator called a junction, where two slightly different types of silicon meet. The two types of silicon are pretty much the same, except each one is "doped" - has a tiny percentage of other materials mixed in. The two types of doping (called n-type and p-type) determine its electrical properties when a random electron reaches the junction.[10]

3. Problems effect

3.1The effect of High Temperature

The increased temperature in the cell leads to an increase in atoms vibration (phonons). In a p-n junction cell, increase and obstruct charge carrier movement which decreases cell efficiency, and this hinders the movement of the charging carriers and reduces the cell efficiency. This is proven by a study conducted on a ploy crystalline PV module on Dhahran east of Saudi Arabia that showed a similar temperature effect. the efficiency decreased from11.6% to 10.4% when the module temperature increased from 38°C to 48°C, which corresponds to 10.3% Fig.2.[2]

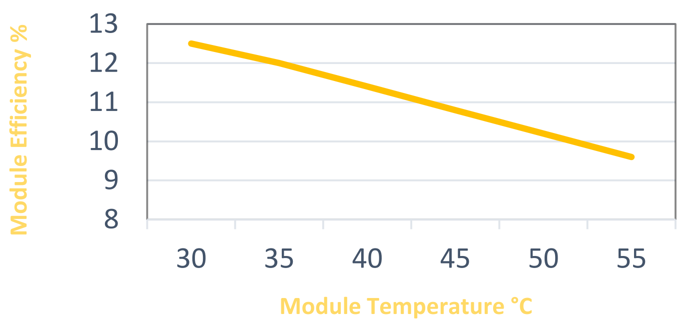

Fig. 2: Correlation between efficiency and module's temperature.

3.2The effect of Dust

The dust accumulation on the surface of the PV module blocks the solar irradiation from reaching cells, and hence impacts on the power output, current-voltage, and characteristics of PV modules.

3.3The Effect of Humidity

On the moisten PV surface the light is scattered either by refraction, reflection or diffraction when it hits water droplets.[3] Moreover, in a hot and humid climate, moisture penetrates into the PV cells through the cracks, causing a significant decrease in cell productivity.[4]

The table below to compared the effect of the problems in the monocrystal line PV and Amorphous PV, the temperature play a vital role in decreasing the efficiency during a day.

However, for a longer period, the effect of dust becomes more and more important and overcome the effects of temperature or Relative Humidity.

	Dust (%)	PV temperature (%)	Relative Humidity (%)
Monocrystal-line PV	0.095	0.15	0.06
Amorphous PV	0.071	0.43	0.18

Table I. - Decrease in efficiency (in %), during a day in Doha, due to increase in dust accumulation, temperature or Relative Humidity for Mono-crystalline and Amorphous Panels [9]

4. Proposed Solutions

- High Temperature

Phase change material (PCM)

This system was named PV–PCM or PV/PCM, a hybrid technology integrating a PV panel and a PCM into a single module to achieve higher module solar conversion.[6]

The PCM reduces the PV temperature thereby increasing its efficiency. Compared to PV using natural or forced air circulation for cooling, PV-PCM module has the advantage of having a smaller module size and offer better integration possibilities on building envelopes. However, the PV–PCM system is still in the infancy stages.[6]

This study was conducted outdoors at the Faculty of Engineering in the University of Syiah Kuala. Three PV panels were used: one of them served as reference, while the second one used paraffin wax as a phase change material (PV-PCM1), and the third one used beeswax as a phase change material (PV-PCM2) Fig3.[6]

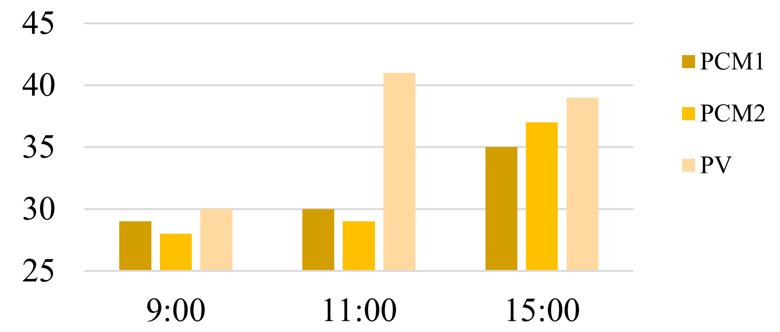

Fig.3: Average temperature at the front surface of the PV,PV-PCM1 and PV- PCM2. paraffin wax (PCM1) bees wax (PCM2).[5]

- Passive Cooling and Active Cooling

The Active Cooling uses energy from the PV solar modules or the external energy source. Such as fans systems that use fans or other means to create airflow and pumps. While, the Passive Cooling is a natural technique such as air ducts, the water tank, and Fins, PV cooling could limit the temperature loss to less than 3%. However, these mechanisms are affected by various variable factors. It was found that different fin sizes have three different effects where larger fins have a greater effect than the smaller ones.

Another mechanism is using air ducts attached to the back of the PV panels. This technique showed more than 10℃ reduction in the panel temperature. Moreover, the water tank below the PV panels could be used to decrease the temperature and resulted in a 12% increase in energy yield. The main disadvantage is that it's heavy weight.

Another way to drop the temperature is flowing water on the top of the surface this solution resulted in an approximately 8-9% increase in energy yield Fig4. The disadvantage of the last two solutions is significant water use, which is a challenge in dry Saudi Arabia conditions. [5]

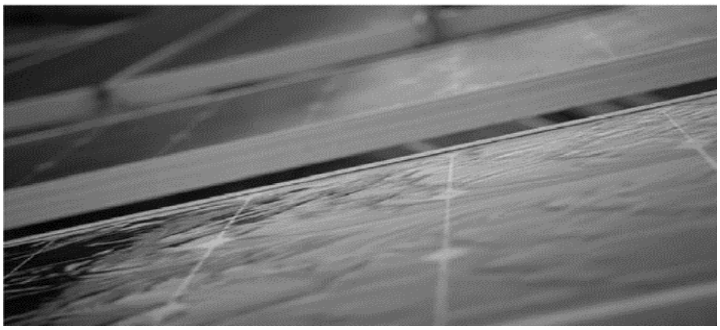

Fig.4: Close-up of the film flowing water at surface.[7]

- Dust & Humidity

Mechanical removal of dust removes the dust by brushing. Saudi Aramco's Research and Development Center (R&DC) produced a low-cost, competitive technology to mitigate the impact of dust on solar panels. The Robotic Dust Mitigation (RDM) project began in 2014 Fig5.

Fig.5: The Robotic Dust Mitigation (RDM) with silicon brush to clean the solar arrays [11]

The version three of the prototype mechanic uses a robotic mechanism with silicon brushes to clean the solar arrays. In term of advantages, the silicon rubber foam, a new type of brush, significantly reduces the cost of the brush and provides highly effective, non-abrasive cleaning.[11]

A smart Coating for Self-Cleaning Application nanofilm covered with self-cleaning; Super-hydrophilicity film the popular super hydrophilicity film is TiO_2 and ZnO Microstructures which has hydrophilicity and photocatalytic activity because of the hydrophilicity, the rainwater will diffuse to the whole surface instead of getting together and rinse the dust. This self-cleaning method cannot be used in a solar cell array in Saudi Arabia because it worked mostly in a desert region with seldom rain.

The super-hydrophobic film, superhydrophobic surfaces such as the leaves of the lotus plant show surface strongly repels water and extremely low wettability. The nanostructures of this surface can enhance the contact angle (CA) to higher than 150°C, so the water droplets that hit the surface would quickly roll off, carrying dust and other particles with them.[8]

5. Conclusion

- The work of solar cells in harsh conditions caused a significant reduction in the efficiency of solar cells.
- The solutions in this paper are some of the propose possible solutions which can increase the efficiency between 10 to 16%.
- The result of solutions depends on a natural factor. By increasing the wind velocity, more heat can be removed from the PV cell surface. On the contrary, wind leads to accumulated dust on the cell surface.

6. References

[1] Salman Zafar (April 6, 2019) Solar Energy in Saudi Arabia: Perspectives, Available at: https://www.ecomena.org/solar-saudi-arabia/ (Accessed: July 6 2019).

[2] M. J. Adinoyi and S. A. M. Said, "Effect of Dust Accumulation on the Power Outputs of Solar Photovoltaic Modules," Renewable Energy 60, 633 (2013).

[3] S. Mekhilef, R. Saidur and M. Kakalisarvestani, "Effect of Dust, Humidity and Air Velocity on Efficiency of Photovoltaic Cells," Renew. Sustain. Energy Rev. 16, 2920 (2012).

[4] Roshen T A Hamdi, Sanaa A. Hafad, Hussein A Kazem, Miqdam T Chaichan"Humidity impact on photovoltaic cells performance: A review" Energy and Renewable Energies Technology Center, University of Technology-Iraq Engineering Faculty, Sohar University, Sohar, Oman(2018)

[5]A.Baras, W. Bamhair, Y. AlKhoshi, M. Alodan King Abdullah City for Atomic and Renewable Energy, J. Engel-Cox Battelle Memorial Institute United States "OPPORTUNITIES AND CHALLENGES OF SOLAR ENERGY IN SAUDI ARABIA"

[6] "Experimental analysis of using beeswax as phase change materials for limiting temperature rise in building integrated photovoltaics"

[7] "Increased electrical yield via water flow over the front of photovoltaic panels"

[8] He, G., Zhou, C., & Li, Z. "Review of Self-Cleaning Method for Solar Cell Array" Procedia Engineering 640 – 645 16 (2011).

[9] F. Touati*, A. Massoud, J. Abu Hamad and S.A. Saeed "Effects of Environmental and Climatic Conditions on PV Efficiency in Qatar" Department of Electrical Engineering, Qatar University, Doha, Qatar

[10] Solarcellcentral.com. 2021. Solar Cell Central - A Comprehensive Solar Energy Site. [online] Available at: <http://solarcellcentral.com/index.html> [Accessed 7 January 2021].

[11] Aramcoexpats.com. 2021. Robot Opens The Door To Improved Solar Energy Opportunities. [online] Available at: <https://www.aramcoexpats.com/articles/robot-opens-the-door-to-improved-solar-energy-opportunities/> [Accessed 7 January 2021].

[12] Pveducation.org. 2021. Absorption Of Light | Pveducation. [online] Available at: <https://www.pveducation.org/pvcdrom/pn-junctions/absorption-of-light> [Accessed 2 January 2021].

11. Renewable Energy Strategies, Policies, Scientists for Future

CONCENTRATING SOLAR THERMAL SYSTEMS IN GREECE: CURRENT STATUS AND FUTURE POTENTIAL

V. Drosou[1], R. Christodoulaki[1], E. Kyriaki[2], A.M. Papadopoulos[2]

[1]Solar Thermal Systems Department, Center for Renewable Energy Sources and Saving, Pikermi, Athens 19009 (Greece)

[2]Process Equipment Design Laboratory, Department of Mechanical Engineering, Aristotle University, 54124 Thessaloniki (Greece)

Abstract

It is a truism that renewable energy sources (RES) facilitate countries to address their objectives regarding a secure, clean, reliable and affordable energy. Greece has committed itself to achieving a renewable energy share of 35% in its aggregate energy mix by 2030, up from 31% presently, which is planned to come mainly from wind, solar and hydroelectric power plants. Concentrating solar thermal (CST) systems have the ability to provide dispatchable power to the grid, due to their inherent thermal storage capacity. Therefore, they are expected to play an important role in the European energy transition plan. Furthermore, CST systems can deliver high temperature process heat for industrial applications. This research work addresses the CST technology and discusses the current status, the national strategy and policy measures, as well as the future potential in the electricity and the industrial sector of Greece.

Keywords: Concentrating solar thermal systems, concentrated solar power, industrial process heat.

1. Introduction

Solar energy is a form of renewable energy which can be converted into useful thermal or electrical energy for use in the residential, commercial and industrial sector. The conversion of solar energy in thermal energy is made with the use of solar thermal systems. The main component of a solar thermal system is the solar thermal collector. Solar thermal collectors may be classified in two categories: with or without sun tracking mechanism. Sun tracking mechanism is used to adjust the collector orientation in a sun-following solar collector system. For low-medium temperature applications, stationary, non-tracking solar thermal collectors are usually used, whereas for medium and high temperature applications, collectors with solar concentration through tracking mechanisms are indicated. Solar concentration is the re-direction of solar radiation to enhance the irradiance received by the absorber or the receiver. Concentrating Solar Thermal (CST) systems use mirrors or lenses with tracking systems to focus a large area of sunlight onto a smaller area.

Solar thermal systems may produce fluid of low ($T < 100$ °C), medium ($100° < T < 400$ °C) and high ($T > 400$ °C) temperatures that can be used directly or be transformed into other forms of energy as mechanical, electrical and chemical.

The most common applications of solar thermal systems are:

- Sanitary hot water production
- Hot air production for space heating and drying
- District heating
- Space heating / cooling
- Solar desalination
- Industrial process heat
- Electricity production

CST systems use a combination of mirrors or lenses to concentrate direct solar radiation to produce heat, electricity

Selection and/or peer review under responsibility of Scientific Committee
doi:10.18086/eurosun.2020.11.01 Available at http://proceedings.ises.org

or fuels. In CST technologies there is a decrease in the absorber area and an increase in the aperture area, allowing an efficient collection of solar light (Mortazavi and Maleki, 2019). Unlike flat plate solar thermal collectors and photovoltaics, CST systems are not able to use diffuse radiation. The most common CST commercial systems configurations are Linear Fresnel Reflector (LFR) and Parabolic Trough Collector (PTC) with linear focus (Fig.1) and Solar Tower and Solar Dish (Fig.2) with point focus mechanism.

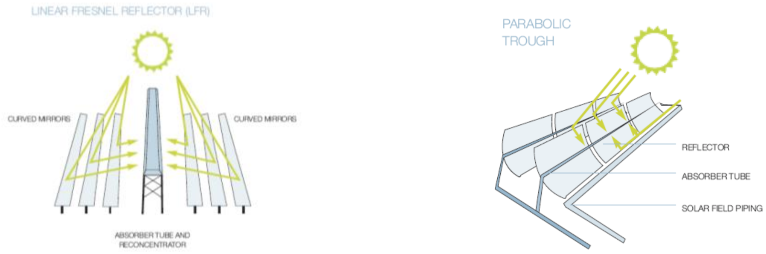

Figure 1: Linear focus CST technologies. Linear Fresnel collectors (left) and Parabolic trough collectors (right)

Figure 2: Point focus CST technologies. Solar tower (left) and Parabolic trough collectors (right)

CST technologies can reach a solar concentration factor from 5 to more than 1000. The increase of the concentration factor from 5 to 1000 increases the operating temperature of the solar plant from 60°C to more than 1000°C, respectively. This technological flexibility allows the adaption of CST technologies to several industrial processes and other emerging applications, such as water desalination, solar chemistry and material processing. The use of CST technologies for electricity production is traditionally known as Concentrating Solar Power CSP or more recently, as Solar Thermal Electricity STE, with the view to differentiate from the concentrating PV plants. These are already tested solutions, relatively cheap and available at high Technology Readiness Levels; for these reasons, CSP is among the most important sustainable technologies that can reduce the fossil fuel consumption of industrial processes and their corresponding carbon footprint (CETP-SRIA, 2020).

Recent data from January 2020 indicates that the world total capacity of CSP plants, either in operation or in advanced construction, is 9267 MW (Fig 3). Parabolic trough collectors hold the greatest share of this figure, as they considered the most bankable for project financing. On the other hand, solar tower designs can reach higher maximum temperatures and hence, increased efficiency for power generation and thermal heat storage. Linear Fresnel technology, another CST line-focusing system, has much lower commercial deployment (415 MW, also in 2019).

In 2019, the commercial CST systems under operation produced 15.6 TWh. This energy production is expected to undergo an exponential increase in the upcoming years; under the Sustainable Development scenario, IEA forecasts that the worldwide energy production from CST will be 53.8 TWh in 2025 and 183.8 TWh (around 60 GW of installed power) in 2030 (IEA, 2020).

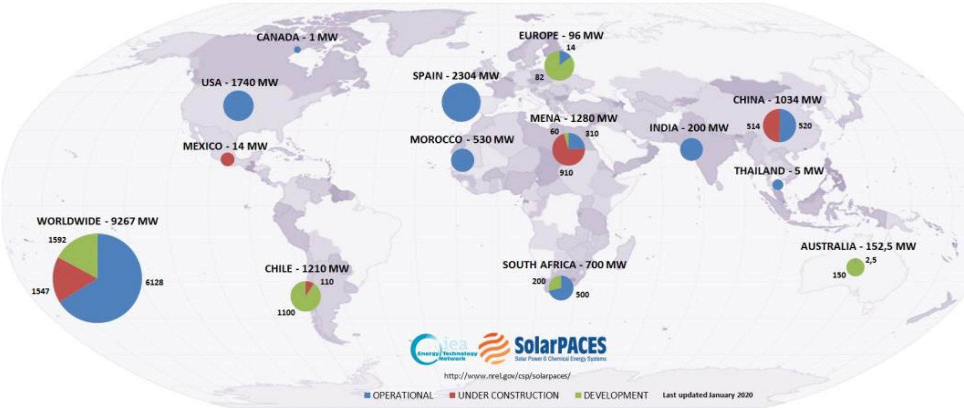

Fig. 3 CSP projects worlwide (SolarPACES, 2020)

The technical potential of CST is much higher, firstly due to its capability to supply industrial heat. According to the International Energy Agency (IEA, 2019), the amount of thermal energy required worldwide by industry was 86 EJ in 2017, which represents about 73% of the total industrial energy consumption. CST can supply most of this heat, since approximately 52% of that heat demand lies in temperatures below 400^{o}C (SolarPayback, 2018). Several industrial sectors can be identified as intensive heat consumers within these temperature ranges. These industries include chemical synthesis, food and beverage, textile, wood processing, pulp and paper, mining and machinery; in processes like evaporation, distillation, pasteurization, cleaning, washing and drying.

Secondly, CST, in contrast to other renewable technologies, can employ heat storage systems efficiently. Following sufficient studies and simulations, the integration of storage technologies can be techno-economically optimized, enabling the matching of the variable solar heat source and the variable load profile. The use of storage concepts further increases the technical potential of the CST technology.

2. Current status in Greece

In this framework, Greece with its inexhaustible solar radiation could not miss out. Today, there are two Greek projects, namely “Maximus” and “Minos”, which have been selected for funding in the first round of EU's NER300 programme, there are other projects waiting for unlocking administrative procedures and there are smaller projects installed in the industrial sector.

“Maximus” project is a large-scale Stirling dish power plant with a total installed capacity of 75.3 MWe, located in the north west of Greece, in the region of Florina. The plant consists of 25160 Stirling dish units, each with 3kW rated power output. The plant is composed of 37 small power plants of modular design, built on different land plots, which will be connected to the grid via a single connection point. The Stirling dish unit consists of a cavity receiver that captures the concentrated solar irradiation from the parabolic-shaped reflector, a free-piston Stirling engine that converts the solar energy to electricity and a closed loop air driven cooling system. The concentrator is mounted on a structure with a two-axis tracking system to follow the sun. This project is on-hold situation.

“Minos” project concerns the implementation and operation of a CSP plant based on central tower technology with a nominal installed electrical capacity of 52MWe that will be built in the southeast of Crete. The project intends to use heliostat mirrors to concentrate the sun irradiation on a solar receiver placed on the top of a tower. The tower system will be based on innovative superheated steam technology in order to increase the efficiency of the present plants with tower technology and saturated steam. The project will be located adjacent to the existing power plant of Atherinolakkos. The planned site has a size of approximately 143 ha, only 1500m from the sea, at an elevation between 50 and 100 m above sea level. It is foreseen 5h thermal storage system with 2 tanks molten salt system. Currently the EPC Engineering – Procurement – Construction selection process has been completed and the EPC contract signing is being finalized. The project construction is expected to start early 2021 with expected operation start in 2023.

Currently, a pilot plant of smaller capacity, namely $0.5MW_{th}$, has already been constructed and has operated in the area of the ‘MINOS’ project (Fig. 4). The pilot plant size with an installed electrical capacity of $50kW_{e}$ consists of $1200m^{2}$ of heliostat area. The pilot plant produces superheated steam of 350^{0}C at approximately $3MP_{a}$. The expected net annual electricity production is estimated at $100kWh_{e}$. In Fig 5 the allocation of pilot plant in relation to the "MINOS" project is seen.

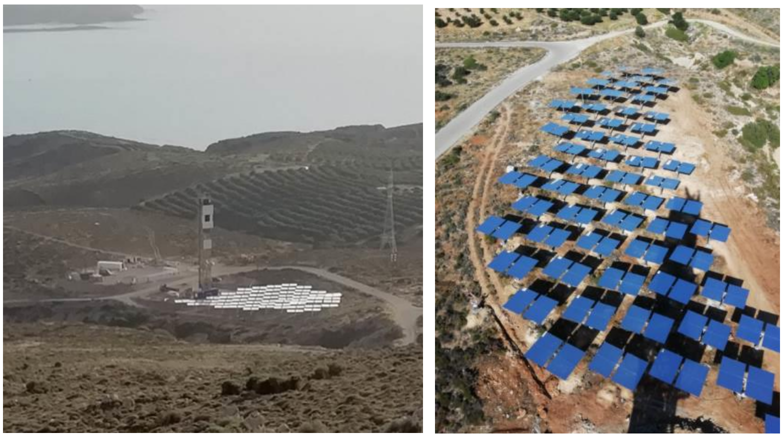

Fig.4 Pilot plant in the area of MINOS project, in Crete.

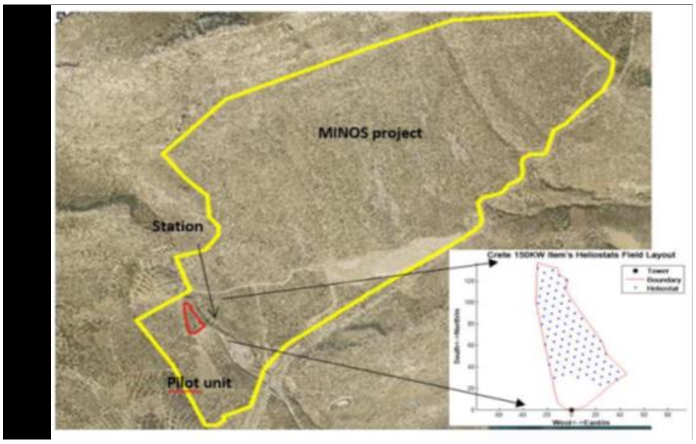

Fig.5 Mapping of the pilot plant, in relation to the 'MINOS' project, in Crete.

A new CSP project, entitled "YPERION-1" has also received approval decision from the Greek Ministry as officially announced on July 2017, with a license of 2+2 years. The owner is the company SOLAR POWER PLANT LASSITHI EPE. It concerns a CSP plant with 70MW installed capacity, with estimated energy production of 168GWh/y. This amount accounts for approximately 10% of the total Crete's energy needs, the total population of which is 630000. The foreseen technology is parabolic trough collectors with oil and molten salt storage. The solar plant will consist of 552552 solar collectors in 138 loops and will occupy about 0.452 km^2. 6 biogas burners of total capacity 186MW for the preheating of heat transfer fluid & molten salt are also foreseen. Fig. 6 indicates the location of YPERION-1, in relation with MINOS project in Crete.

Fig.5 YPERION-1 CSP plant, in relation with 'MINOS' project in Crete

This project is an indicative example of the possible implications that social acceptance has; its installation has been put on hold due to reactions from citizens and local organisations, two years ago. The project now is in marginal timeline position. Recently, an updated Environmental Impact Assessment was submitted for evaluation and acceptance by regional authorities. In the EIA, the project is described to employ parabolic trough collectors by Flagsol GmbH, type SKAL-ET150, in 138 loops and 2 tanks molten salt thermal storage of 2h in nominal load. The project was highlighted by the Prime Minister of the country on September 2019, who stated *"Energy and environment are of particular importance to our country. Energy production must now be combined with the protection of natural resources. The country needs to get on the path to carbon independence; the next inter-ministerial committee on strategic investments will approve a new project solar thermal power generation project* *in Crete, which will cover 10% of the island's needs"*. This clear statement from the Greek Prime Minister, in line with the Greek National Energy and Climate Plan (Hellenic Republic, 2019), is expected to accelerate the construction procedure in the shortcoming period.

To begin with the industrial sector, a small CST plant has been installed in a dairy industry, Koukaki farm. The plant consists of 10m^2 solar concentrating collectors with 7 kW$_{th}$ nominal thermal power. The plant is installed in the roof of the company and it is used for the production of process hot water. It is located in Kilkis region, Northern Greece.

Fig.6 CST in Koukaki farm

Another small CST project has been installed in Colgate-Palmolive, employing parabolic trough collectors from Absolicon Company (Absolicon, 2019). The CST plant consists of a solar field of 100 m^2 T160 Absolicon collectors, for the production of process heat (Absolicon 2018).

Fig.7 CST in Colgate Palmolive Company

3. Potential in electricity sector

At the end of the 2020s, the Greek electricity market is characterized by four main features:

1) The use of lignite, which has been the main fuel for electricity generation since the 1950s and the only indigenous resource, is dramatically shrinking, accounting in 2018 for 33.94% of the total generation, whilst the use of natural gas is respectively increasing, accounting for 33.85%. The use of RES, in the form of wind and PVs, has reached an all-time high of 21.5%, whilst big hydroelectric plants provide another 10.6% (EnExGroup, 2019). RES technologies have become an integral part of the Greek electricity sector: from no more than 300 MW in 2000, 3576 MW of wind generators and 2835 MW of PVs were operational by the end of 2019. Throughout this period, the interest in CST plants was rather marginal, being limited to the aforementioned two projects. And this, despite an attractive Feed in Tariff rate of 284.85 €/MW, provided the CST ensures a storage capacity of 2 hours. The implementation of the Target Model in Greece, in July 2020, is expected to alter the whole renewables market significantly, along with the introduction of Power Purchase Agreements in 2018. The latter may be more suitable to promote a number of CST plants, which would provide the dispatchable capacities that PVs and wind cannot ensure. The ongoing propagation of renewables and natural gas is expected to alter both market structure and electricity generation and transmission costs, but it will impose new burdens on managing the electrical systems and transmission network, especially given the need for keeping reserves and/or storage.

2) The Public Power Corporation PPC still dominates the market, covering in 2019 still 83.9% of the consumers with a market share of 78.5%, with 4 private producers covering another 17.5% of the market and the rest being covered by smaller providers (EnExGroup, 2019). The liberalization of the market, which has begun in the mid-2000s, is based on the use of gas-fired power plants by the 4 main producers.

3) Greece has some of the highest electricity prices in Europe for commercial and industrial clients. In 2018 the average price was 110 €/MWh, with 25% of the price being taxes and another 25% being transmission and

distribution costs. Only Denmark due to its environmental policies and, for entirely different reasons Malta and Cyprus, have more higher tariffs. Even the low voltage tariffs for commercial clients like SMEs and small hotels, was in 2018 on average 175 €/MWh, again with 50% of the price being attributed to taxes and distribution and transmission (HAEE, 2019). Although this price is lower than the respective tariffs in most Northern European member states, it is still placing a considerable burden on the food processing SMEs and the tourism sector, in comparison with competitive Mediterranean countries.

4) Greece has almost 6,000 islands, out of which 117 are inhabited. The non-interconnected islands, host approximately 15% of the Greek population, namely 1.5 million people, and account for 14% of the total electricity consumption. Furthermore, those islands host millions of tourists every year. Prior to the COVID-19 crisis in 2020, more than 18.5 million tourists had visited the islands in 2019 (SETE, 2020), leading to an extremely high seasonal variation of demand and consumption. Electricity generation costs in the non-interconnected islands varies from 120 €/MWh in big islands like Crete and Rhodes to more than 500 €/MWh in the very small islands like Kastellorizo (Papadopoulos, 2020). Although the projects of interconnecting Crete and the Cyclades, covering the overall cost for the islands remains an issue.

It is against this background that one should examine the use of CST and evaluate its feasibility, taking into consideration the increased need for spinning reserves and/or storage due to the increased propagation of RES in the interconnected system and the even more pressing need for meeting generation and demand in the not-interconnected one. As it can be seen in Figure 8, the weighted average cost is varying between 200 and 300 €/MWh, with China only achieving significantly lower values, and with auction prices on average being around 75 €/MWh. However, one has to consider the cost the electrical system operators, and eventually the consumers, have to cover to ensure ancillary services that include (a) Primary control and reserve, (2) Secondary control and range, (3) Tertiary control and spinning reserve, (4) Non-spinning reserve, (5) Standing reserve, (6) Voltage control and (7) Black-start services. This has been so far carried out over the Wholesale and Energy Capacity Assurance Market, which is working on the Day Ahead Scheduling base. The cost of the ancillary services varies on average from 8 to 15% of the system's marginal cost, which in 2019 varied between 45 and 85 €/MWh. However, in peak demand hours generation costs can exceed 125 €/MWh and the cost for replacing unavailable wind or PV plants is considerably higher (IPTO, 2020).

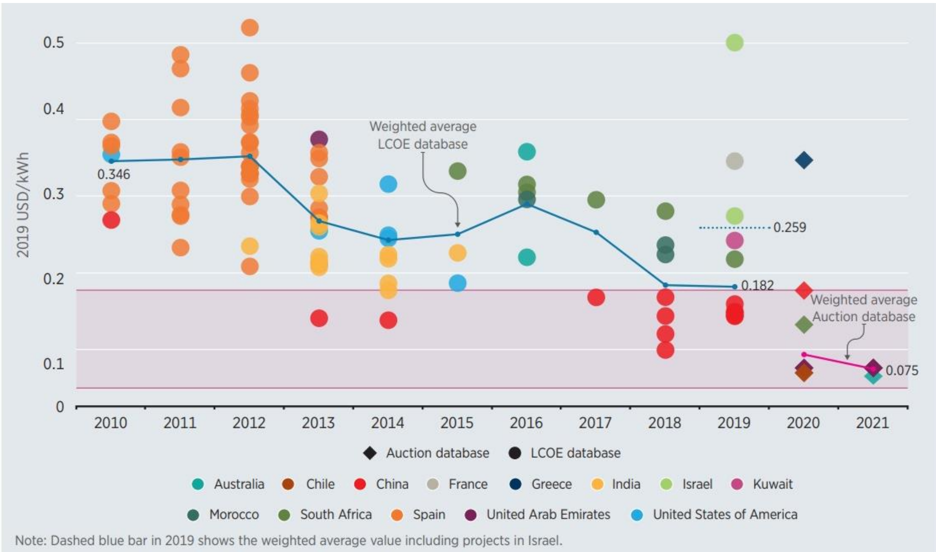

Fig.8 Levelised Cost of electricity and auction price trends for CSP, 2010-2021 (IRENA, 2020)

A CSP plant providing 2 to 6 hours of storage can in that sense be considered as a dispatchable power generation plant, and contribute to reducing the ancillary services costs of the system and this is something which has to be taking into consideration in the new market environment of the Target Model. In the case of non-interconnected systems, like the big islands of Crete and Rhodes, the significance of providing storage is even more important: one the hand there is the stronger impact of the fluctuations in the output of renewables and on the other the variation in the demand. The Value of Lost Load is an important parameter that determines to a great extent the feasibility of alternative energy generation technologies and of energy storage, which can exceed 400 €/MWh (Waterson, 2017; DiSomma et al, 2016). In that case, a CSP investment, which operates as a hybrid generation and storage plant, has a clear advantage over all other RES systems.

4. Potential in the Greek industrial sector

Industrial solar thermal installations with flat plate collectors, have been installed in Greece during the last years with a significant energy saving and environmental benefits. The thermal applications in the Greek industry vary from 60ºC to 200ºC, depending on the process. Flat plate collectors and evacuated tube collectors are ideal for temperatures below 90ºC, whereas for temperatures higher than 100ºC linear focus CST systems are more appropriate. This section discusses the possible configurations of CST systems in industrial process heat applications in Greece along with their technical characteristics and performance evaluation figures.

Presently, process heat applications are suited by a growing range of solar thermal concentrating technologies, all of them presenting products already in pre-commercial or commercial stage (INSHIP, 2018). Integrating solar heat is possible at several points in the heat supply and distribution network of an industrial production site. Nevertheless, the effort for identification of suitable integration points for solar heat as well as the complexity of possible solutions can vary significantly between industrial sectors and factories. The integration of CST in process heat systems must take into account the specificities of end-user´s framework and the development of standardized and modular Balance of Plant (BoP) concepts.

In order to design a solar field layout aimed at steam generation for a specific industrial process, some characteristic parameters should be determined. These parameters can be divided into three different groups depending on the particular subject they are related to: solar technology, location or industrial process. According to this classification, this section describes the main parameters and their effect on a proper design of the solar field layout focusing on medium temperature SHIP applications (150 to 400 ^{o}C) based on steam.

4.1 Solar Field Layouts

- Depending on the steam generation process: Depending on whether the steam is generated directly in the solar field or not, Direct (DSG) or Indirect (ISG) Steam Generation is considered. In the case of DSG, the heat transfer medium circulating through the solar field is water, employing two-phase fluid flow inside the collectors. In the case of DSG, three basic concepts can be considered depending on the specific configuration of the steam generation process in a solar collectors' loop, as seen in Fig. 9 (INSHIP, 2018a). For ISG case, the heat transfer medium is a liquid, typically thermal oil or pressurized water. The solar heat is then transferred to a secondary circuit by means of a heat exchanger an evaporator or a flash tank to generate the steam required by the industrial process.

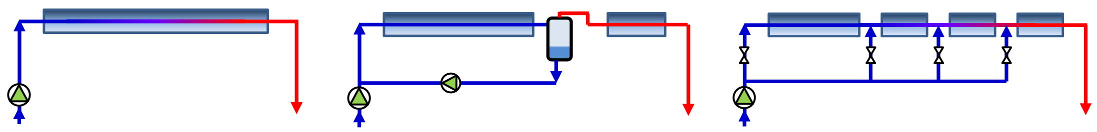

Fig. 9: Basic configurations of the DSG process in a solar collector loop: Once-Through (left), Recirculation (middle), Injection (right)

- Depending on the piping arrangement of the solar field: There are three different options, as seen below. Direct return is the simplest configuration but it involves a misbalance in pressure drop between collector loops because each row has a different pipe length. This results in the increase of the overall pressure loss through the solar field. In reverse return, a certain balance in pressure drop between rows is achieved. This configuration involves less pressure loss than the direct return; however, an extra length of pipe is required. Central supply layout requires regulation valves to balance pressure losses and mass flow rates between rows.

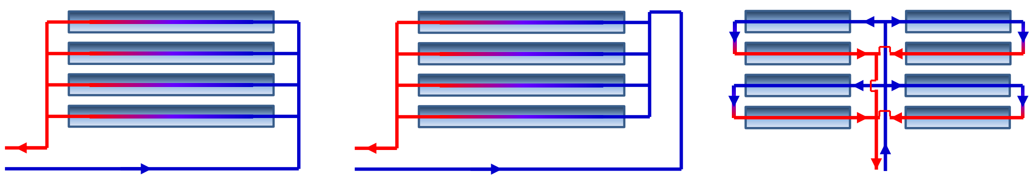

Fig.10 Typical configurations of distribution pipes in a solar field for SHIP applications: Direct return (left), Reverse return (centre), Central supply (right). (INSHIP, 2018a)

4.2 System Layouts

An example of the system layout for a solar ISG application including a storage system is shown in Figure 11 (INSHIP, 2018a). The solar field heats up the working fluid, which can be sent to the storage system or delivered to the industrial process via three-way valves. The heat transfer fluid at high temperature, obtained either from the solar field or the storage system, is used to generate saturated steam by means of a kettle-type evaporator. The steam is then injected into the conventional steam network via a valve, which represents the integration point to the industrial process.

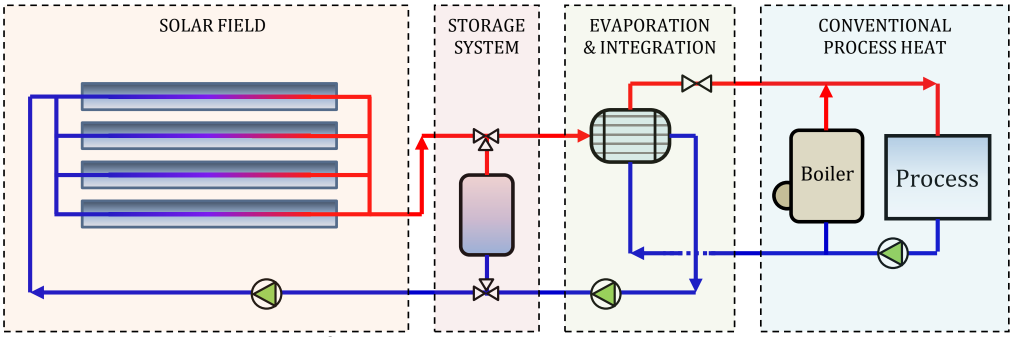

Fig. 11: System layout for a solar ISG application with a storage system (INSHIP, 2018)

Figure 12 shows an example of DSG in a solar field that feeds an industrial process working with superheated steam conditions (INSHIP, 2018a). It is based on the recirculation scheme by means of a common water-steam separator for the evaporation solar field (with 4 rows of solar collectors) and a separate field for steam superheating with 2 rows of solar collectors, including injection valves before the last collector in each row. A set of valves represents the integration point to the conventional steam network. A bypass is also foreseen to enable the stand-alone operation of the solar field for preheating purposes.

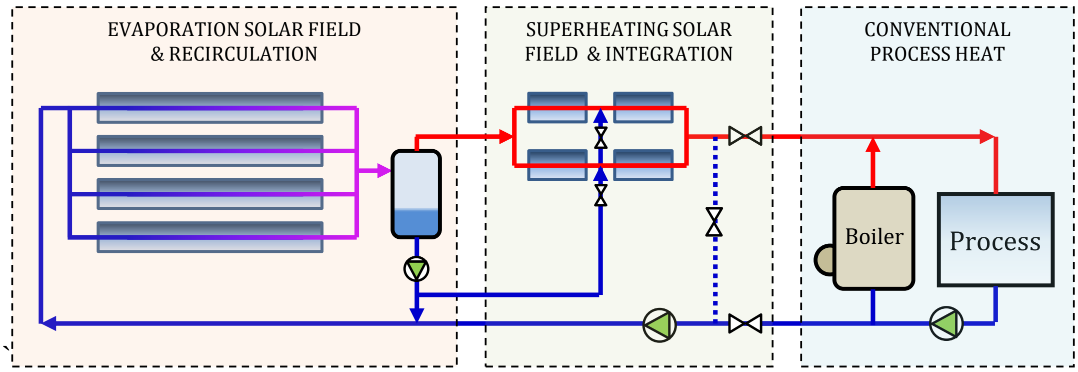

Fig. 12: System layout for a solar DSG application with superheating (INSHIP, 2018a)

Storage charging

Whenever the load profiles at the connected integration points require a storage concept, suitable storage charging and discharging strategies are applied. In SHIP systems, the most common concept is the storage charging via an external plate heat exchanger, because it offers high heat transfer rates.

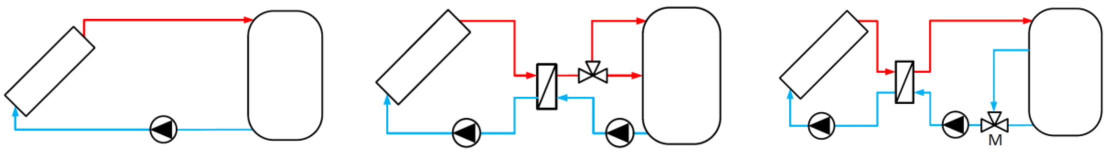

Fig. 13: Different charging concepts a) Direct charging without heat exchanger, b) External heat exchanger with stratification valve, c) External heat exchanger with mixed charging return flow (INSHIP, 2018b).

4.3 Integration point to the industrial process

A possible way for a classification is the distinction between supply and process level. The difference between the integration on supply level and on process level is shown in Fig. 14. Integrating solar thermal heat on supply level is the most common integration method, as it is the easiest possible and has minimum interference with the production process. Integration on process level is much more complex, but has the advantages of higher system efficiency and lower temperature supply.

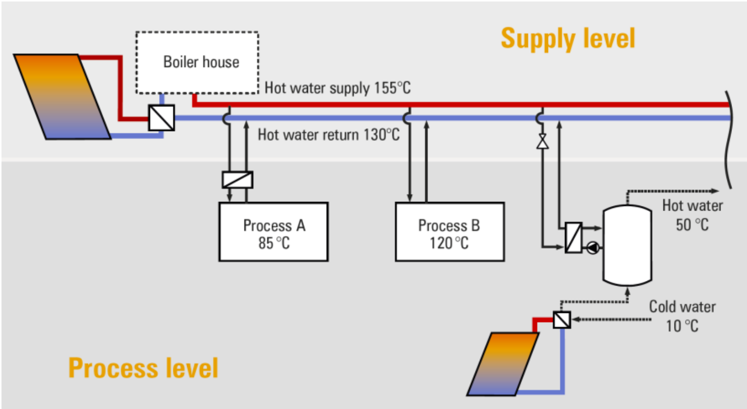

Fig. 14: Possibilities to integrate solar heat on supply level and on process level (Schmitt, 2017).

4.4 Proposed layouts

The authors have studied and simulated various solar heat for industrial processes systems and propose two typical configurations that can be used in most of the Greek industries, as shown in Fig. 15. The proposed system is an Indirect Steam Generation system, employing Parabolic-Trough Collectors with thermal oil as the heat transfer medium. The proposed solar field piping layout is reverse-return, since it involves less pressure losses compared to the other configurations. The evaporator is connected in-parallel and the integration type is on supply level. The two options refer to the presence of a storage tank.

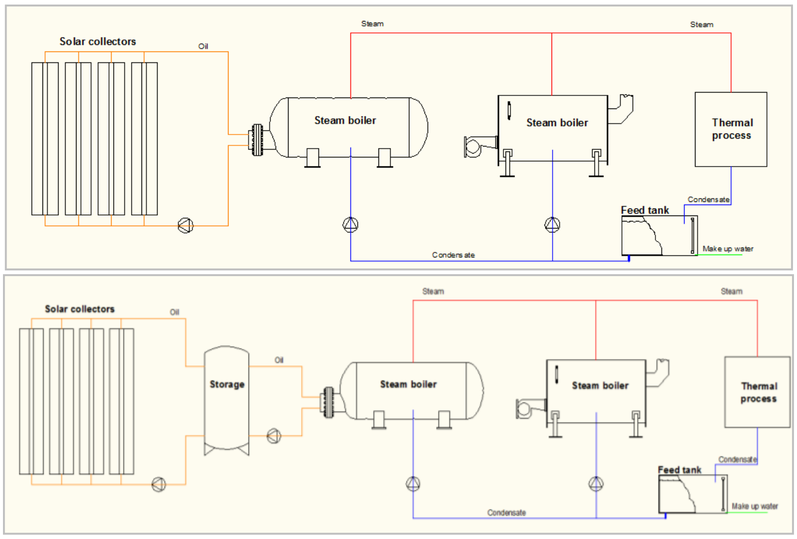

Fig. 15: Proposed SHIP configuration for Greek industries: Supply level, Indirect Steam Generation system, PTC collectors with thermal oil. Up: no storage. Down: with storage.

5. Future potential and Discussion

CST/CSP systems are much more than a highly promising technology. They have become a quite mature integrated energy generation and storage technology, which can provide solutions to a multitude of applications, both considering electricity generation and thermal power requirements. Still, and despite the significant reduction in their initial cost and the increase in their efficiency and reliability, their Levelized Cost of Energy remains high, compared to other renewables, as they are capital intensive investments. This however, is only one aspect, because one has also to consider the integrated storage they provide, which has otherwise to be covered by ancillary services provided by conventional generation plants, by over dimensioned RES systems, by storage or by a combination of all those options. It is against those options that the true feasibility of CST/CSP plants has to be evaluated. One has, however, to keep in mind that until there is a further reduction in these systems' initial cost, it will not be easy to foster their use without some form of incentives.

On the other hand, they are investments that call for a multifaceted evaluation and decision-making procedure that has to take into consideration macroeconomic factors, environmental aspects and eventually, the acceptability by local societies. All those parameters have to be part of an integrated energy and environmental policy that will lead to a regulatory framework for CST/CSP plants and to the elaboration of financial and/or non-financial incentives, which have to be provided in order to foster the energy transition and the de-carbonization of the Greek economy.

6. References

Absolicon, 2018. Absolicon Ongoing projects. Available from: http://www.absolicon.se/om-absolicon/pagaende-projekt/ (accessed on 13 June 2020).

Clean Energy Transition - Strategic Research and Innovation Agenda CETP-SRIA, 2020. Input Paper, Thematic Cluster 1: Renewable Technologies, Concentrated Solar Thermal Energy.

Di Somma M., B.Yan B., N.Bianco N., P. B.Luh P.B., G.Graditi G., L.Mongibello L., Vi.Naso Vi., 2016. , Multi-objective operation optimization of a Distributed Energy System for a large-scale utility customer. , Applied Thermal Engineering, 101, 1 (2016), 752-761.

Energy Exchange Group, 2019. Yearly DAS trading system report, Athens, p.18-27.

Greek Tourism Confederation SETE, 2019. Statistical Bulletin. Available from: https://insete.gr/statistika-deltia/ (accessed on 11 July 2020).

Hellenic Association of Energy Economics HAEE, 2019., Greek Energy Market Report, Athens, 2019, p.46-49

Hellenic Republic, Ministry of the Environment and Energy, 2019. National Energy and Climate Plan. Available from: https://ec.europa.eu/energy/sites/ener/files/el_final_necp_main_en.pdf (accessed on 4 June 2020),2020

IEA International Energy Agency. "Concentrating Solar Power tracking report". Available from: https://www.iea.org/reports/concentrating-solar-power-csp. (accessed on 20 June 2020).

IEA Statistics data browser, 2019. Available from: http://iea.org/statistics (accessed on 2 December 2019)

INSHIP - Integrating National Research Agendas on Solar Heat for Industrial Processes EU project, 2018. Deliverable 3.1 Guidelines for Solar Steam Integration in Steam Networks.

INSHIP - Integrating National Research Agendas on Solar Heat for Industrial Processes EU project, 2018. Deliverable 3.5 Standardization Requirements for BOP.

IPTO, System main indicators, System's monthly marginal prices, https://www.admie.gr/en/market/market-statistics/key-data/sip-vs-smp (in Greek), last accessed August 2020

IRENA International Renewable Energy Agency, 2020. Renewable Cost Database - CSP Summary Charts. Available from: https://www.irena.org/costs/Charts/CSP (accessed on 20 June 2020).

Mortazavi S.M., Maleki A., 2019. A review of solar compound parabolic collectors in water desalination systems, International Journal of Modeling and Simulation, 1–16.

Papadopoulos A.M., (2020),. Renewable energies and storage in small insular systems: potential, perspectives and a case study., Renewable Energy, Vol. 149, 103-114.

Schmitt B., 2017. Solar Process Heat, Low cost and carbon free heat for Industry and Commerce.

Solar Payback project, 2018. Available from: https://solar-payback.com (accessed on 3 June 2020).

SolarPACES, 2019. Available from: https://solarpaces.nrel.gov/ (accessed on 4 June 2020).

Waterson M., 2017. The characteristics of electricity storage, renewables and markets, Energy Policy, 104, 466-473.

Lithuanian Photovoltaic Market between 2010 and 2020, European Background, Current State and Development Perspective

Rokas Valancius[1], Eugenijus Perednis[2], Juozas Vaiciunas[1], and Andrius Jurelionis[1]

[1] Kaunas University of Technology, Faculty of Civil Engineering and Architecture, Kaunas (Lithuania)

[2] Lithuanian Energy Institute, Kaunas (Lithuania)

Abstract

The usage of the Solar Photovoltaic Systems (PV) in Lithuania was commenced during the last decade of the 20th century. They were applied in buildings, yachts, vacation homes, and other facilities to satisfy minor demands of electric power.

The stagnation of the PV's development until 2010 was caused by well-developed electric power distribution infrastructure and relatively large conventional electricity production. The significant increase of installed power from the PV systems and energy they produced was monitored in 2010 when the Government has introduced high rates of purchase of PV produced energy; that lasted till 2013 when high rates were cut down. A two-sided electric power metering system was launched in Lithuania in 2015 and within the next years the cost of PV systems decreased significantly, also the financial support from the state became available. All this gave new impetus to the development of PV systems.

This study aims to review the PV market in Lithuania between 2010 and 2020, the current state and development perspectives.

Keywords: renewable energy, photovoltaic systems, energy prices.

1. Introduction

The renewable energy segment has continued to grow worldwide in recent years, alongside ever increasing global energy consumption and decreasing investment costs for many renewable energy sources. Furthermore, in a lot of countries, the fluctuating price of fossil fuels has had a serious impact on energy security. There are several alternative resources that can provide clean, continuous, and renewable energy, such as solar, wind, biomass, hydro, and geothermal.

In 2019 the solar PV market increased by 12% to around 115 GW. The last decade ended with strong demand in Europe, the United States, and emerging markets. The global total of 627 GW at the end of 2019, compares to a total of less than 23 GW in 2009. Demand for solar PV is spreading and expanding as it becomes the most competitive option for electricity generation for residential and commercial applications and increasingly for utility-scale projects – even without accounting for the external costs of fossil fuels [REN 21].

Lithuania is a Baltic country in the central Europe region, with an area of 65300 km^2 and a population of 2.8 million. The average global solar irradiation in Lithuania is around 1050 kWh/m^2 (2003-2018), similar to Germany, Austria, Denmark, and Poland.

PV systems have been installed in Lithuania for over 20 years, but only in the last decade, the market boomed. Within the recent years, prices of PV systems dropped significantly and a subsidy system was launched for renewable energy sources in single-family houses, public buildings, factories, etc. [Valancius et al. 2018]. Some studies and reports showed that 1 kWp of PV systems can produce around 1000 kWh/year [Valancius et al. 2018a; ENMIN 2020; LSEA 2020]. In 2018, the price of small (up to 10 kWp) PV systems in Lithuania has dropped below 1100 EUR/kWp. At the beginning of 2020, the price PV systems propped again, because of lower PV cells prices. That has increased the interest to PV systems. At the end of 2019 the amount of installed PV power in Lithuania increased to around 100 MW from around 0.018 MW in 2010.

doi:10.18086/eurosun.2020.11.02 Available at http://proceedings.ises.org

Competition in the Lithuanian PV market, as in the rest of the world, increased during the year due to the growing supply of equipment, emerging new manufacturers, and equipment installers. Currently, in 2020, there are three manufacturers in Lithuania producing solar modules from standard to integrated into building facades or roofs: JSC Via Solis Energia, JSC Solet and JSC Intelligent solar. There are also many companies designing and installing a solar power plant.

In 2015 a two-sided electricity accounting scheme was launched in Lithuania, which gave a great impetus to the development of PV systems. This energy accounting scheme works as follows: when a PV of an electricity-producing consumer produces more power than is consumed (for example, when the sun shines in the midday), the electricity produced but not consumed is supplied to the power grid. Later (for example, when you return from work in the evening), when the producing consumer does not have enough of his instantaneous power, the excess electricity accumulated during the day is recovered from the power grid. The bilateral accounting period is scheduled for the calendar year starting from April 1. This means that consumers can also use the excess power produced during the summer in autumn and winter months. In this case, the power grid acts as a battery - it receives electricity when there is a surplus of production and allows to pick up the stored power when an energy-producing consumer lacks it. Power grids charge a fee for storage. The aim is to create clear, transparent pricing that does not have a significant impact on other consumers.

The majority of power consumers in Lithuania are connected to the low voltage grid. Electricity prices in Lithuania currently vary from 0.095 to 0.149 EUR/kWh for households depending on the selected tariff [Ignitis 2020].

Tab. 1. Payment methods and prices (01.01.2020) for producing consumers [ESO 2020].

Payment method	Paid for	Price in low voltage, EUR (including VAT)	Price in medium voltage, EUR (including VAT)
Payment for recovered energy	For a kilowatt-hour of electricity supplied to the grid and subsequently recovered (kWh)	0.05203 Eur/kWh	0.02662 Eur/kWh
Payment for the installed capacity of the PV	For the installed kilowatt of power generated by the PV (kW)	2.6378 Eur/kW/month	1.3552 Eur/kW/month
Hybrid payment	Hybrid payment, i.e. for kilowatt-hours (kWh) of electricity supplied to and subsequently recovered from the power grid and for kilowatt-hours of installed power generated by the PV (kW)	0.02662 Eur/kWh 1.3189 Eur/kW/month	0.01331 Eur/kWh 0.6776 Eur/kW/month
Payment in kilowatt-hours	Payment in kilowatt-hours: a fixed percentage of the amount of energy supplied to the grid (kWh) is left to the operator for the use of network services, the customer will be able to recover free of charge a set percentage of the amount of his production supplied to the grid	36% (64% remains to producing consumer)	21% (79% remains to producing consumer)

For example: if PV produced and supplied 50 kWh to the ESO (company responsible for electrical energy and gas distribution in Lithuania) grid during the month, and the amount consumed was 150 kWh, then for the 50 kWh recovered from the ESO grid, the producing consumer pays according to the prices set for the producing consumers. For the remaining 100 kWh the producing consumer pays according to the tariffs of one-time zone. If during the month it was produced and supplied 50 kWh to the ESO grid, and the amount consumed was 20 kWh, the producing customer pays for 20 kWh recovered from the ESO grid according to the prices of the producing consumers. There is no deficiency (0 kWh) higher than consumed. The accumulated amount of 30 kWh, which is not taxable, is calculated. The accumulated quantity is forwarded to future months and this accumulated quantity can be recovered at any time before 31 March of the following year [ESO 2020].

In order to implement the EU Directive 2010/31/EU on the energy performance of buildings, it was required by the legislation of the Republic of Lithuania that all new buildings constructed after 1 November 2016 comply with energy efficiency class A. This class is granted to buildings that use renewable energy sources for electricity and heat production. It also provided an additional stimulus for the use of PV in urban environments.

2. Residential market

Until 2015 only sporadic PV systems were installed in single-family houses and mostly in the buildings that had no connection to the power grid. The two-sided electric power metering system was commenced in Lithuania in 2015. At the beginning, this system, because of complicated connection procedures and high initial investments, was not popular. After the installation procedures of the PV were simplified in 2017 and installation costs dropped, the number of installed PV started to grow rapidly. More than 1800 new clients were connected between May and November of 2019, in comparison between the years 2015 and 2018 only about 1100 new connections were made. From 2016 to 2020 the number of consumers who produced energy increased from 248 to more than 3000. This number is increasing every week by an average of 80 new producing consumers.

On purpose to promote between population the installation of PV systems in households, the conditions required to become producing consumer were simplified and facilitated in July of 2019. Therefore, presently there is no need to receive a permit for installation of systems with the capacity of less than 30 kW, the simplified connection procedure is applied, and it is enough to submit an application and to apply to an operator of energy distribution [ENMIN 2020a].

Tab. 2. The installation stages of PV with capacity to 30 kWp.

Step	Process	Approx. duration in days
1	Obtaining the connection conditions for PV from ESO	to 5
2	Signing of the connection agreement with ESO	1
3	Installation of PV, submission of the contractor‘s declaration	5-10
4	Signing of a producing consumer‘s contract for the purchase and sale of electricity	to 20
5	Installation of a double-sided metering unit	to 2
	Total:	~40 days

Moreover, starting from 2019 residents have the opportunity to produce and to consume the energy produced by the PV systems that are in different geographic locations. For example, a person that lives in an apartment can purchase a part of a system in the solar PV park managed by third parties. Also, residents are allowed to install a PV system on their sites, for example, in country homesteads and to consume the produced energy in apartments in towns.

The growing popularity of PV is also linked to the support for the installation of heat pumps in households. Although statistics are not collected, it is noticeable that quite often people who install or are installing a heat pump also install a solar power plant.

A natural person who owns a residential building (one or two flats) or a garden building, the construction of which has been completed and registered following the procedure established by legal acts for at least 5 years from the date of the invitation to submit registration forms, may apply for support for the installation of a heat pump. Natural persons are eligible for support if they replace old boilers with efficient renewable energy sources. Requirements for heat pumps: ground-to-water and water-to-water heat pumps with a seasonal efficiency factor (SCOP) of at least 3.5, air-to-water SCOP of heat pumps must be at least 3.0. A natural person is reimbursed with 50% of the amount that is calculated by multiplying the power of the purchased equipment in kilowatts (kW) by the fixed rates of one kilowatt of power, which depends on the type of heating equipment and set of equipment.

3. Large scale market

The significant increase of the installed power from PV systems and the energy they produced was monitored when in 2010 it was started to purchase the energy produced by the PV systems in high rates (0.30-0.52 EUR/kWh) for defined 12 years period, it lasted till 2013 when high rates were cut down. The amount of installed PV power: 0.018 MW in 2010, 0.37 MW – 2011, 7.1 MW - 2012 and 68.01 MW – 2013.

From 2015 legal entities also can become producing consumers. The capacity of PV is selected in such a way that the annual amount of electricity produced is close to the annual demand for energy consumed at the facility, as a company will not be paid for the excess electricity produced. Moreover, the installed capacity of the system has not to exceed permissible power consumption of the facility and has not to be larger than 500 kW.

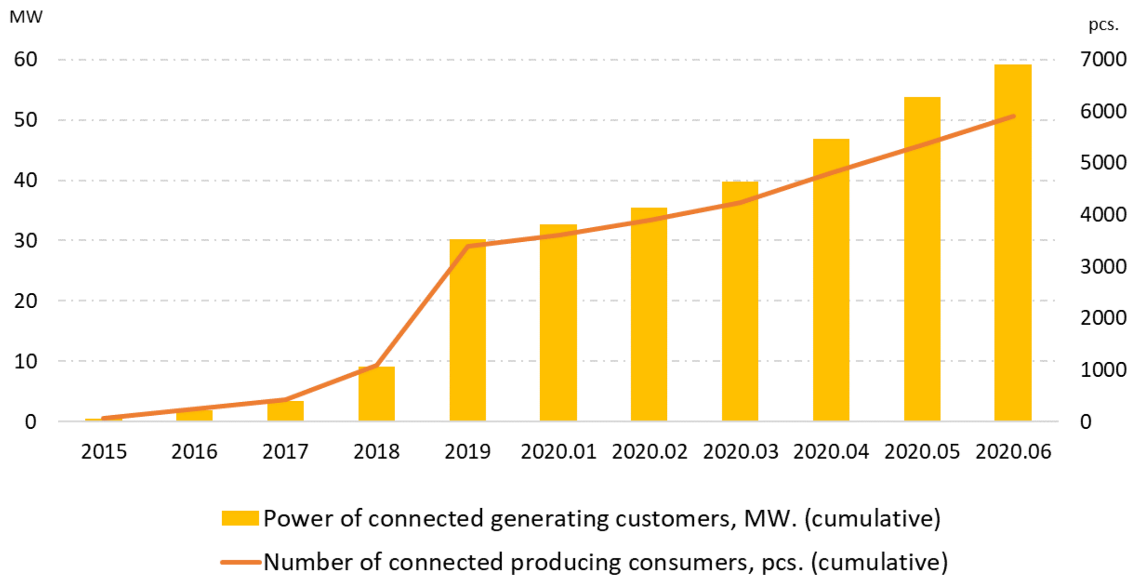

Fig. 1. The statistics concerning the connection of producing consumers [ENMIN 2020a].

The process of installing PV systems larger than 30kWp is much longer [ENMIN 2020a] compared to lower capacity ones and can sometimes take up to half a year or even longer. The steps are described in Table 3.

Tab. 3. The installation stages of PV with a capacity above 30 kWp.

Step	Process	Approx. duration in days
1	Obtaining pre-connection conditions for a PV system from ESO	to 15
2	Obtaining a permit to develop electric power capacity	to 30
3	Obtaining PV connection conditions from ESO	to 3
4	Design activities	30-60
5	Signing of the connection agreement with ESO	to 5
6	Installation of PV system	5-60
7	Inspection of an installed PV system by the National Energy Regulatory Council	to 30
8	Permit to produce electricity issued by the National Energy Regulatory Council	to 30
9	Signing of a producing consumer‘s contract for the purchase and sale of electricity	to 5
10	Installation of a two-sided metering unit	2
	Total:	~7 months depending on a project

The following solar PV systems were the largest ones in Lithuania till the end of 2019: Sitkunai Solar Park – 2.56 MW, Brizgai Solar Park – 1.99 MW, Dausiskiai Solar Park – 1.96 MW. Over the next years, it is planned to build several 3-5 MW solar parks exclusively for residents that want to become producing consumers. The plan is until 2021 to install the first in Baltic region water floating solar plant at Kruonis pumped storage plant. Its capacity at the first stage will be 60 kW. Later, it is planned to increase the capacity to 200-250 kW.

4. Subsidies and prices of photovoltaic systems

The record amount of 9 MM EUR is planned in the 2020s for the subsidies to PV systems. The record subsidies in the amount of 4.5 MM EUR are planned for the installation of remote solar PV or the purchase of the part in solar PV parks. Also, 4.5 MM EUR will be allocated to solar PV in single-family houses. The compensation for 1 kW of installed solar PV capacity is 323 EUR [APVA 2020]. Requirements applied to the equipment:

- it must be new (unused), comply with EU standards and eco-labels normally required for such equipment;

- the product warranty period for solar modules must be 10 years and 80% performance guarantee must be for 25 years, it must have adequate protection against dust and moisture (at least IP 65);
- product warranty period for inverters must be 10 years, it must have adequate protection against dust and moisture (at least IP 65).

Also, the compensation in the amount of 100% of installation cost can be received for schools, hospitals, and other public buildings. Only a feasibility study and a design for the building of a solar PV system have to be prepared on their own expenses. According to the promotional measures for industrial facilities, there is a possibility to receive the support from 30 to 80% of investments to the sustainable resources equipment.

The support in the amount up to 80% is available to state or municipal institutions and bodies, traditional religious communities, religious associations or centres, public institutions owned or partnered by the state, municipality. Not only PV systems but also solar collectors, wind turbines, heat pumps, and other energy-saving measures are supported. The maximum amount of the grant for one applicant who is not engaged in economic and commercial activities is EUR 1,450,000, and for those who are engaged in economic and commercial activities - EUR 200,000. It is considered as an ineligible applicant (beneficiary) if the building where the heat generating installation is to be replaced is connected to the district heating system [APVA 2020].

The support in the amount up to 40% is available to heat supply companies and independent heat producers. The installation of not only PV systems, but also solar collectors, heat storage, heat pumps, absorption heat pumps, and other energy-saving measures is supported. The funding rate per applicant is 30% of the eligible costs (for large enterprises) and 40% of the eligible costs (for small or medium-sized enterprises) may be increased by 10% for investments in specific assisted areas. The maximum grant per applicant is EUR 1 450 000 [APVA 2020].

The support in the amount up to 65% for the installation of renewable energy sources is available to small, medium, and large industrial enterprises. Renewable energy sources are non-fossil energy sources: wind, solar, aerothermal, geothermal and hydrothermal and ocean energy, hydropower, biomass, landfill gas, sewage treatment plant gas and biogas. Investment costs necessary to ensure better environmental protection. If the share of environmental investment costs in the total investment costs can be identified as a separate investment, this part of the environmental costs is an eligible cost. In all other cases, the costs of the environmental investment are determined in comparison with similar less environmentally beneficial investments that would be likely to be made without the aid. The difference refers to the costs related to environmental protection and constitutes eligible costs. The maximum grant per applicant is EUR 868 860 [APVA 2020].

It is obvious that the cost of PV installation has a major impact on its payback period. Prices vary over a wide range depending on the equipment selected, the installation location, and the contractor. The analysis assessed at least 5 proposals that met the minimum requirements for support. Systems larger than 50 kW were not analysed because not enough data was collected. Analysis results is presented in Table 4.

Price composition of the analyzed PV systems is presented in Figure 2. The price of PV panels and inverters systems comprises 67% of the total system price. In recent years there has been a decrease in the prices of PV modules in other hand prices of inverters did not changed. Evidence that the price composition can vary in a wide range, depending on selected equipment, installation place etc.

Tab. 4. Prices analysis of PV systems depending on a size (2020 June).

PV system size	Average price including design and installation cost, EUR (including VAT)	Average price of 1 kWp, EUR (including VAT)	Notes
5 kWp	4979	996	Design and inspection activities are not mandatory
10 kWp	9366	936	
30 kWp	25802	860	Design, permissions and inspection activities are mandatory
50 kWp	40644	813	

Some studies, calculations showed that the payback period of a solar PV in a single-family house varies from 4 to 7 years, if the state support has been received. The payback period for larger facilities is from 3 to 6 years. The payback period depends deeply on the proper selection of the system, the cost of installation and equipment chosen [Valancius et al. 2018a; LSEA 2020].

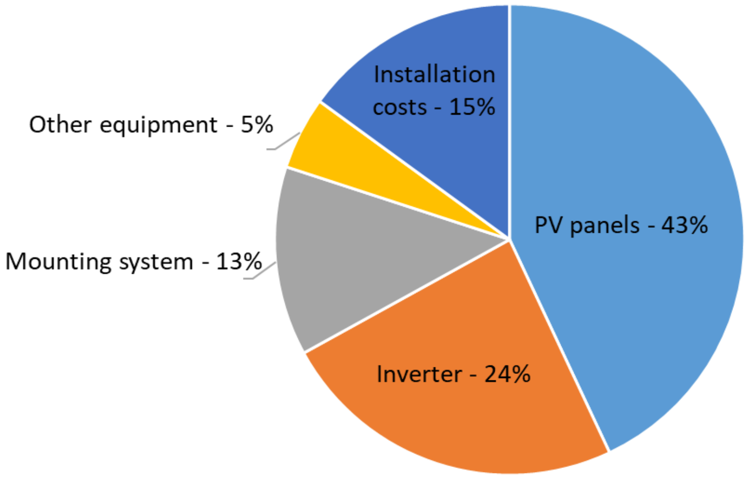

Fig. 2. Price composition of equipment in PV systems from 5 to 10 kWp (2020 June).

5. Discussions and conclusions

Analysis showed that average 1 kWp of small and medium size (5-50 kW) PV system in Lithuania was from 813 to 996 EUR in 2020 EUR. Within the recent years, prices of PV systems dropped significantly and it's expected to decrease slightly in the future.

The goal set by the Ministry of Energy to have 34 000 producing consumers in 2020 is practically unachievable. Although residents, public facilities, and businesses are quite willing to use the support provided for the installation of solar PV systems or to install them without support but a purchase of these systems in solar parks did not receive huge interest from the population.

Obviously simple and clear conditions for connection to a power grid, reduced investments to the equipment, as well as the support of the state to the installation of systems, make a huge impact on the development of the solar PV systems.

References

APVA 2020. Lietuvos Respublikos aplinkos ministerijos. Aplinkos projektų valdymo agentūra. [accessed 14 Juni 2020]. Available from Internet: https://www.apva.lt/naujienos/

ENMIN 2020. Lietuvos Respublikos energetikos ministerija [accessed 25 Juni 2020]. Available from Internet: https://enmin.lrv.lt/lt/veiklos-sritys-3/atsinaujinantys-energijos-istekliai/elektros-energija-gaminantys-vartotojai/dazniausiai-uzduodami-klausimai-apie-elektra-gaminancius-vartotojus

ESO 2020. Energijos skirsymo operatorius [accessed 26 Juni 2020]. Available from Internet: https://www.eso.lt/lt/namams/elektra/tarifai-kainos-atsiskaitymas-ir-skolos/gaminanciu-vartotoju-kainos.html

ENMIN 2020a. Lietuvos Respublikos energetikos ministerija [accessed 25 Juni 2020]. Available from Internet: https://enmin.lrv.lt/lt/veiklos-sritys-3/atsinaujinantys-energijos-istekliai/elektros-energija-gaminantys-vartotojai

Ignitis 2020. Ignitis [accessed 2 Juli 2020]. Available from Internet: https://ignitis.lt/lt/elektros-kainos

LSEA 2020. Lietuvos saulės energetikos asociacija [accessed 25 Juni 2020]. Available from Internet: http://www.lsea.lt/lt/naujienos/aktuali-informacija/saules-elektrine-namu-ukyje-ka-daryti-ir-kiek-tai-uztrunka

REN21. 2020. Renewables 2020 Global Status Report (Paris: REN21 Secretariat). ISBN 978-3-948393-00-7

Valancius, R., Mutiari A., Singh A., Alexander C., De La Cruz, D. A., E del Pozo Jr., F., 2018. Solar Photovoltaic Systems in the Built Environment: Today Trends and Future Challenges. Journal of Sustainable Architecture and Civil Engineering. 23(2), 2018. https://doi.org/10.5755/j01.sace.23.2.21268

Valancius, R., Cerneckiene J., Vaiciunas, J., Jurelionis, A., Fokaides P. 2018a. Solar Thermal Systems vs. Photovoltaic Systems. Case study: Single Family Building in Lithuania. EuroSun 2018 Conference Proceedings. https://doi:10.18086/eurosun2018.01.11

How the European Commission Policy Supports Research and Development in Photovoltaics

A. Rządkowska

European Solar Network, Bruges, Belgium

Institute of International Studies, University of Wrocław, Wrocław, Poland

E-mail: agnieszka.rzadkowska@eusolarnet.org

Abstract

The paper presents an outlook of the European Commission’s policy in supporting research and development (R&D) in photovoltaics (PV) and its mainstream adoption. It analyses the key elements of the EC policy aimed at securing for the European Union leading position in a global competition in PV, including the Strategic Energy Technology Plan, the H2020 Framework Programme and the Energy Union strategy. The paper also analyses the key areas of PV technologies development in Europe as stimulated by R&D funding, the magnitude of investment and particular research topics supported by the EC (with focus on one of the 12 Key Enabling Technologies for the European Union identified as perovskites), as well as the general progress of European PV technology in its international context. Finally the paper addresses the renewables and in particular the role of PV in the European Union COVID-19 pandemic recovery strategy. The paper also discusses the PV R&D potential versus other, traditionally dominating renewable energy sources, such as wind power and hydro power.

Key words: European Union, European Commission, policy, PV, photovoltaics, research and development, renewables

1. Introduction

In 2020 photovoltaic energy may have finally become the cheapest source of the electrical power in developed countries at price of circa 0,014 Euro/kWh (Qatar General Electricity & Water Corporation, 2020 – price agreements for the Al-Kharsaah Solar PV Power Plant), with the solar cells panel prices dropping by one order throughout just the last decade.

This new domination of PV as the most economically viable electrical energy source opens new competition grounds for accelerating transition to sustainable clean energy. It does not mean however that this transition will happen overnight. It is a process of significant costs and efforts that will be however further supported by the EU policy. It is assessed in the European Commission’s Strategic Energy Technology (SET) Plan that the PV competitiveness opens a path to a global transition to sustainable and clean energy which is critical in mitigating global warming. The climate situation is generally perceived very serious by numerous studies and the EU policy. The EU emissions budget for CO_2, in order to meet the 1.5 'C degree limit of temperature rise policy target, would be used up in 2028 if these emissions (mainly associated with energy production and transport) were to remain on the current levels. Utilization of PV as a main source of electrical energy (along with simultaneously developed storage systems and smart grid integrations) is expected to increasingly support the transition process along with the COP21 goals and the EC policy has an important role to facilitate this on the level of R&D.

The PV energy experienced exponential growth over the years, with massive 50% per year in the last 10 years (recently dropping however to 30%) – as reported by the IEA (2020). The installed capacity exceeded 132 GW in the EU alone at the end of 2019 (cf. Jaeger-Waldau 2019). and dynamically growths further on (steadily nearing to a double digit % in the EU electricity demand growing from the 5% level as reported back in 2017). Germany was leading this growth worldwide, followed by China, Japan, Italy and the US (Fraunhofer ISE 2020, World Energy Council 2020).

doi:10.18086/eurosun.2020.11.03 Available at http://proceedings.ises.org

Europe has also became a strong player in PV research and technology development worldwide. In line with deployment on a large scale, the strong R&D position of the EU and price competition from China resulted in PV module prices dropping by about 80% already between 2009 and 2015 (Jaeger-Waldau 2016).

The European SET Plan intends to contribute to further cost reductions and to relaunch PV cell and module manufacturing in the EU. The Energy Union policy set out on basis of the above mentioned European Commission communicated standpoints in particular address the two following goals: 1) putting energy efficiency first and 2) achieving global leadership in renewable energies. The EC has estimated that in order to reach the EU's 2030 climate and energy targets, about €379 billion investments are needed annually over the 2020-2030 period (with €27 billion devoted to public and private research annually) with significant shares needed to be targeted at further development of solar energy and photovoltaics.

The paper studies the current European policy towards PV R&D as defined in the relevant scope of the H2020 Work Programme, the European SET Plan, the Energy Union implementation and the new impetus of the European Green Deal from the newly appointed European Commission.

2. Background of R&D in photovoltaics – the dominating potential of PV

Both in the EU and globally photovoltaics is currently the third renewable energy source in terms of installed capacity (after hydro and wind power). But how the PV potential compares to the two latter renewables?

The potential of the photovoltaics surpasses the potential of hydro and wind power. To visualize the differences, one should point accordingly to calculations done in (Berners-Lee, 2019), that in order to cover the whole current United Kingdom's energy demand with wind power – it would be necessary to cover whole its land surface with wind turbines (and it would still provide just a little over 90% of the required power output). On the other hand to cover the whole current global energy demand with PV it would be required to cover 367 x 367 km^2 area with solar panels (this is only 3% of the EU surface, or just 1.4% of the Sahara desert surface). The global energy demand is ca. 165000 TWh and the UK demand is just 2200 TWh – 1.2%. To cover UK energy demand with PV one would need just below 0.7% of its surface vs. circa 110% of its surface covered by wind turbines. To cover the EU energy use (ca. 16000 TWh) with PV just 0.3% of its area is needed. Here we discuss these calculations under the assumption of using mass-produced, cheap and stable solar cells at only 16% efficiency and an averaged Sun irradiation, so actually in Sahara desert, one of the world's top areas as per the intensity of insolation, it would be even less than 1.4% of its surface.

Cheap and mass-produced 16% efficiency solar panels covering just 0.1% of the Earth land surface can meet the total energy demand today (or as mentioned well below 1.4% of the Sahara desert area). Wind power is no match for this potential (as e.g. to meet the UK's energy demand 110% of its territory would have to be densely covered by wind turbines – solar panels would require ca. 0.7% area – cf. Berners-Lee 2019, Smill 2017, Miller et al. 2011, Peixoto and Oort 1992). Similar situation is with the hydro power. Physical energy estimations in detail presented by Smill (2017) and also discussed by Berners-Lee (2019) prove that if we harness potential and kinetic energy of every droplet of water pulled by gravity from wherever it lands (before it reaches its minimum energy state in the seas or oceans) or in other words, if we would extract all energy from every stream of water moving on Earth (including oceanic waves energy) it would just about meet the current total energy demand on a global scale. Although such an endeavor is in itself unrealistic and impossible to be implemented technically, it would still supply energy at many orders below the above estimated potential of the PV.

PV thus leaves behind the limited wind & hydro power in terms of energy potential and is the best alternative to solve energy problem versus climate change, at least until there is nuclear fusion technology breakthrough.

For the time being however, the proper argument for the policy makers working on the clean energy transition, renewables and mitigating climate change strategies is not by how many times the PV is better energy source than wind and hydro power (and even thermal solar power, especially when it comes to the electricity generation), but rather by how many orders it is better.

PV is also very promising in terms of research and development. The current mainstream PV technologies (mainly Silicon wafers) being at ca. 16% efficiencies are being in a quite fast pace replaced by the so called emerging third-generation solar cells (also cheap but with many advantages, such as lowered sturdiness, flatness of thin-film architectures, elasticity, semi-transparency, etc.). The advanced tandem configurations of new solar cell devices (multi-junction or multi-layer setups) reach almost 50% of the efficiency.

The main aspect of the pronounced R&D efforts in PV is of course reduced to the end price per Watt of power generated, and the technological results as well as objective potential of extracting energy directly from sunlight in a photoelectric effect begin to dominate the spectrum of renewable energy technologies.

3. Current directions in the PV R&D

What are the current directions in photovoltaics research and development? One of the most famous short summarizing-answer to this question is to refer to the National Renewable Energy Laboratory Best Research-Cell Efficiencies graph. The 2020 NREL graph has been placed accordingly with the credited reprinting terms in the Fig.1. (NREL, 2020). It shows how the efficiencies of different PV technologies develop across the recent half-century.

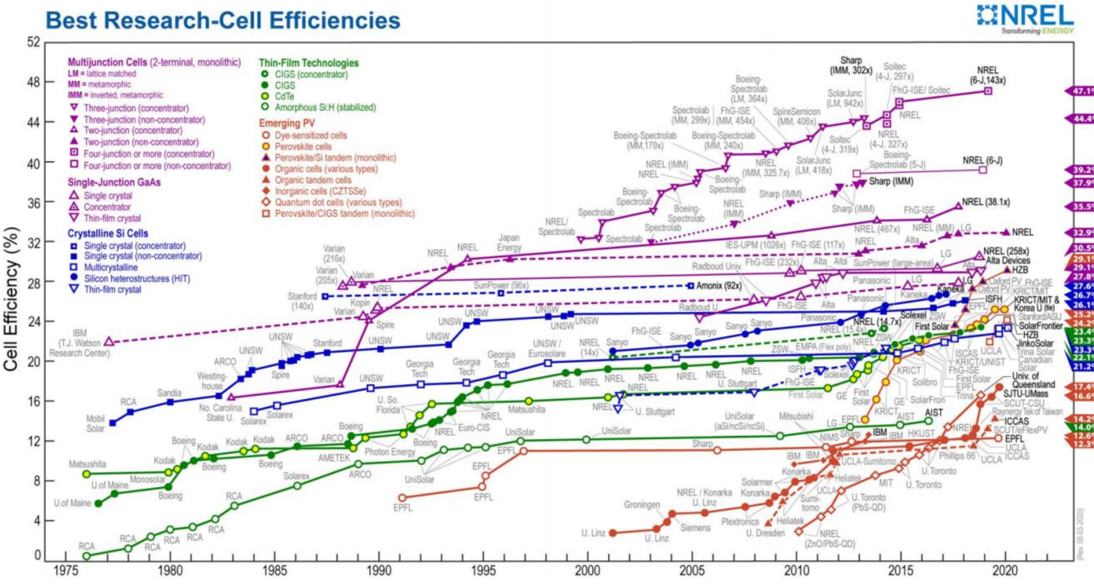

Fig. 1. Summary of the global R&D directions and achievements in PV efficiencies.
Source: National Renewable Energy Laboratory, US Department of Energy, 2020

The colors represent division into main categories of the researched solar cells. The most efficient but also most sophisticated and expensive technologies are the multi-junction (multi-layered) solar cells colored in magenta. These devices combine various other solar cells technologies to stack them up together in the best configuration possible. The most traditional and holding a dominating share (95% - Fraunhofer ISE, 2020) in market and production output are crystalline silicon cells, represented as blue and generally referred to as the first generation solar cells. The green color is reserved for the traditional thin-film cell technologies based on the 3 dominating materials, the copper indium gallium selenide (CIGS) cells, the cadmium telluride cells and the amorphous silicon cells. These technologies are already widely applied in PV power plants and referred to as the second generation solar cells, showing a steady but improving performance over the years similar in magnitude to the first SC generation. Finally the orange color represents the new trends in PV R&D, i.e. so called emerging solar cells technologies, including dye, organic, quantum-dots and perovskite devices. These new material and architecture devices (most commonly in elastic thin-films configurations) are considered the third generation solar cells and their physical operation goes beyond the standard p-n junction model, thus holding a potential to overcome the theoretical Shockley-Queisser limit for the efficiency of a single-junction solar cell. The main advantage of the not-yet commercialized emerging PV technologies are the promise to bring high-efficiency at a low cost of production combined with thin-films advantages.

The key conclusions that one can draw from the NREL graph, is that the upper half of the graph, i.e. values above 30% efficiency (magenta color) are solely reserved for the multi-junction solar cells. This follows directly from the physical Shockley-Queisser limit (cf. Shockley and Queisser 1961), which refers to the calculated maximal theoretical efficiency of a solar cell based on a single semiconductor p-n junction (practically a single solar cell device layer) to employ a photoelectric effect with losses limited only to the radiative recombination. The value of the SQ limit has been calculated at 33.7% efficiency under the normal sunlight conditions (unconcentrated light, perpendicular incidence on the solar cell surface), assuming typical sunlight conditions and the most optimal to the Earth surface sunlight energy spectrum material semiconductor bandgap of 1.34 eV (cf. Rühle 2016 – conditioned by the light absorption in the atmosphere and corresponding to circa 925 nm near-infrared photon wavelength). The semiconductor bandgap refers to the semiconductor material potential energy barrier between the conductive and valence bands, that needs to be aligned to the energy of the incident photon, which when absorbed by the electron from the valence band, gives it the exact energy needed to overcome the potential barrier and conduct electricity in the conductive band – the basis of the photoelectric effect which is generating photocurrent as explained by Einstein in 1905.

From the SQ limit it follows that a single-junction SC theoretical energy efficiency is limited at circa 33%, meaning that from an averaged sunlight energy density of 1000 W/m^2, such cells can maximally harvest about 330 W/m^2. This is where multi-layered (so called multi-junction or tandem architectures) have their say. From the NREL graph one can see the most efficient solar cells researched up to this date are currently the devices incorporating as many as six junctions (layers), horizontally stacked one on the other to reach the 2020 record of 47,1% of the efficiency. The theoretical limit calculated for a model of an infinitely layered multi-junction solar cell is circa 86.8% under the assumption of the concentrated sunlight harvesting design using e.g. optical lensing (i.e. a concentrated photovoltaic system, CPV).

As the multi-junction cells with various materials and architectures stacked one on the other with up to 6 layers are complicated devices their main drawback is cost of the production (increasing unitary cost of energy generated), shortly followed by robustness and durability. These devices are thus less practical for mass applications such as large areas coverings (e.g. in architecture), which is taken into account in R&D planning.

Thus rather more important from the current absolute position of the researched PV technology efficiency on the NREL graph is the recent growth dynamics (i.e. how steeply is the curve going up). On the graph on Fig.1. we can see that the major emerging low-cost PV technology is now the perovskite solar cells (indicated with orange-yellow circles) undergoing spectacular growth from just few % to over 25% efficiency in the last few years. These are thin-film elastic solar cells that caught up in efficiencies with the PV dominating crystalline Si wafers and are easier and cheaper to produce (in the ink-jet printing or roll-to-roll processes well suited for the mass-output production and versatile applications). In more details: the efficiency of these cells has been lifted from 2% (2006) and 3.8% (2009) to 25.3% (2019) and circa 30% (in tandem) and its further increase (up to 40% relative increase as proven in trial experiments) due to metallization incorporating plasmonic-enhancement (cf. Jacak 2020) is highly impressive and carries significant market potential for mainstream proliferation of PV. This is also the PV technology in which the European Union has a very strong research position and the PV technology that holds an important priority context as the KET for the EU.

4. EU Key Enabling Technologies context of the PV R&D

At the end of 2017 the European Union has concluded a study on Key Enabling Technologies for achieving technological global supremacy for the EU (Dervojeda et al. 2017). Upon the relevant studies a total of only 12 promising KETs were identified among all technologies as the ones that hold a potential for the EU to assure through further development that the EU industry in those KETs respective areas will stay ahead of international competition. In energy context the perovskite solar cell technology was defined as one of the KETs for the EU.

Perovskite solar cell is considered the EU Key Enabling Technology mainly due to its excellent efficiency/cost ratio and other key properties such as semi-transparency and elasticity allowing bending and forming these PV devices into different shapes/surfaces coverings, as well as due to the EU securing a leading position in this technology. As buildings are estimated to account for over 40% of the energy demand in the EU, building-integrated solar cells are the primary application for PV. Perovskite in contrast to sturdy Si panels offer simple whole-surface coverings techniques including aspects such as architectural freedom.

What are the main advantages of the thin-film perovskite solar cells? This elastic ultra-thin-film PV technology easily and cheaply ink-jet or screen printed in simple roll-to-roll processes or even sprayed onto large surfaces similarly like ordinary paints that when activated with chemically induced crystallization process make thin-film layers (thickness below 1 μm). These cells are therefore very well suited to mass-output market uptake and vast applications (such as energy smart buildings elevations coverings of variety of geometries, semitransparent or smart windows, roofs coverings, outdoor furniture, vehicles or even clothing external surfaces that may produce enough power to charge a phone). As the efficiencies rose rapidly from just 2% in 2006 to 25.3% in 2019 and up to 30% in tandem, currently these top values come at the cost of the stability and durability problems at higher efficiencies (the mass produced perovskite solar cells are currently stable at ca. 15%-16% efficiency). But the research and investment is dynamic.

The perovskite solar cells enable also advanced applications. E.g. in 2019 NASA announced plans (Herrick 2019) of launching trials with ultra-thin perovskite PV modules transported to orbit or even to the Moon or Mars in liquid form enabling ink-jet printing on-site in space of thin-film modules replacing conventional sturdy panels. Simultaneously new concepts to improve the technology are researched, including the promising metallic nano-modifications for the plasmonic-mediated PV efficiency gain, proven achievable in a relative value of 40% (Laska et al. 2020).

5. How the EU supports R&D in PV

Similar as with all renewable energy sources R&D funding in general, it is the industry which provides most of the research investment in the PV sector in Europe (with estimated 2B Euro in 2020, followed by the public funding from the EU countries, jointly contributing already over 1B Euro).

The joint magnitude of the public support of the European Union Member States towards PV R&D and its annual growth rate are thus significant (at amount of about half of the private investment level).

The European Commission itself in 2019 granted funding for the PV R&D sourced from the EU budget which amounted to over 500M Euro from below 100M Euro back in 2015.

The key overlapping vehicles for this support in the European Union are the:

- Horizon 2020 (H2020) R&D Framework Programme
- Strategic Energy Technology Plan (SET Plan)
- Energy Union Strategy
- European Green Deal

The EU funding of various projects in renewable energy sector is mainly implemented through:

- Cohesion Fund
- Connecting Europe Facility
- Horizon 2020 and Horizon Europe
- European Regional Development Fund
- European Investment Bank and the European Fund for Strategic Investments
- The Just Transition Mechanism
- Financing Energy Efficiency
- The Innovation Fund
- European Energy Programme for Recovery

For more details refer to publication on the European Commission 2020 – Funding Possibilities in the Energy Sector (https://ec.europa.eu/energy/funding-and-contracts/eu-funding-possibilities-in-the-energy-sector_en).
Below an outlook through the main initiatives for the PV R&D support in the EU is given:

5.1. Horizon 2020 and Horizon Europe

The Horizon 2020 is the 2014-2020 financial perspective EU R&D 8th framework program (FP8). The program enables grants for research and innovation projects through open & competitive calls for proposals independently evaluated by relevant experts. H2020 implements the European Environmental Research and Innovation Policy which prioritizes R&D in sustainable energy, including PV.

The H2020 has 3 pillars: Excellent Science (ES), Industrial Leadership (IL), Societal Challenges (SC). PV calls are programmed under the SC pillar in Secure, Clean and Efficient Energy area. Out of H2020 €77 billion budget, €5.9 billion is allocated to non-nuclear energy R&D. PV calls are in Research and Innovation Actions (RIA). Alternatively the advanced scientific proposal on PV R&D may qualify for funding under ES pillar in FET calls (Future and Emerging Technologies).

The H2020 is also supplemented by other funds (e.g. HERMES regional development fund) in transnational member-state programmed bottom-up actions: European Research Area Networks (ERA.NET), (e.g. M-ERA.NET for materials technology or SOLAR-ERA.NET for solar energy technology R&D).

H2020 is programmed within a structure of the so called biannual Work Programmes (3 in total). Horizon Europe is the next planned research framework program to replace Horizon 2020 in the years 2021-2027 with projected R&D spending levels raised by 50%. The Horizon Europe proposed budget is €100 billion and supports the objectives of the EU Green Deal through R&D in sustainable energy.

5.2. SET Plan

The Strategic Energy Technology Plan (SET Plan) sets the primary agenda for the EU energy technology R&D policy. It enhances coordination of national and European research and innovation efforts to position the EU in the forefront of the low-carbon technologies.

SET Plan involves 10 initiatives, including i.a. wind, hydro, bioenergy, CO_2 capture. But the most prospective are currently priorities in solar power (PV and CSP) under Solar Europe Initiative. It promotes cooperation among EU countries, companies and research institutions, aiming to deliver on the main objectives of the Energy Union Strategy. It consists of the SET Plan Steering Group, the European Technology and Innovation Platforms (ETIPs), the European Energy Research Alliance (EERA), and the SET Plan Information System (SETIS). The EERA joins top research institutes in the European Union specializing in energy research and development. SET Plan closely integrates with all key EU activities in energy R&D stimulation involving the Energy Union Strategy, the Clean Energy Strategy, the H2020 energy area programs and the directions in setting the framework of priorities in renewables for the European Green Deal.

5.3. Energy Union Strategy

The Energy Union Strategy of the European Commission launched in 2015 aims to coordinate through investment and development the transformation of the European energy supply. It is sometimes referred to as the biggest energy project since the European Coal and Steel Community and it is rooted in regional insecurities related to geopolitical use of energy resources by Russia.

One of the 5 pillars of the Energy Union Strategy is research and innovation for the competitiveness in sustainable energy sources and electrical grid capacity that includes PV development. The current budget of the projects involved in the Energy Union strategy is approximately 1B Euro, mainly financed by the Connecting Europe Facility. In 2016 the EC presented a comprehensive research, innovation and competitiveness strategy, which supports the objectives of the Energy Union – the Clean Energy Strategy – outlined in the Accelerating Clean Energy Innovation Communication, where energy R&D is recognized as a driver for 3 main goals: EU as a global leader in renewables, energy efficiency first, fair market deal, which accordingly to the arguments presented above, favors PV R&D.

5.4. European Green Deal

The European Green Deal is a set of policy initiatives by the European Commission with the overarching aim of making Europe climate neutral in 2050 and phase out the fossil fuels as much as possible. An impact assessed plan aims to increase the EU's greenhouse gas emission reductions target for 2030 to at least 50% and towards 55% compared with 1990 levels. The policy aims to make Europe the first climate-neutral continent on Earth.

Compared to the proposed Green New Deal stimulus package of the USA, this EU policy is however criticized with too low rate of decarbonisation of the economy, with the EU aiming to become net-zero within three decades instead of within ten years.

In terms of the support for R&D, primarily in most potentially enabled PV technology the policy strongly leans on the Horizon 2020 Framework Programme for further stimulating the private investment and development driving commercialization of emerging solar cells.

Beyond the H2020 the EU plans to finance the Green Deal through InvestEU investment plan forecasting at least €1 trillion budget. It is estimated that to reach the goals of the policy circa €260 billion a year from 2020 to 2030 is needed. In July 2020 the EU Energy System Integration Strategy was published, paying a lot of attention to the PV technology in terms of electricity self-sustainable systems and the so-called PV smart grid integration.

6. COVID-19 response and role of renewables & PV in the recovery strategy

One of the positive circumstance related to the COVID-19 pandemics (if one can speak at all about positives in face of such tragic events) is related to the climate and pollution. We could all observe how the traffic was nulled in the cities and how the lock-downs had frozen air transport during most of the 2020. A little less noticeable were shutdowns of industry production but these too had a profound impact on temporarily stopping the pollution process. In the energy sector we have all witnessed how in the mid of the pandemic the oil prices turned negative for the first time in markets history during spring of 2020. This was due to the costs of the storage of oil which was not needed to fuel airplanes, cars and factories. This situation unveiled another major vulnerability of physically volumetric fossil fuels which is not the property shared by renewable energy sources.

The peaks of epidemic lock-downs in developed countries reduced energy demand by 25%. Simultaneously the energy spent shifted from physical transport and commuting to home-office surging demand for electricity. This favors sustainable electricity production from renewables. International Energy Agency has predicted in 2020 a 6% drop in global energy demand as a consequence of a global lock-downs due to the COVID-19 pandemics. This is a huge drop, which relatively can be compared to being 7 times larger than the drop after the 2008 financial crisis. This drop in energy demand will primarily hit traditional fossil fuels markets (i.e. coal, oil, gas). IEA forecasts that the renewable energy demand will on the other hand grow by 1%.

There are many initiatives in Europe to make renewable energy a key component of the global economic recovery, driving investment and creating jobs in this sector. The weakening of the traditional fossil fuels markets can be a chance in speeding up the clean energy transition process.

The European Council concluded with EU leaders adopting a statement on the EU actions in response to the COVID-19 (Joint statement of the Members of the European Council, 2020), calling on the European Parliament and Commission to *"prepare the measures necessary to get back to a normal functioning of our societies and economies and to sustainable growth, integrating inter alia the green transition and the digital transformation".*

Renewable energy is thus planned to be a key component alongside digital technology in the COVID-19 crisis recovery stimulus package. Members of the European Parliament approved a resolution calling for a €2 trillion recovery fund prioritising EU Green Deal agenda. Major contribution is planned in grants for i.a. R&D with main focus on PV technology.

7. References

Berners-Lee, M., 2019. There is no planet B, A Handbook for the Make or Break Years, first edition, Cambridge University Press

Dervojeda, K., Lengton, M., Koonstra, A., 2017. Perovskite Solar Cells, Report on promising KETs, KETs

Observatory Phase II, EASME/COSME, European Commission

European Commission, 2020. Funding Possibilities in the Energy Sector, https://ec.europa.eu/energy/funding-and-contracts/eu-funding-possibilities-in-the-energy-sector_en

European Commission, 2020. Strategic Energy Technology Plan, European Commission, 2014-2020

European Council, 2020. Joint statement of the Members of the European Council

Fraunhofer ISE, 2020. Photovoltaics Report, Fraunhofer Institute for Solar Energy Systems

Herrick, K., 2019. Building Solar Panels in Space Might be as Easy as Clicking Print, NASA Glenn Research Center, https://www.nasa.gov/feature/glenn/2019/building-solar-panels-in-space-might-be-as-easy-as-clicking-print

IEA, 2020. Snapshot of Global Photovoltaic Markets - International Energy Agency, Photovoltaic Power Systems Programme, https://iea-pvps.org/snapshot-reports/snapshot-2020/

Jacak, W., 2020. Quantum nano-plasmonics, first edition, Cambridge University Press

Jaeger-Waldau, A., 2016. Photovoltaics technology development report 2016. Joint Research Centre, European Commission

Jaeger-Waldau, A., 2019. PV Status Report, Joint Research Centre, European Commission, https://ec.europa.eu/jrc/en/publication/eur-scientific-and-technical-research-reports/pv-status-report-2019

Laska, M., Krzemińska, Z., Kluczyk-Korch, K., Schaadt, D., Popko, E., Jacak, W.A., Jacak, J.E., 2020. Metallization of solar cells, exciton channel of plasmon photovoltaic effect in perovskite cells, Nano Energy

Miller, L.M., Gans, F., Kleidon, A., 2011. Estimating maximum global land surface wind power extractability and associated climatic consequences - Earth System Dynamics

NASA Goddard Space Flight Center, 2011. Solar Radiation - gsfc.nasa.gov

NASA McAuliffe-Shepard Discovery Center, 2009. Solar Intensity

NREL, 2020. Photovoltaic Research: Best Research-Cell Efficiency Chart, National Renewable Energy Laboratory, US Deparment of Energy - https://www.nrel.gov/pv/cell-efficiency.html

Peixoto, J. P., Oort, A.H., 1992. Physics of climate, osti.gov

Rühle, S., 2016. Tabulated values of the Shockley–Queisser limit for single junction solar cells, Solar Energy 130

SCE/SES, 2017. Major New Solar Energy Project Announced By Southern California Edison and Stirling Energy Systems, Inc.

Shockley, W., Queisser, H.J., 1961. Detailed Balance Limit of Efficiency of p-n Junction Solar Cells, Journal of Applied Physics. 32

Smill, V., 2017. Energy Transitions: Global and National Perspectives, first edition, Praeger

Solarpaces.org, 2013. AndaSol Power Plant Projects in Spain

World Energy Council, 2020. https://www.worldenergy.org/data/resources

Qatar General Electricity & Water Corporation, 2020. Kahramaa and Siraj Energy Sign Agreements for Al-Kharsaah Solar PV Power Plant

12. Renewable Energy Solutions for Isolated Systems (i.e. Islands)

EXPERIMENTAL EVALUATION OF LOW-TEMPERATURE ORGANIC RANKINE CYCLE (ORC) ENGINE COUPLED WITH CONCENTRATING PVT SYSTEM

Chrysanthos Golonis[1], Dimitris Manolakos[1], George Kosmadakis[2] and George Papadakis[1]

[1]Agricultural University of Athens, Dept. of Natural Resources and Agricultural Engineering, Athens, Greece

[2]Ricreation IKE, Technological Park “Lefkippos”, PatriarchouGrigoriou&Neapoleos 27,

15341,AgiaParaskevi, Greece

Abstract

A 10 kWp Concentrating (x10) PV-Thermal collectors’ array produces heat at temperatures in the range of 70-90ºC, which is supplied to a low temperature ORC enginedesigned and manufactured for this purpose. The ORC engine converts a fraction of this heat into electricity of about 2to 3 kWewith maximum thermal efficiency in the order of 4.5%, thus ameliorating the performance of CPVT system in terms of additional electricity generation. The paper deals with the presentation of field test results under real operatingconditions. ORC key variables variation according to solar irradiation availability is examined towards maximizing system performance. The results show that the magnitude of electricity produced from the ORC engine is comparable to that of directly generated from the PV and the proposed configuration could be an alternative option forefficient exploitation of CPVT heat that is mostly utilized for domestic heating.

Keywords: Solar Energy, Concentrating PV-Thermal, Organic Rankine Cycle, Scroll expander

1. Introduction

The organic Rankine cycle (ORC) technology has become nowadays a field of intensive research and has proved to be a very promising technology for efficient conversion of low-grade heat into useful power or electricity (Desai, 2009) and (Mago et al., 2008). Some researchers (Algieri and Morrone, 2012) and (Al-Sulaiman et al.,2011)investigated the ORC for agricultural residues and biomass-based power generation and somefocused on the ORC using solar energy (Kosmadakis et al., 2016). Other research works (Zhang et al.,2013) and(Wang et al., 2013)were concentratedon the ORC use for the low-grade waste heat recovery.

ORC technology is suitable for heat recovery applications of temperature even below 100 ºC (Manolakos et al.,2009). At such conditions, its efficiency is rather low, usually in the range of4-6%, but still there are cases where it can be cost effective especially for waste heat recovery. With these range of heat to power conversionefficiency ORC is still the most efficient heat to power generation technology for low temperature heat sources applications and consequently to converting heat to power from CPV-T systems where heat is available at temperatures lower than 90 ºC.

Solar energy has been the fastest-growing energy sector in the last few years. Solar energy is an ideal source of energy because of its worldwide availability (Nazari et al.,2018)and has become a reliable source of power generation on the planet (Mills et al.,2004).Current solar energy generation is increasing a lot due to high investigation in the area and the decreasing cost of their production. Two solar energy decentralized systems are available for electricity generation: photovoltaic solar plants (PV) and concentrated solar power plant (CSP).The efficiency of PV modules is still low, but there have been plenty of improvements in the last years. Photovoltaic cells convert the incident radiation of the sun into electrical energy without producing any pollution or noise. Concentrating Photovoltaic (CPV) technology is one of the growing among the concentrating solar energy technologies. The concentrating photovoltaic (CPV) system is one of the most efficient techniques to reduce the cost of solar electricity.The concentrating photovoltaic/thermal (CPV/T) system is an interesting technique to broaden the field of CPV technology to a higher-efficiency energy system that produces not only electricity but also heat (Bernardo,2011) and (Ong et al., 2012).The final result of this arrangement is the combined production

doi:10.18086/eurosun.2020.12.01 Available at http://proceedings.ises.org

of electricity and heat and a possible improvement of PV efficiency. The PV cells can convert (6%-20%) ofthe incident solar radiation to electricity. The rest of the solar radiation raises the cell's temperature, which causes reduction in PV's efficiency (Dubey and Tay, 2013). Integrating the PV cells with a thermal concentrating solar collector makes the PV cooling necessary to improve its efficiency.

The result of this arrangement is the combined production of electricity and heat with improved PV efficiency.CPV/T systems tend to produce low-temperature heat of less than 80 °C, which is hot enough for domestic hotwater (DHW) applications. The current work investigates experimentally the case where the heat coming from the cooling circuit of a CPV-T system is converted to electricity instead of being used for DHW purposes. The results show that additional electricity of comparable magnitude to that produced directly from CPV-T cells can be produced with this configuration. It is stressed that the ORC engine has been constructed so that to operate also in supercritical conditions so that to investigate the potential increase power generation in this mode, however in this paper operation results from subcritical operation are provided.

2. Description of the system

Figure 1 shows the CPV-T-ORC system layout and a picture of the experimental installation. The solar field has been installed at the campus of the Agricultural University of Athens (AUA),in Greece. Each collector has anelectric capacity of 1 kWp, concentration ratio of around 10, and the nominal heat production is of the order of4.1kWth. The aperture area of each collector is 10.4 m^2. An overview of the CPV-T field is shown in fig. 2. Figure 3 illustrates the ORC engine and the its key components.

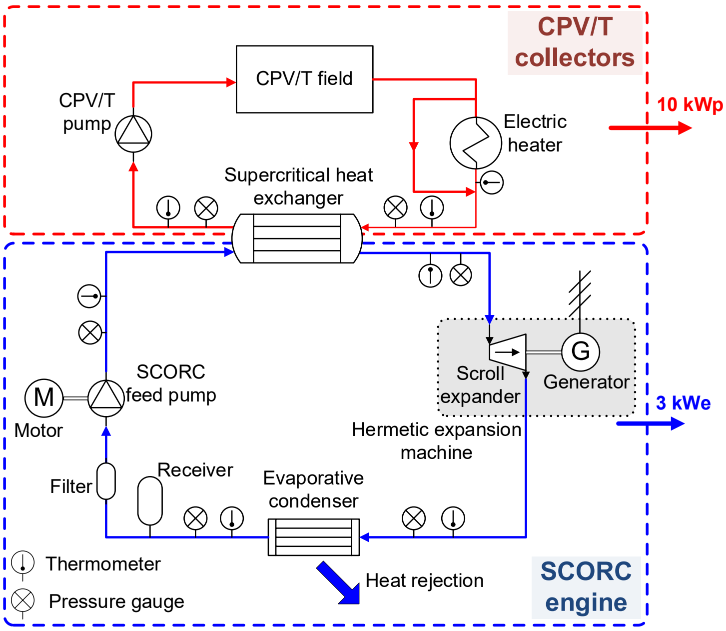

Fig. 1: Schematic representation of CPV-T coupled with ORC system and the experimental installation

Fig. 2: The CPV-T of 10 collectors installed and the ORC engine house

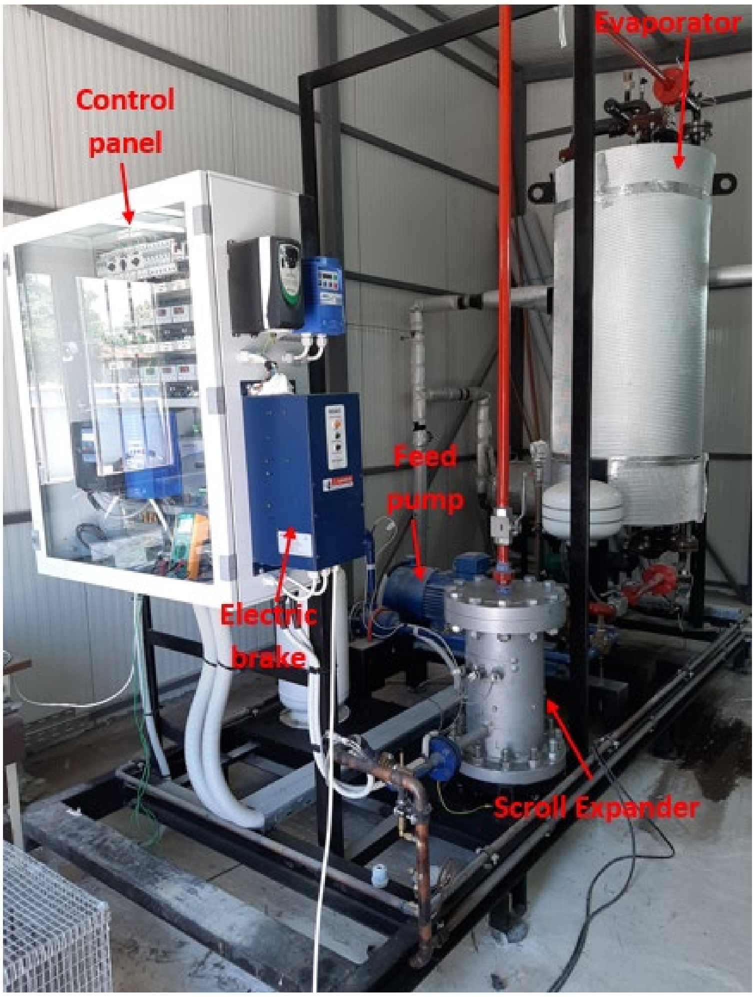

Fig. 3: The ORC engine

The key components of the ORC engine are depicted in Figs. 1 and 3, which are the following:

- The ORC pump: it is a triplex diaphragm pump manufactured byHydra Cell (model G-10X), coupled with a 3 kW induction motor, driven by a 4 kWfrequency inverter.
- The expander: it is a modified (to operate reversely) commercial scroll compressor, (Copeland ZP137KCE-TFD withswept volume of 127.15 cm^3/rev., maximum isentropic efficiency75.2%, and built-in volume ratio of around 2.8 at compressor mode). A new casing was constructed to sustain the high pressures to allow the supercritical operation as well.
- The evaporator: it is of helical coil type with a capacity of 41 kW. This helicalcoil heat exchanger is designed and manufactured specifically for such ORCinstallation, suitable to operate at relatively high pressure andtemperature (capable for both sub and supercritical working conditions).
- The evaporative condenser: it is of 75 kW heat capacity (Condensing 36ºC / Wet-bulb temperature 21ºC)and airflow rate of 10,500 m^3/h.

For small-scale systems with power production lower than around 20 kW, scroll expanders have been widely used and showed adequate performance and expansion efficiency (Lemort et al. 2012). Manolakos et al.(2009) have also used the same expansion technology (both open drive and hermetic ones) and revealed the good performance at a wide range of pressure ratios. This brings confidence that such an expander can be also used at a supercritical cycle, which is the next step of this research. One positive aspect is that for low temperature applications, the pressure ratio is low and usually in the range of 2-4 (Kosmadakis et al. 2015) enabling the scroll expander to operate with good efficiency. An electric brake (heavy duty unit, manufactured by Bonitron),is connected to the frequency inverter of the expander's inductionmotor, to control the test conditions and evaluate theperformance of this expansion machine.

The organic fluid selected is R-404a after screening many potentialfluids using environmental (zero ODP, moderate GWP)and cost criteria. It is stressed that the ORC engine is supposed to operate also in supercritical mode and R-404a is suitable under the temperature regimes imposed by the CPVT (max. temperature ~90 ºC). When operating at low temperature, the condenser also becomes an important component, since thermal efficiency becomes highly sensitive to the temperature of the heat rejection medium.

3. Processing of measured data

For the evaluation of the system, key variables are systematically measured using appropriate instruments for both the CPV-T and the ORC engine.

i. CPV-T

The efficiency $\eta_{\mathrm{col}}$of the collectors' array is given by the equation below:

$$\eta_{\mathrm{col}} = \frac{\dot{Q}_{\mathrm{ev,col}}}{A_{\mathrm{c}} \cdot G_{\mathrm{b,n}}} \cdot 100 \qquad [\%] \qquad \text{(eq. 1)}$$

Where A_c[m^2] is the collectors' aperture area, $\dot{Q}_{\mathrm{ev,col}}$[kW] the heat generatedby the collectors and $G_{\mathrm{b,n}}$ the direct normal solar irradiance. $G_{\mathrm{b,n}}$ is derived by multiplying the direct irradiance G_{b} with the $\cos(\theta)$, where θ [rad], is he angle of incidence on the collectors' surface (eq. 2).

$$G_{\mathrm{b,n}} = G_{\mathrm{b}} \cdot \cos(\theta) \qquad [\mathrm{kW/m^2}] \qquad \text{(eq. 2)}$$

For horizontal E-W axis with N-S tracking collector, $\cos(\theta)$ is defined as:

$$\cos(\theta) = \sqrt{1 - \cos^2(\delta) \cdot \sin^2(\omega)} \qquad [-] \qquad \text{(eq. 3)}$$

Where δ[rad] is the declination of the sun and ω[rad] the angle hour.

G_{b}, is calculated as the difference of total solar irradiance on the collectors' surface$G_{\mathrm{t,track}}$[kW/m^2], minus the amount of diffuse irradiance G_{d} [kW/m^2]:

$$G_{\mathrm{b}} = G_{\mathrm{t,track}} - G_{\mathrm{d}} \qquad [\mathrm{kW/m^2}] \qquad \text{(eq. 4)}$$

From the above equations it is concluded that $G_{\mathrm{t,track}}$ and G_{d} should be known to determine$G_{\mathrm{b,n}}$. For that, two pyranometersare used. A typicalpyranometer is mounted on the collectors' surface to measure the total irradiance ($G_{\mathrm{t,track}}$), while a second with shadow ring (Kipp&Zonen, CM 121) is used for directly measuring the diffuse irradianceat horizontal level (G_{d}).

Finally, the quantity $\dot{Q}_{\mathrm{ev,col}}$ is provided by the formula below:

$$\dot{Q}_{\mathrm{ev,col}} = \dot{m}_{\mathrm{col}} \cdot \mathrm{c_p} \cdot (T_{\mathrm{ev,col\_in}} - T_{\mathrm{ev,col\_out}}) \quad [\mathrm{kW}] \qquad \text{(eq. 5)}$$

$T_{\mathrm{ev,col_in}}$and $T_{\mathrm{ev,col\_out}}$ [ºC]are the inlet and outlet temperatures at the evaporator hot (collectors') side. Thermocouples are used to measure these temperatures. To measure the mass flow rate in the collectors' circuit $\dot{m}_{\mathrm{col}}$ [L/s] a doppler flow meter is used.

ii. ORC engine

The heat supplied to the ORC engine $\dot{Q}_{\mathrm{ev,orc}}$ is expressed as:

$$\dot{Q}_{\mathrm{ev,orc}} = \dot{m}_{\mathrm{p}} \cdot (h_{\mathrm{ev,orc\_out}} - h_{\mathrm{ev,orc\_in}}) \qquad [\mathrm{kW}] \qquad \text{(eq. 6)}$$

$h_{\mathrm{ev,orc\_out}}$ and $h_{\mathrm{ev,orc\_in}}$ [kJ/kg] are the enthalpies at the outlet and inlet of the cold (ORC') side of evaporator. These properties are defined through measuring temperature and pressure at the inlet and outlet of the evaporator using appropriate temperature and pressure transducers. $\dot{m}_{\mathrm{p}}$ [kg/s] is calculated indirectly, through the rotation speed of the ORC feed pump that is a diaphragm pump, is free of volumetric losses and thus rotation speed is linearly related with the mass flow rate.

The net power P_{net} of the ORC engine is:

$$P_{\mathrm{net}} = P_{\mathrm{e,act}} - P_{\mathrm{p,act}} \qquad [\mathrm{kW}] \qquad \text{(eq. 7)}$$

$P_{\mathrm{e,act}}$ and $P_{\mathrm{p,act}}$[kW] are the actual power produced by the expander and absorbed by the pump respectively. Both are directly measured with appropriate instruments (kW-meters).

Finally, the thermal efficiency η_{th} of the ORC engine is expressed as:

$$\eta_{\mathrm{th}} = \frac{P_{\mathrm{net}}}{\dot{Q}_{\mathrm{ev,orc}}} \cdot 100 \qquad [\%] \qquad \text{(eq. 8)}$$

4. Results and discussion

The experimental facility has been designedto assess the ORC engine at both subcritical and supercritical conditions, however in this work, sets of experimental results at strongly diversified subcritical operation conditions are provided once the ORC unit is supplied with heat produced by the solar field, while future work regards supercritical operation as well.Figures4and 5show the variation ofkey variables (thermal efficiency and power generated) as function of the rotational speed of the expander when the fluid pump rotational speed is set at 864 RPM (45 Hz), when heat is supplied by the CPV-T filed. As can be extracted from Fig. 4, thermal efficiency exhibits the highest values in the order of 4.5% at 2000 RPM while heat supply varies within the range of 50-52kWth.The maximum net power generation is calculated by subtracting the power consumed by the pump from that produced by the expander. A maximum of 2.5 kWel at 2000 RPM is observed (see Fig. 3). It is stressed that the direct electricity generation form the CPVT in this condition is about 4-6 kW thus the electricity added by the ORC is about 50%.

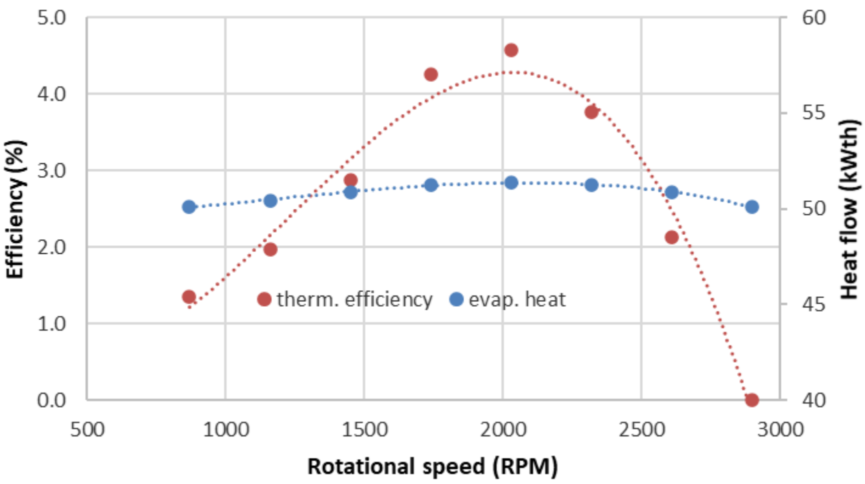

Fig. 4: Variation of thermal efficiency and heat supply at different rotation speed of expander and pump speed at 864 RPM

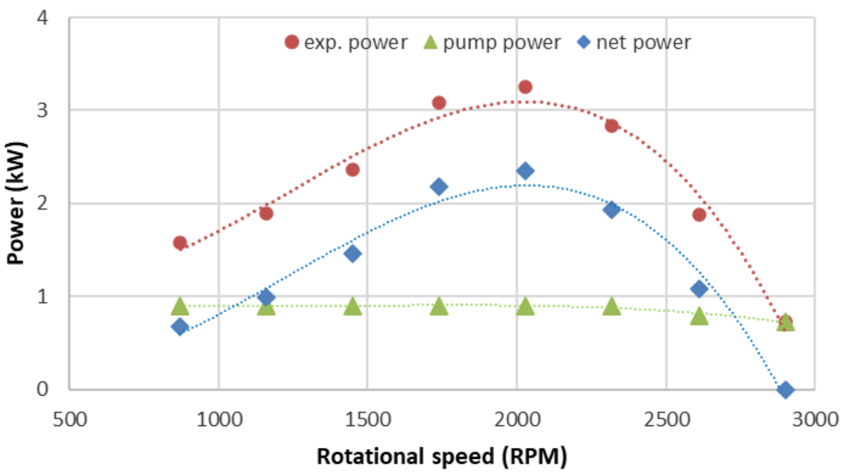

Fig. 5: Variation of power generated by the expander, power absorbed by the pump and net power at different rotation speed of expander and pump speed at 864 RPM

Other key variables that are calculated and assessed for each operatingcondition are the isentropic efficiencies of the pump and the expander, the pressure ratio and the filling factor of the expander. Also, the performance of the CPV-T array in all operating conditions is evaluated.Diagrams similar to the above ones provided for 864 RPM are generated for other values of pump's rotation speed and thus a complete mapping of the ORC engine operation at different heat inputs is achieved.

Next, the variation of selected key parameters is presented during the 4th of July 2020 as function of solar time. It was mostly a clear day with some cloudy intervals appearing late in the afternoon. Figure 6 shows the variation of total, direct and direct normal irradiance on collectors' surface as well as the variation of diffuse irradiance. Maximum values of the total irradiance in the order of 1000 W/m^2 are measured while diffuse radiation ranges between 70 and 90 W/m^2. Direct normal irradiance is the fraction of total irradiance exploited form the collectors' array experiences a maximum in the order of 900 W/m^2 around noon and afternoon.

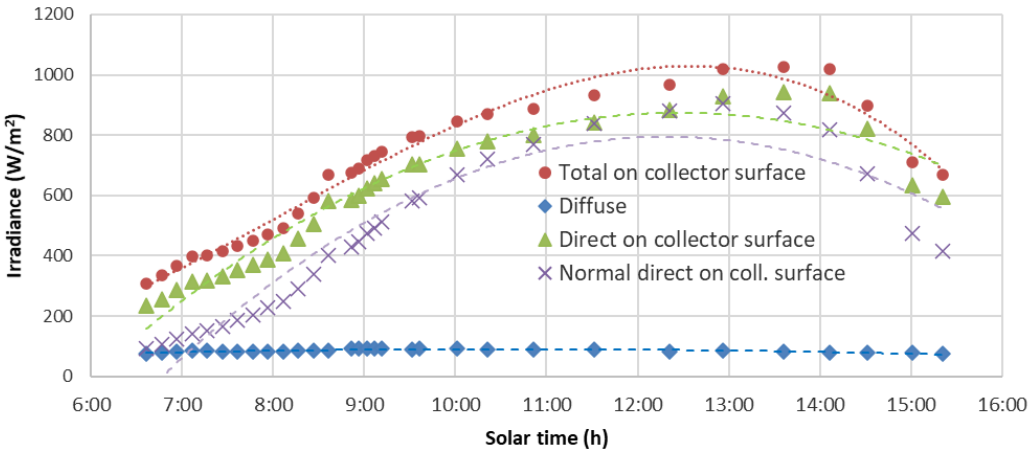

Figure 6: Total, direct, direct normal and diffuse irradiance

Figure 7 shows the variation of the inlet and outlet temperatures in the hot side of the evaporator. A maximum inlet temperature in the order of 85-88 ºC is reached at around 10:00 and slightly varies until 14:00. Afterwards, a decrease of temperature is noticed as the outcome of the reduced heat gain of the collectors' field. The ORC engine operation starts at around 8:30 and hot water temperature linearly increases up to 10:00. Before 8:30 heat generated by the solar collectors' field is used to preheat the water in the collectors' circuit till its temperature reaches about 54 ºCwhich is, the temperature threshold for the ORC engine to start operating (see also fig.8 which details this process). The inlet-outlet temperature difference variation is restricted to few degrees for most of the daily operation. In the beginning of the ORC engine operation, there is a notable increase of this difference (see Figure 9), since this heat is used to increase the temperature ofthe evaporators components in the ORC side.

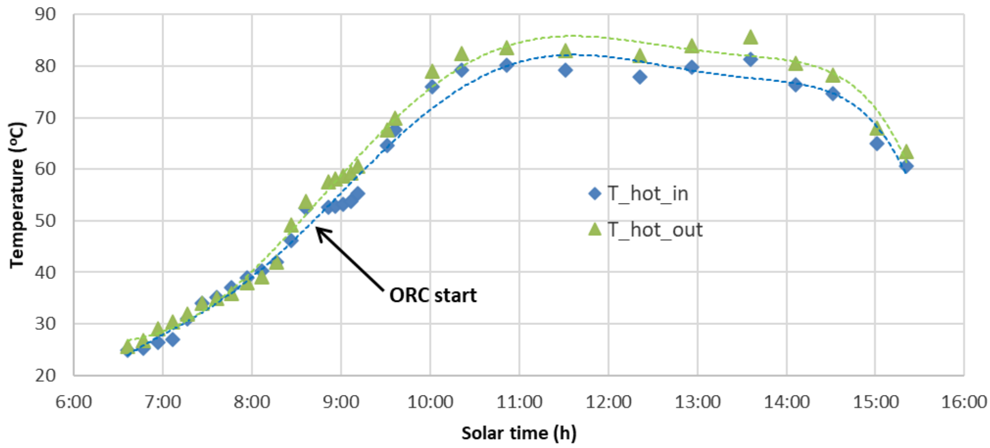

Figure 7: Inlet-outlet temperature of heating water in the evaporator

The processes taking place from the sunrise till the operation of ORC engine is stabilized at the design operation temperature (85 to 90 ºC),are of specific interest and they are analyzed more extensively below. Figure 8 illustrates the temperature variation at the evaporator inlet (hot side) and the heat supplied to the working fluid (water). ORC engine is out of operation until collectors' water is heated up to the appropriate temperature, that according to the experience is of the order of 55 ºC. ORC engine operation starts at around 8.30 a.m. where the water temperature is about 54 ºC. Cumulatively, the collectors' array has produced about 250 MJ of heat till the engine start.

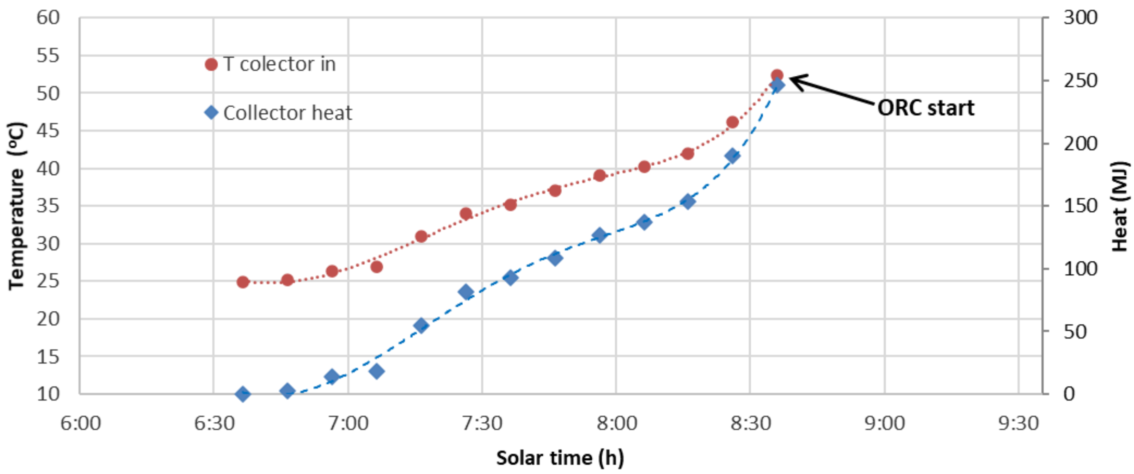

Figure 8: Elevation of temperature and heat at the collectors' array outlet until the engine start

In Figure 9 where the variation of heat flow in the hot (collectors) and cold (ORC) sides of the evaporator is depicted, throughout the ORC operation. In the beginning, the amount of heat is exchanged between the hot (collectors) and cold (ORC) sides of the evaporator to heat up the machinery and the organic fluid of ORC. It escalates fast, and within 15 min reaches to a maximum of 85 kW, while then declines till finally the operation is stabilized, as extracted from the smooth variation of heat flow curves. In the same figure, it is also observed that evaporator losses are considerable. In fact, the heat losses are measured in the range of 16-20 kW, that depending on the operation condition may represent 25 to 50% of the total heat generated. The reason is the high amount of heat being exchanged with the ambient due to the large area of the heat exchanger. Improvement of the insulation could improve the situation to some extent.

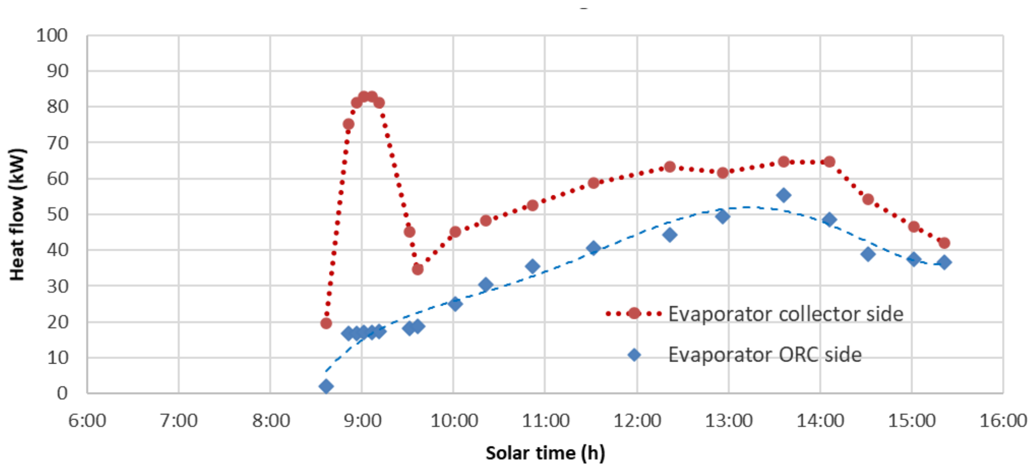

Figure 9: Heat flow in the ORC evaporator's sides

Figure 10 shows the variation of the thermal efficiency of the ORC engine. It is clearly shown that minimum values in the order of 1.5 to 2% are observed at the beginning of the operation. Then the thermal efficiency is gradually increasing and reaches its maximum of about 4-4.5 % between 10:00 to 14:00. Following the reduction of the solar irradiance, thermal efficiency starts to decrease till the system stops operating at about 15:30. The ORC operates at partial load in that case and this is also reflected to the thermal efficiency. The solar collectors' efficiency varies from 52 to slightly above 60% with the upper value to be observed arounf solar noon.

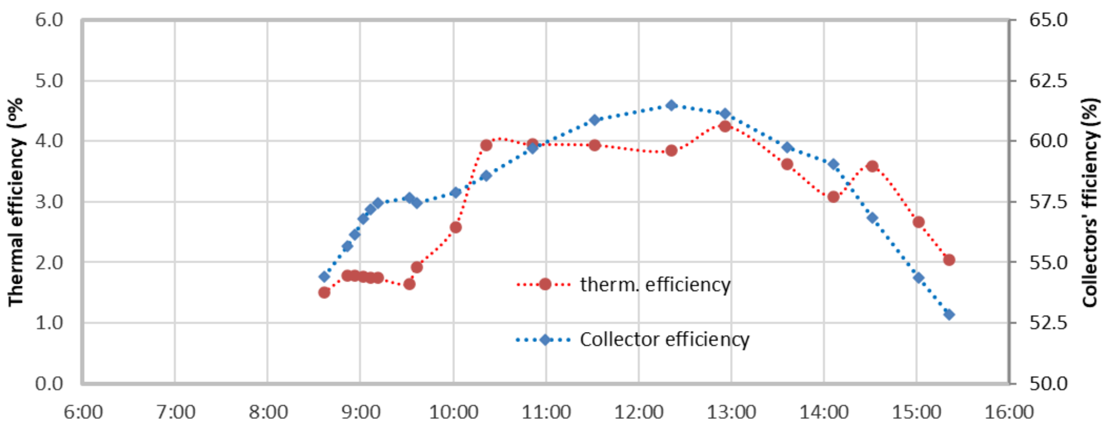

Figure 10: Collectors' and ORC thermal efficiency

Figure 11 presents the variation of expander, pump and net power during the day. Net power experiences low values in the beginning of ORC operation, and then it follows the trend of solar irradiance (Fig. 6). A maximum value slightly above 2 kW is noticed when the solar irradiance is maximized while in the afternoon the net power gradually decreases. This is comparable to the electricity produced directly by the PV cells that varies in the range of 4-6 kWe.

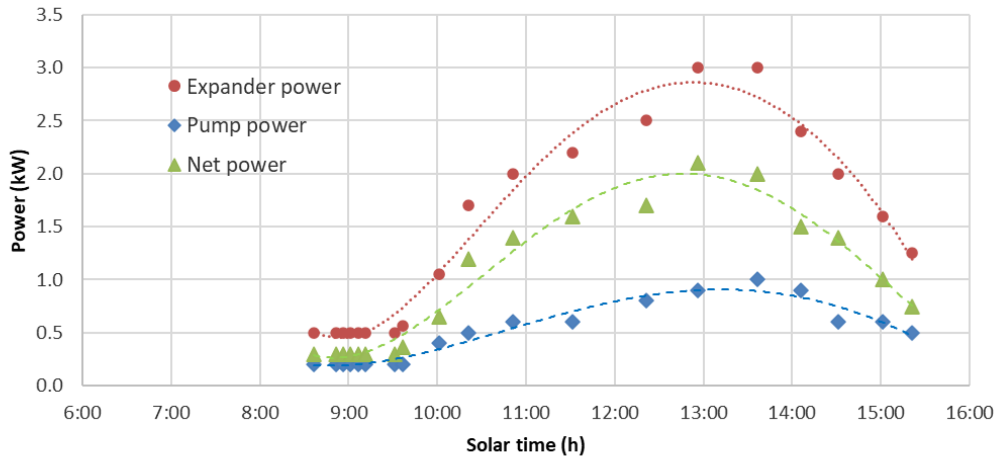

Figure 11: Expander's, pump and net power

After 15:30, the system experiences a radical decrease of net power generation due to the drop of direct normal solar irradiance, resulting from the increase of the angle of incidence and clouds (see fig. 6).

5. Conclusions

The integration of an ORC engine to a CPV-T array was investigated with the purpose of using the heat of the cooling circuit to generate additional electricity.The results prove thatthe coupling of ORC in CPVT systems is a reliable alternative of exploiting the heat production and thus generate additional electricity. In fact, ORC is capable to produce electricity comparable to that being directly offered by the PV cells, since the ORC engine power generation reached 2 kWe while the electricity generation of the CPV ranges from 4-6 kWe.Around solar noon, the ORC engine experienced the higher thermal efficiency, around 4.5%. This value is fair for ORC operating at top temperatures in the order of 80-85 ºC.The integration of an ORC engine canadd flexibility in CPV-T systems application since DHW is seasonally or even daily dependent. Thus, ORC could offer a solution towards diversification in CPV-T heat exploitation that finally can affect effectively to their economic viability.

6. Acknowledgments

The research leading to these results has received funding from the European Union's Seventh Framework Programme managed by REA-Research Executive Agency, under grant agreement no. 315049 [CPV/RANKINE], FP7-SME-2012.

7. References

Algieri A. and Morrone P., 2012. Comparative energetic analysis of high-temperature subcritical and transcritical organic Rankine cycle (ORC). A biomass application in the Sibari district. Appl. Therm. Eng. 36, 236–244.

Al-Sulaiman F. A., Hamdullahpur F., and Dincer I.,2011.Greenhouse gas emission and exergy assessments of an integrated organic Rankine cycle with a biomass combustor for combined cooling, heating and power production. Appl. Therm. Eng. 31, 439–446.

Bernardo, L. R., Perers, B., Hakansson, H. and Karlsson, B., 2011. Performance evaluation of low concentrating photovoltaic/thermal systems: A case study from Sweden. Sol. Energy, 85, 1499-1510.

Desai NB, Bandyopadhyay S., 2009. Process integration of organic Rankine cycle. Energy. 34(no.10):1674-86.

Dubey S, Tay A.,2013.Testingoftwo different typesofphotovoltaic-thermal (PVT) moduleswithheatflowpatternundertropicalclimaticconditions. Energy Sustain Dev.17:1-12.

Kosmadakis G, Landelle A., Lazova M., Manolakos D., Kaya A., Huisseune H., Karavas C., Tauveron N., Revellin R., Haberschill P., De Paepe M., Papadakis G., 2016. Experimental testing of a low-temperature organic Rankine cycle(ORC) engine coupled with concentrating PV/thermal collectors:Laboratory and field tests,Energy. 117, 222-236.

Kosmadakis G, Manolakos D, Papadakis G. 2015. An investigation of design concepts and control strategies of a double-stage expansion solar organic Rankine cycle. Int J Sustain Energy.34(7):446-67.

Lemort V, Declaye S, Quoilin S.,2012. Experimental characterization of a hermetic scroll expander for use in a micro-scale Rankine cycle. Proc Inst Mech Eng A J Power Energy. 226(1):126-36

Mago PJ, Chamra LM, Srinivasan K, Somayaji S., 2008. An examination of regenerative organic Rankine cycles using dry fluids. Appl ThermEng. 28:998-1007.

Manolakos D, Kosmadakis G, Kyritsis S, Papadakis G.,2009. Identification of behavior and evaluation of performance of small scale, low-temperature organicRankine cycle system coupled with a RO desalination unit. Energy. 34(6):767-774.

Mills, D., 2004. Advances in solar thermal electricity technology. Solar Energy. 76 (1–3), 19–31.

Mosaddek H, AHMR Sazedur, Afsana SK, Faruque MMH, Shoeb A., 2017. Systematic assessment of the availability and utilization potential of biomass in Bangladesh. Renew Sustain Energy Rev. 67:94–105.

Nazari MA, Aslani A, Ghasempour R.,2018. Analysis of solar farm site selection based on TOPSIS approach. IJSESD. 9(1):12–25.

Ong, C. L., Escher, W. S., Paredes, A. S., Khalil, G. and Michel, B., 2012. A novel concept of energy reuse from high concentration photovoltaic thermal (HCPVT) system for desalination. Desalination, 295, 70-81.

Othmana M.Y., B. Yatima, Sopianb K., Abu Bakara M.N., 2007. Performance studies on a finned double-pass photovoltaic-thermal (PV/T) solar collector, Desalination, 209, (1-3), 43–49.

Wang D., Ling X., Peng H. , Liu L., and Tao L., 2013. Efficiency and optimal performance evaluation of organic Rankine cycle for low grade waste heat power generation, Energy 50, 343–352.

Wang D., Ling X., and Peng H., 2012. Performance analysis of double organic Rankine cycle for discontinuous low temperature waste heat recovery. Appl. Therm. Eng. 48, 63–71.

Zhang H. G., Wang E. H., and Fan B. Y., 2013. A performance analysis of a novel system of a dual loop bottoming organic Rankine cycle (ORC) with a light-duty diesel engine, Appl. Energy. 102, 1504–1513.

SUSTAINABLE SITING OF OFFSHORE WIND FARMS FOR AN ISOLATED ISLAND SYSTEM

Pandora Gkeka-Serpetsidaki, Theocharis Tsoutsos

Renewable and Sustainable Energy Systems Lab, School of Environmental Engineering, Technical University of Crete, Chania, Crete, 73100, Greece

Abstract

This article highlights a 5-steps methodological framework for evaluating the available marine areas for the installation of offshore wind farms. Furthermore, the study area of our work is the island of Crete, the biggest and most populous island of Greece. The selected area has unique characteristics and great offshore wind potential.

Subsequently, the exclusion and the evaluation criteria are selected in terms of the national and European legislation and according to the study area's characteristics. After that, the evaluation criteria are assessed, through the process of personal interviews and questionnaires, from different groups of stakeholders, and then the AHP method is implemented in order to produce the relative importance of the criteria.

Finally, all exclusion criteria are performed to a unique layer of GIS and the combination emerged constitutes the exclusion map. However, the evaluation criteria are classified to scale from 1 to 5 (5 the higher suitability) and a layer for each criterion is also produced and the final evaluation map with a ranking suitability from 1-5. Eventually, the final suitability map is produced by multiplying the exclusion and evaluation map with Raster calculator.

This work contains an analysis of 4-criteria evaluation and exclusion at the same time. A more analytic and extensive work employing 14-criteria exclusion and 16-criteria evaluation is ongoing.

Keywords: Renewable Energy, Offshore Wind Farms, Sustainable Siting, Insular Environment, Analytical Hierarchy Process (AHP),

1. Introduction

More and more industries and nations/countries are orientated towards the development of Renewable Energy Strategies, Policies, Systems and Solutions nowadays, in order to meet European goals until 2030, concerning the diminution of fossil fuels and as a consequence the reduction of CO_2 emissions (2030 Climate & Energy Framework, Climate Action, 2020). Greece has a high installed capacity of onshore wind energy, surpassing the 3.5 GW (Hellenic Wind Energy Association (HWEA), 2020). Concerning the offshore wind projects, no remarkable progress has been made yet in the country. So, in this context and in order to avoid the additional land-use conflicts (International Energy Agency (IEA), 2019), this work has as a target to indicate the suitable marine areas which hold a high wind potential and meet the socio-economic, environmental and technical demands, simultaneously. Furthermore, this project is implemented in the island of Crete, as it requires a huge annual energy demand, especially in the summer period where the number of visitors is extremely high (Tsoutsos et al., 2015). It is also worth mentioning that a project like this, combined with the electrical interconnectivity, which has been scheduled within the next 2-3 years of the island of Crete with continental Greece could actually offer a variety of advantages for the local and the national economy, too (Independent Power Transmission Operator, 2019).

doi:10.18086/eurosun.2020.12.02 Available at http://proceedings.ises.org

2. Methodology

This work provides a methodological framework based on Multi-Criteria Decision Methods (MCDM) and Geographic Information Systems (GIS). More specifically, the relative weights are extracted from the questionnaires sent to different groups of local groups stakeholders. Consequently, the Analytical Hierarchy Process (AHP) is implemented and along with the use of GIS, the exclusion, as well as the evaluation maps, are exported. The selected criteria are divided into two categories the exclusion and the evaluation, accordingly. Finally, the developed methodology could be adopted by all stakeholders and competent authorities as a decision-making tool, since it could integrate the stakeholders' opinions and result to a sustainable siting of an offshore wind farm, facilitating in this way the transition into the decarbonization era (Höfer et al., 2016; Giamalaki & Tsoutsos, 2019).

In the first step of our method, the indispensable stage of the literature review was conducted. This helped us to acknowledge all the criteria used by the international scientific community in this sector of interest. Subsequently, the criteria which were satisfying the national legislation and were harmonised with the local characteristics of the island were selected as evaluation and placed in the questionnaires. The questionnaires were comprised of a matrix 16 x 16 for pairwise comparisons to become, as the number of evaluation criteria was 16. After that, the answers were received from the experts and the results were processed, based on the method of AHP and the final relative weights were derived for each evaluation criterion. Afterwards, the exclusion stage was taken place, where 14 exclusion criteria were identified (supplementary or not to the evaluation criteria) and the exclusion map with the combined criteria was accrued, so the inappropriate and the suitable areas are now obvious. Finally, the suitable areas are classified into a class from 1 - 5 (the most suitable), based on the weights coming from the stakeholders' opinions, with the aid of the software GIS. In the following Fig. 1 is depicted the summarized process of our methodology.

Fig. 1: Methodological framework for Offshore Wind Farms sustainable siting.

3. Analysis

Crete is the largest and most populous Hellenic island and it disposes an off-grid energy supply system depending mainly on petrol oil. Therefore, the electric interconnectivity with the mainland is under construction, so there will be emerged many advantages; one of these is the fact that the penetration of Renewable energy installations could be achieved more effectively (Fig. 2).

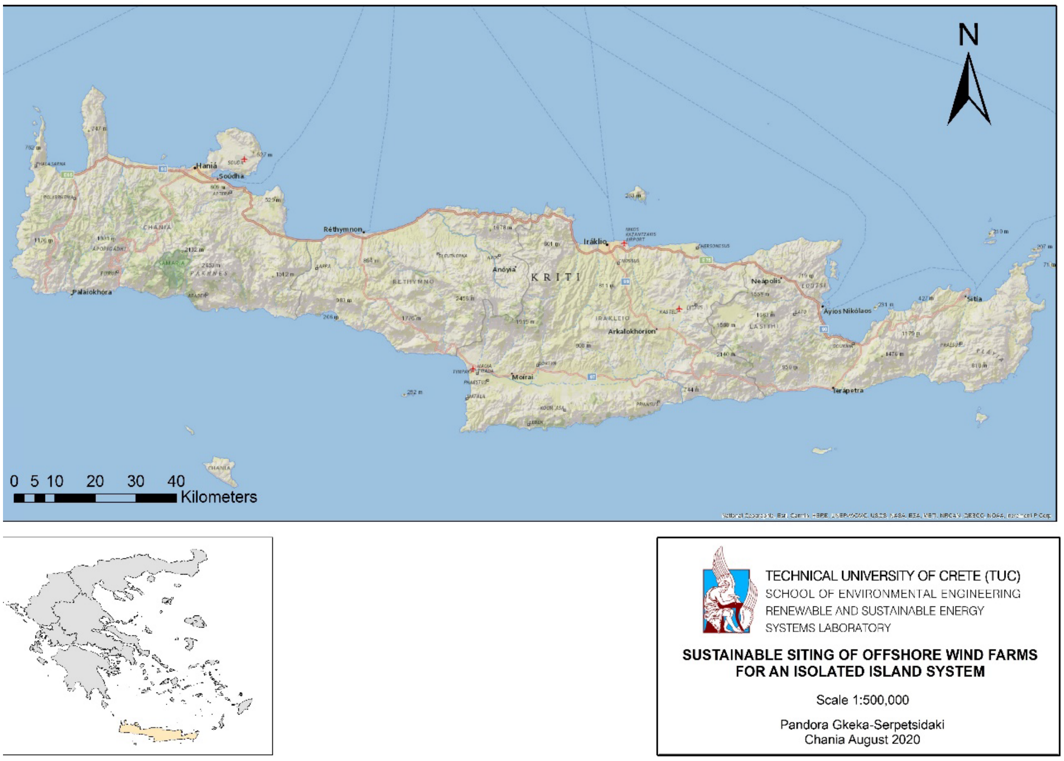

Fig. 2: Study area map, the island of Crete (Greece).

In this stage of our work, it has to be noted that were used fourteen exclusion and sixteen evaluation criteria. These evaluation criteria were assessed by thirty-three involved stakeholders/experts. Consequently, the relative weights of each criterion were calculated through the implementation of AHP method. The final results are actually under further analysis.

In this paper, four out of fourteen basic exclusion criteria were selected to be adapted and highlight our methodology. These criteria are briefly described below:

3.1 Water Depth

The water depth consists a crucial factor to determine where the installations of wind turbines have to be embedded. Today, the fixed wind turbines could reach a maximum depth of 60-80m. Generally, the shallower waters are preferred to deeper because of the great cost. The available marine areas with greater depths than 100m (red colour) are excluded from our study, according to the Fig. 3.

3.2. Environmentally Protected Areas

The environmentally protected areas are a sum of four other subcategories such as the Natura 2000 sites, the Important Bird Areas, the Posidonia oceanica meadows and the migratory corridors of birds. It was considered fair to exclude these areas from our work, because there is no reason to strain the environment further and there are also abundant marine areas for development of Offshore Wind Farms. The excluded marine areas are presented with green/blue colour in the following Fig. 4.

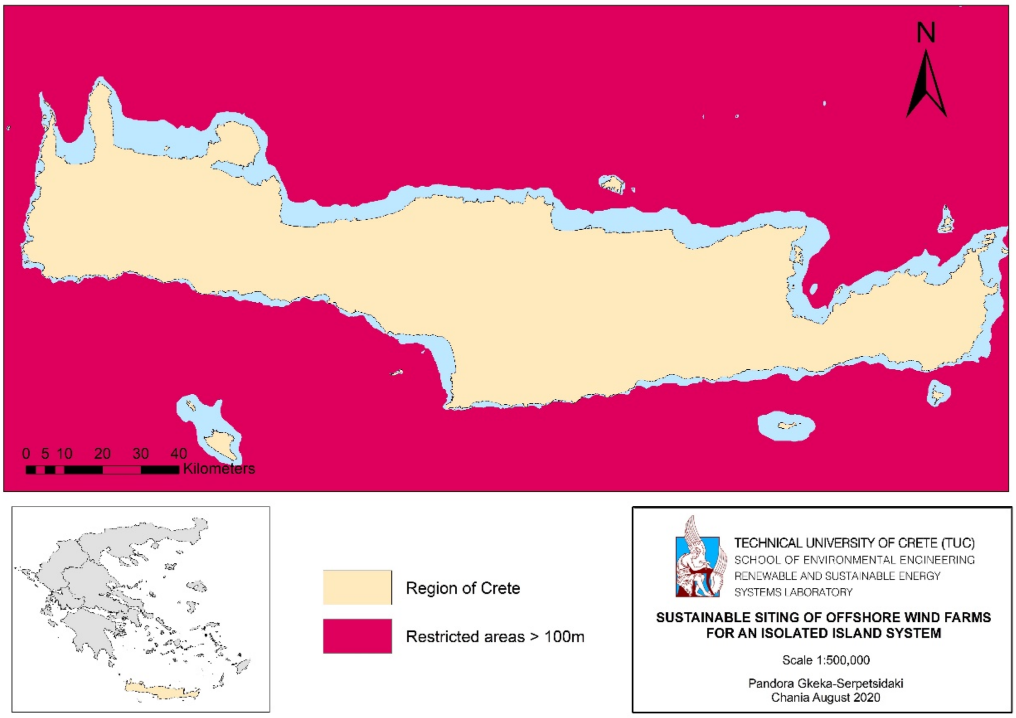

Fig. 3: Constraint of water depth.

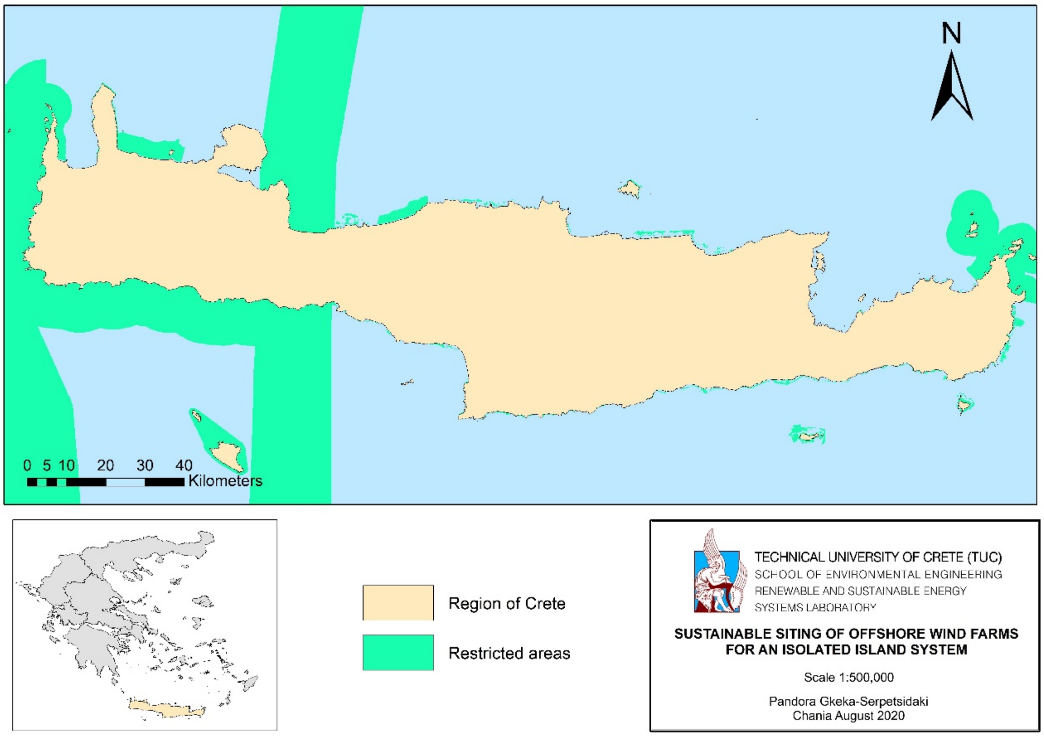

Fig. 4: Constraint of environmentally protected areas.

3.3 Distance from shoreline

This criterion constitutes mainly a legislative criterion and the restriction is that the territorial waters are up to 6miles from the shore. So, all the marine activities have to be taken place into these limits. Furthermore, according to (Hellenic Republic, 2008) the sites very close to the shore should be excluded for safety and aesthetic reasons, so a minimum distance from the shoreline was set to 1500m (e.g. bathing waters restriction). The excluded areas are in the following Fig. 5 with light green colour, whereas the suitable ones with purple colour.

3.4. Wind Velocity

The last essential criterion is the wind velocity and it is from economic and investment aspect, the most important to check for a region. For this reason, the minimum wind speed limit was set to 6 m/s and these areas were excluded from the survey. The green marine areas dispose a wind potential under 6 m/s, so they are excluded (Fig. 6).

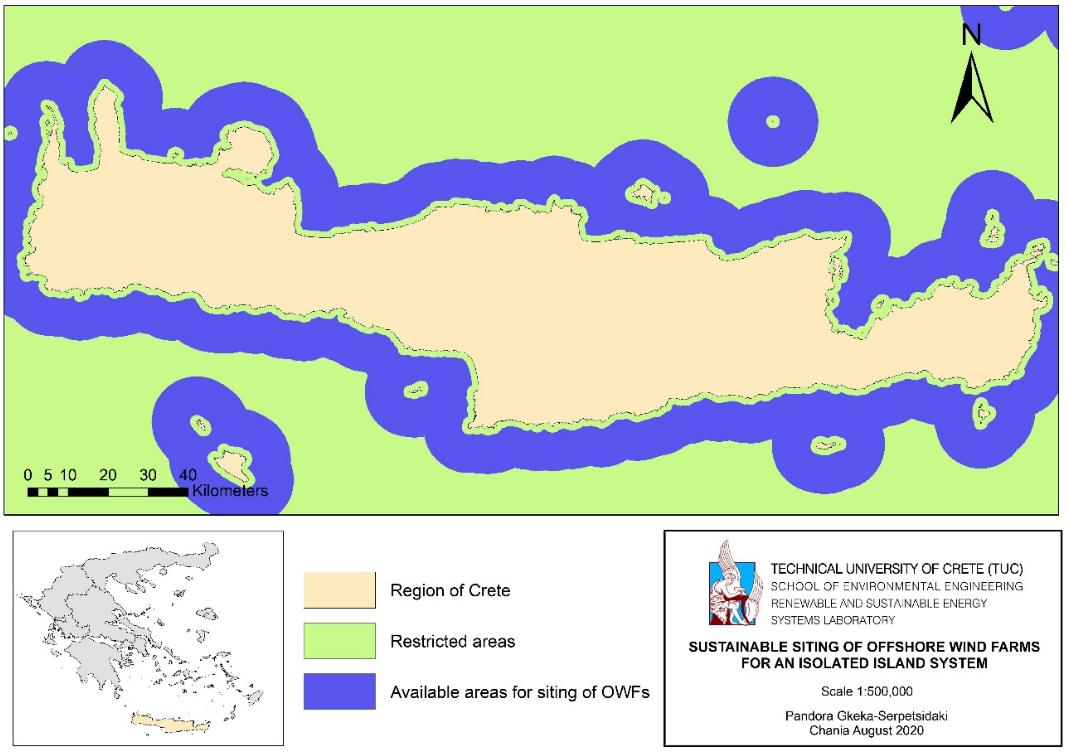

Fig. 5: Constraint of distance from shoreline.

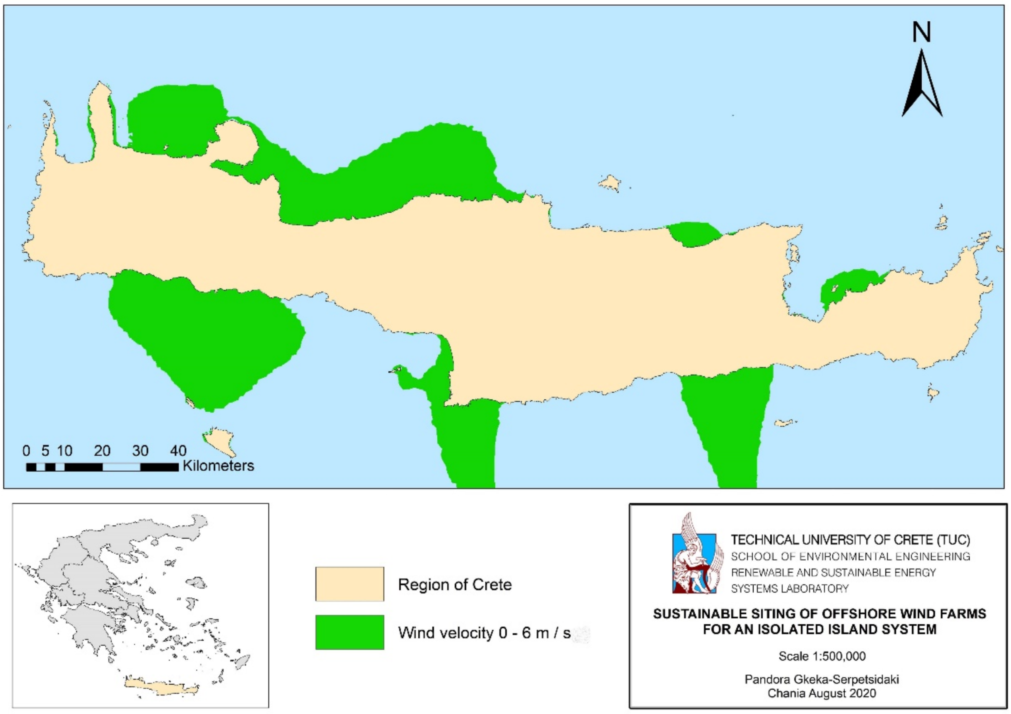

Fig. 6: Constraint of wind velocity.

In Table 1 are presented the digital data used in this work and the relevant source that they were taken from.

Table 1: Digital data used in this study and the source retrieved from.

Data	Source
1. Water Depth	(Hellenic Navy Hydrographic Service (HNHS), 2020)
2. Environmentally Protected Areas	(Hellenic Republic, 2008; Ministry of the Environment and Energy (Greece), 2010)
3. Distance from shoreline	(Hellenic Republic, 2008; Ministry of the Environment and Energy (Greece), 2010)
4. Wind Velocity	(Global Wind Atlas, 2020)

4. Results and Conclusions

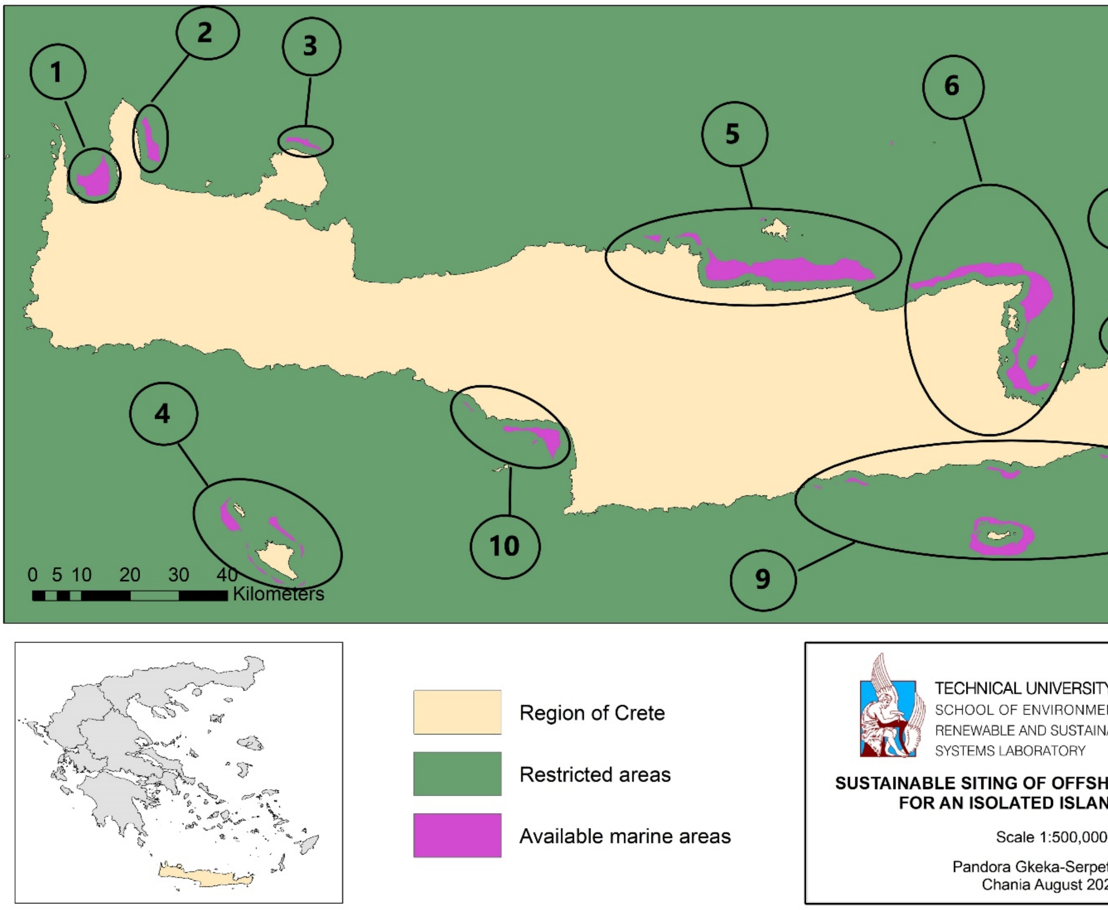

Fig. 7: Indicative results for siting of Offshore Wind Farms.

Table 2: Indicative locations for siting of Offshore Wind Farms and the relevant number of wind turbines fitte

Indicative locations for Offshore Wind Farms siting	Area [km^2]	MHI Vestas Offshore V112 3.3 MW			MHI Vestas Offshore V164 8.0 MW		
		Rotor Diameter	No of Turbines	MW	Rotor Diameter	No of Turbines	MW
LOCATION 1	30.67	112	49	161.7	164	23	184
LOCATION 2	14.58	112	23	75.9	164	11	88
LOCATION 3	6.07	112	9	29.7	164	4	32
LOCATION 4	21.95	112	35	115.5	164	16	128
LOCATION 5	132.52	112	215	709.5	164	100	800
LOCATION 6	113.92	112	185	610.5	164	86	688
LOCATION 7	34.83	112	56	184.8	164	26	208
LOCATION 8	33.53	112	54	178.2	164	25	200
LOCATION 9	58.39	112	94	310.2	164	44	352
LOCATION 10	23.23	112	37	122.1	164	17	136
Sum	469.68		757	2498.1		352	2816

This work describes an analysis of 4-criteria exclusion. A more analytic and extensive work which used 14 exclusion criteria exclusion and 16 evaluation criteria is currently under full analysis.

After the imposition of the exclusion mentioned above criteria, the tool cell statistics from the toolbar spatial analyst, software (ArcGIS 10.5) were used in order to combine all the layers and resulting in the final map presented in Fig. 7.

The total area of suitable marine areas for installations of offshore wind turbines extends to 469.68 km^2 (Table 2). Furthermore, the number of wind turbines of the selected models. The available ten marine areas are analytically described in Table 2, as well as some commercial models of offshore wind turbines that could be fixed in (the number and the MW). The array of offshore wind turbines that adopted for exporting these results was 7 D, where D is the Rotor Diameter of the turbine (Nyserda, 2018). Subsequently, 3 commercial models of Vestas were indicatively selected so as to highlight the capacity of available marine areas for siting of an offshore wind farm, for the island of Crete (MHI Vestas Offshore Wind, 2020).

5. Acknowledgements

All participants in this survey with personal interviews are gratefully acknowledged. Furthermore, we thank Dr. Emmanouil A.Varouchakis and Dr. Georgios Achilleos for their advice and help regarding the software ArcGIS and the provision of digital data.

6. References

2030 climate & energy framework. Climate Action, https://ec.europa.eu/clima/policies/strategies/2030_en [accessed 28 July 2020].

European Environment Agency (EEA). Natura 2000 End 2018 – Shapefile, https://www.eea.europa.eu/data-and-maps/data/natura-10/natura-2000-spatial-data/natura-2000-shapefile-1 [accessed 10 April 2020].

Giamalaki, M., Tsoutsos, T. 2019. Sustainable siting of solar power installations in Mediterranean using a GIS/AHP approach. Renewable Energy, 141, 64–75. https://doi.org/10.1016/j.renene.2019.03.100.

Global Wind Atlas, https://globalwindatlas.info/ [accessed 10 April 2020].

Hellenic Navy Hydrographic Service (HNHS), https://www.hnhs.gr/el/ [accessed 10 April 2020].

Hellenic Ornithological Society, https://www.ornithologiki.gr/index.php?loc=en, [accessed 28 July 2020].

Hellenic Republic. 2008. Law 2464 / B' / 2008. Government Gazette.

Hellenic Wind Energy Association (HWEA), https://eletaen.gr/en/home-eletaen/ [accessed 21 April 2020].

Höfer, T., Sunak, Y., Siddique, H., & Madlener, R. 2016. Wind farm siting using a spatial Analytic Hierarchy Process approach: A case study of the Städteregion Aachen. Applied Energy, 163, 222–243. https://doi.org/10.1016/j.apenergy.2015.10.138.

Independent Power Transmission Operator (IPTO), https://www.admie.gr/sites/default/files/users/dssas/dpa-2021-2030.pdf [accessed 22 April 2020].

International Energy Agency (IEA). Offshore Wind Outlook 2019, World Energy Outlook Special Report 2019, https://www.iea.org/reports/offshore-wind-outlook-2019 [accessed 17 April 2020].

MHI Vestas Offshore Wind, https://www.mhivestasoffshore.com/ [accessed 1 April 2020].

Ministry of the Environment and Energy (Greece). Preliminary procedure for siting of an Offshore Wind Farm, http://www.ypeka.gr/el-gr/, [accessed 22 January 2020].

Nyserda. Analysis of Turbine Layouts and Spacing Between Wind Farms for Potential New York State Offshore Wind Development, file:///C:/Users/Xristos/AppData/Local/Temp/Analysis-Potential-Turbine-Layouts-Spacing-Between-Wind-Farms.pdf [accessed 25 April 2020].

Supplementary files of paper titled "Seagrass mapping in Greek territorial waters using Landat-8 satellite images", https://zenodo.org/record/1120338 [accessed 10 April 2020].

Tsoutsos, T., Tsitoura, I., Kokologos, D., & Kalaitzakis, K. 2015. Sustainable siting process in large wind farms case study in Crete. Renewable Energy, 75, 474–480. https://doi.org/10.1016/j.renene.2014.10.020.

Layout of island power supply based on multi-decadal meteorological sets – reliability discussed in view of inter-annual variability using the case of the Faroe Islands power system

Hams Georg Beyer

University of the Faroe Islands, Tórshavn (Faroe Islands)

Abstract

The layout of renewable power supply systems – the sizing of its generation capacity (here: wind and solar) and its storage capacity - are complicated by the interannual variability of the meteorological conditions. To deal with this problem the use of multiannual sets is mandatory. Here both the sensitivity of the layout parameters on the length of the datasets negotiated, and the reliability of the sizing based on set sections compared to the sizing by a complete set. For this purpose, a 56-year set of daily data of wind speed and solar radiation for the location of the Faroe Islands (North Atlantic) is applied to study the sensitivity of the storage sizing to variations of the number of years considered.

Keywords: island systems, sizing, meteorological data

1 Introduction

To reach the aim of a secure, non-fossil coverage of the load in island grids leads – due to the volatility the wind and solar resource on all temporal scales – to the need for the inclusion of storage capacity and/or a remarkable oversizing of the renewable generation park. The identification of reasonable combinations of storage capacity and oversizing is usually done by use of time step simulations based on at minimum annual data sets of the meteorological conditions. The selection of the these sets – especially their length has been recognized as a critical issue (see e.g. Heide et al 2010, Bryce et. 2018, Pfenninger and Staffell 2016). Here, this issue will be discussed with focus on the sensitivity of the layout identified to the length of subsets selected from a set covering 56 years of wind and solar data. The example will be performed using a simple model that neglects any storage losses and assumes perfect availability of the generation for a full renewable power supply for the Faroe Islands (a group of small Islands in the Northern Atlantic at ~62°N, ~7.5°W). Results are intended to cast a light on the requirements on the quality of predictions of future meteorological conditions to reflect details of the statistics of the data sets.

2 A case study: analysing fully renewable electricity supply for the Faroe Islands using a 56-year data set

A fully renewable power supply for the Faroe Islands is due to its exceptional wind conditions (> 3000 full load hours for wind turbines) expected to by mainly based on wind farms. Starting from this, scenarios (Anonymous 2017, Trondheim et al. 2018, Beyer and Custodio 2018, Katsaprakakis 2019) had been analysed to identify the best mix for a wind/hydro/solar generation mix in combination with a pumped hydro storage scheme with a capacity of about week of average load. All these schemes had been based single year data sets. To widen the perspective and test the reliability of system sizing based on short temporal bases, following Pfenninger and Staffell 2016, Bryce et al. 2018, data sets covering decades are called into service here.

A respective analysis and is tried for a period covering 56 years. For this period system performance is simulated with a daily resolution. The example used concerns the identification of combinations of generation mixes and storage sizes for a fully renewable electricity supply. The results refer to “frozen-in” data of the actual load and hydro-generation of 2017, and wind and solar generation data simulated according to the variability of the meteorological data. The storage is modelled as an ideal one without losses.

doi:10.18086/eurosun.2020.12.03 Available at http://proceedings.ises.org

2.1 Data Base on wind and solar generation

The data base used here applies windspeed data for the years 1958-2013, taken from a hindcast set as described by Reistad et. al. 2011. From this data, given for the synoptic hours, Windfarm power output is simulated using a model derived in Trondheim 2020 form data of a windfarm on the Faroe Islands. Data are aggregated to model daily generation as function of daily mean wind speed.

Long term time of daily irradiance sums for that period are deduced from 1958-1013 station cloud cover data used as proxy. Time parallel satellite derived irradiance data for the years 2005-2013 from the JRC/SARAH data base (Müller et al. 2015) are used to correlate the daily mean cloud cover to the daily irradiance sum for the synoptic hours to set up a respective model. Fig. 5 shows as example 4 years of satellite derived and cloud cover based modelled daily irradiance sums to give an impression of the cloud-cover-based set.

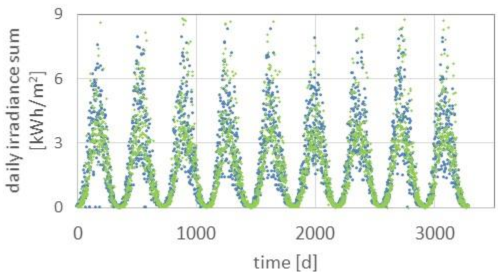

Fig. 1: Series of hourly radiation sums as given by satellite data (blue) and by model based on cloud cover data tuned to the satellite derived data.

For modelling daily PV-generation from daily irradiance sums a correlation scheme derived from the analysis of daily sums stemming from the hourly simulations of the power output of inclined PV modules (see Beyer and Custodia 2018) is used. A first application of the respective scheme was done in Beyer 2019.

2.2 Method for the identification of suitable combinations of generation and storage

The scheme starts with a setting of the generation capacities (minimal sizing of the generation capacity equal the long-term load). For the determination of the storage size required for complete load coverage given a certain generation capacity a method derived from a scheme given by [Haas 94] is used. The storage size required for save supply is estimated by analysing the series of the accumulated balance of generation and load over the (multi) annual period inspected. The storage requirements can be assessed by the analysis of the relative maxima and minima of the balance series.

3 Examples for system sizing

As start a system with wind capacity sized to be capable to equal the long-term average of the remaining load (load – hydro generation) is analysed. This results in a storage capacity equal to about 220 days of load. Double the wind capacity results in a system with required storage size reduced to about 13 days.

Figure 1 gives the 56-years sequence of the storage content for this case. It is remarkable, that the storage is challenged by singular “events”. As shown by Beyer and Custodio 2018, for the conditions at the Faroe Islands a further reduction of the required storage capacity is more easily achieved by adding generation by photovoltaics then by a further increase of the wind capacity. For the current case, an example shows that addition of PV generator giving a long-term generation of 17% of the long-term consumption brings the required storage size down to about 5 days (fig. 2). A remarkable change of the location of the challenging situations is visible

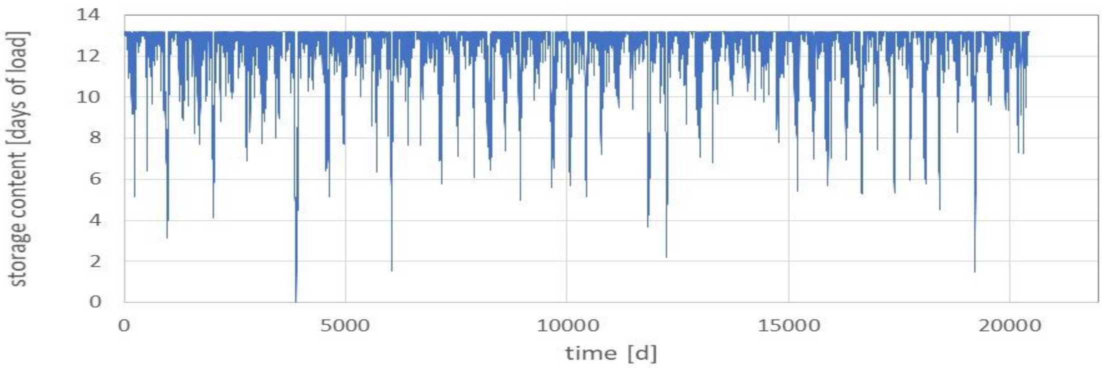

Fig. 2: 56-year time series of the storage content for a system with a wind capacity to equal the annual remaining load (load – hydro generation). Storage capacity set to assure save supply.

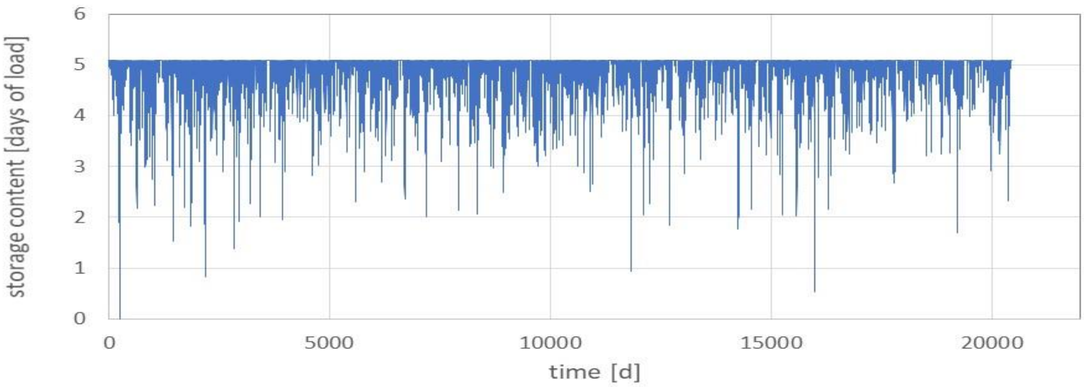

Fig. 3: Same presentation as fig. 3, but for a system with added PV capacity able for a generation of 17% of load consumption.

4 System sizing and time pattern of generation and load

These patterns shown in fig. 2 and fig. 3 give rise to the question whether the storage defining situations can be linked to properties of the balance series to allow for a more direct identification of critical years or time sections.

For this, the long-term evolution of the balance of wind power to remaining load (load - hydro generation) may be presented by its multiply days sliding average for better marking conditions challenging the storage. Fig. 3 and fig. 4 show this for the 365 days average of the balance for the two configurations inspected.

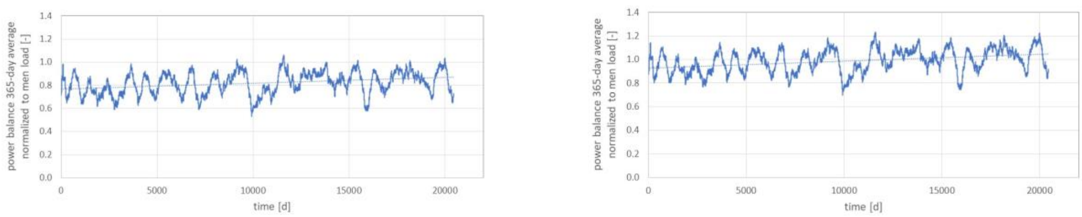

Fig. 4: 55 years time series of the balance (generation -load) presented as sliding 365 days averages. Series refer to the sytems presented in Fig. 2 (left) and 3 (right).

It has to be stated, that there is no obvious link of these average balance series with the storage evolution. This indicates that annually averaged balances do not contain the information needed to analyse a system with the sizing under inspection (oversized generation, storage of about weeks of load).

Thus, averaging over shorter periods (month, weeks) is tested. Results are given in figs, 5 a-c and 6 a-c using the scatter plot of the daily storage content versus the sliding average representing the period before that date.

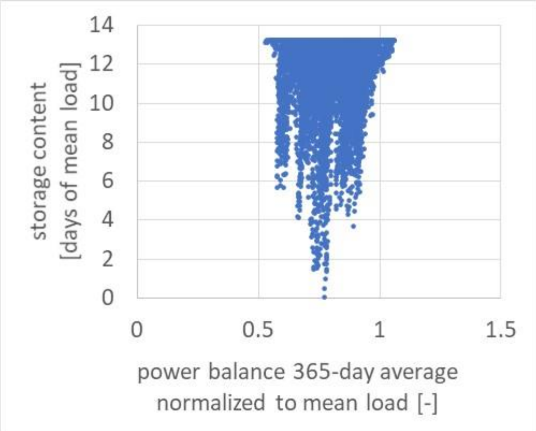

Fig. 5a: Scatter plot of storage content versus 365-day average of the normalized power balance for system presented in Fig, 1.

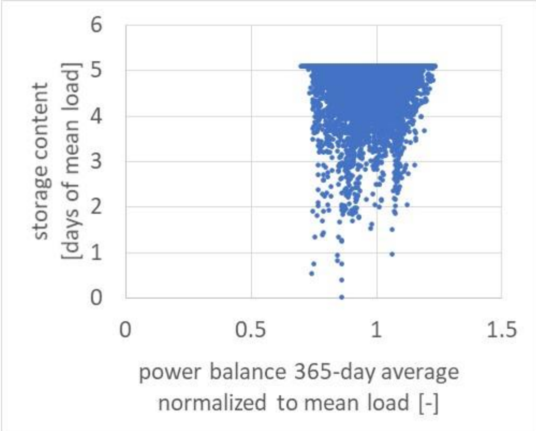

Fig. 6a: Same as 5a, but for system presented in Fig, 2.

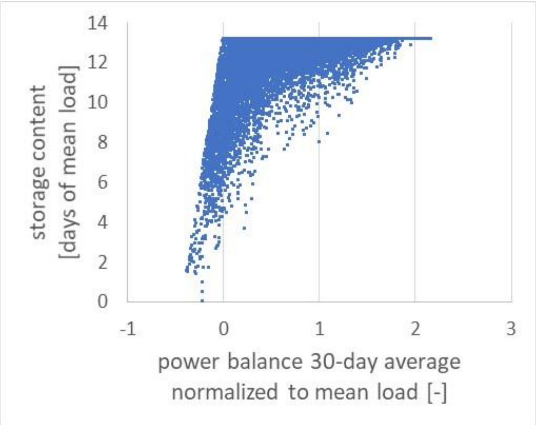

Fig. 5b: Same as 5a but for the 30-day average of the normalized power balance.

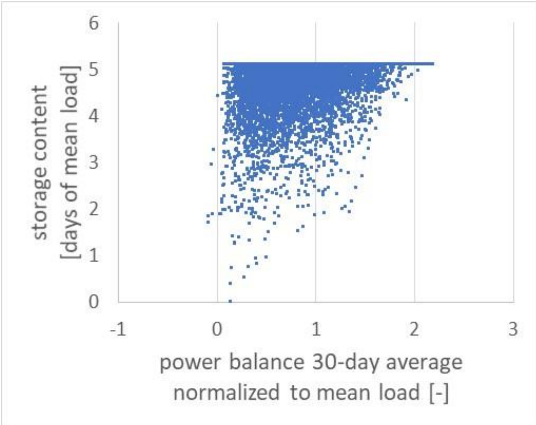

Fig. 6b: Same as 6a, but for the 30-day average of the normalized power balance.

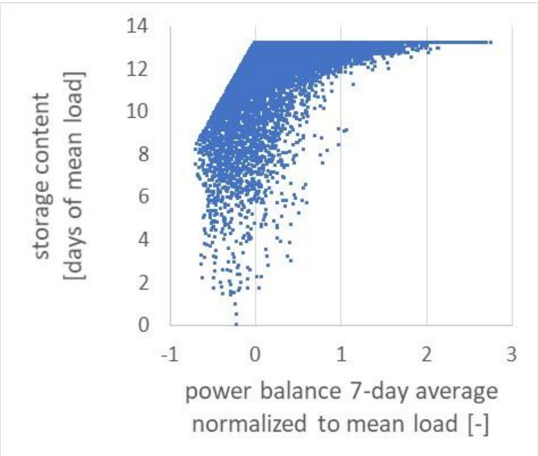

Fig. 5c: Same as 5a but for the 7-day average of the normalized power balance.

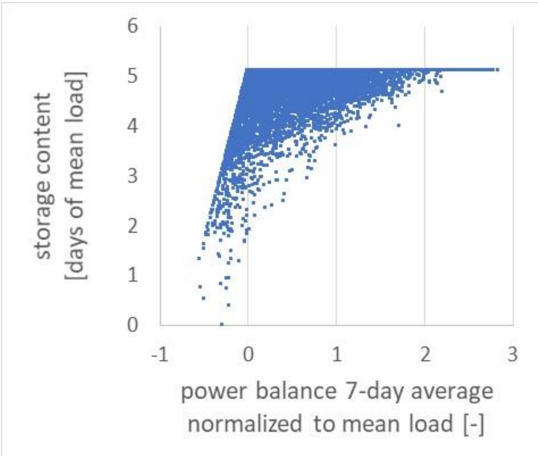

Fig. 6c: Same as 6a, but for the 7-day average of the normalized power balance

It can be remarked that for both configurations inspected, as expected from the time series plots, the lowest (here zero) storage contends appear at unexceptional values of the 365-day averaged balance. For the monthly and weekly balances, the ordinate positions of the points representing depleted storage refer to lower averages of the balance. Thus, averaging the balance over appropriate time sequences can give an indication on when to expect the occurrence of critical storage conditions. For an exact identification of the critical case, a more complex time series analysis or the detailed time series simulation appears unavoidable.

With the system sizing governed by the occurrence of singular event sets the request to data bases used to cover that specific period. Obviously, using but sections will always leave uncertainties of the level of security of supply that can be promised.
As example, the storage histories given in fig. 2 and fig. 3 are used to extract the storage requirement identified when only analysing sections of the set with limited length. Fig. 7 a-c and Fig. 8 a-c 10 show the results when sections of 10-, 5-, and 2-years length are analysed. The values give the storage sizes stemming from the period ending with the ordinate position given.

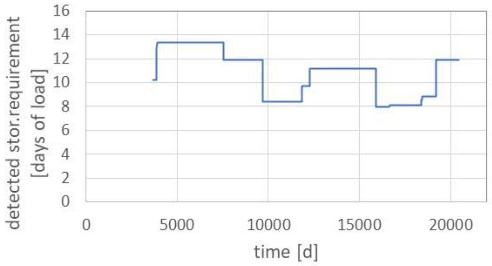

Fig.7a: Storage requirement stemming from the analysis of 10-year sequences of data referring to system shown in Fig.2. The values refer to the period ending with the ordinate position given.

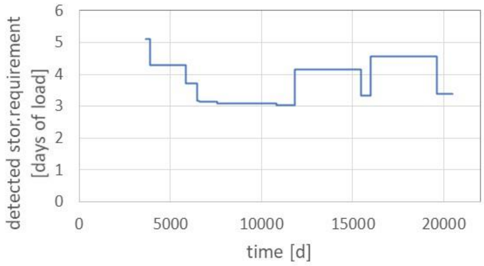

Fig. 8a: Same as Fig. 7a, but data referring to system shown in Fig.3-

.

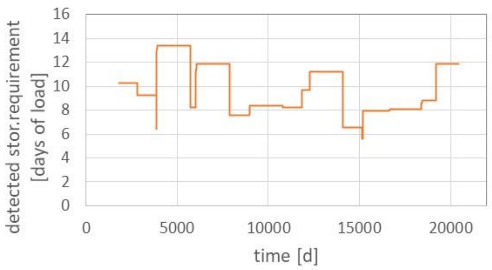

Fig. 7b: Same as Fig. 7a, but for 5-year sequences.

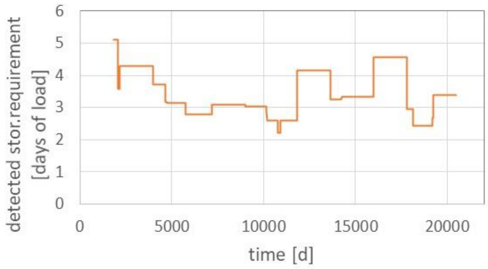

Fig. 8b: Same as Fig. 8a, but for 5-year sequences.

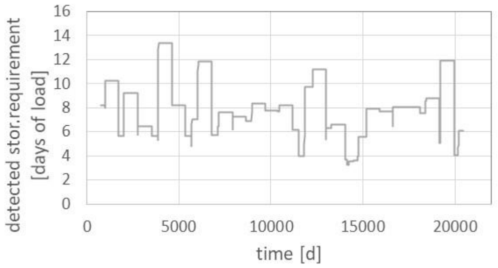

Fig. 7c: Same as Fig. 7a, but for 2-year sequences.

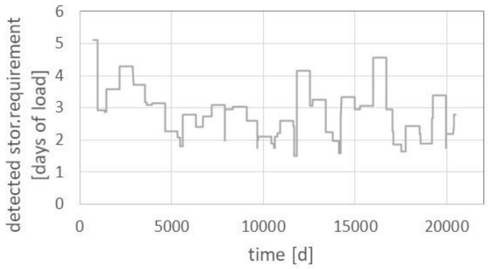

Fig. 8c: Same as Fig. 8a, but for 2-year sequences.

From this information one can derive - in retrospect - e.g. with which probability a randomly selected sequence may return a required storage size which is at minimum 80% of the requirement for the whole period. Table 1 gives respective probabilities for the 2, 5, and 10 years sequences for the two systems analysed.

Table 1: Probability that the use of a randomly selected sequence of 10, 5, and 2 years length would return a required storage size of 80% or more of the requirement stemming from the analysis of the complete set.

Length of sequence/ System	10	5	2
1	0.64	0.36	0.15
2	0.56	0.31	0.12

Thus - given that the variability of the meteorological time series is stable – a layout based on 10-years sequences may lead to remarkably undersized systems when the 100% reliability is the set as goal.

5 Consequences from undersized storage

To analyse the consequences of operating the systems with undersized storage capacity in more details, beyond the fact that there is no full load coverage, the time series of the storage evolution for the systems with the “perfect storage” for 100% coverage shown in figures 2 and 3 can be exploited. Figs. 9 and Fig. 10 give the numbers of days with uncovered load when decreasing the storage size.

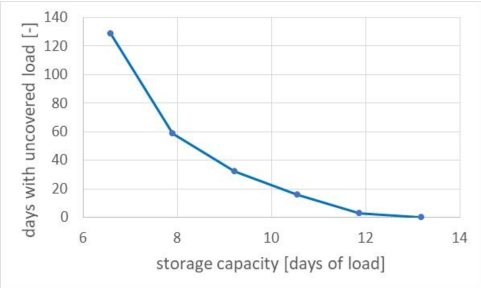

Fig. 9: Number of days with uncovered load in the 56-years sequence for a system as presented in Fig. 2 when reducing the storage size.

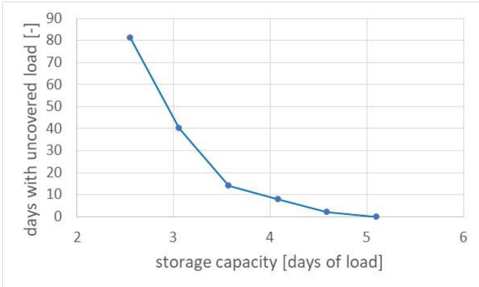

Fig. 10: Same as Fig. 9 but referring to the system presented in Fig. 3.

As indicated by the finding that the storage requirements detected here are determined by singular events, the use of a storage undersized by up to about 20 – 30% of the “complete set”-sizing lead to quite small numbers (with respect to the 56 years base well below 1 day per year)-

Combining this with the information on the probability that the use of short sequences for determining the storage size may result in an under-sizing (see e.g. figs. 7b and 8b) , gives some hope that sequences of about 5 years may be used as manageable basis for the layout. However, measures for handling (rare) events of critical storage states must be prepared.

6 Conclusion

It could be confirmed that the layout of island power supply systems that aim at a secure supply by renewable sources only has to be based on multi-annual data sets. Analysing the application of these sets it gets obvious that the aim of a system design for 100% security of supply or any other exact performance figure seems unreasonable. As this case study is a retrospective study, these results could only be usable for real world application if perfect long-time forecasts would be available. Thus, the uncertainties discussed here will be augmented by the uncertainties of the projections of the future meteorological conditions, Unfortunately the results presented here highlight the fact that the requirements regarding the accuracy of the forecasts go well beyond the correct representation of the long-term average resource.

7 References

Anonymous, 2011, Balancing a 100% renewable electricity system Least cost path for the Faroe Islands, Ea Energy Analyses, Kopenhagen

Beyer, H. G. 2019, Aspects of System sizing for complete autonomy of islands grids, discussed by using the example of PV-integration into the Faroe Islands grid, E-mobility amd solar integration workshop, Dublin

Bryce, R., Losada, I., Kumler, A., Hodge, B., Roberts, B., Martinez-anido, C.B., 2018, Consequences of neglecting the interannual variability of the solar resource : A case study of photovoltaic power among the Hawaiian Islands. Sol. Energy 167, 61–75.

Heide, D., von Bremen, L., Greiner, M., Hoffmann, C., Speckmann, M., Bofinger, S., 2019, Seasonal optimal mix of wind and solar power in a future highly renewable Europe, Renewablw Energy 35, 2483-2489

Katsaprakakis, D., Thomsen, B., I. Dakanali, Tzirakis, K., 2019, Faroe Islands: Towards 100 % R.E.S. peneration,Renewable Energy, 135,473-484

Müller, R., Pfeifroth, U., Träger-Chatterjee C., Cremer, R., Trentmann, J., Hollmann, R., 2015, Surface solar radiation data set - Heliosat (SARAH) - Edition 1. Satellite Application Facility on Climate Monitoring (CM SAF). URL: http://dx.doi.org/10.5676/EUM_SAF_CM/SARAH/V001

Pfenninger, S. and Staffell, I, 2016, Long-term patterns of European PV output using 30 years of validated hourly reanalysis and satellite data, Energy, 114, 1251-1265

Reistad, M., Breivik, Ø, Haakenstad, H., Aarnes, O.J., Furevik, B.R., Bidlot, J.R., 2011, A high-resolution hindcast of wind and waves for the North Sea, the Norwegian Sea, and the Barents Sea, Journal of geophysical research, vol. 116

Tróndheim, H.M., B.A. Niclasen, T. Nielsen, C.L. Bak, F.F. Da Silva (2018), Introduction to the Energy Mixture in an Isolated Grid with 100% Renewable, CIGRE Symposium Aalborg, Denmark 4-7.6

Trondheim, H.M. 2020, personal communication, Helma Trondheim, SEV, Torshavn, Froe islands

Comparative Analysis of Hybrid Renewable Energy Systems Simulation Tools

Panagiotis Triantafyllou, Kosmas A. Kavadias, Georgios Tzanes, Dimitrios Zafirakis

Laboratory of Soft Energy Applications & Environmental Protection, Department of Mechanical Engineering, University of West Attica, Egaleo, Athens, Greece

Abstract

The forthcoming depletion of fossil fuel reserves, currently dominating the global energy fuel mix, along with the continuous growth of electrical demand, have urged the "quest" for alternative energy resources, such as solar and wind energy, to satisfy the current electricity needs, in both urban and remote areas. The aforementioned technologies are considered capital intensive, underpinning the necessity for extensive research on that field in order to reduce costs. On the other hand, Hybrid Renewable Energy Systems (HRES), if properly sized, are considered a proven solution for achieving high economic efficiency, especially for stand-alone applications. Currently, many simulators have been developed aiming to facilitate the HRES stakeholders on planning and on designing better investments, as well as on research activities. Their thorough analysis, although complex, is strongly related to the efficient utilization of renewable energy potential and the careful design of relevant projects. This work assesses the sensitivity of two (2) commercial software packages by examining nine (9) scenarios, based on different combinations of solar and wind energy potential. The results are compared with the ESA (Energy Systems Analysis) Microgrid Simulator, developed by the Soft Energy Applications and Environmental Protection Laboratory (SEALAB) of the University of West Attica. The appraisal of the results provided a detailed assessment of the discrepancies between the selected software.

Keywords: HRES, Hybrid System, Stand-alone, Simulation, RES.

1. Introduction

The forthcoming depletion of fossil fuel reserves, currently dominating the global energy fuel mix, along with the continuous growth of electrical demand – correlated with the global population rise – have urged the "quest" for alternative energy resources, such as solar and wind energy, to satisfy the current electricity needs, in both urban and remote areas (Erdinc and Uzunoglu, 2012). However, the intermittent/stochastic nature of these resources challenges their omnipresent, environmentally-friendly and inexhaustible features, since it introduces difficulties in matching the power generation with the load demand. A common way of dealing with this generation and demand mismatch is the integration of energy storage technologies into the energy systems configurations. Integrating energy storage technologies may -under circumstances- enable maximum exploitation of renewable energy potential prevailing in a specific region (Kavadias, 2016, Kocher-Oberlehner and Peacock, 2014). Nevertheless, the aforementioned technologies are still considered capital intensive, underpinning the necessity for extensive research on that field to achieve further market maturity (Sinha and Chandel, 2014).

Hybrid Renewable Energy Systems (HRES) implemented in this context are considered as one of the most promising and reliable alternatives for the electrification of remote consumers, contributing simultaneously to the mitigation of climate change and minimization of fossil fuels usage (Kavadias, 2012). Various simulation software has been developed under the prism of serving HRES stakeholders' planning, research and development needs (Turcotte et al., 2001). Most of the software packages generate as outcome different combinations of renewable energy systems (RES) depending on the input parameters selected by the user (mainly meteorological and economic data as well as sizing constraints) (Al-Falahi et al., 2012). The different combinations proposed by the various software packages are attributed basically to the diversified control and economic strategies applied (Saiprasad et al., 2018). Their thorough analysis, albeit complex, is strongly related to the efficient utilization of the given renewable energy potential and the careful design of related projects (Kumar, 2016).

The vast majority of scientific papers in this direction analyze two (2) commercial software to conduct the pertinent simulations, namely Hybrid Optimization of Multiple Electric Renewables (HOMER) (various versions) and improved Hybrid Optimization by Genetic Algorithms (iHOGA), developed by the National Renewable Energy

doi:10.18086/eurosun.2020.12.04 Available at http://proceedings.ises.org

Laboratory (NREL) (HOMER Energy LLC, 2020) and the University of Zaragoza (2020) respectively. The present work assesses the sensitivity of the HOMER and iHOGA commercial software on RES potential by examining nine (9) scenarios, based on different combinations of solar and wind energy potential, aiming to cover the electricity needs of a remote domestic consumer. The results are compared with the ESA (Energy Systems Analysis) Microgrid Simulator, developed by the Soft Energy Applications and Environmental Protection Laboratory (SEALAB) of the University of West Attica (PUAS, 2017). ESA examines different hybrid energy system configurations through extensive energy analysis and produces optimized sizing results through the consideration of multiple objectives and criteria. Additionally, and besides the standard sizing algorithms, ESA supports the application of Demand Side Management (DSM) techniques through the configuration of relevant pools of flexible loads such as with the integration of electro-mobility aspects. To that end, the appraisal of the results provided a detailed assessment of the discrepancies between the selected software.

2. Methodology

A HRES comprised of photovoltaic (PV) modules, wind turbine (WT) generators, lead-acid battery banks and a converter/inverter is examined. Three (3) sites representing areas with different renewable energy (both solar and wind) potential are examined. More precisely, these areas were selected to represent low, medium and high renewable energy potential regions of the Greek territory.

The HRES architecture consists of PV modules, WT generators and lead-acid battery banks connected to a common DC busbar. The AC load (connected to the AC busbar) is electrified via an inverter, which also serves as a charge controller. Fig. 1 depicts a schematic overview of the electric circuit used for the simulations.

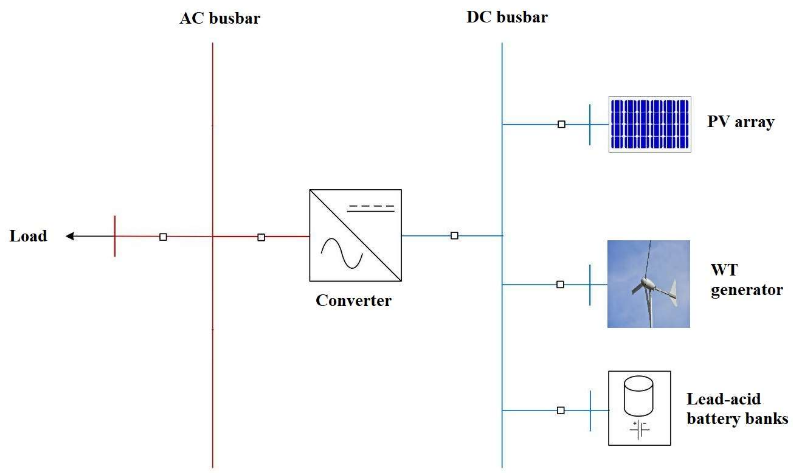

Fig. 1. Schematic overview of the electric circuit used for the simulations.

2.1. Input Data

Three (3) sets of solar irradiation data characterized by different level of potential quality (low, medium and high) were used. The datasets include hourly values of global and diffuse solar irradiation of Typical Meteorological Years (TMY), which were selected by a relevant scientific database developed for the Greek region (Kavadias, 2016). Fig. 2 presents the monthly values of solar energy for the different profiles with annual solar energy values of 1489 kWh/m^2 for the low solar irradiation area, 1686 kWh/m^2 for the medium solar irradiation area and 1732 kWh/m^2 for the high solar irradiation area, correspondingly.

Three (3) sets of wind speed data characterized by different level of potential quality (low, medium and high) were also used (Kavadias, 2016). Fig. 3 presents the wind speed distribution of the selected profiles of annual average values of 5.48 m/s for the low wind speed profile, 6.85 m/s for the medium wind speed profile and 9.16 m/s for the high wind speed profile, respectively.

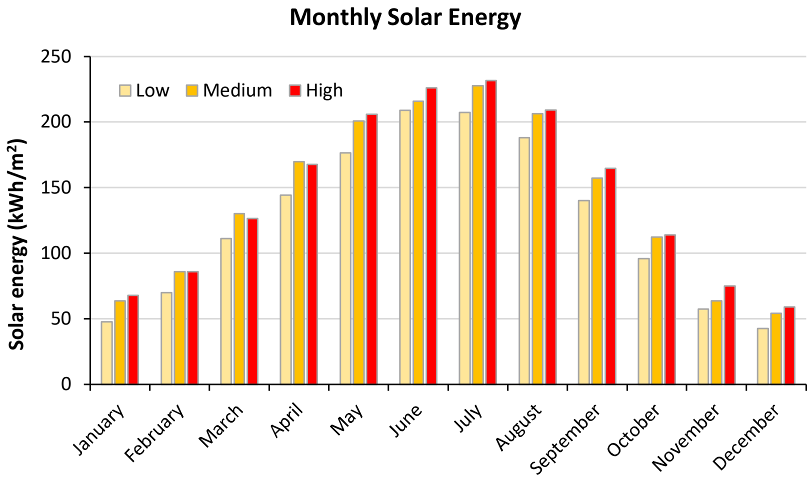

Fig. 2. Monthly solar energy variation for the three (3) selected solar irradiation profiles.

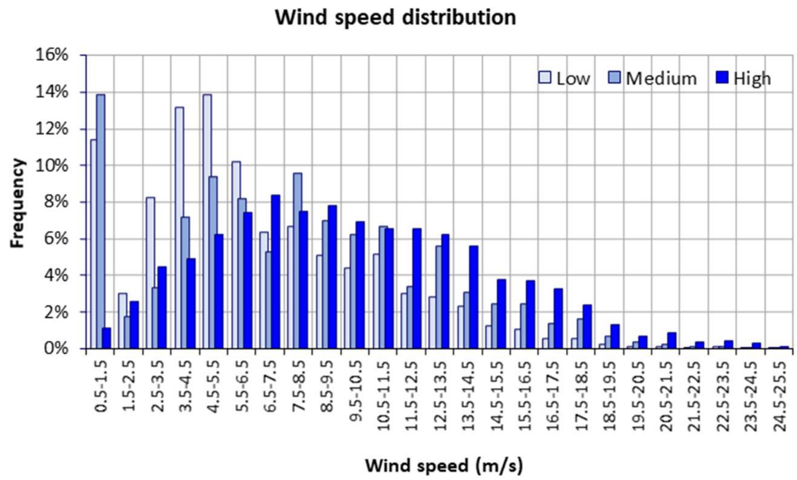

Fig. 3. Wind speed distribution for the three (3) selected wind speed profiles.

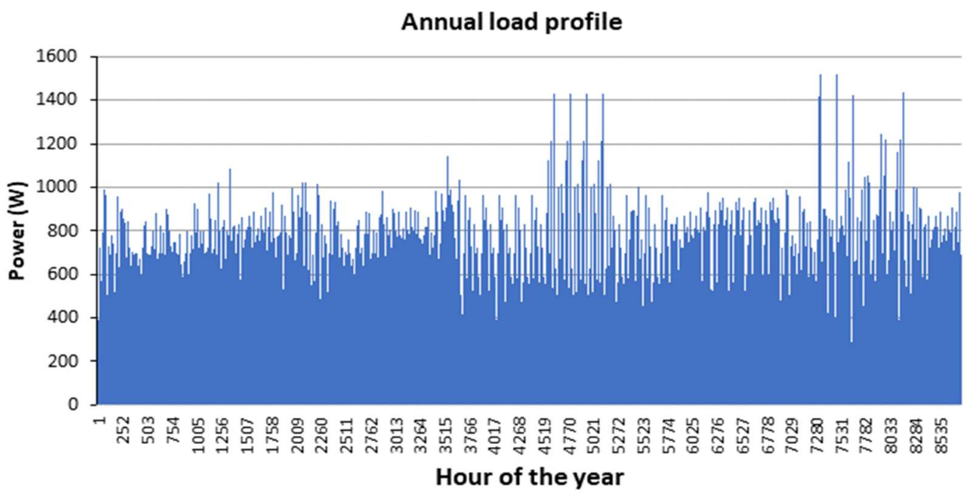

Fig. 4. Annual load profile.

The load profile of a HRES is of paramount importance for its sizing procedure. A 4-member dwelling was examined as a case study, representing a remote off-grid consumer with average energy requirements equal to 9.45 kWh/day. The load dataset includes hourly values of load demand measured at a 4-member dwelling of standard energy consumption and common household appliances. The final time-series were attained by merging typical weekly hourly load profiles for each month of the year (Fig. 4).

Nine (9) different scenarios (Tab. 1) of the aforementioned meteorological data were used as input parameters into the three (3) software and simulated as case studies with an hourly time-step.

Tab. 1 – Renewable energy potential combinations

Scenario	Renewable energy potential data
1	I_T = 1,489 kWh/m^2/year - $\bar{v}$ = 5.48 m/s
2	I_T = 1,489 kWh/m^2/year - $\bar{v}$ = 6.85 m/s
3	I_T = 1,489 kWh/m^2/year - $\bar{v}$ = 9.16 m/s
4	I_T = 1,686 kWh/m^2/year - $\bar{v}$ = 5.48 m/s
5	I_T = 1,686 kWh/m^2/year - $\bar{v}$ = 6.85 m/s
6	I_T = 1,686 kWh/m^2/year - $\bar{v}$ = 9.16 m/s
7	I_T = 1,732 kWh/m^2/year - $\bar{v}$ = 5.48 m/s
8	I_T = 1,732 kWh/m^2/year - $\bar{v}$ = 6.85 m/s
9	I_T = 1,732 kWh/m^2/year - $\bar{v}$ = 9.16 m/s

The system's economic parameters imported into each simulation software for conducting the pertinent analysis are presented in Tab. 2.

Tab. 2 – Data considered for economic analysis

Economic Parameter	Value
Nominal discount rate	7 %
Expected inflation rate	2 %
Project lifetime	25 years

Tab. 3 presents the economic parameters of the components selected for the relevant simulations.

Tab. 3 – HRES components' economic parameters

Component	Economic Parameter	Value
PV modules	Capital cost (€/W)	0.62
	O & M[1] cost (€/W/year)	0.01
	Lifetime (years)	25
WTs	Capital cost (€/W)	4.66
	Replacement cost (€/W)	3.34
	O & M cost (€/W/year)	0.09
	Lifetime (years)	15
Batteries	Capital cost (€/Ah)	0.68
	Replacement cost (€/Ah)	0.64
	O & M cost (€/Ah/year)	0.01
Inverter/Charge controller	Capital cost (€/VA)	0.58
	Replacement cost (€/VA)	0.52
	O & M cost (€/VA/year)	0.06
	Lifetime (years)	10

[1]O & M: Operation & Maintenance

2.2 Simulation Tools

HOMER Pro (Fig. 5) was selected as being a HRES optimization tool used by over 93,000 people worldwide (HOMER Microgrid News, 2020). The users range from energy systems integrators and utilities to military stakeholders and non-profit organizations. The software can perform detailed time-series simulations on different time-scales. The realistic modeling of renewable energy resources with a stochastic/intermittent character, such as wind and solar energy, can be attributed to software's capability for sensitivity analysis, which eliminates the uncertainty associated with input parameters, also increasing the quality of decision-making.

Fig. 5. HOMER Pro graphics user interface.

iHOGA (Fig. 6) is a multi-objective optimization tool, which utilizes comprehensive models of the considered components (University of Zaragoza, 2020, Ganguly et al., 2017). The utilization of cutting-edge genetic algorithms renders the software capable of attaining the optimum system layout with a relatively low computational burden, considering the contradictory optimization constraints of unmet load, costs and emissions. In this context, the quality of decision-making is also enhanced.

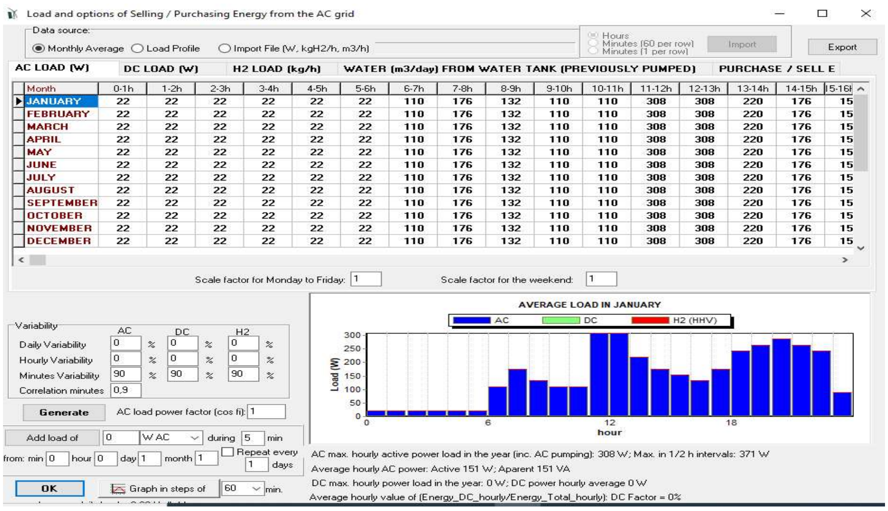

Fig. 6. iHOGA graphics user interface.

ESA Microgrid Simulator (Fig. 7) can examine various hybrid energy system configurations, aiming at their optimization via the application of multiple objectives (PUAS, 2017). Except for HRES sizing, the specific software is able to implement advanced energy management strategies, such as with DSM techniques and relevant embedded elements, e.g. electric vehicles, desalination units, etc. The software was developed in the programming language C# by SEALAB.

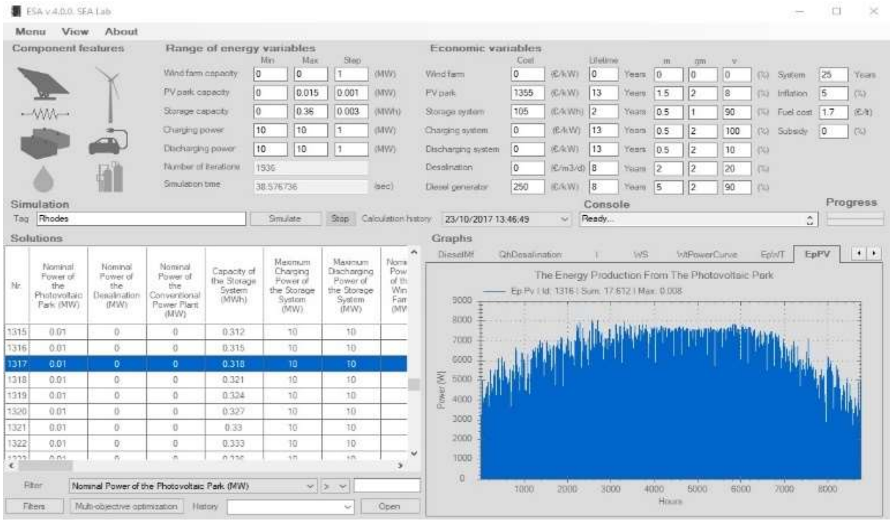

Fig. 7. ESA graphics user interface.

3. Results

3.1 System Sizing for Optimum Economic Results

According to the results obtained, iHOGA maintains both the battery bank capacity and the total nominal wind power constant (except for scenario 9) and therefore their relevant contribution to load requirements (Tab. 4). The software opts for diversifying solar power accordingly to respond to load demand. On the other hand, HOMER Pro adopts a different dispatch strategy. The software retains constant the nominal wind power and opts for diversifying both the solar power and the storage capacity. It is also noticeable that for scenarios 1 and 4 (where low wind potential is present) HOMER Pro has selected only PV panels and battery banks to cover the load demand.

Tab. 4 – Overview of the sizing parameters generated by HOMER Pro and iHOGA for optimum economic results

Scenario	PV power (kW_p)		Wind power (kW)		Storage capacity (kWh)	
	HOMER	iHOGA	HOMER	iHOGA	HOMER Pro	iHOGA
1	10.30	4.26	0	0.66	22.85	31.1
2	5.47	4.26	0.91	0.66	10.55	31.1
3	3.07	1.30	0.91	0.66	10.55	31.1
4	7.47	4.26	0	0.66	15.82	31.1
5	5.09	4.26	0.91	0.66	10.55	31.1
6	2.90	1.30	0.91	0.66	10.55	31.1
7	3.87	4.26	0.91	0.66	15.82	31.1
8	4.07	4.26	0.91	0.66	10.55	31.1
9	2.27	1.30	0.91	1.32	10.55	31.1

For all the scenarios examined, the PV contribution generated by HOMER Pro is higher than the relevant one generated by iHOGA (Tabs. 4 and 5). On the other hand, HOMER Pro has selected a lower storage capacity to respond to load requirements in comparison to iHOGA. Tab. 5 presents the simulation results from both HOMER Pro and iHOGA for the energy distribution of the examined HRES for optimum economic results.

Tab. 5 – Overview of the energy results generated by HOMER Pro and iHOGA for optimum economic results

Scenario	Excess energy (kWh/year)		Energy delivered by PV (kWh/year)		Energy delivered by WT (kWh/year)	
	HOMER	iHOGA	HOMER	iHOGA	HOMER	iHOGA
1	8,908	1,446	12,797	3,917	0	1,775
2	6,163	2,137	6,811	3,917	3,079	2,439
3	4,269	324	3,820	1,205	4,154	3,198
4	6,460	1,844	10,331	4,404	0	1,747

5	6,389	2,570	7,034	4,404	3,079	2,411
6	4,448	563	4,015	1,355	4,154	3,156
7	3,716	1,800	5,373	4,403	2,145	1,747
8	4,997	2,539	5,653	4,402	3,079	2,410
9	3,589	367	3,156	1,354	4,154	3,155

The smaller size of battery banks results in lower values of autonomy as achieved with HOMER Pro compared to iHOGA (Tab. 6), considering two (2) days of autonomy as the calculation base, which are considered as a common engineering practice in such projects. HOMER Pro generates in all cases higher amounts of excess energy (ranging from 2 to over 13 times) in comparison with iHOGA (Tab. 5), which is mainly attributed to the straightforward control strategy adopted by iHOGA (Saiprasad et al., 2018). Tab. 6 depicts the simulation results from both HOMER Pro and iHOGA for the unmet load and the battery bank's autonomy of the examined HRES for optimum economic results.

Tab. 6 – Unmet load and battery banks' autonomy generated by HOMER Pro and iHOGA for optimum economic results

Scenario	Unmet load (kWh/year)		Days of autonomy	
	HOMER Pro	iHOGA	HOMER Pro	iHOGA
1	26.27	96.45	1.93	2.17
2	37.85	73.50	0.89	2.17
3	17.54	150.22	0.89	2.17
4	38.75	44.82	1.34	2.17
5	40.55	46.94	0.89	2.17
6	3.35	24.66	0.89	2.25
7	5.46	21.37	1.34	2.17
8	32.47	34.31	0.89	2.17
9	5.85	99.42	0.89	2.17

The HRES profitability is determined by NPC and LCOE. Tab. 7 accumulates the simulation results from both HOMER Pro and iHOGA for the economic parameters of the examined HRES. These results refer to optimum values produced for the Net Present Cost (NPC) and the Levelized Cost of Electricity (LCOE), respectively. According to Tab. 7, a significant difference is noted between the iHOGA and HOMER Pro in terms of LCOE results. On the other hand, smaller discrepancies are noted in terms of NPC, which however diminish with the improvement of the solar and wind energy potential quality. These discrepancies can be attributed to different control strategies and economic models adopted by each software. More precisely, HOMER Pro uses the real discount rate to account for the time value of money (HOMER Energy LLC, 2020). In contrast, iHOGA considers both the inflation and interest rates for economic calculations. Moreover, iHOGA utilizes advanced models for the battery banks' lifetime calculation, rendering the respective economic results more realistic (University of Zaragoza, 2020).

Tab. 7 – LCOE and NPC values generated by HOMER Pro and iHOGA for optimum economic results

Scenario	NPC (€)		LCOE (€/kWh)	
	HOMER	iHOGA	HOMER Pro	iHOGA
1	40,173	33,171	0.83	0.40
2	37,753	33,171	0.78	0.39
3	33,449	33,138	0.69	0.40
4	37,539	33,171	0.77	0.39
5	37,401	33,171	0.77	0.39
6	33,328	31,808	0.68	0.37
7	37,471	33,171	0.77	0.39
8	36,649	33,171	0.76	0.39
9	33,230	33,138	0.70	0.40

3.2 Power Reliability Calculations for Optimum Economic Results

Each simulation tool has a diversified visualization of the results. Thus, in an attempt to carry out reasonable and justified comparisons, only three (3) Power Reliability Indicators were examined (Guzmán Acuña et al. 2017, Kavadias, 2012, Singh and Bagchi, 2010):

- Loss Of Power Supply Probability (LOPSP):

$$LOPSP = \frac{unmet\ load\ \left(\frac{kWh}{year}\right)}{overall\ energy\ demand\ \left(\frac{kWh}{year}\right)} \qquad \text{(eq. 1)}$$

- Level of Autonomy (LA):

$$LA = 1 - LOPSP \qquad \text{(eq. 2)}$$

- Expected Unserved Energy (EUE), i.e., the sum of the unmet load demand during the simulation year (in kWh/year).

The lower flexibility noted by iHOGA regarding resources allocation led to higher values of annual unmet load compared to the relevant ones generated by HOMER Pro (Tab. 6). In their turn, the higher amounts of unmet load generated by iHOGA, for all the examined scenarios, have a substantial influence on Power Reliability Indicators calculations, hence, leading to smaller levels of autonomy for the stand-alone configurations examined. More precisely, the unmet load values calculated by iHOGA are 1.15 to approximately 17 times greater than the relevant values calculated with HOMER Pro. Figs. 8 - 10 visualize the discrepancies between the values calculated for LOPSP, LA and EUE respectively, based on the simulation results of HOMER Pro and iHOGA.

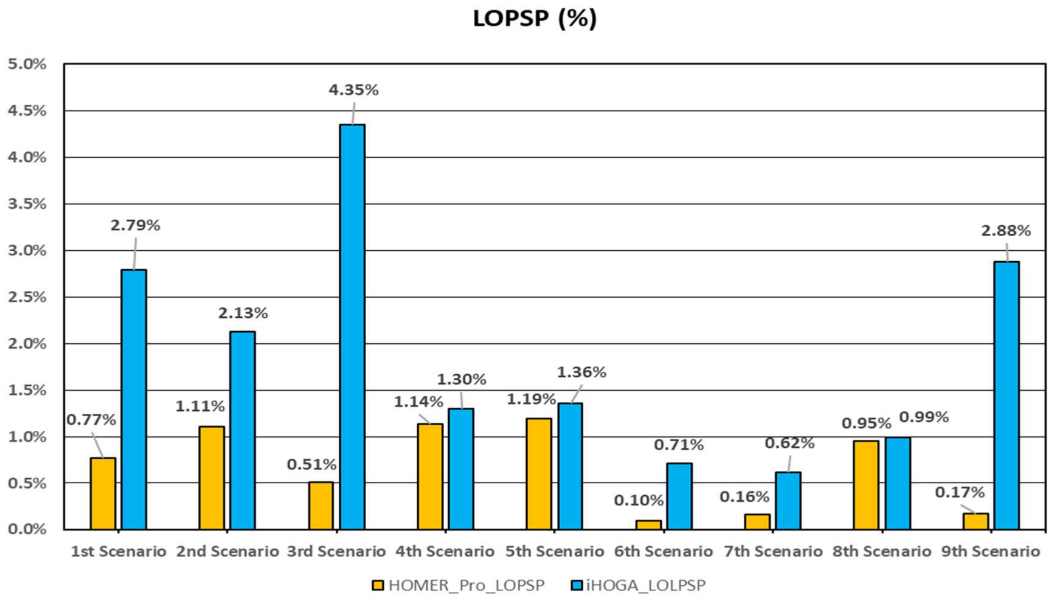

Fig. 8. LOPSP discrepancies for the nine (9) scenarios simulated with HOMER Pro and iHOGA.

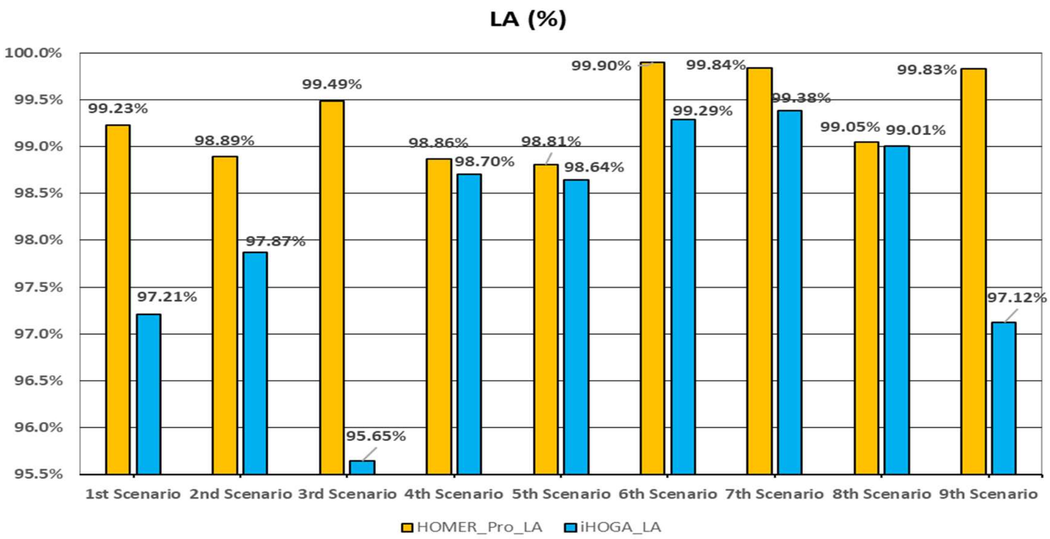

Fig. 9. LA discrepancies for the nine (9) scenarios simulated with HOMER Pro and iHOGA.

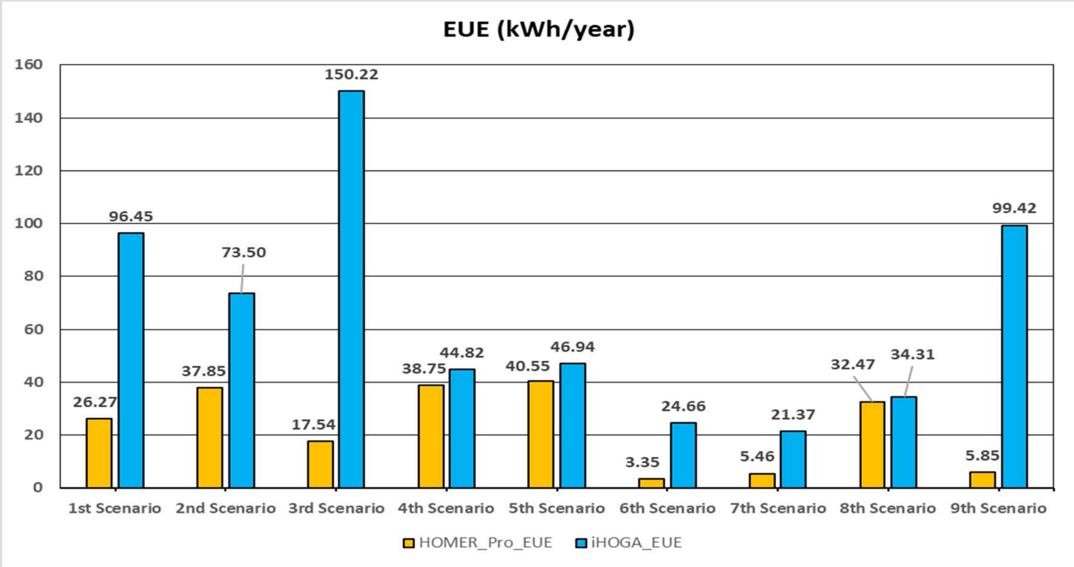

Fig. 10. EUE discrepancies for the nine (9) scenarios simulated with HOMER Pro and iHOGA.

It is noteworthy that the minimum value for LA attained with iHOGA is equal to 95.65%, while the relevant value attained with HOMER Pro is 98.81%. Thus, when power reliability optimization goals are set as a priority, HOMER Pro can be considered preferable than iHOGA, due to its dispatch strategy. The opposite is valid when economic optimization goals are set as a priority.

3.3 System Sizing for Minimum Unmet Load

As also valid for the simulations on the optimum economic results, iHOGA maintains constant both the storage capacity and the total nominal wind power (except for scenario 5) as well as their relevant contribution to load requirement (Tab. 8). The software opts for diversifying the solar power accordingly to respond to load variation. On the other hand, HOMER Pro depicts a different dispatch strategy. The software maintains constant only the nominal wind power (except for scenario 1) and opts for diversifying both the solar power and the storage capacity. Additionally, the configurations generated by both software include all energy resources, in contrast to the simulations for the optimum economic results. Tab. 8 provides an overview of the simulation results generated by both HOMER Pro and iHOGA for the sizing parameters of the examined HRES for a minimum unmet load.

Tab. 8 – Overview of the sizing parameters generated by HOMER Pro and iHOGA for minimum unmet load

Scenario	PV power (kW_p)		Wind power (kW)		Storage capacity (kWh)	
	HOMER	iHOGA	HOMER	iHOGA	HOMER	iHOGA
1	4.61	9.43	1.83	0.66	12.76	31.1
2	5.47	9.10	0.91	0.66	10.55	31.1
3	3.07	4.23	0.91	0.66	10.55	31.1
4	5.42	7.46	0.91	0.66	21.12	31.1
5	5.09	9.10	0.91	1.98	10.55	38.8
6	2.90	4.23	0.91	0.66	10.55	31.1
7	3.87	6.50	0.91	0.66	15.82	31.1
8	4.07	6.50	0.91	0.66	10.55	31.1
9	2.27	4.23	0.91	0.66	10.55	31.1

For all scenarios examined, the PV contribution generated by HOMER Pro is lower than the one generated by iHOGA, in contrast to simulations conducted for the optimum economic results (Tabs. 8 and 9). Moreover, HOMER Pro has selected lower battery banks' capacity to respond to load requirements. In 5 out of 9 scenarios (except for scenarios 1, 2, 5 and 7), HOMER Pro generated higher amounts of excess energy in comparison with iHOGA (Tab. 9). Tab. 9 presents the energy distribution generated by both HOMER Pro and iHOGA for the examined HRES for minimum unmet load.

Tab. 9 – Overview of the energy distribution generated by HOMER Pro and iHOGA for minimum unmet load

Scenario	Excess energy (kWh/year)		Energy delivered by PV array (kWh/year)		Energy delivered by WT array (kWh/year)	
	HOMER	iHOGA	HOMER	iHOGA	HOMER	iHOGA
1	5,577	6,143	5,738	8,738	3,604	1,775
2	6,163	6,575	6,811	8,437	3,079	2,439
3	4,269	2,859	3,820	3,917	4,154	3,198
4	5,832	5,182	7,490	7,792	2,145	1,747
5	6,389	12,522	7,034	9,486	3,079	7,235
6	4,448	3,602	4,015	4,404	4,154	3,156
7	3,716	4,143	5,373	6,775	2,145	1,747
8	4,997	4,873	5,653	6,773	3,079	2,410
9	3,589	3,302	3,156	4,403	4,154	3,155

The differences noted between the NPC values generated by the two (2) software (Tab. 10) follow the same tendency as the one noted during the simulations for optimum economic results. Discrepancies can be noted only for scenarios 2 and 5, under which the NPC values generated by iHOGA are higher than the ones generated by HOMER Pro. On the other hand, for all examined scenarios (except for scenario 5), the LCOE values generated by HOMER Pro are approximately 80% greater than the ones generated by iHOGA. Tab. 10 gives an overview of the simulation results generated by both HOMER Pro and iHOGA for the economic parameters of the examined HRES for minimum unmet load.

Tab. 10 – Overview of the LCOE and NPC generated by HOMER Pro and iHOGA for minimum unmet load

Scenario	NPC (€)		LCOE (€/kWh)	
	HOMER	iHOGA	HOMER	iHOGA
1	43,881	39,378	0.83	0.50
2	37,753	38,980	0.78	0.45
3	33,449	33,171	0.69	0.40
4	37,539	37,052	0.77	0.43
5	37,401	55,370	0.77	0.64
6	33,328	31,842	0.68	0.37
7	37,471	35,883	0.77	0.42
8	36,649	35,883	0.76	0.42
9	33,230	33,171	0.70	0.40

4. Comparison of simulation results with ESA software

For all scenarios examined, ESA opted to cover the load demand only with WTs (Tab. 11). The greater capacity of WTs generated by ESA increased the amount of energy delivered by WTs, compared to HOMER Pro and iHOGA. The storage capacities generated by ESA are higher than the relevant ones generated by HOMER Pro for all scenarios examined (Tab. 11). Tab. 11 presents a comparison of the simulation results for the sizing parameters generated by the three (3) simulation software for optimum economic results.

Tab. 11 – Comparison of the simulation results for the sizing parameters generated for optimum economic results

Scenario	Batteries capacity (kWh)			Energy delivered by WT array (kWh/year)		
	HOMER	iHOGA	ESA	HOMER	iHOGA	ESA
1	22.85	31.1	24	0	1,775	9,989
2	10.55	31.1	30	3,079	2,439	9,989
3	10.55	31.1	20	4,154	3,198	9,989
4	15.82	31.1	32	0	1,747	10,171
5	10.55	31.1	32	3,079	2,411	10,171
6	10.55	31.1	16	4,154	3,156	9,989
7	15.82	31.1	16	2,145	1,747	9,989
8	10.55	31.1	28	3,079	2,410	20,341
9	10.55	31.1	18	4,154	3,155	9,989

On the other hand, except for scenarios 4 and 5, iHOGA generated higher values for the storage than ESA. Except for scenario 8, the excess energy generated by ESA is lower than the one generated by HOMER Pro (Tab. 12). Finally, for all scenarios examined, iHOGA generated smaller amounts of excess energy than ESA. Tab. 12 depicts a comparison of the simulation results for the energy distribution generated by the three (3) simulation software for optimum economic results.

Tab. 12 – Comparison of the simulation results for the energy distribution generated for optimum economic results

Scenario	Unmet load (kWh/year)			Excess energy (kWh/year)		
	HOMER	iHOGA	ESA	HOMER	iHOGA	ESA
1	26.27	96.45	0	8,908	1,446	3,485
2	37.85	73.50	0	6,163	2,137	3,485
3	17.54	150.22	13.80	4,269	324	3,485
4	38.75	44.82	0	6,460	1,844	3,694
5	40.55	46.94	0	6,389	2,570	3,694
6	3.35	18.43	100.08	4,448	563	3,179
7	5.46	21.37	100.08	3,716	1,800	3,179
8	32.47	34.31	131.14	4,997	2,539	9,072
9	5.85	99.42	134.59	3,589	367	3,573

5. Conclusions

The current work provided an overview of the sensitivity and diversified dispatch strategy of two (2) commercial simulation tools by carrying out simulations with nine (9) scenarios of representative renewable energy potentials (solar and wind energy). The two (2) commercial software examined (HOMER and iHOGA) were also compared with the ESA Microgrid Simulator, developed by the SEALAB of the University of West Attica. Two (2) categories of optimization targets were selected (economic and power reliability), leading to different sets of results. The results, concerning mainly the contribution of each RES, the volume of excess energy generated and the relevant volume of unmet load were accumulated in dedicated Tables for further process and analysis. Subsequently, the results were evaluated based on the Power Reliability Indicators selected.

The results have shown discrepancies between the simulation tools, which are mainly attributed to the energy management plan applied in each one of them. Under the precondition of zero load rejection (100% autonomy), the configuration with the minimum LCOE was different between the tools, some proposing higher storage capacity or granting priority to wind power. The results were also impressive in respect of the direct contribution of solar and wind energy to the load demand and the amount of energy directed (attributed) to demand through the storage system. By comparing the proposed configurations for different renewable energy potential scenarios, their sensitivity was assessed, while producing the most cost-efficient HRES configurations on the basis of different dispatch strategies that each software package uses.

Long-term research and development efforts in the scientific field of HRES shall contribute to reduce the gap between emerging technologies and modeling capabilities, rendering possible simulations of increased accuracy. It would be vital to act in advance and incorporate DSM, load control, financial planning and forecasting techniques in the HRES operational control. The implied optimized planning could contribute to further reduction of the total system cost.

In addition, an attempt to model in depth emerging renewable energy technologies that haven't been currently explored in great detail, such as tidal, wave and hydrokinetic energy, shall be performed. Finally, an aspect of long-term work would include the extended simulation of HRES configurations integrating various forms of energy storage technologies.

6. Acknowledgments

The authors would like to thank Mr. Rodolfo Dufo-López of the University of Zaragoza for his valuable assistance during the simulations with iHOGA software.

7. References

Al-Falahi, M. D. A., Jayasinghe, S. D. G., Enshaei, H., 2012. A review on recent size optimization methodologies for stand-alone solar and wind hybrid renewable energy system. J. Energ. Convers. Manage., 143, 252-274.

Erdinc, O., Uzunoglu, M., 2012. Optimum design of hybrid renewable energy systems: Overview of different approaches. J. Renew. Sust. Energ. Rev. 16(3), 1412-1425.

Ganguly, P., Kalam, A., Zayegh, A., 2017. Design an Optimum Standalone Hybrid Renewable Energy System for a

Small Town at Portland, Victoria using iHOGA. *AUPEC 2017*, Melbourne, Australia. 19-22 November.

Guzmán Acuña, L., Vasquez Padilla, R., Santander Mercado, A. 2017. Measuring reliability of hybrid photovoltaic-wind energy systems: A new indicator. Renew. Energ., 106, 68-77.

HOMER Energy LLC, 2020. HOMER - Hybrid Renewable and Distributed Generation System Design Software. https://www.homerenergy.com/ (accessed 2020).

HOMER Microgrid News 2020. https://microgridnews.com (accessed 2020).

Saiprasad, N., Kalam, A., Zayegh, A., 2018. Comparative Study of Optimization of HRES using HOMER and iHOGA Software. J. Sci. Ind. Res., 77(12), 677-683.

Kavadias, K. A., 2016. Modern Solar Map of Greece with application in Hybrid Renewable Energy Systems. University of Ioannina, Greece (Available in Greek only).

Kavadias, K. A., 2012. Stand-Alone, Hybrid Systems, in: Sayigh, A. (Ed.), Comprehensive Renewable Energy. Elsevier B.V., Amsterdam, Netherlands, pp. 623–656. https://doi.org/10.1016/B978-0-0808-7872-0.00222-5

Kocher-Oberlehner, G., Peacock, A., 2014. Demand Management and Energy Storage. Heriot-Watt University, Edinburgh.

Kumar, A. P., 2016. Analysis of Hybrid Systems: Software tools. 2016 *2nd International Conference on Advances in Electrical, Electronics, Information, Communication and Bio-Informatics (AEEICB)*, pp. 327–330, Chennai, India, February. https://doi.org/10.1109/AEEICB.2016.7538302

NASA Prediction Of Worldwide Energy Resources 2020. https://power.larc.nasa.gov (accessed 2020).

PUAS (Piraeus University of Applied Sciences) 2017. Technology Innovation for the Local Scale, Optimum Integration of Battery Energy Storage, TILOS, Innovation Project LCE-08-2014: Local / Small Scale Storage. D7.1 The Validated Microgrid Simulator, Egaleo, Athens.

Singh, C., Bagchi, A. 2010. Reliability Analysis of Power Systems Incorporating Renewable Energy Sources. *16th National Power Systems Conference*, Hyderabad, India. 15-17 December.

Sinha, S., Chandel, S. S., 2014. Review of software tools for hybrid renewable energy systems. J. Renew. Sust. Energ. Rev. 33, 192-205.

Turcotte, D., Ross, M., Sheriffa, F. 2001. Photovoltaic hybrid system sizing and simulation tools: Status and needs. *PV Horizon: Workshop on Photovoltaic Hybrid Systems*, Montreal, Canada, 10 September.

University of Zaragoza 2020. iHOGA – Simulation and optimization of stand-alone and grid-connected hybrid renewable systems. iHOGA. http://ihoga.unizar.es/en/ (accessed 2020).

Solar Sorption System for Extraction of Water from Desert Air Operated in Real Environment

Tomáš Matuška, Vladimír Zmrhal, Bořivoj Šourek, Petr Wolf, Pavel Pelán

Czech Technical University, Prague (Czech Republic)

Abstract

A prototype of solar sorption system for extraction of water from air in hot and dry desert conditions has been designed and built. The system is fully autonomous, the energy for operation is supplied from solar photovoltaic, photovoltaic-thermal and photothermal collectors. Testing of the experimental system was performed in real environment conditions in the desert in central part of the United Arab Emirates. Despite the testing revealed significantly reduced performance of PV system, the potential of water production from the air has been proved. The average autonomous production 80 litres per day during the autumn season was monitored.

Keywords: sorption, photovoltaics, solar thermal

1. Introduction

Extraction of the water from air and its mineralization can be applied as a source of potable water in specific conditions. There is number of methods of water extraction from the air (Wahlgren, 2001), but only two has found practical applications so far: direct condensation of humidity from air and application of sorption process to concentrate humidity. While direct condensation units cannot harvest significant amount of water in case of extremely dry deserts, desiccants are applied in the process to increase the humidity of the processed air.

Water harvesting system based on the adsorption process has been developed. Sorption air handling unit has been tested in laboratory to validate mathematical model for performance simulations (Matuška et al., 2018). Model of the unit has been finally used to design the energy components to power the whole system. To operate the unit autonomously in the desert environment, only renewable energy sources available in the desert were considered. Finally, the experimental prototype has been built to perform testing the autonomous operation in desert climate (United Arab Emirates).

2. Autonomous water extraction system

An experimental system for extraction of water from ambient air consists of number of components, each with a specific function (see Figure 1). The sorption air handling unit uses rotary desiccant wheel with silicagel surface to adsorb the water molecules from ambient air flowrate 2000 m^3/h. Dehumidified air flows back to ambient environment. Ambient air with significantly lower flowrate 1000 m^3/h is used for regeneration of desiccant. Before entering rotary heat exchanger, the air flow is heated to high temperature up to 80 °C. Water molecules are released from the silicagel surface into regeneration air flow. Thus, regeneration air is humidified to higher humidity ratio and cooled down by the physical process (heat recovery, humidification). Humid air finally enters the cooler with low surface temperature (5 °C) and water vapour easily condenses as liquid water.

The whole system was proposed for autonomous operation. Heat recovery and use of local renewable energy were in focus of the design from the beginning. The sorption unit integrates the internal chiller (heat pump) based on the refrigerant R134a in order to achieve high temperatures up to 80 °C for regeneration at condenser side. Variable speed compressor allows a control of the unit at variable conditions and to reduce power input of the unit when needed. The heat from cooling at evaporator is recovered for preheating of the regeneration air. To further reduce the power consumption of the unit additional heat exchangers are applied: a) liquid cooler for precooling of regeneration air after desiccant wheel and b) additional heater to achieve high temperatures of regeneration air

doi:10.18086/eurosun.2020.12.05 Available at http://proceedings.ises.org

at the entrance to desiccant wheel. The additional cooler is connected to cold water storage (2 x 1000 m^3). Solar system with unglazed photovoltaic-thermal collectors (77 m^2) has been designed as a source of renewable cooling energy using the night radiative cooling (towards desert clear sky). The additional heater is connected to hot water storage (1 x 1000 m^3) as a part of solar thermal system based on vacuum flat-plate collectors (22 m^2). These components are complemented with photovoltaic modules (20 m^2) and LiFePO4 battery pack (nominal capacity 33,6 kWh) to balance the electric production and load. The peak power of photovoltaic system (PVT collectors, PV modules) is 16,8 kW_p. Designed water production at autonomous operation of the system is about 100 l/day in extreme desert conditions in yearly average according to simulations (Matuska et al., 2018). Simplified scheme of the system is shown in Figure 1 with indicated temperature level within the process.

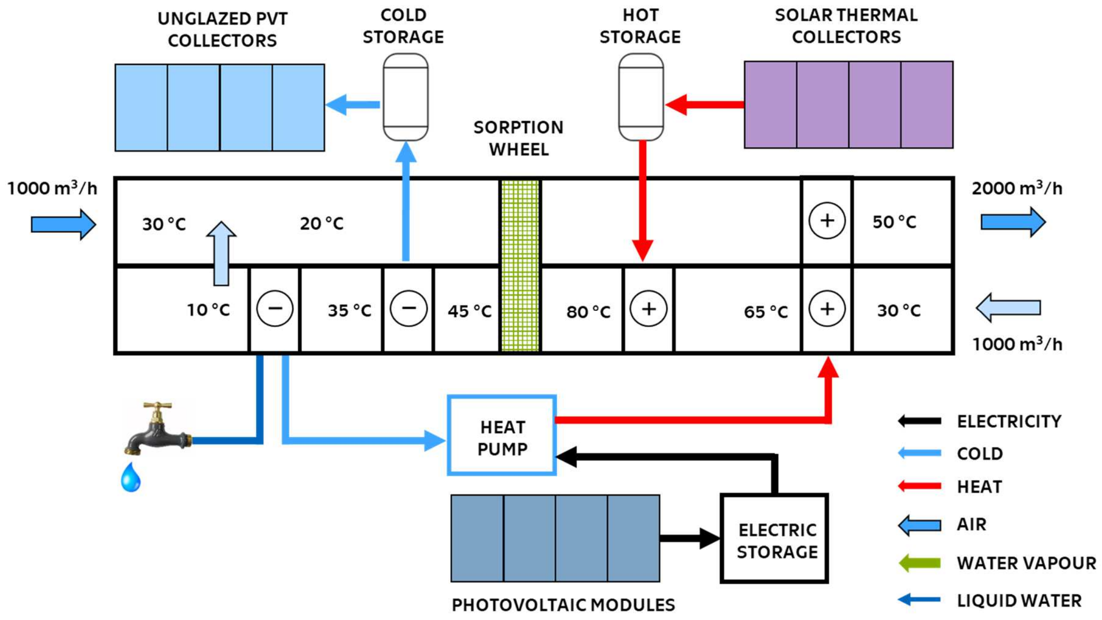

Fig. 1: Scheme of autonomous system for water extraction from desert air

The system has been designed and built as modular with two containers (see Figure 2): production container and energy container coupled with solar roof (solar collectors and PV modules) to be built above both containers. Production container contains the sorption air handling unit, demi-water storage and mineralization unit. It can be operated as potable water generator alone when connected to external electrical grid (3 x 63 A). The energy container together with solar roof is the energy source for production container. It includes battery pack, water storage tanks and hydraulic circuits. Plug and play electric and hydraulic connectors have been used to interconnect the containers.

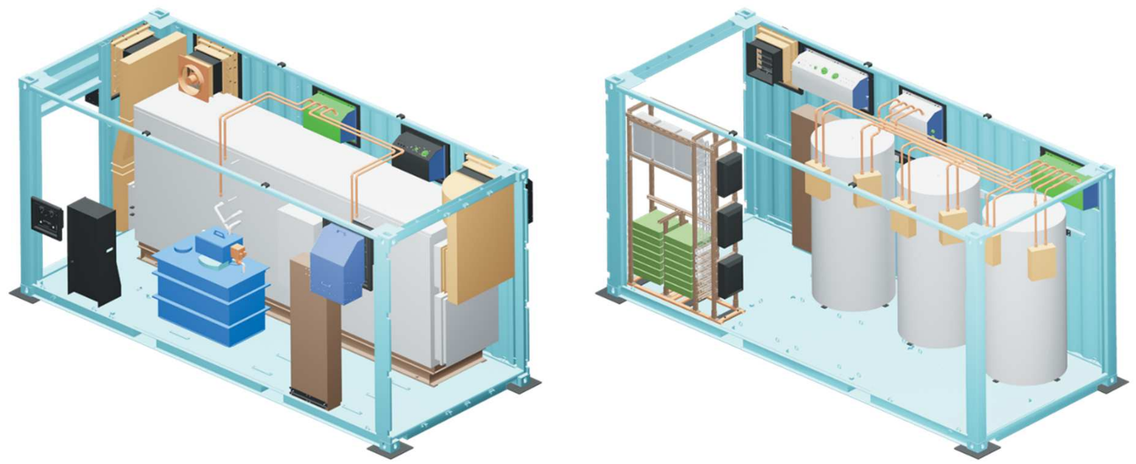

Fig. 2: Water extraction system: production container (left), energy container (right)

Both containers are conditioned by ventilation unit (mainly for night-time) and air-conditioning unit (during sunny day-time) to maintain interior temperature below 35 °C. Containers were equipped with additional internal thermal insulation to reduce the excess cooling load. Container housing for the system has been designed for the shipment of the system to the place of testing in the real environment (United Arab Emirates). Sea transport requires tight, robust and therefore certified containers. The whole system was fitted into 20” containers with floor plan 2,4 x 6,0 m and height 2,9 m. Solar roof demounted to elements (support construction, collectors, modules) was transported inside the containers.

3. Installation and testing

The experimental system has been installed and tested at camel farm near Sweihan (about 100 km from the coast at interior part of United Arab Emirates) with desert conditions to get knowledge on system operation in real environment. Solar roof with PV modules, solar thermal collectors and unglazed PVT collectors has been erected above containers (see Figure 3). Electric and piping connections have been prepared with use of prefabricated components. Despite installation problems due to extreme summer (July-August) conditions in desert and malfunction of one inverter (replaced) the system has been finally commissioned and put to permanent operation in autumn 2019.

Monitoring system focused on sorption process (temperature / humidity of processed and regeneration air), energy performance (PV, PVT and solar thermal system production, system power load), water production at given conditions and reliability of operation (container indoor temperatures, sand filtering).

Fig. 3: Autonomous water extraction system in the front of farm (Sweihan, UAE)

4. Results

The presented results cover two weeks in October 2019 and show the operational characteristics of the experimental system. The main objective of the testing was to gain knowledge on performance potential of individual sub-systems in real operation.

4.1. PV system efficiency

Nominal efficiency of PV modules used in the system is 17,2 %, efficiency of unglazed PVT collectors is 16,9 % (both related to gross area). Daily energy production values and irradiation levels have been evaluated. Daily efficiency of electricity production by whole PV field is between 12 and 14 %. When system losses are included (inverter losses, battery charging-discharging cycles) the total efficiency of PV system results between 10 and 11 %. Low efficiency of PV system is caused by high operation temperature of PV/PVT modules and by electric losses of inverter (both considered in planning phase), but also increased electric losses of battery storage when operated above 25 °C and significant dust accumulation on solar roof (not considered in realistic way in planning phase). These results will be used for further development and design of the system.

4.2. System power load

System power load is given mainly by power input of variable speed compressor of the chiller and fans integrated in sorption air handling unit, devices for air-conditioning of the containers and fans for ventilation of containers. In dependence on operation conditions the load ranges between 5 and 11 kW during operation period of the system. Outside the operation period the power load is low between hundreds of watts during night-time (ventilation, standby) and 2,5 kW during the day (air-conditioning units). Figure 4 shows the PV power production and system power load within two evaluated weeks.

Different control strategies were tested during the testing phase. Basic strategy is to start the system before sun-dawn due to favorable conditions (humidity, lower cooling demand) with minimum power input and to use the residual energy in battery pack from previous day until state of charge is 15 %. Then the controller stops the system and waits until PV system charges the battery pack to 30 %. After this condition is met, system is started again, but power input of the compressor is controlled in a way that state of charge is maintained at value 30 %. The sorption unit is stopped in the afternoon and PV system charges the battery back to state of charge 80 to 100 % to store the energy for next morning. The graph in Figure 4 shows peaks in power load caused by compressor protection when operated at minimum speed. The compressor rotations are repeatably increased time to time to provide the sufficient oil distribution for compressor lubrication.

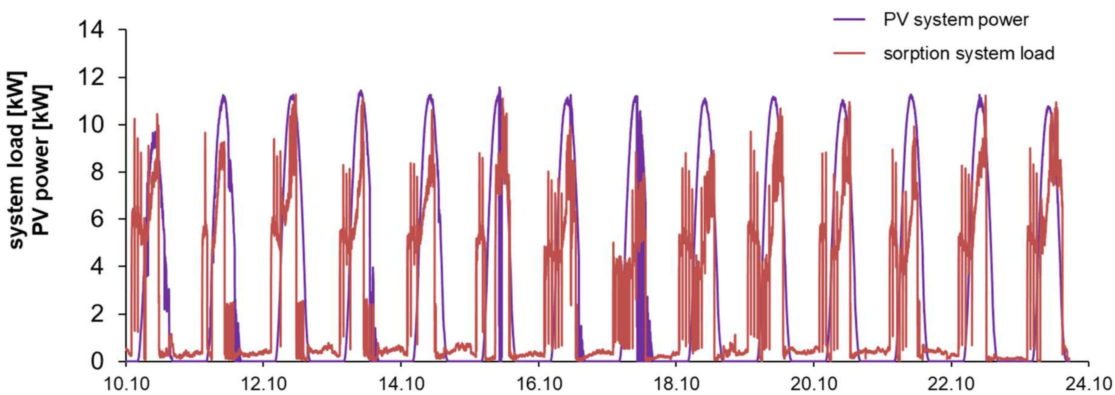

Fig. 4: PV power production and electric load of the system

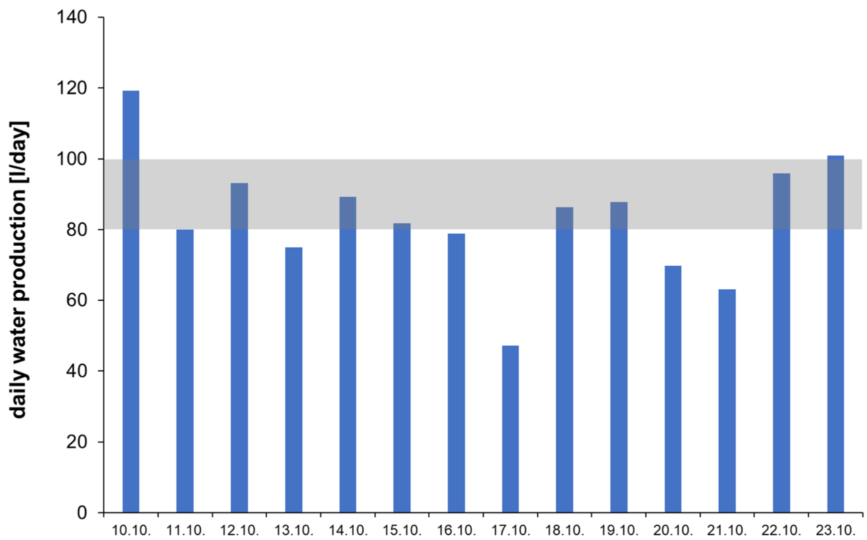

Fig. 5: Production of water in autumn season with a band of expected production

4.3. Water production

The water production (see Figure 5) of the system oscillates between 50 l/day (extreme cloudy day) and 120 l/day (extreme battery state of charge) with average around 80 litres of water per day which corresponds to autumn production potential. Water production is dependent on climate conditions and available energy (precooling from unglazed PVT system, heat for regeneration from solar thermal system, electricity from PV system).

5. Conclusion

The solar sorption system for extraction of water from air has proved functionality and potential to produce the water in desert conditions about 80 litres per day which corresponds to autumn conditions (energy, humidity). The system is fully autonomous with use of local renewable energy, no external energy was used neither for installation/commissioning or operation of the system.

The water production is heavily dependent on available energy. PV system efficiency reduced by high operation temperatures, battery losses and dust accumulation has limited the system performance. The experience from the experiments performed during testing and gained knowledge of system real performance will be used in further development of the system.

6. References

Wahlgren, R.V., 2001. Atmospheric water vapour processor designs for potable water production: a review. Water Resources 35, 1–22.

Matuska, T., Zmrhal, V., Sourek, B., 2018. Development of Solar Assisted Sorption Unit for Extraction of Water from Ambient Air in the Desert Climate. Proceedings of the ISES Eurosun 2018 Conference, Rapperswil (Switzerland), 659-664, doi: 10.18086/eurosun2018.04.22.

Solar Organic Rankine Cycle coupled with Reverse Osmosis and mebrane distillation towards minimizing brine discharge

Erika Ntavou[1], Marina Micari[2], Dimitris Manolakos[1], George Kosmadakis[3] and Chrysanthos Golonis[1]

[1] Agricultural University of Athens, Athens (Greece)

[2] Deutsches Zentrum für Luft- und Raumfahrt (German Aerospace Center), Stuttgart (Germany)

[3] Ricreation IKE, Technological Park "Lefkippos", Athens (Greece)

Abstract

The current research work is focused on the investigation, optimization and identification of key design parameters of a solar-Organic Rankine Cycle (ORC) power generation system coupled with Reverse Osmosis (RO) and Membrane Distillation (MD) desalination units for fresh water production. The core idea is to feed RO and MD units by exploiting both electricity generated by the ORC and the heat dissipated in the ORC condenser respectively. Electricity comes from the direct conversion of heat to power through ORC and is used to drive the system pumps, while heat for MD corresponds to that dissipated during condensation process (heat rejection of the power cycle). By combining RO with MD an increased water recovery ratio from both desalination processes can be achieved, resulting into reduction of the environmentally harmful brine. Further exploitation of the high concentrate is possible to extract sodium chloride crystals. The proposed system can be flexibly combined with other thermal sources (e.g. excess heat from industrial processes) and it is applicable for feed water treatment of different salinities (brackish, seawater etc.). Vacuum tube solar collectors operating at temperature in the order of 130 °C have been considered in the calculations. The condensation temperature where heat is supplied to MD is in the order of 90 °C, Some 90 kWth of heat are rejected in the full load operation, while net power generation from the ORC is about 3 kW with a thermal efficiency slightly above 3.5 %.

Keywords: solar Organic Rankine Cycle, RO desalination, Membrane Distillation, Zero Brine Discharge

1. Introduction

The rapid recent increase in population has created the necessity of intensive water consumption in the human environment. Water desalination appears to be an appropriate technology to cover this increased need. In recent decades, water production has largely shifted to the reverse osmosis (RO) technology, because of its lower energy consumption compared to other desalination technologies (i.e. thermal). The lower consumption has been achieved through the application of energy recovery systems and thanks to the evolution of membranes technology. However, desalination remains an energy-cost intensive water treatment process with serious environmental impacts. In addition to the contribution of desalination to CO_2 emissions, significant environmental burden is incurred due to the rejection of the high concentration of saline solution (brine) as a by-product of the process resulting in soil, aquifer and marine ecosystems pollution. Any effort to mitigate CO_2 and brine disposal environmental effects is of significance towards improving desalination environmental profile and constitutes a complex techno-economical challenge.

Normally, the brine from seawater desalination units using open ocean intakes has the same physical characteristics as the seawater feeding the system since no chemicals are added in the pre-treatment of the RO system, thus increase or decrease in salinity would not result in a severe environmental impact. However, dense concentrate disposal may lead to increased stratification reducing vertical mixing, thus reducing the dissolved oxygen level in water or at the bottom of the ocean in the area of the discharge, which may result in ecological implications (Mickley 2006). Some key environmental issues and considerations linked to the concentrate disposal to surface waters are the increase of salinity over the tolerance barrier of the marine flora and fauna and the discharge of nutrients that trigger a change in the area of the discharge, the ion-imbalance toxicity caused by the mixture of incompatible composition of the desalination plant concentrate and receiving waters and the disturbance in seabed from outfall installation (Voutchkov 2011).

Therefore, a serious concern is growing around the environmental impact of desalination systems and especially the

doi:10.18086/eurosun.2020.12.06 Available at http://proceedings.ises.org

impact on marine life close to the plant intakes and outfalls. Several countries are already discussing strict regulations on seawater desalination concentrate discharge, including zero discharge regulations. As Navar et al. (2019) point out, the interest of policy makers and the industry in understanding the technical and economic implications of zero brine discharge regulations is growing.

At the same time, the CO_2 footprint of the RO plants operation when using conventional energy sources is high. Heihsel et al. (2019) studied the 95% of Australia's RO plants' operation for a decade (assuming that all are using fossil fuels) and pointed out that in both construction and operation, the role of the electricity sector is critical for carbon emissions, each contributing in 69% during the zenith of the construction phase and 96% during the operating phase to the entire emissions, with a total estimation for 2015 at 1193 kt CO_2e.

Recently, much research has been done on seawater RO zero liquid discharge desalination. Tufa et al. (2015) have investigated an innovative approach combining Direct Contact Membrane Distillation (DCMD) and Reverse Electrodialysis (RE), for water and energy production from RO concentrate, thus implementing the concept of low energy and Near-Zero Liquid Discharge in seawater desalination, proving that the DCMD operated on 1 M NaCl RO brine fed at 40–50 °C resulted in a volume reduction factor up to 83.6%. Davis (2006), studied a zero liquid discharge ZLD process for seawater reverse osmosis using electrodialysis (ED) to reduce the salinity of the concentrate from the RO, so that the low salinity reject stream can be recycled to the RO to improve freshwater while producing salable sodium chloride (NaCl), magnesium hydroxide ($Mg(OH)_2$), and bromine (Br_2) from the brine. The results of this study indicated that the use of electrodialysis can reduce the potential detrimental impact of discharging the reject stream to the ocean and if fully implemented, the process could produce high-purity NaCl, Mg $(OH)_2$, Br_2, and mixed dry salts with zero liquid discharge. Al-Obaidani et al. (2015) studied the integration of conventional pressure-driven membranes with the innovative units of membrane contactors such as membrane distillation (MD)/crystallization for concentrate treatment and zero liquid discharge achievement and revealed that the pressure-driven membrane operations were very sensitive to the feed concentration and the cost of electricity consumption, while MD processes were not.

However, the tackling of the high energy and cost of the RO process requires a much more thorough study according to the state of the art. The technology of the Organic Rankine Cycle (ORC) used to convert low grade heat (less than 150 ^{o}C) to electricity, with high conversion efficiency and maturity, in combination to a RO unit has recently started to be investigated. Nevertheless, as the state-of-the-art indicates, there is no research combining the ORC and RO technology towards a near zero liquid discharge.

The current research aims to study, optimize and identify key design parameters of a solar-ORC system combined with RO and MD to maximize the water recovery ratio of the saline feed water. Thus, by exploiting the renewable solar energy, a high value natural resource, water, is produced with a limited environmental footprint for both CO_2 and brine.

2. System description

The current work is the evolution of an already theoretical-experimental work realized within the frame of the research project "Two-stage RO-Rankine", partly funded by the Greek General Secretary of Research and Technology (GSRT), where an autonomous two-stage solar ORC system for RO desalination was investigated. Ntavou et al. (2016 and 2017) have developed and experimentally evaluated a small-scale two-stage ORC engine operating at low temperature, electrically feeding a multi-skid reverse osmosis unit operating at fluctuating power input (see fig. 1). More specifically, a two-stage solar ORC operating with 100 kW_{th} heat input and at around 100-130 °C produced a maximum of ~10 kW of electricity from both stages ($P_{ex,1}$ +$P_{ex,2}$), which operated three identical seawater RO desalination units connected in parallel, of a maximum production of 2,1m^3/h. The RO units were operating with a recovery of 38% and the integrated system was tested for several operation points in different heat input, thus different power input for the RO. The results revealed an efficient operation but the "free" concentrate discharge of the system is still an issue to take into account. Therefore, the system has been further improved by including MD technology that can offer more distilled water by exploiting the heat dissipating from ORC.

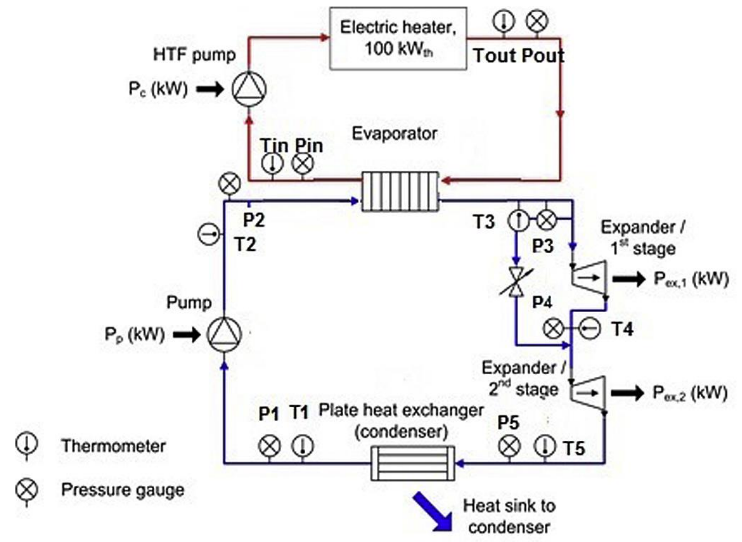

Fig. 1: The two-stage ORC unit

The investigated integrated system layout is depicted in Figure 2 below and is briefly described as follows. Heat is produced from a ~100kW$_{th}$ solar collectors' field. Vacuum tube solar collectors are chosen for this task due to their favorable efficiency in elevated ranges of operation temperature (130-150 ºC). This heat is supplied to the evaporator of the ORC engine and leads to the evaporation of the working fluid (refrigerant) at a slightly lower temperature. The produced superheated vapor at the outlet of the evaporator is driven to the ORC expander (volumetric machine, scroll type in this case), producing electricity that is supplied to ORC feed pump, RO and MD pumps. The RO unit is fed by seawater and produces two water streams: the low salinity (permeate) water and the rejected high salinity (brine) solution which is then directed to the MD unit in order to recover additional fresh water. Thus, in this way, the entire process water recovery ratio can be enhanced.

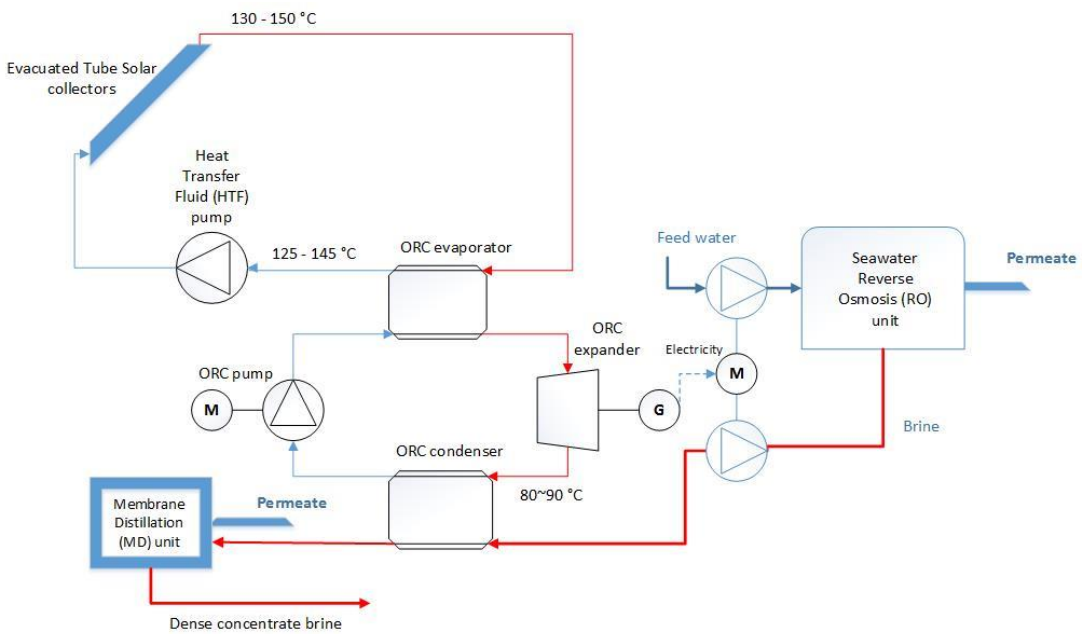

Fig. 2: The integrated solar ORC for RO-MD desalination

The RO unit is equipped with an energy recovery system in order to bring down specific electricity consumption, in the order of ~4-5 kWh/m^3. The heat required for the MD operation is extracted by the condensation process of the ORC at an appropriate temperature range of 80-90°C. This allows the MD unit to operate with hot temperatures between 70 and 80°C, which ensure a high driving force for the vapor flux through the membrane when the cold temperature is around 20°C.

3. System's simulation

Different modelling tools are developed to simulate and optimize the process and technologies involved. An EES steady state model is implemented to simulate the solar collectors and ORC technologies and validated with experimental results, derived from the Two-Stage-Solar ORC. RO is simulated using ROSA software and MD with a multi-hierarchy model, implemented in Python and derived from the work of Micari et al. (2020).

3.1 The solar collectors

For the case under investigation, the Thermomax DF-100, 3m^2 collector's model is considered, with glycol as working fluid. In Table 1, the specific characteristcs of this collector are presented.

Tab. 1: Solar collectors field characteristics

Product	Thermomax collector DF-100 3m^2
Absorber area, A_{abs} (m^2)	3.020
η_o (-)	0.832
a_{c1} (W/m^{2}K)	1.14
a_{c2} (W/m^{2}K^2)	0.0144
Inclination (°)	35
No of collectors, N_c	50
Outlet temperature, $T_{c,out}$ (°C)	133
Inlet temperature, $T_{c,in}$ (°C)	128

To investigate the performance of the vacuum tube solar collector, the definition of the incidence angle modifier (IAM) is crucial to calculate the collector's efficiency and heat generation with more accuracy. In the specification sheet of the specific model, K_b (θ_long), K_b (θ_trans) and K_d (θ) are provided (see table 2).

Tab. 2: Thermomax DF-100 3m^2 IAM

	0°	10°	20°	30°	40°	50°	60°
K_b (θ_trans)	1.00	1.01	1.02	1.03	1.01	0.94	0.80
K_b (θ_long)	1.00	1.00	0.99	0.98	0.96	0.92	0.86
K_d (θ)	0.88						

Accordingly, the collector output is given by the following equation:

$$\dot{q}_{col} = \eta_0 \cdot (K_b(\theta) \cdot G_{bT} + K_d(\theta) \cdot G_d) - a_{c1} \cdot (T_m - T_e) - a_{c2} \cdot (T_m - T_e)^2 \quad [\mathrm{W/m^2}] \quad \text{(eq. 1)}$$

and the total heat produced by the collectors' $\dot{Q}_{col}$array is:

$$\dot{Q}_{col} = N_c \cdot A_{abs} \cdot \frac{\dot{q}_{col}}{1000} \quad [\mathrm{kW}] \quad \text{(eq. 2)}$$

The efficiency η_{col} of the collectors' array can be expressed as:

$$\eta_{\mathrm{col}} = \frac{\dot{q}_{\mathrm{col}}}{G_{\mathrm{tot}}} \cdot 100 \quad [\%] \quad \text{(eq. 3)}$$

G_{tot} [W/m^2] is the total solar irradiance on the collectors' surface.

The mass flow rate of the glycol in the collectors' circuit can then be calculated as:

$$\dot{m}_{\mathrm{col}} = \frac{\dot{Q}_{\mathrm{col}}}{C_{\mathrm{p}} \cdot (T_{c,out} - T_{c,in})} \quad [\mathrm{kg/s}] \quad \text{(eq. 4)}$$

3.2 The ORC engine

As already mentioned, a two-stage ORC system with two scroll expanders in series has already been investigated and the results have been already published. In two-stage operation, however, the organic fluid having expanded further in the second expander, has used more of the available kWth and its saturation temperature drops to around 30°C at the condenser. However, this temperature is very low for the efficient MD operation. Thus, for the ORC only the high-pressure stage operation is considered. Consequently, the new system configuration lacks the power produced by the low-pressure stage on one hand, but the condensation temperature raises to the order of 90 °C that is ideal for the MD efficient operation.

The ORC uses R-245fa as working fluid due to its favorable properties in the selected operation temperature. The cycle is presented at the design conditions in the P- h chart of Fig. 5, which shows the power consumed by the pump (W_p), the power produced from the expander (W_{exp}), the evaporation heat (Q_{ev}) provided by the collectors and the condensation rejected heat (Q_{cond}) which is the driving force for the MD operation. The cycle is considered to operate mostly at constant evaporation-condensation temperature. This can be realized to a considerable extent by regulating appropriately the mass flow rate of the ORC making use of a pump inverter.

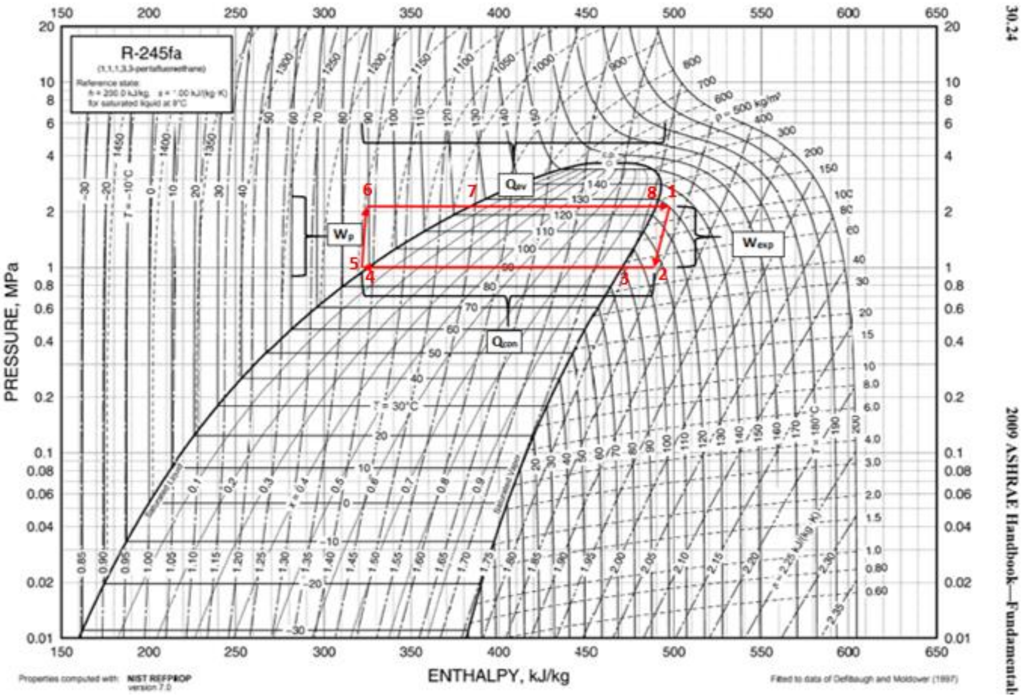

Fig. 3: The ORC cycle on R-245fa P-h chart at design conditions

The states of the thermodynamic cycle of Fig. 5 are illustrated in Table 3.

Tab. 3: States of the cycle

State	S1 (SH vapor)	S2 (SH vapor)	S3 (Sat vapor)	S4 (Sat. liquid)
Temperature (ºC|)	129.8	102.7	89.61	89.61
State	S5 (SC liquid)	S6 (SC liquid)	S7 (Sat liquid)	S8 (Sat. vapor)
Temperature (ºC|)	86.61	87.72	126.8	126.8

SC: sub-cooling SH: Super-heating

In order to evaluate the expander's operation, a polynomial has been derived from the experimental data. More specifically, the isentropic efficiency of the expander is expressed with the following polynomial as a function of pressure ratio (PR) and filling factor (FF) and it is generated by the experimental data derived during testing of the high-pressure expander:

$$\eta_{\exp} = a_0 + a_1 \cdot PR + a_2 \cdot PR^2 + a_3 \cdot FF + a_4 \cdot PR \cdot FF + a_5 \cdot PR \cdot FF^2 + a_6 \cdot PR^2 \cdot FF + a_7 \cdot PR^2 \cdot FF^2 \quad [-] \qquad \text{(eq. 5)}$$

To formulate it, 166 experimental data were processed with a convergence coefficient of R^2=98.26 %. The expression of the isentropic efficiency is valid for PR values in the range between 1.5 and 3.0, and for FF from 1.16 to 9.6. Table 4, summarizes the values of polynomial's factors from a_0 to a_7.

Tab. 4: Expander's isentropic efficiency polynomial factor

a_0	a_1	a_2	a_3
-4.68763263	5.30488508	-1.27035570	1.10352750
a_4	a_5	a_6	a_7
-1.35711599	0.0345269529	0.339770213	-0.0122545150

The power $\dot{W}_{exp}$ generated by the expander is:

$$\dot{W}_{exp} = \eta_{\text{exp}} \cdot \dot{m}_{\text{p}} \cdot (h_1 - h_{2,\text{is}}) \quad \text{[kW]} \quad \text{(eq. 6)}$$

h_1 and $h_{2,\text{is}}$ [kJ/kg] represent the enthalpies at the inlet and the isentropic outlet of the expander.

Concerining the power absorbed by the ORC feed pump $\dot{W}_{pump}$, it is defined as:

$$\dot{W}_{pump} = \frac{\dot{m}_{\text{p}} \cdot (h_{6,is} - h_5)}{\eta_{pump}} \quad \text{[kW]} \quad \text{(eq. 7)}$$

where η_{pump} is the isentropic efficiecny of the ORC feed pump and $h_{6,is}, h_5$[kJ/kg] are the isentropic enthalpy at the outlet and the enthalpy at the inlet of the pump.

The mass flow rate in the ORC engine circuit $\dot{m}_{\text{p}}$ can be calculated by assuming that the evaporator losses are negligible and thus, the total heat gain of the collectors is transfereed to the ORC engine ($\dot{Q}_{orc,ev} = \dot{Q}_{col}$):

$$\dot{m}_{\text{p}} = \frac{\dot{Q}_{\text{orc,ev}}}{h_1 - h_6} \quad \text{[kg/s]} \quad \text{(eq. 8)}$$

The net power produced by the ORC is given by the eqauation below:

$$\dot{W}_{net} = \dot{W}_{exp} - \dot{W}_{pump} \quad \text{[kW]} \quad \text{(eq. 9)}$$

Finally the reject heat $\dot{Q}_{rej}$ that is to drive the MD unit is expressed as:

$$\dot{Q}_{rej} = \dot{m}_{\text{p}} \cdot (h_2 - h_5) \quad \text{[kW]} \quad \text{(eq. 10)}$$

To have a more realistic approach for the real heat supply tot the MD the above expreassion results are combined with the exparimetal values at the same conditions. This comparison indicates a further 10% reduction in the calculateed values, reflecting to the heat losses in the ORC circuit.

4. Results and discussion

Several simulation tests have been conducted for the solar collectors' operation. In Figure 4, the solar irradiance on the inclined collectors' surface and the heat gain are presented for a representative summer day (2nd of July 2019). For that, real meteorological data provided by the National Observatory of Athens were used. The whole system behavior is analyzed for his day.

4.1 Solar collectors

As shown in Fig.4, the solar collectors produce heat for ten hours (from 6:00 to 16:00 UTC), reaching a pick of around 85 kWth. This heat is provided to the ORC engine. The solar irradiance shows a maximum value of the order of 1000 W/m^2

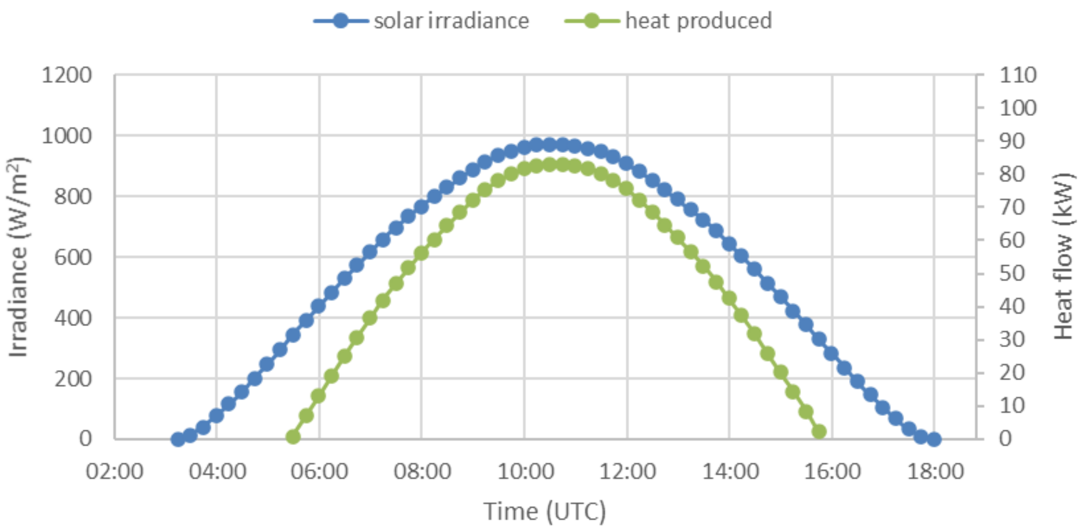

Fig. 4: Solar collectors' heat gain and solar irradiance variation

The collectors' efficiency is presented in Fig. 5, where the glycol mass flow rate in the collectors' circuit is also shown. The maximum efficiency of the solar collectors' is about 55 % and the glycol mass flow rate in the order of 4 kg/s (~14.5 m^3/h) that also constitutes the nominal flow rate of the collectors' circuit pump.

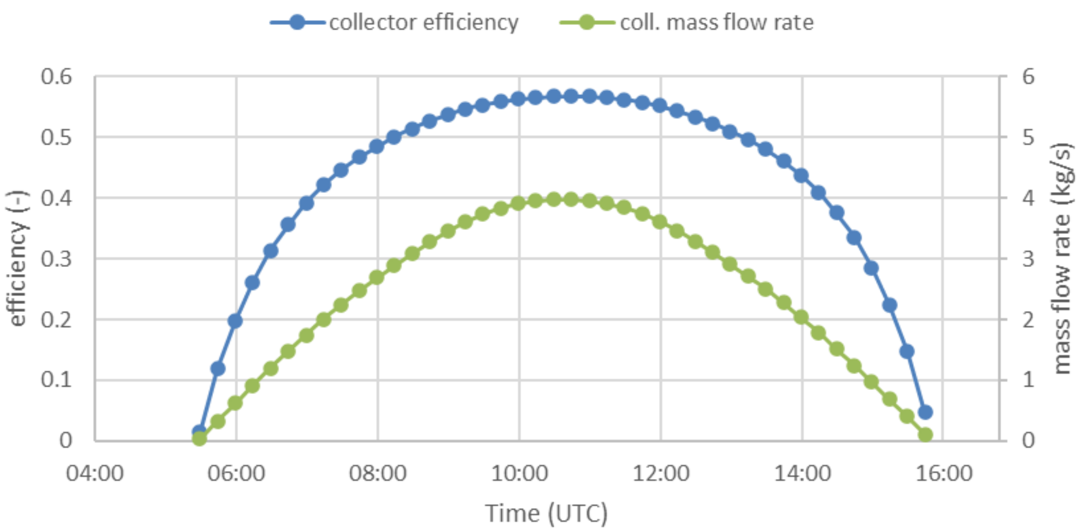

Fig. 5: Solar collectors' efficiency and mass flow rate

4.2 ORC engine

For the ORC cycle of Fig. 3, the pressure ratio is 2.2 (Inlet pressure 22 bar, Outlet pressure 10 bar). The filling factor depends on the mass flow rate of the working fluid, meaning that it is finally a function of the rotation speed. At the design point the filling factor is 1.16 corresponding to a rotational speed of the expander of ~3200 RPM (the working fluid mass flow rate is about 0.5 kg/s in this condition). In the calculations, a feed pump of isentropic efficieny equal to 70% is considered. The isenrropic efficiency of the expander is around 58 % while the thermal efficiecny of the cycle is 3.7 %. Figure 6 shows the variation of the power produced by the expander, the power absorbed by the pump and the net power for the simulation day.

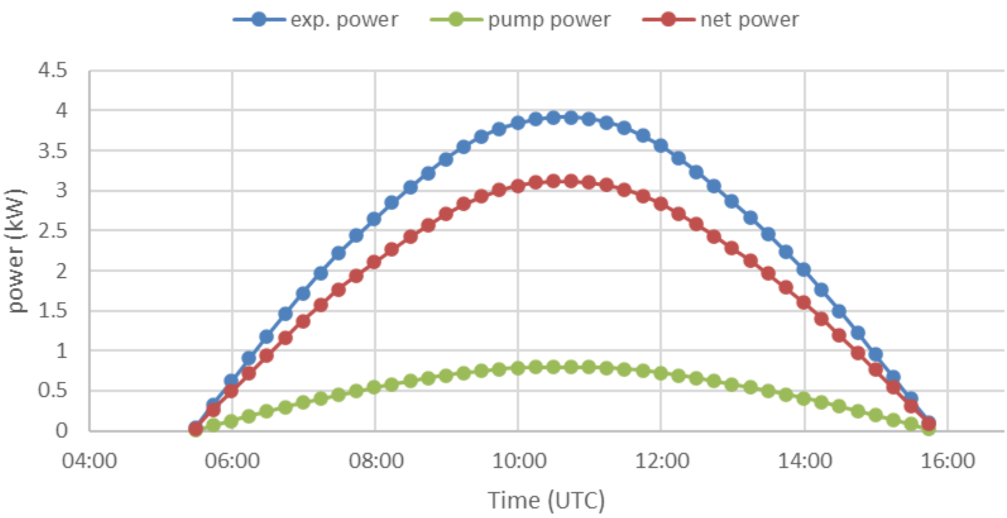

Fig. 6: Expander's, pump's and net ORC power production

While the expander provides a maximum power in the order of 4 kW, the pump absorbs around 0.8 kW and finally the net power avaliable does not exceed the 3.3 kW.

The heat supply to the evaporator, the heat rejected by the condenser and the variation of the mass flow rate of the working fluid are presented in Fig. 7. The heat rejected is supplied to the MD unit. According to Table 3, this heat is mostly available at 89.61 °C since this is the latent heat released by condensation for the phase change process. De-superheating represents no more that 10 % of the global condensation heat.

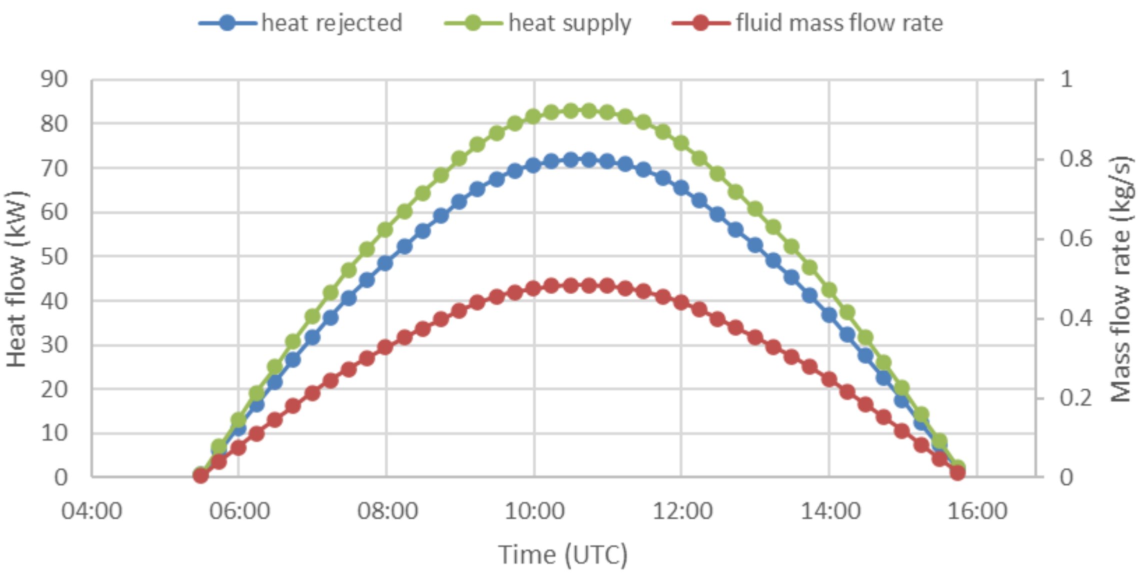

Fig. 7: ORC heat supply, heat rejected and mass flow rate variation

Thus, the MD is designed to operate with heat flow in the order of 70 kWth at a temperature of ~85 °C (considering the temperature difference in the condenser sides).

4.3 The RO unit

The simulation of the RO unit is based on the experimental testing of the three identical sub-units used in the previous project of Ntavou et al. (2016 and 2017). The three units are now replaced by one RO unit, the recovery is 35% and the specific energy consumption 4.3 kWh/m^3, a value that has been experimentally extracted. In Fig. 8, the fresh water and brine generated by the RO for all the power input range from the ORC are presented.

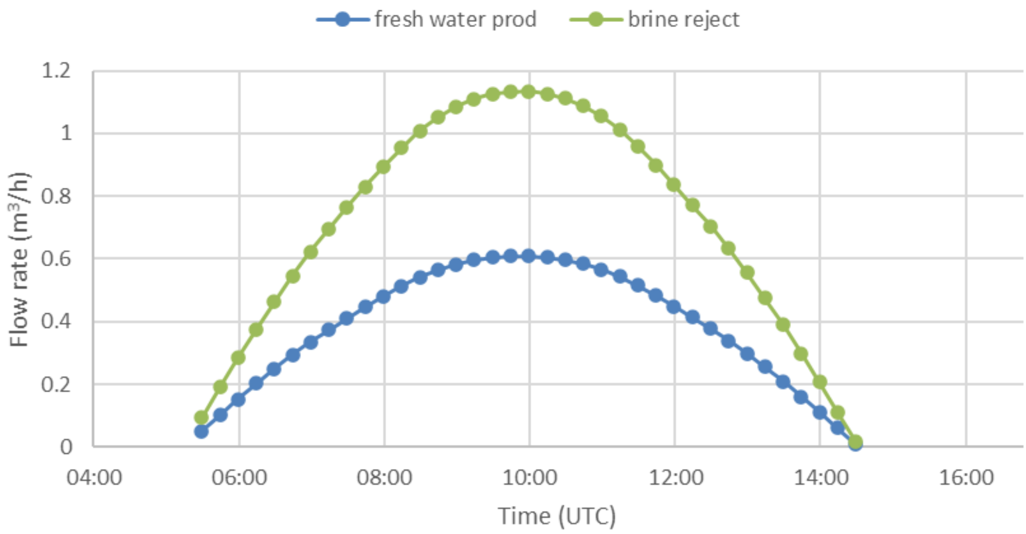

Fig. 8 Fresh water and brine production of the RO unit

The maximum brine flow rate produced by the RO reaches a value of around 1.2 m^3/h. The total concentration of the brine stream is around 65.000 ppm as resulted from the ROSA simulation tool and the expander outlet temperature around 89°C.

4.4 The MD unit

The MD unit is designed based on the brine flow rate generated by the RO unit. This consists of a number of modules in series, each given by 6 membrane sheets with length of 3 m wounded together in a spiral wound arrangement. Each module is designed for a feed flow rate of 1.5 m^3/h, thus, for the present system, only one branch of MD modules in series is required. The feed channel is kept at a temperature of 80ºC, whereas the permeate channel is at ambient temperature (20ºC). The system, with 4 modules in series, is designed to achieve a maximum recovery of around 20%, corresponding to a concentration of the rejected brine of 80,000 ppm. The specific thermal consumption is 700 kWh/m^3, thus, the permeate production varies depending on the heat availability. In Fig. 9, the permeate production of the MD is presented for the specific day of operation of the integrated system.

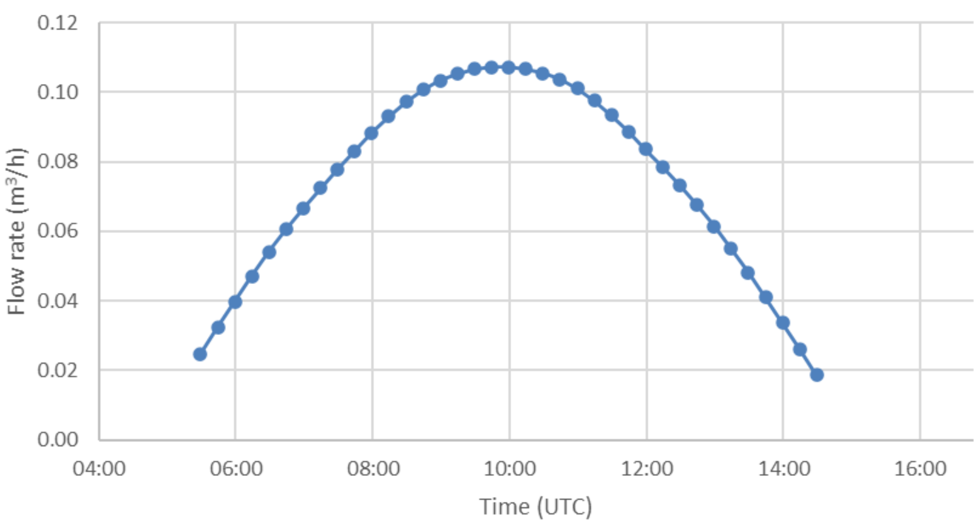

Fig. 9: Contribution on the permeate production from the MD unit

As resulted from the MD operation, the maximum contribution of the MD to the permeate production is around 110L/h. That means that the contribution of the MD system to the RO operation is low, however important. Nevertheless, the goal towards the NZL discharge seems to not be met under the specific conditions and design of the system. The reason for this is that the MD module needs high amounts of available heat in order to operate efficiently, whereas the heat given by the ORC condensation was able to cover only a limited increase in concentration. In addition, in order to produce thermal energy at a temperature suitable to MD operation, only the first expander of the ORC engine was considered, and this led to a power production lower than the one deriving from the initially designed engine, thus to lower fresh water and brine production in the RO unit. However, the system presented in this work is in principle able to meet the target of the NZL discharge and its energy efficiency can be improved by designing a suitable ORC for the energy supply and by including additional steady heat sources to achieve higher recovery in the MD unit.

5. Conclusions

In the current work, an integrated autonomous ORC system combined to a RO unit and an MD unit for the brine treatment has been evaluated to minimize brine discharge. The MD unit exploited the rejected heat of the ORC condensation. According to the results of the simulations based on experimental data, the system provided 3.2 kW of net electricity and 70 kW of thermal energy at 85ºC when the heat supply rate is in the order of 85 kW (i.e. ORC thermal efficiency of 3.7 %). With the electricity provided by the ORC, the RO unit produced a maximum of 0.6 m^3/h permeate when fed by 1.8 m^3/h seawater (feed concentration: 40,000 ppm, water recovery ratio: 35%). Then, the brine (1.20 m^3/h) was fed to the MD, whose operation was driven by the thermal energy supplied by the ORC. In these operating conditions, the MD was able to recover around 0.11 m^3/h of additional distillate. The overall system allowed for recovering 0.7 m^3/h from a feed flow of 1.7 m^3/h (considering a specific heat consumption for MD ~700 kWth/m^3).
As resulted from the current investigation, the MD contribution to the RO fresh water production is low, however important. This is because the heat provided by the ORC condensation was not enough to assure high productivity in the MD unit which is a very energy intensive process. However, this shortcoming is counterbalanced to some extent from the very high quality of the distilled water produced. Moreover, the consideration of only one ORC expander's operation in order to meet the necessary outlet conditions for the MD operation, led to a lower power production from the ORC, thus a lower production from the RO. The intermittent availability of solar energy also imposes operation in part-load. Future work will concern the employment of an independent heat supply to the MD in order to treat the brine more efficiently and to achieve higher fresh water recovery. In this case zero brine discharge could be achieved.

6. Acknowledgments

This research is co-financed by Greece and the European Union (European Social Fund- ESF) through the Operational Programme «Human Resources Development, Education and Lifelong Learning» in the context of the project "Reinforcement of Postdoctoral Researchers – 2nd Cycle" (MIS-5033021), implemented by the State Scholarships Foundation (IKY).
The present work has been based in the previous project of the authors, conducted within the framework of the "*Twostage RO-Rankine*" project No. 09SYN-32-982, partly funded by the Greek General Secretary of Research and Technology (GSRT). The research teams would also like to thank their partners for their work conducted within this project.

7. References

Al-Obaidani S., Al-Abri M., Al-Rawahi N., (2015). Achieving the Zero-Liquid-Discharge Target Using the Integrated Membrane System for Seawater Desalination, in: An Overview: Desalination, Environment and Marine Outfall Systems (pp.53-72)

Davis A.T., 2006. Zero Discharge Seawater Desalination: Integrating the Production of Freshwater, Salt, Magnesium, and Bromine. Desalination and Water Purification Research and Development Program Report No. 111 https://www.usbr.gov/research/dwpr/reportpdfs/report111.pdf

Heihsel M., Lenzen M., Malik A., Geschke A., 2019. The carbon footprint of desalination: An input-output analysis of seawater reverse osmosis desalination in Australia for 2005–2015. Desalination, 454, 71-81.

Micari M., Moser M., Cipollina A., Tamburini A., Micale G., and V. Bertsch. 2020. Towards the Implementation of Circular Economy in the Water Softening Industry: A Technical, Economic and Environmental Analysis. Journal of Cleaner Production. Article number 12029.

Mickley M.C., 2006. Membrane Concentrate Disposal: Practices and Regulation, Desalination and Water Purification Research and Development Program Report N. 123 (Second Edition), U.S. Department of Interior, Bureau of Reclamation, 128.

Nayar G.K., Fernandes J., McGovern K.R., Al-Anzi S.B., Lienhard H.J., 2019. Cost and energy needs of RO-ED-crystallizer systems for zero brine discharge seawater desalination. Desalination, 457, 115-132.

Ntavou, E., Kosmadakis, G., Manolakos, D., Papadakis, G., Papantonis, D., 2016. Experimental evaluation of a multi-skid reverse osmosis unit operating at fluctuating power input. Desalination, 398, 77-86.

Ntavou, E., Kosmadakis, G., Manolakos, D., Papadakis, G., Papantonis, D., 2017. Experimental testing of a small-scale two stage Organic Rankine Cycle engine operating at low temperature. Energy, 141, 869-879.

Voutchkov N., 2011. Overview of seawater concentrate disposal alternatives. Desalination, 273, 205-219.

https://water.custhelp.com/app/answers/detail/a_id/7835/related/1 (01/29/2020)

PV-based Integrated Energy and Water Demand Fulfillment Solution for Very Small Islands

Dedes S., Tzanes G., Papapostolou C., Kondili E., Kaldellis J.K.

Soft Energy Applications & Environmental Protection Lab, University of West Attica

Summary

The current study investigates the prospects of integrated PV-based configurations, devoted to the coverage of both electricity and water needs, with the support also of dedicated water desalination plants. The proposed solution is evaluated in an area of great interest, i.e. the Aegean Archipelagos, focusing on the very small scale islands facing electricity supply and water shortage problems. Emphasis to that end is given on the analysis of both the energy and economic performance of such configurations, as compared to the current status of oil-based power generation and water transfers, challenged also by the scale of application itself. Results obtained to that end derive from the application of the solution to representative, very small scale islands of the Aegean Sea, covering a wide spectrum of island features, which is eventually found to further strengthen the argument on the general applicability and cost-efficient performance of the proposed solution.

Keywords: Non-Interconnected Islands, Water Shortage, Solar Energy, Energy Storage, Desalination

1. Introduction – Position of the Problem

Small island communities all over the world face serious water and energy infrastructure problems that deteriorate the quality of life of the local permanent population. In Greece, there are more than 6,000 islands and islets, 227 of which are inhabited, while approximately 50 of them are very small, having less than 200 inhabitants. The majority of these tiny islands are located in the Aegean Sea. For all these islands the electricity production is almost exclusively based on autonomous power stations (APSs) which consume imported diesel oil and present extremely high electricity generation cost [1]. Another crucial problem of remote islands is the coverage of clean water, which up to now is mainly supported by water tanks delivered to the islands through shipping [2]. The pronounced seasonality of electricity and potable water demand due to tourism is usually handled with difficulty by the local authorities and involved actors [1]. For example, the Greek Public Power Corporation (PPC) transfers portable power generator units between islands in order to cover the corresponding load demand. Moreover, the load demand cannot be always satisfied and insufficient generation problems arise, causing several black-outs, especially during the summer period. On the other hand, the significant water shortage problems are covered mainly with water transfers [2,3] from either bigger, nearby islands, or the mainland at a very high cost, while in some islands, reverse osmosis desalination units have been installed, adding to the local electricity consumption needs [4].

doi:10.18086/eurosun.2020.12.07 Available at http://proceedings.ises.org

2. Proposed Solution-Simulation Results

In order to ameliorate the current situation and to achieve energy autonomy (independence from oil products) in these tiny non-interconnected islands [5], a PV-based system is proposed (Fig.1) in collaboration with energy and water storage infrastructure, able to cover the electricity and fresh water needs of the inhabitants at a rational installation cost [6,7].

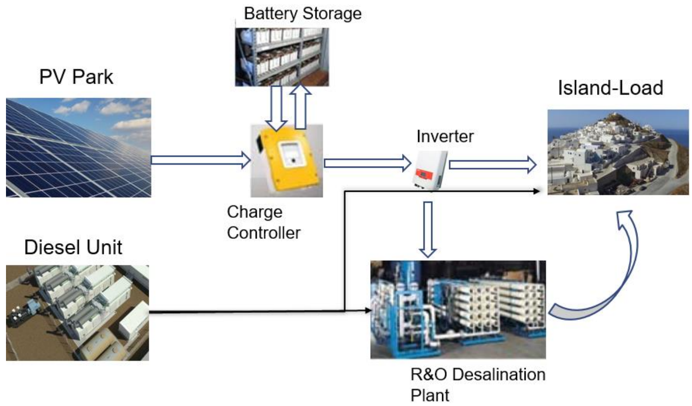

Figure 1: Proposed Energy-Water Solution for Very Small Islands

Accordingly, several representative PV-based configurations have been investigated for selected tiny islands taking also into consideration different water management strategies. According to the results obtained it is obvious that the proposed solution is able to achieve more than 95% energy autonomy for the selected islands, including the water desalination energy requirements, while the corresponding investment pay-back period is less than five years.

The cases examined for each of the configurations are:

- **Case 1:** The island's water load will be treated immediately as electricity load to the R&O plant with a coefficient of 7 kWh/m^3 and will be added to the total electricity load of the island. (steady water profile)
- **Case 2:** The island's water load will be treated separately from electricity. The system will convert the rejected electricity from the PV park that is not able to be stored in the ESS and fill a water tank. In situations that the water tank is unable to meet the demand, excess water will be bought (steady Water profile).
- **Case 1b:** The operational characteristics are the same as in Case 1, but the water profile is different (in accordance to the typical daily water demand profile of a remote island Figure 2) opposite to a constant consumption throughout the day.
- **Case 2b:** Same principles as in case 2 but with the difference in the water profile.

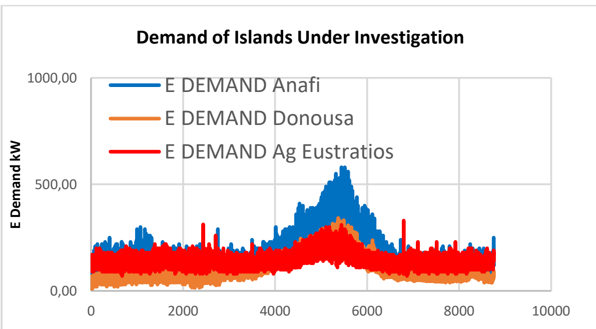

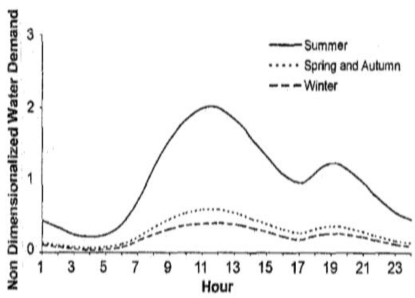

Figure 2: Electricity demand profile and typical daily water demand of the investigated islands

Apart from the 4 cases that refer to the configuration of the demand profiles, there are also 4 cases of economic interest about every island which are:

Case 1 and 1b: A PV unit that will operate as in the previous cases 1 and 1b which means that the water demand will be immediately covered and counted as electricity load.
Case 2 and 2b: A PV unit which operates like in the previous cases 2 and 2b. The water and electricity demand will be treated separately. The electricity load will be covered from the direct production of the PV park and energy stored in the battery system. The water demand will be covered via an installed water tank that will be fed from the desalination plant when the PV park produces excess energy and any deficit will be covered via water transports.

Case 3: A diesel only based unit that will feed the electric network of the island and water needs will be covered via water transports exclusively.
Case 4: A diesel only based unit combined with a desalination unit which will use diesel-produced electricity for the production of fresh water.

To that end, a representative, very small-scale Aegean island, i.e. the island of Anafi, has been selected as the main test-bed for the application of the different cases presented earlier.

Main characteristics of Anafi are given in the following bullets, while for comparison purposes, application results are next obtained for the islands of Agios Eustratios and Donousa as well.

- The population of Anafi according to the 2011 census is 273 people.
- High touristic activity during the summer period.
- The current solution of electricity production is diesel-based with a capacity of 1.15 MW.
- The total demand of Anafi is approximately 1500 MWh_e/year.

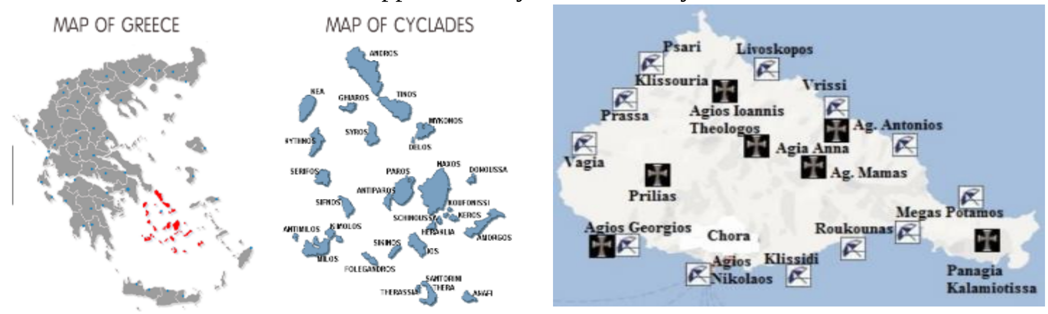

Figure 3: Map of Anafi Island

- For the island of Anafi the selected solution is a PV Park since the island has very low energy needs during the winter and the "heavy" loads are noted in the summer period.
- For this specific installation, a BIOSOL monocrystalline PV module of 265W panel has been selected.
- For the first approximation of the nominal power of the PV park the following equation is being used:

$$Po = \frac{E}{CF * \Delta t * ESS_{efficiency}}$$

Where CF is assumed to be 20% for the first approach and $ESS_{efficiency}$ = 65% which suggests a rather low value

In any case, the percentages of CF and ESS efficiency are estimations chosen in order to have a first sizing of the park.

To that end, energy balance (storage) analysis results together with the resulting diesel fuel consumption are given in Figure 4, for cases 1 and 2 respectively:

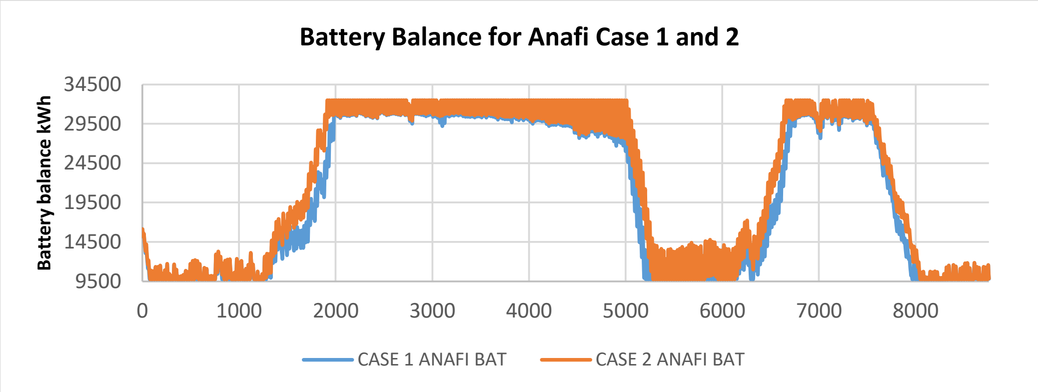

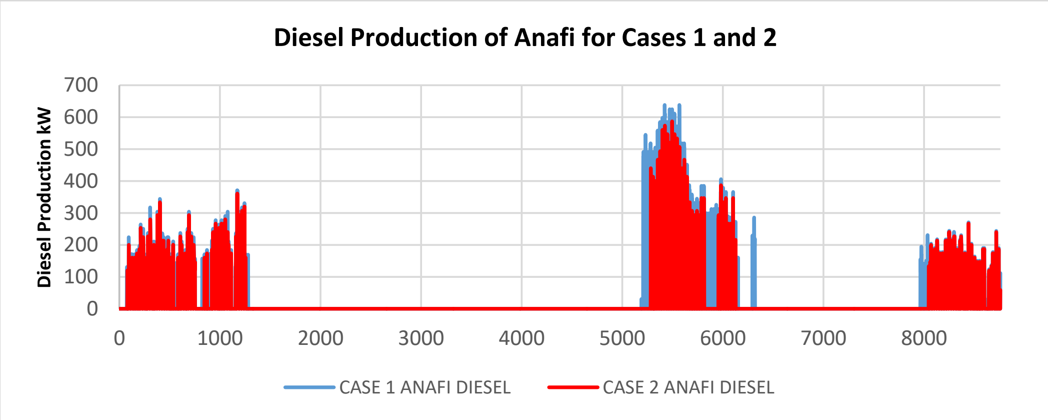

Figure 4: Storage balance and diesel usage for Anafi island, Cases 1 and 2

The batteries that will be used to cover the park will be 6V / 415Ah with DOD at 70% and will be connected in series in order to create each park's corresponding voltage.

For Anafi Island the battery capacity is Q(bat) = 656.25kAh

Cases 1 and 2 for Anafi present 85% and 87% of RES autonomy respectively, while in case 2, the water bought in order to cover the island's water needs is 6500m^3. Some points worth mentioning are the following:

- During the winter period the storage balance remains relatively low since the solar radiation is also low so most of the production of the PV park feeds the demand directly and only a small portion of that can be stored (Figure 4).
- In contrast, for the spring period, because the radiation is much higher than that of the winter season and the demand remains the same, the energy storage system increases its state of charge close to the maximum for the biggest part of the period.
- Lastly, during the summer months the PV park "struggles" to keep up with the demand because it is the touristic period and the demand is much higher than the rest of the year.

For cases 1b and 2b, the results are also being demonstrated below:

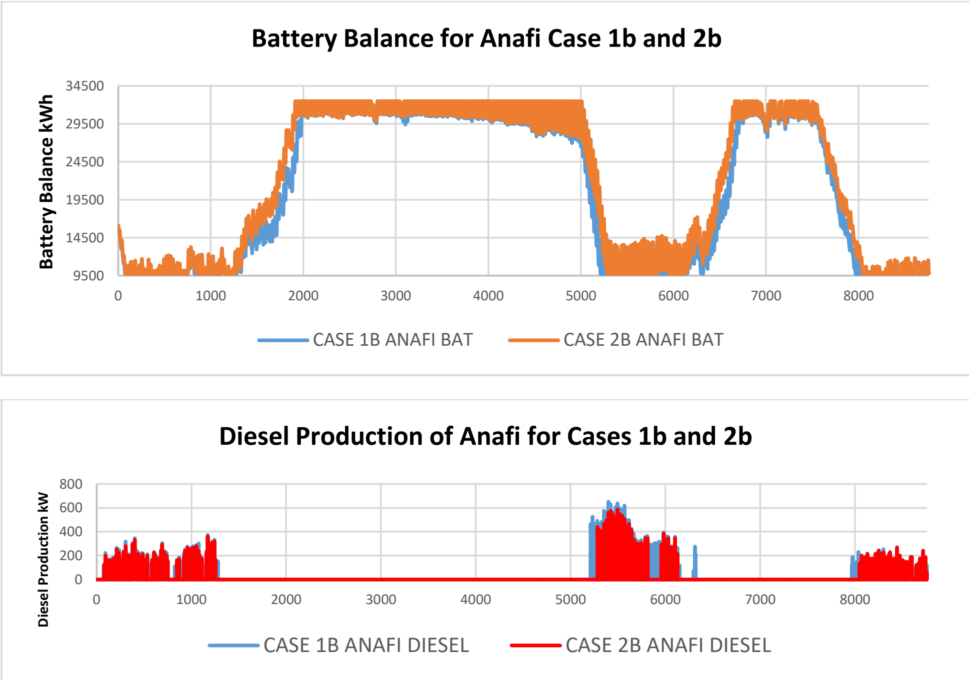

Figure 5: Storage balance and diesel usage for Anafi Island, Cases 1b and 2b

In cases 1b and 2b presented in Figure 5, the profiles are similar to the ones demonstrated in case 1 and 2. The RES autonomy of these cases is 85.2% for case 1b and 87.1% for case 2b.

Considering the water tank balance of cases 2 and 2b there is a graph below that depicts the results on an hourly basis throughout the year.

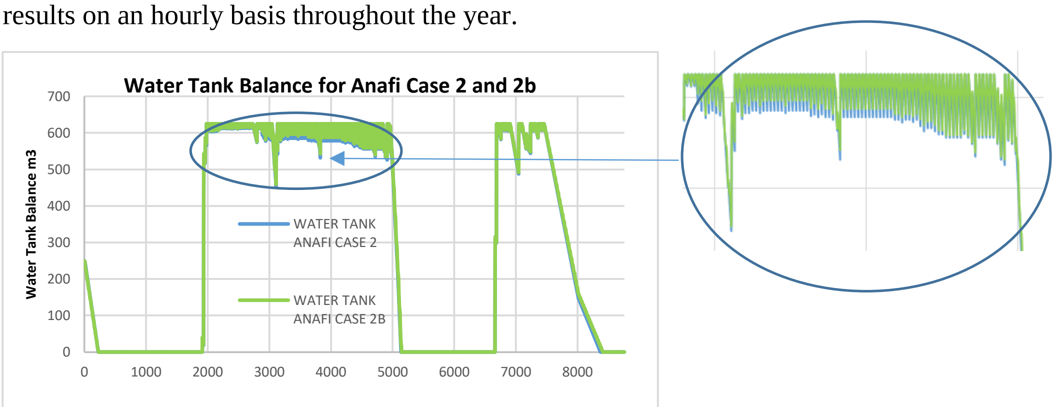

Figure 6: Water tank balance Cases 2 and 2b

The water tank of Figure 6 follows a similar variation profile as the battery storage system. This means that the water tank cannot cover the summer load because the energy demand is so high that there is almost zero excess energy to feed the desalination unit. The total water bought in this case is 6314.4m^3/year.

Economic Scenarios

Cases	PV (MW_p)	DIESEL (MW_p)	ICo M€	Oil Usage (m^3)	Total Cost no Tax M€
1	1.4	1,15	1309840	1544.94	3.24
2	1.4	1,15	1353590	1159.08	3.39
3	0	1,15	100000	1031.,68	8.61
4	0	1,15	0	9610.09	8.64
1b	1.4	1.15	1309840	1501.66	3.20
2b	1.4	1.15	1353590	1159.08	3.38

Table 1: Economic evaluation of Anafi cases

The economic results presented in Table 1 have taken into consideration the following parameters:

a) Each year the energy demand increases by 2% since the trend of increasing energy demand is a common phenomenon in modern societies.
b) The costs of buying water are 2 € / m^3 in the cases 2-2b and 3 which is a low special price and has been selected in order to examine if the lower water costs result in less expenses than case 1
c) The diesel engines are being replaced after 20.000 hours of usage. The capacity factor equation is being used in order to calculate the hours of diesel operation for each year.

$$E = Po * CF * \Delta t => CF = \frac{E}{Po * \Delta t}$$

For example in the 1st year of operation for Anafi, the island's diesel installed power Po is 1.15MW_p, and the energy produced is E=185.5 MWh_e so the CF is 1.84% and the diesel operation hours are 0.018 x 8760=161h.

From the above tables someone can identify that the lowest cost solution is Case 1b. The main reason is that the system is directly treating water demand as an electric load (the desalination plant) which leads to lower energy losses from the storage system. In addition, fluctuating water has better behavior than constant water demand since at nighttime the demand in the fluctuating case is much lower than the one of the constant value. This means that the water demand needed to be covered in the constant demand scenario does not add to the electricity load during the hours that the PV park production is zero.

Taking into consideration the different cases and making economic evaluations about each one of them the conclusion is that case 1b presents the best results, next followed by case 2b. The sensitivity analysis is based on the economic results of case 1b for different values of PV park capacity.

The following figure takes into consideration the cost parameters of each of the cases mentioned above, and a sensitivity analysis of cost vs RES autonomy of the islands in order to conclude on the most beneficial solution regarding the nominal capacity of the PV park.

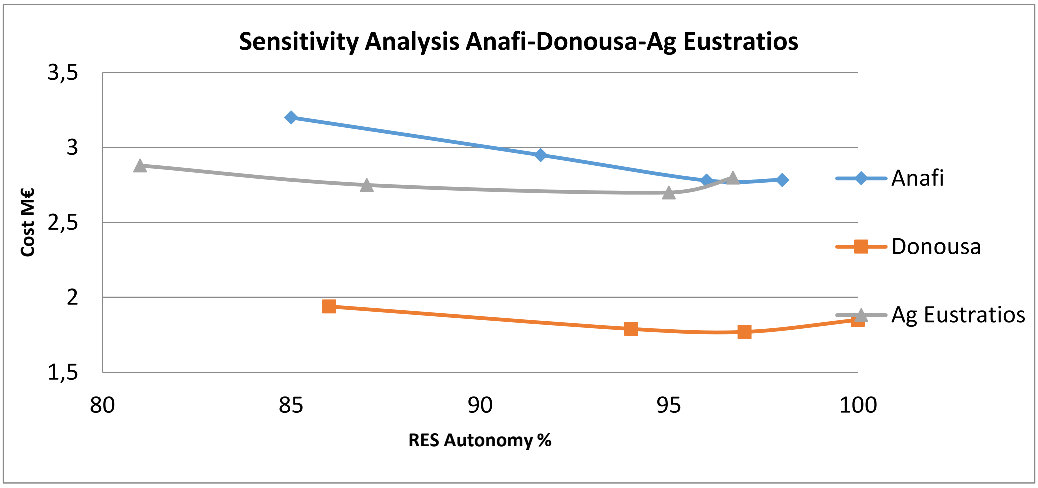

Figure 7: Cost vs RES Autonomy of Anafi, Donousa and Agios Eustratios

- Similar to Anafi island, Donousa and Agios Eustratios present an improvement in the RES autonomy on Figure 7 with the increase of the nominal power of the PV park without any economic "burdens".
- More specifically, for Anafi the optimum economic point appears for 96% autonomy with a cost of 2.78 M€ which results to 1.8MW$_p$ of PV park power, offering 96% autonomy for the island.
- For Agios Eustratios island, the optimum point is at 95% RES autonomy with a cost of 2.7M€ and a 1.8MW$_p$ of PV park power, with an expected autonomy of 95%.
- For Donousa island, the trend of cost reduction stops after 1.2MW$_p$ which yields 97% RES autonomy, while for 100% energy autonomy the cost is increased compared with the 1.2MW$_p$ solution.
- The gradual increase in the PV parks peak power in all islands examined seems to lead to a positive outcome since the cost is reduced and the RES-based energy autonomy of the local remote communities is increased.
- However, the optimum point of each proposed configuration is based on the price comparison between the oil-based and the PV-based solutions.
- The diesel expenses for electricity production are more than the initial and maintenance cost of a larger PV park before the optimum point. After that point the costs of diesel produced electricity has less expenses than adding more PV units to cover the demand.

The following diagrams (Figure 8) represent the results of the proposed solutions that have been analyzed during the sensitivity analysis for each island. These concern cases 1b and 2b with the corresponding battery balance and diesel usage throughout the year. For cases 2b there is also a presentation of the water tank and the water needed for annual operation.

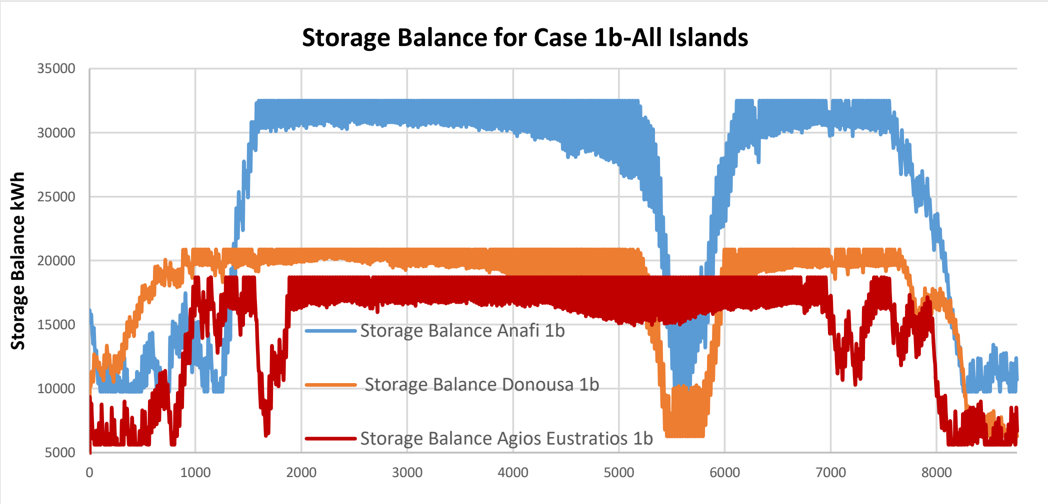

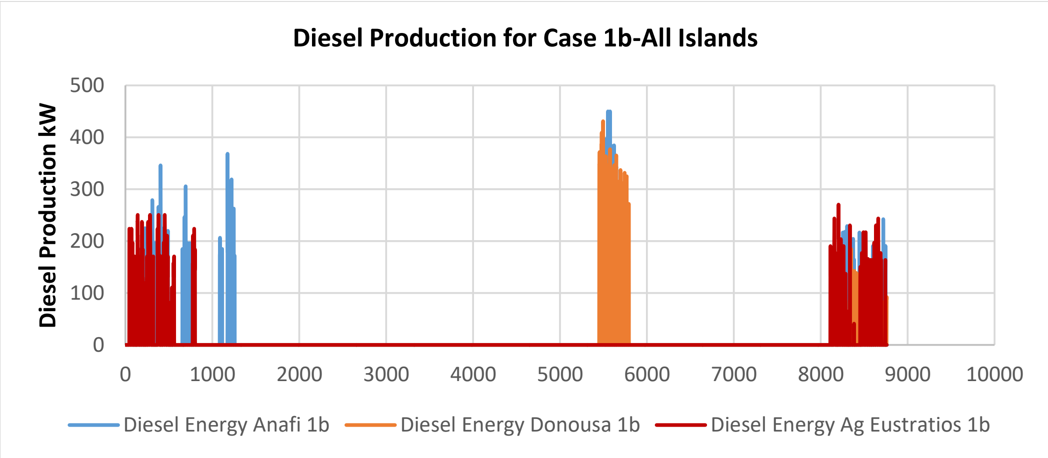

Figure 8: Storage balance and diesel usage for all islands – Analysis of case 1b

After the completion of the sensitivity analysis, the proposed configurations are described in the following bullets:

Anafi Island:

- A PV Park with nominal power of 1.8MW$_p$ is proposed that will cooperate with the current diesel system of the island in order to cover the total water and energy demands.
- This solution leads to 96% of energy autonomy and a reduced cost (2.78M€) compared with the first approach which costs 3.2M€ for a 85% RES autonomy.
- An energy storage system consisting of lead acid batteries and a total capacity of 650 kAh that will be able to cover two (2) consecutive typical summer days is required also.
- Land usage of 18000m^2.
- Oil usage of 19.7tn/year or almost 400tn for the entire 20 years of operation.
- Desalination Unit of 125m /day or 5.2m^3/h

Donousa Island:

- A PV Park with nominal power of 1.2MW$_p$ is proposed that will also be supported by the diesel unit of the island since the autonomy obtained is slightly less than 100% as well as for energy security reasons.
- This solution estimates an expected energy autonomy of 97% and will cost 1.77M€ for a life time of 20 years.
- An energy storage system of lead-acid batteries with a capacity of 435kAh able also to cover the island's needs for two consecutive days during the summer period is also necessary.
- Land usage of 12000m^2
- Oil usage of 8.5tn/year or 170tn for the entire 20 years of operation.
- Desalination unit of 65m^3/day or 2.7m^3/h.

Agios Eustratios Island:

- A PV Park with peak power of 1.8MW$_\mathbf{p}$ is proposed, taking into consideration the necessity of support by the existing diesel generator along with an appropriate energy storage system.
- This solution will provide 95% RES autonomy at the cost of 2.7M€ for 20 years of operation and the diesel usage is expected to be 20.5tn/year or almost 410tn for the entire 20 years of operation.
- An energy storage system (lead-acid batteries) with 390kAh capacity designed to cover the island's needs for two (2) consecutive typical summer days of demand.
- Land usage of 17400 m^2
- Desalination Unit of 125m^3/day or 5.2m^3/h

The battery balance and the diesel usage of the proposed solution mentioned earlier are being demonstrated in Figure 9 for both cases 1b and 2b.The graphs for cases 1b of Anafi and Donousa islands are presenting a similar fluctuation which is justified by the presence of heavy loads during the summer and winter period. In these situations the battery balance reaches its minimum capacity (DOD$_{max}$) and the diesel unit is taking over the electricity production loads in order to cover the island needs.

In the spring and fall periods of the year, the behavior of the battery balance is the same like with the 1.4MW$_\mathbf{p}$ park that was examined for Anafi and the 900kW$_\mathbf{p}$ park for Donousa. The increase in the nominal power of the PV configuration has a better behavior in the load coverage during the summer period.

On the other hand, for Agios Eustratios case 1b, the summer load was not a real problem because the island does not experience high touristic activity like Anafi and Donousa due to its remote location. For this island, the increase of the PV configuration nominal power results in the better handling of the winter loads, while for the rest of seasons the load demand is almost completely covered by the PV park.

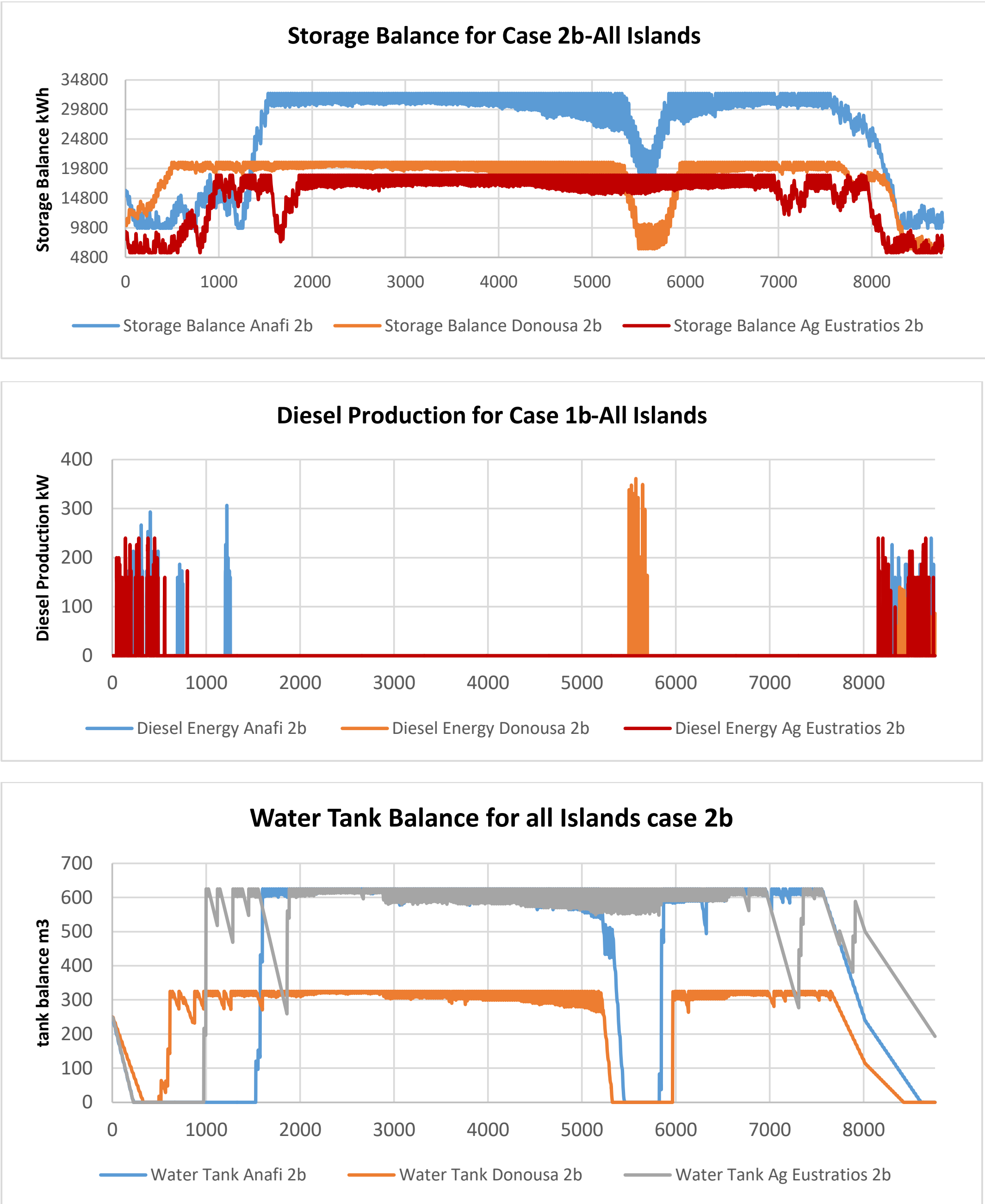

Figure 9: Results for case 2b for all islands

Advantages:

The most critical advantage of the renewable energy solution (on top of the optimum environmental improvement) for the islands examined is the financial performance. For a better understanding there will be a comparison of the costs between the current situation and the renewable based one for each island.

For Anafi, the current diesel costs for producing energy and buying drinkable water are estimated to be 8.64M€ for a 20-year period, while the proposed PV-based one costs only 2.78M€ for the same time period. Donousa's operation provides a total cost for a 20-year lifetime on the basis of the diesel unit equal to 5.37M€ whereas the RES-based proposal cost is expected to be only 1.77M€ for the entire lifetime of the system. Finally, Agios Eustratios's energy production cost for the 20-year period analyzed is 7.2M€ while the corresponding 1.8MW_p PV-park based one will cost only 2.7M€. Summarizing, the total cost of the PV-based solutions for all very small islands examined is almost one third of the expected cost of the current situation for a twenty years operation period and if assuming constant the oil prices in the future.

Apart from the economic factor, which is a very important aspect, there are also advantages concerning the environmental aspect for each island. A renewable proposal will dramatically reduce the diesel oil consumption of the electricity generators because its usage will be minimized. More specifically Anafi's 20 year oil consumption is expected to be 7700 tn while with the proposed solution it will be reduced to only 880 tn for 20 years. For Donousa and Agios Eustratios the current solution will use 4700 tn and 6270 tn for a 20 years operation respectively. The proposed renewable-based solutions will reduce it at 170tn for Donousa and 410 tn for Agios Eustratios, which is a remarkable difference with economic benefits as well. In the environmental spectrum, it is also worth mentioning that since Donousa has protected Natura areas, the addition of renewable energy sources on the island will also benefit this aspect of wildlife.

Finally, another important advantage is the installation of desalination plants for the islands. These units will provide water security for the islands because the current state of buying water that is transported in water tanks with shipment is not very safe. To that end, water deficit can easily occur during adverse weather conditions, when shipments are forbidden.

Disadvantages:

The disadvantages of this proposal are mainly based on the fact that it is a new investment that requires a certain initial capital that may be unattractive for an investor. However, if subsidized by the state or organizations that provide capital support for this type of projects, it can be a very attractive investment on a life cycle analysis.

Another factor to be faced is the land usage. As mentioned above, the PV park for each island requires a certain amount of land usage which may be a problem and create negative feedback from the local community.

3. Conclusions

An integrated energy and water demand coverage solution for very small scale islands has been developed in order to cover the corresponding needs on the basis of RES, and more specifically through the exploitation of the excellent solar potential met across the Aegean Archipelagos. According to the results obtained for selected representative remote islands of very small scale, the proposed solution presents minimum environmental impacts, almost zero diesel oil contribution and rational first investment cost. Actually, and on a life cycle basis, the proposed PV-based configuration proves to be much more cost-efficient than using diesel oil and importing clean water. Finally, it is important to mention that the developed solution may equally well be applied in several other small islands, all around the Mediterranean Sea.

4. References

1. Bertsiou M. , Feloni E. , Karpouzos D. , Baltas E. , (2018), "Water Management and Electricity Output of a Hybrid Renewable Energy System (HRES) in Fournoi Island in Aegean Sea", *Renewable Energy (2018),* Vol.118, pp. 790-798. Available at: www.sciencedirect.com
2. Christopoulos K., Pospotikis N., Kostopoulos Em., Kondili E., Kaldellis J. K., 2018, "Experimental analysis of the water salinity impact on the energy consumption of small desalination plants", *Procedia Structural Integrity*, Vol.10, pp.171-178.
3. Fu, R., Feldman, D., Margolis, R. (2018). "U.S. Solar Photovoltaic System Cost Benchmark: Q1 2018", *National Energy Renewable Laboratory*, Available at: https://www.nrel.gov/docs/fy19osti/72399.pdf
4. Kabir E. , Kumar P. , Kumar S. , Adedeji A. , Adelodun , Kim K-H. (2018), "Solar Energy: Potential and Future Prospects", *Renewable and Sustainable Energy Reviews*, Vol.82, pp. 894-900, Available at: www.elsevier.com
5. Kaldellis J.K., Zafirakis D., 2007, "Optimum Energy Storage Techniques for the Improvement of Renewable Energy Sources-Based Electricity Generation Economic Efficiency", *Energy Journal*, Vol.32(12), pp.2295-2305.
6. Kaldellis J.K., Kavadias K.A., Kondili E., 2004, "Renewable Energy Desalination Plants for the Greek Islands, Technical and Economic Considerations", *Desalination Journal*, Vol.170(2), pp.187-203.
7. Kougias I., Szabo S., Nikitas A., Theodosiou N., (2018), "Sustainable energy modelling of non-interconnected Mediterranean Islands", *Renewable Energy*, Vol.133 (2019), p.p 930-940, Available at: www.sciencedirect.com
8. Kondili E., Kaldellis J.K., Paidousi M., 2013, "A Multicriteria Analysis for the Optimal Desalination-RES System. Special focus: the Small Greek Islands", *Journal of Desalination and Water Treatment*, Vol.51(4-6), pp. 1205-1218.
9. Kaldellis J.K., Gkikaki Ant., Kaldelli El., Kapsali M., 2012, "Investigating the Energy Autonomy of Very Small Non-Interconnected Islands. A Case Study: Agathonisi, Greece", *Energy for Sustainable Development*, Vol.16(4), pp.476-485.
10. Kaldellis J.K., D. Zafirakis, 2020, "Prospects and challenges for clean energy in European Islands".The TILOS paradigm, Renewable Energy, Vol.145, pp.2489-2502.
11. Papapostolou Chr., Kondili E., Kaldellis J.K., 2018, "Optimising the total benefit of water resources management in combination with the local energy systems in remote communities taking into account sustainability considerations", *Computer Aided Chemical Engineering*, Vol.40, pp.2689-2694.

13. Renewable Energy Systems and Spatial Energy Planning

Design and Performance of Landscape Adaptable PV Structures

Caroline Hachem-Vermette, PHD, Associate Prof, University of Calgary, Canada

Abstract

This paper presents an investigation of the electrical output associated with change in shapes of stand-alone adaptable PV structures. The PV structures presented in this work consist of PV plates of different fixed orientations, but adaptable tilt angles according to the time of the day and year, and the orientation of the plates themselves. Adopting fixed but different orientations allows to capture the maximum of solar radiation at different time of the day by a fraction of the structure, without a continuous movement of the plates. The study is carried out for a cold northern climate. The results of the study indicate that it is possible to significantly increase the yearly electrical output of an adaptable PV structure as compared to fixed design.

Keywords: PV structures, Landscape, Adaptable structures, Fixed PV

1. Introduction

Efforts to design and build resilient and low environmental impact communities are multiplying, worldwide. These efforts will become even stronger in the wake of climate related disasters and uncertain economic situations. Reducing reliance of communities on fossil fuels and associated emissions is an important step toward achieving more sustainable and resilient communities. The integration of renewable clean energy, especially solar collectors, including photovoltaic systems, within urban development is attracting considerable interest, in both research and applications, due to their numerous advantages.

Integration of PV in buildings is however limited due to shortage of building surfaces for such integration, potential shading from surrounding buildings, and other architectural and functional considerations. To increase the potential of urban areas to generate solar energy, different methods of integration of PV technologies need to be exploited, including employing PV in urban landscape and open public areas. landscape-integration of PV (Scognamiglio 2016) can be implemented either in agricultural land and remote PV farms, or, on smaller scale installation within urban landscape.

Some issues and opportunities arise in designing landscape integrated PV technologies, both in remote land and in urban areas. A massive and uncontrolled expansion of large-scale PV systems on agricultural land can negatively impact the ecosystem, agricultural productivity of the land, as well as site hydrology (e.g. McDonald et al, 2009; Prados, 2009; Turney and Fthenakis, 2011). In urban setting, significant challenges are posed by the selection of urban landscape to offer adequate solar potential, while avoiding shade from the surrounding buildings. On the other hand, landscape can offer spatial solutions for the installation of PV systems to increase renewable energy generation in remote and urban areas, while presenting environmental co-benefit opportunities.

Although there are some applications of PV technologies in urban landscape, research on landscape PV is mostly targeting large-scale applications, integrated within agricultural or other remote sites. Integration of PV structures in the public landscape provides the opportunity to improve the outdoor thermal comfort of the built environment. PV structures can be designed as integrated part of the spatial design of neighborhoods and its street network to fulfill various supplemental environmental functions, such as weather protection and noise barrier.

Coupling PV electricity generation technologies with structural form finding and deployment methods can improve the overall energy generation throughout the year. The use of moveable and adaptable structures for PV support

doi:10.18086/eurosun.2020.13.01 Available at http://proceedings.ises.org

allows compensation for daily and seasonal variations of solar radiation, as well as for the impact of shading by surrounding buildings in high-density environment. In addition, standalone landscape PV structures can offer flexibility of design, presenting an opportunity to enhance the aesthetics of PV structures, and their acceptability in the built environment. One of the obstacles facing the implementation of PV deployment is the reluctance by designers, architects, planners and the public. Public acceptability can be stimulated by enhancing the aesthetic aspect of PV structures, through appropriate design of their components and choices of color and material while

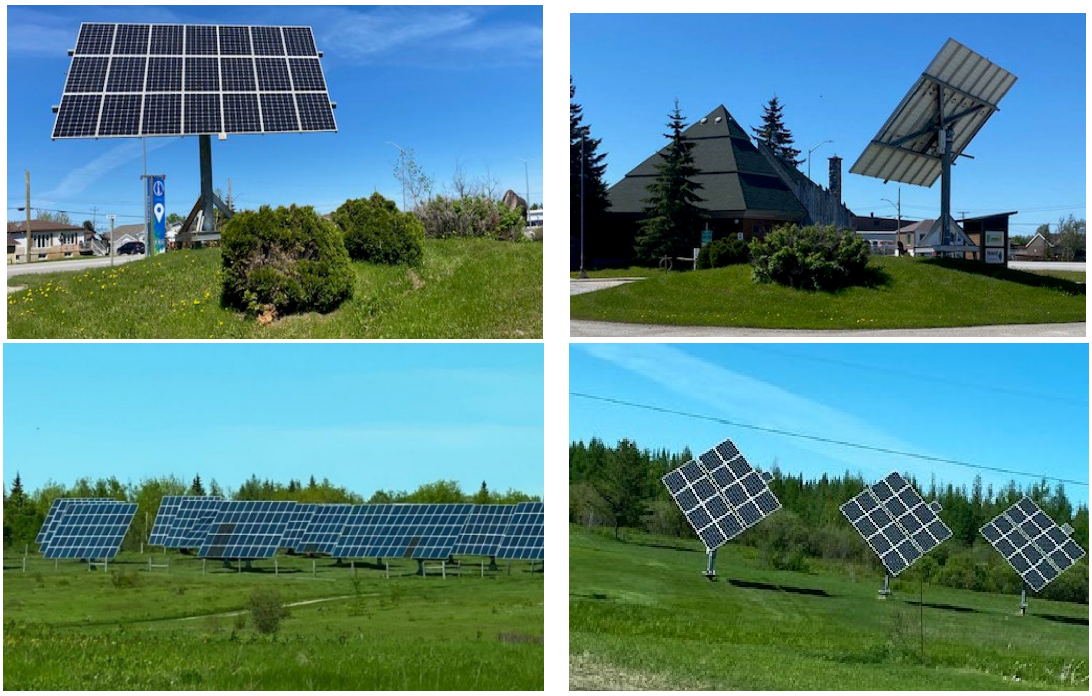

maintaining their performance (e.g. Kapetanakis et al, 2014; Scognamiglio, 2016; Tsantopoulos et al, 2014), Reducing the intrusion of PV structures on landscape, especially in public areas (See Fig.1), can play a key role in increased social acceptance.

Figure 1, examples of PV stand-alone structures, (a) and (b) in public areas, (c) and (d) in farm lands.

A number of methods and approaches are employed in solar tracking, including passive tracking, active tracking and chronological tracking (Khalil et al, 2017). Active trackers employ motors and gears to drive the panels. Two main techniques of solar trackers – single axis and dual axis – are broadly used in PV power systems. While dual axis tracking system is highly accurate, it is associated with high costs and low reliability (e.g. due to wear and tear). Single axis tracking system is associated with lower cost and more reliability; however it is less accurate than the dual axis tracking system. Research on various types of PV technologies employed in tracking systems shows that crystalline or thin film PV cells are not significantly affected by a deviation of the orientation by up to 10^{o} from the sun true location due to diffuse light (Tania and Alam, 2014).

Single axis tracking system is mostly used to track the movement of the sun during the day, by changing the orientation of the panel, so it aligns with the location of the sun. Several studies have been conducted on such systems. For instance, Anuraj et al. (2014) designed a PV prototype with a single degree of freedom solar tracker, which employs Light Dependent Resistors to detect sun light, and to position a PV panel so it receives maximum irradiance. Vertical tracking is usually combined with horizontal tracking in a dual axis tracking system. Mahmood et al. (2013) studied a dual axis solar tracker which employs a programmable logic controller. Optimal vertical and horizontal angles for each day of the year are extracted from numerical models and employed to track the sun, throughout the year. A power gain of 38% is obtained with the proposed system. Afrin and Titirsha (2013) proposed an azimuth-altitude dual axis solar tracker, which allows an overall increase of 50-60% in energy generation as compared to a fixed PV system. In addition, some research had focused on reduced movement of the trackers to reduce the energy consumed by the structure itself (Khalil et al, 2017). Such research aims at proving that increased costs associated with movable PV-arrays can be justified by the increased electrical output (Moghbelli and Vartanian, 2006).

This paper presents the first stage of designing adaptable landscape PV structures (ALPVs) to be implemented in various urban areas. A number of designs are developed and their energy output is simulated to determine the optimal configuration for different times of the year.

2. Methodology

This study investigates two main configurations of adaptable structures, the first design is a single level structure, while the other configuration consists of 2 levels of panels mounted on top of each other. A distance equal to twice the length of the panels is set between the two levels to eliminate shading. For each of these configurations several design alternatives are proposed, comprising different orientations of panels. The designs, within each of these configurations, adopt fixed orientation ranging from full south to full east and west, and variable tilt angles, employing single axis tracking (see below). The study is conducted for a Northern cold climate (51° North).

Conventional PV panels, such as those commercially available are employed in the design. The deployment of PV panels may employ mechanisms of varying complexity, ranging from individual hydraulic pistons to more complex systems, such as cable control, mobile components (e.g. scissors), and others. This work focuses on the PV performance within each design rather than the deployment mechanisms. Figure 2 presents illustrations of the studied single- level adaptable landscape PV structures (ALPVs), while Figure 3 presents an example of application of the basic structure in urban setting. Figure 4 presents a schematic of 2-level ALPVs. The general approach and assumptions in the design of these ALPVs are described below.

2.1. Design approach

The designs explored in this study are described in the following, for the single and 2-level configurations. The total area of PV within the design variations of each of the configurations (i.e. single or double levels) remains fixed. The double-level configurations have double the PV area of the single level configurations.

Single- level design. Three different designs are explored, for the single level configurations, as shown in Figure 2. These designs are the basic structure, a variation on this basic design, and an 8- petals (8P) flower design. The characteristics of each of these designs are summarized below.

- Basic design: consisting of 2 south PV panels, in addition to one east and one west panel (Fig. 2a).
- Variation: consisting of 2 PV panels oriented south and 2 panels oriented 45° from south towards east and west (Fig. 2b). The two south facing PV panels (S1 and S2, Fig 2b), are located on the south and north of the structure, respectively. S2 (located on the north) is tilted toward south, to maximize solar radiation. It is also placed at a higher level than the other panels to reduce potential shading.

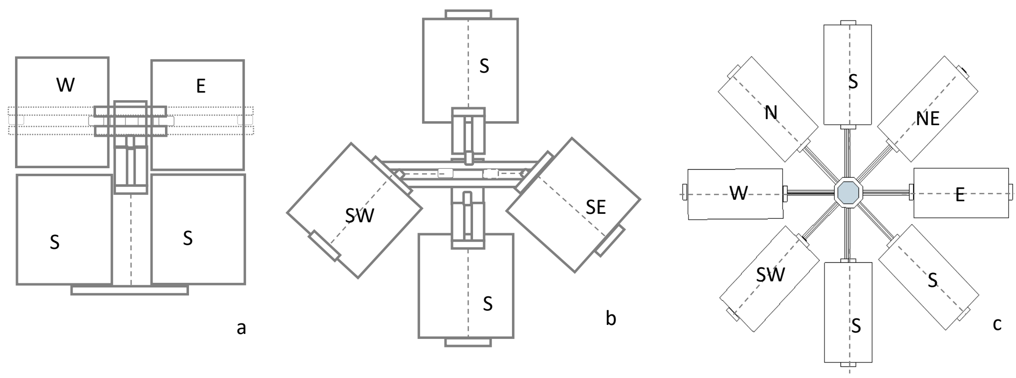

Figure 2, Illustration of the plan view of the single level configurations, (a) basic 4-plates, (b) variation of the basic structure, (c) 8-petal (8P) flower

- Flower design with 8 petals, consisting of 8 rectangular panels. The area of each of these panels is equivalent to half of the panel area employed in the configurations presented above. Panels are oriented south, east and west as well as 45 ° from east and west (Fig. 2c). All panels placed on the north (including north east and north west) in the plan are tilted toward south.

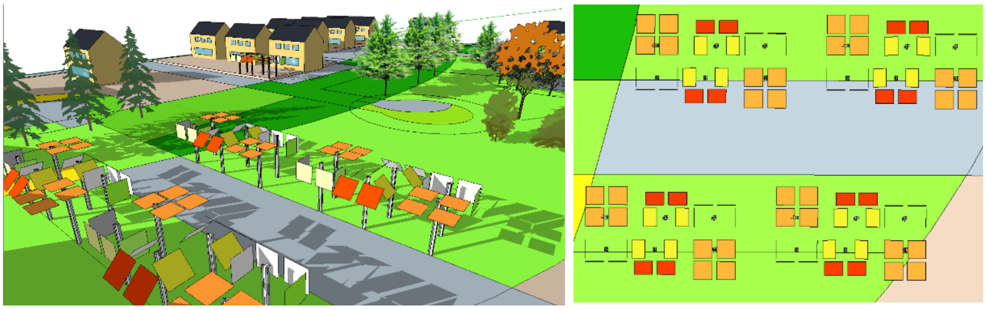

Figure 3, application of the basic structure in urban setting

Two-level designs. The two-level designs combine one or more of the designs developed for the single level configuration, described above. A distance equal to twice the length of the panels is designed between the two levels, to eliminate shading effect. The three design variations are summarized below.

- Basic design consists of the basic 4-plates design (Fig. 2a), employed in both the lower and upper levels (Fig4 a).
- Variation of the basic design (see Fig.4b), employing the variation of 4-plates design described above (Fig 2b) in both levels.
- Combination of basic and variation, consisting of the basic design on the bottom level and the variation on the upper level (Fig.4c).

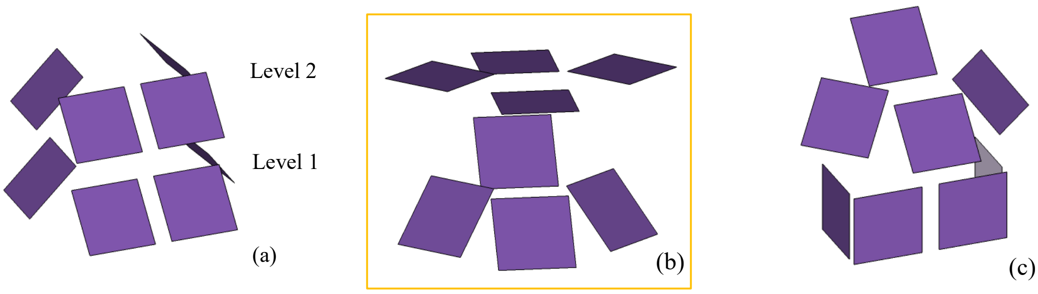

Figure 4, illustration of the PV plates in the 2-level studied structures, (a) Basic, (b) Variation, (c) basic- variation

3. Analysis and Results

The electrical output of these adaptable landscape PV structures (ALPVs) are simulated employing EnergyPlus (Crawly et al, 2000), in conjunction with Scketchup Pluggin (Ellis et al, 2000), employed to generate various geometric shapes. Three main positions of each of the PV panels are analysed – horizontal (0º), inclined (45 º tilt), and vertical (90º). Weather data of Calgary (Canada, 51ºN) is used in the simulations, to obtain daily, monthly and yearly generation. The results are presented for the single level configurations, followed by the 2-level configurations. The results present the yearly, monthly and hourly optimal configurations.

3.1. Single level design

Basic design. Table 1 presents the total yearly generation of the basic 4 plates structure (Fig. 2a), associated with a fixed tilt angle, where the 4 panels of the structure (3 main orientations, south, east and west) assume the same tilt angle year-round (not controlled). Among the main studied positions – horizontal, tilted (45 ^{o}) and vertical – the optimal fixed tilt position is at 45 ^{o}, as expected for the studied location. Controlling the position of the plates to obtain the optimal monthly positions, allows increasing the yearly generation by about 5% as compared to the same structure design with a fixed optimal tilt (of 45^o), and by 16% and 36% as compared to the horizonal (0^o) and vertical (90 ^{o}) positions, respectively. The hourly control allows an increase of generation by 18%, as compared to the 45^o tilt, and by 31% and 53% as compared to the horizontal and vertical positions, respectively.

Table 1[1]: Yearly generation of the basic structure, associated with fixed positions and monthly and hourly change.

Fixed position	Yearly generation	Comparison to optimal	Controlled positions	Generation	Comparison to optimal fixed position (45 ^{o})	Comparison to horizontal position (0 ^{o})	Comparison to vertical position (90^o)
0 ^{o}	5.24E+09	0.90	**Yearly Optimal**	5.8E+09	1.00	1	1
45 ^{o}	5.80E+09	1.00	**Monthly - Optimal**	6.1E+09	1.05	1.16	1.36
90 ^{o}	4.49E+09	0.77	**Hourly - Optimal**	6.86E+09	1.18	1.31	1.53

Variations of the basic 4-plates designs are studied for a fixed tilt position, a monthly controlled and hourly controlled positions. The results are presented in Table 2, and Figs. 5a and 5b. Considering the optimal fixed position (45 ^{o}), the design variation that combines south, south-east and south-west orientations (Fig. 2b), allows an increase of 11%, as compared to the basic design, while the 8P-flower (Fig. 2c) allows a 4% increase.

Table 2: Generation of all single level ALPVs, associated with fixed positions, and monthly and hourly changes

Yearly generation at a fixed position				Yearly generation with controlled positions		
Position	**Basic**	**Variation**	**Flower-8P**	**Configuration**	Monthly -Optimal positions	Hourly - Optimal positions
0	5.24E+09	5.24E+09	5.24E+09	**Basic**	6.10E+09	6.86E+09
45	5.80E+09	6.41E+09	6.04E+09	**Variation**	6.53E+09	7.07E+09
90	4.49E+09	4.96E+09	4.53E+09	**8P-Flower**	6.21E+09	6.95E+09

The comparison of the monthly and hourly optimal positions for all the configurations, to the fixed position (where all plates have the same angle) is presented in Fig. 6a. A monthly change- allowing to change the position only once a month to obtain the optimal generation of the whole month- is significant when compared to the horizontal and vertical fixed position. The increase of generation for the design variations is 25% and 31% as compared to the horizontal and vertical positions (respectively). An increase of generation by 18% and 37% is observed for monthly variation, of the 8P-flower, as compared to the horizontal and vertical position (respectively). The monthly variation of all configurations is not significantly higher than the optimal fixed position (of 45 ^{o} tilt), corresponding to an increase of 5%, 2% and 3% for the basic design, variations and 8P flower respectively.

The hourly change -capturing the optimal generation at each hour of the year- shows a significant increase of generation, for all studied configurations, as compared to all fixed positions. The increase is about 18%, 10% and 15% for the basic, variation and the 8P flower (respectively) as compared to the fixed optimal position. This increase is much more significant when compared to the horizontal and vertical position (reaching difference of 54% for the 8P flower) (see Fig. 5a).

[1] Energy generation is measured in units of Joules (J) in this document.

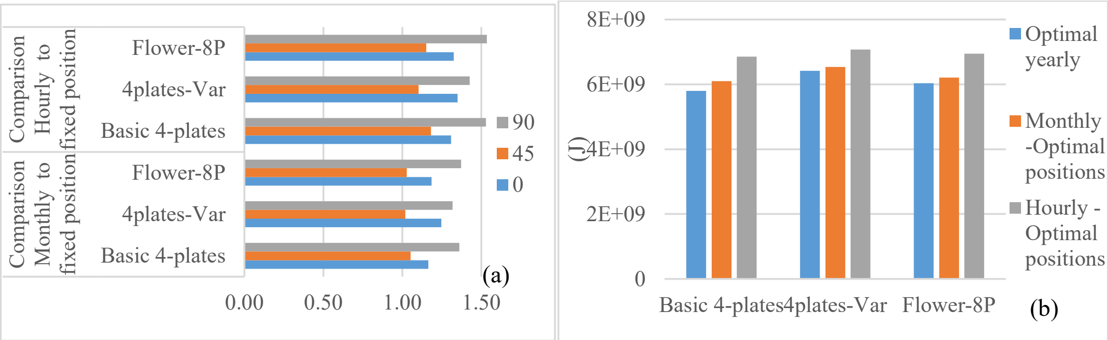

Figure 5, (a) comparison of generation associated with the hourly and monthly change of each structure to the fixed optimal position, (b) total generation of all studied configurations and their positions.

An example of the monthly optimal positions of the plates of the basic configuration is presented in Table 3. It can be observed that while the optimal tilt position of the south plates changes for the different months of the year, the east and west plates have an optimal horizontal position. A vertical position is optimal for the south plates during November-January, and a horizontal position is optimal from May-July. A tilt of 45 º is optimal for the remaining 6 months of the year (Feb-April, and August to October).

Table 3: Monthly variation of energy generation of each panel of the basic 4-plates structure, presented by its position (tilt º) and orientation. The colors indicate the optimal values.

Date/Time	0 º -S [J]	45 º -S [J]	90 º -S [J]	0 º -E- [J]	45 º -E [J]	90 º -E- [J]	0 º -W- [J]	45 º -W	90 º -W
January	3.9E+07	1.0E+08	1.1E+08	3.9E+07	3.6E+07	3.5E+07	3.9E+07	3.7E+07	3.5E+07
February	6.0E+07	1.1E+08	1.1E+08	6.0E+07	5.4E+07	4.6E+07	6.0E+07	5.5E+07	4.7E+07
March	1.0E+08	1.5E+08	1.3E+08	1.0E+08	8.9E+07	6.9E+07	1.0E+08	1.0E+08	8.1E+07
April	1.3E+08	1.6E+08	1.1E+08	1.3E+08	1.3E+08	9.7E+07	1.3E+08	1.2E+08	8.9E+07
May	1.7E+08	1.7E+08	9.9E+07	1.7E+08	1.6E+08	1.2E+08	1.7E+08	1.5E+08	1.1E+08
June	1.8E+08	1.7E+08	9.3E+07	1.8E+08	1.7E+08	1.2E+08	1.8E+08	1.5E+08	1.1E+08
July	2.0E+08	1.9E+08	1.1E+08	2.0E+08	1.8E+08	1.3E+08	2.0E+08	1.8E+08	1.3E+08
August	1.6E+08	1.8E+08	1.2E+08	1.6E+08	1.5E+08	1.1E+08	1.6E+08	1.5E+08	1.1E+08
September	1.1E+08	1.5E+08	1.2E+08	1.1E+08	1.0E+08	8.1E+07	1.1E+08	1.0E+08	8.1E+07
October	8.0E+07	1.5E+08	1.4E+08	8.0E+07	7.4E+07	6.4E+07	8.0E+07	7.9E+07	6.9E+07
November	4.3E+07	9.3E+07	9.6E+07	4.3E+07	3.9E+07	3.4E+07	4.3E+07	4.1E+07	3.6E+07
December	3.1E+07	7.8E+07	8.5E+07	3.1E+07	2.8E+07	2.6E+07	3.1E+07	3.0E+07	2.8E+07

Examples of hourly energy generation of each panel (south (S), East (E)and West (W)) of the 4-plates basic structure, associated with different tilt positions, are presented in Tables 4-7, for the solstice and the equinox days of the year. Since the two south plates yield the same energy generation, only the generation of one of the plates is reported in the tables. In contrast with the monthly results, east and west plates show greater variations of the optimal position during a day while the south plates show less variations.

Table 4: Energy generation variation during the spring equinox

	South (S)			**East (E)**			**West (W)**		
Time	**0 º**	**45 º**	**90 º**	**0 º**	**45 º**	**90 º**	**0 º**	**45 º**	**90 º**
7:00:00	3.1E+03	3.0E+03	2.2E+03	3.1E+03	1.2E+04	1.5E+04	3.1E+03	2.2E+03	1.7E+03
8:00:00	3.1E+04	3.8E+04	2.9E+04	3.1E+04	8.6E+04	9.8E+04	3.1E+04	1.8E+04	1.4E+04
9:00:00	7.6E+04	9.3E+04	7.2E+04	7.6E+04	1.3E+05	1.3E+05	7.6E+04	4.0E+04	3.2E+04
10:00:00	1.5E+05	1.7E+05	1.3E+05	1.5E+05	1.9E+05	1.6E+05	1.5E+05	8.2E+04	6.2E+04
11:00:00	2.2E+05	2.6E+05	2.0E+05	2.2E+05	2.4E+05	1.7E+05	2.2E+05	1.2E+05	9.0E+04

12:00:00	2.6E+05	3.1E+05	2.4E+05	2.6E+05	2.4E+05	1.6E+05	2.6E+05	1.7E+05	1.1E+05
13:00:00	3.1E+05	3.8E+05	2.9E+05	3.1E+05	2.4E+05	1.3E+05	3.1E+05	2.3E+05	1.2E+05
14:00:00	3.5E+05	5.0E+05	4.1E+05	3.5E+05	1.9E+05	1.0E+05	3.5E+05	3.4E+05	2.0E+05
15:00:00	4.1E+05	6.1E+05	5.0E+05	4.1E+05	1.3E+05	1.0E+05	4.1E+05	5.1E+05	3.8E+05
16:00:00	3.4E+05	5.0E+05	4.1E+05	3.4E+05	8.3E+04	8.7E+04	3.4E+05	5.4E+05	4.7E+05
17:00:00	2.3E+05	3.3E+05	2.7E+05	2.3E+05	6.2E+04	6.3E+04	2.3E+05	4.8E+05	4.9E+05
18:00:00	1.1E+05	1.5E+05	1.2E+05	1.1E+05	4.2E+04	3.8E+04	1.1E+05	3.3E+05	3.7E+05
19:00:00	1.5E+04	1.6E+04	1.2E+04	1.5E+04	9.6E+03	7.2E+03	1.5E+04	5.3E+04	6.4E+04

Table 5: Energy generation variation during the summer solstice

	South (S)			East (E)			West (W)		
Time	**0 º**	**45 º**	**90 º**	**Date/Time**	**0 º**	**45 º**	**90 º**	**Date/Time**	**0 º**
5:00:00	7.1E+03	4.1E+03	3.5E+03	7.1E+03	3.6E+04	4.6E+04	7.1E+03	4.0E+03	3.5E+03
6:00:00	5.9E+04	2.0E+04	2.1E+04	5.9E+04	2.2E+05	2.6E+05	5.9E+04	1.9E+04	2.1E+04
7:00:00	1.9E+05	7.7E+04	5.4E+04	1.9E+05	4.7E+05	5.0E+05	1.9E+05	4.9E+04	5.4E+04
8:00:00	3.7E+05	2.6E+05	8.6E+04	3.7E+05	7.2E+05	7.0E+05	3.7E+05	7.0E+04	8.5E+04
9:00:00	5.0E+05	4.5E+05	1.8E+05	5.0E+05	8.2E+05	7.1E+05	5.0E+05	7.3E+04	1.0E+05
10:00:00	6.7E+05	6.7E+05	3.3E+05	6.7E+05	9.2E+05	6.8E+05	6.7E+05	1.2E+05	1.1E+05
11:00:00	7.5E+05	8.1E+05	4.5E+05	7.5E+05	8.7E+05	5.4E+05	7.5E+05	2.9E+05	1.3E+05
12:00:00	6.6E+05	7.3E+05	4.3E+05	6.6E+05	6.4E+05	3.0E+05	6.6E+05	3.7E+05	1.2E+05
13:00:00	3.6E+05	4.1E+05	2.5E+05	3.6E+05	3.0E+05	1.1E+05	3.6E+05	2.9E+05	9.8E+04
14:00:00	3.7E+05	4.1E+05	2.5E+05	3.7E+05	2.3E+05	8.9E+04	3.7E+05	3.6E+05	1.8E+05
15:00:00	5.8E+05	6.3E+05	3.6E+05	5.8E+05	2.4E+05	1.1E+05	5.8E+05	6.7E+05	4.1E+05
16:00:00	5.7E+05	5.8E+05	2.9E+05	5.7E+05	1.1E+05	1.0E+05	5.7E+05	7.7E+05	5.7E+05
17:00:00	4.6E+05	4.2E+05	1.8E+05	4.6E+05	7.1E+04	9.6E+04	4.6E+05	7.4E+05	6.3E+05
18:00:00	2.7E+05	2.0E+05	8.0E+04	2.7E+05	8.0E+04	7.9E+04	2.7E+05	4.9E+05	4.5E+05
19:00:00	2.1E+05	8.1E+04	5.5E+04	2.1E+05	4.8E+04	5.5E+04	2.1E+05	5.3E+05	5.6E+05
20:00:00	1.1E+05	2.9E+04	3.2E+04	1.1E+05	2.8E+04	3.2E+04	1.1E+05	4.3E+05	5.1E+05
21:00:00	1.7E+04	7.6E+03	7.2E+03	1.7E+04	7.4E+03	7.2E+03	1.7E+04	1.1E+05	1.4E+05

Table 6: Energy generation variation during the Fall equinox

	South (S)			East (E)			West (W)		
Time	**0 º**	**45 º**	**90 º**	**Date/Time**	**0 º**	**45 º**	**90 º**	**Date/Time**	**0 º**
7:00:00	2.1E+04	2.5E+04	1.9E+04	2.1E+04	1.5E+05	2.0E+05	2.1E+04	8.1E+03	8.2E+03
8:00:00	1.6E+05	2.4E+05	1.9E+05	1.6E+05	6.1E+05	7.1E+05	1.6E+05	3.2E+04	3.9E+04
9:00:00	3.2E+05	4.8E+05	3.9E+05	3.2E+05	7.5E+05	7.7E+05	3.2E+05	5.7E+04	7.1E+04
10:00:00	4.6E+05	7.0E+05	5.7E+05	4.6E+05	7.8E+05	7.0E+05	4.6E+05	7.1E+04	9.4E+04
11:00:00	5.6E+05	8.6E+05	7.0E+05	5.6E+05	7.3E+05	5.4E+05	5.6E+05	1.4E+05	1.2E+05
12:00:00	6.3E+05	9.6E+05	7.9E+05	6.3E+05	6.2E+05	3.4E+05	6.3E+05	3.0E+05	1.3E+05
13:00:00	6.6E+05	1.0E+06	8.3E+05	6.6E+05	4.5E+05	1.4E+05	6.6E+05	4.8E+05	1.6E+05
14:00:00	6.3E+05	9.8E+05	8.0E+05	6.3E+05	2.7E+05	1.2E+05	6.3E+05	6.5E+05	3.8E+05
15:00:00	5.6E+05	8.6E+05	7.0E+05	5.6E+05	1.1E+05	1.1E+05	5.6E+05	7.6E+05	5.8E+05
16:00:00	4.4E+05	6.7E+05	5.5E+05	4.4E+05	6.9E+04	9.1E+04	4.4E+05	7.9E+05	7.2E+05
17:00:00	2.9E+05	4.4E+05	3.5E+05	2.9E+05	5.3E+04	6.5E+04	2.9E+05	7.2E+05	7.6E+05
18:00:00	1.3E+05	1.8E+05	1.4E+05	1.3E+05	3.3E+04	3.6E+04	1.3E+05	4.9E+05	5.8E+05
19:00:00	1.2E+04	1.2E+04	8.5E+03	1.2E+04	6.0E+03	5.4E+03	1.2E+04	7.8E+04	1.0E+05

Table 7: Energy generation variation during the winter solstice

Date/Time	South (S)			East (E)				West (W)	
	0°	45°	90°	Date/Time	0°	45°	90°	Date/Time	0°
9:00:00	5.8E+03	2.1E+04	2.7E+04	5.8E+03	2.3E+04	2.9E+04	5.8E+03	4.0E+03	3.1E+03
10:00:00	6.3E+04	2.1E+05	2.4E+05	6.3E+04	1.7E+05	2.0E+05	6.3E+04	3.2E+04	2.6E+04
11:00:00	1.6E+05	4.5E+05	5.1E+05	1.6E+05	2.7E+05	2.8E+05	1.6E+05	5.9E+04	5.3E+04
12:00:00	2.4E+05	6.9E+05	7.6E+05	2.4E+05	2.6E+05	2.3E+05	2.4E+05	7.2E+04	6.5E+04
13:00:00	2.5E+05	6.8E+05	7.4E+05	2.5E+05	1.5E+05	9.1E+04	2.5E+05	1.5E+05	9.1E+04
14:00:00	1.9E+05	3.8E+05	3.9E+05	1.9E+05	1.0E+05	7.4E+04	1.9E+05	1.9E+05	1.5E+05
15:00:00	1.3E+05	2.3E+05	2.4E+05	1.3E+05	7.6E+04	5.4E+04	1.3E+05	1.6E+05	1.5E+05
16:00:00	5.9E+04	1.5E+05	1.6E+05	5.9E+04	3.6E+04	2.7E+04	5.9E+04	1.3E+05	1.4E+05
17:00:00	4.6E+03	1.1E+04	1.3E+04	4.6E+03	3.5E+03	2.4E+03	4.6E+03	1.2E+04	1.4E+04

The generation profiles of various tilt positions of the basic configuration, on the four solstice/equinox days are presented in Figure 6. The daily optimal control allows higher generation at each hour of the day, producing, in some cases, substantial increase at specific hours such as mornings and evenings, as compared to the fixed positions.

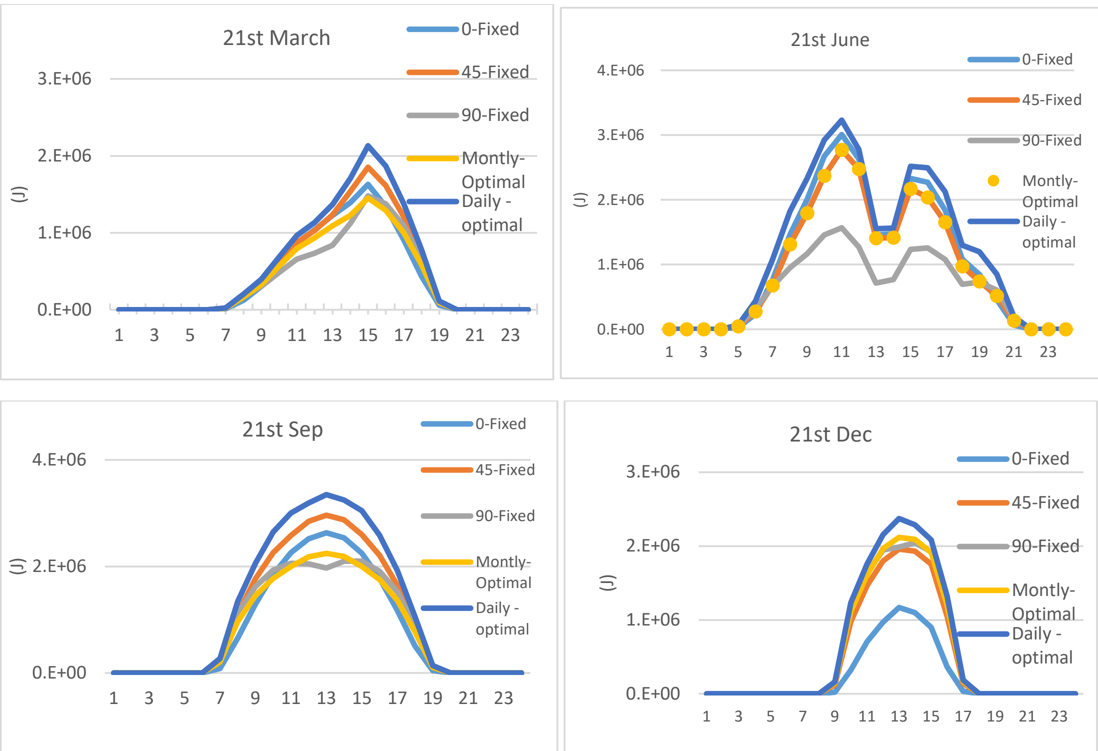

Figure 6, generation of different configurations on the equinox and solstice days

3.2 2-Level configurations

The results of the three studied 2-level configurations –basic, variations, and basic- variation are presented below. Table 8 shows the results of the fixed position of each configuration, as well as the comparison between these configurations. It should be noted that for the fixed positions, the two levels are studied at similar as well as different positions.

The comparison of the variation and basic-variation to the basic design shows that in the majority of cases, these variant configurations outperform the basic configuration. The increase in electrical output reaches 11% for with the 2-level variation with the bottom plates horizontal and the upper plates inclined or vertical. Significant increase (>5%) is highlighted in Table 8.

Table 8: yearly generation of all 2-level configurations associated with various fixed positions of each of plate of the 2 levels, and comparison of these configurations

Position (1st level, 2nd level)	Yearly generation			Comparison	
	Basic	Variation	Basic- variation	Variation/Basic	Basic-Variation/Basic
0 º -0 º	9.80E+09	9.56E+09	9.63E+09	0.97	0.98
0 º -45 º	9.48E+09	1.05E+10	1.06E+10	1.11	1.11
0 º -90 º	8.64E+09	9.38E+09	9.47E+09	1.09	1.10
45 º -0 º	1.08E+10	1.10E+10	1.09E+10	1.01	1.01
45 º -45 º	1.14E+10	1.19E+10	1.21E+10	1.04	1.06
45 º -90 º	1.01E+10	1.10E+10	1.08E+10	1.08	1.06
90 º -0 º	9.61E+09	9.82E+09	9.66E+09	1.02	1.00
90 º -45 º	1.01E+10	1.07E+10	1.09E+10	1.06	1.08
90 º -90 º	8.94E+09	9.24E+09	9.47E+09	1.03	1.06

The yearly generation for optimal monthly and hourly positions for all configurations is presented in Table 9. The comparison of the hourly generation to the optimal fixed position (45º) shows an increase of generation of 13%, 12% and 8% for the basic configuration, the variation and basic-variation configurations, respectively. The optimal monthly position yield less significant change as shown in Table 9. The hourly change as compared to horizontal and vertical fixed position of both levels is about 46% and 56% respectively, for the variation configuration.

Table 9: generation associated with monthly and hourly change, for each configuration and comparison to the generation by the optimal fixed position

Configuration	Generation		Comparison		
	Monthly optimal	Hourly optimal	Monthly to yearly	Hourly to yearly	Hourly to monthly
Basic	1.18E+10	1.32E+10	1.04	1.17	1.13
Variation	1.25E+10	1.38E+10	1.06	1.18	1.12
Basic- variation	1.25E+10	1.33E+10	1.03	1.12	1.08

An example of change of tilt position between the bottom and upper level of the 2-level basic configuration is shown in Table 10. Although the values of the hourly electricity production refer to the panels of the 1st level, the optimal position of the two levels are indicated. For examples a 45 º -90 º E (in the top row of Table 10) corresponds to the east panels, with the first level (bottom) at 45 º and the 2nd level (top) at 90 º.

It should be mentioned that in some cases, several possibilities can be obtained. Although south oriented panels are optimally at vertical position in the winter months, they are subject to more hourly variations during other months of the year. This is also shown for the single level variation presented above (Tables 4-7).

Table 10: Hourly energy generation of the panels with different orientation (S, E and W) of the 2-level basic design during the winter solstice

	Tilt position of the bottom and upper level panels (of the same orientation)							
Time	90º-90 º -S	0 º -0 º -E	45 º-90 º-E	90 º-0 º -E	90 º-90 º-E	0 º-0 º W	45º-90ºW	90 º -0º-W
09:00:00	2.65E+04	5.24E+03	2.30E+04	2.93E+04	2.93E+04	5.20E+03	3.81E+03	3.10E+03
10:00:00	2.43E+05	5.84E+04	1.78E+05	2.05E+05	2.05E+05	5.81E+04	3.03E+04	2.65E+04

11:00:00	5.04E+05	1.50E+05	2.90E+05	2.82E+05	2.82E+05	1.50E+05	5.66E+04	5.26E+04
12:00:00	7.61E+05	2.30E+05	3.08E+05	2.34E+05	2.34E+05	2.30E+05	8.10E+04	6.55E+04
13:00:00	7.40E+05	2.41E+05	1.97E+05	9.08E+04	9.08E+04	2.40E+05	1.96E+05	9.06E+04
14:00:00	3.89E+05	1.77E+05	1.02E+05	7.42E+04	7.42E+04	1.76E+05	2.06E+05	1.52E+05
15:00:00	2.36E+05	1.16E+05	7.22E+04	5.41E+04	5.41E+04	1.15E+05	1.69E+05	1.51E+05
16:00:00	1.63E+05	5.40E+04	3.48E+04	2.69E+04	2.69E+04	5.37E+04	1.29E+05	1.43E+05
17:00:00	1.27E+04	4.12E+03	3.30E+03	2.45E+03	2.45E+03	4.09E+03	1.18E+04	1.41E+04

The comparison between the performance of the 2-levels configurations is presented in Figure 7 for the winter solstice and fall equinox days. While the configurations perform similarly for the summer and spring days, the 2-level variations present more advantageous design for the winter and fall days.

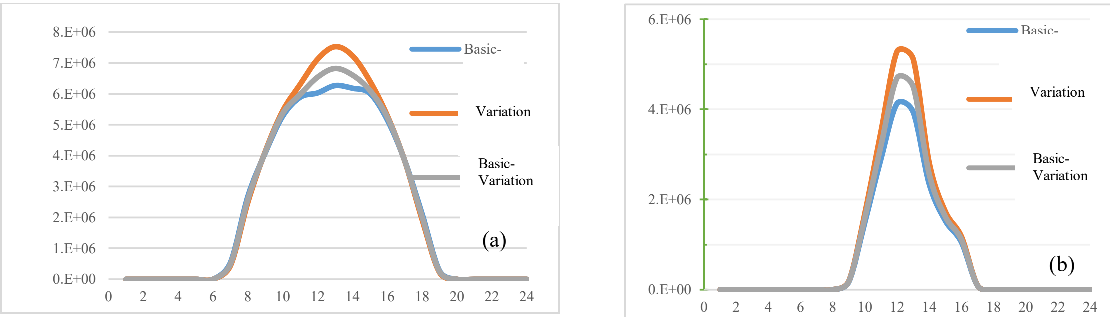

Figure 7, generation profile of all 2-levels configurations: a) Fall equinox; b) Winter solstice.

4. Discussion and Conclusion

This work presents an investigation into the potential of adaptable landscape PV structures (ALPVs), and their performance as compared to fixed structures. Several configurations are designed and their performance in terms of electrical output is analyzed. The designs include a single level structures and 2-level structures, with PV panels stacked on top of each other with a distance in between equal to double of the length of the basic plate of PV. An innovative approach of changing only the tilt of the PV plates, with determined fixed orientation is adopted in this research, in contrast to methods of tracking the sun path all day long. This approach is adopted to reduce the frequency that the plates need to change position and thus reduce associated energy consumption, as well as fabrication and maintenance costs. This investigation is aiming at developing structures that can be incorporated within urban landscape, and can present some architectural and visual interest, while providing multi-functional benefits. The main observations of this investigation are discussed below.

- Monthly variation of the ALPVs, where the plates of different orientations take the optimal position for a specific month, is more beneficial for south plates, while east and west plates are optimal at a 45^{o} tilt. Monthly change increases the performance as compared to a fixed state of optimal tilt (45^{o} tilt) slightly (by up to 5%), but allows a significant increase as compared to the horizontal and vertical PV (16% and 36% respectively). Such design of PV structures can offer supplemental energy generation in existing urban areas where the potential to integrate PV systems in buildings is restricted due to non-optimal surface areas, associated with existing orientation and tilt angles.
- The hourly change of the plates position increases the generation significantly as compared to the fixed tilt position. The fact that the change only happens 3 to 4 times per day and does not occur at every hour as in the case of a rotational motion that follows the daily sun path, reduces the amount of energy required to move the structure. The increase of generation can be very significant, especially if compared to fixed non-optimal position (e.g. horizontal or vertical). This increase in generation ranges between 30-35% for different configurations as compared to the horizontal fixed position and by up to 54% as compared to a

fixed vertical position.

- The concept of designing two levels of PV plates mounted on top of each other, provides an opportunity to increase available areas for PV panels, while occupying the same land area. This concept can be applied to multiple levels, providing significant potential to generate renewable energy in urban areas, where land can be scarce and expensive.
- These ALPVs can present an interesting design especially in public areas, allowing to be better integrated with the landscape and with outdoor comfort. The flexibility of design and changing the shape of the structure reduce the massive aspect that PV structures might take, and therefore their intrusion on the landscape (See Fig 1). This research shows that an improved position for south facing panels is vertical in winter, allowing solar radiation to reach the ground (and people using the space), providing thus more warmth, while in the summer a near horizontal position provides shade to the surrounding. The concept of changing tilt angle of the panels has the potential to adapt to non-optimal situation due to shadow cast by buildings.

This study is a conceptual demonstration of the design of Adaptable Landscape PV structures (ALPVs). Simple designs are presented in this work, to investigate the potential of these structures and flexibility that can be obtained. Variations of the design to respond to various aesthetic and architectural values can be studied in more elaboration, in the future, in order to reduce intrusion on the landscape, both visually and functionally.

5. References

Afrin, F., Titirsha, T., Sanjidah, S., Siddique, A.R.M. and Rabbani, A., 2013, December. Installing dual axis solar tracker on rooftop to meet the soaring demand of energy for developing countries. In 2013 Annual IEEE India Conference (INDICON) (pp. 1-5). IEEE.

Anuraj, A. and Gandhi, R., 2014. Solar tracking system using stepper motor. international journal of electronic and electrical engineering, 7(6), pp.561-566.

Crawley, D.B., Lawrie, L.K., Pedersen, C.O. and Winkelmann, F.C., 2000. Energy plus: energy simulation program. ASHRAE journal, 42(4), pp.49-56.

Ellis, P.G., Torcellini, P.A. and Crawley, D.B., 2008. Energy design plugin: An EnergyPlus plugin for SketchUp. National Renewable Energy Lab.(NREL), Golden, CO (United States).

Kapetanakis, I.A., Kolokotsa, D. and Maria, E.A., 2014. Parametric analysis and assessment of the photovoltaics' landscape integration: Technical and legal aspects. Renewable energy, 67, pp.207-214.

Khalil, F.A., Asif, M., Anwar, S., ul Haq, S. and Illahi, F., 2017. Solar tracking techniques and implementation in photovoltaic power plants: A review. energy, 3, p.4.

Mahmood, O.T., 2013, December. Programmable logic controller based design and implementation of multiple axes solar tracking system. In 2013 International Conference on Electrical Communication, Computer, Power, and Control Engineering (ICECCPCE) (pp. 101-106). IEEE.

McDonald, R.I., Kiesecker, W.M. and Powell, J., 2009. Energy sprawl or energy efficiency: Climate policy impacts on natural habitat for the United States of America. PLoS ONE.

Moghbelli, H. and Vartanian, R., 2006, April. Implementation of the movable photovoltaic array to increase output power of the solar cells. In Proceedings of the International Conference on Renewable energy for developing countries.

Prados, M.J., 2010. Renewable energy policy and landscape management in Andalusia, Spain: the facts. Energy policy, 38(11), pp.6900-6909.

Scognamiglio, A., 2016. ‘Photovoltaic landscapes’: Design and assessment. A critical review for a new transdisciplinary design vision. Renewable and Sustainable Energy Reviews, 55, pp.629-661.

Tania, M.H. and Alam, M.S., 2014, May. Sun tracking schemes for photovoltaic panels. In 2014 3rd International Conference on the Developments in Renewable Energy Technology (ICDRET) (pp. 1-5). IEEE.

Tsantopoulos, G., Arabatzis, G. and Tampakis, S., 2014. Public attitudes towards photovoltaic developments: Case study from Greece. Energy Policy, 71, pp.94-106.

Turney, D. and Fthenakis, V., 2011. Environmental impacts from the installation and operation of large-scale solar power plants. Renewable and Sustainable Energy Reviews, 15(6), pp.3261-3270.

Mapping Priority Energy Intervention Areas in Birmingham (UK)

Helena López Moreno[1,3], Emily Prestwood[2], Grant Wilson[2], Emanuela Giancola[1], María Nuria Sánchez Egido[1], Fco. Javier Neila González[3] and Silvia Soutullo Castro[1]

[1] Energy Department, Energy Efficiency in Buildings Unit of CIEMAT, Madrid (Spain)

[2] Birmingham Energy Institute (BEI), University of Birmingham (UK)

[3] Construction and Architectural Technology, Department of UPM, Madrid (Spain)

Abstract

A reduction of energy consumption and efficient clean solutions in buildings are needed to face the climate change. Thus, a sustainable roadmap should be addressed, fostering urban strategies that reduce energy and social inequalities. However, uncertainties to identify and map households' conditions limit this process

Priority Intervention Areas (PEIA) methodology, based on geographic information systems, characterizes energy deprived areas by overlapping of the lowest values of the Index Energy Deprivation (IED) and the Index Multiple Deprivation (IMD). IED, defined to this aim, locates energy vulnerable areas, facing differences between real and theoretical consumptions associated to user´s behavior. Thus, an urban classification based on building properties and age of construction is developed. IMD deal with socioeconomic and environmental aspects. The city of Birmingham and its east corridor is evaluated as case of study. 23 Lower Layer Super Output Areas (LSOA) has located as PEIA, represented mainly by terraced houses. East Birmingham shows lower values of IED and IMD, identifying 6 PEIA with a higher deprivation intensity compared to the whole city. The proposed method fosters detailed, fair and low carbon strategies to tackle the new climate scenarios.

Keywords: energy poverty, energy performance, socio-economic indices, urban classification, climate change.

1. Introduction

In 2018 the 27% of the final energy consumption in EU belonged to the residential sector, being even superior in the UK reaching the 31% (Eurostat 2018). This fact implies that housing, the second sector with the highest energy consumption after transport, represents one of the crucial areas to face the global warming.

Because of this, positive energy districts and energy retrofitting based on the reduction of energy demands and the use of renewable energy are becoming decisive solutions. To develop these measurements tailored and fair plans are needed. The IPCC report (IPCC 2018) highlights the impact of forecasted extreme climatic events upon vulnerable population. To this end, "green" challenges must consider an energy and a socioeconomic perspective. In that sense, UK government designed the Climate Change Act (CCA 2008). Regionally, the West Midlands area, characterized by a rich industrial heritage, but also for its socioeconomical differences have developed some programs to tackle this situation as the Road Map 2020 (R20 West Midlands)

According to the region forecasts, the Birmingham City Council (BCC) through the Route Zero Taskforce (R20 Taskforce) and BCC´s Green Commission, set out the city´s transition to a future low-carbon roadmap (BCR 2013). It provides a clean framework to reduce total Birmingham´s CO_2 emissions by 60% in 2027. To this aim it is developed an innovative energy system putting together public, commercial, academia and communities sectors in order to become the city more prosperous, healthier, fairer, more resource-efficient and better for business (BEI). One of the main plan´s concerns is the energy poverty, defined as a household which needs to spend more than 10% of its income on fuel to maintain an adequate standard of warm.

Tysely Energy Park (TEP) is one of the projects framed in the described energy transition roadmap. It is founded as a collaborative action between the manufacturing business, council-owned energy plant and the Birmingham University to foster the East Birmingham industrial area through the reuse of waste energy (BU

doi:10.18086/eurosun.2020.13.02 Available at http://proceedings.ises.org

2013). One of the potential scenarios is focused the reuse of heat waste coming from the industry to supply the wasted energy to the communities in this zone. The possible prototype could be carried out through a district network, fostering the circular economy and the deprived East Birmingham neighbourhoods.

The city of Birmingham is notably affected by the fuel poverty phenomena, 1 in 5 households is classed as fuel poverty, considerably higher than the national average of 1 to 10, being even worse in the East Birmingham where the 18% of dwellings have problems to afford the fuel costs or they need an amount higher than the national mean (Sub-Regional). Beyond economical and house quality problems, energy poverty triggers other consequences as health problems (Sanz Fernández et al. 2017). In addition, East Birmingham face other socioeconomic challenges as a low economic activity rates, 3% less than the city average, especially amongst women, high levels of public transport congestion or an habitable house shortage (BCC 2015).

In order to reduce inequalities in this area a tailored, fair and clean energy transition should be developed to ensure the habitability conditions in Birmingham´s city, pointing out a particular attention in the East Birmingham. An impactful and innovative action on climate change will be only secured if it is connected to the householders and communities. However, building sector present shortcomings to deal with these considerations due to the diversity of stakeholders, building typologies and final users that are involved.

Hence, this study presents a methodology to map areas where energy intervention effort is needed because of their vulnerable situation (lower social or economic position, poorer dwelling conditions or both energy poverty situations) (Bouzarovski and Petrova 2015). To this end, the planned objectives for this work are: a) The quantification of real energy consumption and a deep analysis of the theoretical energy consumption according to the building characteristics. b) An index to quantify potential differences between real and theoretical energy consumption. c) An evaluation of the socioeconomic situation though different indicators. d) The location of the Priority Energy Intervention Areas for the city of Birmingham.

2. Priority Energy Intervention Areas methodology (PEIA)

The energy consumption in dwellings depends on buildings characteristics (surface, materials or typology), but social and economic conditions modify this pattern (IEA 2016). A low energy burden is associated to efficient buildings, but it could also be related to a low income. On the contrary, a high energy burden besides user without problems to pay energy bills, could also mean an inefficient household. This complex combination of factors (energy-housing and social-economic perspectives) implies uncertainties to face the energy poverty situations. Priority Energy Intervention Areas method (PEIA) is focused to solve this situation. PEIA is approached by a novel combination of both energy housing perspective through the Index Energy Deprivation (IED) and socioeconomic perspective over the Index Multiple Deprivation (IMD). The lowest IED and IMD zones will be defined as a PEIA, easing the location of households where gas and electricity bills are low because of their socioeconomic situation.

The methodology is developed firstly, studying the region through different areas according to Lower Layer Super Output Area (LSOA) classification by Geographic Information Systems (GIS). Then, the IED and IMD values are defined for each LSOA. The IED is calculated by the relation between the real and theoretical energy consumption. The IMD considers different potential deprivation levels. Finally, the overlapped areas of both the first IED and IMD decile will be considered as a PEIA. The whole city of Birmingham and the east Birmingham area will be analysed separately in order to know the differences between them.

2.1. Birmingham city classification: LSOAs

The city of Birmingham is selected to this study because of its relevance in the UK´s development. After London, it is the largest city and the widest metropolitan economy in United Kingdom. Among its complex urban area diverse cultural, economic and social levels are found, that could be a source of the inequalities. In that sense, the east Birmingham corridor, where is located Tysely Energy Park and the constituencies of Hodge Hill and Yardley, have higher unemployment, lower skills rate and poorer health than other parts of the city.

To quantify and locate these urban differences, the city is studied through LSOAs areas (LSOA), designed for statistical studies in England and Wales. They have been generated with a minimum of 1000 inhabitants and the mean is 1500. The city of Birmingham has 640 LSOAs, which 130 of them belongs to the East Birmingham. They have a mean of 1727 citizens, being the total population of the city 1.1 million inhabitants.

2.2. Energy consumption approaches

The energy consumption characterization could be addresses by different perspectives and factors as follows:

2.2.1. Real energy consumption

A top-down approach based on GIS could be an efficiency tool to analyze globally the potential energy deprivation in an area that could be evaluated more precisely later if it is identified as a susceptible zone. Disaggregated energy consumption provided by UK´s statistics is used for this purpose. Although it is assumed that energy data shouldn´t be provided individually (user´s data protection), this analysis presents some weakness. As it is said, construction characteristics and user patters vary the dwelling´s energy consumption.

That´s means that it is hardly to identify the real reason of high or low energy consumption. High amounts could be related to an inadequate construction system, a poor quality of materials or an inefficiency facility, but also with an unconscious behaviour of energy use because a lack of knowledge or commitment. On the other hand, low energy consumption rates could be associated to a good design, high-tech, high construction quality or energy efficiency systems, including the use or renewable energies. Nevertheless, this low quantity could be linked also to an energy deprivation because of difficulties to afford the cost.

2.2.2. Energy performance simulation

Other procedures to know the energy consumption are based on the calculation of theoretical energy consumption, as the energy performance. This estimated value is got by dynamic energy simulation tools. It defines the quantity of energy that household need under habitability and comfort conditions according with their local climate, construction systems, material properties, facilities and a standard of user´s behaviour.

This bottom-up approach could be more precise defining the energy demand by building or dwelling, instead of a generic area. In addition, it can be transformed in a top-down approach though GIS calculations based on the building geometries and a ratio of energy consumption by surface. However, this procedure also presents shortcomings that limit the priority energy areas identification with discrepancies between the real and theoretical energy consumption. Besides the climate data and building properties, an imprecise user´s patterns could be one of the main reasons behind this problem. In the studies focused on the possible energy vulnerabilities identification, the role of the user´s occupancy and their behaviour are crucial.

2.2.3. Climate, building and user; energy shapers

A common method to characterize the local weather conditions is the typical meteorological year (TMY), that must be based on long term weather variables records (at least 10 years), to ensure the natural climate cycles. Depending on the study, there are diverse methodologies to assess the TMY, varying the weight factor of the meteorological variables(Zarzalejo et al. 1995; Soutullo et al. 2017). These climate data files are usually given by the energy simulation tools or provide by a normative standard. One of the widest climate data are the EPW files, developed by ASRAE and used by the Energy+ software (EnergyPlus) . Other files are necessary for an energy certification as the .MET files developed by the Spanish normative (CTE 2015). Some studies point out possible deviations between real and simulated energy consumption due to outdated climate data files that don't consider the climate change or the urban microclimate effect (Soutullo et al. 2020; Sánchez et al. 2020).

Physical properties of the construction materials are need for the calculation of the thermal transmittance of the building envelope. In addition, the type of zones (acclimatized or not acclimatized) and the performance of the facilities need to be known for the calculation of the heat transference. The time-consuming, complex or invasive process of the material identification, areas and facilities characterisation lead to establish some assumptions. Most of these inferences are based on the urban characteristics, like the type of building or the year of construction. These properties gather similar patterns as the occupancy for residential or not residential buildings, the household morphology depending on the urban archetypes or the facilities efficiency and insulation type according to the construction year. The English Housing Survey (EHS) provides ratios of energy consumption according to these characteristics. Moreover, the LandMap project (LandMap 2012) provides mapped information about building type for many conurbations in the UK. Additionally, the Ordnance Survey (OS) facilitates other geographic information as the residential zones or the high of buildings.

Finally, the occupant behavior style has significant influence on the energy used in heating systems in buildings (Sun and Hong 2017). In addition, the building occupancy patterns have changed, as an example in Spain the number of people how live alone has increased, being most of them elderly women (INE 2014). Due to an undetailed or inexistence of a user´s data base, it is generally used standard and normative occupancy parameters for the energy simulation models. However they don’t incorporate a variety of socio- economical parameters relating to lifestyle, heath condition or family situation (Cuerda et al. 2019).

2.2.4. Index Energy Deprivation (IED)

The development of the Index Energy Deprivation (IED), leads with the found weakness. It is defined as the relation between the real and theoretical energy consumption and it gives an idea of how low or high is the amount of the energy consumed compared to the amount of energy that the same building or household should consume according to the standards (comfort minimum values of indoor temperature, humidity, air ventilation, light or equipment and home appliances use). Values lower than 100% mean that energy consumption is less that it should and could present some vulnerabilities as the energy poverty.

2.3. Socioeconomic indicators

A low Energy Deprivation Index not necessarily means an energy deprivation household per se. Some false positives could be found as an empty dwelling, second or occasional residence or high energy efficiency. In order to avoid these situations, other aspects as economic, social, urban-environmental or health parameters have been considered. It is assumed that citizens who belongs to low socioeconomic profiles with health problems or live in a depressed area could be also be related to energy deprivation.

In that sense, the Index Multiple Deprivation (IMD) addresses different patterns of deprivation per area. It is based on 39 separate indicators, organised across seven distinct domains of deprivation which are combined and weighted (IoD) . The main attended topics and its corresponding weighted relevance are: Income (22.5%), employment (22.5%), health deprivation and disability (13.5%), education, skills training (13.5%), crime (9.3%), barriers to housing and services (9.3%) and living environment (9.3%). Consequently, through the IMD other concerns as the climate data, the quality of buildings or the user behavior could be approached.

The IMD is calculated for every LSOA in England. Their values are ranked according to their level of deprivation relative to that of other areas. High ranking LSOAs can be referred to as the ‘most deprived’ or as being ‘highly deprived’ to aid interpretation, but they are measured on a relative rather than an absolute scale. This fact means that the ranked area as 200th is not twice as deprived as ranked area as 100th, but this number gives an idea of as 100th area should be addressed firstly.

2.4. Definition of Priority Energy Intervention Areas (PEIA)

The combination of both low energy deprivation areas and low multiple deprived areas describe zones which: a) Their energy consumption is lower than a building with its same characteristics conditioned in comfortable conditions. b) Their zones are more deprived in terms of economic, social, health and urban-environmental aspects, that limit the achievement of a minimum of habitability conditions. Therefore, in these neighbourhods, strategies to ensure a good quality and wellbeing are a priority.

In that sense, the Priority Energy Intervention Areas (PEIA) are defined as areas which both the Index Energy Deprivation and the Index Multiple Deprivation belongs to the first decile. This condition gathers the overlapped zones of the lowest IED and IMD conditions.

3. Applied methodology for the city of Birmingham

The Priority Energy Intervention Areas (PEIA) methodology is applied for the whole city of Birmingham (Bham) and more in detail in the East Birmingham (EBham), where is located the Tyseley Energy Park. Firstly, is mapped the real energy consumption (gas and electricity) through LSOA classification. Secondly, it is estimated and located the theoretical energy consumption aggregated by urban typology and year of construction. Then, the Index Energy Deprivation (IED) and the Index Multiple Deprivation (IMD) is defined by LSOA. Finally, the PEIAs are determined by the overlapping of the lowest IED and IMD decile. The number of LSOAs that are classified as PEIA are compared between Birmingham and its East area.

All the data provide by LSOA is calculated by inhabitants (persons) and year to ease the data comprehension. The most updated files considering all data sources, in order to avoid uncertainties between different period times, has been the year 2017. For the calculations is only used the domestic data. No-residential data and areas with no data are not considered and they are indicated on the maps, as well as the Tyseley Energy Park area.

Results are shown by deciles, dividing the number of values in 10 groups with an equal number of LSOAs. As the city of Birmingham has 640 LSOAs, the first decile (decile 1) belongs to the lowest 64 LSOAs (0-64), continuing the classification to the last decile (decile 10) that gather the 64 highest LSOAs values (576-640). This number could be modified if there are LSOAs with no data that will change the total number of LSOAs.

Some figures include a graph in its bottom-left part that aims to know the variability between LSOAs values differentiating Bham (black dots) and EBham (grey dots). In the X axis are located the deciles for the Bham data set and the Y axis represents the LSOAs values. The mean for the total of LSOA values are also represented for Bham (black line) and EBham (grey line).

3.1. Index Energy Deprivation (IED)

For the Index Energy Deprivation (IED) the real and theoretical energy consumption are achieved as follow:

3.1.1. Real energy consumption

The real energy consumption (EC_{real}) for domestic use is provided by the UK statistics of electricity and gas consumption at LSOA layer (Sub-national). The sum of gas and electricity consumption is calculated.

The Figure 1 maps the values of real energy consumption. It is observed differences within the city; north and southeast neighbourhoods present the highest energy consumption values, while west and east zones belong to the lowest deciles. This is also revealed by the total energy means calculations, with 6573 kWh/inh per year for Bham and 5695 kWh/inh per year for EBham, that belongs to the decile 6 and decile 4.There is a high variability between Bham points in the first and last deciles, that is less significant for the last decile of EBham.

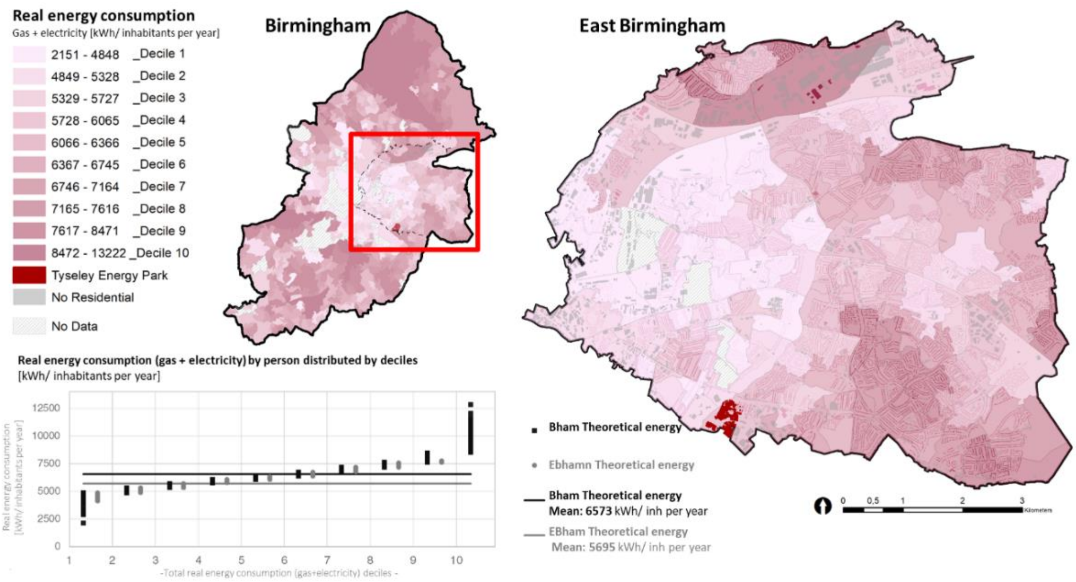

Figure 1. Real energy consumption (gas and electricity) by Bham´s LSOA [kW/inh per year] gathering by deciles.

3.1.2. Urban properties

In order to locate and quantify the theoretical energy consumption for each city´s building, firstly it is necessary define the buildings characteristics and their location. The Cities Revealed Building Class´s datasets (LandMap 2012) classify the main residential buildings grouped by their age and building type, with a total of 9 age categories and 19 type categories. The classification is generated primarily by photo interpretation of high resolution digital aerial photography and the evaluation of different elements as shape and size, materials, etc.

This urban classification allows mapping a detailed urban characterization and geometry, however it doesn´t offer an energy consumption estimation. The English Housing Survey datasets (EHS) incorporates an updated and exhaustive dataset of the energy performance for different urban characteristics based the energy performance building certificates. These data file is divided in diverse levels according to dwellings, areas households and heating and insulation characteristics. Within the dwelling level the energy performance is divided by tenure, occupancy status, dwelling age, dwelling type or total usable area floor.

The combination of the LandMap and EHS analysis allows both the estimation of the theoretical energy consumption (kW/m^2 per year) by urban typology and age of construction and also the location of this attributes. However, they don´t share the same class groups, because of this an on purpose PEIA classification for this study is done based on both LandMap and EHS categories. Figure 2 shows the urban classifications for LandMap (top-left), EHS (top-center) and PEIA (bottom) categorizations and its assumptions (top-right).

A matrix of selected or combined building typologies and age of construction is done. Conducted typologies are flats (high and low), terraced houses (large and small), semidetached houses and detached houses. On the other hand, the period of construction classes are: before 1919, 1919-1944, 1945-1964, 1965-1980, 1981-1999 and after 1999. The PEIA is classified by a total of 29 building typologies. A no classified typology and a no residential categories are included, despite of the fact that the last one is not considered for further analysis.

Previous Urban Classification

LANDMAP PROJECT BUILDING CLSSIFICATON		ENGLISH HOUSING SURVEY	
Urban Typology	Age of construction	Urban Typology	Age of construction
1. Very Tall Flats (point blocks) 2. Tall flats 6 - 15 storeys (slabs) 3. Medium height flats 5 - 6 storeys 4. Lower 3 - 4 storey and smaller flats, detached and linked 5. Tall terraces 3 - 4 storeys 6. Low terraces, 2 storeys with large T-rear extension 7. Low terraces, small 8. Linked and step linked houses, 2 - 3 or mixed 2 - 3 storeys 9. Planned balanced-mixed estates 10. Standard size semis 11. Semi type house in multiples of 4,6,8 etc 12. Large property semis 13. Smaller detached houses 14. Large detached houses 15. Very large detached houses, sometimes now flats 16. Bungalows, both detached and semi detached 17. Single storey small house	1. Historic to end Georgian – 1837 2. Early and Middle Victorian 1837 – 1870 3. Late Victorian/Edwardian 1870 – 1914 4. World War I - World War II 1914 – 1945 5. Post war regeneration 1945 – 1964 6. Sixties/seventies 1964 - 1979 Modern 1979-1999 7. Recent years 2000 - photo date **Property class** 1. No public building 2. public Building	1. Small terrace 2. Medium/large terrace 3. Semi detached 4. Detached 5. Bungalow 6. Converted flat 7. Pb flat, low rise 8. Pb flat, high rise	1. Pre-1919 2. 1919-44 3. 1945-64 4. 1965-80 5. 1981-90 6. Post 1990

Assumptions and criteria for urban typologies (residential buildings)

Surface per floor >35 m^2

Medium height >1.25 m

Floor height values:

- *Year: <1919-64: 2.50 m*
- *Year: >1965: 3.00 m*
- *No_classification: 2.75 m*

Coefficient acclimatized area:

- *Flat: 0.75*
- *Terrace, semi and detached: 0.85*
- *No_classification: 0.80*

Own Classification (combination of previous)

URBAN TYPOLOGY	AGE OF CONSTRUCTION					
	<1919	1919-44	1945-64	1965-80	1981-99	>1999
Res_FlatHieght			Res_FlatHieght1945-64	Res_FlatHieght1965-80	Res_FlatHieght1981-90	
Res_FlatLow	Res_FlatLow<1919	Res_FlatLow1919-44	Res_FlatLow1945-64	Res_FlatLow1965-80	Res_FlatLow1981-90	
Res_TerraceLarge	Res_TerraceLarge<1919	Res_TerraceLarge1919-44	Res_TerraceLarge1945-64	Res_TerraceLarge1965-80	Res_TerraceLarge1981-90	
Res_TerraceSmall	Res_TerraceSmall<1919	Res_TerraceSmall1919-44	Res_TerraceSmall1945-64	Res_TerraceSmall1965-80	Res_TerraceSmall1981-90	
Res_Semidetached	Res_Semidetached<1919	Res_Semidetached1919-44	Res_Semidetached1945-64	Res_Semidetached1965-80	Res_Semidetached1981-90	Res_Semidetached>1990
Res_Detached	Res_Detached<1919	Res_Detached1919-44	Res_Detached1945-64	Res_Detached1965-80	Res_Detached1981-90	
No Classification	Res_NoCalssification					

Figure 2. PEIA building classification (bottom) and its assumptions (top-right) based LandMap (top-left) and EHS.

Figure 3 presents the urban characteristics of the building PEIA classification. Figure 3.a. shows the building typologies (right-top) and the age of construction (righ-bottom) through a georeferenced map. Flats are located in the centre of the city and they are constructed recently. Semidetached and detached houses with a middle-old construction age are sprawled in the suburban neighbourhoods, mainly in the north and south of the city. Finally, terraced houses are located in the west and east areas of Birmingham´s city center. Small-size terraced houses are mainly middle age but most of large-size terraced houses were constructed before 1919.

The PEIA categorization is resembled for the energy performance data provide by the EHS based on dwelling type and age of construction. Then, it is interpolated their values to obtain a value of theoretical energy consumption for each PEIA class. Figure 3.b presents the theoretical energy consumption per surface (left-top and center) and for the whole building and also the representativeness of building typologies (right-bottom)

A notable value of inefficiency is shown for ancient buildings (before 1919 and between 1919 to 1944) and this value is downing along the time (approx. from 290 to 250 kWh/m^2 per year). Small terrace and semidetached typologies present the highest values of theoretical energy consumption around 20 kW/m^2 per year more than low flats and large terraces. Finally, detached houses energy values are the lowest until the middle of the 20th century, when the high flats flourished, with the best energy efficiency performance.

The typology that have the highest energy consumption per building are flats because of their large surface and height based by multiple apartments, specially the flat-high typology. Although its reduction of energy consumption per surface along the years decreases, this value is inverse for the energy consumption by building (reaching values higher than 40MW/ building per year). It could be explained due to the newest high-rise flats are larger. Similar pattern but in a slight manner have the low-rise flats. All single houses have notably lower energy rates, being approximately 2 to 3 MW/ building per year for the 2nd part of the century.

Finally, the quantity of buildings according their typology, give an idea of how the urban growth of the city was. According to the Figure 3.b. current Birmingham was founded on an urban settlement based basically on large terraced houses constructed before the 20´s (first world war). An urban boom took place after this period between 1919-1944 (between world wars periods) with the construction of more than a 100 thousand of semidetached houses and a little number of detached houses. Then, between the years 1945 to 1980 the growth of the semidetached continued, but in much low and stable manner and decreased from the 80´s. Small-size terraced households’ expansion was significant during 1965-1980, approximately 25 thousand were build up. The number of flats is very low compared to the other typologies for all periods, as well as the low number of residential constructions developed from the 21st century.

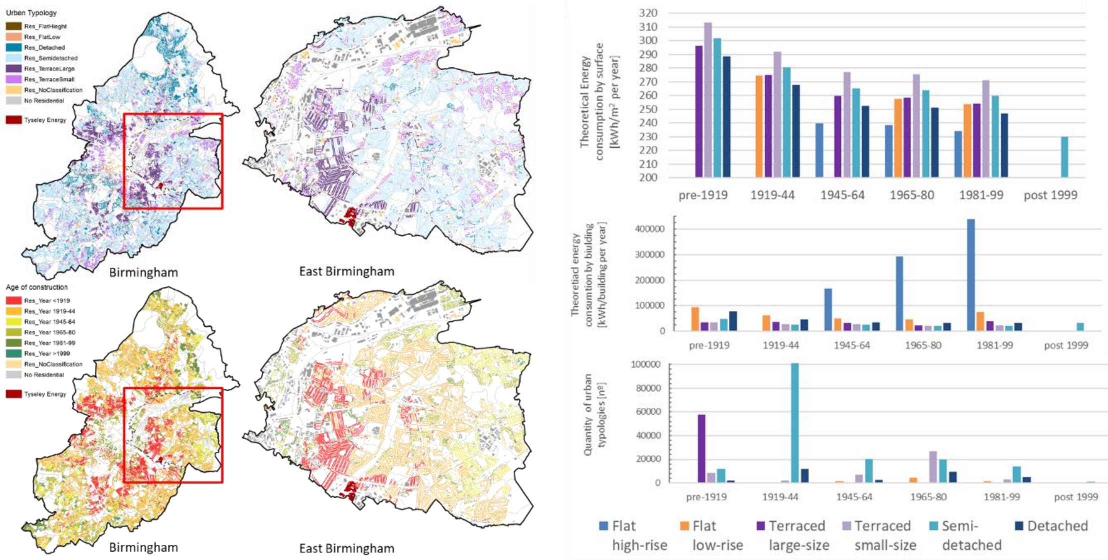

Figure 3. PEIA urban typology classification: a) Georeferenced map for the urban typologies and the age of construction (left) by LSOA classification. b) Theoretical energy characteristics and representaiveness of building typologies (right)

3.1.3. *Theoretical energy consumption*

The theoretical energy consumption (EC_{Th}) it is mapped for the city of Birmingham. This process is developed though the previously calculated theoretical energy consumption per area (EC_{TH_Area}) for each typology and the estimation of the acclimatized surface area per building ($Area_{Acc}$) (eq 1). The assessment of the acclimatized area is addressed by the print area of the building ($Area_{printed}$), provided by georeferenced geometry, the number of floors ($Nº_{floors}$), given by the building height and a coefficient of the acclimatized area ($Coef_{acc}$) (eq 2).

$$EC_{Th} = EC_{Th\_Area} \times Area_{Acc} \text{ [kWh/inh per year]} \qquad \text{(eq 1)}$$

$$Area_{Acc} = Area_{Printed} \times Nº_{floors} \times Coef_{acc} \text{ [m}^2\text{]} \qquad \text{(eq 2)}$$

Some regards are considered in these calculations with the aim of get a better adjustment of the theoretical energy consumption to the reality (Figure 2). Only are considered dwellings with an acclimatized area bigger than 35 m^2 and their mean height is upper than 1.25 m. The height of the buildings used to define the number of building´s floor is 2.5 m for buildings constructed before 1919 to 1964 and 3 m for buildings constructed after 1965. Lastly, a coefficient for acclimatized surface is settled to not include buildings‘ areas which are not heated or cooled as common corridors in flats or garages or storerooms. The acclimatized surface coefficients are 0.75 and 0.85 for flats blocks and single houses.

Figure 4 shows the results of the theoretical energy consumption calculated by the previous criteria gathering the results by LSOAs. Generally, the highest theoretical energy consumption belongs to the north part of the city that corresponds to detached and semidetached houses constructed before 1945. Also, some neighbourhoods located in the southwest, southeast and east of the city center, that are characterized by ancient small terraced houses, show a low efficiency. The north-west and the center buildings of Birmingham have a high ratio of energy efficiency. As it is described previously, the mean theoretical consumption values are lower in EBham than Bham with values of 8316 kW/inh per year and 9196 kW/inh per year respectively, that belongs to the decile 5 and 6 respectively. According to the bottom-left graph, the variability of LSOAs deciles is higher for Bham, especially for the last decile, where there is only a few EBham LSOAs

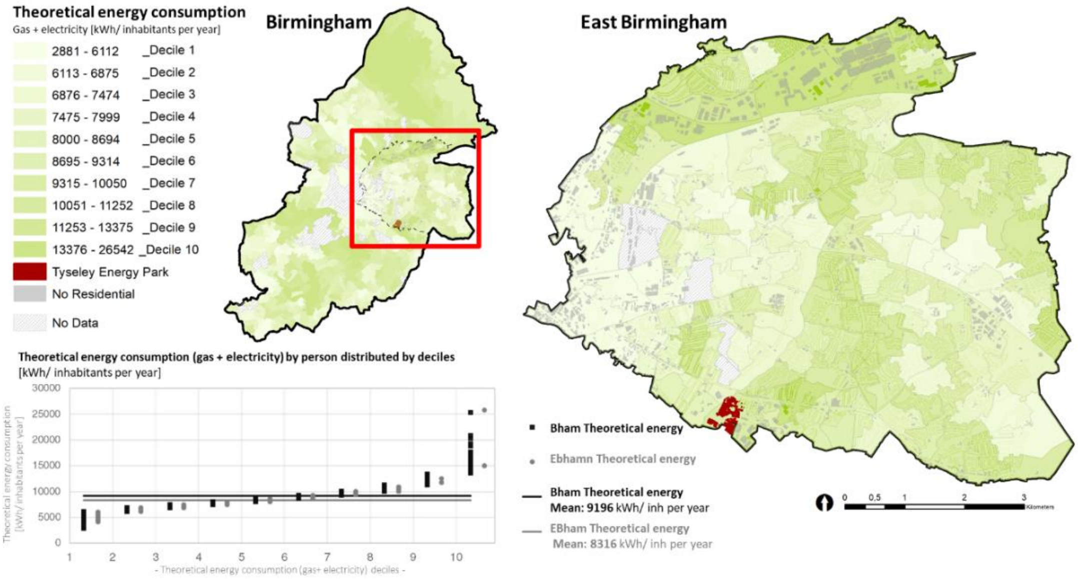

Figure 4. Theoretical energy consumption by Bham´s LSOA [kW/ Inhabitants-year] gathering by deciles

3.1.4. *Energy consumption comparison*

To know the energy behavior generally, the energy consumptions values for Birmingham city are compared to East Birmingham. The Figure 5 shows the LSOAs´ mean of energy consumption by person per the total (left) and relative value (%) for real gas, real electricity, real total and theoretical energy consumption (right).

Comparing the different energy values according with their origin, the means electricity consumptions are the lowest for all cases, being about three times lower than the mean gas consumption. The means of total real energy consumption sum the values of real consumption of gas and electricity. This quantity is lower than the mean theoretical energy consumption for the studied areas of Birmingham with values of 6573 kWh/inh per year and 9196 kWh/inh per year for real and theoretical energy consumption respectively. The mean of the theoretical energy consumption is lower in the EBham (10%) than Bham and its real energy consumption mean is approximately a 13% lower than the total city, highlighting the energy vulnerability in the east corridor.

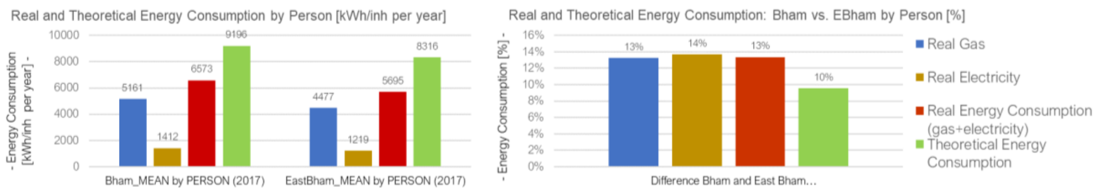

Figure 5. LSOAs´ means of energy consumption by person per the total (left) and relative value (right)

3.1.5. *Index Energy Deprivation*

The final process for the energy approach is the calculation of the Index Energy Deprivation (IED) (eq 3):

$$IED = \frac{EC_{Real}}{EC_{Th}} x100 \ [\%] \qquad \text{(eq 3)}$$

IED values lower than 100 % mean that consumption is lower than expected, associated to a low energy consumption, but not because the buildings of this area presents a higher efficiency than its typology mean. IED values equal to 100 % consume the same as it is expected. Lastly, IED higher than 100 % belongs to areas where the consumption is higher than expected. They would be related to a high energy burdens, but not because the buildings of this area present a lower efficiency than its typology mean.

Figure 6 reveals that the real energy consumption is less that the expected in most parts of the city (IES < 100%). Only a few LSOAs located in the decile 10 consume the same or more than the theoretical values, reaching a maximum of 197.5. Areas closest to the surrounded city center, west, east and southeast zones present the lowest values, including the proximities of the Tyseley Energy Park with values lower than the 50% of desirable energy consumption and reaching minimum values of 20.9% (decile 1). It should be noted that north areas that before presented high energy consumption values, now have areas that belongs to medium deciles. This fact means that the north LSOAs buildings consume more than their mean theoretical typology.

The mean for Bham LSOA´s neighbourhoods consumes an 81% less than the expected by the standards and belongs to the decile 8, being this value even lower for EBham where, the IED value is 73 %, located in the decile 7. This fact is translated as the mean IED for EBham is a 10% lower than Bham. A high variability is shown in the first and last decile, but as is graph most of values are between the IED values of 60 to 80%.

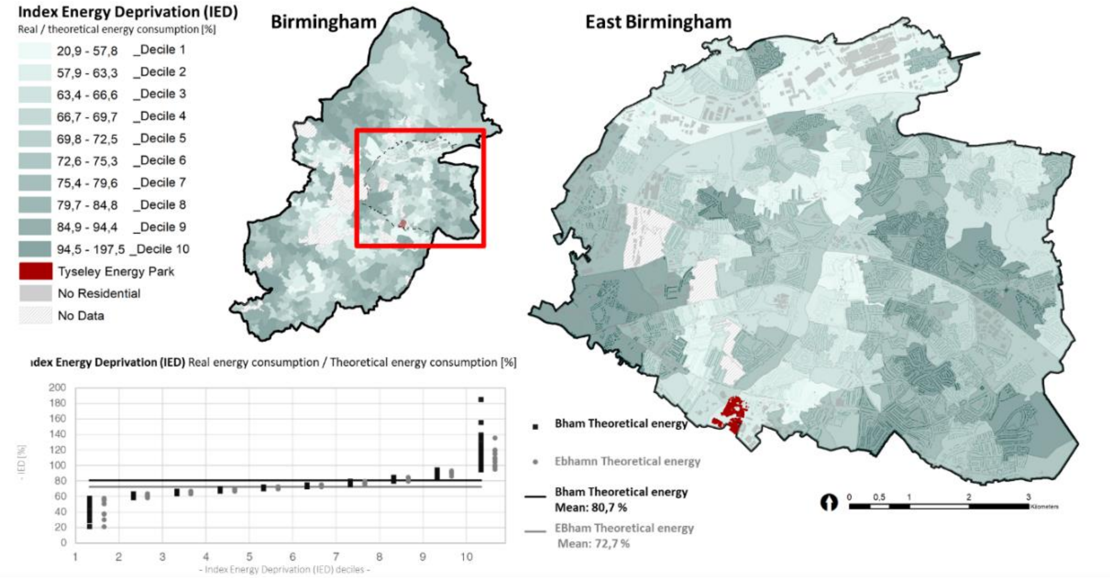

Figure 6. Index Energy Deprivation (IED) by Bham´s LSOA [%] gathering by deciles

3.2. Index Multiple Deprivation (IMD)

The Index Multiple Deprivation (IMD) provided by the English government (IoD 2017) is used to address socioeconomical factors. IMD is based on a scale from 0 to10 points (most to less deprived respectively) that relativizes England LSOAs. Hence, some deciles share the same values as the results are whole numbers.

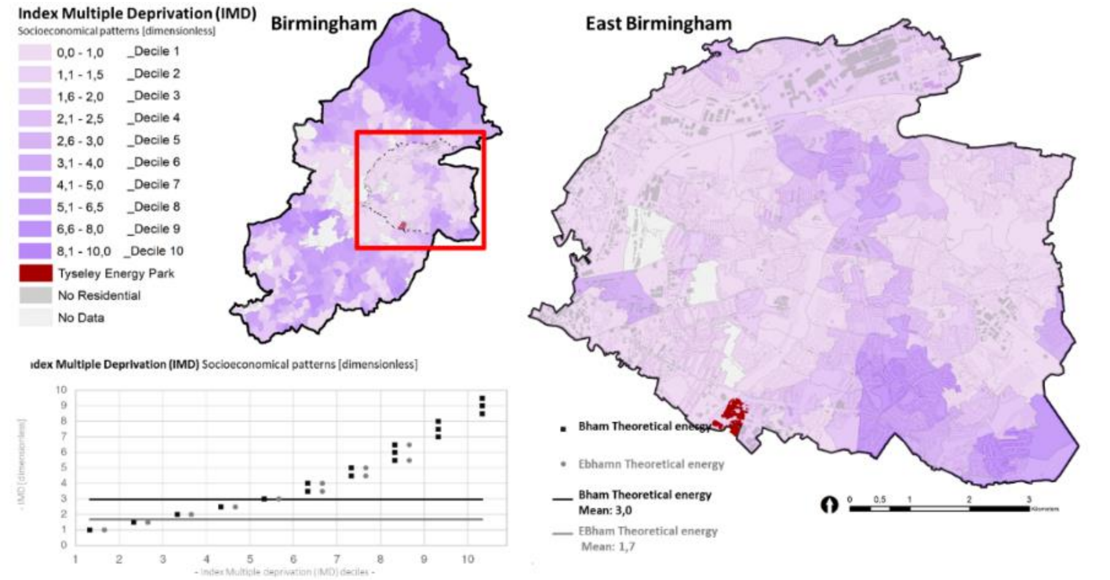

Figure 7. Index Multiple Deprivation (IMD) by Bham´s LSOA [dimensionless] gathering by deciles

Figure 7 present the IMD values aggregated by deciles for the city of Bham. It is observed that mainly the north and the south LSOA´s neighbourhoods are characterized by high IMD, on the contrary, the west and essentially the east of the city have the lowest values. Highlighted differences are found between Bham and EBham, with a mean of IMD values a 43 % lower for EBham (1.7) compared to Bham (2.97). IMD mean value of Bham is classified within the decile 6, while the IMD mean value for EBham corresponds to decile 3.

3.3. Priority Energy Intervention Areas (PEIA)

Finally, LSOA areas where both, IED and IMD correspond to the lowest decile, will be classified as Priority Energy Intervention Area (PEIA), because of their low energy and socioeconomic characteristics. City´s strategies should be address firstly in PEIAs because of the potential risks related to their deprivation situations.

The IED and IMD lowest deciles are mapped in the Figure 8. Green areas correspond to IED LSOAs located in the first decile (20,9 % to 57,8 %.). On the other hand, purple areas correspond to IMD LSOAs placed in the first decile (0 to 1). The overlap of decile 1 for IED and IMD values, reveal 23 PEIA zones located mainly in the west and east of the city. Six of these PEIA are placed in the east Birmingham corridor and three of them in the surrounding areas of Tysely Energy Park. For both Bham and EBham all IMD belongs to 1 value. The number of PEIA located in EBham is lower than the whole city, however they include a high intensity deprivation (fist decile IED mean for Bham is 52.0 versus the value of 49.3 of EBham)

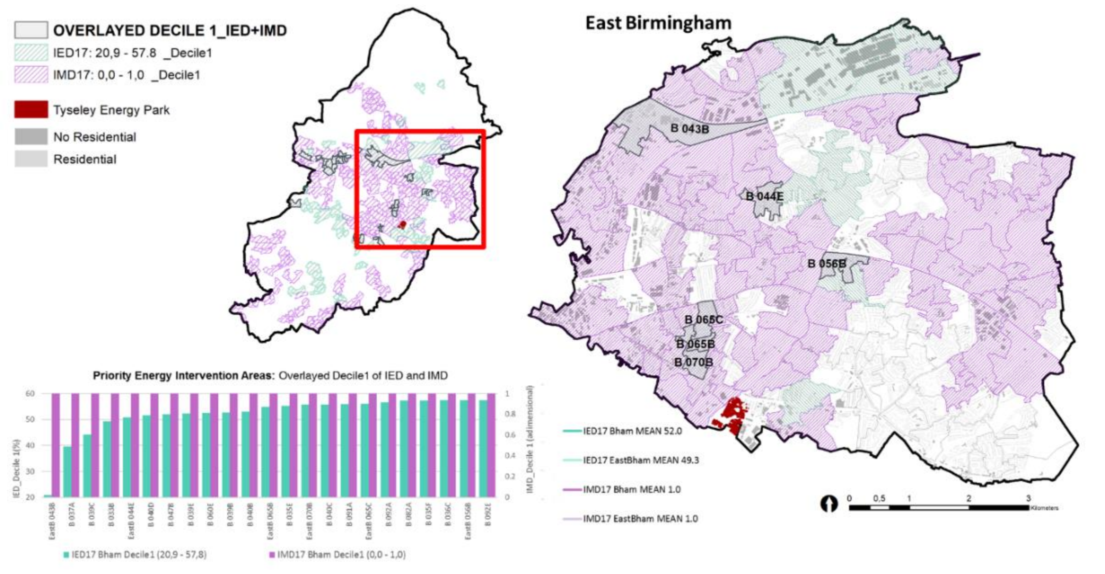

Figure 8. Priority Energy Intervention Areas (PEIA). Overlapped IED (green) and IMD (purple) LSOA´s areas with decile 1.

4. Conclusions

The Priority Energy Intervention Areas (PEIA) methodology is developed for the dwellings placed in the city of Birmigham, focusing especially in the East Birmigham. This top-down approach is based on GIS tools using the Lower Layer Super Output Area (LSOA) classification. This study aims to reduce uncertainties and time-consuming processes for the location of energy deprived areas. Moreover, it fosters to achieve clean, fair and healthier urban environments in these vulnerable areas though the "green" challenge strategies.

To this end, two indexes are used: The Index Energy Deprivation (IED) and the Index Multiple Deprivation (IMD). IED is a proposed index that compares the real and theoretical energy consumption addressing the differences between consumed and the energy performance associated to the user´s behaviour. Other determinant factors in these variations as the climate data or the household´s quality are approached by the IMD that quantify the socioeconomic, health and environment level of the LSOA´s neighbourhoods. The conducted data have been gathered by deciles, defining the overlapping of lowest IED and IMD as PEIA.

The real energy data is calculated as the sum of real domestic gas and electricity for each LSOA. It should highlight the gas energy consumption, which is approximately three times higher than the electricity consumption, which it reveals an elevated dependency of the gas heating facilities.

An on purpose urban classification is carried out to estimate the theoretical energy consumption. It is based on the building typology and construction´s period considering flats, detached, semidetached and terraced houses.

Flats are located in the city center. Their quantity is not that significant compared with other typologies; however they present notably the highest energy consumption per building, specially the high flats with values higher than 40 MWh/inh per year. This is associate to their increasing surface (larger and higher), besides of having the highest values of efficiency. Both low-rise and high-rise categories represent low values of real and energy demand and medium- high rates of IED and IMD.

Detached houses are in the north and southwest zones and have medium-high levels of efficiency. Their real and theoretical energy consumption is high but have medium- high rates of IED and IMD.

Semidetached houses are placed in all the surroundings neighbourhoods of the city, except of the west zone. They widely belong to the most frequent building typology. From 1919 to 1944 were constructed more than a 10 thousand dwellings and have medium-low energy efficiency. Their real energy consumption is medium-high, while the theoretical one is medium. The IED is medium-high but some west city areas have lower ratios.

Terraced houses are mainly in the west and east city center. Most of them (specially the large-size ones) were built up before 1919, but also other representative amount of small-size terraced houses was constructed in during 1965-1980, presenting the worst energy efficiency values. Their real energy consumption is low but their theoretical values are medium-low generating a low IED areas. IMD is also low.

East Birmingham shows lower energy values compared to the whole city for all cases, being a 13% less for the real energy consumption (gas+electricity) and a 10% inferior for the theoretical energy consumption. The same pattern is shown for the indices. IED is a 10 % lower and IMD has a notable reduction of a 43%. It should highlight that almost the whole city consumes less than expected (from 1 to 9 deciles IED is lower than 100%)

Finally, 23 LSOAs have been characterized as Priority Energy Intervention Areas. Their location belongs mainly to terraced houses neighbourhoods, which reveals the worst IED and IMD values. This situation could explain the low IED and IMD values of the east Birmingham corridor, where are located 6 PEIA associated to an intense deprivation ratio. The wasted energy of Tyseley Energy Park industries, could be reused by households located in the three PEIA closest to this area, fostering the innovative energy challenges proposed in the Birmingham´s Carbon Road Map. The west area of the city should be also considered for further energy interventions because of the high number of PEIA found.

The PEIA methodology is proved as an efficient approach to map and quantify the most deprived neighbourhoods from an energy perspective considering also other influence aspects as socioeconomical and environmental levels. Terraced houses should be considered as a preference within the city´s strategy frameworks. This procedure could help stakeholders to improve these areas though further developments based on sustainable and inclusive projects that should be addressed from a deeper urban perspective.

5. References

BCC. 2015. “East Birmingham Prospectus for Growth.” *Birmigham City Council*, no. February.

BCR. 2013. “Birmimingham Carbon Roadmap.” *Birmingham Green Commission. Birmigham City Council*.

BEI. “Birmigham Energy Institute.” Accessed August, 2020. https://www.birmingham.ac.uk

Bouzarovski, Stefan, and Saska Petrova. 2015. “A Global Perspective on Domestic Energy Deprivation: Overcoming the Energy Poverty–Fuel Poverty Binary.” *Energy Research & Social Science* 10 (November): 31–40. https://doi.org/10.1016/J.ERSS.2015.06.007.

BU. 2013. “Power to the People. An Integrated Approach to Clean Energy and Climate Innovation.” *Birmigham University*. Vol. 30. https://doi.org/10.1109/MS.2013.34.

CCA. “Climate Change Act 2008.” Accessed August, 2020. https://www.legislation.gov.uk

CTE. 2015. “Índice Objeto Clima de Referencia Climas de Referencia” *Código Técnico de La Edificación*

EHS. “English Housing Survey. Data on Energy Inefficient Dwellings.” Accessed August 29, 2020. https://www.gov.uk/government/statistical-data-sets/energy-inefficient-dwellings.

Elena Cuerda, Olivia Guerra-Santin, J. J. Sendra & Fco. Javier Neila González. 2019. "Comparing the Impact of Presence Patterns on Energy Demand in Residential Buildings Using Measured Data and Simulation Models." *Building Simulation* 12 (4): 985–88. https://doi.org/10.1017/CBO9781107415324.004.

EnergyPlus. "Weather Data Sources | EnergyPlus." Accessed August 26, 2020. https://energyplus.net

Eurostat. 2018. "Final Energy Consumption by Sector" 2018. https://ec.europa.eu/eurostat

IEA. 2016. "Final Report Annex 53. Total Energy Use in Buildings Analysis and Evaluation Methods." *International Energy Agency Programme on Energy in Buildings and Communities*.

INE. 2014. "Encuesta Continua de Hogares." *Instituto Estadísticon Nacional (Spain)*. http://www.ine.es

IoD. "English Indices of Deprivation 2019." Accessed August, 2020. https://www.gov.uk/government/statistics/english-indices-of-deprivation-2019.

IPCC. 2018. "International Panel of Climate Change, 2018: Global Warming of 1.5°C." *United Union*.

LandMap Project. 2012. "Cities Revealed Building Class Datasets," no. 15: 1–5.

LSOA. "Lower Layer Super Output Area." Accessed August, 2020. https://www.ons.gov.uk

OS. "Specific GIS Mapping Tools Data." Accessed August, 2020. https://www.ordnancesurvey.co.uk

R20-Taskforce. "The Route to Zero (R20) Taskforce, Climate Emergency." Accessed August, 2020. https://www.birmingham.gov.uk/info/20015/environment/2026/climate_emergency/4.

R20, West-Mildland. "Roadmap to 2030." . Accessed August, 2020. https://www.sustainabilitywestmidlands.org.uk

Sánchez, M. N., S. Soutullo, R. Olmedo, D. Bravo, S. Castaño, and M. J. Jiménez. 2020. "An Experimental Methodology to Assess the Climate Impact on the Energy Performance of Buildings: A Ten-Year Evaluation in Temperate and Cold Desert Areas." *Applied Energy* 264 (February): 114730. https://doi.org/10.1016/j.apenergy.2020.114730.

Sanz Fernández, Ana, Gloria Gómez Muñoz, Carmen Sánchez-Guevara Sánchez, and Miguel Núñez Peiró. 2017. "Estudio Técnico Sobre Pobreza Energética En La Ciudad de Madrid," 186.

Soutullo, S., E. Giancola, M. J. Jiménez, J. A. Ferrer, and M. N. Sánchez. 2020. "How Climate Trends Impact on the Thermal Performance of a Typical Residential Building in Madrid." *Energies* 13 (1). https://doi.org/10.3390/en13010237.

Soutullo, S., M. N. Sánchez, R. Enríquez, M. J. Jimenez, and M. R. Heras. 2017. "Empirical Estimation of the Climatic Representativeness in Two Different Areas: Desert and Mediterranean Climates." *Energy Procedia* 122: 829–34. https://doi.org/10.1016/j.egypro.2017.07.415.

Sub-national. "Sub-National Electricity and Gas Consumption 2017 - UK." Accessed August, 2020. https://www.gov.uk/government/statistics

Sub-Regional. "Sub-Regional Fuel Poverty" *Dept of Business, Energy and Industrial Strategy (UK)* 2020

Sun, Kaiyu, and Tianzhen Hong. 2017. "A Simulation Approach to Estimate Energy Savings Potential of Occupant Behavior Measures." *Energy and Buildings* 136: 43–62. https://doi.org/10.1016/j.enbuild.2016.12.010.

TEP. "Tyseley Energy Park." Accessed August 27, 2020. https://www.tyseleyenergy.co.uk/.

Zarzalejo, Luis, Felix Tellez, Elena Palomo del Barrio, and M R Heras. 1995. "Creation of Typical Meteorological Years (TMY) for Southern Spanish Cities." In *International Symposium Passive Cooling of Buildings*.

A Flexible GIS-based Computational Framework for the Early-Design of District Energy Networks

Félix Pouchain[1], Giuseppe Peronato[1] and Guillaume Meunier[2]
Elioth (Egis Concept), [1]Lyon / [2]Montreuil (France)

Abstract

The design of district heating and cooling (DHC) networks is crucial to increase the pooling of energy supply and demand between individual buildings, and thus to reduce the environmental and financial costs of the energy systems. DHC networks are also useful to increase the share of renewable energy sources in cities, their integration being more challenging in high-density environments. This paper presents a novel simulation framework for the optimization of building energy systems connected to a district heating and cooling network. The developed method is based on the open-source Python library PyPSA and is adapted for the early-design exploration of multiple scenarios and their optimization, based on GIS input data. We show the application of the proposed method into a fictitious district in France composed of mixed-use buildings. The results compare two scenarios of energy systems minimizing either greenhouse gas emissions or the energy cost.

Keywords: urban building energy modeling, district heating and cooling (DHC) networks;

1. Introduction

There is a growing interest towards urban energy simulations. Many of these tools fall into the category of urban building energy modeling (Cerezo Davila et al., 2016; Johari et al., 2020) and are generally aimed at the simulation of the building energy needs. Some tools tackle multiple scopes including also the simulation of the building energy systems and of the district energy networks (Fonseca et al., 2016).

We present here a flexible framework for the simulation and optimization of building energy systems and energy sources (including local photovoltaic modules) connected into a district heating and cooling (DHC) network. The simulation framework is constituted of different Python modules, each one performing a specific simulation task while being integrated into a single automated workflow based on the Luigi library (Bernhardsson and Freider, 2019). The optimization routine provides a sizing of the energy systems in the grid in order to optimize different environmental, energy or financial indicators, including both capital and operational expenditures.

Compared to existing urban energy simulation tools, the proposed framework is not bundled as a plugin to existing GIS or CAD modeling tools, but rather conceived as a software-agnostic workflow focusing on the data integration and optimization using open-source Python libraries. The exchange of input/output data between the different modules is performed using standardized formats. This eases the replacement of single modules with other external programs (e.g., a different building performance simulation tool), which could be possibly more adapted to solve specific design situations.

At the current development stage, the framework is particularly adapted for the early-design exploration of energy scenarios of new urban developments, where different design variants can be simulated and compared, with only minimal data input requirements. This is the case of the sample case-study application presented in this paper, where a small fictitious district is used to show the main inputs and outputs of the proposed simulation framework. In particular, two different scenarios minimizing either the environmental (CO_2 emissions) or the financial cost of the district operational energy are evaluated. For each scenario, the framework is used to pre-size the energy systems and the pipework, as well as to simulate the hourly energy demand. This information can be used, for example, to perform a preliminary check of the project compliance with environmental and/or financial objectives.

doi:10.18086/eurosun.2020.13.03 Available at http://proceedings.ises.org

2. Methodology

The proposed framework is composed of six modules bundled as Python packages, which are exchanging data through file-based databases, and form all together a District Energy Modeling tool:

- Weather: translating weather files (EPW and French RT2012 database) into a standard tabular format;
- Geometry: creation of a 3D model from a 2.5D vector GIS model and calculation of the sky view maps for each building surface using the POV-Ray (Cason, 2013) simulation engine;
- Solar: calculation of the PV solar potential based on the PVLIB library (Holmgren et al., 2019, 2018);
- Climelioth: a dynamic building performance simulation tool based on the French building performance regulations (RT, 2012);
- GeoCAD: designing and sizing the district heating & cooling network based on the GeoPandas (Jordahl et al., 2019) and Networkx (Hagberg et al., 2019) libraries;
- Smartgrid: tool to size the energy systems by minimizing either the GHG emissions, the financial cost, the primary energy consumption or a combination of the three metrics, based on the PyPSA toolbox (Brown et al., 2018) and the CBC solver (Forrest et al., 2018).

Because of the use of separate Python modules performing tasks based on a command-line input and standardized files, the components can be easily replaced with other simulation engines, adapted to use different file formats or to solve specific design situations. Building energy needs can for example be computed using IES VE, EnergyPlus, or any equivalent BPS tool, before being used in SmartGrid. It is thus possible to integrate any design parameter available in these tools in the study and design of urban energy systems.

In the next sections, the GeoCAD and SmartGrid modules, composing the actual DHC simulation part of the proposed framework, as well as the workflow management system, will be presented in more detail.

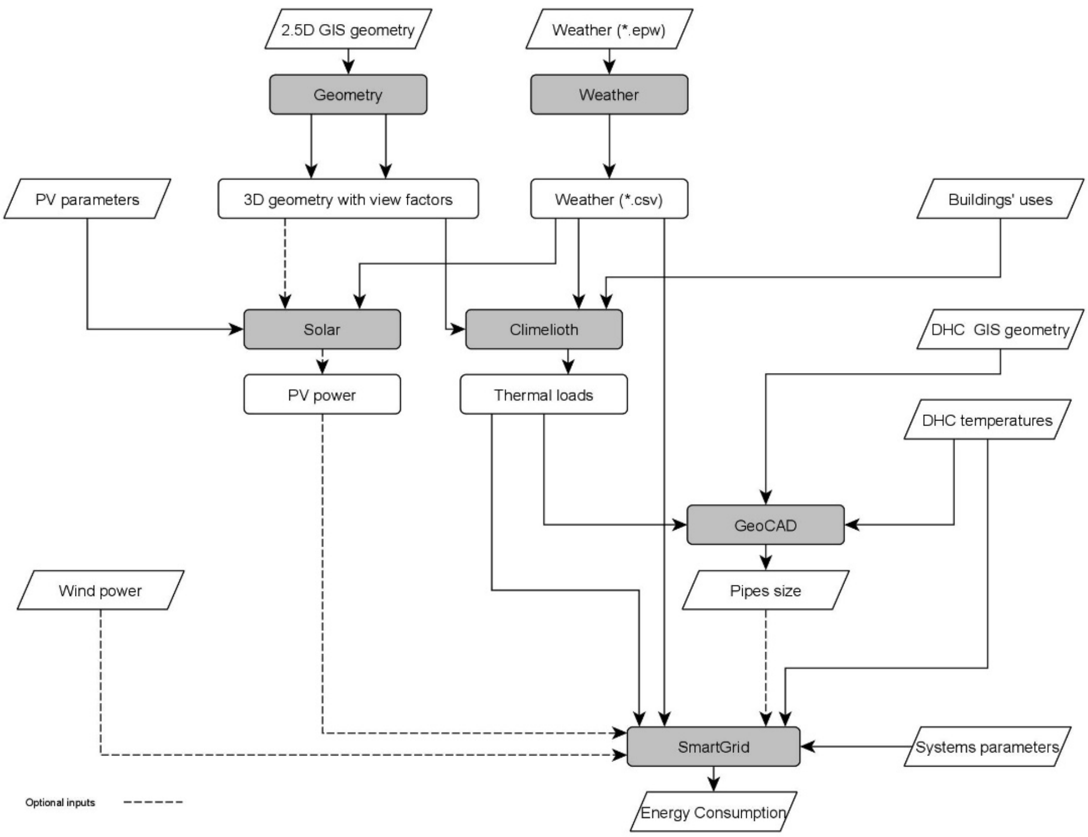

Fig. 1: Flowchart of the proposed simulation framework

3. Workflow Management System

A Python module named "Workflow" and based on the Luigi library (Bernhardsson and Freider 2012) is used as Workflow Management System (WMS) to organize the different simulation modules into a comprehensive and automated workflow.

When running a simulation, the Workflow module checks whether the input data already exist or have to be simulated and, in the latter case, run the modules that are required to produce the missing data inputs. This allows the user to run, for instance, the SmartGrid module, which is at the bottom of the workflow chain shown in Fig.1, with the Workflow module taking care of all missing dependencies in case they have not been already simulated.

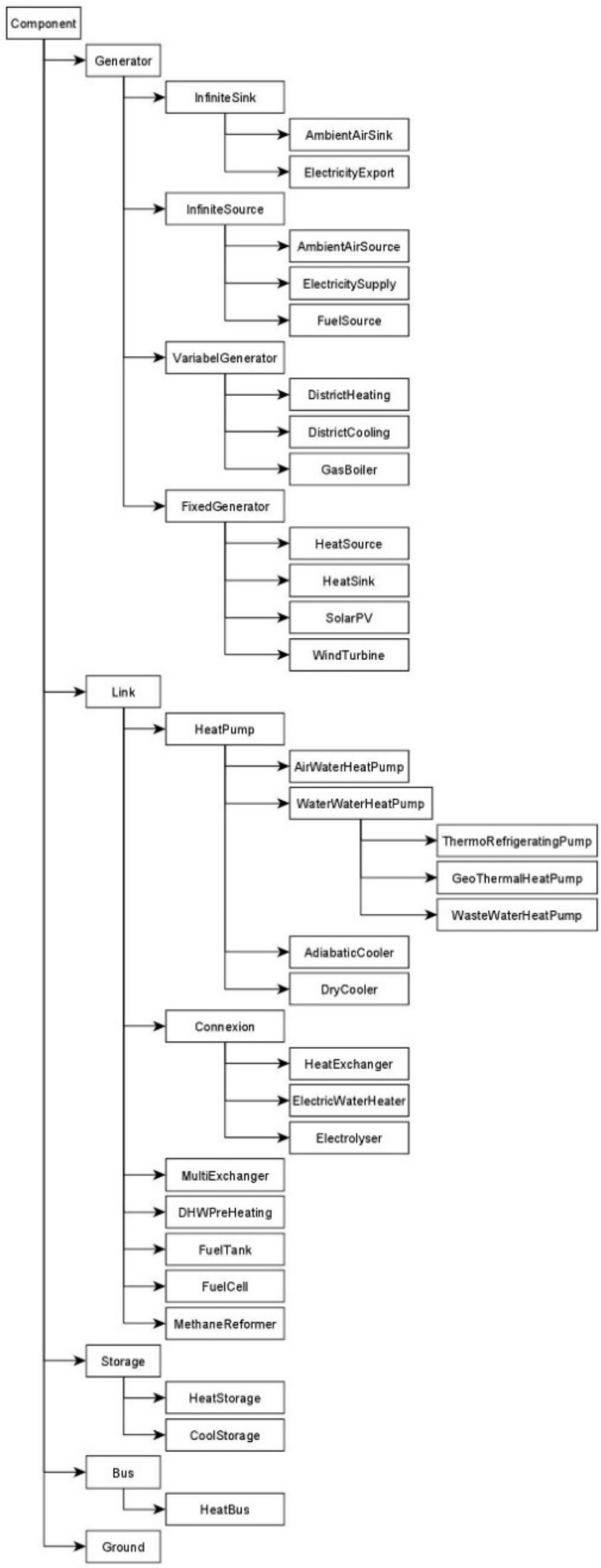

Fig. 1: Tree diagram representing the inheritance of the Python classes of the Smartgrid module.

4. The SmartGrid module

The SmartGrid module is a tool to size the energy systems by minimizing either the GHG emissions, the financial cost, the primary energy consumption or a combination of the three metrics. It is at the bottom of the dependency chain shown in Fig.1 and hence at the core of the developed workflow. It can also be run independently from the other tools, when its mandatory inputs (notably, the building energy needs and network characteristics) are known.

The tool's application goal is twofold: a) modeling the energy systems and pipe network at an hourly timestep to cover the building energy needs, b) finding the combination and size of energy systems that minimize the capital and operational expenditures, in terms of primary energy, financial cost, or GHG emissions. The optimization is conceived as a single-objective problem, while multiple objectives can be weighted into a single one.

The module extends the Python package PyPSA (Brown et al., 2018), which provides basic energy systems components (generator, load, storage, link…) and the ability to optimize power flows given their fixed and marginal costs of use. SmartGrid builds upon these components to provide common buildings and district heating systems (boiler, heat pump, solar panels…). It also provides multiple helper functions, to ease the creation of large systems and the access to simulation results.

As in electricity grid simulation tools, the overall modeling concept revolves around the concepts of buses, links, sources and sinks, while the energy flux, in addition to electricity, can be also of thermal energy. The buildings are typically the sinks of the energy fluxes, while for cooling it is the opposite: the buildings are the sources of the heat waste that is either “sunk” in the environment (modeled here as an infinite sink), recovered by another building connected to the loop or injected into an external district cooling network. Sources and sinks are attached to a bus and the different buses are connected through simple connection links or energy transformation links, which can convert energy between its different forms at a given efficiency rate. Cooling and heating buses are provided with a temperature attribute, which is used to check that the connection is done at the same temperature level in case of simple connection links. Otherwise, the user is prompted to replace the simple connection with an energy transformation link, such as a heat pump, to raise or decrease the temperature to the same level.

The optimization solver implemented into the module solves the problem of the linear optimal power flow within the district energy network, finding the least-cost solution. The cost is expressed in terms of primary energy, financial cost, or GHG emissions and is composed of three components: investment, operational and marginal.

4. 1 Programming paradigm

This module is coded using an Object-Oriented Programming (OOP) paradigm, where each physical component of the DHC network is a Python class.

The attributes of the generic components (bus, generator, load, link and storage) are inherited by the sub-objects and specified with other characteristics (Fig. 1). Each component is based on one or several PyPSA components (StorageUnit, Link, Generator, Bus).

When running a simulation, a SmartGrid object is initialized and the following networks are added:

- *RES*, the network including off-site Renewable Energy Sources, such as large wind power turbines or solar farms.
- *Environment*, used as a source/sink for the air- and ground- heat pumps and chillers. This network includes three thermal buses: ambient_air_source, ambient_air_sink and ground. The ground bus is connected to a storage, which allows the user to define a cyclic storage unit to balance the extractions and injections over the simulation period (for example over the year), while the ambient air source and sink correspond to an infinite source and sink.
- *Network*, the main network to which the shared energy systems are added.
- *Building*, an internal network for each building connected to the district network, to which the building loads are by default connected to, as well as possible building energy systems.

The connections between these networks are defined by the user in the input system parameters file.

4.2 Models

We will briefly describe the main models included in the SmartGrid and GeoCAD modules.

Heat pumps are modeled as PyPSA links connecting two input sources (electricity and a heat bus acting) to an output sink bus, where the efficiency is defined by a variable COP and the nominal electrical power. We use the COP models from (Staffell et al., 2012). The nominal electrical power necessary for the PyPSA model is obtained by diving the nominal thermal power (defined by the used in the input systems parameters file) by a fixed COP. Refrigerating machines can be also modeled as a heat pump, with a source corresponding to the cooling network from which the calories are extracted. A geothermal heat pump can also be modeled and connected to the ground bus, whose temperature can be given in the input weather file or modeled.

The fuel cell is modeled as a cogeneration, which takes as input a dihydrogen flux, and gives as outputs two fluxes: electricity and thermal energy, both proportional to the ingoing dihydrogen flux. The considered efficiencies, corresponding to those of a commercial product, are the following ones:

$$\frac{Heating+Electricity_{out}}{Hydrogen} = 0.95$$

$$\frac{Electricity_{out}}{Hydrogen} = 0.45$$

The energy losses in the piping networks are calculated by a simple Heat Transfer Model, considering the thermal resistance of the pipe (steel and insulation layer), and the average temperature in the thermal loop.

4.3 Input and output

The systems parameters is the module's specific input file, where all energy systems and their parameters are allocated to the district and the building buses. It is structured as a *.csv file and provides the information about the connections of the different energy systems to the buses as well as some of their main design parameters, such as, for example, the nominal power and efficiency.

The input building energy network is in the form of a GeoJSON file, which can be created with the GeoCAD module, containing the geometry and information of the network segments (Origin, Destination, Nominal Diameter). Additional JSON properties are appended to the network input file, to define the depth and soil type, as well as the temperature ranges of all subnetworks (district-wide and building ones). This latter information is compulsory to run the simulation, while the geometry information is only needed to define piping-dependent thermal losses.

The simulation output including the origin, destination, transformation of all hourly energy fluxes is saved into a binary file that can be read through the SmartGrid module. A summary Excel file (including total energy and maximum power) and Sankey diagram are also automatically saved at each simulation.

5. The GeoCAD module

The GeoCAD module can be used for pre-sizing the pipework of heating and cooling networks. The size of the pipes is in fact required to calculate the network losses in the SmartGrid module.

The nominal diameter DN of the pipework components is sized based on the maximum thermal loads in each segment of the network. To this end, the maximum load of each building and each network connected to the network is chosen. This corresponds to a conservative approach, as the buildings are unlikely to have the maximum thermal load simultaneously. The system can be also forced to use the loads at a specific time step as the sizing factor.

The module uses input GIS files that can be created with any GIS software to define the network geometry and the directional flows of the pipes. The GIS files define the buildings (drawn as Points), as well as the networks (drawn as LineStrings) connecting the buildings. The points from where the line starts will be considered as the source of the energy flow, i.e. the position of the district thermal station.

The mandatory attributes for the network geometry are the direction of the flow (supply, return) and the type of network (heating, cooling, medium temperature). However, only the supply pipes are actually considered at this stage, the energy losses in the SmartGrid module being calculated on the average temperature of the supply/return pipes and on the double distance of the supply pipes.

The energy flows are balanced in each network segment using the network simplex algorithm as implemented in the Networkx library (Hagberg et al., 2019).

6. Case-study application

The tool has been already applied in several neighborhood-scale projects at the early-design phase. However, for the scope of this paper, we apply it in a fictitious mixed-use district in Lyon (France) composed of three buildings, which are connected through a local DHC low-temperature network. All systems are centralized in a district thermal station, while a Water-Water Heat Pump is installed in each building to raise the water temperature for domestic hot water. Photovoltaic panels are also installed in one building.

6.1 Description of the case study

The mixed-use district is composed of three buildings named A, B and C, which share the energy systems and are connected through a microgrid (Fig. 2). The energy systems are listed in Tab. 1.

All systems are installed in Building A, while the Water-Water Heat Pump is installed in each building to raise the water temperature and connects hence the heating network to the DHW network. The simulation considers the climate of the H1c zone, including the city of Lyon, from the French building performance regulations (RT, 2012).

Tab. 1: Characteristics of the buildings of the case-study neighborhood: summary of the inputs of the SmartGrid simulation

	A	B	C	Total
Floor area (m^2)	3011	4017	2553	9581
Housing/Office/Retail ($\%_{floor\ area}$)	0/83/17%	0/88/12%	80/0/20%	21/63/15%
Heating needs ($kWh/m^2_{floor\ area}$)	8.2	12.5	6.6	9.6
Cooling needs ($kWh/m^2_{floor\ area}$)	39.7	42.0	7.2	32.0
DHW needs ($kWh/m^2_{floor\ area}$)	1.8	1.9	14.5	5.3
Electricity needs ($kWh/m^2_{floor\ area}$)	14.2	9.0	14.0	11.3
PV generation (kWh)	1 219	-	-	1 219
Heating network temperature (°C supply/return)	47/39	47/39	47/39	47/39
Cooling network temperature (°C supply/return)	8/15	8/15	8/15	8/15
DHW network temperature (°C supply/return)	55/50	55/50	55/50	55/50

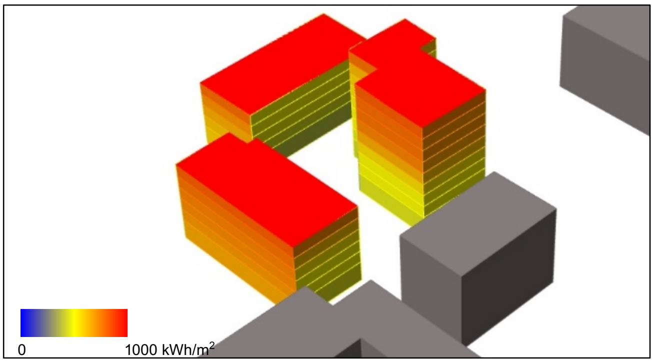

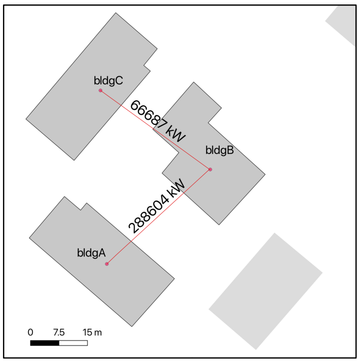

Fig. 2: False color visualization (left) of solar irradiation (based on Climelioth simulation) and map of the max heating power in each segment of the DHC network (based on the GeoCAD simulation)

6.2 Results

We present the results of a study of two simulation scenarios using the same energy sources and systems, while optimizing their use for either minimizing the Environmental Cost (expressed in $gCOe/kWh_{Final\ Energy}$) or Financial Cost (expressed in $Euros/kWh_{Final\ Energy}$). In both cases, we will consider only the marginal cost per unit of energy consumption (kWh) over one year, without considering the investment or operational costs, as presented in the Appendix. However, the SmartGrid module includes the support for power-based capital costs (x/kW) in the simulations.

Tab. 2 shows the size (maximum power) and operating hours per each energy system. The maximum power in some cases exceeds the nominal power, because of the definition of PyPSA efficiency based on a fixed COP (see §4.2). In these cases, the remaining power need is provided by an alternative, yet more expensive, energy source, which is here modeled as "infinite".

In Fig. 3, we can see the monthly energy consumption for the two scenarios. The energy mix is clearly changing between the two scenarios. In the second variant, we notice in particular the use of a natural gas boiler and a chiller as cheaper, yet with a higher CO_2-equivalent content, alternatives to using external district heating and, for most hours, cooling.

Tab. 2: Sizing results of the energy systems for the two optimization goals: Variant 1 – Minimization of CO_2-equivalent emissions (top) and Variant 2 – Minimization of Energy Financial Cost

		Variant 1		Variant 2	
Systems	**Nominal power [kW]**	**Max Power [kW]**	**Annual operating hours [%]**	**Max Power [kW]**	**Annual operating hours [%]**
GasBoiler	Infinite	-	-	365	19
DistrictHeating *DH*	Infinite	329	8	-	-
DistrictCooling *DC*	Infinite	739	2	-	-
Thermorefrigeratingpump *TRP*	50	23	36	23	39
GeoThermalHeatPump (heating)	25	24	73	24	71
GeoThermalHeatPump (cooling)	25	37	6	37	6
AirWaterHeatPump (heating) *HeatPump*	50	42	19	3	0.1
AirWaterHeatPump (cooling) *Chiller*	Infinite	644	18	738	19
WaterWaterHeatPump (heating) *HeatPump_DHW*	Infinite	28	62	28	62

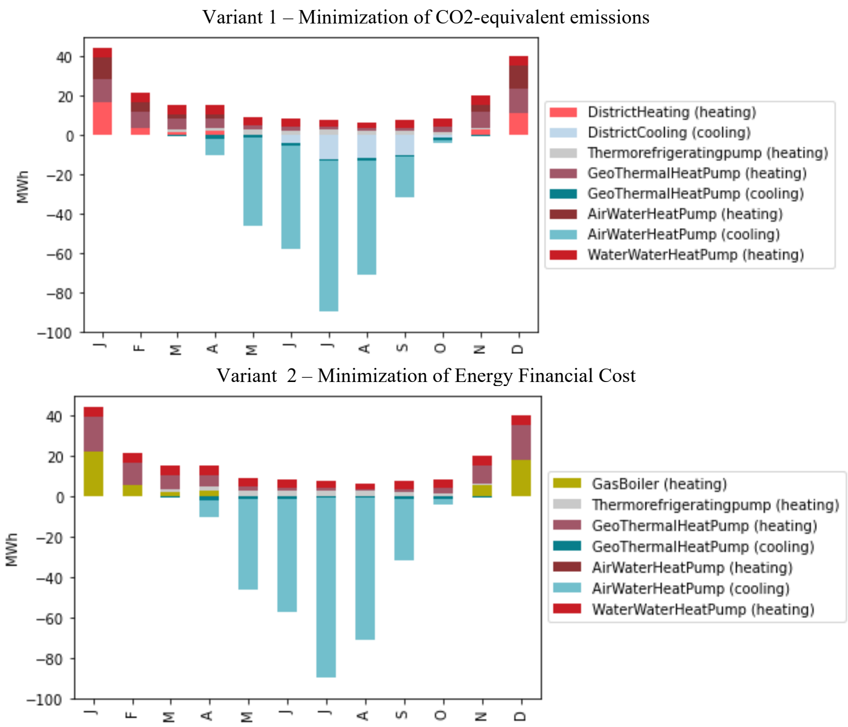

Fig. 3: Monthly thermal energy generation by systems (cooling is represented with negative values)

The Sankey plot representing the annual energy fluxes is also an output of the tool. In Fig. 4, we can see a simplified version, where the original networks and components used in the PyPSA simulation have been simplified to remove unnecessary nodes and the fluxes of building A, B, C have been represented as part of the same building. It can be seen how the heating needs are satisfied in both scenarios with a very diverse energy mix, whose main component is, in Variant 1, the geothermal heat pump.

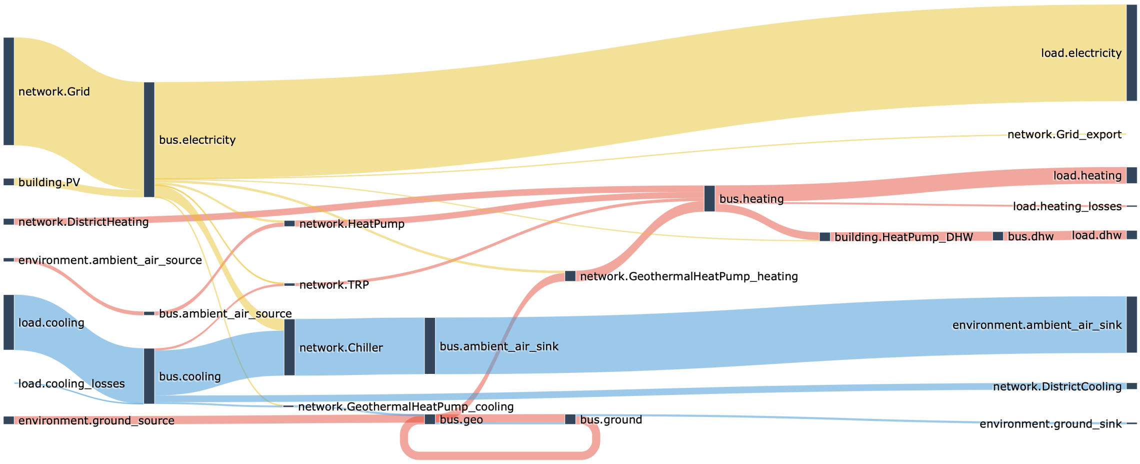

Fig. 4: Simplified Sankey representation of the annual energy fluxes for Variant 1 – Minimization of CO_2-equivalent emissions. The height of each node is proportional to the energy flux.

7. Limitations and future work

The framework we have presented is still under development, and the available components are limited. The integration into the workflow of state-of-the-art energy simulation tools such as EnergyPlus is currently being tested.

Regarding the case-study evaluation presented in this paper, it should be noted that we only considered here environmental and marginal costs for the considered energy sources, while the results could change when analyzing the life-cycle costs.

8. Conclusions

This paper presented a simulation framework for the early simulation of DHC networks. The purpose of this tool is to study the impact of different energy mixes and energy systems on the performance of the network. It also allows a pre-sizing of the pipework and of the energy systems.

We have shown a sample application of this tool, simulating energy scenarios for a DHC network and optimizing its systems given environmental and financial objectives. Thanks to its flexible and platform-agnostic conception and its integration is a workflow automation tool, we argue that this framework is particularly adapted for the exploration of early design scenarios. The tool's source code is released under the GLPv3 license in a Git repository at this address: https://gitlab.com/elioth/DESsim

9. Acknowledgments

The software development presented in this work has been initiated by FP and further conducted by FP, GP and Arnaud Sanson, as part of different projects at Elioth. The authors would like to thank the Egis Group for providing funding to Elioth's "Le lab" R&D activities.

References

Bernhardsson, E., Freider, E., 2019. Spotify/Luigi. Spotify, Stockholm, Sweden. https://github.com/spotify/luigi

Brown, T., Hörsch, J., Schlachtberger, D., 2018. PyPSA: Python for Power System Analysis. J. Open Res. Softw. 6. https://doi.org/10.5334/jors.188

Cason, C., 2013. POV-Ray. http://povray.org
Cerezo Davila, C., Reinhart, C.F., Bemis, J.L., 2016. Modeling Boston: A workflow for the efficient generation and maintenance of urban building energy models from existing geospatial datasets. Energy 117, 237–250. https://doi.org/10.1016/j.energy.2016.10.057
Fonseca, J.A., Nguyen, T.-A., Schlueter, A., Marechal, F., 2016. City Energy Analyst (CEA): Integrated framework for analysis and optimization of building energy systems in neighborhoods and city districts. Energy Build. 113, 202–226. https://doi.org/10.1016/j.enbuild.2015.11.055
Forrest, J., Ralphs, T., Vigerske, S., LouHafer, Kristjansson, jpfasano, EdwinStraver, Lubin, M., Gambini Santos, H., rlougee, Saltzman, M., 2018. coin-or/Cbc. Zenodo. https://doi.org/10.5281/zenodo.1317566
Hagberg, A., Schult, D., Swart, P., 2019. networkx/networkx. NetworkX: Python software for complex networks.
Holmgren, W., Calama-Consulting, Lorenzo, T., Krien, bmu, Mikofski, M., Hansen, C., DaCoEx, konstant_t, Anton Driesse, mayudong, Leland Boeman, Ed Miller, Heliolytics, Marc A. Anoma, jforbess, pyElena21, Volker Beutner, Todd Hendricks, MLEEFS, Johannes Dollinger, Cedric Leroy, Cameron Stark, Kevin Anderson, Jonathan Gaffiot, Johannes Oos, Giuseppe Peronato, Birgit Schachler, Alan Mathew, Alaina Kafkes, 2019. pvlib/pvlib-python. Zenodo. https://doi.org/10.5281/zenodo.2850192
Holmgren, W., Hansen, C., Mikofski, M., 2018. pvlib python: a python package for modeling solar energy systems. J. Open Source Softw. 3, 884. https://doi.org/10.21105/joss.00884
Johari, F., Peronato, G., Sadeghian, P., Zhao, X., Widén, J., 2020. Urban Building Energy Modeling: State of the Art and Future Prospects. Renew. Sustain. Energy Rev. 128, 109902. https://doi.org/10.1016/j.rser.2020.109902
Jordahl, K., Van den Bossche, J., Wasserman, J., McBride, J., Gerard, Tratner, J., Perry, M., Farmer, C., Sean Gillies, Micah Cochran, Matt Bartos, Martin Fleischmann, Lucas Culbertson, Nick Eubank, maxalbert, Aleksey Bilogur, Geir Arne Hjelle, Dani Arribas-Bel, Christopher Ren, Sergio Rey, Martin Journois, Levi John Wolf, Nick Grue, Joshua Wilson, Ömer Özak, YuichiNotoya, 2019. geopandas/geopandas. Zenodo. https://doi.org/10.5281/zenodo.3333010
RT, 2012. Réglementation Thermique 2012. http://rt-batiment.fr
Staffell, I., Brett, D., Brandon, N., Hawkes, A., 2012. A review of domestic heat pumps. Energy Environ. Sci. 5, 9291–9306. https://doi.org/10.1039/C2EE22653G

Appendix

Tab. 1: Factors for the energy sources

	Grid	**DH**	**DC**	**PV**	**Natural gas**
CO2 intensity ($gCO_2eq/kWh_{Final\ Energy}$)	59[a]	98[b]	16[b]	0[c]	243[d]
Cost of energy consumption ($Euros/kWh_{Final\ Energy}$)	0.1324[e]	0.0703[f]	0.15[f]	0	0.03608[g]

[a] Estimation of hourly CO_2 intensity for the French grid based on RTE Eco2mix (https://www.rte-france.com/en/eco2mix) for the 2013-2018 period. The CO_2 intensity of imported electricity has been also included. Hourly values used in the simulations are summarized here by a yearly average.
[b] Average CO_2 intensity in 2018 of district heating and cooling providers in France based on "Base Carbone v17" https://www.data.gouv.fr/en/datasets/base-carbone-complete-de-lademe-en-francais-v17-0/
[c] Photovoltaic modules are considered as part of the building, and, as such, we assume that their footprint will be included in the building's life cycle assessment.
[d] https://www.bilans-ges.ademe.fr, Boiler combustion, E+/C- label
[e] Assumption based on the French regulated price for electricity, non-residential use, "Tarif bleu – option base", 2020, excluding fixed and power-based costs. The gain for the surplus electricity injected into the grid is estimated at 0.06 €/kWh based for installations on buildings (June 2020), excluding other incentives.
[f] Average energy price in 2017 for district heating and cooling providers in France (https://amorce.asso.fr/publications/enquete-sur-le-prix-de-vente-de-la-chaleur-et-du-froid-en-2017-rce31/download). The price includes both energy- and power-based components, with the latter usually representing around 50% of the final energy price.
[g] Assumption based on the French regulated price for natural gas, zone 1, class B1 and B2i, 2020, excluding fixed and power-based costs.

Tyrol 2050 – Scenarios of a Fossil-Free Future

Wolfgang Streicher, Rupert Ebenbichler[2], Markus Mailer[1], Angela Hofmann[3] and Andreas Hertl[2]

[1] University of Innsbruck (Austria)

[2] Wasser Tirol, Innsbruck (Austria)

[3] Management Center Innsbruck /MCI (Austria)

Abstract

The presented study deals with energy scenarios for Tyrol/Austria, how energy systems in 2050 (buildings, production and mobility) could look like without fossil fuel use. For the building sector a course of the needed development is given. All available renewable energy carriers in Tyrol are needed and very high energy efficiency measures have to be taken to reach this goal. Four extreme scenarios and one mix-scenario were calculated. The extreme scenarios are dealing with primarily either electricity (I), hydrogen (II) or green-methane (III and IIIa) as future secondary energy carrier. The mix scenario (IV) is dealing with a more realistic mix of all these. Going for hydrogen and power to methane in an intense way, the electricity demand increases by far and large areas of PV fields on free land are needed.

Keywords: Energy Scenario, Tyrol, Fossil Free.

1. Introduction

The Austrian province of Tyrol intends to become energy autonomous until the year 2050. This means that all fossil energy carriers will have to be replaced by local available renewable energy. In the presented study the useable potential of local available renewable energy sources was evaluated and the future energy demand in 2050 under rigorous energy efficiency measures for the sectors buildings, mobility and production was estimated. Then the impact of different energy conversion technologies on the energy system was calculated. The whole project was accompanied by a stakeholder process in order to achieve a high acceptability in different political, industrial and environmental associations groups.

2. Scenarios and Basic boundary conditions

The energy sectors considered in this study were buildings, transport and production. The starting point was the official statistical data of the year 2016. Four extreme scenarios and one mix-scenario were calculated. The extreme scenarios are dealing with primarily either electricity (I), more hydrogen H2 (e.g. 40 % hydrogen-fuel cells in transportation) (II), or green-methane CH4 (III and IIIa) as future secondary energy carrier. The final mix scenario (IV) is dealing with a more realistic mix of all these.

The current energy flow of Tyrol was taken from official Austrian statistics for the year 2016. The potential of renewable energy carriers available in Tyrol were partly calculated and partly limited due to political restrictions. Hydro power, which is already one of the largest energy sources, was estimated to be increased by 50 %. This is still not the full technical potential, but seems to be today’s maximum political feasible value. Solar energy was estimated to be mounted on 70 % of all roofs with more than 950 kWh/m²a solar irradiation. Thereby a distribution of 90 % to PV and 10 % to solar thermal collectors was assumed due to the price development of the two technologies in the last years. The potential of wood-biomass was derived by combining energetic biomass growing in Tyrol and saw residues from Tyrolian companies, even if the wood they used was originally imported.

doi:10.18086/eurosun.2020.13.04 Available at http://proceedings.ises.org

Biogas, waste etc. was calculated according the available sewage systems and other availabilities. Wind energy is a pure political value. As there are no wind power plants so far in the highly touristic Tyrol installed, only 900 TJ (about 35 wind power plants with 2,5 MW each) were accepted by the stakeholders. Environmental heat for heat pumps was taken unlimited for ambient air and ground coupled systems, ground-water based systems were limited due to available aquifers in populated areas. Photovoltaics on open space is the reserve energy source, but as agricultural land and forest are needed for other purposes, only other land (maybe in the mountains above the tree line) can be used. Deep geothermal energy was not taken into considerations, as there is no major geothermal anomalies available.

Tab.1 sums up the energy flow in Tyrol for 2016 and the potentials of renewable energy sources. Hydro power dominates the potential of renewable energy carriers followed by solar and biomass. All the other reneweable energy sources are minor.

All renewables in their original state are called primary energy in the following.

Tab. 1 Primary energy used in 2016 and the available potential of renewable energy carriers in the province of Tyrol (Ebenbichler, Streicher et. al, 2018)

• Energy Used (2016), Potential (2050)	Use 2016 [TJ]	Potential 2050 [TJ]
Oil	37.314	
Natural Gas	12.788	
Coal	993	
Hydro Power	22.411	30.600
Solar		
Photovoltaics (Potential: 95% of useful roofs >950 kWh/m²a)	259	15.704
Solar thermal (Potential 5% of useful roofs)	891	2.161
Photovoltaics open space	0	not limited
Wood/residues	14.858	15.736
Waste	778	2.262
Wind	0	900
Biogas	401	
from biowaste and green plants		401
from bio fertilizers		549
from sewage gas		266
from energy plantations		0
Environmental heat	489	
Ground water		2.877
Ground coupled		not limited
Air		not limited
Deep geothermal	0	not used

3. Scenario Assumptions

Official statistical data available from 2016 was the starting value for the considerations. The following scenario assumptions were taken:

General

The demand of energy services was taken slightly rising with the population rate. This approach was heavily discussed in the accompanying stakeholder process especially by the environmental organisations. In the end it was agreed, that a reduction of energy services (less mobility, smaller area per person etc.) would make it easier for the energy transition but it would be difficult to “sell” this approach to the public. So taking this approach was staying on the safe (more difficult) side.

The study does not take into account seasonal energy storage or economics. Storage would need even more primary energy due to the storage efficiency. This aspect will be dealt with in a further study.

Trading of electricity is allowed I all scenarios as long as there is a yearly net balance of export/import.

Building sector:

The building sector was differentiated in 6 different building types (single family house (SFH), small and large multi family house (MFH), mixed use, commercial and other use) and 10 classes for the building age. For all buildings the 2016 baseline energy demand differentiated between space heating, domestic hot water and electricity for appliances was taken from previous studies (e.g. Pfeifer, 2017) that were based on a huge number of measured data. The following further assumptions for the scenarios were used:

- Population increase according to official values
- Increase of the useful building area per person from currently 46 to 48 m²/person.
- Starting from 2021 only passive houses for new buildings and a high standard for renovation is allowed. Both values are far better than the current national Austrian building code regulations. The equivalent deep renovation rate was estimated with 1.3 %/a, which corresponds to the historical renovation rate. The way of thinking behind that quite low number is that renovation takes place anyway when something is broken or at the end of life. Then it should be a very high quality renovation. Most of the cost are anyway costs (as the renovation has is done anyway) and only the additional costs for high quality renovation occur. The demolition rate and replacement by new buildings was estimated to be 0.3%.
- The same approach is taken for the exchange of oil and gas burners were an average lifetime of 30 years is assumed. They are replaced at the end of life, with
    - Scenario I, II: mainly heat pumps, minor parts with biomass burners, district heating for larger buildings and direct electric heating.
    - Scenario III, IIIa: all buildings using natural gas 2016 remain on the gas grid (2050 with P2G). The distribution of the rest is similar to the other scenarios.
    - Scenario IV: 5 % of buildings remain n the gas grid (P2G). The distribution of the rest is similar to the other scenarios.
- Starting with 2021 no oil and gas burners for new installations and boiler exchange are allowed.
- The seasonal performance factor (SPF) of the heat pumps is increasing from a current average value of 3 to 3.5 in 2050. Additionally biomass boilers and district heating systems are used.
- The district heating systems will be driven purely by renewables in 2050.
- 1%/a efficiency increase for electric appliances.

Mobility:

- No reduction of the mobility itself. No change in the modal split.
- Passenger und goods transport
- Inner Tyrolian, from/to Tyrol and passing Tyrol mobility is taken into account.
- Switch from fossil driven internal combustion engines driven vehicles depending on the scenario to
    - Scenario I: electric drives (including electrification of motorways for long distance goods transport),
    - Scenario II/IIIa: 40 % fuel cell with hydrogen (mainly goods transport)
    - Scenario III: internal combustion engine with green methane (power-to-gas)
    - (Scenario II to IV).

Production:

- Efficiency increase of 1%/a,
- Increase of production by 0.8 %/a,
- Replacement of fossil fuels by electricity, biomass hydrogen or green gas depending on the scenario.

4. Results

Fig. 1 shows the course of the final energy demand of the building sector including agriculture with the phase out of fossil fuels by 2050 for scenarios I and II. Even with the very high energetic level of new buildings and refurbishment, the final energy demand is only reduced by 32 % (65 % if solar thermal on site and environmental heat is taken as reduction). The additional electricity demand for the heat pumps is compensated by the efficiency increase of the household appliances. District heating stays constant in terms of final energy, this means a 32 % increase in heated area due to the demand reduction. Biomass is strongly reduced because it is needed for industrial processes high temperature heat.

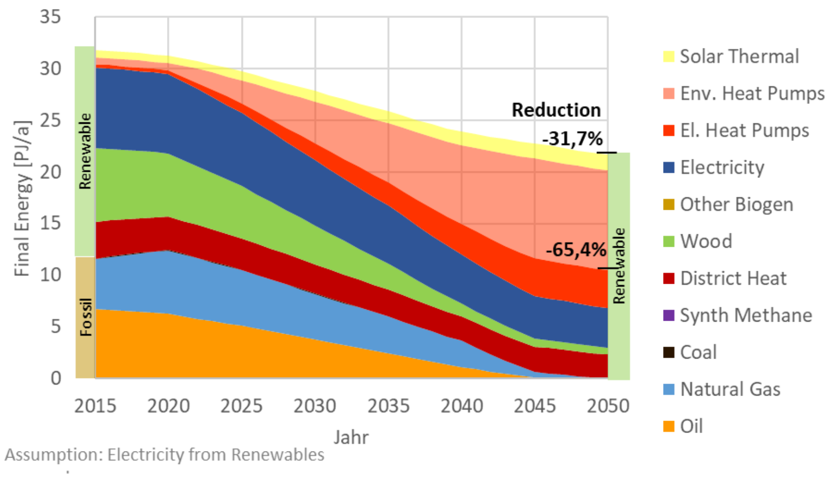

Fig. 1: Development Total Final Energy – all Buildings, (incl. Agriculture without Industry) scenario I&II (Ebenbichler, Streicher et. al, 2018)

Figs. 2 and 3 show the final energy demand distribution for the production and the mobility sector in the year 2016 and in 2050 for the different scenarios. For the production shown in Fig. 2 only a slight reduction of the final energy demand is achieved. This is due to the increase of production and a just little higher increase of efficiency. Nevertheless, there is a complete shift to renewable energies, which means a change in most of the production processes. In the scenario Electr (I) all processes that only need heat or electricity are shifted to electricity or heat pumps for low temperature heat, process that need originally wood are stayed with that and processes that need a flame or carbon are using either bio-coal or biofuels. In the scenarios Hydrogen (II) and CH4 &CH4 adapt (III/IIIA) more hydrogen respectively methan from P2G is used. The Mix scenario (IV) takes a bit of everything but still electricity in the majority.

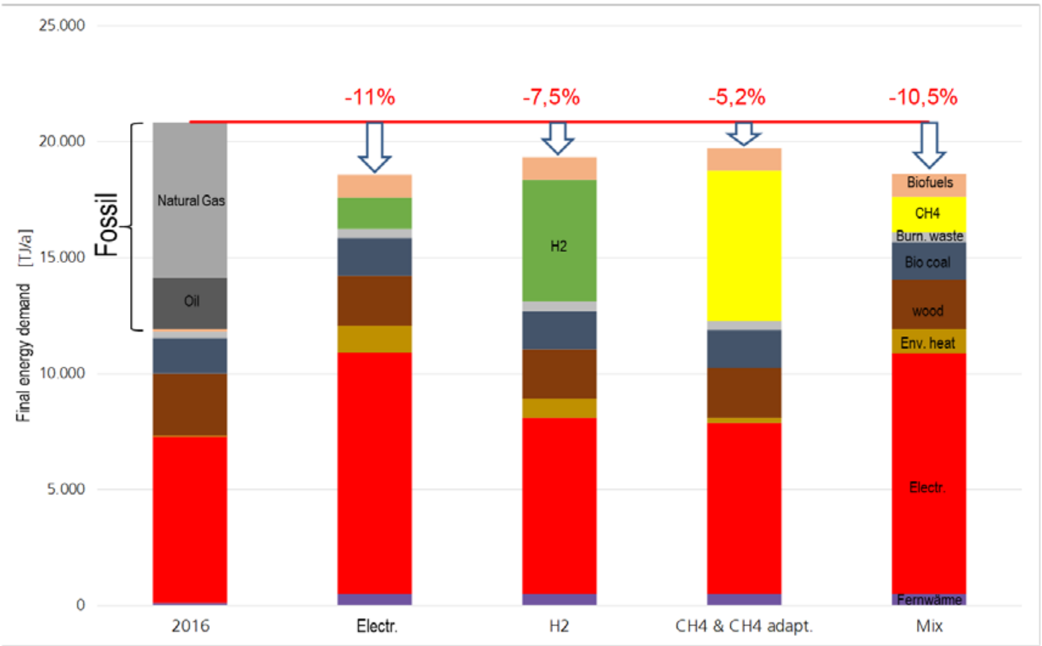

Fig. 2: Final energy demand production – baseline and all scenarios (Ebenbichler, Streicher et. al, 2018)

For the mobility sector the reults look quite diferent. There is a huge reduction of final energy demand for scenarios Electr (I), CH4 adapt (IIIa), H2 (II) and Mix (IV) of around 65 %. This is due to the low average efficiency of internal combustion engine driven cars of around 15% compared to the far higher efficiency of electric and fuel cell driven vehicles.

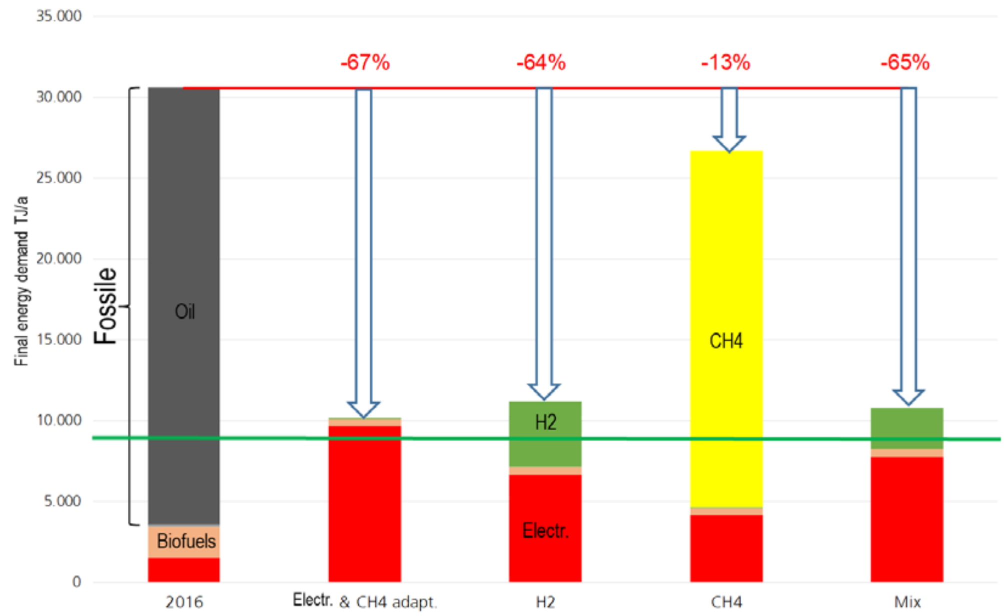

Fig. 3: Final energy demand mobility – baseline and all scenarios (Ebenbichler, Streicher et. al, 2018)

Tab. 2 shows the comparison of the 5 scenarios. Using power–to-methane and hydrogen increases the electricity demand (primary energy) significantly due to the efficiency in the production process, which is assumed to be 50 % for hydrogen production and 40 % for power-to methane (P2G). The highest primary energy demand occurs for Scenario III with bad efficiency for P2G and for internal combustion engine driven vehicles. This scenario should not be further discussed. The lowest demand occurs for the electricity scenario (scenario I) but it has to be admitted that seasonal energy storage was not in the model.

Tab. 2 Comparison of status 2005, 2016 and Scenarios I to IV (Ebenbichler, Streicher et. al, 2018)

	Primary Energy Input*	Losses Energy Input/ Final Energy	Final Energy Distribution by Sectors				Losses Final Energy/ Useful Energy	Useful Energy
			Total	Other (Buildings)	Production	Mobility		
	[TJ]	[TJ]	[TJ]	[%]	[%]	[%]	[TJ]	[TJ]
2005	**101465**	14208	**87257**	42%	24%	34%		
2016	**100481**	13201	**87280**	41%	24%	35%	38125	**49122**
Sc. I	**67758**	13609	**54151**	47%	34%	19%	9834	
Sc. II	**78555**	22640	**55916**	45%	35%	20%	11600	
Sc. III	**147635**	74876	**72761**	36%	27%	37%	28527	**44278**
Sc. IIIa	**103546**	46908	**56640**	45%	35%	20%	12406	
Sc. IV	**73133**	18289	**54845**	46%	34%	20%	10567	

* Excluding electricity import-export, which is net zero in Tyrol.

In Fig. 4 the primary energy demand for the baseline and the different scenarios is plotted. Scenario I (Electr.) is already using up all potentials of renewable energy carriers. Therefor the open space of PV has to be used for the other scenarios to deliver the additional energy due to the efficiencies of hydrogen and power to methane production. As TJ are not understandable by politicians and many other decision makers, the additional PV open space demand was translated to football fields per community. To understand the problematic it should be noted that province of Tyrol has 12.640 km² and 279 communities, which are partly quite small or squeezed in deep valleys between mountains. So the average community size is 44.6 km², a football field has an area of about 7000 m² (0.007 km²). Taken this into account, scenario CH4 (III) along with scenarios H2 (II) and CH4 adapt (IIIa) seem to be quite unrealistic.

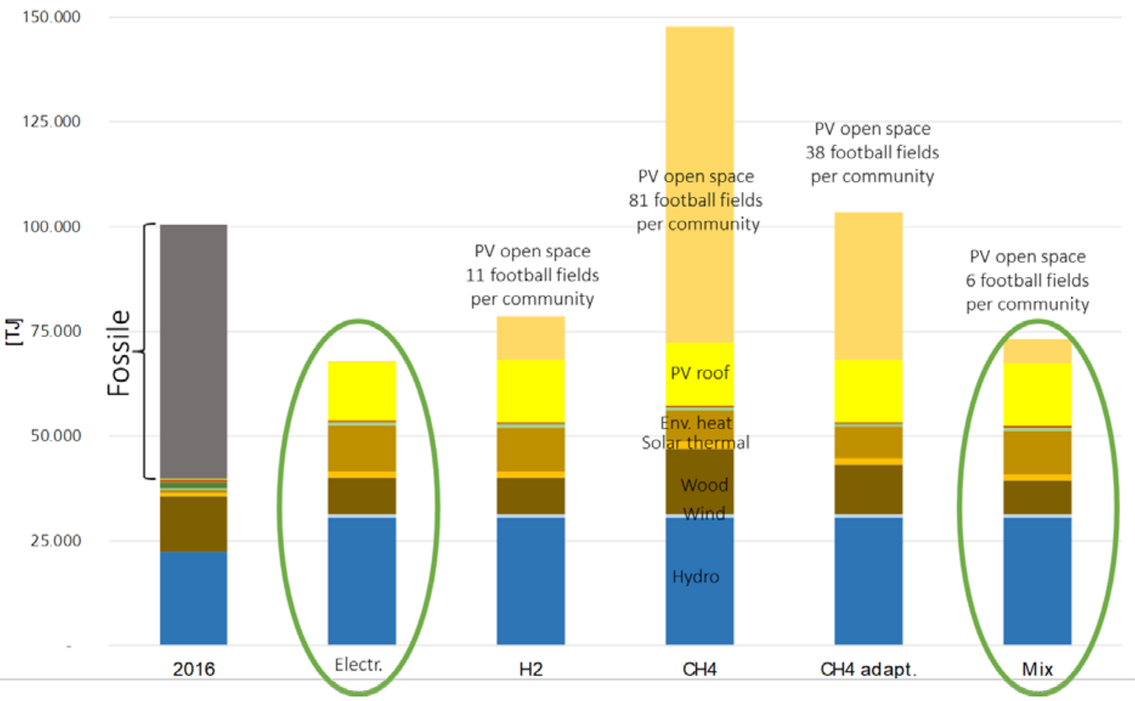

Fig. 4: Distribution of energy carriers – baseline and all scenarios (Ebenbichler, Streicher et. al, 2018)

Concluding it can be stated that the available renewable energy sources in Tyrol can theoretically cover the reduced demand of Tyrol in 2050, if all efficiency measures are implemented. How much of them can be used in reality depends on the political and economic boundary conditions and the acceptance by the people. All scenarios show, that electricity will play a dominant role in the future energy system. To cover the demand, the existing hydropower capacity has to be increased by 50%, the small potential of wind energy has to be fully used, nearly all feasible roofs have to be covered completely with PV or solar thermal plants and additionally free land is used for additional photovoltaic plants. Biomass (wood and biogas) will be used completely, partly in the energy system but also as raw material in industry (paper and pulp, polymers etc.).

5. Acknowledgments

We thank the province of Tyrol for financing the study and all stakeholders involved in the process.

6. References

Ebenbichler, R., Streicher, W., Hofmann, A., Mailer, M., Hertl, A., Fischer, D., Richtfeld, C., Anton, I., Pöham, C., 2018, Ressourcen- und Technologieeinsatz-Szenarien Tirol 2050, https://www.tirol.gv.at/fileadmin/themen/umwelt/wasser_wasserrecht/Downloads/19-03-08_Szenarien-Tirol-2050_Endbericht-Stand-18-10-15.pdf, looked up April 5th 2020.

Pfeifer, 2017, Entwicklung, Untersuchung und Bewertung von Berechnungsmodellen zur Erstellung von kommunalen Energiebilanzen im Gebäudebereich, Dissertation, University of Innsbruck, https://www.uibk.ac.at/bauphysik/lehre/dissertationen/abgeschlossen/documents/pfeifer.pdf, looked up September 4th 2020.

Author Index

A

B

C

H

K

L